# LINAC08 Proceedings

# XXIV Linear Accelerator Conference

# September 29 – October 3, 2008

# Victoria, British Columbia, Canada

## Hosted by TRIUMF

# LINAC08 XXIV International Linear Accelerator Conference

**Victoria, British Columbia, Canada**
**September 29 - October 3, 2008**

**Conference Chair** - Paul Schmor
**Scientific Program Chair** - Robert Laxdal
**Local Organizing Committee Chair** - Amiya Mitra
**Conference Coordinator** - Sandi Miller

**INTERNATIONAL COMMITTEE**

J. Alessi, BNL, USA
J. Barnard, LLNL, USA
W.Barth, GSI, Germany
S. Chattopadhyay, CI, UK
Y. Cho, ANL, USA
M.Fazio, LANL, USA
R. Garoby, CERN, Switzerland
T. Garvey, PSI, Switzerland
H. Hayano, KEK, Japan
S. Henderson, SNS/ORNL, USA
A. Hutton, JLAB, USA
H. Klein, U of Frankfurt, Germany
A. Kolmiets, ITEP, Russia
L. Kravchuk, INR, Russia
L.K. Len, DOE, USA
G. McMichael, ANL, USA
A. Mosnier, Saclay, France
W.Namkung, Postech, Korea
A. Noda, U of Kyoto, Japan
G. Pei, IHEP, China
P. Pierini, INFN/LNL, Italy
M.Popovich, FNAL, USA
R. Ruth, SLAC, USA
P. Schmor, TRIUMF, Canada
S. Schriber, MSU, USA
A. Variola, LAL, France
H. Weise, DESY, Germany
M. White, ANL, USA
Y. Yamasaki, JPARC, Japan

**LINAC08**
**TRIUMF**
**4004 Wesbrook Mall,**
**Vancouver, BC, V6T 2A3 Canada**
**Tel: 1 604 222 7352   Fax: 1 604 222 1074**
**Email: linac08@triumf.ca**
**www.triumf.ca/linac08**

# Foreword

The XXIV International Linear Accelerator Conference, LINAC08, was hosted by TRIUMF and took place during the week of September 29th to October 3rd, 2008 at the Conference Centre in the Canadian city of Victoria, British Columbia. This conference provided a unique opportunity for linear accelerator specialists from around the world to interact professionally and culturally in a relaxed and inspirational atmosphere. Attendance at the conference is by invitation. The large response to the invitations, the quality of the papers and presentations, the participation of many young researchers, the variety of exhibitors and the number of sponsorships all indicate an ongoing and diverse vitality within the Linac community throughout the various world regions.

The venue for the conference was the Victoria Conference Centre and the historic Fairmont Empress Hotel, both located at the heart of the City of Victoria. In order to encourage informal interactions among the delegates, breakfast and lunch were provided in the exhibition floor of the conference centre.

The conference registrations (including the students) totalled 353 from 17 different countries. In addition there were 28 exhibitors with 49 registrations. The conference staff (including the editorial team) totalled 25. Twenty-three students who presented posters at a special session on Sunday were sponsored from conference revenues. These proceedings include 347 of the 382 contributions presented at LINAC08.

Papers were processed during the conference by editors from the JACoW collaboration, under the local leadership of the proceedings coordinator Martin Comyn. We would like to thank the JACoW collaboration for supporting the conference with their well-trained, professional staff. After the conference, Martin together with Jana Thomson and Lorraine King prepared the processed papers for publication. Significant contributions came from Volker Schaa who aided Martin in preparing the proceedings for upload to the JACoW site www.JACoW.org. We apologize for the delay in the circulation of these proceedings; the preparations for the PAC09 conference hosted by TRIUMF proved to be somewhat overwhelming.

One of the goals of the conference programme was to highlight, where possible, young researchers in the field. To this end the conference was opened by Marco Marchetto, a young accelerator physicist from TRIUMF who gave an overview talk on the TRIUMF present and future linear accelerators. In addition, twenty-three students presented their work at a special poster session at the Sunday reception. The winner of the poster session, Joshua Wilson, with his research on twisted waveguides, gave an excellent presentation of his work during the oral programme. There were many significant contributions during the conference from all areas of the linac community. A highlight from the electron community was the progress report on the X-FEL project which promises to be the flag bearer for electron machines over the coming years. The machine is a tremendous technical and industrial challenge and will give the most significant data to date for mass cavity production and performance in the lead up to an ILC decision. On the hadron front there were performance talks from SNS and J-PARC as well as project status presentations from SARAF and SPIRAL-II and future projects Project-X and IFMIF. Several excellent overview presentations summarized the many technical achievements of the community over the last few years. Reports from the fields of laser and plasma acceleration were truly inspiring. The conference was closed by an illuminating address by Nigel Lockyer, Director of TRIUMF, on the significance of the on-going search for the Higgs Boson.

The cultural programme included a reception at the Royal British Columbia Museum where guests were officially welcomed by the City of Victoria and given an opportunity to sample some of the traditional food of the region, a sea excursion to observe first-hand the local whales in their natural habitat and a visit to the spectacular Butchart Gardens. The conference concluded with an opportunity for registrants to visit the TRIUMF laboratory in Vancouver.

The local organizing team under the leadership of Amiya Mitra and the conference coordination under the leadership of Sandi Miller managed the conference logistics professionally.

We wish to thank delegates, exhibitors, students and staff for making this conference a rewarding experience.

Bob Laxdal

Scientific Programme Chair

Paul W. Schmor

LINAC08 Conference Chair

# Contents

## Conference Chair

| | |
|---|---|
| Paul Schmor | TRIUMF |

## Local Organizing Committee

| | |
|---|---|
| Amiya Mitra – Chair | TRIUMF |
| Iouri Bylinskii | TRIUMF |
| Martin Comyn | TRIUMF |
| Lynn DeCaire | TRIUMF |
| Dana Giasson | TRIUMF |
| Mindy Hapke | TRIUMF |
| Mark Keyzer | TRIUMF |
| Corrie Kost | TRIUMF |
| Robert Laxdal | TRIUMF |
| Steven McDonald | TRIUMF |
| Sandi Miller | TRIUMF |
| Alisa Preston | TRIUMF |
| Shirley Reeve | TRIUMF |
| Klaus Reiniger | TRIUMF |
| Paul Schmor | TRIUMF |
| Jana Thomson | TRIUMF |
| Vijay Verma | TRIUMF |

## International Organizing Committee

| | | |
|---|---|---|
| James Alessi | BNL | USA |
| John Barnard | LLNL | USA |
| Winfried Barth | GSI | Germany |
| Swapan Chattopadhyay | Cockcroft Institute | UK |
| Yanglai Cho | ANL | USA |
| Michael Fazio | LANL | USA |
| Roland Garoby | CERN | Switzerland |
| Terence Garvey | PSI | Switzerland |
| Hitoshi Hayano | KEK | Japan |
| Stuart Henderson | ORNL-SNS | USA |
| Andrew Hutton | Jefferson Lab | USA |
| Horst Klein | IAP Frankfurt | Germany |
| Andrei Kolomiets | ITEP | Russia |
| Leonid Kravchuk | INR | Russia |
| LK Len | DOE | USA |
| Gerald McMichael | ANL | USA |
| Alban Mosnier | CEA Saclay | France |
| Won Namkung | Postech | Korea |
| Akira Noda | Kyoto ICR | Japan |
| Guoxi Pei | IHEP Beijing | PR China |
| Paolo Pierini | INFN/LASA | Italy |
| Milorad Popovic | Fermilab | USA |
| Ron Ruth | SLAC | USA |
| Paul Schmor | TRIUMF | Canada |
| Stan Schriber | MSU | USA |
| Alessandro Variola | LAL Orsay | France |
| Hans Weise | DESY | Germany |
| Marion White | ANL | USA |
| Yoshishige Yamasaki | J-PARC | Japan |

## Program Committee

| | | |
|---|---|---|
| Robert Laxdal - Chair | TRIUMF | Canada |
| Chris Adolphsen | SLAC | USA |
| Alexander Aleksandrov | ORNL | USA |
| Giorgio Apollinari | Fermilab | USA |
| John Barnard | LLNL | USA |
| Winfried Barth | GSI | Germany |
| Patrick Bertrand | GANIL | France |
| Carlo Bocchetta | Instrumentation Tech. | Slovenia |
| Bruce Carlsten | LANL | USA |
| Yong Ho Chin | KEK | Japan |
| Yanglai Cho | ANL | USA |
| Byung-Ho Choi | KAERI | Korea |
| Marc Doleans | NSCL | USA |
| Alberto Facco | INFN/LNL | Italy |
| Alexander Feschenko | RAS/INR | Russia |
| David Findlay | STFC/RAL/ISIS | UK |
| Shinian Fu | IHEP Beijing | PR China |
| John Galambos | ORNL-SNS | USA |
| Roland Garoby | CERN | Switzerland |
| Cameron Geddes | LBNL | USA |
| Tomas Junquera | IPN Orsay | France |
| Andrei Kolomiets | ITEP | Russia |
| Geoffrey Krafft | Jefferson Lab | USA |
| Srinivas Krishnagopal | RRCAT | India |
| Matthias Liepe | CLASSE | USA |
| Marco Marchetto | TRIUMF | Canada |
| Peter McIntosh | STFC/DL/ASTeC | UK |
| Sergei Nagaitsev | Fermilab | USA |
| Olivier Napoly | CEA Saclay | France |
| Akira Noda | Kyoto ICR | Japan |
| Yujiro Ogawa | KEK | Japan |
| Peter Ostroumov | ANL | USA |
| Paolo Pierini | INFN/LASA | Italy |
| Joseph Preble | Jefferson Lab | USA |
| Deepak Raparia | BNL | USA |
| Tor Raubenheimer | SLAC | USA |
| Amit Roy | IUAC | India |
| Alwin Schempp | IAP Frankfurt | Germany |
| Paul Schmor | TRIUMF | Canada |
| Tsumoru Shintake | RIKEN | Japan |
| Nikolay Solyak | Fermilab | USA |
| John Staples | LBNL | USA |
| Sami Tantawi | SLAC | USA |
| Akira Ueno | KEK/JAEA | Japan |
| Alessandro Variola | LAL Orsay | France |
| Nikolay Vinokurov | BINP SB RAS | Russia |
| Hans Weise | DESY | Germany |
| Marion White | ANL | USA |
| Yoshishige Yamazaki | J-PARC | Japan |

# Sponsors

| | |
|---|---|
| Linde | Platinum Sponsor |
| PAVAC Industries Inc. | Platinum Sponsor |
| AAPS | Gold Sponsor |
| MDS Nordion | Silver Sponsor |
| Linac Systems, LLC | Bar at Banquet |
| Bruker Biospin Corp. | Wine at Banquet |
| Instrumentation Technologies | Poster Session |
| Richardson Electronics, Ltd. | Prize Donation |
| WC Heraeus GmbH | Student Sponsor |
| Advanced Energy Systems, Inc. | Item in Delegate Bag |
| Advanced Magnet Lab, Inc. | Item in Delegate Bag |
| Alpha Scientific Electronics | Item in Delegate Bag |
| D-Pace, Inc. | Item in Delegate Bag |
| Niowave, Inc. | Item in Delegate Bag |
| RadiaBeam Technologies, LLC | Item in Delegate Bag |

# Exhibitors

Advanced Applied Physics Solutions (AAPS)
ACCEL Instruments GmbH
AccelSoft / G.H. Gillespie
Advanced Energy Systems, Inc. (AES)
Advanced Magnet Lab, Inc.
Amuneal Manufacturing Corp.
Apple Canada
attocube systems AG
Bruker Biospin Corp.
Communications & Power Industries (CPI)
CST of America, Inc.
Diversified Technologies, Inc.
Goodfellow Corporation
Instrumentation Technologies
L-3 Communications Electron Devices
Lambda Americas / Test Force
Muons, Inc.
National Instruments
Neue Technologien GmbH (NTG)
PAVAC Industries Inc.
PLANSEE SE
RadiaBeam Technologies, LLC
Tech-X Corporation
Thales Components Corporation
The Ferrite Company
Toshiba Electron Tubes & Devices
Varian Canada, Inc.
ZTEC Instruments Inc.

## Student Awards and Sponsors

We would like to thank our student sponsors AAPS and WC Heraeus GmbH who helped to bring the following students to Victoria:

| | |
|---|---|
| Adli, Erik | U. Oslo / CERN |
| Franke, Sylvain | TEMF, TU Darmstadt |
| Grassellino, Anna | U. Pennsylvania / TRIUMF |
| Ichikawa, Masahiro | ICR, Kyoto U. |
| Ishibashi, Takuya | RLNR, Tokyo IT |
| Kato, Yuta | RISE, Waseda U. |
| Keung, Justin | U. Pennsylvania |
| Koeth, Timothy | Rutgers U. / Fermilab |
| Kutsaev, Sergey | MEPhI |
| Longuevergne, David | IPN, Orsay |
| Mavric, Uros | Fermilab |
| Paparella, Rocco | INFN/LASA |
| Pfister, Jochen | IAP, Goethe U. Frankfurt |
| Plostinar, Ciprian | JAI / STFC/RAL/ASTeC |
| Posocco, Piero Antonio | Consorzio RFX, INFN/LNL |
| Sakaue, Kazuyuki | RISE, Waseda U. |
| Sugimoto, Takanori | ICR, Kyoto U. |
| Tam, Wai-Ming | Indiana U. / Fermilab |
| Wilson, Joshua | U. Tennessee / ORNL-SNS |
| Yamada, Masako | ICR, Kyoto U. |
| Yan, Fang | TRIUMF |

# Conference Photographs

Photographers: Mindy Hapke (TRIUMF), Corrie Kost (TRIUMF), Volker Schaa (GSI)

# Sunday, 28 September 2008

## Sunday Orientation






## Sunday Student Poster Session

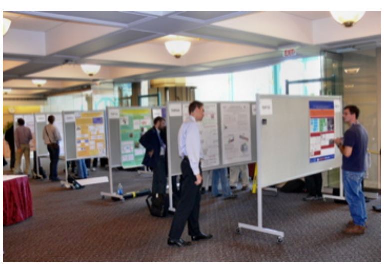
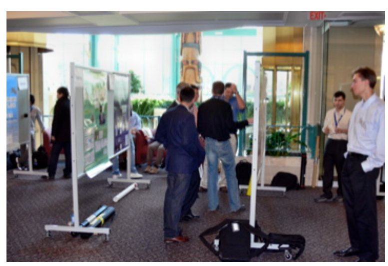


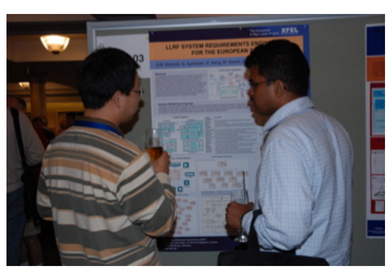
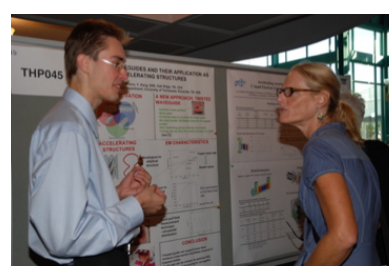

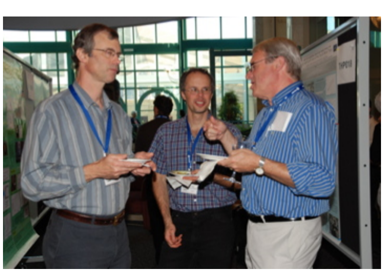
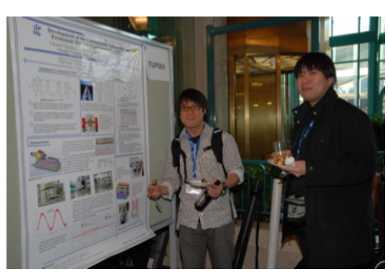



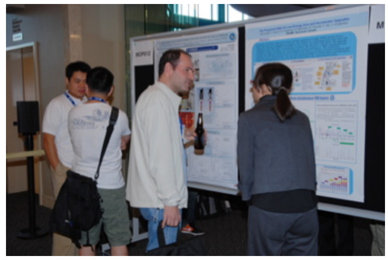
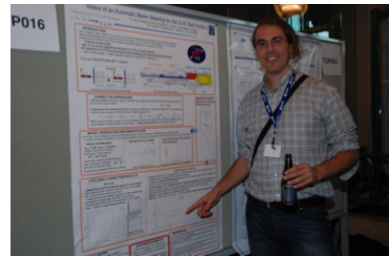


## Sunday Registration

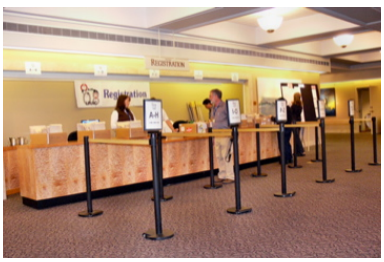





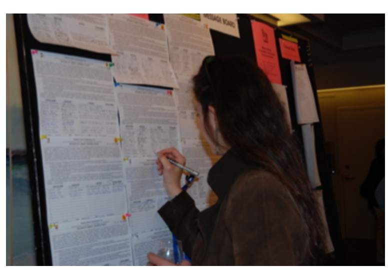
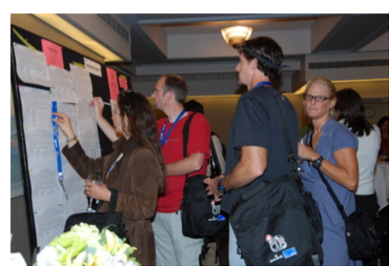



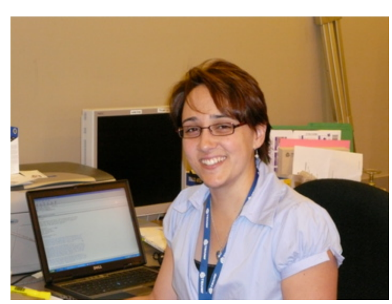

# Sunday Welcome Reception




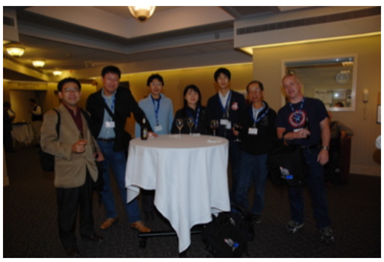



















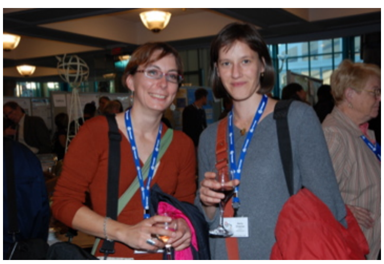




Speaker
Ready Room

Speaker
Ready Room


# Monday, 29 September 2008

## Monday Welcome




## Monday Oral Session MO1

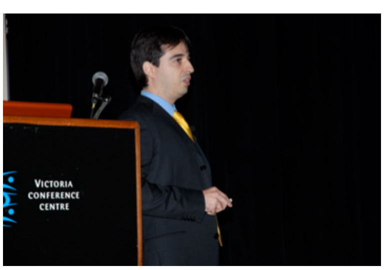



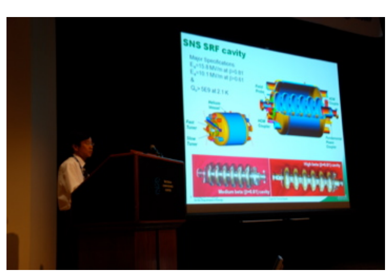

# Monday Coffee Break






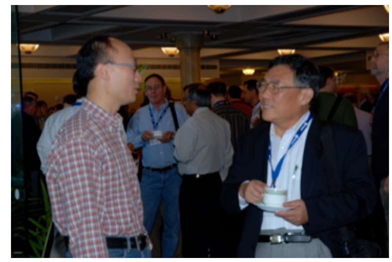


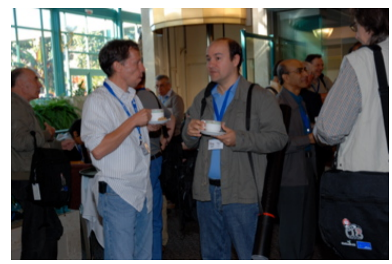





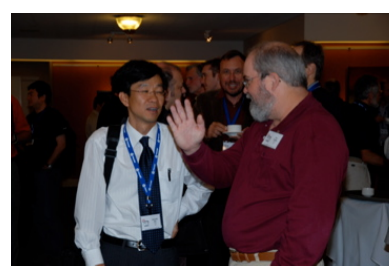




Speaker
Ready Room



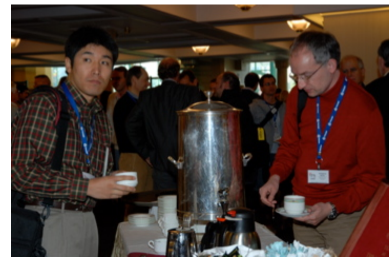

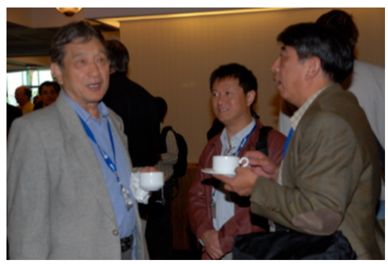

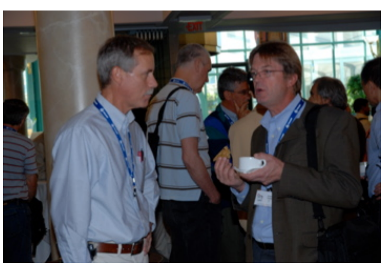




# Monday Oral Session MO2

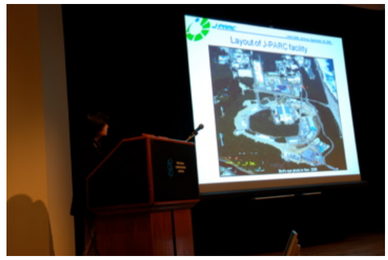


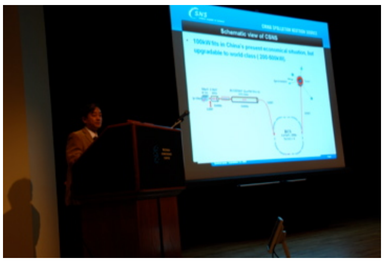

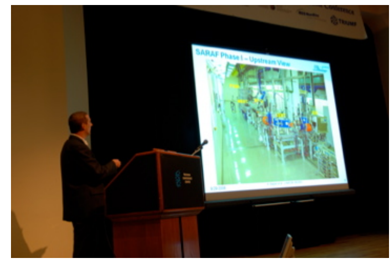



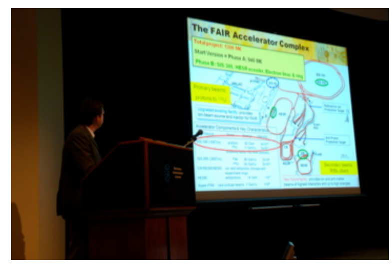



# Monday Lunch




# Monday Oral Session MO3





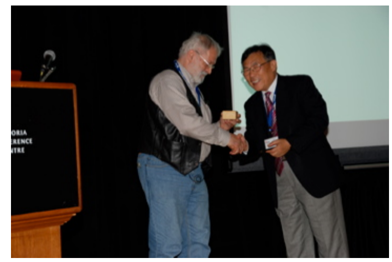
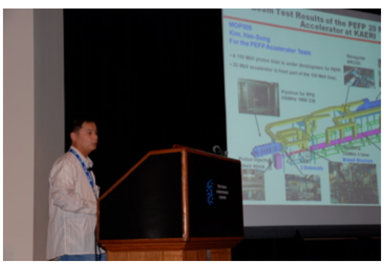



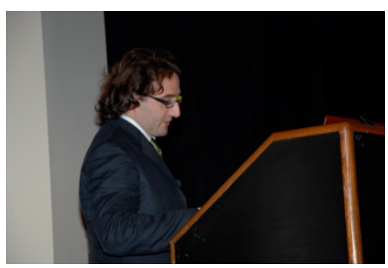

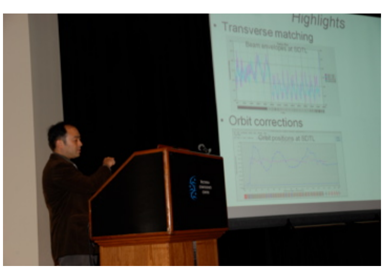

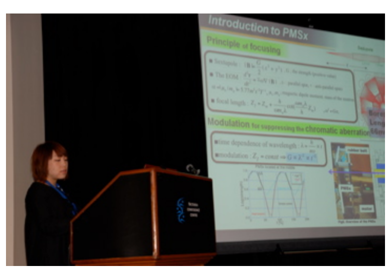

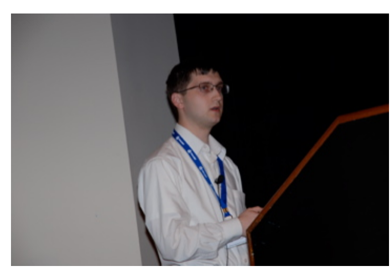
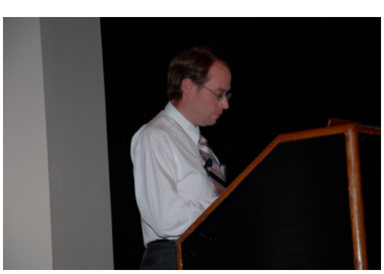

# Monday Poster Session MOP


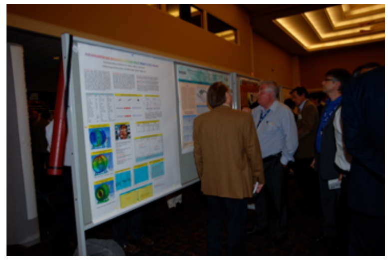

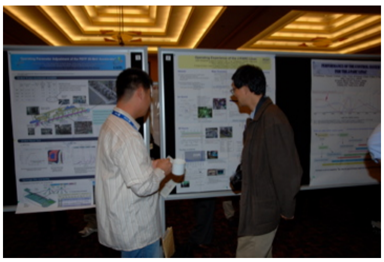
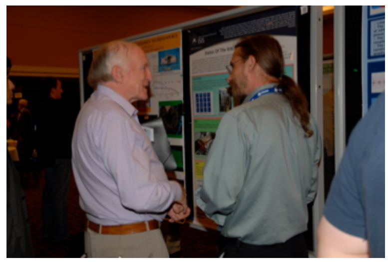
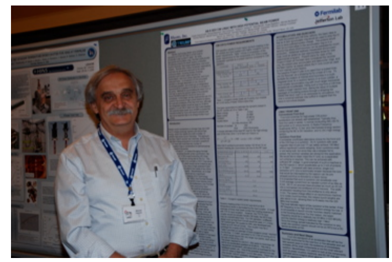

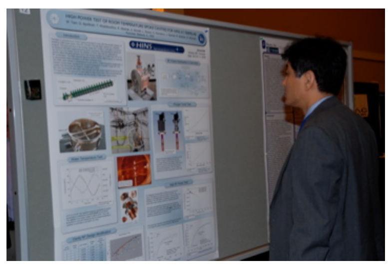


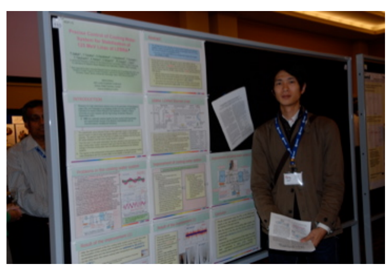
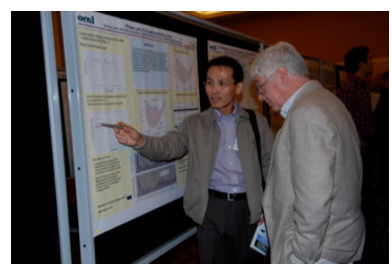


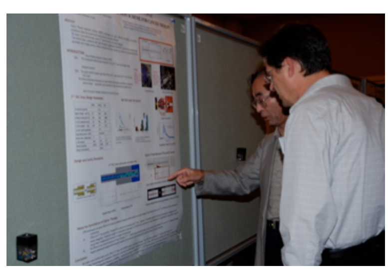
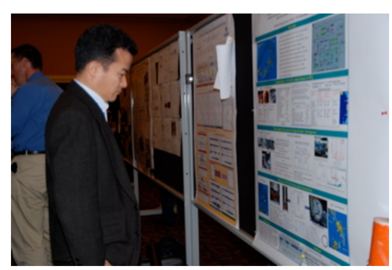
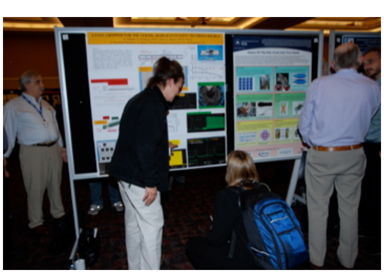


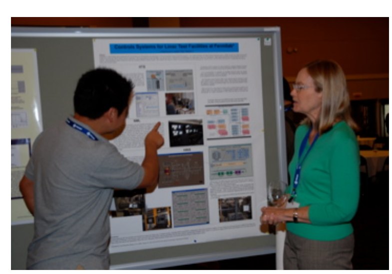

# Monday Chairman's Reception






























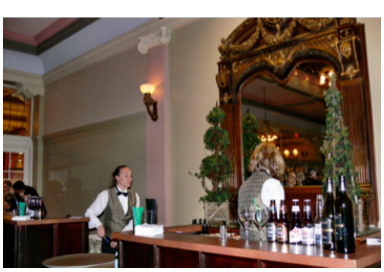

# Tuesday, 30 September 2008

## Tuesday Oral Session TU1

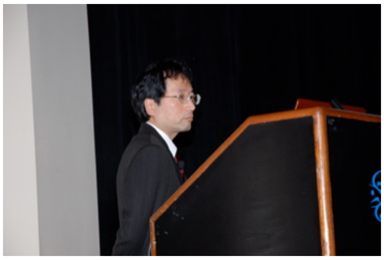

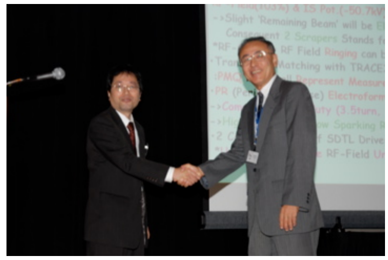

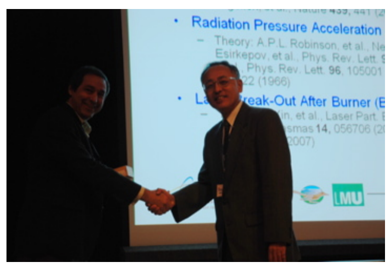


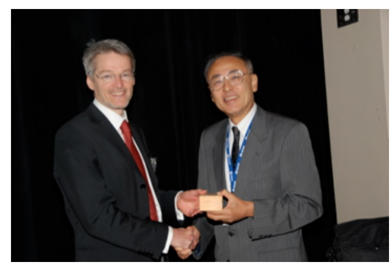

# Tuesday Oral Session TU2

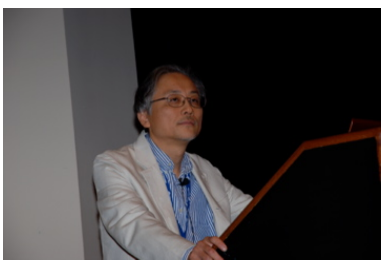

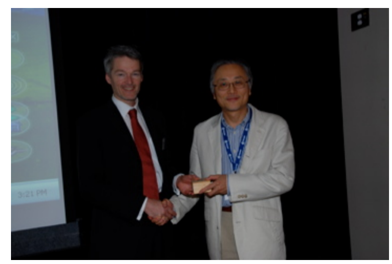

# Tuesday Oral Session TU3

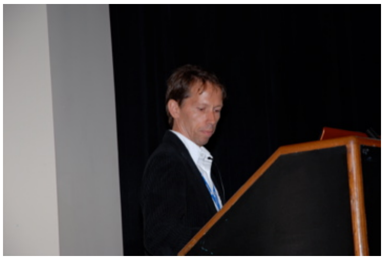



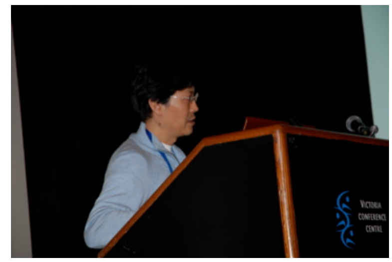



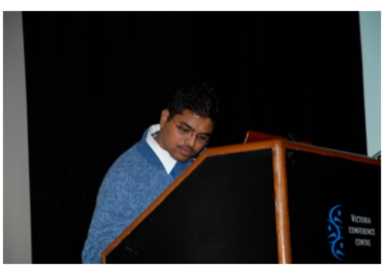


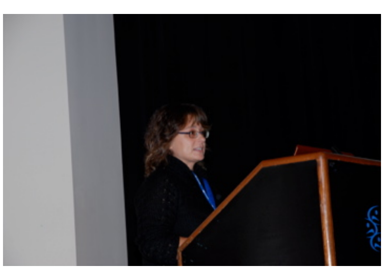


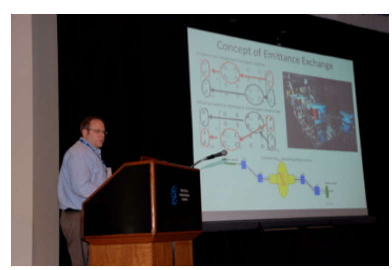



# Tuesday Poster Session TUP

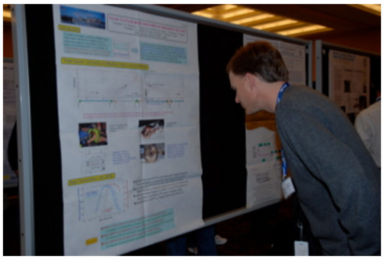
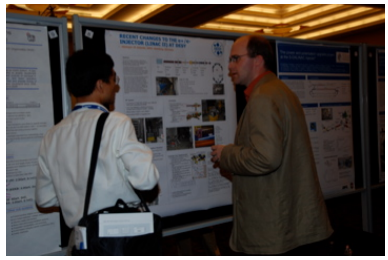
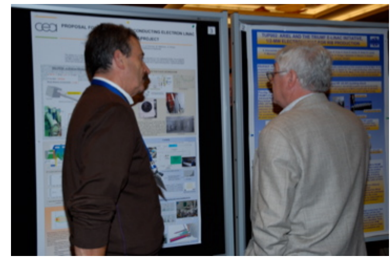
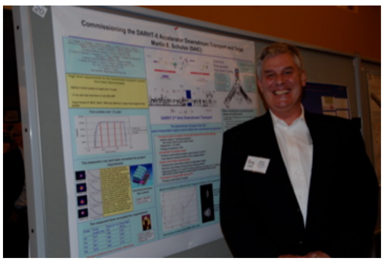
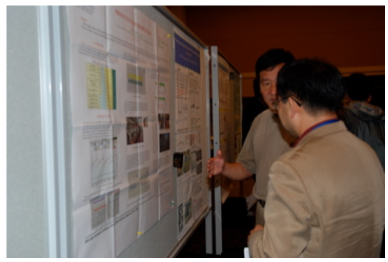
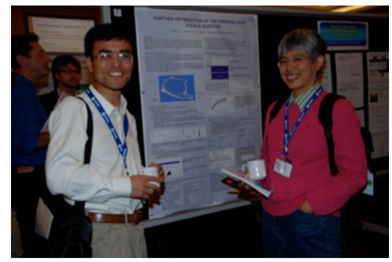
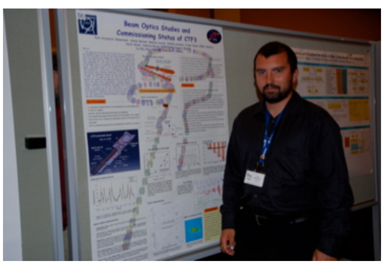
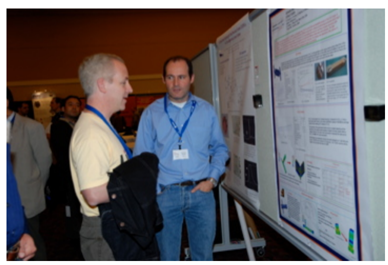
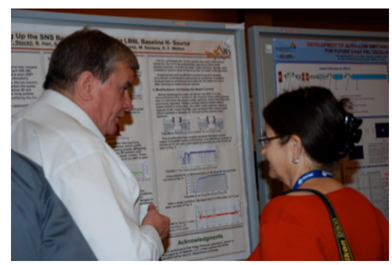
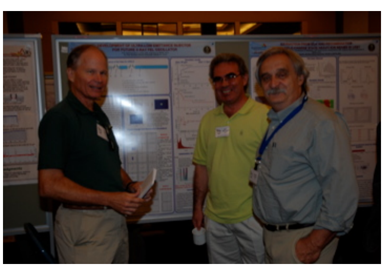
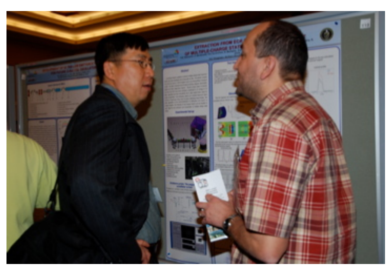
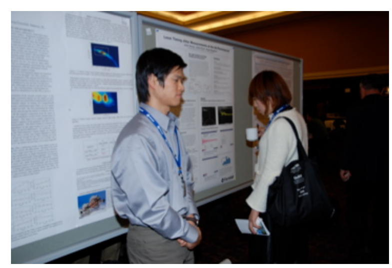
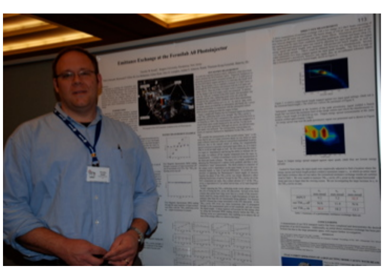
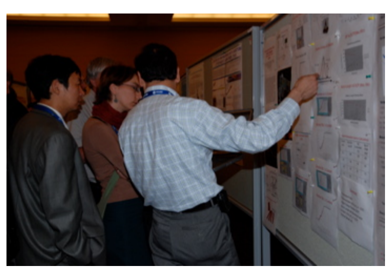
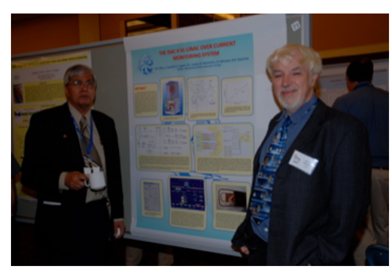

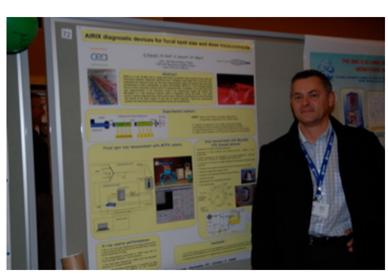
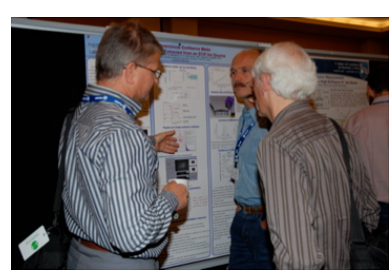

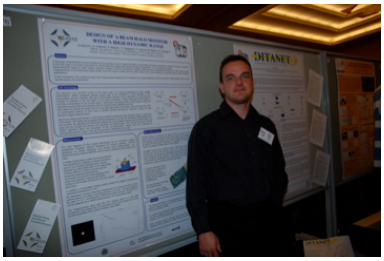
DITANET

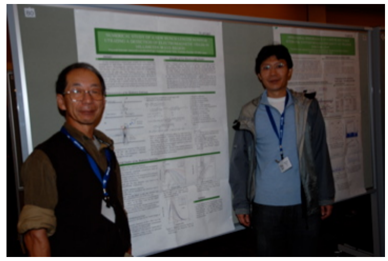

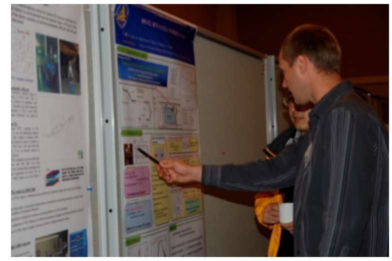

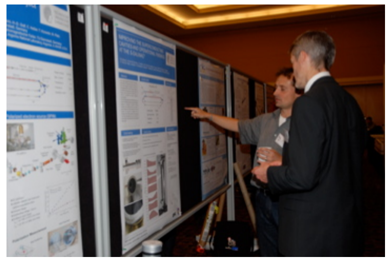

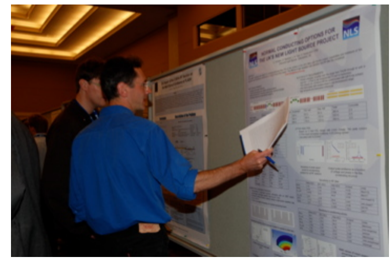
NLS

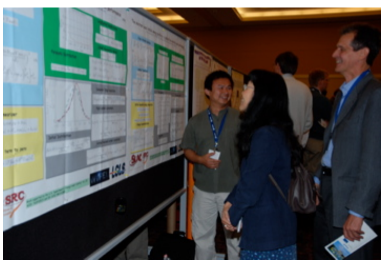
SRC

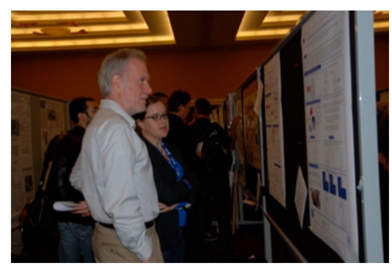

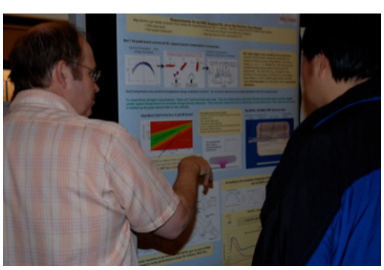

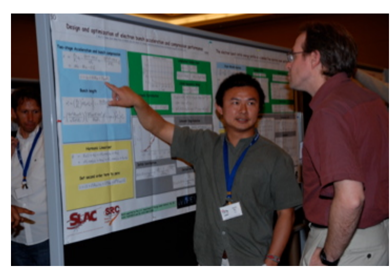
SLAC
SRC

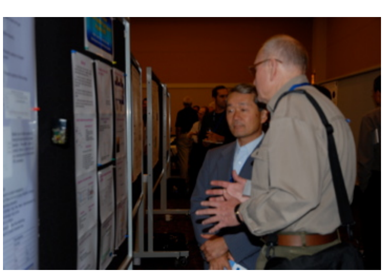

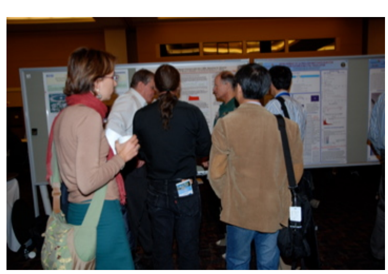

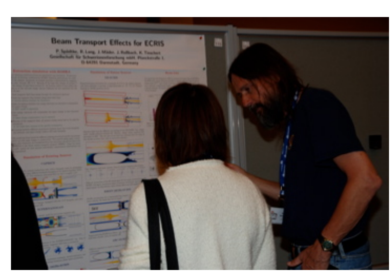
Beam Transport Effects for ECRIS

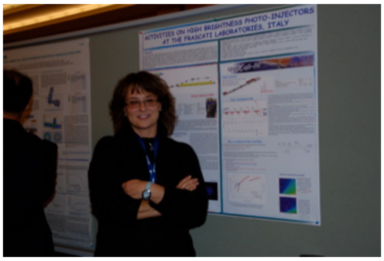
ACTIVITIES ON HIGH BRIGHTNESS PHOTO-INJECTORS
AT THE FRASCATI LABORATORIES, ITALY
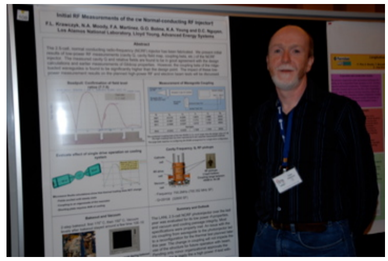
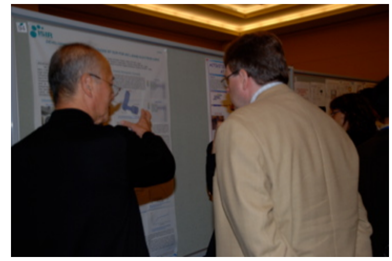
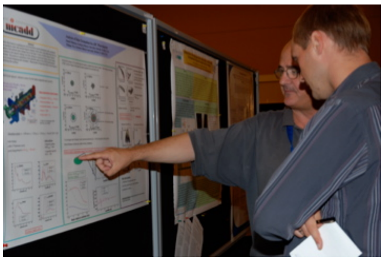
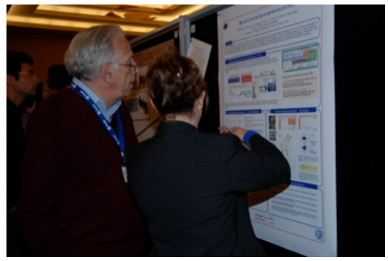
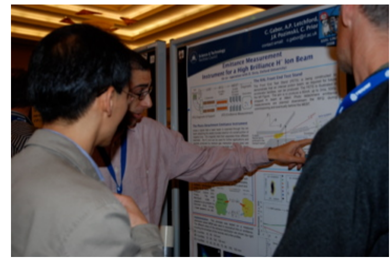
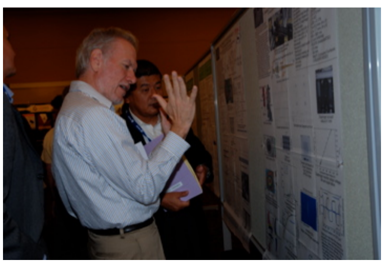


CST

# Wednesday, 1 October 2008

## Wednesday Oral Session WE1


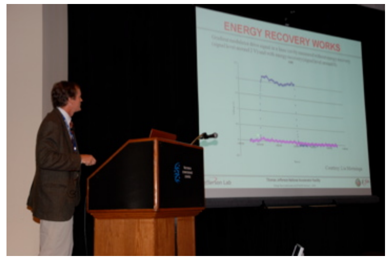










# Wednesday Oral Session WE2

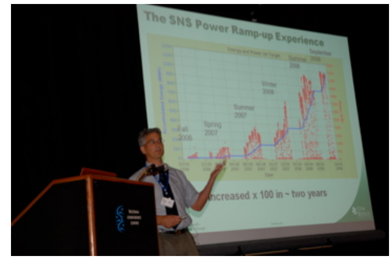


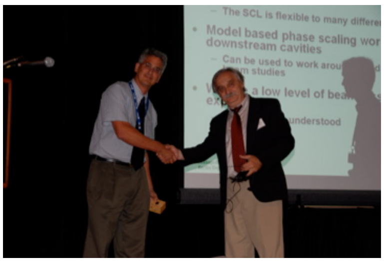

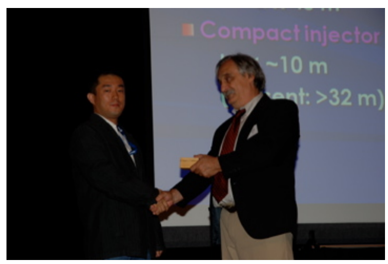


# Wednesday Whale Watching















# Wednesday Butchart Gardens


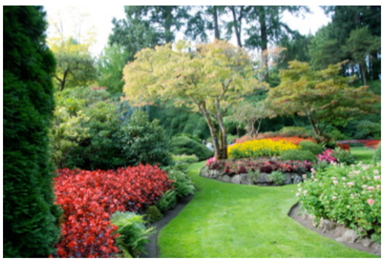

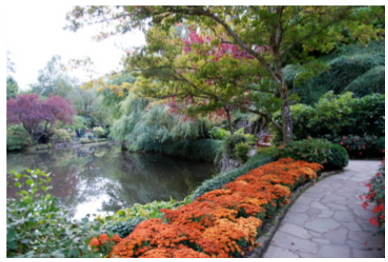

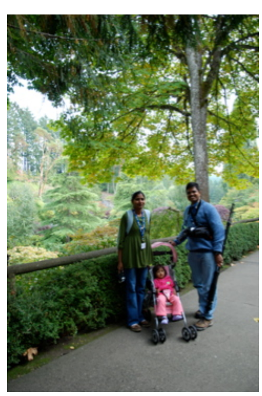









# Wednesday Reception Royal BC Museum





























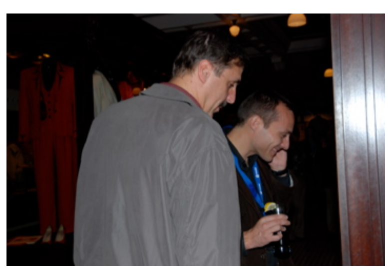


The Terrible Teens


















# Thursday, 2 October 2008

## Thursday Oral Session TH1



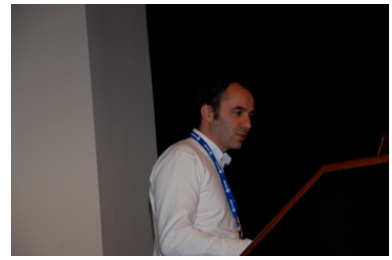

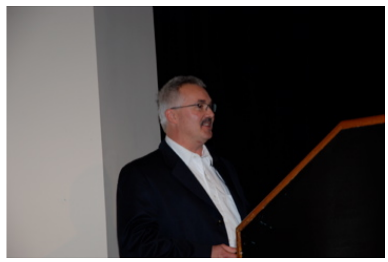

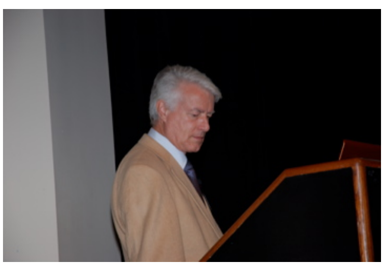

# Thursday Oral Session TH2












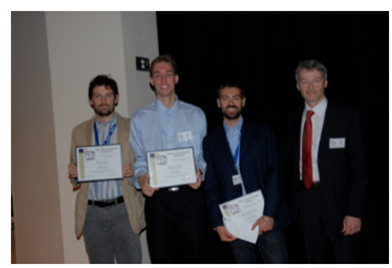

# Thursday Oral Session TH3


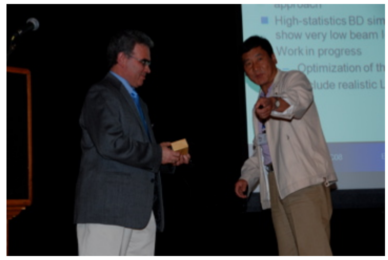




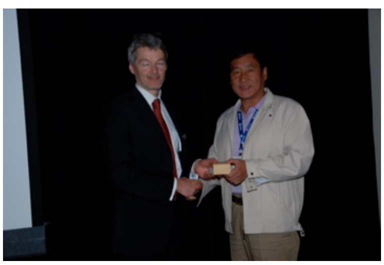
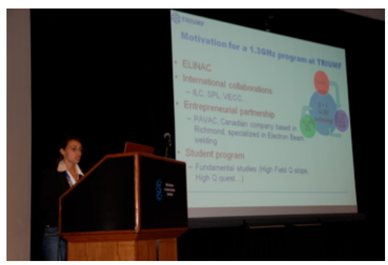



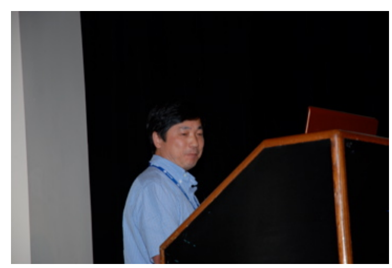

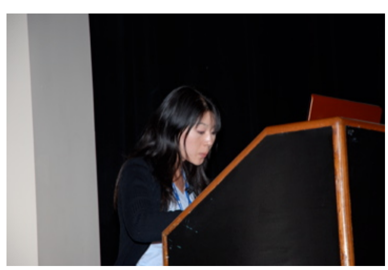
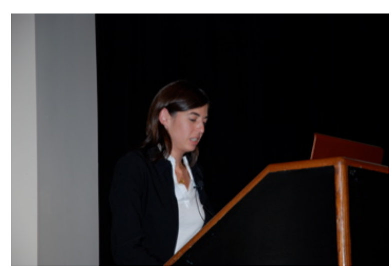

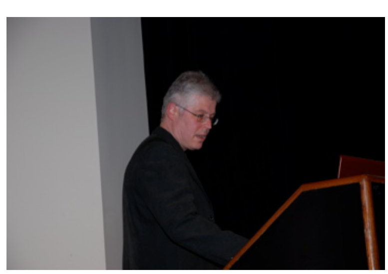



# Thursday Poster Session THP

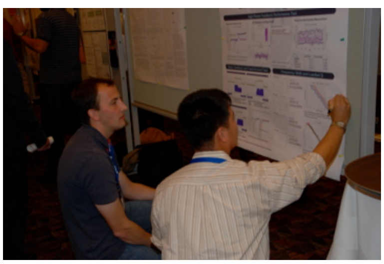

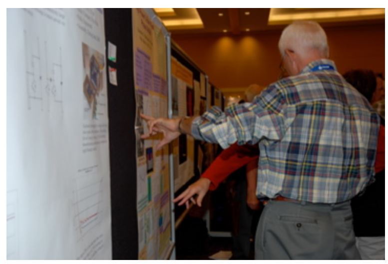

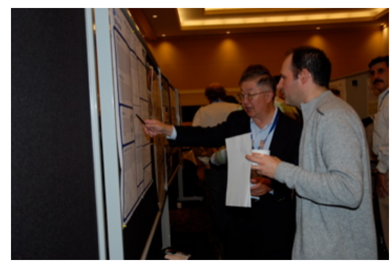

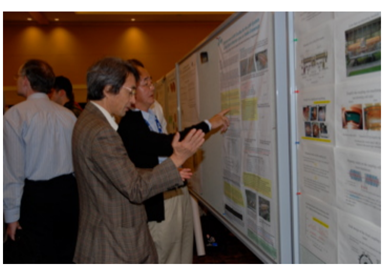

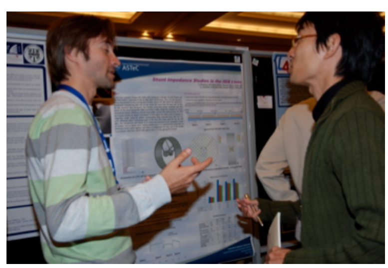

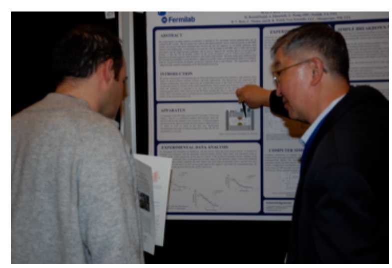

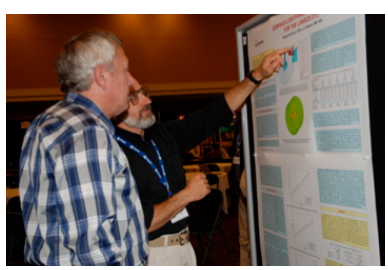

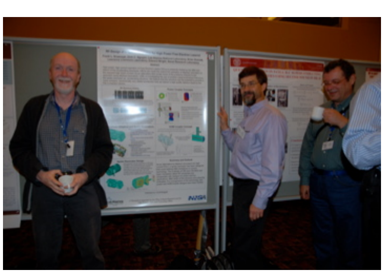

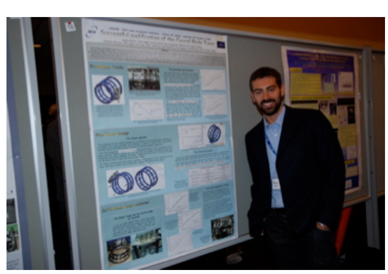

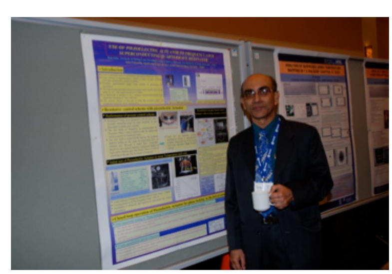


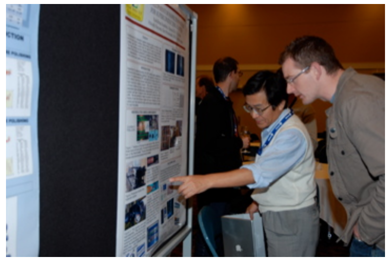

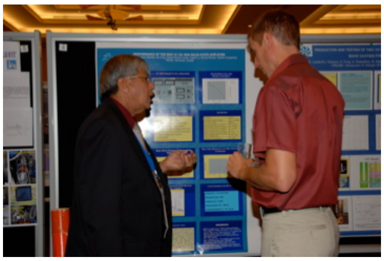
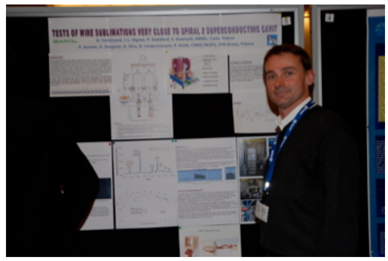
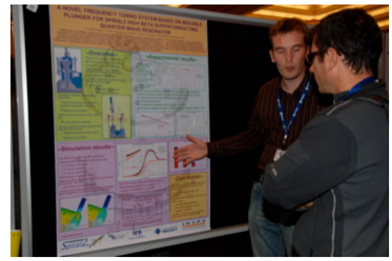
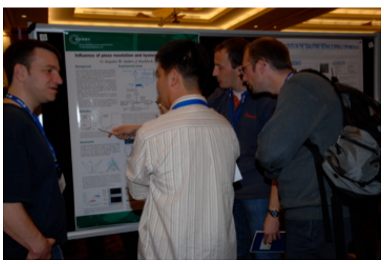
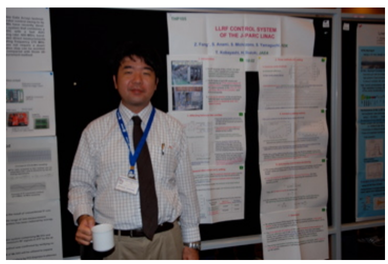
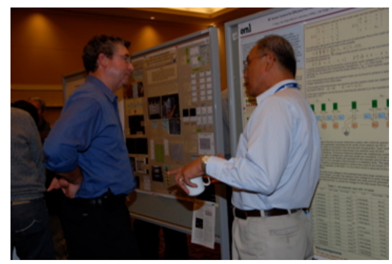
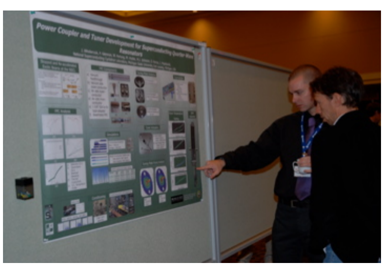


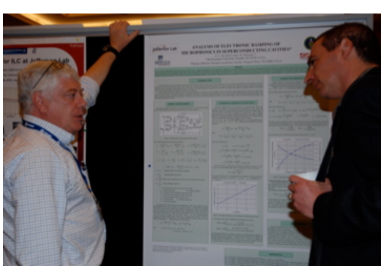
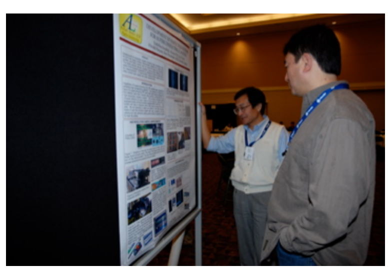
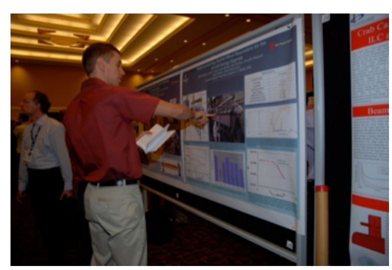
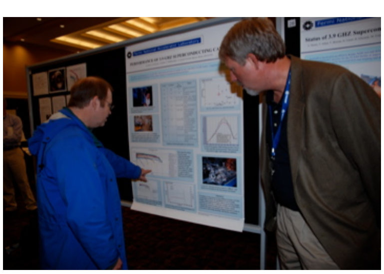
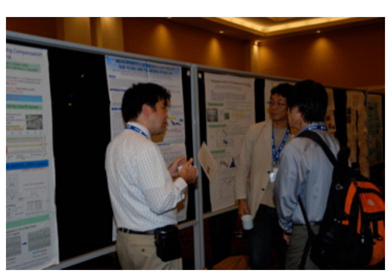
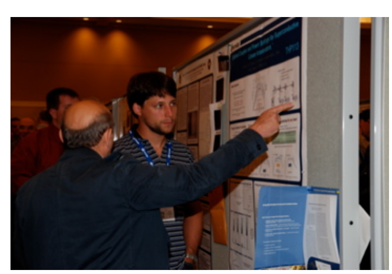


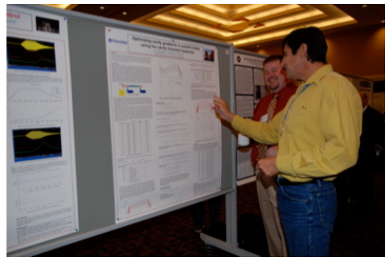
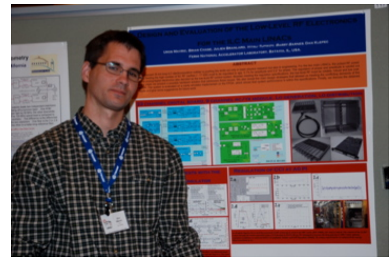
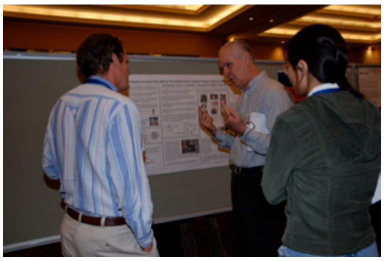
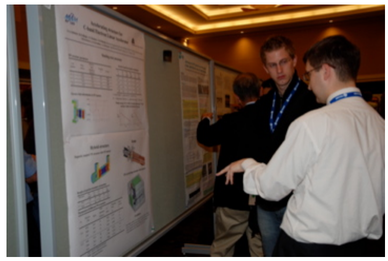

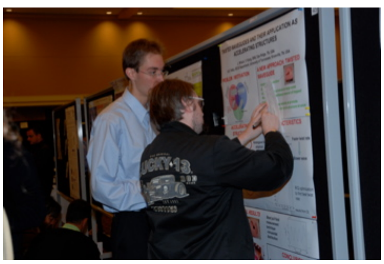

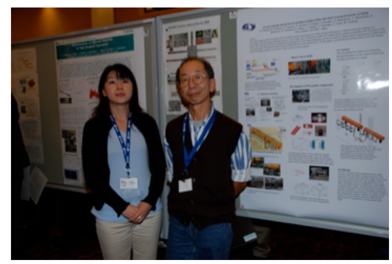
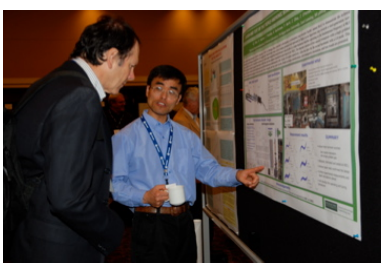


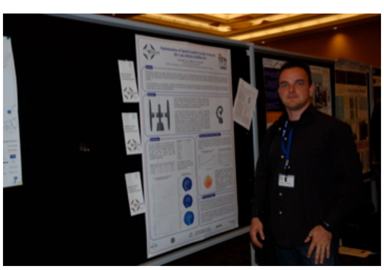

# Thursday Banquet Fairmont Empress Crystal Ballroom







































































# Friday, 3 October 2008

## Friday Oral Session FR1








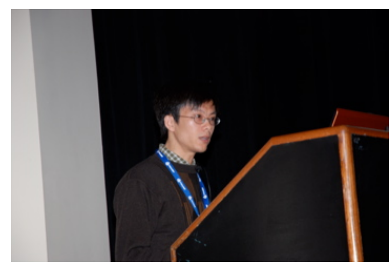
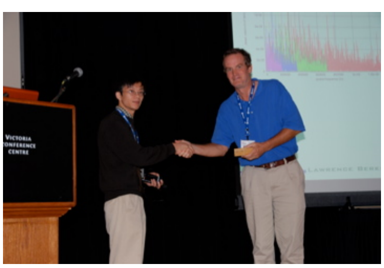


# Friday Oral Session FR2

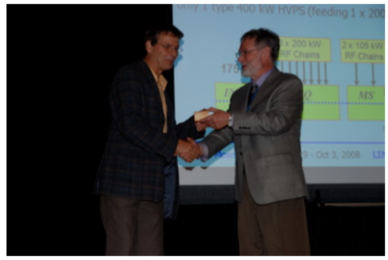

# Friday Closing Remarks



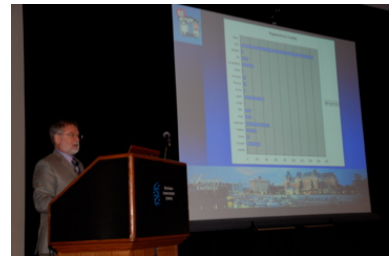










# Friday Hand On to LINAC10

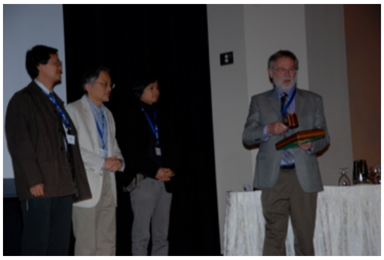

# Other Aspects of the Conference

## Exhibitors












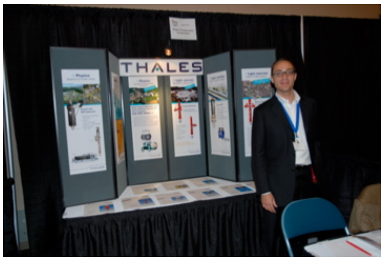
THALES

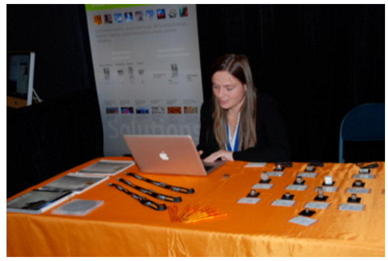


Advanced Energy Systems


amuneal
DESIGN
MATERIALS
FABRICATION
ANNEALING
TESTING
CUSTOM
MAGNETIC SHIELDING


Muons, Inc.

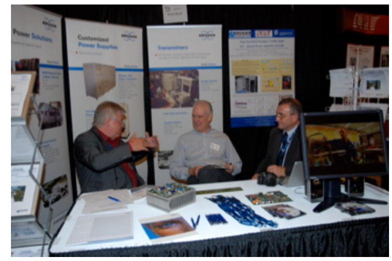


CPI
Communications & Power Industries


CST


PAVAC
INDUSTRIES INC


TOSHIBA
TOSHIBA KLYSTRONS

# Victoria, BC











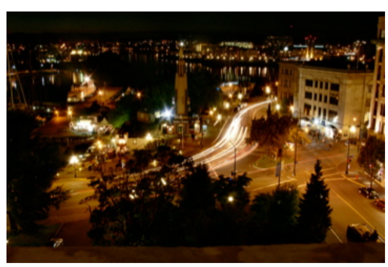

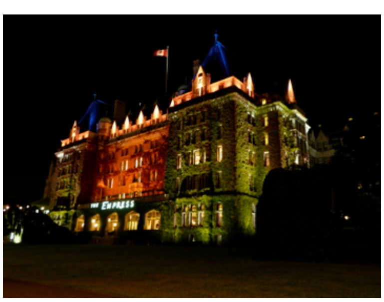

# Victoria Conference Centre








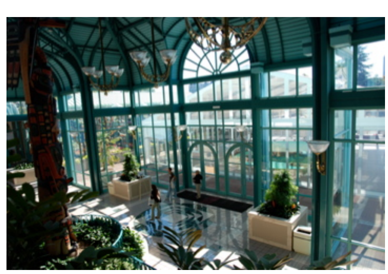

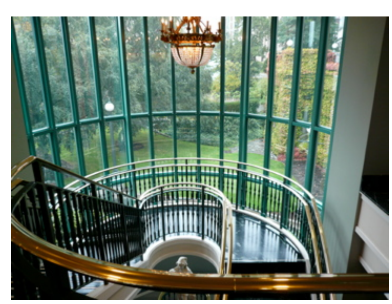

# LOC / JACoW






# JACoW Proceedings Office

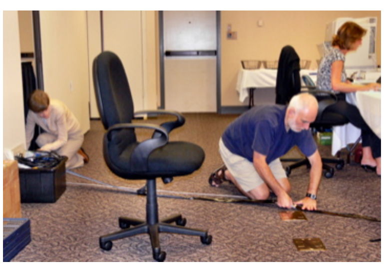
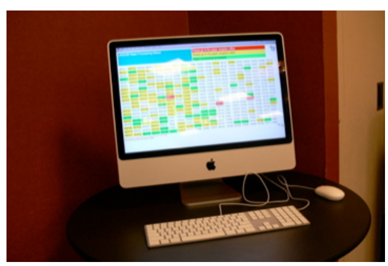

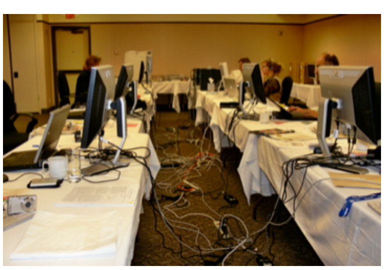
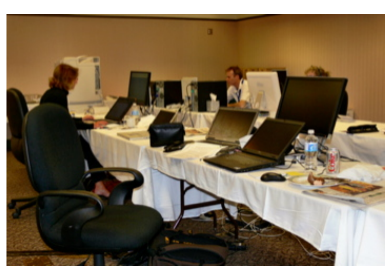



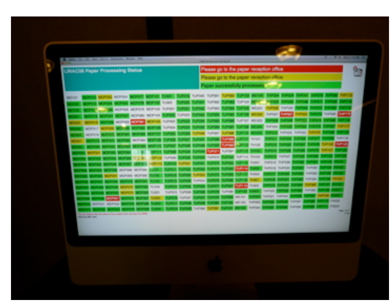

# Group Photographs

# ISAC-II OPERATION AND FUTURE PLANS

M. Marchetto, TRIUMF, Vancouver, BC V6T 2A3, Canada

*Abstract*

The ISAC-II superconducting heavy ion linac now accelerates radioactive ion beams with the highest gradient of any operating SC ion facility in the world and provides a 20 MV boost to the ISAC accelerated beams. The addition of a further 20 MV of SC linac, with cavities made in Canada, will be installed by the end of 2009. The ISAC-III project scheduled to begin in 2010 will see the installation of an additional driver beam of 50 MeV electrons to produce RIBs by photofission, an expanded target area, and new front-end ion accelerators to expand the capability to three simultaneous radioactive beams for experiments.

## INTRODUCTION

ISAC at TRIUMF is one of the major existing facilities for the production of radioactive ion beams (RIB). There are two commonly used methods for RIB production [1].

The first one is the in flight or fragmentation method. The facility using this method has a main accelerator that accelerates heavy ions toward a thin target. The heavy ion breaks apart going through the target producing a variety of radioactive ions. The ions, already at the final velocity, are selected through a fairly complex mass separator system and sent to the experiment.

The second method is the isotope separation on line or ISOL method. In this case an accelerator, called a driver, accelerates light projectiles, the primary beam, toward a thick target. The light projectiles, protons or light ions, break the target nuclei producing neutral radioactive isotopes. These neutral atoms are then transported into a source where they are ionized and extracted at source potential. The radioactive ions are magnetically separated and post accelerated to reach the final energy requested.

The two methods are complementary. The in flight is a fast production method that allows to deliver isotopes of very short half-lives (ms or less) but with a beam of relatively large emittance . The ISOL method on the contrary produces high quality emittances but the complicated and relatively slow process reduces the possibility of extracting isotopes with few ms half-lives. The in flight methods RIB has energy of several tens of MeV/u while the ISOL method can deliver beam of few keV/u.

## ISAC OVERVIEW

The ISAC facility at TRIUMF is an ISOL facility. It has the highest power (50 kW) primary proton beam. The overview of the facility is represented in Fig. 1. The ISAC facility produces the most intense beam for certain species, an example being the exotic $^{11}$Li.

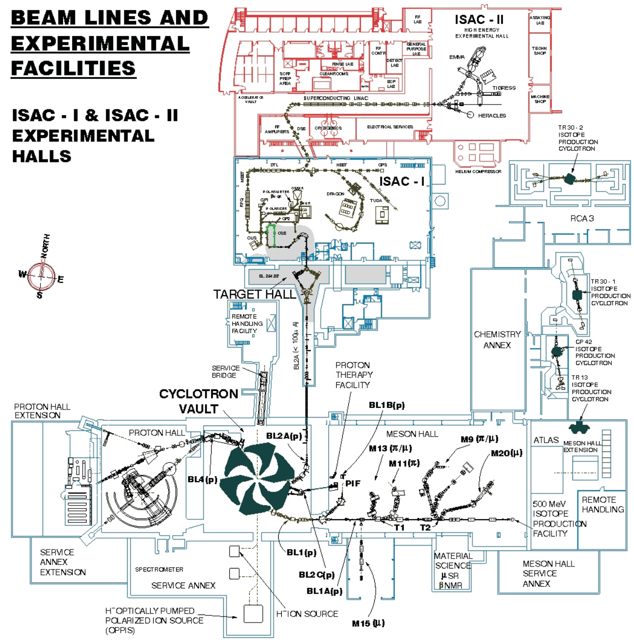


Figure 1: Overview of the TRIUMF site. The main machine is the H$^-$ 500 MeV cyclotron used also as driver of the ISAC facility.

The facility uses silicon carbide or tantalum targets for ion production. Two target configurations are available: low and high power respectively for proton beam powers up to 20 kW and 50 kW. Most recently beam production with a UOx target was successfully completed.

### *Driver*

The TRIUMF H$^-$ cyclotron is the largest cyclotron in the world and has operated for almost 35 years. It accelerates H$^-$ ions up to an intensity of 250 $\mu$A to a maximum energy of 500 MeV. The H$^-$ are then stripped and protons are extracted in three different beam lines at different energies the maximum being 500 MeV. One of these beam line is dedicated for the ISAC radioactive beam production. In this case the beam is extracted at 500 MeV and up to 100 $\mu$A.

The simultaneous extraction of multiple beams with stable delivery is challenging. Nevertheless a 90% availability of the proton beam for the ISAC facility is regularly achieved.

The capability of multiple extractions can be expanded by refurbishing a fourth existing extraction beam line giving two simultaneous proton beams for RIB production [2] as represented in Fig. 2. This possibility together with an upgrade of the cyclotron [3] is one of the goals for the next

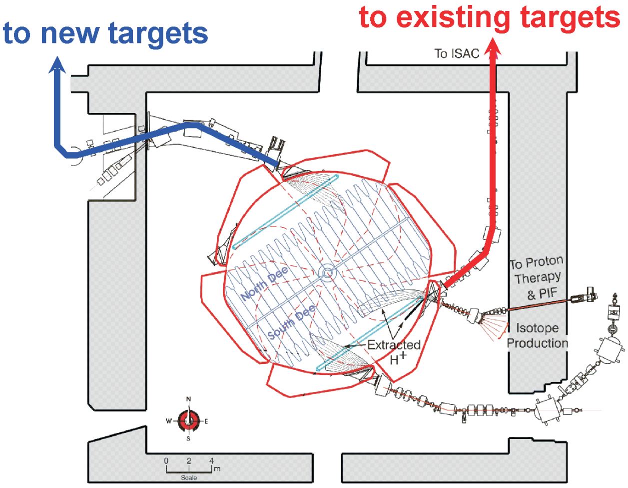


Figure 2: Schematic of the TRIUMF cyclotron. Three operating extraction beam lines in the SE side. One existing extraction beam line in the NW side.

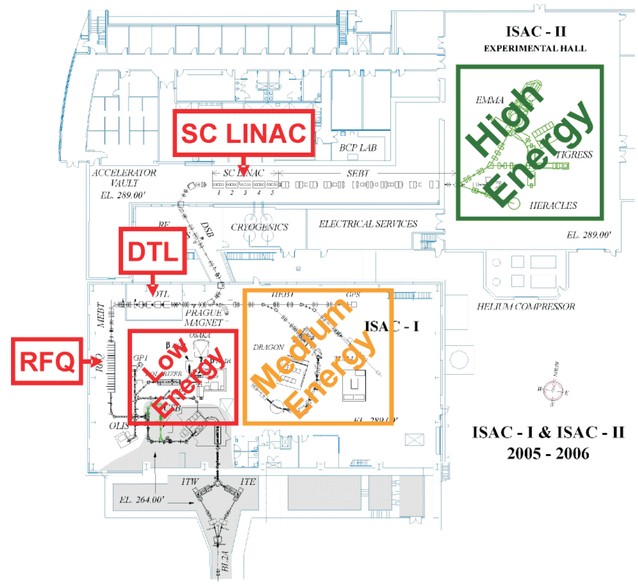


Figure 3: Overview of the ISAC facility at TRIUMF. The ISAC-II linac is superconducting while in ISAC-I the RFQ and the DTL are room temperature machines.

five year plan as explained in the last section of this paper.

### *Target Station and Mass Separator*

The ISAC facility has two independent target stations. This allows service on one target station while producing and delivering radioactive beams with the other.

Each target station is composed of five modules. The entrance module houses the diagnostic and protection monitors for the proton beam. The target module contains the target and the source; this module is routinely removed to change both target and source. Four target modules are available. The beam dump module is located downstream of the target module. The last two are the extraction modules housing the optics elements. They are oriented perpendicular to the proton beam direction.

Downstream of the targets there is a common preseparator. The target modules and preseparator are inside a concrete shielded area. The preseparator reduces the radioactivity transported outside the shielded area in the downstream beam line.

After the preseparator the RIBs are selected using the mass separator. This device is installed on a biased platform to increase the resolution.

After selection it is possible to boost the charge state of the radioactive ion by diverting them through an electron cyclotron resonance ion source (ECRIS). This charge breeder allows post acceleration of masses A>30.

The target stations and the separator area are located underground. Once produced and selected the RIB is then transported to ground level where the post accelerator and experiments are located.

### *Post Accelerators*

The RIBs can be delivered to three experimental areas as represented in Fig. 3: a low energy area where the ions are accelerated at source potential (up to 60 kV),a medium energy area ($\beta$=1.8%$\rightarrow$6%) or a high energy area ($\beta$=6%$\rightarrow$15%) where the ions are post accelerated with linacs.

The first stage of acceleration uses a radio frequency quadrupole (RFQ) acting as an injector [4]. The RFQ boosts the energy from 2 keV/u to 150 keV/u. It can accelerate mass to charge ratio of $3\leq$A/Q$\leq$30. The RFQ is a room temperature CW machine operating at 35.36 MHz. The eight meter long resonant structure is composed of nineteen split rings supporting the electrodes. The RFQ doesn't have a bunching section; the beam is prebunched at the entrance with a three harmonics RF buncher, the fundamental being 11.78 MHz. This configuration produces a high quality longitudinal emittance after the RFQ (0.22 $\pi$ keV/u·ns). Part of the beam transmitted but not accelerated is stopped into a fixed collimator downstream of the RFQ [5]. The beam inside the longitudinal emittance after the slit is around 80% of the injected.

After the RFQ the charge state of the ions is increased by stripping the ions through a thin carbon foil (4 $\mu$g/cm$^2$). As a general rule the most populated charge state is selected using magnetic benders as long as the mass to charge ratio is within $2\leq$A/Q$\leq$6 set by the following drift tube linac (DTL). The efficiency of the stripping foil depends on the mass of the stripped ions; in most of the cases it ranges between 30% to 50%.

The DTL [6] is a variable energy machine covering the entire range of energies 150 keV/u$\leq$E$\leq$1.8 MeV/u. The DTL is a separated function machine composed of five IH interdigital structure accelerating tanks and three split ring bunchers located between the first four tanks. This layout produces good beam quality for each energy. After the fourth tank the beam quality is already sufficient that no buncher is required. The resonance frequency of the tanks and bunchers is 106.08 MHz and they operate at room temperature in CW mode. Transverse focus through the linac is provided by quadrupoles triplets between each tank. The transmission of this linac is greater than 95%. The DTL is also used as an injector for the ISAC-II superconducting (SC) linac.

The SC linac [7] is at present composed of five cryomodules. Each cryomodule houses four superconducting cavities and one superconducting solenoid. The superconducting cavities are bulk niobium quarter wave resonators at 106.08 MHz operating at 4 K. All twenty cavities installed, fabricated in Italy by Zanon, meet or exceed the ISAC specification being 30 MV/m peak surface field at 7 W of helium consumption. In fact the SC linac is now operating for two years at an average gradient of 35 MV/m peak surface field (7 MV/m of acceleration) at 7 W. During this period there is on average no significant degradation in the cavities performance. Each cavity is independently phased at -25° synchronous phase. The transmission through the SC linac is 100%.

### *Beam Delivery*

The post accelerator sections are tuned by means of the pilot beam technique. This technique consists in setting the beam lines and accelerators with a beam of stable ions with the same mass to charge ratio as the RIB. This is necessary because the intensity of the radioactive beam typically ranges between $10^3$ and $10^6$ particle per second. In order to match the radioactive beam coming from the charge breeder an electron cyclotron resonance (ECR) source that can produce stable ions with higher charge states is now installed. The switchover procedure from the pilot beam to the radioactive is straightforward. The transmission of the RIB is checked using several low intensity detectors (like silicon detector, photodiode or channeltron) distributed along the beam line.

The delivery of RIBs is challenging considering the long chain of production, selection and post acceleration. In order to transport the radioactive ions to the experiment every single component has to function properly. The availability of the ISAC linacs is 98%.

## ISAC-II UPGRADE

A linac upgrade is underway [8]. The upgrade consists of twenty more cavities housed in three cryomodules installed downstream of the existing section. The first two cryomodules house six superconducting cavities and one superconducting solenoid while the last one has eight superconducting cavities and a superconducting solenoid.

This upgrade increases the ISAC-II linac voltage capability to 40 MV. This voltage will boost the beam energy above the Coulomb barrier for all masses. Since the SC linac always operates at the maximum possible voltage for stable operation, the final energy depends on the mass to charge ratio of the accelerated species. We anticipate an energy of 22 MeV/u for A/Q=2 and 8 MeV/u for A/Q=6 as represented in Fig. 4 (lower graph).

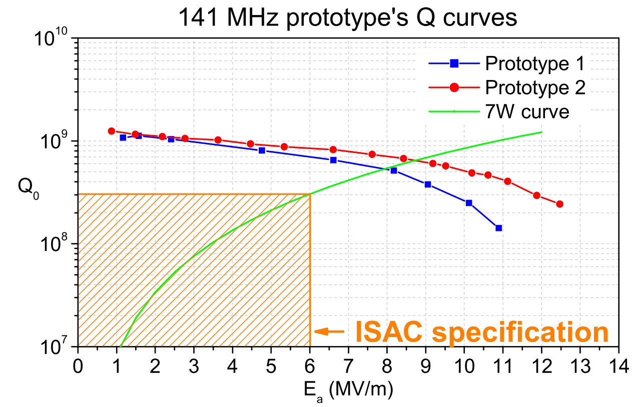


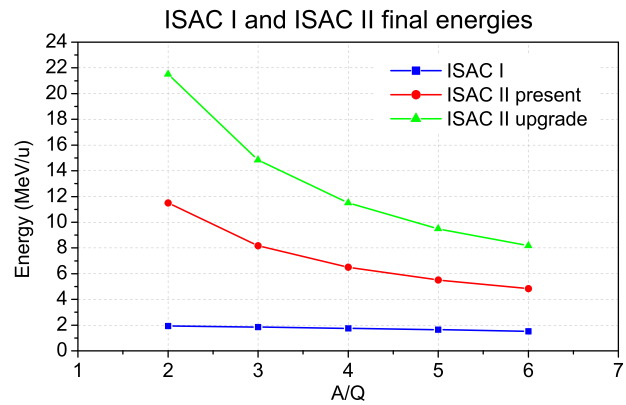


Figure 4: (Upper) Characteristic Q curves of the two new 141 MHz bulk niobium quarter wave resonator fabricated by PAVAC. (Lower) Expected final energies for the ISAC-II SC linac.

Figure 5: The first superconducting cavity produced by PAVAC Industries: the 141MHz quarter wave bulk niobium resonator for the ISAC-II linac upgrade.

The new superconducting cavities are quarter wave bulk niobium resonators operating at the higher frequency of

141.44 MHz.

The fabrication of the new cavities is done through a collaboration between TRIUMF and a local Canadian company, PAVAC Industries. PAVAC machines and electron beam welds the niobium material provided by TRIUMF (see Fig. 5). The pre welding chemical etch, as well as the final etch, is done by TRIUMF. All fabrication steps are followed by TRIUMF experts.

The first two niobium prototypes fabricated by PAVAC are already tested. They both exceed the design specifications of 30 MV peak surface field at 7W of helium consumption. The characteristic Q curves of these two cavities (Fig. 4, upper graph) show that at 7 W the accelerating fields are around 8 MV/m. This result is a significant achievement being the first cavities produced by PAVAC Industries.

The cryomodules are scheduled for installation and commissioning by the end of 2009.

## FUTURE PLANS

TRIUMF is funded in a five year cycle, the next being 2010-15. A proposed upgrade of the ISAC facility, commonly called ISAC-III [9], is contained in the published five year plan.

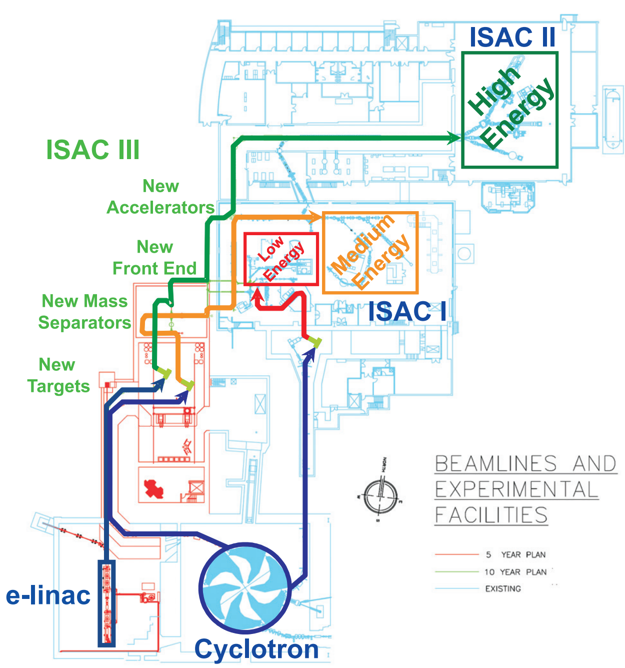


Figure 6: Layout of the proposed ISAC-III upgrade. In the picture a possible delivery schematic of three simultaneous RIBs is outlined.

At present the ISAC facility is limited by the possibility of delivering only one RIB at any given time to one of the twelve experimental stations distributed in the three experimental areas. This limits the development of new radioactive beams since this takes beam time from experiments.

It is then proposed to expand the ISAC facility with two new target stations for RIB production, two new mass separators, and a second post acceleration path (new RFQ and DTL similar to the existing ones) that can inject the beam directly into the SC linac without going through the ISAC-I accelerators.

The expansion foresees also the installation of a new electron driver (e-linac). In this way the new target stations can use as primary beam either the electrons from the new driver (e-linac) or the protons from the fourth extraction beam line (see Fig. 2) of the cyclotron.

Each one of the two new target stations will have a dedicated preseparator inside a shielded area. Two mass separators, one low resolution the other high resolution, are going to be available. The new targets and mass separators are planned to be connected via an electrostatic switchyard that gives the possibility of sending the beam from either target to either mass separator or bypass them.

Another flexible switchyard after the new separators allows to send each of the RIBs to either of the experimental areas.

The layout of the future expanded facility is represented in Fig. 6; in this picture a possible delivery schematic of three simultaneous RIBs is outlined.

The primary goal is to produce three simultaneous radioactive beams making TRIUMF the future leading ISOL facility. Figure 7 show the expected ISAC RIB production in the next decade based on the proposed upgrade.

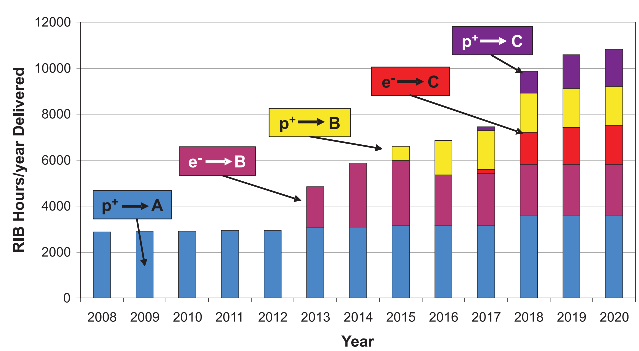


Figure 7: Expected RIB delivery in the next decade for the proposed ISAC-III upgrade. A is one of the two existing target stations, B and C are the new target stations.

### *e-linac*

It is possible to produce radioactive ion beams through photofission [10]. The photons (Bremsstrahlung radiation) are produced by an electron beam. This method produces a higher yield of certain isotopes with respect to proton production, but it doesn't cover the entire nuclide chart as represented in Fig. 8. The two production methods then, photofission and proton induced, are complementary.

In this context an electron driver for RIB production makes ISAC a facility capable of delivery a complete spectrum of radioactive species. The electron driver (e-linac) is

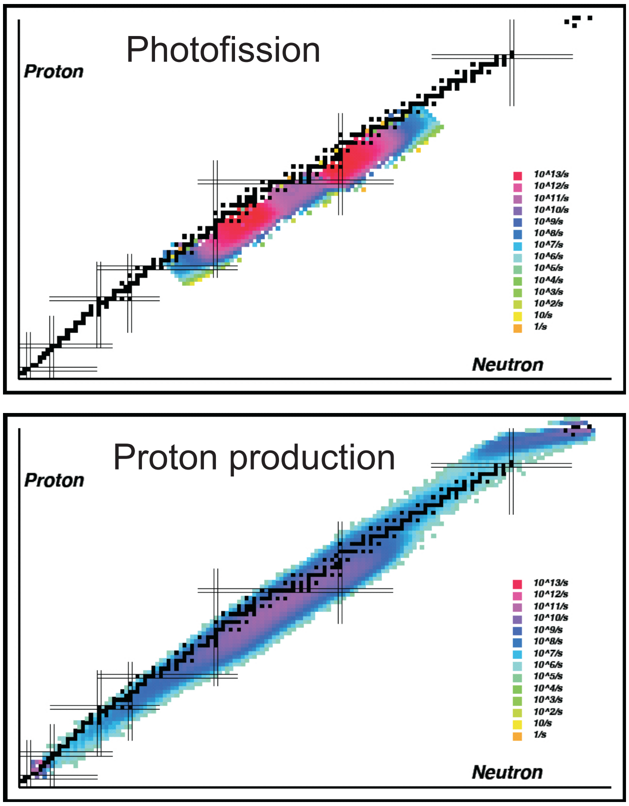


Figure 8: Simulated yield for photofission (upper) and proton (lower).

going to play a fundamental role in making ISAC the future leading ISOL facility.

The e-linac is envisaged as a 0.5 MW machine with a final energy of 50 MeV and an average current of 10 mA [11]. The linac operates in CW mode using superconducting elliptical cavities at 1.3 GHz and operating at 2 K. The layout of the machine foresees an electron gun followed by a buncher, an injector module and an accelerator composed of four nine cells cavities hosted in two cryomodules.

At present the cyclotron is shutdown for four months each year for maintenance. The e-linac is going to be independent from the cyclotron meaning the RIB production can cover the entire year.

### *New SCRF Activities*

TRIUMF has a world class expertise in low $\beta$ superconducting RF (SCRF) gained through the ISAC-II SC linac. This expertise is going to be extended to the $\beta$=1 region with the design and construction of the e-linac.

A new series of SCRF activities are being initiated at TRIUMF [12]: a new vertical cryostat is tested for 2 K operation and being readied for single cavity test. A single cell elliptical cavity test is scheduled this Fall. A RRR measurement apparatus is used to test the electron beam welding quality of niobium material. PAVAC Industries, in collaboration with TRIUMF, is testing fabrication procedures to produce elliptical cavities. All these activities are supported also by external collaborators like the University of Toronto, VECC laboratory in Calcutta and Fermilab.

## CONCLUSION

The ISAC facility at TRIUMF is one of the major ISOL facilities for radioactive ion beam production. It can provide the most intense beams for certain species. Through the next five year plan TRIUMF wants to overcome some existing limitations and become the leading ISOL facility for RIBs. Furthermore TRIUMF has planned to be an R&D center for SCRF activities covering the entire range of $\beta$.

## ACKNOWLEDGEMENTS

I want to acknowledge the scientific committee for the opportunity given to a young physicist, at the beginning of his career, of presenting this talk at the LINAC08 conference. I want also to thank Rick Baartman, Bob Laxdal and Lia Merminga for the comments and suggestions given during the rehearsals of my talk.

## REFERENCES

[1] M. Lieuvin, "Design Issues of Radioactive Ion Beam Facilities", EPAC96, Sitges, SPAIN, June 1996.

[2] G. Dutto et al., "Simultaneous Extraction of Two Stable Beams for ISAC", EPAC08, Genova, ITALY, June 2008 , p. 3505.

[3] I. Bylinskii et al., "TRIUMF 500 MeV Cyclotron Refurbishment", Cyclotrons and Their Application, Giardini Naxos, ITALY, September 2007 , p. 143.

[4] R.L. Poirier et al., "CW Performance of the TRIUMF 8 Meter Long RFQ for Exotic Ions", LINAC2000, Monterey, California, USA, August 2000 , p. 1023.

[5] S. Koscielniak et al., "Beam Dynamics Studies on the ISAC RFQ at TRIUMF", PAC'97, Vancouver, British Columbia, CANADA, May 1997, p. 1102.

[6] R.E. Laxdal et al., "Beam Commissioning and First Operation of the ISAC DTL at TRIUMF", PAC2001, Chicago, Illinoois, USA, June 2001, p. 3942.

[7] R.E. Laxdal, "Commissioning and Early Experiments with ISACII", PAC07, Albuquerque, New Mexico, USA, June 2007, p. 2593.

[8] R.E. Laxdal et al., "ISAC II Superconducting Linac Upgrade - Design and Status", this conference.

[9] R.E. Laxdal et al., "The Proposed ISAC III Low-Energy Area and Accelerator Upgrades", this conference.

[10] W.T. Diamond, "A Radioactive Ion Beam Facility Using Photofission", Nuclear Instruments and Methods in Physics Reserch, A 432 (1999), p. 471-482.

[11] S.R. Koscielnik et al., "Accelerator Design for MW-Class Electron Linac for RIBs and Material Science", this conference.

[12] R.E. Laxdal et al., "The 1.3 GHz Superconducting RF Program at TRIUMF", this conference.

# THE EUROPEAN XFEL SC LINAC PROJECT

R. Brinkmann, Deutsches Elektronen-Synchrotron (DESY), D-22607 Hamburg, Germany for the XFEL Team

*Abstract*

The European XFEL project is entering the construction phase, based on the very successful experience of the TESLA linac technology and the SASE FEL concept, now serving the FLASH user facility at DESY.

The EU-XFEL will be realized by a widespread international collaboration and it is also relevant for the ILC planning. A description of the overall layout of the facility, of the tchnical developments and industrialization efforts for the accelerator components, and of the international collaboration will be given.

## INTRODUCTION

The XFEL was originally proposed as part of the TESLA facility, first in a version integrated with the linear collider using the same linac [1,2], in a later version with its own separate linac [3]. In February 2003 the German Government announced the decision that the XFEL should be realized as a European project, with at least 40% funding contributions requested from partner countries. After this decision an intense preparation phase followed in which DESY, together with partner institutes, pushed forward the work necessary to achieve the status of readiness for start of construction. Besides the optimization of the overall design, main objectives in this phase where preparations for the site and civil construction, industrialization of major technical components and detailed studies of beam physics and the FEL process. The XFEL has a strong link to the FLASH (VUV-FEL) facility at DESY [4 – 6], which is in nearly all respects (accelerator technology, FEL operation, photon beam lines and user experiments) truly a pilot facility for the future project.

The project organization at the international level is supervised by a steering committee (ISC) with members from all countries interested in participating in the project. In 2005 ISC nominated a European Project Team (EPT), with the main charge to deliver the technical and administrative documents required for the process of negotiations and decisions at the political level towards achieving the final go-ahead for the project. In July 2006, an updated Technical Design Report (TDR) was completed [7] and delivered to ISC. The progress in the negotiations with the partner countries on contributions to the project then led to the official go-ahead for project construction on June 5, 2007, on the basis of an initially de-scoped startversion of the facility (see below). The nominal construction cost (in year 2005 prices) of the start version amounts to 850 M€, to which approximately 90 M€ have to be added for project preparation and commissioning.

Up to date, 14 countries have made commitments to contribute to the project (Figure 1), summing up to a total of 1,060 M€ (on year 2005 basis). In addition to covering the cost for the startversion including preparation and commissiong, there remains an overhead which will with first priority be used to cover cost risks, but which may to a limited extent also permit to remove part of the initial de-scoping of the facility.

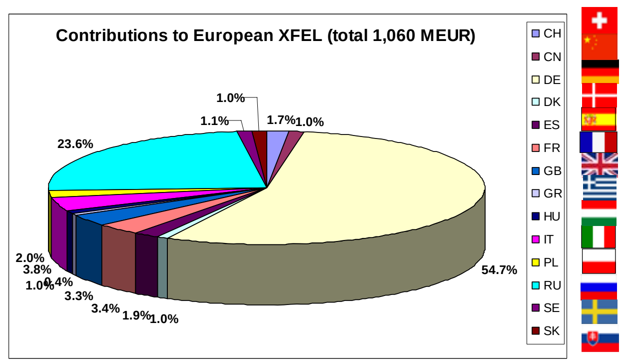


Figure 1: Distribution of funding contributions to the European XFEL project. Contributions are in cash as well as in-kind.

The administrative documents, in particular the Intergovernmental Convention, are essentially ready for signature by the partner countries. After that event, foundation of the XFEL company, of which all partners are shareholders, will take place. The company has the overall supervision and responsibility for the European XFEL and will also manage the civil construction and photon beam systems parts of the project. For the accelerator complex, an international consortium is being set up, which will contribute the entire accelerator and the related technical infrastructure essentially as an in-kind contribution to the project. At present 17 institutes from 10 of the XFEL member states have joined the consortium. DESY will provide approximately 60% of the in-kind contributions to the accelerator complex and act as the consortium coordinator.

## LAYOUT AND PARAMETERS

The main components of the XFEL Facility are the injector, the linear accelerator, the beam distribution system, the undulators, the photon beam lines, and the instruments in the Experiments Hall (see Figure 2).

These components are distributed along an essentially linear geometry, 3.4 km long, starting on the DESY campus in the northwest part of the city of Hamburg, and ending in the neighbouring Federal State of Schleswig-

Holstein, south of the city of Schenefeld, where the Experimental Hall is located. Permission for construction and operation on this site was obtained in July 2006, concluding a so-called Plan Approval Procedure. After the official project start in 2007, the call-for-tender procedure for civil construction was launched. The offers from different civil construction companies are at present being evaluated and placing of the orders for underground construction is expected to happen before the end of 2008.

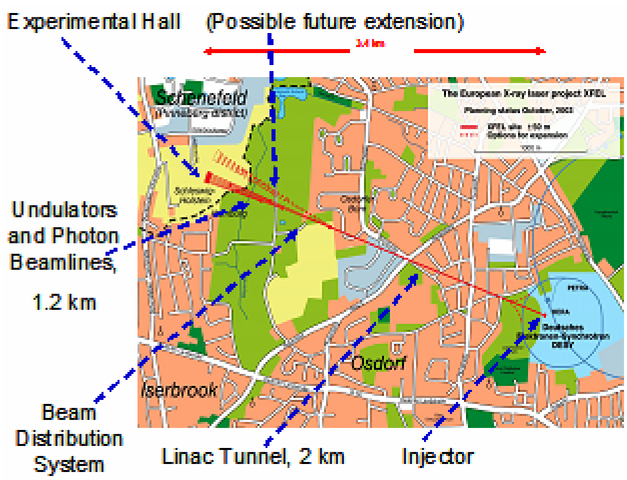


Figure 2: Site and schematic layout of the European XFEL Facility.

The main sections of the facility, as schematically shown in Figure 2, are the following: In the injector, electron bunches are extracted from a solid cathode by a laser beam, accelerated by an electron RF gun and directed towards the linear accelerator with an exit energy of 120 MeV. In the linear accelerator, consisting of a 1.6 km long sequence of superconducting accelerating modules, magnets for beam steering and focusing, and diagnostic equipment, the electrons are accelerated to energies of up to 17.5 GeV, which is the energy foreseen for the standard mode of operation of the XFEL facility at 0.1nm FEL wavelength. The original design energy of 20 GeV was reduced by shortening the linac as part of the initial de-scoping scenario of the startversion. A later upgrade back to the full linac length as foreseen in the TDR remains possible. Along the accelerator, two stages of bunch compression are located, to produce the short and very dense electron bunches required to achieve saturation in the SASE process. At the end of the linac follows a beam transport section with collimation, stabilization feedback and diagnostics systems, after which the individual electron bunches are fed into one or the other of two electron beam lines by the beam distribution system. The linac and beam transport line are housed in a 2.1 km long underground tunnel (Figure 3).

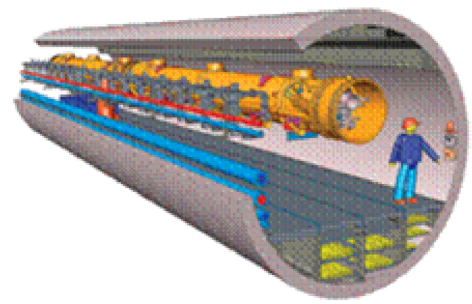

Figure 3: Layout of the 5.2 m diameter linac tunnel.

In the startversion the user facility has 3 SASE-FEL undulator beam lines (Figure 4) with in total 6 experimental stations (Figure 5). The space foreseen for two more undulator beam lines remains initially unoccupied, but since the buildings, technical infrastructure and electron beam line remain unchanged w.r.t. the TDR layout, these beam lines and 4 additional experimental stations can be added at any time as soon as funding permits. Furthermore, the site layout also allows for a later extension of the facility by another 5 beam lines.

Independent wavelength tuning by undulator gap variation is foreseen and, together with electron beam energy variation, a total wavelength range of 0.1 – 5 nm (FEL) can be covered. The peak brilliance of FEL radiation is in the range $10^{32}$ - $5{\cdot}10^{33}$ photons/0.1%bw/s/mm$^2$/mrad$^2$. The baseline operating point for 0.1nm wavelength (SASE1) at 17.5 GeV electron energy has been chosen on the basis of extensive studies of the FEL process with a relatively conservative assumption on the minimum undulator gap (10mm). At the design electron beam emittance of $\varepsilon_N$ = 1.4 mrad·mm very good transverse coherence of the FEL radiation is predicted [8]. The magnetic lengths of the undulators include a safety margin w.r.t. the calculated saturation lengths.

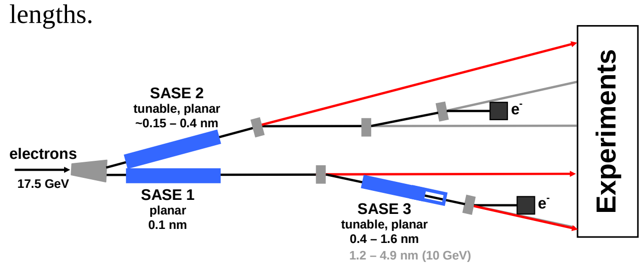


Figure 4: Schematic layout of the beam lines in the user facility.

| | Instrument | Brief description of the instrument |
|---|---|---|
| Hard X-rays | SPB | Ultrafast Coherent Diffraction Imaging of Single Particles, Clusters, and Biomolecules – **Structure determination of single particles: atomic clusters, bio-molecules, virus particles, cells.** |
| | MID | Materials Imaging & Dynamics –**Structure determination of nano- devices and dynamics at the nanoscale.** |
| | FDE | Femtosecond Diffraction Experiments – **Time-resolved investigations of the dynamics of solids, liquids, gases** |
| | HED | High Energy Density Matter – **Investigation of matter under extreme conditions using hard x-ray FEL radiation, e.g. probing dense plasmas.** |
| Soft X-rays | SQS | Small Quantum Systems – **Investigation of atoms, ions, molecules and clusters in intense fields and non-linear phenomena.** |
| | SCS | Soft x-ray Coherent Scattering –**Structure and dynamics of nano-systems and of non-reproducible biological objects using soft X-rays.** |

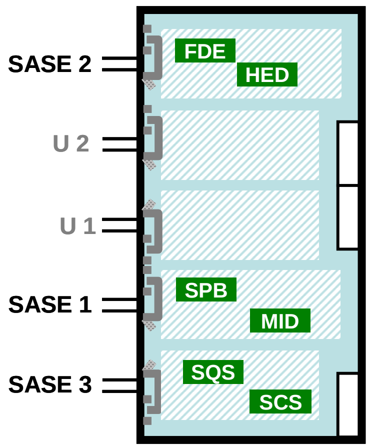


Figure 5: Selection of first scientific instruments and their arrangement in the experimental hall.

## ACCELERATOR COMPLEX

The layout of the accelerator is schematically shown in Figure 6 and its main parameters are summarized in Table 1. The beam energy required for 0.1 nm photon wavelength in the SASE1 and SASE2 beam lines is 17.5 GeV. The required peak power per RF station is well below the limit of the 10 MW multibeam klystrons (for recent test results from one of the three XFEL MBK prototype manufacturers, see [9]. This de-rated mode is beneficial for highly reliable operation on one hand and for an upgrade potential regarding beam energy or duty cycle on the other. Likewise, the cryogenic system is laid out with an overhead of 50% with similar operational benefits.

The electron beam is generated in a laser-driven photocathode RF gun and pre-accelerated in a single superconducting accelerator module. The injector is housed in an underground enclosure separate from the linac tunnel, so that it can be commissioned at an early stage, well before installation work in the linac tunnel is completed. Furthermore, there is space foreseen for a completely separate and radiation-shielded second injector, which can be constructed, commissioned and maintained independently from the operation of the first injector.

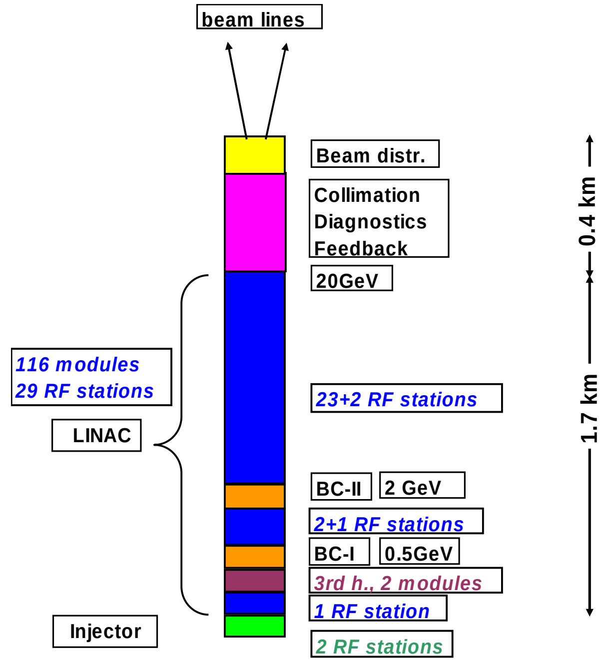


Figure 6: Schematic layout of the accelerator as described in the TDR. In the startversion 4 RF stations and 16 accelerator modules will initially not be installed.

Table 1: Main Parameters of the XFEL Accelerator for the Startversion with 17.5 GeV Design Energy. Numbers in Brackets Correspond to the Full TDR Version

| | |
|---|---|
| Design beam energy | 17.5 GeV *(20 GeV)* |
| # of installed accelerator modules | 100 *(116)* |
| # of cavities | 800 *(928)* |
| Accelerating gradient | 23.6 MV/m |
| # of installed RF stations | 25 |
| Klystron peak power (24 active stations) | 5.2 MW |
| Loaded quality factor $Q_{ext}$ | $4.6 \times 10^6$ |
| RF pulse length | 1.4 ms |
| Beam pulse length | 0.65ms |
| Repetition rate | 10 Hz |
| Max. average Beam power | 600 kW |
| Unloaded cavity quality factor $Q_0$ | $10^{10}$ |
| 2K cryo load (incl. transfer line losses) | 1.7 kW |
| Max. # of bunches per pulse | 3,250 |
| Min. bunch spacing | 200 ns |
| Bunch charge | 1 nC |
| Bunch peak current | 5 kA |
| Emittance (slice) at undulator | 1.4 mm×mrad |
| Energy spread (slice) at undulator | 1 MeV |

The results from simulation studies of the RF gun show that a normalized beam emittance below 1mrad·mm at the design RF field of 60MV/m on the cathode is achievable, even if the thermal emittance is somewhat larger than originally expected, as measurements performed at the PITZ facility (DESY-Zeuthen) indicated [10]. Emittance measurements at PITZ with high gun gradient [11] indicate a beam quality very close to the XFEL design goal [12]. The programme at PITZ continues with emphasis on further optimization of the laser profile and reduction of the gun dark current [13] at high gradients.

After transfer to the main accelerator tunnel (see the layout sketched in Figure 7), the beam is further accelerated by one linac unit (4 accelerator modules with 8 cavities each, driven by one RF station) to an energy of 0.5 GeV before entering the first bunch compression stage. A third harmonic (3.9 GHz) RF system is foreseen to optimize the longitudinal phase space properties. In order to suppress micro-bunching instabilities, the uncorrelated bunch energy spread is intentionally increased by a laser heater [14] after the injector. After acceleration to 2 GeV with three linac units the beam enters the second (final) compression stage, after which the 1nC bunch peak current has increased to 5 kA ($\sigma_z$ = 23μm for a 1nC bunch), a factor of 100 higher than the initial peak current from the RF gun. Considerable attention has been paid to foresee beam diagnostics stations in order to assess the beam phase space properties after the compression process in great detail. Beam simulation studies of the compression system show that the slice emittance growth due to space charge and CSR effects can be kept at a low level and there is room for further parameter optimization beyond the nominal design bunch parameters.

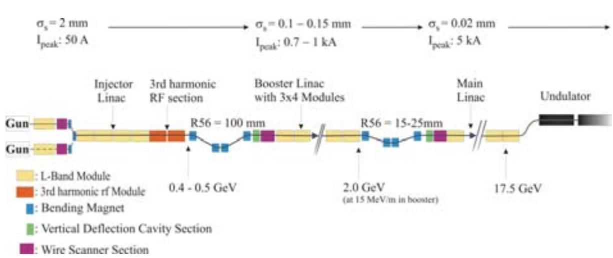


Figure 7: Layout of the XFEL bunch compression system.

The large compression factor and resulting short bunches (70fs rms) require timing, synchronization and diagnostics devices at the fs level as well as excellent RF field control. A considerable R&D program is ongoing in these fields, see e.g. [15 - 21] for recent developments.

Final acceleration to the nominal maximum beam energy of 17.5 GeV takes place in the main part of the linac, consisting of 25 RF stations and 100 accelerator modules in total (an extension to the full scope of the TDR layout with 116 modules and 29 RF stations remains possible). Out of the 25 stations, two are reserve for energy management in case of RF system failures. For the linac technology R&D and industrialization programme, the new cryomodule test bench (CMTB) at DESY, operational since autumn 2006, permits RF tests of cold modules independent from FLASH operation [22]. So far, four modules have passed through extensive test procedures (three of which are now installed at FLASH), a $5^{th}$ module was used for an intentional "crash test" [23]. Besides verifying good performance in terms of accelerating gradient, important results also include short RF coupler processing times and cold-warm cycling without performance degradation. Regarding the 9-cell superconducting Niobium cavities [24], important progress towards industrialization of series production was achieved by successfully commissioning and operating electropolishing facilities at two companies.

Downstream from the linac follows a conventional beam line for installation of the beam collimation and trajectory feedback systems, as well as providing distribution of the beam [25] into the different undulator beam lines, including the connection to a future upgrade of the user facility with more beam lines. A combination of slow and fast switching devices permits to generate bunch trains of different time patterns for different experiments without having to generate and accelerate bunch trains with strongly varying transient beam loading. A fraction of each bunch train will be used to accurately stabilize the following bunches in position and energy by means of a fast feedback system.

In the undulator sections, the effects of undulator gap errors and quadrupole misalignments on the SASE process have been studied [26, 27]. The results show that errors up to a few μm are permitted before the gain length or the peak radiation power are seriously affected. Investigations of quadrupole magnets and on the optimization of the focusing lattice are also ongoing [28, 29].

After having passed through the undulators, the "spent" beam is stopped in radiation shielded solid absorbers. An additional beam dump is installed in the beam distribution shaft XS1, just upstream from the undulator beam lines. It allows to commission or to operate the accelerator while installation or maintenance work is ongoing in the undulator tunnels.

### *Operational Flexibility*

The single set of basic reference parameters in Table 1 does not cover the full range of operational flexibility of the linac. There is, within certain limits, a considerable flexibility regarding operation parameters, based on built-in performance reserves of its technical components. Operation at lower beam energy, thus extending the photon wavelength range to softer X-rays, is an obvious possibility. On the other hand, based on the experience gained with the superconducting TESLA cavities, it can be realistically expected that the linac can be operated at an accelerating gradient somewhat above the specified design value of 23.6 MV/m. An increase of the gradient may thus permit beam energies well above the design value, thus significantly extending the photon wavelength range to harder X-rays, provided that simultaneously also an improved injector beam quality becomes available to be able to maintain saturation of the SASE FEL process. In addition to the possibility of higher beam energies, the available reserve in the RF and cryogenic systems can also be used for increasing the linac repetition rate and thus the duty cycle of the pulsed linac. At sufficiently low beam energy, a 100% duty cycle, i.e. continuous wave (CW), mode of operation is conceivable, an option which is only possible with a superconducting linac. This option (see table 2) is viewed as not being part of the first stage of the XFEL facility but is considered as a future option.

Table 2: Sketch of Possible Parameters for a Future Option of Operating the Linac in CW Mode

| | |
|---|---|
| Beam energy | 7 GeV |
| Accelerating Gradient | 7.5 MV/m |
| # of CW RF stations | 116 |
| RF power per accelerator module | ≈20 kW |
| Beam current | 0.18 mA |
| Loaded quality factor $Q_{ext}$ | $2 \times 10^7$ |
| Bunch frequency | 180 kHz |
| Unloaded quality factor $Q_0$ | $2 \cdot 10^{10}$ |
| 2K cryogenic load | ≈3.5 kW |

## CONCLUSION

After an intense phase of preparation at the scientific-technical, organizational and political level, the European XFEL project is now entering into its realization phase. An approximately 6 year construction phase is lying ahead and we are looking forward to seeing the first photon beam at this facility in 2014.

## REFERENCES

[1] R. Brinkmann, et al., “An X-Ray FEL Laboratory as Part of a Linear Collider Design”, Nucl. Instr. Meth A393, (1997) 86-92.
[2] R. Brinkmann et al. (eds.), ”TESLA Technical Design Report”, DESY-2001-011, March 2001.
[3] R. Brinkmann et al. (eds.), “TESLA XFEL Technical Design report – Supplement”, DESY-2002-167, Oct. 2002.
[4] H. Schlarb, “FLASH Upgraded – preparing for the European XFEL”, Proc. Int. FEL conference, Novosibirsk 2007.
[5] J. Roßbach, “Review of DESY FEL Activities”, Proc. EPAC, Genoa 2008.
[6] K. Honkavaara, “Operation of FLASH as a FEL User Facility”, this conference.
[7] M. Altarelli et al. (eds.), “XFEL Technical Design Report”, DESY 2006-097, http://xfel.desy.de.
[8] E. Saldin et al., “Transverse and Longitudinal Coherence Properties of the Radiation from X-ray SASE FELs”, Proc. Int. FEL Conference, Berlin 2006.
[9] A. Yano et al., “Design and Testing of the Horizontal Version of the Multi Beam Klystron for European XFEL Project”, Proc. EPAC, Genoa 2008.
[10] J. H. Han et al., “Emission Mechanisms in a Photocathode RF Gun”, Proc. PAC, Knoxville 2005.
[11] L. Staykov et al., ”Measurement of the Projected Normalized Transverse Emittance at PITZ”, Proc. Int. FEL Conference, Novosibirsk 2007.
[12] F. Stephan, private communication.
[13] F. Stephan et al., “New Experimental Results from PITZ”, this conference.
[14] G. Angelova et al., “The XFEL Laser Heater”, Proc. EPAC, Genoa 2008.
[15] F. Loehl et al., “Experimental Determination of the Timing Stability of the Optical Synchronization System at FLASH”, Proc. EPAC, Genoa 2008.
[16] F. Loehl et al., “Measurement and Stabilization of the Bunch Arrival Time at FLASH”, Proc. EPAC, Genoa 2008.
[17] P.J. Philips et al, “Single Shot Longitudinal Bunch Profile Measurements at FLASH Using Electro-Optics Detection Techniques”, Proc. EPAC, Genoa 2008.
[18] F. Ludwig et al., “Phase Stability of the Next Generation RF Field Control for VUV- and X-ray Free Electron Lasers”, Proc. EPAC, Edinburgh 2006.
[19] W. Jalmuzna, A. Napieralski and S. Simrock, “Performance of 24 Cavity Vector Sum Controller with Distributed Architecture”, Proc. EPAC, Genoa 2008.
[20] Z. Geng et al., “LLRF System Requirements Engineering for the European XFEL”, this conference.
[21] Z. Geng and S. Simrock, “Evaluation of Fast ADCs for Direct Sampling RF Field Detection for the European XFEL and ILC”, this conference.
[22] D. Kostin et al., “Testing the FLASH Superconducting Accelerating Modules”, 13th SRF workshop, Beijing 2007.
[23] T. Boeckmann et al., “Experimental Tests of Fault Conditions During the Cryogenic Operation of a XFEL Prototype Cryomodule”, Proc. Int. Cryogenic Engineering Conf. ICEC22, Seoul 2008.
[24] L. Lilje and D. Reschke, “Recent Results of Nine-cell Superconducting Accelerating Structures for the European XFEL”, this conference.
[25] W. Decking and F. Obier, “Layout of the Beam Switchyard at the European XFEL”, Proc. EPAC, Genoa 2008.
[26] Y. Li, B. Faatz and J. Pflüger, “Study of Undulator Tolerances for the European XFEL”, Proc. Int. FEL Conference, Novosibirsk 2007.
[27] V. Khachatryan et al., “Effect of Jitter and Quadrupole Alignment Errors on SASE FEL Performance, Proc. EPAC, Genoa 2008.
[28] A. Hedqvist, H. Danared and F. Hellberg, “Field Characterization of XFEL Quadrupole Magnets”, Proc. EPAC, Genoa 2008.
[29] V. Khachatryan et al., “Optimization of the Focusing Lattice for European XFEL”, Proc. EPAC, Genoa 2008.

# SNS SUPERCONDUCTING LINAC OPERATIONAL EXPERIENCE AND UPGRADE PATH*

Sang-ho Kim, ORNL, Oak Ridge, TN 37831, U.S.A.

*Abstract*

The Spallation Neutron Source (SNS) Superconducting Linac (SCL) has been providing a main acceleration in two different accelerating sections with 33 medium beta and 48 high beta superconducting radio-frequency (SRF) 6-cell cavities. The use of superconducting elliptical cavities for particles whose velocity are less than speed of light (beta<1), make this accelerator a very important milestone for learning operating conditions of this type of cavities. Since the SNS SCL is the first large-scale high energy pulsed-superconducting proton linac that provides high beam power utilizing H- beams, many aspects of its performance were unknown and unpredictable. A large amount of data has been collected on the pulsed behavior of cavities and cryomodules at various repetition rates and at various temperatures. This experience will be of great value in determining future optimizations of SNS as well in guiding in the design and operation of future pulsed superconducting linacs. This paper describes the details of the RF properties, performances, path-forward for the SNS power ramp-up goal, and upgrade path of the SNS superconducting linac.

## INTRODUCTION

The SNS accelerator complex consists of a negative hydrogen (H-) RF volume source, a low-energy beam transport (LEBT) line with a first-stage beam chopper, a 4-vane radio-frequency quadrupole (RFQ) up to 2.5 MeV, a medium-energy beam transport (MEBT) line with a second-stage chopper, six drift-tube linac (DTL) tanks up to 87 MeV, four coupled-cavity linac (CCL) modules up to 186 MeV, a superconducting linac (SCL) with 11medium-beta cryomodules (up to 379 MeV) and 12 high-beta cryomodules (up to 1000 MeV), a high energy beam transport (HEBT) line, an accumulator ring with associated beam transport line, a ring-to-target beam transport (RTBT) line, and a mercury target. At a full duty, the linac will produce 38-mA peak, chopped $H^-$ beam for 1-ms long at 60 Hz. In the ring, 700-ns long midi-pulse beam is accumulated over 1060 turns reaching an intensity of $1.5 \times 10^{14}$ protons per pulse. After beam accumulation in the ring, the beam is extracted using the extraction kickers during 300-ns long midi-pulse gap in a single turn is transported to the mercury target through the RTBR line. Figure 1 shows the layout of the SNS.

A series of the beam commissioning, initiated in 2002 and completed in May 2006, was performed in seven commissioning runs for Front-End, DTL Tank 1, DTL Tanks 1-3, CCL, SCL, Accumulator Ring, and beam on target.

* SNS is managed by UT-Battelle, LLC, under contract DE-AC05-00OR22725 for the U.S. Department of Energy

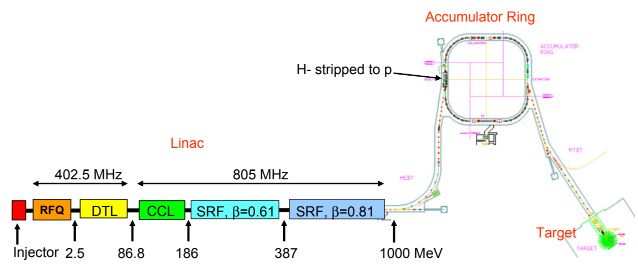


Figure 1: Layout of the SNS accelerator system.

Official SNS operations for scheduled neutron scattering experiments has been started since October 2006. The SNS is now nearly two years into the initial operations phase [1, 2].

The SRF cavities and the cryomodules were designed and developed at Jefferson Lab and installed at the SNS site in 2005. Major parameters are summarized in Table 1. As the first operational pulsed superconducting linac, many of the aspects of its performance were unknown and unpredictable. A lot of experiences and data have been gathered on the pulsed behavior of cavities and cryomodules at various repetition rates and at various temperatures during the commissioning of its components and beam operations. Careful balance between safe operational limits and the study of conditions, parameters and components that create physical limits has been achieved [3, 4]. The SCL is running at about 0.9-GeV output energy and is presently one of the most reliable systems in SNS. Figure 2 shows the accelerating gradients of SCL cavities at 60Hz in 2008 for the neutron production, which is set based on the 60 Hz collective limits achieved. Power ramp up plan to reach the design goal is set and various efforts are in progress.

Table 1: Major Design Parameters of the SNS SCL

| Cryomodule Parameter | β=0.61 Section | β=0.81 Section |
|---|---|---|
| Output Energy (MeV) | 379 | 1000 |
| No. of Cryomodules | 11 | 12 |
| No. of cavities per cryomodule | 3 | 4 |
| **Cavity Parameter** | **β=0.61 Cavity** | **β=0.81 Cavity** |
| Geometric beta | 0.61 | 0.81 |
| EoT (MV/m) | 10.1 at β=0.61 | 15.8 at β=0.81 |
| Epeak (MV/m) | 27.5 | 35.0 |
| Hpeak (kA/m) | 46.2 (580 Oe) | 59.7 (750 Oe) |
| Q*Rs (Ω) | 176 | 228 |
| r/Q at design beta | 279 | 483 |
| Equivalent Cavity Length (cm) | 68.2 | 90.6 |

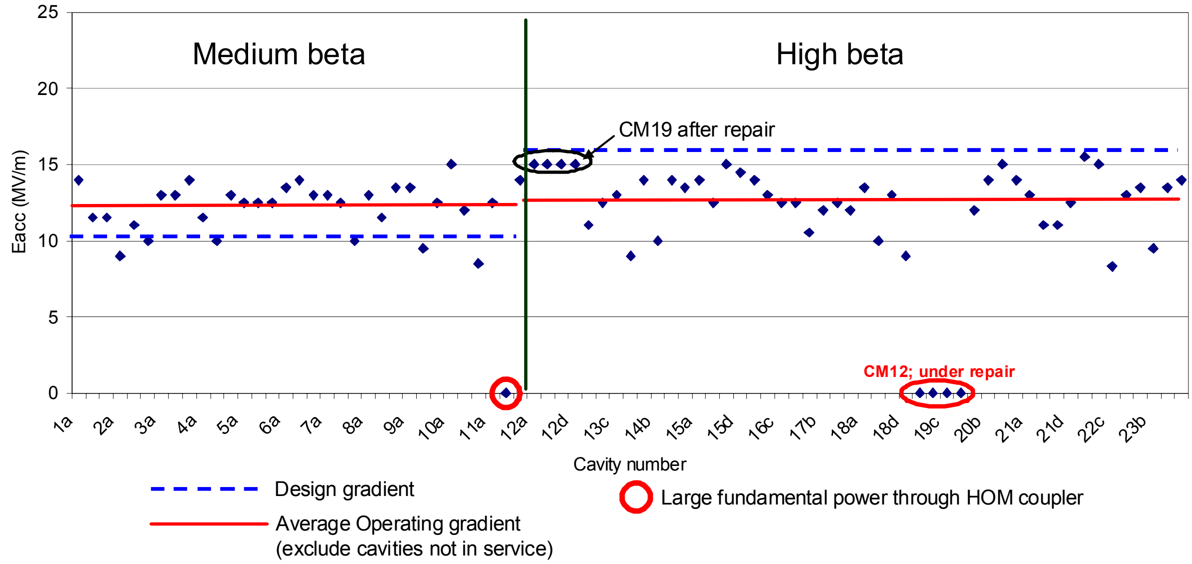


Figure 2: Operating setpoints of SCL SRF cavities at 60 Hz for the neutron production in 2008.

## OPERATIONAL EXPERIENCES

Extensive testing on the SNS superconducting RF modules has been conducted starting in late 2004. Behavior peculiar to the SNS cavities and the overall design, as well as due to the pulse nature of the operation have been observed. These and other limitations have requires extensive studies and close attention in setting gradients which are both necessary for adequate energy gain and for reliable operation.

### *Operational Flexibility*

One of the main characteristics of the superconducting linac is its flexibility and adaptability to adding or removing cavities. In many occasions, cavities' fields had to be temporarily or permanently changed, or in some cases cavities had to be removed from service. The linac flexibility has demonstrated itself in allowing complete retuning and rephrasing of the linac over times of the order of a few minutes. This characteristic is important as not just cavities, but other systems that may be removed temporarily from service and operations interrupted only for a modest amount of time [5].

### *Operating Temperature*

The transient nature of pulsed operation allows larger variation of temperatures within the niobium surface, so that during the pulse the surface resistance of the material can change substantially (see Fig. 3). The operating conditions of the SNS SRF cavities were reviewed and cavity parameters and their interplay were reevaluated, giving details on the possible range of operating parameters which can be achieved at SNS in pulsed conditions [6]. Due mainly to the pulsed nature of the SNS operation and the relatively low operating frequency the cavities can still be operated at 4.2 K up to the critical field. Both calculations and experiments tell us that there's no difference in performances of the SNS SRF cavities as long as the operating temperature is lower than 4.5 K.

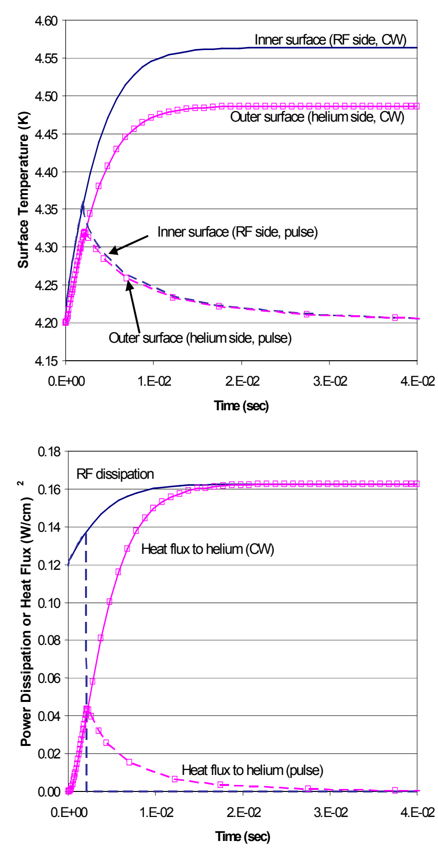


Figure 3: Comparisons of thermal parameters between CW and pulsed operations. Both cases are stable. (solid line; CW operation, dashed line; pulsed operation, lines with symbols; for surface at helium side, lines without symbols; for surface at RF side).

## *Electron Activities and Collective Behaviors at High Repetition Rate*

Most of the cavities exhibit heavy field emission and/or multipacting which directly or indirectly (through heating of end groups) limits the gradients achievable in normal operation with beam. The overall phenomena are complex and the final operational cavity gradients need to be determined individually for each cavity based on the equilibrium between electromagnetic, electron emission and thermal phenomena, each affecting the overall stability of the system on a pulse by pulse basis. In addition to individual cavity field emission limitations, collective effects have been observed which affects neighboring and second neighbor cavities. Bigger heating by these collective effects is clearly observed when the repetition rate is 30 Hz or higher. Heating of cavity elements are driven not only by the amplitude, but also by the relative phase of neighboring cavities. Since in the SCL neighboring cavities' amplitudes and phases are correlated, operation into heavy field emission is prevented by stability concerns, thus limiting the final available energy. Figure 4 compares the average limiting gradients at three different conditions. At low repetition rate (20 Hz or less), individual (powering one cavity at a time) limits are about same as collective limits (powering all cavities in a cryomodule at the same time) at the same low repetition rate, which enabled 1-GeV demonstration at 15 Hz. The difference between limits in open and closed loops results from llrf regulation and much longer duration at the highest field in closed loop.

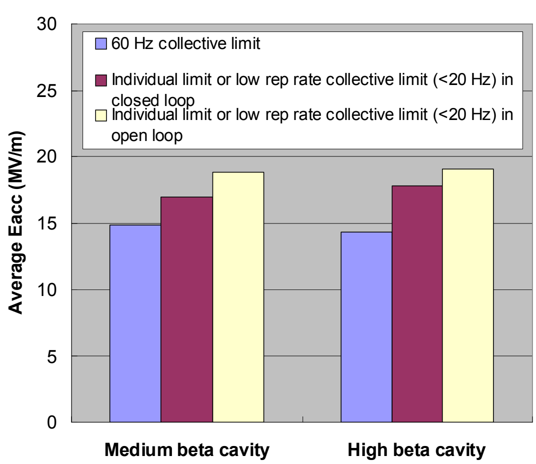


Figure 4: Comparisons of average limiting gradients at 60 Hz collective, individual (or low rep rate collective) in closed loop and that in open loop.

## *Equipment and Sub-components*

Some sub-components have shown peculiar behaviors. The cold cathode gauges, which provide interlock protection to the fundamental power coupler window, have behaved erratically, with a response which is often not correlated at all with other independent measurements of gas pressure at the window.

The Higher Order Mode (HOM) notch RF filters, which are designed to extract RF power at frequencies potentially harmful to the stability of the beam, have shown signs of multipacting, discharges and transient detuning, which can lead to critical components damage.

One high beta cryomodule (CM19) had been removed from the tunnel and been repaired at the SNS SRF test facility by removing HOM coupler feedthroughs from one cavity. Two thermal diodes (TD) were installed where the possible multipacting places according to the analysis as shown in Fig. 5. During the test at the SNS SRF test cave, very aggressive electron activities were observed from the signals of TD ranges from 5 MV/m to 15 MV/m, which led drops of gradients by several percents and detuned cavity bandwidth that corresponds to a few kW deposition of RF power to electrons. All were processed very carefully, which was possible by removing HOM coupler feedthroughs. The first explorer such as the first turn-on, pushing limits, increasing repetition rate must be closely watched and controlled since aggressive multipacting and burst of field emitter could damage weak components. Also we experienced similar situations during subsequent turn-ons after long shutdown and thermal cycle.

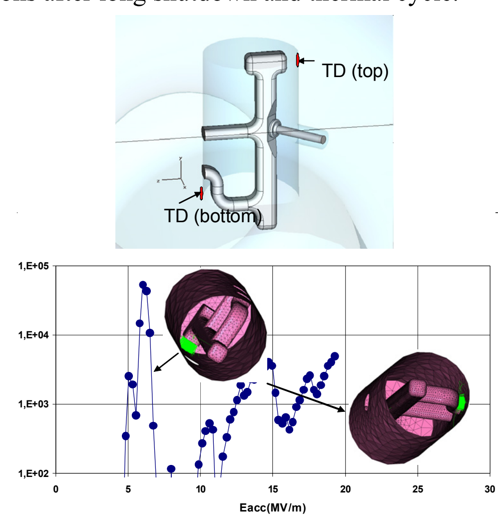


Figure 5: Thermal diodes locations of the 19b after removing the feedthrough (top). Multipacting simulation of the SNS high beta cavity HOM coupler [7] (bottom).

## *Limiting Factors of SRF Cavities*

Statistics of limiting factors achieved during 60-Hz collective tests are summarized in Fig. 6. Two cavities are showing larger mechanical resonances at higher repetition rate while dynamic detuning of all others can be managed by RF feedback and feed-forward only. So far piezo-tuner compensation has not been used in operation. Three cavities are limited by hard quench at a relatively low gradient (around 10 MV/m). One cavity is not in service due to the large power coupling with RF only. The limit tests are stopped for five cavities at about 15 W of fundamental power coupling through HOM coupler. About fourteen cavities are limited by coupler heating, but they are close to the limits by radiation heating. All others are limited by electron loading that leads end group heating, gas burst and quench. Actual operating gradients are set around 85-95 % of limiting gradients achieved at 60-Hz collective tests.

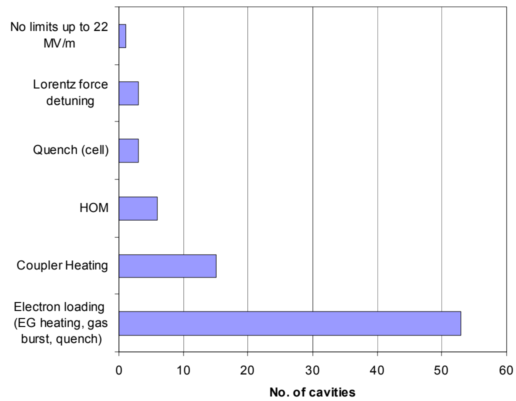


Figure 6: Statistics of limiting factors at 60 Hz collective condition.

### *SRF Cavity Operating Regime*

As seen in Fig. 2 cavities in the medium beta section of the SCL are operating above the design gradient of 10.1 MV/m whereas those in the high beta sections of the SCL are operating below the design one of 15.8 MV/m mainly due to radiations and related heating effects.

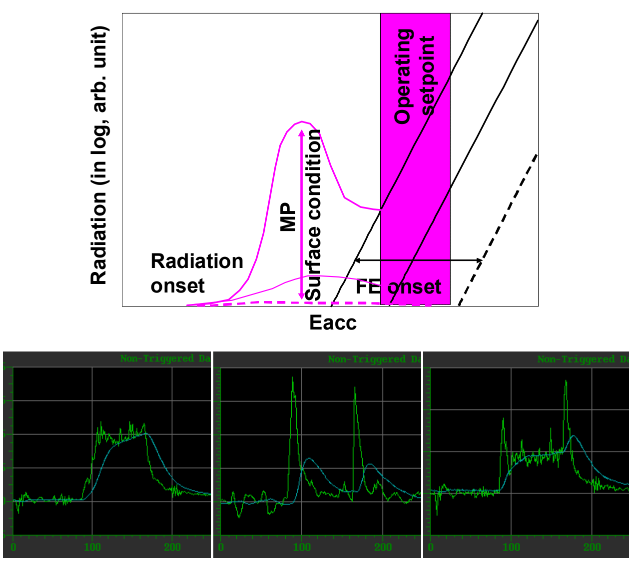


Figure 7: SNS SRF cavity operating regime at 60 Hz and radiation waveforms from RF operations depends on contents of electron activities in a cavity.

Figure 7 is schematically explaining operating regime of most of the SNS SRF cavities, which is higher than big multipacting region and/or lower than the considerable field emission region. During commissioning, testing, and 3-yrs long operation so far, mild contaminations must have been gone, which causes multipacting or mild field emission. In an operational cryomodule, removing a bad contamination is quite difficult. The field emitters on the processed surfaces are known to be very stable. Majority of the SNS SRF cavities are showing radiation waveforms of field emission like the radiation waveform in the bottom left in Fig. 7, while some are showing multi-pacting dominant radiation waveform (bottom center in Fig. 7) and some others are showing both field emission and multipacting (bottom right in Fig. 7).

Since the lack of the final linac output energy, the gradient of each cavity is set to maximize the gradient based on the collective limiting gradients that was achieved through a series of SRF cavity/cryomodule performance test at SNS, rather than having uniform gradients as designed.

## POWER RAMP-UP

Most of equipment in SNS requires substantially higher operational ratings compared to existing accelerators, since the design beam power is almost an order of magnitude higher compared to existing neutron facilities. As beam power increases at higher duty factor during previous runs, down-times of some equipment such as LEBT and high-voltage convertor modulator led lower machine availability than expected. Some systems like the SNS SCL are the first attempt for pulsed operation. Many of the aspects of its performance were unknown and unpredictable, for which it takes time to understand the systems as a whole and/or needs additional performance improvements. A power ramp-up plan has been revised based on the operation experiences and understandings of limits and limiting conditions through extensive studies, which emphasizes more on machine availability (Fig. 8). The plan covers main driving factors for beam power such as chopping efficiency, ion source improvement, high voltage convertor modulator (HVCM) improvement, and SCL output energy. The followings are short descriptions of issues and plans for the power ramp-up at the SCL side.

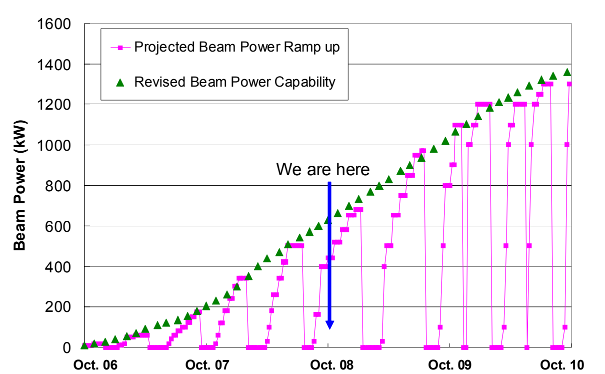


Figure 8: SNS beam power ramp-up history and plan.

The final output beam energy mainly depends on SCL gradients. Presently the SCL is providing output energy of 900 MeV without reserve, which is lower than the design energy due to the facts mentioned in the previous section. The goal of the SCL performances is 1-GeV output energy with 30- to 40-MeV energy reserve for fast recovery of operation from unexpected long-lead down time of not only cavities but also the related systems. Cryomodule repair works are in progress to get all 81 cavities in service [8]. One cavity in the cryomodule 11 is not operable due to the large power coupling through the HOM port from the RF operation. One high beta cryomodule (CM12) was removed from the linac tunnel for repair in the SNS SRF test facility, which had beam line vacuum leaks and showed biggest radiation from RF operation. It is revealed that the beam line leak was resulted from the HOM feedthroughs. Three leaky feedthroughs (plus one feedthrough at the cavity with a leaky feedthrough) were removed out of eight HOM coupler feedthroughs. This cryomodule will be brought in service after RF performance tests in the SNS SRF test facility in the next year. As mentioned above CM19 had been repaired and has been back in service in the slot of CM12 since March, 2008 and is the best performing cryomodule in the SNS SCL. Very recently one cavity, SCL-10b was repaired in the tunnel, which showed noisy field probe signals and had been turned off for about a year at 30- and 60-Hz operations. The final output energy is expected to be about 950 MeV after having all cavities available. For the design energy with some energy reserve like 40 MeV, an active effort for improvement of cavity performance is needed especially for high beta cavities. An R&D program is just started to develop an in-situ surface processing such as helium processing and plasma processing to get about 100-MeV additional output energy.

Each SCL cavity is fed by an individual klystron rated 550-kW RF output at saturation and has independent RF control systems. Eighty one klystrons for the SCL are powered by seven HVCMs; four HVCMs running at 69 kV for twelve klystrons each and three HVCMs running at 71 kV for eleven klystrons each. The voltage of HVCMs needs to be increased up to 75 kV to utilize the rated RF power of the klystrons. To ensure a high intensity beam loading with a good machine availability, a decision was made to have one additional HVCM for the SCL, which is planned to be installed in early next year, so that most of SCL HVCMs will power 10 klystrons at 75 kV with fair reliability.

The beam pulse width is presently major driving factor for the SNS power ramp-up mainly depends on HVCM pulse width and stability of chopper. There will be another beam pulse extension by reducing SCL cavity filling time form 300 μs to 250 μs with the additional HVCM for the SCL mentioned above.

## POWER UPGRADE

Many of the accelerator subsystems are designed to be able to support higher beam intensities and higher beam energy. Upgrades to the SNS accelerator and target systems to increase the beam power to at least 2 MW, with a design goal of 3 MW, are in the planning stages. A beam power upgrade to 3 MW can be achieved by increase the linac beam energy from 1.0 GeV to 1.3 GeV by adding 9 additional high-beta cryomodules in the already prepared empty slots in the linac tunnel and by increasing beam current from 38 mA to 59 mA. The duty factor will be kept at 6 % and most of beam transport lines and ring have capability for 2 MW, 1.3 GeV operations. The newly defined Power Upgrade Project (PUP) includes only the beam energy upgrade portion and the beam current increase and target improvement will be accomplished through R&D activities and so-called Accelerator Improvement Project (AIP). The SNS power upgrade project is waiting for CD-1 approval and the planned project period is from 2011 for about 4 years.

## SUMMARY

The SNS has begun the official operations since October 2006 after completion of the construction project in June 2006. The SNS is in the middle of three-year power ramp-up period to reach the design specifications and high availability for the user services. The presently achieved beam power for the neutron production is about 0.62 MW. From the series of tests and operational experiences more understandings of systems and their limiting conditions in pulsed mode are being obtained at high duty operation. The machine availability is steeply increasing concern as a user facility. The trip rate from the cavity/cryomodule side is now approaching zero and the SCL is providing beam acceleration for the neutron production as one of the most reliable systems. Beam power is keeping on track with the power ramp-up plan that is generated based on the previous operational experiences and studies. The Power upgrade project for energy upgrade from 1 GeV to 1.3 GeV is in planning stage and is waiting for CD-1 approval, which will double the beam power up to 3 MW, incorporated with so-called Accelerator Improvement Project (AIP).

## ACKNOWLEDGEMENT

The author extends his thanks to all his SNS colleagues who have contributed to this work. SNS is managed by UT-Battelle, LLC, under contract DE-AC05-00OR22725 for the U.S. Department of Energy.

## REFERENCES

[1] S. Henderson, Proceedings of European Particle Accelerator Conference 2008 (Genoa, Italy, 2008), p. 2892.
[2] S. Henderson, et al., Proceedings of European Particle Accelerator Conference 2006 (Edinburgh, UK, 2006) , p. 345
[3] S.-H Kim, et al., Proceedings of the 2007 Particle Accelerator Conference (Albuquerque, NM, 2007), p. 2511.
[4] I.E. Campisi, et al., Proceedings of the 2007 Particle Accelerator Conference (Albuquerque, NM, 2007), p. 2502.
[5] J. Galambos, these proceedings, WE202.
[6] S.-H Kim and I.E. Campsi, PRST-AB, 10, 032001 (2007).
[7] I. Gonin, N. Solvak, personal communication.
[8] J. Mammosser, these proceedings, TH103.

# PROGRESS IN THE BEAM COMMISSIONING OF J-PARC LINAC AND ITS UPGRADE PATH

M. Ikegami, KEK, Tsukuba, Ibaraki 305-0801, Japan


## Abstract

The beam commissioning of J-PARC linac was started in November 2006, and its initial stage was completed in October 2007. Since then, we start to provide the linac beam for the beam commissioning of downstream facilities. During this period, we have performed occasional high-power demonstrations, where we have recently achieved the linac beam power of 12.7 kW (210 kW from RCS) for a limited period of time. We have also confirmed that the short-term beam stability and beam availability of the linac have already reached a sufficient level. The final goal of 1 MW from RCS is to be pursued though a staged upgrades.


## INTRODUCTION

J-PARC (Japan Proton Accelerator Research Complex) is a multi-purpose high-intensity proton accelerator facility jointly constructed by KEK (High Energy Accelerator Research Organization) and JAEA (Japan Atomic Energy Agency). J-PARC accelerator consists of a 400-MeV linac, 3-GeV RCS (Rapid Cycling Synchrotron), and 50-GeV MR (Main Ring). Figure 1 shows the schematic layout of J-PARC facilities.

J-PARC linac serves as an injector for the entire J-PARC facility. The output beam from linac is injected into RCS, and that from RCS is delivered to both MR and a neutron production target. We also have a muon production target through which a proton beam penetrates before reaching the neutron target. Meanwhile, MR is accommodated with two beam extraction systems. One is a slow extraction system, and the other is a fast extraction system. The beam extracted with the slow extraction system is utilized for studies on hadron physics, and the fast-extracted beam is delivered to a neutrino production target for a long-baseline neutrino oscillation experiment. The final goal of the project is to deliver a 1-MW beam from RCS and 0.75-MW beam from MR.

To achieve the final goal, a phased approach is taken in the J-PARC project as discussed in a later section. We are currently in the first phase of the project, where the output energy from linac and MR are 181 MeV and 30 GeV, respectively. In this phase, the linac consists of a 50-keV negative hydrogen ion source, 3-MeV RFQ (Radio Frequency Quadrupole linac), 50-MeV DTL (Drift Tube Linac), and 181-MeV SDTL (Separate-type DTL). The schematic layout of the linac is shown in Fig. 2. The operation frequency of these accelerating cavities is 324 MHz, and the RF power is fed by 3-MW klystrons. Aside from these accelerating cavities, we also have two buncher cavities and two chopper cavities in MEBT (Medium Energy Beam Transport) between RFQ and DTL. In addition, two debuncher cavities are installed in the beam transport line between the SDTL exit to RCS, to which we refer as L3BT (Linac-to-3-GeV RCS Beam Transport). In 181-MeV operation, two SDTL tanks are temporarily utilized as debunchers.

At this point, the initial commissioning of RCS is approaching its completion [2]. The first neutron and muon beams were respectively produced in May and September 2008. Then, neutron production runs are to be started in December 2008. The initial commissioning of MR has recently been started with a beam storage mode, and the acceleration up to 30 GeV will be tried in December 2008 [3]. We plan to deliver the beam to the hadron experimental facility by February 2009, and to the neutrino production target by June 2009.

In this paper, we summarize the achieved performance in J-PARC linac after briefly reviewing its commissioning history. We also show the recent situations with emphasis on the stability of the beam operation and the machine activation experienced to date. Finally, we will present an upgrade path planned for J-PARC linac.

## COMMISSIONING HISTORY AND PRESENT SITUATION

The beam commissioning of J-PARC linac was started in November 2006, and its initial stage was completed in October 2007 [4, 5, 6]. During the beam commissioning, the design beam energy of 181 MeV was achieved in January 2007. Then, the output beam power of 1.2 kW (3.3 % of the design value) was demonstrated in June 2007. From February to May 2007, fundamental tunings have been conducted including the phase scan tuning for the RF set-points [7, 8, 9], orbit correction, and transverse match-

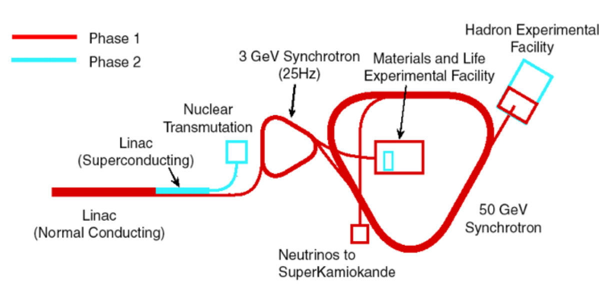


Figure 1: Schematic layout of J-PARC facility.

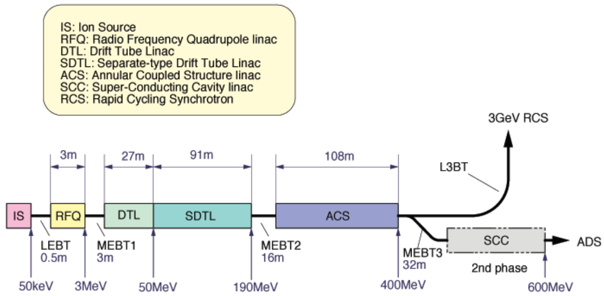


Figure 2: Schematic layout of J-PARC linac.

ing [10]. Subsequently, the output beam from the linac was delivered to RCS in October 2007.

The beam power of 1.2 kW (which corresponds to 20 kW from RCS) is the commissioning goal set for the year 2008, and it is assumed for the initial neutron production run planned in December 2008. Then, we marked the completion of the initial beam commissioning for the linac with achieving 1.2 kW beam power and the beam delivery to RCS without notable beam losses. After completing the initial commissioning for the linac, the beam commissioning of RCS and then MR has been started subsequently [2, 3]. Consequently, the emphasis has been put on the stable beam supply in the linac operation with the minimum beam study for the linac tuning.

As we have focused on the operational stability in this period, some emphasis will be put on this topic in the next section. Needless to say, good stability of the linac is a key to the success in the beam commissioning of the downstream facilities.

## ACHIEVED BEAM PARAMETERS AND THEIR STABILITIES

Currently, the beam power is kept very low for most commissioning runs to avoid excess machine activation at downstream facilities. Then, the high-power operation is performed as a demonstration for limited period of time. The main beam parameters achieved to date are summarized in Table 1. The chopping ratio in this table is defined to be the chopper beam-on ratio during a macro-pulse. Then, parameters with an asterisk is those obtained in a high-power demonstration sustained for only 70 seconds due to a limitation from the beam dump capacity.

The design peak current of 30 mA has already been achieved at the exit of RFQ with the pulse width of 0.25 ms. However, the peak current delivered to RCS is currently limited to around 27 mA. The transmission efficiency is mostly determined by the small aperture of the chopper system in MEBT. Besides, the transmission efficiency of RFQ in this operation was 90 %.

We have performed a high-power demonstration with the reduced peak current of 15 mA. In the demonstration, the macro-pulse width is widened to the design value of 0.5 ms. The repetition rate is also increased to the design value

Table 1: Beam parameters achieved to date

| Parameter | Design | Achieved | Remark |
|---|---|---|---|
| Beam energy [MeV] | 181 | 181 | |
| Peak current [mA] | 30 | 30 | at RFQ ext. |
| | | 27 | at RCS inj. |
| Beam power [kW] | 36 | 3.1 | 27 mA |
| | | 3.4 | 15 mA |
| | | 12.7* | 15 mA |
| Pulse len. / repetition / chop. ratio [ms/Hz/%] | 0.5/25/53 | 0.1/2.5/100 | 27 mA |
| | | 0.5/2.5/100 | 15 mA |
| | | 0.5/25/40* | 15 mA |
| RF width/ repetition [ms/Hz] | ≥0.5/25 | ≥0.5/25 | |

of 25 Hz. Accordingly, the duty factor is the design value of 1.25 %. This operation is sustained for only 70 seconds due to dump capacity limit. The highest beam power from the linac has also been marked in this operation, where the beam power of 12.7 kW is delivered to RCS and 210 kW from RCS with tolerable beam loss rate. The beam intensity of $2.93 \times 10^{13}$ protons per pulse (corresponding to 352 kW with 25 Hz repetition) has also been achieved in a single-shot operation. The stable operation for the neutron target is currently performed with a few kW beam power. The RF source has been operated with the design duty factor since a very early stage of the beam commissioning.

The normalized rms emittance at the SDTL exit is around 0.4 $\pi$mm·mrad with the peak current of 27 mA. The observed emittance is larger than the design value of 0.3 $\pi$mm·mrad due to emittance growth in DTL [11].

As for the stability of beam parameters, we have measured the jitter of the beam centroid energy and the beam centroid position. Figure 3 shows a typical histogram of the measured beam centroid energy, where the energy jitter is monitored for nine hours with TOF (Time Of Flight) measurement utilizing FCT's (Fast Current Transformers). The rms jitters are respectively 39 keV, 15 keV, and 16 keV at the exit of SDTL, the first debuncher, and the second debuncher. The 100 % jitter is sufficiently smaller than the design goal of 333 keV or 0.1 % in momentum.

A typical histogram of the measured beam position is also shown in Fig. 4, where the position jitter is monitored for 30 minutes with two BPM's (Beam Position Monitors). These two BPM's are located at the end of L3BT. The two BPM's are 4.1 m apart with one quadrupole magnet in-between. The rms jitter is found to be around 60 $\mu$m for both BPM's, which is sufficiently small.

It is also noteworthy that the beam availability of J-PARC linac has already exceeds 90 % in recent beam commissioning runs [6, 12].

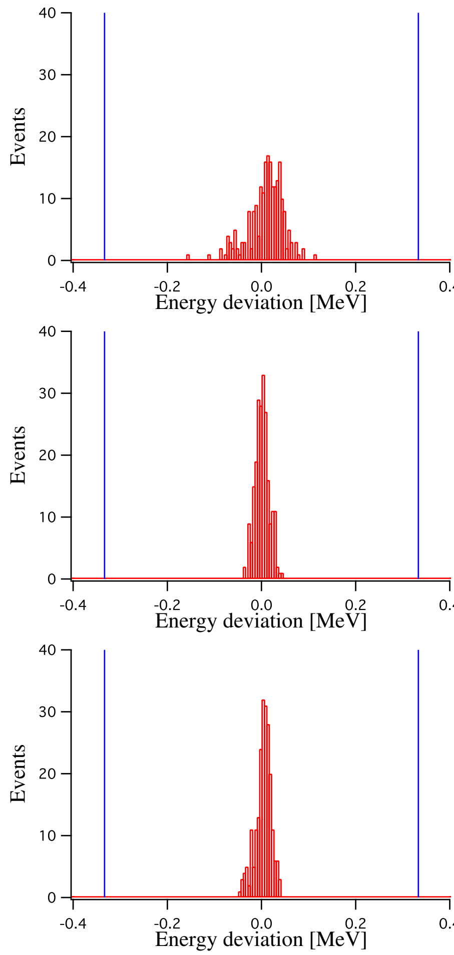


Figure 3: Energy jitter at the SDTL exit (top), the fist debuncher exit (middle), and the second debuncher exit (bottom). The blue vertical lines show the specification of $\pm 0.1$ % in momentum.

## MACHINE ACTIVATION

The machine activation is often the limiting factor for the achievable beam power for a high-intensity accelerator. In spite that the average beam power is mostly kept very low at present, we have already experienced some machine activation due to uncontrolled beam losses.

We have narrow sections at two debunchers installed in L3BT, because the last two SDTL tanks are temporarily utilized for debunchers in 181-MeV operation. Machine activation is mostly localized in the vicinity of the debunchers. We experienced the highest activation when we performed the fine phase-scan tuning for SDTL cavities for the first time with the beam power of 0.12 kW. In that run, the residual radiation level reached 250 $\mu$Sv/h at the second debuncher with contact to the vacuum chamber 6-hour after beam shutdown. Conducting precise tuning of machine parameters, the radiation level was gradually reduced. Then, the typical radiation level at the debunchers became 10 to 40 $\mu$Sv/h at the end of the initial commissioning in spite

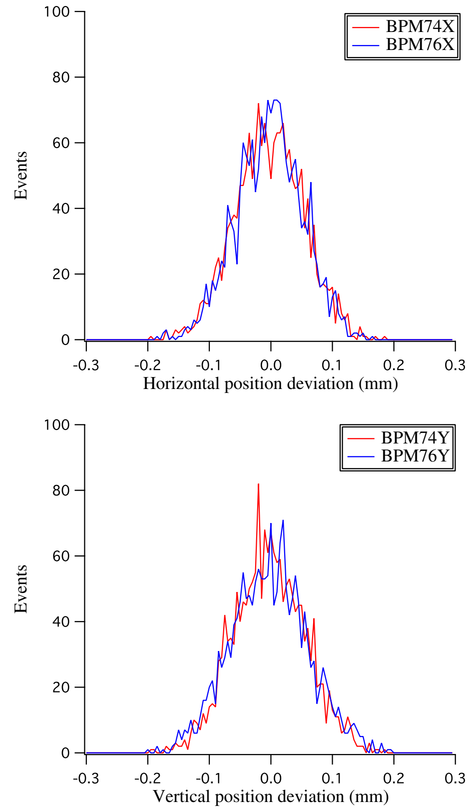


Figure 4: Beam position jitter for the last two BPM's in L3BT. Top: horizontal, bottom: vertical.

of the increased beam power to around 0.6 kW. We also see slight activation in the beam transport line between two debunchers and the arc section after the second debuncher, but it was typically kept below 10 $\mu$Sv/h.

After the commencement of the RCS commissioning, the radiation level has been reduced with the factor of several to ten. However, most of the reduction in the machine activation might be attributable to the single-shot or low-duty factor operations totally employed in the recent runs. As we are entering the stage where we seek beam power ramp-up, we plan to carefully monitor the trend of machine activation in the forthcoming stable beam operations. It is expected to provide valuable information to predict the activation level with the nominal operation with higher beam power.

## BEAM-POWER RAMP-UP

We are now entering the stage where we seek higher beam power in tandem with the further RCS tune-up. The neutron production run will be started in December 2008 with a 20-kW beam delivered from RCS. In the present plan for the beam power ramp-up, the immediate goal is to deliver a 100-kW beam from RCS until February 2009. Then, the next goal is 250 kW until June 2009. The corresponding linac beam power is 6 kW for February 2009 and 15 kW for June 2009. In the present planning, 20 %

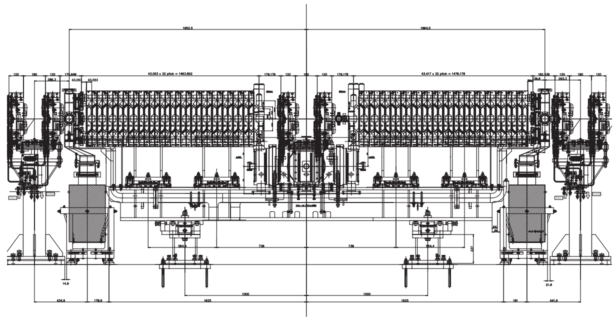

Figure 5: The layout of an ACS module. Two ACS tanks are connected with a bridge coupler. Quadrupole doublets are placed between ACS tanks to provide the transverse focusing.

of the goal beam power is considered to be the minimum requirement for each stage.

The limiting factor for the available beam power is currently the authorized beam dump capacity, and it is to be increased to accommodate the above beam power goals. The machine activation levels and its build-up should also be carefully monitored with a long-term operation.

## UPGRADE PATH

To achieve the final beam power of 1 MW from RCS, we plan to take a phased approach. In the first phase, we start the beam operation of the linac with the lower energy of 181 MeV and the lower peak current of 30 mA. In this phase, the design output beam power from linac is 36 kW and that from RCS is 0.6 kW. We are currently in the beam commissioning stage of this phase.

In the second phase, the linac beam power is increased to 133 kW to achieve the beam power of 1 MW from RCS. The linac output energy is increased to 400 MeV in this phase, and the linac peak current to 50 mA. Instead of moving up to the second phase at a stretch, we plan to take intermediate steps toward the second phase to smoothly ramp-up the output beam power as discussed below.

### [illegible]

In 181-MeV operation, we are aiming at the output beam power of 0.6 MW from RCS. However, this goal is challenging because the space-charge effect is significant in the injection period in RCS. Actually, the space-charge effects in this case is more profound than that in the final stage, where the beam power of 1 MW is aimed with the injection energy of 400 MeV. A simple energy scaling of the space-charge effect results in the beam power of 0.33 MW with 181-MeV injection. Then, we anticipate to face with significant beam losses in achieving 0.6 MW with the injection energy of 181 MeV.

To avoid the potential beam loss problems, we plan to upgrade the linac energy as an intermediate step before proceeding to the second phase. In the energy upgrade, the linac output energy is increased to 400 MeV to ease the space-charge effects in the injection period. Then, the linac output power is increased to 80 kW to achieve the beam power of 0.6 MW from RCS.

The energy upgrade is to be realized by adding an ACS (Annular Coupled Structure linac) section after the existing SDTL section [13]. The ACS is a variation of CCL (Coupled-Cavity Linac), where the emphasis is put on the axial symmetry of its geometry. The J-PARC ACS has been developed based on the former JHF-ACS [14] after an extensive optimization studies with regard to the frequency change [15].

The operation frequency of 972 MHz is adopted for ACS. Then, a 16-m long beam matching section with two buncher modules is to be provided between SDTL and ACS. The primary objective of this matching section is to smoothly absorb the transitional effects due to the three-fold frequency jump [13].

The ACS section consists of 21 ACS modules, and each ACS module is comprised of two ACS tanks. Each ACS module is to be driven by a 3-MW klystron. Figure 5 shows the layout of an ACS module. Three prototype ACS modules have been fabricated and high-power-tested to date [16]. The remaining one and half prototype modules are currently in the final stage of their fabrication. In parallel with the trial manufacturing, the design polishing for the mass production is now under way [17]. Three prototype 972-MHz klystrons have also been fabricated and high-power-tested successfully [18].

We have a four-year plan to fabricate and install ACS modules in the energy upgrade. In the current upgrade plan, it is supposed to take three years to mass-produce the ACS modules. The 972-MHz RF systems, utilities, and cables can be installed during nominal shutdown periods with little interruption of the 181-MeV operation. The ACS modules will be installed in the tunnel during an extended shutdown period. The assumed duration of the extended shutdown period is eight months including that for the following cavity aging and the beam commissioning.

A fraction of the construction budget for ACS has been approved this fiscal year, and we are seeking a government approval of the full construction budget.

### [illegible]

After the energy upgrade, we plan to increase the peak current from 30 mA to 50 mA. Accordingly, the linac output beam power is increased to 133 kW to deliver a 1-MW beam from RCS. The intensity upgrade involves a replacement of the ion source and RFQ. It is also likely to be accompanied with a significant modification of MEBT to accommodate chopper improvement. With increased peak current, the heat load for the chopper system is supposed to be a crucial issue.

As for the 50-mA RFQ, a prototype has been fabricated and low-power-tested successfully [19]. In the trial manufacturing, the upstream one third of the RFQ module has been fabricated.

The 50-mA ion source is naturally the most essential component for the intensity upgrade, for which an extensive R & D has been continued. The peak current of 70 mA has been achieved with a cesium-seeded ion source [20]. However, the available peak current is currently limited to 38 mA without cesium seed [21]. We are continuing the effort to increase the peak current with a cesium-free ion source to avoid potential undesirable effects to the following RFQ.

### [illegible]

In the second phase of the project, it is also foreseen to add an SCL (Super-Conducting Linac) section after ACS to increase the linac output energy to 600 MeV. The 600-MeV beam is not assumed to be injected into RCS, but it will be dedicated to the fundamental studies for ADS (Accelerator-Driven nuclear-waste transmutation System). The 400-MeV beam from ACS will be shared between RCS and SCL. We are planning to increase the linac repetition to 50 Hz, and to utilize 25 Hz of them for ADS studies without reducing the RCS beam power. A prototype cryomodule for SCL has been fabricated and high-power-tested successfully [22].

## SUMMARY

The beam commissioning of J-PARC linac has been started since November 2006, and its initial phase has been completed in October 2007. In October 2007, we started to provide a beam to downstream facilities for their beam commissioning. Since then, the emphasis of the linac operation has been put on providing stable beams to downstream facilities.

In a high-power demonstration for a limited period of time, the beam power of 12.7 kW has been achieved in the linac, which corresponds to 210 kW from RCS. The beam stability and availability of the linac have already reached the sufficient level, and we are entering the stage where we seek beam power ramp-up in tandem with further RCS tuning. We have already experienced a certain machine activation due to uncontrolled beam losses. However, its level is kept sufficiently lower than the tolerable limit.

In J-PARC project, a phased approach is taken to achieve the final goal of 1-MW beam power from RCS and 0.75 MW from MR. In the upgrade path toward the final phase, we plan to take a few intermediate steps for the linac upgrade to smoothly ramp-up the beam power on target. The upgrade is to be started with an energy upgrade by adding ACS section after SDTL. Then, it is followed by an intensity upgrade and another energy upgrade with SCL cavities. Extensive R & D studies are now underway for every front of the staged upgrades. A fraction of the ACS construction budget has been approved this fiscal year, and we are seeking an approval of its full construction.

## REFERENCES


[1] Y. Yamazaki ed., "Technical design report of J-PARC", KEK Report 2002-13; JAERI-Tech 2003-44.

[2] H. Hotchi, "Status of J-PARC commissioning", to be published in Procs. of ICFA-HB2008 Workshop, Nashville, August 2008.

[3] T. Koseki, "Beam commissioning of J-PARC main ring", to be published in Procs. of ICFA-HB2008 Workshop, Nashville, August 2008.

[4] M. Ikegami and A. Ueno, "Commissioning experience and plans for J-PARC linac", ICANS-XVIII, Dongguan, April 2007, p. 61.

[5] K. Hasegawa, "Commissioning of the J-PARC linac", PAC'07, Albuquerque, June 2007, p. 2619.

[6] M. Ikegami, "Transition from commissioning to operation in J-PARC linac", to be published in Procs. of ICFA-HB2008 Workshop, Nashville, August 2008.

[7] G. Shen, M. Ikegami, "Tuning of RF amplitude and phase for the drift tube linac in J-PARC", to be submitted somewhere.

[8] G. Shen, M. Ikegami, "Tuning of RF amplitude and phase for the separate-type drift tube linac in J-PARC", to be published in Nucl. Instrm. Meth. A.

[9] A. Ueno, "Unique features of the J-PARC linac and its performance - Lessons learnt", in these proceedings.

[10] H. Sako et. al.,"Transverse matching and orbit correction at J-PARC linac", in these proceedings.

[11] M. Ikegami et. al., "Measurement and simulation for J-PARC linac", to be published in Procs. of ICFA-HB2008 Workshop, Nashville, August 2008.

[12] K. Hasegawa et. al., "Operating experience of the J-PARL linac", in these proceedings.

[13] M. Ikegami et. al., "Beam dynamics design of the annular-coupled-structure linac and its matching section for the KEK/JAERI joint project", LINAC'02, Gyeongju, August 2002, p. 629.

[14] T. Kageyama et. al.,"Development of annular coupled structure", LINAC'94, August 1994, Tsukuba, p. 248.

[15] V. V. Paramonov, "The annular coupled structure optimization for JAERI/KEK joint project for high intensity proton accelerators", KEK Report 2001-14 (2001).

[16] H. Ao et. al., "First high-power ACS module for J-PARC linac", LINAC'06, Knoxville, August 2006, p. 725.

[17] H. Ao et. al., "Improvement of the ACS cavity design for the J-PARC linac energy upgrade", in these proceedings.

[18] E. Chishiro et. al., "Recent status of RF sources in J-PARC linac", PAC'05, Knoxville, May 2005, p. 1123.

[19] Y. Kondo et. al., "Fabrication and low-power measurements of the J-PARC 50-mA RFQ prototype", LINAC'06, Knoxville, August 2006, p. 749.

[20] H. Oguri et. al., Rev. Sci. Instrum. 73 (2002) 1021.

[21] H. Oguri et. al., Rev. Sci. Instrum. 79 (2008) 02A506.

[22] E. Kako et. al., "High power test of the prototype cryomodule for ADS superconducting linac", PAC'05, Knoxville, May 2005, p. 3579.

# STATUS OF A HIGH CURRENT LINEAR ACCELERATOR AT CSNS

S.N. Fu, H.F. Ouyang, X.J. Yin, J. Li, J. Peng, Z.R. Sun, Y. Cheng
IHEP, Institute of High Energy Physics, Beijing 100049, China

*Abstract*

China Spallation Neutron Source (CSNS) consists of an $H^-$ linac as an injector of a rapid cycling synchrotron of 1.6 GeV. The 324 MHz rf linac is designed with beam energy of 81 MeV and a peak current of 30 mA. The linac design and R&D are in progress. A test stand of a Penning ion source is under construction. RFQ technology has been developed in ADS study, with beam energy of 3.5 MeV, a peak current of 46 mA at 7% duty factor and a beam transmission rate more than 93%. The first segment of the DTL tank is under fabrication. A full-scale prototype of resonant high-voltage pulse power supply for klystron has been successfully demonstrated. This paper will introduce the design and R&D status of the linac.

## INTRODUCTION

The CSNS accelerator is the first large-scale, high-power accelerator project to be constructed in China[1]. CSNS accelerator mainly consists of an H- linac and a proton rapid cycling synchrotron. It is designed to accelerate proton beam pulses to 1.6 GeV kinetic energy at 25 Hz repetition rate, striking a solid metal target to produce spallation neutrons, as schematically shown in Figure 1. The accelerator is designed to deliver a beam power of 120 kW with the upgrade capability up to 500 kW by raising the linac output energy and increasing the beam intensity, as listed in Table 1[2].

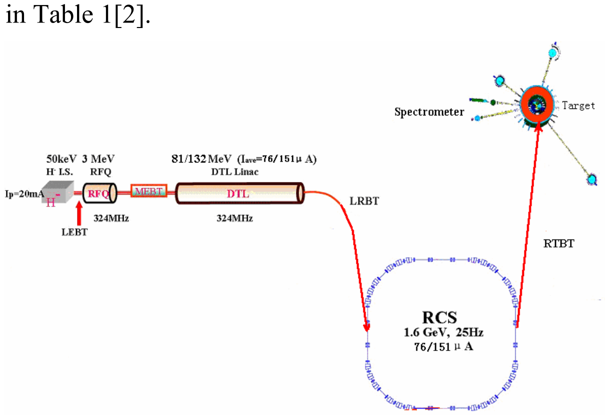


Figure 1: CSNS schematics.

This paper will introduce the design and R&D status of the linac. In the next section, physics design of the linac will be described. Then some R&D activities in the key technology, including ion source, RFQ, DTL and a new type of RF source power supply, will be briefly introduced.

Table 1: CSNS Primary Parameters in Baseline and Upgrade Phases

| Project phase | I | II | II' |
|---|---|---|---|
| Beam ave. power, kW | 120 | 240 | 500 |
| Proton energy, GeV | 1.6 | | |
| Ave. current, *I*, μA | 76 | 151 | 315 |
| Repetition rate, Hz | 25 | | |
| Proton per pulse, $10^{13}$ | 1.88 | 3.76 | 7.83 |
| Pulse length, ns | <500 | | |
| Linac energy, MeV | 81 | 132 | 230 |
| Linac length, m | 50 | 76 | 86 |
| Linac rf freq. , MHz | 324 | | |
| Macro ave. *I*, mA | 15 | 30 | 40 |
| Macro duty factor, % | 1.1 | 1.1 | 1.7 |
| Ring circumference, m | 247 | 247 | 247 |
| Ring filling time, ms | 0.5 | 0.5 | 0.8 |
| Uncontroled loss, W/m | < 1 | | |

## CSNS LINAC PHYSICS DESIGN[3]

CSNS linac consists of an H- ion source, an LEBT, a 3MeV RFQ linac at 324MHz RF frequency, an MEBT and a 324MHz DTL linac. The output beam of the DTL linac is 81MeV with peak current of 15mA in the first phase. CSNS upgrade plan has been taken into the physics design. Beam pulse current will be increase to 30mA or even 40mA, while the beam energy will be increased to 132MeV or even 230MeV respectively so as to keep an acceptable space charge tune spread during the injection into the RCS. Some space in the linac-RCS beam line is now reserved for the additional accelerating structure for the upgraded CSNS linac.

For a low beam loss during the injection to the RCS, injected beam needs to be chopped for pre-bunching in the ring RF bucket. The chopped beam pulse structure is illustrated in Figure 2. To realize such a macro-pulse of 468ns, a pre-chopper is designed in the LEBT. In the case that the chopping is not clear, another fast chopper may be added in the MEBT.

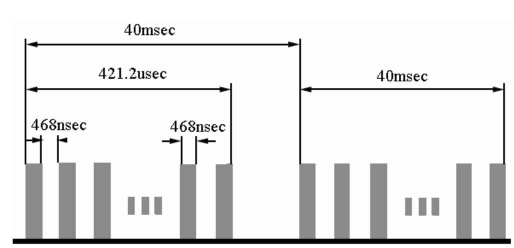


Figure 2: The linac beam pulse structure after chopping.

## *H⁻ Ion Source and LEBT*

CSNS requires the ion source with a high reliability rather than a very high beam current for its first phase. Considering these factors as well as low cost, Penning surface source is preferred. The major design parameters are listed in Table 2. Beam dynamics in extraction was studied with PBGUN code.

Table 2: Major parameters of the ion source

| Ion | $H^-$ |
|---|---|
| Extract energy (keV) | 50 |
| Extract current (mA) | >20 |
| Emittance $\varepsilon_{n,rms}$ ($\pi$ mm-mrad) | <0.20 |
| Rep. frequency (Hz) | 25 |
| Beam duty factor (%) | 1.3 |
| Lifetime (month) | >1 |

The LEBT is mainly composed of three solenoids and an electrostatic chopper for beam matching and chopping, respectively, as shown in Figure 3.The beam from the extraction slit of the ion source is converted to a round beam at the entrance of the RFQ by the three solenoids. To reduce space charge effect, the LEBT is space charge neutralized except for the section of the electrostatic chopper after the last solenoid. Beam optics was studied with TRACE3-D code with 90% neutralization.

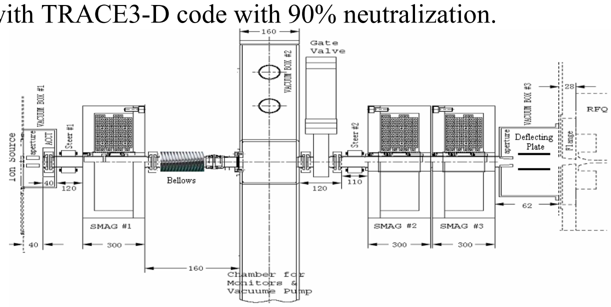


Figure 3: LEBT layout with three solenoids and an electrostatic chopper.

In our previous design, magnetic-alloy loaded induction cavity was design in the LEBT to decelerate the beam for chopping with the following RFQ longitudinal acceptance. Now we proposed to replace the induction cavity with an electrostatic deflector. Correspondingly, the chopper location shifts from the downstream of the first solenoid to the third solenoid, so that the space charge neutralization can be kept in the most space of the LEBT. The transversal acceptance of the RFQ will chop the deflected beam according to PARMTEQ simulation. In this figure, the beam at the RFQ entrance is deviated from the beam axis with x=2.65mm and x'=50mrad. At the exit of the RFQ, no particles emerged, which means the deflected beam is clearly chopped by the RFQ.

The deflector is designed with a length of 40mm and a gap of 30mm. The transit time through the deflector for a 50KeV beam is about 13ns. The applied voltage to generate the beam center deviation of x=2.65mm and x'=50mrad at the entrance of the RFQ is only 3.75kV. Dependence of the RFQ beam transmission on the applied deflecting voltage is plotted in Figure 5. During power source rise time and beam transit time, beam pulse will be partially deflected and thus, chopping becomes unclear. Increase of the deflecting voltage can alleviate this case. Voltage of 3.75kV is so low and so easy to get, and thus we are going to use a higher voltage power supply without much addition cost. In fact, the cost the electrostatic deflector system is much cheaper than our original induction cavity system that requires 150kW pulse power supply for the required decelerating voltage of 8.5kV, while the new deflector requires only 180W pulse power supply at the deflecting voltage of 4.5kV.

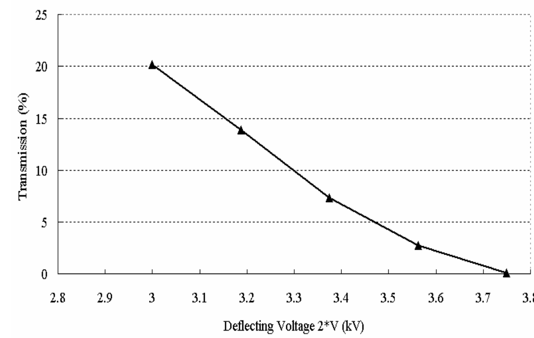


Figure 4: RFQ transmission rate versus deflector voltage.

Most of the deflected beam is lost at the entrance area of the RFQ without further acceleration. So the beam power dumped on the RFQ vanes is rather low, only 25W in average at 50% chopping rate.

## *RFQ Design*

Beam dynamics design with PARMTEQM code indicates a transmission rate higher than 97% for 40mA pulse current. The major design parameters are plotted in Figure 5.

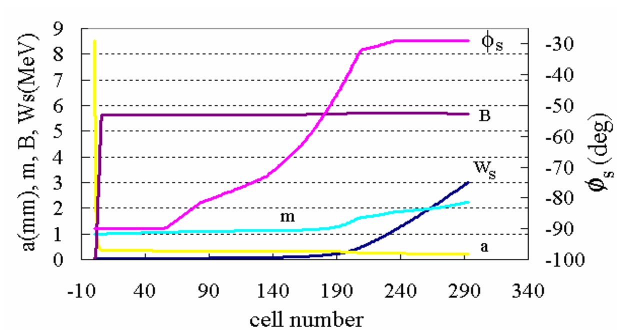


Figure 5: Major parameters along the RFQ.

Four-vane type structure is selected and the total vane length is 3.6m. The cavity is divided into two segments and then resonantly coupled together. Each segment consists two technological modules. Undercut and coupling cell have been carefully designed with 3D code. RF structure design study resulted an acceptable mode separation: the working quadrupole mode has a 3MHz gap from the nearest quadrupole mode and a 5.2MHz gap from the nearest dipole mode. For tuning of the resonant frequency and field distribution, 12 tuners are arranged in each quadrant, as shown in Figure 6. Structure thermal behavior has been studied and some cooling channels are design on the vanes and the cavity wall, as shown in Figure 6. The cooling water serves for two tasks: one for cavity cooling and another for frequency tuning during operation. Simulation indicates that the frequency shift sensitivity on the cooling water temperature is –5kHz/$^0$C.

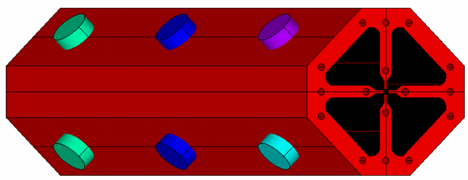

Figure 6: One technological module of the RFQ cavity.

## *MEBT Design*

The major tasks for MEBT are to chop the beam with a fast rise time for low beam loss and to match the beam from RFQ with DTL, again for low beam loss. However, meanwhile fulfilling these two tasks, some beam emittance growth and halo formation may be introduced, resulting in beam loss in the downstream beam transportation. In our case that the chopping task is not demanded in the MEBT in the first phase, we are going to leave a space for a RF chopper in the MEBT, and install it in the second phase for beam power upgrade. RF chopper is preferred so that we can share its successful experience in J-PARC linac.

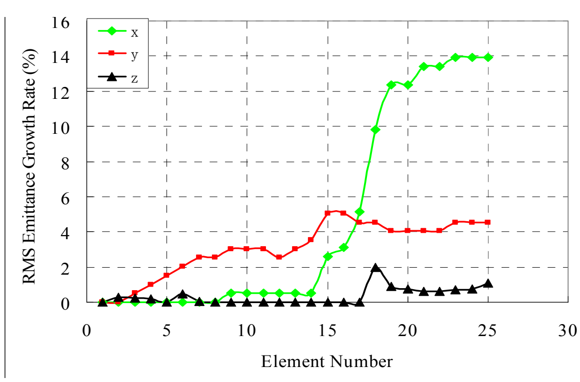


Figure 7: RMS emittance growth in three directions for 40mA beam in MEBT.

RMS emittance growth for 40mA beam is 14%, 4.5% and 1.1% in x, y and z directions respectively, as plotted in Figure 7. In this simulation, beam is chopped in x direction and beam envelope presents a large modulation. Emittance growth in x direction becomes half for half beam current of CSNS first phase linac. MEBT is recognized as most difficult section in the linac in terms of the control of emittance growth and halo formation, due to the combined function of beam chopping and beam matching in three directions.

## *DTL Design*

A conventional DTL was designed with four tanks for 81MeV Phase-I linac and additional three tanks for 132MeV Phase-II linac. Table 3 lists the major parameters of the seven tanks. It is found the field variation pattern given by MDTFISH simulation using the cell data from PARMILA output becomes obviously different from the design value in the PARMILA input file. Cell tuning was hence applied in the tank design to restore the filed distribution back to the PARMILA input data[4] . One of our design goals is to make the RF power consumption in each tank almost the same so as to maximize the utilization efficiency of the RF power source.

Table 3: DTL Tank Parameters

| Tank number | 1 | 2 | 3 | 4 | 5 | 6 | 7 |
|---|---|---|---|---|---|---|---|
| Output energy (MeV) | 21.76 | 41.65 | 61.28 | 80.77 | 98.86 | 115.8 | 132.2 |
| Length(m) | 7.99 | 8.34 | 8.5 | 8.85 | 8.69 | 8.57 | 8.67 |
| Number of cell | 61 | 34 | 29 | 26 | 23 | 21 | 20 |
| Cavity RF power (MW) | 1.41 | 1.41 | 1.39 | 1.45 | 1.45 | 1.45 | 1.49 |
| Total RF power (MW) | 1.97 | 2.01 | 1.98 | 2.03 | 1.99 | 1.96 | 1.98 |
| Accelerating field (MV/m) | 2.2-3.1 | 3.1 | 3.1 | 3.1 | 3.1 | 3.1 | 3.1 |
| Synchronous phase | -30--25 | -25 | -25 | -25 | -25 | -25 | -25 |

FD lattice is chosen for strong focusing with a low envelope modulation, resulting in almost no emittance growth in multi-particle simulation. EMQ is preferred for convenient in beam commissioning. The physics design of the quadrupoles in the DTL drift tubes were conducted with POISSON code.

# KEY TECHNOLOGY DEVELOPMENT

R&D of the key technology in the CSNS linac was started three years ago with a small amount budget from Chinese Academy of Sciences and the site local government of Guangdong Province. It is crucial to make some prototypes for CSNS linac key technology because it has many challenges that we have never touched.

## *R&D of H Ion Source*

We have no experience to make such a high-current, low-emittance and long-lifetime $H^-$ ion source in China. Owing to the collaboration with ISIS, such an $H^-$ ion source is now under development. As a key part of the Penning source, a few source bodies, including discharge chamber and extractor, were fabricated and they were tested at ISIS ion source stand. The results are encouraging. We obtained a beam current of 55mA with beam pulse length of 500 μm at 50Hz., as shown in Figure 8. The emittance measurement gave almost the same value as that of ISIS operating ion source. So we have reason to believe the source can meet for CSNS linac demand.

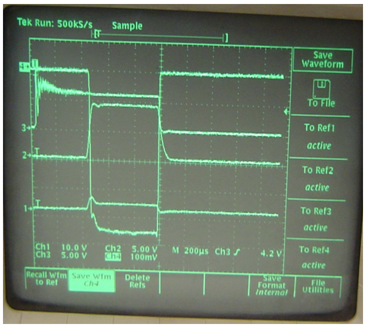


Figure 8: CSNS ion source body tested at ISIS with a beam current of 55mA.

An ion source test stand is now constructed at IHEP. Design of the source was completed (Figure 9) and all elements of the ion source have been fabricated. Assembly of the source is foreseen in recent. Various power sources, high voltage stand, vacuum system, water and gas cooling systems, as well as control system are all in progress.

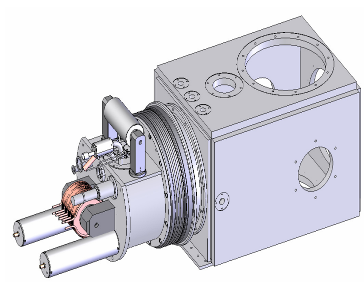

Figure 9: Design of the Penning $H^-$ source for CSNS.

## *LEBT Chopper*

To demonstrate the electrostatic chopper in the space charge neutralized LEBT, we are going to do some experiments on the existing RFQ developed for ADS study at IHEP. The LEBT of the RFQ linac has two solenoids and a beam collimator at the entrance of the RFQ. We will replace the collimator with an electrostatic chopper. It is found a couple of tapered electrostatic plates conforming the shape of the strongly focused beam at the entrance of the RFQ can provide more deflection to the beam at the same applied voltage. The pulse power source has been designed with two solid -state fast switches at the rise and fall ends of the pulse. The switch time is about 8ns at 6kV. A fast beam transformer will also added to the RFQ downstream beam line for beam diagnostics of the chopping effect. By this experiment we want to clarify our concerns: whether the RFQ vane will be damaged by the dumped beam, if spark occurs in the electrostatic chopper which is close to the space charge neutralized region, and if the chopping is fast enough for clear gaps. If it reaches a satisfactory result, we will consider the possibility to omit the MEBT so as to avoid beam degradation in it. In this case, a direct match design between the RFQ and DTL in CSNS linac will be considered.

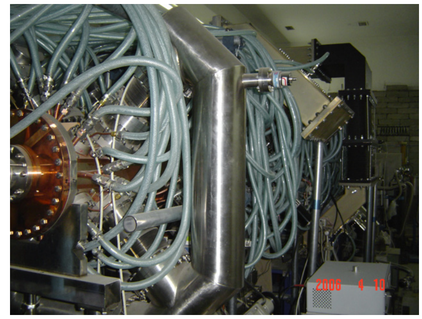

Figure 10. RFQ at 352 MHz for ADS Study.

## *RFQ Developed for ADS Study*

We have no R&D program for CSNS RFQ because we have built a high-current proton RFQ in our ADS research program. The ADS RFQ (Figure 10) has higher beam energy and beam current, and thus all the technology can be applied for CSNS RFQ. .

The major parameters of the ADS RFQ are listed in Table 4. This 3.5MeV RFQ is about 5 $\lambda$ long. To address the longitudinal field stability, it is separated into two resonantly coupled segments. Each segment consists of two technological modules of nearly 1.2m in length. More detailed information about the design and development of the RFQ can be found in reference [5]. From Table 4 it noticed the duty factor is from 6% to 100%. It means the RFQ is designed with 100% duty in terms of the cavity and RF power source, but, as the first step, it was commissioned at 6% duty factor. In the end of this year, we are going to raise its duty factor to 15%. In fact, we have successfully finished high-power RF conditioning at this duty factor in recent. The initial commissioning result will be introduced in the following.

Table 4: RFQ Major Design Parameters

| | |
|---|---|
| Input Energy | 75keV |
| Output Energy | 3.5MeV |
| Peak Current | 50mA |
| Structure Type | 4 vane |
| Duty Factor | 6%-100% |
| RF Frequency | 352.2MHz |
| Maximum $E_s$ | 33MV/m |
| Beam Power | 170kW |
| Structure Power | 420kW |
| Total Power | 590kW |
| Total Length | 4.75 m |

In 2006 we started the beam commission at a low duty factor at IHEP. And gradually the duty factor reached 7% with 1.43ms pulse length at 50Hz. An output beam current of 46mA was obtained with an input beam current of 49mA, resulting in a beam transmission rate more than 93%, as shown in Figure 11. During the operation, the cooling water temperature was tightly controlled for fine tuning of the RFQ cavity resonant frequency. A digital RF control system based on FPGA was developed at IHEP and added to the RF system, which was provided by CERN by kind. With this new feedback system the operation stability became better in the case of long pulse and heavy beam loading. The RF amplitude and phase stability reached $\pm 1\%$ and $\pm 1^0$ respectively.

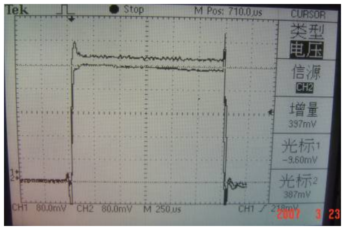


Figure 11: Input and output beam current of the RFQ.

## *R&D on DTL*

A prototype DTL tank was developed. It is the first module of the first tank. This module contains 28 drift tubes with a tank length of 2.9m. Before fabrication, several short tanks were tested to search for the feasible technology. Early attempts to fabricate DTL tank prototypes using the explosive-forming methods failed due to complications in fabrication of various ports on the tank. Periodic reverse electroforming method was successfully adopted by the domestic vendor in the tank fabrication. J-PARC type electromagnetic quadrupoles were fabricated with hollow conductor coils made with PR electroforming method. The drift tube is made of bulk copper and formed with electron-beam welding. Figure 12 shows the DTL tank under final machining of the drift tube holes, a hollow coil in drift tube and a bulk copper drift tube after EBW.

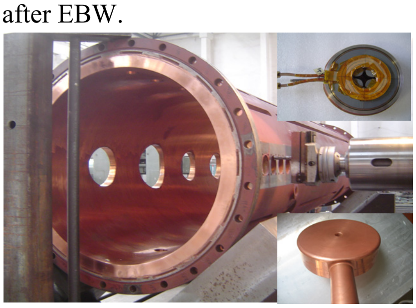

Figure 12: The DTL tank and quadrupole in drift tube of bulk copper.

For the magnetic measurement of the DTL quadrupole, various means, including Hall probe (HP), single stretched wire (SSW), rotating coil (RC), were adopted in order to verify the design specifications and fabrication technology. By carefully adjusting the DTL quadupole position relative to the harmonic coil in the rotating coil measurement, the dipole component can be controlled less than $6\text{X}10^{-4}$, and the magnetic center can be controlled within 0.003mm. More details can be found in a paper for this conference[6].

## *Prototype of Resonant HV Pulse Power Supply*

A new type AC series-resonant high-voltage pulse power supply was proposed by IHEP for the purpose to drive the klystron of the CSNS RF linac. The principle diagram is plotted in Figure 13. This new scheme has no step-up high voltage transformers and multi-phase high-voltage rectifiers. One of obvious advantages of this HV power supply over other types is its simplicity, leading to an easy maintenance and low trip rate during operation.

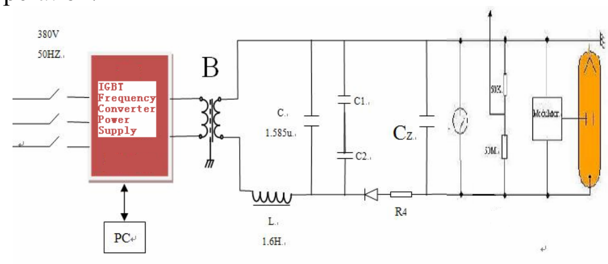


Figure 13: The proposed AC series resonance HV power supply for the klystron.

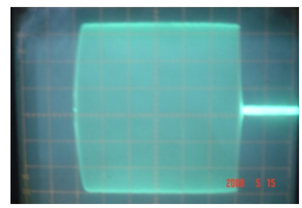

Figure 14: Klystron output pulse (1ms, 420kW) driven by the new prototype pulse power supply.

We have developed a full-scale prototype. Its highest output voltage reached 120 kV, with pulse discharging repetition frequency at 25 Hz or 50 Hz. We obtained an output power of 250 kW. Operation test together with the klystron of ADS RFQ was successful, with an AC-DC conversion efficiency up to 88%, a nice stability and flat-top, as shown in Figure 14. Consequently, the feasibility of the new power supply scheme was demonstrated. In the next step, we will strive for a more compact system.

## ACKNOWLEDGEMENTS

We are very grateful to Y.Yamazaki, K.Hasegawa and F.Naito from J-PARC for their kind assistance and fruitful discussion. Many thanks go to D.Findly, A.Letchford, and D.Faircloth of ISIS for their kind support on the ion source development. We thank all colleagues of CSNS linac team for their great efforts in the design and R&D work.

## REFERENCES

[1] S.X.Fang, S.N.Fu, et al., J. of the Korean Phys. Soc., Vol.48(4), 2006, 697-702.
[2] Jie.Wei, Shouxian Fang, Shinian Fu, An Overview of the Beijing Spallation Neutron Source Accelerators, Proc. of EPAC'06, Edinburgh, UK 26-30 June 2006.
[3] Shinian Fu, Shouxian Fang, Jie Wei, Proc. of LINAC'06.
[4] J.Pen, Z.R.Sun, S.N.Fu, Proc. of LINAC'06.
[5] S.N.Fu,S.X.Fang, et.al., Proc. of LINAC'06.
[6] Yi Cheng, et al. in this proceedings.

# THE SARAF CW 40 MEV PROTON/DEUTERON ACCELERATOR

A. Nagler, D. Berkovits, I. Gertz, I. Mardor#, J. Rodnizki, L. Weissman,
Soreq NRC, Yavne 81800, Israel
K. Dunkel, F. Kremer, M. Pekeler, C. Piel, P. vom Stein,
Accel Instruments GmbH, Bergisch Gladbach 51429, Germany

*Abstract*

The Soreq Applied Research Accelerator Facility, (SARAF) is currently under construction at Soreq NRC. SARAF will be a multi-user facility for basic research, medical and biological research, neutron based non-destructive testing and radio-pharmaceuticals research, development and production. SARAF is based on a continuous wave (CW), proton/deuteron RF superconducting linear accelerator with variable energy (5–40 MeV) and current (0.04-2 mA). The accelerator is designed to enable hands-on maintenance, which implies beam loss below $10^{-5}$ for the entire accelerator. Phase I of SARAF consists of a 20 keV/u ECR ion source, a low energy beam transport section, a 4-rod RFQ, a medium energy (1.5 MeV/u) beam transport section, a superconducting module housing 6 half-wave resonators and 3 superconducting solenoids, a diagnostic plate and a beam dump. Phase II will include 5 additional superconducting modules. The ECR source is in routine operation since 2006 and the RFQ has been operated with ions and is currently under characterization. The superconducting module is installed in the beam line and its RF performance is being characterized. Phase I commissioning results, their comparison to beam dynamics simulations and beam dynamics simulations of Phase II are presented.

## SARAF OVERVIEW

SARAF is currently under construction at Soreq NRC [1]. It will consist of a medium energy (up to 40 MeV) high current (up to 2 mA) RF superconducting linac of protons and deuterons, beam lines and a target hall with several irradiation stations for the abovementioned applications.

The facility schematic layout, its required parameters and a technical description of its components are given in Ref. 2. For a review of its operation concept and control system see Ref. 3.

Due to the technical novelty in the accelerator, the project has been divided to two phases. Phase I includes the ECR ion source, the RFQ, a prototype superconducting module (PSM), the design of the full accelerator (based on beam dynamics simulations [4]) and the design and risk reduction of the foreseen applications. Phase II includes construction of rest of the accelerator and its applications.

This paper presents recent commissioning results of phase I, including comparison to beam dynamics simulations [5], selected results of simulations for Phase II and a calculation of the expected residual activation due to beam loss in Phase II.

#mardor@soreq.gov.il

## PHASE I COMMISSIONING

The SARAF accelerator is designed, manufactured, installed and commissioned by Accel Instruments GmbH [6], in close collaboration with Soreq NRC personnel.

Phase I is fully installed on site, as is shown from 2 views in Figs. 1 and 2.


Figure 1: Upstream view of Phase I as installed on site at Soreq NRC. From right to left: ECR ion source (EIS), Low energy beam transport (LEBT), RFQ and Prototype Superconducting Module (PSM).


Figure 2: Downstream view of Phase I of SARAF. From right to left: PSM, Diagnostic plate (D-Plate), low power (Beam dump 1, copper, 6 kW) and high power (Beam dump 2, tungsten, 20 kW) beam dumps.

In the following sub-sections we describe the commissioning status of each main component.

## *Ion Source and LEBT*

The SARAF ion source is of type ECR, to ensure stable high quality performance and minimal maintenance. The ECR frequency is 2.45 GHz and the plasma is confined via two electromagnetic solenoids.

The ion source is followed by a low energy beam transport line (LEBT) which consists of three focusing solenoids, steerers, a bending magnet, which acts as an ion filter and beam diagnostics, which include two Faraday cups and a slit-wire system for emittance measurement

In Table 1 we show the commissioning results for the ion source. Proton, deuteron and $H_2^+$ beams in the specified range of 0.04 – 5.0 mA have been successfully generated. The emittance of all ion beams in both the X and Y planes was measured by a slit and wire system in the LEBT. Results for protons and deuterons are within the specified value, $\varepsilon_{rms\_norm\_100\%}$ = 0.2 π·mm·mrad. For the $H_2^+$ beam, the emittance is higher.

Table 1: Ion source measured rms, normalized, 100% emittance at both planes for all ions. Emittance for $H_2^+$ at 0.04 mA was not measured.

| Beam current | ε Protons (X/Y) | ε $H_2^+$ (X/Y) | ε Deuterons (X/Y) |
|---|---|---|---|
| [mA] | r.m.s, normalized, 100% [π·mm·mrad] | | |
| 5.0 | 0.20 / 0.17 | 0.34 / 0.36 | 0.13 / 0.12 |
| 2.0 | 0.13 / 0.13 | 0.30 / 0.34 | 0.14 / 0.13 |
| 0.04 | 0.18 / 0.19 | NA | 0.05 / 0.05 |

Possible reasons for the reduced performance for $H_2^+$ are poor ionization efficiency for molecular hydrogen, due to optimization for protons and deuterons, and molecular breakup and ion neutralization of the hydrogen molecules in the beam line's residual gas ($5\times10^{-6}$ mbar H in the LEBT in operation).

Further details on the construction and commissioning of the ion source and LEBT can be found in Ref. 7.

## *RFQ*

The SARAF RFQ is a 176 MHz 4-rod CW RFQ [8]. The main challenge in this RFQ is removing 250 kW from its ~3.8 meter rods, an unprecedented heat density. A high flow water cooling system, including flow inside the rods, has been incorporated in the RFQ.

The RFQ commissioning is comprised of two processes which are being executed in parallel:

- RF conditioning up to 65 kV, the voltage that is required for acceleration of a CW 4 mA deuteron beam to 3.0 MeV.
- Beam commissioning, mainly with protons that require half of the deuteron field.

A few hundred hours of RF conditioning has been performed over the last 2 years in an effort to reach the specified field for CW deuterons. This field implies an input power of approximately 260 kW. Two conditioning schemes were used: setting the input power to a value of 280 kW at a duty cycle of approximately 1% and increasing the duty cycle and starting from a low value of CW power and gradually increasing the power.

So far we were able to reach a 15% duty cycle at 280 kW and CW operation at 195 kW. These values are not stable yet and the sources of these instabilities are currently being investigated. In an effort to improve the slow conditioning progress, several actions were taken at the beginning of 2008:

- The rods were dismantled and sharp edges at their bottom part were rounded off.
- While dismantled, the rods were cleaned with a special cleanser.
- A circuit for fast recovery after sparks was installed.

These measures improved performance for a while but still below the CW deuteron specification. To understand how the input power is converted to the electric field between the rods, the square of the voltage that was measured by one of the RFQ pickups was compared to the input power. The result is shown in Fig. 3.

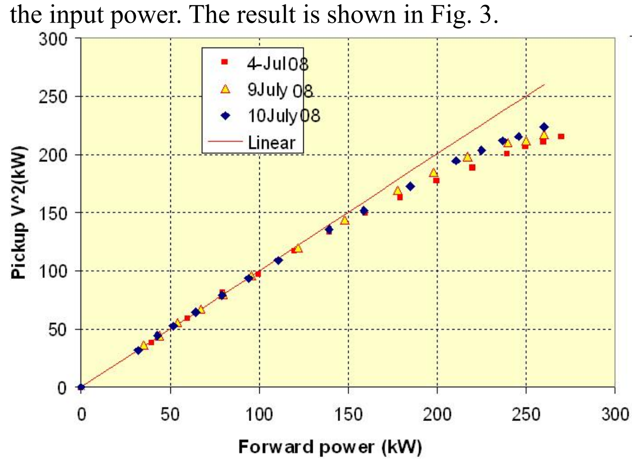


Figure 3: RFQ rod voltage squared versus the RFQ input power. Parting from the linear relation probably indicates onset of dark current due to poor conditioning.

It can be seen that the curve parts from the linear relation below 150 kW. This indicates that the input power generates current that flows between the rods instead of a sustained voltage between them.

The cause of this effect is not certain yet. Following action taken in other installations to circumvent excessive sparking and limited performance (e.g., [9]), an in-situ bake was recently performed by applying ~900 W of CW RF power with the cooling water switched off. The electrode temperature was monitored with PT100 probes that were inserted through the dried water cooling pipes into the rods and rose to 70 – 80 °C, accompanied by a vacuum pressure rise from $5\times10^{-7}$ to $4\times10^{-6}$ mbar. No significant vacuum pressure reduction (such as reported in Ref. 9) was observed after 3 days of baking. The vacuum returned to its base value after turning off the power. The effect of this process on the maximal attainable field in the RFQ will be investigated in the near future.

A description of RFQ beam commissioning, including preliminary results, is given in [10, 11]. Table 2 provides an updated summary of the proton beam performance of the RFQ. Emittance measurements were performed with a low duty cycle beam carrying total power of less than 200W, which is the maximum that the beam intercepting diagnostics can withhold [10]. Energy was measured by the Time-of-Flight (TOF) method using the summed output of beam position monitors in the MEBT and phase probes in the D-Plate. Current was measured by a MPCT and by a FC, both located at the D-Plate.

Table 2: RFQ measured performance. Values in parentheses are the specifications.

| Parameter | Protons |
|---|---|
| Output energy [MeV/u] | 1.5 (1.5) |
| Maximal CW current [mA] | 4.0 (4.0) |
| Transverse emittance r.m.s., normalized, 100% [π·mm·mrad]<br>(at 0.5 mA, closed LEBT aperture)<br>(at 4.0 mA, open LEBT aperture) | <br><br>0.17 (0.30)<br>0.25 /0.29 (0.30) |
| Longitudinal emittance, r.m.s [π·keV·deg/u] (at 3.0 mA) | 30 (120) |
| Transmission [%] (at 0.5 mA)<br>(at 2.0 mA)<br>(at 4.0 mA) | 80 (90)<br>70 (90)<br>65 (90) |
| Required RF power (protons) [kW]<br>(deuterons) [kW] | 62 (55)<br>248 (220) |

The transverse and longitudinal bunch profile measurements were closely followed by beam dynamics simulations [5] using the code TRACK [12]. In Fig. 4 we show the comparison of the measured results with the simulations, which demonstrates good agreement.

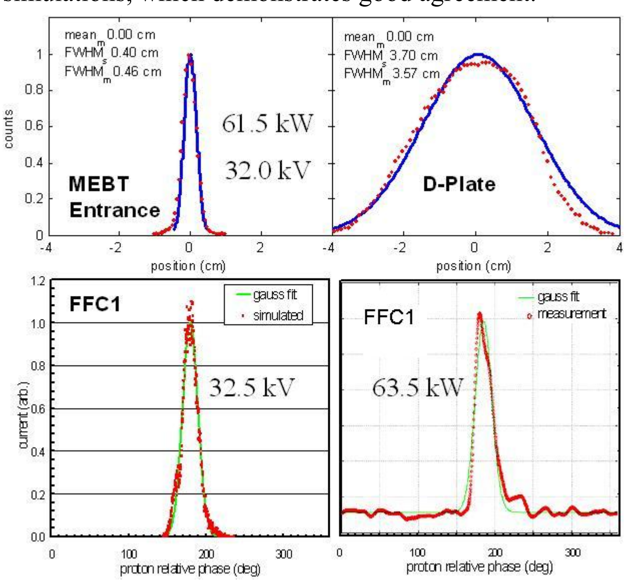


Figure 4: Comparison of post-RFQ measured results and beam dynamics simulations. Top left – Transverse profile at the MEBT entrance. Top right – Transverse profile at the D-Plate. Bottom left – simulated longitudinal profile at the upstream Fast Faraday Cup (FFC) at the D-Plate. Bottom right – measured longitudinal profile.

Short runs of very low duty cycle ($10^{-4}$) deuteron and $H_2^+$ beams were performed. The energy of a $H_2^+$ beam was established to be 3.0 MeV via TOF. The first RFQ transmission measurement for deuterons yielded 70%, without any optimization of LEBT parameters. Further deuteron and $H_2^+$ runs are foreseen following additional conditioning of the RFQ.

### *Prototype Superconducting Module*

The prototype superconducting module (PSM) includes six 176 MHz, β=0.09 half wave resonators (HWR) made of bulk Nb and three 6 T superconducting solenoids inserted amongst them. Further details, along with single cavity vertical cold tests results are described in [13]. RF commissioning results for single cavities inside the PSM, using a voltage controlled oscillator operated at closed loop, are given in [11].

The most recent PSM RF measurements were performed by using the full LLRF system [14], which drives the cavities tuners in a generator driven resonator (GDR [15]) type closed loop. Cavity tuning is based on the forward and transmitted phase signals. An additional coupler was added before the drive amplifier in order to reduce the influence of the reflected signal on forward phase measurements. A further improvement was modification of the tuning loop software in order to include compensation of the piezo tuner hysteresis.

Due to the combination of microphonics, Lorentz force detuning and a possible effect by LHe-pressure variations, which reached peaks of 10 mbar, the cavities frequency variation turned out to be too large for tuning solely by piezo tuners. Therefore, the stepper motor control loop was modified to engage when the voltage input to the piezo approaches 80% of its maximal value.

These modifications enabled PSM operation with the tuners in closed loop. Preliminary results are given in Table 3.

Table 3: PSM RF performance of single cavities. Cavities operated with tuners in closed loop.

| Cavity | $V_{peak}$ [MV] | $E_{peak}$ [MV/m] | Phase stability [°] | Amplitude stability [%] |
|---|---|---|---|---|
| 1 | 0.8 | 23.5 | ±0.3 | 0.5 |
| 2 | 0.7 | 20.6 | ±0.3 | 0.5 |
| 3 | 1.0 | 29.5 | ±0.3 | 0.5 |
| 4 | 0.9 | 26.5 | ±0.3 | 0.5 |
| 5 | 1.14 | 33.5 | ±0.3 | 0.5 |
| 6 | 1.03 | 30.3 | ±0.3 | 0.5 |

The specified $E_{peak}$ for the PSM cavities is 25 MV/m. Cavities 1 and 2 could not be raised to higher fields due to loss of lock. The phase and amplitude stability values are peak-to-peak and are determined by the ADC's least significant bit. It is expected that the actual stability is even better. These values are within specifications.

Operation times in this commissioning run were limited to a few minutes for each cavity, since each cavity was driven separately due to missing couplers.

An additional commissioning run was completed very soon before submission of this paper, where all six cavities were operated simultaneously with the tuners in closed loop. The data is still under analysis, but preliminary qualitative results indicate that it was possible to run the PSM continuously for several hours at an average $E_{peak}$ of slightly less than 20 MV/m .

### *Summary and Outlook*

The commissioning of Phase I of SARAF is on-going. The current challenges include conditioning the RFQ to enable acceleration of CW deuteron and $H_2^+$ beams and optimizing the PSM to enable beam acceleration through it. Beam commissioning of protons and deuterons through the entire Phase I is foreseen for the winter of 2008.

## PHASE II

Phase II of SARAF will include an additional SC accelerating module (SM) similar to the PSM (six β=0.09 HWR cavities and three solenoids) and four additional SMs, including eight β=0.15 HWR cavities and 4 solenoids each.

In this section we shortly describe the extensive beam dynamics simulation effort that is undertaken, in order to ensure that the SARAF design will enable reaching the specified energy, current and emittance, with beam loss that will enable hands on maintenance.

### *Beam Loss Criterion*

The beam loss criterion for the SARAF linac is defined as the beam loss value that generates residual activation of 2 mRem/hr after one year of operation, 30 cm away from the beam line, four hours after accelerator shut down.

In order to generate a conservative criterion, several meticulous assumptions were made:

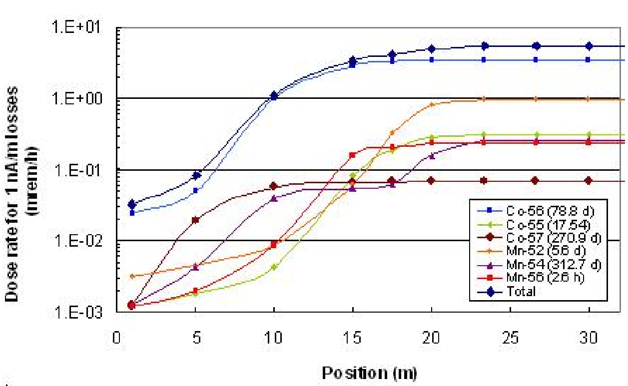


Figure 5: The dose rate along the 22 m long linac and an additional 10 m long beam line, after one year irradiation with beam loss of 1 nA/m, under the meticulous assumptions described in the text.

- The accelerator is operating 365 days per year.
- Only deuterons are accelerated all the time, and to the maximum energy of 40 MeV.
- The accelerator is made entirely of stainless steel.

These assumptions introduce a safety margin of a factor of 2-4. Based on these assumptions, the residual activation per lost deuteron was calculated [16] and this lead to the conclusion that the beam loss criterion is 0.4 nA/m at 40 MeV. As mentioned above, relaxation of the meticulous assumptions that we took may increase this limit by a factor of 2-4. Figure 5 shows the contribution of each isotope, all of which are produced by activation of $^{56}$Fe, to the residual activity assuming beam loss of 1 nA/m. The residual activity is given along the 22 m long linac and an additional 10 m long beam line that leads the beam to the irradiation targets.

### *Beam Dynamics Simulations*

We applied the tail emphasis method [17] in order to study particle losses along the linac. The method is based on the assumption that losses begin longitudinally, and problematic particles begin at the periphery of the longitudinal phase space at the RFQ exit (originate in the boundaries between the downstream bunches at the dc current entering the RFQ buncher section).

This method allows us to calculate losses along the SARAF accelerator at the 1 nA level with limited computational efforts: A Tail Emphasis deuteron beam with 2.1 million macro particles at the RFQ entrance is equivalent to the simulation of 3 bunches containing 42.6 million macro-particles (each 1:10, equivalent to 0.3 nA) for 4 mA CW at 176 MHz.

The reduced computation time allows us to run a large number of simulations in a relatively short span of time. This enables exploration of the effect of manufacturing and operational errors on the beam and estimate losses due to these factors. The values of the errors used on this study are given in [17] and [4].

Figure 6 shows an example of series of 200 simulation runs, each having slightly different manufacturing and operational parameters, which are generated from the distributions described in [17] and [4]. This result is from an application of the tail emphasis method using the simulation code GPT [18].

The result displayed in Fig. 6 is for a 32k/193k core/tail particle distribution of a deuteron beam, which exits the RFQ with a current of 3.4 mA and a normalized rms transverse emittance of 0.23 π·mm·mrad. The outer most macro particle is equivalent to a current of 1 nA. The bore radius is 19 mm within the solenoids and 15 mm everywhere else.

The conclusion from this simulation is that even when considering reasonable manufacturing and operational errors, no beam loss is expected within a simulation resolution of 1 nA. This is consistent with the beam loss criterion for hands on maintenance discussed above.

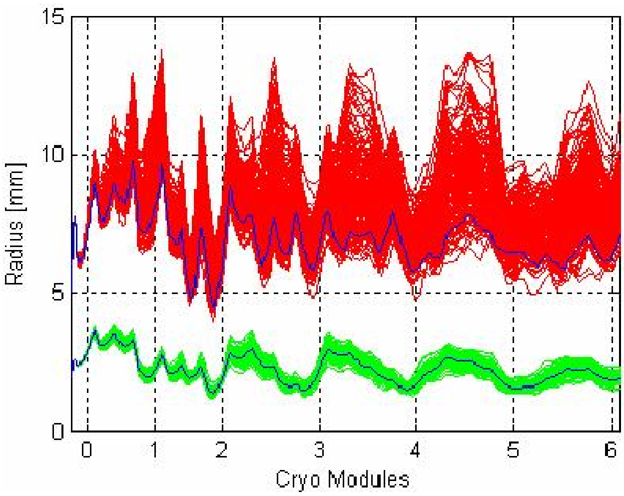


Figure 6: Deuterons transverse envelope (red) and rms radius (green) for a series of 200 error simulation runs through the six SC accelerating modules of the SARAF accelerator.

## SUMMARY AND OUTLOOK

In this paper we presented the current status of the commissioning of Phase I of the SARAF accelerator, and briefly described selected results from the beam dynamics simulation effort which is a major part of the SARAF project.

The commissioning of Phase I is foreseen to be concluded towards the end of 2008 and it is expected that work on Phase II will commence at that time. Currently, Phase II is scheduled to be completed around the year 2013.

## ACKNOWLEDGEMENTS

The authors wish to acknowledge the contribution of B. Bazak, G. Feinberg, S. Halfon, A. Pernick, A. Shor and Y. Yanay to the beam dynamics simulations and the dose rate calculations that are described in this paper.

## REFERENCES

[1] http://www.soreq.gov.il/default_EN.asp

[2] A. Nagler et al., “Status of the SARAF Project”, LINAC'06, Knoxville, August 2006, MOP054, p. 168 (2006).

[3] I. Mardor et al., “The Operation Concept of SARAF”, LINAC'06, Knoxville, August 2006, MOP033, p. 109 (2006).

[4] J. Rodnizki et el., "Lattice Beam Dynamics Study at Low β For SARAF/EURISOL Driver 40/60 MeV 4 mA d&p Superconducting Linac", HB2008, Knoxville, August 2008, WGB15 (2008).

[5] J. Rodnizki et el., "Beam Dynamics Simulation of the 1.5 MeV Proton Beam Measured at the SARAF RFQ Exit", EPAC'08, Genoa, June 2008, THPP038, p. 3458 (2008).

[6] http://www.accel.de

[7] K. Dunkel et al., "Performance of the SARAF Ion Source", PAC'07, Albequerque, June 2007, TUPAN009, p. 1407 (2007).

[8] P. Fischer et al., "Tuning a CW 4-Rod RFQ", LINAC'06, Knoxville, August 2006, THP064, p. 728 (2006)

[9] A. Letchford et al., "Testing, Installation, Commissioning and First Operation of the ISIS RFQ Pre-Injector Upgrade", PAC'05, Knoxville, May 2005, ROPC010, p. 695 (2005).

[10] C. Piel et al., "Beam Operation of the SARAF Light Ion Injector", PAC'07, Alboquerque, June 2007, TUPAN011, p. 1410 (2007).

[11] C. Piel et al., "Phase 1 Commissioning Status of the 40 MeV Proton/Deuteron Accelerator SARAF", EPAC'08, Genoa, June 2008, THPP038, p. 3452 (2008).

[12] P.N. Ostroumov, V. Aseev and B. Mustapha, "TRACK a code for beam dynamics simulations in accelerators and transport lines with 3D electric and magnetic fields", ANL, March 27, 2006.

[13] M. Pekeler et al., “Development of a Superconducting RF Module for Acceleration of Protons and Deuterons at Very Low Energy”, LINAC'06, Knoxville, August 2006, TUP034, p. 321 (2006).

[14] M. Pekeler et al., "Development of Low Level RF Control Systems for Superconducting Heavy Ion Linear Accelerators, Electron Synchrotrons and Storage Rings", PAC'05, Knoxville, May 2005, WPAT068, p. 1 (2005).

[15] S. N. Simrock. "Achieving Phase and Amplitude Stability in Pulsed Superconducting Cavities", PAC'01, Chicago, June 2001, ROAA002, p. 473 (2001)

[16] S. Halfon et el., to be published.

[17] B. Bazak et al., "Simulations of Ion Beam Loss in RF Linacs with Emphasis on Tails of Particle Distributions", Submitted for publication (2008).

[18] General Particle Tracer (GPT), Pulsar Physics, http://www.plusar.nl/gpt/.

# THE INJECTOR SYSTEMS OF THE FAIR PROJECT

W. Barth
Gesellschaft für Schwerionenforschung, D-64291 Darmstadt, Germany

*Abstract*

The present GSI accelerator chain will serve as an injector for FAIR (**F**acility for **A**ntiproton and **I**on **R**esearch). The linear accelerator UNILAC and the heavy ion synchrotron SIS18 should deliver up to $1{\cdot}10^{12}$ $U^{28+}$-particles/sec. In the past two years different hardware measures and a careful fine tuning of the UNILAC resulted in an 35% increase of the beam intensity to a new record of $1.25{\cdot}10^{11}$ $U^{27+}$-ions per 100 µs or 2.3 $10^{10}$ $U^{73+}$-ions per 100 µs. The increased stripper gas density, the optimization of the Alvarez-matching, the use of various newly developed beam diagnostics devices, and a new charge state separator system in the foil stripper section comprised the successful development program. The contribution reports results of beam measurements during the high current operation with uranium beams (beam pulse power up to 0.65 MW). The UNILAC-upgrade for FAIR will be continued by assembling a new front-end for $U^{4+}$, stronger power supplies for the Alvarez quadrupoles, and versatile high current beam diagnostics devices. Additionally, the offered primary proton beam intensities will be increased by a new proton linac, which should be commissioned in 2013. We acknowledge the support of the European Community – Research Infrastructure Activity under the FP6 "Structuring the European Research Area" program (CARE, contract number RII3-CT-2003-506395). Work supported by the European Community INTAS Project Ref. no. 06-1000012-8782.

## INTRODUCTION

Meeting the FAIR science requirements higher intensities have to be achieved in the present GSI-accelerator complex, through faster cycling and, for heavy ions, lower charge state which enters quadratically into the space charge limit (SCL). The desired energy of up to 1.5 GeV/u for radioactive beam production is delivered by the synchrotron SIS 100, which also generates intense beams of energetic protons up to 30 GeV for pbar-


Figure 1: The future accelerator facility FAIR at GSI in Darmstadt [1].

Table 1: FAIR-design Uranium Beam Parameters at UNILAC and SIS 18 Injection [2]

| | HSI entrance | HSI exit | Alvarez entrance | SIS 18 injection | |
|---|---|---|---|---|---|
| Ion species | $^{238}U^{4+}$ | $^{238}U^{4+}$ | $^{238}U^{28+}$ | $^{238}U^{28+}$ | $^{238}U^{73+}$ |
| El. Current [mA] | 25 | 18 | 15 | 15.0 | 5.5 |
| Part. per 100µs pulse | $3.9{\cdot}10^{12}$ | $2.8{\cdot}10^{12}$ | $3.3{\cdot}10^{11}$ | $3.3{\cdot}10^{11}$ | $5.0{\cdot}10^{10}$ |
| Energy [MeV/u] | 0.0022 | 1.4 | 1.4 | 11.4 | |
| ΔW/W | - | $4{\cdot}10^{-3}$ | $\pm1{\cdot}10^{-2}$ | $\pm2{\cdot}10^{-3}$ | |
| $\varepsilon_{n,x}$ [mm mrad] | 0.3 | 0.5 | 0.75 | 0.8 | |
| $\varepsilon_{n,y}$ [mm mrad] | 0.3 | 0.5 | 0.75 | 2.5 | |

production. Highly charged heavy ion beams with a maximum energy of 30 GeV/u have to be accelerated in the slower cycling synchrotron SIS 300. SIS 300 can also be used as a stretcher for radioactive beams, which can be injected, cooled, and stored in a system of rings with internal targets and in-ring experimentation.

In the last years GSI put effort in increasing the uranium intensities delivered to the SIS 18. An advanced upgrade program for the UNILAC is still in progress to meet the FAIR requirements. For uranium (FAIR reference ion) the UNILAC has to deliver $3.3{\cdot}10^{11}$ $U^{28+}$-particles per 100 µs (see Table 1). Besides for a 15 emA $^{238}U^{4+}$ beam from the High Current Injector HSI [2] up to $5.5{\cdot}10^{10}$ $U^{73+}$ particles should be delivered to the GSI heavy ion synchrotron SIS 18 (during 100 µs), while the SIS 18 SCL is reached by a 15 turn injection into the horizontal phase space.

In the 36 MHz-HSI [3] comprising ion sources of MEVVA-, MUCIS- or Penning-type, the IH-RFQ, a short 11 cell adapter RFQ (Super Lens), and two IH-tanks, the beam is accelerated up to 1.4 MeV/u. In the gas stripper section the charge state is increased and after charge separation the high intensity $U^{28+}$-beam is matched to the Alvarez DTL. After acceleration up to the final UNILAC-beam energy the transfer line (TK) to the synchrotron provides for a foil stripper and a new compact charge state separator system.

The UNILAC brilliance for proton beams is at least two orders of magnitude below the FAIR-requirements. For the proposed time sharing scenario proton beam intensities of 35 mA and an energy of 70 MeV are required. Accordingly, a dedicated proton injector linac [4] being designed within FAIR will be operated independently from the existing UNILAC.

The UNILAC serving as a high duty factor heavy ion linac for physics experiments is in operation since more than 30 years. After completion of the FAIR complex in 2015 the running time for the accelerator facility will be 20 years at least, while the UNILAC will then be in operation for more than 60 years. Different proposals for a new advanced short pulse, heavy ion, high intensity, high energy linac, substituting the UNILAC as a synchrotron injector are still in discussion. This new "High Energy-UNILAC" will allow for complete multi-ion-operation, and should provide for reliable beam operation in the future.

The decelerator for HITRAP (Heavy Ion TRAP) is also a (linac-) project providing for ions of selected charge states up to $U^{92+}$ at cryogenic temperatures. One of the HITRAP features will be the ability to decelerate heavy highly-charged ions from 4 MeV/u down to rest after ejection from the Experimental Storage Ring (ESR). After three years of operation at the ESR the HITRAP set-up will be an integral part of FAIR behind the NESR (New Experimental Storage Ring).

## HSI FRONTEND-UPGRADE

Table 2: Main RFQ Parameters

| | New Design | Existing Design |
|---|---|---|
| Voltage, kV | 155.0 | 125.0 |
| Average radius, cm | 0.6 | 0.52-0.77 |
| Electrode width, cm | 0.84 | 0.9-1.08 |
| Maximum field, kV/cm | 312.0 | 318.5 |
| Modulation | 1.012-1.93 | 1.012-2.09 |
| Synch. Phase, degree | -90 to -28 | -90 to -34 |
| Aperture, cm | 0.41 | 0.38 |
| Min. transverse phase advance, rad | 0.56 | 0.45 |
| Norm. transverse acceptance, cm mrad | 0.086 | 0.73 |
| Output energy, MeV/u | 0.120 | |
| Electrode length, mm | 9208.4 | |

The bottleneck of the whole UNILAC is the front-end system of the High Current Injector. It is shown in an upgrade design study that the transverse RFQ-acceptance can be significantly increased while the emittance growth can be reduced. Both goals are achieved with only a moderate change of the RFQ electrode geometry; the intervane voltage rose from 125 kV to 155 kV [5], but keeping the design limit of the maximum field at the electrode surface. The changing resonant frequency can be compensated with a relatively small correction of the carrying rings. The beam parameters in the final focusing elements of the LEBT were optimized together with the improved design of the input radial matcher; the length of the gentle buncher section was considerably increased to provide slow and smooth bunching resulting in a reduced influence of space charge forces. The baseline design was optimized for an $U^{4+}$ beam current of 20 emA and a total transverse emittance of 280 mm·mrad (unnorm.). These values were chosen on the base of the measurements in front of the RFQ (15 mA, 210 mm·mrad) assuming the same brilliance. The main parameters of the new design are summarized in Table 2. [6]

A comparison of the existing and the new RFQ is illustrated in Fig. 2. The beam current inside a given transverse emittance at the RFQ output is shown for both designs. Beam dynamics simulations were done for the same beam current (25 mA) and emittance (210 mm·mrad), but with different matching for each case. The new RFQ design provides for an increase of more than 40 % of the beam current compared to the old design. Higher beam emittance behind the new RFQ is formed by a few percent of the particles, while the core of the beam (20 mm·mrad) contains the required beam current. The HSI-RFQ upgrade will start in spring 2009.

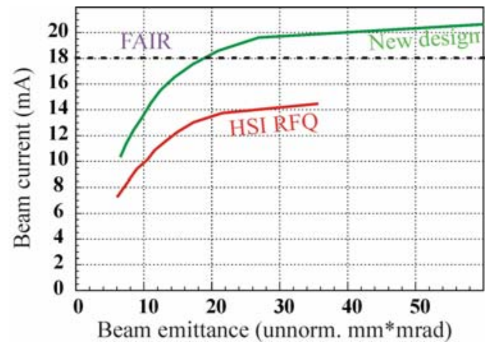


Figure 2: Beam current inside a given emittance at RFQ-output for the existing (red) and the new design (green).

## HSI END TO END SIMULATIONS

The beam dynamics for the HSI were simulated with different codes; the geometry of both RFQ designs were introduced in the DYNAMION-code. Alternatively PARMTEQ-M was used to cross check beam dynamics results; the simulation results of both codes showed high agreement. The DYNAMION macro particle distribution was directly matched to the intertank section comprising a magnetic quadrupole duplet and the super-lens, were the beam is matched to a 20 m IH-section simulated by LORASR. Fig. 3 shows a comparison of the beam performance at the IH-output for the existing and the new RFQ-design. A significant increase of beam brilliance for the total HSI-performance is visible if the new RFQ-design is considered. For a transverse emittance of 20 mm·mrad an $U^{4+}$-current of more than 18 emA is enclosed, meeting the FAIR-requirements. Further simulations will be performed to evaluate the overall improvement at the end of the whole UNILAC. The full FAIR-performance should be reached when the planned installation of ion source terminal and Compact LEBT [7] will be realized (2010-2011).

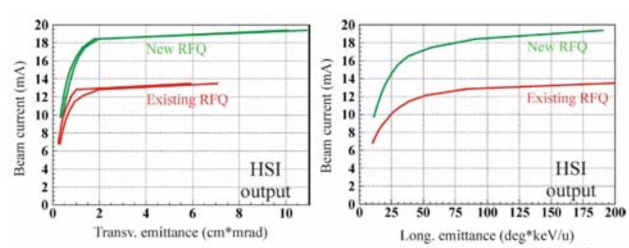


Figure 3: Beam current inside a given transverse (left) and longitudinal (right) emittance at HSI-output for the existing (red) and the new design (green). [6]

## GASSTRIPPER PERFORMANCE

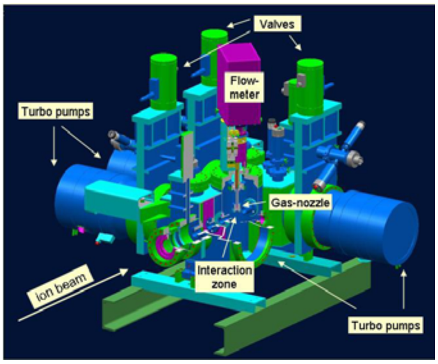


Figure 4: New gas stripper box.

With a reduction of the beam apertures in the old stripper box, it was possible to increase the stripper gas density by 50 %. For medium intense uranium beams this leads to the expected gain for the desired charge state 28+ (up to 12.8 % of the total particle number). The desired equilibrium charge state distribution was reached for a 70 % higher gas density. During long term operation the pumping speed of the old vacuum pumps was not sufficient to compensate this gas load. For high current operation, as required for FAIR, the defocusing effect of the space charge forces leads to particle loss in the transport section after the stripping area. In the new gas stripper box (as shown in Fig. 4) [8] the high stripper gas density for the necessarily enlarged apertures is provided by enhanced vacuum pumping speed.

## BEAM MATCHING TO THE ALVAREZ

The improvement of beam quality at the end of the UNILAC Alvarez DTL section is a major concern with respect to the availability of the design beam parameters. The DTL comprises 177 accelerating gaps and 184 quadrupoles for periodic transverse beam focusing. The high currents arise non-linear space charge forces leading to emittance growth. This emittance growth depends on the beam envelope shape, which can be varied by the transverse phase advance $\sigma$. In case of low currents the zero current phase advance $\sigma_o$ is calculated analytically considering the field strength of the quads.

The beam envelope also depends on the matching to the DTL injection. A beam is matched if its envelope inhabits the same periodicity as the focusing structure, mismatching is quantified by the mismatching factor M. In machine experiments the dependency of emittance growth on $\sigma_o$ and M for the Alvarez DTL was investigated. The design beam for FAIR is 15 emA of $^{238}U^{28+}$ being space charge equivalent to 7.1 emA of $^{40}Ar^{10+}$. Since $^{40}Ar^{10+}$ is available with higher intensity and allows for a larger spectrum of focusing strengths, $^{40}Ar^{10+}$ was used. Phase space distributions were measured in front of the DTL. From the transverse measurements the rms-emittances were extracted. The DTL was set to different values of $\sigma_o$. From the measurement in front of the DTL M was calculated for

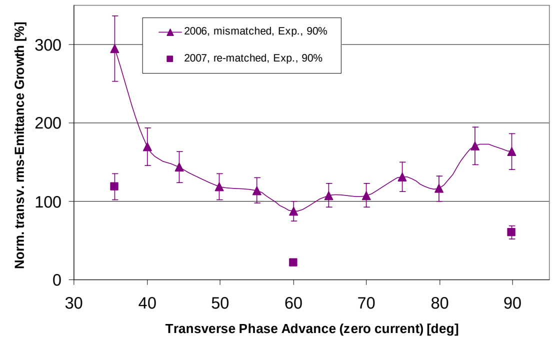


Figure 5: Measured transverse emittance growth as function of the phase advance [9]

each value of $\sigma_o$ and corresponding Alvarez-emittances were measured. Emittance growth rates as function of $\sigma_o$ are plotted in Fig. 5. The mismatch was large for low and for high phase advances. A minimum mismatch occurred at $\sigma_o \approx 55°$, resulting in a minimum emittance growth. Highest growth rates of 300 % were measured at $\sigma_o = 35°$. It decreases down to 100 % at about 60° and increases again to almost 200 % for highest $\sigma_o$. Compared to the 2006-campaign mismatch was reduced for all phase advances. The corresponding emittance growth rates are shown. It was demonstrated that by reducing M, emittance growth rates of just 20 % can be achieved. [9] A sufficient phase advance $\sigma_0 > 50°$ is also required for an improved high current beam brilliance for the SIS-injection of heavy ions. New stron-ger power supplies feeding the quads will be mounted in the winter shutdown 2008/2009 providing for the necessary quadrupole field strength for $U^{28+}$-operation.

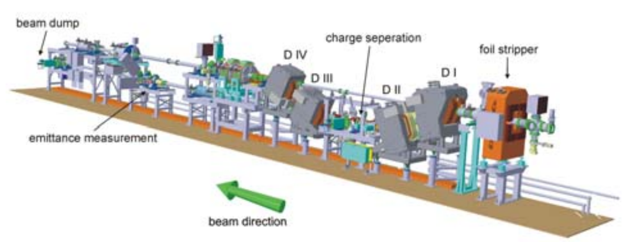


Figure 6: New Charge state separator system, integrated in the TK comprising the foil stripper, the four 35°-Dipole magnets (DI - DIV), and a beam diagnostics bench.

## NEW CHARGE STATE SEPARATOR

A new charge state separator system was installed in the transfer line to the SIS 18 in December 2007. After commissioning of all components, in January 2008 beam commissioning was performed successfully with a medium intensity uranium beam and a high intensity argon beam; the measured beam transmission is close to 100 % for low and high current beams. The sweeper operation was tested with a high intensity argon beam as well as with an uranium beam. In general no emittance growth effects is driven by the sweeper operation. The stripping efficiency measured with the charge separator as a spectrometer is as expected. The improved charge separation capability was simulated with the PARMILA

Transport code and confirmed for heavy ion beams as well as for high current operation. Simulated and measured emittance growth effects for low current operation are caused by small angle straggling; additionally the vertical emittance inside the charge separator is increased by dispersion. Space charge forces act in the short drift length between stripper foil and charge separation in D I only – the space charge influenced emittance growth is 10 % (hor.) resp. 20 % (vert.). [10] The measured high current emittance potentially meets the FAIR requirement. With an advanced beam diagnostics bench behind dipole III high current beam measurements are accomplished to prepare for the injection into the SIS 18. Besides ion current the beam profile and position, the emittance, the beam energy, and the bunch structure can be measured.

## $^{238}$U-BEAM INTENSITIES FOR THE SIS 18

In Fig. 7 the achieved uranium intensities in the UNILAC and TK are summarized (2001-2007), reached by ongoing upgrade measures and by an extended experimental program dedicated to improve the overall UNILAC performance for heavy ion high current operation. In June 2007 an $U^{73+}$ intensity of 2.7 emA (37.1 pμA) was reached for the first time, which corresponds to $2.3 \cdot 10^{10}$ particles per 100 μs. Before foil stripping 5.7 emA (203 pμA) of $U^{28+}$ beam intensity was achieved ($1.25 \cdot 10^{11}$ particles per 100 μs). The optimized total particle transmission through HSI, stripper section,

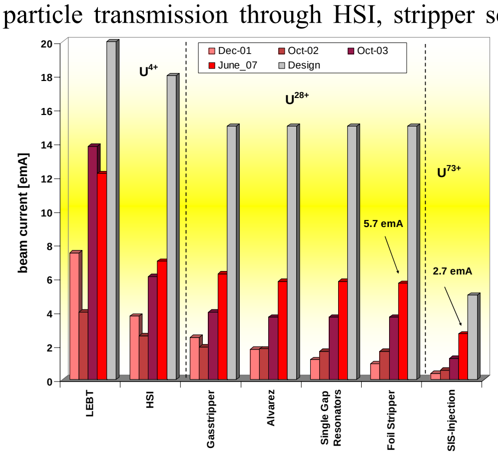


Figure 7: Improvement of the UNILAC-uranium beam intensities during the last three years.

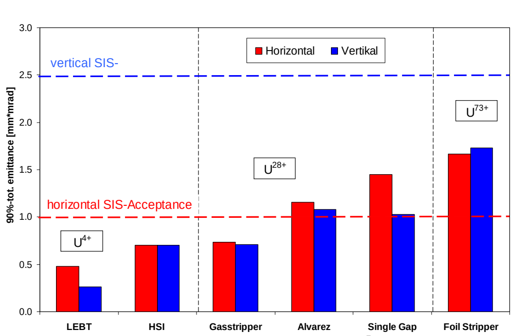


Figure 8: High current beam emittance measured during the measurement campaign in June 2008.

Alvarez DTL, Single gap resonator chain, and TK is larger than 50 % if the particle losses during charge state separation behind the two strippers are taken into account. The measured transverse beam emittance (see Fig. 8) exceeds the acceptance of the synchrotron. The planned front end upgrade and the resulting improvement of the beam brilliance will serve to overcome these bottlenecks.

## LAYOUT OF THE FAIR-PROTON LINAC

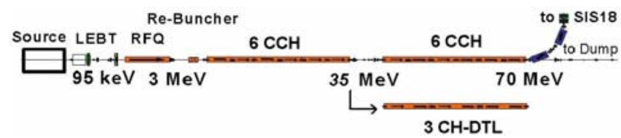


Figure 9: Two proposed schemes for the FAIR p-linac. [11]

To provide the primary proton intensities a dedicated proton linac is planned comprising a proton source, an RFQ, and a DTL, both with an operation frequency of 325 MHz allowing for acceleration up to 70 MeV. For the first time normal conducting Crossed-bar H-cavities (CH) are used. The beam pulses with a length of 36 μs, a current of 35 mA, and total transverse emittances of 7 μm will allow filling the existing synchrotron SIS 18 within a multi-turn-injection up to its SCL of $7 \cdot 10^{12}$ protons. The GSI Proton injector will be the fist machine based on CH-DTL cavities applying a KONUS beam dynamics scheme. The beam dynamics layout has been designed assuming an input current up to 70 mA, twice the value required during operation. Two different layouts are still under investigation, the first design appropriates coupled cavities only and the second makes use of a standard cavity in the high energy section. Beam dynamics investigations including loss studies show that both designs can fulfil the FAIR requirements, and they are robust enough against inevitable errors. At present time technical drawings of the second resonator of the proton injector are in preparation; after validating the coupling scheme with the construction of a scaled model. The construction of the FAIR Proton injector should start in 2010, while the commissioning phase should be finished in 2013. [11]

## COMMISSIONING OF THE HITRAP DECELERATOR

Accelerated and highly stripped heavy ions from the GSI accelerator complex are stored, decelerated down to 4 MeV/u, and finally cooled in the ESR. After beam extraction the ions have to be further decelerated down to 6 keV/u. An IH drift tube cavity and a 4-rod RFQ, both operating at 108 MHz, decelerate the beam down to the final beam energy in two steps. Longitudinal matching to the IH structure is applied by a double-drift-buncher combination comprising a 108 MHz λ/4-resonator and a 2nd harmonic cavity. A third rebuncher of spiral type is located between IH and RFQ. Finally, a low power spiral type debuncher inside the RFQ tank provides for the reduced beam pulse spread sufficient for beam capture in the super conducting penning trap. Within three commissioning periods the technical and physical functionality of the HITRAP-decelerator was proofed (see Fig. 10). No major problems occurred. Additional magnetic steering devices turned out to be necessary for proper beam transport tuning, the setting values were slightly modified by experience, and the working points of the rf-structures were fixed. For improved beam energy analysis a bending magnet and an additional scintillation screen will be installed temporarily behind the IH tank. The RFQ high power conditioning already began. The tank will be finally installed in autumn 2008. HITRAP commissioning will be finished until mid of 2009. [12]

## LONGTERM PERSPECTIVES

After recommissioning of the UNILAC with the highest heavy ion beam intensities, the replacement of the existing Alvarez-DTL is proposed, leading to a sustain operation for the next decades. Additionally a dedicated new cw-Linac could deliver high duty factor beams for the SHIP experiment with energies up to 7.5 MeV/u. A first conceptual layout is shown in Fig. 11. Behind the HSI a new 4 MV/m 108 MHz IH-LINAC (50 m total length) provides a high intensity 5 MeV/u $U^{4+}$-beam. The existing gas stripper section is reused to perform a beam intensity of 24 emA in charge state 42+. The present LINAC-tunnel may house a high efficient 325 MHz-CH-LINAC (35 m), able to boost the beam energy up to 30 MeV/u. In the transfer line to the SIS 18 the foil stripper and the new compact charge state separator will be able to provide for charge state 82+. If the gas stripper will be replaced by a solid state stripper a beam energy of 42 MeV/u (charge state 63+) will be realized. A further upgrade option may provide a second 100 m-CH-LINAC (325 MHz) to enhance the beam energy to up to 100 MeV/u ($U^{41+}$)/150 MeV/u ($U^{63+}$), sufficient to feed the FAIR 100 Tm synchrotron directly. [13]

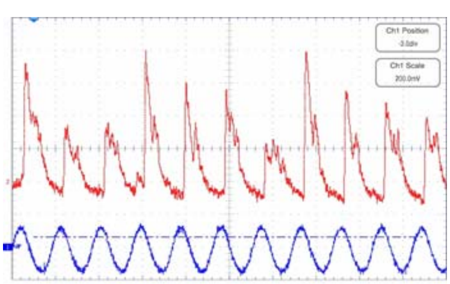

Figure 10: Bunch measurement of a 4 MeV/u $^{20}Ne^{10+}$- beam with the diamond detector (top) and 108 MHz reference signal (bottom) [12]

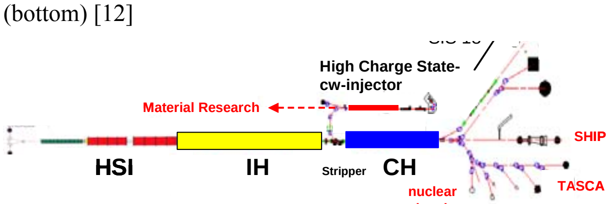


Figure 11: Conceptual layout of a multipurpose high intensity heavy ion linac at GSI [13]

## OUTLOOK

- The UNILAC-upgrade program for FAIR will be finished until 2011; the required $U^{28+}$-beam intensity of 15 emA (for SIS 18 injection) should be available especially after the complete front end upgrade.
- The replacement of the Alvarez-DTL by a new 5 MeV/u, high Bρ IH-DTL and an advanced 30 MeV/u high energy linac is advised to provide a robust and safe operation for the next decades.
- An additional linac-upgrade option sufficient to boost the beam energy up to 150 MeV/u will help to reach the desired heavy ion intensities in the SIS 100.
- An enhanced primary beam intensity at the target is required for different experimental programs with heavy ion beams up to an energy of 7.5 MeV/u. It is recommended to build a cw-heavy heavy ion-LINAC.
- A design study of a multipurpose high intensity heavy ion injector considering all future requirements will be prepared.

## REFERENCES

[1] FAIR Baseline Technical Report, Vol. 2, GSI Darmstadt, Germany, p. 335 (2006)
[2] W. Barth, Commissioning of the 1.4 MeV/u High Current Heavy Ion Linac at GSI, LINAC2000, Monterey, U.S.A., p. 1033 (2000)
[3] U. Ratzinger, The New GSI Prestripper Linac for High Current Heavy Ion Beams, LINAC96, Geneva, Switzerland, p. 288 (1996)
[4] L. Groening, et. al., A Dedicated Proton Linac for the Antiproton Physics Program of FAIR, LINAC04, Lübeck, Germany, p. 42 (2004)
[5] W. Vinzenz, et. al., High Power RF Supplies for the FAIR Injector Linacs, LINAC2008, Victoria, Canada, these proceedings (2008)
[6] A. Kolomiets, Upgrade of the HSI-RFQ, LINAC2008, Victoria, Canada, these proc. (2008)
[7] L. Dahl, et. al., Transport and Injection of heavy ion Beams with High Brilliance for the GSI-HSI, LINAC2002, Gyeongju, Korea, p. 350 (2002)
[8] W. Barth, et. al., UNILAC Status and Development, scientific report 2006
[9] L. Groening, et. al., Benchmarking of measurement and simulation of transverse rms-emittance growth, Phys. Rev. Acc. and Beams 11, 094201, (2008)
[10] W. Barth, et. al., Commissioning of the new GSI-Charge Separator System for High Current Heavy Ion Beams, LINAC2008, Victoria, Canada, these proceedings (2008)
[11] G. Clemente, Investigation of the Beam Dynamics Layout of the FAIR p-Linac, HB2008 Workshop, Nashville, U.S.A., to be published (2008)
[12] L. Dahl, et. al., HITRAP Decelerator Proj. at GSI - Status and Commissioning Report, LINAC2008, Victoria, Canada, these proceedings (2008)
[13] W. Barth, et. al., Long term Perspective for the UNILAC, LINAC2006, Knoxeville, U.S.A., (2006)

# OVERVIEW OF THE HIGH INTENSITY NEUTRINO SOURCE LINAC R&D PROGRAM AT FERMILAB *

R. C. Webber#, G. Apollinari, J. P. Carneiro, I. Gonin, B. Hanna, S. Hays, T. Khabiboulline, G. Lanfranco, R. L. Madrak, A. Moretti, T. Nicol, T. Page, E. Peoples, H. Piekarz, L. Ristori, G. Romanov, C. W. Schmidt, J. Steimel, W. Tam, I. Terechkine, R. Wagner, D. Wildman
Fermilab, Batavia, IL 60510, U.S.A.
P. N. Ostroumov, ANL, Argonne, IL 60439, U.S.A.

*Abstract*

The Fermilab High Intensity Neutrino Source (HINS) Linac R&D program is building a first-of-a-kind 60 MeV superconducting H- linac. The HINS Linac incorporates superconducting solenoids for transverse focusing, high power RF vector modulators for independent control of multiple cavities powered from a single klystron, and superconducting spoke-type accelerating cavities starting at 10 MeV. This will be the first application and demonstration of any of these technologies in a low-energy, high-intensity proton/H- linear accelerator. The HINS effort is relevant to a high intensity, superconducting H- linac that might serve the next generation of neutrino physics and muon storage ring/collider experiments. An overview of the HINS program, machine design, status, and outlook is presented.

## INTRODUCTION

Fermilab has long considered options to replace its aging 8 GeV injector complex to support future accelerator-based physics programs that will demand high intensity proton beams, including neutrino physics and muon storage ring/collider experiments. A technologically advanced, enhanced performance version of the classical Fermilab Linac/Booster system is a natural concept to pursue and a great deal of effort has been invested to develop the physics and engineering details of this option [1][2]. With recent advances in superconducting (SC) RF cavity science and technology, the possibility of a full 8 GeV linac became realistic. Plans for such a machine that would leverage the best aspects of RIA, SNS, and TESLA/ILC developments were born [3] and matured [4].

By late 2005, strong interest in pursuit of the International Linear Collider (ILC) and the U. S. high energy physics community's commitment to PEP-II B-Factory and Tevatron Collider operations left little room to support construction of an 8 GeV linac. Nevertheless, it was recognized that a machine of this caliber might be a key to maintaining a strong U.S. presence in accelerator-based physics before ILC construction. This provided the basis, in the name of neutrino physics, for R&D funding to pursue the novel technical aspects of the linac and thus the Fermilab High Intensity Neutrino Source (HINS) R&D linac.

*Operated by Fermi Research Alliance, LLC under Contract No. DE-AC02-07CH11359 with the United States Department of Energy.
# webber@fnal.gov

## HINS R&D SCOPE

The full scope of the HINS R&D program has included studies of various accelerator physics issues of importance to a facility expected to deliver high intensity, high energy beams for exploration of neutrino physics. With Fermilab steering the overall efforts, collaborating laboratories have also made important contributions. Argonne National Laboratory provides the major resources for the accelerator physics design and particle tracking simulations for both the HINS and the 8 GeV linacs. Argonne's experience in the design and development of SC spoke-type RF cavities [5] [6] serves as the foundation for Fermilab's entry into this technology and Argonne continues to provide resources for cavity processing in the construction phase. Lawrence Berkeley National Laboratory's participation in the HINS program has included studies of electron cloud issues, especially as related to the Fermilab Main Injector and Recycler Rings, development of linac Low Level RF system hardware and firmware, and design and fabrication of two buncher cavities for the HINS 2.5 MeV transport section. Brookhaven National Laboratory has reviewed an 8 GeV H- beam transport line design, provided consultation on H- injection and stripping, and built a prototype H- beam profile monitor based on laser neutralization to be used in the HINS Linac. The Oak Ridge Spallation Neutron Source has provided a copy of their Low Level RF system hardware modified for the HINS frequency.

This paper concentrates on the design, status and outlook for the HINS Linac.

## HINS R&D LINAC OBJECTIVES

The HINS Linac R&D program will address accelerator physics and technology questions for a new concept, low-energy, high intensity, long-pulse H- SC linac. In particular, the specific goals of the program are to demonstrate:

- acceleration of beam using SC spoke-type cavity structures starting at a beam energy of 10 MeV
- use of high power RF vector modulators to control multiple RF cavities driven by a single high power klystron for acceleration of a non-relativistic beam
- control of beam halo and emittance growth with an axially symmetric optics design using solenoid focusing
- performance of a fast, 325 MHz bunch-by-bunch, beam chopper at 2.5 MeV

The plan is to achieve these goals within the context of the once-proposed Fermilab 8 GeV Superconducting Linac Proton Driver front-end design [7]. The 60 MeV HINS Linac, comprising a 50 keV H- ion source, a 2.5 MeV RFQ, a medium energy beam transport section with chopper, a 10 MeV room temperature (RT) linac with SC solenoids, two cryomodules of $\beta = 0.2$ spoke cavities and one cryomodule of $\beta = 0.4$ spoke cavities, is to be constructed and operated. The longer vision is that the HINS Linac itself might eventually become the front-end of a high energy linac. The scope of the HINS linac effort includes development of relevant accelerator design tools, RF and SC RF related technologies, components, and test facilities.

The HINS R&D program seeks to achieve these goals by the end of fiscal year 2012.

## HINS LINAC

### *Parameters*

The basic operating parameters for the HINS Linac, shown in Table 1, are consistent with those for the Proton Driver Linac to deliver 2 MW of 8 GeV beam power.

Table 1: HINS 60 MeV Linac Operating Parameters

| | | |
|---|---|---|
| RF Frequency | 325 | MHz |
| Particles/ Pulse | 37.5* | E13 |
| Pulse Length | 3/1 | msec |
| Average Pulse Current | ~20 | mA |
| Pulse Rep. Rate | 2.5/10 | Hz |
| Chopping ~6% @ 89KHz and 33% @ 53MHz | 0-37.5 | % |
| Bunch Current | 32 | mA |
| Bunch Intensity | 6.1<br>98 | E8<br>pCoul |

* full un-chopped 3 msec pulse at klystron-limited 20 mA

The 325 MHz RF frequency choice is the result of a confluence of influential circumstances. It is the 4$^{th}$ sub-harmonic of the ILC frequency, consistent with the idea that this might be the front-end of a high energy linac based on ILC technology. It is near that of the 345 MHz spoke cavities developed at Argonne. Equally important, minor modifications to the J-PARC 324 MHz high power klystron design provide an economical path to a suitable RF power source.

The Fermilab Proton Driver design was staged for two operational phases: initially, 9 mA in a 3 msec pulse at rates up to 2.5 Hz to support 2 MW beam energy at 120 GeV from the Main Injector; then, with RF system upgrades, 27 mA in a 1 msec pulse to deliver 2 MW at 8 GeV. The HINS Linac can operate in either mode although the maximum current is expected to be klystron power limited at 20 mA. This current, however, can be available for either a 1 or 3 msec pulse length.

Chopping in 2.5 MeV transport line will demonstrate production of a beam time structure ultimately suitable for injection into the Main Injector ring. A 700 nsec chop at 89 kHz preserves an abort gap in the Main Injector with multi-turn injection. Chopping at 53 MHz 'pre-bunches' the beam to match the Main Injector RF frequency.

The desire to include as part of the program at least one cryomodule of $\beta = 0.4$ SC spoke cavities establishes the final energy of the HINS Linac at 60-65 MeV.

### *Design*

The accelerator physics design philosophy of the HINS Linac, described in depth in [8], is naturally tightly coupled to the concepts and technologies the machine is intended to prove. It is punctuated by multiple independent RT accelerating cavities, SC solenoids for axially symmetric focusing, and a transition to SC spoke-type accelerating cavities at 10 MeV. Analysis of the transition energy question indicated an optimum at 10 MeV, where the energy gains per cavity can be equal in the RT and the SC sections and the beam energy is sufficiently high to allow the short drift space necessary to physically accommodate the warm–cold transition.

A 50 keV ion source provides beam to a 2.5 MeV four-vane RFQ with radial matching sections at the input and output ends that form the axially-symmetric beam. The RFQ is followed by a Medium Energy Beam Transport (MEBT) section that provides space for the beam chopper [9] while maintaining desired transverse and longitudinal beam characteristics with two RF buncher cavities and three SC solenoid magnets. The subsequent accelerating section up to 10 MeV comprises 16 RT crossbar H-type (RTCH) cavities [10] and 16 SC solenoid magnets [11]. The first four RTCH cavities are made with three spokes; the remaining 12 have four spokes. As a matter of economics, a subsequent design modification reduced the number of unique RT cavity designs required; nine unique designs fill the complement of 16 RT cavities. The solenoids, even in the RT section of the machine, will be superconducting. Field strengths of six Tesla are necessary to produce the short focal lengths required by the beam optics and for matching into the SC cavity section.

From 10 to 30 MeV, eighteen SC single-spoke cavities of a common $\beta = 0.2$ design are employed [12]. They are foreseen to be divided between two cryomodules. The cavities alternate with eighteen SC solenoids. The final 30 MeV is achieved with a single cryomodule of six solenoids and eleven SC spoke cavities of $\beta = 0.4$ design.

Extensive particle tracking simulations of the HINS and Proton Driver Linacs have been conducted using both TRACK and ASTRA codes [13] [14] [15]. This effort has proven extremely beneficial not only for the machine design, but also for the codes themselves. They have been rigorously benchmarked against each other and improvements in both features and performance have been implemented in each code.

The HINS RF power distribution and control system design is particularly demanding in light of the goal to employ a single high-power klystron to drive multiple cavities accelerating a non-relativistic beam. The physics design calls for each cavity to operate at an individual

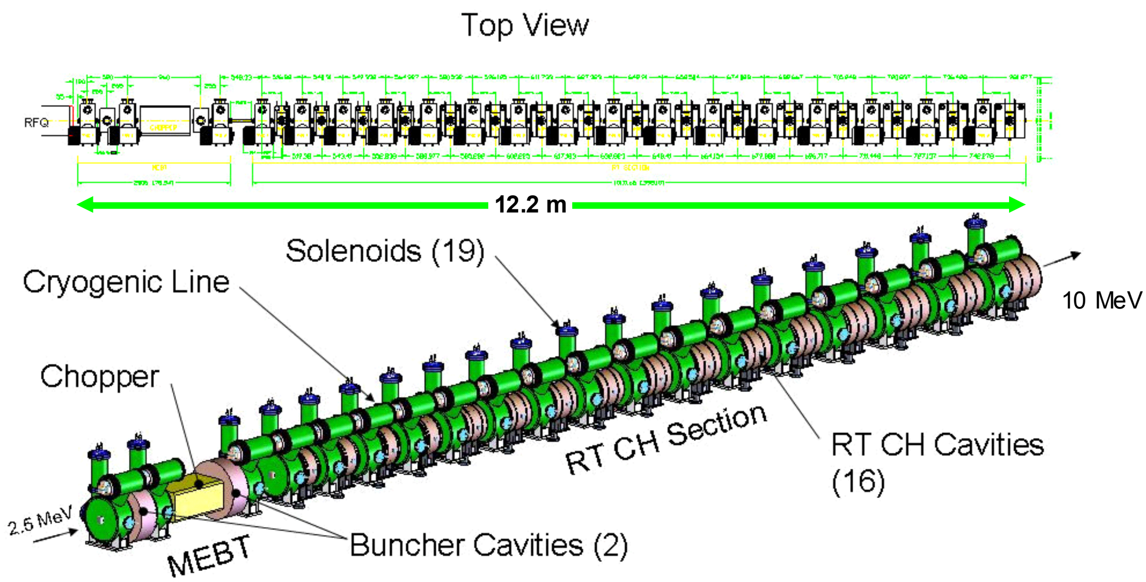


Figure 1. Layout of the first 10 MeV of the HINS linac.

gradient and synchronous phase and thus each experiences different beam loading. To meet tight amplitude and phase tolerances under these dynamic conditions, each cavity requires an individual amplitude and phase control element operating at the full power level of the cavity. This function is served by high power RF vector modulators [16]. Performance simulations of the vector modulator control under realistic RF and beam conditions are on-going. Further complicating the situation, the original HINS concept includes combining both RT and SC cavities on a single klystron. Adding a second klystron to the same modulator to separate the RT from the SC cavities remains a fall-back position.

### *Layout*

The layout of the first 10 MeV of the HINS Linac, including the MEBT and RT section is shown in Figure 1. Conceptual drawings of the SC spoke cavity cryomodules are in Figure 2. The 60 MeV HINS linac, approximately 42 meters in length, followed by a diagnostic beam line with a spectrometer and beam absorber is being assembled in the Fermilab Meson Detector Building. In addition to the linac itself, the Meson HINS facility includes the modulator and klystron RF power system, a

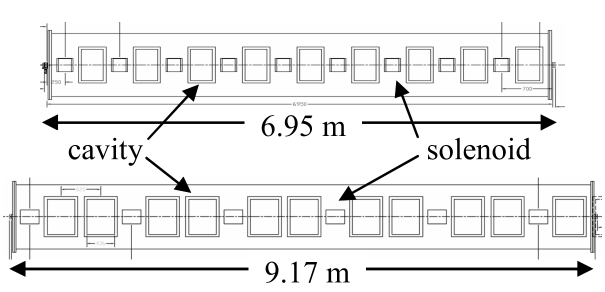


Figure 2. β=0.2 (top) and β=0.4 (bottom) SC spoke cavity cryomodule layouts.

shielded cave supporting both RT cavity testing and a cryostat for dressed SC spoke cavity testing, and an RF shielded high power RF component test area.

### *Status*

The HINS RF power system with one 325 MHz Toshiba E3740A(Fermi) 2.5 MW klystron has been operational since April 2007 to serve vector modulator development and testing of RT cavities.

A 50 keV proton ion source is commissioned and waiting to serve the RFQ. The program will begin beam operations with protons while development of a suitable H- source is completed. H- is expected to be available in mid-2009.

The HINS RFQ [17] [18] [19], pictured in Figure 3, has been manufactured by ACCSYS Technologies, Inc. It is now undergoing final inspections at Fermilab prior to high power RF conditioning that is expected to commence in October 2008.

The two MEBT buncher cavities are being machined at LBL and are expected to be finished in early 2009.

The RTCH cavities are in fabrication. Four are

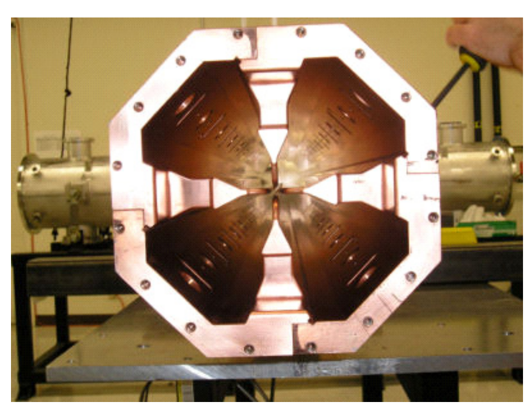

Figure 3. HINS RFQ made by ACCSYS.

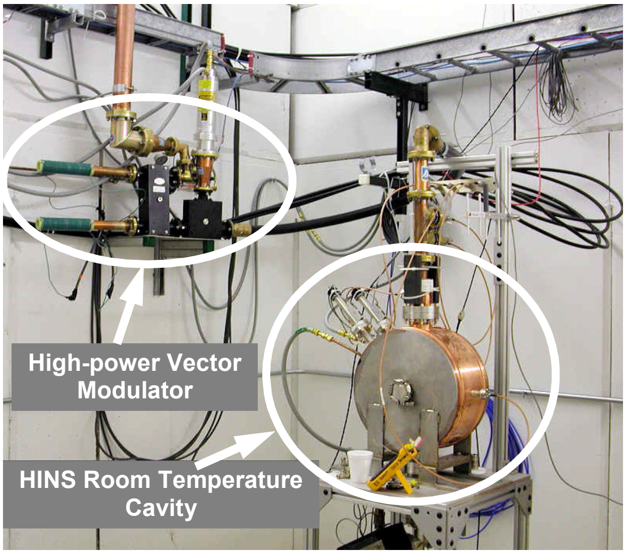


Figure 4. RT cavity coupled with prototype vector modulator on test stand.

completed; three have been successfully RF conditioned to full power [20], the fourth awaits its turn on the test stand. The remaining twelve RTCH cavities are expected to be delivered by this year's end. Figure 4 shows the first RTCH cavity coupled with a prototype vector modulator on the cavity test stand.

Prototype vector modulators for the RTCH cavities have been successfully tested [21] to 70 kW. Phase control rates in excess of 4 degrees per microsecond and an amplitude control range of 13 db have been demonstrated. One very high power vector modulator, for the RFQ, has operated successfully up to >500 kW. Problems have been experienced in obtaining the required high power performance for a companion circulator.

A prototype SC solenoid for the RT section has been successfully tested and production units are now being fabricated [22].

Two $\beta = 0.2$ SC spoke cavities have been fabricated; only one has yet been processed. The processed, bare cavity, pictured in Figure 5, has undergone several test cycles in the Fermilab SC cavity Vertical Test Stand. Results have been very encouraging despite some problems. Figure 6 shows Q vs. gradient performance for three test dates. The two curves starting at Q≈1E10 are for 2°K operation; the other two curves are for 4.4°K. Electron multipacting [23] in the cavity has been observed and overcome at various field levels (see discontinuities in Q curves). The Q slope at 2°K is steeper than expected. Obtaining reproducible results has been complicated by difficulty maintaining acceptable cavity vacuum and, in the latest test, a helium leak into the cavity that was traced to a bad RF antenna feedthrough. Nevertheless, the cavity has achieved an impressive accelerating gradient of 18 MV/m at the HINS operating temperature of 4.4°K. It has performed marginally below the target Q of 5E8 at 10 MV/m. Test results are described in detail in [24]. Further tests are planned.

Figure 5. First SC Spoke Cavity prepared for vertical test.

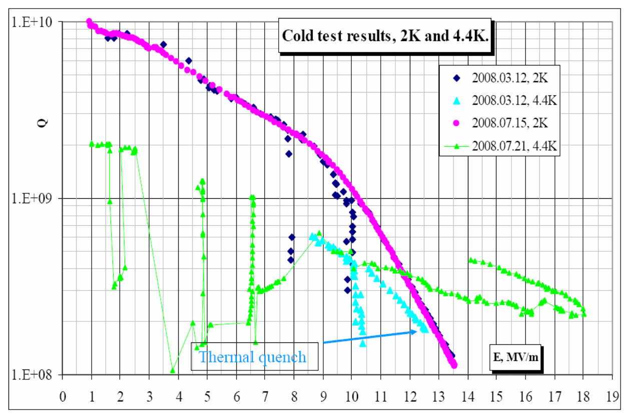


Figure 6. First SC Spoke Cavity Q vs. Gradient results.

## HINS PROGRAM OUTLOOK

Following RF conditioning, the RFQ will be coupled to the proton ion source. The first 2.5 MeV beam is expected by December this year. The linac shielding cave will then be constructed, followed by staged commissioning of the MEBT and RT sections. Full 10 MeV operations are not expected before late 2009. The first beam test of SC spoke cavities is anticipated about one year later using one cryomodule of the $\beta = 0.2$ cavities.

In late 2007, the Fermilab Project X [25] [26] proposal, including an 8 GeV H- linac as a centerpiece, was announced. This followed alignment of important H- linac beam and operating parameters with those of the ILC and a realization that ILC construction is unlikely for a decade. Subsequently, in May 2008, the U.S. Particle Physics Project Prioritization Panel (P5) stated in its ten year strategic plan report [27] "The panel recommends proceeding now with an R&D program to design a multi-megawatt proton source at Fermilab and a neutrino beamline to DUSEL …" Project X is well aligned with this recommendation and Fermilab is now leading a national effort to obtain Department of Energy critical decision approval to carry out the conceptual design.

This will impact the identity of the HINS R&D program. At some stage, it will likely be absorbed into the Project X organizational structure. An evaluation of the HINS technologies, based on performance, cost and risk, will determine how and if these technologies might be incorporated into the eventual Project X Linac design. The current HINS program can positively influence this by delivering on its goals at the earliest possible date.

## SUMMARY

The HINS program has ambitious goals to demonstrate the feasibility and performance of technologies never before applied to a low-energy, high intensity proton or H- linac. The program is actively designing, building, and testing accelerator components to be integrated into a novel 60 MeV superconducting H- linac. It is hoped that this might serve as the front-end to an 8 GeV linac that is a key element of the Project X proposal.

## ACKNOWLEDGEMENTS

The authors wish to acknowledge the persistent efforts of all the individuals, too numerous to name, from Fermilab and collaborating institutions who drive the progress of the HINS program and have contributed to the preparation of this paper.

## REFERENCES

[1] W. Chou et al., (editors), “The Proton Driver Design Study,” Fermilab-TM-2136, Dec 2000.
[2] G. W. Foster et al., (editors), “Proton Driver Study. II. (Part 1),” Fermilab TM-2169, May 2002.
[3] G. W. Foster and J. A. MacLachlan, “A Multi-Mission 8 Gev Injector Linac as a Fermilab Booster Replacement” LINAC02, Gyeongju, Korea.
[4] G. W. Foster et al., “An 8 GeV Superconducting Linac Proton Driver”, Draft Technical Design Study_v56, http://protondriver.fnal.gov.
[5] K.W. Shepard et al, “Prototype Superconducting Triple-Spoke Cavity, PAC2005, Knoxville, 2005.
[6] K.W. Shepard et al, “Superconducting Triple-Spoke Cavity for β=0.5 Ions”, PAC2005, Knoxville, 2005.
[7] P. N. Ostroumov et al., “Design and Development of an 8-Gev Superconducting H– Linac”, HB2006, Tsukuba, Japan, 29 May - 2 Jun 2006.
[8] P.N. Ostroumov, “Physics design of the 8 GeV H-minus Linac, 2006 New J. Phys. 8 281.
[9] R. L. Madrak et al., “A Fast Chopper for the Fermilab High Intensity Neutrino Source (HINS)”, LINAC08, Victoria, BC, Canada, September 2008.
[10] L. Ristori et al., “Design of Normal Conducting 325 MHz Crossbar H-type Resonators at Fermilab”, LINAC06, Knoxville, Tennessee, August 2006.
[11] I. Terechkine et al., “Focusing Solenoid for the Front End of a Linear RF Accelerator”, PAC07, Albuquerque, New Mexico, June 2007.
[12] G. Apollinari et al, “Design of 325MHz Single and Triple Spoke Resonators at FNAL”, LINAC06, Knoxville, Tennessee, August 2006
[13] J. P. Carneiro et al., “Start-to-end Simulations for the Proposed Fermilab High Intensity Proton Source”, PAC07, Albuquerque, New Mexico, June 2007.
[14] P. N. Ostroumov and J.P. Carneiro, “Physics Design of Front Ends for Superconducting Ion Linacs”, HB2008, Nashville, Tennessee, August 2008.
[15] P. N. Ostroumov et al., “Beam Dynamics Studies of the 8 GeV Linac at FNAL”, LINAC08, Victoria, BC, Canada, September 2008.
[16] R. Madrak et al., “New Materials and Designs for High-Power, Fast Phase Shifters”, LINAC06, Knoxville, Tennessee, August 2006.
[17] P. N. Ostroumov et al, “Application of a New Procedure for Design of 325 MHz RFQ”, J. Instrum., JINST 1 P04002.
[18] G. Romanov and A. Lunin, “Complete RF Design of the HINS RFQ with CST MWS and HFSS”, LINAC08, Victoria, BC, Canada, September 2008.
[19] G. Romanov et al., “The Fabrication and Initial Testing of the HINS RFQ”, LINAC08, Victoria, BC, Canada, September 2008.
[20] W. Tam et al., “High Power Test of HINS RT CH Cavities”, LINAC08, Victoria, BC, Canada, September 2008.
[21] R. L. Madrak and D. Wildman, “High Power 325 MHz Vector Modulators for the Fermilab High Intensity Neutrino Source (HINS)”, LINAC08, Victoria, BC, Canada, September 2008.
[22] I. Terechkine et al., “Focusing Solenoids for the HINS Linac Front End”, LINAC08, Victoria, BC, Canada, September 2008.
[23] G. Romanov, “Simulation of Multipacting in HINS Accelerating Structures with CST Particle Studio”, LINAC08, Victoria, BC, Canada, September 2008.
[24] I. Gonin et al., “High Gradient Tests of the HINS SSR1 Single Spoke Resonator”, HB2008, Nashville, Tennessee, August 2008.
[25] S. Nagaitsev, “Fermilab's Project X”, LINAC08, Victoria, BC, Canada, September 2008.
[26] http://projectx.fnal.gov/
[27] Report of the Particle Physics Project Prioritization Panel, “US Particle Physics: Scientific Opportunities: A Strategic Plan for the Next Ten Years”. May 2008. http://www.er.doe.gov/hep/files/pdfs/P5_Report%2006022008.pdf.

# OVERVIEW OF RECENT RFQ PROJECTS *

A. Schempp
Institut für Angewandte Physik, J. W. Goethe-Universität, D-60486 Frankfurt am Main, Germany

RFQs are the new standard injector for a number of projects. The development of the 4-Rod RFQ structure has led to interesting developments, which will be discussed with actual projects as examples. Recent work on the FAIR - p linac, the GSI - high charge state injector upgrade, the GSI - HITRAP, the new BNL - EBIS-RFQ, and the RFQ of the MSU-CW Reaccelerator will be presented and the status of these projects will be discussed.

## INTRODUCTION

Accelerators have been developed as tools for atomic, nuclear and particle physics. From these technologies numerous applied research did develop. The "production" of secondary particles as purpose of a facility was another big step in accelerator technology, because the production rates can be increased by optimizing the beam energy and target arrangement and of course by increasing the beam current to the target.

In case of heavy ion beams the duty factor of the machines had to be large because of the limits of sources for (multiple charged) heavy ions. For protons and deuterons the beam currents from ion sources could be pushed up to the 100 mA region, so the duty factors of the accelerators could be modes tlike for spallation sources with beam powers of up to 1MW and the synchrotron injectors, drivers for neutron production or for sources of radioactive beams with beams of some kW.

Accelerators for radioactive beams have low power beams but require high duty factors for compensation of the low production rates.

The Frankfurt IAP was involved in the planning phase for GSI and the cooperation with GSI in the 70s by post accelerator structure applications (helix, spiral) could be kept up until today with respect to the FAIR project.

A big step were the new ideas about RFQs in the late 70s for low energy acceleration [1,2].

Application for heavy ions and lower frequency and the need for practical solutions led to the development of the 4-rod RFQ structure. First prototyps and beam tests were rather simple, but the big point was the chance to develop and built structures for other labs, at first GSI, DESY and MSI, which pushed the development and besides beam dynamics, the importance of issues like rf- and mechanical technologies and reliability.

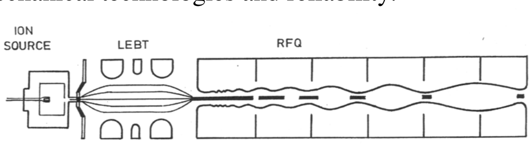


Figure 1: Scheme of a RFQ injector.

*supported by the BMBF

## RFQ DESIGN

The design of RFQs is at first the choice of basic parameters like frequency, input output energy, which are mostly determined by the application or the ion source or the following bigger accelerator system.

Next steps in the beam dynamics design is the choice of electrode voltage U, beam current, input and output energy and emittances ε and the cell parameters along the RFQ: cell length $L_i$, aperture $a_i$, modulation $m_i$. The result is an RFQ with certain total length L and power consumption N which adiabatically bunches and focuses the dc beam from the ion source with small Δε and high transmission [3].

RFQ design is sometimes treated as being completed, when the beam dynamics design is finished. Especially for high power beams it is crucial to have a balanced design which takes into account the special rf-problems as well as the engineering to ensure tolerances, to handle the rf-losses, the beam with losses, the diagnostics and also maintenance possibilities and control.

While for smaller neutron generators RFQ aspects can dominate the choice e.g. of the frequency and length and rf-power consumption to simplify alignment and tuning, for bigger projects the optimization of the total accelerator, the availability of power sources and naturally costs will set some design input parameters and e.g. will increase the frequency to lower the charge per bunch, to avoid funneling and ease emittance growth and matching problems or reduce crucial beam losses.

Reducing losses and emittance growth and high duty factors or beam powers require even new solutions and prototype developments not showing up in beam dynamics simulation which sometimes are described as “physics design”.

To generate the quadrupole fields we use the 4 rod RFQ structure, which we have developed in Frankfurt It can be described as a chain of interlaced λ/2-resonators in π–0-mode. The electrodes can be typical rods, or small vane shaped electrodes. with unchanged rf-properties. The radial dimensions of the 4-rod RFQ are appr. half as for a 4-Vane $TE_{210}$-structure at the same frequency. Beam dynamics and experimental results for emittances and transmission are the same as for 4-Vane RFQs.

While the power consumption is also roughly the same, there are some advantages because the 4-rod structure cannot show dipoles and longitudinal coupling is stronger

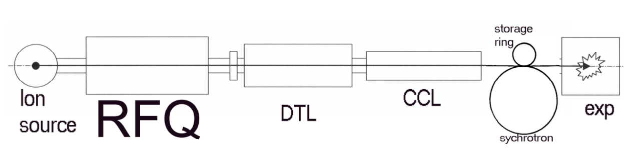


Figure 2: Accelerator system.

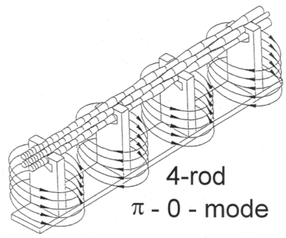


Figure 3: Scheme of a 4-Rod-RFQ resonator insert.

The rf-fields are confined in the resonant insert. A change of tank dimensions results in very little change of the frequency, so ports in the tank and e.g. the top lid along the tank do not change fields and coupling in the structure. So long RFQs can be aligned, tuned and inspected through such a top lid and tank contacts are not critical because less than 10% of the rf-power is dissipated in the tank , most of it close to the insert.

## RFQ PROJECTS

One of the early RFQ- projects was the HLI injector RFQ for GSI. This HLI (108.5 MHz, 2.5keV/u-1.4 MeV/u, U28+) was the first ECR-RFQ-IH combination, which was built and operated. The duty factor was 25%, so also from the duty factor point of view it was a very advanced. It served as example for the Lead Injector of CERN and many other heavy ion machines. Also the injector for the HIT medical synchrotron is a scaled version of the HLI.

The HLI is operating since 1991 routinely with various ions and charge states. Not optimal were the injection with a rather step angle because of the low injection energy.

A new ECR ion source with higher frequency will give higher charge states and beam currents. The extraction energy can be higher and with that the matching problem can be reduced. The maximum cw-power of 60kW can be applied and an optimized cw injector for “superheavy production” can be built [4]. This HLIn is now under construction. Its design is close to the old one, cooling and mechanics are improved using the operational experience.

New beam dynamics design results in a much shorter cavity. The beam should have very small emittance and nearly no emittance growth. The RFQ should be operational in 2009.

### □□□□□□□

In a collaboration with the GSI in Darmstadt an RFQ-Drifttube-Combination for the Heidelberg cancer therapy center HICAT has been designed, built and successfully tested with a H-beam at the IAP Frankfurt. The integration and combination of both an RFQ and a rebunching drifttube unit inside a common cavity forming one single resonant RF-structure has been realized for the first time with this machine.

The 217 MHz RFQ [5] is a part of the HICAT accelerator complex, which consists of a RFQ-IH-linac for pre-acceleration of $^{12}C^{4+}$ up to 7 MeV/u.

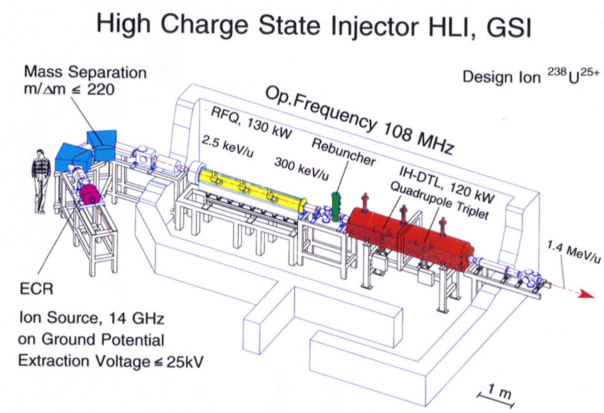


Figure 4: The HLI-injector of GSI.

Table 1: HLI-RFQ Parameters

| PARAMETER | HLI | HLI-n |
|---|---|---|
| Frequency [MHz] | 108.48 | 108.48 |
| A/q | 8.5 | 6 |
| Input Energy [MeV/u] | 0.0025 | 0.004 |
| Output Energy [MeV/u] | 0.3 | 0.3 |
| Inter-ElectrodeVoltage[kV] | 85 | 55 |
| εin norm., rms [π mm mrad] | 0.07 | 0.1 |
| εoutx. n., rms [π mm-mrad] | 0.12 | 0.1009 |
| Electrode Length [cm] | 305 | 199.5 |
| Duty factor [%] | 25 | 100 |

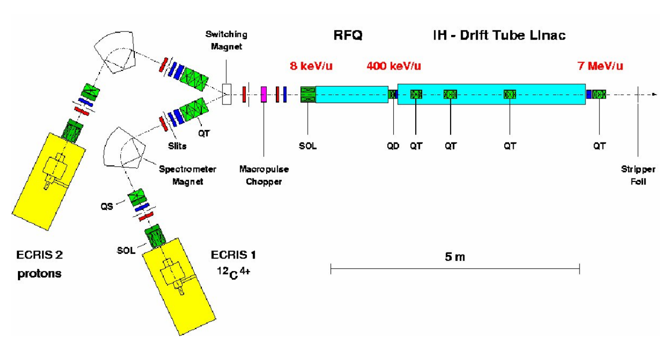


Figure 5: Layout of the HICAT injector.

Table 2: Med-RFQ Parameters

| | |
|---|---|
| Operating frequency | 216.816 MHz |
| Ion species | $^{12}C^{4+}$, protons |
| Length of tank | 1.40 m |
| # of RFQ cells | 219 |
| Input/output energy | 8 / 403 keV/u |
| Input emittance | $\varepsilon_{x,y}$=150 π mm mrad |
| Electrode voltage | 70 kV |
| Power consumption | 165 kW |

In the following synchrotron ring-structure completely stripped $^{12}C^{6+}$ ions are accelerated to final energies between 50 and 430 MeV/u. This linac has been set up and tested at Heidelberg. Also the Synchrotron and the huge Gantry are operational. First patient treatment is planned for Dec.08.

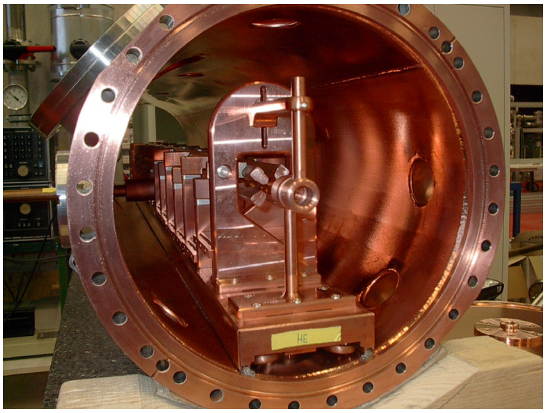

Figure 6: View of the HIT-RFQ with rebunching section.

Three new Med-RFQs have been built by industry since. We have supported by aligning and tuning these twins of the Heidelberg HIT-RFQ, which can be treated as prototype for a chain to clones come?

### □□□□□□-RFQ

The HITRAP-linac at GSI will decelerate ions from 5 MeV/u to 6 keV/u for experiments with the large GSI Penning trap. The ions, provided by the GSI accelerator facility, will be decelerated at first in the existing experimental storage ring (ESR) down to an energy of 5 MeV/u and then injected into a new IH decelerator and decelerated to 500 keV/u. The following 4-Rod RFQ will decelerate the ion beam from 500 keV/u to 6 keV/u. The properties of the RFQ decelerator and the status of the project will be discussed.

The design of the HITRAP 4-rod-RFQ is closely related to the design of the 108 MHz structure of the GSI-HLIn LINAC. The low A/q allows a short structure of 127 cells that is only 1.9 m long. A maximum rod voltage of 77.5 kV is required. The 45° phase spread of the ion bunches extracted from the IH-structure needs to be matched to the RFQ acceptance of 20°. Thus, in the matching section between IH-structure and RFQ two gap-1o8 MHz spiral Rebunchers will be installed [6,7].

### □□□□□□□□□□□□□□

To provide sufficient primary proton intensities a new proton linac is planned for the antiproton physics program for future Facility for Antiproton and Ion Research (FAIR) at GSI-Darmstadt. The proposed linac consists of an ECR proton source, a RFQ, and a normal conducting CH-structure. It will have a final energy of 70MeV and deliver an output current of up to Ip= 90 mA. The operation frequency will be 325 MHz. The RFQ will accept a beam at 95 keV and accelerate to 3 MeV for injection into the IH-type DTL.

### □□□□□□□□□□□□□□□□□□

The new EBIS preinjector at BNL will accelerate ions from the EBIS source with specific mass to charge ratio of up to 6.25, from 17 keV/u to 2000 keV/u to inject into the Booster synchrotron, expanding experimental possibilities for RHIC and NASA experiments [8].

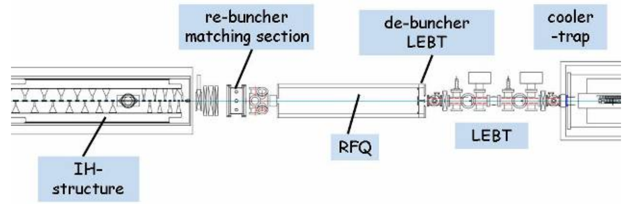


Figure 7: The RFQ section of the HITRAP decelerator.

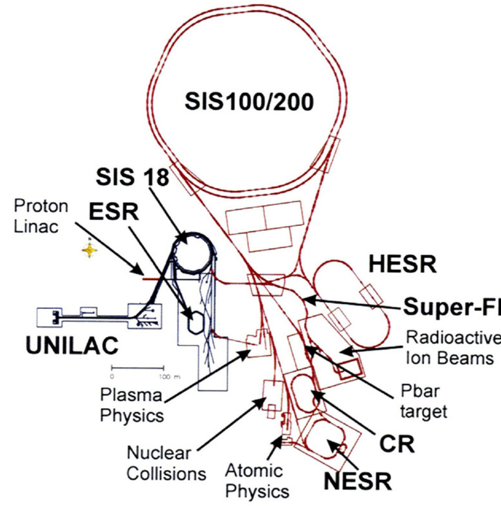


Figure 8: The FAIR project at GSI.

Table 3: Basic Proton-RFQ Parameters

| | |
|---|---|
| Frequency | 325 MHz |
| Input energy | 95 keV |
| Output energy | 3.0 MeV |
| Beam current | 70/90 mA |
| output emittance rms norm. | 0.4 $\pi$ mm mrad |
| energy spread rms | 150 deg keV |
| Electrode voltage | 80 kV |
| RFQ length | 3.22 m |

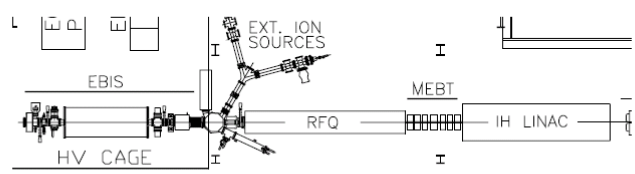


Figure 9: Layout of the EBIS Linac at BNL.

Table 4: BNL-RFQ Beam Dynamics Design Parameters

| | |
|---|---|
| Frequency | 100.625 MHz |
| Input energy | 17 keV/u |
| Output energy | 0.3 MeV/u |
| Mass to charge ratio | 6.25 |
| Beam current | 10 mA |
| Outp trans. emitt rms norm. 90% | < 0.38 $\pi$ mm mrad |
| Output long. emittance 90% | < 220 deg keV/u |
| Transmission | 98% |
| Electrode voltage | 70 kV |
| RFQ length | 3.1 m |

The RFQ has been designed and manufactured. The resonant insert has been aligned with a precision of ±0.03 mm and the flatness is better than ±2%. Tuners and rf-coupler have been built, tested and matched. Vacuum tests have been done and the EBIS-RFQ has been prepared for transport to BNL in the week before LINAC 08 [9].

### [illegible]

The Frankfurt Neutron Source at the Stern-Gerlach-Zentrum (FRANZ) will comprise a short 175 MHz linac sequence consisting of a 1.75 m long 700 keV 4-rod type RFQ [10] followed by a 60 cm IH-DTL for proton acceleration up to 2 MeV to create a nsec pulsed high current beam on a n-target for n production.

The beam current is 200 mA at pulsed and up to 30 mA at c.w. operation. The aim is to have a very compact device driven by only one rf-amplifier to reduce costs and required installation space. A strong coupling between the RFQ and the IH resonators will be realized by a direct connection between the last stems of each resonator through the common end wall. The accelerators could also be driven separately by just removing these brackets. The distance between the end of the RFQ electrodes and the midplane of the first DTL gap is only 5 cm leaving some place for a x-y-steerer. Preliminary rf-simulations have been carried out together with accompanying measurements on rf-models.

The needed high average power levels require improved cooling of the RFQ-resonant insert. A short prototype has been built to develop a structure for such high thermal loads.

### [illegible]

A complete Radio Frequency Quadrupole system presently is designed and fabricated for NSCL [12].. The 4-Rod RFQ structure matches the parameters given by the NSCL beam dynamics layout of the RFQ-electrodes, the 80.5 MHz structure is 3.35 m long and should need less than 150 kW rf-power. The rf-design has been made with the MWS-code and agrees with extrapolations from earlier experiments with 100 and 108 MHz RFQs.

The mechanical design was aiming at a solid structure, similar to the ones we had built recently. Changes had to be made to modify the structure following the request of a minimum number of brazings, water to vacuum and a less complex structure and the question of raw material availability.

Our new layout was using a rectangular cavity, where stems were inserted and sealed from the outside. We modified the cooling of the elctrodes with a cooling tube outside the stem. By this we had only one braze (the rectangular tube-electrode connection and a plug at this end of the electrode). The cooling tube than runs along the stem outside and is sealed at the base plate outside.
Another new feature is the use of a thick wall Al-tank with welded stainless steel flanges, which avoids copper plating and cooling problems at high duty factors.

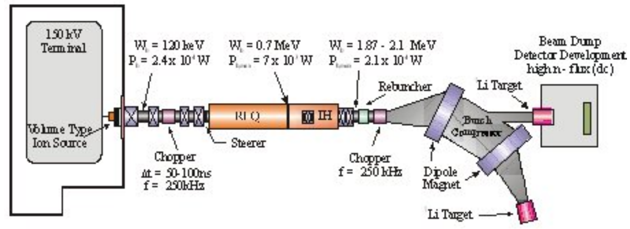


Figure 10: Layout of the FRANZ accelerator

Table 4: FRANZ-RFQ Parameters

| | |
|---|---|
| Frequency | 175 MHz |
| Input energy | 120 keV |
| Output energy | 0.7 MeV |
| Beam current | 150/200 mA |
| output emittance rms norm. | 0.1 $\pi$ mm mrad |
| Long. Emittance | 20keV*30degr. |
| Electrode voltage | 75 kV |
| RFQ length | 1.75 m |
| cell number | 95 |

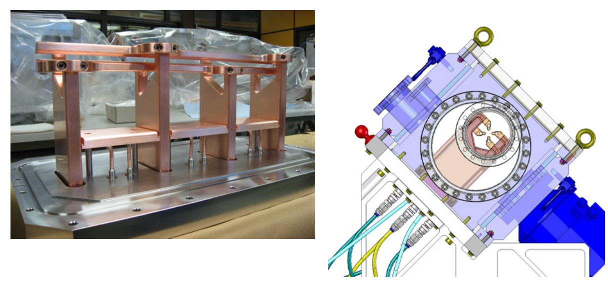

Figure 11: Prototype high power RFQ insert and tank.

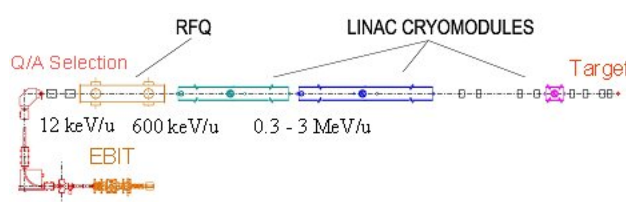


Figure 12: Layout of the MSU reaccelerator.

Table 5: MSU-RFQ Parameters

| | |
|---|---|
| Frequency | 80 MHz |
| Input energy | 12 keV/u |
| Output energy | 0.6 MeV/u |
| Charge to mass ratio | > 0.2 |
| output emittance rms norm. | 0.1 $\pi$ mm mrad |
| Long. Emittance | 30keV/u*degr. |
| Electrode voltage | 87 kV |
| RFQ length | 3.35 m |
| cell number | 93 |

By plugging in the electrode support stems from the outside, all cooling drills are without brazes of the stem and the cooling can be plugged on via Festo/Rectus standard connectors.

Funneling is a method to increase beam currents in several stages. The maximum beam current of a linac is limited by the beam transport capability at the low energy end of the linac: For a given ion source current and emittance the linac current limit is proportional to $\beta =$ [illegible] for electric and to $\beta^3$ for magnetic focusing channels and ideal emittance conservation. The funneling scheme is making use of the higher current limits at higher beam energies.

The Frankfurt Funneling Experiment is a prototype of such a stage. The experimental setup consists of two ion sources with electrostatic lens systems, a Two-Beam RFQ accelerator, a funneling deflector and a beam diagnostic system. The two beams are bunched and accelerated in a Two-Beam RFQ and the last parts of the RFQ electrodes achieve a 3d focus at the crossing point of the two beam axis. A funneling deflector combines the bunches to a common beam axis.

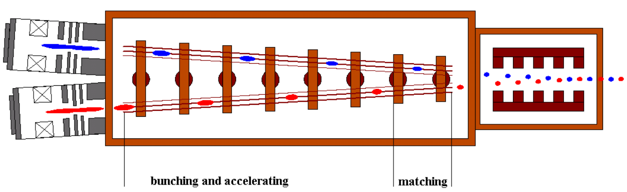


Figure 13: Scheme of the experimental setup.

The two-beam RFQ accelerator consists of two sets of quadrupole electrodes arranged with an angle of 75 mrad in one common resonant structure (fig. 2) [1]. The beams are bunched and accelerated with a phase shift of 180°. The quadrupole sets with a total length of approx. 2 meter are divided into two sections: The first section bunches and accelerates the beam to a final energy of 160 keV. The matching section focuses the beam longitudinally and radially to the beam crossing point at the deflector with low acceleration to 179keV.

The experiments have shown, that the system does funnelling, but beam emittances have to be better to reduce losses. At present the ion sources are improved and the section in front of the deflector is redesigned to give a better focusing at the funnelling section [12].

Other projects are the Saraf-RFQ for the SOREQ sc-linac for 40 MeV p,d beams, were we designed, tuned an CW-RFQ in collaboration with NTG [13]. This cw-RFQ at 175MHz has accelerated protons to 1.5 MeV and now is conditioned for 250 kW cw-operation.

The MAFF-RFQ, an IH-RFQ designed and built by the Munich group for the acceleration of radioactive beams with A/q=6.3 at 100MHz from 3keV/u to 300keV/u, has been set up and beam tests are prepared [14].

For RIKEN we have built a 2 m long RFQ at 100 MHz, which was successfully accelerating a $C^{6+}$ beam of more than 50mA, proving the direct injection scheme with a Laser ion source [15].

## CONCLUSIONS

These projects show the wide range of applications we worked and work on. Besides these projects we have done preliminary designs for advanced medical injectors and compact heavy ion machines and n-generators as well as for high power accelerator projects like IFMIF.

The range of parameters which is characteristic for IFMIF and similar ADS-projects in Asia and Europe comparable with the LANL LEDA project, is requiring power loads and structure length, as basic critical parameters, and efforts in engineering which we cannot provide. Our limited resources force us to work on compact machines.

## ACKNOWLEDGEMENTS

I want to thank my colleagues and our RFQ-group for help and good teamwork, which is necessary for successful projects and thesises. I have to thank the partners in our collaborations for entrusting us with such work, for patience and understanding which sometimes is necessary, because of the special style of University people, old and young ones, and for the Germanenglish.

## REFERENCES

[1] I.M. Kapchinskij, V. Tepliakov, Prib. Tekh. Eksp. 119, No. 219 (1970).
[2] K. Crandall, R.H. Stokes, T.P. Wangler, LINAC79, BNL51134 (1979) 205.
[3] A. Schempp, “Design of Compact RFQs”, LINAC96, p.53.
[4] W. Barth, this conference.
[5] A. Bechtold et al, “Test of a RFQ-Drift tube combination” Linac06, p. 162.
[6] W. Barth et al. this conference.
[7] B. Hofmann et al, Deceleration of highly charged Ions for HITRAP”, PAC07, p.1437.
[8] J. Alessi et al, this conference.
[9] M. Vossberg et al., this conference.
[10] A. Bechtold et al., this conference.
[11] Q. Zhao et al.,” Beam Simulations for the MSU-RIA Driver Linac, Linac06, p. 457.
[12] N. Müller et al., Development of new Ion Sources for Funneling, EPAC08, p. 3596.
[13] NTG, im Steinigen Graben 12, D-63561 Gelnhausen Germany.
[14] A. Bechtold et al, “The MAFF IH-RFQ Test stand at the IAP Frankfurt” EPAC06, p. 1577.
[15] M. Okamura et al.,” Review of Laser driven Sources” PAC07, p. 3761.

# A COUPLED RFQ-DRIFT TUBE COMBINATION FOR FRANZ

A. Bechtold, U. Bartz, M. Heilmann, P. Kolb, H. Liebermann, D. Mäder, O. Meusel, H. Podlech, U. Ratzinger, A. Schempp, C. Zhang, IAP, J. W. Goethe-Universität, Frankfurt, Germany, G. Clemente, GSI, Darmstadt, Germany.

*Abstract*

The Frankfurt Neutron Source at the Stern-Gerlach-Zentrum (FRANZ) [1] will comprise a short 175 MHz linac sequence consisting of a 1.75 m long 700 keV 4-rod type RFQ [2] followed by a 60 cm IH-DTL [3] for proton acceleration up to 2 MeV. The beam current is 200 mA at pulsed and up to 30 mA at c.w. operation. The aim is to have a very compact device driven by only one rf-amplifier to reduce costs and required installation space. A strong coupling between the RFQ and the IH resonators will be realized by a direct connection between the last stems of each resonator through the common end wall. The accelerators could also be driven separately by just removing the coupling. The distance between the end of the RFQ electrodes and the midplane of the first DTL gap is only 5 cm leaving some place for a x-y-steerer. Preliminary rf-simulations have been carried out together with accompanying measurements on rf-models.

## INTRODUCTION

The coupling of different rf-components is very attractive for most recent accelerator development. It leads to more compact devices using a common rf-amplifier and control system. Thus the overall size and the costs of the set up can be reduced drastically.

Many examples are planned or already in existence. For instance a coupled RFQ-drifttube combination that has been developed for medical application at the HICAT (Heavy Ion Cancer Therapy) center in Heidelberg by the IAP, where a 4-rod-RFQ and a 2 gap rebuncher sequence are merged [4]. This concept has been applied recently to other treatment facilities by industry several times [5]. Coupled CH-DTL cavities are a major achievement in the development of the FAIR Proton Injector at GSI [6, 7].

Two coupled rf-systems with same resonance frequency can be driven in 0 or in $\pi$-mode, which can lead to very interesting applications. When they are excited both at the same time, the resulting beat resonance can be used to reduce thermal load where pulsed operation is not feasible like in the case of the former LEP normal conducting accelerator at CERN, where the accelerator cavity was coupled to a low loss spherical resonator [8].

Presently investigations on a resonant coupling between RFQ an IH-DTL for FRANZ are performed. Unlike the aforementioned medicine RFQ, both parts are tuned to the same resonance frequency and are clearly separated by means of a metallic wall.

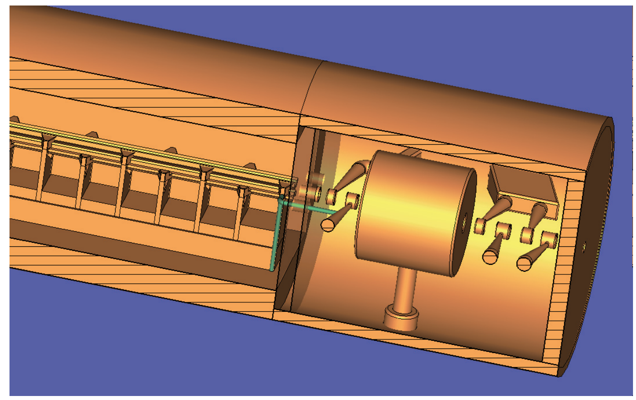

Figure 1: The coupled 4-rod-RFQ-IH-DTL structure. The coupling bridges are colored in green.

Table 1: Main Parameters

| | |
|---|---|
| Operating frequency | 175 MHz |
| Ion species | protons |
| Length of RFQ | 1.75 m |
| Length of IH-DTL | 0.6 m |
| Tank diameter IH | 510 mm |
| Height of RFQ-Stems | 145 mm |
| # of RFQ cells | 97 |
| # of matching in cells | 4 |
| # of IH-gaps | 8 |
| Input energy | 120 keV |
| Input emittance (absolute) $\varepsilon_{x,y}$ | 150 π mm mrad |
| Electrode voltage (RFQ) | 75 kV |
| Max. gap voltage of IH-DTL | 300 kV |
| Exp. Power consumption RFQ | 150 kW |
| Exp. Power consumption IH | 45 kW |
| Current | max. 200 mA |
| Output energy RFQ | 700 keV/u |
| Output energy IH-DTL | 2 MeV |
| Coupling factor $k$ | ≈0.03 |

## COUPLING

The distance between 0 and $\pi$-mode is given by $\Delta\omega = \omega_0 \cdot k$, where $\omega_0$ is the uncoupled resonance frequency and $k$ is the coupling strength. The coupling should be sufficiently strong ($k > 0.01$), to guarantee a good separation between the modes.

As a first approach two galvanic coupling bridges between IH-structure and 4-rod-RFQ were under investigation. They are connecting the last two RFQ stems to the first two DTL stems (fig. 1). Microwave Studio (MWS) [9] simulations resulted in a preliminary coupling factor of $k \approx 0.03$ depending on the exact geometry, which is not fixed in every detail yet. They have to be water cooled at c.w. operation, which could be done by a coaxial cooling system entering at the RFQ side or just by a simple tube geometry with a one way passage of the water. The cavities could also be operated separately by removing the bridges and a subsequent tuning of the RFQ. An alternative coupling over a short external power transition line could also be realized.

## TUNING CONCEPT

One of the most challenging aspects is the tuning of the coupled system during operation. Not only the resonance frequency of the whole system has to be stabilized, the amplitude relation between the cavities has to be kept constant.

The voltage ratio between two coupled resonators can be controlled by a variation of their individual resonance frequency. If the intrinsic resonance frequency of one resonating cell is tuned down, the voltage will increase here and decrease in the other resonator at 0-mode and vice versa at π-mode. This can be shown by treating local frequency detuning within a chain of coupled resonators by means of perturbation theory, which results in field contributions from other unperturbed modes [10]. In the case of the 4-rod RFQ for instance, the field distribution is tuned by means of variable tuning plates. They increase the intrinsic resonant frequency of one cell, which decreases the voltage locally at 0-mode [11].

For the coupled RFQ-DTL combination frequency and amplitude control can be performed by rf-tuning devices (plungers), as illustrated in fig. 2. Both states of the system must be monitored and controlled in separated time slots to avoid instabilities.

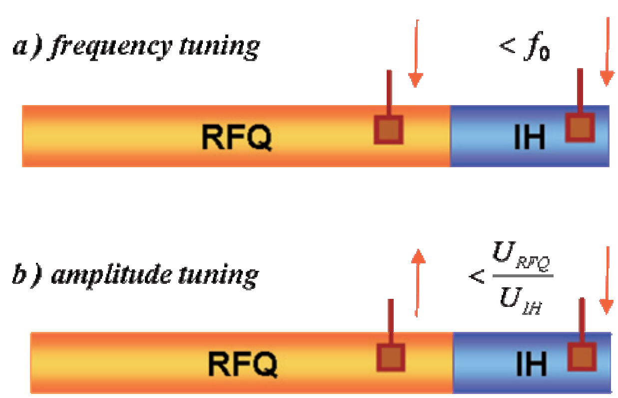


Figure 2: Tuning of frequency and amplitude during operation. Both tuners are acting inductively.

## IMPACT ON RFQ DESIGN

The coupling will have a substantial effect on the field distribution within each cavity. For instance the electrode voltage within the RFQ increases towards the end where the IH-structure is connected to, which can be balanced by tuning plates. For this purpose detailed investigations with MWS have been performed to get information on how the range of the plates respectively the height of the stems has to be extended in comparison to the uncoupled case. To get reliable results it is important to include the aperture progression along the structure implying a sufficient mesh resolution to cover these details. A detailed investigation on the precision of MWS-simulations regarding RFQ-resonators can be found in reference number [12]. Since the exact RFQ beam dynamics is not yet fixed in detail, a reasonable aperture progression with an average of $\bar{a}$ = 5.44 mm for a 1.6 m structure with electrode voltage $U_{el}$ = 85 kV is assumed for these calculations on the basis of a preliminary design proposal [13].

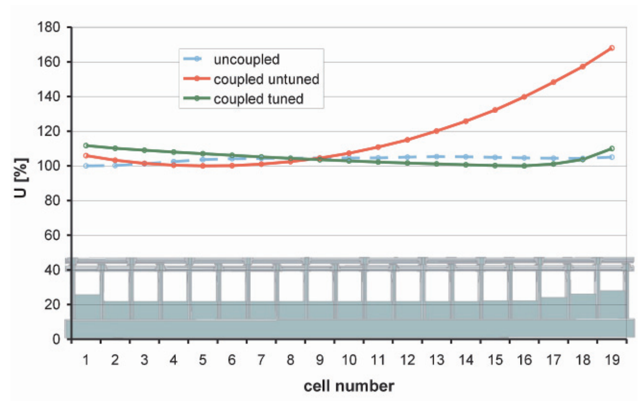


Figure 3: Simulation of the field distribution on RFQ-axis. The different height of tuning plates is indicated for the coupled and tuned case. The aperture is held constant here.

In a first step the positions of the tuning plates for a balanced field distribution were simulated for the uncoupled case assuming a 20 stem structure. Then the coupling was introduced, which gave a field distortion of +70% (fig. 3) towards the end of the RFQ, where it is connected to the IH-structure. To rebalance this disturbing effect, the tuning plates had to be moved up in that region to flatten the field distribution again. To compensate the consequent raise of the resonance frequency, the height of the stems had to be extended by $\Delta s$ = 5 mm which results now in an upper limit for the distance between beam axis and tuning plates of 145 mm, giving some safety margin of 30 mm to cover both cases. It shall be emphasized again that these investigations have been carried out under the assumption of some reasonable but not yet exactly fixed design parameters (aperture progression, number of stems, electrode voltage etc.), which will have to be included successively in future simulations.

## IH-DTL DESIGN

The IH-DTL will comprise eight accelerating gaps and one focussing triplet lens for an energy gain of 1.3 MeV within 60 cm. The structure has been optimized to get maximum field concentration on beam axis. The gap voltages are well tuned to the values given by beam dynamics simulations with LORASR (fig. 4). The field distortion of the IH-structure due to the coupling to the RFQ can be cancelled out by choosing the right position to where the bridges are connected to the IH-stem. The optimum close to the point the voltage corresponds to the voltage on top of the RFQ-stem.

The expected power consumption of the IH-DTL is 45 kW. For c.w. operation it is mandatory to do investigations on power dissipation and thermal load. Cooling of tank and drift tube stems of the IH structure are mandatory. A heating of less than $\Delta T = 20$ K is considered to be uncritical in terms of a stable operation. Thus the maximum acceptable power dissipation on the drift tube averages to $\overline{P}_{DT} = 1.5$ W/cm$^2$ if a direct water cooling of all stems is assumed. Calculations have been executed under the assumption of a linear progression of power dissipation from $P_{\mathrm{DT,max}} = 3$ W/cm$^2$ on bottom to zero on top of the Drifttube (fig.5).

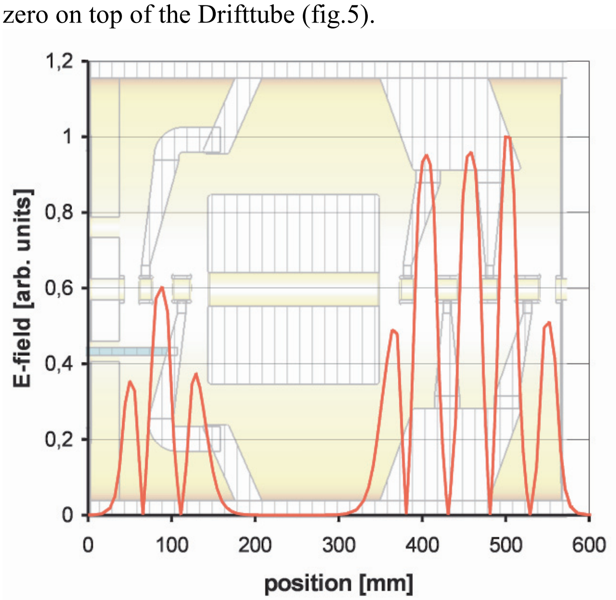


Figure4: Field distribution on beam axis along IH-DTL.

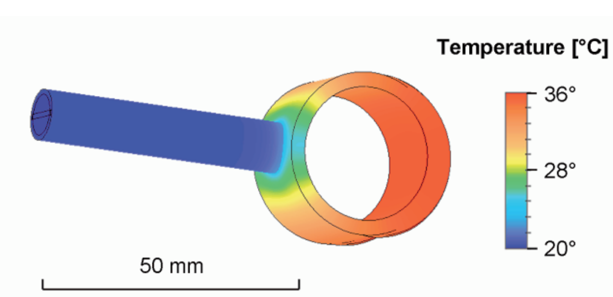


Figure 5: Simulation of thermal load on an IH-drifttube.

## CONCLUSIONS

For the FRANZ project the technique of coupled rf-cavities yields very attractive applications options. Simulations on a coupled RFQ-DTL combination are rather promising. The tuning concept has been demonstrated by means of a "prove of principle" experiment on two coupled pillboxes. It is planned to build up a more sophisticated rf-model that reflects the design of the RFQ-IH-combination more in detail. In addition further investigations on thermal load on the rf-cavities are required. Next step will be the improvement of the coupling design with respect to more detailed beam dynamics simulation data.

## ACKNOWLEDGEMENT

Many thanks to all the people involved to the FRANZ project for inspiring collaboration. We also would like to thank Dipl. Phys. J. Rehberg for making things converging and Dr. P. Fisher for his friendly support on RFQ design. Also thanks to the technicians and the staff of our workshop. This work has been supported by GSI and BMBF under contr. no. 06F134I.

## REFERENCES

[1] O. Meusel et al., "Injector Development for High Intensity Proton Beams at SGZ", these proc.
[2] A. Schempp, "An Overview of Recent RFQ Projects", these proc.
[3] U. Ratzinger, Habilitationschrift, Uni. Frankfurt, 1998.
[4] A. Bechtold, Ph.D. Thesis, Uni. Frankfurt, 2003, http://iaprfq.physik.uni-frankfurt.de.
[5] H. Vormann et al., "Status of the Linac Components fort he Italian Hadrontherapy Centre CNAO", proc. EPAC08, p. 1833 ff.
[6] H. Podlech, Habilitationsschrift, Uni Frankfurt, 2008.
[7] G. Clemente et al., "Development of a Coupled CH Structure for the GSI Proton Injector", proc. PAC07, p. 1428 ff.
[8] P. Brown et al., "Status of the LEP Accelerating Structure", proc. PAC89.
[9] www.cst.de.
[10] T. Wangler, "RF-Linearaccelerators", 1998, p 103 ff.
[11] P. Fischer, Ph.D. Thesis, Uni. Frankfurt, 2007, http://iaprfq.physik.uni-frankfurt.de.
[12] J. Rehberg, Diploma Thesis, Uni. Frankfurt 2008.
[13] C. Zhang, A. Schempp, "Beam Dynamics Studies on a 200 mA Proton Radio Frequency Quadrupole Accelerator", NIM, p. 153-159.

# INJECTOR DEVELOPMENT FOR HIGH INTENSITY PROTON BEAMS AT STERN-GERLACH-ZENTRUM

O. Meusel, A. Bechtold, L.P. Chau, M. Heilmann, H. Podlech, U. Ratzinger, K. Volk, C. Wiesner
IAP, University Frankfurt/Main, Germany

*Abstract*

The Frankfurter neutron source at the Stern-Gerlach-Zentrum (FRANZ) uses a 2 MeV proton LINAC as a driver for the $^7$Li(p,n) neutron production. A volume type ion source will deliver a 120keV, 200mA proton beam continuously. A LEBT section consisting of four solenoids is under construction to transport the beam and to match it into the acceptance of the RFQ. A chopper system between solenoid 2 and 3 will provide beam pulses with a length of about 50 to 100 ns with a repetition rate of up to 250 kHz. The RFQ and the following IH drift tube LINAC will be coupled together to achieve an efficient beam acceleration. Furthermore only one power amplifier will be needed to provide the RF power for both accelerator stages. The Mobley type bunch compressor will merge 8 micro bunches formed in the accelerator module to one single 1ns bunch with an estimated peak current of up to 9.6 A. A rebuncher will provide the post acceleration to final beam energy adjustable between 1.8 and 2.2 MeV. The whole system is optimized for high beam intensity causing high space charge forces. As a consequence new accelerator concepts and beam diagnostic concepts have to be developed.

## INTRODUCTION

FRANZ comprises two experimental areas allow different types of neutron capture measurements. The compressor mode offer time of flight measurements in combination with a 4π $BaF_2$ detector array. The proton beam will be compressed to a 1ns pulse with a peak current of about 9.6 A and a repetition rate of 250 kHz. On the other hand activation mode uses a continuous neutron flux. Primary cw proton beams with a current up to 8 mA on solid targets and up to 30 mA on liquid metal targets as a later option are feasible.

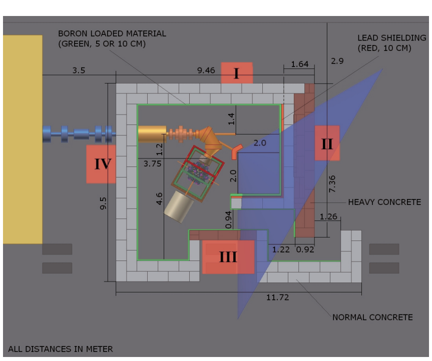


Figure 1: Scheme of the FRANZ facility with targets and detector and iradiation and neutron shielding.

FRANZ is not only a neutron generator but also a test bench for new accelerator and diagnostic concepts for intense ion beams. The envisaged proton beam properties on the target lead into a challenging accelerator design to overcome the space charge forces.

## ION SOURCE

A volume type ion source was chosen for FRANZ to extract the proton beam from a hot filament driven gas discharge plasma [1]. Figure 2 shows this source type. The life time of the filament is limited about one month of operation. On the other hand the plasma temperature of a gas discharge at moderate arc power is as well as the confining magnetic field very low compared with other source types e.g. ECR sources. Therefore the beam emittance is small and gives the possibility to investigate causes of emittance growth during beam transport and acceleration along the whole LINAC.

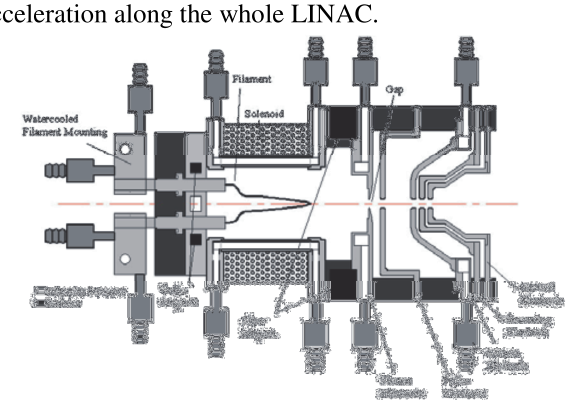


Figure 2: crossectional view of the volume type ion source under construction.

For the planned beam intensities a pentode extraction system keeps quite well the beam emittance during the extraction and pre acceleration phase when compared with other extraction schemes [2]. Figure 3 shows a preliminary numerical simulation of the beam extraction by the use of the IGUN code [3] and under respect of a multi species beam with approximately $H^+$ = 80%, $H_2^+$ = $H_3^+$ 10%.

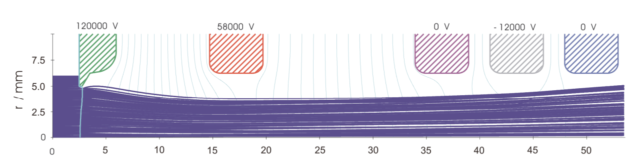


Figure 3: Illustration of a preliminary IGUN calculated beam profile along a pentode extraction system.

The chosen aspect ratio of S = 0.2, an emission area of 0.78 $cm^2$ and an extraction field strength of 6.2 kV/mm result in a beam radius of $r_{beam}$ = 5 mm, $\varepsilon_{rms}$ = 0.06 π mm mrad and a divergence angle of r' = 74.5 mrad.

## LEBT SECTION WITH CHOPPER

The LEBT section consists of 4 solenoids for beam focussing and includes partial of space charge compensation due to residual gas ionisation. Figure 4 shows a scheme of the planned LEBT. The first and second solenoid will be used for separation of ion species and to match the proton beam into the chopper system. Downstream of the chopper two solenoids will focus the beam into the acceptance of the RFQ. Two pumping and diagnostic tanks will be used for several non interceptive diagnostics e.g. optical beam profile measurement and beam potential measurements using a residual gas ion energy analyzer.

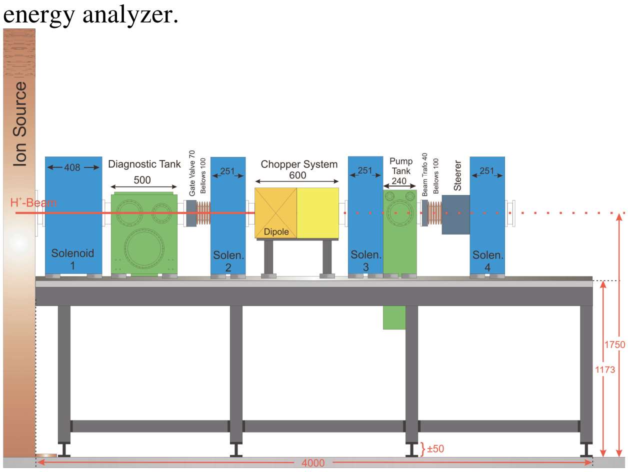


Figure 4: Scheme of the LEBT section with four solenoids and the chopper device.

The chopper system consisting of a kicker and a septum magnet combined with a slit provide the 100 ns proton beam pulses. Figure 5 shows the arrangement of the chopper system.

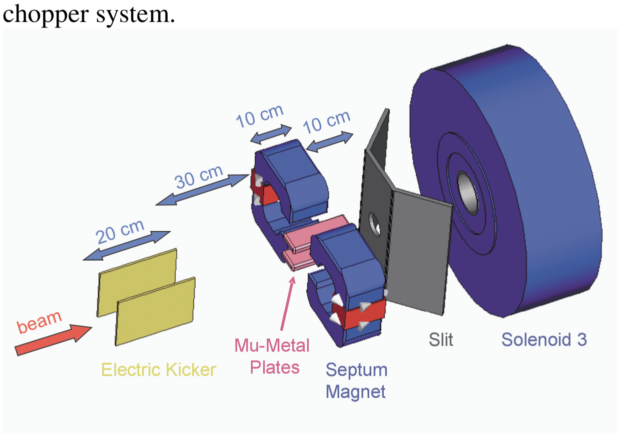


Figure 5: schematic drawing of the chopper system consisting of a fast kicker, a septum magnet and an apertur.

A fast magnetic or electric kicker deflects the beam with a repetition rate of 250 kHz whereas the static septum magnet provides the post separation and a pulse with a flat top of at least 50 ns. Comparison of electric and magnetic kicker systems by the use of numerical simulation shows an influence of secondary electrons. The high production rate of electrons in the chopper system gives the possibility for partial space charge compensation of short beam pulses. Preliminary studies result in approximately 30% of space charge compensation by the use of a magnetic kicker system. For an electric kicker the secondary electrons bear the risk of sparking and sputtering from the electrodes [4]. Beam transport and chopping leads into an emittance growth by a factor of 4. It seems possible to reduce this value by further optimization of beam transport with respect to the filling degree of the solenoids and more detailed description of space charge compensation. Pulsed beam with proton densities of $n_p = 8.2{\cdot}10^{14}\ m^{-3}$, generalized perveance of $K = 3.1{\cdot}10^{3}$ and time structure shown in figure 6 will be injected in the coupled RFQ-IH DTL.

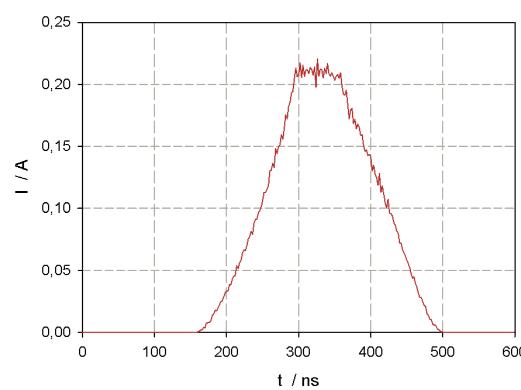


Figure 6: Simulated beam current as a function of time at the entrance of the RFQ, Pulse duration of about 50 ns and repetition rate of 250 kHz.

## COUPLED RFQ-IH DTL

In order to minimize installation costs and to use one compact common rf amplifier a coupling of the RFQ and IH-DTL is foreseen [5]. Figure 6 shows a crossectional view of the coupled accelerator stages. Both of the cavities can also be used separately. The RFQ is 1.75 m long and needs an input power of 150 kW [6]. Numerical simulations using the PARMTEQM [7] code show a beam transmission efficiency of 95 % with acceptable emittance growth at the design current I = 200 mA for an electrode voltage of about 75 kV. Output energy of the RFQ will be 0.7 MeV. The IH-DTL will boost the proton beam to its final beam energy of 2 MeV. The power consumption of the IH cavity is in a range of about 45 kW to establish a gap voltage of 300 kV. Due to the fact that a RFQ acts like a buncher the incoming proton beam will be compressed longitudinally. In result of the beam transport simulation the micro bunch phase width is in a range of 60 degree. The average bunch current increases up to 1.2 A and the resulting compression ratio is η = 6. At beam energy of 2 MeV downstream of the accelerator stages the proton density is $n_p = 8.2{\cdot}10^{14}\ m^{-3}$ and the space charge forces expressed by the generalized perveance decreases of about $K = 2.7 \cdot 10^4$. Figure 7 shows the micro bunch current as a function of time at the exit of the accelerator stages. The average current of one micro bunch is equal to the peak current.

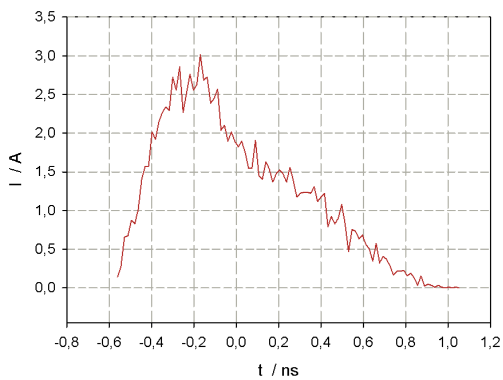


Figure 7: Micro bunch current as a function of time about 1 m behind the LINAC, increase of pulse duration of about 1.2 ns due to the large energy spread and space charge forces.

## BUNCH COMPRESSOR

By applying the bunch compressor concept of the Mobley type [8] for high current beams a split magnetic dipole array include edge focusing was chosen [9]. The periodic deflection by the RF kicker at one focus of the bending system guides up to 8 bunches on different paths to the final focus, where the neutron production target is located. As shown in figure 8 two rebuncher cavities are needed to focus the beam longitudinally.

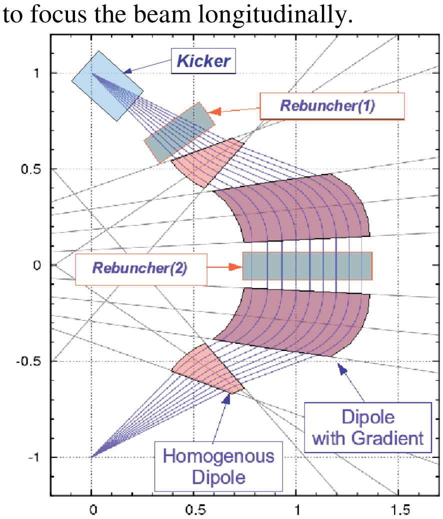


Figure 8: Scheme of the Mobley type bunch compressor.

By choosing adequate parameters all 8 bunches will overlap at the target and produce a 1.1 ns proton pulse with a proton density of $n_p = 8.2 \cdot 10^{14}$ $m^{-3}$. Space charge forces become dominant, the generalized perveance is $K = 2.2 \cdot 10^3$. Figure 9 shows the bunch current as a function of time, the peak current is 9.6 A. The compression ratio downstream of the whole proton injector is of $\eta = 48$.

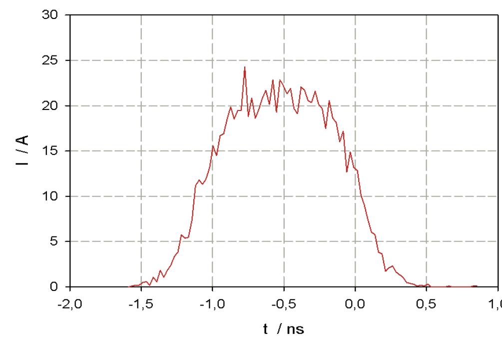


Figure 9: Beam current of the compressed bunch as a function of time at the target, Pulse duration of about 1.1 ns at a repetition rate of 250 kHz.

## CONCLUSIONS

The hardware of the planned proton injector is under construction. More detailed multi particle transport simulations show that the activation mode using a 30 mA cw beam will be limited by the rf power consumption, target power deposition and radiation safety. The compression ratio of the compressor mode is 48. The resulting proton density and space charge force leads into increasing beam spot sizes and pulse duration at the $^7Li(p,n)$ target.

## REFERENCES

[1] R. Nörenberg et al., "Development of a high efficiency proton source for the Frankfurter-Neutronen-Quelle am Stern-Gerlach-Zentrum", Rev. Sci. Instrum. 79, 02B316 (2008);

[2] R. Hollinger, P. Spädtke, "Comparison of different extraction and acceleration systems for a high intense proton beam for the future proton linac at GSI", Rev. Sci. Instrum. 75, 1656 (2004)

[3] R. Becker, W. B. Herrmannsfeldt, "IGUN a program for the simulation of positive ion extraction including magnetic fields", Rev. Sci. Instrum. 63, 2756 (1992)

[4] C. Wiesner et al., "A 250 kHz Chopper for Low Energy High Intensity Proton Beams", Proc. of the Eur. Part. Acc. Conf., Genua (2008).

[5] A. Bechtold et al., "A Coupled RFQ-Drifttube Combination for FRANZ", these proceedings

[6] C. Zhang et al., "Development of a High Current Proton Linac for FRANZ", EPAC'06, ID: 2342 - THPCH007

[7] LANL Manual of RFQ Design Codes (LANL Report No. LA-UR-96-1836), 1996.

[8] R.C. Mobley, "Proposed Method for Producing Short Intense Monoenergetic Ion Pulses", Phys. Rev.88(2), 360-361, 1951

[9] L. P. Chau et al.,"One Nano-second Bunch Compressor for High Intense Proton Beam", Proc. of the Eur. Part. Acc. Conf., Genua (2008).

# PERFORMANCE OF THE CONTROL SYSTEM FOR THE J-PARC LINAC

H.Yoshikawa, T.Suzuki, H.Sakaki, Y.Itoh, Y.Kato, M.Kawase, H.Sako, G.Shen, H.Takahashi, JAEA, Tokai-mura, JAPAN
S.Fukuta, MELCO SC, Tsukuba, JAPAN
S.Sawa, TOSS, Tokai-mura, JAPAN
H.Ikeda, VIC, Tokai-mura, JAPAN.

*Abstract*

LINAC of J-PARC began to operate in November, 2006, and a achieved an initial performance in January, 2007. Afterwards, the beam supply to RCS begins, and it is operating extremely with stability up to now[1]. The fundamental condition of the control system design is to defend the beam loss detecting it as early as possible because it controls the radiation by the large strength beam to the minimum. This requirement influences from the level of the basic function of high-speed interlock to the level of an advanced application that needs the predictive control. It describes what work distribution, how much man power were necessary for the control system construction.

## CONCEPT OF DESIGN

The requirement to minimize the beam loss and to reduce the residual radiation makes large difference from the control system of a past experimental accelerator in the point that operating the trial and error is not permitted. This control system protects LINAC from miss-operation, but flexibility of operation absolutely must be kept for the development of 1MW operation[2]. We set the robustness of protection in the middle-ware, and set the free-stage enclosed that middle-ware for the application.

Basic policies of the strategy are :

- Middle-ware (process communication tools, device drivers, database libraries) gives the perfection as much as possible.
- Least making and maximum recycling by OOP is used.
- End user presents a necessary function of th program, and doesn't make the program itself.

At the debugging, it is severe to find bugs of middle-ware. It takes most of the debugging time that finding the reason of unexpected behaviour of poor libraries or cheep drivers. There is an idea with driver's structure simply to avoid this, too. However, it gives origin to an excessive complexity of a high-level application. We were initially given using EPICS. To make the best use of the advantage of the flat scope of EPICS records, we limited the use of record-link. The use of the record-link is a rapier, and it is necessary to use it under the total management. Even the record file should not be individually described. (Sometimes, the file written at the device test survives still.) The database application that confirmed parsing, matching and grammar was developed. End user, who are the expert of device or equipment, are not always good programmer, and don't know the detail of our function hierarchy. If sharing an individual application by the common device model is attempted, the quiet sleep at the term of all-day operation can be secured. We concentrated on the competent understanding of the function of the application that the user requested.

LINAC components are categorized into :

- Vacuum system (several kind of pumps, vacuum gauge, rough pumping system, gate valve, fast closing valve)
- RF cavity system (cavity, tuner, cooling water, temp meas., )
- High-power RF source (klystron, HV-PS, LLRF, wave-guide, tuner)
- Magnet system (bend, q-singlet, doublet, steer)
- Monitor system (position, profile, current)

And, each device communicates with :

- Timing System (TS)
- Machine Protection System (MPS)
- Personnel Protection System (PPS)
- Parameter Data Base (DB1)
- Measurement Data Base (DB2)

We described all function of each cell in the matrix that is made of device column and sub-system line. On the result of this detailed examination, we aimed at sharing software by adapting low-level application of each device to common skeleton based on the machine model.

MPS and PPS was required very complicated function because J-PARC is a multi-purpose facility. Though it is preferable to achieve it by hardware logic, it is impossible to achieve it only by the relay logic. We decided using PLC for PPS, and FPGA is used for MPS to realize the required response time.

## MAN POWER AND STRATEGY

The control system design started in 2002. It had 4 years to beam operation, but we aimed to use the actual application for factory test of individual equipment after three years. Requested man power was ;

- Five experts those who can develop device driver, process communication.
- Five programmers those who have a experience of medium scale application.

At the beginning, we started 8 members. Fortunately, 4 of us are ex-colleague of SPring-8 LINAC. Machine model, OOP driver and special needs of J-PARC LINAC became our common recognition at once. To cancel the lack of man power, the detailed design of network system was done in outsourcing. And the coverage of the machine model had been expanded to Rapid Cycle Synchrotron, long BT-line and muon magnets.

At the initial phase, new comer tried to adaption of machine model to vacuum component or simple magnet, supervised by the experts. 4 experts, 1 system manager of development system and 3 new programmers changed into 6 experts 2 high-level application developer and 3 OPI programmers.

It worries whether the software by a different method can achieve a necessary function because the person in charge of the devices has an original control specification demand. Especially, the person who takes charge of the device of simple function might see excessive estimation the machine model application for the software sharing. This conflict disappeared when the application in this method showed robustness for the function change in the acceptance test at factory on the devices. The person in charge of the control should make an effort about the device of controlled object to become detailed equally to the person in charge of the device. About the software specification presentation, they are not necessarily the skill people. Even the control people might not describe the software design.

## PERFORMANCE OF CONTROL SYSTEM

At the beginning of LINAC commissioning, we were not able to exclude a local operation completely though we aimed at the achievement of the full remote control.

- All devices of the vacuum system are controlled in remote operation. Changing of gauge values from reference value range signs to operator for attention. Exceeding of the gauge value is signed to operator for attention. Beam line gate-valve are controlled as a device of MPS.
- All interlock and tuner position of RF cavity system are shown and controlled in remote.
- All information of the high-power RF source are monitored and controlled in remote. But Start up sequence after the discharge fault was not fixed yet. Then a RF staff started it up manually. Now, auto-recovery sequence is working well.
- All magnets are controlled in remote at the first operation.
- Data of each monitors acquired in remote, but data processing sequence were not fixed. Some new algorithm are developed to determine the beam energy for the phase scan of every cavity[3]. These data processing are done by high level application.

A part of high-power RF system and the ion-source was left in local control at the first operation. This is caused of the difficulty of treating of discharge event. It is another reason of taking time that many PLC are used. Some PLC were brought in with black-box ladder which made by factory. The cost must be estimated by not only hardware but software including the maintenance.

The subsystem of the whole control system operated from the commissioning beginning well.

- TS worked well. Single shot and arbitral train of pulse repetition was able to be set. This was contributed to effective study to avoid residual radiation. This timing system is operated with scheduled type train. But the delay tables can be written synchronously by using reflective memories, and synchronous delay trimming is enable[4].
- MPS has independent communication bus. Two kind of input modules are developed, and the beam loss monitor signal triggers fast response line to avoid a damage of beam bombardment at the low energy region. Less than 5-micro seconds response is achieved and the noise error is less than 1% of unscheduled downtime( ~5% of operation time)[2].
- PPS has dual network, dual CPU, dual power supply and dual limit switches. PPS is the safety grounds of legal permission of this accelerator.
- DB1 deal with device information and operation parameters. DB1 also works as a record-file generator.
- DB2 is the collector of monitor data, and the data archiver. Data viewer is continuously modified by users request. Now we meet tread off between reducing the size of storage and quick response of viewer cause of data format.

The number of device driver, which is originally developed, is 21.

- 9 kinds of VME IO boards.
- 2 kinds of TS sender/receiver
- 2 kinds of PLC
- 5 kinds of oscilloscope
- 2 kinds of spectrum analyser
- 1 kind of AWG
- Soft IOC

These drivers are working with no bug for two years. Oscilloscope and spectrum analyser for the monitor device are rather complicated, and necessary function is added on fly when it is required. To identify the behaviour of each shot, we brought the shot ID in. The combination of the shot counter, wave-endless recorder (event recorder) and reflective memory network enable to correct shot number between the many measurement devices. This function is prepared to collect data to which the cause of the beam fluctuation was not treated as the statistical data but the causal relation was able to be presumed.

At the initial operation, ideal parameters were calculated by offline simulation code. But XAL and JCE began to run including SAD script interpreter at the second term of the beam operation. Our application is written in JAVA excluding OPI of pilot version. The integrated OPI has so many record connections, and performance tuning is needed. Handling of multi-processing requires high level skill and knowledge of OS behaviour. We control people are shifting high-level application development. The experience of coding primitive software effects quick debagging of the application. Of course most of bugs are found in high-level description.

Feed back of RF amplitude and phase for long time range is started, and its result shows the effect of temperature of klystron gallery. The macro perturbation, caused by atmosphere temperature, cooling water temperature or voltage of electric power station, is quantitatively analysed by a self-regression model. Accelerator control is fundamentally required to stabilize the beam. High precision stability of each devices are inevitable, but achieving the extra-high current beam needs dynamic control for long time span based on the identifying multivariate analysis. The more specialist of the control theory is requested.

## SUMMARY

The control system of J-PARC LINAC successfully established initial requirement. For three to five years from now, this LINAC should aim the 1MW beam power. This control system works as a platform of high-level application. We prepared JCE to merge the components of XAL and other simulation codes. Total analysis of beam behaviour can be done by unified description through LINAC to the ring.

The large scale accelerator is constructed as a project, and keeping the schedule is required. The number of the kind of component of accelerators is not so many, and the state change of each device is not so complex (excluding special destructive monitor).

### *Experimental Accelerator*

If you construct a experimental accelerator of mono-purpose and the life of the accelerator is several years, the control system can be constructed by out-sourcing or by 5 experts of programming. It will take one and half years to make the control system. The middle-ware may make it without sticking to the function hierarchy. Rapid application development must be the first priority. First half year is spent for the design of whole function of the control system. If the number of klystron is greater than 5, the number of control people should be increased. Especially, the variation of monitor device expands quickly. Accessibility of that device has high dependency on bender spec (sometimes it is not opened). There will be many monolithic program described and it is maintained by the author himself. It is not necessary to read the other person’s code. When reading is required, it is ok to write another code.

### *Facility Accelerator*

It is necessary to design the accelerator that operation for users is obligated to integrate the whole in the control system. It doesn’t depend on the scale to construct the control system of this kind of accelerator, and about ten of control people and four years are required. The member must be contained some persons who are expert of :

- OS, compiler and driver design
- Signal, semaphore and Que
- Event driven message procedure

At the beginning of construction, the detail of the specification of each device is not fixed. That is the chance to involve every device to be defined the state flow and machine model in common. It is necessary to spend the first one year on the optimization of a hierarchical distribution of the software function. Do not let the work of the programmer with low skill level be limited to easy application development. The concept can be shared by the initial entire design, the driver design and the function distribution.

Contributing from the development phase of an individual device is indispensable to come to an agreement about the control specification as the person in charge of the device. Finally integrating a lot of machines by which of each produced the control part in an original idea becomes big dangerous for the normal operation securing. The control system can be constructed with the same man power even if it is a LINAC of 100 klystrons scale if succeeding in sharing machine model and the negotiation with the person in charge of the device.

The emphasis is put on the hardware selection, and the importance of the software structure is not recognized enough still. A cheap control equipment is selected, and excessive load is put on the software production, and a lot of examples decreased the entire performance are seen especially in a small-scale accelerator.

The estimation of the performance of the control system is difficult, because that quantitative description of total balance is impossible. Keeping the schedule, suppressing resources and achieving efficiency of operation show that.

## REFERENCES

[1] K.Hasegawa. Other, “Operating experience of the J-PARC LINAC”, MOP004 in this conference.
[2] M.Ikegami, “Progress in the beam commissioning of the J-PARC Linc and its upgrade path”, MO201 in this conference.
[3] H.Sako, Other, “Transverse beam matching and orbit corrections at J-PARC LINAC”, MOP078 in this conference.
[4] A.Ueno, “Unique features of the J-PARC LINAC and its performance – lessons learnt”, TU101 in this conference.

# OPERATING EXPERIENCE OF THE J-PARC LINAC

Kazuo Hasegawa#, H. Asano, E. Chishiro, T. Hori, T. Ito, T. Kobayashi, Y. Kondo, Y. Namekawa, H. Oguri, K. Ohkoshi, H. Suzuki, A. Ueno, M. Yamazaki, J-PARC (KEK&JAEA), JAEA, Tokai, Ibaraki, Japan
S. Anami, Z. Fang, Y. Fukui, K. Ikegami, M. Kawamura, F. Naito, K. Nanmo, H. Tanaka, S. Yamaguchi, J-PARC (KEK&JAEA), KEK, Tokai, Ibaraki, Japan

*Abstract*

The beam commissioning of the J-PARC linac started in November 2006 and 181 MeV acceleration was successfully achieved in January 2007. The linac has delivered beams to the 3 GeV Rapid Cycling Synchrotron for its commissioning, and then, the subsequent Main Ring Synchrotron and the neutron target commissioning. The linac uses a Cs-free $LaB_6$-driven ion source and 20 units of 324 MHz klystrons. As of June 2008, the operation times are about 3,000 and 6,000 hours for the ion source and the RF source, respectively. The operating experience of the linac is described.

## INTRODUCTION

The J-PARC (Japan Proton Accelerator Research Complex) is a multipurpose facility with 1 MW class proton beam[1]. The facility is under construction at the JAEA/Tokai site as a joint project between the Japan Atomic Energy Agency (JAEA) and the High Energy Accelerator Research Organization (KEK). The J-PARC accelerator consists of a linac, a 3 GeV rapid cycling synchrotron (RCS), and a 50 GeV main ring synchrotron (MR). At the initial stage of the project, the linac accelerates a negative hydrogen beam up to 181 MeV with a current of 30 mA, a pulse width of 0.5 msec and repletion of 25 Hz.

The linac consists of an RFQ, a Drift Tube Linac (DTL) and a Separated-type Drift Tube Linac (SDTL). The features of the linac are described in [2]. High power conditioning of the cavities and beam test started in October and November 2006, respectively, then 181 MeV energy acceleration was achieved in January 2007. Since then, the linac beams have been used for the linac commissioning for its own, for the RCS commissioning, for neutron production, and for RF capture experiment at the MR.

We have adopted a three to four weeks commissioning cycle, which consists of a two or three week beam commissioning run and a one or two week interval. Adjusting the terms of intervals to accommodate appropriate maintenance periods, 17 beam commissioning cycles have been experienced from November 2006 to June 2008. Detailed beam commissioning results are described in [3].

## FRONT END

The J-PARC linac uses a Cs-free, $LaB_6$-driven, multicusp $H^-$ ion source[4]. The diameter and the length of the plasma chamber are 100 and 120 mm, respectively. The source plasma is confined by the multicusp magnetic field by 18 rows at the sidewall and four rows at the upper flange. The filament is a cylindrical spiral structure $LaB_6$ and the size is 29.5 mm and 49 mm in diameter and height, respectively.

Figure 1 shows the history of the ion source operation. During intervals between commissioning cycles, we have performed maintenance or ion source study. The pink and green bars denote the typical $H^-$ beam current in the commissioning days and the ion source study days, respectively. The maximum beam current from the ion source is 38 mA at the arc duty factor of 0.8 % (0.32 msec in pulse width and 25 Hz). Since the commissioning tasks doesn't always require a high peak $H^-$ beam current, the ion source has been operated either at the low current mode of 5 mA or at the high current mode of 30 mA. To keep the condition of the plasma chamber surface good, the ion source keeps running of the filament or beam extraction during the nighttime in the commissioning days. Operation time of the source has been reached to 3,360 hours as of June 2008.

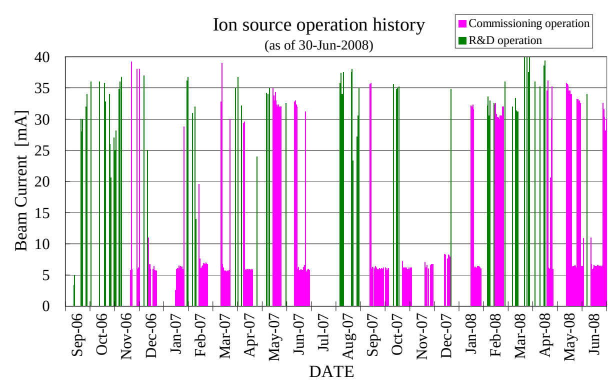


Figure 1: Operation history of the ion source.

On October 6 and December 18, 2006, filament had troubles of short-circuit to the neighboring spirals. The troubles were caused by filament deformation due to the arc power heating. Then the filament shape was modified to have a wider gap between spirals from 0.3 to 0.6 mm. We have not had similar troubles since then.

On August 21, 2007, we had a cutting off of the filament. We consider that the filament was broken by some strong mechanical stress because the filament showed no signs of remarkable consumption. The filament was replaced with a studious care. That filament lasted by June 28, 2008. The beam time was 2,030 hours,

#hasegawa.kazuo@jaea.go.jp

which consists of 780 hours in high current mode and 1,250 hours in low mode. We have not had enough statistics regarding the lifetime, but we have a confidence that the $LaB_6$ filament is of practical use for a few weeks user run.

## DTL/SDTL CAVITIES

The DTL consists of 3 tanks operating at 324 MHz with final output energy of 50 MeV. The transverse focusing is arranged in an FD lattice utilizing electro-magnet. After high-power conditioning of the DTL was completed up to 1.2 times as high as the nominal power level, the beam commissioning of the DTL was achieved in the second run, December 2006[5,6].

We have 32 SDTL tanks but two of them are used as debunchers. The inter-tank sections contain electromagnet quadrupole doublets with beam position monitors inside. Either steering magnet, wire scanner, or gate valve is arranged in between the doublet. The 181 MeV acceleration was achieved on January 24, 2007. We haven't had noteworthy troubles for the DTL/SDTL cavities during the commissioning.

We have 111 and 33 Q-magnet power supplies in the DTL and the SDTL sections, respectively. We had several troubles for these power supplies: replacement of the IGBT unit (2), repair of control unit (2), loose connection of switch (2), and others (1). Some of them happened or found during the maintenance period and not all the failures caused the beam trip. The downtime of the beam is 2 or 3 hours when the failed power supply is replaced by a spare.

We had water leakage in the accelerator tunnel twice due to the flow meter glass breakage. The cause was assumed that small cracks made in the fabrication or in the installation process grew by some shock. All the 64 flow meters, which were the same type of the broken ones, were replaced by commonly used type and installed carefully in summer, 2007. Since then, we have not had the similar troubles.

## RF SYSTEM

Figure 2 shows the RF subsystem. Six high voltage DC power supplies (HVDCPSs) supply the pulsed power to the 20 klystrons. Transmitter systems that control the klystrons and solid-state amplifiers provide RF power to the structures. Stabilization of the cavity fields is well performed with a feed-back and feed-forward control system[7].

The HV trip rate as a function of run number is shown in Fig. 3. At the early stage, we had occasional malfunctions of the crowbar circuit in the HVDCPS. That was improved by replacement of the registers at the current transformer (CT). However, in runs 14 and 15, fault rate increased suddenly. This was caused by discharges between the CT for modulation anode current measurement and the neighbouring wire. The insulator near the CT was replaced as a temporary measure, and we are planning to modify the arrangement around the CTs as a permanent measure.

Other than the power supply itself, HV trips have been caused by timing related matters such as setting error, timing signal failure, 12 MHz master oscillator failure. In these cases, the interlock stops the system because the monitor shows the abnormal state. These issues have been settled one by one based on these experiences.

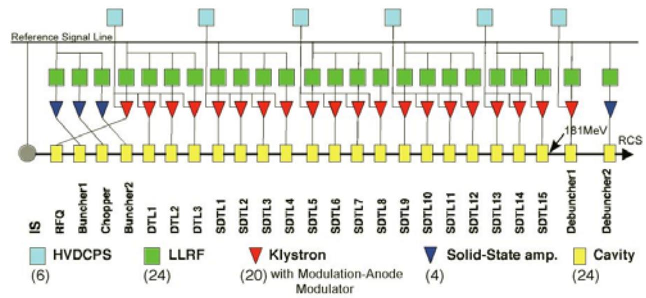


Figure 2: J-PARC linac RF system.

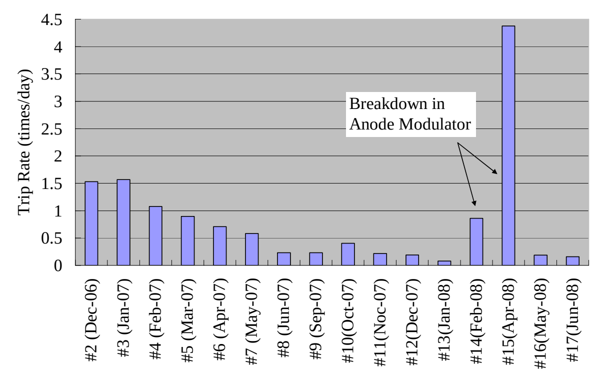


Figure 3: HV trip rate as a function of run number.

We have totally 23 klystrons (Toshiba E3740A) including 3 spares. Figure 4 shows the operation hours of the klystrons in use. The current average operation time is 6,460 LV-on (filament) hours and 5,960 HV-on hours as of June 2008.

Klystrons are consumables (limited lifetime) and costly parts for linac. Reliability engineering approach is taken to estimate the lifetime. So far, we have no failed klystrons, but we can assume the lower limit of Mean Time To Failure (MTTF). If we assume the exponential failure distribution $\alpha=\exp(-\lambda T)$, that refers to the random failure, where $\lambda$, $1-\alpha$ and T are failure rate, confidence level and operation time, respectively. If we take a confidence level of 90 %, failure rate is

$$\lambda = -\ln(1-0.9)/T = 2.30/T \quad (1)$$

If we put the total operation time T=129,292 (hours) for all 20 klystrons, upper limit of failure rate and lower limit of $MTTF_{lower}$ are

$$\lambda_{upper} = 1.78\times10^{-5}\ (1/hour) \quad and$$

$$MTTF_{lower} = 1/\lambda_{upper} = 56{,}200\ (hours)$$

The Poisson distribution denotes probability of klystron failure as the similar manners in [8]

$$f(x) = \frac{\mu^x}{x!} e^{-\mu} \qquad (2)$$

Then, with 20 klystrons and 5,000 hours per year operation, we expect the average number of consumption per year is

$$\mu = N\lambda t = 20 \times 1.78 \times 10^{-5} \times 5{,}000 = 1.78$$

Figure 5 shows the number of failure klystrons after one or two year operation. Above analysis shows that the average consumed number in one year is about 2, but there are high probability of 3 or more klystron failures. It may be said that the 3 spares we have are too short to keep operating for user run. In addition, above estimation would be somewhat optimistic because it is based on the random failure, or constant failure rate (CFR) distribution. This kind of failure tends to follow the increase failure rate (IFR) distribution. Some of them would fail almost simultaneously. In the latest run in September 2008, meaningful emission degradation for 5 klystrons is observed. We should carefully keep an eye on them.

## UTILITIES

We have had unscheduled stop three times due to the cooling water pump trip. This brings almost all the linac system sudden stop including high power RF system. It takes several hours to resume the operation. This pump is for the cooling system of the cavity tanks, which is made of steel. Rust has accumulated and sticks into the magnetic field of the canned pump. Then the line current increases and reaches to the breaker trip level. We have taken a careful quality control of the cooling water and monitoring the pump current for the time being. The type of the pump itself is reconsidered as a permanent measure.

At the initial stage of the beam commissioning, we had occasional stops by the flow rate interlock due to the total cooling water flow decrease and flow balance change. We have had accumulated these operation experiences and the frequency of such failure is going down.

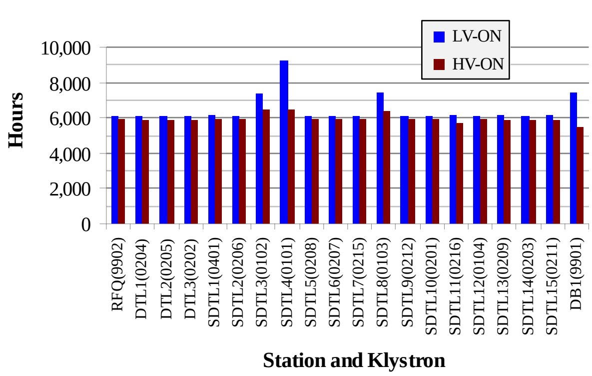


Figure 4: Total klystron operation hours.

## SUMMARY

The J-PARC linac has been successfully commissioned and operational experiences have been accumulated. The Cs-free, $LaB_6$ filament driven ion source demonstrates good performance from a point of view of beam current and lifetime. The DTL and SDTL cavities have been operated without serious troubles. The trip causes are overcome one by one for the RF source and trip rate has been greatly decreased. The average operating hour of the klystrons exceeds 6,000 and the spare issues are discussed. Although we had many cooling water related failures at the initial stage, they are improved and the availability has been increased. Based on these experiences, we will go into a new phase of the user run from December 2008.

## REFERENCES

[1] "Accelerator Technical Design Report for High-intensity Proton Accelerator Facility Project, J-PARC", JAERI-Tech 2003-044, KEK Report 2002-13 (2003).

[2] A. Ueno," Unique Features of the J-PARC Linac and Its Performance - Lessons Learnt", these proceedings, TU-101.

[3] M. Ikegami, "Progress in the Beam Commissioning of the J-PARC Linac and its Upgrade Path", these proceedings, MO-201.

[4] H. Oguri et al.,"Development and operation of a Cs-free J-PARC H$^-$ ion Source", Rev. of Sci. Instr. 79, 02A506 (2008).

[5] F. Naito, "Present Status of J-PARC", APAC2007, MOXMA01, Indore, India (2007).

[6] T. Ito et al., "High Power Conditioning of the DTL for J-PARC", PAC07, p.1517, Albuquerque, USA (2007).

[7] T. Kobayashi et al., "Performance of J-PARC Linac RF System", PAC07, p.2128, Albuquerque, USA (2007).

[8] M. Lynch et al., "The LANSCE 805 MHz RF System History and Status", PAC05, p.2402, Knoxville, USA (2005).

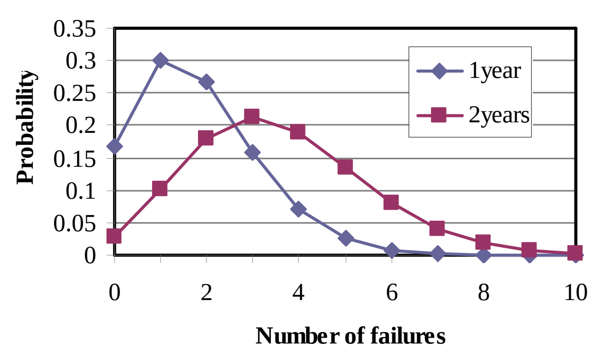


Figure 5: Probability of failure of klystrons in the first and second year.

# BEAM TEST RESULTS OF THE PEFP 20 MEV PROTON ACCELERATOR AT KAERI*

Yong-Sub Cho#, Han-Sung Kim, In-Seok Hong, Ji-Ho Jang, Dae-Il Kim, , Hyeok-Jung Kwon, Bum-Sik Park, Kyung-Tae Seol, Young-Gi Song, Sang-Pil Yun, KAERI, Daejon 305-353, Korea

*Abstract*

A 20 MeV proton accelerator, which consists of a 50 keV injector, a 3 MeV RFQ and a 20 MeV DTL, has been tested by Proton Engineering Frontier Project (PEFP) at Korea Atomic Energy Research Institute (KAERI). The operation conditions are 20 MeV, 20 mA peak current, 50 μs pulse length with a 1 Hz repetition rate due to the limited radiation shielding. The accelerator was tuned to reach to the above operating conditions. Moreover, an irradiation facility with external beam has been installed to supply the proton beam for the user and irradiation test. In this paper, we present results from tuning operation and the irradiation tests.

## INTRODUCTION

The Korean Government launched the Proton Engineering Frontier Project (PEFP) in 2002 to help realize potential applications of high-power proton beams. The primary goal of the project is to develop a high-power proton linear accelerator to supply 100-MeV proton beams and to construct user beam line facilities, whose users can utilize proton beams with a wide range of energies and currents for their research and development programs [1]. In addition, the 100-MeV accelerator can be used as a proton injector for the next-stage high-power accelerators, such as a high-energy linac or rapid cycling synchrotron [2].

A 20-MeV proton linear accelerator has been developed as the front end of the 100-MeV accelerator, which consists of a 50-keV proton injector, a 3-MeV RFQ, a 20-MeV DTL, and RF systems, as shown in Fig. 1.

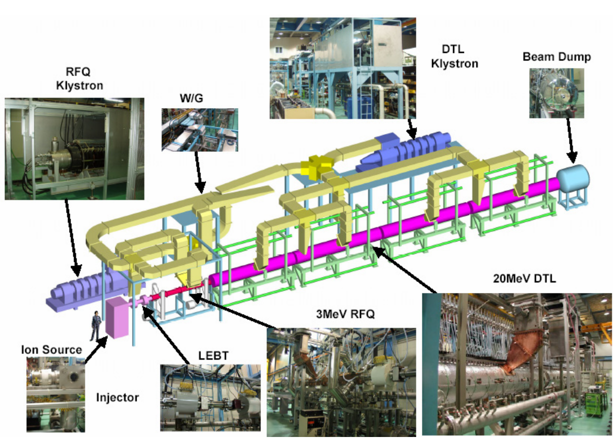


Figure 1: 20MeV proton linac at KAERI.

*Work supported by the Korea Ministry of Education, Science and Technology.
#choys@kaeri.re.kr

## THE 20-MEV PROTON LINEAR ACCELERATOR

### The Proton Injector [3]

The injector includes a duoplasmatron proton source and a low-energy beam transport (LEBT). The beam current extracted from the source reached a current of 50 mA. The extracted beam has a normalized emittance of 0.2 πmm-mrad from a 90% beam current, where the proton fraction is > 80%. To achieve pulsed operation, a high-voltage switch has been installed in the high-voltage power supply, whose rise and fall times are < 50 ns. The pulse length and the repetition rate can be easily changed using this semiconductor switch. The LEBT consists of two solenoid magnets that can filter the $H^{2+}$ ions and two steering magnets that can control the beam's position and angle at the entrance of the RFQ.

### The 3 MeV RFQ [4,5]

The PEFP RFQ is designed to accelerate a 20-mA proton beam using a voltage from 50 keV to 3 MeV and has the usual four-vane-type design. The entire structure is separated into two segments that are resonantly coupled for field stabilization. The RF power is fed into the cavity through two iris couplers in the third section.

A 3-MeV, 350-MHz PEFP RFQ has been fabricated, tuned, installed, and tested. The low-power field tuning satisfied the design requirements. High-power RF conditioning experiments for the RFQ were carried out up to a peak power of 450 kW, a pulse length of 80 μs, and a repetition rate of 1 Hz. The time required for this conditioning was about 8 h. The RF signals shown in Fig. 6 are the signals detected after the conditioning, which were very stable. Beam tests were carried out by adjusting the LEBT and the RF parameters.

### The 20-MeV DTL

The PEFP 20-MeV DTL consists of four tanks that accelerate the 20 mA proton beam from 3 MeV to 20 MeV. The total length of the DTL is about 20 m. The PEFP DTL structures were designed for a beam duty of 24%, and the FFDD lattice configuration has a magnetic field gradient of 5 kG/cm and an effective field length of 3.5 cm.

The DTL was fabricated using electroplating technology for the tanks and e-beam welding technology for the drift tube. A laser tracker was used to align the drift tubes in the tanks. Figure 8 shows the inside of a tank. The tuning goals for the PEFP DTL were such that the deviation in frequency was less than ±5 kHz from the design value, and the field distribution was less than ±2 %

throughout a tank with a tilt sensitivity against perturbations of less than 100%/ MHz.

For the 20-MeV DTL, a single klystron drives four DTL tanks simultaneously. For this multicavity driving concept, temperature control systems and mechanical phase shifters were installed in each tank. High-power RF tests were carried out. The peak RF power to each tank was 150 kW.

### *The RF System [6]*

The accelerator facilities at the KAERI test stand include the 20-MeV accelerator itself, two sets of 1-MW, 350-MHz RF systems, two sets of –100-kV, 20-A DC high-voltage power supplies for the klystron, two sets of 2-MW cooling systems for the cavity, and the RF system. The design duty of the 20-MeV accelerator was 24%, and two 1-MW, 350-MHz klystrons were used to drive the 20-MeV accelerator: one was for the RFQ, and the other was for the DTL. All the other ancillary facilities, such as the klystron power supply and cooling system, were designed for an operational duty of 100%. During the low-duty operational tests at the KAERI test stand, the RF system operated such that the electron beam of the klystron was in the continuous wave (CW) mode, and only the input RF signal was modulated for low-duty pulse operation. TED Model TH2089F klystrons (350 MHz, 1 MW CW, Thales Electron Devices) were used as the RF source for the 3-MeV RFQ and for the 20-MeV DTL. Two high-voltage power supplies and two modulating anode power supplies were fabricated and tested for the klystrons. In addition, iris-type input couplers were developed and installed in the RFQ and the DTL.

The digital LLRF system was developed, and the stability requirements of the RF field were: amplitude = 1% and phase = 1°. Our digital feedback control system was based on a commercial field-programmable gate array (FPGA) card hosted on a virtual machine environment (VME) board. A control logic based on feedback and feed-forward control was implemented in the FPGA by using a very high-speed integrated circuit hardware description language (VHDL).

### *Target Station for 20-MeV Proton Beam Users*

The operational license for the 20-MeV proton linac installed at the KAERI site was issued in 2007 by the Korea Institute of Nuclear Safety (KINS). According to our operational license, a 20-MeV beam with an average current of 1,000 nA can be supplied to users for their applications. At the exit of the 20-MeV DTL, a target station has been prepared to supply beams to the user, as shown in Fig. 2. The 20-MeV proton beams are transported with quadrupole magnets to expand the beam size and change the beam shape, for example, circular shape, and extracted into air through an aluminum beam window. Radiation is shielded with lead and concrete bricks.

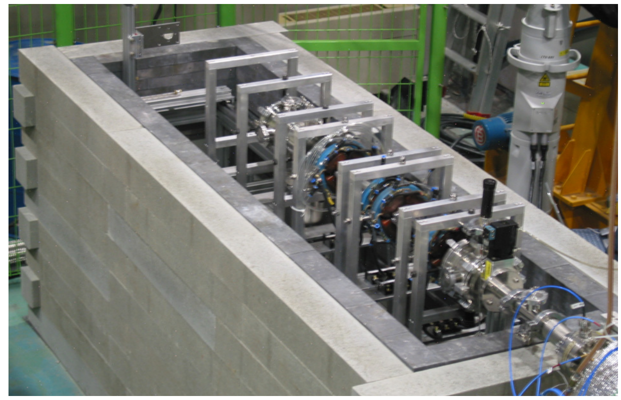

Figure 2: 20MeV proton beam target station.

## BEAM TEST

The beam test of the proton injector and RFQ was done to check the operation characteristics after the slight modification of the front-end system [7]. An ACCT (AC Current Transformer) was installed to measure the input beam current to the RFQ and a Tuned-CT was installed to measure the output beam current from the RFQ. A collimator was installed not only to shield the ACCT from stray magnetic field but also to eliminate the spurious beam signal induced by the secondary electrons. Also an electron trap was installed in front of the RFQ to protect the electron flow from the LEBT. The RFQ output beam current was measured depending on the LEBT parameters – mainly solenoid magnet currents. The results showed typical characteristics of the RFQ transmission. The optimum solenoid current sets were good agreement with the TRACE-3D results within 3%. The beam transmission rate was measured as a function of the RF power. The measured value was compared with the PARMTEQ simulation results as shown in Fig. 3. We could determine the operating set point of the RF power based on the measurement. After the adjustment of the operating parameters such as LEBT steering magnet current, solenoid magnet current, RFQ RF power, we could get 20mA peak current from the RFQ.

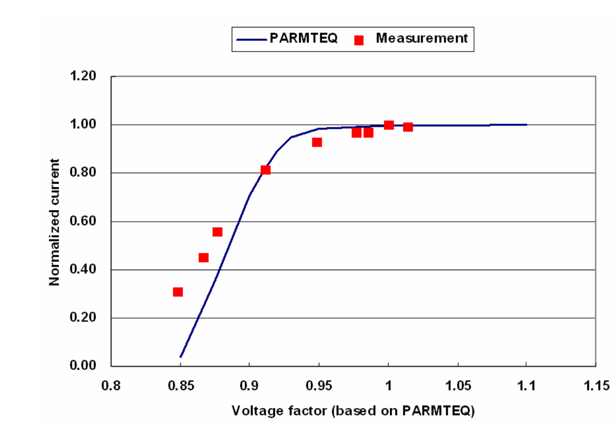


Figure 3: RFQ transmission rate depending on the vane voltage.

After the test of the RFQ, the beam test of the DTL started. The beam transmission through the DTL was about 80%. During test, the beam loss pattern was measured using pocket dosimeter (ALOKA, PDM-192) in every 20cm along the DTL. The result was such that a few numbers of noticeable localized peaks were measured as shown in Fig. 4. A beam dynamics study using PARMILA was done to investigate the cause of the localized beam loss pattern. The results showed that the cause of the first peak was estimated from the polarity reversal of the 30$^{th}$ electromagnet of the 2$^{nd}$ DTL tank. The beam loss pattern after the polarity reversal of the above quadrupole magnet is shown in Fig. 4. It could be seen that the first peak disappeared. In this case, the transmission rate through the DTL was nearly 100%. The second and third peak could not be explained from the polarity reversal of the electromagnet. And the peak could be greatly reduced by the stabilization of the tank resonance conditions. A 20mA peak proton beam could be accelerator up to 20MeV with the above conditions and the typical beam signal is shown in Fig. 5. The beam currents from the proton injector, RFQ and DTL were measured by ACCT, Tuned-CT and FCT respectively. The operating conditions were such that the RF pulse width was 50µs and the repetition rate was 1Hz.

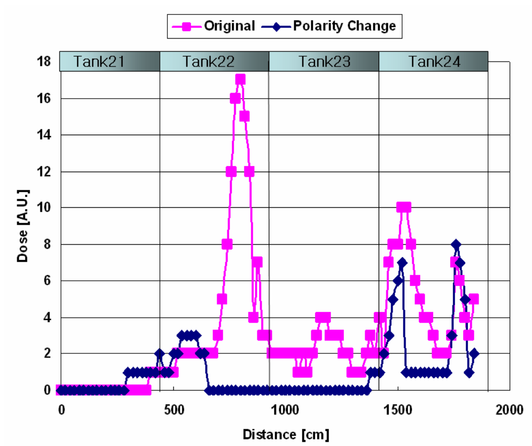


Figure 4: Beam loss distribution along the DTL (original: purple, after polarity change: blue).

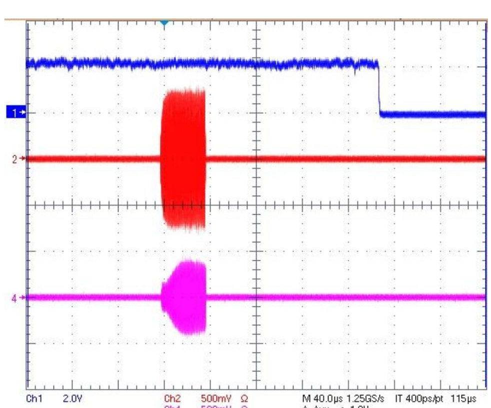

Figure 5: Beam signal of PEFP 20MeV linac (Ch 1: proton injector, Ch 2: RFQ, Ch 4: DTL).

## CONCLUSIONS

We have developed the technology required for the construction of a proton linac. Using this technology, a 20-MeV proton linac was developed and installed at the KAERI site in Daejeon. 20MeV 20mA peak current was achieved at a low duty (1Hz, 50us) and has been used to supply a 20-MeV beam to users with an operational license to supply an average current of 1000 nA.

In April 2009, the ground breaking for the construction will be started and the 20MeV machine will be moved and installed in 2011. In 2012, we will perform the full 24% duty operation of the 20MeV machine. Fig. 6 shows the new site at Gyeonju.

Figure 6: Bird's-eye-view for Gyeonju site.

## REFERENCES

[1] B. H. Choi, in Proceedings of Particle Accelerator Conference 2005 (Knoxville, 2005), p. 576.
[2] Y. Y. Lee, Nuc. Eng. Tech. **37**, 5, 433 (2005).
[3] Y. S. Cho and K. Y. Kim, J. Korean Phys. Soc. **48**, 721 (2006).
[4] H. J. Kwon, H. S. Kim, K. T. Seol, and Y. S. Cho, J. Korean Phys. Soc. **48**, 726 (2006).
[5] H. J. Kwon, H. S. Kim, J. H. Jang , and Y. S. Cho, J. Korean Phys. Soc. **50**, 1450 (2007).
[6] H. S. Kim, H. J. Kwon, and Y. S. Cho, J. Korean Phys. Soc. **48**, 732 (2006).
[7] H. J. Kwon, in Proceedings of the European Particle Accelerator Conference 2008 (Genoa, 2008), p. 3434.

# STABILITY OF NORMAL CONDUCTING STRUCTURES OPERATION WITH HIGH AVERAGE HEAT LOADING

V. V. Paramonov *, INR RAS, 117312 Moscow, Russia

## [illegible]

Instead of proved application of superconducting structures for high energy part of intense linear proton accelerators, Normal Conducting (NC) structures are still considered for medium and low energy parts below $200 MeV$. Operation with accelerating rate of $\sim 4\frac{MeV}{m}$ and duty factor $\sim 5\%$ results for standing wave NC structure in an average heat loading of $\sim 30\frac{kW}{m}$. Due to the high heat loading an operating mode frequency shift is significant during operation. In this paper conditions for field distribution stability against small deviations in time of individual cell frequencies are considered. For $\frac{\pi}{2}$ structures these conditions were formulated by L. Young and Y. Yamazaki. General case of 0, $\frac{\pi}{2}$ and $\pi$ operating modes is considered with common approach.

## INTRODUCTION

In projects of modern particle accelerators NC structures are consideration for application with the strong heat loading due to high average RF power dissipation. It can be the sequence of a high accelerating gradient $E_0T$, or long RF pulse, or high RF pulse repetition rate or combinations of these factors. Together with bi-periodical (or compensated) structures, simple periodical structures with 0 or $\pi$ operating modes are under consideration too due to a simpler design and construction. As it is known well, simple 0 or $\pi$ mode structures are sensitive in electric field distribution to small deviations of cells frequencies. To ensure required accelerating field homogeneity, not so large number of simple structure periods $N_p \sim 5 \div 10$ should be in the cavity and coupling coefficient should be so high, as reasonable.

Nevertheless, let us suppose the cavity with the simple periodic or bi-periodic structure is tuned for required field distribution and another parameters. But during a high RF power operation a question of thermal stability arises.

## THERMAL STABILITY

During a high RF power operation the temperature of the cavity increases and own cavity frequency $f_0$ decreases due to cavity expansion. For the fixed cooling conditions the cavity frequency shift is linearly proportional to the average dissipated RF power. For a heat loading of $\geq 20\frac{kW}{m}$ the cavity frequency shift $df$ can be of $df \geq 2.0 \cdot 10^{-4} f_0$. The cavity frequency for high RF power operation should be adjusted by the change of cooling water temperature.

Suppose we have a steady-state high RF power operation with a reference field distribution in the cavity. Let us suppose, that in one moment the cell with the number $j$ got a small frequency deviation $\Delta f_j$ due to some random reasons. Mostly possible reason is a fluctuation of a turbulent flow in cooling channels, because the turbulent flow is stable in average. For distinctness we will suppose $\Delta f_j < 0$, assuming cooling ability reduction. The small frequency change of the $j-th$ cell immediately will results in the change of the field distribution along the cavity and the change of relative field balance between cells. Depending on the structure dispersion properties, two options are possible.

In the first case the field in the $j-th$ cell relatively decreases. RF power dissipation in this cell decreases, the cell temperature decreases, the cell frequency increases, canceling initial cell frequency deviation. After some time the structure returns to operation with the reference field distribution. Such structures are thermally stable.

In the second case the field in the $j-th$ cell relatively increases. RF power dissipation in this cell also increases, the cell temperature increases, the cell frequency decreases, amplifying initial cell frequency deviation. Self-amplifying process starts. At least, such process can lead to the change in the filed distribution, because the cooling and control systems operate for the cavity as a whole. Such structures are thermally unstable.

## [illegible]

Suppose we know the total set of modes in the reference unperturbed cavity - frequencies $f_\nu$ and field distributions $E_\nu, H_\nu$, normalized as:

$$\int_V Z_0^2 H_n H_\nu^* dV = \int_V E_n E_\nu^* dV = \delta_{n\nu} W_0, \qquad (1)$$

where $Z_0 = \sqrt{\frac{\mu_0}{\epsilon_0}}$ and $V$ is the cavity volume. The field distribution in the cavity with a small dimension deviation $\Delta V$ can be describe as [1]:

$$E = E_n + \sum_{\nu \neq n} E_\nu \frac{f_\nu^2}{f_n^2 - f_\nu^2} \frac{1}{W_0} \int_{\Delta V} (Z_0^2 H_n H_\nu^* - E_n E_\nu^*) dV. \qquad (2)$$

In all periodical accelerating structures the field distribution along the axis can be described as:

$$E_{m\nu} = E_{\nu 0} cos(m\nu\pi), \qquad (3)$$

where $E_{m\nu}$ is the field amplitude in the $m$-th cell, $\nu\pi$ is the phase shift per structure period. Here we assume the phase

* paramono@inr.ru

shift for operating mode $n\pi, n = 0, 1$. Transforming (2) with using perturbation theorem, one can get, remembering frequency detuning only in the $j$-th cell:

$$E = E_n + \sum_{\nu \neq n} 2E_\nu a_\nu \frac{\Delta f_j}{f_j} cos(jn\pi)cos(j\nu\pi), \quad (4)$$

where $a_\nu = \frac{f^2}{f^2 - f_\nu^2}$. The similar relation for descriprion of a field perturbation in the chain of coupled cavities is given in [2] with a matrix form.

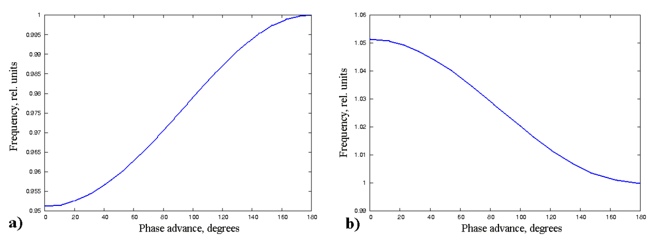


Figure 1: Dispersion curves for simple structures with positive (a) and negative (b) dispersion.

Dispersion curve for a simple periodical chain of coupled cells can be described by the equation:

$$f_\nu = \frac{f_c}{\sqrt{1 + k_c cos(\nu\pi)}}, \quad (5)$$

where $f_c$ is the own cell frequency and $k_c$ is the coupling coefficient. Depending of $k_c$ sign, the chain can have a positive dispersion, $k_c > 0$, $\frac{\partial f}{\partial \nu} > 0$, Fig. 1a, or a negative one, $k_c < 0$, $\frac{\partial f}{\partial \nu} < 0$, Fig. 1b.

Examples of simple structures are shown in Fig. 2. The

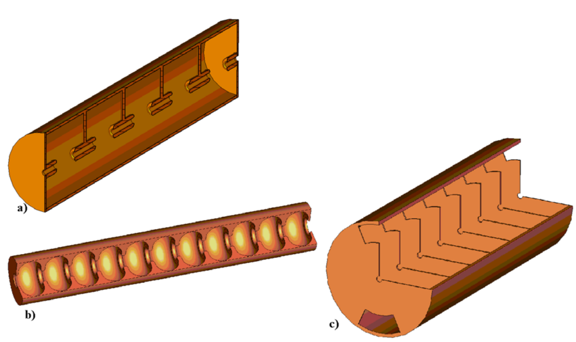


Figure 2: Examples of simple structures.

separated DTL structure [3] with operating 0 mode and positive dispersion is shown in Fig. 2a. Also positive dispersion has the structure with coupling through bore hole and operating $\pi$ mode, [4], Fig. 2b. Negative dispersion has a structure with coupling slots and $\pi$ operating mode, Fig. 2c.

For thermal stability of the structure coefficients $a_\nu$ in (4)

Table 1: Thermal stability of simple structures

| Operating mode | Dispersion | Thermal stabiliuty |
|---|---|---|
| 0 ($2\pi$) | positive | No |
| 0 ($2\pi$) | negative | Yes |
| $\pi$ | positive | Yes |
| $\pi$ | negative | No |

should be positive. With the negative $j-th$ cell detuning and positive $a_\nu$ value the perturbed field value in $j$-th cell will be decreased. One can check it by calculations in (2). It means for operating 0 mode the negative dispersion and for operating $\pi$ mode the positive dispersion. Results of thermal stability definition for all combinations of operating mode type and dispersion sign are summarized in the Table 1.

To confirm this conclusion, direct numerical simulations of the field distribution in $\pi$ mode structures with negative (slot coupled, Fig. 2c) and positive (bore hole coupled, Fig. 2b) dispersion and detuned first cell. Parameters of the structures are - $k_c = -5.0 \cdot 10^{-2}, N_p = 7, \frac{\Delta f}{f} = -5.2 \cdot 10^{-4}$ for slot coupled structure and $k_c = 1.25 \cdot 10^{-2}, N_p = 11, \frac{\Delta f}{f} = -4.4 \cdot 10^{-4}$ for bore hole couples one, where $N_p$ is the number of periods (number of accelerating gaps). Large detuning value, due to conducting cylinder at the cell axis, is chosen to do effect evident. In Fig. 3 the calculated $E_z$ distribution is for the perturbed operating mode are shown. One can see clear filed tilt in the filed distribution. For the $\pi$ mode structure with negative dispersion the field in the detuned cell is larger, Fig. 3a, and this structure is thermally unstable. For the $\pi$ - mode structure with positive dispersion we see the lower field in the detuned cell, Fig. 3b.

Important value is a rate of amplification $\frac{\partial E}{\partial(\Delta f)}$, which

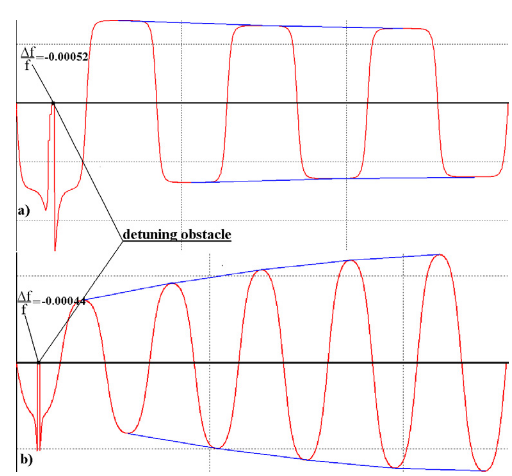


Figure 3: Calculated field distribution in $\pi$-mode structures with negative (a) and positive (b) dispersion with the detuned first cell.

is proportional to $a_\nu$. The main contribution in the field perturbation provides the nearest mode with $a_1$ coefficient. Supposing dispersion curve is described by (5), $a_1 \sim \frac{2N^2}{\pi^2 k}$. For $\pi$ mode structures, considered for Fig. 1, $a_1 = -1.57 \cdot 10^2$ and $a_1 = 1.62 \cdot 10^3$, respectively. Dispersion curve of the separated DTL, Fig. 2a, due to strong coupling is not described well by the relation (5). With direct simulations one can get $a_1 = 1.67$ for $\beta = 0.314$ and $a_1 = 3.75$ for $\beta = 0.553$ - rather small value.

## [illegible]

Let us remember, that a 'compensated' is named a structure in which at operating frequency coincide frequencies of two modes (accelerating $f_a, E_a$ and coupling $f_c, E_c$ modes) with different parities of field distribution with respect to symmetry plane [5]. Examples are well known structures, Side Coupled, Annular Coupled, On-axis Coupled, Disk and Washer, DTL with posts and so on. Dispersion curve of the compensated structure is shown in Fig. 1a, assuming operating $\pi$ mode, and consists from two branches. In practice frequencies of accelerating and coupling modes do not coincide perfectly and between branches there is a stop band with the width $\delta f = f_c - f_a$. The relations for description of dispersion curve (Fig. 4b)

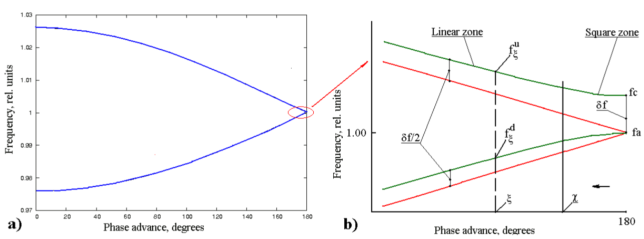


Figure 4: Dispersion curve for compensated structure (a) and behavior in the vicinity of operating point (b).

and field distributions of modes in the vicinity of operating point are given in [6] both for closed $\delta f = 0$ and open $\delta f \neq 0$ stop band.

For $\delta f \neq 0$ in the nearest vicinity of operating point $\xi \leq \chi$, 'square zone', where $\xi = \pi - \nu, \chi = \frac{2\delta f}{k\ f}$, [6], the field distributions for modes at upper $f^u_\xi$ and bottom $f^b_\xi$ branches of dispersion curve strongly differ and should not be modes in this region, $\nu_m = \frac{m\pi}{N}, \xi_m = \pi - \nu_m, \xi_m > \chi$. On the contrary, the structure has no properties of compensated one. It should be done in structure tuning by appropriate stop band width $\delta f$ decreasing.

In the 'linear zone' $\xi \geq \chi$ the behavior of the upper $f^u_\xi$ and the bottom $f^b_\xi$ curve branches is approximated as [6]:

$$f^{u,b}_\xi \approx f_a + \frac{\delta f}{2} \pm \frac{f_a k_c \xi}{4} - \frac{f_a k_c^2 \xi^2}{8}, \quad (6)$$

In this zone the branches of the dispersion curve are shifted at $\delta f/2$ value, but come parallel with respect to the branches for an ideal case $\delta f = 0$. The field distributions for modes at upper and bottom branches of dispersio curve are similar. We have to consider a simultaneous contribution of modes $\xi_m = \pi - \nu_m$ type in the field perturbation (4):

$$a_\xi = a^u_\xi + a^b_\xi = \frac{(f^u_\xi)^2}{f_a^2 - (f^u_\xi)^2} + \frac{(f^b_\xi)^2}{f_a^2 - (f^b_\xi)^2}. \quad (7)$$

Taking into account (7) and (6), considering the main part of the field perturbation due to nearest modes $m = 1, 2, 3...$ in the linear zone, and neglecting second order terms in $\xi_m$ and $\frac{\delta f}{f}$, one can get for perturbed field distribution (4):

$$E = E_a\left(1 + \sum_m \frac{64\delta f \Delta f_a N_p \cos j\theta_m \cos i\theta_m}{f_a^2 m^2 k_c^2}\right) \quad (8)$$

These contributions of nearest modes are partially compensated and a residual is proportional to the $\delta f$ value. As one can see from (8), for thermal stability of the structure should be $\delta f \geq 0$. For compensated structures this conclusion has been done before, [7], [8] basing on coupled circuits approach [2].

Estimating coefficient $a_1$ of contribution for nearest modes into perturbed field distribution, for $k_c = 0.05, N_p = 50, \frac{\delta f}{f} = 10^{-4}$ one gets $a_1 = 32$ - a smaller value as for simple $\pi$ mode structures with the same coupling coefficient but of order smaller number of periods.

## SUMMARY

For compensated, or bi-periodical structures, thermal stable operation all time can be achieved by appropriate structure RF tuning. In simple periodical structures existence or absence of thermal stability is the property of the structure. Thermal run away probability depends on the amplification rate value for field perturbation.

## REFERENCES


[1] B.P. Murin (ed), Ion Linear Accelerators, v.2, Atomizdat, Moscow, 1978, (in Russian)

[2] D.E. Nagle, E.A. Knapp, B.C. Knapp. Coupled cavity model for standing wave accelerator tanks. Rev. Sci. Instr., v. 38, p. 1583, 1967.

[3] T. Kato. Proposal of a Separated-type Proton Drift Tube Linac for a Medium-Energy Structure. KEK Report 92-10, 1992.

[4] J.W. Wang, et al., Studies of Room Temperature Structures for the ILC Positron Source. PAC 2005, p. 2827, 2005.

[5] Linear accelerators /Ed. P.M.Lapostolle and A.L. Septier.- Ams.: North-Holland Publ. Co., 1970.

[6] V.V. Paramonov. General relations for mode parameters of compensated structure in the vicinity of operating point. Proc. Linac2000, p. 401, 2000.

[7] L.M. Young, J. M. Potter. CW Side Coupled Linac for the Los Alamos/NBS Racetrack Microtron. IEEE Trasns. on Nucl. Sci., V. NS-30, n.4, p. 3508, 1983.

[8] Y. Yamazaki, T. Higo, K. Takata. Study of Alternating Periodic Structure Cavities with a Disc Loaded Waveguide Model. Part. Accel. v. 22, p. 273, 1988.

# STATUS OF THE LINAC4 PROJECT AT CERN

M. Vretenar, C. Carli, R. Garoby, F. Gerigk, K. Hanke, A.M. Lombardi, S. Maury, C. Rossi, CERN, Geneva, Switzerland

*Abstract*

Linac4 is a new 160 MeV, 40 mA H- accelerator which will be the source of particles for all proton accelerators at CERN from 2013. Its construction has started in 2008, as part of a programme for the progressive replacement or upgrade of the LHC injectors during the next decade. Linac4 will initially inject into the PS Booster and at a later stage into a 4 GeV Superconducting Proton Linac (SPL), which could ultimately be upgraded to high duty cycle operation. For this reason accelerating structures, RF infrastructure and shielding of Linac4 are dimensioned for higher duty cycle from the initial phase.

Linac4 is normal-conducting, 80 m long and consists of an RF volume ion source, an RFQ, a beam chopping section and a cascade of three different types of 352 MHz accelerating structures. Its main design requirements are high reliability, high beam brightness and low beam loss. The accelerator will be housed in an underground tunnel on the CERN Meyrin site, which can eventually be extended to the SPL, with equipment installed in a surface building above.

The main parameters, the status of the main components, the planning, the project organisation and the civil engineering infrastructure are presented.

## THE CERN INJECTOR UPGRADE

A programme for the progressive replacement or upgrade of the LHC injectors has been recently defined at CERN [1]. The first goal of this programme is to increase the LHC luminosity beyond nominal by improving beam brightness from the injector complex, which is now the main limiting factor towards higher luminosity. A second motivation is the replacement of the present cascade of injectors, which has been built between 1959 and 1978 and in the past few years has been giving rising concerns for its long-term reliability, with a more modern, reliable and easier to maintain system, where transfer energies and beam parameters are optimised for the LHC needs. Moreover, new low energy accelerators can be made compatible with operation at higher beam power that could be required by future physics needs.

The present sequence of accelerators used as LHC injectors is based on a proton linac of a relatively low energy (Linac2, 50 MeV) followed by the 1.4 GeV PS Booster (PSB), by the 26 GeV Proton Synchrotron (PS) and finally by the 450 GeV Super Proton Synchrotron (SPS). The new injector sequence would use an H⁻ high-energy linear accelerator, the 4 GeV Low-Power Superconducting Proton Linac (LP-SPL), whose normal-conducting section of 160 MeV, to be built in a preliminary stage, is called Linac4 [2]. The LP-SPL can be eventually upgraded to a High-Power SPL operating at multi-MW beam power [3]. The SPL will be followed by a new 50 GeV Proton Synchrotron (PS2). Present and future injection lines are schematically presented in Fig. 1.

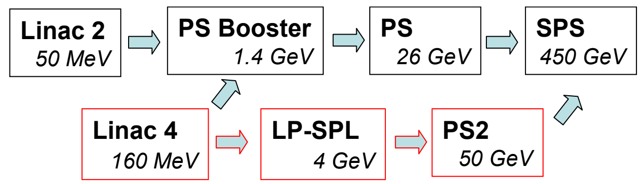


Figure 1: Scheme of the old and new LHC injectors.

A staged construction is possible because Linac4 can inject in a preliminary phase H⁻ ions into the existing PSB. The higher injection energy coupled with the benefits of H⁻ charge exchange injection are expected to increase brightness out of the PSB by a factor of 2, making possible a first increase in the LHC luminosity around 2013, when the nominal luminosity should have been attained in the LHC and a programme of upgrades to the ring and to the experiments aiming at higher luminosity could be implemented.

In June 2007, the CERN Council has approved the construction of Linac4 as a high-priority project for the period 2008-2013. At the same time, it has approved the detailed design of SPL and PS2, whose construction could start in 2012 and be terminated between 2015 and 2017

Linac4 will be housed in a 12 m deep underground tunnel, connected to the Linac2-PSB line. A surface equipment building will house klystrons and linac equipment. The Linac4 tunnel can be later on extended to the SPL. Figure 2 shows a view of the CERN Linac-PSB-PS complex, indicating the position of Linac4 and of the future extension to the SPL. Figure 3 presents the layout of the foreseen Linac4 infrastructure.

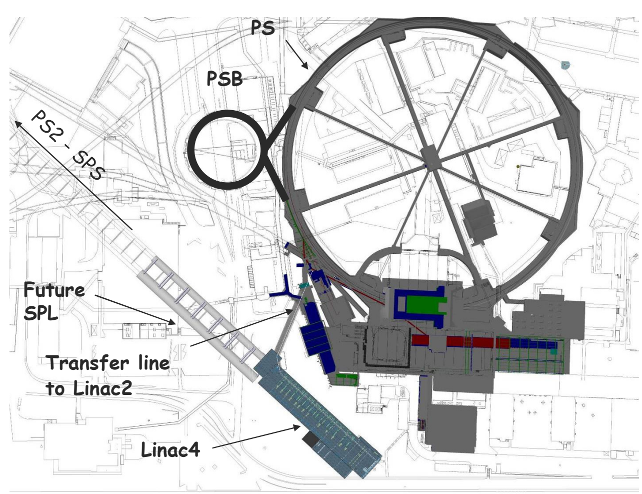


Figure 2: View of the PS Complex at CERN, showing the position of the new Linac4.

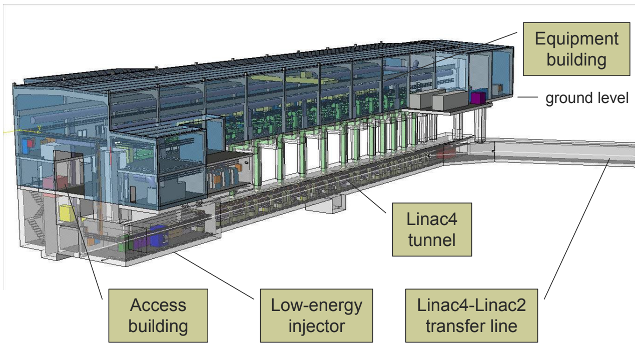


Figure 3: The Linac4 installations.

## LINAC4 DESIGN

The design of Linac4 is dictated by the requirement to operate in three different modes during its lifetime, depending on the characteristics (repetition frequency, pulse current and pulse duration) of the machine that it has to supply with beam:

1. PSB injector, 2013-2017: 1.1 Hz, 40 mA, 400 µs.
2. LP-SPL injector, from 2017: 2 Hz, 20 mA, 1.2 ms.
3. HP-SPL injector, after 2020: 50 Hz, 40 mA, 400 µs.

After a first phase as PSB injector the Linac4 beam pulse length will increase to 1.2 ms, whereas its current will go down by a factor 2. At a later stage, if the high-power programme is approved, Linac4 would operate at 50 Hz with a beam current going up again to 40 mA.

The main consequence on the Linac4 design is that civil engineering and in particular radiation shielding have to be dimensioned from the beginning for high-power operation. Accelerating structures and klystrons will be specified as well for high duty operation, whereas power supplies, electronics, and all electrical and cooling infrastructures will be dimensioned only for low beam power operation and will be replaced or upgraded when required for the SPL at full beam power. Additional space has been foreseen in the surface building for larger power supplies and for the additional SPL equipment.

In the design of machine and infrastructure particular care has been given to solutions providing the high reliability required for the first accelerator in the injection chain. Fault rate should be comparable to that of Linac2, ~1.5% of scheduled beam time. Particular attention has been given to the control of transverse and longitudinal emittance growth, for clean PSB and SPL injection, and of losses along the machine, to limit activation for the full-SPL mode of operation [4]. The main Linac4 design parameters are reported in Table 2.

Table 2: Main Linac4 Design Parameters

| | | |
|---|---|---|
| Output Energy | 160 | MeV |
| Bunch Frequency | 352.2 | MHz |
| Max. Rep. Rate | 2 | Hz |
| Max. Beam Pulse Length | 1.2 | ms |
| Max. Beam Duty Cycle | 0.24 | % |
| Chopper Beam-on Factor | 65 | % |
| Linac pulse current | 40 | mA |
| N. of particles per pulse | 1.0 | $\times 10^{14}$ |
| Transverse emittance | 0.4 | π mm mrad |

Three different accelerating structures will be used in Linac4 after the RFQ, all at 352 MHz frequency [5]. In particular, the Side Coupled Linac (SCL) at 704 MHz foreseen in a previous design [2] has been replaced with a Pi-Mode Structure (PIMS) operating at the basic linac frequency [6]. The Linac4 scheme with the transition energies is reported in Fig. 4.

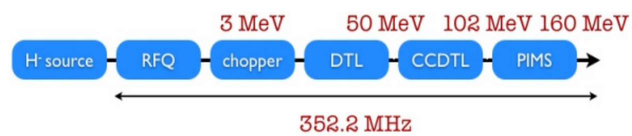


Figure 4: Linac4 layout.

Some 352 MHz klystrons and other equipment from the old LEP accelerator will be re-used for Linac4. In the first stage (Fig. 5, top), 13 old LEP klystrons at 1.3 MW and 6 new pulsed klystrons at 2.6 MW will feed the accelerating structures. Most of the LEP klystrons will be connected in pairs to a single modulator, allowing for the progressive replacement of pairs of LEP klystrons with one klystron of the new type. In the final configuration (Fig. 5, bottom) 9 new klystrons will feed two RF cavities each.

## LINAC4 STATUS

The pre-integration of machine components required for the definition of the building has started in May 2007 and has allowed tendering of the civil engineering works in April 2008. Construction work will start in October 2008; building and tunnel should be delivered at end 2010. In parallel, safety requirements have been addressed, and a preliminary Safety File has been submitted in June 2008 to the CERN Safety Authorities.

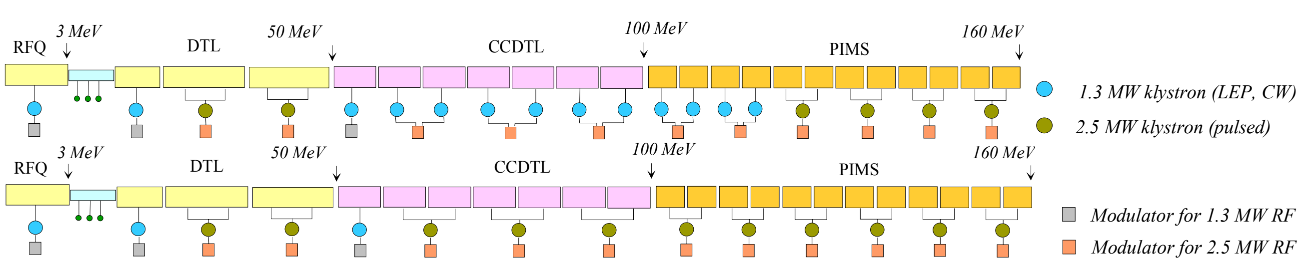


Figure 5: RF power distribution at installation (top) and after the end of the stock of LEP klystrons (bottom).

Construction of the ion source, RFQ [7] and chopper line is progressing. They will be successively installed in the Linac4 Test Stand (Fig. 6), where the Front End beam parameters will be extensively measured before installation in the tunnel. First beam measurements from the RF volume ion source are foreseen for the end of 2008. The chopper line elements have been built and the line is being assembled on its support. First beam tests at 3 MeV are foreseen after installation of the RFQ in March 2010. The prototype modulator and a LEP klystron operating in pulsed mode have been already successfully tested in the Test Stand.

Figure 6: The Test Stand with klystron and modulator (right), ion source cage (top).

The mechanical design of the Drift Tube Linac (DTL) is now completed. The DTL will use Permanent Magnet Quadrupoles mounted in drift tubes precisely aligned inside the tanks, without adjustments after assembly [8]. Construction of a DTL prototype is well advanced, first high-power tests are foreseen for the beginning of 2009 and construction of the first tank will start immediately afterwards. Two prototypes of the first Cell-Coupled DTL (CCDTL) module have been successfully tested at high power and the construction of the complete CCDTL is being organised [9]. The design of the PIMS structure has been completed, and construction of a full prototype of the first module is presently starting in the CERN Workshops [6]. The 70 m long transfer line connecting to the Linac2 line is in the detailed design phase. Procurement of RF and other equipment is starting.

## PROJECT SCHEDULE

The planning of the project (Fig. 7) depends on the schedule of the civil engineering works. After delivery of the building at end 2010, parallel installation of infrastructure and machine components will take place in 2011. In 2012 the different linac sections will be progressively commissioned. The connection of the transfer line and the modifications to the PSB for H$^-$ injection will take place during the 2012/13 CERN machine shut-down. It is foreseen that Linac4 will provide particles to all CERN users from June 2013.

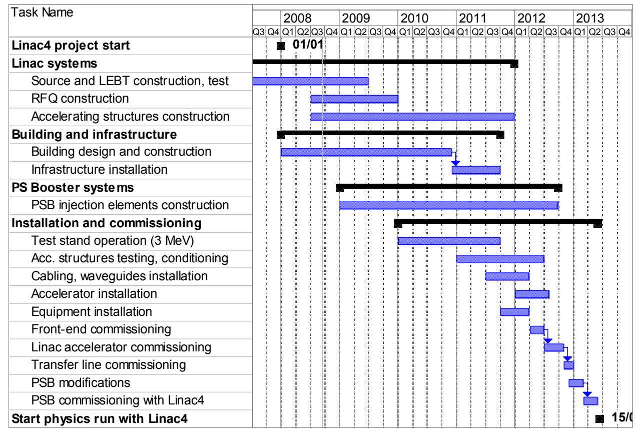


Figure 7: Linac4 Masterplan.

## ACKNOWLEDGEMENTS

We acknowledge the support of the European Community-Research Infrastructure Activity under the FP6 "Structuring the European Research Area" program (CARE, contract number FII3-CT-2003-506395).

## REFERENCES

[1] M. Benedikt, R. Garoby, F. Ruggiero, R. Ostojic, W. Scandale, E. Schaposhnikova, J. Wenninger, "Preliminary Accelerator Plans for Maximizing the Integrated LHC Luminosity", CERN-AB-2006-018.

[2] F. Gerigk, M. Vretenar (eds.), "Linac4 Technical Design Report", CERN-AB-2006-084.

[3] F. Gerigk (ed.), "Conceptual Design of the SPL-II", CERN-2006-006.

[4] G. Bellodi, R. Duperrier, M. Eshraqi, J.B. Lallement, S. Lanzone, A. Lombardi, E. Sargsyan, D. Uriot, "End to End Beam Dynamics and RF Error Studies for Linac4", this Conference.

[5] F. Gerigk, N. Alharbi, M. Pasini, S. Ramberger, M. Vretenar, "RF Structures for Linac4", PAC07, Albuquerque.

[6] M. Vretenar, P. Bourquin, R. De Morais Amaral, F. Gerigk, J.-M. Lacroix, G. Vandoni, R. Wegner, "Development Status of the Pi-Mode Accelerating Structure (PIMS) for Linac4", this Conference.

[7] C. Rossi, P. Bourquin, J.B. Lallement, A.M. Lombardi, S. Mathot, M. Timmins, G. Vandoni, M. Vretenar, S. Cazaux O. Delferriere, M. Desmons, R. Duperrier, A. France, D. Leboeuf, O. Piquet, "The Radiofrequency Quadrupole Accelerator for the CERN Linac4", this Conference.

[8] S. Ramberger, N. Alharbi, P. Bourquin, Y. Cuvet, F. Gerigk, A.M. Lombardi, E. Sargsyan, M. Vretenar, A. Pisent, "Drift Tube Linac Design and Prototyping for the CERN Linac4", this Conference.

[9] M. Vretenar, Y. Cuvet, G. De Michele, F. Gerigk, M. Pasini, S. Ramberger, R. Wegner, E. Kenjebulatov, A. Kryuchkov, E. Rotov, A. Tribendis, "Development of a Cell-Coupled Drift Tube Linac (CCDTL) for Linac4", this Conference.

# DEVELOPMENT OF A CELL-COUPLED DRIFT TUBE LINAC (CCDTL) FOR LINAC4

Y. Cuvet, F. Gerigk, G. De Michele, M. Pasini, S. Ramberger, M. Vretenar, R. Wegner, CERN, Geneva, Switzerland
E. Kenzhebulatov, S. Kryuchkov, E. Rotov, A. Tribendis, BINP, Novossibirsk, Russia
M. Naumenko, VNIITF, Snezhinsk, Russia

*Abstract*

The 352 MHz CCDTL will accelerate the Linac4 beam from 50 to 102 MeV. It is the first structure of this kind that will be used in a proton linac. Three short DTL-type tanks, each having two drift tubes, are connected by coupling cavities and form a chain of resonators operating in the stable π/2 mode. The CCDTL section is made of 7 such 5-resonator chains, each fed by a 1.3 MW klystron. Focusing quadrupoles are placed between tanks, easing their alignment with respect to a conventional DTL thus making the structure less sensitive to manufacturing errors. In order to validate the design and to develop the production technology, two prototypes have been constructed and successfully tested. The first prototype, built at CERN, consists of two half-cavities and one coupling cell, whereas the second, larger one, having two full cavities and one coupling cell, was built at VNIITF and BINP in Russia within the frame of an R&D contract funded by the ISTC Organisation. Both prototypes have been tested at CERN slightly beyond their nominal power level, at the design duty cycle of 10%. In this paper we present the results of high-power tests, the results of the technological developments prior to production, and the final design of the CCDTL.

## INTRODUCTION AND BASIC DESIGN

The Cell-Coupled Drift Tube Linac (CCDTL) was originally developed at LANL as a structure providing higher shunt impedance than conventional Drift Tube Linacs (DTL) for intermediate-velocity particles [1]. In the original design the CCDTL was used at twice the basic linac frequency (800 MHz) and when the principle was tested on a CW prototype it appeared that surface power density was too large for stable operation. To avoid these problems, CERN started to develop a CCDTL at the basic linac frequency of 352 MHz and for applications as the Superconducting Proton Linac (SPL), limited at a duty cycle of less than 10% [2]. Different combinations were analysed and tested, to finally adopt for the Linac4 project [3] the CCDTL configuration shown in Fig. 1. This CCDTL is made of 3-gap DTL-like accelerating tanks, connected by off-axis coupling cells bridging the focusing quadrupoles. Whereas the shunt impedance of this CCDTL configuration remains similar to that of a DTL with permanent quadrupoles, its main advantages are the easy access, alignment and cooling of the quadrupoles and the simpler construction and alignment of the tanks, the drift tube alignment tolerances being no longer dominated by the tight requirements of the quadrupoles.

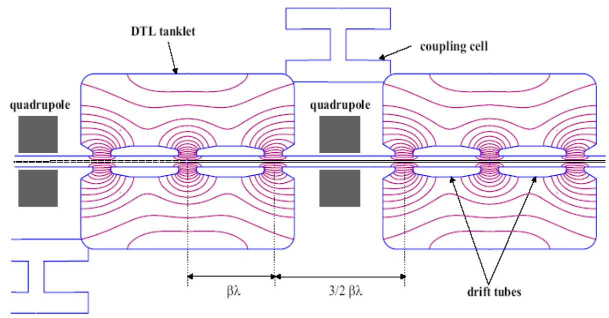


Figure 1: Linac4 CCDTL structure with indication of the electric field lines.

The RF configuration of Linac4 limits the peak power per resonator to about 1 MW. For this reason, the CCDTL tanks are grouped in modules of 3 tanks connected by two coupling cells (Fig. 2). The basic Linac4 CCDTL resonator is therefore made of 5 coupled cells operating in the π/2 mode. The CCDTL starts at 50 MeV, an energy that allows placing quadrupoles within the 3/2 βλ distance between neighbouring gaps. The geometry of the coupling cell and coupling slot is kept constant for all modules to simplify construction. This is achieved by shifting the end-walls of the tanks.

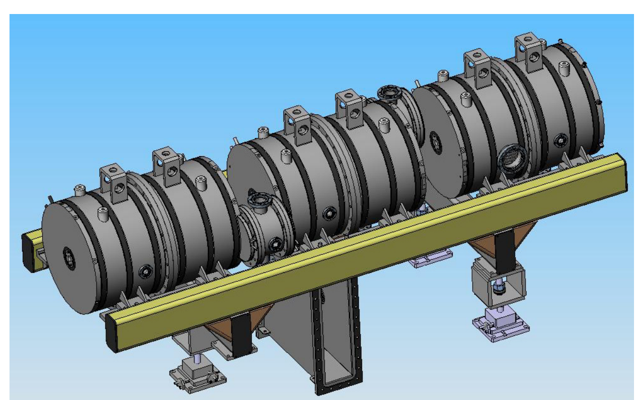

Figure 2: 3D view of a Linac4 CCDTL module with support structure and rectangular RF port.

At higher energies the shunt impedance of the CCDTL falls considerably, together with the coupling factor between CCDTL cells, inversely proportional to the stored energy per tank. Both these factors impose an upper energy limit of about 100 MeV for this structure.

The main parameters of the seven CCDTL modules are given in Table 1. The calculated copper power takes into account the effect of stems and slots and is then increased by a safety factor of 20%. Adding the beam power gives the values quoted in Table 1. The overall length of the CCDTL section is 23.38 m.

Table 1: Linac4 CCDTL Modules

| | $E_{out}$ [MeV] | $G_{acc}$ [MV/m] | $P_{RF}$ [MW] | length [m] | $E_{max}$ [Kilp.] |
|---|---|---|---|---|---|
| 1 | 57.1 | 4.00 | 0.96 | 2.64 | 1.6 |
| 2 | 64.6 | 4.10 | 1.0 | 2.82 | 1.6 |
| 3 | 72.1 | 4.20 | 1.0 | 2.98 | 1.6 |
| 4 | 79.9 | 4.30 | 1.0 | 3.14 | 1.7 |
| 5 | 87.8 | 4.23 | 1.0 | 3.29 | 1.7 |
| 6 | 95.6 | 4.16 | 1.0 | 3.43 | 1.6 |
| 7 | 102.9 | 4.10 | 1.0 | 3.57 | 1.6 |

## RF AND MECHANICAL DESIGN

The diameter of the cells has been optimized for maximum shunt impedance and is fixed for all cavities at 520 mm [4]. Each cavity is then tuned by changing the ratio of gap length over $\beta\lambda$. The gradient has been adjusted to keep the total RF power per cavity at a level of ~1 MW and the maximum surface fields below 1.7 Kilpatrick. Similarly all other geometric parameters were analyzed and the RF properties of the cavities were fully parameterized as a function of the geometric $\beta$ and the accelerating gradient.

A circuit model of a single module has been analysed with PSpice [5] to estimate the voltage errors in the cells due to frequency deviations. These errors can be classified in two types: the first one is caused by residual tuning errors and can be considered as static error; the second one (dynamic errors) comes from, for example, the change of the external temperature or variation of the cooling water temperature or flow speed.

For static errors, we consider the worst case of the CCDTL section, i.e. the last module with a coupling coefficient of k=0.59%. We assume a residual frequency error of ±20 kHz in the cavities using various distribution functions [5]. For this case the tilt sensitivity with respect to the average voltage has been calculated as 10.55%/MHz yielding a maximum field error of 0.2%.

For dynamic errors, the frequency variation due to the maximum expected temperature variation of $\Delta T$=10 K is estimated to be lower than 50 kHz. This variation is compensated with a movable tuner in the central accelerating cavity, requiring a tuner range of 150 kHz. In this condition the maximum voltage error in the accelerating cavities can rise up to 0.4%, which is fully acceptable for beam dynamics. In conclusion only one motorized tuner is necessary for each CCDTL module.

The prototype half-tanks were made by welding (electron beam or TIG) steel cylinders onto the end walls. Two half-tanks are then joined by a Helicoflex® gasket, which provides the RF contact and ensures vacuum tightness. For the series production the half tanks will be made of pre-shaped steel pieces, thus avoiding the welding step, improving the material properties, and speeding up construction. Since the alignment of drift tubes is not as critical as in a DTL, the drift tubes of the prototypes were welded to the tank walls while being fixed into position by a bar penetrating the drift tubes. Since every circular weld has an overlap in the start/end-point, there is a risk of deformation after the alignment bar is taken out. Therefore, for the series production will be adopted an alignment mechanism similar to that of the Linac4 DTL, which relies on the machining tolerances of a “stem holder” in a girder above the tank as shown in Figure 3 [6]. The RF and vacuum contacts between stems and tank are made with Helicoflex® gaskets, which are compressed by the spring-loaded “stem holder”.

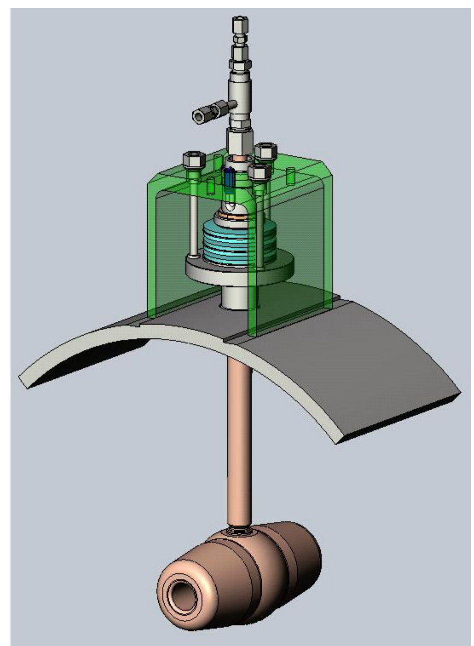

Figure 3: Drift tube fixation on the tank.

A critical point is the vacuum tightness of the rectangular iris, which connects to a rectangular wave-guide stub, and which is used to feed RF power into the central tank. The connection has been studied at VNIITF on a mock-up with HN and HNV type Helicoflex® gaskets using flanges with and without copper plating. The flanges were rectified to a roughness of Ra≈0.3 and cleaned, and after a series of vacuum leak tests it was concluded that the best solution is to use HN type gaskets on non-plated surfaces.

## PROTOTYPE TESTING

Two CCDTL high-power prototypes have been designed and built, both for the critical tanks at low energy (50 MeV). The first prototype, designed and built at CERN, was made of two half tanks closed by flat covers, connected by a coupling cell. This is the minimum configuration required to study RF and thermal properties. The second prototype (see Fig. 4), made of two complete tanks connected by a coupling cell, has been built in Russia by VNIITF (Snezhinsk) and BINP (Novossibirsk) within the frame of an R&D contract funded by ISTC. The mechanical design has been adapted to the production capabilities of the two laboratories. Construction and copper plating of the tanks was done in Snezinsk whereas construction and welding of drift tubes and final assembly and tuning were done in Novossibirsk.

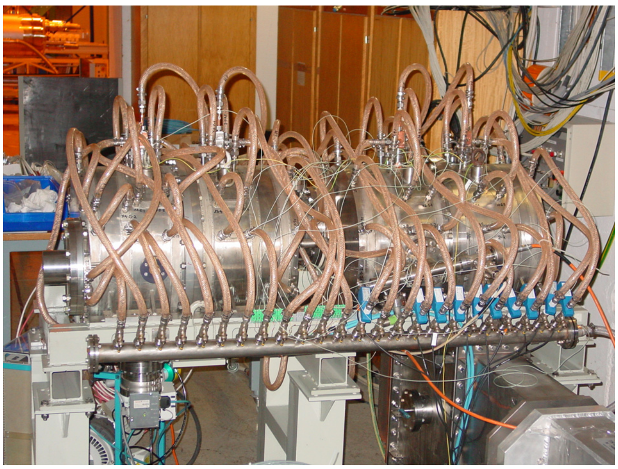

Figure 4: Second CCDTL prototype (VNIITF-BINP).

Both prototypes were tested at CERN, at low power and at high-power at the SM18 Test Stand. Table 2 reports the result of the low-power measurements. The Q-value of the first prototype is lower because the flat covers increase considerably the losses. For the second prototype, the Q-value was about 82% of the calculated one. Field flatness was in both cases within the measurement precision.

Table 2: Results of low-level measurements.

| | CERN prototype | ISTC prototype |
|---|---|---|
| frequency [MHz] | 352.35 | 352.14 |
| coupling factor [%] | 0.86 | 0.90 |
| unloaded Q | 27281 | 36700 |

High-power conditioning up to the Linac4 operating condition was straightforward for both prototypes, and increasing the duty cycle from the Linac4 value (0.1%) to the SPL duty cycle (10%) was relatively easy. No multipacting activity was observed in the first prototype, and only very limited activity was observed in the second one. Conditioning of the first prototype to 290 kW, corresponding to 1.09 times the design voltage, and to the Linac4 duty cycle took less than a day, and extending the duty cycle to 10% took 2 days. The temperature was measured in different critical positions on the tanks by means of thermocouples. The temperature of the drift tube holder, coupling iris and plunger tuner reached 58, 76 and 80 degrees, respectively. Conditioning of the second prototype took about a week. Power levels in excess of 330 kW at both Linac4 (0.1%) and SPL duty cycle (5%) were measured in the cavity, corresponding to 1.03 times the nominal operating level. The temperature monitoring indicated that at 5% duty cycle the temperature on the external part of the drift tube increased by 40 degrees, while the tuners in the accelerating cell (which were not equipped with cooling circuits) went up to 100 degrees. It was possible to stabilize the temperature at 330 kW power level at 11% duty cycle. For a duty cycle of 2.5% the measured temperatures have been compared with ANSYS simulations from VNIITF/BINP and an excellent agreement was found for 10 out of 12 thermocouples.

## CONSTRUCTION PROCEDURE AND PLANNING

It is planned to build the complete CCDTL in the frame of two ISTC projects, one funded entirely by CERN and the other one funded by the ISTC. As for the prototype, tanks and support will be built at VNIITF. After copper plating and pre-assembly the modules will be shipped to BINP. BINP will manufacture and install the drift tubes and take care of the RF tuning. The tuning will be checked after transportation to CERN together with vacuum tightness and a pressure test of the cooling channels. RF conditioning for all the 7 modules will be done at CERN, and installation in the Linac4 tunnel is foreseen from January 2011. Construction is foreseen to start in January 2009, with the first module being delivered to CERN in December 2009. The subsequent 6 modules will be delivered in batches of 2 with the last batch arriving at CERN in December 2010.

## ACKNOWLEDGEMENTS

We acknowledge the support of the European Community-Research Infrastructure Activity under the FP6 “Structuring the European Research Area” programme (CARE, contract number FII3-CT-2003-506395). We further acknowledge the support of the ISTC for the construction of a CCDTL prototype under contract number 2875.

## REFERENCES

[1] J. Billen et al, “A new RF structure for intermediate-velocity particles”, LINAC’94.
[2] F. Gerigk (Ed.),”Conceptual Design of the SPL II”, CERN-2006-006.
[3] http://www.cern.ch/linac4
[4] M. Pasini, “CCDTL design update for LINAC4”, CARE/HIPPI Document-2005-009.
[5] M. Vretenar et al. “CCDTL section for Linac4”, CARE/HIPPI Document-2008-020.
[6] S. Ramberger et al, “Drift tube linac design and prototyping for the CERN Linac4”, LINAC’08.

# STATUS OF THE RAL FRONT END TEST STAND

A.P. Letchford, M.A. Clarke-Gayther, D.C. Faircloth, D.J.S. Findlay, S.R. Lawrie, P. Romano, P. Wise (STFC RAL, Didcot, UK), F.J. Bermejo (Bilbao, Spain), J. Lucas (Elytt Energy, Madrid, Spain), J. Alonso, R. Enparantza (Fundación Tekniker, Elbr, Spain), S.M.H. Al Sari, S. Jolly, A. Kurup, D.A. Lee, P. Savage (Imperial College of Science and Technology, London, UK), J. Pasternak, J.K. Pozimski (Imperial College of Science and Technology, London; STFC RAL, Didcot, UK), C. Gabor, C. Plostinar (STFC ASTeC, Didcot, UK), J.J Back (University of Warwick, Coventry, UK)

*Abstract*

High power proton accelerators (HPPAs) with beam powers in the several megawatt range have many applications including drivers for spallation neutron sources, neutrino factories, waste transmuters and tritium production facilities. The UK's commitment to the development of the next generation of HPPAs is demonstrated by a test stand being constructed in collaboration between RAL, Imperial College London, the University of Warwick and the Universidad del Pais Vasco, Bilbao. The aim of the RAL Front End Test Stand is to demonstrate that chopped low energy beams of high quality can be produced and is intended to allow generic experiments exploring a variety of operational conditions. This paper describes the current status of the RAL Front End Test Stand.

## BACKGROUND

In order to minimise the need for remote or active handling of accelerator components, beam loss in future HPPAs must be kept to levels comparable to those of current facilities. With beam powers an order of magnitude or more greater than those currently achieved, fractional beam loss must necessarily be reduced by a similar factor. Beam chopping is one approach to reducing loss and will be an important feature of the next generation of HPPAs.

### *Beam Chopping*

In circular machines a significant source of beam loss occurs when the continuous linac beam is trapped and bunched in the ring RF bucket. Trapping efficiency can be improved with higher harmonic RF systems but to achieve the improvements necessary for MW scale beams, the linac beam must be chopped at the ring revolution frequency. This chopped beam allows for the ring RF bucket to be precisely filled with little trapping loss. The low levels of beam between bunches also reduces loss at extraction.

Everywhere downstream of the RFQ the linac beam has RF structure, this structure typically being at some 100s of MHz. Partially chopped bunches can occur in the linac if the chopping is not precisely synchronised with the linac beam RF bunch structure. With less charge than normal and possibly off axis or off momentum, these partially chopped bunches may lead to beam loss in the linac. The ideal is perfect chopping where the chopper switches on and off in the time between two successive linac beam bunches which is typically a few ns. This very fast switching requirement coupled with the increasing stiffness and power of the beam at higher energies dictates that chopping is carried out at the front of the linac, downstream of the RFQ at around 2.5 – 3 MeV.

### *Front End Test Stand*

The Front End Test Stand (FETS) project at RAL [1][2][3][4] has several goals. The primary goal is to demonstrate a high quality, high current, chopped $H^-$ beam. This is a generic objective and does not have a single future application in mind. FETS is funded by the Science and Technology Facilities Council (STFC) as part of their HPPA and Megawatt Spallation Source programme [5] and as a generic work package of the UK Neutrino Factory (UKNF) project [6].

A secondary goal of FETS is to encourage the study of accelerator technology within UK universities and foster international collaborations on HPPA research. High energy and particle physics has been well served by UK universities who are enthusiastic users of accelerator facilities and contributors to detector and physics projects however accelerator theory and technology has traditionally been less well served.

## TEST STAND COMPONENTS

The front end test stand consists of an $H^-$ ion source, magnetic low energy beam transport (LEBT), 324 MHz RFQ, medium energy beam transport (MEBT) chopper line and comprehensive diagnostics.

### *Ion Source*

FETS will use an ion source based on the well-proven and highly successful Penning type $H^-$ surface plasma source (SPS) [7] which is in routine operation on ISIS producing currents in excess of 50 mA at a duty factor of ~1%. Its use with an RFQ pre-injector has been previously demonstrated [8].

Following previous work which concentrated on increasing the current and duty factor of the source [9][10][11], recent work has focussed on understanding the beam transport and optics with a view to decreasing the emittance to the FETS specification. Considerable experimental and computational effort, using CST EM & Particle Studies [12] plus General Particle Tracer (GPT) [13], is leading to a much better understanding of the beam behaviour [14][15][16]. Figure 1 shows the predicted and measured beam profile at low extraction voltage.

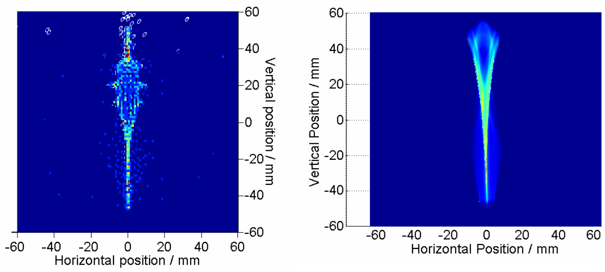


Figure 1: Left, simulated and right, measured beam profile.

In addition to furthering the theoretical understanding, installation of the ion source infrastructure in the FETS building at RAL is nearing completion [17]. Figure 2 shows part of the installation. First beam is anticipated in autumn 2008.

Figure 2: The high voltage cage and 65 kV high voltage platform.

## *Magnetic LEBT*

A 3 solenoid magnetic LEBT has been chosen for FETS [18][19]. In part this decision was informed by the successful combination of such a LEBT with the Penning ion source in the ISIS RFQ pre-injector upgrade [8]. An electrostatic Einzel lens LEBT, although offering some advantages, was rejected for this application due to fears about operating such a LEBT in close proximity to the highly caesiated ion source.

Figure 3 shows the simulated beam envelopes in the LEBT, calculated with GPT and based on the latest ion source measurements. Calculations suggest that from 0 – 100% space charge neutralisation can be accommodated by varying the solenoid fields.

Manufacture of the solenoids has been completed by Elytt/Neureus in Spain.

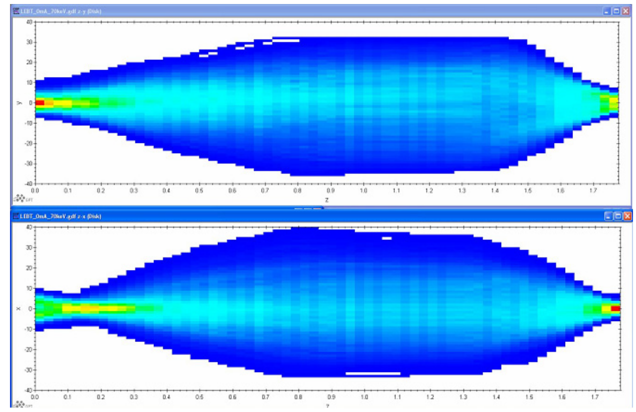

Figure 3: LEBT beam envelopes calculated with GPT.

Design of the LEBT support structures is complete with 2 of the 3 solenoids installed. Figure 4 shows the full LEBT design and one of the completed solenoids.

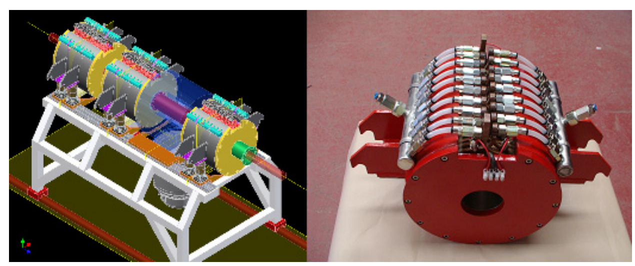

Figure 4: Layout of the FETS LEBT and one of the completed solenoids from Elytt.

## *RFQ*

A frequency of 324 MHz has been chosen for the FETS RFQ, determined by the ready availability of the Toshiba E3740A klystron developed for the JPARC linac [20]. One of these klystrons has been purchased and is at RAL. A contract has been signed for a HV power supply and solid-state modulator from Diversified Technologies, Inc [21] for delivery late in 2008.

A design for a 4-vane RFQ is well advanced with a cold model completed and extensively measured and compared to simulations [22][23][24]. Figure 5 shows the cold model during tests at Imperial College.

## *MEBT and Chopper*

FETS will use the novel fast-slow chopper scheme developed at RAL [25][26]. Having previously demonstrated operation of the 'fast' high voltage pulsers, attention has now focussed on the 'slow' pulsers [27] and prototyping the slow wave deflector structures [28].

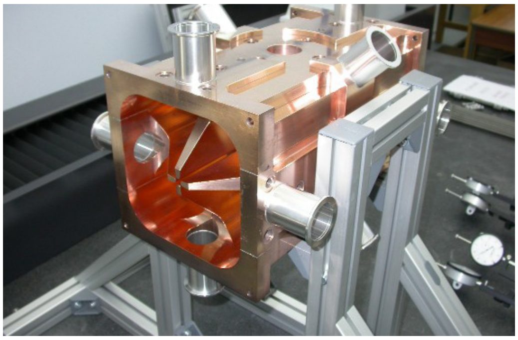

Figure 5: The RFQ cold model under test at Imperial College.

An optical design has been chosen as the FETS baseline for the MEBT. Compact PMQ/EMQ magnets are under investigation [29]. It is hoped to develop cavity cold models soon.

### *Diagnostics*

High quality diagnostics are essential to fully exploit the test stand. In addition to a suite of traditional diagnostics devices, non-destructive laser stripping techniques will also be employed. Non-destructive techniques are attractive due to the high beam power. A laser stripping transverse emittance measurement system is under investigation [30] as is a laser wire beam tomography system for determining beam density profiles [31]. The laser diagnostic vessel is manufactured and ready for installation.

## REFERENCES

[1] D.J.S. Findlay et al, "The RAL Front End Test Stand", Proc. NuFact04, Osaka University, Japan, Aug 2004.

[2] A.P. Letchford et al, "The RAL Front End Test Stand", EPAC'06, Edinburgh, Scotland, June 2006.

[3] J.J. Back et al, "Progress at the RAL Front End Test Stand", Nucl Phys B (Proc Suppl ) 155 309-311.

[4] A.P. Letchford et al, "Status Report on the RAL Front End Test Stand", PAC07, Albuquerque, NM, USA, Jun 2007.

[5] J. Thomason et al, "Megawatt Upgrades for the ISIS Facility", EPAC'08, Genoa, Italy, June 2008.

[6] http://hepunx.rl.ac.uk/uknf.

[7] D.C. Faircloth, et al, "Understanding Extraction and Beam Transport in the ISIS H− Penning Surface Plasma Ion Source", Review Of Scientific Instruments 79, 02b717 2008.

[8] A.P. Letchford et al, "Testing, Installation, Commissioning and First Operation of the ISIS RFQ Pre-injector Upgrade", PAC05, Knoxville, May 2005.

[9] D.C. Faircloth and J.W.G. Thomason, "Extending the Duty Cycle of the ISIS H- ion source, Thermal Considerations", EPAC'04, Lucerne, June 2004.

[10] D.C. Faircloth et al, ."Thermal Modeling of the ISIS H− Ion Source", Review of Scientific Instruments, Volume 75, Number 5, May 2004.

[11] D.C. Faircloth et al, "Practical experience in Extending the Ion Source and Injection System H- Ion Source Duty Cycle", Rev. Sci. Instrum. 77, 03A520 (2006), March 2006.

[12] CST Ltd., Bad Nauheimer Strasse 19, 64289 Darmstadt, Frankfurt, Germany http://www.cst.de.

[13] Pulsar Physics, Burghstraat 47, 5614 BC, Eindhoven,The Netherlands, http://www.pulsar.nl.

[14] D.C. Faircloth et al, "Study of the Post Extraction Acceleration Gap in the ISIS H Penning Ion Source", EPAC'08, Genoa, Italy, June 2008.

[15] S.R. Lawrie et al, "Redesign Of The Analysing Magnet In The ISIS H- Penning Ion Source", 1st International Conference on Negative Ions, Beams and Sources, Aix-en-Provence, France, Sep 2008.

[16] D.C. Faircloth et al, "Multi-Beamlet Study Of Beam Transport In The Isis H- Ion Source Analysing Magnet", EPAC'08, Genoa, Italy, June 2008.

[17] D.C. Faircloth et al, "Installation Of The Front End Test Stand High Performance H− Ion Source", EPAC'08, Genoa, Italy, June 2008.

[18] A.P. Letchford et al, "The RAL Front End Test Stand", EPAC'06, Edinburgh, Scotland, June 2006.

[19] S. Jolly et al, "LEBT Simulations and Ion Source Beam Measurements for the Front End Test Stand (FETS)", EPAC'06, Edinburgh, Scotland, June 2006.

[20] http://www.toshiba-tetd.co.jp/eng/ .

[21] http://www.divtecs.com/.

[22] A Kurup, A.P. Letchford, "Electromagnetic Design of a Radio Frequency Quadrupole for the Front End Test Stand at RAL", EPAC'06, Edinburgh, Scotland, June 2006.

[23] P. Savage et al, "Mechanical Design and RF Measurement on RFQ for Front-end Test Stand at RAL", EPAC'06, Edinburgh, Scotland, June 2006.

[24] D.A. Lee et al, "Detailed Study of the RF Properties of the FETS RFQ Cold Model", EPAC'08, Genoa, Italy, June 2008.

[25] M.A. Clarke-Gayther, "Modulator Systems for the ESS 2.5 MeV Fast Chopper", PAC01, Chicago, USA, June 2001.

[26] M.A. Clarke-Gayther, "A Fast Beam Chopper for Next Generation High Power Proton Drivers", EPAC'04, Lucerne, Switzerland, July 2004.

[27] M.A. Clarke-Gayther, "The Development of a Fast Beam Chopper for Next Generation High Power Proton drivers", EPAC'08, Genoa, Italy, June 2008.

[28] M.A. Clarke-Gayther, "Slow-wave chopper structures for next generation high power proton drivers", PAC07, Albuquerque, NM, USA, Jun 2007.

[29] C. Plostinar, M.A. Clarke-Gayther, "Hybrid Quadrupoles Designs for the RAL Front End Test Stand (FETS)", EPAC'08, Genoa, Italy, June 2008.

[30] C. Gabor et al, "Laser-based Beam Diagnostic for the Front End Test Stand (FETS) at RAL", EPAC'06, Edinburgh, Scotland, June 2006.

[31] D.A. Lee et al, "Laser-based Ion Beam Diagnostics for the Front End Test Stand at RAL", EPAC'08, Genoa, Italy, June 2008.

# A FAST CHOPPER FOR THE FERMILAB HIGH INTENSITY NEUTRINO SOURCE (HINS)*

R. Madrak, D. Wildman, FNAL, Batavia, Illinois, 60510, U.S.A.
A. Dymokde-Bradshaw, J. Hares, P. Kellett, Kentech Instruments Ltd., Wallingford, U.K.

*Abstract*

A fast chopper capable of kicking single 2.5 MeV $H^-$ bunches spaced at 325 MHz, at rates greater than 50 MHz is needed for the Fermilab High Intensity Neutrino Source (HINS) [1]. Four 1.2 kV fast pulsers, designed and manufactured by Kentech Instruments Ltd., will drive a 0.5 m long meander made from a copper plated ceramic composite. Test results showing pulses from the first 1.2 kV pulser and meander results will be presented.

## INTRODUCTION

As a demonstration of the feasibility of a high intensity 8 GeV proton source, Fermilab is constructing a 60 MeV $H^-$ linac (HINS). This would serve as the front end to a superconducting 8 GeV linac, which would deliver beam to the Main Injector. Since the operating frequency of this linac is 325 MHz, not a multiple of the Main Injector's 53 MHz, we are compelled to chop out approximately one out of every six beam bunches. This avoids beam losses due to bunches which would not be captured in a Main Injector RF bucket.

The chopping is to be done in the 2.5 MeV (MEBT) section of the linac. This requires extremely fast (width < 6 ns) high voltage (±2.4 kV) pulses which propagate at the same speed as the beam ($\beta$=0.073) along a two plate deflecting "meander" structure. The requirement on the width is such that only one bunch at a time may be removed.

The two meander structures are 50 cm long, each with an impedance of 100 ohms. To obtain the necessary deflection, the beam must be kicked by the electric field (due to the high voltage pulse) for the entire length of the meander.

## FAST PULSER

Fermilab has procured from Kentech Instruments, Ltd. [2] a prototype 500V pulser, in June 2006, and a 1.2 kV pulser in November 2007. The average chopping rate imposed by the HINS pulse parameters is close to 1MHz however the switching losses in high voltage (kilovolt) semiconductor switching devices becomes excessive at these pulse rates. In order to obtain fast rise and fall, together with a high pulse repetition rate, the output is generated from an array of custom packaged low voltage (100 volt) semiconductor switches. These relatively low voltage parts have a bandwidth of ~500MHz allowing nanosecond rise and fall times.

The 1.2 kV pulser is based on an array of twenty four 50V pulse cards. The cards are floating, each with an output impedance of ~2 ohms. This output from each card is transported by 12 parallel 25 ohm semi-rigid coax cables and is taken to a summing point. When combined, this yields the 1.2 kV, 50 ohm output.


Figure 1: Kentech 1.2 kV pulser.

Each card has a floating power supply together with PECL trigger logic, burst width and duty cycle limit circuitry and power supply monitoring, all of which are remotely controlled. The TTL burst pattern input trigger signal is regenerated in PECL circuitry on each card before being amplified to a 50V pulse output. Individual cards can be enabled or disabled for testing purposes and the correct operation of the card can be confirmed via the link.

The pulser incorporates load fault detection (open or short circuit) and has an embedded controller for set up and control functions. It may be operated in either a 1 ms or 3 ms mode, triggered by an arbitrary TTL pattern with the option of a 325MHz clocked data input. The maximum total on-time during a 1 ms burst is 0.75 ms. A photograph of the 1.2 kV pulser is shown in Fig. 1. Figure 2 shows the pulser output (attenuated by 60dB). The top scope photo shows several 1.2 kV pulses spaced by ~20 ns. The bottom shows a full 3 ms burst of this pulse pattern.

*Operated by Fermi Research Alliance, LLC under Contract No. DE-AC02-07CH11359 with the United States Department of Energy.

## MEANDER STRUCTURES

We began our meander R&D with a $Z_0 = 50\Omega$ prototype structure given to us by F. Caspers (CERN) [3]. This is a double meander structure printed onto alumina substrate ($\varepsilon$=9.8). We scaled this design (by scaling the width of the trace pattern) to account for the difference in $\beta$ of ~8%. The new scaled structure is the first shown in Fig. 3.

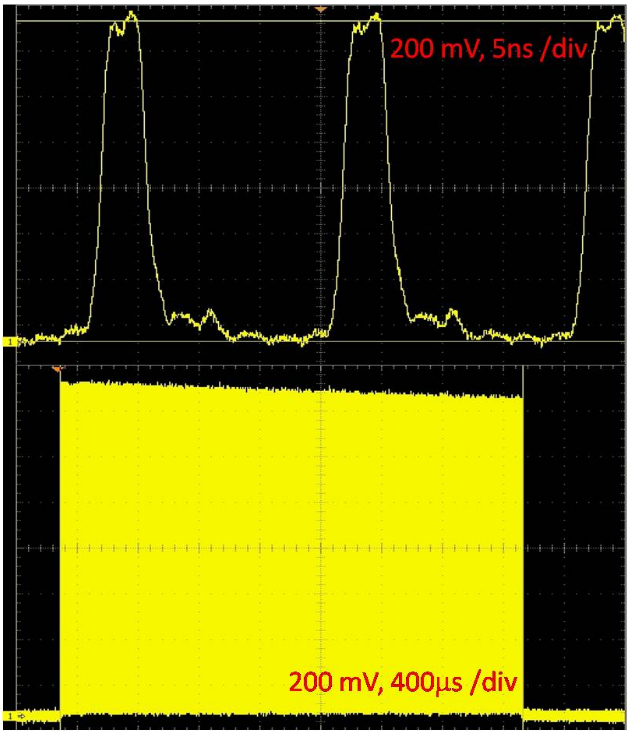


Figure 2: Kentech 1.2 kV pulser output, with 60dB attenuation. The top trace shows several 1.2 kV pulses with ~20 ns spacing. The bottom trace shows this pattern repeated for 3 ms.

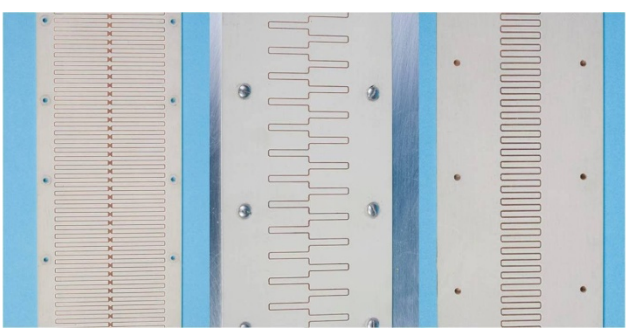

Figure 3: Double meander (left, $Z_0 = 50\Omega$), low dispersion single meander (middle, $Z_0 = 100\Omega$) and high coverage factor single meander (right, $Z_0 = 100\Omega$).

Rogers TMM10i was chosen instead of alumina for the new meander structure. This material also has $\varepsilon$=9.8, however, the material allows for complete meanders to be made very quickly. Laminates may be procured in 18x24″ sheets with copper cladding on one or both sides. The meander pattern can then be quickly routed out on a small programmable milling machine for PC boards which is available in-house.

To test for suitable behavior of Rogers TMM10i in vacuum, we baked a 24x13 cm sample for 90 hours at 170 C. After the bakeout we obtained a pressure of 8E-08 torr at 55 C (the predicted operating temperature of the meander, given losses) with a relatively low pumping speed of 0.63 L/s. Given that the surface area of the sample is a factor of 3 lower than that of the two meanders which will comprise the final chopper, we expect to be able to attain vacuum levels on the order of $10^{-8}$ torr. (using a larger vacuum pump) without much difficulty.

We have explored three designs for the meander structure. The first, already mentioned, is a 50 ohm double meander structure. The second and third have a single trace with 100 ohm impedance. These are shown in Fig. 3 and are termed the 'low dispersion single meander' (LDSM) and the 'high coverage factor single meander' (HCSM). Each structure uses ⅛″ thick Rogers TMM10i High Frequency Laminate Circuit Material with 70 µm Cu cladding. The prototype structures are 18″ (46 cm) long. The transverse extent of the traces is 78 mm for the double meander, 40 mm for the LDSM and 20 mm for the HCSM. In each case the width of the trace is 0.015″.

### *Pulse Behavior*

Figure 4 shows the pulse behavior at the beginning, middle and end of the three meanders. Also shown is the (low voltage) input pulse. Both single meanders show little increase in the pulse width as it progresses down the structure, though the degradation is the least in the LDSM.

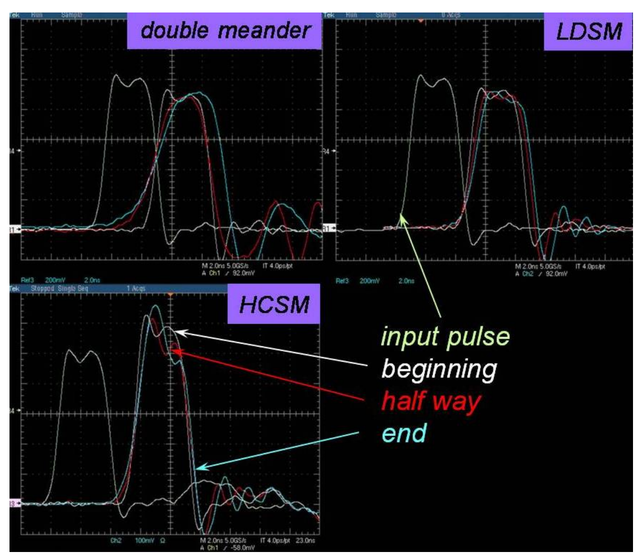


Figure 4: Pulse behavior along the meander structure.

### *Coverage Factor*

Since the metal traces of the meander are not solid conductor (on the scale of the beam size), the effective electric field is less than the voltage difference between two structures divided by their separation. The leads to the definition of the coverage factor, which is $E/(\Delta V/d)$, where E is the actual electric field between the plates, $\Delta V$

is the voltage difference, and d is the separation. We have measured the coverage factor as a function of transverse position for each meander, using the fixture shown in Fig. 5, along with a network analyzer. This is an $S_{21}$ measurement with Port 1 connected to the meander traces and Port 2 connected to a HP85024A high frequency probe which serves as a pickup. The probe tip is the same distance away from the meander surface as the beam (8 mm) and is surrounded by a ground plane. The probe is mounted on micrometer adjustable stages so that it may be moved in the x and z directions.

For normalization, a wide (25 mm) stripline is used. In this case, the probe tip is located at one of the stripline groundplanes. Each groundplane is 8mm from the stripline center conductor. Measurements for 100 ohm meanders are corrected for reflection due to the impedance mismatch between the network analyzer and the meander. For the double, LDSM and HCSM we measure coverage factors of 71%, 48%, and 74%. We also measure the coverage factor for the double meander in a slightly different configuration: with 0.062″ spacers between the double meander and groundplane. Here the double meander has 100 ohm impedance; we measure a coverage factor of 87%. Simulations of the CERN SPL double meander chopper structure [3], which has the same trace density as the double meander discussed here predict a coverage factor of 80%. Microwave Studio (MWS) simulations at FNAL predict a slightly lower coverage factor of 75%. Figure 6 shows measurements of the coverage factor versus transverse position on the meander.

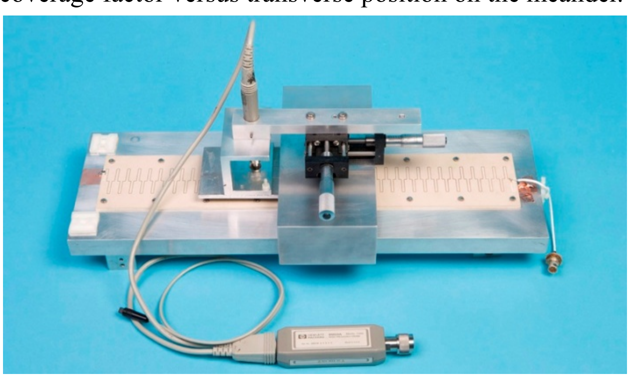

Figure 5: Coverage factor measurement fixture.

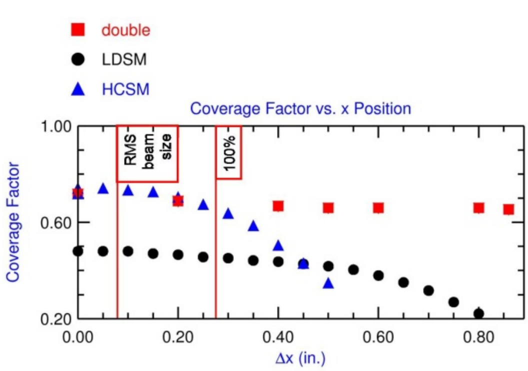


Figure 6: Coverage factor vs. transverse position.

## FINAL DESIGN

The final chopper will consist of two 50 cm long meander structures with a spacing of 16 mm. Obtaining the necessary beam deflection angle of 24 mRad imposes the requirement $\Delta V$(plates) = 4.8 kV (accounting for a coverage factor of 80%).

Figure 2 shows that a high quality 53 MHz 1.2 kV pulser is possible. Thus, we plan to combine the output of two 1.2 kV/50 ohm pulsers into one 2.4 kV/100 ohm pulser. This can be done for both polarities (for ± 2.4 kV) and will yield the desired 4.8 kV, when used with a 100 ohm meander structure. It is this reasoning which initially led us to explore the 100 ohm meander design as opposed to the more common 50 ohm version. Of the 100 ohm single meanders, the LDSM exhibits the best pulse behavior along the length; however, the coverage factor is much too low. Thus we have chosen for our final design the HCSM, which has good pulse behavior along the length of meander as well as a high coverage factor.

We have built a combiner, or coaxial cable impedance transformer, using 46 turns of Andrew FSJ2-50, ⅜″ heliax superflexible foam coaxial cable, wrapped around five 1″ thick cores. These are MN60 cores with an OD and ID of 11″ and 4.5″. We have tested the combiner using the Kentech 0.5 and 1.2 kV pulsers. We obtain good quality output pulses of approximately 1.6 kV, shown in Fig. 7.

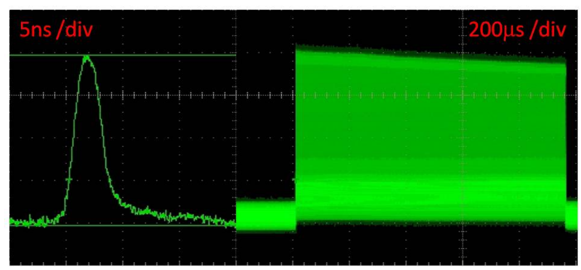


Figure 7: Combiner output.

## ACKNOWLEDGEMENTS

We wish to thank F. Caspers (CERN) for many useful discussions and for providing the double meander structure with which we began our studies.

We also wish to thank Gennady Romanov (FNAL) for the MWS simulation predicting the coverage factor for the meander structure, and Terry Anderson (FNAL) for performing the TMM10i vacuum test.

## REFERENCES

[1] R. Webber, "Overview of the High Intensity Neutrino Source Linac R&D Program at Fermilab", LINAC08, Victoria, BC, Canada, September 2008.

[2] Kentech Instruments Ltd., Isis Building, Howbery Park, Wallingford, Oxfordshire, OX10 8BA. U.K., http://www.kentech.co.uk/index.html.

[3] F. Caspers, A. Mostacci, S. Kurennoy, "Fast Chopper Structure for the CERN Superconducting Proton Linac", EPAC'02, Paris, June 2002, THPLE027, p. 873 (2002).

# AN 8 GeV CW LINAC WITH HIGH POTENTIAL BEAM POWER*

Charles Ankenbrandt[a,c], Richard Baartman[b], Ivan Enchevich[a], Rolland P. Johnson[a#], Alfred Moretti[c], Sergei Nagaitsev[c], Michael Neubauer[a], Thomas Peterson[c], Milorad Popovic[c], Robert Rimmer[d], Gennady Romanov[c], Nikolay Solyak[c], Vyacheslav Yakovlev[c], Katsuya Yonehara[c]

[a]*Muons, Inc., Batavia, IL, USA*
[b]*TRIUMF, Vancouver, BC, Canada*
[c]*Fermi National Accelerator Laboratory, Batavia, IL USA*
[d]*Thomas Jefferson National Accelerator Facility, Newport News, VA, USA*

*Abstract*

Modern technology allows us to consider operating an 8 GeV SC linac in a CW mode to accelerate a high-current $H^-$ beam. By using appropriate accumulation rings, the linac could provide simultaneous beams for direct neutrino production, neutrino factories, fixed target experiments, and muon colliders. Several other unique accelerator applications could also be served and improved by the same continuous beam, including studies of energy production and nuclear waste reduction by transmutation, rare muon decay searches, and muon catalyzed fusion. A comparison of CW and pulsed operation is strongly dependent on the choice of accelerating gradient, and a first look at refrigeration requirements for a gradient of 20 MV/m is included in this study. Methods for accumulating the beam from a CW linac to serve the special needs of the potential future Fermilab programs mentioned above are considered. In this paper we also examine the use of a cyclotron as a source of high current beams to reduce the cost and complexity of the linac front end. Although the refrigeration system would be large for 20 MV/m gradient, a 3 mA CW $H^-$ beam at 8 GeV looks feasible, with potential beam power up to 24 MW to access the intensity-frontier for muon and neutrino physics and also be an essential step to an energy-frontier muon collider.

## INTRODUCTION

Modern proton accelerators or storage rings use multi-turn $H^-$ charge exchange injection and strip at high energy, where the Laslett tune shift is smaller, to achieve high proton bunch intensities. This approach has been used in several new machines, and the next step that is being proposed is to provide a powerful 8 GeV $H^-$ linac that could feed any number of accumulation rings or accelerators for planned and as yet undreamt-of purposes.

A plan for Project-X [1], to replace the aging Fermilab 8 GeV rapid cycling Booster proton synchrotron, has centered on a 1.3 GHz superconducting (SC) linac, which could also act as a string test for the ILC. The purpose of this paper is to consider a CW $H^-$ linac as an option for Project-X, which would not be limited by any ILC constraints and, by virtue of high potential 8 GeV beam power, be best suited to the needs of any future Fermilab research program. Nevertheless, as a large-scale SRF system, it would act as a significant demonstration of many aspects of ILC technology.

Since its design in the late 1960's, the Fermilab Booster has at times been both the world's most intense proton source and almost always the bottleneck in the Fermilab research program, where proton economics have determined which experiments could be scheduled or even were possible. If the Booster is replaced as planned, it will have served in this way for about 45 years. It is quite likely that its replacement will have a similar function for a similar time.

Recent studies of proton driver requirements for muon colliders and neutrino factories [2] have indicated that the present parameters for Project-X may limit these machines because the proton beam power will be insufficient and the repetition rate too low. Even with optimistic muon collection and cooling efficiencies, at least 4 MW of 8 GeV proton power will be required for muon collider designs. The natural repetition rate for muon machines is suggested by the muon lifetime in its final storage ring. For a 5 TeV center of mass collider, for example, the muon lifetime is about 50 ms so that the natural repetition rate is about 20 Hz. For lower energy storage rings, the natural repetition rate is higher.

For the study reported here, the RF gradient G has been chosen to be low enough such that resistive losses, proportional to $G^2$, are not too large. In the next section we calculate the wall-plug power for the case of G=20 MV/m for ILC-like RF structures. This is to be compared to the 25 to 30 MV/m presently favored by Project-X. A gradient of 20 MV/m implies a linac that would be about 27/20 times longer than the baseline, but has the compensating virtue of easier technology for the RF cavities and klystrons.

## CW CRYO POWER REQUIREMENTS

CW operation results in much higher dynamic heating in the RF cavities and input couplers and higher cryogenic cooling power requirements. Table 1 shows a comparison of the power requirements for the components of a TESLA linear accelerator operated as a pulsed machine compared to CW operation.

*Supported in part by the US DOE under contracts DE-AC02-07CH11359 and DE-AC05-84ER40150 and STTR grant DE-FG02-08ER86350.
#rol@muonsinc.com

Table 1: cryogenic power loads per 8-cavity cryomodule for a CW versus Pulsed TESLA-style linac.

| Cryomodule | TESLA | | CW | |
|---|---|---|---|---|
| | Static | Dynamic | Static | Dynamic |
| Temperature Level | 2K | | | |
| Static, dynamic sum | 1.1 | 7.6 | 1.3 | 159 |
| 2K Sum [W] | 8.8 | | 160 | |
| | | | | |
| | 5K - 8K | | | |
| Static, dynamic sum | 11.7 | 7.0 | 10.6 | 58 |
| 5K Sum [W] | 18.7 | | 68 | |
| | | | | |
| | 40K - 80K | | | |
| Static, dynamic sum | 91.5 | 82.7 | 59.1 | 2870 |
| 40K Sum [W] | 174.1 | | 2930 | |

The basic parameters to estimate the dynamic losses in the RF cavities at 2 K in Table 1 are:

1. Beam energy U 8 GeV
2. Beam power W 20 MW
3. Gradient G 20 MV/m
4. Quality factor Q $\sim 2\times 10^{10}$ (ILC-like structure, 2K)
5. Number of cavities N 350
6. R/Q 1050 Ohm/cavity

A simple estimate of the total RF load for the high energy part of the linac (from 1 to 8 GeV) at 2 Kelvin is:

$$P = \frac{G^2}{Q\times(R/Q)} N = 19W/cavity \times 350 = 6700W.$$

Note that 8 cavities/cryomodule implies 152 W at 2 K of dynamic heating per cryomodule just due to the RF load.

Table 2: Cryogenic system power requirements

| Temperature level | 40 K to 80 K | 5 K to 8 K | 2 K |
|---|---|---|---|
| Total cryomodule heat load (W) | 2930 | 68 | 160 |
| Number of cryomodules | 44 | 44 | 44 |
| Total linac heat load (kW) | 129 | 3 | 7 |
| Conversion factor to wall plug power | 16.5 | 200 | 700 |
| Power at each level (MW) | 2.1 | 0.6 | 4.9 |
| Total operating power (MW) | 7.7 | | |
| Cryogenic system margin | 1.5 | | |
| Total installed power (MW) | 11.5 | | |
| Installed 4.5 K equivalent (kW) | 52.3 | | |

Dynamic heating at the 5 K to 8 K and 40 K to 80 K temperature levels is dominated by the input coupler. A rough estimate of those heat loads comes from scaling experience with TTF-III input couplers. However, the TTF-III input coupler would not actually handle CW loads; the 40 K heat may be overestimated here. For CW operation, a different design such as that from Cornell [3] would be used. A 1.3 GHz, CW coaxial-type TW coupler for ERL was developed and tested up to 61 kW at Cornell. This coupler may be a prototype for a cavity of the CW linac.

Table 2 provides an estimate of total cryogenic power required for the linac, 11.5 MW, equivalent to 52.3 kW of cooling at 4.5 K, which would require two very large cryoplants, each about the size of that of the LHC.

The power required for one ILC – like cavity is more than 50 kW for an acceleration gradient of 20 MV/m. Fifty kW is required for acceleration, and about 20% is overhead for the feedback system, etc. One of the possible options is to use CW IOT tubes to feed each 1 m ILC-like cavity. There are 1.3 GHz 30 kW, CW IOT available, developed by CPI [4]. The CPI Company has offered to examine technical feasibility of a CW operating 1.3 GHz tube providing output power of 60 and 120 kW. Very preliminary modeling shows no fundamental technical difficulty to build such a tube [4].

## ACCUMULATORS AND BUNCHERS

In both the pulsed and CW linac options, the basic idea is that an 8 GeV accumulator ring would be used to strip the $H^-$ ions to store sufficient proton charge. The protons would then be bunched either in the accumulator ring or in a second ring where short bunches can be extracted for muon production. Additional relatively inexpensive accumulator rings could be added as new opportunities arose for new experimental programs. Present plans for uses of the Project-X beam at Fermilab have considered the recycler ring, the present pbar accumulator and debuncher rings, and the Main Injector as places where the $H^-$ ions could be used to form intense proton beams.

The baseline Project X plan is to inject from a pulsed linac into the Recycler via a stripping foil for a total of 3 ms. To facilitate the creation of intense short bunches in a multi-megawatt driver for a neutrino factory or a muon collider, a much smaller accumulation ring with much larger transverse acceptances is preferable. Filling such a ring from a CW linac implies a longer injection time, raising the issue of multiple passages of circulating protons through a stripping foil. Ideally that issue ought to be addressed by simulations. For now a numerical example may suffice to suggest that the issue is not a show-stopper.

A repetition rate of 100 Hz implies an injection time of 10 ms compared with 3 ms in the Recycler. If the accumulation ring is ~5 times smaller than the Recycler, then the circulating beam passes through the injection region 5*10/3~17 times more than in the Recycler. However, the multi-megawatt accumulation ring must have transverse acceptances ~10 times larger than the Recycler in order to control transverse space-charge effects. Painting into both transverse planes then implies 100 times more phase-space volume to work with. So the number of times that each circulating proton passes through the stripping foil might be lower than in the Recycler by a factor of ~100/17~6. Alternatively, the development of magnetic plus laser stripping may solve the problem [5].

## LINAC FRONT END

### *Conventional Front End*

Front end schemes for high-power CW proton accelerators are already well established [6,7]. Typically they have four parts in series: 1) normal conducting (NC) 50-75 keV proton or $H^-$ minus source, 2) Radio-Frequency Quadrupole (RFQ), 3) low- and intermediate-energy section containing the NC to SC transition, and 4) (SC) high energy section.

The proton beam out of the source is a continuous beam that needs to be bunched at (a subharmonic of) the frequency used for the intermediate and high energy sections of the accelerator. This task, and an initial acceleration boost up to a few (5 to 7) MeV is performed by an RFQ. Several CW proton RFQs have been built or designed recently [8,9,10].

While there is a wide international consensus on the use of an Electron Cyclotron Resonance (ECR) $H^-$ source and RFQ for energies up to 5 to 6 MeV, different ideas have been pursued for the intermediate energy section up to approximately 100 MeV. Many projects have used different combinations of traditional normal conducting RF systems such as classical Drift Tube, Coupled Cavity Drift Tube, and Coupled Cavity Linacs. However, the use of SC cavity technology seems to be most promising in terms of the needed accelerator plug power efficiency. Some projects have investigated the possibility of extending the SC part of the accelerator down to low energies with independently phased low-velocity SC cavities, where the most promising are spoke and re-entrant SC cavities because of their simplicity and good RF parameters. The choice of NC or SC technology for the intermediate acceleration stages may be an issue for pulsed machines, but for CW beams the intermediate velocity SC structures are favored. Also a very big advantage of CW operation is the absence of Lorentz force detuning problems, which are especially severe for low-beta SC cavities in pulsed mode.

### *Cyclotron Front End*

A somewhat unorthodox alternative choice for the front end of the CW linac is a cyclotron. An $H^-$ cyclotron with peak magnetic field of just over 1T can safely achieve 100 MeV without significant Lorentz stripping. Such cyclotrons exist or are being built, but since they use a stripper foil to extract, the common varieties are wrong for this application. We would like to retain intact the $H^-$ ions, so a separated turn scheme is required. This can be achieved with sufficient RF voltage. A good example of such a machine is the PSI Injector 2 [11], which accelerates up to 2 mA of protons to 72 MeV. Compared with bare protons, single turn extraction of $H^-$ ions is technically simpler because the ions that would be intercepted by the septum can be pre-stripped and thus re-directed to a beam dump.

It is projected that such a cyclotron can accelerate over 3 mA average current [12] from an injected current of as little as 9 mA. DC $H^-$ ion sources have provided as much as 20 mA into a normalized rms emittance of 0.4 microns [13]. The width at extraction resulting from this emittance is only about 3 mm. The space charge effect in an isochronous machine is to create round bunches; this means bunch lengths are also about 3 mm, allowing them to fit easily into the 325 MHz linac buckets.

The most delicate region of the cyclotron is the center. If the RF frequency is too high and the injection energy too low, it is not possible to launch circular bunches cleanly matched to the focusing structure. For this reason, the beam frequency would be a relatively low 54 MHz (=325 MHz/6), and the injection energy a relatively high 1 MeV.

Since the energy spread tolerated by the cyclotron is very small, the cyclotron injector should not be an RFQ but a DC device as exists at PSI.

## NEXT STUDIES

From the standpoint of an accelerator that will be the Fermilab workhorse for the next four or five decades and will take several years to build, the existence of immediately available off the shelf components is not the most relevant question. Nevertheless, it is useful to look at the components such as power couplers, klystrons, and SC RF that are available and to imagine which devices could be improved with an appropriate amount of R&D.

To extend the studies reported here, all linac system parameters (RF frequency, and other cavity, klystron, and coupler choices, refrigeration system, the conventional construction and infrastructure, etc.) will be examined as a function of accelerating gradient to arrive at a CW system to compare to the pulsed option for Project-X. Other, more speculative approaches are also being considered, such as the use of a Jefferson Lab style recirculating linear accelerator, the use of lower energy protons for muon and neutrino production, and the possibility to use the proton accelerator to simultaneously accelerate cooled muons [14].

## REFERENCES

[1] S. Nagaitsev et al., this conference
[2] C. M. Ankenbrandt and R. P. Johnson, HB2008
[3] S. Belomestnykh, SRF 2007
[4] J. Sekutowicz, EUROFEL – Report 2006 - DS5 - 015, RF-source (Report 5.20)
[5] V. Danilov and S. Assadi HB2008
[6] A. Mosnier, LINAC2002
[7] J. David Schneider, EPAC2000
[8] D. Schrage, et al., PAC97
[9] M. Comunian et al., EPAC 2000
[10] J. M. Han et al, LINAC98
[11] M. Seidel, HB2008
[12] P. A. Schmelzbach et al., PAC2005
[13] Proc. ICIS
[14] M. Popovic and R. P. Johnson, NuFact05

# HIGH POWER TEST OF ROOM TEMPERATURE SPOKE CAVITIES FOR HINS AT FERMILAB *

W-M. Tam #, G. Apollinari, T. Khabiboulline, R. Madrak, A. Moretti, L. Ristori, G. Romanov, J. Steimel, R. Webber, D. Wildman, Fermilab, Batavia, IL 60510

*Abstract*

The High Intensity Neutrino Source (HINS) R&D program at Fermilab will build a new 65 MeV test linac to demonstrate new technologies for application in a high intensity hadron linac front-end. The HINS warm section is composed of an ion source, a radio frequency quadrupole, a medium energy beam transport and 16 room temperature Crossbar H-type (RT-CH) cavities that accelerate the beam to 10 MeV ($\beta$=0.1422). The RT-CH cavities are separated by superconducting solenoids enclosed in individual cryostats. Beyond 10 MeV, the design uses superconducting spoke resonators. In this paper, we illustrate the completion of four RT-CH cavities and explain latest modifications in the mechanical and radio frequency (RF) designs. Cavities RF measurements and tuning performed at Fermilab are also discussed. Descriptions of the HINS R&D Facility including high power RF, vacuum, cooling and low level RF systems will be given. Finally, the history of RF conditioning and the results of high power tests of RT-CH cavities will be discussed.

## INTRODUCTION

Fermilab is considering an 8 GeV superconducting H- linac with the primary mission of enabling 2 MW beam power from the 120 GeV Fermilab Main Injector for a neutrino program [1]. The front end linac in the energy range from 10 MeV to 400 MeV is foreseen as based on 325 MHz superconducting spoke resonators. New paradigms introduced into the front end design include the adoption of short, high field SC solenoids as primary lattice focusing elements and a low energy transition at 10 MeV from RT to SC RF acceleration. The HINS R&D program is underway to demonstrate these concepts in a 65 MeV prototype linac [2].

Our studies show that the most appropriate RT accelerating structure in the energy range 2.5-15 MeV is a CH type cavity [3, 4] operating at 325 MHz. We have successfully fabricated, fully dressed and high power tested the first three RT-CH resonators. The next one is now ready for high power tests. We are currently fabricating the remaining twelve resonators.

## CAVITY RF DESIGN

The RF design of the RT-CH cavities is reported in [2, 3]. In order to accelerate the manufacture of the remaining twelve cavities, five different designs are used instead of twelve. So there are 2-3 identical cavities in each of the five groups. Due to the reduction in the overall efficiency of acceleration, the power loss in the warm section is increased by 2%.

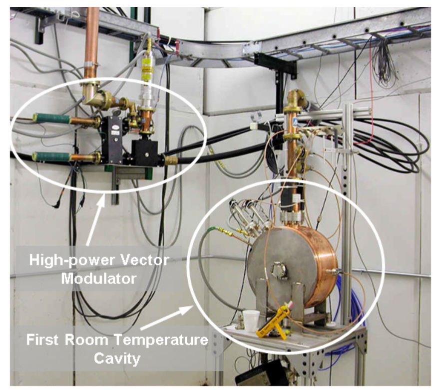


Figure 1: Cavity completed with coupler, tuners, cooling pipes, vacuum, and vector modulator.

## RF POWER SYSTEM AND TEST STAND

The cavity under test is completed with a power coupler, a pair of motor-driven tuners (now reduced to one) and cooling pipes and is mounted on a test stand sitting inside a cavity test cave for radiation shielding purpose (See Fig.1). This cavity assembly is then leak-checked with helium and is connected to low conductivity water (LCW), vacuum pumps and gauges, high power RF directional coupler and cable, and low-level RF (LLRF) signal cables.

RF power is supplied by a 325 MHz 2.5 MW Toshiba E3740A klystron which is protected by a 2.5 MW circulator (See Fig.2). Two RF power lines, 25 kW and 250 kW, are available for the cavity test cave. The 25 kW line was used in the test.

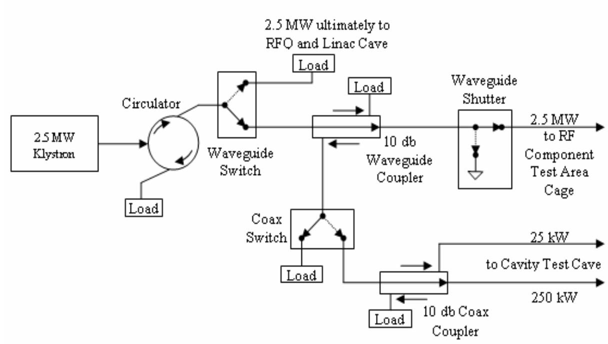


Figure 2: RF power and distribution system diagram.

*This work was supported by the U.S. Department of Energy under contract number DE-AC02-76CH03000.
#watam@fnal.gov.

LCW is maintained at a temperature of approximately 97.0 ± 0.5 $^0$F by a heater feedback circuit and at a flow rate of about 1 gal/min. A turbo molecular pump is attached to the cavity for pump-down, after which an ion pump alone can maintain cavity vacuum. An ionization vacuum gauge and the ion pump current provide monitors of the vacuum pressure. A base pressure of $2\times10^{-7}$ Torr before application of RF power was considered acceptable for beginning power tests.

Reflected power from the cavity, vacuum pressure, and water flow rate are part of the fast interlock system which is capable of inhibiting the RF power to protect the cavity assembly and the RF power system from being damaged in case of abnormal behavior.

## HIGH POWER TESTS

The first three of the sixteen RT-CH cavities have been successfully RF conditioned and tested. These tests include measuring the tuning range provided by motor-driven plunger tuners and deducing the cavity resonant frequency sensitivity to coolant temperature and RF power level. Detail is described in this section.

### *RF Conditioning*

The RF conditioning of RT-CH#1 was done by gradually increasing the RF power to the conditioning target, 8 kW, 3 ms and 2 Hz. Multipacting was observed at several power levels. The cavity was allowed to pump down overnight in case of persisting multipacting behavior. Vacuum trips occurred occasionally when power or pulse length increase; this is normal behavior resulting from high emission inside cavity due to imperfections such as unclean surface. This cavity took a total of 34 hours of RF power to complete conditioning.

The second cavity, RT-CH #2, was baked for 4 days at 300 $^0$F before conditioning. The target for this cavity is 13.5 kW, 3.5 ms and 2 Hz. Although multipacting and vacuum trips were still observed, the total conditioning time was significantly shortened to 6 hours plus one overnight pump down. It is believed that the baking contributes to this improvement.

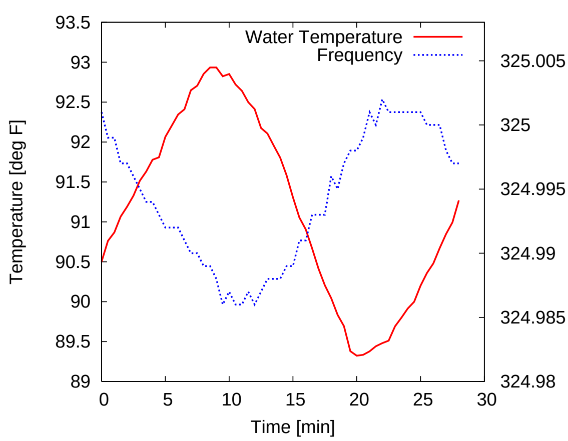


Figure 3: Cavity resonant frequency measured against coolant temperature.

### *Temperature Dependence of Resonant Frequency*

Temperature dependence of cavity resonant frequency was studied for RT-CH #1 at zero power. The temperature of LCW was measured with a temperature probe about 1 m upstream from the cavity in the cooling circuit. The resonant frequency was tracked using a simple phase locked loop.

The scaling constant, α, was measured for the scaling law: $\Delta f = \alpha\Delta T$, where $\Delta f$ and $\Delta T$ are the change in resonant frequency and the change in water temperature respectively (see Fig.3). At 91.0 ± 2.0 $^0$F, α was measured to be 8.0 kHz/K. An estimation of α, by assuming uniform expansion of cavity volume and using the linear expansion coefficient for copper, is 5.4 kHz/K. It is believed that the discrepancy is due to non-uniform cavity expansion and the presence of stainless steel plates mounted on the two end-walls of the cavity. Further study will be carried out to understand this discrepancy.

The stability of our water system is about ±0.5$^0$F. Thus, the fluctuation in resonant frequency due to coolant temperature variation is controlled to be within ±2.2 kHz.

### *RF Power Dependence of Resonant Frequency*

The designed nominal power is different for each RT-CH cavity. The highest one can go as high as 40 kW. This suggests an average power consumption of 400 W with a 1% duty factor. This will result in a significant heat load on the cavity which would cause a shift in its resonant frequency. The behavior of the cavity under high power should be studied to assure normal operation. The resonant frequency sensitivity to RF power is measured for RT-CH #2 (see Fig. 4).

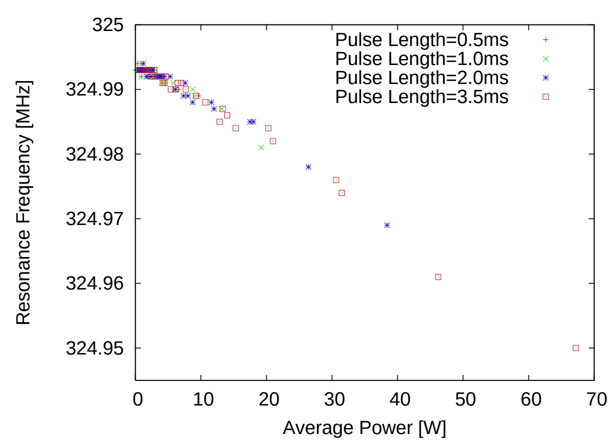


Figure 4: Cavity resonant response to RF power.

The resonant frequency of the cavity was measured for average RF power ranging from zero to about 68 W. The average RF power was controlled by adjusting the repetition rate (0.2 to 2.0 Hz), the pulse width (0.1 to 3.5 ms), and the nominal peak power (1.2 to 9.6 kW). The shift in the resonant frequency was measured to be about 43 kHz and responded linearly to the change in average power. The corresponding sensitivity is about 632 Hz/W. Notice that the change in resonant frequency does not depend upon the way in which the average power is being adjusted. Similar studies will be carried out on the rest of the RT-CH cavities.

The dynamical response of the resonant frequency to a jump in average RF power was also studied (see Fig.5). The repetition rate was set at 0.5 Hz and the nominal peak power at 8.0 kW while the pulse width was set to jump from 0.5 to 3.5 msec. This is equivalent to an average power jump from 2 to 14 Watts. The time constant of the response of the frequency was measured to be 73 sec.

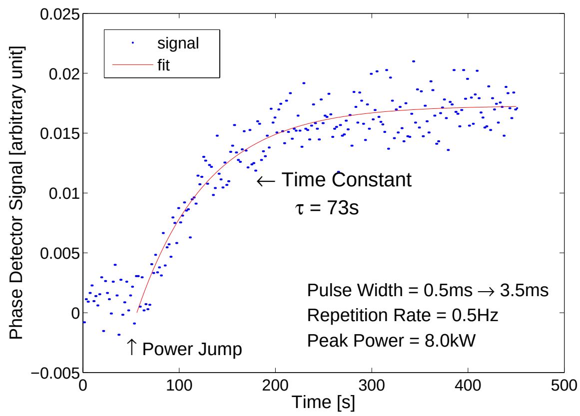


Figure 5: Dynamic measurement of cavity resonant response to RF power.

## *Plunger Tuner Test*

A pair of identical motor-driven tuners was installed on RT-CH #1. The full stroke, or the plunger active length, is about 42 mm or 106,000 motor steps. The resonant frequency of the cavity was measured by a network analyzer. With identical movement for both tuners, the tuning range was measured to be 1290.6 kHz. Resonant frequency responded linearly to the tuner position. The corresponding sensitivity is 30.7 kHz/mm or 12.2 Hz/step (see Fig. 6).

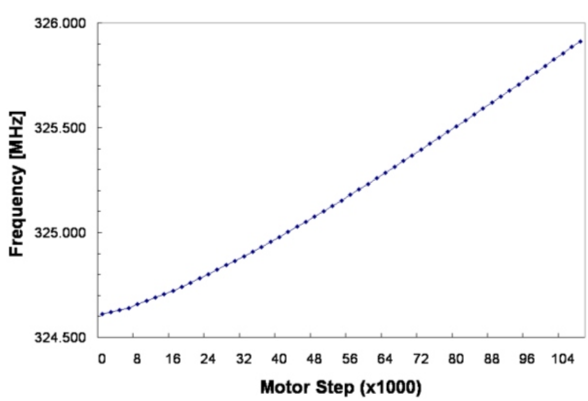


Figure 6: Cavity resonant frequency versus tuner position.

In a design revision the number of tuners is reduced to one and the full stroke of the tuner is cut by a half to 21 mm to improve the tuner's mechanical performance. The new design is sufficient to provide a reasonable tuning range.

## *RF Power Test with Vector Modulator*

Eventually these RT-CH cavities will be powered by a single klystron. To ensure control over the phase and the amplitude of individual cavities, a vector modulator (IQM) is required by each of them. A high power test of the cavity with IQM is performed (see Fig. 7).

By manipulating the drives (yellow and blue) of the IQM, the amplitude (red) of the cavity can be controlled within 13 dB. Detailed discussion on the design and performance of these IQMs can be found in this conference [5].

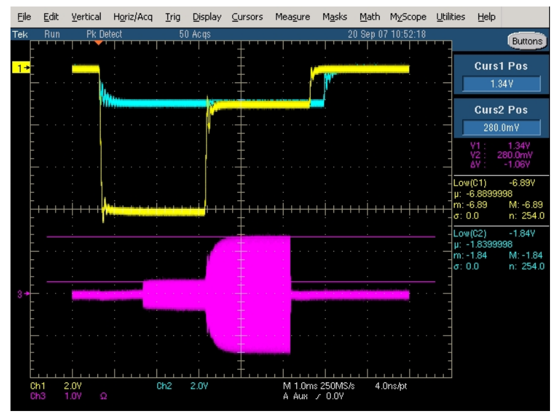


Figure 7. Amplitude control with IQM for a 6 kW 3.5 msec RF pulse. The red trace is cavity RF amplitude; the blue and the yellow are modulator bias currents.

# CONCLUSIONS

The first three of the sixteen HINS RT-CH cavities are complete and tested. These cavities have met all of the design requirements. The time needed to condition up to full power for RT-CH #2 is significantly shortened as a result of baking. Cavity sensitivity to coolant temperature, tuner position, RF power and IQM bias has been measured. These results are useful for RF control design and cavity performance improvement effort.

# REFERENCES

[1] S. Nagaitsev, "Fermilab's Project X", this conference
[2] R.Webber, "Overview of the High Intensity Neutrino Source Linac R&D Program at Fermilab", this conference
[3] L. Ristori et al., "Design of Normal-Conducting 325 MHz Crossbar H-type Resonators at Fermilab", LINAC'06, Knoxville, Tennessee, USA, TUP072, August 2006
[4] L.Ristori et al., "Fabrication and Test of the First Normal-Conducting Cross-Bar H-Type Accelerating Cavity at Fermilab for HINS", PAC'07, Albuquerque, New Mexico, USA, WEPMN110, 2007
[5] R. Madrak and D. Wildman, "High Power 325 MHz Vector Modulators for the Fermilab High Intensity Neutrino Source (HINS)", this conference

# FOCUSING SOLENOIDS FOR THE HINS LINAC FRONT END*

I. Terechkine#, G. Apollinari, J. DiMarco, Y. Huang, D. Orris, T. Page,
R. Rabehl, M. Tartaglia, J. Tompkins, FNAL, Batavia, IL 60510, U.S.A.

## ABSTRACT

The low energy part (front end) of a linac for the High Intensity Neutrino Source (HINS) project at Fermilab will use superconducting solenoids as beam focusing elements (lenses). The lenses for the conventional (room temperature) drift tube-type accelerating section of the front end require individual cryostats; in the superconducting accelerating sections, solenoids will be installed inside RF cryomodules. Some of the lenses in the conventional and superconducting section are equipped with horizontal and vertical steering dipoles. Lenses for the room temperature section are in the stage of production with certification activities ongoing at Fermilab, and a prototype lens for the superconducting section has been built and tested. Since each lens will be installed in the transport channel of the accelerator so that its magnetic axis is on the beamline, testing has also included alignment measurements.

This report summarizes design features, parameters, and test results of the focusing lenses.

## INTRODUCTION

As part of the High Intensity Neutrino Source (HINS) program at Fermilab, building a high power H⁻ RF linac is under consideration [1]. At present, main R&D efforts are concentrated on development of accelerating and transport elements for the front end of the linac. To reduce beam losses through mitigation of halo formation in the front end (see [2]), superconducting solenoids will be used as focusing lenses [3]. There are three sections of the front end, which are identified by the type of 325 MHz RF structure used for acceleration. The first section uses low-beta, room temperature Crossbar H-type (CH) structures [4]; in this section, each focusing lens is in its own cryostat. For higher energies, superconducting spoke resonators are used with several of them in one cryostat [5]; focusing lenses in these sections are mounted in the same cryostats. There exist two types of superconducting sections in the linac: SS1 and SS2; focusing lenses for these sections differ in strength.

One of the major requirements for focusing lenses in the superconducting sections of the linac is low fringe field. To limit the power loss in walls of accelerating cavities, it is desirable to keep the magnetic field on the walls below 10 μT [6].

*Work supported by the U.S. Department of Energy under contract No. DE-AC02-07CH11359.

#terechki@fnal.gov

In each section of the linac, two styles of lenses are required: with and without embedded steering dipoles for horizontal and vertical correction of beam position.

A total of 53 focusing lenses will be built for the linac (including spares). Solenoids for the CH section are in the production stage, solenoids for the SS1 section are being prototyped, and design work is ongoing for the SS2 system.

## CH SECTION FOCUSING SOLENOID

Focusing length of a solenoid-based focusing lens is given by the following expression:

$$f = \frac{8mU}{q^2 \int_{-\infty}^{+\infty} B^2 dz}$$

where ***m*** is mass, ***q*** is charge, and ***U*** is the kinetic energy of the particles in the beam. For high intensity ion beams, it is essential to have the focusing period small; this requires high magnetic field, that only can be generated by superconducting systems. Basic requirements for the focusing lens include 20 mm warm bore diameter, the squared magnetic field integral $\int B^2 dz$ of ~1.8 $T^2$-m, with an effective length less than 0.1 m (normalized to the maximum magnetic field). Steering dipoles must have an integrated strength of ~0.25 T-cm to be able to compensate for uncertainties in the solenoid magnetic axis positioning of ~0.3 mm. Due to lack of space in the beamline, the dipoles must be placed inside of some of solenoids. To solve the fringe field problem, each solenoid is made of a main coil and two bucking coils with the direction of magnetic field opposite to that of the main coil. Design of the solenoid is described in [7] and [8]. Several prototypes of the focusing solenoid were tested before serial production started. Magnetic field distribution of a solenoid with embedded steering coils in the central and the fringe area is shown in Fig. 1. Here the measured field is compared to a model prediction; the data points from both sides of the magnet are overlaid. The squared field integral at 200A is 2.5 $T^2$-m, versus the predicted value of 2.4 $T^2$-m. The maximum current in the system (quench condition) is ~240 A; the required value of 1.8 $T^2$-m can be achieved at 170 A.

The measured magnetic field in the fringe field region (outside the solenoid) is also very close to the expected. At the nominal current of 170 A, for the solenoids with the embedded steering coils, the magnetic field in the area of the accelerating cavity (~150 mm from the solenoid center) is ~0.03 T; it is ~0.01 T for the solenoids without the steering coils. Additional shielding is needed if the accelerating cavity test shows that this field is too high.

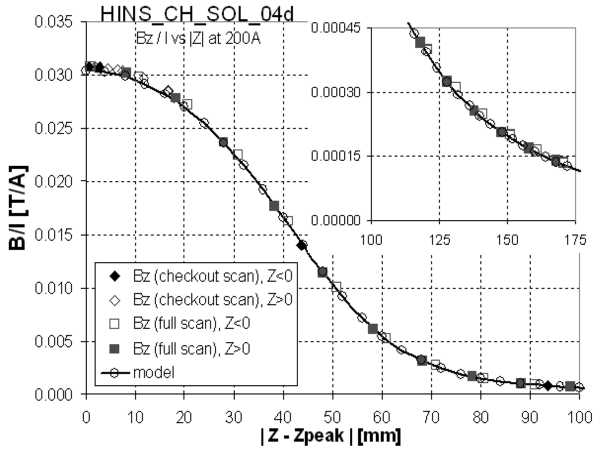


Figure 1: Comparison of measured and predicted axial magnetic field transfer function profiles for CH section solenoid at 200A in the central and fringe regions.

Each steering dipole was made by placing a one-layer winding on the surface of a G-10 cylinder. NbTi 0.8 mm strand was used for both the horizontal and vertical dipole. The steering dipole assembly is placed inside the main coil with the horizontal dipole inside the vertical one; the total radial thickness of the assembly was ~4.8 mm. The magnetic field integral ∫□□□≈ 1 T-cm was measured in both steering coils of the first production lens at 200 A. The required integrated strength of 0.25 T-cm is achieved at ~50 A.

Assembled and tested cold masses are to be placed in cryo-vessels at FNAL to form completed focusing lenses (see Fig. 2).

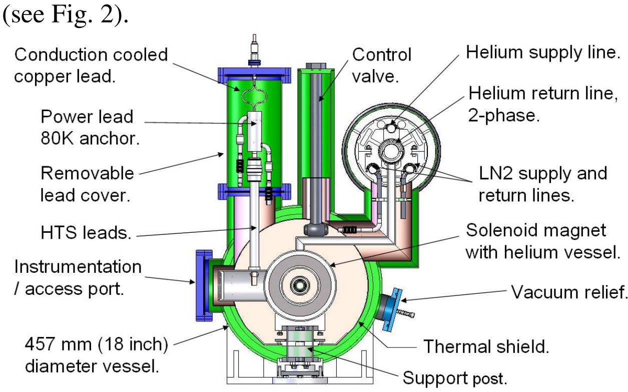


Figure 2: Cross section through CH solenoid cryostat

Description of the cryostat design can be found in [9]. All 19 cryostats in the beamline of CH section will be connected in series mechanically and in parallel cryogenically using a "header" – a pipe that contains LHe and LN2 supply and return lines. The first cryostat has been assembled with the prototype solenoid and tested to show good performance [10].

One of the most important aspects of using the solenoid-based focusing lenses is their alignment in the transport channel. During certification process at FNAL, it was found that positions of the geometric axis and the magnetic axis of a solenoid can differ by ~0.5 mm. Alignment of the lenses in the linac must be done to place the magnetic axis within ~0.25 mm of the beamline. To ensure this accuracy of alignment, the Single Stretched Wire (SSW) system is used to find the magnetic axis position relative to external fiducials [10]. This measurement is made at different stages: warm solenoid at atmospheric pressure and after pumping out the air, the solenoid cooled to 4.2 K without current, and powered solenoid at different current levels. Several cycles of these measurements were made with the first prototype lens to understand reproducibility of the magnetic axis positioning. Preliminary results show that reproducibility of the alignment is on the order of ±100 μm.

## SS SECTION FOCUSING SOLENOIDS

Main requirements for the SS1 section focusing solenoids are: 30 mm cold bore diameter, integrated focusing strength of ~3 $T^2$-m, and effective length less than 0.15 m (normalized to the maximum magnetic field). Each steering dipole must have an integrated strength higher than 0.5 T-cm. From the experience of building and testing CH section lenses, it was clear that a refined design was needed to meet the fringe field requirement. Some help comes from the fact that there is no need for individual cryostats, so the solenoid coil inner diameters could be made smaller. Nevertheless, a new steering coil design was needed to make the assembly "slim" to allow further reduction of the inner diameter of the solenoid. A new coil winding technique was developed that employed 0.3-mm NbTi strand. The reduced radial thickness of the steering dipole assembly was ~2.5 mm including the thickness of the main coil barrel; this made it possible to have identical solenoid geometry for both styles of the solenoid: with and without steering coils. Main design features of the SS-1 focusing solenoid are described in [11]. A prototype lens has been built and tested. Fig. 3 shows a comparison of the measured and predicted fringe field for the solenoid without steering coils [12].

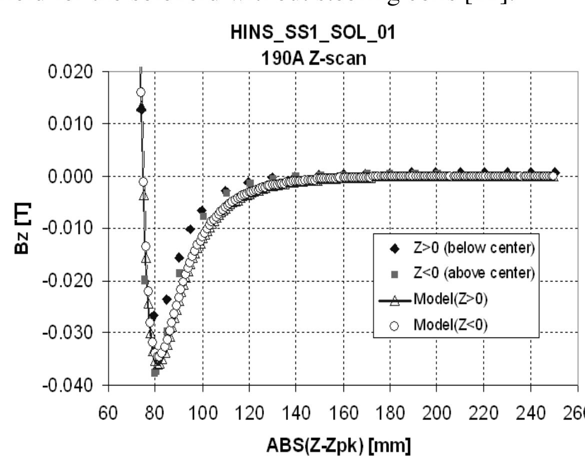


Figure 3: Predicted and measured axial magnetic field in the fringe region at 190A for SS1 prototype solenoid

Expected magnetic field on the walls of the spoke cavities is ~20 µT, and additional shielding will be needed to bring it to the level below the recommended 10 µT.

Alignment issues for the lenses in the superconducting sections of the linac are more demanding than they are in the CH section. The lenses will be installed inside RF cryomodule, and special techniques and procedures must be developed to align the lenses and follow the drift of the magnetic axis in time. An approach to solving this problem has been developed (e.g. see [13]), but specifics of the design will require a lot of work to implement a known solution or to find a new one. This part of the solenoid lens R&D is in the initial stage; a prototype cryostat is to be built to address the issue.

Design of the SS2 section focusing solenoid is similar to that of the SS1 solenoid except it is much stronger: the required squared field integral for this solenoid is 5 $T^2$-m. As a result, this solenoid stores more energy, and quench protection solution becomes more complicated in comparison with the SS1 and CH systems, that can absorb all the stored energy safely.

## SOLENOID QUENCH PROTECTION

Quench training is part of testing performed on each assembled lens. As in each focusing solenoid, a main coil and two (much) smaller bucking coils are connected in series, quenching in one of the bucking coils can result in an unacceptable temperature rise. Protection of focusing solenoids was the subject of several studies (e.g., see [14], [15], and [16]). A proper protection scheme should prevent the temperature and voltage to ground in the coils from going too high: $T_{max}$< 300 K, $V_{max}$< 300 V. Reliability of the protection dictates choosing a simple solution from many possible ones. CH and SS1 focusing solenoids appear to be self-protected; this means that if the energy stored in the system is fully dissipated by the quenching coil, the temperature and the voltage are still below the allowed limits in any part of the coil. Nevertheless, to reduce heat dissipation within LHe bath, we use an external dump resistor, that, if chosen correctly, helps to lower the voltage and temperature spikes. For solenoids of the SS2 section, using a dump resistor alone does not solve the problem. A solution to this problem is still to be found and tested.

## SUMMARY

To build a solenoid-based transport system for the front end of the HINS linac under construction at FNAL, a focusing solenoid R&D program has been initiated. The focusing lens design and fabrication technology development efforts within the R&D are close to completion. The CH series of lenses is in production with the final assembly and certification activities taking place at FNAL. Ongoing tests of SS1 prototype lenses will be followed by production in 2009. Quench protection issues for SS2 lens is under study, and design activities are in progress. A shift in the R&D is now being made towards development of adequate procedures for testing and installation of SS1 and SS2 lenses.

## REFERENCES


[1] R. C. Webber, "Overview of the High Intensity Neutrino Source Linac R&D Program at Fermilab", LINAC08, Victoria, BC, Canada, Sept. 2008.

[2] Dong-o Jeon, et al "Halo Formation and its Mitigation in the SNS Linac", LINAC 2002, Proceedings, pp. 121 – 123.

[3] P. Ostroumov, "Physics Design of the 8-GeV $H^-$ Linac", New Journal of Physics, 8 (2006) 281.

[4] L. Ristori, et al, "Design of normal Conducting 325 MHz Crossbar H-Type Resonators at Fermilab", LINAC 2006, Proceedings, pp. 710 – 712.

[5] G. Apollinari, et al, "Design of 325 MHz Single and Triple Spoke Resonators at FNAL". LINAC 2006, Proceedings, pp. 707 – 709.

[6] T. Khabiboulline, I. Terechkine, "Superconducting Cavity Magnetic Field Requirements", FNAL TD note TD-08-006, FNAL, 2008.

[7] G. Davis, et al, "Designing Focusing Solenoids for Superconducting RF Accelerators", IEEE Transactions on Applied Superconductivity, vol. 17, no. 2, pp. 1221 – 1224, June 2007.

[8] G. Apollinari, et al, "HINS Linac Front End Focusing System R&D", ASC-08, Chicago, 2008, report 4LA02; see also FERMILAB-CONF-08-323-TD.

[9] T. Page, et al, "High Intensity Neutrino Source Superconducting Solenoid Cryostat Design", Proceedings of CEC-07, Chattanooga, TN, 2007.

[10] T. Page, et al., "HINS Superconducting Lens and Cryostat Performance", ASC-08, Chicago, 2008, rep. 1LPC06; see also FERMILAB-CONF-08-266-TD.

[11] G. Davis, et al, "HINS Linac SS-1 Section Prototype Focusing Solenoid Design", FNAL TD note TD-08-010, FNAL, March 2008

[12] G. Davis, et al, "HINS_SS1_SOL_01 Fabrication Summary and Test Results", FNAL TD note TD-08-012, FNAL, April 2008.

[13] G. Stanford, et al, "Engineering and Cryogenic Testing of the ISAC-II Medium Beta Cryomodule", LINAC 2004, Proceedings, pp. 630 – 632.

[14] I. Terechkine, P. Bauer, "Focusing Solenoid Quench Protection Studies; Part 1: Method description and First Iteration", TD-06-003

[15] I. Terechkine, "CH Section Focusing Solenoid Quench Analysis", TD-06-067

[16] I. Terechkine, V. Veretennikov, "Normal Zone Propagation in Superconducting Focusing Solenoids and Related Quench Protection Issues", IEEE Transactions on Applied Superconductivity, vol. 18, no. 2, pp. 1325-1328, June, 2008.

# STATUS OF THE LANSCE REFURBISHMENT PROJECT*

John L. Erickson, Kevin W. Jones and Michael W. Strevell
Los Alamos National Laboratory, Los Alamos, NM 87545, U.S.A.

*Abstract*

The Los Alamos Neutron Science Center (LANSCE) accelerator is an 800-MeV proton linac that drives user facilities for isotope production, proton radiography, ultra-cold neutrons, weapons neutron research and various sciences using neutron scattering. The LANSCE Refurbishment Project (LANSCE-R) is an ambitious project to refurbish key elements of the LANSCE accelerator that are becoming obsolete or nearing end-of-life. The conceptual design phase for the project is funded and underway. The 5 year, $170M (US) project will enable future decades of reliable, high-performance operation. It will replace a substantial fraction of the radio-frequency power systems (gridded tubes and klystrons) with modern systems, completely refurbish the original accelerator control and timing systems, replace obsolete diagnostic devices, and modernize other ancillary systems. An overview of the LANSCE-R project will be presented. The functional and operating requirements will be discussed, the proposed technical solutions presented, and the plan for successful project execution while meeting annual customer expectations for beam delivery will be reviewed.

## INTRODUCTION

The LANSCE User Facility accelerator is capable of simultaneously accelerating protons or negative hydrogen ions to beam powers of up to 800 kW. A beam switchyard allows tailored time-structured beams to be delivered to the five distinct experimental areas.

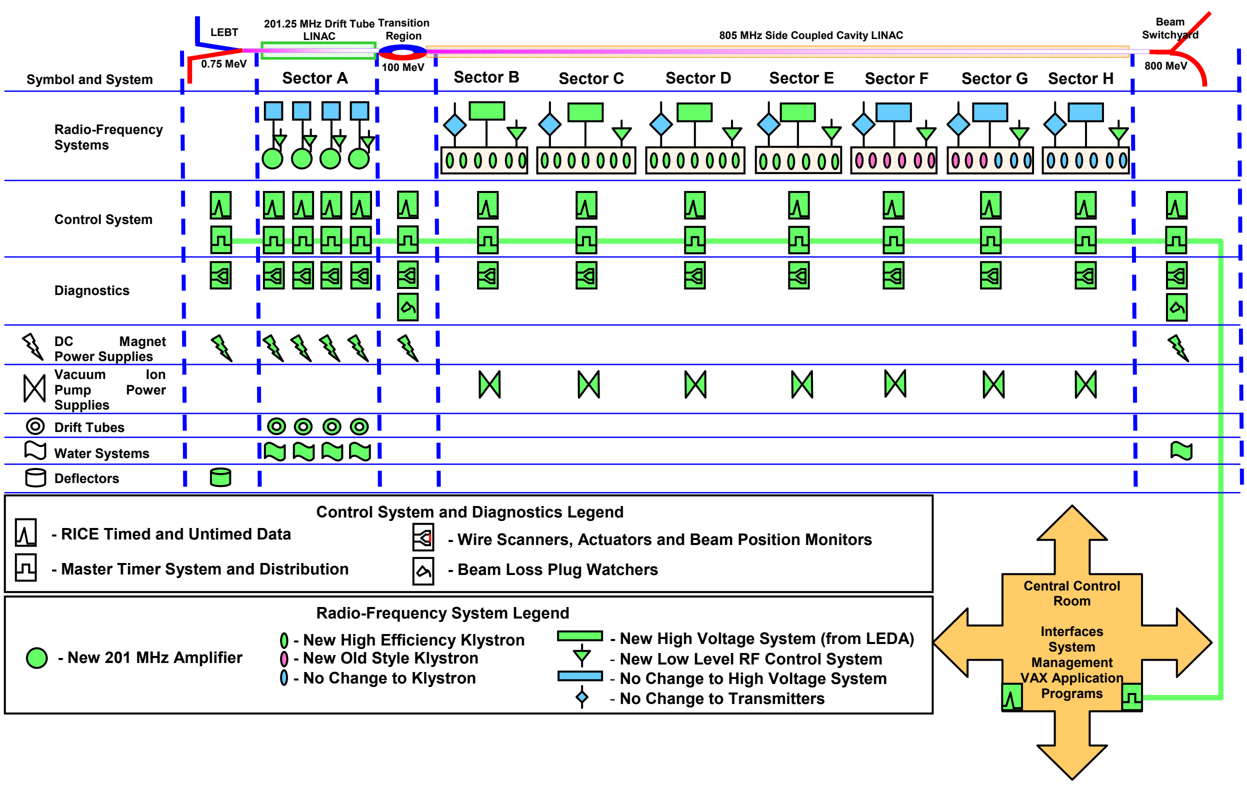


Figure 1: A summary diagram showing the scope of LANSCE-R.

## *Vision and Goals*

LANSCE produces one of the highest beam currents in the world of medium energy protons to irradiate experimental targets directly or to produce intense pulses of spallation neutrons. LANSCE performs state-of-the-art experiments in proton radiography, nuclear science, and materials science.

Our goal is to provide safe, secure, environmentally-compliant, cost-effective performance in beam delivery that meets or exceeds metrics prescribed by our customers.

*Work supported by the U. S. Department of Energy, National Nuclear Security Administration, Contract No. DE-AC52-06NA25396 – Publication Release LA-UR-08-06209

The LANSCE Refurbishment Project (LANSCE-R) ensures that the LANSCE User Facility will continue to be the premier neutron science facility at Los Alamos National Laboratory, providing NNSA with critical data in support of its Defense Programs mission. A schematic of the project scope is shown in Figure 1.

### *Assumptions*

Operation of the scientific program will continue during the refurbishment project in a tailored way to meet customer expectations to the extent possible while simultaneously implementing the refurbishment project during scheduled operational outages. Refurbishment elements will be pre-assembled, staged, and tested to the greatest extent possible prior to possible multi-shift installation evolutions.

## STRATEGIES AND PROJECTS

### *Implementation Strategies*

The overall implementation strategy is to integrate ongoing LANSCE User Facility operation with the execution of the LANSCE-R project. The operations organization for LANSCE is both well established and strong. Capital projects have a successful history of integration with the operating facility. The recent experience of integrating the construction of the Isotope Production Facility is an example of strong cooperation between a project and the operating facility.

The overall success of both LANSCE Operations and the LANSCE-R Project rests on the ability of the responsible organizations to retain and, where appropriate, develop the skilled technical staff needed to support ongoing operations, maintenance and related improvements as well as the conceptual, preliminary and final designs of LANSCE-R sub-systems, oversight of component procurement, acceptance testing, pre-installation assembly and testing, and final installation and commissioning.

The following key operational elements are essential for the integrated model to be successful:

- A commitment to schedule at least 3,000 hours of beam operation for users each fiscal year from FY2008 through FY2014 and beyond, with appropriate allocation of sole-use and beam development time.
- No more than one cold-start facility turn-on in each fiscal year.
- An appropriate distribution of extended outages of several months duration to accommodate both a modular approach to LANSCE-R sub-system installation and other operations-funded system improvements as well as appropriate cool-down times for routine maintenance on activated equipment in areas such as the Proton Storage Ring and the 1L Target.
- A disciplined approach to configuration management for accelerator and beam delivery systems to minimize return to service after short and extended outages.
- Continuous certification of the Radiation Security System to minimize the time required for resumption of production beam operation.

The following elements are essential for LANSCE-R to be successful:

- Proposed equipment and system upgrades are focused on those current LANSCE capabilities required to support Weapons Program needs.
- A design, acquisition, and assembly strategy that optimizes preparation for focused equipment installation during scheduled operational outages.
- An appropriate balance between refurbishment of the LANSCE User Facility real property and installed equipment through the Facility Infrastructure Recapitalization Program (FIRP) and refurbishment of essential accelerator sub-systems through the LANSCE-R project.
- A project execution time line that permits performance of the full scope of work in no more than five to seven years.

### *Facility and Infrastructure Projects*

Weapons Program GPP funding and the Facility Infrastructure Recapitalization Program (FIRP) have effectively been used at the LANSCE User Facility to replace Radioactive Liquid Waste handling, cooling towers, and the chilled water plant to ensure that the real property and installed equipment remain capable of supporting long term operation through 2020. These projects have been completed on schedule and within budget, with the work being carefully planned within extended accelerator maintenance outages. Additional work is needed, and replacement of electrical distribution system and certain process water systems are being undertaken in FY09.

A strong FIRP program is essential to underpin the ongoing success of LANSCE operations and the refurbishment scope planned in LANSCE-R. Out-year projects (FY09-FY11) encompass multiple electrical distribution system upgrades, process cooling water upgrades, roof replacements, and HVAC replacements.

### *LANSCE-R Preferred Scope*

The preferred scope that was included to support the Mission Need for the LANSCE-R Project will enhance cost effectiveness by system refurbishments or improvements that reduce operating costs and will improve decreasing facility reliability by replacing systems that have an impact of 15% or greater on reliability for those systems.

The full LANSCE-R project will also eliminate the following sources of operational inefficiencies that should improve operational effectiveness:

- Single-point failures with an estimated time to repair of greater than 30 days,

- Equipment that is beyond its predicted end-of-life that could severely impact facility operations,
- Obsolete equipment for which no spare parts are available,
- ES&H or code compliance issues necessary to continue safe operation.

The baseline refurbishment project consists of replacing the 201 MHz RF systems, updating about 75% of the 805 MHz RF systems, modernizing the control system, and replacing or refurbishing a variety of diagnostics and accelerator subsystems.

The RF and power supply scope includes the following:

- Magnet Power Supplies – Approximately 12 different power supply replacement projects.
- Pulsed Power – Solid State Replacement for Ground Level Deflectors
- 201 MHz RF for the Drift Tube Linac – All new 201 RF except for High Voltage
- Low Level RF – All new LLRF in the 201 MHz and 805 MHz subsystems
- 805 MHz Klystrons – 4 sectors of new high efficiency klystrons and 1.5 sectors of new old style klystrons (leaving 1.5 sectors of klystrons not replaced)
- High Voltage Power Systems – 4 sectors of new high voltage systems.

The Controls replacement scope is limited to the replacement of the control and instrumentation functions implemented by the RICE systems, DEC MicroVAX and workstation computer systems, and application software that comprise the current LANSCE Control System (LCS). The LCS provides control and data monitoring for most devices in the LINAC and for some of its associated experimental-area beam lines. The overall Control and Instrumentation scope includes the following:

- Replace Linac Beam Position Monitors and incorporate phase measurements
- Replace the Delta T system
- Replace 95 Wire scanners in the linac
- 18 IR loss monitor systems & 5 GD systems
- Replace VAXs and VAX applications
- Replace RICE systems (Remote Instrumentation Control Equipment systems)
- Replace Master Timer System.

The accelerator sub-systems scope includes:

- Cooling Water distribution and monitoring
- Vacuum system equipment and monitoring
- Linear accelerator copper structures, Drift Tubes.

The preferred scope being proposed is a self-consistent approach to maintaining reliability and addressing single point failures in the LANSCE facility that serves the NNSA/SSP Defense Programs mission. It generally assumes that the current facility capability will be maintained. LANSCE-R includes only scope to support NNSA/SSP mission research at 120 Hz and 625 µs beam gate. It only includes beam delivery elements common to pRad, WNR and Lujan Center that all have NNSA/SSP mission deliverables. It does not include refurbishment of equipment /systems from the end of the accelerator to WNR and the Lujan Center, including Line D and the PSR. In addition, LANSCE-R does not include equipment changes to support current or future H+ operations to Isotope Production or Area A/MTS. This approach is consistent with guidance received from NNSA.

## IMPLEMENTATION OF A SEVEN-YEAR PLAN FOR FY09-FY15

### *Operations Objectives for Project:*

- Operate for approximately 3,000 hours exclusive of development, documentation, and sole use operation consistent with operations in FY2008.
- Retain key staff required to perform both operations and LANSCE-R implementation at the same time.

### *LANSCE-R Current Year – FY2008-9*

- Conduct the agreed-upon scope of work for conceptual design and obtain approval of the final CD-1 Critical Decision. This will include project management, project controls, and technical writing in support of the CD-1 package development.

### *LANSCE-R Future Years – FY2010-15*

Given the funding scenario that is ultimately determined, we will manage the work to be accomplished in each annual outage (each an identified subproject) to achieve the highest priority items first within budget and funding profile constraints, while making progress on all sub-projects.

Integration of new hardware will occur during the extended outages that occur each calendar year. These will be approximately 6 months in duration and will be integrated into the operating schedule well in advance. Installation, checkout and commissioning of the first module of upgraded 201 MHz RF systems will take place in FY12 with the next two modules to follow as soon as possible after that.

Each outage will constitute a sub-project in itself that can be integrated with planned routine plant maintenance and scheduled FIRP projects. Each annual outage will include required activities with checkout and verification of interlock systems, operations manual updates, and commissioning time commensurate with extent of changes. For example, LLRF system testing requires cooling water, RF power, and control system interfaces.

Ancillary system upgrades will be planned to minimize disruption, and will begin with systems that have the least impact to gain experience and improve project estimation for more complex installations. For example, network infrastructure should be put in place and commissioned before final upgrades are made to the Master Timing system. High voltage system work for refurbishment of the 805 MHz systems should precede acquisition and installation of new or rebuilt klystrons.

# OPERATIONAL STATUS AND FUTURE PLANS FOR THE LOS ALAMOS NEUTRON SCIENCE CENTER (LANSCE)*

Kevin W. Jones and Kurt F. Schoenberg, Los Alamos National Laboratory, Los Alamos, NM 87545, U.S.A.

*Abstract*

The Los Alamos Neutron Science Center (LANSCE) continues to be a signature experimental science facility at Los Alamos National Laboratory (LANL). The 800 MeV linear proton accelerator provides multiplexed beams to five unique target stations to produce medical radioisotopes, ultra-cold neutrons, thermal and high-energy neutrons for material and nuclear science, and to conduct proton radiography of dynamic events. Recent operating experience will be reviewed and the role of an enhanced LANSCE facility in LANL's new signature facility initiative, Matter and Radiation in Extremes (MaRIE) will be discussed.

## INTRODUCTION

The Los Alamos Neutron Science Center (LANSCE) is a unique multidisciplinary facility for science and technology. The core of the facility is an 800-MeV linear accelerator system with demonstrated 1MW capability that presently accelerates up to 100kW of negative hydrogen ions with unique and highly variable timing patterns suitable for a wide variety of experimental programs. Five experimental areas form the core of the user facility. Four areas utilize the 800-MeV negative hydrogen ion beams directed by appropriate pulsed kicker systems: at the Manuel Lujan Jr. Neutron Scattering Center (Lujan Center) sixteen flight paths utilize pulsed thermal and epithermal neutrons produced at 20Hz by intense 0.29μs bursts of protons incident on a tungsten spallation target and moderated by water or liquid hydrogen; the Weapons Neutron Research Facility (WNR) provides the most intense source of high-energy neutrons in the world for neutron nuclear science and is an accepted world standard for irradiation of semiconductor electronics; the Proton Radiography Facility (pRAD) provides a unique facility for the study of shock-induced dynamic processes where shocks are driven by high explosives or projectiles; and the Ultra-Cold Neutron (UCN) facility uses a moderated solid deuterium target to generate intense pulses of ultra-cold neutrons for fundamental science research. The Isotope Production Facility (IPF) at 100 MeV utilizes a proton beam of up to 275 μA to produce proton-induced isotopes for medical imaging diagnostics and fundamental research. LANSCE continues a disciplined approach to both operations and maintenance that maintains operational performance and user satisfaction in a constrained funding environment.

*Work supported by the U. S. Department of Energy, National Nuclear Security Administration, Contract No. DE-AC52-06NA25396 – Publication Release LA-UR-08-06170

## THE LANSCE USER FACILITY

The Lujan Center provides 11 neutron scattering instruments capable of studying materials structures of diverse items such as proteins, machinery components, powders, and single crystals using both elastic and inelastic techniques. Nuclear science is supported by three flight paths, one of which is equipped with a 4π detector used to measure thermal neutron capture cross sections on unstable nuclei. This suite of instruments applies and advances neutron scattering for both defense and academic research. Beam current to the Lujan target is nominally 100μA but can be as high as 125μA depending on ion source and accelerator optimization.

The WNR facility receives beam at 40-100Hz with a variable micro-pulse spacing (typically 1.8μs) to address the needs of LANSCE Users in the areas of basic and applied nuclear science. The pulse spacing permits resolution of frame overlap in the neutron spectra. This white neutron source (Target 4) is the most intense source of high-energy (<760 MeV) neutrons worldwide and is equipped with six flight paths that determine neutron energy using time-of-flight techniques. A key flight path used principally by industry users provides a neutron spectrum essentially identical to that of cosmic-ray neutrons to permit accelerated studies of single-event-upset sensitivity for the electronics and avionics industries. A related facility (Target 2) provides direct access to proton beams with energies up to 800 MeV for studies of proton-induced reactions and target irradiations for materials testing. This target station is also equipped with five neutron flight paths.

The pRAD facility provides a unique experimental technique for studies of dynamic processes. Up to 37 pulses of protons, each with approximately $10^9$ particles per pulse, temporally spaced at appropriate intervals, are directed at a dynamic object. The scattering characteristics of each pulse are imaged by a collimator and magnetic lens system and recorded by a camera. This technique permits multi-frame radiographs of dynamic events driven by gas guns or high explosives. These radiographs permit the study of material dynamics and failure mechanisms under shock conditions.

The UCN facility accepts several full charge (~5μC) accelerator pulses separated by a period suitable for the moderation and bottling of the neutrons and compatible with average current limits, typically about 5-7 seconds. The ultra-cold neutrons are then directed through a guide to a decay volume where beta-decay parameters are measured.

The IPF irradiates source materials to produce proton-induced isotopes for applications in medical diagnostic imaging and research. Most notable is the production of $^{82}$Sr used for cardiac imaging, and other isotopes for the calibration of PET scanners. The operation of this facility is interleaved with others around the world to assure a constant supply of the necessary isotopes.

A schematic representation of the facility and its operating characteristics is given in Figure 1.

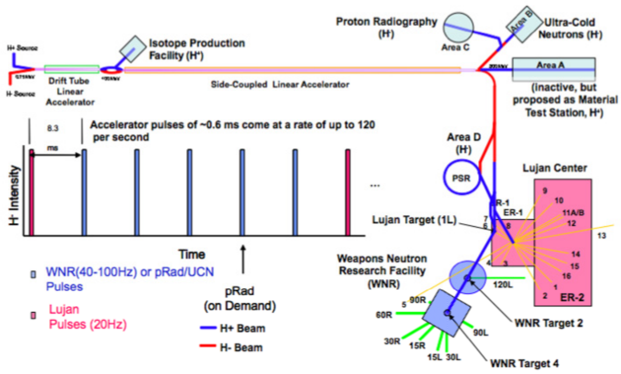


Figure 1: Schematic layout of the LANSCE User Facility

## OPERATIONS PERFORMANCE

Integrated performance for the LANSCE User Facility has been remarkably consistent since the year 2000. This is best illustrated by reliability data for the Lujan Center from 1991 to 2007 as shown in Figure 2. This represents the most complex beam delivery system including the injectors and linac, the proton storage ring, and beam transport lines.

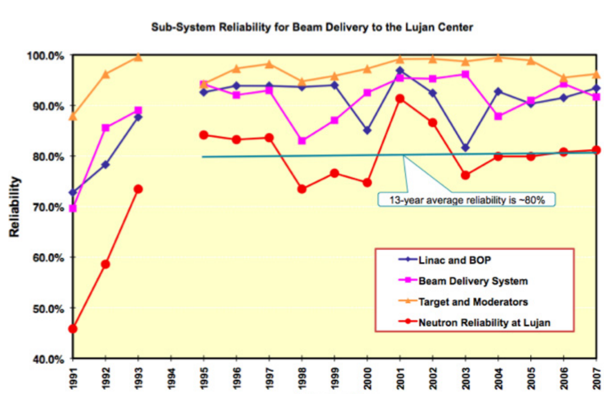


Figure 2: Sub-system reliability for beam delivery to the Lujan Center

These data illustrate that the 13-year average reliability from 1995 to 2007 is slightly over 80% which is remarkable for a facility that is now 36 years old with much of the original equipment still in service.

Operating hours from 1989 to 2007 are illustrated in Figure 3.

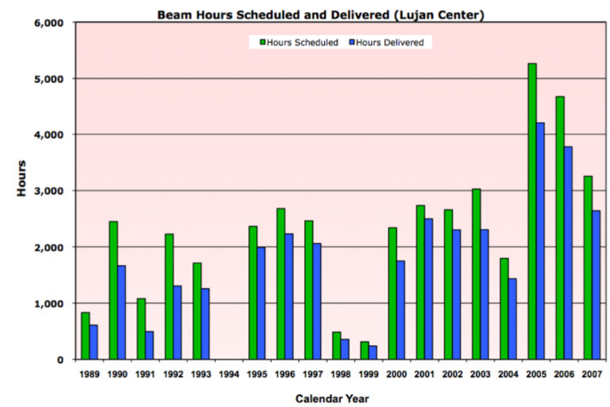


Figure 3: Operating hours for the Lujan Center illustrating recent gains.

Strong efforts have recently been made to increase the number of operating hours for the facility, but budget constraints coupled with increasing power costs dictate that future operating schedules be limited to 3,000 hours per calendar year. This operating scenario is consistent with that planned for the LANSCE Refurbishment Project discussed elsewhere at this conference [1].

Sub-system down time is recorded throughout each scheduled operating period with 1-minute resolution. Historical data allow for careful trending and allocation of scarce maintenance resources. These data have proved valuable in the definition of the scope of the LANSCE Refurbishment Project [1], and are shown in Figure 4.

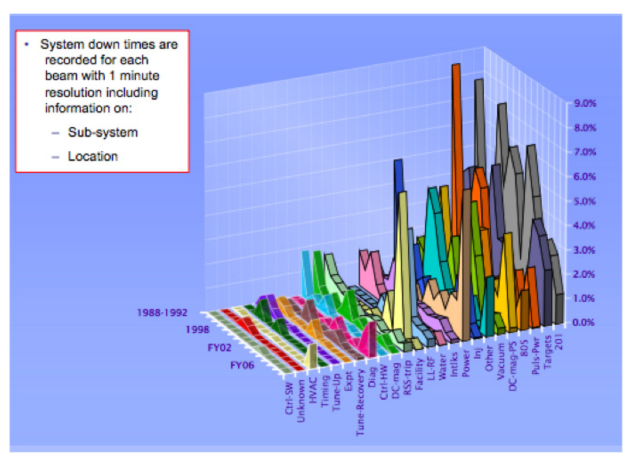


Figure 4: Historical sub-system down time for beam delivery to the Lujan Center

Average operating performance over recent years for the principal facilities at LANSCE is summarized in Table 1.

Table 1: Recent average operating performance for the principal facilities at LANSCE

| Facility | Reliability |
|---|---|
| Lujan Center | 81.6% |
| WNR Target 4 | 84.7% |
| pRAD | 89.5% |
| IPF | 83.7% |

## FUTURE PLANS

Substantial effort has been invested in the LANSCE Refurbishment Project (LANSCE-R) that is discussed elsewhere at this conference [1]. The National Nuclear Security Administration (NNSA) investment in LANSCE-R is planned to be ~$150M (US).

Another core element of facility refurbishment is replacement of electrical, water, and HVAC utilities in the linac service building. This has been done for one of the eight sectors of the accelerator, Sector B. This replacement project for the remaining 7 sectors and budgeted at $22M is planned for FY09-FY12.

Two partner organizations also plan significant investment in the facility. The DOE Office of Science/Basic Energy Sciences plans to enhance the materials science instrument suite at the Lujan Center to emphasize utilization of cold neutrons and improve compatibility with the Spallation Neutron Source at Oak Ridge National Laboratory. This will also involve a new design of the moderator suite for the target-moderator-reflector system that serves the Lujan Center. This work is underway.

The DOE Office of Nuclear Energy plans to install a Material Test Station (MTS) in the decommissioned high-power beam end-station, Area A, which in the past housed the pion and muon production targets and experimental stations for the original LAMPF nuclear physics program. Site preparation in Area A has begun and the shielding doors surrounding the production targets have successfully been opened after 15 years. The MTS will provide a target facility capable of accepting at least 800kW of proton beam power to irradiate fast-fission spectrum fuel elements for material science studies, and will be designed to accept beam powers of up to 3.6MW. The planned budget for this facility is ~$75M with construction scheduled from FY10-FY12.

Several other facility enhancements proposed by work-for-others programs are being considered. A proton interrogation test facility for remote cargo interrogation is in the conceptual design phase. This initiative would utilize single micro-pulses accelerated to 1GeV in a high-gradient superconducting afterburner accelerator for delivery down a 600m external flight path to examine prototypical cargo containers for materials of interest. This project is one of several projects at the conceptual design phase using accelerated particle beams aimed at improving national security. Other projects underway at Los Alamos also consider the use of muon beams for this purpose.

The Proton Storage Ring (PSR) beam may be utilized in different ways. Recent successful development activities have focused on modifications to the PSR to allow accumulation of stacked micro-pulses rather than the 290ns pulse intended for the Lujan Center. These stacked micropulses would be delivered to WNR Target 4 and would enhance the neutron spectrum from the white source in a region of significant interest to the neutron science program. A second concept would extract high-charge (~10μC) pulses from the PSR and deliver them to a new low-enriched sub-critical assembly where the proton burst would drive the assembly to generate a substantial neutron burst, essentially emulating a short-pulse critical assembly. This facility could replace the Short Pulse Reactor facility at Sandia National Laboratory that had been used to study neutron-induced radiation effects on materials and electronics. The estimated cost of such a facility, which is in the conceptual design stage, is ~$70M.

The Los Alamos National Laboratory is developing conceptual plans for a new signature experimental facility, MaRIE. LANSCE will form the foundation for this new facility. Plans include an increase in power capacity for the present linac from 1MW to 1.8-3.6MW for enhanced operation of the MTS. Plans also include a 35GeV high-gradient electron linac and FEL facility that will produce radiation of ~50keV for enhanced material science capabilities.

The LANSCE User Facility is the subject of resurgent interest in the spectrum of science accessible at the facility, and the future is bright.

## REFERENCES

[1] J. Erickson, K. Jones and M. Strevell, "Status of the LANSCE Refurbishment Project," Linac08, Victoria, BC, MOP014 (2008); http://www.JACoW.org.

# OPERATIONAL EXPERIENCE OF THE SNS FRONT END AND WARM LINAC

A. Aleksandrov

Oak Ridge National Laboratory, Oak Ridge, TN 37830 USA

*Abstract*

The Spallation Neutron Source accelerator complex uses set of pulsed linear accelerators of different types to accelerate beam to 1GeV. The 2.5 MeV beam from the Front End is accelerated to 86 MeV in the Drift Tube Linac, then to 185 MeV in a Coupled-Cavity Linac and finally to 1 GeV in the Superconducting Linac. In the process of the commissioning and beam power ramp up many technical systems, as well as tuning algorithms, have deviated significantly from the original design. Our understanding of beam behavior has been evolving continuously and resulted in a steady reduction of fractional beam losses in the linac. In the same time new unexpected problems have been discovered, which are still in the process of investigation. In this paper we summarize our experience up to date and report on the current directions of experimental study, simulations, and development of tuning methods.

## INTRODUCTION

The SNS Front End and warm linac consist of an $H^-$ injector, capable of producing one-ms-long pulses with 38 mA peak current, chopped with a 68% beam-on duty factor and a repetition rate of 60 Hz to produce 1.6 mA average current, an 87 MeV Drift Tube Linac (DTL), a 186 MeV Coupled Cavity Linac (CCL), and associated transport lines. After completion of the initial beam commissioning at a power level lower than the nominal, the SNS accelerator complex is gradually increasing the operating power with the goal of achieving the design parameters in 2009 [1]. Results of the initial commissioning can be found in [2], and of the initial operation experience in [3]. At the time of this writing the Front End and warm linac routinely provides beam at 40% of the design average power.

## FRONT-END PERFORMANCE

The front-end for the SNS accelerator systems is a 2.5 MeV injector consisting of the following major subsystems: an RF-driven $H^-$ source, an electrostatic low energy beam transport line (LEBT), a 402.5 MHz RFQ, a medium energy beam transport line (MEBT), a beam chopper system, and a suite of diagnostic devices. The front-end is required to produce a 2.5 MeV beam of 38 mA peak current at 6% duty factor. The 1 ms long $H^-$ macro-pulses are chopped at the revolution frequency of the accumulator ring (~1 MHz) into mini-pulses of 645 ns duration with 300 ns gaps.

### *Ion Source and LEBT*

The ion source has been capable of satisfying peak and average beam current requirements for the power ramp up goals. At the time of this writing it produces 32mA 750us pulses at 60Hz. We do not expect significant difficulties in expanding the pulse width to the design value of 1200us. Increasing peak current to the nominal 38mA is more challenging but peak current higher than 40mA in 800us pulses has been demonstrated recently in dedicated tests [4].

The RF antenna life time and the possibility of catastrophic antenna failures still remains a concern. We implemented several interlock mechanisms to prevent a possible water leak into the LEBT chamber in case of antenna failure and have not had such events for the two last run periods. An external antenna source is being developed as a long term solution and the first experimental tests have shown promising results [4].

The long standing problem of electrical breakdowns in the electrostatic LEBT has not been fully resolved yet. An improved LEBT design, which does not have glue joints and has a better isolation between the chopper electrodes and the rest of the LEBT, was installed before the last run and demonstrated significant reduction of arc related chopper failures. As a long term solution we plan to use a magnetic LEBT which is in the early stages of development.

### *Chopper Systems*

Beam chopping is performed by two separate chopper systems located in the LEBT and MEBT. The last lens in the LEBT is split into four quadrants to allow electrostatic chopping using the RFQ entrance flange as a chopper target. The LEBT chopper removes most of the beam charge during the mini-pulse gaps, and the traveling-wave MEBT chopper further cleans the gap to a level of $10^{-4}$ and reduces the rise and fall time of the mini-pulse to 10 ns. A chopper controller provides different patterns of chopped beam: “regular chopping”, “single mini-pulse”, “every n-th mini-pulse”, “blanking-off”, and “ramp up”. The chopper systems demonstrated design parameters during commissioning for the nominal chopping pattern at low average beam power. We encountered serious problems with both the LEBT and the MEBT choppers at higher beam power.

The main problem of the LEBT chopper is frequent damage to the high voltage switches by arcs in the electrostatic LEBT. Serial resistors were installed in the chopper circuitry for protection, resulting in significant increase of the chopper rise time. We change the resistor value in the range from 750 Ohm, for the case of high arcing rate, to 175 Ohm, for the case when the LEBT electrodes are well conditioned, and the arc rate is low. Even in the latter case the chopper rise time is ~80ns, which is still significantly longer than the design requirement of <50 ns. At the time of this writing we have 450 Ohm resistor installed resulting in rise/fall time in excess of 100ns as shown in Fig.1. Quite surprisingly, we are able to deliver up to 550 kW of beam power on the target with acceptable losses everywhere in the machine even with such poor chopping quality. The redesigned high voltage switch with more robust protection from the arcs is planned to be installed in January of 2009.

The MEBT chopper high voltage switches had poor reliability in early runs, and the kicker structure had to be redesigned [5]. A number of small evolutionary improvements in the high voltage electronics design resulted in significant improvement in reliability, which, together with using a new kicker, allowed using the MEBT chopper for extraction loss reduction during neutron production runs. The kick strength provided by the prototype structure of the new design is about 15% below the original design specification. Results of the kick strength measurement are shown in Fig.1. The chopper rise time of ~16 ns is still longer than the design specification. The final version of the chopper kicker, which we plan to install in January of 2009, will have a 25% stronger kick and an 8ns rise time. Figure 2 demonstrates the effect of the MEBT chopper on the ring extraction losses in one of the experiments. Just inserting the chopper target reduces losses by factor of 2 due to scraping of the vertical halo, when the chopper is on the losses are reduced by another factor of 5. In the later experiments we discovered that ion source alignment has a significant effect on the LEBT chopper efficiency. With improved alignment procedure we are able to run with negligible extraction losses even with the MEBT chopper off. We do see effects of the slow chopper rise time, most notably in bunch position and phase variation along the pulse and effective beam size increase. We have not found evidence of additional losses in the linac associated with the slow chopping.

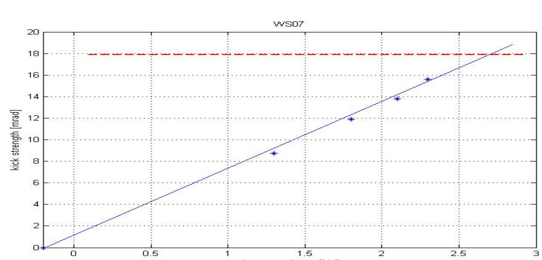


Figure 1: Chopper kicker strength vs. kicker voltage calculated from the profiles in Fig.1. Red dashed line shows the design requirements.

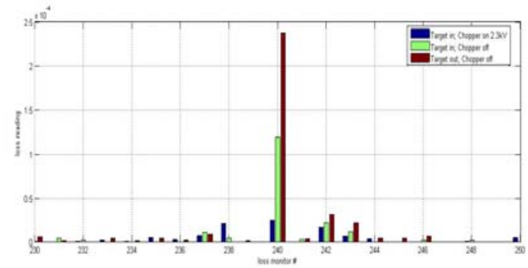

Figure 2**:** Effect of the MEBT chopper on the ring extraction losses. Bar chart is BLM readings: the brown bar– chopper is off, target is out; the green bar – chopper is off, target is in; the blue bar – chopper is on, target is in.

## DTL AND CCL PERFORMANCE

The Drift Tube Linac consists of six accelerating tanks operating at 402.5 MHz with output energy of 87 MeV. The transverse focusing is arranged in a FFODDO lattice utilizing permanent-magnet quadrupoles. Some empty drift tubes contain BPMs and dipole correctors. The Coupled Cavity Linac (CCL) consists of four 12-segment accelerating modules operating at 805 MHz with output energy of 187 MeV. The inter-segment sections contain electromagnet quadrupoles arranged in a FODO focusing lattice, BPMs, wire scanners, and Beam Shape Monitors.

The original plan for the transverse beam matching was to use profile measurements in several places along the linac. So far we have not achieved any significant progress in using wire scanner data for loss reduction. We set all quadrupole magnet strengths to the design values and manually tweak some of them within 1-2% range to minimize beam losses.

Longitudinal tuning of the linac had been routinely done using PASTA phase scan algorithm [6]. Measured longitudinal rms Twiss parameters were close to the design values and we did not observe significant beam losses in the warm linac [7]. However, with the increased average beam power we started seeing unexpectedly large losses in the Super Conducting Linac (SCL). These losses depended weakly on the transverse focusing parameters but were very sensitive to the RF phase settings of the warm linac cavities. One of the strange experimental findings was that minimum losses were achieved by shifting some of the RF phases away from the nominal set points found from the PASTA phase scans. For example, DTL6 phase had to be shifted by 6 degrees. In the process of resolving this puzzle we developed a beam based measuring technique, which allows us to measure the deviation of accelerating gradients from the design value with high accuracy. For this measurement the phase of the beam is shifted by several degrees at the entrance of a selected cavity, and the phase shift at all available BPMs downstream is recorded. The period of the resulting synchrotron oscillation inside the longitudinal separatrix depends on the accelerating field amplitude. By fitting the model to the measurements it is possible to deduce the RF amplitude errors, as illustrated by an example in Figs. 3 and 4. We found that our standard PASTA scans produced RF amplitude set points overestimated by 1-2% for each cavity. The cumulative effect of these relatively small errors led to significant deviation from the design longitudinal phase advance. After correction of the set points the minimum of the losses corresponded to the nominal set points found from the phase scans, and no DTL phase tweaking is required.

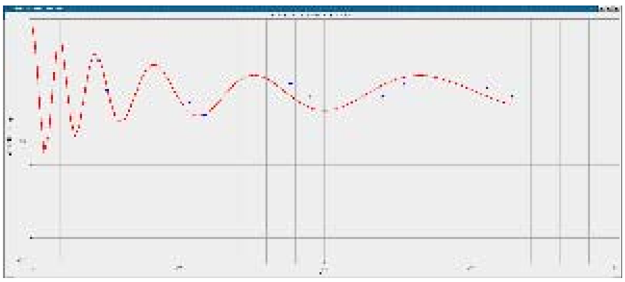

Figure 3: Synchrotron bunch oscillation in the DTL. Solid line is simulation result for the nominal cavity amplitudes; points are measured values for the case of 2.7% error of the DTL2 amplitude.

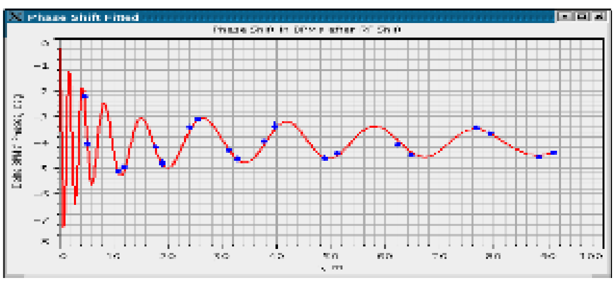

Figure 4: Synchrotron bunch oscillation in the DTL and CCL. Solid line is simulation result for the nominal cavity amplitudes; points are measured values for the case of good linac tuning.

### *Beam Loss in the Warm Linac*

There is no reduction in beam current along the linac detectable by the beam current monitors. Beam loss monitors (BLMs) based on ionization chambers are used to detect prompt radiation due to beam losses.

The integrated radiation dose recorded by the BLMs during a typical 10 day run with 400 kW beam on target is shown in Fig. 5. The result of the activation survey after 2 days of cool down period is shown in Fig. 6. There is a good correlation between the activation levels and prompt radiation doses; therefore we can use BLM data reliably in machine tuning. We associate the main hot spot in the beginning of the CCL with particles falling out of the longitudinal DTL separatrix due to large energy and/or phase deviation at the entrance. In order to fix this problem we will have to improve longitudinal beam quality in the Front End. The first step will be to increase the available RF power for the MEBT rebunchers, which is currently limited at about 75% of the nominal design level.

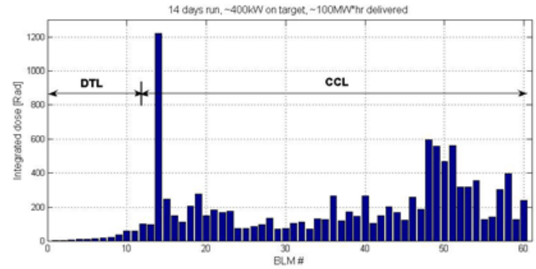


Figure 5: Measured distribution of prompt radiation due to beam loss in the warm linac.

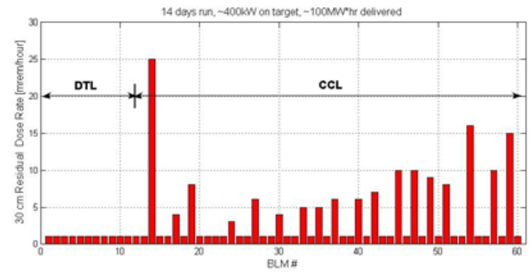


Figure 6: Measured distribution of the residual radiation in the warm linac after 36 hours of cool down period.

## CONCLUSIONS

The SNS Front End and warm linac has been successfully keeping up with the requirements of the beam power ramp up plan. We continue to refine the tuning algorithms. The most significant technical problem at the moment is inadequate chopping quality due to the electrical breakdowns in the electrostatic LEBT. Transition to a magnetic type LEBT is seen as the long term solution and various design improvements are being implemented on the existing LEBT as a temporary fix. The new MEBT chopper deflector has been successfully tested and is in use. In general, losses in the warm linac itself are well under control and should not present any limitations to increasing the average beam power to the design level. A bigger concern is losses in the downstream parts of the machine, possibly caused by the halo generated in the Front End and warm linac. This is a subject of an ongoing research.

## ACKNOWLEDGEMENT

ORNL/SNS is managed by UT-Battelle, LLC, for the U.S. Department of Energy under contract DE-AC05-00OR22725.

## REFERENCES

[1] S. Henderson, Proc. EPAC 2008, p.2892.
[2] A. Aleksandrov, Proc. PAC 2005, p.97
[3] A. Aleksandrov et al., Proc. PAC 2007, p.1820
[4] R. Welton et al., Rev. Sci. Instrum. **79**, 02C721 (2008)
[5] A. Aleksandrov et al, Proc. PAC 2007, p.1817
[6] J. Galambos et al., Proc. PAC 2005, p.1491
[7] A. Feschenko et al, Proc. PAC 2007, p.2610

# THE PROPOSED ISAC-III (ARIEL) LOW-ENERGY AREA AND ACCELERATOR UPGRADES

R.E. Laxdal, F. Ames, R. Baartman, M. Marchetto, M. Trinzcek, Fang Yan,
V. Zvyagintsev, TRIUMF*, Vancouver, BC, V6T2A3, Canada

*Abstract*

The ISAC-III proposal (now called ARIEL) is a ten year plan to triple the amount of radioactive ion beam (RIB) time at the facility. The plan includes the addition of two new independent target stations, a second 500 MeV proton beam line from the TRIUMF cyclotron and a new 50 MeV electron linac as a complementary driver to provide RIBs through photo-fission. A new mass-separator and low-energy beam-transport complex is foreseen to deliver the additional beams to the ISAC experimental facilities. A new linear accelerator section would provide the capability for two simultaneous accelerated RIBs to experimenters. This paper will describe the proposed installations in the low-energy transport and accelerator sections of the ISAC complex.

## INTRODUCTION

In the ISAC-I facility[1] 500 MeV protons from the cyclotron at up to 100$\mu$A impinge on one of two production targets to produce radioactive isotopes. The isotopes are ionized and the resulting beam is mass-separated and transported in the low energy beam transport (LEBT) electrostatic beamline to either the low energy experimental area or through a series of room temperature accelerating structures (RFQ, DTL) to the ISAC-I medium energy experimental area. The RFQ accelerates ions with A/q$\leq$30 to 150 keV/u and the post-stripper variable energy DTL accelerates ions with A/q$\leq$6 up to 1.8 MeV/u. The accelerated beam can also be transported to the ISAC-II Superconducting Linear Accelerator (SC-linac)[3] for further acceleration above the Coulomb barrier. An ECR charge breeder (CSB) is presently being added to extend the mass range beyond A=30.

The cyclotron provides the highest power driver beam (50 kW) of any operating ISOL based facility. Two 50 kW target stations are available to reduce the switchover time between targets. But the present scientific output is oversubscribed with more experiments requested than available beam time would allow. The aim of the ISAC-III (ARIEL) proposal is to get more RIBs on target to produce more physics. Fundamental to the plan is the eventual delivery of three simultaneous RIBs to three experimental areas. The expansion requires the addition of two new driver beams - one from a second cyclotron proton beamline and one from a new high power electron linac[2]. Two new target areas with independent separators and a flexible beam delivery system would allow simultaneous operation of three production sources. A new accelerator front end including a second charge breeder provides a second simultaneous accelerated beam capability. The TRIUMF site with the prosposed addition is shown in Fig. 1.

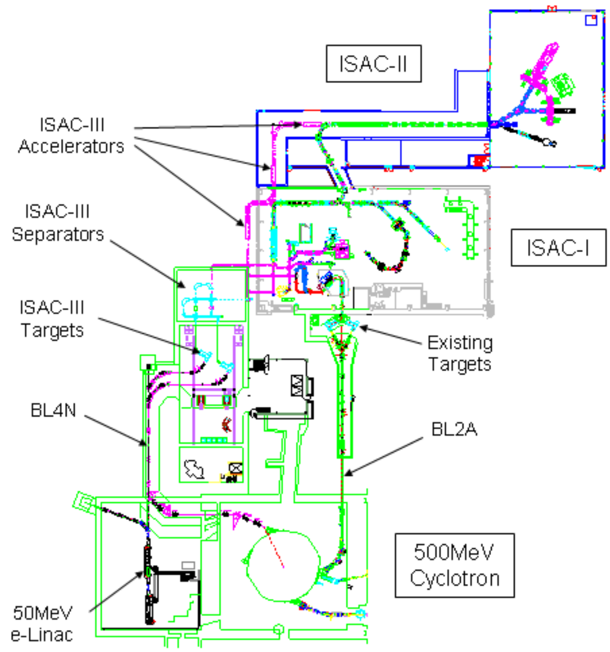


Figure 1: The TRIUMF site including the cyclotron, ISAC-I and ISAC-II and the proposed ISAC-III (ARIEL) facility. BL2A is the present proton line and the BL4N tunnel is proposed for the new ISAC-III driver beams.

## MASS-SEPARATOR SWITCHYARD

It is useful to consider a switchyard that is capable of either low resolution, medium resolution or high resolution separation schemes depending on the experiment. In general reduced resolution schemes are desired since they reduce the tuning time required. The proposed configuration is shown in Fig. 2. Here each of the two target/source units has a pre-separator and individual transport lines directing the beams to a mass-separator switchyard. The beams after separation are directed to either one of two new vertical sections VS-2 or VS-3 for delivery to the upstairs experimental area. Standard ISAC LEBT electrostatic components are used to deliver the beam to either a Medium Resolution Spectrometer (MRS) or a High Resolution Spectrometer (HRS). The medium resolution leg has a resolution of ~2500 while the high resolution leg has a resolution

* TRIUMF receives funding via a contribution agreement through the National Research Council of Canada

of ∼15000. The high resolution leg is equipped with an rf cooler to reduce the transverse emittance and energy spread of the beam before separation. The switchyard is designed with sufficient flexibility that each of the targets can pass beams through the HRS while the beam from the other target is sent to the MRS. In addition a bypass line is available so that if not required a beam with pre-separation only can be sent to the experimental area. A first stage would require only the MRS section and vertical section to transport the single new RIB beam upstairs from the first target.

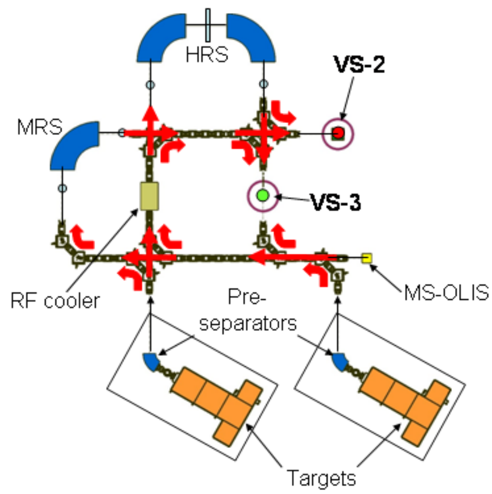


Figure 2: ISAC-III target stations and mass-separator switchyard. The red arrows indicate possible beam paths. An off-line source (MS-OLIS) is available for separator tuning.

## LOW ENERGY BEAM TRANSPORT

The LEBT is the all electrostatic transport that takes the beam at source potential (≤60 kV) from the downstairs target/separator area to the upstairs experimental floor for delivery to the low energy areas or to the accelerators. Substantial LEBT transport has already been installed in ISAC. The design of the new installation will copy the standard building blocks that comprise the present installation. The new installation is designed to provide enough flexibility that any of the target stations, existing or new, can deliver beams to any of the three experimental areas, low energy, medium energy or high energy, so that the RIB beams from each target can be optimized for a given experiment. A second path to the low energy experimental area is provided since this is where there is the largest inventory of experimental infrastructure. The ground floor LEBT for ISAC-III is shown in Fig. 3.

A second charge state booster (CSB2) is added in Stage 1 to increase the charge state of beams selected for acceleration. An extra line is added so that beams from the existing target area can also be boosted in CSB2 if preferable. A second accelerator path is available with the addition of RFQ2 positioned beside the existing ISAC RFQ1.

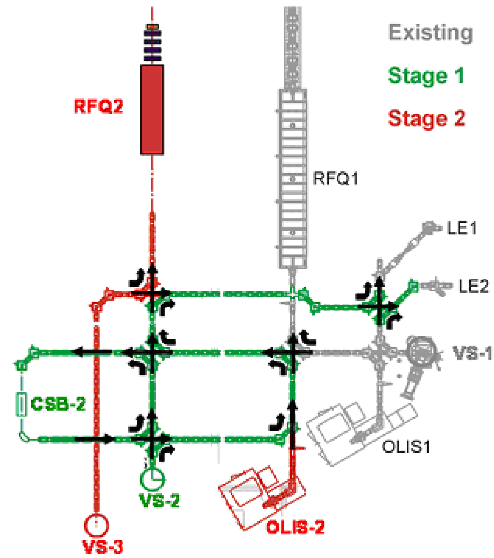


Figure 3: The new ground level LEBT (low energy beam transport) for ISAC-III. The existing section appears in grey. The first stage installation is shown in green and the second stage is shown in red. The black arrows indicate the available beam paths.

A second off line ion source (OLIS2) allows tuning of either accelerator line while delivering RIBs to the other. The LEBT vacuum normally reaches 2e-7 Torr. For transporting the higher charge states from the CSBs the vacuum will be improved to <5e-8 Torr to reduce transmission losses.

## NEW ACCELERATOR LEG

The technique of accelerating a 1+ beam through a series of stripping and acceleration steps was considered but abandoned due to the high total accelerating voltages required. Instead a second charge breeder (CSB2) will be added to boost the 1+ ions from the on-line source. The technical choice for the ISAC-III CSB2 between an EBIS or an ECRIS charge breeder will be made by 2010 after the on-line performance of CSB1 (Phoenix 14.5 GHz ECRIS) with RIB delivery can be evaluated. TRIUMF also has a working EBIS on-site with the TITAN experimental installation. CSB1 produces charge states compatible with A/q≤9 for all masses and this sets the mass specification for the second accelerator leg.

The proposed accelerator addition is shown in Fig. 4. A new RFQ compatible with accelerating ions up to A/q=9 takes the beam to 150 keV/u. A new beamline running north of the existing RFQ will provide separate paths for ISAC-I and ISAC-II accelerated beams avoiding the ISAC-DTL1 bottleneck of 2 ≤ A/q ≤6. A new medium energy transport section incorporates a switchyard that allows sending either of the RFQ1 or RFQ2 beams to either of ISAC-I or ISAC-II simultaneously. The new beamline to ISAC-II will include a room temperature drift tube linac (DTL2) to boost the energy from 0.15 MeV/u to 0.7 MeV/u for beams up to A/q=9. A new low beta cryomodule (SCA) at 106 MHz would further boost the energy to at least 1.5 MeV/u for injection into the existing SC-linac. An optional stripper could be employed between DTL2 and SCA to boost the charge state to achieve a higher final energy.

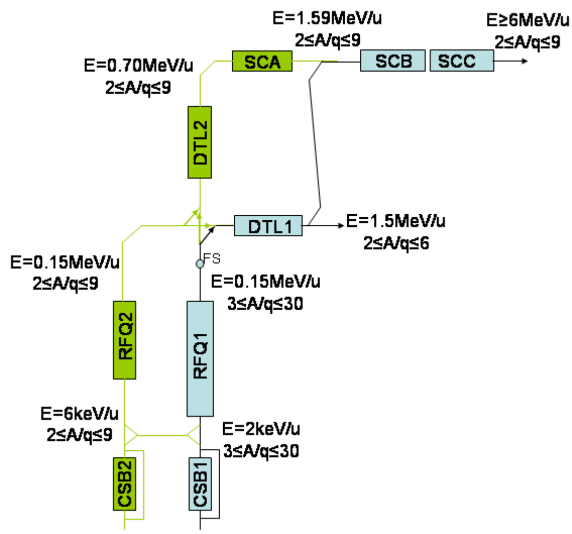


Figure 4: The existing ISAC-1 and ISAC-II accelerator chain in (blue) and the upgrade of the ISAC-III accelerator system in green.

RFQ2 is a room temperature device that accelerates beams from 6 keV/u to 150 keV/u for ions up to A/q=9. The rf structure has not yet been chosen but preliminary beam dynamics have been completed. The rf is specified at 70 MHz with $\Delta$V=1.3 MV. A length of 3.2 m is estimated.

DTL2 is presently specified as a room temperature device at 106 MHz. A four tank IH structure is chosen with magnetic triplets in between tanks for transverse focussing. Design values for number of gaps and rf parameters are shown in Table 1. The DTL is designed to accelerate at 0° synchronous phase with -60° bunching sections in the first several gaps of each tank.

Table 1: DTL2 tank design parameters.

| Tank | $N_{\text{gap}}$ | L(m) | D(m) | V(MV) | P(kW) |
|---|---|---|---|---|---|
| 1 | 10 | 0.28 | 0.92 | 0.83 | 6.1 |
| 2 | 16 | 0.55 | 0.7 | 1.66 | 10.8 |
| 3 | 18 | 0.75 | 0.7 | 2.25 | 11.9 |
| 4 | 21 | 1.04 | 0.7 | 3.13 | 14.3 |

The SCA accelerator section represents the low energy front end to the ISAC-II linac. The injection energy is 0.7 MeV/u and the section accelerates A/q values up to 9. The SCA section is comprised of one cryomodule with eight cavities and three superconducting solenoids for transverse focussing. The cavities are 70 MHz with a design geometry corresponding to $\beta_0 = 4.6\%$.

Initial beam simulations from RFQ2 to the end of the SC-Linac have been completed. The transversal RMS envelopes are shown in Fig. 5. The initial Twiss parameters for the simulation at the exit of RFQ2 are $\alpha_x = 1.3$, $\beta_x = 0.202$ (mm/mrad), $\alpha_y = -1.65$, $\beta_y = 0.283$ (mm/mrad), $\alpha_z = -0.5$, $\beta_z = 10$ (degree/%) with normalized emittances of $\epsilon_{x,y} = 0.3\pi$ mm-mrad, $\epsilon_z = 0.6\pi$ keV/u-nsec. Emittance growth of 10% and 6% are estimated for the full acceleration in the transverse and longitudinal dimensions respectively.

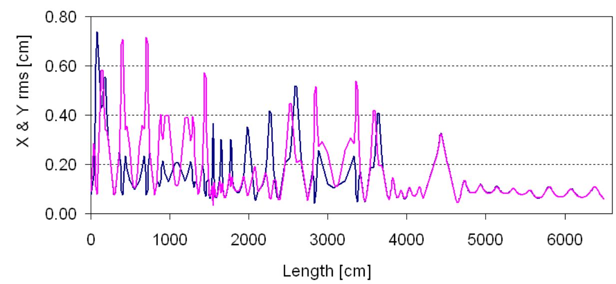


Figure 5: The x (magneta) and y (blue) beam envelopes from RFQ2 to the end of the ISAC-II SC-linac.

## STAGING

The first stage comprising the period 2010-2015 includes the additions of the e-Linac to 50 MeV, 1 mA (50 kW) capability; 25 MeV by the end of 2012, the completion of the new proton line to a capability of 500 MeV, 200$\mu$A (100 kW) by the end of 2014, one new target station with 50 kW electron/proton capability by April 2013, a new medium resolution mass separator (MRS) and low energy beam transport (LEBT) to deliver beams from the new target station to the low energy area by April 2013 and CSB2 and LEBT to allow the acceleration of beams from the new target area by the end of 2014. The second stage through 2015-2020 would include the addition of the upgrade of the e-Linac to 50 MeV, 10 mA (500 kW), a second new target station with 500 kW electron capability, an expanded low energy section with high resolution separator (HRS) allowing simultaneous beams from the two new target areas and a new accelerator front end to allow two simultaneous accelerated beams. Presently ISAC runs at ~2900 RIB hours a year. With ISAC-III this is expected to rise to 6500 by the end of 2014 with a further rise to 10700 by the end of 2019.

## REFERENCES

[1] P. Schmor, et al, "Development and Future Plans at ISAC", LINAC2004, Lubeck, Germany, Aug. 2004.

[2] S. Koscielniak, et al, "ARIEL and the TRIUMF e-Linac Initiative, a 0.5 MW Electron Linac for Rare Isotope Beam Production", these proceedings.

[3] R.E. Laxdal, et al, "The ISAC-II Superconducting Linac Upgrade - Design and Status"

# ISAC-II SUPERCONDUCTING LINAC UPGRADE - DESIGN AND STATUS

R.E. Laxdal, R.J. Dawson, M. Marchetto, A.K. Mitra, W.R. Rawnsley,
T. Ries, I. Sekachev, V. Zvyagintsev, TRIUMF*, Vancouver, BC, Canada,

*Abstract*

The ISAC-II superconducting linac, operational since April 2006, adds 20 MV accelerating potential to the ISAC Radioactive Ion Beam (RIB) facility. An upgrade to the linac, in progress, calls for the addition of a further 20 MV of accelerating structure by the end of 2009. The new installation consists of twenty 141 MHz quarter wave cavities at $\beta_0$=11%. The cavities will be housed in three cryomodules with six cavities in the first two cryomodules and eight cavities in the last. A second Linde TC50 refrigerator has been installed and commissioned to provide cooling for the new installation. The design incorporates several new features as improvements to the existing cryomodules. A summary of the design and the current status of the cryomodule production and supporting infrastructure will be presented.

## INTRODUCTION

The Radioactive Ion Beam (RIB) facility, ISAC, includes an ISOL production facility and a post-accelerator for delivery of beams from 150 keV/u to beyond the Coulomb barrier.[1] The post-accelerator consists of two room temperature devices, a 35 MHz RFQ for acceleration of ions with A$\leq$30 to 150 keV/u and a 106 MHz post-stripper DTL to energies fully variable from 0.15 to 1.8 MeV/u. A superconducting heavy ion linac[2] was added in 2006 to add a further 20 MV to the ISAC beam energy. The installation known as ISAC-II is the first phase in a planned three phase installation. The Phase I linac consists of 20 bulk niobium quarter wave cavities housed in five cryomodules. Each cryomodule consists of four cavities and one superconducting solenoid arranged symmetrically along the beamline with a diagnostic box and steering magnet located between the modules at the beam waist. Routine average operating gradients of 7 MV/m corresponding to peak surface fields of 35 MV/m are achieved. Eight of the cavities (the first two cryomodules) are $\beta$=0.057 and the other twelve are $\beta$=0.071.

A second phase now in progress will see the addition of another 20 MV of accelerating potential to extend the present energy range by the end of 2009. The new installation consists of twenty 141 MHz quarter wave cavities at $\beta$=0.11. The cavities will be housed in three cryomodules with six cavities in the first two cryomodules and eight cavities in the last. The cavities and cryomodules are now in fabrication. The plan is to install the completed and tested cryomodules during an extended shutdown of ISAC-II starting in Sept. 2009. The layout of ISAC-I and ISAC-II is shown in Fig. 1.

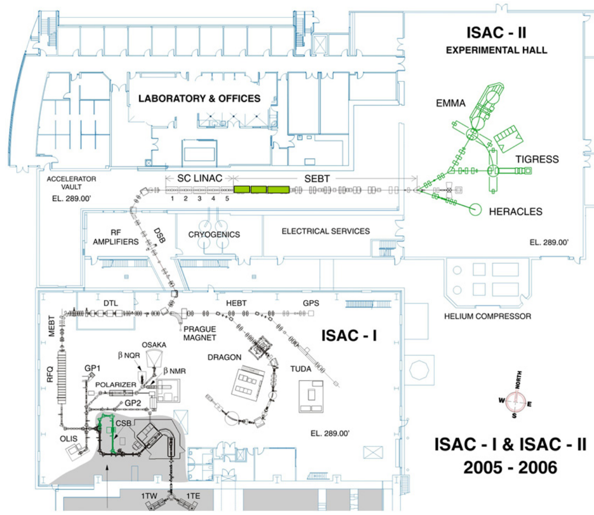


Figure 1: The layout of ISAC-I and ISAC-II. The Phase II SC-linac is highlighted.

## CRYOMODULE DESIGN AND STATUS

The Phase II cryomodules are identical in many respects compared to the Phase I cryomodules. A key design choice was to maintain the philosophy of incorporating a single vacuum space for thermal isolation and beam/rf volumes. This has been the historic choice in the low-beta community (ATLAS, INFN-Legnaro, JAERI) but recent proposed facilities in development or assembly have chosen separated vacuum systems (SARAF, SPIRAL-II, FRIB). The decision to maintain a single vacuum comes from our experience with Phase I operation of the SC-linac. We have seen very little evidence of degradation in cavity performance over the first two years of operation even after repeated thermal and venting cycles. Procedures are followed to help mitigate cavity degradation: 1. Initial cavity treatment and overall assembly using HPWR and clean conditions 2. Vacuum materials and components to be free from particulate, grease, flux and other volatiles 3. Maintain a LN2 cooled cold trap upstream and downstream of the linac to prevent volatiles migrating from the beamline into the cryomodule 4. Cryomodule venting with filtered nitrogen 5. Pumping and venting of modules at slow rates to avoid turbulences.

All cryomodules are assembled in a ‘dirty’ assembly area to check the fitting of all components. Next the assembly is completely dismantled, all parts are cleaned in

* TRIUMF receives funding via a contribution agreement through the National Research Council of Canada

an ultrasound bath, rinsed with 18 MΩ water at high pressure and dried in a clean room before assembly.

There are some differences between the Phase I and Phase II cryomodules that either address small deficiencies in the Phase I design or are required due to the longer size of the Phase II cryomodules: 1. The vacuum tanks are essentially the same with dimensional differences to accommodate the internal components. The eight cavity SCC3 has an extra set of ribs on the lid and sides to reduce vacuum deformation on the larger areas. The mounting footprint is also elongated to give more stability. 2. The cavities and solenoid are supported from a rigid strongback that is in turn supported from the tank lid by support rods. In the SCB cryomodules a three point mounting system was used to suspend the strongback. The decision here is to adopt a four point system to reduce the freedom in the movement of the cold mass. The strongback assembly is considerably more robust than in the SCB due to the increased cold mass and length. 3. In the SCB the LN2 cooling for the side shields and the coupling loop is one series circuit. In the SCC the delivery to the coupling loops is achieved with parallel channels to reduce the size of the fittings on the coupling loop. 4. The solenoid mounting system is completely modified in SCC and is based on a linked strut system to aid in alignment. 5. The helium reservoir is redesigned with thicker wall material and a purchased tee section. Bulkheads are incorporated into the weld seams to make all welds external. The service stack for the helium space is now outfitted with a 12.5 cm high spool piece with the feedthroughs and ports for all of the cryogenic and vacuum diagnostics. Provision for level sensor replacement has been added with ports on the top of the reservoir. Cables and He distribution lines are installed before final weld on each end of the reservoir. The welding is done in place of the SCB indium seals that were prone to cold leaks. 6. The mu metal thickness has been increased from 1 mm to 1.5 mm.

### *Present Status*

All three vacuum chambers and lids have been received. Mu metal has been installed on two of the vacuum chambers. The LN2 side shields panels have been fabricated and the shield box assembly is almost complete. Dirty assembly of the first cryomodule is underway. The effect of the mu metal has been characterized and reaches the specified remnant field criterion of <20mG.

## SUPERCONDUCTING CAVITIES

The cavities for Phase II are quarter wave bulk niobium with features similar to the Phase I cavities. In this case the rf frequency of 141.4 MHz (the 12th harmonic of the bunch frequency 11.8 MHz) allows to keep the same outer conductor dimension while increasing the design velocity to $\beta$=0.11. The cavity has been outfitted with a beam tube (donut) to symmetrize the transverse rf fields and improve the transit time factor. The cavity is shown in Fig. 2.

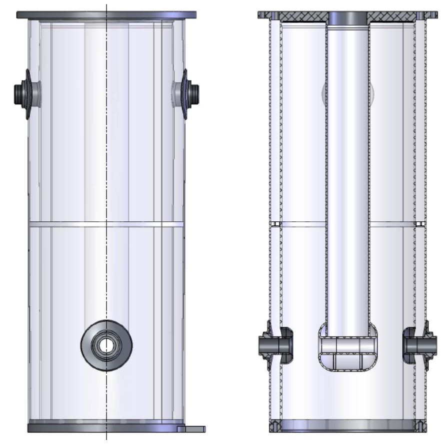

Figure 2: The 141.44MHz rf cavity for Phase II.

The cavities are being produced by Pavac Industries of Richmond BC Canada. The development included the manufacture of two full size copper models to study all of the machining, assembly, tuning and welding steps. Two Niobium cavities have been produced.[3] The cold test results of the two prototypes are shown in Fig. 3. Note that the ISAC-II specification of $E_a = 6$ MV/m at 7W ($E_p$=30 MV/m) is exceeded by a comfortable margin with average values of $E_a = 8.5$ MV/m ($E_p > 40$ MV/m). PAVAC is presently completing the first six production cavities as well as machining the rest of the parts for the remaining fourteen cavities in preparation for welding.

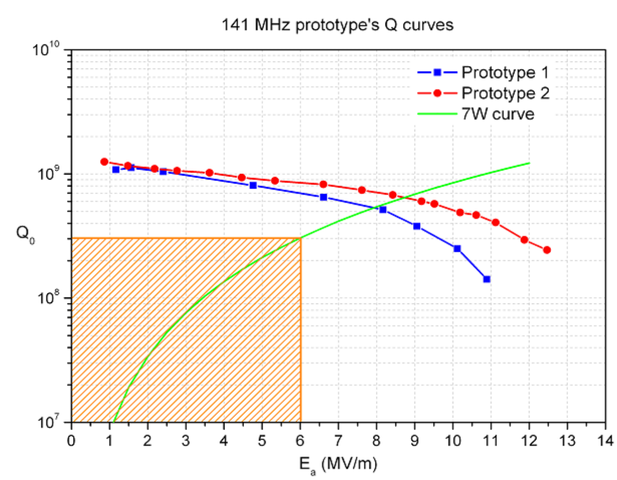


Figure 3: Characterization curves of the two 141 MHz QWR cavities.

## RF ANCILLARIES

### *Amplifiers*

As part of the upgrade of the ISAC-II superconducting linac, twenty solid state amplifiers have been ordered with QEI Corporation, NJ, USA. A prototype amplifier has been tested thoroughly prior to series production. The gain of the amplifier, the 3 dB bandwidth and output power were measured and are within the specification. Gain linearity is within $\pm 0.5$ dB and phase linearity is within $\pm 2.0$ dB for the output power range from 1 to 250 watts. The amplifier gain is measured to be $65 \pm 0.75$ dB, which is 10 dB higher than specified. The phase noise of the prototype amplifier is estimated by tests into both a dummy load and one of the prototype cavities. These measurements are compared to the same values using a tube amplifier. The solid state amplifier is significantly less noisy than the tube amplifier. For the solid state amplifier the average noise value is 0.0044° rms in the frequency range of 2-200 Hz. The average noise for the tube amplifier in the same frequency range is 0.098° rms. The integrated value of phase noise in the bandwidth of $2 - 200$ Hz was specified to be less than 0.3° rms. These amplifiers will be installed in the power supply room adjacent to the accelerator vault.

### *Mechanical Tuner*

In the Phase I system the cavities are tuned by a lever arm that pushes against a tuner plate on the bottom end of the cavity. The lever arm is actuated by a long push rod that extends to the top of the cryomodule through a bellows to a linear servo motor[4]. The system works well and provides high performance tuning for high gradient operation. The tuner motor is an expensive item and development work subsequent to the Phase I installation has resulted in a new design using a ball screw drive to replace the linear motor. The brush-less servomotor contains its own single turn absolute sine encoder. The power and encoder signals are connected through long cables to a matched digital servo-amplifier. The output shaft of the motor is connected directly to the anti-backlash internally preloaded precision ball screw nut, through a stiff bellows coupling. The anti-backlash nut is fixed rigidly to the anti-backlash liner guides that provide perfectly reproducible vertical straight-line motion resulting in a vertical position resolution of at least 0.03 $\mu$m with a positioning bandwidth of at least 30 Hz. The interface connections are designed to retrofit the SCB low beta SRF tuner rod connector design.

### *Coupling Loop*

The SCB variable coupling loop[5] uses a Teflon bearing but side loads from the LN2 cooling lines cause some stiffness in the mechanical motion at cold temperature. A redesigned coupling loop with non-magnetic cross-roller bearings and symmetric loading has greatly improved the mechanical motion and the new design is being employed in SCC.

## CRYOGENIC SYSTEM

The Phase I cryogenic system consists of a Linde TC50 cold box configured with a 79 gm/sec KAESER compressor. Helium produced in the cold box is fed to a 1000 liter dewar. The LHe is delivered to the cryomodules at 4K through vacuum jacketed LN2 cooled helium transfer lines with a slight overpressure in the dewar. The cryomodules are fed in parallel from a main supply manifold (trunk) through variable supply valves. The level in the cryomodules is used to control the opening of the supply valves. The vapour from the cryomodules is returned either in a warm return line direct to the compressor during cooldown or through a cold return line back to the cold box during normal operation.

The Phase II addition of the cryogenic system (shown in Fig.4) essentially duplicates the Phase I system. A second Linde plant has been installed identical in every respect to Phase I except that a second recovery compressor was not ordered. The system has been installed by TRIUMF and commissioned. The measured liquefaction with LN2 precool is 240 ltr/hour and the refrigeration power is 600 W. The stability of the helium pressure is within $\pm 7$ mBar.

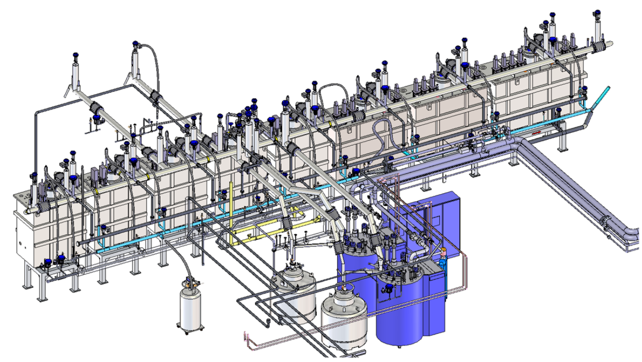

Figure 4: The cryogenics system for ISAC-II Phase I and II.

## SUMMARY

The phase II system is on schedule for completion by the end of 2009. The first six cavities are expected by the end of October. The cavities will be processed (BCP) and tested at TRIUMF before mounting into the first cryomodule for cryogenic and alignment tests. The other two cryomodules will follow with full installation by Dec. 2009.

## REFERENCES


[1] P. Schmor, "Development and Future Plans at ISAC/TRIUMF", LINAC2004, Lubeck, Germany, Aug. 2004, p. 251.

[2] R.E. Laxdal et al, "Commissioning and Early Experiments with ISAC-II", PAC07, Albuquerque, New Mexico, USA, June 2007, p. 2593.

[3] R.E. Laxdal, et al, "Production and Testing of Two 141MHz Prototype Quarter Wave Cavities for ISAC-II", this conference.

[4] T. Ries, et al, "A Mechanical Tuner for the ISAC-II Quarter Wave Superconducting Cavities", PAC03, Portland, Oregon, USA, May 2003, p. 1488.

[5] R. Poirier, et al, "RF Coupler Design for the TRIUMF ISAC-II Superconducting Quarter Wave Resonator", LINAC2004, Lubeck, Germany, Aug. 2004, p. 228.

# THE HITRAP DECELERATOR PROJECT AT GSI - STATUS AND COMMISSIONING REPORT

L. Dahl#, W. Barth, P. Gerhard, F. Herfurth, M. Kaiser, O. Kester, H.-J. Kluge, S. Koszudowski, C. Kozhuharov, G. Maero, W. Quint, A. Sokolov, T. Stöhlker, W. Vinzenz, G. Vorobjev, D. Winters
Gesellschaft für Schwerionenforschung, D-64291 Darmstadt, Germany

B. Hofmann, J. Pfister, U. Ratzinger, A. Sauer, A. Schempp
Goethe University, D-60438 Frankfurt, Germany

*Abstract*

For injection into the ion trap facility HITRAP, the GSI accelerator complex has the unique possibility to provide beams of highly stripped ions and even bare nuclei up to Uranium at an energy of 4 MeV/u. The HITRAP facility comprises linear 108 MHz-structures of IH- and RFQ-type to decelerate the beams further down to 6keV/u for capturing the ions in a large penning trap for cooling purpose. The installation is completed except the RFQ.

During commissioning periods in 2007 $^{64}Ni^{28+}$ and $^{20}Ne^{10+}$ beams were used to investigate the beam optics from the experimental storage ring extraction to the HITRAP double-drift-buncher system. In 2008 the IH-structure and the downstream matching section were examined with $^{197}Au^{79+}$ beam. Comprehensive beam diagnostics were installed: Faraday cups, tubular and short capacitive pick ups, SEM grids, YAG scintillation screens, a single shot pepper pot emittance meter, and a diamond detector for bunch shape measurements. Results of the extensive measurements are presented.

## INTRODUCTION

Within the HITRAP project (Heavy Ion Trap) [1] trapped and cooled highly charged ions up to $U^{92+}$ will become available for a variety of attractive experiments in atomic physics. As presented in Fig.1 heavy ions are produced, accelerated, and stripped in the GSI accelerator complex and are stored, decelerated, and cooled in the ESR (Experimental Storage Ring) down to 4 MeV/u. After extraction from the ESR, the ions have to be further decelerated down to 6 keV/u by 108.408 MHz structures [2,3]. An IH drift tube cavity operating in the H11(0) mode reduces the ion energy to 0.5 MeV/u and a 4-rod RFQ [4] degrades it finally to 6 keV/u. Phase matching into the IH structure is prepared by a DDB (Double-Drift-Buncher combination) of λ/4-resonators whereof the second one works at 216 MHz. A third rebuncher of spiral type is located between the decelerator tanks. Finally a low power spiral type debuncher integrated into the RFQ tank at the beam exit end reduces the beam energy spread for efficient beam capturing in the super conducting penning trap. The linear decelerator as sketched in Fig. 1 is installed in the re-injection channel between ESR and SIS (Heavy Ion Synchrotron).

## STATUS OF INSTALLATIONS

Until September 2008 the HITRAP decelerator was being constructed except the RFQ tank. Magnet power

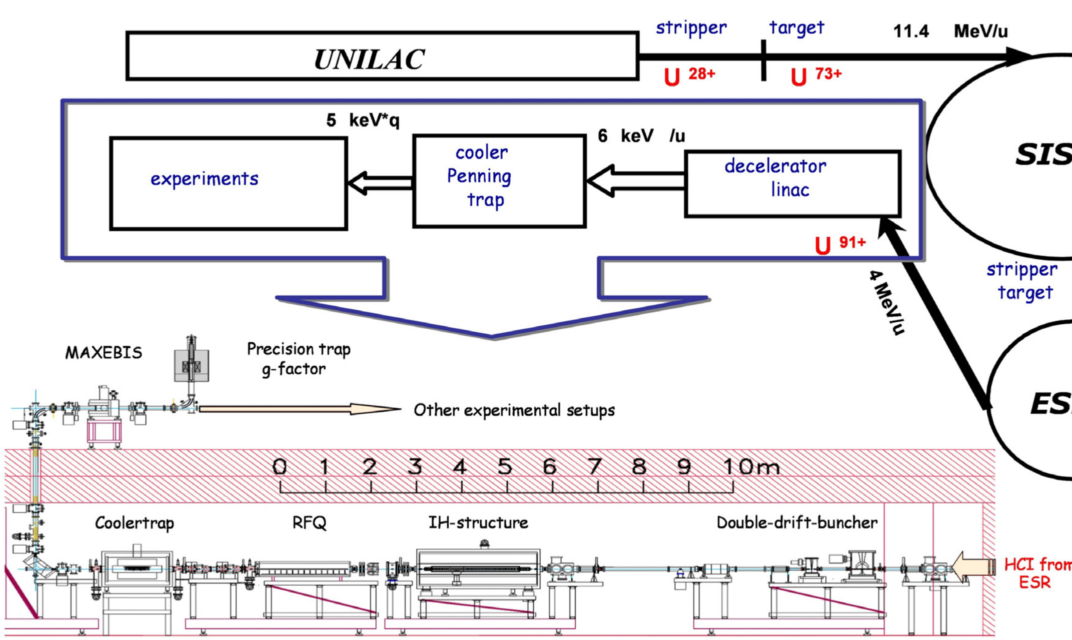


Figure 1: Production process of bare nuclei and HITRAP decelerator.

# l.dahl@gsi.de

converters and rf amplifiers are in operation as well as beam diagnostics and controls. The bunchers are fed by solid state amplifiers up to 5 kW power and could be commissioned without major problems. The decelerator cavities run by 200 kW tube amplifiers from GSI stock.

The commissioning of the IH tank [5] including bead pull measurements and rf power conditioning was done in a rather short time. Fig. 2 shows the gap voltage distribution as calculated by MWS® (Micro Wave Studio) compared to the measured one. The drop corresponds to the position of the inner quadrupole triplet lens. The deviations cause an output energy 30 keV/u higher than the 500 keV/u design value. Final adjustment of the voltage distribution will be done later by undercut tuning. The overall effective deceleration voltage is 10.5 MV.

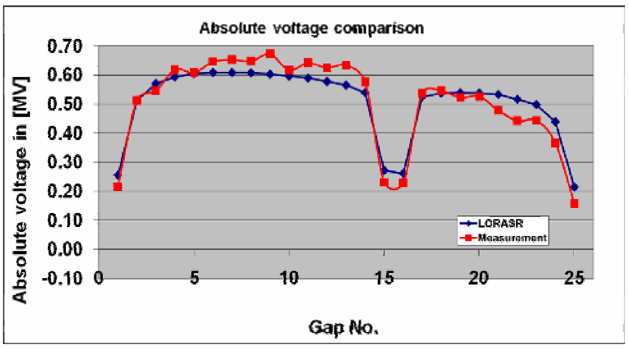


Figure 2: Measured (red) and calculated (blue) field distribution of the IH decelerator.

Table 1 shows the rf parameters of the IH structure. The measured values are very close to the calculated ones. The rf power consumption for the highest beam rigidity of mass/charge = 3 including 10 % reserve stays clearly below the limit of performance of the existing amplifiers.

Table 1: Parameters of the IH Decelerator Tank

| Parameter | layout geometry calculated | actual geometry calculated | measured |
|---|---|---|---|
| f [MHz] | 108.408 | 108.69 | 108.661 |
| Z eff [MΩ/m] | 263.3 | 264.9 | 270.2 |
| rf-power [kW] | 179.6 | 178.5 | 174.9 |
| $Q_0$ (MWS) | 21,948 | 22,163 | 22,529 |

Table 2: Measured RF Parameters of Bunchers and RFQ

| Resonator | Q | Zeff [MΩ/m] | Ueff [kV] | required rf power [kW] |
|---|---|---|---|---|
| DDB 108 MHz | 10,950 | 51.70 | 220.00 | 1.99 |
| DDB 216 MHz | 11,100 | 43.01 | 76.00 | 0.56 |
| Re-buncher 108 MHz | 5,300 | 28.60 | 105.00 | 1.92 |
| RFQ 108 MHz | 3,700 | 138.00 | 77.50 | 82.69 |
| De-buncher 108MHz | 2,700 | 15.50 | 0.40 | 0.00015 |

The RFQ tank is already placed in the HITRAP cave apart from the beam axis for high power rf conditioning. Table 2 summarizes measured properties of the bunchers and the RFQ and the resulting rf power consumption.

## COMMISSIONING MEASUREMENTS

The beam line from the ESR extraction to the HITRAP DDB section contains comprehensive beam diagnostics: Faraday cups, one tubular and two short capacitive pick-ups, three SEM grids, and four YAG scintillation screens. A single-shot pepper pot emittance meter [6] was used in the final temporary diagnostic setup containing also a diamond detector for pulse shape measurements.

In the first commissioning period in May 2007 the functionality of all components and controls was checked. The $^{64}Ni^{28+}$ beam was transported through the DDB without rf operation as an acceptance test. Operational experience showed that two additional vertical steering magnets are necessary to improve the beam transmission through a diaphragm mounted to decouple the ESR vacuum of ~$10^{-9}$ Pa from the ~$10^{-6}$ Pa in the decelerator.

During the second commissioning period in August 2007 with a $^{20}Ne^{10+}$ beam of 2 μA pulse current and 1.6 μs length the bunchers were in operation. No beam loss was measured up to the tubular pick-up behind the diaphragm. Negligible losses occurred at the narrow apertures of the buncher cavities. The capacitive pick-ups between the two bunchers and behind the second buncher generated bunch signals according to the 108 MHz operating frequency (Fig. 3).

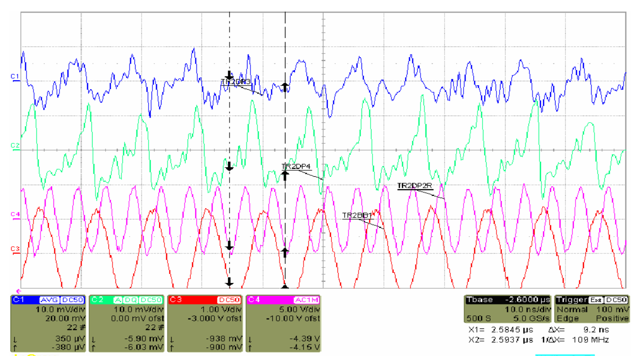

Figure 3: Top: two pick-up signals, bottom: rf signals of the 108 and 216 MHz bunchers.

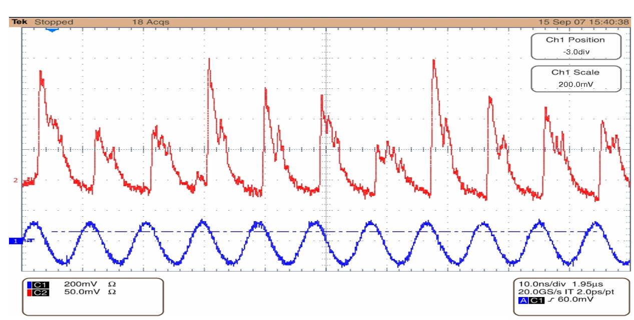

Figure 4: Top: 108 MHz bunches measured with the diamond detector, bottom: the 108 MHz reference signal.

The diamond detector turned out as an excellent diagnostic tool to optimize the bunch length. The extended fall time of the bunch signals (Fig. 4) is caused by amplifier discharge. The transverse emittance was measured by two methods, pepper pot [6] and scintillation screen combined with quadrupole variation. The results of $\varepsilon_{xrms}$ = 1.7 and $\varepsilon_{yrms}$ = 2.0 mm·mrad for 90 % of the intensity are in agreement with calculations. The successful commissioning of the DDB section allowed following up the installation of the IH tank and the matching section downstream.

For the third commissioning period in August 2008 a cooled $^{197}Au^{79+}$ beam was provided by the ESR. The investigations focused on the beam deceleration through the IH tank. Unfortunately the beam intensity at ESR extraction was only 300 nA and 200 nA at the final diagnostics station for both cases, with and without rf cavity operation. Nevertheless, using four YAG scintillation screens (Fig. 5) matching of the beam through the whole HITRAP with several narrow drift tube aperture limitations was possible comfortably.

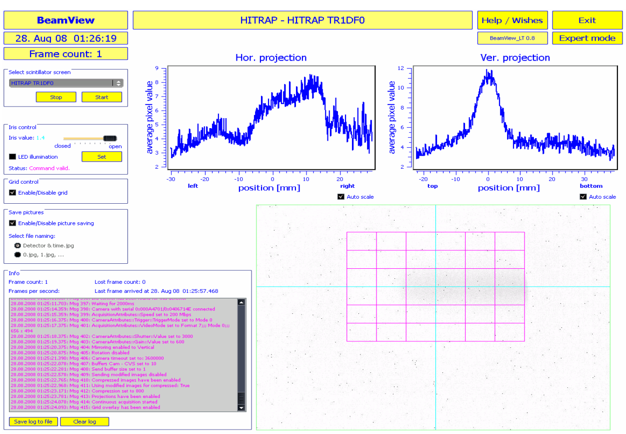


Figure 5: Screen shot of a YAG scintillation target.

The beam intensity was too low for proper capacitive pick-up signals. Therefore calibration measurements were done mainly by diamond detector signals. Fig. 6 shows typical oscilloscope signals of the tubular pick-up in front of the DDB and a Faraday cup behind the IH tank.

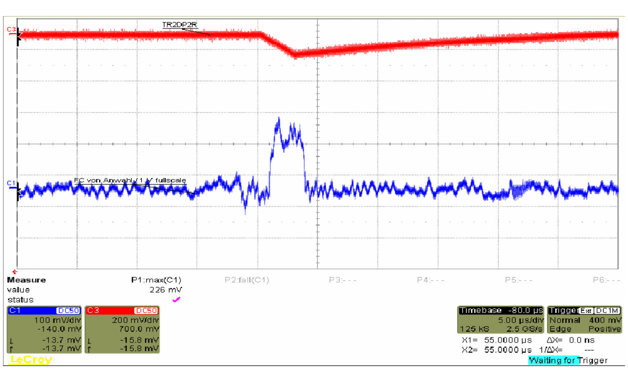


Figure 6: Top: signal of the tubular pick-up in front of the DDB, bottom: signal of a Faraday cup behind the IH tank.

In an elaborate procedure the working points of the DDB were determined by measuring the bunch width behind the IH tank. Afterwards rf power for the IH cavity was switched on and phase and amplitude settings were scanned to determine the working point of this structure. In the meantime the amplifiers of the diamond detectors were exchanged resulting in shorter fall times. Fig. 7 shows the decelerated and well shaped bunches in time distances of 9 ns for the working point settings of the DDB and IH cavity.

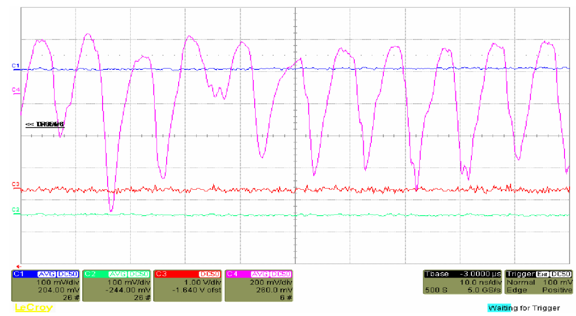


Figure 7: Inverted diamond detector signal of a 108 MHz bunch series behind the IH tank, DDB and IH switched on.

## CONCLUSIONS AND OUTLOOK

Within the three commissioning periods the technical and physical functionality of the HITRAP was proofed. No major problems occurred. Additional magnetic steerers turned out to be necessary for proper beam transport tuning. The setting was slightly modified by experience, and the working points of the rf structures were fixed. An uncertainty of the IH decelerator output energy remained. The next commissioning period in October 2008 will focus on this subject. For improved energy analysis a bending magnet and an extra scintillation screen will be installed behind the IH tank. Due to an expected higher beam intensity of the $^{64}Ni^{28+}$ beam also capacitive pick-up signals will be evaluable. The RFQ high power conditioning already began. The tank will be installed on beam axis in autumn. The final HITRAP commissioning beam time focusing on the last deceleration stage by the RFQ will take place in the first months in 2009.

## REFERENCES

[1] Th. Beier, et al., HITRAP Technical Design Report, GSI Darmstadt, Germany, (2003)

[2] O. Kester, et al., Deceleration of highly charged ions for the HITRAP project at GSI, Proc. of the LINAC06, Knoxville, Tennessee, USA, (2006)

[3] L. Dahl et al., The HITRAP decelerator project at GSI, Proc. of the EPAC2006, Edinburgh, UK, (2006)

[4] A. Schempp, An overview of recent RFQ projects, these proceedings

[5] U. Ratzinger, et al., The IH Cavity for HITRAP, LINAC, Lübeck, Germany, (2004)

[6] J. Pfister et al., Commissioning of the HITRAP decelerator using a single-shot pepper pot emittance meter, these proceedings

# POST-ACCELERATOR LINAC DEVELOPMENT FOR THE RIB FACILITY PROJECT AT VECC, KOLKATA

Arup Bandyopadhyay, M. Mondal, H. K. Pandey, T. Mandi, A. Chakrabarti
Variable Energy Cyclotron Centre, 1/AF Bidhan Nagar, Kolkata 700064, India


## [illegible]

An ISOL (Isotope Separator On Line) type of RIB (Rare Ion Beam) facility is being developed at our centre. The post-acceleration scheme will consist of a Radio Frequency Quadrupole (RFQ) followed by a few IH LINAC cavities - further augumentation of energy using SC QWRs will be taken up at a later stage.

The first two IH cavities have been designed for 37.6 MHz frequency like the preceding RFQ to keep the RF defocusing smaller. Explosively bonded copper on steel has been used for the fabrication of the IH cavities and the inner components have been from of ETP grade (UNS C11000) copper. Also, we have adopted an octagonal cross-section for the cavity structure to avoid fabrication complicacies. The first and second cavity have inside lengths of 0.62 and 0.97 m respectively and the inside separation between two opposite sides of the octagon is 1.72 m.

Thermal analysis of the cavities has been carried out and cooling configurations have been optimized accordingly to control the temperature rise of the LINACs. Detailed mechanical analysis has been carried out to reduce the deflection of the LINAC components under various loads.

Design and fabrication aspects of these two cavities and results of the low power tests will be reported in this paper.


## INTRODUCTION

Rare Ion Beams (ions of $\beta$-unstable nuclei) offer many new possibilities in different branches of accelerator based research. An ISOL type of RIB facility is being developed at our centre [1]. Light ion beams ([illegible], $\alpha$) from the K=130 cyclotron will be used as a primary beam for this facility. Also an electron LINAC is being developed at present which will open up the possibility of producing RIBs using photofission route. The primary reaction products will be ionised using an on line ion source and mass separated to choose the RIB of interest from the other reaction products. The RIBs will be accelerated from 1-97.5 keV/u using a heavy ion RFQ [2, 3, 4] operating at 37.6 MHz. Further acceleration up to 1.2 MeV/u will be done using IH LINAC cavities. The first two of these cavities have been designed and fabricated. Low power tests have also been performed. Design and fabrication aspects of these two cavities and results of the low power tests will be reported in this paper.

## DESIGN REQUIREMENTS

The initial energy of the RIBs after the mass selection is 1.7 keV/u. The RIBs will be accelerated in stages - the first post-accelerator is a RFQ which accelerates up to about 98.7 keV/u at 37.6 MHz, followed by two IH cavities at the same frequency to reach 287 keV/u - all of them are designed for $q/A \geq 1/14$. This will be followed by one IH cavity designed for 75.2 MHz to reach 409.1 keV/u. There will be a charge stripper at this stage and this will be followed by three more IH cavities designed for $q/A \geq 1/7$ to reach around 1.2 MeV/u. Further acceleration using QWRs are being planned at present.

The intensity of RIBs is a prime concern as it is significantly lower than stable ion beams in most of the cases. So, the LINACs have been designed for high transmission efficiency of the ions. Many experiments require measurement of parameters at various energies and therefore the aim is to continuously vary the energy of the beam without significant loss of intensity or degradation of beam quality (spot size and energy width).

## DESIGN PRINCIPLE

The acceleration method adopted in our design consists of classical negative synchronous phase small length LINACs with transverse focusing quadrupole triplets in between the cavities. Buncher cavities will also be accomodated where need arises. The cell parameters of the LINACs have been calculated by tracking trajectory of an ion having designed values of phase and velocity by integrating its equation of motion using static electric field obtained from [illegible] code for a particular drift tube geometry – ignoring the details of the drift tube supports, ridges and cavity. With this drift tube (DT) and gap geometry, the cavity parameters have been optimised using [illegible] The detailed beam dynamics have been studied using interpolated field from [illegible] using [illegible] code. Details of this design principle has been reported elsewhere [5].

The important parameters for the first two IH cavities are shown in Table 1. The frequency of first two LINACs has been kept same as that of RFQ to keep the RF defocusing smaller for low input energy. The shunt impedance and Q-values of the table are [illegible] results and the power has been calculated for a 60% shunt impedance value. The beam energy can be veried without any significant loss of intensity or degradation of beam quality. Fig. 1 shows two possible tunes for 286.8 keV/u energy - the case for good transmission (top) and good beam quality (bottom). This has of course still room for improvement by reducing the inter-tank separation.

Table 1: Important parameters of frst two IH cavities

| Parameter | Unit | LINAC-1 | LINAC-2 |
|---|---|---|---|
| Frequency | MHz | 37.6 | 37.6 |
| q/A | | $\geq 1/14$ | $\geq 1/14$ |
| $T_{in}(\beta_{in})$ | keV/u | 98.8(1.46) | 183.6(1.98) |
| $T_{out}(\beta_{out})$ | % | 183.6(1.98) | 286.8(2.48) |
| Gaps | | 9 | 10 |
| DT ID | mm | 25 | 25 |
| DT OD | mm | 69.5 | 60 |
| Gap length | mm | 29.2 | 39.8 |
| Peak potential | kV | 101.24 | 107.5 |
| Max. field | $E_{Kil}$ | 1.4 | 1.3 |
| Sync. phase | | -24° | -25° |
| Cavity length | m | 0.618 | 0.871 |
| Accln. gradient | MV/m | 2.102 | 1.79 |
| Shunt impedance | MΩ/m | 342 | 432 |
| Q-value | | 13765 | 18963 |
| RF power | kW | 19.9 | 16.4 |

The two cavities have been fabricated using explosively bonded copper (grade ETP or UNS C11000) on steel (grade SS304L or UNS S30403 ). Also, bending of copper bonded with steel has been avoided using an octagonal cross-section of the cavity. Each of the ridges and drift tubes have been fabricated from single block of ETP grade copper.

The thermal load on the cavity has been calculated from RF analysis and used for the optimisation of cooling channels of the LINACs using adequate safety factor. A typical example of such analysis is shown in Fig. 2. In the worst case scenario, there may be a temperature rise of about 15°C at some locations within the cavity. The LINACs are subjected to loads due to atmospheric pressure, gravity and temperature distribution. The deformations may affect the alignment of the drift tubes and the end gaps of the LINACs. The thickness of the materials of the cavity and the end covers have been optimised to reduce this effect. In addition, circular reinforcements have been incorporated on the end covers and optimised to further minimise this effect. A typical simulation is shown in Fig. 3.

## FABRICATION & ALIGNMENT

The cavity has been fabricated by full penetration TIG welding of the steel plates by removing copper close to the welding joints. Adequate precautions have been taken to minimise the distortion during welding. After the fabrication, the faces of octagon on which ridges are supported have been machined to get the desired flatness, parallelism and equal distance from the centerline. Entire final machining job of the cavity with end plates have been done in a single setting of CNC machine. All inner components have also been machined using CNC. After the machining, the drift tubes were placed and their center line deviations were measured using optical theodolite with proper target fixtures. The final machining of drift tube bases were done based on the initial measurement data. The drift tubes could be aligned within an accuracy of 150 $\mu$m and the drift tube gaps have been maintained within $\pm 50$ $\mu$m. Fig. 4 shows the LINAC-1 during final assembly.

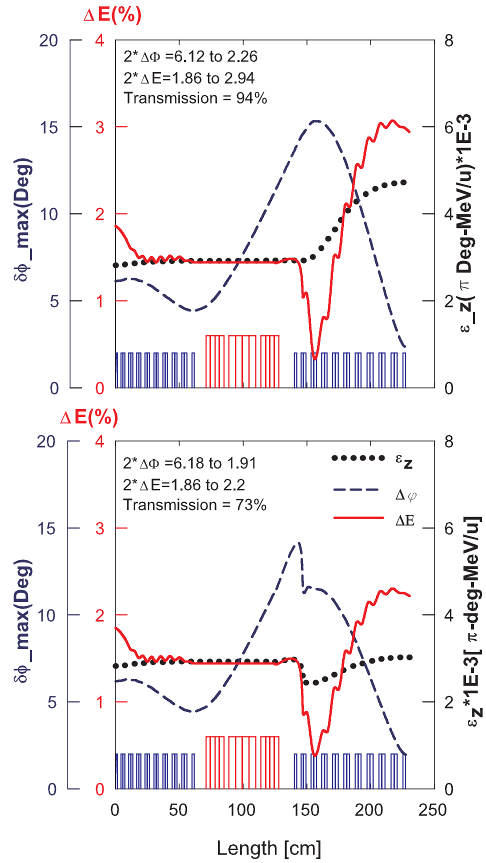


Figure 1: A typical tune through two LINAC cavities showing the variation of rms energy width, phase width and longitudinal emittance growth.

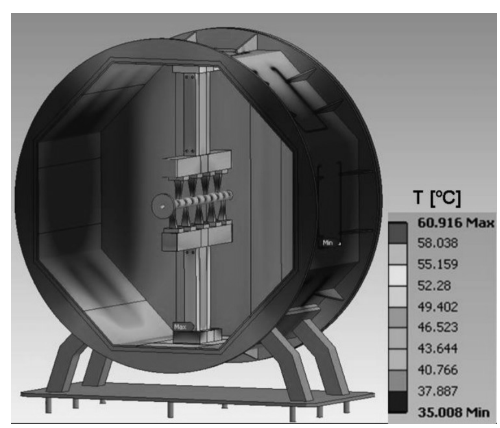


Figure 2: Temperature profile of LINAC-2 calculated using ANSYS.

Both LINAC-1 and LINAC-2 have passed the vacuum

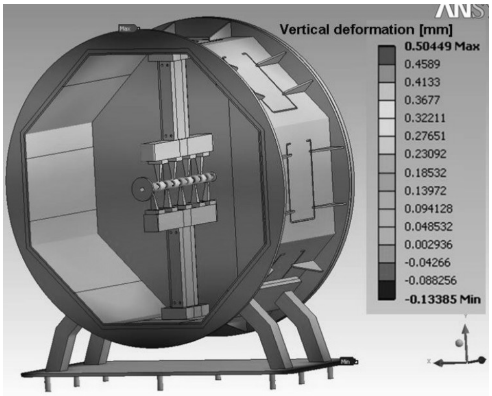


Figure 3: Structural deformation of LINAC-2 calculated using ANSYS.

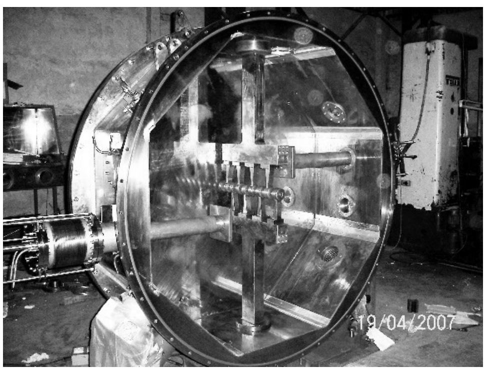


Figure 4: LINAC-1 during assembly.

performance test. Each of the LINACs with their inner components have been leak tested and no local leak could be traced up to a level of 1E-9 mbar-LPS. Both of them have been pumped using two 500 LPS turbo drag pumps after initial pumping using dry pumps. LINAC-1 reached a vacuum of 1.4E-6 mbar after about 1 week of pumping after the final cleaning. LINAC-2 reached a vacuum of 2.7E-6 mbar after about 24 Hours of pumping at manufacturer's site before the final cleaning. The performance is likely to improve significantly after the RF conditioning.

## LOW POWER TEST

Both LINAC-1 and 2 were initially assembled at manufacturers site and RF measurements were done. LINAC-1 has been throughly cleaned in our site and assembled again and RF tests have been repeated again and it is ready for putting into operation. Results of these measurements are shown in Table 2. The frequency measurements are within 0.3% of the calculated values. The measured $Q_0$ values for LINAC-1 and 2 are 59% and 35% of the calculated values. A significantly lower value of $Q_0$ for LINAC-2 is due to the facts that many of its inner components were not having the required surface finish at the time of testing and also no RF springs were used during testing. The $Q_0$ value has significantly increased to 71% of the calculated value when LINAC-1 has been assembled after through cleaning and putting RF contact at all joints. We expect similar result for LINAC-2 also.

Table 2: Important parameters of frst two IH cavities

| LINAC | Freq. [MHz] | | $Q_0$-value | |
|---|---|---|---|---|
| Number | Calc. | Meas. | Calc. | Meas. |
| 1 | 37.695 | 37.75 | 13765 | 8073 |
| 2 | 37.861 | 37.75 | 18963 | 6687 |

The electric field on the axis of LINAC-1 has been measured using bead perturbation technique. In which a dielectric bead was made to move along the drift tube axis in small steps and the frquency deviation was calculated using network analyser. Results of this measurement is shown in Fig. 5 where the □□□□□calculated field is also shown.

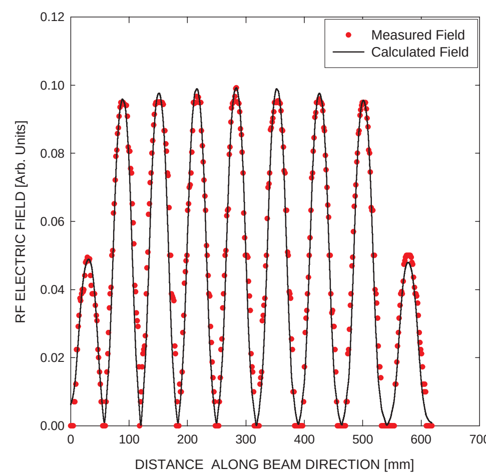


Figure 5: Results of bead perturbation measurement of LINAC-1.

## REFERENCES

[1] Vaishali Naik, Alok Chakrabarti et al., "Towards the Development of Rare Isotope Beam Facility at VECC Kolkata", these proceedings.

[2] Alok Chakrabarti, Vaishali Naik et al., "The design of a four rod RFQ LINAC for the VEC-RIB facility", Nucl. Instr. & Meth. 535 (2004) 599.

[3] Alok Chakrabarti, Vaishali Naik et al., "33.7 MHz heavy-Ion radio frequency quadrupole linac at VECC Kolkata", Rev. Sci. Instr. 78 (2007) 043303.

[4] Siddhartha Dechoudhury, Vaishali Naik et al., "Heavy ion radio frequency quadrupole LINAC for VEC-RIB facility", these proceedings.

[5] Arup Bandyopadhyay, O. Kamigaito et al., "Design of LINAC post-accelerator for VECC RIB facility using realistic field", Nucl. Instr. & Meth. 560 (2006) 182.

# TOWARDS THE DEVELOPMENT OF RARE ISOTOPE BEAM FACILITY AT VECC KOLKATA*

Vaishali Naik, Alok Chakrabarti, Arup Bandyopadhyay, Manas Mondal, Siddharta Dechoudhury, Hemendra Kumar Pandey, Debasis Bhowmick, Dirtha Sanyal, Tapatee Kundu Roy, J.S. Kainth, Tapan Kumar Mandi, Mahuya Chakrabarti, Prasanta Karmakar
Variable Energy Cyclotron Centre, 1/AF Bidhannagar, Kolkata, India

*Abstract*

An ISOL type Rare Isotope Beam (RIB) Facility is being developed at VECC, Kolkata around the existing K=130 room temperature cyclotron. In the first stage, the beam energy will be about 400 keV/u using an RFQ pos-accelerator and three modules of IH-linacs. Subsequently the energy will be boosted to about 1.3 MeV/u. A separate LEBT line for material science experiments is planned. Some of the systems have already been installed and made operational. The LEBT line has been tested and stable ion beams accelerated to 29 keV/u with high efficiency in a 1.7 m RFQ. A 3.4 m RFQ and the first IH Linac tank are under installation in the post-acceleration beam line. In this contribution an overview of the present status of the facility will be presented.

## INTRODUCTION

An ISOL type RIB facility is presently under construction at VECC Kolkata [1]. The K=130 cyclotron at VECC will act as mother accelerator for this facility. A schematic layout of the facility is shown in figure 1. The 1+ radioactive ions will be produced inside a thick target integrated ion-source, injected into an on-line Electron Cyclotron Resonance Ion source (ECRIS) for high charge state ionization, mass separated and then post accelerated in a Radio Frequency Quadrupole (RFQ) Linac and IH-Linacs. The production target and ECR based charge-breeder system lead to two beam lines. The first one, a low energy beam transport (LEBT) line is already installed and presently delivers stable ion beams of 29 keV/u energy at the end of a 1.7m RFQ linac. The second, post-acceleration beam line will accelerate the beams to 1.3 MeV/u using a longer, 3.4 m RFQ and a series of IH linear accelerators. In the first stage, the beam energy will be about 400 keV/u using three modules of linacs.

## DESCRIPTION OF RIB FACILITY

### *Target Ion-Source*

The first component is the Integrated Ion source. Radioactive nuclei will be produced inside thick targets using proton and α-particle beams from the K=130 cyclotron at VECC and ionized to 1+ charge state in the integrated surface ionization source. A possibility of using a multiple target Electron Beam Plasma ion-source is also being worked out. The low energy 1+ ion beam from the first ion-source will be injected into the ECR ion source for higher charge state (n+) production in the *charge breeder*.

We have undertaken a target R&D programme as we need to develop many kinds of thick targets for our facility. Since diffusion of radioactive species out of the target increases with temperature one usually selects refractory target compounds such as oxides and carbides for the target. Target materials can be deposited on Graphite matrices (RVCF fibres) that can withstand high temperature and have sufficient porosity to allow radioactive atoms to diffuse out [2].

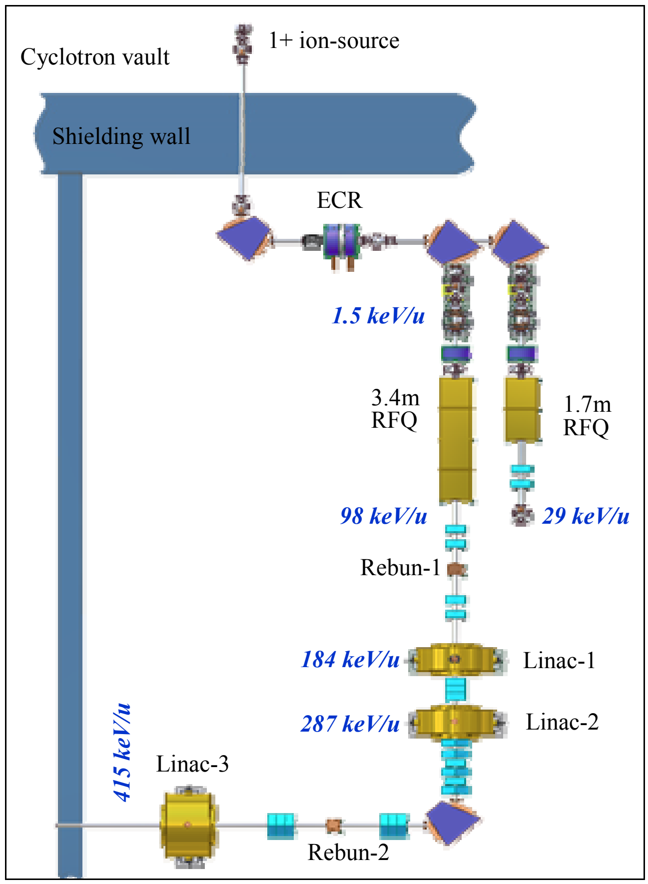


Figure 1: Layout of RIB facility.

Sintering & grain growth due to beam heating hinders the release of radioactive ions. Studies have shown that grain growth stays within limiting range if one starts with grain size of nano-metre range. Recent studies in case of ZnO have revealed that formation of a composite phase (Zinc silicate) resist the grain growth within the permissible limits even for 6 hrs heating at 1300 C[3].

*This is a VECC-DAE project

### *The Charge Breeder*

The radioactive ions have to be ionized to higher charge state with good enough efficiency in order to accelerate a wide range of RI beams. In the "two-ion source" concept the beams are ionized to 1+ charge in the integrated target-ion source and then injected into the on-line ECRIS for further ionization to higher charge state n+.

The beam transport line between the integrated target surface ionization source and the *ECRIS* incorporates a dipole, for selection of $1^+$ beam. The beam transport design ensures that the beam extent lies within the plasma region of ECR and also $1^+$ beam get properly trapped in the ECR [4]. To keep the ECR volume large we have chosen a 6.4 GHz on-line ECR ion source as the charge breeder. This ion-source has been operated for both gaseous and metallic beams. A typical spectrum for iron ions produced using the MIVOC [5] technique is shown in Fig 2. Also for heavier ions, a charge breeder with ECR operating in 10+14 GHz dual frequency mode has been designed [6].

In addition to this, new R&D on efficient & fast transport and ionisation of radioactive atoms irrespective of their chemical nature has been started. The ECRIS can be exploited as a universal $1^+$ ion-source. However, with an internal or close vicinity target the radiation damage to the permanent magnet drastically reduced the lifetime of the ion-source [7]. A possible alternative could be the Helium-jet coupled ECR ion-source with multiple thin target system (figure 3). This *universal charge breeder* option is highly attractive especially for the fission production route. Transport efficiencies of 50-60% can be obtained from the He-jet recoil method [8] for most of the elements. Assuming a typical skimmer efficiency of 50% and ionization efficiency of 50% for $1^+$ in ECR, one can expect a total transport and ionization efficiency in the range 10 – 15 % for almost all the elements.

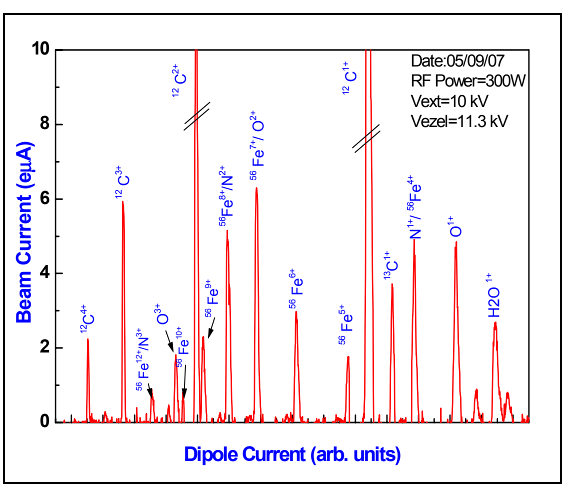


Figure 2: ECR spectrum.

### *The Heavy-Ion RFQ Linac*

Radio Frequency Quadrupole Linac would be the first post accelerator of our RIB facility. It has been designed for q/A=1/14 and input energy of 1.7 keV/u .The four-rod type RFQ is 3.4m long (vane length ~ 3.2m) and operates at the resonance frequency of 37.8 MHz. The development of RFQ has been done in phases. In the first phase we have developed a 1.7 m RFQ capable of accelerating beams up to 29 keV/u. This RFQ operates at a resonance frequency of 33.7 MHz. It has already been installed and operational since the year 2005. Transmission efficiencies of about 85% were measured for $Ar^{4+}$ and other beams like $O^{2+,3+,4+}$ and $N^{3+,4+}$ through the RFQ. The details of this RFQ and results of beam tests are reported in ref [9].

The post-acceleration RFQ is almost identical to the 1.7m RFQ but is longer to achieve higher output energy of 98 keV/u. This RFQ is also completely indigenously designed and constructed. The resonant structure including the vanes and supporting posts is made from OFHC copper and has been machined at Central Mechanical Engineering Research Institute (CMERI), Durgapur located about 200 km north of Kolkata. The top cover (cavity) has been Copper plated and built by Danfysik. A photograph of the 3.4m RFQ during installation is shown in fig. 3. In the preliminary test, beam transmission efficiency of 90% has been measured for O3+ in the RFQ. Further details about the RFQ system are presented in another contribution in Linac08 conference [10].

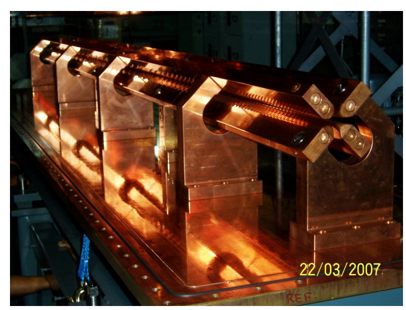


Figure 3: The 3.4m RFQ post-accelerator.

### *ECR to RFQ Beam-Line*

The beam transport line from the ECR ion-source to the RFQ consists of an Einzel lens, a 90 degree, 0.25 Tesla dipole magnet for *q/A* selection, and a solenoid magnet lens downstream of the dipole magnet to ensure proper matching of the ion-beam at the entry of the RFQ. The ion optics of this low energy transport line has been designed using the computer code TRANSPORT. The separation stage is designed for a dispersion of 1.84 cm. The magnification in the dispersive plane is -0.88. The RFQ demands converging beam in both the planes. A reasonable match could be obtained using a solenoid magnet length of 30 cm and a maximum magnetic strength of 0.65 Tesla

### *RFQ to LINAC Beam-Line*

The RFQ to LINAC-1 beam line has been designed to match the RFQ beam with the longitudinal & transverse acceptance of Linac1. A 4-gap, 37.8 MHz Re-buncher will be placed between the RFQ and Linac1 to obtain a beam of desired phase and energy width at the entry of the Linac. For transverse focusing we would be using two quadrupoles upstream and two downstream of the Re-buncher. A fortran code was written to optimize the position of Re-buncher & voltages on the drift tube. In order to recheck the results of our code we have simulated using SIMION, the time varying voltage on the drift tube of the Re-buncher and calculated the bunching property both in phase and energy, due to the applied RF voltage.

RF simulation of the Re-buncher was done using ANSYS. The height of the movable short was optimized to obtain the desired resonant frequency of 37.8 MHz. Experimentally found out value are in good agreement with calculated resonating frequency using ANSYS. The mechanical fabrication of the Re-buncher including major components such as inductive coupler, capacitive pick-up and tuner is almost complete. A photograph of the Re-buncher during assembly is shown in Fig 4.


Figure 4: The Re-buncher during assembly.

### *The IH-LINAC Post-Accelerators*

After the initial stage of acceleration in the RFQ linac the subsequent acceleration of beams will be done in LINAC tanks [11]. For these low-$\beta$ and low q/A RI beams the IH-LINAC structure is the preferred choice. In this type of structure, the LINAC cavities are excited in TE mode. Three IH-Linac cavities would accelerate the 98 keV/u beam from RFQ to about 415 keV/u. The beam energy is expected to be 184 keV/u and 287 keV/u after the first and second Linacs respectively. A photograph of the first Linac cavity is shown in Fig. 5. It is an octagonal cavity made of 25 mm thick SS304L steel cladded with 5mm thick ETP Copper. The cavity has been tested at low power. The measured frequency and Q values match reasonably well with calculated value. The axial component of the RF electric field was measured using bead perturbation technique using an insulating teflon spherical ball. The arrangement allowed us to measure frequency deviation at a step of 5 mm. The detailed design and results of Linac cavity has been presented in another contribution in Linac08 conference [12].

## SUMMARY & OUTLOOK

The status of ISOL type Rare Isotope Beam facility development at VECC Kolkata has been presented. The facility is at present delivering stable heavy-ion beams of energy 29 keV/u. Experiments can be performed at two experiment stations – one at the ECR mass separator focal point and the other at the end of the 1.7m RFQ. The longer post-accelerator RFQ is also installed and very soon the beam tests will be conducted for Linac-1.

The present RIB facility has been planned around the existing K=130 cyclotron. We are also exploring the possibility for using the photo-fission route for the production of neutron rich RI beams. For this purpose we have undertaken a programme to develop a 50 MeV, 100 kW super-conducting electron Linac. In the first phase we have received funding to construct a Horizontal Test Cryostat (HTC) cavity. Recently, a memorandum of understanding was signed between VECC and TRIUMF for the joint HTC development.

## REFERENCES

[1] Alok Chakrabarti, Nuclear Instrument.and Method. B **261** (2007)1018.
[2] Debasis Bhowmick et al, Nuclear Instrument.and Method. A **539** (2005) 54.
[3] Tapatee Kundu Roy et. al, Ceramics International **34** (2008) 81.
[4] V. Banerjee et.al , Nuclear Instrument. and Method. A **539** (2005) 54.
[5] M.Koivisto et al, Nuclear Instrument and Method B **94** (1994) 291.
[6] Damayanti Naik et. al., Nuclear Instrument and Method A **547** (2005) 270.
[7] A.C. C. Villari, Nucl. Instrum. & Method B **126** (1997) 35.
[8] A. Chakrabarti et. al, Nucl. Instrum. & Meth. A **263** (1988) 421.
[9] A. Chakrabarti et. al, Review of Scientific Instrum.**78** (2007) 043303.
[10] S. Dechoudhury et. al. these proceedings. [11] A. Bandhyopadhyay et. al, Nuclear Instrument. and Method A 560 (2006)182.
[12] A. Bandhyopadhyay et. al. these proceedings.

# THE ALPI SUPER-CONDUCTING ACCELERATOR UPGRADE FOR THE SPES PROJECT*

P. A. Posocco†, Consorzio RFX, Padova and INFN/LNL, Legnaro, ITALY
G. Bisoffi, A. Pisent, INFN/LNL, Legnaro, ITALY

*Abstract*

The SPES project at Laboratori Nazionali di Legnaro foresees the construction of a RIB facility based on a fission target driven by a 40 MeV proton beam. After the $^{238}$U carbide target the 1+ charged ions will be selected by a high resolution mass spectrometer, charge enhanced by a charge breeder and accelerated up to 10 MeV/A for $^{132}$Sn. The present configuration of the Legnaro super-conducting accelerator complex (PIAVE injector and ALPI main accelerator) fits the requirements for SPES post acceleration too. Nevertheless an upgrade of its performances both in overall transmission and final energy is needed and a solution which minimizes the impact on the present structures will be presented.

## INTRODUCTION

The super-conducting linac ALPI [1] is injected either by a XTU tandem or by the s-c PIAVE injector [2][3]. The linac (at the present 64 cavities and a total voltage of 48 MV) is build up in two branches connected by an achromatic and isochronous U-bend (Fig. 1). ALPI period consists in one triplet and 2 cryostats (4 cavities in each cryostat), and a diagnostic box (profile monitor and Faraday cup) in between.

The PIAVE-ALPI complex is able to accelerate beams up to A/q = 7. Higher A/q ions suffer from a too low injection energy to the medium-β cryostats, where the RF defocusing is too strong and the beam gets easily lost onto the cavity beam ports. In the last few years the average cavity accelerating field ($E_{acc}$) has been enhanced by more than a factor of two with respect to the original design value [4]. The strength of the focusing lenses on the other hand, has remained the same (20 T/m). Therefore, even for 6 < A/q < 7 it is hard to design a proper longitudinal beam dynamics such that it will not cause problems on the transverse plane. To fully exploit the available acceleration gradient, some improvements are required in the layout of both PIAVE and ALPI.

Referring to the cavity performances of Tab. 1 (expected in the next years), three subsequent upgrade scenarios may be envisaged, each one representing a step forward in the final energy (Fig. 2) and beam quality: 2009 for stable beams (funded), an intermediate and a final upgrade within the SPES project (not yet officially funded). For SPES, the Radioactive Ion Beam at 37.1 keV/A will be injected into PIAVE line upstream the SRFQs.

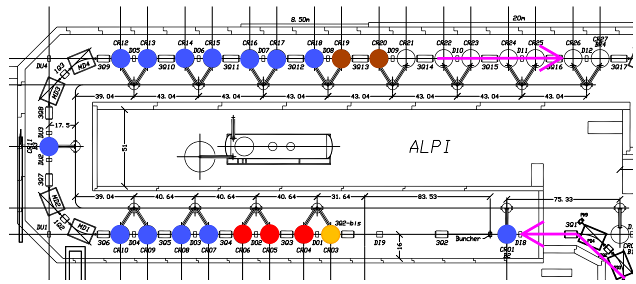

Figure 1: ALPI plan for 2009. The beam coming from PIAVE injector passes through the low-β (in orange and red), medium-β (blu) and high-β (brown) cryostats.

The beam dynamics of each scenario has been optimized for 4 < A/q < 7 thanks to several runs of PARMELA [5]: the beam behavior in the low-energy branch is highly non-linear due to the high gradients and strong Bessel components of the fields inside the cavities, therefore, in such conditions, simulation programs like Trace3D are simply ineffective.

Table 1: ALPI cavity performances for the upgrade scenarios. $E_{acc}$ in MV/m.

| cryostat | # | 2009 | inter | SPES I | SPES II |
|---|---|---|---|---|---|
| *low-beta* ($\beta_o$ = 0.047 *and* $\beta_o$ = 0.056), 80 MHz | | | | | |
| CR01-02 | 8 | n/a | n/a | 6 | n/a |
| CR03 | 4 | 5 | 6 | 6 | 6 |
| CR04-06 | 12 | 3.5 | 6 | 6 | 6 |
| *medium-beta* ($\beta_o$ = 0.11), 160 MHz | | | | | |
| CR07-18 | 44 | 4.2 | 4.5 | 4.5 | 4.5 |
| *high-beta* ($\beta_o$ = 0.13), 160 MHz | | | | | |
| CR19-20 | 8 | 5.5 | 5.5 | 5.5 | 5.5 |
| CR21 | 4 | n/a | 5.5 | 5.5 | 5.5 |
| CR22-23 | 8 | n/a | n/a | n/a | 5.5 |
| total number | | 68 | 72 | 80 | 80 |

## THE 2009 STATUS

The first ALPI cryostat (CR03) gently focuses the beam coming from PIAVE to the following cryostat. Hence, only a small acceleration is given to the beam by CRO3. The $E_{acc}$ values of the following low-energy branch cavities are

* http://www.lnl.infn.it/ spes/
† piero.antonio.posocco@lnl.infn.it

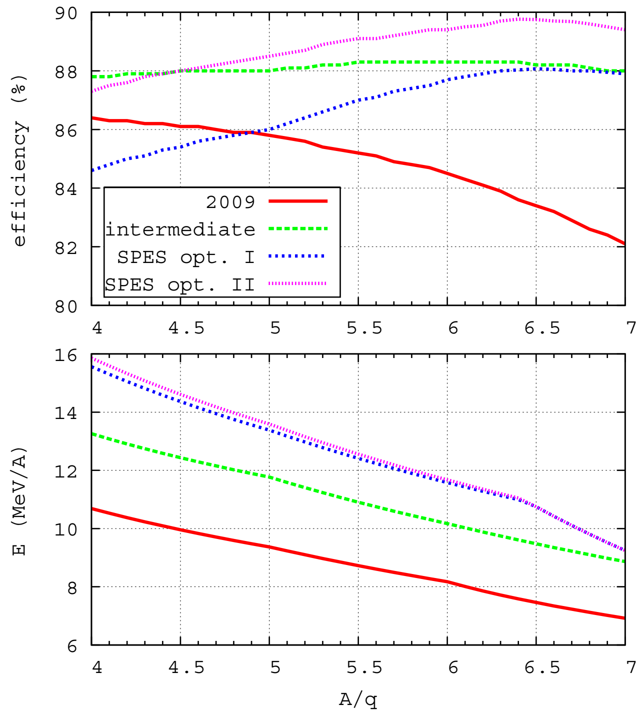


Figure 2: Accelerator efficiency and final energy for the different scenarios. The efficiency is here defined as E [MeV/A] * A/q * V$^{-1}$. For A/q ≥ 6.4 the final energy is limited by the 3 T·m max. rigidity in dipoles.

chosen as function of the A/q and the beam dynamics has been optimized for A/q = 7, where its main limit is the maximum gradient of the magnet before the last period (3Q5). For 6 < A/q < 7, the $E_{acc}$ of CR09 and CR10 are raised and the maximum field is obtained for the configuration of A/q = 6. For 5 < A/q < 6, the $E_{acc}$ is lowered by a less steep function than the linear A/q scaling, because the longitudinal match can be found by changing specific synchronous phases. For A/q = 5 the beam dynamics limit (i.e. long. phase advance and RF defocusing) is reached. Finally, for 4 < A/q < 5 $E_{acc}$ scales like A/q. Given this optimization, it results that for A/q = 4 the acceleration efficiency is at its maximum. More low-β cavities are needed in order to accelerate larger A/q in a more comfortable way.

## THE INTERMEDIATE UPGRADE

To enhance the low-β gradient, a new 80 MHz buncher is needed in front of the first ALPI period. Consequently an additional quadrupole triplet must be placed before CR03. The first period $E_{acc}$ values are scaled by A/q up to A/q = 6, whereas the remaining ALPI low-energy branch $E_{acc}$ are scaled up to A/q = 5. The acceleration is much more efficient than before and the final energies exceed 9 MeV/A. The higher beam rigidity requires the triplets to be replaced (20 T/m→30 T/m) both in the low and in the high-energy branch.

## THE FINAL UPGRADE

The present PIAVE layout (Fig. 4(a)) is very compact, with the SRFQ cryostat immediately followed by the two QWR cryostat periods with external doublet focusing. The period is kept as short as possible, especially to reduce the longitudinal phase advance. This solution presents a weak point: the lack of a separate function matching line between the two sections. In the present set-up the first cavity is used as buncher and this results in a residual longitudinal emittance increase; as a consequence, the first part of the acceleration in ALPI is troublesome and longitudinal losses cannot be avoided. Moreover, the transverse transport is such that it causes 40% vertical emittance increase (Tab. 2). Finally, the first available beam diagnostics is located only after the second QWR period.

### *New Injector Layout*

To improve the situation, a new layout (see Fig. 4(b)) of the line downstream the SRFQs is proposed.

*Bunching section.* A new low-energy n-c buncher and a quadrupole singlet must be installed. The singlet must be placed at the x-plane waist between the SRFQs and the buncher itself, in order to reverse the transverse beam divergence without affecting the quadrupole symmetry. This means that the beam dimensions are almost equal inside the cavity. After the buncher, 2PQ5 doublet focuses the beam at the first QWR cavity and the round condition should be achieved while setting the singlet field appropriately.

*New cryostats.* In the present PIAVE beam dynamics the synchronous phases are employed in a alternating "funnel" scheme, (−90| + 60| + 30| − 25) (−20| − 20| − 20| + 20) and, in order to obtain the required longitudinal acceptance, the QWRs are set to lower $E_{acc}$ values than the best achieved cavity performances. To overcome the problem, a shorter longitudinal and transverse period must be designed. A good solution is the periodic structure à la ISAC-II (TRIUMF) [6]: each cryostat houses 4 QWRs and a compact s-c solenoid (max 9 T) in the middle. Because of the dimensions of the cryostat and the solenoid, the effective longitudinal period comprises two cavities and it is half the transverse one. Hence, all the synchronous phases can be set to −30 and $E_{acc}$ ≃ 5.2 MV/m for A/q = 7 are employed. Moreover, a short space for beam diagnostics is available between the modules. This diagnostic box, combined with

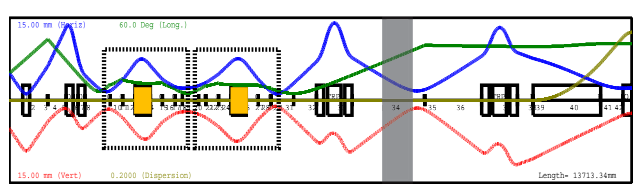

Figure 3: Beam dynamics for the new PIAVE layout from the SRFQ output to the quad singlet of the achromatic bend to ALPI.

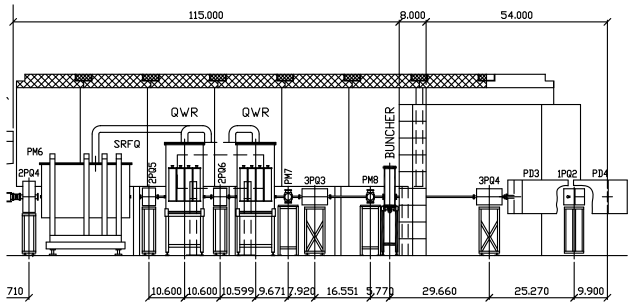


(a) Present layout.

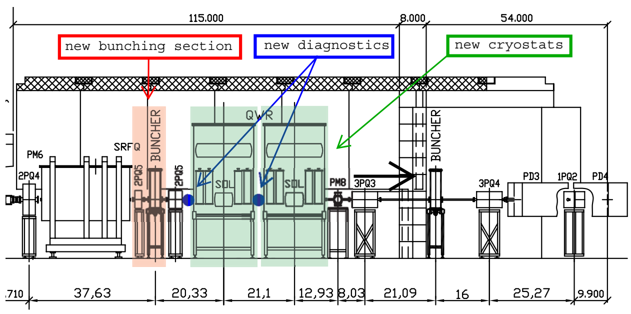


(b) New layout.

Figure 4: PIAVE injector layout comparison.

the one placed after 2PQ5, will be used for checking the transverse match parameters and, in particular, the roundness of the beam before it enters the first cryostat. Table 2 shows the results for the new layout: the even envelopes (Fig. 3) inside the cavities do not produce the any significant emittance growth and the final energy is increased by $\sim 20\%$.

*New HEB1 location.* The n-c rebuncher HEB1 will be slightly moved downstream in order to obtain a parallel longitudinal beam transport along the bend to ALPI.

Table 2: PIAVE beam dynamics results. Emittances are in mm.mrad.

| | SRFQs | present | new | *var.* |
|---|---|---|---|---|
| $\varepsilon_{x\ rms\ norm}$ | 0.100 | 0.102 | 0.105 | *+3%* |
| $\varepsilon_{y\ rms\ norm}$ | 0.100 | 0.138 | 0.105 | *-24%* |
| $\varepsilon_{z\ rms\ norm}$ | 0.060 | 0.163 | 0.066 | *-60%* |
| E (MeV/A) | 0.59 | 1.24 | 1.45 | *+17%* |

### *ALPI Upgrade Options*

I. Low-β upgrade. The new period before CR03 can be filled with the two cryostats recovered from PIAVE. The last two low-β cryostats can be required to work at $E_{acc}$ = 6 MV/m up to A/q = 5. This way, the acceleration efficiency would be favorable to the heaviest ions, whereas the lightest ones would suffer from an excess of low-β cavities. However, this allows to transport the beam efficiently even if some low-β cavities were out of order.

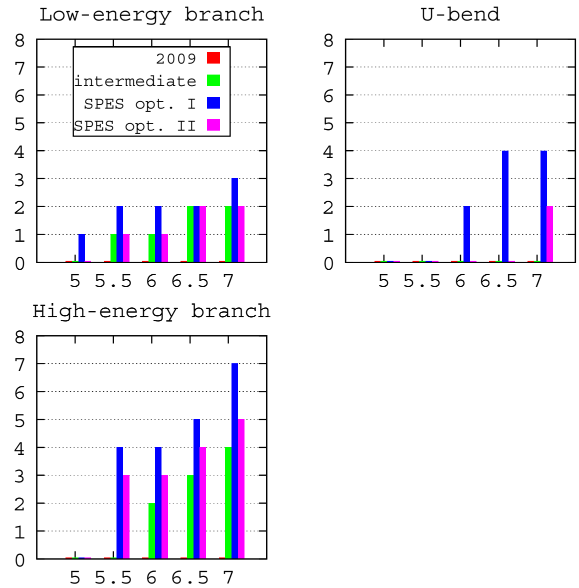


Figure 5: Number of quadrupole triplets that need to be replaced (20 T/m→30 T/m) in the various scenarios as function of A/q.

II. High-β upgrade. Alternatively, the two cryostats could be placed downstream the high-energy branch. This way, the number of cavities would be more effectively divided among the three optimum betas an the final energy for the lightest ions would be slightly enhanced.

## CONCLUSIONS

As shown in Fig. 2, in the second and third scenario the heaviest ions are accelerated in a increasingly efficient way. It is worth to point out, however, that the maximum magnetic field of the dipoles (1.6 T) in ALPI and in the extraction lines limits the performances of the SPES scenario for A/q ≥ 6.4.

SPES option I is the most demanding scenario from the point of view the magnetic quadrupole replacement (Fig. 5). The only way to keep the existing magnets in both the U-bend and the high-energy branch is to use a stripper foil, as described in [7]. As a major consequence of this, the final energies increase by 30% at the cost of a lower transmission, depending on the selected charge state probability (15 ~ 20% for the heaviest ions).

## REFERENCES

[1] A. Dainelli and al., NIM A382 (1996), p. 100.

[2] A. Pisent, Proc. of the 8th HIAT, no. 473, p. 214.

[3] A. Pisent and al., Proc. of LINAC2006, p. 227.

[4] G. Bisoffi and al., Proc. of SRF2007, MO404.

[5] K. Crandall and L. Young, PARMELA.

[6] R. E. Laxdal and al., Proc. of PAC05, p. 3191.

[7] P. A. Posocco, these Proceedings.

# PRESENT STATUS OF RIKEN HEAVY-ION LINAC

O. Kamigaito*, E. Ikezawa, M. Kase, M. Fujimaki, T. Fujinawa, N. Fukunishi,
A. Goto, H. Haba, Y. Higurashi, M. Kidera, M. Komiyama, R. Koyama†,
H. Kuboki, K. Kumagai, T. Maie, M. Nagase, T. Nakagawa, J. Ohnishi, H. Okuno,
N. Sakamoto, Y. Sato, K. Suda, T. Watanabe, K. Yamada, S. Yokouchi, Y. Yano,
RIKEN Nishina Center for Accelerator-Based Science, Wako-shi, Saitama 351-0198 Japan

**Abstract**

The RIKEN heavy-ion linac (RILAC) has been used as an injector for the RIKEN RI-Beam Factory (RIBF) since 2006. Results of the acceleration tests of $^{48}$Ca and $^{238}$U performed recently in the RIBF are reported; we got 270 pnA of $^{48}$Ca at an energy of 114 MeV/u after the Intermediate-stage Ring Cyclotron (IRC). On the other hand, the intensity of the uranium beam is still far below the design goal. Therefore, we are planning to install a superconducting ECR ion source, which is under construction, on the high-voltage platform of the Cockcroft-Walton pre-injector. It will be possible to test this new pre-injector in April 2009. A plan to construct an alternative injector for the RIBF, consisting of an ECR ion source, an RFQ, and three DTLs, is also illustrated, which aims at independent operation of the RIBF experiments and super-heavy element synthesis.

## INTRODUCTION

The RIKEN heavy-ion linac (RILAC), which has been operated since 1981, accelerates various kinds of ions by changing the rf frequency from 18 to 38 MHz in the continuous-wave (cw) mode. The voltage gain is 16 MV in the whole frequency range, and the acceptable mass-to-charge ratio ($m/q$) of the ions ranges from 5.5 at 38 MHz to 25 at 18 MHz. The original Cockcroft-Walton pre-injector to the RILAC was replaced by an RFQ pre-injector equipped with an 18-GHz ECR ion source in 1996.

In 2001, a booster linac for the RILAC was constructed, which consists of two variable-frequency resonators and four fixed-frequency resonators; the maximum energy of the RILAC facility has been increased to 5.8 MeV/u [1]. By using the high-intensity beams from the booster, experimental study has been started for searching super-heavy elements (SHE) since 2002. The beam time provided for the SHE experiments so far has exceeded 10,000 hours. The present layout of the RILAC facility is illustrated in Fig. 1.

On the other hand, commissioning of the RI-Beam Factory (RIBF) [2] started in 2006 [3], where the RILAC is used as an injector. Results of the acceleration tests performed recently in the RIBF are given in the next section, as well as a brief introduction of the RIBF accelerators.

## RILAC AS RIBF INJECTOR

Figure 2 shows a conceptual layout of the accelerator chain of the RIBF, which consists of the RILAC injector and four booster cyclotrons (RRC, fRC, IRC and SRC) in a cascade. The fRC is exclusively used for very heavy ions such as uranium and xenon, where the rf frequency of the RILAC is fixed to 18.25 MHz and the beam energy at the exit of the SRC is 345 MeV/u. For medium-mass ions such as calcium and krypton, the fRC is skipped; it is possible to operate the accelerator chain in the variable-energy mode. There is another acceleration mode in the RIBF, where the AVF cyclotron (K70 MeV) is used as an injector for the acceleration of light ions such as deuteron and carbon.

In this year, acceleration tests were performed up to the exit of the IRC using $^{48}$Ca and $^{238}$U beams.

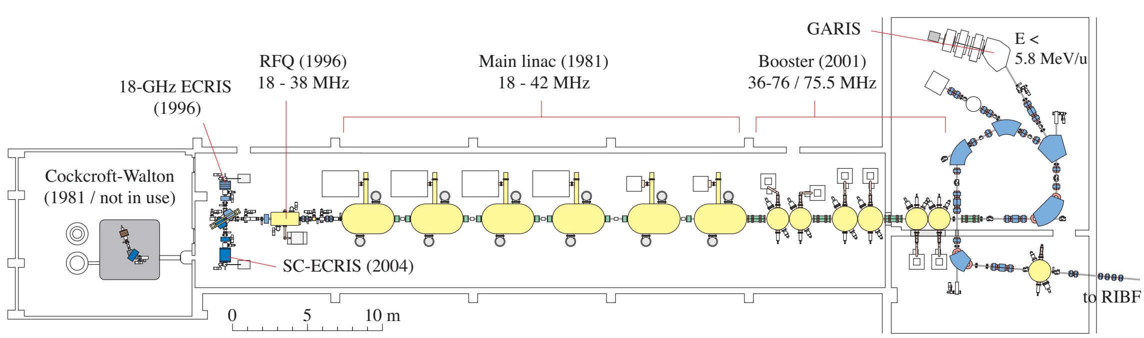


Figure 1: Plan view of the RIKEN Heavy-Ion Linac (RILAC).

* kamigait@riken.jp
† SHI Accelerator Service, Ltd.

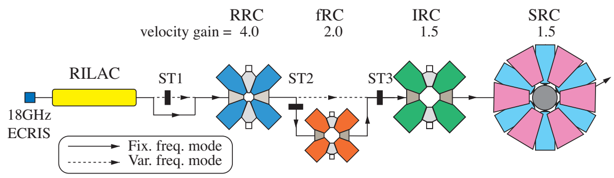


Figure 2: Conceptual layout of the accelerator chain of the RI-Beam Factory (RIBF). The RILAC injector is followed by the booster cyclotrons: RRC (RIKEN Ring Cyclotron, K540 MeV), fRC (fixed-frequency Ring Cyclotron, K570 MeV), IRC (Intermediate-stage Ring Cyclotron, K980 MeV), and SRC (Superconducting Ring Cyclotron, K2600 MeV). The charge strippers are indicated by ST1 - ST3.

## [illegible]

The acceleration test was carried out in June using the $^{48}Ca^{10+}$ ions from the 18-GHz ECR ion source. The rf frequency of the RILAC was 36.5 MHz, which corresponds to the beam energy of 114 MeV/u at the exit of the IRC.

The calcium ions were generated from a $^{48}CaO$ rod with support gas of $O_2$ in the ion source. At the extraction voltage of 16.0 kV, the beam current was 40 e$\mu$A at the first Faraday cup after the analyzing magnet. The charge state was changed into 17+ with a carbon foil of 40 $\mu$g/cm$^2$ at the beam energy of 2.7 MeV/u after passing through the RILAC . The transmission efficiency through the RILAC was 53 % and the stripping efficiency was 35 %. We used another stripper of carbon foil of 1 mg/cm$^2$ after the RRC, which fully stripped the calcium ions with an efficiency of 87 % at the energy of 46 MeV/u. Finally, we got 270 pnA at the exit of the IRC, corresponding to $1.6\times10^{12}$ pps. In the test, we used a beam attenuator of 50 % after the RILAC in order to keep the beam current below 300 pnA, which is the maximum intensity allowed by the operating license.

The rf system of the RILAC and the charge strippers were stable throughout the beam study. We are planning to accelerate the calcium beam through the SRC in November 2008.

## [illegible]

We performed the test using the $^{238}U^{35+}$ ions from the 18-GHz ECR ion source in May and July. The rf frequency of the RILAC was 18.25 MHz, corresponding to the beam energy of 114 MeV/u at the exit of the IRC.

We used a rod of metallic uranium with support gas of helium in the ion source. The beam current at the first Faraday cup was 2 e$\mu$A at the extraction voltage of 5.7 kV, and the transmission efficiency through the RILAC was 30 %. The beam was injected directly into the RRC without charge stripping. As shown in Fig. 2, the extracted beam from the RRC went through two charge strippers placed on both sides of the fRC. The final beam current at the exit of the IRC was 0.35 pnA, which corresponds to $2\times10^9$ pps.

One of the reasons for the low transmission efficiency through the RILAC comes from the mismatch of the emittance of the output beam from the ion source to the acceptance of the RFQ. We also found the vacuum pressure in the low energy part of the RILAC is not sufficient for the highly charged ions like $^{238}U^{35+}$.

During the acceleration, the rf voltage, rf phase and beam phase were measured with a monitoring system which has been newly developed based on lock-in amplifiers [4]. The measured data shows that the rf voltage and phase of the first four resonators of the RILAC sometimes moved out of the required range of $\pm0.1$ % and $\pm0.1\,^\circ$, respectively, and the beam phase in the following accelerators was influenced by these fluctuations. The origin of the variation of the rf systems is under investigation.

## NEW PRE-INJECTOR FOR RILAC

From the operational status mentioned in the previous section, it is clear that we need more beams from the ion source, especially for the uranium acceleration. To increase the intensity, we are constructing a new superconducting ECR ion source capable of the microwave frequency of 28 GHz [5]. It is designed to have as large plasma volume as 1100 cm$^3$.

The superconducting coil system of this ion source consists of six solenoids and a set of sextupole coils to make a confinement magnetic field. The maximum axial magnetic fields are 3.8 T at the rf-injection side and 2.2 T at the beam-extraction side. The inner solenoid coils are used for introducing a flat magnetic field region between the mirrors. The coils use a NbTi-copper conductor and are bath-cooled in liquid helium. The superconducting coils were already assembled and the excitation test is under progress. After the test, the assembling of the cryostat for these superconducting coils will be started. The ion source will be brought to RIKEN in December 2008.

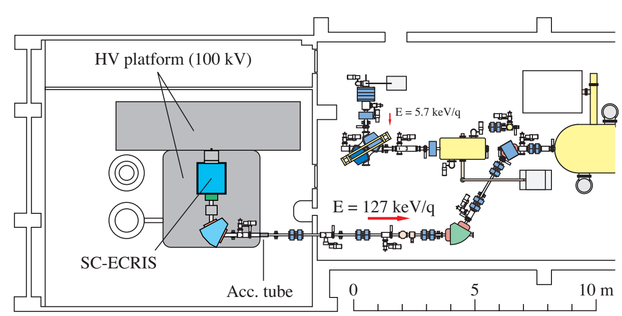


Figure 3: Configuration of the new pre-injector for the RILAC.

Low frequency operation of the RILAC at 18.25 MHz requires, however, such low extraction voltage as 5.7 kV in the $^{238}U^{35+}$ acceleration. High power beams of 5.7 kV surely grow up due to their space charge forces in the low-energy transport line. On the other hand, RILAC requires such low injection energy as 127 kV. Therefore, we decided to put the superconducting ECR ion source as well as the analyzing magnet [6] on the high-voltage terminal of the original Cockcroft-Walton pre-injector so that extracted beam from the source can be directly injected to the RILAC, skipping the RFQ , as shown in Fig. 3. We expect that the emittance growth can be suppressed in the beam transport system.

The design study of the medium-energy beam transport system is under progress, for which we plan to use recycled magnets. The original power generator of 50 kVA will be used for the devices on the platform as well as an additional power transformer of 50 kVA. We expect to start the test of the superconducting ECR ion source in April 2009.

## NEW LINAC INJECTOR FOR RIBF

The recent success in the synthesis of SHE [7] using the GARIS (gas-filled recoil ion separator) system in the RILAC facility strongly encourages us to further pursue the search for the heavier elements and to more extensively study physical and chemical properties of SHEs. This compels us to provide a longer machine time for these experiments. However, the SHE research and RIBF research conflict with each other, because both of them use the RILAC.

Therefore, a new additional injector linac to the RRC has been proposed [8], which will make it possible to conduct the SHE and RIBF research studies independently. The new injector, which will be placed in the AVF-cyclotron vault, will be used exclusively to produce primary beams of 345 MeV/u from the SRC.

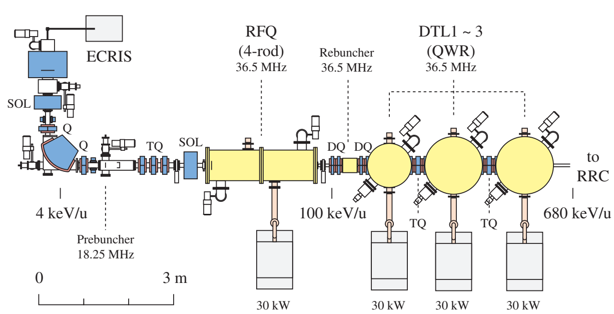


Figure 4: Schematic layout of the new injector.

The injector is designed to accelerate ions with a mass-to-charge ratio of 7, aiming at heavy ions such as $^{136}Xe^{20+}$ and $^{238}U^{35+}$, up to an energy of 680 keV/u in the cw mode. It consists of an ECR ion source, a low-energy beam transport system including a pre-buncher, an RFQ linac based on the four-rod structure, and three DTLs based on the quarter-wavelength resonator (QWR), as shown in Fig. 4. The rf resonators are supposed to be operated at a fixed rf frequency of 36.5 MHz. Strong quadrupole magnets will be placed into the beam line between the rf resonators. The output beam will be injected to the RRC without charge stripping.

In November 2007, an RFQ system including two post accelerators and their rf amplifiers was transferred to RIKEN through the courtesy of Kyoto University, as shown in Fig. 5 This RFQ system was originally developed by Nissin Electric Co., Ltd. in 1993. [9] Since the termination of its acceleration tests in the company, the RFQ system has been maintained in the Advanced Research Center for Beam Science, Kyoto University for several years.

Figure 5: Photograph of the four-rod RFQ settled in the RIBF building for high power tests.

The RFQ linac, based on a four-rod structure, accelerates heavy ions of $m/q$ = 16 up to an energy of 84 keV/u in the cw mode with an rf frequency of 33.3 MHz. When the RFQ resonator is modified so as to have a resonant frequency of 36.5 MHz, it becomes possible to accelerate ions of $m/q$ = 7 to 100 keV/u, which is the required energy in the new injector system, without changing the vane electrodes.

We plan to perform high-power tests of the RFQ resonator at the original frequency of 33.3 MHz in this year, after reassembling the rf amplifier.

## REFERENCES

[1] O. Kamigaito et al., Rev. Sci. Instrum. **76**, 013306 (2005).

[2] Y. Yano, Nucl. Instr. & Meth **B 261**, 1007 (2007).

[3] A. Goto et al., "Commissioning of RIKEN RI Beam Factory", Cyclotrons'07, Giardini Naxos, Sep. 2007, p. 3, http://www.JACoW.org.

[4] R. Koyama et al., "Beam Phase and Rf Fields Monitoring System using Lock-in Amplifier for RIKEN RIBF", EPAC'08, Genoa, June 2008, TUPC052, p. 1173, http://www.JACoW.org.

[5] T. Nakagawa et al., Rev. Sci. Instrum. **79**, 02A327, (2008).

[6] D. Leitner et al., gProgress and Perspective for High Frequency, High Performance Superconducting ECR Ion Sourcesh, Cyclotrons'07, Giardini Naxos, Sep. 2007, p. 265, http://www.JACoW.org.

[7] K. Morita et al., J. Phys. Soc. Jpn. **73**, 2593 (2004).

[8] O. Kamigaito et al., "Design of New Injector to RIKEN Ring Cyclotron", PASJ3-LAM31, Sendai, Japan, Aug. 2006, WP78, p. 502.

[9] H. Fujisawa, Nucl. Instrum. Methods **A 345**, 23 (1994).

# LOW ENERGY SPREAD BEAM DYNAMICS AND RF DESIGN OF A TRAPEZOIDAL IH-RFQ *

Y.R. Lu†, Y.C. Nie‡ ,C.E. Chen, Z.Y.Guo, X.Q.Yan, K.Zhu, S.L.Gao, J.X.Fang
State Key Lab of Nuclear Physics and Technology, Peking University, 100871

*Abstract*

The methodology for a low energy spread RFQ beam dynamics design has been studied for $C^{14+}$ AMS application This paper will present a low energy spread beam dynamics and RF design for a trapezoidal IH-RFQ (abbreviated T-IH-RFQ) operating at 104MHz at Peking University. $^{14}C^{+}$ will be accelerated from 40keV to 500keV with the length of about 1.1m. The designed transmission efficiency is better than 95% and the energy spread is as low as 0.6%. Combining the beam dynamics design, a T-IH-RFQ structure was proposed, which can be cooled more easily and has better mechanical performance than traditional RFQ. The electromagnetic field distribution was simulated by CST Microwave Studio (MWS). The simulation results show such T-IH-RFQ has higher operating frequency than normal four rods RFQ and/or IH-RFQs. The specific shunt impedance and the quality factor were also compared to these RFQ structures.

## INTRODUCTION

RFQ, proposed by I.M.Kapchinsky and V.A.Teplyakov in 1970[1], has been used widely for many applications. It can focus, bunch and accelerate low energy beam, extracted from ion sources directly, over a mass range from proton to heavy ions such as uranium based on the RF electrical field of a modulated quadruple transport channel [2]. RFQ was used to $^{3}H$ Accelerator Mass Spectroscopy (AMS) firstly by LLNL in USA because of its inherent compact size [3]. RFQ based $^{14}C$ AMS application has been studying in recent years at the Institute of Heavy Ion Physics (IHIP), Peking University [4, 5]. The most critical problem is that the energy spread of full width at half magnitude (FWHM) for traditional RFQ is usually larger than 2% because of the process of adiabatic bunching and phase oscillation, which is too high for the particle identification in an AMS detector. So, ways must be found to reduce the energy spread of the output $^{14}C$ beam. The highest beam current of RFQ used for AMS $^{14}C$ facility is lower than 200μA, which is such low that the space charge effects can be ignored. Non-adiabatic bunching method should be used to make output beam energy spread low. A physical design of RFQ with 0.6% energy spread has been obtained through external bunching method by previous work at IHIP. A pre-buncher will be necessary in the injection system before RFQ to bunch beam length in the range of [-20°, 20°]. However, the bunching efficiency of a pre-buncher can only be 70~80%. As a result, the total transmission will be lower than most tandems based AMS facility even though no particle is lost in RFQ. An internal discrete bunching proposed by J.W.Staples at LBNL [6] is used to save additional RF power supply and buncher cavity. The low energy spread beam dynamics design for $^{14}C^{+}$ RFQ will be presented in this paper.

On the other hand, an IH-RFQ acceleration structure was proposed and studied. The four electrodes are supported by erect boards connected to the external cavity up and down. This new structure was named trapezoidal IH-RFQ according to its appearance. The trapezoidal IH-RFQ is easily cooled and will have good mechanical performance. Moreover, it will have higher resonant frequency than traditional IH-RFQ [7]. Simulations of the electromagnetic fields have been completed by CST Microwave Studio (MWS). RF characteristics is investigated, and geometrical parameters are optimised initially to make the shunt impedance and the quality factor as large as possible.

## BEAM DYNAMICS DESIGN

According to Staples' method, the whole RFQ beam dynamics design is divided into five sections, radial matcher, buncher section, drift section, transition section and accelerator section. The radial matcher is similar to that of four-step method developed at LANL [8], which matches DC input beam to the time-varying transverse envelope at the entrance of RFQ. The buncher section is distributed over several cells while the modulation parameter $m$ ramps from zero to a maximum and then back down to zero, which performs the function of bunching as a non-adiabatic buncher. The following several unmodulated cells make up of the drift section which allows the ideal beam bunch to form. In the transition section, the beam is accelerated slowly as the synchronous phase varies from -90º to its final value -30º. Finally, the designed energy is reached in the acceleration section. Significantly lowered longitudinal output emittance and slightly lowered transverse emittance can be obtained by this new design technique compared to previous methods, which has been proved by PARMTEQM.

* Supported by NSFC(19775009)
† Corresponding author yrlu@pku.edu.cn
‡ Current institute: Institute of Applied Physics, Frankfurt University, Frankfurt, Germany

There is another approach to reduce the RFQ energy spread further more, which can be shown by

$$\Delta w_{\max} = \left[2A\xi V_0 e w_s(\varphi_s \cos\varphi_s - \sin\varphi_s)\right]^{1/2} \quad (1)$$

Where $\Delta w_{\max}$ is the separatrix height that indicates the maximum beam energy spread, $\xi$ is the charge-to-mass ratio of the ion, $e$ is the charge of an electron, and $w_s$ the energy per nucleon of the synchronous particle. The formula shows that energy spread can be decreased by reducing acceleration coefficient $A$, inter-vane voltage $V_0$ and synchronous $\varphi_s$, where lower $A$ means lower $m$.

From above we can see apparently that $\varphi_s$ should be as large as possible in order to obtain low energy spread, but not be kept at -30º. On the other hand, the focus parameter $B$ should increase during the first stage of the transition section and then keep constant, whereas at the acceleration section it should decrease slowly in order to receive the constant transverse phase advance to keep the beam matched, minimize the emittance growth and related beam loss [9]. The above two aspects can be realized by MATCHDESIGN [10], a code developed at IHIP taking matching equations, equipartition condition and constant transverse beam size into account to avoid emittance growth and beam loss.

Integrating all the above points, we are capable of performing beam dynamics design in pursuit of low energy spread. The design parameters were given by MATCHDESIGN, and then the internal non-adiabatic buncher was designed by the code of J.W.Staples. On one hand $V_0$ should be as low as possible to reduce power consumption; on the other hand $V_0$ should be large enough to achieve sufficient focusing. Finally $V_0$ was chosen to be 60kV, meanwhile $m$ should be increased very slowly, otherwise particles will not be focused effectively and some of them will then be lost. The main dynamics parameters of the RFQ are plotted in figure 1 and listed in Table 1. Energy spectrum of ion beam output from this RFQ is shown as figure 2.

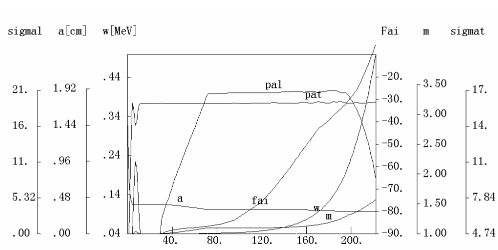


Figure 1: The main dynamics parameters (sigmal is longitudinal phase advance, sigmat is transverse phase advance, Fai is synchronous phase, a is aperture radius, w is ion kinetic energy and m is modulation respectively).

Table 1: The Main Dynamics Parameters

| | |
|---|---|
| Ion | $^{14}C$ |
| Charge number $q$ | 1 |
| Operating frequency $f$ (MHz) | 104 |
| Electrode voltage $V_0$ (kV) | 60 |
| Input energy $W_i$ (keV) | 40 |
| Output energy $W_o$ (keV) | 500 |
| Modulation $m$ | 1.0–1.57 |
| Minimum aperture radius $a$ (mm) | 2.93 |
| Maximum focusing factor $B$ | 3.44 |
| Synchronous phase $\varphi_s$ (degree) | -90 to -6 |
| Electrode length $L$ (mm) | 1091.3 |
| Transmission $T$ (%) | 97.6 |
| Energy spread (%) | 0.6 |

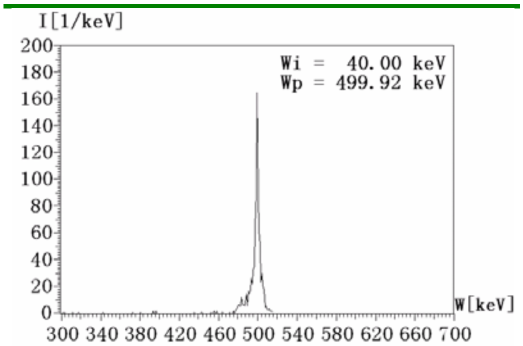


Figure 2: Output beam energy spectum.

The total length of the RFQ is about 1.1m, and further more $m$ is small to make particles be focused sufficient in the whole acceleration process and to obtain low energy spread. However, the low energy spread beam dynamics design method introduced in this paper will undoubtedly simplify the RFQ based AMS in compare to external non-adiabatic bunching. The maximum surface field is about 25MV/m, so the Kilpatrick coefficient is about 2.1 which can be accepted in the case of weak beam current. The transmission efficiency is about 97.6%, which is much better than that of external bunch design.

## RF DESIGN

A cavity model was built using MWS, given by figure 3. Intuitively, a trapezoidal IH-RFQ has great mechanical capability and will simplify the cooling system very much.

Figure 3: Model of trapezoidal IH-RFQ

The RF design includes resonance frequency, electromagnetic field distribution and RF efficiency. The field distribution illustrated that the trapezoidal IH-RFQ structure was a cavity operated at $H_{21(n)}$ mode shown in figure 4, not $H_{11(n)}$ mode like classical IH-RFQ. As a result, the trapezoidal IH-RFQ has higher resonant frequency than traditional RFQ and IH-RFQ when they have same transverse dimension. It is suitable for not only light particles such as proton and deuteron but also heavier ions such as $^{14}C^{+}$. The longitudinal field distribution un-flatness is less than 5%.

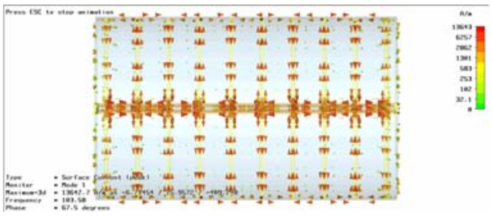

Figure 4: Current flow for T-IH-RFQ.

In order to reduce RF power loss, the specific shunt impedance and quality factor were optimized for different geometric parameters, such as shape of electrode, width and thickness of the support boards, spacing between support boards and cavity diameter. The simulated cavity frequency is a bit lower than 104MHz to keep the tuning margin, and the conductivity is set to $5.0\times10^{7}$s/m. Considering the cavity is relatively short, the whole cavity was simulated. The distance between neighbouring two support boards is almost equivalent to the amount of support boards since the total length has been confirmed by beam dynamics design. If it is large, the electrode length per module increases which leads to large capacitance, whereas a small distance means significant capacitive loading between the support boards [11]. Taking mechanical factor into account, 10 support boards were used and the distance was chosen to be 115mm. Finally, the simulated quality factor is around 5192, and the specific shunt impedance is optimized to reach about 110kΩ•m, which means the designed RF power is 36kW. The optimized structure parameters are listed in table 2.

Table 2: The Optimized Structure Parameters

| | |
|---|---|
| RF frequency $f$ (MHz) | 103.6 |
| Cavity length $L$ (mm) | 1111.3 |
| Number of support boards | 10 |
| Distance between support boards (mm) | 115 |
| Width of support boards (mm) | 112 |
| Thickness of support boards (mm) | 13.5 |
| Cavity diameter (mm) | 680 |
| Quality factor | 5192 |
| Specific shunt impedance (kΩ•m) | 110 |
| RF power (kW) | 36 |

Comparing T-IH-RFQ to traditional four rods RFQ and IH-RFQ with the same mechanical dimensions, T-IH-RFQ has the highest frequency and lowest RF shunt impedance. Their performances are shown in Table 3.

Table 3: Comparing Three Different RFQs

| | T-IH-RFQ | IH-RFQ | Four Rod RFQ |
|---|---|---|---|
| Frequency/MHz | 103.6 | 46.5 | 77.9 |
| Shunt impedance /kΩ•m | 110 | 300 | 170.9 |
| Quality Factor | 5192 | 5934 | 5077 |

Cold model cavity will not be necessary because good agreement between simulation results and the cavity measurements. The real trapezoidal IH-RFQ power cavity will be manufactured directly based on MWS design.

## CONCLUSION

Internal discrete bunching method was used to simplify the RFQ based $^{14}C$ AMS and improve the transmission. The non-adiabatic buncher section functioned as the pre-buncher before RFQ. All dynamics parameters were designed and modified repeatedly by MATCHDESIGN, the code of Staples and PARMTEQM. After a satisfying beam dynamics design was obtained, we proposed the trapezoidal IH-RFQ operating at $H_{21(n)}$ mode illustrated by MWS simulations. It has higher resonant frequency and great mechanical performance. After optimization, the quality factor and the specific shunt impedance for the trapezoidal IH-RFQ are initially satisfied.

Further optimization will be carried out for RF design mainly aimed to decrease power consumption. A trapezoidal real IH-RFQ power cavity will be constructed under the support of NSFC (19775009) and be tested next year.

## REFERENCES


[1]. Kapchinsky M, Teplyakov V A. Prib. Tekh. Eksp., 1970, (2): 19-22

[2]. Wangler T P. Principles of RF Linear Accelerators. New York: John Wiley & Sons, 1998. 225-257

[3]. Roberts M L, Hamm R W, Dingley K H et al. Nucl. Instr. & Meth., B, 2000, 172(1-4): 262-267

[4]. GUO Zhi-Yu, LIU Ke-Xin, YAN Xue-Qing et al. Nucl. Instr. & Meth., B, 2007, 259(1): 204-207

[5]. GUO Zhi-Yu, XIE Yi, LIU Ke-Xin et al. HEP & NP, 2006, 30(Supp.I): 114-116 (in Chinese)

[6]. Staples J W. Proc. of LINAC1994, 755

[7]. Ratzinger U, Kaspar K, Malwitz E et al. Nucl. Instr. & Meth. A, 1998, 415: 281-286

[8]. Crandall K R, Stokes R H, Wangler T P et al. Proc. of LINAC1979, BNL-51134, 205-220

[9]. YAN Xue-Qing, FANF Jia-Xun, GUO Zhi-Yu et al. HEP & NP, 2006, 30(Supp.I): 19-21 (in Chinese)

[10]. YAN Xue-Qing, Jameson R A, LU Yuan-Rong et al. Nucl. Instr. & Meth., A, 2007, 577(3): 402-408

[11]. Bricault P G, Schneider H R, Vancouver B C. Proc. of PAC1995, IEEE96, 1125-112

# AN INTERMEDIATE STRUCTURE SFRFQ BETWEEN RFQ AND DTL*

Y. R. Lu, J. E. Chen†, K. Zhu, X. Q. Yan, Z. Wang, Z. Y. Guo,
M. L. Kang, M. Zhang, J. Zhao, S. L. Gao, S. X. Peng, J. X. Fang
State Key Lab of Nuclear Physics and Technology, Peking University, 100871

*Abstract*

SFRFQ is an intermediate accelerating structure, which combines RFQ and DTL together, it can increase the accelerating efficiency at RFQ exit part by inserting gap acceleration between RFQ electrodes while providing strong focusing by RFQ focusing field. One prototype cavity has been manufactured and been used as a post accelerator of ISR RFQ to accelerate O+ from 1MeV to 1.6MeV in 1meter. A code SFRFQCODEV1.0 was developed for the beam dynamics design. The RF conditioning and full RF power test has been carried out. The intervane or gap voltage have reached 86kV at 29 kW with 1/6 duty cycle and repetition frequency 166Hz. The initial beam test results will also be presented in this paper.
PACS numbers: 29.20.Ej

## INTRODUCTION

RFQ accelerators have been widely used in many applications. Because of increasing of the beam energy, beam accelerating efficiency goes down rapidly. Actually, Longer the RFQ length is, lower kinetic energy gain per unit length is; lower the injection energy of DTL is, much higher accelerating efficiency is; more accelerating gaps at DTL entrance means stronger transverse focusing is needed for the beam. Therefore several different accelerating structures, such as SP RFQ [1] in Russia and RFD [2] in U.S.A., have been studied in last decade to improve accelerating efficiency. The novel idea of Separated Function RFQ (SFRFQ) was first proposed by the RFQ group of IHIP (Institute of Heavy Ion Physics) at Peking university[3], based on the experience of ISR-RFQ 1000 (Integral Split Ring RFQ) [4][5][6]. Initial results of electro-magnetic calculation and dynamics proved the possibility and higher RF accelerating efficiency of SFRFQ structure[7].

To verify accelerating feasibilities of the SFRFQ structure, a simulation code SFRFQCODEV1.0[8] was developed for beam dynamics design. The prototype SFRFQ cavity will be used as a post-accelerator for ISR RFQ-1000 and accelerate O+ beam with ~mA peak current from 1MeV to 1.6MeV. This paper will present the beam line setup and related experimental results.

## SFRFQ BEAMLINE SETUP

SFRFQ accelerating system consists of a 2.45GHz ECR ion source and LEBT, 1MeV ISR RFQ-1000, Magnetic Triplet, SFRFQ cavity, Analyzing Magnet and three beam Faraday cups. It is shown in Fig.1. Figure 2 shows the 2.45GHz ECR ion source and LEBT. 2.45GHz ECR ion source was made by permanent magnet. It can generate the axial magnetic field of 90~100mT in microwave discharging chamber, which is about 50mm in diameter and 50mm in length. LEBT consists of two electrostatic lenses with diameter of 80mm and 120mm respectively. The total extracted beam current can reach 5mA with extraction voltage 22kV, extraction aperture diameter of 5mm, $O_2$ gas inlet of 0.15sccm, electrostatic focusing voltage 19.6kV and 16.7kV respectively. The extracted $O^+$ ratio is about 0.6 and LEBT transmission is about 80%[9]. The beam emittance is about 0.12~0.16mm·mrad measured by Allison emmitance equipment.

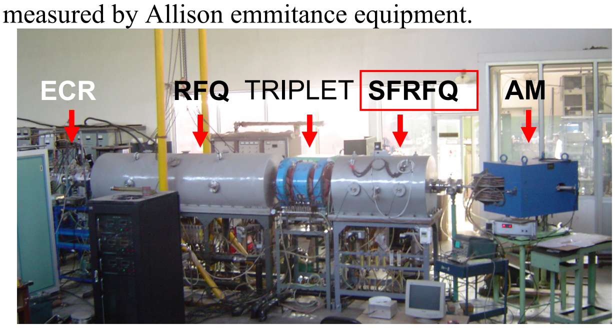


Figure 1: SFRFQ beam line setup.

The triplet has been designed to realize the beam matching in transverse. The figure 2 shows the magnetic gradient distribution along the triplet axis. It is only regret that longitudinal bunched beam length was expanded to nearly 150degree because of beam energy spread and longitudinal drifting. It asks an additional buncher to bunch the beam.

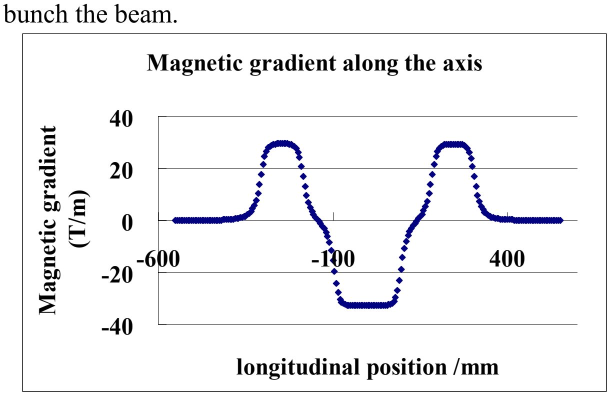


Figure 2: Magnetic gradient along the triplet axis.

The upgrade of beam test for 1MeV ISR-RFQ has been performed. The maximum output peak beam current at RFQ exit i.e. at the entrance of triplet is 2mA with sample

---

* Supported by NSFC 10455001

† Corresponding author: Chenje@pku.edu.cn

resistor of 1kΩ. This was shown in figure 3. The needed RF power is more than 32.5kW.

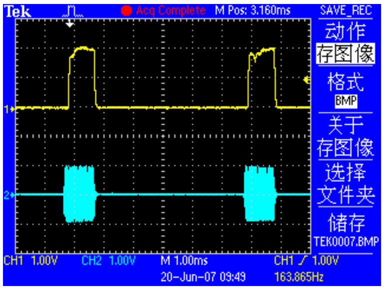


Figure 3: 2mA output peak current for 1MeV ISR RFQ with RF peak power 32.5kW, duty factor 1/6, and RFQ transmission of about 80%.

## SFRFQ AND FULL RF TEST

SFRFQ is a hybrid structure of RFQ and DTL accelerator, the inner structure is shown in figure 4. The RFQ parts are for the transversal alternating gradient focusing, gaps between diaphragms are for acceleration. As we mentioned in last section, the particles' phase are expanded to 150º in triplet drifting. The synchronous phase in SFRFQ should be set gradually from phase -87º to - 20 º (refer to figure 5). The detailed optimization for SFRFQ cavity design was referenced to[10] . In reference [10], the manufacturing tolerance for inner structure has been also studied very carefully.

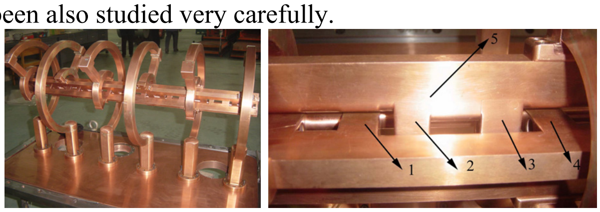


Figure 4: SFRFQ inner structure (left), 1,2,3,4 diaphragms and 5 RFQ electrodes (right).

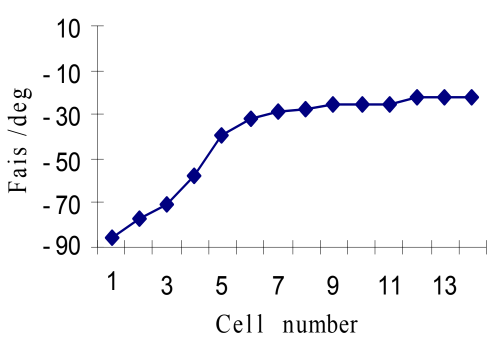


Figure 5: Synchronous phase versus cell number.

A capacitance tuner is installed on the top of tank cover. It has a frequency tuning ability from 26.42MHz to 25.95MHz when it is moved from 0 to depth of 25mm, while the unloaded quality factor goes down from 2480 to 2340. Up to now the capacitance tuner position is controlled by step motor and worked at open loop, because the cavity detuning is about 3 kHz per hour, this is easily controlled manually to decrease the influence of tuning device vibration. The electric field distribution $E^2$ along the axis was measured by bead pull measurement [10], it fits the field simulation results.

The RF systems, shown in figure 6, consist of two 30kW CW final amplifier made by FU105Z3 which is cooled by circulating distilled water. They can deliver 45kW in pulse mode operation with duty factor 1/6. Each of them includes a 20W (3-30MHz) short wave broadband preamplifier, 1kW driver made by FU100 cooled by air. The electric field gradient in the cavity is stabilized by an AGC feedback system independently. The RF system for SFRFQ cavity includes a voltage controlled phase shifter[10], it can control the RF field phase in SFRFQ cavity and keep it be synchronous with the particles. The shifted phase versus controlled voltage is shown in figure 7. The voltage standing wave ratio is less than 1.1 under the RF power test. The principal parameters for RFQ cavity can be referenced in [6], and that for SFRFQ is listed in Table 1. The RF test results are listed in Table 2. TABLE II lists the results of RF power test with the duty factor 1/6. Here $V_o$ is the intervane voltage, $\rho = \frac{V_0^2}{p} \cdot l$ is the specific shunt impedance, where $p$ and $l$ is the RF power and length of the cavity. Figure 8 gives an example of intervane voltage measurement by using high purity Ge detector. The specific shunt impedance is about 270.8kΩm.

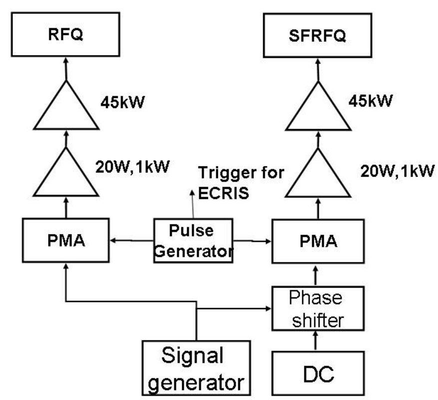


Fig. 6 RF system

Table 1: Principal Parameters of SFRFQ

| | Prototype |
|---|---|
| Ion species | $O^+$ |
| F(MHz) | 26.07 |
| $W_{in}$(keV) | 1000 |
| $W_{out}$(keV) | 1620 |
| Cavity Length(cm) | 105.8 |
| Diameter(cm) | 70 |
| $V_o$(kV) | 70 |
| Duty factor | 1ms/6ms |

Table 2: The Results of SFRFQ RF Power Test

| Power/kW | $V_o$/kV | $\rho$ /k$\Omega$ ·m |
|---|---|---|
| 16.2 | 65.81 | 276.2 |
| 20.7 | 73.16 | 265.7 |
| 23.4 | 78.06 | 269.8 |
| 28.8 | 86.22 | 266.6 |
| 33.3 | 91.02 | 257.1 |

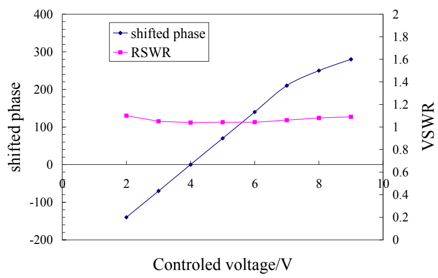


Figure 7: Shifted phase versus control voltage.

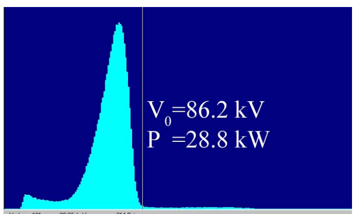


Figure 8: Roentgen spectrum at 28.8 kW RF powers.

## INITIAL BEAM TEST

Because 1MeV ISR RFQ has no frequency tuning system, RF test for total accelerating system is rather difficult at the beginning of RF conditioning. At first nearly 35kW pulse power with duty cycle of 1/6 at 166Hz repetition frequency is feed into RFQ cavity, several minutes later, and the cooling water temperature of RFQ cavity has balanced with RF feeding power. The RFQ frequency finally is kept at 26.075MHz. This is actually the working point of SFRFQ. This fits the impedance matching (figure 9) of in-coupling loop. After feeding about 20kW into SFRFQ cavity, and changing controlled voltage of phase shifter to 4.9V, setting triplet coils currents to 65A,47.5A and 65A respectively, the first beam comes at the SFRFQ exit, it is nearly about 162μA. The energy spectrum of output beam is also measured by analysing magnets. The maximum beam current is corresponding to the beam energy of 1.86MeV. It is rather higher than the designed 1.62MeV. The energy spectrum will be calibrated by nuclear reaction and beam transport will be optimized in the further experiments.

## CONCLUSION

Initial results show the SFRFQ cavity can have higher acceleration efficiency and can also stand 91kV intervane voltage. Although the output beam energy is higher than the designed value and output beam current is not yet good optimized for the final operation. The RF synchronous phase and RF power level will greatly influence the output beam current and beam energy. The triplet parameters have also great influence on the beam transport.

The authors would like to thank Prof.Dr.Klein and Prof.U.Ratzinger for their helpful discussions about H type DTL linac.

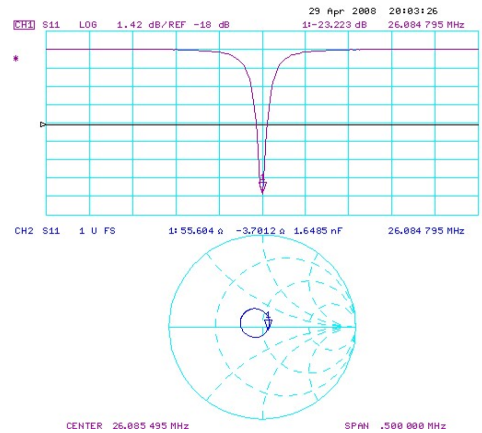


Figure 9: The Impedance Matching of RF Feeder.

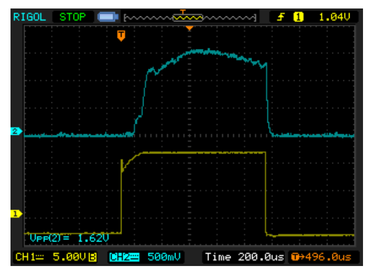


Figure 10: Output Macro-pulse Beam Current (sample resistor 10kΩ).

## REFERENCE

[1] S.Minaev, Nuclear Instruments and Methods in Physics Research, a, Issue: 1-3, August 21, 2002, pp. 45-58
[2] D.A.Swenson, et al., Proceedings of the 1998 LINAC Conference, Chicago, IL, 1998, p. 648
[3] C.E.Chen, J.X. Fang, et al. Progress on Natural Science, Vol. 12, No.1, 23, 2002
[4] C.E.Chen, J.X. Fang, et al., Proc. of EPAC 1994
[5] Y.R.Lu, J.F.Guo, et al., NIM.A, 420 (1999)
[6] Y.R.Lu,C.E.Chen,J.X.Fang,et al. NIMA,A515(2003): 394-403
[7] X.Q.Yan, J.X. Fang, et al., Nuclear Inst. and Methods in Physics Research, A, 506(1-6)
[8] Z. Wang, et al, NIMA, 572,2007,596-600
[9] S.X.Peng,M.Zhang et al.,Review of Scientific Instrument, **79**, 02B706 _2008, DOI: 10.1063/1.2802200
[10] Z. Wang, Peking university dissertation, 2008
[11] Lu Yuanrong, W Gutowski, Acta Scientiarum Naturalium Universitatis Pekinensis, Vol.38, No.1, P. 49-56, (Jan,2002)

# HEAVY ION INJECTOR FOR NICA/MPD PROJECT

V.V.Kobets, A.I.Govorov, G.V.Trubnikov, E.E.Donets, E.D.Donets, A.O.Sidorin, V.A.Monchinsky, I.N.Meshkov, JINR, Dubna, Russia

O.K.Belyaev, A.P.Maltsev, Yu.A.Budanov, I.A.Zvonarev, IHEP, Protvino, Russia

*Abstract*

General goal of the NICA/MPD project under realization at JINR is to start in the coming 5÷7 years an experimental study of hot and dense strongly interacting QCD matter and search for possible manifestation of signs of the mixed phase and critical endpoint in heavy ion collisions. The Nuclotron-based Ion Collider fAcility (NICA) and the Multi Purpose Detector (MPD) are proposed for these purposes. The NICA collider is aimed to provide experiment with heavy ions like Au, Pb or U at energy up to 3.5 x 3.5 GeV/u with average luminosity of $10^{27}$ $cm^{-2} \cdot s^{-1}$ and to provide collisions of light ions in the total energy range available with the Nuclotron. New injector designed for efficient operation of the NICA facility is based on Electron String Ion Source providing short (< 10 μs) and intensive (up to 10 mA) pulses of $U^{32+}$ ions, one section of RFQ and four sections of RFQ Drift Tube Linac accelerating the ions at Z/A ≥ 0.12 up to 6.2 MeV/u of the kinetic energy. General parameters of the injector are discussed.

## INTRODUCTION

General challenge of the NICA facility is to achieve a high luminosity level of heavy ion collisions in a wide energy range starting with about 1 GeV/u. To reach this goal the NICA injection chain has to deliver a single bunch of fully stripped heavy ions ($U^{92+}$, $Pb^{82+}$ or $Au^{79+}$) at intensity of about $1 \div 1.5 \cdot 10^9$ ions [1]. The existing Nuclotron injection complex consists of HV fore-injector and Alvarez-type linac LU-20. The LU-20 accelerates the protons up to the energy of 20 MeV and ions at Z/A ≥ 0.33 up to the energy of 5 MeV/u [2]. Because of the limitation in charge to mass ration the LU-20 can not be used effectively for operation as a part of the NICA facility. Additionally, an effective stripping of the ions before injection into the Nuclotron requires their preliminary acceleration to an energy of a few hundreds of MeV/u. Therefore, realization of the NICA project presumes design and construction a heavy ion injector and intermediate booster synchrotron as new elements of the NICA collider injection chain. The injection chain optimization was started from the choice of an ion source and formulation of requirements to the linear accelerator.

## ION SOURCE AND REQUIREMENTS FOR LINAC

We have considered a few types of the heavy ion sources – namely the Laser Ion Source (LIS), the Electron Beam Ion Source (EBIS), the Electron String Ion Source (ESIS) and the Electron Cyclotron Resonance (ECR) ion source.

The LIS has limitations in the kind of ions that can be produced. Additional obstacles, such as large beam emittance due to a large energy spread, target erosion and coating of mirrors, state of the art laser requirements, and very large pulse-to-pulse fluctuations of the beam current, set one thinking seriously about development of this type of the ion source presently.

The EBIS ion source chosen as the base of the new RHIC injector [3] has parameters close to the required ones and expected for the ESIS. General disadvantage of the EBIS is very high DC power of the electron beam. So, the EBIS proposed for the new RHIC injector requires of about 300 kW DC power for the operation and maximum charge state is limited because of the electron energy limitations. At the same time, the maximum DC power of the electron beam in the ESIS is about 200 W. By contrast to the EBIS, the ESIS source can provide heavy ions in very high charge states, like $Au^{51+}$ or $U^{64+}$ at practically same intensity as $Au^{30+}$ or $U^{32+}$. The repetition frequency of ESIS operation in this mode is at the level of 1 Hz.

In view of the facts described above the decision to use the development of the ESIS as the baseline for the NICA project has been taken.

The possibility to work with ECR ion source as reserve option for the NICA facility operation is considered as well. To realize it the linac has to accelerate long heavy ions pulse generated in an ECR source for multiturn injection into the booster.

To provide optimization of the heavy ion injection chain and cover the polarized program of the NICA facility the injector-linac has to provide the following options of the operation:

- acceleration of the heavy ions at the charge state of 30+ ÷ 32+ at the intensity of $(2 \div 4) \cdot 10^9$ ions and the pulse duration of 7 μs (the ion revolution period in the booster);
- acceleration of the heavy ions like $Au^{51+}$ and $U^{64+}$ at the intensity of $(2 \div 4) \cdot 10^9$ and the pulse duration of 7 μs;
- acceleration of the heavy ions at the charge state of about 30+ ÷ 32+ at the current of 0.1 ÷ 0.2 mA and pulse duration up to 100 μs (operation with ECR source);
- acceleration of the polarized $D^-$ ions at the current up to 1 mA and the pulse duration of about 1 ms.

The first option is chosen as the baseline for realization of U-U collision experiment. The pulse of $4 \cdot 10^9$ $U^{32+}$ ions at 7 μs duration corresponds to the peak current of about

3 mA. Maximum ion current corresponds to the second option and it is about 6 mA. To provide required technical reserve the linac has to have good efficiency of the heavy ion acceleration at the current up to 10 – 15 mA.

## LINAC AND INJECTION CHAIN

The RFQ section was chosen as the initial part of the injector linear accelerator. At low ion velocity RFQ permits a continuous acceleration and perfect adiabatic conditions to produce a very good bunching efficiency (~ 100%). For the main part of the injector linac we considered four versions:
1) Alvarez-type accelerator,
2) an accelerator with the Alternative Phase Focusing (APF) [4],
2) hybrid type of the focusing proposed at GSI [5],
3) RFQ DTL developed in IHEP (Protvino) [6].

*1st version* assumes installation of an RFQ accelerator instead of the existing HV fore-injector and replacement of the drift tubes system of the LU-20 by a new one. However, in the ion energy range of a few MeV/u the peak RF power required for the Alvarez structure is about three times larger than for the structures based on H-cavities. Furthermore, the drift tube length in E-cavity structure has to be long enough to place a quadrupole lens inside it. This leads to low acceleration rate in the initial part of the structure and to decrease of the accelerator efficiency.

*2nd version*. The APF accelerator provides high acceleration rate and is simple in operation. However, its maximum ion current is below 1 mA.

*3rd version*. In the GSI type structure the strength of the transverse focusing of the APF is sufficiently increased by using quadrupole triplets located in a few large drift tubes. Such structure is used for lead ion acceleration in CERN and is planned as the main part of the new RHIC injector [3]. However, up to now such accelerators were used with ECR ion sources and their application to acceleration of a high current ion beam has been never demonstrated yet experimentally.

*The 4rd version* - the RFQ DTL, in contrast to the APF structures utilizes focusing by quadrupole components of the accelerating field and provides a strong focusing in both longitudinal and transverse planes. As result, the maximum ion beam current can reach of about 100 mA. The IHEP group (founded by one of the inventors of the RFQ accelerator Vladimir Teplyakov) has more than 30 years experience in design and construction of such structures.

Finally, *the 4d version* - RFQ DTL has been chosen as the basis for the main part of the new linac design and construction. On the basis of conceptual design of the RFQ and the RFQ DTL prepared by the IHEP group the optimization of the NICA injection chain (Fig. 1) was done. The booster maximum energy is limited by available room in the existing building and maximum magnetic field of its bending magnets. The injection chain satisfies to the requirements of the heavy ion program and provides technical reserve for the facility development.

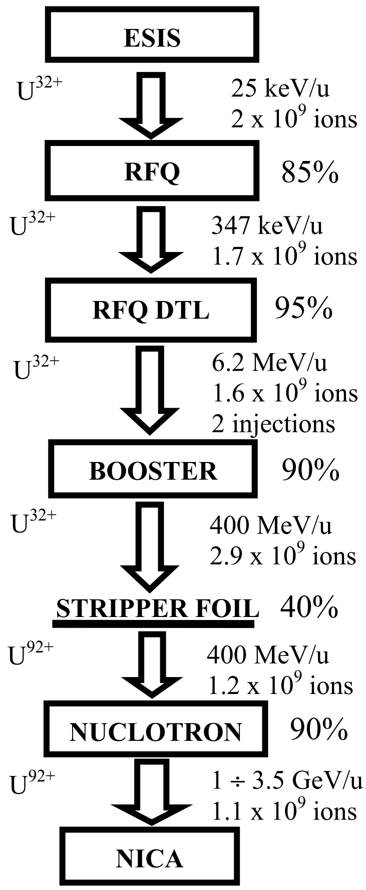


Figure 1: Injection chain of the NICA collider based on ESIS source and RFQ linac.

## STRUCTURE AND PARAMETERS OF THE INJECTOR

The injector delivers ions in wide atomic number range – from polarized deuterons to $^{238}U^{32+}$ at the energy of 6.2 MeV/u. Its total length is of 30 m. The injector will be constructed in the existing so called UFTI building (a very preliminary design is shown in the Fig. 2) in order to provide its assembly and commissioning without interruption of the Nuclotron operation.

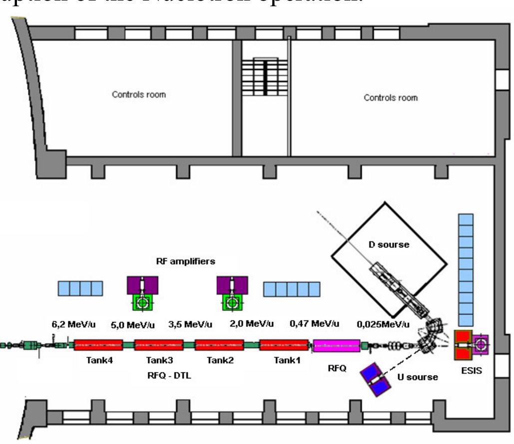


Figure 2: Injector location in the existing building.

The injector includes the following elements:
- Electron String Ion Source (ESIS);
- External uranium ion source;
- Source of polarized $D^-$ ions (POLARIS or CIPIOS);
- Low Energy Beam Transport (LEBT) to match the beam with the entrance of the linear accelerator;
- Linear accelerator consisting of the RFQ section and four sections of the RFQ DTL;
- High Energy Beam Transport (HEBT) from the exit of the linac to the injection point of the booster. This line includes also a debuncher system.

## ESIS

Electron beam ion sources (EBIS) invented at JINR [8] are used widely in many accelerator centers for production of highly charged ions. In the reflex mode of the EBIS operation the electrons do not reach electron collector after one pass through the drift space of the source. Instead they are reflected back towards the electron gun, where are reflected again near the gun cathode, travel one more to the reflector, and so on. Thus, the electrons are bouncing between the cathode and the reflector of the source and can be used for generation of highly charged ions much as a direct electron beam does.

It was found that in certain conditions the ”cloud” consisting of the multiply reflected electrons confined in a strong solenoid magnetic field exhibits properties similar to a phase transition. It leads to a stepwise increase of the confined electron plasma density in a new steady state called "the electron string". Various highly charged ion beams have been produced with the ESIS “KRION-2” constructed at JINR (Fig. 3) and used in two Nuclotron runs during recent years [9].

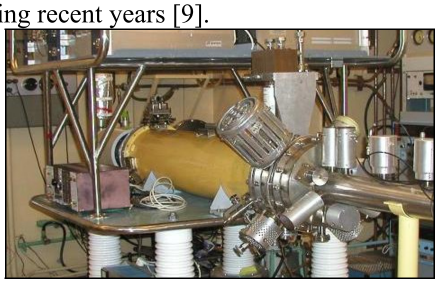

Figure 3: ESIS “KRION-2” operated at JINR.

New stand ESIS “KRION-6T” aimed to achieve parameters required for NICA (Table 1) is under construction now.

Table 1: Main Parameters of the ESIS Sources

| | “KRION-2” achieved to date | “KRION-6T” expected |
|---|---|---|
| Magnetic field, T | ≤ 3 | ≤ 6 |
| Electron energy, keV | ≤ 8 | ≤ 25 |
| Ions | $Au^{30+}$ | $Au^{32+}$ ($U^{32+}$) |
| Ionization time, s | $2 \cdot 10^{-2}$ | 0.015 |
| Work frequency, Hz | 40 | 50 |
| Number of ions per pulse (at given charge state) | $5 \cdot 10^{8}$ | $2 \cdot 10^{9}$ |
| Extraction time, μs | 8 | 6 - 8 |

## RFQ AND RFQ DTL

The RF frequency in both accelerators - the RFQ and the RFQ DTL - is equal to 75 MHz. The accelerator is designed to accelerate the beam of initial normalized rms emittance of 0.1 π·mm·mrad and the emittance growth during acceleration does not exceed two times. To avoid electron load of the cavity (cold emission) the maximum electric field at the electrode surface RFQ is chosen to be limited by the value of 350 kV/cm for RFQ DTL. The accelerator consists of the RFQ section (of the length of about 6 m) and four RFQ DTL sections (of the length of about 4.5 m, Fig. 4). The section number and length are determined by technological reasons.

The RF, water cooling, vacuum systems and the beam diagnostics along the accelerator will be designed and constructed on the basis of the IHEP long experience in the design, construction and exploitation of RFQ structures. All the elements of the linear accelerator can be fabricated in Protvino at the IHEP workshop.

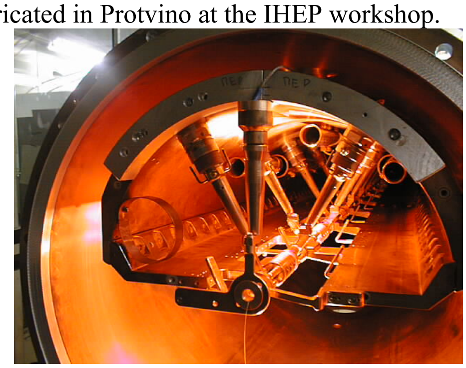

Figure 4: RFQ DTL proton linac in IHEP.

## REFERENCES


[1] NICA Conceptual Design Report, JINR, January 2008. http://www.jinr.ru/

[2] Govorov A.N., Kovalenko A.D., Monchinsky V.A. et al., Linac LU-20 as injector of NUCLOTRON, Proc. of LINAC-96, 394 – 396.

[3] Electron beam ion source pre-injector project (EBIS), Conceptual Design Report, under edition by J. Alessi, BNL-73700-2005-IR.

[4] M.L.Good, Phase-reversal in linear accelerators, Phys. Rev., v.92, N 2, p. 538 (1953), Fainberg I.B., Alternating Phase Focusing, In: Proc. Symp. on High Energy Accelerators and Pion Physics, V. 1. Geneva, CERN, 1956, p. 91-100.

[5] http://www.gsi.de/portrait/Broschueren/Therapie/index_e.html

[6] O.K. Belyaev A.P. Maltsev,, V.B. Stepanov, et. al., RFQ Drift-Tube proton linacs in IHEP, Proceedings of LINAC 2004, Lübeck, Germany

[8] E.D.Donets, in "Physics and Technology of Ion Sources", Ed. by I.G. Brown, Wiley &Sons, NY, 1989, p. 245.

[9] E.D. Donets et al., Electron string source of highly charged ions: Studies and the first test on a synchrotron, in Proc. of EPAC-2002, Paris, June 3-7, 2002 p.1700-1702.

# A SC UPGRADE FOR THE REX-ISOLDE ACCELERATOR AT CERN

M. Pasini*, S. Calatroni, N. Delruelle, M. Lindroos, V. Parma, P. Trilhe,
D. Voulot, F. Wenander, CERN, Geneva, Switzerland
R. M. Jones, Cockcroft Institute, Daresbury, UK and University of Manchester, Manchester, UK.
P. McIntosh STFC/DL/ASTeC, Daresbury, Warrington, Cheshire, UK

[illegible]

The High Intensity and Energy ISOLDE (HIE-ISOLDE) proposal is a major upgrade of the existing ISOLDE and REX-ISOLDE facilities with the objective of increasing the energy and the intensity of the delivered radioactive ion beam. For the energy increase a staged construction of a superconducting linac based on sputtered quarter wave cavities is foreseen downstream of the present normal conducting linac. A funded R&D program has been launched at the end of 2007 in order to prepare a full Technical Design Report covering all the issues of such linac, including cavity prototyping and testing, cryomodule design, beam dynamics and beam diagnostics. We report here on the status and planning of the R&D activities for the SCREX-ISOLDE linac.

## INTRODUCTION

Radioactive ion beam production at the ISOLDE facility at CERN is based on the ISOL (Isotope Separation On-Line) method where a max 2.8 kW proton beam, extracted at 1.4 GeV from the Proton-Syncrotron Booster (PSB), impinges upon a thick, high temperature target. The radioactive nuclei can be produced in two different target stations (GPS and HRS) via spallation, fission or fragmentation reactions. ISOLDE has been continuously developing targets and ion sources for four decades, introducing several new technologies (e.g. the resonance ionization laser ion source) so that there are now available more then 700 radioisotopes from 65 elements. These beams are accelerated to 60kV and steered to different experimental stations. In the present REX-ISOLDE facility [1] the RIBs are accelerated to higher energies with a compact Normal Conducting (NC) linac, making use of a special low energy preparatory scheme where the ion charge state is boosted so that the maximum mass to charge ratio is always $3 < A/q < 4.5$. This scheme consists of a Penning trap (REXTRAP), a charge breeder (REXEBIS) and an achromatic A/q separator of the Nier spectrometer type. The NC accelerator is designed with an accelerating voltage for a corresponding maximum A/q of 4.5 and it delivers a final energy of 3 MeV/u for $A/q < 3.5$ and 2.8 for $A/q < 4.5$. After charge breeding, the first acceleration stage is provided by a 101.28 MHz 4-rod Radio Frequency Quadrupole (RFQ) which takes the beam from an energy of 5 keV/u up to 300 keV/u. The beam is then re-bunched into the first 101.28MHz interdigital drift tube (IH) structure which increases the energy to 1.2 MeV/u. Three split ring cavities are used to give further acceleration to 2.2 MeV/u and finally a 202.56 MHz 9-gap IH cavity is used to boost and to vary the energy between $2.2 < E < 3$ MeV/u. Fig. 1 illustrate the scheme of the present linac.

The HIE-ISOLDE project contains three major parts: higher energies, improvements in beam quality and flexibility, and higher beam intensities. This requires developments in radioisotope selection, improvement in charge breeding and target-ion source development, as well as construction of the new injector for the PSB, LINAC4 [2]. The most significant improvement in the physics program [3] will come from the energy upgrade which aims at reaching a minimum energy of 10 MeV/u.

The present NC machine was developed in order to deliver beams at specific energies whilst taking advantage of the high accelerating gradient that pulsed NC IH structure could achieve. This concept is nevertheless not without some limitations: 1) limited energy variability; 2) operation restricted to pulsed mode; 3) inefficient use of the installed power when running light ions; 4) non variable longitudinal beam parameters, such as energy spread and bunch length.

To overcome the above limitations and to open the possibility of different longitudinal beam parameters, a superconducting linac based on Nb-sputtered SC Quarter Wave Resonators (QWRs) has been proposed [4]. The fact of having 2-gaps cavity independently phased assures both a very high flexibility in term of velocity acceptance and at the same time a small number of cavity types to cover the whole energy range.

## THE SUPERCONDUCTING LINAC

The superconducting linac is designed to deliver an effective accelerating voltage of at least 39.6 MV with an average synchronous phase $\phi_s$ of -20 deg. This is the minimum voltage required in order to achieve a final energy of at least 10 MeV/u with $A/q = 4.5$. Because of the steep variation of the ions velocity, at least two cavity geometries are required in order to have an efficient acceleration throughout the whole energy range. A total number of 32 cavities are needed to provide the full acceleration voltage. The geometries chosen corresponding to [illegible] ($\beta_0 = 6.3\%$) and [illegible] ($\beta_0 = 10.3\%$) "$\beta$" cavities maintain the fundamental beam frequency of 101.28 MHz and their design parameters are given in Table 1. The design accelerating gradient aims at reaching 6 MV/m with a power consumption of 7 W per low $\beta$ cavity and 10 W per high $\beta$ cavity. These values have been already achieved by the two avail-

* matteo.pasini@cern.ch

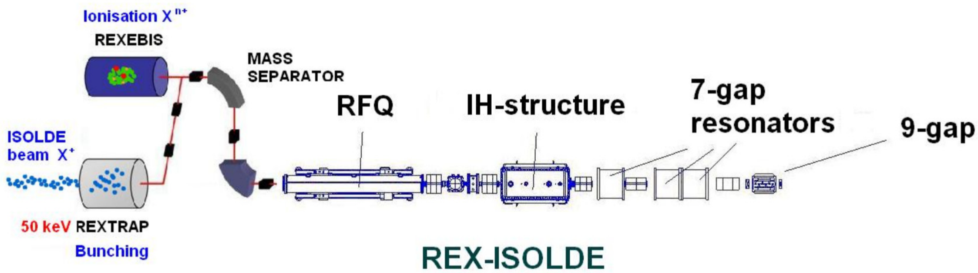


Figure 1: REX-ISOLDE present scheme.

able technologies for the QWRs, namely the □□□□Nb and the □□□□□□□□cavity [5], [6].

Table 1: Cavity Design Parameters

| Cavity | Low $\beta$ | high$\beta$ |
|---|---|---|
| No. of Cells | 2 | 2 |
| f (MHz) | 101.28 | 101.28 |
| $\beta_0$ (%) | 6.3 | 10.3 |
| Design gradient $E_{\text{acc}}$(MV/m) | 6 | 6 |
| Active length (mm) | 195 | 300 |
| Inner conductor diameter (mm) | 50 | 90 |
| Mechanical length (mm) | 215 | 320 |
| Gap length (mm) | 50 | 85 |
| Beam aperture diameter (mm) | 20 | 20 |
| $U/E_{\text{acc}}{}^2$ (mJ/(MV/m)$^2$ | 73 | 207 |
| $E_{\text{pk}}/E_{\text{acc}}$ | 5.4 | 5.6 |
| $H_{\text{pk}}/E_{\text{acc}}$ (Oe/MV/m) | 80 | 100.7 |
| $R_{\text{sh}}/Q$ ($\Omega$) | 564 | 548 |
| $\Gamma = R_{\text{s}} \cdot Q_0$ ($\Omega$) | 23 | 30.6 |
| $Q_0$ for 6MV/m at 7W | $3.2 \cdot 10^8$ | $5 \cdot 10^8$ |
| TTF max | 0.85 | 0.9 |
| No. of cavities | 12 | 20 |

Because each cavity is independently phased, we can apply the maximum voltage available in each cavity so that lighter ion will reach higher final energies. Figure 2 shows a plot of the energies reached by the ions with different A/q. The focussing scheme foresees the employment of SC solenoids, which allows a higher mismatch factor tolerance with respect to standard triplet or doublet focussing scheme [7]. The low $\beta$ cavities have been grouped into two cryomodules of six cavities each, while the high $\beta$ cavities have been grouped in four cryomodules of five cavities each. Beam dynamics studies are ongoing to assess optics parameters and to optimize emittance growth control [8].

## □a□□□□□□□□□□□□□□

The Nb sputtering technology wil be used for the HIE-LINAC cavities. A distinct advantage of the sputtering technology is that, because of the dominant copper base, the cavities can be made with thick walls so to ensure high thermal conductivity and a high mechanical stability. The former guarantees an excellent thermalization of the cavity avoiding hot spots that could break the superconducting state. The latter allows substantial simplification of the tuning system. A prototype cavity is under fabrication and a detailed study for the mechanical assembly and procedures has been performed in order to avoid any copper annealing so to maintain the mechanical rigidity of the copper [9]. The established procedures allows a substantial reduction of the cost of the copper material, and critical e-beam weldings have all been tested. An important part of the cavity manufacturing is the actual sputtering of the Nb layer onto the copper base. The bias technology developed at LNL-INFN will serve as a starting point [10] but a development towards magnetron sputtering is planned. The plan foresees the completion of the copper base manufacturing by the end of October 2008, chemical treatment and Nb deposit by the end of the year. First cold tests are expected beginning 2009.

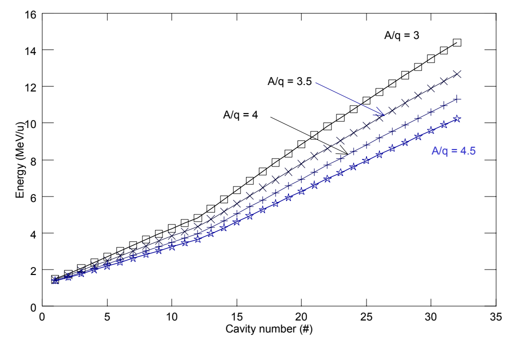


Figure 2: Beam energy as a function of the cavity number. For the $A/q = 3$ the maximum energy achieved is 14.4 MeV/u.

## □□□□□□□□□□□

The choice of having a SC solenoid as focusing element allows to reduce the intermodule distance with respect to a scheme where the focusing elements are made of warm quadrupoles. The advantage is a more compact linac, saving precious space for the experiments and simplify the longitudinal beam dynamics. The result of this scheme sets

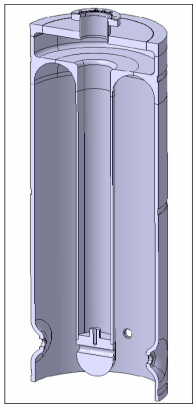

Figure 3: High $\beta$ cavity 3-D section.

several constraints on the cryomodule layout, for which a conceptual design is ongoing. An important design issue of low energy SC ion linacs is whether the beam vacuum is shared with the insulation vacuum or not. This former brings as a consequence a strict control on the fabrication and cleaning procedures, as well as the assembly. The latter brings as a consequence an additional layer of interconnection with an increased engineering complexity. Details about the conceptual design are reported in ref. [11].

### [illegible]

The cryoplant needed to supply liquid helium at 4.5 K will require an additional building - located next to the experimental hall - to house the compressor station and its cold box. We are looking at the possibility of reusing an existing refrigerator which was connected to the ALEPH magnet during the LEP operation from 1989 to 2000. The cold box was capable in 1989 to provide an isothermal refrigeration power of 630W at 4.5K plus an additional shield load of 2700 W between 55K and 75K. Fig. 4 shows a first concept design of the cryoplant. The total heat load of the system required for the complete ISOLDE energy upgrade is very close to the maximum power that the cold box can provide. Nevertheless, we have to evaluate precisely this possibility as it would allow a substantial cost saving with respect to the purchase of a new unit. The transfer line needed to supply the liquid helium is 35 m long and will be equipped with 6 [illegible] modules (one per module) to allow the isolation of each module from the common distribution line without interruption on the remaining modules.

## INSTALLATION PLAN

The first stage of the upgrade plan consists of installing two [illegible] $\beta$ cryomodules downstream the present NC linac so to reach a final energy of a least 5.5 MeV/u. The position of these two cryomodules is set to be also the final one, so that no additional removal will be required for the installation of the complete linac. Accordingly, a modular transfer line will be in place in order to accomodate the beam transport as the linac energy will increase. The position of the experimental facilities like Miniball and the planned recoil spectrometer will also be fixed at the position of the full installation. Assuming the financing is approved by mid of 2009 the first stage of the upgrade is planned to be completed in the fall 2012. The remaining high and low $\beta$ cryomodules will then be installed subsequently with the aim of completing the commissioning of the HIE-LINAC by mid 2013.

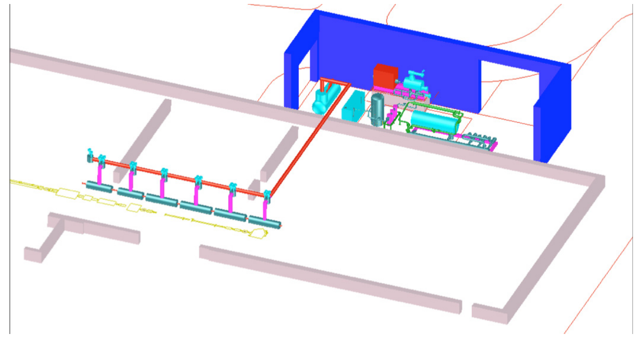

Figure 4: Cryoplant 3-D layout.

## ACKNOWLEDGEMENTS

The cavity design and the reference linac design have taken great contribution from the work performed by Enzo Palmieri and Anna Maria Porcellato of INFN-LNL. Indeed many ideas and a solid starting point have come from them.

## REFERENCES

[1] D. Voulot, et al., Radioactive beams at REX-ISOLDE: Present status ..., Nucl. Instr. and Meth. B (2008), doi:10.1016/j.nimb.2008.05.129

[2] M. Vretenar, et al., Status of the LINAC4 project at CERN, these proc.

[3] K. Riisager, et al., HIE-ISOLDE: the scientific opportunities, CERN-2007-008

[4] http://hie-isolde.web.cern.ch

[5] R. Laxdal, Initial Commissioning Results from the ISAC-II SC Linac, LINAC06, Knoxville, US

[6] A.M. Porcellato, et al., Proceedings SRF workshop 2005, Cornell, US

[7] R. Laxdal, et al., Progress in the Conceptual Design of the ISAC-II Linac at TRIUMF, PAC2001, Chicago, US

[8] M. Pasini, et al., Beam Dynamics Studies for the SCREX-ISOLDE Linac at CERN, these proceedings

[9] M. Pasini, et al., SC Nb Sputtered QWRs for the REX-ISOLDE Accelerator at CERN: Prototype Design and Manufacturing, these proceedings

[10] V. Palmieri, et al., [illegible], ICEC supplement, Vol. 34, p.773

[11] V. Parma, et al., Concept Design Study of the HIE-ISOLDE Cryomodules at CERN, these proceedings

# BEAM DYNAMICS STUDIES FOR THE SCREX-ISOLDE LINAC AT CERN

M. Pasini*, D. Voulot, CERN, Geneva, Switzerland
M. A. Fraser, R. M. Jones, Cockcroft Institute, UK and University of Manchester, Manchester, UK

## Abstract

For the REX-ISOLDE upgrade a superconducting linac based on 101.28 MHz Quarter Wave Resonators (QWRs) is foreseen downstream of the normal conducting (NC) linac. Currently the REX-ISOLDE linac can accelerate ions with a mass to charge ratio in the range of $3 <$ A/q $< 4.5$ up to an energy of 2.8 MeV/u. The upgrade aims to reach a minimum final beam energy of 10 MeV/u for A/q=4.5 in two main stages. The first stage consists of installing two cryomodules loaded with 10 cavities able to reach 5.5 MeV/u at the end of the present linac and the second consists of replacing part of the existing NC linac and adding further cryomodules. We report here on a beam dynamics study of the accelerator for the two installation stages.

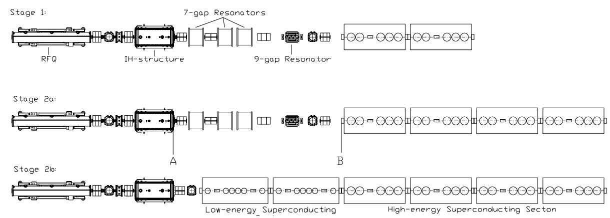


Figure 1: A Schematic of the HIE-ISOLDE linac stages. Stage 1 is shown at the top, while stage 2 can be split into two sub-stages depending on the physics priorities: the low energy cryomodules will allow the delivery of a beam with better emittance; the high energy cryomodule will enable the maximum energy to be reached.

## INTRODUCTION

The REX-ISOLDE linac for the ISOLDE Radioactive Ion Beam facility at CERN [1] consists of a normal conducting linac where the RIB gets accelerated in different stages: a 101.28 MHz 4-rod Radio Frequency Quadrupole (RFQ) takes the beam from 5 to 300 keV/u, a 101.28 MHz interdigital drift tube (IH) structure boosts the beam energy up to 1.2 MeV/u, three 101.28 MHz split ring cavities accelerate to reach 2.2 MeV/u and a final 202.56 MHz IH structure is used to vary the energy between 2.2 and 3 MeV/u. The HIE-ISOLDE project [2] looks at the overall upgrade of the facility, i.e. an increase of the final energy of the radioactive ion beam, an improvement of the beam quality and flexibility and an increase of the beam intensity. The linac upgrade will consist of a superconducting machine [3] providing 39.6 MV of effective accelerating voltage with an average synchronous phase $\phi_s$ of -20 deg. utilising 32 101.28 MHz QWRs split into two families: [illegible] and [illegible] $\beta$ cavities. The first stage of the upgrade plan consists of installing 10 high $\beta$ cavities grouped in two cryomodules downstream of the present NC linac (stage 1). The second stage will be installed in two parts. Firstly, two more high $\beta$ cryomodules will be added (stage 2a) downstream from those in stage 1 and secondly the split ring cavities and the 202.56 MHz IH cavity will be replaced with 12 low $\beta$ cavities grouped in 2 cryomodules (stage 2b). Figure 1 shows a schematic of the different installation stages. The final energy for stage 1 and stage 2 is respectively 5.5 MeV/u and 10 MeV/u for A/q=4.5.

The focusing scheme foresees the employment of 200 mm long SC solenoids, which allow a high mismatch factor tolerance with respect to a standard triplet or doublet focusing scheme [4]. This brings a significant advantage for the tuning and operation of the machine. In fact, RIBs accelerators in general make use of a [illegible] intensity stable beam as a pilot beam with an A/q ratio that is as close as possible to the A/q of the wanted RIB. This is in fact necessary, since the very low RIB's intensity is practically invisible to conventional beam instrumentation. Once the pilot beam is established, a scaling action is performed and a focusing lattice with high mismatch tolerance guarantees better beam transport in the machine after scaling, where possible beam mismatch can occur. In addition, because SC solenoids allow the intermodule distance to be minimized, the longitudinal acceptance of the linac is not reduced and multi-charge state acceleration can be performed [5]. A schematic of the two cryomodules is shown in Figure 2. With this configuration the beam diagnostics instruments are ideally positioned at the beam waist location in the inter-cryomodule region where a pair of steering magnets will also be installed.

## BEAM DYNAMICS SIMULATIONS

For the simulations of the complete HIE-LINAC (stage 2b) a 1 m long matching section with 4 quadrupoles between the first IH-structure and the first cryomodule is taken into account. It is important to keep this section as short as possible in order to minimize the longitudinal beam debunching. The input beam parameters for the simulations are constrained by the IH-cavity output beam and were calculated using TRACE3D [6]. The resonators were set to operate at a synchronous phase of -20 deg., and to increase the longitudinal phase spread capture at injection, the first resonator was phased at -40 deg. The last resonator in the first cryomodule was also re-phased, at -30 deg., in

* matteo.pasini@cern.ch

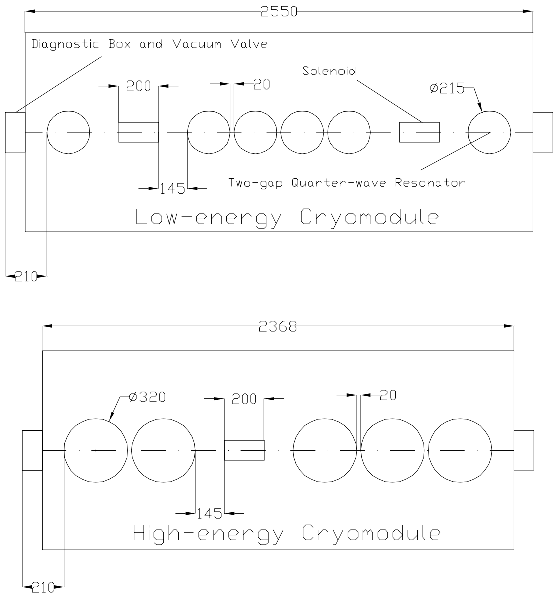


Figure 2: Schematic of the cryomodules design. On the top the low $\beta$ cryomodule and on the bottom the high $\beta$ cryomodule.

order to further decrease the longitudinal phase spread of the beam after the first cryomodule. The simulations were implemented to first-order in `LANA` [7] using a square field distribution for the cavities and solenoids and the results confirmed with `Path Manager` [8], which uses a thin-lens approximation for lattice elements. Two thousand particles were simulated and space-charge forces neglected because of the low beam intensity.

The solenoidal magnetic fields were adjusted to achieve matched beams along the HIE-LINAC. The three solenoids in the second and third cryomodules were used to match the beam across the transition region between the low and high-energy sections. Matched solutions were found for different values of the phase advance per cryomodule $\mu$ in the low-energy section and the resulting transverse emittance growth along the HIE-LINAC investigated. The source of transverse emittance growth comes essentially from the beam phase spread inside the RF gap, as can be seen from the expression for the RF defocusing impulse, $\Delta p$, acting on a single particle, and the growth can be controlled by choosing an appropriate phase advance:

$$\Delta p \propto \frac{\sin(\phi)}{\beta\gamma} r \qquad (1)$$

where $r$ is the particles radial displacement, $\phi$ is its average longitudinal phase and $\beta\gamma$ are the relativistic factors associated with its motion. From (1), a monotonic decrease in transverse emittance growth would be expected as the phase advance increases and the extent of the beam in the transverse plane shrinks, provided the spread in any of the other variables does not dominate. The results of this preliminary survey are shown in Figure 3, which shows a decrease of emittance growth with phase advance per cryomodule above 80 deg, as expected, but anomalous behaviour below 80 deg.

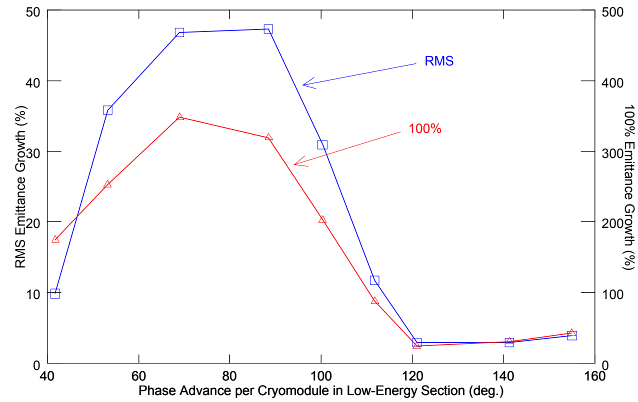


Figure 3: Final emittance growths in the HIE-LINAC with phase advance per cryomodule in the low-energy section.

The variables in Equation 1 are well controlled in the simulations and, in particular, the spread of the longitudinal phase of the beam does not vary enough to account for this anomalous behaviour at low phase advance. This anomalous behaviour was investigated by isolating the low and high-energy sections of the HIE-LINAC and simulating the behaviour of the transverse emittance growth, with phase advance, separately. The input beam parameters for the low-energy section were identical to the previous simulations but the input parameters for the high-energy section were calculated at point B in Figure 1, (i.e. 1664 mm downstream from the 9-gap). The RMS emittance behaves as expected, as shown in Figures 4 and 5, and the transverse emittance growth reduces as the transverse beam size shrinks.

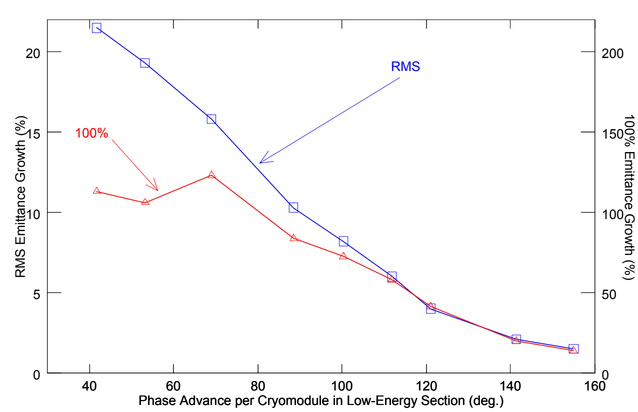


Figure 4: Emittance growth with phase advance in low-energy section.

We conclude that the anomalous behaviour in Figure 3 results from the matching region between the two sections

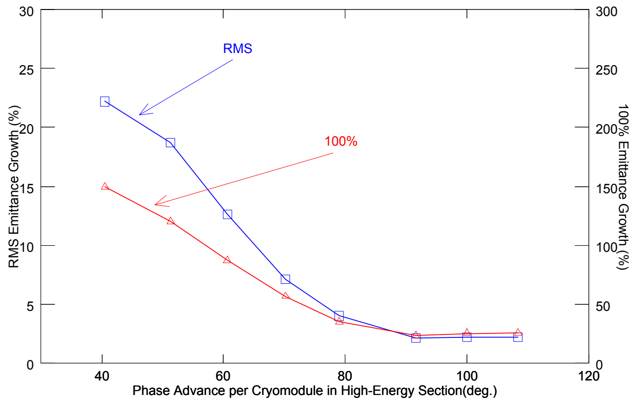


Figure 5: Emittance growth with phase advance in high-energy section.

of the HIE-LINAC. In order to confine the beam at higher phase advance, larger magnetic fields must be used in the focusing elements. We proceed with the beam dynamics study by selecting the matched solution which provides minimal emittance growth without demanding excessively high solenoidal magnetic fields.

## CONCLUSION

Due to the development of the cryomodule design, the inter-cryomodule distance, i.e. the distance from the last cavity in one cryomodule to the first cavity in the following one, was increased to 800 mm; a modification which would have little impact on the findings of our preliminary survey. Both stage 1 and stage 2 scenarios were simulated and the results of the full linac installation are shown in Fig. 6. The chosen matched solution requires 130 deg. phase advance in the first section, and 90 deg. in the second. Both the RMS transverse and longitudinal emittance grow no more than 4% throughout the HIE-LINAC, and, even with the re-phasing of the first and sixth resonators, the target energy of 10 MeV/u is reached, with A/q = 4.5.

The input and output beam parameters are listed in Table 1 for the two installation stages. The average solenoidal magnetic field in the low-energy section is 5.1 T and 7.4 T in the high-energy section.

Future study will aim to better understand the anomalous behaviour observed above. Additional simulations studying the effect of the intrinsic dipole component [9] of the QWRs and higher order effects of the focussing lattice are anticipated. These simulations will focus on field mappings for both the cavity and the solenoids.

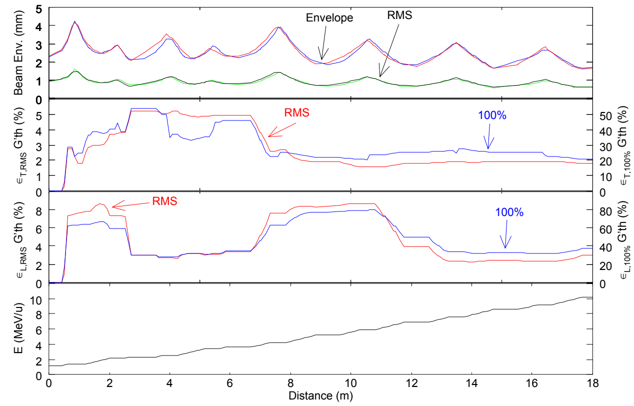


Figure 6: Beam dynamic for a simulation with phase advance of 130 and 90 deg. in the low and high-energy sections, respectively. From top to bottom: max and rms envelope, 100% and rms transverse emittance growth, 100% and rms longitudinal emittance growth, beam energy as a function of the linac length.

Table 1: Beam Parameters

| Parameter | Input | Output |
|---|---|---|
| Stage 1 | | |
| $\alpha_T$ | -0.150 | -0.165 |
| $\beta_T$ (cm/mrad) | 0.100 | 0.132 |
| $\epsilon_{T,100\%,\text{norm}}$ ($\pi$ cm mrad) | 0.030 | 0.037 |
| $\alpha_L$ | 1.425 | -0.355 |
| $\beta_L$ (deg/keV) | 0.027 | 0.038 |
| $\epsilon_{L,100\%,\text{norm}}$ ($\pi$ ns keV/u) | 2.000 | 2.517 |
| Stage 2 | | |
| $\alpha_T$ | -0.200 | -0.209 |
| $\beta_T$ (cm/mrad) | 0.100 | 0.138 |
| $\epsilon_{T,100\%,\text{norm}}$ ($\pi$ cm mrad) | 0.030 | 0.036 |
| $\alpha_L$ | 1.281 | 1.013 |
| $\beta_L$ (deg/keV) | 0.035 | 0.044 |
| $\epsilon_{L,100\%,\text{norm}}$ ($\pi$ ns keV/u) | 2.000 | 2.746 |

## REFERENCES

[1] http://isolde.web.cern.ch/ISOLDE/

[2] M. Lindroos, et al., HIE-ISOLDE : the technical options, CERN-2007-008

[3] M. Pasini, et al., A SC upgrade for the REX-ISOLDE accelerator at CERN, these proc.

[4] R. Laxdal, et al., Progress in the Conceptual Design of the ISAC-II Linac at TRIUMF, PAC2001, Chicago, US

[5] M. Pasini, et al., Beam Dynamics Studies on the ISAC-II Post-Accelerator at TRIUMF, EPAC2002, Paris, France

[6] K.R. Crandall et al., Trace 3-D Documentation, LA-UR-97-886

[7] D. V. Gorelov, P. N. Ostrumov, Application of LANA Code for Design of Ion Linac, Proc. of Linac Conference 1996

[8] A. Perrin and J.F. Amand, Travel v4.06, user manual, CERN (2003).

[9] P. N. Ostroumov and K. W. Shepard, Physical Review STAB, **4**, 110101 (2001)

# MULTIPLE USER BEAM DISTRIBUTION SYSTEM FOR FRIB DRIVER LINAC*

D. Gorelov# , V. Andreev, S. Chouhan, X. Wu, R. C. York,
NSCL/MSU, East Lansing, MI 48824, U.S.A.

## ABSTRACT

The proposed Facility for Radioactive Ion Beams (FRIB) [1] will deliver up to 400 kW of any stable isotope to Rare Isotop Beam (RIB) production target. Operational efficiency could, under certain conditions, be improved by a system that can distribute the beam current, variable in a large dynamic range, to several independent targets simultaneously. A possible FRIB Beam Switchyard (BSY) utilizes an RF kicker with subsequent magnetostatic septum system to split the beam on micro-bunch to micro-bunch basis. The micro-bunches can be differentially loaded at the front-end of the Driver Linac [2]. The detailed analysis of the beam dynamics performance in the proposed BSY system is presented.

## INTRODUCTION

The effective use of the proposed FRIB facility [1] can under certain conditions be benefited by the ability to support simultaneous experiments. The stable isotope beams from the Driver Linac can be used for production of Radioactive Ion Beams (RIBs) using either Isotope Sepatation On Line (ISOL) or In-flight Particle Fragmentation methods to maximize yield of the corresponding species.

The discussed Beam Switchyard (BSY) will allow separation of the continuous stable ion beam from the Driver Linac into two independent channels on a micro-bunch by micro-bunch basis using an RF kicker followed by magnetic septum system.

The performance of this system was explored in details using three-dimensional electromagnetic fields for the RF kicker and a magnetostatic field distribution in septum magnet. As an alternative to the RF kicker, a DC septum magnet consisting of an array of thin wires and two electrodes can be used for lighter ions.

## BEAM SWITCHYARD (BSY) SYSTEM

A proposed FRIB BSY design uses an RF kicker, an alternative DC bending dipole, and a septum magnet along the beam transport channel to either split the incoming stable beam into two beam lines with 50% intensity in each branch or to supply a single target with the full beam intensity (100 %) any of two production targets. The intensity of the two branches can be varied from 0% to 50% total beam intensity independently using the additional system of differential beam loading [2]. Figure 1 shows the layout of the proposed BSY system.

To minimize beam loss, quadrupole magnets in front of the RF kicker are provided to achieve reduced horizontal beam size at the entrance of the septum magnet. Both the RF kicker and the DC dipole have the same design deflection angle of ±1.5 mrad and will be used interchangeably for either splitting the incoming beam into two segments or direct all beam into one of the following beam lines. Given the beam micro-bunch frequency of 80.5 MHz, an RF kicker frequency of 120.75 MHz is appropriate to split the beam into two segments by kicking every other bunch in opposite transverse directions. A 10 m long drift space after the initial splitting point in RF kicker is required to generate enough spatial separation to accommodate a 10 mm thick septum in the septum magnet.

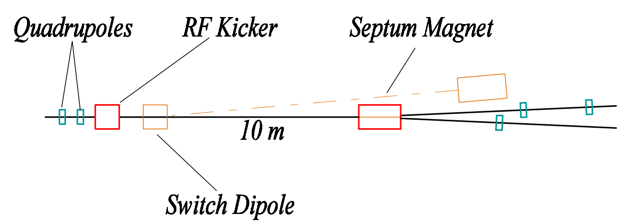


Figure 1: Layout of a proposed FRIB BSY system.

The performance of the proposed BSY system was evaluated by detailed beam dynamics simulations using the realistic three-dimensional (3D) distributions of the electromagnetic RF and magnetostatic fields in the system elements.

## RF KICKER

The electromagnetic (EM) field calculations for the RF kicker were done using the computer code MAFIA. The resonant structure of the RF kicker is shown in Figure 2 and represents a “lumped circuit” consisting of two parallel plates (capacitance) and four stems (inductors).

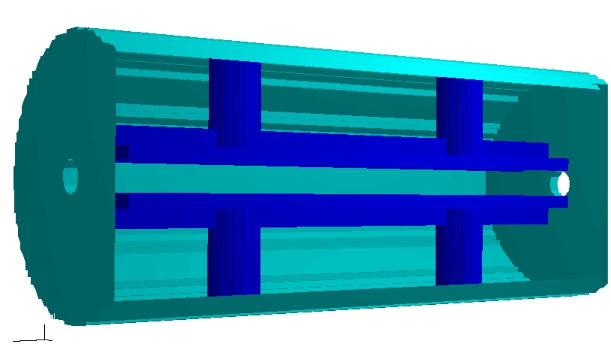

Figure 2: Three-dimensional view of the RF kicker.

The transverse electric field created between the plates deflects the beam in the direction perpendicular to the planes and parallel to the stems. Using two stems improves stiffness of the structure, simplifies cooling, and helps to equalize the longitudinal electric field

*Work was supported by the US DOE grant DE-FG02-04ER41324.
#gorelov@msu.edu

distribution. Selected parameters of the RF kicker are listed in Table 1.

Table 1: RF Kicker Structure Parameters

| | |
|---|---|
| Beam bunch frequency | 80.5 MHz |
| RF kicker harmonic | 3/2 |
| RF kicker frequency | 120.75 MHz |
| Deflection angle | ±1.5 mrad |
| RF power | 28 kW |
| RF voltage | 170 kV |
| Tank diameter | 0.4 m |
| Stem diameter | 0.08 m |
| Plate width | 0.12 m |
| Plate thickness | 0.02 m |
| Plate length | 0.88 m |
| Gap | 0.05 m |

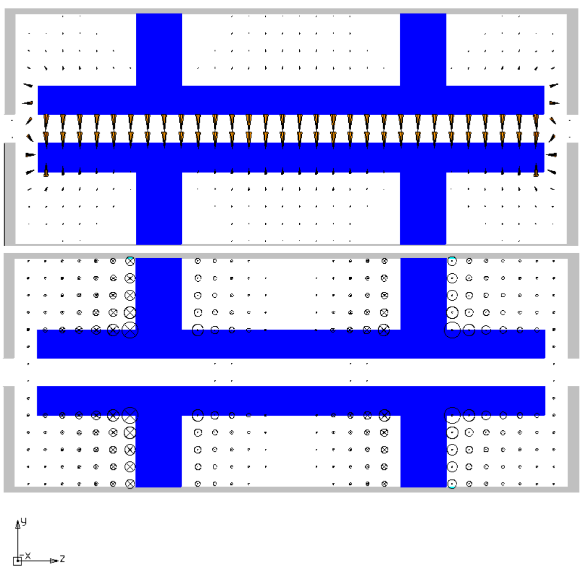

Figure 3: Electric (top) and magnetic (bottom) field distribution in a central vertical cross-section along the beam axis of the RF kicker structure.

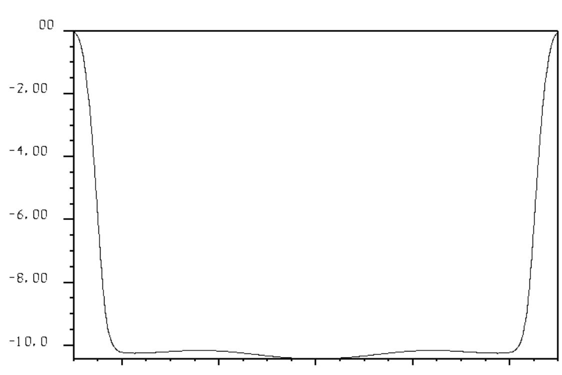


Figure 4: Transverse electric field profile in the RF kicker along the beam axis.

Electric and magnetic field distributions of the resonant structure are shown in Figure 3. Transverse electric field has variance of less then 5 % on the 80 cm of total effective length of the RF kicker deflecting plates as shown in Figure 4. Transverse electric field in the Extent of the direction orthogonal to the beam direction and plane of deflection has a variance of less then 1 % over a width of ± 4 cm Power dissipation inside the resonant structure versus inter-plate voltage is shown in Figure 5.

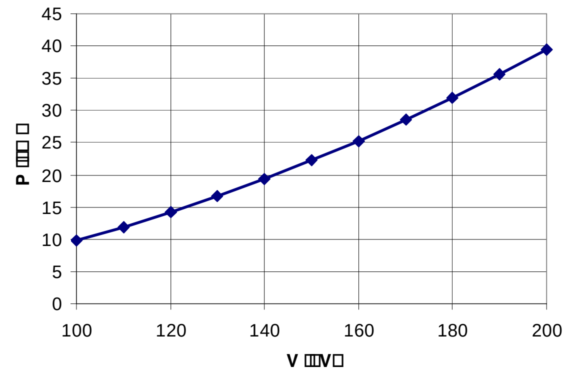


Figure 5: RF power losses in the structure vs. inter-plate voltage.

## [illegible]

The magnetic field of the septum magnet was modeled using the OPERA computer code. Table 2 lists the main parameters of the septum magnet. Figure 6 shows the 3D view of septum magnet.

Table 2: Septum Magnet Main Parameters

| | |
|---|---|
| Septum thickness | 0.16 m |
| Bending angle | ±2.5 ° |
| Full gap | 0.062 m |
| Peak field | 0.22 T |
| Excitation current | 5500 A |
| Current density | 3000 A/cm$^2$ |
| Effective length | 1.814 m |
| Coils cross-section | 30 mm x 6 mm |

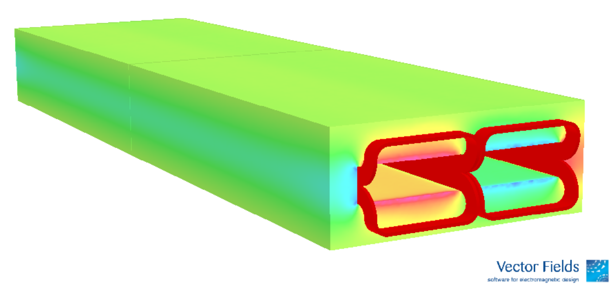


Figure 6: Three-dimensional view of the septum magnet.

## BEAM DYNAMICS SIMULATION RESULTS

Beam dynamics analysis of the proposed BSY was done using the LANA code [3]. The detailed analysis of the beam dynamics in the septum magnet was also done in parallel using the KOBRA code. The results from KOBRA and LANA were found to be in agreement within model accuracy. In all simulations, the three-dimensional electromagnetic field of the RF kicker and the magnetostatic field of septum magnet were used with the field distributions obtained from the MAFIA and OPERA computer codes respectively.

The initial beam parameters obtained from end-to-end beam simulations for the driver linac used in the BSY simulation are given in Table 3. Four quadrupole magnets before the RF kicker were used to obtain the required beam phase space at the RF kicker entrance.

Table 3: BSY Input Beam Parameters

| | | | |
|---|---|---|---|
| Energy | 400 MeV/u | $\varepsilon_Z$ | 27.6 $\pi$ ns keV/u |
| Q | 89+ | $\alpha_Z$ | 0 |
| A | 238 | $\beta_Z$ | 20.0 degree/% |
| $\varepsilon_X$ | 1.6 $\pi$ mm mrad | $\varepsilon_Y$ | 1.6 $\pi$ mm mrad |
| $\alpha_X$ | 0 | $\alpha_Y$ | 0 |
| $\beta_X$ | 1.0 | $\beta_Y$ | 1.0 |

The RF kicker is used to create an initial spatial separation between sequential (every other) bunches. To deflect every other bunch into two different trajectories, the operating frequency of the rf kicker can be any odd half-integer of the bunch frequency. The 3/2 harmonic, which corresponds to a frequency of 120.75 MHz, was chosen (see Table 1).

The septum magnet is used to further separate two beams in space. The septum magnet is placed 10 meters downstream the RF kicker where the two beams are sufficiently separated. The main beam dynamics parameters of the septum magnet are given in Table 2.

The resulting separation of the beam bunches in the bending plane for the design settings of the system parameters are summarized in the Table 4.

Table 4: Bunch Separation in the Bending Plane

| Separation | After RF kicker | Before septum | After septum |
|---|---|---|---|
| x (±) [mm] | 0.8 | 15.7 | 73.1 |
| x` (±) [mrad] | 1.53 | 1.53 | 48.5 |

Table 5: Estimation of the Total Emittance Growth in the BSY

| Relative emittance growth [%] | After RF kicker | At the end of BSY |
|---|---|---|
| $\delta\varepsilon_X/\varepsilon_X$ | <0.1 | ~2.0 |
| $\delta\varepsilon_Y/\varepsilon_Y$ | 0 | <0.5 |
| $\delta\varepsilon_Z/\varepsilon_Z$ | 0 | 0 |

From simulation, the effective emittance growth in the proposed BSY was negligible except in the bending plane. The variation of the emittance in the other planes was comparable to the simulation model accuracy. The summary of the emittance growth is given in the Table 5. The beam path inside the septum magnet is shown in Figure 7.

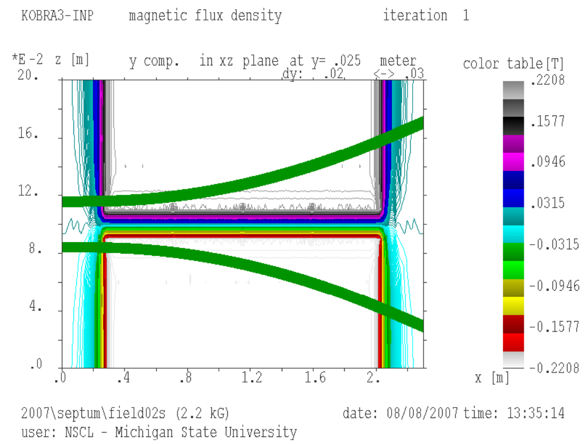


Figure 7: The path of the two separated bunches and the magnetic field distribution in the septum magnet.

The smearing of the beam due to fast amplitude variation of the RF field in the kicker (jitter) will lead to an additional emittance growth. This additional growth, however, is several times smaller than the static growth. The effect of the corresponding RF phase jitter on the final beam emittance for all three phase space projections was found to be negligible in all simulations.

## CONCLUSION

A proposed FRIB beam switchyard using an RF kicker and magnetic septum system to split the beam into two downstream beam lines on a micro-bunch by micro-bunch basis provides high quality beam on targets. It is possible to enhance the efficacy of this system by differentially loading the micro-bunches by employing a system in the Medium Energy Beam Transport system.

A dc septum system consisting of an array of thin wires and two cathodes could be used to split the beam but only for oxygen ions or lighter.

## REFERENCES

[1] D. Gorelov, T. Grimm, W. Hartung, F. Marti, H. Podlech, X. Wu and R.C. York, “Beam Dynamics Studies at NSCL of the RIA Superconducting Driver Linac”, proc. of EPAC 2002, Paris, France, 2002.

[2] M. Doleans, V. Andreev, X. Wu R. C. York, “Beam Distribution System for the MSU-RIA Driver Linac”, proc. of LINAC 2006, Knoxville, TN, USA, 2006.

[3] D.V.Gorelov and P.N.Ostroumov, “Applications of the LANA Code for Design of Ion Linacs”, Proc. of the EPAC’96 Conf., Sitges, Spain, (1996) p.1271.

# ESTIMATES OF ENERGY FLUENCE AT THE FOCAL PLANE IN BEAMS UNDERGOING NEUTRALIZED DRIFT COMPRESSION*

J. J. Barnard, LLNL, Livermore, CA 94550, USA, P. A. Seidl, J. E. Coleman, D. Ogata, LBNL, Berkeley, CA 94720, USA, D. R. Welch, Voss Scientific Corp., Albuquerque, NM, 87108, USA

*Abstract*

We estimate the energy fluence (energy per unit area) at the focal plane of a beam undergoing neutralized drift compression and neutralized solenoidal final focus, as is being carried out in the Neutralized Drift Compression Experiment (NDCX) at LBNL. In these experiments, in order to reach high beam intensity, the beam is compressed longitudinally by ramping the beam velocity (i.e. introducing a velocity tilt) over the course of the pulse, and the beam is transversely focused in a high field solenoid just before the target. To remove the effects of space charge, the beam drifts in a plasma. The tilt introduces chromatic aberrations, with different slices of the original beam having different radii at the focal plane. The fluence can be calculated by summing the contribution from the various slices. We develop analytic formulae for the energy fluence for beams that have current profiles that are initially constant in time. We compare with envelope and particle-in-cell calculations. The expressions derived are useful for predicting how the fluence scales with accelerator and beam parameters..

## INTRODUCTION

Recently, experiments have been carried out on the Neutralized Drift Compression Experiment (NDCX) at Lawrence Berkeley National Laboratory to investigate the use of injected plasma into a final drift compression line, final focus magnet, and target chamber to eliminate the effects of space charge [1], which, in turn, allows for maximum longitudinal compression and transverse final focusing. These beams have short final pulse duration $\Delta t_f$ and small focal spot radius $r_{spot}$ (defined at $2^{1/2}$ times the rms radius, when averaged over all beam particles). Because of the possibility of creating high beam intensities in a short pulse, the beams are being used to generate so called warm dense matter (WDM) conditions [2,3]. The main figures of merit for experiments are the beam fluence (beam energy per unit area integrated over the pulse) $E$ and $\Delta t_f$, since the attainable temperature is determined by $E$ as long as $\Delta t_f$ is much shorter than the hydrodynamic timescale for expansion. In this paper, we provide an analytic estimation of $E$ which can be useful for designing experiments that maximize $E$.

In the following sections, we first describe a simplified model for a final drift and focus section. We then outline the derivation of the estimate and.compare with more detailed numerical calculations (envelope and particle in cell), and finally we describe how we have used these three approaches to help design experiments for NDCX at LBNL.

## MODEL FOR ANALYTIC ESTIMATE

We assume that after the beam is accelerated to final velocity $v_0$, and energy $qV_0$ with charge state $q$, the beam exits the accelerator with 4 rms unnormalized transverse emittance $\varepsilon$. The beam passes through an induction bunching module gap that increases the velocity of the tail to $v_t$ and decreases the velocity of the head to $v_h$. The "tilt" is defined as $\Delta \equiv (v_t-v_h)/v_0$. The beam drifts a distance $L$ to the target, longitudinally compressing as it propagates, due to the tilt. A distance $f$ from the target, when the beam has radius $r_0$ the beam enters a solenoid of strength $B_{sol}$ and length $l_{mag}$, and exits the solenoid with the envelope converging angle $r_1'$ and radius $r_1$, setting the beam onto a final trajectory that focuses onto the target with radius $r_{spot}$. (Throughout this paper, envelope radii $r$, with or without subscripts, are defined as $2^{1/2}$ times the rms radius). A plasma is assumed to fill the drift section, the final solenoid and the target chamber (that includes the distance between the target and the solenoid). We further assume that the plasma density sufficiently exceeds the beam density so that the space charge forces within the beam are negligible. This implies that each slice of the beam retains the velocity $v \equiv v_0(1+\delta)$ it obtained in the bunching gap, and so each slice will have a slightly different focal length, and hence slightly larger focal spot at the target than the focal spot of the longitudinal center of the beam ($\delta$=0). Although formal analytic solutions to the kinetic equations describing drift compression have been obtained [4], exact closed form-scaling relations for the fluence have not, as of yet, been derived.

## ANALYTIC ESTIMATE OF FLUENCE $E$

The envelope equation for the beam radius $r$ for a beam without space charge may be written: $r'' = -\frac{k_c^2}{4}r + \frac{\varepsilon^2}{r^3}$. Here $k_c = qB_{sol}/(mv)$, and prime is derivative with respect to longitudinal position $z$. Within the solenoid, the emitttance term is small relarive to the focusing term, so we may solve the envelope equation: $r_1 = r_0 \cos\frac{k_c z}{2} + \frac{2r_0'}{k_c}\sin\frac{k_c z}{2}$ . We assume that $r_0'=0$, as the change in $r'$ going through the solenoid is expected to be large. The condition that the beam comes to a focus at a distance after the magnet $f-l_{mag}$ is: $r_1' = \left(r_0/\left(f-l_{mag}\right)\right)\cos k_c l_{mag}/2 = (k_c r_0/2)\sin k_c l_{mag}/2$ . This may be expressed as: $\eta_{mag} = \theta\tan\theta/\left(1+\theta\tan\theta\right)$. Here $\eta_{mag} = l_{mag}/f$, and $\theta = k_c l_{mag}/2$. The contribution to the spot size from the emittance is thus: $r_{spot}^2\big|_{\text{emittance}} = \frac{\varepsilon^2}{r_1'^2} = \frac{\varepsilon^2 f^2}{r_0^2}F_1(\theta)$.

Here $F_1(\theta) = 1/(\cos\theta+\theta\sin\theta)^2$. For "off-momentum" slices the beam spot will be larger by the amount $dr_{spot} = r_1' df$ where the focal length is given by: $f = r_1/r_1'$ so the change in focal length for off-momentum particles is: $df = dr_1/r_1' - r_1 dr_1'/r_1'^2$. The contribution to the spot size from chromatic aberrations is thus $dr_{spot}\big|_{\text{chromatic}} = (\theta/\sin\theta) r_0\delta$. So the spot radius from both emittance and chromatic aberrations can be written:

$$r_{spot}^2(\delta) = r_{spot}^2\big|_{\text{emittance}} + dr_{spot}^2\big|_{\text{chromatic}} = \varepsilon^2 f^2 F_1(\theta)/r_0^2 + r_0^2\delta^2 F_2(\theta)$$

Here $F_2(\theta) = (\theta/\sin\theta)^2$. For the "thin lens" approximation $\theta \ll 1$, $F_1(\theta) \approx 1$ and $F_2(\theta) \approx 1$, and the "thick lens" approximation $\theta = \pi/2$, $F_1(\theta) = 4/\pi^2$ and $F_2(\theta) = \pi^2/4$. A more direct derivation of $r_{\text{spot}}(\delta)$ may be obtained by expanding the envelope equation in $\delta$ and integrating.

To calculate the central fluence $E(r=0)$, we must integrate the intensity from each slice. Since the phase space at the focus is rotated by $\sim\pi/2$ relative to the beginning of the soleonid, we expect (and assume) the spatial distribution for each slice to be close to a gaussian distribution in radius with an rms radius equal to $r_{\text{spot}}/2^{1/2}$ (for each $\delta$). This amounts to adding many different gaussians with different widths, yielding a non-gaussian distribution. The number of particles per unit area $n(r)$ at radius $r$ at the focus integrated over the pulse is thus:

$$n(r) = \int_{-l_b/2}^{l_b/2} \frac{dn(r)}{ds} ds = \int_{-\Delta/2}^{\Delta/2} \frac{dn(r)}{ds}\frac{ds}{d\delta} d\delta = \frac{l_b}{\Delta}\int_{-\Delta/2}^{\Delta/2} \frac{dn(r)}{ds} d\delta$$

Here $l_b$ is the length of the bunch before compression, and $ds$ is an element of beam along the beam length corresponding to an element of velocity tilt $d\delta$. Note that we are assuming that the velocity tilt imposed on the beam in the induction gap is linear, so that $\delta/\Delta = s/l_b$. By assumption:

$$\frac{dn(r)}{ds} = \frac{N_0/l_b}{\pi\sigma^2}\exp[-r^2/\sigma^2]$$

Here $\sigma = r_{\text{spot}}/2^{1/2}$, and $N_0$ is the total number of particles in the bunch, so that $N_0 = 2\pi\int_0^\infty dr\, r\, dn(r)/ds$. The bunch here is assumed to be constant current before bunch compression. The integral for $n(r)$ may be expressed:

$$n(r) = \frac{4N_0}{\pi f\varepsilon\Delta\sqrt{F_1(\theta)F_2(\theta)}}\int_1^{\sigma_{\max}/\sigma_{\min}} \frac{\exp[-r^2/(u^2\sigma_{\min}^2)]}{u\sqrt{u^2-1}} du$$ where

$$\sigma_{\min} = \frac{1}{\sqrt{2}}\frac{\varepsilon f\sqrt{F_1(\theta)}}{r_0} \text{ and } \sigma_{\max} = \frac{1}{\sqrt{2}}\sqrt{\frac{\varepsilon^2 f^2 F_1(\theta)}{r_0^2} + \frac{r_0^2\Delta^2 F_2(\theta)}{4}}.$$

For $r=0$, the integral may be carried out:

$$n(r=0) = \frac{4N_0}{\pi f\varepsilon\Delta\sqrt{F_1(\theta)F_2(\theta)}}\tan^{-1}\left(\frac{r_0^2\Delta\sqrt{F_2(\theta)}}{2f\varepsilon\sqrt{F_1(\theta)}}\right). \quad (1)$$

In the limit, that $\Delta$ approaches zero, the central integrated density is just that of an uncompressed emittance limited beam $n(r=0,\Delta=0) = 2N_0 r_0^2/[\pi f^2\varepsilon^2 F_1(\theta)]$. The fluence $E$ is given by $E \approx qV_0\, n(r=0)$. In figure 1, we have plotted the fluence normalized to the fluence at $\Delta=0$, as a function of the argument of the inverse tangent to show potential gains if the chromatic aberrations were corrected (as in a time dependent correction concept now under study for NDCX). For the NDCX experiments listed in Table 1 (cases b and c), the argument has a range of 4 to 16, with corresponding values of $n(r=0)/n(r=0,\Delta=0)$ ranging 0.31 to 0.092, respectively, indicating potential fluence increases of 3 to 11, respectively if chromatic aberrations are corrected.

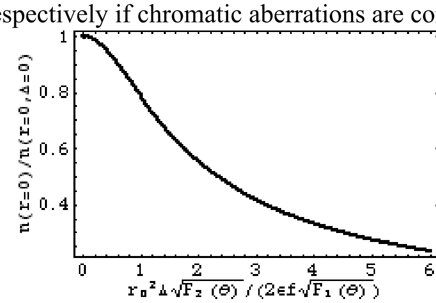


Figure 1. Fluence normalized to $\Delta=0$ fluence as function of quantity $r_0^2\Delta\, F_2(\theta)^{1/2}/[2\varepsilon f F_1(\theta)^{1/2}]$.

We may also estimate the spot radius of the integrated pulse. Integrating over all slices, the radius of the integrated pulse is given by:

$$r_{spot}^2 = \frac{\varepsilon^2 f^2}{r_0^2}F_1(\theta) + r_0^2\eta^2\Delta^2 F_2(\theta) \quad (2)$$

Here $\eta \equiv \left(\int_{-l_b/2}^{l_b/2} I(s)(\delta(s)/\Delta)^2 ds\right)^{1/2} / \left(\int_{-l_b/2}^{l_b/2} I(s) ds\right)^{1/2}$, where $I(s)$ is the current as a function of longitudinal position $s$ along the beam before drift compression, with $s=0$ corresponding to the center of the beam. For $I(s)$=constant, then $\eta = 1/12^{1/2} \approx 0.29$. (For a parabolic pulse $\eta = 1/20^{1/2} \approx 0.22$). The quantity $r_{\text{spot}}$ is minimized when $r_0$ is such that the two terms in the equation for $r_{\text{spot}}^2$ are equal, namely: $r_{0\_\text{opt}}^2 = \varepsilon f[F_1(\theta)F_2(\theta)]^{1/2}/(\eta\Delta)$ for which $r_{\text{spot\_opt}}^2 = 2\varepsilon f\eta\Delta[F_1(\theta)F_2(\theta)]^{1/2}$. Note that, although there is an optimum $r_{0\_\text{opt}}$ that minimizes the rms radius of the integrated spot $r_{\text{spot\_opt}}$[5], increasing $r_0$ increases $E$ monotonically, only saturating as the inverse tangent in eq. 2 approaches $\pi/2$. However, the area over which $E$ is large decreases as $r_0$ increases beyond $r_{0\_\text{opt}}$.

There are a number of assumptions that are built into equation (1). One assumption is that $r_0$ is constant for all $\delta$. When we rederive equation 1 replacing $r_0$ with $r_0 + \alpha L\delta$, where $\alpha$ is a constant (as can be expected from aberations from the induction bunching module), we find that the integral for $n(r=0)$ is unchanged, to lowest order in the parameter $\alpha L\delta/r_0$ as long as $\alpha L\delta/r_0 \ll 1$, with finite correction only in second order. Another assumption in the model, is that $r_0'$ is small, which usually is true relative to $r_1'$, but its impact on $r_{\text{spot}}$ has not yet been quantified analytically.

## COMPARISONS WITH NUMERICAL RESULTS

We have compared our analytic model with predictions of an envelope model and a particle in cell code LSP. The envelope model makes the same assumption as the

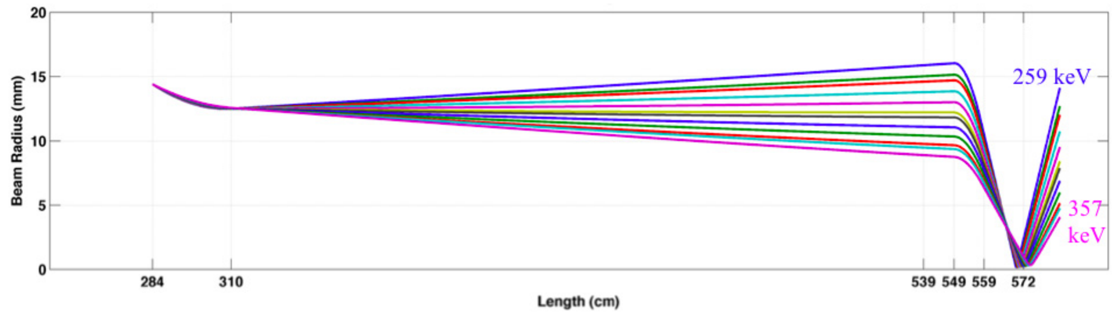


Figure 2. Calcuation of E using an envelope/slice model. Each color represents the trajectory of a different slice with different d. See text for further details.

Table 1. Comparison of *E* calculated using envelope model, LSP, and Eq. (1)

| | $B_{sol}$ (T) | Initial pulse t(ns) | $qV_0$ (keV) | $r$ $z$=284 (mm) | $r'$ z=284 (mm) | $I$ at focus (A) | Δt_f (ns) | L (cm) | Δ | $f$ (cm) | r_0 (mm) | $E$ en-velope (J/cm$^2$) | $E$ LSP (J/cm$^2$) | $E$ Eq. (1) (J/cm$^2$) |
|---|---|---|---|---|---|---|---|---|---|---|---|---|---|---|
| a | 0 | 200 | 300 | 21.5 | -23.80 | 3.08 | 1.69 | 144 | 0.17 | | | 0.06 | | |
| b | 8 | 282 | 300 | 9.55 | -9.82 | 4.01 | 1.83 | 144 | 0.24 | 23 | 19.2 | 0.39 | 0.30 | 0.59 |
| c | 8 | 400 | 300 | 14.40 | -13.70 | 3.23 | 3.22 | 288 | 0.17 | 23 | 11.8 | 0.82 | 0.69 | 0.94 |

analytic model at the focal spot. Namely, take the spot radius for each slice as calculated by a numerical integration of the envelope equations, and assume a gaussian intensity profile for the slice at the target plane, summing the intensities over slices numerically. The advantage of the envelope model is that the finite $r'$ induced by the induction bunching module can be used as an initial condition at the beginning of the drift; the finite region where the beam is non-neutral can be accounted for; and so there are no assumptions about $r_0$ and $r_0'$.

The most detailed and accurate description of the drift compression and final focus is obtained using the LSP code [6,7]. LSP is a particle in cell code that includes fringe fields of the magnets and bunching module and models for calculating the plasma density and flow. The calculation includes first principle simulations of the beam through accelerator, drift, final focus, and chamber.

In figure 2, we plot an example of an envelope calculation using parameters from the NDCX experiment. The beam is 300 kV, 27 mA, singly charged potassium. The envelope calculation is initialized at $z$ = 284 cm, at the exit of the induction bunching module gap. The envelope slices are calculated assuming full space charge contribution, until the entrance to the neutralized section at $z$=310 cm. The beam propagates assuming full neutralization through the final focusing solenoid (549 < $z$ < 559 cm) to the focal plane ($z$= 572 cm).

Table 1 compares the final fluence $E$ for the numerical calculation of the envelope; LSP; and analytic model (eq. 1). The first row (a) corresponds to experiments without a final focusing solenoid. The second and third rows correspond to beamlines using a new NDCX induction bunching module, the final focusing solenoid (Bsol = 8 Tesla) and two beamline configurations: (b) with the present drift compression length ($L$=144 cm), and (c) with twice the drift compression length ($L$=288 cm) as the present setup. The two cases (b) and (c) show the effect of using a bunching module with a shorter bunch length (and relatively large tilt) with short drift length (since $L \approx l_b/\Delta$) versus using a larger bunch length and smaller tilt (and large drift length). This approximately keeps the "Volt-seconds" (roughly proportional to $\Delta\, l_b$) of the bunching module constant, which is constrained by the finite size of the induction core. As can be seen from the table the simulation yields somewhat smaller values of $E$, than the envelope results or analytic results, possibly due to imperfect neutralization, or effects of fringe fields, but the analytic calculation demonstrates the trends and scalings that can be useful for quick design estimates.

## CONCLUSION

We have estimated the energy fluence in a beam undergoing neutralized drift compression and neutralized solenoidal final focus, (eq. 1) and have compared it to envelope and particle in cell simulations. We find that the estimate is useful for understanding the general scaling of fluence on beam and accelerator parameters and for estimating system performance when alternative experiments are being considered.

## ACKNOWLEDGMENTS

This work was performed under the auspices of the U.S. DOE by LLNL under contract DE-AC52-07NA27344, and the Univ. of California, LBNL under Contract Number DE-AC02-05CH11231.

## REFERENCES

[1] P.A. Seidl et al, Proceedings of LINAC08 (these proceedings).
[2] F.M. Bieniosek et al, Nucl. Inst. Methods in Phys. Res. A, (submitted) 2008.
[3] J.J. Barnard et al, Nucl. Inst. Methods in Phys. Res. A.**577**, 275-283, (2007)
[4] R. C. Davidson and H.Qin, PRSTAB **8**, 064201 (2005).
[5] J.J. Barnard et al, Proceedings of the 2005 Part. Accel. Conf, 2568 - 2570 (2005).
[6] D.R. Welch et al, PRSTAB, **11**, 064701 (2008).
[7] A.B. Sefkow, et al, Nucl. Inst. Meth. in Phys. Res. A, 577, 289-297 (2007)

# UPGRADE OF THE UNILAC HIGH CURRENT INJECTOR RFQ

A. Kolomiets, S. Minaev, ITEP, Moscow, Russia
W. Barth #, L. Dahl, H. Vormann, S. Yaramyshev, GSI, Darmstadt, Germany

*Abstract*

For the operation of the GSI-accelerator chain as an injector for the future FAIR facility a considerable increase of the heavy ion beam intensity of up to a factor of 5 at the end of the UNILAC is required. The bottleneck of the whole UNILAC is the front-end system of the High Current Injector. It is shown that the transverse RFQ-acceptance can be significantly increased while the emittance growth can be reduced. Both goals are achieved with only a moderate change of the RFQ electrode geometry; the intervane voltage raised from 125 kV to 155 kV, but keeping the design limit of the maximum field at the electrode surface. The changed resonant frequency can be compensated with a relatively small correction of the carrying rings. The beam parameters in the final focusing elements of the LEBT were optimized together with the improved design of the input radial matcher; the length of the gentle buncher section was considerably increased to provide slow and smooth bunching resulting in a reduced influence of space charge forces. DYNAMION simulation with the modified electrode design resulted in an increase of the $U^{4+}$-beam current of up to 20 emA. It is planned to start the upgrade measure in spring 2009.

## INTRODUCTION

In 1999 UNILAC passed a substantial upgrade - the Wideroe structure was replaced by the High Current Injector (HSI) [1]. The HSI consists of IH-type RFQ and two IH-DTL structures. The main goal of the upgrade project was to increase the $U^{4+}$ beam current up to 15 emA. However the measured $U^{4+}$ beam current behind the HSI never exceeded 6.5 mA. Detailed computer simulations using the DYNAMION code were performed to determine the source of beam intensity limitations [2]. The simulations were verified by beam parameters, measured during the whole period of HSI operation. The most important limitations were the following:

– lower brilliance of the injected beam in comparison with the design value;
– considerably mismatched beam at the RFQ-entrance due to the too high beam convergence required by original design;
– fast beam bunching in the RFQ gentle buncher section, leading to transverse emittance growth;
– strongly limited rf-voltage during the $U^{4+}$ operation.

As a result, a partial RFQ upgrade program took place in 2004. It was mainly directed to the improvement of the rf-performance, but also included the new design of the input radial matcher (IRM), dedicated to optimize the beam dynamics in the focusing elements in front of the RFQ and to improve the matching itself [3].

The rf-performance of the HSI-RFQ was significantly improved after replacement of the electrodes. Minor changes in the IRM lead to 15% increase of the maximum beam intensity at the RFQ output (with the same beam, coming from the ion source). More than this, the results of the numerically calculated optimization of the RFQ electrode profile was confirmed and the beam dynamics codes were approved.

The FAIR program [4] requires increased beam intensities for the UNILAC as an injector. The HSI $U^{4+}$ beam current has to be increased up to 18 mA. All previously obtained beam dynamics results confirmed that an essential RFQ electrode profile upgrade could provide for such requirements.

## DESIGN OF THE HSI RFQ PROFILE

The main conditions for the new design are:

– maximum field at electrode surface should not exceed 320 kV/cm (existing design, $U^{4+}$ -operation);
– total length of the electrodes must be exactly the same as in the existing design;
– operation frequency and other essential rf-parameters of the cavity must be kept, only minor adjustments of the resonant structure are acceptable.

It is clear, that an increase of the RFQ output beam current, keeping parameters of an injected beam, can be provided only by a corresponding increase of its transverse acceptance. The normalized transverse acceptance of the RFQ $\boldsymbol{V_k}$ can be expressed as:

$$V_k = \frac{1}{\lambda}\left(\frac{2}{m+1}\ \frac{R_0}{\rho_{\max}}\right)^2 \tag{1}$$

with $\boldsymbol{\lambda}$ - wave length, $\boldsymbol{m}$ - modulation, $\boldsymbol{R_0}$ - average distance from axis to electrode, $\boldsymbol{\rho_{max}}$ - maximum value of the normalized matched envelope. The value of $\boldsymbol{\rho_{max}}$ is defined mainly by the focusing parameter $\boldsymbol{B}$, expressed through the maximum field at the electrode surface $\boldsymbol{E_{\max}}$ :

$$B = \frac{Ze}{A}\frac{1}{E_0}\frac{E_{\max}}{\chi R_0}\lambda^2 \tag{2}$$

with $\boldsymbol{\chi}$ - field enhancement factor, $\boldsymbol{A,Z}$ - mass and charge numbers, $\boldsymbol{E_0}$ - rest energy. For flat electrodes with semicircular tips $\boldsymbol{R_e}$ it can be calculated by the formula

$$\chi = \sqrt{\frac{1}{2}\left(1+\frac{R_e}{R_0}\right)^2 + \frac{2T}{\pi}k\,R_0\,I_0\left(k\frac{R_0+R_e}{\sqrt{2}}\right)^2} \tag{3}$$

with $\boldsymbol{T}$ - transit-time factor, $\boldsymbol{k = 2\pi/\beta\lambda}$ - wave number, $\boldsymbol{\beta}$ - relative velocity of the particle, $\boldsymbol{I_0}$ - modified Bessel function [5]. It follows from the expressions above, that the only way to keep the focusing parameter $\boldsymbol{B}$ constant,

# Presenting author
W.Barth@gsi.de

while $\boldsymbol{R_0}$ increases, is to keep the $\boldsymbol{\chi R_0}$ value. The last condition can be satisfied by decreasing the $R_e/R_0$ ratio.

The electrode geometry for the existing RFQ design (dotted lines) and the new one (dashed lines) is shown in Fig.1. The bottom lines represent the electrode curvature radius $R_e$, the middle lines the average radius $R_0$ and the upper ones the $R_e/R_0$ ratio.

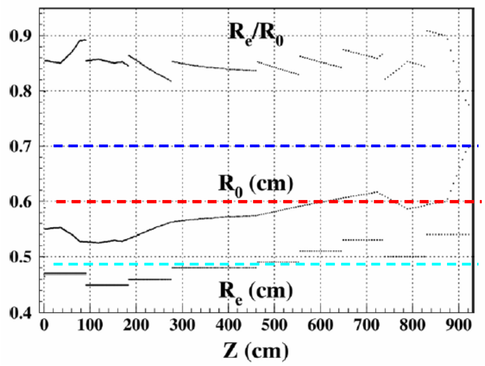


Figure 1: Electrode parameters of existing (dotted) and new (dashed) designs; the blue line represents the $\boldsymbol{R_e/R_0}$ ratio, the red line - $\boldsymbol{R_0}$ and the magenta line - $\boldsymbol{R_e}$.

The HSI-RFQ was designed with a variable $\boldsymbol{R_0}$ and $\boldsymbol{R_e}$ and with a constant voltage $\boldsymbol{U}$ along the structure. The design voltage of the existing RFQ ($\boldsymbol{U}$=125 kV) is limited by $\boldsymbol{R_0}$ near cell #100 (Fig. 1). According (2), it determines in total the relatively low acceleration rate and low focusing parameter $\boldsymbol{B}$ in the main part of the RFQ. The new electrode geometry is designed with constant $\boldsymbol{R_0}$ (6 mm) and $\boldsymbol{R_e/R_0}$ (0.7) along the whole RFQ structure. It allows to increase the voltage keeping the maximum field $\boldsymbol{E_{max}}$. The higher voltage allows to reduce the modulation in the main part of the RFQ and to optimize the beam dynamics in the gentle buncher to prevent excessive transverse emittance growth.

An increase of the high order terms in the RFQ electrical field due to the lower $\boldsymbol{R_e/R_0}$ ratio was investigated and a minor influence of this effect to the particle transmission (< 1.5%) was demonstrated.

The new RFQ-channel was designed using the DESRFQ code [6]. Modulation and synchronous phase for each RFQ-cell were chosen to provide the following conditions:

– capture of the particles into acceleration is not less then 90 %;
– separatrix is filled in the beginning of the gentle buncher as uniformly as possible;
– transverse phase advance is almost constant along the gentle buncher;
– tune depression in gentle buncher is almost equal its initial value.

The baseline design was optimized for $U^{4+}$ beam current of 20 mA and a total transverse emittance of 280 mm*mrad (unnorm.). These values were chosen on the base of the measurements in front of the RFQ (15 mA, 210 mm*mrad) assuming the same brilliance of the high current beam coming from the ion source. The main parameters of the new design are summarized in Tab. 1.

Table 1: Main RFQ Parameters

| | New | Existing |
|---|---|---|
| Voltage, kV | 155.0 | 125.0 |
| Average radius, mm | 6.0 | 5.2 ÷ 7.7 |
| Electrode width, mm | 8.4 | 9.0 ÷ 10.8 |
| Max. field, kV/cm | 312 | 318 |
| Modulation | 1.012 ÷ 1.93 | 1.001 ÷ 2.09 |
| Synch. Phase, degree | -90 ÷ -28 | -90 ÷ -34 |
| Aperture, mm | 4.1 | 5.5÷3.8÷4.8 |
| Min. transverse phase advance, rad | 0.56 | 0.45 |
| Norm. transverse acceptance, mm*mrad | 0.86 | 0.73 |
| Electrode length, mm | 9217.4 | 9217.4 |

## SIMULATION RESULTS

The beam dynamics simulations for the final RFQ design were additionally carried out with the DYNAMION code. The RFQ output beam current in dependence on the input current (15 ÷ 30 mA) is shown in Fig. 2 for the case of a constant input emittance (210 mm*mrad, green line); additionally for the input emittances increased proportionally to the beam current (210 ÷ 420 mm*mrad, red line).

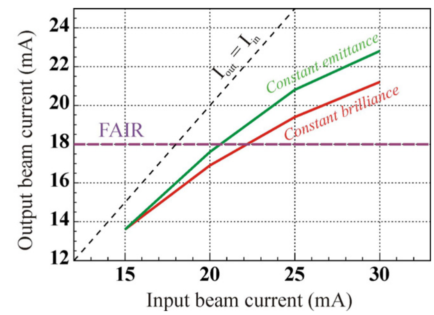


Figure 2: Simulated beam current at RFQ output in dependence on input current.

A comparison of the existing and the new RFQ channels is illustrated in Fig. 3. A beam current inside a given transverse emittance at the RFQ-output is shown for both designs. Beam dynamics simulations were done for the same beam current (25 mA) and emittance (210 mm*mrad), but with matched Twiss-parameters for each case.

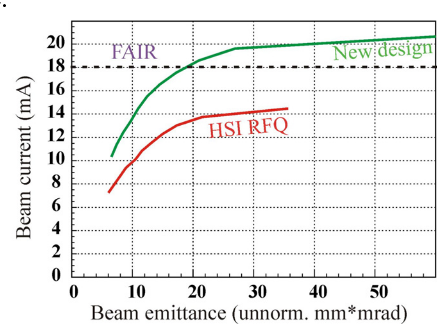


Figure 3: Beam current inside a given emittance at the RFQ-output for the existing design (red) and the new design (green).

The new RFQ design provides for more than 40% of the beam current compare to the old design. Higher beam emittance behind the new RFQ channel is formed by a few percent of the particles, while the core of the beam (20 mm*mrad) contains the required beam current.

An additional cross-check of the beam dynamics for the new RFQ was performed with the PARMTEQM code; a good coincidence of the results was demonstrated [7].

## RESONANT STRUCTURE

For improved beam dynamics the average channel aperture $R_0$ and the electrode half-width/curvature $R_e$ have been specified constant along the channel. It leads to a different capacitive load, the appearing frequency shift must be compensated by other channel parameters. For the existing IH-RFQ a frequency of 35.96 MHz was calculated, what is in good agreement with the experimentally measured value. Then the height of the electrode "shoulder" $h$ and the ring length $L$ (Fig. 4) were used as free parameters to achieve the design frequency for the new channel.

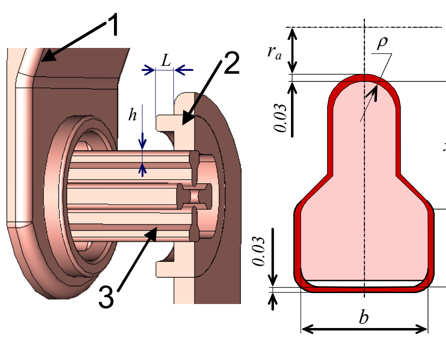


Figure 4: Regular cell of IH-RFQ structure (left) and electrode cross-section (right). 1 - stems; 2 - carrier rings; 3 - electrodes (mini-vanes).

The length of the carrier rings is the most efficient parameter for frequency adjustment, available at every cell of the structure. The frequency dependence on the length of the carrier ring edge, calculated for the structure with the modified channel, is shown in Fig. 5.

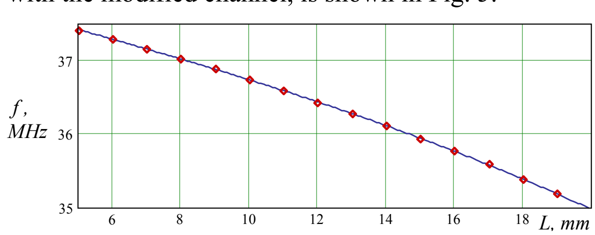


Figure 5: IH-RFQ frequency as a function of the length of the carrier ring edges.

A desired frequency of 35.96 MHz without tuners may be realized with the structure cell parameters given in the Tab. 2, while the operating frequency of 36.136 MHz will be reached with inductive tuning plungers.

Table 2: Main Dimensions of the IH-RFQ Cell

| $R_0$, mm | $R_e$, mm | b, mm | h, mm | L, mm |
|---|---|---|---|---|
| 6.0 | 4.2 | 16.0 | 7.0 | 14.8 |

In order to reduce dark current contributions [3], the electrode surface has to be covered by a 0.03 mm layer of electrolytic copper (Fig. 4, right). The electrodynamics simulations for the final geometry showed that additional 10 micrometers of copper layer lead to a frequency shift of about 0.023 MHz, which is comparable to the effect of one plunger. The frequency sensitivity to the radial displacement of the electrode is considerably less (0.0006 MHz/μm).

## CONCLUSION

The new electrode profile for the HSI-RFQ was designed with higher transverse acceptance and phase advance, keeping the maximum field at the electrode surface of the recently operating machine. The new design of the Input Radial Matcher allows for an improved beam matching to the RFQ by means of the LEBT quadrupole lenses. Beam dynamics in the beginning of the gentle buncher was optimized to provide for rapid and uniform (as possible) separatrix filling. To avoid an excessive rf-defocusing and a significant space charge influence, the modulation and the synchronous phase in the gentle buncher increase considerably slower compare to the existing RFQ-design. The maximum modulation in the main RFQ part is also reduced.

The shift of the resonant frequency of the cavity with increased average radius and reduced electrode thickness can be compensated with minor changes of the topology of the mini-vane and the connecting ring.

Beam dynamics in the new channel were studied with the DYNAMION code. It could be shown, that the beam intensity at the HSI-RFQ output (18 mA of $U^{4+}$ ions), required for the FAIR program, can be reached.

## ACKNOWLEDGMENTS

Authors would like to express sincere acknowledgments to our colleagues from the IAP Frankfurt, Prof. U. Ratzinger, Prof. A. Schempp and Dr. R. Tiede for fruitful discussions and supporting simulations [8].

Work is supported by EU: INTAS contract Ref. Nr 06-1000012-8782.

## REFERENCE

[1] W. Barth, "Commissioning of the 1.4 MeV/u high current heavy ion linac at GSI", LINAC 2000, USA.
[2] S. Yaramishev et al., "Development of the versatile multi-particle code DYNAMION", NIM A, 2005.
[3] S. Yaramyshev et al., "Upgrade of the high current heavy ion front-end system of the GSI UNILAC", IWCPA 2005, Prob.Atomic Sci.Technol., 2006.
[4] W. Barth et al., "Upgrade Program of the High Current Heavy Ion UNILAC as an Injector for FAIR", ICAP 2006, NIM A, 2007.
[5] A. I. Balabin, Preprint ITEP 81-107, 1981.
[6] Physical Review Vol. 5, 060101 (2002).
[7] A. Schempp, IAP Int. Rep. UF-IAP-S-08-1307.
[8] R. Tiede, IAP Int. Rep. IAP-DYNA-010708.

# THE NEW EBIS RFQ FOR BNL

M. Vossberg, J. Schmidt, B. Hofmann, A. Schempp, C. Zhang, IAP, Univ. Frankfurt, Germany
J. Alessi, D. Raparia, L. Snydstrup, BNL, Upton NY, U.S.A.

*Abstract*

A new RFQ is being built as a part of the new EBIS-Linac at BNL. The RFQ accepts highly charged ions from the EBIS ion source with energy of 17 keV/u and ion currents of up to 10 mA. The operation frequency will be 100.625 MHz. The design had been optimized to get a rather short structure with $L_{RFQ} = 3.1$ m with moderate electrode voltages of $U_Q = 70$ kV. The resonant insert has a cooled base plate and solid stems and vane-electrodes. The mechanical design is very stiff, with a precise base-structure. The top lid along the RFQ allows installation, alignment, inspection and maintenance.
After the mechanical alignment of the electrodes the longitudinal electrode voltage distribution will be adjusted with tuning plates between the stems. The properties of the RFQ, the results of the tuning and the status of the project will be discussed.

## INTRODUCTION

Availability for beams for high energy heavy ion physics is limited by the properties and performance of the accelerator chain especially the low energy part, where beam intensities and emittances are set.

At RHIC the injector consists of a Tandem whose beam is transported to the AGS. The limitations of that injector, a combination of a dc, low beam current heavy ion machine, a long transport line with a typical pulsed proton high energy machine are obvious. Starting with negative ions, the mass range is also limited.

Plans for a new injector making use of the new developments of ion sources as well as rf-linacs have been discussed for a number of years. Now that modern injector scheme is being set up at BNL, which will lead to more reliable operation and improved capability especially for the RHIC and NSRL programs [1].

The EBIS ion source is perfectly matched to the operation pattern with its pulsed beam of highly charged ions. The RFQ accepts a low energy heavy ion beam, and bunches and accelerates it with high efficiency and low emittance growth [2]. The IH structure has been applied for heavy ion machines e.g. at GSI and CERN which have demonstrated operation with very high gradients resulting in a very efficient compact ion injector for a Synchrotron [3,4].

Figure 1 shows a layout of the new heavy ion injector linac with total length of appr. 12 m, which will provide ions with 2 MeV/u for a mass to charge ratio of up to A/q = 6.25.

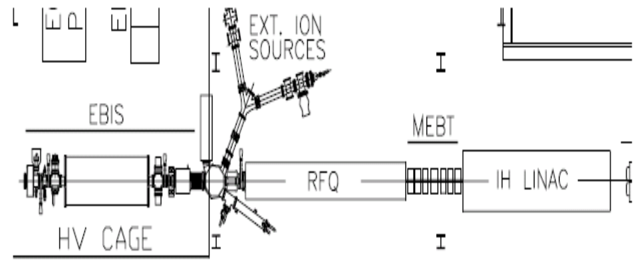


Figure 1: Layout of the EBIS Linac at BNL.

## RFQ

The RFQ for the new EBIS-linac at BNL accepts highly charged ions from the EBIS ion source with energy of 17 keV/u and ion currents of up tp 10 mA. The operation frequency will be 100.625 MHz.

### *Beam Dynamics*

The beam dynamics design does an adiabatic variation of the RFQ parameters to shape, bunch and accelerate the beam [5]. We optimized the design to get a rather short structure with $L_{RFQ} = 3.1$ m with moderate electrode voltage of $U_Q = 70$ kV.

Table 1: RFQ Beam Dynamics Design Parameters

| | |
|---|---|
| Frequency | 100.625 MHz |
| Input energy | 17 keV/u |
| Output energy | 0.3 MeV/u |
| Mass to charge ratio | 6.25 |
| Beam current | 10 mA |
| Outp trans. emitt rms norm. 90% | < 0.38 π mm mrad |
| Output long. emittance 90% | < 220 deg keV/u |
| Transmission | 98% |
| Electrode voltage | 70 kV |
| RFQ length | 3.1 m |
| Cell number | 189 |
| Aperture min - max | 2.96-5.25 mm |

Results of particle dynamics simulations show the RFQ output transmission and emittances for different beam input emittances and currents show low emittance growth and very high transmission also for I = 10 mA

*Work supported by the US Department of Energy and the National Aeronautic and Space Administration.

Table 2: RFQ Beam Emittances

| $\varepsilon_{in}^{trans.,un., real}$ [π mm-rad] | Transm. [%] | $\varepsilon_{out}^{z, rms}$ [MeV-deg] 100% | $\varepsilon_{out}^{xy, rms}$ [π mm mrad] 100/90% |
|---|---|---|---|
| 0.05790 I=0 | 99.2 | 0.284 | 0.064 / 0.0271 |
| 0.08685 I=10 | 96.7 | 0.243 | 0.09 / 0.038 |
| 0.11580 I=0 | 98.4 | 0.27 | 0.126 / 0.053 |
| 0.11580 I=10 | 98.7 | 0.33 | 0.15 / 0.060 |

Beam dynamics simulations have been done with Parmteqm Vers. 3.07. This allows applying a Crandall-Output cell with low divergence of the beam. The final design has good emittances in both axial and radial direction, a very high transmission.

The beam dynamics design is very flexible; it allows rather large variations of the input beam parameters and has good output beam quality.

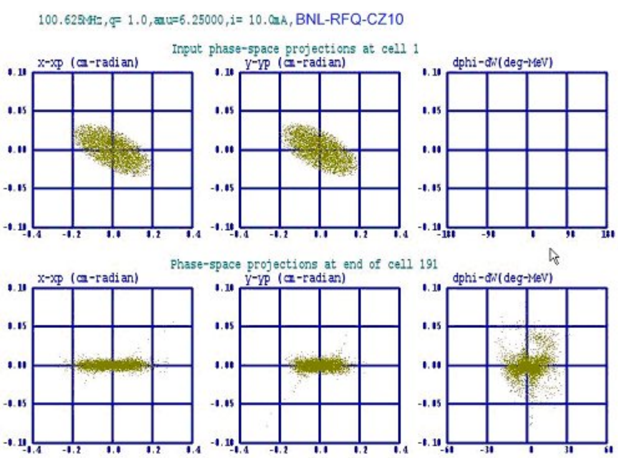


Figure 2: RFQ emittances for I = 10 mA.

## *4-Rod-RFQ-Structure*

The 4-Rod-RFQ consists of a chain of λ/2 resonators which are operated in π-0-mode, to have opposite voltage on the adjacent electrodes and constant voltage along the RFQ. It is possible to describe the basic cell of the 4-Rod-RFQ as a capacitively loaded line, at which the electrodes are the capacity and the stems the inductivity resp. the short line.

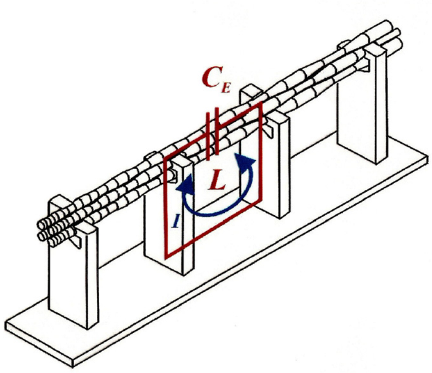


Figure 3: Basic cell of the 4-Rod RFQ structure.

Table 3: 4 Rod Structure Parameters

| | |
|---|---|
| 4-Rod-RFQ | 100.625 MHz |
| Tank diameter | 350 mm |
| Tank length | 3100mm |
| Beam axis height | 147 mm |
| Stem number | 20 |
| Stem distance / thickness | 158 mm / 10mm |
| Aperture | 5.2-2.96 mm |
| Modulation factor | 1-1.99 |

Based on MWS-simulations and experimental results of similar RFQs the structure power for the EBIS-RFQ is $P_S$ = 105 kW. Two inductive tuners will perturb the field in the plane between the stems. The 3-1/8" power line will be fed in by a central coupling loop.

The RFQ-cavity is made out of a 5 cm thick wall tube, copper plated, with inner diameter of 350 mm. The resonant insert has a cooled base plate and solid stems and sloped-electrodes. The support stand structure is 70 cm wide and allows horizontal adjustment.

The mechanical design is very stiff, avoids much welding for stress free, precise basic structure and by the use of the top lid allows rather easy installation, alignment, inspection and maintenance.

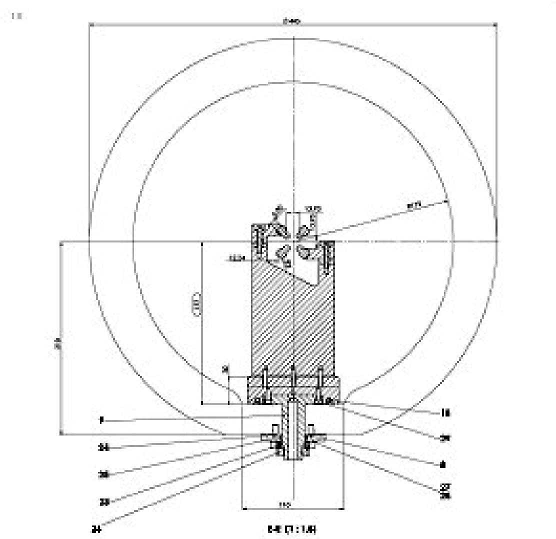

Figure 4: BNL 4-Rod RFQ Cross section.

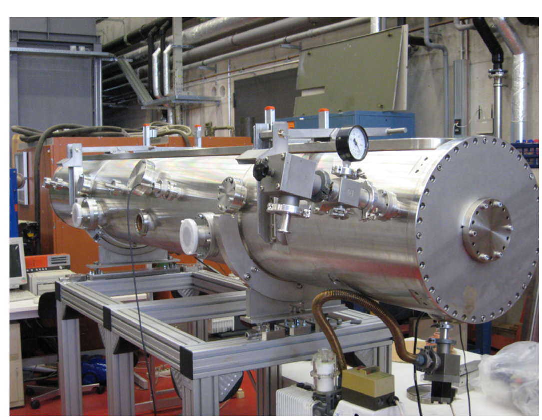

Figure 5: BNL 4-Rod RFQ set up.

### *Mechanical Alignment and Tuning*

The first step for the mechanical alignment is to mount the stems onto the base plate and insert this set-up into the cavity. For alignment in the tank, measurements of the distance between the backsides of the electrode bridge heads and the minima of the aperture are needed. This is done with a Tesla meter in vertical and horizontal plane. Afterwards the electrodes are attached on the stems in the tank. To align them silver plated shims with a size of 4mm up to 6mm are fixed between the electrodes and the stems. They can easily be changed in order to adapt the proper vertical position. To align the electrodes horizontal we can change their position by shifting them. The top flange of the tank serves as reference for these measurements. Our measurement equipment for the alignment in the tank is the FARO Gage plus meter with which we can quantify distances of planes easily. The results of measurement show, that the positions is better than ±0,03 mm.

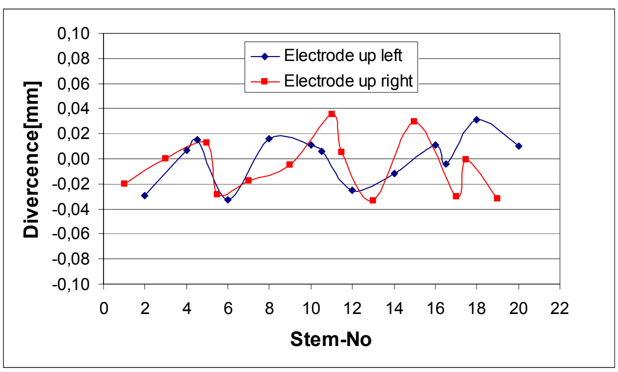


Figure 6: Results of Alignment.

A constant voltage on the electrodes of the RFQ is required for correct operation according to the beam dynamics design. For electrodes with no modulation and constant capacity a simulation of the whole structure was done. In structures with length design of 3,1 meters, the voltage difference from the mean voltage ranges between +11,8 % and -5,4 %. To balance this unflatness, tuning plates are inserted between the stems. They will change the local eigenfrequency of about 15 kHz per mm and correct the voltage differences, what is measured with a network analyzer. So each tuning plate is positioned at an individual height. As results of our tuning the quadrupole voltage (flatness) is better than ± 2 %.

Table 4: Position of Tuningplates in the BNL-RFQ

| Cell No. | Height | Cell No. | Height |
|---|---|---|---|
| 1 | 48.4 mm | 12 | 23.3 mm |
| 7 | 36 mm | 13 | 38.3 mm |
| 8 | 30 mm | 19 | 44.2 mm |

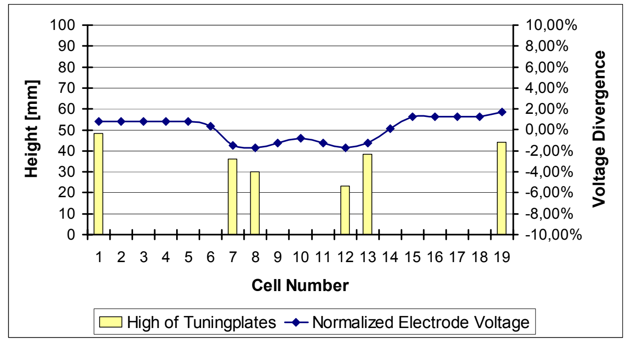


Figure 7: Results of Tuning.

The tuning plates change not only the local eigenfrequency but also the general one. For the precise adjustment of the resonance frequency, two inductive piston tuners are used. They enhance the resonance frequency up to 0.4 MHz dependent to the depth of the tuner.

## STATUS

The resonant structure is inserted into the cavity. We have done the alignment with a precede of ±0.03 mm and the flatness is better than ±2 %. Leak tests have been done and the EBIS- RFQ will be prepared for transport to BNL in the week before LINAC 08.

## REFERENCES

[1] J. Alessi et al., “Status of the EBIS Project at Brookhaven”, Proc. of the 2006 LINAC Conf., Knoxville, Tennessee, USA, p.385.
[2] A. Schempp “New developments in High Duty Cycle High Current RFQs” Linac 02, Korea,p541
[3] N. Angert et al., “The IH Linac of the CERN Lead Injector”, Proc. of the 1994 LINAC Conf., Tsukuba, Japan, p.743.
[4] U. Ratzinger, “The New High Current Ion Accelerator at GSI and Perspectives for Linac Design Based on H-mode Cavities”, Proc. of the 2000 EPAC Conf., Vienna, p.98.
[5] A. Schempp, “Design of Compact RFQs”, Proc. of the 1996 LINAC Conf., Geneve, p.53.

# HEAVY ION RADIO-FREQUENCY QUADRUPOLE LINAC FOR VEC-RIB FACILITY

Siddhartha Dechoudhury, Vaishali Naik, Arup Bandyopadhyay, Manas Mondal, Hemendra Kumar Pandey, Tapatee Kundu Roy,Dirtha Sanyal, Debasis Bhowmick, Alok Chakrabarti

Variable Energy Cyclotron Centre,1/AF Bidhan Nagar, Kolkata 700 064, India

*Abstract*

Post acceleration of ion beams would be done in Radio Frequency Quadrupole (RFQ) LINAC for the upcoming Radioactive Ion Beam (RIB) facility at Variable Energy Cyclotron Centre (VECC), India. A 33.7 Mhz RFQ capable of accelerating stable as well as RI beams of q/A≥1/16 to about 30 keV/u has already been constructed and operational since September 2005. This has been installed in a dedicated beam line for doing material science experiments. Another 3.4 m long RFQ resonating at 37.8 Mhz and capable of accelerating heavy ion beams upto 98 keV/u have been fabricated which is to be installed in the beam-line for the VEC-RIB facility. The physical parameters, rf test along with the measurements of accelerated beams from RFQ would be presented.

## DESIGN OF RFQ

We plan to accelerate beams with mass ranging up to A=150 in the VEC-RIB facility[1]. The radioactive atoms would be ionized in Electron Cyclotron resonance ion source(ECRIS) operating in "High B-mode". The ions would be then subsequently mass separated and accelerated in RFQ and Linac tanks[2]. ECRIS in principle would be able to deliver beams of around $15^+$ for uranium even in the on-line mode .Thus q/A≥ 1/14 seems to be a judicious choice for our RFQ. Normalized emmittance of ion beam has been taken to be 0.05 π cm mrad. Characteristic radius of 0.71 mm for the RFQ ensured a good transmission of the RI beams through the RFQ. The four-rod type structure have extended vanes supported on posts similar to the structure developed by Fujisawa[3]. The rods are placed at an angle of $45^o$ with respect to conventional horizontal and vertical axes.

The beam dynamics simulation has been done using GENRFQ and PARMTEQ code. Optimization of different physical parameters was done keeping in mind the goal to achieve the desired acceleration with minimum vane length and maximum transmission efficiency. Initially the RFQ was decided to design for input beam of energy of 1keV/u and input bunch width of $\pm 42^o$ and final energy of 86 keV/u[4]. The RFQ was designed to resonate at frequency of 35 MHz. A half scale cold model was fabricated for RF measurements. The results show good agreement with the simulation using MAFIA. In the next stage we have designed and fabricated 33.7 MHz RFQ delivering beam of 29 keV/u to be installed in the dedicated beam line for material science experiments . As the first post accelerator, using the experience and expertise gathered with 33.7 MHz RFQ final 3.4 m RFQ accelerating RIB's to 98 keV/u have been fabricated.

## 33.7 MHz RFQ

### *Design Parameters*

The RFQ is designed for an input dc beam of 1.38 keV/u, *q/A*=1/ 16, and resonant frequency of 33.7 MHz. The intervane voltage has been chosen to be 45.9 kV, which is about 1.12 times the Kilpatric limit for cw operation. With the interelectrode potential of 45.9 kV the calculated output energy comes out to be 29.06 keV/u for a vane length of 1.552 m. The radial matching section consists of 6 rf cells, and a total of 119 cells are needed to reach the energy. The synchronous phase in the acceleration section is chosen to be −30°. The calculated transmission efficiency is 95.8% for a beam current of 1 mA. The optimized physical parameters are shown in Fig.1. Energy width of the beam at the exit of RFQ is ± 0.67 keV/u.

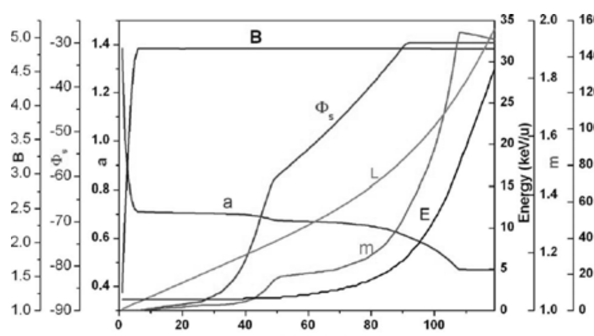


Figure 1: Optimised physical parameters variation along length of 33.7 MHz RFQ.

### *RF Analysis*

MAFIA estimates resonant frequency, *Q*, and *Rp* values for the structure with unmodulated electrodes of the same characteristic radius to be 35 MHz, 9830, and 174 kΩ respectively. The measured resonating frequency is 33.7 MHz. The Q value measured using pick ups under 99% power reflection method is 5200.The tuning range of the tuner has been measured to be 100 KHz.

### *Beam Energy Measurement*

Low energy beam transport line from ECRIS to RFQ consists of einzel lens,$90^o$dipole for q/A selection and solenoid as matching element. The separation stage is designed for a dispersion of 1.84 cm. The ions are extracted from ECRIS at 1.38 keV/u. In the downstream of RFQ a QQD configuration has been installed for energy measurement. The quadrupole and dipole magnet strengths are calculated using TRANSPORT for RFQ beam energy of 29.06 keV/u, as theoretically predicted by PARMTEQ. The 5.4 m long beamline is designed for dispersion of 1.9 cm. The magnetic strengths of the quadrupoles and the dipole magnet are tuned so as to achieve maximum beam current on the Faraday cup (with electron suppression) placed upstream of the dipole after the RFQ. The beam tests have been carried out using oxygen ($^{16}O^{2+}$, $^{16}O^{3+}$, $^{16}O^{4+}$), nitrogen ($^{14}N^{3+}$, $^{14}N^{4+}$), and argon ($^{40}Ar^{4+}$).Typical transmission efficiency for most of the beams is 85% & 80% respectively for un analyzed and analyzed beam[5]. A plot of beam current measured on Faraday cup before RFQ as a function of vane voltage measured pickup voltage, proportional to vane voltage is shown in Fig.2.The transmission falls drastically when the vane voltage is reduced to a value lower than roughly 86.6% of the voltage corresponding to maximum transmission, as expected for the chosen synchronous phase of −30°.

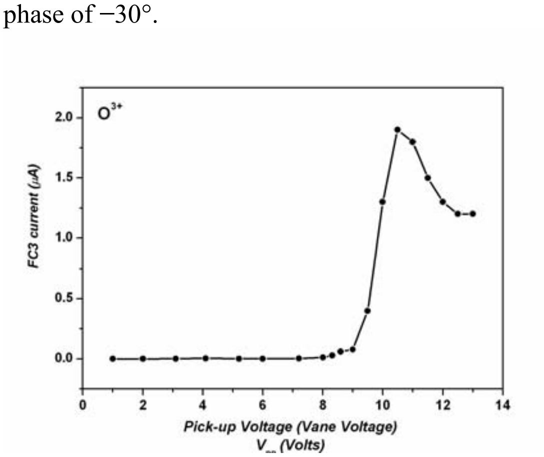


Figure 2: Variation of beam current with vane voltage for $^{16}O^{3+}$ beam.

## 37.8 MHz RFQ

### *Design Parameters*

The RFQ has been designed for DC beams with input energy of 1.7 keV/u. The vane voltage of 53.7 kV accelerates the beam to energy of 98 keV/u over a length of 3.12m. This voltage is around 1.12 times of Killpatric Voltage of 47.65 kV. RFQ consists of 6 radial matching sections (RMS) and in all 147 cells. The potential formulation in the RMS is similar to that proposed by Yamada [6], where the focusing strength (B) obeys a sinusoidal variation over the length of RMS. The calculated efficiency for 1mA beam comes out to be ~96% The variation of the optimized physical parameters along the length of RFQ is shown in Fig 3.The minimum aperture radius is 4.1mm while the maximum modulation parameter is 1.388. Energy width of the output beam through the RFQ is around ± 0.3% of the final energy. Output beam distribution as calculated by PARMTEQ, both in longitudinal & transverse phase space is shown in Fig 4.

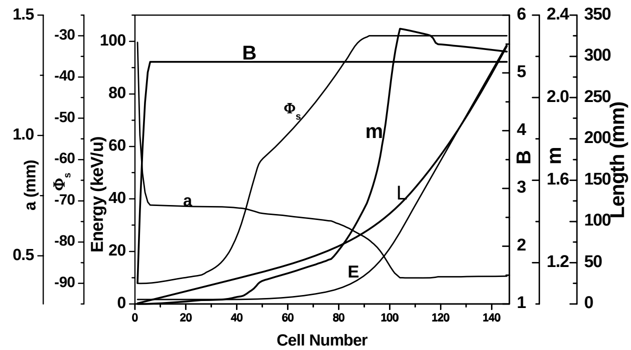


Figure 3: Variation of optimised physical parameters along the length of RFQ.

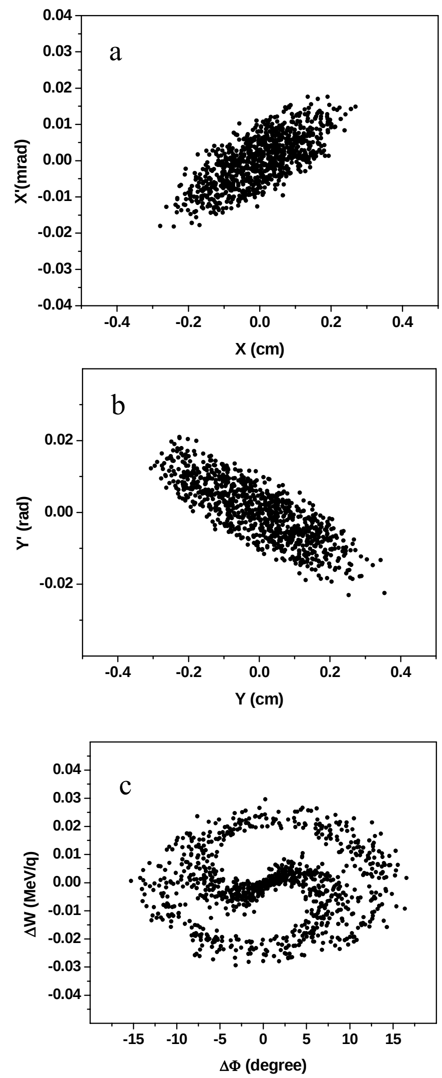


Figure 4: Longitudinal and transverse beam distribution at the exit of RFQ.

### *RF Analysis*

The RF structure design was done using the code ANSYS. The resonant frequency, Q and $R_p$ value simulated with unmodulated vanes having same characteristic radius are 37 MHz, 9763 and 78 kΩ respectively. Estimated power loss for 53.7 kV is around 18 kW. The resonance frequency is measured to be 37.8 MHz which is about 2% higher than simulated from ANSYS. The Q-value (Unloaded) measured using two pick-up loops under more than 98% reflection of power (-56 dB) is about 3705 (fig 5). The shunt impedance Rp was measured using both capacitance variation method (fig 6) and input admittance variance method. From both the methods Rp value comes out to be 53.65 KΩ and 53.9 KΩ which are about 68% of the calculated value.

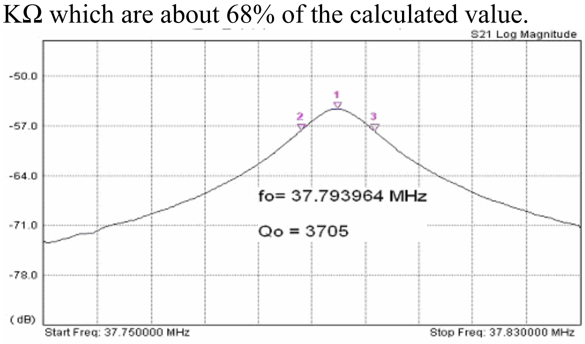


Figure 5: Unloaded Q value measurement using pick-up probes.

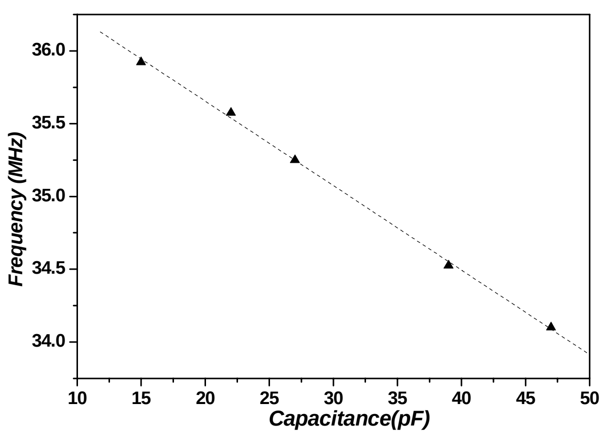


Figure 6: Rp/Q value measurement using capacitance variation method.

### *Beam Transmission Efficiency*

The acceleration performance of RFQ has been measured with O(5+) beam extracted from ECRIS at 1.7 keV/u. After selection through 90 degree dipole magnet the solenoid is tuned in order to match the beam with RFQ. The ion optics has been calculated using TRANSPORT code. The strength of both the Dipole magnet and solenoid has been tuned accordingly. The transmission efficiency has been measured by taking the ratio of currents for faraday cups placed upstream and downstream of RFQ. Unanalysed efficiency is close to 90% for $O(^{5+})$ beam.

## Discussion

33.7 MHz RFQ have been successfully built and we are able to accelerate beam to 29keV/u with high enough efficiency through it. We have also succeeded in accelerating heavy ions such as $Fe^{5+}$ through the RFQ for material science experiments. 3.4 m long RFQ have already been installed in the beam-line for accelerating heavy ion RI beams to 98 keV/u.Beam line after RFQ is in process of installation. A QQD configuration will be installed to assess the analysed beam transmission efficiency, in due course of time.

## Acknowledgement

The authors would like to acknowledge Osamu Kamigaito, Akira Goto, and Yashushige Yano from RIKEN Accelerator Research Facility, Japan, for their help during design and development of the RFQ. Authors would like to thank the teams of CMERI and SAMEER for their valuable technical support in this work.

## REFERENCE

[1] Vaishali Naik et. al " Development of Rare Isotope Beam Facility at VECC Kolkata" **LINAC 08** conference

[2] Arup Bandhyopadhyay et. al "Post-Accelerator LINAC Development for the RIB Facility Project at VECC, Kolkata" **LINAC 08** Conference

[3] H. Fujisawa,Nuclear Instrument.and Methods. A **345** (1994)23.

[4] A. Chakrabarti et. al , Nuclear Instrument and Methods A **535** (2004) 599

[5] A. Chakrabarti et. al , Review of Scientific Instruments **78** (2007) 043303

# THE IFMIF-EVEDA RFQ: BEAM DYNAMICS DESIGN

M. Comunian, A. Pisent INFN/LNL, Legnaro (PD) Italy, E. Fagotti (Consorzio RFX, Padova)

*Abstract*

The IFMIF-EVEDA (Engineering Validation and Engineering Design Activities) project foresees the construction of a high intensity deuteron accelerator up to 9 MeV, with the characteristics required for the actual IFMIF facility. The linac will be installed in Rokkasho, and INFN is in charge of the construction of a 5 MeV, 125 mA, deuteron RFQ operating at 175 MHz. In this article the beam dynamics design of this challenging RFQ is described, namely the design, the main outcomes in terms of beam particles physics, and finally the study of mechanical and rf field error tolerances. The RFQ design method has been aimed to the optimization of the voltage and R0 law along the RFQ, the accurate tuning of the maximum surface field and the enlargement of the acceptance in the final part of the structure. As a result this RFQ is characterized by a length shorter than in all previous design, very low losses (especially at higher energy) and small RF power dissipation[1][2][3].

## RFQ PARAMETERS AND DESIGN

The IFMIF EVEDA RFQ specification and the main design parameters are listed in Table 1.

Table 1: IFMIF RFQ Parameters

| | | |
|---|---|---|
| Particles | D+ | |
| Frequency | 175 | MHz |
| Input Current | 130 | mA |
| RMS Input tr. emittance | 0.25 | N.mmmrad |
| Input/Output Energy | 0.1/5 | MeV |
| Max Surface Field (1.82 Kp) | 25.6 | MV/m |
| Length L | 9.78 | m (5.7 λ) |
| Voltage Min/Max | 79/132 | kV |
| Total Power with margins | 1.6 | MW |
| Mean aperture $R_0$(min/max) | 4.1 / 7.1 | mm |
| Trans. (WaterBag÷Gauss)* | 99.1÷95.7 | % |
| Power Loss(WaterBag÷Gauss)* | 253÷1007 | Watts |
| RMS Output Long. Emittance* | 0.197 | MeVdeg |
| RMS Output Tr. Emittance* | 0.26 | N.mmmrad |

*Average of 10 Toutatis runs with $10^6$ particles.

The design of such high current RFQ is very challenging due to the necessity to limit deuteron losses, keeping in particular extremely low the losses in the high energy part. The aim is to minimize the neutron production and the consequent activation of the RFQ structure.

Due to the high space charge effect at low energy. The value of input energy has been chosen of 0.1 MeV to maintain the value of maximum transverse current up to 200 mA until the end of Gentle Buncher;, this large margin guarantees small losses along the buncher formation process.

All the RFQ simulations here reported has been made by using the CEA code "Toutatis" [4].

### *Transverse Parameters Characterization*

The IFMIF EVEDA RFQ beam dynamics study was aimed at minimizing beam losses at high energy, reducing the RFQ length and power consumption. The main parameters are plotted in fig. 1, the focusing force "B" at the beginning of RFQ is about 7, i.e. a very high value to compensate the high space charge force and keep the beam in a linear force fields. It is not possible to ramp the value of "B" in the shaper because we get a larger beam size and due to that same losses in the gentle buncher process. The normalized transverse acceptance of the RFQ in smooth approximation is defined by:

$$Acc = \frac{a^2\sigma_{T0}}{2\lambda}\sqrt{\left(1-\frac{B}{4\pi^2}\right)^3 / \left(1+\frac{B}{4\pi^2}\right)}$$

with λ the wavelength *a* small aperture,$\sigma_{T0}$ phase advance at zero current and "B" the focusing factor expressed by:

$$B = \frac{qV}{mc^2}\frac{\lambda^2}{R_0^{\,2}} \quad and \quad \sigma^2_{T0} = \Delta_{RF} + \frac{B^2}{8\pi^2}$$

The variation of acceptance and "B" is therefore strictly connect to voltage and average aperture $R_0$ along the RFQ. For that reason a closed-form and continuous up to the 2$^{nd}$ derivative voltage law V(z) and $R_0$(z) was used.

$$V(z) = V_1 + (V_2 - V_1)\left(\frac{1}{2} + \frac{15}{8}\left(-\sin(\Delta z_{12}) - \frac{1}{3}\sin(3\Delta z_{12}) + \frac{1}{5}\sin(5\Delta z_{12})\right)\right)$$

$$R_0(z) = R_{01} + (R_{02} - R_{01})\left(\frac{1}{2} + \frac{15}{8}\left(-\sin(\Delta z_{34}) - \frac{1}{3}\sin(3\Delta z_{34}) + \frac{1}{5}\sin(5\Delta z_{34})\right)\right)$$

$$with \quad \Delta z_{12} = \frac{\pi}{6} - \frac{\pi(z-z_1)}{3(z_2-z_1)} \quad and \quad \Delta z_{34} = \frac{\pi}{6} - \frac{\pi(z-z_3)}{3(z_4-z_3)}$$

In this way it is possible to increase the voltage in a smooth way in the accelerator part and to have continuous variation of the phase advance per meter along the RFQ. The R0 and the voltage V are ramped after the Gentle Buncher, the V is increased for 4.4 meters instead the R0 are changed for 4.5 meters to reduce the surface fields and smoothing the phase advance change rate. The final value of the voltage $V_2$ is limited by the total available RF power, the final value of R0 allows to avoid the resonance $\sigma_T = \sigma_L$.

In the final 3 meters of accelerator almost all the parameters are kept constant. It's done to avoid small losses and to limit the part of the RFQ where the full 3D machining modulation is needed.

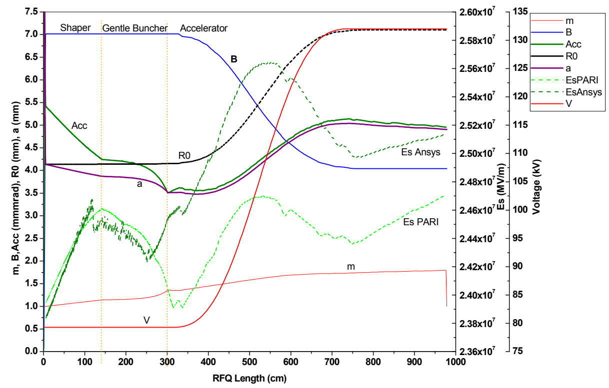


Figure 1: Modulation, Focusing factor B, Acceptance, Mean aperture "R0", minimum aperture "a", Surface Fields "Es" and voltage profile along the RFQ.

The ratio of V/R0 also is limited by the surface fields Es. The increase of R0 and "a" produce the increase of acceptance. The ratio of ρ/R0 is kept constant at 0.75 to reduce the surface fields, at the price of higher multipoles components. The modulation law chosen was the "2TERM" type, allows to manage successfully the non linearities.

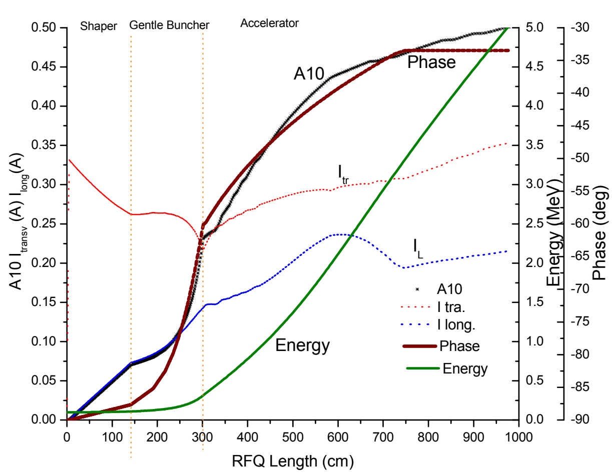


Figure 2: Energy, Acceleration coefficient A10, Synchronous phase, Current Limit Transverse and Longitudinal along the RFQ.

## *Longitudinal Parameters Characterization*

Due to the strong longitudinal space charge phenomena during the separatrix formation, also with the presence of filamentations, the shaper section of the RFQ is very long, about 1.4 meters, this guarantees with an relative high number of cells, the high longitudinal beam capture. The bunching process is so done in as smooth as possible way to capture as much as possible particles. The particles capture indicate by RFQuick was 100% in a large range of GB energy but with the multiparticles tests the real useful zone in energy was very small, so the selected GB final energy was 0.31 MeV, and at the end of GB the synchronous phase is -60 deg, this is the maximum phase possible keeping in account the longitudinal current limit. In the accelerator part the synchronous phase is increased linearly, respect to the cell, from -60 to -33.5 deg, if it is increase more rapidly part of the beam go out of the separatrix. The energy gain per meter in the accelerator part is about 0.7 MeV/m. The plot of Fig. 3 show the final phase space with a gaussian input beam distribution, very few particles on 106 are making longitudinal halo.

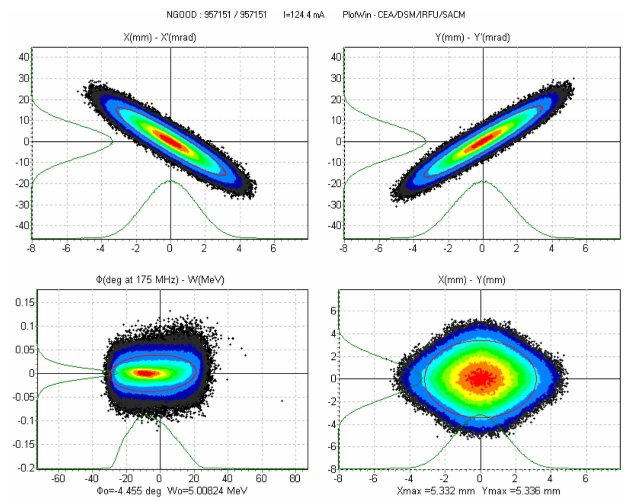


Figure 3: Phase Space at RFQ output with input Gaussian beam distribution of 130 mA, ε=0.25 RMS N. mm mrad.

## ERRORS STUDIES

### *Alignment Between Modules*

The RFQ structure will be made by fundamental elements 550 mm long; such elements are either brazed of flanged with a short longitudinal discontinuity. For that reason a study of tranverse misalignment at transition is mandatory. Vanes shape with an error on profile value $x_p(z)$ were generated, according to:

$$xp(z) = xp_0(z) \pm r\Delta X \quad with \quad -1 \le r \le 1$$

where $\Delta X$ is the maximum vane error amplitude considered and the random value "r" is regenerated for each element (Fig. 4). This procedure are made with 10 different RFQs, to accumulate statistics, and with a range from 0 to 100 μm of $\Delta X$ (Fig.5). It appears to be possible to handle errors on segmented RFQ in the order of ±50 μm, without a too large impact on transmission and power beam losses.

Due the huge numbers of runs to do, the errors study has been made by using Toutatis on a Linux cluster with about 20 nodes.

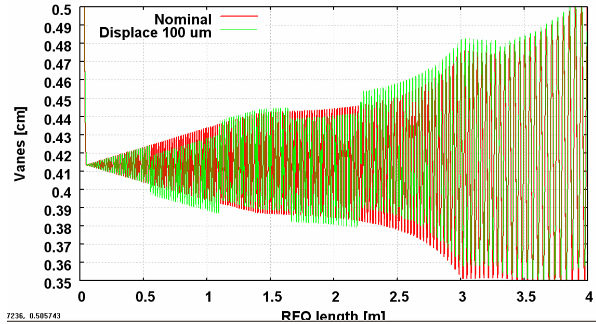


Figure 4: Vanes profile nominal and segmented in 550 mm pieces, along the first 4 meters of RFQ.

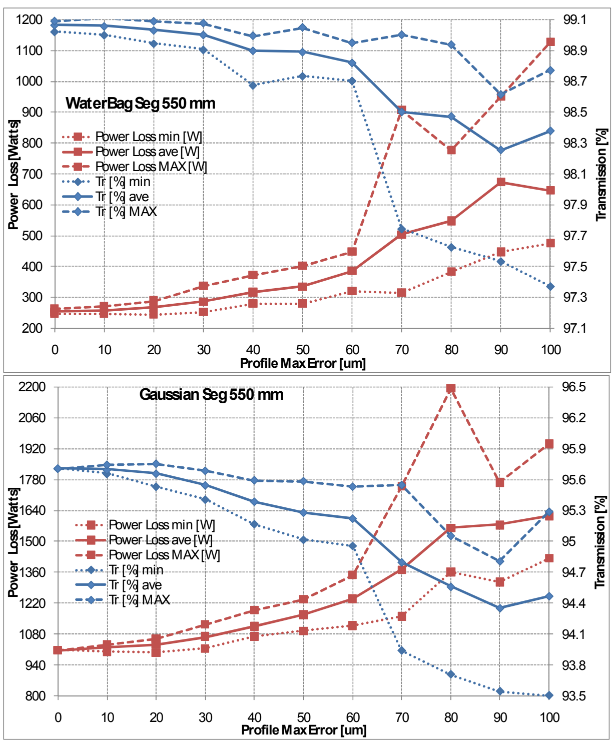


Figure 5: Transmission and Power loss due to the segmentations applied with gaussian and waterbag input beam distribution.

## *Voltage Tilt*

To study the RF errors a tilt on voltage respect to the nominal value has been generated, (fig. 6), corresponding to a non null component of the first perturbing quadrupole.

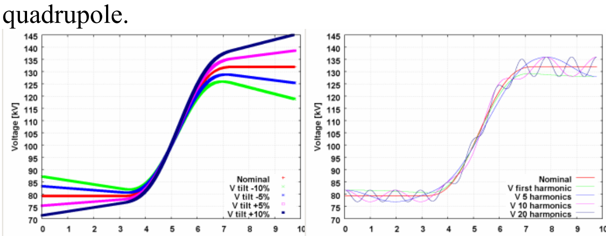


Figure 6: Tilted Voltage profile and harmonics profiled Voltage along the rfq.

The results of tilted voltage are in fig. 7, a positive tilt means a lower value of voltage at RFQ beginning. The power loss remains below 1.6 kW for very large range of values of tilted voltage.

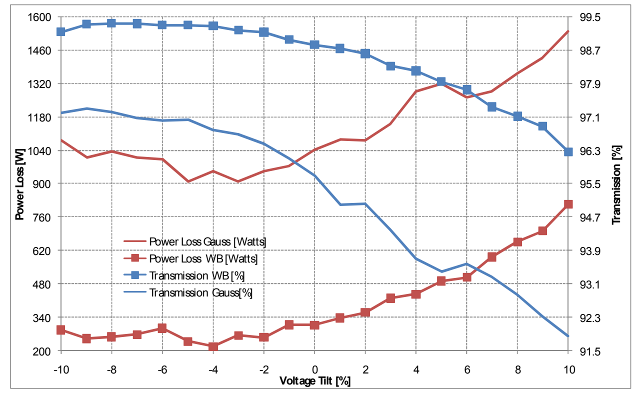


Figure 7: Voltage tilts effects on Transmission and Power loss with gaussian and waterbag input beam distribution.

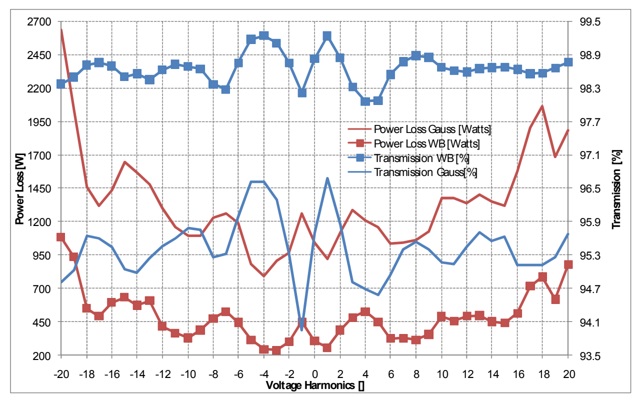


Figure 8: Voltage harmonics effects on transmission and power loss with gaussian and waterbag input beam distribution.

## *Residual Voltage Error*

We have then simulated the residual voltage error after RFQ tuning by introducing higher order harmonics according to:

$$V_r(z) = V_0(z) + \mathrm{sgn}(n)\cdot\Delta V\cdot\cos(n\cdot\frac{\pi}{2}\cdot z / L_{rfq})$$

where $n$ is integer and $\Delta V$=3% of the nominal voltage (Fig. 6). The results show very little dependence from the applied voltage harmonics. From the results on tilted voltage and harmonics analysis it seems to be possible to handle a maximum error of ±3% on voltage (Fig. 8).

## REFERENCES

[1] A. Mosnier, et. al. "The IFMIF-EVEDA Accelerator Activities", EPAC 2006, Genoa (Italy).
[2] A. Pisent, et. al. "IFMIF-EVEDA RFQ Design", EPAC 2006, Genoa (Italy).
[3] M. Comunian, et. al. " Beam Dynamics of the IFMIF-EVEDA RFQ", EPAC 2006, Genoa (Italy).
[4] R. Duperrier, "TOUTATIS: A radio frequency quadrupole code", Phys. Rev. Vol.3, 124201(2000).

# RF DESIGN OF THE IFMIF-EVEDA RFQ

F. Grespan, A. Palmieri, A. Pisent INFN/LNL, Legnaro (PD) Italy

*Abstract*

The RFQ of IFMIF-EVEDA project is characterized by very challenging specifications, with 125 mA of deuteron current accelerated up to 5 MeV. Upon beam dynamics studies, it has been chosen a law for the variation of $R_0$ and voltage along the structure; this law provides a significant reduction in terms of structure length, beam losses and rf power consumption. Starting from these outcomes, the rf study of the RFQ, aimed at determining the optimum design of the cavity shape, was performed. The stabilization issues were also addressed, through the analysis of the RFQ sensitivity to geometrical errors, by means of perturbative theory-based algorithms developed for this purpose . Moreover the determination of the main 3D details of the structure was also carried out. In this article the results of the rf studies concerning the above-mentioned topics are outlined.

## RFQ PARAMETERS AND CAVITY DESIGN

The main RFQ parameters are listed in Table 1, and the 3D layout in Figure 1.

Table 1: IFMIF RFQ Input Design Parameters

| | | |
|---|---|---|
| Particles | D+ | |
| Frequency | 175 | MHz |
| Input Current | 130 | mA |
| Energy (in-out) | 0.1-5 | MeV |
| Max Surface Field | 25.2 | MV/m (1.8 Kp) |
| Length L | 9.78 | m |
| Voltage min/max | 79/132 | kV |
| Mean aperture $R_0$ | 4.1 / 7.1 | mm |
| Pole tip radius ρ | 3.08/5.33 | mm |

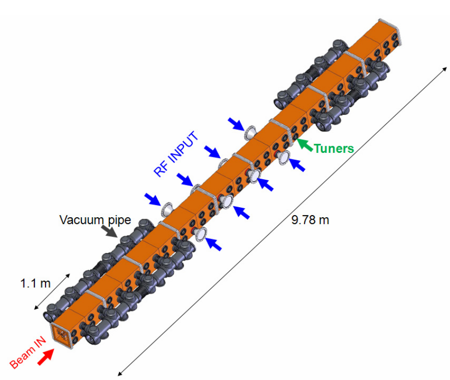


Figure 1: IFMIF RFQ schematic layout.

The IFMIF EVEDA RFQ beam dynamics study[1] was aimed at minimizing beam losses at high energy, reducing the RFQ length and power consumption. A closed-form and continuous up to the 2nd derivative voltage law V(z) was used. In this way it is possible to increase the voltage smoothly along the accelerator part and to have continuous cut-off frequency variations.

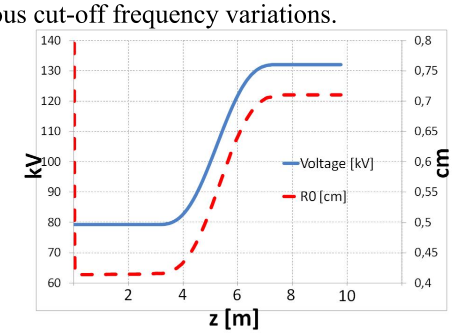


Figure 2: Mean aperture and voltage profile along the RFQ.

The goal of the cavity design was the optimization of the transverse section in order to match the local cut-off frequency with respect to local $TE_{21}$ cut-off frequency f(z) variation due both to voltage and aperture variation, by varying the Vane Base Width 2·W1 along the RFQ with the usage of the RFQFISH routine. The minimum W value (1 cm) was chosen in order to allow cooling channel positioning and the maximum W1 value (1.5 cm) to avoid mechanical oscillations during machining. The upper flat surfaces H1 and H2 (9 cm) allow the positioning of tuners and RF couplers (Fig.3). Moreover the choice of the section was also dictated by the fact that a “square” shape of the RFQ cross-section allows, for a given frequency and $R_0$, a better volume/surface ratio and a subsequent Q improvement (about 10%) with respect to a “triangular” shape.

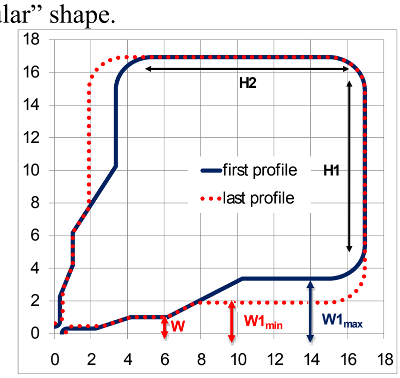


Figure 3: The variable shape of the RFQ section.

The main parameters obtained from the SUPERFISH optimization are summarized in Table 2.

Table 2: SUPERFISH Results

| | | |
|---|---|---|
| $Q_0$ (SF) (z=0-z=L) | 15100-16700 | |
| 2D Power (SF) | 450 | kW |
| Stored Energy | 6.6 | J |
| Max H field (z=0-z=L) | 3000-4500 | A/m |
| Max. Power Density (z=0-z=L) | 1.6-3.1 | W/cm$^2$ |
| Total power $P_d$ | 1.345 | MW |

The $P_d$ is related to the 2D power calculated by SUPERFISH, $P_{SF}$, by means of the relationship

$$P_d = P_{SF}\alpha_{3D}\alpha_v + P_b$$

where $\alpha_{3D}$=1.3 (for 3D losses), $P_b$ is the beam power at 130 mA and $\alpha_v$ = 1.21 ( = 1.1$^2$) for Voltage enhancement The sensitivity with respect to geometrical errors was addressed both numerically and analytically, and it was found that the maximum [minimum] sensitivity $\chi$ is located in the initial [final] section of the RFQ, where $\Delta f/\Delta R_0$=11.8 MHz/mm [7.5 MHz/mm].

## FIELD STABILIZATION ISSUES

Geometrical errors in the RFQ section produce perturbations on the nominal voltage profile $U_0(z)$ via capacitance perturbations. General beam dynamics considerations prescribe that $|\Delta U(z)/U_0(z)|< 0.01$ and $|U_{qd1,qd2}(z)/U_0(z)|$<0.02 [2] where $\Delta U(z)$ and $U_{qd1,qd2}(z)$ are the voltage perturbations due to upper quadrupole modes and the two kinds of dipole modes respectively. In order to reach such goal, it is necessary to use a system of $N_T$ slug tuners per quadrant of radius $a$ and depth $h$ variable in the interval [0, $h_{max}$]. Each tuner can vary the resonant frequency of the RFQ of an amount equal to $\Delta f_t = \chi_t h$ $\chi_t$ being the tuner sensitivity related to the magnetic field on the upper RFQ wall. The idea is that the tuning range (the frequency interval that can spanned by the tuners) $\Delta f_{TR} = 2N_T\chi_t h_{\max}$ should be able to correct for frequency shifts induced by geometrical error $\Delta f_q$ with appropriate margin, that is $\Delta f_{TR} = k\Delta f_q$ with k>1. If $f_c$ is the average cut-off frequency of the RFQ and $f_0$ is the operating frequency, the tuning range is symmetric around $f_0$, in the sense that $\Delta f_{TR}=f_0- f_c$. If all tuners, couplers and vacuum ports are placed along, say, H1 surface, then the number of tuners is determined by the space constraints Looking at the structure of IFMIF RFQ (Figure 1), there are $N_T$=22 longitudinal locations per quadrant available for tuners. However, $N_T$ can be increased to 24 or 27, by placing the tuners in H2 surface and all the other ancillaries along H1 (see Figure 3), thus permitting the tuners to be periodically spaced. In the following the effectiveness of tuning will be discussed by comparing the case of coupled and uncoupled RFQs in terms of tuning range required, with the coupling element is located at L/2. For simplicity let us assume that the RFQ is uniform with $R_0$=4.1 mm, a=45 mm and $\chi_t$= 800 Hz/mm. In order to understand better the meaning of the tuning range, let us suppose to have a geometric perturbation $\Delta R_0$=0.04 mm if 0<z<L/2 and $\Delta R_0$=0 mm otherwise and equal in all the four quadrants. ($\Delta U(z)\neq 0$, $U_{qd1,qd2}(z)=0$). For this kind of perturbation, we have a local frequency variation equal to 500 kHz. The corresponding $\Delta U(z)/U_0(z)$ functions for the case of coupled and uncoupled RFQ are shown in Figure 5. Now, let us suppose that our tuning system is rated for $\Delta f_{TR} = 1MHz$ corresponding to $h_{max}$=28.6 mm and k=2. It is possible to show that, in this case, the voltage variation can be reduced to ±1.5% in one tuning step without exploiting the whole tuners depth capability, both for coupled and uncoupled RFQ's (Figures 4 and 5).

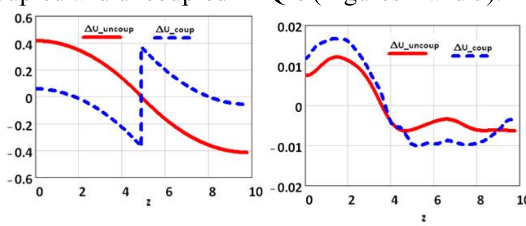


Figure 4: The $\Delta U/U_0$ function before (left) and after (right) one tuning step.

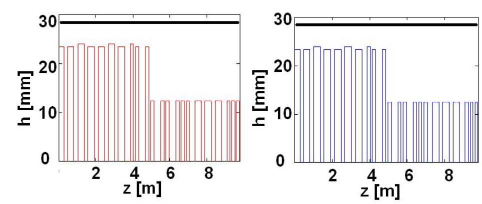


Figure 5: The tuner depths needed for the uncoupled (left) and coupled (right) case vs. tuner locations.

The situation is different if the tuning range is such that k=1. In fact, in this case, the tuning range is halved, and therefore all tuner depths saturate to $h_{max}$=14.3 mm in the first half of the RFQ and the voltage variation does not reduce less than 7.5% for the coupled case and 8.8 % for the uncoupled case. In conclusion, for our L/λ ratio, the usage of a coupling element does not reduce significantly the tuning range needed and the chosen tuning range seems to be effective to contrast perturbations also with an unsegmented structure. This is somewhat in agreement with the fact that the SNS RFQ (which is only 15% shorter than IFMIF RFQ in terms of L/λ) does not use any coupling cell.

As for the dipoles, the minimum sensitivity to dipole errors vs. boundary conditions for coupled and uncoupled structures is substantially the same. This can be shown by comparing in both cases the minimum value of the quantity $h_{dip}$ as a function of the voltage slope $s_a$= $U'_{qd1,d2}(0)/U_{qd1,d2}(0)$ (boundary condition) at the beginning of the RFQ [6]. Such quantity is defined as the maximum value with respect to z and $z_0$ of

$U_{qd1,d2}(z)/U_0(z)$ in the case of a delta capacitance perturbation located in z=$z_0$ (Figure 6).

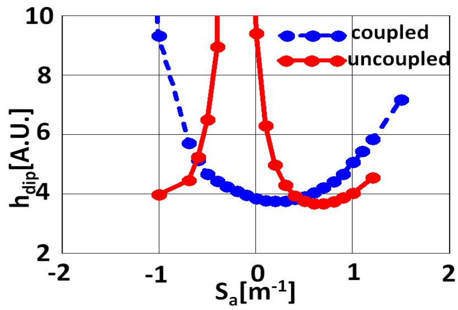


Figure 6: $h_{dip}$ comparison for IFMIF RFQ.

The tuning system effectiveness will be experimentally tested on a real-scale aluminium model of the RFQ, which will allow also the possibility of introducing a coupling element in between.

## 3D MODELING OF THE RFQ AND RELATED HFSS SIMULATIONS

The study of the 3D details of the RFQ, performed with the code HFSS v. 11.1 was concentrated mainly on the following aspects: voltage law validation, end cell design and study of the vacuum grid. In the following the power densities are calculated by using the $\alpha_{3D}\alpha_v$ margins defined before.

The validation of the voltage law was made by comparing the magnitude of the electric fields in a point ($X_0$, $Y_0$) = (1cm, 1 cm) along the symmetry axis of the quadrant given by SUPERFISH and HFSS. The agreement between the two field profiles is within 4% and the Q value calculated by HFSS is equal to 15400. Moreover, it was also possible to calculate the value of the longitudinal surface currents that are non vanishing, since the voltage profile is not constant. This component intercepts discontinuities due to modularity of RFQ, but its value (~4 A/m ) is negligible respect to the transverse component (~2000 A/m).

The design of the end cells was accomplished too, by determining the dimensions of the vane undercuts that assure the achievement of the proper boundary conditions at the RFQ extremities. For such structure, the power density was checked in view of the 3D thermo-structural calculation. In Figure 7 the geometry of the matched Low Energy undercut is shown, as well as the power density profile.

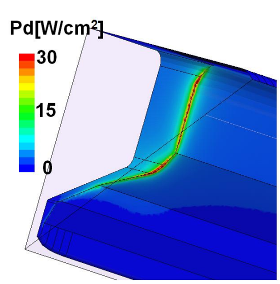


Figure 7: Power density profile along the end-cell.

As for the vacuum grids, they introduce a discontinuity in the upper wall of the RFQ, that creates a frequency shift and an enhancement in current density. In order to understand the amount of such effects, simulations on a 27.5 cm RFQ slice were performed for the grid model of Figure 8, in which the slit distance δ was varied. The results are summarized in Table 3 and Figure 9.

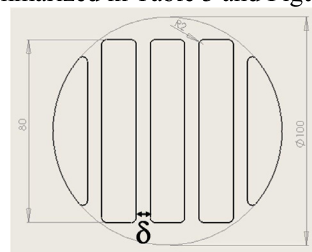


Figure 8: The vacuum grid model.

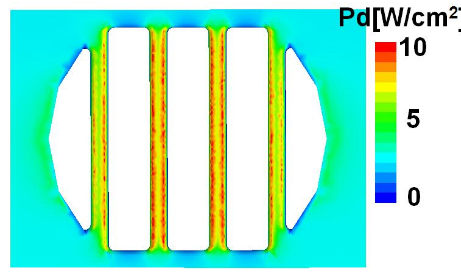


Figure 9: Power density in the vacuum grid for δ=6.5 mm.

Table 3: Vacuum Grid Main Parameters

| case | δ[mm] | f[MHz] | Pd grid [W] |
|---|---|---|---|
| nominal | No grid | 174.375 | 153 (on the flat surface to be occupied by the grid) |
| 1 | 6.25 | 174.245 | 186 |
| 2 | 7.25 | 174.267 | 187 |
| 3 | 8.25 | 174.289 | 188 |
| 4 | 9.25 | 174.312 | 179 |

The Q drop due to the vacuum grid keeps under 1% and the power density enhancement due to the grid is about 3 with respect to the flush wall. The validation of the current layout of the grid will be given upon thermal simulations whose input data are the above calculated power densities.

## REFERENCES

[1] M. Comunian, et. al. " Beam Dynamics of the IFMIF-EVEDA RFQ", EPAC 2006, Genoa (Italy).
[2] M. Comunian, et. al. this conference.
[3] A. Pisent, et. al. " IFMIF-EVEDA RFQ Design", EPAC 2006, Genoa (Italy).
[4] A. Ratti et al, Proc. LINAC98, Chicago, (USA), August 1998, p. 276.
[5] A. Pisent et al. “The TRASCO-SPES RFQ” LINAC 2004 conference, Lübeck (Germany).
[6] A. France, LNL colloquium 16 July 2007.

# FABRICATION AND TESTING OF TRASCO RFQ

E. Fagotti, Consorzio RFX, Padova, Italy and INFN/LNL, Legnaro, Padova, Italy
M. Comunian, A. Palmieri, A. Pisent, C. Roncolato, INFN/LNL, Legnaro, Padova, Italy
F. Grespan, Università degli studi di Milano, Milano, Italy and INFN/LNL, Legnaro, Padova, Italy
S. J. Mathot, CERN, Geneva, Switzerland.

## Abstract

The Legnaro National Laboratory (LNL) is building the 30 mA, 5 MeV front end injector for the production of intense neutron fluxes for interdisciplinary application. This injector comprises a proton source, a low energy beam transport line (LEBT), a radio frequency quadrupole (RFQ) and a beam transport line designed to provide a 150 kW beam to the beryllium target used as neutron converter. The RFQ, developed within TRASCO project for ADS application, is designed to operate cw at 352.2 MHz. The structure is made of OFE copper and is fully brazed. The RFQ is built in 6 modules, each approximately 1.2 meter long. This paper covers the mechanical fabrication, the brazing results and acceptance tests for the various modules.

## INTRODUCTION

The high intensity RFQ under construction at LNL, developed within TRASCO project[1] for ADS study, will be devoted to the application of Boron Neutron Capture Therapy (BNCT) for the treatment of skin melanoma[2]. The main RFQ nominal parameters are listed in Table 1.

Table 1: Main RFQ parameters

| Parameter | Value | Unit |
|---|---|---|
| Energy In/Out | 0.08/5 | MeV |
| Frequency | 352.2 | MHz |
| Proton Current (CW) | 30 | mA |
| Emit. t. rms.n. in/out | 0.20/0.21 | mm-mrad |
| Emit. l. rms. | 0.19 | MeV-deg |
| RFQ length | 7.13 | m (8.4 λ) |
| Intervane Voltage | 68 | KV (1.8 Kilp.) |
| Transmission (Waterbag) | 98.5 | % |
| Q (70% of SF result) | 7000 | |
| Beam Loading | 0.148 | MW |
| RF Power dissipation | 0.847 | MW |

The RFQ consists of three electromagnetic segments 2.4 meters long resonantly coupled via two coupling cells in order to reduce sensitivity to machining errors. Each module consists of two 1.2 meters long modules, which are the basic construction units.

In order to accelerate the 30 mA CW proton beam up to 5 MeV, the maximum amount of power expected to be delivered to the RFQ is about 995 kW (148 kW beam power + 847 kW dissipated power). The possibility of a ten percent voltage increase respect to the nominal is considered in the dissipated power value. The power is generated by one klystron and supplied to the RFQ by a WR2300 waveguide system. Due to the fact that each RF coupler is rated for a maximum of 140 kW[3], the RF power is split in eight ways via magic-Tee dividers. An artistic view of the integration of the RF distribution, vacuum system and support is presented in Fig.1.

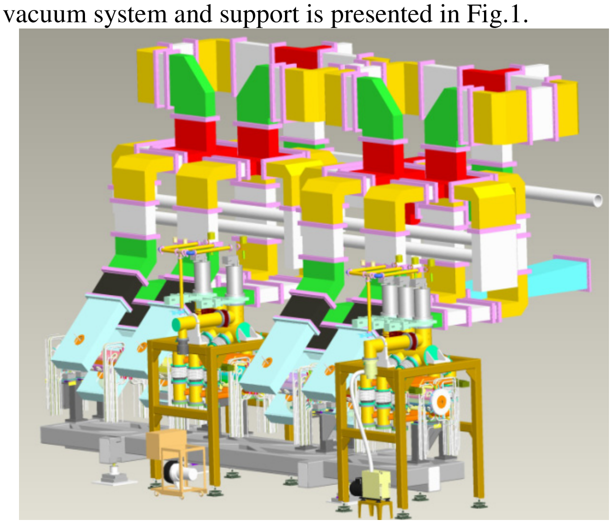

Figure 1: Integration of RFQ with ancillaries.

## MECHANICAL FABRICATION AND BRAZING

Each module, built in OFE copper, is made of four main parts. The head flanges between modules and the rectangular vacuum flanges are made of SS (LN316). To reduce the number of brazing joints, the longitudinal cooling passages are deep-hole drilled from one side and closed with brazed plugs on the flat surfaces of the RFQ module (opposite to the coupling or end cells). Moreover, the vacuum grids with their cooling channels are directly machined on the copper bulk.

Two brazing steps occur. In the first the four main parts are brazed in horizontal position in a horizontal vacuum furnace, as well as the OFE plugs for the cooling channels. The brazing alloy is Ag68CuPd-807/810 (57.3% at., 38,4% at., 4.3% at.) and the brazing temperature is 815°C. After first brazing, housings for the head flanges and the flat end surfaces (where the cooling channel plugs are located) are machined. In the second brazing cycle the head SS flanges, the inlet and outlet cooling water SS tubes, the SS supports for vacuum ports flanges and the SS flanges for couplers are brazed in vertical position in a vertical vacuum furnace. The brazing alloy is Ag72Cu-779 (40% at.) and the brazing temperature is 785ºC.

Maximum temperature of the OFE copper stabilization cycle before finishing turned out to be extremely important to avoid deformation after brazing. For the first two modules this temperature was 250ºC. After brazing both the modules showed a two hundreds microns longitudinal bending (banana shape). Moreover the module 2 presented an important displacement in one transversal direction that entailed the opening of eight more tuner holes for frequency recovery. Relaxation of stress induced during machining was identified as the main effect in comparison with the deformations due to the brazing heat treatment.

Consequently machining procedure changed. For the remaining modules a full annealing at 600 °C preceded finishing. In addition finishing was as soft as possible in order to minimize induced stress. The success of the new procedure was evident after the brazing of the third module (Fig.2). Banana shape and transversal movements generated by brazing heat treatment turned out to maintain nominal tolerances (±20 µm). Almost the same results were obtained after brazing of RFQ4 and RFQ5.

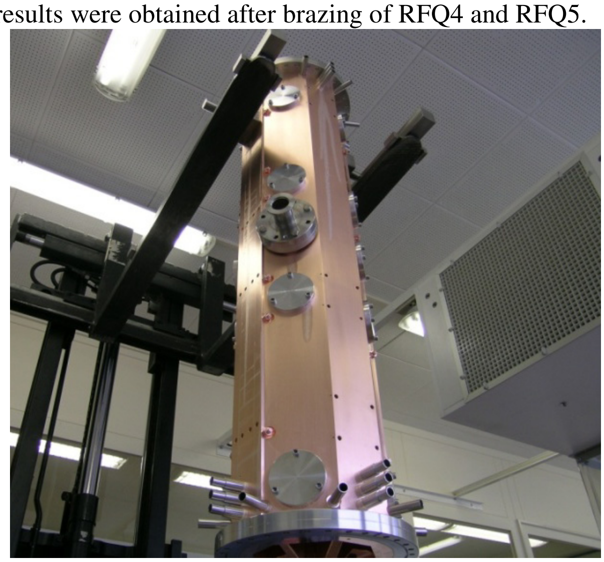

Figure 2: Module 3 after vertical brazing.

Some minor problems characterized the brazing of module 3 and 4. Module 3 experienced a vacuum leak after vertical brazing. Leak was caused by a bad nickelization process of the head SS flanges. A repairing brazing was attempted before summer without success. This will force to remove the head flanges and to repeat the vertical brazing with new nickelized flanges. Regarding RFQ4, the water channel plugs experienced some problem of brazing alloy flow. Plugs with not visible brazing alloy were removed and re-brazed in the vertical brazing last week. RFQ6 is currently under first brazing.

The plan for the next future foresees the brazing completion before the end of the year.

## ACCEPTANCE TESTS

RF and mechanical measurements allow checking the correctness of each fabrication step.

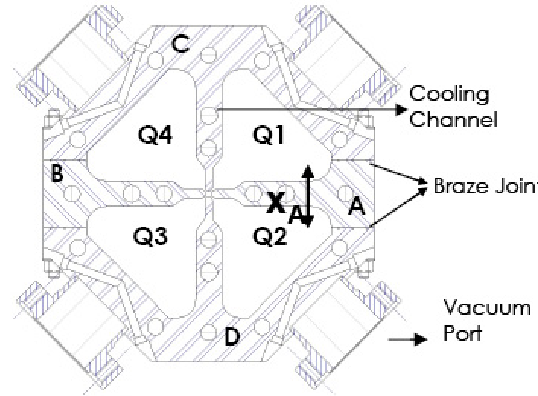


Figure 3: Nomenclature for electrodes and quadrants.

With reference to Fig.3, let $\Delta x$ be the extra thicknesses of the electrodes A and B, with respect to their nominal values $\Delta y$ the amount of extraction of the electrodes A and B with respect to their nominal position. The initial values of such parameters are $\Delta x$=50µm and $\Delta y$=0µm. The first measurement step foresees the determination of the quadrupole and dipole frequency {fQ, fD1, fD2} in such configuration and with tuners set at the nominal penetration. Then $\Delta y$ is varied by means of the application of calibrated spacers and a new set of {fQ, fD1, fD2} is found. The knowledge of these two sets permits us to determine the values of $\Delta x^*$and $\Delta y^*$ that fulfil the conditions fQ= 352.2 MHz and fD1=fD2 within the precision limits of the spacers and of the milling machine (±10µm). Then the thickness $\Delta x^*$ is removed from the electrodes A and B and the definitive spacers are applied. With this configuration the tuning operations (based on bead-pulling measurements) are performed up to the achievement of an overall ±5% longitudinal uniformity of the electric fields in all quadrants.

The modules RFQ2 to RFQ6 successfully underwent such characterization before 1st brazing step with the values for $\Delta x^*$ and $\Delta y^*$ presented in Table.2. Concerning RFQ1 the $\Delta y$ tuning was not yet introduced; as a result the quadrupole mode was tuned, but the two dipoles were splitted by about 2 MHz.

For RFQ1 and RFQ2 the entire set of RF measurements (including bead pulling) was repeated at CERN immediately before brazing. The reproducibility found allowed to skip this step for the following modules.

After brazing, a set of mechanical measurements is foreseen in order to check the effect of brazing upon some important parameters, namely the reference plane distance (directly related to $R_0$) and the width of the coupling gap. Then the tuning procedure is repeated up to the achievement of the above-mentioned specifications.

Table 2: Pre-braze setting for the RFQ modules.

| Module | $\Delta x^*$[µm] | $\Delta y^*$[µm] |
|---|---|---|
| RFQ2 | 70 | 20 |
| RFQ3 | 50 | 50 |
| RFQ4 | 70 | 50 |
| RFQ5 | 65 | 40 |
| RFQ6 | 60 | 15 |

To date modules up to RFQ3 underwent such characterization, with somewhat different outcomes. As for RFQ2 a quadrupole frequency increase of 700 kHz and a ± 20% dipole content on the operational mode were observed after brazing. Such a unexpected voltage variation, related to the abnormal bending discussed in the previous paragraph, could not be completely recovered with standard tuners. Therefore eight additional holes for tuners (four in Quadrant 1 and four in Quadrant 4) were machined and the required voltage flatness was recovered. As for the other modules, the RF measurement and tuning procedure was carried out without any particular problem.

## RF MEASUREMENTS ON THE 1ST RFQ SEGMENT (RFQ1+RFQ2)

The first RFQ segment was mounted at LNL for low power RF and vacuum tests (Fig.4). Prior to the vertical assembling of the two modules, the beam axis of each RFQ was characterized, and the necessary reference planes and pins were machined.

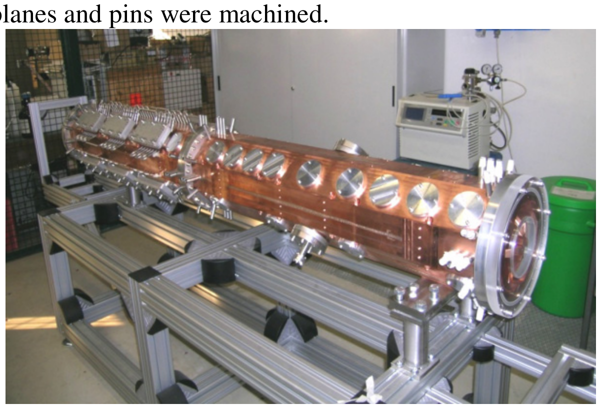

Figure 4: The 1st RFQ segment mounted at LNL.

In order to allow a complete RF characterization, the segment was equipped on low and high energy sides with two aluminum Tunable End Cells (Fig.5) equipped with variable dipole stabilizing rods (DSR). The RF measurements were performed in steps: first the optimum length and transverse position of DSRs that guaranteed the maximum dipole-free region (about ±7 MHz) around the operating mode were determined: the optimum DSR length are equal to Then, the boundary conditions for the $TE_{210}$ mode were tuned by inserting the octagon in the RFQ volume.

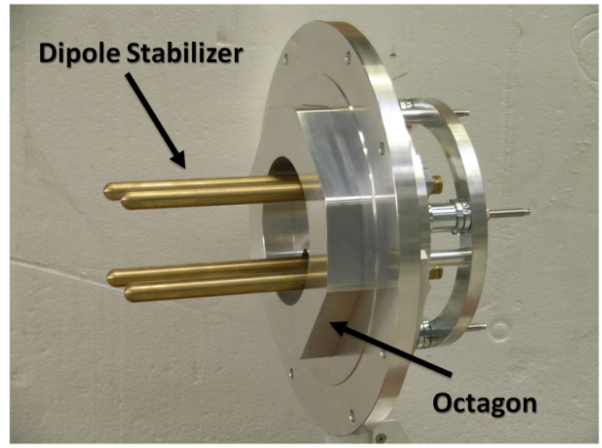


Figure 5: The Tunable End Cell.

Finally the bead pull measurements and the tuning operations (based on an on-purpose developed algorithms making use on the RFQ modal expansion) were performed. The effectiveness of the tuning algorithms is shown in the following two figures, where the voltage perturbations due to upper quadrupole modes and the two kinds of dipole modes □(□)/□$_0$ and □$_{□□1,□□2}$(□)/□$_0$ are shown before and after tuning (Fig. 6 and 7).

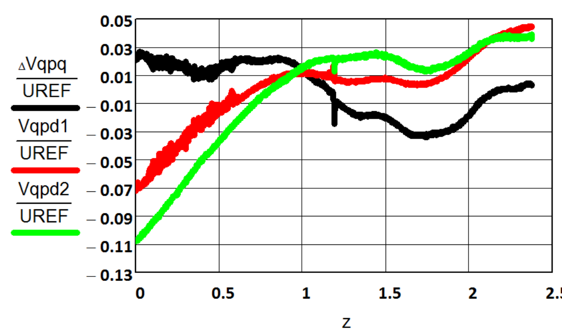


Figure 6: Perturbative quadrupole (black) and dipole (red and green) components before tuning.

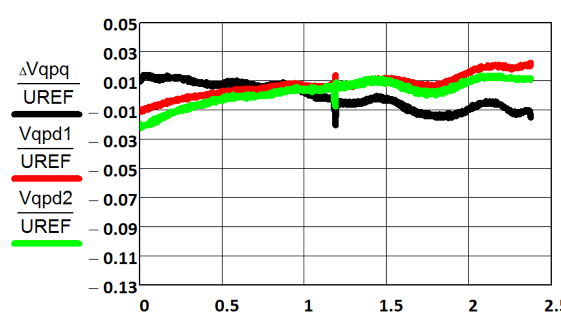


Figure 7: Perturbative quadrupole (black) and dipole (red and green) components after tuning.

## REFERENCES


[1] SPES proposal 2007
[2] A.Pisent, et al LINAC04, Lübeck, Germany. p. 69
[3] A.Palmieri, et al., Proc. of the XXI Linac Conference, Gyeonju (Rep. of Korea), 18-22 August 2002.

# DESIGN OF A 2-BEAM TYPE IH-RFQ LINAC FOR HIGH INTENSE HEAVY ION BEAM ACCELERATIONS IN LOW ENERGY REGION

Takuya Ishibashi#, Noriyosu Hayashizaki, Toshiyuki Hattori,
Research Laboratory for Nuclear Research, Tokyo Institute of Technology, Tokyo, Japan

*Abstract*

For generating high intense ion beams from a linear accelerator (linac) stably, it is necessary to suppress the defocusing force between the charged particles. The defocusing force is extremely strong in low energy and high intense beams. Therefore, high intense ion beam acceleration in the low energy region is one of the most difficult conditions to achieve. One of the solutions is to suppress the defocusing force by dividing the high intense beam into several beams. Thus, a multibeam IH type Radio Frequency Quadrupole (IH-RFQ) linac has been proposed for the low energy and high intense beam acceleration. In particular, we have been developing a 2-beam type IH-RFQ cavity as a prototype of the multibeam type IH-RFQ.

## INTRODUCTION

High intense ion beam acceleration in the low energy region is one of the most difficult conditions to achieve due to the space charge effect. As a solution for this problem, an idea has been proposed to divide a single, high intense beam into several beams, and merge these beams into a single high intense beam with higher energy. Toward this end, an accelerator technology for a heavy ion inertial confinement fusion driver has been studied [1-3].

There is a HIBLIC in Japan that serves as a conceptual design of the inertial confinement fusion reactor [1]. The design requires 16 RFQ linacs for the first acceleration stage because the maximum output current limit is estimated to be 35 mA in the conventional RFQ linac. In this case, a beam is accelerated in a cavity conventionally. Thus, if several beams can be accelerated in a cavity towards a cascade acceleration, this method would be better than the existing systems in terms of space and cost economy.

Therefore, multibeam type linacs, which consist of several beam channels in one cavity, have been studied. For instance, a multibeam type RFQ linac with an IH structure was proposed at GSI in Germany [4]. However, there have been no previous cases in which the actual machine was manufactured. Consequently, we have developed an IH-RFQ linac with two beam channels in one cavity as a prototype for the multibeam type linac.

## DESIGN AND PARAMETERS

The external appearance of the 2-beam type IH-RFQ cavity is shown in Fig. 1, which consists of two sets of quadrupole electrodes. The RF electromagnetic field is stimulated by the $TE_{111}$ mode as well as the IH cavity. The RFQ electric field is generated by four rods installed in each of the stems taking the polarity into consideration. We adopted a structure separated into three parts, a main frame and two semi cylinders, for ease in fabrication and modification of the electrodes.

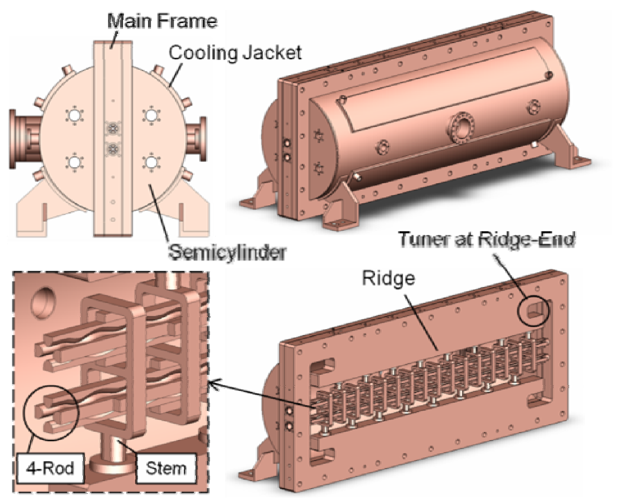


Figure 1: External appearance of the 2-beam type IH-RFQ.

The RFQ cavity can replace a resonance circuit equivalently, and the four gaps between the quadrupole electrodes in the RFQ are represented as the electrical capacitance in the resonance circuit. The resonance frequency is proportional to $(LC)^{-0.5}$. $L$ and $C$ are inductance and electrical capacitance in the cavity respectively. The electrical capacitance of the 2-beam type IH-RFQ cavity increases compared to the single beam type because the 2-beam type structure has two sets of quadrupole electrodes. This allows a comparatively low frequency to be achieved within a small cavity diameter. The cuts at the end of the ridge adjust the resonance frequency by changing the area of the magnetic flux surface and the inductance in the cavity.

Acceleration properties of the 2-beam type and the single beam type IH-RFQ linac were simulated [5]. The results demonstrated that the cavity diameter and length of the 2-beam type cavity are more compact than those of the single beam type cavity. The transmission of the 2-beam type cavity is 34% larger than that of the single beam type cavity, which has double the cross section of the beam channel in the 2-beam type. However, the beams from the multibeam type cavity need to be merged because the total emittance of the several output beams is too large for most applications to handle. There is a

# ishibashi.t.aa@m.titech.ac.jp

possibility that a portion of the ion beams are lost due to beam funneling, so beam funneling technology with efficiency is required for multibeam acceleration.

The accelerated particles were set to q/A≥1/6, and $C^{2+}$ beams will be accelerated in the test of this linac. The resonance frequency in this cavity is 46.2 MHz in MW-Studio calculation. The input energy is 5 keV/u considering beam dynamics simulations and the voltage at which the beam will be extracted from an ion source. Taking into consideration the maximum output of the RF power source, the wall loss is saved less than about 80 kW including beam loading. A Kilpatrick factor of the maximum field at inter-rod is 1.8 which is the ratio of electric field to the Kilpatrick criterion.

Table 1 shows the main parameters for the 2-beam type IH-RFQ linac. The computer code RFQUICK was used to generate the cell parameters for the PARMTEQM calculation [6]. The RFQUICK is suitable for the design of RFQ linacs whose output beam currents exceed 10 mA. The computer code PARMTEQM was used to simulate the beam dynamics in the RFQ. The electromagnetic simulation software MW-Studio was used to calculate the resonance frequency, the Q value and the wall loss of the cavity.

Table 1: Main Parameters for the 2-beam Type IH-RFQ

| | |
|---|---|
| Chargh to mass ratio (q/A) | 1/6 |
| Input energy (keV/u) | 5 |
| Output energy (keV/u) | 60 |
| Resonance frequency (calculated by MW-Studio) (MHz) | 46.2 |
| Rod-tip type | $0.75r_0$ |
| Modulation type | Standard |
| Average bore radius, $r_0$ (cm) | 0.76 |
| Minimum bore radius, $a_{min}$ (cm) | 0.41 |
| Cavature radious of rod-tip (cm) | 0.57 |
| Focusing strength, $B$ | 8.754 |
| Defocusing strength (at exit of the gentle buncher section), $\|\Delta\|$ | 0.216 |
| Synchronous phase, $\phi_s$ (degree) | -90 → -30 |
| Rod length (cm) | 148.12 |
| Total number of cells | 104 |
| Cavity length (cm) | 150 |
| Cavity diameter (cm) | 49.2 |
| Maximum field at inter-rod (Kilpat.) | 1.8 |
| Q value (calculated by MW-Studio) | 7500 |
| Wall loss (at normalized inter-rod voltage, 80% Q) (kW) | 25 |

## BEAM DYNAMICS SIMULATION

Table 2 shows the parameters of the input beam for the beam dynamics simulations. $\alpha_t$ and $\beta_t$ refer to twiss parameters, and $\varepsilon_t$ refers to the emittance at the transverse direction. The parameters were determined under the assumption that a laser ion source with a direct plasma injection scheme would be adopted as the injection system for the linac [7]. The particle distribution of the 4-D waterbag exhibits a uniform phase and a random energy spread [6].

Table 2: Parameters of the Input Beam for the Beam Dynamics Simulation

| | |
|---|---|
| Beam current (mA) | 60 |
| Number of particles | 10000 |
| $\alpha_t$ | 3.4 |
| $\beta_t$ (cm/rad) | 12.7 |
| $\varepsilon_t$ (π mm.mrad, RMS, normarized) | 0.1 |
| Distribution | 4-D waterbag |
| phase | uniform |
| energy | 5keV/u, random |

Figure 2 shows the output beam profile at the end of the 4-rod. The emittance and the twiss parameters at the end of the rods are shown in Table 3. When a beam current of 60 mA from an ion source is injected into a beam channel, the 2-beam type IH-RFQ linac accelerates an output current of 43.6 mA per beam channel. As a result, when the total beam current of 120 mA is injected into the two beam channels, the total output current from the cavity will be 87.2 mA.

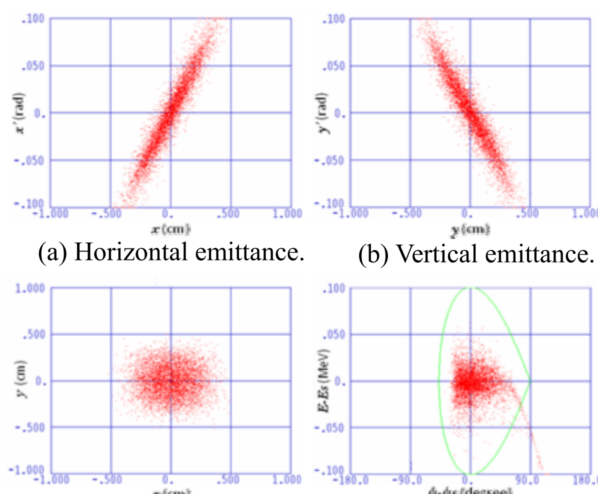

(a) Horizontal emittance. (b) Vertical emittance.

(c) Particle distribution on the real plane. (d) Longitudinal emittance.

Figure 2: Beam profile at the end of the 4-rod.

Table 3: Parameters of the Output Beam from a Beam Channel

| | |
|---|---|
| Transmission (%) | 72.7 |
| Output current (mA) | 43.6 |
| $\alpha_x$ | 1.8 |
| $\beta_x$ (cm/rad) | 14.8 |
| $\varepsilon_x$ (π mm.mrad, RMS, normarized) | 0.25 |
| $\alpha_y$ | -1.6 |
| $\beta_y$ (cm/rad) | 10.5 |
| $\varepsilon_y$ (π mm.mrad, RMS, normarized) | 0.23 |
| $\alpha_z$ | 0.69 |
| $\beta_z$ (degree/MeV) | 1473 |
| $\varepsilon_z$ (π MeV.degree, RMS, normarized) | 0.33 |

The output current against the input current in this design is shown in Fig. 3. The output current saturates when the input beam current reaches 120 mA and above. Figure 4 shows the output current against the Kilpatrick factor at the inter-rod. The output current can rise to about 8% by increasing from 1.8 to 2.2 Kilpatrick factor.

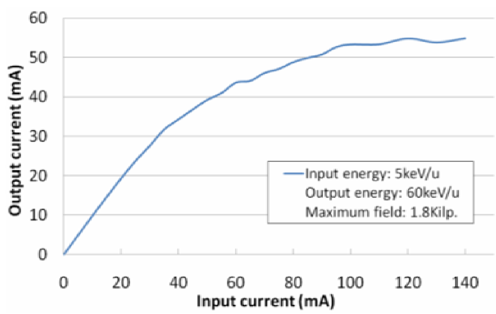


Figure 3: Output current versus the input current per beam channel.

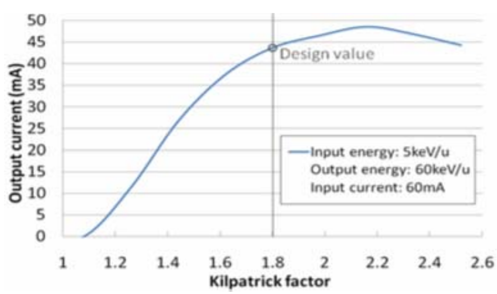


Figure 4: Output current per beam channel versus Kilpatrick factor.

## RF MEASUREMENT

As shown in Fig. 5., the actual machine of the 2-beam type IH-RFQ cavity was manufactured, and the low power RF property of the cavity in room air was measured by using a network analyzer (E5070B made by Agilent Technologies, Inc.). At the time of the measurement, the room air temperature, the cavity temperature and the humidity were 31.2°C, 30.4°C and 51.5% respectively. The $S_{21}$ parameter in $TE_{111}$ mode is shown in Fig. 6. The resonance frequency and the Q value were about 46.99MHz and about 5900 respectively.

Figure 5: Low power RF measurement of the 2-beam type IH-RFQ cavity.

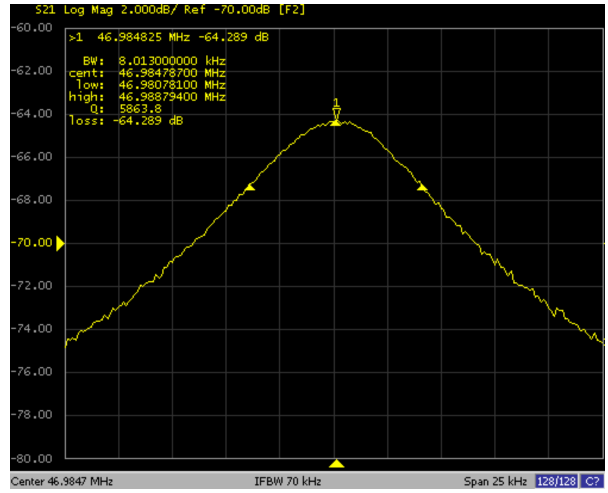


Figure 6: $S_{21}$ parameter in $TE_{111}$ mode.

The Q value in the real cavity goes down to about 80% from the calculated value because electrical contacts and surface roughness of the elements in the cavity are less than perfect. In the case of a 2-beam type RFQ with a π-0 mode structure, the Q value in the real cavity was 2000-3000 [8]. This indicates that the 2-beam type IH-RFQ is more power-efficient than the type with the π-0 mode structure because the power loss per RF cycle in the cavity is in inverse proportion to the Q value.

## CONCLUSION

We have studied a multibeam type IH-RFQ linac that is a practical and efficient method to accelerate high intense and low energy ion beams and developed a 2-beam type as the prototype. The actual machine of the 2-beam type IH-RFQ has been manufactured, and the RF property has been measured.

The results of the beam dynamics simulations demonstrated that the total output current from the 2-beam type IH-RFQ linac is 87.2 mA to yield a total input current of 120 mA in q/A=1/6 particle acceleration. The output current from the 2-beam type IH-RFQ can exceed that from the conventional RFQ.

## REFERENCES


[1] Y. Fujiie, *et al.*, Research Report Institute of Plasma Physics Nagoya University, HIBLIC-heavy ion fusion reactor, Rep. IPPJ-663 (1984).

[2] I. Hofmann, Nucl. Instr. Meth. A 415 (1998) 11.

[3] HIBALL-A Conceptual Heavy Ion Beam Driven Fusion Reactor Study, Kahlsruhe, Germany KfK-3202, UWFDM-450, (1981).

[4] U. Ratzinger, *et al.*, Nuclear Instruments and Method in Physics Research A, 415 (1998) 281.

[5] Takuya Ishibashi, *et al.*, Nuclear Instruments and Methods in Physics Research B, 266 (2008) 2146.

[6] K.R. Crandall, *et al.*, LA-UR-96-1836 (2005).

[7] M. Okamura, *et al.*, Proc. LINAC2002 (2002) 91.

[8] A. Firjahn-Andersch, *et al.*, Proc. Particle Accelerator Conference 1997 (1997) 1081.

# THE RADIOFREQUENCY QUADRUPOLE ACCELERATOR FOR THE LINAC4

C. Rossi, P. Bourquin, J.-B. Lallement, A. M. Lombardi, S. Mathot, M. Timmins, G. Vandoni, M. Vretenar ,CERN, Geneva, Switzerland.
S. Cazaux, O. Delferriere, M. Desmons, R. Duperrier, A. France, D. Leboeuf, O. Piquet, CEA, Saclay, France.

*Abstract*

The first stage of acceleration in Linac4, the new 160 MeV CERN H$^-$ injector, is a 352 MHz, 3-m long Radiofrequency Quadrupole (RFQ) Accelerator. The RFQ will capture a 70 mA, 45 keV beam from the RF source and accelerate it to 3 MeV, an energy suitable for chopping and injecting the beam in a conventional Drift Tube Linac. Although the RFQ will be initially operated at low duty cycle (0.1%), its design is compatible with higher duty cycle (10%) as the front-end for a possible high-intensity upgrade of the CERN linac facility.

The RFQ will be of brazed-copper construction and will be built and assembled at CERN. Beam dynamics design allows for a compact structure made of a single resonant unit. Field symmetry is ensured by fixed tuners placed along the structure. In this paper we present the RF and mechanical design, the beam dynamics and the sensitivity to fabrication and to RF errors.

## INTRODUCTION

In Linac4 an RFQ is required to capture the beam extracted from the H$^-$ ion source and accelerate it to an energy suitable for injection in the following DTL [1]. This energy must also be compatible with the operation of a chopper line, used to create a microstructure in the beam pulse. The initial Linac4 plans considered using the RFQ developed and built by CEA and IN2P3, for their IPHI project [2].

The possibility to adopt a lighter design, by reducing the injection energy and adopting a different acceleration profile, made CERN decide in 2007 to build a dedicated RFQ, which could profit from the tools and experience developed at CEA within the IPHI and SPIRAL2 projects, thus reducing the R&D cost and time. Besides, CERN has recently brazed the RFQ for the TRASCO project and therefore has contributed to the related mechanical design and gained access to this manufacturing experience [3].

## BEAM DYNAMICS CONSIDERATIONS

The RFQ must initially be able to operate in Linac4 to fill the PS Booster, delivering beam pulses of 400 µs at 1.1 Hz, and, at a later stage, to fill a Superconducting Proton Linac (SPL) operated as LHC injector (1.2 ms, 2 Hz). In case a high intensity beam programme would be approved, the option is left open to operate with 400 µs, 50 Hz pulses. These different requirements represent an additional complication to the design. The specification parameters are listed in Table 1.

Table 1: Main Design Specification for the Linac4 RFQ, with rms Values of Emittance in the Two Planes

| Linac4 RFQ Parameter | Min | Max | Units |
|---|---|---|---|
| Beam energy | 3.0 | 3.0 | MeV |
| Operating frequency | 352.2 | | MHz |
| Peak beam current (pulse) | 10 | 80 | mA |
| RF duty cycle | 0.08 | 7.5 | % |
| Transverse emittance (in) | 0.20 | 0.35 | π mm mrad |
| Longitudinal emittance (out) | 0.11 | 0.20 | π deg MeV |

The decision to designing a dedicated RFQ came after the chopper line elements had already been procured and assembly plans made. The output beam parameters of the new RFQ have to be similar to the IPHI ones or at least compatible with the existing chopper line. Other constraints on the design are the requirement to limit the RF power to 0.8 MW peak, corresponding to a single LEP klystron with a sufficient safety margin, and to keep the RFQ length around 3 m. This allows dividing the RFQ into 3 segments of 1 meter while keeping the overall length at 3.5 λ, thus allowing the direct coupling of the three RFQ sections without using coupling cells between sections.

The results of the redesign is a compact RFQ (3 m vs 6 m of IPHI) with an intra-vane voltage of 78 kV and a peak surface field of 34 MV/m (1.84 times the Kilpatrick limit). The main design parameters are shown in Figure 1.

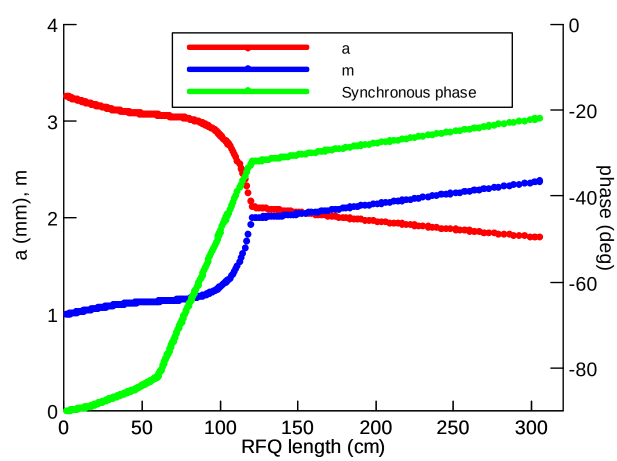


Figure 1: Graph of the synchronous phase, with the RFQ aperture a and modulation parameter m.

The considerable reduction in length was made possible by the lower injection energy, a higher focusing factor and a compromise on the current limit (80 mA vs. 100 mA). The beam quality for the nominal current is equivalent to that of the 6 m long IPHI RFQ. The value for the peak surface field appears acceptable as it is reached over a short section and the RFQ is not meant to work in CW mode.

The minimum value for the aperture a is 0.18 cm and the maximum modulation factor m is 2.38.The main beam parameters, evaluated for 70 mA of beam current, are summarized in Table 2.

Table 2: Summary of the Main Beam Dynamics Parameters for the Linac4 RFQ (rms Values of Emittance)

| RFQ Beam Parameter | Value | Units |
|---|---|---|
| Beam input energy | 0.045 | MeV |
| Beam output energy | 3.0 | MeV |
| Nominal beam current | 70 | mA |
| Average aperture $r_0$ | 0.33 | cm |
| Ratio $\rho/ r_0$ | 0.85 | |
| Focusing parameter | 5.77 | |
| Input emittance (norm) | 0.25 | $\pi$ mm mrad |
| Acceptance at zero current | 1.7 | $\pi$ mm mrad |
| Longitudinal emittance (out) | 0.13 | $\pi$ deg MeV |
| Transmission | 95 | % |
| Transverse emittance growth | 0 | % |

## RF DESIGN

The RFQ cavity design has been driven by the aim of keeping the design as simple as the project requirements could allow.

The 2D section of the RFQ cavity has been kept constant over the full RFQ length, in order to simplify the mechanical fabrication. The intra-vane voltage is also constant at 78 kV and the tuning of the accelerating field profile is left to 12 tuners per quadrant distributed over the accelerator length. Table 3 shows the 2-dimensional electrical parameters for the quadrupole cut-off frequency mode, i.e. without tuner and end-cell contributions.

Table 3: RFQ Electrical Parameters (2D Simulation)

| RFQ Electrical Parameter | Value | Units |
|---|---|---|
| Vane voltage | 78.27 | kV |
| Quality factor (unloaded) | 10269 | - |
| Stored energy | 0.372 | J/m |
| Dissipated power | 78.738 | kW/m |
| Magnetic field (max) | 5444 | A/m |

The design of a short RFQ has helped in minimizing the RF power requirements from the klystron and one klystron should be sufficient to drive the RFQ in all conditions. This also allows the use of a single input RF coupling port: an iris coupled ridged waveguide connecting the WR2300 reduced height RF window to the RFQ cavity.

The impact of the vane modulation on the cut-off frequency of the transmission line modes has been studied by means of 3D simulations, showing a frequency reduction of 0.208 MHz for the quadrupole mode and of 3.871 MHz for the fundamental dipole mode when the modulation is taken into account.

The frequency separation between the accelerating quadrupole mode and the adjacent dipole modes is about 5 MHz, which should guarantee sufficient stability during operation in all conditions. The study for the tuning of the end cells has shown that dipole rods are not required to displace the dipole modes which are closer to the accelerating mode due to the favourable length of this design. The proper tuning of the end-cells should guarantee a voltage error in the RFQ not exceeding ±1 %.

First simulations have shown that eight cooling channels should be sufficient to allow temperature stabilization of the RFQ cavity, because of the limited dissipated power in pulsed mode. The dynamic tuning strategy is based on two cooling circuits, one using four channels drilled inside the vane pole tips and the other using four channels in the RFQ body. The dynamic tuning of the RFQ cavity is obtained by regulating the water temperature difference between the two circuits.

Thirty-two fixed tuners (80 mm diameter) plus the RF and the dummy RF ports will allow achieving a flat electrical field for the quadrupole accelerating mode. The nominal tuner position has been set at 15 mm inside the cavity to allow linear frequency variations as a function of the tuner penetration. The total peak power dissipated in the tuners will be less than 100 kW.

## MECHANICAL DESIGN

The RFQ cavity is made of three sections, each one-meter long, directly coupled. Each of the three sections results from the assembly of two major vanes and two minor vanes. A CAD picture of the RFQ is shown in Figure 2.

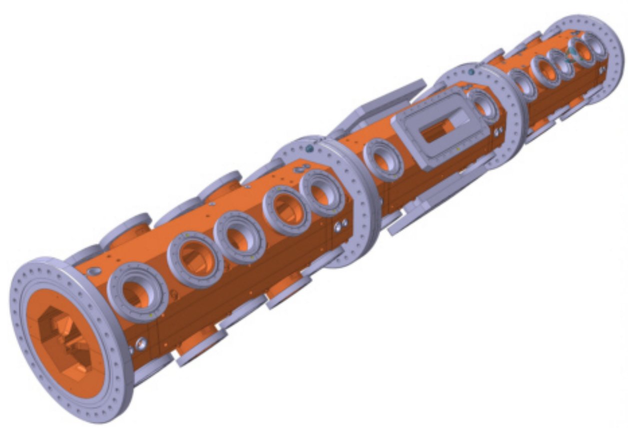

Figure 2: Linac4 RFQ.

The structure is equipped with a total of thirty-two circular apertures, 82 mm diameter, to host the fixed tuners; four rectangular apertures have been designed in the central section for the RF input(s). The first and last section holds eight circular apertures that have been designed to host the vacuum pumping ports. The design of the vacuum system takes into account that the main gas load is coming from the LEBT gas injection used for neutralization and is estimated at 1.1 $10^{-3}$ mbar l/s, whereas the gas load from outgassing is only 1.5 $10^{-5}$ mbar l/s. By using eight diode ion pumps and four turbo molecular pumps the effective pumping speed of 2700 l/s is obtained, which allows to keep the dynamic vacuum level of the RFQ in the range of $10^{-7}$ mbar.

The vane modulation is achieved by a milling machine using a wheel shaped cutting tool. The assembly of the RFQ cavity will be performed by means of a two-step brazing procedure that has been developed at CERN during the fabrication of the IPHI and TRASCO RFQs [4].

The first assembly step of the four poles is made by brazing in the horizontal position, at 825 °C, which allows a uniform diffusion of the brazing material, by capillary action. The second assembly step, performed in a vertical oven at 790 °C, brings the stainless steel flanges and end-flanges onto the RFQ cavity.

The OFE copper used for fabrication has been submitted to a severe 3D forging, in order to obtain the maximum of homogeneity in the raw material. A detailed procedure, alternating machining phases to thermal annealing cycles has been established in order to stabilize the material and avoid deformations and possible displacements of the vanes, especially on the occasion of the first brazing step.

The machining and assembly tolerances have been defined following an error study simulation campaign, which showed that the beam dynamics design adopted is relatively insensitive to errors. The most important contributions come from section tilts and electromagnetic field errors. The set of errors considered is summarized in Table 4, while Table 5 shows how such errors affect the beam dynamics.

Table 4: RFQ Mechanical and Field Tolerances

| **Linac4 RFQ Tolerances** | **Value** | **Units** |
|---|---|---|
| Machining error | ± 20 | μm |
| Vane modulation error | ± 20 | μm |
| Vane tilt over 1 m | ± 100 | μm |
| Vane positioning error (displacement h+V) | ± 30 | μm |
| Vane thickness error | ± 10 | μm |
| Contiguous section gap | 100 ± 15 | μm |
| Section tilt over 1 m | ± 30 | μm |
| Klystron error | ± 1 | % |

Table 5: Beam Degradation Due to Mechanical and Field Errors

| | Losses % | EmitX % | EmitY % | EmitZ % |
|---|---|---|---|---|
| Average | 1.674 | 2.034 | 2.146 | 3.497 |
| Min | -0.940 | -1.839 | -1.573 | -3.442 |
| Max | 5.098 | 6.813 | 6.508 | 17.107 |
| StDev | 0.940 | 1.337 | 1.239 | 3.093 |

## ORGANISATION, STATUS AND PLANNING OF THE PROJECT

The RFQ project has been organized in two work packages: the first is responsible for establishing the general design (beam dynamics, RF design, thermal loads) and performing the RF measurements, tuning and final commissioning, while the second is in charge of the mechanical design and of the fabrication (raw material procurement, machining, assembly). The first work package relies on the contribution from CEA for the RF design, the thermo-mechanical calculations, the RF measurements and the final tuning.

The general design is now complete and execution drawings are being prepared. The 3D forged copper has been purchased and delivered; first machining tests have started at the CERN workshop. The start of the machining of the first section is expected before the end of 2008.

The Linac4 RFQ is expected to become available earlier than needed for Linac4 installation. It will be installed in a dedicated 3 MeV Test Stand to test the beam dynamics of the Linac4 low energy end [5]. Since all emittance increase and beam degradation occurs before 3 MeV, three aspects of beam dynamics must be carefully studied: the space charge control at low energy, the beam chopping and re-matching to the DTL and the beam matching to the RFQ in the presence of neutralization. Studies cannot be performed any more once the front end has taken its place in the Linac4 tunnel. The 3 MeV Test Stand is already in an advanced stage of preparation, the klystron and the prototype modulator that will be used for feeding RFQ have already been tested. The ion source is presently being assembled and the LEBT and chopper lines are in the installation phase. The RFQ schedule is shown in Figure 3.

The Linac4 RFQ will accelerate beam at the Test Stand during 2010 and the first half of 2011. In order to achieve this goal, the RFQ construction has to be completed in the first months of 2010.

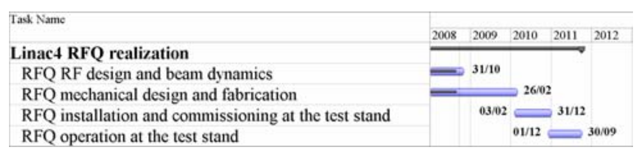


Figure 3: Linac4 RFQ project schedule.

## REFERENCES

[1] M. Vretenar, C. Carli, R. Garoby, F. Gerigk, K. Hanke, A.M. Lombardi, S. Maury, C. Rossi, "Status of the Linac4 Project at CERN", this conference.

[2] P.-Y. Beauvais, "Recent Evolutions in the Design of the French High Intensity Proton Injector (IPHI)", EPAC04, Lucerne, Switzerland.

[3] E. Fagotti, M. Comunian, F. Grespan, S. Mathot, A. Palmieri, A. Pisent, C. Roncolato, "Fabrication and Testing of TRASCO RFQ", this conference.

[4] S. Mathot, "RFQ Vacuum Brazing at CERN", EPAC08, Genova, Italy.

[5] A.M. Lombardi, M. Baylac, G. Bellodi, R. Duperrier, J.-B. Lallement, S. Lanzone, E. Sargsyan, D. Uriot, "End-to-end Beam Dynamics for CERN Linac4", HB2006, Tsukuba, Japan (2006).

# THE FABRICATION AND INITIAL TESTING OF THE HINS RFQ*

G.Romanov#, G.Apollinari, B.Hanna, T.Khabiboulline, A.Lunin, A.Moretti T.Page, J.Steimel, R.Webber, D.Wildman, Fermilab, Batavia, IL 60510, USA
P.Ostroumov, ANL, Argonne, IL 60439, USA

*Abstract*

Fermilab is designing and building the HINS front-end test facility. The HINS proton linear accelerator consists of a normal-conducting and a superconducting section. The normal-conducting (warm) section is composed of an ion source, a 2.5 MeV radio frequency quadrupole (RFQ), a medium energy beam transport, and 16 normal-conducting crossbar H-type cavities that accelerate the beam to 10 MeV. Production of 325MHz 4-vane RFQ is recently completed. This paper presents the design concepts for this RFQ, the mechanical design and tuning results. Issues that arose during manufacturing of the RFQ will be discussed and specific corrective modifications will be explained. The preliminary results of initial testing of RFQ at the test facility will be presented and comparisons with the former simulations will also be discussed.

## INTRODUCTION

Within the framework of the High Intensity Neutrino Source (HINS) program at FNAL, we plan to build and operate a portion of the Front End (up to energies of 90 MeV) as a technical feasibility proof of the proposal. A detailed description of the project and the current status is given in [1]. In the Front End test stand a four vane 325 MHz Radio Frequency Quadrupole (RFQ) will be used for bunching the beam and accelerating it from 50 keV to 2.5 MeV.

The technical specifications for the RFQ were developed by ANL/FNAL collaboration and are presented in Table 1.

Table 1. Initial Specifications for the RFQ Design

| | |
|---|---|
| Input energy | 50 keV |
| Output energy | 2.5 MeV |
| Frequency, MHz | 325 |
| Accelerating beam current, mA | 40 |
| Peak surface field, kV/cm | <330 |
| Acceleration efficiency,% | >95 |
| Pulsed power losses in copper, kW | <450 |
| Duty factor, % | 1 |
| Total length of vanes | 302.428 cm |
| Average bore radius | 3.4 mm |
| Input rms transverse emittance, normalized π mm mrad | 0.25 |
| Transverse emittance growth factor | <1.1 |
| Longitudinal rms emittance, π keV deg | <150 |
| Separation between operating and nearest dipole modes | >4 MHz |

*This work was supported by the U.S. Department of Energy under contract number DE-AC02-76CH03000.
#gromanov@fnal.gov.

In this collaborative effort ANL was responsible for complete beam dynamic design resulting in a vane tip modulation table for machining. RF design with computational support from FNAL, mechanical design and manufacturing, preliminary tuning were delivered by AccSys Technology, Inc. Serious issues arose during manufacturing of the RFQ that prevented proper preliminary tuning. Intensive study has been undertaken to address the problem and specific corrective modifications have been done. Final RF measurements and testing of recently arrived RFQ have been performed by FNAL. The preliminary results of initial testing of RFQ at the test facility are presented.

## DESIGN FEATURES

Similar to many other linear accelerators, the HINS proton accelerator requires an RFQ for initial acceleration and formation of the bunched beam structure. The HINS RFQ will operate at 325 MHz. The initially projected acceleration of ~40 mA pulsed current is considered a relatively moderate problem in the physics design of the RFQ. The design of the RFQ, MEBT and whole proton accelerator lattice has been iterated several times to satisfy more advanced RFQ beam specifications. Particularly, the longitudinal phase space beam emittance must be halo free to avoid excessive beam loss in the high energy section of the accelerator. As a part of this approach, axial-symmetric beam was requested at the RFQ output.

For RFQs longer than ~3l rf wavelengths, it is difficult to stabilize the operating field and damp field errors. To address this problem, modern RFQ designs include p-mode stabilizing loops (PISLs) [2]. PISLs complicate the resonator design and increase its cost; therefore we proposed to minimize the length of the RFQ resonator to allow using the end-wall dipole mode tuners for field

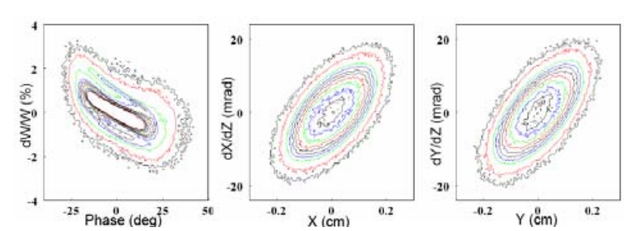


Figure 1: Phase space plots of accelerated beam. The outmost isoline contains 100%, the next one contains 99%.

stabilization that were successfully applied to several RFQs.

For the beam dynamics design, the RFQ is divided into three main sections: an input radial matcher, a main modulated vane section where bunching and acceleration occur, and an output radial matcher. The emittance and profile of the beam exiting the RFQ obtained from TRACK simulation of $10^6$ particles are shown in Fig. 1

The complete beam dynamics design, resulting in a vane tip modulation table for machining, is described in [3].

## RFQ MECHANICAL DESIGN

The RFQ resonator was fabricated using AccSys patented Univane technology [4]. The four identical univanes were each fabricated from solid copper billets (Fig. 2). The univanes are bolted together (Fig. 3) and can be disassembled and re-assembled to facilitate repairs, surface cleaning etc, if necessary. This mechanical design feature turned out to be very useful.

Figure 2: CMM measurements of the univane at SLAC.

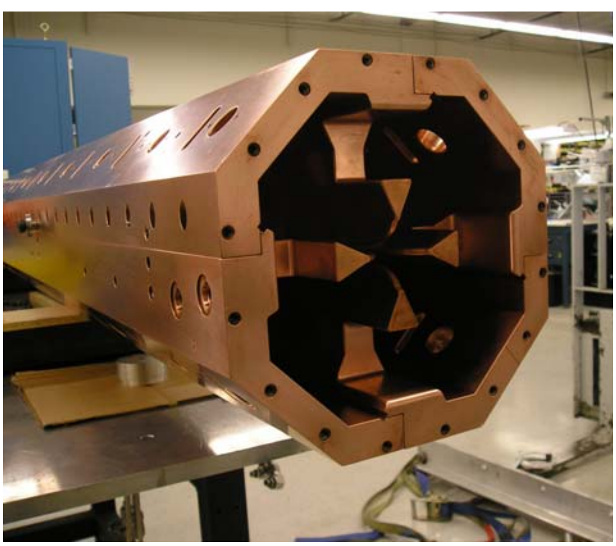

Figure 3: Assembled RFQ resonator. Output end.

Twelve cooling water passages were gun-drilled through the full length of the structure. The cooling passages near vane tips are isolated from passages in outer part of the body to allow RFQ resonant frequency control by adjusting the differential water temperature between the two circuits. The RFQ resonant frequency may also be adjusted using a moveable slug tuner located at the midpoint of the cavity.

Two 3 1/8 inch RF drive loops are used to keep the RF losses in the loops low and also to allow the coupling to be easily adjusted. To operationally monitor and control field distribution in the RFQ, 12 pick-up electrodes (3 per quadrant) are provided. Tuning of the structure at assembly is achieved by means of 64 fixed slug type tuners (16 per quadrant at evenly distributed locations).

Since RFQ resonator cavity does not serve as a vacuum chamber, it is placed in a stainless steel vacuum chamber with vacuum feedthroughs for the RF drive loops, the water cooling and RF pick-up loops (see Fig. 4). Two ports are located on the bottom for mounting vacuum pumps to maintain an operating pressure in the chamber less than $1x10^{-8}$ Torr.

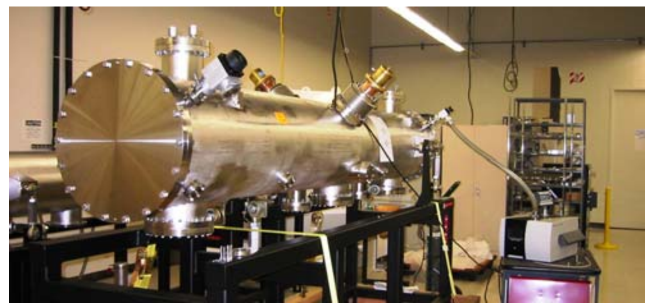

Figure 4: RFQ in the vacuum chamber.

## DESIGN CORRECTIONS AND TUNING

During the initial tuning of the RFQ it turned out impossible to correct (flatten) the resonator's quadrupole field without exceeding the nominal operating frequency by 2-3 MHz. The quadrupole field measurements showed an extreme tilt of field distribution along the resonator, approx. 80%. This was beyond the range of normal correction (i.e. end tuners and slugs) and indicated a fundamental geometry error in the RFQ.

Extensive numerical simulations of the RF properties of the RFQ were performed at FNAL with the use of MWS and HFSS to understand the problem and find a solution [5, 6, and 7]. It was determined that the main problem was the result of a mis-tuned output matcher. The output radial matcher is designed to form axially symmetric beam exiting the RFQ, and because of this special function it is different than the input radial matcher. An error in the final dimensions of the matcher was not realized before univane machining and the resultant matcher local frequency went too high. Simulations indicated that fixing the problem without affecting fields in the matching area meant disassembly and re-machining of the univanes (see Fig. 5).

Also during simulations it became understood that there is an additional distortion of the quadrupole field distribution due to the local frequency variation along the RFQ associated with very specific vane tip modulation. This frequency variation was a potentially serious problem as well, but could be avoided by proper assembly and tuning. This meant reducing the bore radius by 50-70 microns using shims of appropriate thickness (see Fig. 6).

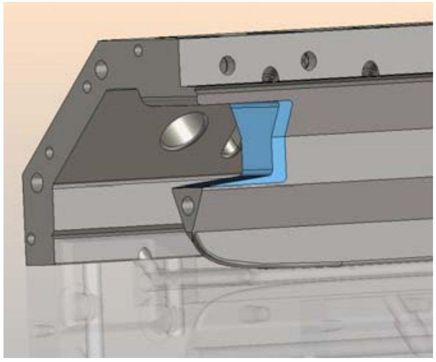

Figure 5: The blue volume has been removed during the univanes re-machining to tune output matcher.

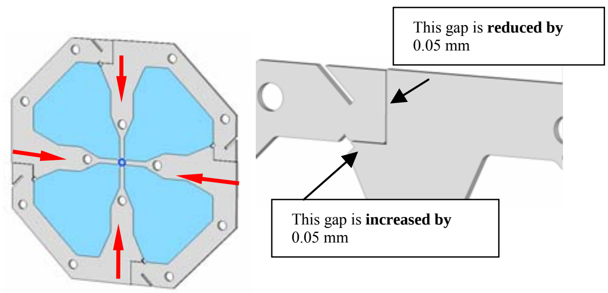


Figure 6: The shims of appropriate thickness reduced bore radius by 50 microns.

After all recommended corrections were done, the tuning went smoothly and RFQ met all design requirements. Fig. 7 shows the evolution of the field distribution. Overall final flatness of field distribution is in ±2% interval.

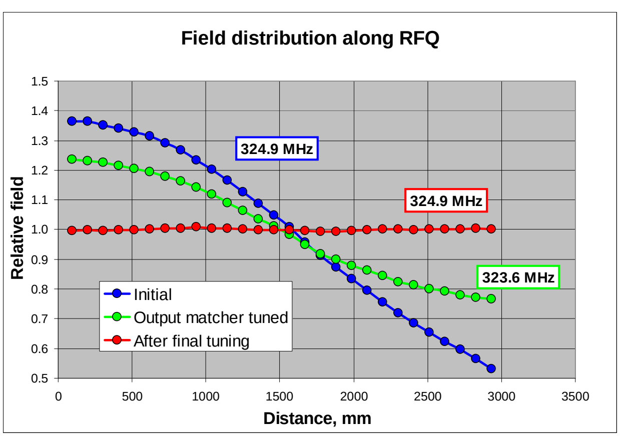


Figure 7: Measurements of field distribution along RFQ resonator at different stages of tuning (average over four quadrants).

Frequency spectra measured at room temperature of 22°C and air filled cavity are given in MHz in Table 2.

Table 2

| Mode | Q | D1 | D2 |
|---|---|---|---|
| 0 | 324.942 | 313.249 | 312.731 |
| 1 | 328.693 | 319.226 | 319.594 |
| 2 | 339.837 | 330.378 | 330.608 |
| 3 | 357.102 | 348.062 | 347.797 |

Nearest dipole modes are located symmetrically in respect to operating frequency with separation more than 5 MHz. Measured unloaded quality factor was Q=9650 compare to the simulated figure of 10750.

## TESTING

The RFQ was delivered to Fermilab this month. Receiving inspections, alignment measurements, and final cold tests are now under way prior to high power RF conditioning expected to commence in October 2008.

The HINS 325 MHz RF power system is operational and ready for the RFQ. A proton ion source and low energy beam transport line is installed and waiting. Following RF conditioning, the source and RFQ will be coupled. The first 2.5 MeV beam is expected by December this year.

## CONCLUSIONS

The HINS RFQ has been fabricated and has passed all mechanical and low power RF tests. The excellent agreement between comprehensive numerical simulations and the RFQ structure's behavior in response to re-machining and during final assembly and tuning offers confidence that the RFQ will perform as designed with beam.

## REFERENCES


[1] R.Webber, Overview of the High Intensity Neutrino Source Linac R&D Program at Fermilab, this conference.

[2] A. Ueno and Y. Kondo, RF-Test of a 324-MHz, 3-MeV, H- RFQ Stabilized with PISL's, LINAC'00, Monterey, California, TUD02, 2000.

[3] P.Ostroumov et al., Application of a new procedure for design of 325 MHz RFQ, JINST 1 P04002, April 2006.

[4] U.S. Patent No 5,315,120

[5] G. Romanov, A. Lunin and T. Page. Analysis on AccSys RFQ resonator model, Fermilab, Technical division technical note TD-08-007, February 2008.

[6] G. Romanov, A. Lunin and R. Webber. Recommendations on RFQ Final Tuning, Fermilab, Technical division technical note TD-08-008, February 2008.

[7] G. Romanov and A. Lunin, Complete RF design of the HINS RFQ with CST MWS and HFSS, this conference.

# COMPLETE RF DESIGN OF THE HINS RFQ WITH CST MWS AND HFSS*

G. Romanov[#], A.Lunin, Fermilab, Batavia, IL 60510, USA.

*Abstract*

Similar to many other linear accelerators, the High Intensity Neutron Source requires an RFQ for initial acceleration and formation of the bunched beam structure. The RFQ design includes two main tasks: a) the beam dynamics design resulting in a vane tip modulation table for machining and b) the resonator electromagnetic design resulting in the final dimensions of the resonator. The focus of this paper is on the second task. We report complete and detailed RF modeling on the HINS RFQ resonator using simulating codes CST Microwave Studio (MWS) and Ansoft High Frequency Structure Simulator (HFSS). All details of the resonator such as input and output radial matchers, the end cut-backs etc have been precisely determined. Finally in the first time a full size RFQ model with modulated vane tips and all tuners installed has been built, and a complete simulation of RFQ tuning has been performed. Comparison of the simulation results with experimental measurements demonstrated excellent agreement.

## INTRODUCTION

Within the framework of the High Intensity Neutrino Source (HINS) program at FNAL, we plan to build and operate a portion of the Front End (up to energy of 62 MeV) as a technical feasibility proof of the proposal. A detailed description of the project and the current status is given in [1]. In the Front End test stand a four vane 325 MHz Radio Frequency Quadrupole (RFQ) will be used for bunching the beam and accelerating it from 50 keV to 2.5 MeV.

The complete beam dynamics design, resulted in a vane tip modulation table for machining, is described in [2]. The mechanical design concepts for this RFQ, tuning results, manufacturing of the RFQ in industry and the preliminary results of initial testing of RFQ at the Front End test stand are discussed in [3].

The electromagnetic design of RFQ resonators is rather complicated and requires essentially three-dimensional modeling. That, and also an additional complication with RF tuning because of some blunder made in the mechanical design of RFQ, urged us to develop a full length 3D RFQ model for simulation. Modern three-dimensional electromagnetic codes are now available and successfully used for RFQ design [4, 5, and 6]. This paper focuses exclusively on the computational technique of electromagnetic design. We report complete and detailed RF modeling on the HINS RFQ resonator using simulating codes CST Microwave Studio (MWS) and Ansoft High Frequency Structure Simulator (HFSS).

*This work was supported by the U.S. Department of Energy under contract number DE-AC02-76CH03000.

#gromanov@fnal.gov.

## RFQ MODEL FOR ELECTROMAGNETIC SIMULATION

The basic parameters of the RFQ are given in table 1.

Table 1

| | |
|---|---|
| Input energy | 50 keV |
| Output energy | 2.5 MeV |
| Frequency | 325 MHz |
| Total length of vanes | 302.428 cm |
| Average bore radius | 3.4 mm |

The RFQ design has several features that have been taken into account during electromagnetic simulations.

Instead of π-mode stabilizing loops (PISLs) usual for RFQs longer than ~3λ, where λ is the rf wavelength [7], FNAL's RFQ design uses the end-wall tuners - field stabilizers simpler than PISLs [8]. This method requires a precise knowledge of dipole mode spectrum, so simulating full length RFQ with end-wall tuners installed was needed.

Modulation of the vanes in the regular accelerating section of the RFQ is shown in Fig. 1. A variable modulation changes capacitive loading and therefore local frequency along RFQ as also reported elsewhere [4, 9, and 10]. In our RFQ the local frequency variation due to the modulation is significant, so the vane tip modulation has been included in the model.

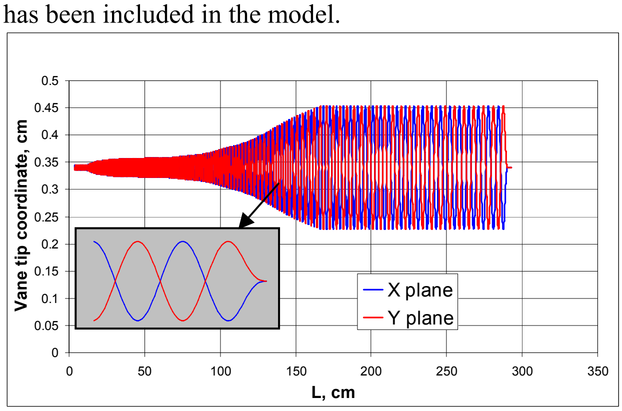


Figure 1: Vane tip modulation along RFQ. Radial matchers are excluded.

The output radial matcher is designed to form axially symmetric beam exiting the RFQ, and because of this special function it is different than the input radial matcher. Fig. 2 shows profile of the output radial matcher and imposed profile of the input matcher to compare with. The RFQ ends (cutbacks) can be tuned in simulations individually, but their combined effect on field flatness must be evaluated. Besides the end-wall tuners have different tuning range and sensitivity for input and output ends of the RFQ. So again, for proper RFQ end design a full length model had to be considered.

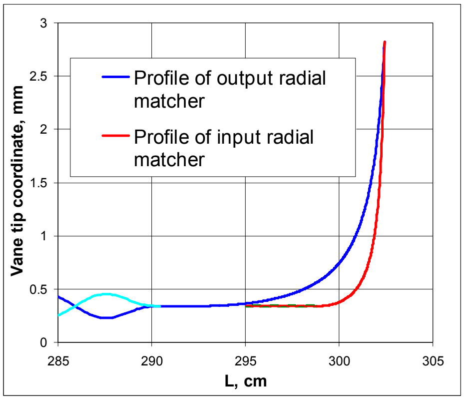

Figure 2: The Radial Matcher Profiles.

The basis of the 3D RF model prepared for simulation was a solid engineering model built in SolidWorks and stored in SAT format. The SAT file was then imported into CST Microwave Studio. CST MWS has its own well developed tools to work with solid models and to heal imported objects, so the RF model was completely prepared directly in MWS environment.

## PERIODS OF RFQ

Many basic RFQ parameters can be obtained and defined with 2D approach. CST MWS and HFSS are entirely 3D codes, but RFQ “slices” with thickness of one mesh step were effectively used to define the basic RFQ parameters. Some RF features like PISLs and slug tuners can be studied with periods of RFQ [6]. The period of RFQ defined by the slug tuner spacing was simulated to evaluate slug tuning sensitivity. Also magnetic field distortion around slug tuners was investigated since the bumps created by the tuners were visible at the bead pull axis which was close to the tuners.

The specific vane tip modulation (see Fig. 1) attracted attention as a possible reason of the local frequency variation. To check whether the vane tip modulation affects local resonant frequency, one accelerating period with modulated vane tips (see Fig. 3) has been simulated. The frequency of the model was found to be 324.7 MHz, while the frequency of the same model with identical average bore radius and no modulation was 323.5 MHz. The difference of 1.2 MHz is significant for such a long RFQ and must be taken into account.

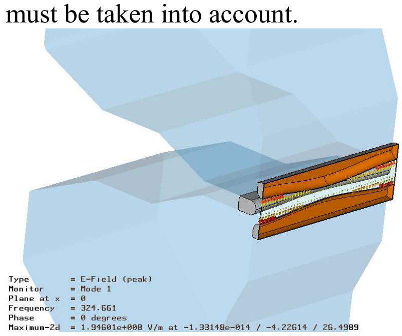

Figure 3: A model of accelerating period #267.

## RFQ END TUNING

Field flatness is always one of the most important tasks for RFQ tuning. This parameter is very sensitive (especially in long RFQs) to proper vane terminations. The RFQ ends are supposed to be tuned by appropriate geometry and dimensions of undercuts and the errors are usually hard to fix.

In the RF 3D model the end-wall tuners were set to a default value of 25.4 mm of penetration as it was during the initial RF measurements. The tuning slugs were flush with the inner wall of the RFQ cavity, so the slugs were not included in RF model for the vane end tuning. Each RFQ end can be tuned separately, so applying appropriate boundary conditions we used 1/8 of the full model, which is equivalent to full length RFQ with two input or two output ends. Actually the model can be of any length for this tuning, but we prefer to use field flatness as a tuning criterion which is more sensitive for longer cavity. If a local frequency is used as a tuning criterion, a reasonably short model should be used for higher sensitivity.

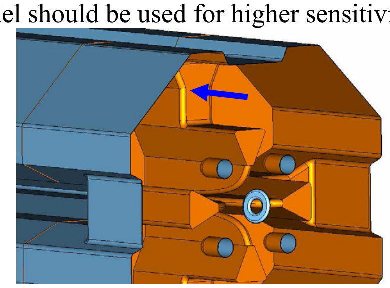
Figure 4: A model of RFQ output end. The back wall (marked by arrow) is moved for tuning.

After main dimensions of cut-backs have been found, the back wall as the most influential parameter was being moved inward (i.e. “removing” of material) for fine tuning (Fig. 4). We monitored the electric field distribution of quadrupole mode along RFQ at 4 mm and 45° off the axis (in the gap between tips). The field distribution changes with cut-back variation as it is shown in Fig. 5, and it gets flat at optimal cut-back of 65.6 mm.

## COMPLETE SIMULATION

Initially the full length model was used to obtain realistic spectrum of quadrupole and dipole modes with end-wall tuners installed, since the exact mode spacing is a key for field stabilization in the RFQ. Then it was realized that the vane tip modulation cannot be ignored, and this feature has been added to the full length model.

The attempts to perform the simulation of the full model with MWS were not successful. It was decided to transfer the problem into HFSS. Using powerful MWS modeler the vane tip modulation was prepared in faceted representation of shape that is more appropriate for triangulated surface meshing in HFSS (see Fig. 6).

The model parameters were set in accordance with actual initial RFQ settings during RF measurement just after final assembly [11]. Fig. 7 shows the field distributions as simulated with and without vane modulation in comparison to the previous actual

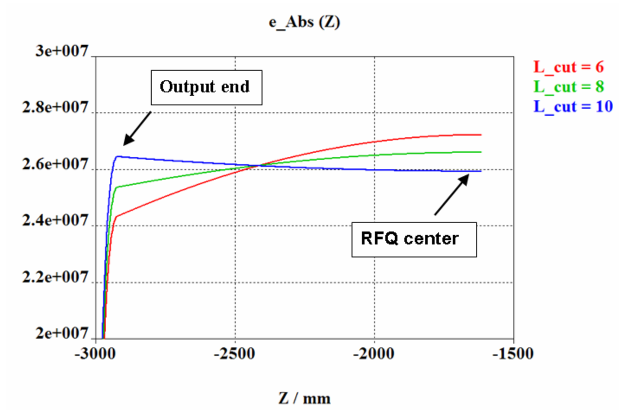


Figure 5: Field distribution with varying cut-back depths.

measurements. With the vane tip modulation included in the model, the simulation reproduces the measurements with high accuracy, including both total field distribution tilt and sinus-like shape. Therefore, the theory that the vane tip modulation is responsible for the additional field distribution distortion is supported. Without modulation, the field tilt in the simulation is due only to the detuned output matcher.

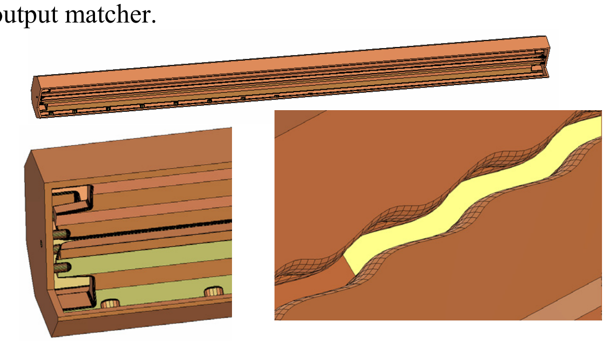

Figure 6: Full length RFQ model with vane tip modulation, radial end matchers, end-wall tuners and slug tuners.

To check final RFQ tuning in simulation, the output matcher cut-back dimensions in the solid model were set to the specified values and slug tuners were introduced. Skipping intermediate simulations of the tuning process with slug tuners, the result is summarized in Fig. 9.

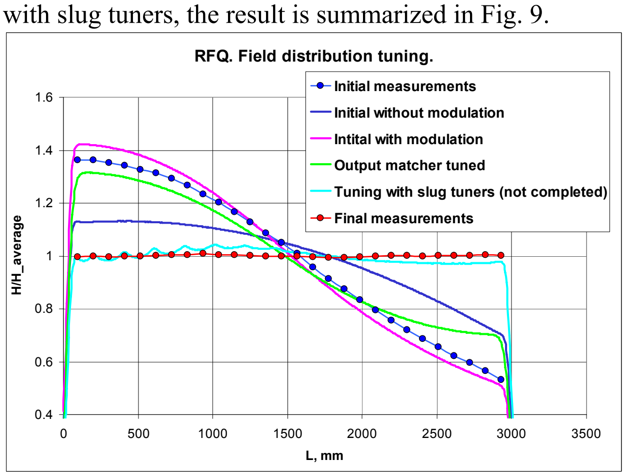


Figure 7: Evolution of field distribution. Lines – simulations, points – measurements. Due to the axial symmetry H-field distributions for only one quadrant are shown.

The slug tuners can only increase the local and overall frequency. After field flattening in the simulation, the RFQ frequency was well above required value of 325 MHz. To decrease the initial frequency of the resonator a reduction of the average bore radius by 50-70 µm was recommended after test simulations.

The results of simulations and the recommendations were taken into account during the final vane machining, RFQ assembly and tuning [4].

## CONCLUSIONS

In the first time a full size RFQ model with modulated vane tips and all tuners installed has been built, and a complete simulation of RFQ tuning has been performed. Results of this complete simulation are in excellent agreement with the measurements made on the RFQ during initial assembly and tuning. All recommendation and predictions were proven correct by the final tuning results.

This work is an important step toward entirely computational RF modeling on RFQ structures.

## ACKNOWLEDGEMENTS

Special thanks to G.Apollinary, T.Page and R.Webber.

## REFERENCES

[1] R. Webber , Overview of the High Intensity Neutrino Source Linac R&D Program at Fermilab, this conference.
[2] P. Ostroumov et al., Application of a new procedure for design of 325 MHz RFQ, JINST 1 P04002, April 2006.
[3] G. Apollinari et al., The fabrication and initial testing of the HINS RFQ, this conference.
[4] D. Li et al., Detailed Modeling of the SNS RFQ Structure with CST Microwave Studio, LINAC'06, THP008, Knoxville, Tennessee, USA, 2006.
[5] A. Kurup et al., Electromagnetic Design of a Radio Frequency Quadrupole for the Front end Test Stand at RAL, EPAC'06, MOPCH116, Edinburgh, Scotland, 2006.
[6] A. France et al., Design of Slug Tuners for the SPIRAL2 RFQ, PAC'07, Albuquerque, New Mexico, USA, TUPAN006, 2007.
[7] A. Ratti et al., Conceptual design of the SNS RFQ, Proc. of the LINAC 98, p. 276.
[8] L.Young, 25 Years of Technical Advances in RFQ Accelerators, PAC'03, Portlend, Oregon, USA, MOPB001, 2003.
[9] A. Ueno and Y. Kondo, RF-Test of a 324-MHz, 3-MeV, H- RFQ Stabilized with PISL's, LINAC'00, Monterey, California, TUD02, 2000.
[10] O. Delferriere et al., A New RF Tuning Method for the End Regions of the IPHI 4-vane RFQ, EPAC'06 Edinburgh, Scotland, MOPCH105, 2006.
[11] G. Romanov, A. Lunin and R. Webber. Recommendations on RFQ Final Tuning, Fermilab, Technical division technical note TD-08-008, February 2008.

# SIMULATION OF MULTIPACTING IN HINS ACCELERATING STRUCTURES WITH CST PARTICLE STUDIO*

G. Romanov #, Fermilab, Batavia, IL 60510

*Abstract*

Recently high power tests of the room temperature cross-bar H-type resonators (CH resonators) and high gradient tests of a superconducting single spoke resonator (SSR) have been performed under the High Intensity Neutrino Source (HINS) project at Fermilab. The resonators have shown a tendency of having multipacting at various levels of input power and therefore longer processing time. To provide insights for the problem, detailed numerical simulations of multipacting for these resonators have become necessary. New generation of accelerating structures like superconducting spoke resonators and room temperature CH resonators need a full 3D treatment. Simulations and study of multipacting in the resonators have been carried out using CST Particle Studio. The problematic regions and power levels have been identified for both types of resonators. This presentation will give the result of simulations and comparison with experimental data.

## INTRODUCTION

Within the framework of the High Intensity Neutrino Source (HINS) program, we plan to build and operate a portion of the Front End (up to energy of 62 MeV) as a technical feasibility proof of the proposal. A detailed description of the project and the current status is given in [1]. The Front End of HINS, operating at 325 MHz, uses a mixture of warm copper structures and superconducting spoke resonators. After a standard RFQ [2], room-temperature crossbar H-type resonators are used to accelerate the beam from 2.5 to 10 MeV [3]. The use of short normal conducting resonators up to ~10 MeV reduces the number of different types of SC cavities and provides adiabatic beam matching. Three types of superconducting spoke resonators are used to accelerate protons from 10 MeV to 400 MeV [4].

Recently high power tests of the room temperature cross-bar H-type resonators (CH resonators) and high gradient tests of a superconducting single spoke resonator (SSR) have been performed [5,6]. The resonators have shown a tendency of having multipacting at various levels of input power and therefore longer processing time. To provide insights for the problem, detailed numerical simulations of multipacting for these resonators have become necessary. Simulations and study of multipacting in the resonators have been carried out using CST Particle Studio. Since CST PS is probably the first commercial code that can simulate realistic electron multiplication, the result of study is useful also as the code benchmarking.

## MODEL PREPARATION

A general approach for mulipacting simulation was developed a while ago and it can be mapped to the three steps. These steps are performed in every case, with variations in execution, strategies for detailed implementation and numerical methods. The first step is the definition of the geometry and the calculation of the RF and static fields in this geometry. In a second step, a motion of large number of particles is tracked in the structure. And in a third and final step a multipacting behavior in the collection of particle tracking data is identified [7]. In CST PS, all three steps are smoothly integrated in one code.

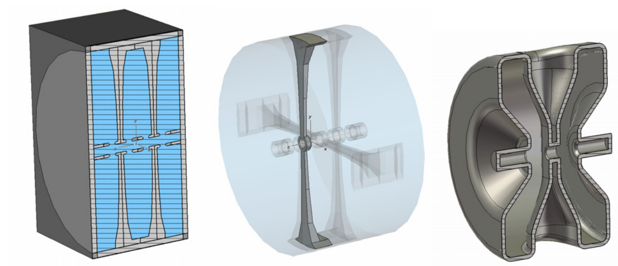

Figure 1: RT CH model consisting of background PEC, cavity components and vacuum filling is on the left. In the center a separate half of spoke is shown. Model of single spoke superconducting cavity SSR is on the right.

RF design for all HINS cavities was done with CST MicroWave Studio. The standard “vacuum” solid models from MWS can not be used “as is” in PS and additional manipulations are needed. First of all, the models before importing into PS from MWS had to be converted to more realistic models with metal walls (or developed from scratch). This is because the secondary emission properties in PS can be assigned to metal surface only, and PS does not recognize Perfect Electric Conductor background as a metal surface. Besides creating a model with metallic walls it is recommended to fill it with vacuum and make background of PEC as shown in Fig.1. This eliminates parasitic mode simulation outside a cavity. Usually several locations are suspicious as MP ones, so it is useful to build a cavity model consisting of separate parts and provide them with independent initial particle sources. It helps to evaluate MP on different surfaces independently.

The prepared models were imported first into MWS for field calculations (it is preferable because MWS has more

*This work was supported by the U.S. Department of Energy under contract number DE-AC02-76CH03000.

#gromanov@fnal.gov.

advanced eigenmode solvers than PS), and then into PS for particle tracking.

In this study the Furman probabilistic model of secondary emission for copper was used with default PS parameters. Usually 50 generations of secondary electrons were tracked and maximum of secondaries per hit was 1.5-2.5. The particle sources provided the simulations with primary electrons uniformly distributed over source area and uniformly distributed over the energy range of 0-4 eV. Number of primary electrons per source was from 200 to 5000. Unfortunately there is no possibility to distribute primary electrons in time, so all initial electrons were launched simultaneously at the same phase of RF field.

## MULTIPACTING IN CH RESONATORS

The goal of MP simulations is to find a location of multipacting activity in a cavity and determine the RF power levels or zones where MP conditions are fulfilled. After analyzing field pattern and trying particle sources on different surfaces, a location of stable multipacting activity in RT CH was found in area shown in Fig.2.

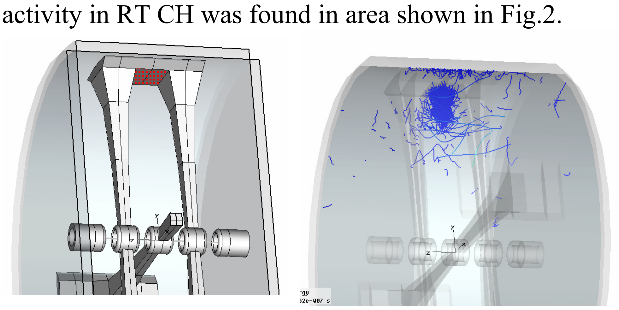

Figure 2: Initial electron source and particle trajectories in CH1 after 40 RF periods (crashed particles are not shown).

PS evaluates particle number in a cavity volume vs time, which is a natural parameter to indicate and verify electron multiplication (see Fig.3).

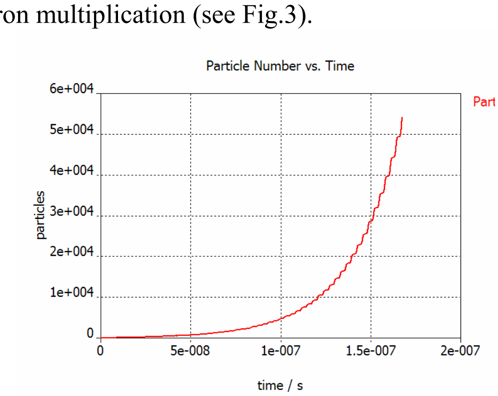


Figure 3: Exponential growth of particle number in a cavity when MP conditions are fulfilled.

PS stores information on emission and collision for every separately defined surface. This data allows to calculate integral secondary emission yield defined as <SEY>=(Total Number of Secondaries)/(Total Number of Hits) and evaluate MP probability, its intensity and zones for each separate surface. Simulations for all RT CH cavities have been performed and shown essentially similar MP behavior. Typical curves <SEY> vs input power are shown in Fig. 4.

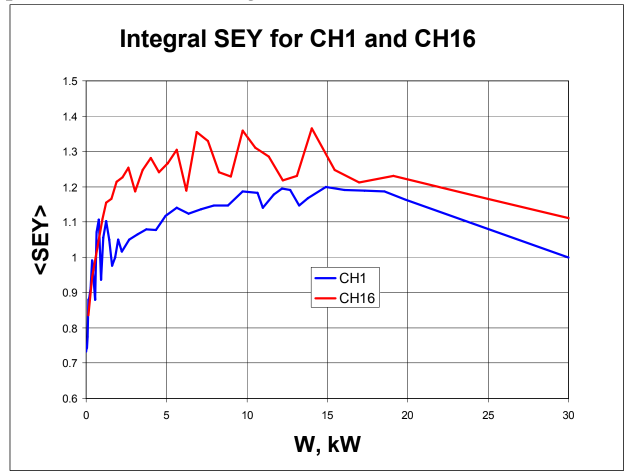


Figure 4: Results of the MP simulations in CH1 and CH16.

Single trajectory simulations show that multipacting is of 5-6 order, and therefore the MP can not be very powerful. It can exist only due to the specific field “trap” for electrons plus flat surface between spokes. In practice it takes time to process a CH resonator first time through 2-10 kW barrier, but eventually MP disappears [5].

## MULTIPACTING IN SSR1

Multipacting seems to be a common problem for low beta SC spoke cavities. Once a particular case of multipacting was simulated in a single spoke cavity [8], but existence of several levels of MP and its broad band character were not explained.

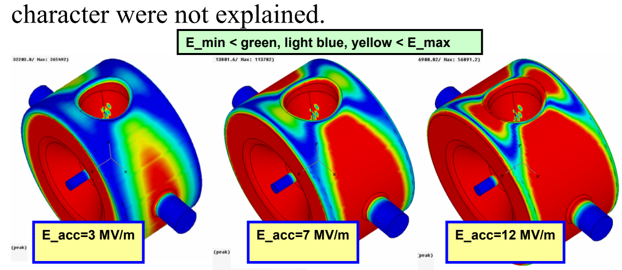


Figure 5: Electric surface field distribution at different accelerating gradients.

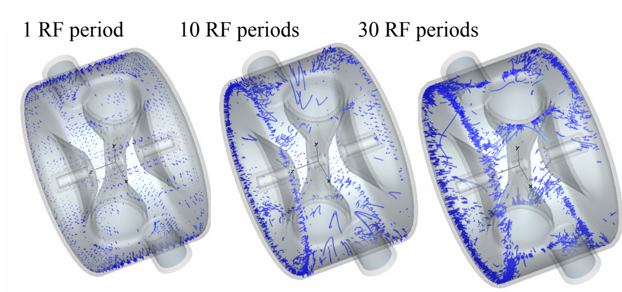


Figure 6: Development of multipacting in time at accelerating gradient of 7 MV/m.

To understand locations of multipacting in SSR1 the upper and lower limits of RF electric field, where MP can exist, were defined in accordance with [9]. Corresponding areas, where electrons can gain right incident energy, are shown at different accelerating gradients in Fig.5. These areas are just approximate locations of potential MP because only surface field is considered. But since MP is a near surface process it is an accurate approximation.

In Fig.6 development of multipacting in the cavity is shown. Uniformly distributed initial electrons were launched from cylindrical surface of the cavity. After 30 RF periods the MP concentration reproduced the surface field pattern. So, the surface field distribution predicts correctly probable locations of multipacting, and one can conclude that MP should migrate from one area to another with accelerating gradient increase.

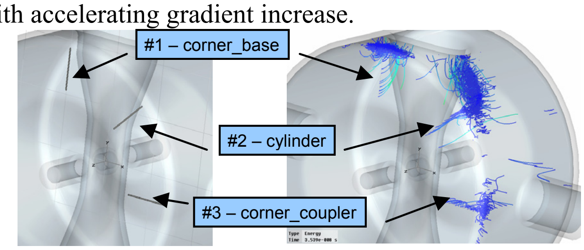


Figure 7: The initial electron sources in different locations.

To evaluate MP in different locations and track the MP migration around the cavity three sources of initial electrons were introduced (Fig.7). Each source allows studying MP in particular area. Simulations were performed for all sources simultaneously and the trick was to stop simulation before MP spreads over the cavity. Then the integral secondary emission yield can be calculated for each source separately.

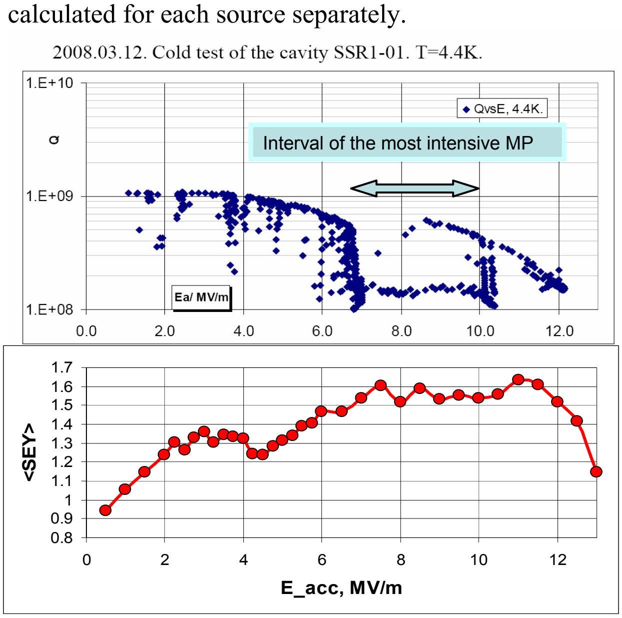


Figure 8: Comparison with experiment.

The simulations confirmed that the most intensive spot of multipacting migrates from location to location with accelerating gradient increase. While moving to the new areas the spot sees “fresh” unconditioned parts of surface and this explains the broad interval of mulipacting. The spatial stability of MP is poor, so rather high re-emision coefficient (>1.7) is required to sustain the process. The intensity of multipacting drops when areas with favorable for MP conditions start shrinking due to high fields (see Fig.5).

Combined <SEY> for all three sources is plotted in Fig.8 along with quality factor Q measurements made during first high gradient test of SSR1 cavity [6]. The drops of Q correspond to the MP levels and zones. The simulations correctly indicate that MP zones.

## CONCLUSIONS

The multipacting in CH resonators and SSRs is a broadband phenomenon. There are not many chances to rid of it by reshaping the problem spots because it is related to the operating field distribution and basic geometry. Fortunately, the MP is not persistent and very powerful in both cases due to the mentioned above reasons, so the effect is no show stopper, but just annoying for operation/start-up.

CST PS proved to be a good tool for MP study. To make it more effective a development of tracking in real time, distributing of primary electrons over RF phases and more advanced evaluation of particle data to identify multipacting, is recommended.

## ACKNOWLEDGEMENTS

Special thanks to T.Khabiboulline for the SSR1 high gradient test data.

## REFERENCES

[1] R.Webber, Overview of the High Intensity Neutrino Source Linac R&D Program at Fermilab, this conference.

[2] G.Apollinari et al., The Fabrication and Initial Testing of the HINS RFQ, this conference.

[3] L.Ristori et al., “Fabrication and Test of the First Normal-Conducting Cross-Bar H-Type Accelerating Cavity at Fermilab for HINS, PAC’07, Albuquerque, New Mexico, USA, WEPMN110, 2007.

[4] G.Lanfanco et al., Production of 325 MHz Single Spoke Resonators at FNAL, PAC’07, Albuquerque, New Mexico, USA, WEPMN099, 2007.

[5] G.Romanov et al., High Power Test of HINS RT CH Cavitites, this conference.

[6] I. Gonin et al., “High Gradient Tests of the HINS SSR1 Single Spoke Resonator”, HB2008, Nashville, Tennessee, August 2008.

[7] F.L.Krawczyk, Status of Multipacting Simulation Capabilities for SCRF Applications, Proceedings of the 10th Workshop on RF Superconductivity, Tsukuba, Japan, 2001.

[8] L.V.Kravchuk, G.V.Romanov and S.N.Tarasov, Multipactoring Code for 3D Accelerating Structures, LINAC’00, Monterey, California, THB12, 2000.

[9] В.Г.Мудролюбов, В.И.Петрушин, Обобщённые соотношения для областей существования модификаций резонансного ВЧ разряда с учётом кулоновского поля, ЖТФ, т.XL, вып.5, май 1970, стр.1017.

# STATUS OF DPIS DEVELOPMENT IN BNL*

M. Okamura**, BNL, Upton, NY 11973, U.S.A.

J. Tamura**, Tokyo Inst. Tech, Meguro, Tokyo, 152-8550, Japan

T. Kanesue**, Kyushu University, Ito, Fukuoka, Ito, 819-0395, Japan

**RIKEN, Saitama, 351-0198, Japan

*Abstract*

Direct injection scheme was proposed in 2000 at RIKEN in Japan. The first beam test was done at Tokyo Institute of Technology using a $CO_2$ laser and an 80 MHz 4 vane RFQ in 2001, and further development continued in RIKEN. In 2006, all the experimental equipments were moved to BNL and a new development program was started. We report on our recent activities at BNL including the use of a frozen gas target for the laser source, low charge state ion beam production and a newly developed laser irradiation system.

## INTRODUCTION

A laser ion source (LIS) is a leading candidate of heavy ion sources for providing intense highly charged beams for high-energy accelerators. The laser power can be deposited within a tiny area of the target material's surface and the evaporation process starts. Successively the evaporated gas absorbs the laser power and becomes plasma. Since the large laser power goes into a very limited volume, huge amount of the highly charged ions are produced. An emission from a table top small laser easily produce more than$10^{12}$ W/cm$^2$ on a target surface and the total induced current reaches more than a few hundred A.

We have studied LIS since 2000. We proposed direct plasma injection scheme which enables high current heavy ion beam acceleration. More than 60 mA of carbon [1] and aluminum beam accelerations by an RFQ were demonstrated. We have also examined several laser systems and many targets species [2]. Using the measured plasma data, almost any desired species can be used for the LIS except helium gas.

In 2006, our group moved from RIKEN, Japan to BNL, USA with all the experimental equipments and we started a new development program in BNL. In this report, we briefly introduce our current activities related LIS and DPIS.

## LASER EMISSION CONTROL

The laser emission control is important to gain good ion beam stability. We are currently using a tabletop Nd-YAG laser system, Thales-SAGA 230/10. When we started to use this laser, we were suffered by laser leakages. The laser consists of two laser cavities, a master oscillator and a power amplifier, and a Q-switch is installed at the oscillator to make a short pulse. The Q-switch controls a polarization and adjusts laser-firing timing. The laser media is pumped by flash lamps. A typical emission of the flash lamps is indicated as red curve in Fig. 1. The flash lamp emission lasts more than 200 μs and the Q-switch selects certain timing for releasing the pumped energy to maximize laser emission power.

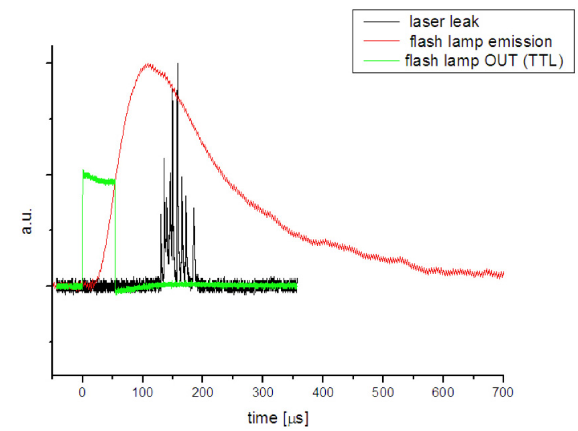


Figure 1: Flash lamp timing and laser leakage.

The laser emission pulse width is typically 6 ~ 9 ns. The flash lamps are always operated at 10 Hz for good stability and the laser emission is only controlled by the Q-switch. While the Q-switch is off position, the laser should not be emitted. However even Q-switch is turned off, very week laser emission exists. This leakage could not be sensed by a power meter. We observed the leakage by directly seeing the light from the plasma using an IR viewer. The leaking laser energy is very small but is enough to make plasmas and can damage the surface of the target since the leaked energy is concentrated onto a pinpoint by a focusing mirror. To avoid the pre-damage of the target due to the laser leakage, we installed a fast mechanical shutter in the laser path to the ion source. The shutter closes or opens within several ms and this speed is adequate to choose any desired laser pulses because the flash lamps are blinking at 10 Hz. So that the laser shots caused only by the Q-switch are transported to the ion source. Un-desired laser leakages from the un-fired blinking of the flash lamps are blocked. The ion beam stability was dramatically improved. However the laser shutter is not enough to eliminate the negative effects completely. Again in Fig. 1, you see the black plot which shows the time structure of the laser leakage when the Q-switch closed. The leakage still exists even in the same fired laser pulse. The Q-witch timing is usually selected to maximize the laser emitting power and typically around 180 μs behind the flash lamp control signal triggered.

*Work supported by U.S. DOE and RIKEN

However as it is shown in the figure, before 180 μs, the leakage starts. The leakage in a single laser pulse is weak and we cannot observe any foot print on the target surface, however this small leakage just before the main pulse of the laser shot has enormous effect to the plasma heating condition. Let us note that this leakage is not considered as "pre-lasing," since this is usually too weak and cannot be detected while you are measuring the main laser pulse. Therefore the Q-switch timing should be selected before the leakage starts or after the leakage ends. Base on our experience, it is suggested to wait for more than several μs past after the leakage ends for the Q-switch timing. The behavior of the laser leakage depends on the type of Q-switch. The careful timing settings are required for the good ion beam stability. The further investigations of the performance of the Q-switch and its timing are presently performed.

## FROZEN TARGET

Although LIS had only used solid target materials, we started to induce plasma from rare gaseous. The idea is quite simple. We used a cryo-cooler head, Sumitomo RDK-408D2, to condense gases and the solidified targets were tested in BNL. Ar and Ne were successfully used to provide intense beams. We also tried hydrogen, but the cooling power or a heat shield was not enough and could not get stable beams. Figure 2 shows the detected charge states from the Ar experiment.

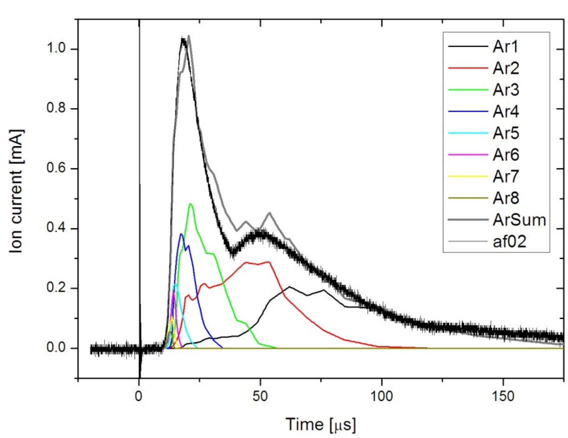


Figure 2: Analyzed Ar plasma. The currents are measured at 2.4 m from the target. The aperture size of the Faraday cup was 10 mm in diameter. The laser was set to 1200 mJ with a second harmonic crystal (532 nm). The applied laser power density on the target was about $5x10^9$ W/cm$^2$.

The cryo head could be cooled down to 4.5 K that temperature was low enough for almost any gases except helium. At the beginning of the experiment, the gases were fed by a thin plastic pipe, less than 1 mm in diameter, to spray directly to the target surface however this structure was not necessary. The gas could be fed into the vacuum chamber without the nozzle and the pressure was controlled not to exceed $10^{-4}$ Pa. The residual gas was mostly the fed molecules and those were caught by the cold surface automatically. The cold surface was coated by several layers of the molecules and those were enough to provide the desired plasmas. Once laser was shot, the surface became clean and the surrounding area was also flashed by the conducted heat. The accumulated layers always started on the fresh cold surface and were in same condition for every laser shot. The reproducibility was quite good. On the other hand, rapid cycle was not applicable and more than a few seconds were needed as an interval. To increase the repetition rate, a differential pumping system will be required. We plan to accelerate the rare gas atoms by an RFQ in the near future.

## LOW CHARGE STATE BEAMS

By controlling the laser power density on the target, a charge states distribution can be shifted. We are studying low charge ion beam production from the LIS. Generally lower laser power density is better to produce low charge state beam, however there is a threshold value of the density to make a plasma. We tested many materials and most of the material have almost same thresholds which are about $10^8$ W/cm$^2$. Only carbon graphite showed higher threshold.

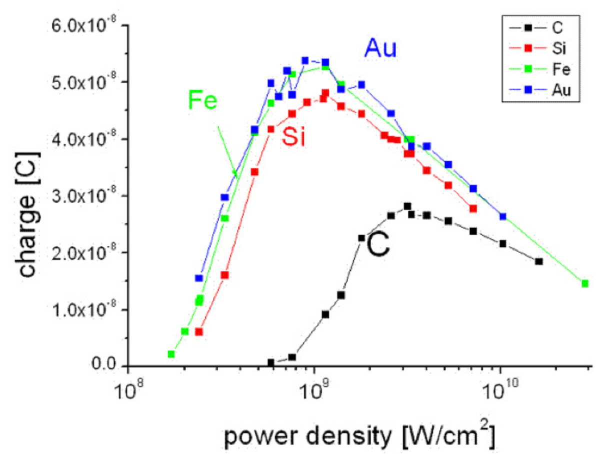


Figure 3: The measured total charges. The laser power density was controlled by changing the position of the focusing lens. The lower density also implies a larger exposure area.

By measuring the velocity distribution of the plasma, the initial plasma temperature was estimated and the obtained temperature was consistent with the first ionization energy of the atoms except the carbon case. We can provide intense low charged ions to the RFQ with the DPIS. This is suitable approach for "heavy ion inertial fusion." Unfortunately we do not have an adequate RFQ to capture the very low charge to mass ratio particles. In the next step we plan to inject the $Au^{1+}$ beam to our existing 100 MHz RFQ to examine just the transverse motion of the beam.

The low charge state beam from the LIS has another superior advantage. We measured the emittance of the extracted beam and the obtained values were dominated by an emittance measurement system [4]. The plasma was produced under the high temperature condition but it is adiabatically expanded before the ion extraction process. This means the extracted beam is cold and it might be useful for other applications.

## IMPROVED DPIS-LIS

The mechanical structure of the ion source is also developing. To accelerate many kinds of species, the plasma drift length is adjustable in our newly designed DPIS chamber. The plasma drift length is the distance between the target surface and the extraction point where is the entrance of the RFQ linac. The dense plasma is diluted while it travels over the drift length and becomes a required density at the extraction point. To obtain good matching condition of the extracted beam to the acceptance of the RFQ, the length needs to be optimized for a desired current, species and charge states. Our recent study indicated that more than 200 mA of carbon 6+ beam can be matched into the acceptance of the existing RFQ. Also the position of the final focusing element can be adjusted. We had used concave mirrors as final focusing element, however a focused image of the laser light on the target were elliptical. To avoid this effect, a convex lens will be used instead of the concave mirror. The focal distance was shortened from 100 mm to 50 mm and the laser power density can be increased. Unlike ion beam optics, there is a diffraction limit for the laser light as the minimum spot size, however we still expect a reasonable improvement. Figure 4 shows the new ion source vacuum chamber which is being constructed in BNL. We also developed a winding system to roll a plastic tape which protect the final focusing lens from the plasma exposure.

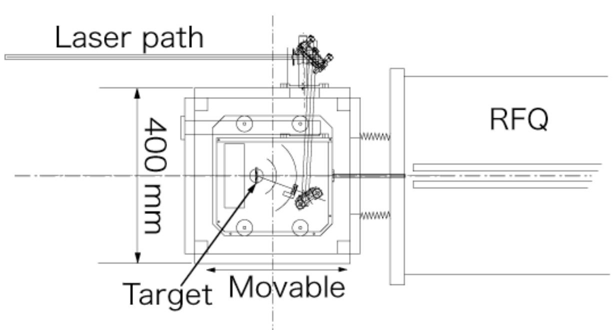


Figure 4: New DPIS set-up.

## RFQ

The existing RFQ was designed and fabricated in 2003 [5]. Due to a limitation of a radiation safety regulation in a facility where the beam commissioning was carried out. The output energy was restricted to 100 keV/u, however the acceleration is achieved within the first 1.42 m of the RFQ. The rest of the RFQ length is 0.5 m and this secsion has un-modulated vanes. In the un-modulated section, only transverse confinement force exists and consequently longitudinal bunch structure is completely lost.

In BNL, this RFQ is already connected to a 300 kW RF power amplifier and the high power test was done. At 220 kW RF power input, X-ray emission was measured as 120 μrem/h at the tank surface near the RF coupler. Now we are waiting for an approval for the beam operation in BNL. Using newly optimized condition, carbon beam will be produced and accelerated in next month.

The RFQ has 4 rod structure and the resonator including vanes can be replaceable. The next version of the resonator was already fabricated. The basic parameters of the existing resonator and the new one are listed in Table 1.

Table 1: Basic Parameters of the DPIS RFQ

| | Type I | Type II |
|---|---|---|
| Design beam | $C^{4+}$ 100 mA | $Ag^{15+}$ 15 mA |
| Frequency | 100 MHz | 100 MHz |
| Duty factor | 0.1 % | 0.1 % |
| Inter vane voltage | 120 kV | 73 kV |
| Injection energy | 20 keV/u | 8.3 keV/u |
| Output energy | 100 keV/u | 270 keV/u |
| Cell number | 118 | 143 |

## SUMMARY AND PLAN

As mentioned above, the intensive plasma extraction studies were done in BNL. The feasibility of the frozen gas target was also proved. Many small but important improvements were adopted in the new ion source chamber. A higher current and higher quality beam is expected using the DPIS in BNL.

## ACKNOWLEDGEMENT

We thank all the collaborators and friends in BNL, RIKEN, JAEA, KEK, TITech, NIRS and IAP-Frankfurt.

## REFERENCES

[1] M. Okamura, R. A. Jameson, H. Kashiwagi, T. Hattori, N. Hayashizaki, K. Sakakibara, K. Yamamoto, and T. Kanesue, Radiat. Eff. Defects Solids **160**, 10 (2005)
[2] S. Kondrashev, T. Kanesue, M. Okamura, K. Sakakibara, JOURNAL OF APPLIED PHYSICS 100, 103301 (2006)
[3] J. Tamura, M. Okamura, T. Kanesue and S. Kondrashev, APPLIED PHYSICS LETTERS **91**, 041504 (2007)
[4] T. Kanesue, J. Tmura, M. Okamura, EPAC08, mopc147, 421-423 (2008)
[5] M. Okamura, H. Kashiwagi, K. Sakakibara, J. Takano, T. Hattori, N. Hayashizaki, R.A. Jameson, K. Yamamoto REVIEW OF SCIENTIFIC INSTRUMENTS 77, 03B303 (2006)

# DESIGN STUDY OF A DPIS INJECTOR FOR A HEAVY ION FFAG *

M. Okamura#, D. Raparia, BNL, Upton, NY 11973, U.S.A.
K. Ishibashi, Y. Yonemura, T. Kanesue, Kyushu University, Ito, Fukuoka 819-0395, Japan

*Abstract*

A new heavy ion injector linac is proposed for providing heavy ion beams to a fixed field alternating gradient (FFAG) accelerator in Kyushu University. A combination of the new intense laser source based injector and the FFAG will be able to accelerate high current ion beams with 100 Hz of a repetition rate. The planned average current reaches 7 µA with carbon 6+ beam.

## A NEW INTENSE PULSED ACCELERATOR

To obtain large beam power within a limited space, cyclotrons have been chosen since they provide CW beams even with relatively small peak beam current. In this report, we propose a new approach to utilize comparatively large beam power using a laser ion source and a FFAG synchrotron accelerator.

Generally a synchrotron can have larger peak current than cyclotron has, however most of the time is occupied for ramping up and down the bending magnets in the operation and the beam pulse width is very limited. To increase the total beam power, it is effective to have high repetition rate. The maximum repetition rate is about 1 to 25 Hz for normal conducting synchrotrons [1]. Recently FFAG accelerators are being focused as high repetition synchrotrons and some FFAGs have already been built by KEK and Kyoto University groups both lead by Y. Mori [2]. It has been proved to operate it at 100 Hz in KEK and possibly it will run at 1 KHz. Also FFAG has large transverse acceptance and is expected to deliver large current.

A laser ion source (LIS) has an advantage to induce a powerful pulsed beam and can operate at high repetition rate which is restricted by a driver laser system. A typical flash lamp pumped solid laser can reach 100 Hz and a LED pumped laser easily achieves above 1 kHz operation with good stability. Hence both a laser source and a FFAG are operational at same high frequency range. Since a LIS can provide large current, beam losses in a transport line which connects from the ion source to a first stage accelerator, typically RFQ, was always tough issue. To overcome this difficulty caused by space charge effect, direct plasma injection scheme (DPIS) has been studied. Using the DPIS, several tens of mA heavy ion beams have been accelerated effortlessly in an RFQ [3]. A rapid cycle LIS with DPIS and a high current heavy ion RFQ suit a FFAG well to boost the beam power.

In Kyushu University, a new facility called "Center for accelerator and beam applied science" is established [4]. A new building was already constructed to accommodate a FFAG accelerator which was originally designed and constructed in KEK as a prototype 150 MeV FFAG. The installation of the FFAG to the new building is in progress. A small proton cyclotron will be used as an injector in the first stage and in the next stage we plan to install a new injector system to provide heavy ions for various application including medical, engineering studies and educational activities. A photo of the FFAG and its design parameters are shown in Fig. 1 and Table 1.

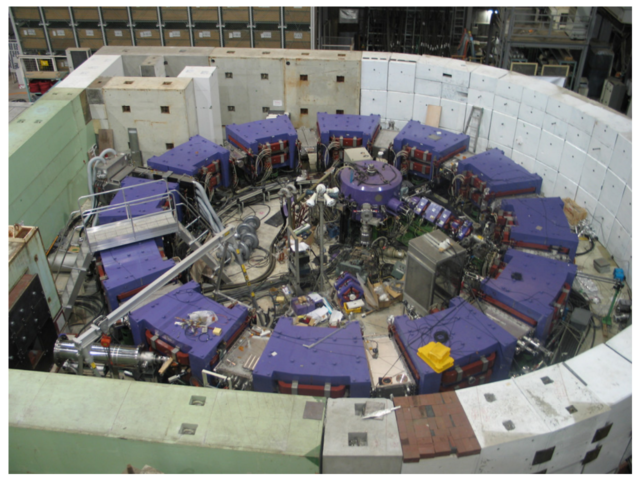

Figure 1: 150 MeV FFAG in KEK.

Table 1: Design Parameters of 150 MeV FFAG

| | |
|---|---|
| Energy | 10 – 125 MeV (proton)<br>2.5 – 31 MeV/u ($C^{6+}$) |
| Type of magnet | Triplet radial (DFD) |
| Number of cell | 12 |
| Average radius | 4.47 – 5.20 m |
| Magnetic field | Focus: 1.63 T<br>Defocus: 0.78 T |
| Revolution Frequency | 1.5 – 4.2 MHz (proton)<br>0.78 – 2.3 MHz ($C^{6+}$) |
| Repetition rate | 100 Hz (2 RF cavities) |

The proposed heavy ion injector will accelerate fully stripped ion beams up to 2.5 MeV/u with the highest available current which will be induced by a conventional table top laser system with the DPIS.

## LASER ION SOURCE

### *Beam Pulse Width*

The harmonic number of the FFAG ring is one and revolution period at the injection energy is 1.28 µs. With single turn injection scenario, the required beam pulse

*Work supported by U. S. DOE
#okamura@bnl.gov

width is about 1.2 - 1.3 μs with adiabatic beam capturing which can build up the distributed beam over the 360 degree of the injection RF cycle. Using the DPIS, we can provide sufficient number of particles with the short period. In this case, we can assume the acceleration RF phase of the FFAG at the beam injection. If the Separatrix occupies 150 degree of phase acceptance, the required beam pulse width is 0.53 μs. The LIS was designed to produce slightly longer than 0.53 μs of the pulse duration.

### *Laser System*

We assumed a flush lamp driven Nd-YAG laser as a driver since it is commercially available and has good stability (typically a few %). To provide fully stripped ions from light to medium species efficiently, more than 1 J per shot of the laser energy is recommended. To obtain 100 Hz operation, it may need to have multiple oscillators. Table 2 shows the planned laser parameters for the injector.

Table 2: Laser Parameters for FFAG LIS

| | |
|---|---|
| Media | Nd - YAG |
| Wave length | 1064 nm |
| Oscillator | 2 stages (multiple) |
| Pulse width | 5 - 7 ns (Q switched) |
| Energy | 1.5 J |
| Repetition rate | 100 Hz |

### *Induced Ions from the DPIS Geometry*

A LIS consists of a laser, a target material and extraction electrodes. Particularly in the DPIS, RFQ vanes are used as negative electrodes of the extraction system. The positive electrode, plasma target and the space between them are all biased to high voltage which corresponds to the injection energy of the RFQ. Firstly a plasma induced by a laser shot on the target. The plasma is started to expand and is ionized during laser irradiation, typically in several ns. After ionization, the plasma keeps expanding like a cloud and the gravity center of the cloud moves perpendicular to the target surface. All these processes appear in the enclosed space by a high voltage cage. At the beam extraction point, the ion beam begins when the head of the plasma cloud reaches and ends when the tail passes. The moving velocity of the plasma and its distribution are determined by a laser power density on the target. However we have the minimum laser power density since fully stripped ions, like $C^{6+}$ is required. The laser power density should be more than $10^{12}$ W/cm$^2$. To optimize the beam pulse width, the drift length is adjusted around 0.5 m. The expected peak current of the $C^{6+}$ beam reaches about 300 mA assuming the positive extraction hole of 8 mm in diameter.

### *Expected Beam Characteristics*

Assuming the irradiation condition, we measured charge states distributions from a carbon graphite target in BNL. Thales – SAGA 230/10 laser system was used and the laser energy was set to 1.5 J. A convex mirror were placed 100 mm from the target surface. The incident angle to the target was 15 degree off from the perpendicular line. Figure 2 shows the expected charge distribution and the currents converted from the measured data. The pulse length of $C^{6+}$ beam was 0.63 μs (above 10% of the peak value). The experimental setup was same as described in ref. [5].

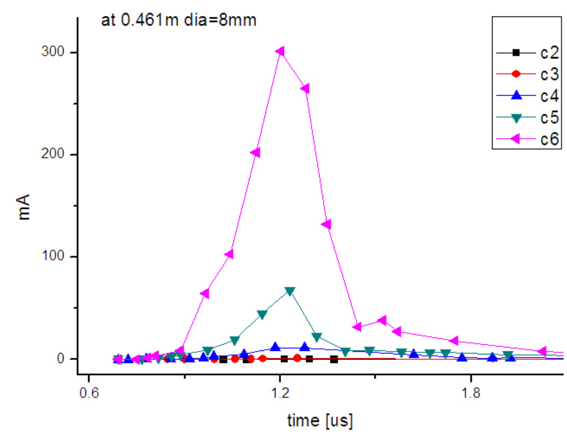


Figure 2: Re-constructed currents based on the measurements.

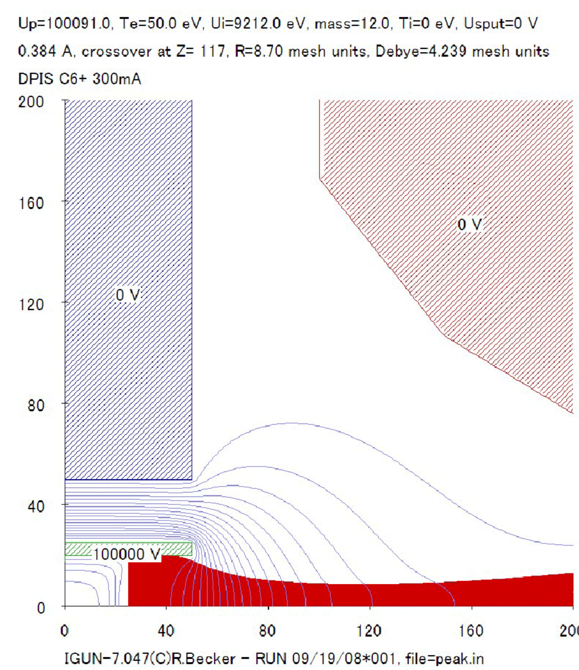


Figure 3: Beam extraction simulation by IGUN.

The beam extraction condition of $C^{6+}$ beam with small fractions of other charge states was simulated by using IGUN [6]. The applied bias voltage is 100 kV to obtain a matched condition of the extraction. Table 3 shows the Twiss parameters of the predicted beams at the peak current. The study of other species production is in progress.

Table 3: The Simulated Extracted Beams

| | Current (mA) | ε rms (mm mrad) | α | β (mm/rad) | γ (rad/mm) |
|---|---|---|---|---|---|
| $C^{4+}$ | 11.9 | 35.7 | 1.16 | 63.7 | 0.0369 |
| $C^{5+}$ | 62.1 | 35.5 | 1.16 | 63.7 | 0.0368 |
| $C^{6+}$ | 300 | 35.5 | 1.16 | 63.7 | 0.0368 |

## RFQ

The RFQ was designed to be fit into the inside of the FFAG ring. By adopting the DPIS, the ion source part can be made very compact. The plasma drift length is about 0.5 m and the entire source part needs around 0.7 m in length. The injection energy was given by the plasma extraction condition as 100 kV (50 keV/u). The kilpatrik limit factor (14.7 MV/m at 200 MHz) was set to 2.3 supposing a vane tip curvature equals to the average bore radius. Since the required beam pulse length is short and the probability of RF break down will be small even adopting a high bravery factor. Also by controlling the multpole components in the field, a smaller vane tip curvature can be applied and the electric field strength can be reduced. The operation RF frequency was chosen as 200 MHz due to an availability of an existing RF amplifier. The design parameters of the RFQ are summarized in Table 4.

Table 4: DPIS RFQ for FFAG

| | |
|---|---|
| Energy | 0.05 – 2.5 MeV/u |
| Cell number | 215 |
| Vane length | 4.28 m |
| Frequency | 200 MHz |
| Inter-vane voltage | 140 kV |
| Average bore radius | 5.0 mm |
| $m_{max.}$ | 2.25 |
| $a_{min.}$ | 2.9 mm |

The power consumption was estimated as 580 kW by scaling from an existing 4-rod DPIS RFQ. The beam pulse is much shorter than the RF build up time, so that the duty factor of the RFQ is determined by a Q value of the cavity. Assuming 5000 of the Q value, the duty factor is about 2.5 %. Since the beam pulse is only 0.5 µs, the effect of the beam loading will be negligible. The tracking simulations in the RFQ were done by using PARMTEQ [7] and Pteq-HI [8]. In the Pteq-HI calculation, three charge state ions, $C^{4+}$, $C^{5+}$ and $C^{6+}$, were tracked simultaneously. The peak currents shown in Table 3 as the input beam condition resulted 205 mA of the accelerated $C^{6+}$ current. The beam spread in the longitudinal phase space is shown in Fig. 4.

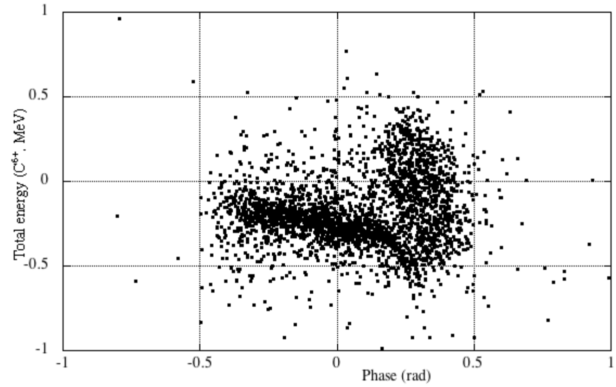


Figure 4: Simulated $C^{6+}$ output beam in longitudinal phase space.

The simulation based on the above discussion predicted that the RFQ provides average current of 8 µA to the FFAG.

## CONCLUSION

A new injector using DPIS was designed to accelerate $C^{6+}$ beam with a 200 MHz RFQ. The laser ion source will provide 300 mA $C^{6+}$ beam and the RFQ will provide 186 mA at peak. If we assume 10 % and 5 % beam losses at the beam injection and extraction of the FFAG The average output current will be 7 µA. The total beam power will be 400 W. Let us note that we adopted 100 Hz as the repetition rate of the entire accelerator system in the discussion, however it can be increased up to 1 KHz by modifying the RF system of the FFAG and the laser system.

## REFERENCES

[1] H. Suzuki, "Rapid cycling synchrotron of J-PARC" APAC'04, Gyoneju, 2004, WEM303, p. 499 (2004)
[2] Y. Mori, K. Okabe, "development of FFAG accelerators in Japan" Cyclotrons and Their applications 07, p. 177 (2007)
[3] S. Kondrashev, et al., "Acceleration of intense beams of highly charged ions using direct plasma injection scheme." HB2006, Tsukuba, Japan, THBY01 (2006)
[4] Y. Yonemura, et al., "Status of Center for Accelrator and Beam Applied Science of Kyushu University." EAPC'08, Genoa, Italy, 2008, THPP070 (2008)
[5] K. Sakakibara, et al., "Properties of Laser-Produced highly charged heavy ions for Direct Injection Scheme," PAC'05, Knoxville, USA, TPPE027 (2005)
[6] R. Becker, www.egun-igun.com
[7] Los Alamos Accelerator Code Group (LAACG)
[8] R.A. Jameson, IAP Universität Frankfurt/M, Germany

# COMMISSIONING OF THE NEW GSI-CHARGE STATE SEPARATOR SYSTEM FOR HIGH CURRENT HEAVY ION BEAMS

W. Barth, L. Dahl, L. Groening, P. Gerhard, S. Mickat, M. Kaiser
Gesellschaft für Schwerionenforschung, D-64291 Darmstadt, Germany

*Abstract*

A dedicated charge separator system has been installed in the transfer line to the GSI synchrotron SIS18, replacing charge separation with a single 11 degree dipole magnet after a 25 m beam transport section. This was not adequate to meet the requirements during high current operation for FAIR: it only allows for charge state separation of low intensity and low emittance beams. With the new compact charge separator system emittance blow up and undesired beam losses for high intensity beam operation will be avoided. Additionally, a new beam diagnostics test bench is integrated to measure beam parameters (ion current, beam profile, beam position, transversal emittance, bunch structure and beam energy) for the injection into the SIS 18 in parallel to the routine operation in the transfer line. Results of commissioning with high intensity argon beams as well as with an uranium beam will be reported. We acknowledge the support of the EU-Research Infrastructure Activity under the FP6 "Construction of infrastructure for the FAIR-project" (co.-number 515876).

## INTRODUCTION

In the transfer line (TK) to the GSI synchrotron SIS 18 the beam is stripped to higher charge states in a carbon foil, if high final energies from the SIS 18 are required. The TK is operated at 3 Hz pulse to pulse mode at maximum, with beams of different ion species and intensities, with or without stripping. A high current $U^{28+}$-beam of 15 emA (FAIR requirement) has a power of 1.5 MW (≤300μs pulse length). After stripping, undesired charge states with 85 % of the beam power must be separated and dumped. A newly developed stripper foil (with enlarged width) is loaded with 3 % of the beam power. To avoid evaporation in a single beam pulse, the beam is rapidly swept over its width of 55 mm. The UNILAC delivers beam emittances in the range of 5 to 20 μm, depending on the beam current. Emittance growth in the TK is caused by small angle scattering in the stripper foil, and by space charge forces, mainly in the section between the stripper and the charge separator (see Fig. 1). To minimize emittance growth, a narrow, vertically elongated beam spot (4 mm · 20 mm) is prepared, and the distance to the separator is kept as short as possible. [1]

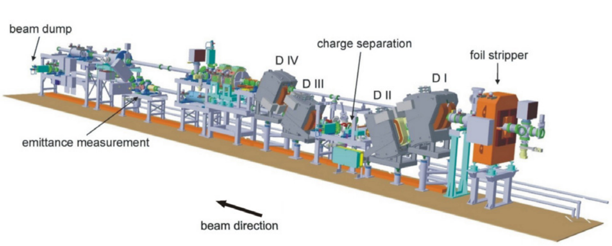


Figure 1: New charge state separator system integrated in the TK comprising the foil stripper, the four 35°-Dipole magnets (DI - DIV), and a beam diagnostics bench.

## THE NEW CHARGE STATE SEPARATOR SETUP

The vertical magnetic bending system of the new charge state separator system consists of four 1.6 T-dipole magnets providing high resolution and a field homogeneity ≥ 99.97 %. Each of the four 35° H-type dipole magnets (D I - D IV) has a bending radius of 1.1 m. The first two dipoles have the same vertical and horizontal aperture, as well as D III and D IV. Rogowski profiles at the beam entrance and the beam exit assure independence of the magnetic flux density (up to 1.6 T) from the effective magnetic length. The gyration number of each coil is chosen to make use of three equal power supplies (650 A/380 V); the last two dipole magnets (with reduced gap height) are operated in a serial mode. All coils are equipped with correction coils to compensate remaining fields. [2] With a beam diagnostic bench behind D III high current beam measurements are accomplished to prepare for the injection of high intensity heavy ion beams into the synchrotron. Besides ion current the beam profile and position, the emittance, the beam energy and the bunch structure can be measured. Additionally, beam focusing using a quadrupole duplet and the correction of beam positions is provided in the 12 m diagnostic line. [3]

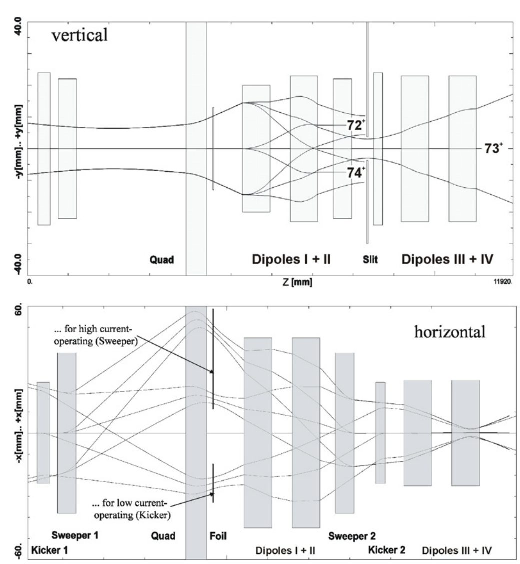


Figure 2: Beam dynamics layout of the new charge state separator system.

## BEAM DYNAMICS LAYOUT

Beam envelopes [3] are shown in Fig. 2. Well focused beams, passing the stripper in horizontal off-axis positions, are bend back by a quadrupole magnet into the horizontally 90 mm wide gaps of the first two dipoles of the analysing system. The beams are realigned to the ion optical axis in a sweeper or a kicker magnet, respectively. In the vertical plane, the rather wide, divergent beam striking the stripper is charge states separated by the first magnet. Simultaneously, it is focused by the magnets upstream pole face rotation angle of -20° onto the analysing slit. Ions from neighbouring charge states hit the jaws of the slit and even the magnet chambers. These components were designed for a high thermal surface load and low radiation activation. The charge resolution q/Δq is about 100. The slot width is 10 mm; the dispersion in this point is 7.5 mm/%. The dispersion of the complete system is zero.

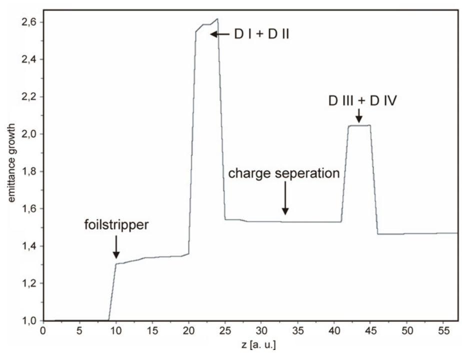


Figure 3: Vertical emittance growth in the charge separator.

PARMILA Transport simulations were performed to investigate the influence of space charge effects on the beam dynamics layout. As shown in Fig. 3 the vertical rms emittance increases by 50 %. Besides small angle scattering in the stripper foil, the emittance growth in vertical as well as in horizontal plane is caused by coulomb interactions.

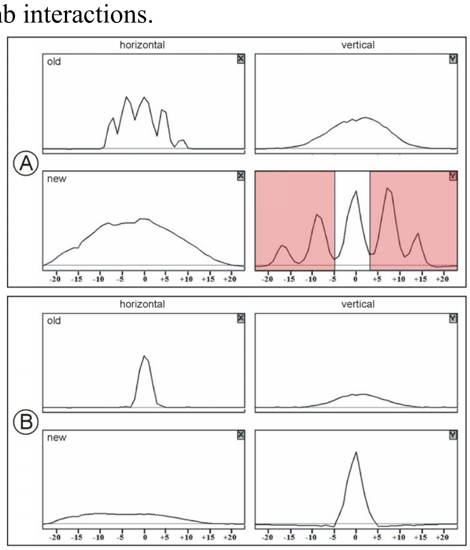


Figure 4: Measured uranium beam profiles with opened (A) and closed (B) separation slits.

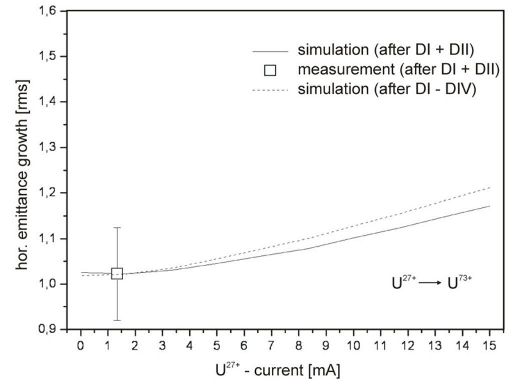


Figure 5: PARMILA Transport beam simulations for different uranium beam intensities; emittance growth measured for low and medium intensities.

## COMMISSIONING RESULTS

After mounting the magnetic charge state separator and the beam diagnostics bench in the TK (December 2007), commissioning of all subsystems and components was performed until January 2008, followed by a three weeks period of beam commissioning with a high intensity $^{40}Ar^{11+}$ beam (7 emA) and a $^{238}U^{27+}$ beam with a beam intensity of up to 2 emA. The uranium beam was used to investigate the separation capabilities of the system. Fig. 4 shows the measured uranium beam profile inside the charge separator and at the position of former charge separation. For the new charge separator an improved charge resolution (factor of 2) is clearly visible, especially when the separation slits are closed.

The simulated horizontal rms emittance growth is presented in Fig. 5. Behind D II as well as behind the whole charge separator system the maximum growth factor is less than 20 % (for 15 emA). Emittance growth for low intensities is confirmed by measurements with a 1.5 emA $U^{27+}$-beam. High and low current argon beam emittance measurements were performed along the whole transfer line. As an example Fig. 6 shows measured transverse beam emittances behind D II. For the high current case the emittance is significantly increased in both transverse planes (65 % horizontally, 30 % vertically). When the beam is passing D III and D IV the dispersion becomes zero – the measured transverse emittance decreases significantly.

The space charge induced emittance growth is reduced to less than 10 % horizontally and less than 20 % vertically. The total horizontal normalized rms emittance was measured with 0.22 mm*mrad, meeting the FAIR-requirements. The beam transmission in the charge state separator system and the adjacent beam transport lines to the emittance measurement devices is close to 100 %.

Table 1: Measured $^{40}AR^{18+}$-beam Emittances (90 %)

| ($4 \cdot \varepsilon_{rms}$ [µm]) | high current | | low current | |
|---|---|---|---|---|
| | hor. | vert. | hor. | vert. |
| behind D II | 9,0 | 17,6 | 6,9 | 7,1 |
| SIS injection | 5,5 | 8,1 | 5,9 | 5,6 |

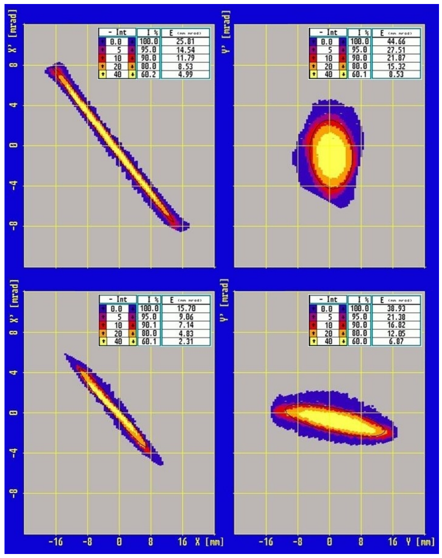

Figure 6: High (top) and low (bottom) current argon beam emittance behind D II.

Emittance measurements for low and high intensity argon beams were also performed for different stripper foil thicknesses. The equilibrium charge state distribution is reached for 400 μg/cm². For this reason space charge induced emittance growth for high current argon beams hitting thicker targets is much higher as for the 200 μg/cm² stripper foil. The 600 μg/cm² foil is sufficient for the operation with heavy ions; e.g. $U^{73+}$ is stripped with high efficiency (15 %). For the argon beam additional emittance growth is measured, while the stripping efficiency stays constant. As simulated with the PARMILA Transport code the horizontal emittance growth is below 50 % for low and high current, while the vertical emittance increases by 70 %. In both transverse planes the space charge dominated beam transport from the stripper foil downstream to the first dipole magnet (D I), where charge separation reduces the space charge forces, increases the emittance area significantly.

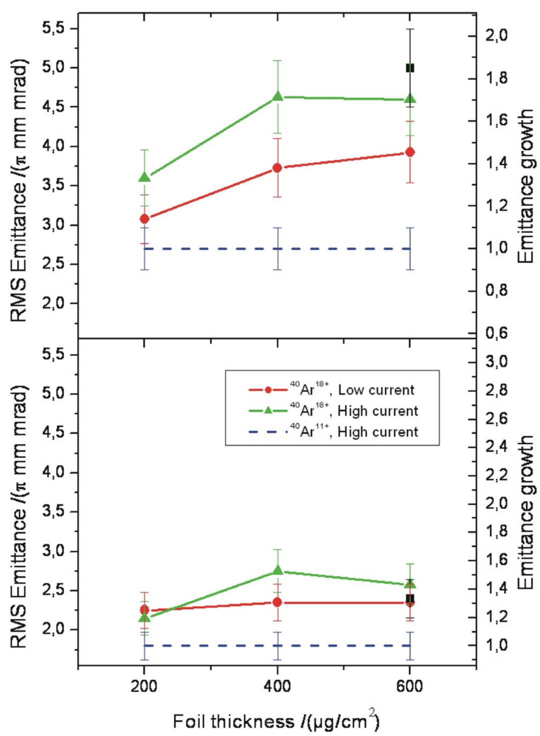


Figure 7: High and low intensity argon emittance measure-ments for different stripper foil thicknesses in horizontal (bottom) and vertical (top) plane; additionally measure-ments with $U^{73+}$ (600 μg/cm²) are shown in black.

## SUMMARY

The new charge separator system was installed in the transfer line to the GSI SIS 18 in December 2007. After commissioning of all components, beam commissioning was performed successfully with a medium intensity uranium beam and a high intensity argon beam. The measured beam transmission is close to 100 % for low and high current operation. For the high current heavy ion beam operation newly developed stripper foils of extended size are in use. The sweeper operation was tested with a high intensity argon beam as well as with an uranium beam. In general emittance growth is not induced by the sweeper devices. The stripping efficiency measured with the charge separator as a spectrometer is as expected. The improved charge separation capability was confirmed for heavy ions as well as for high current operation. Simulated and measured emittance growth effects for low current operation are caused by small angle straggling. Additionally, the vertical emittance inside the charge state separator is increased by disper-sion. Space charge forces act in the short drift length between stripper foil and charge separation in D I only – the space charge influenced emittance growth is 10 % (hor.) resp. 20 % (vert.). The measured high current emittance potentially meets the requirement defined by the FAIR project [4]. We acknowledge the support of GSI expert divisions involved in the charge separator project.

## REFERENCES


[1] J. Glatz, B. Langenbeck, A high duty Foil Stripper System in the Injector Line to the Heavy Ion Synchrotron SIS, 5th European Particle Accelerator Conference, Sitges, Spain, p. 2406 (1996).

[2] B. Langenbeck, J. Glatz, The High Current Stripper, the Charge Separator, and their Magnets for the Beam Transfer Line to the Heavy Ion Synchrotron SIS, 17th International Conference on Magnet Technology, Geneve, Suisse(2001)

[3] J. Eschke, DIRAC-Phase -1, Construction of New Infrastructur (Charge separator, SIS18-6), Annual Report 2007, GSI-Darmstadt, Germany, (2007)

[4] W. Barth, L. Dahl, J. Glatz, L. Groening, S. Richter, S. Yaramishev, Development of the UNILAC towards a Megawatt Beam Injector, LINAC 2004, Lübeck, Germany, p. 246-250 (2004)

# QUADRUPOLE MAGNET DEVELOPMENT FOR 132 MEV DTL OF CSNS

Yi Cheng, Xuejun Yin, Zhirui Sun, Keyun Gong, Shinian Fu
[1]IHEP, Institute of High Energy Physics, Chinese Academy of Sciences, Beijing 100049, China

*Abstract*

In the China Spallation Neutron Source (CSNS) linac, a conventional 324 MHz drift-tube linac (DTL) accelerating an H- ion beam from 3 MeV to 132 MeV has been designed with 1.05% duty, consisting of 7 tanks with a total length of approximately 59.6 m. Currently, R&D work has focused on the first module of Tank 1, which will have 29 drift-tubes (DT) each housing an electro-magnet quadrupole (EMQ). Some EMQs with SAKAE coil have been fabricated and are under rigorous magnetic measurements by means of Hall probe (HP), single stretched wire (SSW), rotating coil (RC) in order to verify the design specifications and fabrication technology. Magnetic measurements on the EMQs with iron cores made from the electrical-discharge machining (EDM) and the stacking method will be compared and discussed. Work has been implemented to reduce the alignment discrepancies between the geometric center of the DT and magnetic center of EMQ to within +/- 50 µm.

## INTRODUCTION

Currently, a prototype cavity of the 1st module of Tank 1, of the 132MeV drift tube linac (DTL) for the proton linear accelerator for the CSNS has been constructed. A frequency of 324 MHz and a duty factor of 1.05% have been chosen for the RF structures. The design of the DTL was presented in reference [1]. Alongside with the construction of the DTL RF cavity, R&D work has also focused on the drift-tubes (DT) and the electro-magnet quadrupoles (EMQ). Presently, six EMQs with J-PARC type SAKAE coils [2] have been fabricated and are under rigorous magnetic measurements that includes the Hall probe (HP), single stretched wire (SSW) and rotating coil (RC) measurements, to verify the EMQ design specifications and fabrication technology and capabilities in the Institute of High Energy Physics (IHEP), Beijing. The design parameters for the EMQs and DTL Tank-1 are listed in Table 1.

Table 1: Design Parameters for EMQ and DTL Tank-1

| EMQ | | Tank 1 of DTL | |
|---|---|---|---|
| Parameter name | Parameter values | Parameter name | Parameter values |
| Beam aperture[mm] | 15 | Output energy [MeV] | 21.76 |
| Core outer diameter[mm] | 59 | Length [m] | 7.99 |
| Core length[mm] | 35 | Number of DTs | 61 |
| Magnetic field gradient[T/m] | 75 | RF power for each cell[MW] | 1.41 |
| Magnetic field effective length[mm] | 40.96 | Total RF power[MW] | 1.97 |
| Maximum excitation current[A] | 530 | Accelerating field strength[MV/m] | 2.2-3.1 |
| Field integral, *GL*[T] | 3.07 | | |
| Coil resistance [mΩ] | 9.08 | | |

## THE ELECTRO-MAGNET QUADRUPOLES (EMQ)

The six EMQ-magnets constructed consists of 3 EMQs with their iron cores made using the Stamped-Stacking Method (SSM), and 3 EMQs with their iron cores made using the Electrical Discharge Machining (EDM). DQ1#DW is the only EMQ that has its water gasket installed as shown in Figure 1.The results of the magnetic measurements for both EDM-made and SSM-made iron core EMQs will be presented, in order to illustrate their magnetic parameters' similarities and differences.

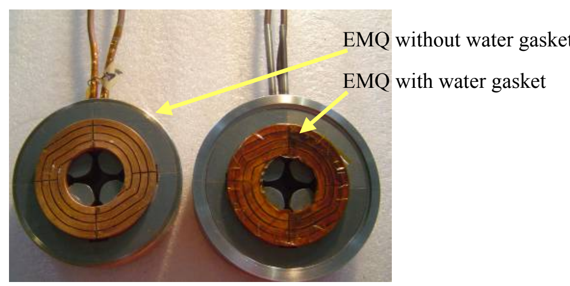


Figure 1: Photos of EMQ.

## MAGNET MEASUREMENTS

### *Hall Measurements*

From the HP measurement, the magnetic field profile along the beam-axis of the EMQ can be obtained at different x and y transverse positions. A typical result from the HP measurement is shown Figure 2.

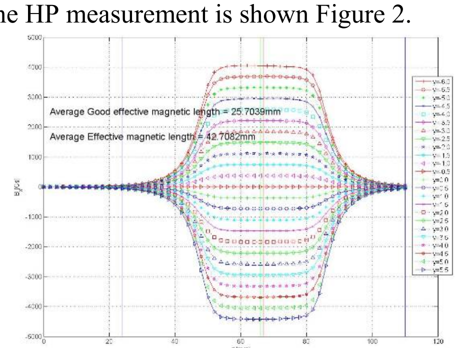


Figure 2: Typical HP measurement result on an EMQ.

The average effective magnetic length, $\overline{L_{eff}}$ , is computed by taking the average of all the effective magnetic length obtained from each profile along the transverse x or y direction. The good effective magnetic length is the region where only field strengths are within 5% from the maximum field strength. The magnetic field profiles obtained from all the EMQs are smooth within the good field region. The averaged effective magnetic length is about 42.64mm. No significant difference in magnetic length was observed between iron cores made from SSM and EDM.

Next, the field gradient distribution of the EMQs was investigated. The gradient value was then evaluated using the expression below:

$$g_{meas} = \frac{A_{i+1} - A_i}{d_{i+1} - d_i} \quad (1)$$

where $A$ and $d$ can be either $Bx$ and $y$ or $By$ and $x$ respectively, and the subscripts i stands for the i-th position along x or y axis respectively for $By$ or $Bx$.

The flatness of the gradient distribution was calculated by implementing the idea of field flatness from [3],

$$FF = \frac{g_{\max} - g_{\min}}{\frac{1}{N}\sum_{i=1}^{N} g_i} \text{ x } 100\% \quad (2)$$

where $FF$ is the flatness percentage; $g_{\max}$ and $g_{\min}$ are the maximum and minimum gradient respectively; denominator of $FF$ is the mean gradient. The required field flatness for the gradient distribution in the transverse direction is $FF \leq 1\%$.

Figure 3 shows some of the results obtained from evaluating all the gradient profile of the magnets. A decision was made to implement upper and lower limits to eliminate data which were considered to be incorrect due to measurement errors. The limits were implemented to be 5% from the mean of each profile. Data points within the limits are taken into consideration to replot the gradient profiles of all magnets and evaluate the flatness of the profiles.

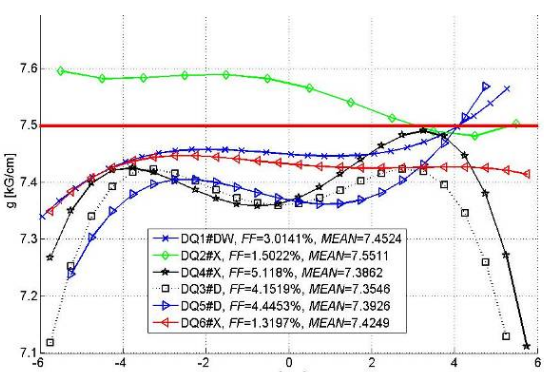


Data Set 1 (Average *FF*: 3.26%)

Figure 3: Example of field gradient distribution along x-axis.

As shown in Figure 3, the field gradient distribution is not entirely constant or smooth along the transverse direction for all EMQs. The *FF* for most of the EMQs are higher than 1%, which is not acceptable.

The reasons for poor field flatness in the transverse field gradient profile are speculative. One can argue that there is high systematic error contribution due to mechanical misalignments and measured data acquisition. There is a need to accumulate the systematic errors of the measuring probe and probe positioning errors in order to verify such suspicions. Furthermore, repeatability of the HP measurement results should be investigated in order to eliminate or understand the systematic errors as suspected.

One other important difference between the EDM-made and SSM-made iron cores is that, the EDM-made laminations are short-circuited at the magnet pole tip. Since the EMQs will be supplied with pulse currents, the EDM-made laminations will not be suitable for this operation mode because eddy-currents will be significant and will affect the performance of the EMQs.

## *SSW Measurement Results*

The SSW measurement results on all the EMQs are presented in this section. The measurements are performed within a range of ±5mm in the x- and y-axis from the magnetic field center.

Table 3: Quadrupole Magnetic Field Center Deviation from Mechanical Center on Each EMQ

| | Magnet names | Δx [mm] | Δy [mm] | $\theta_{role}$ [mrad] |
|---|---|---|---|---|
| SSM-made Iron Core | DQ1#DW | -0.270 | 0.300 | -0.403 |
| | DQ3#D | 0.500 | 0.080 | 0.897 |
| | DQ5#D | 0.610 | 0.260 | 1.233 |
| EDM-made Iron core | DQ2#X | 0.200 | 0.025 | -0.074 |
| | DQ4#X | 0.060 | 0.158 | -0.165 |
| | DQ6#X | 0.255 | -0.205 | -0.537 |

The mechanical center was determined by aligning the wire via motors to the optical alignment instruments. The magnetic center of quadrupole mode was measured by the SSW measurement. From Table 3, it suggests that the deviation between the mechanical center and magnetic field center are significantly large, where the largest deviation is 0.61mm. This indicates that the drift tube housing must have at least 0.65mm of material to machine in order to reduce the deviation within ±50μm. This requirement is achievable.

Currently, it is believed that poor mechanical reference points contributed to the mechanical misalignment of the EMQ, and hence the large deviation between mechanical center and magnetic field center. Mechanical assembly details and measurements have to be reviewed to further verify the above suspicions and to make proper improvements.

To determine the operating current, $I_o$, for each EMQ, the required field integral, $GL = G \text{ x } L_{eff}$, has to be determined for each EMQ using their individually measured $L_{eff}$. With the required $GL$ value, the required $I_o$ can be determined from the excitation curve of the EMQs.

Table 4: Field Integral for Magnets

| | SSM-made Iron Core | | | EDM-made Iron core | | |
|---|---|---|---|---|---|---|
| Magnet names | DQ1#DW | DQ3#D | DQ5#D | DQ2#X | DQ4#X | DQ6#X |
| $L_{eff}$ [mm] | 42.42 | 42.72 | 42.64 | 42.78 | 42.40 | 42.87 |
| Field integral *GL* [T] | 3.18 | 3.20 | 3.20 | 3.21 | 3.18 | 3.21 |

Table 4 tabulates the $L_{eff}$ results obtained from HP measurements, and their corresponding *GL* value that must be achieved to meet the required G, which will be used to determine the magnets' $I_o$ from the excitation curves.

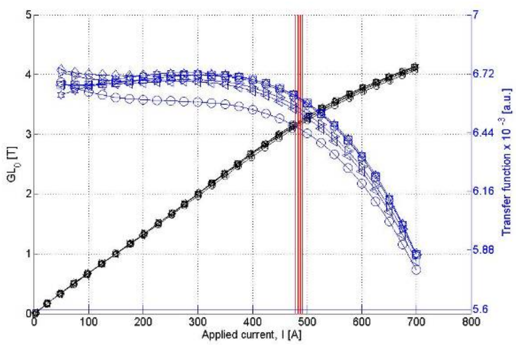


Figure 5: Quadrupole excitation curve.

Figure 5 shows the excitation curves and transfer function coefficient curves for all EMQs, curve-fitted with a polynomial of the 6th degree. It is worth noting that, the curves for EMQs with EDM-made and SSM-made iron cores are similar. Furthermore, the EMQs with EDM-made iron cores seemed to need a lower $I_o$ value to achieve the required *GL*.

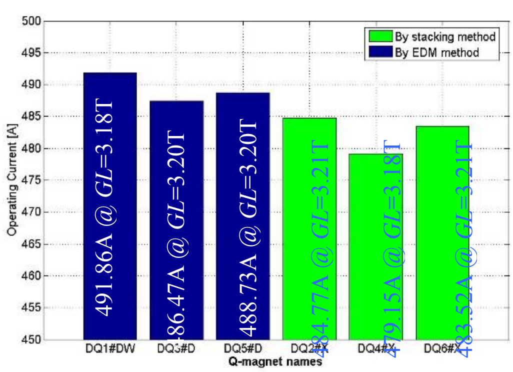


Figure 6: Operating current required for EMQs.

Figure 6 shows a bar chart of the operating current required for the EMQs. It indicates that the EMQs with EDM-made iron cores requires less current to achieve their corresponding *GL* value in order to meet the gradient specification. So, one advantage from using EDM-made iron cores is the reduction of electrical supply cost to operate such an EMQ.

## DEVELOPMENT OF RC MEASUREMENT SYSTEM

The RC system has been developed, as shown in Figure 7, which includes a harmonic coil and a measurement stand. One EMQ is put onto the driving stand which can be adjusted along the x and y in the horizontal plane. The driving axis where the harmonic coil connected with can be moved vertically, so the harmonic coil can be push into the magnet aperture. A stepper motor and an angular encoder are connected with the driving axis in series. As the coil rotates inside the magnet aperture, the integral field, field harmonic contents and the magnetic center are measured at the same time. By carefully adjusting the EMQ position relative to the harmonic coil, the normalized magnitude of the dipole component can be reduced to less than $6 \times 10^{-4}$, and the magnetic center adjusted to within ±3μm. Figure 7 shows a screenshot for the software interface and the measurement results.

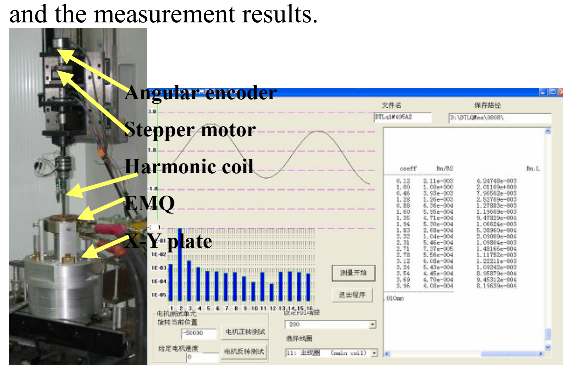


Figure 7: Harmonic measurement system and shot of measurement results.

## CONCLUSIONS

Six EMQs for the eventual DTL test cavity has been manufactured and tested for its assembly reliability in IHEP. Current results suggest that many mechanical fine tuning has to be done. A review in the manufacturing process of the EMQ should be underway. Magnet measurement systems for the sole-purpose to develop these EMQs are within completion. The SSM-made iron core EMQs will be used.

## ACKNOWLEDGEMENTS

We would like to acknowledge C. T. Shi, C. Yuan, L. Li, B. G. Yin, Q. L Peng and Z. Zhang of the Magnet Group for their assistance and help in magnet measurements, and Z. Z. Zhang and his fellow technicians for their continuing effort in producing the EMQs.

## REFERENCES

[1] J. Peng et al, 'Design of 132MeV DTL FOR CSNS', LINAC2006.
[2] H. Ino et al, 'Advanced Copper Lining for Accelerator Components', LINAC2000.
[3] An Sun et al., "Effect of the tuner on the field flatness of SNS Superconducting RF Cavities", LINAC 2004.

# DTL TANK DEVELOPMENT OF 132 MeV LINAC FOR CSNS

Zhirui Sun, Xuejun Yin, Keyun Gong, Jun Peng, Shinian Fu
IHEP, Institute of High Energy Physics, Beijing 100049, China

*Abstract*

A conventional 324 MHz DTL has been designed for China Spallation Neutron Source (CSNS) to accelerate $H^-$ ion beam from 3MeV to 81MeV and up to 132MeV in its second phase. There are 7 tanks in the 132MeV DTL and currently the R&D of the first tank is under progress. In the design, tank-1 has a tilt field distribution partial for obtaining the most effective energy gain and keeping the low Kilpatrick parameter. This tank is under fabrication and the manufacture technique was verified by the measurement results. Concerning of the difficulty of tuning a partial tilt field distribution, the complex RF measuring and tuning procedure is introduced.

## INTRODUCTION

China Spallation Neutron Source (CSNS) mainly consists of an $H^-$ linac and a rapid cycling synchrotron of 1.6GeV[1]. The DTL linac are designed in two phases, with energy of 81MeV for phase I and 132MeV for phase II. R&D program for some key technologies involves a prototype of the first unit of the DTL tank, which is the most difficult section in the whole DTL linac. A 3-meter module covers an energy range from 3MeV to 8.9MeV. The tilt field is designed in this module with an electrical field from 2.2MV/m to 3.1MV/m. The electrical field will keep 3.1MV/m after tilt part through whole DTL tank. Concerning the difficulty in tuning this kind of RF field, a procedure for measuring and tuning the tank is designed. In this paper, we will introduce the progress of module tank fabrication and RF tuning procedure.

## DTL CAVITY DESIGN

The main parameters of the CSNS DTL are listed in Table 1. There are four tanks for phase I and additional three tanks for phase II. The first tank is composed of three short module tanks, and the first module tank is under manufacturing.

Table 1: DTL main parameters

| | CSNS-I | CSNS-II |
|---|---|---|
| Input Energy (MeV) | 3 | 3 |
| Output Energy（MeV） | 81 | 132 |
| Chopping rate （%） | 50 | 50 |
| Average I（μA） | 75 | 150 |
| Pulse Current（mA） | 15 | 30 |
| RF frequency (MHz) | 324 | 324 |
| Repetition frequency(Hz) | 25 | 25 |
| Duty factor（%） | 1.05 | 1.05 |

Mechanical parameters for this unit are listed in Table 2. In the drift tube, the electromagnetic quadrupole (EMQ) is used to supply a gradient 75T/m focusing strength in maximum. The focusing periods are designed as the FD lattice and each drift tube contains one quadrupole.

Table 2: The parameters of first module tank

| | |
|---|---|
| Tank length (m) | 2.85 |
| Energy range (MeV) | 3-8.88 |
| Average $E_0$ (MV/m) | 2.2 ~ 3.1 |
| Synchronous phase (deg) | -30 ~ -25 |
| Tube face angle (deg) | 0 ~ 9 ~ 14 |
| Tank inner diameter(mm) | 566.27 |
| Cells number | 29 |
| No. of Slug tuners | 4 |
| Bore radius (mm) | 6 |
| DT diameter (mm) | 148 |

## TANK MANUFACTURE

The tank body was made of carbon steel with a copper inner surface. To develop the technology, we tried various approaches with some short test tanks. At the beginning, an explosive bonding technology was tested. A thin copper plate was tightly bonded with a steel tank in the inner surface. Since the tank had many ports and holes for vacuum and for holding drift tubes, here the bonding condition was not as good as the inner surface, resulting in vacuum leakage at some ports. Then we turned to adopt the technology of the Periodic Reverse (PR) copper electroforming method. It has been successful for both inner surface and all ports/holes. Figure1 shows the 2.8m tank module after electroforming. The inner copper surface was polished and the ports are now under fine machining for high accuracy and high flatness. There are twelve straight water cooling channel embedded into tank out-wall. Size of the channel is 26mm×13mm. The tank end plate is separated into two parts for water cooling with opposite water flow direction. Water channels on the end plate are shown in Figure 2.

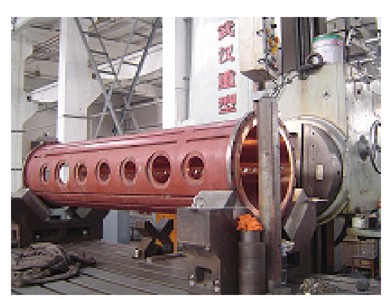

Figure 1: The first module tank is under fine machining after copper electroform.

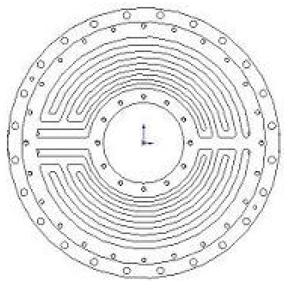

Figure 2: Water channels inside of end plate.

Elements in the first module tank are consist of 28 drift tubes with stems, 14 post couplers, 4 slug tuners, 3 vacuum ports, 1 vacuum detecting port, 4 pickups, 1 viewing window and 29 quadrupoles. There are 29 physical cells in this module tank. The downstream ending plate is made of aluminium as a dummying end plate and thus there is no magnet in the half drift tube. Concerning the permanent magnets hardly have a good uniformity, all the quadrupoles in DTL are electromagnetic quadrupole. The magnets cores have the same thickness of 34mm and the same gradient of 75T/m. The magnet coil is the SAKAE type made by electroforming method which was used in J-PARK DTL linac[2]. Figure 3 shows the magnet inside with the half copper drift tube.


Figure 3: Magnet with SAKAE coil inside the drift tube.

Some field measurements have been carried out with six model magnets in IHEP. The effective length, magnet field gradient in transverse plane, B-H curve and magnet field centre were measured and analyzed. Detailed results can be found in another paper in this conference[3].

The magnet installed into drift tube has a concentric tolerance of less than 50μm error. The mechanical centre is fixed by a set of supporting structure on the rotating coil measurement system. Then beam pipe and outer diameter of the drift tube are machined in accordance with the magnetic centre which is defined as the position with a minimum dipole component. The supporting structure is shown in Figure 4.

## OFC DRIFT TUBE MANUFACTURE

The drift tube of DTL for CSNS is made of oxygen free copper (OFC). The advance is there is no electroplating after electron beam welding (EBW) of the two halves of a drift tube, and the surface machining demands only one time according to the mechanical centre fixed from magnetic measurement, saving a lot of time in mass production.

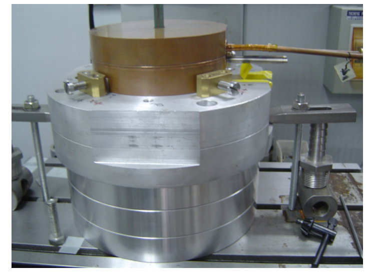

Figure 4: Supporting structure for rotating coil measurement.

In fact, a stainless steel drift tube was constructed in the early R&D stage. The welding deformation was more than 1mm, which was thought bigger than expected. Then we tried to manufacture drift tube with OFC. By using OFC drift tube, the deformation in EBW is 0.4mm, and this error will be corrected by fine machining after welding.

However the major concern is its intensity of OFC drift tube in comparison with stainless steel one. We have done two experiments to check the intensity of OFC drift tube. The first is to check the deformation of the drift tube surface under a giving high air pressure inside the welded drift tube, as shown in Figure 5. The result was 0.02mm deformation when the air pressure was increased from 0 to 1.5kg/cm$^2$, while it recovered back to 0 when no air pressure was applied. The second is to check deformation of the total length of the stem with an additional hanging load for a long time, as shown in Figure 6. The result was 0.01mm length change with a 150kg hanging load for 23 hours, while it became 0 when taking away the load. These tests demonstrate the intensity of OFC is high enough for our design.

Figure 5: Deformation check of an OFC drift tube under a high air pressure.

Figure 6: DT Deformation test with a hanging heavy load.

## DESIGN OF THE ELECTRICAL FIELD

In the analysis of tilt field design of the first tank, the accelerating field distribution generated by MDTFISH code is different with the design data[4]. Figure 7 shows the difference between these two fields. This difference will cause beam property completely different with the design, especially beam loss. In order to recover the electrical field as designed, a cell gap adjustment in special position is adopted. The modified field becomes nearly the same as the designed field, as plotted in Figure 8, but on the other hand it causes the beam synchronous phase in adjusted cells different with the design. As a result, the beam energy is 0.2% lower than the design value in simulation.

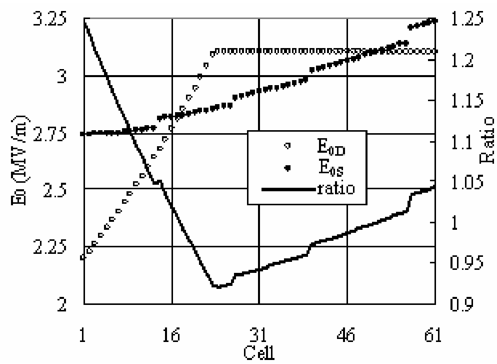


Figure 7: The code generated field before adjusting

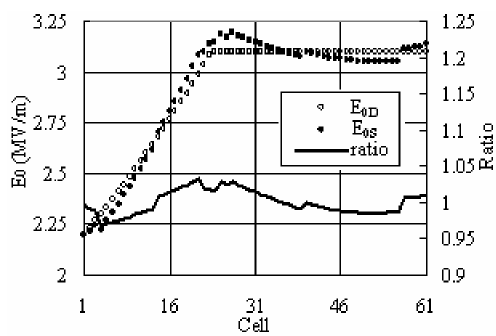


Figure 8: The code generated field after adjusting.

## RF TUNING DESIGN

In the RF tuning of DTL for CSNS, the field is required to be no more than 1% different from the design one. There are several procedures on RF tuning for that goal. First, separate the perturbation of slug tuners and post couplers. Second, adjust the slug tuners by calculating the transfer matrix for field modification. Third, check the sensitivity of RF field in a 5% tilt field. And last, check the effects of the movable tuners both on field tilt and on field flatness.

According these procedures, the RF tuning of DTL is designed for three aims: resonant frequency, flatness and field sensitivity. The most concerned issue is how to get the designed field distribution for both tilt field section and flat field section. While the sensitivity in different sections, including movable tuners effect on tilt part, is also under thorough detecting.

In the tank 1 there are 12 fixed tuners and 2 movable tuners, as shown in the Fig 10. All the 14 slug tuners have a 150mm diameter and 10mm corner radius. The maximum penetrating depth is 100mm. Frequency adjustment is designed as ±1MHz.

**1. Frequency tuning** The designed field is complicated, so the tuning of post couplers is separated from frequency tuning with slug tuners. The frequency shift caused by the insertion of the post couplers is 486.34 kHz in simulation. Here the simulated post couplers are fixed in length and have no tip angle. In the frequency tuning, post couplers are all pulled out. The slug tuners penetrate into tank with different length to obtain the required field distribution as designed at the resonant frequency. And the position changes of slug tuners for ±5% are recorded to check the sensitivity afterwards.

**2. Flatness tuning** When the frequency is proper and field is flat, post couplers are inserted in a same length and same tip angle. According to the frequency shift and field perturbation, the post couplers are tuned in several groups with different length. Flatness tuning is an iterating process between resonant frequency and designed flatness approach.

**3. Sensitivity tuning** The sensitivity is judged by 2 points. Firstly, 5% field change introduced from fixed tuners has a perturbation on designed field. Rotate the post couplers angle until the perturbation has no effect on field distribution. Secondly, check the waveform by bead pulling system to ensure the RF field as designed. After the post couplers adjustment, movable tuners perturbation is measured with 1% field variation.

For the RF tuning of DTL for CSNS, the target field distribution is different from any other design. So the RF tuning, especially the flatness and sensitivity, is more difficult. After the module tank is manufactured, more experiment will be conducted to check the design.

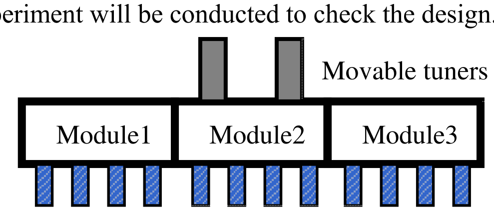


Figure 9: Tuner distribution on the first DTL tank

## ACKNOWLEDGEMENTS

We are grateful to K. Hasegawa and F. Naito of J-PARC for their great support. Many discussions with them are instructive for our work.

## REFERENCES

[1] S.N.Fu, et al., “Status of High Current Linear Accelerator at CSNS”, this conference MO202
[2] F.Naito, et al. “JHF Accelerator design study report”, Chapter 4.5
[3] Y.Cheng, et al., “Quadrupole Magnet Development for 132MeV DTL of CSNS”, this conference MOP047
[4] J.Peng, et al. “A new tuning procedure for the DTL RF field”, Chinese Physics C. 2008.

# DRIFT TUBE LINAC DESIGN AND PROTOTYPING FOR THE CERN LINAC4

S. Ramberger, N. Alharbi, P. Bourquin, Y. Cuvet, F. Gerigk, A.M. Lombardi, E. Sargsyan, M. Vretenar, CERN, Geneva, Switzerland, A. Pisent, INFN/LNL, Legnaro, Italy


## Abstract

The Drift Tube Linac (DTL) for the new linear accelerator Linac4 at CERN will accelerate H⁻-ion beams of up to 40 mA average pulse current from 3 to 50 MeV. It is designed to operate at 352.2 MHz and at duty cycles of up to 10 %, if required by future physics programmes. The accelerating field is 3.2 MV/m over the entire length. Permanent magnet quadrupoles (PMQs) are used as focusing elements. The 3 DTL cavities consist of 2, 4 and 4 section of about 1.8 m each, are equipped with 35, 41 and 29 drift tubes respectively, and are stabilized with post-couplers. Several new features have been incorporated in the basic design. The electro-magnetic design has been refined in order to reduce peak field levels in critical areas. The mechanical design aims at reducing the complexity of the mechanical structure and of the adjustment procedure. Drift tubes and holders on the tanks that are machined to tight tolerances do not require adjustment mechanisms like screws or bellows for drift tube positioning. A scaled cold model, an assembly model and a full-scale prototype of the first half section have been constructed to validate the design principles. The results of metrological and RF tests are presented.


## INTRODUCTION

The Linac4 DTL will accelerate H⁻-ion beams of up to 40 mA average pulse current from 3 MeV to 50 MeV in 3 accelerating cavities over a length of 18.7 m. The RF cavities operating at 352.2 MHz and at duty cycles of up to 10% are 520 mm in diameter with drift tubes of 90 mm diameter and 20 mm beam aperture.

The drift tubes are equipped with permanent magnet quadrupoles (PMQ) with an FFDD lattice in cavity 1 and an FD lattice in cavity 2 and 3. PMQs have the advantage of small size at medium magnetic gradients without the need for current supply wires or power converters. To ease matching for beam currents below nominal, electro-magnetic quadrupoles are placed in each of the intertank sections. Latest design parameters are shown in Table 1.

## ELECTRO-MAGNETIC DESIGN

The electro-magnetic design aims at an acceleration with high constant average field $E_0$ of 3.2 MV/m over all gaps with a high effective shunt impedance per unit length $ZT^2$. While it is a typical DTL concept to ramp $E_0$ in the first cavity in order to adiabatically capture the beam longitudinally [1], the choice of high constant $E_0$ aims at maximizing the energy acceptance to the incoming beam and leads to a more compact design [2].

Table 1: DTL Cavity Parameters

| Parameter | Cavity 1 / 2 / 3 |
|---|---|
| Cells per cavity | 36 / 42 / 30 |
| Maximum surface field | 1.6 / 1.4 / 1.3 Kilp |
| Synchronous phase | -30 to -20 / -20 / -20 deg |
| RF peak power per cavity | 0.95 / 1.92 / 1.85 MW |
| RF beam / peak power | 1.88 MW / 4.7 MW |
| Focusing scheme | FFDD / FD / FD |
| Quadrupole length | 45 / 80 / 80 mm |
| Number of sections | 2 / 4 / 4 |
| Length per cavity | 3.63 / 7.38 / 7.25 m |

A particular advantage of ramping $E_0$ are lower peak fields at lower beam energies where earlier designs showed increased breakdowns [3]. Several parameters might be of influence: comparably large surfaces of flat opposing faces on consecutive drift tubes, more outgassing due to larger overall surfaces including the cavity end-wall, an incoming beam with a higher number of stray particles, magnetic fields close to surfaces of shorter drift tubes.

Recent studies for muon cooling where strong accelerating and magnetic fields have to be combined, emphasize the importance of the latter [4]. The PMQs that will be used for the DTL design have a peak magnetic surface field of 0.5 T which in the shortest drift tubes falls close to the area of peak electric fields.

In order to reduce breakdown probability in the first cells, the peak electric field therefore has been reduced by 30% by increasing the gap length. The cells are tuned by the face angle. At longer drift tubes the peak electric field can be ramped to values that allow for optimum effective shunt impedance (Fig. 1). In this way, the same advantage of lower peak fields in the first cells is achieved as when ramping $E_0$.

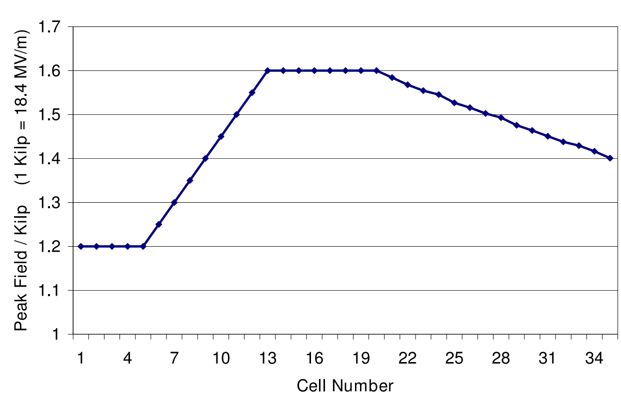


Figure 1: The peak field is reduced in the first cells.

The minimum gap length increases by 40 % from about 8.5 mm to 11.9 mm. As a further advantage also longitudinal mechanical tolerances increase by the same relative amount. The consequences on the effectiveness of the structure remain low. Energy gain in the first cells decreases by 4.1% but only 1% in beam energy over the first cavity is lost.

## ALIGNMENT TOLERANCES

The required alignment tolerances were defined by error studies on beam dynamics [5]. Limits for transversal and rotational positioning of quadrupoles are tight (Table 2). The longitudinal magnet position is less critical.

Table 2: Alignment Tolerances Between Drift Tubes

| Error Type | Max. Amplitude |
|---|---|
| Transverse horiz. & vert. (x,y) | ±0.1 mm |
| Magnet rotation, all axes | ±3 mrad |

The tolerances are tight but following advances in machining quality, they are considered feasible without any further adjustment mechanism. In consequence, all critical parts have to undergo metrology before assembly. Considerable advantage of this strategy is that the assembly becomes straightforward and that positioning cannot degrade by accidental movement of screws. It is worth noting that on other DTLs like the Linac2 at CERN, the drift tube positions have never been corrected after their first alignment even though the design had foreseen this explicitly [6].

## MECHANICAL DTL STRUCTURE

The DTL cavities consist of a steel cavity, an aluminium girder, drift tubes assembled from pre-machined copper pieces, and accessories for mounting drift tubes in girders as well as for tuning, stabilization, support, vacuum pumping and alignment of the structures (Fig. 2).

The cavities are made from 50 mm thick mild steel cylinders that provide the rigidity to achieve the required tolerances when placed on supports. The cavity is segmented into 2 sections in the first cavity, and 4 sections in the second and third cavity that are aligned with precisely machined rings after assembly of each section. Mild steel is the material of choice due to its thermal conductivity, mechanical strength, and comparably low price [1].

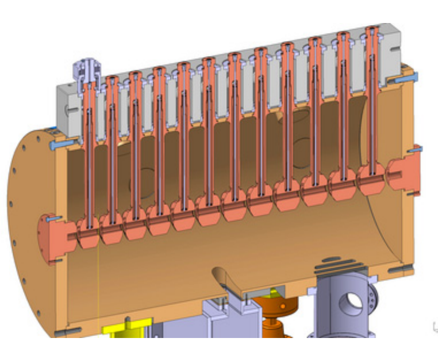

Figure 2: DTL prototype cut along the beam axis.

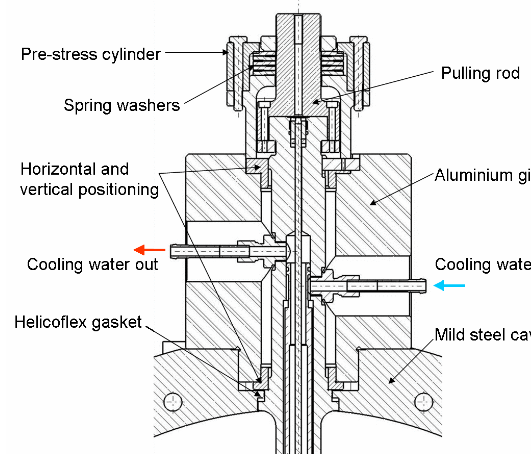


Figure 3: Drift tube mount assembly.

The steel cylinders of about 1.8 m length are precision machined in order to correctly position rectangular aluminium girders on top. The girders are pre-machined for each drift tube and stainless steel rings are inserted into the openings from above and below. The steel rings are remachined for precise drift tube positioning.

## DRIFT TUBE MOUNT ASSEMBLY

The completed girder is placed on the steel cylinder and provides the reference for drift tube mounting (Fig. 3). The horizontal position of the drift tube is defined via the lever arm between upper and lower steel rings whereas the vertical position is given by the stop position on the lower ring.

At the top, the copper drift tube is extended by a stainless steel pulling rod as the length of the drift tube shaft that can be installed in the cavity is limited by the diameter of the cavity. The Helicoflex® gasket rests on a stop on the drift tube and provides for vacuum tightness and RF continuity towards the copper plated mild steel cavity. Spring washers at the top of the drift tube provide the required force via a nut to compress the Helicoflex® gaskets.

For the installation of the spring washers a pre-compression socket is assembled in advance with the lower support socket. This pre-assembly is placed over the pulling rod and rests on the upper stainless steel ring. The nut is placed on the extension rod and just locked on the spring washers. The pre-compression cylinder is released in a way that the compression force is transferred uniformly to the drift tube through the nut and the extension rod.

## MANUFACTURING PROCEDURE

The manufacturing procedure for drift tubes is critical in order to reach the required high precision at assembly:

- Machining of drift tube parts with main references
- Assembly of drift tube with stem by e-beam welding
- Vacuum test of cooling circuit
- Final machining of magnet holder and references
- Insertion of PMQ

- Closure of drift tube by e-beam welding
- Metrology

After assembly of each cavity section, the position of drift tubes to reference surfaces is checked by a laser tracker.

## THE PROTOTYPES

A full-scale pre-prototype with two drift tubes has been built to test the mount assembly. Laser tracker measurements compared to dimensional metrology data show that the vertical positioning is within 0.01 mm. The horizontal positioning is within 0.1 mm longitudinally and within 0.05 mm transversally with respect to the cylinder axis.

Currently a full-scale prototype of a half section with 12 drift tubes without PMQs is being constructed at CERN (Fig.4). The purpose is to gain a small representative statistic sample on drift tube mechanics and to test technologies such as copper plating, e-beam welding, vacuum sealing, as well as tuning, stabilization, and operation at high RF power. At a later stage, few drift tubes with PMQs will be installed. All the prototype component machining has been provided by INFN/LNL, a contribution in view of a possible application for a radioactive ion beam facility driver in the SPES project [7].

A scaled cold model has been manufactured in order to study stabilization with post-couplers considered to be critical because of the drift tube to tank distance of $1.01\ \lambda/4$ and the 1 in 3 post-coupler scheme in the first cavity [8]. The model could be easily stabilized. Figure 5 compares bead-pull measurements with and without post-couplers after detuning by shifting the half drift tubes at either end.

## CONCLUSIONS

The DTL design for the Linac4 at CERN incorporates new features in a basic design: Peak fields are ramped in the first cavity in order to reduce probability for breakdown

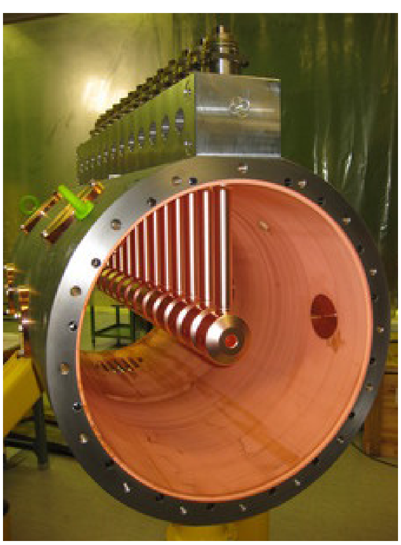

Figure 4: DTL prototype in the assembly stage.

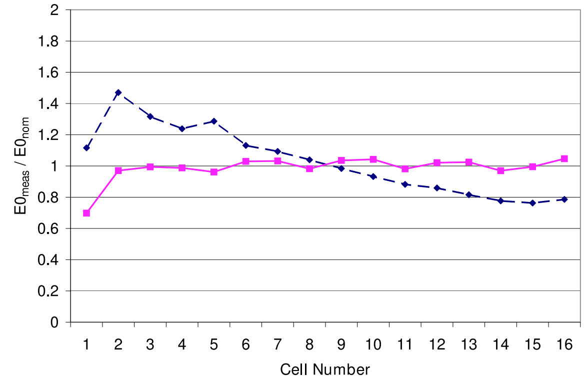


Figure 5: Accelerating voltage per cell in the cold model without (dashed) and with post-couplers (continuous).

while the accelerating field $E_0$ is kept constant over the whole structure. A new mounting mechanism is described that does not require any adjustment after assembly. Both features aim at a robust and reliable construction and operation. First results of metrological and RF tests demonstrate the current progress of prototyping.

## ACKNOWLEDGEMENT

Construction of the prototypes relies on the CERN central workshops for assembly and finishing technologies. The cold model has been financed and manufactured by KACST, Riad, Saudi Arabia.

We acknowledge the support of the European Community-Research Infrastructure Activity under the FP6 “Structuring the European Research Area” programme (CARE, contract number RII3-CT-2003-506395).

## REFERENCES

[1] J. Stovall, “Low and Medium Energy Beam Acceleration in High Intensity Linacs”, Proc. EPAC 2004, Lucerne, Switzerland, 2004, pp. 108–112.

[2] A. M. Lombardi et al., “End-to-End Beam Dynamics for CERN LINAC4”, Tech. Rep. CERN-AB-2007-001 / CARE-Conf-06-039-HIPPI, CERN, Geneva, Aug 2006.

[3] P. M. Lapostolle and A. L. Septier, Linear accelerators, North-Holland, Amsterdam, 1970.

[4] A. Moretti et al., “Effects of high solenoidal magnetic fields on rf accelerating cavities”, Phys. Rev. ST Accel. Beams 8 (2005) 7, p. 072001.

[5] A. M. Lombardi et al., “Loss Control and Steering Strategy for the CERN LINAC4”, Tech. Rep. AB-Note-2007-033 / CERN-AB-Note-2007-033, CERN, Geneva, Aug 2007.

[6] E. Boltezar, “Mechanical Design of CERN New Linac Accelerating Structure”, Proc. 1979 Linear Accel. Conf., vol. BNL51134, Montauk, New York, 1979, pp. 392–395.

[7] A. Pisent et al., “Design of the High Current Linac of SPES Project”, Proc. EPAC’08, Genoa, Italy, 2008, pp. 3545–3547.

[8] N. Alharbi, F. Gerigk and M. Vretenar, “Field Stabilization with Post Couplers for DTL Tank1 of Linac4”, Tech. Rep. CARE-Note-2006-012-HIPPI, CARE, 2006.

# DEVELOPMENT OF INVESTIGATIONS ON THE MILAC HEAVY ION LINEAR ACCELERATOR

V.O.Bomko, O.F.Dyachenko, O.M.Yegorov, A.P.Kobets#, M.S.Lesnykh, K.V.Pavlii, Z.Ye.Ptukhina, V.M.Reshetnikov, S.S.Tishkin, O.V.Zabotin, B.V.Zajtsev, B.M.Zinchenko, V.G.Zhuravlev, National Science Center "Kharkov Institute of Physics and Technology", Kharkov, Ukraine

*Abstract*

On the Kharkov heavy ion linear accelerator MILAC works are carried out with heavy ion beams accelerated to 8.5 MeV/u, and development of new methods for acceleration and investigations on modernization of accelerating structures [1].

## MILAC LINEAR ACCELERATOR

The Kharkov ***multicharge ion linear accelerator*** (MILAC) is a unique physical and technology complex that consists the first prestripping section PSS-15 (Fig. 1, p. 2), second prestripping section PSS-4 (Fig. 1, p. 5), main section MS-5 (Fig. 1, p. 3) and the system of the ion irradiation (Fig. 1, p. 8). The structural scheme of the accelerator is given in the Fig.1.

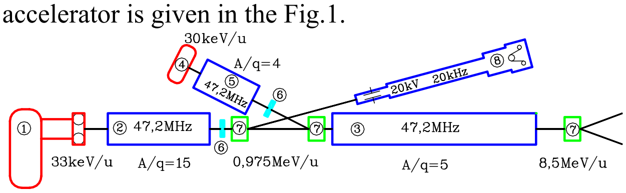


Figure 1: The structural scheme of the MILAC.

At the main and two pre-stripping sections of the MILAC linear accelerator the accelerating DTL structure on the H-wave of interdigital type (IH-structure). was applied [2].

The characteristic feature of the main section MS-5 (Fig. 1, p. 3) is its electrodynamic characteristics. An effective method was developed for adjusting the cells of the accelerating structure using additional current-carrying rods located at an angle to the supporting rod (Fig.2).

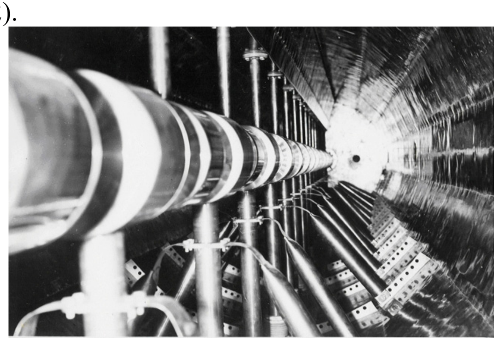

Figure 2: Accelerating structure MS-5.

This method of adjusting the inductive accelerating cell parameters allowed formation of a uniform accelerating field distribution along the structure. From one hand, this allowed to increase significantly the acceleration rate, and from the other, to form the paths of the uniform filed distribution of the controllable extension which gives a possibility to obtain the beams of intermediate energies [3]. Additionally, a method was developed for adjusting the field distribution using the ending resonance adjusting device, which represent quarter wave oscillators; on the side of the oscillator facing the side wall of the cavity a control piston is placed which can move in longitudinal direction. Such systems are installed on the input and output ends of the cavity.

The main section MS-5 11 m in length with 42 drift tubes, of which 21 contain magnetic quadrupoles gives a possibility to accelerate ions with A/q≤5 from 0.975 to 8.5 MeV/u. Total acceleration rate in the prestripping section is 3.2 MeV/m.

Second pre-stripping section PSS-4 (Fig. 1, p. 5) for accelerating only light ions with A/q≤4 from 30 keV/u to 1 MeV/u is developed. In this new section irregular interdigital (IH) accelerating structure with beam focusing by radiofrequency field (alternating phase focusing with stepped changing the synchronous phase along the focusing period) are used. After stripping this beam will be output on the acceleration line of the main MILAC section (Fig. 1, p. 3) and accelerated up to 8.5 MeV/u.

The problem of adjustment accelerating structure PSS-4 was especially difficult in connection with the non-uniform of lengths of cells mention above in structure of the focusing periods and increasing character of distribution of an accelerating field along the accelerator. Therefore it was required to apply a combination of various tuning methods The new effective inductance-capacitor tuning devices (contrivance) as rods located on the drift tube side, opposite to their holders are developed [4]. At the certain design the exact local tuning of cells is possible for carrying out not only selection of contrivance length, but also by change of a corner of their disposition concerning an axis of drift tube holders (Fig.3.).

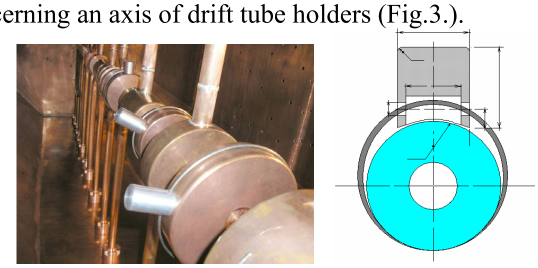

Figure 3: Accelerating structure PSS-4 with contrivance.

The high efficiency such inductance-capacitor tuning system allows to receive required electro-dynamic characteristics of accelerating structure at an identical small diameter of drift tubes, that considerably simplifies

#kobets@kipt.kharkov.ua

their design, reduces a radiating background around of the accelerator and prevents occurrence of the multypaction high-frequency discharges.

## INVESTIGATIONS ON MILAC

Introduction on MILAC linear accelerator IH accelerating structures of various modifications considerably expand a scientific and applied range of researches. Experimental investigations with heavy ions beams for obtaining track-etched membranes, production of unique radionuclides, developments of proton and ion therapy, studying of radiating characteristics of constructional materials of nuclear power, research processes of fusion-fission superheavy nucleus and other problems of nuclear physics are carried out.

### *Track-Etched Membranes*

Presently, on MILAC experimental investigations on irradiation the polymer films with heavy ion beams with the aim of obtaining track-etched membranes [5]. In the MILAC prestripping section triple-charge $Ar_{40}^{3+}$ ions were accelerated to the energy of 1 MeV/u with the intensity of $10^{10}$ particles/s; PETF films 6 – 10 μm thick were irradiated, and after subsequent physical and chemical treatment it was possible to obtain experimental samples of track-etched membranes with through pores from 2 to 0.05 μm in diameter (Fig.4).

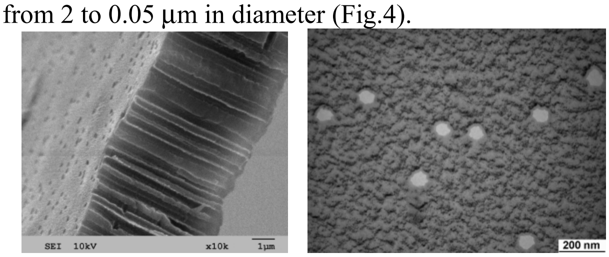


Figure 4: Pores at the cross section and the surface track-etched membrane.

To provide uniform track distribution in the polymer film with the specified density and orientation a system for ion irradiation of polymer film with horizontal beam scanning with the frequency of 20 kHz and sinusoidal voltage up to 20 kV was developed.

### *Radiation Investigations on Structural Materials*

In connection with the forthcoming termination of the design service life of some energetic blocks at nuclear power plants in Ukraine it is necessary to develop a scientific and engineering substantiation for extending the operating lives of NPP units. The use of accelerated charged particles allows one to imitate quite completely the processes involved by radiation effects in the reactor cores under steady-state and transient operating conditions.

In experiments the ions of helium, neon and argon are accelerated at the accelerator MILAC in the two prestripping sections PSS-15 and PSS-4 to energy of 1 MeV/nucleon and in the main section MS-5 to energy of 8.5 MeV/nucleon. Thus, it is possible to imitate the process of irradiation with heavy ions of fuel element materials and other structural materials used in energetic blocks.

For investigations on the mechanical characteristics of structural materials a complex of experimental devices was developed. It is designed to study the creep, stress relaxation and active straining of samples after irradiation with accelerated ions.

A device permitting to study the creep, stress relaxation, active straining and dimension stability directly in the process of irradiation with accelerated ions was designed. In Fig.5 given are the schematic presentation and the photograph of the experimental device for investigations of plastic properties of structural materials exposed to the ion beam.

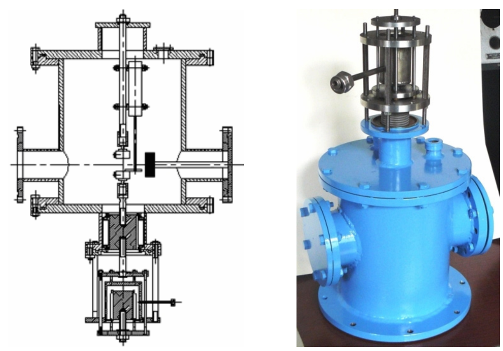

Figure 5: Chamber for investigations of plastic properties of structural materials exposed to the ion beam.

Using the developed methods and experimental devices at the accelerator MILAC it will be possible to investigate the structural materials directly in the process of irradiation with heavy ions, as well as, after irradiation.

### *Development of Investigations on the Nuclear Fusion of Heavy Particles*

At present, 1.5 tens of supeheavy elements are obtained, but there are no direct reactions to produce, for example, a stable isotope of the element-114 with an atomic number 298 for lack of neutrons.

To produce new superheavy elements and to study their properties in the field of the assumed stability island it is necessary to develop new experimental techniques. For arrangement of experiments on studying the reactions of deep inelastic transfers during interactions of heavy ions, with a maximum yield of interesting isotopes, the choice of an initial target-beam isotope combination and kinetic beam energy is a determining factor. The most realistic description of the process of nuclear fusion is proposed in the concept of a double nuclear system. Basing on this system a series of models are constructed being successfully applied in the description of the processes of fusion-quasi-fission of heavy nuclei.

We have calculated the number of protons and neutrons in the fragments of the double nuclear system and considered possible variants of transitions which are controlled by the potential energy and are determined by its minimum value. The dynamics of transitions in the reaction of isotopes *Fe*, *Ni* and *Co with* $^{238}U$ for ±n, ±p, ±(n+p) allowed transitions is calculated. With a correct choice of the target-beam isotope configuration, taking into account the nucleon emission and excitation energy changing, there is a probability to direct the reaction into the channel of nucleon transfer for production of superheavy nuclei.

Using the accelerator MILAC it is planned to accelerate the ions of iron, cobalt, nickel, copper and zinc to the energy of 8.5 MeV/nucleon. In experiments the target of uranium, bismuth, lead and other heavy metals will be used. When carrying out experiments on the study of the reactions of deep inelastic transfers there is a need for heavy ion accelerators with controlled beam energy. The team of specialists working at the accelerator MILAC facility has a wide theoretical and experimental experience in smooth variation of ion energy, including the beam ion energy of the main section MS-5 [3].

## *Radionuclides for PET Diagnostic*

For investigation with PET it is important to choose a radionuclide having a low maximum energy of $\beta^+$-particles which provides high resolution of the image. $^{18}$F having the maximum energy of $\beta^+$-particles of 635 keV is the best among the other radionuclides. Ideally, average period of life of radionuclides should be of the same order as the time necessary for investigating

$^{18}$F is relatively long living among short living isotopes ($T_{1/2}$=109.7 minutes) which radiopharmaceutical preparation takes the main part in the development of positron-emission tomography. PET investigations requires from 1 to 4 hours for scanning from the moment of the admission of the preparation.

Production of considerable amount of fluorine-18 (about 1 curie per an hour) at linear accelerator MILAC is possible with $^{18}O(p,n)^{18}F$ and $^{16}O(\alpha,pn)^{18}F$ reactions with energies 8.5 and 34 MeV for protons and helium ions, respectively. In the Fig. 6. the function for excitation of $^{16}O(\alpha,pn)^{18}F$ reaction is shown. It is easily seen that at the energy of 34 MeV it has the maximum.

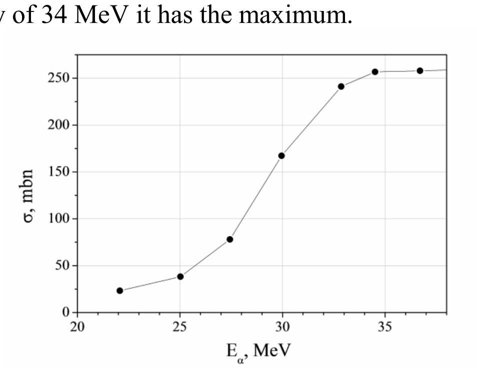


Figure 6: The function for excitation of $^{16}O(\alpha, pn)^{18}F$.

After start prestripping section PSS-4 on linear accelerator MILAC acceleration of ions of helium up to energy 34 MeV at an average intensity of helium ion beam up to 10 μA is planned.

A system for target irradiation was created; in the targets nuclear reactions run. Production process of $^{18}$F radioactive fluorine from $CeO_2$ oxide respectively to the nuclear reaction $^{16}O(\alpha, pn)^{18}F$ was studied.

## *Ion Therapy*

In Ukraine medical centers of proton and ion therapy are not at all. The oncological disease and mortality rate in our country is highest throughout Europe and the survival rate is lower by a factor of 2.5 then in other countries. Widespread investigations demonstrated that the best method of overcoming the tumor resistivity is the use of a close-ionizing radiation with linear energy losses of 50÷100 KeV/μm. Practical results revealed a high efficiency of radiation treatment with carbon ions. In many cases the effective treatment is ensured by the combined use of proton and ion beams. Therefore, the most complete center of radiotheraphy should provide the radiation treatment by carbon ions and protons.

After starting the new prestripping section PSS-4 at the linear accelerator MILAC it will be possible to accelerate protons to energy of 8.5 MeV, helium ions to energy of 34 MeV and carbon ions to energy of 102 MeV. For further acceleration of above mentioned ions it is necessary to construct a synchrotron having 20 m in diameter. Then ions could be accelerated to the controlled energy from 50 to 400 MeV/nucleon being necessary for the ray therapeutics. Establishing of the center of radiotherapy has a reason, as it is located near the accelerator MILAC of the research institute of medical radiotheraphy possessing a necessary therapeutic base and highly qualified personnel having a great experience in treatment of oncological patients by surgical, chemotherapeutical and radiation methods.

## REFERENCES

[1] B.O.Bomko, A.P.Kobets, Ju.P.Mazalov, B.I.Rudyak. Linear Accelerator of the Heavy Ions KIPT// Ukr. Phis. Journal, v.43, # 9 (1998), p.1144.

[2] V.A. Bomko, N.I. Demchuk, A.F. Dyachenko et al. Interdigital Accelerating H-structure in the Multicharged Ion Linac (MILAC) // Review of Scientific Instruments and Methods, v. 69, # 10 (1997), p. 3537–3540.

[3] V.A. Bomko, A.F. Dyachenko, A.F. Kobets, Yu.P. Mazalov, B.I. Rudyak. Smooth variation of ion energy in the interdigital accelerating H-structure // Nuclear Instrumens & Methods in Physics Research, A 406 (1998), p. 1–5.

[4] V.A. Bomko, Y.V. Ivakhno. A new technique of tuning interdigital accelerating structure of the ion linear accelerator // Nuclear Instrumens & Methods in Physics Research, A 582 (2007), p. 374–377.

[5] V.A. Bomko, A.F. Burban, A.F. Kobets et al. Initial stage of etching through pores in PET films irradiated by Ar ions //Nuclear Instrumens & Methods in Physics Research, B 266 (2008), p. 256–261.

# LINAC OPERATIONS AT FERMILAB

L. Allen, FNAL, Box 500, Batavia, IL 60510 USA

The Fermilab Linac has been delivering unprecedented amounts of beam for HEP. The addition of Main Injector, three high intensity high repetition rate experiments and the 120 GeV Fixed Target Programs have increased the repetition rates from 0.33Hz. to a maximum of 7.5 Hz. and it is expected to increase further. The intensity accelerated by the Booster is 5 E12 protons per pulse. The effects on radiation levels and operational reliability and developments helping both to cope with the higher rates and make the beam more useful to Booster will be discussed.

## THE PROBLEM

As the demand for higher booster intensity and repetition rate began to ramp up, the Booster was operating at about 65% efficiency. Because the Linac discards the first ten μsec of beam it needed to accelerate almost 1 E13 H- ions per pulse. Today after many improvements to the Linac and Booster, booster efficiency is 90% and only 7.7 E12 per pulse are required from Linac.

## IMPROVEMENTS

In the late 1990's Milorad Popovic [1] accurately modeled the high energy linac quadruples. Using this data he was able to make significant reductions in losses. The match to the Booster was also improved.

In 2001 an experiment [2] was performed measuring the effect of linac beam current on booster efficiency. At that time the Linac normally accelerated 50ma. and injected 11 turns into the Booster. During the experiment, linac beam current was reduced to 30ma. and The Booster was tuned with up to 20 turns injected. The Booster operated at the same or better efficiency at the lower current. As a result, linac beam current was reduced to 40 ma. and as a result of further booster improvements to 36 ma.

As a result of these improvements, linac beam losses have decreased dramatically. The parameter D7LMSM is the sum of all the loss monitors in the RF area. In 2000 D7LMSM was >20. The improvements noted plus constant tuning has reduced the total losses to the 10 to 12 region for the H- ion source and less than ten for the I- ion source.

To get a better measurement of the linac energy on a day to day basis a device called the Velocity Meter [3] has been installed in the 400 MeV Line. By measuring the beam phase between two Griffin [4] detectors it measures flight. While it is not calibrated in energy, it does alert one to energy changes. Before this monitor was installed it was impossible to determine if an energy drift was causing booster efficiency to decline.

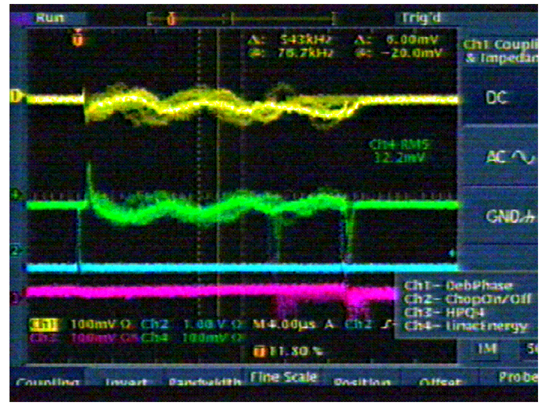


Figure 1: Velocity meter scope traces.

The output signal (in green) viewed on an oscilloscope can detect an energy swing during the pulse or an overall energy shift. The computer reads this parameter and automatically changes the RF phase in the final RF module to correct the energy. Using this method has stabilized the linac energy and made booster tuning more repeatable.

A Bunch Length Monitor [5] was also installed in the 400 MeV Line. It has been empirically determined that booster needs this device to read less than .85 nsec. for good operation. Linac has been tuned so that it averages approximately .83 nsec. The low energy buncher. medium energy buncher and the phase difference between the Low Energy Linac(LE Linac) and High Energy Linac(HE Linac) are the most common adjustments to control this.

## CONTINUING PROBLEMS

Looking at the trace in Fig. 1 one notices an oscillation. The oscillation is at approximately 130 kHz and is a real energy effect. We can see this in the HE Linac RF phase and at times in the gradient. There is a program underway, lead by Ken Quinn, to locate and repair the source of this oscillation.

There is a slow drift of some parameter in the LE Linac. The signature of this drift indicates that it is RF related. The gradients have independent readings but intertank phase does not. The drift does not appear to be the gradient because the independent readings do not change at the same time. The lack of independent readings has made looking at phase difficult. The fix is to vary the phase of LE Tank 5. This both changes the output energy of the LE Linac and the phase difference between the LE Linac and the HE Linac.

As mentioned earlier the Linac discards the first 10μsec. of beam each pulse. This is the time it takes for the feedback systems in the LE Linac to settle in. During this time the beam is unreliable and dumped. This beam usually has slightly higher losses than the later beam sent to booster and should not be necessary. The HE Linac settles in about two µsec.

To address the LE RF drift and the 10 µsec. throwaway there is a program ongoing to replace the LE Linac LLRF System [6,7]. The new system replaces the current Intertank Phase Error reading with a phase measurement between the cavity and reference line. This will provide proper read-backs and control of the amplitude and phase of the RF. It will hold the accelerating gradient to within .3 percent and the phase being held to less than .3 deg. and settle in two µsec. The effect of this will be to eliminate the LE Linac RF drift and cut the 10 µsec. of beam thrown away to two µsec. These improvements improve linac stability and losses.

## RELIABILITY

Overall linac reliability has decreased over the last few years. Before the upgrade in 1993 uptime was 98%. So far in 2008 it is 95.6%, in 2007 it averaged 94.8%. Over the period of Run II from 2001 to 2005 it was 97%. From June, 2006 through August, 2008 it was 95%.

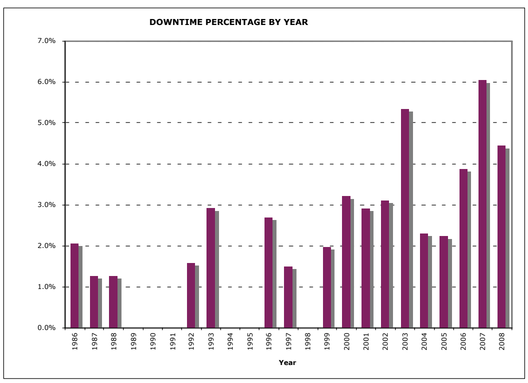


Figure 2: Linac downtime percentage by year.

In the time period of 2001 through 2005 there were 1160 hours of downtime or 3.03% of the total scheduled time from 6621 entries. In the period from June 2006 through August of 2008 there are 908.5 hours or 5.035% on 4986 entries.

Table 1: Percent of Downtime By Major Subsystem.

| | 2001-2005 | 2006-2008 |
|---|---|---|
| **LRF TOTAL** | 36.78% | 38.77% |
| **KRF TOT.** | 32.92% | 19.55% |
| **PREAC** | 8.38% | 10.78% |
| **MISC. TOT.** | 19.27% | 28.34% |
| **SAFETY** | 1.10% | 1.17% |
| **CONTROLS** | 1.45% | 1.39% |

Table 1 shows the distribution of downtime by major subsystem. The differences are small between the 2001-2005 and 2006-2008 time periods. There are however more incidents of longer duration in the 2006-2008 time period. There were an average of 131 events per month from 2001 to 2005, while the average for 2006 to 2008 is 191.

There are several reasons for the decrease in reliability. Components are aging and require more maintenance. The retirement of a the last technician who was here from the beginning The decrease in the lifetime of some components coupled with Fermilab's policy of not scheduling regular maintenance periods.

The water flow meters for the Klystron RF Systems are an example of aging components. They operated without major problems for several years, but are now sticking and causing the systems to trip. Each trip causes from 2 to 5 minutes of downtime.. A program to replace them has been going on for some time with limited success.

In the period around 2001 to 2003 the lifetimes of the 7835 triodes decreased dramatically. There was a time when the lifetime was less than the time needed to build or rebuild them. Fermilab had to borrow tubes from other laboratories to continue operating. The manufacturer, Burle Industries, has made great strides in modernization and quality control. As a result, average lifetimes have increased but there is still a wide spread in tube lifetime. While not back to the pre 2000 levels, the last few years have shown an upward trend.

The policy of not scheduling maintenance periods also contributes to lower linac reliability. While this maintenance policy does work for the laboratory as a whole, there are so many users that the Booster must be broken for Linac to get maintenance time. The result is that the Linac has trouble stretching problems until a maintenance period.

Most linac downtimes are less than two minutes. Since June, 2006 downtimes of two minutes or less account for 61.25% of the total entries. Events lasting 14 minutes or less account for 90% of the total number of downtime entries. Forty six percent of the total downtime results from entries of less than 2 hours. Some serious problems do not always result in one long downtime but can be many short ones.

A recent example of this type of problem was a long series of Klystron Charging Supply Trips. The downtime from each was generally less than four minutes. The frequency started out low, one or two trips per day, and ramped up to as many as nine per day. The problem took almost six months to get to the point of being noticeable. It turned out that the temperature in the charging supply was to low causing the ignitron to self-fire. The total cost was 39.2 hours down on 1096 incidents.

## SUMMARY

The Fermilab Linac has been made to run in a way that makes it possible for the Booster to operate very efficiently. These improvements are mostly the result of diagnostics developed by the Booster Group. Using these diagnostics, both in automatic loops and manual tuning, has stabilized the Linac. The underlying problems are still there but we now have solutions in progress and are close to being able to implement them.

## REFERENCES

[1] Personal Communication with Milorad Popovic.
[2] D. P. Moehs et al, Fermilab Booster Charge as a Function of Linac Intensity, LINAC 2002, Gyeongju, Korea
[3] Local Documentation W. Pellico, Fermilab Batavia, IL
[4] Local Documentation W. Pellico, Fermilab Batavia, IL
[5] C. Drennan, Booster Bunch Length Monitor, Fermilab Internal Document, Nov. 22, 2004
[6] T. A. Butler et al, Proposed LLRF Improvements for Fermilab 201.25 MHz Linac, Proc. LINAC 2006, Knoxville Tennessee USA
[7] T. A. Butler et al, New LLRF System for Fermilab 201.25 MHz Linac, Proc. LINAC 08, Victoria British Columbia, Canada

# RE-PHASING OF THE ISAC SUPERCONDUCTING LINAC WITH COMPUTED VALUES

M. Marchetto, R.E. Laxdal, Fang Yan TRIUMF, Vancouver, BC V6T2A3, Canada


## Abstract

The ISAC superconducting linac is a fully operational machine that routinely provides beam to experiments. The linac consists of twenty superconducting independently phased cavities housed in five cryomodules. The initial tune is done manually aided by MATLAB routines to phase the linac and set the correct optics. From the initial tune we calculate the gradient at which each cavity operates based on the energy gain, the transit time factor and the geometry of the cavity itself. Then in the event of a gradient change of one or more cavities we can calculate the RF phase shift of each downstream cavity using the initial gradients, the known geometry of the entire linac and assuming linearity of the RF controls. This possibility has been investigated and we have demonstrated that the calculated phase shift can be implemented automatically thus avoiding a complete retune of the machine. In this paper we will present the calculations and the results of the online tests.


## INTRODUCTION

The ISAC facility at TRIUMF (Fig. 1) has at present the most intense driver available for ISOL based radioactive ion beams (RIB) production. The RIBs can be delivered to three experimental areas; one using the beam at source potential (60 kV), the other two using post accelerated beam.

In the ISAC I facility the beam is accelerated through a chain composed of an RFQ injector followed by an IH drift tube linac (DTL). The DTL is design as an energy variable machine [1] being able to deliver all the energies ranging between 150 keV/u and 1.8 MeV/u. The DTL injects also the beam in the ISAC II linac at 1.5 MeV/u.

In the ISAC II facility the beam is accelerated by means of a superconducting (SC) linac operating at 106.08 MHz [3]. The present installation of the SC linac is composed of five cryomodules each housing four superconducting cavities and one superconducting solenoid. The cavity voltages are set to operate each at a fixed power of 7W, for a total of ∼20MV of acceleration. The twenty cavities are independently phased at -25° synchronous phase in sequence starting from the first one. The number of cavities turned on determines the final energy. The tuning time for the SC linac can be as long as four hours although tuning algorithms are being developed to reduce this time. The ISAC II linac is going to be upgraded by the end of 2009 adding twenty more cavities housed in three cryomodules [2]. In this case there is an increased motivation to look for more tuning aids.

In order to maximize the integrated beam at the experiment it is essential to reduce the downtime as much as possible. One possible source of downtime is the retuning of

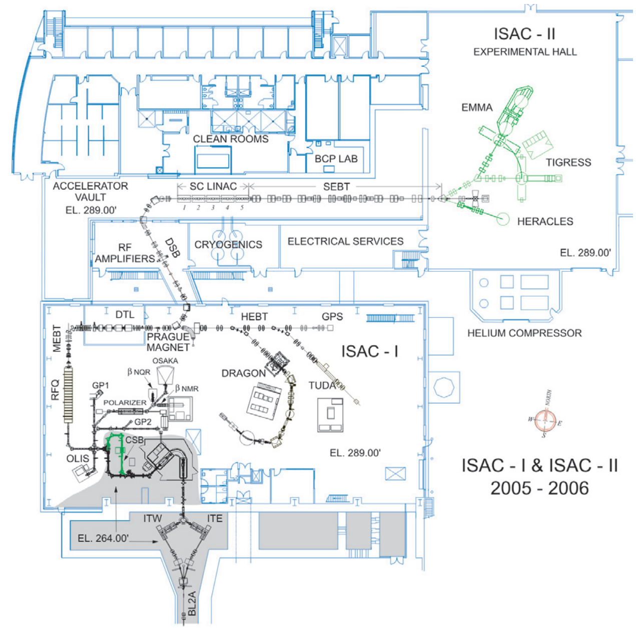


Figure 1: Overview of the ISAC facility at TRIUMF. The ISAC II linac is superconducting while in ISAC I they (RFQ and DTL) are normal conducting.

the superconducting linac in case one cavity (or more) experiences a drop of the accelerating gradient. In this paper we call this generic event a cavity failure without specifying the cause. In this case it is possible to recalculate the difference in time of flight and hence the shift of the RF phase for each cavity downstream of the faulty one. In order to calculate the phase shifts we need to know the geometry of the linac, the transit time factor of the cavities and the accelerating gradients. The transit time factor is known from radio frequency simulations of the cavity geometry. The geometry of the linac is also known by design. The operating gradients of each cavity are calculated based on the energy gain measured from the initial tuning of the linac.

## ONLINE MEASUREMENT

In order to validate the calculated values of the rephasing routine the first cavity is turned off and online RF phases are manually reset for the nineteen cavities downstream. Four separate runs are completed using different ion beams, meaning also that the energy gain after each cavity is different from one run to another due to different A/Q. These four series together with their original phase setting give the online phase shift for cavity one off. Fig. 2 represents the calculated time of flights (TOF) before and after cavity one failure for a $^{22}Ne^{4+}$ beam. In the same figure the calculated phase shift, relative to the TOFs, are plotted as well as the measured (online) phase shift for the same type of ion. The comparison of the calculated versus the online values shows a discrepancy in some cases of more than ten degrees.

These discrepancies between the online (measured) and the calculated values are the phase errors of the calculated values themselves. The discrepancy data of the four runs are binned and the distribution of the binned phase errors is represented in Fig. 3; it has $\sigma$=6.5 deg.

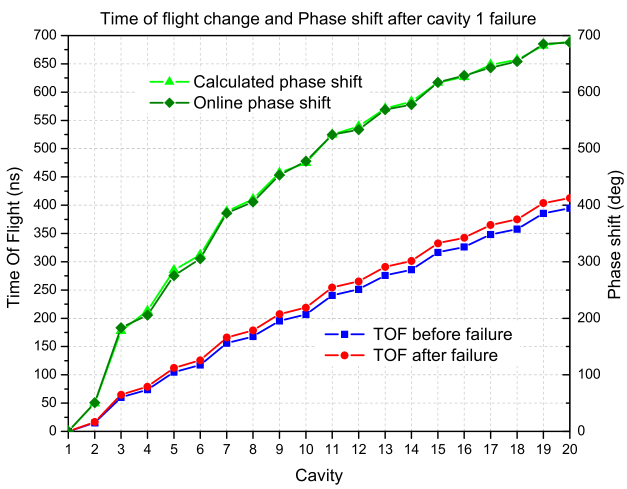


Figure 2: The plot represents the time of flights (TOF) before and after the failure for a $^{22}Ne^{4+}$ beam. The relative phase shifts are also plotted together with the online measured phase shifts.

We can identify three possible sources of error for the discrepancy. First of all the distances between cavities have some systematic error. Second, the gradient of the cavities is calculated through the energy gain, and the measurement of the energy is affected by a random error. These two errors contribute to the error of the calculated values. In addition the rephasing routine assumes the cavity has no dimension meaning the acceleration happens instantly at the center of the cavity. Third, the phasing method we use [4], by cosine fitting the energy gain versus the RF phase curve, has also a random error estimated to be $\pm 3°$. This last error affects the phases set manually. Both series of phases (manual set and calculated) contain some uncertainties meaning none of them are the absolute RF phases. Nevertheless the online measurements can be considered as the actual values for the phasing the linac.

## BEAM SIMULATION

In order to analyse the effect of the random phase error we simulate the longitudinal emittance growth for different cases. The phase errors distribution produced by the calculated values (see Fig. 3) is then associated to an emittance growth. The emittance growth is also compared with

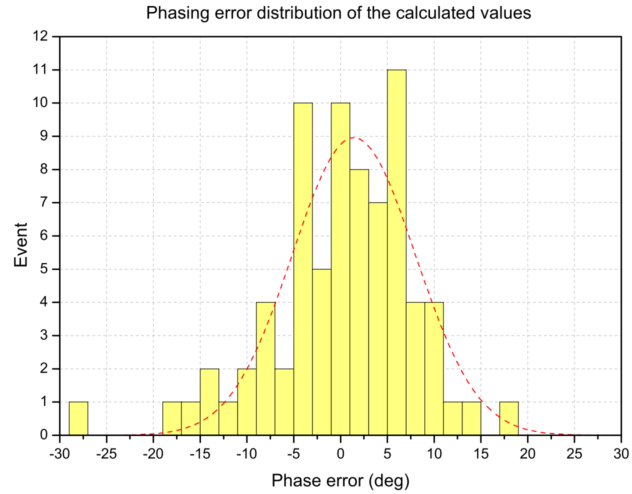


Figure 3: The plot shows the distribution of the phase error we commit when we use the rephasing calculated values. The distribution $\sigma$=6.5 deg.

the acceptance of the linac. Both the emittance growth and the acceptance are estimated via simulation done with the LANA code [5].

The beam dynamics of the ISAC linacs are simulated using the LANA code. The LANA models of our linacs well match the online measurements at the machines. We therefore use this code model to characterized the SC linac in terms of emittance growth and acceptance of the linac. The ion we simulate has A=3, Q=1 and $E_{in}$=1.5 MeV/u.

### [illegible]

The longitudinal emittance of the injected beam we use for the simulation is 1.5 $\pi$ keV/u·ns (this emittance is the design one, the measured emittance of the real beam is around 1 $\pi$ keV/u·ns).

The error we commit in the RF phase setting of the twenty cavities is assumed to be random with normal distribution centered around the synchronous phase we want to set, for us being -25°. In the simulations we consider four different distributions with $\sigma$ values of 2.5°,5°,10° and 15° centered around -25°. For each distribution we run 300 seeds (each seed corresponding to a LANA simulation run) of twenty RF phase. For each seed we record the final emittance and the final energy. For each distribution we then collect the final longitudinal emittance distribution and the final energy distribution.

The energy distribution can be fitted with a gaussian curve and therefore characterize the spread of the final energy in terms of $\sigma$ .

The longitudinal emittance distribution is instead asymmetric with a minimum value represented by the initial longitudinal emittance. In this case we calculate the rms value to characterize each error distribution.

The final results are plotted in Fig. 4. The longitudinal emittance growth is normalized to the initial emittance. In the graph it can be noticed that at 0° spread, meaning no error in the set up of the RF phase, the emittance slightly grows to a value of 1.04.

For $\sigma$=6.5 deg the emittance growth factor is ∼1.4.

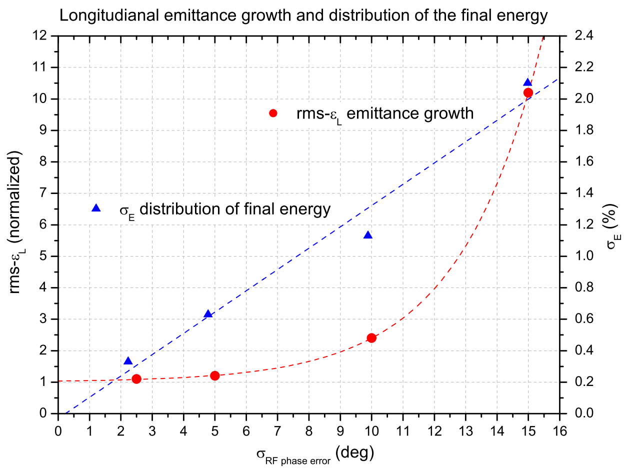


Figure 4: A plot of the longitudinal emittance growth and the spread of the final energy as a function of the RF phase error spread. The longitudinal emittance growth is normalized to the initial emittance.

## [illegible]

An estimate of the acceptance of the linac can be simulated by injecting a beam with a large longitudinal emittance and noting those particles that are transmitted to the end. The surviving particles are then mapped back to the original distribution.

The initial beam distribution for the simulation runs is uniformly distributed over 360 degree with a ±15% energy spread. The cavity accelerating gradient is set to 6MV/m.

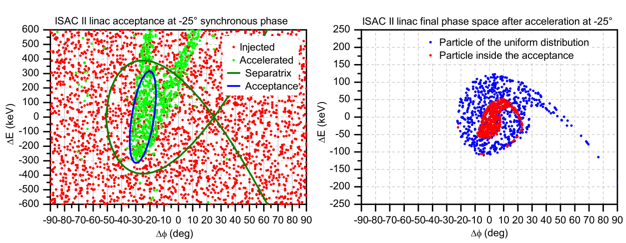


Figure 5: (Right) The red and green dots represent the injected and the accelerated particle of the initial phase space. The drawn ellipse is the acceptance. (Left) The phase space after acceleration at -25° synchronous phase. The final energy is 20.31 MeV. The red dots represent the accelerated particles inside the acceptance.

The acceptance is the maximum emittance that can be accelerated through the linac without loss. The acceptance is estimated fitting an ellipse to the initial reconstructed phase space. The acceptance and final phase space for -25° synchronous phase are represented respectively in Fig. 5.

The estimated acceptance at -25° synchronous phase is 22 $\pi$ keV/u·ns. For comparison we recall that the measured longitudinal emittance of the injected beam is ∼1 $\pi$ keV/u·ns. At -10° the estimated acceptance is 6 $\pi$ keV/u·ns.

## CONCLUSION

Based on the estimated emittance growth (see Fig. 4) we expect to have less than 50% emittance growth when using the calculated phase shift of the rephasing routine. This means that if ∼1 $\pi$ keV/u·ns emittance is injected, a ∼1.5 $\pi$ keV/u·ns emittance is expected at the exit of the linac. This longitudinal emittance is more than one order of magnitude lower with respect to the acceptance of the linac at -25°. The analysis shows that even though the rephasing values are affected by an error it is acceptable to rephase the linac in case of cavity failures. The first beam test using $^{22}Ne^{4+}$ successfully demonstrated the utility of the rephasing routine.

## REFERENCES

[1] R.E. Laxdal, "A Separated Function Drift Tube Linac for the ISAC Project at TRIUMF", PAC'97, Vancouver, May 1997, p. 1194

[2] R.E. Laxdal et al., "ISAC II Superconducting Linac Upgrade - Design and Status", this conference.

[3] R.E. Laxdal, "Initial Commissioning Result From The ISAC II SC Linac", LINAC2006, Knoxville, Tennessee, USA, August 2006, p. 521.

[4] M. Marchetto et al., "Upgrade of the ISAC DTL Tuning Procedure at TRIUMF", EPAC08, Genoa, July 2008, p. 3440

[5] D.V. Gorelov et al., "Use of the LANA Code for the Design of a Heavy Ion Linac", PAC'97, Vancouver, May 1997, p. 2621

# THE SPIRAL 2 SUPERCONDUCTING LINAC

R. Ferdinand, T. Junquera, SPIRAL2/GANIL Caen
P. Bosland, PE Bernaudin CEA Saclay
H. Saugnac, G. Olry IPN Orsay
Y. Gómez-Martínez LPSC Grenoble

*Abstract*

The SPIRAL 2 superconducting linac is composed of 2 cryomodule families, basically one of low beta, called Cryomodule A, and one of high beta, called Cryomodule B. The low beta family is composed of 12 single cavity cryomodules. The high energy section is composed of 7 cryomodules hosting 2 cavities each. According to beam dynamics calculations all the cavities will operate at 88 MHz: one family at $\beta$=0.07, and one at $\beta$=0.12. The design goal for the accelerating field Eacc of the SPIRAL 2 QWRs is 6.5 MV/m. The configuration, cavities and cryomodule tests and status are described.

## INTRODUCTION

The GANIL's SPIRAL 2 Project [1] aims at delivering high intensities of rare isotope beams by adopting the best production method for each respective radioactive beam. The unstable beams will be produced by the ISOL "Isotope Separation On-Line" method via a converter, or by direct irradiation of fissile material.

The driver will accelerate protons (0.15 to 5 mA – 33 MeV), deuterons (0.15 to 5 mA – 40 MeV) and heavy ions (up to 1 mA, Q/A=1/3 14.5 MeV/u to 1/6 8.5 MeV/A). It consists of high performance ECR sources, a RFQ, and the superconducting light/heavy ion linac. The driver is also asked to provide all the energies from 2 MeV/u to the maximum designed value.

Figure 1 : SPIRAL2 superconducting linac – 2 QuaterWave Resonator (QWR) families.

The superconducting linac is composed of cryomodules type A developed by CEA-Saclay, and cryomodules type B developed by IPN-Orsay. Both types of cavities will be equipped with the same power coupler specified for a maximum power into the cavity of 12.8 kW@6.5MV/m, which is developed in a third laboratory, LPSC-Grenoble. The coupler must handle 100% reflected power at maximum incident power.

All the components of the series (cavities and cryomodules) will be fabricated in the industries. Couplers conditioning, cavities chemical treatments, HPR rinsing in clean room, assembly, and RF tests of the cavities in vertical cryostat and RF power tests of the cryomodules will be made in the respective 3 labs.

## CRYOMODULES A - $\beta$=0.07

Details of the cavity and cryomodule design were described in [2,3].

The cavity tuner works by cavity deformation perpendicularly to the beam axis. This design saves room in the beam axis direction. The cavity mechanical design was optimized in order to reach a full tuning range of ±25 kHz at 4 K, without plastic deformation of the niobium cavity.

Figure 2 : Cavity A with MLI and B in clean room.

Each cavity A will be feed by 5 to 10 kW solid state RF amplifier [4]. The first cavities of this low beta section working at low accelerating field (≈ 0.49 MV/m, 0.5 kW) will require less power than the last cavities of the section.

At present, one cavity prototype and a qualifying cavity have been tested in vertical cryostat. Whereas the prototype reached the specifications, the qualifying cavity performances were not as good as expected. The maximum accelerating field, 11 MV/m, was much higher that needed, but the $Q_0$ value was a factor 10 below the acceptable value, about 2 $10^8$ (see Figure 3).

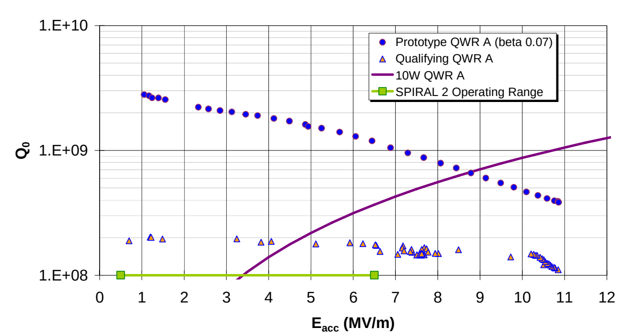


Figure 3: prototype and qualifying QWR A cavity in vertical cryostat.

Several tests were performed to localise the dissipating defects without success. We could determine that this defect is not located at the cavity extremities, at the maximum $B_{peak}$ region, or at the dismountable bottom plate. It may be located at middle height of the cavity. At about 11 MV/m the cavity dissipates more than 100 W. Fortunately small gradients are required at the beginning of the LINAC, and the dissipations can be kept bellow the 10 W limit ($E_{acc} < 4.5$ MV/m).

As consequences of these low performances, the different tests induced delays, and a new call for tender was restarted for the series of the cavities, inducing more delays. The new procedure asks for 2 new cavities with 2 different manufacturers, ZANON and SDMS. A stop point exists after the cavity welding and before the helium tank welding for tests. The 2 manufacturers allow us to speed up the process while being confident on the cavity design. The remaining series cavities of this order will then be manufactured with one or both companies. These 2 first cavities are expected in February 2009. The last cavities are expected in September 2010.

The qualification cryomodule has been assembled with the faulty cavity. Because of the small size of the Saclay clean room, the clean assembly took place in two phases. At first the HPR was performed at Saclay and all components prepared for clean assembly. Secondly, the cavity and associated components, where mounted in the vacuum tank in the large clean room at CERN.

A severe vacuum leak occurred during assembling and prevented us to perform the RF power tests as expected. Only low level RF measurements and cryogenic analyses could be made. The measured static consumption of the cold mass @ 4K of the cryostat is about 7 W, within the expected value. 21 W is dissipated on the copper screen at 77 K. The valve box, cryogenic lines and cryomodule dissipate about 25 W @ 4 K, little more than expected.


Figure 4: qualification type A cryomodule ($\beta$=0.07).

Preliminary analyses of the microphonics were performed. The resonance of the stem oscillation was observed at 39 Hz as expected, and vibrations generated by the pumping systems were detected around 100 Hz. Further analysis is still needed to determine if the microphonics observed are dangerous or not and to confirm if a damping system is required.

At present the qualification cryomodule is being dismounted. It will be remounted using the IPN-Orsay SUPRATECH clean room, now available.

The RF power tests with the cryomodule in the accelerator configuration are expected in November this year.

The call for tender of the cryostat series is ongoing. The order should take place late in December this year or January 2009. The test of the last assembled cryomodule A is scheduled in March 2011.

## CRYOMODULES B - $\beta$=0.12

A first “qualifying” cryomodule has been manufactured and tested with success in early 2008. The serial production of the 6 remaining cryomodules is under way.


Figure 5 : qualification type B cryomodule (2×$\beta$=0.12).

### *Resonators*

At present time, one prototype, 2 pre-series cavities and one series cavity has been tested. The first qualification resonator equipped with its Titanium helium tank has been tested in vertical cryostat in May 2007, the second one had a vacuum leak revealed by the chemical treatment and is lost.

The ACCEL Company is manufacturing the cavities series. Three series cavities are in hand at present time. The first one has some mechanical default but was tested with excellent result. The ACCEL Company improved the mechanical manufacturing of the two other ones. They are under chemical treatment and will be tested very soon. A stop point was decided in order to validate the design with a complete set of cavities. The company will then be able to finish the manufacturing. The remaining resonators should all be in hand before the end of 2009.

The first qualification cavity, and the first series cavity named “Erentrude” on the curve Figure 7, showed good electro-magnetic performances. Another good sign is that we observe a slight improvement from the prototype to the first series production. Design gives $E_s/E_{acc}$ = 5.51 and $B_s/E_{acc}$ = 10.19 mT/MV/m, for a $\beta\times\lambda$ accelerating length of 0.41 mm). Despite modification of the electric field area shape, multipacting barriers, identical to the ones observed on the prototype, are measured. One barrier (around 1.3 MV/m) can be easily processed while two or more barriers at very low field (between 30 and 80 kV/m) cannot. These barriers were observed at about the same fields on the 2 cavity types (A and B).

The cavity cold tuning is performed using superconducting plungers inserted on the top of the cavity inside the magnetic volume [5].

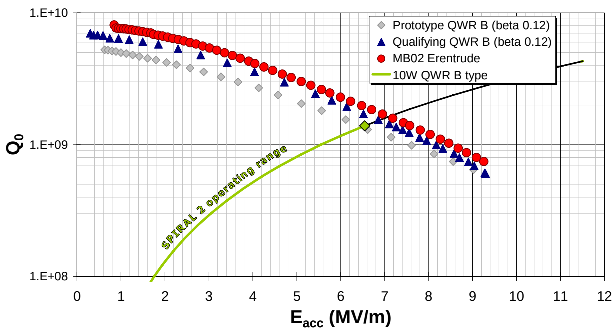


Figure 7 : $Q_0$ curve of the first type B cavities.

### *Cryostat*

The call for tender of the cryostats is started. The offer will be analysed and the contract should be signed by the end of the year.

The qualification cryomodule was first used to validate the design. As the second qualifying cavity was not useable it was tested with the prototype cavity with an antenna at the critical coupling ($\beta$=1) and with the first qualifying equipped with a power coupler. In this configuration, 8 MV/m was reach in the cryomodule. The specified main performances was achieved, Eacc = 6.5 MV/m with a dissipated power < 10 W @ 6.5 MV/m, without magnetic shielding. The static dissipation was 13 W for 11 W specified, with possibilities for improvements. Good results were obtained with the power coupler, the 10 kW solid state amplifiers [4], microphonics and the cold tuning system mentioned above. Very interesting pollution tests were performed to validate the surrounding warm sections of the cryomodules [6] and the possible use of interceptive diagnostics close to the cavities. The low field multipactor problem was solved with the use of the power coupler. See details in [7].

The cryostat has been disassembled; the cavities cleaned are under re-assembly in the final configuration with the terrestrial magnetic shielding. It will be tested in November this year, focusing on microphonics, alignment repeatability, digital low level RF and usability of the power amplifier at low power.

## COUPLERS

The RF couplers have to provide 12.8 kW CW power to the cavities at 88.05 MHz for the design goal accelerating field of 6.5 MV/m [8].

The coupler has a fixed coaxial antenna with a disc-shape ceramic (6 mm thickness). The coupling will be fixed, and the RF system will have to manage some reflected power. Coupler prototypes have been tested (head to head) up to 40 kW CW with good results.

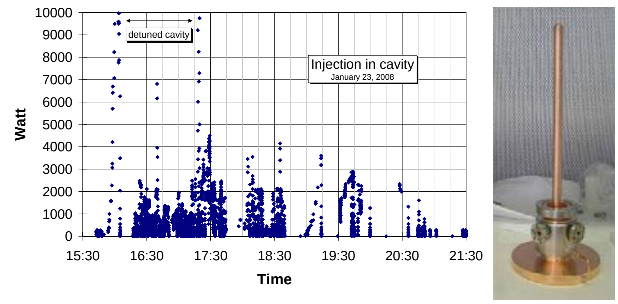


Figure 6 : Power test with the cryomodule.

The transport of three qualification couplers showed some weakness and the design has been recently improved. RF simulations, mechanical and thermal simulations were carried out.

As previously describe, the full power RF test was performed using the B type cryomodule (see Figure 6). The coupler was warm and cold conditioned, we observed some low level multipactor, as with the critical coupling, but we had no difficulties to pass them.

The tender of the series was won by the SCT Company in France. The kick off meeting of the series the production was in September this year. The completion of this production is foreseen in 2010.

## CONCLUSION

The different teams of each laboratory involved in this project are now preparing the industrialization. Installation in the linac tunnel is foreseen in 2011.

## REFERENCES

[1] T. Junquera, “Status of the Construction of the SPIRAL2 Accelerator at GANIL”, this conference
[2] P-E. Bernaudin, P. Bosland, S. Chel, P. de Girolamo, G. Devanz, P. Hardy, F. Michel, “Design of the Low-Beta, Quater-Wave Resonnator and its Cryomodule for the SPIRAL2 Project”, EPAC’06, Lucerne, July 2004, p.1276.
[3] G. Devanz, “SPIRAL2 Resonators”, 12th SRF Workshop 2005, Cornell University, July 2005.
[4] M. Di Giacomo et al., “RF power amplifiers for the SPIRAL 2 driver: requirements and status”, this conference
[5] D. Longuevergne et al. “A Novel Frequency Tuning System Based on Movable Plunger for SPIRAL2 High-Beta Superconducting Quarter-Wave Resonator” this conference
[6] R. Ferdinand et al, “Tests of wire sublimations very close to SPIRAL 2 superconducting cavity”, this conference.
[7] H. Saugnac et al, “RF cryogenic tests on the “qualifying” beta = 0.12 SPIRAL2 cryomodule, this conf.
[8] Y. Gomez Martinez, “SPIRAL2 10 kW CW RF Coupler Design and Test”, this conference.

# EXPERIENCE WITH STRIPPING CARBON FOILS IN ALPI SUPER-CONDUCTING ACCELERATOR

P. A. Posocco*, Consorzio RFX, Padova, and INFN/LNL, Legnaro, ITALY
D. Carlucci, A. Pisent, M. Poggi, INFN/LNL, Legnaro, ITALY

*Abstract*

The super-conducting linac ALPI, injected either by a XTU tandem or by the s-c RFQ of PIAVE, is composed by 3 cryostats of bulk-Nb cavities ($\beta_o$ = 0.056) and 13 cryostats of Nb-sputtered-on-Cu cavities ($\beta_o$ = 0.11 and $\beta_o$ = 0.13), for a total of 64 cavities and an equivalent voltage of 35 MV. The linac is build up in two branches connected by an achromatic and isochronous U-bend. In January 2007 a stripping station equipped with carbon foils of different thickness was placed after 6 cryostats, before the U-bend, to test the feasibility of acceleration and transport of a charge enhanced beam. The study was performed with 4 different beams (Ca, Ar, Zr and Xe) and a complete data analysis has been carried out.

## INTRODUCTION

ALPI (Acceleratore Lineare Per Ioni) [1] is a super-conducting linac running since 1995 at LNL, Legnaro. The structure of this booster (see Fig. 1) is comprised of two branches (low and high-energy branch) connected by an achromatic and isochronous U-bend. There are three families of cavities, 12 $\beta_o$ = 0.056 of bulk Nb, 44 $\beta_o$ = 0.11 and 8 $\beta_o$ = 0.13 of Nb-sputtered-on-Cu, 4 cavities in each cryostat. At present the low-$\beta$ cryostats reach an average accelerating field of 3.5 MV/m, the medium-$\beta$ 4.2 MV/m and the high-$\beta$ 5.5 MV/m, resulting in a total available voltage of 48 MV [2]. The effective voltage reaches $\sim$ 35 MV due to a careful beam dynamics optimization.

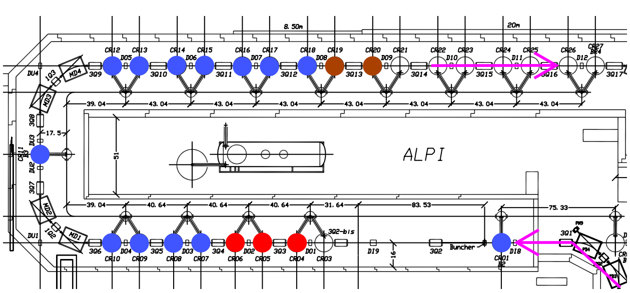


Figure 1: ALPI plan. The beam coming from PIAVE injector passes through the low-β (in red), medium-β (blu) and high-β (brown) cryostats.

The linac period is made by one triplet and 2 cryostats with a diagnostics box (profile monitor and Faraday cup) in between. In January 2007 it was decided to place a stripper station in the center of the low-energy branch period, at the both transverse and longitudinal focal point in order to reduce undesired emittance growths. Hence, the diagnostics box DO4 was modified to held the device.

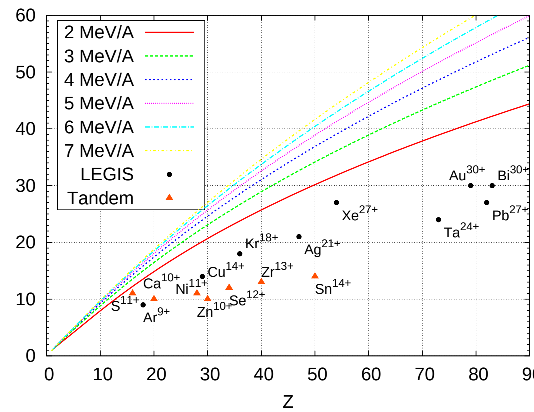


Figure 2: Most probable charge state from stripper as function of Z and energy compared to some examples of available ions out of LNL Tandem injector or foreseen for the new LEGnaro ecrIS (LEGIS).

The position along the accelerator was chosen to optimize the overall energy gain: the energy before the stripping is about 3 MeV/A, enough to enhance the charge state by 50% for the medium/high mass ions (see Fig. 2), and the remaining accelerating voltage is 2/3 of the total voltage. This means that the final energy of the stripped beam is 20 $\sim$ 30% higher than the unstripped one.

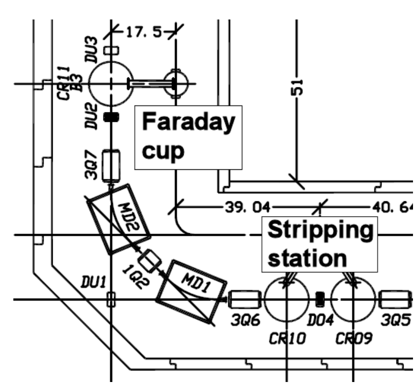


Figure 3: ALPI layout around the stripper station. The beam focalized in the diagnostic box D04 is stripped and then selected by the two dipoles MD1 and MD2.

* piero.antonio.posocco@lnl.infn.it

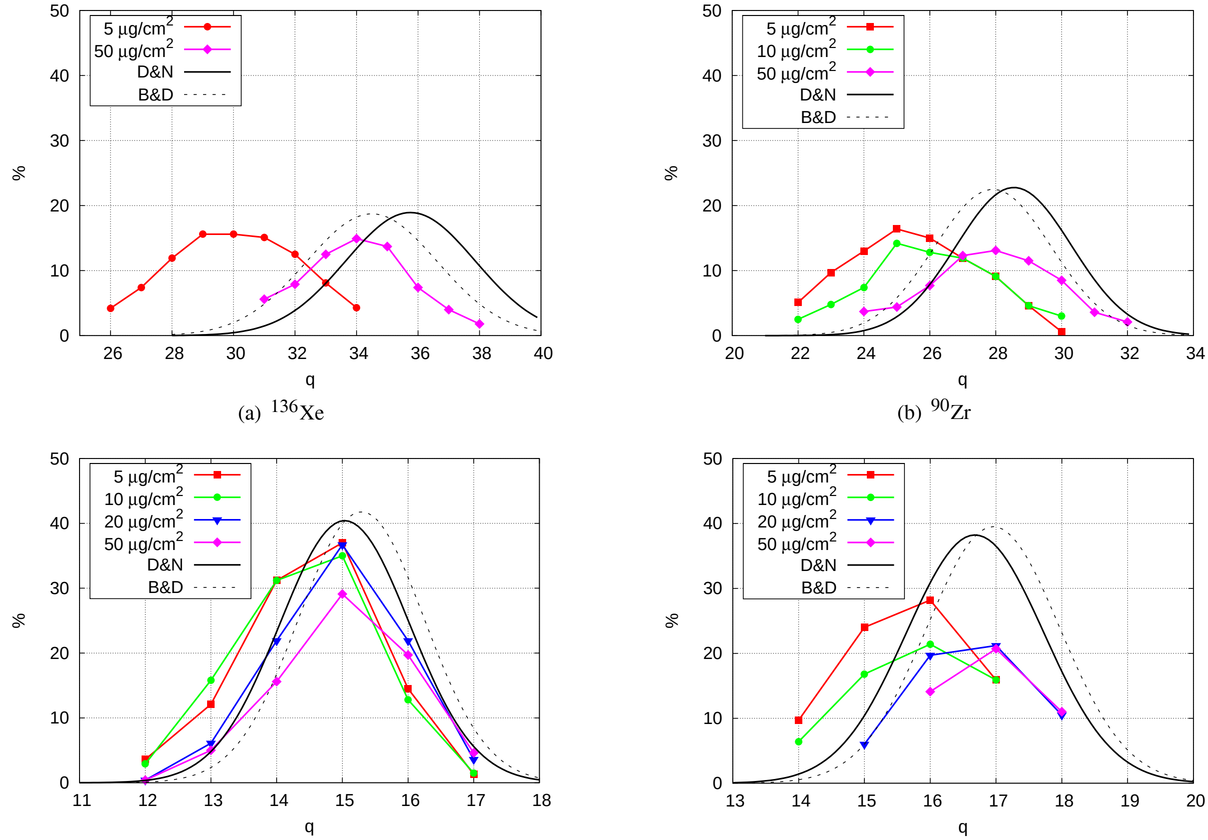


(a) $^{136}$Xe (b) $^{90}$Zr (c) $^{36}$Ar (d) $^{48}$Ca

Figure 4: Stripping probability as function of the target thickness. Semi-empirical formulas predictions are added as comparison. The data are normalized on the beam current before stripping.

## EXPERIMENTAL SET-UP

The stripper station foresees a carousel equipped with a hundred stripper foil of various thickness values (5-10-20-50 µg/cm$^2$) preceded by a collimator, which ensures a proper beam focusing at the foil plane. The system is remote-controlled via PC. Downstream the stripper station the beam is focalized by 3Q6 triplet and bent by MD1 and MD2, whose magnetic field is measured by a Tesla-meter with a precision of $1/10^6$. The beam passes through 3Q7 triplet (set to off) and is then monitored relatively to its position and current in the diagnostics box DU2, in the middle of the U-bend. This way, the first half of the U-bend acts as a spectrometer. The overall scheme is shown in Fig. 3.

The procedure consists in recording dipole field and current of both the collimated unstripped beam and of the different stripped charge states, which are selected by the dipoles. The procedure is repeated for the different foil thicknesses.

## STRIPPING DATA ANALYSIS

If $N(q)$ is the number of ions having charge state $q$ after being stripped, the charge state fraction is defined by $P(q) = N(q)/\sum_q N(q)$. Figure 4 shows the evolution of the charge state fractions for $^{90}$Zr, $^{48}$Ca (from Tandem) and $^{136}$Xe, $^{36}$Ar (from PIAVE) as a function of the carbon target thickness $t$. As the thickness is increased, the $P(q)$ curve moves towards higher charge states. The equilibrium thickness $t_\infty$ is reached when the average charge state $\bar{q} = \sum_q P(q)$ stops raising.

The $\bar{q}$ as function of $t$ (Fig. 5) can be fitted by

$$\bar{q}(t) = q_0 + (\bar{q}_\infty - q_0)\ e^{-\frac{t}{k}}, \tag{1}$$

where $q_0$ is the charge of the beam before stripping and $\bar{q}_\infty$ is the most probable charge state for $t_\infty$. This formula, already used in [3], is misleading because the beam loses part of its energy as it passes through the foil, resulting in a drop of $\bar{q}$ for $t >> t_\infty$. Nevertheless, for low thickness it is very useful and it is easy to get the $\bar{q}_\infty$. From the fit it possible to obtain an estimate of the $t_\infty$ as well. Assuming that $t_\infty \simeq 5\ k$, the results are reported in Tab. 1.

Equilibrium distributions may be approximately represented by a normal distribution,

$$P(q) = \frac{1}{d\sqrt{2\pi}} \exp\left(-\frac{(q-\bar{q}_\infty)^2}{2d^2}\right)$$

with $d^2 = \sum_q (q-\bar{q}_\infty)^2 P(q) - 1/12$.

A large collection of data from stripping experiments was analyzed by H. D. Betz in [4]. In particular he summarizes all the semi-empirical formulas for $\bar{q}_\infty$ and $d$ published up to that time, listing them by stripper material, Z of the ions and energy range. Among those, only two fit the conditions for the present experiment (Carbon foils, medium/high Z, E ∼ 3 MeV/A): Dmitriev and Nikolaev (D&N) and Baron and Delaunay (B&D). The predictions by these formulas (Tab. 1) match both the maximum $\bar{q}$ found in the data distributions and the $\bar{q}_\infty$ from the fit.

Concerning the beam energy loss through the stripper, the data in Fig. 6 are linearly fitted by

$$\Delta\mathrm{E}(t) = \delta\mathrm{E} + \Delta\mathrm{E}/\Delta\mathrm{x} \cdot t, \quad (2)$$

where ΔE/Δx is the stopping power and δE is the error on the beam energy before stripping (see Tab. 1). For all the four beams, the former perfectly matches the value calculated via SRIM program [5]. On the contrary, the latter is not compatible with zero: a systematic error was clearly committed in the energy measurement, probably due to a slight misalignment of the beam line. The problem will be investigated promptly.

## CONCLUSIONS

- $^{136}$Xe$^{34+}$ was easily transported to the experiment: the final energy reached 1.1 GeV (8.1 MeV/A), 20% more of the energy of the unstripped beam (923 MeV). The beam current on target was greater than 1 pnA, but the transmission in the ALPI high-energy branch was limited to 50%, probably due to an unexpected longitudinal emittance growth. A better control over the longitudinal focusing at the foil plane is therefore mandatory.

- $^{90}$Zr$^{28+}$ was transported only up to half of the high-energy branch. Due to the low current of the selected charge state (< 1 pnA), the cavity setting was extremely difficult and the right synchronous phase setting could not be guaranteed.

Table 1: Data analysis. The equilibrium thickness is in [µg/cm$^2$], energy in [MeV/A] and the stopping power in [keV/µg/cm$^2$].

| | $^{136}$Xe$^{23+}$ | $^{90}$Zr$^{13+}$ | $^{36}$Ar$^{8+}$ | $^{48}$Ca$^{9+}$ |
|---|---|---|---|---|
| E | 2.475 | 2.614 | 3.206 | 3.487 |
| max $\bar{q}$ | 33.9 ± 0.4 | 27.9 ± 0.7 | 15.0 ± 0.4 | 16.9 ± 0.3 |
| D&N | 35.8 | 28.5 | 15.0 | 16.7 |
| B&D | 34.5 | 27.9 | 15.3 | 17.0 |
| $\bar{q}_\infty$ | 33.9 | 27.9 ± 0.7 | 14.8 ± 0.1 | 16.6 ± 0.2 |
| $t_\infty$ | 24 | 13 ± 3 | 9 ± 3 | 15 ± 3 |
| ΔE/Δx | 78.8 | 62 ± 6 | 18 ± 3 | 22 ± 6 |
| SRIM | 82.9 | 58.1 | 19.4 | 22.7 |
| δE (‰) | 8.6 | 4.6 ± 0.8 | 7.7 ± 0.5 | 2.1 ± 1.5 |

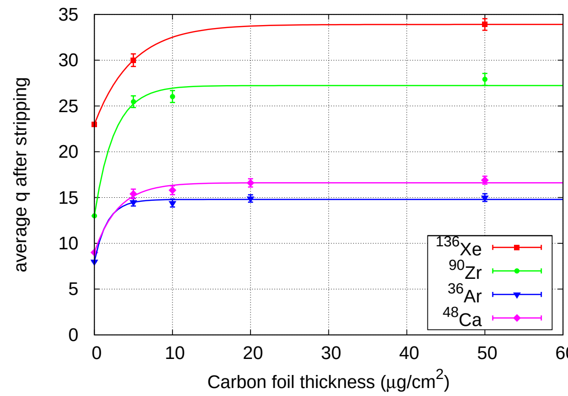


Figure 5: Beam average charge $\bar{q} = \sum_q P(q)$ as a function of target thickness. Fit by Eq. 1.

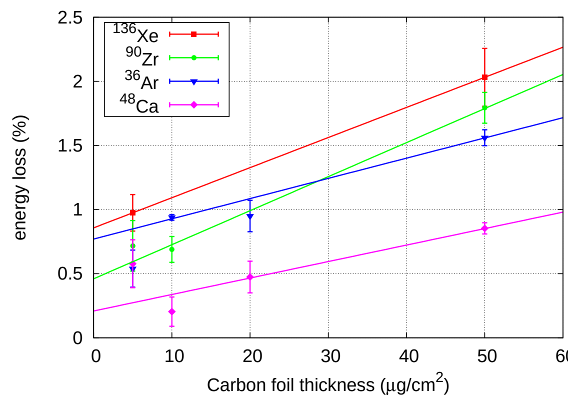


Figure 6: Beam energy loss as a function of the target thickness. Fit by Eq. 2.

- $^{36}$Ar$^{15+}$ was transported to the experiment with some troubles due the failure of the last cryostat before the stripper station. The final energy reached 450 MeV, whereas the energy without stripping was 300 MeV. The lack of the four cavities did not allow to focus longitudinally the beam at the foil plain and the transmission of the high-energy branch was extremely low (20%).

- $^{48}$Ca$^{17+}$ was not transported since the current was too low for the synchronous phase setting.

The acceleration was successful only for the beams coming from PIAVE thanks to the high current provided by the ECRIS ion source. The low-energy branch beam dynamics must be carefully optimized to obtain a strong longitudinal focusing at the foil plane.

## REFERENCES

[1] A. Dainelli and al., NIM A382 (1996), p. 100.
[2] G. Bisoffi and al., Proc. of SRF2007, MO404.
[3] E. Baron and B. Delaunay, Phys. Rev. A 12 (1975), p. 40.
[4] H. D. Betz, "Heavy Ion Charge States", Applied atomic collision physics, Academic Press (1983).
[5] J. F. Ziegler, J. P. Biersack, and U. Littmark, SRIM.

# PLANS FOR A SUPERCONDUCTING H$^-$ LINAC (SPL) AT CERN

O. Brunner, S. Calatroni, E. Ciapala, R. Garoby, F. Gerigk , A.M. Lombardi, R. Losito, V. Parma, C. Rossi, J. Tuckmantel, M. Vretenar, W. Weingarten, CERN, Geneva, Switzerland

*Abstract*

As part of the upgrade of the LHC injector complex at CERN, the construction of a 4 GeV Superconducting Proton Linac (the SPL, in fact an H$^-$ accelerator) is planned to begin in 2012. Depending upon physics requests, it should be upgradeable to 5 GeV and multi-MW beam power at a later stage. The construction of Linac4, its low energy front end, has started at the beginning of 2008. A full project proposal with a cost estimate for the low power version of the SPL aimed at improving LHC performance has to be ready for mid-2011. As a first step towards that goal, essential machine parameters like RF frequency, cooling temperature and accelerating gradient have recently been revisited and plans have been drawn for designing and testing critical components.

## INTRODUCTION

The foreseen upgrade of the LHC injector complex [1] will entail the construction of PS2, a new 50 GeV synchrotron and of the SPL as its injector. The SPS will not be replaced, but it will be significantly upgraded. The layout of these new accelerators on the CERN site has been decided [2] and Linac4 [3], the SPL front-end, is being built at its final location (Fig. 1).

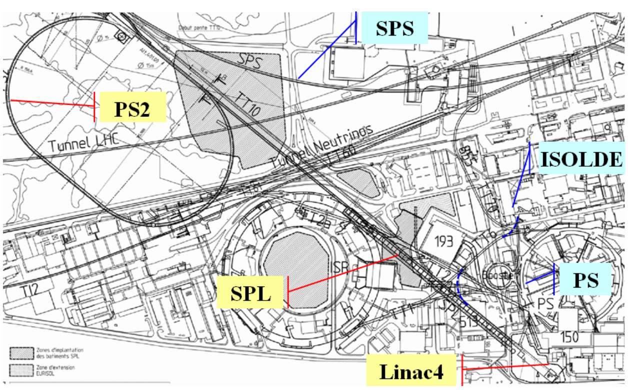


Figure 1: Layout of the new injector complex.

The flexibility and the potential of evolution of the SPL will make it an important asset for physics in the future [4]. As injector of PS2, only a 4 GeV low power version of the SPL is needed ("the "LP-SPL"). For a neutrino facility, the LP-SPL would have to be upgraded to 5 GeV and 4 MW of beam power, and accompanied with an accumulator and a compression ring to meet the required time structure of the beam [5]. For a Radioactive Ion Beam Facility of the next generation [6], a similar beam power would also be required at 2.5 GeV. A summary of the specifications of the accelerator in its different possible phases of implementation is given in Table 1.

As a first step in the preparation for the project proposal to be submitted to the CERN Council by mid-2011, the choice of the basic parameters of the SPL [7] has been revisited during the past months in view of optimizing synergy with the worldwide development effort on superconducting accelerating structures cavities. The RF frequency was therefore reconsidered, as well as the cooling temperature of the superconducting cavities and the foreseeable accelerating gradients [8, 9, 10].

Table 1: Main Characteristics of the Successive Phases of Realization of the SPL

| | LP-SPL | SPL (5 GeV) | SPL (2.5 GeV) |
|---|---|---|---|
| Users | PS2 ISOLDE | + ν facility | + RIB facility |
| T [GeV] | 4 | 5 | 2.5 |
| $P_{beam}$ [MW] | 0.2 | 4 | 4 |
| $F_{rep}$ [Hz] | 2 | 50 | 50 |
| $I_{source}$ [mA] | 40 | 80 | 80 |
| Chopping | yes | yes | no |
| $I_{av}$ [mA] | 20 | 40 | 40 |
| $T_{pulse}$ [ms] | 1.2 | 0.4 | 0.8 |

## DESIGN OPTIONS

The RF frequency of 352 MHz has been selected for Linac4, because it is very well matched for use in the low energy front end of a proton linac and because of the large inventory of RF hardware available at that frequency since the decommissioning of LEP. Hence only harmonics of 352 MHz can be considered for acceleration after Linac4 (160 MeV). The three design options which have been compared [9] (Table 2) were especially aimed at analysing the interest of 1408 MHz which is close to the frequency used in the ILC and X-FEL projects.

An updated survey of recent experimental results, confirmed the 2006 conclusion [7, 10] that the maximum accelerating gradient of bulk Niobium cavities only depends on geometry ($\beta_{geometrical}$) and on the quality of the surface treatment techniques, and not on the RF frequency. It is therefore assumed when comparing the length of the different options that the superconducting elliptical cavities operate at an accelerating gradient corresponding to the same peak surface field of 50 MV/m, as in a β=1 cavity with an accelerating gradient of 25 MV/m. Their characteristics are given in Table 3.

The "Nominal" option in Table 2 is a slightly improved version of the SPL design published in 2006 [7]. It uses only 2 types of 5 cell elliptical cavities and has a length of 439 m.

Table 2: SPL Design Options

| | Nominal | High frequency | Hybrid |
|---|---|---|---|
| Frequency [MHz] | 704 | 1408 | 352/1408 |
| Type of cavities | elliptical | elliptical | spoke/elliptical |
| $\beta_{geometrical}$ | 0.65/0.92 | 0.6/0.76/0.94 | 0.67/0.8/0.94 |
| Number of cells/cavity | 5/5 | 7/9/9 | 4/5/9 |
| Input energies/section [MeV] | 160/581 | 160/357/884 | 160/392/758 |
| Accelerating gradient* [MV/m] | 19.4/24.2 | 18.1/21.7/24.2 | 8.5/9.5/24.2 |
| Number of cavities/focusing period | 3/8 | 2/4/8 | 3/4/8 |
| Number of cavities | 42/200 | 30/40/208 | 27/24/216 |
| Total number of cavities | 242 | 278 | 267 |
| Length of sc linac | 439 | 499 | 485 |

* Normalized for elliptical cavities to a peak surface field of 50 MV/m.

Table 3: Estimated Characteristics of SC Cavities

| f [MHz] | $\beta_{geometric}$ | R/Q [Ω] | $Q_0$ [$10^9$] @4.5/2 K | $E_{acc}$ [MV/m] |
|---|---|---|---|---|
| 704 | 0.65 | 285 | 0.3/5.8 | 19.4 |
| 704 | 0.92 | 501 | 0.4/7.7 | 24.2 |
| 1408 | 0.60 | 441 | 0.1/2.3 | 18.1 |
| 1408 | 0.76 | 671 | 0.12/2.5 | 21.7 |
| 1408 | 0.94 | 931 | 0.15/3.2 | 24.2 |

In the “High frequency” option, 1408 MHz elliptical cavities are used immediately after Linac4. To preserve comparable real-estate gradient, cavities with more cells must be used, which reduces their energy range and forces to have three different types. Moreover, the accelerator length has to be 60 m longer because of the longer matching section needed by the x4 frequency jump.

In the “Hybrid” option, the transition to 1408 MHz is done at 758 MeV only, using spoke cavities operating at 352 MHz immediately after Linac4. Two different types of Spoke and one type of elliptical cavities are needed. The total length remains 46 m longer than in the nominal case.

## ANALYSIS

### *Beam Dynamics*

Similar design principles are used in all options, using similar focusing periods and avoiding space charge resonances by keeping an approximately constant ratio between transverse and longitudinal phase advances. Beam dynamics performance is compared in terms of r.m.s. emittance growth and sensitivity to RF field errors.

Transverse emittance growth is small in all cases [between 1.5 (5.3) and 5.6 (8.2) % for $\varepsilon_X$ (resp. $\varepsilon_Y$)], with a slight advantage for the “hybrid” option. The situation is more contrasted in the longitudinal phase plane where the “high frequency” option is clearly worse (12 % blow-up instead of 6.8 % and 2.5 % in the “nominal” and “hybrid” cases). This is confirmed by the analysis of the effect of RF field errors and energy/phase jitter of the Linac4 beam, 4.2 % of the simulation runs showing particle loss with the “high frequency” option.

### *Impact of Frequency on Cavity Parameters*

The characteristic impedance R/Q of a one cell elliptical cavity with a given geometry is independent of its resonant frequency f. The impedance per unit of length is then proportional to f.

The stored energy, for the same accelerating gradient, scales like the volume as $1/f^3$. Hence the energy stored in a 1408 MHz multi-cell cavity is ¼ of the energy stored in a 704 MHz cavity of the same length (and less cells). Since SPL cavities are pulsed, filling them with RF field uses four times more wall-plug power at 704 MHz.

For longitudinal High Order Modes (HOM), similar reasoning shows that the short range wake-field is 4 times larger in a 1408 MHz multi-cell cavity. The impedance for long range longitudinal wake-fields is between 8 and 16 times larger, depending upon the mode. The impedance for transverse long range dipole modes is between 8 and 32 times larger, resulting in a reduction by the same factor of the threshold for the onset of beam break-up.

In the case of real/imperfect structures, the production scatter in the individual cell frequencies and end-cell correction for the fundamental mode disturbs the HOM field profiles. This makes their coupling and hence their damping more uncertain by a factor 2 to 4 in the 1408 MHz case.

### *Impact of Frequency on RF Hardware*

RF equipment is more compact at higher frequency, which increases the difficulty to dissipate the heat generated at ~10 % duty cycle. 1 MW class hybrids and amplitude & phase modulators will be especially challenging to design at 1408 MHz. For klystrons, manufacturers have clearly expressed their reluctance for similar reasons.

### *Cryogenics Issues*

The design of the SPL cryomodule will re-use as much as possible of the state-of-the-art development made for the ILC. Static cryogenic losses are minimized using a long cryomodule with a high packing factor and containing the helium supply and return pipes. The pumping return line is also a structural element securing the alignment of the cavities and magnets. It is however impossible to duplicate exactly the ILC device because of the 1.7 % slope of the SPL (ILC: 0.6 %), and because of the 10 times higher duty factor of the SPL which imposes new designs for the RF and HOM couplers.

The quality factor $Q_0$ estimated [9] at the indicated gradient for the different types of superconducting elliptical cavities is shown in Table 3. It is more than 20 times larger at 2 K than at 4.5 K, independently of frequency, and more than 2.5 times higher at 704 than at 1408 MHz. Taking these estimates and static loads [7] into account, the equivalent cryogenic load of the 5 GeV-4 MW SPL for the "nominal" and high frequency" options is given in Table 4. Electrical power consumption imposes clearly to operate cavities at much lower temperature than 4.5 K.

Table 4 also shows the power required by RF which is ~9 MW larger at 704 MHz because of the larger stored energy in the cavities (see above).

Table 4: Cryogenic load and electrical consumption of the 5 GeV/4 MW SPL

| Option [see Table 2] | $T_{cryo}$ [K] | $Q_{eq\ @\ 4.5\ K}$ [kW] | $P_{el}$ (cryo) [MW] | $P_{el}$ (RF) [MW] |
|---|---|---|---|---|
| "Nominal" | 2 | 20.8 | 5.2 | 25.5 |
| "Nominal" | 4.5 | 95.4 | 23.9 | 25.5 |
| "High frequency" | 2 | 18.3 | 4.6 | 16.3 |
| "High frequency" | 4.5 | 81.9 | 20.5 | 16.3 |

### *Achievable Gradient*

The performance of cavities recently built for SNS and at DESY has been analysed [10]. For a yield of 90 %, the maximum achievable equivalent gradient in β=1 cavities is between 16 MV/m (SNS) and 23 MV/m (DESY). Higher gradients like the 25 MV/m presently assumed in the SPL can only be achieved after reprocessing a large number of cavities and/or with an improved surface treatment (electro-polishing). It is therefore important to design and build SPL-type superconducting cavities in the near future to arrive at a realistic estimate.

## CONCLUSION AND PLANS

The main advantage of the "high frequency" option is its smaller power consumption which may be balanced against its longer length and larger number of cavities and cavity types with respect to the "normal" option. For a high power proton accelerator where beam losses have to be minimized, it suffers however from less tolerance to energy/phase jitter of the Linac4 front end. Moreover, the high power RF components that it requires are much more difficult to design/build/buy. The "hybrid" option suffers from the same drawbacks, plus the need to develop an additional family of cavities (spokes). 704 MHz is hence confirmed as the correct choice for the frequency and ~2 K for the cooling temperature of the SPL. Although valuable for the LP-SPL, these choices are mandatory for the foreseen high power/ high duty cycle extensions.

The accelerating gradient that can be expected with a reasonable yield deserves further investigation.

The main goals of the next 3 years will hence be to:

- optimize the overall design of the SPL,
- build and test 704 MHz superconducting cavities to better estimate the achievable accelerating gradient,
- design and test a solution for stabilization of the field in pulsed mode,
- progress in the development of an $H^-$ ion source,
- design, assemble and characterize a complete high energy cryomodule.

## REFERENCES


[1] R. Garoby, "Upgrade Issues for the CERN Accelerator Complex", EPAC'08, Genoa, June 2008, FRYAGM01, p. 3734, http://www.JACoW.org.

[2] J.L. Baldy et al., "Site Layout of the Proposed New Hadrons' Injector Chain at CERN", CERN-AB-2007-061-PAF.

[3] M. Vretenar et al., "Status of the Linac4 Project at CERN", this conference.

[4] R. Garoby, M. Benedikt, A. Fabich, F. Gerigk, "Comparison of Options for the Injector of PS2", CERN-AB-2007-014-PAF.

[5] M. Aiba, "Feasibility Study of Accumulator and Compressor for the 6-bunches SPL based Proton Driver", CERN-AB-2008-060.

[6] EURISOL report 2004 http://www.ganil.fr/eurisol/Final_Report/EURISOL-REPORT.pdf.

[7] F. Gerigk (ed.), "Conceptual Design of the SPL-II", CERN-2006-006.

[8] Workshop on "Status of Analysis of SPL RF Frequencies and Cooling Temperature", 2008, CERN http://indico.cern.ch/conferenceDisplay.py?confId=32631.

[9] F. Gerigk et al., "Choice of Frequency, Gradient, and Temperature for a Superconducting Proton Linac", HB'08 workshop, August 2008, Nashville, USA.

[10] W. Weingarten, "Performance of Superconducting Cavities as required for the SPL", to be published as CERN-AB-2008 -RF.

# THE STATUS OF THE MSU RE-ACCELERATOR (ReA3)*

X. Wu[†], C. Compton, S. Chouhan, M. Doleans, W. Hartung, D. Lawton,
G. Machicoane, F. Marti, P. Miller, J. Ottarson, M. Portillo, R. C. York, A. Zeller and Q. Zhao
National Superconducting Cyclotron Laboratory, Michigan State University, E. Lansing, MI 48824, U.S.A.

Abstract

The Re-accelerator ReA3 [1] being developed at the Michigan State University is a major component of a novel system proposed to first stop the high energy Rare Isotope Beams (RIBs) created using Coupled Cyclotron Facility (CCF) by the in-flight particle fragmentation method in a helium filled gas system, then increase their charge state with an Electron Beam Ion Trap (EBIT) charge breeder, and finally re-accelerate them to 3 MeV/u to provide opportunities for an experimental program ranging from low-energy Coulomb excitation to transfer reaction studies of astrophysical reactions. The accelerator system consists of a Low Energy Beam Transport (LEBT) with an external multi-harmonic buncher, a radio frequency quadrupole (RFQ), a superconducting linac, and a High Energy Beam Transport (HEBT). The superconducting linac will use quarter-wave resonators with $\beta_{opt}$ of 0.041 and 0.085 for acceleration and superconducting solenoid magnets for transverse focusing. The paper will discuss the recent progress of R&D and beam dynamics studies for ReA3.

## INTRODUCTION

Isotope Separation On-line (ISOL) and Projectile Fragmentation (PF) are the two methods used to produce high quality RIBs for the nuclear science. Since 1989, the NSCL has been using the PF method with great success to produce fast RIBs for nuclear structure and nuclear reaction experiments, especially after the completion of the CCF and the A1900 Fragment Separator in 2001. For ReA3, RIBs from the EBIT will have an initial energy of 12 keV/u and an initial emittance of 0.6 $\pi$ mm-mrad. The ReA3 is required to accelerate RIBs with charge-to-mass ratios (Q/A) ranging from 0.2 to 0.4 and to achieve a final energy ranging from 0.3 to 3 MeV/u. The nuclear astrophysics experimental program requires the beam bunch width and the energy spread for the RIBs on the experiment target within 1 ns and 1 keV/u, respectively, which corresponding to a small longitudinal emittance of ~0.25 $\pi$ keV/u-ns. The ReA3 accelerator system consists of four segments: a Low Energy Beam Transport (LEBT) system to transport, bunch and match the RIBs from the EBIT to the RFQ, an RFQ for initial beam acceleration and focusing, a superconducting linac system for RIBs acceleration to the desired energy, and a High Energy Beam Transport (HEBT) system to deliver the RIBs to an experimental area with the required beam parameters. The entire ReA3 accelerator system will be located on a balcony in the NSCL high bay area.

*Work supported by Michigan State University and NSF
[#]xwu@nscl.msu.edu

## LEBT

The ReA3 LEBT will transport, bunch and match RIBs from the EBIT into RFQ. An electrostatic triple Bender is implemented in the LEBT in order to allow a stable ion source (SIS) on a high voltage platform to deliver $^4He^{1+}$ beam into the RFQ for SC linac tuning and diagnostics calibrations. It is also capable to deliver RIBs from the EBIT directly to a low energy experiment area as well as accept RIBs from a possible 2nd EBIT in the future upgrade. Figure 1 shows the layout of the ReA3 LEBT. Electrostatic quadrupoles and a solenoid magnet are used to provide transverse focusing for both RIBs and stable beam. In addition, there are four beam diagnostics stations in the LEBT for proper beam transverse and longitudinal matching into the RFQ. To achieve a small longitudinal emittance, an external Multi-Harmonic Buncher (MHB) is used in the LEBT, which has been constructed and tested at MSU recently [2].

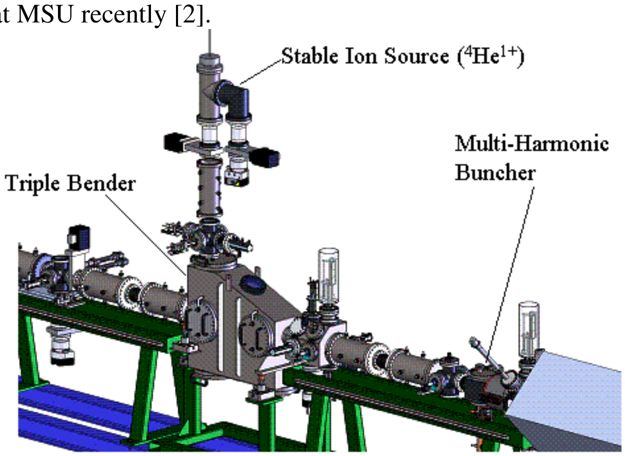


Figure 1: The layout of the ReA3 LEBT.

Figure 2 shows the structure of the triple bender. It consists of three 75° spherical benders and two 15° parallel plate kickers. The spherical bender has a bend radius of 250 mm and a gap of 80 mm. For a maximum initial accelerating voltage of 60 kV, potentials of ±19.2 kV are required to bend beam by 75°. The parallel plate kicker has a gap of 120 mm, and requires potentials of ±9.3 kV to deflect beam by ±15°. Herzog shunt plates grounded to the vacuum chamber are used for limiting the fringe electric fields at the entrance and exit of the electrodes. A gap of 12 mm separates the shunt plates and the electrodes. COSY INFINITY [3] and SIMION [4] were used for beam simulations and optimizations of the shape of the electrodes and the shunt plates.

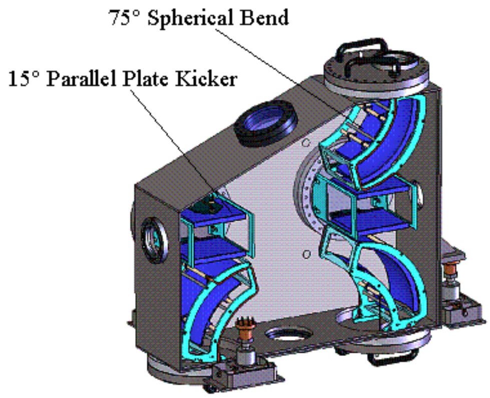


Figure 2: The structure of the triple bender in LEBT.

The beam simulations for RIBs from the EBIT and the $^{4}He^{1+}$ beam from the stable ion source were performed and results show both were well matched transversely and longitudinally into the RFQ. Figure 3 shows the beam envelopes in the LEBT. The triple bender was active only for the stable beam.

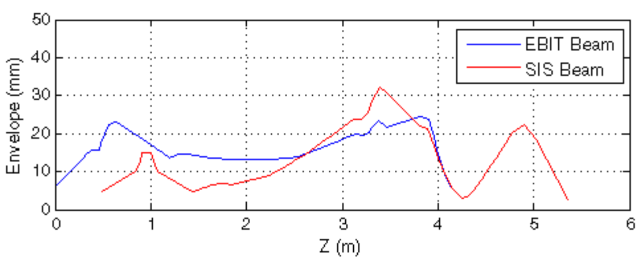


Figure 3: Beam envelopes in the LEBT for RIBs from the EBIT and He beam from the stable ion source.

## RFQ

The ReA3 RFQ [5] will accelerate RIBs from 12 keV/u to 600 keV/u with a Q/A ratio of 0.2 to 0.4. The 4-rod structure, CW, room temperature RFQ is currently under design and construction at Frankfurt University [6]. Table 1 lists the main parameters of the RFQ. Together with the external MHB in the LEBT, the ReA3 RFQ will achieve a 90% longitudinal emittance of ~0.29 π keV/u-ns in order to meet the beam requirement for ReA3. The transmission efficiency of the RFQ is about 82%. The RFQ will have an Aluminum tank and improved cooling channels. The delivery of the RFQ, and initial RF and beam tests are expected in 2009.

Table 1: Main RFQ Parameters

| | |
|---|---|
| Frequency (MHz) | 80.5 |
| Length (m) | 3.5 |
| Mid-cell radial aperture (mm) | 7.3 |
| Vane tip radius (mm) | 6.0 |
| Inter-vane voltage (kV) | 86.2 |
| Peak field ($\square_{kilpatrick}$) | 1.6 |
| Peak electric field (MV/m) | 16.7 |

## SUPERCONDUCTING LINAC

The ReA3 superconducting linac will provide the acceleration or deceleration of the RIBs from RFQ output energy of 600 keV/u to the desired final energies ranging from 0.3 to 3 MeV/u on target. The SC linac consists of a total of three cryomodules with fifteen 80.5 MHz λ/4 SRF cavities. Eight superconducting solenoid magnets inside cryomodules will provide the transverse focusing. Each solenoid will have two dipole coils to provide alignment error corrections. Figures 4 and 5 show the structures of the λ/4 SRF cavities and the layout of cryomodules of the ReA3 SC linac. Four beam diagnostics stations located in the warm region between cryomodules will be used for beam and SC linac tuning.

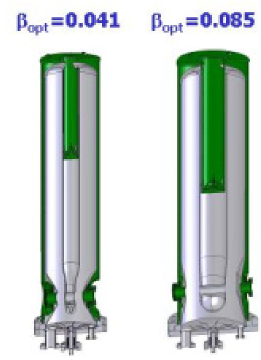


Figure 4: λ/4 SRF cavities used in ReA3 SC linac.

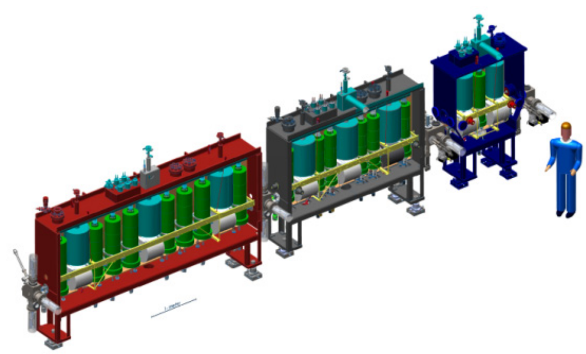

Figure 5: The layout of the cryomodules of the ReA3 SC Linac.

Both λ/4 SRF cavities have been prototyped and tested at MSU, and the RF test results show both cavities exceeding the design field levels by a comfortable margin. A prototype cryomodule consisting of a 80.5 MHz $\beta_{opt}$ = 0.085 λ/4 cavity and a 322 MHz $\beta_{opt}$ = 0.285 λ/2 cavity, with helium vessels made of titanium, was fabricated and tested at the NSCL recently. The superconducting focusing magnets inside the cryomodule consist of a 9 T solenoid with an integrated steering dipole and a 31 T/m quadrupole. In addition, a coaxial probe-type rf fundamental power coupler for both λ/4 SRF cavities and a prototype niobium tuning plate for $\beta_{opt}$ = 0.041 cavity been designed, fabricated and tested at MSU. The detailed test results for the prototype cryomudule, tuner and power coupler will be discussed in separate papers [7, 8].

## HEBT

The REA3 HEBT will transport RIBs from the SC linac to the experiment area. Figure 6 shows the layout of the proposed HEBT for ReA3. Two achromatic bending sections were used to bring RIBs from the mezzanine floor to the ground floor while limit the beam emittance growth. A cryomodule with a single λ/4 SRF cavity with $\beta_{opt}$ = 0.041located between the achromatic bending sections was used to rotate the beam longitudinal phase space, minimizing the final beam energy spread in order to achieve the required beam bunch width and the energy spread for the RIBs on the experiment target within 1 ns and 1 keV/u.

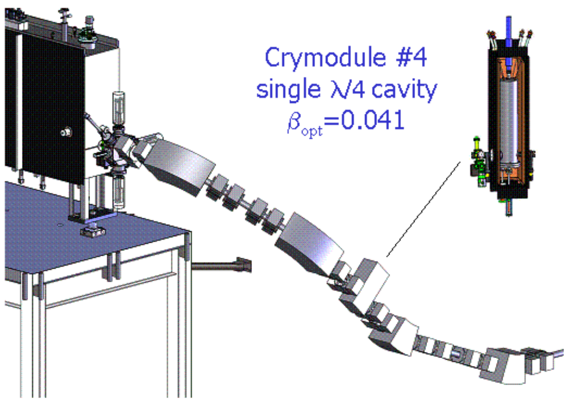


Figure 6: The layout of the ReA3 HEBT.

The beam envelope in the SC linac and HEBT for RIBs accelerated to 3 MeV/u with a Q/A of 0.25 is shown in Figure 7. Beam simulations show that the performance for the RIBs decelerated to ~300 keV/u was similar. About ~88% of beam on target was found to be within the required bunch width and energy spread.

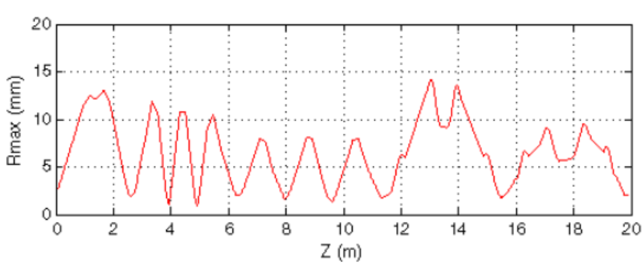


Figure 7: Beam envelope in the SC linac and HEBT.

## BEAM DIAGNOSTICS

Many of the beam diagnostic devices for ReA3 are similar to those in use at the ISAC-II accelerator at TRIUMF [9, 10]. They are deployed in various combinations at four diagnostic stations in the LEBT, and the other four in the SC linac section. Because of intensity requirements, many of the devices are usable only with a stable ion beam from either the stable ion source in the LEBT or the EBIT. The preliminary tuning of the RFQ and SC linac will be performed using such a stable beam of the same charge-to-mass as the RIBs.

A movable slit plate containing a vertical and a horizontal slit can be scanned through the beam to provide transverse beam profiles using the beam current registered on the Faraday cup behind it. A phosphor viewer plate is used in diagnostics stations in the LEBT to display the beam cross section. A series of grids for attenuation of the beam current may be inserted if needed to control the stable ion beam intensity. There is provision for installing an emittance rig in one of the diagnostics stations in the LEBT. A 2-dimensional Allison type scanner similar to those used in the CCP injection line will be used for initial beam studies for ReA3.

Downstream from the MHB in the LEBT, there are up to 5 diagnostics stations where a high-resolution timing detector [9] can be used to characterize the longitudinal phase space distribution of the beam and to measure the beam velocity. The beam particles release secondary electrons from a biased coaxial wire inside a metal cylinder, some of which are detected by a multi-channel plate behind a hole in the cylinder wall. The time structure of the beam is directly indicated by the time distribution of the electrons. In addition, up to four scattered particle monitors [10] based on Si heavy ion detectors measuring the energy of elastically scattered beam from a thin gold foil.

## REFERENCES


[1] X. Wu et al. "MSU Re-accelerator – the Re-acceleration of Low Energy RIBs at the NSCL", Proceedings of the 13th Workshop on RF Superconductivity, Beijing, China (2007).

[2] Q. Zhao et al, "Design and Test of the Triple-Harmonic Buncher fro the NSCL Re-accelerator", these proceedings.

[3] M. Berz, J. Hoefkens, K. Makino, "COSY INFINITY 8.1 Programming Manual". MSUHEP-200703, Michigan State University, 2002.

[4] D.A. Dahl, Int. J. Mass Spectrom. Ion Processes 200, 3 (2000).

[5] Q. Zhao et al. "Design Studies of the Reaccelerator RFQ at NSCL", Proceedings of 2007 Particle Accelerator Conference, Albuquerque, New Mexico, USA, June 2007.

[6] A. Shempp, "An Overview of Recent RFQ Projects", these proceedings.

[7] W. Hartung et al, "Superconducting Quarter-Wave Resonator Cavity and Cryomodule Development for a Heavy Ion Re-accelerator", these proceedings.

[8] J. Wlodarczak et al, "Power Coupler and Tuner Development for Superconducting Quarter-Wave Resonators ", these proceedings.

[9] M. Marchetto, A. Bylinskii, R. E. Laxdal, "Beam Dynamics Studies on the ISAC II Superconducting Linac," Proceedings of the LINAC2006, Knoxville, Tennessee, USA (2006).

[10] V. A. Verzilov, R. E. Laxdal, M. Marchetto, W. R. Rawnsley, "Time Domain Diagnostics for the ISAC-II Superconducting Heavy Ion Linac," http://felino.elettra.trieste.it/papers/WEPB07.pdf

# LINAC FRONT-END UPGRADE AT THE CANCER THERAPY FACILITY HIT

M. Maier[#], W. Barth, B. Schlitt, A. Orzychevkaya, H. Vormann, S. Yaramyshev

GSI, Darmstadt, Germany

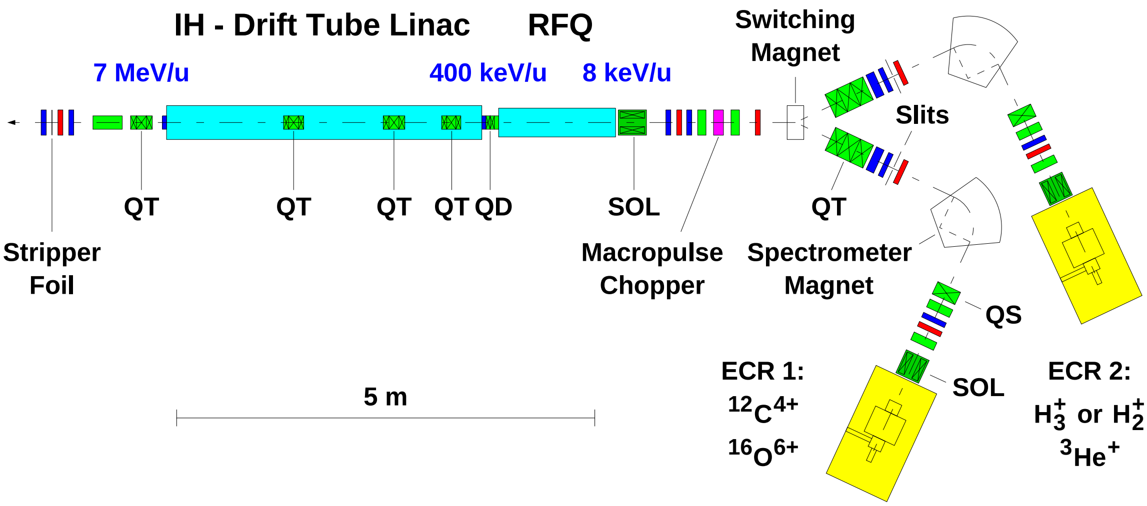


Figure 1: Layout of the Injector Linac [1]. QS = Quadrupole singulet, QT = Quadrupole triplet, SOL = solenoid, magnetic focusing and steering magnets (green), profile grids and the tantalum screen (red), and the beam current monitors (blue).

*Abstract*

A clinical facility for cancer therapy using energetic proton and ion beams (C, He and O) has been installed at the Radiologische Universitätsklinik in Heidelberg, Germany [1]. It consists of two ECR ion sources, a 7 MeV/u linac injector, and a 6.5 Tm synchrotron to accelerate the ions up to 430 MeV/u. The linac [2] comprises a 400 keV/u RFQ [3] and a 7 MeV/u IH-DTL [4] operating at 216.8 MHz and has been commissioned successfully in 2006 [5]. Yet the overall achieved transmission through the injector linac did not ecxeed 30 % due to a mismatch of the beam at the RFQ entrance. Thus a detailed upgrade programm has been started to exchange the RFQ with a new radial matcher design, to correct the missalignment and to optimize beam transport to the IH-DTL. The aim is to achive a sufficient overall linac transmission above 60%. Since August 2008 the new RFQ is at a test setup in Risø, Danmark. There a test bench comprising a full ion source and LEBT setup to commission the RFQ has been installed by Danfysik.

## INTRODUCTION

The commissioning of the injector Linac [5] shown in Figure 1 was performed in three consecutive steps for the LEBT, the RFQ, and the IH-DTL.

Because of the low transmission (~30 %) achieved for the injector Linac an upgrade program was initiated in 2007. The timeline of the commissioning and the upgrade program is given in Table 1.

Table 1: Timeline of the HIT Linac Commissioning and the Linac Front-end Upgrade Program

| | |
|---|---|
| 2006 Apr.-Dec. | HIT Linac commissioning |
| 2007 Aug. | RFQ design study measurements and solenoid exchange |
| 2007 Nov. | New stiffened tank copper plated |
| 2007 Dec. | RFQ input radial matcher design ready and approved |
| 2008 May | Machining of the electrodes at NTG workshop |
| 2008 Jun. | Assembly and RF tuning at the Univ. of Frankfurt |
| 2008 Sep.–Oct. | Rebuncher adjustment and commissioning in Risø, Danfysik |
| **Outlook** | |
| 2009 | Integration of the new RFQ at HIT |

## LINAC FRONT-END UPGRADE

As a result of the Linac commissioning and excessive beam dynamics simulations the reasons for the low RFQ transmission were found to be:

- The poor performance of the ion sources,
- field errors of the Solenoid matching the beam to the RFQ,
- RFQ input radial matcher section and
- the deformed electrodes due to mechanical stress on the tank.

As first the Solenoid matching the beam to the RFQ has been exchanged and the result is shown in Figure 3.

During this solenoid exchange a measurement campaign was performed to obtain sufficient data for optimization of the input radial matcher design.

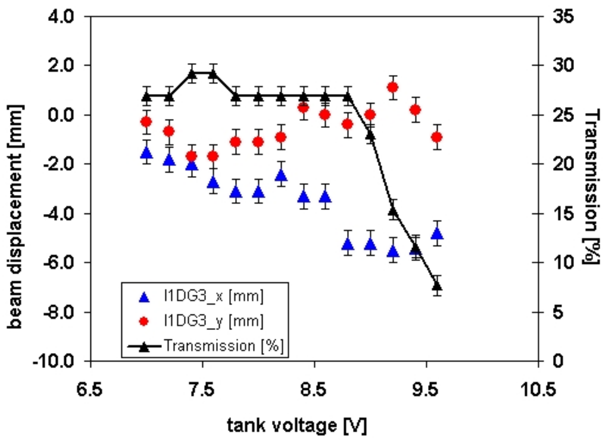


Figure 2: Transmission and beam displacement of the RFQ measured during commissioning in 2006.

Yet, because of unstable conditions of the ion sources this data could not be used. Instead, from the emittance measurements of the commissioning in 2006 a particle distribution was generated (Figure 4) and used for simulation with the simulation code Dynamion [6].

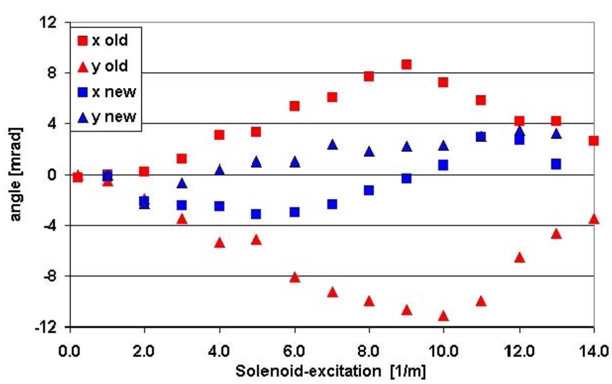


Figure 3: Steering of the beam behind the old and new Solenoids depending on their field strengths.

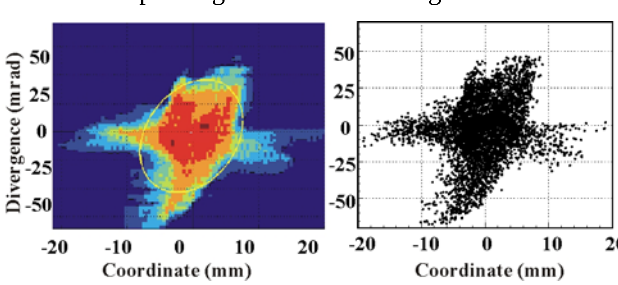


Figure 4: Measured $^{12}C^{4+}$ emittance at the RFQ entrance (left) and generated particle distribution to be used for simulation.

This distribution was transformed backwards through the solenoid. By varying the field strength in the transformations forward it was found that it is not the total emittance but the mismatch of the Twiss-parameters that leads to the beam losses. The possible improvement changing the input radial matcher is shown in Figure 5.

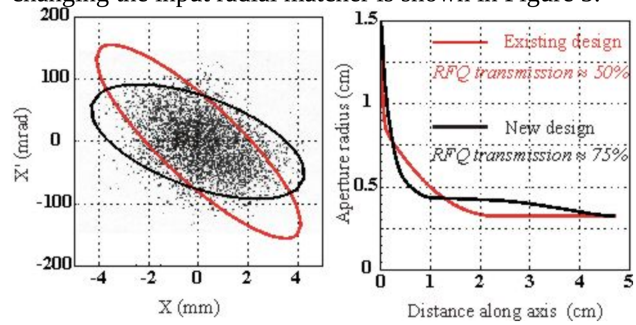


Figure 5: Dynamion simulation of the transmission improvement through the old and the new input radial matcher design using the particle distributions generated from the measured emittances (Figure 4).

During commissioning the alignment of the electrodes has been checked and a strong bending due to mechanical stress on the structure was found. A measurement of this deformation is shown in Figure 6 for the CNAO RFQ [7], a copy of the HIT RFQ. This deformation most likely happened during the alignment procedure and is of the same order of magnitude for both RFQs. A new stiffened tank design with thicker walls (6 mm instead of 4 mm), extra supports and 3 instead of 4 fixation points should solve this problem for the new RFQ design.

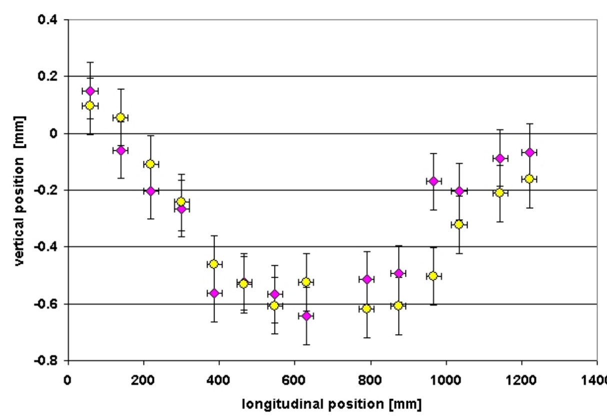


Figure 6: Vertical deformation of the CNAO RFQ electrodes measured on the upper and lower rods for a fixed (red) and loosened (yellow) tank.

Before the electrodes for the new design of the RFQ were machined, test pieces have been prepared to check the machining procedures for their feasibility. After the whole RFQ has been assembled, aligned and RF tuned it was shipped to a test setup of Danfysik in Risø, Denmark. This type of RFQ has an integrated rebuncher section (Figure 8) which has to be adjusted in a first commissioning step as described in [8]. The adjustment of the rebuncher voltage, which is a necessary prerequisite to commission the RFQ, has highest priority.

Besides an investigation of the high energy end of the RFQ is foreseen. The data obtained during commissioning in 2006 indicates that there might be particle losses also in the rebuncher section.

Figure 7: Final test piece of the RFQ radial matcher section to check the production procedures.

Beam losses definitely occurred in the doublet following the RFQ. Yet this fact does not allow for simulating the data further back as at this point all information about the transversal beam properties are lost.

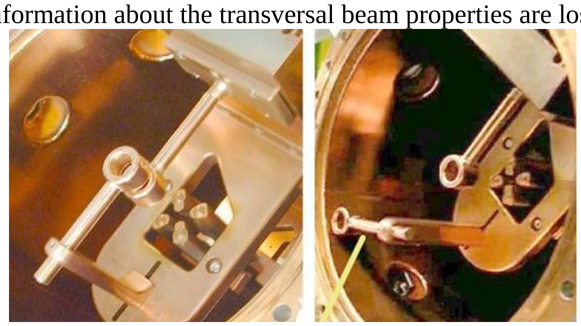

Figure 8: Rebuncher structure as mounted for operation (left) and in a dummy position to measure the output energy of the RFQ itself (right).

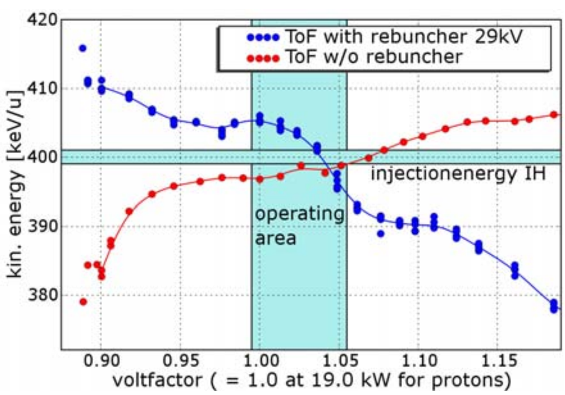


Figure 9: Measurement to adjust the rebuncher gap voltage [6].

The measurement campaign in Risø has started in September 2008 and for the first part the test bench shown in Figure 10 is equipped with three pickups a profile grid and an end cup for electron suppression. With this equipment the first energy scan without the rebuncher section shown in Figure 11 could be obtained.
Presently the rebuncher is adjusted to the design position continuing the beam energy measurements. After the rebuncher setting is fixed it is foreseen to change the test bench setup to allow for beam current and emittance measurements. Due to narrow apertures in front of the pickups it is not possible to do so with the provided setup for energy measurements.

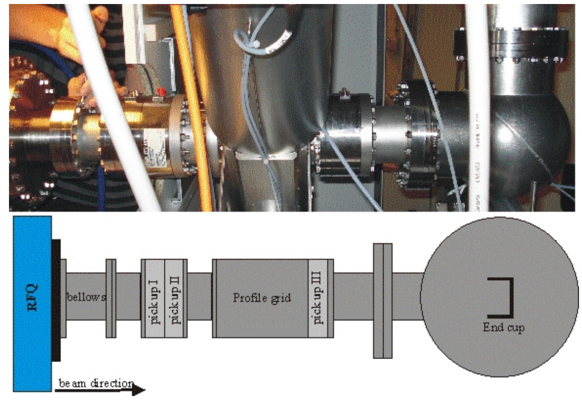


Figure 10: A photo of the diagnostics test bench as currently installed at Risø for RFQ energy measurements (top) and a schematic drawing (bottom).

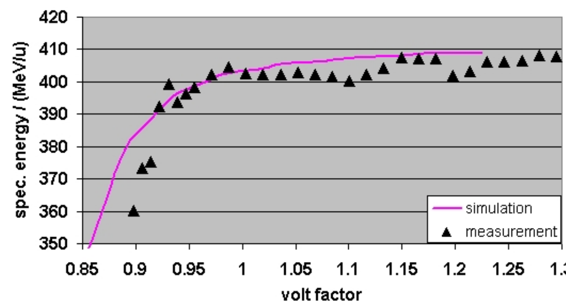


Figure 11: The RFQ energy scan with the rebuncher in the dummy position (blue) and the theory curve (red).

The planed second setup will consist of a beam current monitor, an emittance scanner and an end cup.

## OUTLOOK

After the commissioning of the RFQ at the test bench in Risø in autumn 2008 it will be shipped to Heidelberg and included in the system during the first available shutdown period. A significant improvement in the overall Linac transmission up to 60% is expected.

## ACKNOWLEDGEMENTS

The authors would like to express their gratitude to the fruitful collaboration with the Heidelberg Ion therapy HIT and IAP Frankfurt as well as towards the companies NTG, Danfysik and Siemens for their contribution.

## REFERENCES

[1] H. Eickhoff et al., Proc. EPAC 2004, p. 290.
[2] B. Schlitt et al., Proc. Linac 2004, p. 51.
[3] A. Bechtold et al., Proc. PAC 2001, p. 2485.
[4] Y. Lu et al., Proc. Linac 2004, p. 57.
[5] M. Maier et al., Proc. PAC 2007, p. 2734
[6] S. Yaramishev et al., NIM A, 2005.
[7] S. Rossi, Proc. EPAC 2006, p. 3631
[8] C. Kleffner et al., GSI annual report 2005.

# $C^{6+}$ ION HYBRID SINGLE CAVITY LINAC WITH DIRECT PLASMA INJECTION SCHEME FOR CANCER THERAPY

Toshiyuki Hattori, Taku Ito, Noriyosu Hayashizaki, Takuya Ishibashi, Liang Lu, Jun Tamura, Rui Kobori, Masahiro Okamura[1)], E.Osvath[2)], D.Biro[2)], D.Hollanda[2)], L. Kenez[2)]
Research Laboratory for Nuclear Reactors, Tokyo Institute of Technology,Tokyo, Japan
1) Collider-Accelerator Department, Brookhaven National Laboratory, New York, USA
2) Sapientia –Hungarian University of Transylvania, Tirgu-Mures, Romania

*Abstract*

We succeeded to accelerate more than 18mA of $C^{6+}$ ions with Direct Plasma Injection Scheme (DPIS) of YAG laser in 2004. We believe that these techniques are quite effective for pulse accelerator complexes (linac and synchrotron) such as heavy ion cancer therapy. We study a new hybrid single cavity $C^{6+}$ linac for heavy ion cancer therapy. This hybrid linac, combined with radio frequency quadrupole (4rod-RFQ) electrodes and drift tube electrodes into a single cavity, is able to downsize the linac system and reduce the peripheral device. High intensity beam of $C^{6+}$ by DPIS have many advantage for the synchrotron of heavy ion cancer therapy. We will present the design procedures of this hybrid linac, which is base on a three-dimensional electromagnetic field simulation.

## INTRODUCTION

In order to verify DPIS, accelerator test was carried out using Tokyo Institute of Technology (Titech) RFQ heavy ion linear accelerator and $CO_2$ laser heavy-ion source in 2001. The accelerated carbon beam obtained 9.2mA of $C^{4+}$ was much higher than designed currents. [1-4 ] To confirm the capability of the DPIS, we designed and fabricated a new RFQ linac to accommodate 100mA of carbon beam collaboration The Institute of Physical and Chemical Research and Frankfurt University. We succeeded to accelerate very intense carbon ions with the DPIS in 2004. The peak current reached more than 60mA of $C^{4+}$ and 18mA of $C^{6+}$ by CO2 and YAG laser, respectively [5-9]. Fig. 1 shows photographs of Titech RFQ linac and 100 mA Test RFQ linac. We believe that these techniques are quite effective for pulse accelerator complexes such as linear accelerator and synchrotron. The accelerator complexes are heavy ion cancer therapy and heavy ion inertial fusion.

We are studying a new hybrid single cavity linac [10] for Boron Neutron Capture Therapy. This hybrid linac, combined with radio frequency quadrupole electrodes and drift tube electrodes into an interdigital-H (IH) type single cavity, is able to downsize the linac system and reduce the peripheral device. From these matters, we propose a small Hybrid Single Cavity (HSC) linac for injector of heavy ion cancer therapy.

Titech RFQ linac 100 mA Test RFQ linac

Figure 1: Titech RFQ linac in 2001 and 100 mA Test RFQ linac in 2004 succeeded to accelerate high intensity beam by DPIS.

## ND-YAG LASE ION SOURCE

A Nd-YAG laser with a wavelength of 1060nm is used for this ion source. The pulse duration is 15ns(FWHM) and its energy is 400mJ. Fig.2 shows charge state distribution of Carbon ion with about 400mJ. Fig.3 shows laser power dependence of charge state distribution of Carbon ion. From these data, $C^{6+}$ ions were produced 40%. $C^{6+}$ ion beam have pulse width of about 2 $\mu$ s and about 200mA at injection point of 4 rod of RFQ.

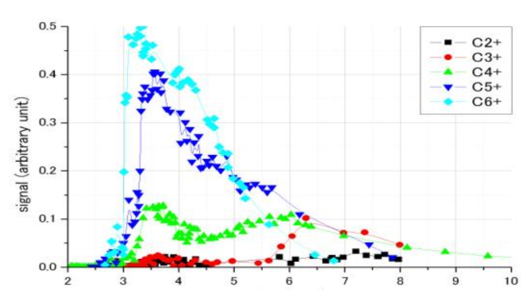


Figure 2: Charge state distribution of the Carbon ion with about 400mJ of YAG laser.

---
[#] thattori@nr.titech.ac.jp

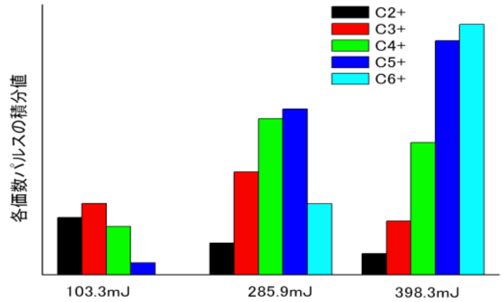


Figure 3: Laser power dependence of the charge state distribution of Carbon ion.

## DESIGN AND PARAMETERS

The accelerated particles are set to $C^{6+}$ more than 10 mA ( more than $2\times10^{10}$ particles/pulse) with YAG laser ion source. The operation frequency in this linac is 80 MHz. The HSC linac accelerate from 25keV/amu up to 2MeV/amu, see Table 1.

Table 1: Main parameters of $C^{6+}$ HSC Linac.

| | RFQ | BTL | DT |
|---|---|---|---|
| Accelerate particle | | $C^{6+}$ | |
| Input energy (keV/u) | 25 | 160 | 160 |
| Output energy(keV/u) | 160 | 160 | 2000 |
| Cavity diameters(cm) | 40 | 80 | 80 |
| Cavity length (cm) | 104 | 35 | 134 |
| Cavity total length(cm) | | 273 | |
| Operation power (kW) | | lower 80 | |
| Beam bore radius(mm) | 5 | 12 | 7 |
| Cell number | 160 | (10) | 15 |
| Beam focusing | RFQ | TQM | APF |
| Beam current | | 10 mA | |

The computer code RFQUICK was used to generate the cell parameters for the PARMTEQM calculation [11]. The computer code PARMTEQM was used to simulate the beam dynamics in the RFQ section. Drift tube structure section was calculated by computer code PARMIRA. Beam maching of RFQ and Dorift tube section were calculated by computer code Trace-3D.

The 3D electromagnetic simulation software MW-Studio [12] was used to calculate the resonance frequency, the electric field, the Q value and the wall loss of the cavity.

## DESIGN AND CAVITY SIMULATION

The electric field distribution of the HSC(IH) cavity must be constant through out the beam line. However the electric field of the inner IH cavity is increased towards the beam injection side. Because, capacitances of the RFQ section are larger than that of DT section. To adjust this unequal field distribution, we improved the IH cavity geometry. First, in order to modify the cavity diameter at the DT section, the field distribution was spread along the beam output side. Secondly, as the End Ridge Tuner (ERT) length was adjusted, the cavity was made to adopt a constant resonance frequency along the cavity. The electric-field strength was investigated by means of field simulations. Adjustments of realizing cavity at the ERT length were performed. Fig.4 shows modified cavity diameter and End Ridge Tuner.

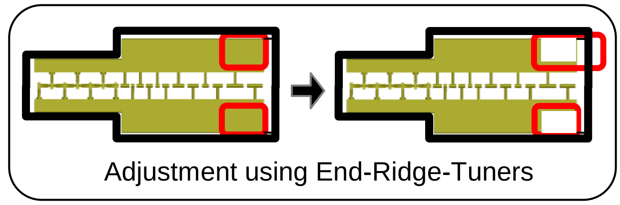


Figure 4: Modified cavity diameter and End Ridge Tuner.

The more the diameter of DT section was increased, the more the frequency of both sides were approached, and electric field was excited from input side to output side when inside diameter was 80-90cm. We calculated the electric field distribution from 280 to 360mm at 20mm intervals of ERT at the exit of the cavity. The optimum electric-field distribution was obtained with ERT length of 320mm as shown in Fig.5,6,7.

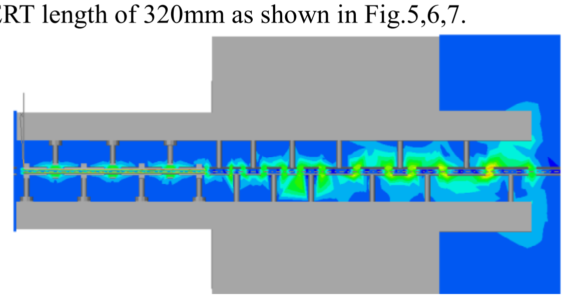

Figure 5: $C^{6+}$ HSC linac cross section and electric field.

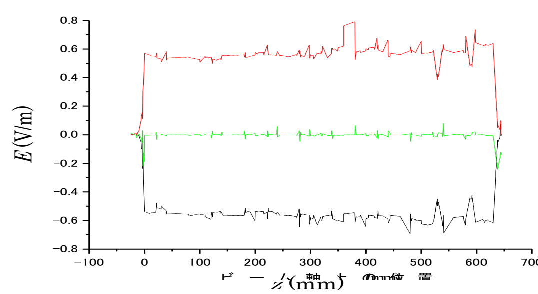


Figure 6: Electric-field distribution of RFQ section.

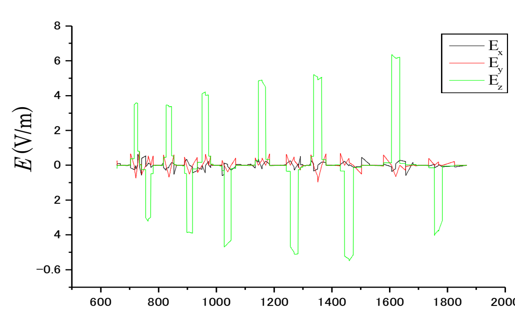


Figure 7: Electric-field distribution of DT section.

## ELECTRIC-FIELD BETWEEN RFQ AND DT SECTION

In the HSC linac, electric-field distribution in the gap region between the back-end of the 4-rod(RFQ) and injection side of DT region must be considered as shown in Fig.8-A. This electric-field have a negative effect on the acceleration beam as shown in Fig.9-A. We studied an improved electrode of drift-tube shape in which three quadrupole magnets, was inserted into this gap as shown in Fig.8-B. The electrode was able to reduce the excitation of the electric-field at the gap between 4 rods and drift tube as shown in Fig.9-B.

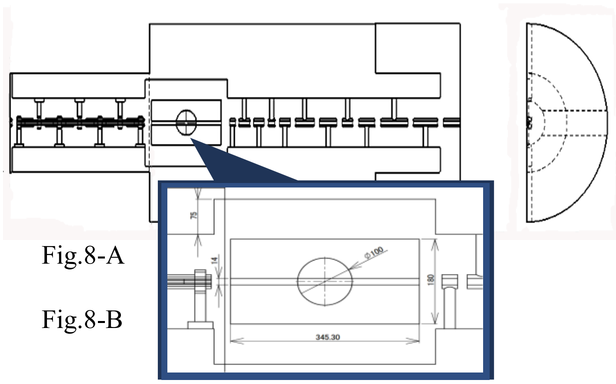

Fig.8-A

Fig.8-B

Figure 8: $C^{6+}$ HSC linac cavity cross section (A) and inserted electrode (B).

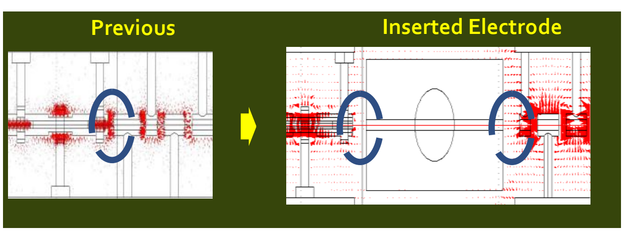


Fig.9-A Fig.9-B

Figure 9: Excited electric-field at the gap between 4 rods and drift tube. A: Previous; B: Inserted Electrode.

## HEAVY ION SYNCHROTRON OF CANCER THERAPY

DPIS techniques are quite effective for pulse accelerator complexes (linac and synchrotron) such as heavy ion cancer therapy. High intensity beam of $C^{6+}$ by DPIS have many advantage for synchrotron.

A) Effects of $C^{6+}$ ion injection

1.Striper foil system is not necessary by $C^{6+}$ ion injection. 2.Emittance growth is decrease by decrease of energy loss and energy straggling. 3.Injection energy of synchrotron is decrease to 2-3 MeV/u by no decrease of ions. 4.Operation of synchrotron is easy with no change of energy that is happened by decrease of stripper foil thickness.

B) Effects of one turn by injection of high intensity $C^{6+}$

1. Mulch turns injection system is not necessary by more than $10^9$ ions of $C^{6+}$. 2. Magnets (bending magnet, quadrupole magnet and sextapole magnet) of synchrotron are compacted by small size beam of one turn injection.

The heavy ion synchrotron is compact and use low electric power. Therefore facility of heavy ion cancer therapy will be able to smaller than present size.

## CONCLUSION

We study a new hybrid single cavity (HSC) $C^{6+}$ linac with DPIS for heavy ion cancer therapy. This HSC linac accelerate $C^{6+}$ ion from 25keV/amu up to 2MeV/amu.

Electromagnetic simulation of the cavity was done by MW-Studio. Acceleration cavity is 40cm (RFQ section) and 80cm (DT section) in diameter and 273cm in length. The operation frequency is 80MHz. Acceleration current is 10mA of $C^{6+}$ ( $2x10^{10}$particles/pulse). For this beam intensity of $C^{6+}$, The heavy ion synchrotron is compact and use low electric power. Therefore facility of heavy ion cancer therapy will be able to smaller than present size.

## REFERENCES

[1] M.Okamura, T.Takeuchi, T.Katayama, T.Hattori, Review of Scientific Instruments, 73(2002)761-763
[2] T.Takeuchi, T.Katayama, M.Okamura, T.Hattori, Review of Scientific Instruments, 73(2002)764-766
[3] M.Okamura, T.Katayama, R.Jameson, T.Takeuchi, T.Hattori and N.Hayashizaki, Nucl, Inst. and Meth., in Physics Research B188(2002)216-230
[4] T.Takeuchi, T.Katayama, M.Okamura, T.Hattori, N.Hayashizaki and R.A.Jameson, Nucl, Inst. And Meth., in Physics Research B188(2002)233-237
[5] H.Kashiwagi, T.Hattori, N.Hayashizaki, M.Okamura,R.A.Jameson, N.Meschryakov, Review of Scientific Instruments, 75 (2004)1569-1571
[6] T. Hattori, H. Kashiwagi, N. Hayashizaki, K. Yamamoto, S. Ueda, T. Nagae, J. Takano, Proc. of Symposium on the Application of Accelerator and Related Technology, 6(2004) 43-46.
[7] M. Okamura, R.AJameson, H. Kashiwagi T.Hattori, N.Hayashizaki,K.Sakakibara,K.Yamamoto, Radiation Effects & Defects in Solids, 160, (2005), 445-449.
[8] M. Okamura, H. Kashiwagi, K. Sakakibara, T.Hattori, N. Hayashizaki, R. A. Jameson, Review of Scientific Instruments, 77 (2006) 03B303-1/03B303-3.
[9] H. Kashiwagi, M. Fukuda, M. Okamura, R. A. Jameson, T. Hattori, N. Hayashizaki, J. Takano, K. Sakakibara, K. Yamamoto, Review of Scientific Instruments, 77 (2006) 03B305-1/03B305-4
[10] T.Ito, N.Hayashizaki, T.Ishibashi, T.Hattori, Nucl, Inst. and Meth. in Physics Research B261(2007) 17-20
[11] K.R. Crandall, *et al.*, LA-UR-96-1836 (2005).
[12] Computer Simulation Technology (CST), Micro Wave Studio Version2008 (http://www.cst.dec/)

# QUALITY IMPROVEMENT OF LASER-PRODUCED PROTONS BY PHASE ROTATION AND ITS POSSIBLE EXTENSION TO HIGH ENERGIES*

Akira Noda, Yoshihisa Iwashita, Hikaru Souda, Hiromu Tongu, Akihisa Wakita
ICR, Kyoto University, Gokano-sho, Uji-city, Kyoto, 611-0011, Japan
Hiroyuki Daido, Masahiro Ikegami, Hiromitsu Kiriyama, Michiaki Mori, Mamiko Nishiuchi, Koichi Ogura, Satoshi Orimo, Alexander Pirozhkov, Akito Sagisaka, Akifumi Yogo
JAEA/Kansai, 8-1, Umemidai, Kizugawa-city, Kyoto, 619-0215, Japan
Toshiyuki Shirai, NIRS, 4-9-1, Inage-ku, Chiba-city, Chiba, 263-8555, Japan

*Abstract*

Energy spread compression scheme for laser-produced ions by phase rotation with the use of an RF electric field synchronized to the pulse laser has been proved in principle for rather lower energies up to ~2 MeV. Its extension to higher energy around 200 MeV has been investigated with multi-gap structure assuming higher frequency of L-Band (~1.3 GHz). RF defocusing effect worried about at lower energy was found to be manageable at such a higher energy if the laser-produced-protons are well treated just after production at the target

## INTRODUCTION

Based on recent rapid development of high-power short-pulse laser with the use of Chirped Pulse Amplification, laser-produced ion beam has been proposed to be utilized as an injection beam of a medical synchrotron for cancer therapy replacing the RF linac as shown in Fig.1 [1]. For that purpose, however, the characteristics of laser-produced ion beam are not well suited. The energy spread of the laser-produced ion beam has been almost 100 % without a rather sophisticated treatment of the production target [2] or additional radial focusing scheme [3], which seems not to be suitable for operation by a tolerable repetition (~1 Hz) with good reproducibility as is required from medical use.

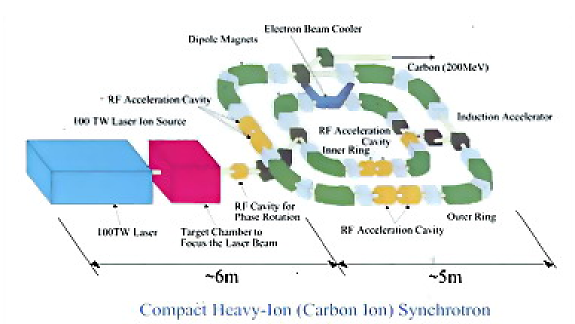


Figure 1: Layout of a medical synchrotron for cancer therapy replacing an injector linac by laser-produced ion beam.

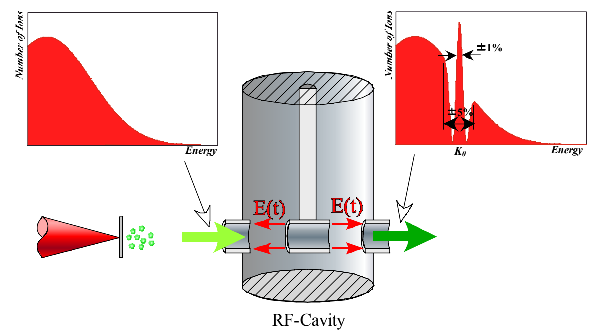


Figure 2: Illustration of the phase rotation principle.

In order to manage such a situation, a phase rotation scheme of the laser-produced ion beam with the use of an RF electric field synchronized to the pulse laser has been proposed [1]. In Fig.2, a basic concept of the phase rotation of phase rotation is illustrated. Utilizing the phase difference caused by the speed difference among ions with different energies, faster and slower ions are decelerated and accelerated, respectively in order to be put together into a central peak. Such an idea of energy spread compression of laser-produced ions by phase rotation has already been experimentally demonstrated with use of a rather smaller peak power (~10 TW) pulse laser, J-LITEX [4, 5]. Recent experiments with use of higher peak power (~100TW) laser, J-KAREN, has extended the energy of laser-produced proton up to ~4 MeV and also given us the information on the radial focusing/defocusing of such protons by the RF electric field created with the phase rotation cavity [6]. In the present paper, capability of multi-gap structure cavity for phase rotation has been considered for the case of

Table 1: Main Parameters of the Two Gap Resonator

| | | |
|---|---|---|
| Structure | | λ/4 with 2 gaps |
| RF Frequency | | 80.6MHz (83.7MHz) |
| Applied Power | | <30kW |
| Dimension | Outer Conductor | ID200mm×~1100mm |
| | Inner Conductor | ϕ40 mm×~700 mm |
| | Drift Tube | ID50×100mm |
| | Gap | 20mm |
| RF Tuner | | Cover ~250 kHz |
| Water Cooling | | Keep Temperature with in 0.5° |

*This work has been supported by Advanced Compact Accelerator Development from MEXT of Japanese Government and the 21st COE of Kyoto University, Center for Diversity and Universality in Physics.
#noda@kyticr.kuicr.kyoto-u.ac.jp

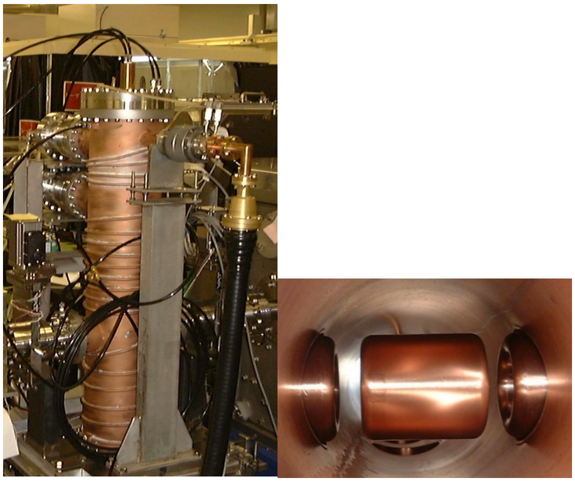

Figure 3: Fabricated two gap resonator for phase rotation of an injection beam for synchrotron with lower energy (~2 MeV).

extension to the higher energy (~200 MeV) applicable to cancer therapy directly. In the process, not only energy compression, but also radial oscillation amplitude is taken into account.

## PHASE ROTATION FOR INJECTION BEAM

For the scheme to utilize the laser-induced proton beam as the injection beam of a synchrotron to replace an injector linac, a two gap resonator with quarter wave-length as shown in Fig. 3 has been fabricated [4]. The main parameters of the cavity are listed up in table 1. The cavity is designed to enable phase rotation of the ion beam with the kinetic energy of up to 2 MeV/u for such ions as $^{12}C^{6+}$ with a charge to mass ratio of 1/2 [1].

### *Creation of Energy Peak*

The first phase rotation experiment with the use of J-KAREN has been performed with the set up as shown in Fig. 4. Due to the limited available time of J-KAREN, the energy spectrum of the laser-produced protons has been measured by their time of flight between production target and TOF detector, which, however, has been found to give a correct spectrum only for the case of without phase rotation, because due to energy change by the electric field of phase rotation cavity, time of flight of proton does not uniquely corresponds to its energy. So as to obtain correct energy spectrum of phase

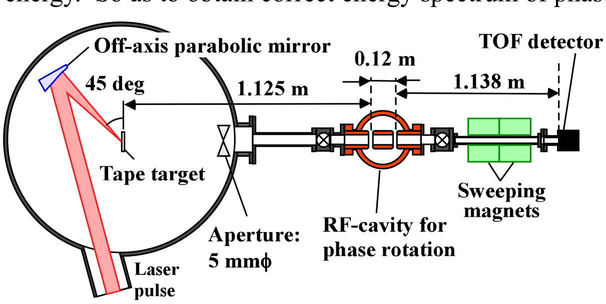


Figure 4: Experimental setup of proton-beam production and its phase rotation with the use of J-KAREN.

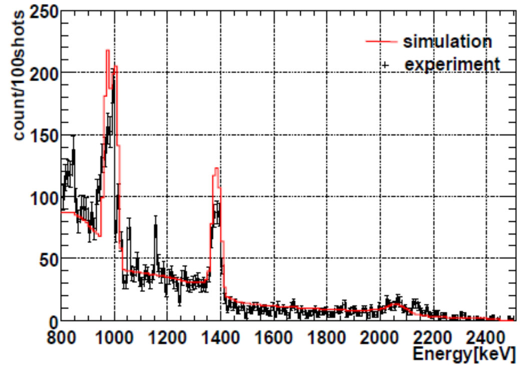


Figure 5: Energy spectrum of phase rotated laser-produced proton beam detected by a Thomson parabola. Clear peak creation has been observed at ~1.0MeV and ~1.4 MeV.

rotated protons, the next experiment with J-KAREN was performed by replacing TOF detector in Fig. 4 by a Thomson Parabola using CR39, which can give us correct energy information of detected protons. In Fig. 5, clear energy peaks formed by phase rotation are shown around 1.0 and 1.4 MeV [5]. It is shown that these peak positions coincide with the ones expected from simulation, which also coincide with the ones observed by the TOF method [6].

### *Radial Focusing Effect*

Through the experiments of phase rotation of proton beam produced by J-KAREN utilizing a two gap cavity above mentioned, radial focusing and defocusing effects as shown in Fig. 6 is observed Images of the mesh set 387 mm downstream from the production target were observed by CR39 detectors set at the positions 0.491 m down stream from the second gap of the phase rotation cavity (1.736 m downstream from the target). With

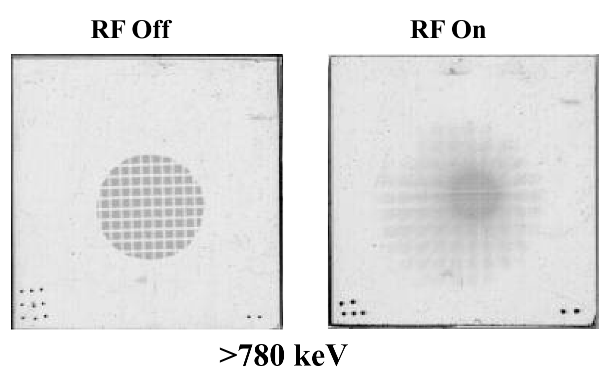


Figure 6: Observed radial focusing/defocusing effects on laser-produced protons by the electric fields of the phase rotation cavity located 1.125 m down stream from the production target. Images of the mesh set 387 mm downstream from the production target observed by CR39 detectors at the positions 1.736 m are shown for both cases with and without RF voltage of the phase rotation cavity.

application of phase rotation voltage, focusing and defocusing effects in radial motion are observed corresponding to various phases applied for protons with various energies. This is considered to be due to curved structure of the applied electric field at the phase rotation cavity, which results in the radial components of the electric field.

## MULTI-GAP STRUICTURE FOR HIGHER ENERGIES

The scheme to utilize the laser-produced protons by application of phase rotation and electron beam cooling as an injection beam of a synchrotron for cancer therapy [1] has been proved in principle up to now [4,5]. It, however, is considered a little bit complex compared with a scheme to produce directly a beam with the desired energy for cancer therapy by laser ion production and the latter scheme is eagerly pursuit although the energy attained with direct production by laser-plasma interaction is rather limited (~ 4 MeV) at the moment.

Even for proton beam, the desired energy for cancer therapy is rather high as >180 MeV for human body treatment and ~70 MeV for eye treatment. Extension of the energy of laser-produced ion has been under elaborate investigation all over the world to respond the urgent needs for wide spread use of effective cancer therapy. In addition to the increase of the attained ion energy, improvement of the characteristics of the laser-produced ion with good energy resolution and good reproducibility is one of the most important items to be investigated. For such a purpose, we have proposed to extend our previous two gap resonator to a multi-gap structure in order to increase the applicable energy to higher value without causing spark problem at the RF cavity. Expecting rapid increase of laser-produced protons, we have investigated the capability of applying the phase rotation scheme to laser-produced ions with such a higher energy (~200 MeV) as can directly be applied for cancer therapy.

### *Selection of RF Frequency*

As the RF frequency of the two gap resonator for phase rotation, we have adopted the same frequency as the source laser (~ 80 MHz) [4]. As the sparking limit of the RF electric field is proportional to square root of the frequency, it is preferable to select as high frequency as possible from this point of view, which, however, needs to be compromised with the practical aspects of hardware construction. Considering the easiness of synchronization between the RF electric field and the pulse laser together with the above requirement, we have selected the frequency of the integral (16 times) multiples of the source frequency of the pulse laser, [80.6 MHz (83.7 MHz)], in the L-Band [1290 MHz (1339 MHz)].

### *Multi-Gap Structure*

For the reference design of phase rotation of laser-produced proton to be directly applicable for cancer therapy, its energy is assumed at 200 MeV. In case we want to collect protons in the energy region of ±5% of this energy, maximum needed energy correction at a single passage through the resonator is 10 MeV. It seems to be well applicable by 12 cell resonator considering the so-called “Kilpatric limit” [7]. For the frequency ~1.3 GHz, the distance between the centres of adjacent two gaps is to be 130 mm if 200 MeV proton is assumed to pass through with the same phase. The energy compression is expected for the passage with the phase where the RF voltage is increasing, while the RF defocusing is anticipated with this phase. So as to suppress this radial defocusing, a scheme to utilize alternating phases at successive gaps has been proposed for lower energy [6]. Such radial focusing/defocusing effect, however, was found to be less dominant at the higher energy as -200 MeV from the computer simulation and it is considered to be manageable if enough focusing action has been applied before phase rotation. So it is possible to utilize every gap with the phase to compress the energy spread. Thus, the length of the phase rotation multi-gap cavity is expected to be around 1.5 m, which seems to be well compact for real medical applications.

## SUMMARY

With the use of multi-gap cavity with the frequency of L-Band (~1.3 GHz), energy peak creation by phase rotation is also expected for higher energy as ~200 MeV.

## REFERENCES


[1] A. Noda et al., “Ion production with a high-power short-pulse laser for application to cancer therapy”, Proc. of EPAC2002, Paris, France, pp.2748-2750..

[2] B. M. Hegelich et al., “Laser acceleration of quasi-monoenergetic MeV ion beams”, Nature: 439 (2006) 441-444.
H. Schwoerer et al.: “Laser–plasma acceleration of quasi-monoenergetic protons from microstructured targets”, Nature 439 (2006) 445-448.

[3] T. Toncian et al.: “Ultrafast Laser-Driven Microlens to Focus and Energy-Select Mega-Electron Volt Protons”, Science, 312 (2006) 410-413.

[4] A. Noda et al., “Creation of peaks in the energy spectrum of laser-produced ions by phase rotation”, Proc of LINAC2006, Knoxville, Tennessee, USA, (2006); pp. 97-99
S. Nakamura et al., “High-Quality Laser-Produced Proton Beam Realized by the Application of a Synchronous RF Electric Field”, Japanese Journal of Applied Physics, 46, pp.L717–L720 (2007).

[5] A. Wakita et al., “Characteristics of Laser-Produced Proton Beam Improved by a Synchronous RF Field”, submitted to Nucl. Instr. & Meth. in Phys. Res.

[6] M. Ikegami et al., “Radial focusing and energy compression of a laser-produced proton beam by a synchronous rf field”, submitted to Phys. Rev. St AB.

[7] W. D. Kilpatrick, Criterion for Vacuum Sparking Designed to Include Both rf and dc, Rev. Sci. Instrum. 28, p.824 (1957).

# THE FEASIBILITY OF LOW-ENERGY ELECTRONUCLEAR POWER PLANT

Yu.A. Svistunov, M.F. Vorogushin (D.V. Efremov Institune, 196641, St.Petersburg, Russia),
I.V. Kudinovich (A.N. Krylov Shipbuilding Research Institute, 196158, Moskovskoye Shosse, 44, St.Petersburg, Russia)

*Abstract*

There are examined prospects and challengers associated with the development of low-energy electronuclear power plant eliminating any possibility of uncontrolled chain fission reaction through fission in subcritical reactor with an additional neutron source. The neutron source is anticipated to be a heavy-element target irradiated with a beam of protons accelerated to several hundreds of mega-electron-volts. The intensity of external neutron source for an electronuclear reactor rated under 200-400 MW may be much less than for greater ones, and that allows reducing accelerator performances to limits that are already run in the world industry. Potential applications of such electronuclear plants include municipal, industrial and other electricity, and heat supply utilities in remote areas. The same engineering philosophy may be used on solving of the nuclear waste transmutation problem.

## INTRODUCTION

Thermal power $N_T$ which is picked out in active zone of a subcritical reactor with an outer neutron source and effective multiplying factor $K_{ef}$ is determined by formula

$$N_t = \frac{I_p n_0}{e} \cdot \frac{K_\infty}{1-K_{ef}} \cdot \frac{E_f}{\nu} \quad (1)$$

where $E_f$ - energy which is picked out under fussion of one fuel nucleus; $\upsilon$ - average number of neutrons from one act of fission; $K_\infty$ - multiplying factor of infinite reactor; $I_p$ - average current of accelerator; $n_0$ - number of neutrons which are produced by one particle after interaction with target. It is supposed now that for save of nuclear safety $K_{ef}$ must be not more than 0.98. During the active zone campaign $K_{ef}$ can decrease due to change of the fuel isotope composition (fuel burning out, toxic effect etc.) One expect $K_{ef}$ will decrease to 0.95 for fast neutron reactor. Results of modeling of active zones of gas-cooled reactor with multiplying target and $K_{ef}$ =0.96 give release of thermal power 200 MW for intensity of outer source $4.2\cdot 10^{17}$ n/s. This intensity may be achieved for $I_p$ =5mA and yield of neutron $n_0$ =13. Such yield neutrons can obtain from (UN+W) target under proton energy $E_p$ =200-400 MeV. 200 MeV spread depend on incompleteness of experimental data, possibilities to use $K_{ef}$ >0.96, cascade zone etc. There is consider proton linac as outer source of neutrons. Alternative variant is to use cyclotron as energy amplifier. Among contemporary cyclotrons PSI (or such type cyclotron) may provide 1 MW beam and required conversion "proton-neutron". But cost of such machine and weight will be well higher than 200-400 MeV, 5 mA proton linac. On the other hand cyclotron with energy 400 MeV and 5 mA current could consider as alternative of rf linac for stationary nuclear power station. Conclusions of workshop [1] show that at present creation of 5 mA cyclotron has more problems than creation of rf linac with the same current.

## LINEAR ACCELERATOR

A probable scheme of such proton linac is given on fig.1 It includes: RF volume source, LEBT, 4-vane spatially-homogeneous strong focusing structure (RFQ), alternating phase focusing structure (APF DTL), coupled cavity linac structure (CCL). APF DTL structure is IH-cavity with thick holders turned on right angle in each following sell and magnetic lenses in drift tubes [2].

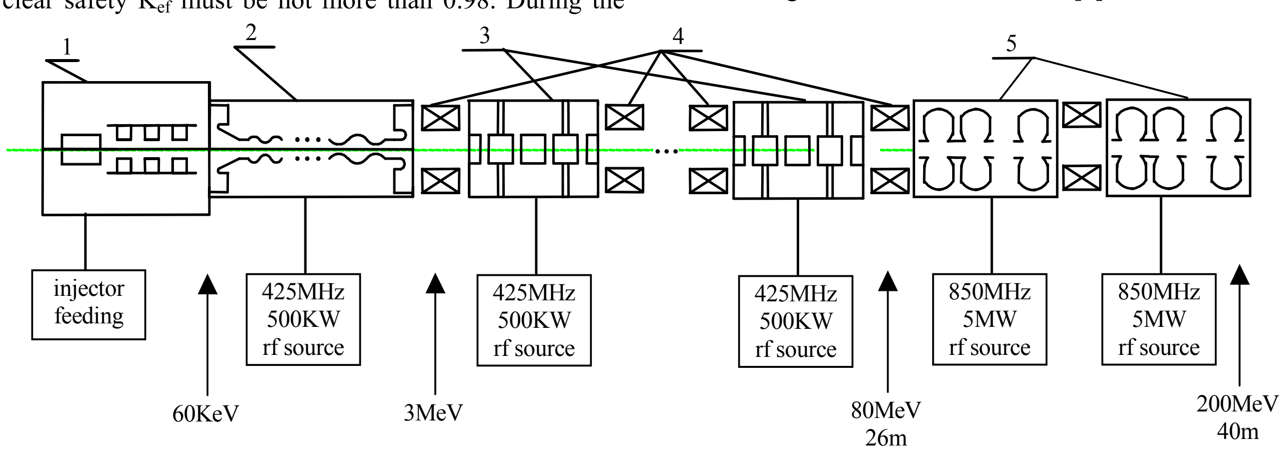


Figure 1: Layout of linac. 1 - ion source and LEBT 2 - spatially-homogeneous strong focusing structure (RFQ) 3 - alternating phase focusing structure (APF DTL) 4 - coupled cavity linac structure (CCL) 5 - focus lenses

Main parameters of linac are given in table 1.

Table 1: Main Parameters of Linac

| | |
|---|---|
| Output energy, MeV | 200-400 |
| Average current, mA | 5 |
| Duty Factor, % | 10 |
| Possible frequency range of RFQ and DTL, MHz | 402.5-433 |
| Beam power, MW | 1-2 |
| Working frequency of CCL, MHz | 805-866 |
| Number of RFQ | 1 |
| Number of APF DTL resonators | 20 |
| Number of CCL module | 4 |

Presented parameters are based on achievements of accelerator technologies of the last twenty five years [3], [4], [5].

## HIGH TEMPERATURE GAS-COOLED REACTOR

To compensate decreasing of $K_{ef}$ during long reactor working one need increase accelerator current. Therefore it is expediently reactor with hard spectrum of neutrons to use for LEEPP where diapason of $K_{ef}$ change much less than the same in thermal neutron reactors. There is considered high-temperature gas-cooled fast neutron reactor (HTGCR) [6] as reactor of LEEP. Gaseous heat-carrier captures neutrons weakly therefore fuel reproduction is improved and change of reactivity is lowered in fast neutron reactors. So that risk of inlet of positive reactivity because of heat-carrier lost is absent. Helium is chosen as heat-carrier of gas-cooled reactor of LEEPP since helium has best thermal properties than other than other gaseous heat-carriers. Advantages of helium are chemical inertness preventing corrosion of constructional materials and absence of activation under action of neutron irradiation. It raises radioactive safety of LEEPP. HTGCR design of LEEPP is shown on fig. 2. Active zone of LEEPP reactor may be created on base of elements developed for ship HTGCR. Active zone consists of cylindrical heat assemblings (diameter 42 mm) with ball-shaped elements of HRA. Heat releasing elements (HRE) (diameter 2-4 mm) include fuel core from mononitrid of uranium covered by tangsten. HRE take place in inside HRA as backfill in ring gap between two coaxial pipes of niobium. Cooling of HRE is released by transversal stream of helium via ball-shape backfill. Reactor of thermal power 200 MW active zone sizes are: outer diameter 1.6 m, height 1.5 m. These sizes are determined by energy intensity 70 $MW/m^3$. It proves safe elimination of heat from active zone. Results of modeling show that in active zone with multiplying target (UN+W) (diameter 0.4 m) power heat releasing 200 MW may be achieved for $K_{ef}$ 0.96 and source intensity $4.2\cdot10^{17}$ n/s.

## NEUTRON-PRODUCING TARGET

In this report one proposes design of target with tubular irradiated elements (fig.3). Three of coaxially-located shells form vessel. Inner carrier shell, connected with ion transport channel, is insulated from heat-carrier and has good vacuum. Target is cooled by heat-carrier of reactor - helium. Middle and outer shells of vessel prove circulation of cooling heat-carrier in the target. The middle shell has holes inside surface which are connected with inner pipe of suitable irradiated elements via adapter. Radial clearances between shells are used as collectors of heat carrier which are cooling neutron-producing target.

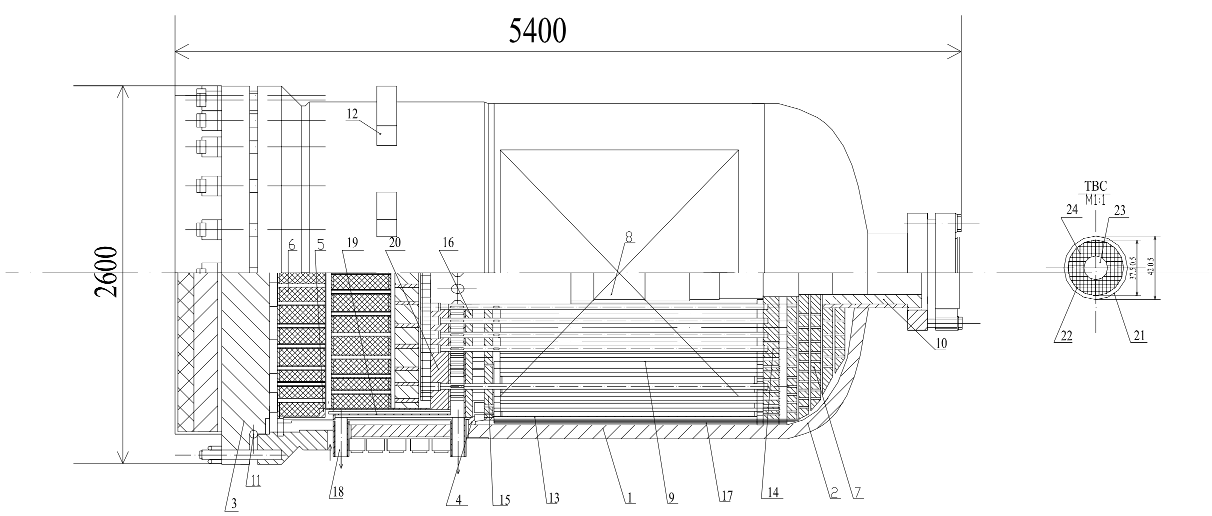


Figure 2: Design of high-temperature gas-cooled reactor. 1 - vessel 2 - bottom 3 - cap 4 - holder of active zone 5 - holder of heat releasing assembling (HRA) 6 - upper shield plug 7 - edge-joint screens 8 - neutron-producing target 9 - active zone 10 - cooled socket for target strengthening 11 - tubular thickening 12 - elements of strengthening of bio-protection 13 - carrying shell 14 - bottom bearing plate 15 - intermediate plate 16 - dividing plate 17 - sidelong screen 18 - sockets "pipe in pipe" type 19 - shell of HRA holder 20 - upper plate of HRA holder 21, 22, 23 - tube of HRA 24 - ball-shaped elements of HRA

Each tubular irradiated element consists of two coaxial pipes with thin walls.

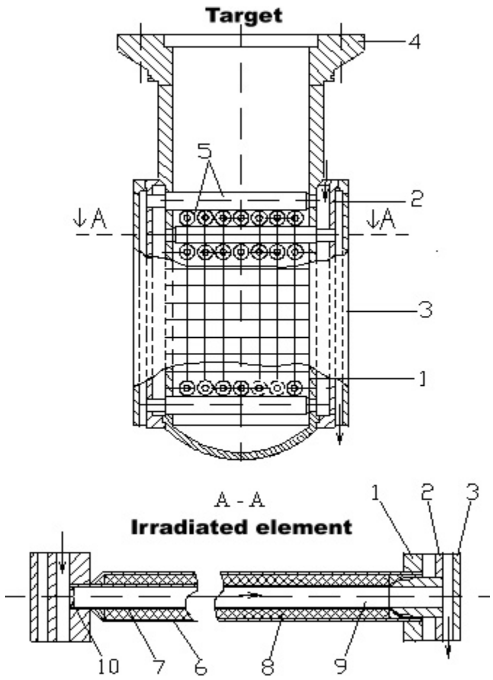


Figure 3: Neutron-producing target. 1, 2, 3 - shells of vessel, forming channel of heat carrier 4 - ion supply channel 5 - irradiated elements of target 6, 7 - shells of irradiated element 8 - neutron-producing material 9 - heat-carriers channel 10 - choke element

Between walls is placed neutron producing material. Such structure of irradiated element allows to use neutron-producing substance in different form (tablets, powder etc.) and to decrease requirements to radiative and heat resistance. It is proposed uranium compound UN to use as neutron-producing material. It is heat-resistance and multiplying target allows to obtain heat power in activ zone 1.5 times as much as unmultiplying one. Experimental data of neutron yields from targets of finite sizes presented in publications have essential distinctions. Modeling of neutron yield from UN 60 cm diameter target for 400 MeV protons gives more than 20 n/p.

## CONCLUSION. DESIGN LEEPP

Scheme of principle placement of basic equipment is given on fig. 4. It is possible to place installation in protected container with diameter 10 m and length 25 m. It is according to sizes of atomicship's compartments. linac and power equipment of LEEPP are placed in same enclosed space to reduce length of protected container. Longitudinal size of linac may be reduced under 180° turn of accelerator tract. Turbocompressor with start system, power turbine, heat-exchanger and main electric generator are forming rigid construction. they are placed inside power vessel connected with reactor. Foundation of construction is attached to protected container's vessel. Linac is placed on foundation which is integral whole construction. It help to prevent deformations of beam tract due to vibrations of mechanical equipment of LEEPP. Blocks of linac RF system may be placed in special chambers protected from radiation. It proves possibility of their servicing under working LEEPP.

## REFERENCES

[1] M.K. Graddock. Critical Beam-Intensity Issues in Cyclotrones - overview of the Santa-Fe workshop // Proc. of Conference "Cyclotrons and their Application", 1998, Caen, p. 377

[2] Yu.A. Svistunov, S.A. Minaev, S.A. Silaev. Modelling and and Testing of APF Cavity RF Field // Proc. of workshop BDO-95, St.Petersburg, Russia, 1995, pp.130-137

[3] K.F. Johnson et al . Operational Characteristics of 100mA 2MeV RFQ // 1992 Linear Accel.. Conf. Proc., Chalk River Lab. Report, AECL-10728, p.64

[4] J. Stovall. Low and Medium Energy Beam Acceleration in High Intensity Linacs // Proc. of EPAC 2004, Lucerne, Switzerland, pp. 108-111

[5] Commissioning and Initial Operating Experience with the SNS 1GeV Linac // Proc.of LINAC 2006, Knoxville, Tennessee, USA, pp.1-5

[6] L.N. Gerasimov, I.V.Kudinovich, Yu.A. Svistunov, V.P. Struev. Compact Electronuclear installation. Possible Technical Solutions // Proc. of Russian Academy of Science. Energetics. N2, 2005, pp.3-16 (in Russian)

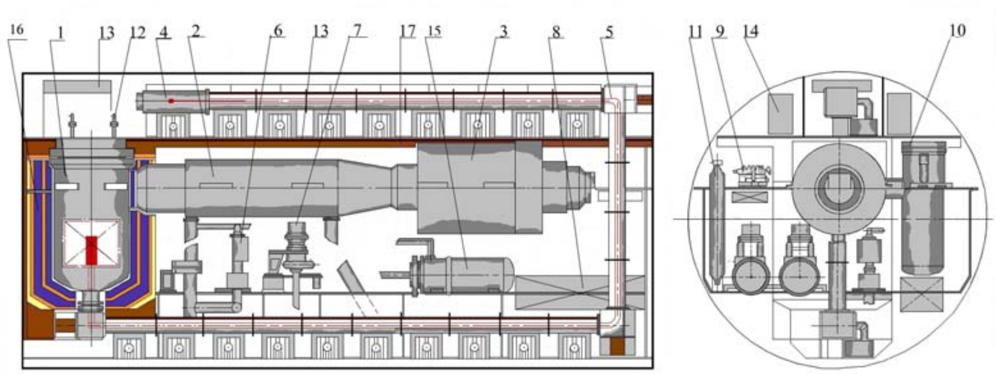


Figure 4: Configuration of electronuclear installation in protecting container. 1 - reactor 2 - turbocompressor with heat exchanger 3 - main electricity-generating 4 - accelerator 5 - bending magnets 6, 7 - pumps of cooling system 8 - water storage tank of cooling system 9 - vacuum aggregate 10 - aggregate of emergency shut-down cooling 11 - helium balloons 12 - monitors 13 - electrical equipment 14 - blocks of RF source 15 - heat-exchanger 16 - bio and heat shielding.

# CW PROTON LINAC FOR THE BNCT APPLICATION

Donald A. Swenson, Linac Systems, LLC, Albuquerque, NM

*Abstract*

A 2.5-MeV, 20-mA, cw, proton linac for the Boron Neutron Capture Therapy medical application is under construction at Linac Systems. The system consists of a 25-keV microwave ion source, a solenoid lens based low energy beam transport system, a 0.75-MeV RFQ linac, a 2.5-MeV RFI linac, and the necessary service systems. Because of the superb low energy capabilities of the RFI structure, the RFQ linac need only go to 0.75 MeV, resulting in a cavity dissipation of 74 kW for the RFQ section. Because of the high rf efficiency of the RFI structure, the cavity dissipation is only 35 kW for the RFI section. Extensive thermal studies have been made to accommodate these cw heat load. The beam power is 50 kW. The rf power system is designed for an average power output of 200 kW. The RFQ and RFI sections are coupled into a single resonant unit by a quarter-wave-stub resonant coupler. The combination is driven at a single point in the RFQ structure. The total length of the linac is 2.84 meters.

## INTRODUCTION

There are very few cw linacs in the world. Our proprietary linac structures offer the best chance to realize a commercially viable cw linac product. Features of our patented Rf Focused Interdigital (RFI) linac structure make it practical to consider cw linac systems for applications requiring very high average beam intensities. BNCT and Isotope Production are two such medical application. Solid state materials modification is another such application.

A 2.5-MeV, 20-mA, cw, proton linac for the Boron Neutron Capture Therapy (BNCT) medical application is under construction at Linac Systems. The system consists of a 25-keV microwave ion source, a solenoid lens based low energy beam transport (LEBT) system, a 0.75-MeV RFQ linac, a 2.5-MeV RFI linac, and the necessary service systems. This 2.84-m linac system is shown in Fig. 1.

The largest engineering challenge for cw operation is the removal of the heat generated by the cw operation. To mitigate this problem, we have performed extensive thermal management studies on the critical parts of the system. The highest power density in the RFQ linac structure is the RFQ bar supporting strut. The highest power density in the RFI structure is the main drift tube support stem.

Because of the superb low energy capabilities of the RFI structure, the RFQ linac need only go to 0.75 MeV, resulting in a cavity dissipation of only 65 kW (30% beyond theoretical) for the RFQ section. Because of the high rf efficiency of the RFI structure, the cavity dissipation for the RFI section is only 35 kW (30% beyond theoretical). The beam power is 50 kW. The

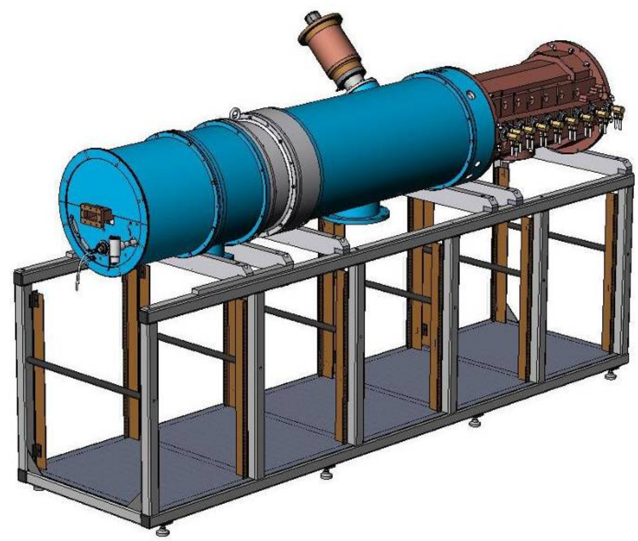

Figure 1: Cw proton linac.

total rf power required is 150 kW. The two linac structures are resonantly coupled, providing a single drive point for the combination. The details of this coupler are presented in another paper at this conference[1].

Abundant quantities of epithermal neutrons are produced when the 50 kW, 2.5-MeV proton beam falls on a solid lithium target, which is under design and fabrication at Linac Systems. The details of this target are presented in another paper at this conference[2].

## THE INJECTION SYSTEM

The first section of this accelerator is an ion source and low-energy beam transport (LEBT) system. The ion source is a microwave ion source which produces a 25-keV, 30-mA, dc, proton beam with low emittance and high proton fraction. A drawing of the injection system is shown in Fig. 2. The total distance from the ion source to the RFQ is 540 mm.

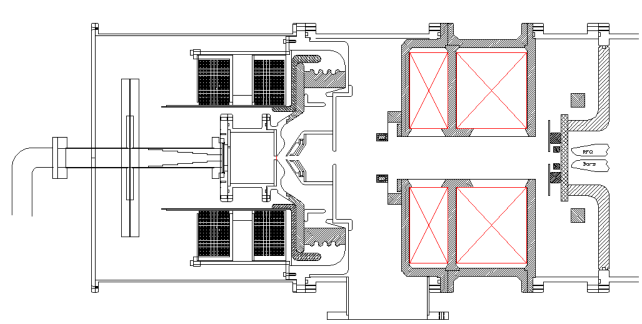

Figure 2: Injection system.

The focusing element in the LEBT is a novel dual-solenoid magnet utilizing two separate tape-wound, edge-cooled coils. The upstream coil produces 25,000 Amp-turns for a current of 85 A. The downstream coil produces twice the Amp-turns for the same current. An x,y steering magnet is suspended a few centimeters in front of the solenoid.

## THE RFQ LINAC

The next section of this accelerator is the RFQ linac, which accelerates the beam from the ion source energy of 25 keV to an output energy of 0.75 MeV, in a length of 1.04 m. The RFQ a four-bar RFQ of the Radial Strut design, where the individual bars are supported by radial struts emanating from the walls of the cavity with four-pole symmetry. A significant advantage of the Radial Strut design is that the rf dipole mode is 6 MHz above the quadrupole mode and does not present a problem with rf field stability.

The rf efficiency of the RFQ is expressed in terms of a transverse shunt impedance, $Z_{TR}$ (MΩ-m), defined as $V^2/P_L$, where V is the bar-to-bar voltage and $P_L$ is the rf power per unit length in the structure. The shunt impedance of the radial strut design is 0.12 MΩ/m, about twice the value of conventional four-bar RFQs.

## THE RFI LINAC

The Rf-Focused Interdigital (RFI) linac structure represents an effective combination of the interdigital (Wideröe) linac structure and the rf electric quadrupole focusing used in the Radio Frequency Quadrupole (RFQ) and Rf-Focused Drift tube (RFD) linac structures. This linac structure is three to four times more efficient and three times smaller in diameter than the conventional Drift Tube Linac (DTL) structure in the energy range from 0.75 to 6 MeV. It is ten times more efficient than the RFQ linac structure in the 0.75 to 6 MeV range.

In the RFI structure, when the accelerated particles enter the drift tube, the electric fields are near their maximum. When the accelerated particles are three quarters of the way through the drift tube, the electric fields are zero and changing sign. As a result, the focusing action must be pushed upstream to lie as close to the leading edge of the drift tube as possible, leaving the latter portion of the drift tube solely as a drift action (no focusing, no acceleration). Hence, the drift tubes of the RFI linac structure are asymmetrical, consisting of a minor piece and a major piece.

The rf focusing is introduced into the RFI linac structure by configuring the drift tubes as two independent pieces operating at different electrical potentials as determined by the rf fields of the linac structure. Each piece supports two fingers pointed inwards towards the opposite end of the drift tube forming a four-finger geometry, which produces an rf quadrupole field along the axis of the linac for focusing the beam.

The assembly and alignment procedure goes as follows. After the tank and stems are fabricated, the stems (major and minor) are installed in their hard socket prior to attachment of the major and minor drift tube bodies. Socket for the drift tube bodies are precision machined into the major and minor stems using an extended wire EDM facility that can span the entire length of the tank (≤750mm). In this way, the relative alignment of the drift tube bodies is very good. Following this EDM process, the stems are removed, the drift tube bodies are soldered into their sockets and the stems are re-installed. A picture of this multi-cell structure is shown in Fig. 3.

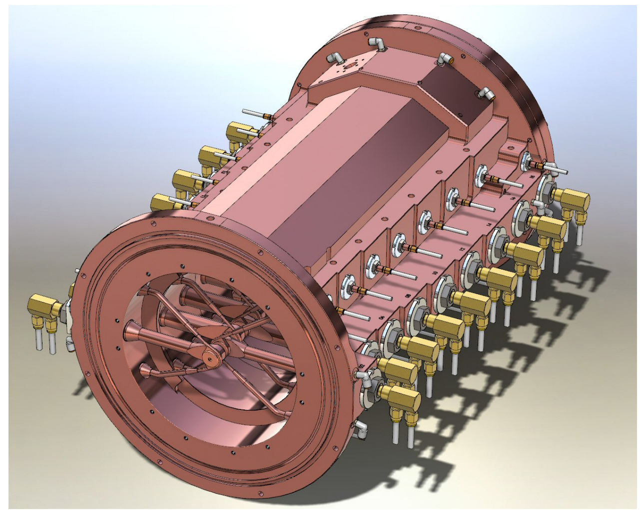

Figure 3: Multi-cell RFI linac structure.

Our first RFI structure was built as a series of unit cells, each containing a major drift tube body mounted on a supporting stem and a minor drift tube body mounted on a supporting stem[1]. Alignment shoulders on each cell provided cell-to-cell alignment. The drift tube alignment was achieved by machining sockets in the major and minor stems for the major and minor drift tube parts, relative to the alignment shoulders, by a precision wire EDM process.

Our present fabrication scheme results in multi-cell RFI tank sections. In this scheme, the tank sections are precision machined with "hard socket" for all major and minor stems. The basic requirement on the hard socket is that the stem location be reproducible – that is, that the stem can be removed and replaced to the same location with considerable precision (~25 microns).

## RF POWER SYSTEM

The rf power system is designed to produce a cw power of 200 kW at 200 MHz, and consists of a Low Level Rf chassis, a Solid State Amplifier, an Intermediate Power Amplifiers, and a Final Power Amplifier. The rf systems are designed and built by JP Accelerator Works, Inc.

## POWER AND COOLING REQUIREMENTS

The short, 0.75-MeV RFQ linac structure and the very efficient RFI linac structure present a manageable power and cooling requirement for this cw linac system.

The total structure power for the RFQ linac structure is 65 kW. Seventy percent of this power (45.5 kW) is dissipated in the bar/strut assemblies. There are a total of 20 parallel cooling circuits, implying about 2.3 kW per cooling circuit. The majority of this power is in the struts, where we employ a conical spiral cooling path for heat transfer. In all, the RFQ is cooled by 30 parallel cooling circuits. Some cooling circuits are shown in Fig. 4.

The total structure power for the RFI structure is 35 kW. This power is evenly split between the cavity wall and the drift tube stems. The highest power dissipation is in the 18 major drift tube stems, where the power per stem is about 0.8 kW. Each of these stems is cooled by a parallel cooling circuit. In all, the RFI is cooled by 52 parallel cooling circuits. Some cooling circuits are shown in Fig. 5.

## CW TEST CAVITY TESTS

The two most difficult components of this linac system to cool are the RFQ strut and the RFI main stem. Both of these components were tested in a Test Cavity set up for this purpose. To expose the main stem to its design level of dissipation required 1162 W of rf power in the Test Cavity. We chose to supply this power as 116.2 kW of power at a 1% duty factor. To expose the strut to its design level of dissipation required 5932 W of rf power. We chose to supply this power as 118.64 kW of power at a 5% duty factor. Both components survived the tests with no sign of damage.

## THERMAL CALCULATIONS

Both linac structures are cooled by multiple, parallel, cooling circuits between supply and return manifolds as seen in Figs. 4 and 5. Thermal and flow dynamics calculations were made on all typical cooling circuits. Pressures like 20 psi and flow velocities like 3 m/s keep the temperature rise in the coolant to less than 8 C.

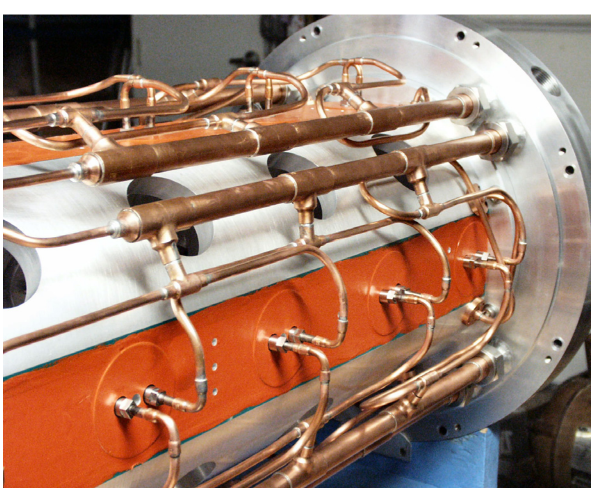

Figure 4: RFQ cooling circuits.

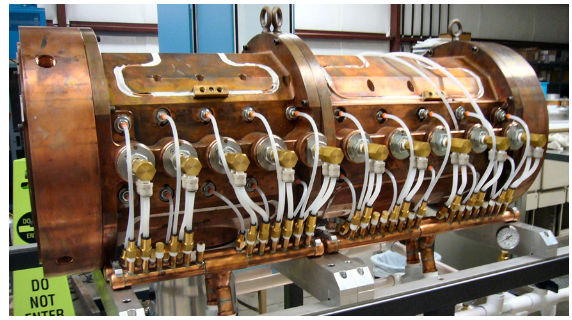


Figure 5: RFI cooling circuits.

## ACKNOWLEDGMENTS

The author wishes to acknowledge the assistance of Joel Starling, Ken Crandall, Jim Potter, Frank Guy, John Lenz, Joe Sherman, and Carl Willis.

## REFERENCES

[1] D.A. Swenson, “RF-Focused Drift-Tube Linac”, 1994 International Linac Conf., Japan, 1994.

[2] D.A. Swenson, “CW RFD Linacs for the BNCT Application”, Fourteenth International Conference on the Applications of Accelerators in Research and Industry, Denton, TX, 1996.

[3] D.A. Swenson, “An RF Focused Interdigital Linac Structure”, 2002 International Linac Conf., Korea, 2002.

[4] D.A. Swenson, “An Rf Focused Interdigital Ion Accelerating Structure”, CAARI 2002, Denton, TX.

[5] D.A. Swenson, W.J. Starling, F.W. Guy, and K.R. Crandall, “Continued Development of the RFI Linac Structure’, PAC2003.

[6] D.A. Swenson and W.J. Starling, “Status of the RFI Prototype”, 2004 International Linac Conference.

# HIGH-POWER LITHIUM TARGET FOR ACCELERATOR-BASED BNCT

Carl Willis*, John Lenz, Donald Swenson, Linac Systems LLC, Albuquerque, NM 87109, USA

*Abstract*

A water-cooled conical target for producing neutrons via the $^{7}Li(p,n)^{7}Be$ reaction at 2.5 MeV is under development at Linac Systems. The target is intended to accept an expanded 50-kW beam from an rf linac, and is predicted to meet the intensity requirements for practical accelerator-based boron neutron capture therapy (BNCT) in concert with Linac Systems' CW RFI linac[1]. Lithium metal targets present well-known physical and mechanical challenges at high beam power density that are addressed in our design. CFD modelling indicates that the peak lithium temperature can be held below 150°C with a water flow rate near 80 kg $min^{-1}$ and corresponding pressure drop of 170 kPa. The target prototype has been fabricated and is undergoing thermal-hydraulic testing using an electron beam at the Plasma Materials Test Facility, Sandia National Laboratories.

## INTRODUCTION

The $^{7}Li(p,n)^{7}Be$ reaction on lithium metal, at energies in the range of 1.9-3.0 MeV, has desirable properties as a potential source of neutrons for BNCT. Yield is high, typically reported in the range of $8\text{-}9 \times 10^{14}$ n $A^{-1}$ $s^{-1}$ at 2.5 MeV. Neutron energy is low; at 2.5 MeV, the flux-weighted mean neutron energy is only 330 keV.

Despite nuclear advantages, lithium presents thermal challenges in a high-power-density target. The solid is preferable on account of the corrosive and mobile nature of the liquid, but its 180°C melting point necessitates careful cooling. Recent experimental attempts at using solid lithium in targets have elucidated other difficulties. Taskaev[2] operated a 10-cm-diameter planar copper-backed lithium target with a 25-kW beam, finding that blistering of the copper substrate by beam-implanted hydrogen limited target lifetime to under a day.

Linac Systems is developing a unique solid lithium target for a 2.5-MeV, 20-mA beam. In this paper we focus on the target prototype mechanical design and some results of experiment and modelling pertaining to the thermal hydraulics of the heat removal system.

## TARGET DESIGN AND FABRICATION

### *Design Criteria and CFD Modelling*

Several basic functional requirements for our target were stipulated to guide the design:

- The proton beam is an 8-cm-diameter stationary (i.e. not rastered or rotated), magnetically-expanded, "waterbag" distribution produced by an rf linac.
- Peak surface temperature must not exceed 150°C to keep lithium layer solid (including safety margin).
- Liquid water coolant will be used with inlet temperature of 20-30°C, outlet pressure of 101 kPa.
- Symmetry of target system about the beam axis is desirable to simplify neutron dosimetry and treatment planning calculations.

The concept born from these requirements consists of a 10-cm diameter conical heat exchanger with water channels on the exterior that mates with a coolant manifold. This concept is illustrated in Figure 1.

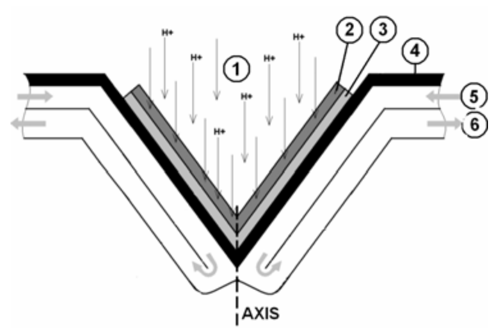


Figure 1: Protons (1) strike a 50-μm lithium metal layer (2) that is deposited on a Pd anti-blistering substrate (3), supported by a channelized conical heat exchanger (4). Coolant (5) flows through a conical-annular duct that encompasses the channels of the heat exchanger; reverses at the apex; returns via an outer conical-annular duct, and exits (6).

Design of the channelized heat exchanger was carried out with the aid of the CFD packages FLUENT, CFDesign, and COSMOS FloWorks. Simulations examined the effects of channel dimensions, number of channels, heat exchanger material, and apex-region geometry upon the coolant flow, pressure drop, and pumping power needed to meet the target surface temperature requirement. Initial studies focused on designs with straight tangential channels, but we determined that helical channels would offer superior performance (Figure 2). Copper was selected as the only viable heat exchanger material. In simulations comparing identical aluminium and copper heat exchangers, copper conferred a ~40°C target temperature improvement over aluminium for given coolant flow rates.

Modelling concluded with the acceptance of a copper heat exchanger design with 20 2-mm helical channels. According to the FloWorks models, this design will hold the target surface temperature below 150 °C by means of 80 kg $min^{-1}$ of water flow with 170 kPa pressure drop. Such a requirement is easily met with a small centrifugal pump.

*Willis.219@osu.edu

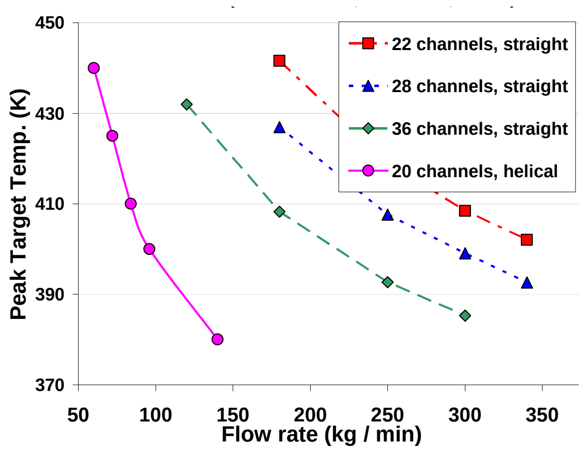


Figure 2: Predicted maximum target temperature as a function of coolant flow for various copper heat exchangers. Maximum design temperature is 420K.

Our proposed antidote to the blistering problem is a ~10-µm substrate of electroplated palladium interposed between the lithium and the heat exchanger, of sufficient thickness to encompass the Bragg peak of the beam and dissipate hydrogen either by storage or diffusion. Palladium electroplating on copper is routine. Lithium readily alloys with palladium[3], indicating that adherence is likely to be good, but raising the possibility of destructive solid phase changes.

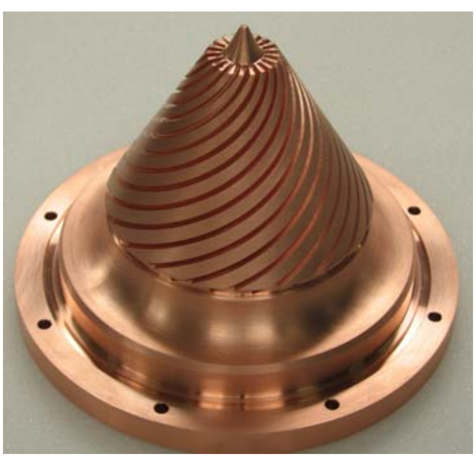

Figure 3: Channelized heat exchanger.

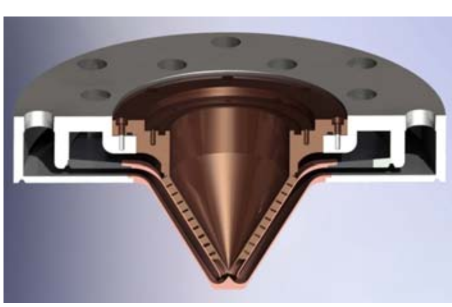

Figure 4: Manifold with target heat exchanger installed.

### Prototype Fabrication

A prototype target heat exchanger (Figure 3) and manifold (Figure 4) were constructed to experimentally validate our CFD thermal-hydraulic predictions.

The conical heat exchanger is OFE copper, while the manifold is mostly aluminium that has been electroless-nickel-plated internally to prevent galvanic corrosion. Components in the apex region of the manifold, where coolant flow is rapid and potentially erosive, are solid copper joined to the plated aluminium with low-temperature silver solder. These joints have so far proven reliable. Water enters and exits the manifold through 16 3/4-inch (1.9 cm) pipe fittings in the upstream face.

## EXPERIMENTS AND RESULTS

The prototype BNCT target has undergone limited electron-beam thermal testing with the 50-kW EB-60 electron gun at the Plasma Materials Test Facility, Sandia National Laboratories, Albuquerque, and further testing is planned. The capabilities of this unique user facility are described in detail by Youchison[4]. Linac Systems has used a homemade flow loop for preliminary hydraulic testing at its own laboratory.

### Preliminary Hydraulic Testing

A test cooling loop at Linac Systems is based upon a small centrifugal pump (Chemflo-1, MP Pumps, Inc.), transit-time ultrasonic flow meter, pressure transducers, and data-logging computer. The target and manifold were connected to this loop to produce pressure-vs.-flow data that is in good agreement with the FloWorks predictions (Figure 5).

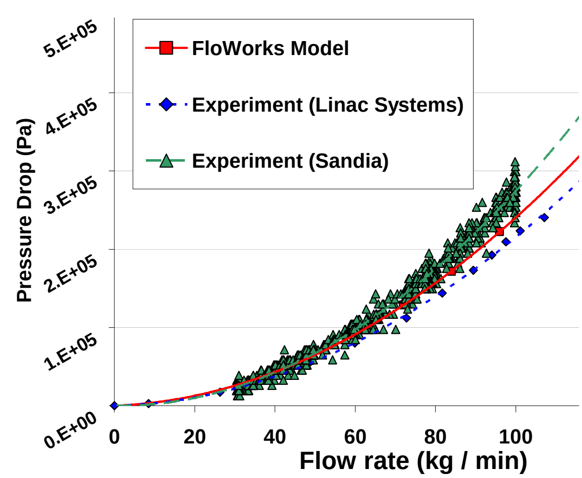


Figure 5: Pressure-flow characteristics of 20-helical-channel heat exchanger, with both CFD and experimental results. Design flow is 80 kg $min^{-1}$.

### PMTF Experiment

Manifold, target, and associated plumbing have been placed in the PMTF EB-60 vacuum chamber for testing. In this facility, a 20-keV electron gun scans a raster pattern representing the intended “waterbag” power density distribution onto the conical target surface. According to plan, two series of data will be collected: surface temperature as a function of beam power with fixed coolant flow rate; and temperature as a function of flow rate for fixed beam power. Water from a high-purity loop is used to cool the target. Absorbed power measurements are made by calorimetry on this coolant, the inlet and outlet feedthroughs being fitted with platinum RTDs.

Target surface thermographs are collected using IR cameras observing the target through ZnSe viewports. To account for the emissivity of the surface and calibrate the cameras, thermocouples are mounted in a section of the target wall.

Thus far, results from e-beam testing have been limited by some practical difficulties: a leaky weld on the manifold, and an apparent inability to produce more than 10 kW from the EB-60 gun. Alternatively, the latter observation may suggest problems with calorimetry, since the electron gun power supplies indicated that up to 30 kW has been developed.

Figures 6 and 7 show an example thermograph and radial temperature profile, respectively, of the target surface. Conditions in that experiment were 9.3 kW absorbed power, 36.7 kg min$^{-1}$ coolant flow.

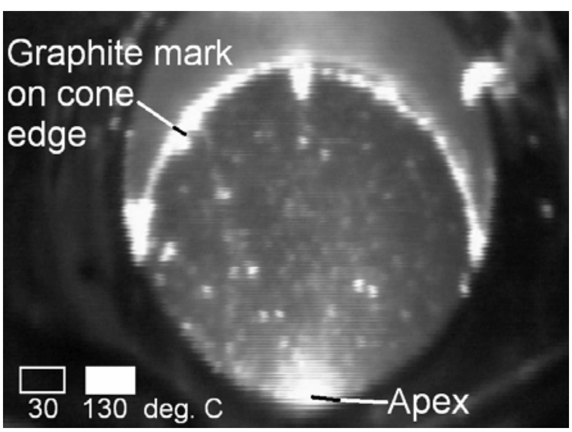


Figure 6: Thermograph of target surface.

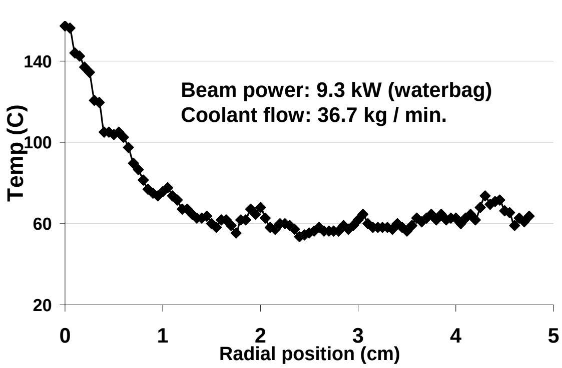


Figure 7: Target surface temperature vs. position.

## CONCLUSIONS

Electron-beam heating is an attractive tool to validate CFD models of high-power accelerator targets, particularly those whose operation would be associated with significant hazards to personnel and equipment. Linac Systems' experience with e-beam heating at PMTF is only in the incipient phase and there may be limits to the utility of the technique. These include variations in surface emissivity during testing; inaccurate power-density distributions on the concave conical surface resulting from electron scattering; or simply the inability of the PMTF guns to deliver required beam power (which so far has remained below 10 kW). We are also sceptical of the calorimetry at PMTF in our tests to date. More work needs to be done to allow us to trust thermal data from e-beam heating.

Pressure-flow characteristics of the target heat exchanger match CFD predictions. We were concerned that the fast (~ 10 m s$^{-1}$), turning flows in the apex region would be prone to cavitation, but after an estimated 10 hours of exposure to high-flow testing—including flow rates 20% higher than the estimated requirement—the target and manifold components show no signs of erosion.

In the present work we have focused on the heat removal problem. Of course many other aspects of design must be considered before a high-power lithium target for BNCT can enter clinical service, including neutronics, shielding, and the target preparation and replacement procedures. We hope to publish detail on our work in these areas soon.

## ACKNOWLEDGEMENTS

The authors are grateful for the assistance of Dennis Youchison and his staff at PMTF, Sandia National Laboratories; and the mechanical design contributions of David Sattler on this project. Carl Willis acknowledges the USDOE NE Graduate Fellowship for prior support of his work, and thanks his faculty advisors at Ohio State University for their guidance.

## REFERENCES

[1] D. Swenson, "An rf focused interdigital linac structure", Proc. LINAC2002, p. 227 (2002)
[2] S. Taskaev and B. Bayanov, "Development of lithium target for accelerator based neutron capture therapy", Proc. ICNCT-12 p. 292 (2006)
[3] T. Nohira and Y. Ito, "Thermodynamic properties of Pd-Li alloys", J. Electrochem. Soc. 125(3) p. 785 (1998)
[4] D. Youchison and J. McDonald, "High heat flux testing capabilities at Sandia National Laboratories, New Mexico", Proc. ASME Heat Transfer Division, HTD-Vol. 301, p. 31 (1994)

# BENT SOLENOID TUNING SIMULATIONS FOR THE COMET BEAMLINE.*

A. Kurup, Imperial College London, UK / FNAL, Batavia, USA

*Abstract*

The COMET experiment beamline uses bent superconducting solenoids for the muon transport and the spectrometer used to analyse the decay electrons from stopped muons. The bent solenoid includes not just a solenoid field but also a vertical dipole field. It is therefore important to have the ability to tune the field distribution. However, since the field distribution is mainly determined by the geometry it is difficult to adjust once the solenoids have been constructed. A cost effective method to provide tuning capability of the field distribution of the bent solenoids is proposed and the results of simulations presented.

## INTRODUCTION

The COMET [1] experiment aims to investigate COherent Muon to Electron Transitions by nuclear capture. This requires having a very precisely controlled muon momentum spectrum on a target that will stop the muons and the electron momentum spectrum produced by coherent $\mu \rightarrow e$ transitions needs to be accurately measured. The COMET experiment utilises bent solenoids for the muon transport and the electron spectrometer. However, helical trajectories in a curved solenoid drift in the vertical direction. In order to compensate for this vertical drift an additional dipole field in the vertical direction is applied. In the COMET design this is done in a cost effective way by tilting the solenoids. The downside to using this method is that the relative magnitude of the vertical dipole field component is given by the geometry, which is fixed after the solenoid has been manufactured. It may be necessary to tune the magnitude of the vertical dipole component after manufacture to correct for manufacturing tolerances and thermal contraction due to cooling the magnets to superconducting operating temperatures.

This paper investigates the possibility of having some control over the vertical dipole component by powering alternate solenoids with a different current. The simulations presented aim to demonstrate whether this method could provide the ability to control the momentum distribution, vertical dispersion and composition of the beam at the stopping target. For these simulations, only the muon transport has been considered and only the simple scenario where all solenoids in the bent transport channel have identical geometries and only two different power supplies are used.

* This work has been supported by The Royal Society as a joint project between Imperial College London and Osaka University. The author would also like to thank the members of the COMET collaboration for all their help.

## G4BEAMLINE FIELD DISTRIBUTION

Initial simulations were done using G4Beamline [2] by taking the existing baseline design of the COMET beamline. The geometry was altered to include the tilt of the solenoids but all other parameters were kept the same. Figure 1 shows the model that was simulated and Fig. 2 shows the tilt of the solenoids, which is $1.43°$. All the solenoids

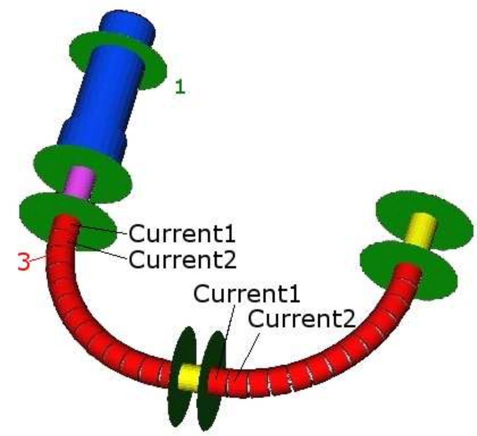


Figure 1: G4Beamline model of the muon transport channel. The blue solenoids are the pion capture channel, the red solenoids are the bent, tilted solenoids for pion decay and muon transport and the final yellow solenoids end just before the stopping target. The virtual detector (green circle) labelled 1 shows the position of the pion production target. Alternate solenoids in the transport channel (in red) were powered with a different current. Field measurements were made at the centre of the solenoid labelled 3.

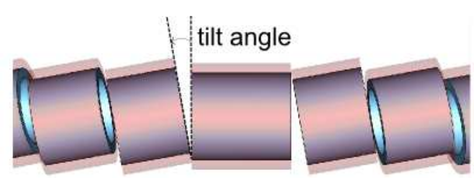


Figure 2: Drawing of the bent, tilted muon transport channel of the COMET beamline showing the tilt used to produced the vertical dipole field. The tilt angle shown here is exaggerated as the angle used in the simulations is $1.43°$.

in the G4Beamline simulations are ideal solenoids composed of infinitely-thin current sheets. Four different scenarios for powering the bent, tilted solenoids were investigated, see Table 1.

Table 1: Values for Current1 and Current2 used in the simulations. Current1 was applied to every other solenoid starting with the first one and Current2 was applied to the other solenoids, see Fig. 1.

| | **Current1 (A)** | **Current2 (A)** |
|---|---|---|
| 1 | 631890 | 631890 |
| 2 | 758268 | 758268 |
| 3 | 631890 | 1263780 |
| 4 | 631890 | 315945 |

Figure 3 shows the $B_x$, $B_y$ and $B_z$ field components at the centre of the third solenoid (labelled 3 in Fig. 1) for the different powering schemes. The $z$ direction is parallel to the axis of each solenoid and the $x$ axis is in the plane of the bend. As can be seen, by supplying alternate solenoids with a different current it is possible to adjust, to some extent, the vertical dipole component (i.e. $B_y$) independently.

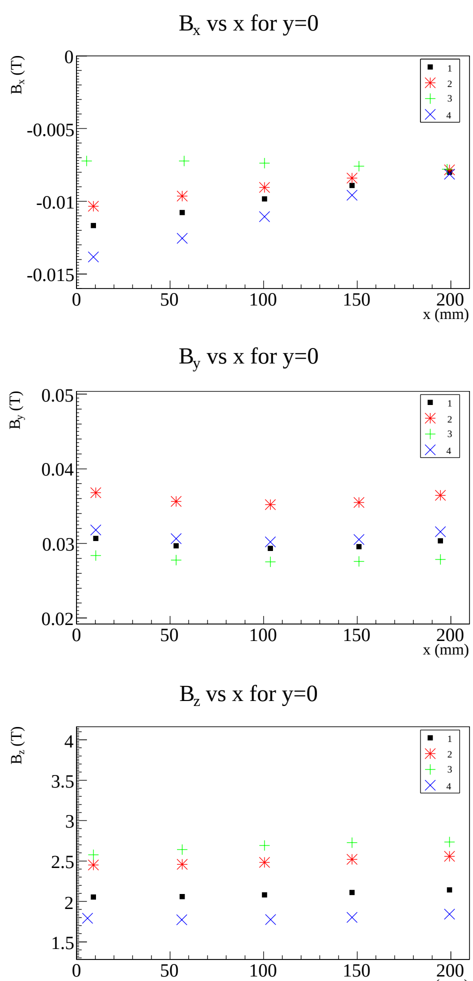


Figure 3: Results of the G4Beamline simulation. The plots show the $B_x$,$B_y$ and $B_z$ components as a function of x for the different powering schemes described in Table 1.

## EM STUDIO FIELD DISTRIBUTION

To obtain a more accurate field distribution of the beamline, a 3-D magnetostatic simulation using EM Studio [3] was done. The geometry was kept the same as in the G4Beamline simulations. Preliminary designs of the superconducting solenoids have a non-magnetic steel wall inside the coils and an iron yoke outside. To obtain a comparison with the G4Bemaline model the iron yoke was not considered and the permeability of the steel was set to 1.

Figure 4 shows the $B_x$, $B_y$ and $B_z$ field distributions, for the same location as in the G4Beamline simulation, for the same four current scenarios listed in Table 1. The

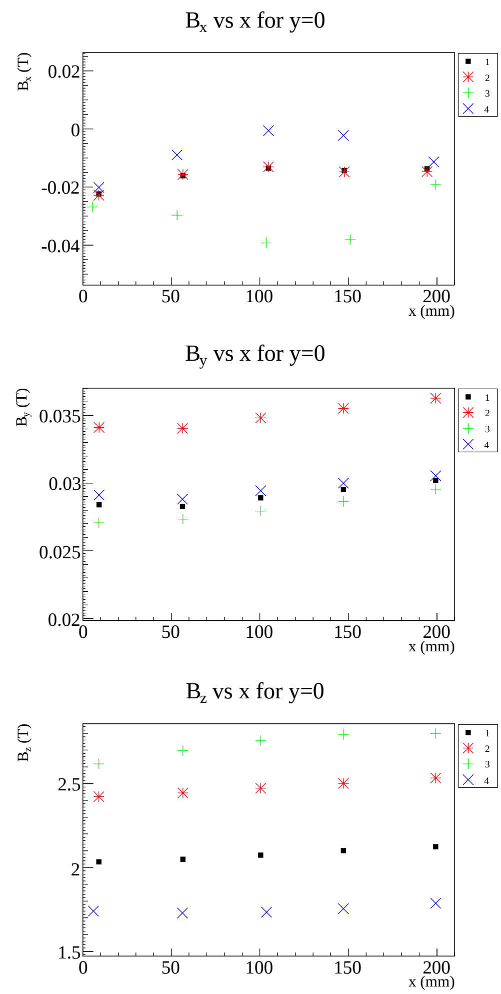


Figure 4: Results of the EM Studio simulation. The plots show the $B_x$,$B_y$ and $B_z$ components as a function of x for the different powering schemes described in Table 1.

$B_y$ and $B_z$ components show good agreement with the G4Beamline simulation but the $B_x$ component shows significant differences, though the absolute magnitude of the differences are small. This is likely due to the way in which fringe fields are considered in G4Beamline. However, the fact that the $B_x$ component in the EM Studio simulations does not follow the same trend as in the G4Beamline simulations will complicate tuning the beam transported by the channel.

## PARTICLE TRACKING

To understand the effect of altering the field in the solenoids, some preliminary tracking studies have been done using the G4Beamline model of the muon transport channel. Initially, a simple muon beam was tracked through $90°$ of the bent solenoid. The input beam contained on-axis, parallel muons with a momentum range of 10–150 $MeV/c$. Figure 5 shows the momentum distribution as a function of the vertical position after the muons were tracked through half of the bent solenoid. This figure shows that it is possible to affect the vertical dispersion produced by the transport channel by powering alternate solenoids with a different current.

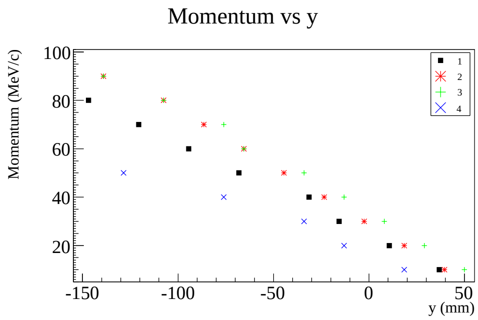


Figure 5: Momentum as a function of vertical position for an on-axis,parallel muon beam with a momentum range of 10–150 $MeV$.

Since the COMET experiment requires a very low background rate it is important to track particles using a realistic beam to determine to composition of the beam at the stopping target. An input beam produced by a MARS [4] simulation of 8 $GeV/c$ protons on a graphite target was tracked through the whole G4Beamline model. Figure 6 shows the momentum distribution of muons and Table 2 shows the composition of the beam at the stopping target for the different current scenarios.

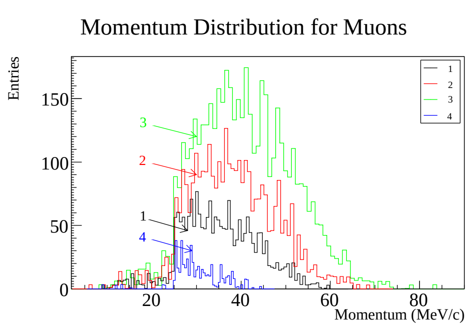


Figure 6: Momentum distribution of muons at the end of the muon transport channel for the different scenarios.

Table 2: Fractional beam composition at the stopping target for the four different scenarios.

| | $\mu^-$ | $\mu^+$ | $e^-$ | $e^+$ | $\pi^-$ | $\pi^+$ | $p^+$ |
|---|---|---|---|---|---|---|---|
| 1 | 0.89 | 0.02 | 0.055 | 0.030 | 0 | 0 | 0.0024 |
| 2 | 0.89 | 0.011 | 0.072 | 0.029 | 0 | 0 | 0.001 |
| 3 | 0.91 | 0.014 | 0.063 | 0.009 | 0 | 0 | 0.0006 |
| 4 | 0.96 | 0.027 | 0 | 0 | 0.018 | 0 | 0 |

Although it is possible to affect the momentum distribution of muons at the stopping target by powering alternate solenoids with a different current, the change in the muon yield is quite significant. This may be detrimental if tuning the solenoid requires reducing the current.

## CONCLUSIONS

By powering alternate solenoids with a different power supply it is possible to independently control the vertical dipole component of the bent, tilted solenoids. The simulations using EM Studio show deviations of the $B_x$ component compared to the G4Beamline solenoid model. To make the model more accurate it will be necessary to include the iron yoke. The effect of this on the transport of particles will need to be investigated. Thus, tracking with a field map from the EM Studio simulations is essential.

It is also important to study the mechanical forces applied to the support structure of the solenoid as having significantly different currents in adjacent solenoids may put significant additional stress on the support structure.

As the next step, it will be useful to study the effect of thermal contraction on an optimised version of the muon transport channel, tuning of the momentum spectrum to obtain the best yield and apply this method to the electron spectrometer to allow tuning of the momentum selection.

## REFERENCES

[1] The COMET Collaboration, "An Experimental Search for Lepton Flavor Violating $\mu^- \to e^-$ Conversion at Sensitivity of $10^{-16}$ with a Slow-Extracted Bunched Proton Beam", http://j-parc.jp/NuclPart/pac_0801/pdf/Kuno.pdf

[2] Thomas J. Roberts *et al.*, "G4beamline Particle Tracking in Matter-Dominated Beam Lines", EPAC'08, Genoa (2008), p. 2776.

[3] Computer Simulation Technology (CST) Electro-magnetic Studio, http://www.cst.com/Content/Products/EMS/Overview.aspx

[4] N.V. Mokhov, S.I. Striganov, "MARS15 Overview", AIP Conf. Proc. **896** (2007), p. 50.

# STATUS OF MICE: THE INTERNATIONAL MUON IONIZATION COOLING EXPERIMENT

Dazhang Huang#, Daniel M. Kaplan, IIT, Chicago, IL 60616 USA
Michael S. Zisman, LBNL, Berkeley, CA 94720 USA

*Abstract*

A key unanswered question in particle physics is why the universe consists only of matter. It is believed that CP violation in the lepton sector is the answer. The best tool to find this is a muon-based neutrino factory. Muons can also be used for an energy-frontier collider that would fit on an existing laboratory site. Since muons are produced as a tertiary beam, their phase space and energy spread are large and must be reduced (cooled) to create a usable beam. Ionization cooling, comprising momentum loss in material followed by RF reacceleration, is the only suitable technique. A transverse cooling channel is merely a linac with absorbing material in the beam path. To demonstrate an understanding of the physics and technology issues, MICE will test a section of cooling channel exposed to a muon beam derived from the ISIS synchrotron at RAL. The muon beam line is now installed and commissioning is under way. Fabrication of cooling-channel components and the required detector systems has begun. A successful demonstration will go a long way toward proving the value of muon beams for future accelerator-based particle physics experiments.

## INTRODUCTION

Muon ionization cooling is the only practical method for preparing high-brilliance beams needed for a neutrino factory or muon collider. It reduces the transverse phase space of muons sufficiently to permit subsequent acceleration and storage in a practical acceleration system. This key enabling technology will be demonstrated experimentally for the first time in the Muon Ionization Cooling Experiment (MICE).

MICE is an experimental program to establish the feasibility and performance of ionization cooling. The approach is to measure precisely the emittance of 140–240 MeV/c muon beams both before and after an ionization-cooling cell. Implementing such a system will tell us about the subtleties of fabrication of the required components and, after comparing our results with detailed simulation predictions, will provide a validated tool for designing and optimizing the performance of a future neutrino factory and/or muon collider cooling channel.

The experiment is currently under construction at the Rutherford Appleton Laboratory (RAL) in the UK.

## MICE BEAM LINE AND SCHEDULE

The secondary muon beam line at RAL's ISIS synchrotron is being built to meet the needs of MICE. The line will provide muon beams in the range of 140–240 MeV/c momentum, with normalized transverse emittance values in the range of 1–10 π mm-rad. The muon beam will be momentum-selected and transported to the MICE apparatus (see Fig. 1). Particle identification ensures better than 99.9% muon purity. Via magnet settings and a Pb diffuser of adjustable thickness, the transverse emittance of the input muon beam can be tuned. The input 6D emittance is measured [1] in a magnetic spectrometer comprising a five-station scintillating-fiber tracker mounted within a 4 T superconducting (SC) solenoid. The tracker determines $x$, $x'$, $y$, $y'$, and particle energy. The time-of-flight (TOF) counters measure the sixth phase space coordinate, $t$. The cooling cell consists of low-$Z$ absorbers and normal conducting (NC) RF cavities, along with SC coils to provide strong focusing for the beam. The final emittance is measured in a second spectrometer system identical to the first one. Electrons from muon decay are eliminated from the data by calorimetry.

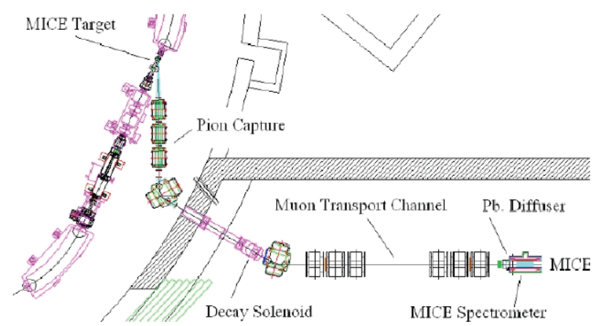


Figure 1: MICE beam line at ISIS, with two bending magnets and three quadrupole triplets.

The most important part of MICE is the cooling cell (see Fig. 2). It comprises three absorber–focus-coil (AFC) modules [2,3] and two RF–coupling-coil (RFCC) modules [4] (Fig. 3). Each hydrogen absorber contains about 20 L of liquid and is enclosed within a pair of room-temperature safety windows (Fig. 4) [5].

A pair of focus coils is employed to focus the muon beam, which results in a low equilibrium emittance for the channel. While hydrogen is best, for emittance far from equilibrium, a more practical absorption medium may be LiH, or Be. MICE is therefore designed to test both liquid and solid absorbers over a range of beta-function values. Critical hydrogen system issues are:

1. safety
2. use of the thinnest possible metal containment windows
3. hydrogen storage

A commercial metal-hydride storage system will be tested at RAL.

# huangd@iit.edu

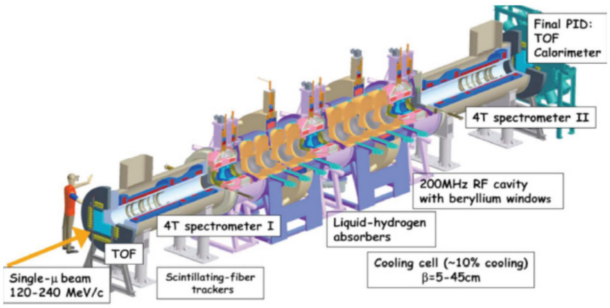


Figure 2: Cutaway view of the MICE cooling channel.

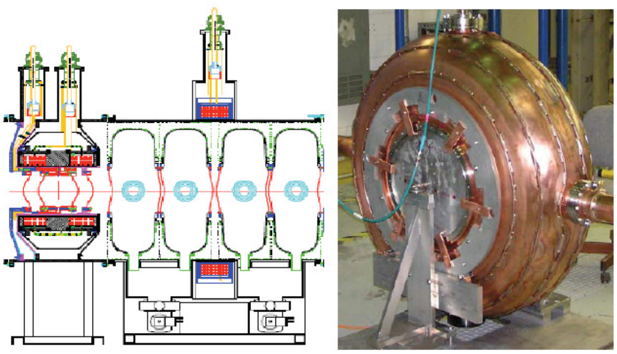

Figure 3: (left) Schematic diagram of AFC module connected to RFCC module, with cavities closed by curved Be windows; (right) a photo of the 201 MHz prototype cavity.

Since the beam to be cooled is large, the RF frequency must be low; due to the focusing magnetic field, NC cavities must be used to restore the energy lost in cooling. The eight 201 MHz RF acceleration cavities are very similar to the prototype cavity being tested in the MuCool Test Area (MTA) at Fermilab, and each will have Be windows on the beam apertures to close the cavity electro-magnetically. This is acceptable in a muon channel since the muons only interact weakly with material in their path. Compared with an open-cell cavity design, this method greatly improves the accelerating gradient of the cavity and is able to achieve ~18 MV/m in the 201 MHz cavity and ~40 MV/m in an 805 MHz ¼-scale prototype cavity with no magnetic field.

Although conceptually simple, both ionization cooling and its experimental verification pose challenges:

1. Operation of high-gradient (≈16 MV/m), low-frequency (201 MHz) RF cavities in strong (1–3 T) magnetic fields.
2. Safe designs employing substantial amounts of $LH_2$ near potential ignition sources.
3. The small effect (≈10%) of an affordable cooling device that leads to the goal of $10^{-3}$ emittance precision, requiring single-particle measurements rather than standard beam instrumentation.

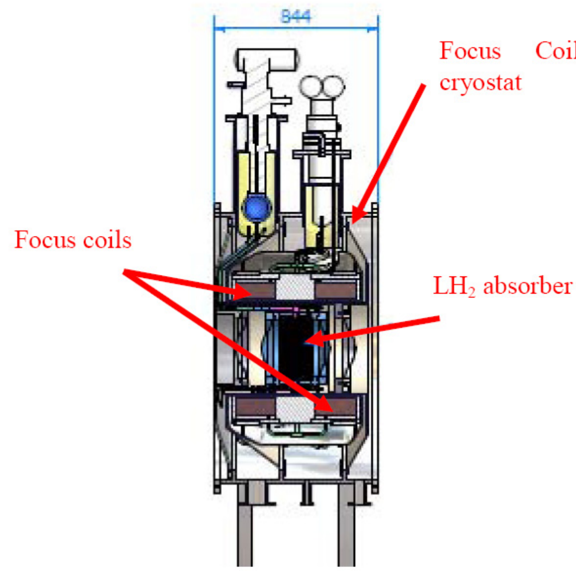


Figure 4: Side view of absorber–focus-coil module.

The staging of MICE (Fig. 5) allows careful calibration at each step and also reflects funding realities. Beam characterization and data acquisition have begun. Measurements of particle momenta and emittance will be possible once the first spectrometer solenoid is available. In Step III, up- and downstream emittance measurements will be precisely compared, which allows a precise determination of biases and testing of the required correction procedures. Step V will test "repeatable" cooling, in which the momentum lost in the absorbers is restored in the RF cavities. Step VI will test the full cooling cell.

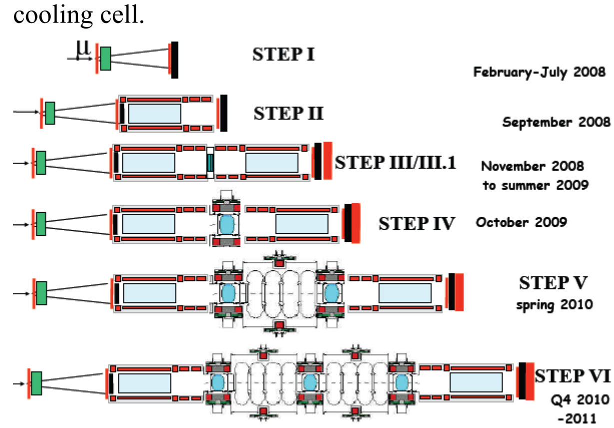


Figure 5: The planned stages of MICE.

## CURRENT STATUS

The beam line is now operational. The pions from a small, movable Ti target grazing the ISIS proton beam during its 2 ms flattop are captured by a quadrupole triplet and momentum-selected by a dipole magnet. Muons from pions decaying within a 5 T solenoid of 5 m length and 12 cm bore are momentum-selected in a second dipole at a momentum about half that of the pions. Two aerogel

Cherenkov counters and TOF0 (Fig. 6) are placed between quadrupole triplets 2 and 3. Three two-layer scintillator-hodoscope TOF stations each provide 50 ps resolution.

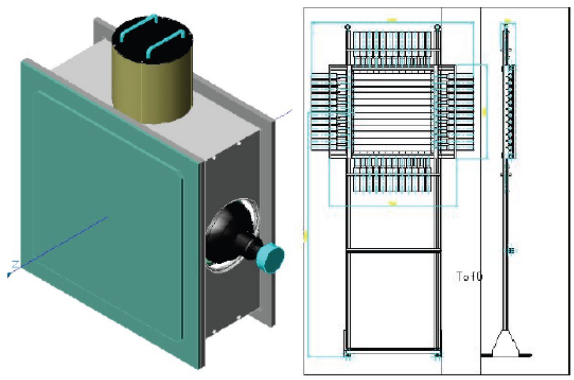

Figure 6: MICE upstream (Cherenkov and TOF) particle ID detectors.

The 2-m-long spectrometer solenoids (Fig. 7) will provide 4 T over a 1-m-long, 20-cm-radius tracking volume. Two end coils ensure <1% field non-uniformity and two matching coils at one end match optics in and out of the cooling cell. The magnets are on order for late-2008 delivery. This will be followed by field measurement and installation at RAL. Magnet sensors will monitor the field. Scintillating-fiber tracker 1 is completed and undergoing cosmic-ray testing and tracker 2 is in final assembly.

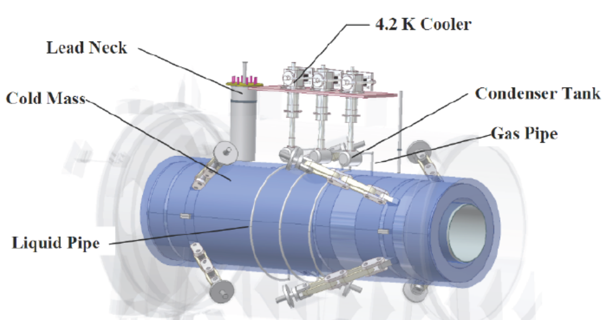


Figure 7: Schematic of spectrometer solenoid.

Downstream particle ID comprises TOF2 and a calorimeter to distinguish muons from decay electrons. A Pb–scintillating-fiber sandwich layer precedes a ≈1 $m^3$, fully sensitive, segmented scintillator block. The sandwich layer degrades electrons; the scintillator block precisely measures muon range. Prototypes have been tested and assembly of final detectors is in progress.

Currently, a CERN-refurbished 4 MW RF power source plus two 2-MW RF sources donated by LBNL give 8 MW in total, allowing 23 MeV of acceleration in MICE Step VI. The coupling coils are being constructed at the Institute of Cryogenics and Superconductivity Technology (ICST) of the Harbin Institute of Technology in China, in collaboration with LBNL. Crucial high-magnetic-field cavity tests await delivery of the first coupling coil.

MICE will run at ≈ 1 Hz and record up to 600 muons in each 1 ms beam burst. RF amplitude and phase, absorber mass, and other parameters must be precisely known for comparison with predictions and simulations. State-of-the-art instrumentation will monitor and record the relevant parameters.

MICE beam line commissioning started in February, 2008. The production rates of various particles, such as protons and pions, have been measured and particle identification has been made by means of Cherenkov light and time-of-flight measurements. Some representative results are given in Fig. 8, which demonstrates particle identification of both protons and pions.

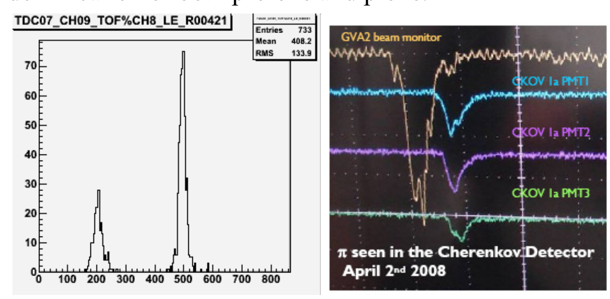


Figure 8: Representative MICE results. (left) Pions and protons separated through the time-of-flight with 414 MeV/c proton momentum at the first bending magnet; the left peak is pions, and the right peak is protons. (right) Cherenkov photomultiplier tube signals in coincidence with pulses from the second scintillating paddle indicating the passage of pions [6].

## ACKNOWLEDGMENTS

Work supported by Department of Energy under contract DE-AC02-05CH11231, DE-FG02-01ER41159 and National Science Foundation grant PHY-031737

## REFERENCES

[1] T. Hart and D. Kaplan, “Emittance Measurement in MICE,” ICHEP08, 2008.
[2] M. Cummings and S. Ishimoto, “Progress on the Liquid Hydrogen Absorber for the MICE cooling Channel,” PAC05, May 2005.
[3] S. Q. Yang *et al.*, “Progress on the Focus Coil for the MICE Channel,” PAC05, May 2005.
[4] D. Li *et al.*, “Progress on the RF Coupling Coil Module Design for the MICE Channel,” PAC05 May 2005.
[5] M. Zisman, “Status of the International Muon Ionization Cooling Experiment (MICE),” PAC07, June 2007.
[6] T. Hart, “MICE: The International Muon Ionization Cooling Experiment: Diagnostic Systems,” EPAC08, June, 2008.

# HIGH GRADIENT EXCITATION AND RF POWER GENERATION USING DIELECTRIC LOADED WAKEFIELD STRUCTURES*

M.E. Conde#, S. Antipov, F. Franchini, W. Gai, R. Konecny, W. Liu, J.G. Power, Z. Yusof, ANL, Argonne, IL 60439, U.S.A.
F. Gao, IIT, Chicago, IL 60616, U.S.A.
C. Jing, Euclid Techlabs LLC, Solon, OH 44139, U.S.A.

*Abstract*

Dielectric loaded wakefield structures are being developed to be used as high gradient accelerator components. The high current electron beam at the Argonne Wakefield Accelerator Facility (AWA) was used to excite wakefields in cylindrical dielectric loaded wakefield structures in the frequency range of 8 to 14 GHz, with pulse duration of a few nanoseconds. Short electron bunches (13 ps FWHM) of up to 86 nC drove these wakefields, and accelerating fields as high as 100 MV/m were reached. Similar structures were used to extract RF power from the electron beam; however, in this case they were traveling-wave structures, driven by electron bunch trains of up to 16 bunches. RF pulses of up to 40 MW were measured at the output coupler of these structures. The AWA electron beam was also used to drive the cavity modes in a metallic standing-wave structure designed and built by SLAC / KEK (originally meant to be powered by a klystron).

## INTRODUCTION

The Argonne Wakefield Accelerator Facility (AWA) is dedicated to the study of electron beam physics and the development of accelerating structures based on electron beam driven wakefields [1]. In order to carry out these studies, the facility employs a photocathode RF gun capable of generating electron beams with high bunch charges and short bunch lengths (up to 100 nC with a bunch length of 13 ps FWHM). This high intensity beam is used to excite wakefields in the structures under investigation. The wakefield structures presently under development are dielectric loaded cylindrical waveguides with operating frequencies between 8 and 14 GHz.

The facility is also used to investigate the generation and propagation of high brightness electron beams, and to develop novel electron beam diagnostics.

The AWA electron beam is also used in laboratory-based astrophysics experiments; namely, measurements of microwave Cherenkov radiation and beam induced fluorescence of air [2].

## AWA FACILITY

The AWA high intensity electron beam is generated by a photocathode RF gun, operating at 1.3 GHz. This one-and-a-half cell gun typically runs with 12 MW of input power, which generates an 80 MV/m electric field on its Magnesium cathode surface. A 1.3 GHz linac structure increases the electron beam energy, from the 8 MeV produced by the RF gun, to 15 MeV. The charge of the electron bunches can be easily varied from 1 to 100 nC, with bunch lengths of 2 mm rms, and normalized emittances of 30 to 200 $\pi$ mm mrad.

The AWA laser system consists of a Spectra Physics Tsunami oscillator followed by a Spitfire regenerative amplifier and two Ti:Sapphire amplifiers (TSA 50). It produces 1.5 mJ pulses at 248 nm, with a pulse length of 2 to 8 ps FWHM and a repetition rate of up to 10 pps. A final KrF Excimer amplifier is optionally used to increase the energy per pulse to 15 mJ. The generation of electron bunch trains (presently up to 16 bunches) requires each laser pulse to be divided by means of beam splitters into a laser pulse train.

## HIGH GRADIENT WAKEFIELD GENERATION

We have recently built and tested four dielectric loaded wakefield structures. Each one consists of a cylindrical dielectric tube inserted into a cylindrical copper waveguide. The dielectric material is either a ceramic known as cordierite, or quartz. The insertion of metallic end-pieces with a cut-off frequency above the operating frequency, makes these devices operate as standing-wave structures. A weakly coupled field probe (-60 dB) near the outer diameter of the dielectric cylinders serves to monitor the wakefields generated by the driving electron bunches, and to verify the absence of electric breakdown. Table 1 shows some parameters of four wakefield structures tested.

Table 1: Parameters of Standing-Wave Structures

| SW Structure | # 1 | # 2 | # 3 | # 4 |
|---|---|---|---|---|
| Material | Cordierite | Cordierite | Cordierite | Quartz |
| Dielectric constant | 4.76 | 4.76 | 4.76 | 3.75 |
| Freq. of TM01n | 14.1 GHz | 14.1 GHz | 9.4 GHz | 8.6 GHz |
| Inner radius | 5 mm | 5 mm | 2.75 mm | 1.9 mm |
| Outer radius | 7.49 mm | 7.49 mm | 7.49 mm | 7.49 mm |
| Length | 102 mm | 23 mm | 28 mm | 25.4 mm |
| Maximum charge | 46 nC | 86 nC | 86 nC | 75 nC |
| Maximum gradient | 21 MV/m | 43 MV/m | 78 MV/m | 100 MV/m |

*Work supported by the U.S. Department of Energy under contract No. DE-AC02-06CH11357.
#conde@anl.gov

Table 1 also lists the maximum bunch charge that traversed each structure, and the accelerating gradient generated in the structure by its passage. These values of gradient result from numerical calculations with the software MAFIA, using the known parameters of the structures and of the electron bunches. The amplitude of the field probe signals are not a reliable way to measure the field gradients, because the calibration of the probe cannot be made accurately enough for the different modes supported by the structures. Thus, the field probe signals are used solely to monitor possible electric breakdown events in the structures.

The field probe signal can be sent directly to a high bandwidth oscilloscope (Tektronix TDS-6154C; 15 GHz bandwidth). Figure 1 shows this signal and its FFT, as seen when electron bunches propagate through structure #4. Due to the field probe geometry, its signal is basically proportional to the radial electric field present at the tip of the probe. A comparison of the FFT of the signal with numerical simulations allows the different peaks to be identified with the various modes supported by the structure.

## POWER EXTRACTOR FOR TWO-BEAM-ACCELERATION

The development of the necessary components for two-beam-acceleration experiments is being pursued. Thus, we recently tested a decelerating structure, which has an RF power output coupler as an integral part of the structure. The drive beam of a two-beam-accelerator (TBA) would traverse this so-called power extractor, and the generated RF power would then be coupled out of the decelerator and into the accelerating structure.

This power extractor was installed on the AWA drive beamline, and a calibrated bi-directional RF coupler was connected to its output coupler, to enable the measurement of the RF power generated by the beam.

Single electron bunches were initially put through this structure, generating short RF pulses (about 2 ns FWHM) with a frequency spectrum centered at 7.8 GHz. A maximum peak power of 30 MW was generated by electron bunches of 66 nC. Subsequently, bunch trains consisting of 16 electron bunches were used to generate longer RF pulses; these electron bunches were either spaced by six RF periods of the 7.8 GHz wakefield (one RF period of the 1.3 GHz RF gun), or by twelve periods of the 7.8 GHz wakefield (two RF periods of the 1.3 GHz RF gun). Due to the finite group velocity of the RF packets in the structure, the superposition of the RF fields of the individual bunches involves fewer bunches when they are spaced further part. Figure 2 shows a series of oscilloscope traces from the bi-directional coupler signal, for an increasing number of electron bunches, each separated by six RF periods. Obviously, the larger number of bunches generate longer RF pulses, with narrower frequency spectra. Figure 3 shows the bi-directional coupler signal generated by bunch trains in which the bunches are separated by twelve RF periods. In this case, longer RF pulses are generated, but due to the effective superposition of fewer pulses, the amplitude of the RF pulse is smaller, for a given bunch charge.

The highest power generated by this structure was 44 MW, of which 40 MW were actually coupled out, the difference being accounted for by losses in the output coupler. This was achieved with four electron bunches spaced by six RF periods, with a total charge of 107 nC; in this case the pulse length was approximately 4 ns FWHM.

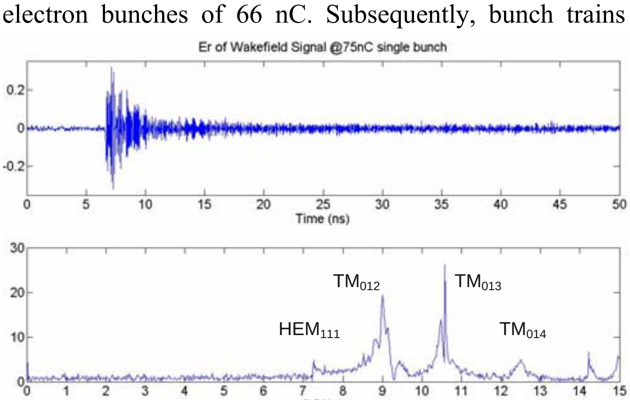


Figure 1: Measurement of the radial electric field driven by a 75 nC electron bunch, using the field probe on Structure 4: (a) temporal profile of the radial electric field; (b) the FFT of the signal.

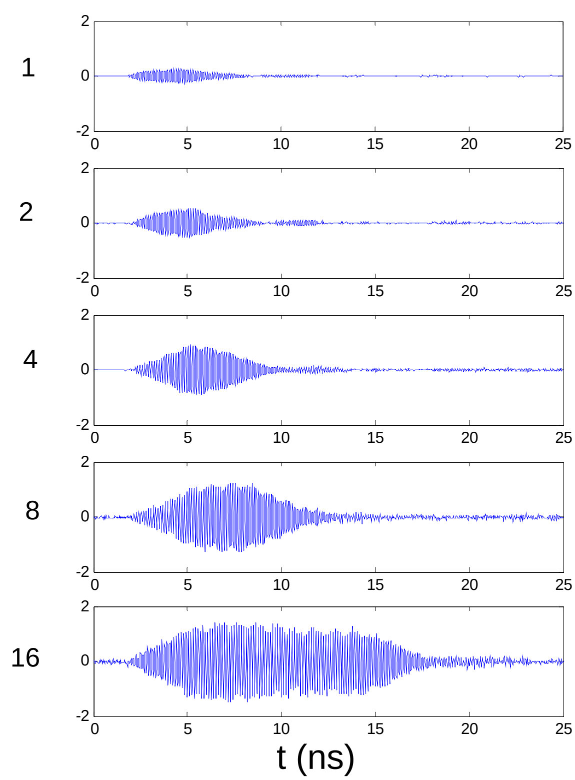


Figure 2: Oscilloscope traces showing the RF pulses sampled by the bi-directional coupler. The number on the left side of the plots indicates the number of electron bunches that propagated through the power extractor.

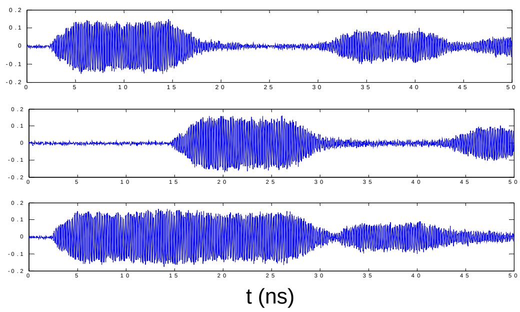


Figure 3: Oscilloscope traces showing the RF pulses sampled by the bi-directional coupler: (a) eight bunches spaced by twelve RF periods; (b) later set of eight bunches spaced by twelve RF periods; (c) sixteen bunches spaced by twelve RF periods.

## SLAC / KEK STRUCTURE

Recently, we have performed an experiment at AWA using a metallic iris loaded standing wave X-band structure developed by SLAC and KEK, which was originally meant to be powered by a klystron. The structure, installed in the AWA drive beamline, is shown in Fig. 4. A bidirectional coupler at the coupling port allows the measurement of the wakefields excited by the passage of the drive electron bunch (Fig. 5). The estimated peak wakefield generated is about 50 MV/m for a bunch charge of 80 nC. Also from the figure, a loaded quality factor Q of about 5500 can be estimated. Figure 6 shows the peak electric field measured at the bidirectional coupler as a function of the drive bunch charge; the deviation from the initial linear dependence is due to the slight bunch lengthening that occurs as the bunch charge is increased. One could increase the gradient to much higher levels by using a multiple bunch drive beam. We believe this is an effective way to test properties of high gradient structures, including the excitation of higher order modes.

## NEXT STEPS

In the immediate future, the development of dielectric loaded structures will proceed, as well as the testing of more X-band metallic structures driven as wakefield devices: a photonic band-gap structure and more iris loaded standing wave structure (built by SLAC / KEK). A

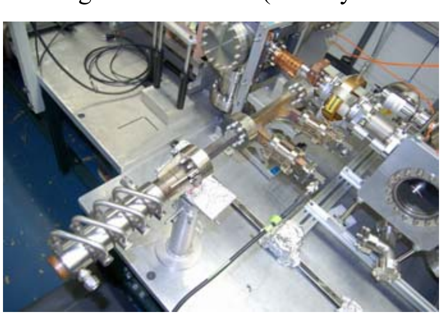

Figure 4: SLAC / KEK X-band structure installed at the AWA beamline.

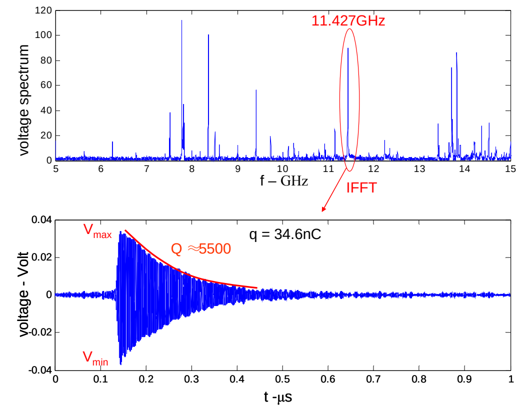


Figure 5: Wakefields observed at bidirectional coupler: (a) FFT of voltage signal; (b) IFFT of 11.4 GHz component only.

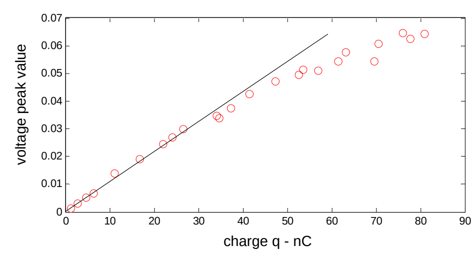


Figure 6: Peak electric field measured at the bidirectional coupler as a function of the drive bunch charge.

new RF power station, now under fabrication, with an additional 30 MW L-band klystron (on loan from LANL – many thanks!) will greatly increase the capabilities of the AWA facility, by increasing the drive beam energy and enabling experiments with smaller diameter structures. This additional RF power will also allow the operation of a second RF gun, now under fabrication, which will provide the witness beam to directly probe the generated wakefields. The development of a Cesium Telluride photocathode fabrication chamber, now in its final stages, will enable the generation of longer electron bunch trains, with high charge per bunch, which will produce longer wakefield RF pulses with even higher amplitude. The goal is to reach gradients on the order of 0.5 GV/m, and to be able to generate RF pulses with GW power level.

## REFERENCES

[1] M.E. Conde et al., “The Argonne Wakefield Accelerator Facility: Capabilities and Experiments,” Proceedings of the 2004 Advanced Accelerator Concepts Workshop, June 2004.

[2] M. Ave et al., “Measurement of the pressure dependence of air fluorescence emission induced by electrons,” Astropart. Phys. 28 (2007) 41.

# TRAINS OF SUB-PICOSECOND ELECTRON BUNCHES FOR HIGH-GRADIENT PLASMA WAKEFIELD ACCELERATION

P. Muggli, UCLA, Los Angeles, California;
M. Babzien, BNL, Upton, Long Island, New York;
M.J. Hogan, SLAC, Menlo Park, California;
E. Kallos, USC, Los Angeles, California;
K. Kusche, J.H. Park, V. Yakimenko, BNL, Upton, Long Island, New York

*Abstract*

In the plasma wakefield accelerator (PWFA), high quality accelerated electron bunches can be produced by injecting a witness bunch behind a single drive bunch or a train of N bunches. To operate at large gradient the plasma density must be in the $10^{17}$/cc range, corresponding to a typical bunch separation of the order of the plasma wavelength or ~100$\mu$m. We have demonstrated that such a subpicosecond temporal bunch structure can be produced using a mask to selectively spoil the emittance of temporal slices of the bunch*. The bunches spacing, as well as their length can be tailored by designing the mask and choosing the beam parameters at the mask location. The number of bunches is varied by using an adjustable width energy limiting slit. The bunches spacing is measured with coherent transition radiation interferometry. Experimental results will be presented and compared to simulations of the bunch train formation process with the particle tracking code ELEGANT.

* P. Muggli *et al.*, to appear in Phys. Rev. Lett. (2008).

**CONTRIBUTION NOT RECEIVED**

# BEAM DYNAMICS SIMULATIONS FOR A 15 MEV SUPERCONDUCTING ELECTRON LINAC COUPLED TO A DC PHOTO-INJECTOR

D. Guilhem, J-L. Lemaire, S. Pichon
CEA, Département de Physique théorique et Appliquée
Bruyères Le Châtel, 91297 Arpajon, Cedex, France


## Abstract

A 15 MeV accelerator scheme based on a DC photo-injector and a RF superconducting linac has been proposed as a new facility for radiography applications.

The beam operating condition is a limited number of bunches up to twenty electron micro-pulses of 100 ps time duration and 200 nC bunch charge at 352 MHz repetition rate.

The overall beam dynamics simulation process based on LANL POISSON-SUPERFISH and PARMELA codes, is presented and the results will be reviewed.


## INTRODUCTION

A new versatile scheme based on well-tested technologies has been studied in the purpose to produce flash X-ray pulses from very intense electron beams impinging a high Z material target [1].

This machine consists to a DC photo-injector coupled to a RF superconducting accelerator. A final beam transport allows tight beam focusing on the target. Electrons bunches are emitted from a photocathode driven by a 266 nm wavelength laser and extracted up to the_energy of 2.5 MeV in a DC gun. The beam is accelerated in a 352 MHz RF-cavity to a final energy of 15MeV (Fig. 1). Among several applications, one requires a total accelerated charge of 1μC. In this scope, we studied two beam distributions in time: either ten electron bunches carrying 100 nC each (pulse time duration of 28 ns) or five electron bunches carrying 200 nC each (pulse time duration 13 ns).

Beam dynamics have been computed using a simulation chain based on LANL codes POISSON-SUPERFISH [2] and PARMELA [2]. The optimizations of the photo-injector beam transport and the final focusing on the target are presented. The results for the whole machine simulation are reviewed for the two different configurations.

## BEAM DYNAMICS CHART

Our beam dynamics study is based on the LANL POISSON-SUPERFISH and PARMELA codes. We have linked them together through a graphical interactive interface which was developed specifically for this use (Fig. 2). POISSON-SUPERFISH first computes electromagnetic field maps of the photo-injector, the RF cavity and final focusing. These results are used as input data in PARMELA to calculate the beam dynamics along the machine. We have developed coupling and post processing tools compatible with CEA-PLOTWIN software (*.plt) [3] which allows powerful, interactive and friendly viewing of the beam behaviour.

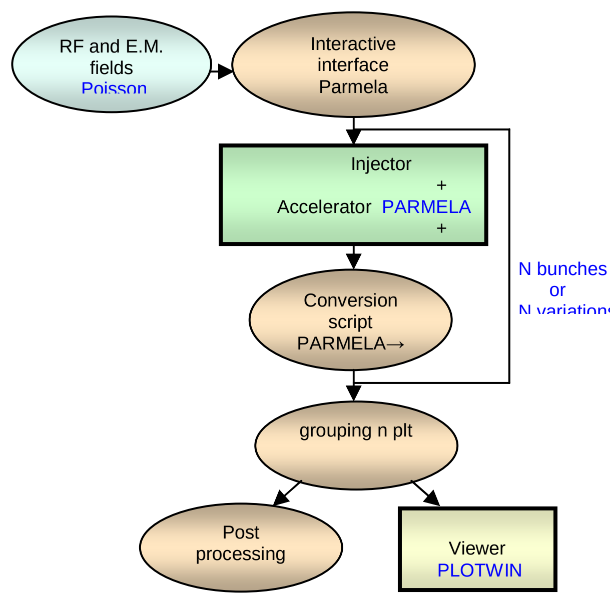


Figure 2: Beam dynamics simulation chart.

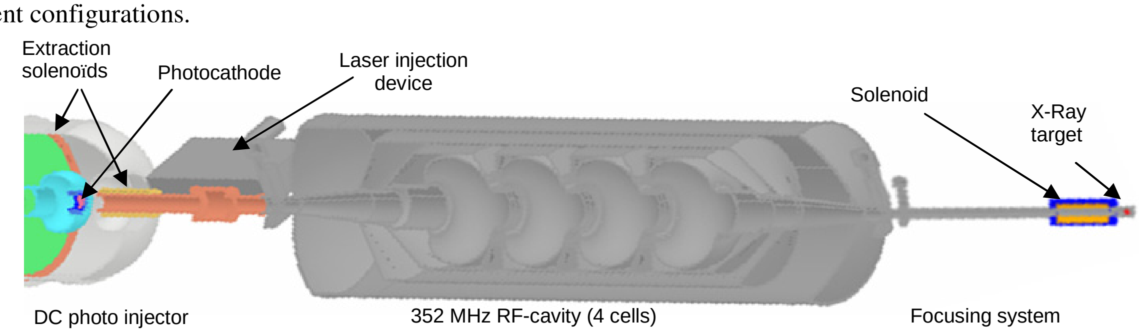


Figure 1: Scheme for the 15MeV RF proposed machine.

For identical beam input conditions, comparisons with other codes (MAGIC, PARTRAN) and experimental validations have been carried out in order to validate this beam simulation scheme.

## PHOTO-INJECTOR OPTIMIZATION

The photo-injector [4] delivers to the linac the required 2.5 MeV pulsed e-beam with the smallest achievable emittance. Every bunch is emitted at 352 MHz and has an initial uniform transverse distribution as well as a 100 ps FHWH time Gaussian distribution.
The photocathode shape, the electrode geometry and the focusing lens contribute to the beam quality (Fig. 3). A cathode recess and the magnetostatic focusing system have been optimized to deal with the space charge effect at the emission and during extraction.

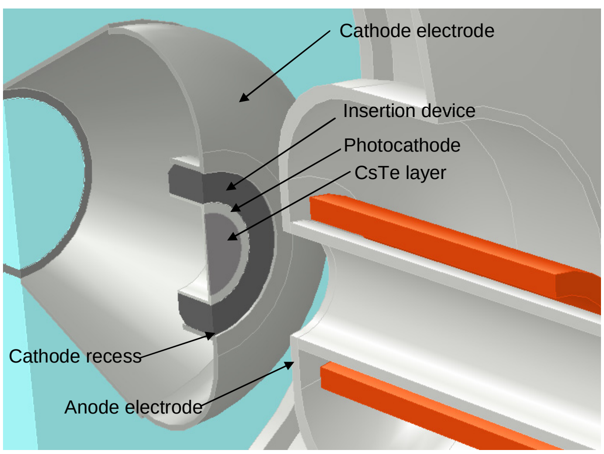


Figure 3: Cathode electrode with photocathode structure.

### [illegible]

The emitive surface of the photocathode has a 40 mm diameter $Cs_2Te$ deposit layered on a 50 mm diameter molybdenum substrate. The photocathode assembly is mechanically inserted by remote handling under ultra high vacuum.

We have performed beam dynamics simulations for different cathode recess values. The cathode recess locally curves the electric field lines. This effect induces a transverse electric field component which contributes to transverse focusing. Since the electron beam is early focused at emission, the space charge is under better control and nonlinear effects are limited.

The beam dynamics has been optimized to provide a parallel beam at the linac entrance (Fig. 4). The best beam transport (lowest emittance) is obtained for a 4 mm length cathode recess. The net gain in emittance is close to 30%.

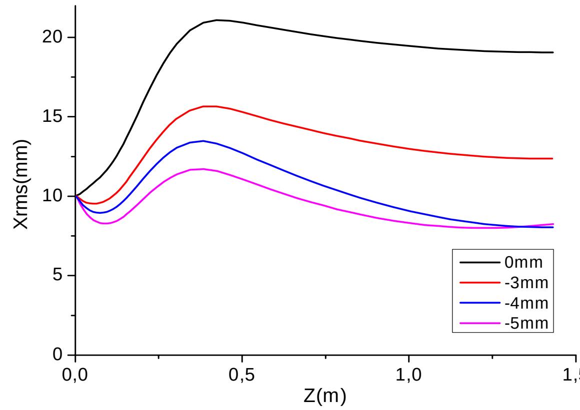


Figure 4: RMS beam envelope for different cathode recess.

### [illegible]

The magnetostatic focusing at extraction is based on a solenoid lens. Two options were considered. The first one is made of a main solenoid surrounding the anode vacuum tube and a bucking coil at the cathode surrounding the vacuum vessel. Initial momentum condition is then nil and increase in emittance is limited. The second option consists to a single solenoid which has been magnetically shielded. This last solution produces a stronger magnetic field localized in a restricted volume and acts as a short magnetic lens (solenoids must be considered as long magnetic lenses). In addition, no need for a bucking coil is required in this case. Tune is consequently eased.

Former results (Fig. 5) showed that the solenoid location along the beam axis is a critical parameter. After optimization of the two options, the second one (shielded coil) leads to a decrease of the beam emittance by about 10%.

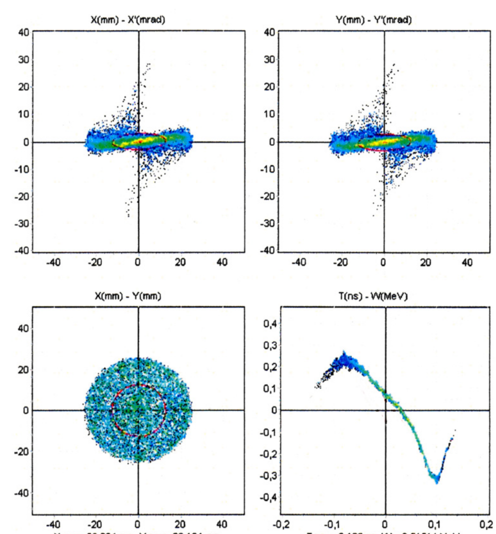


Figure 5: Phase space diagrams with the optimized shielded coil at the linac entrance.

## SIMULATION RESULTS OF THE WHOLE ACCELERATOR MACHINE

Beam dynamics of the whole accelerator machine has been carried out thanks to the simulation chain described above. The optimized values of the photo-injector are used. The linac RF cavity phase is tuned to provide the lowest RMS beam energy spread. The final focusing system is adjusted to provide the smallest spot on the target. Two different bunch configurations have been studied: 5 bunches of 200nC/bunch and 10 bunches of 100nC/bunch. Differences between these configurations are essentially the total beam duration from 13 ns to 28 ns, the space charge effects and the beam loading in the RF cavity.

The beam envelopes and the phase space diagrams on the target are shown on the figures below (Figs. 6-8).

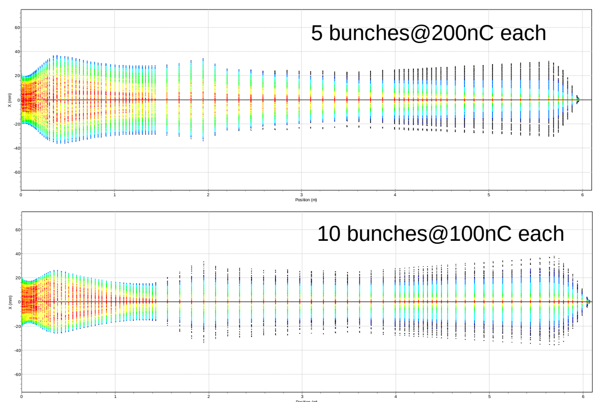


Figure 6: RMS beam envelope for the two configurations.

Although the number of bunches and charge per bunch are very different, the simulations for the two accelerated beam configurations give very close results (difference of only 5% on the spot size). The larger energy spread due to the beam loading of the 10 bunches train configuration carrying 100 nC each is balanced by the higher space charge effect of the 5 bunches train configuration carrying 200 nC each.

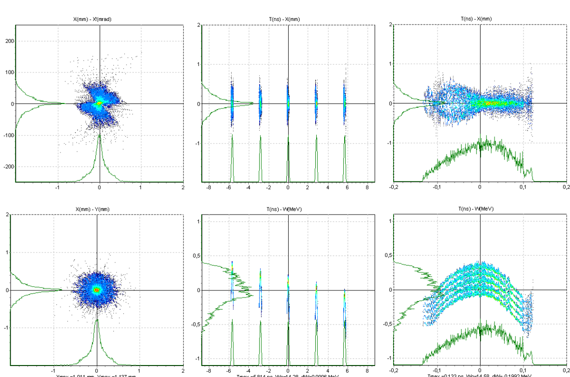

Figure 7: Phase space diagrams on the target for the 5 bunches@200nC per bunch configuration.

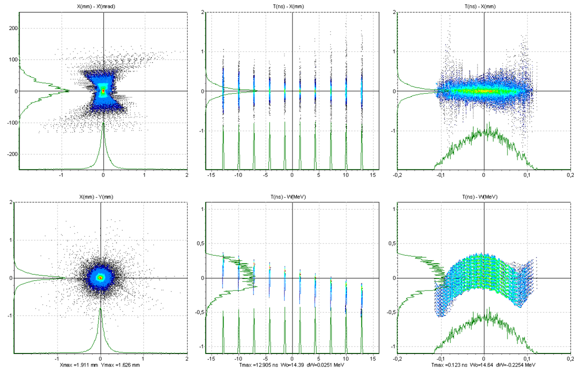

Figure 8: Phase space diagrams on the target for the 10 bunches@100 nC per bunch configuration.

The 5 bunches train configuration @200nC leads to faster radiographic imaging (13 ns) at same spot size and dose. In addition, the total length of the high voltage generator part of the photo-injector is shorter allowing a more compact overall radiographic facility.

## CONCLUSION

Beam dynamics simulations for a new X-ray radiographic project have been performed with an interactive, fast and accurate chain simulation codes based on POISSON- SUPERFISH and PARMELA .

Photo-injector beam transport calculations have showed that a single shielded solenoid achieves best beam qualities (10% reduction in beam emittance) than the usual focusing configuration using long solenoid and bucking coil. Thanks to a cathode recess, the early space charge effect is limited in the photo-injector. In consequence the beam emittance is lowered by 30% for a 4 mm optimized cathode recess.

The whole machine simulations for a 1μC total charge beam have been carried out for two beam configurations: 5 bunches of 200 nC each and 10 bunches of 100 nC. Quite similar beam characteristics are obtained on the target. Spot size and dose are the same. The 5 bunches train configuration @200nC allows faster radiographic imaging (13 ns). The total length of the high voltage generator part of the photo-injector is also shorter allowing a more compact radiographic facility.

## REFERENCES

[1] "Beam Dynamics simulation and DC photo-injector Design for CEA RF Accelerator", S. Pichon, D. Guilhem, Pulse Power Conference 2007.
[2] http://laacg1.lanl.gov/services/.
[3] CEA/DSM/DAPNIA/SACM, didier.uriot@cea.fr.
[4] "A 2.5 MeV Pulsed Photo-Injector Demonstrator for Radiographic Applications", J-L. Lemaire, IPMC 2008, Las Vegas, USA.

# BEAM DYNAMICS AND ERROR STUDIES OF THE SPIRAL2 DRIVER ACCELERATOR

P. Bertrand, GANIL, Caen, France
J-L. Biarrotte, L. Perrot, CNRS / IPN Orsay, France
D. Uriot, CEA Saclay, France.

*Abstract*

After a detailed design study phase (2003-2004), the SPIRAL2 project at GANIL (Caen, France) was officially approved in May 2005, and is now in its phase of construction, with a project group including the participation of many French laboratories (CEA,CNRS) and international partners. The SPIRAL2 facility is composed of a multi-beam driver accelerator (5mA 40MeV deuterons, 5mA 33Mev protons, 1mA 14.5MeV/u heavy ions), a dedicated building for the production of Radioactive Ion Beams, the existing cyclotron CIME for the post acceleration of the RIBs, and new experimental areas. In this paper we focus on the beam dynamics and error studies dedicated to the SPIRAL2 accelerator part of the project, from the ECR sources to the High Energy Beam Lines which have been recently updated.

## INTRODUCTION

The SPIRAL2 facility is now in its construction phase with huge progress for many parts of the machine as explained in [1]. In parallel, many beam dynamics calculations have been performed in order to extend the possibilities of the accelerator, and to take into account new demands of experimental physics.

As indicated table 1, the Spiral2 accelerator will deliver a huge variety of beams, at various intensities and energies, which constitutes a great challenge.

Table 1: Beam Specifications

| beam | P+ | D+ | ions | ions |
|---|---|---|---|---|
| Q/A | 1 | 1/2 | 1/3 | 1/6 |
| Max. I (mA) | 5 | 5 | 1 | 1 |
| Min. output W (Mev/A) | 2 | 2 | 2 | 2 |
| Max output W (Mev/A) | 33 | 20 | 14.5 | 8 |
| CW Max. beam power (kW) | 165 | 200 | 44 | 48 |

Our beam dynamics reference program is the well known TRACEWIN code [2]. It allows us to simulate the machine from the source to the final target, with a huge number of pseudo-particles. All the simulations can use 3D electromagnetic maps of magnets and cavities which are presently under construction, and the beam optimization uses the set of diagnostics which will be effectively used in the real machine. Moreover we project to incorporate (part of) TRACEWIN into the control system as an essential component of the tuning process.

## SPIRAL2 INJECTOR

### *LEBT Lines and RFQ*

The beam dynamics of the LEBT has been explained in detail in [3] and there is no recent modification. However we have investigated in detail the behaviour of the beam for various estimated values of the space charge compensation: this aspect is crucial when we manage the duty cycle and keep perfect bunches with a combination of ECR source, slow chopper and RFQ pulsations.

The 88 MHz 4-vane RFQ accepts charge/mass ratio between 1 and 1/3, and is designed for a very high transmission, in particular in the case of Deuterons at full intensity. We have checked that the 99% transmission was kept with or without space charge.

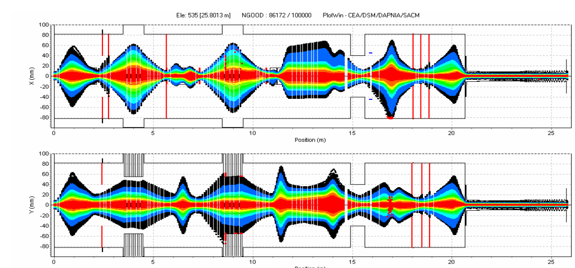

Figure 1: LEBT transport and RFQ acceleration for 1mA 1/3 heavy ions.

### *MEBT Line*

The SPIRAL2 MEBT (Fig. 2) is a complex 8 meters transfer line with the following fundamental functions:

- Transverse/longitudinal matching into the linac
- Fast chopping system and associated beam stop
- Drift for a future connexion of a q/A=1/6 injector
- Movable slits for halo elimination.

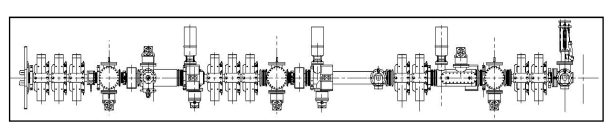

Figure 2: SPIRAL2 MEBT design.

The MEBT beam energy is fixed to 0.75 Mev/u, which corresponds to 7.5 kW for 5mA D+. Beam dynamics have been performed for all types of ions, using particle distributions from LEBTs and the RFQ, using quadrupole and rebuncher 3D maps and with linac matching (fig.3).

Calculations with use of the fast chopper have been performed in parallel with the development of the device.

We have checked that using a static magnetic deviator combined with an RF electric wave did not generate a significant emittance growth (Fig. 4).

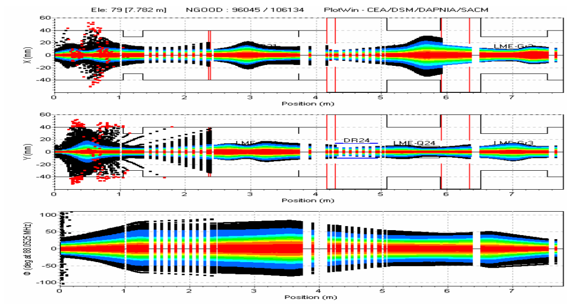

Figure 3: LME nominal (x,y, $\phi$) optics for 5mA D+ beam.

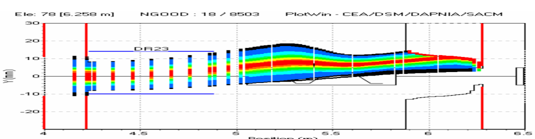

Figure 4: LME fast chopper and beam stopper (7.5 kW).

## SUPER-CONDUCTIONG LINAC

The SPIRAL2 linear accelerator [4] is composed of 2 families of 88 MHz SC QWR cavities ($\beta_0$=0.07, $\beta_0$=0.12), which permits the acceleration of all ions and energies mentioned in table 1. Between each cryomodule, beam focusing is performed by means of 2 warm quadrupoles with short vacuum/diagnostics boxes in between.

### *Linac Tuning*

Thanks to the regular geometry of the linac, it is possible to put the quadrupole strengths in such a way to obtain a continuous phase advance per meter and a continuous transverse focusing channel. We match the beam to the Linac by adjusting the 2 last MEBT quadrupoles and the first Linac doublet (Fig. 5).

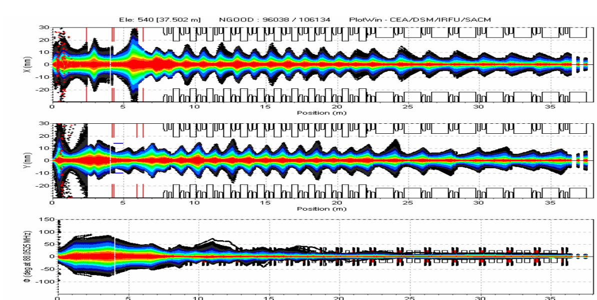

Figure 5: 5 mA $D^+$ nominal (x,y,$\phi$) optics in MEBT and the linac (40 Mev at exit).

The control of the transverse beam matching in the periodic sections is done by using the quadrupolar moment of the Beam Position Monitors. The non interceptive BPMs are located inside the first quadrupole of each lattice, where envelopes are different in x and y. The longitudinal matching is tuned by applying a similar method based on the adjustment of the 3 MEBT re-bunchers, in association with beam phase length diagnostics located in the first Linac periods.

### *Output Energy Tuning*

Physics requirements impose the Linac output energy to be adjustable between 2 and 20 MeV/u, with the beam kept bunched (<0.5ns) at target in some cases. In the low energy cases, the $\beta_0$=0.07 cavities are tuned to obtain 2 MeV/u, while $\beta_0$=0.12 cavities are off except one or two, in order to keep the beam bunched at the linac exit.

### *Error Studies*

The TRACEWIN code can pilot a heterogeneous collection of computers including PCs and clusters. We use this feature to simulate more than 1400 linacs with $10^6$ macro-particles for each one, and study very precisely the losses occurring in the full linac, following the Extreme Value Theory detailed in [5]. For each linac the procedure is the following: the parameters are initialized with theoretical perfect values. A set of random "*static errors*" is applied: cavity/quads misalignments, amplitude errors due to tuning or machining imperfections... and the standard corrections scheme is performed, typically the beam centring with steerers associated with BMPs, beam size adjustment with envelope measurement and quads. In a second step, a set of random "*dynamic errors*" is applied: RF jitter, mechanical vibrations, diagnostic noises or errors…Finally the simulation with $10^6$ particles is done from the output ECR source to the linac exit, using a Gaussian initial beam distribution. Most of elements are simulated using a 3D electromagnetic field maps. Then, statistical information concerning emittance growth, centroid behaviour and losses are available. In the case of 5mA 40MeV $D^+$, average Linac-integrated losses are 0.2W, with 0.26W deviation (Fig. 6).

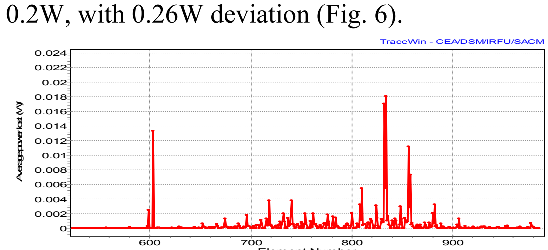


Figure 6: Average beam loss distribution for $D^+$.

## HEBT LINES

HEBT have been recently updated, according to the evolution of physics demands and implantation of buildings and experimental areas:

The "red" production cave (separate building) is dedicated to the production of radioactive nuclides using D+ beam, neutron converter and UCx target production. RIBs will be used in a low energy hall (DESIR) or/and accelerated with the existing CIME cyclotron.

The Super Separator Spectrometer (S3) is dedicated to experiments using heavy ion beams from LINAC (super-heavy and very-heavy nuclei, spectroscopy at and beyond the drip-line, isomers and ground state properties…)

Neutrons For Science hall (NFS) is dedicated to cross-section measurements (TOF or irradiation techniques) and fundamental physics. It concerns transmutation of nuclear waste, design of future fission and fusion reactors, nuclear medicine and tests and development of new detectors.

SRI facility is dedicated to atomic physics research.

HEBT lines are designed with a limited number of repeated structures:

- Matching sections composed of 4 quadrupoles, used at Linac exit, for the beam dump, and at the entrance of each experimental room,
- Triplet sections for transport, with repetitive transverse waists and periodic envelopes,
- Achromatic double deviations for beam distribution and protection of targets against energy fluctuations.

HEBT beam dynamics scheme is such that we have always the same radial envelopes, up to a homothety, according to the type of beam and the final energy (fig. 7). In some cases, very short bunch time lengths are needed on target (<0.5 ns for $S^3$and NFS). We will use a set of 2 SC cavities (probably $\beta_0$=0.07) installed between triplet sections, where the beam diameter is minimum. The SPIRAL2 beam dump is located in the straight line of the LINAC. For safety and radioprotection reasons, beam dump entrance is located around 6meters from the last matching quadrupole. An optimized beam-dump geometry profile limits the power deposition density to 400W/cm² and permits a 200kW beam (5mA $D^+$, 40MeV), although we will always limit the duty cycle to around 5% during the tuning of the accelerator.

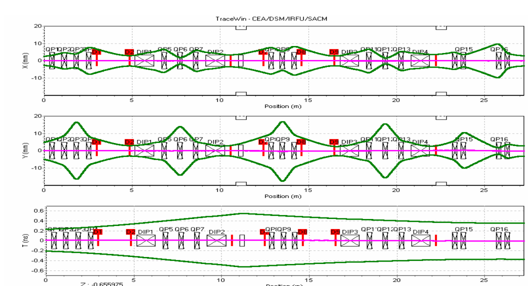

Figure 7: 5rms HEBT envelopes of Q/A=1/3 1mA ion beam at 14.5MeV/u between linac and $S^3$.

Ideally, HEBT beam error and beam loss studies must be done for all beam lines, all species and for minimum and maximum energies. By decreasing artificially the beam tube diameter, the worst case appears to be the 33MeV protons beam: beam losses are located in the middle of triplet sections, where the vertical envelope is maximal, and also at the output of the re-buncher. (Fig.7).

Recent activation calculations confirm that dose rate obtained with stainless steel vacuum chamber would be higher than with aluminium, for deuterons or even protons. Moreover, the decrease after beam put off is much favourable in the case of aluminium. In order to permits hands-on maintenance and reduce exposure, we are looking carefully at the best compromise in term of beam tube diameter and material, collimators and beam loss monitors along the HEBT lines.

## OPERATION MODES

It is fundamental to protect the machine from thermal and activation problems during the tuning as well as at full nominal beam power. The best way is certainly to dispose of a dedicate software/hardware which gives successive authorizations to increase the beam power, depending upon the part of the machine we consider.

However in the case of SPIRAL2, the problem is very complex, because it also depends of the type of accelerated beam (D+, p+…) and of the required final energy. Moreover we have many possible paths for the beam (2 ECR sources, many experimental halls…) and we must distinguish various types of targets (with or without neutron convertor in the red cave for example…)

In order to have a clear idea of what we are doing during the tuning and avoid dangerous mistakes, we propose to introduce a "tuning mode 3D-Matrix", with 3 axis corresponding to the following basic modes:

- The "beam-type mode", corresponding to the type of beam we want to accelerate,
- The "machine-path mode", corresponding to the path of the beam and the intermediate beam stop or final target we consider,
- The "beam-power mode", corresponding to a maximum authorized beam power at a given step.

Once the 3D (sparse) matrix obtained is filled according to the relevant combinations, and given a beam type at a given final energy, we can extract the corresponding 2D matrix automatically and determine the succession of safe steps to increase the beam power along the machine.

## CONCLUSION

Beam dynamics calculations for the SPIRAL2 driver accelerator have been performed on various aspects, with results giving more and more confidence in the machine capability to ensure a safe and flexible beam operation. Further studies are on-going, especially concerning the final definition of the HEBT lines, the management of operation modes, and the role to be played by the TRACEWIN code into the control-command process of the real machine.

## REFERENCES

[1] T. Junquera, "Status of the Construction of the SPIRAL2 Accelerator at GANIL", LINAC 2008, Vancouver, Canada.

[2] R. Duperrier, N. Pichoff, D. Uriot, "CEA Saclay codes review", ICCS Conference, Amsterdam, 2002.

[3] J.L. Biarrotte, P. Bertrand, D. Uriot, "Beam dynamics studies fort the spiral2 project", EPAC 2006, Edinburgh, Scotland.

[4] R. Ferdinand et al. "The SPIRAL2 superconducting Linac", LINAC 2008, Vancouver, Canada.

[5] R. Duperrier, D. Uriot, Phys. Rev. ST Accel. Beams 9, 044202 (2006).

# BEAM DYNAMICS SIMULATION OF THE LOW ENERGY BEAM TRANSPORT LINE FOR IFMIF/EVEDA

N. Chauvin*, O. Delferrière, R. Duperrier, R. Gobin, P.A.P. Nghiem, D. Uriot,
CEA, IRFU, F-91191 Gif-sur-Yvette, France.

*Abstract*

The purpose of the IFMIF-EVEDA (International Fusion Materials Irradiation Facility-Engineering Validation and Engineering Design Activities) demonstrator is to accelerate a 125 mA cw deuteron beam up to 9 MeV. Therefore, the project requires that the ion source and the low energy beam transport (LEBT) line deliver a 140 mA cw deuteron beam with an energy of 100 keV and an emittance of 0.25 $\pi$.mm.mrad (rms normalized) at the entrance of the RFQ. The deuteron beam is extracted from a 2.45 GHz ECR source based on the SILHI design. A LEBT with a two solenoids focusing system is foreseen to transport and adapt the beam for the RFQ injection. In order to validate the LEBT design, intensive beam dynamics simulations have been carried out using a parallel implementation of a particle-in-cell 3D code which takes into account the space charge compensation of the beam induced by the ionization of the residual gas. The simulations results (in particular from the emittance growth point of view) performed under several conditions of gas species or gas pressure in the beam line are presented.

## INTRODUCTION

The International Fusion Materials Irradiation Facility (IFMIF) will produce a high flux ($10^{18}$n.m$^{-2}$.s$^{-1}$) of 14 MeV neutron dedicated to characterization and study of candidate materials for future fusion reactors. A solution based on two high power cw accelerator drivers, each delivering a 125 mA deuteron beam at 40 MeV to a liquid lithium target, is foreseen [1].

In the first phase of IFMIF, called EVEDA (Engineering Validation and Engineering Design Activities), a 125 mA cw/9 MeV deuteron demonstrator accelerator will be constructed, tested and operated at Rokkasho-mura, in Japan [2]. This accelerator is composed by an ECR (Electron Cyclotron Resonance) ion source, a low energy beam transport (LEBT) line, a RFQ (100 keV to 5 MeV) [3], a matching section, a superconducting Half Wave Resonator cavities section (5 MeV to 9 MeV), and a high energy beam line equiped with diagnostic plate and a beam dump. This paper will focused on the LEBT section of the EVEDA project.

The purpose of the LEBT is to transport the 140 mA/100 keV deuteron beam extracted from the ECR source to the RFQ. In order to design the LEBT parameters and to optimize the beam injection in the RFQ, beam dynamics simulations have been performed.

* Nicolas.Chauvin@cea.fr

## LOW ENERGY BEAM LINE LAYOUT

### *ECR Ion Source and Extraction System*

The beam intensity and reliability required for the IFMIF project have lead to the choice of an ECR ion source to produce the deuteron beam. The IFMIF source, based on the SILHI design, will operate at 2.45 GHz [4]. The extraction system has been optimized to increase the total beam intensity from 150 mA to 175 mA in order to meet the 140 mA $D^+$ requirements, as $D_2^+$ and $D_3^+$ are also produced in the ECR source. The extraction energy has also been increased from 95 keV to 100 keV, and a four electrode system has been calculated to minimize the $D^+$ divergence. In order to decrease the risk of high voltage breakdown, the maximum of the extraction electric field has been kept around 100 kV/cm.

Table 1: Beams Parameters after the Extraction System

| Extracted Species | Intensity (mA) | Emittance ($\pi$ mm.mrad) |
|---|---|---|
| $D^+$ | 141 | 0.064 |
| $D_2^+$ | 26.5 | 0.043 |
| $D_3^+$ | 8.8 | 0.042 |

The particle distributions after the source are derived from their tracking through the extraction system. Those beam distributions, of which main parameters are summarized in table 1, have been taken as inputs for the LEBT simulations. More precisely, the simulations start with a part of source extraction system, computed with AXCEL-INP [5], in order to get relevant boundary condition.

### *Low Energy Beam Transport Line*

The optics for the LEBT is based on a dual solenoids system. The 3D magnetic field maps of the solenoids (pole length: 300 mm), computed by finite elements method, have been included in the simulations.

The total length of the beam line, from the plasma electrode to the RFQ entrance is 2.05 m (see Fig.1). A pumping system and beam diagnostics as movable Faraday cup and emittance measurement could be inserted between the two solenoids. A regulating valve is also foreseen in order to inject a controlled flux of a specific gas in the beam line.

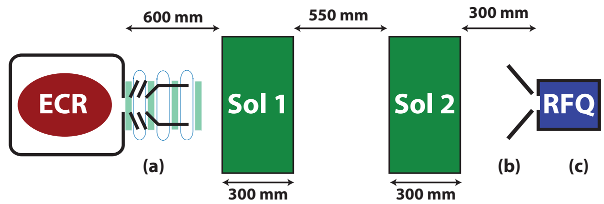


Figure 1: Scheme of the IFMIF-EVEDA LEBT. (a): ECR extraction system - (b): RFQ injection cone - (c): first RFQ segment.

## SIMULATION AND OPTIMIZATION

### Codes Used

For this work, three different numerical codes have been employed.

First, the modeling of the extraction system of the ECR source has been done with a commercial code, called AXCEL-INP.

In order to achieve realistic beam transport simulations in the 100 keV energy range and with such a high intensity, it is necessary to take into account the space charge compensation of the beam on the residual gas. For that, a 3D particle-in-cell (PIC), called SOLMAXP, has been recently developed at CEA/Saclay and has been employed for this work. The basics of this code are briefly described in the next section.

Finally, the optimization of the LEBT optics parameters for the beam injection in the RFQ has been performed with TraceWin [6].

### SOLMAXP: A 3D PIC Code

In this code, the motion of the macro-particle (each of them carrying an equal fraction of the overall beam intensity) is integrated on a time step basis. The simulation region is divided into a 3D grid. At each time step, the following procedure is done:

- weighting of the position of the particle to assign a charge density on the grid nodes.
- calculation of the potential and electric field from the charge density, by solving the Poisson equation.
- weighting of the forces (from the **B** and **E** self-generated fields and external fields) at the position of the particles.
- calculation of the new velocity and the position of the particles by integration of the equation of motion.
- simulation of collisions (ionization and neutralization) between particles, with the help of a Monte-Carlo algorithm.

This procedure is repeated until the emittance at the end of the LEBT has reached its steady-state.

### Optimization Method

A first calculation is made with TraceWin, considering around 70 % of space charge neutralization, to find the beam transport and focalization that met the required Twiss parameters for the injection in the RFQ. In our case, the goal is to find magnetic field values applied by the two solenoids of the LEBT.

Then, a calculation is made with SOLMAXP, with the beam line parameters found with TraceWin. SOLMAXP is run until the steady-state of the space charge compensation is reached. The code outputs are the particle distribution (ions, electrons, neutral atoms) and the electric field map derived from the potential created by the space charge along the beam line. A projection of a space charge potential map is represented in Fig. 2.

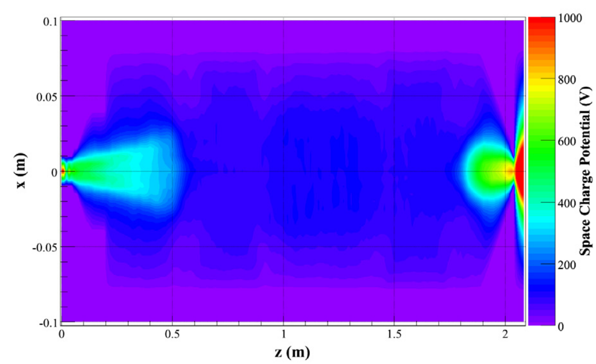


Figure 2: Two dimension projection in (z0x) plane of a space charge potential map.

For the TraceWin calculation, this space charge electric field map is then superimposed to those of the beam line elements. So, the RFQ injection optimization is now performed with space charge compensation through the LEBT. During that TraceWin optimization process, the optics parameters are modified and consequently, the space charge compensation should vary, because of the new particle distribution. Thus, another simulation has to be done with SOLMAXP.

After a few steps of that back and forth process between the two codes, the convergence toward the optimized solution is reached.

## SIMULATION RESULTS

One of the most critical beam parameter in the IFMIF LEBT, is the emittance growth. The emittance values presented in the following section are derived from the particle distributions calculated with SOLMAXP.

### Gas Pressure

Previous measurements performed with the SILHI source and LEBT [7] showed that beam emittance can be improved by injecting some gas in the beam line. Furthermore, this improvement seems to depend strongly on the gas species.

Preliminary simulations were done, with a shorter and simplified beam line, for pressure values of deuteron gas of $4\times10^{-4}$ hPa and $4\times10^{-5}$ hPa. The results showed clearly that with the higher pressure, the obtained emittance is 45% lower.

But, in the IFMIF LEBT, the pressure has to be kept around several $10^{-5}$ hPa to minimize the high voltage breakdowns and ion losses on neutral gas. Then, we chose a total pressure value of $5\times10^{-5}$ hPa. Nevertheless, according to reference [7], a lower emittance could be obtained by adding a heavier gas like krypton in the beam line.

Assuming that the residual $D_2$ gas contibution to the total pressure in the beam line is $10^{-5}$ hPa, two simulations were done by adding a partial pressure ($4\times10^{-5}$) of either $D_2$ or krypton, all the other parameters remaining constant. The results are presented in table 2.

Table 2: Simulations Results for Two Gas Species Injected.

| $D_2$ partial pressure (hPa) | Kr partial pressure (hPa) | Final Emittance ($\pi$ mm.mrad) |
|---|---|---|
| $5\times10^{-5}$ | 0 | 0.41 |
| $1\times10^{-5}$ | $4\times10^{-5}$ | 0.31 |

These simulation results confirm that the emittance is lowered with kryton injection, as it has been observed experimentally. Then, we can recommend that some krypton has to be injected in the IFMIF LEBT.

Finally, we have to consider the loss rate due to the $D^+$ beam neutralization by the gases. With these pressure conditions, the loss rate is around 2.4%.

### *Focalization*

In the preliminary optimization process, it has been determined that the Twiss parameters required for the beam injection in the RFQ could be reached with two different beam focalization types: with or without a beam waist between the two solenoids (respectively called “strong” and “weak” focalization).

Simulations have been performed for these two cases, with a gas pressure of $5\times10^{-5}$ hPa ($D_2$ and Kr). Fig. 3 shows the emittance results.

This results shows that the “weak” focalization should be adopted for the IFMIF LEBT in order to get a final emittance value of $0.31\pi$ mm.mrad. The magnetic field values on the two solenoids are respectively 0.36 T and 0.4 T

### *Space charge compensation steady-state*

The simulations with SOLMAXP make possible to determine when the space charge compensation steady-state is reached. This information can be useful for an operation in pulsed mode, during the commissioning phase, for example. In this case, the pulsed mode has to be representative of the cw mode from the space charge compensation point of view.

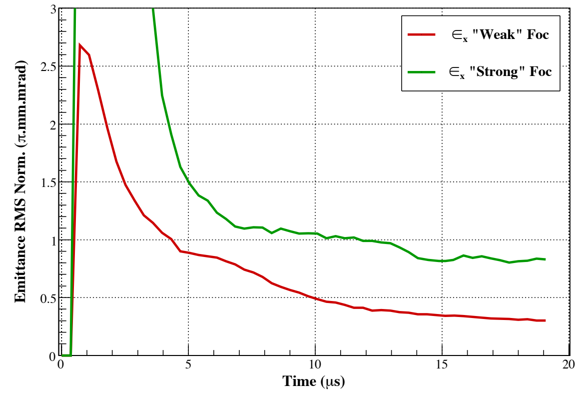


Figure 3: Emittance evolution as a function of time, for the two type focalisation conditions. The simulation starts at time t=0.

From Fig 3, one can deduce that the space charge compensation steady-state is reached after around 15 $\mu$s.

## CONCLUSIONS AND PERSPECTIVES

The beam dynamics simulations for the IFMIF LEBT have been achieved with a 3D PIC code developed at CEA/Saclay to compute the space charge compensation of the beam by the ionization of the residual gas.

The calculated beam emittance value at the end of the LEBT is still higher than the RFQ requirements. However, the optimization process, in order to adapt the beam for its injection in the RFQ is currently in progress. The preliminary results are promising and further optimization may lead to a lower beam emittance value than the current one. Otherwise, the final beam emittance can also be lowered by increasing slightly the krypton pressure in the beam line or by reducing the distance between the two solenoids.

## REFERENCES

[1] P. Garin, *IFMIF: Status and developments*, Proc. of EPAC 2008, Genoa, Italy.

[2] A. Mosnier et al, *The IFMIF-EVEDA Accelerator Activities*, Proc. of EPAC 2008, Genoa, Italy.

[3] M. Comunian et al, *Beam Dynamics of the IFMIF-EVEDA RFQ*, Proc. of EPAC 2008, Genoa, Italy.

[4] R. Gobin et al, Rev. Sci. Instrum. **79** (2008) 02B303.

[5] INP, P. Spädke, Junkernst. 99, 65205 Wiesbaden, Germany, e-mail: p.spaedtke@inp-dme.com.

[6] R. Duperrier, N. Pichoff and D. Uriot, *CEA Saclay codes review*, Proc. of ICCS 2002, Amsterdam, Netherlands.

[7] P.-Y. Beauvais et al, Rev. Sci. Instrum. **71** (2000) 1413.

# PARAMETER DESIGN AND BEAM DYNAMICS SIMULATIONS FOR THE IFMIF-EVEDA ACCELERATORS

P. A. P. Nghiem*, N. Chauvin, O. Delferrière, R. Duperrier, A. Mosnier, D. Uriot,
CEA/DSM/IRFU, 91191 Gif-sur-Yvette Cedex, France
M.Comunian, INFN/LNL, Legnaro, Italy. C. Oliver, CIEMAT, Madrid, Spain.

*Abstract*

One major system of IFMIF (International Fusion Materials Irradiation Facility) is its accelerator facility, consisting of two 175 MHz CW accelerators, each accelerating a deuteron beam of 125 mA to the energy of 40 MeV. This high power beam, 10 MW, induces challenging issues that lead to plan a first phase called EVEDA (Engineering Validation and Engineering Design Activity), where only the portion up to 9 MeV of one accelerator will be constructed and tested. For these accelerators, the Parameter Design phase is about to be completed. Particular efforts have been dedicated to minimise the space charge effect that can strongly increase the beam size via the halo, and the losses that can prohibit the requested hand-on maintenance. This paper presents the status of these studies.

## INTRODUCTION

In the future Fusion Demonstration Reactor (DEMO), the materials surrounding the plasma will be submitted to a very intense neutron flux, so that their atoms can be displaced up to hundreds of times more than with those of present fusion materials. In order to test and qualify the material behaviour under such severe irradiations, the International Fusion Materials Irradiation Facility (IFMIF) is planned, with the purpose of delivering an intense neutron flux, generated by the impact of an accelerated deuteron beam on a liquid lithium target. One major system of IFMIF is its accelerator facility, consisting of two 175 MHz CW accelerators, each accelerating a deuteron beam of 125 mA to the energy of 40 MeV. The total power delivered at the target is 10 MW. One important challenging specification of these accelerators is therefore their very high intensity, which must nevertheless be reconciled with the requested hands-on maintenance imperative. That is why a first phase called Engineering Validation and Engineering Design Activity (EVEDA) is now starting, where a prototype accelerator will be constructed and tested, consisting of only the portion up to 9 MeV of one IFMIF accelerator. For these accelerators, the parameter design and beam dynamics simulations are now well engaged. Two topics have been particularly scrutinised: characterisation and minimisation of the space-charge effect, very critical in the low energy part, and of the losses, very critical in the high energy part. Different solutions have been studied, and the choices between them are either done or underway. In this paper, after having given the general layout, the status of those studies is presented for each accelerator section.

## LAYOUT & CHALLENGING ISSUES

The layout and general parameters of IFMIF and EVEDA accelerators are given in Fig.1. D+ particles are extracted from the ion source at 100 keV, then properly focused by the LEBT in order to be injected into the RFQ where they are bunched and accelerated to 5 MeV. The MEBT matches the RFQ output beam in transverse and longitudinal to that required by the superconducting HWR-Linac. Composed of 4 cryomodules housing solenoids and accelerating cavities, the Linac accelerates particles to the final energy of 40 MeV, where the HEBT transports the beam to the lithium target while giving it the required dimensions and homogeneity. For the prototype accelerator, only the first cryomodule will be constructed, and a special HEBT sends the resulting 9 MeV beam with the right dimensions to a beam dump, while allowing to measure its characteristics.

For Beam dynamics studies, the TraceWin package code(including PARTRAN and TOUTATIS) [1] is used as the common code between the different sections, where multiparticle trackings are performed under a strong space charge regime. Given the very high

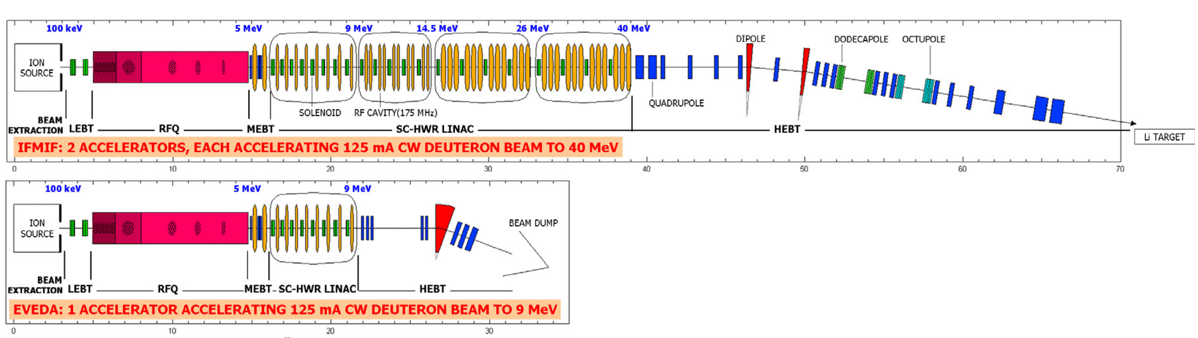


Figure1: General layout of the IFMIF-EVEDA accelerators.

intensity involved, any linear calculation is even useless. Indeed, space charge forces always overtake magnetic forces. The tune depression parameter is 0.4-0.5 in the RFQ, and 0.2-0.5 in the HWR-Linac. It results a high compactness for the accelerator so that available space for beam equipments and diagnostics has been dramatically reduced.

The high intensity impacts also strongly on beam losses considerations. To allow hands-on maintenance, losses should not exceed 1W/m for particles at energies beyond 5 MeV. Table 1 lists the beam power at different positions along the accelerator and the corresponding beam fraction per meter allowed to be lost. We can see that it concerns a really tiny part of the beam. Let us consider for example the 23 m long HWR-Linac. If we adopt an accepted loss average current of 100 nA/m, it means that, no more than 2 $10^{-5}$ of the beam can be lost for the whole Linac. This demonstrates how carefully should be considered the beam loss problem for IFMIF. In particular, beam dynamics studies must be made with $10^6$ macroparticles downstream the LEBT, and total losses of more than two dozens of macroparticles should be avoided. Losses in case of errors, tunings or accidents should also be precisely examined.

Table 1: Beam Energy, Beam Power and Allowed loss/m (Beam Fraction or Current) at Different Locations

| End of | Energy (MeV) | Power (MW) | Allowed loss (fraction/m) | Allowed loss (nA/m) |
|---|---|---|---|---|
| RFQ | 5.0 | 0.625 | 1.6 $10^{-6}$ | 200 |
| 1$^{rst}$ Cryo | 9.0 | 1.125 | 9.0 $10^{-7}$ | 100 |
| 2$^{nd}$ Cryo | 14.5 | 1.813 | 5.5 $10^{-7}$ | 70 |
| 3$^{rd}$ Cryo | 26.0 | 3.250 | 3.1 $10^{-7}$ | 38 |
| 4$^{th}$ Cryo | 40.0 | 5.000 | 2.0 $10^{-7}$ | 25 |

## BEAM EXTRACTION

The beam extraction system is designed following that of the SILHI source [2]. To extract a higher flux from the ion source, the diameter of the plasma electrode hole is enlarged from 10 to 12 mm. To reduce the space charge effects, the overall length of extraction electrodes has been shortened by reducing their number from 5 to 4. Their spacing has been adjusted to keep a maximum electric field not exceeding too much 100 kV/cm. As a result, the extracted beam emittance is 0.06 $\pi$mm.mrad (normalised RMS), at the current of 140 mA (D+) in anticipation of some losses in the low energy sections. The beam distribution is not Gaussian. The density is rather flat, except on a thin part near the edge where it is higher. This is due to the beam size, in the very first extraction steps, which spreads into non linear focusing zones so that the external part is folded toward interior. For a same emittance, this distribution is more compact than a Gaussian one and should not be unfavourable.

## LEBT

In this low energy section, the strong space charge is partially compensated by residual gas electrons. A fine calculation of the resulting space charge potential is thus necessary, and it has been performed with a home made code [3], taken into account the ionisation and the dynamics of ions and electrons. It has been found with this code that the space charge is better compensated within a quadrupole than within a solenoid. But for this line, quadrupoles induce more emittance growth because the distance source-quadrupole is so huge that a bigger beam enveloppe is induced than with solenoids that focus in both planes at the same time. For solutions with two solenoids, it has also been noted that a strong focusing scheme (with a waist in between them) leads to a stronger emittance growth. Finally, a configuration with 2 solenoids has been adopted in the weak focusing scheme. The 2.1m total length can admit various technical equipments and diagnostics, of which an emittance measurement. No beam loss occurs in this section, excepting the neutralisation induced by the addition of Krypton gas aiming at producing a more linear space charge. Nevertheless, the output emittance is higher than expected. This value can be lowered as first further optimisations have shown. Otherwise, either higher Krypton pressure has to be added, or the distance between the solenoids has to be reduced. The matching of the output beam to the RFQ channel is being performed by means of the TraceWin code.

## RFQ

From this section, calculations begin to be made with $10^6$ macroparticles, and losses should begin to be carefully managed. For that, the design [4] has adopted a "2TERM" geometry type combined with a strong electric focusing to produce extremely linear transverse fields around the beam. At the end of the Gentle Buncher, about the first third of the RFQ, an abrupt decrease of the aperture is intended to loose out-of-energy particles that are not bunched, in order to prevent them from being accelerated to higher energy. On the contrary, in the last third of the RFQ all parameters are let unchanged to avoid losses at an energy approaching 5 MeV. Therefore, losses are concentrated in the first part and concern mainly particles at low energy around 100 keV. Notice that only 3 particles out of $10^6$ with energies between 3.5 and 4.5 MeV are not bunched and will be lost in the next sections. These calculations have been made with the PARMTEQM code [5], cross-checked with the TOUTATIS code. The overall transmission of the 9.78 m long RFQ depends on the beam current, emittance, and distribution type at input. We can remember that for 130 mA, 0.25 $\pi$mm.mrad at input, the transmission is 95.7 % for a Gaussian distribution, and 99.1% for a Waterbag one. The emittance growth is insignificant because here the tiny lengths of focusing lattices forbid any space charge manifestation.

## MEBT

This section has been re-designed from the initial IFMIF Conceptual Design Report, in order to reach a more realistic 1.36 m long section, in which can be now installed essential beam diagnostics along with 3 quadrupoles and 2 buncher cavities. These last elements must have enough focalisation strength in transverse and longitudinal to be capable to match the beam from a very short focusing lattice (cm) of the RFQ to a much longer one (m) of the HWR-Linac.

## HWR-LINAC

The design of the superconducting HWR-Linac has been performed under many constraints of energy, length, RF power, feasibility, and more particularly of emittance growth and beam losses [6]. The beam dimensions, in transverse as well as in longitudinal, have to be kept as small and regular as possible along the 22.8 m long Linac. To further improve the transition between consecutive cryomodules, the lattice lengths in each cryomodule have been progressively made longer. But these considerations about 3RMS beam size are not enough. A precise examination of the beam halo is necessary to prevent particle losses. For that, the very external fringe of the beam has to be considered. We arrive then to a solution where there is no loss over $10^6$ macroparticles, and where the contour line encircling 100% of particles occupies 60-80% of the aperture, with a comfortable room in longitudinal acceptance. This result remains to be further improved. On the other hand, the emittance growth is not negligible; it reaches 50%, of which 40% occurs at the MEBT and the first meter of the first cryomodule.

The aim now is to keep this no-loss result in the presence of errors which remain to be simulated. While errors of the HWR-Linac alone could be not critical, errors combined from the ion source down to the accelerator end could enhance losses. Re-tuning of the Linac could be necessary in real operation. The point is that the above described tuning allowing to avoid losses is based on the knowledge of beam sizes. But in order to limit emittance and halo growths, focusing lattices need to be the shortest possible, and thus no place is available for beam size measurements. Therefore this question of managing losses in the real machine has to be addressed and simulated.

A possible solution that can help is the use of quadrupoles instead of solenoids. Thanks to the now different horizontal-vertical sizes, and provided that Beam Position Monitors can be installed inside the quadrupoles, difference of squared transverse sizes can be measured, and would be useful to match the beam [7]. That is why a Linac configuration with quadrupoles has also been simulated, and it gives equivalent results than with solenoids. The choice of the final configuration will depend on current feasibility studies of SC quadrupoles with BPM inside.

## HEBT-EVEDA

For the prototype accelerator, the HEBT line transports the 9 MeV beam output from the first Linac cryomodule to a beam dump [8]. At this point, the beam is expanded at optimised size and divergence in order to spread the energy deposition. Another goal is to allow beam characterisation by a 3m long diagnostic plate. Given the high space-charge regime, the beam is very quickly debunched, and the use of a buncher is necessary for any longitudinal measurement. For the same reason, the transverse emittance measurement by varying quadrupole strengths is no longer possible by linear calculations. A minimisation code remains to be made, calling the multiparticle TraceWin code. For the moment, we have verified that variations of horizontal and vertical beam sizes by a factor of 6 and 3 are possible without any loss. Simulations along the 10m long HEBT have also shown that 100% of the beam occupies 50-70% of the aperture.

## HEBT-IFMIF

For the IFMIF accelerator, the HEBT line has to guide the 5 MW beam to the target with precise specified dimensions and homogeneity. Until now, only a feasibility study has verified that with the beam output from the above HWR-Linac, it is possible to obtain roughly a beam footprint of 5x20 cm as required, with relatively hard edges and good homogeneity. All that with a ~40m long line containing quadrupoles, octupoles and dodecapoles. But it seems that results are very sensitive to the input beam. More detailed studies remain to be done.

## CONCLUSIONS

The design and simulations of the IFMIF-EVEDA accelerators are challenging due to its very high beam power. A true competition between focusing and space-charge forces has to be managed. A detailed examination of each particle loss is necessary to allow the required hands-on maintenance. This paper has summarised the status of these studies, by pointing out the specific hot topics for each section, and the choices made or to be made to solve them.

## REFERENCES

[1] R. Duperrier, N. Pichoff and D. Uriot, Proc. of ICCS 2002, Amsterdam, Netherlands.
[2] O. Delferrière et al., Proc. of ICIS 2007, Jeju, Korea
[3] N. Chauvin et al., Proc. of LINAC 2008, Victoria, Canada
[4] M. Comunian, Proc. of LINAC 2008, Victoria, Canada
[5] K.R. Crandall et al., LA-UR-88-1546.
[6] N. Chauvin et al., Proc. of LINAC 2008, Victoria, Canada (and also EPAC 2008).
[7] R. Duperrier, D. Uriot, IFMIF report, 2008.
[8] C. Oliver et al., Proc. of EPAC 2008, Genoa, Italy.

# BEAM DYNAMICS SIMULATIONS OF SUB-PS ELECTRON BUNCH PRODUCED IN A PHOTO-INJECTOR

R. Roux
LAL, bâtiment 200, Université Paris-Sud, 91898 Orsay, France.

*Abstract*

A growing number of experiments require low emittance ultra-short electron bunches in the 100 fs range (rms value) for the production of coherent light or the injection into a plasma for laser-plasma acceleration. Especially in the last case it is highly desirable to have a compact accelerator; hence a strong experimental activity is carried out to get such a beam directly from a photo-injector. We have performed beam dynamic simulations using the PARMELA code to study the performances of the alphaX photo-injector installed in the University of Strathclyde in UK*. This RF gun is aimed to produce electron bunches which have 100 pC of bunch charge, 100 fs bunch length and 1 π mmmrad transverse emittance. We will show the results of systematic parametric studies as a function of charge and laser pulse duration as well as the natural evolution of the beam phase space as a function of the distance from the photo-cathode.

## INTRODUCTION

Up to now the preferred way to get very short bunch is to use a magnetic chicane but this could lead to a degradation of the emittance due to the emission of coherent synchrotron radiation. Moreover it is difficult to make a compact beamline in such a scheme. Some experiments as alphaX [1] in the University of Strathclyde strive to produce X ray in the SASE [2] regime with a very short accelerator which the length is roughly 7 meters. The idea is to inject a very short electron bunch coming from a photo-injector into a laser-plasma [3] accelerating cell to bring it at 1 GeV over few millimeters instead of ≈ 30 m in classical linear accelerators. In order to get an efficient acceleration in the plasma, the specification on the bunch length must be absolutely fulfilled. So the purpose of this study is to investigate the behaviour of sub-ps electron bunches directly issued from the photo-injector using numerical simulations.

## PARMELA SIMULATIONS

PARMELA is a well-known code used for beam dynamics in linacs which takes into account the space charge force effect. It was created by Los Alamos National Laboratory and modified at LAL by B. Mouton to include, for instance, the photo-injectors.

*We acknowledge the support of the European Community-New and Emerging Science and Technology Activity under the FP6 "Structuring the European Research Area" programme (project EuroLEAP, contract number 028514).

### *AlphaX Photo-injector*

The alphaX photo-injector is made of 2.5 cells at 3 GHz resonant frequency. This gun designed at the Eindhoven University of Technology [4] exhibits two noticeable features. First, the shape of irises is elliptical because, according to the RF simulations, the surface electrical field is reduced by a factor 2 with respect to the more usual cylindrical shape. So one hopes to operate the gun at gradient higher than 100 MV/m without electrical breakdowns. Secondly the RF power is sent to the gun via a coaxial "doorknob" antenna in a coupler at the output of the gun. In this way the gun keeps a perfect cylindrical symmetry in order to avoid possible degradation of the emittance rising in non-symmetric coupling.

Simulations in PARMELA are performed with the electrical field of alphaX calculated with the 2D RF code SUPERFISH. Results are shown in table 1 for 6000 macro-particles used in the simulation.

Table 1: Results of PARMELA simulations at the output of the gun, input parameters are (rms value): Q = 100 pC, laser has a Gaussian profile, radius = 1.4 mm cut at 10 mm and pulse duration = 100 fs cut at 500 fs. The peak electrical field is 92 MV/m and the phase is chosen to optimise the energy gain, rms value.

| | |
|---|---|
| Beam radius (mm) | 3.1 |
| Bunch length (fs) | 206 |
| Energy (MeV) | 6.2 |
| Normalized Emittance (πmmmrad) | 4.2 |
| Energy spread (%) | 0.172 |

In this case the specifications are not fulfilled, the emittance being 4 times higher and the bunch length 2 times bigger. About the emittance there is a way to significantly reduce the effect of the space charge forces thanks to a uniform transverse profile instead of a Gaussian shape for the laser. The same technique can be applied along the longitudinal axis. But before to show the results of the improvements with a square distribution, one may wonder about the validity of these calculations. Indeed most of simulations are usually performed with electron bunches which the length is in the picosecond range.

### *Test of PARMELA*

Up to now there are no measurements of sub-ps bunches produced directly from the gun to compare with PARMELA simulations. But it is possible to check if the results of PARMELA are at least in agreement with the physics of charged beam. For instance the scaling of the emittance as a function of the bunch charge depends on the space charge forces. Normally the repulsive force applying on each electron is proportional to the total charge. In figure 1 we tested this scaling law for 2 bunch lengths, 10 ps and 100 fs.

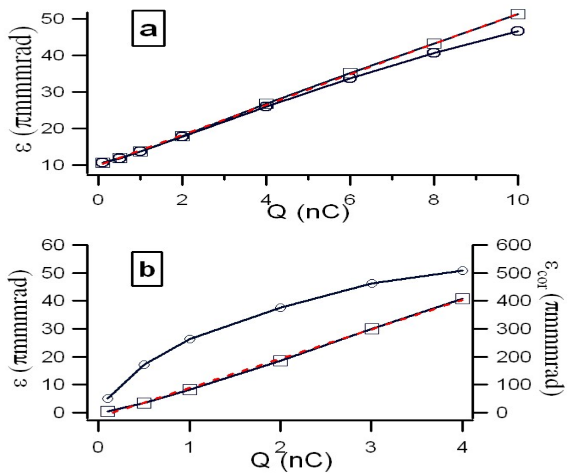


Figure 1: normalized emittance as a function of the total charge. In a), the laser pulse duration is 10 ps; in b), it is 100 fs. Lines with circle are raw PARMELA results, lines with squares are corrected data and dashed red line is a linear fit. In the case of b), the value of the corrected data is reported on the right axis.

In the case of the long bunches, 10 ps, the growth of the emittance becomes non-linear for charges above 4 nC and this change even occurs below 1 nC for the 100 fs bunches. This is due to the fact that the space charge force is proportional to the electronic density. So when it becomes stronger, the bunch length increases leading to a reduction of the space charge force and therefore the emittance growth is slowed down. To remove this effect, we multiplied the emittance by a corrective factor which is the ratio of the bunch length at the output of the gun over the bunch length at zero charge. The corrected data fit perfectly with a linear law for fs bunches as well as for ps bunches. So PARMELA seems to be still reliable for short bunches and we can look for better performances with 100 fs bunches.

## EMITTANCE OPTIMISATION

It is now usual to make a flat shape of the laser distribution in order to decrease the space charge forces. After optimisation, the best parameters for the laser are: in transverse plane, $\sigma_r$ = 4 mm, $r_{max}$ = 1.2 mm and no change in the longitudinal axis, results are given in table 2. The emittance is reduced by 33 % with respect to the case of the laser with a Gaussian profile (table 1). However it was impossible to find a set of longitudinal laser parameters which allows one to further decrease the emittance. It is a first visible difference with respect to the ps bunches where using also a flat longitudinal pulse leads to a supplementary reduction of the emittance.

Table 2: Results of PARMELA simulations for Q = 100 pC in rms value (6000 macro-particles) for a laser flat transverse profile and 2 accelerating fields.

| | 92 MV/m | 120 MV/m |
|---|---|---|
| Beam radius (mm) | 1.6 | 1.5 |
| Bunch length (fs) | 283 | 196 |
| Energy (MeV) | 6.2 | 8 |
| Normalized Emittance (πmmmrad) | 2.8 | 2.4 |
| Energy spread (%) | 0.43 | 0.32 |

Moreover the bunch length and the energy spread are enhanced while it should be the opposite. One way to overcome these difficulties is to increase the accelerating gradient. But it seems to profit mainly to the bunch length which is reduced of 30 % while it is only 14 % for the emittance. Of course only the experiment can tell if the gun can be operated at such high gradient with a good stability. So unless to relax the specification on the bunch length it seems difficult to get the 1 πmmmrad for 100 pC and 100 fs bunch length.

## LONGITUDINAL DYNAMICS

For some applications the bunch length is a parameter of a paramount importance and one must investigate how evolves a bunch with a length of 100 fs.

### *Natural Behavior*

Plotting the evolution of the bunch length as a function of the longitudinal distance, a special feature of the short bunches appears, as illustrated in figure 2.

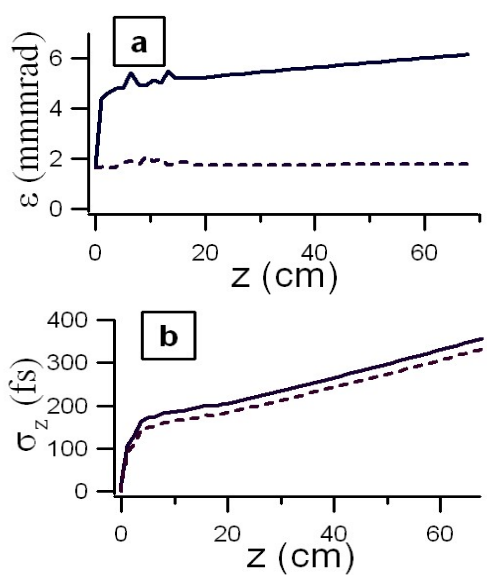


Figure 2: a), emittance as a function of the longitudinal distance z; b), bunch length as a function of z. Plain line is the simulation taking into account the space charge forces, dashed line is without space charge. Parameters of the simulations are the same as used in table 1 except number of macro-particles, 1000 in this case.

In the drift space after the gun, there is a slow increase of the emittance while the bunch is lengthened by a factor 2. In the case of the emittance it is clearly the consequence of the space charge forces. At the opposite the major part of the bunch lengthening even occurs without the inclusion of the space charge forces. The latter give a very weak contribution to the bunch length. This bunch lengthening was already investigated by previous studies [5] with the GPT code and is a pure geometrical effect. External electrons have higher divergence with respect to electrons on axis. Therefore they follow a longer path than electrons in the centre of the bunch and accumulate a time lag which means they go to the tail of the bunch. With longer bunch, 10 ps, a drift of the external electrons of 0.1 ps is completely absorbed in the overall bunch.

### *Behavior with Vertical Focussing*

To transport the electron beam or to focus it for an experiment, the use of a solenoid or quadrupole is unavoidable. Usually the longitudinal dynamic is not coupled to the transverse motion, except in a dipole. But for fs bunches it is not true anymore. We performed a simulation with a quadrupole focussing in the horizontal plane, results are shown in figure 3.

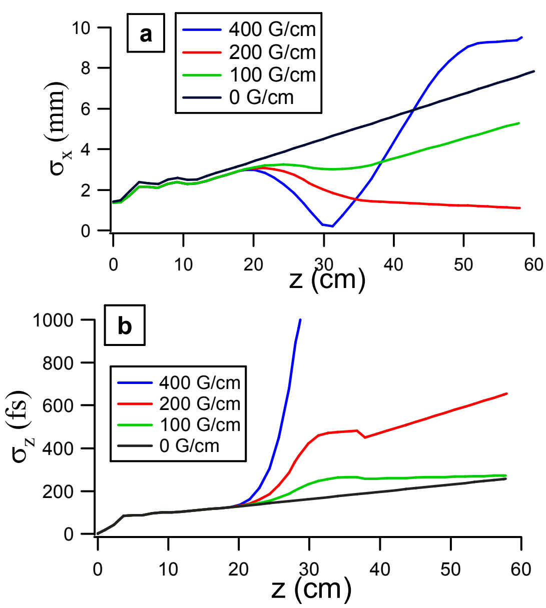


Figure 3: simulations without space charge, same parameters for the laser (see table 1), a horizontal quadrupole is placed at z = 20 cm; in a), horizontal sizes (rms) and in b) the bunch lengths (rms) for several values of the quadrupole gradient.

When one tries to focus the electron beam, the bunch length quickly increases. When the beam passes through the quadrupole, external electrons have a longer path to go to the focus point with respect to the on axis electron. It is a critical issue because if it is really required to focus the beam at a size below 0.2 mm (to inject in a capillary for instance) the bunch length inflates, from 130 fs up to 4 ps, 40 cm after the gun. Simulations performed with a solenoid give the same results as the quadrupole ones. So every time the beam is transported or focused with magnets the bunch length strongly increases.

The only way to compensate this bunch lengthening is to use a curved photo-cathode [6] made in such a way that external electrons are emitted in first with respect to on axis electrons.

### *With a Laser at Non-zero Incidence*

Usually in the simulations, one neglects the angle of incidence of the laser onto the photo-cathode because it is very small, ≈ 3° in our case. In figure 4 is reported the result of a simulation with an incident angle of 3° and compared with the case at normal incidence.

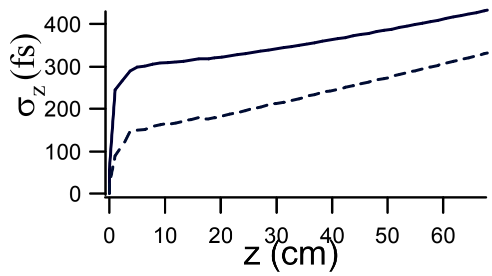


Figure 4: bunch length as a function of the longitudinal distance. The parameters of the simulations are those used in table 1; plain line: angle of laser incidence is 3°, dashed line: normal incidence on the photo-cathode.

The result is rather clear: for femtosecond bunches one must not neglect the angle of incidence anymore. Even with only 3° it induces a bunch lengthening of 120 fs.

## CONCLUSION

A study of femtosecond bunches based on PARMELA simulations has been performed which shows that the handling of such beam produced from a photo-injector is rather difficult. External electrons have a longer path to travel than the core electron; a drift space or magnets used to transport or focus the beam induce inevitably a bunch lengthening. The minimization of the emittance thanks to a flat transverse profile of the laser is obtained at the expense of a degradation of the bunch length and energy spread.

## REFERENCES

[1] T. Garvey *et a*l, EPAC'06, Edimburgh, June 2006, TUPCH113, p. 1277 (2006); http://www.JACoW.org.

[2] J. Andruszkow *et al*, Phys. Rev. Lett. 85 (2000) 18.

[3] J. Faure, Y. Glinec, A. Pukhov, S. Kiselev, S. Gordienko, E. Lefebvre, J. Rousseau, F. Burgy and V. Malka, Nature (London) **431**, 541 (2004).

[4] F. Kiewiet, "Generation of Ultra-short, High Brightness Relativistic Electron Bunches", Eindhoven University of Technology thesis, ISBN 90-386-1815-8, 2003

[5] W. H. Urbanus, W. van Dijk, S. B. van der Geer, G. J. H. Brussard and M. J. van der Weil, Jour. of Appl. Phys. **99**, 114501 (2006).

[6] M. J. de Loos *et al*, Phys. Rev. ST Accel. Beams. **9**, 084201(2006).

# BENCHMARKING OF MEASUREMENT AND SIMULATION OF TRANSVERSE RMS-EMITTANCE GROWTH ALONG AN ALVAREZ DTL

L. Groening, W. Barth, W. Bayer, G. Clemente, L. Dahl, P. Forck, P. Gerhard,
I. Hofmann, G. Riehl, S. Yaramyshev, GSI, D-64291 Darmstadt, Germany
D. Jeon, SNS, ORNL, Oak Ridge, TN 37831, USA
D. Uriot, CEA IRFU, F-91191 Gif-sur-Yvette, France

*Abstract*

Transverse emittance growth along the Alvarez DTL section is a major concern with respect to the preservation of beam quality of high current beams at the GSI UNILAC. In order to define measures to reduce this growth appropriate tools to simulate the beam dynamics are indispensable. This paper is on benchmarking of three beam dynamics simulation codes, i.e. DYNAMION, PARMILA and PARTRAN against systematic measurements of beam emittance growth for different machine settings. Experimental set-ups, data reduction, the preparation of the simulations, and the evaluation of the simulations will be described. It was found that the mean value of final horizontal and vertical rms-emittance can be reproduced well by the codes.

## INTRODUCTION

In the last decades many beam dynamics computer codes were developed [1] in order to simulate emittance growth along a linac. Several benchmarking studies among codes have been performed [2, 3, 4] generally assuming idealized conditions as initial Gaussian distributions, equal transverse emittances, matched injection into a periodic lattice, and small longitudinal emittance with respect to the rf-bucket size. In case of an operating linac most likely non of these conditions is met. To apply simulation codes to a realistic environment a benchmark activity was started aiming at the simulations of beam emittance measurements performed at a DTL entrance and exit, respectively. The studies were performed at the GSI UNILAC [5]. For the simulations three different codes were used: DYNAMION [6], PARMILA (V 2.32) [7], and PARTRAN [8]. A more detailed description of the campaign is given in [9].

## EXPERIMENT SET-UP AND PROCEDURE

Intense beams are provided by MEVVA, MUCIS, or CHORDIS sources at low charge states with the energy of 2.2 keV/u. An RFQ followed by two IH-cavities (HSI section) accelerates the ions to 1.4 MeV/u using an rf-frequency of 36 MHz. A subsequent gas-stripper increases the average charge state of the ion beam. Final acceleration to 11.4 MeV/u is done in the Alvarez DTL section operated at 108 MHz. The increase of rf-frequency by a factor of three requires a dedicated matching section preceding the DTL. It comprises a 36 MHz buncher for longitudinal bunch compression, a 108 MHz buncher for final bunch rotation, a quadrupole doublet for transverse compression, and a quadrupole triplet for final transverse beam matching.

The Alvarez DTL comprises five independent rf-tanks. Transverse beam focusing is performed by quadrupoles in the F-D-D-F mode. Each drift tube houses one quadrupole. The periodicity of the lattice is interrupted by four intertank sections, where D-F-D focusing is applied. Acceleration is done -30° from crest in the first three tanks and -25° from crest in the last two tanks.

Figure 1 presents the schematic set-up of the experiments. Beam current transformers are placed in front of

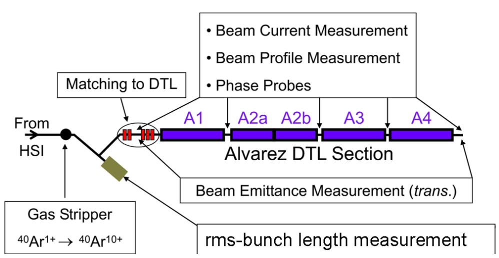


Figure 1: Schematic set-up of the experiments.

and behind the DTL as well as horizontal and vertical slit/grid emittance measurement devices. The total accuracy of each rms-emittance measurement including its evaluation is estimated to be 10%. A set-up to measure the longitudinal rms-bunch length is available in front of the DTL [10]. It measures the time of impact of a single ion on a foil. This time is related to a 36 MHz master oscillator. The resolution is 0.3° (36 MHz).

The HSI was set to obtain 7.1 mA of $^{40}Ar^{10+}$ in front of the DTL being space charge equivalent to the UNILAC design beam of 15 mA of $^{238}U^{28+}$. Horizontal and vertical phase space distributions were measured in front of the DTL. The longitudinal rms-bunch length was measured at the entrance to the DTL. The DTL quadrupoles were set to zero current transverse phase advances $\sigma_o$ ranging from 35° to 90° in steps of 5°. Due to space charge the phase advances in all three dimensions were depressed. The transverse depression reached from 21% (90°) to 43% (35°). Afterwards the quadrupoles and bunchers preceding the DTL were set to obtain full transmission and to minimize low energy tails of the beam. For each value of $\sigma_o$ horizontal and vertical beam emittances were measured at the exit of the DTL with a resolution of 0.8 mm in space and 0.5 mrad in angle.

Each emittance measurement delivers a two dimensional matrix of discrete slit-positions and discrete angles. The data are processed by the measurement & evaluation program PROEMI [11]. Fractional emittances can be extracted as well since in practical cases it is beneficial to focus on the "inner" 95% of the particles. The emittance containing a given percentage $p$ of the full distribution is extracted as follows: (i) The sum $\sum_{100}$ of all pixel contents is calculated. (ii) The pixels are sorted by their content starting from the largest one. (iii) Starting from the largest content the sum of all pixel contents is built as long as this sum is less or equal to the percentage $p$ of $\sum_{100}$. (iv) Those pixels that contributed to the sum are considered for the rms-evaluation. Simulation deliver a set of six dimensional particle coordinates. This ensemble is projected onto a pixel-grid having the same characteristics as the slit/grid device used for the measurements. The grid is read by the measurement evaluation program PROEMI such that data reduction was done in the same way as for measured data.

## INPUT FOR SIMULATIONS

From the transverse emittances measured in front of the DTL normalized 100%-rms-emittances of 0.12 and 0.23 mm mrad were evaluated horizontally and vertically, respectively. Measuring the rms-bunch length in front of the DTL a value of 25 mm was found corresponding to a phase spread of 20° at 36 MHz.

The reconstruction of the initial distribution is done in two steps. First the 100%-rms-Twiss parameters are determined. In the second step the type of distribution is reconstructed. The transverse rms-measurements and the longitudinal rms-measurements on the initial distribution, done at different locations along the beam line (Fig. 2), had to be combined.

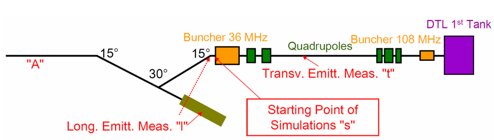


Figure 2: Reference points used for reconstruction of the initial phase space distribution.

This was achieved by attaching to the transverse rms-parameters measured at location "t" such longitudinal rms-parameters that result in the measured rms-bunch length measured at location "l", after rms-tracking the distribution from "t" to "s". The tracking implies the assumption that the virtual transport from "l" to "s" can be approximated by a simple drift including space charge. The length of this drift is given by the difference of the distances ("A", "l") and ("A", "s"), i.e. 0.4 m. Additionally, the recombined distribution must result in longitudinally matched injection into the DTL in accordance with the measurements. Eventual longitudinal mismatch could have been observed experimentally by transmission loss and the occurance of low energy tails.

The reconstruction of the type of distribution is based on evaluation of the brilliance curve, i.e. the fractional rms-emittance as function of the fraction (Fig. 3). Different

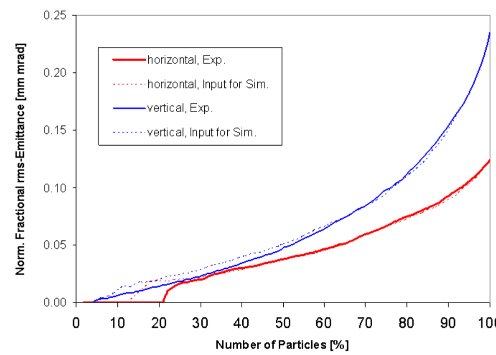


Figure 3: Brilliance curves of the phase space distribution in front of the DTL. Bold: from measurement; dashed: from initial distribution for simulations

amounts of halo have been found in the two transverse planes as indicated by the horizontal and vertical curvatures. For proper modelling of the initial distribution, both curvatures must be reproduced. This was achieved by using a distribution function as

$$f(R) \;=\; \frac{a}{2.5\cdot 10^{-4}\,+\,R^{10}},\quad R\leq 1 \qquad (1)$$

and $f(R)$=0 for $R > 0$ with

$$R^2 \;=\; X^2+X'^2+Y^{1.2}+Y'^{1.2}+\Phi^2+(\delta P/P)^2\,, \quad (2)$$

where $a$ is the normalization constant and the constant in the demoninator results from the cut off condition at $R$ = 1. By defining the radius $R$ using different powers for different sub phase spaces the halos within the planes could be modelled. Since for the longitudinal phase space distribution no measurement but on the rms-bunch length is available, a Gaussian distribution cut at $4\sigma$ is assumed. This can be achieved by setting the respective powers in the definition of $R$ to a value of 2.

## COMPARISON OF RESULTS

For all phase advances full beam transmission was observed through the DTL in the experiment. The codes revealed losses of about 2%. Figure 4 displays final horizontal phase space distributions at the DTL output as obtained from measurements and from simulations for three different values of $\sigma_o$. The simulated final distributions look quite similar. Simulations could reproduce the wings attached to the core measured at highest phase advances. But the codes did not show the asymmetric distributions measured at lowest phase advances. Final 95%-rms-emittances

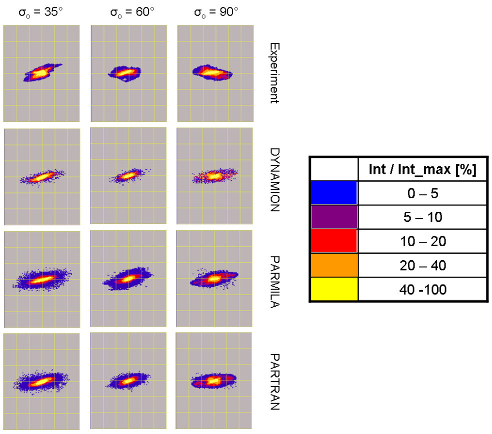


Figure 4: Top to buttom: horizontal phase space distributions at the DTL exit. Left: $\sigma_o$ = 35°; centre: $\sigma_o$ = 60°; right: $\sigma_o$ = 90°. The scaling is $\pm$ 24 mm (horizontal axis) and $\pm$ 24 mrad (vertical axis), respectively.

are presented in Fig. 5 to Fig. 7 as function of the transverse phase advance $\sigma_o$. The measurements and the simulations revealed lowest emittances at $\sigma_o \approx 60°$. In general good agreement among the codes was found. However, the codes slightly underestimate the emittance growth. This is reasonable since the codes assume a machine without errors causing additional growth [12].

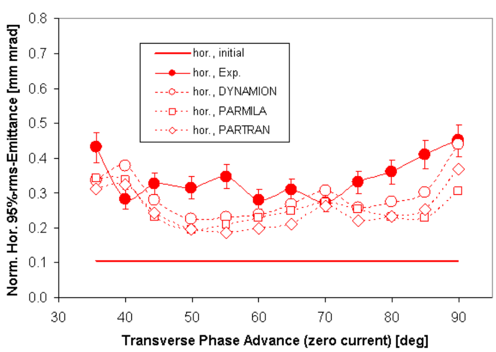


Figure 5: Horizontal 95%-rms-emittance at the end of the DTL as function of $\sigma_o$.

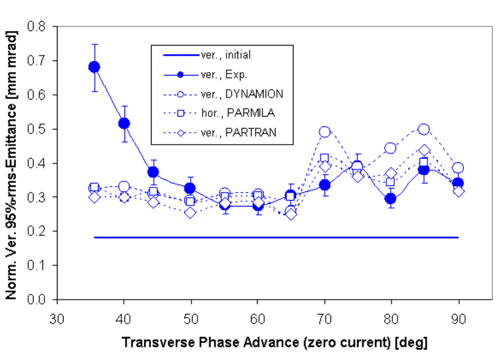


Figure 6: Vertical 95%-rms-emittance at the end of the DTL as function of $\sigma_o$.

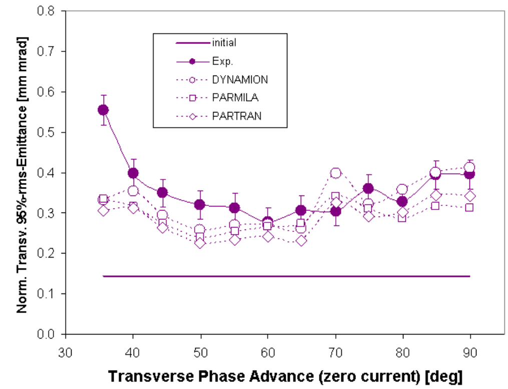


Figure 7: Mean value of horizontal and vertical 95%-rms-emittance at the end of the DTL as function of $\sigma_o$.

## ACKNOWLEDGEMENT


We acknowledge the support of the European Community-Research Infrastructure Activity under the FP6 "Structuring the European Research Area" programme (CARE, contract number RII3-CT-2003-506395).

The participation of D. Jeon to this work was made possible partly by the support of ORNL/SNS (managed by UT-Battelle, LLC, for the U.S. Department of Energy under contract DE-AC05-00OR22725).


## REFERENCES


[1] R. Ryne et al., Proc. of the HB2008 workshop, Nashville, U.S.A., (2008).

[2] S. Nath et al., Proc. of the 2001 Part. Accel. Conf., Chicago, U.S.A., (2001).

[3] A. Franchi et al., Proc. of the XXIII Linac Conf., Knoxville, U.S.A., (2006).

[4] A. Franchi et al., http://www-dapnia.cea.fr/Phocea/file.php?class=std&&file=Doc/Care/note-2006-011-HIPPI.pdf

[5] W. Barth et al., Proc. of the XXII Linac Conf., Lübeck, Germany, (2004).

[6] S. Yaramyshev et al., Nucl. Instrum. & Methods in Phys. Res. A **558**, 1, (2006).

[7] J.H. Billen and H. Takeda, PARMILA Manual, Report LAUR-98-4478, Los Alamos, 1998 (Revised 2004).

[8] R. Duperrier et al., ICSS 2002 Conf., Amsterdam, The Netherlands, (2002).

[9] L. Groening et al., Phys. Rev. ST Accel. Beams **11**, 094201 (2008).

[10] P. Forck et al., Proc. of the XX Linac Conf., Monterey, U.S.A., (2000).

[11] G. Riehl, *PROEMI: An emittance measurement and evaluation code.* The manual is available from the code author on request (g.riehl@gsi.de).

[12] K.R. Crandall, AOT Division Technical Note LA-CP-96-16, January 22, 1966.

# INTEGRATION OF FRINGE FIELD ALPHA MAGNETS INTO THE V-CODE BEAM DYNAMICS SIMULATION TOOL*

Sylvain Franke**, Wolfgang Ackermann, Bastian Steiner, Thomas Weiland,
Technische Universität Darmstadt, Institut für Theorie Elektromagnetischer Felder,
Schlossgartenstraße 8, 64289 Darmstadt, Germany,

Joachim Enders, Christoph Heßler, Yuliya Poltoratska,
Technische Universität Darmstadt, Institut für Kernphysik,
Schlossgartenstraße 9, 64289 Darmstadt, Germany

## Abstract

The design process and the operation of particle accelerator machines can advantageously be assisted by fast online beam dynamics simulations because of its flexible parameter variation combined with nearly simultaneous solution responses providing a detailed insight into the actual machine status. Based on the moment approach a fast tracking code named V-Code has been implemented at TEMF. At the Superconducting DArmstädter LINear ACcelerator S-DALINAC the V-Code is used during the design process of the injector for the new 100 keV polarized electron source but is also supposed to be employed at the control system. For these purposes an implementation of fringe field alpha magnets is mandatory. In this paper a summary of issues regarding the implementation complemented with simulation results will be provided.

## INTRODUCTION

At the Superconducting DArmstädter LINear ACcelerator (S-DALINAC) a new 100 keV polarized electron source is currently being installed. Therefore, a new low energy injection concept has to be designed. The most important components of the injector are a polarized electron source, an alpha magnet and a Wien filter used for spin rotation together with various beam forming elements. The polarized electrons extracted vertically from a photo cathode are bent into the horizontal injector beam line with the help of an alpha magnet. Unlike a classical alpha magnet designed as a half quadrupole given for example in [1], the hyperbolic poles of the installed alpha magnet are supplemented by a dipole like extension in order to achieve a 90° bending angle. In Fig. 1 a schematic computational model of the realized alpha magnet is visualized. Within the V-Code simulation tool the beam line is represented as a consecutive alignment of separate independent beam line elements. This procedure allows to simulate even a very long beam line with minimum requirements to the computer memory. In order to be able to simulate the hole injector an implementation of alpha magnets was missing so far.

* Work supported by DFG through SFB 634.
** franke@temf.tu-darmstadt.de

## NUMERICAL MODEL

The V-Code simulation tool is based on the moment approach to beam dynamics. Instead of using the particle distribution itself this method applies a discrete set of moments of the particle distribution. The time evolution of each moment can be deduced from the VLASOV equation when suitable initial conditions are given and all essential external forces are known. These forces are given by the LORENTZ equation in combination with the distribution of electric and magnetic fields obtained during a preprocessing step.
The required three-dimensional field distribution in the immediate vicinity of the particle trajectory can be reconstructed from extracted one-dimensional field components by means of a TAYLOR series expansion. This allows to considerably reduce the size of the required field data inside a specific beam line element.
A precise description of the numerical model is given in [2]. Details about its implementation in V-Code are published for example in [3] and [4].

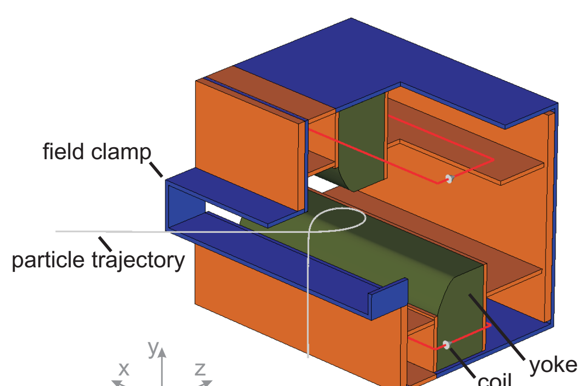


Figure 1: Schematic computational model of an $\alpha$-magnet including the excitation coils and the high permeable yoke. For visualization reasons the upper corner of the housing and the yoke have been cut away. Additionally, a typical particle trajectory is specified as a reference path.

### [illegible]

The particle tracking in external magnetic fields requires the detailed knowledge of the local field distribution which can be determined for example with the magnetostatic solver included in the CST Design Environment. From the precise field data one can extract the necessary multipole components and provide those information in a very efficient manner for further usage. In V-Code the full field can be reconstructed and evaluated particularly in the vicinity of the bunch trajectory. Due to the layout of the magnet it is sufficient to evaluate the field along the longitudinal axis z while it is assumed to be constant in transversal direction. In Fig. 3 the important vertical component of the magnetic flux density is displayed.

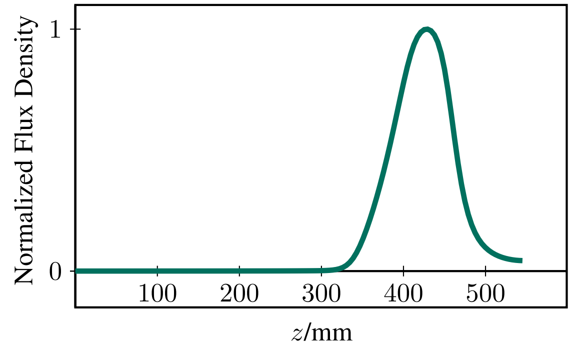


Figure 3: Vertical component of the magnetic flux density inside the $\alpha$-magnet normalized to the absolute maximum. Geometric details are specified in Fig. 1.

### [illegible]

In order to determine the components which have to be considered in the multipole expansion, one can analyze the tangential field component on concentric circles of different radii along the longitudinal axis of the alpha magnet. In Fig. 2 the calculated multipole coefficients are shown in logarithmic scale. From the plot one can see that the sextupole part forms the most eminent disturbance to the dipole field. Since the magnitudes of all higher order multipoles are at least two orders of magnitude smaller than the dominant dipole component even for the pessimistic evaluation radius $r = 6$ mm we neglect all multipole parts except the dipole field in the following.

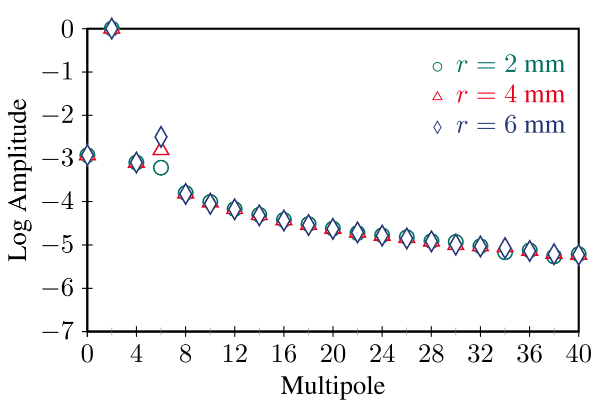


Figure 2: Normalized multipole moments of the magnetic flux density evaluated on concentric circles of different radii in the center of the $\alpha$-magnet.

### [illegible]

Within the V-Code simulation tool the entire beam line is represented as a straight line directed along the z axis. This requires for a beam line element like the alpha magnet the definition of a curved reference path, determining the nominal length inside the beam line. A suitable reference path can be attained for example by tracking a single particle with proper initial conditions in the provided magnetic field.

## IMPLEMENTATION

For accuracy reasons it is not advisable to calculate and visualize the bunch evolution in the same successively rotated coordinate system. A more accurate proceeding avoiding the accumulation of errors due to rotation is illustrated in Fig 4. At the beginning a coordinate transformation is performed to align the global primed coordinate system with the unprimed system in which the field components are reconstructed and the bunch evolution is calculated. The simulated bunch parameters are plotted in the visualization pane relative to the reference path using the double primed coordinate system. For this purpose the normal projection from the actual bunch position $(z_1, x_1)$ onto the reference path $(z_s, x_s)$ and a local coordinate transformation for the first and second order moments is performed. At the end a final transformation from the unprimed to the triple primed coordinate system is necessary in order to orient the global system along the subsequent beam line.

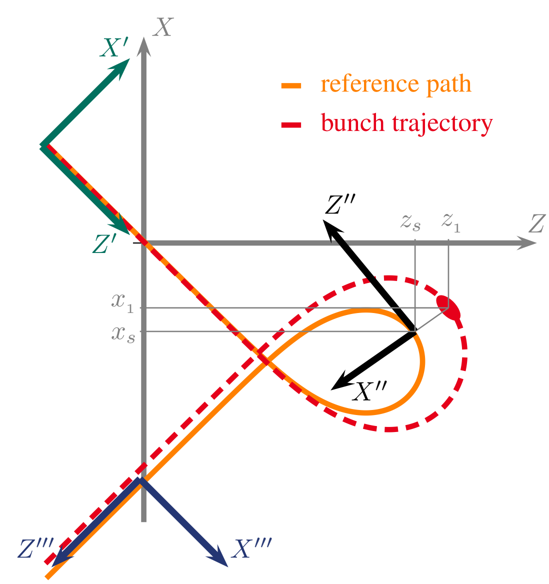


Figure 4: Typical projected bunch trajectory together with the predefined reference path for the $\alpha$-magnet setup specified in Fig. 1.

## SIMULATION

In order to study the applicability of the preprocessing steps and the implementation of the proposed scheme the simulation results from V-Code are compared to simulation results obtained with a reference tracking code based on the so called Boris algorithm [6] as well as results extracted from the particle tracker integrated in the CST Design Environment.

In Fig. 5 and Fig. 6 the evolution of the center of mass of a nearly point-like bunch equipped with a vertical offset of 1 mm from the reference path is tracked with V-Code and is compared to trajectories of individual particles calculated with the Boris algorithm and with the CST particle tracker.

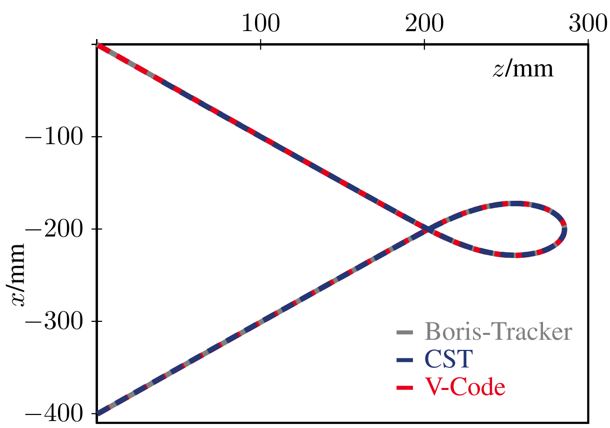


Figure 5: Simulation of the horizontal evolution of two individual particles with 1 mm vertical offset from the symmetry plane within the $\alpha$-magnet.

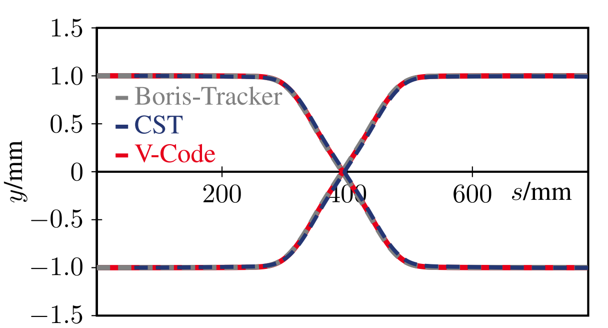


Figure 6: Simulation of the vertical evolution of two single particles with 1 mm vertical offset from the symmetry plane within the $\alpha$-magnet.

In Fig. 7 and Fig. 8 the focusing behavior inside the alpha magnet is illustrated. From the CST Design Environment the bunch dimensions were obtained by tracking a bunch of particles through the build-in particle monitors placed orthogonal to the reference path inside the alpha magnet. In V-Code the horizontal and vertical bunch dimensions are calculated from the global coordinates by means of coordinate transformations as explained in the previous section. In all tracking routines space charge effects are neglected.

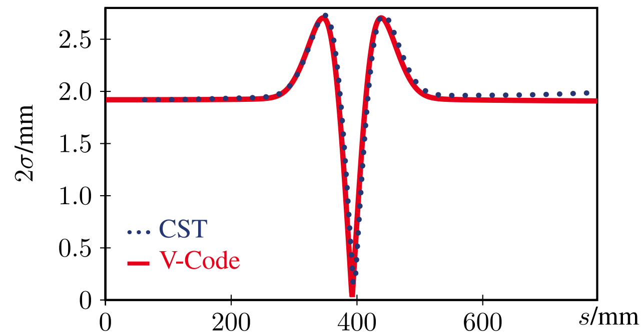


Figure 7: Simulation of the horizontal focusing behavior within the $\alpha$-magnet.

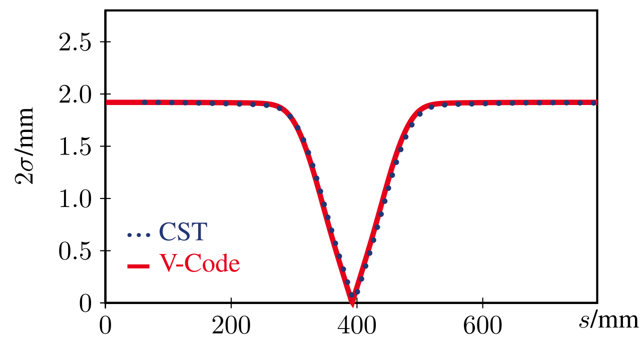


Figure 8: Simulation of the vertical focusing behavior within the $\alpha$-magnet.

The provided charts show that the center of mass as well as the transversal beam dynamics are precisely modeled in the new beam line element in V-Code.

## REFERENCES

[1] M. D. Borland, A High-Brightness Thermionic Microwave Electron Gun, Thesis (PH.D.), SLAC-R-402, Stanford University, 1991.

[2] P. J. Channell, The Moment Approach to Charged Particle Beam Dynamics, [illegible], NS-30, No. 4, Page 2607, 1983.

[3] W. Ackermann, T. Weiland: Data Base Extension for the Ensemble Model using a Flexible Implementation, presented at the 2005 Particle Accelerator Conference (PAC05), Knoxville, Tennessee, USA, May 16-20, 2005, 19.05.2005.

[4] S. Franke, W. Ackermann, B. Steiner, T. Weiland, J. Enders, C. Hessler, Y. Poltoratska: Implementation of Fringe Field Dipole Magnets into the V-Code Beam Dynamics Simulation Tool, Proceedings of the 11th European Particle Accelerator Conference (EPAC 2008), Genoa, Italy, June 23-27, 2008.

[5] CST - Computer Simulation Technology, Bad Nauheimer Str. 19, D-64289 Darmstadt, Germany, http://www.cst.com.

[6] J. Boris, Relativistic Plasma Simulation - Optimization of a Hybrid Code, Proceedings of the 4th Conference on the Numerical Simulation of Plasmas, Washington, D.C., November 2-3, 1970.

# BEAM DYNAMICS STUDIES ON THE EURISOL DRIVER ACCELERATOR

A. Facco, A. Balabin, R. Paparella, D. Zenere, INFN-Laboratori Nazionali di Legnaro, Padova, Italy; D. Berkovits, J. Rodnizki, SOREQ, Yavne, Israel; J. L. Biarrotte, S. Bousson, A. Ponton, IPN Orsay, France; R. Duperrier, D. Uriot, CEA/Saclay, France; V. Zvyagintsev, TRIUMF, Vancouver, Canada

*Abstract*

A 1 GeV, 5 mA cw superconducting proton/$H^-$ linac, with the capability of supplying cw primary beam to up to four targets simultaneously by means of a new beam splitting scheme, is under study in the framework of the EURISOL DS project which aims to produce an engineering-oriented design of a next generation European Radioactive beam facility. The EURISOL driver accelerator would be able to accelerate also a 100 μA, $^3$He beam up to 2.2 GeV, and a 5 mA deuteron beam up to 264 MeV. The linac characteristics and the status of the beam dynamics studies will be presented.

## INTRODUCTION

The EURISOL-DS project [1] aims at the design of a last generation Radioactive Ion Beam (RIB) facility for nuclear physics experiments, based on the ISOL method, to be constructed in Europe [2]. This facility is based on a 1 GeV, 5 mA primary proton beam feeding 4 RIB production targets. One of them (the high power target) will include a 4 MW neutron converter, able to receive most of the beam power and to create an intense neutron flux to the RIB target. The three remaining ones will accept a proton beam up to 100 kW for RIB production through direct reactions. The radioactive ions will be then extracted from the sources, selected and post-accelerated to the required energy (up to 150 MeV/A) by means of a superconducting linac.

One of the main requirements for the driver accelerator is the possibility of feeding more than one target in parallel, possibly in cw mode with finely tunable intensity to avoid destructive thermal shocks. No apparatus was available for this operation when the EURISOL-DS study started.

New requirements for the Driver, proposed after the first year of studies by the Beam Intensity Calculations Task group with the aim of opening new lines of experiments, are the possibility of delivering to the direct targets a 2 GeV, 100 μA $^3$He beam, and to a new target station a 250 MeV, 5 mA deuteron beam. This could be accomplished with a rather limited effort taking advantage of the structure of the EURISOL Driver, based on short, independently phased cavities, which allows a rather wide beam velocity acceptance.

## EURISOL DRIVER LAYOUT

The EURISOL Driver is a superconducting (SC) linac that includes 5 different sections: Injector, Low-β section, medium-β section, high-β section and CW Beam Splitter (Fig. 2). The lengths of the injector and of the SC part are 12 m and 247 m, respectively, while the 4-way beam splitting section is 55 m long. An additional extraction sector is located at the beginning of the high-β section, giving a beam line for 264 MeV deuterons. All cryostats are planned to work at 4.5K.

### *Injector*

The injector design is rather similar to the SARAF one [3], with modifications required by the different beam types (Fig. 1). Two ion sources are used. The first one is a TRIUMF-type multicusp $H^-$ source [4], located in the straight LEBT line. The second one is an ECR source for production of Deuterons (5 mA) and doubly charged $^3$He (0.1 mA) beams, located in the 90° LEBT branch to allow A/q selection. The minimum beam parameters at the sources output are listed in Table 1.

Table 1: LEBT Input Beams Specifications

| beam | $H^-$ | $^3He^{++}$ | $D^+$ |
|---|---|---|---|
| E (keV/A) | 20 | 20 | 20 |
| I (mA) | 6 | 0.2 | 6 |
| $\varepsilon_x$, $\varepsilon_y$ (π mm mrad rms norm.) | 0.125 | 0.125 | 0.1 |

The LEBT includes 6 solenoids and one dipole. An electron trap is foreseen at the RFQ injection.

The 176 MHz RFQ, resembling the SARAF one, is 3.8 m long and must be able to operate in cw mode. It allows acceleration up to 1.5 MeV/A, requiring a maximum power of 300 kW for acceleration of the Deuteron beam.

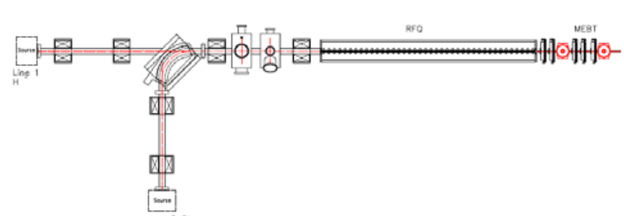


Figure 1: Injector RFQ and MEBT schematic layout.

Little emittance growth and relatively small size and cost are its main characteristics, at the price of a not spectacular transmission (92% accelerated beam for $H^-$ and 95 % for D and $^3$He). However, this appears to be fully acceptable for our application. The transmitted, but not accelerated RFQ particles (about 3%) are lost in the MEBT which is used to match the RFQ beam to the superconducting linac in order to prevent halo formation. The MEBT includes 5 quadrupole magnets and 2 normal conducting HWR bunchers.

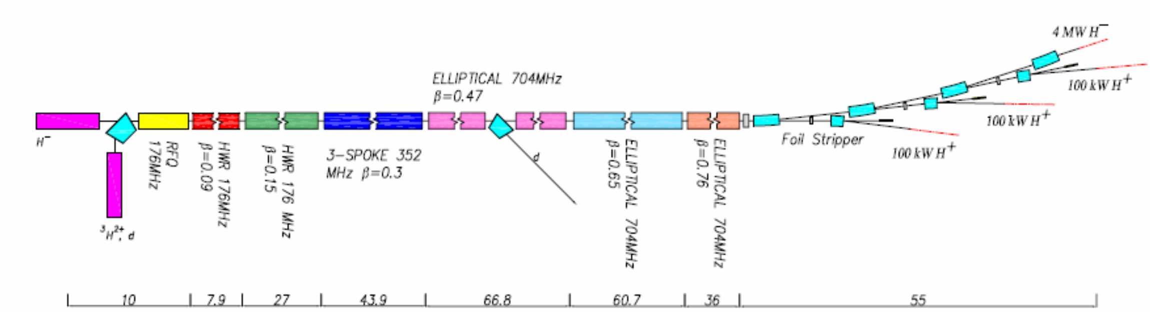


Figure 2: EURISOL Driver schematic layout (not in scale) and length of the different sections.

### *Low-β Section*

The low-β section consists of 9 cryostats, containing 8 176 MHz Half-Wave resonators (HWRs) each.

The required resonators are of 2 types, with $\beta_0$=0.09 and 0.15, working at the conservative gradient of 4.5 and 5.5 MV/m, respectively. They are being developed in the EURISOL Task 8 framework [5]. SARAF resonators [6] might also be adapted to this linac. The HWR geometry was chosen because it is steering free. In the first two cryostats every resonator is alternated with one superconducting solenoid; from the third cryostat on, there is one solenoid every two HWRs. The beam vacuum and the vacuum required for thermal insulation are in common to minimize cost. Until now, the most performing low-β heavy ion linacs in operation working at similar or lower rf frequency, are of this type.

### *Medium-β Section*

The medium-β section is based on 36, 352 MHz triple-spoke resonators, also developed in the EURISOL Task 8 framework, with β=0.3 and a specified gradient of 8 MV/m [7]. The architecture has been optimized with the GenLinWin code [8]. The cryostats contain three resonators each, and in this case, as usual for this rf frequency value, the beam vacuum and the insulating vacuum are separated. Transverse focusing is provided by conventional quadrupole doublets. The matching between the low- and the medium-β sections is achieved by replacing the first medium-β doublet with a triplet.

### *High-β Section*

The high-β section is based on 112, 5-cells elliptical cavities with 3 different optimum β of 0.47, 0.65 and 0.76. These β have been optimized to minimize the length of the linac with the GenLinWin code. The cavities are of the type developed in previous projects and the specified gradients of 12, 18 and 18 MV/m, respectively, were chosen, taking into account the experimental results of the on-line SNS cavities [9]. Transverse focusing is done by conventional quadrupole doublets. In the first subsection, one of the cryostats is replaced by a dipole magnet which allows the deuteron beam extraction at 264 MeV.

## THE 1 GeV, CW BEAM SPLITTER

A unique peculiarity of the EURISOL driver is its possibility of delivering parallel cw proton beams to different targets with low losses [10]. This is achieved by using a $H^-$ primary beam (up to 5 MW), neutralizing part of it (up to 100 kW) by magnetic stripping, and then displacing the unneutralized $H^-$ ions to a different beam line by means of a dipole magnet (Fig. 3). When the two beams are sufficiently separated, the neutral one is transformed into a proton beam by means of a stripper foil. From here on, the H- and H+ beams can be transported independently. The 100 kW limit of the extracted beam is dictated by the present RIB direct target technology. The beam losses, mainly due to the stripper foil efficiency, can be limited to a few tens of Watts and collected by a small beam dump. The splitting operation can be repeated by adding more splitting sections, providing multiple cw beams.

A critical component of the system is the special magnetic neutralizer, a simple and unconventional chicane made of 3 short dipoles that can provide partial neutralization without affecting the primary beam emittance and without producing unwanted $H^+$ ions. Since the neutralization rate is determined by the magnetic field intensity, it is possible to raise slowly the field (thus the secondary beam current) to avoid thermal shocks in the direct RIB targets.

## BEAM DYNAMICS

The linac beam dynamics was studied using the TRACEWIN code developed at CEA Saclay [8]. The transport of all the beams ($H^-$, $D^+$ and $^3He^{++}$) was simulated from the exit of the ion source to the target (except for D which was stopped at its extraction point) with macroparticles. All the cavities and the solenoids have been simulated with their computed EM field maps.

We chose to use conservative specifications for the linac components (cavity gradients, magnet fields) in order to achieve a reliable design without depending on future technological breakthroughs. We kept the transverse and longitudinal phase advance per period below 90° along the linac, and carefully tried to avoid parametric resonances. The continuity of the phase advance per meter has been also an important criterion in

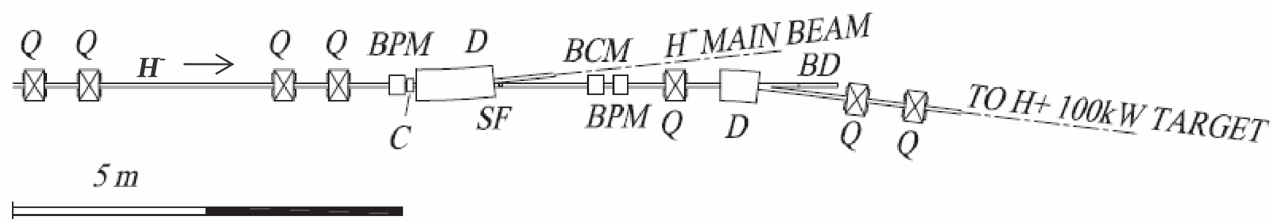


Figure 3: CW beam splitter layout (1 section). The main $H^-$ beam (coming from left) is partially neutralized in a small magnetic chicane (C). In the first bending magnet (D), the main $H^-$ beam is guided to the next splitter section, while the $H^0$ particles move straight to the stripper foil (SF), to be stripped into $H^+$ and then transported to the target. Q=quadrupole magnet; BD=beam dump; BCM=beam current monitor; BPM=beam profile monitor.

order to simplify the matching at transition. This point is especially relevant to transport different beam currents in a common linac. The frequency jump from 352 to 704 MHz was managed according to the technique described in [11] in order to avoid a longitudinal bottleneck just before the high energy section. Beam losses could be confined below 1.5 MeV, before entering the superconducting linac.

A special effort was required for transporting the 5 mA $H^-$ beam in the low-β section, where cryostats with different structure introduce discontinuities in the lattice. However, the final layout could allow transport with satisfactory acceptance and emittance growth for all beams (Tab. 2, Fig. 4 and 5). Studies performed in an earlier version of the HWR section showed a moderate (25%), further increase in emittance growth after introduction of errors in the lattice [12]. Error study for the whole accelerator will begin in autumn 2008.

Table 2: Source-to-target rms Emittance Growth for Each Beam (Longitudinal: from RFQ Output to Linac End)

| beam | $H^-$ | $^3He^{++}$ | $D^+$ |
|---|---|---|---|
| Tr. emittance growth (%) | 75 | 20 | 80 |
| Lg. emittance growth (%) | 43 | 12 | 0 |

## CONCLUSIONS

The EURISOL Driver design has achieved its beam dynamics specifications. The linac, which is only based on the RF superconducting technology above 1.5 MeV/A, is able to accelerate 5mA beams to 1GeV/q (for 1 ≤ A/q ≤1.5) and to 264 MeV (for A/q ≤2). A novel splitting scheme allows to distribute the primary $H^-$ output beam in 4 parallel cw beams which can be used independently in different beam lines.

## ACKNOWLEDGMENTS

We acknowledge the financial support of the European Community under the FP6 ‘‘Research Infrastructure Action-Structuring the European Research Area’’ EURISOL DS Project Contract No. 515768 RIDS.

## REFERENCES

[1] http://www.eurisol.org/site01/index.php
[2] Y. Blumenfeld, proc. of EPAC08, Genova, Italy, 2008.

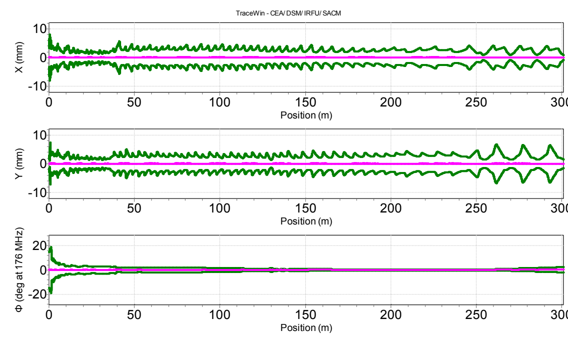


Figure 4: X, Y and phase envelopes for the proton case from the output of the RFQ to the last target location.

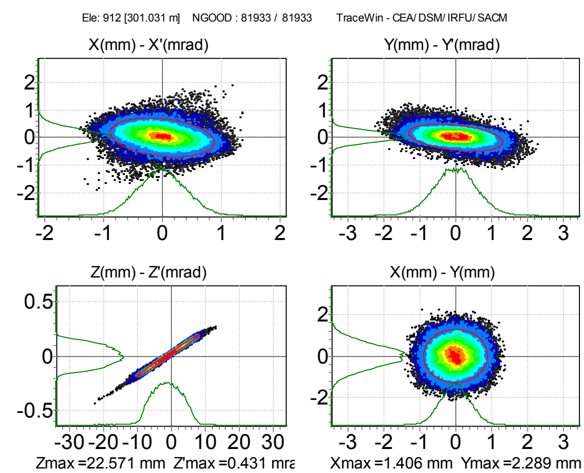


Figure 5: Proton beam at target in the phase spaces.

[3] A. Nagler et al., Proc. of LINAC06, Knoxville, Tennessee, USA, 2006, p. 168.
[4] T. Kuo et al., Rev. Sci. Instr. Vol. 69 N. 2, Feb. 1998.
[5] A. Facco et al., PRST-AB 9, 110101 (2006)
[6] M. Pekeler, K. Dunkel, C. Piel, P. vom Stein, Proc. of LINAC06, Knoxville, Tennessee, USA, p. 321.
[7] S. Bousson et al., Proc. of LINAC 06, Knoxville, Tennessee, 2006, p. 706.
[8] R. Duperrier, N. Pichoff, and D. Uriot, in Proceedings of the International Conference Computational Science, Amsterdam, 2002.
[9] Y. Zhang et al., Proc. of EPAC08, Genova, Italy, 2008, p. 3461.
[10] A. Facco et al., PRST-AB 10, 091001 (2007).
[11] R. Duperrier et al. PRST-AB 10, 084201 (2007).
[12] J. Rodnizki, Proc. of LINAC06, Knoxville, Tennessee, USA, p. 426.

# TRANSVERSE BEAM MATCHING AND ORBIT CORRECTIONS AT J-PARC LINAC

H. Sako#, A. Ueno, T. Ohkawa, Y. Kondo, T. Morishita, JAEA, Tokai, Japan
M. Ikegami, H. Akikawa, KEK, Tsukuba, Japan

## [illegible]

In high intensity $H^-$ beam of J-PARC LINAC, precise control of transverse beam dynamics is extremely important to suppress beam loss. Transverse matching has been performed at several matching sections in LINAC, which consist of knob quadruple magnets (QM's) and wire scanners (WS's) for profile measurements. Mismatch factors of less than 5% have been achieved. Matching of Twiss parameters and dispersion at the RCS injection point has been also done with quadruple magnets at L3BT injection region with beam profiles measured with WS's and also multi-wire profile monitors (MWPM's) at RCS. Orbit corrections along the whole LINAC have been done with steering dipole magnets in the upstream of beam position monitors (BPM's). Orbit deviations were suppressed within 1mm in the whole LINAC.

## TRANSVERSE MATCHING

The strategy of the LINAC transverse matching is as follows;

1. At MEBT1, we fit transverse and longitudinal Twiss parameters and emittance at the MEBT1 entrance.
2. Then, using the beam parameters, an initial QM field pattern at matching sections through LINAC and electric field and phase settings of Buncher 1 and 2 at MEBT1 is calculated requiring matching conditions with a model (TRACE3D).
3. Applying the calculated settings to QM's and Bunchers, we measure beam profiles from most upstream (MEBT1) to most downstream (L3BT injection section) in turn at each matching section. At sections after MEBT1 QM field is corrected to fulfil matching conditions.

The LINAC has 7 matching sections, each of which consists of 4 or more upstream QM's and 4 or more downstream WS's. At MEBT1, only fitting of initial beam parameters is done. At RCS injection section, special matching procedure is performed which is described later. At the rest of matching sections; SDTL entrance, MEBT2, L3BT straight, L3BT arc, L3BT collimator sections, lattices are periodic at each WS position; where the following common procedure has been applied.

1. Fit the XAL online model [2, 3] to measured horizontal and vertical beam widths at 4 WS's by varying ($\alpha_x$, $\alpha_y$, $\beta_x$, $\beta_y$, $\varepsilon_x$, $\varepsilon_y$) at an upstream position from the QM's. The fit is done with a response matrix calculated with the model.
2. Corrections of 4 QM field are calculated to require that $\alpha_x$, $\alpha_y$, $\beta_x$, $\beta_y$ agree at each WS. The calculation is done by applying the response matrix calculated with XAL [2].
3. The above procedures 1 and 2 are iteratively applied until convergence.

In MEBT1, Procedure 1 is replaced by 1';

1'. In addition to transverse parameter ($\alpha_x$, $\alpha_y$, $\beta_x$, $\beta_y$, $\varepsilon_x$, $\varepsilon_y$), longitudinal parameters ($\alpha_z$, $\beta_z$, $\varepsilon_z$) are varied to fit simultaneously beam widths at 4 WS's at MEBT1 and transverse emittance and Twiss parameters measured at a double-slit emittance monitor at MEBT1 bend line [4].

In L3BT injection section, Procedure 2 is replaced by;

2'. QM's after the collimator section (L3BT QM62-79) are used to tune transverse Twiss parameters and dispersion at the RCS injection point of the charge exchange foil.

These procedures are done with a newly developed application called "matcher" [2].

## [illegible]

Measured emittance is shown in Fig. 1 at 5 mA and 30 mA at all sections. At 5 mA, measured 1 σ emittance at 5 mA is 0.17 πmm-mrad and 0.25 πmm-mrad at 30 mA.

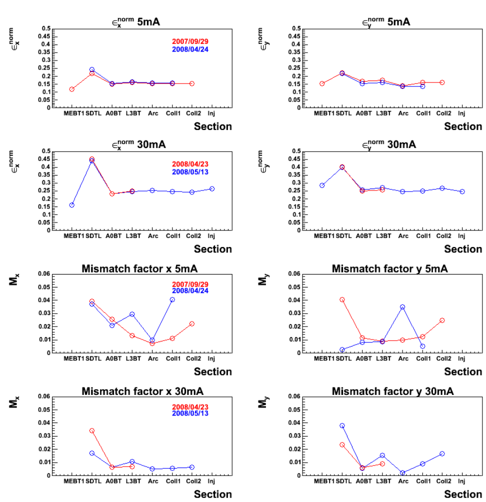


Figure 1: Normalized 1 σ emittance at 5mA (first row) and 30 mA (second row) in horizontal (left) and vertical (right) directions. Mismatch factors at 5 mA (third row) and 30 mA (forth row) in horizontal (left) and vertical directions (right).

Red and blue lines show matching results at two different periods, which proves good reproducibility of the matching procedure. Emittance growth at the SDTL entrance has been observed 5 mA and more enhanced at 30 mA. Mismatch factors of less than 5% have been achieved at 5 mA and 30 mA.

Figure 2 shows fit of beam widths measured from L3BT straight section to L3BT collimator sections to XAL. The XAL model without emittance growth describes very well the data at L3BT.

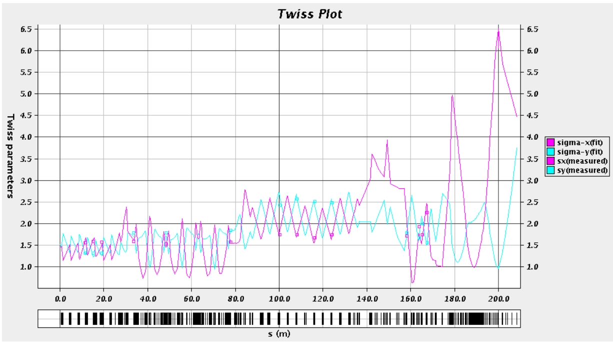


Figure 2: Horizontal (pink) and vertical (blue) 1 σ beam widths [mm] at L3BT fit to XAL model at 30 mA.

## [illegible]

The main goal of this section is to determine transverse and longitudinal beam parameters. Using above method 1', we have fit beam widths at WS's in the straight line, and emittance and Twiss parameters at the emittance monitor at the bend line.

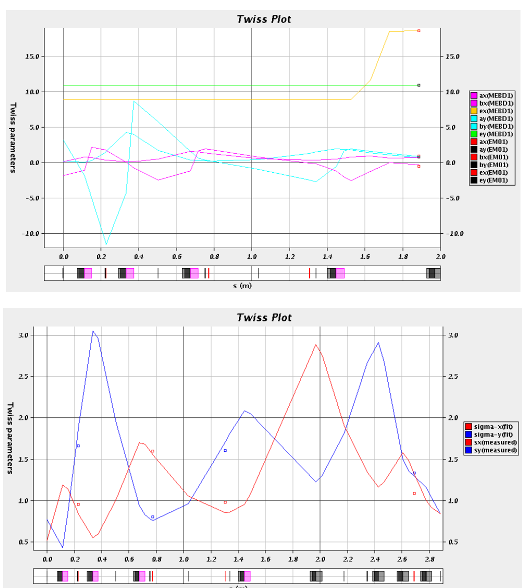


Figure 3: Top: measured transverse emittance and Twiss parameters with the double-slit emittance monitor at MEBT1 bend line. Bottom: measured profile widths with wire scanners at MEBT1. The curves show simultaneous fit with entrance transverse and longitudinal emittance and Twiss parameters.

Reasonable fit has been obtained as shown in Fig. 3. The resulting 5 σ longitudinal emittance at 5 mA and 30 mA is 582 and 477 π deg-keV. The values are similar to preliminary PARMTEQM calculations [7] of 550 and 410 π deg-keV.

## [illegible]

This section tunes Twiss parameters and dispersions at the RCS injection point. The following three sets of beam parameters and QM configurations have been set and measured;

1. "Matched" setting where ($\alpha_x$, $\alpha_y$, $\beta_x$, $\beta_y$) are matched with those of RCS circulating beam.
2. "Dispersion matched" setting where [illegible] and [illegible] at the foil.
3. "Half-matched" setting" which is a default setting with Twiss parameters and dispersions between "Matched" and "Dispersion matched" settings.

Figure 4 shows results of "Half-matched" configuration and fit to the XAL model, which shows beam parameters can be actually controlled by LINAC QM's.

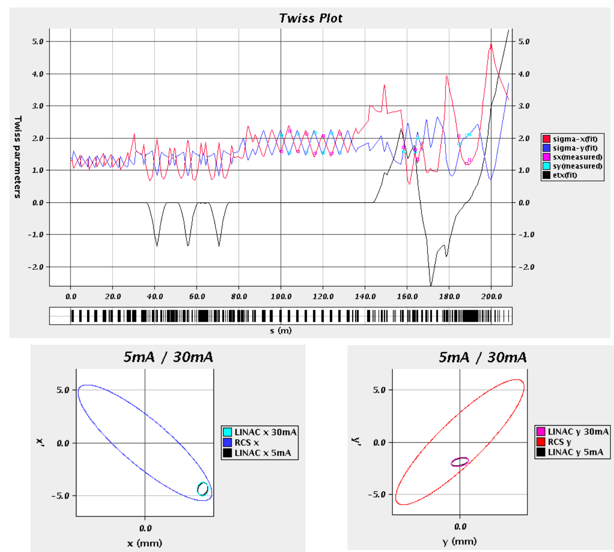


Figure 4: Top: Horizontal (red line) and vertical (blue line) envelopes fit to profile widths (points) and dispersions (m) (black line) calculated by the model at different sets of QM field for "Half-matched" setting at 5 mA. Bottom: Horizontal (left) and vertical (right) phase ellipses of LINAC beam at the injection point at 5 mA and 30 mA with "Half-matched" setting compared to RCS phase ellipse.

# EMITTANCE GROWTH AT SDTL AND COMPARISON WITH IMPACT

In order to understand the observed evolution of emittance from MEBT1 to SDTL exit, we have compared the data with IMPACT simulation [6] at 30 mA. The initial particle phase space distributions are Gaussian with initial Twiss parameters and emittance from the measured values at MEBT1. Figure 5 shows comparison of measured profiles at the second WS in MEBT1, the first WS in SDTL entrance, and the third WS at the MEBT2 section with IMPACT. Another distributions with $\alpha_x$, and $\alpha_y$ deviated by ~25% to make mismatch by ~30% at the DTL1 entrance are also simulated. In that case, IMPACT does not deviate from measured profile data very much. IMPACT in both cases apparently underestimates the beam width at the SDTL entrance, and fails to create tails at the SDTL exit.

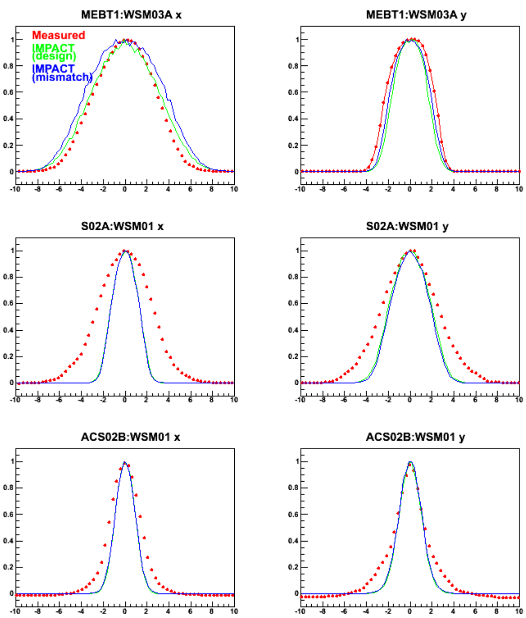


Figure 5: Horizontal (left) and vertical (right) beam profiles at MEBT1 (top), SDTL entrance (middle), and SDTL exit (bottom). Red dots show measured data with WS's. Blue lines show IMPACT calculations with the initial beam parameters from fit at MEBT1. Green lines show IMPACT calculations mismatched at the entrance of DTL1 by deviating initial Twiss parameters

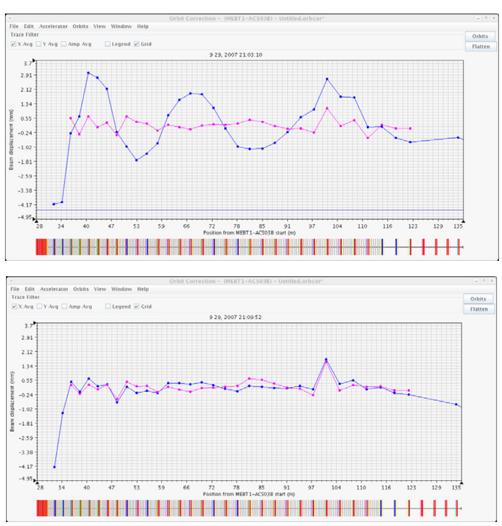

Figure 6: Horizontal orbit positions as a function of a distance at SDTL before correction (top) and after correction (bottom). Blue lines show measured beam positions, and pink lines show predicted positions.

## ORBIT CORRECTIONS

Orbit corrections are performed for good beam transport and beam loss suppression. Main sources of orbit deviations are alignment errors of magnets, and magnetic and electric field errors. Beam positions are measured with beam position monitors (BPM's), and orbits are corrected with dipole steering magnets. The corrections are calculated with XAL in the application "orbitcorrect" as shown in Fig. 6 [5]. Orbit references and steering field patterns are saved, and orbit corrections are started with the restored field patterns and the orbit references. After the corrections, the orbit deviations are suppressed within 1 mm. The dipole field patterns have been stable at different runs.

## CONCLUSIONS

Procedures of transverse matching in the whole LINAC have been established. At MEBT1, longitudinal and transverse initial beam parameters have been obtained. From SDTL to L3BT collimator sections, mismatch factors less than 5% have been achieved with good reproducibility. Twiss parameters at the RCS injection point have been controlled by QM's at LINAC. Emittance enhancement has been observed at SDTL entrance, and profile tails have been developed after SDTL. They are not reproduced by IMPACT by causing mismatch by varying initial transverse Twiss parameters in the constraint of profile data at MEBT. This problem is not critical for beam loss and emittance enhancement. However, to solve this problem it is necessary to improve precision of geometry, magnetic and electric field at MEBT1, DTL and SDTL. Orbit corrections have been successfully performed with orbit deviation within 1 mm.

## REFERENCES

[1] J. Galambos, et al., "XAL Application Programming Framework", ICALEPCS 2003, Gyeongju, Korea.
[2] H. Sako, et al., "Transverse Beam Tuning and Injection to RCS at J-PARC LINAC", WP086, 5th Annual Meeting of Particle Accelerator Society of Japan, Hiroshima, Aug. 2008.
[3] C. K. Allen, et al., "XAL Online Model Enhancements for J-PARC Commissioning and Operation", MOPAN029, PAC07, Albuquerque, USA.
[4] M. Ikegami, et al., "Beam Commissioning of the J-PARC Linac Medium Energy Beam Transport at KEK", pp 1509, PAC03, Portland, USA.
[5] H. Sako, et al., "Development of Commissioning Software System for J-PARC LINAC", MOPAN044, PAC07, Albuquerque, USA.
[6] J. Qiang, et al., J. Comput. Phys. 163, 434 (2000).
[7] K. R. Crandall et al., "RFQ Design Codes", LA-UR-96-1836.

# DEVELOPMENT OF MODULATING PERMANENT MAGNET SEXTUPOLE LENS FOR FOCUSING OF PULSED COLD NEUTRONS*

Masako Yamada, Yoshihisa Iwashita, Masahiro Ichikawa, Hiromu Tongu, Hiroshi Fujisawa (ICR, Kyoto University, Uji Kyoto Japan), Hirohiko M. Shimizu, Takashi Ino, Kenji Mishima, Kaoru Taketani, Takahiro Morishima, Suguru Mutou, Tamaki Yoshioka (KEK, Ibaraki Japan), Takayuki Oku, Kenji Sakai, Takenao Shinohara, Jun-ichi Suzuki (JAEA, Ibaraki, Japan), Katsuya Hirota, Yoshie Otake, Hiromi Sato (RIKEN, Wako, Saitama), Yoshichika Seki (Kyoto University, Kyoto), Sinsuke Kawasaki, Hidetoshi Otono, Sachio Komamiya (The University of Tokyo), Satoru Yamashita, Yoshio Kamiya (ICEPP, Tokyo), Peter Geltenbort (ILL, Grenoble, France)

*Abstract*

Cold neutron beams can be focused by a strong sextupole magnetic field. A permanent magnet sextupole lens whose focusing strength can be synchronously modulated at the rate of pulsed cold neutron beams is under development. This device should keep the focal point for pulsed neutron beams whose wavelength spreads as a function of time of flight. This kind of device improves the utilization of valuable neutrons and saves experiment time and costs. It will raise linac based small neutron sources as a good counter part to large powerful neutron facilities. Experimental results that were obtained at Institute Laue-Langevin (ILL) are also described.

## INTRODUCTION

Neutron beams are well known as powerful probes for both material science and fundamental physics. The applicable research field, however, is limited by the low intensity of the neutron beams. Meanwhile, the efficiency of a neutron beam has recently been much improved by techniques such as neutron optics [1-6], time of flight (TOF) method, and so on.

Among such neutron optics devices, a magnetic lens can focus neutron beams on such targets as samples and/or detectors by using interaction between the neutron's magnetic dipole moment and the sextupole field. When we apply the TOF method to pulsed neutrons for increasing the efficiency of each experiment, the wavelength range to be covered is in the order of a few times. The time dependence of the wavelength λ is proportional to $t$ (time of flight of a neutron). Then we should modulate the field gradient proportional to $t^{-2}$ in order to keep the focal length $Z_f$ fixed independent of $\lambda$. With these aspects, we are developing a modulating permanent magnet sextupole lens (PMSx) for focusing of pulsed neutron beams with chromatic aberration suppressed. The sextupole lens is composed of permanent magnets (NdBFe) because they can generate a strong magnetic field within limited space.

This lens increases the intensity of neutron beams on a target to reduce an experiment time with sufficient count rate and to increase the spatial resolution. Then neutron probe applications can be widely extended, for example, even the linac-based small neutron source now under development becomes practical.

## FOCUSING OF PULSED NEUTRONS BY SEXTUPOLE MAGNET

The origin of the focusing force is the interaction between neutron's magnetic dipole moment and the external magnetic field [7-9]. A sextupole component of magnetic field B can be written as:

$$|B| = G'/2\left(x^2 + y^2\right) \qquad (1)$$

where $G'$ is a positive value indicating the strength of the gradient of magnetic field. In the sextupole field, neutrons feel the thrusting force proportional to the distance from the magnetic centre and their equation of motion is a simple harmonic oscillator described as

$$\frac{d^2x}{dt^2} = -\omega^2 x,\quad \frac{d^2y}{dt^2} = -\omega^2 y,\quad \frac{d^2z}{dt^2} = 0 \qquad (2)$$

where $\omega^2 = G'\alpha$, $\alpha = |\mu_n/m_n| = 5.77$ m$^2$ s$^{-2}$ T$^{-1}$, $\mu_n$ is magnetic dipole moment and $m_n$ is the mass of neutron, in case the neutron spin is parallel to the local magnetic field [7-8]. When the ambient magnetic field is strong and changes slow enough (adiabatic condition), the spin direction follows the magnetic field direction. Because the magnetic dipole moment of the neutron is connected to the spin, the polarity of the force changes in accordance

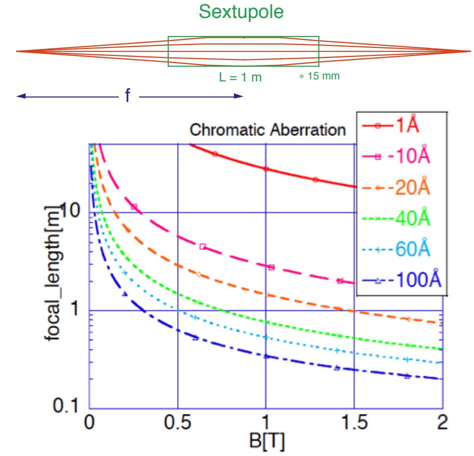


Figure 1: Focusing of neutrons by sextupole magnet and chromatic aberration.

*Work partially supported by the Ministry of Education, Science, Sports and Culture, Grant-in-Aid for Scientific Research (A), 18204023(2006) and 19GS0210.

with the spin polarity. The focal point is described as

$$Z_f = Z_m + \frac{h}{\omega m_n \lambda} \cot\left(\frac{\omega m_n \lambda}{h} Z_m\right). \tag{3}$$

When $\lambda$ is close to zero, Eq. 5 can be rewritten as

$$Z_f = \frac{2}{3} Z_m + \frac{1}{Z_m G \alpha}\left(\frac{h}{m_n \lambda}\right)^2, \tag{4}$$

where $h$ is Plank constant. The focal length of the magnetic lens depends on the wavelength (momentum) of the neutrons and field gradient (Fig. 1). For pulsed neutrons, we can apply the Time of Flight method for effective use of valuable neutrons. In that case, we need to modulate the field gradient according to the wavelength change in time. In order to keep the focal length constant independent of the $\lambda$ proportional to t, in other words, to suppress the chromatic aberration, we need to follow the relation:

$$G' \propto \lambda^{-2} \propto t^{-2}. \tag{5}$$

## FABRICATION OF THE PROTOTYPE

We have fabricated a prototype of magnetic lens using permanent magnets as mentioned before (see Fig. 2). In order to adjust the strength, the magnet is divided into two nested co-axial rings, where the inner ring is fixed and the outer ring can be rotated (see Fig. 3). Synchronizing the modulation with neutron beam pulse suppresses the chromatic aberration. Strictly speaking, the modulation is not proportional to $t^{-2}$ but sinusoidal. But we can use a part of the descending slope.

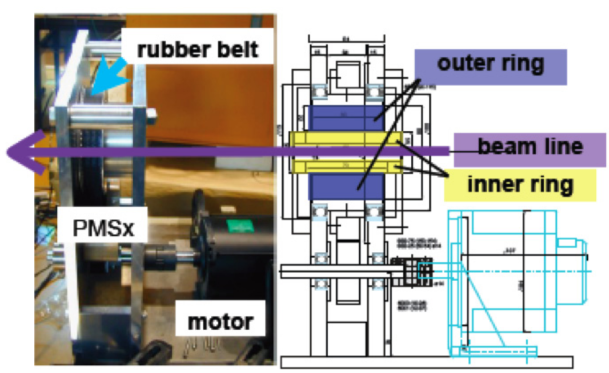


Figure 2: The overview and cross section of the prototype of PMSx

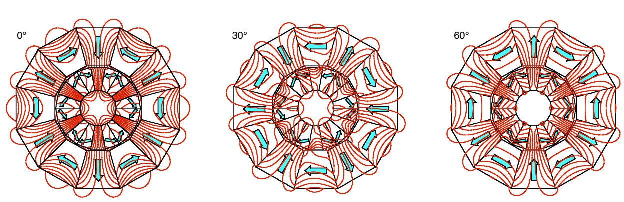


Figure 3: Sextupole with two-nested ring structure. (a) maximum strength position where the outer ring is in phase with inner ring (b) 30° rotated (c) minimum strength position where the outer ring is out of phase (60°). The arrows indicate the easy axes of the magnet pieces. The pieces without arrows are made of soft magnet material.

The magnet has Extended Halbach configuration, where one of the soft magnetic materials, Permendur, is used as pole material to generate stronger field [10]. The outer ring is composed of 12 magnet pieces and the inner ring is composed of 12 magnet pieces and 6 Permendur ones (18 pieces total). The magnetic field changes three times in one revolution of the outer ring. The diameter of the bore is 15mm, the repetition rate of the magnetic field modulation is 25Hz (the same as J-PARC), and the magnet length is 66mm. The strongest magnetic field (rotation angle is determined as 0º) measured by single axis tesla meter (Group-3 DTM151) at the surface of poles showed 1.65 T, $G = 5.69 \times 10^4$ [T/m$^2$], and the focal length is calculated to be about 0.5m for $\lambda$=40Å, which is a practical value (see Fig. 4).

The temperature rise during the operation has been reduced [11] and is under improvement further beyond.

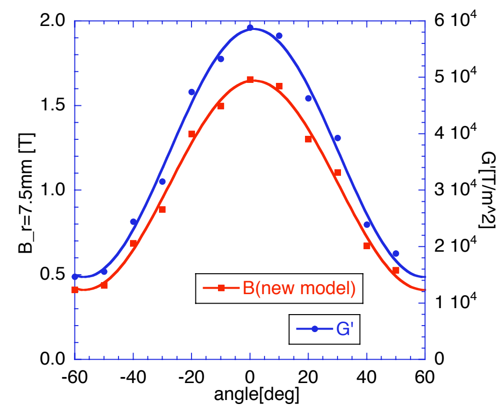


Figure 4: The measured magnetic field modulation and derived its field gradient.

## EXPERIMENTS WITH VCN

We carried out experiments on focusing of pulsed VCN with TOF method in PF2 beam line at ILL. In this experiments, we fixed the outer ring rotation angle at 0º, 31.7º and 60º (see Fig. 4). The setup is shown in Fig. 5. The disc-chopper (see Fig. 5 right) chops the continuous neutron beams to be pulsed, around 20~60Å in their wavelengths. The detector has time resolution and 2D spatial resolution, which is composed of a scintillation screen and 2D-PMT. The polarising super mirror selects neutrons with parallel spins to the magnetic field, thus only the images of focused neutrons are detected. After the ø1mm slit, in order to satisfy the adiabatic condition as mentioned at Eq. (2), we placed two dipoles to keep the polarization. The magnetic field from the mirror to the PMSx was not less than 15G. We obtained the wavelengths (momentum, energy) from their time of flight when neutrons are focused by PMSx, and compared with the field gradient.

The results are shown in Fig. 6 and Table 1. The results are consistent with the calculation. We confirmed that neutrons are focused depending on the strength of magnetic field. However, the timing offset ($t_0$) is not considered in this analysis. We plan to determine the $t_0$ pre-

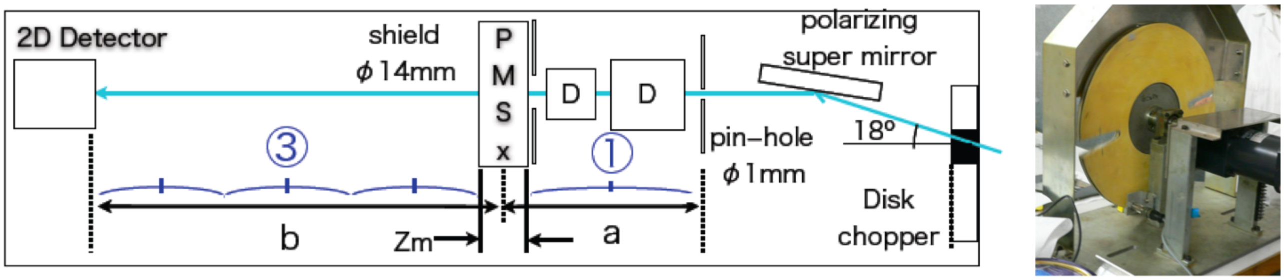


Figure 5: (left): The set up of experiments: a=720mm, b=2140mm, then $Z_f$=540mm. (right): The disk-chopper making the VCN beam pulsed.

Table 1: the results compared with calculation

| angle [deg] | B(r=7.5mm) [T] | $G'\times10^4$ $[T/m^2]$ | λ[Å] (calc.) | λ[Å] (meas.) |
|---|---|---|---|---|
| 0 | 1.65 | 5.88 | 38 | 39 |
| 31.7 | 0.89 | 3.15 | 49 | 50 |
| 60 | 0.41 | 1.48 | 75 | out of focus |

cisely soon. It should be mentioned that we might see the effect of gravity from the vertical movements of the centre (see Fig. 6 - right).

## FUTURE PROSPECTS

We are going to develop a practical PMSx this year. Firstly, we will have the pole sliced thinner and annealed for less eddy currents and hysteresis losses, while keeping the strength of the magnetic field as good as possible. Secondly, we are going to incorporate a technique for smooth rotation of the outer ring such as a torque canceller.

The first application of this device would be Small Angle Neutron Scattering (SANS) for material science. Dr. Bleuel has carried out some focusing-SANS experiments with our PMSx after our experiments [12]. The idea of PMSx can be extended widely when we use the time harmonics. It will ease the adjustment of time variation of the focusing strength.

## REFERENCES

[1] P.S. Farago, Nucl. Instr. and Meth. 30 (1964) 271.

[2] H.M. Brash et al., Proc. Roy. Soc. Edinburgh A 68 (part. 2) (1969) 158.

[3] G.I. Terekhov, Pis'ma Zh. Tekh. Fiz. 3 (1977) 1275 [Sov. Tech. Phys. Lett. 3 (1977) 526].

[4] J.H. Coupland, R.V. Stovold, Sixth International Conference on Magnet Technology, Bratislava, Czechoslovakia, 29 Aug.}2 Sep. 1977, p. 558.

[5] W.G. Williams, Polarized Neutrons, Clearendon Press, Oxford, 1988.

[6] Z.J. Yang, D.J.W. Geldart, R.A. Dunlap, Phil. Mag. B 68 (1993) 713.

[7] H.M. Shimizu, et al., Physica B 241–243 (1998) 172.

[8] H.M. Shimizu, et al., Nucl. Instr. and Meth. A 430 (1999) 423.

[9] J. Suzuki, et al., Nucl. Instr. and Meth. A 529 (2004) 120

[10] Y.Iwashita, et al, Nucl. Instr. and Meth. A 586 (2008) 73

[11] M.Yamada, et al, EPAC08, WEPC164 (2008)

[12] M. Bleuel, et al, PNCMI2008 Poster B26 (2008)

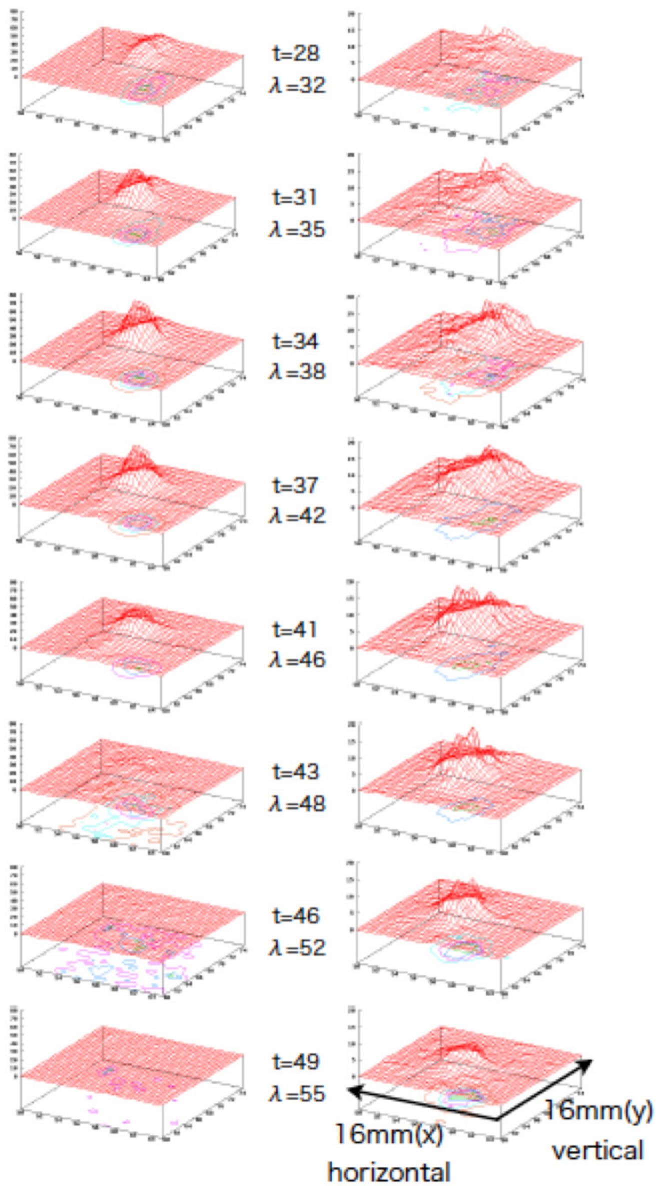


Figure 6: Neutron intensity map on the 2D detector: the vertical axis shows counts. (left) fixed angle; 0° (strongest G') (right) fixed angle; 31.7° (weaker G'). We confirmed that the neutrons with specific wavelengths are focused according to the strength of magnetic field.

# MULTIPACTING SIMULATION IN RF STRUCTURES

M.A.Gusarova, V.I.Kaminsky, S.V.Kutsaev, M.V.Lalayan, N.P.Sobenin, MEPhI, Moscow, Russia
L.V.Kravchuk, S.G.Tarasov, INR, Moscow, Russia

*Abstract*

A new computer code for 3D simulation of multipacting phenomenon in radio frequency (RF) structures is developed. Simulation results in various RF devices are compared with theoretical calculations and experimental measurements.

## INTRODUCTION

Design of accelerating cavities, input power couplers and other RF devices for the charged particle accelerators should provide the conditions of multipactor discharge elimination or suppression. The multipactor effect is a phenomenon in radio frequency (RF) devices (cavities, waveguides and others), where, under certain conditions, secondary electron emission in resonance with an alternating electric field leads to exponential electron multiplication, possibly damaging and even destroying the RF device.

Currently, there are three general approaches for suppressing multipactor discharge: conditioning of the components by the discharge, coatings and other surface treatments, and geometrical modifications. Proper design and geometry choice are the most powerful methods for multipactor suppression. Geometry modification results in electromagnetic field pattern changes. Latter leads to electrons trajectories distortion that breaks resonant conditions for multipactor discharge.

The code MultP–M is a tool that allows the analysis of multipacting in fully 3 dimensional RF structures and the modification for multipactor suppression

## MULTP-M

The main window MultP-M is presented on Fig. 1. The code was programmed using Object Pascal in Delphi environment.

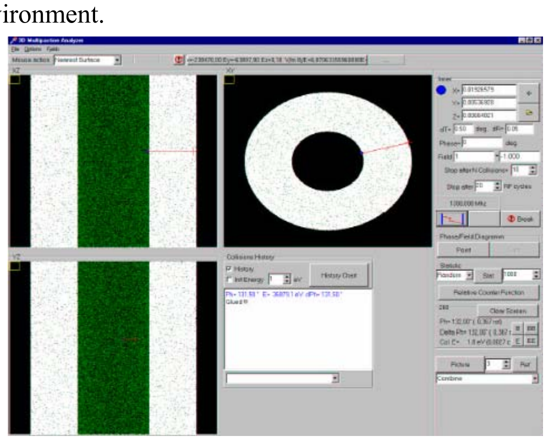

Figure 1: The main window. Example: single trajectory in a coax cavity.

MultP–M is the succeeding code for MultP [1, 2]. The latter was upgraded to get more functionality.

The code MultP–M is a tool that allows the analysis of multipacting in fully 3-dimensional RF structures. It solves the non-relativistic equation of motion of electrons in time harmonic rf fields. MultP–M does not contain a field solver, but it provides an interface to import the field-map from a text-file. The external field solver must be able to export field-maps to text-files, and it is strongly recommended that it uses a conformal mesh (mesh-points coincide with the boundary). MultP-M takes into account the RF device operation mode and allows simulation both for standing and traveling waves.

The resulting trajectories can be analyses by means of electron counter function and various statistics (statistics - particle counter, statistics - impact energy distribution, statistics - distribution of impact phases, statistics - the collision counter, statistics - finding trajectories with more than n impacts). All parameters used in the calculation (field level ranges, SEY, initial energy of electron, electron emission phases, initial number of particles, minimal collision, frequency, and limitation of number of field periods for calculation) are assigned by user.

The final decision whether multipacting is possible or not is up to the user.

### *Testing of MultP-M*

As the test several narrow rectangular waveguides were simulated. For the narrow rectangular waveguides it is possible to do the theoretical estimation of the electric field strength threshold providing the conditions to multipactor discharge (equation 1). Resonance sizes of discharge gaps h(k) can be calculated using expression (2).

$$E_0 = \frac{\omega}{e}\sqrt{\frac{W_1 m}{2}} \quad (1) \qquad h^{(k)} = \frac{eE_0 k\pi}{m\omega^2} \quad (2)$$

Here h - distance between the wide walls of waveguide, k - multipactor order, $W_1$ - energy of primary electron providing SEY > 1. These equations are rather simple and leave out the electron's initial phase and velocity spread.

Two rectangular waveguides were studied namely copper waveguides of 70x3.5 mm and 70x2.1 mm operated on 1.3 GHz.

Fig. 2 illustrates direct modeling results for 70x3.5 mm waveguide presented in two cross sections in xy and yz planes. The region subject to multipactor electrons burst is marked with dark blue.

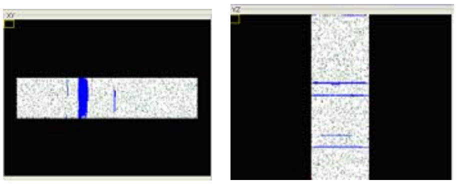

Figure 2: Multipactor discharge region in narrow rectangular waveguide.

The results of theoretical calculation of electrical field strength threshold and simulation done by MultP–M code are summarized in table 1.

Table 1: The Results of Theoretical Calculation of Electrical Field Strength Threshold and Simulation Done by MultP–M.

| Narrow waveguide (normal conducting, Cu) 70×3.5 mm | | |
|---|---|---|
| | Theoretical calculations | MultP–M |
| Field strength, kV/m | 450 | 448 |
| Order of the multipacting | 5 | 5 |
| Narrow waveguide (normal conducting, Cu) 70×2.1 mm | | |
| | Theoretical calculations | MultP–M |
| Field strength, kV/m | 450 | 447 |
| Order of the multipacting | 3 | 3 |

It is seen that the results are in good agreement within ±3 kV/m. This divergence can be caused by constant secondary electron emission yield value for impact energy 200 eV, used for analytical calculation, whereas the entire yield on energy dependence was used in numeric simulation.

## EXAMPLES SIMULATION

In order to illustrate MultP-M usage let us consider accelerating cavity (standing wave mode) and ceramic window (traveling wave mode) analysis

### *RF Cavity*

The superconducting accelerating cavity for Energy Recovery Linac [3] is good choice to illustrate multipactor simulation in standing wave device. Its model made in MultP-M is shown on Fig. 3.

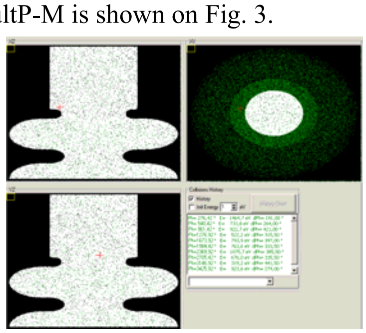

Figure 3: Cavity model in MultP-M.

Electromagnetic field distribution used for simulation had values defined for Nx=100 $N_y$=100 $N_z$=300 nodes. Electron energy providing SEY>1 was 50 to 1500 eV. Simulation made for 1000 initial particles. The results of simulation done by MultP–M are presented on Fig. 4 – 6.

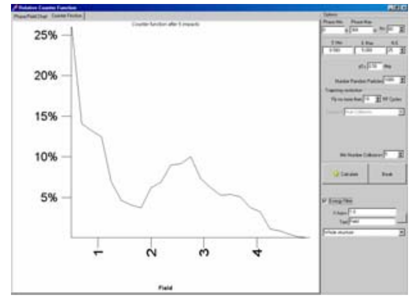


Figure 4: MultP-M, Electron Counter Function; (1= 11.635 MV/m).

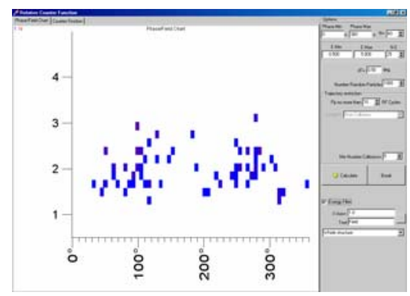


Figure 5: MultP-M, Phase/Field Diagram; (1= 11.635 MV/m).

From simulation results namely Electron Counter Function and Phase/Field diagram presented on Fig. 4. It is seen that about 10% of the primary particles remain in the structure for the field strength ~ of 21 - 36 MV/m (normalized value 1.8 – 3.1). Impact energy distribution study for this field strength range showed that electrons impact energy corresponds to SEY value exceeding one.

Electron trajectories thorough analysis showed the resonant conditions exist in rounded interconnection area between cell and drift tube. These trajectories are shown on Fig. 6 exist for electric field strength on axis ranging from 22 to 36 MV/m.

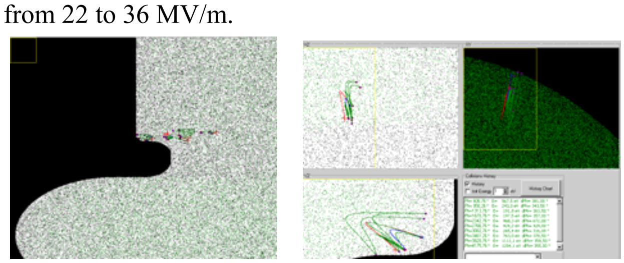

Figure 6: Resonance electron trajectories.

Summarizing the results described above one could conclude that this structure is subject to multipactor discharge on drift tube to cell interconnection region. Multipactor is most possible to occur for on-axis electric field strength range 22–36 MV/m. This result obtained using MultP-M code agrees with published data [3].

## *Ceramic RF-windows*

Ceramic vacuum windows are traveling wave operating devices. It is to be noted that usually there are at least two different materials featuring diverse SEY values used in design. In order to simulate multipactor in this case MultP-M allows assigning different properties for all materials used in single model.

Some results of Energy Recovery Linac [4] RF-coupler cold window simulation using MultP-M code are presented below. The cold window model used for simulations included the ceramics, upstream coaxial line from warm window (D=62 mm, d=28.8 mm) and the downstream one to cavity (D=62 mm, d=22.8 mm).

Fig.7 - 8 illustrates the direct modeling results for multipactor discharge at 100 and 700 kW transmitted power.

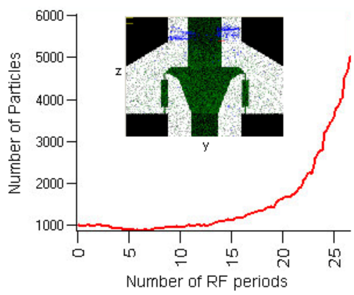


Figure 7: Statistical simulation results for ceramic window operated at 100kW.

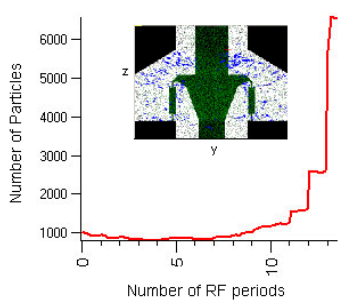


Figure 8: Statistical simulation results for ceramic window operated at 700 kW.

The statistical simulations were made using 1000 initial particles of 1eV energy. Secondary electron emission yield for metal was equal to 3 and for the ceramics was 6. Electromagnetic fields were obtained using Microwave studio run for model with 30.000 nodes. The area where multipactor occurs is marked with dark (blue) fill.

The simulation results showed that the multipactor could occur when power > 50kW. It is seen, that for low power less than 200 kW the dangerous areas located close to coaxial waveguides Fig. 7 whereas the discharge in the ceramics vicinity could occur for higher power Fig. 8.

## CONCLUSIONS

MultP–M code is a convenient tool designed for multipactor discharge simulations in RF devices of a complicated 3D shape. The results obtained using MultP-M code are agree with theoretical and experimental data. MultP–M makes the modification, optimization and design available for RF components used in the charged particle accelerators.

## REFERENCES

[1] L.V.Kravchuk, G.V.Romanov, S.G.Tarasov, “Multipacting Code for 3D Accelerating Struc-tures”, XX International Linac Conference, Monterey, California. 2000

[2] M.A.Gusarova, V.I.Kaminskii, L.V.Kravchuk, S.V.Kucaev, M.V.Lalayan, S.G.Tarasov, N.P.Sobenin “Evolution of 3D simulation multipactoring code MultP”, XX International Workshop on Charged Particle Accelerators, Ukraine, Alushta, 2007

[3] S. Belomestnykh, V. Shemelin, “Multipacting-free transitions between cavities and beam-pipes”, SRF 080415-01

[4] 11. M.A.Gusarova, A.A.Zavadtsev, D.A.Zavadtsev, A.A.Krasnov, M.W.Lalayan, N.P.Sobenin,” Input coupler development for superconducting cavity 500kW CW power feed”, Problems of atomic science and technology, 2006, #3,P.101-103.

# ANALYSIS OF INPUT COUPLER ASYMMETRY INFLUENCE ON BEAM DYNAMICS IN ACCELERATORS WITH SUPERCONDUCTING CAVITIES

S.V.Kutsaev, M.V.Lalayan, V.A.Makarov, N.P.Sobenin, MEPhI, Moscow, Russia
V.I. Shvedunov, SINP MSU, Moscow, Russia
A.A.Krasnov, A.A.Zavadtsev, ScanTech Sciences, LLC, Affiliate in Russia, Moscow

*Abstract*

An investigation of input coupler asymmetry influence on electron beam dynamics in energy recovery linacs (ERL) with superconducting cavities was carried out. There were several types of input power couplers – coaxial and waveguide, asymmetric and symmetric considered. Using numerical simulation the electromagnetic fields distribution in accelerating cavity with input coupler was found and transverse deflecting impulse was calculated. RTMTRACE code was adapted for beam dynamics modeling.

## INTRODUCTION

Choice of asymmetric geometry for RF-power input coupler for accelerator leads to transverse components of EM-field on the beam axis, which are responsible for a transverse impulse deflecting particles from the axis and making the beam emittance grow. To estimate the influence of the current effect on beam dynamics a notion of the beam kick is introduced. Numerically it is characterized by a ratio of Lorenz force integral normalized by charge and integral of longitudinal accelerating component of EM-field. Integration is made along the trajectory of the beam center. One must also take into account transit-time factor.

$$kick = \frac{V_t}{V_{acc}} = \frac{\int \left(E_y + eH_x\right)dx}{\int E_z dz} \qquad (1)$$

Calculation of beam emittance change due to field asymmetry in the beam region can be performed by analytical formula, which is given in [1]. More precise results can be obtained by modeling of beam dynamics, i.e. by solving motion equations for all beam particles in the field distribution obtained. RTMTRACE software was used for that task. It was originally designed for electron beam dynamics simulation in microtron [2]. Further developments made it possible to use RTMTRACE for calculation of other accelerating structures. One has to provide EM-field calculated using external software and exported to file in a special format for dynamics modeling. Also, to calculate structures considered below initial program was modified and compiled to produce an executable file.

## COAXIAL INPUT COUPLER

Calculations were made for structures with coaxial and waveguide input couplers presented in Fig. 1.

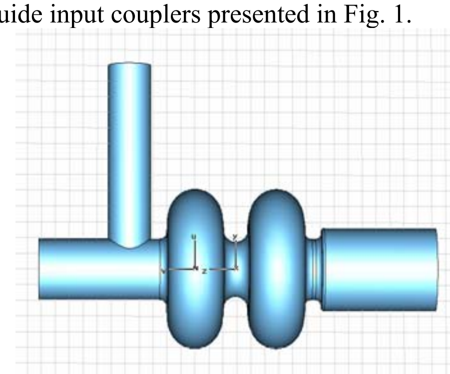

a

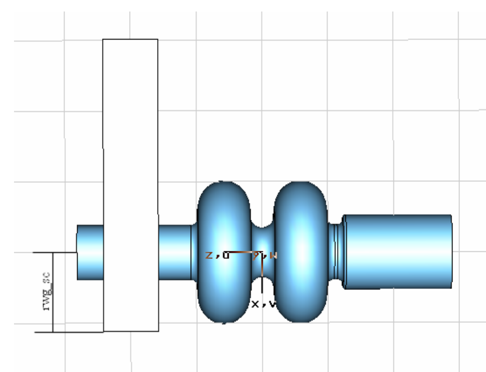

b

Figure 1: Coaxial and waveguide input couplers.

Calculation for a structure with a single coaxial input coupler (Fig.1, a) was performed to compare results with those given in [1]. During field calculation manual mesh optimization was performed in order to increase the number of mesh nodes in the beam region. Finally mesh with 160000 elements was used for field calculation, 10000 nodes corresponded to the beam region. Fig.2 presents the components of EM-fields in asymmetric coaxial input coupler calculated for perfect electric wall set as boundary condition. Similar calculations were made for a perfect magnetic wall.

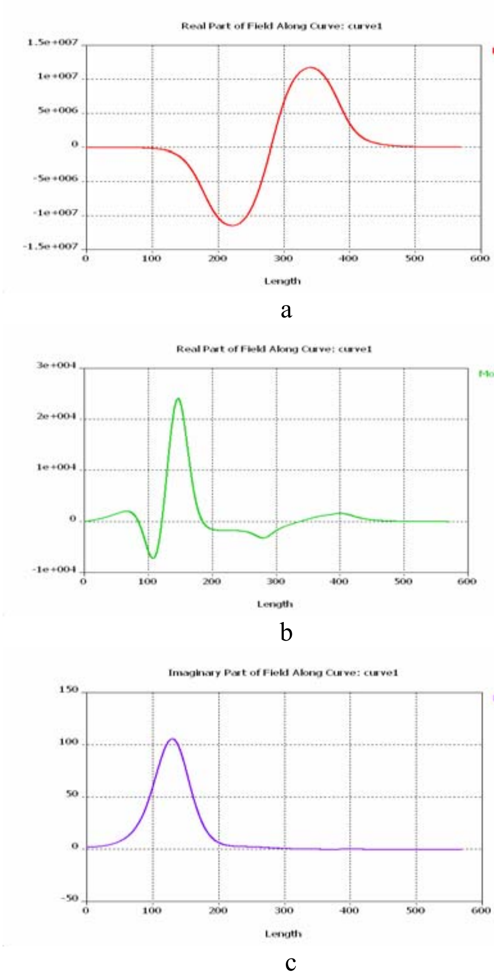


Figure 2: Longitudinal (a), transverse (b) components of electric field and transverse component of магmagnetic field (c) on structure axis for electric wall boundary condition.

Table 1 gives values of peak electric and magnetic field components values, obtained by calculation with two boundary conditions (E-wall and H-wall). In order to determine kick in two-cell buncher of ERL by using these data normalization was made to get effective accelerating voltage in the cavity equal to 1 MV. The kick calculation method gave kick = 0.0014 – 0.0018i. The following parameters of ERL injector were used: operating frequency is 1.3 GHz, initial beam energy 4 MeV, accelerating voltage 1 MV, beam current 0.1 A, charge 77 pC, transverse beam radius $\sigma_{x,y}$=2 mm, beam length $\sigma_я$=0.6 mm, and initial emittance $\varepsilon_0$=1 mm*mrad. Beam emittance growth calculated by the analytical formula [1] for kick value obtained was 12% for one of the five accelerating cavities. The difference from the result of 20% given in [1] can be explained by mesh effects, and by different software used to compute fields.

Beam dynamics modeling by RTMTRACE in cavity with the single coaxial input coupler was done for two various electron bunches. Results are given in Table 2.

Table 1: EM-Field Components Peak Values on Beam Axis

| Component | Peak value | |
|---|---|---|
| | E-wall | H-wall |
| $E_z$ [V/m] | $1.1\cdot10^7$ | $1.1\cdot10^7$ |
| $E_y$ [V/м] | $2.6\cdot10^4$ | $5.6\cdot10^4$ |
| $c\cdot B_x$ [V/m] | $4.0\cdot10^4$ | $4.0\cdot10^4$ |

Table 2: Electron Beam Dynamics Modeling Results

| Bunch | q [pC] | $\varepsilon_0$ [mm·mrad] | $\sigma_z$ [mm] | $\sigma_{x,y}$ [mm] | emittance growth, % |
|---|---|---|---|---|---|
| 1 | 77 | 1 | 0.6 | 2 | 5 |
| 2 | 8 | 0.1 | 0.6 | 0.6 | 12 |

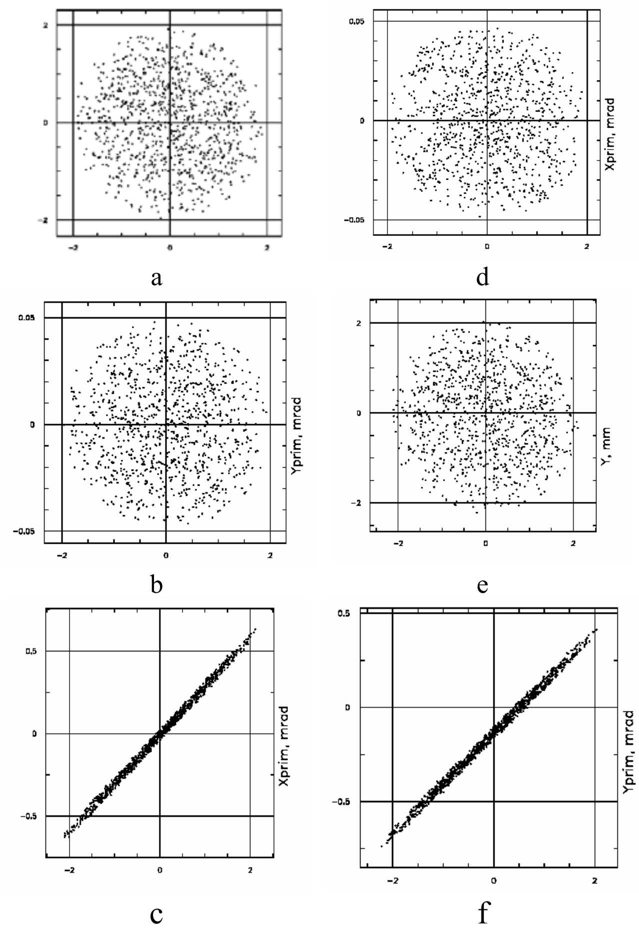


Figure 3: Beam parameters before (a – cross-section, b – phase plane x-xp, c– phase plane y-yp) and after passing the accelerator (d– cross-section, e – phase plane x-xp, f – phase plane y-yp).

Beam characteristics obtained using RTMTRACE before and after passing the accelerator are presented on Fig.3. Here are some other output parameters of beam dynamics modeling: energy spread – 6.23%, maximum particle deflection – 2.25 mm from axis, bunch length – 1.05º.

Structure with symmetric coaxial input coupler was also used to determine beam dynamics with RTMTRACE. Two cases given in Table 2 were considered. For either case the emittance growth did not exceed 4%.

## WAVEGUIDE INPUT COUPLER

Waveguide input coupler, shown in Fig. 1, b is proposed as a good alternative to coaxial coupler if geometric asymmetry does not lead to considerable transverse components values of EM-field in the beam region. Analysis of the structure using MWS showed that on-axis field distribution is strongly affected by the length of short-circuited waveguide, which is noted as *rwg_sc* in Fig. 1, b. Table 3 gives values for peak fields on structure axis for two values of *rwg_sc* – 111 mm and 145 mm.

Table 3: Peak Field Values on Structure Axis with Various Lengths of Rectangular Waveguide

| Boundary | Parameter | | |
|---|---|---|---|
| | $E_z$ [V/m] | $E_y$ [V/m] (min./max) | $cB_x$ [V/m] |
| | Peak value, for rwg_sc = 110 mm | | |
| E-wall | $1.15\cdot10^7$ | $(3.6/4.1)\cdot10^3$ | $1.6\cdot10^4$ |
| H-wall | $1.15\cdot10^7$ | $(3.1/3.8)\cdot10^5$ | $1.4\cdot10^6$ |
| | Peak value, for rwg_sc = 145 mm | | |
| E- wall | $1.15\cdot10^7$ | $(1.4/1.6)10^3$ | $6.4\cdot10^3$ |
| H- wall | $1.15\cdot10^7$ | $(7.0/8.0)\cdot10^3$ | $3.1\cdot10^4$ |

In both cases the estimation of beam emittance growth was made for the bunch (see Table 2) center being in phase with the accelerating wave. The following values were obtained for kick and emittance growth: for rwg_sc = 110 mm кick = 0.0638 – 0,0241i and emittance growth is 154%; for rwg_sc = 145 mm kick = 0.0009 – 0.0006i and emittance growth is 3.8%.

For rwg_sc = 145 mm the transverse components are considerably lower. Obviously, smaller waveguide length leads to a local field perturbation.

## CONCLUSIONS

The results obtained are evaluative; the calculations did not take into account transverse dependence of electromagnetic fields. However, the following conclusions can be made:

the asymmetric structure with coaxial input coupler cannot provide low beam emittance growth;

the asymmetric structure with waveguide rectangular input coupler with some size optimization can provide quite low emittance growth (3,8%).

## REFERENCES

[1] V. Shemelin, S. Belomestnykh and H. Padamsee, “Low-lick Twin-coaxial and Waveguide-coaxial Couplers for ERL”, Cornell Lepp Report SRF 021028-08 (November 28, 2002).

[2] V.I.Shvedunov at al., RTMTRACE, VINITI, N 183-B89, 1989

# CALCULATIONS OF TARGETS FOR ADS USING GEANT-4

R.S. Kolevatov, I.V. Kudinovich, A.N. Krylov Shipbuilding Research Institute,
Moskovskoe Shosse 44, 196158, St. Petersburg Russia
Yu.A. Svistunov, D.V. Efremov Research Institute of Electrophysical Apparatus,
Metallostroy Road 3, 196641 Metallostroy, St. Petersburg, Russia

*Abstract*

Calculations of neutron production in metallic targets bombarded by protons with energies up to 1 GeV in framework of GEANT-4 are presented. Calculations of neutron production in targets of large size, dependencies of neutron yields on target dimensions and spatial distribution of energy deposited in the target, intended for working out ADS targets with multiplying blankets are also presented.

## INTRODUCTION

Accelerator driven systems (ADS) as powerful spallation sources of neutrons can find their application in nuclear power engineering for transmutation of long-living radioactive waste, production of new elements and substances with fission capability and for power generation. In hybrid reactor also called energy amplifier (EA) - fission reaction takes place in sub-critical reactor while the necessary density of neutron flux is provided by the spallation neutron source.

Costs, dimensions and weights as well as power consumption of accelerators required in a large extend depend on the output power of EA. Installations with high (about 1GW) power output for their operation require beams of protons accelerated up to the energies of 1GeV and higher with intensities of hundreds of mA. Beams of charged particles with mentioned characteristics one can get only using unique expensive accelerator machines. However EA of 200-400MW output require substantially lower intensities of neutron sources. This fact allows one to make use of accelerators producing beams of several hundred MeV and few mA current which can be copiously produced by industrial means.

In our work on the basis of calculations performed within GEANT-4 framework (v.9.1) we present neutron yield for different metal targets (Cu,Fe,Ta,W, Pb) bombarded by proton beam with energies from 300 MeV up to 1 GeV and spatial distribution of heat deposited in target.

GEANT-4 (v.9.1) developed by CERN is a program package (a set of C++ libraries) designed for modelling particle interactions with matter on the Monte-Carlo basis [1]. GEANT-4 can be used with different types of projectiles, materials and geometry of targets (detectors) and user is free to choose models for physical processes involved according to the task, which he is working at.

In our calculations we take into account electromagnetic processes, i.e. multiple scatterings off nuclei and ionization losses of charged particles, together with nuclear processes. For modelling of high-energy hadron—nucleus interactions we choose Bertini intranuclear cascade model for the very first cascade stage of interaction (approx. $10^{-23}$ s). Excited nucleus formed after this first stage rather emits hadrons (cascade-exciton and evaporation models are used respectively for pre-equilibrium and equilibrium states of excited nucleus) or breaks up instantly (multifragmentation or Fermi break-up for light nuclei). Interaction of neutrons having energies lower than 20 MeV with matter is described by parameterization-driven models based on ENDF/B-IV neutron cross section libraries.

Interaction of particles with matter within GEANT-4 is modelled on step-by step basis, at each step characteristics of generated track can be extracted and processed. To obtain our results we process up to 10000 of primary proton tracks.

Computation error was determined according to root mean square deviation (RMS) of the quantity of interest, determined using same set of values for the quantity obtained by Monte-Carlo. That is, for $N$ events and RMS value of $D$ computation error on 3σ level for quantity $X$ can be determined according to central limit theorem as

$$\Delta X = 3D / \sqrt{N} \qquad (1)$$

Table 1 represents comparison of experimental data on neutron yields from target bombarded by protons with GEANT-4 computations.

Table 1: Average Neutron Yield m from Cylindrical Lead Targets per 1 Proton

| Target dimensions D×L cm | $E_p$, MeV | *m*, n/p GEANT-4 | *m*, n/p experimental data | Reference (experimental data ) |
|---|---|---|---|---|
| 10.0×60 | 17 | 3.65±0.52 | 3.13±0.06 | [2] |
| 10.2×61 | 70 | 7.53±0.80 | 8.0±0.4 | [3] |
| | | | 6.4±0.3 | [2] |
| | 40 | 9.47 ±0.87 | 9.0 | [4] |
| | 20 | 14.99±1.02 | 11.8±0.6 | [3] |
| | | | 11.7±0.4 | [2] |
| | | | 13.3 | [4] |
| | 60 | 21.28±1.19 | 16.6±0.8 | [3] |
| | | | 16,8±0,5 | [2] |
| | | | 17.7 | [4] |
| 0.4×61 | 70 | 8.46±0.88 | 8.7±0.4 | [5] |
| | 20 | 16.24±1.14 | 13.9±0.7 | [5] |
| | 60 | 24.63±1.38 | 20.3±1.1 | [5] |

Comparison of GEANT-4 evolved quantities confirms a possibility to apply the toolkit for practical calculations of targets for ADS.

## NEUTRON GENERATION IN TARGET

Neutron yield from the target depends on parameters of the charged particles beam, target composition and dimensions. Bombardment by high-energy particles produces a hadron-electromagnetic cascade in target matter. Accelerated primaries induce fission of atomic nuclei and creation of secondary particles which in their turn can also induce fission and create new generations of particles (protons, neutrons, mesons and γ-quanta). High-energy particles can induce fission not only of those nuclei for which fission can be induced by low-energy neutrons (e.g. uranium) but also of other heavy elements (e.g. tantalum, lead, tungsten). The latter ones can be used as the neutron-producing material of the target.

In Fig. 1 we present total number of neutrons produced in different metal targets as a function of the incident primary proton energy. Calculations are performed for infinite targets.

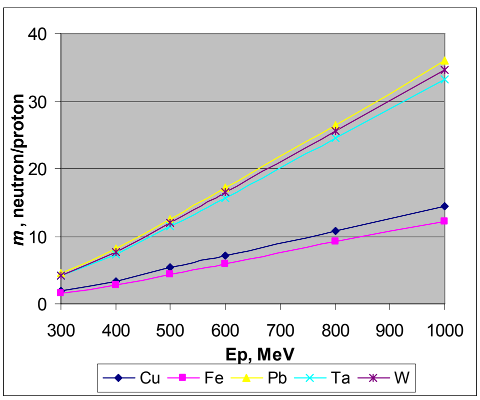


Figure 1: Total number of neutrons produced in infinite target.

Yields of neutrons (number of neurons which escape from the target) for finite targets depend on both beam characteristics and target dimensions. When dimensions are small a substantial part of secondary particles capable to induce fission with additional neutron production escapes form the target without interaction. At the same time in large target neutron radiative capture plays an important role.

For cylindrical target an optimal diameter with respect to neutron yield corresponds to few (2-3) characteristic inelastic interaction lengths $\lambda_{in}$. Due to anisotropy in particle production for inelastic proton scatterings in the lab frame (most of particles are produced in forward direction), the target length $L$ should be somewhat larger than its radius, at the same time value of $L$ has minor effect on the neutron multiplicity provided $L>D>\lambda_{in}$. Substantial part of neutrons escapes through the front butt-end of the target block, so neutron yield is maximal for comparatively small deepening of the beam injection point $z_0 \approx 0.3\lambda_{in}$.

In Table 2 we present calculated values for optimal dimensions of cylindrical target, Fig. 2 represents maximum neutron yields for them obtained via GEANT-4.

Table 2: Optimal Dimensions of Cylindrical Target

| Material | D, sm | L,sm | Beam injection point, $z_0$ ,sm |
|---|---|---|---|
| Fe | 40 | 50 | 5 |
| Cu | 30 | 50 | 5 |
| Ta | 20 | 50 | 2.5 |
| W | 20 | 50 | 2.5 |
| Pb | 40 | 50 | 7.5 |

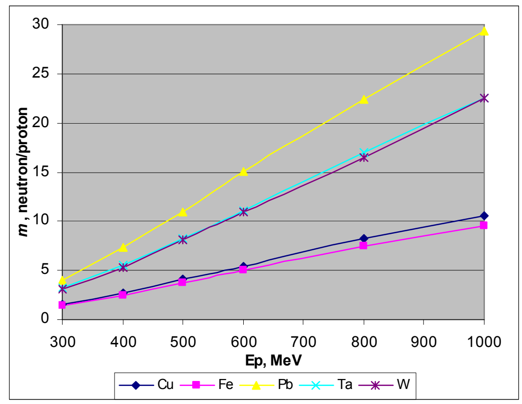


Figure 2: Maximal neutron yields for cylindrical targets. Target dimensions according to Table 2.

Energy spectrum of the neutrons obtained by electronuclear method is close to the fission spectrum. Specific energy spent for a single neutron production first drops with growth of beam energy $E_p$ and stays approximately constant afterwards (see Fig. 3).

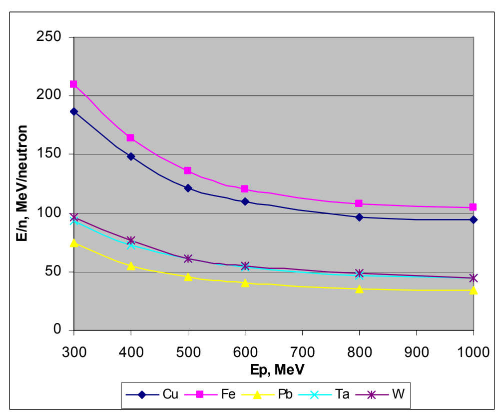


Figure.3: Specific energy spent for a single neutron yield. Target dimensions according to Table 2.

Power capacity of sub-critical reactor ($N_T$) with external neutron source spatial distribution similar to fission neutron one (reference external neutron source) is evaluated as

$$N_T = S_0 \cdot \frac{k_{eff}}{1-k_{eff}} \cdot \frac{1}{\nu} \cdot E_f \qquad (2)$$

where $S_0$- intensity of reference external neutron source, $k_{eff} < 1$ – multiplication factor, ν – mean number of neutrons per fission , $E_f$ – energy released per fission.

From (2) it follows that for a subcritical reactor with 200 MW power output and $k_{eff}$ =0.98 that ensures critical safety the needed intensity of the neutron source is $S_0=4.2\cdot10^{17}$n/s. It is possible to reduce intensity of external neutron source locating one in the center of core and hence decrease neutron leakage. In case of cylindrical core the intensity of central neutron source ($S$) may be twice lower than reference source intensity ($S_0$).

Intensity of the electronuclear neutron source

$$S = \frac{I_p m_0}{e} \qquad (3)$$

with $I_p$ standing for an average current of accelerator, $m_0$ – average neutron yield out of the target per single accelerated beam particle, $e$ – charge of the accelerated particle.

Intensity $S=2.1\cdot10^{17}$n/s can be reached for 5mA accelerator current if the yield is about $m_0 = 6.5$ neutrons per one primary accelerated particle. Our calculations (fig.2) show that the corresponding neutron yields can be reached for proton beam energies larger than 400 MeV for Pb target and larger than 450 MeV for Ta and W targets.

## HEAT DEPOSITION IN TARGET

To determine temperature field in the target and for calculations of cooling system one should possess data on a heat deposition in target bombarded by charged particle beam. Heat deposition in target is due to ionization losses of charged particles, (electromagnetic interaction of charged particles with material), inelastic interaction of cascade hadrons (neutrons, protons, $\pi$-mesons) with nuclei of the target, fission of nuclei of target material.

Figure 4 represents results on relative heat deposition (ratio of total rate of heat deposition $Q$ to beam power $N_{beam}$) in different materials (targets of optimal size w.r.t. the yield) at different proton beam energies.

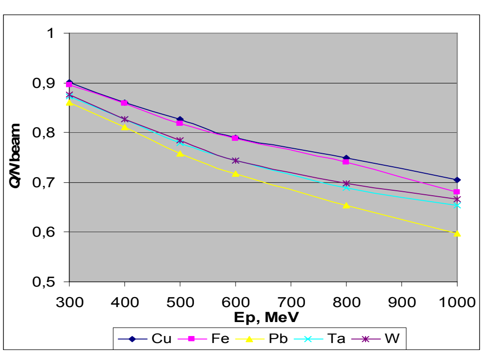


Figure 4: Relative total heat deposition in target.

Specific heat deposition is maximal along the beam injection axis. The maximum values of the specific heat deposition for a narrow beam are presented in Fig. 5.

In Fig. 6 we show calculated values for longitudinal heat deposition in copper target in comparison with experimental data [6]. The figure shows satisfactory correspondence of calculations with experiment.

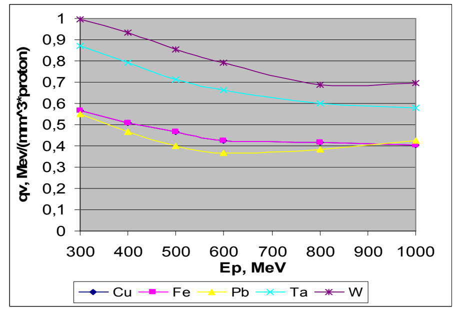


Figure 5: Maximal specific heat deposition for different targets.

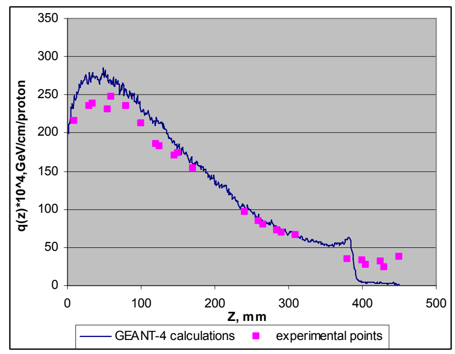


Figure 6: Longitudinal heat deposition in copper target. Proton energy 800 MeV.

## CONCLUSION

1. Comparison of GEANT-4 calculations with experimental data confirms its applicability for ADS target calculation and design.
2. For EA with sub-critical reactor with power output of 200 MW at $k_{eff}$ = 0.98 and 5mA accelerator current neutron yield should be as large as 6.5 neutrons/proton which can be achieved for heavy metal targets and beam energies slightly above 400-450 MeV.
3. For cylindrical targets optimal dimensions with respect to neutron yield are: diameter D=2...3 $\lambda_{in}$ , length $L \approx D$, deepening of beam injection point $z_0 \approx 0.3\lambda_{in}$ .
4. GEANT-4 gives a fair description of heat deposition in metal targets.

## REFERENCES

[1] Physics reference manual, version GEANT 4 9.1, (2007)
[2] D. West, B. Wood, Canad.J.Phys.49,2061 (1971)
[3] “The AECL Study for an Intence Neutron Generator”, AECL-2600, Chalk River, Ontario,1966
[4] J.S. Fraser et al. Phys. In Canada 21, N 2,17 (1965)
[5] P. Tunnicliffe, “High current proton accelerators and nuclear”. In Proc. Information Meet. on Accelerator-Breeding. BNL, CONF-770107, 1977, p.69-84.
[6] V.I. Belyakov-Bodin et al., “Heat deposition in targets bombarded by medium-energy protons”. Nucl. Instr. And Meth. A35 (1993) 30-36.

# END TO END BEAM DYNAMICS AND RF ERROR STUDIES FOR LINAC4

G. Bellodi, M. Eshraqi, J-B. Lallement, S. Lanzone, A.M. Lombardi, E. Sargsyan, CERN, Geneva, Switzerland
R. Duperrier, D.Uriot, CEA, Gif-sur-Yvette, France

Linac4 is a normal conducting $H^-$ linac to be built at CERN as a new injector to the PS Booster and later on as a front end of a possible MultiMegaWatt Linac Facility. The layout consists of a $H^-$ RF source, a magnetic LEBT, a RFQ (accelerating the beam from 45 keV to 3 MeV), a chopper line, a conventional Drift Tube Linac (from 3 MeV to 50 MeV), a Coupled Cavity Drift Tube Linac (from 50 MeV to 102 MeV) and a π-mode structure (PIMS, from 102 to 160 MeV), all operating at a frequency of 352 MHz. End-to-end beam dynamics simulations have been carried out in parallel with the codes PATH and TRACEWIN to optimise the design and performance of the accelerator and at the same time to guarantee a cross-check of the results found. An extensive statistical campaign of longitudinal error studies (static and dynamic) was then launched for validation of the proposed design and to assess the maximum level of RF jitter/inaccuracies (in both phase and amplitude) the system can tolerate before beam quality at injection in the PS Booster - and later in the Superconducting Proton Linac (SPL)- is compromised.

## LINAC4 LAYOUT

A 2 MHz RF volume source and 1.9m long 2-solenoid LEBT supply the initial $H^-$ beam at 45 keV (a 400 µs long pulse at 2 Hz repetition rate for 80 mA current). This is first accelerated to 3 MeV by a 352 MHz RFQ, before entering a 3.6 m long chopper line consisting of 11 EM quadrupoles, 3 bunchers and 2 deflecting plates. Here micro-bunches are removed from the pulse to achieve a cleaner injection of the Linac4 beam in the PS Booster ring downstream. The beam is then accelerated to 50 MeV by a 352 MHz conventional Drift Tube Linac (DTL), composed of 3 separate tanks each fed by one klystron. There are 111 drift tubes, each equipped with a Permanent Magnet Quadrupole. The DTL is followed by a Cell-Coupled Drift Tube Linac, which takes the beam to 102 MeV through a series of 7 modules (21 tanks coupled by 3's) operating at 352 MHz and powered by individual klystrons. Transverse focusing is provided by 21 electromagnetic quadrupoles placed between tanks. Acceleration to the final energy of 160 MeV is then carried out by 12 Pi-Mode Structure (PIMS) tanks at 352 MHz, each composed of 7 cells, and 12 EM quadrupoles. The first 4 tanks are powered individually, while the last 8 are coupled in pairs onto a same klystron. The last 2 tanks have a lower nominal accelerating field, to allow for the possibility of energy painting at injection in the PSB [1]. The layout here described is the result of several revisions of previous designs [2], the main changes being in the values of the transition energies and in the final choice for one single frequency (352 MHz), to make for a simpler design.

## END-TO-END BEAM DYNAMICS

Each section of Linac4 has been studied and optimized independently before a campaign of end-to-end simulations was launched to identify overall bottlenecks and limitations. The codes PATH[3], TRACEWIN[4], TOUTATIS[5], and PARMTEQ[6] have been used for these studies, providing mutual crosscheck of the results.

The $H^-$ beam pulse current from the source is 80 mA, and the duty cycle is 0.1% in an initial phase when Linac4 is used as injector of the PS Booster ring, and a duty factor of 6% for a later use as front end for the SPL (value used for the safety and loss studies).

Space charge effects dominate at low energy, causing some beam degradation and losses in the RFQ and chopper line. The RFQ can accelerate with <5% losses beams in the 20-100 mA range, with 8% transverse emittance growth for 70 mA current. The chopper line consists of two deflecting plates housed inside quadrupoles and driven at an effective voltage of 500V to remove 133/352 micro-bunches in the pulse, which are kicked onto a conical shaped dump. About 5% of the unchopped beam is lost here, whereas the fraction of chopped beam that is transmitted past the dump into the Linac, and might need to be eliminated at the lowest possible energy is ~0.05%. The beam current available at the end of the chopper line would thus be 65 mA per pulse without chopping, and 40mA with chopping on.

After the dump the beam is matched into the first tank of the DTL, with a FFDD focusing scheme. Most of the transverse emittance growth (almost 20%) occurs at this transition, when after a relatively slow phase advance

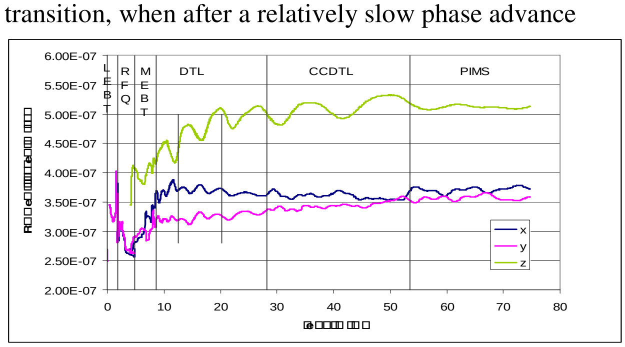


Figure 1: Transverse and longitudinal RMS emittance growth along the chopper line and Linac.

regime in the chopper (1 FODO per 10 βλ), the beam is compressed back in volume to fit a faster phase advance focusing channel (see Fig.1). The synchronous phase is ramped from -30 to -20 deg in Tank1 and then kept constant in the rest of the DTL (where the focusing scheme changes to a FODO type). At 50 MeV the beam is transferred to a CCDTL structure, composed of 3-gap cavities with an average phase of -20 deg, 4 MV/m accelerating field and a focusing period of 7βλ. Finally at 102 MeV a 352 MHz Pi-Mode Structure has been eventually adopted, with -20 deg average synchronous phase and a 9βλ focusing period.

Accurate matching between different types of structures allows for a very smooth variation of phase advances and good control over potential emittance growth. The evolution of the RMS emittances in the 3 planes is shown in Fig.1 for PATH calculations with a 2D space charge model. TRACEWIN results for a 3D model only differ by up to 10%. A measure of the design solidity is given by the aperture over RMS beam size ratio, shown for the transverse and longitudinal planes in Fig.2 and 3. The longitudinal acceptance has been defined in an "equivalent" way to the transverse one, as ratio between the phase and energy width of the linearised bucket, and the RMS beam phase and energy spread.

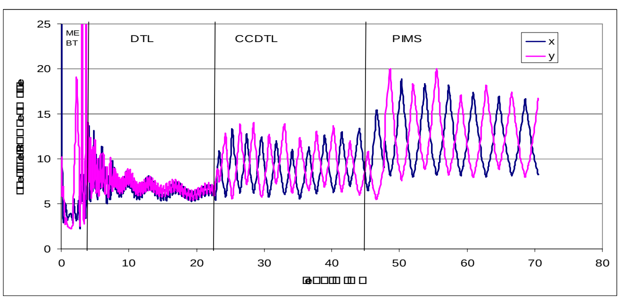


Figure 2: Aperture over RMS beam size ratio for chopper-DTL-CCDTL-PIMS.

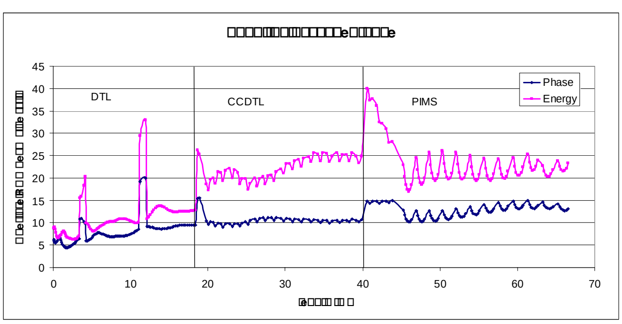


Figure 3: Longitudinal acceptance over RMS beam size ratio for DTL-CCDTL-PIMS. The bucket phase and energy width are taken as: $\Delta\phi=\pm 3/2\phi_s$ and $\Delta W=\pm 2\sqrt{[qmc^3\beta^3\gamma^3 E_0 T(\phi_s\cos\phi_s-\sin\phi_s)]/\omega}$.

The transverse acceptance bottleneck is located in the RFQ and chopper line, whereas for the longitudinal plane both the phase and energy acceptance minima are at the input of the DTL.

## EFFECTS OF RF ERRORS

The beam dynamics results shown so far are for the case of a nominal, perfect machine. Beam degradation induced by machine imperfections has been the subject of a campaign of error studies, aimed at assessing the maximum level of inaccuracies the system can tolerate before beam quality at PS Booster injection is compromised. Several hundred to a few thousand runs were carried out with both PATH and TRACEWIN for a typical 50k particles input beam population for several error scenarios, and results for beam loss, emittance growth, average energy and phase jitter have been statistically analysed. The criteria followed to establish maximum tolerances are:

- maximum average losses (transverse) of 1W/m at 6% duty cycle (shielding requirements)
- maximum longitudinal losses (un-accelerated particles) of 5%
- maximum emittance growth of 15-20% at 2σ level (PSB budget)
- maximum energy jitter at 160MeV (1σ) below ±100keV (transfer line acceptance)

Transverse error studies and steering strategies have been described in detail in [7]. RF errors can be classified as either dynamic or static. To the first category belong klystron phase and energy jitters, varying in time and affecting several gaps at once (all the ones connected onto the same RF supply). In the static category, we have gap amplifier errors mainly due to tuning or machining imperfections. These do not vary in time, they are uncorrelated from gap to gap and can be mitigated by adjusting the RF power around the nominal value.

Table 1: Results of dynamic RF error studies for the DTL (RMS quantities).

| Errors | Phase jitter [deg] | Energy jitter [keV] | 90% emittance [deg MeV] |
|---|---|---|---|
| 0% - 0deg | - | - | 0.734 |
| 0.5%-0.5deg | 0.82 | 13 | 0.745±0.014 |
| 0.5% - 1deg | 0.88 | 18 | 0.751±0.017 |
| 0.5% - 2deg | 1.14 | 31 | 0.774±0.034 |
| 1% - 0.5deg | 1.6 | 23 | 0.757±0.024 |
| 1% - 1deg | 1.6 | 28 | 0.762±0.027 |
| 1% - 2deg | 1.77 | 36 | 0.786±0.047 |
| 2% - 0.5deg | 5.12 | 43 | 0.794±0.07 |
| 2% - 1deg | 5.66 | 46 | 0.799±0.07 |
| 2% - 2deg | 8.55 | 49 | 0.830±0.1 |

Table 1 shows the results of RF klystron error studies for the DTL; the most left-hand column lists all the scenarios examined (amplitude and phase error), with uniformly distributed random errors within the given intervals. The output beam phase jitter is dominated by the klystron field amplitude errors, whereas the output energy deviation is more sensitive to phase errors, though these become negligible when the amplitude jitter is large enough (effects are even more balanced for the longitudinal emittance growth). The 1%-1deg case beam energy error is then propagated as input energy jitter downstream to the following structures (3σ uniformly distributed errors). Tables 2 and 3 list the equivalent results for the CCDTL and PIMS. In the PIMS case the sensitivity to the initial beam jitter is strong only for RF errors smaller than the 1%-1deg level. Above this threshold, klystron errors are the most significant source of deviation from nominal values. For this reason a balance should be kept between the two effects, and similar levels of RF tolerances specified for all types of structures. The criteria to be met at injection in the PSB impose that klystron phases and amplitudes be controlled ideally at the 0.5%-0.5 deg level (but 1%-1deg would still be acceptable).

Table 2: Results of dynamic RF error studies for the CCDTL (RMS quantities).

| Errors | Phase jitter [deg] | Energy jitter [keV] | 90% emittance [deg MeV] |
|---|---|---|---|
| 0. -0.deg | - | - | 0.769 |
| 0.5%0.5deg | 0.5 | 39 | 0.771±0.013 |
| 1% - 1deg | 1 | 63 | 0.773±0.018 |
| 2% - 2deg | 2 | 115 | 0.780±0.030 |
| 5% - 2deg | 4 | 237 | 0.794±0.047 |

Table 3: Results of dynamic error studies for the PIMS (RMS quantities).

| Errors | Phase jitter [deg] | Energy jitter [keV] | 90% emittance [deg MeV] |
|---|---|---|---|
| 0% - 0deg | - | - | 0.740 |
| 0.3%0.3deg | 0.3 | 83 | 0.741±0.001 |
| 0.5%0.5deg | 0.4 | 94.6 | 0.741±0.002 |
| 1% - 1deg | 0.66 | 135 | 0.741±0.003 |
| 2% - 1deg | 0.85 | 225 | 0.742±0.004 |
| 3% - 1deg | 1.1 | 329 | 0.742±0.005 |

RF static error studies have been carried out, assuming either uniformly spread random errors (DTL) or a correlated tilt, i.e. a linear distribution of the errors over all the gaps in one tank, with the central gap at the nominal value (CCDTL) or an elliptical distribution with the nominal value for average (PIMS). The field error amplitude was varied between ±2% and ±10%. Results are summarized in Table 4. Unlike klystrons dynamic errors, that are relevant for causing a beam energy and phase jitter, in the case of gap errors, which are more similar to a systematic imperfection, energy and phase deviations can be adjusted by varying the level of the RF power supplied. What cannot be corrected for is the longitudinal emittance growth, which is therefore the quantity of interest when assessing beam quality degradation. Also, for dynamic errors, it only makes sense to consider RMS effects, whereas the impact of static errors is best evaluated by looking at extreme cases. The results in Table 4 show the different sensitivities of the Linac4 RF structures to gap errors (decreasing with beam energy). A tolerance budget of ±2% field variation for the DTL and CCDTL gaps and ±5% for the PIMS gaps has been assumed as RF specification. No significant beam losses have been observed in any of the error cases examined (both dynamic and static).

Table 4: Gap error studies: average emittance growth with respect to nominal and worst case deviation in no of σ .

| Structure | Gap errors (±) | RMS average emitt. growth[%] | RMS emitt Std dev [deg MeV] |
|---|---|---|---|
| **DTL** | Spread 2% | 5.4 | 0.011 |
| | Spread 5% | 31.1 | 0.076 |
| **CCDTL** | Linear 2% | 2 | 0.0025 |
| | Linear 5% | 1.5 | 0.0044 |
| | Linear10% | <0.1 | 0.0086 |
| **PIMS** | Linear 2% | 0.6 | 0.00083 |
| | Linear 5% | <0.1 | 0.00084 |
| | Linear10% | 0.6 | 0.00089 |
| | Ellipt. 2% | 0.18 | 0.0002 |
| | Ellipt. 5% | 0.4 | 0.0002 |
| | Ellipt.10% | 0.79 | 0.0003 |

## CONCLUSIONS

Nominal beam dynamics for Linac4 has been studied with two different codes, indicating good performance. An extensive statistical campaign of longitudinal error studies has allowed to establish a tolerance budget on RF phase and amplitude errors that should guarantee good beam quality at PS Booster injection.

## REFERENCES


[1] M.Aiba et al, TUPAN093, PAC'07, NM, USA, 2007.

[2] A.M. Lombardi et al., HB2006 proceedings, Tsukuba, Japan, August 2006.

[3] A. Perrin, J.F. Amand, Travel User Manual (2003).

[4] R. Duperrier, N. Pichoff, D. Uriot, ICCS 2002 Proceedings.

[5] R. Duperrier, Phys. Rev. ST Accel. Beams 3, 124201 (2000).

[6] K. Crandall, T. Wangler, AIP Conf. Proc. Vol. 177, pp. 22-28 (1988)

[7] A.M. Lombardi ☐☐a☐ CERN-AB-Note-2007-033.

# STATUS OF LONGITUDINAL BEAM DYNAMICS STUDIES IN CTF3

H. Shaker, Institute for research in fundamental science, Iran; CERN, Switzerland
E. Adli, University of Oslo, Norway; CERN, Switzerland
R. Corsini, A. Dabrowski, A. Latina[*], T. Lefevre, P. K. Skowronski, F. Tecker, P. Urschutz[#], CERN, Switzerland

*Abstract*

The aim of the CLIC Test Facility CTF3, built at CERN by an international collaboration, is to address the main feasibility issues of the CLIC electron-positron linear collider technology by 2010. One key-issue studied in CTF3 is the generation of the very high current drive beam, used in CLIC as the RF power source. It is particularly important to simulate and control the drive beam longitudinal dynamics in the drive beam generation complex, since it directly affects the efficiency and stability of the RF power production process. In this paper we describe the ongoing effort in modelling the longitudinal evolution of the CTF3 drive beam and compare the simulations with experimental results. Our study is based on single bunch simulation.

## INTRODUCTION

The result of PARMELA [1] for the injector (see Fig. 1) was used as the input for PLACET [2] simulation code and for a 1-D analytical model using MathCAD. By these simulation codes, the CL (CTF3 Linac) from girder 3 in the injector (see Fig. 1), CT and CTS lines (See Fig. 1) were simulated. Measurements of the bunch length in CT and CTS lines by using RF deflector of delay loop in the CT line and OTR screen in the CTS line were done and were compared to the result of the simulation.

Table 1: Simulation Codes Comparison

| PARMELA | MathCAD | PLACET |
|---|---|---|
| Injector, Chicane | Girder 3, Chicane, DBA†, CT & CTS lines | DBA, INFN-Frascati chicane |
| Space charge | No space charge | No space charge |
| No wake field | Wake field | Wake field |
| Longitudinal & Transverse | Longitudinal | Longitudinal & Transverse |
| No CSR‡ | No CSR | CSR |

## SIMULATION

*Injector*

In the Injector, the electron beam is produced by a DC electron gun, is bunched at 1.5 or 3 GHz by the bunching system and is accelerated to about 18 MeV.

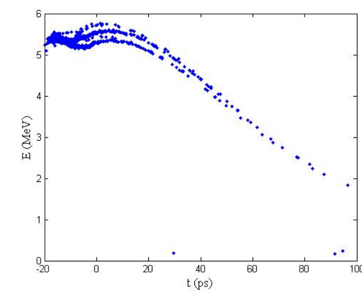


Figure 2: The result from PARMELA after girder 2 and the input for MathCAD.

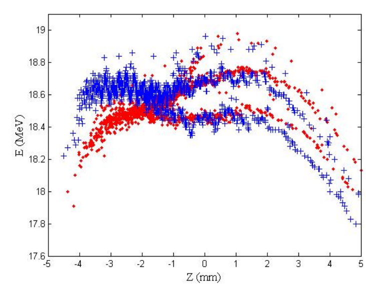


Figure 3: The result from MathCAD (no wake field) and PARMELA (+) after the injector, between z=-5 and z=5 mm. The rest will be cut in the chicane of girder 4.

Fig. 3 shows a good agreement between MathCAD and PARMELA result. In Fig. 13 you will see a little difference in the final bunch length, after the INFN-Frascati chicane.

The main reason for this difference is the space charge effect that is included in PARMELA and it is not included in MathCAD. The space charge effect is even less and hence insignificant in other parts of the machine where the energy is higher.

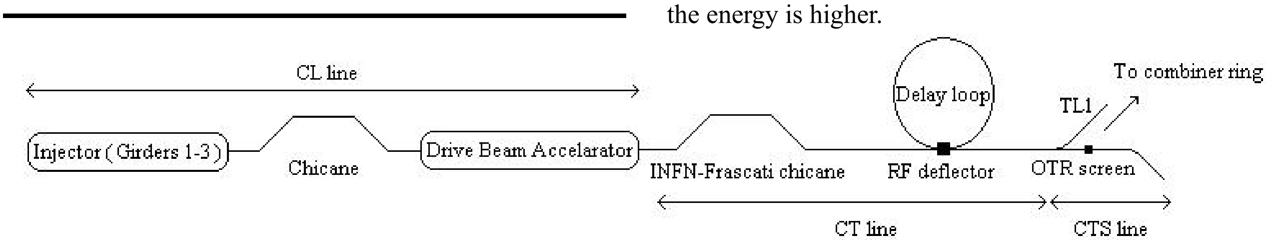


Figure 1: Layout of CTF3 from the injector to the combiner ring.

[*]Presently at Fermilab, [#]Presently at Siemens, †Drive Beam Accelerator, ‡Coherent Synchrotron Radiation.

### *Chicane*

Chicane (in the girder 4) is used for two reasons:

1- To cut the low energy tail of the bunch: Each particle in the bunch travels in a different orbit related to its energy then by using an adjustable slit in chicane it is possible to stop the particles of a chosen energy.

2- To change the bunch length: $R_{56}$=15.2 mm. The simulation shows that the minimum bunch length after the chicane is obtained by the phase of the input RF power source feeding the accelerating structure on girder 3 equal to -3 degree from crest.

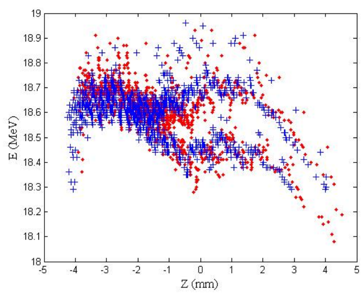


Figure 4: The result from MathCAD (no wake field) and PARMELA (+) after chicane starting from the end of the injector. Input is from PARMELA.

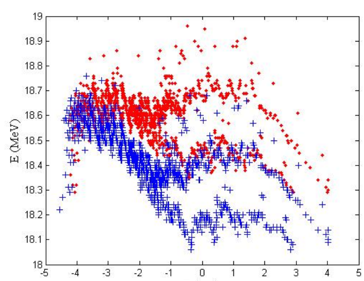


Figure 5: The result from the MathCAD after the chicane with wake field (+) (input for the MathCAD) and without wake field.

### *Drive Beam Accelerator (DBA)*

In the Drive Beam Accelerator (girders 5-15), the electron beam is accelerated to about 120 MeV by structures located in girders 5,6,7,11,12,13,15. Each of these girders has two accelerating cavities and each of these cavities contains 34 cells [3]. (See Fig. 5, 6, 7).

### *INFN-Frascati Chicane*

The INFN-Frascati Chicane is used to change the bunch length ($R_{56}$=0.46 m (calculated by MadX and PLACET), $T_{566}$=-1.14 m (calculated by PLACET)). The optimum bunch length should be around 2 mm r.m.s. that means not too short because of the coherent synchrotron radiation in the delay loop and the combiner ring and not too long because of acceptable injection into the delay loop and the combiner ring. (See Fig. 8, 9).

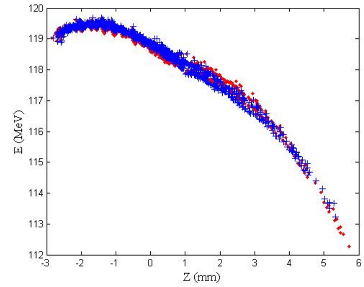


Figure 6: The result from MathCAD and PLACET after the DBA. Input is from PARMELA.

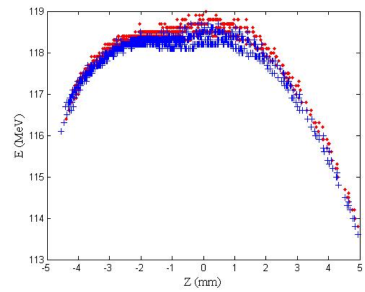


(+)

Figure 7: The result from MathCAD after the DBA with wake field (+) and without wake field. Input is from MathCAD.

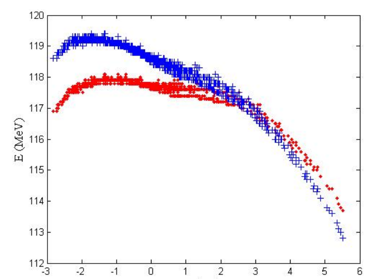


Figure 8: The result from MathCAD before the INFN-Frascati chicane with changing the phase by -20 degree in girder 15 from crest and without changing the phase (+). For both: σ=1.62 mm. Input is from MathCAD.

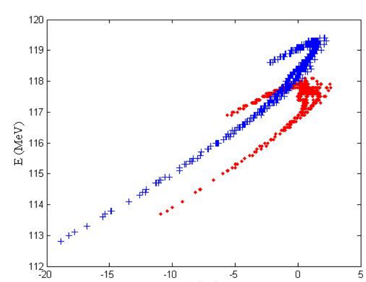


Figure 9: The result from MathCAD after the INFN-Frascati chicane with changing the phase by -20 degree in girder 15 from crest (σ=1.47mm) and without changing the phase (+) (σ=2.43mm). Input is from MathCAD.

## BUNCH LENGTH MEASUREMENT

The RF deflector is a cavity in TE mode that gives a transverse kick to the electron bunch. The RF deflector is used to inject the electron beam into the delay loop but if it is used near zero crossing is useful for the bunch length measurement, making a correlation between transverse and longitudinal positions in the bunch. (See Fig. 10). Therefore the transverse shape on the OTR screen, give the information of longitudinal shape too. [5, 6, 7].

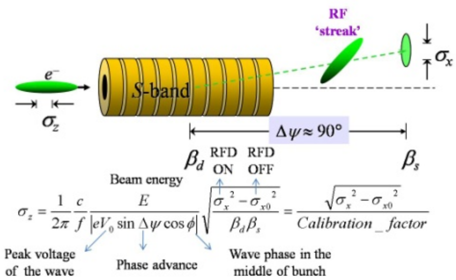


Figure 10: Using RF deflector for bunch length measurement [4]. f=1.5 GHz.

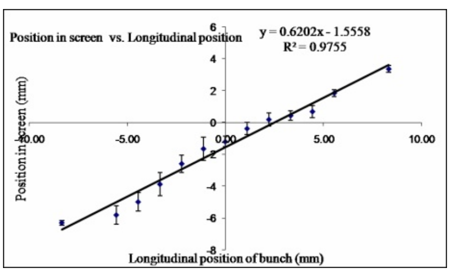


Figure 11: The method for finding the calibration factor that shows the relation between the screen position unit and the longitudinal position unit.

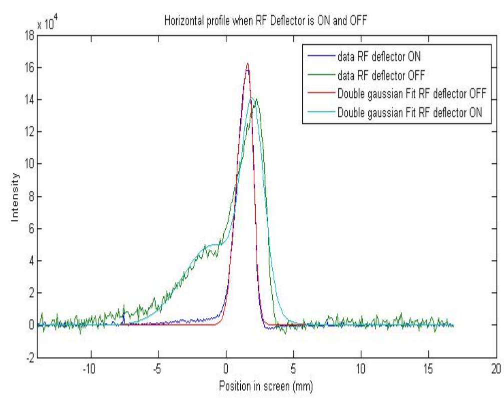


Figure 12: This shows the horizontal profile on screen when the RF deflector is ON and when it is OFF. ($\sigma > \sigma_0$).

In this method the horizontal size of beam on the screen is measured when RF deflector is on ($\sigma$) and off ($\sigma_0$). Instead of finding the magnitude of each parameter in the equation in the Fig. 10, the calibration factor is calculated by a measurement of the beam position on the screen versus RF deflector phase. Fig. 11 shows the result of one measurement. It shows a good linear fit. The slope is the calibration factor. Fig. 13 shows the result of one measurement for different wave phase in the girder 15 (last girder of DBA).

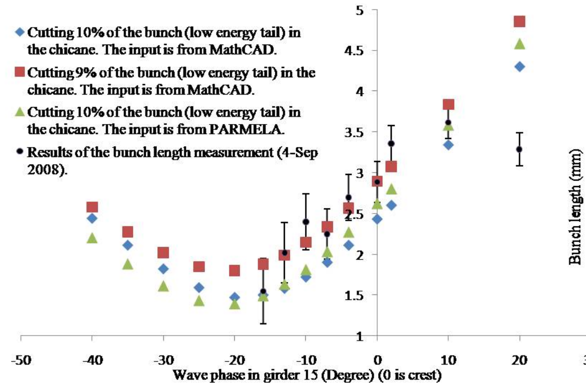


Figure 13: The result of bunch length measurement by RF deflector and the result of different simulations.

## CONCLUSION

Fig. 13 shows a good agreement between simulations by MathCAD and bunch length measurement by RF deflector. The errors in measurement, mainly, are from the jittering of beam on the screen. RF deflector and electron gun are the main source of this jittering. Non-linearity of OTR screen is another reason of errors. The measurement was done by RF pickup too but it didn't show a good agreement but more or less the same shape. The work will continue to find the root of this difference.

## REFERENCES

[1] A. Yeremian, R.Miller, R.Ruth, H. H. Braun, G. Geschonke,L. Groening, L. Rinolfi, L. Thorndahl, I. Wilson, F. Zhou, "CTF3 Drive-Beam Injector Design",EPAC'02, June 2002, Paris.

[2] https://savannah.cern.ch/projects/placet/.

[3] G. Geschonke and A. Ghigo (editors), "CTF3 design report", CERN/PS 2002-008, LNF-02/008, May 2002

[4] P. Emma, "Electron Bunch Measurements with a Transverse RF Deflector", ICFA XFEL 2004 Workshop, SLAC, July 2004.

[5] D.Alesini, R.Corsini, D.Filippetto, A.Ghigo, F.Marcellini, B.Preger, "CTF3 Bunch Length Measurement with the 1.3 GHz RF Deflector", CTFF3-010, Frascati, January 2007.

[6] P. Emma, J. Frisch, P. Krejcik, "A Transverse RF Deflecting Structure for Bunch Length and Phase Space Diagnostics ", LCLS-TN-00-12, SLAC, August 2000.

[7] D. Alesini, C. Biscari, R. Corsini, A. Ghigo, F. Marcellini, "Longitudinal phase space characterization of the CTF3 beam with the RF Deflector", EPAC 2004, Lucerne, Switzerland.

# PARTICLE DYNAMICS CALCULATIONS AND EMITTANCE MEASUREMENTS AT THE FETS *

J. Pozimski[1+2 #],A. Letchford[2] , J. Back[3], Dan Faircloth[2], S. Jolly[1] C. Gabor[4], C. Plostinar[4]
[1]Imperial College London, United Kingdom, [2]Rutherford Appleton Laboratory, Oxford, United Kingdom, [3]Warwick University, Coventry, [4]ASTeC United Kingdom

## Abstract

In order to contribute to the development of high power proton accelerators in the MW range, to prepare the way for an ISIS upgrade and to contribute to the UK design effort on neutrino factories [1,2], a front end test stand (FETS) is being constructed at the Rutherford Appleton Laboratory (RAL) in the UK [3]. The aim of the FETS is to demonstrate the production of a 60 mA, 2 ms, 50 pps chopped beam at 3 MeV with sufficient beam quality. The results of numerical simulations of the particle dynamics from the charge separation dipole behind the ion source to the end of the MEBT will be presented. Previous measurements showed that the emittance of the beam delivered by the ion source exceeded our expectations by more than a factor of three [4]. Since then various changes in the beam extraction/post accelerator region reduced the beam emittance by nearly a factor of two. Simulations of the particle dynamics in the FETS based on distributions gained from recent measurements of the transversal beam emittance behind the ion source will be presented and the results for different input distributions discussed.

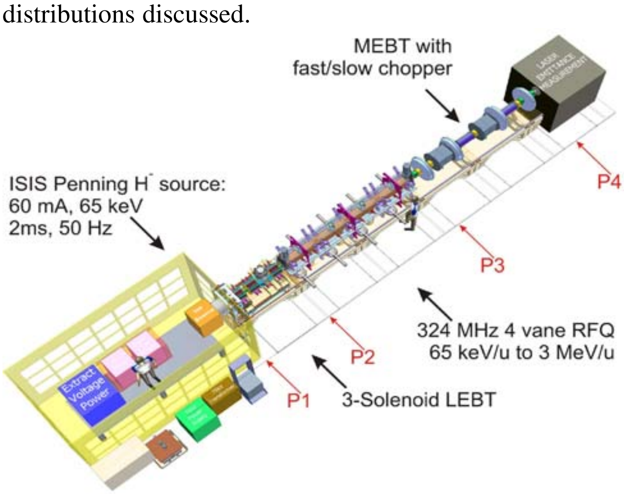


Figure 1: Schematic layout of the FETS set up. For the positions indicated (P1 behind post acceleration at the entrance of the LEBT [z=0mm], P2 at the entrance of the RFQ [z=1770mm], P3 at the RFQ exit [z=5770mm] and P4 at the end of the MEBT [z=10580mm]) the phase space distribution of the beam has been determined with GPT and TRACEWIN.

## INITIAL PARTICLE DISTRIBUTION

The ion source development program, based on the highly successful ISIS $H^-$ ion source at RAL, has already shown encouraging results. The aim is to increase the ion current from 35mA to 70mA, to increase the pulse length from 250μs to 2ms and to improve the beam quality [5]. In order to compare the recent status of the improvement of the ion source emittance and the consequences for the beam transport through the FETS end-to-end simulations have been performed for an idealized (shown in figure 2) and a real measured space phase distribution (shown in figure 3) based on pepper-pot emittance data.

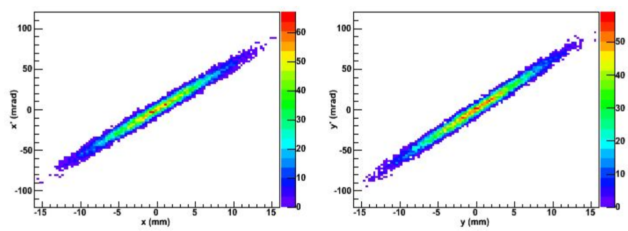

Figure 2: Input particle distribution into the LEBT (P1) for an ideal waterbag beam (input 1) ($\varepsilon_{x,rms}$=0.25 πmmmrad; $\varepsilon_{y,rms}$=0.25 πmmmrad).

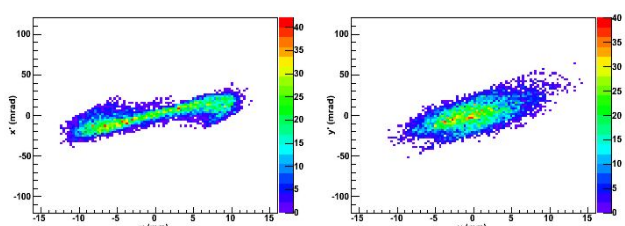

Figure 3: Input particle distribution into the LEBT (P1) for a measured beam distribution (input 2) ($\varepsilon_{x,rms}$=0.58 πmmmrad; $\varepsilon_{y,rms}$=0.52 πmmmrad).

## LEBT SIMULATION AND RESULTS

A 3 solenoid LEBT system similar to the one used at the ISIS injector is under construction and the calculated 3D field distribution of the solenoids (figure 4) is used for particle transport simulation of the LEBT using the GPT code [6, 7].

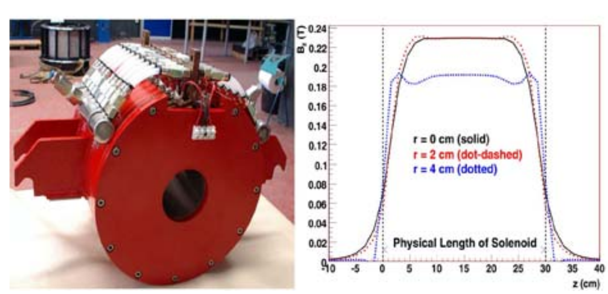


Figure 4: Left: one of three LEBT solenoids for FETS. Right: Magnetic field distribution in the z direction for different radii.

The field strengths of the three solenoids are chosen to optimise beam injection into the RFQ. The result of these optimisations for input distribution 1 is shown in figure 5. The estimated acceptance of the RFQ is drawn as an ellipse in the transversal phase space plots. There is no transversal beam loss in the LEBT and the total transmission (including stripping) into the RFQ acceptance is predicted to be above 90%.

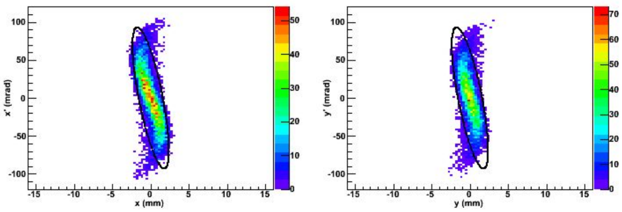


Figure 5: Phase space distributions in the transversal plane at the exit of the LEBT (P2) for input 1 ($\varepsilon_{x,rms}$=0.33 $\pi$mmmrad; $\varepsilon_{y,rms}$=0.33 $\pi$mmmrad).

The beam envelope in both transversal planes in the LEBT using distribution 2 is shown in figure 6 and the phase space distribution is shown in figure 7. Again the acceptance of the RFQ is drawn.

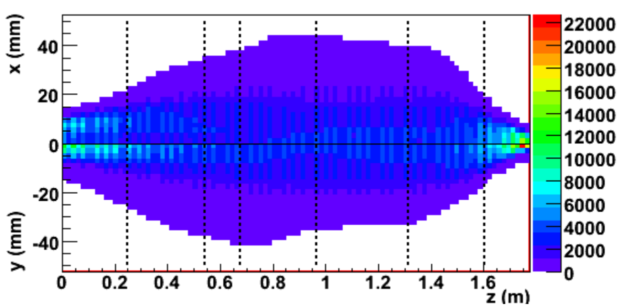


Figure 6:Beam envelope along the length z of the LEBT using the input distribution from the measured beam. Dotted vertical lines show the drift and solenoid sections.

Due to the relatively large size of the beam in the solenoids compared to their aperture (80%) non linear fields cause aberrations (already indicated by the slightly S-shaped phase space distribution in figure 5) and emittance growth. While the absolute increase of the emittance for the waterbag input distribution with $\Delta\varepsilon_{x,y,rms}$=0.08 $\pi$mmmrad is smaller than for the real beam ( $\Delta\varepsilon_{x,rms}$=0.11 and $\Delta\varepsilon_{y,rms}$=0.12 $\pi$mmmrad), the penalty seems to be rather moderate.

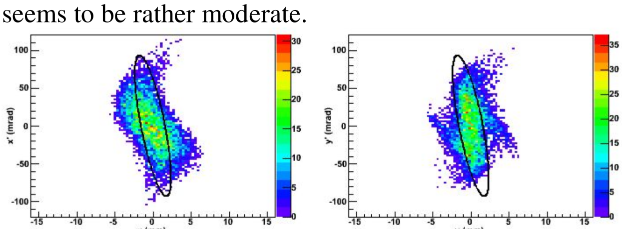


Figure 7: Phase space distributions in the transversal plane at the exit of the LEBT (P2) for input 2 ($\varepsilon_{x,rms}$=0.69 $\pi$mmmrad; $\varepsilon_{y,rms}$=0.64 $\pi$mmmrad).

Even for the presented very preliminary first data the result is surprisingly good and a total transmission into the RFQ acceptance is predicted to be 50%. The simulations performed also show that, independent of the degree of space charge compensation and using the available measured beam emittances, it is always possible to inject the core of the beam into the RFQ by just tuning the solenoid strengths.

## PARTICLE TRANSPORT CALCULATION IN THE RFQ

A preliminary design of the 324 MHz RFQ has been used for particle dynamics simulations. The variation of the RFQ parameters along z is shown in Figure 8. The design was made for an optimized transmission of more than 90% under the estimate of an input beam emittance of 0.25 $\pi$mmmrad. In a first run the particle distribution gained from the GPT simulations of the LEBT with generated data was used for input into the RFQ.

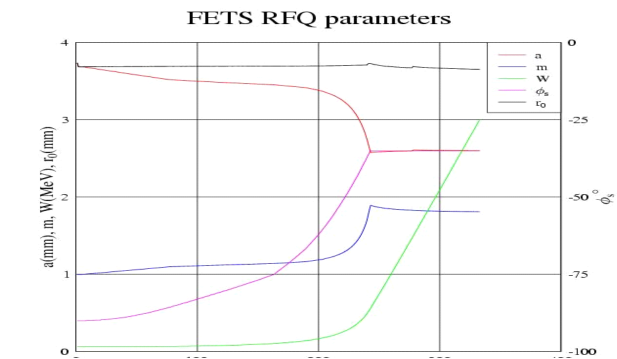


Figure 8: Development of the main RFQ parameters for the FETS along z.

The output distributions of this simulation are shown in figure 9. The transmission through the RFQ was ~96% for all energies and ~91% for an energy of 3MeV. The reduction of the emittance by 15% is caused by the particle losses. Considering this input distribution the design is likely to fulfil the requirements for the FETS.

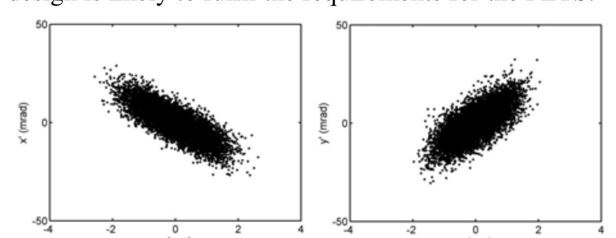


Figure 9: Particle distribution behind the RFQ (P3) for input 1 ($\varepsilon_{x,rms}$=0.28 $\pi$mmmrad; $\varepsilon_{y,rms}$=0.27 $\pi$mmmrad).

Using the second data set and taking into account that, while improved by nearly a factor of two over the last year, the input emittance is still a factor of two larger than the one used for the design, the achievable RFQ transmission of ~52% for all energies (50.5% for 3 MeV) seems to be reasonable but fails to meet the FETS specifications. The transversal output distributions are shown in figure 10. The emittance is reduced by up to 44 % due to the large particle losses but still 30 % larger compared to the results for the waterbag input

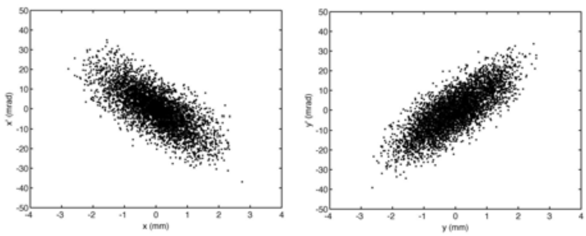

Figure 10: Particle distribution behind the RFQ (P3) for input 2 ($\varepsilon_{x,rms}$=0.46 πmmmrad; $\varepsilon_{y,rms}$=0.47 πmmmrad).

## PARTICLE TRANSPORT CALCULATION IN THE MEBT

A preliminary design of the MEBT consisting of 11 quadrupoles, 4 bunching cavities and a slow and fast chopper with accompanying beam dumps is shown in Figure 11 [8].

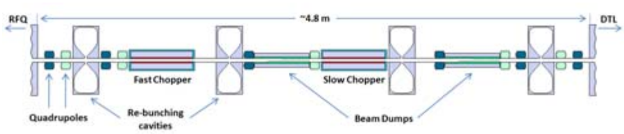


Figure 11: Design of the MEBT.

The output distributions of the simulation are shown in figure 12 and 13. For the ideal case the emittance growth is ~7% in x,x' and ~20% in y,y'. The transmission is ~98%.

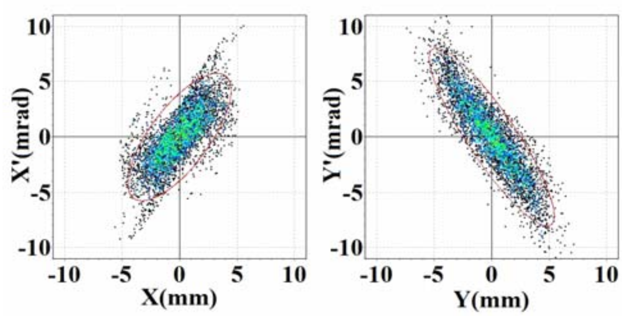


Figure 12: Particle distribution at the end of the MEBT (P4) for input distribution 1 ($\varepsilon_{x,rms}$=0.30 πmmmrad; $\varepsilon_{y,rms}$=0.34 πmmmrad).

For the real beam the emittance growth is -13% in the x,x' space (due to losses) and 4 % in the y,y' space. The transmission is reduced to ~89%.

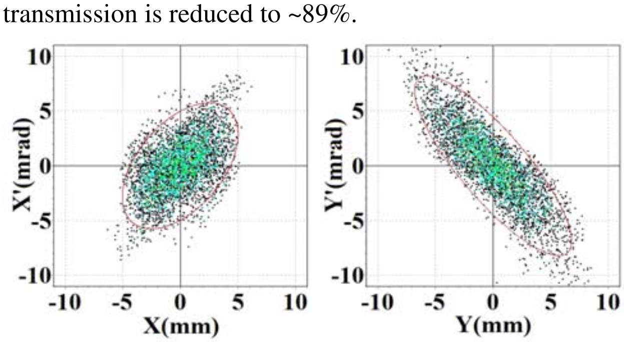


Figure 13: Particle distribution at the end of the MEBT (P4) for input distribution 1 ($\varepsilon_{x,rms}$=0.40 πmmmrad; $\varepsilon_{y,rms}$=0.49 πmmmrad).

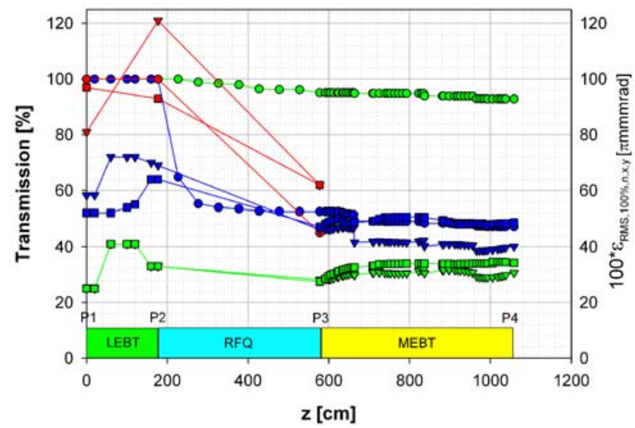


Figure 14: Development of Transmission (solid, circles), and transversal emittances (x is dashed, triangles, y dotted, squares), along beam propagation for ideal (green), initial (red) and new (blue) real input distributions.

## DISCUSSION

The first simulations from the ion source exit to the output of the MEBT show a mixed picture. The presented results based on an artificial input distribution are quite encouraging and with a total transmission from the source to the exit of the MEBT of >90% (100% in the LEBT, 95% in the RFQ and 98% in the MEBT, see figure 14) the goals are nearly reached. This result further proves that the design of the individual sections is sound and the joint performance is satisfactory. On the other hand, the latest results using a measured initial distribution show a dramatic increase of the beam emittance with fatal consequences on beam transmission. For the current status the transmission is expected to be ~46% (100% in the LEBT, 52% in the RFQ and 89% in the MEBT). Due to the large beam losses in the RFQ the total emittance growth is moderate (-10% in x and 23% in y). Serious efforts to reduce the ion source emittance and improve the RFQ acceptance are under way and recent work has already increased the transmission through the RFQ by 10%, but further progress is required.

## REFERENCES

[1] T R Edgecock, 6th Int. Workshop Neutrino Factories & Superbeams (NuFact04), July/August 2004, Osaka
[2] Neutron News, vol. 15 (2004), ISSN 1044-8632. See also http://www.isis.rl.ac.uk/.
[3] Alan Letchford et al., EPAC06, June 2006, Edinburgh
[4] J. Pozimski et al, Proceedings of LINAC 2006, Knoxville, Tennessee USA, p 403 ff
[5] S Lawrie et al, Proceedings of NIBS2008, Aix en Provence, France, to be publ. (AIP)
[6] John Back et al, EPAC2006, June 2006, Edinburgh
[7]GPT User Manual, Pulsar Physics, http://www.pulsar.nl/gpt/
[8] C. Plostinar et al., Proc. of PAC'07, Albuquerque, NM, USA, June 2007, p 1646 ff

# BEAM DYNAMICS AND WAKE-FIELD SIMULATIONS FOR HIGH GRADIENT ILC LINACS

C.J. Glasman & R.M. Jones; Cockcroft Institute, Daresbury, WA4 4AD, UK; University of Manchester, Manchester M13 9PL, UK

*Abstract*

Higher order modes (HOMs) are simulated with finite element and finite difference computer codes for the ILC superconducting cavities. In particular, HOMs in KEK's Ichiro type of cavity and Cornell University's Reentrant design are focused on in this work. The aim, at these universities and laboratories, is to achieve an accelerating gradient in excess of 50 MV/m in 9-cell superconducting cavities whilst maintaining a high quality and stable electron beam. At these gradients, electrical breakdown is an important cause for concern and the wakefields excited by the energetic electron beams are also potentially damaging to the beam's emittance. Here we restrict the analysis to performing detailed simulations, on emittance dilution due to beams initially injected with realistic offsets from the electrical centre of the cavities. We take advantage of the latest beam dynamics codes in order to perform these simulations.

## INTRODUCTION

The main superconducting (SC) linacs of the ILC will accelerate electron (positron) beams from energies of 5 (15) GeV to a center of mass energy of 500 GeV at collision. Efficient operation of the machine demands high luminosity collisions which are achieved by accelerating a train of 2625 low emittance bunches particles. This low emittance must of course be preserved in transport through the main linacs and beam delivery system to the interaction point.

Here we consider the main positron linac where the beam quality can be degraded and the emittance can be diluted due to a number of factors including energy spread, phase jitter in cavities, beam position feedback errors, quadrupole magnet misalignments and wakefield effects. We focus on the dilution in the transverse emittance due to long range transverse wakefields. In this case the wakefields are excited by the relativistic particle beam and consist of a series of higher order modes [1]. These wakefields have the potential to not only dilute the emittance, but can also cause a beam beak up instability (BBU) [2].

The ILC will employ superconducting cavities operating at gradients at 31.5 MV/m. It is envisaged that the cavity design will be the TESLA type which has been developed at DESY over a long period [3]. TESLA is a relatively mature design, however there are still significant concerns regarding the limited yield and reproducibility of high gradient cavities.

There is also a concerted international effort focused on increasing the gradient of the SC cavities. Reshaping the cavity has allowed the accelerating gradient to be increased without pushing the magnetic field past the quenching limit (~180 mT) on the walls of the cavity [4]. This has allowed cavity designs which in theory will sustain accelerating gradients in excess of 50 MV/m. There is also a recent design which minimizes both the electric field as well as the magnetic field on the walls of the cavity [5].

In practice only single-cell cavities have reached these gradients, at Cornell University [6] with the Reentrant design and at KEK with the Ichiro design [7]. Complete 9-cell cavities are in the process of being fabricated and tested for both designs with a view to achieving similar gradients. The new high gradient designs operate at the same accelerating frequency as the baseline TESLA design. Furthermore the cavity shapes are similar to that of the TESLA design.

However, the perturbations of the cavity geometry are expected to give rise to a modification of the mode distribution. With this in mind, we carefully investigated the kick factors and mode frequencies in the alternative designs. The transverse long range wakefield experienced by the bunch train is given by:

$$W_T(t) = 2\sum_p K_p \sin(\omega_p t) e^{\frac{-\omega_p t}{2Q_p}}$$

where $\omega_p/2\pi$, $K_p$ and $Q_p$ are the modal frequencies, kick factors [1] and damping Qs respectively for the dipole mode $p$.

These modes have been simulated in detail [8, 9] using parallel finite difference and finite element codes GdfidL [10] and Analyst [11] and this data has been used as input for beam dynamics simulations presented herein, using the codes Lucretia [12] and Placet [13]. The codes track particle bunches through the lattice of the linac in which the energy is increased from 15 GeV to 250 GeV.

The envelope of the transverse long range wakefield is displayed in Fig. 1 with a damping Q imposed on all modes of $10^5$ for the Ichiro cavity. Here it is evident that after 500 bunches (~50 km) the wake has decayed by 6 orders of magnitude. Thus, in all beam dynamics simulations 500 bunches is sufficient to account for the interaction between the wakefield and the multi-bunch train. We report on the results of these simulations in the next section.

## BEAM DYNAMICS SIMULATIONS

In constructing the main linacs of ILC approximately 16,000 cavities will be required. Fabrication of these cavities is expected to introduce random errors in the geometry and thereby alter the modal frequencies and kick factors for each cavity. These errors are in fact necessary in order that the beam receives a random kick from cavity to cavity. A linac made up of identical

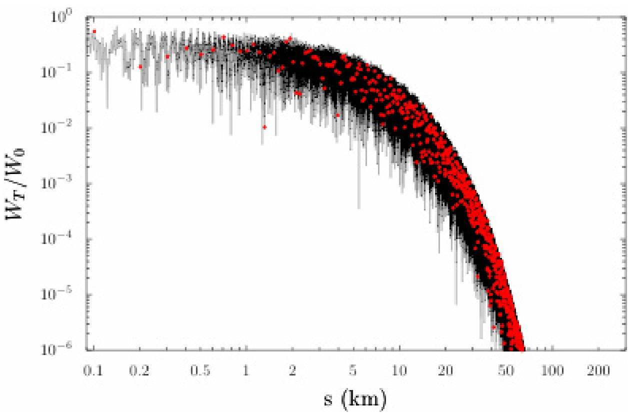


Figure 1: Envelope of long range transverse wakefield for the Ichiro cavity with Q=$10^5$, $W_0$=0.1472 V/pC/mm/m. Points show the location of the bunches.

cavities would impart the same kick coherently on the beam from cavity to cavity. This would resonantly drive beam break up and lead to severe emittance dilution.

The simulations described here are preformed with the Matlab-based code Lucretia. All simulations incorporate manufacturing errors by generating 100 sets of dipole mode frequencies in which each mode has been shifted by a random number generated according to a normal distribution; these define 100 different cavity types. These cavity types are then randomly distributed throughout the linac prior to tracking the beam down the linac. We applied a 1 MHz RMS spread in the dipole mode frequencies and a uniform damping Q of $10^6$. Each bunch was subjected to an injection offset of $\sigma_y$ (~ 6 μm) and trains of 500 bunches were subsequently tracked down the linac at the nominal bunch spacing of 369ns [14]. Placet simulations were also performed, although in this case the cavity mode randomization is achieved in a somewhat different manner; in this case all modes are shifted by the same random factor for each cavity in the linac. Fig.2 illustrates the dilution in the projected emittance for the bunch train at each beam position monitor position in the lattice that results from tracking down 40 machines. Each curve results from a different random seed, and the frequency distributions are distributed randomly over the complete linac. Figs. 3 and 4 present the results for machines consisting of Reentrant and Ichiro cavities, respectively. Fig. 5 displays a comparison of the mean value of the emittance dilution for each cavity type, together with the results of Placet simulations for the Ichiro cavity.

There is a discrepancy between the Lucretia and Placet results for the linac made up of Ichiro cavities. The difference between individual tracking simulations, for Lucretia, illustrated in Fig. 4, was small (~1%) for all cavity types simulated with Placet.

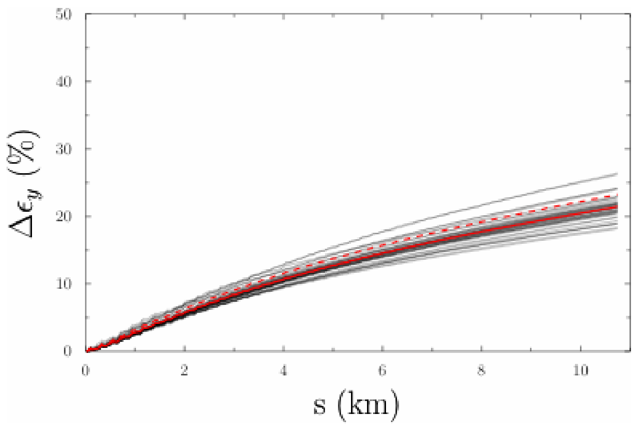


Figure 2: Emittance dilution simulated with Lucretia for 40 machines consisting of TESLA cavities. The mean dilution over all machines is displayed in red, with one standard deviation dashed.

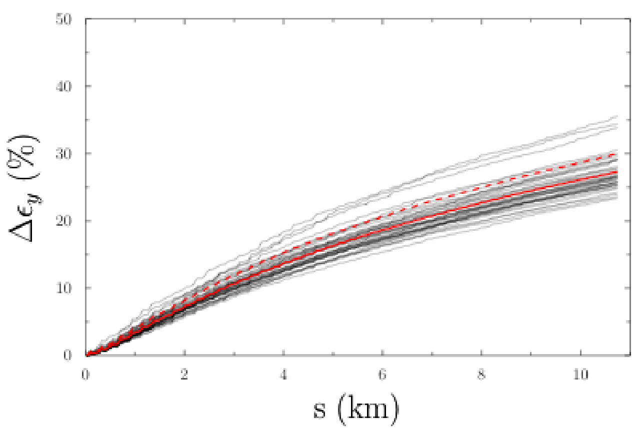


Figure 3: Emittance dilution simulated with Lucretia for 40 machines consisting of Reentrant cavities. The mean curve is displayed in red, with one standard deviation dashed.

The beam dynamics simulations described above incorporated random cavity fabrication errors but did not consider systematic effects.

In practice, superconducting cavities are squeezed to tune and to optimally achieve field flatness in the 1.3 GHz accelerating mode. This process changes the cell geometry and gives rise to a shift in the designed dipole mode frequencies. This tuning effect and those resulting from an amalgam of relaxed tolerances in the manufacturing process can readily make the dipole frequencies significantly detuned. This leads to both systematic and random frequency errors in the dipole modes. The sinusoidal dependence in Eq. 1 indicates that the wakefield time coordinate is determined by the bunch spacing. Consequently shifts in the bunch spacing are to a large extent equivalent to a shift in modal frequencies. Shifting the modal frequencies can push the beam dynamics into a region in which resonant BBU occurs. Clearly these regimes need to be predicted prior to fabrication of the complete linac.

The onset of this instability is predicted by the RMS of the sum wakefield which can be evaluated for small shifts in bunch spacing. Fig. 6 reveals a series of resonances associated with the Ichiro cavity. Applying heavier damping, changing the Qs from $10^6$ to $10^5$, suppresses these resonances significantly.

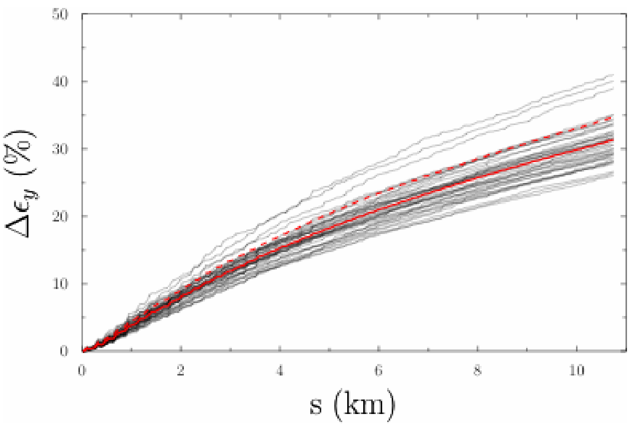


Figure 4: Emittance dilution simulated with Lucretia for 40 machines consisting of Ichiro cavities including the effects of random errors attributed to the manufacturing process. The mean curve is displayed in red, with one standard deviation dashed.

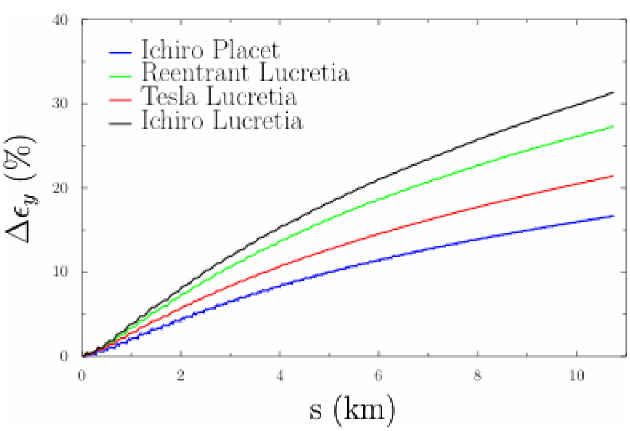


Figure 5: Comparison of the mean emittance dilution for each cavity type simulated with Lucretia. A single simulation undertaken with the code Placet for a linac comprising of Ichiro cavties is displayed in blue.

Earlier work has indicated that severe emittance dilution will occur should the machine be operating close to one of these resonances [15].

## CONCLUSIONS

Beam dynamics simulations have indicated that, with damping with Q~$10^6$, emittance dilution due to long range wakes in the Ichiro and Reentrant cavities is less than 50% at the end of the linac. Increasing This is tolerable performance similar to that of a linac made up of the ILC baseline TESLA cavities.

These simulations assume a bunch spacing of 369ns as detailed in the ILC Reference Design Report however, small deviations in this bunch spacing or equivalent systematic shifts in the HOM frequencies can lead to resonant wakefield effects, as illustrated in Fig. 6.

The damping required to preserve a high quality beam will be investigated with beam dynamics work including different levels of random detuning and systematic shifts to the HOM.

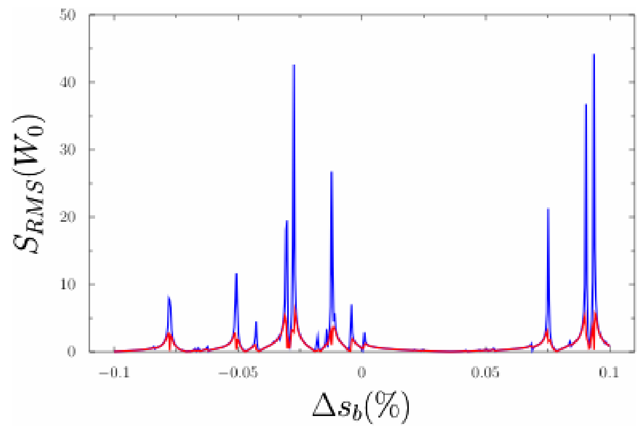


Figure 6: RMS of the sum wakefield as a function of fractional deviations in the bunch spacing. For Q=$10^6$ (blue) and Q=$10^5$ (red).

We note the importance of understanding the inconsistency between the Lucretia and Placet simulations. In order to shed light on the present discrepancy we intend to modify the mode randomization scheme to be consistent between both codes. Additional research is in progress on simulations of emittance dilution issues using Lucretia and including the short range wakefield due to cavity and coupler geometries and realistic component misalignments.

## REFERENCES

[1] P.B. Wilson, SLAC-PUB-4547, 1989.
[2] K. Yokoya, DESY Report 86-084, 1986..
[3] B. Aune et al. 2001, (PRST-AB Vol. 3, 092001)
[4] R.L. Geng, Cornell SRF060209-01.
[5] Z. Li and C. Adolphsen, THP038, this conference.
[6] R.L. Geng et al. WEPMS006, PAC07,2007.
[7] T. Saeki et al. MOPP029 EPAC08, 2008
[8] R.M. Jones & C.J. Glasman, PAC07, 2007.
[9] C.J. Glasman et al., SRF2007, 2007.
[10] W. Bruns , www.gdfidl.de.
[11] J. DeFord et al., www.staarinc.com
[12] P. Tenenbaum et al. www.slac.stanford.edu/accel/ilc/codes/Lucretia
[13] D. Schulte et al., https://savannah.cern.ch/placet
[14] International Linear Collider Reference Design Report, 2007, www.linearcollider.org/rdr/
[15] C.J. Glasman & R.M. Jones, EPAC08, 2008.

# SCATTERING MATRIX SIMULATIONS OF FIELDS AND DISPERSION RELATIONS IN SUPERCONDUCTING CAVITIES FOR XFEL AND ILC

I. Shinton and R.M. Jones; Cockcroft Institute, Daresbury, WA4 4AD, UK;
University of Manchester, Manchester, M13 9PL, UK

*Abstract*

The globalised cascaded scattering matrix technique is a well proven, practical method that can be used to simulate large accelerating RF structures in which realistic fabrication errors to be incorporated in an efficient manner without the necessity to re-mesh the entire geometry. The globalised scattering matrix (GMS) technique allows one to obtain the scattering matrix for a structure. The method allows rapid e.m. field calculations to be obtained. Results are presented on monopole mode fields and dispersion relations calculated from direct and analytical methods. Analytical approximate results are also presented for the equivalent shunt susceptance of an iris loaded structure.

## INTRODUCTION

In large accelerating structures such as the ILC beam break up and emittance dilution are major design concerns; hence the need to be able to accurately model large fractions of these structures in which effects such as wakefields, trapped modes, coupler kicks have been taken into consideration. GSM has been shown in previous works [1-3] to be capable of being employed to accurately model such large scale structures.

## MODE MATCHING USING GSM

Mode matching is an established technique [4-5] which has been applied to various accelerator problems for sharp transitions consisting of adjoining wide narrow (WN) sections [6-10]. The mode matching technique relies upon splitting the structure into a series of sub-regions (WN or NW regions) in which an analytical solution of Maxwell's equations is given in terms of a series expansion over a set of orthogonal modes. The field solutions are then obtained by matching the field at the interfaces. In principle there are an infinite number of modes excited at a junction. In a practical application of the technique we truncate the series with an appropriate ratio of the modes in the narrow to wide section. Indeed, numerous studies have been preformed on the relative convergence phenomena to determine the optimal ratio of modes [11].

## A MODE MATCHING GSM TECHNIQUE FOR FIELD DETERMINATION

The mode matching procedure presented here differs from previous studies. We will consider the case for a propagating monopole mode launched form one port. We derive an analytical relation for the S matrix for a WN or a NW junction. Let us consider the circular WN junction with n modes in region I (wide) and m modes in region II (narrow) where m<=n. We shall denote "b" as the radius of the wide region and "a" as the radius of the narrow region. Analytical electromagnetic fields $\vec{e}$ in a circular beam waveguide are provided in [12]. The characteristic scalar product is given by $\bar{a}_{nm} = \int_S e_n \cdot \hat{e}_m \partial\Gamma$ (over the aperture S) and this evaluates to:

$$\bar{a}_{nm} = \frac{2a^2 \chi_n J_0(\chi_{0n} a/b)}{b^2 J_1(\chi_{0n})\left((\chi_{0n} a/b)^2 - \chi_m{}^2\right)} \tag{1}$$

where $\chi_{0n}$ is the nth root of $J_0(\chi_{0n})$. For a = b the normalisation in [12] corresponds to $\bar{a}_{nm} = \delta_{nm}$ (where $\delta$ is the Kronecker delta function). The S matrix at the transition is obtained by mode-matching the fields in terms of the modal amplitudes at each transition:

$$S_{21} = 2\left(U + \hat{Z}\bar{a}^t Y \bar{a}\right)^{-1} \hat{Z}\bar{a}^t Y \tag{2}$$

$$S_{11} = \bar{a} S_{21} - U \tag{3}$$

$$S_{22} = 2\left(U + \hat{Z}\bar{a}^t Y \bar{a}\right)^{-1} - U \tag{4}$$

$$S_{12} = \bar{a}\left(U + S_{22}\right) \tag{5}$$

In the above equations U, $Z = Y^{-1}$ is the identity and impedance matrix, respectively. Using Eqs. 1-5 the S matrix of a structure decomposed into WN and NW transitions can be obtained. The e.m field in any structure can be subdivided into one of three different regions, as depicted in Fig. 1. Region 1 lies between z=0 and z=1, here the S matrix consists of the GSM formed z=z1 and z=z3.

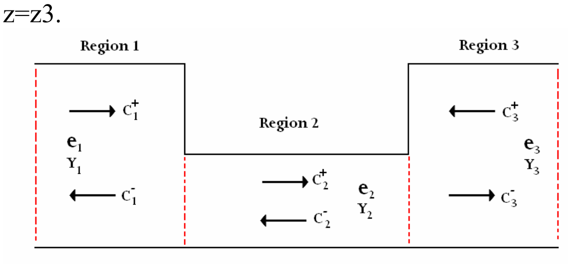


Figure 1: Sketch of WNW transition illustrating incident and reflected modes.

Any subsection of a structure will be classified as a region 2 section, only the first and last sections are classified as region 1 and 3 respectively. The S matrix of any region 2 subsection consists of a propagating matrix representing the infinite propagating wave series $S_{21}^0$ and a reflected matrix $S_{11}^0$ representing the infinite reflected wave series both which are decaying within the subsection [3]. Here the superscripts I and II represent the GSM's left and right of the subsection respectively, $T_z = \delta_{nm} e^{-ik_n z}$ and g is the length of the subsection. Region 3 lies between z=z2 and z=z3, here the S matrix consists of the GSM between z=0 and z=z2. Since the S matrices are directly proportional to the modal amplitudes then after applying the mode matching procedure we obtain the following formulae for the three regions:

Region 1 electric field

$$E_{\parallel} = e_{n1} e^{ik_{n1}(z-z1)} - \sum_{n1=1}^{N} S_{11}(n1,1)\bar{e}_{n1} e^{ik_{n1}(z-z1)} Y_{n1} \quad (6)$$

$$E_{\perp} = e_{n1} e^{ik_{n1}(z-z1)} + \sum_{n1=1}^{N} S_{11}(n1,1)\bar{e}_{n1} e^{ik_{n1}(z-z1)} \quad (7)$$

Region 2 electric field

$$S_{21}^{0} = T_z\left[U - S_{22}^{I} T_g S_{11}^{II} T_g\right]^{-1} S_{21}^{I} \quad (8)$$

$$S_{11}^{0} = T_{-z}\left[U - T_g S_{11}^{II} T_g S_{22}^{I}\right]^{-1} T_g S_{11}^{II} T_g S_{21}^{I}$$

$$S_{11}^{0} = T_{-z}\left[U - T_g S_{11}^{II} T_g S_{22}^{I}\right]^{-1} T_g S_{11}^{II} T_g S_{21}^{I} \quad (9)$$

$$E_{\perp} = \sum_{n_2=1}^{N}\left(T_z S_{21}^{0} + T_{-z} S_{11}^{0}\right)\bar{e}_{n_2} \quad (10)$$

$$E_{\parallel} = \sum_{n_2=1}^{N}\left(T_z S_{21}^{0} - T_{-z} S_{11}^{0}\right)\bar{e}_{n2} Y_{n_2} \quad (11)$$

Region 3 electric field

$$E_{\parallel} = \sum_{n_3=1}^{N} S_{21}(n_3,1) e_{n_3} e^{-ik_{n_3}(z-z2)} Y_{n_3} \quad (12)$$

$$E_{\perp} = \sum_{n_3=1}^{N} S_{21}(n_3,1) e_{n_3} e^{-ik_{n_3}(z-z2)} \quad (13)$$

To verify the essential behaviour of the fields a wide-narrow-wide (WNW) junction is considered. A 2D field plot showing the radial dependence of the field is presented in Fig. 2. This simulation is very efficient as it required no more than a few seconds of CPU time in a PC compared to up to an hour on a comparable PC with a conventional numerical finite element code.

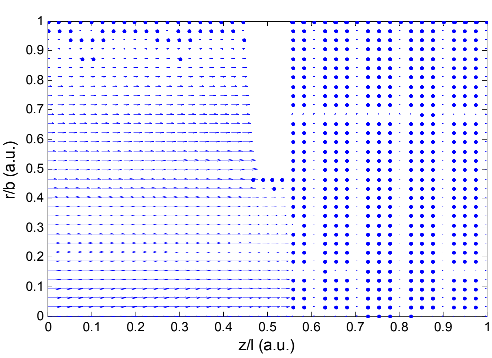


Figure 2: Axial electric $E_z$ for WNW transition as a function of radius and axial position.

## ANALYTICAL FORMULAE FOR DISPERSION CURVES

Combining GSM and mode matching in conjunction with the Bethe hole coupling perturbation theory [5,13] allows exact analytical expressions to be obtained for the normalised susceptance $\overline{B}$ of a structure. We note that $\overline{B}$ is equivalent to the coupling constant κ or fractional bandwidth of the mode. Let us consider the case of a monopole accelerating mode. From circuit theory [14] we can express the relationship between angular frequency ω and phase advance per cell Φ in the thin iris approximation (where κ<<1 ) as:

$$\omega = \omega_{\pi/2}\left(1 - \frac{\kappa}{2}\cos\Phi\right) \quad (14)$$

where $\omega_{\pi/2}/2\pi$ is frequency as a phase advance of π/2. The relationship between phase and susceptance can be derived using either transmission line theory or from considering the ABCD matrix representation [4]:

$$\cos\Phi = \cos(k_z l) - \frac{\overline{B}}{2}\sin(k_z l) \quad (15)$$

In Eq. 15 l is the cavity length and $k_z$ is the propagation constant of the dominant mode: $k_z = \sqrt{(\omega/c)^2 - (\chi_{01}/b)^2}$ (where b is the radius in the cavity region and $\chi_{01}$ is the first root of the Bessel function $J_0$). Provided $k_z l << 1$ then to first order in $k_z l$ Eq. 15 is simplified to:

$$\cos\Phi = 1 - \frac{\overline{B}}{2} k_z l \quad (16)$$

A Bethe hole coupling analysis [5, 13] allows the fractional bandwidth to be obtained as:

$$\kappa = \frac{4a^3}{3\pi l b^2 J_1(\chi_{01})} \quad (17)$$

In Eq. 17 $a$ is the iris radius. Rewriting and comparing Eqns. 15 and 16 in terms of $\cos\Phi$ allows the following equation to be derived in the thin iris approximation:

$$\overline{B} = \frac{3\pi b^4 J_1(\chi_{01})^2 k_z}{2a^3\chi_{01}^2} \quad (18)$$

An exact formulation for the dominant mode can also be obtained by considering a susceptance placed symmetrically and in parallel with a transmission line. The susceptance normalised to the transmission line impedance is then obtained in terms of the reflection coefficient of $S_{11}(1,1)$ the dominant mode: [4]:

$$\overline{B} = \frac{2iS_{11}(1,1)}{S_{11}(1,1)+1} \quad (19)$$

The dispersion curve is obtained from the combination of Eqns. 15 and 18 have a limited domain of applicability due to the thin iris approximation used in obtaining it. An alternative method which circumvents this limitation is to consider the S matrix of a cell in an infinite periodic structure (obtained from GSM):

$$\begin{pmatrix} b_1 \\ b_2 \end{pmatrix} = \begin{pmatrix} S_{11} & S_{12} \\ S_{21} & S_{22} \end{pmatrix} \begin{pmatrix} a_1 \\ a_2 \end{pmatrix} \tag{20}$$

In Eq. 20 a represents the incident waves and b the reflected waves on each port, the subscripts refer to the ports. Applying the Floquet condition:

$$b_2 = e^{-i\Phi} a_1 \tag{21}$$

$$b_1 = e^{-i\Phi} a_2 \tag{22}$$

Eqns. 20-22 represent an eigen-mode problem. Provided the field is evaluated sufficiently far away from the junction such that all evanescent modes have decayed to leave only the dominant propagating mode, we can solve for the phase advance. The solution for Φ in terms of the dominant propagating mode scattering matrix parameters is obtained:

$$\cos\Phi = \frac{1 + S_{21}(1,1)^2 - S_{11}(1,1)^2}{2S_{21}(1,1)} \tag{23}$$

The analytical equation for obtaining a dispersion curve using the thin iris approximation (Eqns. 15 and 18), reveals there is little discrepancy between the two methods provided the iris is sufficiently thin (see Fig. 3). However for irises thicker than t=50 μm the Bethe hole coupling formula that the analytical susceptance formula, which Eq. 18 was based on, is no longer valid.

The analytical equation derived by considering the S matrix of a cell in an infinitely periodic structure (Eq. 23) is of course not limited by the thin iris approximation. However, it does require all evanescent modes to be small compared to the dominant mode. A Brillouin diagram is displayed in Fig. 4 from a calculation based on three methods. The transverse mode matching method developed herein is in good agreement with results based on the longitudinal mode matching code KN7C [15,16]. However, there is some discrepancy between HFSS and the other methods. The bandwidth obtained from all three methods is: 1.074%, 1.100% and 1.066% for KN7C, analytical model and HFSS, respectively.

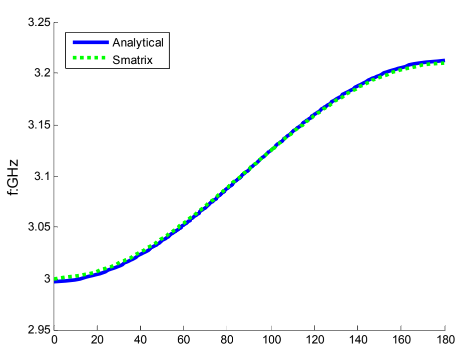


Figure 3: Brillouin diagram calculated using Eq. 15 for a = 7.5 mm, b = 38.23 mm, t = 0.10 mm, l = 6.1 mm. The analytical approximation corresponding to Eq. 18 is given in blue together with the exact model provided by Eq. 19 in green.

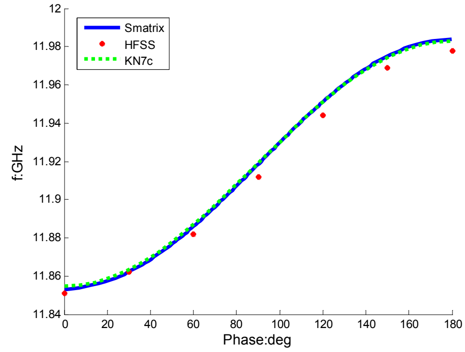


Figure 4: Brillouin diagram calculated using an analytical (Eq. 23 blue) and numerical approaches (HFSS red and KN7c green) for an idealised CLIC_G cell. This structure has been represented as a simplified NWN transition with cell parameters: a = 2.619 mm, b = 9.783 mm, t = 1.202 mm, l = 8.332 mm.

## DISCUSSION

The transverse mode matching method developed herein provides an efficient and accurate means of characterising the fields and dispersion relation of accelerator structures. The analytical dispersion relation and analytic formula for iris suspectance can be applied to specific accelerator cells. However, the geometrical dependence of the analytical formula provides a rapid means of designing accelerator cells with sufficiently thin irises. It is planned to extend the mode matching method to consider aggregate accelerator structures.

## REFERENCES

[1] I.R.R. Shinton and R.M. Jones, PAC, 2007, p2218
[2] I.R.R. Shinton and R.M. Jones, 13th International workshop on RF Superconductivity, 2007, WEP80
[3] I.R.R. Shinton and R.M. Jones, EPAC, 2008, p619
[4] R.E. Collin, Foundations for microwave engineering,1966
[5] R.E. Collin, Field theory of guided waves, 1991
[6] U. van Rienen, AIP Conf. Proc, 1997, Vol 391, p89
[7] S.A. Heifets and S.A. Kheifets, SLAC-PUB-5907
[8] S.A. Heifets and S.A. Kheifets, SLAC-PUB-5562
[9] V.A. Dolgashev, ICAP, 1998, p149
[10] V. Dolgashev, T. Higo, Proceedings of the 8th international workshop on linear colliders, LC97,1997.
[11] L. Carin, Computational analysis of cascaded coaxial and circular waveguide discontinuities, Masters thesis, University of Maryland, 1986
[12] N. Marcuvitz, The wave guide handbook, 1986
[13] H. Henke, TET-Note 96/04, August 1996
[14] R.M. Jones et al., SLAC-PUB-9247, 2002
[15] L.F. Wang, Y.Z. Lin, T. Higo and K. Takata, PAC, 2001, pg 3045
[16] E. Keil, CERN Report ISR-TE/69-49, 1969

# END-TO-END SIMULATION OF THE SNS LINAC USING TRACK*

B. Mustapha#, P.N. Ostroumov
Argonne National Laboratory, 9700 S. Cass Ave, IL 60439, U.S.A.

D. Jeon
Oak Ridge National Laboratory, 1 Bethel Valley Rd, Oak Ridge, TN 37831, U.S.A.

*Abstract*

To simulate the SNS linac using the beam dynamics code TRACK and to benchmark the results against the recent commissioning data, we have updated TRACK to support SNS-type elements such as DTL's and CCL's. After successfully implementing and simulating the DTL section of the SNS linac, we have implemented the CCL section and the high energy superconducting (SCL) section up to 1 GeV. Results from end-to-end TRACK simulations of the SNS linac including the RFQ will be presented and discussed.

## INTRODUCTION

In an effort to benchmark the beam dynamics code TRACK [1] againt experimental data from existing linacs, such as the SNS linac, we have updated the code to support new elements such as DTLs and CCLs. We previously reported the results of TRACK simulations for the SNS MEBT and DTL [2]. Recently, we implemented a new subroutine for the simulation of CCL tanks. After building the CCL, SCL and HEBT lattices, we were able to perform end-to-end simulations from the RFQ to the HEBT right before the stripping foil.

After briefly describing the SNS linac lattice, results of the RFQ simulations using TRACK are presented and compared to simulations using the RFQ design code Parmteq [3]. The method of implementing CCL tanks is then presented followed by results of end-to-end simulations of the linac from the MEBT to the HEBT. Possible future developments are discussed at the end.

## THE SNS LINAC

The SNS accelerator facility [4] is designed to provide a 1 GeV, 1.4 MW proton beam to a liquid mercury target for neutron production. The accelerator complex consists of a H− injector capable of producing 38 mA peak current, a 1 GeV linac, an accumulator ring and associated beam transport lines to experimental areas. The linac consists of a 2.5 MeV, 38mA H− front-end injector, a six-tank 402.5 MHz DTL to accelerate the beam to 87 MeV, a four-module 805 MHz Coupled Cavity Linac (CCL) to accelerate the beam to 187 MeV, and a superconducting linac (SCL) to accelerate the beam to 1 GeV. Figure 1 shows a schematic layout of the SNS linac.

* This work was supported by the U.S. Department of Energy, Office of Nuclear Physics, under Contract No. DE-AC02-06CH11357.
# mustapha@phy.anl.gov

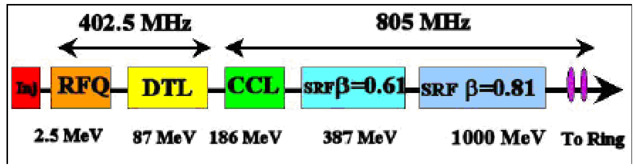


Figure 1: Schematic layout of the SNS linac.

## SIMULATIONS OF THE RFQ

The design parameters of the SNS RFQ [5] are summarized in Table 1. According to these parameters the RFQ lattice was generated using Parmteq from which the TRACK lattice was derived. The simulations were performed using both Parmteq and TRACK. Table 2 compares the calculated transmissions for a 0 mA beam and the actual operating current of 32 mA [6]. We notice differences between TRACK and Parmteq that should be further investigated. However, the two codes agree reasonably well on the output beam parameters. Figure 2 compares the phase space plots at the end of the RFQ and Table 3 compares the values of the normalized rms emittances.

Table 1: Design parameters of the SNS RFQ.

| | |
|---|---|
| **Type** | 4 vane |
| **RF Frequency** | 402.5 MHz |
| **Voltage** | 83 kV |
| **N. Of Cells** | 448 |
| **Length** | 3.723 m |
| **Beam** | H- |
| **Input Energy** | 65 keV |
| **Output Energy** | 2.5 MeV |
| **Peak Output Current** | 52 mA |
| **Long. Emittance** | 103 deg-keV |
| **Trans. Emittance: N-RMS** | 0.21 mm-mrad |
| **Design Transmission** | > 90 % |

Table 2: RFQ transmission for different beam currents calculated using both Parmteq and TRACK.

| Current | Parmteq | TRACK |
|---|---|---|
| 0 mA | 99.4 % | 98.5 % |
| 32 mA | 97.3 % | 91.4 % |

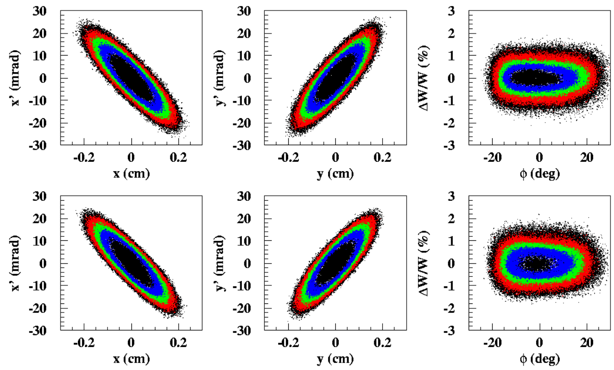


Figure 3: Phase space plots for a 32 mA H- beam at the end of the RFQ. The top three plots are the results of Parmteq and the bottom ones are obtained from TRACK.

Table 3: Normalized RMS beam emittances at the end of the RFQ from both Parmteq and TRACK for 32 mA .

| Emittance: N. RMS | Parmteq | TRACK |
|---|---|---|
| $\varepsilon_x$ (mm-mrad) | 0.213 | 0.204 |
| $\varepsilon_y$ (mm-mrad) | 0.211 | 0.203 |
| $\varepsilon_z$ (deg-keV) | 99.63 | 105.86 |

We have also simulated the RFQ with three different beam currents: 0 mA, 32 mA and 60 mA. The results are shown in Fig. 4. We clearly notice the compression of the longitudinal phase space with increasing beam current. The beam envelopes and emittances along the RFQ are shown in Fig. 5 for a 32 mA H- beam.

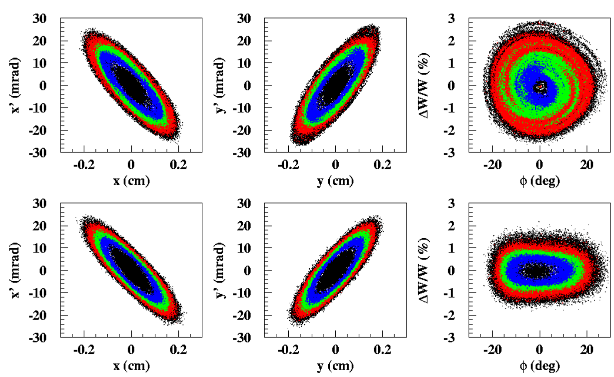


Figure 4: Phase space plots at the end of the RFQ for different beam currents: 0 mA (top) and 32 mA (bottom).

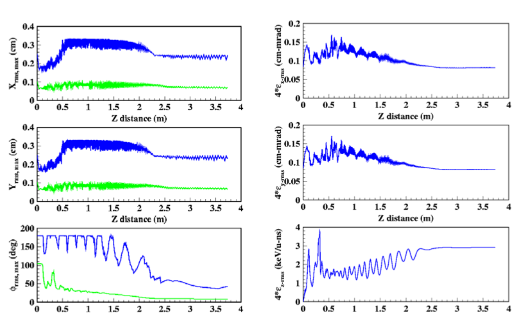


Figure 5: Envelopes and emittances along the SNS RFQ for a 32 mA H- beam.

## IMPLEMENTATION OF THE CCL

As was done for the DTL [2], a new TRACK subroutine was developed for particle tracking in a CCL tank. Unlike a DTL, a CCL has external focusing and several CCL tanks are usually powered by a single Klystron. A special attention should be paid to the phasing of the CCL tanks. Every CCL tank has two input files, one for the cells data and one for the field data. The fields are 2D tables calculated using Superfish [7].

## END-TO-END SIMULATIONS OF THE LINAC

After building the lattices for the CCL, SCL and HEBT we performed end-to-end simulations of the linac from the MEBT to the HEBT right before the stripping foil. Figure 6 shows the envelopes and emittances along the linac for a 32 mA H- beam while Fig. 7 shows the phase space plots at the exit of the linac. We notice how the phase width of the beam expands for injection into the accumulator ring operating at a lower frequency.

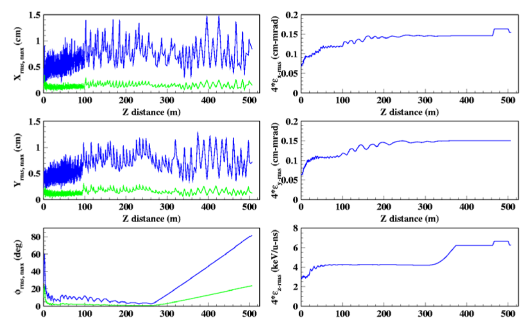


Figure 6: Envelopes and emittances along the SNS linac for a 32 mA H- beam.

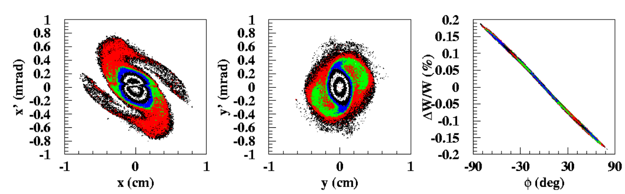


Figure 7: Phase space plots at the exit of the SNS linac; end of HEBT right before the stripping foil. The beam is a 32 mA H- beam.

## SUMMARY AND FUTURE WORK

We have successfully implemented and simulated all the sections of the SNS linac, from the RFQ to the HEBT, using the beam dynamics code TRACK. Future work will focus on end-to-end simulations including machine errors and beam loss analysis in order to compare the results with the experimental data. This is an important step towards the realization of the concept of model driven accelerator.

## REFERENCES

[1] V.N. Aseev et al, Proceedings of PAC-05 Conference, Knoxville, Tennessee, May 16-20, 2005.
[2] B. Mustapha et al, Proceedings of LINAC-06 Conference, Knoxville, Tennessee, August 21-25, 2006.
[3] Parmteq: RFQ design code by LANL @ http://laacg1.lanl.gov/laacg/software
[4] N. Holtkamp, Proceedings of PAC-03 Conference, Portland, Oregon, May 12-16, 2003.
[5] A. Ratti et al, Proceedings of EPAC-00 Conference.
[6] A. Aleksandrov, private communication.
[7] J.H. Billen and L.M. Young, Poisson-Superfish Manual, Report LA-UR-96-1834, Los Alamos, 1996 (Revised 2005).

# MONTE CARLO SIMULATION OF TOUSCHEK EFFECTS IN A LINAC BEAM *

A. Xiao†, M. Borland, ANL, Argonne, IL 60439, USA


## Abstract

We present a Monte Carlo method implemented in the code `elegant` [1] for simulating Touschek scattering effects in a linac beam. The local scattering rate and the distribution of scattered electrons can be obtained from the code. In addition, scattered electrons can be tracked to the end of the beamline and the local beam loss rate and beam halo information recorded. This information can be used for beam collimation system design.


## INTRODUCTION

The Touschek effect is a single Coulomb scattering effect between charged particles in a beam. For a relativistic beam, a small change of transverse momentum results in a much larger change of longitudinal momentum, as the momentum change is increased by the Lorentz factor $\gamma$. When the change exceeds the machine's momentum acceptance, the scattered particle is lost.

The Touschek effect is well understood in storage rings and has been largely ignored for linac beams in the past due to the negligible loss rate. However, this is not the case for an intense electron bunch with ultra-low emittance and very short bunch length that passes through a linac with a very high repetition rate, as occurs in proposed Energy Recovery Linacs (ERLs) [2]. This is a concern for a possible ERL upgrade of the APS, since the radiation shielding of the ring is not designed for high continuous loss rates [3].

Previously, a preliminary theoretical analysis [4] was performed using Piwinski's formula [5]. To better determine the scattered electron distribution and determine precisely the electron loss rate and loss position, we have included a Monte Carlo simulation method in `elegant` for studying the Touschek scattering effect.

In this paper, we review the theory of Touschek scattering, then describe the method used for the Monte Carlo simulation. The scattering rates calculated from the Monte Carlo simulation and Piwinski's formula are compared. The strategy used for calculating beam loss rate and location in `elegant` is then explained. Finally, we give an application example to a proposed APS ERL lattice design.

## THEORY DESCRIPTION

In the center-of-mass (CM) system [1], the probability of one of the two encountered electrons being scattered into a solid angle $d\Omega^*$ is given by the differential Møller cross section [6]

$$\frac{d\sigma^*}{d\Omega^*} = \frac{r_e^2}{4\gamma^{*2}}\left[\left(1+\frac{1}{\beta^{*2}}\right)^2\frac{4-3\sin^2\Theta^*}{\sin^4\Theta^*}+\frac{4}{\sin^2\Theta^*}+1\right], \tag{1}$$

where $r_e$ is the classical electron radius; $\gamma^*$ and $\beta^*$ are the relative energy and velocity of scattered electrons in the CM system, respectively; $\Theta^*$ is the angle between the momenta before and after scattering; and $d\Omega^* = \sin\Theta^* d\Theta^* d\Psi^*$.

The total scattering rate $R$ is given by the integration over all possible scattering angles and over all electrons in the bunch. In the CM system,

$$R^* = 2\int |v^*|\sigma^*\rho(\vec{x}_1^*)^*\rho(\vec{x}_2^*)^* dV^*, \tag{2}$$

where $v^*$ is the scattered electrons' velocity, $\sigma^*$ is the total Møller cross section, $\vec{x}^* = (x^*, y^*, z^*, p_x^*, p_y^*, p_z^*)$, $\rho(x_i^*)^*$ is the electron phase-space density, and $dV = dx^*dy^*dz^*dp_{x1}^*dp_{y1}^*dp_{z1}^*dp_{x2}^*dp_{y2}^*dp_{z2}^*$. $\sigma^*$ is integrated over the solid angle $d\Omega^*$ with $\Theta^* \in (0, \frac{\pi}{2}]$, $\Psi^* \in [0, 2\pi]$:

$$\sigma^* = \int_0^{2\pi}\int_0^{\pi/2}\frac{d\sigma^*}{d\Omega^*}\sin\Theta^* d\Theta^* d\Psi^*. \tag{3}$$

The reason for $\Theta^* \in (0, \frac{\pi}{2}]$ is that, if one electron is scattered into the region $0 < \Theta^* \leq \frac{\pi}{2}$, then the other is scattered into the region $\frac{\pi}{2} \leq \Theta^* < \pi$. The factor "2" in Equation (2) includes both regions.

For the problem we are interested in, we assume that $p_x \ll p_z$ and $p_y \ll p_z$, which means that the Lorentz transformation is mainly taking place along the $z$ direction, and $\sigma^*$ is parallel to the $z^*$-axis. Transforming to the laboratory coordinate system gives

$$|v|\sigma = \frac{|v^*|}{\gamma}\frac{\sigma^*}{\gamma} \tag{4}$$

and

$$R = 2\int |v|\sigma\rho(\vec{x_1})\rho(\vec{x_2})dV, \tag{5}$$

with

$$dV = dx_\beta dy_\beta d\Delta z dx'_{\beta 1}dx'_{\beta 2}dy'_{\beta 1}dy'_{\beta 2}d\Delta p_1 d\Delta p_2. \tag{6}$$

Ignoring coupling, for an electron bunch with Gaussian distribution, the electron's density in phase space $(x_\beta, x'_\beta, y_\beta, y'_\beta, \Delta z, \Delta p/p_0)$ is given by

$$\rho = \frac{N\beta\ \beta}{8\pi^3\sigma\ \sigma\ \sigma^2\ \sigma^2}\exp\left\{-\frac{\Delta z^2}{2\sigma^2}-\frac{1}{2\sigma^2}\frac{\Delta p^2}{p_0^2}\right\}$$
$$\times\exp\left\{-\frac{x^2+(\alpha\ x\ +\beta\ x')^2}{2\sigma^2}-\frac{y^2+(\alpha\ y\ +\beta\ y')^2}{2\sigma^2}\right\}, \tag{7}$$

* Work supported by the U.S. Department of Energy, Office of Science, Office of Basic Energy Sciences, under Contract No. DE-AC02-06CH11357.

† xiaoam@aps.anl.gov

[1] For clarity, we use (*) to denote all quantities in the CM system, as opposed to quantities in the laboratory coordinate system.

where $N$ is the total number of electrons in the bunch; $\beta_{x,y}$ and $\alpha_{x,y}$ are the local optical functions; $\sigma_{x\beta,y\beta}$ are the transverse beam sizes for on-momentum electrons; $\sigma_z$ is the bunch length; and $\sigma_p$ is the energy spread. A scattering event happens when the following conditions are satisfied

$$\begin{aligned} \Delta z_1 &= \Delta z_2, \\ x_{\beta 1} + D_x \frac{\Delta p_1}{p_0} &= x_{\beta 2} + D_x \frac{\Delta p_2}{p_0}, \\ y_{\beta 1} + D_y \frac{\Delta p_1}{p_0} &= y_{\beta 2} + D_y \frac{\Delta p_2}{p_0}, \end{aligned} \tag{8}$$

where $D_{x,y}$ are the dispersion functions.

Equation (5) is a general expression for the Coulomb scattering rate. The Touschek scattering rate (beam loss rate) is $R_T = R(|\Delta p/p_0| > \delta_m)$, where $\delta_m = \Delta p_m/p_0$ is the machine's local momentum aperture, i.e., the momentum aperture relevant to particles scattered at a specific location.

## MONTE CARLO SIMULATION

The method used in `elegant` for simulating electron scattering processes is modified from S. Khan's work for BESSY II [7, 8]. For each simulated scattering event, a total of 11 random numbers are generated and used to determine the position of the scattering event $(x, y, z)$; the momenta of electron 1 $(x'_1, y'_1, \Delta p_1)$; the momenta of electron 2 $(x'_2, y'_2, \Delta p_2)$; and the scattering angles $(\Theta^*, \Psi^*)$. Dispersion corrections are included in the process of assignment. The electron's momenta after scattering are calculated and saved. We compute the integral in Equation (5) using Monte Carlo integration with $N$ uniform distributed samples in the n-dimensional volume $V$, e.g.,

$$\int_V f(\vec{x}) d\vec{x} \approx \frac{V}{N} \sum_{i=1}^{N} f(\vec{x_i}). \tag{9}$$

The average scattering rate is thus given by

$$R_M(|\delta| > \delta_m) = \frac{V}{N} \sum_{k=1}^{M} \left[ \frac{v^*}{\gamma^2} \frac{d\sigma^*}{d\Omega^*} \sin\Theta^* \rho(\vec{x_1}) \rho(\vec{x_2}) \right]_k, \tag{10}$$

where $N$ is the total number of simulated scattering events; M is the total number of scattered electrons with $|\delta| > \delta_m$ (one scattering event may generate one or two electrons with $|\delta| > \delta_m$, and they are counted individually); and $V$ is the total volume in $(x, y, z, x'_1, y'_1, dp_1, x'_2, y'_2, dp_2, \Theta^*, \Psi^*)$ space from which the events are selected. When $M$ is large enough, the simulated scattering rate converges to the analytical scattering rate, see Figure 1. In `elegant`, we use $5 \cdot 10^6$ as the default value of $M$.

Figure 2 shows the excellent agreement in the local scattering rates calculated from Piwinski's formula [5] and our Monte Carlo simulation. The lattice used here is the turn-around arc (TAA) cell of the APS-ERL lattice [9].

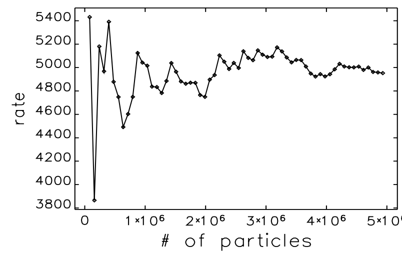


Figure 1: Simulated scattering rate vs. number of simulated scattered electrons.

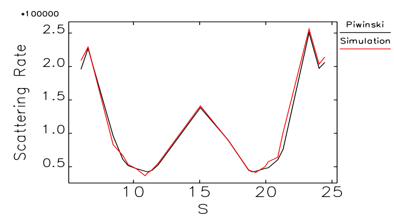


Figure 2: Local Touschek scattering rate: Piwinski formula (black) and Monte Carlo simulation (red).

## BEAM LOSS CALCULATION

To simulate beam loss due to Touschek scattering, we combined Piwinski's formula and the Monte Carlo method in `elegant`. First, the entire beamline is divided into $N_s$ short segments by inserting `TSCATTER` elements as separators. For each segment, we use Piwinski's formula to calculate the total scattering rate (integrated scattering rate $\int R_{Piwinski,i}$) for that segment. The scattered electron distribution at each `TSCATTER` element is generated from the Monte Carlo simulation. Each simulated scattered electron represents many electrons with a local scattering rate $r_i$. Let the total rate each represents for that [illegible] be $R_i$, given by

$$R_i = \frac{r_i}{\sum r_i,} \times \int R_{Piwinski}. \tag{11}$$

The beam loss rate and location can then be calculated through tracking those scattered electrons through the beamline and recording all lost electrons, with $R_i$ providing a weight for each simulated electron's contribution to the total loss rate.

As we pointed out in the previous section, to obtain a reliable scattering rate and a smooth scattered electron distribution, $M$ has to be large enough ($\sim 5 \cdot 10^6$). We also require a large number of segments, $N_s$. That means that we need to track $M \times N_s$ electrons, which requires significant CPU time. This motivated a search for an alternative strategy to reduce the simulation burden. We examined the scattering rate that each simulated electron represents and, not surprisingly, found a large variation. Some simulated electrons represent very likely scattering events, while some represent very low probability events. We sorted all simulated electrons by the associated scattering rate. Figure 3 illustrates the sum of the scattering rate ($\sum r_i$) vs. the number of simulated electrons ($\sum_i$).

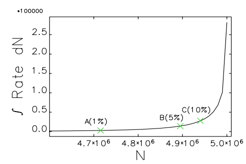


Figure 3: Integrated scattering rate vs. number of simulated electrons. Electrons are sorted with increasing associated scattering rate.

From this plot we can see that about $5\%$ of simulated electrons represent about $99\%$ of the scattering rate, which means that we may track a small portion of simulated electrons and get a fairly good beam loss information. Figure 4 compares the computed loss rate for tracking scattered electrons with $95\%$, $99\%$, and $100\%$ of the total scattering rate, respectively. It's clear that the differences are small and that this strategy can greatly speed up simulation with little sacrifice of accuracy. In `elegant` we use 99% as a default value.

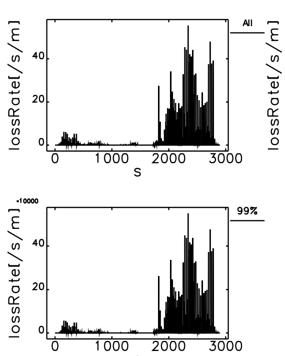


Figure 4: Simulated loss rate vs. position for various values of the scattering rate cut-off.

## APPLICATION TO APS-ERL DESIGN

APS has an eye on a future ERL upgrade, but we are concerned about beam loss issues since the APS tunnel is already built. The allowed beam loss in the APS ring is about 170 pA / 1100 m [10], i.e., 0.15 pA/m. We applied the Monte Carlo simulation to the APS-ERL lattice [9]. We assumed geometric rms emittances of 22 pm, 0.01% rms energy spread, 0.6 mm rms bunch length, 77 pC/bunch, and a 1.3 GHz repetition rate (giving 100 mA average current). Figure 5 shows the beam loss rate from Touschek scattering without sextupole correction in the TAA section. This is well above what is tolerable. A sextupole correction along the TAA section was then added to the lattice by maximizing the minimum value of the local momentum aperture. Figure 5 shows that this significantly reduces the beam loss rate, so that the average loss rate (0.018 pA/m) is well below the desired value.

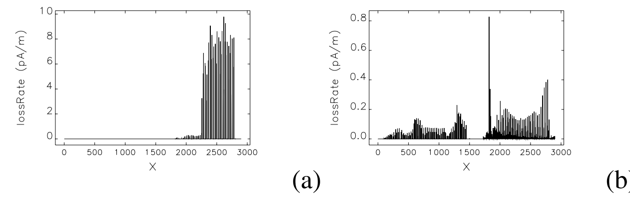


Figure 5: Simulated loss rate vs. position for APS-ERL without sextupole correction in TAA (a) and with optimized sextupole correction (b).

## CONCLUSION

A Monte Carlo simulation of Touschek scattering for a single-pass system (linac or transport line) was implemented in `elegant`. We compared the simulated local scattering rate with the rate from Piwinski's formula and found good agreement that confirms our simulation is correct. We also developed a strategy to speed up the simulation by tracking only those simulated scattered particles that represent the bulk of the scattering events. The application to a proposed APS-ERL lattice shows that the Touschek scattering effect is serious in an intense high-brightness electron beam. An optimized sextupole correction must be employed to lower the beam loss to a safe value. This simulation can also provide information for beam collimator design and verify the collimator system's efficacy.

## REFERENCES

[1] M. Borland, "elegant: A Flexible SDDS-Compliant Code for Accelerator Simulation," Advanced Photon Source LS-287, September 2000.

[2] M. Tigner, Nuovo Cimento **37**, 1228 (1965).

[3] M. Borland et al., NIM A 582, 54 (2007).

[4] A. Xiao and M. Borland, "Touschek effect calculation and its application to a transport line," Proc. of PAC2007, 3453 (2007).

[5] A. Piwinsiki, "The Touschek effect in strong focusing storage rings," DESY 98-179, Nov. 1998.

[6] W. T. Ford, A. K. Mann and T. Y. Ling, "Beam Polarization Effects in High Energy Electron-Positron Storage Rings," SLAC-158, 1972.

[7] S. Khan, "Simulation of the Touschek Effect for BESSY II: A Monte Carlo Appproach," Proc. of EPAC1994, 1192 (1994).

[8] S. Khan, private communication.

[9] M. Borland et al., Proc. of AccApp'07, 196 (2007).

[10] "Advanced Photon Source Safety Assessment Document, APS-3.1.2.1.0 Rev. 3, July 2006.

# STUDY OF IBS EFFECTS FOR HIGH-BRIGHTNESS LINAC BEAMS *

A. Xiao†, ANL, Argonne, IL 60439, USA


## ABSTRACT

Intrabeam scattering (IBS) may become an issue for linac-based fourth-generation light sources such as X-ray free-electron lasers and energy recovery linacs (ERLs), both of which use high-brightness electron beams with extremely small emittance and energy spread. Any degradation of this extremely high beam quality could significantly reduce the machine's performance. We present here a strategy first used in the code `elegant` [1] for simulating IBS effects for high-brightness linac beams. We also present an application to a possible ERL upgrade of the Advanced Photon Source.


## INTRODUCTION

Particles in a beam exchange energy between transverse and longitudinal oscillations due to Coulomb scattering. Depending on the scattering angles, the process leads to a diffusion in beam size (intrabeam scattering or IBS) or beam loss (Touschek effect).

The theory of IBS is discussed in several publications [2, 3]. A number of codes (e.g., ZAP [4], MAD-X [5]) have been developed for calculating the beam size growth rates. In the past, particle densities were not very high, so the growth times were much longer than the time spent traversing a typical linac. Thus, codes were designed for the stored beam case only with a constant beam energy. Linac-based fourth-generation light sources, such as X-ray free-electron lasers and Energy Recovery Linacs (ERLs [6]), require a high-brightness electron beam with extremely small emittance and energy spread. Any degradation of the beam quality could significantly reduce the machine's performance. Since the IBS growth time becomes much shorter for a high-brightness beam, IBS effects may become an issue even for a linac beam.

To investigate this issue, we modified the IBS calculation in `elegant` to include vertical dispersion effects and added the ability to handle acceleration. We applied our code to a proposed APS-ERL [7, 8] upgrade lattice also. Our results show that the IBS effects is moderate with the designed beam parameters.

## CALCULATION OF IBS GROWTH RATES

A detailed formalism for intrabeam scattering, taking into account the variation of lattice functions with azimuth, has been developed by Bjorken and Mtingwa [3]. The expression of emittance growth rate $\tau_d$ in the direction $d$ ($x$, $y$, or $z$) is given by (3.4) in [3] as:

$$\frac{1}{\tau} = \frac{\pi^2 c r_0^2 m^3 N ln\Lambda}{\gamma\Gamma} f,$$

$$f = \left\langle \int_0^\infty \frac{\lambda^{1/2} d\lambda}{\sqrt{|A|}} \left\{ TrL^d Tr[A^{-1}] - 3Tr[L^d (A)^{-1}] \right\} \right\rangle, \tag{1}$$

where $c$ is the speed of light, $r_0$ is the classical particle radius, $m$ is the particle mass, $N$ is the number of particles per bunch (or in the beam for unbunched case), $ln\Lambda$ is a Coulomb logarithm, $\gamma$ is the Lorentz factor, $\Gamma$ is the 6-dimensional invariant phase-space volume of the beam,

$$\Gamma_B = (2\pi)^3 (\beta\gamma)^3 m^3 \varepsilon_x \varepsilon_y \sigma_p \sigma_z \qquad (bunched)$$

$$\Gamma_U = 4\pi^{5/2} (\beta\gamma)^3 m^3 \varepsilon_x \varepsilon_y \sigma_p (2\pi R) \quad (unbunched), \tag{2}$$

and $A = (L + \lambda I)$, with

$$\begin{aligned} L &= L^x + L^y + L^z, \\ L^x &= \frac{\beta}{\varepsilon} \begin{pmatrix} 1 & -\gamma\phi_x & 0 \\ -\gamma\phi_x & \gamma^2(\frac{D^2}{\beta^2} + \phi_x^2) & 0 \\ 0 & 0 & 0 \end{pmatrix}, \\ L^y &= \frac{\beta}{\varepsilon} \begin{pmatrix} 0 & 0 & 0 \\ 0 & \gamma^2(\frac{D^2}{\beta^2} + \phi_y^2) & -\gamma\phi_y \\ 0 & -\gamma\phi_y & 1 \end{pmatrix}, \\ L^z &= \frac{\gamma^2}{\sigma^2} \begin{pmatrix} 0 & 0 & 0 \\ 0 & 1 & 0 \\ 0 & 0 & 0 \end{pmatrix}. \end{aligned} \tag{3}$$

Here, $\phi_{x,y} = D'_{x,y} + \frac{\alpha\ ,\ D\ ,}{\beta\ ,}$; $\varepsilon_{x,y}$ and $\sigma_{p,z}$ are beam distribution related quantities; and $\beta_{x,y}, \alpha_{x,y}, D_{x,y}, D'_{x,y}$ are local optical functions.

Equation (3), which includes vertical dispersion effects, is used in `elegant` for calculating the beam size growth rate. We found there are missing terms in MAD-X in the expressions for $a_{x,y}$ and $b_{x,y}$ used in formula (8) in [9], as confirmed by the developer [10]. The following equations show the differences between $a_x$ in `elegant`,

$$\begin{aligned} a_x &= 2\gamma^2 \left( \frac{H}{\varepsilon} + \frac{H}{\varepsilon} + \frac{1}{\sigma^2} \right) - \frac{2\beta}{\varepsilon} - \frac{\beta}{\varepsilon} \\ &\quad - \frac{\beta\ H}{H\ \varepsilon} + \frac{\beta}{H\ \gamma^2} \left( \frac{2\beta}{\varepsilon} - \frac{\beta}{\varepsilon} - \frac{\gamma^2}{\sigma^2} + \frac{6\beta}{\varepsilon} \gamma^2 \phi_x^2 \right) \end{aligned} \tag{4}$$

* Work supported by the U.S. Department of Energy, Office of Science, Office of Basic Energy Sciences, under Contract No. DE-AC02-06CH11357.

† xiaoam@aps.anl.gov

and $a_x$ in MAD-X,

$$
\begin{aligned}
a_x \quad &= 2\gamma^2 \left( \frac{H}{\varepsilon} + \frac{H}{\varepsilon} + \frac{1}{\sigma^2} \right) \\
&- \frac{\beta}{H} \frac{H}{\varepsilon} + \frac{\beta}{H} \frac{}{\gamma^2} \left( \frac{2\beta}{\varepsilon} - \frac{\beta}{\varepsilon} - \frac{\gamma^2}{\sigma^2} \right)
\end{aligned} \tag{5}
$$

with

$$
H_{x,y} = \frac{D_{x,y}^2 + \beta_{x,y}^2 \phi_{x,y}^2}{\beta_{x,y}}.
$$

To further improve accuracy, we also moved the Coulomb logarithm $ln\Lambda$ into the average bracket in Equation (1), since it varies with location also.

To test the code, we simulated the emittance growth rate using the APS1nm [11] lattice and compared our results with ZAP and MAD-X. The beam parameters used in simulation are given in Table 1 (varied parameters are show in a bold face).

Table 1: Parameters used in Code Comparisons

| Index | Energy GeV | $N_b$ $10^{10}$ | coupling | $\sigma_p$ $10^{-3}$ | $\sigma_z$ mm |
|---|---|---|---|---|---|
| 0 | **3.0** | 2.0 | 0.01 | 1.11 | 6 |
| 2 | **5.0** | 2.0 | 0.01 | 1.11 | 6 |
| 4 | **7.0** | 2.0 | 0.01 | 1.11 | 6 |
| 5 | 7.0 | **2.0** | 0.01 | 1.11 | 6 |
| 7 | 7.0 | **6.0** | 0.01 | 1.11 | 6 |
| 9 | 7.0 | **10.0** | 0.01 | 1.11 | 6 |
| 10 | 7.0 | 2.0 | 0.01 | **1.11** | 6 |
| 12 | 7.0 | 2.0 | 0.01 | **3.0** | 6 |
| 14 | 7.0 | 2.0 | 0.01 | **5.0** | 6 |
| 15 | 7.0 | 2.0 | 0.01 | 1.11 | **2** |
| 17 | 7.0 | 2.0 | 0.01 | 1.11 | **6** |
| 19 | 7.0 | 2.0 | 0.01 | 1.11 | **10** |
| 20 | 7.0 | 2.0 | **0.01** | 1.11 | 6 |
| 22 | 7.0 | 2.0 | **0.03** | 1.11 | 6 |
| 24 | 7.0 | 2.0 | **0.05** | 1.11 | 6 |

Figure 1 shows results from `elegant`, ZAP, and MAD-X. It shows that our results agree with the other two codes very well in a large range of parameters. The differences due to the missing terms are minor and negligible in our test run, as are the differences due to variation in $ln\Lambda$.

To verify the calculation with non-zero vertical dispersion, we performed the following test: first we set $\epsilon_x = \epsilon_y = \epsilon_0$ and computed the horizontal growth rate; then we exchanged the horizontal and vertical plane optical functions and computed the vertical growth rate. The resulting vertical growth rate should be the same as the original horizontal growth rate. Figure 2 shows simulation results before and after exchange of the optical functions, demonstrating that our vertical dispersion implementation is correct.

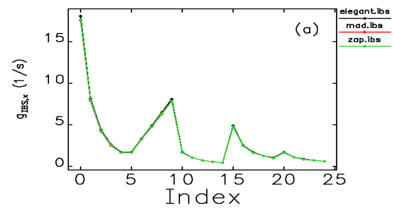


Figure 1: Comparison of calculated IBS growth rate from `elegant`, MAD-X, and ZAP. See Table 1 for the meaning of the Index.

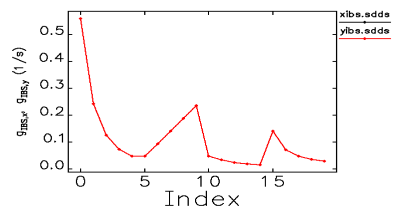


Figure 2: Demonstration that the vertical dispersion calculation is correct (xibs.sdds and yibs.sdds have their horizontal and vertical optical functions exchanged).

## IBS GROWTH RATES FOR ACCELERATING BEAM

To calculate the IBS growth rates for a beam with acceleration is straightforward. First, we calculate the IBS growth rates locally with local beam energy and emittance, then integrate over the beam's path length $s$. Note that, since there are no synchrotron oscillations in a linac, the formula for unbunched beam should be used and results in a factor of 2 increase in the longitudinal growth rate [12]:

$$
\frac{1}{\tau_z}\left[Unbunched\right] = 2\frac{1}{\tau_z}\left[Bunched\right]. \tag{6}
$$

The evolution of beam size is simulated through tracking using a specially designed element, `IBSCATTER`. First the entire beamline is divided into several segments by inserting `IBSCATTER` elements between selected existing elements. The normalized beam emittance is assumed constant within each segment, and the integrated IBS growth rates are calculated using the input beam parameters (for the first `IBSCATTER` element) or the parameters at the exit of the previous `IBSCATTER` element. The scattering action takes place at each `IBSCATTER` and the beam parameters are updated. This is done either by inflating the beam phase-space coordinates by factors that provide the equivalent size changes, or by adding appropriately scaled random values to the simulation particle coordinates. This is continued until the end of the beamline. Since the growth rates depend on beam size, the user needs to perform tests to determine how many `IBSCATTER` elements are needed. For example, in a linac the IBS growth rates are much higher in the low-energy region compared to the high-energy region.

Because the IBS growth rates are energy dependent, special caution is needed for calculations for accelerating beam. At the beginning of acceleration, the beam energy varies significantly. Figure 3 illustrates the energy change along the first sector of an APS-ERL design [7, 8]. We don't have an analytical method to calculate the IBS growth rate in this case. The integration is done using the local IBS rate at each element and the distance between elements. In such a case, the user needs to split their accelerating cavity into several pieces, so that $\gamma$ has no large changes between elements. We split our rf cavities into 100 pieces. It's not necessary to put an `IBSCATTER` element after each element, since the effects of IBS on the beam size will only manifest themselves some distance downstream. The code will take care of beam size change vs. energy in computing the local IBS growth rate.

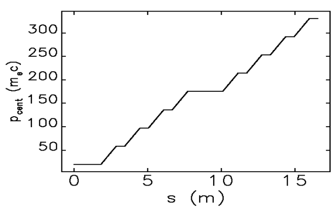


Figure 3: Energy vs. $s$ at the first sector of APS-ERL.

## EXAMPLE

In this section we present an example of an IBS calculation for an APS-ERL design. We assumed that the 10 MeV beam from the pre-injector has normalized emittances of 0.1 $\mu$m, 0.1% rms energy spread, 0.6 mm rms bunch length, and 19 pC/bunch. Figure 4 shows the beam size evolution as the beam passes through the beamline to the exit of the APS. We see a moderate but noticeable bunch lengthening due to IBS effects. But the normalized emittance dilution is minor compared to the emittance dilution from other effects, such as quantum excitation.

## CONCLUSION

A more general IBS growth rate calculation including vertical dispersion effects and beam energy variation was added to `elegant`. The code was benchmarked with ZAP and MAD-X for vertical dispersion equal to zero and against itself by exchanging the horizontal and vertical plane parameters. Insertion of many scattering elements, `IBSCATTER`, allows simulation along a transport line or a linac. An application was made to a possible APS-ERL upgrade. Results show that the IBS effects are moderate with the proposed beam parameters.

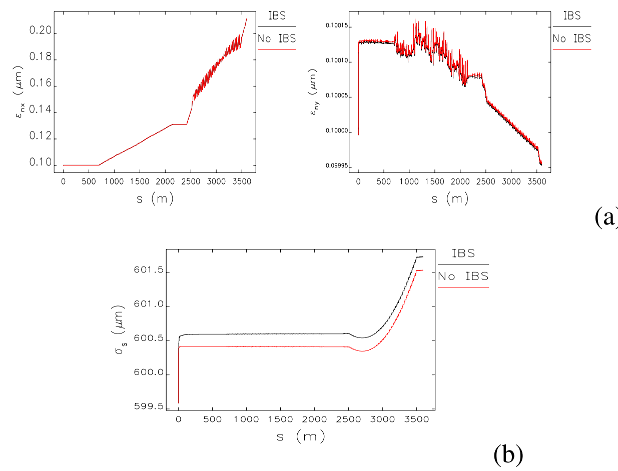


Figure 4: Evolution of beam dimensions for a proposed APS-ERL lattice, with and without IBS. (a) Effective normalized emittance. (b) Bunch length.

## REFERENCES

[1] M. Borland, "elegant: A Flexible SDDS-Compliant Code for Accelerator Simulation," Advanced Photon Source LS-287, September 2000.

[2] A. Piwinski, "Intrabeam Scattering," Proceedings of the 9th International Conference on High Energy Accelerators, p. 405.

[3] J.D. Bjorken, S.K. Mtingwa, "Intrabeam Scattering," Part. Acc. **13** (1983) 115.

[4] M. Zisman, S. Chattopadhyay, J. Bisognana, "ZAP User's Manual," LBL-21270, 1986.

[5] "The MAD-X Program," http://mad.web.cern.ch/mad/.

[6] M. Tigner, Nuovo Cimento **37** (1965) 1228.

[7] M. Borland *et al.*, NIM A **582** (2007) 54.

[8] M. Borland *et al.*, Proc. of AccApp'07, p196 (2007).

[9] F. Zimmermann, "Intrabeam scattering with Non-Ultrarelativistic Corrections and Vertical Dispersion for MAD-X," CERN-AB-2006-002, Jan. 2006.

[10] F. Zimmermann, private conversation.

[11] A. Xiao, M. Borland, and V. Sajaev, "A 1 nm Emittance Lattice for the Advanced Photon Source Storage Ring," Proc. of PAC2007, p 3447 (2007).

[12] A. Piwinski, "Intra-beam Scattering," CERN Accelerator School, p. 226, (1991).

# ORTHOGONAL BASIS FUNCTION APPROXIMATION OF PARTICLE DISTRIBUTION IN NUMERICAL SIMULATIONS OF BEAMS *

Balša Terzić†, NICADD, Northern Illinois University, DeKalb, IL 60115, USA

Numerical simulations of charged particle beams require an approximation to the particle distribution being simulated. We present a mathematical formalism for approximating two-dimensional (2D) particle distribution using a basis composed of scaled and translated Gauss-Hermite (STGH) functions. It is computationally efficient, because it only requires the values of the particle distribution at $(N+1)\times(M+1)$ nodes, where $N$ and $M$ are the highest basis function retained in the expansion in each coordinate. After outlining the mathematical formalism for the expansion, we compare it to the cosine expansion which is currently used in a code simulating coherent synchrotron radiation. The advantages of the STGH approximation over the cosine expansion are demonstrated by comparing the computational costs and execution times, as well as manifesting that unphysical fluctuations in the tail of the approximation which plague cosine expansion are not a factor in the new method. All these features make the STGH approximation valuable for $N$-body codes simulating the dynamics of multiparticle systems.

## INTRODUCTION

The normalized Gauss-Hermite functions are given by

$$\psi_n(v) = \frac{1}{\sqrt{2^n n! \sqrt{\pi}}} H_n(v) e^{-v^2}, \qquad (1)$$

where the $H_n(v)$ are the Hermite polynomials. They are orthonormal on $(-\infty, \infty)$ with the weight $w(v) = e^{v^2}$:

$$\int_{-\infty}^{\infty} \psi_n(v)\psi_m(v) e^{v^2} dv = \delta_{nm}, \qquad (2)$$

where $\delta_{nm}$ is a Kronecker delta. The basis composed of Gauss-Hermite functions $\{\psi_n\}_{n=0}^{N}$ are often used in various areas of physics, because of their relationship to normal distribution. The Gauss-Hermite spectral methods, while possessing some useful properties, only yield good approximation when scaled. Scaled Gauss-Hermite functions have been used earlier in the context of beam simulations [1, 2, 3]. While most of our motivation and justification for using scaled Gauss-Hermite function coincides with theirs, the mathematical formalism and computational implementation we present here are different. In the new method: (i) no underlying ellipsoidal distributions are assumed; (ii) the computation of the scaled Gauss-Hermite expansion here is done in a more direct and efficient way; (iii) the Poisson equation and the self-fields are directly obtained, without an expensive multidimensional integration. The results reported in the earlier work – most notably appreciable increase in accuracy and computational efficiency over the existing particle-in-cell (PIC) codes – gives us a reasonable expectation that the approach we present here is indeed superior to the existing gridless approaches. The efforts to integrate this 2D formalism into an existing 2D beam simulation code, as well as extending it to 3D and implementing a full 3D gridless $N$-body code as an alternative to PIC codes, are currently underway [4].

## SCALED AND TRANSLATED GAUSS-HERMITE BASIS

The 2D gaussian-type functions (i.e., functions which decay at infinity at least like $\exp\left(-px^2 - qy^2\right)$, with $p, q$ some positive constants) can be well-approximated by a finite Gauss-Hermite expansion

$$f(x,y) = \sum_{n=0}^{N}\sum_{m=0}^{M} a_{nm}\psi_n(\alpha_1(x-\bar{x}))\psi_m(\alpha_2(y-\bar{y})), \qquad (3)$$

where $\alpha_1, \alpha_2 > 0$ and $\bar{x}$, $\bar{y}$ are constants. In solving differential equations, it is important to be able to express derivatives of the function in the same basis. This is achieved via recurrence relations of Gauss-Hermite polynomials [6]:

$$\begin{aligned} H_{k+1}(z) &= 2zH_k(z) - 2kH_{k-1}(z), \\ H'_k(z) &= 2zH_{k-1}(z). \end{aligned} \qquad (4)$$

This ability to express coefficients of the derivatives of the function in terms of coefficients of the function itself renders solving the Poisson equation in this basis trivial.

In pseudo-spectral methods, such as the collocation method used in [5], the optimal pseudo-spectral points are the roots of the $H_{N+1}(x)$ and $H_{M+1}(y)$, denoted by $\{\gamma_j\}_{j=0}^{N}$ and $\{\beta_k\}_{k=0}^{M}$, respectively. The collocation points are arranged in descending order, i.e., $\gamma_0 > \gamma_1 > ... > \gamma_N$ and $\beta_0 > \beta_1 > ... > \beta_M$. If the eq. (3) is satisfied at the collocation points, then it can be written as

$$f(\tilde{\gamma}_j, \tilde{\beta}_k) = \sum_{n=0}^{N}\sum_{m=0}^{M} a_{nm}\psi_n(\gamma_j)\psi_m(\beta_k), \qquad (5)$$

where $0 \le j \le N$, $0 \le j \le M$, and

$$\tilde{\gamma}_j = \frac{\gamma_j}{\alpha_1} + \bar{x}, \qquad \tilde{\beta}_k = \frac{\beta_k}{\alpha_2} + \bar{y}. \qquad (6)$$

* Work supported by the Department of Defense under contract N00014-06-1-0587 with Northern Illinois University.
† bterzic@nicadd.niu.edu

It is now convenient to take advantage of the following relation for Hermite polynomials [6]:

$$\sum_{k=0}^{n} \frac{H_k(x)H_k(y)}{2^k k!} = \frac{H_{n+1}(x)H_n(y) - H_n(x)H_{n+1}(y)}{2^{n+1}n!(x-y)}, \tag{7}$$

which, for $0 \le i, j \le N$ and $0 \le k, l \le M$, leads to

$$\sum_{n=0}^{N} \psi_n(\gamma_i)\psi_n(\gamma_j) \sum_{m=0}^{M} \psi_m(\beta_k)\psi_m(\beta_l) = C_{ik}\delta_{ij}\delta_{kl}. \tag{8}$$

From eq. (8) it follows for $0 \le i \le N$ and $0 \le k \le M$:

$$C_{ik} = \sum_{n=0}^{N} [\psi_n(\gamma_i)]^2 \sum_{m=0}^{M} [\psi_m(\beta_k)]^2 \tag{9}$$

after which we finally we obtain the expression for coefficients $a_{nm}$, with $0 \le n \le N$ and $0 \le m \le M$:

$$a_{nm} = \sum_{j=0}^{N}\sum_{k=0}^{M} \frac{1}{C_{jk}} f(\tilde{\gamma}_j, \tilde{\beta}_k)\psi_n(\gamma_j)\psi_m(\beta_k). \tag{10}$$

By utilizing the property in eq. (7), evaluation of the expansion coefficients $a_{nm}$ no longer requires integration over the entire distribution function, but only its value at the nodes. Combining eqs. (5) and (10) yields a STGH approximation to function $f$.

The scaling factors $\alpha_1$ and $\alpha_2$ for the normalized distribution function $f$ are computed from the standard deviation in $x$- and $y$-coordinates:

$$\alpha_1 = \frac{1}{\sqrt{2}\sigma_x}, \qquad \alpha_2 = \frac{1}{\sqrt{2}\sigma_y}, \tag{11}$$

while $\bar{x}$ and $\bar{y}$ are simply first moments of the DF in $x$- and $y$-coordinates, respectively.

## APPLICATION TO SIMULATIONS OF MULTIPARTICLE SYSTEMS

The STGH expansion is well-suited in the context where one needs an analytical approximation to the microscopic Klimontovich density distribution:

$$f(x, y) = \frac{1}{N_{\text{part}}} \sum_{i=1}^{N_{\text{part}}} \delta(x - x_i)\delta(y - y_i), \tag{12}$$

where $N_{\text{part}}$ is the number of macroparticles. The STGH expansion can be tailored to the 2D gridless $N$-body simulation of charged-particle beams [7, 8] in which:

1. discretely-sampled macroparticle distribution is analytically approximated by a cosine expansion;
2. the Poisson equation is solved to obtain corresponding potential and forces acting on each macroparticle;
3. each macroparticle is advanced a small time-step $\Delta t$.

The STGH seeks to improve on computationally expensive cosine expansion in Step 1, while providing an efficient way to compute the potential and forces.

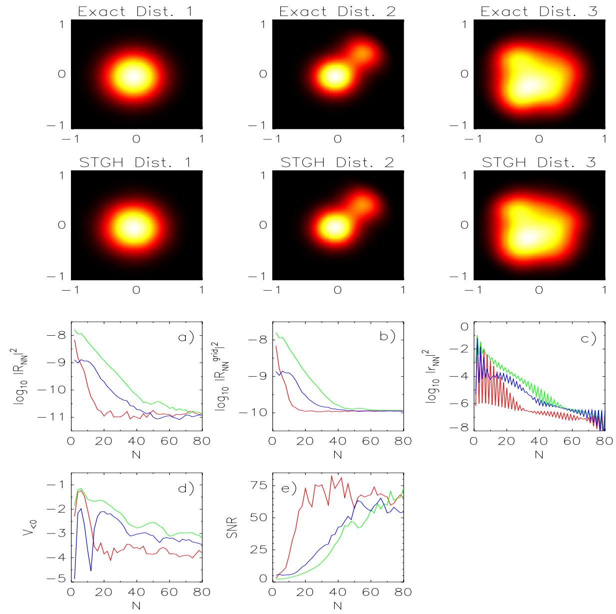


Figure 1: Three "toy" analytical distributions (superpositions of 1, 2 and 50 gaussians): exact (top row); approximated by STGH with $N = M = 80$ (second row); convergence estimators $|R_{NM}|^2$, $\left|R_{NM}^{\text{grid}}\right|^2$, $|r_{NM}|^2$ versus the number of expansion coefficients $N = M$; fraction of negative volume (panel d) and signal-to-noise ratio (panel e).

## [illegible]

The STGH algorithm for computing coefficients $a_{nm}$ can be outlined as follows:

1. tabulate unchanging quantities $\frac{\psi\ (\gamma\ )\psi\ \ (\beta\ )}{C}$;
2. compute scaling and translation factors $\bar{x}$, $\bar{x}$, $\alpha_1$, $\alpha_2$;
3. evaluate $f\left(\tilde{\gamma}_j, \tilde{\beta}_k\right)$;
4. compute coefficients $a_{lm}$ [eq. (10)].

Steps 2-4 are repeated at each time-step of the simulation. Evaluation of $f\left(\tilde{\gamma}_j, \tilde{\beta}_k\right)$ in Step 3 is the key to the STGH approximation. It can be done by counting the number of particles in some small neighborhood of the node ([illegible]), and normalizing it. We also tested alternative adaptive estimators, but the difference was not appreciable enough to warrant substantial increase in computational effort.

## [illegible]

Convergence and accuracy of the STGH can be quantified using several quantities.

### [illegible]

(i) $L_2$-norm of the difference between the exact and approximated distributions:
$R_{NM}(x, y) = f_{NM}^{\text{apx}}(x, y) - f^{\text{ex}}(x, y)$;
(ii) signal-to-noise ratio (SNR):

$$SNR \equiv \left[\sum_{i=1}^{K}\sum_{j=1}^{K}\left(f_{ij}^{\mathrm{apx}}\right)^2\right]^{\frac{1}{2}}\left[\sum_{i=1}^{K}\sum_{j=1}^{K}\left(f_{ij}^{\mathrm{ex}}-f_{ij}^{\mathrm{apx}}\right)^2\right]^{-\frac{1}{2}}.$$

(Figure 1 shows these for three analytical "toy" distributions.)

[illegible] not [illegible]

(i) $L_2$-norm of the difference between the approximated and gridded distributions:
$R_{NM}^{\mathrm{grid}}(x,y) = f_{NM}^{\mathrm{apx}}(x,y) - f^{\mathrm{g}}(x,y)$;
(ii) correction to the expansion from one step to another:
$r_{NM}(x,y) = f_{N-1M-1}^{\mathrm{apx}}(x,y) - f_{NM}^{\mathrm{apx}}$.

## STGH VS. COSINE EXPANSION: ACCURACY AND EFFICIENCY

We compare the cosine and STGH expansion on a set of particle distributions containing $10^6$ macroparticles, generated from realistic simulation [9].

[illegible] As quantified by $|R_{NM}^{g}|^2$, $|r_{NM}|^2$, the STGH is at least as accurate as the cosine expansion (Fig. 2, second and third row).

[illegible] STGH expansion is considerably faster than cosine expansion – by about 5-25 times – because it does not require expensive trigonometric function evaluations, and each coefficient does not require integration (summation) over all particles in the distribution (Fig. 2, fourth row).

[illegible] Fraction of negative particle distribution for STGH expansion is considerably lower – by at least an order of of magnitude (Fig. 2, fifth row; Fig. 3). This is because the cosine basis functions are non-decaying, while the STGH basis functions decay exponentially.

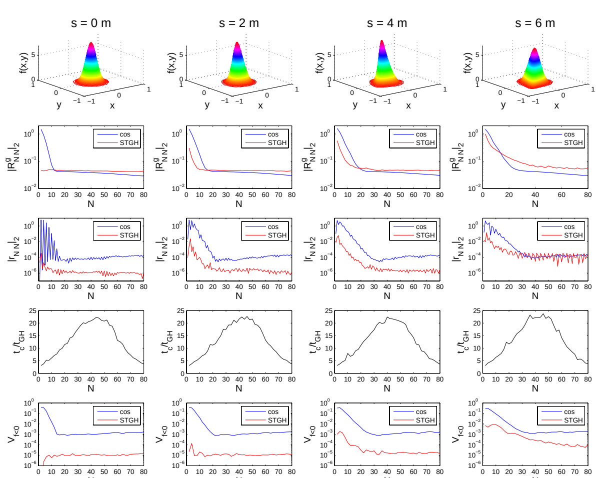


Figure 2: Particle distribution from a beam simulation with $N_{\mathrm{part}} = 10^6$ macroparticles at $s = 0, 2, 4, 6$m, gridded on a $128 \times 128$ grid. For the cosine (blue lines) and the STGH (red) expansion: second and third rows show convergence estimators $\left|R_{NM}^{\mathrm{grid}}\right|^2$, $|r_{NM}|^2$; fourth ratio of execution speeds; and fifth fraction of negative volume.

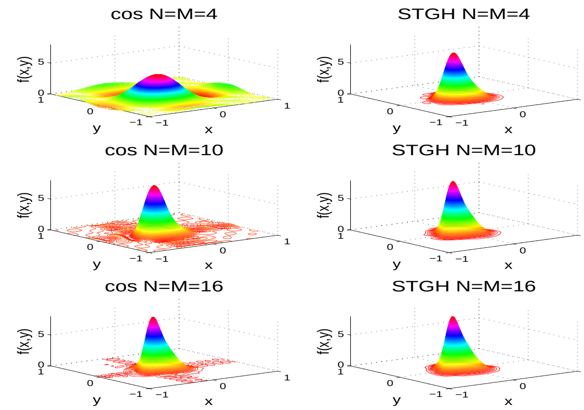


Figure 3: Approximations to the particle distribution from a beam simulation with $N_{\mathrm{part}} = 10^6$ macroparticles at $s =$ 4m with the cosine expansion (left column) and the STGH (right column), with $N = M = 4$ (first row), $N = M = 10$ (second row), $N = M = 16$ (second row).

## CONCLUSION

We presented the STGH expansion which is well-suited when an analytical approximation of the distribution sampled by $N_{\mathrm{part}}$ macroparticles is needed. We have shown that in the context of simulations of charged particle beams, the STGH approximation is more accurate and about an order of magnitude faster than the cosine approximation. It is also immune to a problem of unphysical wiggles in the tails of the distribution, which is intrinsic to cosine expansion. Therefore, the STGH provides a more accurate approximation in the tails of the distribution, which is of pivotal importance to beam halo simulations. Overall, the STGH represents a significant improvement over the existing analytic approximations used in beam simulation codes.

## REFERENCES

[1] P. Lapostolle, A.M. Lombardi, E. Tanke, S. Valero, R.W. Garnett, T.P. Wangler, Instr. Meth. Phys. Res. A 379, (1996) 21.

[2] P. Lapostolle, A.M. Lombardi, E. Tanke, S. Valero, R.W. Garnett, T.P. Wangler, Proc. LINAC (1996).

[3] E. Tanke, S. Valero, A.M. Lombardi, Proc. LINAC (2002), Garnett, T.P. Wangler, Proc. LINAC (2002), 656.

[4] B. Terzić, in preparation (2008).

[5] T. Tang, SIAM J. Sci. Comput. 14, (1993) 594.

[6] M.R. Spiegel, [illegible] McGraw-Hill, New York (1997).

[7] R. Warnock, G. Bassi, J.A. Ellison, Nucl. Instr. and Meth. in Phys. Res. A 558 (2006) 85.

[8] G. Bassi, J.A. Ellison, K. Heinemann, Proc. PAC (2007).

[9] G. Bassi, private communication (2007).

# THE OPEN ARCHITECTURE SOFTWARE INTEGRATION SYSTEM (OASIS) FOR CREATING PBO LAB MODULES

G. H. Gillespie and B. W. Hill
G. H. Gillespie Associates, Inc., P. O. Box 2961, Del Mar, CA 92014, USA

A specialized software package has been developed that enables the rapid implementation of custom beam optics modules that run in the Particle Beam Optics Laboratory (PBO Lab™). PBO Lab is a commercially available software application that supports a suite of accelerator codes for design, operations, and personnel education. The intuitive and easy-to-use graphic user interface (GUI) is largely responsible for the popularity of PBO Lab. The Open Architecture Software Integration System, or OASIS, builds upon the capability of PBO Lab to host a suite of different codes. OASIS provides an innovative framework that allows users to readily create new PBO Lab modules without writing or compiling any source code. OASIS has been used to develop several new modules for PBO Lab. This paper presents a summary of the OASIS framework and describes some of the features used in creating a new PBO Lab module for one example optics code.

## INTRODUCTION

PBO Lab has been used to support beamline design, personnel training, and accelerator operations for over a decade and delivers a suite of Application Modules that implement a variety of trusted optics codes [1]. The PBO Lab GUI provides a common graphic user interface for creating and editing iconic object-based computer models of accelerators and beamlines.

OASIS leverages the mature software framework utilized by PBO Lab [2], and extends its capabilities to provide users with a familiar environment from which to create their own PBO Lab Application Modules [3]. The PBO Lab Beamline Object Model [4] is the underlying persistent representation that allows multiple optics codes with varying input/output requirements to utilize a single beamline model description. Multiple optics codes run side by side in PBO Lab's sophisticated drag-and-drop graphic user interface. PBO Lab generates the native input and processes the native output, for the different optics codes, from a single beamline model.

## THE OASIS FRAMEWORK

The OASIS framework is a collection of abstract and concrete classes, and their interfaces which comprise a generic subsystem used to implement Application Modules in PBO Lab. It provides a reusable, generic OASIS Module, or "OModule," that encapsulates the user interface and data interface functionality required for running in the multi-module PBO Lab environment. Figure 1 illustrates the abstract layer diagram for the PBO Lab/OASIS application framework. User developed Application Modules are implemented dynamically in PBO Lab with this generic reusable Application Module (OModule) design pattern.

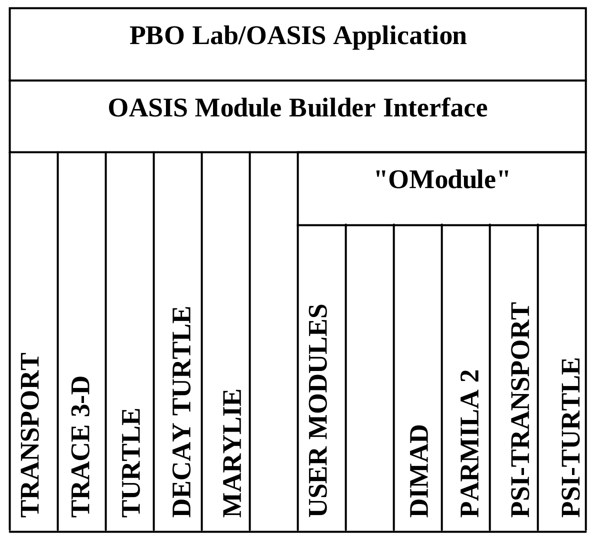


Figure 1: Layer diagram for PBO Lab Framework and Open Architecture Software Integration System.

An OModule has both a user interface component and a computational component. The user interface component is created in the OASIS Module Builder Interface which is an extension to the drag-and-drop PBO Lab GUI. The computational component may be a library (.dll) or executable (.exe) application. No source code needs to be compiled or linked to use the Application Module in PBO Lab.

## OASIS MODULE BUILDER

The OASIS Module Builder Interface, used to create PBO Lab Application Modules, is an intuitive extension of the standard PBO Lab interface, providing users with a familiar environment to create custom Application Modules that run seamlessly in the PBO Lab GUI without writing or compiling any source code. The OASIS Module Builder is itself a very specialized PBO Lab Module: it is a Module for the specification of other Application Modules. The OASIS Module Builder provides an interactive environment to incrementally create and test Application Modules in the PBO Lab GUI. Detailed specifications to fully define the requirements for the generation of a native input file for an optics code are accomplished through the familiar PBO Lab GUI, which has been extended to support the OASIS Module Builder Interface.

Application Modules are exported from the OASIS Module Builder for use in PBO Lab using a PBO Lab module definition (.omod) file. Figure 2 illustrates the process. The module definition file utilizes an enhanced version of the PBO Lab persistent Beamline Object Model representation [4]. The object model has been expanded to include specifications that define the native input/output requirements for a given optics code, and to include a variety of other specifications and constraints that encapsulate the operations and commands of the target optics code.

Iconic representations (Piece Components) of physical beamline elements and non-physical beamline operations, in the Module Builder Interface, are used to access and specify most input requirements for a target optics code.

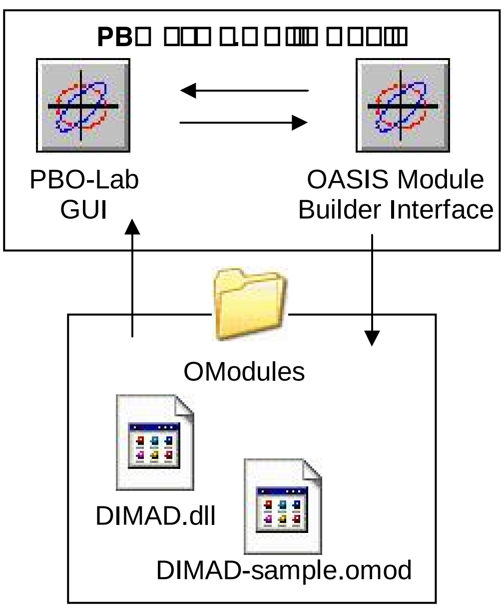


Figure 2: Application Modules can be interactively developed and executed in the Module Builder Interface and exported for use directly in the PBO Lab GUI as (.omod) OModule definition files.

## MODULE BUILDER EXAMPLE

Piece Components are categorized into three types, Optics Pieces, Parameter Pieces and Command Pieces. Optics Pieces are used to represent physical beamline elements and include a variety of standard Pieces available in the PBO Lab Palette Bar [5]. Customizable Optics Pieces can be used to add additional optics elements. The Parameter Piece type provides a customizable generic interface and is typically used to support parameters not associated with any particular physical optics element. Command Pieces are used to implement Application Module commands or operations supported by the target optics code. Command Pieces provide a versatile method of encapsulating the wide variety of commands that can be specified for a given optics code. Command Pieces do not represent physical beamline elements, although they can be located at specific locations in the beamline model, where they are evaluated sequentially to produce the appropriate command instructions in the native input file for the given optics code.

Each optics code has its own unique “commands” or “operators” that encapsulate the computational capability for that code. This code-specific functionality is implemented in an Application Module using a set of Command Pieces. An example of such a Command Piece, created for a DIMAD Application Module, is illustrated here.

The DIMAD program [6] was developed to study particle motion in both beamlines and circular machines. The code uses a matrix formalism through second order. It is perhaps most commonly used at facilities operating electron accelerator systems.

There are several Command Pieces defined for the DIMAD Application Module. For illustrative purposes, the implementation of DIMAD's Least Squares Fit operation will be described here. (The Least Squares Fit operation is described in Section 2.15 of reference [6].)

The DIMAD Application Module “Least Squares Fit…” Command Piece implements a variety of native instructions required to direct the DIMAD computation engine to perform a particular fitting operation [6]. The definition of the “Least Squares Fit…” Command Piece in the OASIS Module Builder Interface involves both the specification of the required input parameters and the syntax used to generate instructions for the DIMAD native input file.

A generic Command Piece serves as a template and is initially created on the Work Space [5] of the Module Builder Doc Window using a menu command that prompts the user to name the new Command Piece. The named piece can then be dragged to the Model Space [5] where double-clicking the piece icon will open its Command Piece Specification Window. From there, additional windows are accessed that provide for the definition of input parameters and the specification of the native syntax required for the command to be processed by the target optics code (i.e. DIMAD). Once the Command Piece is defined, it will be available for use with the DIMAD Application Module in PBO Lab. Figure 3 shows two of the input parameter tab pages defined in this way for the “Least Squares Fit…” Command Piece.

The “Least Squares Fit…” Command Piece is added to a PBO Lab beamline to direct the DIMAD computation engine to perform the prescribed fitting operation. From the DIMAD Command Menu, the “Write and Run DiMadInput” command is used to generate the native DIMAD input, execute the DIMAD computation engine, and open the resulting output file.

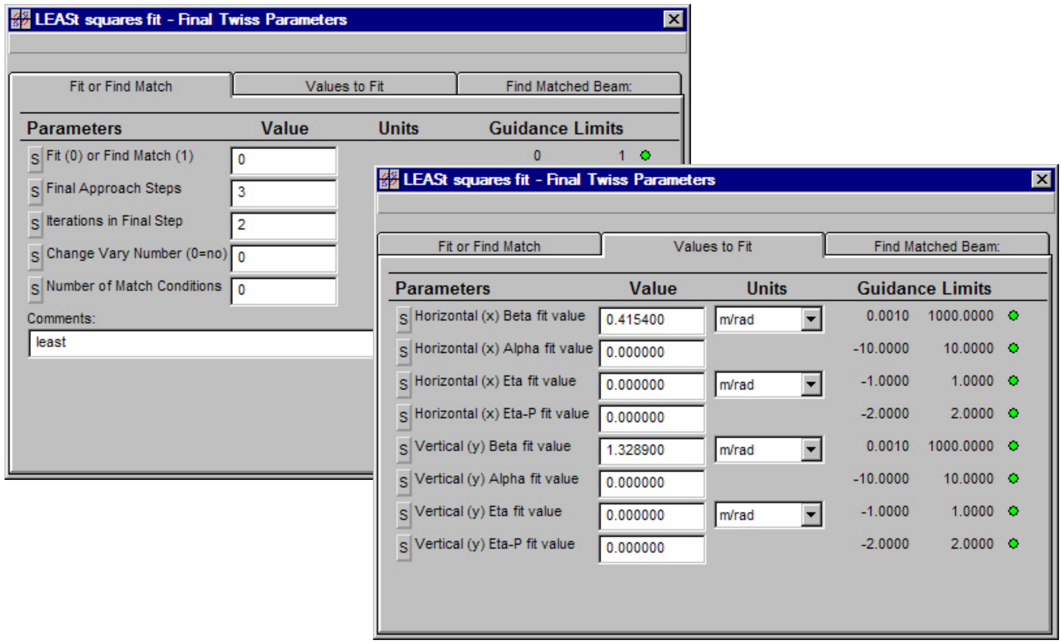


Figure 3: Input parameter tab pages for the “LEASt Squares Fit…” Command Piece window.

The first four letters of the Command Piece name, "LEASt squares fit ..." are intentionally capitalized: those letters represent the DIMAD keyword for this operation. However, users need not know this keyword, nor learn any of the other input file syntax and format for DIMAD's least squares fitting operation. The Command Piece Window (Figure 3) provides text descriptions of all parameters. The OASIS Module Builder syntax specification for this Command Piece provides PBO Lab with the necessary instructions needed to write the parameters in the correct format, and in the correct location, to the DIMAD input file. Users simply set the fitting goals using the parameters of the Command Piece Window illustrated in Figure 3.

The least squares fitting computation is just one example of available operations implemented for the DIMAD Application Module. A variety of other calculations are also implemented using other DIMAD Command Pieces.

## SUMMARY

A specialized software package has been developed called the Open Architecture Software Integration System, or OASIS, that can be used to create custom Modules for the Particle Beam Optics Laboratory (PBO Lab). OASIS builds upon the capability of PBO Lab to host a suite of different codes, and provides an innovative framework that enables users to rapidly implement custom beam optics modules. The custom modules will run in PBO Lab without writing or compiling any source code.

## ACKNOWLEDGEMENT

Parts of this work were supported by the U. S. Department of Energy Small Business Innovative Research program under grant number DE-FG02-04ER83961.

## REFERENCES

[1] PBO Lab is available from AccelSoft Inc., San Diego, California, http://www.ghga.com/accelsoft.

[2] B. W. Hill, H. Martono, J. M. Moore and J. S. Gillespie "An Application Framework and Intelligent Graphic User Interface for Multiple Accelerator Codes," Proc. 1998 Intern. Comp. Accel. Phys. Conf., SLAC-R-580, 92-96 (1998).

[3] G. H. Gillespie and B. W. Hill, "Open Architecture Software Integration System (OASIS) for the Particle Beam Optics Laboratory (PBO Lab)," Proc. 2007 Particle Accelerator Conf., paper THPAS037 (2007).

[4] B. W. Hill, H. Martono and J. S. Gillespie "An Object Model for Beamline Descriptions," AIP Conf. Proc. 391, 361-365 (1996).

[5] G. H. Gillespie, B. W. Hill, H. Martono, J. M. Moore, N. A. Brown, M. C. Lampel and R. C. Babcock, “The Particle Beam Optics Interactive Computer Laboratory for Personal Computers and Workstations,” Proc. 1997 IEEE Part. Accel. Conf., Vol. 2, 2562-2564 (1997).

[6] R. V. Servranckx, K. L. Brown, L. Schachinger, D. Douglas and P. G. Tenenbaum, "Users Guide to the Program DIMAD," SLAC Report (2004).

# AN INNOVATIVE GRAPHIC USER INTERFACE FOR PARMILA 2

G. H. Gillespie and B. W. Hill
G. H. Gillespie Associates, Inc., P. O. Box 2961, Del Mar, CA 92014, USA

## [illegible]

A new graphic user interface (GUI) has been created for the PARMILA 2 program. PARMILA 2 is an advanced version of the historical PARMILA program originally developed to design and model drift tube linear (DTL) accelerators. PARMILA 2 expands upon that capability to support the design and simulation of coupled cavity linear (CCL) accelerator structures, coupled-cavity drift tube linac (CC-DTL) structures, superconducting accelerator structures, as well as DTL structures and transport lines that can include magnetic, radiofrequency and electrostatic beam optics elements. A new software package called the Open Architecture Software Integration System, or OASIS™, has been used to develop an innovative graphic interface for the PARMILA 2 program. OASIS provides a framework for developing custom modules for the Particle Beam Optics Laboratory (PBO Lab™) software. The framework can be used to create new PBO Lab modules [illegible] *a* [illegible] Tools in the OASIS software were utilized to define the GUI features of the new PARMILA 2 module. Existing PARMILA 2 executables, including Parmila.exe, Lingraf.exe and readdst.exe, have been linked to GUI commands utilizing other tools within the OASIS framework. This paper presents an overview of the new PARMILA 2 module and illustrates some of the GUI features.

## INTRODUCTION

PARMILA (Phase and Radial Motion in Ion Linear Accelerators) is a well established computer code [1] used for the design and simulation of proton (and heavier particle) linear accelerators. The program has a long history and the version 2 developed at the Los Alamos National Laboratory includes design capabilities for drift tube linacs (DTLs), coupled cavity linacs (CCLs), coupled cavity drift tube linacs (CCDTLs) and several types of superconducting linac structures [2, 3]. One challenge to users of PARMILA has been acquiring a good knowledge of the detailed input file format required by the program. The development of an intuitive, easy-to-use graphic interface for PARMILA 2, as an Application Module of the Particle Beam Optics Laboratory (PBO Lab), directly addresses that challenge.

PBO Lab is a modular suite of commercial software applications which has Application Modules that support a variety of particle beam optics programs and other accelerator-related codes [4]. Each optics program Application Module incorporates a specific particle beam optics modeling or simulation program. Available modules include TRANSPORT [5], TURTLE [6], MARYLIE [7], TRACE 3-D [8] and DECAY-TURTLE [6]. Other modules are also available, including an Optimization Module utilizing the NPSOL [9] and MINOS [10] nonlinear constrained optimization programs, and specialized modules for modeling electrostatic elements [11] and traveling wave accelerator components [12]. PBO Lab provides a common graphic user interface (GUI) for constructing and editing iconic object-based computer models of accelerators and beamlines. The common GUI for optics programs in PBO Lab simplifies the task of carrying out calculations for a given beamline. PBO Lab assures that the input files for every optics program represent the same beamline, and PBO Lab will automatically display graphical results that may otherwise require post-processors. Users do not need to construct input files in the format required by a specific program -- PBO Lab takes care of all the needed bookkeeping, and the object model automatically creates the necessary input files following simple menu commands issued by a user.

## PBO LAB PARMILA-2 MODULE

The requirements to develop a workable GUI for PARMILA were outlined some years ago [13] and a prototype concept was described at the 1994 Linac Conference [14]. For a variety of reasons, further progress was limited until a new approach for creating optics code GUIs for PBO Lab became available. The new approach was provided by the Open Architecture Software Integration System, or OASIS. Developed under the auspices of the U. S. DOE Small Business Innovation Research (SBIR) program, OASIS [15] provides the type of reusable framework required for rapidly creating PBO Lab Application Modules without the need to write any new source code, for either the GUI (PBO Lab) or the associated physics code (e.g. PARMILA). In brief, OASIS is a new PBO Lab Module that is used to create additional PBO Lab Modules, where the GUI and related object model themselves provide the creative framework.

The document (or start up) window for the PARMILA-2 Module is basically the same as that for any other PBO Lab Module. Figure 1 illustrates an example document window which has an iconic description of a drift tube linac (DTL) model displayed. The DTL model was created by using the "drag and drop" construction kit of the PBO Lab software. Several custom features of the PARMILA-2 Module are pointed out in Figure 1.

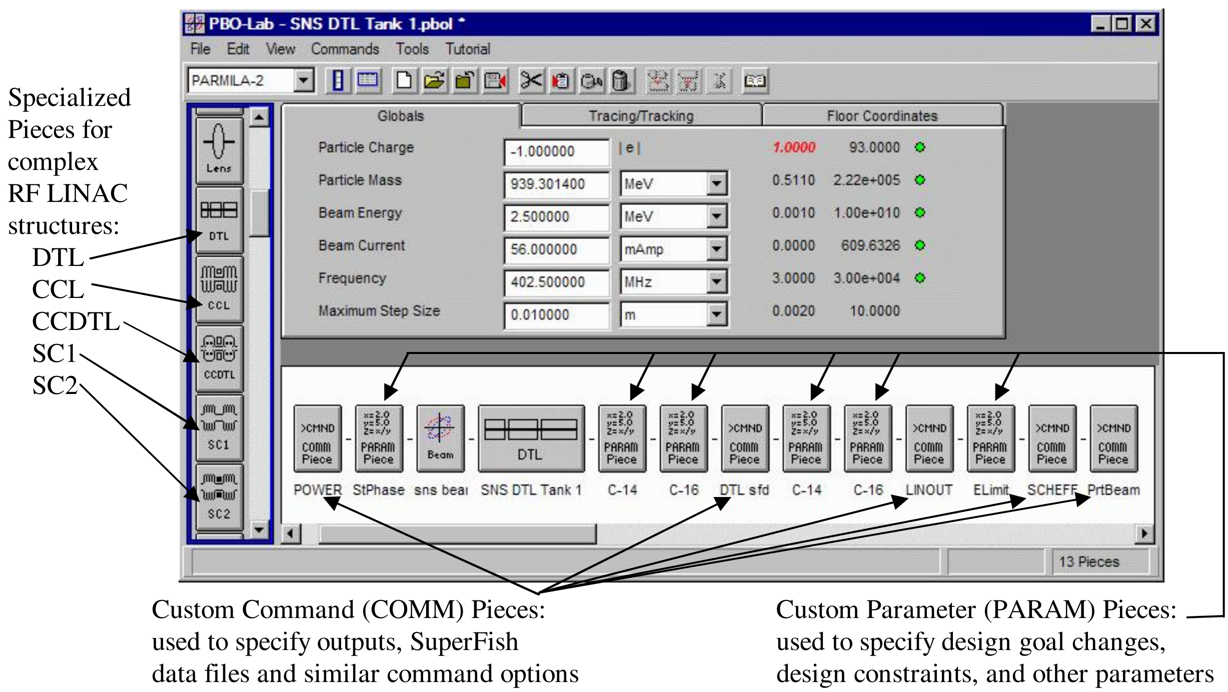


Figure 1: The standard PBO Lab Document Window is used for the PARMILA-2 Module. This example shows a beamline model for a single-tank drift tube linac (DTL) accelerator.

Figure 1 shows a number of icons representing new PBO Lab Pieces created for the PARMILA Module. The new Pieces are of three types: Palette Pieces, Command (COMM) Pieces and Parameter (PARAM) Pieces. Each of the newly created Pieces corresponds to specific lines in a PARMILA 2 input file [3]. Table 1 summarizes most of the new Pieces. The entries listed for the COMM and PARAM Pieces give the corresponding PARMILA keywords implemented for those Piece types.

The PBO Lab data input windows (Piece Windows) provide a complete description of the command or parameter that will be utilized -- not just the keyword. It is beyond the scope of this paper to describe the implementation in detail here, but an example illustrates how this assists users. Figure 1 illustrates the use of several PARMILA "Change" types. These are identified by the Piece comments "C-14" and "C-16" which appear as labels below the corresponding PARAM Pieces.

In constructing a PARMILA-2 beamline, a scrolling list window is used to select Pieces that contain Change types. Figure 2 shows the list window for the PARMILA-2 Parameter Pieces. All PARAM Pieces are given brief word descriptions. Figure 2 illustrates the selection "m. Ramp Quads w Energy" which corresponds to Change type 14, discussed in the PARMILA 2 documentation in subsection "m" of the Change section. Similarly, the item "o. Gradient of First DTL Quad" corresponds to Change type 16. A Change type PARAM Piece, that is selected and created using the "Create Piece" button shown in Figure 2, will have a default label (e.g. "C-12") which identifies the Change type that will appear in the PARMILA 2 input file (e.g. "CHANGE 12"). Users need not look up any Change type code, or the format for a Change type, in order to implement a specific type of Change. Users simply select from the descriptions appearing in the PARMILA-2 Parameter Piece list window (Figure 2).

Table 1: Examples of custom PBO Lab Pieces developed for the PARMILA 2 Module using the OASIS framework. PARMILA 2 keywords implemented through COMM and PARAM Pieces are listed under the respective columns.

| Palette Pieces | Command (COMM) Pieces | Parameter (PARAM) Pieces |
|---|---|---|
| DTL, CCL | SCHEFF, LINOUT, POWER, | Change Types (20+ Pieces) |
| CC-DTL | PrtBeam, SFDATA, TRANSPORT, | ExQ Types (7+ Pieces) |
| SC1, SC2 | Quad OPTIONS, MPOLES, … | Elimit, StartPhase, ErrorSeed, … |

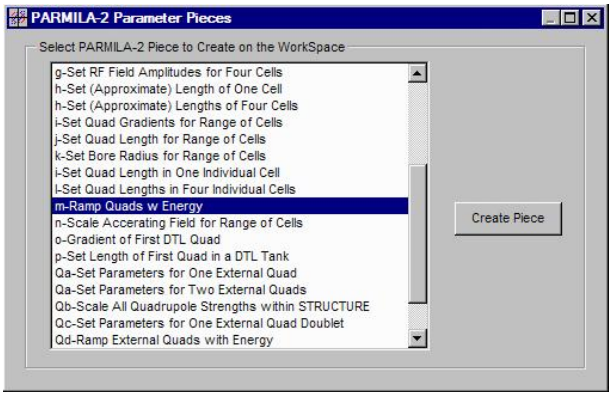


Figure 2. Scrolling list window used for selecting and creating PARMILA-2 Parameter Pieces.

Other custom Command and Parameter Pieces developed for the PARMILA-2 Module provide simple text descriptions of their function. The corresponding Piece Windows likewise provide descriptive information useful for specifying any needed input parameters. The format and syntax for each line in the PARMILA 2 input file is automatically handled by the PARMILA-2 Module.

Standard transport elements supported by PARMILA 2 (i.e. drifts, quadrupoles, bends, etc.) are implemented using the standard PBO Lab Pieces for those elements, requiring no additional objects in the PBO Lab object model. In a few cases, additional parameters have been added to the standard Pieces in order to support specific PARMILA capabilities, such as specifying the number of times space charge forces are computed in a drift element.

The PARMILA program can be used in a design mode or a simulation mode, and the new Module has been developed to support both modes. Location specific commands and parameters are set up using the custom created Command and Parameter Pieces.

## SUMMARY

An innovative GUI has been developed for the PARMILA 2 accelerator design code, implemented as an Application Module for the Particle Beam Optics Laboratory. This new PBO Lab PARMILA-2 Module was created using the Open Architecture Software Integration System.

## ACKNOWLEDGEMENT

Parts of this work were supported by the U. S. Department of Energy Small Business Innovative Research program under grant number DE-FG02-04ER83961. Other parts of the effort were supported by G. H. Gillespie Associates, Inc. Independent Research and Development (IR&D) funds.

## REFERENCES

[1] G. Boicourt and J. Merson, "PARMILA Users and Reference Manual," Los Alamos Nat. Lab. report LA-UR-90-127, Revised, 141 pp (1992).

[2] H. Takeda and J. H. Billen, "Recent Developments in the Accelerator Design Code PARMILA," Proceedings of the XIX International Linac Conference, ANL 98/28, Vol. 1, 156-158 (1998).

[3] H. Takeda and J. H. Billen, "Parmila," Los Alamos Nat. Lab. report LA-UR-98-4478 Rev, 159 pp (2005).

[4] PBO Lab is available from AccelSoft Inc., San Diego, California, http://www.ghga.com/accelsoft.

[5] D. C. Carey, K. L. Brown and F. Rothacker, "Third-Order TRANSPORT with MAD Input - A Computer Program for Designing Charged Particle Beam Transport Systems," SLAC-R-530, 316 pp (1998).

[6] D. C. Carey, "TURTLE with MAD Input (Trace Unlimited Rays Through Lumped Elements), a Computer Program for Simulating Charged Particle Beam Transport Systems, and DECAY-TURTLE Including Decay Calculations," Fermilab-Pub-99/232, 196 pp (1999).

[7] A. J. Dragt, et al, "MARYLIE 3.0 User's Manual, A Program for Charged Particle Beam Transport Based on Lie Algebraic Methods," 901 pp (2003).

[8] K. Crandall and D. Rusthoi, "TRACE 3-D Documentation," LA-UR-97-886, 106 pp (1997).

[9] P. E. Gill, W. Murray, M. A. Saunders, M. H. Wright, "User's Guide for NPSOL 5.0: A Fortran Package for Nonlinear Programming," Stanford Univ. Dept. Op. Res., Rpt. SOL 86-2R, 44 pp (1998).

[10] B. A. Murtagh and M. A. Saunders, "MINOS 5.5 User's Guide," Stanford Univ. Dept. Op. Research, Rpt. SOL 83-20R, 145 pp (1998).

[11] T. A. Brown and G. H. Gillespie, "Optics Elements for modeling electrostatic lenses and accelerator components: III. Electrostatic deflectors," NIM **B** 172, 338-343 (2000) and references cited therein.

[12] M. C. Lampel, "A self-consistent beam loaded traveling wave accelerator model for use in TRACE 3D," Proc. 1998 Particle Accelerator Conf., Vol. 2, 2615-2617 (1998).

[13] G. H. Gillespie, B. W. Hill and J. S. Gillespie, "Making PARMILA Easy to Use - [illegible] Proc. 10th Intern. Conf. on High Power Beams, NTIS PB95-144317, Vol. 2, 626-633 (1994).

[14] G. H. Gillespie and B. W. Hill, "An Interactive Graphical User Interface for the Linac Beam Dynamics Code PARMILA," Proc. 1994 Intern. Linac Conf., KEK Report Vol. 2, 517-519 (1994).

[15] G. H. Gillespie and B. W. Hill, "Open Architecture Software Integration System (OASIS) for the Particle Beam Optics Laboratory (PBO Lab)," Proc. 2007 Particle Accelerator Conf., paper THPAS037 (2007). See also paper MOP098 of these proceedings.

# SIMULATION OF EMITTANCE GROWTH USING THE UAL STRING SPACE CHARGE MODEL

Richard Talman, Cornell University, Ithaca, NY, USA, Nikolay Malitsky, Brookhaven National Laboratory, Upton, NY,USA, and Frank Stulle, CERN, Geneva, Switzerland

*Abstract*

Evolution of short intense electron bunches passing through bunch-compressing beamlines is simulated using the UAL (Unified Accelerator Libraries) string space charge formulation.[1] Excellent agreement is obtained with results obtained experimentally at CTF-II, the CERN ``Compact Linear Collider" test facility[2]. The 40 MeV energy of these data is low enough for Coulomb and Biot-Savart forces to be important and high enough for coherent synchrotron radiation and centrifugal space charge forces to be important. UAL results are also compared with CSRtrack [3] results for emittance growth in a 50 MeV "standard" chicane. Vertical space charge forces are found to be important in this (low energy) case.

## CALCULATIONAL MODEL

Particles are treated as strings as regards their fields but as points as regards their dynamics. Bunch evolution is treated as standard tracking but with intrabeam scattering. The force on particle A due to the (properly-retarded) field of the string associated with particle B is expressed in terms of (closed-form) elliptic integral functions. In the (rare) case when the bunch straddles a magnet edge all particles are assumed to be on the same side of the edge as A. All results have become essentially independent of the number N of macroparticles for N>400, but N-values as great as 3200 have been used in some cases. Summed over all B, for every particle A there are N impulses, making N-squared calculations per evolution step. Even so, all calculations have been done on a laptop.

CSR (coherent synchrotron radiation) results from self-work of the bunch acting on itself---validity of Newton's third law requires the inclusion of field momentum. All static (electric and magnetic) forces plus all coherent longitudinal (CSR) and transverse CSCF (centrifugal space charge force), as well as radiative effects, are included. Since there is no need for "regularization" to suppress singularity, bends and drifts are treated homogeneously. Extreme relativistic approximations (such as neglect of vertical forces) are avoided.

## SIMULATION OF CTF-II MEASUREMENTS

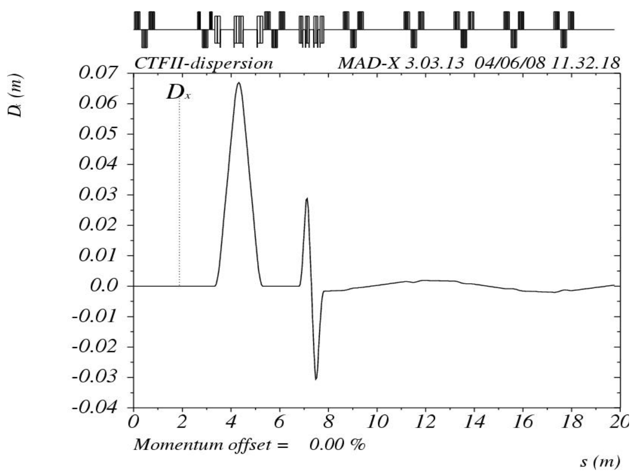


Figure 1: Beamline dispersion, showing "compressor" chicane (C shape) and "shielded" chicane (S shape).

Emittance growth in a bunch compressor has been studied experimentally[2] at the CTF-II (CERN Compact Test Facility), shown in Fig. 1, using electrons of energy 40 MeV. No shielding of CSR by vacuum chamber walls was detected, and the present simulation assumes this to be true. Input and output momentum spectra are shown in Fig. 2. Substantial momentum spreading is visible.

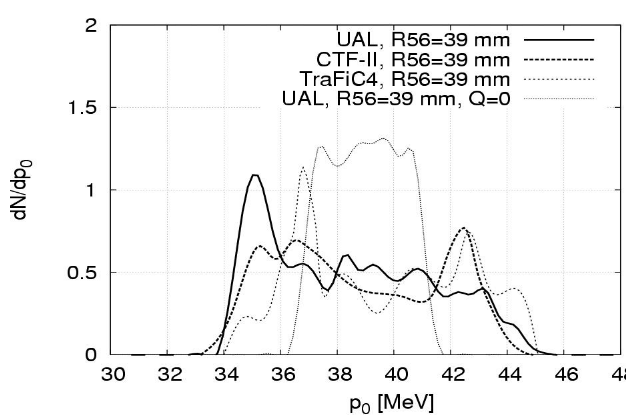


Figure 2: Bunch momentum spread at beamline output with no space charge (narrow square pulse) and with Q=10nC, as measured (label CTF-II) and as simulated by UAL and by (an early version of) TraFiC4.

Dependence of CSR energy loss on bunch length and on R56 value at S-chicane location, was measured for Q=15nC. See Fig. 3. The present simulation, having no empirically adjustable parameters, agrees well within error bars with the measurements. This confirms theoretical expectations concerning CSR.

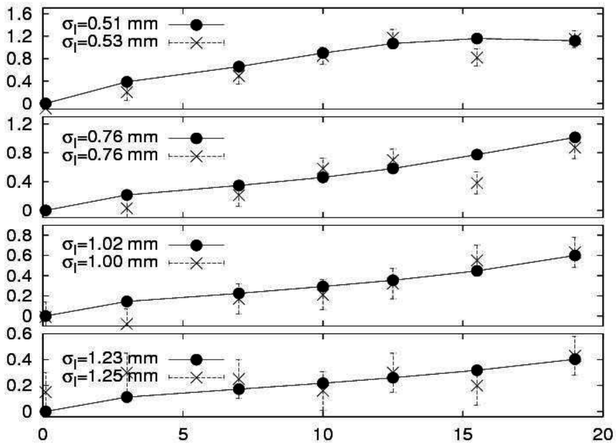


Figure 3: Energy loss in MeV as function of S-chicane R56 value in mm, for the four values of r.m.s. bunch length (adjusted using the C-chicane) labeling the figures. The measured values have error bars.

An unexpected (at the time) result reported was a quite strong increase in horizontal emittance for small beta function values at the C-chicane location (with S-chicane turned off). The data and simulation is shown in Figure 4. The present simulation agrees at least semi-quantitatively with the measurements.

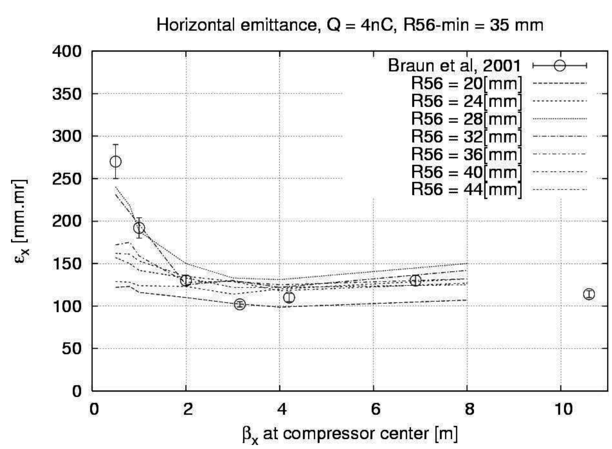


Figure 4: Dependence of output horizontal emittance on horizontal beta function at the C-compressor.

## UAL CSRTRACK COMPARISON

To enable controlled comparison of UAL with the CSR-aware code CSRtrack[3], the 50 MeV benchmark chicane shown in Fig. 5 was designed. Parameters are given in Table 1. All distributions are Gaussian.

Table 1: Chicane and Beam Parameters

| Chicane Parameters | Symbol | Value, Unit |
|---|---|---|
| Dipole length | $L_B$ | 0.50 m |
| Drift length | $L_D$ | 5.00 m |
| Drift length | $L_i$ | 1.00 m |
| Total chicane length | $L_{\text{tot}}$ | 13.00 m |
| Nominal bending angle | $\alpha_0$ | 2.77 deg |
| Nominal momentum compaction | $R_{56}$ | -25.00 mm |

| Electron Beam Parameters | Symbol | Value, Unit |
|---|---|---|
| Electron energy | $E_0$ | 50 MeV |
| Bunch charge | $Q_0$ | 1.0 nC |
| Initial rms bunch length | $\sigma_{s,i}$ | 200 $\mu$m |
| Initial peak current | $I_{p,i}$ | 600 A |
| Initial uncorrelated rms energy spread | $\sigma_{E,rms}/E_0$ | 0.01 % |
| Initial energy-position correlation | $1/E_0\, dE/ds$ | -20.1 m$^{-1}$ |
| Initial normalized emittance | $\epsilon_{n,x}$ | 1.0 mm mrad |
| | $\epsilon_{n,y}$ | 1.0 mm mrad |
| Twiss functions at chicane entrance | $\beta_{x,i}$, $\alpha_{x,i}$ | 80.41 m, 6.254 |
| | $\beta_{y,i}$, $\alpha_{y,i}$ | 22.80 m, 3.110 |

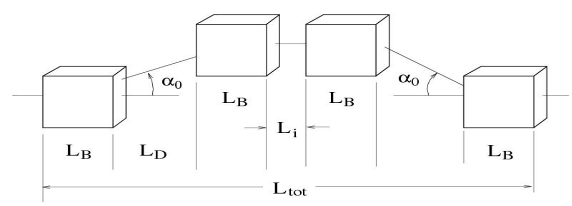


Figure 5: Chicane sketch.

Due to the low energy but high bunch intensity this benchmark case is deliberately made extreme regarding CSR emission and emittance blow-up.

To emulate CSRtrack (which neglects vertical intrabunch forces) the UAL simulation was run with all vertical intrabunch forces suppressed. This simplification is justified at high electrons energies since then the electromagnetic fields are confined to a narrow cone, i.e. vertical and also horizontal field components are small. But it should breakdown at low energies. Table 2 shows excellent agreement of simplified UAL and CSRtrack simulations for the benchmark case; the output vertical emittances 74.1 and 72.6 mm.mrad, differ by 2 percent. Figure 6 shows final horizontal phase space distributions. The most striking difference is the speed advance of UAL over CSRTrack by several orders of magnitude.

Table 2: UAL CSRtrack Comparison

| Quantity | Unit | CSRtrack | UAL-NoVert | UAL-True |
|---|---|---|---|---|
| $\epsilon_{x,n}\|_{in}$ | mm.mrad | 1.005 | 0.982 | 0.982 |
| $\epsilon_{x,n}\|_{out}$ | | 74.10 | 72.6 | 57.2 |
| $\epsilon_{y,n}\|_{in}$ | mm.mrad | 1.0 | 1.04 | 1.04 |
| $\epsilon_{y,n}\|_{out}$ | | 1.0 | 1.04 | 3.50 |
| $\sigma_E\|_{in}$ | % | 0.402 | 0.40 | 0.40 |
| $\sigma_E\|_{out}$ | | 0.532 | 0.56 | 0.48 |
| $\sigma_l\|_{in}$ | $\mu$m | 200.2 | 199 | 199 |
| $\sigma_l\|_{out}$ | | 190.3 | 191 | 184 |

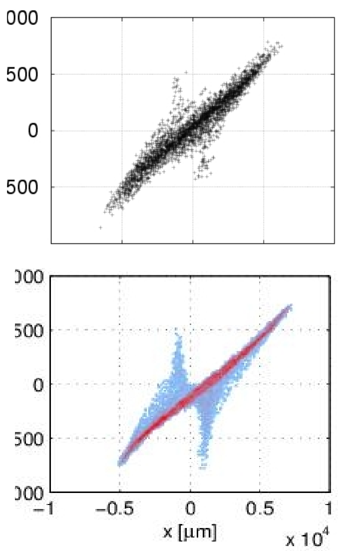


Figure 6: Output phase space distributions, UAL above, CSRtrack below, agree very well (except for a tiny relative horizontal displacement). Residual linear dispersion has been subtracted in these plots.

To investigate the effect of vertical forces, the UAL simulation was also run with all forces, including vertical, retained. According to this simulation the horizontal emittance increase, shown in Table 2, from 57.2 to 72.6 mm.mrad is an artefact of the neglect of vertical forces. Note the substantial increase in vertical emittance, from 1.04 to 3.50 mm.mrad, that accompanies the inclusion of vertical forces.

## ACKNOWLEDGEMENTS

This work is partially supported by the NSF, by the DOE, and by the Commission of the European Communities under the 6th Framework Programme ``Structuring the European Research Area'', contract number RIDS-011899. The Paul Scherrer Institut and the Swiss National Supercomputing Center (CSCS) provided access to a Cray XT3 supercomputing facility.

## REFERENCES

[1] R. Talman, String Formulation of Space Charge "Forces in a Deflecting Bunch", PRST-AB, **7**, 100701, 2004. N. Malitsky and R.Talman, "UAL Implementation of String Space Charge Formalism", WEPLT154, EPAC Conference, Lucerne, Switzerland, 2004. R. Talman, "Accelerator X-Ray Sources", Chap. 13, Wiley-VCH, Weinheim, 2006

[2] L. Groening, M. Borland, H. Braun, S. Doebert, and A. Kabel, "Experiments on the Effect of CSR on the Electron Beam of CTF II", PAC 2001, Chicago, p.164

[3] M. Dohlus and T.Limberg, "CSRtrack: Faster Calculation of 3-D CSR Effects", Proc. 2004 FEL Conference, 18-21, 2004

# ELECTRON BEAM DYNAMICS IN THE DARHT-II LINEAR INDUCTION ACCELERATOR*

Carl Ekdahl, E. O. Abeyta, P. Aragon, R. Archuleta, G. Cook, D. Dalmas, K. Esquibel, R. Gallegos, R. Garnett, J. Harrison, J. Johnson, E. Jacquez, B. Trent McCuistian, N. Montoya, S. Nath, K.Nielsen, D. Oro, L. Rowton, M. Sanchez, R. Scarpetti, M. Schauer, G. Seitz, V. Smith, and R. Temple, LANL, Los Alamos, NM 87545, USA

H. Bender, W. Broste, C. Carlson, D. Frayer, D. Johnson, C. Y. Tom, C. Trainham, and J. Williams, NSTec, Los Alamos, NM 87544, USA

B. Prichard and M. Schulze, SAIC, San Diego, CA 92121, USA

T. Genoni, T. Hughes, and C. Thoma, Voss Scientific, Albuquerque, NM 87108, USA

*Abstract*

The DARHT-II linear induction accelerator (LIA) accelerates a 2-kA electron beam to more than 17 MeV. The beam pulse has a greater than 1.5-microsecond flattop region over which the electron kinetic energy is constant to within 1%. The beam dynamics are diagnosed with 21 beam-position monitors located throughout the injector, accelerator, and after the accelerator exit, where we also have beam imaging diagnostics. We discuss the tuning of the injector and accelerator, and present data for the resulting beam dynamics. We discuss the tuning procedures and other methods used to minimize beam motion, which is undesirable for its application as a bremsstrahlung source for multi-pulse radiography of explosively driven hydrodynamic experiments. We also present beam stability measurements, which we relate to previous stability experiments at lower current and energy.

## INTRODUCTION

The 2-kA, 17-MeV DARHT-II linear induction accelerator (LIA) is unique in that its beam pulse has a long, 1.6-μs flattop during which the kinetic energy varies by less than ±1%. A kicker cleaves four short pulses out of this long pulse, and these are converted to bremsstrahlung for multi-pulse flash radiography of high explosive driven hydrodynamic experiments.

The long-pulse 2-kA beam is produced in a 2.5-MV diode. A diverter switch (crowbar) is incorporated to shorten the 2-μs flat-top pulse to as little as 200 ns flat-top (Fig. 1). After leaving the diode, the beam is accelerated by six induction cells to ~3.5 MeV, and then enters a transport zone designed to scrape off the long rise time, off-energy beam head. As in previous experiments [1,2,3], this beam-head clean-up zone (BCUZ) was configured to pass almost the entire beam head. The main LIA has 68 induction cells that have been upgraded to provide enough potential to accelerate the beam to more than 17 MeV. Each accelerating cell incorporates a solenoid to provide the focusing field for beam transport, as well as dipoles for beam steering.

The solenoids in the injector cells are tuned so that none of the off-energy electrons in the ~500-ns beam head are lost, even in the absence of accelerating fields. The solenoids through the main accelerator were tuned to transport a matched beam through a field increasing to more than 1 kG on axis to suppress beam breakup (BBU).

The tunes for the DARHT-II magnetic transport were designed with two envelope codes, XTR [4] and LAMDA [5]. These solve the beam-envelope differential equations keeping terms that are dropped from the usual paraxial approximation [6]. Initial conditions for XTR and LAMDA were provided by simulations of the space-charge limited diode using the TRAK gun-design code [7] and the LSP particle-in-cell code [8].

Non-invasive DARHT-II beam diagnostics, such as beam position monitors (BPM), are used on every shot [2,3]. Invasive diagnostics, such as a magnetic spectrometer and beam current profile imaging, are only occasionally used [1,2,9].

## RESULTS

There was no loss of beam current through the LIA during the time that the accelerating cells were energized, as shown in Fig. 1, which is an overlay of beam current measurements though the injector and accelerator for a single shot. The ~7-MHz oscillation on the beam head is the result of large capacitances and inductances on the diode structure. The loss of some current in the beam head as it transited the BCUZ is evident. For these data, the current was terminated by the crowbar, which was timed to coincide with the end of the accelerating cell pulse. The red cursors in Fig. 1 delineate the 1.6-μs flattop used for the four radiography pulses. Slight beam loss in the BCUZ during the risetime is evident. Figure 2 shows the electron kinetic energy measured with our magnetic spectrometer. The kinetic energy of the accelerated beam exceeds 17.0 MeV for more than 1.6 μs. For this measurement five of the LIA cells were turned off, which reduced the energy by ~1.3 MeV from that expected with all 74 cells.

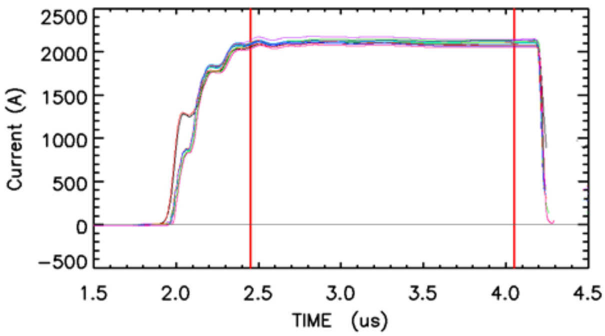


Figure 1: Overlay of beam current measurements in injector and accelerator. Red cursors indicate the 1.6-µs flattop region used for the four radiography pulses.

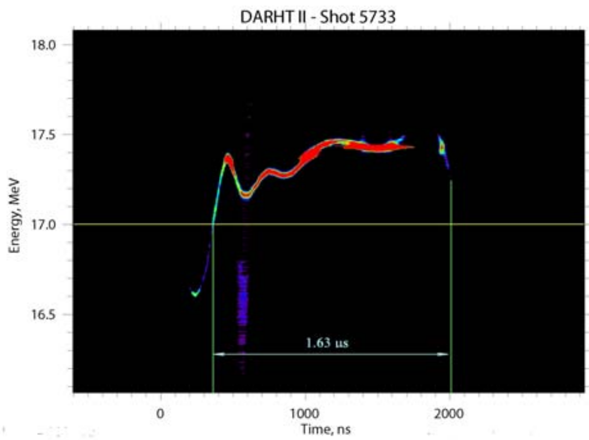


Figure 2: Magnetic spectrometer measurement of electron kinetic energy.

Low frequency beam motion at the exit of the accelerator was dominated by an energy dependent sweep. This sweep is undesirable because it effects the locations of the four radiography pulses, so we must understand it, and reduce its amplitude . While head-to-tail sweep is a characteristic of the resistive wall instability, we believe it unlikely that this instability is responsible for the sweep in DARHT-II. In a uniform strong solenoidal focusing field the distance for an initial perturbation to exponentiate is approximately $L = 3.1Ba^3/I_b/(\tau\rho)^{1/2}$, where $a$ is the pipe radius in cm, $B$ is the field in kG, $I_b$ is the beam current in kA, $\tau$ is the pulse-length in µs, and $\rho$ is the pipe resistivity in µΩ-cm [10]. Based on this theory, we estimate that the growth of an initial perturbation in DARHT-II is less than 60% over the length of the LIA. Moreover, in a strong solenoidal focusing field like DARHT-II the growth is independent of energy, in contradiction to our sweep data, which show a strong correlation with the energy variation illustrated in Fig. 2. The other likely cause of sweep is corkscrew, or the interaction of the energy-varying beam with a few accidental dipoles. Indeed, the observed sweep amplitude can be fit to a model of dipole deflection resulting from the observed energy variation (Fig. 3). Suppression of corkscrew by using steering dipoles has been demonstrated on other LIAs [11]. In an initial attempt to reduce our sweep amplitude, we used only a few of the available steering dipoles. We were able to reduce the sweep to an amplitude acceptable for commissioning the multi-pulse radiography target, and for our first radiographs of an upcoming hydrodynamic test. This initial attempt reduced the sweep amplitude by ~40% over the 1.6-µs flat top (Fig. 4). We anticipate further improvements in the future by using more of our dipoles.

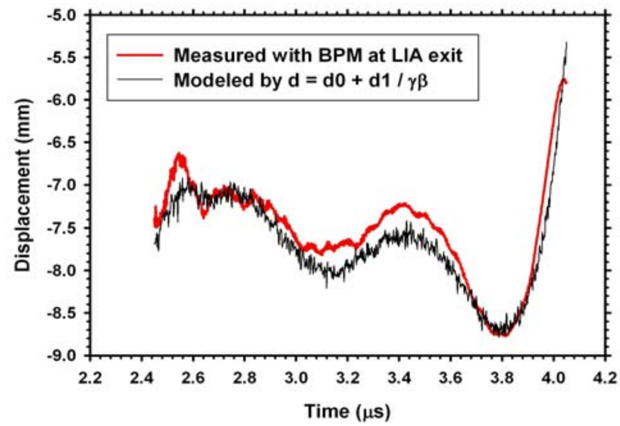


Figure 3: Comparison of measured sweep with model of sweep caused by beam energy variation interacting with a single accidental dipole.

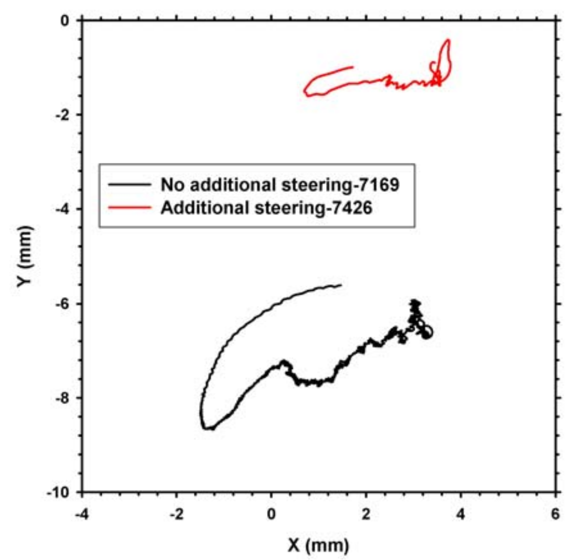


Figure 4: The beam sweep at the accelerator exit was reduced by using additional steering dipoles. Two different shots are shown. Black (lower): nominal steering. Red (upper): additional steering.

High-frequency motion due to low-amplitude BBU was observed at the accelerator exit [12]. For the DARHT-II LIA parameters theory predicts that the BBU amplitude saturates at $\xi(z)=(\gamma_0/\gamma)^{1/2}\xi_0\exp(\Gamma_m)$, where subscript zero denotes initial conditions, and $\gamma$ is the usual relativistic mass factor, and $\Gamma_m = I_b N_g Z_\perp \langle 1/B \rangle / 3\mathrm{x}10^4$ [13]. Here $I_b$ is the beam current in kA, $N_g$ is the number of gaps, the transverse impedance $Z_\perp$ is in $\Omega$/m, and the average focusing force $\langle 1/B \rangle$ is in $\mathrm{kG}^{-1}$. This theoretical prediction was confirmed in earlier experiments with legacy cells [3], and those results were used to design a tune with magnetic field strong enough to suppress the BBU to amplitude small enough that it did not significantly affect the measured radiographic spot size [15]. The observed BBU with this tune agrees with the earlier measurements and with this theory as shown in Fig. 5.

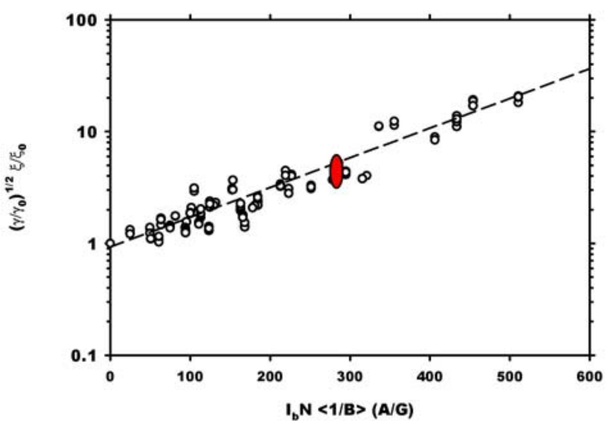


Figure 5: BBU growth in DARHT-II. Open circles: data obtained in low-current, low-energy experiments with legacy cells [3]. Filled oval: range of data obtained during commissioning the 2-kA, 18-MeV accelerator incorporating upgraded cells. The dashed line corresponds to the transverse impedance of the legacy cells.

In conclusion, we have now operated the DARHT-II accelerator at its fully rated current, energy, and pulse width. Even at the full 2-kA current, the solenoidal magnetic field of the tune was strong enough to suppress the BBU to acceptable amplitude. After some additional steering to reduce the sweep, the beam was stable enough for us to proceed with commissioning the multi-pulse kicker and bremsstrahlung converter for radiography.

This work was supported by the US National Nuclear Security Agency and the US Department of Energy under contract W-7405-ENG-36.

## REFERENCES


[1] Carl Ekdahl, et al., "First beam at DARHT-II," in Proc. 2003 Part. Accel. Conf., (2003), pp. 558-562

[2] Carl Ekdahl, et al., "Initial electron-beam results from the DARHT-II linear induction accelerator," IEEE Trans. Plasma Sci. 33, (2005), pp. 892-900.

[3] Carl Ekdahl, et al., "Long-pulse beam stability experiments on the DARHT-II linear induction accelerator," IEEE Trans. Plasma Sci. 34, (2006), pp.460-466.

[4] Thomas P. Hughes, David C. Moir and Paul W. Allison, "Beam injector and transport calculations for ITS," in Proc. 1995 Part. Accel. Conf., (1995), pp. 1207-1209

[5] Thomas .P. Hughes, et al., "LAMDA User's Manual and Reference", Voss Scientific technical report VSL-0707, April 2007

[6] E. P. Lee and R. K. Cooper, "General envelope equation for cylindrically symmetric charged-particle beams," *Part. Acc. 7*, (1976), pp. 83-95

[7] Stanley Humphries Jr., "TRAK – Charged particle tracking in electric and magnetic fields," in Computational Accelerator Physics, R. Ryne Ed., New York: American Institute of Physics, (1994), pp. 597-601 .

[8] T. P. Hughes, R. E. Clark, and S. S. Yu, "Three-dimensional calculations for a 4 kA, 3.5 MV, 2 microsecond injector with asymmetric power feed," Phys. Rev. ST Accel. Beams 2, (1999), pp. 110401-1 – 110401-6

[9] H. Bender, et al., "Quasi-anamorphic optical imaging system with tomographic reconstruction for electron beam imaging," Rev. Sci. Instrum. 78, (2007), pp. 013301

[10] G. J. Caporaso, W. A. Barletta, and V. K. Neil, "Transverse resistive wall instability of a relativistic electron beam," Particle Accelerators, vol. 11, 1980, pp. 71-79

[11] J. T. Weir, J. K. Boyd, Y.-J. Chen, J. C. Clark, D. L. Lager, and A. C. Paul, "Improved ETA-II accelerator performance," in *Proc. 1999 Particle Accelerator Conf.*, New York, NY, March, 1999, pp. 3513-3515.

[12] Carl Ekdahl, et al., "Electron beam dynamics in the long-pulse, high-current DARHT-II linear induction accelerator," in Proc. 2008 European Part. Accel Conf., (2008) pp. 968-970

[13] V. K. Neil, L. S. Hall, and R. K. Cooper, "Further theoretical studies of the beam breakup instability," Particle Accelerators, vol. 9, 1979, pp. 213-222.

[14] R. Briggs and W. Waldron, "Transverse impedance measurements of the modified DARHT-2 accelerator cell design," LBNL Report #59199, November, 2005

[15] Martin Schulze, et al., "Commissioning the DARHT-II Accelerator Downstream Transport and Target," in Proc. 2008 Linear Accel. Conf. (these proceedings).

# ARTIFICIAL INTELLIGENCE RESEARCH IN PARTICLE ACCELERATOR CONTROL SYSTEMS FOR BEAM LINE TUNING*

Martin Pieck†, Los Alamos National Laboratory, NM 87544, USA

*Abstract*

Tuning particle accelerators is time consuming and expensive, with a number of inherently non-linear interactions between system components. Conventional control methods have not been successful in this domain, and the result is constant and expensive monitoring of the systems by human operators. This is particularly true for the start-up and conditioning phase after a maintenance period or an unexpected fault. In turn, this often requires a step by step restart of the accelerator. Surprisingly few attempts have been made to apply intelligent accelerator control techniques to help with beam tuning, fault detection, and fault recovery problems. The reason for that might be that accelerator facilities are rare and difficult to understand systems that require detailed expert knowledge about the underlying physics as well as months if not years of experience to understand the relationship between individual components, particularly if they are geographically disjoint. This paper will give an overview about the research effort in the accelerator community that has been dedicated to the use of artificial intelligence methods for accelerator beam line tuning.

## BEAM LINE TUNING

A typical accelerator beam line includes trim magnets for steering, quadrupole magnets for focusing, Faraday cups and stripline detectors for measuring current, and profile monitors for measuring beam size and position. Beam loss monitors give information about loss of beam through miss-steering. Unfortunately, real systems rarely work as they are designed. Problems arise from imperfect beam production, residual magnetic fields, poorly modeled beam behavior, misplaced or flawed control elements, and changes to the design or use of the facility after it has been built. Beam line designers consider these problems and build diagnostic components into the beam lines. Profile monitors and current detectors are used to measure beam parameters throughout the line to provide information for verifying or correcting beam characteristics. Even so, imperfect detectors, system errors, and noise due to various effect cause beam line control to be difficult at best. Surprisingly, few attempts have been made to apply intelligent accelerator control techniques to help with beam tuning, fault detection, and fault recovery problems.

*This work has benefited from the use of the LANSCE at LANL. This facility is funded by the US DOE and operated by LANS for NSSA under Contract DE-AC52-06NA25396.

† pieck@lanl.gov

## PREVIOUS AI ATTEPMPTS TO ACCELERATOR CONTROL

An early example of AI technology applied to accelerator control can be found in Higo et al. [1]. In this work a rather simple objective of maintaining a given system or operation condition has been discussed. AI is relevant here for dealing with the complex problems of generalized hysteretic and stochastic effects.

Weygand [2] reports on a development for a knowledge-based, domain specific expert system at Brookhaven National Laboratory. The purpose of the expert system is to aid in the control of the Heavy Ion Transfer line (HITL) and in turn to minimize down time after a change in running conditions or the start of a new run. Due to the complexity of the expert system it was divided up into three domains (control, device beam influence, and device cause and effect segment). Separate from that is the goal-solving mechanism of the program. This goal-solving function takes a specified high level goal, and then, by developing a tree of sub-goals, attempts to solve the given goal via a hill-climbing technique. However, the system doesn’t take into account that conditions may change during the execution of the solution.

Other attempts at intelligent control for accelerators include the ISIS tune advisor (Schultz et al. 1990), the LAMPF Beam Loss Expert (Clearwater et al. 1986), and a learning system based on RL4 (Clearwater et al. 1990). The ISIS tune advisor and LAMPF Beam Loss Expert were both expert systems for indirect control which were never implemented as general or real-time control solutions. The learning system used knowledge-based induction for off-line learning of beam position monitor placement, but was not implemented as a general learning algorithm.

Neural networks have been applied to accelerator control for actual manipulation of control parameters as well as for simulation. Howell et al. [3] used neural networks for modeling and control of a negative-ion accelerator source at Los Alamos National Laboratory to predict the beam characteristics of the source for given changes in control settings. However, the success was rather limited.

Brown [4] developed an automated controller based on an artificial neural network and evaluated its applicability in a real-time environment. This capability was developed within the context of a small angle negative ion source on the Discharge Test Stand at Los Alamos National Laboratory. Using no knowledge of operating conditions, the controller begins acquiring rough snapshot of the operational condition. Once the rough approximation of the condition has been determined, the network formulates a model from which it determines the best operating point. The controller takes the ion source to that operating point for a reality check. As real data is fed in, the model of the operating surface is updated until the neural network's model agrees with reality. The controller then uses a gradient ascent method to optimize the operation of the ion source. Mead (1994) presents some successful control examples of the above application.

The SETUP program developed at CERN (Bouche 1995) is representative of efforts to apply AI techniques to small subsystems. SETUP is only used for pre-control equipment setup. The program uses an object-oriented description language for representing control actions. The reasoning system searches the oriented graph defined by an object description to make decisions about equipment setup without human assistance. The program provides a good example of using object models for control decision making. It does not attempt to perform real-time control or use on-line feedback from the system.

Arruat [5] reports on symbolic computing programs that address not only the manipulation of mathematical functions, but also process control. He uses symbolic computing as a tool for developing algorithmic engines that can be fully integrated in the controls environment and facilitates modular design of control systems. He reports that this technique has been applied to a special class of accelerator problems, namely the beam steering in transfer lines and accelerator rings in the CERN PS Complex.

In his Ph.D. dissertation Jennings [6] developed and implemented a new model of multi-agent coordination, called *Joint Responsibility*, based upon the notion of joint intentions. The Responsibility framework was devised specifically for coordinating behavior in complex, unpredictable and dynamic environments such as particle accelerator control. Jennings contribution was that he noticed that in a distributed multi-agent system when anything unexpected happened (i.e. new information invalidated existing goals, synchronization between actions was disrupted or agents had misinterpreted the situation) the multi-agent community would act incoherently. This incoherence occurred because agents did not embody sufficient knowledge about the process of team problem solving. Jennings provided agents with an explicit model of joint problem solving about which they could reason when deciding how to interact with others. This new development found its application in ARCHON.

ARCHON (1993-1996) was Europe's largest ever project in the area of Distributed Artificial Intelligence (DAI) and applied to CERN control systems for controlling and diagnosing faults in one of their particle accelerators (called the Proton Synchrotron (PS)). The Archon-project, which Jennings was in charge of, provided the architecture for integrating multiple pre-existing expert systems to exchange information and, therefore, increase the overall performance.

Another application of AI techniques in operating a larger system is in the field of fault detection and system diagnosis. Leger et al. (1996) points out that in order to operate a successful plant, continues improvement must be made in the areas of safety quality and reliability. Central to this continuous improvement is the early or proactive detection and correct diagnosis of process faults. The paper examines the feasibility of using cumulative summation control charts and artificial neural networks together for fault detection and diagnosis (FDD). The control chart and neural network are linked by using a characteristic fault signature pattern for each fault, which is to be detected and diagnosed.

In one of the first papers from Klein and Luger [2] on beam tuning, a framework of a general purpose intelligent control system for a particle accelerator has been presented. Results of coupling neural network and expert systems technology to solve several standard accelerator tuning problems based on realistic simulations have been discussed. The authors also examine the effectiveness of additional heuristic search techniques such as genetic algorithms. However, the algorithm did not converge towards specific solution methods to create the desired result. To solve the problem, the authors also examined the capabilities of an analytic control algorithm, fuzzy logic (FL) control, and genetic algorithm searches. It was noticed that the accuracy of the FL solution depended greatly on the quality of the knowledge the author placed in the system. The genetic algorithm is an appropriate heuristic for focusing control because it can search large solution spaces in non-linear domains.

In continuation of their earlier work Klein and Luger (Klein et al. 1997(a)) have identified two different sources of control information that must both be incorporated into any successful automated control system. The first source includes analytic domain knowledge necessary for modeling the accelerator and beam line. The second, equally important source is experiential knowledge about the specific facility and group of components being controlled.

Stern (Stern et al. 1997) reports on the continuing work of Klein on coordinating the activity of the control subsystems to adaptively execute sustained sequences of control actions of the type required to tune the whole accelerator in a coordinated fashion. The discussed control system employs a multi-layer organization in which knowledge–based decision making is used to dynamically configure a lower level optimization and control algorithm. An object-oriented physical access layer supported by a distributed control system allows abstraction from the lower level details of hardware manipulation, signal processing, and synchronization.

This hybrid architecture integrates a variety of methodologies, including teleo-reactive trees for dynamic exception handling and re-planning.

In Klein's last paper [7] he discusses the results of their research on the use of Teleo-Reactive programming as a high level control mechanism. According to the authors, control of particle accelerators requires a hybrid architecture which includes methodologies for planning, intelligent search, and pattern recognition. The author's suggestion is that control must be distributed and hierarchical to utilize parallel problem-solving in the face of time-sensitive control requirements and to decompose complex control problems into more manageable subtasks. As a high level control mechanism, the authors used a planning technique known as Teleo-Reactive (TR) programming developed by Nils Nilsson at Stanford. TR programming combines the responsiveness of an analog feedback loop and the goal-oriented behavior of a production system, to allow the control system to govern the execution of its tasks in a dynamic environment. The system has been successfully tested at both the Brookhaven National Laboratory ATF and at the ATLAS facility at Argonne National Laboratory.

Fiesler [8] reports on a suit of tests on predictive algorithms to determine their ability to learn from and find relationships between large numbers of variables. In particular, they used COMFORT, a particle accelerator simulator, to generate large amounts of data. They eventually compared the results among several fundamentally different types of algorithms, including least squares and hybrid neural networks with real data that were obtained from Brookhaven National Laboratory.

## SUMMARY

It seems surprising that virtually all research on AI applied to particle accelerator stopped around the year 2000. This certainly can't be explained with the Y2K problem. Nevertheless, it seems like interest and/or funding must have stopped around that time. The alternative is, of course, that the research in the area wasn't promising or the problem was so complex that researchers did not find the return of investment very appealing to them.

Nevertheless, the author of this paper sees a great chance for AI to make its comeback in accelerator control rooms. The first and foremost reason is that running these machines has become a time and cost critical issue. The older an accelerator gets the more maintenance/upgrade work needs to be invested. This is in turn creates a problem since users/experimenters are paying to do their experiments and extensive maintenance/upgrade work reduces experimental time. With less time for experiments less money comes in for maintenance. However, less maintenance means that the accelerators become more error/fault prone. Therefore, managers have to balance down time vs. beam time and try to minimize conditioning, start-up time and fault recovery time. In addition, managers increase their attention to preventive maintenance (predicting when something might happen and then to something beforehand).

Speeding up beam tuning, advanced fault detection, and preventive maintenance (sometimes referred to as structural health) are areas where AI can and has already made an impact. Specifically applied to accelerator controls, expert beam tuning systems have been around for more than a decade, fault recovery programs got more attention at the end of the century. On the other hand preventive maintenance has never been applied to accelerator facilities. So, there is a chance here to lead the way.

## REFERENCES

[1] Higo T., Shaoee H., and Spencer J.E., "Some application of AI to Problems of Accelerator Physics", *Proceedings of the IEEE Particle Accelerator Conference*, Washington D.C. (1987).

[2] Weygand D.P., "Artificial Intelligence and Accelerator Control", Proceedings of the IEEE Particle Accelerator Conference, Washington DC, (1987).

[3] Howell, J. A., et al.., *"Control of a negative-ion accelerator source using neural networks "*, Nuclear Instruments and Methods in Physics Research Section A, Volume 293, Issue 1-2, p. 517-522.

[4] Brown, S. K., et al., "Optimization and control of a small angle ion source using an adaptive neural network controller (invited) ", Review of Scientific Instruments, Volume 65, Issue 4, April 1994, pp.1411-1415.

[5] Arruat M., et al., *"Integration of symbolic computing in accelerator control"*, International Journal of Modern Physics C (Physics and Computers); Aug. 1995; vol.6, no.4, p.475-80, Fourth International Workshop on Software Engineering, Artificial Intelligence, and Expert Systems for High Energy and Nuclear Physics, 3-8 April 1995, Pisa, Italy

[6] Jennings N. R., et al., "Using ARCHON to develop real-word DAI applications for electricity transportation management and particle accelerator control", IEEE Expert, (1996).

[7] Klein, W.B., et al., "Teleo-Reactive Control for Accelerator Beamline Tuning". In *Proceedings of the IASTED International Conference*. Zurich: IASTED/ACTA Press (2000).

[8] Fiesler, E., Campbell, S., "*Hybrid neural networks and their application to particle accelerator control"***,** Proceedings of the SPIE - The International Society for Optical Engineering; 1999; vol.3812, p.132-42, Proceedings of the 1999 Applications and Sciences of Neural Networks, Fuzzy Systems, and Evolutionary Computation II; Jul 19-Jul 20 1999; Denver, CO, USA

# PARALLEL 3D FINITE ELEMENT PARTICLE-IN-CELL CODE FOR HIGH-FIDELITY RF GUN SIMULATIONS*

A. Candel†, A. Kabel, L. Lee, Z. Li, C. Limborg, C. Ng,
G. Schussman, R. Uplenchwar and K. Ko
SLAC, Menlo Park, CA 94025, USA

*Abstract*

SLAC's Advanced Computations Department (ACD) has developed the first high-performance parallel Finite Element 3D Particle-In-Cell code, Pic3P, for simulations of RF guns and other space-charge dominated beam-cavity interactions. As opposed to standard beam transport codes, which are based on the electrostatic approximation, Pic3P solves the complete set of Maxwell-Lorentz equations and thus includes space charge, retardation and wakefield effects from first principles. Pic3P uses advanced Finite Element methods with unstructured meshes, higher-order basis functions and quadratic surface approximation. A novel scheme for causal adaptive refinement reduces computational resource requirements by orders of magnitude. Pic3P is optimized for large-scale parallel processing and allows simulations of realistic 3D particle distributions with unprecedented accuracy, aiding the design and operation of the next generation of accelerator facilities. Applications to the Linac Coherent Light Source (LCLS) RF gun are presented.

## INTRODUCTION

The Office of Science in the U. S. DOE is promoting the use of High Performance Computing (HPC) in projects relevant to its mission via the 'Scientific Discovery through Advanced Computing' (SciDAC) program which began in 2001 [1]. Since 1996, SLAC has been developing a parallel accelerator modeling capability, first under the DOE Grand Challenge and now under SciDAC, for use on HPC platforms to enable the large-scale electromagnetic and beam dynamics simulations needed for improving existing facilities and optimizing the design of future machines.

## METHODS

In the following, a brief introduction to the employed methods for solving the full set of Maxwell's equations in time domain in the presence of charged particles is given.

### *Maxwell Finite Element Time-Domain*

In our approach, Ampère's and Faraday's laws are combined and integrated over time to yield the inhomogeneous vector wave equation for the time integral of the electric field:

$$\varepsilon \frac{\partial^2}{\partial t^2} \int_{-\infty}^{\mathbf{t}} \mathbf{E}\, \mathrm{d}\tau + \nabla \times \mu^{-1} \nabla \times \int_{-\infty}^{\mathbf{t}} \mathbf{E}\, \mathrm{d}\tau = -\mathbf{J}, \quad (1)$$

where $\mathbf{E}$ is the electric field intensity, $\mathbf{J}$ is the electric current source density, and $\varepsilon$ and $\mu$ are the electric permittivity and magnetic permeability.

The computational domain is discretized into curved tetrahedral elements and $\int_{-\infty}^{t} \mathbf{E}\, \mathrm{d}\tau$ in Eq. (1) is expanded into a set of hierarchical Whitney vector basis functions $\mathbf{N_i}(\mathbf{x})$ up to order $p$ within each element:

$$\int_{-\infty}^{t} \mathbf{E}(\mathbf{x}, \tau)\, \mathrm{d}\tau = \sum_{i=1}^{N} e_i(t) \cdot \mathbf{N_i}(\mathbf{x}). \quad (2)$$

For illustration, $N_2 = 20$ and $N_6 = 216$. After accounting for boundary conditions at domain boundaries and between neighboring elements, a global number of expansion coefficients is obtained, representing the field degrees of freedom (DOFs) of the system.

Substituting Eq. (2) into Eq. (1), multiplying by a test function and integrating over the computational domain $\Omega$ results in a matrix equation, second-order in time. The unconditionally stable implicit Newmark-Beta scheme [2] is employed for numerical time integration. The resulting sparse positive definite system matrix is distributed over the compute nodes and is either factorized with a direct solver for smaller problems, or the linear system is solved iteratively at each time step with a conjugate gradient method with suitable preconditioners.

At a given moment in time, the electric field $\mathbf{E}$ and the magnetic flux density $\mathbf{B}$ are then easily obtained from the solution vector $\mathbf{e}$:

$$\mathbf{E}(\mathbf{x}) = \sum_{\mathbf{i}} (\partial_{\mathbf{t}} \mathbf{e})_{\mathbf{i}} \cdot \mathbf{N_i}(\mathbf{x}) \quad (3)$$

and

$$\mathbf{B}(\mathbf{x}) = -\sum_{\mathbf{i}} (\mathbf{e})_{\mathbf{i}} \cdot \nabla \times \mathbf{N_i}(\mathbf{x}). \quad (4)$$

* Work supported by the U.S. DOE ASCR, BES, and HEP Divisions under contract No. DE-AC002-76SF00515.

† candel@slac.stanford.edu

### *Particle-In-Cell (PIC)*

Numerical charge conservation is critical during the self-consistent simulation of charged particles and electromagnetic fields. If the discrete analogs of the two Maxwell divergence equations $\nabla \cdot \mathbf{B} = \mathbf{0}$ and $\nabla \cdot \mathbf{E} = \rho$ are satisfied at $t = 0$, then it is sufficient to fulfill the discrete versions of wave Eq. (1) and the continuity equation

$$\frac{\partial \rho}{\partial t} + \nabla \cdot \mathbf{J} = \mathbf{0}$$

in order to maintain charge conservation at all times. In our approach, these conditions are satisfied by using Whitney basis functions and starting with a charge-free simulation domain.

Freely moving charges are modeled by a number of macro particles specified by position $\mathbf{x}$, momentum $\mathbf{p}$, rest mass $m$ and charge $q$ attributes. The total current density is then approximated as

$$\mathbf{J}(\mathbf{x}, t) = \sum_i \rho(\mathbf{x} - \mathbf{x_i}, t) \cdot \mathbf{v_i}(t),$$

with $\mathbf{v} = \frac{\mathbf{p}}{\gamma m}$, $\gamma^2 = 1 + |\frac{\mathbf{p}}{mc}|^2$ and $\rho$ the macro particle charge density, currently implemented for point charges and Gaussian line currents (which act as smoothing filter). The macro particles obey the classical relativistic collisionless (Newton-Lorentz) equations of motion,

$$\begin{aligned} \frac{d\mathbf{r}}{dt} &= \mathbf{v}, \\ \frac{d\mathbf{p}}{dt} &= q(\mathbf{E} + \mathbf{v} \times \mathbf{B}), \end{aligned}$$

which are integrated using the standard 'Boris' pusher, an explicit method splitting the momentum update into two accelerations and one rotation [3].

### *Causal Moving Window*

FE methods are most efficient when using (adaptive) $hpq$-refinement, where $h$ stands for the mesh resolution, $p$ for the polynomial order of the basis functions and $q$ for the degree of mesh curvature. Our current implementation supports static $h$- and $q$-refinement ($q$=1,2) as well as adaptive $p$-refinement ($p$=0...6), where each element is assigned an independent value of $p$ and its basis functions that are shared with neighboring elements are restricted to the highest common order. This requires a consistent set of hierarchical FE basis functions.

Higher-order elements not only significantly improve field accuracy and dispersive properties [4], but they also generically lead to higher-order accurate particle-field coupling equivalent to, but much less laborious than, complicated higher-order interpolation schemes commonly found in finite-difference methods.

Orders of magnitude in computational resources can be saved, while preserving full simulation accuracy, by restricting higher-order $p$-refinement to regions that are inside the causal range of the particle bunch. Since a change of the selected basis functions requires reassembly of the system matrix, adaptive $p$-refinement is usually only done from time to time, in accordance with the particle dynamics. Fig. 1 shows a Minkowski spacetime diagram indicating the causal domain for a bunch transiting through a compact structure. The causal domain can be determined from the bunch emission and exit spacetime positions, and non-causal fields are neglected by not including their elements in the computation. A resulting parallel partitioning after dynamic load balancing is shown in Fig. 2.

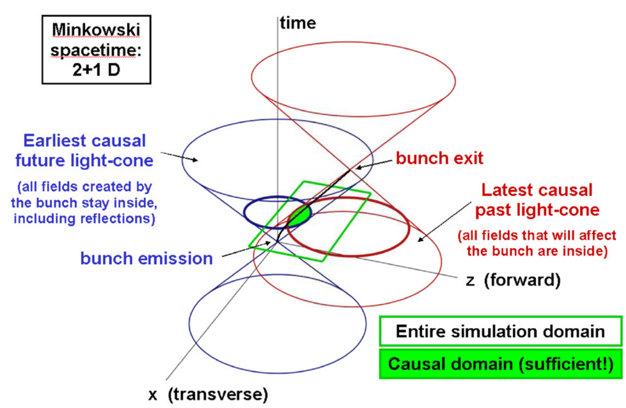


Figure 1: 2+1D spacetime diagram indicating the causal field domain for an accelerated particle bunch inside the gun at a snapshot in time.

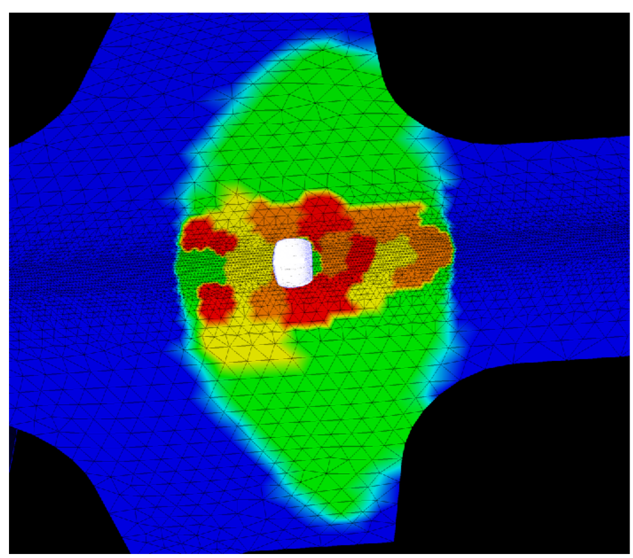

Figure 2: Example of a Pic3P simulation employing the causal moving window technique. Elements outside the causal domain are neglected in the field computations and are indicated by the blue color. Elements and fields in the causal domain are partitioned onto all CPUs with dynamic load balancing and are indicated by different colors. Macro particles are distributed among all CPUs and are shown in white.

## RESULTS

PIC simulations of the 1.6 cell S-band LCLS RF gun are presented [5]. In the simulations, the gun is driven by the $\pi$-mode with a peak accelerating field gradient of 120 MV/m at the cathode (the cavity wall). A cold, uniform, 10 ps long (flat-top), cylindrically symmetric electron bunch of 1 mm radius is emitted, centered around a phase of -58° with respect to the crest. Solenoidal focusing fields are neglected for simplicity. These parameters allow comparisons between the 3D codes Pic3P and PARMELA and the 2D codes Pic2P and MAFIA.

For Pic3P simulations, a conformal, unstructured 3D (1/4) mesh model with 305k tetrahedral elements is used, with $h$-refinement along the beam trajectory. High fidelity cavity modes are obtained with ACD's parallel FE frequency domain code Omega3P and directly loaded into Pic3P. Fig. 3 shows the evolution of the normalized transverse RMS emittance during transit through the gun for different bunch charges. There is excellent agreement between Pic3P and the 2D results from Pic2P and MAFIA, as expected from the high cylindrical symmetry in the fields and the convergence behavior of the codes. PARMELA results differ as space charge effects are significant, presumably because it ignores wakefield and retardation effects, as detailed in a previous study[6]. By using the causal window technique in Pic3P (cf. Fig. 1 and 2), the problem size was reduced by one order of magnitude without a loss of simulation accuracy. Note that Pic3P is able to solve problems that are several hundred times larger than what is needed here in order to reach convergence in the bunch emittance. Parallel dynamic load balancing and excellent scalability to thousands of CPUs result in fast turn-around times. Results on large-scale, realistic 3D simulations have been presented in the past [7].

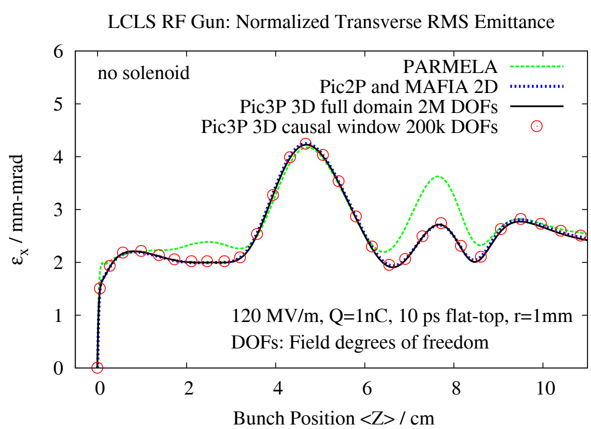


Figure 3: Comparison of normalized transverse RMS emittance as a function of beam position in the LCLS RF gun as calculated by PARMELA, Pic2P and MAFIA 2D (both agree), and Pic3P, where the causal window technique reduces the problem size by one order of magnitude.

## CONCLUSIONS

The parallel Finite Element 3D electromagnetic PIC code Pic3P, the first such successful implementation, was used to model space charge effects in the LCLS RF gun from 1$^{st}$ principles, including space charge, wakefield and retardation effects. On a cylindrically symmetric benchmark case, Pic3P shows excellent agreement with 2D codes such as MAFIA and Pic2P. Results from the electrostatic code PARMELA differ as wakefield and retardation effects are neglected.

Pic3P employs state-of-the-art parallel Finite Element methods on conformal, unstructured meshes with unconditionally stable time integration and self-consistent higher-order particle-field coupling. In combination with novel causal moving window techniques and dynamic load balancing, Pic3P allows parallel 3D PIC simulations of high-brightness, low-emittance electron injectors with unprecedented accuracy, aiding the design and operation of the next generation of accelerator facilities.

## ACKNOWLEDGMENTS

This work was supported by the U.S. DOE ASCR, BES, and HEP Divisions under contract No. DE-AC002-76SF00515. This research used resources of the National Energy Research Scientific Computing Center, which is supported by the Office of Science of the U.S. Department of Energy under Contract No. DE-AC02-05CH11231. We also acknowledge the contributions from our SciDAC collaborators in numerous areas of computational science.

## REFERENCES

[1] Cho Ng et al., "Design and Optimization of Large Scale Accelerator Systems through High-Fidelity Electromagnetic Simulations", Invited Talk given at SciDAC 2008 Conference, Seattle, Washington, July 13-17, 2008.

[2] N. M. Newmark, "A method of computation for structural dynamics", Journal of Eng. Mech. Div., ASCE, vol. 85, pp. 67-94, July 1959.

[3] J. P. Boris, "Relativistic plasma simulation-optimization of a hybrid code", Proc. Fourth Conf. Num. Sim. Plasmas, Naval Res. Lab, Wash. D.C.,pp. 3-67, Nov. 2-3, 1970.

[4] M. Ainsworth, "Dispersive properties of high-order Nedelec/edge element approximation of the time-harmonic Maxwell equations", Philos. trans.-Royal Soc., Math. phys. eng. sci., vol. 362, no. 1816, pp. 471-492, 2004.

[5] L. Xiao et al., "Dual Feed RF Gun Design for the LCLS", Proc. PAC 2005, Knoxville, Tennessee, May 15-20, 2005.

[6] A. Candel et al., "Parallel Higher-order Finite Element Method for Accurate Field Computations in Wakefield and PIC Simulations", Proc. ICAP 2006, Chamonix Mont-Blanc, France, October 2-6, 2006.

[7] A. Candel, "Parallel 3D Finite Element Particle-In-Cell Simulations for the LCLS RF Gun", LCLS Seminar Talk, Stanford Linear Accelerator Center, March 25, 2008.

# BEAM DYNAMICS AND WAKE-FIELD SIMULATIONS FOR THE CLIC MAIN LINACS

V. F. Khan, R.M. Jones, Cockcroft Institute, Daresbury, WA4 4AD, UK
and University of Manchester, Manchester, M13 9PL, UK

*Abstract*

The CLIC linear collider aims at accelerating multiple bunches of electrons and positrons and colliding them at a centre of mass energy of 3 TeV. These bunches will be accelerated through X-band linacs, operating at an accelerating frequency of 12 GHz. Each beam readily excites wake-fields within the accelerating cavities of each linac. The transverse components of the wake-fields, if left unchecked, can dilute the beam emittance. The present CLIC design relies on heavy damping of these wake-fields in order to ameliorate the effects of the wake-fields on the beam emittance. Here we present initial results on simulations of the long-range wake-fields in these structures and on beam dynamics simulations. In particular, detailed simulations are performed, on emittance dilution due to beams initially injected with realistic offsets from the electrical centre of the cavities.

## INTRODUCTION

The CLIC scheme aims at colliding electrons and positrons at a centre of mass energy of 3 TeV. The main accelerating cavities of CLIC are normal conducting copper structures, designed to operate at 12 GHz. As the beam transits these accelerating cavities it receives a tranverse momentum kick which has the potential to result in serious beam disruption. This kick is proportional to the $a^3$, where "a" is the iris dimension. It is interesting to note that for the CLIC scenario the average iris is ~3.0 mm compared to 35 mm for the ILC superconducting cavities (which operate at an L-band frequency of 1.3 GHz). Thus, the kick imparted to the beam in the CLIC design is a factor of 1600 greater than that of the ILC cavities. Clearly, the wake-field will require careful suppression and the impact on emittance dilution will necessitate a beam dynamics study including realistic fabrication tolerances.

The present baseline design for CLIC relies on heavy damping (with Qs as low as 10) in order to suppress these wake-fields. The wake-field suppression in this case entails locating the damping materials in relatively close proximity to the location of the accelerated beam. Here a strategy originally employed for the NLC [1] in which moderate damping is imposed (Q~500) together with detuning of the characteristic modes of the structure is used. The potential advantage of this alternative method lies in the ability to locate the damping materials outside the immediate vicinity of the beam and to provide a means of diagnosing the location of the beam and cell misalignments from the radiation at the damping ports [2].

We have already considered a design in which we prescribed a Gaussian dipole mode distribution with an optimised bandwidth of 3.3 GHz for the first band together with interleaving of successive structures [3]. The detuning resulted in a wake-field which was suppressed by almost two order of magnitude at the first trailing bunch in the CLIC train of 312 bunches. In this work we focus on the parameters of the present baseline design known as CLIC_G which consists of 24 cells. We retain the dimensions of the end cells and the intermediate cells are modified with a view to enforcing a Gaussian distribution in the kick factor weighted distribution [1]. Enforcing a fixed geometry to the end cells results in a reduced dipole mode bandwidth. As a consequence of this fixed dipole bandwidth the wake-field at the first few trailing bunches is insufficiently damped. Interleaving successive structures results in an improved overall suppression in the wake-field. Nonetheless, even with 8-fold interleaving of structures the envelope of the wake-field is still unsatisfactory. To ameliorate the effect of this wake-field on emittance dilution we have modified the structure geometry with a view to locating the first few trailing bunches at the zero crossing point in the wake-field. To assess the practicality of this method we have undertaken a series of beam dynamics simulations entailing tracking the beam through the complete CLIC main linac. We present initial results on this study herein. The RMS of the sum wake-field also provides evidence as to whether beam break up (BBU) is occurring and we study this parameter also.

## BASELINE CLIC STRUCTURE

The fundamental parameters of the present baseline structure known as CLIC_G are delineated in Table 1. From an analysis of electrical breakdown the group velocity of the fundamental mode should be kept as small as is commensurate with a practical filling time. With this in mind, the geometry of the end cells is invariant to within a factor of ~10%. Intermediate cells are varied in

Table 1: Parameters of updated CLIC baseline structure CLIC_G [4].

| Structure | CLIC_G |
|---|---|
| Frequency (GHz) | 12 |
| Average iris radius/wavelength $\langle a\rangle/\lambda$ | 0.11 |
| Input /Output iris radii (mm) | 3.15, 2.35 |
| Input /Output iris thickness (mm) | 1.67, 1.0 |
| Group velocity (% c) | 1.66, 0.83 |
| Number of cells per cavity | 24 |
| Bunch separation (rf cycles) | 6 |
| Number of bunches in a train | 312 |

order to enforce a Gaussian distribution of the kick factor weighted distribution. The resulting wake-field for a structure of N cells is calculated from the modal summation:

$$W(t) = 2\,\mathrm{Im}\left\{\sum_{p=1}^{N} K_p \exp\left[i\omega_p t\left(1+\frac{i}{2Q_p}\right)\right]\right\} \quad (1)$$

where for the p[th] mode $\omega_p/2\pi$, $K_p$ is the coupled mode frequency and kick factor, respectively. A damping factor $Q_p$ has also been incorporated. Furthermore, it is convenient to display the maximum excursion in the wake-field and this is obtained by replacing the Im factor in Eq. (1) with the absolute value.

Our design focussed on a 24 cell structure and 8-fold interleaving of the structure (making the structure effectively 192 cells). We investigated a Gaussian kick factor weighted distribution with a standard deviation $\sigma$ from the central value $\omega_c/2\pi$. The optimised design features a bandwidth of $\Delta\omega/2\pi = 3\sigma = 5.8\%\ \omega_c = 1$ GHz. The envelope of the wake-field for a single, non-

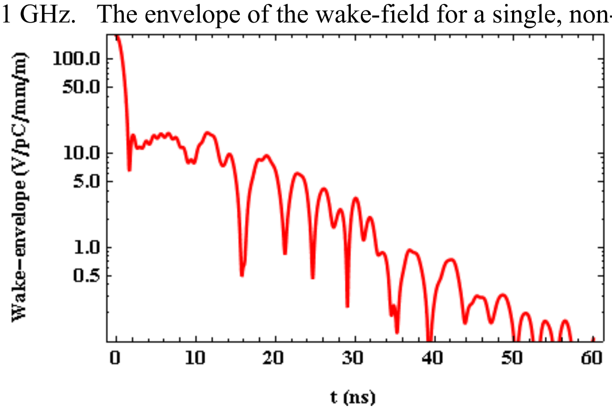


Figure 1: Envelope of the wakefield of 24 cell structure, CLIC_ZC with Q ~500.

interleaved structure is illustrated in Fig. 1. For this bandwidth, the wake-field is insufficiently damped as at the first trailing bunch it is 74% of the peak value (~177 V/pC/mm/m). Interleaving structures reduces the amplitude of the wake-field experienced by the first trailing bunch is reduced to ~ 26% of the peak value. The amplitude of the wake-field for the first 4 trailing bunches is displayed in Fig 2.

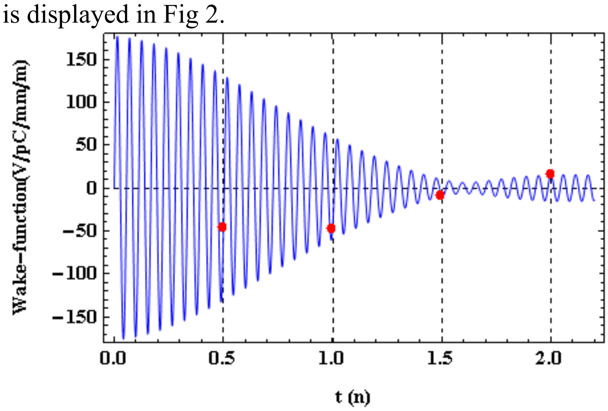


Figure 2: Wake-function of a modified CLIC_G structure, representing the wake at first four trailing bunches.

## PERTURBED BASELINE STRUCTURE

The wake felt by the bunch is obtained with Eq. 1. The oscillations in the wake-field amplitude are due to the corresponding sinusoidal term. We adjust the mode frequencies to force the bunches to be located at the zero crossing in the wake-field. This can be achieved in a straightforward manner for the first few trailing bunches by shifting the mode frequencies of all cells. In practise this is achieved by systematically shifting all cell dimensions (aperture and cavity radius). The parameters of 7 fiducial cells of a 24 cell structure, which we refer to as CLIC_ZC, are presented in Table 2. Here a is the iris radius, b is the cavity radius, t is the iris thickness, $v_g/c$ is the group velocity of the fundamental mode and $\omega_1/2\pi$ is the first band dipole frequency. The ratio of average iris radius to wavelength ($\langle a\rangle/\lambda$) is 0.103. In order to maintain the group velocity of CLIC_G it was necessary to change the first cell iris radius by 160µm and the last cell iris radius by 220µm.

The group velocities of the fundamental mode are retained within the tolerable limits of 10% [5] by modifying the iris thickness of the cells accordingly. The wake-envelope of the detuned CLIC_ZC structure is relatively invariant with respect to the shifted perturbation in cell parameters.

Table 2. Parameters of the detuned CLIC_ZC structure.

| Cell. | a (mm) | B (mm) | t (mm) | Vg/c (%) | $\omega_1/2\pi$ (GHz) |
|---|---|---|---|---|---|
| 1 | 2.99 | 9.88 | 1.6 | 1.49 | 17.57 |
| 4 | 2.84 | 9.83 | 1.4 | 1.38 | 17.72 |
| 8 | 2.72 | 9.80 | 1.3 | 1.29 | 17.85 |
| 12 | 2.61 | 9.78 | 1.2 | 1.18 | 17.96 |
| 16 | 2.51 | 9.75 | 1.1 | 1.06 | 18.07 |
| 20 | 2.37 | 9.73 | 0.96 | 0.98 | 18.2 |
| 24 | 2.13 | 9.68 | 0.7 | 0.83 | 18.40 |

However, there is a considerable difference in the wake-field experienced by the first trailing bunch, which is 1.7 % of peak value in this case. The corresponding wake-field is illustrated in the Fig. 3 for the first 4 trailing bunches.

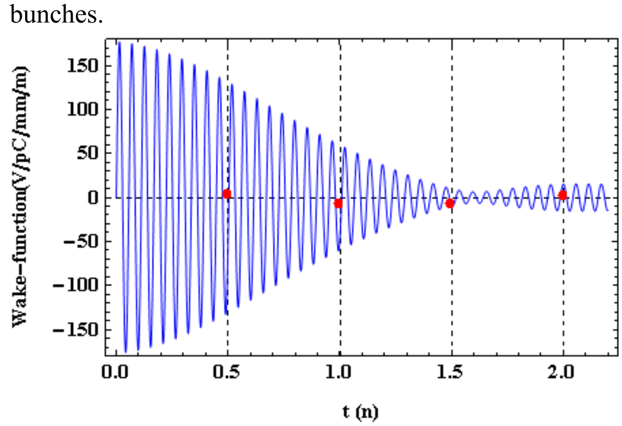


Figure 3: Wake-field of the CLIC_ZC structure. The wake-field at the location of the bunch is indicated by the dots.

In order to further improve wake-field suppression we incorporated 8-fold interleaving of the mode frequencies of successive structures and this is illustrated in Fig. 4. for a Q of 500, it is notable that the wake-field is below unity after approximately 15 ns, i.e. 30 trailing bunches.

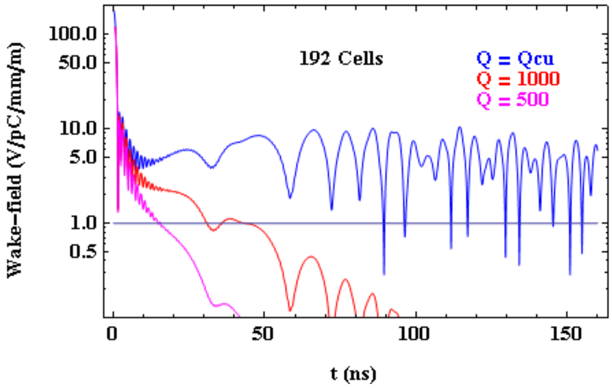


Figure 4: Envelope of wake-field for an 8-fold interleaving of dipole mode frequencies in the CLIC_ZC structure.

## BEAM DYNAMICS SIMULATIONS

The emittance dilution due to these long-range wake-fields is evaluated by tracking the progress of the beam throughout the complete linac. For this purpose we utilised the code PLACET [6]. However, an indication as to whether BBU occurs is also provided by the RMS of the sum wake-field, $S_{RMS}$ [7]. This is a direct and straightforward calculation. As a prelude to full beam dynamics tracking simulations we investigated the sensitivity of $S_{RMS}$ to small fractional errors in the bunch spacing. This is illustrated in Fig. 5 for both a single structure and an interleaved structure. At the nominal bunch spacing $S_{RMS}$ is ~33 V/pC/mm/m for a single structure and it is reduced to ~7 V/pC/mm/m for an 8-fold interleaved structure.

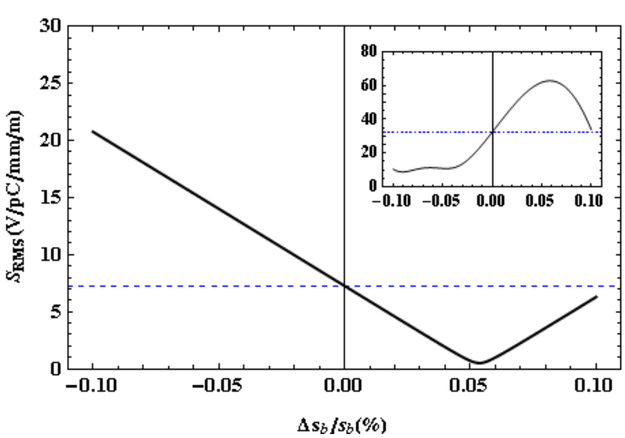


Figure 5: $S_{RMS}$ of a 24 cell structure interleaved 8-fold with a damping Q of 500. The 24 cell non-interleaved structure result is shown inset.

We also tracked the beam through the complete linac and computed the projected emittance of the beam. The results of this initial study indicate that a single, non-interleaved structure gives rise to a huge emittance growth, as expected. However, for an 8-fold interleaved structure the emittance dilution is reduced to ~ 70% at the nominal bunch spacing. This is still not acceptable

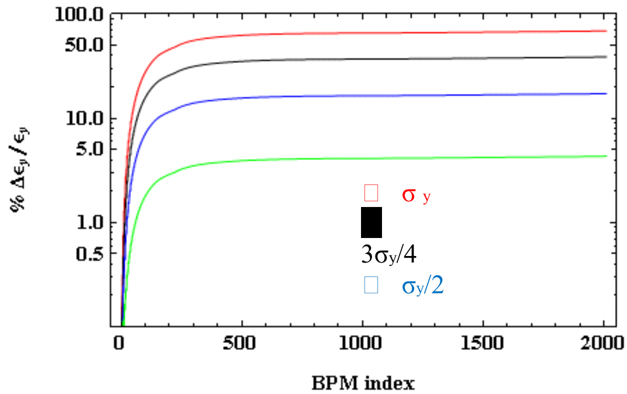


Figure 6: Emittance dilution in an 8-fold interleaved CLIC_ZC structure for various beam offsets.

from the perspective of the impact on beam luminosity. However, further optimisation may lead to a further reduction in the beam emittance. Detailed results on this study are displayed in Fig. 6. in which the emittance dilution down the linac is evaluated for several injection offsets in the beam from the centre of the linac.

## DISCUSSION

Interleaving the dipole frequencies of successive structures reduces the overall emittance dilution significantly. A beam subjected to a $\sigma_y$ injection offset results in an emittance dilution of ~70% at the nominal bunch spacing. Additional simulations conducted on the sensitivity of the emittance dilution to systematic fabrication errors indicate a strong sensitivity. However, a more careful randomisation of the zero crossing point in groups of structures has the potential to reduce the emittance dilution.

## ACKNOWLEDGMENTS

We have benefited from valuable discussions with W. Wuensch and A. Grudiev regarding the recent structures and with D. Schulte, B. Dalena and A. Latina on the beam dynamics code PLACET.

## REFERENCES

[1] R.M. Jones, 2006, Phys. Rev. STAB, **9**, 102001.
[2] R.M. Jones et al, 1997, SLAC-PUB 7539, PAC97.
[3] V.F. Khan, R.M. Jones, 2008, WEPP089, EPAC08.
[4] A. Grudiev, 2008, The nominal CLIC accelerating Structures: CLIC_G; 2nd Collaboration Meeting on X-band Accelerator Structure Design and Test-Program.
[5] A. Grudiev, private communication.
[6] D. Schulte, The Tracking Code PLACET, 2008.
[7] R.M. Jones e*t al*, 2002, SLAC-PUB-9407, LINAC02.

# PREDICTION OF 4ν=1 RESONANCE OF A HIGH INTENSITY LINAC*

D. Jeon#, SNS, ORNL, Oak Ridge, TN 37831, U.S.A.
I. Hofmann, L. Groening, G. Franchetti, GSI, Darmstadt, Germany

*Abstract*

The 4ν=1 resonance of a linac is demonstrated when the depressed tune is around 90°. It is observed that this fourth order resonance is dominating over the better known envelope instability and practically replacing it. Simulation study shows a clear emittance growth by this resonance and its stopband. Experimental measurement of the stopband of this resonance is proposed and conducted in 2008 using the UNILAC at GSI. This study will serve as a benchmarking and guidance for the experiment.

## INTRODUCTION

Recently many high intensity linacs have been designed or constructed like the SNS (USA) [1], J-PARC (Japan) [2], or people are trying to increase the intensity of existing linacs such as the UNILAC of GSI (Germany) [3]. For the high intensity linacs, it is the utmost goal to minimize the beam loss of halo particles by avoiding or minimizing contributions of various halo formation mechanisms. One such mechanism is the envelope instability [4]. So far the high intensity linac design such as the SNS linac has avoided the $\sigma_{ot}$ = 90° phase advance because of the envelope instability [1].

Until 1998, mismatch was the primarily studied mechanism of halo formation. Late 1998, Jeon found a case of halo formation induced by the $2\nu_x$-$2\nu_y$=0 resonance from the space charge potential in the ring [5]. Further studies of halo formation and/or emittance growth by space charge and resonances are reported in [6] and by space charge coupling resonance studies of linac such as [7]. Besides these, halo formation by non-round beam was reported [8] and halo formation by rf cavity [9].

In this paper, we will report about a collaborative effort between FAIR-GSI and SNS concerning the 4ν=1 resonance of a high intensity linac. We are preparing for an experiment to measure the stop-band of this resonance using the UNILAC at GSI. Numerical simulation is performed with 50 000 to 100 000 macroparticles with the PARMILA code [10]. Space charge tune shift is about -20°.

## THE LINAC FOURTH ORDER RESONANCE

The study shows that the 4ν=1 resonance occurs when the phase advance with space charge σ is slightly lower than 90° for a linac just like a ring through the space charge octupole potential for a variety of beams including Gaussian, waterbag, etc.. For the phase advance with space charge σ > 90°, no resonance effect is observed, as shown in Fig. 6.

### *Crossing the Resonance from Below 90 °*

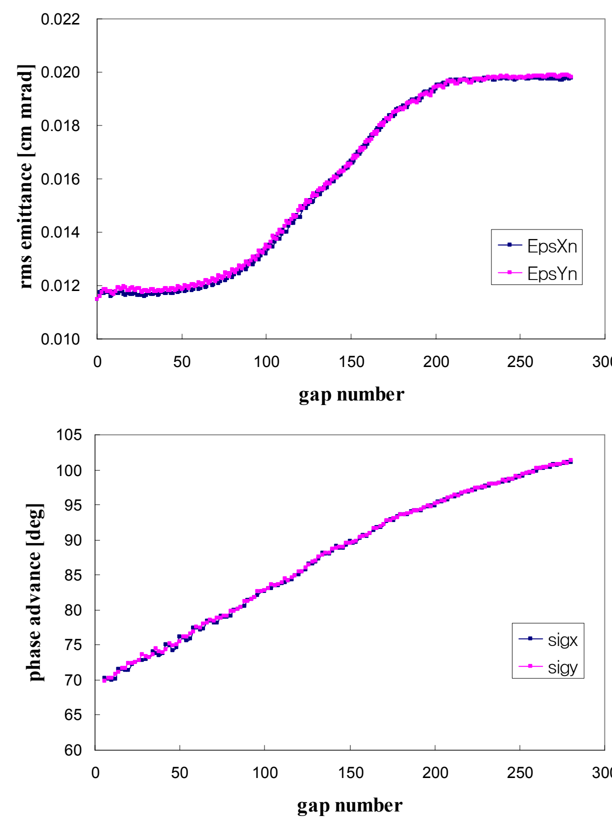


Figure 1: Top plots display rms emittance vs gap number and bottom plots the phase advance with space charge when the beam crosses the resonance from below.

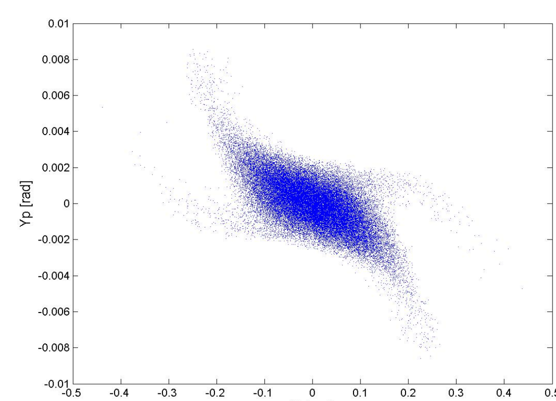


Figure 2: Plot of the beam distribution in Y phase space at the 96th gap. Transport of beam particles along the separatrices is observed.

* See acknowledgement
#jeond@ornl.gov

We performed a simulation of beam crossing the resonance from below 90°. Fig. 1 shows the normalized rms emittance growth as the beam crosses the 4ν=1 resonance together with the variation of the depressed phase advance σ. When the depressed phase advance with space charge σ reaches about 75°, emittance starts to grow. The initial beam is a well matched Gaussian beam to the linac and the emittance growth is solely due to the resonance crossing. The same phenomenon is observed with waterbag beam.

When the beam crosses the resonance from below 90°, the stable fixed points move from afar to the origin and beam particles are transported along the separatrices, not captured by the stable islands. This is well illustrated in Fig. 2.

### *Crossing the Resonance from Above 90 °*

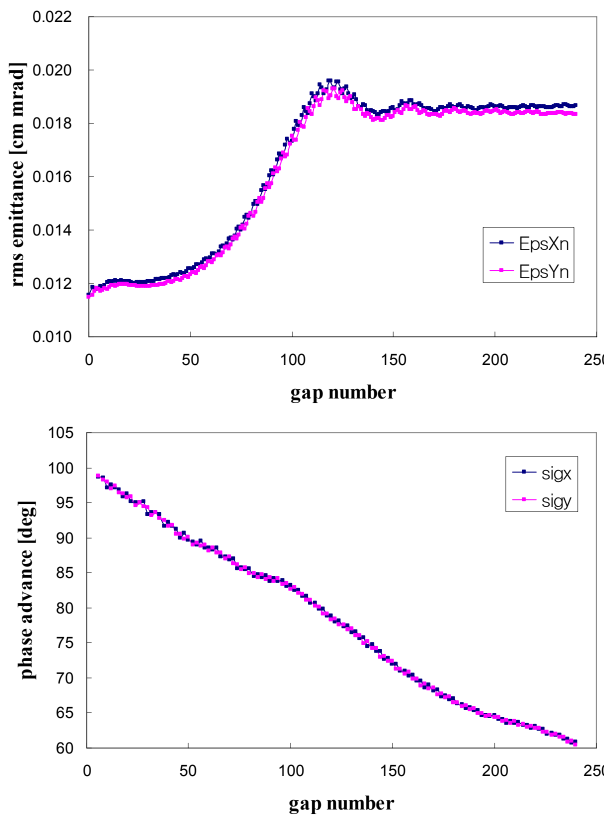


Figure 3: Top plots display rms emittance vs gap number and bottom plots the phase advance with space charge, when the beam crosses the resonance from above.

We performed a simulation of beam crossing the resonance from above 90°. Fig. 3 shows the normalized rms emittance growth as the beam crosses the 4ν=1 resonance along with the variation of the depressed phase advance σ. As the depressed phase advance σ crosses 90°, emittance starts to grow. The initial beam is a well matched Gaussian beam to the linac. For σ > 90°, there is no resonance effect.

When the beam crosses the resonance from above 90°, stable fixed points move away from the origin to afar. Unlike rings, tune change rate is not slow enough for adiabatic capture of beam particles by the stable islands. So beam particles are not entirely captured as illustrated in Fig. 4.

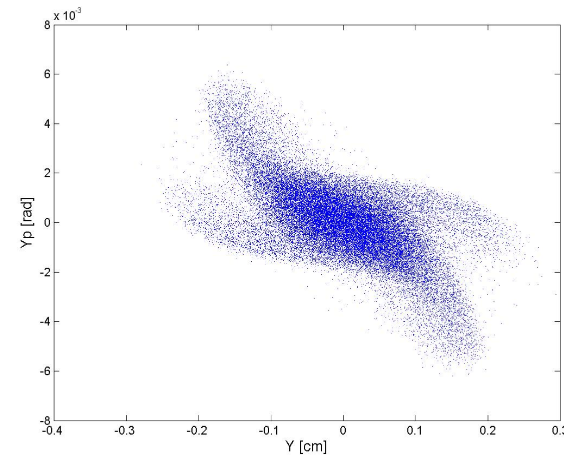


Figure 4: Plot of the beam distribution in Y phase space at the 88$^{th}$ gap.

### *Measurement of the Stopband*

We are preparing for an experiment to measure the stop-band of the 4ν=1 resonance with an emittance scanner installed right after the first DTL tank A1 of the UNILAC. Figure 5 displays the simulation of the sum of transverse rms emittances vs. zero current phase advance. About 45% of rms emittance increase is anticipated due to the resonance.

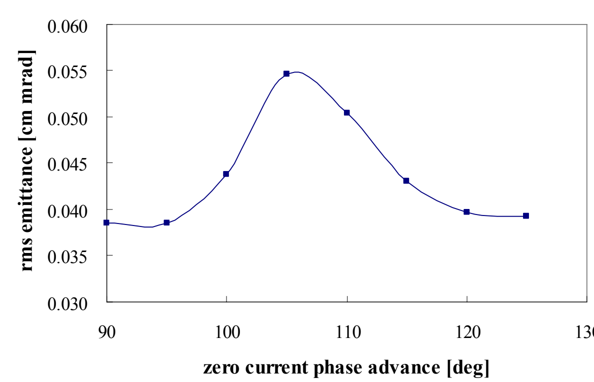


Figure 5: Plot of the sum of the normalized rms emittance $\varepsilon_x + \varepsilon_y$ vs. zero current phase advance.

### *Envelope Instability??*

High intensity linac design has avoided the 90° phase advance because of the well known envelope instability. Our study indicates that the 4ν=1 resonance is dominating over the envelope instability and practically replacing it. We did not observe the envelope instability during the simulation for the phase advance around 90° as shown in Fig. 5. For $90° \leq \sigma_o \leq 95°$, no appreciable emittance growth is observed. It should be noted that the initial beam is well matched to the linac.

Considering this, it should be stated that the high intensity linac design should avoid 90° phase advance because of the 4ν=1 resonance rather than the better known envelope instability. The effect of the envelope instability can actually be minimized – in theory - by nearly perfect envelope matching, whereas the 4ν=1 resonance is independent of the rms matching.

### *Rms Emittance vs. Phase Advance*

Simulation is done to study the equilibrium rms emittance as a function of the depressed phase advance σ. For this simulation, σ is kept constant throughout the linac. Figure 6 shows plots of the ratio of the final transverse emittance over the initial emittance as a function of the depressed phase advance σ. Rms emittance grows as a power of 3.5 up to 90° and there is no emittance growth beyond 90°. Two cases are simulated and plotted; one is with a tune depression of -23° and the other -20°.

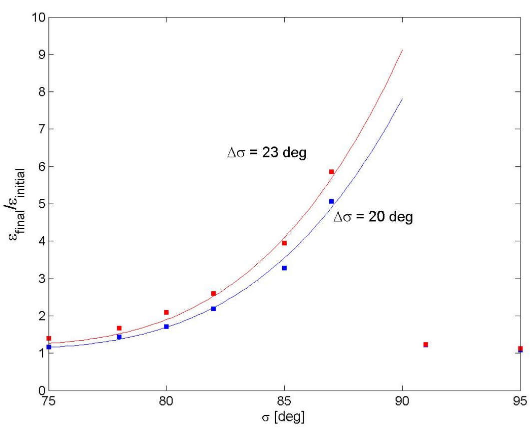


Figure 6: Plots of the rms emittance vs. the depressed phase advance σ. No emittance growth occurs for σ > 90°.

### *Effect of Mismatch*

When strong mismatch is applied to the initial beam distribution, the effect of mismatch is manifested on top of the 4ν=1 resonance, as shown in Fig. 7. Obviously the fourth order resonance remains dominant, and there is not enough time for the envelope instability to take over. In both planes, initial $\beta_x$ and $\beta_y$ are increased by 40%.

## CONCLUSION

The 4ν=1 resonance of a linac is demonstrated through space charge potential when the depressed tune is around 90°. It is observed that this fourth order resonance is dominating over the better known envelope instability and practically replacing it. It needs to be rephrased that the high intensity linac design should avoid 90° phase advance because of the 4ν=1 resonance rather than the better known envelope instability.

## ACKNOWLEDGEMENT

This work is a result of the collaboration between GSI-FAIR and SNS. One of the authors (D.J) is grateful for the hospitality of GSI and the support through the EU-FP6 CARE-HIPPI (contract number RII3-CT-2003-506395). SNS is managed by UT-Battelle, LLC, under contract DE-AC05-00OR22725 for the U.S. Department of Energy.

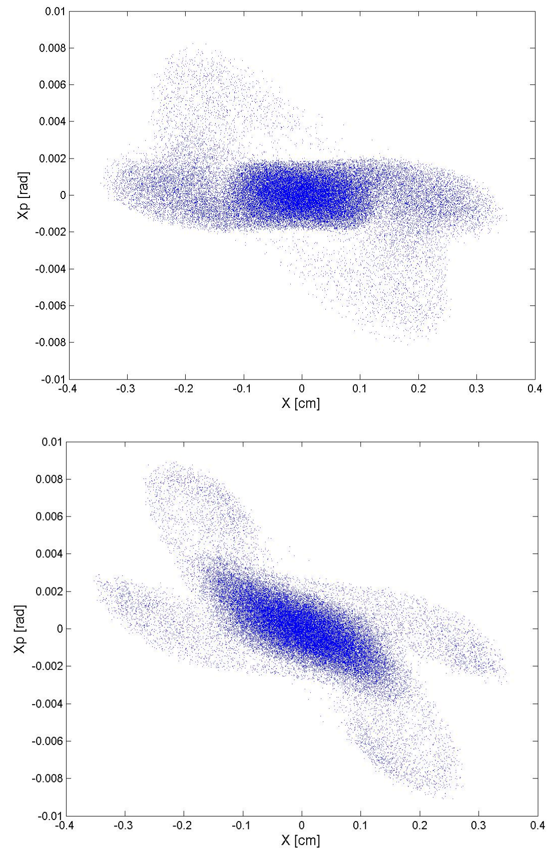


Figure 7: Plots of Beam distribution with mismatch (upper plot) and without mismatch (lower plot).

## REFERENCES

[1] J. Stovall et al., Proc. of 2001 Part. Accl. Conf., Chicago, USA, p. 446.

[2] Y. Yamazaki, Proc. of 2003 Part. Acc. Conf., Portland, USA, p.576.

[3] W. Barth et al, Proc. of 2004 LINAC Conf., Luebeck, Germany, p.246.

[4] I. Hofmann, L.J. Laslett, L. Smith, I. Haber, Part. Acc **13**, 145 (1983).

[5] D. Jeon et al, Phys. Rev. E **60**, 7479 (1999).

[6] G. Franchetti et al, Phys. Rev. ST AB **6**, 124201 (2003).

[7] G. Franchetti, I. Hofmann, D. Jeon, Phys. Rev. Lett. **88**, 254802 (2002).

[8] D. Jeon, Proc. of 2007 Asian Part. Accel. Conf., Indore, India, p.333.

[9] M. Eshraqi, private communication CERN.

[10] J.H. Billen and H. Takeda, PARMILA Manual, Report LAUR-98-4478, Los Alamos, 1998 (Revised 2004).

# TRANSVERSE MATCHING OF THE SNS LINAC BASED ON PROFILE MEASUREMENTS *

Dong-o Jeon#, Oak Ridge National Laboratory, Oak Ridge, TN37831, U.S.A.

*Abstract*

For a high intensity linac such as the SNS linac, it matters to match transversely adequately to minimize the beam mismatch and potential beam loss. The technique of doing the matching using the wire-scanners in series was employed [1]. It was verified that matching was improved through the matching technique based on the beam profile measurements from wire-scanners in series.

## INTRODUCTION

The Spallation Neutron Source (SNS) linac accelerates intense $H^-$ beams to energy of 1-GeV, delivering more than 1.4 MW of beam power to the neutron production target [2]. Being a high intensity linac, a primary concern is the uncontrolled beam loss and radio activation of accelerator components. Mismatch generating beam halo, it is important to accomplish adequate level of transverse matching between sections of linac.

When emittance measurement device is available, minimization of rms emittance proves to be effective in doing the matching as for the SNS DTL (Drift Tube Linac) tank 1 commissioning [3].

Alternatively wire-scanners installed in series can be used to transversely matching between two different structures of the SNS linac [4,1]. During the beam operation runs, the matching technique based on beam profile measurements was tested and the results are presented here. The previous work [5] was for a relatively low beam current around 15 mA. This study is focused on the performance for high current (~ 32 mA) and for an incoming beam with a large envelope oscillation.

## MATCHING DTL TO CCL

We applied the technique based on profile measurements to matching the Drift Tube Linac (DTL) to the Coupled Cavity Linac (CCL). The beam energy is 86.6 MeV coming out of DTL. The peak beam current used for the measurement was 34 mA. We performed a Gaussian fit to the measured beam profile and obtained its beam size $\sigma$. By fitting the beam envelope from the Trace3D code to the wire-scanner profile data, we obtained the input beam Courant-Snyder parameters $\beta$ and $\alpha$, and the beam emittance $\varepsilon$, as shown in Fig. 1. With the beam parameters of the incoming beam determined, the matching quadrupoles are optimized using the Trace3D code to do the matching.

The first four wire-scanners were used by the matching program to predict a better matching. This matching technique is robust for quite high peak current beam. Figure 1 shows the data before the matching exercise and Fig. 2 the data after the matching. The solid circles in Figs. 1 and 2 represent profile measurements from wire-scanners in CCL module 1 and 2. The blue color represents the x beam size and the red the y beam size. It is clear that the matching in x plane is improved significantly and that a slight improvement is observed in y plane (y plane was already close to well matched condition). We observe an overall improvement in matching. The measured normalized rms emittances are $\varepsilon_x$=0.283 and $\varepsilon_y$=0.320 [mm mrad] of the equivalent uniform beam distribution having the same rms beam size as the beam profile.

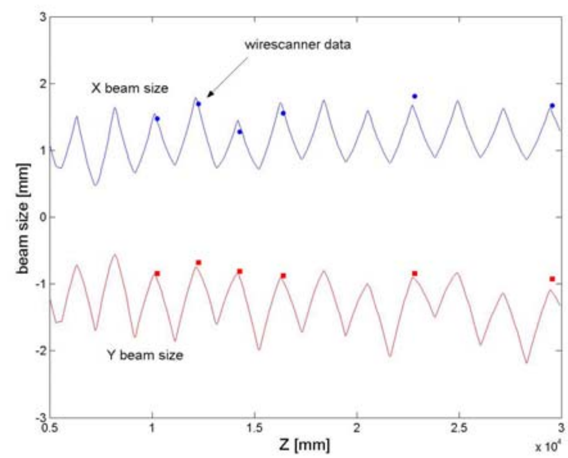


Figure 1: Plots of beam profiles before matching DTL to CCL. Solid lines are plots of beam size $\sigma$ [mm] from the Trace3D program and solid circles are wire-scanner profile data. The peak beam current is 40 mA.

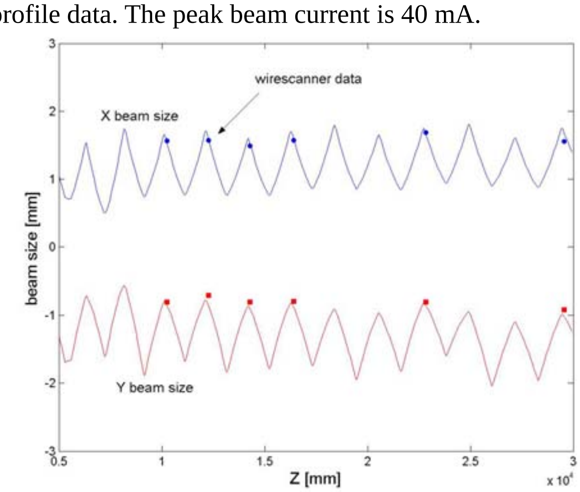


Figure 2: Plots of beam profiles after matching DTL to CCL. Solid lines are plots of beam size $\sigma$ [mm] from the Trace3D program and solid circles are wire-scanner profile data.

* SNS is managed by UT-Battelle, LLC, under contract DE-AC05-00OR22725 for the U.S. Department of Energy.
#jeond@ornl.gov

In the previous work [5], when matching in one plane is improved significantly, matching of the other plane degraded slightly. We improved fitting routine with a modified figure of merits. This routine seems to be robust to a high current beam or to a beam with a significant envelope oscillation as shown in the following section.

## MATCHING SCL TO HEBT

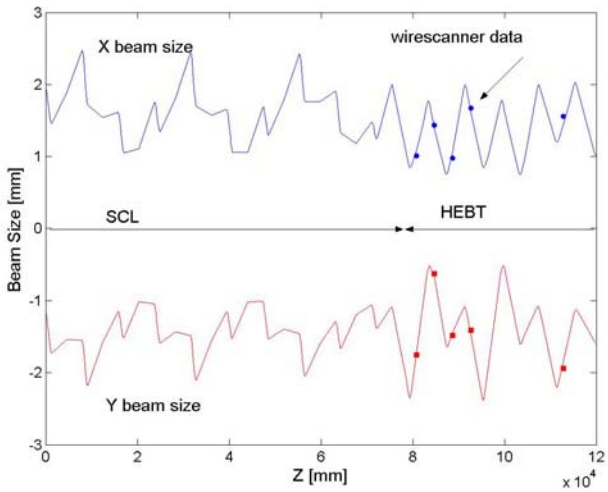


Figure 3: Plots of beam profiles before matching SCL to HEBT. Solid lines are plots of beam size σ [mm] from the Trace3D program and solid circles are wire-scanner measurement data.

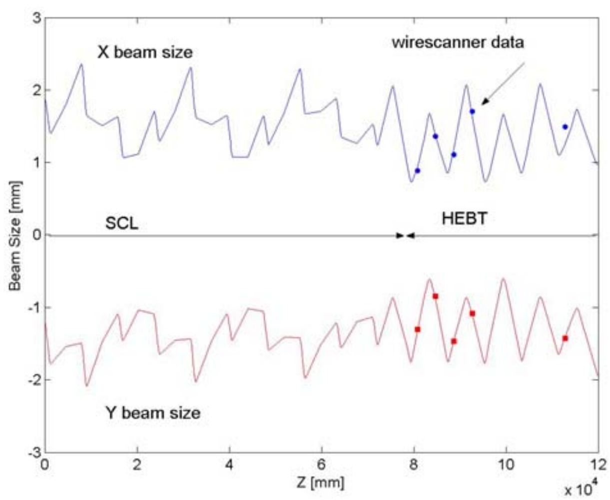


Figure 4: Plots of beam profiles after matching SCL to HEBT. Solid lines are plots of beam size σ [mm] from the Trace3D program and solid circles are wire-scanner measurement data.

We applied the same technique to matching the Superconducting Linac (SCL) to the High Energy Beam Transport (HEBT). The focusing of SCL is provided by doublets and HEBT by FODO. The solid circles in Figs. 3 and 4 represent the beam profile data from the wire-scanners in the HEBT and the solid lines represent simulated beam profile obtained from the Trace3D code. The blue color represents the x beam size and the red the y beam size. It should be noted that there is a mild beam envelope oscillation at the SCL.

By fitting the beam envelope from the Trace3D code to the wire-scanner profile data, we obtained the input beam Courant-Snyder parameters β and α, and the beam emittance ε, as shown in Fig. 3. Table 1 lists the input beam parameters at Z=0 in Fig. 3. $\varepsilon_x$=0.420 and $\varepsilon_y$=0.358 are the normalized rms emittance [mm mrad] of the equivalent uniform beam distribution having the same rms beam size as the beam profile. Figure 3 shows the data before the matching exercise and Fig. 4 the data after the matching. The envelope oscillation in the SCL is pretty severe, resulting in relatively high rms emittance values.

The matching exercise primarily improves the matching in the plane where the mismatch is pronounced. This routine proves to be quite robust even when there is a significant mismatch/envelope oscillation to the incoming beam, as demonstrated in this case.

Table 1: Input Beam Parameters

| | **X plane** | **Y plane** |
|---|---|---|
| ε [mm-mrad] | 0.420 | 0.358 |
| β [m] | 15.107 | 6.556 |
| α | -1.938 | -0.544 |

## CONCLUSION

A study of transverse matching of the SNS linac is performed. Positive results are obtained showing that the matching is improved for high current and significant mismatch. Further matching study will be conducted for other sections of the SNS linac.

## REFERENCES

[1] Dong-o Jeon and J. Stovall, J. Proc. of the 2003 Part. Accel. Conf. (Portland, 2003), p. 2652.
[2] J. Wei et al, Proc. of the 2001 Part. Accel. Conf. (Chicago, 2001), p. 319.
[3] D. Jeon et al, Proc. of the 2004 European Part. Accel. Conf. (Lucerne, Switzerland, 2004), p. 1536.
[4] D. Jeon and J. Stovall, Proc. of the 2002 LINAC Conf. (Gyeongju, Korea, 2002), p. 88.
[5] D. Jeon and P.Chu, Proc. of the 2007 Asian Part. Accel. Conf. (Indore, India, 2007), p. 250.

# PHASE LAW OF A HIGH INTENSITY SUPERCONDUCTING LINAC*

D. Jeon# and J. Galambos, SNS, ORNL, Oak Ridge, TN 37831, U.S.A.

*Abstract*

The importance of a proper phase law is recognized to tune the synchronous phase of each superconducting cavities of a high intensity proton superconducting linac such as the SNS linac. The factors to be optimized are 1) maximizing the longitudinal acceptance 2) better matching throughout the linac and 3) achieving maximum beam energy. The driving force behind this study is how to effectively control the large voltage fluctuation from cavity to cavity, achieving low beam loss and high beam quality.

## INTRODUCTION

Recently many high intensity linacs have been designed or constructed like the SNS (Spallation Neutron Source) [1], and J-PARC (Japan) [2]. Part of the SNS linac is a pulsed superconducting linac (SCL) accelerating from 186 MeV to 1 GeV. There is a significant spread of the cavity field from cavity to cavity as shown in Fig. 1. Besides, there are cavities turned off for various reasons. If the synchronous phase is set to design values which assumes uniform cavity voltage, cavity field variation and off cavities lead to significant perturbation to the beam, potentially leading to beam loss. So the goal is how to 1) preserve beam quality, 2) minimize beam loss and 3) get as high beam energy as possible. In this paper, we report the important factors to be considered in achieving the three goals.

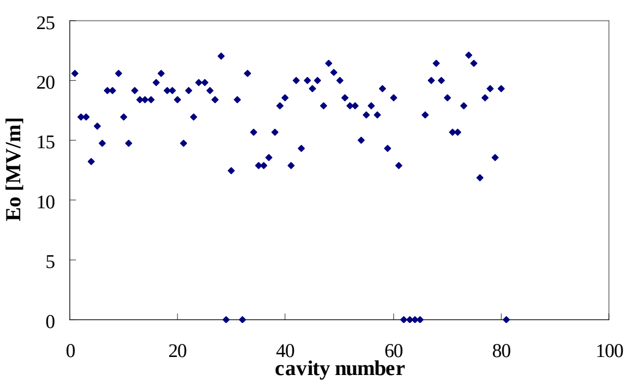


Figure 1: Plot of cavity field Eo vs. cavity number. Quite significant variation is observed besides that six cavities are off.

## IT MATTERS HOW TO SET THE PHASE

Each superconducting cavity of the SNS linac is fed by individual klystron, leaving us a lot of freedom how to set the phase of each cavity. One approach is to vary the synchronous phase $\phi_s$ of each cavity to compensate the variation of Eo from cavity to cavity, hoping to provide smooth focusing across the superconducting linac. We call this method "Smooth Focusing Optics (SFO)" for the sake of convenience. The other approach is to fix the synchronous phase of most of the cavities to design values and vary the phase of a handful of carefully chosen cavities only. We call this method "Constant Phase Optics (CPO)". Figure 2 shows how the synchronous phase of each cavity is set for the two optics.

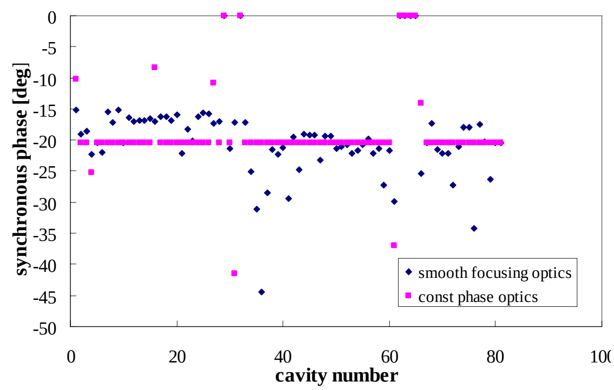


Figure 2: Plot of synchronous phase of the smooth focusing optics in blue and that of the constant phase optics in magenta. Phase of cavities that are off is set to zero in the plot.

### *Longitudinal Acceptance Matters*

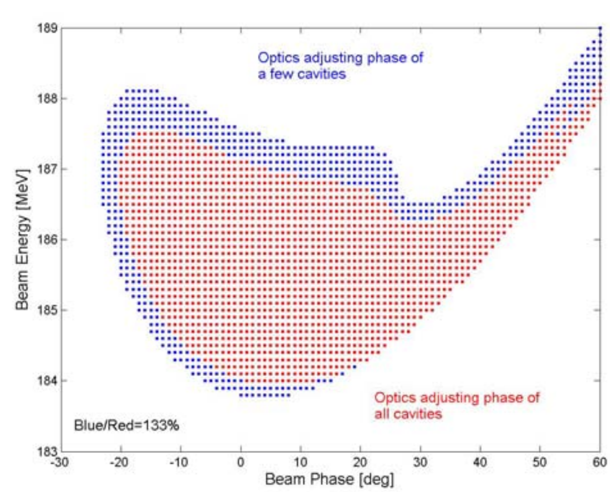


Figure 3: Longitudinal acceptance of the two optics. The constant phase optics in blue produces 33 % bigger acceptance than the smooth focusing optics in red.

* SNS is managed by UT-Battelle, LLC, under contract DE-AC05-00OR22725 for the U.S. Department of Energy.
#jeond@ornl.gov

One of the primary advantages of setting the phase of each superconducting cavities according to the constant phase optics is that we can get bigger longitudinal acceptance, even though the output beam energy is the same (less than 0.5 MeV different). As shown in Fig. 3, the acceptance of the constant phase optics produces about 33 % bigger acceptance than the smooth focusing optics. The blue solid squares represent the acceptance of the constant phase optics and the red squares the smooth focusing optics.

At the end of each beam operations, survey of residual activation throughout the entire accelerator is routinely performed. Figure 4 shows the residual activation of the superconducting linac measured at 30 away. The 11/26/2007 120 kW run was performed with the “Constant Phase Optics (CPO)”, while the 08/13/2007 run and 08/27/2007 run with 150 kW and 160 kW of beam power with the “Smooth Focusing Optics (SFO)”. Radiation survey indicates that the residual activation of 340 kW run is comparable to that of 160 kW run.

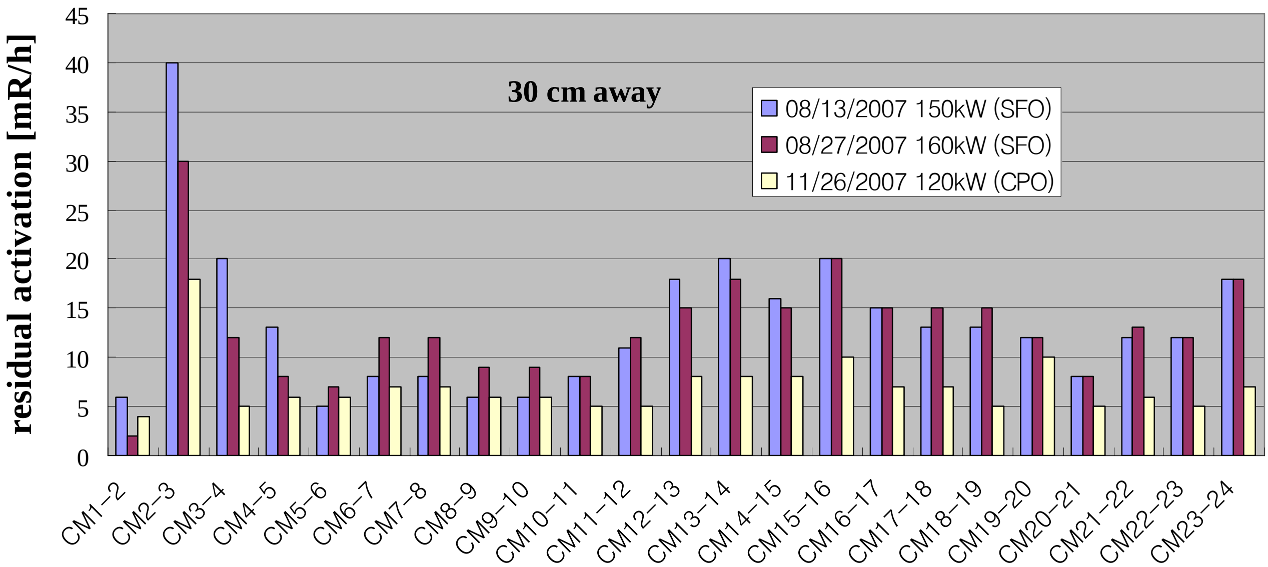


Figure 4: Plots of the residual machine activation 30 away after the beam operation for three different run periods. The 150 kW (08/13/2007) run and the 160 kW (08/27/2007) run used the “Smooth Focusing Optics (SFO)”, while 120 kW (11/26/2007) run the “Constant Phase Optics (CPO)”. CM1-2 means that between the cryo-module 1 and 2.

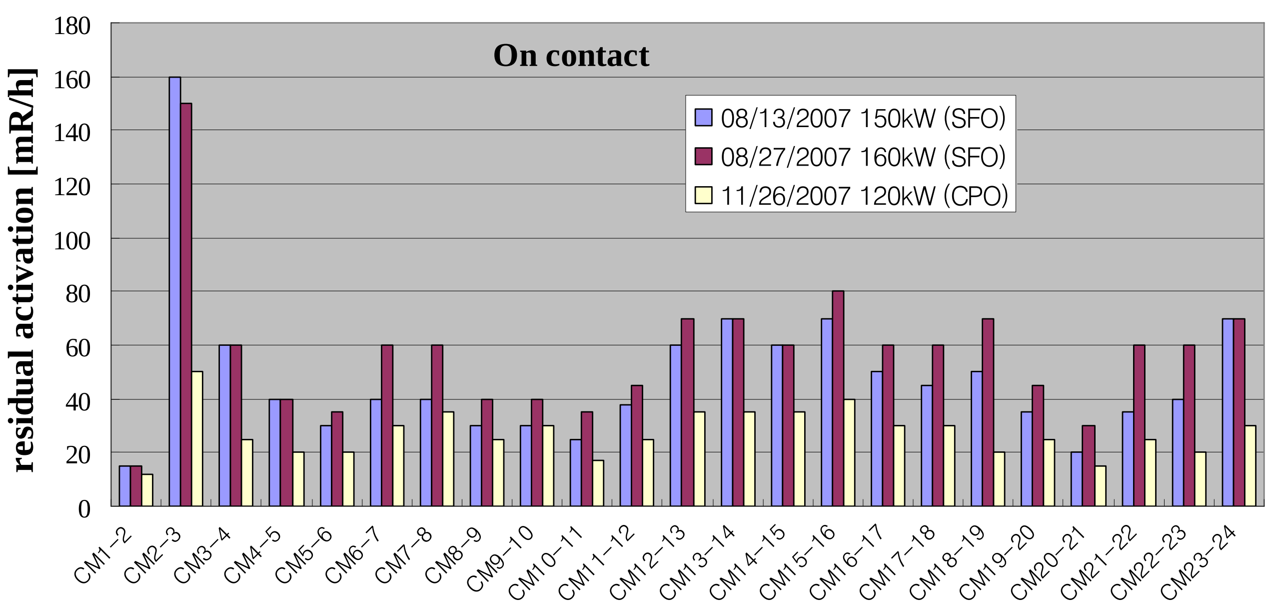


Figure 5: Plots of the residual machine activation on contact after the beam operation for four different run periods. The 150 kW (08/13/2007) run and the 160 kW (08/27/2007) run used the “Smooth Focusing Optics (SFO)”, while 120 kW (11/26/2007) run the “Constant Phase Optics (CPO)”.

Table 1: Cumulative Beam Power

| | **Cumulative beam power** | **Time lapsed for survey** |
|---|---|---|
| 08/13/2007 | 27970 kWh | 40 hours |
| 08/27/2007 | 25350 kWh | 63 hours |
| 11/26/2007 | 22450 kWh | 49 hours |

Table 1 lists the cumulative beam power delivered to the target in [kWh] and the time between the radiation survey and the production run for each period listed on the left.

### *Matching Matters*

Matching is also an important factor as shown in Fig. 6. Without proper matching, the orientation of the acceptance may not line up with the beam distribution, more prone to spilling beam particles outside the rf bucket, even though the overall area of the acceptance may remain the same. The acceptance in Fig. 3 is for well matched case. It should be noted that the difference primarily in orientation and also in shape.

Figure 7 shows the Trace3D envelope profiles for the constant phase optics used in the November, 2007 run and for the smooth focusing optics used in the August, 2007 run. The cavity field and phase are shown in Figs 1 and 2. For these runs, six superconducting cavities were off. Judging from the longitudinal beam envelope, the longitudinal matching from the medium beta section to the high beta section is marginal for the smooth focusing optics used then.

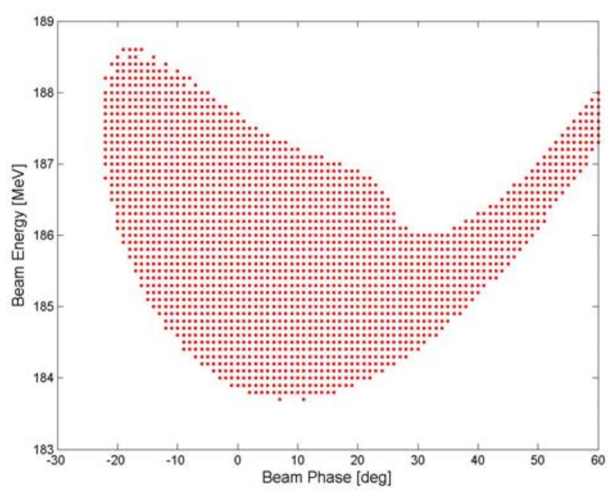


Figure 6: Plot of the longitudinal acceptance when the phase of all cavities are set to the design values without any matching.

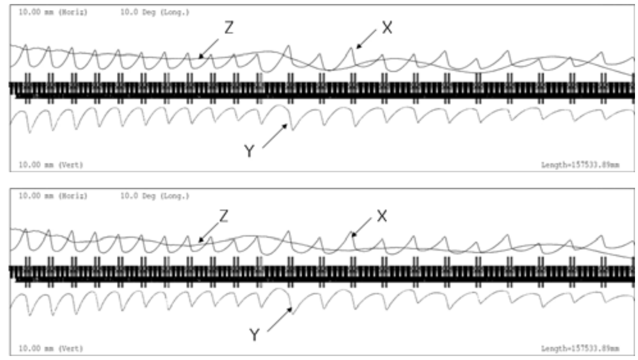


Figure 7: Trace3D envelope profiles for the smooth focusing optics (upper plot) and those for the constant phase optics (lower plot).

## CONCLUSIONS

Study shows that it is important to get as big a longitudinal acceptance as possible while maintaining reasonable matching throughout the superconducting linac in order to minimize beam loss for the SNS superconducting linac.

## REFERENCES

[1] J. Stovall et al., Proc. of 2001 Part. Accl. Conf., Chicago, USA, p. 446.
[2] Y. Yamazaki, Proc. of 2003 Part. Acc. Conf., Portland, USA, p.576.

# PRECISE CONTROL OF COOLING WATER SYSTEM FOR STABILIZATION OF 125 MEV LINAC AT LEBRA*

T.Sakai#, T.Kuwada, M.Inagaki, I.Sato, ARISH, Nihon University, Tokyo, 102-8251, Japan
T.Tanaka, K.Hayakawa, Y.Hayakawa, Y.Takahashi, K.Nakao, K.Nogami, LEBRA, Nihon University, Funabashi, 274-8501, Japan

## Abstract

The 125-MeV linac at the Laboratory for Electron Beam Research and Application (LEBRA) in Nihon University has been used for the generation of the near-infrared FEL and the Parametric X-ray Radiation (PXR). Currently the FELs from 0.855 to 6μm and the PXR X-rays from 5 to 20keV are available at LEBRA.

Precise experiments using the light sources require a high stability in both the wavelength and the intensity of the lights. Though the linac was operated with the cooling water stabilized at 30±0.2°C, periodical fluctuation of the electron beam energy and the beam orbit suggested that the stability of the cooling water temperature was not sufficient. With this condition a large fluctuation (±15%) was observed for the PXR intensity.

After the improvement of the fine cooling water system and the water flow path, fluctuation of the cooling water temperature at the supply head of the accelerating tubes and the electromagnets was suppressed to within ±0.01°C. As a result of the improvement the PXR intensity fluctuation at the X-ray output port has been suppressed to within ±2% for the operation over several hours.

## INTRODUCTION

Research of a high performance electron linac for the generation of Free Electron Laser (FEL) and Parametric X-ray Radiation (PXR) has been continued at the Laboratory for Electron Beam Research and Application (LEBRA) of Nihon University as a joint research with the High Energy Accelerator Research Organization (KEK) [1],[2]. The experiments using coherent X-rays or FELs generally require a high stability electron beam in order to keep high spatial definition and stability of wavelength and intensity.

The electron beam from the linac at LEBRA was stabilized with the klystron RF phase feedback and the beam energy feedback systems [3]. Then the work on the beam stabilization has been devoted to the improvement of the linac cooling water system, because it was found that the effect of the temperature change in the linac cooling water was not sufficiently suppressed by the feedback systems. This paper reports on the achievement of the precise stabilization for the accelerator cooling water temperature and the resultant effect on the stability of the light sources.

*Work supported by Nihon University Research Grant for Assistants and Young Researchers (2007), and "Academic Frontier" Project for Private Universities: matching fund subsidy from MEXT, Japan, 2000-2004 and 2005-2007.
#sakai@lebra.nihon-u.ac.jp

## LEBRA 125MEV ELECTRON LINAC

The linac consists mainly of the 100kV DC electron gun, the pre-buncher, the buncher and the three 4m long regular accelerating structures. The accelerating RF has been powered by two S-band klystrons (the peak output power of 20MW has been achieved at the repetition rate of 12.5Hz and the pulse duration of 20μs) [4]. After the improvement of the linac cooling system the accelerating structures, the bending magnet coils and the PXR Si target crystal have been cooled with the water precisely controlled by a single fine cooling unit. On the other hand, the klystrons, the klystron focus coils and the RF dummy loads have been cooled with the coarse cooling water. The layout of the LEBRA electron linac is shown in figure 1, and the specifications of the linac are listed in table 1.

The saturated FEL lasing has been obtained in the wavelength region of 0.855-6μm, with the maximum macropulse output energy of approximately 60mJ/pulse at a wavelength of 1725nm [1]. The PXR generator covers the X-ray energies from 5 to 20 keV by using Si(111) planes as the target and the second crystals[2]. These light sources have been used for the variety of user's experiments [2],[5].

Table 1: Specifications of the LEBRA Electron Linac

| | | |
|---|---|---|
| Maximum Energy | 125 | MeV |
| DC gun voltage | -100 | kV |
| Accelerating RF frequency | 2856 | MHz |
| Klystron peak RF power | 30 | MW |
| Number of klystrons | 2 | |
| Macropulse duration | 5~20 | μs |
| Repetition rate | 2~12.5 | Hz |
| Macropulse beam current | 200 | mA |
| Energy spread(FWHM) | 0.5~1 | % |

## PROBLEMS IN THE COOLING WATER SYSTEM

The diagram of the original water flow path in the cooling system for the LEBRA linac is shown in figure 2. The water temperature in the fine cooling system was 30 ±0.2°C at the normal operation. The fluctuation of the PXR intensity measured using an ion chamber was approximately ±15% of the average value, strongly depending on the change in the cooling water temperature. By adjusting the control parameters of the fine cooling

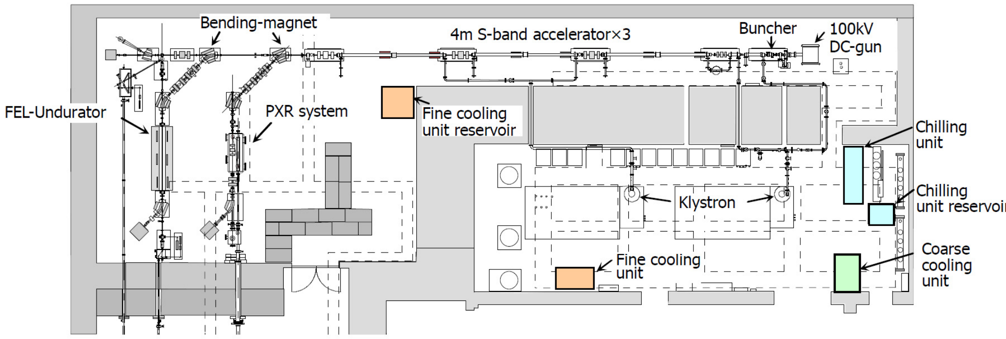


Figure 1: Layout of the 125MeV electron linac at LEBRA.

system the fluctuation of water temperature was suppressed to within ±0.1°C and the dependence of the X-ray intensity became insignificant. Then, however, the main source of the intensity fluctuation still as large as ±10% was found to be the vibration of the Si target caused by the high pressure flow of the cooling water.

The investigation of the water flow path revealed another problem of the fine cooling system. The fast change in the temperature of the chilled water caused by on/off of the compressor was found to be transmitted instantly from the chilling unit to the accelerating tubes and the bending magnets, which resulted in the fluctuation of the energy and the position of the electron beam. This implied that the action of the three-way valve was not sufficiently fast to compensate the rapid change of the chilled water temperature.

The stability of the coarse cooling water temperature was sufficiently good for a coarse cooling system. However, the klystron output RF phase was obviously

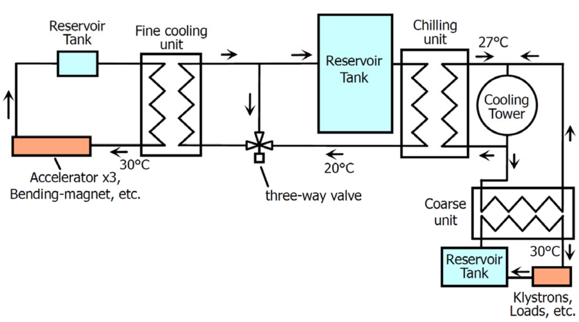


Figure 2: The diagram of the original water flow path in the cooling system for the LEBRA linac.

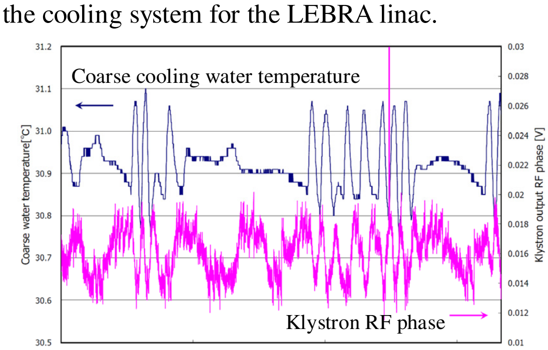


Figure 3: The behaviours of the coarse water temperature and the klystron output RF phase.

depending on the coarse cooling water temperature as shown in figure 3. The temperature of the coarse cooling water at the normal operation was controlled by the action of the three-way valve following to the changes in the temperature of the coarse cooling water itself and the water recirculated through the cooling tower. A rapid change in the temperature of the water from the cooling tower was caused by on/off of the compressor in the chilling unit as well as the cooling fan in the cooling tower. Therefore, the action of the chilling unit had a strong effect on the fluctuation of the output RF phase of the klystron.

## IMPROVEMENT OF COOLING WATER TEMPERATURE STABILITY

### [illegible] C[illegible] Wa[illegible] S[illegible]

Improvement of the cooling water system was undertaken in two steps. In the first step, the setup of the fine cooling system was changed as follows. An additional three-way valve was placed in order to regulate the temperature of the chilled water recirculating through the fine cooling unit. The direction of the fine cooling water flow was reversed so that the rapid change of the water temperature induced in the heat exchanger was reduced in the reservoir tank before flowing through the accelerating tubes and so on, which worked quite effectively in combination with the increase of the reservoir tank volume from 120L to 800L. Then, the cooling water for the PXR Si target was separated from the main path, directly returned to the reservoir tank in order to bypass the high pressure water pump and avoid

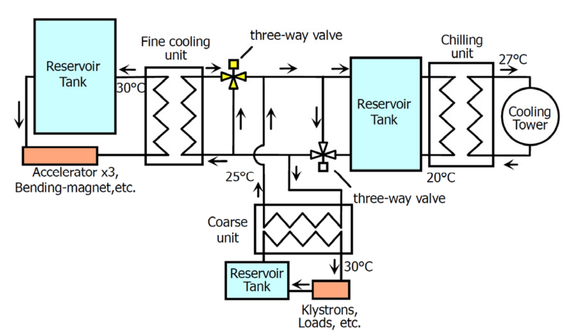


Figure 4: The diagram of the improved cooling water system.

the vibration of the target.

In the second step, the setup of the coarse cooling system was changed. The cooling water from the cooling tower was replaced by the chilled water, because the fluctuation of the regulated chilled water temperature was less than ±0.1°C which was far more preferable than the former for the precise control of the coarse cooling water temperature. The diagram of the cooling water system after the improvement is shown in figure 4.

## [illegible]/[illegible]

After the improvement of the fine cooling water system and the water flow path, the fluctuation of the cooling water temperature at the supply head of the accelerating tubes and the electromagnets was stabilized to 30±0.01°C. On the other hand, the coarse cooling water temperature was stabilized to 30±0.05°C. The behaviours of the cooling water temperatures over a few hours in the original and the improved setups for the fine and the coarse cooling water systems, respectively, are compared in figure 5. The water temperature was measured using an Extremely-Thin-Platinum-Resistance-Thermometer (ETPRT, 0.2 mmt). As shown in figure 6, the X-ray intensity fluctuation measured at the X-ray output port has been reduced from ±10% to ±2% by the improvement of the fine cooling water system. Due to a high stability of the electron beam and the X-ray intensity, the X-ray image by the diffraction enhanced imaging (DEI) method has been obtained clearly. The DEI image of a tetra fish is shown in figure 7.

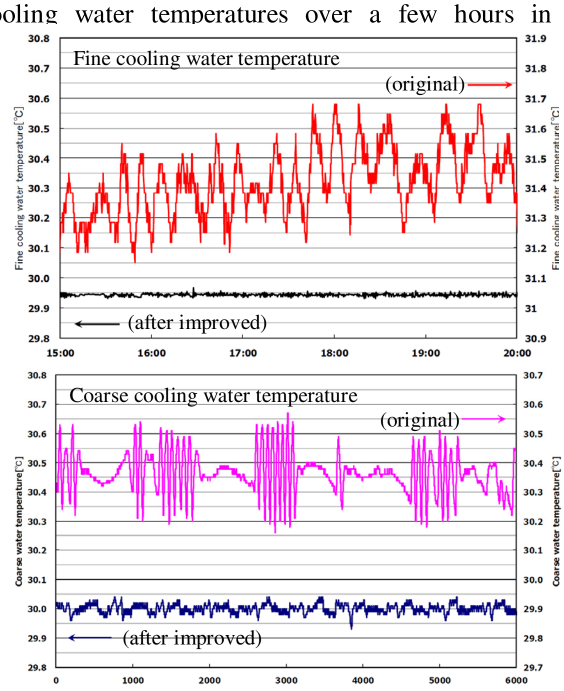


Figure 5: The comparison of the water temperature between the original and the improved setups for the fine and the coarse cooling system, respectively.

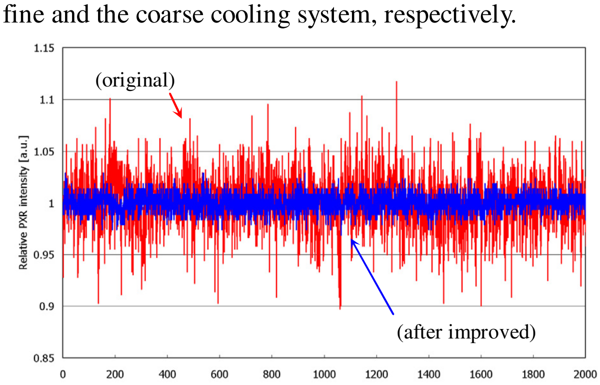


Figure 6: The comparison of the X-ray intensity fluctuation between the original and the improved fine cooling system.

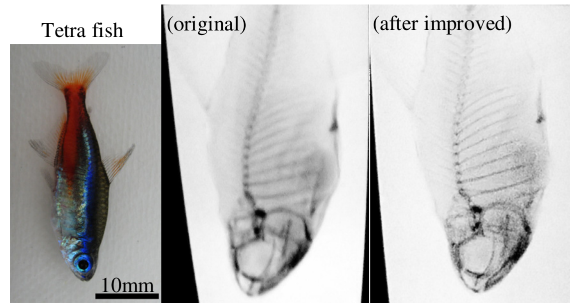


Figure 7: DEI images of a tetra fish taken with the original and the improved cooling water system, respectively (16keV, exposure time 15min (net 21ms) using the IP.).

## CONCLUSION

Precise experiments using the FEL or the PXR beam require a very high stability in both the wavelength and the intensity of the light sources. After the improvement of the cooling water system, the temperatures of the fine and the coarse cooling water systems were stabilized to 30±0.01°C and 30±0.05°C, respectively. Combined with the improvement of the water flow path, the PXR intensity fluctuation at the X-ray output port has been suppressed to within ±2%, resulting in appreciable effect in the DEI experiment using PXR.

## REFERENCES


[1] K.Hayakawa, et al,. "Operation of Near-infrared FEL at Nihon University", Proceedings of FEL 2007, Novosibirsk, Russia, p114-117.

[2] Y.Hayakawa, et al,. "Dependence of PXR beam performance on the operation of the pulsed electron linac", NIMB, Vol 266, Issue 17, 2008, p.3758-3769.

[3] K.Nakao, et al,. "Control and support system for LEBRA FEL Operation", the 30th International Conference on Free Electron Laser 2008, (Geyongju, Korea), in submission.

[4] T.Sakai, et al,. "S-Band Klystron for Long Pulse Operation", Proceedings of the 21st International Linear Accelerator Conference (LINAC2002, Gyeongju, Korea, 2002.8), p.712-714.

[5] T.Sakae, et al,. "Wavelength Dependency and Plasma Ablation of Free Electron Laser Irradiation to Dental Hard Tissues",JJSLSM,Vol.29 No.2(2008)p.106-111.

# CONTROL SYSTEMS FOR LINAC TEST FACILITIES AT FERMILAB*

J. Patrick and S. Lackey, Fermilab, Batavia, IL, U.S.A.

*Abstract*

Fermilab is constructing superconducting RF test facilities for development of technologies to be used in future linear accelerator projects. Two of these facilities, the High Intensity Neutrino Source, (HINS) and the New Muon Laboratory, (NML) are proto-type linacs which will run with beam. Originally the NML facility was primarily an R&D facility for the proposed International Linear Collider. Now both HINS and NML are focused on R&D for the Project X [2] high intensity proton linac proposed for Fermilab. The requirements for these facilities vary but all involve collaboration and flexibility for integrating various new instruments. Tight timing requirements and automation are also required. Some facilities require integration into the existing Fermilab controls system. The controls also must be robust so as not to interfere with the main purpose of the facilities. We will outline the plan for accomplishing this task as well as the current status.

## STATUS AND REQUIREMENTS

### *HINS*

HINS (High Intensity Neutrino Facility) [2] is a 60 MeV proton or H- accelerator being built in the Meson Detector Building at Fermilab. It consists of an ion source, RFQ, room temperature and superconducting RF cavities, focusing solenoids, and diagnostic instrumentation. It is initially using an instance of the SNS low level RF system [3] to control the klystron. This =and a desire to create graphical user interfaces easily without programming resulted in the decision to use EPICS for the HINS control system. The SNS LLRF system will be replaced with a new design within a year to accommodate longer pulse lengths and control multiple cavities per klystron using vector modulators.

As in any pulsed machine, it is important to be able to correlate data from the various front ends and instruments. Special time stamping which includes either pulse identification and/or synchronization across computers will be required.

### *NML*

The NML facility is intended to test cryomodules developed for the ILC or the proposed Project X linac. Initially RF testing on a single cryomodule will be performed with no beam. Eventually the facility will support electron beam operation through 3 cryomodules at energies up to 750 MeV. The NML facility is a stand alone system which will not have to interoperate with the rest of the Fermilab complex. The low level RF system presently in use is from DESY and was developed in the DOOCs control system. There may be equipment which other laboratories may bring for testing purposes but the main objective of this facility will be the testing of the cryomodules themselves. The correlation of data by RF pulse is a requirement for NML as well.

The aggressive schedule demands that especially the cryogenic system and RF system be controllable this fall. Depending on the funding profile, beam will come somewhat later. For this reason, the Fermilab Control System will be used at NML.

There is an NML control room with operator consoles but it will most likely not be manned 24 hours per day so some oversight at least during off hours will be required.

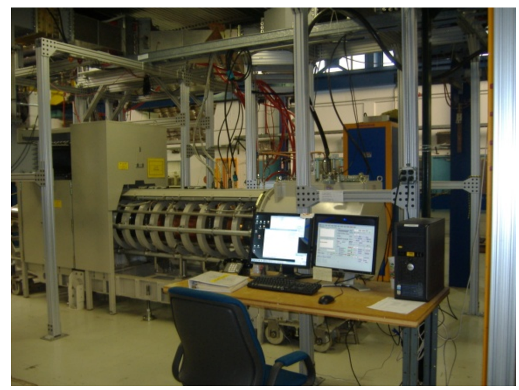

Figure 1: HINS Console and Klystron.

### *HTS*

The Horizontal Test Stand is also in the Meson Detector Building and has been operating for the past year. The purpose of this facility is to test dressed cavities at full RF power before they are installed in cryomodules. It makes use of the DOOCs based low level RF system as well as EPICs input/output controllers for processing loops and interfacing to systems such as vacuum and high level RF interlocks and control.

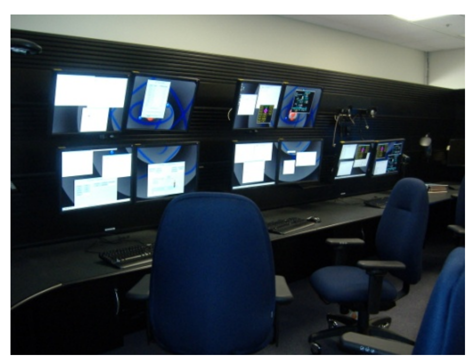

Figure 2: NML Control Room.

* Operated by Fermi Research Alliance, LLC under Contract No. DE-AC02-07CH11359 with the United States Department of Energy

### *Operational Considerations*

From the view point of the Operations Department as well as the Controls Department, it is much preferred that one control system be used to control all of these areas rather than multiple, parallel control systems; one alarm handler, one method of data logging, one database, one graphical user interface, etc. The operations staff will be located in one location, the Accelerator Division Main Control Room.

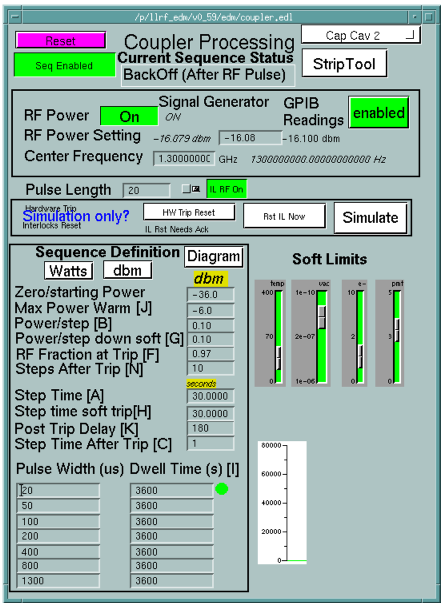


Figure 3: HTS Coupler Processing GUI

## PHILOSOPHY AND GOALS

Accelerator control systems are often required to integrate disparate systems such as LabView or SCADA systems into one global, cohesive control system.

It is our preference to maintain one standard protocol within the system rather than incorporate a variety of protocols. This implies that the integration be accomplished at the lowest level possible.

The Fermilab Control System offers some facilities that are lacking in some other systems which we find extremely useful. These include most importantly, the logging of settings, the parameter page, fast time plots and snapshots, and a central device database.

There are however some aspects of other control systems which would be very useful to add to our system such as a modern graphical display builder, built in mechanisms for simple automation or PID loops, and easy to use front end builders. Extending our controls protocol to enable data correlation is also a goal.

These test areas can be the opportunity to incorporate new functionality into our system while the complex is operating without adversely affecting operation of the collider and neutrino programs.

If successful, the HINS linac may become the front end of the Project X linac. In which case, the HINS control system would need to interface with the rest of the Fermilab controls system.

Project X also is a collaborative effort which means instruments and equipment will be developed at other institutions to be integrated into the system at Fermilab. Many of these institutes already use and understand EPICS and would be more comfortable supplying EPICS drivers for their equipment. All of this implies integration of EPICS into the Fermilab control system in some fashion.

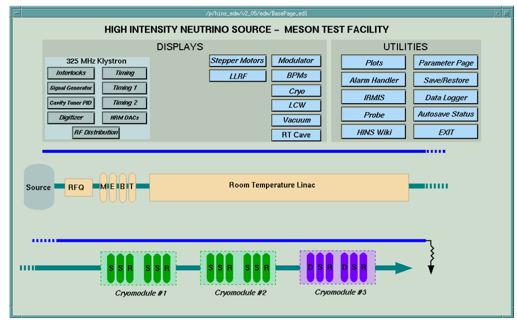


Figure 4: HINS Controls Base Page.

## POSSIBLE SOLUTIONS

The TINE control system in use at DESY has solved a similar problem by incorporating a TINE task in the EPICs IOCs and DOOCs front ends [4]. We are investigating how to implement a similar approach in our system.

We have a graphical user interface builder which has been in use for some time but has functional limitations. We are increasing the functionality of our GUI builder. Also an extension for the EPICs GUI builder, edm, has been created to interface directly with the Fermilab control system protocol.

## SUMMARY

Superconducting RF Test facilities at Fermilab have been run using a mix of control systems, including EPICS and DOOCS, independent of the main accelerator complex. As these efforts have become focused on R&D for the future Project X linac at Fermilab, it has become a goal to provide more commonality and interoperability between these facilities and the main Fermilab control system. It is planned to support EPICS IOCs and selected tools in the main system for cases where that may be the appropriate choice for some subsystem. These facilities will provide a test bed for the future Project X linac control system.

## ACKNOWLEDGEMENTS

This work is the result of the efforts of people from the Accelerator, Computing and Particle Physics Divisions at Fermilab. The authors would like to also thank those from Argonne, DESY and the Spallation Neutron Source who have answered many EPICS, DOOCs and TINE questions.

## REFERENCES

[1] S. Nagaitsev, "Fermilab's Project X", this conference; http://projectx.fnal.gov.

[2] R. Webber, "Overview of the High Intensity Neutrino Source Linac R&D Program at Fermilab", MO301, this conference.

[3] M. Champion, et. al., "The SNS Accelerator Low Level RF Control System", Proc. Particle Accelerator Conference, Portland, OR, June 2003.

[4] P. Duval, et. al., "The Babylonization of Control Systems", Proc. ICALEPCS 2003, Gueongju, Korea, October 2003.

# THE DARHT DATA ACQUISITION, ARCHIVAL, ANALYSIS, AND INSTRUMENT CONTROL SYSTEM (DAAAC), AND NETWORK INFRASTRUCTURE.*

R. Archuleta, L. Sanchez, LANL, Los Alamos, NM 87545, USA

*Abstract*

The Dual Axis Radiographic Hydrodynamic Test Facility (DARHT) at Los Alamos National Laboratory is the world's most advanced weapons test facility. DARHT contains two linear accelerators for producing flash radiographs of hydrodynamic experiments. High-speed electronics and optical instrumentation are used for triggering the accelerators and collecting accelerator data. Efficient and effective diagnostics provide basic information needed to routinely tune the accelerators for peak radiographic performance, and to successfully monitor the accelerators performance. DARHT's server and network infrastructure is a key element in providing shot related data storage and retrieval for successfully executing radiographic experiments. This paper will outline the elaborate Data Acquisition, Archival, Analysis, and Instrument Control System (DAAAC), as well as the server and network infrastructure for both accelerators.

## INTRODUCTION

The DARHT facility consists of two accelerators, DARHT-I and DARHT-II. The data acquisition systems are elaborate and heavily instrumented with beam and pulse power diagnostics. Since accelerator data storage and retrieval is crucial in monitoring and executing radiographic experiments, the server and network infrastructure must be isolated and reliable.

## DATA ACQUISITION SOFTWARE

DARHT-I and DARHT-II use the Data Acquisition, Archival, Analysis, and Instrument Control System (DAAAC, V4.0) software package from Voss Scientific [1]. This software is used for automating remote instrumentation setup and control, documentation, data archival, and data analysis. The DAAAC software runs on computers running the Windows XP operating system.

The user interface consists of five modules; Archive, Acquire, Analyze, CalMan, and NetCom which operate as one system (see Figure 1).

* This work supported by the US National Nuclear Security Agency and the US Department of Energy under contract DE-AC52-06NA25396

LA-UR-08-06026

The Archive module is the database management tool which allows users to select databases, import or export data, and organize and transfer data. This module manages the various databases that have been created under DAAAC. It provides access to waveforms, images, single point data, informational notes, and accelerator diagnostic data logs that have been stored into a particular database. The Analyze module is the data analysis display tool which is used for examining and processing waveforms, single point data, images, informational notes, and accelerator diagnostic data logs.

Raw and processed data is shown by this module after the data is captured by the Acquire module and processed by the CalMan module. Once the data is displayed by this module it can be examined using tools that apply directly to the data presentation. These tools include such mechanisms as cursors, combining data into single plots, sub-sampling data or computing Figures of Merit (FOMs). In addition to FOMs, there are other tools for performing various mathematical functions. The Acquire module manages instrumentation communication, and controls acquisition sequence and automatic data processing. The CalMan module is used for documenting every channel's signal path, providing a graphical display of the test setup, and organizing the signal line components. The NetCom module is the mechanism that coordinates actions between the other DAAAC modules and the Microsoft Structured Query Language (SQL) Database. The DAAAC architecture uses inter-process communication (IPC) to exchange information between the five modules to operate as a single integrated system [1].

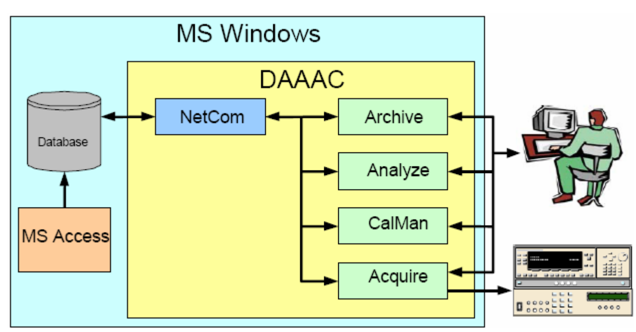


Figure 1: The DAAAC modules.

An additional DAAAC embedded piece of software is the Data Migration tool which migrates data from each accelerator SQL database into Microsoft Access database files. This migration allows for remote users to access the data without having SQL software to poll data from the SQL database elevating the risk of data loss and corruption of the database. The migrated Access databases are also used as a backup to the SQL database. If the accelerator's SQL database data becomes corrupt or lost it can be fully restored using the Access databases causing minimal accelerator down time. DARHT-I and DARHT-II DAAAC software produces binary data files (FlatFiles) on a per shot basis for further analysis using software created with IDL, a data visualization and analysis software development tool. These FlatFiles are available on a website for user specific access which allows internal and external laboratory collaborators to access accelerator data.

Both DARHT-I and DARHT-II run DAAAC in "Networked" mode which supports several data acquisition stations, each running its own copy of DAAAC (see Figure 2). Each data acquisition station controls and acquires data from its own set of connected instruments. DARHT-I has seven dedicated data acquisition stations and DARHT-II has nineteen dedicated data acquisition stations. Each accelerator has a test director which is the primary DAAAC station that instructs the other stations to perform an acquisition and to transmit data. All data is acquired by data acquisition stations and stored in a database. DAAAC stations running the Analyze module retrieve data from the database for analysis and display. Running DARHT-I and DARHT-II in networked mode allows the test director to perform ganged calibrations on the remote dedicated data acquisition stations. The capabilities of running in a network mode with a test director allows for modifications to the accelerators timing sequence through the test director to the associated data acquisition equipment.

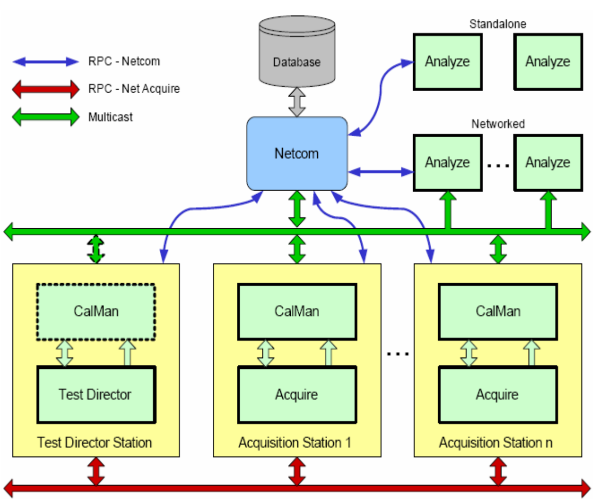


Figure 2: Networked dataflow and communication protocols.

Communication protocols used by Netcom and NetAquire is inter-process communication (RPC) technology that allows a computer program to cause a subroutine or procedure to execute in another address space (commonly on another computer on a shared network) without the programmer explicitly coding the details for this remote interaction. Multicast is the delivery of information to a group of destinations simultaneously using the most efficient strategy to deliver the messages over each link of the network only once, creating copies only when the links to the multiple destinations split. Internet Protocol (IP) Multicast is a technique for a one to many communication over an IP infrastructure, which the implementation occurs on the IP routing level.

## DATA ACQUISITION HARDWARE

The Data Acquisition system for the DARHT accelerators is elaborate and heavily instrumented. Table 1 and Table 2 illustrate the amount of instruments we are using for recording data from and controlling instruments on both DARHT-I and DARHT-II accelerators.

Table 1: DARHT-I Data Acquisition Hardware

| | |
|---|---|
| Server | 1 |
| DAAAC Acquire Stations | 7 |
| DAAAC Analysis Stations | 5 |
| Recording Instruments (45 DC271 Digitizers, and 11 TDS684 Digital scopes) | 56 |
| Digital Delay Generators | 29 |

Table 2: DARHT-II Data Acquisition Hardware

| | |
|---|---|
| Server | 1 |
| DAAAC Acquire Stations | 19 |
| DAAAC Analysis Stations | 9 |
| Recording Instruments (70 DC440, 32 DC282, and 140 DC271 Digitizers) | 242 |
| Digital Delay Generators | 28 |

The type of equipment used for the accelerators are the Compact PCI 21 and 8 slot Acqiris crates from Agilent Technologies which are populated with DC271, DC440, DC282, and DC271V digitizer modules. These crates communicate to our DAAAC Acquire stations using high speed MXI-3 interfaces. The DC271 is a 4 channel, 1 GHz bandwidth and 1-4 Giga Sample per second (GS/s) sampling rate Acqiris digitizer with oscilloscope characteristics. The DC440 is a high-resolution, high-speed dual-channel digitizer for frequency domain applications (2-channel, 100MHz, 400 MS/s and 4 Mpoint acquisition memory). The DC282 is a 4 channel, 2-8 GS/s high-speed digitizer. We also use Stanford Research Systems (SRS) Digital Delay Generators (DG535) for accelerator triggering and timing. These DG535s use the general purpose interface bus (GPIB) communication protocol for interfacing to the DAAAC stations. In addition to the DG535s we use Tektronix TDS 684 oscilloscopes on DARHT-I which also use the GPIB communication protocol.

DARHT diagnostics provide basic information needed to routinely tune the accelerators for peak radiographic performance. Beam position monitors (BPMs) are used to measure beam current and position for both accelerators. DARHT-I has a total of 26 BPMs, and DARHT-II has a total of 31 BPMs which are used on every beam shot. In addition to the BPMs both accelerators use cell voltage monitors (CVM) which are used to measure induction cell accelerating potential. DARHT-I has a total of 64 CVMs, and DARHT-II has a total of 74 CVMs which are also used on every beam shot.

Information needed to monitor the accelerators performance is provided by our diagnostics. DARHT I and DARHT II both have 20 Injector diagnostic parameters including voltages and currents which are used on a per shot basis.

## DARHT SERVER/NETWORK INFRASTRUCTURE

Storage and retrieval of DARHT accelerator data is crucial in monitoring and executing radiographic experiments. The server and network infrastructure must be isolated and reliable.

DARHT-I relies on a data storage server running the NetCom module which is the interface between DAAAC and the Structured Query Language (SQL) Database. This server is running a Microsoft SQL 2005 database which is the repository for DARHT-I diagnostic data and station configurations. DARHT-I and DARHT-II severs are Microsoft Windows 2003 servers which are configured with 1 terabyte of data storage, 4 gigabytes of memory and has a 3.7 gigahertz dual core processor.

DARHT-II also relies on a data storage server running the NetCom module. This server is running a Microsoft SQL 2005 database which is the repository for DARHT-II diagnostic data and station configurations.

DARHT-I and DARHT-II also have a server running a Microsoft SQL 2005 database for storing and retrieving accelerator controls data. These accelerator control parameters such as; pulse power, magnet, and vacuum controls data for both accelerators for monitoring performance.

There are over 90 controls and data acquisition stations throughout the facility. The servers and stations are on a local are network (LAN) (see Figure 3). They are isolated from the outside network. The DARHT accelerators have two domain controllers which are running the Microsoft Windows 2003 Server operating system with Active Directory service installed. Active Directory enables centralized, secure management of the DARHT facility local area network. This network was established to enhance and secure crucial accelerator data and to avoid other network traffic. All diagnostic and control systems within the DARHT facility local area network are on a 1 gigabit per second fiber network which allows for speedy storage and retrieval of accelerator data.

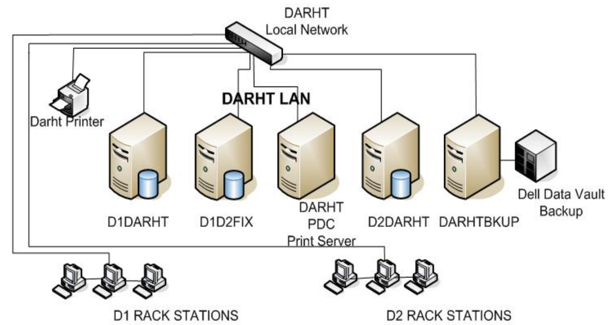


Figure 3: DARHT accelerators local area domain.

A bridge server (see Figure 4) was added as part of the DARHT facility local area network to allow specific users on the Los Alamos National Laboratory open network and the Windows Active Directory (WIN) Domain to access a copy of the accelerator's diagnostic and controls data. This data on the bridge server is synchronized with the data on the data acquisition servers using PeerSync commercial software. To accomplish data storage and retrieval across the DARHT facility local area network and the Laboratory open network the bridge server is configured to operate with dual 1 gigabit per second fiber network interfaces. This bridge server is a Microsoft Windows 2003 file server which is configured with 6 terabytes of data storage, 4 gigabytes of memory and 2.3 gigahertz quad core processor. To insure proper data storage we maintain our own backup system via a tape library storage unit which uses 800 gigabyte (compressed) tapes.

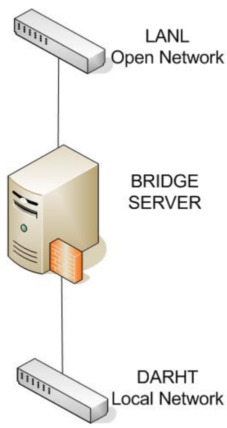


Figure 4: DARHT accelerators bridge and file server.

## SUMMARY

The DARHT accelerator's triggering and data collection is elaborate and heavily instrumented with state-of-the-art diagnostics, server, and network equipment. Efficient and effective diagnostics, server, and network infrastructure is crucial for successfully executing radiographic experiments at DARHT.

## REFERENCES

[1] Voss Scientific Inc., "DAAAC 4.0 User's Manual." Voss Scientific Inc., New Mexico, August 2007, pgs. 1-170, http://www.vosssci.com.

# THE DUAL AXIS RADIOGRAPHIC HYDRODYNAMIC TEST (DARHT) FACILITY PERSONNEL SAFETY SYSTEM (PSS) CONTROL SYSTEM*

E. Jacquez, LANL, Los Alamos, NM 87545, U.S.A.

*Abstract*

The mission of the Dual Axis Radiograph Hydrodynamic Test (DARHT) Facility is to conduct experiments on dynamic events of extremely dense materials.

The PSS control system is designed specifically to prevent personnel from becoming exposed to radiation and explosive hazards during machine operations and/or the firing site operation. This paper will outline the Radiation Safety System (RSS) and the High Explosive Safety System (HESS) which are computer-controlled sets of positive interlocks, warning devices, and other exclusion mechanisms that together form the PSS.

## BASIC OPERATIONAL OVERVIEW

Physical barriers and alarms are interlocked to the PSS. Door interlocks are located throughout the building. Other physical barriers include the Firing Point boundary fence, interlocked firing point gates, and perimeter warning lights and sirens.

The PSS logic is shown in Figure 1. The PSS is passive in that no external arming, conditioning, or operator intervention is required other than selecting the operational mode and executing the sweep.

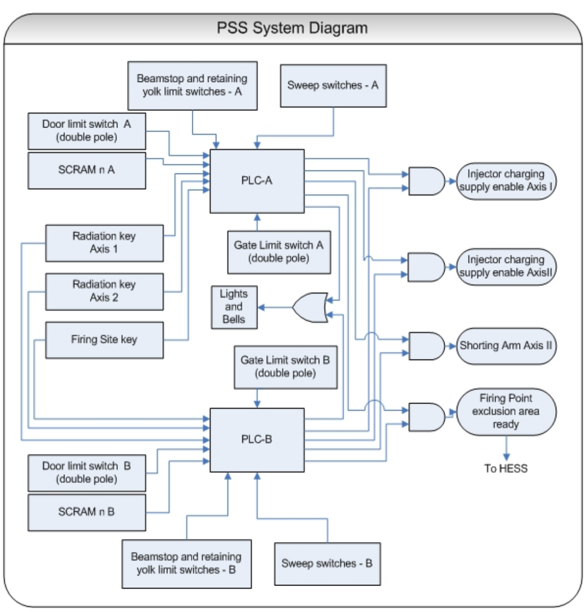

Figure 1: System diagram of PSS.

*This work supported by the US National Nuclear Security Agency and the US Department of Energy under contract DE-AC52-06NA25396
LA-UR-08-06022

A physical inspection, or sweep, of all exclusion areas ensures that affected hazardous areas are clear of personnel before any hazardous operation begins.

SCRAM actuators that inhibit radiation production are located throughout all potential radiation areas.

Located before the beam exit of each accelerator hall, the beamstop is designed to block the beam from reaching beyond the thick-walled accelerator halls. The beamstops allow beam production internal to the accelerator halls and inhibit radiation from reaching the firing point.

The PSS inhibits radiation production and explosive permissions depending on the modes of operation selected. The modes of operation for each axis are described below in Table 1.

Table 1: Operations Modes

| Mode | Activities |
|---|---|
| 0 | beam off |
| 1 | beam in the accelerator hall |
| 2 | beam in the hall and on the firing point |
| 3 | beam in the hall on the firing point in combination with explosives operations on the firing point |

The entire facility operation must be defined by the mode for each axis i.e., Mode 1, 1 (Axis I Mode 1, Axis II Mode 1; Mode 1, 3 (Axis I Mode 1, Axis II Mode 3); etc). The mode of operation defines the requirements for personnel exclusion in an area and therefore procedural sweep patterns. The PSS software controls are programmed to allow certain modes for each axis depending on the mode of the other axis. The modes of operation are shown below in Figure 2.. Up to two modes may be selected simultaneously, depending on the modes selected in Table 1 of this document.

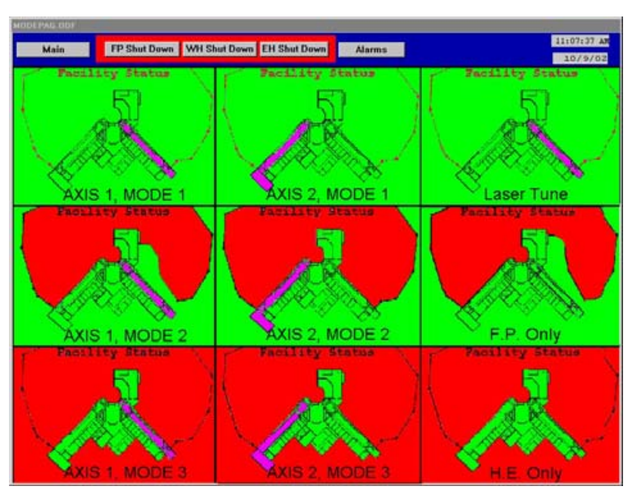

Figure 2: Mode select page.

# PSS CONTROL FUNCTION OVERVIEW

The two safety systems (RSS / HESS) that make up the PSS share hardware, software, and have similar sweep protocols. Input hardware mechanically fails in the safe position or condition. The PSS has three subcomponents: 1) the computer systems; 2) the field device hardware, including the interlocks and wiring for buttons and switches; and 3) redundant Programmable Logic Controllers (PLC's). (Operator PCs interface with PLCs.)

The PSS ensures that proper exclusion areas are secured and boundaries are maintained, depending on the mode of operation. The RSS maintains the exclusion areas around the accelerator where radiation production is the hazard. The HESS limits the manner in which the DARHT Detection Chamber (DDC) executes arming and detonation hardware for explosive tests.

The system provides a signal to inhibit beam production if access control to exclusion areas is lost. Requirements associated with these functions are determined by modes of operations in Table 1 of this document.

## *Radiation Safety System*

The RSS is integral to both axes of DARHT. When combined with administrative controls, the RSS eliminates the potential of personnel accessing areas in which they may receive exposure during beam production.

The RSS consists of those elements of the PSS that limit access to areas around the accelerator. Included in the RSS are: administrative controls, Standard Operating Procedures, Hazard Control Plans (HCPs), and a passive computer-based series of hardwired interlock devices.

The system monitors the physical barriers that prevent personnel from entering a radiation area while the injector is capable of producing radiation as illustrated in Figure 3. The RSS provides an interface between the operators and the machine environment to ensure that the hazard area is clear of personnel when a radiation hazard is present and monitors and detects access after a sweep and search process. The safety relays that permit the charging of each injector is controlled by redundant PLC units. These units must agree before the relay permits charging of the injector.

## *High Explosive Safety System*

When combined with administrative controls, the HESS limits the potential of injury to personnel from high explosives by monitoring interlocks.

The high explosive firing system uses a conventional modular capacitive discharge unit (CDU) system. The modular CDU system contains up to 12 CDUs, or 24 CDUs when two units are used together. The system fires only when commanded and with no time delay to meet the usual demands on a CDU system. The safety features prohibit charging of the capacitor until safety interlocks are complete. If an interlock is breached or control of the exclusion area is lost, the safety features discharge the capacitor, and the detonator will not fire. The CDU control system stops on any error and must return to the start of the control sequence.

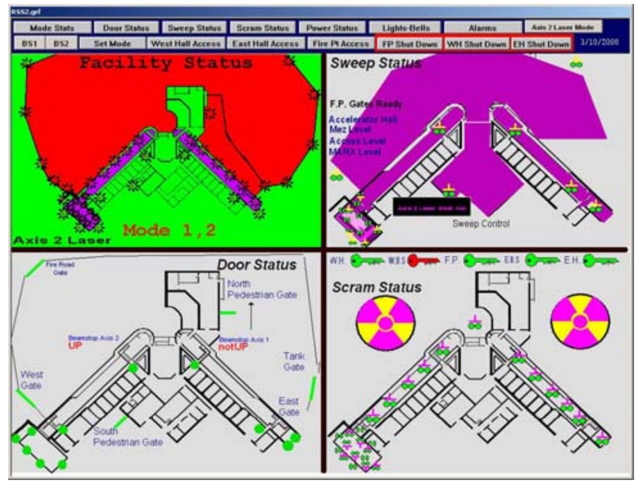


Figure 3: Facility status page.

# PSS SYSTEMS, SUBSYSTEMS, AND MAJOR COMPONENTS

Several of the PSS major subsystems and components are described in the following subsections.

## *PLC Hardware*

The dual PLC hardware system consists of two identical Modicon PLCs and I/O field interface hardware that provide redundant inhibit paths. The PLCs provide protection for both axes in an integrated fashion, depending on the mode selected. Each PLC executes identical programmed logic which manages the interlock hardware.

The computerized PSS control hardware is based on Modicon "Quantum" PLC's and remote "Quantum" I/O hardware from Schneider Electric. The PLC executes safety-system logic independently of the DARHT PSS display screen (HMI).

## *Software*

The software consists of Concept by Schneider Electric for the PLCs, GE Fanuc® iFIX™ automation software for the Human-Machine Interface (HMI), Windows®XP, and I/O driver software. Application specific software is developed in-house. The modular programming software, Concept, provides the platform for application specific software. The HMI software, iFIX™, provides operator visibility. Together, the PLC and HMI software monitor such activities as doors opening and engagement and disengagement of other interlocks and switches. HMI software allows process visibility to the operators. The HMI graphically presents the condition of the interlocks, progress of the sweep, SCRAM button status, beamstop position, and other elements of the safety system in the control room.

The HMI applications software has been successfully used at the integrated test stand during development and on Axis I and Axis II of the DARHT Facility. The HMI software offers third-party integration compatibility for even greater application potential such as VP-Link, simulator software used to test modifications offline and to qualify the PSS software on the integrated test stand. It is flexible and reliable configurable for I/O management and visibility.

The software was developed using DOE Order 1330.1D as a guideline. Documentation includes a software Development Plan, HMI/PLC Test Procedure, and a Software Backup Plan. A Functional Verification Checklist is used to ensure that the system functions as intended.

### *Hardware*

PSS Hardware and ANSI colored signs mark entrances to hazard areas. Hardware is verified during semiannual testing of the PSS. Lights and bells overlap in their visible and audible coverage and are evaluated for operation during each sweep in addition to the semiannual verification.

The PSS uses a dual set of I/O communication lines and applies error checking to ensure the integrity of communication to the I/O as seen in Figure 3. Two separate and independent configurations of the interlock hardware are installed to provide redundant inhibit paths. A power loss will result in a PSS fail-safe position that inhibits the high explosive and accelerator interlocks.

### *Keys*

There are individual keys for each axis and a separate key for the firing point that in conjunction with the PSS provide protection for authorized entries into exclusion areas, inadvertent production of radiation, and or high explosive events. The beamstop locks are a separate core.

Each accelerator axis has a Radiation Key that must be properly positioned before charging of the respective injector can take place. The Axis I or Axis II Radiation Keys lock/unlock the doors to the Axis I or Axis II accelerator halls. For radiation production, the Axis I or Axis II key must be inserted in a PSS cored switch located in the accelerator control room at the main console. The Axis I and Axis II keys have unique lock cores.

A Firing Point Key is used to control access to the mode 2 exclusion area. This key locks/unlocks the pedestrian/vehicle gates around the outside perimeter. The core is unique from the Axis I and Axis II Radiation Keys. The key must be inserted in a PSS cored switch located in the accelerator control room at the main console before charging of the injectors can take place in modes 2 or mode 3 for either axis. This key is not used if both accelerator axes are in Mode 0 or 1.

The beamstop keys are used at the location of the Axis I and Axis II beamstops to allow the raising of the respective beamstop. Its core is also unique from that of the other three keys. When the beamstop is lowered into the path of the electron beam for Mode 1 operation, the key is removed from the beamstop core and will remain inserted into the beamstop DARHT operations key control console. For Mode 0, the keys remain in the controlled key lockbox located in the accelerator control room. For mode 2 and mode 3, the respected beamstop key remains in the beamstop lock located on the side of the beamstop.

## SUMMARY

The PSS is designed specifically to include a combination of engineering and administrative controls. The hardware is designed in a redundant fail-safe manner that ensures optimal safety of DARHT personnel. The system is verified on a semiannual basis or whenever a modification is made. The multiple modes of operation allow for each axis to run independently or in combined modes of operation which benefits the diverse experiments which occur at the DARHT facility.

## REFERENCES

[1] W. Spencer, D. Schmitt, E. Jacquez, “DARHT Personnel Safety System Design Description”, HX6, May 2007, p. 1-34.

# UNIQUE FEATURES OF THE J-PARC LINAC AND ITS PERFORMANCE - LESSONS LEARNT

A. Ueno#, J-PARC, JAEA, Tokai, Naka, Ibaraki, 319-1195, Japan


*Abstract*

The J-PARC (Japan Proton Accelerator Research Complex) linac has been successfully commissioned up to its design energy of 181MeV and almost the first stage design peak intensity of 30mA. The following unique methods and hardware features adopted in the J-PARC linac are explained and those results are presented in this paper. The surface production dominating Cs-free $H^-$ IS (Ion Source) with magnetic focus LEBT (low energy beam transport), macro-beam-pulse shaping method related with the J-PARC 30mA-RFQ (Radio Frequency Quadrupole linac) design, a stable one-shot operation method, beam suspending method for machine protection, RF-chopper system related with the operation parameter of the RFQ, one-turn injection into the following J-PARC RCS (Rapid Cycling Synchrotron), transverse matching using TRACE3D PMQ (Permanent Magnet Quadrupole) elements approximating the fringe field effects of the electro-quadrupole magnets, PR (Periodic Reverse) electroforming for high-duty compact DTQ (Drift Tube Quadrupole) coil and thick pure plating of DTL (Drift Tube Linac) and SDTL (Separated-type DTL) and 2 cavity behaviour of SDTL fed with one Klystron.


## OVERVIEW OF J-PARC LINAC

As shown in Fig. 1, the J-PARC linac consists of 34 accelerating cavities (RFQ, DTL1~3, SDTL1A~15B), IS, LEBT, MEBT1 (Medium Energy Beam Transport 1) and beam transport to RCS [1]. Since the uncoupled SDTLnA and B (n=1~15) are fed RF-power by one klystron, 19 klystrons are used for acceleration. At the J-PARC first stage, the J-PARC linac accelerates an $H^-$ beam with a peak intensity of 30mA up to the energy of 181MeV with a pulse width of 500μs and a repetition rate of 25Hz.

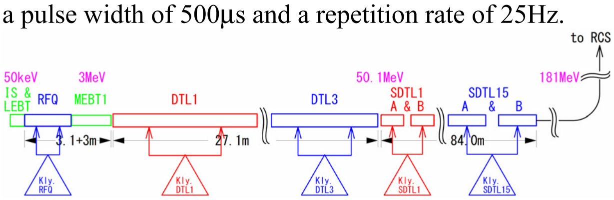


Figure 1: Scheme of J-PARC linac.

## SURFACE PRODUCTION DOMINATING CS-FREE IS & MAGNETIC FOCUS LEBT

In almost all of IS's for high intensity $H^-$ accelerators, Cs is seeded on PE (Plasma Electrode) in order to increase $H^-$ production efficiency. Since the thickness of the Cs layer affects to the efficiency greatly, it is not so easy to keep $H^-$ intensity constant with the Cs seeded $H^-$ IS. Also the frequency of sparking in high-voltage gaps of IS or RFQ is increased by the Cs. For stable operation, Cs-free IS is adopted for J-PARC. In order to minimize emittance growth by using SCN (Space-Charge Neutralization) measured as more than 90% [2], the magnetic focus LEBT composed of two solenoid and one ejection angle correction magnets is adopted. A schematic drawing of the IS and LEBT is shown in Fig. 2.

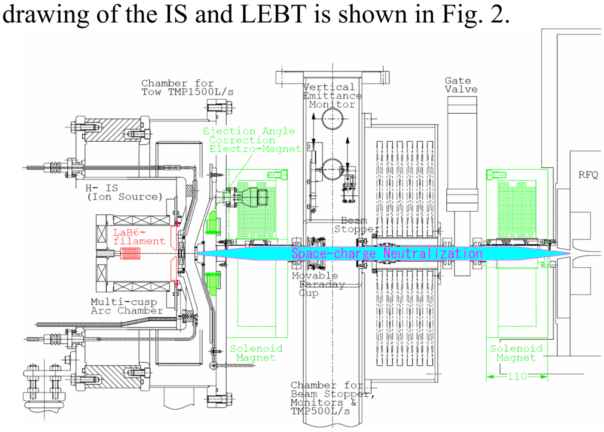


Figure 2: Schematic drawing of IS and LEBT.

On 1995, in a Cs-free IS, a 16mA $H^-$ beam was produced by using a cylindrical arc-chomber (D150mm, L150mm), a $LaB_6$-filament, a PE shown as Fig.3(a) and an arc-current of 220A [3]. Although the plasma density was increased by using a smaller arc-chamber (D100mm, L125mm) and a higher arc-current of 290A, the intensity had been limited to 16mA by using the PE shown as Fig. 3(b), for two years. After the success of 4mA intensity increase by only increasing the temperature of PE with a thermal insulator ceramics flange shown as Fig. 3(c), various shapes of PE's shown in Fig. 3 were examined by the assumption of that surface $H^-$ production was dominating. Finally, a 38mA $H^-$ beam was produced by using PE shown as Fig.3(h) [4]. The $H^-$ production efficiency seems to be increased mainly by the deoxidization of PE surface made of Mo with the high temperature measured as about 500°C in $H_2$ gas.

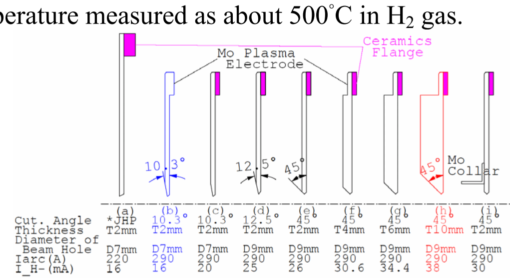


Figure 3: Various shapes of PE's examined.

## MACRO-BEAM-PULSE SHAPING & BEAM SUSPENDING METHODS

In order to avoid emittance rotation problem during the rise-time of SCN, macro-beam-pulse shaping by kicking the beam transversely is not available in magnetic focus

#akira.ueno@j-parc.jp

LEBT. Therefore, macro-beam-pulse is shaped by using RFQ longitudinal acceptance with modulating the injection energy in J-PARC. As shown in Fig. 4, RFQ acceleration starts after more than 100μs from IS arc pulse start and SCN established by low-energy unaccelerated beam transported through the LEBT. The end of macro-beam-pulse is determined by the end of RFQ-RF pulse since its fall-time is fastest. The macro-beam-pulse also ends by ending the RFQ-RF responding to MPS (Machine Protection System) fast interlock [5], for example DTL sparking and so on. In order to suspend beam acceleration for MPS reset time or one-shot operation, only IS arc pulse timing is delayed 0.2 ms after RFQ-RF pulse end where IS extraction voltage is switched off. As shown in Fig.5, no acceleration was observed for the beam with 10keV lower energy than the design energy of 50keV. IS signals {potential, arc voltage, arc current, $H^-$ beam measured by FC(Faraday Cup)} and RFQ RF-field are shown in Fig. 6.

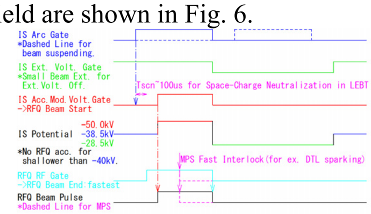


Figure 4: Timing-Chart of J-PARC IS & RFQ.

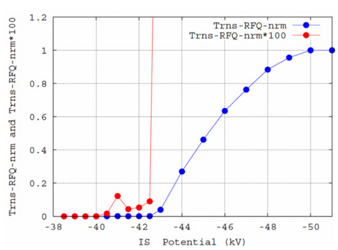


Figure 5: Measured Relationship between IS Potential and RFQ Transmission.

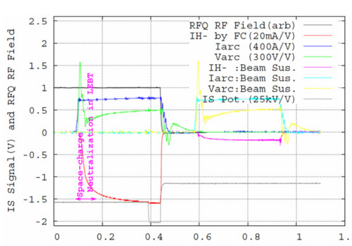


Figure 6: IS Signals and RFQ RF Field.

## *J-PARC 30mA-RFQ Design and Manufacturing*

In order to make the above macro-beam-pulse shaping available and the RFQ as emittance filter in both longitudinal and transverse motions, the RFQ is designed by using codes KEKRFQ [6] and PARMTEQm [7]. By using KEKRFQ, longitudinal and transverse acceptances including space-charge effect are kept constant in GB (Gentle Buncher) section (synchronous phase $\phi_s$= –88°→–30°) and accelerator section ($\phi_s$= –30°), respectively. The designed cell parameters of energy, modulation factor 'm', minimum bore radius 'a' and $\phi_s$ are shown as the functions of longitudinal position in Fig. 7(a). Since 'm' and 'a' change rather rapidly in GB, the accelerating field should be as accurate as possible. The approximated accelerating field used in PARMTEQm is shown as Eq. (1) whose parameters are explained in Fig. 7(b). In the equation, incorrect cell length Lc(i+1) is used to calculate A(i+1). The accelerating field is more accurately approximated by using Eq. (2). In order to stabilize the accelerating quadrupole field of the RFQ against the dipole-mode mixing, PILS's (π-mode Stabilizing Loops) are installed in the RFQ as shown in Fig. 8(a) [8, 9]. The electric field near beam axis is modified as shown in Fig. 8(b), in which the field distribution of one PISL cell length between pares of vertical and horizontal PISL rods calculated by MAFIA [10] are shown.

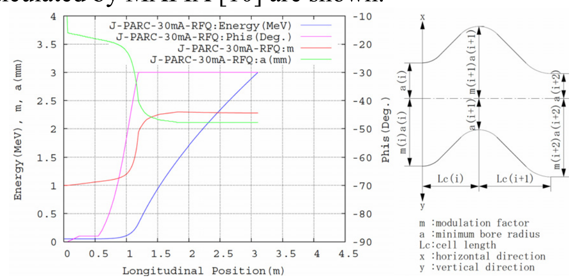


(a) (b)

Figure 7: (a) Designed Cell Parameters and (b) Explanation of 'a', 'm' and 'Lc'.

$$E_z(z)=\{A(i)+\frac{A(i+1)-A(i)}{L_c(i)}dz\}e(L_c(i),z) \quad \text{where} \quad A(i)=\frac{m(i)^2-1}{m(i)^2 I_0(\frac{\pi a(i)}{L_c(i)})+I_0(\frac{\pi m(i)a(i)}{L_c(i)})} \tag{1}$$

$$E_z(z)=\{A_0(i)+\frac{A_1(i)-A_0(i)}{L_c(i)}dz\}e(L_c(i),z) \quad \text{where} \quad A_0(i)=\frac{m(i)^2-1}{m(i)^2 I_0(\frac{\pi a(i)}{L_c(i)})+I_0(\frac{\pi m(i)a(i)}{L_c(i)})},$$

$$\text{and} \quad A_1(i)=\frac{m(i+1)^2-1}{m(i+1)^2 I_0(\frac{\pi a(i+1)}{L_c(i)})+I_0(\frac{\pi m(i+1)a(i+1)}{L_c(i)})} \tag{2}$$

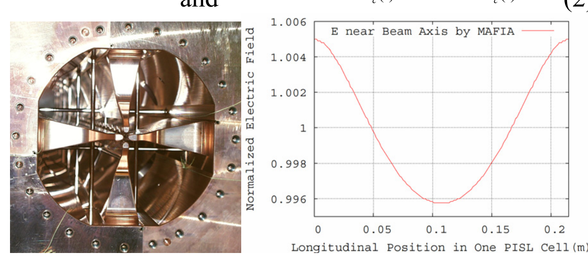


(a) (b)

Figure 8: Inside View of RFQ and Field Distribution near Beam Axis in One PISL Cell Calculated by MAFIA.

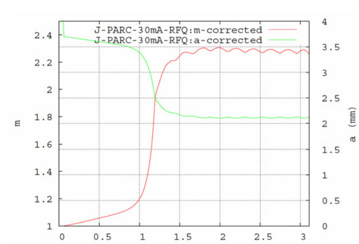


Figure 9: 'm' and 'a' for Design Accelerating Field.

The RFQ was manufactured with corrected 'm' and 'a' shown in Fig. 9.

## RF-CHOPPER & RFQ OPERATION PARAMETER SUITABLE FOR IT

In Figs. 10 and 11, the schematic drawing of MEBT1 and the inside-view of 2 coupled RF-chopper cavities are shown. Beam is deflected and dumped on a movable scraper made of graphite by the RF-field in RF-chopper. By switching RF-power to the RF-chopper, it is possible to produce arbitrary width and number of intermediate-beam-pulses [11, 12, 13]. Although the range of 3MeV-H$^-$ beam is very short (a few μm) and therefore energy density depositing on it is very high, it is confirmed experimentally that graphite stands for design beam duty (30mA*270μs*25Hz) of the J-PARC first stage.

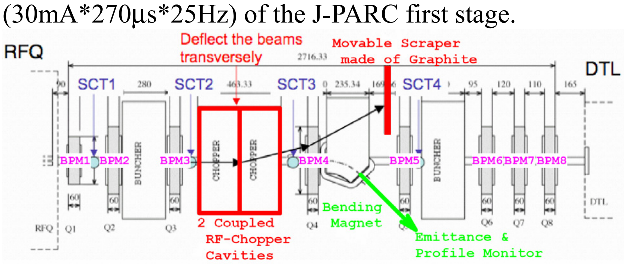


Figure 10: Schematic Drawing of MEBT1.

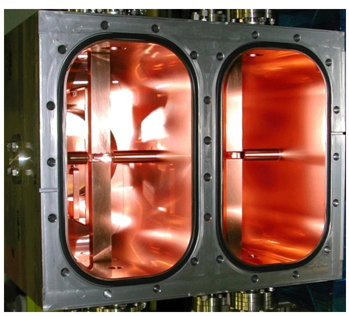

Figure 11: Inside View of RF-Chopper Cavities.

The 'remaining beam' which is deflected by the RF-chopper but undumped and accelerated by the following accelerators should be reduced as small as possible, in order to reduce residual radiation in the RCS. Early in the J-PARC linac commissioning, it was difficult to reduce the 'remaining beam' lower than measurement accuracy especially for high peak intensity beam about 30mA. In order to minimize the longitudinal halo of the beam accelerated with the RFQ, RFQ RF-field and IS potential are searched to minimize the horizontal beam size at the position with dispersion downstream of the bending magnet in MEBT1. The result is shown in Fig. 12.

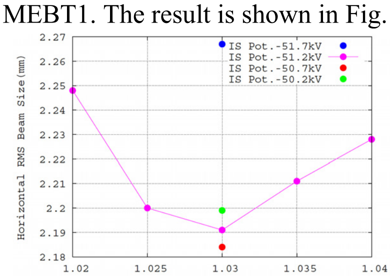


Figure 12: Relationship between RFQ RF-Field & IS Potential and Horizontal RMS Beam Size at Position with Dispersion.

By setting the RFQ RF-field at 3% higher than the design value and the IS potential at –50.7kV, the 'remaining beam' can be reduced lower than the measurement accuracy of linac monitor. By using RCS BLM (Beam Loss Monitor) [14] at the position with dispersion, the 'remaining beam' can be measured most accurately as shown in Fig. 13 in which very slight beam is measured (red line), although all of the beam is deflected by the RF-chopper. The 'remaining beam' due to longitudinal halo will hopefully be eliminated by RF-chopper with half resonant frequency of 162MHz.

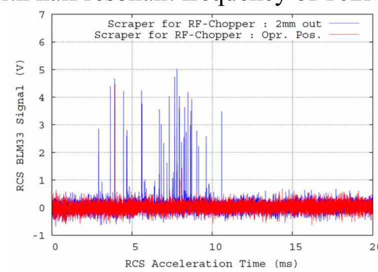


Figure 13: BML Signal during RCS Acceleration Time at Position with Dispersion.

The measured LEBT and MEBT1 SCT signals and RFQ RF-field are shown in Fig. 14. The rise-time of the macro-beam-pulse (blue line) measured by MEBT1-SCT3 (upstream of RF-chopper) is rather short (about 3μs) which is the proof of SCN establishment in the LEBT. The fall-time is much faster than it (about 1μs) since it is determined by 80% of the RFQ RF-field (black line). Two type of chopped beam measured by MEBT1-SCT5 (downstream of RF-chopper) are shown with green (112ns, 22turn) and red (560ns, 1turn) lines artificially.

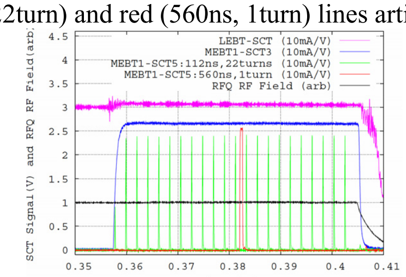


Figure 14: LEBT and MEBT1 SCT Signals and RFQ RF-Field.

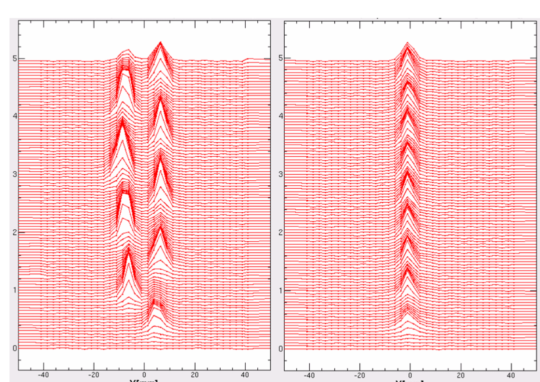


(a) (b)

Figure 15: Mountain Plots of RCS Vertical IPM Signals before (a) and after (b) Injection Error Correction.

One turn injection into the RCS makes injection error correction possible. The beam position and profile measured by an RCS IPM (residual gas Ionization Profile Monitor) as mountain plots during the first 9turns are shown in Fig. 15(a)(before correction) and (b)(after correction).

The RF-field in the RF-chopper, MEBT1-BPM right and left signals are shown as red, blue and green lines, respectively in Fig. 16. The ringing of RF-field at RF on/off transient-time due to RF-power flow between the 2 coupled cavities is observed. The shit of beam position due to the ringing is also observed for about 50ns after beam rise-time. If the affect of the ringing is significant, it can be eliminated by driving each RF-chopper cavity independently with two RF-sources.

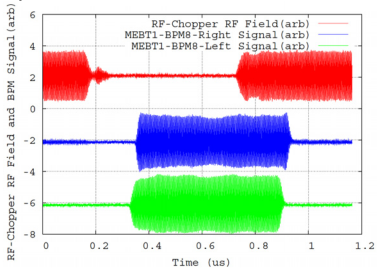


Figure 16: RF-Chopper RF-Field and Right- and LEFT-BPM Signals of MEBT1.

## TRANSVERSE MATCHING WITH TRACE3D PMQ APPLOXIMATION

As reported in the paper of LINAC2002 [17], the fringe field of Q(quadrupole)-magnets should be taken into account. By using 20-pieces of hard-edge magnets (red line of Fig. 17) for each Q-magnet, the ellipses measured in the MEBT1 test setup are reproduced.

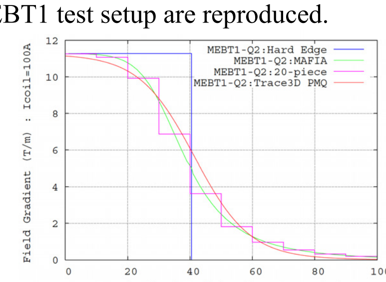


Figure 17: Various Field Distributions of MEBT1-Q2 Used for TRACE3D Calculations.

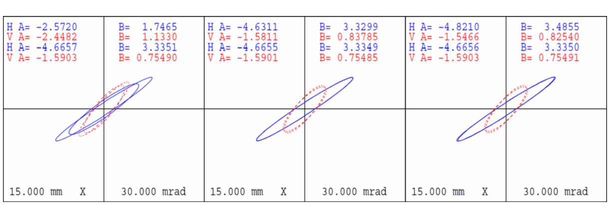

(a) (b) (c)

Figure 18: Measured and Calculated Ellipses in MEBT1 Test by Using Hard Edge Field (a), 20-Pieces Field (b) and TRAC3D PMQ Field (c).

Instead of 20-pieces of hard-edge magnets, PMQ element (magenta line of Fig. 17) of TRACE3D [18] can also reproduce the experimental result as shown in Fig. 18(c). In Fig. 18(a), (b) and (c), measured and calculated ellipses are shown for hard-edge field, 20-pieces field and PMQ field, respectively. Since online control of the J-PARC linac is done by using XAL [19], the PMQ element has been transplanted into XAL [20]. All of Q-magnets in J-PARC linac are treated as PMQ elements.

## DTQ-COIL & CAVITY-PLATING USING PR-ELECTROFORMING

PR(Periodic Reverse)-electroforming, in which electroforming and short electro-polishing is reiterated without any brightening agent, is able to produce thick and pure plating comparable with OFC (Oxygen Free Copper). Compact DTQ-coil shown in Fig. 19(a) was produced with it and is able to be operated with high magneto-motive-force and high-duty (3.5turn, 600A, DC) [21]. As shown in Fig. 19(b), each inside of DTL or SDTL cavity was plated with PR-electroforming. All of DTL and SDTL cavities were successfully high-power RF-conditioned up to 20% higher powers of the design values. [22, 23]

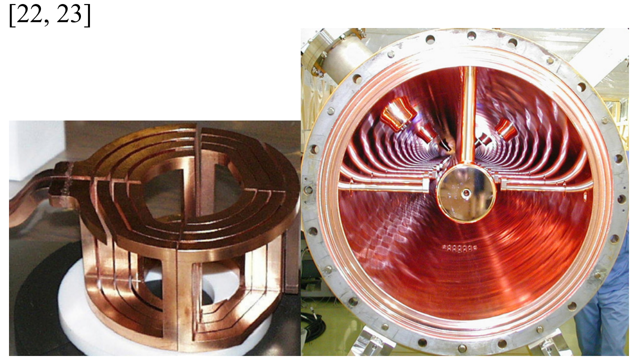

(a) (b)

Figure 19: Photos of DTQ-Coil (a) and Inside View of DTL1 (b).

## 2 CAVITY BEHAVIOR OF SDTL

Each pair of SDTLnA and B (n=1~15) is driven by one klystron. The vector-sum of the two RF-fields is feedback-controlled [24]. However, unexpectedly high RF-field unbalances caused by beam loading are observed in several of the pairs. In Fig. 20, the measured maximum (SDTL03) and minimum (SDTL12) unbalances are shown when a 28mA-beam with 100ms pulse width is accelerated.

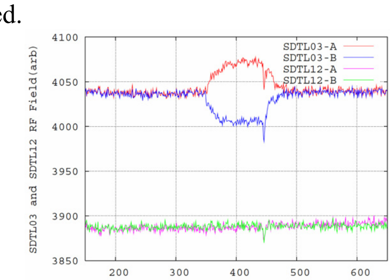


Figure 20: RF-Fields in SDTL03A&B and 12A&B while Accelerating 28mA- and 100µs-Beam.

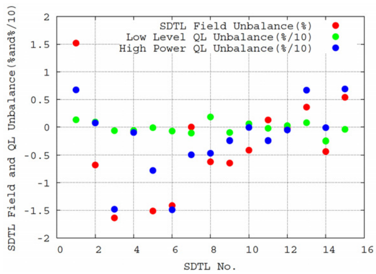


Figure 21:SDTL QL Unbalance (Preliminary) & RF-Field Unbalance while Accelerating 28mA- and 100µs-Beam.

In Fig. 21, the RF-field unbalance UBRF due to beam-loading and the QL (Loaded Q-value) unbalance UBQL calculated with following equations are shown.

UBRFn=(RFnA-RFnB)*2/(RFnA+RFnB)
UBQLn=(QLnA-QLnB)*2/(QLnA+QLnB)

In the latest beam acceleration, preliminarily, each QLnA and QLnB was measured by measuring RF decay-time during high-power operation as shown with blue circles in Fig. 21. The RF-field unbalance due to beam-loading seems to have some relationship with the unbalance of the high-power loaded Q-value, although more accurate measurements are necessary. If the change of the loaded Q-value is correct, multipacting is one candidate of the causes.

## SUMMARY

The following unique methods and hardware features adopted in the J-PARC linac are explained and the performances and problems of them are presented.

- Surface production dominating Cs-free $H^-$ IS
- succeeded in produce more than 30mA stably.
- Macro-beam-pulse shaping by using RFQ longitudinal acceptance with magnetic focus LEBT
- succeeded in producing the pulse with rather high rise- and fall-time. It also makes possible stable one shot operation, fast beam suspending for MPS and so on.
- RF-chopper
- succeeded in reducing the ‘remaining beam’ lower than the measurement accuracy of linac monitor by searching the RFQ operation parameter. One turn injection with it into the following RCS is essential for injection error correction. Two RF-sources are necessary to eliminate the measured RF-ringing. The RF-chopper with half resonant frequency of 162MHz will eliminate the ‘remaining beam’ and makes possible beam intensity double by inevitably used two scrapers.
- Transverse matching with TRACE3D PMQ
- succeeded in representing the fringe field effects. All of Q-magnets in the J-PARC linac are treated as PMQ in XAL and TRACE3D.
- PR (Periodic Reverse) electroforming.
- succeeded in producing high-duty compact DTQ-coil and thick pure plating of DTL and SDTL.
- 2 cavity behaviour of SDTL fed with one Klystron.
- unexpectedly high RF-field unbalance between the 2 cavities are observed. The RF-field unbalance due to beam-loading seems to have some relationship with the unbalance of the high-power loaded Q-value (preliminarily measured).

## REFERENCES

[1] K. Hasegawa, Proc. of PAC2007, 2619(2007).
[2] S. Fujimura and A. Ueno, Proc. of LINAC1996, 343(1996).
[3] A. Ueno et al., Proc. of LINAC1996, 293(1996).
[4] A. Ueno et al., Rev. Sci. Instrum. 75, 1714(2004).
[5] H. Sakaki et al., Proc. of APAC2004, 622(2004).
[6] A. Ueno and Y. Yamazaki, Proc. of LINAC1990, LA-12004-C, 329(1991).
[7] K. R. Crandall et al., LA-UR-96-1836, (1998).
[8] A. Ueno and Y. Yamazaki, Nucl. Instr. and Meth. A300, 15(1991).
[9] A. Ueno and Y. Kondo, Proc. of LINAC2000, 545(2000).
[10] T. Weiland, Part. Accel., 17, 227, (1985).
[11] S. Fu and T. Kato, Nucl. Instr. And Meth. A 440, 296(2000).
[12] S. Wang, S. Fu and T. Kato, Proc. of LINAC2004, 770(2004).
[13] T. Kato et al., Proc. of PAC2003, 1455(2003).
[14] K. Yamamoto et al., Proc. of EPAC2008, 382(2008).
[15] K. Satou et al., Proc. of EPAC2008, 1275(2008).
[16] H. Hotchi, “Status of J-PARC Commissioning”, Proc. of ICFA-HB2008.
[17] A. Ueno et al., Proc. of LINAC2002, 356(2002).
[18] K. R. Crandall and D. P. Rusthoi, LA-UR-97-886, (1997).
[19] J. Galambos, et al., Proc. of ICALEPCS2003, 332(2003).
[20] C. K. Allen, et al, Proc. of PAC2007, 218(2007).
[21] K. Yoshino et al., Proceedings of LINAC2000, 569(2000).
[22] H. Ino et al., Proceedings of LINAC2000, 1015(2000).
[23] F. Naito, Proc. of APAC2007, 1(2007).
[24] T. Kobayashi et.al., Proceedings of PAC2007, 2128(2007).

### *Acknowledgement*

The author express sincere thanks to the members of J-PARC linac and RCS for their works.

# STATUS OF THE CONSTRUCTION OF THE SPIRAL2 ACCELERATOR AT GANIL

Tomas Junquera # on behalf of the Spiral 2 project team, IPN (CNRS/IN2P3, Univ. Paris Sud)
91400 Orsay, France

*Abstract*

The Driver Accelerator for the SPIRAL2 Radioactive Ion Beam facility at GANIL (Caen, France) is in the construction phase. Following the initial phase of prototyping development, the series production of major components was recently launched. Important decisions have also been recently taken concerning buildings, RIB operational aspects and related safety requirements.

## INTRODUCTION

The GANIL laboratory (CNRS-CEA) in Caen (France) is one of the major radioactive and stable-ion facilities for nuclear physics, astrophysics and interdisciplinary research in the world. Since the first beams delivered in 1983 the performances of the GANIL accelerator complex, was constantly improved with respect to the beam intensity, energy and available detection systems. A major improvement was the construction of a new Cyclotron dedicated to the production and acceleration of Radioactive Ion Beams (RIB), the Spiral 1 project, which entered into operation in 2002.

Following the recommendations of international committees, the French Minister of Research took the decision in May 2005 to construct a new facility (Spiral 2) in order to enlarge the range of accelerated ions by production of high intensity RIB. On the 1st of July 2005, the construction phase of SPIRAL2 was launched within a consortium formed by CNRS, CEA and the region of Basse-Normandie in collaboration with French, European and international institutions.

The importance of the availability of Radioactive Ion Beams (RIB) has been often underlined in the last years. NuPECC (Nuclear Physics European Collaboration Committee) and ESFRI (European Strategy Forum on Research Infrastructures) established roadmaps and recommendations for the next generation of facilities in Europe. FAIR in GSI laboratory in Darmstadt (Germany) and Spiral 2 in GANIL laboratory are among the selected projects. Both projects are complementary and are based on two different RIB production methods: FAIR is based on In-Flight Fragmentation techniques, while Spiral 2 uses the Isotope Separation on Line (ISOL) techniques.

## THE SPIRAL 2 PROJECT

The radioactive neutron rich beams will be mainly produced via the fission process induced by fast neutrons in a depleted Uranium Carbide (UCx) target (11g/cm3 density), with the aim of $5.10^{13}$-$10^{14}$ fissions/s [1]. For this purpose a high intensity CW driver accelerator will deliver 40 MeV (5 mA) to a thick Carbon target (Converter), and produce a very high neutron flux on the UCx target. The fission process will release radioactive atoms which are ionized and extracted from a target/ion-source system. The produced RIB are finally sent to either a low energy experimental hall, or driven towards a charge breeder and post-accelerated by the existing CIME cyclotron (Spiral 1).

The possibilities offered by the driver accelerator, with its capability to accelerate a large range of high intensity CW ion beams (Table 1 and 2), have opened new complementary opportunities to the Spiral 2 project:

- High intensity stable beams, i.e. Ar, Kr, etc
- Neutron experiments, i.e. time of flight
- Interdisciplinary researchs, i.e. solid state, biology, etc

Table 1: Driver Accelerator Beams

| beam | p+ | D+ | ions | ions |
|---|---|---|---|---|
| Q/A | 1 | 1/2 | 1/3 | 1/6 |
| I (mA) max. | 5 | 5 | 1 | 1 |
| Womin(Mev/A) | 2 | 2 | 2 | 2 |
| Womax(Mev/A) | 33 | 20 | 14.5 | 8.5 |
| CW max beam power (KW) | 165 | 200 | 44 | 48 |

Table 2: Driver Accelerator Characteristics

| |
|---|
| **Total length: 65 m (without HE lines)** |
| **D+ : ECR ion source** |
| **Heavy Ions: ECR Ion Source** |
| **Slow and Fast Chopper** |
| **RFQ (1/1, 1/2, 1/3) & 3 re-bunchers** |
| **12 QWR beta 0.07 (12 cryomodules)** |
| **14 QWR beta 0.12 (7 cryomodules)** |
| **1 KW Helium Liquifier (4.2 K)** |
| **Room Temperature Q-poles** |
| **30 Solid State RF amplifiers (10 & 20 KW)** |

## PROGRESS IN THE CONSTRUCTION OF THE SPIRAL 2 FACILITY

During the last two years (oct. 2006-sept 2008) the activities have evolved in two main directions:

1. Preparation and adoption of decisions around the project phases, considering the different beam users and the main project goals, the consequences on buildings and the safety aspects.

2. Construction and tests of main components of the driver accelerator, essentially the Injector and the SC Linac

# junquera@ipno.in2p3.fr

The new buildings: Driver Accelerator, RIB Production, and two new Experimental Halls, are illustrated in Fig. 1, close to the present buildings (in blue). New experimental halls will be dedicated to high intensity stable beams, neutron experiments, interdisciplinary physics, and low energy RIB experiments.

The production building, which will host the RIB production caves and the RIB transport lines, will be a nuclear class building. The safety requirements imply a double confinement in the whole building that will host the UCx production cave as well as the transport lines for the radioactive beams composed of fission products. The whole vacuum system will be connected to the gas storage system, and a public enquiry will be launched to get the authorization to release gas from the storage facility, after a suitable period of radioactivity decrease.

For the construction of these buildings, and strongly related to the safety authorisation procedures, two phases have been proposed:

1. Driver Accelerator and first experimental areas
2. RIB Production building and associated experimental areas

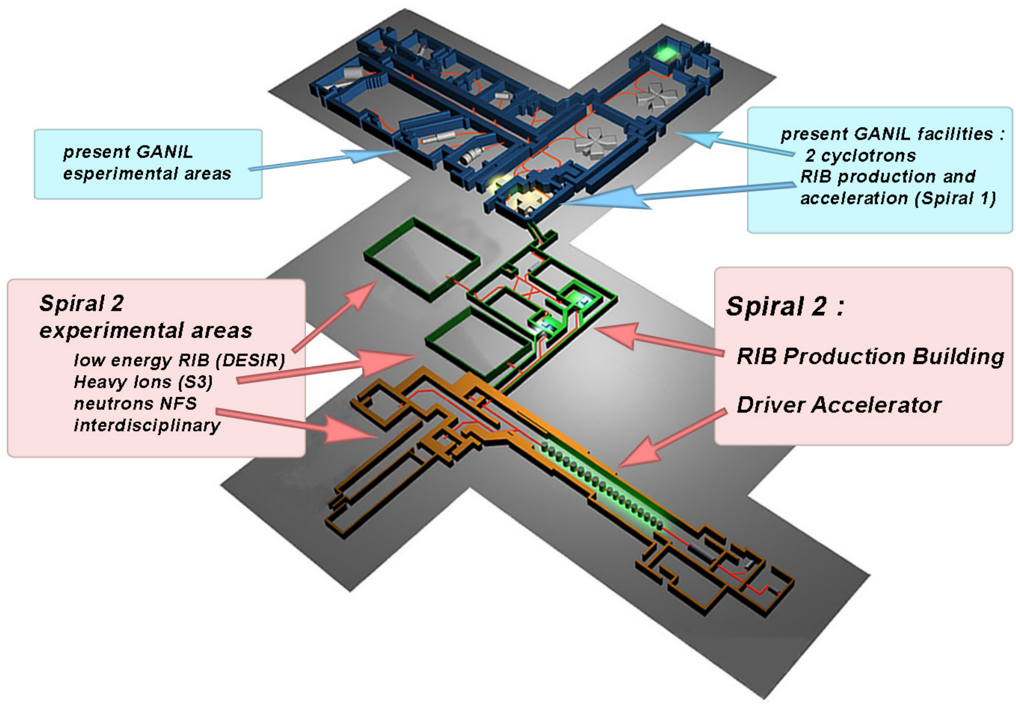


Figure 1: Present facilities at GANIL laboratory and new buildings for SPIRAL 2 Driver Accelerator and associated Experimental Areas.

GANIL is a nuclear facility and, for Spiral 2 authorizations, it is considered as an extension of the existing facility. During the last two years, together with preliminary safety studies, initial talks with the National Nuclear Safety Agency have resulted in a final agreement for the licensing procedure: A global safety report (DAM report) leading to a single Ministry Authorisation Decree with several steps.

This report must include:

- Preliminary Safety report of the two phases
- Operating ranges of the whole facility
- Study of the impact on the environment

The reports to be delivered were defined by a very recent new regulation law (2007) and Spiral 2 is the first major facility for nuclear research to be concerned by these new regulations.

## *Spiral 2 Schedule*

The general schedule of the project is presented in Fig 2, showing the major milestones:

- October 2008: Phase 1 buildings contracts.
- Beginning of 2011 accelerator building available
- Beginning of 2012 for the first beams in the stable ion experimental hall and the neutron time of flight hall
- Mid 2013 for the first RIB and the low energy experimental hall.

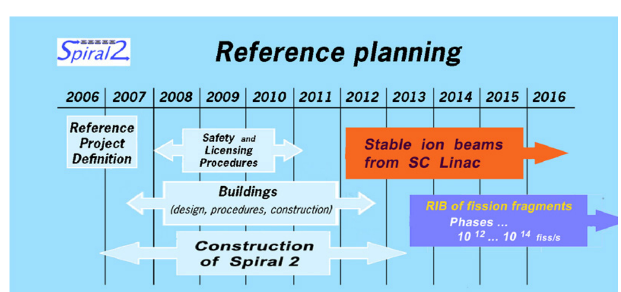


Figure 2 : Spiral 2 schedule.

## BEAM LOSSES AND SAFETY ASPECTS

A complete beam dynamics study of the Linac Driver Accelerator has been completed. It includes the two injectors, the SC Linac and a preliminary version of the High Energy Beam Lines ( Fig 3).

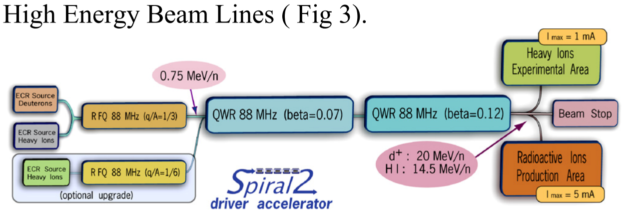


Figure 3: Driver accelerator layout.

Very extensive calculations of mutiple-ion-type beam transport using 3D maps have been performed with various conditions of space charge, and various hypothesis of space charge compensation (including solenoids 3D map) [2]. A dedicated poster covering all the beam dynamic studies is presented in this conference [3].

Two codes were used for this computing: Toutatis for the RFQ and TraceWin/Partran for the Linac . Distributed computing was performed using 40 PC in a client/server network. Errors were introduced in a statistical way for 1400 different Linac configurations and 1 million macro-particles trajectories were analyzed for each configuration. The matching and correction schemes were applied for each Linac.

The main goal of these calculations was to limit the beam losses for safety and machine protection. One important result was to define the precise position of slits in the low energy sections (Fig. 4)

- 3 slit systems to control input emittance in the RFQ and remove beam halo coming from LEBT line.About 40 W beam losses on slits (for 5 mA deuteron beam)
- 6 slit systems to remove beam halo coming from the RFQ before the entrance of the SC linac. About 6x125 W beam losses on slits (for 5 mA deuteron beam).

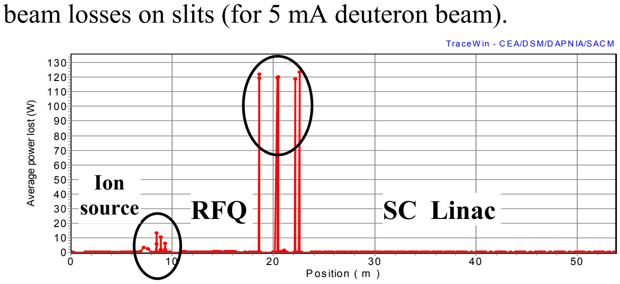


Figure 4: Beam losses on the slits.

The errors introduced in these calculations are of two types:

- Corrected (alignment, QWR steering effects, etc)
- Uncorrected (vibrations, stability of magnet currents, RF voltage, phase, etc)

The uncorrected errors are responsible for a very low level of losses: 0.20 W for the SC linac (average value of 1400 computed linacs), this corresponds to 0.2W for a length of 30m, ~6 mW/m.

Most of these losses are located in the firsts QWR of both low and high energy sections (Fig. 5)

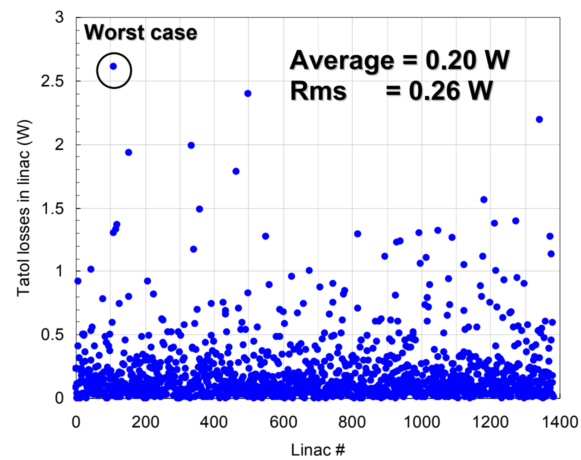


Figure 5: Statistical study of Linac losses.

Based on preliminary experience in other high intensity accelerator projects and performed calculations, a reasonable level of losses goal of ~1 W/m could be adopted. In order to stay well inside this level of losses in the Spiral 2 project, the decision was taken to install a big number of beam diagnostic systems, special mechanical adjustments systems for all the components and magnetic correcting devices all along the Linac.

The safety goals, in terms of dose rates for the Spiral 2 project are shown in the following table:

Table 3: Safety Goals in Terms of Dose Rates

| | Technical Staff | People/Environment |
|---|---|---|
| Normal operation | < 2 mSv/year | < 10 µSv/year |
| Incidental situation | < 10 mSv/year | < 10 µSv/incident |
| Major incident | < 20 mSv/incident | < 100 µSv/incident |
| Major accident | Variable according to situation and potential impact | < 1 mSv/accident |

The limit dose for offices, labs and workshops where permanent activity is foreseen, is 7.5 µSv/h, the limit for a zone where maintenance operations are possible is 100 µSv/h and zones where dose rates are greater than 10 mSv/h are not accessible.

Activation and dose rates calculation are based on two codes: MCNPX 2.5 for deuteron and neutron transport and Fispack 2007 for activation inventory. All the Linac components were modelled with high degree of geometric detail and material composition.

Two major contributions were studied for the more critical beam: 5 mA deuteron beam at 40 MeV:

1) interaction between deuterons and materials
2) interaction between the generated neutron yield and materials.

Both mechanisms originate high material activation, and the main contributing isotopes were identified: Co56, Fe55, Co57, Mn54, CO58 and Cr51 (for stainless steel material). Hands on maintenance operation conditions are presently under study, taking into account different levels of beam losses along the Linac and considering reasonable decay times after beam shutdown.

## BUILDINGS STUDIES AND CONSTRUCTION

During the last year an intensive work has been developed for the definition of the buildings technical specifications, followed by a call for tenders and the analysis of proposals. At the present time we are very close to final contract agreement for the phase 1 (driver accelerator and stable ions experimental areas). The major decision was to install all these facilities underground. The level of Linac tunnel floor will be -9 m with a beam line at -7.5 m and an available tunnel height of 6 m. A technical tunnel running parallel to the Linac tunnel will allow installing cables, water cooling and some RF and electronics components that must be located in the linac proximity.

All the technical activities (labs and workshops, including the SC cavities preparation area, clean room and cryogenics tests) will be installed at the ground level. The RF amplifiers and the Helium liquefier will be also installed on top of the Linac minimising the distances to the cryostats and RF couplers. Total surfaces of the two levels, including the wall thickness are 8300 m2. Figure 6 shows a preliminary sketch of the underground tunnel. The height of the tunnel is 6 m and the width is 4.5 m, a crane covers all the tunnel length for manipulation of heavy components like cryomodules and Q-poles. The access to the Linac tunnel for components installation is made through special pits and elevators.

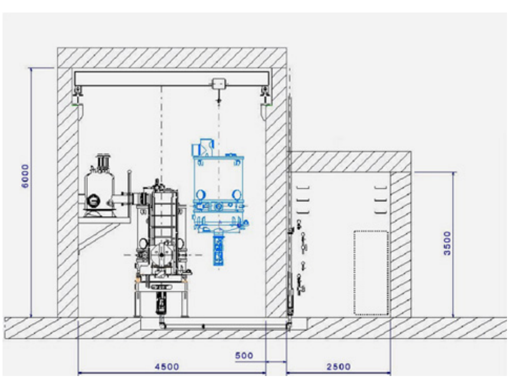


Figure 6: Underground Linac tunnel sketch.

## PROGRESS IN THE CONSTRUCTION OF ACCELERATOR COMPONENTS

### *Injector*

Complete tests of the two ion sources and the RFQ cavity are planned before the buildings completion and final installation of the components in the Linac tunnel. The Heavy Ions source with its mass analyzer and beam diagnostics will be tested in the CNRS/LPSC laboratory in Grenoble. The assembly has presently started and the first Ion Source measurements will start in January 2009.

The light ion source (proton and deuteron) with its beam transfer line and diagnostics will be tested in the CEA/Saclay laboratory, starting in mid-2009.

The construction of the RFQ cavity has started this year and after a final assembly and preliminary RF tests at the end of 2010, the cavity will be installed on the low energy deuteron line for beam tests in 2011.

### *SC Linac*

All (12+14) SC QWR contracts are presently placed in two different companies. The first series QWR for the high energy sections (β=0.12) have been delivered. The performances reached for the first cavity in a recent test in July 2008 are shown in Fig. 7. After some conditioning needed to overcome multipacting barriers, a very high gradient was reached (9 MV/m, for a max. nominal operating gradient in the accelerator of 6.5 MV/m) and the losses at 4 K were well inside the expected range. The low energy (β=0.07) QWR prototypes exhibit also very good performances, gradients higher than 10 MV/m. The contract for the manufacturing of the series QWR is already agreed and the first cavities will be delivered starting in March 2009.

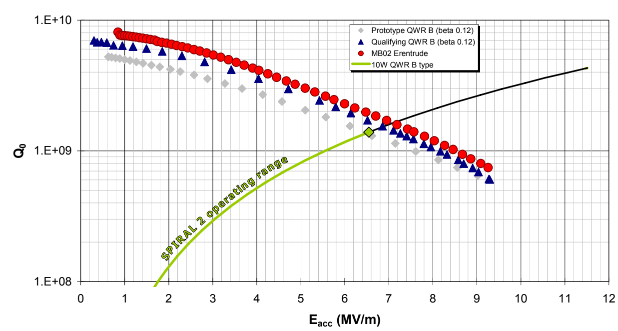


Figure 7: Accelerating gradient performances of β=0.12 QWR ( 2 prototypes and first of serial production).

Concerning the RF power couplers, the CNRS/LPSC laboratory in Grenoble developed a two years long prototyping program. Several prototypes models were tested at high power (40 KW) and a careful study of the multipacting and conditioning aspects was completed. These couplers have a fixed coupling position on the cavities, so the Qext adjustment must be done for the maximum current to be accelerated (5mA). The nominal CW RF operating power ranges between 5 KW and 15 KW.

### *First Cryomodules Tests in Orsay and Saclay Laboratories*

The two first crymodules, low and high energy, have been assembled and tested at 4 K integrating all RF (power couplers, amplifiers, tuners) and cryogenic interfaces (valve boxes and He transfer lines). The results obtained (CNRS/IPN Orsay laboratory, Fig. 8) with the high energy cryomodule (including two β=0.12 cavities) are completely satisfactory, a gradient of 8 MV/m was obtained with the power coupler, all the cryogenic measurements have confirmed a low level of static losses (13 W at 4 K), a new tuner system using a movable piston was also successfully operated. All the cryogenic interfaces operates very satisfactorily allowing the launch of all the series components contracts.

The low energy cryomodule, which integrates only one cavity is presently in the final test period at the CEA/Saclay laboratory Fig. 9. The initial cryogenic tests have confirmed a good performance for the static cryogenic losses, 7 W at 4K, and a very satisfactorily operation of all cryogenic interfaces. The complete test with power coupler, amplifier and tuning system will be performed next month.

A poster covering all the technical aspects and tests performed is presented in this conference [4].

Figure 8: High Energy cryomodule tested at CNRS/IPN Orsay laboratory.

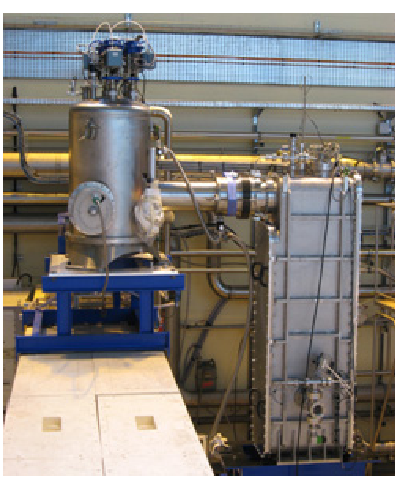

Figure 9: Low Energy cryomodule tested at CEA/Saclay laboratory.

### *RF Systems*

Two types of RF amplifiers have been studied :

- RFQ amplifiers: 4 x 60 KW tube amplifiers
- QWR amplifiers : 12 x 10 KW and 14 x 20 KW solid state amplifiers.

One model of each amplifier type was constructed for prototyping purpose. All the prototypes were successfully tested, reaching the nominal power and exhibiting stable operation behaviour during long term tests. A dedicated poster is presented in this conference [5] giving all the results of tests and technical specifications

Between the RFQ and the first QWR of the superconducting Linac, a long Medium Energy Beam Transfer line imposes the installation of 3 re-bunchers to to optimize the beam longitudinal phase length.

An original 3-gap cavity has been designed with very large beam holes (diameter 60mm) providing up to 120 kV of effective voltage. A poster describing this design is presented in this conference [6].

The control of all RF cavities of the Driver Accelerator will be performed by a new Digital Low Level RF system which is presently under development and will cover all the particular needs in terms of independent amplitude and phase of each cavity, as well as the accurate control of its associated tuning system.

## ACKNOWLEDGEMENTS

This work is the result of a large Project Team composed of people from GANIL and associated CEA and CNRS laboratories. It is also the result of an exceptional international collaborative effort of many accelerator experts in the world. Peer reviews, technical meetings, workshops, etc. have largely contributed to assess and establish the grounds for the design and construction of this new facility.

## REFERENCES

[1] M-G Saint-Laurent on behalf of the Spiral2 project group, "Future opportunities with Spiral2 at GANIL", AccApp07, Pocatello, Idaho, July 30-August 2nd, 2007.
[2] R. Duperrier, D. Uriot,, Phys. Rev. ST Accel. Beams 9, 044202 (2006).
[3] P. Bertrand et al. "Beam Dynamics and Error Studies of the Spiral 2 Driver Accelerator", paper MOP070, this conference.
[4] R. Ferdinand et al., "The Spiral 2 Superconducting Linac", paper MOP053, this conference.
[5] M. DiGiacomo and B. Ducoudret, "RF Power Amplifiers for the Spiral 2 Driver", paper THP048, this conference.
[6] M. DiGiacomo and al., "Design of the MEBT Rebunchers for the Spiral 2 DriverRF Power", paper THP047, this conference.

# CERN LINAC UPGRADE ACTIVITIES

A. M. Lombardi, CERN, Geneva, Switzerland.

*Abstract*

In its June 2007 session the CERN Council has approved the White Paper, which includes construction of a 160 MeV $H^-$ linear accelerator called Linac4, and the study of a 4 GeV Superconducting Proton Linac (SPL). Linac4 will initially replace Linac2 as the injector to the PS Booster, improving its performance up to the levels required for producing the ultimate LHC luminosity. In a later stage, Linac4 is intended to become the front-end of SPL in a renewed injection chain for the LHC, which could be progressively constructed over the next decade. After briefly introducing the motivations and layout of the new injector chain, the talk will present the characteristics of the new linacs and give an overview of their main technical features and the R&D activities pursued within the HIPPI Joint Research Activity.

## INTRODUCTION

In its June 2007 session the CERN Council has approved the White Paper "Scientific Activities and Budget Estimates for 2007 and Provisional Projections for the Years 2008-2010 and Perspectives for Long-Term", which includes construction of a 160 MeV $H^-$ linear accelerator called Linac4, and the study of a 5GeV, high beam power, superconducting proton Linac (SPL).

Both those activities aim at rejuvenating the present proton injectors which –although well-performing for the time being - date from the 60-70s and are working, since some years, well beyond their design intensity and very close to their technical limits.

## PRESENT LHC INJECTORS

All the protons at CERN are produced by a duoplasmatron ion source giving in excess of 300 mA of beam current, composed by about 2/3 of protons [1]. The source provides a 100-150 µs beam with a repetition rate of 1.1 Hz. The beam, extracted at 90 keV, is further accelerated by a Linac (Linac2) up to 50 MeV and then injected in the 4 rings of a 25 m radius synchrotron, called the CERN PS Booster (PSB). The PSB, commissioned in 1972, brings the beam energy to 1.4 GeV and injects in another synchrotron, 100 m in radius, called the Proton Synchrotron (PS). CERN PS was commissioned in 1959 and accelerates the beam up to 26 GeV. All the above accelerators are located on the original CERN Meyrin site and serve several experimental facilities like ISOLDE, the antiprotons facility (AD), nTOF and the experiments in the East Area [2].

A fraction of the proton pulses from the PS is sent to the Super Proton Synchrotron (SPS), 1000 m in radius, to be accelerated to 450 GeV and then, amongst other, be injected in the Large Hadron Collider (LHC). The SPS was commissioned in 1976. A sketch of the present CERN accelerator is shown in Fig 1.

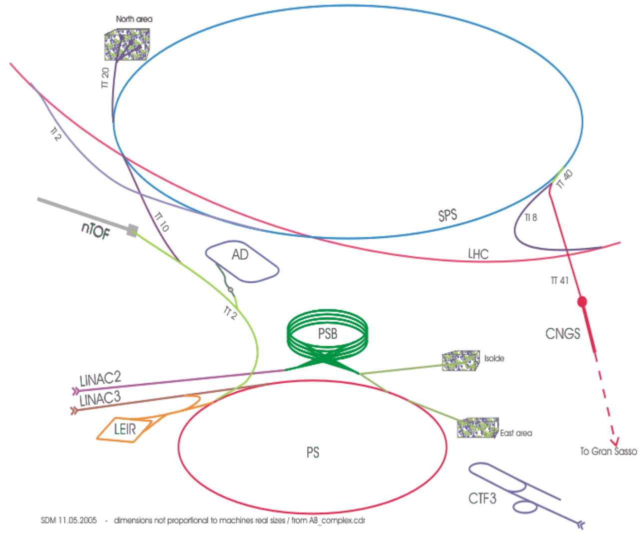


Figure 1: Layout of the present LHC proton injectors.

### *Linac2 and the Reasons for Its Upgrade*

Linac2 [3] was commissioned in 1978 and it consists of a three Alvarez-type Drift Tube Linac (DTL) tanks, operating at the frequency of 202.56 MHz. Electromagnetic quadrupoles are housed inside the 128 drift tubes necessary to bring the beam energy from 0.75 to 50 MeV. Until 1993 the pre-injector was a 750 kV Cockcroft-Walton, which was then replaced by a 4-vane Radio Frequency Quadrupole (RFQ2) [4], capable of delivering almost 200 mA of protons to the DTL. Linac2 is working at a current well beyond its design limit (150 mA) and the RF hardware is working at its technical limit. Besides, the output energy of 50 MeV is too low for any further current increase in the PSB, limited by space charge detuning at injection.

All the above reasons motivate the construction of Linac4 [5], accelerating $H^-$ to an energy of 160 MeV, which halves the space charge detuning at PSB injection and allows charge exchange injection.

### *Upgrade of the Injectors*

Linac4, which is approved to provide $H^-$ for the PSB operation in 2013, can be the first stage of a more global injector upgrade, which includes a Superconducting Proton Linac (SPL) [6] delivering a 4 GeV beam to a new synchrotron (PS2). PS2 could inject in the SPS at 50 GeV opening the potential for a higher proton beam flux from the SPS [7]. A technical design study on SPL and PS2 are due to be completed by 2011 when a decision on further upgrades could be taken. The layout on the Meyrin site [8] is shown on Fig.3. In the next two sections the ongoing activities for Linac upgrades will be described.

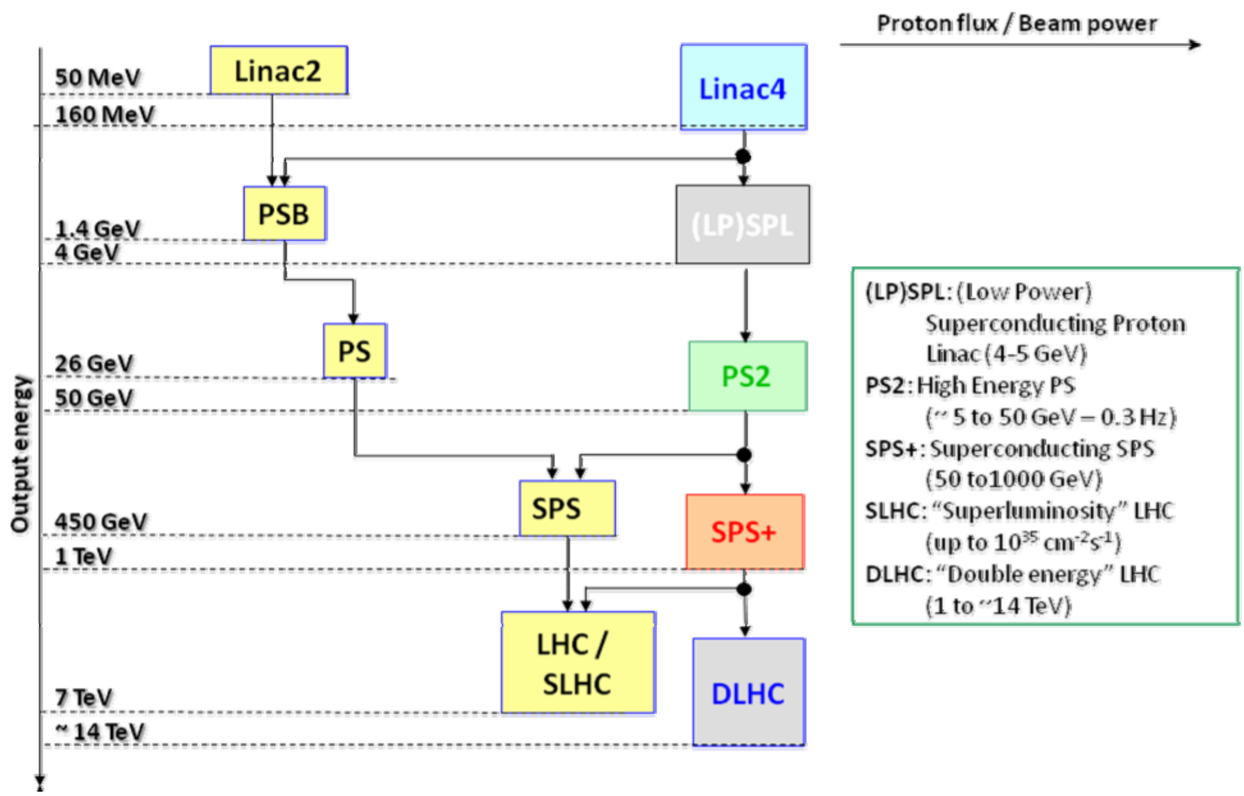


Figure 2: Block diagram of the present CERN proton injectors (left) and the possible staged upgrade (right).

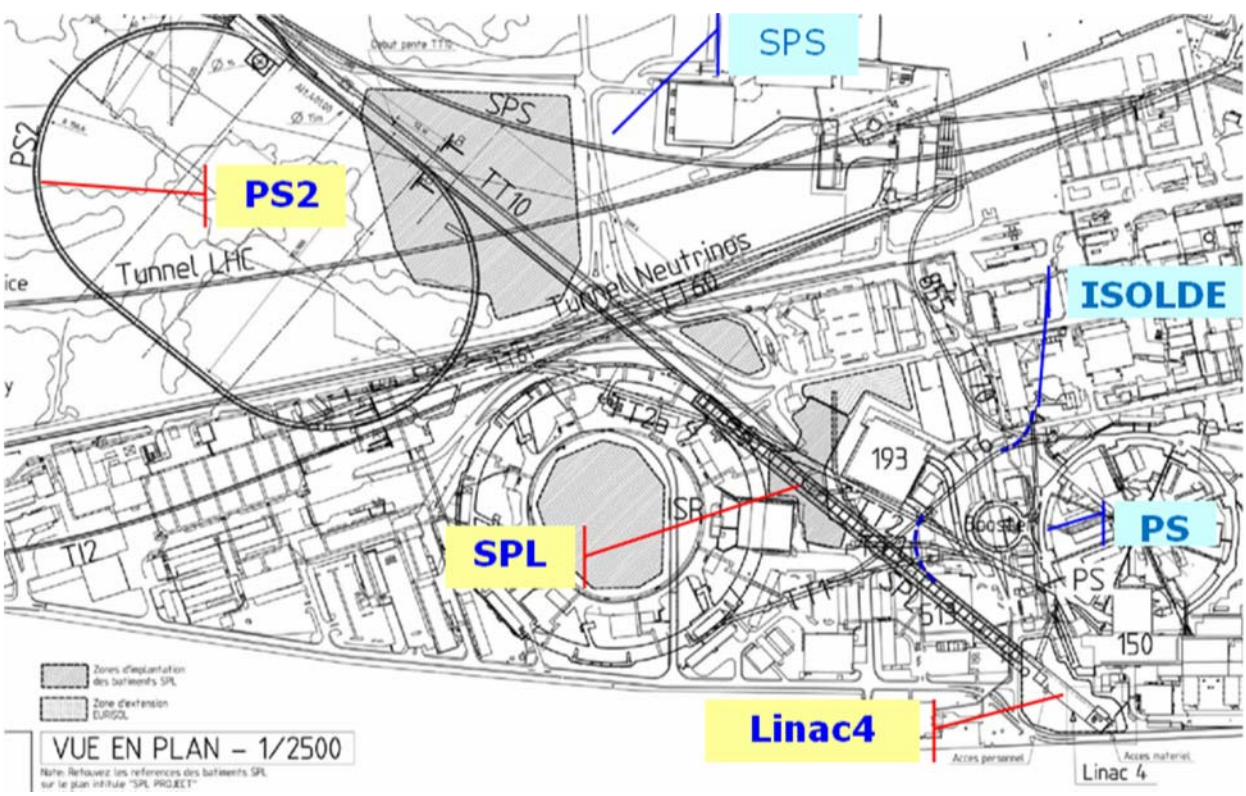


Figure 3: Layout of the new injector on the CERN Meyrin site.

.

## LINAC4

The Linac4 project started officially in January 2008 with the goal of having a Linac injecting 160 MeV $H^-$ beam in the PSB by 2013. The main characteristics of the beam from Linac4 are summarised in Table 1. In brackets the values to be achieved for future (Low Power-)SPL operation.

Table 1: Linac4 Beam Characteristics

| Ion species | $H^-$ |
|---|---|
| Output kinetic energy | 160 MeV |
| Bunch frequency | 352.2 MHz |
| Max. repetition rate | 1.1 (2) Hz |
| Beam pulse duration | 0.4 (1.2) ms |
| Chopping factor (beam on) | 65% |
| Source current | 80 mA |
| Linac current | 64 mA |
| Average current during beam pulse | 40 mA |
| Average beam power | 2.8 kW |
| Particles / pulse | $1.0\ 10^{14}$ |
| Transverse emittance in -rms | 0.25 mm mrad |
| Transverse emittance out - rms | 0.4 mm mrad |

### *Linac4 Layout*

Linac4 is a normal conducting linear accelerator operating at the frequency of 352MHz. The first element of Linac4 is a 2MHz RF volume source [9] which provides a 400 µs 80 mA $H^-$ beam at 45 keV with a repetition rate of 2 Hz. The first RF acceleration (from 45 keV to 3 MeV) is done by a 3 m long Radio Frequency Quadrupole [10]. At 3 MeV the beam enters a 3.6 meter long chopper line, consisting of 11 quadrupoles, 3 bunchers and two sets of deflecting plates. The beam is then further accelerated to 50 MeV in a conventional Drift Tube Linac (DTL). The DTL, subdivided in 3 tanks, is 19 meters long. Each of the 111 drift tubes is equipped with a Permanet Magnet Quadrupole (PMQ). The acceleration from 50 to 100 MeV is provided by a Cell-Coupled Drift Tube Linac (CCDTL). The CCDTL is made of 21 tanks of 3 cells each for a total length of 25 meters. Three tanks are powered by the same klystron, and constitute a module. The focusing is provided by electromagnetic quadrupoles placed outside each tank, with the option of using Permanet Magnet Quadrupoles between coupled tanks. The acceleration from 100 to 160 MeV is done in a π-Mode structure. The PIMS is made of 12 tanks of 7 cells each for a total of 22 m. Focusing is provided by 12 Electromagnetic Quadrupoles (EMQ). A 60 m long transfer line, composed of 2 horizontal and 2 vertical bendings, 15 quadrupoles and a debuncher cavity connects the Linac4 tunnel to the present Linac2 to PSB transfer line.

### *Prototyping Activities*

Prototyping activities have been going on since 2004, in order to prepare the Linac4 technical design report and to help choosing the most reliable technology and the best engineering solution for the components of Linac4. Prototyping activities include the realisation of a chopper device complete with its driver; two prototypes for the DTL; three prototypes of PMQ for the DTL; two prototypes for the CCDTL and a cold model of the PIMS structures. A list of the issues addressed and the achievements of the past and ongoing prototyping activities is given in the following:

- Chopper structure: a meander type structure printed on alumina substrate has been realised in collaboration with industry. Electrical and vacuum tests have confirmed the final choice of material and geometry. Assembly in a quadrupole has been demonstrated. [11]
- A driver for the chopper plates has been realised in house and a commercial amplifier has been bought and tested. Both solutions present advantages and disadvantages. The required voltage and repletion rate for LP-SPL operation has been achieved. The ultimate repetition rate operation (40 MHz) is still to be fully demonstrated. [12]
- A cold model of the DTL has been realised to test the tuning capability [13]
- A mechanical model of the DTL has been realised to test the mechanical tolerances achievable with the chosen assembly procedure [13]
- Two models (1 and half cell) of CCDTL have been tested at high power [14]
- A cold model for the PIMS is undergoing RF measurements[15]
- A klystron test stand has been set-up to demonstrate the operation of decommissioned LEP klystron in pulsed mode.

### *The 3 MeV Test Stand*

Experience with other Linacs and dedicated beam dynamics studies [16] show that the most difficult part to master in a high intensity Linac is the low energy part, where the beam is slow and under the influence of strong space charge. Besides, issues like neutralisation at the lowest energy and non-standard beam distribution can result in beam parameters that severely differ from computational prediction. In order to have enough time to study and master the low energy beam a test stand including the source, the Radio Frequency Quadrupole and the chopper line is being put in place in the PS south hall, with the aim of being operational by 2010, before the final Linac4 building will be available. The 3 MeV test-stand will be equipped with a dedicated diagnostics line and a state-of-the-art device capable of detecting the population of adjacent microbunches (spaced by 2.8 ns) with a dynamic range of $10^6$[23]. The goal of the 3 MeV test stand is to demonstrate the capability of delivering a 70 mA , 400 µs long, beam at 3 MeV of energy, matched to the DTL and adapted to the 1 MHz PSB bucket, i.e. with 123 over 352 pulses removed and intercepted by the in-line beam dump [17].

# SUPERCONDUCTING PROTON LINAC

The location [8] of Linac4 has been chosen to allow using Linac4 as the front end of a Superconducting Proton Linac delivering a 4-5 GeV beam. The SPL could initially be configured for "low power" and serve as injector for a new 50 GeV Synchrotron (PS2) and later be configured for high power and serve as a multi-megawatt proton facility for future physics needs, e.g. a neutrino factory. The LP-SPL (and PS2) would complete the re-juvenation of the CERN LHC injectors while leaving 50% of the pulses available for nuclear physics experiments, e.g. an upgraded ISOLDE. Linac4 can work as front end for the LP-SPL without major modification, whereas for the SPL a new source and new electronics and power supplies should be procured. The shielding, the alignment and the correction system of Linac4 is designed to work at the highest possible beam duty cycle, 6%.

The goal of the SPL activities is to complete a Technical Design Report by the year 2011 when a decision on the construction of the SPL and PS2 could be taken. Should this decision be positive a LP-SPL could be available in 2017.

The main parameters of LP-SPL and SPL are listed in Table 2.

Table 2: SPL Parameters

| | **LP-SPL** | **SPL** |
|---|---|---|
| Energy [GeV] | 4 | 5 |
| Beam power [MW] | 0.192 | >4.0 |
| Repetition rate [Hz] | 2 | 50 |
| Average pulse current [mA] | 20 | 40 |
| Source current [mA] | 40 | 80 |
| Chopping ratio [%] | 62 | 62 |
| Beam pulse length [ms] | 1.2 | 0.4-1.2 |
| Beam duty cycle [%] | 0.24 | 2.0- 6.0 |
| Number of klystrons (704 MHz, 5 MW) | 24 | 53 |
| Geometric cavity beta | 0.65/1.0 | 0.65/1.0 |
| Number of cavities | 42/160 | 42/200 |
| Cavities/klystron | 8 - 16 | 4-8 |
| Cavities/cryostat | 6/8 | 6/8 |
| Length including Linac4 [m] | 459 | 534 |

## *Nominal Layout*

The layout of the SPL is based on 704 MHz 5-cell elliptical cavities. Two building blocks are used in the layout: a low-beta module (beta=0.65, Eacc=19MV/m) and a high-beta module (beta=0.92, Eacc=25 MV/m), see Fig. 4 and 5. A low beta module contains 6 cavities and two quadrupole doublets (2 periods), a high beta module contains 8 cavities and one doublet. Seven low beta modules are used to bring the energy from 160 MeV to 589 MeV and 20/25 high beta modules bring the energy to 4/5 GeV. Special attention has been paid in the beam dynamics design to achieve a proper matching between the two sections.

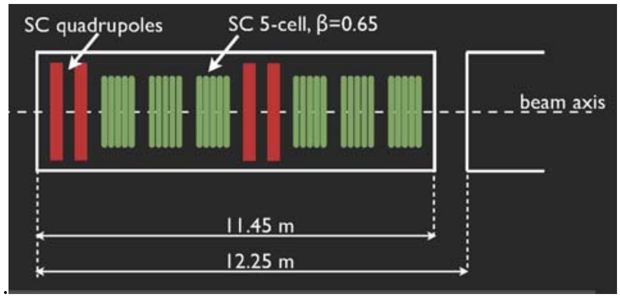


Figure 4: Low beta module.

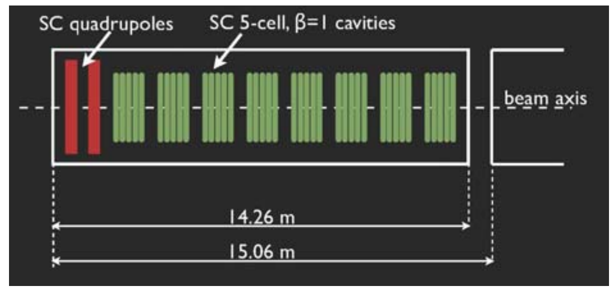


Figure 5: High beta module.

## *Research Activities*

Several themes have been identified for the R&D necessary to complete a Technical Design Report for the SPL. The main activities are listed in the following:

- Tests of surface treatment techniques on a 704 MHz, low beta single cell cavity from CEA are expected for 2009. The goal of this test is to verify the efficiency of electro-polishing low beta cavities.
- Prototypes of β=0.65 and β=0.92 5-cell cavities are to be developed with the aim to demonstrate the gradients of 19 MV/m and 25 MV/m, which have so far been assumed in the beam dynamics design.
- The design of a cryostat adapted to house 704 MHz cavities.
- Ideally, equip a cryostat with 8 cavities 5-cell Beta=0.92 and perform for high power RF tests.
- Development of a plasma generator for the 2 MHz RF source as a part of the European FP7 activities.
- Development of a low level RF system.

# ACTIVITIES WITHIN HIPPI

HIPPI (High Intensity Pulsed Proton Injector) is a Joint Research Activity in the framework of CARE [18] (Coordinated Accelerator Research in Europe), within the 6$^{th}$ European Framework Program (2004-2008). Ten European laboratories participate in HIPPI and the projects supported within HIPPI are Linac4, FAIR and the ISIS upgrade.

The scientific work in HIPPI is organized in 4 work packages addressing the issues of normal conducting structure (WP2), superconducting structures (WP3), chopping (WP4) and beam dynamics (WP5).

A lot of the prototyping work for Linac4 was fostered by HIPPI. In particular in the work package normal conducting structure activities on CCDTL prototyping were very instrumental to the choice of an optimised design for the structure [19].

The original design of Linac4 considered a 704 MHz Side Coupled Linac Structure for the energy 90-160 MeV. Prototyping work and studies were carried out on this structure which wasn't eventually retained [20].

Part of the work in WP3, the study of superconducting spoke cavities [21], was the basis for the study of an alternative Superconducting layout for the high energy part of Linac4. This solution was also discarded with the reason that a short superconducting section added unnecessary complexity for Linac4 itself, but it allowed to explore all possibilities.

For the chopper prototyping, the work within HIPPI was fundamental for the developing of a meander structure adapted to 3 MeV and its integration in the 3 MeV beam line. The prototyping activity was fully covered by HIPPI [22]. The system is ready to be tested at the 3 MeV test-stand.

The work within WP5 included beam dynamics and instrumentation. The development of a time resolved device [23] able to access the efficiency of the chopper is instrumental to the measurement program of the 3 MeV test stand.

## ACKNOWLEDGEMENTS

We acknowledge the support of the European Community-Research Infrastructure Activity under the FP6 "Structuring the European Research Area" programme (CARE, contract number RII3-CT-2003-506395).

We acknowledge the support of ISTC projects 2888 and 2875 for DTL and CCDTL prototyping activities.

We acknowledge the support of the IPHI projects in the mechanical, RF and beam dynamics design of the RFQ and for the diagnostic line of the 3MeV test-stand.

## REFERENCES

[1] C.E. Hill, M. O'Neil "The High Voltage System for the High Intensity CERN Proton Source". LINAC98, Chicago, IL, USA ,ANL-98/28, 1998

[2] K. Schindl "The injector chain for the LHC", Chamonix IX, 25-29 Jan 1999

[3] E. Boltezar, H. Haseroth, W. Pirkl, G. Plass, T. Sherwood, U. Tallgren, P. Tetu, D. Warner, M. Weiss,"The New CERN 50 MeV Linac" 1979 LINAC Montauk, NY, USA. BNL51134, 1979.

[4] M. Weiss, "The RFQ2 complex : the future injector to CERN Linac 2",CERN-PS-92-34-HI.- Geneva : CERN, 1992.

[5] M. Vretenar ed., LINAC4 technical Design Report, CERN-AB-2006-084 ABP/RF (2006).

[6] F. Gerigk ed., SPL Conceptual Design Report CERN-2006-006 (2006).

[7] R. Garoby, "Upgrade Issues for the CERN Accelerator Complex", EPAC'08, Genoa, June 2008, FRYAGM01, p. 3734 (2008).

[8] J.L. Baldy et al., "Site Layout of the Proposed New Hadrons' Injector Chain at CERN", CERN-AB-2007-061-PAF.

[9] D. Küchler, Th. Meinschad, J. Peters, R. Scrivens, "A RF driven $H^-$ Source for LINAC4", CERN-AB-2007-073.

[10] C. Rossi, P. Bourquin, J.B. Lallement, A.M. Lombardi, S. Mathot, M. Timmins, G. Vandoni, M. Vretenar, S. Cazaux O. Delferriere, M. Desmons, R. Duperrier, A. France, D. Leboeuf, O. Piquet, "The Radiofrequency Quadrupole Accelerator for the CERN Linac4", this Conference.

[11] F.Caspers et al., "The CERN-SPL Chopper Concept and Final Layout", EPAC'04 Proceedings (2004)

[12] M. Paoluzzi et al., CERN-AB-Note-2008-040 (2008)

[13] S. Ramberger, N. Alharbi, P. Bourquin, Y. Cuvet, F. Gerigk, A.M. Lombardi, E. Sargsyan, M. Vretenar, A. Pisent, "Drift Tube Linac Design and Prototyping for the CERN Linac4", this Conference.

[14] M. Vretenar, Y. Cuvet, G. De Michele, F. Gerigk, M. Pasini, S. Ramberger, R. Wegner, E. Kenjebulatov, A. Kryuchkov, E. Rotov, A. Tribendis, "Development of a Cell-Coupled Drift Tube Linac (CCDTL) for Linac4", this Conference.

[15] M. Vretenar, P. Bourquin, R. De Morais Amaral, F. Gerigk, J.-M. Lacroix, G. Vandoni, R. Wegner, "Development Status of the Pi-Mode Accelerating Structure (PIMS) for Linac4", this Conference

[16] A.M. Lombardi et al; "Beam dynamics in Linac4 at CERN", HB2008 Proceedings, Nashville, USA (2008)

[17] J-B. Lallement et al., "Measurement strategy for the CERN Linac4 chopper line", HB2006 Proceedings, Tsukuba, Japan (2006).

[18] http://care.lal.in2p3.fr/

[19] G. De Michele, F. Gerigk M. Pasini, M. Vretenar, A. Tribendis, "CCDTL section for Linac"4 CARE-Report-08-021-HIPPI

[20] J.-M. De Conto, J.-M. Carretta, Y Gomez-Martinez, R Micoud," Development of Side Coupled Cavities",CARE-Report-08-11-HIPPI

[21] H. Glückler, W. Günther, M. Pap, R. Tölle, E. Zaplatin,G. Olry, G. Michel, S. Bousson, P. Szott, F. Eozenou, Y. Gasser, "The Julich triple spoke resonator "CARE-Report-08-015-HIPPI

[22] F. Caspers, T. Kroyer, M. Paoluzzi, "Cern chopper final report", CARE-Report-08-020-HIPPI

[23] M. Hori, K. Hanke, "Design and Construction of a Beam Shape and Halo Monitor for the CERN SPL", CARE-Note-2005-013-HIPPI

# LASER ACCELERATION OF QUASI-MONOENERGETIC MeV-GeV ION BEAMS

J.C. Fernandez, LANL, Los Alamos, New Mexico

*Abstract*

Laser interactions with thin solid targets can produce sheath fields of tens of TV/m, which have been used to accelerate ions to several MeV with ps pulse lengths, high currents, and low transverse emittance. While previous results have had 100% energy spread, recent experiments using foils coated with a few monolayers have produced quasi-monoenergetic beams with 17% energy spread near 3 MeV. Such beams may be of interest as injectors or sources. Simulations show the potential for acceleration to hundreds of MeV or GeV energies using very thin foils.

**CONTRIBUTION NOT RECEIVED**

# LINAC R&D FOR THE ILC TECHNICAL DESIGN REPORT

M. C. Ross, Fermilab, Batavia


## Abstract

The International Linear Collider (ILC) Technical Design Report (TDR) is scheduled for publication in 2012. The TDR will include an updated ILC baseline technical design description, results from critical R&D programs in support of key parameter choices, and one or more models for a Project Implementation Plan with an associated value estimate. The focus of linac R&D is to: 1) achieve the specified superconducting rf cavity accelerating gradient of 35 MV/m with a corresponding production yield, 2) design and test cryomodule assemblies that include "plug-compatible" sub-components with specified interfaces, and 3) demonstrate system performance with nominal ILC high intensity beams. In keeping with the international nature of the project, R&D is underway at ILC partner institutions with results and infrastructure that are shared throughout the project effort. This paper describes the technical challenges to be addressed and summarizes ongoing activities and plans.


**CONTRIBUTION NOT RECEIVED**

# ILC SITING IN MOSCOW REGION NEAR DUBNA AND ILC RELATED ACTIVITY AT JINR

Yu. Budagov, Yu. Denisov, I. Meshkov, G. Shirkov, A. Sissakian, G. Trubnikov, JINR, Dubna, 141980, Russia

*Abstract*

The investigations on ILC siting in the Dubna region and ILC technical activity at JINR are presented. International intergovernmental status of JINR, stable geological and plain relief conditions, comfortable location and well developed infrastructure create a set of advantages of the JINR site in the neighborhood of Dubna. The shallow layout of accelerator tunnel makes it possible to use a communication gallery at the surface instead of second one. This is an effective way of significant cost reduction of all conventional facilities and explicit labor of the project.

Besides JINR physicists take part in several fields of activity in ILC: works on photo injector prototype, participation in design and construction of cryomodules, laser metrology, etc. [1].

## INTRODUCTION

The last Global Design Effort (GDE) and ILC Steering Committee (SC) meetings took place at JINR, in Dubna on June 3-7, 2008. These meetings were dedicated to ILC convention facilities and siting and were focused at proposals of JINR [2]. The meetings finished with helicopter flight for leaders of ILC SC and GDE along the ILC possible layout (Fig. 1).

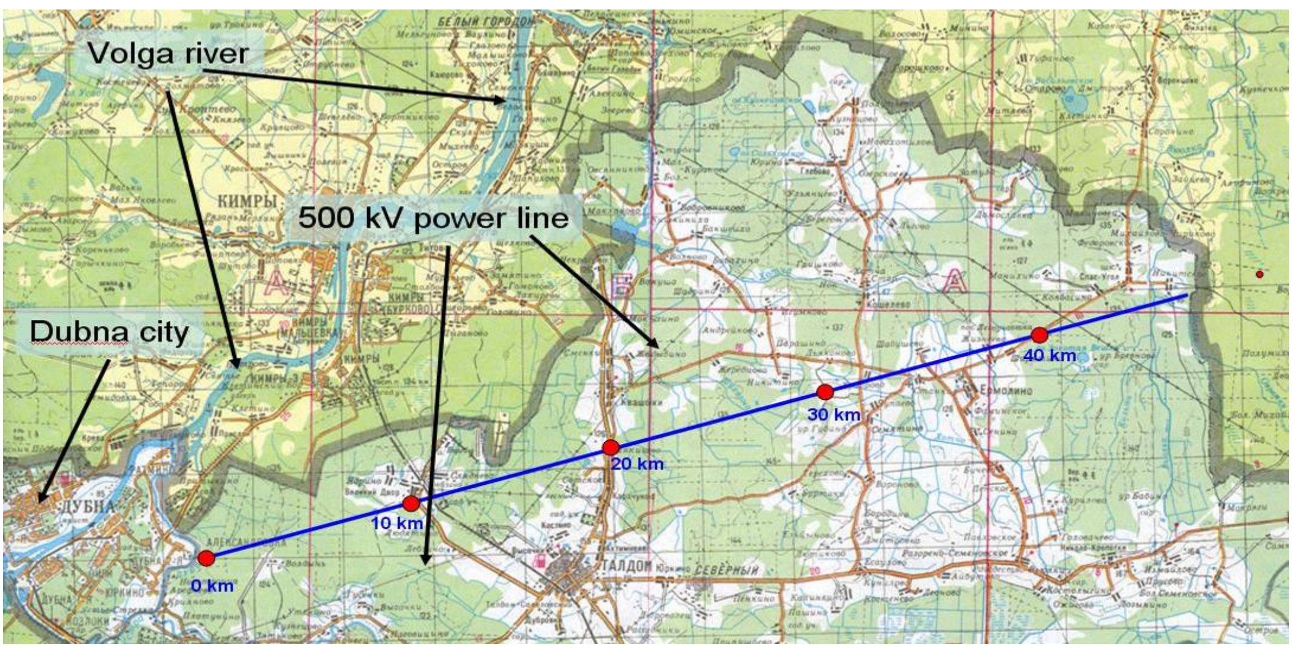


Figure 1: Planned location for ILC near Dubna, Moscow region.

The international scientific community has demonstrated a considerable interest to the proposal of ILC construction in Russia, in Dubna region, where JINR has essential benefits and privileges as an International Intergovernmental Organization and has a unique experience of organization and successful realization of large-scale research projects based on wide cooperation of scientific centers and industrial enterprises of many countries.

Taking into account that the ILC project is considered by the international scientific community as a strategic priority in the field of high energy physics after the LHC era, the International Scientific Council of the JINR has supported the idea of ILC siting in the Dubna region and has recommended to take part in preparation of the collider project. These recommendations had been approved by the Committee of Plenipotentiaries of the JINR Member States. The ILC project and it's siting in the Dubna region have been discussed and supported at different meetings of the Russian Academy of Sciences (RAS).

The initiative to host the ILC in the Dubna site has been strongly supported by the Moscow region governor B. Gromov.

## DUBNA SITE DESCRIPTION

The ILC linear accelerator is proposed to be placed in the northern part of Moscow region to the north-east from the existing scientific center JINR in the town Dubna (Fig. 1). This area is thinly populated, the path of the accelerator traverses only two small settlements and a railway with light traffic between the towns Taldom and

Kimry at the distance up to 50 km from Dubna. The region is mainly covered with forest with small inclusions of agricultural lands (see Fig. 2) and it is uniform along the line of 150-200 km in this direction.

Figure 2: The typical view of ILC proposed area from helicopter.

This area is situated within the Russian plate, a part of the Eastern European ancient platform, is a stable, steady structural element of the earth's crust. The characteristic feature of this territory is the uniformity, monolithic character of the surface. The existing rises of the relief in the form of single hills and ridges have smoothed shapes, soft outlines and small excesses. The territory of the area is waterlogged. The absolute marks of the surface range from 125 to 135 m with regard to the Baltic Sea level (see Fig. 3).

The ILC area is located in the southern part of a very gently sloping saucer-shaped structure – the Moscovian syneclise. Alluvial deposits are bedded above, i.e. fine water-saturated sands, 1-5 m of thickness. Below one can find semisolid drift clay of the Moscovian glaciations with inclusions of detritus and igneous rocks. The thickness of moraine deposits is 30-40 m. Under the moraine of the Moscovian glaciations fluvioglacial water-saturated sands and loams of the Dnieper glaciations are bedded. Jurassic clays and carboniferous limestone of the platform mantle are spread under the overburdens at the depth of 50-60 m. This has been confirmed by the geological survey carried out during the selection of site for construction of the U-70 accelerator.

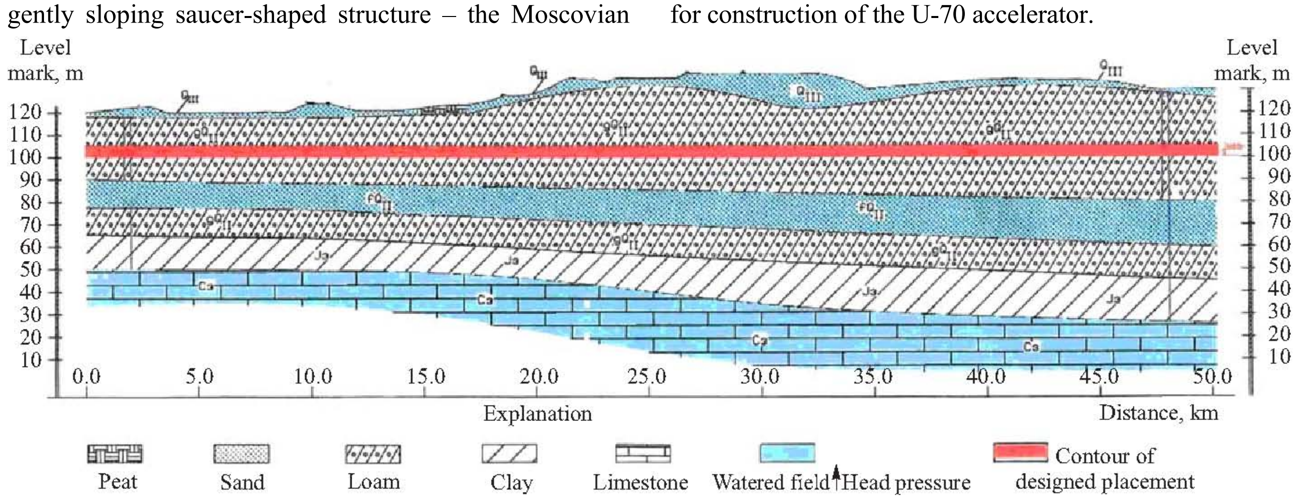


Figure 3: Engineering-geological sectional view along the ILC path axis.

The ILC linear accelerator is proposed to be placed in the drift clay at the depth of 15÷25 m so that below the tunnel there should be watertight soil preventing from the underlying groundwater inrush. This will make it possible to construct tunnels of the accelerating complex using tunnel shields with a simultaneous wall timbering by tubing or falsework concreting. Vertical shafts, experimental and service halls, and some other underground service volumes could be constructed in the cut and cover way and this should sufficiently reduce the price of civil engineering construction.

JINR and Dubna have at their disposal all the necessary infrastructure to accommodate specialists for the period of the accelerator construction, to accumulate the equipment, to provide for the project-production support during manufacturing of the special-purpose equipment at the enterprises located in Dubna and the region. The town Dubna possesses all the necessary means of transport to deliver all kinds of the equipment of the accelerator itself and its technological systems: highways, railways, waterways (the Volga River and Moscow channel). The international airport "Sheremetyevo" is situated at the distance of 80 kilometers from Dubna.

The northern part of Moscow region and the neighboring regions have enough of objects of generation, transmission and distribution of electrical energy. There are first-rate generating stations: the Konakovo electric power station and the Udomlia atomic power plant. Two trunk transmission lines with the voltage 220 and 500 kV pass through the territory of Dubna and along to the possible ILC line. The preliminary study of the existing possibilities of the power supply for the accelerator and its infrastructure with the total power up to 300 MW resulted in the convenient variant: construction of the 220 kV power line, 35-40 km long, directly from the center of generation – the Konakovo power station to the central experimental zone of the accelerator.

## ONE TUNNEL SOLUTION

A possible one-tunnel solution for the accelerator structure and convention facilities for Dubna site is presented in Fig. 4. The scheme is as follows:

- the main technological tunnel with accelerating structures, magnetic elements for beam focusing and diagnostics means will be put on depth of ~ 20м so that from below and above the tunnel there will be an impermeable stratum preventing break of underground waters;
- communication tunnel (collector) will be placed directly above the technological one near the ground surface at the depth of 3-4 m practically following its form. This tunnel is necessary for power supplies, RF power sources, data storage devices, electronic and control systems, etc.;
- technological connection between the accelerator tunnel and collector will be provided by vertical shafts of various diameters made by drilling;
- connection of ground and underground structures will be provided by vertical and horizontal shafts (stairs, elevators, etc).

The one-tunnel design is economically and technically preferable for a number of reasons:

- communication tunnel practically can be of any size to discharge the basic tunnel. Moreover it can be made by open way that is rather inexpensive;
- vertical communication service lines (service ducts) can be made by means of drilling that is rather cheaper then underground horizontal lines; their number and sizes can be optimized, and waterproofing will not be required as well;
- export of ground waters will be performed directly on the surface without pumping facilities;
- operation of communication tunnels will be substantial simplified;
- technological and cable communications between the communication tunnel and ground buildings and constructions will be considerably reduced.

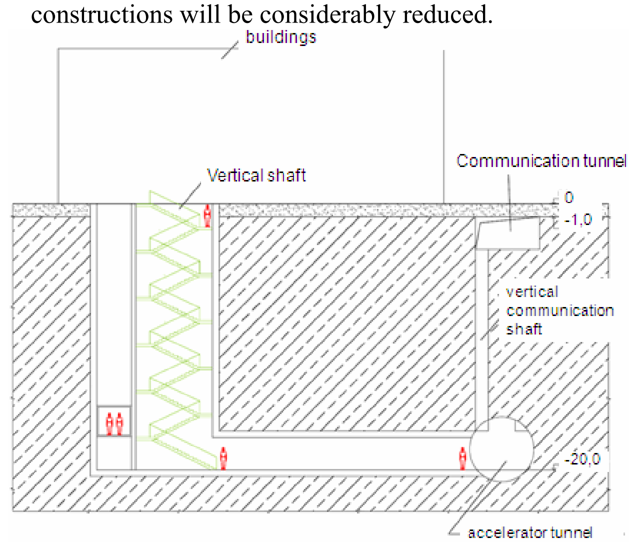


Figure 4: One tunnel solution.

## ILC ACTIVITY AT JINR

The JINR is carrying out active work to develop international cooperation in the ILC project and in the related projects, in the XFEL and CLIC projects in particular. The scientists from JINR participate in all international forums and committees on the ILC. JINR has successfully organized wide cooperation in Russia in order to perform experimental and theoretical investigations on the project with Russian research centers: BINP of Siberian Brunch of RAS, Institute for Applied Physics (IAP) of RAS (Nizhniy Novgorod), GSPI, Physical Institute of RAS etc.

JINR in collaboration with KEK (Japan), DESY (Germany) and IAP of RAS is carrying out research and design works for creation of the injector, an electron source on the base of a photoemissive gun. Creation of the test bench to study properties of photocathodes, new materials and also creation of new unique laser system are planned (Fig. 5). The test bench on the base of the linear accelerator of electrons LINAC-800 for adjustment of beam diagnostics tools will be made in JINR. The injector will be a part of the bench.

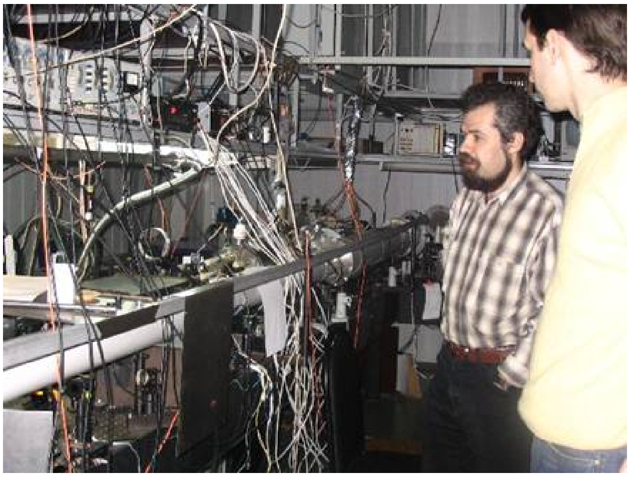

Figure 5: JINR and IAP experts at the superpower laser system at IAP of RAS in Nizhniy Novgorod.

Specialists from JINR and VNIIEF (Sarov) have studied the production of bimetal tubes (stainless steel and titanium) by explosion welding (Fig. 6). The tube is used as a transitional load-bearing element in the 4th generation cryomodule construction for the ILC.


Figure 6: Explosion welding of bimetal tubes.

The R&D works have result in developing the pilot technical process for production of bimetal billet of the tube by explosion welding and researching a micro-structure of the weld joint.

JINR develops a test bench at CERN for the precise laser metrology. The precision of 1.0 micron of laser beam position is achieved on the base of 100 m. At JINR it is planned to set this system at the LINAC-800 accelerator complex on the base of 2 x 250 m.

DR magnetic system simulations and magnet prototype construction in collaboration with SLAC are in progress. The aim is to design and possibility to construct and to test at JINR a series of magnetic system elements (dipole magnets) of ILS damping ring.

A series of activities in the field cryogenic engineering and diagnostics has been started and well developed at JINR.

## CONCLUSION

The main advantages of the ILC construction in Dubna are as follows:

- JINR as a basic international intergovernmental organization.
- Prevalent legal practice makes it possible to get the land of the ILC location to permanent free use just as it has been done for JINR, according to the agreement between JINR and the RF government.
- The proposed territory is extremely thinly populated and practically free of industrial structures, rivers and roads.
- The area is absolutely steady seismically and has stable geological characteristics.
- A flat relief and geological conditions allow to place ILC on a small depth in the dry drift clay and to perform construction of tunnels, experimental halls and other underground objects with the least expenses, including cut-and-cover.
- The only one shallow tunnel with accelerator structures and communication gallery on the surface
- Sources of the electric power of sufficient capacity.
- The developed system of transport and communication services.
- Presence of a modern network and information infrastructure, including one of the largest Satellite Communication Center.
- The special economic zone of Dubna with preferential terms for high technology technical production.
- A powerful scientific and technical potential of Dubna town.

Realization of such a wide scale project namely in Dubna will let Russia to become in a perspective future by a leader and center of attraction for scientists from Russia and neighbor countries. Another obvious factor is an attraction of significant investments and financial resources at all stages of the project including further exploitation of the new accelerator center during long years. Creation of ILC accelerator complex as international collaboration will raise prestige of the fundamental science in a total and the role of Russia as one of the world leader.

## REFERENCES

[1] G. Trubnikov, Yu. Budagov, Yu. Denisov et al. ILC. International Linear Collider, JINR Communication D9-2008-78, edited by A.Sissakian and G.Shirkov, Dubna, JINR, (2008), 15.

[2] http://www.linearcollider.org/.

# STATUS AND FUTURE PROSPECTS OF CLIC

S. Döbert, for the CLIC/CTF3 collaboration, CERN, Geneva, Switzerland

*Abstract*

The Compact Linear Collider (CLIC) is studied by a growing international collaboration. Main feasibility issues should be demonstrated by 2010 with the CLIC Test Facility (CTF3) constructed at CERN. The CLIC design parameters have recently been changed significantly. The rf frequency has been reduced from 30 GHz to 12 GHz and the loaded accelerating gradient from 150 MV/m to 100 MV/m. A new coherent parameter set for a 3 TeV machine will be presented.

The status and perspectives of the CLIC feasibility study will be presented with a special emphasis on experimental results obtained with CTF3 towards drive beam generation as well as progress on the high gradient accelerating structure development.

The frequency change allows using high power x-band test facilities at SLAC and KEK for accelerating structure testing at 11.4 GHz. The design gradient of 100 MV/m has been achieved in a recent test at SLAC with a very low breakdown-rate.

## INTRODUCTION

There is a consensus in the community of high energy particle physicists that LHC physics results need to be complemented in the future by experiments done with a high-energy lepton collider in the TeV centre-of-mass energy range [1]. A promising candidate for such a facility is CLIC, a linear collider aiming at a centre-of-mass energy of 3 TeV and a luminosity in the range of $10^{34}$ $cm^{-2}$ $s^{-1}$ presently studied by a large international collaboration [2, 3].

In a linear collider the particles have to be accelerated in a single pass to the final energy, 80% of the facility length is used for acceleration. Naturally the emphasis for the R&D on CLIC is on the rf system which has to reach a maximum accelerating gradient and efficiency to keep the length and cost limited. The CLIC scheme uses high-frequency normal conducting accelerating structures and a two beam scheme to cope with these challenges. In 2007 the rf frequency has been reduced from 30 GHz to 12 GHz and the accelerating gradient from 150 MV/m to 100 MV/m for CLIC. This change was motivated by high gradient constraints found experimentally which made the ambitious goal of 150 MV/m unrealistic. A general optimization study taking into account these rf constraints showed that the new parameters represent an optimum with respect to luminosity and cost [3].

The CLIC Test Facility CTF3 [4] is being built at CERN by the CTF3 collaboration to investigate and demonstrate the key technical issues of the CLIC scheme. This feasibility study should conclude in 2010 with a Conceptual Design Report for CLIC.

## COMPACT LINAER COLLIDER CLIC

The compact linear collider CLIC uses high-frequency high-gradient normal conducting rf accelerating structures to accelerate the electrons. An accelerating gradient of 100 MV/m at 12 GHz allows to keep such a facility bellow a length of 50 km. The 12 GHz rf power needed to energize the accelerating structures is extracted from a drive beam running parallel to the main beam. This two beam scheme is an efficient and less costly way to provide the rf power needed for acceleration as compared to the use of 12 GHz klystrons. In order to achieve the luminosity needed for the experiments the electrons and positron beams need to be produced with extremely small emittances, accelerated and transported without significant degradation and finally focused to spot sizes in the nm range. The main parameters of CLIC can be found in table 1.

Table 1: CLIC Main Parameters

| | | |
|---|---|---|
| Centre of mass energy | 3 | TeV |
| Luminosity (in 1% energy) | $2*10^{34}$ | $cm^{-2}$ $s^{-1}$ |
| Number of particles per bunch | $3.72*10^{9}$ | |
| Bunch separation | 0.5 | ns |
| Number of bunches per train | 312 | |
| Proposed site length | 48.4 | km |
| AC to beam power efficiency | 7.2 | % |

### *The Facility Layout*

A schematic layout of CLIC is shown in figure 1. A central injector complex prepares the ultra low emittance beams needed for high luminosity collisions. The complex contains the positron and polarized electron sources, pre-damping and damping rings, bunch

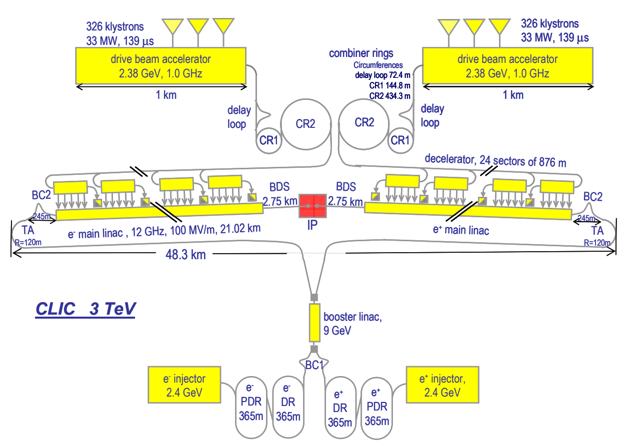


Figure 1: Schematic CLLC layout (not to scale).

compressors and a 9 GeV booster linac. These beams are then transported by a long transfer line to both ends of the linear collider. The corresponding drive beams providing the rf power for acceleration are also generated in a central location. The high-current low-energy drive beams are than decelerated along the main linacs transferring the power to the main beam which is accelerated in parallel.

### Drive Beam Generation

A unique feature of the CLIC scheme is the rf power source using a high current drive beam. A long 139 µs long pulse train with 4.2 A average current and a 500 MHz bunch spacing is accelerated efficiently to 2.38 GeV using 1GHz klystrons and fully loaded accelerating structures. This bunch train is then combined into 24 beam pulses with a pulse length of 240 ns with 100 A average current and 12 GHz bunch spacing in a sequence of delay loop and combiner rings. The details of the beam combination are explained in the test facility section below. The generated drive beam pulses are then sent along the linac towards the extremities and then with precision timing injected into the corresponding decelerator section (see layout). The drive beam can be seen as a very efficient rf pulse compression system which allows to transform the rf power generated efficiently with low peak power and long pulse length into short pulses with high peak power needed for acceleration. The drive beam parameters are listed in table 2.

Table 2**:** Drive Beam Parameters

| | | |
|---|---|---|
| Drive Beam Linac | | |
| Linac RF frequency | 999.5 | MHz |
| Beam energy | 2.38 | GeV |
| Klystron peak power | 33 | MW |
| Number of klystrons | 326*2 | |
| Pulse length (bunch train) | 139 | µs |
| Beam current | 4.2 | A |
| RF-to-beam efficiency | 93 | % |
| Compressed beam | | |
| total compression factor | 24 | |
| Pulse length | 240 | ns |
| Beam current | 100 | A |
| Beam energy after deceleration | 240 | MeV |
| Number of pulses per cycle | 24 | |

### Decelerator

Each decelerator sector is designed to extract 90% of the drive beam energy. During this process the size and the energy spread of the beam increases significantly.

The key equipment of the decelerator sector is the Power Extraction and Transfer Structure (PETS) [5]. These structures are large-aperture travelling wave structures resonant at 12 GHz with an active length of 21 cm. They have a high group velocity ($v_g/c$ =48%) and are equipped with damping slots all along the structure loaded with rf damping material. Each PETS extracts 136 MW of 12 GHz rf power to feed a pair of accelerating structures. A total of 36000 of these structures are needed for CLIC. Prototypes of these unconventional structures fabricated in octants have been built and will be high power tested this fall both with klystrons at 11.4 GHz and with beam in CTF3 at 12 GHz. The CTF3 program includes a test beam line to study and bench mark the challenging beam dynamics of the CLIC decelerator.

### Accelerating Structure

A sophisticated optimization procedure taking into account constraints from beam dynamics, cost and high gradient constraints resulted in a new accelerating structure for CLIC [3]. An optimum was obtained at 12 GHz with a loaded gradient of 100 MV/m. The structure has a constant gradient design with a rather small aperture and a group velocity of only 1.7 % at the entrance of the structure. The rf pulse length needed to accelerate the 312 bunches is 240 ns including the filling time. This requires strong higher order mode damping provided by four waveguides in each cell. The low power consumption and the short bunch spacing made possible by the HOM damping results in a high rf-to-beam power efficiency of 27.7% for this structure. A total of 30 km active acceleration will be needed for both linacs which imposes a trip rate better than 3 $10^{-7}$ per meter. The main parameters of the CLIC accelerating structure are listed in table 3.

Table 3: Accelerating Structure Parameters

| | | |
|---|---|---|
| RF frequency | 11.994 | GHz |
| Loaded acceleration gradient | 100 | MV/m |
| Input Power for 100 MV/m | 64 | MW |
| Maximum surface field | 245 | MV/m |
| Active structure length | 0.23 | m |
| $\langle a/\lambda \rangle$ | 0.11 | |
| RF to beam efficiency | 27.7 | % |

A recent high power test of a low group velocity prototype at 11.4 GHz reached 100 MV/m unloaded gradient with a pulse length of 230 ns and a trip rate below $10^{-7}$/m [7]. The structure tested had a constant loaded gradient design with a strong tapering of the aperture towards the end. The electrical surface field reached therefore more than 300 MV/m.

### Beam Quality Issues

One of the biggest challenges for the CLIC scheme is to generate the ultra low emittance beams required to achieve the high luminosity. The normalized emittance needed at the IP is 660 nm in horizontal and 20 nm in the vertical plane. The beam has to be focused down to a spot size of 40 nm in horizontal and 1 nm in vertical. The damping ring is designed to reach emittances of 381 nm in the horizontal plane and 4.1 nm in the vertical plane using high field wigglers [8]. Therefore the beam transport and acceleration allow only very small emittance growth. This imposes very strict alignment and jitter tolerances. CLIC will have to rely extensively on beam based alignment procedures and active vibration stabilisation of focusing elements. The most severe constraints are on the final focus quadrupoles which have to be stabilized in the sub-nm range for frequencies above 4 Hz. Some R&D has been done already showing a proof of principle stabilization of a quadrupole to the level of 0.5 nm [9].

## THE CLIC TEST FACILTY CTF3

The CLIC scheme comprises a number of novel concepts and challenging parameters which have to be validated experimentally. Therefore the CLIC Test Facility was designed to demonstrate the feasibility of the following key issues until 2010.

- The feasibility of the CLIC rf power source: Generating a drive beam using bunch combination with rf deflectors with high efficiency.
- Demonstrating the main linac rf structures by operating a two-beam acceleration sub-unit at nominal rf parameters.
- Validating the CLIC decelerator concept by operating several deceleration modules in series and extracting 12 GHz power.

The test facility was constructed in stages starting in 2001 re-using equipment and infrastructure from the former LEP pre-injector. The layout of the facility is shown in figure 2. A thermionic electron gun provides a beam current of nominal 3.5 A. The beam is subsequently bunched by a 1.5 GHz subharmonic system and by a 3 GHz travelling wave buncher. The high-bandwidth 1.5 GHz buncher cavities allow the phase coding of the beam by switching the phase of their TWT-drivers by 180 deg. This results in a 1.2 μs long bunch train which consists of eight 140 ns long sub-trains captured alternately in odd or even buckets of the following 3 GHz rf acceleration system. A total of 16 accelerating structures are used to accelerate this beam up to 150 MeV at the end of the linac. The one meter long acceleration sections have been optimized for full beam loading at nominal current and are equipped with strong higher order mode damping in each cell [10] to avoid beam break up in the linac. At the end of the linac a magnetic chicane allows for bunch compression or stretching. The nominal operation mode foresees bunch stretching to avoid coherent synchrotron radiation effects in the rings. After the rings the bunches are compressed again in the second transfer line (TL2 [11]) for efficient rf power production. The phase coded 140 ns long sub-trains are alternately injected into the delay loop with 1.5 GHz deflectors. After one turn the bunches of the delayed trains are interleaved in between the bunches of the following sub-train. After the delay loop the beam consists of four 140 ns long sub-trains with an average current of 7 A and 3 GHz bunch spacing and a 140 ns gap between them. A second stage of bunch combination and frequency multiplication is done in the combiner ring. Here 3 GHz rf deflectors are used to create a time-dependent closed orbit bump, which allows to interleave the bunches of four subsequent sub-trains into one. Finally the fully generated drive beam has a pulse length of 140 ns with an average current of 28 A and 12 GHz bunch spacing. This beam is then sent to the CLIC Experimental hall (CLEX), where 12 GHz rf power is extracted by power extraction structures (PETS). The CLEX area comprises an independent 200 MeV probe beam (Califes [12]) which will be used for the two beam acceleration demonstration experiments in the two beam test stand (TBTS [13]). One PETS will be powering up to two accelerating structures. In addition a test beam line (TBL) [14] will be installed consisting out of 16 deceleration modules which will produce a total of 2.4 GW of 12 GHz rf power by extracting roughly 50 % of the drive beam energy. This experiment will be used to validate the CLIC decelerator concepts. CTF3 cannot achieve CLIC parameters in all aspects due to the financial constraints of this R&D effort but is believed to demonstrate the key technical issues and provide relevant bench marks for scaling to the nominal CLIC parameters. Table 4 shows the main differences between CTF3 and CLIC parameters.

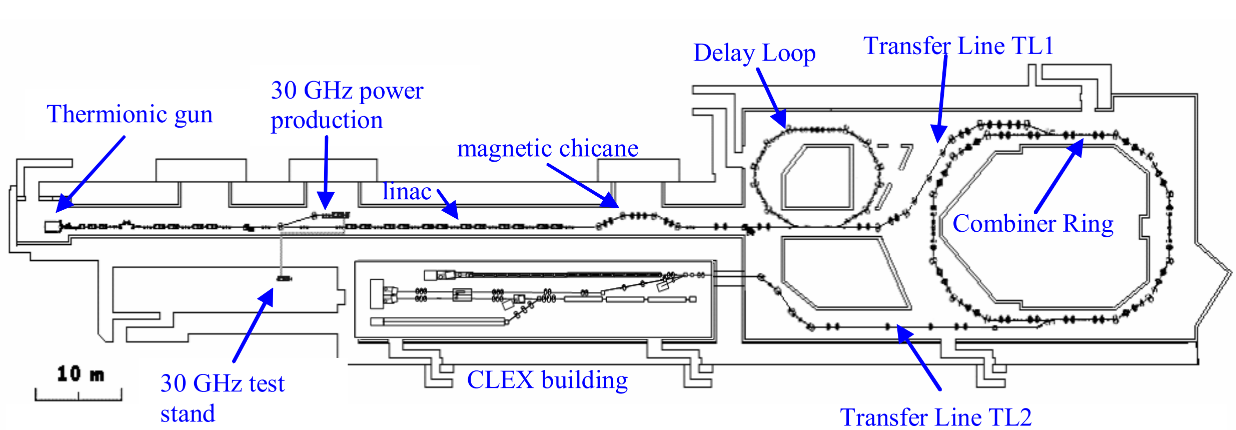


Figure 2: Layout of CTF3.

Table 4: Comparison CLIC-CTF3

| | CLIC | CTF3 |
|---|---|---|
| Drive Beam energy | 2.4 GeV | 150 MeV |
| Drive Beam current | 100 A | 28 A |
| Drive Beam RF Frequency | 999.5 MHz | 3 GHz |
| Train length in linac | 139 μs | 1.5 μs |

## STATUS AND FIRST RESULTS

The construction of CTF3 is advancing according to schedule. This installation of TL2, the two beam test stand and the probe beam have been completed and commissioning with beam started in CLEX this summer. The first PETS in the two beam test stand and the prototype module in TBL are scheduled to be tested this fall. The remaining 15 modules of TBL will be installed in stages during 2009 and 2010. This will complete the installation of the CTF3 base line program. The facility is operated routinely for about 7 months a year. A number of milestones towards a feasibility demonstration of the CLIC scheme have been already achieved.

### *Full Beam Loading Operation*

It is essential for the CLIC scheme that the rf power source reaches a high efficiency. Therefore the drive beam accelerator is operated with full beam loading. An efficiency of power transfer to the beam of 95.3% has been measured [15]. Figure 3 shows the measured rf power signals with full beam loading. Each structure provides 6.5 MV/m of acceleration for 30 MW input power. The shape of the rf signals before the beam are caused by an rf pulse compression system, which will, however, not be used in CLIC. The CTF3 linac is routinely operated with full beam loading for several years and no signs of beam break up have been found thanks to the strong high order mode damping in each cell of the drive beam accelerator structures.

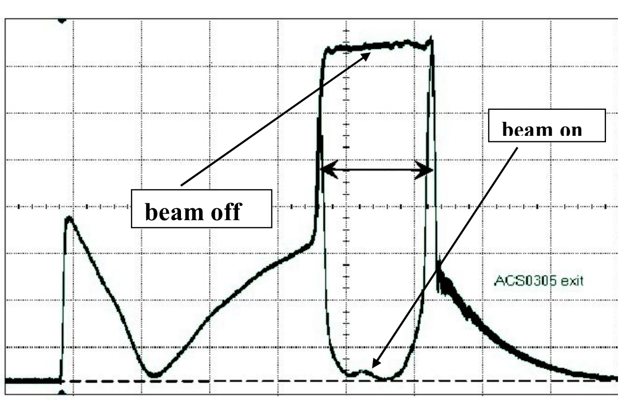


Figure 3: Demonstration of full beam loading.

### *Bunch Phase Coding*

The phase coding of bunches within sub-trains with a sub-harmonic bunching system was commissioned in 2005 [16]. The rf phase of these bunches can be switched by 180 deg in about 4 ns. The bunching process is not perfect yet and produces satellites in the wrong 3 GHz bucket with about 8% intensity of the main bunch. These satellites are lost during recombination in the delay loop. This inefficiency can be avoided in CLIC if a photo-injector is used and the phase coding can be done by the laser.

### *Delay Loop Operation*

Every other phase coded sub-train can now be delayed and combined with the following one as shown in figure 5. A 1.5 μs long bunch train consisting out of ten 140 ns long sub-trains was combined by separating the odd trains with the 1.5 GHz rf deflector and interleaving them with the even sub-trains, again with the rf deflector after one turn in the delay loop. In this example the combination was done for 5 sub-trains. The missing intensity in the delay loop is the 8% satellites from the bunching process which are lost later on.
The delay loop has an isochronous lattice to avoid bunch lengthening and uses a wiggler magnet to fine tune the path length of the beam to be an integer of the rf wavelength.

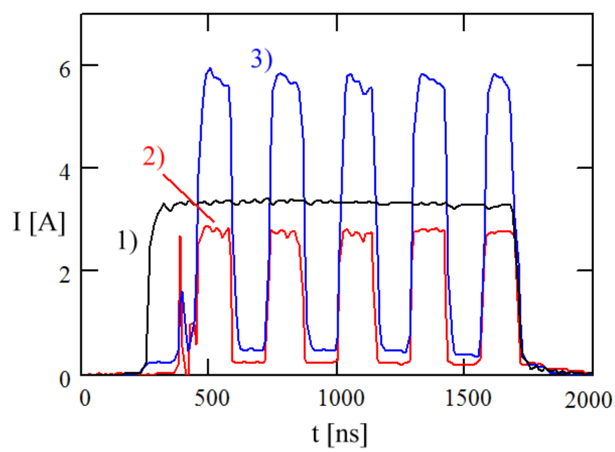


Figure 4: Beam current as function of time, measured: 1) before, 2) in, 3) after the delay loop. The sub-trains combined are 140 ns long.

### *Combiner Ring Commissioning*

The last step of the drive beam generation in CTF3 is done by the combiner ring. Four 140 ns long sub-trains with 3 GHz bunch spacing are combined to a current of 28 A. Two 3 GHz rf deflectors are used in the ring to inject the bunch trains and to keep them on a closed orbit while circulating in the ring. A wiggler magnet is used to adjust the path-length of the ring to insure the correct phasing in the rf deflectors.

For initial commissioning a 1.2 μs long 3 GHz bunch train was used straight from the linac without going through the delay loop, it has therefore no gaps between the sub-trains. A combination of such a beam is shown in figure 6, where 2.6 A beams from the linac were interleaved to reach 8.5 A. The combination suffered from a vertical instability discovered during commissioning. The instability is caused by the vertical deflecting mode of the rf deflectors. This mode had been shifted by polarising rods but not actively damped. HOM-damping has to be incorporated in a new set of deflectors required to demonstrate combination at full current. More details on the combiner ring commissioning can be found in [17].

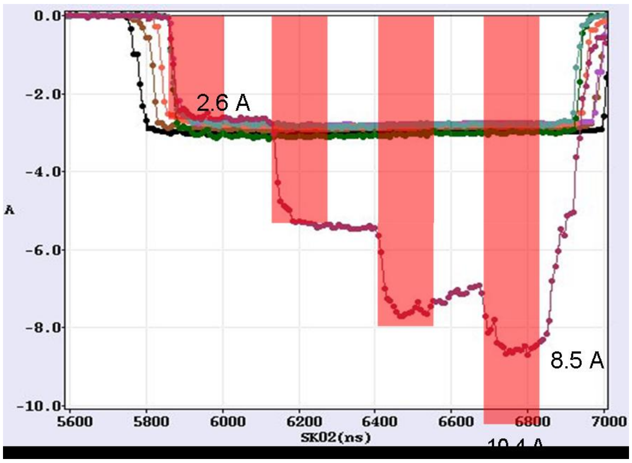


Figure 5: Interleaving of 4 bunch trains.

## CONCLUSIONS AND OUTLOOK

The CLIC collaboration has worked out a new consistent parameter set for CLIC with a luminosity in the range of $2*10^{34}$ $cm^{-2}$ $s^{-1}$ at 3 TeV, using 12 GHz rf and 100 MV/m accelerating gradient. First very promising results from a prototype test of a CLIC type accelerating structure at 11.4 GHz have been already obtained. Currently a conservative parameter set for a 500 GeV machine together with an upgrade scenario to 3 TeV is under development [2].

The CTF3 project is on schedule to fulfil its objective to demonstrate the feasibility of the main issues for CLIC by 2010. A number of questions have already been answered, such as full beam loading operation of the Drive Beam linac, and the bunch interleaving scheme.

A CLIC conceptual design report is scheduled to be finished by end 2010. The detailed technical design is expected to take another five years after this.

## ACKNOWLEDGEMENT

This work is done by the CTF3 collaboration currently consisting of the following institutes: Ankara University Group (Ankara and Gazi), Budker Institute of Nuclear Physics (BINP), CEA (IRFU Saclay), CERN, CNRS IN3P3 (LAL, LAPP, LURE ), DAE India (RRCAT) DOE USA (Northwestern Univ. Illinois, SLAC, JLAB), Helsinki Institute of Physics (HIP), IAP Nizhny Novgorod, INFN Frascati, JINR Dubna, MEC Spain (CIEMAT Madrid, IFIC Valencia, UPC Barcelona) NCP Pakistan, Norwegian Research Council (University of Oslo), PSI Switzerland, STFC UK (J.Adams Inst., Royal Holloway London), Ukraine Nat. Acad. Sci (IAP NASU), Uppsala University.

## REFERENCES

[1] http://council-strategygroup.web.cern.ch/council-strategygroup
[2] http://clic-study.web.cern.ch/CLIC-Study/
[3] F .Tecker, ‘CLIC 2008 Parameters’, CLIC-Note 764, (2008)
[4] G.Geschonke, “Results from the CLIC Test Facility CTF3 and update on the CLIC Design”, Proc. EPAC 2008, Genoa, Italy (2008)
[5] I. Syratchev,” CLIC rf High Power Production Testing Program”, Proc. EPAC 2008, Genoa, Italy (2008)
[7] S. Doebert, “High Power test of a low group velocity X-band accelerator structure for CLIC’, this conference
[8] Y. Papaphilippou et al, “Parameter Scan for the CLIC damping rings”, Proc. EPAC 2008, Genoa, Italy (2008)
[9] R. Assmann,”Colliding Nanobeams in CLIC with Magnets stabilizedto the sub-nm level”, CERN-AB-2003-011, CLIC Note 563, (2003)
[10] E. Jensen, ‘CTF3 Drive Beam Accelrating Structures, Proc. LINAC 2002, Korea, (2002)
[11] A. Sharma et al, “Design of the Transfer Line 2 for the CTF3 at CERN”, Proc. APAC 2007, Indore, India (2007)
[12] F. Peauger,” Status of the CTF3 Probe Beam Linac CALIFES”, this conference
[13] R. Ruber, “ The CTF3 Two-Beam Test-Stand Installation and Experimental Program”, Proc. EPAC 2008, Genoa, Italy (2008)
[14] S. Döbert, “Progress on the CTF3 Test Beam Line”, Proc. EPAC 2006, Edinburgh, Scotland (2006)
[15] P. Urschütz et al., “Efficient Long Pulse Fully Loaded CTF3 Linac Operation”, Linac 2006
[16] P. Urschütz,’Beam dynamics and first operation of the sub-harmonic bunching system in the CTF3 injector”, Proc. EPAC 2006, Edinburgh, Scotland (22006)
[17] P. Skowronski, “Beam Optics Studies and Commissioning Status of CTF3”, this conference

# DESIGN AND PERFORMANCE OF L-BAND AND S-BAND MULTI BEAM KLYSTRONS

Y. H. Chin, KEK, Tsukuba, Japan.

*Abstract*

Recently, there has been a rising international interest in multi-beam klystrons (MBK) in the L-band and S-band, with active development taking place. These MBKs are developed by industries such as Toshiba, Thales and CPI for the European X-FEL project or at the Naval Research Laboratory for high-power, low-voltage, broadband radar/radio communication systems. Some of them are already in operation at full specification and are commercially available. MBKs have distinctive advantages to conventional single-beam klystrons in their ability to produce high power with high efficiency and large bandwidth at lower voltage in compact body. This paper reviews the design and performance of these multi-beam klystrons, and describes future development plans.

## INTRODUCTION

Klystrons have been always the major sources of high power RF in particle accelerators. The development of new types of klystrons has made large and important contributions in achieving significant advances in energy outreach of linear accelerators. The historical growth in klystron power in the past 60 years since WWII shows that the output power increases 10-fold every 14 years. Recent projects and proposals of high-energy super-conducting linacs demand high power klystrons with high efficiency (60-70%) and long pulse duration (an order of 1ms). The peak power delivered by a long pulse Single-Beam Klystron (SBK) is limited by the high voltage that its gun can withstand. A lower cathode voltage (more exactly speaking, the maximum surface electric field in the gun region) is desirable to ensure reliable operation without gun arching or voltage breakdown. However, in a single-beam klystron, the simultaneous optimization of output power, voltage and efficiency is nearly impossible, since the pervenace determines the relationship of all other operating parameters and even an achievable maximum efficiency of the tube.

When one designs a single-beam klystron for a given output power $P_{out}$, he first has to choose the pervenace, p, given by $p=I/V^{3/2}$, where I is the beam current from a cathode and V is the cathode voltage. The pervance indicates how much beam current comes out of the cathode when the voltage V is applied between the cathode and the anode. There is the empirical relation between the perveance and the achievable highest efficiency, $\eta_{max}$, given by [1]

$$\eta_{\max}(\%) = 78 - 16 \times p\,(\mu\text{-perveance}). \quad (1)$$

Figure 1 illustrates this relationship. This figure indicates that a lower perveance beam with weaker space-charge forces enables stronger bunching and thus consequently higher efficiency.

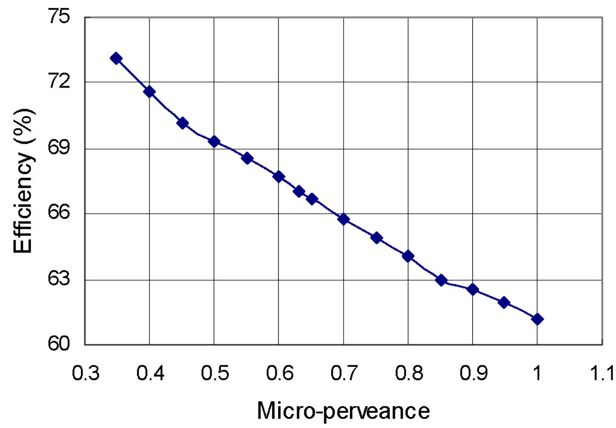


Figure 1: The empirical relation between the perveance and the achievable highest efficiency, $\eta_{max}$.

Once the efficiency ($\eta \le \eta_{\max}$) of the tube is assumed, the cathode voltage is determined from the relation

$$P_{out} = \eta IV = \eta p V^{5/2}. \quad (2)$$

In this circumstance, only way to increase the output power without increasing the voltage, or reduce the voltage without reducing the output power, is to increase the perveance, i.e., the beam current. However, a high perveance is strongly undesirable since (1) it provides a lower efficiency (2) it requires a larger cathode current loading resulting in a shorter cathode lifetime (see Fig.2) (3) it requires stronger magnetic fields for beam focusing which can lead higher system volume and weight (4) it has a higher risk of gun oscillation and gun arching. In conclusion, the choice of perveance in a single-beam klystron is always a compromise between high power and efficiency and tube reliability.

A breakthrough solution to this gridlock is to use multiple low perveance beamlets in parallel in the same vacuum envelop. The number of beamlets introduces a new degree of freedom in parameter space. In a Multi-Beam Klystron (MBK), a high current electron beam is separated into multiple parallel beamlets,

- each with a sufficiently low current density (perveance) to ensure efficient electron bunching and a high efficiency,
- while the high total perveance of beam current provides the required high output power.

The co-existence of these two different perveances in the same device is the great advantage of MBK to SBK, which allows simultaneous optimization of efficiency and output power. Each beamlet propagates in individual drift tube, paralleled to, but isolated from each other and are allowed to interact only in common RF cavities. Schematic presentation of MBKs is shown in Fig.3

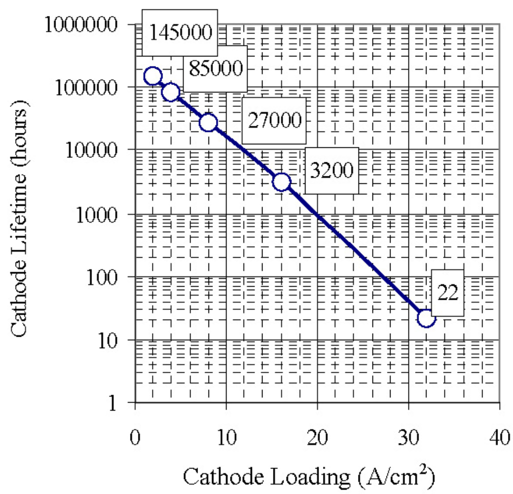


Figure 2: Empirical relation between the cathode loading and expected lifetime of the cathode.

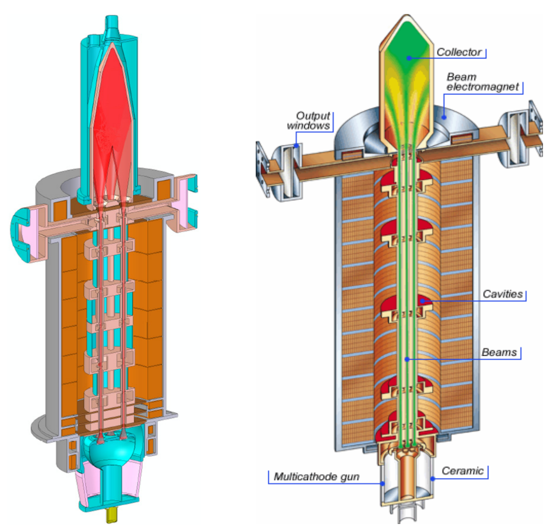


Figure 3: Schematic presentation of MBKs (Toshiba E3736: left and Thales TH1801: right).

For a given output power, a lower cathode voltage is required in a MBK compared to a SBK. The combination of high total beam current and lower beam-induced voltage in a common output cavity makes it possible for a lower external Q-factor, facilitating higher bandwidth operation.

## HISTORICAL BACKGROUND

The concept of multi-beam klystron is not new. It was proposed as early as the middle of the 20th century in both the Former Soviet Union and France. MBK development in the US all but ceased after the early 1960s, since it was thought that potential benefits of MBK technology did not overweight the added device complexity and associated cost [2]. In the last three decades, MBK development has occurred primarily in the Former Soviet Union for mobile ground-based, airborne and space-based radar and radio-communication systems because of its advantages in high power, efficient, broadband operation capability at lower voltage in compact and lightweight body. Few details were published to outside world before the end of Cold War, as they were developed primarily for military applications. Recently, other countries have revived their activities in MBK for similar applications.

Under the renewed interest in US, Naval Research Lab recently built a broadband (6%), S-band, 600kW, 8-beam MBK for shipboard radar/communication systems [2]. Table 1 summarizes its parameters and measurement results. They employ the typical design of MBK for a large instantaneous bandwidth, with eight clustered beamlets around the geometric axis, interacting with four common $TM_{010}$ cylindrical cavities (see Fig. 4).

Table 1: Parameters and Measurement Results of Naval Research Lab's S-band, 600kW, 8-beam MBK

| **Parameter** | **Measured** | **Unit** |
|---|---|---|
| Central Frequency | 3.2 | GHz |
| Peak Output Power | 600 | kW |
| Beam Voltage | 45 | kV |
| Beam Current | 32 | A |
| RF Pulse Duration | 5 | µs |
| Efficiency | 39 | % |
| Bandwidth | 6 | % |
| Gain | 30 | dB |

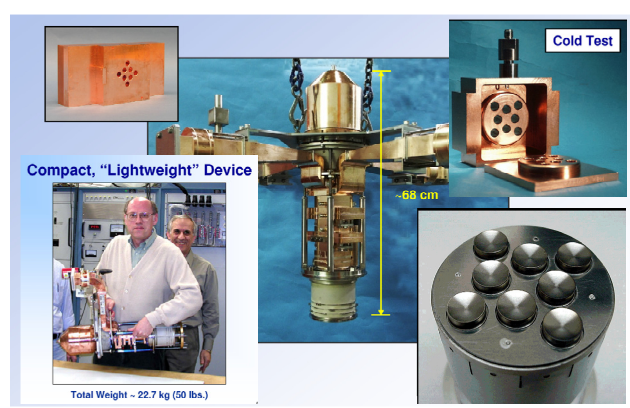


Figure 4: Naval Research Lab's S-band, 600kW fundamental-mode, 8-beam MBK.

## L-BAND 10MW MBK FOR TESLA

Recently, there has been a rising international interest in MBK for applications in particle accelerators, with active development taking place, in France, US, and Japan. That began about 10 years ago, when DESY started its efforts to develop an L-band 10MW MBK with Thales (France) for the TESLA [3] (now XFEL [4] and ILC) project. Thales started the design work in late 1990, and the full power test of the first MBK was done successfully at DESY in May 2000 [1]. CPI joined this effort with its own design in 2001 [5] and the test of the first CPI MBK was done at DESY in September 2005. At last but not least, Toshiba joined the worldwide effort of MBK development with its own design in 2002. Although it was late start, they built and successfully tested the vertical MBK at DESY in June 2006 [6]. They then built the first horizontal MBK for XFEL and the full power test was done successful at DESY in February 2008 [7].

The major challenges to design and operation of L-band (1.3GHz) MBK for TESLA are (1) “super-high” peak (10MW) and average (150kW) power requirements (2) a high efficiency (≥65%) required at this power level (3) multiple and uniform beam cathodes that stably sustain long beam pulse operation (1.7ms at 115kV at 10Hz repetition rate) with long tube lifetime (>60,000hrs). However, the required instantaneous -1dB bandwidth is only 3MHz unlike a broadband MBK for radars. At acceptance test at DESY, a tube has to satisfy all requirements for operation parameters. Transfer curves (RF output power vs. RF drive power) need to be smooth without any discontinuity, meaning no sign of multi-pactoring or parasitic oscillation. 24 hours continuous operation without fault by gun or window arching is also required at the end of test.

## DESIGN AND PERFORMANCE

Development of “super-high” power MBKs is relatively new area, and there is no standard design model yet. In fact, the all three MBKs (Thales, CPI and Toshiba) have different designs with their own pros and cons. Success of any MBK among them will greatly help to establish a design model for future MBKs in a centimetre-wavelength band. The following assessments are based on the author’s analysis of pros and cons of different design approaches when he made the basic design of the Toshiba MBK in 2002, which later became Toshiba E3736.

### *Thales MBK TH1801*

Thales design is the conventional “clustered-beam approach” for a radar requiring a large instantaneous bandwidth. This design uses 7 beamlets (6 on a circle and 1 at the center), each with 0.5 μ-perveance [1]. They enter the center of cylindrical common cavities operating in the fundamental ($TM_{010}$) mode through individual drift tubes. Figure 5 shows the photograph of the multi cathode gun (left) and the cross sectional view of $TM_{010}$ cylindrical cavity. This design provides the most compact and lightweight MBK. The primary drawback to this design is that clustered beamlets are closely packed near the center of the tube. The consequent small cathodes and poor beam area compression (9:1) lead to high cathode loading (5.5A/cm$^2$), which in turn results in the relatively short cathode lifetime (36,000hrs). Use of recent long-life, high emission current density cathodes may ease this concern.

In reality, the lifetime of a tube is likely to be determined by, not the cathode loading itself, but deposition of Barium, evaporated from cathodes, on focus electrode or anode. For this reason, lower operating temperature of cathodes (lower cathode loading), and larger deposition area of Barium (larger focus electrode and larger anode) help to significantly extend the arc-free lifetime of a tube. In this sense, the Thales design may inherit the typical problem of relatively short lifetime of MBK for radar/radio-communication systems.

Another characteristic of Thales design is the conflicting role of the center beamlet. If only off-axis beamlets are used, the pervenace of each beamlet will be 0.58μ-perveance, and the achievable highest efficiency is 68.7%, according to the relationship (1). Addition of the center beamlet helps to reduce the single beam pervenace to 0.5μ-perveance, and increase the achievable highest efficiency to 70%. The current loading of each cathode is also reduced, benefitting longer cathode lifetime. On the other hand, the center beamlet experiences a larger voltage across the gap of a cavity than the off-axis beamlets due to the field shape, and the R/Q of the center gap is 40% higher than those of the off-axis gaps. Therefore, the center beamlet will develop different bunching from other beamlets, which will perturb coherent excitation of $TM_{010}$ modes at the cavities, in particular at the output cavity. As will be seen soon, the measured efficiency of Thales TH1801 is 65%, 5% lower than the achievable highest efficiency of 70%. A challenge of this design is to find methodology for improvement of efficiency and peak power.

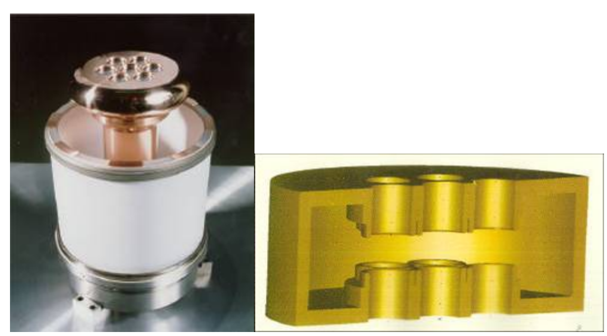

Figure 5: The multi cathode gun (left) and the cross section of $TM_{010}$ cavity (right) of Thales TH1801.

Eight Thales TH1801 tubes have been built and successfully tested (except #2) at DESY. Figure 6 shows its photograph. The typical test results are summarized in Table 2. The early two TH1801 tubes showed gun arching problems. The small cathodes and the large cathode loading were suspected as the causes. However, thoroughly investigation at Thales revealed that the cause was a gun oscillation and the problem was fixed. Since then, no sign of degradation has been observed. The horizontal version, which fits in the accelerator tunnel, is almost ready to be delivered for testing at DESY in fall 2008.

Figure 6: Thales TH1801.

Table 2: Typical test results of Thales TH1801 at DESY.

| Parameter | Measured | Unit |
|---|---|---|
| Peak Output Power | 10.2 | MW |
| Beam Voltage | 117 | kV |
| Beam Current | 131 | A |
| RF Pulse Duration | 1.5 | ms |
| Repetition Rate | 10 | Hz |
| Efficiency | 65 | % |
| Bandwidth | >10 | MHz |
| Gain | 48.2 | dB |

## *CPI MBK VLK-8301*

CPI takes a unique approach [5]: Their MBK has six weakly-coupled single-beam klystrons in parallel, sharing the same modulator, but with its own cathode, collector and individual cylindrical $TM_{010}$ cavities except for input and output cavities. They are coupled by large common input and output cavities operating in the higher-order ($TM_{020}$) mode. The beamlets are set on a large bolt circular diameter (26.7cm) and interact with the second radial peak of the axial electric field in the $TM_{020}$ cavities.

The advantage of this design is the ability to use large cathodes with small cathode current loading (2.2A/cm$^2$) and resulting long cathode lifetime (>100,000hrs).

The disadvantage is an increase of the complexity of the tube, in particular, in design of proper focusing system to provide minimum radial fields for 13.4cm off-axis beamlets. The tube has high volume (a major diameter of 53cm) and is heavyweight: the tube weights 900kg, three times heavier than Thales TH1801 (300kg). Use of large $TM_{020}$ cavities also increases a number of parasitic modes and a risk of their undesirable oscillation.

Use of intermediate individual cavities raises concern on efficiency degradation. In a klystron, the beam-induced voltages in cavities amplify the bunching in beams. The induced voltage is a function of the cavity characteristics (R/Q, resonant frequency, etc.) and the beam characteristics (beam current, size, etc.). In a MBK, the currents and sizes of individual beamlets will not in general be exactly balanced. Therefore, even if all the cavities are exactly same, the beam-induced voltages at each individual $TM_{010}$ cavity will differ, depending on the characteristics of each beamlet. As a result, each beamlet will develop slightly different bunching, and this difference will be amplified as they interact with successive intermediate individual cavities. If the cavities are not balanced either, say, due to deformation during bake-out or heating during operation, the synergy effects of unbalanced beamlets and unbalanced individual cavities will further deviate the synchronous bunching of beamlets. When all beamlets meet at the common output cavity, a loss in synchronization of bunching in amplitude and phase will degrade the efficiency. In Thales and Toshiba designs, they use only common cavities where all beamlets excite the same $TM_{010}$ modes together and receive the same voltages together. Therefore, they are less susceptible to unbalance in beamlets and cavities.

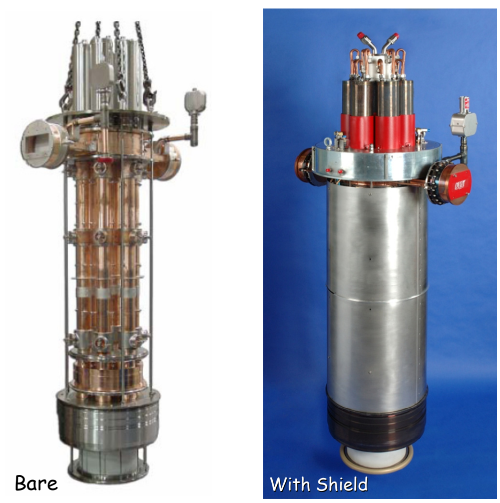


Figure 7: CPI VLK-8301. Bare (left), shielded (right).

VLK-8301 was tested at DESY in September 2005. It did not make full 10MW peak power at full pulse length. The best result was 8.1MW peak power at 1.3ms pulse length at 10Hz repetition rate with efficiency of 53.5%. It attained 9MW peak power at a short pulse length of 0.3ms. The test results are summarized in Table 3. The tube is now in use at DESY for the cryomodule test stand.

Table 3: Test Results of CPI VLK-8301 at DESY in 2005.

| Parameter | Measured | Unit |
|---|---|---|
| Peak Output Power | 8.1 | MW |
| Beam Voltage | 115 | kV |
| Beam Current | 131 | A |
| RF Pulse Duration | 1.3 | ms |
| Repetition Rate | 10 | Hz |
| Efficiency | 53.5 | % |
| Bandwidth | >5 | MHz |
| Gain | 48 | dB |

CPI is currently developing a second-generation, horizontal version of MBK, VKL-8301B. In this new design, they utilize 7 ring-shaped cavities operating in the fundamental $TM_{010}$ mode, just like the Toshiba design, instead of $TM_{020}$ cylindrical cavities used in the first generation. The horizontal VKL-8301B is expected to be delivered to DESY in fall 2008.

### *Toshiba MBK E3736 and E3736H*

Toshiba approach is a “simple and symmetric” design [6]. They use common ring-shaped cavities for all cavities, operating in the fundamental $TM_{010}$ mode, to ensure sufficient beam separation (spaced on a diameter of 12cm, not 26.7cm like CPI), while still keeping the overall size small to reduce cost and complexity. The 6cm separation of beamlets allows to use large cathodes (a diameter of 38mm), and the cathode current loading is 2.1A/cm$^2$, as small as CPI VLK-8301 for long lifetime (>100,000hrs).

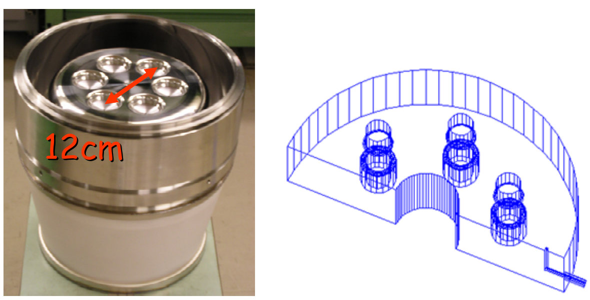


Figure 8: The multi cathode gun (left) and the ring-shaped $TM_{010}$ cavity (right) of Toshiba E3736 and E3736H.

The distinctive advantage of this design is the ability to optimize the cavity structure, the beam separation, the cathode diameter and the number of beamlets for optimum operational performance of the tube, by adjusting the overall sizes of ring-shaped cavities: the diameter of ring is a relatively free parameter, while the width of ring is constrained by the operation frequency of 1.3GHz. Despite of great benefits of the sufficient beam separation and the large cathode size, the tube weights only 340kg, 13% heavier than Thales Th1801. An added advantage of the fundamental mode operation is to make the tube more tolerant to manufacturing errors and cavity deformation due to bake-out or heat deposition.

The first tube, the vertical E3736 (Fig. 9 left), was successfully tested at DESY in June 2006 to full peak and full average RF power at full pulse length [6]. The second tube, the horizontal version, named E3736H (Fig. 9 right), was also tested successfully at DESY in February 2008[7]. Their test results are summarized in Table 4.

Toshiba E3736H was the first horizontal MBK for the XFEL project, delivered, successfully tested and accepted by DESY. The vertical version has been operated for more than 750 hours at the full power in about 80% of time. The horizontal version has been operated for more than 850 hours, in use for investigation of RF behaviour such as temperature stability, harmonic level, and phase stability, etc., which will be of great help for XFEL operation.

Figure 9: Toshiba vertical E3736 (left) and horizontal E3736H (right).

Table 4: Test Results of Toshiba E3736 and E3736H Measured at DESY in 2006 and 2008, Respectively

| Parameter | E3736 | E3736H | Unit |
|---|---|---|---|
| Peak Output Power | 10.2 | 10.1 | MW |
| Beam Voltage | 115 | 118 | kV |
| Beam Current | 134 | 130 | A |
| RF Pulse Duration | 1.5 | 1.5 | ms |
| Repetition Rate | 10 | 10 | Hz |
| Efficiency | 66 | 65.4 | % |
| Bandwidth | 3.5 | 3.5 | MHz |
| Gain | 49 | 48 | dB |

## CONCLUSIONS

The good performance of the Thales and Toshiba L-band MBKs operating in the fundamental modes of cylindrical cavities (Thales) or ring-shaped cavities (Toshiba) demonstrates that their design approaches are sound and valid in this wave-length band. The Toshiba design is more advantageous in a shorter wave-length, because of greater flexibility in design of the gun region. In a longer wave-length, Thales design is an attractive choice, since it provides a compact and low-cost tube. The MBK technology and its distinctive advantages over SBK will greatly benefit and advance linear accelerators.

## REFERENCES


[1] A. Beunas, G. Faillon and S. Choroba, http://tdserver1.fnal.gov/8gevlinacPapers/Klystrons/Thales_multi_beam_Klystron_MDK2001.pdf

[2] D. K. Abe, et al., IVEC08, p.423.

[3] TESLA Technical Design Report, March 2001. http://tesla.desy.de/new_pages/TDR_CD/start.html

[4] S. Choroba, PAC07, p.841.

[5] A. Balkcum, et al., PAC05, p.2170.

[6] Y. H. Chin, et al., PAC07, p.2098

[7] A. Yano, et al., EPAC08, p.544.

# POSITRON BEAMS PROPAGATION IN PLASMA WAKEFIELD ACCELERATORS

Patric Muggli
University of Southern California, Los Angeles, CA 90089, USA

*Abstract*

Preservation of beam emittance is a concern in all accelerators. The formation of a beam charge halo in a plasma wakefield accelerator (PWFA) driven by a single positron bunch is observed. This phenomenon is also observed in numerical simulations. These simulations indicate that it results in significant emittance growth of the positron bunch. We discuss theses results as well as possible means to preserve the positron emittance.

## INTRODUCTION

In conventional accelerators using magnetic optics and rf waves in resonant cavities to focus and accelerate particles, positive and negative charge particles can be accommodated by merely a change of current sign in the magnets and phase in the rf.

In plasma-based accelerators (PBAs) the plasma itself sustains the focusing and the accelerating fields. Plasmas are composed of particles of opposite charge, electrons and protons or ions, but of very different mass. Therefore, the light electrons are the mobile species, while the heavier ions are usually considered as immobile on the time scale of an electron plasma period. In the linear theory of PBAs where the relative plasma density perturbations $\delta n/n_e$ ($n_e$ the background plasma density) and wakefield amplitudes are small, the plasma wave is also symmetric for opposite sign charges, providing a simple 90° phase shift of the wave or wake.

However, the nonlinear or blowout regime of PBAs [1] offers some striking advantages over the linear regime for accelerating electrons. In this regime all the plasma electrons are blown out of a volume encompassing the drive and the witness beam. This regime is reached when the drive particle bunch density $n_b$ is much larger than the plasma density: $n_b >> n_e$, or when the drive laser intensity exceeds a threshold value. In this regime the accelerated beam propagates in a pure ion column that acts as a long focusing element free of geometric aberrations. Also, the accelerating field ($\approx\delta n/n_e$) is larger than in the linear regime. In fact, all current PBA experiments operate in this regime. These experiments have shown emittance preservation of the incoming beam [2,3], matching of the beam to the plasma focusing [3], and energy doubling of 42 GeV incoming electrons in only 85 cm of plasma [4], all the above in beam driven PBAs or plasma wakefield accelerators (PWFAs). Acceleration of electron bunches to hundreds of MeVs with narrow energy spread was also demonstrated in this regime in PBAs driven by intense laser pulses or laser wakefield accelerators (LWFAs) [5,6,7]. In this case, access to the nonlinear regime is necessary since the source for the accelerated beam is the trapping of the plasma electron triggered by the breaking of the plasma wave. In recent all these experiments the accelerating gradient exceeded 50 GV/m.

## POSITRON BEAMS IN PLASMAS

The situation is very different for the acceleration of positron beams in plasmas. No blowout regime exists because the mobile plasma species is still the electrons, and to focus the positron beam by partial charge neutralization the plasma electrons have to flow through the positron bunch. As a result, in uniform plasmas the electrons do not form a large region (of the order of the plasma wavelength cubed as in the case of an electron bunch) where the wakefield can be uniform enough to accelerate the positron bunch with low energy spread and to focus it while preserving its low incoming emittance. This is true whether the drive beam is a laser pulse or a particle bunch. For instance, simulations indicate that the accelerating field driven by single bunch positron beams is smaller [8] than that driven by an electron bunch with similar parameters. Also, emittance growth of the incoming bunch along the plasma is expected as a consequence of the non-linear focusing force exerted by the plasma onto the bunch. Acceleration and propagation of positron beams in plasmas have not been studied as extensively as they have been with electrons. This is of course due primarily to the fact that short, high current positron bunches are not readily available, except at the Stanford Linear Accelerator Center (SLAC).

The acceleration of positrons in the wakefield driven by a single positron bunch has been demonstrated [9]. The focusing of a positron beam by a short, high-density gas jet plasma was also demonstrated [10]. The effect of the propagation of the same positron beam along a $L_p$=1.4 m, low density ($<10^{12}$ cm$^{-3}$) plasma column was studied in detail with picosecond time resolution along the ≈10 ps long bunch [11]. However, in these experiments the product of plasma density and plasma length ($n_eL_p<3\text{x}10^{12}$ m$^{-2}$) was too small for the beam to significantly evolve in its transverse dimensions along the plasma.

In order to gain large amounts of energy (>10 GeV) the positron beam will have to propagate through a long ($L_p$>2 m), dense ($n_e>10^{16}$ cm$^{-3}$) plasma, since accelerating gradients of 5 to 10 GV/m are desirable. The effect of the non-ideal wakefield will therefore accumulate and emittance preservation is an open question.

We present here some experimental and simulation results demonstrating the formation of a beam halo around a single positron bunch propagating through a 1.4-

m-long plasma, as well as the corresponding emittance growth [12].

## EXPERIMENTAL SETUP

Figure 1 shows a schematic of the experimental set up. The ultra-relativistic ($E_0$=28.5 GeV, $\gamma$≈56,000) beam available at the SLAC Final Focus Test Beam [13] facility with ≈1.8x$10^{10}$ positrons is focused near the entrance of the plasma. The typical transverse beam size at the waist is $\sigma_{r0}$≈25 $\mu$m (round beam). The bunch length is $\sigma_z$≈700 $\mu$m (or 2.3 ps). Because of scattering in the entrance beryllium window, the upstream optical transition radiation (OTR) foil and the thin pellicle mirror that makes the ionizing laser pulse collinear with the positron beam, the normalized emittances at the plasma entrance are $\varepsilon_{Nx}$≈380 and $\varepsilon_{Ny}$≈80 mm-mrad. Here the $x$ direction is in the horizontal plane, and $y$ in the vertical plane. The beam propagates along $z$. The beam transverse size and shape are monitored ≈1 m upstream and downstream of the plasma using OTR. The visible OTR light is imaged onto CCD cameras to record images for each bunch.

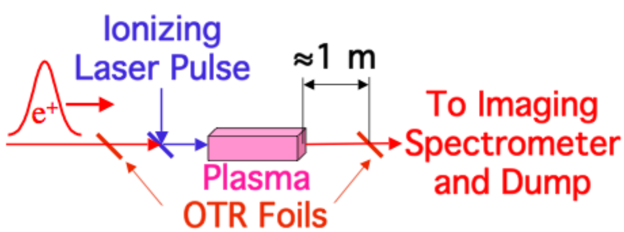


Figure 1: Schematic of the experimental setup. The beam transverse size and shape are monitored ≈1 m upstream and downstream of the plasma using optical transition radiation (OTR).

The plasma source consists of a hot lithium (Li) vapor contained in a heat-pipe oven [14,15]. A 20 ns uv laser pulse with a wavelength of 193 nm (6.4 eV/photon) ionizes the low ionization potential (5.4 eV) Li. The laser beam, and therefore the plasma, is made collinear with the positron beam by reflection off a 45°, 150 $\mu$m-thick glass pellicle coated for high reflectivity at 193 nm. The laser beam is also focused along the lithium vapor column to compensate for the uv photons absorption and thereby maintain a constant (±5%) plasma density over the column length. The plasma density is obtained from the measurements of the lithium neutral density and absorbed uv energy. The measurements of the positron characteristics with plasma ($n_e$>0) are acquired with the positron bunch traveling along the plasma 200 ns after the laser pulse. Every fourth event is recorded with the laser firing after the positron bunch ($n_e$=0) in order to continuously monitor the incoming beam characteristics. The plasma length is $L_p$=1.4 m, and $n_e$ is varied between ≈$10^{13}$ cm$^{-3}$ and ≈5x$10^{14}$ cm$^{-3}$ by adjusting the laser pulse energy. The maximum ionization fraction is ≈13%.

## HALO FORMATION, EXPERIMENT

Figure 2 show two images of the beam recorded at the downstream OTR foil location. With $n_e$=0 (Fig. (a)) the beam transverse shape is elliptical because of the round transverse size at the beam waist and the unequal emittances. The projections of the beam along the $x$ and y directions are Gaussian to a good approximation. The corresponding transverse sizes are $\sigma_x$≈1430 $\mu$m (large) and $\sigma_y$≈310 $\mu$m (low emittance plane).

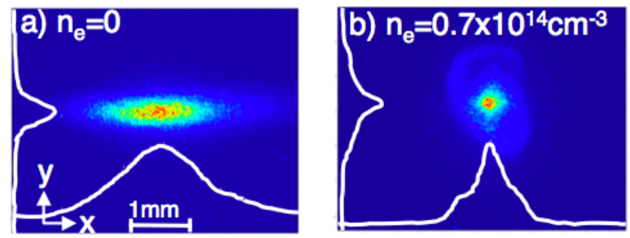


Figure 2: Experimental images of the beam recorded at the downstream OTR foil location. The white lines show the transverse beam profiles obtained by summing the images along the perpendicular direction. (a) With $n_e$=0, the beam profiles are Gaussian to a good approximation. The different $x$ and $y$ sizes are the result of the different emittances. (b) With $n_e$=0.7x$10^{14}$ cm$^{-3}$, the image and the profiles exhibit a dense core surrounded by a charge halo (from [12]).

Figure 2 (b) shows an image of the beam after traveling through the $n_e$=0.7x$10^{14}$ cm$^{-3}$ plasma. This image shows that the beam has a tightly focused core, with a strong reduction of the beam transverse size in the $x$, large emittance plane. A halo of charge also appeared in the two planes, but is most noticeable in the $y$, low emittance plane. The transverse profiles are not Gaussian anymore, but instead reflect the core and halo structure. In order to describe these non-Gaussian profiles, a two-triangle fit [16]] is used to quantify the bunch core size as well as the relative amount of charge in the core and halo.

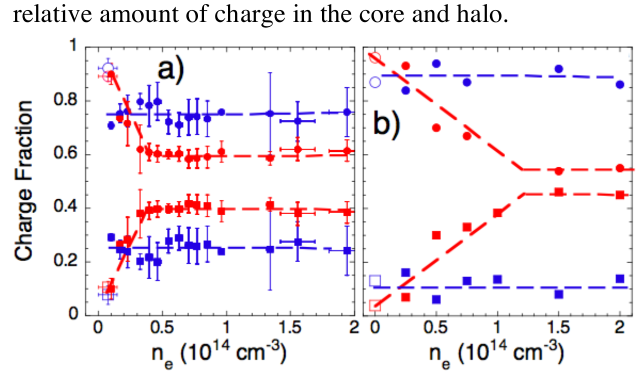


Figure 3: Charge fraction in the beam core (circles) and halo (squares) in the $x$ (blue symbols) and y plane (red symbols) as a function of $n_e$ obtained (a) from experimental OTR images (see Fig. 2) and (b) from simulations generated images. The beam parameters are those of the experiment. The lines are added to suggest trends.

Figure 3(a) shows the relative amount of charge in the focused core and in the halo as a function of $n_e$ for densities up to $2x10^{14}$ cm$^{-3}$. These measurements are obtained from OTR images such as those on Fig. 2. In the $y$ plane charge transfers from the core to the halo from $n_e$=0 to ≈$0.3x10^{14}$ cm$^{-3}$. Then the charge fractions remain approximately constant at 60% and 40% in the core and halo, respectively. In the $x$ plane the charge fractions remain at 75% and 25% for all $0<n_e<2x10^{14}$ cm$^{-3}$.

## HALO FORMATION, SIMULATION

The numerical code QuickPIC [17] is used to simulate the propagation of the positron bunch along the plasma. The positrons are then ballistically propagated a distance of one meter to generate images to be compared with those measured in the experiment at the location of the downstream OTR foil. Figure 4 show the evolution of the beam transverse size along the plasma obtained from one of these simulations. The beam parameters are those of the experiment, and the plasma density is $n_e=10^{14}$ cm$^{-3}$. Over the first 10 cm the plasma focuses the beam. This effect is similar to the size reduction measured downstream from the plasma in ref. 11. The $n_eL_p$ product is small, $10^{13}$ cm$^{-2}$ in this case, and the plasma focusing force nonlinearities have not yet strongly spoiled the beam transverse phase space. The beam size is therefore reduced. Note that this focus occurs at a distance into the plasma that is shorter than the distance an electron beam with identical parameters would focus at. The betatron wavelength for electrons in a pure ion column with an ion density equal to $n_e$ is $\lambda_\beta=2\pi(2\gamma)^{1/2}c/\omega_{pe}$, where $\omega_{pe}=(n_e e^2/\varepsilon_0 m)^{1/2}$ is the electron plasma angular frequency. The focus would appear at $\lambda_\beta/4$≈28 cm. This shorter focusing length reflects the fact that the plasma electron charge density can exceed the background density $n_e$ and therefore the focusing force exceed that experienced by an electron beam in the same situation.

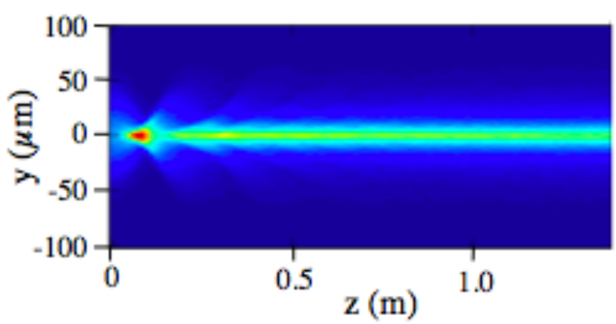


Figure 4: Beam transverse distribution ($y$, low emittance plane) along the $L_p$=140 cm, $n_e=10^{14}$ cm$^{-3}$ plasma obtained from numerical simulations. The beam parameters are those of the experiment.

After the first pinch the beam expands again, but does not come to a clear second pinch. Instead, the beam profile has a focused core on axis surrounded by charge in a beam halo, as seen on Fig. 2, and as seen on simulated images [12]. The beam profile then remains essentially constant over the length of the plasma from $L$=0.5 m to $L_p$=1.4 m, and $n_eL_p=1.4x10^{14}$ cm$^{-2}$.

Figure 3 (b) shows the charge fraction in the beam core and halo at the downstream OTR location as a function of $n_e$ and can be compared to the experimental result of Fig. (a). Similarly to Fig. (a), Fig. (b) also shows a continuous transfer of charge from the core to the halo. However, this transfer process extends over a higher density range than observed in the experiment, up to ≈$1.2x10^{14}$ cm$^{-3}$. At higher $n_e$ the fractions remain at 55% and 45% in the core and halo, respectively, values similar to those measured in the experiment. Beam transverse size measurements show excellent agreement with the sizes calculated from simulations images [12]. They also indicate that the beam exits the plasma with approximately equal transverse sizes.

The formation of the halo is the result of the nonlinear focusing force from the non uniform neutralization of the positron space charge by the plasma electrons rushing through it. The halo formation is therefore expected to lead to emittance growth. The bunch emittance is obtained from simulation results.

## EMITTANCE GROWTH, SIMULATION

The normalized rms emittance of the beam in the $x$ plane is calculated from the particles position $x$ and momentum $p_x$ as:

$$\varepsilon_{Nx} = \gamma\left(\left\langle x^2\right\rangle\left\langle x'^2\right\rangle - \left\langle xx'\right\rangle^2\right)^{1/2}$$

where $x'=p_x/<p_z>$, <.> stands for the quantity average, and $<p_z>$ is the beam average longitudinal momentum. A similar expression is used for the $y$ plane normalized emittance.

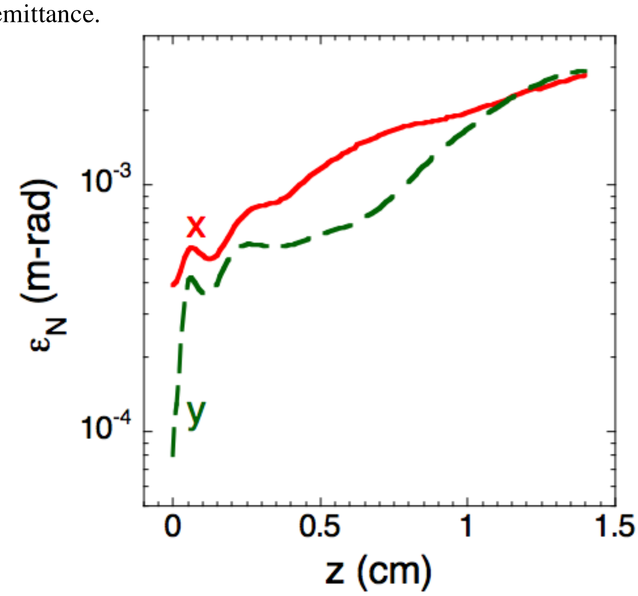


Figure 5: Evolution of the beam emittances ($x$ plane, red continuous line, $y$ plane green dashed line) along the plasma with $n_e=2x10^{14}$ cm$^{-3}$ obtained from numerical simulations. Both final emittances are ≈$3x10^{-3}$ m-rad, corresponding to an emittance growth by a factor of ≈8 in the $x$-plane and 38 in the $y$-plane. The beam parameters are those of the experiment.

Figure 5 shows the evolution of the positron bunch normalized emittance in both transverse planes along the plasma. In the low emittance $y$ plane the emittance quickly grows from the incoming 80 mm-mrad over the first few centimeter of plasma, to become approximately equal to the $x$ emittance. After that the two emittances grow together and remain approximately equal. Both final emittances are $\approx 3\text{x}10^{-3}$ m-rad, corresponding to an emittance growth by a factor of ≈8 in the $x$ plane and 38 in the $y$ plane. As noted before, the beam transverses sizes are also about equal (as for example on Fig. 2 (b)).

## EMITTANCE PRESERVATION

The results presented here above show charge halo formation and emittance growth when a single positron propagates in a uniform plasma suitable for acceleration of trailing particles [9]. However, future plasma-based linear collider will use a drive/witness bunch scheme. In that scheme, a first bunch (electron or positron) drives the wake and loses energy, while a witness bunch, following about a plasma wavelength behind the drive bunch, only gains energy. A similar scheme will be used in a laser-driven PBA, with the drive bunch replaces by a laser pulse. The emittance preservation of a positron witness bunch has not been studied in a two-bunch scheme and will be the subject of future simulation work. However, the use of a plasma with an on-axis hollow channel has been proposed to increase the accelerating gradient in the single positron bunch case [18]. Hollow plasma channels may also have an effect on the emittance of the bunch. Hollow plasma channels also have advantageous effects for laser-driven PBAs [19]. Preliminary results seem to indicate that a plasma hollow channel guides the positron beam and minimizes the beam distortion [20]. The challenge is to find a configuration that generates a region of the wake large enough to encompass a high charge positron bunch, a region in which the accelerating gradient is large and uniform, and the focusing force linearly increasing with radius. An alternative approach is to shape the witness bunch in its transverse and longitudinal dimensions in order to compensate for the non uniformities of the wake fields.

## POSITRONS ON ELECTRON WAKE

Short, high-charge positron bunches are difficult to produce. It may therefore be advantageous to accelerate the positron witness bunch in the wake driven by an electron bunch [21,22]. This scheme would increase the efficiency of a future PBA $e^-/e^+$ collider by avoiding the generation of a positron drive bunch. It is also similar to that of a positron bunch in the wake driven by a laser pulse. The scheme is shown on Fig. 6. The positron bunch is placed right after the density spike created by the expelled plasma electrons returning on axis, the region where the wakefield is both accelerating and focusing for positrons. This region becomes narrower as the wake is made more nonlinear. A scheme was recently proposed [22] to create the positron beam inside the plasma, thereby avoiding all the issues associated with the generation, transport and timing of a positron bunch ≈100 $\mu$m behind an electron bunch. The positron bunch is generated by $e^-/e^+$ pair creation in a high-Z foil embedded into the plasma, The incoming electron beam is split in a drive/witness bunch train using for example a mask technique [23]. After the foils, two positron bunches overlap in space and time with the two incoming electron bunches. The plasma wakefields act to select and preserve only the drive electron bunch and the positron witness bunch or positron beam load. The positron beam load size must be adjusted to fit inside the favorable wake volume. Simulations show that $\approx 10^8$ positrons with energies >5 MeV can be injected into, and trapped by the plasma wake. They can be accelerated to ≈5 GeV in one meter with a relative energy spread of ≈8%. The positron beam load normalized emittances are 20 and 25 mm-mrad in the $x$ and $y$ plane, respectively.

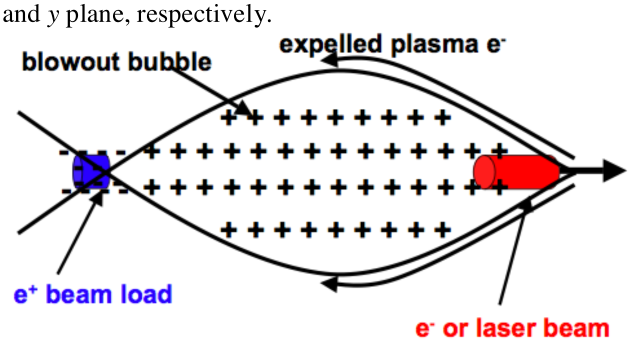


Figure 6: Schematic of the acceleration of a positron bunch ($e^+$ beam load) on the wake driven by an electron bunch or a laser pulse, from ref. 22.

## SUMMARY

The acceleration of positron bunches in high-gradient PBAs while preserving the quality of the incoming bunch is key for a future plasma-based $e^-/e^+$ high-energy collider, whether driven by a laser pulse or a particle bunch. Experimental results obtained with a single positron PWFA show the appearance of a beam charge halo after the propagation through a 1.4 m-long plasma with a density in the 0.5-5x$10^{14}$ cm$^{-3}$ range. Simulations show that this halo formation is the indicator of emittance growth along the plasma. Halo formation and emittance growth are the result of the nonlinear force exerted by the plasmas onto the positron bunch. Unlike in the case of an electron bunch whose emittance can be preserved in the nonlinear blowout regime, the preservation of the emittance of a positron beam in a plasma is more challenging. This issue must be studied using full-scale numerical simulations and confirmed by experiments. Possible solutions include the use of a hollow plasma channel and the careful placing of the positron bunch in a lower plasma density, more linear-like wake.

## ACKNOWLEDGEMENTS

This work is supported by the U.S. Department of Energy, Grant No. DE-FG02-92ER40745.

## REFERENCES

[1] J.B. Rosenzweig, *et al.* , Phys. Rev. Lett. 58, 555 (1987).
[2] C. E Clayton et al., Phys. Rev. Lett. 88, 154801 (2002).
[3] P. Muggli *et al.*, Phys. Rev. Lett. 93, 014802 (2004).
[4] I. Blumenfeld *et al.*, Nature 445, 741 (2007).
[5] S. P. D. Mangles *et al.*, Nature 431, 535–538 (2004).
[6] C. G. R. Geddes *et al.*. Nature 431, 538–541 (2004).
[7] J. Faure *et al.*, Nature 431, 541–544 (2004).
[8] S. Lee, *et al.*, Phys. Rev. E 64, 045501 (2001).
[9] B.E. Blue *et al.*, Phys. Rev. Lett. 90, 214801 (2003).
[10] J. S. T. Ng, *et al.* , Phys. Rev. Lett. 87, 244801 (2001).
[11] M. J. Hogan *et al.*, Phys. Rev. Lett. 90, 205002 (2003).
[12] P. Muggli et al., Phys. Rev. Lett. 101, 055001 (2008).
[13] V. Balakin *et al.*, Phys. Rev. Lett. 74, 2479 (1995).
[14] C. R. Vidal and J. Cooper, J. Appl. Phys. 40, 3370 (1969).
[15] P. Muggli *et al.*, IEEE Trans. Plasma Sci. 27, 791 (1999).
[16] P. Muggli *et al.*, Proceedings of the 2003 Particle Accelerator Conference, Portland OR, p. 1915, www.jacow.org.
[17] C.H. Huang, *et al.*, J. Comp. Phys., 217(2), 658, (2006).
[18] S. Lee *et al.* , Phys. Rev. E 64, 045501 (2001).
[19] T. C. Chiou et al., Physics Of Plasmas, 2(1), 310 (1995).
[20] K.A. Marsh *et al.*, Proceedings of the 2003 Particle Accelerator Conference, p. 731, www.jacow.org.
[21] K. V. Lotov, Phys. Plasmas 14, 023101 (2007).
[22] X. Wang *et al.*, accepted for publication in Phys. Rev. Lett.
[23] P. Muggli et al., Phys. Rev. Lett. 101, 054801 (2008).

# CONTROL, STABILITY AND STAGING IN LASER WAKEFIELD ACCELERATORS

D. Panasenko, LBNL, Berkeley, California


## Abstract

Laser driven plasma wakefields have recently accelerated electron beams with quasi-monoenergetic energy distributions and with gradients of ~100 GV/m. Stabilization and optimization of beam quality are now essential. Recent LBNL experiments have demonstrated control of self trapping, resulting in reproducible bunches at 0.5 GeV. Further optimization has been demonstrated using plasma density gradients to control trapping, producing beams with very low absolute momentum spread at low energies. Simulations indicate that use of these beams as an injector greatly improves accelerator performance and experiments are now underway to demonstrate such staging, which will be a crucial technology for laser driven linacs. This talk will cover recent progress in LWFAs to obtain more reproducible, higher quality beams and also cover staging prospects for high energy laser linacs.


**CONTRIBUTION NOT RECEIVED**

# STATUS AND UPGRADE PLAN OF 250 MeV LINAC AT CLS

X.F. Shen, M.S. de Jong, L.O. Dallin, R.M. Silzer and T. Summers

CLS Inc., University of Saskatchewan, Saskatoon, SK S7N 0X4, Canada

### [illegible]

The Canadian Light Source (CLS) 250 MeV linac, originally constructed in the 1960's, serves as the injector for the 2.9 GeV synchrotron radiation facility [1] located on the University of Saskatchewan campus. The linac has operated reasonably well for routine operation of the light source. However, the long-term goal of operating the CLS storage ring in top-up mode will place increased demands on the linac for stability and availability that cannot be met with the existing system.

Consequently, an upgrade is planned over the next two years to get higher beam stability, reliability and reproducibility. In this paper, the existing linac system will be described and the planned upgrade will be reported.

## INTRODUCTION

The 150 MeV linac, with three Varian accelerating sections, was originally constructed in the mid-1960's for nuclear physics research in the Saskatchewan Accelerator Laboratory. In the 1980's, the linac was upgraded to 300 MeV with the addition of three SLAC-type accelerating sections.

In 1999, the nuclear physics research program was shut down, and the linac was incorporated into the injection chain for the 2.9 GeV synchrotron storage ring of Canadian Light Source. In this upgrade the control system was partially modified to use the EPICS system with the exception of the electron gun and modulator high voltage control. The timing, trigger system and instrumentation were also upgraded. Linac operation for the injector only requires short bunch trains (less than 200 ns) with repetitions rates less than 2 Hz. Extensive changes to the modulators were made including the pulse-forming-networks (PFNs) the high voltage power supplies and thyratrons. Some ion pumps and CCGs were upgraded in the vacuum system. About 15% of the magnet power supplies were changed to fit new requirements. The video deflector was modified to produce bunch train lengths of up to 136 ns, corresponding to 68 bunches at 500 MHz. Figure 1 shows the 250 MeV linac tunnel with the 220 kV electron gun.

## LINAC STATUS

### [illegible]

The linac consists of a high-current gun with a buncher section (manufactured by Haimson) and six 2856 MHz rf sections, and is operated at 250 MeV. After the linac, there is an Energy Compression System (ECS), which reduces the 1% energy spread from the linac by a factor of 10, followed by a transport line to the 2.9 GeV booster synchrotron for the main storage ring.

The electron gun can provide up to 1A beam current at 220 keV. In normal operation, the gun emits 125 mA peak beam current. The buncher section compresses the bunch phase to about 12º and increases beam energy to 13 MeV [2]. Beam current at this point is about 70 mA. There are three Varian style acceleration sections that can provide approximately 50 MeV and three SLAC style sections which provide 40 MeV per section. Each section is supplied RF power by an ITT 8568 klystron.

The linac main parameters are listed in Table 1. The linac is shown in Fig. 1. The linac control schematic is shown in Fig. 4.

Table 1: General parameters of the CLS injector linac.

| | |
|---|---|
| Type of structure | TW disc-load WG |
| Frequency | 2856 MHz |
| Length of section | 3 m and 5 m |
| Total number of section | 3(3m) & 3 (5m) |
| ***RF source*** | |
| Peak power of klystron | 20 MW |
| Number of klystrons | 6 |
| RF pulse length | 2.5 μs |
| ***Main Linac Beam*** | |
| Energy | 250 MeV |
| Beam Current | 60 mA |
| Beam Pulse Length | 2 ns ~136 ns |
| Repetition Rate | 1 Hz |
| Energy spread (without ECS) | <1.0% |
| Energy spread (with ECS) | 0.1% |


Figure 1: CLS 250 MeV linac.

## [illegible]

After four years of operations following commissioning of the storage ring, routine injections use a 250 MeV, 60 mA beam, and 2 ns to 136 ns variable bunch train length. The bunch length is selected by a video deflector, corresponding to the requirements of the storage ring injection or the light source users. Figure 2 shows the beam currents from the linac. The red (top) trace is the signal picked up from a toroid, located just after the end of the linac, which has some distortions at the rising and falling edges caused by the toroid slow time response. The blue (bottom) trace shows the signal from a FCT installed after the small rf section used for the Energy Compression System (ECS). The current uniformity along the bunch train is quite good, with typically less than 10% variation.

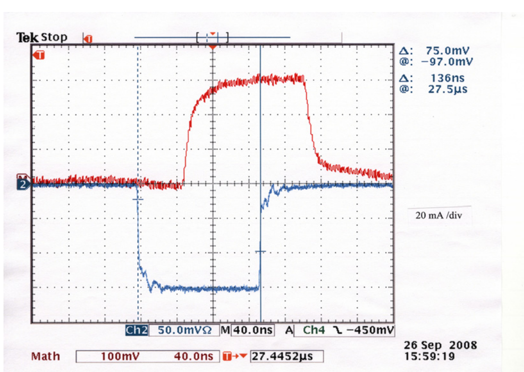


Figure 2: Linac beam current.

During normal storage ring operations, the linac is used only for about 15 minutes every 12 hours. Figure 3 shows the typical daily performance of CLS storage ring. In addition, an in-line beam stop can be placed in the linac-to-booster transport line to allow independent linac operation between storage ring injections. When operated in this mode, the linac operation has been quite reliable with less than 10% of storage ring down-time attributable to the linac.

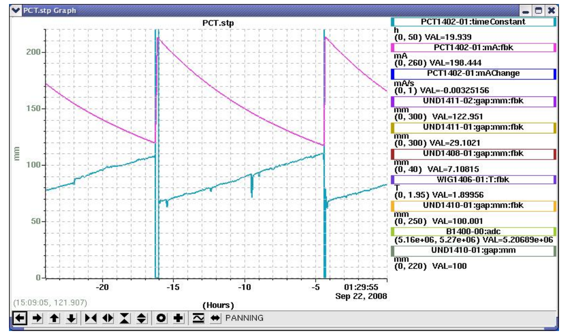


Figure 3: CLS storage ring daily performance. Current is routinely filled to 250 mA every 12 hours. The top trace shows the current decay between refills. The bottom trace shows the beam lifetime.

However, after a period of a few weeks, the operating point for the linac tends to drift, resulting in reduced injection efficiency into the storage ring and requiring some time to re-optimize the linac operation. As well, some linac and rf system components are over 40 years old and are nearing or at the end of their useful operating lifetime. CLS is now considering top-up operation of the storage ring, which requires continuous operation of the linac at a very low repetition rate (~ 0.01 Hz). This places much greater demands on the stability and reliability of the linac.

Thus, most of the following issues need to be addressed for good long-term operation in top-up mode:

- Linac average output energy changes slightly over time.
- The beam energy spread grows over time reducing injection efficiency.
- Beam energy changes from shot to shot, resulting in large variations in current injected into the storage ring.
- Some acceleration sections are quite old and were operated with bad vacuum conditions for many years,.
- Several rf power source parts have no available replacements.
- The Varian section’s expected lifetime was about 20 years, but now they have already worked for over 40 years.
- Unfortunately, because of space limitations in the 1980’s upgrade, the six modulators were installed into the original three modulator cabinets, which has caused serious cross-talk between modulator pairs.
- Electron beam diagnostics are inadequate for automatic control and effective optimization.

## UPGRADE PLAN

A linac upgrade plan has been developed to address these problems for future operation, and will be implemented over the next two years.

### [illegible]

- Four new acceleration sections will replace the existing three Varian sections and a vacuum-contaminated SLAC section. This will both reduce the VSWR trips and solve bad vacuum condition problem.
- A new solid-state RF drive amplifier will replace the existing klystron amplifier.
- All high-voltage modulators will be replaced to stabilize the beam energy jitter which is caused by cross-talk in the modulator triggering circuits.
- Phase detectors and a feedback system will be incorporated to stabilize the beam energy.

### [illegible]

- All controls will be upgraded to the EPICS system.

### [illegible]

- All toroids used to measure the beam currents will be replaced by either fast toroids or fast current transformers.
- All beam profile monitors will be replaced.
- An Emittance measurement device will be considered.

### [illegible]

- Replacement of all old ion pumps and ion pump controllers.
- Installation of more CCGs and TCGs to monitor pressure in all sections,
- Replacement of all vacuum valves.

### [illegible]

- All old DC magnet power supplies will be replaced to stabilize the beam parameters and increase the operation reliability.

## REFERENCES

[1] L. Dallin, R. Berg, J. Bergstrom, M. de Jong, X. Shen, R.M. Silzer and J.M. Vogt, "The Canadian Light Source Status and Commissioning Results", EPAC2004, p. 2269.

[2] J. Haimson, "13 MeV Injection Linear Accelerator Model HRC-735 Instruction and Maintenance Manual", August 1989.

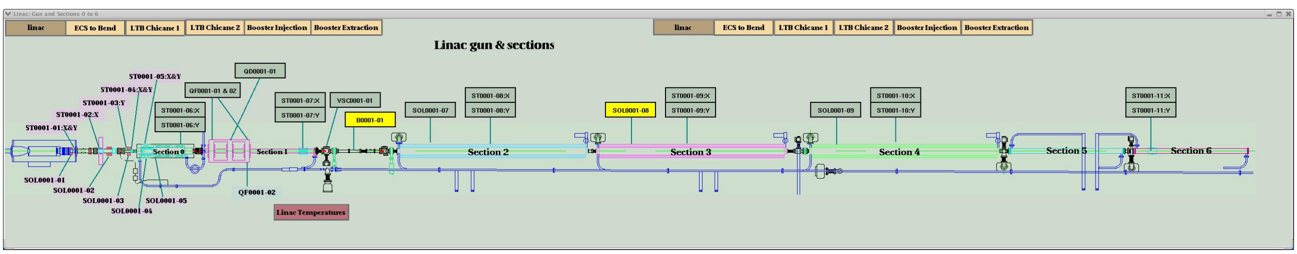


Figure 4: Layout of the CLS linac as shown on the control consul. Layout shows linac sections, steering magnets, and focusing magnets. Gun and buncher controls need to be updated to be part of the EPICS operating system.

# ARIEL AND THE TRIUMF E-LINAC INITIATIVE, A ½-MW ELECTRON LINAC FOR RARE ISOTOPE BEAM PRODUCTION

S. Koscielniak, F. Ames, R. Baartman, R. Dawson, J. Drozdoff, Y. Bylinsky, K. Fong, A. Hurst, D. Karlen, R. Keitel, R. Laxdal, F. Mammarella, M. Marchetto, L. Merminga, A.K. Mitra, K. Reiniger, T. Ries, R. Ruegg, I. Sekachev, G. Stinson, V. Verzilov
TRIUMF*, 4004 Wesbrook Mall, Vancouver, BC V6T 2A3, Canada

*Abstract*

TRIUMF, in collaboration with university partners, proposes to construct a megawatt-class electron linear accelerator (e-linac) as a driver for U(γ,f) of actinide targets for nuclear astrophysics studies, and $^{9}Be(\gamma,p)^{8}Li$ for beta-NMR materials science. The e-linac is part of a broader proposal for an expansion of the TRIUMF rare isotope beams capability through a new facility to be named ARIEL. The e-linac design and prospects for funding are elaborated.

## INTRODUCTION

TRIUMF, in its Five Year Plan 2010-2015 proposes to build the Advanced Rare IsotopE Laboratory (ARIEL) to augment the Rare Isotope Beam (RIB) science program at the ISAC facility. ARIEL, Figure 1, will have four major components: (i) an electron linac photo-fission driver, (ii) a new target hall to be located in a western extension of the existing ISAC building, (iii) a new proton beam line from the H- cyclotron, and (iv) a new RIB "front end". The accelerators and target station(s) will be connected by new 60 metre long beam lines in a common tunnel. The project will be staged. In the first stage, a 100 kW capable linac, a single target station, the e and p beam lines, ion sources and mass analyzers and RIB transport lines to the existing ISAC RFQ and linacs will be constructed. The second stage occurs in the 2015-2020 Plan: the electron linac and target station are upgraded to the full 1/2 –MW capability, an additional target station is added, and the "front end" is completed by the addition of new RIB accelerators, thus facilitating up to three simultaneous RIB, two of which may be accelerated beams. The science program is sketched in Ref.[1] and concepts for the e-linac design and RIB front end are presented in Refs.[2,3].

**Ariel** is a fictional sprite who appears in Shakespeare's play *The Tempest*. The counterpart of Ariel's master *Prospero* is the ISAC science program with its suite of world-class experimental apparatus eager to command the production of more beams and new beams. Adding the electron linac will double the RIBs, and adding the new proton beam line and second target station will triple the RIB production and science output. The '-el' ending of Ariel translates in Hebrew as 'God,' placing Ariel inline with benevolent spirits; and indeed the new accelerator will bring many benefits to TRIUMF.

*TRIUMF receives federal funding via a contribution agreement through the National Research Council of Canada.

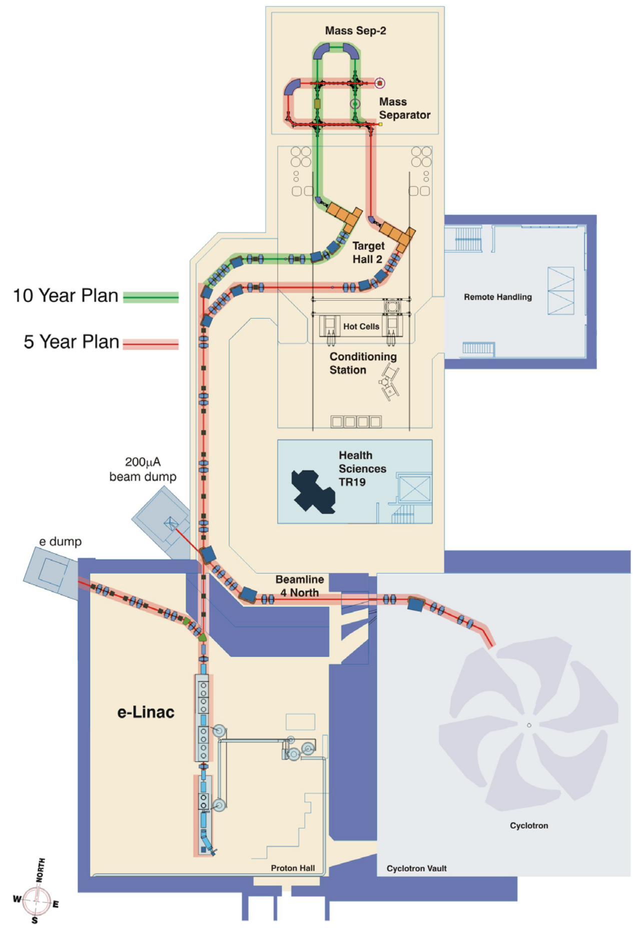


Figure 1: ARIEL infrastructure and layout.

- New Science: nuclear physics with neutron-rich RIBs, and $^{9}Be(\gamma,p)^{8}Li$ production for β-NMR studies in Materials and Molecular Sciences.
- An independent driver for RIB production that complements the cyclotron proton driver.
  - Implements strategy of multiple beams (e, p) to multiple users to accelerate science output.
  - E-linac will operate through annual cyclotron shutdowns providing a strong year-round RIB experimental program.
- Leverages valuable existing infrastructure:
  - Proton Hall, shielded vault with services
  - World-class experimental apparatus (detectors)
  - Builds further SCRF expertise base from β«1, 100 MHz, 4K quarter-wave structures to β=1, 1 GHz, 2K elliptical structures.

- Prepares Canada for SCRF projects world-wide (e.g. CERN-Superconducting Proton Linac, ILC).
- Qualifies a Canadian commercial partner (PAVAC) to build SCRF elliptical cavities.
- Test bed for 4th generation light source technologies.

The centre piece of this program is the high average current continuous-wave electron linear accelerator (e-linac) founded on superconducting RF technology.

## E-LINAC DESIGN OVERVIEW

Three goals have shaped the conceptual design of the e-linac: (1) the utilization of existing technology wherever possible; (2) c.w. operation at high average power; and (3) flexibility toward operation and re-configuration.

From the outset we have opted to base the e-linac design around Tesla Test Facility (TTF) technology developed for TESLA, XFEL [5] and ILC[6]. This is for two reasons: to benefit from the extensive SRF development for these accelerators, and to prepare Canada for participation in high-energy physics projects such as CERN-SPL and the International Linear Collider. However, if given free rein we would have come to similar conclusions.

The TESLA/ILC cavity unit has become a building block for SRF linac design. Though it is the starting point for the e-linac design, commonality with the ILC stops at the cavity level and does not extend to cryovessel or RF power sources. The ILC is a low duty factor machine whose design is limited by the achievable gradient. The e-linac design is driven by the challenges of continuous operation at high average current. Particular challenges are the input coupler design and the 2 Kelvin heat loads. For example, the average power sustained by an ILC input coupler is ≤ 16 kW. In the fission-driver linac, 500 kW of CW RF power has to propagate through the input couplers and cavities into the electron beam. CW operation poses some challenges compared with XFEL or ILC designs, but these challenges are starting to be met in light source designs[4].

Basing the design on existing technology, the e-linac adopts a High-Level RF (HLRF) building block of one 130 kW klystron, two 60 kW couplers and one 9-cell cavity. Five such units operated at 10 MV/m coupled with 10 mA beam current consume 100 kW/cavity and result in a beam energy of 50 MeV. Though the gradient planned for e-linac is a modest 10 MV/m, we intend to leave an upgrade path to an Energy Recovery Linac (ERL) or Recirculating Linear Accelerator (RLA) operated at 20 MV/m; and the cavity fabrication and niobium surface preparation will be consistent with that goal.

The baseline configuration splits the entire e-linac into a low energy injector and the main linac; driven by one and four HLRF blocks, respectively. This choice would allow the linacs to be re-configured at some later date, by the insertion of return arcs, as a test bed for ERL (20 mA, 80 MeV) or RLA (2 mA, 160 MeV) technology. With marginal incremental investments, e-linac could serve as a test-bed for a Compton Scatter Source of hard x-rays or a staging post to an IR or THz FEL or Coherent Synchroton Radiation source. The return arcs are not costed in this proposal, nor a photo-cathode gun; but HOM absorbers, variable coupling ratio and piezo tuners form part of the baseline design.

## E-LINAC TECHNICAL DESIGN

The 50 MeV, 10 mA, capable CW linac is based on TTF super-conducting radio-frequency (SRF) technology at 1.3 GHz and 2K; and consists of an electron gun, buncher, injector cryomodule, and two main-linac cryomodules. Figure 2 shows the e-linac baseline layout as it will appear in 2017. The injector module contains a capture section, followed by acceleration in a 9-cell cavity to a few MeV. Each of the main linac cryomodules, accelerating by 20 MeV, contains two 9-cell cavities.

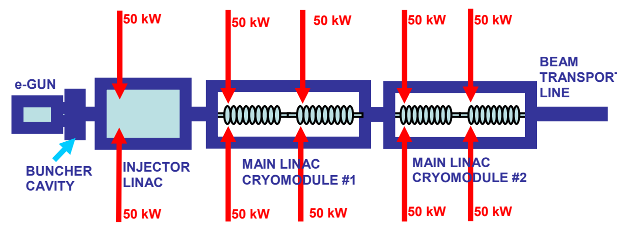


Figure 2: E-linac layout and power distribution.

In the first stage, to be completed mid-2013, the injector the first of the main linac modules, and single IOT and klystron drivers are installed providing 25 MeV, 4 mA. In the second stage, to be implemented 2017, the second of the main linac modules is added along with additional high-power RF sources to achieve the final ½-MW goal. The decision to divide the main linac into two modules stems mainly from the anticipated funding envelope.

We now focus on some technical details of the e-linac. Multiple stages of bunching are required to prepare the beam for on-crest acceleration in the main linac. There is progressive bunching at the source, buncher cavity and capture section at entrance of the injector linac.

### *Electron Source*

The fission-driver specification is more relaxed than a comparable ERL injector to a Free Electron Laser. Light sources need 6D high-brilliance beams. By contrast, the fission driver eliminates its beam on target and so a 100 kV thermionic gun (30 µm normalized) is employed. A diode type gun has been received from TJNAF and will be converted to triode operation; modulating the grid causes the gun to be conducting for ≤ 45° of the RF cycle allowing the beam to emerge pre-bunched at the anode.

Figure 3 shows the gun test bed at TRIUMF; vacuum components and HV power supplies are on order. The final source will output 170 ps FW bunches each of 16 pC with a bunch repetition rate of 650 MHz.

### *Buncher Cavity*

The buncher cavity is used to prepare the beam for the injector linac. The buncher is a normal conducting RF cavity excited at 650 MHz with an amplitude of 15 kV and phased at 90° with respect to the beam. The power requirements are modest and are met with a commercial solid-state amplifier.

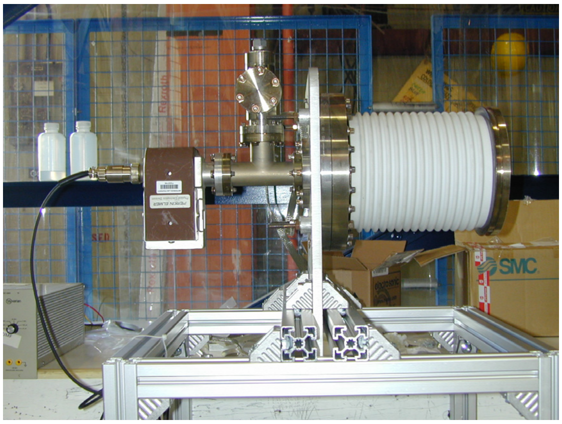


Figure 3: Ex-TJNAF thermionic gun at TRIUMF.

## *Injector Linac*

The injector linac is composed of a capture section, followed a 9-cell SRF cavity. The injector terminates in an electron beam analysis section. A short, 2-magnet dog-leg is envisioned immediately downstream of the injector linac for compatibility with later ERL or RLA options.

Injecting a 100 keV beam ($\beta$=0.55) directly into a $\beta$=1 RF structure results in inefficient acceleration because of the mis-match in transit time. There are also possible deleterious transverse effects associated with such low energy injection into a high-gradient SRF structure. So the capture section performs two functions: additional bunching and modest acceleration. The capture section could be implemented as either a graded-beta structure; or independently phased cells. Both NC and SC structures are possible; cost favours the latter. A detailed analysis will be performed leading to a final choice between these options. The capture section is driven by Inductive Output Tubes (IOTs).

## *Main Linac*

The main linac consists of four 9-cell TTF-style SRF cavities housed in two cryomodules. The cavities operate at 10 MV/m, and each has an active length of 1 m.

We confine the gradient options to ≤ 20 MV/m because this is the limit achievable with buffer chemical polishing (BCP) alone of the niobium surfaces. BCP is readily available at TRIUMF, whereas electro-polishing is not. The e-linac cavities will be constructed in collaboration with a BC-based engineering company, PAVAC, with the intention of introducing to Canada the capability to fabricate and process elliptical Nb cavities. The company presently makes bulk-niobium quarter-wave cavities [7] for the ISAC-II project.

## *RF Power Source*

A variety of manufacturers offer pulsed klystrons rated at up to 5 MW peak and 100–250 kW average power, but the reduced duty factor means they are not applicable to the fission driver. Several manufacturers at present have the capability to build a 120 kW CW klystron, but only *e2V* has recently delivered such a product – six units for the Cornell ERL injector[4]. The *e2V* K3415LS klystrons match the e-linac baseline specification. However, *e2V* has recently redirected its business strategy and ceased production of these klystrons. For the e-linac RF source we rely on the offer from *CPI Microwave Power Products*. Their device will be based on the 1.5 GHz, 110 kW klystron developed for the FEL injector at TJNAF. With minor modification, this will be capable to deliver up to 150 kW of RF power at 1.3 GHz in CW operation.

At present, the highest power-rated commercially available CW input coupler at 1.3 GHz is the 60 kW Cornell-designed coaxial coupler available from *CPI-Eimac*; and this is chosen for the baseline.

## *Funding Prospects*

The ARIEL facility is a major component of the 2010-2015 TRIUMF Five Year Plan (5YP), and its funding will be pursued in that context with the National Research Council Canada. There exists also another funding route for e-linac: the Canada Foundation for Innovation (CFI) which proceeds by bi-annual competitions. The University of Victoria, TRIUMF and other Canadian universities actively propose to obtain CFI funding to leverage the 5YP and submitted the Letter of Intent January 15th 2008.

On June 23rd, CFI designated the e-linac proposal as a National Project Application, not subject to institutional caps. On June 30th, a collaboration of 14 universities submitted the official Notification of Intent, and CFI responded by inviting the submission of the Full Proposal by October 3rd 2008, the final day of this conference. The CFI competition results are to be made public in June 2009, and an announcement of the TRIUMF five year funding is expected in February 2010.

## *Conclusion*

E-linac will be an exemplar CW high-power, high-current linac. Due to the intrinsic power efficiency of SRF technology and the compactness and high accelerating gradient of L-band structures, their adoption provides a cost effective approach to a MW-class fission driver. Many of the major sub-system components have been identified. There are cell, cavity, input coupler, klystron, mechanical tuner, HOM damper and cryostat designs either pre-existing or close to the e-linac requirements; and their adoption will speed project completion and reduce R&D costs.

## REFERENCES

[1] S. Koscielniak *et al*, Proc. EPAC 2008, Genoa, Italy, p 985.
[2] S. Koscielniak *et al*, ibid p 2728.
[3] R.E. Laxdal *et al*, ibid p 3635.
[4] S. Belomestnykh *et al*, ibid p 832.
[5] H. Weise: Proc. EPAC2004, Lucerne, Switzerland, p 11.
[6] B. Barish: Proc. EPAC 2006, Edinburgh, Scotland, p 1.
[7] R.E. Laxdal *et al*, these proceedings THP003.

# PROPOSAL FOR A 15 MeV SUPERCONDUCTING ELECTRON LINAC FOR THE DEINOS PROJECT

J-L. Lemaire, P. Balleyguier, D. Guilhem, J-L Flament, V. Le Flanchec, M.Millerioux, S. Pichon
CEA, DAM, DIF, Bruyères le Châtel, 91297 Arpajon, Cedex, France

The design of a 15 MeV, 2 kA peak current, electron accelerator for the DEINOS project is presented. It is dedicated to a new radiographic facility. The accelerator is based on a DC photo-injector and a RF superconducting linac. Up to twenty electron micro-pulses, 100 ps time duration and 200 nC bunch charge are emitted at 352 MHz repetition rate from a $Cs_2Te$ photocathode and accelerated to 2.5 MeV in the DC diode before injection into a superconducting linac.

A general description of the main accelerator components and the beam dynamics simulations are presented.

## INTRODUCTION

The former DEINOS project which name stands for "**DE**monstrateur d'**IN**jecteur **O**ptimisé pour un accélérateur **S**upraconducteur**"** was consisting of a DC photo-injector coupled to a RF superconducting accelerator (Fig. 1). It is a new versatile scheme based on rather well tested technologies. It has been proposed to produce flash X-ray pulses from very intense electron beams impinging on a high Z material target. A final beam transport allows tight beam focusing on the conversion target [1].

In order to meet the specifications of the radiographic need, 2 µC- 51 MeV- 60 ns, compactness and low cost, the machine could be made of the assembly of a 352 MHz RF linear accelerator and a photo-injector, provided the photo-injector delivers the proper bunches.

Electrons bunches are emitted from a $Cs_2Te$ photocathode driven by a 266 nm wavelength laser and extracted in a DC gun. A pulsed power supply made of a prime power, a Blumlein and coaxial transmission lines drives the diode accelerating voltage.

The voltage applied to the accelerating gap of the diode can reach a value up to 2.5 MV. Time duration of the voltage plateau is set by the Blumlein to be 60 ns.

A short drift section between the photo-injector and the linac allows room for the injection of the photocathode laser beam, a vacuum valve and beam diagnostics.

Optimizations of the photo-injector, the RF accelerator and radiographic parameters led to a design for which the accelerator machine could deliver 20 bunches at 352 MHz. Each bunch of 100 ps time duration would carry 100 nC. This can be done with a UV laser illuminating the photocathode in synchronism with the linac RF in order to recapture the bunches in the RF cavities without any losses.

All the main technical issues that were identified to building the photo-injector (large size diameter and high quantum efficiency $Cs_2Te$ photocathodes, UH Vacuum level - $10^{-10}$ mbar, high voltage insulator barrier, electron gun and diode geometry, stability of the high voltage driver and stability of the laser) could be worked out with this new demonstrator, at lower budgetary cost. A new orientation has been decided for the project in order to build a reduced scale model.

Then a 15 MeV accelerator scheme based on the early architecture consisting of a DC photo-injector and a superconducting RF linac made of only one cavity, has been proposed as a new facility for radiography applications.

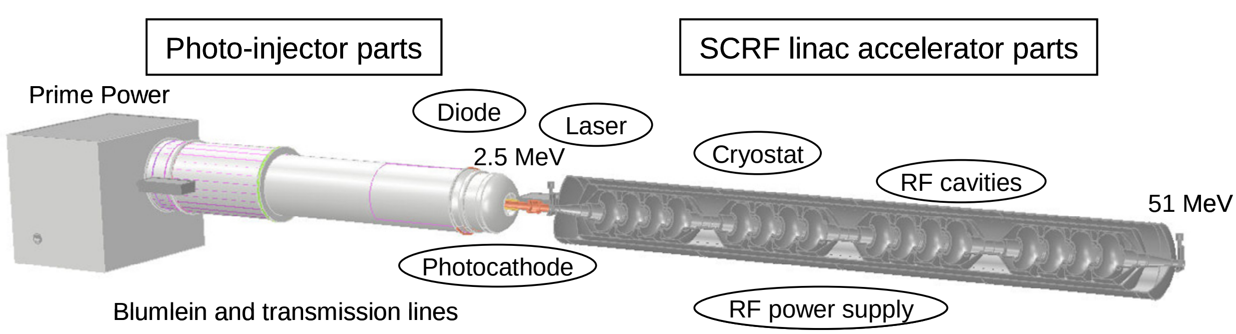


Figure 1: Artist's view of the DEINOS project.

## PHOTO-INJECTOR

The photo-injector consists of a pulsed DC high voltage gun diode under UH Vacuum. High voltage can be tuned from 1.5 to 2.5MV.

The diode is followed by a solenoid lens either to propagate the beam through a short beamline along which various beam diagnostics are installed (emittancemeter, Faraday cup, pulsed current transformer, Cerenkov screen, streak camera), or to focus the beam at a waist before entering the next SCRF accelerator module, a 266 nm laser illuminating a removable $Cs_2Te$ 40 mm diameter emissive size photocathode which is inserted under vacuum through remote handling and a high voltage pulse power generator [2].

### [illegible]

Most of the subsystems needed for the high voltage generator are spare pieces from the PIVAIR prototype injector of AIRIX induction radiographic machine. Some have been rebuilt, some have been modified or replaced to deal with the present need. The prime power consists of a 1 µF capacitor bank, which is switched through the primary of an iron-core high voltage pulse transformer (Stangenese manufacturing).

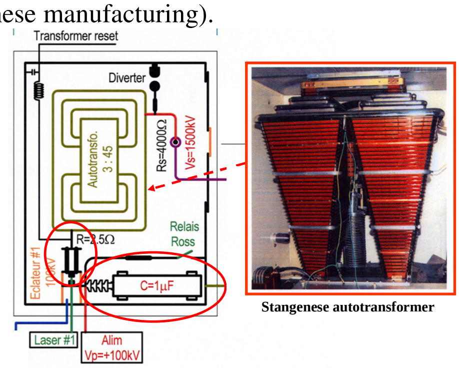


Figure 2: Prime power.

The secondary of the transformer is electrically tied to the Blumlein which is charged to a maximum voltage of 1.5 MV. The outer leg of the Blumlein is switched out with a laser triggered SF6 gas switch. Coaxial transmission lines also called output lines finally transform the output voltage to the required maximum 2.5 MV voltage on diode and parallel resistor load. Figure 2 shows parts of the prime power refurbishing, which is now completed.

### [illegible]

The interface separating the oil medium insulator inside the coaxial transmission line from the vacuum of the diode part is a major component of the photo-injector. The insulator design is a challenge as far as fabrication is concerned. Compatibility between the high voltage hold off, the mechanical size and stresses and the attainable vacuum as low as $10^{-10}$ mbar during static operation (beam off) requires specific materials. Optimized geometries and shapes must be manufacturable from candidate like ceramic or borosilicate materials. Feasibility comparisons have been carried out. We ended up to a vacuum insulator stack made of alumina rings and intermediate metallic washers as shown in Fig. 3.

Electrode geometries have been optimized to achieve lowest and constant E peak field values on surface of electrodes. Voltage hold off must be safe up to the maximum accelerating voltage of 2.5 MV applied for a time duration of 100 ns.

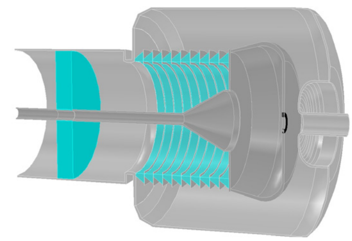

Figure 3: Reversed axial ceramic stack HV insulator.

### [illegible]

The driving laser must provide a maximum of bursts of 20 topped hat pulses of 100 ps FWHM separated by 2.84 ns. The laser system is shown in Fig. 4. It consists of a 500 mW, 1064 nm wavelength Nd:$YVO_4$ SESAM oscillator.

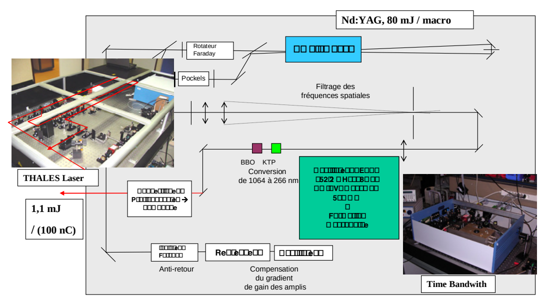


Figure 4: Laser chain.

It is actually able to deliver 2 separated in time trains. Each train of 60 ns time duration carries 20 bursts. After pulsed shaping, amplification and frequency quadrupling, the energy to be delivered to the photocathode is 25 µJ per burst at 266 nm. Rms jitter value is 2 ps and achieved value of beam homogeneity is 4% rms.

### [illegible]

Robust photoelectric cathodes are being investigated and fabricated in a separated photocathode bench. Transfer from this preparation chamber and the photo-injector is done thanks to a transportation system that moves cathodes one by one in a unit chamber tight to the diode vessel. A set of 3 cathodes is stored. The cathodes are kept under UHV wait then to be loaded in the DC gun using the remote handling device. Photocathode fabrication has started with 30 mm diameter molybdenum cathode. Tellure is first evaporated for 8 nm thickness followed by cesium deposition. Deposition is stopped when the measured photocurrent reaches a maximum and stays constant (Cs thickness is then about 50 nm). So far Q.E is not yet reproducible enough for our application mainly due to CO pollution. It varies from 1 % to 16 %

(Fig. 5). A parametric study is been carried on over several parameters such as cathode temperature value during deposition process, speed of evaporation, thickness of cesium deposit on tellure, surface emission homogeneity. Robustness of $Cs_2Te$ photocathodes against specific gas pollution will be tested next before going to nominal larger size diameter cathodes.

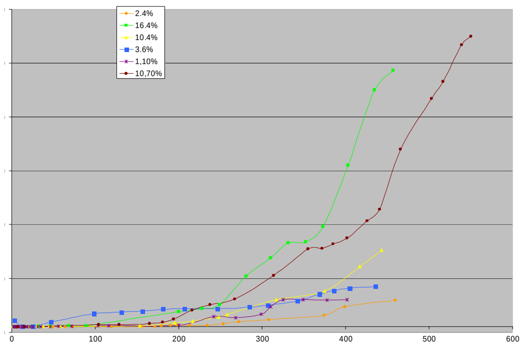


Figure 5: Q.E. vs Cs thickness deposit (x100A°).

## SC-LINEAR ACCELERATOR

Superconducting accelerator structures give more compact machine for equivalent energy stored in the cavity than room temperature ones. To compensate for the loading in order to accelerate properly the high charged bunches, the linear accelerator has to be superconducting. Therefore mean beam energy from bunch to bunch decreases. Beam dynamics must deal with the resulting energy spread of the beam to be delivered on target.

### [illegible]

The SC-Linac is a close replica of a 4 cells superconducting LEP2 module. We have presently chosen the niobium deposit on to copper manufacturing. The accelerating field of 7.5 MV/m fits the design. $Q_0$: 3.2 $10^9$. Total stored energy: 160 J and beam loading requirement is 1.2 J/ bunch@100 nC. Effort is being done to low down the static cryogenic losses.

### [illegible]

Solid-state RF power supply can be used and requires 20 kW of RF power. A prototype unit of 2.5 kW was constructed successfully.

### [illegible]

Beam dynamics of the whole accelerator machine has been carried out thanks to the simulation chain described in [3]. The linac RF cavity phase is tuned to end up with the lowest rms beam energy spread. Two different machine configurations have been studied: 10 bursts of 100nC/bunch and 5 bursts of 200nC/bunch which accelerated beam simulation is shown in Fig. 6.

The two configurations give very close results (difference of only 5% in the spot size value). The 5 bursts train configuration @200nC per bunch allows a short radiographic imaging (13 ns) at same spot size for a 2 kA, 15 MeV beam delivering an integrated X-ray dose of 1.7 Rad. The radiographic facility is very compact.

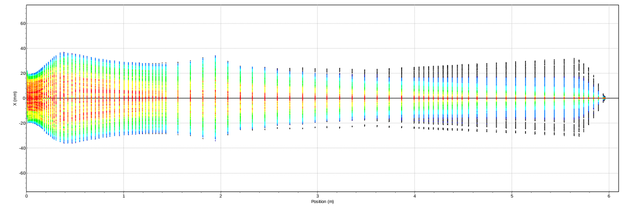

Figure 6: Beam envelope 5 bunches @200 nC per bunch.

## FINAL FOCUSING

One drawback with the large energy spread of the accelerated beam comes from the spot size enlargement due to the chromaticity of the final focusing lens. Three parameters drive this effect:

- space charge of the high charge in every bunch,
- beam loading in the RF-cavity reducing continuously the net accelerating field,
- large longitudinal beam extension over the RF phase, generating RF energy spread.

In order to limit these effects, we have studied a conical solenoid geometry (figure 7).

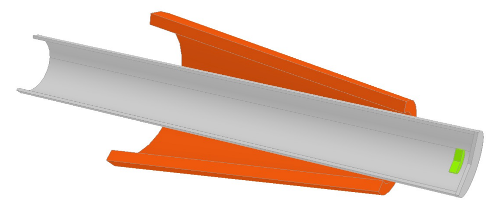

Figure 7: Conical solenoid geometry.

Beam dynamics simulations have showed that the beam spot size on the target can be decreased by about 15 to 20% for large energy spread.

## CONCLUSION

We focused on the description of the accelerator components, achieved, under construction or to be fabricated in order to be used in view of a reduce scale demonstrator for a radiography applications. This new machine is made of a photo-injector, a superconducting RF accelerator and a final focusing. The whole machine simulations have been carried out for a 1µC total charge beam. Two beam configurations were considered: small spot sizes, short time exposure imaging as low as 13 ns can be obtained with electron bunches carrying 200 nC of charge.

## REFERENCES

[1] "Design of a RF accelerator demonstrator for driving X-ray source", J-L Lemaire and al, Pulse Power Conference 2005, Monterey, USA.
[2] "A 2.5MeV pulsed photo-injector demonstrator for radiographic applications", JL. Lemaire, IPMC2008, Las Vegas, USA.
[3] "Beam dynamics simulations for a 15 MeV superconducting electron linac coupled to a DC photo-injector", D. Guilhem, J-L Lemaire, S. Pichon, these proceedings.

# STATUS OF THE CTF3 PROBE BEAM LINAC CALIFES

F. Peauger, D. Bogard, G. Cheymol, P. Contrepois, A. Curtoni, G. Dispau, M. Dorlot, W. Farabolini, M. Fontaine, P. Girardot, R. Granelli, F. Harrault, JL. Jannin, C. Lahonde-Hamdoun, T. Lerch, PA. Leroy, M. Luong, A. Mosnier, F. Orsini, C. Simon, DSM/Irfu, CEA Saclay, France, S. Curt, K. Elsener, V. Fedosseev, G. Mcmonagle, J. Mourier, M. Petrarca, L. Rinolfi, G. Rossat, E. Rugo, L. Timeo, CERN, Geneva, Switzerland, R. Roux, LAL, Orsay, France

*Abstract*

The CLIC project based on the innovative Two Beams Acceleration concept is currently under study at CTF3 where the acceleration of a probe beam will be demonstrated. This paper will describe in details the status of the probe beam linac called CALIFES. This linac (170 MeV, 0.9 A) is developed by CEA Saclay, LAL Orsay and CERN. It has been installed in the new experimental area of CTF3 to deliver short bunches (1.8 ps) with a charge of 0.6 nC to the CLIC 12 GHz accelerating structures. We report new results of beam dynamic and RF simulations considering the new CLIC parameters. The construction of CALIFES in the CLEX building is presented. Recent measurements from the laser system are discussed. Details about the HV modulator tests and the power phase shifter fabrication will be described and the start of commissioning will be also reported.

## INTRODUCTION

The electron linac CALIFES [1] (Figure 1) will produce both single bunch and bunch train spaced by 0.66 ns to X-band structures in order to perform various tests such as beam kick due to RF breakdown or dipole mode excitation, in addition with the Two Beam Acceleration demonstration. The main linac parameters have been updated and are shown in Table 1.

Table 1: CALIFES main parameters.

| Parameters | Value |
|---|---|
| Final linac $e^-$ energy | 170 MeV |
| Emittance rms | < 20 $\pi$ mm.mrad |
| Energy spread (single bunch) | < ± 2% |
| Energy / Phase deviation (multi-bunch) | < ± 1% / < 10 ° at 12 GHz |
| Number of bunches Nb | 1 – 32 - 226 |
| Bunch charge (single/ multi bunch) | 0.6 nC / 6 nC/Nb |
| Initial/final bunch length | 5.3 / 1.8 ps, 1.6 / 0.5 mm |
| Transverse beam size | 0.6 mm x 0.6 mm |
| Bunch spacing | 0.66 ns / 1.5 GHz |
| Train length | 21 – 150 ns |
| Train spacing (rep. rate) | 5 Hz |

## BEAM DYNAMIC AND TRANSIENT RF SIMULATIONS

Due to fact that the flat top duration of the compressed RF pulse (1.3 µs) is close to the structure filling time (1.23 µs), the accelerating field profile must be precisely computed (Figure 2). With a drive frequency slightly above the centre frequency (+ 150 MHz), the filling of the structure is nearly complete after a pulse propagation of 5.5 µs. A quasi steady state is reached and no major changes of the beam quality are expected.

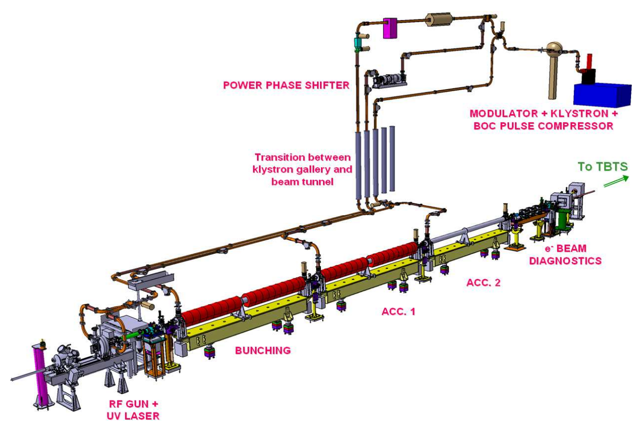


Figure 1: 3D layout of CALIFES.

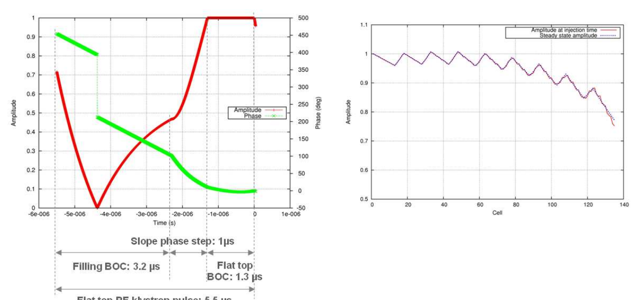


Figure 2: RF pulse shape after compression (left) and amplitude field profile after 5.5 µs (right).

In single bunch operation, simulations showed that the transverse profile at the end of the linac are $x_{rms} \sim y_{rms} \sim 0.6$ mm. The bunch length at the end of the linac is $z_{rms} = 0.176$ mm and the emittance is 13.04 mm.mrad. The final linac energy is 169.6 MeV/c with an energy spread of $\Delta P/P =$ 1.006 %.

In multi bunch operation, we calculated a total energy deviation between the first and last bunch of 5.4 % at 170 MeV and a phase deviation of 15.5° at 12 GHz. The bunch charge will be reduced with the number Nb of bunches, Qb < 6 nC / Nb, such a way that both energy and phase deviations are smaller than respectively 1% and 10° at 12 GHz.

## INSTALLATION IN THE CLEX BUILDING

While the CLEX building was still under construction, a pre-installation of the linac began in Nov. 2006 in building 182 at CERN for two S-band structures re-used from the former LEP injector linac. These elements were transferred in CLEX in June 2007 and the beam stopper, the spectrometer dipole magnet and some supports were quickly installed. All the elements were pre-aligned in less than 1 mm. The BPMs and the dipole steerers are supported by a common girder and alignment support. There were connected to the accelerating sections in Oct. 2007 to allow first alignment procedure and vacuum tests (Figure 3).

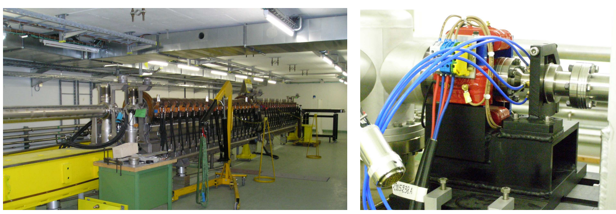

Figure 3: Accelerator sections (left), dipole steerer and BPM (right) installed in November 2007.

After being fine tuned in laboratory, the Video Profile Monitors (VPM) and laser beam line components were progressively installed between Dec. 2007 and May 2008. The high voltage modulator including the oil tank, the PFN rack and the auxiliary power supplies were installed in Dec. 2007 and tested with its dedicated klystron in April 2008. The RF gun was delivered in May 2008 from LAL and a final frequency tuning was completed directly on the linac in June 2008 (Figure 4).

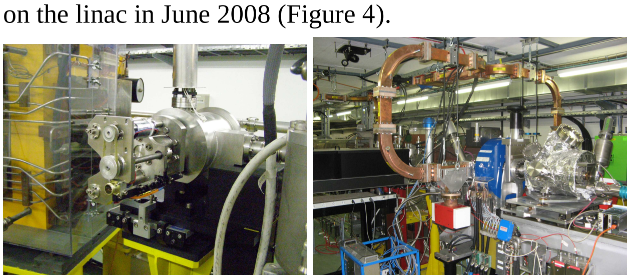

Figure 4: VPM n°2 and RF Gun installed between Dec. 2007 and June 2008.

Some alignment problems for the structures and the beam diagnostic elements were identified, mainly through visual inspection and metrological measurements. The misalignment issues were caused by errors in alignment input data and accidental manipulation of the elements. The final alignment (~ 0.1 mm) has been completed in May 2008.

Finally, the RF network including splitters, windows, couplers and loads were progressively installed during summer 2008 (Figure 5).

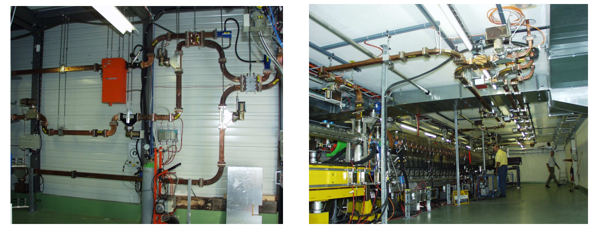

Figure 5: RF network in the klystron gallery (left) and the beam tunnel (right) installed during summer 2008.

## LASER SYSTEM

Since both drive and probe beams must be synchronous, the 10 ps width pulses created in IR at 1.5 GHz for the drive beam are derived after a double amplification. The diode pumped Nd:YLF based amplifiers enhance the laser energy up to 10 µJ per pulses before being gated to create from 0.4 to 150 ns pulse train (pulse pickers). The laser beam is then converted from IR to green by a KTP crystal (10 mm) and from green to UV (261 nm) by a BBO crystal (12 mm) with a specified conversion efficiency of around 35% each.

A transport path of 80 m long under vacuum has been built to deliver the UV pulses to the photocathode. 25% losses are expected in the pulse picker and transport line each. A final UV nominal energy of 370 nJ would give a bunch charge of 0.6 nC considering a quantum efficiency of 1%.

Experiments done in March 2008 showed that the amplified IR pulses energy was limited to 4.3µJ, and that the crystal efficiencies were respectively 13% and 4.3%. This leads to a UV pulse energy of 15 nJ on the photocathode, giving 0.03 nC and 45 mA instead of 900 mA.

The main hypothesis to explain the low conversion efficiency is a presence of a significant DC component around the 10 ps pulses. Remarkably improvements have been achieved very recently, in Sept. 2008 by the CERN team. The UV energy per pulse reached 133 nJ, giving 0.26 nC and 390 mA.

The UV beam transport down to the photocathode has been demonstrated (Figure 6). The oval profile of the beam is mainly due to the high walk-off (85 mrad) combined with the low diameter (130 µm) of the green beam focused on the BBO.

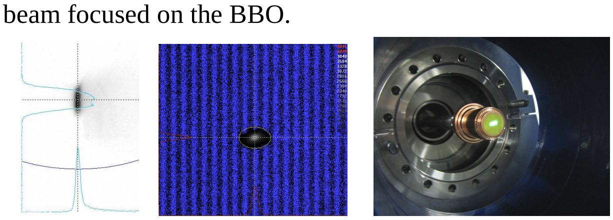

Figure 6: UV beam after the second crystal (left), on the virtual photocathode (middle) and on the photocathode itself (right).

The Pulse Picker has been installed and tested in July 2008. Rise and fall times are fast enough to select the desired number of bunches (Figure 7). The transmission is

81% and no discontinuity has been observed during the flat top.

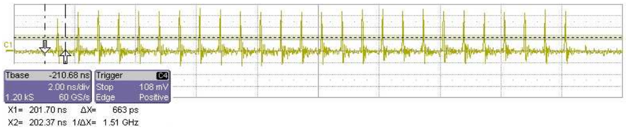

Figure 7: Train of 26 pulses spaced by 0.66 ns gated by the Pulse Picker system.

## BEAM DIAGNOSTICS

The video profile monitors and the five BPM are widely described in [2] and [3]. They have been calibrated and installed in the linac.

For these two diagnostic systems, the control command interface is in progress in order to be able to check the beam profile as well as its position in the control room.

## RF SYSTEM

### *Modulator*

The modulator has been fabricated by PPT (Germany). It delivers quasi-rectangular pulses of 300 kV - 300 A - 7.6 µs at 5Hz to a 45 MW S-band klystron. It has been commissioned first at factory on a dry load at low repetition rate and tested at nominal values on two different klystrons at CERN. A pulse quality problem was discovered during the first high power tests. A ripple of ±4% was measured on the cathode voltage flat top. The problem was identified to be a superposition of a long wave on the flat top and a high frequency noise at the beginning of the voltage pulse. The long wave oscillation has been efficiently removed by a fine tuning of the PFN. The HF noise is believed to be due to fast oscillations in the voltage divider used to measure the pulse in the oil tank. This hypothesis has been confirmed by pulse quality measurements with the RF pulse. The klystron has been driven at saturation up to 42 MW and a remarkably good voltage ripple of ±0.3 % has been deduced from the RF pulse ripple measurement. No signs of HV breakdown were observed.

### *Power Phase Shifter*

The power phase shifter aims at tuning the off crest RF phase of the first section for velocity bunching. This new component is made of three sliding circular waveguides working on the $TE_{01}$ mode. The mode conversion is done by two “wrap around” mode launchers. During its fabrication, the first brazing operation of the two main parts failed. A leakage has been detected and some drips of the brazing alloy appeared. Experiments on samples at different temperatures showed that the chosen alloy was very sensitive to temperature variation during brazing melting period. The converter has been re-used to a scale one prototype to validate a new brazing alloy and check the thermal behaviour of the assembly during the temperature ramping. In particular, the temperature probes inserted in two of the four posts (74 mm height) confirmed that a strong temperature gradient occurs in this region. The cleaning procedure and alignment mechanism have also been improved. The prototype shown in Figure 8 has been successfully brazed in March 2008. The assembly is tight and the join did not produce any drips neither lacks. Two new converters are now under construction and will be available for high power test in March 2009.

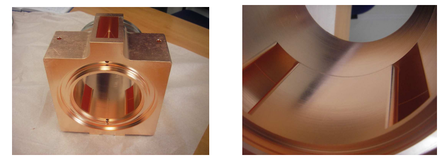

Figure 8: Mode converter prototype for a qualification test of the brazing process.

### *RF Conditioning*

The RF conditioning has started in Sept. 2008. An RF pulsed power of 43 MW – 1µs – 5 Hz has been reached in less than 2 hours. The waveguide pressure stayed below $0.5.10^{-8}$ mbar and only few RF breakdowns were observed on the scope, identified by a fast increase of the reflected power. The filling time of the structures was measured by the time delay between the input and the output incident RF pulse (Figure 9). It is 1.2 µs and in a good agreement with our predictions.

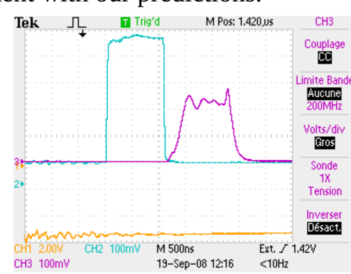


Figure 9: Incident RF pulse at the input (blue) and output (pink) of the 1st travelling wave accelerating structure.

## CONCLUSION

The electron beam line, the laser transport line and most of the RF network are now under vacuum. The RF conditioning will continue during October and the start of operation with beam is planned in Nov. 2008.

## ACKNOWLEGMENTS

We would like to thank our colleagues from CERN for their large contribution on the CALIFES project.

## REFERENCES

[1] A. Mosnier et al., “The Probe Beam Linac in CTF3”, Proceedings of the EPAC 2006 conf., Edinburgh

[2] W. Farabolini et al., “Video Profile Monitors Developments for the CTF3 Probe Beam Linac”, EPAC 2008, Genoa

[3] C. Simon et al., “Beam Position Monitors using a re-Entrant Cavity”, DIPAC 2007 Workshop, Venice

# THE NEW SINGLE BUNCH INJECTOR FOR ELSA

F. Klarner, S. Aderhold, O. Boldt, W. Hillert,
Electron Stretcher Accelerator, Physikal. Institut, Nussallee 12, 53115 Bonn

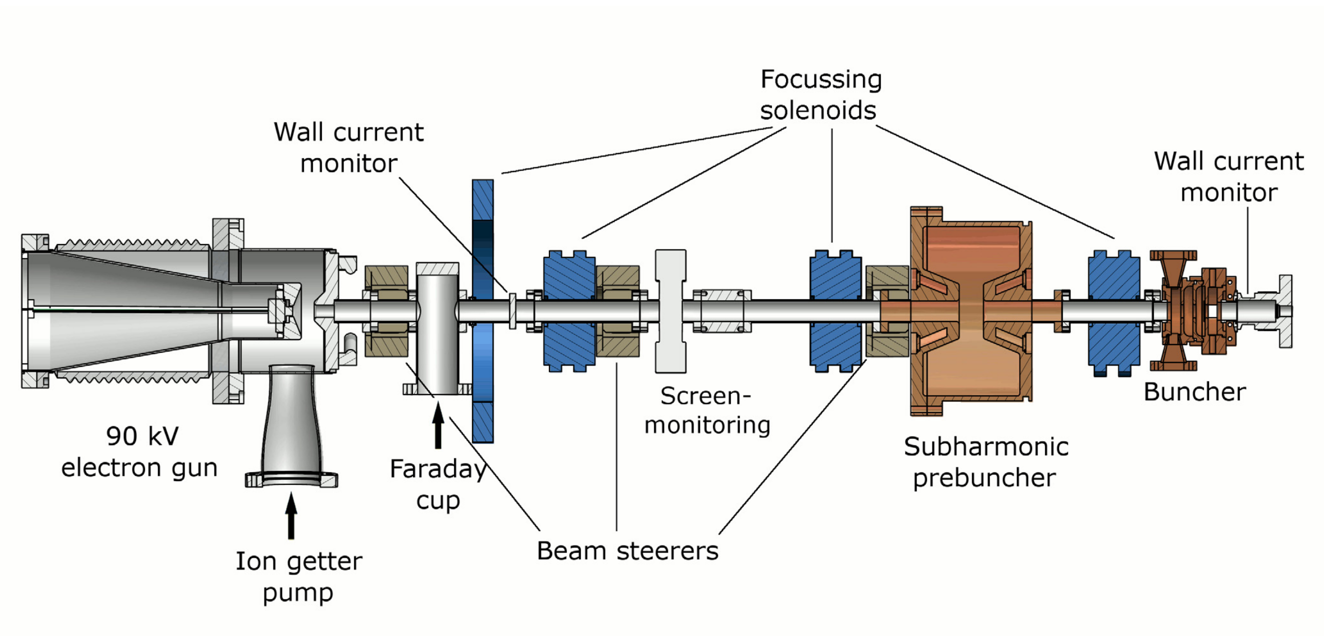


Figure 1: Overview of the new injection system which will be installed at the linear accelerator LINAC I at ELSA.

*Abstract*

Since 1966 a Varian manufactured injector is in use at the ELSA accelerator facility of the University of Bonn for several experiments investigating the subnuclear structure of matter.

The new injector for Linac 1 currently under construction at ELSA is expected to operate in a single bunch mode of 2 A beam current. This mode gives the possibility of deeper background studies in the experimental setup of the CB experiment sponsored by the "Deutsche Forschungsgesellschaft" and to investigate single bunch instabilities within the Helmholtz alliance "Physics at the Terascale". Also, a 2 μs long pulse mode of 500 mA beam current will be available for normal thermionic electron service. The injector delivering a single bunch was designed and optimised with EGUN and numerical simulations based on the paraxial equations. The compression of the pulses created by a pulsed thermionic 90 kV gun is achieved by a 500 MHz prebuncher as well as a β-matching travelling wave buncher running at the linac frequency.

## 90 KV ELECTRON GUN

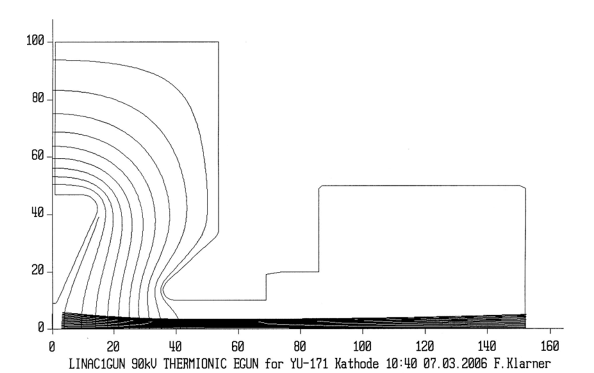


Figure 2: Gun geometry $r$ vs. $z$ in mm with equipotential lines and space charge limited electron rays calculated with EGUN for an anode voltage of 90 kV.

The 90 kV gun is based on a design used in the SBTF test facility at DESY. The design of the cathode conus was adjusted with the computer code EGUN to fulfill the requirements of 2 A single pulse and 500 mA long pulse operation. With a 34 mm wide anode cathode gap this gun has a perveance of 0.16 $\mu A/V^{3/2}$ and delivers a 4.3 A space charge limited current at 90 kV. The EGUN calculated beam propagation is shown in figure 2. The cathode is carried by a conical metallic tube that runs through the 250 mm long ceramic and is flanged at the high voltage end of the isolator. The gun needs a grid electrode near the cathode in order to be pulsed. The EMAC Y-171 cathode-grid assembly, which emits from a circular area of 1 cm² equivalent to 5.64 mm in radius, is used here. The normalized emittance for a 2 A pulse at the gun exit is $\varepsilon = 22.8\ \pi$ mm mrad. Pulsing the cathode will be done by a fast gun pulser housed inside the conical tube right behind the cathode. In single pulse mode the gun, together with this pulser, is expected to deliver FWHM ≤ 2 ns pulses with a peak current of 2 A.

## PREBUNCHING

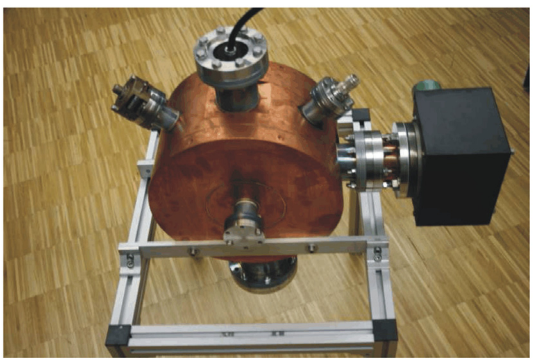

Figure 3: 500 MHz prebuncher.

The 40 mm wide gap of the 500 MHz nosecone prebuncher is centred at $z$ = 112 cm. In order to weaken the requirements for the gun this frequency has to be as low as possible, but nevertheless has to match with the time structure of the bunch train in the stretcher ring ELSA. Therefore in our case the prebuncher has to work at 500 MHz, which implies that the gun pulse for the single bunch has a length in the order of 2 ns. The chosen prebuncher has an untuned resonance frequency of $\nu_0$ = (499.819 ± 0.001) MHz, an unloaded quality factor of $Q_0$ = 15220 ± 196 and a shunt impedance of

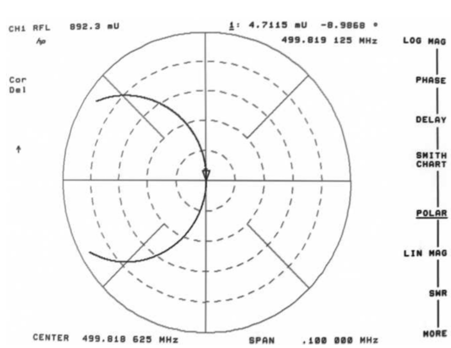


Figure 4: Polar plot of the complex reflection factor close to the first resonace of the prebuncher.

$R_s$ = (1.63 ± 0.05) MΩ. With an injected RF power of 400 W a gap voltage of 36 kV is excited. For a critical RF coupling a new coupling loop has been designed. In figure 4 the measurement of the new coupling loop into the cavity at the first resonance is shown [1].

## TRAVELLING WAVE BUNCHER

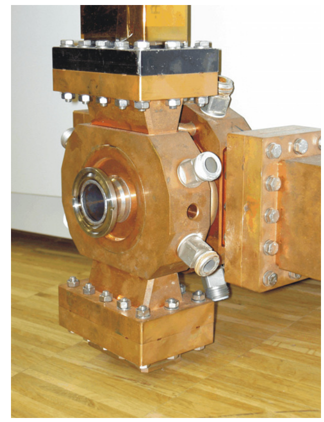

Figure 5: The travelling wave buncher with a view of the exit of the structure. On top a waterload is flanged. On the right hand side is the input of the accelerating RF.

The first cell of the travelling wave buncher is centred 34 cm behind the center of the prebuncher. The 4 cell, 6.7 MV/m structure further compresses the bunches and matches the beta to $\beta = 0.891$ at the exit of the structure. The design of the buncher implements a phase velocity of $v_p$ = 0.0575 c and a group velocity of $v_g$ = 0.010 c. The structure is driven by 2 MW RF power coupled from the linac RF. The passband of the structure is shown in figure 6. After a drift space of 8 cm beyond the buncher the beam is injected into the linac section.

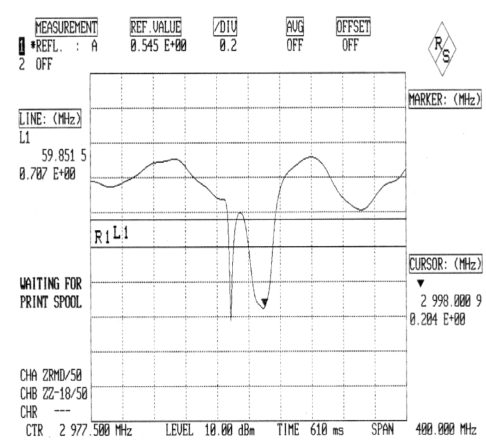


Figure 6: Plot of the reflected power against the RF frequency. The plot shows the passband of the structure.

## TRANSVERSE BEAM DYNAMICS

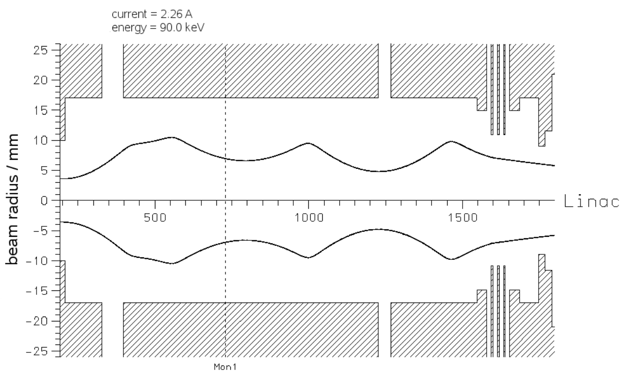


Figure 7: Simulation of a 2 A beam propagating through the beam guiding elements based on the paraxial equations.

The beam pipe has an inner diameter of 34 mm along the injector. Just in front of the entrance of the linear accelerator the aperture is reduced to 21 mm in order to minimize RF leakage out of the linac. Transverse focussing of the beam is achieved by four solenoids. The position and the strength of the solenoids were determined by numerical calculations based on the paraxial equations. The resulting beam propagation is shown in figure 7. Three solenoids with a diameter of 37 mm and a length of 75 mm produce a longitudinal field of 110 Gauss/A.
Due to spacing problems the first solenoid has a diameter of 150 mm. This causes a produced field of 1.1 Gauss/A. Additionally the field is set to zero at the gun cathode by means of a bucking coil.

## MONITORING

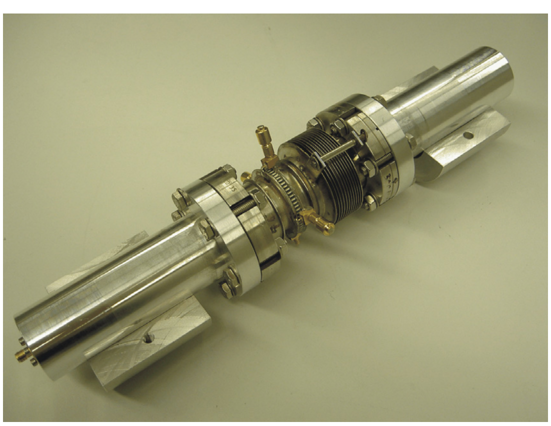

Figure 8: Wall current monitor with a bandwidth of 3 GHz, mounted on a special measurement setup to determine the bandwidth.

The driftspace in front of the prebuncher is used for beam instrumentation to measure the position, the current and the emittance as well as the beam profile. A wall current monitor with higher bandwidth up to 3 GHz is used in order to measure the charge distribution of a single bunch [2]. In figure 8 the wall current monitor is shown on a special measurement setup to determine the bandwidth of the monitor. The measurement has shown that the monitor is useable for signals up to 3 GHz.

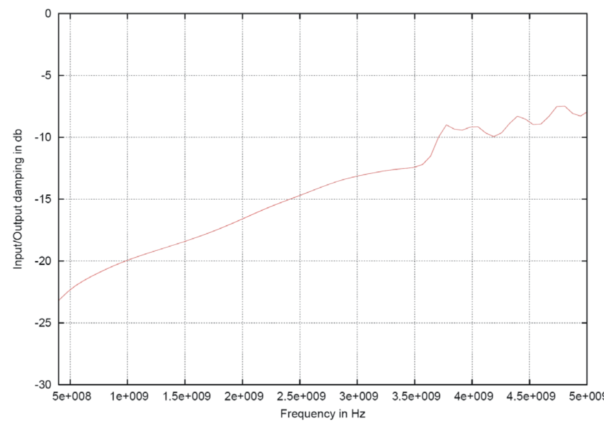


Figure 9: Measurements of the bandwidth of the wall current monitor. The results give an estimate of the bandwidth of the monitor. It appears, that the monitor will be useable for a range up to 3 – 3.5 GHz.

## CONCLUSION

In order to achieve the possibility of operating ELSA in a single bunch mode a new injector is designed and still under construction. The design of the injector for Linac 1 at ELSA is based on a conservative scheme using a thermionic high intensity pulsed gun, one subharmonic bunchercavity and a travelling wave buncher. The bunching is expected to compress the bunches to less than 0.1 ns before entering the linear accelerator. To specify the real bunch length deeper studies with a computer code like PARMELA are necessary. Unwanted transverse dynamics are compensated by solenoid fields and correctors. The bunch leaves the injector with an energy of about 615 keV.

## REFERENCES

[1] S. Aderhold, “Ein System zur Puls- und Energiekompression am Elektronenbeschleuniger ELSA”, University of Bonn, Germany, January 2008, http://www-elsa.physik.uni-bonn.de/Publikationen/
[2] O. Boldt, personal notice, September 2008 in preparation of “Ein Breitband-Wandstrom-Monitor für ELSA”, University of Bonn, Germany

# IMPROVING THE SUPERCONDUCTING CAVITIES AND OPERATIONAL FINDINGS AT THE S-DALINAC*

R. Eichhorn#, A. Araz, M. Brunken, J. Conrad, H.D. Graef, M. Hertling, F. Hug, C. Klose, C. Liebig, M. Konrad, T. Kuerzeder, M. Platz, A. Richter, S. Sievers and T. Weilbach
S-DALINAC, Institut fuer Kernphysik, TU-Darmstadt, D-64293 Darmstadt, Germany

*Abstract*

After 15 years operating the S-DALINAC the design quality factor for the superconducting cavities has still not been reached. Currently, the cavities are heat treated at 850 C in an UHV furnace installed in Darmstadt three years ago. We will report about the furnace, the heat treatment procedure and the results of subsequent surface resistance measurements.

Prior to the heat treatment the field flatness of some of the 20 cell elliptical cavities has been measured, leading to unexpected operational findings to be reported: operating and frequency-tuning the cavity for several years led to heavy distortions of the field flatness. This might be an indication that the frequency tuning of the cavity done by compressing the cavity longitudinally, does not act uniformly on each cell even though the cavity is only supported at the end cells. The paper will close with a status report on machine operation and modifications undertaken during the last two years.

## INTRODUCTION

The superconducting Darmstadt electron linear accelerator S–DALINAC was put into operation in 1987. It consists of ten superconducting 20 cell niobium cavities, operated at 2 K at a frequency of 2.9975 GHz. With a design accelerating gradient of 5 MV/m and a design quality factor of $3 \cdot 10^9$ in cw operation, the final energy of the machine is 130 MeV which is reached when the beam is recirculated twice [1]. The layout of the S–DALINAC is shown in Fig. 1.

The first set of cavities was built in the 80's at Interatom using low RRR material, so the observed performance regarding the gradient and the quality factor was rather poor [2]. Accordingly, a second set of cavities was ordered in the 90's made from RRR 300 material.

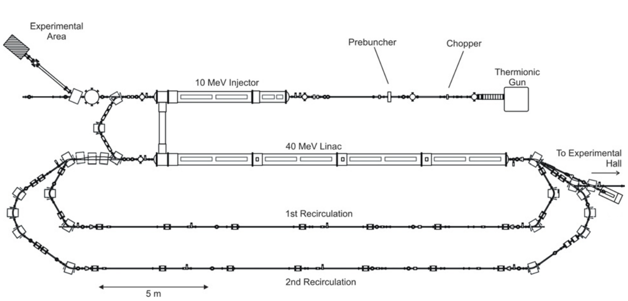


Figure 1: Floor plan of the S-DALINAC.

These cavities, welded at Dornier, are used since then. All of them reach the design gradient, some exceeding it by more than 50% [3]. The accelerator performance however did not benefit from this improvement: Due to the limited refrigerator power of some 100 Watt and the rather low Q of the cavities (typically below $1 \cdot 10^9$) the cavities have to be operated below their maximum gradients. Many measures have been taken in the past [4], all of them helped improving the Q but none was able to solve the problem completely.

## CAVITY FIRING

The high temperature vacuum firing has proven to be an inherent part of the surface preparation of superconducting cavities. This procedure is applied to stress anneal the niobium and to remove hydrogen from the material inoculating cavities against the "Q disease" during their operation. The S-DALINAC niobium cavities were heat treated at 750 C after their commissioning as well. However recent studies have shown that the niobium is still contaminated by hydrogen which can be explained by doubting the temperature measurement during the first firing.

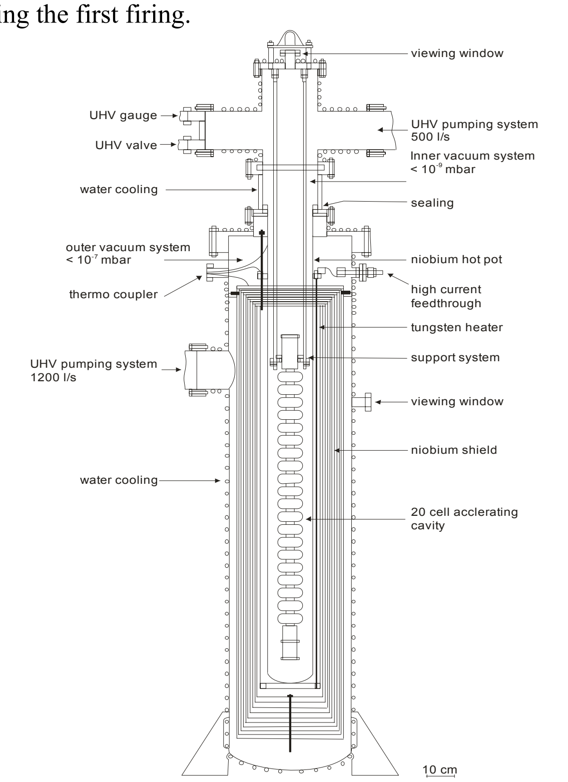


Figure 2: Side view of the UHV furnace in Darmstadt.

*Work supported by the DFG through SFB 634
#eichhorn@ikp.tu-darmstadt.de

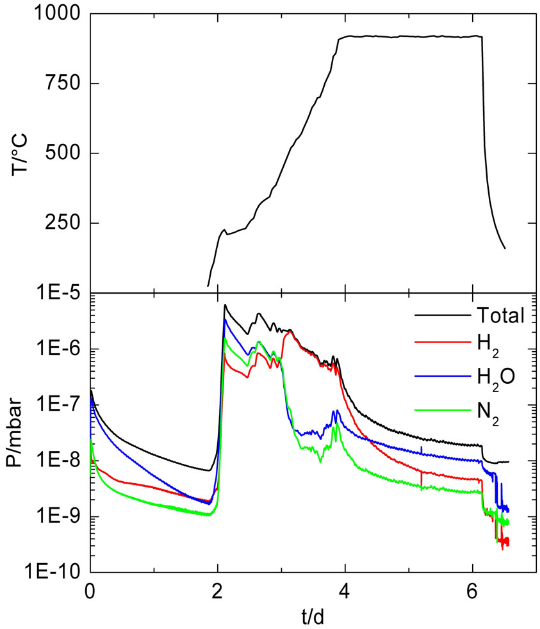


Figure 3: Temperature and partial pressure of the residual gas inside the furnace during the firing procedure. At 300 C hydrogen becomes dominant indicating a huge reservoir.

The high temperature vacuum furnace shown in Fig. 2 allows temperatures of up to 1800 C. It was put into operation at Darmstadt in 2005 after relocation from Wuppertal. Its construction and basic parameters are described in [5]. Up to now a total of 7 cavities were heat treated.

Once the cavity was mounted inside the furnace, the temperature was increased steadily up to 800 C, keeping the vacuum pressure below $1{\cdot}10^{-5}$ mbar. The residual gas in the furnace was analyzed using a mass spectrometer; the temperature was measured with a pyrometer. The heat treatment procedure lasted typically 8 to 10 days. A typical temperature and gas profile is shown in Fig. 3.

By taking the throughput of the ion getter pump, the integrated partial pressure and the amount of niobium, a hydrogen contamination of the cavity of some 30 ppm could be estimated - values above 2 ppm are thought to cause Q-disease [6]. After the heat treatment, the cavities were taken out of the furnace and mounted directly inside the accelerator cryostat without any intermediate preparation step. After cooling down to 2 K, the quality factor improved from $7{\cdot}10^8$ to $1.5{\cdot}10^9$ by this treatment being still below design. Unfolding the contributions to the quality factor leads to a residual resistance of 60 nΩ.

For cavities contaminated with hydrogen a high residual resistance would be expected, but for cavities fired at 800 C lower values are anticipated.

Out of the data two objectives can be deduced: First, the contribution coming from the frozen magnetic flux is in the order of the BCS value. This has to be improved by adding additional shielding against the earth magnetic field. Second, the residual resistance is even higher and exceeds values achieved elsewhere by far. This indicates that the process of preparing and/or mounting of the cavities still need to be improved, for example by applying a hydrofluoric acid polishing after the heat treatment. Both will be addressed in the future.

## FIELD FLATNESS CHANGES

When the cavities had been installed more than 10 years ago, all cavities were tuned to a flat field profile to ensure optimum performance. During operation, continual measurements of the pass-band frequencies indicated a change in field profile which only could be quantified by dismounting the cavities. So before the cavities were heat treated as described above, a field profile was measured with a bead-pull measurement set- up. The field distribution of six cavities measured so far is shown in Fig. 4.

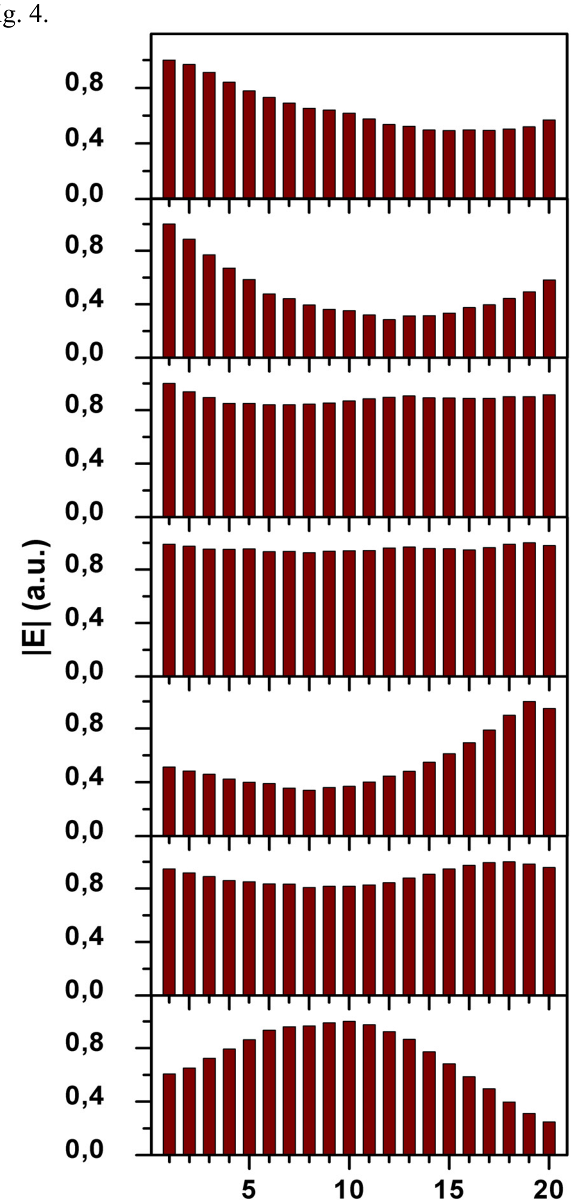


Figure 4: Measured field flatness of six cavities being in operation for some 10 years. Some cavities display a heavily distorted field profile that could be restored during the tuning procedure.

Obviously, the field flatness of some cavities is heavily distorted after several years of operation, while other cavities are still more or less field flat.

During operation the cavity frequency is adjusted by a tuner changing the overall length of the cavity. The tuner acts on the cut-off tubes of the cavity only, while the elliptical cells hang freely in between. This should lead to a uniform distribution of the forces along the cavity and thus to an undisturbed field profile, which seems to be true for some cavities but wrong for the others (with distorted field profile). The measurement shown in Fig. 4 suggests that the tuning force does not act uniformly over the cavity length for all cavities, which might be caused by two reasons: Some friction between the cavity support frame and the cavity reducing the forces from cell to cell might be one explanation. The other, which seems to be more attractive, is that the elliptical cells have different mechanical spring constants making the cavity itself mechanically inhomogeneous.

Investigations on this findings will go on, however it could be stated that tuning the cavity by changing the total length – commonly used in other places too – in our case leads to unwanted distortions in the field profile differing from cavity to cavity.

However, all cavities could be retuned to a flat field profile by squeezing the individual elliptical cells.

## COLD LEAK PROBLEMS

During last year's operation, several cold leaks developed, degrading the cavity performance and disrupting the accelerator operation. After several time consuming investigations the reason for these cold leaks could be determined: The HELICOFLEX® gasket used to seal the cavity flange against the coupler (see Fig. 5) became untight, especially after an insitu-baking procedure followed by an immediate cool-down to 2 K. After checking all parameters to lie within specifications the reason for this was localized: the HELICOFLEX® gasket made out of aluminum was hard enough to cave the flat cavity flange (made out of RRR30 Niobium) after many years of operation, some 50 thermal cycles and approximately 10 replacements of the gaskets. As the tightness of this gasket is ensured by pressing it to a nominal thickness which is ensured by a nose-piece in the coupler flange, the score mark in the cavity flange reduces the compression of the gasket and thus explains the failure in tight sealing.

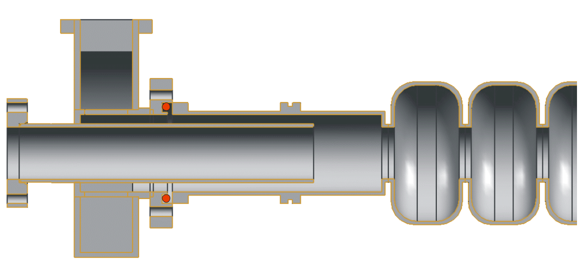

Figure 5: Cross section of the coupler to cavity transition. The HELICOFLEX® gasket used is marked red.

Currently, all HELICOFLEX® gaskets are replaced by gaskets with overmeasure (by adding the depths of the score to the gasket thickness), not solving the principle problem but ensuring tightness without machining the ultraclean surface of the cavity or the coupler.

Figure 6: Picture of the cavity flange displaying an obvious score mark.

## REFERENCES

[1] A. Richter, "Operational Experience at the S-DALINAC", EPAC '96, Sitges (1996) 110.

[2] K. Alrutz-Ziemssen, D. Flasche, H.-D. Graef., V. Huck, M. Knirsch, W. Lotz, A. Richter, T. Rietdorf, P. Schardt, E. Spamer, A. Stascheck, O. Titze, W. Voigt, H. Wiese and W. Ziegler, "Performance of the Accelerating Cavities at the S-DALINAC", SRF '89, Tsukuba (1989) 53.

[3] J. Auerhammer, H. Genz, H.-D. Graef, V. Huck, C. Luettge, A. Richter, T. Rietdorf, P. Schardt, E. Spamer, K. Rühl, A. Stascheck, F. Thomas, O. Titze, J. Toepper and H. Weise, "Latest of the superconducting Darmstadt Electron Accelerator S-DALINAC", SRF '91, Hamburg, (1991) 110.

[4] A. Araz, M. Brunken, M. Gopych, H.-D. Graef, J. Hasper, M. Hertling, M. Platz, A. Richter, S. Watzlawik, H. Kunze, W. Mueller, S. Setzer, T. Weiland, W. Bayer and U. Laier, "Recent Results and Developments from the S-DALINAC", SRF '05, Ithaca (2005).

[5] G. Mueller, Dissertation WUB-DI 83-1 BUGH Wuppertal (1983).

[6] H. Padamsee, J. Knobloch, T. Hays, "RF Superconductivity for Accelerators", John Wiley and Sons, New York (1998).

# THE POWER AND POLARISATION UPGRADE PROJECT AT THE S-DALINAC INJECTOR*

R. Eichhorn#, R. Barday, U. Bonnes, M. Brunken, C. Eckardt, J. Conrad, J. Enders, H.D. Graef , C. Heßler, T. Kuerzeder, C. Liebig, M. Platz, Y. Poltoratska, M. Roth, S. Sievers, T. Weilbach, S-DALINAC, IKP, TU Darmstadt, Germany
W. Ackermann, W. F. O. Mueller, B. Steiner, T. Weiland, TEMF, TU Darmstadt, Germany
K. Aulenbacher, IKP. University of Mainz, Germany
J. Fuerst, ANL, Argonne, IL 60439, U.S.A.

*Abstract*

The current upgrade for the injector mainly involves the superconducting rf part. In order to increase the maximum current from 60 µA to 150 or 250 µA the power coupler design had to be modified, resulting in major changes in the whole cryo-module.

Second, an additional polarized electron source (SPIN) has been set-up at an offline test area. There, the polarized electrons are produced by photoemission at a strained GaAs cathode on a 100 kV platform. The test beamline includes a Wien filter for spin manipulation, a Mott polarimeter for polarization measurement and additional diagnostic elements. We will give an overview to the project, report on the status and present first measurement results including the proof of polarisation.

## INTRODUCTION

The superconducting Darmstadt electron linear accelerator S-DALINAC [1] is a recirculating linac, using ten superconducting niobium cavities at a frequency of 2.9975 GHz. It was first put into operation in 1987. Running at a temperature of 2 K the main acceleration is done by ten 20 cell elliptical cavities with a design accelerating gradient of 5 MV/m. The first pair of those cavities is used in the injector section of the machine. Behind this section it is possible to use the beam for nuclear physics experiments with a maximum energy of 10 MeV or the beam can be bent into the main linac. With its two recirculations and an energy gain of 40 MeV per pass the maximum design energy of the S-DALINAC is 130 MeV which can be used for several experiments in the adjacent experimental hall. The layout of the machine is shown in Fig. 1.

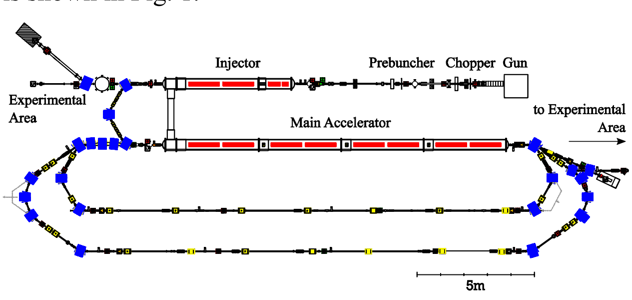


Figure 1: Floor plan of the S-DALINAC.

*Work supported by the DFG through SFB 634
#eichhorn@ikp.tu-darmstadt.de

## POWER UPGRADE

The S-DALINAC uses cryostat-modules with two cavities per module. Each cavity has an rf input coupler, which is capable of a maximum power of 500 W. Assuming a 5 MV/m gradient the beam current is limited to 60 µA for the injector and 20 µA for the main linac, which might be higher for lower beam energies.

For future astrophysical experiments behind the injector, beam currents of 150 µA and above as well as energies of up to 14 MeV are demanded. Therefore, modifications in the injector linac had to be made.

### *New Power Couplers*

The first step was to design and build new power couplers providing the necessary rf power of up to 2 kW to the cavities. While the existing couplers are coax-to-coax couplers [2] and limited to 500 W, the newly designed couplers are of waveguide-to-coax type [3]. One essential design feature of the old coupler was kept, namely the minimized transversal fields being a major concern in the low energy part of the accelerator. This was accomplished by using two diaphragms, reducing the excitations of the transverse electromagnetic fields in the beam pipe below -40 dB.

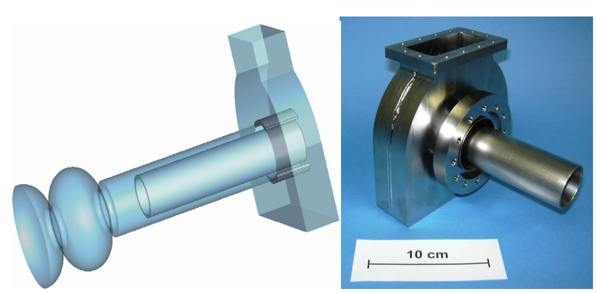


Figure 2: The design and the finally fabricated waveguide-to-coax coupler for the injector upgrade.

Figure 2 gives on the left side an impression, how the coupling from waveguide to coax and to the cavity along its cut-off tube is realized. The external quality factor of $5{\cdot}10^6$ ensures acceleration of beam currents ranging from 150 to 250 µA.

The coupler was made out of bulk niobium. The fabrication including the EB-welding was done by the FZ Juelich. Currently, the chemical cleaning of the couplers is underway.

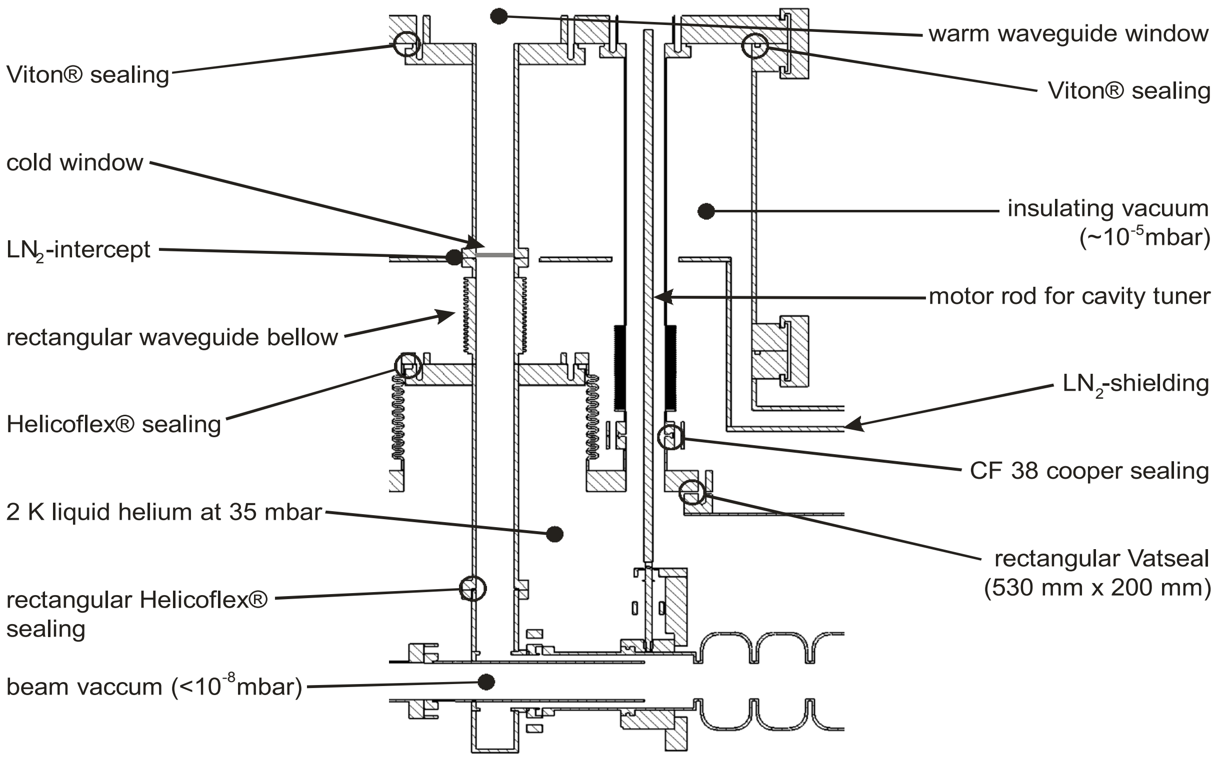


Figure 3: 2-D cut of the cross-section of the waveguide transition line surrounding from the helium vessel through the whole module. The different pressure stages and the position of sealings and other elements are shown.

## *Design of the New Cryostat*

In the current design, the rf transmission line to the power couplers has a diameter of only 21 mm. For the new couplers, a WR-284 waveguide (cross area 72×34 mm$^2$) has been chosen. Accordingly the existing cryostat-module had to be modified:

The cavities together with their tuners and the couplers are located inside the helium vessel. The vacuum inside the beam-pipe is below $10^{-8}$ mbar, while the pressure in the liquid helium is at 35 mbar (2 K operation). The thermal shield between the helium vessel and the outer vessel is cooled by liquid nitrogen. Together with the insulation vacuum of $10^{-5}$ mbar and some 20 layers of super-insulation a minimum heat transfer is ensured (being 4 W per cryo-module currently).

The actual design consists of a complex waveguide which will be flanged to the coupler. Welded to this waveguide is a circular flange sealing the helium vessel. The counter-flange provides a bellow to compensate small vertical and angular displacements while oversized holes are planned to have additional freedom in the horizontal direction. To avoid vacuum forces on the coupler this bellow can be fixed by threaded rods.

To seal between insulating vacuum and atmospheric pressure Viton® gaskets are intended. To keep the static heat losses per transition line below 0.4 W it has a thermal intercept to the nitrogen-shield behind the waveguide bellow. Furthermore, a cold waveguide window could be installed at this position to reduce the heat radiation from the ambient window to be installed outside the cryo-module.

Figure 3 shows the cross-section of the module allowing an insight to the positions of the gaskets, bellows and the different pressure vessels. The big apperture of the helium vessel has to be sealed by a customized VATSEAL® gasket. An additional tube holds a rod for coarse tuning of the cavity. Its motor is placed outside the module at ambient. In addition, the cabling of the magneto-restrictive (fine-) tuner and other electrics like temperature sensors or heaters are located inside that tube.

# POLARIZED ELECTRON SOURCE

To complement the present experimental program with polarized electron and photon scattering experiments a new source for polarized electrons, the S–DALINAC Polarized INjector SPIN, is developed [5]. Therewith, experiments are planned studying parity violation in nuclei or measuring the fifth structure function in electron scattering. With these experiments results obtained at other accelerator laboratories can be extended to lower momentum transfer values.

## *Test-Stand Set-up*

The new source consists of a cathode on a HV platform, a chopper and prebuncher system, a Wien filter and a Mott polarimeter for spin manipulation and polarization measurement. To set-up and test the electron source independent from the accelerator operation of the

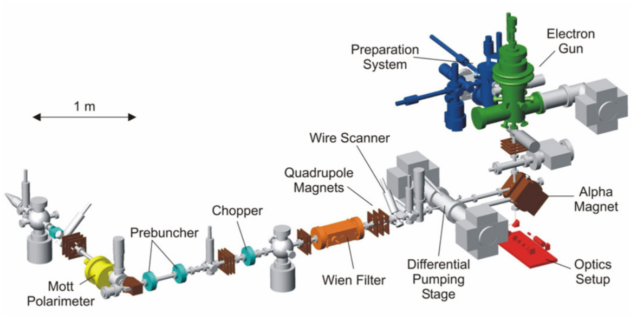


Figure 4: Schematic drawing of the SPIN test-stand. A laser beam focused onto the cathode produces a polarized electron beam by photoemission. After pre-acceleration to 100 keV it is injected into the horizontal beam-line where its properties can be studied. The chopper and prebuncher system is currently installed.

source independent from the accelerator operation of the S–DALINAC, an offline-test-stand has been built.

Figure 4 gives an overview about SPIN. The electrons are produced inside an ultra-high vacuum chamber at a GaAs cathode. For the first tests, bulk GaAs cathodes were used, whereas strained-superlattice cathodes will be used for regular operation. A laser beam is focused from an optics setup below the electron source onto the photocathode and produces the electrons by photoemission. These electrons are accelerated by the platform voltage to 100 keV and bent by an alpha magnet into the horizontal beam-line, where the beam properties can be measured. The whole design is based on the MAMI polarized source [6], but is compared to it more compact due to the limited space in the accelerator hall.

### *Recent Results*

After extracting the first beam, the transverse properties were measured using a wire scanner. The beam profile was determined to have approximately a gaussian shape with an x/y beam radius of .44/.41 mm, respectively. The normalized transversal emittance has been determined to $\varepsilon_{n,x} = (0.146 \pm 0.037)$ mm mrad and $\varepsilon_{n,y} = (0.197 \pm 0.089)$ mm mrad respectively being comparable with the MAMI source. The beam current reached so far was 3 μA.

The polarization of the electron beam was measured by Mott scattering where one uses the effect that the Coulomb potential has a term which is proportional to the scalar product of the angular momentum and the spin of the incident electron (spin-orbit interaction). This results in a right-left asymmetry of the angular distribution of the scattered electrons which is proportional to the polarization P of the electron beam. The Mott polarimeter used houses four silicon surface barrier detectors which are oriented in two perpendicular scattering planes to measure both transverse polarization components simultaneously.

As targets, self-supporting gold foils of the thickness in the range from 42.5 nm to 500 nm are used. From the left/right asymmetry measured, the degree of polarization was determined to be (33.4±1.6)% which agrees very well with common values for bulk GaAs cathodes. For the superlattice photocathode to be used during accelerator operation, the polarization was determined to be (72.1 ± 2.1)%.

## SUMMARY AND OUTLOOK

Currently, the design of the cryo-module for the power upgrade is finalized. The chemical treatments for the waveguide couplers are underway and three new cavities have been ordered to complete the module (one cavity spare). Including tests of all components and completion of construction, the timetable aims for a first test in spring 2009.

At that time, the installation of the polarized electron source and its subsystems at the S–DALINAC accelerator vault is planned. Currently, the test stand is completed by adding the chopper and prebuncher system and improvements on the laser system to increase the beam current are pursued.

First results of both upgrade projects, the polarized source and the power upgrade of the injector are expected in late summer 2009.

## REFERENCES

[1] A. Richter, “Operational experience at the S-DALINAC”, EPAC’96, Sitges (1996) 110.

[2] J. Auerhammer, R. Eichhorn, H. Genz, H.-D. Graef, R. Hahn, T. Hampel, C. Hofmann, J. Horn, C. Luettge, A. Richter, T. Rietdorf, K. Ruehl, P. Schardt, V. Schlott, E. Spamer, A. Stascheck, A. Stiller, F. Thomas, O. Titze, J. Topper, T. Wesp, H. Weise, M. Wiencken, T. Winkler, “Progress and status of the S-DALINAC”, SRF’93, Newport News (1993) 1203.

[3] M. Kunze, W.F.O. Müller, T. Weiland, M. Brunken, H.-D. Graef, A. Richter, “Electromagnetic design of new rf power couplers for the S-DALINAC”, LINAC ‘04, Luebeck (2004) 736.

[4] J. Auerhammer, H. Genz, H.-D. Graef, V. Huck, C. Luettge, A. Richter, T. Rietdorf, P. Schardt, E. Spamer, K. Rühl, A. Staschek, F. Thomas, O. Titze, J. Toepper, H. Weise, “Latest of the Superconducting Darmstadt Electron Accelerator S-DALINAC”, SRF’91, Hamburg (1191) 110.

[5] C. Heßler et al., “Status of the Polarized–Electron Gun at the S–DALINAC”, EPAC’06, Edinburgh (2006) 3173.

[6] K. Aulenbacher et al., “The MAMI source of polarized electrons”, Nucl. Instrum. Methods in Phys. Research A 391 (1997) 498.

# RECENT CHANGES TO THE $e^+/e^-$ INJECTOR (LINAC II) AT DESY

M. Hüning#, M. Schmitz, DESY, Hamburg, Germany


*Abstract*

The Linac II at DESY consists of a 6A/150kV DC electron gun, a 400 MeV primary electron linac, an 800 MW positron converter, and a 450 MeV secondary electron/positron linac.

The Positron Intensity Accumulator (PIA) is also considered part of the injector complex accumulating and damping the 50 Hz beam pulses from the linac and transferring them with a rate of 6.25 Hz or 3.125 Hz into the Synchrotron DESY II. The typical positrons rates are $6{\cdot}10^{10}$/s.

DESY II and Linac II will serve as injectors for the two synchrotron light facilities PETRA III and DORIS. Since PETRA III will operate in top-up mode, Linac availability of 98-99% is required. DORIS requires positrons for operation. Therefore during top-up mode positrons are required for both rings. In order to maintain its reliability over the operation time of the new facility PETRA III, the major components of the linac were renovated. Some components were redesigned taking into account experience from 30 years of operation.


## INTRODUCTION

The Linac II was built in the late 1960s to provide electrons and positrons for the Deutsches Elektronen Synchrotron (DESY) at higher energies (200 MeV) than the at that time existing linac (50 MeV) [1]. It consisted of 14 S-band travelling wave structures operating at 2.998 GHz and 20 MW input power and 4 µs pulse duration. The setup was modified since by introducing SLED (SLAC energy doubler) cavities for pulse compression and injecting into the Particle Intensity Accumulator (PIA). PIA was built to achieve short damping times for the positrons to be injected into the electron/positron storage ring collider PETRA. The pulse compression scheme enabled an energy increase to 450 MeV and allowed reduction of RF stations to 12, but required together with the high revolution frequency of PIA a reduction of beam pulse duration.

Today DESY II with its injector Linac II provides electrons and positrons for the synchrotron radiation facility DORIS, the synchrotron radiation facility under construction PETRA III, and for test beam targets inside DESY II. The injection into HERA via PETRA II is shut off, but there is an option to inject directly into HERA if there is the requirement by future projects.

## LINAC OVERVIEW

### *Injection System*

The primary electron beam is produced by a 120 kV pulsed DC diode gun. Beam pulses of up to 6 A and 4 µs duration are produced. The cathode is made by a thoriated tungsten plug, heated by a 3 kV, 1.2 kW bombarder. For best performance the cathode plug has to be carborized.

An electrostatic chopper forms beam pulses of 2 ns to 30 ns duration, depending on the operation conditions. In electron mode the primary beam is used directly, which reduces the required average beam current. A 2.998 GHz prebuncher cavity is fed by a portion of the first structure's forward RF power drawn from a directional coupler. The beam then enters the first accelerator section, which is not tapered.

### *Accelerator Sections*

The linac sections are 5.2 m long travelling wave S-band structures, operating at 2.998 GHz. They are constant gradient structures with an on-axis load. Therefore the last six of their 154 cells are coated with an absorbing material and add little to the total accelerating voltage. The fill-time of the structures is 740 ns. The original structures were replaced by a design made for the S-Band Linear Collider Test Facility [2].

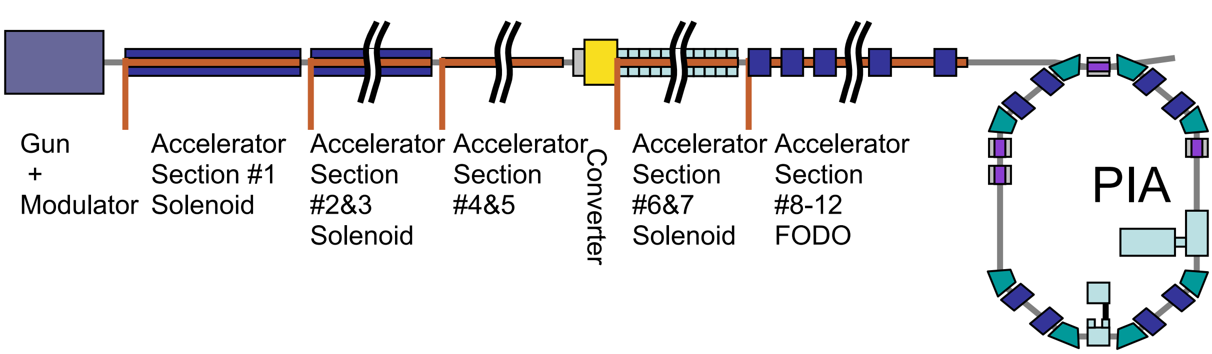


Figure 1: Schematic layout of the Linac II at DESY. The 6 A primary beam is produced in a 120 kV pulsed DC gun and directed onto a converter target at approximately 400 MeV. The secondary beam is accelerated to 450 MeV and injected into the Positron Intensity Accumulator (PIA).

# corresponding author: markus.huening@desy.de

All but one RF stations are equipped with SLED cavities for pulse compression, increasing the peak power from 20 MW to 90 MW. With this the structures achieve an average gradient of 18 MV/m or 90 MV/structure. The klystron drive is provided by the RF station number 9, which therefore cannot use the SLED scheme. Phase and amplitude are adjusted via high power phase shifters and adjustable attenuators. The phase jump for the SLED is produced individually by PIN-diodes in the drive of each klystron.

### Converter

At approximately 400 MeV there is the converter target. The beam current at this point usually is 2 A. The target consists of a tungsten plate with a thickness of 7 mm. An 1.8 T pulsed solenoid coil serves for focusing the secondary beam into the following acceleration sections, which in turn are surrounded completely by 0.4 T solenoid magnets. An off-axis hole in the target allows the primary beam to be steered through the target to be used directly in electron mode.

Six linac sections are available to bring the secondary beam energy to 450 MeV. Out of these six one usually is in stand-by mode and two are used off-crest with variable opposite phases to allow for adjustment of the final energy.

### PIA

The electrons or positrons at 450 MeV are injected into the PIA ring. The revolution frequency in PIA is 10.4 MHz and so is the frequency of its RF system [3]. The beam is damped longitudinally with only the 10.4 MHz RF system to 1.2 ns (RMS) [4]. A second RF system at the $12^{th}$ harmonic produces a bunch length of 380 ps (RMS). The damping time of the synchrotron oscillation is 12.9 ms, the damping time of the betatron oscillation is 23.6 ms. The theoretical horizontal emittance is 300 nm, the vertical emittance is 15 nm.

One full accumulation lasts 160 ms or 320 ms, depending on the mode of operation. This corresponds to 8 or 16 pulses of the linac. Only 4 respectively 12 shots are injected, the other 20 ms cycles are: 1 empty, 1 additional damping with only 10.4 MHz RF, 2 damping with 10.4 MHz and 125 MHz RF.

In the 3.125 Hz mode of operation $2{\cdot}10^{10}$ positrons can be accumulated routinely. This corresponds to an efficiency of 4‰ from beam on target to accumulated particles.

## MAJOR CHANGES

### RF System

The klystrons are powered by line-type modulators which are switched with a thyratron. The thyratrons were successively changed from CX1168 to CX1836A, which can handle higher voltages. Although the switching voltage (up to 38 kV) is within the specifications of the old thyratron, a better lifetime and reliability is expected with the new one. Experience over 270000 hours of operation confirms this.

### Converter

The target and its surroundings were rebuilt completely to remove technical risks and to allow better handling of the radioactive target after use. Firstly, all movable parts were eliminated because the high radiation levels around the target quickly destroy all motors and end-switches. Even the mechanical parts of the movers tend to suffer from corrosion. Secondly all braze joints of water filled parts were avoided or designed outside the vacuum. This applies especially to the vacuum feedthroughs of the solenoid coil and the water cooling of the target itself. Here the design benefits from the reduction of movable parts.

The output port was connected with a clamp-flange to minimize the time needed for dismounting the activated target. This turned out to be problematic for tightening the vacuum system. So in the new design a standard CF type flange is used. The copper seal at the same time serves as a collimator.

Handling the activated target after a few years of operation used to be a problem. Therefore the new target is equipped with a permanent shielding. A first layer of 20 cm Aluminium serves to reduce activation in the proximity of the converter while being little activated itself. A second layer of 5 cm lead protects persons working near the target.

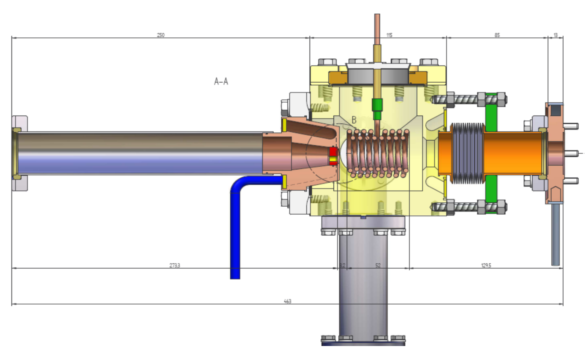

Figure 2: CAD model of the modified positron converter. In comparison to the old design all movable parts were eliminated and there are no more braze joints of water filled parts in vacuum.

A removable rail system eases the handling of the whole unit. Fixed end-points serve as references for the installation of prealigned converter targets.

### Vacuum System

In places where it had not been done already, the vacuum chambers of aluminium and with DIN-type flanges were replaced by stainless steel with CF-flanges. In the wake of these works BPMs were introduced.

### *Beam Position Monitors*

While PIA was equipped with BPMs from the beginning, the linac and the adjacent transport lines were not. In the recent shutdown Button-BPMs [5] were added to the transport line between linac and PIA (LP-Weg) and the transport line between PIA and DESY II (L-Weg). The BPM in the second straight – at 7 meters from the septum – was replaced by a new type of higher bandwidth.

Because of sensitivity and noise restrictions in the readout electronics, only damped bunches with high peak current can be resolved. For the BPMs before PIA and for the first turn in PIA readout electronics based on filtering the 3 GHz component of the button signal is being developed. For the first turn in PIA this adds the benefit of being able to distinguish the injected beam bunched at 3 GHz from the 10.4 MHz bunches already circulating in the ring.

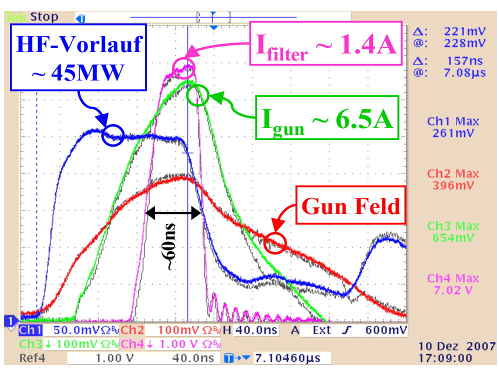


Figure 3: Scope traces of RF-gun pulses. At very high forward power of 45 MW over 160 ns filtered beam currents of 1.4 A are achieved

### *Gun*

One problem connected with the current gun is the ceramic high voltage isolator at the same time sealing the vacuum against the oil of the modulator. Should this ceramic break, it would cause irreparable damage to probably the whole linac. Second, it is becoming increasingly harder to find suppliers for the carborized cathode plugs. Third, due to the bunching scheme a substantial portion of the primary beam is lost at high energies along the linac.

To remedy these problems a replacement of the gun is being considered. In the moment a design by MAX-Lab [6] is being evaluated. This is an RF-gun with thermionic cathode. To avoid beam losses along the linac, an energy filter is used to cut away low energy electrons. The required beam pulses are much shorter than the time constant of the gun cavity. Therefore very high forward power is used to power the gun.

At 20 MW forward power stable beam current of 900 mA has been achieved over 1 month of continuous operation. Since this current was measured behind the energy filter, it is assumed that it would reach the converter target. At higher forward power self-enhancement by back bombardment occurs. Higher beam currents are achieved at the cost of unstable operation.

With slightly reduced performance 900 mA are acceptable for the Linac II, nevertheless tests with laser enhancement are planned.

## CONCLUSION

The Linac II provides electrons and positrons for the synchrotron and the storage rings at DESY. It has been renovated and upgraded to sustain its stable and reliable operation. The converter was completely redesigned, a new gun is still being evaluated.

## ACKNOWLEDGEMENTS

Work described in this paper was funded through the PETRA III project. The authors would like to thank MAX-Lab for providing an RF-gun and energy filter for testing.

## REFERENCES


[1] A. Febel et al., “General description and Performance Measurement of the DESY Linac II Electron-Positron Injector”, Proc of PAC 1971

[2] R. Brinkmann, G. Materlik, J. Rossbach, A. Wagner (eds.) “Conceptual Design of a 500 GeV e+ e- Linear Collider with Integrated X-Ray Laser Facility”, DESY 97-48, ECFA 97-182, 1997

[3] W. Ebeling et al., “The Radiofrequency Systems of PIA”, Proc. of PAC 1981, Washington, DC, 1981

[4] A. Febel, G. Hemmie, “PIA, the Positron Intensity Accumulator for the PETRA Injection”, PAC 1979, IEEE Trans on Nucl Sci Vol. NS-26, No 3, 3244

[5] G. Kube et al., “Overview of the Diagnostics Systems of PETRA III”, Proc. of EPAC 08, Genoa, 2008

[6] B. Anderberg et al., “The Design of a 3 GHz thermionic RF-Gun and Energy Filter for MAX-Lab”, Nucl Instr Meth A 491 (2002) 307

# DEVELOPMENT OF TIMING AND CONTROL SYSTEMS FOR FAST BEAM SWITCH AT KEK 8 GeV LINAC

K. Furukawa*, M. Satoh, T. Suwada, KEK, Tsukuba, 305-0801, Japan
T. Kudou, S. Kusano, MELCO SC, Tsukuba, 305-0045, Japan
A. Kazakov, GUAS/SOKENDAI, Tsukuba, 305-0801, Japan
G. Lei, G. Xu, IHEP, Beijing, 100049, China

*Abstract*

The 8 GeV Linac at KEK provides electrons and positrons to Photon Factory (PF) and B-Factory (KEKB). Simultaneous top-up injections have been considered for both PF and KEKB rings in order to improve the injection efficiency and the experimental stability. Therefore, fast beam-switching mechanisms are being implemented, upgrading the timing and control systems. While the old timing system provides precise timing signals for 150 devices, many of the signals are now dynamically switched using an event system. A new scheme has been developed and tested to enable double-fold synchronization between rf signals. Fast controls of low-level rf, beam instrumentation, kickers, a gun, and beam operation parameters are also upgraded for fast and precise tuning of those parameters. The system has been developed since 2006, and is being deployed under the beam operation in 2008.

## INTRODUCTION

The KEK Linac injects electron and positron beams with different characteristics into four storage rings, KEKB-HER, KEKB-LER, PF and PF-AR. It takes 30 seconds to 2 minutes in order to switch the beam modes, depending on the magnet standardization [1]. When the beam development study is performed at PF ring for example, the experiment at KEKB is disturbed. Especially with the crab cavities installed at KEKB, the luminosity tuning is sensitive to the constant beam conditions at the both HER and LER rings and simultaneous injection to those rings is preferable. At the same time, the top-up injection is increasingly demanded at the PF ring in order to achieve higher-quality experimental data.

Thus, the fast beam-mode switching system has been designed and implemented [2]. In the system many hardware pieces of equipment are installed including pulsed magnets, fast rf system, and so on. Beam optics development is also performed in parallel to support the wide dynamic range of beam energy and charge, namely 3-times different energy and 100-times different charge.

Control and timing systems is upgraded as well to meet the requirement of the beam-mode switch in 50Hz (20ms). In order to notify the switching event globally along the 600-m Linac, an event system has been introduced [3]. It has been tested since 2006 and installed for the operation in autumn 2008. The system enables fast switching of many parameters of timing-signals, magnets, microwave systems, and beam instrumentations.

## FAST BEAM-MODE SWITCHING

There are a few beam modes defined at the Linac. It took more than 30 seconds for more than 20 items to switch. And it is considered important to switch at least following beam modes.

- KEKB HER : 8 GeV electron, 1.2-nC, 2 bunches.
- KEKB LER : 3.5 GeV positron, 1.2 nC, 2 bunches (10-nC primary electron).
- PF ring : 2.5 GeV electron, 0.1 nC, 1 bunch.

Here, 2 bunches in a pulse are separated by 96 ns. A fast switch of those beam modes is challenging because the dynamic range of the beam characteristics is very large. An adaptive beam optics scheme is being developed. In order to enable this scheme several hardware components had to be improved. And following parameters are changed within 20ms.

- Magnet: a pulsed bending magnet, several pulsed steering magnets, and a pulsed positron capture coil.
- Microwave: phase and timing of low-level rf, timing of high-power rf.
- Gun: grid-pulser selection, bias voltage, pico-second timing.
- Beam instrumentation: synchronized and fast beam-position-monitor read-out, pulse selection for wire-scanners and streak-cameras.
- Injection: selection of septa and kickers, interface to bucket selection systems.
- Operation: beam stabilization feedback, beam mode sequence pattern generation, mode-dependent parameter manipulation and archiving.

In order to achieve synchronized controls over Linac and beam transport lines for KEKB and PF, a global event notification system has been installed. Errors are not allowed because of safety reasons as the beam power varies 10 to 100 times [4]. The parameters for each mode have to be manipulated easily to optimize the beam tuning and the physics experiment conditions. It almost corresponds to building of three virtual accelerators.

* <kazuro.furukawa@kek.jp>

## EVENT DISTRIBUTION SYSTEM

In the old system beam-modes were notified through two mechanisms. Four separate cables were connected to important control stations in order to indicate four independent pulse characteristics, such as the beam existence and the synchronized beam measurement. More detailed information was transferred via normal control features through control networks. Timing signals were transferred to 15 timing stations through a coaxial cable, which provides a 50 Hz pulse and a 571 MHz clock [5].

When the beam mode was changed, more than 500 parameters were changed. It took more than 30 seconds mainly because many magnets had to be standardized.

In the new system, it was decided to introduce the series-230 event system that was developed for Diamond light source [6]. With an event generator (EVG230) installed at the central station, event receivers (EVR200/EVR230RF) can receive information through an optical fiber connection. EVRs can provide,

- Sequence of programmed events in a pulse,
- Regenerated clock signal (114.24 MHz in our case),
- Up to 14 delayed timing signals (with precision less than 10 ps),
- Shared data buffer up to 2 k bytes.

Because they are transferred through a single fiber connection, the maintenance is expected to be straightforward.

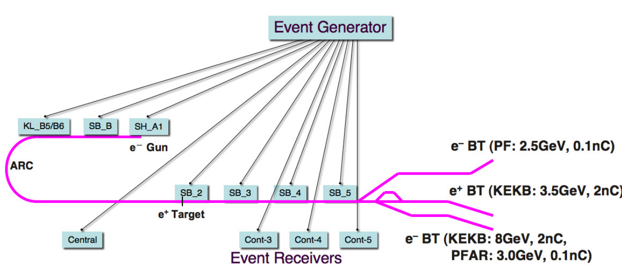


Figure 1: Layout of new event system.

Figure 1 shows 11 EVRs installed along the Linac. They are believed to be enough to control three beam-modes. Seven of those EVRs reside close to the existent timing stations, whose functionalities are being moved to EVRs. The number of components is reduced as an EVR can generate 14 precise delayed timing signals. Thus, most of the remaining old timing stations will be replaced by EVRs near future. Some devices, such as streak cameras, require better timing precision, so that a precise re-synchronization module is being developed.

The event rate is chosen to be 114.24 MHz, which is same frequency as the first sub-harmonic buncher and 1/25 of the main Linac frequency. The rf signal of 114.24 MHz is fed into EVG and used to transfer events and other data to EVRs in a star-like topology. Most of the EVR stations are connected through fan-out modules with multi-mode optical fibers, which were laid more than 10 years ago. Some of further stations are connected with single-mode optical fibers, replacing small-form-factor pluggable (SFP) modules at the fan-out module and EVRs.

The EPICS driver software is employed, and is extended to support new features of the series-230 system. The CPUs and the operating system of the VME computers are MVME5500 and VxWorks-5.5.1, respectively. The combination was chosen to satisfy the realtime performance requirements to the system and to enable the maximum coherence of the resources in KEK and EPICS community [7].

## BEAM MODE PATTERN GENERATION

Approximately 50 event codes are defined so far. Some of them are directly related to one of the beam modes, and some others are related to one of the accelerator equipment. Each beam pulse, every 20 ms, is accompanied with a sequence of several event codes, which contains at least an event related to the beam mode of the present pulse and that of the next pulse. Some event codes received at an EVR system trigger EPICS software to control equipment connected.

Some of the equipment can respond to 50 Hz controls, however, others impose restriction rules in choosing pulses. The beam repetition request from each ring may vary depending on the beam and experimental conditions in the ring. Thus, it is complicated to arbitrate and design the pattern of the beam-mode pulse train. At the same time, however, it should be flexible.

As the modification of the software on the EVG system may interrupt the beam operation, it was decided to generate the pattern in a separate program. The present pattern generation scheme is developed in a scripting language for rapid prototyping.

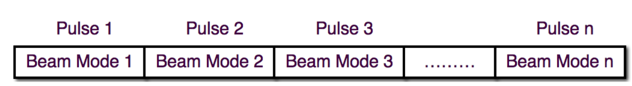


Figure 2: Beam-mode pulse pattern. A certain beam mode is assigned to each beam pulse, and several event codes accompany each beam mode.

The pattern such as Fig. 2 is designed in the program. The length of the pattern can be any number less than 500 (10 seconds), and it can be downloaded any time into the EVG system. Once it is loaded, it repeats forever until the next one is loaded, then the previous one is replaced at the end of the pattern. The EVG system generates a related event code sequence automatically following the pattern.

## EQUIPMENT CONTROLS

EVR modules directly drive timing signals, responding to event codes. The pulse widths are normally fixed, however, the timing delays are modified dependent on the event codes that correspond to one of the beam modes. Those timing signals are connected to devices such as pulsed magnets, low-level rf, high-power sources, beam instrumentation, and injection systems in order to switch the beam and to adjust the beam characteristics.

The phase values in the low-level rf systems (LLRF) are essential in order to define the profile, absolute value and spread of the beam energy. At the end of each pulse LLRF parameters are changed to prepare the next LLRF pulse as in Fig. 3.

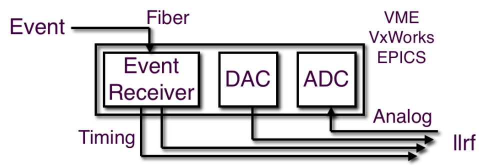


Figure 3: Six LLRF stations are controlled by EVR systems.

Currently, six pulsed magnets are installed in Linac, a bending magnet to feed the beam to the transport lines, a pulsed coil to efficiently capture the positron, and pulsed steering magnets to create a beam orbit bump to guide a beam around the positron target. They are separately triggered by timing signals from nearby EVR systems depending on the beam modes.

Beam instrumentations are also important to ensure the beam properties. Approximately 100 beam-position monitors (BPM) are utilized to monitor, stabilize and analyze the beam [8]. The old system reads the information only once a second. However, it is required to read every pulse if we switch the beam.

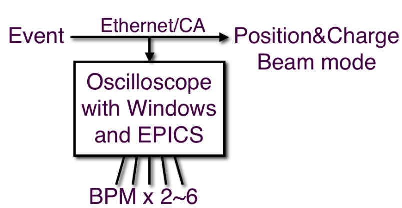


Figure 4: 24 oscilloscopes are installed to read 100 BPMs in 50 Hz distinguishing the beam modes.

The new system employs 24 oscilloscopes (Tektronix DPO7104) [9]. EPICS software is embedded on to those oscilloscopes with Windows. They can acquire the BPM signals in 10 Gsample/s and analyze the beam properties applying more than 20 coefficients per BPM. They can process the signals every pulse recognizing the beam modes and distinguishing two bunches 96 ns apart. Because the event system cannot be embedded on oscilloscope, events are delivered through the normal control network.

For some of the beam instrumentations such as streak cameras that do not recognize 50 Hz switched signals, a timing signal for only a selected beam mode is delivered.

## RF SYNCHRONIZATION

Both of the ring rf frequencies are independently and continuously adjusted in order to compensate the ring circumference variations. KEKB and Linac frequencies have a common source because the tolerance of the injection timing jitter is less than 30 ps. For PF ring, double-fold synchronization module was developed to choose a timing that synchronizes within a certain jitter between PF revolution frequency and Linac frequency. Currently, the jitter is set to 300 ps.

## CONCLUSION

The features of this new event-based control system is being validated under the beam operation. It is proved to satisfy the fast switch requirements. The system is expected to realize a sensitive and stable tuning of KEKB with crab cavities for a higher luminosity and a top-up injection at PF ring, simultaneously. More software development may be needed to support the beam operation with those three virtual accelerators enabled by the event system. An integrity monitor of the system is being developed as well to ensure the correct operation.

## ACKNOWLEDGMENTS

The authors would like to thank Dr. E. Björklund at LANL, Dr. T. Korhonen at PSI, and Mr. J. Pietarinen at MRF for their providing us EPICS event software and for valuable discussions.

## REFERENCES

[1] K. Furukawa *et al.*, "Beam Switching and Beam Feedback Systems at KEKB Linac", *Proc. LINAC2000*, Monterey, USA., 2000, p. 633.

[2] M. Satoh *et al.*, "Present Status of the KEK Injector Upgrade for the Fast Beam-Mode Switch", *these proceedings*.

[3] K. Furukawa *et al.*, "Timing System Upgrade for Top-up Injection at KEK Linac", *Proc. EPAC2006*, Edinburgh, U.K., 2006, p. 3071.

[4] T. Suwada *et al.*, "Operational Performance of a New Beam-Charge Interlock System for Radiation Safety at the KEKB Injector Linac", *these proceedings*.

[5] K. Furukawa *et al.*, "The Timing System of KEKB 8-GeV Linac", *Proc. ICALEPCS2003*, Gyeongju, Korea, 2003, p. 130.

[6] <http://www.mrf.fi/>.

[7] <http://www.aps.anl.gov/epics/>.

[8] K. Furukawa *et al.*, "Beam Feedback Systems and BPM Read-Out System for the Two-Bunch Acceleration at the KEKB Linac", *Proc. ICALEPCS2001*, San Jose, USA., 2001, p. 266.

[9] M. Satoh *et al.*, "Fast BPM DAQ System Using Windows Oscilloscope-based EPICS IOC", *Proc. ICALEPCS2007*, Knoxville, USA, 2007, p. 469.

# PULSE-TO-PULSE MODE SWITCHING OF KEKB INJECTOR LINAC

T. Kamitani*, K. Yokoyama, T. Sugimura, K. Kakihara, M. Ikeda, A. Shirakawa, S. Ohsawa, T. Suwada, K. Furukawa, M. Satoh, M. Kikuchi, T. Mimashi, N. Iida,
KEK, Tsukuba, Japan


## [illegible]

Electron and positron injections from the KEKB injector linac to storage rings have been switched in a typical cycle of five minutes. The switching involves a mechanical movement of a positron production target from and to a beam line. It prevents from faster switching, like pulse-to-pulse switching. A target assembly with a small hole beside a target material and four pulse steering magnets are installed. For positron injection pulses, the pulse steering magnets are off and electron beams irradiate the target to produce positrons. While, for electron injection pulses, the pulse steering magnets are excited to create a orbit bump in order for the electron beams to go through the hole and bypass the target. This paper describes details of a system for the pulse orbit bump and results from recent beam studies.


## INTRODUCTION

The KEKB injector linac supplies electron and positron beams to the KEKB storage rings HER (8.0 GeV e-), LER (3.5 GeV e+) and to the two synchrotron radiation facility rings PF (2.5 GeV e-) and AR (3.1 GeV e-) as well. Each ring requires different beam properties; a time-structure, a particle charge, an energy and an intensity. Parameter setting of the linac, called as "injection mode", is switched for an appropriate beam to be generated, accelerated and sent into a selected ring. In this mode switching, parameters like a choice of the pre-injector, electron gun settings, magnet currents, acceleration phases, rf pulse timings and so forth are changed. Mode switching between the electron and the positron injection for HER and LER rings is frequent in typically 5 minutes cycle. Each switching takes 30 seconds in completing to change parameters. Most of the linac operation time is occupied for KEKB continuous injection. It is interrupted by injections to PF (once a day) and to AR (twice a day), each takes 15 minutes to fill up the storage ring. Switchings from KEKB to PF or AR and its reverse have taken a few minutes until recently, since it needed to change a current slowly for a large bending magnet to keep its hysteresis cycle. However, recently, a demand of continuous PF injection was brought up for keeping its storage current constant. It is beneficial for some synchrotron radiation users, but it was not compatible with the KEKB continuous injection. To solve this issue, much efforts have been made to realize quasi-simultaneous electron injection to KEKB HER and to PF [1]. It can be achieved by injecting both beams from the same pre-injector, installing a pulse bending magnet and a new beam transfer line for PF, pulse-to-pulse switching of acceleration rf phases for 8.0 GeV and 2.5 GeV beam energies, setting up focusing and steering magnets compatible for these different beam energies [2]. This unification of these two injection modes has almost been completed and it will be used for an autumn run this year (2008).

Next step of the unification is that of the KEKB electron and positron injections. Positrons are produced by irradiating a metal target with electron beams. A target is placed on a beam line halfway across the KEKB linac. The target is retracted from the beam line during an electron injection and inserted during a positron injection. Mechanical movement of the target takes a few seconds. It is desirable keep constant storage currents in both of electron ring and positron ring for a beam collision tuning to achieve superior luminosity. To realize pulse-to-pulse switching of the electron and positron injection modes, it was proposed to use a target assembly with a small hole beside a target material in order to fix it on a beam line and to let electron beams bypass through the hole with pulse steering magnets only for electron injection pulses.

In the following chapters, details of the target assembly, the pulse steering magnets and recent results of beam studies are given.

## TARGET BYPASS ORBIT FOR PULSE-TO-PULSE MODE SWITCHING

### [illegible]

In designing a bypass orbit to avoid the target retraction, first considered has been a large orbit bump to bypass not only the target but positron focusing solenoids and a capture system. It needed an independent bypass beam line apart more than 300 mm from the original beam line and also huge pulse magnets to bend 4-GeV electron beams in large angle. Thus, it was too costly. More practical and economical solution was to make a small hole in a target assembly beside the target material and to make a bump orbit of only some millimeters height. This small orbit bump can be contained in a present beam ducts and in apertures of accelerating structures. Fig. 1 shows a bypass orbit bump and a beam line layout around the positron production target. A component denoted as PT21T in the figure is a positron production target and the thick green lines show an aperture of the target hole. Center of the hole is 5.2 mm aside horizontally from a beam line center. Focusing quadrupoles setting is based on a candidate beam optical calculation which is compatible for HER and PF injections. A purple line shows a bump orbit and red

* takuya.kamitani@kek.jp

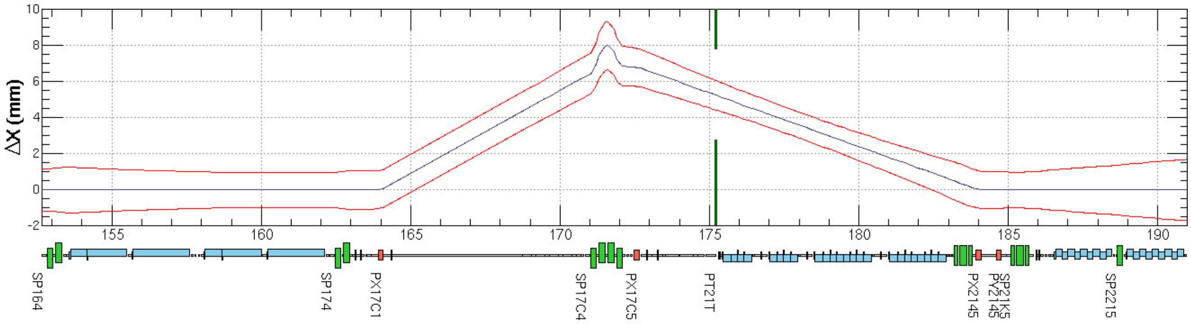


Figure 1: Target bypass orbit and beam-line component layout around the positron production target.

lines show a beam envelope in 3-sigma extent assuming a design emittance of electron beam for HER injection: $\gamma\epsilon = 1.0 \times 10^{-4} m$. A envelope of PF injection beams is not described here since its size is typically much less than that of HER beam. About 3 meters upstream of the target, there is a quadrupole quartet (illustrated in green rectangles) to focus electron beam onto the target. At just downstream of the target, there is a positron-focusing solenoid region in 8 meters long and capture accelerating structures (blue rectangles) in it. Three horizontal pulse steering magnets (PX17C, PX17C5, PX2145) and a vertical steering (PY2145) are installed (orange rectangles). Horizontal steering magnets make a closed orbit bump to let electron beams go through the hole. Since the focusing quadrupole quartet is inside the bump, it contributes to kick the beam toward the beam line center and help the second steering magnet. The vertical steering magnet is used to compensate a vertical kick from edges of the solenoidal field.

## [illegible]

For positron production, 4.0-GeV electron beam (beam intensity 10 nC/bunch, 1 or 2 bunches/pulse, maximum pulse repetition 50 Hz) irradiates a tungsten target. A 14-mm thick amorphous tungsten had been used as a target material. Recently, a 10-mm thick crystal tungsten has been developed for practical use, which resulted in 25% increase of the positron intensity [3]. Transverse cross section of the crystal tungsten is a square in shape, 4.5 mm on a side. The target is combined in a copper support by the hot isostatic pressing method. Cooling water pipe is wound around the support and connected by brazing. In a present injection mode switching, the target assembly is mechanically moved. The target is retracted from a beam line for electron beams to pass through during electron injections, and it is inserted in the beam line for positron production during positron injections. The target is driven by a pressurized air and it takes a few seconds to complete the movement. A cycle period of the retraction and the insertion is limited to be longer than 5 minutes for avoiding a breakage of a vacuum bellows in a long-term operation. To realize a beam mode switching without moving the target, a hole 5.0 mm in diameter is penetrated beside the target as shown in Fig. 2.

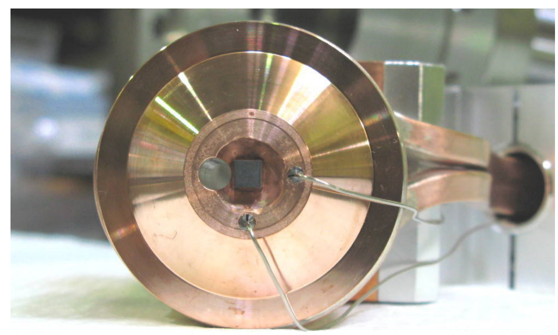

Figure 2: Positron production target assembly with a hole.

## [illegible]

To make a bump height of the target bypass orbit sufficient for the target hole, pulse steering magnets should generate 1.0-mrad transverse kick angle for the 4-GeV electron beam. To achieve this specification, modification of used magnets in the TRISTAN accelerator was considered. The candidate magnet has dimensions of 330 mm in yoke width, 280 mm in yoke height and 170 mm in pole length. This size is suitable for installing into available spaces in the linac beam line. It could generate 0.0593 Tesla dipole field with a maximum DC current of 10 A, which corresponds to 0.56-mrad kick angle for 4.0 GeV beam. To meet the specification requirement on the field strength, a pole gap of the magnet was modified from 70 mm to 35 mm, by fabricating additional pole head and welding to an existing pole. It doubled the field strength at the same current to meet the specification. This modification resulted in significant increase of a coil inductance from 32 mH to 57 mH. In this situation, the maximum current which can be supplied to the magnet is limited by a induction voltage a power supply can manage. We use a sine-like pulse shape with a offset to make an initial and a final time derivates of the supplied current to be zero, because an edged shape of the pulse current give larger induction voltage. Bipolar pulse power supplies, BP4610 and BP4620 of the NF corporation are used as amplifiers of input pulses from function generators. The power supplies can tolerate an induction voltage by a pulse longer than 40-ms cycle. Thus, it can excite a bump orbit at maximum repetition of 25 Hz. In a case of 50 Hz injection, we will switch the power supplies to a DC mode. A timing of the orbit bump excitation with respect to beam arrival has 0.5 ms jitter from a constraint in bucket selection.

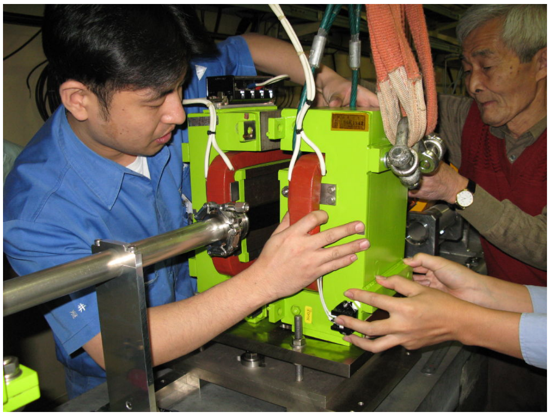

Figure 3: Pulse steering magnet for target bypass orbit

## [illegible]

Preliminary beam studies have clarified some issues on this scheme of mode switching using a bump orbit through the target hole:

- When the bump height is large, certain beam loss occurs because some fraction of electrons hit vacuum ducts around the region of the quadrupole quartet. Vacuum ducts whose inner shape was a circle of 10.0 mm in radius was replaced by that of elliptical shape whose major axis is 14.5 mm.
- Preliminary target hole diameter 3.0 mm was not sufficiently tolerant for beam transmission. It was enlarged to 5.0 mm in the most recent target.
- Setting of the pulse steering magnets for the bump orbit and beam transmission performance are dependent upon a focusing strength of the quadrupole quartet. In the most promising optical setting in views of beam transmission and matching to a downstream optics, the quadrupole strength was set to a medium value between that for an previous HER injection optics and that for optimum focusing onto the target [2].

Beam studies are performed quite recently to measure a beam transmission performance after these improvements. Fig. 4 shows beam transmission ratios for 1st and 2nd bunches of the HER injection beam and for the PF beam. We define a standard charge by a beam charge measured at a downstream of the bump orbit when bump height is zero and the target extracted. The transmission ratio in vertical axis of the figure is calculated as a measured beam charge divided by the standard charge. The bump height in horizontal axis is defined as a difference of an orbit position at the target from that when pulse steering magnets are off. It should be noticed that these values are not absolute orbit position. Dashed the blue and aqua lines show measured beam transmission ratio of two bunches of a HER beam with the target extracted. Degradation in a right-hand shoulder is caused by beam loss at vacuum ducts. While, the solid lines in same colors are those for the case the target is inserted. At each bump height of the maximum transmission for the first and second bunches, differences of the values for the cases with and without the target is less than 5%. Thus, it shows that 95% of the beams can be pass through even with an aperture limited by the hole. Optimum bump heights for the first and second bunches of the HER coincides in a range of 0.1 mm. It shows that the orbits for them are very close in 0.1 mm and a common bump height can achieve a transmission close to the optimum. Dashed and solid red lines show the transmission for PF beams. The optimum transmission for PF beam is better than 95%, but the optimum bump height differs about 0.6 mm from those of HER beams. This significant orbit difference forces a compromised bump height in order to make it common for the HER and PF beams. It results in slightly degraded transmission. It need more careful tuning to make these orbit to be closer for better tranmission. If the tuning cannot improve the situation, pulse-to-pulse variation of the bump height will be necessary and requires some upgrades in the pulse power supply control system. After all, even in a compromised bump height, 90% transmission is achieved both for HER beams and for PF beam.

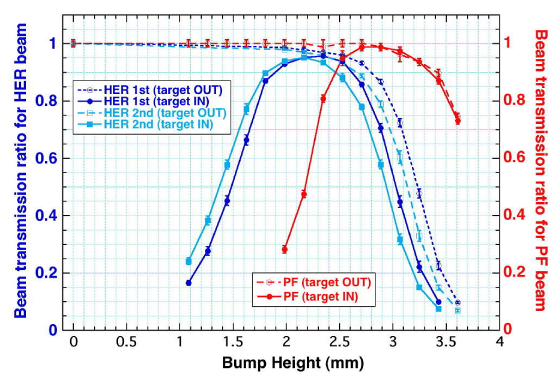


Figure 4: Measured beam transmission performances.

# REFERENCES

[1] M. Satoh, et al., "Present Status of the KEKB injector upgrade for the Fast Beam-Mode Switch", LINAC'08, Victoria, Canada, September 2008, TUP013.

[2] Y. Ohnishi, et al., "Design and Performance of Optics for Multi-energy Injector Linac", LINAC'08, Victoria, Canada, September 2008, TUP012.

[3] T. Suwada, et al., "First application of a tungsten single-crystal positron source at the KEK B-factory", Phys. Rev. ST Accel. Beams 10, 073501 (2007).

# OBSERVATIONS OF TWO MICROBUNCHES AFTER A 180-DEGREE ARC SECTION AT THE KEKB LINAC

Y. Ogawa#, M. Yoshida, KEK, Tsukuba, Japan


*Abstract*

The KEKB linac [1] continuously injects 8-GeV electron and 3.5-GeV positron beams into the KEKB rings: HER (high energy ring) and LER (low energy ring). The energy spread of the 8-GeV electron beam, which is accelerated to an energy of 1.7-GeV at a 180-degree arc section and reaccelerated after this arc to a final energy of 8 GeV, is optimized by adjusting rf acceleration phases so as to assure efficient injections. When rf phases after the arc are slightly changed or drifted for some reasons, the beam not only shows larger energy spreads but also indicates two clusters on a beam profile monitor located at large energy dispersions. In this connection, a longitudinal beam profile was measured before and after the arc section with streak-camera systems utilizing OTR (Optical Transition Radiation). The observed bunch shape clearly shows a two-microbunch structure, suggesting that it could be generated in the arc section. Various experimental data as well as some CSR-related speculations are presented.


## INTRODUCTION

In high-luminosity machines like the KEKB factory, stable beam injections are absolutely essential to retaining the optimum luminosity. The injection efficiency is quite dependent upon the quality of injected beams, especially upon the energy spread. Thus the energy spread of the electron beam for the KEKB has been always kept at a minimum enough for stable injection by adjusting rf acceleration phases.

The KEKB electron beam is accelerated to an energy of 1.7-GeV at a 180-degree arc section and reaccelerated after the arc to a final energy of 8 GeV (Fig. 1). During tuning processes of the energy spread, we have found that the energy profile at the end of the linac shows peculiar behaviour, splitting into two clusters if the rf phases after the arc are not optimized, while we have not observed the same phenomenon before the arc section. Although the phenomenon itself is quite stable and reproducible, we examined as a first step the rf system looking for some unstable components, but did not find any causes attributed to the rf system. Meanwhile we have taken various observation data concerning this phenomenon, which are reported in this paper together with some CSR-related speculations.

## EXPERIMENTAL CONFIGURATION

A schematic view of the experimental setup is shown in Fig. 2. The parameters relevant to the 8-GeV single-bunched electron beam are summarized in Table 1. The energy profile of the beam is observed by a screen monitor using an alumina fluorescent plate (AF995R, Desmarquest Co.) located at the 8-GeV energy-analyzer line; the energy separation of the two clusters is measured by changing rf phases of appropriate accelerator sections corresponding to an energy range of about 5 GeV. The time structure of the bunch is investigated with streak-camera systems (Hamamatsu Photonics K. K.) utilizing OTR located before and after the arc, which have a time resolution of two or three picoseconds.

Table 1: Beam Parameters

| | |
|---|---|
| Energy | 8 GeV |
| Acceleration Frequency | 2856 MHz |
| Charge | 1 nC (single bunch) |
| Bunch Length (σ) | 4.7 ps (single bunch) |
| Energy Spread (σ) | 0.05 % |
| Emittance $\gamma\beta\varepsilon$ (σ) | 0.31 mm |
| Maximum Repetition | 50 pps |
| Energy at the Arc Section | 1.7 GeV |

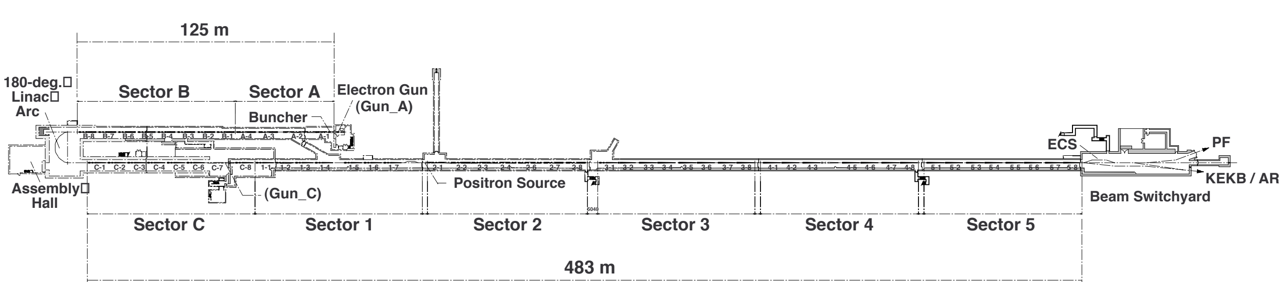


Figure 1: Layout of the KEKB linac. The KEKB electron beam is accelerated to an energy of 1.7-GeV at a 180-degree arc section and reaccelerated after the arc to a final energy of 8 GeV.

#yujiro.ogawa@kek.jp

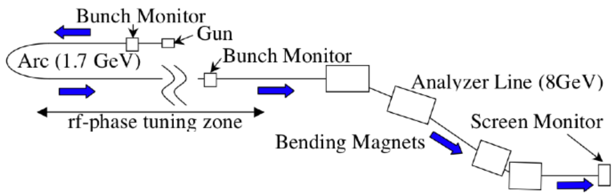


Figure 2: Schematic view of the experimental setup. The longitudinal phase space of the single-bunched electron beam is diagnosed by two methods: one with the bunch monitors before and after the arc, the other utilizing the 8-GeV energy analyzer line located at the end of the linac.

## EXPERIMENTAL RESULTS

### *Observation on the Screen at Large Dispersions*

Fig. 3 shows the photographs of energy profiles observed on the screen monitor located at the energy-analyzer line in two cases: Fig. 3a for the single bunch in optimum rf acceleration phases and Fig. 3b for those split into two clusters in non-optimum rf phases. Since the alumina fluorescent plate has a long image lag when irradiated by charged beams, the beam repetition was decreased to 0.5 Hz so as to check if two clusters shine at the same time. This has verified that the observed phenomena are not caused by some energy-jitter effects but due to the real two independent clusters with different energies.

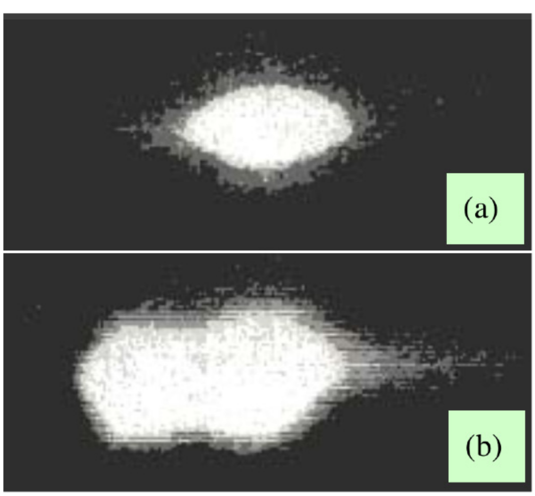


Figure 3: Energy profiles observed on the screen monitor at large dispersions: (a) for the single bunch in optimum rf acceleration phases and (b) for those split into two clusters in non-optimum rf phases.

### *Measurements of the Bunch Structure*

This fact has pushed us to figure out time structures of the bunch with streak-camera systems utilizing OTR located before and after the 180-degree arc section. The results are shown in Fig. 4; one observed before the arc (a), the others after it (b, c). Fig. 4b and 4c clearly indicate a two-microbunch structure with a time interval of about 20 ps irrespective of rf phases, while the bunch shape before the arc (Fig. 4a) has just a single peak. Since the measurements were carried out in integration modes of the streak camera systems to improve S/N ratios for a small charge of 1 nC or 2 nC, it remains unclear whether the results could conclude the actual existence of two microbunches after the arc, which might hint that the phenomena should take place during passage through the arc.

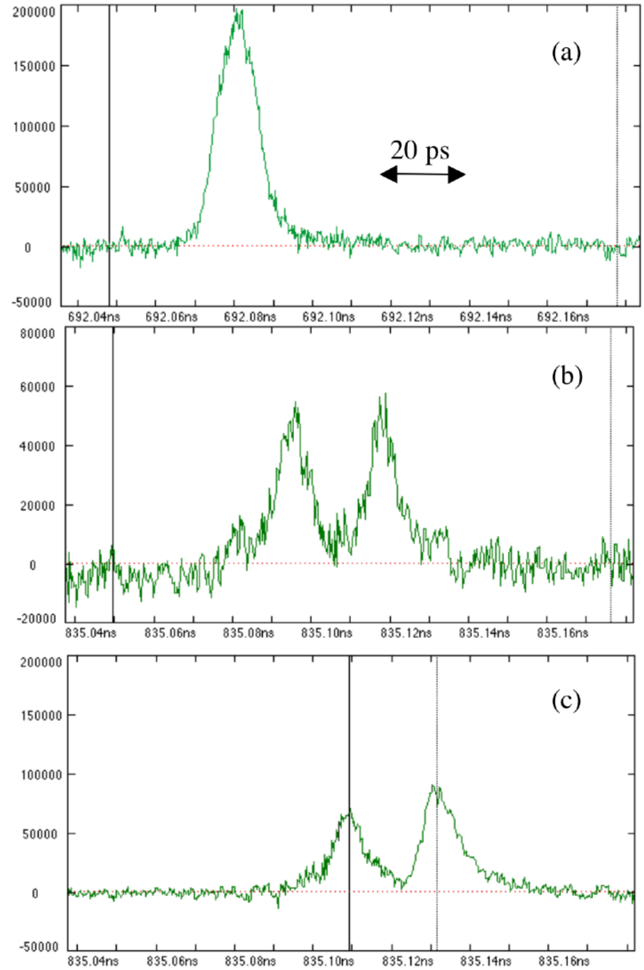


Figure 4: Bunch structure measured with streak-camera systems utilizing OTR located before and after the 180-degree arc section: (a) observed before the arc, (b) and (c) after the arc. (a) and (b) are the cases for a charge of 1 nC, while (c) is for 2 nC.

We also checked the charge dependence of the phenomena anticipating the wake-field issue, but the time interval of the two microbunches shows weak or no dependence on the charge (Fig. 4c).

### *Energy Separation as a Function of rf Phases*

In order to clarify the two-microbunch structure, we have examined whether the energy separation of the two clusters seen by the screen monitor at large dispersions really varies with rf phases. Fig. 5 shows unequivocal dependences of the energy separation of the two clusters on the rf acceleration phases confirming the existence of two microbunches.

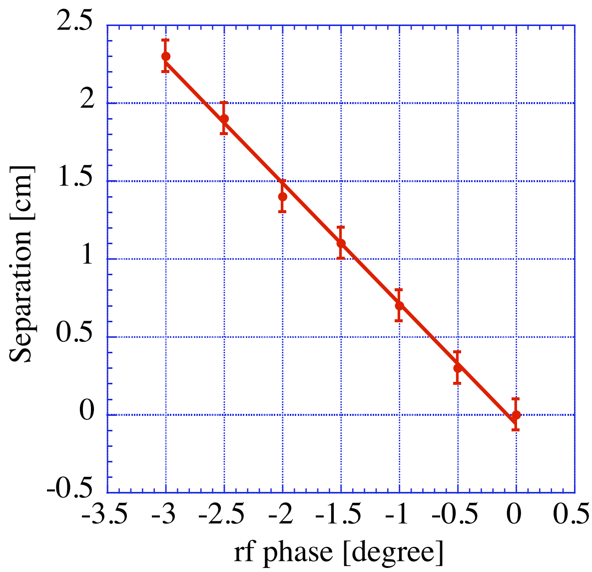


Figure 5: Energy separation of the two microbunches as a function of the rf phases. The data points are fitted with the function $x$ given in the text.

## DISCUSSIONS

### *Cross-Check of the Measurements*

The measurements by the bunch monitor after the arc (Fig. 4b) shows that the time interval of the two microbunches is about 20 ps, which should be compared with the value obtained from the rf-phase dependence of the energy separation of the two clusters (Fig. 5). If the two microbnches really exist, their energy separation $\delta E$ is written as,

$$\frac{\delta E}{E} = \frac{E_{rf}}{E_0}(\cos\phi_2 - \cos\phi_1),$$

where $E_{rf}$ is the corresponding energy of the sections for rf phase tuning, $E_0$ the total energy (8 GeV), $\phi_1$ the rf phase of the first microbunch, $\phi_2$ that of the second microbunch. The observed separation on the screen ($x$) is proportional to $\delta E$,

$$x = A\eta_x \frac{\delta E}{E},$$

where $\eta_x$ is the dispersion function at the measurement point, $A$ the calibration factor. Defining the following quantities,

$$\phi_{rf} = \frac{\phi_1 + \phi_2}{2},\ \ \delta\phi = \phi_2 - \phi_1,$$

$x$ is represented by

$$x(\phi_{rf}) = -2A\eta_x \frac{E_{rf}}{E_0} \sin\frac{\delta\phi}{2} \sin\phi_{rf}.$$

The data points in Fig. 5 are fitted with this function on the assumption that

$$A = 0.8,\ \ \eta_x = 400\ cm,\ \ E_{rf} = 5.25\ GeV,$$

from which we obtain $\delta\phi$ :

$$\delta\phi = 12 \pm 1\ [\text{degree}],$$

corresponding to the time interval $\delta t$ :

$$\delta t = 12 \pm 1\ [\text{ps}].$$

This is to be compared with the value (20 ps) obtained by the bunch monitor, showing a certain amount of difference, which should be attributed to the uncertainties concerning the calibrations of the streak camera systems and the factor $A$.

### *Some Speculations on CSR Effects at the Arc*

The experimental results suggest that the observed phenomena might originate at the arc section, which is designed to be achromatic and isochronous. The CSR effects could be primarily not the issue because the bunch length is not so small and not even compressed in the arc. During passage of the arc, however, it might happen that an initial density fluctuation with a characteristic length much shorter than the bunch length could radiate coherently, leading to microbunching phenomena observed in our linac if the CSR effects are enhanced in the arc [2]. The simulations based on the CSR effects are in preparation and will be reported elsewhere.

## CONCLUSIONS

We have observed peculiar phenomena in the energy profile of the KEKB 8-GeV electron beam during rf phase tuning, splitting into two clusters like microbunches. In order to check the existence of microbunches, we performed a series of experiments. The results surely indicate that microbunching happens at the 180-degree arc section when the rf acceleration phases are not optimized for an energy spread. Further experiments as well as some simulations related to CSR effects are to be carried out in the near future.

## REFERENCES


[1] I. Abe et al., “The KEKB injector linac”, Nucl. Instr. and Meth. A499 (2003) 167.

[2] M. Huning et al., “Observation of longitudinal phase space fragmentation at the TESLA test facility free-electron laser”, Nucl. Instr. and Meth. A475 (2001) 348.

# DESIGN AND PERFORMANCE OF OPTICS FOR MULTI-ENERGY INJECTOR LINAC

Y. Ohnishi*, T. Kamitani, N. Iida, M. Kikuchi, K. Furukawa, M. Satoh, K. Yokoyama, and Y. Ogawa,
KEK, Tsukuba, Japan

*Abstract*

KEK injector linac provides an injection beam for four storage rings, KEKB high energy electron ring(HER), low energy positron ring(LER), PF-AR electron ring, and PF electron ring. The injection beams for these rings have different energies and intensities. Recently, a requirement of simultaneous injection among these rings arises to make a top-up injection possible. Magnetic field of the DC magnets to confine the beam to the accelerating structures can not be changed during a pulse-to-pulse, although the beam energy can be controlled by fast rf phase shifters of the klystrons. This implies that a common magnetic field of the bending magnets and the quadrupole magnets should be utilized to deliver beams having different characteristics. Therefore, we have designed a multi-energy optics for the KEKB-HER electron ring(8 GeV, 1 nC/pulse), the PF electron ring(2.5 GeV, 0.1 nC/pulse), and the KEKB-LER positron ring(3.5 GeV, 0.4 nC/pulse). We present a performance of the multi-energy injector linac for the PF ring and the KEKB-HER.

## INTRODUCTION

A new injection scheme has been developed, which is so called a pulse-to-pulse injection with multi-energy linac for the KEKB-HER, the KEKB-LER, the PF ring. The pulse-to-pulse injection means that the beam can be switched and injected to the desired rings within 20 msec at a minimum duration. However, the beam energy is different among these rings. Difficulties arise from that most of magnets can not change the magnetic field by a pulse-to-pulse duration. Therefore, we have developed a new optics to use a common magnetic field for the different beam energies, such as 2.5 GeV for the PF and 8 GeV for the KEKB-HER. The KEKB-LER injection has been still tested and under development in this scheme, however, the strategy is a similar way of the PF and the KEKB-HER.

The injector linac has 7 sectors, A-sector and B-sector before 180° arc(J-arc) and 1-sector to 5-sector after the J-arc. The energy of the J-arc is 1.7 GeV and the multi-energy scheme focuses on the region from the C-sector to the 5-sector. A pulse bend is placed in the 5-sector and the 2.5 GeV beam is kicked out to the transport line of the PF ring, while the 8 GeV beam passes through the ECS(the energy compression system) to the KEKB-HER transport line.

* Email: yukiyoshi.onishi@kek.jp

## OPTICS

A fundamental block of the linac is an acceleration unit that consists of an S-band klystron and four 2 m-long accelerating structures. The klystron drives these accelerating structures which have a common phase of the microwaves. The accelerating structures in the acceleration unit have the same field gradient in principle. Eight acceleration units make a sector, typically. A sub-booster supplies microwaves to each klystron in the sector and adjusts the phase for a beam passage.

A doublet or a triplet of quadrupole magnets is placed in every one or two acceleration unit and makes a cell of a periodic lattice. In the case of an electron injection, an electron beam is accelerated from 1.7 GeV up to 4.8 GeV between the C-sector and the 3-sector. A positron target to make a positron beam is placed in the 2-sector. In the case of a positron injection, a primary electron beam hits the positron target and positrons are generated by means of electro-magnetic showers. On the other hand, a small hall($\phi$=3 mm) is placed in the vicinity of the target so that an electron beam can pass through the positron target for the electron injection. In order to make this possible, it is necessary to squeeze the beta function at the hall as small as possible and to make a local bump orbit by using pulse steerings in the horizontal plane.

The electron beam injected to the PF ring is decelerated down from 4.8 GeV to 2.5 GeV between the 3-sector and the 5-sector, while the electron beam is accelerated up to 8 GeV for the KEKB-HER. In the multi-energy region, the phases of the sub-boosters are shifted by 180° approximately between the acceleration and the deceleration. In practice, an off-crest phase typically shifted by 6° from the crest phase is used to compensate the energy difference between the head and the tail of a bunch due to the wake field. The deceleration phase is

$$\phi_{dec} = \phi_{acc} + 180^\circ - 2\Delta\phi, \quad (1)$$

where $\Delta\phi$ is the phase shift from the crest phase. Further more, a few klystrons in the 3-sector would be a stand-by mode to adjust the beam energy so as to be 2.5 GeV. The stand-by mode implies an off-timing trigger for the beam passage. Both the 2.5 GeV and 8 GeV beam would be adjusted by the energy-feedback system[1] precisely. The energy feedback system consists of a set of two klystrons and adjust the phase. The off-crest phases are used in the opposite side of the crest for each klystron to compensate the energy spread. Those sub-boosters and the energy feedback system utilize a phase shifter with a solid-sate device and can change the phase by a pulse-to-pulse duration.

The DC magnets are used in the lattice for the quadrupole and steering magnets. Therefore, the beams which have a different energy must be transported with a common magnetic field from the 3-sector to the 5-sector(multi-energy region). The optics is designed for the 2.5 GeV beam as a base line since there is a matching section in the transport line for the KEKB ring and not for the PF ring. The beta functions and beam energies for the 2.5 and the 8 GeV beams are shown in Fig. 1. The betatron phase advance of the cell is 90° typically in most sectors. However, the phase advance in the multi-energy region should be optimized so as to make the beta function enough small for the the different beam energy. In the 2.5 GeV optics, the phase advance for each cell is designed to be 108° approximately in the 4-sector and the 5-sector. While, the phase advance of the cell would become 40°∼50° for the 8 GeV optics. The optics design would suppress a large beam size in the multi-energy region for the both 2.5 and 8 GeV beam.

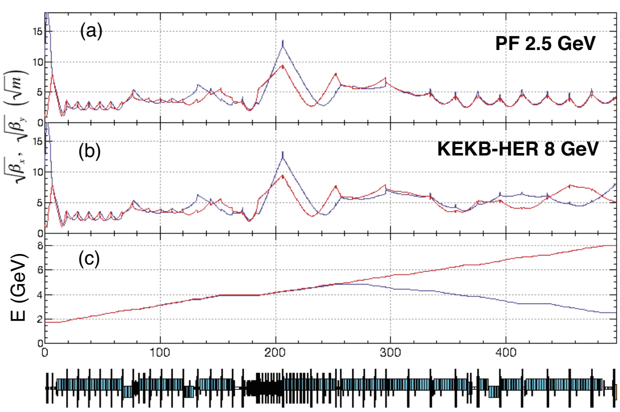


Figure 1: Optical parameters for (a) 2.5 GeV PF, (b) 8.0 GeV KEKB-HER, and (c) beam energy.

In the optics calculation, the SAD code[2] is utilized. We assumed that the beam energy at the exit of the buncher section in the A-sector would be 20 MeV which is measured by a energy analyzer cosists of a well calibrated bending magnet and a beam screen monitor. The beam energy is calculated by using a peak acceleration field of an accelerating structure, a phase, a klystron status[3]. The calculated energy would have errors due to a characteristic of the accelerating structure and the beam loading. Therefore, the absolute value of the beam energy should be adjusted to be the desired energy at the end of linac for each injection. A normalization factor is used to scale the beam energy to 1.7 GeV at the J-arc, 2.5 GeV for the PF ring, and 8 GeV for the KEKB-HER. The relative energy among the accelerating structures should be kept since the relartive error of the energy gain from the accelerating strucure would be small. Although the normalization factor is an overall factor, the normalization factor of 8 GeV is used for the 2.5 GeV beam in the common energy region which is between the J-arc and the entrance of the multi-energy region.

Twiss parameters at the entrance of the C-sector are matched so as to be the design values using the matching section in the J-arc. The matching procedure is based on emittance measurements with wire scanners[4]. From the C-sector to the 5-sector, k values correspond to the magnetic field of the quadrupoles are determined so that the beta functions become the design values by means of a fitting procedure with the SAD code.

## CORRECTION OF OPTICS

The optics is corrected by a single-kick method. A single-kick orbit induced by a steering is measured by beam position monitors(BPM) which are placed next to each quadrupole magnet. Since the single-kick orbit is a relative orbit displacement by a single steering, we do not have to consider an absolute beam position.

The measured orbits are compared with the design orbits calculated by optical parameters based on the k value of the quadrupoles and the calculated beam ebergy described in the previous section. A fudge factor is introduced to correct the k value so that the measured orbits agree with the design orbits. The definition of the fudge factor, $a_f$, applied to the k value is written by

$$K_{ps} = a_f \cdot K_d, \tag{2}$$

where $K_{ps}$ is a k value set to the real magnet and $K_d$ is a k value of the design value. The deviation from the design of the k value of the $m$-th quadrupole can be estimated by solving following equations:

$$\Delta x_i^{(j)} = \sum_{m=1}^{M} R_{y,im}^{(j)} \Delta K_m \tag{3}$$

$$\Delta y_i^{(j)} = \sum_{m=1}^{M} R_{x,im}^{(j)} \Delta K_m \tag{4}$$

where $\Delta x_i^{(j)} = x_{m,i}^{(j)} - x_{d,i}^{(j)}$, $x_{m,i}^{(j)}$ and $x_{d,i}^{(j)}$ are the measured and the design orbit at the $i$-th BPM induced by the $j$-th steering in the horizontal plane, and $y$ is the same as $x$. The response matrix, $R_{x,y}$ is calculated by the SAD code. The fudge factor is $a_{f,m}^{-1} = 1 + \Delta K_m / K_{d,m}$ and includes not only a field gradient error but also an energy error. Here, $xy$ couplings are ignored because it is a higher order effect and it should be small.

In the optics correction, we use 22 kinds of single-kick orbits typically to obtain fudge factors of the quadrupole magnets and the fudge factors are determined at the 2.5 GeV lattice. During the optics correction, we found a miss connection of power supplies to quadrupole magnets. In this case, both a large fudge factor and a large field gradient error are appeared at a specified quadrupole magnet(QD484, QF484). In this manner, the single-kick method is also effective to find a machine error. The fudge factor after fixing the connection problem is shown in Fig. 2(c). The fudge factors are within 3%. Figure 2 shows a comparison of the measured and the design single-kick orbit for the 2.5 GeV beam before and after the optics correction. Introducing the fudge factors, the measured single-kick orbit is consistent with the design orbit. All other single-kick orbits are similar to Fig. 2 and consistent with each design orbit.

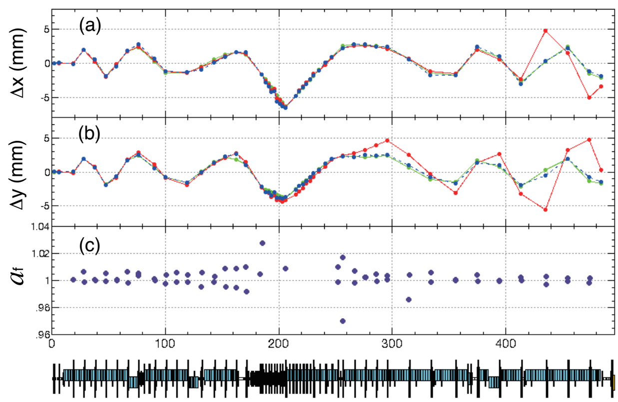


Figure 2: (a): Horizontal orbits for design(green), measured before correction(red), and measured after correction(blue). (b): The vertical orbits are the same as the horizontal. (c): Fudge factors for quadrupoles.

The optics is evaluated by the wire scanner in the 5-sector. The measured optical parameters for 2.5 GeV in front of the pulse bend are listed in Table 1. The optical parameters are well matched to the design values since the B$_{mag}$ parameters are very close to 1.

Table 1: Optical parameters for 2.5 GeV measured by the wire scanner in the 5-sector.

| | **horizontal** | **vertical** | unit |
|---|---|---|---|
| Beta function | 10.36 | 13.08 | m |
| Normalized emittance | 288 | 161 | nm |
| B$_{mag}$ | 1.01 | 1.05 | |

## ORBIT CORRECTION AND FEEDBACK

Beam orbits are required to be fixed and stable at the end of linac. A position and an angle of the 2.5 GeV beam should be zero at the pulse bend. At the same time, a position and an angle of the 8 GeV beam should also be zero at the ECS. We have developed a tuning technique to adjust both orbits for 2.5 GeV and 8 GeV simultaneously by using a common magnetic field of DC steerings. In order to adjust the orbit for 8 GeV, a local bump method is utilized. While the local bump is closed at 2.5 GeV, the local bump is not closed at 8 GeV in general. Therefore, the orbit for 8 GeV can be adjusted independent on the 2.5 GeV orbit. On the other hand, the beam orbit for 2.5 GeV is controlled by two steerings. However, these two steerings would affect the orbit for 8 GeV. In spite of this, the orbit response of two steerings can be canceled by adjusting the local bump height. The orbits for 2.5 GeV and 8 GeV can be adjusted by solving a following equation:

$$\begin{pmatrix} \Delta x_1 \\ \Delta x_2 \\ \Delta X_1 \\ \Delta X_2 \end{pmatrix} = \begin{pmatrix} m_{11} & m_{12} & 0 & 0 \\ m_{21} & m_{22} & 0 & 0 \\ n_{31} & n_{32} & n_{33} & n_{34} \\ n_{41} & n_{42} & n_{43} & n_{44} \end{pmatrix} \begin{pmatrix} \theta_1 \\ \theta_2 \\ h_1 \\ h_2 \end{pmatrix}, \quad (5)$$

where $x$ and $X$ are a beam position for 2.5 GeV and 8 GeV, respectively, $\theta$ is a kick angle of a steering, and $h$ is a local bump height. The orbit response matrix, $m_{ij}$ and $n_{ij}$, is calculated by the SAD code. Vertical positions, $y$ and $Y$, are adjusted by the similar way of the horizontal positions. In this procedure, the positions at two BPMs is necessary at least to adjust the position and the angle. We use two local bumps and two steerings to control the orbits. The phase advance between two local bumps is about 90° which corresponds to two cells of the lattice in the case of 8 GeV.

We consider the orbit feedback system by using this technique. This is a slow orbit feedback since the steerings are DC magnets and beam positions measure by BPMs for 2 sec intervals so far. The slow orbit feedback for the multi-energy beam can suppress an orbit drift for a long term .

## CONCLUSION

We have present the optics designed for the multi-energy injector linac. The beams which have the different energies, such as 2.5 GeV and 8 GeV, can be successfully transported to the end of linac with a common magnetic field of the quadrupoles and steerings. As the next step, the multi-energy injector linac together with the positron injection to the KEKB-LER, the beam energy of 3.5 GeV, is under development.

## ACKNOWLEDGMENT

We would like to thank K. Oide and A. Enomoto who have supported the program for the pulse-to-pulse injection to the PF and the KEKB rings.

## REFERENCES


[1] K. Furukawa et al., ICALEPCS '99, p.248-250.

[2] `http://acc-physics.kek.jp/SAD/`.

[3] T. Kamitani at al., EPAC 2000, p.1507-1509.

[4] N. Iida et al., EPAC 2000, p.1738-1740.

# PRESENT STATUS OF THE KEK INJECTOR UPGRADE FOR THE FAST BEAM-MODE SWITCH

M. Satoh# for the IUC* Accelerator Laboratory, High Energy Accelerator Research Organization (KEK), 1-1 Oho, Tsukuba, Ibaraki, 305-0801

*Abstract*

The KEK Linac provides the four different quality beams for the four independent rings. The KEK Linac upgrade aiming a fast beam-mode switch operation is now in progress so that the KEKB continuous injection and PF top-up injection can be carried out at the same time. In this paper, we will report the present status of the KEK Linac upgrade in detail.

## INTRODUCTION

The KEK Linac provides the beams of the different modes sequentially with four storage rings (KEKB 3.5 GeV positron/ 8 GeV electron, Photon Factory (PF) 2.5 GeV electron and Advanced Ring for pulse X-rays (PF-AR) 3 GeV electron).

For a typical operation, the PF and PF-AR need the beam injection twice a day on scheduled time. On the other hand, the KEKB rings are operated by the continuous injection mode (CIM) for keeping the stored current almost constant. In the CIM operation, the switch time between the electron and positron modes takes about a half minute so that all settings of magnet power supplies, RF phases and timings should be changed according to the electron and positron beam properties. In the near future, the PF top-up operation will be started to enhance the integrated photon flux. For these reasons, the linac upgrade is strongly required for a fast beam-mode switch [1, 2, 3 and 4].

Figure 1 shows the schematic drawing of ultimate fast beam-mode switch operation. In this operation scheme, we will change only the minimum parameters of the timing signals and Low-Level RF (LLRF) phases, and all the rest of parameters like DC magnet settings are never changed even for the different beam-mode. In the final stage of the linac upgrade, the beam mode can be changed in every 50 Hz of an arbitrary beam-mode pattern.

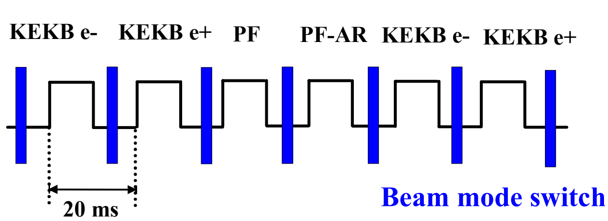


Figure 1: Schematic drawing of fast beam mode.

# masanori.satoh@kek.jp

* Injector Upgrade Committee: Cross-functional team for the injector upgrade from PF/ KEKB and Linac members

## UPGRADE PLAN

### *Outline*

This project is a phased upgrade, and the phase-I has been already completed in the summer of FY2005. The detailed upgrade phases are shown in following sub-sections.

### *Phase-I*

In the phase-I, the new PF-BT line has been constructed for shortening the beam-mode switch time between the KEKB and PF modes. Here, the initialization procedures of the energy compensation system (ECS) bends are required since the original DC switch bend was placed downstream of the ECS bends. In order to bypass the ECS, a new DC switch bend has been installed by removing four accelerating structures, and a new PF-BT line of 60-m-long has been constructed [5].

After the phase-I, the beam-mode switch between the KEKB and PF modes does not need to change the ECS parameters. The round trip mode switch time including PF injection was reduced by half from 5.5 min. to 2.5 min. In addition, the beam injection efficiency has been increased.

### *Phase-II*

The phase-II aims to perform the fast beam-mode switch between the KEKB electron and PF modes up to 50 Hz. For the phase-II and later, we will use the new operation scheme called “Multi-Energy Linac” [6 and 7]. In this scheme, the common magnet settings are used for the different beam modes. The adjustment of the beam energy is performed by a fast control of LLRF phase. Though PF ring injection requires the 2.5 GeV electron, the beam is accelerated up to about 5 GeV in the multi-energy scheme. After then, the beam energy is adjusted to 2.5 GeV by using the deceleration RF phases. This method is effective for enlarging the common optics region. The result of a preliminary machine study shows that this scheme is feasible for a realistic beam operation. In this autumn, the more detailed machine study will be carried out to develop the daily operation parameters.

### *Phase-III*

In the phase-III, the fast beam-mode switch will include the KEKB positron mode. In the current operation, the positron production target is controlled by a mechanical movement. For the fast beam-mode switch between the electron and positron modes, the positron target with a hole will be used. In this scheme, the fast beam-mode switch will be performed by a fast control of the electron beam orbit at upstream of the positron target.

The tungsten crystalline target with a hole has been installed as shown in Fig. 2. A centre of a hole is placed 4.5 mm apart from that of a crystalline tungsten target. The diameter of a hole is about 5 mm. The electron beam goes through the inside of a hole for the electron mode, whereas the electron beam hits the centre of target for the positron mode.

In the machine study, it was measured that almost 100% of the electron beam can traverse the inside a target hole in comparison with a normal operation (target removed). We convinced that this scheme is applicable to the practical beam operation. For a fast control of the beam orbit upstream target, the pulsed steering magnets have been installed in the winter of FY2007.

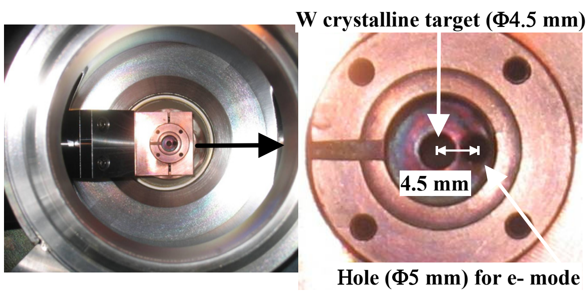


Figure 2: Photograph of tungsten crystalline positron production target with a hole.

### *PF-AR Injection*

The full energy injection of PF-AR is very difficult since the current beam energy at AR-BT is limited up to 3.1 GeV. One solution is to use the 3.5 GeV positron beam of KEKB positron mode for the PF-AR injection, though this scheme involves the installation of a pulsed bend and the improvement of two power supplies at the AR-BT line. In addition, all quadrupole magnets and vacuum chambers should be remodelled for increasing magnetic field. The detailed design study is now in progress, and its result will be reported elsewhere.

## PULSED BEND SYSTEM

For the fast beam-mode switch, the PF beam should be selectively kicked out toward the PF-BT by using the pulsed bend. The DC switch bend installed in the phase-I was replaced by the new pulsed bend system in the last winter maintenance. Table 1 shows the main parameters of the pulsed bend system. The photograph of pulsed bend is shown in Fig. 3.

Though the 2.5 GeV electron are used for the PF injection, the pulsed bend was designed for the beam operation up to 3 GeV. The maximum beam repetition is 25 Hz, and its output current has the half-sinusoidal shape of 200 μs. The both at long and short term stability of power supply output current was satisfied less than 0.1%.

The 1200-mm-long ceramic chamber has been also installed, and its cross-section is a race track-shaped. To avoid the heating, the inner wall of ceramic chamber was coated with 1-μm-thick Ti.

In the first week of February 2007, the PF top-up test operation has been successfully performed during single-bunch user operation. Figurer 4 shows the stored current stability of the PF ring. In this machine study, we can achieve the stability of $10^{-3}$ by using a newly installed slit at the PF-BT. The pulsed bend has worked well during the one week continuous operation without any problem.

Table 1: Main Parameters of Pulsed Bend System

| | | |
|---|---|---|
| Pulsed bend: | | |
| | Beam bending angle: | 7 deg. (up to 3 GeV) |
| | Max. magnetic field: | 1.36 T |
| | Gap: | 157 x 30 mm (W x H) |
| | Coil: | 1 tuen |
| Power supply: | | |
| | Max. current: | 32 kA (12.5 Hz) |
| | | 27 kA (25 Hz) |
| | Pulse width: | 200 μs (half-sinusoidal) |
| | Stability: | 0.1% |
| Ceramic chamber: | | |
| | Length: | 1200 mm |
| | Coating: | Ti (1 μm) |

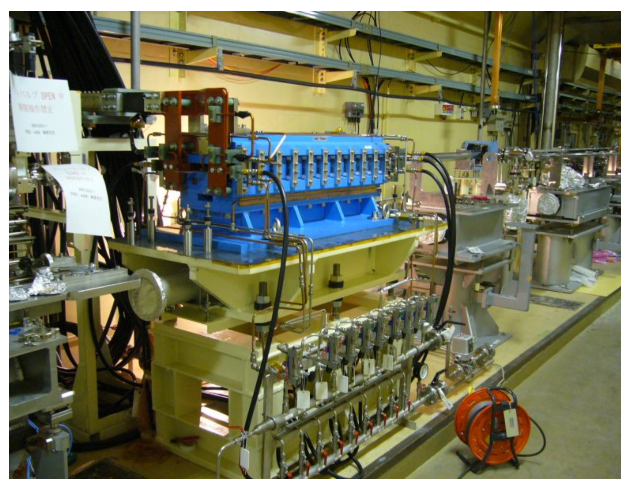

Figure 3: Photograph of pulsed bend.

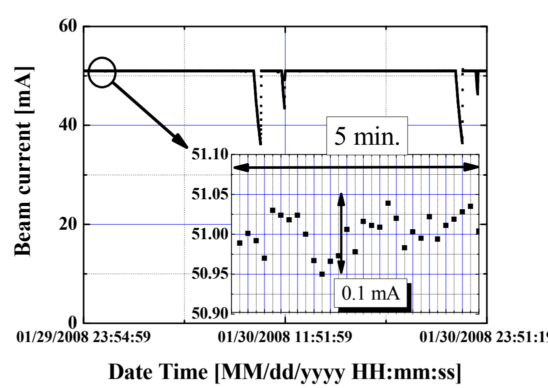


Figure 4: Stability of stored beam current at PF ring for single-bunch Top-up injection study.

## OTHER NEW SUBSYSTEMS

### *Beam-Charge Interlock System*

Toward the fast beam-mode switch operation, a new PLC-based beam-charge interlock system was developed for radiation safety [8]. This system restricts a regulated amount of integrated beam charges traversing through at several locations for machine protection, and it also monitors the amount of integrated beam charges delivered to the four different storage rings at the linac beam switchyard.

The beam charges delivered from an electron gun are measured with the beam-charge interlock system. This system consists of the wall-current monitors, beam-charge integration circuits, and a PLC-based control system. This system sends the beam abort signals directly to another radiation safety system with hard-wire cables when the amount of the integrated beam charges is beyond the prescribed threshold level. This system has been already used for a daily operation.

### *Timing System*

In the present timing system, about 150 timing delay modules based on VME-bus and CAMAC (TD4V/ TD4) are used for controlling the timing signals distributed to the many different types of local controllers. The timing system upgrade is indispensable since it is very difficult for the current system to realize a fast timing control.

The event generator and receiver (EVG/EVR) system based on VME64x-bus was adopted as a new timing system [9, 10, 11 and 12]. In the new system, one EVG and eleven EVRs are connected via optical fibre. The event information (beam-mode), RF clock (114 MHz), timestamp and data buffer can be quickly transferred from EVG to EVR. In addition, the number of used module for the timing system can be drastically reduced by using the EVG/EVR system. This can gratefully increase the reliability of timing system and beam operation. The operation software based on EPICS system has been already developed. One EVR and nine EVRs are already utilized for the beam operation. In the near future, the overall system test will be carried out for the practical operation after the two rest EVRs will be installed.

## SUMMARY AND FUTURE PLAN

The KEK injector upgrade aiming the fast beam-mode switch is in progress so that the KEKB CIM and PF top-up injection can be simultaneously performed. For this upgrade, the pulsed steering and bend system have been already installed. The almost part of new timing system works for a beam commissioning. In addition, many software development and update are going on. This upgrade will be very effective to increase the beam operation efficiency of KEK Linac. Eventually, the operational availability of each ring will be also greatly enhanced.

## REFERENCES

[1] M. Sato, et al., “KEK injector linac upgrade for fast beam-mode switch (II)”, Journal of Particle Accelerator Society of Japan, Vol.5, No.2 (2008).

[2] M. Sato, et al., “KEK injector linac upgrade for fast beam-mode switch”, Journal of Particle Accelerator Society of Japan, Vol.3, No.2 (2006).

[3] M. Satoh, et al., “THE KEK INJECTOR UPGRADE FOR THE FAST BEAM-MODE SWITCH”, in Proceedings of EPAC2006, Edinburgh, UK, 26-60 June 2006, pp.855-857 (2006).

[4] M. Satoh, et al., “The KEK Linac Upgrade for the Fast Beam Mode Switch”, Proc. of EPAC 2006, Edinburgh, 26-30 June 2006, pp.855-857 (2006).

[5] N. Iida, et al., “NEW BEAM TRANSPORT LINE FROM LINAC TO PHOTON FACTORY IN KEK”, Proc. of EPAC 2006, Edinburgh, 26-30 June 2006, pp.1505-1507 (2006).

[6] Y. Ohnishi, et al., “Design and Performance of Optics for Multi-Energy Injector Linac”, Proc. of LINAC2006, Knoxville, 21-25 August 2006, pp.46-48 (2006).

[7] Y. Ohnishi, "Design and Performance of Optics for Multi-energy Injector Linac", these proceedings.

[8] T. Suwada, E. Kadokura, M. Satoh, and K. Furukawa, "New beam-charge interlock system for radiation safety at the KEKB injector linac", Review of Scientific Instruments, Vol.79, 023302 (2008).

[9] K. Furukawa, T. Suwada, M. Satoh, E. Kadokura, A. Kazakov, “TIMING SYSTEM UPGRADE FOR TOP-UP INJECTION AT KEK LINAC”, Proc. of EPAC 2006, Edinburgh, 26-30 June 2006, pp.3071-3073 (2006).

[10] K. Furukawa, et al., “Development of Timing and Control Systems for Fast Beam Switch at KEK 8 GeV Linac”, these proceedings.

[11] S. Kusano, et al., “DEVELOPMENT OF SOFTWARE FOR EVENT SYSTEM IN KEK LINAC”, Proc. of The 5th Annual Meeting of Particle Accelerator Society of Japan and the 33rd Linear Accelerator Meeting in Japan, Higashihiroshima, 6-8 August 2008.

[12] T. Kudou, et al., “Parameter management in KEK Linac”, ibid.

# PRESENT STATUS OF THE BEPCII LINAC

Pei Guoxi* for BEPCII-Linac Group
Institute of High Energy Physics, IHEP, Beijing, P. O. Box 918, 100049, China

*Abstract*

After the major upgrades in 2005, the BEPCII injector linac has been commissioning and working smoothly for more than two years. A 1.89GeV, 61.5mA positron beam at the linac end has been obtained, and the highest injection rate into the ring of 80mA/min. at 50pps is reached, much higher than the design goal of 50mA/min. The machine is working stably, and the mal function was only about 2% in the past two years, including the system test and the commissioning.

## INTRODUCTION

The BEPCII [1] is a factory type $e^-e^+$ collider with a luminosity of $1\times10^{33}\,cm^{-2}s^{-1}$ in the Tau-Charm energy region (2-5 GeV). On-energy injection scheme with an injection rate of > 50mA/min (almost twenty times of BEPC number) for $e^+$ beam requires the existing BEPC injector linac be upgraded with higher performance [2]. The BEPCII linac major upgrades were completed in 2005, and we got the first positron beam of ~50mA on March 19th. On December 23rd, 2007, an acceptance test group organized by the Chinese Academy of Sciences has fully checked the linac beam performance. The measured beam energy, current, emittance, energy spread, orbit and energy stabilities were well reached their design goals, as shown in Table 1.

Table 1: The Design and Reached Beam Performance

| | | Design | Reached |
|---|---|---|---|
| Beam Energy（GeV） | | 1.89 | 1.89 |
| Beam Current（mA） | $e^+$ | 37 | 66 |
| | $e^-$ | 500 | 550 |
| Emittance（1σ,μm) | $e^+$ | 0.40 | 0.35 (x) 0.27(y) |
| | $e^-$ | 0.10 | 0.097 (x) 0.079 (y) |
| Energy spread（1σ,%） | $e^+$ | 0.50 | 0.37 |
| | $e^-$ | 0.50 | 0.30 |
| Repetition rate (Hz) | | 50 | 50 |
| Beam orbit stability(mm) | | 0.30 | ≤0.15 |
| Beam energy stability (%) | | 0.15 | ≤0.05 |
| $e^+$ injection rate(mA/min.) | | 50 | 61.5 |

## OPERATIONAL STATUS

From October, 2006, up to now, the BEPCII only had two shut down time [3, 4, 5]. One was from early August to early October, 2007, which was for the BEPCII interaction region installation. We also took this chance to replace 5# RF unit's waveguide, which was badly damaged and confined the high power transmission. The other one was from March to May, 2008, for the BESIII installation. General speaking, in almost 20 months, the linac performance was excellent. The mal function including those happened at system test and commissioning time was only about 2%. The positron beam current at the linac end exceeded 60mA, which is good for a much higher injection rate. The injection rate of 61.5mA/min. listed in Table 1 was an average number. Actually, the peak value often reached 80mA/min. at 50pps as mentioned in the abstract, which indicates the injector linac's capability. The switch time for electron and positron modes change was less than 10 seconds. And the highest electron energy has reached 2.7GeV, so in the operation for the BERF early this year the top off injection at 2.5GeV with one RF unit stand-by has been adopted as shown in Fig. 1.

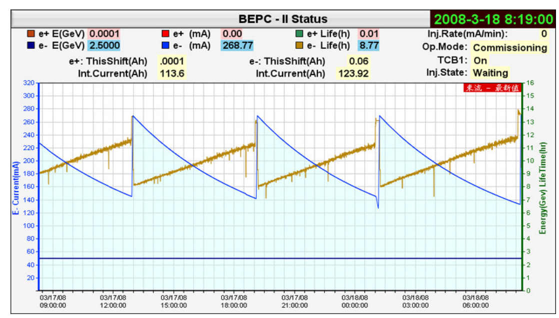


Figure1: The plot for top off injection.

In what follows we will present some details concerning the beam as well as machine stability issues.

### *Beam Orbit Stability*

There are 19 BPMs along the linac. With these BPMs we can easily observe the beam position and the orbit stability. Figure 2 shows a good electron orbit at BPM5 and BPM14, the jitter is less than 0.1mm (1σ).

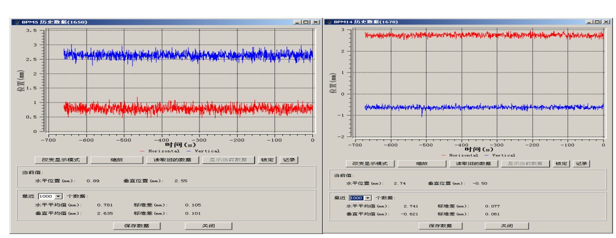

BPM5 BPM14

Figure 2: Beam position stability at BPMs 5 and 14.

### *Beam Energy Stability*

The beam energy stability can be measured by the BPMs located at a large dispersion region in the beam transfer line. Figure 3 shows the plot of beam position varied within ±1.0mm, seen by a BPM in the e- beam transport line, where the dispersion function is 2.0m. It indicated that the beam energy jitter was about ±0.05%, much smaller than the beam energy spread (±0.5%).

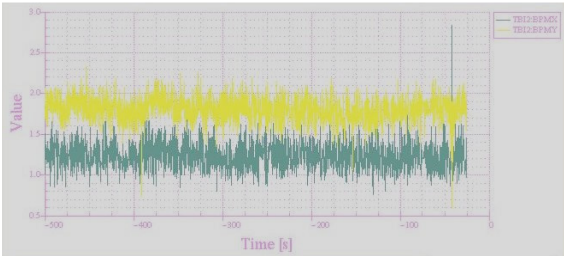


Figure 3: Beam energy stability.

Usually, the energy jitter comes from modulator's beam voltage pulse to pulse jitter, and the voltage stability within ±0.15% is essential. To reach the goal, a lot of measures have been used, including using a De-Qing circuit to stabilize the charging voltage, using a Thyristor voltage regulator with feedback control to stabilize the modulator DC voltage, and using a high precision stabilizer for the klystron filament.

### *The Problems Encountered*

1) The unit 5# RF system arcing was a BEPC times' problem, and because of the tight budget we didn't replace them during the BEPCII linac major upgrades while hoped the problem could be solved through high power processing. After several times processing both in 2006 and 2007, the problem was still there. In July 5~6, 2007 we made an experiment again to identify the arcing place, and found it was at a branch waveguide right downstream the 3dB high power splitter, not in the RF structures as guessed before by analyzing the RF waveforms at different places as shown in Fig. 4.

Figure 4: The schematic of unit $5^{\#}$ RF system.

2) In middle of December, 2006, a big beam orbit oscillation (8~10mm) was observed at TEBPM1, a BPM located at the dispersion region (2m) of the electron transfer line. Because no correlated orbit oscillation was found at other linac BPMs, so we identified it was an energy jitter. After many correlation experiments we found that the arcing of a directional coupler load at the RF drive line caused 6º phase jitter of the 6# and down stream RF units, which agreed well with the observed orbit oscillation at TEBPM1. Figure 5 is the correlation plot between the phase of the 6# RF unit and orbit oscillation at TEBPM1.

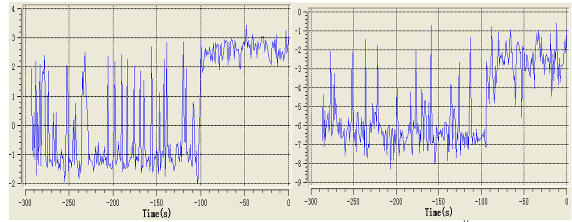


Figure 5: Correlation experiment plots of $6^{\#}$ phase jitter (left) and orbit oscillation at TEBPM1 (right).

3) In February, 2008, the machine worked at 5pps for the BSRF operation, and we found an energy jitter of 0.3~0.5% which came from linac, and electron energy was also lower than before. The phases and amplitudes of all the RF power sources, the timing system as well were checked with no problems. But when investigating beam voltage jitter at the first RF power source we found the RF pulse width was shorten because the modulator high voltage pulse was delayed by 0.7μs. The source was power line loose connection for the thyratron. After fixed the problem, the energy jitter disappeared.

4) Over Current Protection (OCP) sometimes occurred at the BEPCII modulators, which is a common problem for the conventional (resonant charging type) modulator, caused by continues conduction of the thyratron and will shut off main breaker of the modulator. The main causation of continues conduction is that it's difficult for a conventional modulator circuit to ensure enough recovery time for the thyrstron. For reducing thyratron continues conduction, normally we tune the reservoir voltage and operate it at lower gas pressure.

## FUTURE PLAN

The existing BEPCII bunching system consists of an S-band pre-buncher and a buncher, and beam pulse width from the gun is about 1.6ns (bottom width). So the linac is not single bunch operation, while with one main bunch and some satellite bunches. The satellite bunches are troublesome and make operation not clean, and cause the beam instability. The sub-harmonic bunching system can solve all these problems with higher transmission efficiency. Figure 6 shows the compassion between the present bunching system and the system with two SHBs. Except the solid state RF amplifiers are under test, almost all the system constructions are completed, and waiting for installation. Figure 7 shows the SHB cavity tuning at the laboratory, pre-installation and alignment. Figure 8 is the pictures of SHB RF amplifier under test.

Once the SHB system completed, we can hope to adopt the two bunch acceleration mode so as to double the injection rate into the ring. The pulse generator and timing system are ready.

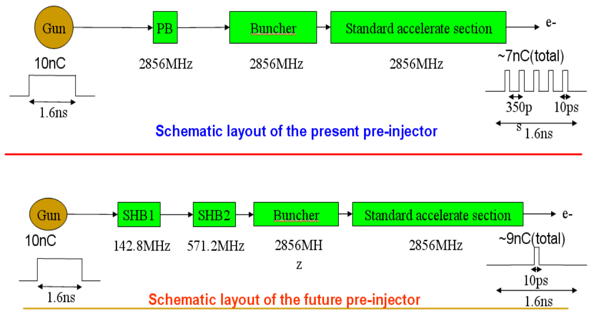


Figure 6: Bunching system compassion.

Figure 7: SHB cavity tuning (left) and system pre-installation (right).

Figure 8: Pictures of RF amplifier under test.

Recently, high energy physicists have interests in the energy region of 2.1~2.3GeV, and strongly request the BEPCII injector linac energy be upgraded to 2.3GeV. The design positron energy for the present linac is 1.89GeV, but can be increased up to 2.1GeV because of design margin. In order to realize 2.3GeV top off injection for positron beam, we need further upgrade the machine, and the simplest way is replacing four 50MW RF power sources with 80MW ones. The linac energy upgrade proposal has been submitted to Chinese Academy of Sciences, and waiting for approval.

## SUMMARY

In last two runs, the BEPCII injector linac worked excellently for both the BSRF operation and the ring commissioning. All the design goals have been reached and passed the acceptance test organized by the Chinese Academy of Sciences. The highest injection rate into the ring even reached 80mA/min. at 50pps, much higher than the design goal of 50mA/min.

The SHB system as one of the second phase upgrades is in progress, but a little bit delayed and missed the chance to be installed during last machine shut-down. Now the system is almost ready, and waiting for next chance installation, hopefully in 2009 summer shut-down.

## ACKNOWLEGEMENT

The work is supported by the BEPCII project headquarters. Thanks to all members of the BEPCII linac group for their great contributions to the successful linac upgrades and operations. Thanks also go to S.Ohsawa, K. Furukawa and T. Suwada of KEK for their helpful discussions on the beam instability issues.

## REFERENCES

[1] C. Zhang et al., BEPCII—the Second Phase Construction of Beijing Electron Positron Collider (BEPC), Proceedings of PAC05, Knoxville, Tennessee, USA, May 16-20, 2005.

[2] G. X. Pei et al., Design Report of the BEPCII Injector Linac, IHEP-BEPCII-SB-03-02, November 2003.

[3] G. X. Pei for linac group, Upgrade Status and Commissioning of BEPCII Linac, Proceedings of LINAC06, Knoxville, Tennessee, USA, August 21-25, 2006.

[4] S. H. Wang et al., BEPCII Linac Beam Commissioning and operation, High Energy Phys. & Nucl. Phys. 31 (11) (2007) 1067.

[5] S. H. Wang, *et al.*, BEPCII Injector Linac Upgrade and Beam Instabilities, Chin. Phys. Lett, Vol.25, No.5(2008)1636.

# STATUS OF AN AUTOMATIC BEAM STEERING FOR THE CLIC TEST FACILITY 3*

E. Adli†, R. Corsini, A. Dabrowski, D. Schulte, S.H. Shaker,
P. Skowronski, F. Tecker, R. Tomas, CERN, Geneva, Switzerland

*Abstract*

An automatic beam steering application for CTF 3 is being designed in order to automatize operation of the machine, as well as providing a test-bed for advanced steering algorithms for CLIC. Beam-based correction including dispersion free steering have been investigated. An approach based on a PLACET on-line model has been tested. This paper gives an overview of the current status and the achieved results of the CTF3 automatic steering.

## INTRODUCTION

The Compact LInear Collider (CLIC) study has shown that advanced beam-based correction will be needed to reach nominal performance of several parts of the collider [1], [2]. The CLIC Test Facility 3 (CTF3) has been constructed at CERN in order to demonstrate feasibility of several key concepts of CLIC [3]. New areas are added to CTF3 for each new phase, making operation more complicated, and it is therefore of significant interest to ease the operation of this machine. The purpose of the work described here is thus two-fold:

- test of correction algorithms devised for CLIC on a real machine
- aid operation of CTF3 by automating beam steering (currently performed by hand)

## CORRECTION APPROACHES

The correction algorithms investigated here are "all-to-all" (A2A) and dispersion-free steering (DFS) [4]. In this paper we use "correction" and "steering" interchangeably. Both algorithms can be implemented using response matrices. Their effect when applied to a defined lattice segment is ideally:

- A2A: steers the beam to get BPM zero-readings, by simply inverting the response matrix of the nominal machine optics
- DFS: minimizes the difference of dispersive trajectories, using responses corresponding to optics with different $\Delta p/p$; weighted against A2A

Matrix inversion for both candidates is performed in the Least-Squares sense, using SVD. Smoothing can be introduced by taking out corrector modes corresponding to small singular values, effectively smoothing out noise effects. Furthermore, defect BPMs and/or correctors can be taken easily into account by zeroing rows and/or columns of the response matrix. A2A and DFS then find the global solution within the defined lattice segment (this is why we say "all-to-all" rather than "1-to-1").

For quick and effective correction computer model generated responses are needed. With model-based steering, one can perform all-to-all steering for a lattice segment in few tens of seconds. In comparison, to obtain machine responses in CTF3 takes from 1/4 h to 1/2 h per optics, per plane, totaling to hours if one wants to do dispersion-free steering. On the other hand, model-based steering require a good correspondence model/machine, and obtaining the needed model accuracy might be challenging.

## TEST-CASE: THE CTF3 LINAC

The CTF3 linac, characterized by operation with full beam-loading [5], was chosen as "test-lattice", because of higher applicability wrt. [1], [2]. We apply correction on a straight part of the linac, with regular lattice structure consisting of 11 girders ("nr. 5" to "nr. 15"), where each girder supports a quadrupole triplet, one corrector coil, and one BPM, as shown in Figure 1. For girders 5,6,7,11,12,13 and 15 there are in addition two accelerating structures, fed by one klystron, located between the corrector and the BPM.

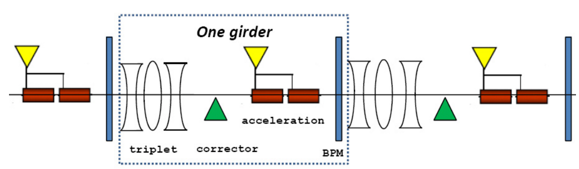


Figure 1: Structure of the CTF3 linac (not to scale).

### *Dispersion and Emittance Growth*

Dispersion measurement and DFS were in this work performed by scaling magnet currents. We therefore consider only dispersion building up from the start of the test-lattice (we do not consider, and cannot mitigate, upstream dispersion). There are no powered dipoles in the test-lattice, so the dispersion comes mainly from parasitic dispersion due to quadrupole offsets (we also get a small contribution from the correctors, dispersion due to incoming beam offset/angle and due to transverse wakes). We note that our 11 cell lattice accomodates little more than a single betatron-oscillation, and we therefore expect dispersion to be small, even for the uncorrected case (no resonant build-up possible). The CTF3 component alignment tolerance is 100 $\mu$m

* Work supported by the Research Council of Norway and the Commission of the European Communities under the 6th Framework Programme 'Structuring the European Research Area', contract number RIDS-011899.
† Erik.Adli@cern.ch, University of Oslo and CERN

rms. PLACET simulations estimate the resulting dispersion growth to 5 mm (rms of 100 seeds). By simulation we estimate emittance growth without correction, assuming a bunch-length of 1.6 mm and an initial normalized emittance of 100 $\mu$m, to be in the order of percent, and an ultimate test of DFS would be to compare emittance growth before and after correction.

## MODEL IDENTIFICATION

A linac model implemented in PLACET was to be used for the model-based correction. It was decided to verify and eventually improve the model before using it for steering. An attempt to use "LOCO-type" global identification [6] was initiated (not applied to the linac before), and a new identification code was written in Octave for this purpose. Improvement of the model with this method turned out to be difficult because of the triplet cells (see below) combined with imprecise response measurement (the same response point was found to vary up to 10% rms, due to beam jitter, different working points, hysteresis etc).

### *Triplet Cells*

The linac focusing is done with quadrupoles in triplets, powered 2+1 or 1+1+1, with a single BPM and corrector per triplet cell (see Figure 1). The similarity of difference orbit when changing either of the outer quadrupoles, as well as almost opposite orbit of the middle quad, leads to near degeneracies which becomes difficult to resolve with imprecise data. Quantitatively we see this by error propagation through the covariance matrix $(\frac{\partial E}{\partial K}^T \frac{\partial E}{\partial K})^{-1}$ [7]; inputting the imprecision of the response points, the standard uncertainty of the parameter estimates is for many of the quadrupoles of the same order as the parameter itself, even when disregarding the first few triplet cells (the least constrained ones). As comparison, with quadrupole currents frozen, the uncertainty of the corrector gains is $\sim 1\%$. The phase-difference between model and machine was shown to be reasonable small by direct SVD analysis, and it was therefore decided to go on with quadrupole parameters frozen. The trustworthiness of individual corrector gain identification with quadrupoles frozen is not clear, and therefore the only parameters fitted before correction was global scaling + the ratio of the calibration factor of the two different corrector types in the test-lattice.

### *Requirement for Model-machine Correspondence*

After identification we still have a certain mismatch between model and machine. We want to estimate, by simulation, the error accepted on the model parameters while still achieving adequate correction. To study this, A2A was applied to a perturbed model using ideal model responses. Each quadrupole strength was randomly scaled by an rms value of $\sigma_{\Delta k}$ %. The maximum resulting BPM readings after 5 iterations of A2A, averaged over 100 machines, are shown in Table 1. For strength rms error of up to 12%, A2A still converges to BPM readings $< 100\mu$m (Perfect BPMs were assumed for these simulations).

Table 1: Correction Convergence with Model Discrepancy

| $\sigma_{\mathbf{\Delta k}}[\%]$ | 4 | 6 | 8 | 10 | 12 | 14 | 16 | 20 |
|---|---|---|---|---|---|---|---|---|
| **y [mm]** | 0 | 0 | 0.02 | 0.04 | 0.1 | 0.3 | 0.7 | 3.6 |

## CORRECTION RESULTS

### *All-to-all*

Using machine responses both planes were corrected to within 0.15 mm rms in two iterations (this illustrates some imprecision in the machine responses and/or machine jitter). Then, correction was performed using responses calculated from the PLACET model. The calculation of the responses takes less than 5 seconds. Both planes did converge, but needed up to to four iterations before reaching the convergence criterion, showing that the model of the linac is not perfect but good enough for steering. Each iteration takes from 10 to 20 seconds, depending on whether a corrector has to switch polarity or not.

Non-functioning correctors or BPMs can be taken into account by first identifying them (e.g manually or from machine responses). A device is disregarded by the algorithm by simply setting the corresponding row or column to zero. One corrector was very unreliable during this work (DVD1420), and was turned off and the corresponding column set to 0. The resulting system is under-actuated (10 correctors and 11 BPMs), and instead of trying to achieve zero BPM readings A2A finds the least-square solution. The result after model-based A2A correction, with one defect corrector in the vertical, is show in Figure 2. The oscillatory pattern in the vertical corresponds to the uncorrectable BPM mode, belonging to the zero singular value which is due to the defect corrector. Dispersion after A2A steering was measured to less than 5 mm (error margin of about 0.5 mm). This is comparable to dispersion measured after manual correction of the machine. We conclude that model-based all-to-all correction seems to work well, is reasonably fast, and robust wrt. corrector or BPM defects.

### *Dispersion Free Steering*

Since A2A correction gives a very small residual dispersion (showing reasonably small misalignments), we do not expect to improve this result, given the beam jitter and limited BPM resolution of 10 $\mu$m. As test-case we instead *simulate* misalignment of 3-6 mm for a few BPMs. A2A will now steer the beam into the simulated centre, creating a position bump in the real trajectory. The red line of Figure 3 shows the position bump (the plot shows *real* BPM readings, as opposed to the readings with *simulated* misalignments that the correction algorithm sees). This bump increases the local dispersion by a factor 3, up to 15 mm, as shown in red in Figure 4.

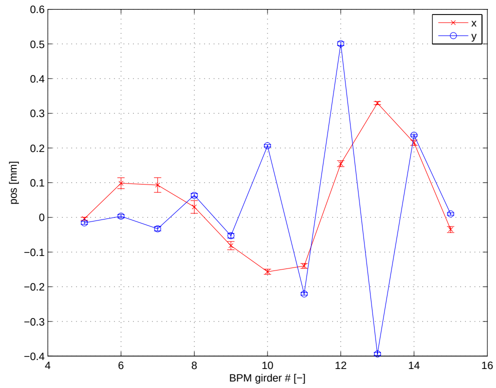


Figure 2: Model-based A2A (BPM readings for both planes).

One of the salient features of dispersion-free steering is that absolute BPM position readings are mostly disregarded, and instead difference readings are used to minimize the difference of dispersive trajectories. We therefore expect a successful DFS to find an orbit with smaller dispersion than A2A, while being mostly oblivious to the simulated BPM misalignment. However, the performance of the DFS depends on the precision with which the difference orbit can be obtained. We had dispersion of $\sim 10$ mm and a dispersion measurement precision of $\sim 0.5$ mm for $\Delta p/p = 10\%$, with present machine conditions. It was therefore not straightforward to find a good solution for DFS, but after substantial trials with different weighting wrt. the zero-reading ($w_1/w_0$=10 used), different SVD-cuts (70% used) and different $\Delta p/p$ (0.2 used), solutions were found that clearly indicates how the dispersion and position bump is reduced, shown in blue in Figure 3 and 4. The BPM readings including the simulated misalignments (seen by our correction algorithms) would show a large bump after the DFS, giving operators indications of large BPM misalignment. Finally, we note that applying DFS without simulated BPM misalignment gave similar performance as with these misalignments.

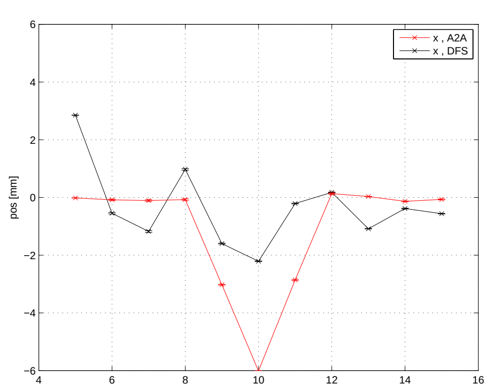


Figure 3: DFS versus A2A (*real* BPM readings after correction).

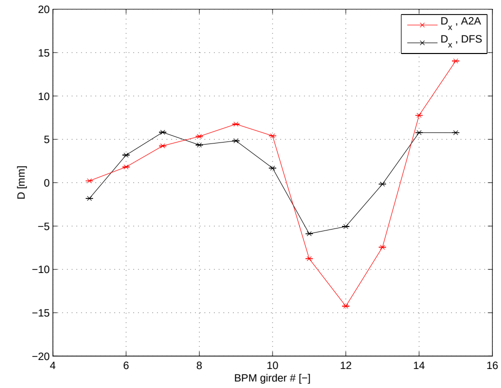


Figure 4: DFS versus A2A (dispersion after correction).

The initial large offset after DFS is due to incoming beam offset/angle (reproduceable in simulations). Machine-based responses were used for the dispersion-free steering. The results show that when dispersion is significant after A2A correction, for instance due to large BPM misalignment, DFS can provide a solution with lower dispersion and at the same time indicating the source of the problem. However, as correction algorithm for CTF3, DFS does not give a clear advantage over A2A.

## CONCLUSIONS

The triplet structure impeded further model improvement. Model-based A2A has been applied successfully in a robust way to the CTF3 linac. DFS performance was superior to A2A in a test-case with artificially large BPM misalignment. However, for nominal linac operation we recommend A2A because of its faster execution.

## ACKNOWLEDGEMENTS

Helpful discussions with A. Latina, K. Fuchsberger, S. Stapnes and V. Ziemann are gratefully acknowledged.

## REFERENCES


[1] D. Schulte, Different Options for Dispersion Free Steering in the CLIC Main Linac, *Proceeding of PAC 2005* (2005)

[2] E. Adli and D. Schulte, Beam-Based Alignment for the CLIC Decelerator, *Proceeding of EPAC 2008* (2008)

[3] I. Wilson for the CLIC Study Team, CLIC Accelerated R&D, CLIC-Note 620 (2005)

[4] T.O. Raubenheimer and R.D. Ruth, A dispersion-free trajectory correction technique for linear colliders, **NIM** A302 (1991) 191-208

[5] R. Corsini et al., First Full Beam Loading Operation with the CTF3 Linac, *Proceeding of EPAC 2004* (2004)

[6] J. Safranek, Experimental Determination of Storage Ring Optics using Orbit Response Measurements, **NIM** A388 (1997) 27-36

[7] W.H. Press et al., Numerical Recipes, 3rd Edition, Cambridge University Press (2007)

# DESIGN OF THE TAIL CLIPPER COLLIMATOR FOR CTF3

R. Chamizo, H. H. Braun, N. Chritin, D. Grenier, J. Hansen, Y. Kadi, L. Massidda, Th. Otto, R. Rocca, R. Zennaro, CERN, Geneva, Switzerland.

*Abstract*

The CERN CLIC Test Facility (CTF3) aims at assessing the feasibility of the future multi-TeV Compact Linear Collider (CLIC). The CTF3 Tail Clipper Collimator (TCC) will serve to adjust the bunch train length of the beam extracted from the combiner ring, in combination with a fast kicker magnet. In addition, the TCC will operate, when required, as an internal beam dump. The challenge of the TCC design is to meet the requirements of both collimation and dump operational modes for a low energy $e^-$ beam (100-300MeV) of 35A peak intensity. The TCC collimator will be installed in January 2009 in the TL2 transfer line of CTF3. This paper describes the final design of the TCC and the main issues related to its integration in the line.

## INTRODUCTION

The CTF3 facility [1] is a demonstrator of the technical feasibility of the key concepts of the novel CLIC RF power source, e.g., generation of high-charge, high-frequency electron bunch trains by beam combination and operation with a fully-loaded drive-beam accelerator. The CTF3 facility includes a 70 m long linac followed by a 42 m delay loop, an 84 m combiner ring (CR) and a CLic EXperimental area (CLEX). The TCC is a combined collimator/dump and will be installed in the transfer line from the CR to the CLEX. It will serve to shorten the pulse length of the accelerated beam for 12 GHz RF generation in the CLEX (collimation mode). A fast kicker magnet [2] will deflect vertically an adjustable fraction of the pulse length. The TCC will absorb the deflected pulse while the rest will be transferred to the CLEX. The TCC will also serve to intercept the full beam (dump mode) for safe installation work in the CLEX. The main beam parameters considered for the design of the TCC are summarized in Table 1.

Table 1: CTF3 Beam Parameters Relevant for the TCC Design

| | | |
|---|---|---|
| Particles | $e^-$ | |
| Beam energy @ TCC | 150 | MeV |
| Repetition rate | 0.8 – 5.0 | Hz |
| Incoming pulse duration | 140 | ns |
| Peak beam pulse current | 35 | A |
| Beam size range (rms, 1σ) | σh=2-5; σv=1 | mm |
| Beam deflection @ TCC | >6 | mm |
| Average beam power | 3.7 | kW |

## THE TCC DESIGN

### *Thermo-Mechanical Considerations*

The dump mode of the TCC represents the most demanding case of operation from the thermo mechanical point of view and it has been considered as the determining condition for the design. The TCC will intercept a 150MeV $e^-$ beam of average power equal to 3.7kW. In the collimation mode, the absorbed power will be less than this.

In order to determine the most appropriate material for the TCC jaw, detailed studies with the Monte-Carlo code FLUKA were performed for assessing the amount of energy deposited on the TCC. Fig. 1 shows the temperature profile (instantaneous) in the jaw after one pulse impact (beam: 150MeV, 5 pulses/s, 3.7kW) for Aluminium, Graphite and Glidcop® jaws.

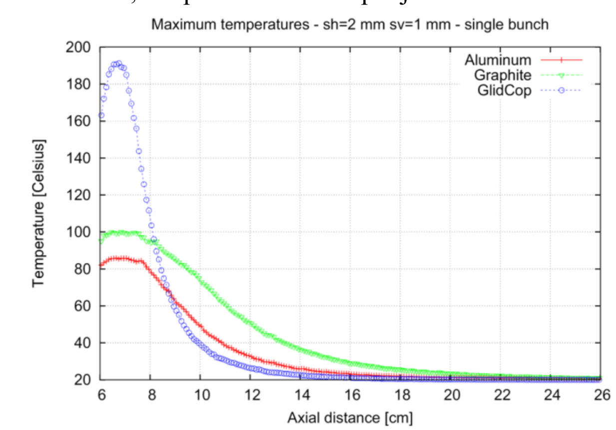


Figure 1: Temperature profile in the TCC jaw after one pulse impact for the studied materials.

Previous thermo-mechanical studies [3] have concluded that, structurally, the most critical case of impact occurs during an impact placed below 1.3mm from the jaw surface. The thermal loads calculated with FLUKA were given as input to an ANSYS® FE model of the TCC jaw, reproducing this particular case. The results obtained are summarized in Table 2.

Table 2: Temperature and Internal Stresses Obtained by ANSYS Simulation for the Studied Materials

| $e^-$ beam (σh=2 - σv=1, mm), 150Mev, 3.7kW, 5 pulses/s | Al | Glidcop | Graphite |
|---|---|---|---|
| Yield Strength (MPa) | 55 | 255 | 30 |
| ΔT (140ns) (ºC) | 58 | 166 | 78 |
| Maximum stress (140ns) (MPa) | 79 | 265 | 2 |

The instantaneous increase of temperature (ΔT) due to the pulse impact originates high internal stresses in the jaw. Graphite was considered as the most convenient material for the jaw since the maximum stress is well below the yield strength value.

### The Active Part - Jaw

The active part of the TCC will be made of a high-density graphite jaw held inside a water-cooled copper vacuum chamber. The high outgassing rate of graphite makes it critical to limit its increase of temperature in order to respect the vacuum requirements of the line ($10^{-8}$ mbar).

A first solution with the graphite block shrink-fitted inside the copper was considered too risky. In fact, in order to limit the temperature increase and avoid dangerous internal stresses in the graphite, the tolerance of the shrink fitting obtained by a coupled thermo-structural simulation in ANSYS was in the range of 10-20μm. A hypothetical sudden thermal contact between graphite and copper could compromise the integrity of the graphite due to the high internal stresses generated by the thermal gradient. An alternative solution was selected, forcing a gap between the graphite and copper and creating a continuous thermal contact by means of a copper foil acting as a spring. Fig. 2 shows the design of the active part of the TCC.

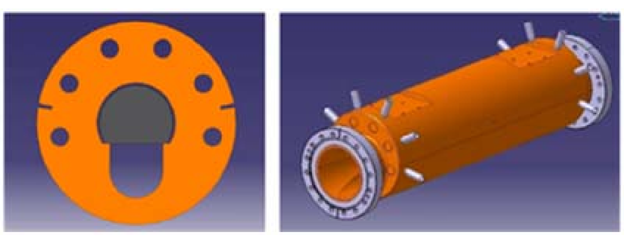

Figure 2: Front view (left) and isometric view (right) of the active part of the TCC.

Even though the thermal contact is not as efficient as a direct contact, the temperature of the graphite will be well under control. The maximum temperature in the graphite is 112°C (in steady state) as shown in Fig. 3.

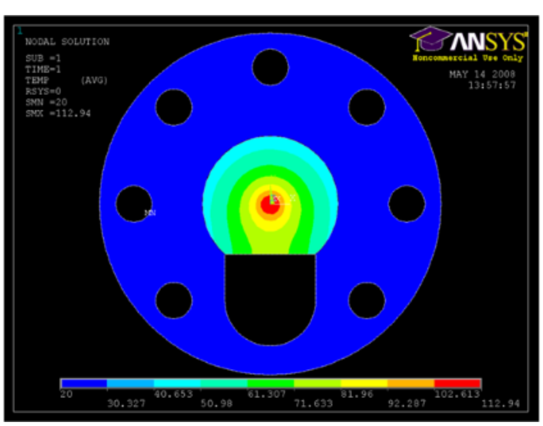


Figure 3: Temperature distribution in TCC active part during dump operation.

### Wakefield Calculation

The possible presence of wake fields induced by the beam passing through the TCC has been computed with GDFIDL [4], which provides the time domain computation of a wake generated by a single bunch. By combining the results with the appropriate delay it is possible to see if a multi-bunch beam could generate a build-up of the wake; see Fig. 4.

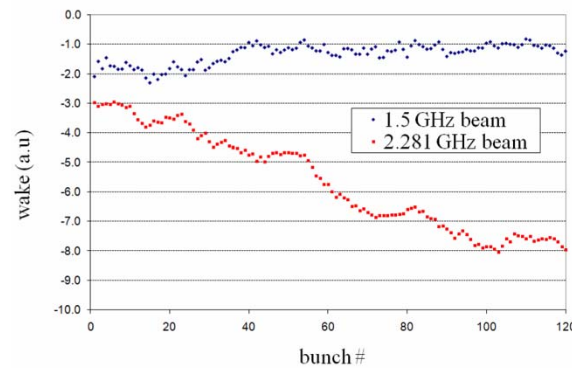


Figure 4: The wake seen by different bunches. The value for bunches with a spacing of 1.5 GHz (real operation) is constant. An artificial bunch frequency of 2.281 GHz served to validate the method; in this case the build-up is evident.

For a frequency of 1.5 GHz or multiples the wake does not build up. A successive FFT of the wake has provided the impedance of the device, and no indication of a resonance at a multiple of 1.5 GHz has been found. Anyhow the presence of a dipole mode at 2993 MHz required a careful study. The impedance of the mode (R=300 Ohm) was computed with HFSS [5]. For a 3 GHz beam of 100 MeV and a current of 35/4 A the normalized transverse kick induced by this mode is only 0.06 mrad.

### Actuator System

In the collimation mode, the jaw must be movable, in the vertical plane (plane of deflection of the beam), between +20 and -10 mm, with respect to the reference beam trajectory. In the dump mode, the jaw must completely block the beam aperture. In addition, the TCC is a fail-safe mechanism and the dump position can be reached by cutting the electrical current.

The TCC is supported by two movable tables that provide the movement range needed for the collimation and dump modes. The upper table enables the movement for the operation in the collimation mode. The movement is provided by a stepper motor connected to three screw jacks. The motor system gives a positioning accuracy and resolution well within the TCC specification (0.3 and 0.1 mm respectively). The displacement is also monitored by one potentiometer that will serve to detect any motor failure. A pneumatic cylinder attached to the lower table lifts the ensemble to the collimation mode position (up). For dump operation, the compressed air inside the cylinder is released and the TCC reaches the dump position (down) by its own weight.

End switches and mechanical stops limit the maximum and minimum ranges of movements for both collimation and dump operation.

## INTEGRATION ISSUES

A detailed FLUKA simulation of the operation in dump mode (150MeV e- beam, 3.7kW, 5 pulses/s) was performed in order to study the effect of the radiation on other components of the beam line.

The TCC will be installed 50cm upstream of a set of quadrupole magnets. Experimental results [6] show an important degradation of the mechanical properties of the insulating resin (Araldite) used in the manufacturing of the quadrupole coils when irradiated above 3MGy. The FLUKA analysis concluded that the absorbed dose in the quadrupole was mainly due to photons. Although the average energy of photons and neutrons are of the same order (9.7MeV for photons and 1.8MeV for neutrons), the fluence of photons at 5Hz is four orders of magnitude higher than that of neutrons ($10^{15}$ $cm^{-2}s^{-1}$ for photons, while for neutrons is $10^{11}$ $cm^{-2}s^{-1}$). The predicted absorbed dose in the quadrupole magnet was equal to 27MGy after one-year operation (1000 hours at 5 Hz), much higher than the absolute limit of 3MGy.

In order to preserve the integrity of the quadrupole, a combined internal-external shielding of the TCC was foreseen. Inside the TCC assembly, a copper block, as shown in Fig. 5, will shield the graphite jaw.

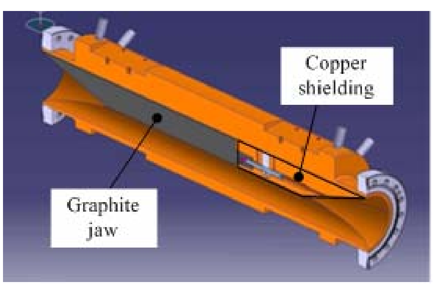


Figure 5: Final bi-material jaw of the TCC.

Fig. 6 shows the final layout of the TCC in the TL2 line of the CTF3 facility.

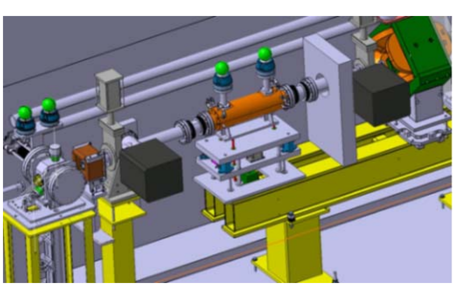

Figure 6: Layout of the TCC in the CTF3 facility.

The external shielding will consist of a 10cm lead plate placed between the TCC and the quadrupole magnet. The predicted absorbed dose in the quadupole in this configuration is equal to 0.1MGy, much lower than the mentioned threshold (Fig. 7).

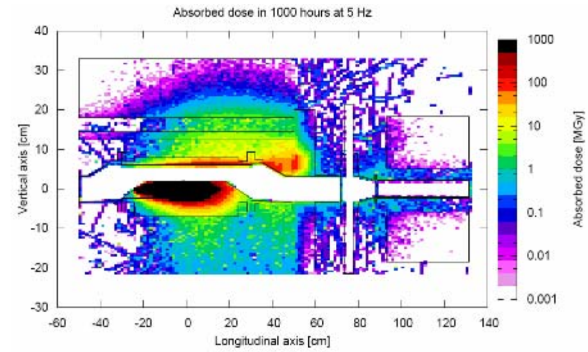


Figure 7: Absorbed dose in the TCC and downstream quadrupole after internal and external shielding.

In addition, the analysis of the ambient dose equivalent rates [7] in the accessible areas surrounding the facility led to the design of an iron local shielding that will fully enclose the TCC in order to respect the radiation protection regulations.

## CONCLUSIONS

The TCC will be installed in the CTF3 facility by January 2009 and it will operate in both collimation and dump modes with a 150MeV e- beam of 35A peak intensity. The design of the active part responds to the thermo-structural constraints for both operation modes. The design intends to minimize any degradation of the vacuum quality in the line due to the outgassing of the graphite during the beam impacts. Additional aspects concerning the integration of the TCC in the facility and the impact on the surrounding equipments during its operation have been treated. The adopted multi-shielding solution guarantees the integrity of the equipments and respects the radiation protection regulations in the adjacent accessible areas.

## ACKNOWLEDGEMENT

The authors would like to thank L. Bruno, A. Ferrari, C. Kharoua and K. Samec for their helpful discussions.

## REFERENCES

[1] G. Geschonke, A. Ghigo, “CTF3 Design Report”, CERN/PS 2002-008 (RF).
[2] M.J. Barnes, T. Fowler, G. Ravida, A. Ueda, “Design of the Modulator for the CTF3 Tail Clipper Kicker”, CERN-AB-2007-055.
[3] L. Massida, F. Mura “Thermal and Mechanical Analysis of the LHC Injection Beam Stopper (TDI)”, Tech. Rep. CRS4-TECH-REP-03/, CRS4, 2003.
[4] www.gdfidl.de/
[5] www.ansoft.com/products/hf/hfss/
[6] H. Schönbacher, M. Tavlet, “Absorbed doses and radiation damage during the 11 years of LEP operation”, CERN-TIS-2002-010-DI-PP.
[7] Th. Otto, “Radiation Protection Shielding of the CTF3 Tail Clipper”, CERN-SC-2008-051-RP-TN.

# THE 150 MeV PULSE ELECTRON LINAC WITH 1 mA AVERAGE CURRENT*

M.I. Ayzatsky, A.N. Dovbnya, V.N. Boriskin, I.V. Khodak, S.G. Kononenko, V.A. Kushnir, V.V. Mytrochenko, S.A. Perezhogin, Yu.D. Tur. Kharkov, NSC/KIPT, Kharkov, 61108, Ukraine

*Abstract*

The project of the accelerator driven subcritical assembly facility is under development in the National Science Center "Kharkov Institute of Physics and Technology". The important component of the facility is an electron linac with the particles energy of 100…200 MeV and average beam current of 1 mA. In this paper we focus on the S-band electron linac design. The accelerator scheme includes the injector based on evanescence waves, RF chopper, five accelerating structures and energy compression system. The calculation results of accelerating structure performances and linac systems are considered in the paper.

## INTRODUCTION

The developing facility consists of the linac, the system of the beam transport to the target complex, the neutron-producing target and the subcritical assembly of the fuel elements.

Using of the linac as the subcritical assembly driver makes a number of demands. The electron energy at the linac exit must be 100-200 MeV. On the one hand, it provides rather high yield of the neutrons, and on the other hand - the volume of the neutron target will be large enough for the energy density decrease and the target cooling conditions improve. The existing high-frequency linac power supplies and the injector systems allow obtaining the average current at such linac exit in the necessary electron energy range near 1 mA. Considerable average beam power (about 100 kW) obviously demands minimizing the high-energy particles loss during their acceleration and transport.

## THE FACILITY POSITION AND STRUCTURE

The linac will be placed in the building of the linac LU-2000 in NSC KIPT. Such placing of the complex doesn't need the new fundamental construction, allows using the existing engineer infrastructure after its major reconstruction. The existing power system allows power supplying of all systems of the linac. New equipment placing is possible after the demounting of the existing equipment. The accelerating sections of the developing linac will be placed after the 36$^{th}$ section of the linac LU-2000. The layout of the linac main parts is presented in Fig. 1.

The accelerator itself consists of the electron source, injector (I), five S-band accelerating sections (1s-5s) and the system of energy compression (SEC). The system of energy compression includes the debuncher (D) and the compensation accelerating section (CS). At the accelerator exit there are placed the magnetic electron energy analyzer (M1) and the dipole magnet (M2), providing the electron beam injection into the transport system to the target complex. The main elements for the beam focusing are the short solenoid on the first section (S) and the doublets of the quadruple lenses, placed on each section. The beam current transformers and the beam position monitors will be placed after the injector and each section exit.

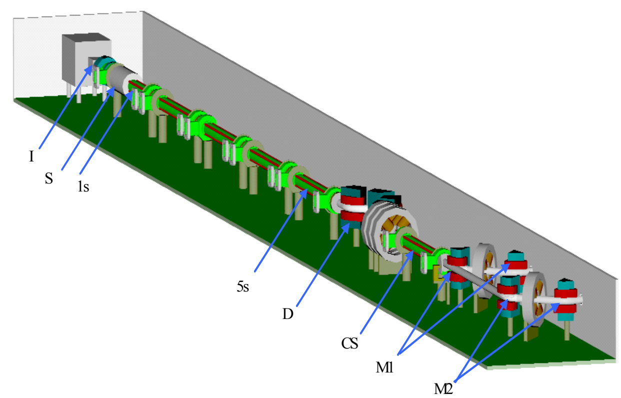


Figure 1: Placing of the accelerator main elements.

The accelerator RF power supply system is planned to be created at the base of six klystrons SLAC 5045 (produced by SLAC, USA). Proceeding from the average beam power 100 kW, the current pulse repetition rate and the pulse duration are chosen 300 pps and 3.0 µs respectively. In this context the standard mode of the klystron SLAC 5045 will have to be changed (see Table 1).

Table 1: Klystron parameters

| Parameter | Standard mode | Required mode |
|---|---|---|
| RF frequency, MHz | 2856 | 2856 |
| Pulse repetition rate, pps | ≤ 180 | 300 |
| Max. pulse RF power, MW | 67 | 29.9 |
| RF pulse duration, µs | 3.5 | 3.2 |
| Average RF power, kW | 37 | 31.2 |

* Work supported by STCU project P233

## INJECTOR

One of the main conditions of obtaining the minimal energy electron spread at the accelerator exit is the demand of the length and form of the electron bunch, formed in the initial part of the facility – in the injector. We suppose to use the bunching system on the evanescent oscillations [1]. The prototype injector for the developing linac is the accelerator electron injector for the storage ring H-100M [2]. According to the calculations and the preliminary testing of the injector prototype such system allows to form effectively the electron bunches at the pulse current up to 1.5 A and at energy of particles of about 1 MeV.

The code POISSON/SUPERFISH [3] has been applied for the calculations of the injector resonance and magnet system characteristics. The particle dynamics in the bunching system has been simulated using PARMELA code [4]. The electron injector (see Fig.2) with operating frequency 2856 MHz provides the minimal bunch phase size at the minimal energy spread and the electron current up to 1.5 A at the injector exit.

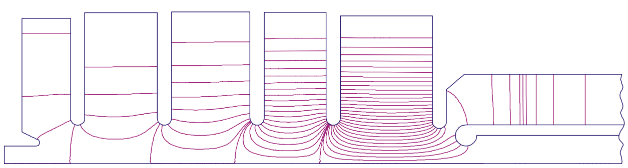

Figure 2: The injector resonance system geometry and the longitudinal RF electric field distribution.

The simulation has been held taking into account space charge forces for the electron beam with the initial energy 25 keV and the current 1.2 A. To decrease the radial beam size the injector is equipped with a solenoid. At the pulse current 1.07 A at the bunching system exit the beam has the following parameters: normalized emittance ($1\sigma$), $\varepsilon_{rms\ x,y}$=21 mm·mrad; phase spectrum width $\Delta\varphi$=9.8° (for 70% of the particles); energy spread $\Delta W/W$=6.3%, (for 70% of the particles); energy at the spectrum maximum W=1.2 MeV; beam size d=1.55 mm. The phase-energy electron beam distribution at the injector exit is shown in Fig. 3.

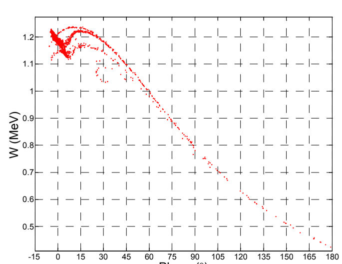


Figure 3: The phase-energy particle distribution at the injector exit.

However, in the interval between the bunching system and the accelerating section the bunch phase duration is increased. At that the phase distribution of the particles has the extended "tail". As the numerical simulation has shown, those periphery particles form the energy halo. That's why it is important in this case to apply the additional methods for the phase compression or phase selection. After the analysis we have considered the possibility to use the chopper system [5, 6]. This system is composed of a RF cavity, a drift tube and a collimator. The most simple is to use the cylindrical cavity with the $TM_{110}$ mode. We have carried out the numerical simulation of the particle motion in the injector system with such chopper. It is shown (see Fig. 4) that using of that device allows to decrease substantially extension of the "tail".

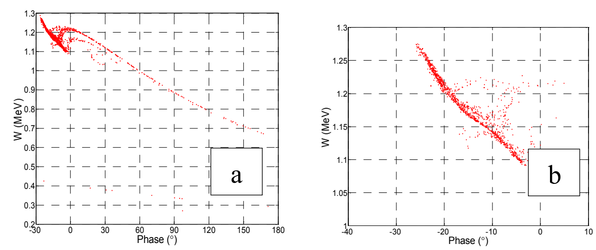


Figure 4: The phase-energy particles spread at the input of the first accelerating section without chopper (a) and with chopper (b).

In general, the main disadvantage of this method is the increase of the transverse beam emittance. However, if during the bunch forming the particles motion in different phase planes is connected, the inverse picture can be observed – in the chopper the particles with bad radial characteristics are also chopped off. Thus, in our case, the particle losses are 29.4% of the particles at the injector exit and the decrease of rms emittance of the chopped beam in a beam scanning plane up to 12 mm·mrad is observed.

## ACCELERATING SECTIONS

The accelerating system of the accelerator includes five accelerating sections, where the electron beam with the pulse current up to 1 A, pulse duration 3 µs and the repetition rate 300 pps should gain energy about 150 MeV. When choosing the section parameters the simulation of the particle dynamics in the injector and the sections in the steady state mode has been carried out with the PARMELA program. On the base of simulation the homogenous travelling wave accelerating structure with the $\pi/2$ phase advance per cell has been chosen. The length of each of five accelerating sections and the filling time are 4.15 m and 0.368 µs respectively, shunt impedance is 52.8 MOhm/m, attenuation is 0.088 1/m, Q-factor is 11200. For suppression of BBU the radial slots in the accelerating wave-guide irises will be used. The length of the slots and their orientation will vary along the accelerating section. At the supplying RF power for each section of 28.8 MW the electrons energy at the fifth section exit is 154 MeV at the pulse current 0.75 A. The other parameters are shown in Table 2.

To decrease the energy spread there has been settled the system of energy compression at the fifth section exit. It consists of the «magnetic chicane» type debuncher and the additional accelerating section. For the correct operating of such device at the accelerator exit

Table 2: Beam parameters at the fifth section exit

| | d, mm | $\varepsilon_n$ mm·mrad | $\Delta\varphi$° | $\Delta W/W$ % |
|---|---|---|---|---|
| 70% of particles | 1.4 | 15 | 14 | 4,9 |
| 99% of particles | 3.3 | 170 | 24 | 8 |

there has been formed a special phase-energy electron distribution. The preliminary calculation of the system of energy compression (SEC) has been carried out with the MADX program [7]. The final calculation of SEC and the accelerator as a whole has been carried out with the PARMELA program. The simulation results are presented in Fig. 5.

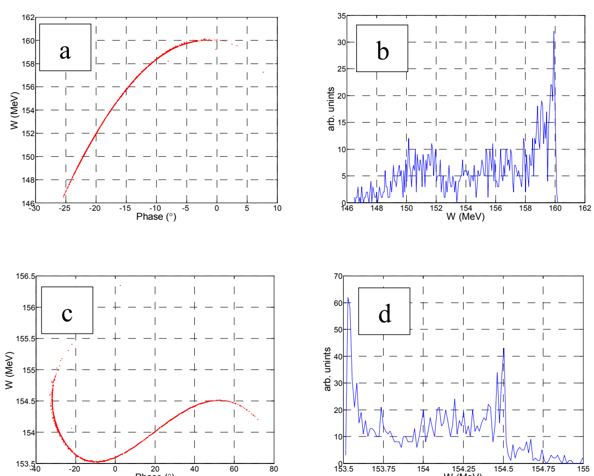


Figure 5: Phase-energy distribution and the energy spectrum at the fifth section exit (a, b) and the SEC exit (c, d).

It is seen, that SEC allows to decrease the energy spread of 99% of the particles from 8 % to 0,7% . At that the normalized emittance of the beam doesn't exceed 180 mm·mrad, and the beam loss are absent in that system. At the same time it should be noted that the work of that system taking into account the beam loading of the compensating accelerating section needs further study.

## BEAM MONOCHROMATIZATION IN THE TRANSIENT MODE

The beam energy spread as a whole is determined by both the acceleration steady state mode (considered above) and the beam loading effect. Decrease of influence of transient has been achieved by the selection of the optimal current pulse delay relative to RF pulse. As the results of the calculations we have obtained the optimal values of the pulse delay time for each of five sections: 0.399 µs, 0.323 µs, 0.23 µs, 0.139 µs, 0.045 µs. From the calculation results (see Fig.6) it follows that the particles accelerated during the transient (about 15% of all particles) have the energy spread at the linac exit less than 1%.

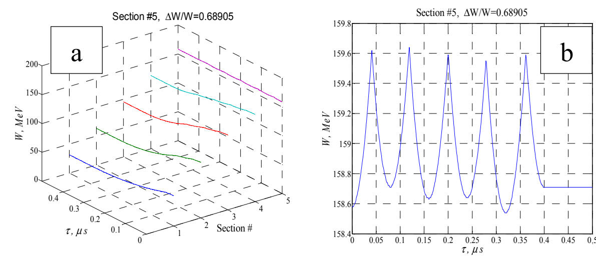


Figure 6: Electron energy during the transient at each section's exit (a) and at the accelerator exit (b).

## SUMMARY

Researches on design of the high power pulse linac for the neutron source on the base of a subcritical assembly is under way in NSC KIPT. The simulation results show that the chosen accelerator scheme allows obtaining the beam with the required for the facility work parameters: W=154 MeV, $\Delta W/W<1\%$, $P_{cp}$ =104 kW.

## REFERENCES


[1] M.I. Ayzatsky, E.Z. Biller, V.A. Kushnir et. al., "Bunching systems of electrons on base evanescent waves", PAC'03, Portland, 2003, p. 1605-1607.

[2] M.I. Ayzatsky, K.Yu. Kramarenko, I.V. Khodak, et. al., "Performance of Compact Electron Injector on Evanescent Oscillations", EPAC`08, Genoa, July 2008, MOPP100, p. 790 (2008); http: //www.JACoW .org.

[3] J.H. Billen, L.M. Young, "POISSON/SUPERFISH on PC compatibles", PAC'93, Washington, 1993, p.790–792.

[4] L.M. Young PARMELA . – Los Alamos: 1996. – 93 c. (preprint / Los Alamos National Laboratory, LA-UR-96-1835).

[5] A.I. Zykov, G.D. Kramskoi, E.K. Ostrovsky et al., The forming of short electron bunches in an injector linac// Pribory I tekhnika experimenta. –1968. -№4. – P.22-25 (in Russian).

[6] Y. L. Wang, T. Emoto, M. Nomura et al A Novel Chopper System with Very Little Emittance Growth. Proceedings of the EPAC 1994. p. 1373; http://www.JACoW.org.

[7] W. Herr, F. Schmidt, M. "A MAD-X Primer", CERN-AB-2004-027-ABP.

# INJECTOR OF INTENSE ELECTRON BEAM

M. Ayzatskiy, V. Mytrochenko NSC/KIPT, Kharkov, 61108, Ukraine


## ABSTRACT

The results of beam dynamic simulation in a S-band injector that can be used for creation of the powerful electron linac are presented in the report. The injector consists of a diode electron gun with beam current of up to 2 A at energy of electrons of 25 keV, the klystron type prebuncher and the three cavity buncher. In the buncher, due to the special choice of eigen frequencies of resonators, maximal amplitude of the field on the axis of resonators exponentially increases from the first (downstream of the beam) resonator to the last resonator. It allows to realize an effective bunching the intensive electron beam and accelerating it to relativistic velocities. For achievement a low transversal beam emittance the injector is placed into the external magnetic field. The injector provides more than 1 A of beam current with particle energies of about 1 MeV. Attention is paid to research of transients and stability of injector work.


## INTRODUCTION

Often it is necessary to provide ampere range beam at an exit of the pulsed electron S-band linacs with high beam power because a duty factor of pulsed klystron amplifiers is about 0.1%. Use of relatively low voltage electron guns (several tens of kilovolts) in a linac injector facilitates obtaining high reliability of the linac at compact linac dimensions. Bunching system based on evanescent waves (see for example [1]) is very suitable to generate electron bunches from continuous beam emitted from a cathode of such low voltage gun as well as to accelerate particles to relativistic velocities. The above mentioned bunching system comprised of five cells has exponential rise of on-axis field from the entrance of the electron beam into the buncher to the it exit. This rise is provided by correspondent choice of cell dimensions. To provide flexibility of the system at bunching and accelerating of the ampere range electron beam it was decided to change the first two cells of the buncher with a klystron type prebuncher and drift space. To prevent degradation of transversal beam emittance the prebuncher and buncher are placed into solenoidal magnetic field. This paper is devoted to brief description of simulation algorithms of beam dynamics in a system comprised of the prebuncher and the three cell buncher as well as to review of simulation results.

## SIMULATION ALGORITHMS

The POISSON/SUPERFISH [2] group of codes was used to calculate characteristics of resonance and magnetic systems of the injector. Simulation of electron motion in the injector was performed using the PARMELA [3] code. Beam parameters of the ampere range diode gun [4] was calculated with EGUN [4] code. Study of unsteady self consistent beam dynamics in the injector were performed both with technique [6] and with developed by us program COUPLRES. Technique [6] solves self-consistent equations of field excitation in axially symmetrical cavities both by an electron beam and by an external RF generator. The PARMELA code is used in this technique to simulate particle motion in evaluated field to get needed data at each temporal step of the equation solution. This technique takes into account only one mode of a cavity field.

COUPLRES (COUPLing RESonators) allows to describe unsteady processes arising at interaction of electron beam with electromagnetic systems that can be represented as a chain of coupled cavities. This code is elaborated on a base of mathematical model that is development of the coupled cavity model by correct taking into account self-consistent beam dynamics in fields excited both by external sources and by particles itself. At the moment the model takes into account only fields that are symmetrical relatively the main direction of beam propagation. The base of the model is decomposition of a considered electromagnetic system into closed volumes and representation of fields inside of the volumes as an expansion into a series of eigen functions (solenoidal and potential) of closed cavities. Particles are injected into a simulated system at certain moments of time. A set of equations to be analyzed consists of particle motion equations and equations for expansion amplitudes (differential equations for basic oscillations and algebraic ones for non-resonant modes).

A developed variant of the code is applicable to describe systems that can be decomposed into cylindrical volumes. In this case there are analytical expressions for the eigen functions. The Runge-Kutta method is used to solve both equations of motion and equations for amplitudes of basic oscillations. At solution of the last equations values of current and charge integrals are kept constant over RF period of the fundamental frequency. Quasi-coulomb fields are represented as expansion into series of solenoidal and potential functions and are evaluated at frequencies $\omega \approx 0$ and $\omega \approx \omega_0$, where $\omega_0$ is frequency of a RF source.

The merit of the code is a possibility to take into account influence of all eigen modes at simulation of time beam dynamics. This feature allows to make an analysis of injector operation stability at bunching and accelerating of intense electron beams.

## SIMULATION RESULTS

Simulations were carried out to attain two aims. On the one hand in was necessary to find configurations both the resonance and magnetic system of the injector that provide effective bunching of the ampere range electron beam at minimal degradation of the transversal emittance. On the other hand stability of the each considered configurations against excitation of parasitic oscillation in the buncher was checked. As a result of preliminary researches we chose injector structure that provides on-axis field distributions shoved in Fig. 1 and Fig. 2.

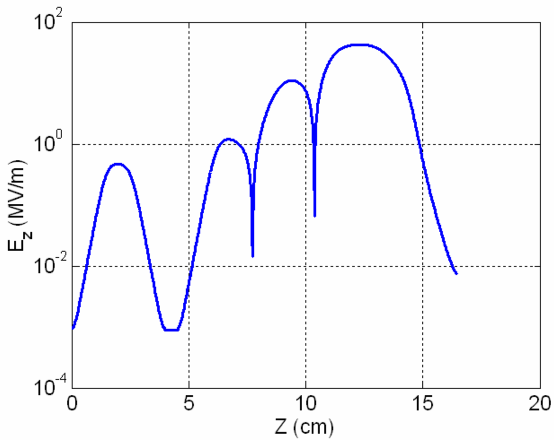


Figure 1: On-axis distribution of the electromagnetic field.

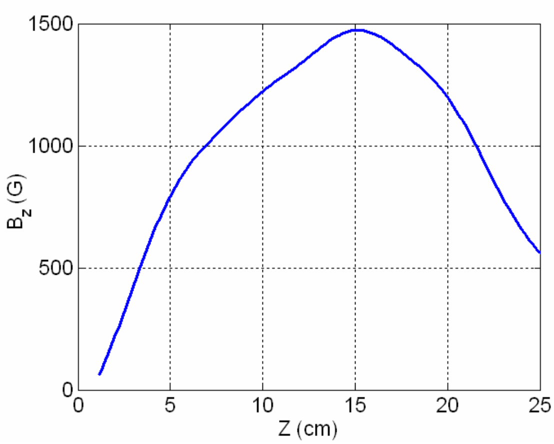


Figure 2: On-axis distribution of the static magnetic field.

Injector parameters and data obtained in self-consistent beam dynamic simulation with technique [6] are listed in Table 1. Beam parameters are given taking into account transients. The COUPLEREZ code gives similar results. It can be seen from Table 1 that the injector provides enough short bunch length at formation of an ampere range beam. High energy of particles allows injection directly into acceleration section with phase velocity that is equal to velocity of the light. We are going to optimize field distribution in the buncher with technique [7] to get shorter bunch in near future.

Some simulated signal waveforms that characterize injector operation are shown in Fig. 3 through Fig. 5.

Analysis of simulation results has shown that some part of electrons uncaptured into process of acceleration in the buncher goes backward through the prebuncher cavity. Current of such electrons can reach 0.15 A at average energy of 0.1 MeV. Interaction of these electrons with prebuncher field sets a feedback loop by beam. For the described injector configuration the feedback does not notably change beam parameters at the exit of the injector, but transient times in cavities are high compare with the case when we do not take back motion into account.

Table 1: Injector Specification

| | |
|---|---|
| Gun current, A | 1.5 |
| Output beam current, A | 1.34 |
| Bunch repetition rate, MHz | 2797.15 |
| RF power supply of prebuncher, W | 570 |
| RF power supply of the buncher, MW | 1.8 |
| RF pulse length, μs | 2.9 |
| Current pulse length, μs | 2.4 |
| Normalized root mean square (RMS) emittance $\varepsilon_{rms\ x,y}$, π·mm·mrad, (1 σ) | 12 |
| RMS beam size ($4\sigma_{x,y}$), mm | 2.8 |
| Bunch phase length (for 70% of particles), ° | 18 |
| Energy spread width (for 70% particles), % | 5.4 |
| Energy of particles, keV | 948 |

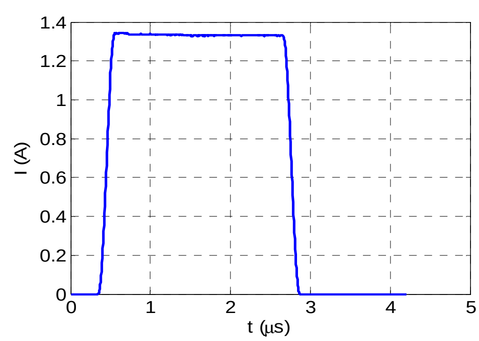


Figure 3: Output current pulse.

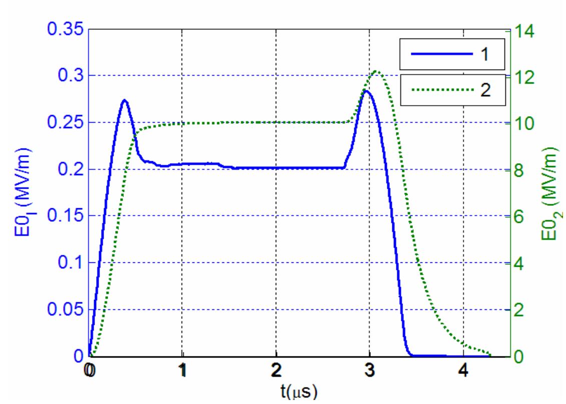


Figure 4: Waveforms of average on-axis field in the prebuncher (1) and in the buncher (2).

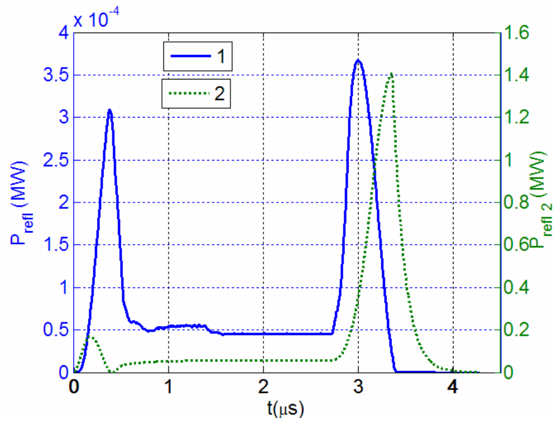


Figure 5: Waveforms of reflected waves from the prebuncher (1) and the buncher (2).

Increase of transient time due to the beam induced feedback can be seen in Fig. 4 and Fig. 5 at temporal interval from 0.5 to 1.5 μs. If we do not include backward propagated electron into consideration, above mentioned features will disappear.

At interaction of intense electron beam with multicavity system there is possibility of field excitation on adjacent modes that can cause unstable operation of the injector. The COUPLRES code was used to analyze stability of considered injector operation at bunching and accelerating electron beam with current up to 2.5 A. It is necessary to note that on-axis field distribution for nearest adjacent modes in the buncher has inverse dependence compare with shown in Fig. 1. That is field amplitude in the first cell has about the maximal level while that in the last cell has very small level. Therefore excitation of the adjacent modes will influence mostly field amplitude in the first cell of the buncher. Fig. 6 shows time dependence of a value that is proportional to field amplitude of $\square_{010}$ oscillation in the first cell of the buncher at no beam load and at acceleration of 1.5 A beam (current pulse length was 4.5 μs in this case). It can be seen decreasing field amplitude at beam injection but after transient is over the steady state regime is established. Therefore a process of bunching and acceleration is stable at such beam current.

## SUMMARY

As a result of carried out simulation we determined configurations of both the resonance and magnetic system of the injector that provide effective bunching of the ampere range electron beam at minimal degradation of the transversal emittance. The injector with the chosen configuration is stable against excitation of parasitic oscillation in the buncher at input currents up to 1.5 A. It was shown that backward propagated electrons interact with the prebuncher and increase transient time.

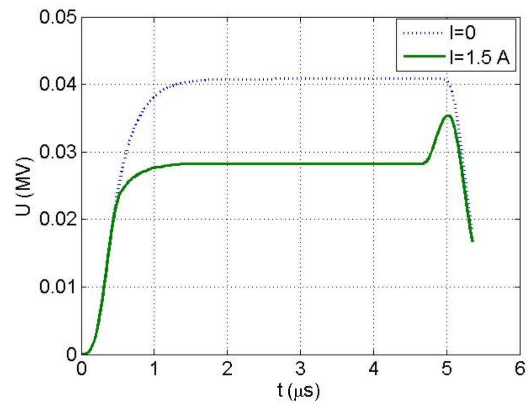


Figure 6: Voltage over the gap of the first buncher cell.

The injector can provide more than 1 A of output current at particle energies about 1 MeV and normalized RMS (1 σ) transverse emittance of 12 π·mm·mrad.

## REFERENCES

[1] M.I. Ayzatsky, E.Z. Biller, V.A. Kushnir et. al., Bunching systems of electrons on base evanescent waves, PAC'03, Portland, 2003, p 1605-1607.

[2] J.H. Billen and L.M. Young, POISSON/SUPERFISH on PC compatibles, PAC'93, Washington, 1993, p.790–792.

[3] L.M. Young, PARMELA, Preprint LANL LA-UR-96-1835, Los Alamos, USA, 1996, 93p.

[4] W.B. Herrmannsfeldt. EGUN: Electron Optics Program, Preprint, Stanford Linear Accelerator Center SLAC-PUB-6729, Stanford, USA, 1994.

[5] M.I. Ayzatsky, V.A. Kushnir, V.V. Mytrochenko et al., Problems of atomic science and technology, Ser. Nuclear Physics Investigation, 2, 2006, p. 94–96.

[6] V.V. Mytrochenko, A. Opanasenko, □□□ □558□ 2006, p. 235 – 239.

[7] S.A. Perezhogin, N.I. Ayzatsky, K.Yu. Kramarenko et. al., The optimization of the electron injector resonant system based on the evanescent oscillations, PAC'05, Knoxville, 2005, p. 3170.

# COMMISSIONING THE DARHT-II ACCELERATOR DOWNSTREAM TRANSPORT AND TARGET*

Martin Schulze, SAIC, Los Alamos, NM 87544, USA
E. O. Abeyta,, R. Archuleta, J. Barazza, D. Dalmas, C. Ekdahl, W. Gregory, J. Harrison, J. Johnson, E. Jacquez, P. Marroquin, B. Trent McCuistian, R. Mitchell, N. Montoya, S. Nath, K. Nielson, R. Ortiz, L. Rowton, R. Scarpetti, G. Seitz, M. Schauer,
Los Alamos National Laboratory, Los Alamos, NM 87545, USA
R. Anaya, G Caporaso, F. Chambers, Y.J. Chen, S. Falabella, G. Guethlein, B. Raymond, R. Richardson, J. Watson, J. Weir
Lawrence Livermore National Laboratory, Livermore, CA 94550
H. Bender, W. Broste, C. Carlson, D. Frayer, D. Johnson, and C. Y. Tom,
N.S. Tech, Los Alamos, NM 87544, USA
T. P. Hughes, C. Thoma,
Voss Scientific, Albuquerque, NM 87108, USA

*Abstract*

The DARHT-II accelerator [1] produces a 2-kA, 17-MeV beam in a 1600-ns pulse. After exiting the accelerator, the pulse is sliced into four short pulses by a kicker and quadrupole septum and then transported for several meters to a tantalum target for conversion to x-rays for radiography. We describe the commissioning of the kicker, septum, transport, and multi-pulse converter target. The results of beam measurements made during the commissioning of the downstream transport are described.

## INTRODUCTION

The DARHT–II accelerator beam parameters are 17-MeV and 2.0 kA with a flattop of 1.6 microseconds. The DARHT–II downstream transport was commissioned at reduced energy and current in early 2007 [2]. The beam parameters were 8-MeV and 1.1 kA with a flattop of 1.6 microseconds.

The downstream transport system for the DARHT-II accelerator is designed to extract four short pulses (20-100 nsec) from the 1.6 microsecond beam and deliver these pulses to an x-ray production target for radiography. Figure 1 provides a schematic illustration of the downstream transport beamline.

The high level requirements imposed on the downstream transport are outlined below:

- Deliver four pulses over 1.5-1.6 μsec
- Spot sizes less than 2.3 mm 50% MTF
- Dose format exceeding 100 R, 100 R 100 R and 300 R in each successive pulse

Each of these requirements were met and reproduced over multiple shots. These results will be described. High quality radiographic images with the DARHT-II accelerator impose additional requirements on the beam quality, in particular, the beam motion over flattop. This issue and the methods used to minimize the that have been used to address them are discussed.

*Work supported by USDOE under contract DE-AC52-06NA25396

## LAYOUT AND OPTICS

The beam from the accelerator is focused using the first and third solenoids to produce a small waist at the entrance to the quad septum. This effectively decouples the accelerator from the remainder of the downstream transport. The beam enters the kicker and is either directed downward to the beam dump with a DC bias dipole magnet or the fast kicker is energized to direct the beam straight ahead. The bias dipole deflects the beam by 1-1.5 degrees. This deflection is magnified with a large aperture septum quadrupole tuned to defocus the beam in the vertical plane resulting in a net deflection of about 15 degrees. This also results in a large beam size on the dump which reduces the power density to acceptable levels. A dipole magnet further deflects the beam into the dump. The kicked beam enters the septum quadrupole on axis and the nominally round beam profile becomes elliptical. The function of the small Collins quadrupoles following the septum quadrupole is to transform this elliptical beam back to a round profile. The purpose of the remaining solenoid is to transport the beam to the final focus solenoid which delivers a tightly focused beam to the target.

There are four semi-independent regions in the downstream transport. The first region is from the accelerator to the septum quadrupole and the settings of the first and third solenoids. The second region is the transport to the septum dump. This defines the required settings of the bias dipole, septum quad and the septum dipole. The third region includes the four Collins quadrupoles that are used to return the beam back to round. The forth region consists of a transport solenoid and a final focus solenoid to produce a small beam size on target. The last transport solenoid was not used.

Beam position and current measuring diagnostics are located throughout the downstream transport. Beam profile imaging stations were located at the accelerator exit, between the 1$^{st}$ and 2$^{nd}$ Collins quadrupole magnets, and after the 4$^{th}$ solenoid.

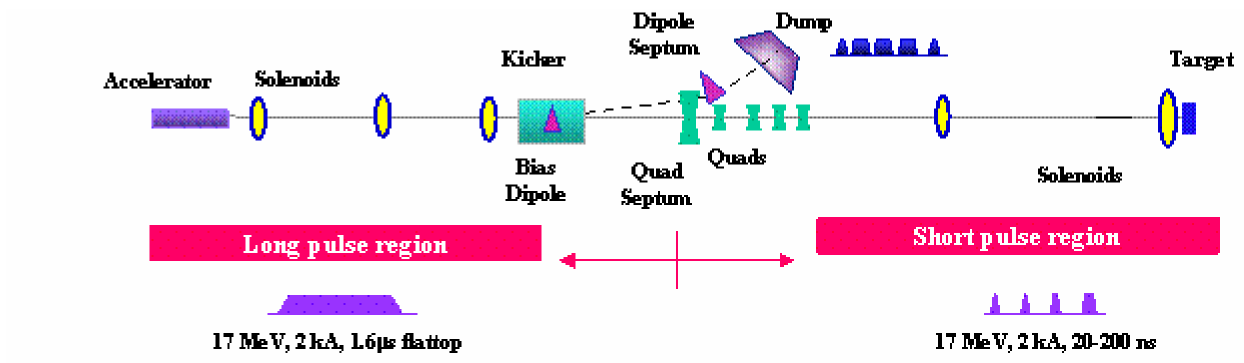


Figure 1: Schematic layout of DARHT 2nd Axis downstream transport.

## COMMISSIONING

The beam profile of the beam exiting the accelerator could not be measured due to the high power density of the beam. As a result, it was necessary to tune S1 and S3 based on beam profile measurements at the imaging station between the 1st and 2nd Collins quadrupole magnets. The desired beam profile was an upright ellipse with a vertical to horizontal aspect ratio of about 2:1. This was achieved as shown in the left image in Figure 2. The right image in Figure 2 shows the transverse beam distribution after S4.

The beam envelope and entrance conditions in the downstream were inferred from the magnet settings and images. Figure 3 shows the resulting beam envelope.

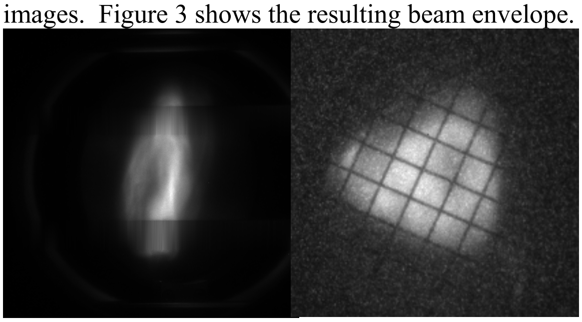

Figure 2: Beam images between the 1st and 2nd Collins quadrupoles (left), and after the 4th solenoid (right).

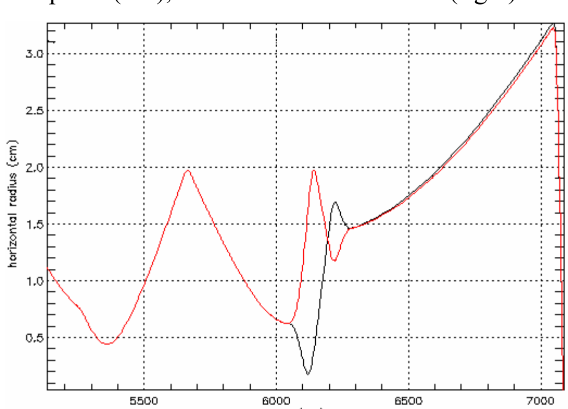


Figure 3: Beam envelope in the downstream transport based on initial conditions inferred from magnet settings and beam profile measurements.

## RESULTS

We will report results on the beam transport of four pulses to the target, and spot size and dose measurements of these pulses. through the kicker and quadrupole region, kicker performance, estimates of the emittance growth through the kicker and quadrupole region, stability of the kicked beam parameters at the beginning and end of flattop, studies of beam induced gas desorption at the septum edge, and spot size measurements of the four beam pulses on target.

### *Kicker Performance*

The kicker is nominally programmed to kick up to four pulses spaced over the flattop. The pulse lengths can be adjusted from 20 to 250 nsec. Figure 4 shows a typical beam current profile at the injector (black), accelerator exit (blue) and target (red). The four kicked pulses have lengths of 35, 40, 40, and 100 nsec respectively. The beam current is about 2 kA. The spacing from the beginning of P1 to the end of P4 is 1.5 usec demonstrating the first high level requirement.

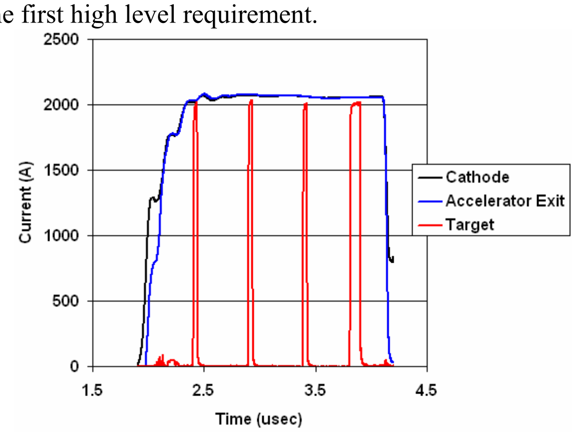


Figure 4: Beam current profile at injector, accelerator exit and target showing four kicked pulses.

### *Beam Size on Target*

The size of the x-ray spot on the target was measured using the Time-Resolved-Spot-Size camera as described by McCuistian et al. [3]. A series of measurements were made using the pulse format shown in Figure 4. The x-ray images and the calculated 50% MTF (Modulation-Transfer-Function) are presented in Figure 5. The values for the 50% MTF of the four pulses are all significantly smaller than the second high level requirement of 2.3 mm and are comparable to or less than the measured beam size for the DARHT 1st axis. The plots on the right side of the images compare the MTF of the single pulse from the first axis (grey) with that calculated for the corresponding second axis pulse (black). The larger high frequency or wave-number structure in the 2nd axis x-ray images translates directly into higher quality radiographic images.

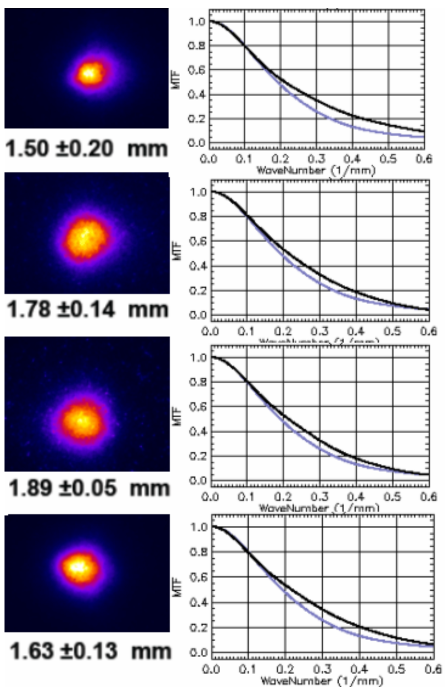


Figure 5: X-ray images of a four pulse target shot with measured 50% MTF and calculated MTF.

### *Dose Measurement*

The dose was measured with a diamond radiation detector (DRD) located approximately 30 cm downstream from the x-ray target. Measurements were made on the DARHT 1st and 2nd axes and the DRD is described by Bender [4]. The dose on the 1st axis was also measured using a calibrated dose calorimeter [5]. This provides a calibration for the DRD measurements. Table 1 presents the pulse length, dose and dose rate for the pulse format presented in Figure 4. The measurements correspond to five beam shots taken under identical conditions. The standard deviation in the dose and dose rate was less than 1%. This result exceeds the third high level requirement.

Table 1: Pulse Format and Dose

| Pulse | Pulse length (ns) | Dose at 1 m (R) | Dose Rate (R/ns) |
|---|---|---|---|
| P1 | 34.4 | 169 | 4.92 |
| P2 | 37.1 | 186 | 5.00 |
| P3 | 36.1 | 170 | 4.71 |
| P4 | 93.9 | 444 | 4.73 |

### *Beam Motion Over Four Pulses*

The beam motion of the four pulses at the x-ray production target must be kept to a very small fraction of the x-ray spot size. Studies of the beam transport from the accelerator exit to the target were performed and resulted in beam motion requirements of less than 2 mm and 2 mrad in both transverse planes at the accelerator exit. This was achieved in accelerator commissioning as described by Ekdahl et al.[6]. The measured beam motion between P1 and P4 was about 0.3 mm in both transverse planes. Subsequent studies have shown that the beam trajectory through the kicker can significantly alter the beam motion over flattop due to the action of image currents and charges on the kicker electrodes. Beam induced kicker steering is described by Caporaso et al [7]. Beam motion in the vertical plane can be minimized by independent controls on the kicker voltage for the four pulses. The horizontal beam motion on the target will be defined by the initial beam motion at the accelerator exit and the beam trajectory through the kicker. Beam studies have demonstrated that the trajectory through the kicker can be adjusted to reduce the horizontal beam motion in target. Further studies are required determine the minimal beam motion on target.

## CONCLUSIONS

The DARHT-II scaled accelerator downstream transport and target systems were successfully commissioned. The high level requirements for pulse length, spot size and dose were successfully demonstrated.

## REFERENCES

[1] Scarpetti, R.D., Status of the DARHT-II Accelerator, Proceedings of PAC07, Albuquerque, New Mexico, USA, p 831.
[2] Schulze, M.E., et al., Commissioning the DARHT-II Scaled Accelerator, Proceedings of PAC07, Albuquerque, New Mexico, USA, p 2627.
[3] McCuistian, B.T., et al., Temporal Spot Size Evolution of the DARHT First Axis Radiographic Source, Proceedings of EPAC08, Genoa, Italy, p 1206.
[4] Prasad, R.R., Diamond Radiation Detectors, Alameda Applied Science Corporation.
[5] Watson, S., et al., AIP Conference Proceedings Volume 333, 6th Annual Beam Instrumentation Workshop, MacKenzie, G.H. et al., editors 1994, pp. 307-313.
[6] Ekdahl, C., et al., Electron-Beam Dynamics in the DARHT-II Linear-Induction Accelerator, these proceedings.
[7] Caporaso, G.J., et al., Transmission line analysis of beam deflection in a BPM stripline kicker, Proceedings of PAC97, Albuquerque, New Mexico, USA, p 1861.

# DIGITALLY CONTROLLED HIGH AVAILABILITY POWER SUPPLY

David MacNair, Stanford Linear Accelerator Center, Menlo Park, CA


## *Abstract*

This paper reports the design and test results on novel topology, high-efficiency, and low operating temperature, 1,320-watt power modules for high availability power supplies. The modules permit parallel operation for N+1 redundancy with hot swap capability. An embedded DSP provides intelligent start-up and shutdown, output regulation, general control and fault detection. PWM modules in the DSP drive the FET switches at 20 to 100 kHz. The DSP also ensures current sharing between modules, synchronized switching, and soft start up for hot swapping. The module voltage and current have dedicated ADCs (>200 kS/sec) to provide pulse-by-pulse output control. A Dual CAN bus interface provides for low cost redundant control paths. Over-rated module components provide high reliability and high efficiency at full load. Low on-resistance FETs replace conventional diodes in the buck regulator. Saturable inductors limit the FET reverse diode current during switching. The modules operate in a two-quadrant mode, allowing bipolar output from complimentary module groups. Controllable, low resistance FETs at the input and output provide fault isolation and allow module hot swapping.


## OVERVIEW

The next linear collider will require several thousand magnet power supplies. This is a far greater number then any linear accelerator has used to date. To achieve equivalent or better availability of the beam will require improved availability of all systems. Significant increases in availability can come from improved reliability of modules, but an order of magnitude improvement can only come from redundant modules.

Power supplies will consist of parallel power modules in a N+1 redundant arrangement. Individual modules can fail without causing the power supply to lose regulation of the magnet current. Individual modules must provide for fault isolation to allow the power supply to operate with a failed module. The isolation will also allow for hot swapping of modules.

The individual modules will be autonomous so that there is no single point of failure. A digital controller will provide module control and fault detection. The controller provides a dual CAN bus interface for redundant power supply control.

## POWER MODULE

The power supply architecture is based on shared central bulk AC-DC power supplies with redundant buck regulators for each load. The power supplies are assumed to be in the 5 to 50 kW range consisting of redundant 1 to 10 kW modules. The modules will provide a voltage regulated output set by CAN bus broadcast messages from redundant magnet current regulators. The modules will use buck regulators with FETs in place of free wheeling diodes. This provides lower conduction losses and eliminates the non-linear discontinuous conduction region at low current. The two quadrant operation allows two power supplies operating with complimentary outputs to drive bipolar loads.

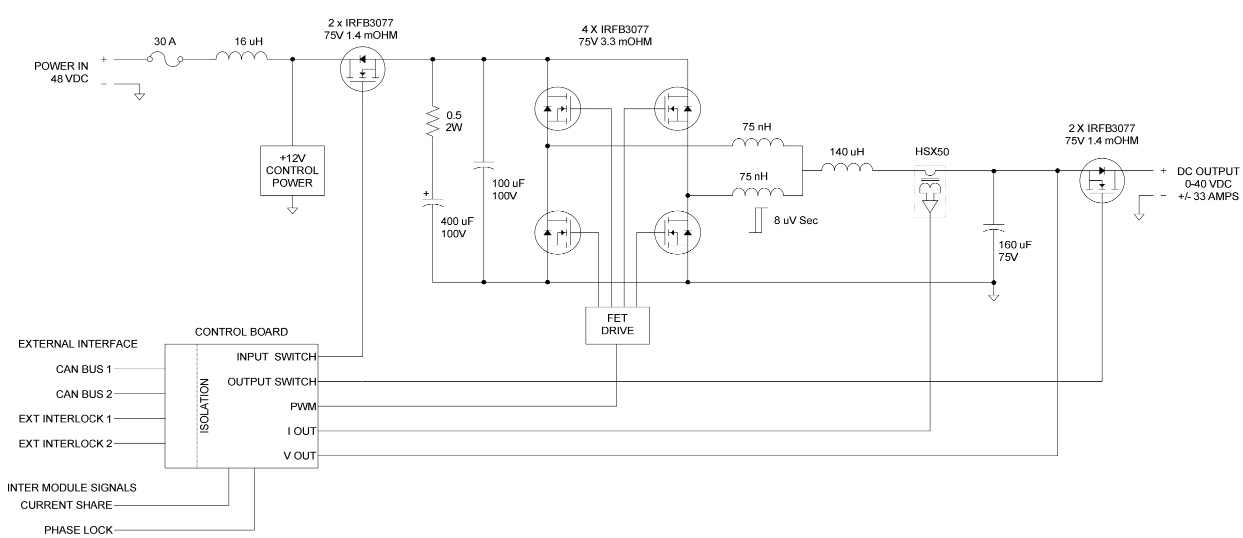


Figure 1: Two quadrant DC-DC converter with input and output FET switches.

*Work supported by the U.S. Department of Energy under contract number DE-AC02-76SF00515. SLAC-PUB-13415

Each module has FETs on the input and output. These allow failed modules to be isolated from the power source and load, and also allow modules to be replaced (hot swap) while the power supply is operating. Since the FETs ON resistance has a positive temperature coefficient, they can be easily paralleled to lower the conduction losses.

Ideally the upper and lower switching FETS would be driven synchronously, one turning on exactly as the other is turning off. This technology exists for low power (<100 watts) devices, but not for the high power devices. If the FETs are switched at the same time, there is a period where both are conducting (shoot through). This current is wasted as heat in the FETs. The existing FET drivers do not control the propagation delays and rise times to the extent needed for synchronous switching.

Adding a delay between turn ON and turn OFF eliminates shoot through losses, but adds losses from the FET body diode. When a FET with reverse current flowing is turned off, the current is shunted to the FET body diode. The diode has a large reverse recovery charge that increases with current and temperature.

## *Four FET Buck Regulator*

The buck regulator topology chosen uses 4 FETs instead of the usual 2. This allows for two small saturable ferrite chokes to be included. These provide a 100 nanosecond delay to allow the FET diodes conducting reverse current to recover before seeing the full bulk voltage. This greatly reduces the reverse current and switching losses in the FETs, and reduces the snubber circuit requirements.

The power supply controller sets the FET turn on sequence according to the polarity of the output current. For positive output current, the bottom two FETs will be carrying current in the reverse direction. When a bottom FET turns off, the opposite side upper FET turns on. When a top FET turns off, the bottom FET on the same side turns on. For negative output current, the top two FETs will be carrying current in the reverse direction. When a top FET turns off, the opposite side bottom FET turns on. When a bottom FET turns off, the top FET on the same side turns on. The module controller senses the polarity of the output current with a hall effect current sensor in series with the output inductor.

## *Digital Module Controller*

A major goal of this project is to design a power module control board that can be used with a power supplies with a large range different outputs. This will provide a common interface for most of the power supplies needed for the NLC.

The power module controller for redundant modules has to address the following requirements;

- Stability: Operate in a stable manner in parallel with other modules under all possible load conditions.
- Load Sharing: The output current of each module should be within 10% of other modules.
- Failure Detection: The controller needs to be able to sense and report a module that is not operating properly.
- Soft Start: The controller needs to be able to smoothly turn on and off a single module in a power supply without disturbing the power supply output.
- Autonomous Operation: The controller needs to be independent of all other module controllers to eliminate any single point failures.
- Redundant Communications: The controller will support dual CAN bus interfaces for redundant control.
- Module Synchronization: Each controller will provide a delay lock loop to lock the switching frequency and phase to the other modules.

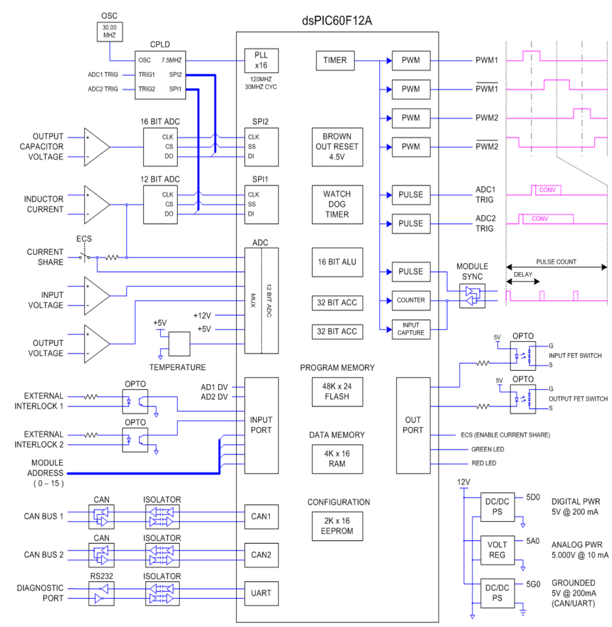


Figure 2: Power module controller block diagram.

## *Module Controller*

The processor used for the project is a Microchip dsPIC60F12A. It offers a high performance processor with a large array of external interfaces in a small inexpensive package. The processor executes 30 MIPs, or 300 instructions per cycle for a 100 kHz switching rate. It has a Harvard architecture with a 24 bit instruction path, and 16 bit data paths. It has two 40 bit accumulators with automatic limiting (saturation) of results. This eliminates range checking of results in the PID algorithms. The external interfaces include a dual CAN bus, UART, 8 PWM outputs, 2 SPI interfaces, and a 12 bit ADC with 16 input channels.

The maximum switching frequency for the design is 100 kHz (10 μs period), but may be programmed to be as low as 20 kHz. Two external serial ADCs are used to allowing reading the output voltage and output current on each cycle. A 16 bit ADC is used for the output voltage, and a 12 bit ADC for the output current. The noise from the hall effect current transducer limits the current resolution to less about 10 bits. The analog input to the ADCs is allows for under and over range conditions. All zero's or one's from an ADC is considered as a hardware fault.

The controller is referenced to the negative output of the power module. The CAN bus interfaces and diagnostic UART use digital isolators to provide a ground referenced control interface.

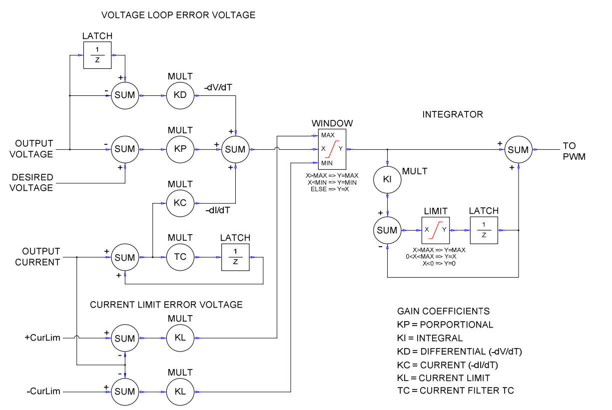


Figure 3: Control algorithm.

## *Controller Algorithm*

The controller uses a modified PID algorithm. The Proportional and Derivative terms are combined to form an error signal. The error signal is integrated to generate the Integral term. The error signal and integral are summed to generate the PWM on time.

The current limit operates as a window function for the error signal. The controller determines the minimum and maximum error signals that will keep the output current in range. The voltage and current loops share the same integral term to allow glitchless switching between voltage control and current limit.

The controller uses two derivative terms; dV/dT and dI/dT. The main function of the derivative term is to damp the response of the output LC filter. Using two derivatives allows better response for all possible load conditions.

The PWM outputs of the dsPIC processor have a 33 ns resolution. The input to the PWM algorithm is a 12 bit integer. The actual resolution of the PWM ranges from 8 to 10 bits, depending on the frequency. The input signal is truncated before being applied to the PWM, with the remainder from the truncation being applied to future cycles. This extends the resolution of the ADC, but adds some small lower frequency harmonics to the output.

The PWM algorithm allows setting minimum and maximum duty cycles. When a value less then the minimum is requested, the PWM maintains the minimum pulse width, but skips cycles to maintain the average value equal to the requested value. The on time remains constant, but the frequency changes to provide the correct average value.

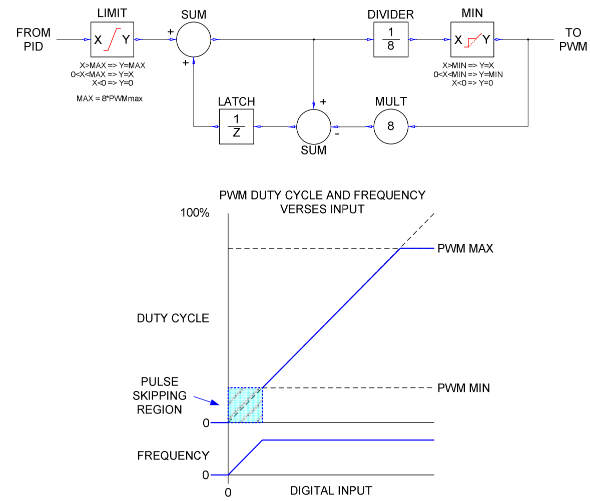


Figure 4: PWM algorithm.

## TEST RESULTS

To date, 5 test power modules have been built. They have been tested with using Microchip development boards that use the internal 12 bit ADC. The losses in the module were less then 22 watts for a 33 amp output. This puts the full load efficiency of the power section at better then 98%. The unit requires 3 watts of control power, and another 3 watts for the input and output FET switches. The complete module full load efficiency should be better then 97%. More then half of the losses are due to the resistance of the inductors, PCB traces, and FETs. The FET switching losses are a minor contribution.

The circuit design and PCB layout of the controller has been completed. When the controllers are built, they will allow testing of the parallel and redundant operation of the power modules.

## CONCLUSION

Power supplies with high efficiency and reliability that support redundant operation are technically strait forward. There are additional costs involved with additional hardware for redundant operation, and over sizing of components to improve efficiency and reliability.

Redundant power supplies are becoming available for high availability computer systems, but these fixed output voltage and low power make them inappropriate for powering magnets. There is currently not adequate demand for redundant 1 to 100 kW power supplies to have commercial sources available.

This project will continue to develop the power supply controller to demonstrate a power supply made from redundant modules. This will provide a better understanding of the issues involved in providing ultra reliable power supplies for the next linear collider.

# RF CONTROL AND LONGITUDINAL BEAM STABILITY IN ENERGY RECOVERY LINACS

A. Neumann, M. Abo-Bakr, J. Knobloch, BESSY GmbH, Berlin


## Abstract

Most concepts for next generation light sources base on linear accelerators (linac) due to their excellent beam properties. In case of high electron energies and extreme average currents Energy Recovery Linacs (ERL) are mandatory. In this paper we investigate the rf field stability in a generic superconducting, cw operated ERL. By using rf control cavity simulations and longitudinal beam dynamics the influence of rf field stability on the energy recovery process is analyzed. Since the ERL aims for a small net beam loading cavities are operated at a high loaded quality factor. Therefore they are operated at a low bandwidth and are very susceptible to microphonics detuning. We considered the field stability under the influence of limited rf power, mechanical cavity detuning, varying beamloading, synchronization deviations and varying bunch parameters at injection into the linac. The resulting temporal and energy jitter at the linac end will be transformed in the return arc and leads to rf phase deviations on the return path. Implications of varying beam loading on the ERL performance are examined.


**CONTRIBUTION NOT RECEIVED**

# OPTIMIZATION OF LATTICE FOR AN ERL UPGRADE TO THE ADVANCED PHOTON SOURCE*

M. Borland†, V. Sajaev, ANL, Argonne, IL 60439, USA

*Abstract*

An Energy Recovery Linac (ERL) is one possibility for an upgrade to the Advanced Photon Source (APS). In addition to the linac itself, our concept involves a large turn-around arc (TAA) at 7 GeV that would eventually accommodate many new beamlines. Previously, we based the TAA design on isochronous triple-bend achromat (TBA) cells, since these are expected to provide some immunity to the effects of coherent synchrotron radiation. In the present work, we compare the previous TBA-based design to a new design based on double-bend achromat (DBA) cells, in terms of emittance growth, energy spread growth, and energy recovery. We also explore the trade-off between optimization of the beta functions in the straight sections and minimization of emittance growth.

## INTRODUCTION

An ERL [1] upgrade to the APS promises a revolutionary improvement in x-ray properties. In previous work [2] we made use of a TBA-based cell design for the TAA for the ERL upgrade. This choice was inspired by the desire to make an isochronous system with cancellation of coherent synchrotron radiation (CSR) effects [3, 4]. However, we found that CSR effects were very small, even as we increased the charge in the beam. Hence, we hypothesized that perhaps a simpler cell design might be acceptable. In this paper, we show results for a DBA-based design and compare these to the previous TBA-based design. (The APS ring portion of the ERL is necessarily DBA, since we don't propose to replace the APS ring. However, for simplicity we'll refer to "TBA" or "DBA" designs based on the optics design used for the non-APS portions.)

We also noted previously that with smaller beta functions at the insertion devices, x-ray brightness might be increased beyond what was predicted in [2]. In the second part of this paper, we explore the potential benefit and issues related to smaller beta functions.

## NEW ARC DESIGN

To develop the new arc design, we started with the APS cell including the Decker distortion[5], since this cell design is close to what we want. We then used `elegant` [6] to evolve this cell as follows: (1) Bending angle per cell of $\pi/24$ (48 cell turn around), just as for the TBA design. (2) $\eta_x = \eta'_x = 0$ in straights. (3) Increase space for insertion devices (IDs) from 4.8 m to 8 m. (4) $\beta_x \approx \beta_y \leq 5\text{m}$ at center of ID straights. (5) Mean arc radius of 230 m, just as for the TBA design. (6) Minimize the $I_2$, $I_3$ and $I_5$ radiation integrals. (7) Similar maximum lattice beta functions as the TBA design, e.g., $\sim 25\text{m}$. As Figure 1 shows, it was possible to make $\beta_x \approx \beta_y \approx 3\text{m}$, which has advantages for brightness compared to the $\beta_x = 12\text{m}$ and $\beta_y = 4.7\text{m}$ values for the TBA. It is likely this could be achieved in the TBA only by moving away from the CSR canceling tunes and perhaps giving up isochronicity.

We attempted to simplify the DBA cell by having doublets on each side of the ID instead of triplets. We did not find a solution that had satisfactory emittance growth and beta functions. Hence, the promise of the DBA to simplify the cell structure didn't bear fruit. We eliminate one dipole magnet, but the dipoles are longer.

We also performed a DBA-based design of the arcs ("transport arcs") that bring the beam into and out of the APS ring. The constraints are very similar to those just listed, except there is no need for long straight sections. The mean radius was 75 m with a total bending angle of 72 degrees in 8 cells, as in the TBA design.

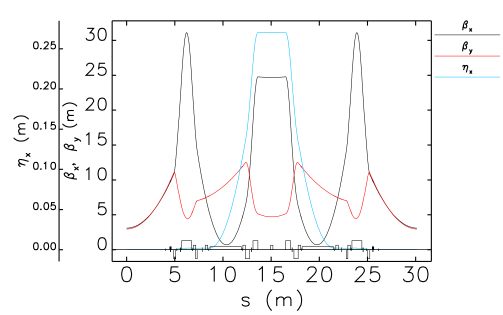


Figure 1: Optics for turn-around arc DBA cell.

## TRACKING COMPARISON

The next step is to compare tracking results for the DBA and TBA designs. We are interested in absolute energy loss, energy droop (deviation from reference), energy spread increase, and emittance increase. Mechanisms involved are classical, incoherent, and coherent synchrotron radiation. All the tracking studies used `Pelegant` [7] and the high-coherence-mode beam parameters [8], i.e., 0.1 $\mu$m initial normalized emittance with a 2-ps rms bunch length. For consistency with previous work, we assumed an initial

* Work supported by the U.S. Department of Energy, Office of Science, Office of Basic Energy Sciences, under Contract No. DE-AC02-06CH11357.
† borland@aps.anl.gov

energy spread of 0.1% rms, which is very likely too large but which doesn't impact our results.

We found that neither design has a worrisome energy droop. As Figure 2 shows, the DBA design is superior overall in terms of energy spread growth. This is in spite of larger growth in the TAA and results from very low growth in the transport arcs. Clearly, we might combine the TBA-based TAA with our DBA-based transport arcs if we wished. The emittance grows more rapidly in the DBA version of the TAA, then at about the same rate in the transport arcs and the APS itself. These differences are negligible.

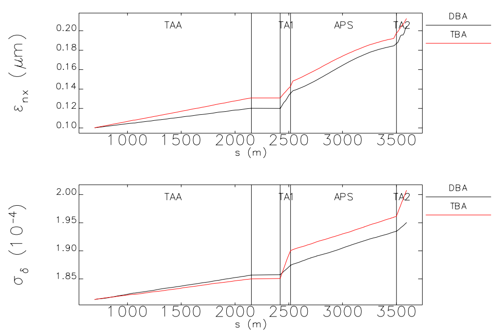


Figure 2: Evolution of normalized rms horizontal emittance and rms fractional momentum spread in 7-GeV portion for the two designs.

For the deceleration phase, increasing fractional energy spread and beam size may lead to beam loss. The final longitudinal distribution, shown in Figure 3, exhibits low- and high-energy tails, resulting from non-isochronous transport. The effects are worse in the all-DBA design, but still present in our "TBA" design because the APS portion is still DBA. This can be mitigated by moving the rf phase in the deceleration stage, at the cost of less efficient energy recovery. This is shown in Figure 3 for a deceleration phase that is 0.5 degree off trough. The average final momentum increases by only 1.5%.

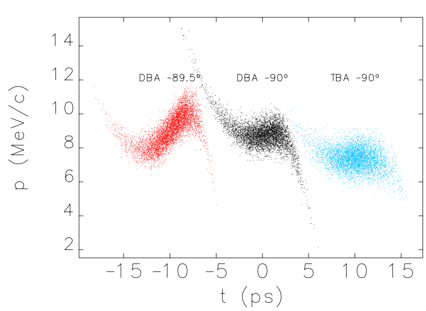


Figure 3: Comparison of final longitudinal phase space for three cases. Data are offset horizontally for clarity.

In passing, we note that one advantage of the TBA design is that the $R_{56}$ is adjustable. Hence, we could perhaps adjust the total $R_{56}$ of the 7-GeV transport lines to be zero, something we can't do with an all-DBA system. This would result in lower post-deceleration energy spread.

Next, we performed tracking with CSR to compare the DBA and TBA lattices. We are most interested in the 25 mA high-coherence mode [8], which has 19 pC per bunch. We also looked at the high-flux mode, which has 77 pC per bunch, leaving the emittance fixed for simplicity in comparisons (in reality the emittance is expected to increase four-fold). As seen from Figure 4, the effects of CSR are quite modest. This is the same result as we saw for the TBA-based design. Of course, these studies are for a very smooth initial distribution. Since the all-DBA lattice has considerable path-length dispersion, we must look carefully at possible microbunching instabilities [9]. This is the subject of another paper in these proceedings.

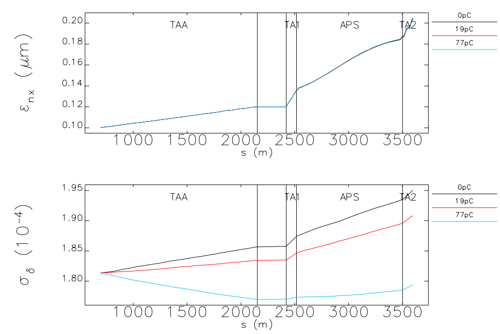


Figure 4: Evolution of normalized rms horizontal emittance (top) and rms fractional momentum spread (bottom) in 7-GeV portion of DBA design for three charge levels.

We next used `sddsanalyzebeam` and `sddsbrightness` [10] to compute the x-ray brightness for U33 undulators of various lengths at various locations, including emittance and energy spread growth. We found that the DBA-based design is about 70% brighter than the TBA-based design in the TAA, and basically indistinguishable in the APS itself. The improvement in the TAA results from the smaller beta functions in the straight sections.

## BRIGHTNESS OPTIMIZATION

The brightness improvement from the DBA cell design is, of course, not inherent in the DBA but results simply from the improved beta functions. Ideally, the beta function of the electron beam would be the same as the beta function of the single-electron undulator radiation. The latter is $\beta_r = \epsilon_r/\sigma_{r'}^2$, where $\epsilon_r = \lambda/(4\pi)$ is the intrinsic radiation emittance, $\sigma_{r'} = \sqrt{\lambda/(2L)}$ is the intrinsic radiation divergence, $\lambda$ is the radiation wavelength, and $L$ is the undulator length [11]. The result, $\beta_r = L/(2\pi)$, is quite small and not easily obtained in a storage ring. With the greater optical freedom of a single-pass system, it might be feasible.

Toward this end, we used `elegant` to rematch the APS DBA cell for a grid of target $\beta_x$ and $\beta_y$ values at the ID. We included the following constraints: (1) $\eta_x = \eta'_x = 0$ at

ID. (2) Maximum beta functions under 70 m in both planes, in order to reduce beam motion, halo generation, and optics sensitivity to the orbit. That 70m is necessary and sufficient is an educated guess at this point. (3) Acceptable emittance growth, implemented by constraining the cell's equilibrium emittance $\epsilon_0$ to less than 10 nm. Although the equilibrium emittance is not of course directly relevant, it provides an intuitive way to constrain $I_5$.

The maximum beta function constraint proved difficult. By introducing small gradients in the dipoles, we reduced this problem and got significantly smaller beta functions in the straight sections. We limited ourselves to $|K_1| \leq 0.05\mathrm{m}^{-2}$, which might require only pole-face windings.

In an attempt to ensure that chromatic effects are manageable, we eliminated all solutions for which our present maximum sextupole strength of $K_2 = 31.5\mathrm{m}^{-3}$ was insufficient to correct the chromaticity to zero. We also removed all solutions for which $\max(\beta_{\{x,y\}} \geq 75$ m and $\epsilon_0 \geq 11$ nm. This eliminated about 17% of the solutions.

Following matching, we chose to compute the x-ray brightness at Sector 35 (the end of the APS portion of the ERL), since it is the most sensitive to emittance increase. To save computation, instead of tracking we estimated the emittance using [12]

$$\Delta\epsilon_x = \frac{55 r_e \hbar}{48\sqrt{3} m_e c}\gamma^5 I_5, \quad (1)$$

where $I_5$ is the radiation integral for 35 sectors. Similarly, the fractional energy spread growth is [13]

$$\Delta\sigma_\delta^2 = \frac{55 r_e \hbar}{24\sqrt{3} m_e c}\gamma^5 I_3. \quad (2)$$

We checked these equations against tracking with `elegant` for the nominal design and got good agreement.

The beam parameters at the entrance of the APS portion are $\epsilon_x = 10.9$ pm, $\epsilon_y = 7.1$ pm, and $\sigma_\delta = 0.0186\%$. After computing the beam properties at Sector 35, we used `sddsbrightness` to determine the brightness for the first three harmonics assuming at 4.8-m undulator and 25 mA average beam current. We found the largest improvement in brightness for $\beta_x = 1.0\mathrm{m}$ and $\beta_y = 1.1\mathrm{m}$, the smallest we could get in both planes (see Figure 5). This solution is close to the limits for maximum beta functions, emittance increase, and sextupole strength. As Figure 6 shows, the improvement in brightness relative to the reference case is a factor of 2.5.

## CONCLUSION

Based on an analysis of emittance growth including coherent synchrotron radiation, we found no advantage to a TBA-based design for the turn-around arc and transport arcs in an APS ERL upgrade. Even for 77 pC/bunch, the use of CSR-canceling optics appears to be unnecessary, which relaxes several constraints on the lattice. This would allow, for example, optimization of the beta functions at the insertion devices, giving significantly improved brightness.

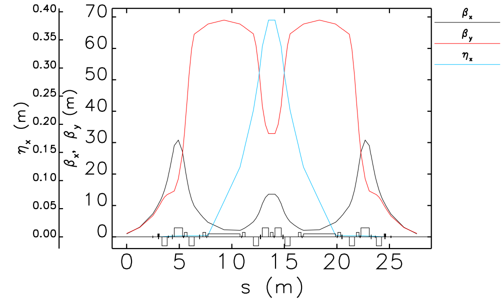


Figure 5: Optics for optimized APS DBA cell.

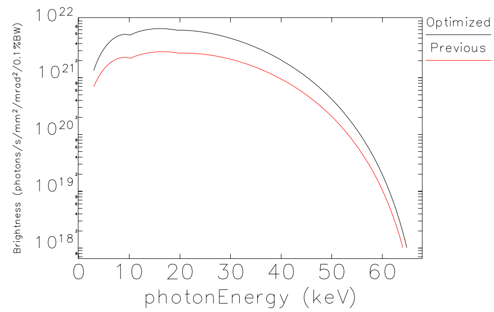


Figure 6: Comparison of brightness for the optimized APS DBA cell and the previous solution.

We showed an example of applying this, albeit to the APS DBA cell only, gaining a factor of 2.5 in the brightness. Strong path-length dispersion in the all-DBA design may increase the growth of microbunching in the beam, which is the subject of another paper in these proceedings.

## REFERENCES

[1] M. Tigner, Nuovo Cimento **37**, pp 1228-1231 (1965).

[2] M. Borland *et al.*, NIM A 582 (2007) 54-56.

[3] J. Wu *et al.*, Proc. of PAC 2001, 2866-2868 (2001).

[4] G. Bassi *et al.*, NIM A 557 (2006) 189.

[5] G. Decker and O. Singh, Phys. Rev. ST Accel. Beams 2, 112801 (1999).

[6] M. Borland, Advanced Photon Source LS-287, September 2000.

[7] Y. Wang and M. Borland, Proc. of PAC 2007, 3444-3446 (2007).

[8] G. Hoffstaetter, "Status of the Cornell ERL Project," FLS 2006 Workshop, working group 2.

[9] M. Borland *et al.*, Proc. of PAC 2001, p 2707 (2001).

[10] M. Borland *et al.*, Proc. of PAC 2003, 3461-3463 (2003).

[11] K. Kim in *Physics of Particle Accelerators*, M. Month and M. Dienes eds., AIP 184, 565-632 (1989).

[12] H. Wiedemann in *Handbook of Accelerator Physics and Engineering*, section 3.1.4.3, second edition, A. W. Chao and M. Tigner eds (1999).

[13] M. Sands, SLAC-121, November 1970.

# GROWTH OF DENSITY MODULATIONS IN AN ENERGY RECOVERY LINAC LIGHT SOURCE DUE TO COHERENT SYNCHROTRON RADIATION AND LONGITUDINAL SPACE CHARGE*

M. Borland †, ANL, Argonne, IL 60439, USA

*Abstract*

An Energy Recovery Linac (ERL) is one possibility for an upgrade to the Advanced Photon Source (APS). Such a system involves not only a long linac, but also long transport lines with many dipole magnets. Since the bunches are short, we may expect that coherent synchrotron radiation (CSR) and longitudial space charge (LSC) will have an effect on the beam dynamics. Although previous studies have shown minimal effects for an initially quiet beam distribution, the possibility of a microbunching instability seeded by initial density modulation must be evaluated. We present and discuss simulation results showing the growth of density modulations in two possible lattices for an ERL upgrade of the APS.

## INTRODUCTION

The first hint that CSR could amplify initial density modulations in a beam in a single-pass system came from modeling [1] of the Linac Coherent Light Source (LCLS) with `elegant` [2]. Subsequently, theoretical analysis [3] for the TESLA Test Facility predicted an even more severe problem when LSC was included. This was subsequently confirmed by modeling with `elegant` for the LCLS [4]. What is critical in the LCLS and other similar systems is the alternation between long linear accelerators in which LSC effects accumulate and one or more bunch compression systems in which CSR effects act.

An ERL [5] upgrade to the APS promises a revolutionary improvement in x-ray properties. We have developed a concept for an "ultimate" ERL upgrade to the APS [6] that involves a long, single-pass 7-GeV linac and a large 7-GeV turn-around arc. The potential for build-up of CSR and LSC effects in such a system seems clear, due to the length of the linac and transport line, as well as the large number of dipole magnets. In addition, the bunch duration is relatively short ($\sim$2 ps rms) and the normalized emittance is very small ($\sim 0.1\ \mu$m), as is the rms fractional momentum spread ($\sim 0.02\%$). Like the LCLS and other high-performance injectors, the ERL injector is likely to be driven by a shaped laser pulse [7], which opens up the possibility that significant density ripples will be imparted to the beam at the cathode. Hence, in spite of the low charge (under 100 pC), there is reason to be concerned about potential microbunching growth.

We've investigated this for two possible optical configurations of the ERL: (1) The original "TBA" configuration [6, 8], with triple-bend-achromat (TBA) cells outside the APS and double-bend-achromat (DBA) cells inside the APS. (2) A new DBA configuration, with DBA cells throughout. A comparison of these configurations is offered elsewhere in these proceedings.

In the present work, we begin our simulations at the 10-MeV point. Full simulations starting at the cathode are obviously desirable, but beyond our scope at this time.

## SIMULATION METHODS

The approach we have taken is very similar to what was done for LCLS and FERMI [9, 4, 10], where we obtained a growth curve for density modulations. We performed a series of simulations for various bunch charge, modulation wavelength, and modulation depth with CSR, LSC, and linac longitudinal wakefields. CSR was included using `elegant`'s line-charge model [11, 12], including CSR in drift spaces. This model includes the transient build-up of CSR in each dipole, but does not include shielding. Shielding will in fact have some effect on the "bulk CSR," i.e., CSR at the wavelengths related to the overall bunch length [13]. However, it will have a significantly diminished effect at the shorter wavelengths corresponding to density modulations.

LSC was included using an impedance-based method [4]. An LSC kick was added after each linac structure as well as at the center of each ID straight section. This made use of a newly-added feature in `elegant`, namely, the ability to insert an LSC kick that integrates the effect of an LSC applied over a user-specified length of the beamline. This approach is valid as long as the relative longitudinal motion of particles is not too great, which is the case when we place kicks at each ID straight section.

Control of noise is essential to getting reliable results. We followed the algorithm in [4, 10] fairly closely: 1. Choose a density modulation wavelength and depth. We used depth values between 0 and 10%, inclusive. The 0% runs are helpful in baselining the effects of noise. 2. Choose the bin size to be 1/24$^{\rm th}$ of the wavelength. This means the Nyquist frequency is 12 times the wavelength. 3. Set the low-pass noise filter cutoff to 1.5 times the modulation frequency. Combined with item 2, we smooth and interpolate features at the modulation frequency on the

* Work supported by the U.S. Department of Energy, Office of Science, Office of Basic Energy Sciences, under Contract No. DE-AC02-06CH11357.

† borland@aps.anl.gov

scale of the bin size. 4. Choose the number of particles such that there are at least 1000 particles per bin in the center of the distribution. This provides additional control of binning noise. 5. Generate a distribution with the desired modulation and the required number of particles. The distribution is Gaussian in the longitudinal coordinate $z$, with the modulation imposed by multiplying the Gaussian distribution function by $1 + d \cos 2\pi\lambda z$, where $\lambda$ is the modulation wavelength and $d$ is the modulation depth. 6. Perform tracking, recording time histograms along the system. Unlike the LCLS case, we are in principle interested in the modulation at each straight section. We recorded histograms after each set of linac structures (typically eight cavities) after each achromat in the turn-around arc (TAA), input transport line, APS, and output transport line.

The initial beam parameters were 19 pC/bunch, 0.01% rms energy spread at 10 MeV with a normalized emittance of 0.1 $\mu$m [7, 14, 15]. Gaussian distributions were used in all six phase space coordinates. For tracking, we used `Pelegant` [16], the parallel version of `elegant`. Typically 42 processors were used with up to 7.2 million simulation particles, requiring up to 24 hours for a single run. We also performed tracking with 77 pC/bunch and the same initial beam parameters, although in reality the emittance and initial energy spread would be higher.

Analysis of the simulation data used power spectral densities (PSDs) of the longitudinal histograms along the accelerator. For each location $s$, modulation depth $d$, wavelength $\lambda$, and charge $q$, we integrated the PSD between $0.9f_0$ and $1.1f_0$ to get a value $E(s, d, \lambda, q)$, where $f_0$ is the frequency corresponding to $\lambda$. The quantity $E'(s, d, \lambda, q) = E(s, d, \lambda, q) - E(s, 0, \lambda, q)$ is the adjusted value, with any contribution from noise removed. The quantity $G = \sqrt{E'(s, d, \lambda, q)/E'(0, d, \lambda, q)}$ is the gain relative to the initial modulation strength.

## RESULTS AND DISCUSSION

Figures 1 and 2 show the results for the all-DBA lattice, while Figures **??** and **??** show the results for the TBA lattice. What's plotted is the maximum gain seen at any location as a function of the initial modulation wavelength, for several values of the initial modulation depth. Varying the modulation depth helps ensure that results have converged and that we are in the linear regime.

The results of our analysis show the same general features as those for FEL driver linacs: low gain for long wavelengths and increasing gain for shorter wavelengths, but with a cutoff at very short wavelengths. For most cases, we don't see any significant difference as the initial modulation depth is varied. This is typical when the gain is small. However, for the all-DBA lattice with 77 pC/bunch, the gain is somewhat high and it doesn't appear that the results have fully converged. Apparently the maximum gain is $\sim$ 5, so for 1% initial modulation, the depth is only $\pm 5\%$. More work is needed to determine why this hasn't converged, since it should be in the linear regime.

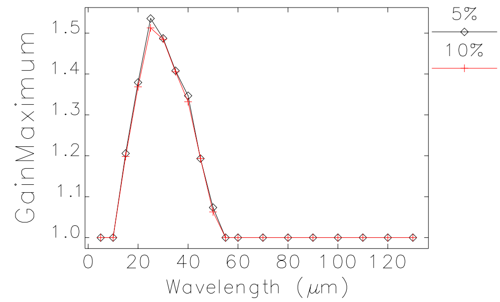


Figure 1: Maximum microbunching gain for 19 pC/bunch in the DBA lattice.

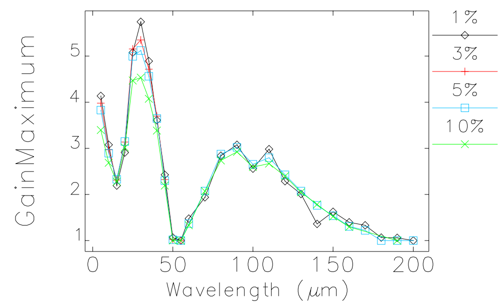


Figure 2: Maximum microbunching gain for 77 pC/bunch in the DBA lattice.

Comparing the results for 19 pC/bunch, the DBA lattice shows about 15% higher maximum gain than the TBA lattice. This is perhaps not unexpected given the larger $R_{56}$ of the all-DBA lattice (0.57m compared to 0.24m).

For 77 pC/bunch, the results are not too different for wavelengths above 50 $\mu$m, with the DBA lattice showing about 25% higher maximum gain. However, for short wavelengths the DBA lattice is significantly worse, with maximum gain of $\sim$ 5 compared to $\sim$ 2. Note that the short-wavelength gain for 77 pC/bunch is overstated because we used unrealistically small emittance and energy spread. Exploration of this effect is in progress.

Although the maximum gain is not small, it should not degrade performance for users. For example, Figure 5 com-

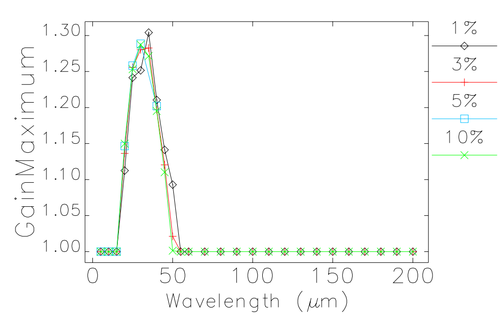


Figure 3: Maximum microbunching gain for 19 pC/bunch in the TBA lattice.

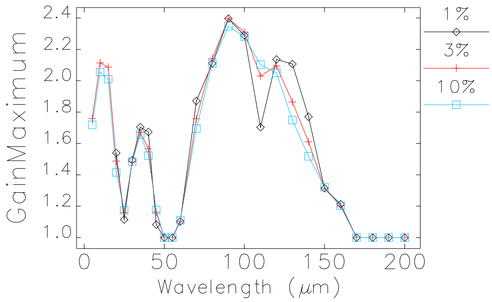


Figure 4: Maximum microbunching gain for 77 pC/bunch in the TBA lattice.

pares the normalized horizontal emittance at the ID straight sections for the DBA lattice with 77 pC/bunch for three cases: 5% and 10% initial modulation depth at 30 $\mu$m, and no initial modulation. We see that the effect is negligible.

More interesting, although still negligible, is the effect on the energy spread, shown in Figure 6. We see that the bulk CSR effect (0% modulation) results in a decrease in the energy spread in the turn around arc (TAA), followed by an increase in subsequent sections. That some decrease may occur is plausible given that the initial energy spread of the beam is dominated by rf curvature effects. Bulk CSR tends to flatten the sinusoidal distribution in time-momentum space, resulting in lower energy spread. This can't happen indefinitely and the energy spread begins to increase when the beam transits the stronger dipoles in the Transport Arc into the APS. That this effect would be stronger when a short-wavelength density modulation is present was not expected and is still surprising

Inspection of the longitudinal distribution after deceleration shows no significant effect of the initial modulation. Hence, we have no added concerns about transporting the decelerated beam efficiently.

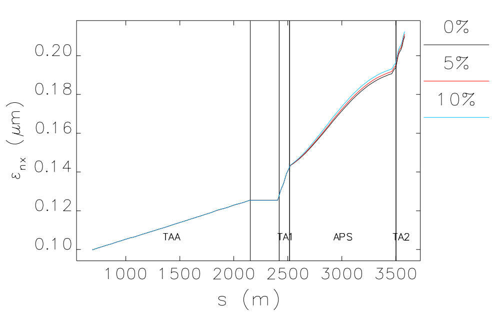


Figure 5: Effect of an initial 30-$\mu$m density modulation on the normalized rms horizontal emittance seen at the ID straight sections, for 77 pC/bunch. The line for 5% initial modulation is only slightly above that for 0% modulation. The labels refer to the TAA, input and output transport arcs (TA1 and TA2), and the APS ring.

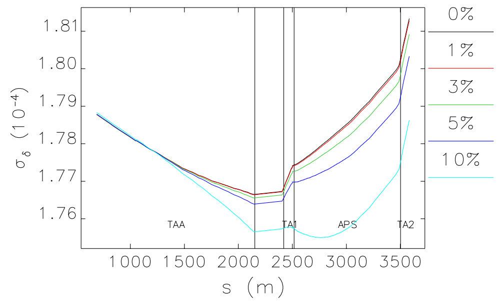


Figure 6: Effect of an initial 30-$\mu$m density modulation on the rms fractional energy spread seen at the ID straight sections, for 77 pC/bunch, for various initial modulation depths. See Figure 5 for an explanation of the labels.

## CONCLUSION

We have used `Pelegant` to model the propagation of initial density modulations from the 10-MeV point in an APS ERL upgrade. Although significant gain, up to 30-fold, was found for 77 pC/bunch in the all-DBA lattice, it appears this will have little or no impact on the beam quality seen by users. Density modulation growth does not appear to be a strong reason to favor the TBA-based design over the all-DBA design. Additional modeling is needed to extend the simulations to the cathode.

## ACKNOWLEDGEMENT

The author wishes to thank Yusong Wang for his efforts in parallelizing `elegant`, which made this work possible.

## REFERENCES

[1] M. Borland *et al.*, Proc. of PAC 2001, 2707-2709 (2001).
[2] M. Borland, Advanced Photon Source LS-287, Sept. 2000.
[3] E. Saldin *et al.*, DESY Report No. TESLA-FEL-2003-02 (2003).
[4] Z. Huang *et al.*, Phys. Rev. ST Accel. Beams 7, 074401 (2004).
[5] M. Tigner, Nuovo Cimento **37**, 1228-1231 (1965).
[6] M. Borland *et al.*, NIM A 582, 54-56, (2007).
[7] I. Bazarov *et al.*, Phys. Rev. ST Accel. Beams 8, 034202 (2005).
[8] M. Borland *et al.*, Proc. of AccApp'07, 196-203 (2007).
[9] M. Borland, Proc. of LINAC 2002, Gyeongju, Korea, 11-15 (2002).
[10] M. Borland, Phys. Rev. ST Accel. Beams 11, 030701 (2008).
[11] M. Borland, Phys. Rev. ST Accel. Beams 4, 070701 (2001).
[12] G. Stupakov *et al*, Proc. of EPAC 2002, 1479-1481 (2002).
[13] Y. Wang and Y.-C. Chae, private communication.
[14] Y. Sun *et al.*, these proceedings.
[15] G. Hoffstaetter, "Status of the Cornell ERL Project," FLS 2006 Workshop, working group 2.
[16] Y. Wang *et al.*, Proc. of 2007 PAC, 3444-3446 (2007).

# EXPLORING BENEFITS OF USING RF DEFLECTION FOR SHORT X-RAY PULSE GENERATION FOR AN ENERGY-RECOVERY LINAC UPGRADE TO THE ADVANCED PHOTON SOURCE*

V. Sajaev#, M. Borland, ANL, Argonne, IL 60439, U.S.A.

*Abstract*

One option for the Advanced Photon Source (APS) upgrade is an energy-recovery linac (ERL). In its main operating mode, the ERL rms bunch length would be two picoseconds. Even though this bunch length is already a factor of 20 shorter than the present APS bunch length, some experiments might benefit from even shorter x-ray pulses. For the APS storage ring, we plan to use an rf deflection technique [1] to generate one-picosecond-long x-ray pulses. In this approach, an rf cavity is used to deliver a longitudinally dependent vertical kick to the electron beam and then a pair of slits is used to slice the vertically streaked x-ray beam (see Figure 1). Here, we investigate the possibility and benefits of utilizing this technique to generate shorter x-ray pulses in an ERL.

## ANALYSIS

Let's consider the beam motion after the first cavity, which provides time dependent vertical kick:

$$y_0'(t) = \frac{V}{E}\sin(\omega t) \approx \frac{V}{E}\omega t \, ,$$

where $V$ is the deflecting cavity voltage, $\omega$ is the deflecting cavity frequency, $E$ is the beam energy, and we have assumed that the beam is short enough to stay within the linear part of the rf waveform. At the location of the undulator, the beam will have the following coordinates [2]:

$$y_{ID}(t) = \frac{V\omega t}{E}\sqrt{\beta_{RF}\beta_{ID}}\sin(\psi) \, ,$$

$$y_{ID}'(t) = \frac{V\omega t}{E}\sqrt{\frac{\beta_{RF}}{\beta_{ID}}}\left(\cos(\psi) - \alpha_{ID}\sin(\psi)\right) ,$$

where $\beta$ and $\alpha$ are Twiss functions, and $\psi$ is the betatron phase advance. These equations describe the vertical position and angle of the beam slice located at longitudinal position $t$. Each beam slice has beam size $\sigma_y$ and divergence $\sigma_{y'}$. Considering the undulator radiation divergence $\sigma_\theta$, the photon beam position and its vertical size a distance $L$ down the beamline are

$$y_L(t) = y_{ID}(t) + y_{ID}'(t)\cdot L =$$

$$= \frac{V\omega t}{E}\left(\sqrt{\beta_{RF}\beta_{ID}}\sin(\psi) + L\cdot\sqrt{\frac{\beta_{RF}}{\beta_{ID}}}\left(\cos(\psi) - \alpha_{ID}\sin(\psi)\right)\right),$$

$$\sigma_L^{\,2} = \sigma_y^{\,2} + L^2\left(\sigma_{y'}^{\,2} + \sigma_\theta^{\,2}\right).$$

At this point, an asymmetrically cut crystal can be used to compress the photon pulse as shown in Figure 2. Such a crystal performs horizontal sheering as shown by the red arrows, and the resulting minimum pulse length after the crystal is $\sigma_s = \sigma_y / \tan(\vartheta)$. The same length can be achieved by using slits instead of the crystal to slice the beam along the horizontal axis. The minimum achievable pulse length is

$$\sigma_t = \frac{\sigma_L}{dy_L(t)/dt} =$$

$$= \frac{\frac{E}{V\omega}\sqrt{\sigma_y^{\,2} + L^2\left(\sigma_{y'}^{\,2} + \sigma_\theta^{\,2}\right)}}{\left(\sqrt{\beta_{RF}\beta_{ID}}\sin(\psi) + L\cdot\sqrt{\frac{\beta_{RF}}{\beta_{ID}}}\left(\cos(\psi) - \alpha_{ID}\sin(\psi)\right)\right)} .$$

There are two phase-advance values between the cavity and the undulator that simplify the expression above by zeroing the sine or cosine term. One can see that having *sin(ψ)* equal zero rather than *cos(ψ)* allows for achieving shorter pulses assuming reasonable values for beta functions and distance to the beamline optics. The expression can be simplified for this case as follows:

$$\Delta t = \frac{E}{V\omega}\sqrt{\frac{\beta_{ID}}{\beta_{RF}}}\sqrt{\sigma_{y'}^{\,2} + \sigma_\theta^{\,2}} \, . \qquad (1)$$

This expression is the same as obtained in Ref. [3] with the addition of a beta function ratio. Looking at this equation, one can see what steps are necessary to achieve as short a pulse as possible: higher rf voltage and frequency, smaller ratio of beta functions, and smaller electron beam size divergence and undulator radiation divergence.

Figure 1: Schematic of the rf deflection approach to producing a short pulse.

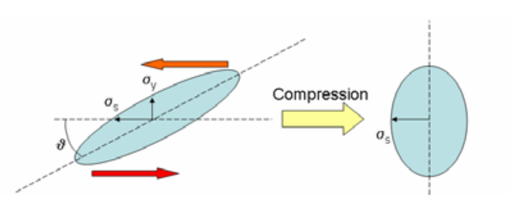


Figure 2: Illustration of pulse compression and minimum achievable pulse length.

---

* Work supported by the U.S. Department of Energy, Office of Science, Office of Basic Energy Sciences, under Contract No. DE-AC02-06CH11357.

#sajaev@aps.anl.gov

Extensive optimization of all parameters for achieving short pulses was performed for the APS storage ring [4]. Simulations rather than analysis of Eq. (1) were used for a number of reasons: the bunch length of the APS (70 ps rms) was comparable to the rf wavelength, making the rf kick strength nonlinear with the particle position in the bunch; vertical beam emittance was dependent on the deflecting rf voltage due to nonlinear coupling in the sextupoles; and second harmonic radiation in undulator affected the achievable pulse length.

For the ERL beam, the electron bunch duration (2 ps rms) is much shorter than the rf period, which keeps the entire beam in the linear region of the rf waveform. Sextupoles can be safely removed from the lattice between the cavities, thus removing beam emittance dependence on the rf voltage. For a longer undulator, the effect of the second-harmonic radiation also becomes less important. For the APS ring, having initial large vertical beam size presents difficulties for pulse compression using asymmetrically cut crystals [5], which is much less of an issue for the ERL since the beam size and divergence at the crystal will be smaller. Therefore, we will first analyze Eq. (1) and then perform simulations for cases of interest.

First, we will write Eq. (1) using expressions for the electron beam divergence and photon beam divergence:

$$\Delta t = \frac{E}{V\omega}\sqrt{\frac{\beta_{ID}}{\beta_{RF}}}\sqrt{\frac{\varepsilon_y}{\beta_{ID}} + \frac{\lambda}{2L_U}}\ ,$$

where $\lambda$ and $L_U$ are radiation wavelength and undulator length respectively, and we assumed that the beta function slope is zero in the middle of the undulator. According to this equation, the minimum pulse length depends on seven different parameters (we don't consider beam energy $E$ as a parameter – it is always 7 GeV).

For our analysis here we assume the following fixed parameters: $\beta_{ID}$=2 m, $\beta_{RF}$=20 m, $\varepsilon_y$=10 pm. The beta function choice is somewhat arbitrary (but reasonable). The emittance value was given by ERL gun simulations [6]. To analyze the effect of the undulator length on the achievable pulse duration, we further assume the following values for rf and radiation wavelength: V=6 MV, $\omega=2\pi\cdot 2.8$ GHz, and $\lambda$ =1.2 Å (photon energy 10 keV). Figure 3 shows the dependence of the pulse length on the undulator length. One can see that there is definitely a benefit in increasing undulator length from 2.4 m (standard APS undulator length) to at least 5 m. Considering also that longer undulators provide more photons, for our further analysis we chose an undulator length of 10 m. Figure 4 shows the dependence of the pulse length on the photon energy for three different rf settings: 4 MV and 1.4 GHz, 6 MV and 2.4 GHz, and 8 MV and 5.6 GHz. One can see that pulse length shows little change after about 10 keV, but different rf settings (different curves on the plot) affect pulse length significantly. For the most extreme rf values of 8 MV and 5.6 GHz, an rms pulse duration of about 25 fs could be achieved. Figure 5 shows pulse length as a function of rf voltage and frequency for 10-keV photon energy to demonstrate possible trade-offs between rf voltage and frequency.

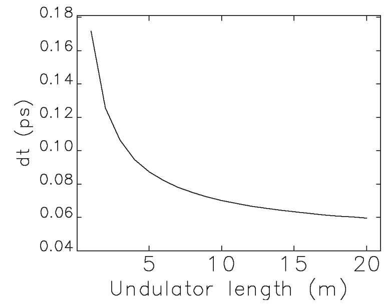


Figure 3: Minimum pulse length dependence on the undulator length for V=6 MV, $\omega=2\pi\cdot 2.8$ GHz, and $\lambda$ =1.2 Å.

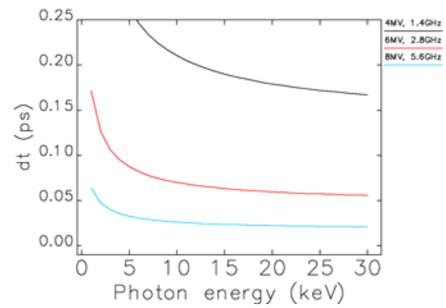


Figure 4: Minimum pulse length dependence on the photon energy for different rf voltages and frequencies.

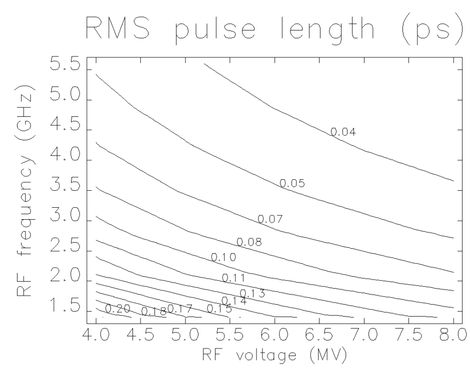


Figure 5: Minimum pulse length as a function of rf frequency and voltage.

## SIMULATIONS

We performed detailed simulations for the particular set of parameters shown in Table 1.

Table 1: Parameters Used in Simulations

| | |
|---|---|
| Beam energy | 7 GeV |
| RF voltage | 6 MV |
| RF frequency | 2.8 GHz |
| ID beta function | 2 m |
| RF beta function | 20 m |
| Vertical emittance | 10 pm |
| Undulator length | 10 m |
| Photon energy | 10 keV |

A description of the ERL lattice can be found in [7]. The insertion with deflecting cavities was placed at the end of the turn-around arc (TAA). For simplicity, we used TAA sectors for insertion but removed the dipoles and sextupoles. Deflecting cavities and the undulator were located in successive ID straight sections. The full insertion consists of four sectors with the symmetry point in the middle. The first sector brings the vertical beta function to 20 m at the first deflecting cavity, a second sector brings the beta functions to 2 m at the undulator, and the rest is reflectively symmetric. The vertical phase advance of each sector was tuned to 0.5 and the natural chromaticity was also minimized. The accelerator code `elegant` [8] was used for lattice matching and particle tracking.

For the initial particle distribution we used the results of a gun simulation with 0.1-micron normalized emittance [6]. The bunch was then tracked through the entire linac and TAA. At the insertion entrance, the vertical beam emittance was close to 11 pm·rad. At the undulator location, the photon distribution was generated by combining the electron distribution and the single-electron radiation pattern. The photon distribution was then propagated 30 m to a point where either an asymmetrically cut crystal can be used to compress the pulse or a slit can be used to slice it. Figure 6 shows the pulse shape before and after compression. The resulting rms pulse duration after compression was 62 fs. If calculated using Eq. (1), the pulse duration would be 70 fs.

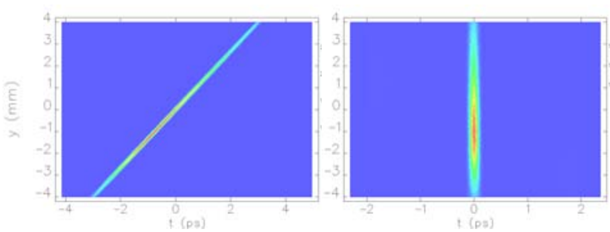


Figure 6: Photon pulse shapes before (left) and after (right) compression.

Figure 7 shows the pulse profile. One can see small peaks at around ±2 ps. These are produced by the second-harmonic undulator radiation. The intensity of the peaks is about 0.3% of the main peak intensity.

From our previous analysis of the rf deflection for the APS storage ring [3], we know that the vertical kick can increase the vertical beam emittance due to magnet nonlinearities and chromaticity between the cavities. Figure 8 shows the emittance at the exit of the insertion after the second cavity, as a function of rf frequency for two different rf voltages. A diamond symbol represents the point corresponding to the parameters in Table 1. The increase in this case is 6%, which can be tolerated. However, if one considers increasing the voltage and frequency, then the emittance increase might present a challenge and might require special study to mitigate the problem.

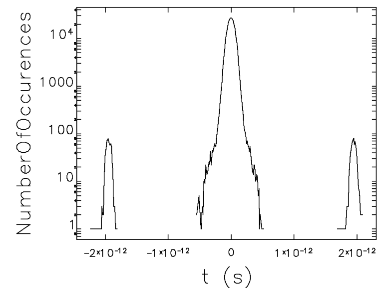


Figure 7: Photon pulse profile. The rms pulse length is 62 fs. Small peaks at around ±2 ps are produced by the second-harmonic radiation.

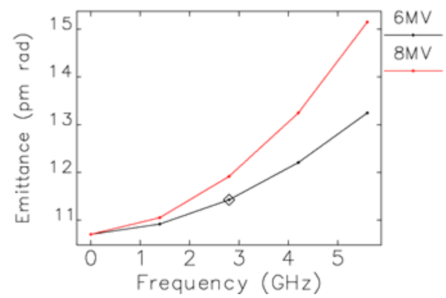


Figure 8: Vertical beam emittance after the second deflecting cavity for different rf frequencies and voltages. A diamond symbol shows the point corresponding to the parameters in Table 1.

## CONCLUSION

We have studied the application of an rf deflection scheme for achieving short pulses at an APS ERL. We have found that an rms pulse duration of 62 fs can be achieved with the beam and rf parameters shown in Table 1, which are very similar to those considered for the APS storage ring. We confirmed through tracking that vertical emittance of the beam does not increase significantly after the second cavity. We also have found that for some extreme rf parameters (8 MV and 5.6 GHz), the rms pulse length can be decreased to 25 fs.

## REFERENCES

[1] A. Zholents et al., Nucl. Instrum. and Methods A 425 (1999) 385.
[2] H. Wiedemann, Particle Accelerator Physics I, 2003, Springer
[3] M. Borland, Phys. Rev. ST Accel. Beams 8 (2005), 074001.
[4] M. Borland and V. Sajaev, Proceedings of PAC 2005, 3886 (2005).
[5] K. Harkay et al., Proceedings of PAC 2005, 668 (2005).
[6] Yin-e Sun, these proceedings.
[7] M. Borland, G. Decker, A. Nassiri, Y. Sun, and M. White, Proc. of AccApp'07, 196 (2007).
[8] M. Borland, “elegant: A Flexible SDDS-Compliant Code for Accelerator Simulations,” Advanced Photon Source LS-287, September 2000.

# SIMULATION OF LINEAR LATTICE CORRECTION OF AN ENERGY-RECOVERY LINAC DESIGNED FOR AN APS UPGRADE*

V. Sajaev#, ANL, Argonne, IL 60439, U.S.A.

*Abstract*

An energy recovery linac (ERL) is a possible candidate for an upgrade of the Advanced Photon Source (APS). Our ERL design includes full-energy linac, large turn-around arc that could accommodate new x-ray beamlines, and APS itself. In total, the beam trajectory length would be close to 3 km. The ERL lattice has a strong focusing to limit emittance growth, and it includes strong sextupoles to keep beam energy spread under control and minimize beam losses. As in storage rings, trajectory errors in sextupoles will result in lattice perturbations that would affect delivered x-ray beam properties. In storage rings, the response matrix fit method is widely used to measure and correct linear lattice errors. Here, we explore the application of the method to the linear lattice correction of ERL.

## INTRODUCTION

Linear optics measurement and correction using response matrix fit is well known and widely used on modern circular machines. The purpose of this work is to simulate the application of the same method to a non-closed beamline.

Theoretically, there is no big difference between response matrix measurement for closed and non-closed beamlines. The orbit equations are well-known and look similar (top equation is for non-closed trajectory and bottom is for closed trajectory, $\theta$ – is the kick strength):

$$x(s) = \theta\sqrt{\beta_s\,\beta_\theta}\,\sin(\psi_s - \psi_\theta),$$

$$x(s) = \frac{\theta}{2\sin(\pi\nu)}\sqrt{\beta_s\,\beta_\theta}\,\cos(\psi_s - \psi_\theta - \pi\nu)\,.$$

The measured trajectories in both cases depend on beta functions and phase advances and therefore could be used to derive linear optics. The main practical difference is that in the case of non-closed beamline, the response matrix is triangular with zeros in the top right triangle.

## SIMULATION DETAILS

At APS, we have been using response matrix fit method for many years [1]. We added an option of working with non-closed trajectories to our existing program. From our experience, we know that at APS the main source of focusing errors are non-zero orbits in sextupoles and we also know that the focusing errors from sextupoles cannot be precisely represented by nearest quadrupoles [2]. Therefore we decided to include sextupole displacements in error simulation. The following set of errors was used for simulations:

* Work supported by the U.S. Department of Energy, Office of Science, office of Basic Energy Sciences, under Contract No. DE-AC02-06CH11357.

#sajaev@aps.anl.gov

Table 1: Errors used in Calculations

| | |
|---|---|
| Quadrupole gradient error | 0.1 % |
| Quadrupole tilt | 0.001 rad |
| Sextupole X and Y displacement | 1 mm |
| Corrector calibration error | 5 % |
| Corrector tilt | 0.001 rad |
| BPM calibration error | 2 % |
| BPM tilt | 0.001 rad |
| BPM measurement noise | 1 μm |

Sextupole displacements were chosen rather large because trajectory errors in sextupoles are defined not by the accuracy of sextupole alignment but by the accuracy of nearest BPM offset which could be large. The errors were generated using Gaussian distribution with 2 sigma limit.

For optics correction simulation we used only APS portion of the ERL because the Turn-Around Arc design has not been finalized to a level of BPM and corrector locations. The lattice of the APS portion is described in [3], the lattice functions of one APS sector are presented in Figure 1. The main difference from the present APS storage ring lattice is zero dispersion in ID straight sections to decrease electron beam size dependence on energy spread. The APS consists of 40 nearly identical sectors.

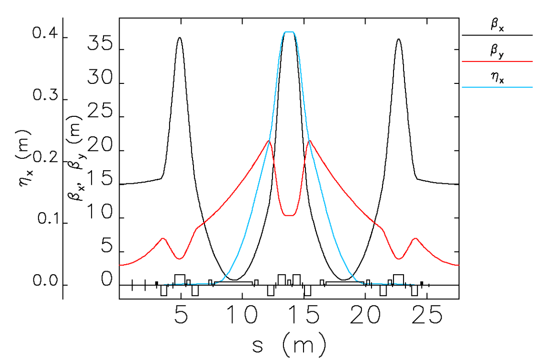


Figure 1: Lattice functions of one sector of the APS portion of the ERL.

Special attention was paid to the choice of correctors used for response matrix measurement in our simulations. APS storage ring has 8 correctors and 11 BPMs per sectors (in most sectors). Presently, for real measurements we use only 27 correctors in each plane (out of 320) evenly distributed along the ring and all BPMs. We limit the number of correctors in order to save measurement time and also to limit the size of the fitting problem. If all the correctors were used, the size of the response matrix derivative would be 15 Gb, which would be too big. Our experience shows that with 27 correctors we still have enough data for an accurate fit. In case of a circular machine, the location of correctors used for the response matrix measurement is not important as long as they are separated by some phase advance. However, the situation is different for a non-closed beamline where measured trajectory is affected only by elements that are located after the steering magnet. Therefore, for a non-closed beamline, different steering magnets provide different amount of useful information. Obviously, one would want to use as many steering magnets in the beginning of the beamline as possible while keeping them at some phase space distance. For our simulations, we used 27 correctors in each plane spread over first six sectors (out of forty) and none after that.

The following procedure was used to simulate the entire process of measurement and optics correction (`elegant` [4] was used for all beta function and trajectory calculations):

- `elegant` parameter file is generated with element errors;
- trajectory is corrected (because the sextupole displacements could lead to large trajectory errors) using 2 correctors per sector;
- "measured" response matrix and dispersion are calculated on the corrected orbit, response matrix is generated from two trajectories for each corrector using the same plus-minus delta approach that we use in real measurements;
- response matrix fit is calculated (dispersion included);
- quadrupole gradient errors opposite to those found in the response matrix fit are applied to correct the optics, and the resulting beta functions are compared with the ideal beta functions

The entire process was run 100 times with different error seeds. Figure 2 shows typical beta functions before beta function correction. For each case, we have calculated relative beta function difference between actual and ideal beta functions and its rms value (the rms value is calculated using all beta function points along the beamline). Figure 3 shows histogram of rms of relative beta function errors before correction. Average rms of the relative beta function difference over all cases is 0.71 for horizontal and 0.47 for vertical plane.

## CORRECTION RESULTS

All APS quadrupole magnets have separate power supply. Therefore, the straightforward way to correct the optics is to apply opposite quadrupole gradients. However, this method has some drawbacks that prevent us from using it in real life. To achieve the best possible response matrix fit, we use as many singular values in matrix inversion as possible. This might lead to appearance of large quadrupole errors in the solution. After we calculated beta functions using quadrupole errors from the response matrix fit, we use inverse beta function response matrix to correct the difference between measured and ideal beta functions. We also adjust the number of singular values in this inversion until we get satisfactory correction accuracy while still keeping quadrupole changes small. This allows us to minimize real quadrupole changes during optics correction at APS storage ring.

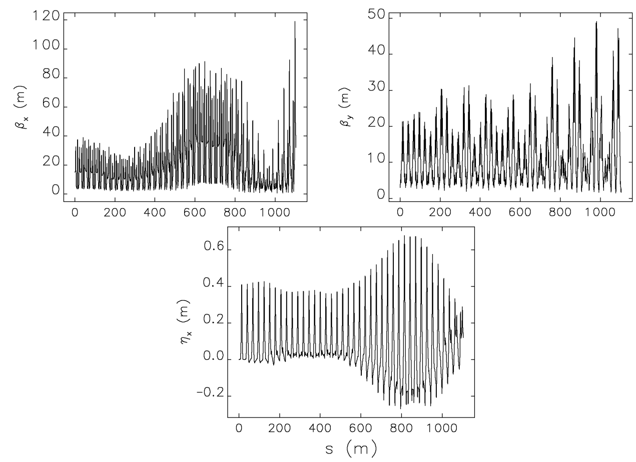


Figure 2: Typical beta functions before beta function correction. Top left – horizontal, top right – vertical, and bottom is dispersion.

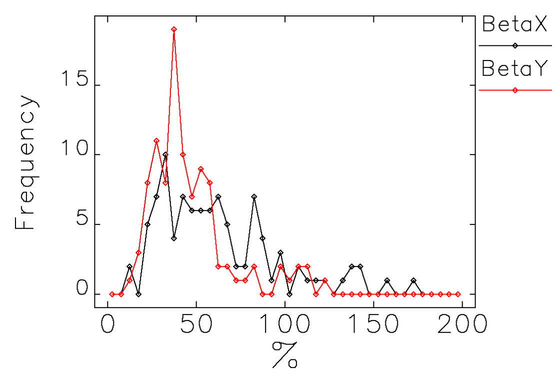


Figure 3: Histogram of the relative beta function error rms before beta function correction. Histogram is calculated over the set of 100 different error seeds. For every seed, the relative beta function error was calculated, and then rms was calculated using all beta function points along the beamline.

However, these arguments are not important for the optics correction simulation here, so we used the straightforward approach to keep our simulations simple. Figure 4 shows histogram of rms of relative beta function errors after correction. Average rms of the relative beta function difference over all cases is 0.03 for horizontal and 0.02 for vertical plane. Figure 5 shows typical lattice functions after correction.

We can estimate the effect of residual dispersion perturbation on the beam size using typical ERL parameters: $\varepsilon$=10pm and $\sigma_E$=0.02%. Maximum beam size increase at ID location due to energy spread contribution using dispersion on Figure 5 (bottom plot) is about 15%. If such accuracy of dispersion correction turns out to be not satisfactory, it can be corrected separately afterwards since the dispersion (unlike beta functions) can be directly measured by scanning beam energy.

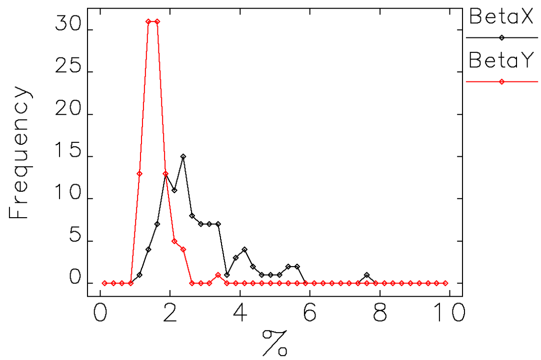


Figure 4: Histogram of the relative beta function error rms after beta function correction. See Figure 3 for comment on plot units.

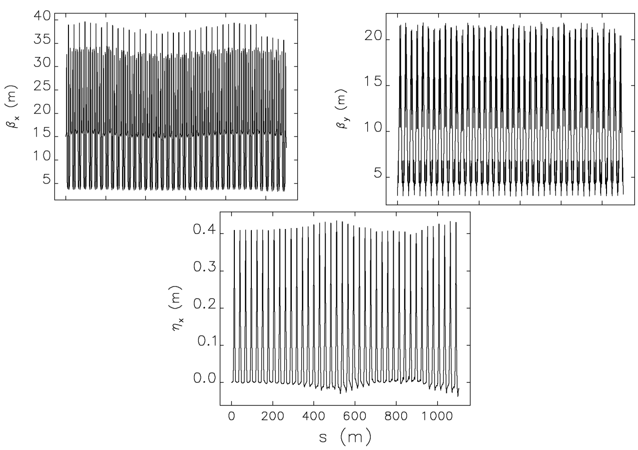


Figure 5: Typical beta functions after beta function correction.

One can ask why the correction is not perfect. Two reasons are obvious – due to BPM noise the response matrix measurement is not accurate and due to the fact that the focusing errors come from sextupoles but are corrected using quadrupoles in different locations. These reasons are likely to explain short-scale perturbations in beta functions. But we can also see a long-scale smooth variation in the horizontal beta function on Figure 5. The reason for that is inaccurate determination of focusing errors in the very beginning of the lattice because the first quadrupoles and sextupoles have only few trajectories going through them. If this argument is true, then the beta function variation can be corrected by adjusting initial beta functions at the entrance of the lattice. Figure 6 shows horizontal beta functions that were obtained by varying incoming beta function and its slope. A small change in initial beta function conditions allows correcting the long smooth variation seen on top left plot of Figure 5 thus confirming that quadrupole errors in the beginning of the beamline were not determined correctly. To improve accuracy for first elements of the measured beamline, one might use several correctors upstream of measured portion of the beamline.

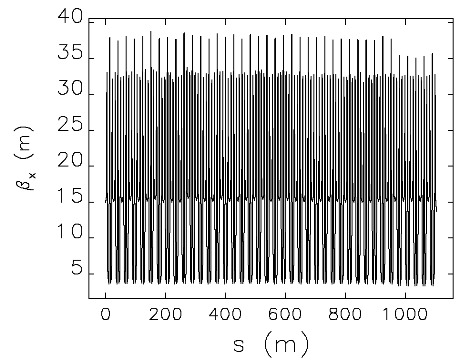


Figure 6: Horizontal beta function with adjusted initial conditions (to be compared with the top plot of Figure 5). A step change at the last 5 sectors is due to sector design difference.

During our simulations, we have also found that if the focusing errors of the lattice are large enough, sometimes the response matrix fit does not converge because the initial approximation (ideal lattice) is too far from the lattice with errors. We have tested the following procedure that helps in case of convergence problem: split lattice in pieces and perform response matrix fit piece by piece (not necessarily to be done to a very accurate level) and apply corrections from piece by piece solutions. After this step, the new lattice with errors is closer to the initial lattice and therefore can be solved without problems. This piece by piece approach will probably have to be used anyway when correcting optics of the entire ERL just to avoid long measurements and huge matrices. We have tested and confirmed that one can measure and correct only a part of the non-closed beamline.

## CONCLUSION

We have simulated optics correction for non-closed beamline using response matrix fit. As example we used suggested APS lattice in ERL mode. We have found that response matrix fit can be used to measure and correct linear lattice successfully. We have confirmed that one can measure and correct only a part of non-closed beamline which will be useful for large ERLs.

Author would like to thank M. Borland for useful discussions.

## REFERENCES

[1] L. Emery, V. Sajaev, “Determination and Correction of the Linear Lattice of the APS storage ring,” Proceedings of EPAC 2002.
[2] M. Borland, private communication.
[3] M. Borland, G. Decker, A. Nassiri, Y. Sun, and M. White, “Potential and Challenges of Upgrading the Advanced Photon Source to an Energy Recovery Linac," Proc. of AccApp'07, pp. 196-203, 2007.
[4] M. Borland, “elegant: A Flexible SDDS-Compliant Code for Accelerator Simulations”, Advanced Photon Source LS-287, September 2000.

# STATUS OF HIGH CURRENT R&D ENERGY RECOVERY LINAC AT BROOKHAVEN NATIONAL LABORATORY *

D. Kayran#, D. Beavis, I. Ben-Zvi, M. Blaskiewicz, J.M. Brennan, A. Burrill, R. Calaga, P. Cameron, X. Chang, A. Drees, G. Ganetis, D.M. Gassner, J. Grimes, H. Hahn, L. Hammons, A. Hershcovitch, H.-C. Hseuh, A. Jain, R. Lambiase, D. Lederle, V.N. Litvinenko, G. Mahler, G. McIntyre, W. Meng, T.C. Nehring, B. Oerter, C.-I. Pai, D. Pate, D. Phillips, E. Pozdeyev, J. Reich, T. Roser, T. Russo, A. Sharma, Z. Segalov, J. Smedley, K.S. Smith, T. Srinivasan-Rao, Tuozzolo, G. Wang, D. Weiss, N.W. Williams, Q. Wu, K. Yip, A. Zaltsman, BNL, Upton, NY, USA,
H.P. Bluem, M. Cole, A. Favale, D. Holmes, J. Rathke, T. Schultheiss, AES, Medford, NY, USA,
A. Todd, AES, Princeton, NJ, USA,
J. Delayen, W. Funk, L. Phillips, J. Preble, JLab, Newport News, VA, USA


## Abstract

An ampere class 20 MeV superconducting Energy Recovery Linac (ERL) is under construction at Brookhaven National Laboratory (BNL) [1] for testing concepts for high-energy electron cooling and electron-ion colliders. One of the goals is to demonstrate an electron beam with high charge per bunch (~ 5 nC) and extremely low normalized emittance (~ 5 mm-mrad) at an energy of 20 MeV. Flexible lattice of ERL loop provides a test-bed for testing issues of transverse and longitudinal instabilities and diagnostics of intense CW e-beam. The superconducting 703 MHz RF photoinjector is considered as an electron source for such a facility. At first we develop the straight pass (gun -- 5 cell cavity -- beam stop) test for the SRF Gun performance studies. Then the novel injection line concept of emittance preservation at the lower energy will be tested at this ERL. In this paper we present the status and our plans for construction and commissioning of this facility.


## INTRODUCTION

The R&D ERL facility at BNL aims to demonstrate CW operation of ERL with average beam current in the range of 0.1-1 ampere, combined with very high efficiency of energy recovery. The ERL is being installed in one of the spacious bays in Bldg. 912 of the RHIC/AGS complex.

The ERL R&D program is started by the Collider Accelerator Department (C-AD) at BNL as an important stepping-stone for 10-fold increase of the luminosity of the Relativistic Heavy Ion Collider (RHIC). Furthermore, the ERL R&D program extends toward a possibility of using 10-20 GeV ERL for future electron-hadron/heavy ion collider, eRHIC [2].

Future RHIC upgrades define the goals for the R&D ERL development to test: 1) Test the key components of the High Current ERL based solely on SRF technology; 2) 703.75 MHz **SRF gun** test with 500 mA current; 3) 5-cell **SRF linac** test with HOM absorbers; 4) Single turn - 500 mA test the beam current stability criteria for CW operation; 5) Test the attainable ranges of electron beam parameters in SRF ERL; 6) Demonstrate beam quality close to that required for RHIC electron cooling and scalability to eRHIC.

## GENERAL LAYOUT OF R&D ERL

The R&D ERL design (shown in Fig. 1) has one turn: electrons are generated in the superconducting half-cell gun and injected into the main superconductive linac. Linac accelerates electrons up to 15-20 MeV, when electron bunch pass through a one turn re-circulating loop with achromatic flexible optics [3].

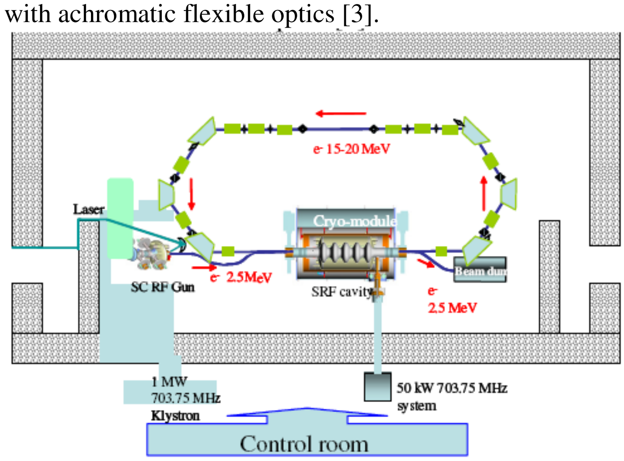


Figure1: Layout of the R&D energy recovery linac in the shielded vault.

The photocathode is located in a high electric field for immediate acceleration of the electrons to as high energy as possible, reducing emittance degradation due to strong space charge force. Furthermore, liner part of space charge effects is compensated by applying a suitable external solenoid magnetic field.

In nominal recovery operation regime the path-length of the loop provides for 180 degrees change of the RF phase, causing electron deceleration (hence energy recovery) down to injection energy. The decelerated beam separates from the higher energy beam and goes to the beam-dump.

## ERL INJECTOR

The electron injector is a central part of any ERL that

* Work performed under the auspices of the US Department of Energy
# dkayran@bnl.gov

has to deliver high brightness electron beam. The BNL R&D ERL injector (see Fig. 2) consist of ½ cell superconducting RF gun with photocathode inside [4], solenoid, four dipoles and two solenoids turned on in opposite direction. The 4th dipole mergers the high and low energy beams. One of the novel systems we plan to use for the R&D ERL is a merging system providing achromatic condition for space charge dominated beam and compatible with the emittance compensation scheme. Focusing of the bending magnets in the merging section has significant effect on the low energy electrons. Different focusing in vertical and horizontal planes (astigmatism) makes impossible simultaneous emittance compensation. Hence, the use of combined function magnets with equal focusing strength in x- and y-direction is necessary.

Table 1: Electron Beam Parameters of the R&D ERL

| **Mode** | **High current** | **High charge** |
|---|---|---|
| Charge per bunch, nC | 1.4 | 5 |
| Injection energy, MeV | 2.5 | 3 |
| Maximum beam energy, MeV | 20 | 20 |
| Average e-beam current, mA | 500 | 50 |
| Bunch rep. rate, MHz | 350 | 9.38 |
| Normilized emittance, mm*mrad | 2.3/2.3 | 4.8/5.3 |
| Rms energy spread, % | 0.5 | 1 |
| Rms bunch length, ps | 20 | 30 |

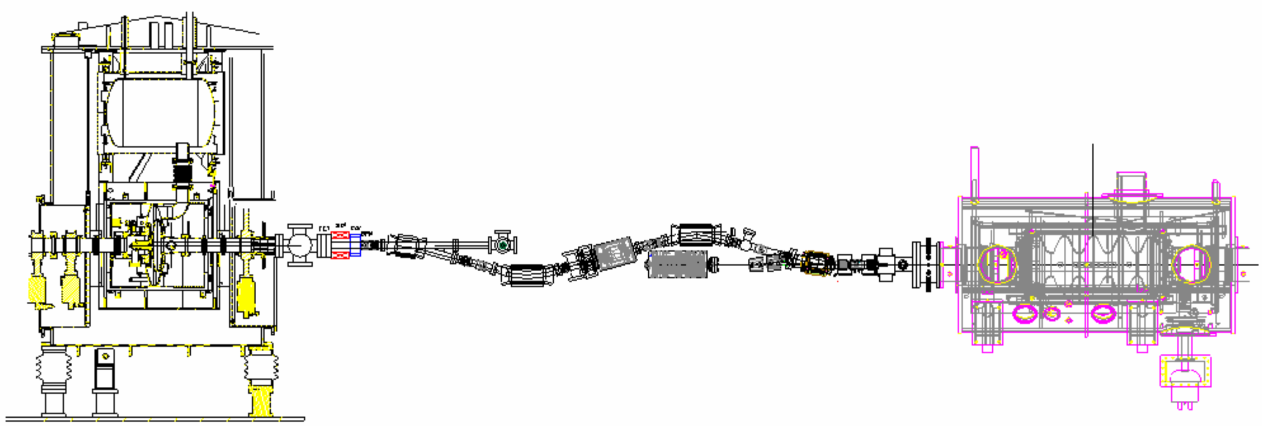

Figure 2: Detailed drawing of SRF Injector for the BNL R&D ERL.

Beam dynamics simulation shows that for Z-merger both vertical and horizontal emittances at the end of the linac can be the same [5].

The main expected electron beam parameters for the BNL R&D ERL obtained by PARMELA [6] simulations are listed in Table 1.

Due to the bends in vertical direction the effect of vertical emittance growth is clear. But at the exit of Z-merger both: vertical and horizontal emittances become almost equal. In case of 5 nC per bunch this equality is broken, the next order nonlinearity start playing a role.

## 5 CELL SRF LINAC

The heart of the ERL facility is 5-cell SRF linac, which is designed for operating with ampere-class CW beam current [7]. The cavity was designed as a “single-mode” cavity, in which all Higher Order Modes (HOMs) propagate to HOM ferrite absorbers through the large beam pipe. Measurements of the damped Q and R/Q of the HOMs and simulations show that in nominal operation regime the cavity is stable to over 20 amperes in a one pass ERL and over 2 amperes for two passes ERL.

The 5-cell SRF linac successfully went through vertical test at Jlab and the 20 MeV/m accelerating voltage was demonstrated [8]. We are finishing of the cryostat assembly (see Fig .3) and the cavity will go through a horizontal (a normal mode of an operation) cold-emission test (CET) in the ERL cave in November 2008.

Figure 3: 5-cell cavity in the cryomodule.

## GUN 5-CELL CAVITY TEST

We will start ERL commissioning from gun through 5-cell cavity (G5) beam test in 2009. The layout of G5 test is shown in Fig. 4.

During the G5 test we will have two modes of measurements:

1) in straight ahead mode: the quadrupole scan and flag will be used to measure projected emittances transverse halo and;
2) turning on bending magnet mode gives the nice opportunity to measure longitudinal parameters of

the electron bunch:: bunch length, longitudinal tails. Slice emittance will be measured using off crest RF operation and slits.

All flags will be driven by multi-position pneumatic actuators, and will have both YAG and OTR capability at each location. Images will be viewed off the ERL plane via mirrors.

The expected parameters for G5 test are summarized in Table 2.

Table 2. Main Parameters of Electron Beam for G5 Test

| | |
|---|---|
| Charge per Bunch: | 0.05-5 nC |
| Gun Energy: | 2.5 -3 MeV |
| Maximum Energy: | 20 MeV |
| Energy spread on crest | 3% ,off crest 15% |
| Max. Average current: | 500 nA |
| Max. Rep Rate: | 100 Hz |
| Average Power: | < 10 W |

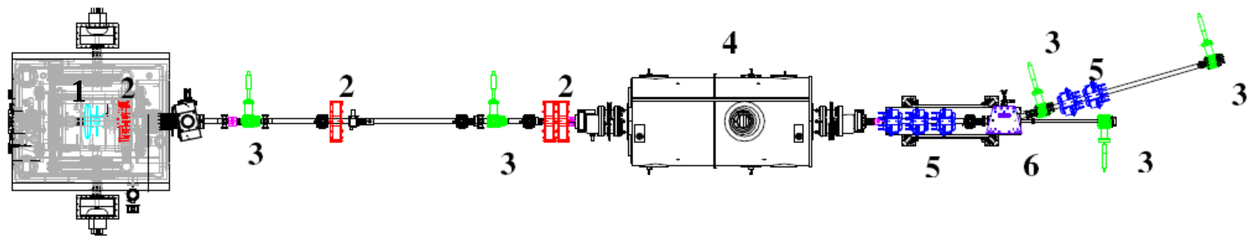


Figure 4: Detailed drawing of G5-test: 1 - 703MHz SRF gun; 2 – solenoids; 3 - beam profile monitors; 4- 5cell SRF cavity; 5-quadrupoles; 6-dipole magnet. 2.5 MeV electron beam from SRF gun propagates through a straight section with beam diagnostics: BPMs, pepper-pot, YaG/OTR screens. Then beam is accelerated in 5-cell cavity to 20 MeV.

## STATUS AND PLANS

Many of the ERL subsystem and most of its infrastructure had been installed in the Bldg. 912 of the CAD complex:

- 5-cell Cavity is being processed and tested at JLAB, cold emission test 5-cell cavity in cryostat at BNL in November 2008
- 1 MW Gun klystron and 50 kW 5-cell cavity transmitter are installed, tested with dummy load at 0.6 MW level
- Recirculation loop magnets and vacuum system components are ready for installation
- Gun drive laser is been procured, will arrive in October 2008
- RF control will be based on the new digital RHIC LLRF. The LLRF system is currently under development.
- Machine protection system is being designed (BLMs, DCCTs)
- Gun is under construction at AES

BNL starts commissioning of the R&D ERL in 2009:

1) the straight pass (G5 test) or the beam quality studies.
2) test concept of emittance preservation in a beam merger in the same configuration as above
3) complete recirculation loop, demonstrate energy recovery with high charge per bunch and high beam current
4) study beam and stability issues relevant for high current ERLs

The availability of high current electron beam with low emittance (see Table 1) opens new perspective of using BNL R&D ERL as an electron beam provider for free electron laser [9]

After the testing main components of ERL in building 912 we are planning to use 20 MeV BNL R&D ERL to do a CeC proof-of-principle experiment to cool Au ions in RHIC at ~ 40 GeV/n [10]. As an example, the layout of CeC proof-of-principle test installed at RHIC IR2 is shown in Fig. 5 PoP CeC experiment using this ERL at RHIC could be possible in 2012

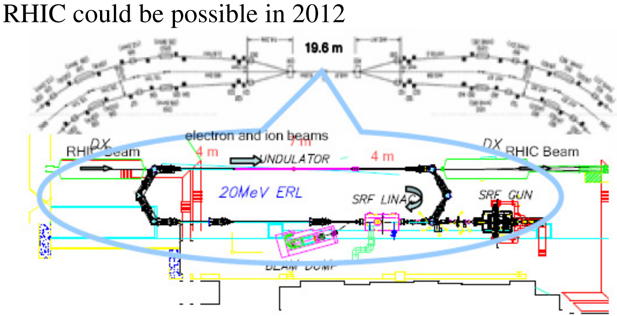


Figure 5: Coherent electron cooling proof-of-principle layout at RHIC IR2.

## REFERENCES

[1] I. Ben-Zvi at al., Proceeding of PAC'05. p. 1150
[2] T. Hallman, T. Kirk, T. Roser and R.G. Milner, http://www.bnl.gov/henp/docs/NSAC_RHICII-eRHIC_2-15-03.pdf
[3] D. Kayran et al, Proceeding of PAC 2005, p. 1775.
[4] A. M. M. Todd et al., Proceeding of PAC'05, p.2292.
[5] V.N. Litvinenko, R. Hajima, D. Kayran, NIM A 557, (2006) p. 165.
[6] L. M. Young, J. H. Billen, "Parmela documentation", LA-UR-96-1835.
[7] R. Calaga et al., "High Current Superconducting Cavities at RHIC", TUPKF078, Proceedings of EPAC-2004, Geneva, Switzerland, July 5-9, 2004
[8] A.Burrill et al., Proceeding of PAC'07, p.2541,
[9] D. Kayran et al. Proceeding of FEL 2007, p. 232.
[10] V.N. Litvinenko, Y.S. Derbenev, Proceeding of EPAC'08, pp. 2560

# ELECTRON LINAC BASED COHERENT RADIATION LIGHT SOURCE PROJECT AT OPU*

S. Okuda#, Y. Sakamoto, R. Taniguchi, T. Kojima, Radiation Research Center, Osaka Prefecture Univ., Sakai, Osaka 599-8570, Japan

*Abstract*

The coherent radiation from an electron bunch of a linear accelerator (linac) has continuous spectrum in a submillimeter to millimeter wavelength range and has an intense pulsed electric field. The purpose of the present work is to establish a new light source of the coherent synchrotron and transition radiation from the electron beams of a 18 MeV S-band linac at Osaka Prefecture University (OPU). The pulse shape of the radiation has been evaluated from the electron bunch shape. The system of the light source has been optimized. The light source will be applied to the excitation of various kinds of matters and to the pump-probe experiments using the electron beam and the coherent radiation.

## INTRODUCTION

The coherent radiation from a short electron bunch of a linac has continuous spectrum in a submillimeter to millimeter wavelength range at a relatively high peak-intensity. After the first observation of the coherence effect in synchrotron radiation the radiation processes have been investigated.

The peak intensity of the coherent radiation is extremely high compared with those of the other light sources. The coherent synchrotron and transition radiation light sources have been applied to absorption spectroscopy for various kinds of matters [1-4], especially for matters with relatively strong light absorbance. Recently, the absorption spectroscopy system using the coherent transition radiation from the electron beams of the L-band electron linac under relatively simple configurations has been established at Kyoto University Research Reactor Institute [5], and has been generally used for experiments.

As well as the applications as probes the high peak intensity and the short pulse shape of the radiation are expected to be used for excitation of matters and time-resolved experiments. Such applications are not performed so far.

The present work has been performed to establish the new coherent radiation light source applied to the excitation of matters and the pump-probe experiments.

## COHERENT RADIATION LIGHT SOURCE

Synchrotron and transition radiation from short electron bunches of a linac becomes coherent and highly intense at wavelengths longer than the bunch length. It has a continuous spectrum in a submillimeter to millimeter wavelength range. The wavelength range of the radiation is determined by the length and the shape of the electron bunch. In general cases the wavelengths correspond to the terahertz and the lower frequencies of light. The peak intensity of the coherent radiation is extremely high compared with those of the other terahertz light sources.

The coherent synchrotron radiation is emitted as a linearly polarized, unipolar and pulsed electric field. The pulse shape of the electric filed is determined by the electron bunch shape. In our previous work investigating the electron bunch form factors from the coherent radiation spectra the bunch shape of an linac beam has been found to be approximated as triangular [6]. The light pulse has a short length corresponding to the bunch length, typically within a few picosecond in the case of the electron bunch of an S-band linac. It might be possible to use the coherent transition radiation for obtaining the similar pulsed light as well as the coherent synchrotron radiation.

The coherent radiation induces intense pulsed electric field in a matter and results in the excitation of it. In the case of the coherent radiation the electric field induced in a matter is expected to be more than 10 MV/cm.

## LIGHT SOURCE SYSTEM

The new light source for the excitation of matters and the pump-probe experiments by using a 18 MeV S-band electron linac at OPU has been investigated.

### *OPU Electron Linac*

The accelerator system of the OPU S-band linac is schematically shown in Fig. 1. Pulsed electron beams are injected from a thermionic triode gun with a cathode-grid assembly. The maximum energy, pulse lengths, the maximum pulse repetition rate of the beam are 18 MeV, 5 ns-5 μs and 500 pulses/s, respectively. The accelerated beam is bent to an underground irradiation room, where the energy spectrum of the beam is measured. In this

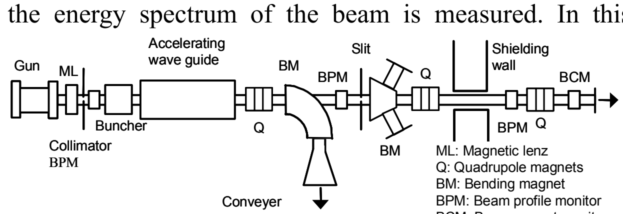


Figure 1: Schematic diagram of the OPU electron linac system.

*Work supported in part by the program of KEK for supporting accelerator research activities in universities, and KAKENHI (20360421).
#okuda@riast.osakafu-u.ac.jp

room a beam scanner for the irradiation over a relatively large area of samples is installed.

The beams transported to the straight direction through a hole in a concrete shielding wall are used in the other irradiation room for various experiments such as irradiation experiments with narrow beams and pulse radiolysis experiments. The present system for the new light source is located in the end of the straight beam line.

The operational conditions of the linac components such as waveguides and the beam steering magnets are optimized to obtain the highest intensity of radiation at the light detector. In this process relatively strong bunch compression in accelerator waveguides results in the increase of the radiation intensity by two or three orders of magnitude. Such conditions have been previously investigated [7]. While the energy spectrum of the electron beam slightly spreads in the operational conditions, this does not affect the straight beam transportation to the light source as shown in Fig. 1.

In order to perform the time-resolved experiments the grid pulser of the electron gun of the linac has been improved for generating short pulse electron beams at a length of 5 ns. It will be improved to be shorter to obtain a single-bunch beam. The trigger system for the pump-probe experiments has already been established for the pulse radiolysis experiments.

### *Evaluation of the Coherent Radiation*

In the usual cases the radiation is suppressed in the relatively long wavelength range because of the limited space of the vacuum chamber made of conductor [8]. The absorption of the light in the path of transportation possibly causes the deformation of the pulse shape. In order to establish a new light source the characteristics of the radiation has been evaluated. The pulse shape of the

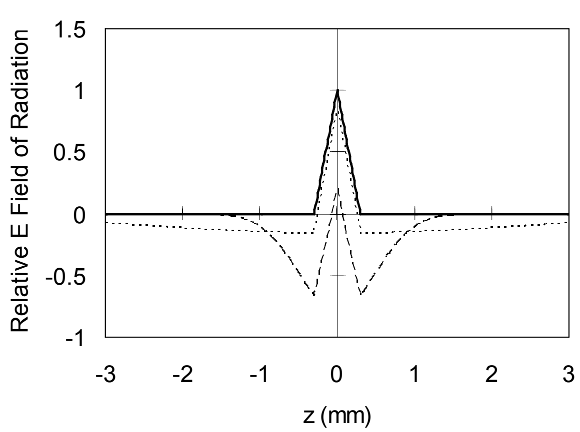


Figure 2: Pulse shape of the electric filed of the coherent synchrotron radiation obtained by calculation for the isosceles triangular electron bunch at a FWHM length of 1 ps. No suppression (solid line) and suppression of radiation at wavelengths longer than a cutoff wavelength of 1 (dashed line) and 5 (dotted line) mm have been assumed.

electric filed of the coherent radiation obtained by calculation for the triangular electron bunch at a FWHM length of 1 ps is shown in Fig. 2. The complete suppression of radiation at wavelengths longer than a cutoff wavelength has been assumed in the calculation. As shown in this figure the peak electric field decreases with the cutoff wavelength. From these results it has been found that the cutoff of radiation at wavelengths shorter than 5 mm should be avoided in order to obtain sufficient peak field intensities of radiation.

The electric field induced in matters by the coherent radiation has been estimated to be higher than 1 MV/cm.

### *Setup for Pump-Probe Experiments*

The important applications of the coherent radiation light source are pump-probe experiments, where matters are excited with the electron beams or the pulsed coherent radiation in a short period which corresponds to the bunch length and is typically within a few picosecond in the case of S-band linac. In the light source project at OPU the system schematically shown in Fig. 3 is established. In this system the coherent synchrotron and transition radiation is used as light sources. The sample is excited by pulsed electrons used for the source of light or by the pulsed radiation. A part of the radiation synchronized with the pumping beam is used as a probe to perform the time-resolved absorption spectroscopy after the excitation. On the path of light a delay line is installed.

The grid pulser of the electron gun of the linac will be improved for generating single-bunch electron beams in the near future.

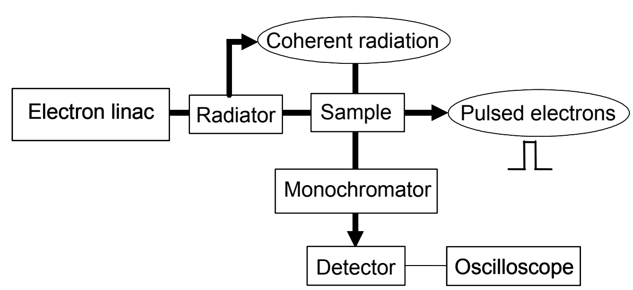


Figure 3: Schematic diagram of the pump-probe experimental setup.

## CONCLUSIONS

Study has been made to establish a new light source of the coherent synchrotron and transition radiation from the electron beams of a 18 MeV S-band linac at OPU. The pulse shape of the radiation has been evaluated from the electron bunch shape. The system of the light source has been optimized. The light source will be applied to the excitation of various kinds of matters and to the pump-probe experiments using the electron beam and the pulsed coherent radiation.

## REFERENCES

[1] T. Takahashi, T. Matsuyama, K. Kobayashi, Y. Fujita, Y. Shibata, K. Ishi and M. Ikezawa, Rev. Sci. Instrum. 69 (1998) 3770.
[2] K. Yokoyama, Y. Miyauchi, S. Okuda, R. Kato and T. Takahashi, Proc. 20th Int. Free-Electron Laser Conf. (Williamsburg, USA, 1998) pp. II17-18.
[3] S. Okuda, M. Nakamura, K. Yokoyama, R. Kato and T. Takahashi, Nucl. Instrum. Meth. A445 (2000) 267.
[4] S. Okuda, M. Takanaka, M. Nakamura, R. Kato, T. Takahashi, S. Nam, R. Taniguchi and T. Kojima, Radiat. Phys. Chem. 75 (2006) 903.
[5] S. Okuda and T. Takahashi, Infrared Phys. Technol. 51 (2008) 410.
[6] M. Nakamura, M. Takanaka, S. Okuda, T. Kozawa, R. Kato, T. Takahashi and S. Nam, Nucl. Instum. Meth. A475 (2001) 487.
[7] S. Okuda, M. Nakamura, M. Takanaka, T. Kozawa and S. Nam, Proc. 23rd Int. Free-Electron Laser Conf., Darmstadt, Germany, 2001, II-49.
[8] R. Kato, T. Nakazato, M. Oyamada, S. Urasawa, T. Yamakawa, M. Yoshioka, M. Ikezawa, K. Ishi, T. Kanai, Y. Shibata and T. Takahashi, Phys. Rev. E 57 (1998) 3454.

# ENHANCEMENTS TO THE DIAMOND LIGHT SOURCE PRE-INJECTOR LINAC

C. Christou, S. J. Singleton and V. C. Kempson, Diamond Light Source, Oxfordshire, UK

*Abstract*

Modifications have been made to the Diamond pre-injector linac to improve beam stability and to increase the scope of operation of the system. New modes of operation are described and RF stability studies are presented. Operational experience is summarised, and options for future development are considered.

## MODES OF OPERATION

The DLS pre-injector is a 3 GHz, 100 MeV linac delivering up to 3 nC in a bunch train of up to 1000 ns, or a single bunch of up to 1 nC. It has a bunching section and two identical accelerating structures driven by two Thales TH2100 klystrons, and a thermionic DC gun [1].

Beam from the linac is delivered through a full-energy booster to the 3 GeV storage ring. For user operation, beam is injected as required, usually topping up twice a day to the present operating level of 225 mA. During fills the linac and booster are cycled together at 5 Hz

Linac single-bunch operation has recently been incorporated into the Diamond top-up application [2] and into an automated single bunch filling routine for the storage ring, both implemented in Python. For both applications, the linac gun and booster extraction timing is set each shot so that the bunch is injected into the bucket with lowest charge relative to a programmed fill pattern. Linac bunch charge is kept constant for top-up, but is programmed during the single bunch fill to generate a smooth fill in the minimum time: high-charge bunches are first injected into empty buckets, and charge is reduced as the bucket approaches its target. Bunch charge is controlled by setting the bias on the triode gun, as illustrated in Figure 1. Top-up uses low bunch charge, whereas single bunch fill covers the entire range. Single bunch injection efficiency into the booster is 80% at low bunch charge falling to below 50% at high bunch charge. Injection efficiency studies are continuing, with attention being paid to booster chromaticity on injection [3].

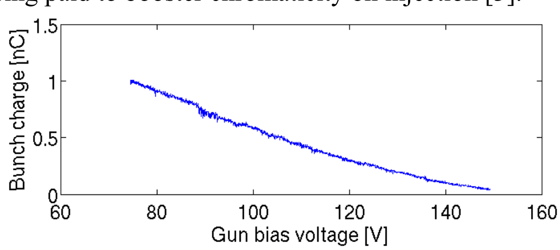


Figure 1: Single bunch charge as a function of gun bias.

Since the beginning of user operations in January 2007 most storage ring fills for user operation have used the multibunch mode of the linac, with trains of 144 buckets injected every 120 buckets over two-thirds of the ring. The 24 bucket overlap overcompensates for the 30 ns rise-time of the linac long-pulse envelope, and generates small peaks in the storage ring fill pattern [4]. The single bunch fill generates a very smooth fill, as shown in Figure 2. The smooth fill from buckets 100 to 600 is much better than that could be achieved by multibunch injection. This figure also illustrates the hybrid fill, which can be routinely generated for users on request. Hybrid fill may be generated by a multibunch two-thirds fill followed by single bunch injection, or by using the single bunch fill for the entire fill. Switching fill modes is quicker, because of the higher charge available in multibunch mode, but the automatic single bunch fill is simpler to carry out.

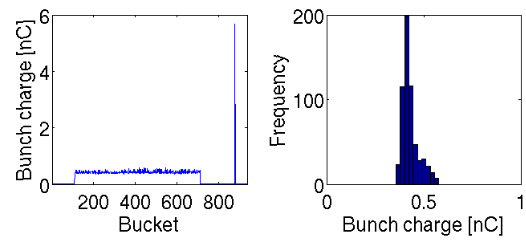


Figure 2: Hybrid fill generated using single bunch fill and histogram of bunch charge over two-thirds fill.

Long-duration tests of linac and booster reliability have been carried out in preparation for routinely offering top-up to users. Figure 3 summarises a continuous linac and booster run (with three short breaks for storage ring fills), showing a very reliable bunch charge delivered to the booster with a mean and standard deviation of 0.125 nC and 0.014 nC respectively over 24 hours.

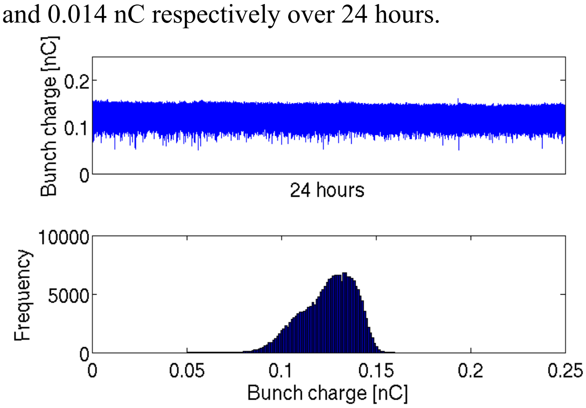


Figure 3: 24 hour run of linac and booster showing the beam delivered to the booster (top) and histogram of bunch charge (bottom).

A recent test of the complete top-up application is summarised in Table 1. At the start of top-up the gun bias was set so that the number of shots per top-up cycle was around 10 to reduce the variation in charge along the bunch train to 10% or less while minimising the disturbance of the stored beam. The number of shots to be fired in each cycle is calculated by the top-up software from the loss of current during the previous cycle, using the average charge injected per shot over the last 10 cycles. Linac bunch charge was consistent over the test, and resulted in a stable, reproducible top-up cycle.

Table 1: Summary of Top-Up Operation Test

| | |
|---|---|
| Duration of test | 7 hours |
| Fill pattern | Two-thirds fill |
| Mean storage ring current | 199.875 mA |
| Storage ring current range | 199.652 mA - 199.875 mA |
| Period between top-ups | 2 minutes |
| Average shots per top-up | 9.22 |
| Current stability | 0.043% |
| Mean charge in BTS | 0.068 nC |
| Mean BTS to SR efficiency | 73.05% |

## STABILITY AND RELIABILITY

A stable linac beam is essential for reliable operation of Diamond with minimum beam losses at booster injection. Continuous application of a constant phase, constant power RF signal to the prebuncher cavity has cured multipacting there, and locking the gun heater power supply and booster dipole to a common 50 Hz oscillator derived from the timing system rather than the mains supply removed the largest variation in booster injection efficiency[4]. A slow variation of booster current still remained after these improvements, with the standard deviation of a moving sample of booster current increasing when the mains frequency drifted from 50 Hz. This was a linac energy effect and is shown in Figure 4.

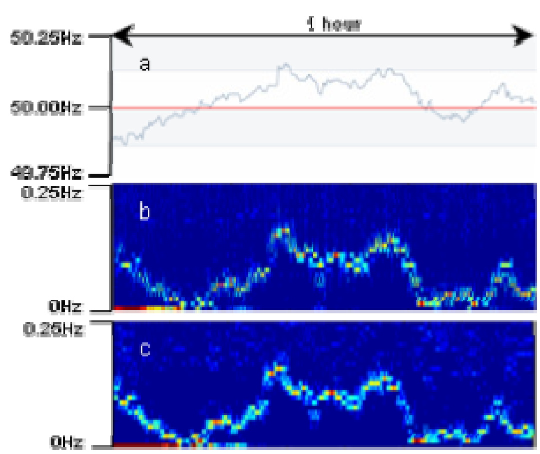


Figure 4: (a) Mains frequency, (b) frequency spectrum of booster current and (c) frequency spectrum of linac beam energy recorded over one hour.

The frequency spectrum of the booster current and the linac energy measured at a BPM in a dispersive part of the LTB correlate strongly with the deviation of the mains frequency from 50 Hz. No such oscillations were seen in the klystron preamplifier, and so it was clear that the oscillation was generated in the klystrons.

Locking the mains-driven klystron filament heaters to the same 50 Hz signal as the gun and the booster dipole removed this effect, as can be seen from Figure 5 in which one klystron filament heater is driven from the mains, and one is driven from the 50 Hz oscillator; the spectral content of the klystron locked to the 50 Hz signal has been removed.

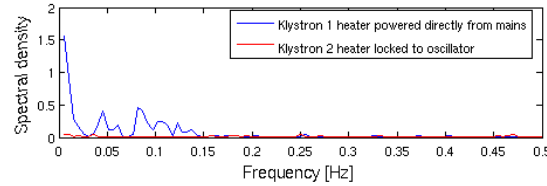


Figure 5: Comparison of klystrons with heater powered by mains (blue) and locked to the timing oscillator (red).

Sensitivity of the linac LLRF to the operating temperature in the controls rack has been noted and is controlled by enhanced cooling of this rack [4]. Further analysis of klystron operation in Figure 6 shows that klystron amplification is roughly linear over the range used in normal operation, usually > 30 W. If the preamplifier output is increased then the klystrons can be moved towards saturation and so the effect of the preamplifier thermal droop will be reduced. Preamplifer output is currently limited by cable losses at 3 GHz. Reconfiguration of the LLRF to reduce losses will also have the benefit of reducing the operating voltage of the klystrons and therefore reduce klystron arcing further.

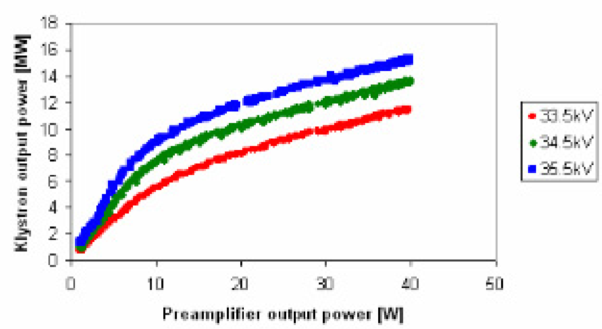


Figure 6: Klystron operation at different values of modulator PFN charging voltage.

Minimisation of klystron arcing is essential for reliable operation of top-up. At the moment klystron arcing is only a problem during klystron start-up following a machine shut-down, when the voltage must be brought up in a slow controlled manner to recondition the gun. A Matlab script has been developed for this. Klystron reconditioning takes roughly ten minutes, after which the arc rate is low, for example there were no arcs in either klystron in either the 24 hour injector test or seven hour top-up tests above. The operating point of the klystron filament is also reviewed annually to minimise arcing, and the filament voltage has been dropped twice in 2 V increments since initial commissioning of the klystrons.

Lifetime is monitored by calculation of klystron perveance during operation. The perveance record of one of the two klystrons since beginning of user operations is shown in Figure 7, showing no significant drop in perveance over this period. The spikes on the plot are artefacts recorded during klystron turn-on and turn-off. The performance of the second klystron is similar.

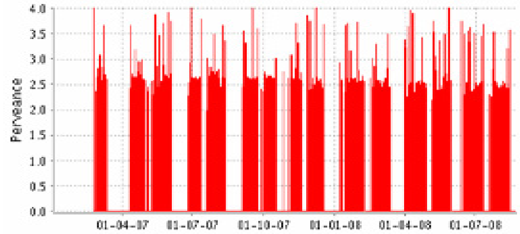


Figure 7: Klystron perveance record.

## SINGLE KLYSTRON OPERATION

Perveance monitoring can be used to give early warning of klystron cathode failure, allowing replacement in a shutdown as far as possible, but unexpected klystron failure may still occur during user operation. One spare klystron is held on site, but standard operation is impossible for the duration of the klystron change and recommissioning. Operation of the injection system with one klystron has therefore been investigated, and injection of beam into the storage ring has been achieved with low-energy single klystron linac operation. Table 2 is a comparison of linac beams generated by one and two klystrons. Some increase of beam energy is possible by running the single klystron at a higher power.

Table 2: Single and Double Klystron Operation

| | One klystron | | Two klystrons | |
|---|---|---|---|---|
| Energy | 44.9 MeV | | 99.9 MeV | |
| Energy spread | 0.3 % | | 0.3 % | |
| | x | y | x | y |
| $\varepsilon_N$ [mm.mrad] | 32.7 | 42.6 | 39.6 | 39.2 |
| α | -1.28 | -0.22 | -1.11 | -0.50 |
| β [m/rad] | 5.89 | 0.72 | 2.47 | 2.60 |

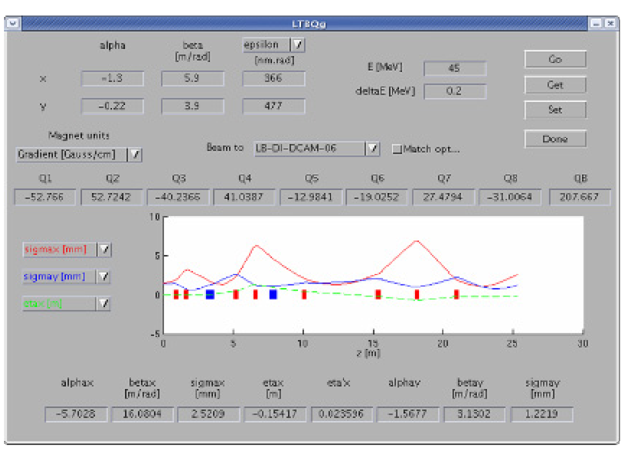


Figure 8: LTB quadrupole current tool.

Operation of the linac with one klystron requires changes to LTB and booster. Quadrupole settings for the LTB at reduced energy were calculated with the LTBQg tool, which performs a least-squares minimisation of the beam size along the transfer line whilst constraining the Twiss parameters at the LTB entrance and exit [5]. Figure 8 shows LTB parameters calculated using this tool.

Injection into the booster was achieved by scaling all magnets at injection according to the reduced beam energy and then empirically optimising the values, this involved modifying the quadrupole power supplies to operate at a lower start value for the ramp. Injection efficiency into booster and storage ring is currently much lower for single klystron operation, but it is expected that this can be improved by further optimisation of operating parameters. Again, booster chromaticity on injection is being studied.

Single klystron operation is only possible by powering the first accelerating structure and drifting through the second structure, and so studies are underway to introduce a switching mechanism in the WR284 waveguide network at the output of the klystrons as shown in Figure 9. This would allow accelerating structure 1 to be powered from klystron 2. Such a switching network is installed in other pre-injector linacs [6, 7].

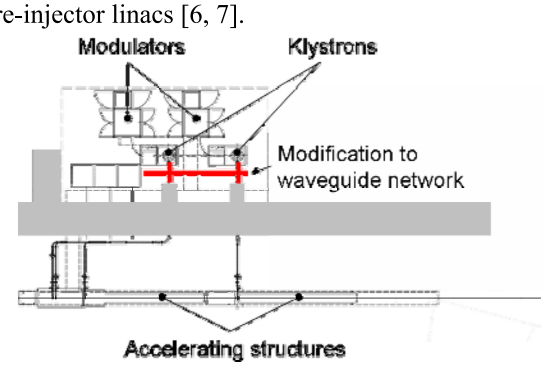


Figure 9: Waveguide modification for klystron switching.

## SUMMARY

Two new modes of operation have been developed in the second year of operation of Diamond: firstly, the Diamond pre-injector linac has been fully incorporated into top-up operation, and secondly high-uniformity storage ring fill has been delivered to users by operating the linac in a programmed single bunch mode. A new fault-mode of operation using one of the two linac klystrons is also under development. Linac stability has been improved by modification of the klystron filament power circuit, and options for further stability and reliability enhancements have been identified in both low-level RF and high-power RF distribution.

## REFERENCES


[1] C. Christou, et al, EPAC 2006, Edinburgh, p 3187.
[2] R. P. Walker et al, EPAC 2008, Genoa, p 2121.
[3] C. Christou et al, EPAC 2008, Genoa, p 2157.
[4] C. Christou et al, PAC 2007, Albuquerque, p 1112.
[5] R. Bartolini et al, EPAC 2006, Edinburgh, p 3065.
[6] B. Pottin et al, PAC 2005, Knoxville, p 755.
[7] G. D'Auria et al, EPAC 2008, Genoa, p 2160.

# NORMAL CONDUCTING OPTIONS FOR THE UK'S NEW LIGHT SOURCE PROJECT

C. Christou, R. Bartolini, J.-H. Han, H. Huang and J. Kay
Diamond Light Source, Oxfordshire, UK

*Abstract*

This paper considers the design of a normal-conducting linac FEL in the context of the UK's New Light Source project. Capabilities and limitations of this approach are illustrated by reference to a 3 GeV S-band linac design. The effects of high repetition rate operation and RF jitter are considered.

## THE NEW LIGHT SOURCE PROJECT

The UK's New Light Source (NLS) project [1] was launched in April 2008 to consider the scientific case and develop a conceptual design for a possible next generation light source. The outline facility design will be agreed by January 2009 following consultation with the user community throughout 2008 after which a design report and proposal for funding will be prepared for submission in October 2009.

A high (> 400 Hz) repetition rate of single pulses demands superconducting linac technology operating in continuous-wave. Normal conducting linac technology is however significantly cheaper, allowing a higher energy to be reached for a given cost. Design studies are ongoing for both normal conducting and superconducting linacs. This paper reviews the options for a normal conducting NLS design; a companion paper reviews the superconducting approach [2].

## LINAC LIGHT SOURCE PROJECTS

There has been much recent interest in the use of normal conducting technology for linac FELs. Most projects in construction or development use the well-proven S-band technology used at SLAC for several decades whereas SCSS exploits C-band technology developed in the JLC(C) programme. LCLS and SCSS are scheduled for completion in 2009 [3] and 2011 [4] respectively. The study presented here considers an S-band linac for NLS, although X-band technology has not been ruled out, particularly considering possible technology developments following the decision to change the CLIC design frequency to 12 GHz [5].

## NORMAL CONDUCTING TECHNOLOGY

Virtually all high-power klystrons operating today are driven by line-type modulators using a reactive pulse forming network (PFN) and a thyratron switch. The line-type modulator can be the dominant cost driver in a linac [6]. The self-terminating nature of the line-type discharge limits the modulator operation: the pulse length can only be changed by switching the connections to multiple PFNs, and the trailing edge of the pulse is usually not sharp since it depends on the discharge of multiple reactive elements. The modulator cannot drive loads of different impedances, and the thyratron has a limited operational lifetime. The overall efficiency of a line-type modulator is as low as 50% to 60% and the thyratron is a single-point of failure of the modulator.

An approach that would mitigate many of these problems in NLS is the use of an Insulated Gate Bipolar Transistor (IGBT) switch together with a solid state induction modulator: this is a stack of small pulse transformers in which the primaries of the cores are driven in parallel by separate sets of IGBT switches and capacitors operated at relatively low voltage (2-4kV). The high voltage is developed at the secondary in series [7].

Repetition rate of a line type modulator and klystron is limited by modulator charging rate or thyratron recovery time. Incorporation of an IGBT switch increases the available repetition rate from the modulator and power dissipation in the klystron is then the limiting factor.

Table 1: High Power Klystrons of Interest to NLS

| Manufacturer | Thales | Toshiba | SLAC |
|---|---|---|---|
| Model | TH2155 | E3730A | XL4 |
| Waveband | S-band | S-band | X-band |
| Frequency | 2998 MHz | 2856 MHz | 11.42 GHz |
| Peak power | 45 MW | 50 MW | 50 MW |
| Efficiency | 44% | 45% | 40% |
| Gain | 54 dB | 51 dB | 50 dB |
| Pulse length | 3.5 μs | 4 μs | 1.5 μs |

Table 1 shows high power klystrons available in S-band and X-band. S-band klystrons already exist that separately satisfy high average and high peak power demands. The enhanced collector cooling that is provided in the former needs to be combined with a high peak power klystron, and manufacturers have indicated their readiness to supply this; repetition rates of up to 400 Hz are envisaged. A redesign of the klystron gun to reduce the arcing rate is also being discussed.

Table 2: Comparison of the DESY Type II Linac and SLAC 3 m Accelerating Structures available at 2998 MHz

| Property | DESY structure | SLAC structure |
|---|---|---|
| Length | 5.2 m | 3.0 m |
| Shunt impedance | 51.5 MΩ/m | 52 MΩ/m |
| Attenuation | 0.5 Neper | 0.49 Neper |
| Mode | 2π/3 | 2π/3 |
| Q | 14000 | 12500 |
| Filling time | 740 ns | 690 ns |
| Number of cells | 156 | 89 |

The two main types of S-band accelerating structure that are readily available are the DESY type II and SLAC 3 m ones; these structures are compared in Table 2.

Performance of the structures is similar, and the 3 GeV NLS requirements can be met by either design with an accelerating gradient of around 20 MV/m.

The power delivered by the klystron can be compressed with a SLED cavity. Figure 1 shows the increase in acceleration through a DESY structure achievable with a SLED cavity with $Q_0=10^5$ and β=6.7, together with power dissipation in a single pulse.

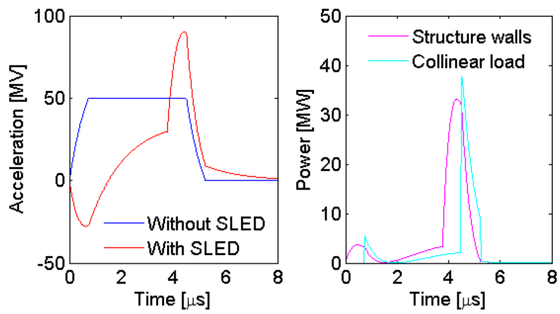


Figure 1: Acceleration through a DESY structure with and without SLED (left) and powers dissipated in structure and collinear load in a single pulse with SLED (right).

400 Hz repetition rate at 20 MV/m is much higher than operating rates of 120 Hz at SLAC and 50 Hz at DESY for similar gradients. At this rate, average klystron power is 70 kW. Average power dissipation limits have not been explored for either structure or for SLED cavities, and further work is required to determine what repetition rate is achievable. As a first estimate of the capability of an S-band structure to withstand such power levels, a thermal model has been developed. SUPERFISH was used to solve for the two accelerating modes in a 3 GHz structure, based on an adaptation of the SLAC 2856 MHz design, and shown in Figure 2 (dimensions in inches). Power transfer at the walls for these two modes was then taken as an input for a thermal model shown in Figure 3, demonstrating that with suitable water cooling on the outer surface of the structure, the temperature of a normal cell can be kept at an average of 30°C to 35°C.

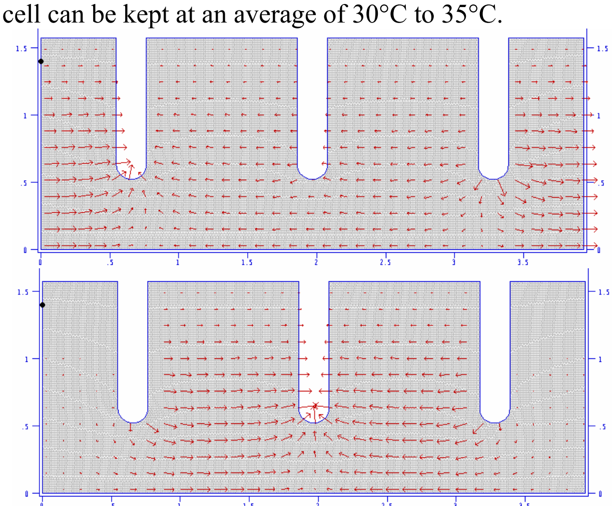

Figure 2: Accelerating modes in an S-band structure.

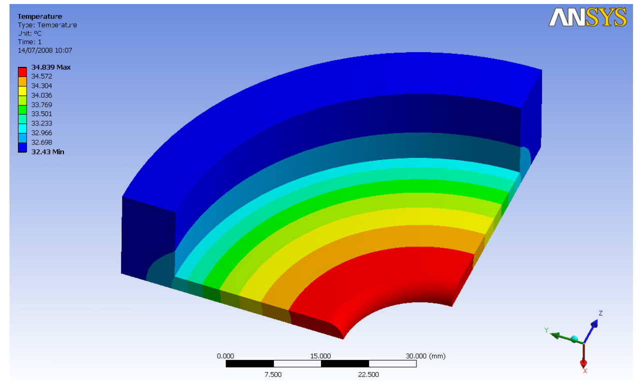


Figure 3: Equilibrium temperatures in an S-band structure operating at 400 Hz: blue is 32.4°C, red is 34.8°C.

The main design difference between the DESY and SLAC structures is the use of a collinear load in the DESY structure and an external load in the SLAC structures. While the DESY approach preserves the symmetry of the structure, it may prove to be more difficult to adapt the cooling to cope with the high power dissipated in the collinear load, as 38% of the total power must be dissipated in the final 8 cells of the structure. A full thermal model of the whole structure is needed before the impact of the intense heating can be fully assessed, but problems may arise in the matching of the load to the main part of the structure because of the existence of a longitudinal temperature gradient. Rapid thermal cycling of the load cells may also be problematic, as the SLED cavity delivers a very high power pulse to the load, as shown in Figure 1 and the cyclic stress may lead to metal fatigue. For fully annealed OFE copper the temperature rise required to initiate fatigue stress has been measured to be between 40 K [8] and 110 K [9]. Heat dissipation in the resistive coating in the load cells is a particular point of concern. We have therefore provisionally selected the SLAC structure for beam dynamics simulations and layout considerations.

## LINAC BEAM DYNAMICS

A suitable NLS 3 GeV design consists of 12 RF stations operating at 2998 MHz, each driving up to 4 SLAC structures, plus one X-band linearising structure, two bunch compressors (at 460 MeV and 1.2 GeV) and one dog-leg immediately before the undulator section The beam dynamics in the linac have been calculated with ELEGANT, taking CSR and wakefields into account [10]. Input is from an ASTRA model of a new S-band gun [11]. Initial simulations have been carried out with a charge of 0.2 nC, showing that the linac can deliver a 3 GeV beam with of peak current 7 kA, 0.7 mm mrad normalised emittance and 0.2% energy spread [12].

The sensitivity of the linac to jitter in RF phase and accelerating gradient of the structures has been studied in order to generate a baseline specification for modulator stability and low-level RF. This first stage analysis considers beam at the exit of the linac.

Figure 4 shows the change of peak linac current for a one percent change in gradient at all RF stations along the linac including the X-band structure. The first S-band plant is considered part of the injector and so is not studied here. Sensitivity is highest for RF stations S2 and S3 before BC1, smaller for S4 to S6 between the bunch compressors and smaller again after BC2.

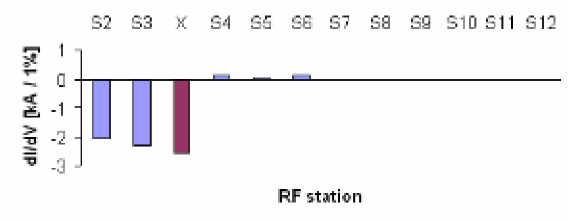


Figure 4: Sensitivity of peak beam current to accelerating gradient for all RF stations.

More detailed study of station S2 shown in Figure 5 shows the effect of changes in gradient, or accelerating voltage, on emittance. Large phase changes affect the bunch compression such that the peak beam current increases rapidly to tens of kA and horizontal emittance blows up through CSR effects. The figure shows perturbation of ±5% and ±5° about the working point.

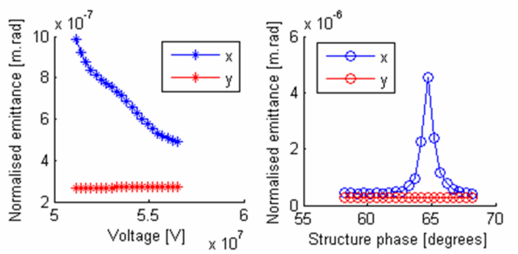


Figure 5: Output pulse emittance as a function of voltage and phase in the first accelerating structure.

The sensitivity of the different RF stations to small changes in RF voltage and phase are summarised in Table 3. In general, effects are greatest on the X-band structure and before the first bunch compressor.

Table 3: Sensitivity of Individual RF Stations to RF Errors

| | Before BC1 | BC1-BC2 | After BC2 | X-band | Units |
|---|---|---|---|---|---|
| dE/dV | 1.64 | 2.44 | 3.03 | -0.30 | MeV/1% |
| dE/dφ | -0.43 | 1.81 | 0.038 | 1.245 | MeV/1° |
| $d\varepsilon_{nx}/dV$ | -0.076 | 0.01 | 4e-4 | -0.04 | mm.mrad/1% |
| $d\varepsilon_{nx}/d\varphi$ | 0.87 | 0.08 | 2e-4 | -0.61 | mm.mrad/1° |
| dI/dV | -2.18 | 0.11 | -7e-3 | -2.56 | kA/1% |
| dI/dφ | 19.7 | 1.77 | 0.055 | -12.3 | kA/1° |

Summaries of the distributions of 10000-particle runs through the ELEGANT model with up to 500 runs at each point are shown in Figure 6. This demonstrates how the beam jitter grows with RF jitter. For comparison, the rms energy of a single 100000 particle distribution with no jitter is 7.0 MeV and the rms in arrival time is 28 fs. Jitter of 0.5° in S-band phase and 0.4% in accelerating structure gradient leads to a 0.1% jitter in beam energy.

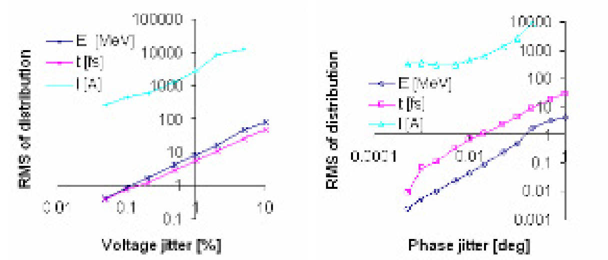


Figure 6: RMS values of mean energy, arrival time and peak current with voltage and phase jitter as displayed.

Similarly, the effect of small physical displacements on the RF structures can be calculated by inserting a lateral displacement or by introducing a kick into the lattice in ELEGANT. Results are summarised in Table 4.

Table 4: Sensitivity of RF Structures to Positioning Errors

| | Before BC1 | BC1-BC2 | After BC2 | X-band | Units |
|---|---|---|---|---|---|
| dE/dx | 9e-3 | -0.01 | 4e-4 | 0.29 | MeV/mm |
| $d\varepsilon_{nx}/dx$ | -8e-3 | 7e-3 | 2e-3 | -.13 | mm.mrad/mm |
| dI/dx | 0.46 | 1.36 | 1.76 | -1.5 | kA/mm |
| $dE/d\alpha_x$ | -2.39 | 0.47 | 2e-3 | 0.48 | MeV/mrad |
| $d\varepsilon_{nx}/d\alpha_x$ | 1.63 | -0.64 | 0.44 | 0.27 | mm.mrad/mrad |
| $dI/d\alpha_x$ | 6.53 | -8.66 | 1.10 | 3.42 | kA/mrad |

Positioning errors of the X-band structure have a large effect on the beam. For this reason, the X-band structures in the NLC design were designed to be mounted on moveable supports to align with the beam; this approach is recommended for the NLS.

## SUMMARY

Recent advances in solid state modulators, together with the adoption of well proven S-band linac technology offer the prospect of a reliable, cost effective normal conducting linac FEL for the UK New Light Source project operating at repetition rates previously impossible for such an approach. A 3 GeV linac design has been developed and the issues of power dissipation and RF stability have been considered.

## REFERENCES

[1] http://www.newlightsource.org/
[2] P. A. McIntosh et al, this conference.
[3] J. N. Galayda, EPAC 08, Genoa, p1939.
[4] T. Shintake, EPAC 08, Genoa, p136.
[5] G. Geschonke, EPAC 08, Genoa, p2912.
[6] ILC Technical Review Committee 2nd Report (2003).
[7] R. L. Cassel et al, PAC 01, Chicago, p3744.
[8] D. P. Pritzkau et al, SLAC-PUB-8013 (1998).
[9] O. A. Nezhevenko, PAC 97, Vancouver, p3013.
[10] We gratefully acknowledge the initial work carried out on the S-band design optimisation by Y. J. Kim.
[11] J.-H. Han, this conference.
[12] R. P. Walker et al, EPAC 08, Genoa, p142.

# SIMULATIONS ON IMPACT OF THE 3.9 GHZ RF SECTION ON THE MULTI BUNCH EMITTANCE AT FLASH

Y. Kot, DESY, Hamburg, Germany.

*Abstract*

In order to compensate nonlinear distortions of the longitudinal phase space a RF section operated at three times the 1.3 GHz frequency of the existing TTF cavities is foreseen in the next phase of FLASH. Four modules of a nine cell 3.9 GHz cavities will be installed right after the first accelerating module ACC1. These cavities could cause additional long-range wake fields which would affect the multi bunch (MB) beam dynamics leading to increase of the MB emittance. The MB emittance at the end of the linac is determined by the strength of the transverse wake fields in the RF system. These so called higher order modes appear after any off-axis moving bunch, which could happen either due to the cavities misalignment, or by transverse position fluctuations of the injected bunches. It is intended to damp them by means of the HOM couplers, which can reduce the damping time by factor of $10^5$. The misalignment of the cavities offsets is expected to be limited by 0.5 mm rms. The paper describes the results of the simulations on the dependence of the MB emittance on cavities misalignment offsets and damping strength of the HOM couplers in the planned 3.9 GHz RF section.

## INTRODUCTION

In the next phase of FLASH it is planned to install four modules of a nine cell 3,9GHz cavities right after the ACC1 at 14-19meter. These cavities would cause additional long-range wake fields which could affect the multi bunch beam dynamics leading to the increase of the multi bunch emittance.

It is transverse long-range wake fields which determine the multi bunch emittance at the end of the LINAC. They appear after any off-axis moving bunch which could happen either due to the cavities offset misalignment, or by transverse position fluctuations of the injected bunches. According to the design of the cavities setup the precision of 0.5mm rms could be achieved, whereas the fluctuations of the transverse positions of the injected bunches could be kept well below this value.

In order to damp the wake fields HOM couplers will be installed which will reduce the damping time by the factor of $10^{-5}$. The MB emittance blow up is also mitigated due to the RF focussing since each cavity acts as a focussing quadrupole in both vertical and horizontal planes simultaneously. This effect could play an important role if the change of the energy per cavity is not negligible compared to the bunch energy.

Thus the resulting transverse multi bunch emittance is a subject to equilibrium between the strength of the transverse wake fields due to bunch positions offsets from the cavity axis on the one side and damping strength of the wake fields due to HOM couplers on the other side.

We have simulated the MB beam dynamics for the FLASH beam line with the new 3rd harmonic RF section. The meaning of the RF focussing for the MB dynamics at FLASH has been also investigated. The results will be shown in this paper.

## THEORY AND MODEL

### *Formulas and Theory*

The technical characteristics of both 1,3GHz and 3,9GHz cavities has been described in [3] and [1,2] respectively.

The calculations of the wake fields have been fulfilled according to the following formulas:

$$W_{\parallel}^{(m)}(s) = -\sum_n \omega_n \left(\frac{R^{(m)}}{Q}\right)_n \cos\left(\omega_n \cdot {s}/{c}\right) \exp\left(-{1}/{\tau_n} \cdot {s}/{c}\right)$$

$$W_{\perp}^{(m)}(s) = c\sum_n \left(\frac{R^{(m)}}{Q}\right)_n \sin\left(\omega_n \cdot {s}/{c}\right) \exp\left(-{1}/{\tau_n} \cdot {s}/{c}\right)$$

where $W_{\parallel}^{(m)}$ and $W_{\perp}^{(m)}$ are the longitudinal and transverse wake fields accordingly, $\omega_n = 2\pi f_n$ - the frequency of the mode, $R^{(m)}$ the impedance, Q the quality factor and $\tau_n$ the lifetime of the mode. In the simulations the lowest four passbands of the monopole (m=0), dipole (m=1) and quadrupole (m=2) modes for the longitudinal and dipole (m=1) and quadrupole (m=2) modes for the transverse wake fields has been considered.

The strength of the wake fields decays in time according to the natural mode lifetime $\tau_{n0}$. If the external damping of the higher order modes provided, the lifetime reduces according to:

$$\tau_n \rightarrow dampingfactor \cdot \tau_{n0}$$

The energy deviation and the transverse kick of the bunch j due to the wake fields of the previous bunches can be then computed as:

$$\Delta E(s_j) = -eq\sum_{i<j} W_{\parallel}^{(0)}(s_j - s_i) - eq\sum_{i<j}(x_j x_i + y_j y_i) W_{\parallel}^{(1)} + \mathrm{K}$$

$$\vec{\theta}_j = \frac{eq}{E_j}\sum_{i<j}\left(x_i \vec{e}_x + y_i \vec{e}_y\right) W_{\perp}^{(1)}(s_j - s_i) + \ldots$$

### *Assumptions and Parameters*

We have simulated the MB dynamics during the beam transport through the LINAC at FLASH beginning at the quadrupole Q9ACC1 (13m) right after the ACC1 and ending at the entrance into the Undulator 1 at the BPM at 203m (Q22SEED). The 3.9GHz cavities have been supposed to be installed between V10ACC1 at 14m and 1UBC2 at 19m.

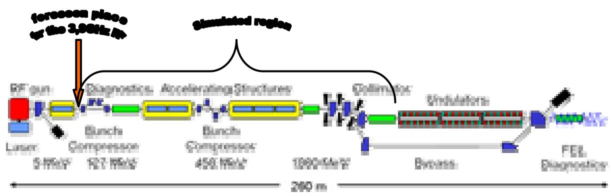


Figure 1: Schematic plan of the FLASH. Simulated region of the linac and the supposed place for the 3.9GHz RF section marked.

One particle model has been assumed for the bunch. Therefore single bunch effects were not considered. All bunches were assumed to be ideally injected on axis without multi bunch slope or position divergence. For each measurement we have taken 100 linacs with random offsets and averaged the results.

Other parameters are given in the table 1:

Table 1: Assumed Parameters in the Simulations

| | |
|---|---|
| Bunch charge | 1nC |
| Bunches per train | 600 |
| Bunch spacing | 200ns |
| Pulse length | 120µs |
| Cavities misalignment | 0.5-5.0 mm rms |
| Cavities detuning | 0.1% rms |

## SIMULATIONS WITHOUT RF FOCUSSING

In the simplified model the RF focussing in the cavities has been neglected. A simple drift transfer matrix has been used to perform the transfer of a bunch between two neighbour cavities. The impact of the long range wakes was described by a transverse kick and energy change in the middle of each cavity. For the transfer between modules the optics from [4] has been used.

The results of the simulations with the simplified model are shown in the figure 2. Here is the normalized multi bunch emittance at the end of the linac in dependence from the damping order of the higher order modes in the 3,9GHz cavities plotted. The design value of 0.5mm rms has been assumed for the cavities offset misalignment in this simulation.

An effective damping of the multi bunch blow up can be achieved if the damping order stronger than 3 (or damping factor smaller than $10^{-3}$) provided. The both extreme cases without no external damping of the HOM and with the damping provided by the HOM couplers results in the normalized multi bunch emittance of 1.8mm mrad and $4.4 \cdot 10^{-4}$ mm mrad respectively. Compared to the design single bunch emittance of 1.4 mm mrad one can say that the multi bunch emittance blow up would become a serious problem if no damping of the HOM provided, whilst the damping as it is foreseen by the HOM couplers would make this phenomenon negligible.

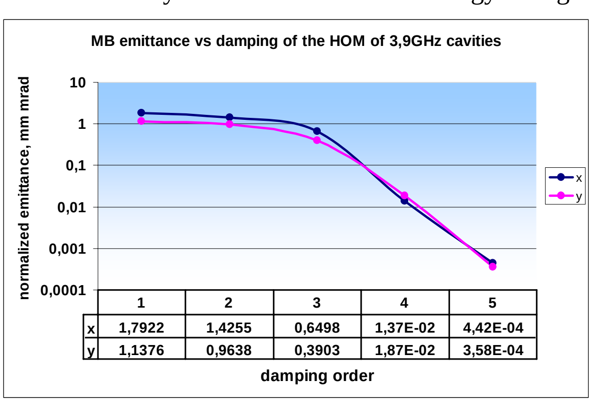


| | 1 | 2 | 3 | 4 | 5 |
|---|---|---|---|---|---|
| x | 1,7922 | 1,4255 | 0,6498 | 1,37E-02 | 4,42E-04 |
| y | 1,1376 | 0,9638 | 0,3903 | 1,87E-02 | 3,58E-04 |

Figure 2: Multi bunch emittance in the simplified model.

## SIMULATIONS WITH RF FOCUSSING

The simplified model which is described in the previous chapter implies the drift transfer between the centres of two neighbouring cavities. This could be a good approximation only if the energy of bunches is significantly larger than the energy gain pro cavity. However this condition isn't fulfilled for FLASH, since the energy gain pro cavity reaches about 20MeV whereas the energy of bunches is between 127MeV and 700MeV. Therefore one can expect a noticeable effect from the RF focussing which would mitigate the MB emittance blow up.

In the modified model the transfer between two neighbouring cavities in the same module has been fulfilled by means of the transfer matrixes as they follow from the optics [4]. The simulations have been done for different damping factors and cavities misalignment offsets of 0.5mm, 2.5mm and 5.0mm. For each measurement 100 linacs have been simulated and

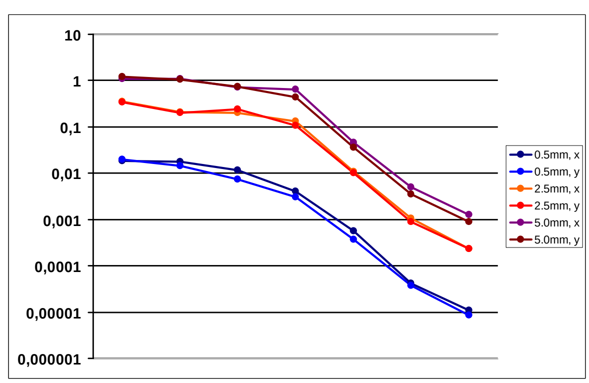


Figure 3: Normalized multi bunch emittance in the model with RF focussing as a function of damping of the higher order modes at the 3,9GHz cavities for different cavities misalignment offsets.

averaged.

Figure 3 shows the results of the simulations for the MB emittance. For the design cavities offset misalignment the MB emittance doesn't exceed 0.02 mm mrad even if the HOM remain undamped. This is reasonably smaller than the single bunch emittance. It is also about 50 times smaller than the results of the simulations in the simplified model without RF focussing.

It has been found that the MB emittance increases to the values between $10^{-3}$ mm mrad and 0.35mm mrad (with and without HOM couplers) if the cavities offset misalignment reaches 2.5 mm rms. For the cavities offset misalignment of 5.0 mm rms the MB emittance increases up to the range of $3.0 \cdot 10^{-3}$ - 1.2mm mrad. However even in that case the HOM couplers would damp the MB emittance blow up effectively.

The results of the simulations with and without HOM couplers for different cavities offset misalignments are summarized in the table 2.

Table 2: Multi Bunch Emittance for Extreme Cases

| | With HOM couplers | Undamped |
|---|---|---|
| 0.5 mm | $10^{-5}$ | 0.02 |
| 2.5 mm | 0.001 | 0.35 |
| 5.0 mm | 0.003 | 1.20 |

## THE EVOLUTION OF THE MB EMITTANCE ALONG THE LINAC

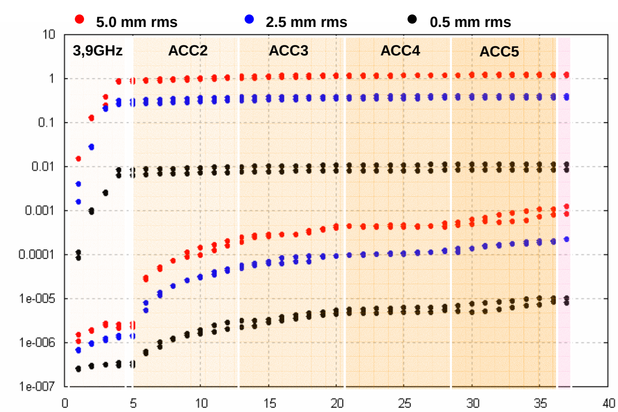


Figure 4: Multi bunch emittance along the linac. The multi bunch emittance (horizontal and vertical planes) along the linac for different cavity offset misalignments. Upper plots correspond to the case in which the higher order modes remained undamped, the lower plots – if the higher order modes are damped by HOM couplers.

The evolution of the MB emittance during the transport through the linac is shown in the figure 4 for different cavities offset misalignments.

It could be seen that the MB emittance blow up happens already in the 3,9GHz RF section if the higher order modes remain undamped. In the following sections ACC2 -> ACC5 the multi bunch emittance remains almost unchanged for all cavities misalignment offsets.

In the presence of the HOM couplers the multi bunch emittance is slightly increasing also during the passage through the 1,3GHz cavities. Nevertheless it remains negligible all the time.

## CONLCLUSIONS AND DISCUSSION

The multi bunch emittance at FLASH depends crucially on the damping factor of the HOM modes at 3.9GHz cavities. The damping factor of $10^{-5}$ as it is foreseen by the HOM couplers provides suitable bunch train quality with negligible multi bunch emittance for the cavity misalignment offset up to 5.0mm rms. If the 3.9GHz cavities are operated without damping of the HOM, the multi bunch emittance still remains reasonably smaller than the single bunch emittance. However the bunch train may become unusable since a lot of bunches arrive too far away from the average position of bunches in the phase space.

The RF focussing plays an important role by damping the multi bunch emittance expansion. The simulations in which the RF focussing has been taken into account indicate the multi bunch emittance 50 times smaller than in the case where the RF focussing has not been considered.

If the HOM are not damped or only weak damped, than the emittance blow up occurs at the very beginning of the linac, mostly during the passage through the 3,9GHz cavities.

## REFERENCES

[1] T. Khabibouline, N. Solyak, R. Wanzenberg "Higher Order Modes of a 3rd Harmonic Cavity with an Increased End-cup Iris", FERMILAB-TM-2210, TESLA-FEL 2003-01, May 2003.

[2] J. Sekutowicz, R. Wanzenberg, "A Design of a 3rd Harmonic Cavity for the TTF 2 Photoinjector",

[3] R. Wanzenberg, "Monopole, Dipole and Quadrupole Passbands of the TESLA 9-Cell Cavity"

[4] V. Balandin, N. Golubeva "Matlab Functions for Calculations of the Linear beam Optics of FLASH Linac"

# LATTICE STUDIES FOR THE XFEL-INJECTOR

Y. Kot, V. Balandin, W. Decking, C. Gerth, N. Golubeva, and T. Limberg,
DESY, Hamburg, Germany

*Abstract*

The XFEL injector building has a length of 74.3 meters and is divided by 2.5m long concrete shielding wall. The section upstream the shielding wall will have a length of 42.3m and give place for the gun, accelerating module, a possible 3rd harmonic section, laser heater and the beam diagnostics section. At its end the possibility for the beam dump is foreseen so that the tuning of the beam in the injector becomes possible without any impact on the subsequent parts of the XFEL. Each of these components sets certain requirements on beam optics which may compete with each other.

Since there are two injectors foreseen for the XFEL the injector will be vertically displaced by 2.75 m from the linac. The displacement of the beam line takes place downstream the shielding over the distance of 20m by means of the so called dogleg – a combination of two four cells arcs (8 cell system). It is important there to optimize cells in such an order that the chromatic effects don't impact the beam quality noticeably. In this paper we describe the solution for the beam optics at the XFEL injector.

## INTRODUCTION

The XFEL injector plays a crucial role for the beam quality along the subsequent transport of the beam through the XFEL. Therefore it is important to have the possibility for both the understanding of the beam parameters at the injector as well as for the flexible change of the beam parameters there. For the tuning and analysis of the beam parameters the section upstream the shielding wall is foreseen. At the end of this section a possibility for a separate beam dump will be given so that the tuning of the beam may proceed without any impact on the actions at the other sections of the XFEL. The section is about 42.3m long and has to give place for numerous components. They are the gun and gun diagnostics, accelerating module, 3rd harmonic RF section, laser heater, transverse deflecting structure (TDS) and the diagnostics section with four OTR monitors. Besides, a spare place of about 2.4m at the end of the section is needed in order to provide the change of the absorber body. Each of these components sets certain requirements on the beam optics, which may compete with each other. Since a very short length of the beam line of less than 40 meters for this purpose available the design of the beam optics at the injector becomes a challenging problem for the investigations.

Downstream the shielding wall the beam will be vertically displaced by 2.75m over the beam line length of 20m. Since the vertical displacement takes place one has to be cautious with the choice of the magnet arrangement there so that the optics doesn't affect the chromatic features of the beam noticeably.

We describe the possible optics solution for the XFEL injector in which these considerations and requirements of each component on the optics have been taken into account.

## REQUIREMENTS ON OPTICS AT THE LASER HEATER

The purpose of the laser heater is to enhance the uncorrelated energy spread of the electron beam which would lead to the increase of the Landau damping and thus reduce the sensibility of the beam to the sources of the instabilities during the bunch acceleration and transport through the linac [1].

However not only the net value of the uncorrelated energy spread plays an important role for the effectiveness of the Landau damping but also the form of the energy distribution in the bunch. It has been found [1] that the laser beam size has to be equal or slightly larger than the transverse size of the electron beam to provide an effective Landau damping. This condition would require a reasonable matching of both laser and electron beams and thus sets constraints on the optics at the laser heater.

The possibility to suppress the microbunching instability by means of the laser heater has been discussed in [1]. The design of the laser heater for the XFEL injector has been described in [2]. It was found that the optics at the laser heater has to been chosen in such a way that the electron beam size doesn't change a lot during the transport through the undulator. Since the length of the undulator is L=0.5m the change of the beta-function along the undulator can be than roughly estimated according to the formula:

$$\Delta\beta[m] \approx -2\alpha L = -\alpha$$

The transverse beam size goes as $\sqrt{\beta}$ so that the reduction of the beta function by factor of 2 (i.e. $\alpha=0.5\beta$) causes the change of the transverse beam size by approximately 30%. This boundary, though floating, has been proven to be a reasonable limitation on the $\alpha$-function at the laser heater.

The smallest acceptable value for the beta function at the undulator is set by the condition of the stable laser beam spot size. The Rayleigh length shouldn't be shorter than the undulator length. Furthermore both beams should have the same transverse size. If one assumes the smallest possible transverse size of the laser and therefore also of the electron beam one gets for the design emittance of 1.0mm mrad that the beta function shouldn't be smaller than 7m along the undulator.

The upper limit for the beta function is given by the highest possible laser beam power. However it is expected that the laser will be powerful enough to provide matching for any reasonable electron beam size.

## REQUIREMENTS ON OPTICS AT THE DIAGNOSTICS SECTION

The diagnostics section consists of the transverse deflecting structure and the OTR monitors section. According to the formula [3]:

$$\beta_y \geq \left( \frac{\lambda}{\pi\sigma_z} \cdot \frac{1}{eV_o \sin\phi_y} \right)^2 pc \cdot mc^2 \varepsilon_N \tag{1}$$

the beta function has to be not smaller than 1.0m at the TDS. Further requirement concerns the phase advance between the TDS and the OTR screens which could be described by

$$\prod_{i=1}^{4} \sin\left(\phi_y\left(TDS, OTR_i\right)\right) = \max \tag{2}$$

Besides the allowed transverse size of the electron beam as it passes through the OTR screen is determined by the resolution of the OTR monitors on one hand and the size of the streaked beam on the other hand. A reasonable assumption for the resolution of the OTR monitor is given by 12μm [4] whereas the streaked beam should not be larger than 25mm. These conditions set borders for the beta function at the OTR stations as

$$0.9m \leq \beta_{x,y} \leq 5.9m \tag{3}$$

## OPTICS SOLUTIONS FOR THE DIAGNOSTICS SECTION

Three different options for the implementation of the optics in the diagnostics section have been considered. The simplest one is the so called "waist" solution in which the OTRs are placed in a common drift section. Hereby the beta function is adjusted in such a way that it assumes a parabola form with the vertex in the middle of the diagnostics section. The OTR monitors are arranged then symmetrically around the vertex in such an order that the phase advance between the neighbour OTRs reaches 45°. This option, though the simplest one, has been found not to be flexible enough to provide a good matching for all expected initial values of the beta function at the entrance. Besides, it was not possible to get a suitable phase advance between the TDS and OTR screens so that the condition (2) could be satisfied.

Another option, a 45° FODO lattice, uses FODO cells to control the phase advance between the OTR screens. One OTR screen per FODO cell is used in so that total 3.5 cells are necessary to house all OTRs. Contrary to the waist solution an additional matching section between the undulator and OTR section is needed, which allows to choose a suitable place for the TDS so that condition (2) could be fulfilled easily.

In the third option, a 76° FODO lattice, there are two OTR screens per cell, so that 1.5 FODO cells are required. Therefore the whole solution becomes more compact and suitable for injector.

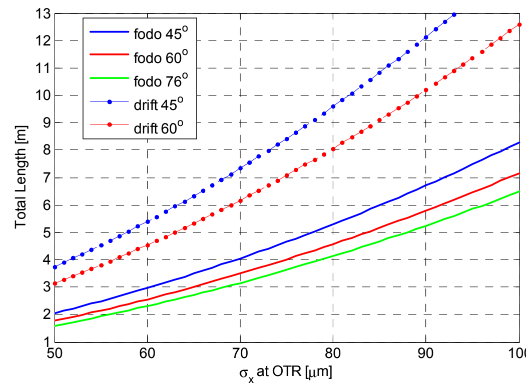


Figure 1: length needed by the diagnostics section for different solutions. Though FODO solutions require less space an additional matching section (not taken into account here) in front of the diagnostics would be needed. Nevertheless the FODO 76° solution even together with the matching section requires less space than other solutions and offers enough flexibility for the beam optics.

## OPTICS AT THE DOGLEG

### *General Requirements and Preliminaries*

The magnet lattice of a dogleg has to fulfill a number of requirements, both in terms of beam dynamics as well as geometry considerations:

- Provide a vertical displacement of the beam for a distance 2.75m at the length 20m as measured along linac axis.
- It should be able to accept (matched) bunches with different energies (up to 10% from nominal energy) and transport them without deterioration of transverse beam parameters.
- First order momentum compaction (r56 matrix coefficient) should be zero.

### *Dogleg as Combination of Two, Four Cell Arcs (8 Cell System)*

Solution considered in this section is constructed using the idea presented in [5]. The dogleg is formed by two arcs, where the second arc is made from the first arc by taking magnets of the first arc in reverse order and switching polarities of all odd multipoles (dipoles and sextupoles). Besides that each arc is mirror symmetric with respect to its center. The symmetries involved in design of such a system guarantee that if one makes the arc to be a second order achromat, the nonlinear dispersions will be automatically zero at least up to fifth order.

The only difference with systems considered in [5] is that for constructing second order achromatic arc we use not four identical cells, but the symmetry FRFR as in [6]

Note that again as in [5], it is sufficient to correct only horizontal (deflecting plane) motion and the good beam transfer properties for the vertical dynamics can be provided simply by small betatron functions and properties of the linear achromat. So both sextupoles are working only for horizontal motion. Additional optimizations made to obtain so good beam transfer properties include finding right balance between positive and negative dipole angles (it is important not only for r56 control, but also for effective sextupole usage), positioning of dipoles and central quadrupole (which is not in the cell center), positioning and strength reduction of sextupoles.

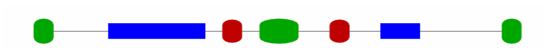

Figure 2: Forward cell of the dogleg. The cell length is about 2.53m as measured along curved beam path. Blue, green and red colours mark dipole, quadrupole and sextupole magnets, respectively.

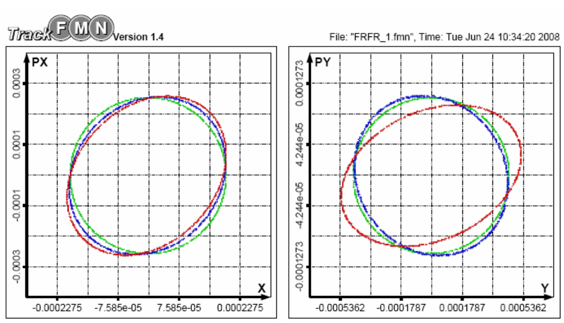


Figure 3: Phase space portraits of monochromatic $3\sigma_{x,y}$ ellipses (matched at the entrance) after tracking through the dogleg. The relative energy deviations are equal to -15%, 0% and +15% (red, green and blue ellipses respectively).

## PRELIMINARY OPTICS SOLUTION

Figure 6 shows preliminary optics solution for the XFEL injector. It begins at the entrance of the 3,9GHz RF section with design values for the initial optics functions ($\beta_x=\beta_y=45.0$m and $\alpha_x=\alpha_y=0$). After it follow the laser heater, TDS, diagnostics section with a FODO 76° solution, shielding and dogleg. The optics is well-defined after the matching section between the laser heater and TDS. Simulations have also shown that the matching is possible for any values of the initial beta-functions from the expected range (20-100m).

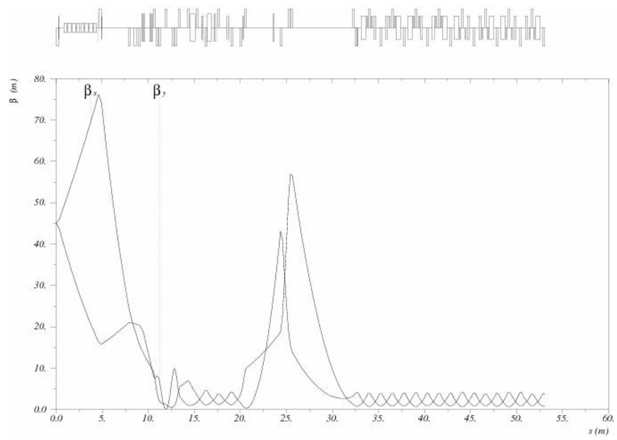


Figure 4: Preliminary optics solution for the XFEL injector.

## REFERENCES

[1] Z. Huang, M. Borland, P. Emma, J. Wu, C. Limborg, G. Stupakov, and J. Welch "Suppression of Microbunching Instability in the Linac Coherent Light Source", Physical Review Special Topics – Accelerator and Beams, Vol. 7, 074401 (2004).

[2] Y. Kot and T. Limberg "Laser Heater Integration into the XFEL injector", Unpublished Note

[3] R. Akre, L. Bentson, P. Emma and P. Krejcik „A Transverse RF Deflecting Structure for the Bunch Length and Phase Space Diagnostics" SLAC-PUB-8864, June 2001

[4] A. Cianchi, L. Catani, E. Chiadroni, M. Raparelli, M.Castellano, G. Di Pirro and K. Honkavaara "Commissioning of the OTR Beam Profile Monitor System at the TTF/VUV-FEL Injector" Proceedings of EPAC 2004, Lucerne, Switzerland

[5] V. Balandin and N. Golubeva "Preliminary Consideration Toward XFEL Injector Dogleg" Unpublished Note, June 03, 2008

[6] V. Balandin, R. Brinkmann, W. Decking and N. Golubeva "Optics Solution for the XFEL Post-Linac Collimation Section" TESLA-FEL 2007-05, May 2007

# STATUS OF THE 3RD HARMONIC SYSTEMS FOR FLASH AND XFEL IN SUMMER 2008

E. Vogel[3], A. Bosotti[2], W. Decking[3], M. Dohlus[3], H. Edwards[1], E. Harms[1], M. Hoffmann[3], M. Huening[3], J. Iversen[3], K. Jensch[3], T. Khabiboulline[1], G. Kreps[3], T. Limberg[3], A. Matheisen[3], W.-D. Moeller[3], P. Pierini[2], K. Rehlich[3], A. Schmidt[3], J. Sekutowicz[3], D. Sertore[2] and W. Singer[3] for all third harmonic collaborators

[1]Fermi National Accelerator Laboratory (Fermilab), Batavia, Illinois, 60510 USA

[2]Istituto Nazionale di Fisica Nucleare (INFN), LASA, 20090 Segrate (Milano), Italy

[3]Deutsches Elektronen Synchrotron (DESY), Notkestraße 85, 22607 Hamburg, Germany

*Abstract*

Ultra short bunches with high peak current are required for the creation of high brilliance coherent light in the VUV and x-ray range in undulators. At the Free Electron Laser in Hamburg (FLASH) and the European x-ray free electron laser (XFEL) they are obtained by a two stage bunch compression scheme based on acceleration off the rf field crest and transverse magnetic chicanes. The deviation of the rf field's sine shape from a straight line leads to long bunch tails and reduces the peak current. This effect can be eliminated by adding a third harmonic rf system [1, 2, 3]. This paper gives an overview on the actual status of the beam dynamical examinations, as well as on the development of the third harmonic sub-systems like modules, cavities and radio frequency systems for FLASH and the XFEL. For an basic overview on the activities we refer to [3].

## INTRODUCTION

At the linear accelerator based free electron lasers FLASH and XFEL bunches are generated by a normal conducting photocathode rf gun and then accelerated by a superconducting linear accelerator. While passing through undulators the bunches emit high brilliance coherent light. The emission process requires high electron peak currents and small transverse emittances. Collective effects restrict the minimum full width bunch length obtained from the photocathode rf gun. The high peak currents are obtained by compressing the bunch length in the first part of the superconducting accelerator (Fig. 1).

Accelerating the bunches off the rf field crest results in an energy chirp from the bunch head to the tail. In the bunch compressors the trajectory of the bunch head becomes longer than the trajectory of the bunch tail resulting in a compressed bunch due to the different transit time. Both the sinusoidal accelerating wave and non-linear collective effects lead to asymmetric bunches with reduced peak current and long tails. By adding a higher harmonic rf system, the voltage seen by the bunches and the collective effects may be linearised. The bunch compression becomes much more effective.

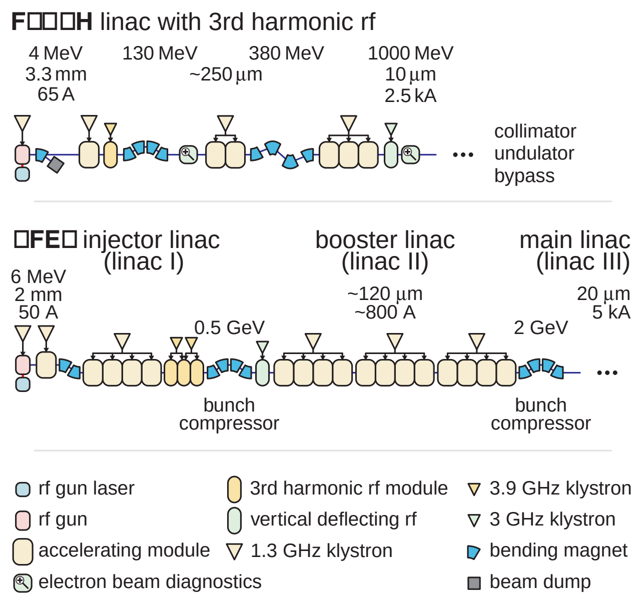


Figure 1: Sketch of the FLASH accelerator and the first part of the European XFEL accelerator.

## BEAM DYNAMICS

Beam passing a third harmonic section suffers from coupler kicks, short range (intra bunch) and long range (bunch to bunch) effects. For the XFEL we decided to use a coupler arrangement where every second cavity is rotated around the cavity longitudinal axis [3, fig. 4] resulting in a transverse beam blow up in the order of 2%. The FLASH configuration or all couplers at the same side would result in a blow up by 40% and 100%, respectively. The r.m.s. of the difference between the cavity cell centre and the beam trajectory has to be below 0.3 mm for keeping the transverse blow up due to transverse wake fields below 5%. Long range effects caused by the lower frequency higher order modes (HOMs) are damped by the cavity HOM absorbers. Higher frequency HOMs can be trapped in a string of cavities with different spectra for the frequencies above 10 GHz. The effects on the beam are expected to be cured by an arrival time feedback system [4] and we can go without beam pipe HOM absorbers inside modules. Absorbers between modules should be sufficient.

At FLASH, beam steering in the 3.9 GHz (ACC39) section for reducing 3.9 GHz coupler kick and wake field effects can be done using a steering magnet after the gun and at the end of the first 1.3 GHz (ACC1) module. We have started to study the effect of ACC1 on the beam while generating orbit bumps at the later ACC39 position for comparison with the future situation when ACC39 is installed.

## FLASH 3RD HARMONIC MODULE

The principal development work for the third harmonic rf is performed at Fermilab by developing and building the module ACC39 for FLASH [5]. It consists of four 3.9 GHz cavities of which one has been horizontally tested. The gradient of 22 MV/m is well above the desired operational gradient of 14 MV/m. Additional cavities will soon be tested horizontally [6].

A number of tests have been performed to study the potential consequences of the module transportation from Fermilab to DESY. Therefore the module and cold mass has been equipped with four mock-up cavities showing the weight of the original cavities. After transportation of this module by truck from Fermilab to the Chicago airport O'Hare and back the cavity alignment was unchanged within the required limits.

Before installation into the FLASH accelerators, we plan to test the module at the cryo-module test bed (CMTB) at DESY. It will be the first cold test of the assembled module. The preparation required for this test has been started.

## HIGH POWER RF

At Fermilab the first built 3.9 GHz klystron is operated for coupler processing and for the horizontal cavity tests. The second built klystron is foreseen to operate ACC39 at the CMTB and in FLASH at DESY. Operation tests for this klystron take place these days.

We started the call for tender process to purchase a modulator for the third 3.9 GHz rf station. It is required for processing the couplers for the XFEL 3.9 GHz prototype cavities. Beside for coupler processing it serves for XFEL module tests at the CMTB followed by the 3rd harmonic operation at the XFEL.

The results of the klystron test at DESY and the operational experience from the Fermilab klystron may be used to propose improvements for future 3.9 GHz klystrons. Therefore, purchasing the klystron for the third rf station will first start after the DESY klystron tests.

## RF CONTROL

The rf field is controlled by an EseCon controller at the horizontal 3.9 GHz cavity tests at Fermilab. At FLASH the SimCon controller [7] is used to control the 1.3 GHz rf field in the injector part (rf gun and ACC1). It is also foreseen for the later modules. For keeping the future maintenance effort low, SimCon has also been chosen for 3.9 GHz rf control at the CMTB and FLASH. This requires the development of down converters as interface between the 3.9 GHz rf and the ADCs of the controller.

A collection of the requirements on the individual parts and the control loops [3, fig. 7] is in progress. Discussions on the control system interfaces has just started. Nevertheless, a first initial laboratory setup of an SimCon controller adapted to 3.9 GHz exists.

## XFEL CAVITY PROTOTYPES

About one year ago, we ordered three 3.9 GHz cavities [8] built and surface treated by industry with the goal to industrialize the cavity production. Within this process we exchange and examine ideas for design changes with the vendor to simplify the production and to ease the survey. Some of the changes are desirable due to the different the electron beam welding apparatus available to Fermilab and by the vendor. As a result we look into topics like the magnetic shielding and the effectiveness of the tuner. To verify the changes are uncritical we prepare everything to perform horizontal tests with this XFEL type 3.9 GHz cavities. We revise and procure parts like the He-vessels, tuner, magnetic shielding, power-coupler and so on.

## XFEL CRYOMODULE

The cryo-modules for the XFEL differ from the older cryo-module designs used in the FLASH injector area. In the FLASH injector, the two phase helium line is between the cavities and the He return pipe. Due to the smaller diameter of the new outer vessel, the two phase line is shifted sideways in the newer designs also foreseen for the XFEL. This results in two types of dressed 3.9 GHz cavities because of the alternating coupler positions.

Our baseline inner third harmonic module design consists of a string of eight cavities, a quadrupole magnet, a beam position monitor and valves at the beginning and the end. Between those modules beam pipe HOM absorbers are foreseen. The module together with the beam pipe absorber covers a length of 5.8 m. Three of these modules, with a total of 24 cavities, will be used to build up the third harmonic voltage of 108 MV [3]. Two rf stations, each driving 12 cavities ($1\frac{1}{2}$ modules) are foreseen.

We skipped the option enabling a cavity alignment in the cold as mentioned in [3]. An r.m.s. of 0.3 mm for the cavity to cavity alignment seems to be feasible without such a complicating feature.

## SUMMARY AND OUTLOOK

Due to the smaller diameter and higher frequency of the third harmonic rf, the influence on the beam is substantially higher than at the 1.3 GHz accelerating sections. After calculating these effects we have a clear picture on the required arrangement of the cavities and coupler positions in the module. Some questions like the heat load induced by trapped HOMs are still under investigation.

At the construction and assembly of the FLASH third harmonic module at Fermilab two cavities are nearly ready for string installation and four other cavities are in the queue for being tested horizontally soon. Module transportation tests show quite promising results so that we can hope ACC39 arrives at DESY without any damage for being cold tested, installed an operated.

FLASH operation requires the 3.9 GHz rf station present at DESY. To enable parallel coupler processing, horizontal and CMTB tests, we already started to purchase an additional 3.9 GHz rf station. The development of the 3.9 GHz rf control based on the SimCon technology is on going.

Three 3.9 GHz cavities are on the way to being built and surface treated by industry. Within this context some design changes appear desirable to simplify the production by the vendor. The resulting XFEL 3.9 GHz cavities will be horizontally tested to verify the changes are uncritical.

The over all design of the XFEL third harmonic cryomodule has not been started. Nevertheless, our baseline is eight cavities with alternating coupler positions per module plus a package of a quadrupole magnet and a beam position monitor.

## ACKNOWLEDGEMENTS

The principal development work for the third harmonic rf of FLASH and the European XFEL is performed at Fermilab by developing and building the third harmonic rf module for FLASH. Therefore we would like to thank T. Arkan, L. Bellantoni, V. Bocean, G. Cancelo, H. Carter, B. Chase, C. Cooper, M. Foley, M. Gonin, U. Mavric, M. McGee, D. Mitchell, D. Olis, P. Pfund, A. Rowe, W. Schappert, N. Solyak and A. Hocker. The XFEL third harmonic studies group consists also of the following experts from INFN Milano: S. Barbanotti, N. Panzeri, R. Paparella and from DESY Hamburg: N. Baboi, A. Brinkmann, T. Buettner, K. Floettmann, P.-D. Gall, N. Golubeva, M. Hoffmann, J. Iversen, A. Janke, J. Kahl, W. Koprek, G. Kreps, R. Lange, L. Lilje, F. Ludwig, N. Mildner, P. Morozov, E. Prat, J. Prenting, D. Proch, P. Pucyk, D. Reschke, M. Schloesser, J. Thomas, R. Wanzenberg, H. Weise and I. Zagorodnov. We are grateful to them.

## REFERENCES

[1] K. Flöttmann, T. Limberg, Ph. Piot, 'Generation of Ultrashort Electron Bunches by cancellation of nonlinear distortions in the longitudinal phase space', TESLA-FEL Report No. TESLA-FEL 2001-06, 2001

[2] Massimo Altarelli, Reinhard Brinkmann, Majed Chergui, Winfried Decking, Barry Dobson, Stefan Düsterer, Gerhard Grübel, Walter Graeff, Heinz Graafsma, Janos Hajdu, Jonathan Marangos, Joachim Pflüger, Harald Redlin, David Riley, Ian Robinson, Jörg Rossbach, Andreas Schwarz, Kai Tiedtke, Thomas Tschentscher, Ivan Vartaniants, Hubertus Wabnitz, Hans Weise, Riko Wichmann, Karl Witte, Andreas Wolf, Michael Wulff, Mikhail Yurkov (Editors), 'The Technical Design Report of the European XFEL', DESY Report DESY 2006-097, (July 2006); http://xfel.desy.de/tdr/index_eng.html

[3] E. Vogel, M. Dohlus, H. Edwards, E. Harms, M. Huening, K. Jensch, T. Khabiboulline, A. Matheisen, W.-D. Moeller, A. Schmidt and W. Singer, 'Considerations on the third harmonic rf of the European XFEL', *Proc. of SRF2007*, Peking University, Beijing, China 2007

[4] F. Loehl, V. Arsov, M. Felber, K. Hacker, B. Lorbeer, F. Ludwig, K. Matthiesen, H. Schlarb, B. Schmidt, W. Jalmuzna, J. Szewinski, S. Schulz, A. Winter and J. Zemella, 'Measurement and Stabilization of the Bunch Arrival Time at FLASH', *Proc. of EPAC07,* Genoa, Italy, 2008

[5] E.R. Harms, T.T. Arkan, V. Bocean, H. Carter, H. Edwards, M.H. Foley, T.N. Khabiboulline, M. McGee, D. Mitchell, D. Olis, A. Rowe, N. Solyak, 'Status of 3.9 GHZ Superconducting RF Cavity Technology at Fermilab', *Proc. of LINAC 2008*, Victoria, Canada, 2008

[6] E.R. Harms, H. Edwards, I.V. Gonin, A. Hocker, T.N. Khabiboulline, N. Solyak, 'Performance of 3.9-GHZ Superconducting Cavities', *Proc. of LINAC 2008*, Victoria, Canada, 2008

[7] W. Giergusiewicz, W. Jalmuzna, K. Pozniak, N. Ignashin, M. Grecki D.V.M., D. Makowski, T. Jezynski, K. Perkuszewski, K. Czuba, S. Simrock, R. Romaniuk, 'Low latency control board for LLRF system - SIMCON 3.1', *Proc. of SPIE Vol. 5948*, 2005

[8] P. Pierini, A. Bosotti, N. Panzeri, D. Sertore, J. Iversen, W. Singer, E. Vogel, H. Edwards, M.H. Foley, E.R. Harms and D. Mitchell, 'Third harmonic superconducting cavity prototypes for the XFEL', *Proc. of LINAC 2008,* Victoria, Canada, 2008

# NEW EXPERIMENTAL RESULTS FROM PITZ*

F. Stephan#, G. Asova§, J. Bähr, C. Boulware, H.J. Grabosch, M. Hänel, L. Hakobyan$, Y. Ivanisenko, M. Khojoyan$, M. Krasilnikov, B. Petrosyan, S. Riemann, S. Rimjaem, T. Scholz, A. Shapovalov&, R. Spesyvtsev, L. Staykov§, DESY, 15738 Zeuthen, Germany
K. Flöttmann, S. Lederer, DESY, 22607 Hamburg, Germany
D. Richter, BESSY, 12489 Berlin, Germany
J. Rönsch, Hamburg University, 22761 Hamburg, Germany
F. Jackson, STFC Daresbury Laboratory, United Kingdom
P. Michelato, L. Monaco, C. Pagani, D. Sertore, INFN Milano – LASA, 20090 Segrate, Italy

The **P**hoto **I**njector **T**est facility at DESY, **Z**euthen site, (PITZ) was built to develop and optimize high brightness electron sources for Free Electron Lasers (FELs) like FLASH and the European XFEL. Last year, an electron beam with a very low transverse projected emittance of 1.26 mm mrad for 1 nC charge (100% RMS) was demonstrated [1, 2, 3]. In the shutdown last winter, a major upgrade of the facility took place where many new diagnostics elements were installed and almost all components in the beamline were repositioned. In addition, a new RF gun cavity with improved water cooling was installed and conditioned. It is the first RF gun where the surface cleaning was done with a dry-ice technique instead of high-pressure water rinsing. It showed a 10 times lower dark current emission than its precursor gun, even at cathode gradients as high as 60 MV/m. Also a new photo cathode laser system with higher bandwidth was installed, which so far has produced Gaussian laser pulses of 2.1 ps FWHM.
This contribution will summarize the transverse emittance measurements in 2007, the upgrade of the facility, dark current measurements from the new dry-ice cleaned RF gun cavity and quantum efficiency measurements of $Cs_2Te$ photo cathodes.

## INTRODUCTION

SASE-FELs for short photon wavelengths require electron sources providing particle beams with very good beam properties. Therefore, DESY is operating and continuously extending a photo injector test facility at its Zeuthen site (PITZ). It contains an 1½ cell L-band RF gun with cathode load-lock system and solenoids for space charge compensation, a laser system able to generate trains of electron pulses including temporal and transverse laser beam shaping, a booster cavity and many beam diagnostics systems for the characterization of the electron beam at different beam energies.

In the first section of this paper measurements of very low transverse emittance are summarized. These data have been taken in summer 2007 with a facility setup that was mainly unchanged since beginning of 2006. From autumn 2007 to spring 2008 a major upgrade of the facility took place and the current setup is shortly described in the second section. During the shutdown a new RF gun cavity treated with a dry-ice surface cleaning technique was commissioned at an accelerating gradient of 60 MV/m which is reported in the third section. In the fourth section recent quantum efficiency measurements of $Cs_2Te$ photo cathodes are presented.

## EMITTANCE MEASUREMENTS FROM SUMMER 2007

The transverse normalized projected emittance is of paramount importance for electron sources driving FELs. In summer 2007 it was measured at a bunch charge of 1 nC for gun cavity prototype 3.2, which was the first RF gun operated at PITZ with about 60 MV/m maximum accelerating gradient at the cathode. This cavity was cleaned with high-pressure water rinsing. Although the level of dark current at the maximum gradient was high (see details in commissioning section) this did not have a major influence on the emittance measurements when using the single slit measurement technique at a distance of 4.3 m from the photo cathode. Details of the measurement procedure and the data analysis are described in references [1, 2, 3]. An extensive experimental scan of different machine parameters resulted in an absolute minimum of the transverse normalized projected emittance for the following conditions: The gun was operated at a maximum accelerating gradient at the cathode of about 60 MV/m. The RF phases for gun and booster where set to maximum mean momentum gain. The beam momenta were 6.44 MeV/c downstream the gun and 14.5 MeV/c downstream the booster. The $Cs_2Te$ cathode number 90.1 was used with a laser beam of about 0.36 mm rms spot size (approximate flat-top transverse shape) and an approximately flat-top temporal distribution of about 20 ps FWHM with 6-7 ps rise/fall time. The main scan parameter is the main solenoid current. A bucking magnet is always used to zero the magnetic field on the cathode. The measurement results of two different shift crews are shown in Figure 1. The repeatability is a few percent.

* This work has partly been supported by the European Community, contracts RII3-CT-2004-506008 and 011935, and by the 'Impuls- und Vernetzungsfonds' of the Helmholtz Association, contract number VH-FZ-005.
# Frank.Stephan@desy.de
§ on leave from INRNE, Sofia.
$ on leave from YERPHI, Yerevan.
& on leave from MEPHI, Moscow.

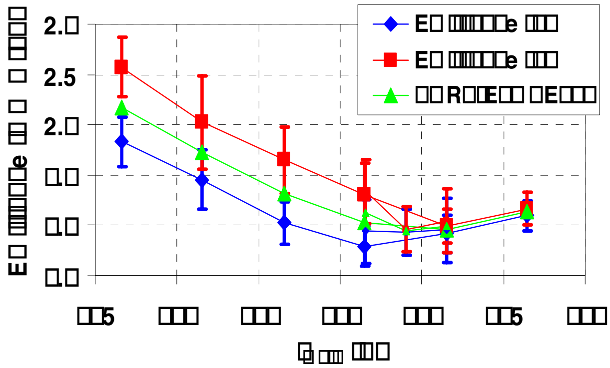

Figure 1: Transverse normalized projected emittance for different main solenoid currents at a bunch charge of 1 nC. Relevant machine parameters are given in the text. The numbers represent 100% RMS values.

The absolute emittance minimum is obtained at a main solenoid current of about 372.5 A with $\varepsilon_x$ = 1.25 ± 0.19 mm mrad in the horizontal and $\varepsilon_y$ = 1.27 ± 0.18 mm mrad in the vertical plane. Maximum effort has been performed to minimize intrinsic cuts in the particle distributions for the measurements by using highly sensitive screens, 12 bit signal resolution, large enough areas of interest to cover whole beam distributions and so on. Therefore, the numbers presented here can be considered as 100 % RMS emittance. The error bars represent the statistical fluctuation of the particle distributions during the measurements. As discussed elsewhere [3] there is an additional systematic uncertainty of the emittance numbers of about 20 %.

While the results presented above have been obtained with scanning 11 slit positions over the whole beam size additional measurements with more than 40 beamlets were performed at the point of minimum emittance found before. The horizontal phase space is shown in Figure 2.

The 100% RMS emittance is strongly dependent on the tails of the particle distributions. If for example particles below a certain phase space density in Figure 2 are removed from the analysis, then neglecting a charge fraction of only 10% will result in an emittance reduction of more than 30%, yielding 0.9 mm mrad [3]. Since these particles in the tails of the distribution will most probably not contribute to the lasing of the FEL this is considered to be the first demonstration of the beam quality required for the European XFEL.

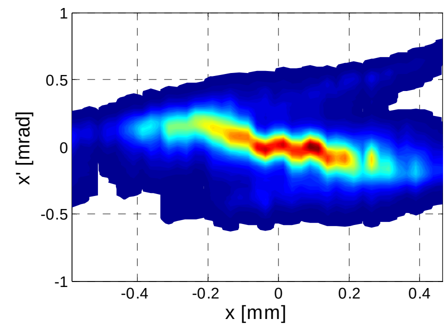


Figure 2: Detailed sampling of the horizontal phase space at the smallest emittance shown in Fig. 1 ($I_{main}$ = 372.5 A).

## UPGRADE OF THE PITZ FACILITY

At the end of August 2007 a major upgrade of the PITZ facility was started where many new diagnostics elements were installed and almost all components in the beamline were moved to new locations. The current setup is schematically shown in Figure 3. Downstream the new gun cavity (described in the next section) a new RF shielded vacuum valve and a new diagnostics cross were mounted to reduce wakefield effects and especially improve the vacuum conductivity. A new low energy dipole was installed to cure aperture problems at low main solenoid currents present before. Due to the increased maximum gun gradient of 60 MV/m, the booster cavity was moved to a larger distance from the photo cathode. Downstream the booster cavity, quadrupoles and a new, multi-purpose 180-degree spectrometer system below the main beamline were installed. Three emittance measurement systems (EMSYs) were located at the exit of the booster, the end of the beamline and in between. Also the Cherenkov radiators with streak readout for measurements of the longitudinal phase space were repositioned. In addition, a new photo cathode laser system with higher bandwidth was installed. This system has mainly produced Gaussian laser pulses of 2.1 ps FWHM up to now and with a new pulse shaper will be able to create flat-top temporal laser shapes of ~20 ps FWHM with ~2 ps rise/fall time [4]. More details on the new setup can be found in [5].

## COMMISIONING OF A NEW RF GUN

In winter 2007/2008 the RF gun prototype 4.2 was commissioned at PITZ [6]. There are two major

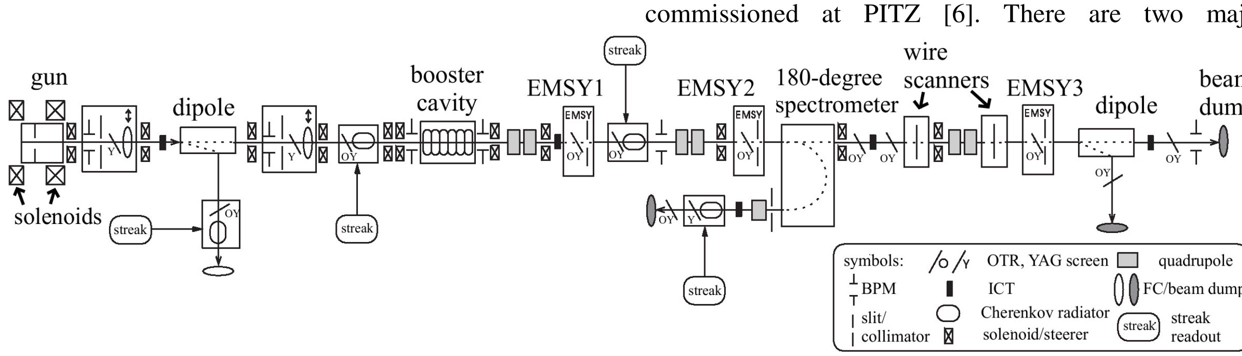


Figure 3. Layout of the upgraded photo injector test facility in Zeuthen (setup PITZ-1.7).

differences between this cavity and earlier prototypes: A) Instead of two there are now 14 independent water input channels which allow a detailed control and monitoring of the water flow rate in the different parts of the cavity cooling. B) The particle free cleaning of the inner surface of this cavity was for the first time done with $CO_2$ snow instead of the high-pressure water rinsing (HPWR) technique used up to now. The new dry-ice technique is effectively removing particles down to 100 nm without placing any water on the copper surface [7]. This led to a major improvement of the vacuum conditions in the gun and a major reduction of the emitted dark current by a factor of more than 10 as demonstrated in Figure 4. The dark current presented here is always the maximum dark current emitted during a main solenoid scan between 0 and 500 A for a given RF power in the gun cavity. As visible from Figure 5, the dark current in general goes further down with more conditioning time at longer RF pulse length and there is no major difference between pure molybdenum cathodes and those with $Cs_2Te$ coating. In addition, Figure 5 demonstrates that gun prototype 4.2 has been operated with more than 7 MW at 700 µs flat-top RF pulse length. Since the repetition rate was 10 Hz and the RF fill time was set to 32 µs, the average RF power stored in the gun was more than 50 kW.

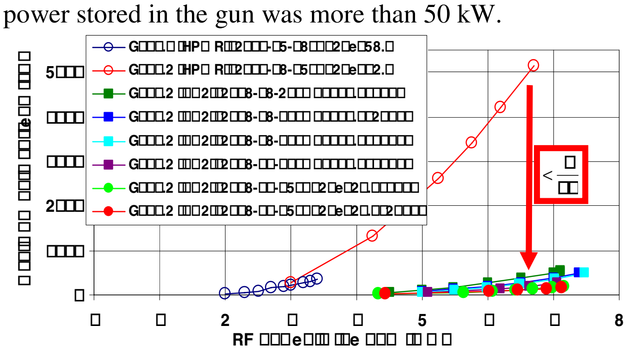

Figure 4: Maximum dark current for different gun cavities treated with different cleaning techniques.

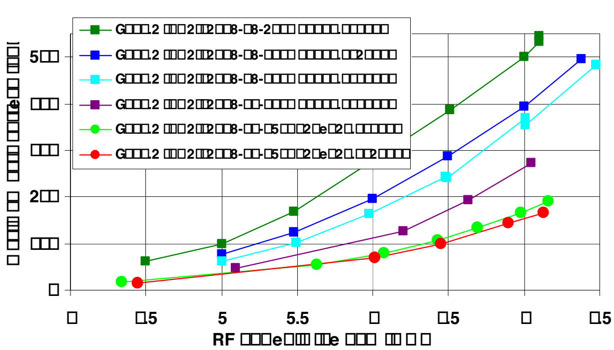

Figure 5: Maximum dark current for different RF pulse lengths and cathodes, ordered in sequence of data taking.

## QUANTUM EFFICIENCY

The quantum efficiency is regularly measured at PITZ. Figure 6 shows different measurements as a function of the accelerating field during electron emission. The full line represents a fit including a Schottky-like model for lowering the work function by the electric field.

Figure 7 shows the transverse distribution of the QE over the cathode surface. The scan was done with an RMS laser spot size of about 0.18 mm. The QE homogeneity in the central part is better than ±10 % which is within the measurement accuracy.

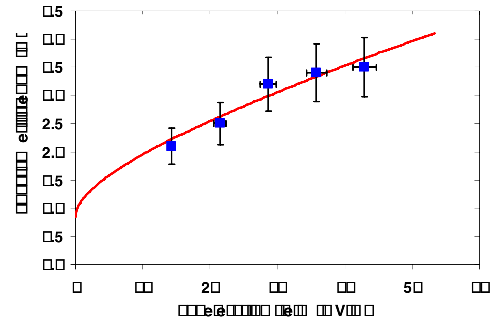

Figure 6: Quantum efficiency of $Cs_2Te$ cathode #23.3 as a function of the accelerating field at the photo cathode.

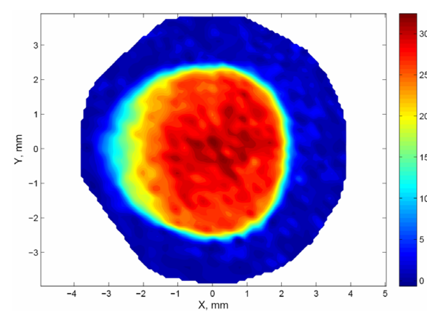


Figure 7: Quantum efficiency map of $Cs_2Te$ cathode #23.3. The colour code gives relative information only.

## REFERENCES

[1] L. Staykov et al., “Measurements of the Projected Normalized Transverse Emittance at PITZ”, FEL’07, Novosibirsk, Russia, August 2007.

[2] L. Staykov, “Characterization of the transverse phase space at the photo-injector test facility in Zeuthen”, PhD thesis, University of Hamburg, November 2008.

[3] F. Stephan al., “Detailed characterization of electron sources at PITZ yielding first demonstration of European XFEL beam quality”, to be submitted to PRST-AB in 2008.

[4] I. Will, G. Klemz, “Generation of flat-top picosecond pulses by coherent pulse stacking in a multicrystal birefringent filter”, OpticsExpress 16 (2008), pp. 14922-14937.

[5] C. Boulware et al., “Latest Results at the Upgraded PITZ Facility”, FEL’08, Gyeongju, Korea, August 2008.

[6] S. Rimjaem et al., “Tuning and Conditioning of a New High Gradient Gun Cavity at PITZ”, EPAC2008, Genoa, Italy, June 2008.

[7] A. Brinkmann, D. Reschke, J. Ziegler, “Various Applications of Dry-Ice Cleaning in the Field of Accelerator Components at DESY”, THP013, LINAC2008, Victoria, Canada, Sept./Oct. 2008.

# MIR-FEL WITH 4.5-CELL THERMIONIC RF-GUN

T. Kii#, H. Zen, K. Higasimura, R. Kinjo, K. Masuda, H. Ohgaki

Institute of Advanced Energy, Kyoto University, Gokasho, Uji, Kyoto 6110011, JAPAN

*Abstract*

We have constructed a compact Mid-Infrared Free Electron Laser (MIR-FEL) facility, Kyoto University FEL (KU-FEL) for advanced energy researches. The KU-FEL, consisting of an S-band thermionic RF gun, a 3 m accelerator tube and a planer undulator, aims to generate 4-13 µm tunable FEL. The most serious problem in using the thermionic RF gun for FEL facilities is unstable beam loading owing to back-streaming electrons in the RF gun. In order to overcome the problem, we have developed beamloading compensation methods realized by amplitude modulated RF and slight detuning of the resonant frequency of the RF gun. The first lasing was successfully achieved on March, 2008 at 12.4 µm and the FEL power saturation at 13.6 µm was observed on May. 2008.

## INTRODUCTION

A tunable and coherent light source in the MIR (mid-infrared) range is useful tool for a research on molecular dynamics, designing a functional material, which are key techniques for "sustainable energy science". Thus in the Institute of Advanced Energy, Kyoto University, we have developed a compact MIR-FEL (Free Electron Laser) facility[1] with a thermionic RF gun. A use of the thermionic RF gun is aimed to realize a cost effective, compact, easily operable FEL facility.

### *Facility Design*

The FEL system has been constructed in the Laboratory for Photon and Charged Particle Research, Institute of Advanced Energy, Kyoto University. Schematic drawing of the FEL facility is shown in Fig. 1. Total area of the facility is 350 m$^2$ including klystron gallery, control room and experimental hall. In order to reduce a construction cost, height of a radiation shielding wall made of concrete is reduced to 2.5 m and stairs are used to access to the accelerator room instead of a shielding door. Part of the shielding wall consists of cubic concrete blocks of 1 m$^3$ which can be moved to install large devices in the accelerator room. The KU-FEL was constructed in 2006[2] and commissioning was started in Dec. 2007.

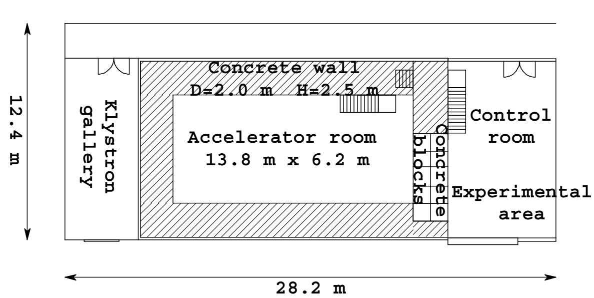


Figure 1: Schematic drawing of the KU-FEL facility.

### *KU-FEL System*

The FEL system consists of an S-band 4.5 cell thermionic RF gun driven by a 10 MW klystron, a 3 m travelling wave accelerator structure driven by a 20 MW klystron, beam transport system, a Halbach type undulator of 1.6 m, and an optical resonator. Figure 2 shows a schematic drawing of the system. The FEL wavelength of from 4 to 13 µm is expected with electron-beam energy of from 20 to 40 MeV.

A thermionic RF gun is a key device for constructing economical and compact FEL facility, because it does not need any expensive multi-bunched stable short pulsed UV laser for a photocathode RF gun or additional beam bunching system for a DC RF gun. However, a serious problem of back-bombardment limits macro-pulse duration. The back-bombardment problem is described as follows. Some electrons which escape from acceleration phase change their direction in the RF gun. And the cathode surface temperature increases due to bombardment of the back-streaming electrons. As a result, the number of extracted electron increases, and the beam loading increases. Then the beam energy decreases. In case for our 4.5 cell thermionic RF gun, the maximum pulse duration which can pass the 'dog-leg' section shown in Fig. 2 was less than 1 µs, when the cathode temperature was set to extract the electron beam more than 100 mA at the exit of the 'dog-leg' section.

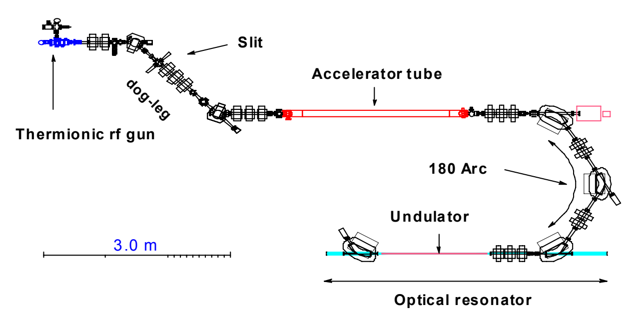


Figure 2: Layout of KU-FEL system.

## BEAMLOADING COMPENSATION

In case of a low-gain resonator linac FEL, which consists of an undulator and a couple of mirrors, an

#kii@iae.kyoto-u.ac.jp

spontaneous radiation emitted from electron bunch is amplified by the FEL interaction with following electron bunches. Thus, macropulse duration of the electron beam is quite important to obtain saturated FEL output. In case for the KU-FEL, the required pulse duration was at least 3 µs [3]. In order to obtain the long-pulse electron beam, we have developed and applied several techniques to reduce the back-streaming electrons and to reduce the influence of the back-bombardment.

### *Transverse Magnetic Field on the Cathode Surface*

Application of transverse magnetic field on the cathode surface[4] is the most popular technique to reduce the back-streaming electrons. We have applied the transverse magnetic field of about 10 G using a dipole magnet located behind the RF gun[5]. Although the temperature increase during the macropulse was reduced, the effect was not enough to obtain the electron beam longer than 1 µs, because too large magnetic field also diverge the extracted electron beam and the electrons were lost in the RF gun.

### *Amplitude Modulation to the Input RF*

In order to compensate the energy degradation due to the cathode heating by the back-streaming electrons, we applied amplitude-modulated RF pulses to the RF gun[6] and the accelerator tube. Remotely tunable reactors in a pulse forming network (PFN) of a klystron modulator[7] were used to form the optimized RF pulse shape. Phase advance due to the change of the velocity of the electrons in the klystron tube was carefully compensated by using a electric phase shifter. The block diagram of the RF supply system is shown in Fig. 3. The temporal evolutions of the applied voltage to the klystron for the RF gun, the input and reflected RF pulse from the RF gun, and the beam current at the exit of the RF gun are shown in Fig. 4. Although the transverse magnetic field was applied on the cathode surface, the extracted current increased from 200 to 500 mA. In this condition, the RF amplitude was changed from 6.4 to 8.0 MW during the macropulse. The temporal evolutions of the energy distribution extracted from the RF gun with and without modulated RF input are shown in Figs. 5 a), b). The energy degradation during the macropulse due to the increase of the beamloading was successfully compensated. The energy degradation was reduced from 10 to 0.7 %.

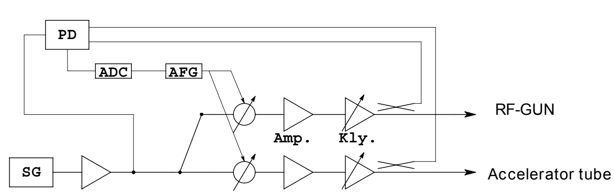


Figure 3: Block diagram of the RF system. The RF phase and the amplitude are independently controlled for the RF gun and the accelerator tube.

As the results, the first lasing of the KU-FEL at 12.4 µm was successfully observed[8]. The same RF amplitude modulation method was also introduced to the accelerator tube. The energy degradation after the accelerator tube was also reduced from 6.0 to 0.8 % as shown in Figs. 6 a), b). The macropulse duration was extended by the amplitude modulation technique from 0.8 to 4.0 µs.

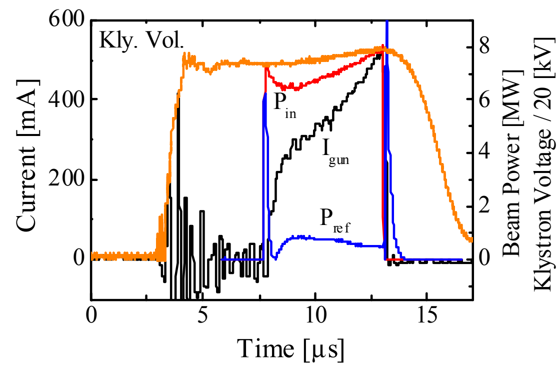


Figure 4: Temporal profiles of the klystron voltage (Kly. Vol.), input RF to the RF gun ($P_{in}$), extracted current from the RF gun ($I_{gun}$), and reflected RF from the RF gun ($P_{ref}$).

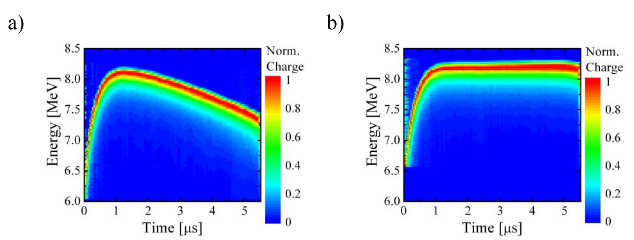


Figure 5: Temporal evolutions of the energy distribution extracted from the RF gun. a): flat RF b): modulated RF.

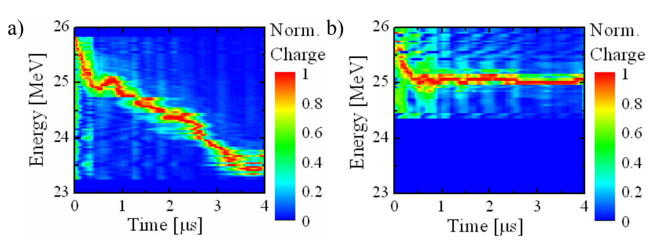


Figure 6: Temporal evolutions of the energy distribution at the exit of the accelerator tube. a): flat RF b): modulated RF.

### *RF Detuning in a Thermionic RF Gun*

Although the macropulse duration was successfully increased, the FEL power was not saturated due to the inadequate macropulse duration, because the tuning range of the RF amplitude was limited to about 20% due to the mechanical limitation of the variable reactors of the PFN circuit. Thus we have introduced new beamloading compensation method which is realized by feeding a RF power with slightly higher frequency than the resonant frequency of the gun[9]. The energy degradation due to the reduction of the cavity voltage was successfully mitigated, and the macropulse duration at the undulator section was extended from 4.2 µs to 5.5 µs as shown in Fig. 7. In this case, the detuning was 290 kHz.

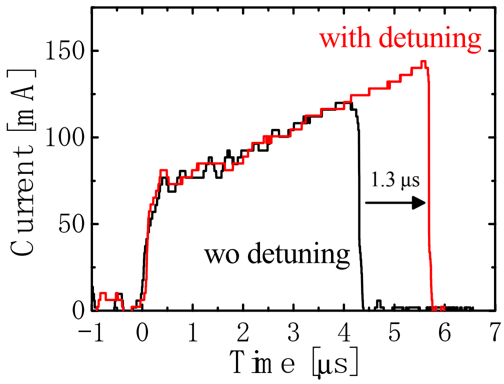


Figure 7: Current profiles of the electron beam at the undulator section. The detuning of 290 kHz was applied.

### *FEL Performance*

A lasing experiment has been carried out using the optimized electron beam. The beam parameter under the lasing experiment is shown in Table 1. The FEL wavelength was 13.2 µm. The temporal evolutions of the FEL output and the current profile at the undulator section are shown in Fig. 8. At the end of the macropulse, power saturation of the FEL was observed. The peak FEL power was expected to be about 2 MW when we assumed the optical pulse duration was 1 ps. The FEL gain and the optical loss were evaluated as 22 % and 11 % respectively from the power evolution of the FEL output.

Table 1: Electron Beam Parameters in the Saturation Experiment

| Parameter | Value |
|---|---|
| Energy (MeV) | 24 |
| $\sigma_E/E$ (%) | 0.8 |
| Bunch length (ps in rms) | 2 |
| Macropulse length (µs) | 5.5 |
| Average current (mA) | 115 |

## CONCLUSION

We have constructed a compact MIR FEL facility, KU-FEL consisting of an S-band thermionic RF gun, a 3 m accelerator tube and a planer undulator. A serious back-bombardment problem in using the thermionic RF gun for FEL facilities was successfully solved by the energy compensation techniques. The first lasing of the KU-FEL was achieved by the RF amplitude modulation for the RF gun. By introducing a new detuning method realized by feeding a RF power with slightly higher frequency than the resonant frequency of the RF gun, the macropulse duration reached to 5.5 µs and the FEL power saturation at 13.6 µm was successfully obtained.

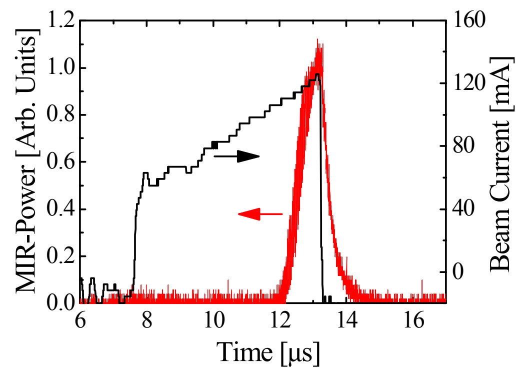


Figure 8: Current profile of the electron beam at the undulator section and power evolution of the FEL output.

## REFERENCES


[1] T. Yamazaki, H. Ohgaki, K. Masuda, T. Kii, S. Amazaki, T. Horii, H. Toku, and K. Yoshikawa: Proc. 23rd Int. Free Electron Lasers Conf., / 8th FEL User Workshop, (2002), pp. 13-15.

[2] H. Zen, T. Kii, K. Masuda, H. Ohgaki, and T. Yamazaki: Infrared Phys., Technol., Vol. 51, Issue 5, (2008) pp.382-385.

[3] S. Sasaki, H. Zen, T. Shiiyama, T. Kii, K. Masuda, H. Ohgaki, Proc. of FEL2007 (2008), pp. 394-397.

[4] C.B. McKee and John M.J. Maday, Nuclear Instruments & Methods in Physics Research, A296 (1990), 716-719.

[5] T. Kii, K. Yamane, I. Tometaka, K. Masuda, H. Ohgaki, K. Yoshikawa, and T. Yamazaki, Nuclear Instruments and Methods in Physics Research A507 (2003), 340-344.

[6] T. Kii, Y. Nakai, T. Fukui, H. Zen, K. Kusukame, N. Okawachi, M. Nakano, K. Masuda, H. Ohgaki, K. Yoshikawa, T. Yamazak, AIP Proc., SRI2006, 248-251, (2006).

[7] E. Oshita, et al., IEEE Proceedings of PAC'95, Dallas, May 1-5, (1995) pp. 1608-1610.

[8] H. Ohgaki et al., Japanese Journal of Applied Physics, in press. (2008).

[9] H. Zen, K. Higashimura, T. Kii, R. Kinjo, K. Masuda, H. Ohgaki, Proc. of FEL2008, in press. (2008).

# STATUS OF THE LINAC-800 CONSTRUCTION AT JINR

N.I. Balalykin, V.V. Kobets, A.G. Kobets, I.N. Meshkov, V.F. Minashkin, G.I. Sidorov, V.G. Shabratov, G.D. Shirkov, G.V. Trubnikov
JINR, Moscow region, 141980, Dubna, Russia

*Abstract*

800 MeV electron linac (LINAC-800) is under construction at JINR. It will be used as a driver for Volume FEL and as a test bench for commissioning of elements of the ILC. Presently the electron injector is commissioned and the electron beam of 50 keV of the energy at current of about 15 mA was obtained. The results of the injector operation at nominal parameters (400 keV, 300 mA) and commissioning of the first accelerating section at 20 MeV are discussed.

## THE LINAK-800 PROJEKT

The LINAC-800 project is being under development at the JINR, Dubna, Russia. It is based on an accelerator facility presented to JINR by the NIKHEF, Amsterdam.

Project will be accomplished with the construction of a complex of free electron lasers covering continuously the spectrum from far infrared down to ultraviolet (of about 150 nm) [1]. The far-infrared coherent source will cover continuously the submillimeter wavelength range.

Realization of this project will not require a significant modification of the JINR infrastructure. In Table 1 we present a summary of the radiation properties from coherent radiation sources being planned to build in project. Notations G1-G4 refer to the FEL oscillators, and FIR stands for the far-infrared coherent source.

## ACCELERATOR LINAC-800

The electron beam with necessary parameters for the Free Electron Laser will be generated with the electron linac, which is a modified version of the Medium Energy Accelerator (MEA) transferred to JINR from NIKHEF[2]. The energy of electrons at the linac exit is 800 MeV and peak current of 30-60 A, with subharmonic buncher of the frequency of 476 MHz, a buncher at the frequency of 2856 MHz and 24 acceleration sections, which are combined in 14 acceleration stations (A00 – A13). To operate FEL, one needs an injector with a special subharmonic prebuncher. Such an injector has to be developed at JINR.

### *MEA Injector*

To start the linac operation and test its condition, we plan to use the MEA injector consisting of an electron gun, chopper, prebuncher and buncher [2].

The electron gun (Table 2) has a dispenser thermocathode with the diameter of 8 mm. Its heater current is 15 A at the heater filament voltage of 12 V. The cathode lifetime is of the order of 20 thousand hours. The gun optics elements contain Pirce electrode at the cathode potential, control electrode and acceleration tube, which has 15 diaphragms forming homogeneous acceleration field. Linear potential distribution along the tube is provided with the divider, the voltage between two neighbour diaphragms is of the order of 30 kV. One can "close" the gun by applying the voltage of –150 V between the cathode and control electrode. The gun is operated in a pulsed mode by applying voltage pulses of +6 kV amplitude between the cathode and control electrode.

Table 1: Summary of Radiation Properties from Coherent Radiation Sources in Project

| | FIR | G1 | G2 | G3 | G4 |
|---|---|---|---|---|---|
| Radiation wavelength [μm] | 150-1000 | 20-150 | 50-30 | 1-6 | 0.15-1.2 |
| Peak output power, [MW] | 10-100 | 1-5 | 1-5 | 3-15 | 10-20 |
| Micropulse energy, [μJ] | 500 | 50-200 | 25-100 | 25-100 | 50-100 |
| Micropulse duration (FWHM),[ps] | 5-10 | 10-30 | 10 | 10 | 3-5 |
| Spectrum bandwidth (FWHM),[%] | | 0.2-0.4 | 0.6 | 0.6 | 0.6 |
| Micropulse repetition rate, [MHz] | | | 19.8/ 39.7/ 59.5 | | |
| Macropulse duration, [μs] | | | 5-10 | | |
| Repetition rate, [Hz] | | | 1-100 | | |
| Average output power (max.), [W] | 10-50 | | 0.2-1 | | |

Table 2: The Electron Gun Parameters

| Scheme | Triode |
|---|---|
| Type of cathode:<br>Diameter, [mm]<br>Heater: voltage, [V]<br>current, [A] | Dispenser<br>8<br>0-12<br>0-15 |
| Electron energy, [keV] | 400 |
| Peak current, [A] | 0.45 |
| Cathode current stability | $1.5 \cdot 10^{-3}$ |
| Beam diameter, [mm] | 1.5 |
| Normalized emittance (1σ), [π·mm·mrad] | 8 |

### *Buncher*

The MEA buncher system (Table 3) contains three elements, and the first of them is the chopper.

Table 3: The Buncher System

| | | |
|---|---|---|
| **Chopper** | Scheme | RF-cavity ($TM_{110}$) |
| | Frequency, [MHz] | 2856 |
| | Amplitude of transverse deflection, [mm] | 16 |
| | Drift space Length, [cm] | 50 |
| | Quality factor (unloaded) | 4000 |
| | Transmission efficiency, % | 20 |
| | Peak RF power input,[kW] | 3.0 |
| **Prebuncher** | Scheme | RF-cavity ($TM_{010}$) |
| | Frequency, [MHz] | 2856 |
| | Mode | 2π/3 |
| | Peak electric field at the gap center, [kV/cm] | 10.3 |
| | Bunch phase length at the prebuncher exit:<br>at 10 mA current<br>at 20 mA current | <br><br>6°<br>10° |
| | Distance between chopper collimator and the buncher entrance, [cm] | 98.7 |
| | Distance between prebuncher exit and the buncher entrance, [cm] | 132.7 |
| **Buncher** | Frequency, [MHz] | 2856 |
| | Mode | 2π/3 |
| | Number of cavities | 38 |
| | Shunt impedance, [MΩ/m] | 51.2 – 55.1 |
| | Length at 24° C, cm] | 127.77 |
| | Bunch phase length at the buncher exit:<br>at 10 mA current<br>at 20 mA current | <br><br>≤ 1°<br>≤ 2° |
| | Electron energy, [MeV] | 6 |

It is a deflector cavity of S-band type with collimator. The peak RF power consumed by the chopper is of 3 kW.

The prebuncher cavity is installed just after the chopper cavity. It is fed with RF of 2 kW power from klystron of the first acceleration section through attenuator and phase shifter.

The buncher is actually the short acceleration section of the accelerator structure. The bunch phase length at the buncher exit is of 6°. Its structure is supplied with RF power of 2 MW from the first klystron. The RF power is transmitted from the buncher exit through phase shifter to the first acceleration section.

### *Acceleration Sections*

The MEA linac contains acceleration waveguide sections of six types. They are similar in mechanical features, but differ in RF-parameters (Table 4). Each section contains eleven uniform 2π/3-mode segments. The numbering of the sections is done with the alphanumeric identifiers, in which first letter symbol (A or B) means the way of RF-feeder connection to the section: symbol A indicates that the feeder is connected to the top of the section, the symbol B – to the bottom. The last symbols (one or two) mean the type of the section. Besides, double letter symbol AA or BB indicates the short section, single letter A, B, C, D – a long section. The short sections have the length of 3.6 m, they are immersed in constant solenoidal magnetic field of the order of 500 Gauss. The long sections of the length of 7.35 m have no magnetic field. All the acceleration sections are combined in acceleration stations that comprise an RF-power source (klystrons with modulators), waveguide, acceleration section and drift section. The drift section is used as a place of disposition of beam diagnostic devices (monitoring of the electron energy, beam current, size, position and emittance).

Table 4: The Parameters of Acceleration Sections

| Type of section | Short | Long |
|---|---|---|
| Number of sections | 3 | 18 |
| Number of cells per sections | 105 | 210 |
| Section length, [m] | 3.673 | 7.346 |
| Frequency, [MHz] | 2856 | |
| Traveling-wave mode | 2π/3 | |
| Acceleration gradient, [MeV/m] | 5 | |
| Filling time, [μs] | 1.3 | |
| Beam load, [MeV/mA] | 2.6 | |
| Shunt impedance, [MΩm] | 56.5 - 48 | |
| Aperture: diameter, [mm]<br>thickness, [mm] | 32<br>5.84 | |

## FEL INJECTOR

Generation of an electron beam with the parameters suitable for feeding of FEL requires significant upgrade of the linac injector. The requirements to the FEL electron beam listed in Table 5 can be satisfied using a subharmonic bunch compressor (SBH) described in Ref. [4]. It contains in our case (Figure 1) an electron gun, a cavity operating at subharmonic frequency, a drift section and the first acceleration section of the linac.

The electron gun has a modulation grid, which provides generation of short electron bunches with the duration of 0.5 ns. The electrons emitted from the dispenser thermocathode are accelerated in the electric field of the gun electrodes up to energy of the order of 400 keV and are formed in the injector elements – prebuncher, drift section and acceleration section[5].

Table 5: Parameters of Electron Beam after Injection and Acceleration in the First Linac Section

| | |
|---|---|
| Energy, [MeV] | 7 |
| Peak current, [A] | 50-70 |
| Micropulse duration, [ps] | 20 |
| Normalized emittance, [πmm·mrad] | ≤ 30 |
| Electron energy spread, [%] | < 3 |
| Micropulse frequency, [MHz] | 19,8/39,7/59/5 |
| Macropulse duration, [μs] | 5-10 |
| Repetition frequency, [Hz] | 1-100 |

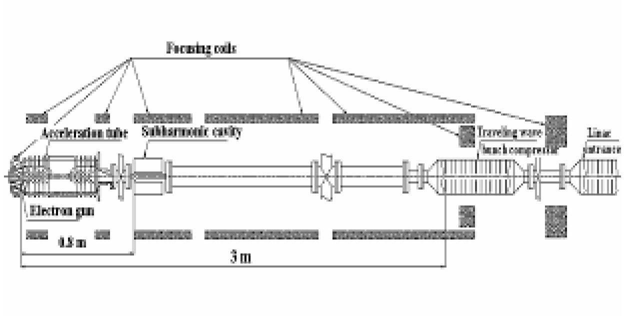


Figure 1: Injector layout.

Three first linac sections have focusing solenoids with magnetic field of 500 G. In the FEL injector the most critical position for beam space charge influence is the exit part of the drift section and the entrance part of the first linac section. There $I_{peak} \approx 36$ *A*. The value of the solenoid magnetic field has to exceed the level of so-called Brillouin field.

$$B_{Brillouin} \approx 500 \text{ G}.$$

Keeping in mind future development of the injector, we have chosen maximum value of drift section magnetic field equal to 1 kG.

## RESULTS OF THE WORK

During realization of LINAC-800 project the injector of electrons with buncher, short accelerating section and four long accelerating section have been assembled (Figure 2). The injector and accelerating sections power supply units were installed.

The control system of the injector was upgraded. As a result of the fulfilled works the vacuum pressure in the injector of $10^{-8}$ Torr has been achieved. The injector commissioning was done. In the first experiments on the injector commissioning the voltage on the accelerating tube was 50 kV. The current at of the accelerating tube output up to 12 mA in the pulse duration up to 10 μs was achieved (Figure 3). The works aiming to increase the voltage up to 400 kV and current up to design value are in progress.

After launching the electron injector at 50 keV these works are continued. The reconstruction of the HV transformer and its control systems was performed, the pressure of nitrogen in the transformer tanks achieved at 6 bar, now we provide works aiming to achieve voltage of 400 kV at injector. Besides that on the first accelerating station the klystron was mounted, forming lines were tested and prepared, commissioning works have been started.

Figure 2: The injector of electrons with buncher, short accelerating section and four long accelerating section.

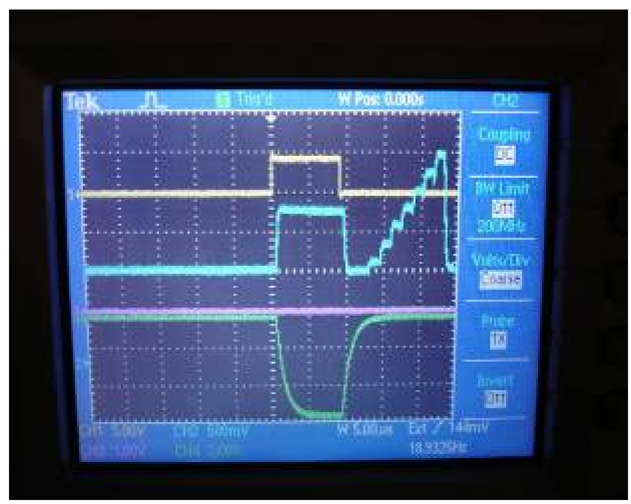


Figure 3: Beam current signal from injector.

## REFERENCES

[1] G. Arzumanian, N. Balalykin, V. Kobets et al., Conceptual Design Report, Dubna, 2001.

[2] F.B. Kroes, Electron Linac MEA, Compedium of Scientific Linacs, LINAC′96, 1996.

[3] F.B. Kroes et al., Improvement of the 400 kV Linac Electron Source of AMPS, Proc.of EPAC′92, p.1032.

[4] T. Tomimasu, Y. Morii, E. Oshita et al., NIM A 407 (1998) 370.

[5] V. Kobets, I. Meshkov et al, Optimization of subharmonic injector for LINAC-800, Physics of articles and Nuclei Letters, Vol. 2, No. 3, 2005, pp. 158-163.

# LINEAR ACCELERATOR FOR THE PSI-XFEL FEL3 BEAMLINE

Y. Kim*, A. Adelmann, B. Beutner, M. Dehler, R. Ganter, R. Ischebeck, T. Garvey
M. Pedrozzi, J.-Y. Raguin, S. Reiche, L. Rivkin, V. Schlott, A. Streun, and A. F. Wrulich
Paul Scherrer Institute, CH-5232 Villigen PSI, Switzerland

*Abstract*

To supply coherent, ultra-bright, and ultra-short XFEL photon beams covering a wide wavelength range from 0.1 nm to 7 nm, three FEL beamlines will be constructed in the planned PSI-XFEL facility. The FEL1 beamline will use a 6 GeV normal conducting S-band linac to generate hard X-rays from 0.1 nm to 0.7 nm, while the FEL2 beamline will use a 3.4 GeV linac to supply X-rays from 0.7 nm to 2.8 nm. However, the FEL3 beamline is designed to supply spatially as well as temporally coherent soft X-rays from 1.8 nm to 7 nm with the High-order Harmonic Generation (HHG) based seeded High Gain Harmonic Generation (HGHG) scheme. In this paper, we describe an injector, bunch compressors, beam diagnostic sections, and linacs for the FEL3 beamline, which is based on a 2.5 cell S-band RF gun and a 2.1 GeV linac.

## INTRODUCTION

Since 2003, the Paul Scherrer Institute (PSI) has been developing two key technologies to realize the advanced and compact PSI-XFEL facility within about 930 m long space [1]. One is the high voltage pulser based advanced Low Emittance Gun (LEG), and the other is the Cryogenic Permanent Magnet in-vacuum Undulator (CPMU) with a small gap of about 5 mm and a short period of about 15 mm [2]. A prototype CPMU will be installed at the Swiss Light Source in 2011. Since required slice beam parameters for FEL1 and FEL2 beamlines are challenging, we have been concentrating our efforts to develop the advanced LEG [1]. In 2007, a 500 kV pulser based LEG test facility was constructed at PSI, and recently, we have performed various machine studies there [1–3]. In parallel, a 250 MeV injector test facility will be constructed by the end of 2009 to develop advanced accelerator technologies for the future 6 GeV PSI-XFEL project [1, 4]. In the first phase of the 250 MeV injector test facility, a CTF3 RF gun based photoinjector will be tested, and in its second phase, a 1 MV pulser based advanced LEG will be tested. Additionally, an upgrade of the HHG based seeding with a CPMU in the 250 MeV injector test facility is under discussion. To saturate the FEL3 beamline effectively, a low slice energy spread is more important than a low slice beam emittance. Due to a much lower overall bunch length compression factor, the CTF3 RF gun is expected to supply a lower slice energy spread than the advanced LEG. Therefore the RF gun will be used as a dedicated gun to drive the FEL3 beamline. However, the advanced LEG will be used to drive the FEL1 and FEL2 beamlines, where a low slice emittance is the most critical beam parameter to get saturation with 60 m long undulators. In this paper, we describe the CTF3 RF gun based linac to drive the PSI-XFEL FEL3 beamline.

* Mail : Yujong.Kim@PSI.ch

## OPTIMIZATION OF DRIVING LINAC

From our recent thermal emittance measurements at the LEG test facility, we find that the thermal emittance of a diamond turned copper cathode is about 0.2 $\mu$m for an rms laser spotsize on the cathode of about 330 $\mu$m at 40 MV/m [2, 3]. To optimize the CTF3 RF gun based injector, we used the measured value. Since the thermal emittance depends on the rms laser spotsize and the gradient on the cathode by the Schottky effect, the thermal emittance in the CTF3 RF gun was re-scaled to about 0.2 $\mu$m by choosing a smaller rms laser spotsize of about 270 $\mu$m at 100 MV/m [2, 4]. To compensate the projected emittance growth due to the linear space charge force in a drift space between the gun and the booster linac and to satisfy two special conditions for the invariant envelope matching in the booster, we have optimized the gradient of the RF gun, the magnetic field of the main gun solenoid, and gradients of the booster linac [4,5]. Details on the optimization of the CTF3 RF gun based injector are described in reference [4], and its optimized beam parameters are summarized in Table 1 where all emittances are normalized rms values, and all energy spreads are rms ones. According to ASTRA simulations, the optimized normalized projected and central slice emittance before the first bunch compressor (BC1) are about 0.35 $\mu$m and 0.32 $\mu$m, respectively.

Since the initial peak current from the RF gun is about 22 A, the peak current is increased to about 1.6 kA by two bunch compressors (BC1 and BC2) as shown in Figs. 1, 2, 3, and 4(middle left) and as summarized in Table 1. To minimize the projected and slice emittance growth due to the space charge forces, the bunch length is initially compressed from 840 $\mu$m to 55 $\mu$m by BC1 at 256 MeV. Then the beam is accelerated to a much higher beam energy of about 1469 MeV, where the bunch length is re-compressed down to 14 $\mu$m by BC2. To control the emittance growth at BC1 due to Coherent Synchrotron Radiation (CSR), we used special optimization methods which are described in references [4, 6]. Additionally, to control the horizontal emittance growth at BC2 due to CSR, we chose a higher horizontal beta-function of about 65 m in front of BC2 and a strong focusing horizontal beta-function in BC2 to make a beam waist at the end of the fourth dipole as shown in Fig. 2(bottom) [6]. Since the projected energy spread is

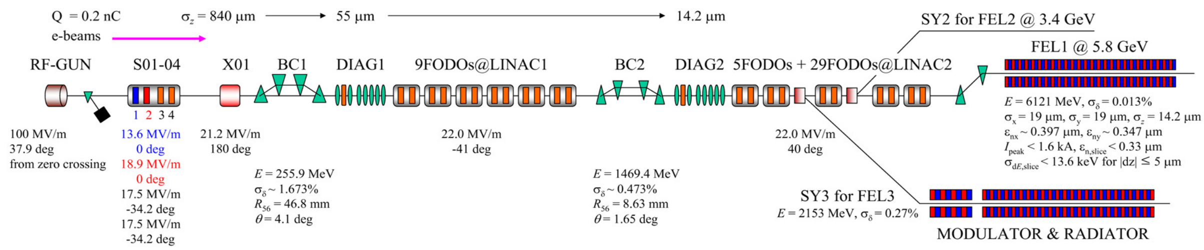


Figure 1: An optimized layout of the CTF3 RF gun based linac for the PSI-XFEL Project.

Table 1: Parameters of an optimized FEL3 driving linac.

| Parameter | unit | value |
|---|---|---|
| single bunch charge $Q$ | nC | 0.2 |
| gun and S-band linac RF frequency | MHz | 2998 |
| maximum repetition rate | Hz | 100 |
| gun cell number | cell | 2.5 |
| rms laser spotsize on cathode $\sigma_{\mathrm{laser}}$ | $\mu$m | 270 |
| laser pulse length (FWHM) | ps | 9.9 |
| laser pulse rising and falling time | ps | 0.7 |
| normalized thermal emittance | $\mu$m | 0.195 |
| gun solenoid max longitudinal field | T | 0.206 |
| gun maximum gradient | MV/m | 100 |
| gun RF phase from zero crossing | deg | 37.9 |
| S01 accelerating gradient | MV/m | 13.6 |
| S01 RF phase from on crest | deg | 0.0 |
| S02 accelerating gradient | MV/m | 18.9 |
| S02 RF phase from on crest | deg | 0.0 |
| length per FODO in LINAC1 / LINAC2 | m | 10.3 / 10.4 |
| phase per FODO in LINAC1 / LINAC2 | deg | 60 / 60 |
| max $\beta$-function in LINAC1 / LINAC2 | m | 17.3 / 18.8 |
| length of QM in LINAC1 / LINAC2 | m | 0.15 / 0.2 |
| max QM gradient in LINAC1 / LINAC2 | T/m | 6.5 / 23.2 |
| projected emittance before BC1 / BC2 | $\mu$m | 0.35 / 0.39 |
| central slice emittance before BC1 / BC2 | $\mu$m | 0.32 / 0.32 |
| rms bunch length before BC1 / BC2 | $\mu$m | 840 / 55 |
| beam energy before BC1 / BC2 | MeV | 256 / 1469 |
| projected E-spread before BC1 / BC2 | % | 1.7 / 0.47 |
| central slice E-spread before BC1 / BC2 | keV | 0.3 / 2.6 |
| full slice E-spread before BC1 / BC2 | keV | 1.4 / 30.5 |
| projected emittance after BC2 / SY3 | $\mu$m | 0.40 / 0.40 |
| central slice emittance after BC2 / SY3 | $\mu$m | 0.33 / 0.33 |
| rms bunch length after BC2 / SY3 | $\mu$m | 14 / 14 |
| beam energy after BC2 / SY3 | GeV | 1.469 / 2.153 |
| projected E-spread after BC2 / SY3 | % | 0.47 / 0.27 |
| projected E-spread after SY2 / SY1 | % | 0.12 / 0.01 |
| central slice E-spread after BC2 / SY3 | keV | 13.6 / 13.6 |
| full slice E-spread BC2 / SY3 | keV | 147.6 / 147.6 |

about 0.47% and the bunch length is already compressed by BC1, we can avoid the chromatic effects around BC2 though the beta-function is somewhat large. To control CSR and Incoherent Synchrotron Radiation (ISR) effects at BCs effectively, a higher bunch compression factor of about 15 is selected at BC1 where CSR and ISR effects are

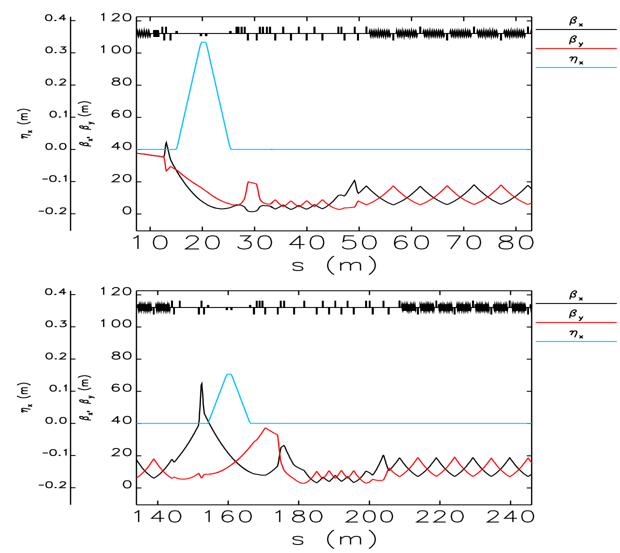


Figure 2: Optics around BC1, DIAG1, and LINAC1 (top), optics around BC2, DIAG2, and LINAC2 (bottom). Here TDSs will be installed at about 30 m and about 170 m.

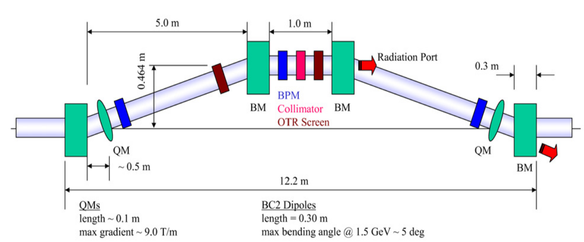


Figure 3: Layout of BC2 for the PSI-XFEL project.

weaker due to a somewhat longer bunch length and a lower beam energy. Then the bunch length is slightly compressed further with a lower bunch compression factor of about 4 at BC2 where CSR and ISR effects are stronger due to a much shorter bunch length and a higher beam energy.

As shown in Figs. 1 and 2, two special diagnostic sections (DIAG1 and DIAG2) are designed after BCs to measure the slice emittance, slice energy spread, bunch length, longitudinal phase space, arrival timing jitter, projected emittance, and Twiss parameters without changing optics during FEL operations. The diagnostic sections consist of five main parts: The first part is the five quadrupoles (QMs) to match optics between BCs and a transverse deflection cavity (TDS). The second part is the TDS to streak beams vertically. The third part is another five quadrupoles to match optics between the TDS and following three FODO cells. The fourth part is three FODO cells with seven quadrupoles to generate a wide-range phase advance along seven OTR screens in the FODO cells. The fifth part is the one dipole magnet after three FODO cells to generate a required dispersion for the longitudinal phase space measurement. To get a high time resolution of about 20 fs (FW), the vertical beta-functions at those TDSs should be high enough as shown in Fig. 2. Additionally, to get a high resolution in slice and projected emittance measurements, an asymmetric optics is used for three FODO cells where the horizontal and vertical phase advances per FODO cell are 55 degree and 25 degree, respectively.

After bunch length compression, the electron beam is accelerated by LINAC1 and LINAC2 as shown in Figs. 1 and 2 and as summarized in Table 1. To avoid any emittance growth due to chromatic effects, LINAC1 and LINAC2 use optimized FODO cells with a phase advance per FODO cell of 60 degree and the maximum beta-function smaller than 20 m. In each FODO cell in LINAC1 and LINAC2, there are two quadrupoles, two 0.7 m long drift spaces to host beam diagnostic components and steerers, and two 4.3 m long S-band tubes as shown in Fig. 2.

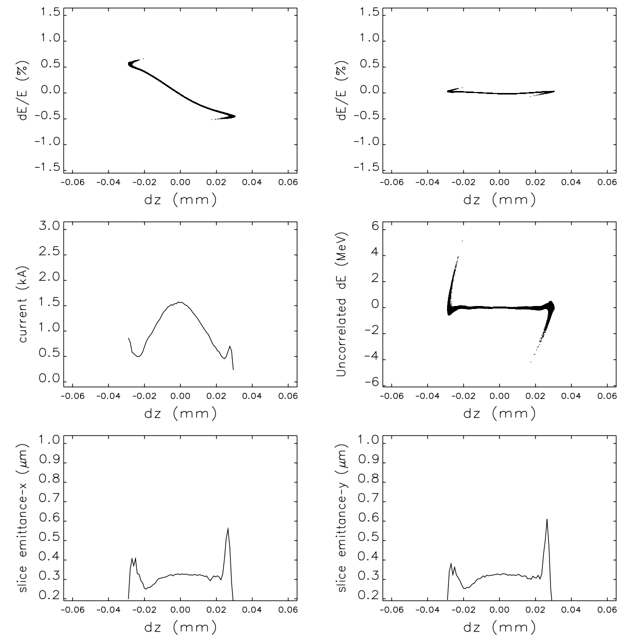


Figure 4: Longitudinal phase space at the FEL3 (top left) and at the FEL1 (top right), peak current (middle left) and slice beam parameters at the FEL1, FEL2, and FEL3 beamlines (middle right and bottom). Here positive $dz$ corresponds to the head part of an electron bunch.

## OVERALL PERFORMANCE

To check the overall performance of the CTF3 RF gun based FEL driving linac, we have performed start-to-end (S2E) simulations from the cathode to the end of LINAC2 with the ASTRA and ELEGANT codes. Here, all main emittance dilution effects such as space charge effects up to 150 MeV, short-range transverse and longitudinal wakefields in all linac structures, CSR and ISR in BC dipoles, and fringe-field and chromatic effects in all magnets are considered. As summarized in Table 1 and as shown in Figs. 1 and 4, the emittance growth along the whole linac is well suppressed, and the final projected emittance and central slice emittance at a switching yard 3 (SY3) for the FEL3 beamline are about 0.40 $\mu$m and 0.33 $\mu$m, respectively. Although the projected energy spread is about 0.27% at SY3 and the energy chirp is somewhat large as shown in Fig. 4(top left), its rms slice energy spread is smaller than 150 keV over the whole bunch. In particular, the central rms slice energy spread is only about 14 keV for a 5 $\mu$m long central slice. The large linear energy chirp is helpful to reduce the sensitivity of the energy jitter in the seeded FEL3 beamline. As shown in Figs. 1 and 4(top right), by continuously accelerating the electron beam with an off-crest RF phase of 40 degree in LINAC2, the large projected energy spread is effectively damped down to 0.01% by the action of short-range longitudinal wakefield in LINAC2. This ultra-small projected energy spread and ultra-flat energy chirp is helpful to increase the intensity of FEL photon beams and to reduce the bandwidth of the FEL photon beam spectrum in the SASE based FEL1 beamline. Note that the growth of the slice beam parameters along LINAC2 is negligible. Therefore the slice beam parameters at the FEL1 beamline are same as those at the FEL3 beamline.

## SUMMARY

The CTF3 RF gun based linac can supply sufficient beam quality to drive the FEL3 beamline with the help of four main optimization methods; compensation of projected and slice emittances with the invariant envelope matching in the booster, careful suppression of CSR and ISR in BCs, reduction of chromatic effects in the LINACs with the optimized FODO cells, and control of energy chirp and energy spread by the action of the short-range longitudinal wakefields in LINAC2. From the full S2E simulations with the ASTRA, ELEGANT and GENESIS codes, we have checked that the power of the FEL1 beamline can be saturated even at 0.1 nm with this optimized beam quality, and a promising spectrum bandwidth of about 0.05% can be obtained by the ultra-flat energy chirp.

## REFERENCES

[1] http://fel.web.psi.ch

[2] Y. Kim *et al.*, in *Proc. FEL2008*, Gyeongju, Korea.

[3] M. Pedrozzi *et al.*, in *Proc. EPAC2008*, Genoa, Italy.

[4] Y. Kim *et al.*, in *Proc. EPAC2008*, Genoa, Italy.

[5] Y. Kim *et al.*, in *Proc. LINAC2006*, Knoxville, USA.

[6] Y. Kim *et al.*, *Nucl. Instr. and Meth. A* **528** 421 (2004).

# SUPERCONDUCTING OPTIONS FOR THE UK'S NEW LIGHT SOURCE PROJECT

P.A.McIntosh#, R.Bate, C.D.Beard, D.M.Dykes and S.Pattalwar, STFC Daresbury Laboratory, Warrington, WA4 4AD, UK

*Abstract*

The UK's New Light Source (NLS) project was officially launched on April 11th 2008 [1], which will be based on advanced conventional and free electron lasers, with unique and world leading capabilities. User consultation exercises have already been initiated to determine the fundamental photon output requirements for such a machine. In order to match possible requirements for high repetition rates (> 1 kHz), a series of Superconducting RF (SRF) linac options have been investigated, reflecting varied beam loading conditions and possible beam energy scenarios.

## INTRODUCTION

Superconducting RF (SRF) is becoming the technology of choice for the next generation of particle accelerators, both for basic energy science programmes such as conventional synchrotron radiation sources (i.e. diamond, TLS, SSRF and SOLEIL), and also for high energy physics collider machines (i.e. LHC and ILC). This paper assesses possible existing SRF cryomodule design solutions for a number of SRF linac based accelerators that have been developed specifically for FEL applications around the world; which include single-pass (XFEL and BESSY-FEL), recirculating (CEBAF) and energy recovery (ALICE) configurations. A companion paper deals with alternative normal conducting linac solutions for NLS [2].

The design requirements for an SRF linac differ for every application, as typically for single pass configurations, beam-loading is relatively weak and RF infrastructure costs are not as significant compared to more heavily beam-loaded linacs. It then becomes more cost effective to recirculate and/or to remove the beam-loading component completely by operating in energy-recovery mode. Dynamic RF cryogenic loads will typically dominate for these types of linacs and so considerable cost savings can also be gained using multi-pass schemes to attain higher energies. A recirculating option is also being investigated for NLS in order to assess potential capital and operational cost savings.

## CEBAF UPGRADE CRYOMODULE

A series of three cryomodules have been constructed as part of JLab's efforts to increase CEBAF's availability and reliability. These provide additional acceleration for the FEL and produce prototypical cryomodules for the 12 GeV Upgrade. The first two constructed were based on the initial "Upgrade Cryomodule" design [3,4]. Both containing 7-cell cavities based on the original CEBAF cavity cell shape operating at 1.5 GHz, with a design expectation of > 70 MeV of acceleration. The third cryomodule, dubbed "Renascence," incorporates several design changes in order to provide more than the 108 MeV capability required for the 12 GeV upgrade of CEBAF [5] (see Figure 1).

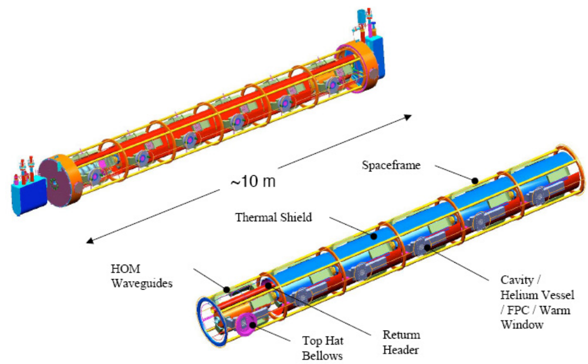


Figure 1: JLab Renascence Cryomodule.

## XFEL CRYOMODULE

The XFEL Cryomodule consists of eight TESLA cavities in a string with a large helium gas return pipe as the backbone of the structure which the cavities are supported from (see Figure 2). Optimisation of the cryomodule design has been taken place to develop the module capable of reaching nearly 280 MV of acceleration, fed by a MW class multibeam klystron. In order to minimise the cryogenic load, XFEL is pulsed with a 1% duty factor to achieve a final operating energy of 20 GeV [6].

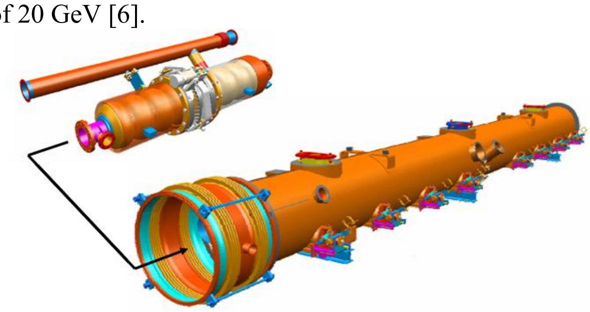

Figure 2: XFEL Cryomodule.

## BESSY-FEL CRYOMODULE

The TESLA/XFEL cavity and cryomodule technology was developed for pulsed operation, although most of the system is equally suited for CW mode. There are a number of modifications that must be implemented to

#p.a.mcintosh@dl.ac.uk

achieve modest CW gradients and BESSY's approach has been to maintain the TESLA design philosophy and only make changes were necessary; to sustain reliable CW operation, and/or if significant cost savings can be realised [7].

Since the BESSY-FEL has a much reduced final beam energy of 2.3 GeV, optimisation of the cryogenic load and analysis of the construction cost versus gradient and helium temperature, lead to a relatively flat optimum between 15 – 18 MV/m. (15.4 MV/m actually chosen) at a $Q_0$ of 2e10, with an operating temperature of 1.8 K. Since it is intended to run the module CW and at a higher $Q_0$, the cavities are very sensitive to microphonics and in order to mitigate this, the diameter of the helium fill pipe is increased to allow a higher heat load to be dissipated. Modifications to the existing XFEL coupler are also planned in order to achieve the higher average powers required for the BESSY-FEL linac.

## ALICE CRYOMODULE

The remit of the ALICE facility is to provide a R&D facility for advanced accelerator systems; from high-intensity electron sources, CW SRF linac cryomodules, short pulse FEL undulators, to Electro-Optical diagnostics [8]. The SRF cryomodule employed on ALICE (see Figure 3) was developed in collaboration between FZD-Rossendorf and Stanford University, and first operated on the SCA facility at Stanford University in 1979, then at the ELBE facility from 2001 and is now commercially licensed by ACCEL GmbH in Germany. It comprises two, 1.3 GHz 9-cell cavities; each having a pair of HOM couplers (á la XFEL), modified to utilise sapphire ceramics (developed at JLab [9]) to improve the power handling capability upto 10 W (from the original 5W), plus a single non-adjustable 10 kW CW coaxial input coupler.

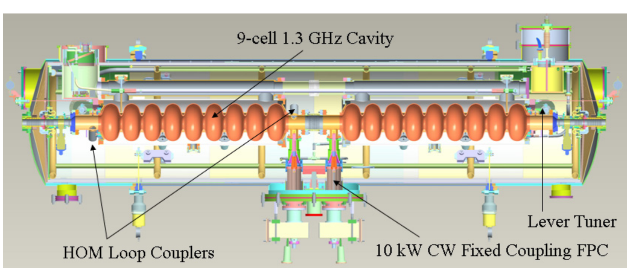


Figure 3: ALICE Cryomodule.

## DARESBURY INTERNATIONAL CRYOMODULE COLLABORATION

A collaboration between Daresbury Laboratory, Stanford and Cornell Universities, LBNL and FZD Rossendorf has been developed to design and build an improved cryomodule, which can facilitate modest CW gradients and provide increased power handling capability, with improved field stability control. The intention is to develop a cryomodule design, based upon the ALICE cryomodule. The reason for choosing this module is to enable its installation on the ALICE facility to allow for full beam test validation on an operational ERL accelerator, albeit at relatively low average beam current (~13 µA). These tests will enable the evaluation of modest accelerating gradients (up to 20 MV/m) with an input coupler $Q_{ext}$ reaching beyond $10^8$, at temperatures down to 1.8 K.

Modifications to this cryomodule (see Figure 4) include adopting two 7-cell TESLA super-structure cavities and widening its beam pipes to allow improved propagation of the HOMs, which are then dissipated in beam-pipe ferrite based HOM absorbers developed by Cornell. The Cornell ERL injector coupler is also adopted, which is optimised for lower average power (~25 kW). Finally, an upgrade to the tuning system will allow piezo actuators to be introduced, to allow fast tuning of the cavity to compensate for microphonics [10].

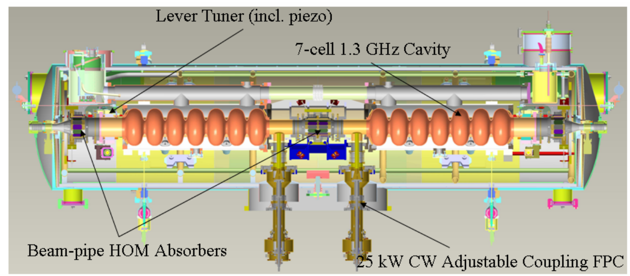


Figure 4: DICC Collaboration Cryomodule.

## MODULE SUMMARY

Comparing the operational parameters for each of the cryomodule designs highlighted here, we can see when applied to what may be needed for NLS (at 1 GeV), an active linac length of ~ 100 m would be required for ¾ of the CW optimised cryomodules (see Table 1). The BESSY FEL cryomodule clearly provides the most optimum solution overall; requiring fewer SRF cryomodules, the shortest active linac length and a significantly lower total linac dynamic load.

Table 1: SRF Module Comparison and NLS Application

| Accelerator | CEBAF Upg. | XFEL | BESSY FEL | ALICE | DICC |
|---|---|---|---|---|---|
| Average Cavity Gradient (MV/m) | 19.2 | 23.6 | 15.4 | 13 | 20 |
| Frequency (GHz) | 1.5 | 1.3 | 1.3 | 1.3 | 1.3 |
| Qo | 8.0E+09 | 1.0E+10 | 2.0E+10 | 5.0E+09 | 1.0E+10 |
| Input coupler Qe | 2E+07 (fixed) | 4.6E+06 | 3.0E+07 | 5E+06 (fixed) | 1E+07 – 1E+08 |
| Max Input Coupler Power (kW) | 13 | 169 (pulsed) | 5 | 10 | 25 |
| Cavities per cryomodule | 8 | 8 | 8 | 2 | 2 |
| Module Energy Gain (MeV) | 108 | 196 | 128 | 27 | 32 |
| Cryomodule Length (m) | 10 | 12 | 12 | 3 | 3 |
| | Application on NLS | | | | |
| Number of Cryomodules (1GeV) | 10 | PULSED | 8 | 48 | 32 |
| Active Length of Linac (m) | 100 | | 96 | 144 | 96 |
| Dynamic RF load per cryomodule (W) | 199.8 | | 98.6 | 70.3 | 64.7 |
| Total Linac Dynamic load (W) | 1997.6 | | 788.9 | 3372.9 | 2069.2 |
| Cryomodule dynamic load/energy gain (W/MeV) | 1.8 | | 0.8 | 2.6 | 2.0 |

## POTENTIAL NLS REQUIREMENTS

The NLS project is very much in its infancy in terms of machine layout and defined parameters. Figure 5 shows a possible NLS machine layout for 1 GeV operation, based upon a BESSY-FEL cryomodule, operating at 17.2 MV/m; chosen to ensure at low energies (for $\phi_b = \pm 30^o$) that peak gradients do not exceed 20 MV/m.

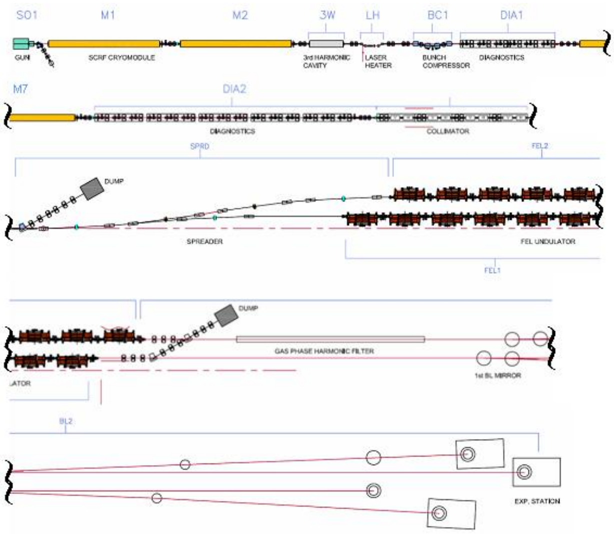


Figure 5: Possible NLS facility layout (1 GeV shown).

This review of many existing and/or under development cryomodules, potentially suitable for an FEL based light source has highlighted a clear understanding of the capabilities for each. For NLS, operating at possible repetition rates of between 1 kHz and 1 MHz, Table 2 shows how the nominal SRF parameters would vary for a linac based upon the BESSY-FEL type cryomodule, operating at 1, 2 and 3 GeV.

Table 2: Possible SRF Linac Parameters for NLS

| | 1GeV | | 2GeV | | 3GeV | | Units |
|---|---|---|---|---|---|---|---|
| RF Frequency | 1.3 | 1.3 | 1.3 | 1.3 | 1.3 | 1.3 | GHz |
| Bunch Charge (max) | 200 | 200 | 200 | 200 | 200 | 200 | pC |
| Repetition Rate (max) | 1 | 1000 | 1 | 1000 | 1 | 1000 | kHz |
| Average Current (max) | 0.0002 | 0.2 | 0.0002 | 0.2 | 0.0002 | 0.2 | mA |
| Number of cells/cavity | 9 | 9 | 9 | 9 | 9 | 9 | |
| Number of Cavities | 56 | 56 | 112 | 112 | 168 | 168 | |
| Number of Modules | 7 | 7 | 14 | 14 | 21 | 21 | |
| Cavity R/Q | 1036 | 1036 | 1036 | 1036 | 1036 | 1036 | Ω |
| Qo | 2.0E+10 | 2.0E+10 | 2.0E+10 | 2.0E+10 | 2.0E+10 | 2.0E+10 | |
| Energy Gain | 1 | 1 | 2 | 2 | 3 | 3 | GeV |
| Eacc | 17.2 | 17.2 | 17.2 | 17.2 | 17.2 | 17.2 | MV/m |
| Qe | 5.0E+07 | 5.0E+07 | 5.0E+07 | 5.0E+07 | 5.0E+07 | 5.0E+07 | |
| Cavity Filling Time | 6.121 | 6.121 | 6.121 | 6.121 | 6.121 | 6.121 | ms |
| RF Power per Cavity | 6 | 6 | 6 | 6 | 6 | 6 | kW |
| Total RF Power per Linac | 0.345 | 0.345 | 0.689 | 0.689 | 1.034 | 1.034 | MW |
| Dynamic load per Cavity | 14.3 | 14.3 | 14.3 | 14.3 | 14.3 | 14.3 | W |
| Dynamic load per Linac | 803.0 | 803.0 | 1606.0 | 1606.0 | 2408.9 | 2408.9 | W |
| Static load per Linac | 70 | 70 | 140 | 140 | 210 | 210 | W |
| Total CW load at 1.8K | 873.0 | 873.0 | 1746.0 | 1746.0 | 2618.9 | 2618.9 | W |
| Total Linac Active Length | 84 | 84 | 168 | 168 | 252 | 252 | m |
| Total Machine Length | 370 | 370 | 510 | 510 | 640 | 640 | m |

For the 200 pC bunch charge and 1 kHz and 1 MHz repetition rates, beam loading is relatively low, with average beam currents ($I_b$) of only 0.0002 mA and 0.2 mA respectively, which for on crest acceleration ($\phi_b = 0^o$) gives an optimum Qe of 8.6e10 and 8.6e7 using Equation 1:

$$Q_e = \frac{V_{acc}}{R/_Q \, I_b \cos\phi_b} \tag{1}$$

For LLRF and microphonics stability reasons, Qe's at this level will be difficult to sustain and so a conservative value of 5e7 is proposed for each repetition rate. For information, Cornell have demonstrated stable operation at Qe = 1e8 on the JLab IR-FEL [11].

Whilst the use of SRF technology minimises the amount of RF power required to generate the accelerating voltage, the total efficiency gain is also dependant on the load to the cryogenics. Table 2 also highlights the anticipated module count and total cryogenic load at 1.8K (Qo = 2e10) for 1, 2 and 3 GeV final operating energies. Note that these figures do not include the customary operational safety factor (typically 50%), to ensure machine performance can be maintained.

## CONCLUSIONS

Having compared the various cryomodules available for potential use on NLS, a number of important issues have been identified. The first of which being that pushing up the CW gradient in these cryomodules impacts heavily on the dynamic capacity needed from the cryogenic system. The second being the maximum energy gain a module can deliver, whilst minimising its real estate footprint. On both counts, the proposed BESSY-FEL cryomodule appears to be the most optimum choice of extensively developed cryomodules available at present, which could effectively match possible high repetition rate operation for NLS in the UK.

## REFERENCES

[1] http://www.newlightsource.org/.

[2] C. Christou et al, "Normal Conducting Options for the UK'S New Light Source Project", these proceedings.

[3] J. R. Delayen et al., "Upgrade of the CEBAF Acceleration System," PAC99, pp. 3498 – 3500.

[4] J. P. Preble et al., "Cryomodule Development for the CEBAF Upgrade," PAC99, pp. 934 - 936.

[5] L. Harwood and C. Reece, "CEBAF at 12 and 25 GeV," Proc. 2001 SRF Workshop, KEK, Japan, 2001.

[6] R. Brinkmann et al. (eds.), TESLA Technical Design Report – Part II: The Accelerator, DESY 2001-011, pp. II-19, March 2001.

[7] BESSY-FEL Technical Design Report, March 2004.

[8] M. W. Poole et al, "4GLS and the Prototype Energy Recovery Linac Project at Daresbury", EPAC04, Lucerne, 2004, pp. 455 – 457.

[9] P. Kneisel et al, "First Cryogenic Tests with JLab's New Upgrade Cavities", Linac04, Lubeck, pp. 216-218.

[10] P.A. McIntosh et al, "Development of a Prototype Superconducting CW Cavity and Cryomodule for Energy Recovery", EPAC'06, Edinburgh, June 2006, pp. 436 – 438.

[11] M. Liepe et al, "Pushing the Limits: RF Field Control at High Loaded Q", PAC'05, Knoxville, 2005, pp. 2642-2644.

# HIGH REPETITION RATE ELECTRON INJECTORS FOR FEL-BASED NEXT GENERATION LIGHT SOURCES

B.L. Militsyn*, C.D. Beard, J.W. McKenzie, STFC Daresbury Laboratory, Warrington, UK.


### *Abstract*

Several laboratories concentrate their efforts on the development of high repetition rate FEL-based next generation light sources. One particular concept under development at STFC Daresbury Laboratory specifies high brightness electron bunches with a charge of 0.2 nC which arrive with a repetition rate of up to 1 MHz. As emittance of the bunches should not exceed 1 mm·mrad, traditional grid modulated thermionic injectors, similar to the ones used at ELBE or FELIX, may not be used. We consider three options of high repetition rate injectors based on photocathode guns - a high voltage DC gun, a 3½-cell superconducting RF gun and a normal conducting VHF gun, recently proposed at LBNL. We analyse practical injector schemes for all three guns and provide the results of beam dynamic simulations. We also discuss the photocathodes which may be used in each gun, as this critical component defines achievable beam parameters and operational efficiency of the injectors.


## INTRODUCTION

High brightness electron beams which are required for the operation of next generation light source may be delivered by three types of electron injectors – a high voltage DC photocathode gun, a very high frequency NCRF gun and a SRF gun. The first two options deliver relatively low energy (500-750 keV) beams and require additional velocity bunching and acceleration with a booster to an energy of 10 MeV in order to inject into the main linac. A SRF gun delivers beams with the required energy without additional acceleration. However, this leads to less flexibility in emittance compensation at different bunch charges. We consider the injectors for operation in CW mode with high beam repetition rate with a bunch charge of 200 pC as is the case for the UK's New Light Source (NLS) project [1].

### *Simulations*

Beam dynamic simulations have been carried out for the three guns considered using ASTRA through the injector system to 10 MeV, then through the first module of the main linac to 120 MeV. Initial thermal emittance was included in all the simulations.

The main linac module consists of eight 9-cell TESLA-type 1.3 GHz superconducting cavities. All cavities except the first have been set to provide an average accelerating gradient of 17 MV/m and a phase of -20° to provide a beam with the necessary longitudinal phase space profile for the bunch compression system. There are two quadropoles to match the beam from the injector into the main linac. The injector parameters were optimised using a multi-objective genetic algorithm with a non-dominated sorting approach.

## HIGH VOLTAGE DC GUN

High voltage DC guns with GaAs photocathodes illuminated with laser light of wavelength 532 nm are used at a number of laboratories worldwide to feed energy recovery linac (ERL) based FELs. These include TJNAF [2] and Daresbury Laboratory [3]. An extra high voltage gun is under development at Cornell University [4]. Originally designed for operation at high (up to 100 mA) average currents, DC guns may be relatively easily adopted for operation at low (typically less than 1 mA) currents specific for NLS.

One disadvantage of DC guns is that the field strength on the cathode is restricted to 10-12 MV/m in order to minimise field emission. This rules out obtaining high emission current density and limits the minimum beam size at given bunch charges. However, the low energy spread of emitted electrons from GaAs photocathodes allows high brightness beams to be produced.

GaAs based photocathodes require XHV vacuum conditions to avoid surface contamination which restricts the cathode lifetime. Under ideal vacuum conditions the operational life time is defined by ion back-bombardment, which is proportional to the total extracted charge. Experiments have shown that the maximum charge extracted does not exceed a few hundred coulombs [5] which means that for an average current of 0.2 mA the operational life time will be at a level of 1–2 months. This is acceptable as modern guns are equipped with integrated load-lock photocathode preparation facilities [6] that allow replacement of the photocathode within half an hour and reduce the possibilities of vacuum contamination.

Alkali photocathodes operating in visible light are more stable to vacuum contaminations than GaAs [7]. For example, their lifetime in the presence of oxygen is two orders of magnitude higher than GaAs. However, their resistance to ion back-bombardment is not known, and investigation of their operation in DC photocathode guns is now in progress at Daresbury.

### *Simulations*

A 500 keV DC electron gun with a focussing electrode was modelled in CST Studio/POISSON [8] and the on-axis field map was used as an input to ASTRA. The initial laser pulse used has a 4 mm diameter flat-top transverse profile and a 20 ps flat-top longitudinal profile.

DC guns provide electron bunches with a temporal profile similar to that of the initial laser pulse but quickly

*b.l.militsyn@dl.ac.uk

lengthen during acceleration, therefore a buncher cavity is required to reduce the bunch length to less than 2 mm.

Solenoids are located on either side of the buncher to provide transverse focussing and emittance compensation. A booster module increases the energy of the beam from the 500 keV of the gun to a level around 10 MeV for injection into the main linac. A superconducting module containing two 9-cell TESLA-type cavities operating with peak gradients of lower than 10 MV/m is appropriate for this purpose. Figure 1 shows the evolution of emittance along the injector and Fig. 2 shows the slice emittance of the beam at the exit of the injector.

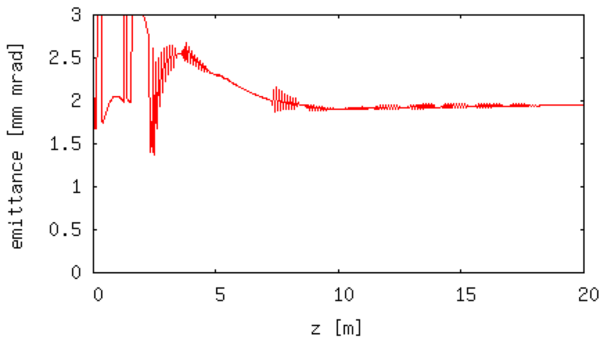


Figure 1: Evolution of emittance along the DC injector.

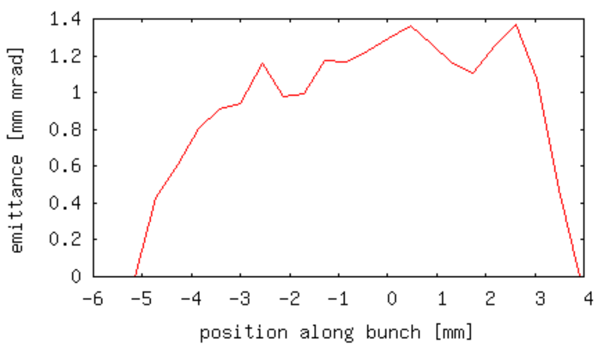


Figure 2: Slice emittance at the exit of the DC injector.

## NORMAL CONDUCTING VHF GUN

An interesting design of a high repetition rate gun has been proposed by LBNL [9]. A normal conducting copper cavity is driven with a frequency of around 100 MHz and is able to deliver bunches over a broad range of repetition rates, varying from a few hertz to the RF driving frequency. The cavity is based on mature normal conducting technology but requires installation of a dedicated RF power supply. The total RF power required for accelerating of the beam to 750 keV should be about 100 kW. This corresponds to a maximum field strength on the cathode of 20 MV/m. Operation at relatively low frequencies allows significant reduction in the power density dissipated in the gun walls to 10 W/cm$^2$, which significantly simplifies the cooling system. The gun uses $K_2CsSb$ or similar alkali-antimonide photocathodes which operate at a wavelength of 532 nm and require extra high vacuum, which can be provided by an array of NEG strips installed on the periphery of the gun cavity.

### *Simulations*

Since the gun delivers bunches with a similar profile and energy to DC guns, a similar injector layout can be used, with the addition of an extra solenoid and a bucking coil to zero the magnetic field on the cathode. The higher field strength allows a smaller laser spot to be used than in the DC case. The following simulations use a laser pulse with a 2 mm diameter flat-top transverse profile and a 20 ps flat-top longitudinal profile with rise and fall times of 2 ps. Figure 3 shows the evolution of emittance along the injector and Fig. 4 shows the slice emittance of the beam at the exit of the injector.

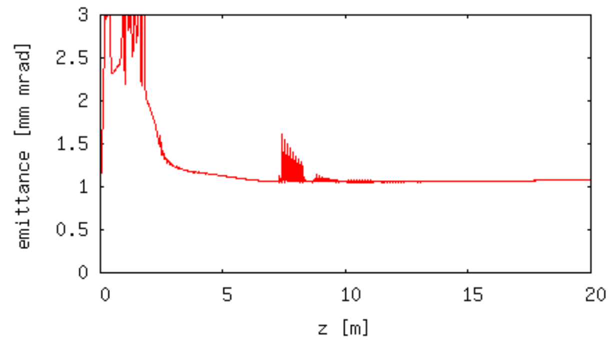


Figure 3: Evolution of emittance along the VHF injector.

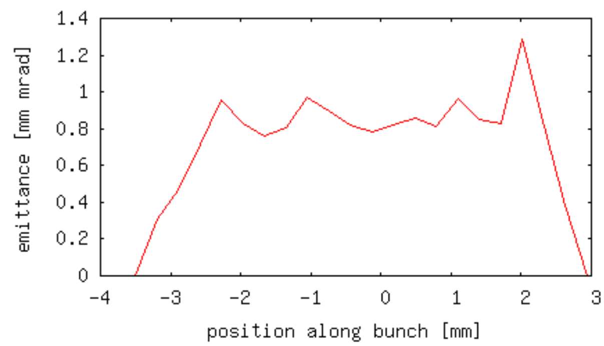


Figure 4: Slice emittance at the exit of the VHF injector.

## SUPERCONDUCTING RF GUN

Studies of a suitable 3½-cell SRF gun have been carried out at Daresbury Laboratory [10]. The gun consists of two cavities: a 1½-cell launch cavity with a proposed design largely adopting the TESLA cavity shape, and an adapted Cornell 2-cell booster cavity [11]. The cavities are placed in one cryomodule and are fed via individual RF couplers. If the gun is operated at high repetition rate, an optional High Order Mode (HOM) absorber may be installed between the cavities. The beam pipe diameters are widened to allow the HOMs to propagate and are then absorbed by a broad band absorber [12] consisting of a series of ferrite and ceramic plates which can absorb over 200 watts of RF power over a frequency range of 1 to 40 GHz. Further assessment of the geometry has to be carried out to evaluate the HOM excitation and extraction.

The absence of ohmic losses in SRF cavities provides an option for delivering high beam current with significantly less RF power than for an equivalent normal conducting gun. The hard limit is therefore the maximum power of CW RF source available at 1.3 GHz L-band klystrons are able to provide over 160 kW CW, with an IOT equivalent capable of rising to 90 kW pulsed.

For a beam energy of 10 MeV, the power required is easily achievable with a standard IOT amplifier. An output beam power of 2 kW simplifies the RF input coupler scheme which often restricts the maximum beam power of SRF accelerating systems. If the gun operates at the frequency of the main linac, it easily integrates with the RF and cryogenic infrastructure and does not require non-standard RF power supplies.

At 1 MHz, existing laser systems are not able to drive metallic photocathodes so alkali photocathodes have to be considered. A SRF gun using $Cs_2Te$ photocathodes is under commissioning at FZD [13] and a SRF gun using $K_2CsSb$ photocathodes is under development at BNL [14] to operate in CW mode with an average current of 0.5 A.

### *Simulations*

Operating at 50 MV/m peak field strength, the 3½-cell gun accelerates electrons to 10 MeV, thus no additional accelerating modules are required before the main linac. A buncher cavity is not required as the SRF gun alone can provide electrons with an rms bunch length lower than 2 mm. The laser pulse used in the ASTRA simulations has a 1 mm diameter flat-top transverse profile and a 20 ps flat-top longitudinal profile with rise and fall times of 2 ps. Fig. 5 shows the evolution of emittance along the injector line and Fig. 6 shows the slice emittance of the beam at the exit of the injector.

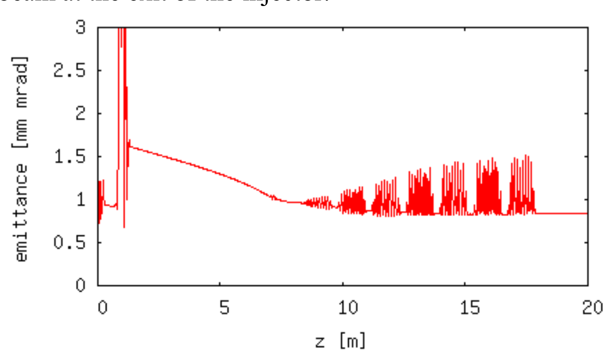


Figure 5: Evolution of emittance along the SRF injector.

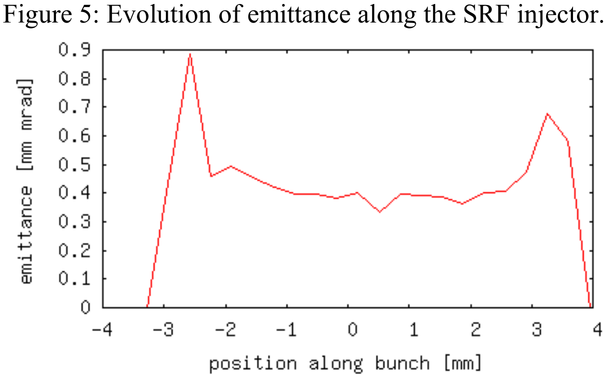


Figure 6: Slice emittance at the exit of the SRF injector.

## JITTER

An important aspect of FEL-based light sources is synchronisation, particularly when multiple sources are used such as in pump-probe experiments or in HGHG schemes where the FEL interacts with light from an external laser. Any instability of the RF phase and amplitude of the various cavities causes the arrival time of the electron bunches to differ. An analysis was carried out on the contribution to arrival time jitter in the VHF gun case. For phasing instabilities, the buncher contributes 5.1 ps per degree and the first cavity 1.0 ps per degree. Any instability of the gradients in the cavities contributes a minor amount, only 0.1 ps for each percent offset. The largest contribution comes from the buncher phase jitter. Since the injector layout is the same, the DC gun jitter follows these trends however, since the SRF gun does not require additional bunching and boosting modules, the jitter is solely determined by that of the drive laser.

## SUMMARY

The results of beam dynamics simulations of the proposed injector designs are summarised in Table 1. As may be seen the best beam parameters are delivered by the SRF gun, though development of the particular design requires extensive R&D.

Table 1: Beam parameters at the exit of the injectors.

| | DC | VHF | SRF |
|---|---|---|---|
| Projected emittance (mm·mrad) | 1.95 | 1.08 | 0.84 |
| Slice emittance (mm·mrad) | 1.2 | 0.8 | 0.4 |
| Bunch length (mm) | 1.72 | 1.3 | 1.67 |
| Longitudinal emittance (keV·mm) | 295 | 115 | 198 |
| Beam energy (MeV) | 120 | 117 | 118 |

## ACKNOWLEDGMENTS

The authors would like to thank A.A. Zholents for fruitful discussions.

## REFERENCES

[1] P.H. Williams et al., Proceedings of EPAC'08
[2] T. Siggins et al., Nucl. Instr. And Meth. A 475 (2001) 549
[3] B.M. Dunham et al., Proceedings of PAC'07
[4] D.J. Holder et al., these proceedings
[5] J. Grames et al., Proceedings of PAC'07
[6] B.L. Militsyn et al., Proceedings of EPAC'08.
[7] P. Michelato et al., Proceedings PAC'95.
[8] J.W. McKenzie et al., Proceedings of EPAC'08.
[9] J.W. Staples, al., Proceedings of PAC'07.
[10] C.D. Beard et al, Proceedings of EPAC'08.
[11] M.Liepe et al., Proceedings of PAC'05
[12] V.Shemelin et al., Proceedings of EPAC'06
[13] J. Teichert, et al., Proceedings of EPAC'08
[14] R. Calaga et al., Physica C441 (2006)159-172

# DEVELOPMENT OF A BEAM LOSS MONITOR SYSTEM FOR THE LCLS UNDULATOR BEAMLINE*

W. Berg#, J. C. Dooling, A. Pietryla, and B.-X. Yang, Advanced Photon Source, Argonne National Laboratory, Argonne, IL 60439 USA
H.-D. Nuhn, Linac Coherent Light Source, Stanford Linear Accelerator Center, Menlo Park, CA 94025 USA

*Abstract*

A beam loss monitor (BLM) system based on the detection of Cerenkov radiation has been developed at the Advanced Photon Source (APS) for the Linear Coherent Light Source (LCLS) free-electron laser (FEL). The electron beam will vary in energy from 4.6 to 13.6 GeV with a bunch charge of 0.2 to 1.0 nC and a maximum repetition rate of 120 Hz. In order to limit radiation-induced demagnetization of the undulator permanent magnets, the BLM will provide beam-loss threshold detection as part of the Machine Protection System (MPS). The detector incorporates a large-volume (30 $cm^3$) fused-silica Cerenkov radiator coupled to a photo-multiplier tube (PMT). The output of the PMT is conditioned locally by a charge amplifier and then digitized at the front end of the MPS electronics. During commissioning, the device will be calibrated by inserting a 1-micron aluminum foil into the beam, upstream of the undulator magnets. Tests of a prototype BLM system showed that the detector and electronics are functional. Initial results from computer simulations support the proposed calibration scheme and indicate of the need for a dense population of BLM devices.

## INTRODUCTION

APS is developing a beam loss monitor detector as a component of the LCLS Machine Protection System. The BLM is intended to protect the FEL undulator magnets from potential damage resulting from localized and distributed electron beam losses. Detection of a loss event above threshold will limit the beam pulse rate. A secondary usage of the BLM system is to track and archive the radiation dose. The data will be analyzed for correlation to any observed demagnetization or damage in the undulator magnets.

Initially, five detector modules will be distributed throughout the length of the 33 undulator magnets. Calibration of the system will be based on computer simulation using MARS [1, 2] and empirically verified during machine commissioning. Some of the relevant specifications of the electron beam are listed in Table 1.

## SYSTEM OVERVIEW

Electron beam loss is measured by collecting Cerenkov radiation generated in a quartz radiator from a high-energy electron shower. The Cerenkov light propagates through the radiator to the UV glass entrance window (185-850 nm) of a single PMT for detection. The PMT output is conditioned locally by an interface module (IM) incorporating a charge amplifier. The amplifier integrates the PMT charge output pulse and converts the signal to a voltage pulse. The output of the amplifier is transmitted over a coaxial line to the MPS instrumentation racks, where signal filtering and a/d conversion is performed. Further signal processing, distribution, threshold detection, and system validation is handled by the MPS.

Table 1: Electron Beam Specifications

| Beam Parameter | Value |
|---|---|
| Max. repetition rate | 120 Hz |
| Beam charge | 0.2 - 1.0 nC |
| Normalized emittance | 2.0 - 3.0 µm rad |
| Beam energy | 4.6 - 13.6 GeV |
| FWHM bunch duration | 0.25 - 0.48 ps |

## BEAM LOSS DETECTOR

The detector design shown in Fig 1 is conceptually derived from a design for the PEP II B-Factory at SLAC [3]. A quartz Cerenkov radiator was chosen over conventional scintillation materials for better immunity to scintillation effects from the high-power x-ray beam emanating from the undulator. The radiator is cut from a single boule of synthetic crystalline quartz. Military-grade fused silica (MIL-G-174B) is used to limit impurities that may result in premature browning of the material from radiation exposure. The tuning fork geometry was chosen so the radiator would cover the surface area of the

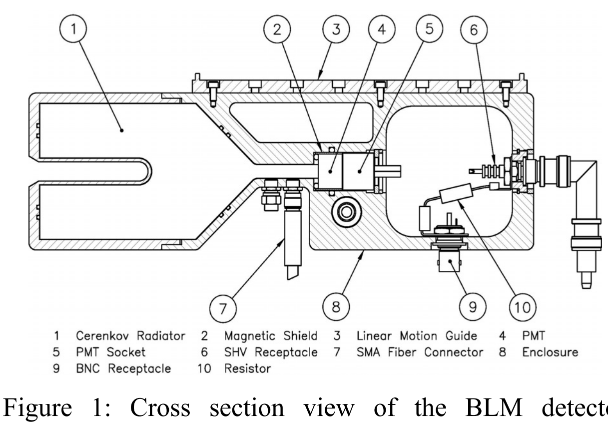


Figure 1: Cross section view of the BLM detector configuration with the component call outs.

*Work supported by U.S. DOE, Office of Science, Office of Basic Energy Sciences, under contract number DE-AC02-06CHI11357.
#berg@aps.anl.gov

undulator pole pieces and still deliver the Cerenkov light to a single PMT. The raw substrate is water-jet rough cut, flame polished, annealed, and lap polished to the final surface figure before plating with an aluminum reflector and protective overcoat.

The detector can be positionally configured to remain at the static home location or to track with the undulator's horizontal motion. This change is accomplished by relocating a capture screw to the undulator field shunt end plate. The BLM housing is mounted to a linear bearing to provide the 100 mm of stroke required. This configuration is intended for when the detector is operated as a dosimeter for tracking exposure levels to the adjacent undulator magnet [4].

## SIGNAL CONDITIONING

The BLM interface module (IM) is designed to provide the interface between the PMT and the LCLS MPS link node chassis [5]. The interface electronics are housed in an RFI enclosure located in the tunnel, below the girder. The IM provides three functions: PMT high voltage (HV) supply, signal conditioning, and heartbeat circuit. The interface signals between the IM and the link node chassis are carried by an individually shielded twisted pair cable harness (see Figure 2). The conditioned signal is transported to the link node chassis via 300' of low-loss LMR coaxial cable.

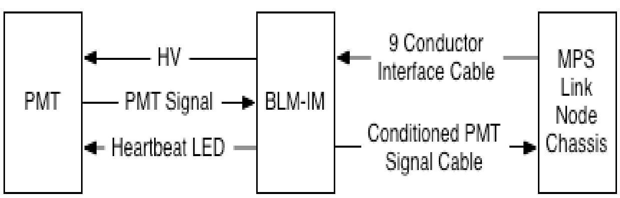


Figure 2: System-level block diagram.

The high-voltage circuit for the PMT is an Emco CA10N [6] module with an output ranging from 0 V to 1000 V. The HV output is set by a 0- to 5-V control signal. The output signal of the PMT is a negative current pulse, approximately 1.8 ns wide, whose integrated charge is proportional to the loss detected. A charge-sensitive amplifier, Cremat CR-112 [7], will integrate this current pulse, providing an output voltage pulse amplitude proportional to the charge. The charge amplifier selected has a decay time constant of 50 µs with an output ranging from 0-1.5 V when terminated with 50 Ω.

The heartbeat signal is a 120-Hz optical pulse sent over a short fiber bundle to the PMT before each beam pulse. The resulting PMT signal is then processed and compared to a fixed threshold. If the heartbeat is not detected, the MPS system will inhibit beam.

Bench testing of the heartbeat circuit was performed to optimize its signal. The heartbeat pulse should be detected over a PMT voltage range of –400- to –900 V representing a large dynamic range (~ 48 dB) for the PMT output. A nominal pulse width of 600 ns allows the heartbeat pulse to be detected when the PMT is operating at –400 V but the charge amplifier output is saturated when operating at –900 V. A choice of a pulse width between 200 ns and 1000 ns is provided.

## TEST AND CALIBRATION

A prototype of the beam loss monitor has been constructed with a small quartz Cerenkov radiator block (~ 1.0 cm$^3$) and tested using stored electron beam in the APS storage ring. The radiator was mounted in 9-ID, approximately 13 mm above the beam and 85 cm from the entrance of the chamber. For stored beams, most of the electrons are lost through Touschek scattering and strike the entrance of ID chambers one electron at a time. The charge amplifier output was sent to an Amptek digital pulse processor/multichannel analyzer (MCA PX4) [8] to analyze the amplitudes of these step pulses and to make the data set into a histogram, as shown in Fig. 3 below.

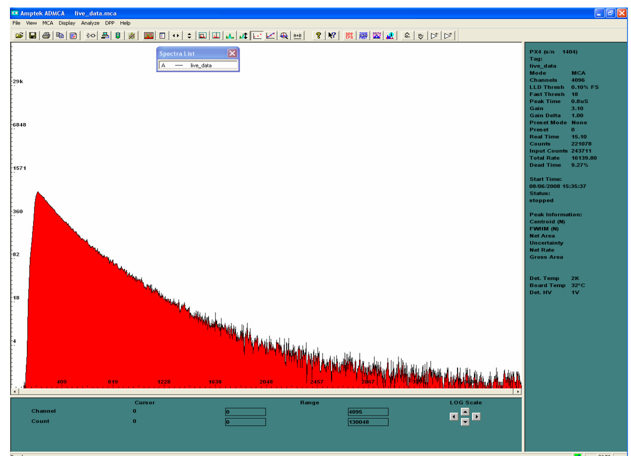

Figure 3: Loss monitor spectrum of stored beam.

Table 2 shows the instrument settings and derived MCA calibration of 10.5 fC/channel. The first moment for the MCA spectrum,

$$Q(N_o) = \sum_{N_o}^{N} n f_n \ , \tag{1}$$

is the total PMT charge collected during the experiment, where N=4096, $f_n$ is the number events in channel n, and $N_o$ is the cutoff channel. Using the well-behaved portion of the spectrum ($N_o$>400), the Q ($N_o$) is extrapolated back to channel 0 to recover the low-energy contribution. This procedure corrects for the effect of the finite-discriminator level and yields an integrated charge of 7.6 µC. Combining this result with the 40-c/s count rate of the existing APS Cerenkov detector [9] and the 9-fC/c calibration of the detector, we arrive at the sensitivity of the LCLS-BLM prototype detector as

$$Q_{\text{LCLS-BLM-Prototype-S9}} = 1.4\times10^5 Q_{\text{Loss-7GeV-S9}} \ . \tag{2}$$

These tests not only validate the detector and electronics with the electron beam, but also produce an absolute calibration that can be used to validate the computer simulations performed for these detectors. This calibration has an estimated error of a factor of two.

Table 2: Calibration of LCLS BLM Prototype

| Quantity | Values |
|---|---|
| MCA input sensitivity<br>-MCA preamplifier gain = 3.1<br>-MCA digitizer full scale = 1.00 V<br>-MCA histogram width = 4095 channel | 78.8 μV/channel |
| CA-MCA input charge sensitivity<br>-Charge amplifier gain = 7.5 V/nC | 10.5 fC/channel |
| Integrated charge (after corrections)<br>-Total charge sum = 4.6 μC<br>-Extrapolation correction of discriminator cutoff leads to 6.9 μC<br>-Dead time = 9.27% | 7.6 μC |
| Lost electron beam charge<br>-APS Cherenkov detector rate = 40 c/s<br>-Cherenkov detector calibration = 9.1 fC/c<br>-Total acquisition time = 15 seconds | 5.5 pC |
| Loss monitor sensitivity this test | $1.4 \times 10^5$ |

## BEAM-LOSS SIMULATIONS

Monte Carlo simulations of the beam losses and detector signals in both the LCLS undulator and in the APS test site are being performed using the program MARS [1, 2]. In the first case studied, a 1-μm Al foil was used as the scatterer at LCLS OTR-33 station. Beam transport downstream of the foil includes quadrupole magnets and a collimator, with a beam aperture of (0.86 cm $\times$ 0.43 cm).

Figure 4 shows the calculated high-energy electron fluence in the LCLS-BLM radiators along the undulators. The fluence is expected to be proportional to the detector signal. When all quads are off, the beam loss can be used to calibrate the monitors. When all quads are on, simulation show a possible axial loss distribution during FEL operations. Unlike the field-free case, the radiation dose can be localized to within one or two undulators. Hence, a sparse distribution of BLM detectors may not be sufficient to measure the beam losses for realistic loss scenarios. Figure 5 shows the calculated electron fluence in the undulator magnets, which are expected to correlate with damage to the undulators. A comparison of Figs. 4 and 5 shows that the signal level of the BLM is correlated with the dose rate in nearby undulators, but is not strictly proportional to it. We also note that the magnetic lattice transports most of the scattered electrons out of the undulator chamber and the dose rate in the undulator is 10- to 100-fold lower than that estimated from the field-free calculation. Model calculations for the test geometry at the APS are in progress and will be reported elsewhere.

## CONCLUSIONS

Installation of the BLM hardware will take place this coming fall with commissioning to follow during the first quarter of 2009. Initially, the undulator magnets will not be installed until the machine is tuned and the undulator system components are tested. At the conclusion of this first phase of commissioning in March 2009, the undulator magnets will be installed, and the LCLS will begin generating x-rays. The authors would like to acknowledge our many collaborators at SLAC and our support personnel at ANL for their in-depth input and discussions.

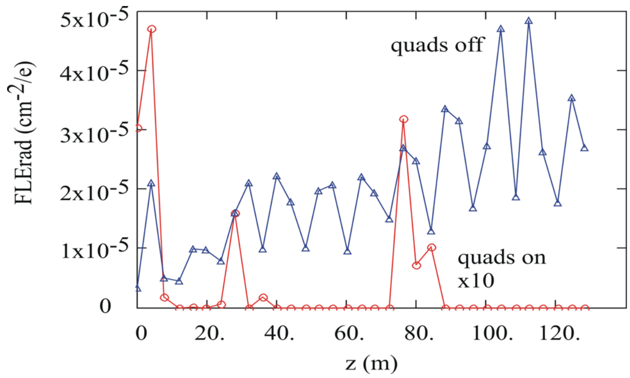


Figure 4: Electron fluence per incident electron in the LCLS BLM radiators with and without quadrupole fields.

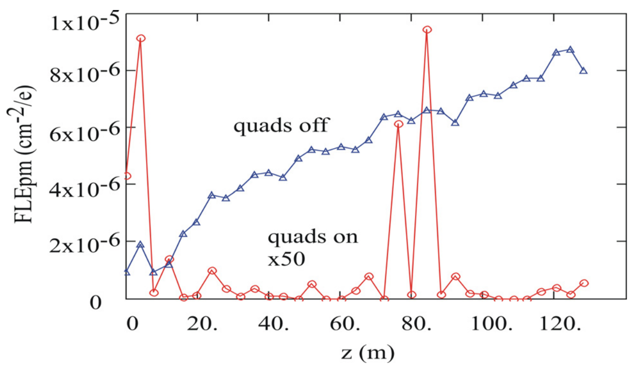


Figure 5: Electron fluence per incident electron in the LCLS undulators with and without quadrupole fields.

## REFERENCES

[1] N. V. Mokhov and S. I. Striganov, “Mars15 overview,” Technical Report Fermilab-Conf-07/008-AD, 2007.
[2] N. V. Mokhov et al., AIP Conf. Proc. 769, 1618-1623 (2004).
[3] A. Fisher et al., AIP Conf. Proc. 390, 248-256 (1996).
[4] H.-D. Nuhn, Undulator Beam Loss Monitor, LCLS PRD 1.4-005-r0, September 2007
[5] S. Norum, LCLS Machine Protection System, ESD 1.1-315-r1, January 2007.
[6] Emco High Voltage Corporation; http://www.emcohighvoltage.com
[7] Cremat, Inc.; http://cremat.com
[8] Amptek digital pulse processor PX4 datasheet; http://www.amptek.com/px4.html
[9] A. Pietryla et al., Proc. of PAC2001; Chicago, IL, 1622-1624 (2001); http://www.JACoW.org.

# THE NPS-FEL INJECTOR UPGRADE*

J.W. Lewellen#, W.B. Colson, S.P. Niles, Naval Postgraduate School, Monterey, CA
W.S. Graves, Massachusetts Institute of Technology, Cambridge, MA
T.L. Grimm, A.E. Bogle, Niowave, Inc., Lansing, MI
T.I. Smith, Stanford University, Stanford, CA

*Abstract*

The Naval Postgraduate School (NPS) has begun the design and assembly of the NPS Free-Electron Laser (NPS-FEL). As part of this effort, the original DC gun-based injector system from the Stanford Superconducting Accelerator has been moved to NPS and is being refurbished and upgraded to operate as a photoinjector. Design work has begun on a new, SRF, quarter-wave resonator based cavity that can serve as either an energy booster or photocathode gun.

The overall NPS-FEL design parameters are for 40-MeV beam energy, 1 nC bunch charge, and 1 mA average beam current, built as an energy-recovery linac in its final configuration [1]. As we move towards this goal, the injector system will be incrementally upgraded to add photocathode capability, have a higher final beam energy, and improve the beam brightness, to meet the needs of the overall experimental program.

## OVERVIEW

The NPS-FEL is based around key components from the Stanford Superconducting Accelerator (SCA). These include:

- two, Stanford/Rossendorf cryomodules, each of which contains two, TESLA-type 9-cell 1.3-GHz cavities;
- four, 10-kW 1.3-GHz CW klystrons;
- a 240-kV gridded DC thermionic injector, with subharmonic buncher;
- the FIREFLY electromagnetic undulator; and
- assorted power supplies and magnets.

At present, the 240-kV SCA injector has been moved to NPS and is being prepared for beam in a temporary facility. This will serve as a platform for initial experiments while the main NPS-FEL vault is being constructed.

The nominal voltage gain in the TESLA structures is 10 MV per structure. The structures are matched for $\beta\sim1$, so injecting a 240-kV beam ($\beta\sim0.73$) results in significant phase slip and consequent reduction of maximum beam energy, as was observed at the SCA [2]. An injection voltage of 1.5 MV ($\beta\sim0.97$) will significantly reduce the phase slip during injection into the first linac structure, increasing final voltage and probably also helping to preserve beam quality. Higher injection beam energies are also desirable from the standpoint of constructing ERL return-loop beam merges.

Also, while reliable and robust, the gridded DC injector places limits on both the charge per bunch that can be extracted, and on the quality of the beam produced.

For these reasons, we intend to gradually upgrade the NPS-FEL injector system, including diagnostics, from the original 240-kV DC gun to a superconducting RF photoinjector capable of generating nC bunches at 1.5 MeV (kinetic), with good transverse beam quality.

The incremental upgrade process will also allow us to continually perform experiments of interest in low-energy beam transport and cathode characterization.

## DC GUN

The original SCA injector beam source is a 2-stage, 240-kV DC gun with a Pierce-type geometry and gridded cathode, shown schematically in Figure 1.

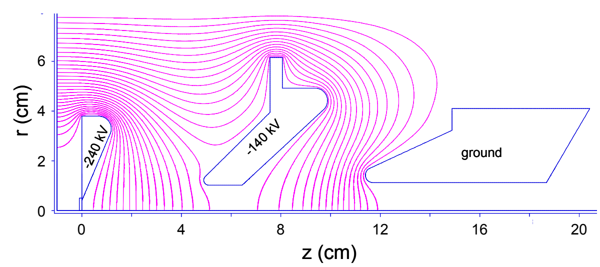


Figure 1: SCA DC-gun electrode geometry and equipotentials.

In the nominal configuration, with a potential difference of 100 kV between the cathode and first anode, the gradient at the cathode center is ~ 1.4 MV/m. The maximum radius of the cathode is 4mm, defined by the inner radius of the Pierce-type electrode ring.

### *Initial Configuration*

As installed in the SCA, the gun was followed by a 260-MHz prebuncher and series of focusing solenoids, with approximately 3m from the cathode to the entrance of the first TESLA-type cavity. To configure the line as a photoinjector, the first solenoid lens and prebuncher will be moved downstream by approximately 13 cm (5") to install a laser injection port. For the initial series of experiments, the prebuncher will be removed and replaced with diagnostics, such as screens and slits for emittance measurement.

The first drive laser will be a Continuum Minilite-II Q-switched Nd:YAG laser [3]. This laser has a maximum repetition rate of 15 Hz, and a relatively long (relative to the RF period of the linac) pulse duration of ~ 5 ns (FWHM). The laser is appropriate for an initial series of

* Funding for this work was provided by the Office of Naval Research, and the High-Energy Laser Joint Technology Office
# jwlewell@nps.edu

experiments to study photothermal cathodes, and will allow us to refine our laser injection system, operational procedures, safety protocols, etc., before installation of a higher-power, higher-repetition-rate drive laser system. Based on other studies making use of this type of laser, we expect bunch charges of up to 5 nC per pulse [4].

### *Simulation Studies*

The transverse placement of the laser injection mirror is critical: too close to the beam axis and the mirror will cause wakefield effects on the beam and, potentially, intercept a portion of the beam; too far from the axis and the laser beam will be clipped.

To address this, a series of simulations was conducted using General Particle Tracer (GPT) v2.8. Beam charges of 0.5, 1.0 and 1.5 nC were assumed, with uniform transverse and either uniform or quadratic longitudinal distributions. The laser spot radius was varied between 1 and 4 mm, and the bunch duration between 0.1 and 1.5 ns. These simulations were used to find the maximum radius of the electron beam 30 cm from the cathode, the nominal mirror location.

Given a maximum laser beam radius of 4 mm, and a clear aperture radius of 1.1 cm at the exit anode 18.8 cm from the cathode, the laser injection angle can be a maximum of approximately 2 deg. At 30 cm, this corresponds to a distance from the inner edge of the mirror to the beam axis of 6 mm (for a 4 mm laser spot radius). The results of the simulations are shown in Figure 2 for 0.5-nC bunch charge, and a quadratic temporal profile.

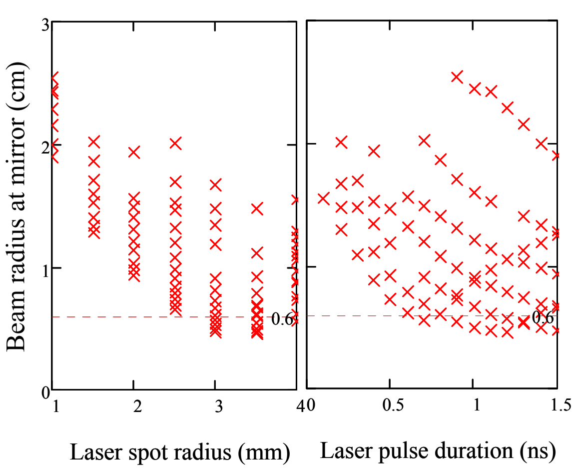


Figure 2: Electron beam radius at mirror location, as a function of laser spot radius (left plot) and pulse duration (right plot) at cathode for a quadratic temporal profile.

Similar results are obtained for 1.0 and 1.5 nC simulations. Generally speaking the mirror clearance is less at these charges, but beam should not be intercepted at the longer laser pulses and spot radii. Depending on experimental results, we will consider adding additional focusing coils near the gun to help contain the beam during initial transport.

The emittance of the beam was also calculated at the mirror position, and is shown in Figure 3.

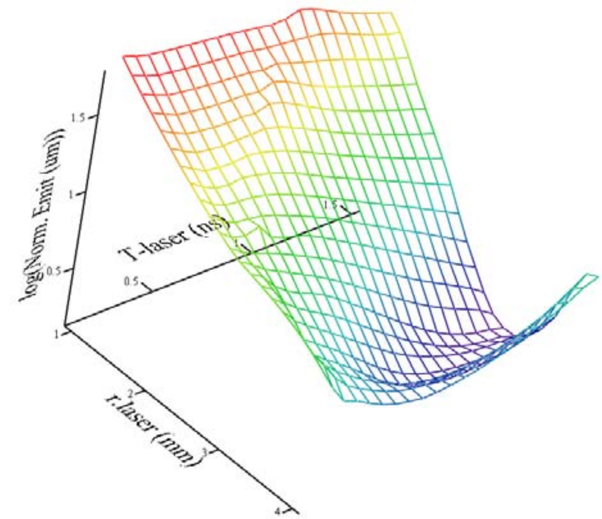


Figure 3: Normalized emittance at the mirror location as a function of laser spot size and pulse duration at the cathode. The emittance axis is plotted on a log scale and is normalized to 1 μm.

The GPT simulations indicate that, theoretically, normalized emittances on the order of 2 μm are possible (not including thermal emittance). Simulations with the particle-in-cell code **spiffe** [6] show similar results.

## QUARTERWAVE GUN

There has been increasing interest in the use of reentrant-type structures for high-brightness, high-current CW injectors [7]. Compared to pillbox-type structures, these geometries offer a number of advantages, including more efficient use of RF power and smaller outer wall radii for a given frequency.

For the NPS-FEL, we have selected a quarter-wave superconducting resonator geometry with a nominal instantaneous gap voltage of 1.5 MV, and an operating frequency of 500 MHz. This allows for a maximum injection rate of 100 MHz into the 1.3-GHz linac cavities. With a nominal beam current of 1 mA, this injection frequency would correspond to a bunch charge of 10 pC, sufficient to be of interest for several studies. The structure will be designed to have a removable cathode insert, allowing the resonator to be used as both a beam source in its own right (which application we focus on below), and as an energy booster for an external beam source such as the DC injector. Given a small transit-time factor (or ratio of realizable to instantaneous voltage), phase slip effects can be minimized in this application.

A key tradeoff in this geometry is the gap length, or distance between cathode (or input beamport) and exit aperture. By decreasing the gap, the transit time factor and peak field at the cathode are both increased; this is good in terms of emittance preservation and minimization of the beam energy spread, but bad in terms of peak surface fields, field emission, etc.

Using MathCAD to perform 1-d particle tracking, we calculated the transit time factor, peak cathode field, and beam launch phase for maximum energy gain, for a variety of cathode-to-exit port distances, given a nominal instantaneous voltage of 1.5 MV.

Another parameter of interest is the launch window, defined here as the spread in phase over which a particle gains at least 99% of the maximum possible voltage. The results are summarized in Table 1. A plot of exit beam energy as a function of launch phase is shown in Figure 4.

Table 1: 1-d Tracking Results for Various Cathode-Beamport Gaps

| Gap [cm] | Cathode gradient [MV/m] | Transit-time factor | $KE_{max}$ phase [deg] | Launch window [deg] |
|---|---|---|---|---|
| 2 | 63 | 0.993 | 78 | 16.2 |
| 4 | 37 | 0.985 | 70 | 16.4 |
| 6 | 27 | 0.973 | 62 | 16.9 |
| 7 | 24 | 0.965 | 59 | 17.1 |
| 8 | 22 | 0.957 | 56 | 17.3 |

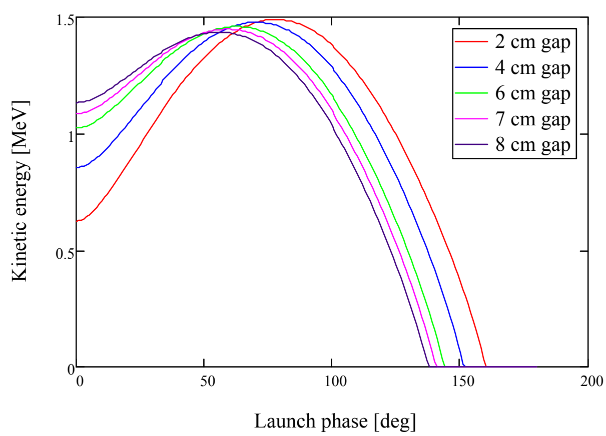


Figure 4: Kinetic energy as a function of launch phase, for various cathode-to-beamport gaps.

The free-space wavelength corresponding to 500 MHz is 0.6 m. A typical RF gun design has a cathode cell length on the order of $\lambda/4$; the cell lengths examined above thus correspond to $\lambda/30$ – $2\lambda/15$, or less than half the length of a typical cathode cell. This is the principal reason the transit-time factor is so high, along with the relatively wide launch windows for low energy spreads. In effect, the quarter-wave resonator "looks" more like a DC gun than an RF gun, for the time the beam is in the gap.

A first-cut design of a quarter-wave resonator geometry for the NPS injector upgrade is shown in Figure 5.

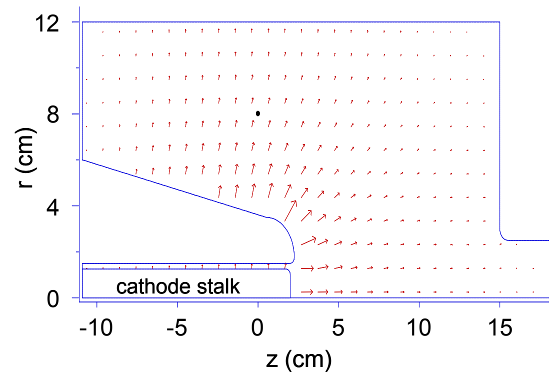


Figure 5: First-cut design for the NPS QW cavity.

We are still in the process of optimizing the gap and nosecone shape to obtain a good balance between peak surface electric and magnetic fields, transit-time factor, and gap. Detailed beam simulations will be conducted following the cavity parameter optimization, both in "injector" mode and "booster" mode.

## CONCLUSIONS

The NPS-FEL project has formally begun with the installation of the SCA DC-gun injector line at NPS. The line is now under vacuum, and we are preparing to modify the gun for photocathode operation.

The quarter-wave resonator design process has also begun. Initial calculations indicate that cathode-to-beamport gaps of 8 – 10 cm may provide a good balance between peak fields and transit-time factors. Detailed beam dynamics calculations will begin shortly, when the cavity design has been further refined to balance these factors. The calculations will study the anticipated performance of the quarter-wave cavity as both an energy booster and as a stand-alone photoinjector.

## REFERENCES

[1] J.W. Lewellen et.al., "Status of the NPS Free-Electron Laser," these Proceedings.
[2] T.I. Smith, private communication, 2006.
[3] http://www.continuumlasers.com/products/pdfs/minilite_II.pdf
[4] Y.-E. Sun and J.W. Lewellen, "Photothermal cathode measurements at the Advanced Photon Source," Proc. 2006 LINAC Conf., Knoxville, TN (pp. 349-51).
[5] www.pulsar.nl
[6] www.aps.anl.gov/Accelerator_Systems_Division/Operations_Analysis/
[7] See, for instance, R. Legg, et.al., "Half Wave Injector Design for WiFEL," Proc. EPAC08, Genoa, Italy (pp. 469-71).

# GENERATION OF FEMTOSECOND BUNCH TRAINS USING A LONGITUDINAL-TO-TRANSVERSE PHASE SPACE EXCHANGE TECHNIQUE*

Yin-e Sun[1], Philippe Piot[1,2]
[1]Accelerator Physics Center, Fermi National Accelerator Laboratory, Batavia IL 60510, USA
[2] Department of Physics, Northern Illinois University, DeKalb, IL 60115, USA

*Abstract*

We demonstrate analytically and via numerical simulations, how a longitudinal-to-transverse phase space manipulation can be used to produce a train of femtosecond electron bunches. The technique uses an incoming transversely-modulated electron beam obtained via destructive (e.g. using a multislits mask) methods. A transverse-to-longitudinal exchanger is used to map this transverse modulation into a temporal modulation. Limitation of the proposed method and scalability to the femtosecond regime are analyzed analytically and with the help of numerical simulation. Finally, a proof-of-principle experiment is discussed in the context of the Fermilab's A0 photoinjector.

## INTRODUCTION

Modern applications of the accelerator often call for certain phase space distribution which sometimes can be achieved from the phase space manipulation within one or two degrees of freedom. For example, the production of comb bunches, i.e. a bunch consisting of a train of microbunches, could open the path toward compact light source operating in the super-radiant regime at a wavelength comparable or larger than the typical density modulation. The generation of such beams by shaping the photocathode drive laser of a photoemission electron source were explored via numerical simulations [1, 2]. An alternative method using an interceptive mask located in a dispersive section was experimentally demonstrated [3]. Each of these methods has its limitations: the method based on shaping the photocathode drive laser distribution is prone to space-charge effects which are prominent at low energy and wash out the impressed modulation; the other techniques have limited tunability. In this paper, we present a more general technique for tailoring the current profile to follow certain distribution: first the transverse beam profile is modulated using a mask in the beamline, then beam goes through a longitudinal-to-transverse phase space exchange [4, 5, 6], resulting in a longitudinally modulated beam.

* Work supported by by the Fermi Research Alliance, LLC under Contract No. DE-AC02-07CH11359 with the U.S. Department of Energy and by Northern Illinois University under Contract No. DE-AC02-76CH00300 with the U.S. Department of Energy.

## THEORETICAL BACKGROUND

Our method is illustrated in Fig. 1: an incoming electron bunch is transversely intercepted by a mask with transmission function $T(x, y)$. The mask can have different patterns for various desired beam current profiles. In order to generate the comb bunches, we use a plate with multi vertical slits located upstream of an emittance exchanger beamline. The exchanger beamline consists of a dipole mode rf cavity flanked by two identical doglegs [5, 6]. The beam horizontal projection is mapped into the longitudinal (temporal) current density profile at the end of the emittance exchanger.

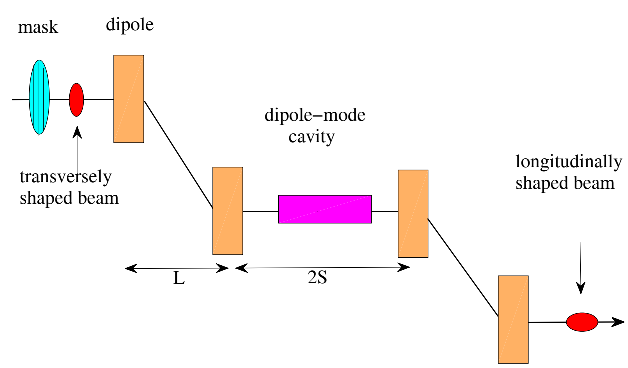


Figure 1: Overview of the proposed technique to produce relativistic electron bunch with arbitrary current profile.

A simple model based on the thin lens approximation for the transfer matrix associated to the dipole and cavity can be elaborated to give insights on the technique. In (x, x′, z, $\delta$) phase space, the transfer matrix of a dogleg is

$$M_D = \begin{pmatrix} 1 & L & 0 & -L\alpha \\ 0 & 1 & 0 & 0 \\ 0 & -L\alpha & 1 & L\alpha^2 \\ 0 & 0 & 0 & 1 \end{pmatrix}, \qquad (1)$$

where $L$ is the drift distance between the two dipoles, and $\alpha$ is the bending angle. The matrix associated to a dipole-mode cavity with strength $k$ is

$$M_C = \begin{pmatrix} 1 & 0 & 0 & 0 \\ 0 & 1 & k & 0 \\ 0 & 0 & 1 & 0 \\ k & 0 & 0 & 1 \end{pmatrix}. \qquad (2)$$

Under the emittance exchange condition [5, 6], we have $k + \alpha L = 1$. The exchanger matrix simplifies to the block anti-diagonal form

$$\mathrm{M} = \begin{pmatrix} 0 & 0 & \frac{L+S}{\alpha L} & \alpha S \\ 0 & 0 & \frac{1}{\alpha L} & \alpha \\ \alpha & \alpha S & 0 & 0 \\ \frac{1}{\alpha L} & \frac{L+S}{\alpha L} & 0 & 0 \end{pmatrix}. \quad (3)$$

where $2S$ is the separation between the middle two dipoles (see Fig. 1). The final phase space coordinates relates to the initial ones via

$$\begin{pmatrix} x \\ x' \\ z \\ \delta \end{pmatrix}_f = \mathrm{M} \begin{pmatrix} x \\ x' \\ z \\ \delta \end{pmatrix}_i = \begin{pmatrix} \frac{L+S}{\alpha L} z_i + \alpha S \delta_i \\ \frac{1}{\alpha L} z_i + \alpha \delta_i \\ \alpha x_i + \alpha S x'_i \\ \frac{1}{\alpha L} x_i + \frac{L+S}{\alpha L} x'_i \end{pmatrix}. \quad (4)$$

From Eq. (4), we see that in order to replicate the initial $x_i$ structure in the final coordinate $z_f$, we want the contribution to $z_f$ from the term $x'_i$ as small as possible. This can be done by (1) designing the beamline to minimize the bending angle $\alpha$, and/or the drift space between the two center dipole magnets $2S$; (2) tuning the initial beam parameters such that the initial divergence of the beam, $x'_i$, is as small as possible. For a given emittance, this means increasing the betatron function at the beam waist in (x, x′) phase space. It is also apparent that the correlation in an individual beamlet ( for which the $x_i$ is constants for an infinitely narrow slit in the multislit mask) in the longitudinal phase space at the end the exchange is given by

$$\frac{\Delta z}{\Delta \delta} = \frac{z_f - \alpha x_i}{\delta_f - x_i/\alpha L} = \frac{LS\alpha^2}{L+S} = \frac{M_{52}}{M_{62}}. \quad (5)$$

and is independent of the incoming Courant-Snyder parameters of the beam. A magnetic compressor with $R_{56} = -\frac{\Delta z}{\Delta \delta}$ can exploit the local correlation and further compresses the beamlets.

## NUMERICAL SIMULATIONS

The emittance exchange beam line is composed of four rectangular magnets of length $L_b = 0.288$ m and bending angle $\alpha = 22.5\,°$. The dipole mode cavity is the 3.9 GHz $\mathrm{TM}_{110}$ 5-cell copper cavity currently in operation at the A0 photoinjector in FermiLab [7]. The drift distances (see Fig. 1) are $L = 0.869$ m, $S = 0.400$ m.

The longitudinal chirp of the beam before it enters the emittance exchanger is chosen such to achieve the best possible emittance exchange as prescribed in Reference [8]; while the transverse Courant-Snyder parameters are tuned to obtain femtosecond bunch trains at the end of the exchanger; one set of initial conditions for the simulation is shown in Table 1.

The simulations are performed using `GPT` [9] and space charge is ignored for these simulations. A mask with vertical slits intercepts the beam in front of the emittance exchanger. The projection of the beam in the horizontal direction ($x$) is modulated; see the top picture in Fig. 2. At the end of the emittance exchanger, the beam intensity becomes modulated in the longitudinal direction ($z$) as a result of the swapping between the horizontal and longitudinal phase spaces. The modulation pattern is determined by the mask dimension as well as the lattice and the initial beam parameters, as shown in Eq. (4). Using the parameters shown in Table 1, the beam at the end of the emit-

Table 1: Parameters Prior to the Emittance Exchange

| | |
|---|---|
| beam energy (MeV) | 15 |
| bunch charge (pC) | 100 |
| normalized horizontal emittance ($\mu$m) | 1 |
| normalized longitudinal emittance( $\mu$m) | 27 |
| horizontal beta function (m) | 20 |
| longitudinal chirp $\partial\delta/\partial z$ (m$^{-1}$) | -4.5 |
| rms bunch length (mm) | 0.9 |
| slit width ( $\mu$m) | 80 |
| slit separation ( $\mu$m) | 300 |

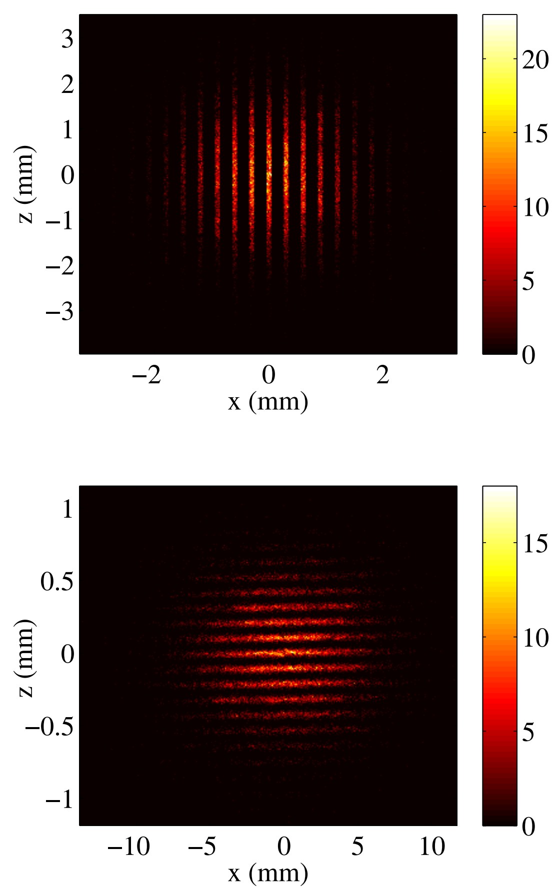


Figure 2: Beam projection in the x-z configuration space right after the mask (top) and at the end of the emittance exchanger (bottom).

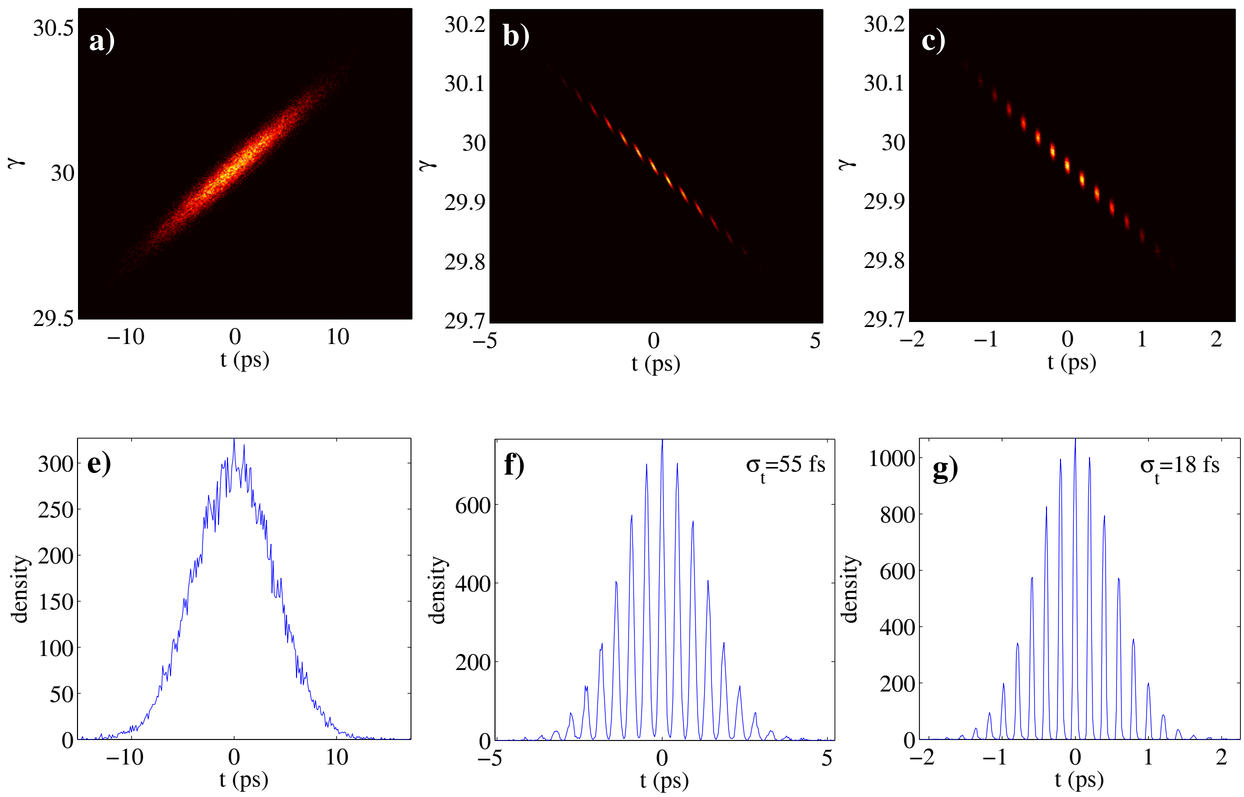


Figure 3: Longitudinal phase spaces (top) and their corresponding projections onto the time axis (bottom): a) & e) beam after the mask, at the entrance of the emittance exchanger; b) & f) beam at the end of the emittance exchanger; c) & g) beam downstream of a dogleg used to compress the beamlets. The bunch head corresponds to $t > 0$.

tance exchanger has a train of micro pulses with rms length around 55 fs. The separation between two neighbor micro pulses is about 350 fs; see Fig. 3 b) and f). The individual beamlets have a slope (correlation between energy and position) that is given by Eq. (5), which is different from the slope of the whole bunch train. In order to further compress the beamlet, one can use a two-dipole achromatic single dogleg compressor [10],which has the opposite $R_{56}$ sign as a conventional four-dipole chicane magnetic compressor. The absolute value of $R_{56}$ is given by Eq. (5). Upon the removal of the correlation in the longitudinal phase space within the beamlet, pulses with rms lengths of 18 fs and 120 fs separations are achieved; see Fig. 3 c) and g).

## FUTURE PLANS

In our simulations, the input beam parameters and lattice used are very close to those available at the A0 photoinjector Laboratory, with the exception of the non-existing single dogleg compressor after the emittance exchanger. However it is not essential for a proof-of-principle experiment. We are therefore preparing an experiment at the A0 photoinjector aimed at demonstrating the concept presented in the preceding sections. A tungsten plate will be used to intercept the beam before the emittance exchanger and coherent transition radiation detected by a cryogenically-cooled InSb bolometer will provide information on the pulse structure downstream of the exchanger. The bolometer will be used to directly detect the radiation with a set of band-pass mesh filters and as part of a Michelson interferometer. The planned parametric studies include the variation of the width, separation and number of the slits.

## REFERENCES

[1] M. Boscolo *et al.*, Nucl. Instrum. Methods A **577**, 409 (2007).

[2] Y. Li *et al.*, PRST-AB **11**, 080701 (2008).

[3] P. Muggli *et al.*, Phys. Rev. Lett. **101**, 054801 (2008).

[4] M. Cornacchia and P. Emma, PRST-AB **5**, 084001 (2002).

[5] K.-J. Kim and A. Sessler, AIP Conf. Proc. **821**, p. 115 (2006).

[6] P. Emma *et al.*, PRST-AB **9**, 100702 (2006).

[7] T. Koeth *et al.*, in Proc. of PAC 2007, pp. 3663 - 3665 (2007).

[8] Y.-E Sun *et al.*, in Proc. of PAC 2007, pp. 3441 - 3443 (2007).

[9] http://www.pulsar.nl/gpt.

[10] H. Wiedemann, “Particle Accelerator Physics I”, second edition, p. 173, Spinger (1999).

# LINAC DESIGN FOR AN ARRAY OF SOFT X-RAY FREE ELECTRON LASERS*

A.A. Zholents#, E. Kur, G. Penn, Ji Qiang, M. Venturini, R. P. Wells, LBNL, Berkeley, CA 94720, U.S.A.

*Abstract*

The design of the linac delivering electron bunches into ten independent soft x-ray free electron lasers (FELs) producing light at 1 nm and longer wavelengths is presented. The bunch repetition rate in the linac is 1 MHz and 100 kHz in each of ten FEL beam lines. Various issues regarding machine layout and lattice, bunch compression, collimation, and the beam switch yard are discussed. Particular attention is given to collective effects. A demanding goal is to preserve both a low beam slice emittance and low slice energy spread during acceleration, bunch compression and distribution of the electron bunches into the array of FEL beamlines. Detailed studies of the effect of the electron beam microbunching caused by longitudinal space-charge forces and coherent synchrotron radiation (CSR) have been carried out and their results are presented.

## LATTICE AND DESIGN PARAMETRS

The accelerator is schematically shown in Figure 1. It consists of an injector, a laser heater, a bunch compressor, two main linacs, a harmonic linearizer linac, and a beam switch yard (spreader) into ten FELs (not shown).

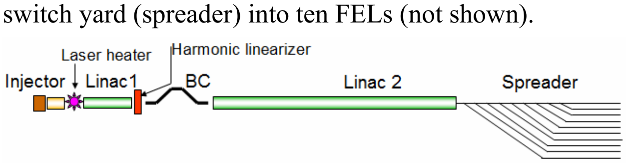


Figure 1: A schematic of the accelerator. Elements of the machine include the injector, laser heater, first linac, harmonic linearizer, bunch compressor, second linac, and spreader. The entire length of the machine is ~ 650 m.

The electron beam energy after injector at the entrance of the laser heater (LH) is ~ 40 MeV and the peak current is ~ 70A. The electron peak current after bunch compressor (BC), located behind the first linac (L1) and harmonic linearizer (HL) at a ~ 250 MeV beam energy point, is ~ 1 kA. The requirement for tunability of FELs outputs using APPLE-II undulator with adjustable helicity, in particular the FELs covering wavelengths from 1.5 nm to 1 nm, largely determines the lowest final beam energy ~ 2.4 GeV at the exit of the second linac (L2). However, surprisingly, this energy only weakly depends on a size of a minimal gap in APPLE-II undulator [1] (see Figure 2).

According to the user requirements the accelerator must accommodate with sufficient flexibility three operation modes depending on the x-ray pulse length, i.e the long pulse from 500 fs to 100 fs, the medium pulse from 100 fs to 10 fs and the short pulse of 10 fs and shorter. Because of a limited space, only the long pulse option requiring the long electron bunch is discussed here in detail. Other important electron beam parameters include the normalized slice electron beam emittance < 1 µm and the slice rms energy spread ~ 100 keV.

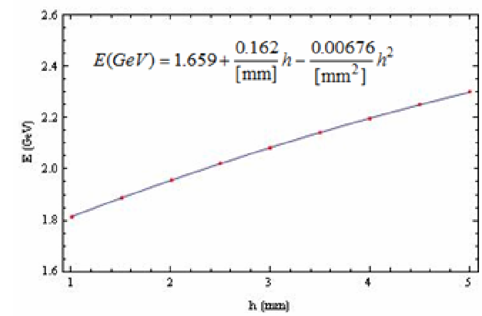


Figure 2: The electron beam energy that supports production of the x-rays within the range of wave lengths from 1 nm to 1.5 nm as a function of the size of the beam-stay-clear gap $h$ in APPLE-II undulator.

Figure 3 shows one plausible alignment for a linac tunnel leading into the array of FELs located on the existing flat site in LBNL previously occupied by BEVATRON. It is also possible to begin the tunnel at a further point allowing more space for a linac.

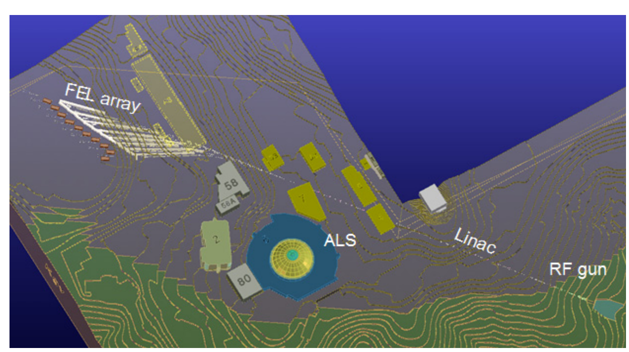


Figure 3: Bird view on East tunnel option for a linac, spreader and FEL array.

The linac lattice functions beginning from the end of the injector are shown in Figure 4. Large beta-functions are used in several locations along the L2 for convenience of the collimation of halo particles. This is important as we plan for up to 1 mA average electron current. A small horizontal beta-function <10 m is used at the forth bending magnet of the bunch compressor in order to minimize the impact of CSR on the beam emittance. It is considered that TESLA cryomodules with 1.3 GHz linac structures will be used in L1 and L2 with the energy gain

*Work supported by the U.S. Department of Energy under Contract No. DE-AC02-05CH11231.
#AAZholents@lbl.gov

of 13.5 MeV/m in the active part. However, it is worth pointing out that cryomodules with 1.5 GHz linac structures under development for the CEBAF upgrade could also be used.

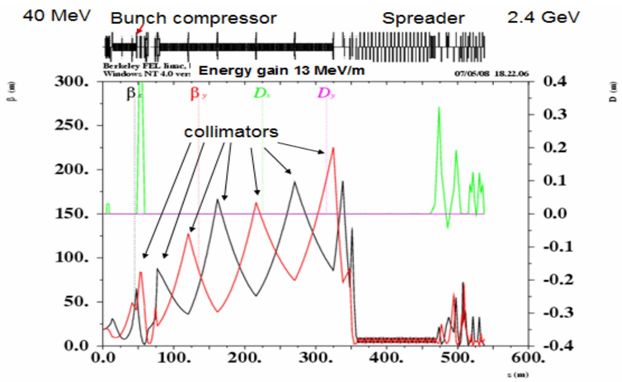


Figure 4: Linac lattice beginning from the end of the injector.

L1 is followed by HL which is a 3.9 GHz superconducting linac with the energy gain of 5 MeV/m and a total energy of ~ 30 MeV. HL is used to decelerate the electrons and (together with L1) to produce the linear energy chirp in the electron bunch in front of the BC. BC has a large R56=0.135 m and produces bunch compression increasing the electron peak current up to 1 kA. Fine tuning of the rf amplitudes and phases in L1 and HL is needed in order to obtain a desirable compression as seen in Figure 5. BC is followed by L2 and the spreader, which distributes electron bunches into ten independent FEL

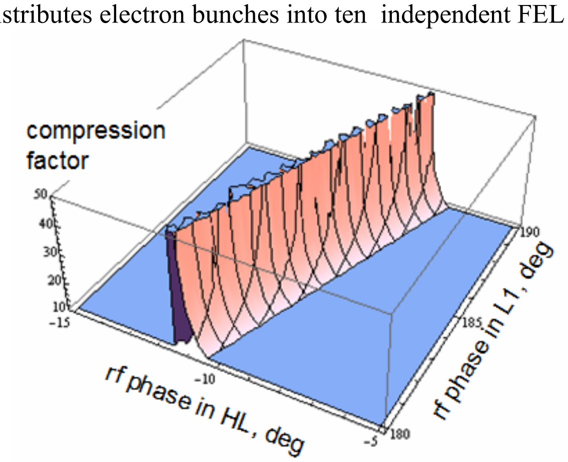


Figure 5: Compression factor (CF) as a function of the rf phases in linac L1 and HL. Steep rise of CF indicates high sensitivity to all parameters.

undulator lines. The maximum bunch repetition rate in the linac is 1 MHz and it is 100 kHz in each of ten FELs .

Figure 6 shows a schematic of the beam take-off section of the spreader. Each beamline has a 2 m long stripline kicker with a 5 mm gap providing maximum kick of 3 mrad at a 100 kHz pulse repetition rate and a 2 m long electromagnet septum located at a 90° betatron phase advance with respect to the kicker and providing 27 mrad turn to the beam. The septum is followed by three quads, bending magnet another three quads and another bend magnet (see, Figure 7). All these plus the kicker and a septum make the triple bend achromatic and isochronous lattice. This is considered to be important in order to minimize the impact of the bending on the beam microbunching [2].

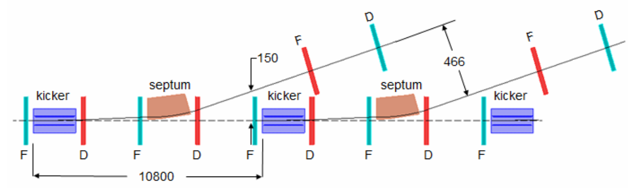


Figure 6: Beam take-off section of the spreader. Only two out of ten neighboring beamlines are shown.

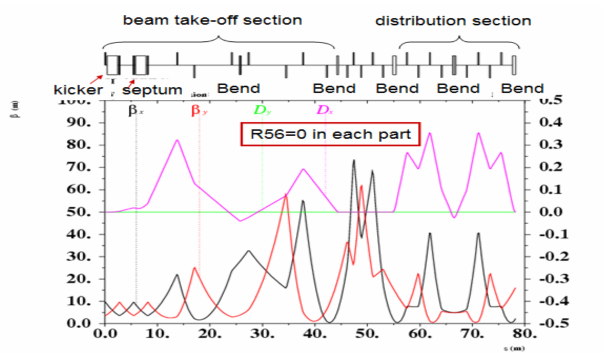


Figure 7: Lattice of the beam take-off section of the spreader. The downstream beam distribution section is also shown. This section is specific for each FEL and is used to fan out all FEL lines by turning the electron beam at various angles, but all of them have a similar design and are achromatic and isochronous.

## COLLECTIVE EFFECTS

A major emphasis in the linac design was given to understanding, characterization and control of collective effects caused by the space charge, rf structure wakefields, and CSR. The approach taken include analytical estimations, reverse tracking in longitudinal phase space [3], fine tuning by tracking of a small number of macroparticles in 3D phase space and performance validation with tracking up to one billion macroparticles. For these tasks we used a package of computer codes: LiTrack [4], Elegant [5], Vlasov solver [6], CSRTrack [7], and IMPACT [8].

First we verified a concept of the spreader lattice by tracking particles from the end of BC to the end of the linac and through the spreader using a flat top, 0.8 ps long electron bunch with 1 kA peak current. We found no evidence for slice emittance growth and for microbunching instability.

The result of the particle tracking through the entire machine beginning from the end of the injector is shown in Figures 8 and 9. The simulation was carried out for a 0.8 nC electron bunch with 70 A initial peak current and parabolic density distribution. It is assumed that LH will be used for control of the energy spread after injector and 5 keV rms energy spread was used in simulation. We note that after accounting for a compression factor of ~ 20, the modulation period due to microbunching instability seen

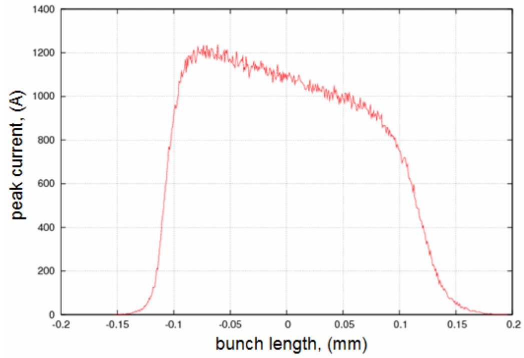


Figure 8: Peak current distribution at the end of the spreader obtained in tracking of 1B macroparticels through the entire machine beginning from the end of the injector using IMPACT.

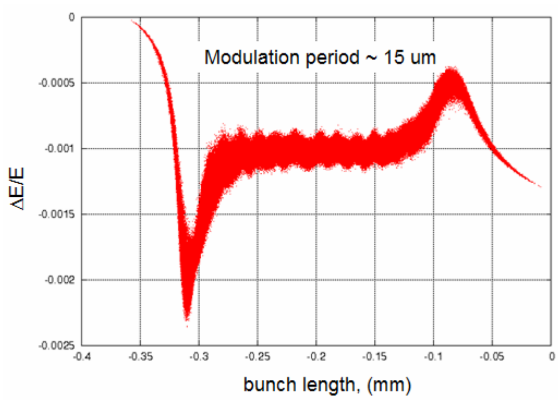


Figure 9: Longitudinal phase space at the end of the spreader obtained in tracking of 1B macroparticels through the entire machine beginning from the end of the injector using IMPACT.

in Figure 9 is in a good agreement with analysis of the gain of the microbunching instability performed on the basis of the linear theory [9] (see, Figure 10).

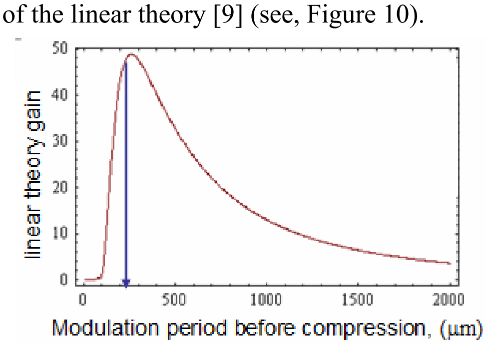


Figure 10: Gain of the microbunching instability. Arrow indicates modulation period obtained in macroparticle tracking (after accounting for a compression factor).

Figure 11 shows the normalized slice emittance at the end of the spreader which is the same as 0.45 μm initial emittance assumed in this simulation.

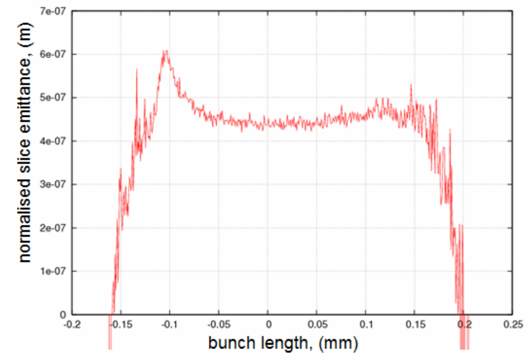


Figure 11: Normalized slice emittance at the end of the spreader obtained in tracking of 1B macroparticels through the entire machine beginning from the end of the injector using IMPACT.

Finally, Figure 12 shows the rms slice energy spread at the end of the spreader. For the most part of the bunch it is simply defined by the bunch compression and is not affected by microbunching instability. The large increase at the tail of the bunch is due to off-set of the central slice energy seen in Figure 10.

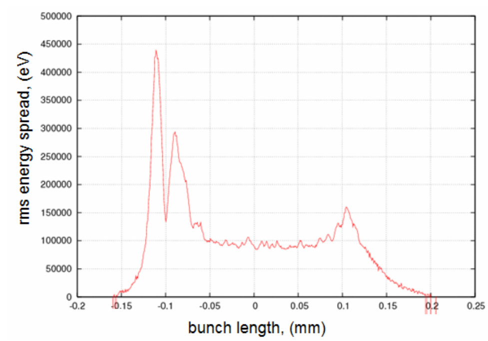


Figure 12: Slice rms energy spread at the end of the spreader obtained obtained in tracking of 1B macroparticels through the entire machine beginning from the end of the injector using IMPACT.

In conclusion, we have produce a design for an accelerator satisfying performance requirements for soft x-ray FEL array. Testing this design by particle tracking indicates that all adverse collective effects are well managed. This allows the electron beam transport from injector to FELs without deterioration of the slice emittance and slice energy spread.

## REFERENCES

[1] A. Zholents, CBP Tech. Note – 381, (2007).
[2] M. Venturini , A. Zholents, NIM A**, 593**, 53(2008).
[3] M. Cornacchia *et. al.*, PRST-AB, **9**, 120701(2006).
[4] K. L. F. Bane and P. Emma, Proc. Part. Acc. Conf., Knoxville, Tennessee, 4266(2005).
[5] M. Borland,, APS Tech. Note LS-207, (2000).
[6] M. Venturini, *et al.,* PRST-AB, **10**, 05403 (2007).
[7] M. Dohlus, TESLA-FEL-2003-05, DESY, 2003.
[8] J. Qiang, *et. al.*, J. Comp. Phys. **163**, 434 (2000).
[9] S. Heifets, *et al.,* PRST-AB, **5**, 064401 (2002).

# MANIPULATING THE TWO-STREAM INSTABILITY FOR EFFICIENT TERAHERTZ GENERATION*

K. Bishofberger, B. Carlsten, R. Faehl; LANL, Los Alamos, NM 87544

*Abstract*

Particle beams have exhibited a two-stream instability for many decades; this undesirable trait has been well-understood for many years. We propose creating a scheme that uses a beam of electrons with two distinct energies that will develop the two-stream instability as a bunching mechanism. By controlling the beam parameters and seeding them with a low-level rf signal, a gain as high as 2.5 dB per centimeter is predicted. We show the theory behind this concept and recent progress in a developing experiment.

## INTRODUCTION

Terahertz-frequency sources have been the holy grail of mm-wave research for many years now. In the recent past, a great deal of emphasis has been placed on developing these sources for a variety of applications [1].

Terahertz generally refers to a range of several hundred GHz through perhaps 10 THz, which lies in a band that has shorter wavelengths than electronics and conventional structures, yet longer than the atomic scale. Because of this, sources in this band have eluded conventional electronics and atomic techniques (e.g. lasers) and remain an unexplored region of the EM spectrum.

Yet the number of applications of terahertz manipulation is vast and growing. Typically, these include remote sensing, communications, three-dimensional imaging, and directed energy. Discussions of THz applications are published frequently; they will not be regurgitated here [1,2].

The most common approach to building a high-power source that reaches to 1 THz is typically a TWT-type device, where an electron beam is pushed through a comb-like structure, and the coupling of the beam with the vanes generates traveling waves of a wavelength nearly matching that of the structure. However, the structure and the efficiency of coupling scale very poorly to short wavelengths.

We propose a terahertz-generation scheme that eliminates the need for any problematic structure while providing high-average power output to satisfy the desires of the THz-based applications.

## PHYSICAL DESCRIPTION

Figure 1 shows a three-dimensional model of the experiment currently being fabricated. The total beamline length, represented by the blue and red lines, is only a couple feet long. Two electron guns produce electron beams of slightly different energy. These beams are bent by a (green) dipole so that they merge and co-propagate. Then they get bent again and collected in a large-aperature collector.

The next section describes the theory of the interaction, and shows that Coulombic bunching should occur during the mixing process. These space-charge waves will radiate via coherent synchrotron radiation at the second bend. Instead of being dependent on shot noise to begin the process, we expect to steal a small percentage of the output radiation and reflect it back on the initial beam using one (yellow) mirror and a diffraction grating.

Seeding the beams at a specific frequency will allow that mode to self-select in the amplification process. Meanwhile, the majority of the radiative beam will be collected and analyzed. A number of variations are possible (frequency-modulated input, multi-mode mixing, etc), but in all cases, the setup is significantly less complex than conventional TWT-type techniques.

## LINEAR THEORY

We start by separating out the dc and ac components of each beam's density and velocity:

$$\eta_j = \eta_{0j} + \tilde{\eta}_j \,,\; v_j = v_{0j} + \tilde{v}_j \,, \text{and } E = E_0 + \tilde{E} \,,$$

The continuity equation, Lorentz' law, and Poisson's equation can be written:

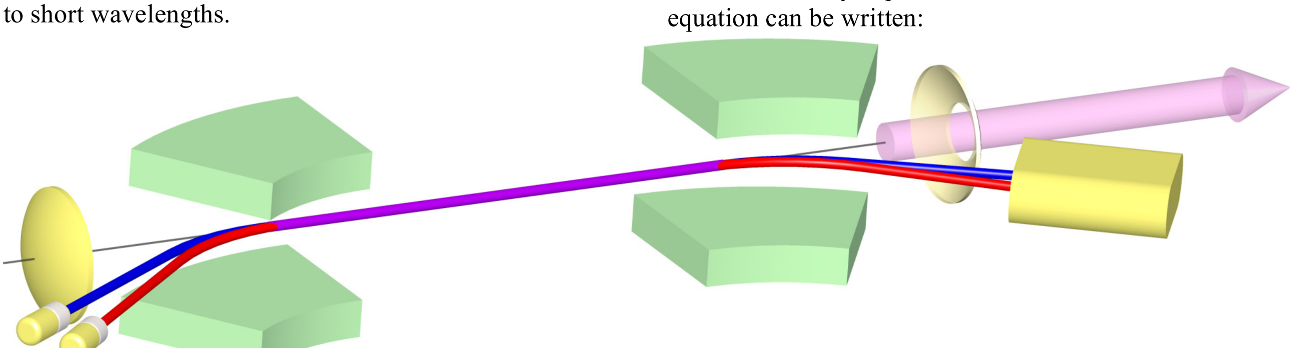

Figure 1: Model of the experimental beam layout. The two electron guns generate beams of slightly higher (blue) and lower (red) energies, which are then mixed (purple) through the interaction region. This middle portion is about 10-cm long, and the total apparatus is less than one meter in length.

$$\frac{\partial \eta_j}{\partial t} = -\frac{\partial}{\partial z}\eta_j v_j$$

$$\frac{\partial v_j}{\partial t} + v_j \frac{\partial}{\partial z} v_j = \left(\frac{q}{m}\right)\left(\vec{E} + \frac{\vec{v}}{c} \times \vec{B}\right)_z$$

$$\frac{\partial E}{\partial z} = \frac{q}{\varepsilon_0}\sum_j \eta_j .$$

Considering only longitudinal motion, these equations become:

$$\left(\omega - k v_{0j}\right)\tilde{\eta}_j = k\eta_{0j}\tilde{v}_j$$

$$-i\left(\omega - k v_{0j}\right)\tilde{v}_j = \left(\frac{q}{m}\right)\tilde{E}$$

$$ik\tilde{E} = \frac{q}{\varepsilon_0}\sum \tilde{\eta}_j .$$

If we define the average and difference quantities as:

$$\bar{v} \equiv \frac{v_{01} + v_{02}}{2}, \quad \Delta \equiv \frac{v_{01} - v_{02}}{2}, \text{ and } \Omega \equiv \omega - k\bar{v},$$

then the linearized equations can be rewritten as:

$$\left(\Omega - k\Delta\right)\tilde{\eta}_1 = k\eta_{01}\tilde{v}_1$$

$$\left(\Omega + k\Delta\right)\tilde{\eta}_2 = k\eta_{02}\tilde{v}_2$$

$$\left(\Omega - k\Delta\right)\tilde{v}_1 = i\left(\frac{q}{m}\right)\tilde{E}$$

$$\left(\Omega + k\Delta\right)\tilde{v}_2 = i\left(\frac{q}{m}\right)\tilde{E}$$

$$ik\tilde{E} = \frac{q}{\varepsilon_0}\left(\tilde{\eta}_1 + \tilde{\eta}_2\right).$$

Now the dispersion relation can be evaluated:

$$\left(\Omega - k\Delta\right)^2 \tilde{\eta}_1 = \omega_{p1}^2\left(\tilde{\eta}_1 + \tilde{\eta}_2\right)$$

$$\left(\Omega + k\Delta\right)^2 \tilde{\eta}_2 = \omega_{p2}^2\left(\tilde{\eta}_1 + \tilde{\eta}_2\right),$$

where $\omega_{p(1,2)}^2 \equiv q^2\eta_{0(1,2)} \big/ \varepsilon_0 m$ are each beam's plasma frequencies.

Combining both parts of the last equation and assuming $\omega_{p1}^2 \approx \omega_{p2}^2$, we generate the dispersion relation:

$$\Omega^4 - 2\Omega^2\left(\omega_p^2 + k^2\Delta^2\right) + k^4\Delta^4 - 2k^2\Delta^2\omega_p^2 = 0 .$$

If $\Gamma$ is defined as:

$$\Gamma^2 \equiv \sqrt{1 + k^2\Delta^2\left(2\omega_p^2 - k^2\Delta^2\right) \Big/ \left(\omega_p^2 + k^2\Delta^2\right)^2} - 1 ,$$

then the solution of the dispersion relation becomes $\Omega = \pm i\Gamma\sqrt{\omega_p^2 + k^2\Delta^2}$ or $k\bar{v} = \omega \pm i\Gamma\sqrt{\omega_p^2 + k^2\Delta^2}$. The velocity separation and growth approximation can thus be rewritten as:

$$k = \frac{\omega}{\bar{v}} \pm i\frac{\omega_p}{\bar{v}}\left(\frac{2-\sqrt{3}}{\sqrt{2}}\right)$$

and

$$\frac{\omega_p}{\bar{v}} = \frac{2}{b}\sqrt{\frac{I}{\beta^3 I_A}} .$$

Putting these together, the gain (in decibels) over a length $L$ becomes:

$$G = 20 \cdot \log\left(\exp\left(\frac{2L}{b}\sqrt{\frac{I}{\beta^3 I_A}}\left(\frac{2-\sqrt{3}}{\sqrt{2}}\right)\right)\right)$$

$$G \approx 3.29\frac{L}{b}\sqrt{\frac{I}{\beta^3 I_A}} .$$

For a beam of one-millimeter radius and one ampere, this is about $0.25\,\mathrm{dB/mm}$.

## CURRENT PROGRESS

For the past several months, 3D simulations have been analyzing the two-stream amplification process more completely than the linear theory. One-dimensional simulations have produced impressive results, which have been published elsewhere.

Simultaneously, the experimental demonstration of this method is nearly finished fabrication and assembly. Beam mixing and bunching is expected in the next year.

## REFERENCES


[1] M. Rosker, "Progress Towards a THz Imager," IMS 2007 Workshop (2007); www.darpa.mil/mto/ programs/tift/pdf/MTT_THz_Workshop.pdf.

[2] B. Carlsten, K. Bishofberger, R. Faehl, "Compact two-stream generator of mm and sub-mm wave radiation," Physics of Plasmas 15, 073102 (2008).

[3] K. Bishofberger, B. Carlsten, and R. Faehl, "Generation of millimeter and sub-millimeter radiation in a compact oscillator utilizing the two-stream instability," International Vacuum Electronics Conference 2008, April 2008, 164 (2008).

# IDENTIFYING JITTER SOURCES IN THE LCLS LINAC*

F.-J. Decker, R. Akre, A. Brachmann, W. Colocho, Y. Ding, D. Dowell, P. Emma, J. Frisch, S. Gilevich, G. Hays, P. Hering, Z. Huang, R. Iverson, K.D. Kotturi, A. Krasnykh, C. Limborg-Deprey, H. Loos, S.D. Molloy, H.-D. Nuhn, D. Ratner, J. Turner, J. Welch, W. White, J. Wu,
SLAC, Stanford, CA 94025, USA

*Abstract*

The beam stability for the Linac Coherent Light Source (LCLS) Free-Electron Laser (FEL) at Stanford Linear Accelerator Center (SLAC) is critical for good X-Ray operation. Although stability tolerances are met or very close to the specification [1,2], there is some transverse and longitudinal jitter in the beam [3]. Here we discuss identifying these jitter sources by different methods like correlations, frequency spectrum analysis or other methods for finally eliminating or reducing them.

## MECHANICAL SOURCES

Understanding some of the jitter sources for the LCLS requires going back in history and looking at the sources and their solutions, which played out during running the SLC (SLAC Linac Collider) [4-7]. There was 10 Hz structural quadrupole vibration, which coupled from the longitudinal to the vertical 100 times stronger, since the quadrupole was mounted not below its center of gravity [4,5]. Additional clamps stiffened that motion and eliminated this frequency. Early frequency checks on the LCLS motion indicated some jitter power at 10 Hz, which could be traced to some clamps fallen in disrepair, like not be tightened down or even missing altogether, which was quickly fixed. The main sources, which drive this motion with mainly white noise jitter, are big accelerator structure water pumps. The asynchronous motors run at 3540 rpm 59 Hz [6,7], which when unbalanced, can be directly seen, or with 30 Hz beam rate aliased down at 1 Hz (see Fig. 1). 12% of the jitter power is at 1 Hz (8% at 4.4, 5% at 7 Hz).

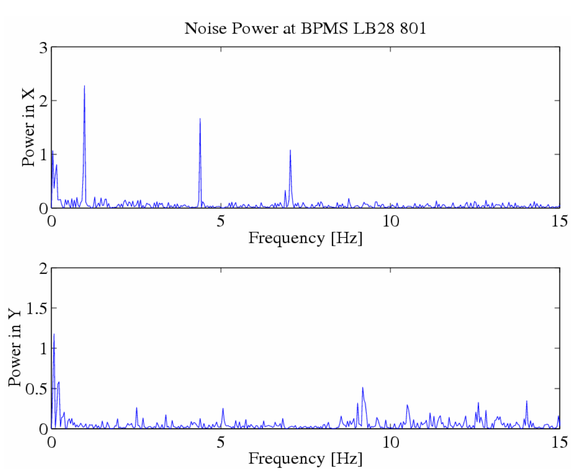


Figure 1: Power spectrum of a Beam Position Monitor (BPM) in the Linac indicates noise at 1.0, 4.4 and 7.0 Hz.

* Work supported by US DOE contract DE-AC02-76SF00515.

By plotting just the power at 1 Hz versus the length of the Linac $z$ [6], we can pinpoint the location where a pump might be bad. Direct vibration data measured on top of the quadrupole can confirm this, and excessive variations of the pump water pressure can be even measured during running the beam.

### *Quantitative Analysis*

A more quantitative approach is achieved in the following way. Only the 1-Hz-component of the FFT power spectrum (Fig. 1) is selected and the inverse FFT is taken. This gives a cleaned up 1-Hz sin curve (with some modulation, if more than one frequency bin was chosen). Now we take the peak-to-peak (p-p) difference (max – min) and plot this 1-Hz-difference orbit for all BPMs versus $z$ or versus the BPM number (Fig. 2).

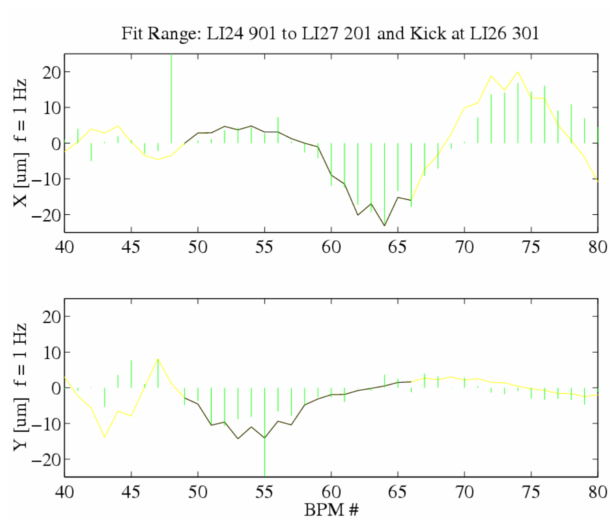


Figure 2: BPM orbit difference for only the 1 Hz component. A part (black curve) was fitted to the data allowing a kick at BPM # 59 (Li26 301).

The fitted kick angle was $\theta$ = -0.52 µrad in $x$ and -0.18 µrad in $y$ for a problem at Li26 301 BPM. The observed quadrupole vibration on top of the magnet was 2.3 µm RMS. These two numbers can be compared using the following equation

$$\theta = \frac{0.03}{E\,[\mathrm{GeV}]} * BL\,[\mathrm{kG\text{-}m}] \qquad (1)$$

where $E$ (6.2 GeV) is the energy at that point and $BL$ is the integrated field strength of an effective dipole kick. This kick is assumed to be produced by a nearby quadrupole $B$ (-9.4 kG) and a vibration offset $\Delta y$. Using the above numbers $\Delta y$ results to 11.4 µm (p-p).

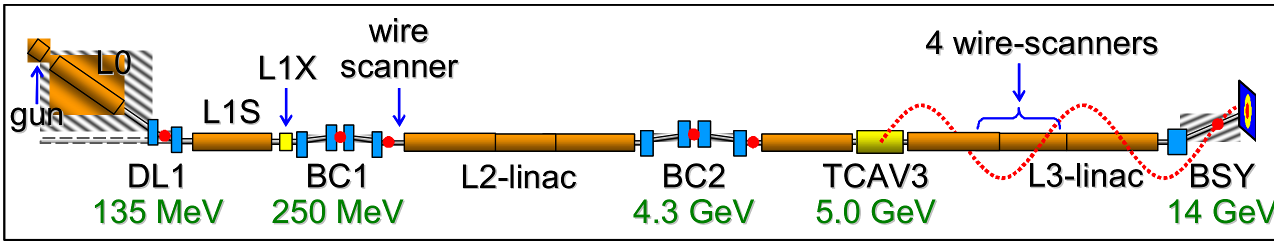


Figure 3: LCLS schematic layout of Linac sections L0, L1, L2, and L3 with the two bunch compressors (BC). There are four energy BPMs in the four dispersive sections: DL1 (Dog Leg), BC1, BC2, and BSY (Beam Switch Yard).

To get the amplitude of the 1 Hz sin wave we have to divide the p-p number by two (5.7 µm), and finally the RMS of a sin wave is still $1/\sqrt{2}$ smaller resulting in 4.0 µm RMS. For sin wave we have:

$$2.0\ (\text{p-p}) \equiv 1.0\ (\text{ampl.}) \equiv 0.707\ (\text{RMS}) \qquad (2)$$

This is still a factor of 1.7 higher than 2.3 µm. The quadrupoles in Sector 26 showed an average vibration level of 1.2 µm, while a "good" Sector can have an average below 0.5 µm RMS in $x$ and 0.15 µm RMS in $y$ [8]. The quadrupoles next to 301, namely 201 and 401, had 0.7 and 1.5 µm RMS quadrupole vibration which could have added coherently to 4.0 µm RMS. This is especially likely since the power cables of only Quad 301 were found resting on a vibrating rectangular waveguide.

Normally it could be argued in the opposite direction that the eight quadrupoles per Sector (driven by one pump) should cancel partly their motion due to focusing and defocusing quadrupoles and about half a betatron oscillation over a Sector. The incoherent addition of 8 quads with 0.1 µm gives 0.28 µm, while coherently four times: +0.10 and -0.06 µm gives 0.16 µm and the phase advance reduces this further to 0.12 µm. So a coherent motion of all eight magnets loosens the jitter tolerance by 2.3, so a 0.10 µm tolerance becomes 0.23 µm. There is still a discrepancy of about a factor of two between this tolerance [1] and the measured beam jitter (15% in $x$, 10% in $y$ [3]) and the vibration measurement on top of the quadrupoles (0.5 µm RMS in $x$, 0.15 µm RMS in $y$). It could be explained by the center of the quadrupoles (beam axis) moving about half of the on top of magnet vibration numbers, making the different measurement nearly consistent.

## RF SOURCES

The new EPICS RF system for LCLS had many teething problems concerning jitter and many problems got already identified and fixed [3]. So we concentrate on some new findings. Besides the 1 Hz line in Fig. 1, there is a 4.4 Hz line which turned out to be mainly longitudinal. Looking at Fig. 3 we have four dispersive sections where energy BPMs can pick up any energy jitter. Figure 4 shows the 4.4 Hz line p-p orbit difference along the Linac. With the design dispersion the energy BPMs give the following p-p energy jitter (at 4.4 Hz): DL1: -0.45‰, BC1: -0.38‰, BC2: 0.70‰, BSY: 0.18‰.

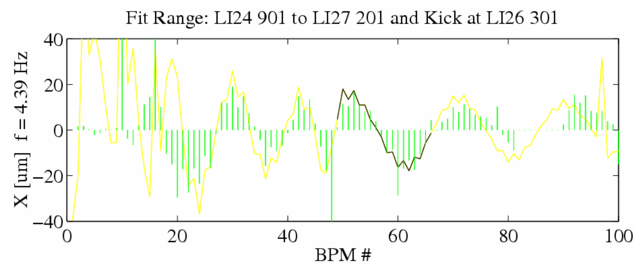


Figure 4: Horizontal p-p orbit difference for the 4.4 Hz line, indicating an energy jitter problem early in the Linac and non-matched dispersion after BC1 and BC2. Most energy BPMs are off-scale: DL1 (#10): 119 µm, BC1 (#16) 88µm, BC2 (#48) -256 µm, and BSY (#100) -15 µm.

Again, these numbers are $2\sqrt{2}$ bigger than RMS. The energy change is not the whole story, there was some phase jitter, but mainly the R56s of the chicanes (and dogleg) explain the energy ratios or even the sign flip after BC1. A lower energy of -0.38‰ in BC1 will give rise to a 17 µm longer path (R56 = -45mm), the effective L2 phase will move from -37° to -36.94° resulting in a +0.71‰ energy change at BC2, as measured. Figure 5 shows the culprit, mainly an amplitude jitter of the L0B klystron, although the jitter is 0.052%, below the tolerance of 0.1%.

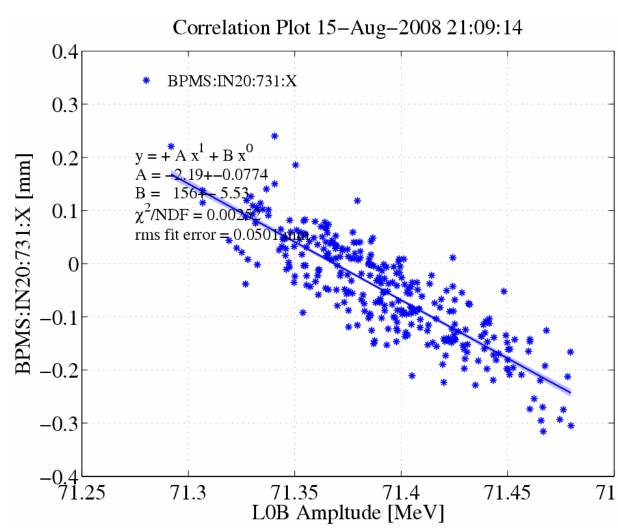


Figure 5: The BPM in DL1 (IN20:731) shows a strong correlation to the amplitude variation of the L0B klystron.

The square of the correlation coefficient ($r$ = -0.85) is equal to the power (73%) in the correlation

$$r^2 = p, \tag{3}$$

while the reduced jitter amplitude is

$$j_r = j_o * \sqrt{1-p}\,. \tag{4}$$

So the jitter in the BPM $x$ (RMS = 96 µm) could be reduced to 50 µm. Another way to get this reduced number is to look at the rms fit error (see Fig. 5), which is the projection along the fitted line. To compare how much jitter comes from different sources it is best look at the power fractions, since they just add (not add in quadrature like the amplitudes). Table 1 lists some jitter sources and their fraction of the jitter power, which correlates with energy, phase, bunch length (BL), and transverse measurements (73% of DL1 $\Delta E$ is from L0B).

Table 1: Fractional Jitter Power [in %] of Four Sources

| Source:→ Measurement ↓ | L0B amplitude | L1S phase | L1S ampl. | L0A ampl. |
|---|---|---|---|---|
| DL1 energy | 73 | 0 | 0 | 12 |
| BC1 energy | 10 | 4 | 1 | |
| BC2 energy | 12 | 26 | 5 | |
| BSY energy | 13 | 24 | 5 | |
| Li21beamphase | 4 | 9 | 2 | |
| BL Li21_A | 3 | 17 | 2 | |
| BL Li21_B | 11 | 31 | 5 | |
| Li28 401 x | 15 | 8 | 6 | all |
| Li28 801 x | 9 | 13 | 3 | in % |

The phase jitter of L1S (only 0.09° RMS) has no special frequency component. It is white noise, most likely a random instability in the klystron itself. It causes the highest down stream energy and bunch length jitter, and even contributes about the same amount to the transverse jitter (13%) compared to the 1 Hz pump jitter from Fig. 1 (12%). This is also an indication that the dispersion after the chicane is not perfectly canceled.

### *SVD Method*

Besides the FFT approach, looking at the special frequency component and plotting it versus $z$, or correlating an observed jitter with a suspecting source, there is the singular value decomposition (or SVD):

$$[U, S, V] = \text{svd}(X), \tag{5}$$

where $X$ is a big matrix off about 400 variables at 400 to 800 consecutive time intervals. The variables were for 101 BPMs ($x$, $y$, charge) and about 100 RF klystron and sub-booster phases. This gives about 400 eigenvalues $S$, which are orthogonal to each other, and depending on the orientation of $X$, $U$ is the time eigenvector and $V$ is the variable eigenvector. Just plotting the first 100 elements (equals to $x$) of the four biggest eigenvectors $V$ reveals big excursions at 10, 16, 48 (see Fig. 6), where the energy BPM are located, indicating at least 4 independent sources.

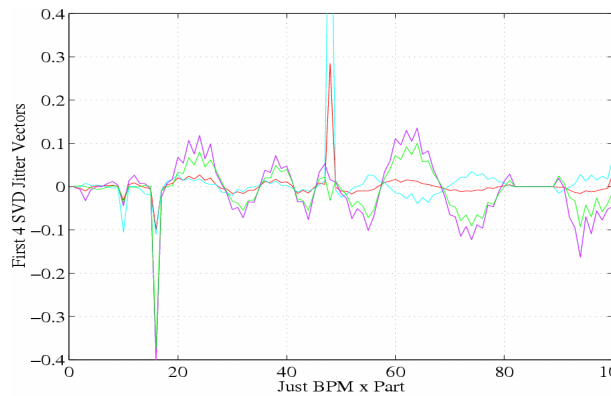


Figure 6: The first 4 eigen values using the SVD method point to different jitter sources, all concerning energy. Although they have the same sign at the energy BPMs and after BC1, the sign of one mode is opposite after BC2.

A small bump was also seen on L0B phase. The FFT of the time eigenvector $U$ turned up one eigenvector with 4.4 Hz indicating the L0B problem (magenta $V$-vector in Fig. 6). The others mainly had a slow drift.

How to "scale" the data and get the most important jitter sources is still under investigation. For example the charge in units of number of particles (4E9 = 250 pC) had to be divided by 1E10, otherwise these eigenvector would have dominated. Maybe scaling by RMS jitter for each device is an option, but was not checked yet. The other problem is that the energy BPMs have more absolute jitter compared to transverse jitter say in Li28, so the 1 Hz line was not sticking out as a problem.

## SUMMARY

Three methods to identify jitter sources were discussed: frequency content, correlation, and singular value decomposition. They helped to find vibrating pumps, phase noise in the RF system and trouble with certain klystrons, finally bringing the jitter numbers within spec.

## REFERENCES


[1] P. Emma, J. Wu, "Trajectory Stability Modeling and Tolerances in the LCLS", EPAC06, Edinburgh, p. 151.

[2] P. McIntosh et al., "Overview of the RF Systems for LCLS", PAC'05, Knoxville, p. 2753.

[3] R. Akre et al., "Beam Stability Studies in the LCLS Linac", FEL08, Korea, Aug 2008.

[4] J.L. Turner et al., "Vibration Studies of the Stanford Linear Accelerator", PAC95, Dallas, 1995, p. 665.

[5] R.E. Stege, J.L. Turner, "Beam Jitter and Quadrupole Motion in the Stanford Linear Collider", BIW98, Palo Alto, May 1998.

[6] F.-J. Decker et al., "Characterizing Transverse Beam Jitter in the SLC Linac", EPAC 98, Stockholm, p. 457

[7] J.L. Turner, R. Stege, "Vibration of Linac Quadrupoles at 59-Hertz", SLAC-CN-399, Oct 1995.

[8] J. Turner et al., "LINAC Quadrupole Vibration Measurements", LCLS Engineering Note #1.0-003, May 2008.

# THE ELECTRON BUNCH INITIAL ENERGY PROFILE ON A SEEDED FREE ELECTRON LASER PERFORMANCE*

Juhao Wu†, Alexander W. Chao, SLAC, Menlo Park, CA 94025, USA
Joseph J. Bisognano, Synchrotron Radiation Center, UW-Madison, Stoughton, WI 53589, USA

## [illegible]

A single-pass high-gain x-ray free electron laser (FEL) calls for a high quality electron bunch. In particular, for a seeded FEL, and for a cascaded harmonic generation (HG) FEL, the electron bunch initial energy profile is crucial for generating an FEL with a narrow bandwidth. After the acceleration, compression, and transportion, the electron bunch energy profile entering the undulator can acquire temporal non-uniformity. We study the effects of the electron bunch initial energy profile on the FEL performance.

## VLASOV-MAXWELL ANALYSIS FOR AN INITIAL VALUE PROBLEM

The photoinjector generated electron bunch has a very small energy spread and small emittance. During the acceleration, bunch compression, and transportation, the electron bunch can acquire RF curvature, second order effect in the chicane, and collective effects, which will all lead to energy profile to be nonuniform. Further more, the electron bunch is subject to microbunching instability [1]. Thus, the electron bunch coming into the undulator can have an energy modulation. We study the energy profile nonuniformity on the free electron laser (FEL).

To analyze the start-up of a seeded FEL amplifier we use the coupled set of Vlasov and Maxwell equations which describe the evolution of the electrons and the radiation fields [2]. This approach is used as well for the Self-Amplified Spontaneous Emission (SASE) FEL [3]. We will work with a one-dimensional system analytically.

### [illegible]

We follow the analysis and notation of Refs. [3, 4, 2]. Dimensionless variables are introduced as $Z = k_w z$, $\theta = (k_0 + k_w)z - \omega_0 t$, where $k_0 = 2\pi/\lambda_0$, $\omega_0 = k_0 c$, and $k_w = 2\pi/\lambda_w$ with $\lambda_0$ being the radiation wavelength, $\lambda_w$ being the undulator period, and $c$ being the speed of light in vacuum. We also introduce $p = 2(\gamma - \gamma_0)/\gamma_0$ as the measure of energy deviation, with $\gamma$ the Lorentz factor of an electron in the electron bunch, and $\gamma_0$ the resonant energy defined by $\lambda_0 = \lambda_w(1 + K^2/2)/(2\gamma_0^2)$, for a planar undulator, where the undulator parameter $K \approx 93.4 B_w \lambda_w$ with $B_w$ the peak magnetic field in Tesla and $\lambda$ the undulator period in meter. The electron distribution function is $\psi(\theta, p, Z)$ with $\psi_0(\theta, p, Z)$ describing the slow varying unperturbed component. The FEL electric field is written as $E(t, z) = A(\theta, Z)e^{i(\theta - Z)}$ with $A(\theta, Z)$ being the slow varying envelope function.

The one-dimensional linearized Vlasov-Maxwell equations are,

$$\frac{\partial \psi}{\partial Z} + p\frac{\partial \psi}{\partial \theta} - \frac{2D_2}{\gamma_0^2}\left(Ae^{i\theta} + A^* e^{-i\theta}\right)\frac{\partial \psi_0}{\partial p} = 0, \quad (1)$$

and,

$$\left(\frac{\partial}{\partial Z} + \frac{\partial}{\partial \theta}\right) A(\theta, Z) = \frac{D_1}{\gamma_0} e^{-i\theta} \int dp \psi(\theta, p, Z), \quad (2)$$

where in SI units, $D_1 = e a_w n_0 [JJ]/(2\sqrt{2} k_w \varepsilon_0)$, $D_2 = e a_w [JJ]/(\sqrt{2} k_w m c^2)$, with $e$ and $m$ being the charge and mass of the electron; $\varepsilon_0 \approx 8.85 \times 10^{-12}$ F/m being the vacuum permittivity; $n_0$ being the electron beam density; and $[JJ] = J_0[a_w^2/2(1 + a_w^2)] - J_1[a_w^2/2(1 + a_w^2)]$ where the dimensionless rms undulator parameter $a_w \equiv K/\sqrt{2}$. Equation (1) gives a general solution as

$$\begin{aligned} &\psi(\theta, Z, \gamma) \approx \psi_0(\theta - pZ, \gamma) \\ + \quad &\int_0^Z dZ' \frac{2D_2}{\gamma_0^2} A[\theta - p(Z - Z'), \gamma] e^{i[\theta - p(Z - Z')]} \\ \times \quad &\frac{\partial \psi_0[\theta - p(Z - Z'), \gamma]}{\partial p}. \end{aligned} \quad (3)$$

Plugging Eq. (3) into Eq. (2), we have

$$\begin{aligned} &\left(\frac{\partial}{\partial Z} + \frac{\partial}{\partial \theta}\right) A(\theta, Z) = \frac{D_1}{\gamma_0} e^{-i\theta} \int dp \psi_0(\theta - pZ, \gamma) \\ + \quad &(2\rho)^3 e^{-i\theta} \int dp \int_0^Z dZ' A[\theta - p(Z - Z'), \gamma] \\ \times \quad &e^{i[\theta - p(Z - Z')]} \frac{\partial \psi_0[\theta - p(Z - Z'), \gamma]}{\partial p}, \end{aligned} \quad (4)$$

with $(2\rho)^3 = (2D_1 D_2)/\gamma_0^3$, the Pierce parameter $\rho$ [5, 6].

### [illegible]

To model an energy imperfectness in the electron bunch coming into the undulator, we assume that the initial distribution function is

$$\psi_0 = \delta[p + g(\theta_0)] = \delta[p + g(\theta - pZ)], \quad (5)$$

where $g(\theta_0)$ is a general function.

* Work supported by the US DOE contract DE-AC02-76SF00515.
† jhwu@SLAC.Stanford.EDU

The Maxwell equation is further rewritten after performing a partial integral

$$\left(\frac{\partial}{\partial Z}+\frac{\partial}{\partial \theta}\right)A(\theta,Z)=\frac{D_1}{\gamma_0}\sum_j e^{-i\theta\ +ig(\theta\ )Z}\delta(\theta-\theta_j)$$
$$+i(2\rho)^3\int_0^Z dZ'(Z-Z')e^{ig(\theta)(Z-Z')}A(\theta,Z'),(6)$$

where the initial discrete radiators (electrons) are modeled as $\sum_j\delta(\theta-\theta_j)$ for the longitudinal coordinates.

To further work on Eq. (6), we now introduce the Laplace transform,

$$f(\theta,s)=\int_0^\infty dZe^{-sZ}A(\theta,Z). \qquad (7)$$

With this, Eq. (6) is now casted in the frequency domain as

$$\begin{aligned}\frac{\partial f(\theta,s)}{\partial\theta} &+ \left(s-\frac{i(2\rho)^3}{[s-ig(\theta)]^2}\right)f(\theta,s)\\ &= A(\theta,0)+\frac{D_1}{\gamma_0}\sum_j\frac{e^{-i\theta}\ \delta(\theta-\theta_j)}{s-ig(\theta_j)}, \qquad (8)\end{aligned}$$

which yields the general solution as

$$\begin{aligned}f(\theta,s)=&\int_{-\infty}^{\theta}d\theta' e^{-s(\theta-\theta')+\int_{\theta'}^{\theta}\frac{(2\rho)^3}{[\ -\ \ (\theta'')]^2}d\theta''}\\ &\times\left[A(\theta',0)+\frac{D_1}{\gamma_0}\sum_j\frac{e^{-i\theta}\ \delta(\theta'-\theta_j)}{s-ig(\theta_j)}\right]. \qquad (9)\end{aligned}$$

Notice that, in the square bracket in Eq. (9), the first term $A(\theta,0)$ characterizes the initial seed for a seeded FEL, while the second term models the Self-Amplified Spontaneous Emission (SASE) FEL. In the following, let us focus on a seeded FEL, so that the second term in the square bracket will be neglected.

**Initial Sinusoidal Energy Modulation** For electron bunch experienced microbunching instability, there can be an energy modulation as

$$\gamma=\gamma_0+\varepsilon_m\sin[\omega_m(t-t_0)], \qquad (10)$$

where $\omega_m$ characterizes the energy modulation. The initial distribution function is then

$$\Psi_0=\delta[p+\eta\sin(\omega_\eta\theta_0)], \qquad (11)$$

where $\eta\equiv 2\varepsilon_m/\gamma_0$ and $\omega_\eta\equiv\omega_m/\omega_0$. For such a sinusoidal modulation, we have

$$\begin{aligned}\int_{\theta'}^{\theta}\frac{i(2\rho)^3}{[s-i\eta\sin(\omega_\eta\theta'')]^2}d\theta''&\approx\frac{i(2\rho)^3(\theta-\theta')}{s^2}\\ +\quad\frac{2\eta(2\rho)^3\left[\cos(\omega_\eta\theta)-\cos(\omega_\eta\theta')\right]}{\omega_\eta s^3}&. \qquad (12)\end{aligned}$$

Up to this stage, let us throw away the SASE term, and keep only the seed in Eq. (9).

$$\begin{aligned}f(\theta,s)\approx&\int_{-\infty}^{\theta}d\theta' A(\theta',0) \qquad (13)\\ \times\quad& e^{-s(\theta-\theta')+\frac{(2\rho)^3(\theta-\theta')}{2}+\frac{2\eta(2\rho)^3\left[\cos(\omega_\eta\theta)-\cos(\omega_\eta\theta')\right]}{\omega_\eta\ ^3}}.\end{aligned}$$

The inverse Laplace transform then gives us the FEL field envelope as

$$\begin{aligned}A(\theta,Z)&=\int_c\frac{ds}{2\pi i}e^{sZ}f(\theta,s)\\ &\approx\int_c\frac{ds}{2\pi i}e^{sZ}\int_{-\infty}^{\theta}d\theta' A(\theta',0) \qquad (14)\\ &\times\quad e^{-s(\theta-\theta')+\frac{(2\rho)^3(\theta-\theta')}{2}+\frac{2\eta(2\rho)^3\left[\cos(\omega_\eta\theta)-\cos(\omega_\eta\theta')\right]}{\omega_\eta\ ^3}}.\end{aligned}$$

Obviously, once we know the initial seed field envelope $A(\theta,0)$, we can obtain the seeded FEL field envelope $A(\theta,Z)$ along the undulator.

The double integral in Eq. (14) can be evaluated by first performing the contour integral to get,

$$A(\theta,Z)=\int_0^\infty d\xi A(\theta-\xi,0)\,\mathcal{G}(\theta,\xi,Z,s,\eta), \qquad (15)$$

with the Green function $\mathcal{G}(\theta,\xi,Z,s,\eta)$ and the corresponding phasor $\mathcal{F}(\theta,\xi,Z,s,\eta)$ defined as

$$\begin{aligned}&\mathcal{G}(\theta,\xi,Z,s,\eta)\\ \equiv&\int_c\frac{ds}{2\pi i}e^{s(Z-\xi)+\frac{(2\rho)^3\xi}{2}+\frac{2\eta(2\rho)^3\left[\cos(\omega_\eta\theta)-\cos[\omega_\eta(\theta-\xi)]\right]}{\omega_\eta\ ^3}}\\ \equiv&\int_c\frac{ds}{2\pi i}\exp\left[\mathcal{F}(\theta,\xi,Z,s,\eta)\right]. \qquad (16)\end{aligned}$$

The Green function can be estimated by saddle point approximation. The saddle point $s_s$ is found from

$$\left.\frac{d\mathcal{F}(\theta,\xi,Z,s,\eta)}{ds}\right|_{s=s}=0, \qquad (17)$$

and the Green function is approximated as

$$\begin{aligned}\mathcal{G}(\theta,\xi,Z,s,\eta)\approx&\frac{\exp\left[\mathcal{F}(\theta,\xi,Z,s_s,\eta)\right]}{\left[2\pi\mathcal{F}''(\theta,\xi,Z,s_s,\eta)\right]^{1/2}} \qquad (18)\\ \simeq&\frac{-e^{i\pi/12}e^{i^{1/3}2\rho Z-\frac{1/3\,9(\theta-\ /3)^2\rho}{2}-\frac{2\eta\{\cos(\omega_\eta\theta)-\cos[\omega_\eta(\theta-\xi)]\}}{\omega_\eta}}}{\sqrt{2\pi Z/\rho}}.\end{aligned}$$

For an initial Gaussian seed,

$$\begin{aligned}&E(t,z=0)=E_0e^{-i\omega_0t-\alpha_0t^2}=E_0e^{i\theta-\theta^2\alpha_0/\omega_0^2}\\ \Longrightarrow\quad&A(\theta,0)=E_0e^{-\theta^2\alpha_0/\omega_0^2}, \qquad (19)\end{aligned}$$

where $\alpha_0=1/(4\sigma_{t0}^2)$ with $\sigma_{t0}$ being the initial seed rms pulse duration. According to Eq. (15), the FEL pulse is

$$A(\theta,Z)=E_0\frac{-e^{i\pi/12}}{\sqrt{2\pi Z/\rho}}e^{i^{1/3}2\rho Z-\frac{1/3\,9(\theta-\ /3)^2\rho}{2}-\frac{2\eta\cos(\omega_\eta\theta)}{\omega_\eta}}$$

$$
\begin{aligned}
&\times \quad \int_{-\infty}^{\theta} d\theta' e^{-\frac{\theta'^2 \alpha_0}{\omega_0^2}+\frac{2\eta\cos(\omega_\eta\theta')}{\omega_\eta}} \\
&\approx \quad E_0\omega_0 \frac{-e^{i\pi/12}}{\sqrt{2\alpha_0 Z/\rho}}\left(1+\frac{i2\eta}{\omega_\eta}e^{-\frac{\omega_0^2\omega_\eta^2}{4\alpha_0}}\right) \\
&\times \quad e^{i^{1/3}2\rho Z-\frac{1/3\,9(\theta- \quad /3)^2\rho}{2}-\frac{2\eta\cos(\omega_\eta\theta)}{\omega_\eta}}. \qquad (20)
\end{aligned}
$$

It is interesting to find that to the first order in $\eta$, in the exponential function, the microbunching energy modulation only leads to a pure phase modulation, but does not affect the power, except the small correction term $(i2\eta/\omega_\eta)\exp[-\omega_0^2\omega_\eta^2/(4\alpha_0)]$ in front of the exponential function.

**Bandwidth** As we find above, the first order correction is a pure phase modulation, we would like to investigate this phase modulation on the FEL coherence. Recall that, one of the most important purposes of a seeded FEL is to generate transform limited light, let us now find the FEL spectrum:

$$
\tilde{E}(\omega,z) \equiv \frac{1}{\sqrt{2\pi}}\int dt E(t,z)e^{i\omega t}. \qquad (21)
$$

Notice that $E(t,z) \sim e^{-i\omega_0 t}$, hence the Fourier transform is defined as in Eq. (21).

First, we rewrite $E(t,z)$ to have $t$-dependence explicit, ,

$$
\begin{aligned}
E(t,z) \quad &\approx \quad E_0\omega_0\frac{-e^{i\pi/12}}{\sqrt{2\alpha_0 Z/\rho}}\left(1+\frac{i2\eta}{\omega_\eta}e^{-\frac{\omega_0^2\omega_\eta^2}{4\alpha_0}}\right) \\
&\times \quad e^{ik_0 Z/k \quad -6i^{1/3}k_0\rho Z/k \quad -9i^{1/3}k_0^2\rho Z/(2k^2 \ )} \\
&\times \quad e^{[9i^{1/3}\rho\omega_0/(v \ \ k \ \ )-i]\omega_0 t-9i^{1/3}\rho\omega_0^2 t^2/(2Z)} \\
&\times \quad \left[1-\frac{i\eta}{\omega_\eta}\left(e^{i\omega_\eta\theta}+e^{-i\omega_\eta\theta}\right)\right] \\
&\equiv \quad \mathcal{A}(z)e^{[9i^{1/3}\rho\omega_0/(v \ \ k \ \ )-i]\omega_0 t-9i^{1/3}\rho\omega_0^2 t^2/(2Z)} \\
&\times \quad \left[1-\frac{i\eta}{\omega_\eta}\left(e^{i\omega_\eta\theta}+e^{-i\omega_\eta\theta}\right)\right] \\
&\equiv \quad \mathcal{A}(z)e^{i^{1/3}\mathcal{B}z^2/v^2}e^{-i\omega_0 t-i^{1/3}\mathcal{B}(t-z/v \ \ )^2} \\
&\times \quad \left[1-\frac{i\eta}{\omega_\eta}\left(e^{i\omega_\eta\theta}+e^{-i\omega_\eta\theta}\right)\right], \qquad (22)
\end{aligned}
$$

where $v_g = \omega_0/(k_0+2k_w/3)$.

Completing the integral in Eq. (21), we have

$$
\begin{aligned}
\tilde{E}(\omega,z) &= \frac{\mathcal{A}(z)}{\sqrt{2\mathcal{B}i^{1/3}}}e^{\frac{\ \ 5/3\left[(\omega-\omega_0)-\frac{2 \ \ 4/3\mathcal{B}}{\quad}\right]^2}{4\mathcal{B}}} \\
\times &\quad \left\{1-\frac{i\eta}{\omega_\eta}e^{i^{5/3}\omega_0^2\omega_\eta^2/(4\mathcal{B})}\right. \qquad (23) \\
\times &\quad \left[e^{iz(k_0+k \ \ -\omega_0/v \ \ )\omega_\eta-i^{5/3}(\omega-\omega_0)\omega_0\omega_\eta/(2\mathcal{B})}\right. \\
+ &\quad \left.\left. e^{-iz(k_0+k \ \ -\omega_0/v \ \ )\omega_\eta+i^{5/3}(\omega-\omega_0)\omega_0\omega_\eta/(2\mathcal{B})}\right]\right\}.
\end{aligned}
$$

The FEL energy density is then $\mathcal{I}(\omega,z) \equiv \tilde{E}(\omega,z)\tilde{E}^*(\omega,z)$, where $\tilde{E}^*(\omega,z)$ is the complex conjugate of $\tilde{E}(\omega,z)$.

We can then compute

$$
\begin{aligned}
\langle\omega(z)\rangle &\equiv \frac{\int\omega\mathcal{I}(\omega,z)}{\int\mathcal{I}(\omega,z)} \qquad (24) \\
&\approx \omega_0\{1+2\eta e^{-\frac{\omega_0^2\omega_\eta^2}{4\sqrt{3}\mathcal{B}}}\sin[(k_0+k_w-\omega_0/v_g)\omega_\eta z]\}.
\end{aligned}
$$

Likewise, the standard deviation is

$$
\begin{aligned}
\sigma_\omega(z) &\equiv \sqrt{\frac{\int\omega^2\mathcal{I}(\omega,z)}{\int\mathcal{I}(\omega,z)}-(\langle\omega(z)\rangle)^2} \\
&\approx \frac{2\mathcal{B}-\eta\omega_0^2\omega_\eta e^{-\frac{\omega_0^2\omega_\eta^2}{4\sqrt{3}\mathcal{B}}}\cos[(k_0+k_w-\omega_0/v_g)\omega_\eta z]}{\sqrt{2\sqrt{3}\mathcal{B}}} \\
&\equiv \frac{2\mathcal{B}-\mathcal{C}\cos[(k_0+k_w-\omega_0/v_g)\omega_\eta z]}{\sqrt{2\sqrt{3}\mathcal{B}}} \\
&\equiv \frac{2\mathcal{B}+\mathcal{D}}{\sqrt{2\sqrt{3}\mathcal{B}}}. \qquad (25)
\end{aligned}
$$

Notice that, for $\eta = 0$, $\sigma_\omega(z) = \sqrt{3\sqrt{3}\rho\omega_0^2/(k_w z)}$ is the well-known rms bandwidth of the FEL Green function for a coasting electron beam [3, 7, 8].

To be explicit, we have

$$
\frac{\mathcal{C}}{2\mathcal{B}} = \frac{\eta\omega_\eta k_w z}{9\rho}e^{-\frac{\omega_\eta^2}{18\sqrt{3}\rho}}. \qquad (26)
$$

Recall that $\omega_\eta = \omega_m/\omega_0$, the ratio of the microbunching frequency to the FEL frequency, the most serious degradation will be at the first stage, where the FEL frequency is the lowest. Also, due to the $n^2$ amplification, the first stage is always the most serious stage. Also notice that, the ratio in Eq. (26) is maximum at $z = 18\sqrt{3}\rho/(k_w\omega_\eta^2)$.

As an conclusion, in this paper, we study the effect on a seeded FEL performance due to an initial energy non-uniformity when the electron bunch enters the undulator.

## REFERENCES


[1] Z. Huang, J. Wu, and T. Shaftan, ICFA Beam Dynamics Newslett, Vol.38, p.37-51, 2005.

[2] J. Wu, J.B. Murphy, P.J. Emma, X. Wang, T. Watanabe, and X. Zhong, J. Opt. Soc. Am. B **24**, 484 (2007)

[3] J.-M. Wang and L.-H. Yu, Nuc. Instrum. and Methods in Physics Research A **250**, 484 (1986).

[4] S. Krinsky and Z. Huang, Phys. Rev. ST Accel. Beams **6**, 050702 (2003).

[5] R. Bonifacio, C. Pellegrini, and L.M. Narducci, Opt. Commun., **50**, 373 (1984).

[6] J.B. Murphy, C. Pellegrini, and R. Bonifacio, Opt. Commun. **53**, 197 (1985).

[7] K.J. Kim, Nuc. Instrum. and Methods in Physics Research A **250**, 396-403 (1986).

[8] K.J. Kim, Phys. Rev. Lett. **57**, 1871-1874 (1986).

# DESIGN AND OPTIMIZATION OF ELECTRON BUNCH ACCELERATION AND COMPRESSION*

Juhao Wu†, Paul J. Emma, SLAC, Menlo Park, CA 94025, USA,
Robert A. Bosch, Kevin J. Kleman,
Synchrotron Radiation Center, University of Wisconsin – Madison, Stoughton, WI 53589, USA

*Abstract*

For electron bunches driving a hard x-ray free electron laser, the electron bunch high qualities should be preserved as well as possible in the acceleration and compression. For typical configuration, the electron bunch is accelerated in RF cavity and compressed in magnetic chicane. Besides the RF curvature and high-order optics terms in a chicane, the collective effects during the bunch acceleration, transportation, and compression can further distort the phase space. Among these collective effects, the coherent edge radiation dominates and governs the macroscopic bunch property. We study these effects and discuss their implication to general LINAC design and optimization.

## TWO-STAGE LINAC BUNCH COMPRESSOR SYSTEM

After the electron bunch born from the cathode, it is accelerated and compressed by bunch compressors to achieve high peak current for x-ray free electron laser (FEL) [1]. Typically, there are two bunch compressor chicanes to achieve good stability. In the following, we will use BC1 to stand for the first chicane, and BC2 for the second. The accelerator RF waveform introduces RF curvature on a finite electron bunch, which needs a harmonic cavity to linearize the longitudinal phase space. The bunch compressor also introduces second order effect. Besides, the collective effects: geometric wakefield in LINAC, and coherent radiation wakefield in a bunch compressor will also affect the bunch compression. Recently, it was identified that the coherent edge radiation (CER) is the main source of impedance to govern the electron bunch macroscopic properties [2]. To illustrate the related concepts for RF acceleration and bunch compression, we first show some details of one stage of acceleration and bunch compression.

The electron beam is first accelerated, hence $E(z_0) = E_0(1+\delta_0) + eV\cos[\varphi + kz_0]$, where $z_0$ is the longitudinal coordinate of a certain electron with respect to the reference electron, $z_0 < 0$ is in the head, and $z_0 > 0$ is in the tail; $k = 2\pi/\lambda$ is the RF wavenumber for a wavelength of $\lambda$. We define the energy of the reference electron as $E_1 = E_0 + eV\cos[\varphi]$, so that the relative energy deviation of the electron with longitudinal coordinate $z_0$ is

$$\begin{aligned}\delta &\approx \frac{E_0}{E_1}\delta_0 - \frac{2\pi eV\sin\varphi}{\lambda E_1}z_0 - \frac{2\pi^2 eV\cos\varphi}{\lambda^2 E_1}z_0^2 \\ &\equiv \mathcal{A}\delta_0 - \mathcal{B}z_0 - \mathcal{C}z_0^2. \end{aligned} \tag{1}$$

Now, the beam is chirped and sent through the chicane. In the thin lens approximation, the path length difference after the chicane reads $\Delta s \sim [\theta_0/(1+\delta)]^2 L_2$, where $L_2$ is half of the drift distance for a symmetric chicane, and $\theta_0$ is the bending angle. Hence, after the chicane, the particle internal coordinate reads

$$z = z_0 + \delta(R_{56} + T_{566}\delta), \tag{2}$$

where in the thin lens approximation, $T_{566} = -3R_{56}/2$. In a 4-dipole (or 3-dipole) magnetic chicane, the high energy particle travels a short path, hence for compression, the tail particles should have higher energy than that of the head particles. For convention of the tail with coordinate $z$ larger than that of the head, this means that the chirp slope $-\mathcal{B} > 0$, so that $R_{56} < 0$.

To find the bunch length after the chicane, we plug Eq. (1) into Eq. (2) to get

$$z \approx \mathcal{A}R_{56}\delta_0 + (1 - \mathcal{B}R_{56})z_0 + (\mathcal{B}^2 T_{566} - \mathcal{C}R_{56})z_0^2. \tag{3}$$

Assuming a longitudinal uniform beam, we have

$$\begin{aligned}\sigma_z^2 \approx \left(\frac{E_0}{E_1}\right)^2 R_{56}^2\sigma_{\delta_0}^2 + \Bigg[\left(1 - \frac{2\pi R_{56}eV\sin\varphi}{\lambda E_1}\right)^2 \quad (4)\\ + \left(\frac{6\pi^2 R_{56}eV}{\sqrt{5}\lambda^2 E_1}\right)^2\left(\frac{2T_{566}eV\sin^2\varphi}{R_{56}E_1} - \cos\varphi\right)^2\sigma_{z_0}^2\Bigg]\sigma_{z_0}^2,\end{aligned}$$

where $\langle z_0^4\rangle = (9/5)\sigma_{z_0}^4$. Seen in Eq. (4), even if we choose a right $R_{56}$ to minimize the bunch length according to the term quadratic in $\sigma_{z_0}$, the term quartic in $\sigma_{z_0}$ will change the bunch length. This is brought up by the RF curvature. To remove the RF curvature effect, for LINAC Coherent Light Source (LCLS) setting, we install a X-band cavity, which is operated at the $4^{th}$ harmonic of the other S-band cavities. After L0- and L1- and the LX-linac, the energy of the electron reads

$$\begin{aligned} E &= E_0(1+\delta_0) + eV_0\cos[\varphi_0 + kz_0] \\ &+ eV_1\cos[\varphi_1 + kz_0] + eV_x\cos[\varphi_x + k_x z_0]. \end{aligned} \tag{5}$$

This leads to

$$\delta \equiv \frac{E - E_2}{E_2} \approx \mathcal{D}\delta_0 + \mathcal{E}z_0 + \mathcal{F}z_0^2 + \mathcal{G}z_0^3, \quad \text{where} \tag{6}$$

$$E_2 = E_0 + eV_0\cos(\varphi_0) + eV_1\cos(\varphi_1) + eV_x\cos(\varphi_x), \tag{7}$$

$$\mathcal{E} = -\frac{e}{E_2}[kV_0\sin(\varphi_0) + kV_1\sin(\varphi_1) + k_xV_x\sin(\varphi_x)], \tag{8}$$

$$\mathcal{F} = -\frac{e[k^2V_0\cos(\varphi_0) + k^2V_1\cos(\varphi_1) + k_x^2V_x\cos(\varphi_x)]}{2E_2}, \tag{9}$$

* Work supported by the US DOE contract DE-AC02-76SF00515.
† jhwu@SLAC.Stanford.EDU

and $\mathcal{D} = E_0/E_2$. Now, plug Eq. (6) into Eq. (2), we have

$$z = (1 + \mathcal{E}R_{56})z_0 + (\mathcal{F}R_{56} + \mathcal{E}^2 T_{566})z_0^2. \qquad (10)$$

In principle, there should be multiple solutions for $V_x$ and $\varphi_x$ to set the term $\propto z_0^2$ to zero.

## COLLECTIVE EFFECT

In above, we illustrate the design concepts with emphasis on the RF curvature and second order effect in the chicane. Besides, the collective effects have to be considered, *i.e.*, the LINAC geometric wakefield, the coherent synchrotron radiation (CSR) and the coherent edge radiation (CER) in a chicane, and space charge effect [2]. It was identified that CER is the dominating effect governing the electron bunch macroscopic properties [2]. In the following, we will discuss the geometric wakefield and the CER.

### *RF LINAC Geometric Wakefield: Longitudinal Double-horn Distribution*

For LCLS Linac, the wakefield is approximated as [3]

$$w(z) = \frac{Z_0 c}{\pi a^2} e^{-\sqrt{z/s_0}} \qquad (11)$$

where $s_0$ is a characteristic length, and $a$ is the iris radius; radius. For S-band SLAC cavity, $s_0 = 1.32$ mm, and $a = 11.6$ mm and for X-band, $s_0 = 0.77$ mm, and $a = 4.72$ mm. The wakefield given in Eq. (11) is in units of $V/c/m$. The induced voltage along the bunch is $V(z) = -NeL\int_{-\infty}^{z} w(z-z')f(z')dz'$, where $L$ is Linac length, $N$ is the bunching electron population, and $e$ is the charge of the electron.

The double-horn structure is originated from the cubic term in the $\delta$-$z$ plot. It is easy to check that, for LCLS design parameters, the RF waveform induced cubic term is small, while the wakefield combined with the parabolic distribution leads to the cubic term. The normalized parabolic distribution function reads $f(z) = 3/(4\sqrt{5}\sigma_z)[1 - z^2/(5\sigma_z^2)]$, where $\sigma_z$ is the rms bunch length. Given this parabolic distribution, and the wake Green function in Eq. (11), the wakefield induced voltage along the bunch is

$$\begin{aligned} V_{w,2}(z) = \mathcal{H}\Big\{&\Big[8\left(15 + 15\sqrt{\eta} + 6\eta + \eta^{3/2}\right)e^{-\sqrt{\eta}} \\ -\;& (120 - 12\eta + \eta^2)\Big]\, s_0 \\ +\;& 2\sqrt{5}\left[2\left(3 + 3\sqrt{\eta} + \eta\right)e^{-\sqrt{\eta}} + (\eta - 6)\right]\sigma_z\Big\}, \\ \equiv\;& \mathcal{H}\bar{V}_{w,2}(z) \end{aligned} \qquad (12)$$

where $\mathcal{H} = -(3NeLZ_0cs_0^2)/(10\sqrt{5}\pi a^2\sigma_z^3)$, and $\eta = z/s_0$. Note that $z \in (0, \Delta z \equiv 2\sqrt{5}\sigma_z)$. Hence after L2, the acceleration together with the wakefield gives

$$\begin{aligned} E_2(z) &= E_1 + eV_2\cos\left(\varphi_2 + \frac{2\pi z}{\lambda_2}\right) + eV_{w,2}\left(z + \frac{\Delta z}{2}\right) \\ &= eV_2\left[E_{r,1} + \cos(\varphi_2 + k_2 z) + \epsilon\bar{V}_{w,2}\left(z + \frac{\Delta z}{2}\right)\right], \end{aligned} \qquad (13)$$

where $E_{r,1} = E_1/(eV_2)$, $k_2 = 2\pi/\lambda_2$, and $\epsilon = e\mathcal{H}/(eV_2)$. We have assumed that $E_1$ is a constant due to the large acceleration in L2. Also, we have shifted the definition domain so that $z \in (-\Delta z/2, \Delta z/2)$.

Now, BC2 gives the following transformation $E \to E$ and $z \to z + R_{56,2}(E - E_2(0))/E_2(0)$. Assume that the intrinsic energy spread is extremely small, the longitudinal phase space distribution before BC2 is

$$f(z,E) = \frac{3}{4\sqrt{5}\sigma_z}\left(1 - \frac{z^2}{5\sigma_z^2}\right)\delta\left[E - E_2(z)\right]. \qquad (14)$$

After BC2, the distribution function is transformed into

$$\begin{aligned} f(z,E) &= \frac{3}{4\sqrt{5}\sigma_z}\left\{1 - \frac{\left[z - R_{56,2}\frac{E-E_2(0)}{E_2(0)}\right]^2}{5\sigma_z^2}\right\} \\ \times\quad & \delta\left[E - E_2\left(z - R_{56,2}\frac{E - E_2(0)}{E_2(0)}\right)\right] \end{aligned} \qquad (15)$$

Integrating out the energy, the final distribution function is

$$f(z) = \frac{\frac{3}{4\sqrt{5}\sigma}\left\{1 - \frac{\left[z - R_{56,2}\frac{(\;)-\;_2(0)}{_2(0)}\right]^2}{5\sigma^2}\right\}}{\left|\frac{\partial g(z,E)}{\partial E}\right|_{E=E\;(z)}} \qquad (16)$$

where $E_s(z)$ is determined by $g[z, E_s(z)] = 0$, with

$$\begin{aligned} g(z,E) &\equiv E - E_1 \\ -\quad & eV_2\cos\left(\varphi_2 + k_2\left[z - R_{56,2}\frac{E - E_2(0)}{E_2(0)}\right]\right) \\ -\quad & eV_{w,2}\left[z - R_{56,2}\frac{E - E_2(0)}{E_2(0)} + \frac{\Delta z}{2}\right]. \end{aligned} \qquad (17)$$

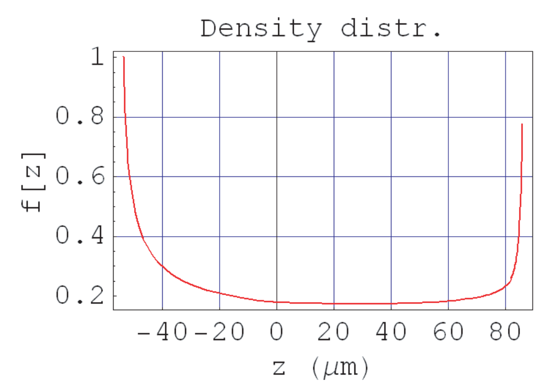


Figure 1: Double-horn structure in current profile.

With the nominal parameters [1], the longitudinal current profile after BC2 is double-horn as in Fig. 1.

### *CSR and CER Effect*

We assume that the initial electron bunch distribution before BC1 is a linearly energy chirped bunch

$$f_0(z,\delta) = \frac{1}{\sqrt{2\pi}\sigma_{z_0}}e^{-\frac{2}{2\sigma^2\;_0}}\frac{1}{\sqrt{2\pi}\sigma_{\delta_0}}e^{-\frac{(\delta-\;_1\;)^2}{2\sigma_{\delta_0}^2}}, \qquad (18)$$

where $\sigma_{z_0}$ and $\sigma_{\delta_0}$ are the electron rms bunch length and rms energy spread, respectively. The first bunch compressor BC1 then introduce a transformation as $z \to z+R_{56,1}\delta$, which leads to $\sigma_{z_1} = \sqrt{(1-h_1R_{56,1})^2\sigma_{z_0}^2 + R_{56,1}^2\sigma_{\delta_0}^2}$ and $\sigma_{\delta_1} = \sqrt{h_1^2\sigma_{z_0}^2 + \sigma_{\delta_0}^2}$. The current profile is simply $I_1(z) = ecN/(\sqrt{2\pi}\sigma_{z_1})e^{-z^2/(2\sigma^2{}_1)}$, where $e$ is the electron charge, $N$ is the number of electrons in the bunch, and $c$ is the speed of light in vaccum.

Downstream of the BC1 magnet, the wake primarily results from CER. For $k > 0$, the integrated resistive CER impedance in a drift space of length $L_d$ is modeled as [2]

$$\int Z_{\mathrm{CER}}(k) = \frac{Z_0}{2\pi}\ln\left\{\frac{\min[L_d, \lambda\gamma^2/(2\pi)]}{\rho^{2/3}\lambda^{1/3}}\right\} \equiv \mathcal{Z}_{\mathrm{CER}}, \quad (19)$$

for wavelengths where the right-hand side (rhs) of Eq. (19) is positive. For typical chicane parameters ($\gamma \sim 1000$, $\rho \sim 1$ m, $\lambda/(2\pi) \sim \sigma_z \sim 100$ $\mu$m, $L_d \sim 10$ m), the integrated CER impedance is $\sim Z_0$. Due to the weak logarithmic dependence in Eq. (19), an integrated impedance of $\sim Z_0$ might be a good approximation for a wide range of parameters. The voltage induced along the electron bunch is then $V_1(z) = \mathcal{Z}_{\mathrm{CER},1}I_1(z)$. This leads to a relative energy deviation of

$$\frac{eV_1(z)}{E_2} = \frac{e\mathcal{Z}_{\mathrm{CER},1}}{E_2}I_1(z) \equiv \varepsilon_1 e^{-z^2/(2\sigma^2{}_1)}, \quad (20)$$

where $E_2$ is the electron nominal energy at the entrance of BC2, and

$$\varepsilon_1 = \frac{e^2cN\mathcal{Z}_{\mathrm{CER},1}}{\sqrt{2\pi}\sigma_{z_1}E_2}. \quad (21)$$

For the LCLS low charge operation mode, the charge is 250 pC, $\sigma_{z_1} = 100$ $\mu$m, $E_2 = 4.3$ GeV, and $\mathcal{Z}_{\mathrm{CER},1} \sim Z_0$, we have $\varepsilon_1 \approx 2.6 \times 10^{-5}$.

Assuming that the electron bunch acquires additional linear chirp in the LINAC between BC1 and BC2, the total linear chirp on the electron bunch is then $h_2$. The electron bunch distribution function at the entrance of BC2 is

$$\begin{aligned} f_{1,2}(z,\delta) &\approx \frac{e^{-\frac{2}{2\sigma^2{}_1}-\left[\delta-h_2z-\varepsilon_1 e^{-\ {}^2/(2\sigma^2{}_1)}\right]^2/(2\sigma_{\delta_1}^2)}}{2\pi\sigma_{z_1}\sigma_{\delta_1}} \\ &\approx \frac{e^{-\frac{2}{2\sigma^2{}_1}}}{\sqrt{2\pi}\sigma_{z_1}}\delta_D\left[\delta - h_2z - \varepsilon_1 e^{-\frac{2}{2\sigma^2{}_1}}\right], \quad (22) \end{aligned}$$

where $\delta_D(x)$ is the Dirac Delta-function.

The electron bunch is then transport through BC2, *i.e.*, $z \to z + R_{56,2}\delta$. Integrated out $\delta$, we have the current profile as

$$I_2(z) = \frac{ecN}{\sqrt{2\pi}\sigma_{z_2}}e^{-\frac{2}{2\sigma^2{}_2}}\left[1-\varepsilon_1\frac{2R_{56,2}z}{\sigma_{z_2}^2}e^{-\frac{2}{2\sigma^2{}_2}}\right], \quad (23)$$

where $\sigma_{z_2} = \sigma_{z_1}/\mathcal{C}_2$, with $\mathcal{C}_2 \equiv (1-h_2R_{56,2})^{-1}$ being the compression factor in BC2. According to Eq. (23), the electron current profile will be enhanced at the head or the tail when $2\varepsilon_1R_{56,2}/\sigma_{z_2}$ is not negligibly small. Since the quantity $\varepsilon_1$ in Eq. (21) is positively defined, the current will be enhanced at the tail of the electron bunch. For typical machine design as for WiFEL [2], this CER wakefield can cause a distortion of the longitudinal current profile as in Fig. 2, leading to an asymmetric distribution.

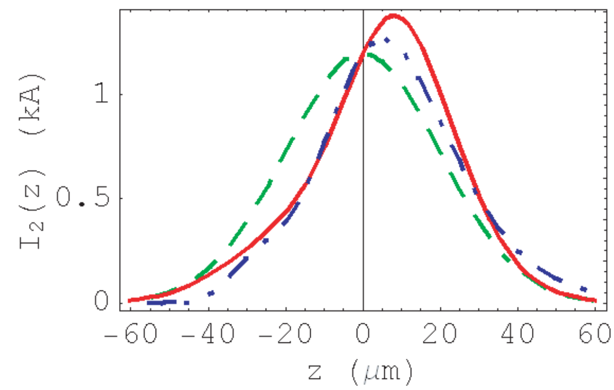


Figure 2: Illustration of the CER wakefield effect on the longitudinal current profile. The ideal case without CER effect is shown as dashed green curve, the case with the CER effect is shown as the red solid curve, and the case with the CER and also a second order curvature is shown as the blue dot-dashed curve.

To reduce the effect of the CER wakefield, we can deliberately mismatch the harmonic cavity to have some residual second order RF curvature before entering the BC1. This is to modify the distribution function in Eq. (22) to be

$$f_{1,2,m}(z,\delta) \approx \frac{e^{-\frac{2}{2\sigma^2{}_1}}}{\sqrt{2\pi}\sigma_{z_1}}\delta_D\left[\delta - h_2z - g_2z^2 - \varepsilon_1 e^{-\frac{2}{2\sigma^2{}_1}}\right], \quad (24)$$

where $g_2$ represents the residual second-order curvature effect. As an illustration, in Fig. 2, the blue dot-dashed curve is for $g_2 = -5 \times 10^4$ m$^{-2}$. One sees that the bunch profile can be restored to certain degree, but will lead to some ripple in the large $z$ head and tail region.

As an conclusion, in this paper, we discuss the key design issues for a two-stage acceleration and compression system for x-ray FEL. The emphasis is on the RF curvature cancelation, chicane second order effect, the LINAC geometric wake, and CSR/CER effect.

## REFERENCES

[1] P. Emma, in SLAC Report No. SLAC-R-593 (2002).

[2] R.A. Bosch, K. J. Kleman, and J. Wu, Phys. Rev. ST Accel. Beams, **11**, 090702 (2008).

[3] K. Bane, P. Wilson, Proceedings of the 11th Int. Conf. on High Energy Accelerators, CERN (Birkhuser Verlag, Basel, 1980), p. 592.

# DESIGN OF MICROWAVE UNDULATOR CAVITY*

Muralidhar Yeddulla, Sami Tantawi, SLAC, Menlo Park, CA 94061, USA


*Abstract*

Static magnetic field undulators are capable of producing quasi-monochromatic synchrotron radiation of very high brightness. However, it is not possible to quickly change the properties such as polarization of the radiation in a static undulator. It is possible to construct an undulator using microwaves instead of static magnets where the electron beam is undulated by both electric and magnetic fields of an rf wave. A major advantage with a microwave undulator is that the radiation properties can be changed very quickly. The biggest challenge in developing a microwave undulator is in keeping the rf losses low. We are designing a microwave undulator with the aim of achieving at least a tenth of the flux obtained by the BL13 static magnetic field Elliptical Polarized Undulator in the SPEAR ring. We have considered circular waveguide modes and hybrid $HE_{11}$ mode in a corrugated waveguide as possible candidates for the microwave undulator. It is found that a corrugated waveguide has the lowest rf losses with a very desirable field profile. It is also possible to use this device for a linac driven FEL. Our analysis of the corrugated waveguide cavity for the rf undulator will be presented.


## INTRODUCTION

In general, an undulator consists of a highly relativistic electron beam wiggled in the presence of a periodic undulating magnetic (or electromagnetic) fields producing synchrotron radiation. Highly successful modern undulator based synchrotron sources are based on periodic permanent magnetic fields. However, due to the intrinsic limitations of magneto static fields the polarization of the radiation fields and the undulator period cannot be controlled. These limitations can be overcome if high power rf waves are used instead of static magnetic fields in the undulator. However, the necessary rf power sources required to realize a microwave undulator capable of delivering synchrotron radiation comparable to a magneto static undulator was not available in the past. Recently a 500 MW X-band rf source was developed for the Next Linear Collider [2]. Combined with the advances in overmoded rf components and systems [3] led to the idea of the possibility of a practical rf undulator presented in this work. The same idea can be extended to LINAC driven rf FEL.

We are designing a microwave undulator for the SPEAR3 storage ring at SLAC. In a storage ring a static undulator would be *on* all the time giving rise to higher brightness. In order to be competitive, the microwave undulator we are designing should generate at least a tenth of circularly polarized radiation flux that can be generated by a static undulator. We have considered smooth wall circular waveguide structures operating in the $TE_{11}$ and $TE_{12}$ modes and a corrugated waveguide operating in the $HE_{11}$ - mode as possible candidates for the design of the undulator [4]. Our study has shown that the $HE_{11}$ - mode offers superior loss characteristics compared to other modes and can be operated at relatively lower power levels.

In order to generate the necessary field strength to undulate the 3 GeV electron beam in the storage ring, the rf power flow in the waveguide would be in the order of giga watts. To achieve such power levels rf energy can be stored inside a waveguide cavity to obtain the required levels of field strength by only compensating for the waveguide losses which can be within achievable power levels. It is a computationally intensive problem to design a corrugated waveguide cavity using numerical methods such as Finite Element Methods (FEM). As the corrugated waveguide can be regarded as a series of smooth cylindrical waveguides with discontinuities in radius, it can be analyzed using mode matching techniques that require moderate computational resources which is presented in this work.

## RADIATION IN A MICROWAVE UNDULATOR

In a Circularly Polarized Standing Wave (CPSW) microwave undulator, due to the fact that the rf energy is confined in a cavity, the electron beam interacts with both the forward and backward wave with respect to the electron motion inside the cavity. The transverse electron velocity (normalized to speed of light in free space) is given by [1],

$$\beta_x(z) + i\beta_y(z) = -\frac{K}{\gamma}\sum_{n=-\infty}^{\infty}\left[J_n(\delta) + J_{n+1}(\delta)\right] \cdot \exp\left\{i\left[k/\bar{\beta}_{||} + (2n+1)k_{||}\right]z\right\}, \tag{1}$$

where

$$\delta = \frac{K^2}{2\gamma^2}\frac{k}{k_{||}}, \tag{2}$$

$K = eE_w/m_0c^2k_{||}$ is the normalized amplitude of the rf wave, $E_w$ is the amplitude of the rf wave, $m_0$ is the mass of an electron, $c$ is the speed of light in free space, $\gamma$ is the relativistic factor, $k$ is free space wave number and $k_{||}$ is the axial wave number of the rf wave inside the waveguide.

From Eq. (1) we see that a CPSW microwave undulator, in general, is a combination of several harmonic motions and would radiate in several harmonics unlike a static

* Work supported by Department of Energy, USA

undulator. However, for a highly relativistic electron beam, such as one in the SPEAR3 ring, the value of $\delta$ (Eq. (2)) would be small when operated far from cutoff and higher order terms may be neglected and only $n = 0$ and $n = -1$ terms which are the contributions of the backward and forward wave respectively are dominant. If these conditions are not met, then the beam would radiate in higher harmonics also. Propagation far from cut-off necessitates the use of waveguide cavities with very large transverse dimensions. An advantage of large waveguide dimension is that the surface heat density will be low. However, a large waveguide will be highly overmoded and it will be challenging to excite only the required rf mode in it.

## CHOICE OF WAVEGUIDES AND MODES

The microwave undulator should have a very strong transverse field strength (both electric and magnetic) near the axis of the waveguide where the electron beam is placed to undulate the beam. At the same time the waveguide losses of the rf field should be low as the feasibility as well as cost of the rf source is critically dependent on keeping the waveguide losses low.

The microwave undulator we are designing is required to produce at least a tenth of radiation flux of the proposed BL13 static magnetic undulator. To be conservative we are designing the microwave undulator to produce a fifth of the radiation flux as the BL13 static undulator. A circular cylindrical waveguide operating in the $TE_{11}$ - mode, which is the easiest to excite, satisfies the condition that the field near the axis is strongest. For the undulator we are designing, the power loss per meter length of the waveguide for a $TE_{11}$ - mode is over 5 MW to produce a fifth of the radiation flux with a radiation energy of 700 eV of the BL13 static undulator [4]. A $TE_{12}$ - mode in a cylindrical waveguide has the same field structure near the axis of the waveguide as a $TE_{11}$ - mode. The loss per meter length of the waveguide for a $TE_{12}$ - mode would be 1.6 MW to produce the same radiation as a $TE_{11}$ - mode. We see that there is a significant reduction in waveguide loss if the undulator is operated in the $TE_{12}$ - mode instead of the $TE_{11}$ - mode.

We have also considered another waveguide structure and mode, a hybrid $HE_{11}$ - mode in a corrugated waveguide. This mode is typically used in transporting high power millimeter waves in applications such as Electron Cyclotron Resonance Heating in tokomaks due to their low attenuation characteristics. The corrugated waveguide is a cylindrical waveguide with periodic corrugations as shown in Fig. 1a. The $HE_{11}$ - mode which is a cylindrical waveguide $TM_{11}$ - mode (with $H_z = 0$) near cutoff undergoes a transformation due to the corrugations in the waveguide in to a rf field with both an electric and magnetic field ($E_z \neq 0, H_z \neq 0$)in the axial direction as we move away from the waveguide cutoff. Under conditions known as the "balanced hybrid conditions", when the axial electric field is equal to the axial magnetic field times free space

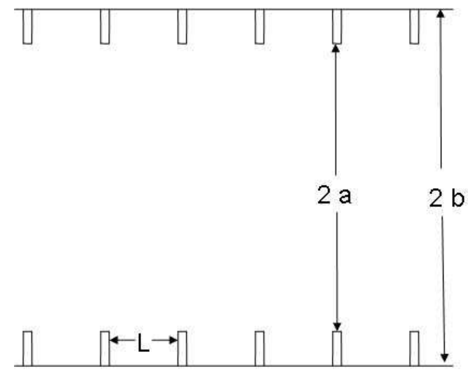


(a)

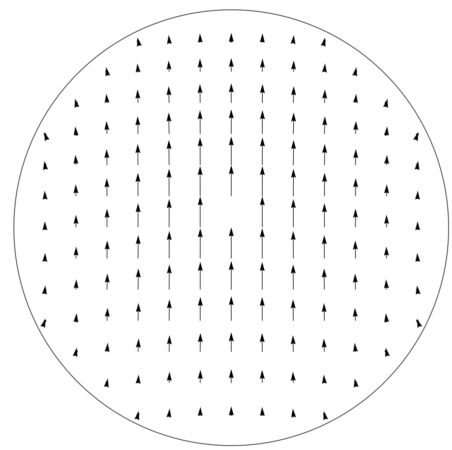

(b)

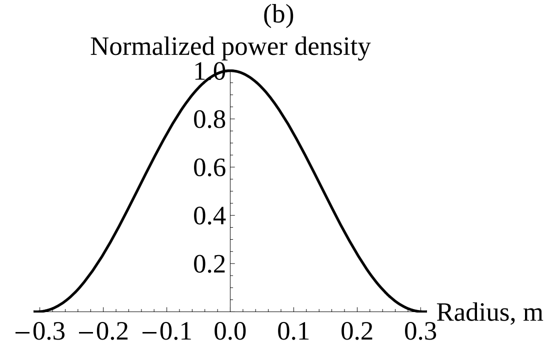


(c)

Figure 1: (a) Corrugated waveguide, (b) Cross section of transverse electric field in a $HE_{11}$ - mode in a corrugated waveguide under balanced hybrid conditions, (c) Normalized power density of a balanced hybrid $HE_{11}$ - mode.

impedance, the transverse electric field is strongly polarized as shown in Fig. 1b. Figure 1c shows the normalized power density as a function of radius over a cross section of the corrugated waveguide which approximates a gaussian curve under balanced hybrid conditions. As can be seen from Fig. 1c the power density is very low near the waveguide walls which lead to very low attenuation for this mode. As can be seen from Fig.1b the rf field is strongest near the axis of the corrugated waveguide as required for undulator operation. Another significant advantage of a $HE_{11}$ - mode in a corrugated waveguide over the $TE_{11}$ and $TE_{12}$ modes

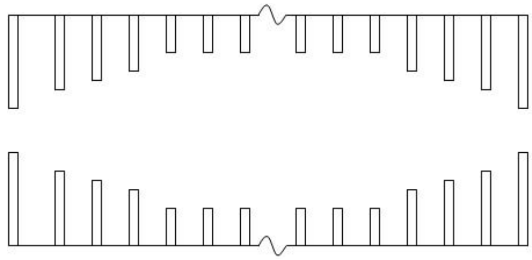

Figure 2: Schematic of a corrugated cavity with non uniform end corrugations for mode conversion and reflection of a $HE_{11}$ - mode.

in a smooth cylindrical waveguide is that the fields are very strongly polarized in one direction. Therefore, cross polarization in a $HE_{11}$ mode is very low.

## MODE MATCHING ANALYSIS OF A CORRUGATED WAVEGUIDE

To study the feasibility of using a corrugated waveguide working in the $HE_{11}$ - mode in a microwave undulator, we used boundary matching analysis of the corrugated waveguide neglecting space harmonics. This analysis was presented in [4] and verified with simulations in HFSS. Our studies show that a corrugated waveguide $HE_{11}$ - mode is a promising mode for the microwave undulator.

The foregoing analysis assumed that the corrugated waveguide is uniform and matched on both ends of the waveguide. However, we are designing a standing wave undulator in which the rf energy should be reflected at both ends of the corrugated waveguide cavity. Moreover, the cavity would include a mode converter in order to excite the $HE_{11}$ - mode. Hence, corrugations in the ends of the corrugated waveguide cavity will necessarily be not uniform. A rough schematic of how the corrugated waveguide cavity would be is shown in Fig. 2. Note that the end corrugations shown in Fig. 2 are only for illustration purposes to show the corrugation dimensions vary near the ends of the cavity and not necessarily how the final design would be.

The analysis and design of a corrugated waveguide cavity with a mode converter is a computationally intensive problem for numerical techniques such as FEM. The corrugated waveguide cavity can be treated as a series of uniform waveguides with discontinuities in wall radius at each corrugation. Therefore, the structure can be analyzed using Mode Matching (MM) techniques (for example see [5]) which can be much less computationally intensive than FEM techniques. Moreover, the MM techniques include space harmonics in the analysis making it more accurate than the analysis given in [4].

## RESULTS AND DISCUSSION

In [4] we have estimated that a corrugated waveguide with an outer radius of 34 cm and a corrugation depth of 3.4 cm gives the lowest waveguide loss for the undulator being designed. We have now developed a mode matching code to design the complete cavity including mode conversion from a mode in a smooth cylindrical waveguide to a $HE_{11}$ - mode. Figure 3 shows the dispersion curves for the $EH_{11}$, $HE_{11}$ and $EH_{12}$ modes for the above dimensions. Near cutoff, the $EH_{1n}$ - mode is the same as a $TE_{1n}$ - mode while a $HE_{1n}$ - mode is the same as a $TM_{1n}$ - mode in a circular cylindrical waveguide. Therefore, our approach to excite a $HE_{11}$ - mode in the corrugated waveguide is to transform a $TM_{11}$ - mode in a smooth cylindrical waveguide through a mode converter. At present we are in the process of designing such a mode converter by gradually tapering the corrugations from a smooth waveguide to the corrugation depth required. Results of the design will be published in a future work. After designing this mode converter, we will work on the excitation of a $TM_{11}$ - mode in a smooth cylindrical waveguide suitable for the microwave undulator we are designing. The design will also include reflection of this mode to confine the power inside the waveguide cavity.

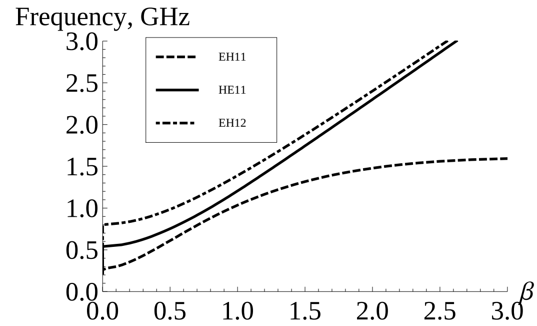


Figure 3: Dispersion curves calculated using mode matching method for a corrugated waveguide. $\beta$ is the product of the axial wave number and the pitch of corrugations.

## REFERENCES


[1] T. M. Tran, B. G. Danly et al. “Free electron lasers with electromagnetic standing wave wigglers”, IEEE Journal of Quantum Electronics. Vol. QE-23, NO. 9, pp. 1578-1589, 1987.

[2] Sami G. Tantawi, *et al*, “A high-power multi mode X-band rf pulse compression system for future linear colliders”, Physical Review Special Topics - Accelerators and Beams, 8, 042002, April 2005.

[3] Sami G. Tantawi, *et al*, “Evaluation of the $TE_{12}$ - mode in circular waveguide for low-loss high-power rf transmission,” Phys. Rev. ST Accel. Beams 3, 082001 (2000), pp. 21, Issue-8, August 2000.

[4] Muralidhar Yeddulla , Huiping Geng, Zhiyu Ma, Zhirong Huang, Sami Tantawi, “Waveguide Structures for RF Undulators with Applications to FELs and Storage Rings”, EPAC’08, Genoa, Italy, June 2008.

[5] Greame L. James, “Analysis and design of a $TE_{11}$ - to $HE_{11}$ corrugated cylindrical waveguide mode converters”, IEEE Transactions on microwave theory and techniques, Vol. MTT-29, No. 10, October 1981.

# STATUS OF THE NPS FREE-ELECTRON LASER*

J.W. Lewellen[#,1], W.B. Colson[1], S.P. Niles[1], T. Smith[1,2]
[1] Naval Postgraduate School, Monterey, CA 93943
[2] Stanford University, Stanford, CA 94305

*Abstract*

The Naval Postgraduate School (NPS) is in the process of designing and constructing a free-electron laser (FEL) laboratory to pursue FEL-related research and introduce students to modern accelerator and FEL technology. The laboratory will pursue research on high-brightness injectors, fundamental and applied beam dynamics, energy recovery linear accelerators, as well as FEL experiments.

The accelerator will be based around two, Stanford-Rossendorf type cryomodules, each of which houses two, 9-cell TESLA-type cavities. RF power will be provided by four, 10-kW CW L-band klystrons. With a nominal beam current of 1 mA, this provides an energy gain of 10 MV per structure. Intended operating modes include single-pass, energy recovery linac, and 2-pass microtron.

This paper provides an introduction to the NPS-FEL program goals, site and vault layout, and preliminary experimental plan.

## PROGRAM GOALS

The Naval Postgraduate School has committed to the construction and operation of a free-electron laser and accelerator physics laboratory, NPS-FEL.

One of the primary missions of the NPS-FEL will be student education. NPS grants Master's and Ph.D. degrees in a variety of disciplines, including physics, mechanical and electrical engineering. Accelerators by their nature require multidisciplinary efforts to construct, operate and characterize; thus, the NPS-FEL represents an opportunity for cross-disciplinary study and research.

The NPS-FEL experimental program is intended to address technical challenges relevant to next-generation accelerator, light source and FEL design, and study topics of fundamental interest in accelerator physics. There is, naturally, substantial overlap, such as beam merger design, coherent synchrotron radiation effects, beam halo formation, etc.

## FACILITY

### Location

The NPS-FEL laboratory will be located at an existing building at the Monterey Pines golf course, a Navy-owned facility adjacent to the NPS main campus (see Figure 1). The NPS-FEL laboratory building is one of several research buildings at Monterey Pines, including a jet-engine test laboratory, several wind tunnels, oceanographic laboratories, machine shops, and a flash X-ray facility.

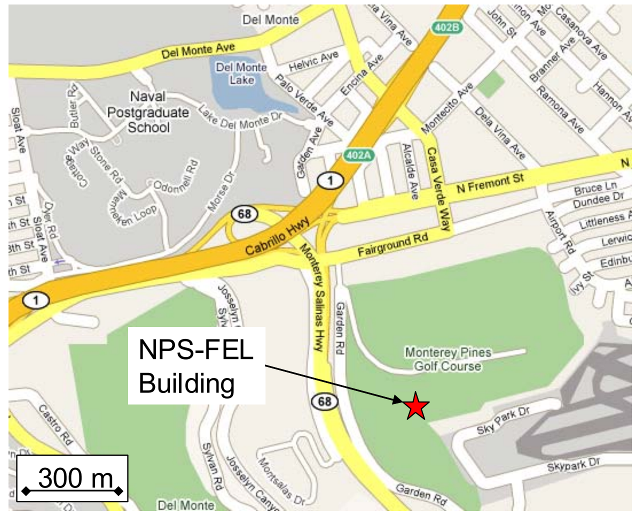


Figure 1: NPS-FEL facility location relative to the Naval Postgraduate School campus.

### Site Preparation

The laboratory building is a metal-frame structure with steel side-panel walls and a concrete slab foundation, which until recently served as a laboratory and repair bay for an autonomous underwater vehicle (AUV) research program. The AUV laboratory move was completed in June 2008.

Site preparation began in early 2008 with the installation of a new electrical substation near the building, capable of supplying an additional MW for power supplies, cryogenic systems, and RF power sources.

Renovation for the NPS-FEL will include addition of an on-grade radiation shield vault, replacement and insulation of the building skin, and reconstruction of the interior laboratory and office space.

### Interior Layout

The building is a rectangle approximately 40' (12.2 m) wide by 162' (49.4 m) long. There is a secondary pad to one side of the main foundation, approximately 22' (6.7 m) square, that will serve as a base for the eventual cryogenics plant.

The shield vault will take approximately half of the building, with the remaining half being dedicated to laboratory and office space. Figure 2 shows a conceptual sketch of the building layout; the vault design and interior space allocation have not been finalized as of this writing, however.

* Work supported by the Office of Naval Research and the Joint Technology Office for High-Energy Lasers
# jwlewell@nps.edu

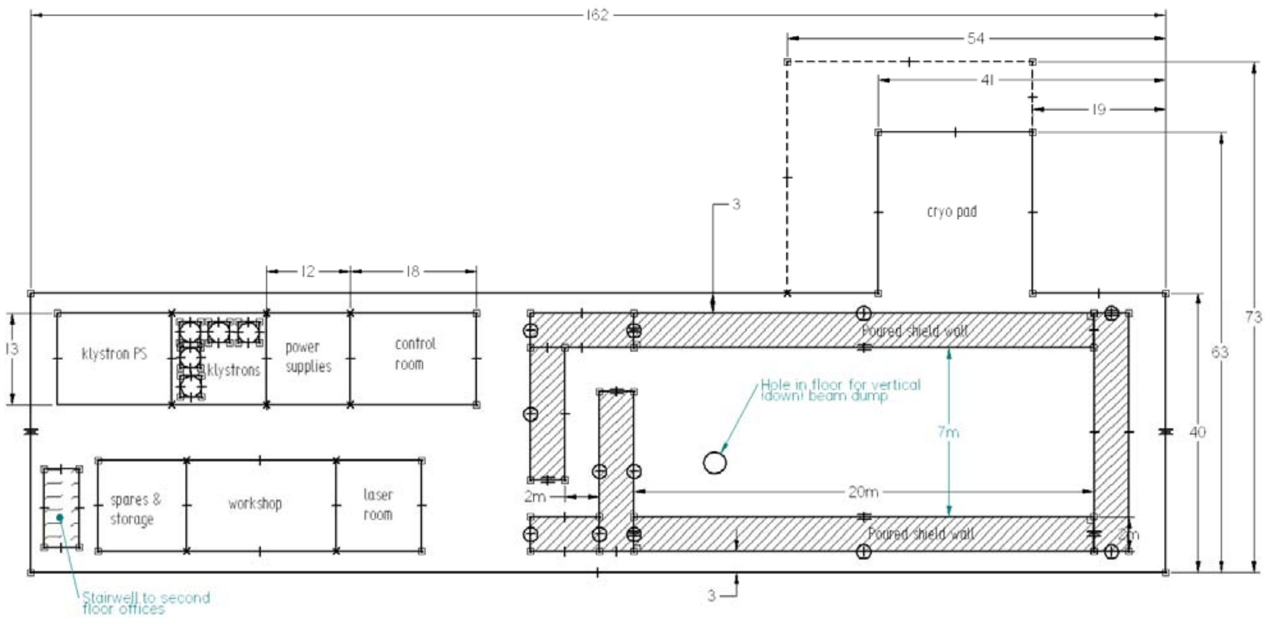


Figure 2: Preliminary layout of the NPS-FEL laboratory building. All dimensions without units are in feet.

### *Shield Design*

Based on the nominal RF power to be installed, and the capability of the structures to run CW, the maximum electron beam power will be 40 kW. The shield has been designed based on the assumption that, when operating at full beam power, transport losses are minimal and the beam is directed into a well-shielded beam dump. The design targets are for a maximum radiation level of less than 2 mRem / hour and less than 500 mRem / year [1] at the exterior of the shield vault at ground level.

Four beam loss scenarios were considered: a major beam excursion and total loss at maximum beam energy; halo effects during injector testing at low voltage; halo effects at full beam energy; and beam misalignment at full energy. The first scenario assumes the beam will be shut down within 200 µs of the excursion; the others assume CW operation. Beam loss monitors and radiation monitors will be included into the safety interlock system to force a shutdown should average current losses exceed acceptable limits, or external dose rates exceed the thresholds listed above.

The baseline shield design is for 3’ (0.9 m) thick walls, and a 2’ (0.61 m) thick ceiling, of normal-density concrete (approximately 2400 kg/m$^3$). The thinner ceiling shield allows equipment placement above the vault, but will not be occupied when the FEL is in operation.

The mass of the shield will require modifications to the building foundation. We are considering making the foundation capable of supporting 4’ (1.2 m) thick walls, but initially installing the planned 3’ thick walls. This will allow us to easily add supplemental shielding in the event beam losses are larger than anticipated, or to more readily accommodate a higher-average power machine in the future, should there be interest in doing so.

The interior vault dimensions are intended to accommodate several potential machine configurations. There is also the possibility of pursuing independent operation of two separate accelerator lines, or a dedicated injector test area.

## ACCELERATOR

The initial configuration for the NPS-FEL will be a traditional in-line arrangement, without energy recovery. This will allow commissioning of most major subsystems with minimal ambiguity and startup difficulties. It is also probably the most straightforward configuration to use when performing high-brightness injector testing.

### *Folded ERL*

The conceptual folded ERL arrangement is shown in Figure 3. The intent of the design is to minimize the length of the ERL, at the expense of the width. For wavelengths in the 1 – 10 µm range, this is a potential option for a more compact arrangement compared to more traditional designs.

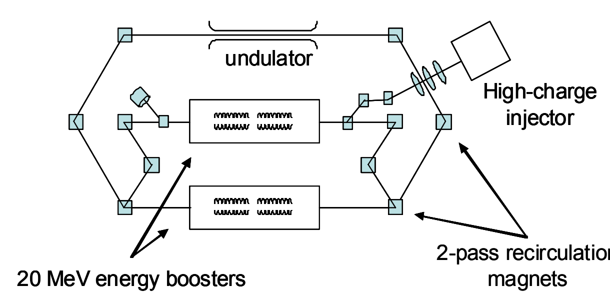


Figure 3: Conceptual layout of folded ERL.

The folded ERL configuration also presents many opportunities for studying effects such as coherent synchrotron radiation, beam merge, and optimal bunch compression methodology in compact FELs.

### *Injector System*

The initial injector for the NPS-FEL will be the 230-kV ($\beta \sim 0.75$) DC gun and subharmonic buncher, previously installed at the Superconducting Accelerator (SCA) at Stanford University [2].

As installed at Stanford, the SCA injector used a gridded thermionic cathode, and injected beam directly into one of the speed-of-light, 9-cell TESLA-type structures. Phase slip was significant and limited voltage gain through the first cavity.

The DC gun is presently being retrofitted to operate with a photothermal cathode [3] and will serve as a platform for initial experiments in a temporary facility until the NPS-FEL vault is completed.

Design has also begun on a 2-MV energy booster cavity. This will effectively eliminate the phase slippage, and will deliver a reasonable beam energy for ERL merger testing. A conceptual sketch of the injector layout is shown in Figure 4.

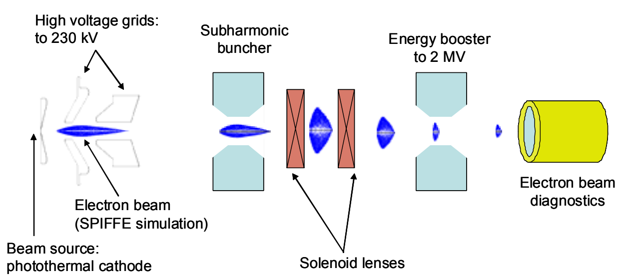


Figure 4: Conceptual layout of modified DC injector for the NPS-FEL.

Injector studies are expected to commence by the third quarter of 2008, focusing mainly on photothermal cathode performance and other cathodes of interest. The 2-MeV energy booster is expected to start testing in mid-2009.

## FREE-ELECTRON LASER

In both the in-line and folded-ERL configurations, the NPS accelerator will be used to drive a free-electron laser. In both cases the maximum beam energy will be approximately 40 MeV, with the initial FEL configuration as an oscillator.

The existing FIREFLY electromagnetic undulator has 25 periods, with a K-value of 1 and a 6-cm period [4]. The resulting optical radiation will be 9.5 μm, given a 40-MeV electron beam energy.

We would like to extend the FEL operation to shorter wavelengths, via the use of a shorter-period undulator. Also, exploration of novel undulator technology, such as solenoid-derived, variable-period undulators, is of interest [5]. Given an undulator period of 1 cm, and K-parameter of 0.7, wavelengths down to approximately 1 μm may be achievable. A fixed-period solenoid-derived unduator with these parameters [6] has already been used in a far-infrared FEL.

## CONCLUSIONS

Construction has started on the Naval Postgraduate School free-electron laser laboratory, NPS-FEL. The laboratory will be capable of hosting a 40-MeV, 40-kW electron accelerator in any of several configurations.

The initial injector for the NPS-FEL, a 230-kV DC gun, is being retrofitted to support photocathode operation. A 2-MeV energy booster is being designed and is expected to begin commissioning in mid-2009.

Lattice design for the NPS-FEL ERL configuration has begun, and will emphasize support for experiments on electron beam merger techniques, coherent synchrotron radiation, and other topics relevant to compact, high-power ERL design.

## ACKNOWLEDGEMENTS

A project of this magnitude is the work of many people, and properly listing our friends and colleagues who have helped and encouraged us this far would more than fill the paper. That being said, we would like to give special thanks to:

- David Douglas of Jefferson Laboratory, for inspiration and insight into lattice design; and
- President Daniel Oliver and Provost Leonard Ferrari of the Naval Postgraduate School, for their unswerving dedication and support for bringing an FEL to the School.

## REFERENCES

[1] NAVMED P-5055 chapter 6-2.
[2] Dee, for instance, T. I. Smith, "Development of the SCA/FEL for Use in Biomedical and Materials Science Experiments", Nucl. Instr. And Methods, A259 (1987) 1-7.
[3] Y.-E. Sun et.al., "Photothermal cathode measurements at the Advanced Photon Source," Proc. 2006 Lin. Acc. Conf., Knoxville, TN, USA (pp. 349-351).
[4] K.N. Ricci and T.I. Smith, "Longitudinal electron beam and free electron laser microbunch measurements using off-phase rf acceleration," Phys. Rev. ST – AB, vol. 3, 032801 (2000).
[5] G.K. Shenoy et.al., "Variable-period undulators as synchrotron radiation sources," J. Sunchrotron Rad (2003), **10**, 205-213.
[6] Y.C. Huang et.al., "A staggered-araray wiggler for far-infrared, free-electron laser operation," IEEE Journ. Quantum. Elect., vol. 30, no. 5, May 1994 (1289-94).

# EXPERIMENTAL CHARACTERIZATION AND OPTIMIZATION OF HIGH-BRIGHTNESS ELECTRON BEAM AT THE NSLS SDL

X. Yang, J. B. Murphy, H. Qian, S. Seletskiy, Y. Shen, and X. J. Wang,
National Synchrotron Light Source, BNL, Upton, NY 11973, U.S.A.

*Abstract*

The Source Development Laboratory (SDL) at the National Synchrotron Light Source (NSLS) is a laser linac facility dedicated for laser seeded FEL and beam physics R&D. The SDL consists of a RF synchronized Ti:sapphire laser, a BNL photocathode RF gun, a four-magnet chicane bunch compressor, and a 300 MeV linac. To further improve the performance of the laser seeded FEL at the NSLS SDL, we have carried out a systematic experimental characterization of the high-brightness electron beam generated by the photocathode RF gun. We will present the experimental studies of transverse emittance of electron beam as a function of RF gun phase and solenoid magnet for electron beam charge ranging from 350 pC to 1 nC.

## INTRODUCTION

Small transverse emittance, high peak current, and small energy spread are keys for achieving high energy gains in the seeded FEL experiments. The electrons with a small energy spread and low space-charge-induced emittance are emitted from the photocathode surface with a strong RF field (~100MV/m). The quick acceleration of the electron beam in a photoinjector prevents thermalization of the beam's phase space. However, the emittance growth, due to the RF and the space-charge effects, occurs in the RF gun. In particular, the transverse emittance increases close to the cathode surface due to transverse defocusing space-charge force. We use a spatial laser shaping to produce a nearly flat-topped charge density electron beam, and a 9ps long Gaussian laser pulse to reduce the longitudinal space charge force. As an example, after a 1.6-cell RF gun with a space-charge emittance compensation solenoid magnet developed in the Brookhaven National Laboratory (BNL) [1,2], a transverse normalized rms emittance of 4 mm•mrad with 1nC of bunch charge was obtained.

Optimization of operating parameters of the RF gun, such as the laser injection phase and the space-charge compensation are required for the generation of a high-brightness electron beam. We have carried out a systematic experimental characterization of the transverse emittance of electron beam as a function of RF gun phase and solenoid magnet for electron beam charge ranging from 350 pC to 1 nC.

## EXPERIMENTAL SETUP

The SDL accelerator features a 6MeV BNL gun, two SLAC-type traveling-wave accelerating structures providing 70MeV followed by a 4 dipole chicane and three more accelerating structures with a final energy of up to 250MeV [3]. A spectrometer dipole after the last structure enables energy spectra and time resolved measurements [4]. The RF gun consists of a half cell and a full cell. A magnesium cathode is located on the side of the half cell. A single solenoid magnet is mounted at the exit of the RF gun to compensate for the transverse emittance growth due to the space-charge effect.

The beam transverse emittance was measured downstream of the 4th accelerating structure with a standard quadrupole scan technique. The beam size was measured on a YAG crystal downstream of a quadrupole magnet which was varied so that the beam passed and a data translation 8-bit frame grabber both synchronized

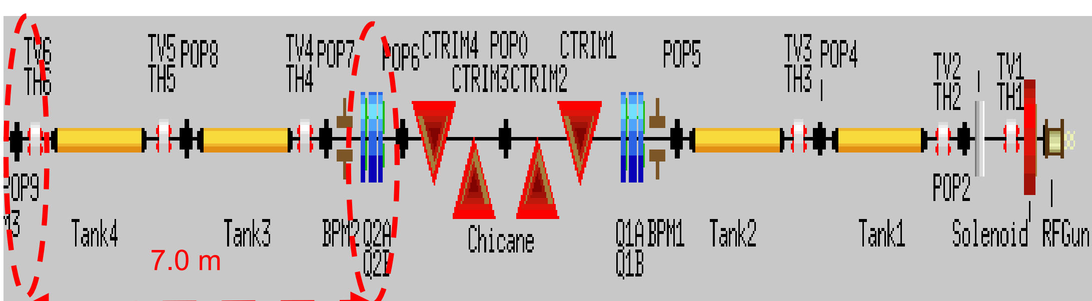


Figure 1: Schematic diagram of the experimental arrangement.

to the electron beam for a single-shot measurement. The combination of a polarizer and a half-wave plate was used to increase the dynamic range of the CCD camera. The beam waist of a 1nC bunch on the YAG screen can be as small as ~10pixels before the image saturates. The resolution on the CCD camera was achieved to be 24.1μm/pixel.

The beam size on a screen at a distance $L$ from a quadrupole is given by Eq. (1):

$$x = x_{\min}\sqrt{1+\left(\frac{L}{x_{\min}}\right)^4\left(\frac{\varepsilon_{un}}{f_w}\right)^2\left(1-\frac{f_w}{f}\right)^2} \qquad (1)$$

where $\varepsilon_{un}$ is the un-normalized rms emittance, $f$ is the quadrupole's focal length, and $f_w$ is the focal length producing the minimum spot size $x_{min}$ [5]. Longer the drift distance $L$ is, larger the range of spot size variation on the YAG screen is. So we chose the quadrupole and YAG screen pair indicated by red dash ellipses in Fig. 1 to measure the emittance, the drift distance is 7.04m. The beam size at each quadrupole setting is measured by averaging 5 different images. The image is truncated outside the manual bounding box. Gaussian fit is applied to the intensity histogram of the image, and the background level is set to 1.5 sigma. After applying the background subtraction to the image, the first and second integrated moments are calculated. The transport matrix from the quadrupole to YAG screen is calculated based upon the quadrupole setting and the drift distance. Based upon the measured sigma matrix at YAG screen and the transport matrix, the initial sigma matrix is obtained by least square fit [6].

## MEASUREMENTS

The quantum efficiency and the electron charge in the bunch were measured as a function of the laser injection phase on a charge monitor downstream of the solenoid magnet and upstream of the linac, as shown in Fig. 2. The laser injection phase is the RF phase when the center of a laser pulse arrives at the cathode surface. The data was taken at a constant laser energy of 11.9μJ and a cathode field of ~105MV/m. The laser spot size at the cathode was fixed to 2mm in diameter. The solenoid field was fixed at 1.91kG. When the laser injection phase is smaller than 70°, the data agrees very well with the fitted curve using Eq. (2) [7]:

$$QE = a\times\left(\hbar\omega - W_0 + b\sqrt{\beta E\sin\theta}\right) \qquad (2)$$

where $QE$ is the quantum efficiency, $\hbar\omega$ is the photon energy, $W_0$=3.66eV is the work function of the Mg cathode at zero field, $E$≈105MV/m is the peak electric field on the axis at the cathode, $\beta$ is the field enhancement factor, and a and b are material-dependent fitting parameters. Eq. (2) is obtained in the case that quantum efficiency is dominated by the Schottky effect. However, we observed a sharp drop on the bunch charge when the laser injection phase was above 73°. This can be explained by the charge loss in beam transport due to a significant decrease in beam energy when the laser injection phase is above 70°.

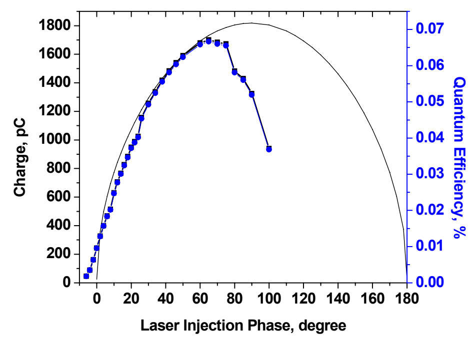


Figure 2: Electron charge and quantum efficiency as a function of laser injection phase.

Inside the RF gun, the beam is dominated by the space-charge effect. However, the transverse emittance growth due to the linear space-charge effect can be compensated with an optimal solenoid magnetic field. The horizontal emittance *vs*. the solenoid field at a bunch charge of ~300pC is shown in Fig. 3. The red and blue curves are the data taken before and after the cathode cleaning respectively. There was a factor of ~2.5 improvement on the transverse emittance after the cathode cleaning. Also, we observed a factor of ~10 improvement on quantum efficiency after the cathode cleaning. The data shown in Fig. 2 is after the cathode cleaning. In both cases, the optimal solenoid fields were ~1.47kG.

In order to investigate the contribution to the emittance growth due to the RF field in the gun, we measured the normalized transverse emittance as a function of the laser injection phase at the optimal solenoid field of 1.47kG. Laser energy was varied in the measurement in order to keep the charge constant. Emittance measurements were carried out at three different charges of 300pC, 500pC, and 1nC, and they are shown in Fig.4 as the black, red, and green curves respectively.

Since the charge was kept constant at each measurement, the contribution to the emittance growth due to the space-charge effect was constant. The RF-induced emittance growth starts to increase with the laser injection phase when it's above 30°. The emittance grows faster when the bunch charge increases.

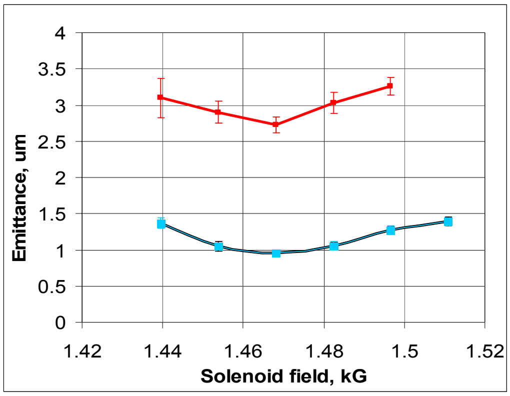


Figure 3: Normalized rms transverse emittance as a function of solenoid magnetic field at the bunch charge of ~300pC and laser injection phase of 25°. The red and blue curves are the data taken before and after the cathode cleaning respectively.

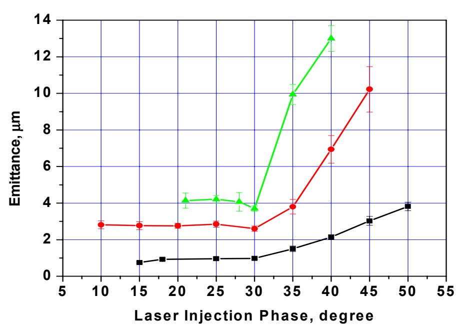


Figure 4: Normalized rms transverse emittance as a function of laser injection phase for constant solenoid field and constant charge at 300pC (black), 500pC (red), and 1nC (green).

## CONCLUSIONS

The transverse emittance was investigated experimentally for high brightness electron beam generation. The transverse emittance growth due to the RF and the space charge effects in the RF gun were measured as functions of the laser injection phase. Normalized rms transverse emittances of 1µm, 2.8µm, and 4µm are achieved at the charge of 300pC, 500pC, and 1nC respectively when the solenoid field is set at the optimal.

Comparing the cases before and after the cathode cleaning, we observed a factor of ~10 improvement on quantum efficiency, and a factor of ~2.5 improvement on the transverse emittance.

We will upgrade the frame grabber from 8-bit to 12-bit to improve the image resolution, and also investigate the uncertainty of the emittance measurement.

## ACKNOWLEDGEMENT

The authors would like to thank B. Podobedov for useful discussions and Pooran Singh for technical support.

## REFERENCES

[1] D. T. Palmer et al, Proc. Particle Accelerator Conf., Canada, 1997, p. 2687.
[2] X. J. Wang and I. Ben-Zvi, Proc. Particle Accelerator Conf., Canada, 1997, p. 2793.
[3] W. S. Graves et al, Proc. Particle Accelerator Conf., Chicago, June 2001, p.2860.
[4] W. S. Graves et al, Proc. Particle Accelerator Conf., Chicago, June 2001, p.2224.
[5] B. E. Carlsten et al, Nucl. Instr. and Meth. A 331 (1993) 791.
[6] H. Loos, Manual: "The SDL control Software Package".
[7] J. Yang et al, Jpn. J. Appl. Phys., Vol. 44, No. 12 (2005).

# DEVELOPMENT OF THE CONTINUOUSLY ADJUSTABLE PERMANENT MAGNET QUADRUPOLE FOR ATF2

Takanori Sugimoto, Yoshihisa Iwashita, Masahiro Ichikawa, Masako Yamada, Ichiro Kazama (ICR Kyoto Univ. Uji Kyoto) and Toshiaki Tauchi (KEK, Ibaraki)

*Abstract*

A quadrupole magnet for the final focus system of the International Linear Collider (ILC) is required specific properties, that is comparatively 'compact' (because the crossing angle of the Interaction Point (IP) of ILC is planned to be very small (~14mrad) and so out-going beam-line is installed passing close by the Final Focus Quadrupole (FFQ)), 'solid and stable' (so that beams with the very small beam-size at IP (~several nm in y-plane) needed can be realized and be handled stably) and so on. A super-conducting magnet scheduled now is not always suitable for that, for instance because of a huge cryostat needed outside of it (since it may have the mechanical vibrations due to liquid helium flow and also the magnet. This may prove not to be good). Since the continuously field-strength adjustable Permanent Magnet Quadrupole (PMQ) designed by Gluckstern [1][2] satisfies these properties, we are developing FFQ of this type for ILC, and for ATF2 (the Acceleration Test Facility 2) firstly.

However the magnet of this type has a risk of x-y coupling more greatly influenced than magnets of other types. For it is five discs singlet, which comprises five PMQ discs with appropriate skew each other. A nominal beam for ILC has different scales in x-plane and y-plane, so we need to avoid x-y coupling sufficiently.

We estimated the effect of field-error brought by skew of each PMQ disc. Then we used the way of calculation of transfer matrices neglecting fringe field and multipoles except for Q. In addition we produced this type of the magnet experimentally and measured field-strength and harmonics in the magnet. Then we fabricated an instrument measuring harmonics of fields in the magnets. The harmonic analysis is discussed compared with the estimation above.

We explain these schemes and show the conclusion. At the same time we are adjusting and aligning the magnets for reducing errors. We fabricated a jig then, so we explain it too.

## INTRODUCTION

Since recent development for a PMQ enables high degree of field strength, a PMQ can be used as a focus magnet for a high-energy beam. However a focus magnet requires the tuning of field strength for the sake of practical beam energy and focal length. A five-discs-singlet configuration proposed by Gluckstern works as a PMQ, whose strength is continuously adjustable. Each disc of a Gluckstern's PMQ comprises a PMQ, and the field strength in it is altered by rotating the discs with respect to each other (Fig. 1). Though x-y coupling effect caused by a skew of each disc can be theoretically cancelled in this design, fabrication errors and rotation errors alter the situation. The effect of x-y coupling may prove fatal to a beam whose size in x-plane and y-plane are considerably different as in a case at IP of ILC.

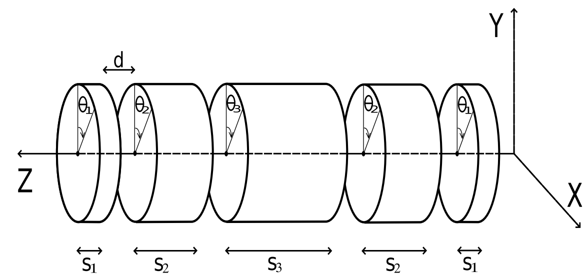


Figure 1: A Gluckstern's PMQ.

Though six parameters exist in the five-discs-singlet, five conditions constrain these parameters. So only one parameter is free. Using this parameter total field strength is continuously adjustable. The five constraint conditions are as follows.

- The absolute values of three rotation angles of five discs are the same. It should be noted that this statement represents two constraint conditions. The statement is namely
$$\theta \equiv \theta_1 = -\theta_2 = \theta_3 . \tag{1}$$
- The minimum of the total focusing force is decided. Here we chose the minimum zero, and strength of focusing is approximated in proportion to length of the magnetic filed. Then this constraint condition is
$$2s_1 - 2s_2 + s_3 \equiv S_0 . \tag{2}$$
We decided $S_0$ to be zero here.
- The maximum of the total focussing force is decided. We chose the maximum the value needed by ATF2. The total focussing force is represented as the total length when field gradients of discs are the same and decided. By the way, with the aim at ILC we are planning to choose the same total length and smaller bore of discs.
$$2s_1 + 2s_2 + s_3 \equiv S_t . \tag{3}$$
Here $S_t$ is 220mm.
- In order to cancel the effect of x-y coupling at all angles of discs, the proportion of the lengths of discs should be optimized. In this optimization we used the proportion of the length of first and fifth discs to the total length.
$$\lambda \equiv s_1 / S_t . \tag{4}$$
Here $\lambda$ is 0.07877.

## ESTIMATION OF ERRORS

We estimated an x-y coupling effect caused by three types of errors associated with each disc, namely a rotation error, a length error and a shift. This estimation includes the calculation of transfer matrices neglecting fringing field and multipole components [3].

The effect of an x-y coupling can be calculated with nominal parameters at IP in ILC. When nominal beam size and divergence at IP is represented as $\boldsymbol{X}$, practical beam size and divergence at IP can be represented as $\boldsymbol{X}^*$, nominal transfer matrix of FFQ is $\boldsymbol{M_Q}$ and the practical transfer matrix of a Gluckstern's PMQ as FFQ is $\boldsymbol{M_Q}^*$, and so on. Namely $\boldsymbol{X}$ and $\boldsymbol{X}^*$ are defined as follows,

$$X = M_{DS} M_Q X_0$$
$$X^* = M_{DS} M_Q{}^* X_0. \tag{5}$$

The effect of an x-y coupling at IP, $\boldsymbol{\Delta X}$ is

$$\Delta X = X - X^* = M_{DS}\left(E - M_Q{}^* M_Q{}^{-1}\right) M_{DS}{}^{-1} X. \tag{6}$$

### A Rotation Error

We calculated with ILC parameters $\boldsymbol{\Delta X}$ when a rotation error $\delta\theta$ exists on each disc of a Gluckstern's PMQ with ILC parameters. Then we fixed length of a Gluckstern's PMQ to 220 mm, and used the optimum length as a length of each disc. For $\boldsymbol{\Delta X}$ is to be less than 10 percent of $\boldsymbol{X}$, $\delta\theta$ on each disc has to be less than the value shown in Table 1. We can say that the x-y coupling effect is about in proportion to the length of each disc.

Table 1: Nominal $\delta\theta$ on each disc

| **Disc** | **Optimum length [mm]** | **Nominal $\delta\theta$ [rad]** |
|---|---|---|
| First | 17.33 | $< 2.2 * 10^{-4}$ |
| Second | 55.00 | $< 7.0 * 10^{-5}$ |
| Third | 75.34 | $< 5.3 * 10^{-5}$ |
| Forth | 55.00 | $< 7.6 * 10^{-5}$ |
| Fifth | 17.33 | $< 2.5 * 10^{-4}$ |

### A Length Error

It was found that a length error of each disc has to be less than 100 µm for $\boldsymbol{\Delta X}$ be within less than 10 percents of $\boldsymbol{X}$. Since a fabrication error can be controlled within 100 µm, the x-y coupling caused by a length error isn't as bad as a rotation error. When fringing field in edges of each disc exists, since effective length of the field is changed a little, it is also shown the cause of the x-y coupling at IP never affected a change of the field length derived from fringing field.

### A Shift

A shift of a disc does hardly affect x-y coupling at IP in ILC, but shifts the position of interaction of beams instead. If the shift at IP less than 1 nm is wanted, a shift of each disc must be less than 1 µm. It is understood that a shift of each disc less than 1µm is difficult to realize but not impossible. As a first step, we measured the shift of a disc experimentally. It was found that the shift was in an order of 10 µm. This value is rather large and is attributable to fabrication errors. It can be improved so the shift less than 1 µm is not impossible.

## MEASUREMENT

We fabricated only two discs (disc-3 whose length is 70mm and disc-4 whose length is 55mm). Though we fabricated more two discs precisely, for adjustment we disassembled or took to pieces those discs. Here we mentioned about only two discs assembled now.

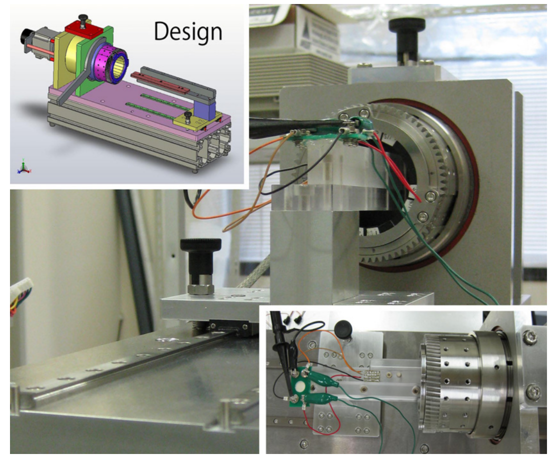


Figure 2: The Rotation Magnet Instrument

We fabricated an instrument for measuring harmonics of fields (Fig. 2). The instrument can measure voltage of two induction coils inserted in a disc as rotating the disc. One coil has the area twice as larger as the other's and its rolled number is a quarter of the other's (Fig. 3). Since the difference of induced voltages of two coils does not include the quadrupole component theoretically, other components still more little than the quadrupole component can be measured more accurately. A blue line in the upper picture of Figure 3 shows the position of the axis of symmetry of a disc when the coils are inserted in the disc.

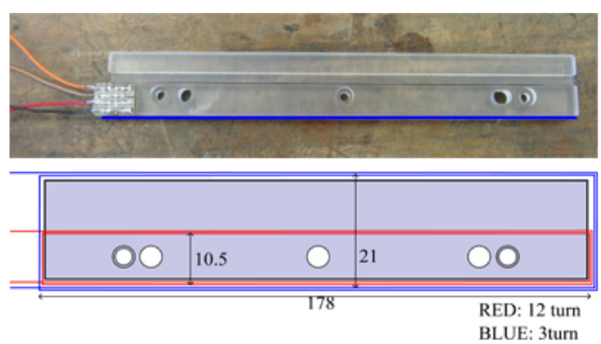


Figure 3: the Coils of the Rotation Magnet Instrument

In practice filed strength as complex expression in perpendicular plane to the axis of symmetry of a disc $B(r,\theta)$ is written as follows,

$$B = B_r + iB_\theta = \sum_n \frac{B_n r^{n-1}}{(n-1)!} \exp[in\theta], \tag{7}$$

where $B_n$ is a complex coefficient of 2n-pole component. Therefore induced voltage $V$ is

$$
\begin{aligned}
V &= -\oint_C E dl = \int_S \frac{d}{dt} B_\theta d\sigma \\
&= N\omega L_{eff} \int_0^R \mathrm{Re}\left[\sum_n \frac{nB_n r^{n-1}}{(n-1)!}\exp[in\theta]\right] dr \\
&= N\omega L_{eff}\, \mathrm{Re}\left[\sum_n \frac{B_n R^n}{(n-1)!}\exp[in\theta]\right],
\end{aligned}
\tag{8}
$$

where $N$ is a turn number of a coil, $\omega$ is a angular frequency of a disc, $L_{eff}$ is an effective length of magnetic field along the axis of symmetry of the disc and $R$ is defined that $RL_{eff}$ is the effective field area of the coil.

We analyzed harmonics with the FFT (Fast Fourier Transfer) after smoothing of the plane data measured. The smoothing is the filter that equates the duration of 0.01 seconds around each point and that means the low pass filter of 100 Hertz. With this filter we removed a noise caused by the pulse motor in the plane data at first.

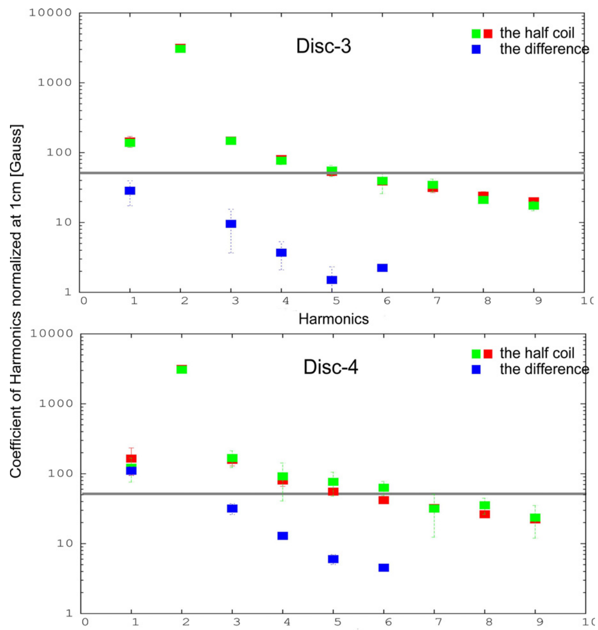


Figure 4: The analysis of harmonics.

We measured induced voltage three times with oscilloscope. Each measurement includes the data of 16 periods. Induced voltage of the half coil (red one in Fig. 3) was measured twice, and the difference of induced voltages of the full coil (blue one) and the half was measured once (see Fig. 4). The oscilloscope we used has only the accuracy of few percent, so when the data includes quadrupole component other components, which are more little influenced than one percent of quadrupole component, cannot be measured precisely. The gray lines in Fig. 4 show this mechanical accuracy limit. By the way of measuring the difference, since quadrupole component is not included theoretically, with the accuracy of few percent of dipole component, which is the secondary component of the field, other components can be measured precisely. Values in Tab. 2 show multipole components obtained the third measurement but normalized where the distance from the centre of the discs is one centimeter. Quadrupole component in Tab. 2 is however the mean of previous two measurements.

Table 2: Harmonics and Shift Measured

| Disc | Dipole (Err) [G] | Quadrupole (Err) [G/cm] | Shift (Err) [μm] |
|---|---|---|---|
| Third | 29 (11) | 3120 (10) | 91.5 (36.3) |
| Fourth | 110 (16) | 3120 (10) | 353 (52) |

## ADJUSTMENT

We fabricated a jig adjusting and aligning pieces of magnets (see Fig. 5). We think an error of alignment of each piece of magnet of a disc is dominant to the shift error (or dipole component) of the disc. Though magnetic pieces were fixed by the force of outside screws, this time we developed a jig which can make force from the inside the pieces to the outside of them. The outside diameter of the jig is changed by the taper of the jig (the red part in Fig. 5) going up and down.

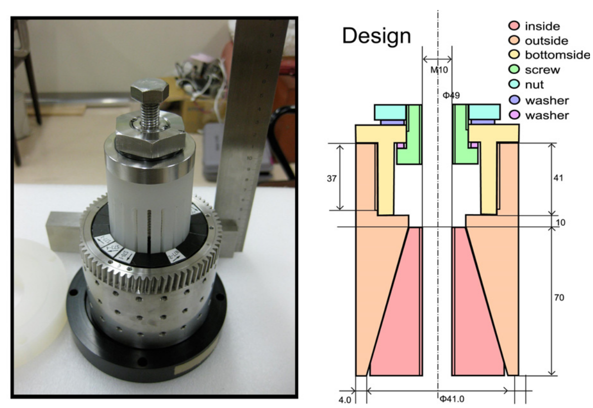


Figure 5: The jig adjusting magnetic pieces.

## CONCLUSIONS

We fabricated an instrument measuring harmonics and estimated shift errors of discs (the third disc and the fourth disc). It was found that when we measured induced voltage including quadrupole component other components could not be estimated precisely.

We fabricated a jig adjusting and aligning magnetic pieces. We think using the jig we can force magnetic pieces into appropriate places, as the result we can reduce other components including dipole.

## REFERENCES

[1] R.L.Gluckstern et al, "Variable Strength Focussing with Permanent Magnet Quadrupole", Nucl. Instrum. Meth., **187**, 119, (1981)

[2] R.L.Gluckstern et al, "Adjustable Strength REC Quadrupole", IEEE Trans. on Nucl. Sci., **30**, 3226, (1983)

[3] T.Sugimoto et al, "Continuously Adjustable Permanent Magnet Quadrupole for a Final Focus", EPAC08, MOPP015, (2008)

# OPTIMUM FREQUENCY AND GRADIENT FOR THE CLIC MAIN LINAC ACCELERATING STRUCTURE

A. Grudiev, H. H. Braun, D. Schulte, W. Wuensch, CERN, Geneva, Switzerland

*Abstract*

Recently the CLIC study has changed the operating frequency and accelerating gradient of the main linac from 30 GHz and 150 MV/m to 12 GHz and 100 MV/m, respectively. This major change of parameters has been driven by the results from a novel main linac optimization procedure. The procedure allows the simultaneous optimization of operating frequency, accelerating gradient, and many other parameters of CLIC main linac. It takes into account both beam dynamics (BD) and high power RF constraints. BD constraints are related to emittance growth due to short- and long-range transverse wakefields. RF constraints are related to RF breakdown and pulsed surface heating of the accelerating structure. The optimization figure of merit includes the power efficiency, measured as a ratio of luminosity to the input power, as well as a quantity proportional to total cost.

## INTRODUCTION

From almost the very beginning of CLIC [1] the operating frequency of the main linac accelerating structure was 30 GHz which gave a compromise between the efficiency and peak power, and and machinability and wakefield considerations. The original gradient was 80 MV/m for a 2 TeV collision energy. Eventually it was increased to 150 MV/m [2] in order to reach the CLIC design luminosity and energy (~$10^{35}$ $cm^{-2}sec^{-1}$ and 3 TeV, respectively) in a power-efficient way and with an affordable site length. Since then several attempts have been made to find a better choice of the frequency and gradient for CLIC [3, 4].

In [4], a new optimization procedure has been used which is based on the interpolation of the accelerating structure parameters allowing millions of structures to be analyzed. The demanding beam dynamics requirements, a short-range transverse wakefield limit and long-range transverse wakefield suppression, are taken into account as well as high-power rf effects such as, rf breakdown and rf pulsed surface heating. The results indicated that 18 GHz and 100 MV/m are a better choice for CLIC if the ratio luminosity to the input power is considered to be paramount. Two things limited the validity of the results: first was the absence of a cost analysis and second was the lack of high gradient experimental data at 30 GHz. The latter difficiency called into question the frequency scaling of the rf breakdown constraints used in the optimization.

In this report, the extension of the optimization procedure described in [4] to include both a parameterized cost model and updated rf constrains is presented. Finally, the results of the CLIC main-linac accelerating structure using the new optimization are presented and discussed.

## PARAMETERIZED COST MODEL

In the new parameterized cost model , the total cost is given by the sum of the investment cost and the exploitation cost for 10 years. It is calculated as a function of several parameters of the linac: the repetition frequency $f_{rep}$, the RF pulse energy for the whole linac $W$, the accelerating gradient $E_{acc}$, the structure length $L$, the operating frequency $f$ and the rf phase advance per cell $\Delta\varphi$.

The model uses as a reference point a cost estimate which was done for a 30 GHz, 150 MV/m machine as described in [5]. Cost are scaled with the assumption that the cost per meter of accelerating structure varies according to the function

$$C_{\mathrm{acc}} = C_{mat} \cdot (f\,/\,30\mathrm{GHz})^{-3/2} + C_{mach} \cdot (f\,/\,30\mathrm{GHz})^{3/2} \cdot (\Delta\varphi\,/60^0)^{-2/3}$$

$C_{acc}$ is the cost per meter of accelerating structure, $C_{mat}$ *is* the material cost per meter of accelerating structure of the reference and $C_{mach}$ is the cost of structure machining and assembly of the reference. This rule is based on scaling the required machining time and material mass and was benchmarked with the procurement costs of prototype structures at 30 GHz and 11.4 GHz. The effect of structure length $L$ was modeled assuming that costs per meter of accelerator scale in proportion to $L^{-2/3}$. For other quantities like tunnel, magnet and instrumentation costs a simple linear scaling with cost ~$E_{acc}^{-1}$ is assumed. The main cost of the drive beam the is determined by the total RF energy per machine pulse, which directly affects the number of required klystrons and modulators. The average RF power affects the total required charging power supply capacity. Electricity costs are based on the integrated consumption over 10 years of operation with 200 days per year and 95% up-time. The same unit costs were used as in estimates for the ILC [6].

## UPDATED RF CONSTRAINTS

The following three rf constraints have been used in the optimization:

1. Surface electric field: $E_{surf}^{\max} < 380$ MV/m
2. Pulsed surface heating: $\Delta T^{\max} < 56$ K
3. Power: $P_{in}\,/C\cdot\tau_p^{1/3}\cdot f < 156$ MW/mm/ns$^{2/3}$

Here $E_{surf}^{\max}$ and $\Delta T^{\max}$ refer to maximum surface electric field and maximum pulsed surface heating temperature rise in the structure respectively. $P_{in}$, $\tau_p$ and $f$ denote input power, pulse length and frequency respectively. $C$ is the circumference of the first regular iris. The value used for the power constraint (3) is different from the one used in the previous optimization [4].

The original concept of power over circumference (P/C) as a limit for travelling wave rf breakdowns [7] which was used in [4] has been improved in several respects. First, the limiting value has been reduced in order to correspond to the CLIC nominal breakdown rate (BDR) of ~$10^{-7}$ per pulse. The value is based on the available data for X-band Cu-structures and typical scaling of breakdown rate versus gradient [8]. Second, new experimental data obtained at 30 GHz [9, 10] have shown that P/C measured at (or scaled using typical scaling laws to) the same pulse length and BDR is inversely proportional to the frequency. This is directly related to an experimental observation that scaled X-band and 30 GHz structures reach approximately the same gradient at the same pulse length and BDR [11].

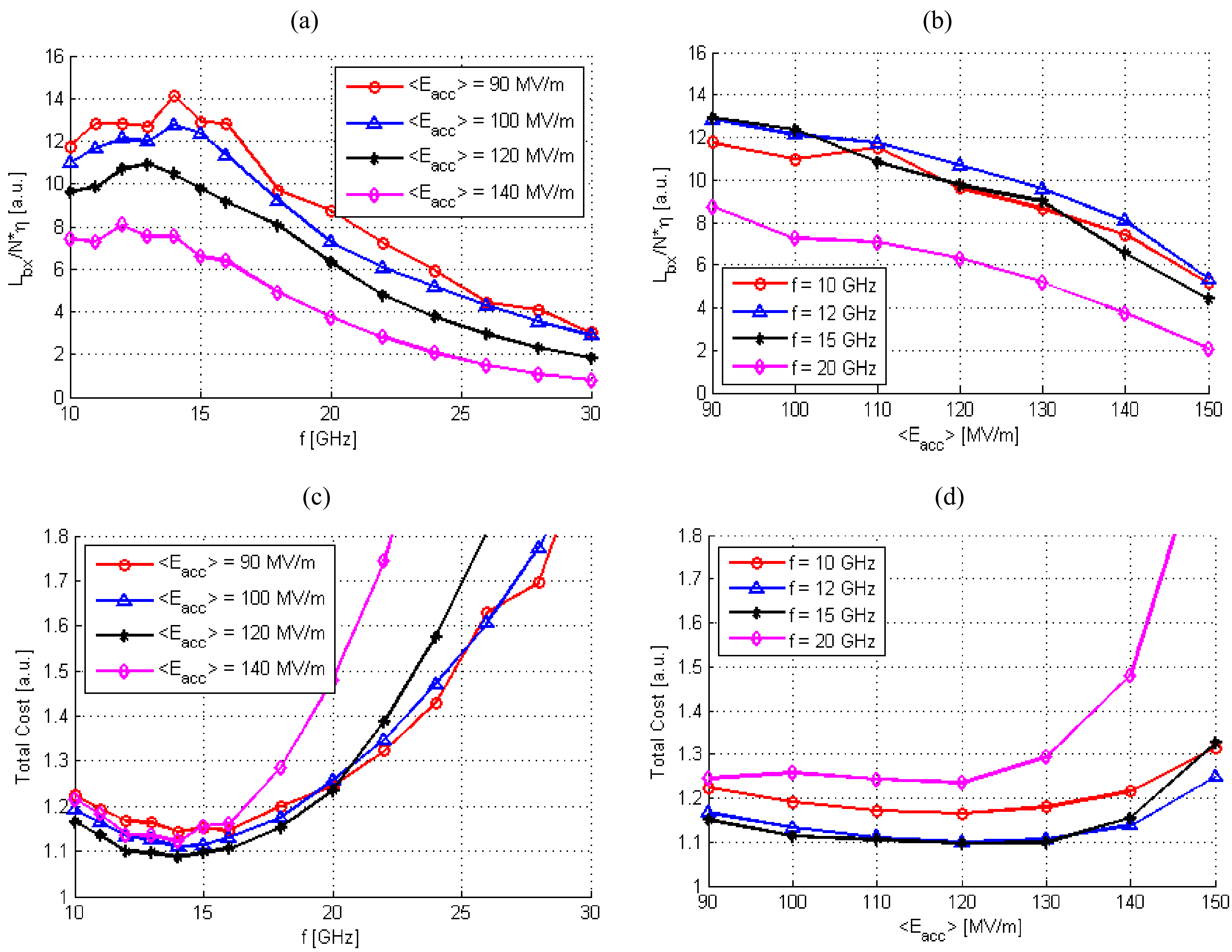


Figure 1: The results of optimization are presented both FoM on the top and for the total cost at the bottom.

## OPTIMIZATION RESULTS

The CLIC main linac accelerating structure optimization has been performed in a range of $f$ from 10 to 30 GHz and $\langle E_{acc}\rangle$ from 90 to 150 MV/m for two different quantities. The first, the figure of merit (FoM) $\eta L_{b\times}/N$ has been maximized as in [4], where $\eta$ is rf-to-beam efficiency, $L_{b\times}$ is luminosity per bunch crossing within 1 % of the energy spectrum and $N$ denotes the bunch population. Then the total cost, calculated using the parameterized cost model described above, has been minimized. The results are presented in Fig. 1. The figure clearly shows that 150 MV/m and 30 GHz are not optimum parameters for CLIC. In Fig. 1 (a) and (c), the FoM and the total cost are shown as a function of frequency for different gradients. Both point to the same optimum frequency range of 12 to 15 GHz for all gradients considered. Finally, based on other considerations, mainly the availability of a frequency with extensively developed hardware, 12 GHz is chosen from the range as the best choice for CLIC.

The optimum gradient is not so obvious from the results of the optimization. In Fig. 1 (b), the FoM is shown as a function of gradient for different frequencies. Again as in [4], it indicates that for the whole frequency range considered, the lowest gradient gives the highest performance of the collider. However the gain becomes smaller at lower gradients, and is marginal at gradients below 110 MV/m. The dependence of total cost on gradient, which is shown in Fig. 1 (d), for different frequencies has different behavior. This has a minimum around 120 MV/m though it is rather flat, so the cost does not increase significantly even below 100 MV/m. Taking both the performance and the total cost considerations into account, a gradient of 100 MV/m is considered to be the best choice for CLIC. The lower gradient would increase the cost considerably, while the higher one would reduce the performance.

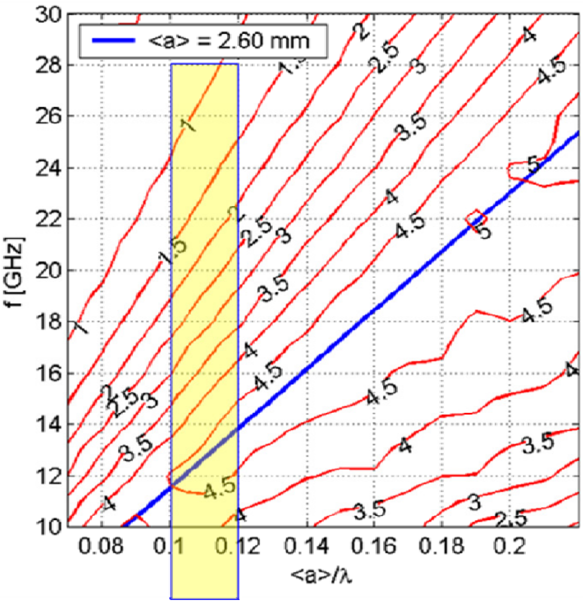


Figure 2: Lines of constant luminosity per bunch crossing normalized to the bunch population are plotted versus frequency and average ratio of aperture to the wavelength.

A closer look at the luminosity in 1 % of energy spectrum per bunch crossing normalized to the bunch population $L_{b\times}/N$ is useful to get more of an insight into the mechanisms driving the optimum. This very important parameter represents the beam dynamics requirements in the FoM. It is plotted in Fig. 2 as function of $f$ and the average ratio of structure aperture to rf wavelength $<a>/\lambda$. The lines of constant values of $L_{b\times}/N$ are shown in red. Higher values are better for beam dynamics. At each frequency, there is a maximum of $L_{b\times}/N$ which gives the optimum aperture at the frequency. In fact, this optimum aperture coincides very well with the straight blue line which shows the value of $<a>/\lambda$ versus frequency for a structure with $<a>$ = 2.6 mm. In other words, an accelerating structure with average aperture radius of 2.6 mm is the best from the beam dynamics point of view *independent of frequency*. The high gradient limitations have a different type of optimum. According to the presently available experimental data [11], scaled accelerating structures with the same $<a>/\lambda$ show roughly the same gradient. This is shown in Fig. 2 by the yellow band covering range of $<a>/\lambda$ from 0.1 to 0.12 and representing the area where a gradient of 100 MV/m can be achieved. The intersection of the blue line and the yellow band gives a range of frequencies where an accelerating structure with the optimum aperture providing gradient of 100 MV/m can be realised. Going lower in frequency reduces both the $L_{b\times}/N$ and the rf-to-beam efficiency of the structure.

## CONCLUSIONS

The CLIC main linac accelerating structure optimization procedure taking into account complex interplay between beam dynamics and rf performance has been developed over the past few years. Recently new experimental data both at 30 GHz and at X-band have been obtained as well as a parameterized cost model of CLIC.Taking into account these last two ingredients, an optimization of CLIC frequency and gradient has been done which, together with some other considerations, resulted in major change of CLIC parameters from 150MV/m at 30GHz to 100MV/m at 12GHz. Following this change a new CLIC parameter set is under preparation [12]. The details of a new CLIC X-band accelerating structure design are presented in [13].

## REFERENCES

[1] W. Schnell, “Radio-Frequency Acceleration for Linear Colliders”, In: AIP Conf. Proc.: 156 (1987), pp.17-36.
[2] The CLIC Study Team (edited by G. Guignard), CERN Report 2000-008.
[3] H. H. Braun and D. Schulte, “Optimum Choice of RF Frequency for Two Beam Linear Colliders”, PAC’03, Portland, May 2003.
[4] A. Grudiev et al., “Optimum Frequency and Gradient for the CLIC Main Linac Accelerating Structure”, EPAC’06, Edinburgh, June 2006.
[5] F. Tecker (ed.), “Updated CLIC parameters 2005,” CLIC note 627, 2005.
[6] ILC RDR, Vol. 3, p.264. 2007.
[7] W. Wuensch, “The Scaling of the Travelling-Wave RF Breakdown Limit”, 2006, CLIC-Note-649.
[8] S. Doebert et al., “High Gradient Performance of Prototype NLC/GLC X-band Accelerator Structures”, PAC’05, Knoxville, May 2005.
[9] R. Corsini et al., “A High-Gradient Test of 30 GHz Copper Accelerating Structure”, LINAC’06, Knoxville, August 2006.
[10] J. Rodriguez et al., “30 GHz High-Gradient Accelerating Structure Test Results”, PAC’07, Albuquerque, June 2007.
[11] S. Doebert et al., “High Power Test of an X-band Slotted-Iris Accelerator Structure at NLCTA”, PAC’07, Albuquerque, June 2007.
[12] F. Tecker (ed.), “CLIC 2008 Parameters”, CLIC-Note-764, to be published.
[13] A. Grudiev et al., “Design of X-band accelerating structure for the CLIC main linac”. This conference.

# BEAM OPTICS STUDIES AND COMMISSIONING STATUS OF CTF3

P. K. Skowronski, R. Corsini, S. Bettoni, S. Doebert, F. Tecker, CERN, Geneva, Switzerland
D. Alesini, C. Biscari, INFN/LNF, Frascati, Italy
Yu-Chiu Chao, TRIUMF, Vancouver, Canada

*Abstract*

The objective of the CLIC Test Facility CTF3 is to demonstrate the feasibility issues of the CLIC two-beam technology. CTF3 consists of an electron linac followed by a delay loop, a combiner ring and a two-beam test area. One issue studied in CTF3 is the efficient generation of a very high current drive beam, used in CLIC as the power source to accelerate the main beam to multi-TeV energies. The beam current is first doubled in the delay loop and then multiplied by a factor four in the combiner ring by interleaving bunches using transverse deflecting rf cavities. The combiner ring and the connecting transfer line have been put into operation in 2007, and the remaining parts, namely decelerating section, probe beam linac and test beam line in 2008. In this paper we give the status of the commissioning, present the results of the combination tests and illustrate in some detail the beam optics measurements, including response matrix analysis, dispersion measurement and applied orbit correction algorithms. We discuss as well the observation of a vertical beam break-up instability which is due to the vertical transverse mode in the horizontal RF deflectors used for beam injection and combination. We outline the attempted methods to mitigate the instability and their effectiveness.

## THE CTF3 COMPLEX

The CLIC technology [1] is believed to be the only practical path to multi-TeV colliders. The experimental program of the present CLIC Test Facility (CTF3) [2], aims to confirm its feasibility. In particular the generation and use of the high-current drive beam [3].

CTF3 is build at CERN by an international collaboration which at present includes 24 institutes from 14 countries [4]. Its construction is almost completed and a large part of the facility is already commissioned. It re-uses the infrastructure and most of the hardware of the former LEP Pre-Injector, LPI (see Fig. 1).

CTF3 consists of a 70 m long drive-beam linac followed by two rings, where the beam current is multiplied by a factor eight: a 42 m delay loop and an 84 m combiner ring. The drive beam is then delivered to the CLic EXperimental area (CLEX) to produce 12 GHz RF power for structure tests. In the same area, the CALIFES linac provides a probe beam for a Two-Beam Test Stand (TBTS) and a decelerator (Test Beam Line – TBL) will be used for drive beam stability studies. The detailed description of the facility can be found in [2,5].

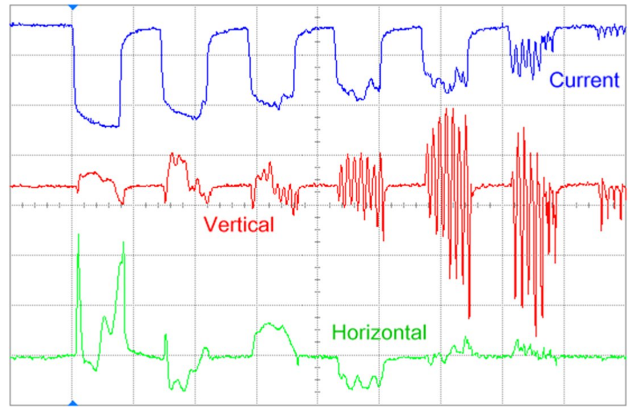


Figure 1: Traces of the beam current (upper line), vertical position (middle) and horizontal position (lower) in the ring, a clear indication of the vertical instability.

## COMMISSIONING STATUS

In 2003-2004 the injector, the linac, the mid-linac power station and the end-of-linac magnetic chicane were installed and commissioned. Full beam-loading operation was established [6]. The resulting beam is remarkably stable, with no sign of beam break-up. An RF-to-beam efficiency of 94 % has been experimentally verified later on [7]. The first part of the linac is routinely used since 2005 as a source of 30 GHz RF power. Up to 100 MW can be produced in the PETS, and transported to the test stand with ~ 70 % efficiency. The delay loop was installed during 2005 and commissioned in 2006. Five 140 ns long bunch-trains were injected into the delay loop and combined with the following train, thus doubling the beam current [8]. In 2006 a short period was dedicated to the commissioning of the newly installed TL1. Short pulses of 200 ns were used. The beam was rapidly transported to the end of the line and a current of 3 A could be injected in the ring first straight section.

The combiner ring installation was completed at the beginning of 2007. Commissioning of the combiner ring began in 2007, with several interruptions for repairs and installation work [9], and still continues with the goal to reach nominal beam parameters. Several problems in the hardware and in the optics model were identified, mainly through beam measurements, and eventually fixed, including wrong BPM calibration and connections, quadrupole cabling errors, switched polarities and wrong current calibrations. The alignment of magnets and vacuum chamber elements was also re-checked and corrected when necessary. During 2007 we could finally obtain a beam circulating for several turns in the ring, albeit with non-negligible losses. A fast beam instability in the vertical plane (see Fig.1) was indeed discovered

[10], which gives rise to growing vertical beam oscillations and eventually to beam loss.

The instability is believed to be caused by the vertical deflecting mode in the RF deflectors, excited by the beam [11]. This mode is shifted in frequency by 48 MHz with respect to the horizontal deflecting mode by polarising rods in the deflector cells, but it is not damped. New RF deflectors are being built, to be installed in October 2008. At the end of the 2007 run, a recombination test over four turns was performed anyway, bypassing the delay loop (see Fig. 2). In 2008 the ring commissioning restarted.

In August this year the last part of the drive beam installation was completed. Currently the TL2 line, which transports the beam to CLEX area and also TBTS are being commissioned. The beam was already successfully transported to the end of TBTS, however, with only half of the initial current. More detailed study is ongoing which aims to find the remaining problems.

The construction of the probe beam linac was also completed in August. Currently its CALIFES gun and accelerating structures undergo the RF conditioning process. The start of CALIFES commissioning is foreseen for November this year.

## MEASUREMENTS

Detailed beam optics measurements had to be performed in order to identify discrepancies between the model and the real machine. Furthermore, they were necessary to try to control the vertical instability by a proper choice of the vertical tune in the ring and of the β-function in the RF deflectors [10]. Indeed, we have found that bringing the vertical tune close to half integer reduces the instability growth time. However, we have not yet managed to damp it enough to achieve nominal beam parameters. During these machine studies, we were severely limited by beam jitter induced by gun voltage fluctuations. Recently we have ameliorated the performance of the gun, and at present further studies on this subject are being performed.

Among others, the following optics measurements were done:

1. Standard quadrupole scans, used to check the optics and perform re-matching of the different beam lines.
2. Determination of transverse response matrix elements by orbit measurements with kick excitation. The data obtained were paramount in order to identify and correct errors in the quadrupole families and also insufficiently precise modelling of combined function magnets, in which magnetic lengths of dipolar and quadrupolar components are different.
3. Dispersion, typically measured by varying the strength of all magnetic elements over a 1% range and taking the orbit difference. Such technique is simpler then a beam energy change and has the additional advantage that dispersion can be measured locally, not being sensitive to incoming residual dispersion. A good agreement was found in all machine areas (see an example in Fig. 3).

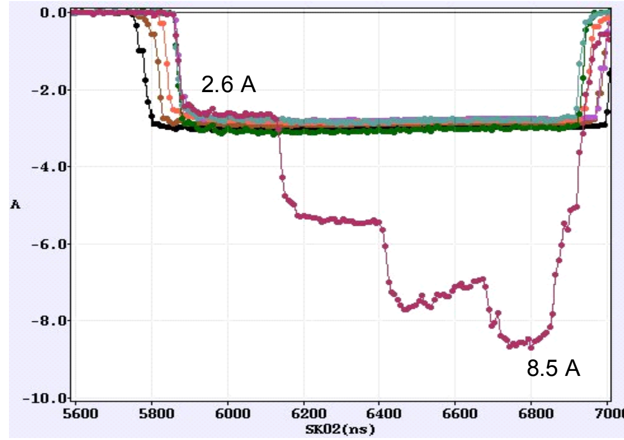


Figure 2: Beam current multiplication in the combiner ring. The traces show the beam current measured in several BPMs in the linac and TL1, and in one ring BPM. The incoming pulse has four times the ring length (4×280 ns). Losses from instability in the last two turns don't allow to reach a full factor four in current gain.

Additionally we have implemented on-line dispersion monitoring by means of beam energy jitter measurement. We can perform such a measurement since the precision and sensitivity of our beam monitors is high enough to observe beam displacement induced by the energy jitter from shot to shot, which is in our case the primary factor of the beam position variation. Dispersion is directly proportional to the position spread at a given location. The calibration is made at a chicane in the linac where dispersion is well known and controlled.

4. Tune measurements, by FFT of horizontal and vertical signals of the ring BPMs (see Fig.4). Together with dispersion and kick-orbit studies this enabled us to find, and later correct, disagreements with the MAD model.

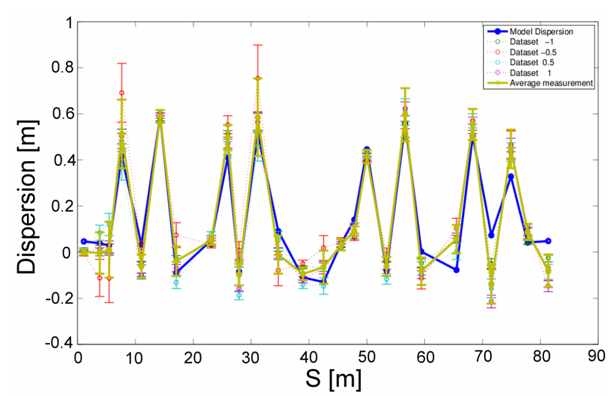


Figure 3: Results of dispersion measurements in the combiner ring (yellow line) compared with predictions from the MAD model (blue line).

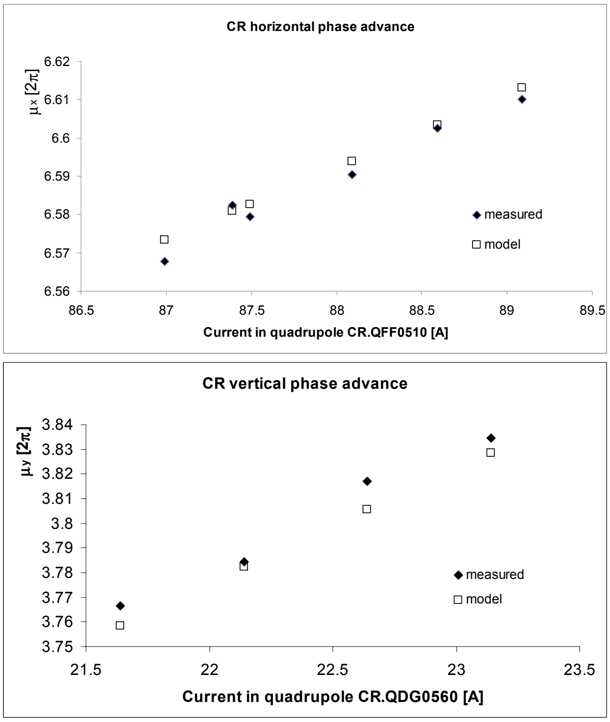


Figure 4: Example of tune measurement results for different setting of a quadrupole current compared with the predictions of the model.

5. Determination of the closed orbit. A first estimate is done by averaging the first few turns. The injection is then optimized to minimize the turn-to-turn difference. An automatic closed orbit correction program is still under test. The main limiting factor is low number of turns which is again related to the instability.

6. Measurement of the ring length, fundamental since the recombination process relies on a precise control of the revolution time, to the $10^{-5}$ level. The measurement was done using a 3 GHz RF phase monitor. An FFT of the signal gives the ring length modulo the RF wavelength (see Fig.5). The ring was found to be 1.5 mm longer than nominal. A good closed orbit correction (not applied then) may in principle reduce the discrepancy, which is however within the limits of the needed operational range (corresponding to 4-turn to 5-turn recombination). The path length variation as a function of the path length tuning wiggler current behaved exactly as expected.

## CONCLUSIONS

The CTF3 project is the main facility to demonstrate feasibility of the CLIC scheme, in particular the generation of the high-current drive beam. A number of issues have already been addressed, such as full beam loading operation and the bunch phase coding and interleaving scheme. Commissioning of the combiner ring is in progress and a full combination test is expected after installation of the new RF deflectors, needed to damp the fast vertical instability which is the present limiting factor. The construction of the facility is completed now and commissioning of the newly delivered parts is ongoing.

We have summarized the optics measurements that we performed in order to find the discrepancies between the model and the machine.

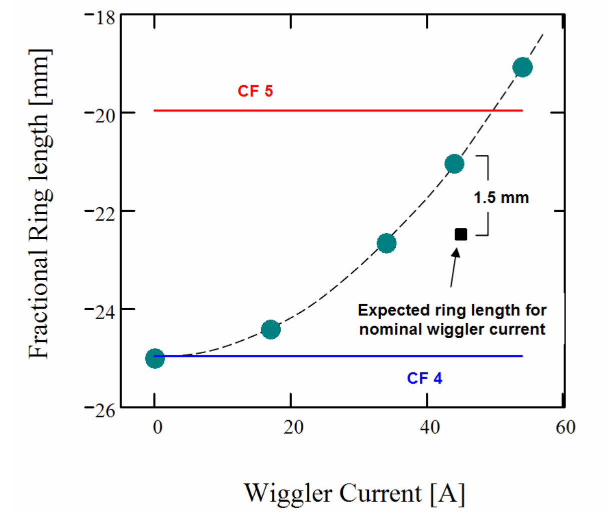


Figure 5: Ring length as a function of the tuning wiggler current. The actual length is an integer number of 3 GHz wavelengths, plus the fractional part shown here. The circles are measured values and the dashed line the expected variation. The black square is the nominal value and the horizontal lines mark the operational range.

## REFERENCES


[1] G. Guignard (Ed.), “A 3 TeV e+e- linear collider based on CLIC technology”, CERN 2000-008, 2000.
[2] G. Geschonke and A. Ghigo Eds, “CTF3 Design Report”, CERN/PS 2002-008 (RF).
[3] R. Corsini (Ed.), “The CLIC RF power source”, CERN 99-06, 1999.
[4] http://clic-meeting.web.cern.ch/clic-meeting/CTF3_Coordination_Mtg/Table_MoU.htm
[5] R. Corsini et al., “Experimental studies on drive beam generation in CTF3”, Proc. EPAC’08.
[6] R. Corsini et al., “First full beam loading operation with the CTF3 Linac”, Proc. EPAC’04 and CLIC note 604.
[7] P. Urschütz et al., “Efficient long-pulse fully-loaded CTF3 linac operation,” Proc. LINAC’06 and CLIC note 697.
[8] D. Alesini et al., “Commissioning status of the CTF3 delay loop”, Proc. EPAC’06 and CLIC note 675.
[9] F. Tecker et al., “CTF3 combiner ring commissioning”, Proc. PAC’07 and CLIC note 718.
[10] R. Corsini et al., “Fast Vertical Beam Instability in the CTF3 Combiner Ring”, Proc. EPAC’08.
[11] D. Alesini et al., “Analysis of the Vertical Beam Instability in CTF3 Combiner Ring and New RF Deflector Design”, Proc. EPAC’08.

# DESIGN AND FABRICATION OF CLIC TEST STRUCTURES

R. Zennaro, A. Grudiev, G. Riddone, A. Samoshkin, W. Wuensch, CERN, Geneva, Switzerland
S. Tantawi, J. W. Wang SLAC, Menlo Park, USA
T. Higo KEK, Tsukuba, Japan

*Abstract*

Demonstration of an accelerating gradient of 100 MV/m at a breakdown rate of $10^{-7}$ is one of the key feasibility issues of the CLIC study. A high power RF test program both at X-band (SLAC and KEK) and 30 GHz (CERN) is under way to develop accelerating structures which reach this performance. The centrepiece of the testing program is the nominal CLIC accelerating structure [1], but also includes structures with different RF parameters, with and without wakefield damping waveguides and made with different fabrication technologies. The latter structures address as directly as possible the different aspects of the nominal CLIC structure. The design and objectives of the various X-band and 30 GHz test structures are presented and their fabrication methods and status are reviewed.

## INTRODUCTION

The accelerating structure test program is one of the highest priority activities of the CLIC study [2]. The two main aims of the testing program are to validate the present CLIC structure design, CLIC_G [1], and to acquire data from different structures which can be used to both improve the understanding of and validate models of fundamental high power limits [3, 4, 5] and the effect on performance of different aspects of the design, such as the presence of HOM damping waveguides.

One of the main objectives for the structure is a loaded gradient of 100 MV/m with a $10^{-7}$ breakdown rate at the design pulse length. A second important objective is that the long range transverse wakefields be suppressed at the position of the second bunch to $W_{t,2} \leq 6.6$V/pC/mm/m for a bunch population $N=4*10^9$. In the CLIC structure this suppression is provided by combination of HOM damping waveguides located in each accelerating cell and detuning. Finally, the short range wakefield, which is determined by the aperture of the irises and is proportional to the bunch charge must remain below the threshold provided by the beam dynamics study.

The test structures can be organized into four groups: the VG1 family which is based on the design of the former nominal CLIC structure, CLIC_G family which is based on the present CLIC structure, the C10 family which is used to investigate specific issues in a simple constant impedance design with reusable couplers and 30 GHz structures which are now dedicated to the study of new ideas and to acquire more data for the understanding of the breakdown physics.

## THE VG1 FAMILY

The design of vg1 is derived from the CLIC_C, a former CLIC nominal structure CLIC_C is strongly tapered with a group velocity which drops from 2.4%c to 0.65%c (values for the damped versions). The tapering results in a surface electric field of 300 MV/m in the last cell for the unloaded case as shown in Figure 1. Vg1 is a shortened version of CLIC_C, and is composed of the first 18 regular cells in order to limit the field on the surface to 265 MV/m for the unloaded case. The surface field for the loaded case is anyhow equivalent in the two cases as shown in Figure 1.

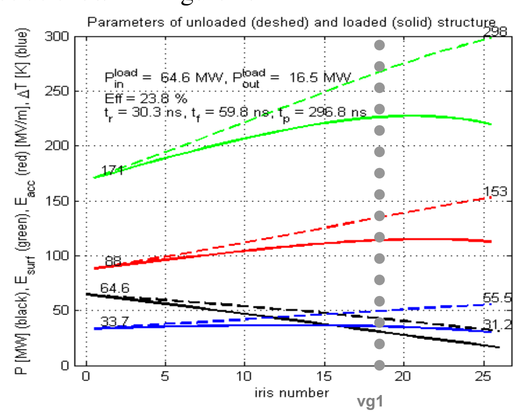


Figure 1: CLIC_C with accelerating gradient (MV/m, red), field on surface (MV/m, green), power (MW, black) and pulsed surface heating (K, blue) along the structure. vg1 extends to cell 18.

The reduction in the number of cells has as consequence not only in the reduction of peak surface electric field, but also a reduction in the efficiency of the structure which drops to only 18% from the original 24% of CLIC_C as shown in Table 1.

Table 1: Vg1 main parameters (undamped version).

| Name | T18_vg2.6_disk |
|---|---|
| Frequency (GHz) | 11.424 |
| N cell | 18+2 |
| Phase advance/cell (deg) | 120 |
| Iris aperture ain,out (mm) | 4.06/2.66 |
| Iris thickness din,out (mm) | 2.897/1.314 |
| Vgin/out (%c) | 2.61/1.02 |
| Tfilling (ns) (full structure) | 36 |
| Pin unloaded (MW) (100 MV/m) | 55.5 |
| Pin loaded (MW) (100 MV/m) | 63.7 |
| Pulse length (ns) | 267.4 |
| P/c (Wu) | 15.0 |
| Efficiency (%) | 17.7 |

The basic vg1 design has been used to address a number of basic structure features, experimental issues, and technology choices. The first question the structure addresses is the achievable gradient given the iris dimensions. A first structure (T18_vg2.4_disk) made using diamond turning and bonding techniques developed by the NLC/JLC program has been tested [6] and has produced excellent results largely in agreement with predictions. In order to demonstrate the reproducibility of the results another four equivalent structures are being fabricated.

The test of T18_vg2.4_disk demonstrates the potential of the structure but without the complication of the damping waveguides. The damping waveguides result in a surface magnetic field enhancement ($H_s/E_a$) of about 4.5 mA/V (~2.5 mA/V for the undamped case), a group velocity change of about 15% and may influence the dynamics of breakdown in an unknown way. For this reason a damped version of the vg1 (TD18_vg2.4_disk) is next most important step in the test programme. A picture of an undamped disk of the test structure is shown in Figure 2.

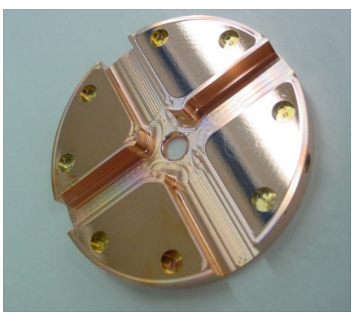

Figure 2: A single disk of TD18_vg2.4_disk.

The TD18_vg2.4_disk machined with a combination of diamond turning for the cell iris and disk faces and milling for the outer cavity wall and damping waveguides. Three structures are under production. Two of them will be brazed at SLAC at high temperature (~1015 deg) in a hydrogen furnace. The brazing will be followed by conventional vacuum baking at 650 deg to remove hydrogen from the bulk. The third structure will be brazed at 820 degrees in a vacuum oven and no successive baking is required.

Another two units of the damped version of the vg1 are under fabrication but in this case using the technology of clamped quadrants (TD18_vg2.4_quad) as shown in Figure 3.

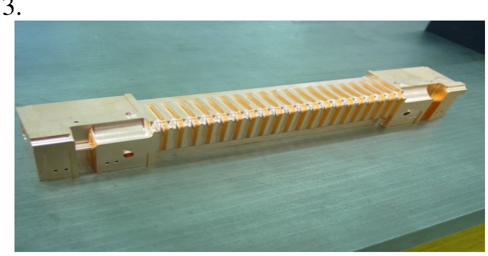

Figure 3: A single quadrant of TD18_vg2.4_quad.

The advantage of clamped quadrants is to give the possibility to avoid the heating associated with brazing and thus gives the possibility of using high-strength copper alloys. Alloys such as copper zirconium (Zr ~0.2% in weight) have a much higher fatigue strength than normal OFE copper [7]. The estimated fatigue limit for cold worked copper zirconium is much larger than the one of pure copper allowing a pulsed temperature rise of ΔT=77K instead of 48K. Even in case of brazing, copper zirconium still has better thermal fatigue strength than cold worked pure copper although its conductivity drops to only 80% of the conductivity of copper. To compare the breakdown performances of copper zirconium and conventional OFE copper, one of the two units of TD18_vg2.4_quad is made out of copper zirconium and the second is made out of OFE copper.

## THE CLIC_G FAMILY

CLIC_G is the present nominal CLIC structure. Compared to CLIC_C, it has a lower peak surface electric field, 245 MV/m instead of 294 MV/m, and lower pulsed surface heating, 53 K instead of 71 K. The reduction of the peak electric field is due to a weaker tapering and the reduction of the pulsed surface heating is related to shorter pulses with 240 ns instead of 296 ns.

The value of the 64 MW input power is nearly the same as for CLIC_C as is the value of P/C.

Both damped and undamped versions have been designed for 11.424 GHz and also for 11.994 GHz, the nominal CLIC frequency. The 12 GHz versions will be tested in the two beam test stand at CERN [8].

The basic parameters of the undamped test structure in disk at 11.424 GHz (T24_vg1.8_disk) are presented in Table 2.

Table 2: CLIC_G main parameters (undamped version).

| Name | T24_vg1.8_disk |
|---|---|
| Frequency (GHz) | 11.424 |
| N cell | 24+2 |
| Phase advance/cell (deg) | 120 |
| Iris aperture ain,out (mm) | 3.307/2.467 |
| Iris thickness din,out (mm) | 1.753/1.050 |
| Vgin/out (%c) | 1.82/0.93 |
| Tfilling (ns) (full structure) | 59 |
| Pin unloaded (MW) (100 MV/m) | 44.2 |
| Pin loaded (MW) (100 MV/m) | 55.7 |
| Pulse length (ns) | 239 |
| P/c (Wu) | 14.7 |
| Efficiency (%) | 30.5 |

All the X-band test structures currently under production make use of mode launcher couplers to pass from rectangular to circular waveguide which is axially coupled to the structure. This can be seen in Figure 3 Mode launcher couplers require additional length so cannot be used in CLIC. A compact coupler is currently being developed. A version of CLIC_G with waveguide feeders directly connected to the matching cell via magnetic coupling has been developed and a damped test structure will follow. The matching cell of the coupler is equipped with four waveguides, two for damping and two dual purpose waveguides for RF input plus damping. The coupler design has a magnetic field enhancement which is lower than in the regular cells for an equivalent accelerating gradient.

A damped version of CLIC_G in copper-zirconium is also included in the test program for comparison to pure copper. In this case the structure is made out of disks and requires high temperature bonding. The resistivity of the copper will be increased by 25% which requires an additional RF power of respectively 6% and 12% for loaded and unloaded cases.

## THE C10 FAMILY

The role of C10 structures are to provide a standard and well benchmarked geometry that is simple and inexpensive to build and exploits the reusable couplers already developed at SLAC. Features of structures such as iris diameter, damping features and material can all be directly tested. In addition the constant impedance geometry provides a clear geometrical reference point without the effect of tapering. C10s will provide information on the direct effect of geometrical parameters on the breakdown rate. Four different designs based on different combination of radius and thickness have been considered and summarized in table3.

Table 3: C10 main parameters; *a* is iris radius and *d* is iris thickness.

| | a (mm) | d (mm) | Vg (%c) |
|---|---|---|---|
| C10_vg0.7 | 2.53 | 1.66 | 0.7 |
| C10_vg1.35 | 3 | 1.66 | 1.35 |
| C10_vg2.25 | 3.88 | 2.79 | 2.25 |
| C10_vg3.3 | 3.88 | 1.66 | 3.3 |

At least two structures of each design are under fabrication. The test of repeatability will provide much information on the performance of C10_vg_1.35 that is produced in four units; for this reason it is taken as undamped reference for testing the effect of damping features on the breakdown rate. A version of C10_vg_1.35 with damping waveguides is already designed (CD10_vg_1.35) and a second structure, which has radial choke damping, has been proposed.

## 30 GHz TEST STRUCTURES

The programme for 30 GHz structures makes use of the CTF3 facility [9] and emphases the test of novel ideas. For example the so called "speed bump" has recently been tested, although not yet analyzed. The particularity of the speed bump, which is a constant impedance structure, is the use of the TM03 mode for the input matching cell in order to locally reduce the group velocity. In the structure regular cells group velocity is 4.7% but is only 1.7% in the matching cell. This drop of the group velocity reduces the bandwidth which is expected to diminish the damage due to the breakdown in the first regular cell by limiting the transient feeding of power to the breakdown. The first cell is normally the one most damaged by breakdown. Apart from the matching cell the structure is identical to the $2\pi/3$ Cu [10] which was tested in 2006.

Another structure which has been produced in 2008 is the so called "TM02" which has regular cells that are identical to the ones of the $2\pi/3$Cu with the exception of the diameter which is very large in order to use the TM02 propagating mode. This mode has the the same P/C, the same electric field enhancement and the same Sc but different group velocity, which drops from 4.7%c to 2.0%c. The use of the TM02 mode drastically changes the group velocity without modifying local fields near the iris. The test of the TM02 could provide good indications on the eventual direct effect of the group velocity on the breakdown rate.

The final structure of the planned testing program is a scaled version of the NLC T24 structure which is currently under test in SLAC is also scheduled in order to check the effect on the breakdown rate of frequency scaling.

## CONCLUSION

The possibility to reach 100 MV/m at $10^{-7}$ repetition rate for the nominal pulse length has been demonstrated by the T18_vg2.6_disk. The testing program continues with the objective to reach the same gradient with a higher efficiency structure (CLIC_G) and with the HOM damping waveguides. Studies on different technologies and materials are underway to address the issue of pulsed surface heating.

## REFERENCES


[1] A. Grudiev, "Design of X-band accelerating structure for the CLIC main linac". This conference.

[2] http://clic-study.web.cern.ch/CLIC-Study/.

[3] A. Grudiev "A new local field quantity describing the high gradient limit of accelerating structures". This conference.

[4] W. Wuensch, Progress in Understanding the High Gradient Limitations of Accelerating Structures, CLIC-Note-706 - Geneva, CERN, 08 Mar 2007.

[5] O.A. Nezhevenko, "On the Limitations of Accelerating Gradient in Linear Colliders Due to the Pulsed Heating," Proceedings of PAC97, Vancouver 1997, p.3013.

[6] S. Doebert et al., "High Power test of a low group velocity X-band Accelerator Structure for CLIC". This conference.

[7] S. Heikkinen, "Study of High Power RF Induced Thermal Fatigue in the High Gradient Accelerating Structures", Helsinki University of Technology, 2008 (pending).

[8] http://ctf3-tbts.web.cern.ch/ctf3-tbts/.

[9] http://ctf3.home.cern.ch/ctf3/CTFindex.htm.

[10] R. Corsini et al., "A High-Gradient Test of a 30-GHz Copper Accelerating Structure" Proceedings of LINAC96, Knoxville, Tennessee USA 1996, p.761.

# A KICKER DRIVER EXPLOITING DRIFT STEP RECOVERY DIODES FOR THE INTERNATIONAL LINEAR COLLIDER

F. Arntz, M.P.J.Gaudreau, M. Kempkes, Diversified Technologies, Inc., Bedford, MA USA
A. Krasnykh, Stanford Linear Accelerator Center
A. Kardo-Sysoev, Ioffe Institute of Physics, Russia

## ABSTRACT

Diversified Technologies, Inc. (DTI), under a SBIR grant from the U.S. Department of Energy[1], is developing a driver for a kicker TEM strip-line deflector which inserts and extracts charge bunches to and from the electron and positron damping rings of the International Linear Collider. The ultimate ILC damping ring kicker driver must drive a 50 Ohm load (a 50 Ohm terminated TEM deflector blade) at 10 kV, with 2 ns flat-topped pulses at a 3 MHz rate, within one-millisecond bursts occurring at a 5 Hz rate. The driver must also effectively absorb high-order mode signals emerging from the deflector itself.

In this paper, DTI describes the design of the kicker driver involving high voltage DSRDs (Drift Step Recovery Diodes) and high voltage MOSFETs. The development system will produce 5 kV pulses, which otherwise will satisfy the ILC requirements, as a precursor to the full 10 kV system. Because of the high 3-MHz pulse rate required, this design employs an all-electronic, rather than magnetic, approach to pulse compression.

## BACKGROUND

Every particle accelerator requires "kickers" – electromagnetic deflectors that pulse on to divert (kick) bunches of particles out of their trajectory onto new beam paths, targets, detectors, or other instrumentation. Kickers must reach the intended deflection field between particle bunches, control that field for a finite time, and return to zero field to avoid affecting the next bunch. The drivers for these kicker deflectors, therefore, must be capable of providing the required current pulses into the kicker impedance at demanding rates.

This effort is focused on the use of very fast Drift Step Recovery Diodes (DSRDs), driven by a MOSFET pulser, to obtain bursts of identical energetic pulses at a 3-MHz pulse rate - well beyond that attainable by magnetic pulse compression.

The pulse rate must be 3 MHz for a burst duration of one millisecond, with a bursts repetition rate of 5 Hertz (i.e. the average PRF is 15,000 Hertz). The essential objective of the project is to develop highly repetitive, high-voltage, 2 ns pulses for deflecting packets of electrons and positrons from their respective damping rings (6 km circumference rings) into the 40-km long ILC linear collider, and for nearly simultaneous replenishing of the packets of charge in the damping rings. An increment of deflection will be imparted by a symmetric pair of shaped parallel deflection blades of 30-cm length, pulsed in opposition at 10 kV each for two nanoseconds.

(Ten stages of such deflection will be necessary to produce the overall "kick" required.) Within each guide comprised of the two 30-cm deflector blades and their environment, each TEM wave produced by the two pulse generators traverses from the entrance to the terminus of the guide. Matching 50-Ohm resistors terminate the deflector blades, to avoid creation of secondary traveling waves.

## OVERVIEW OF THE APPROACH

The project itself is structured to achieve three critical milestones, (1) development of fabrication of DSRD diode stacks by an established semiconductor device manufacturer (in particular Voltage Multiplier Inc of Vaisala CA), (2) development of instrumentation and methods for characterizing the deflection pulses with sufficient accuracy, and (3) development of a reliable and jitter-free source for producing 40-to-50 nanosecond "pump" pulses at the rate of 3 MHz. These are compressed to 2 nanosecond pulses by the DSRD and one-nanosecond delay line - see Figure 2.

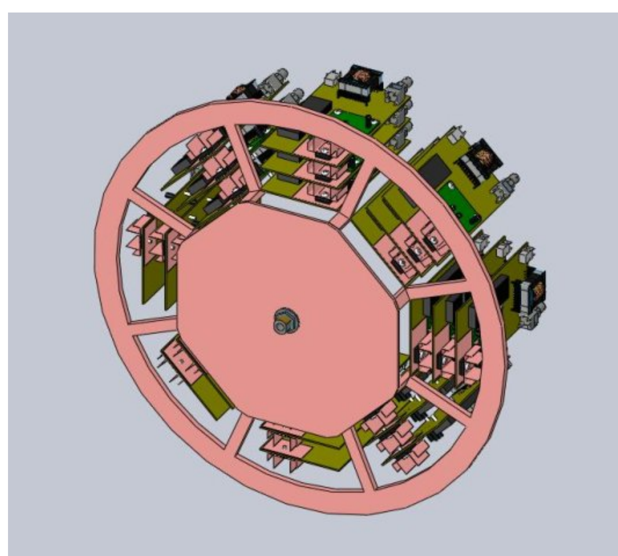

Figure 1: Basic configuration of ILC damping ring pulse generator. Unified 3MHz power/ pulse-synchronization supply and fiber-optic coupled controller are not shown. The one nanosecond delay line emerges from center of plate.

[1] This work supported in part under U.S. Department of Energy SBIR Grant DE-FG02-06ER84459.

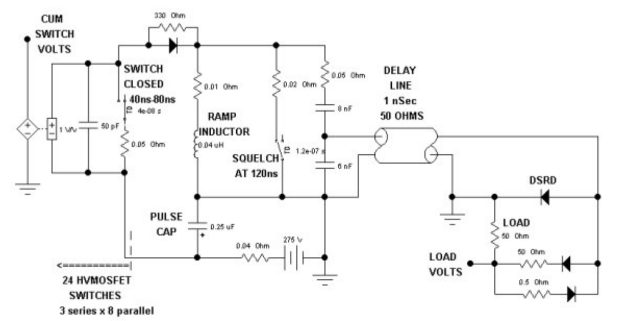


Figure 2: Schematic design of kicker driver, DSRD and load at right.

Various system designs were explored for producing desired pulse wave forms by exploiting the extremely abrupt opening of DSRD switches. The favored embodiment of the overall pulse generator, illustrated in Figure 1, is based on measurements, circuit modeling and practical considerations regarding component performance in the sub-nanosecond regime. The original design, first described at PAC07, has been changed substantially to adequately address the demanding constraint on pulse-to-pulse variation. Furthermore, the physical configuration has been revised to take advantage of symmetries. In this case an eight-fold symmetry is exploited, as shown in Figure 1. Each of the octal sections is comprised of three MOSFET switch cards arranged in series.

The overall pulse generation and compression network is presented in Figure 2. This represents the principal schema, with variants on this approach readily possible. The key components are exhibited in this figure including:

- A high voltage MOSFET switch array capable of delivering 25 ns, 400 A, 1 kV pulses at 3 MHz in one millisecond bursts, at a burst rate of 5 Hz; this switch array having a withstand capability of 4 kV or more.
- A DSRD diode stack initially capable of exhibiting 5 kV upon opening (but capable of 10 kV), able to open within 500 picoseconds, and interrupt 400 A reverse current.
- A one-nanosecond 50 Ohm delay line, together with an input circuit that presents a near-electrical-short to the line for frequencies greater than 10 MHz.

The presence of the delay line is essential. Its inductance ensures the input current pulse is maintained at the DSRD for a full two nanoseconds with little sag, and its high-frequency shorted input is expressed at the DSRD (and load) only after a round-trip of two nanoseconds, abruptly terminating the output pulse. Because this feed delay line is in parallel with the 50 Ohm load (actually a transmission line, terminated by the 50 Ohm TEM deflector) the DSRD stack must interrupt 400 A to produce 10 kV pulses.

The operation of the overall network shown in Figure 2 starts when the pump circuit to the left applies 780 V to the 25 nH transfer inductor for 25 ns. During and immediately after this brief pumping interval, a moderate forward current is established in the DSRD stack at the right, establishing narrow, highly concentrated minority carrier populations on both sides of the physical PN junctions within the DSRD diode stack. When the pump switch (the HV MOSFET array) opens, a large portion of the current that has been established in the transfer inductor must be suddenly drawn ***from*** the 1-nanosecond delay line, reversing the current in the conducting DSRD which, by design, opens extremely abruptly after a few nanoseconds delay (i.e. after the plasmas on both sides of the PN junctions collapse). The opening of the DSRD switch causes the reverse current of 400 A to redirect, splitting it equally between the 50 Ohm load and a reflection back into the 50 Ohm source line (i.e. the 1 ns delay line). This condition persists only for the 2 ns round-trip in the delay line, after which the pumping source appears to the DSRD - and the load in parallel with

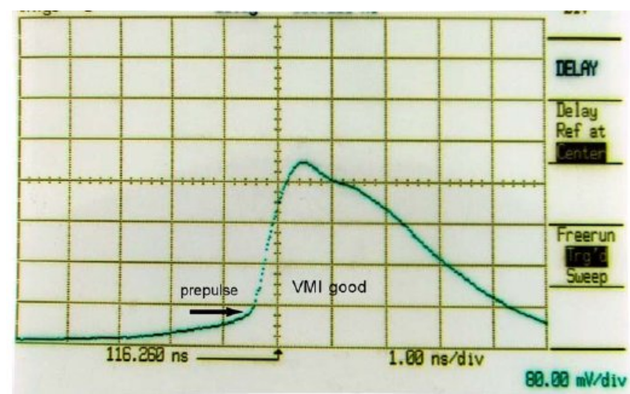


Figure 3: Reverse voltage pulse of VMI fabricated DSRD diode. Forward pumping is 100 nanoseconds in duration. Avalanche occurs above 550V. Time-axis: one-nanosecond per division.

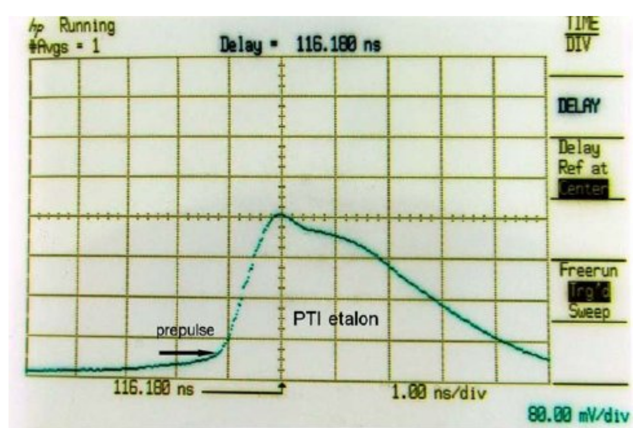


Figure 4: Reverse voltage pulse of Ioffee Physics Institute's PTI etalon DSRD diode. Forward pumping is 100 nanoseconds in duration. Avalanche occurs at 500V. Time-axis: one nanosecond per division.

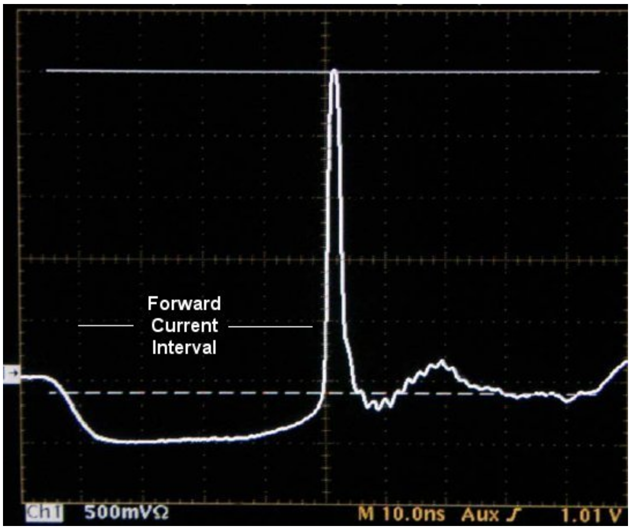


Figure 5: Pump and step recovery switching performance of DSRD stack provided by Ioffe Institute of Physics, compliments of Professor Alexei Kardo-Sysoev. Time axis 10ns/division. Peak voltage 1000V; one-nanosecond delay line employed.

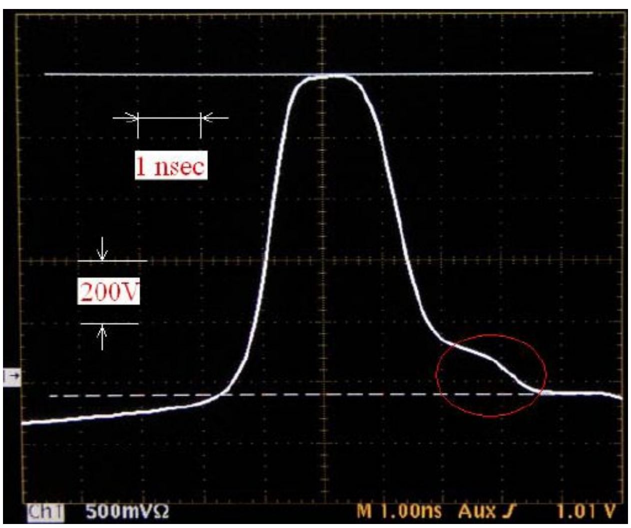


Figure 6: Step recovery switching performance of DSRD stack, time axis; one-nanosecond per division.

it - as a short circuit, which terminates the 2 ns pulse impressed on the load. Delivery of a 10 kV pulse to the load requires that the MOSFET switch array must withstand a voltage of 3.5 kV upon opening.

Fabrication of DSRD diodes at VMI has been accomplished, and these DSRD diodes have been assembled into stacks and successfully tested at Ioffe Institute of Physics in St. Petersburg Russia. Professor Alexei Kardo-Sysoev of this institute has been instrumental in developing the silicon processing at VMI and in the build and testing of the resulting DSRD modules. VMI has proven high-volume technology for producing passivated high-voltage diode stacks, and will soon be producing these from its DSRD diodes as well. Figure 3 and Figure 4 compare of the pulse properties of the VMI produced DSRD diodes with the "PTI etalon" DSRD diodes of Ioffe Physics Institute.

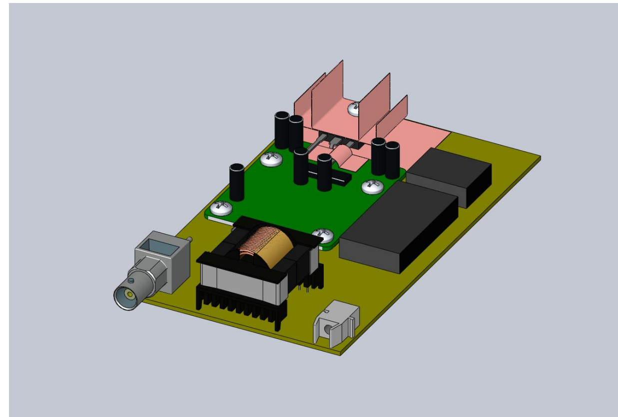

Figure 7: Illustration of individual MOSFET switching card. The pump system will employ eight parallel ranks of three (or four) of these in series. The series arrangement is required to withstand 2.5 kV opening voltage.

Development of instrumentation and methods for characterizing DSRD modules is underway. Dr. Anatoly Krasnykh, coauthor, has been employing a DSRD module provided by Ioffe Physics Institute to prove these capabilities. Figure 5 shows a complete pump and blocking cycle for this device with a 50-Ohm parallel load, and pumped via a one-nanosecond long delay line as shown in principle in Figure 2. Figure 6 shows the principal pulse in higher resolution.

The design of the pump circuitry has been revised substantially. Modeling indicated that extraordinary measures would be required to adequately prevent AC ripple from influencing pulse repeatability within the 1-millisecond bursts. Rather than employing brute force filtering techniques to accomplish this, we have chosen to adopt 3-MHz RF as means of powering the switching logic and gate drivers for the MOSFET switches. Optical fiber will only carry the signals delineating the bursts, but will not affect pulse timing. Each switch card in each series stack of three will be isolated from its neighbors by common mode chokes, which carry the 3-MHz power and synchronizing waveforms. Testing of a breadboard version of the MOSFET switching card, illustrated in Figure 7, is underway. It employs a 800V HV MOSFET as the principal switching component.

## SUMMARY

Development of a fully capable DSRD kicker driving is successfully proceeding, with excellent results obtained from our first commercially produced DSRDs, and a refined circuit for the MOSFET driver. In the next year, the DSRDs will be produced in diode stacks, and combined with the MOSFET driver to demonstrate the full pulse operation required by the ILC.

# DEVELOPMENT OF A NEW HIGHLY BRIGHT X-RAY GENERATOR

Satoshi Ohsawa#, Ikeda Mitsuo, Takashi Sugimura, KEK, Tsukuba, Japan
Noriyoshi Sakabe, KEK, FAIS, Tsukuba, Japan

A new type of rotating anticathode X-ray generator has been developed, in which the electron beam irradiates the inner surface of a U-shaped anticathode. We have achieved emission of X-rays 10 times more brilliant than can be attained by a conventional rotating anticathode. The development is still in progress. New results are reported in details.

## INTRODUCTION

The U-shaped rotating anticathode X-ray generator has achieved highly brightness by means of using heat of fusion. The electron beams are focused so strong that anticathode material, cupper, is being melted in operation [1]. A high-flux electron beam is focused on the inner surface by optimizing the shape of the bending magnet [2, 3]. In order to minimize the sizes of the X-ray source, the electron beam is focused in a short distance by the bending magnet which is small and is close to the rotating anticathode. The power of the electron beam can be increased over the melting point, because a strong centrifugal force fixes the melting part on the inner surface not to be splashed.

## SOUCE SIZE AND RESOLUTION

The electron beam focus size on the U-shaped rotating anticathode was measured using a 10 mm-diameter Au pinhole and a chilled CCD camera with fluorescent film.

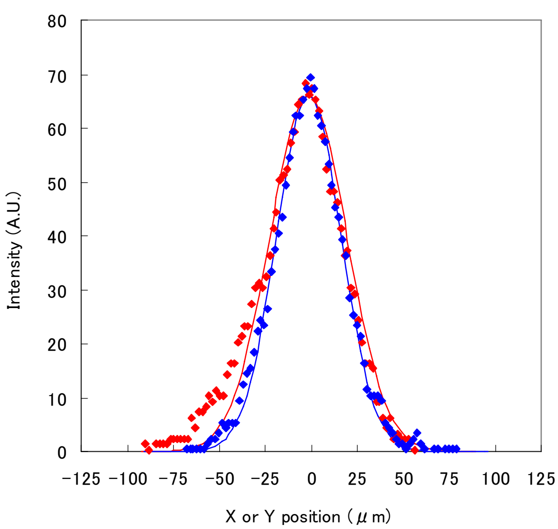


Figure 1: X-ray source distribution on the anticathode.

Figure 1 shows a typical example of the focused electron distribution observed at the takeout angle of 6 degrees from the rotation surface. Each distribution in x and y directions has a FWHM size less than 50μm.

In order to estimate resolution, we took an X-ray enlarged picture of a MFT chart, of which line numbers and width are listed in Table 1. Figure 2 shows an example with a magnifying power of 4.7.

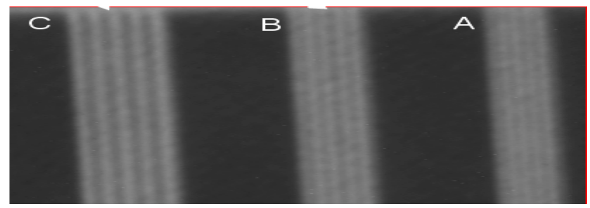


Figure 2: X-ray figure of a MTF chart.

Table 1: MFT chart parameter

| Type | Line density | Line width (μm) |
|---|---|---|
| A | 20 line pairs/mm | 25 μm |
| B | 16 line pairs/mm | 31 μm |
| C | 12.5 line pairs/mm | 40 μm |

## BRIGHTNESS AND CURRENT

Figure.3 presents examples of the achieved brightness

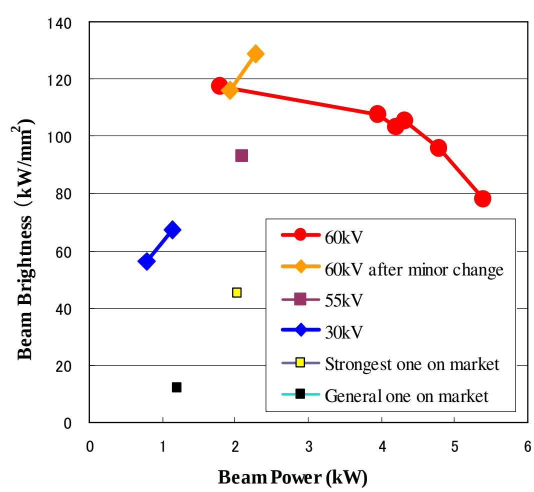


Figure 3: Beam power dependence of brightness.

#satoshi.ohsawa@kek.jp

by the new X-ray generator. Two values of other systems seen in the figure. It would be one of the major subjects to improve ability in the high energy region.

The measured source sizes are plotted in Fig. 4, which correspond to the data shown in Fig. 4. The focus sizes obviously increases linearly or more rapidly in high current region. This is the reason why the brightness decreases in the high power region in Fig. 3. It would be necessary to improve the final focusing.

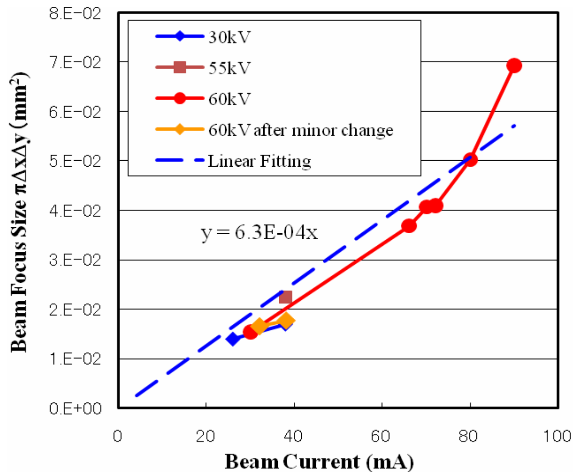


Figure 4: Current dependence of focus size.

## TEMPERATURE OF ANTITARGET

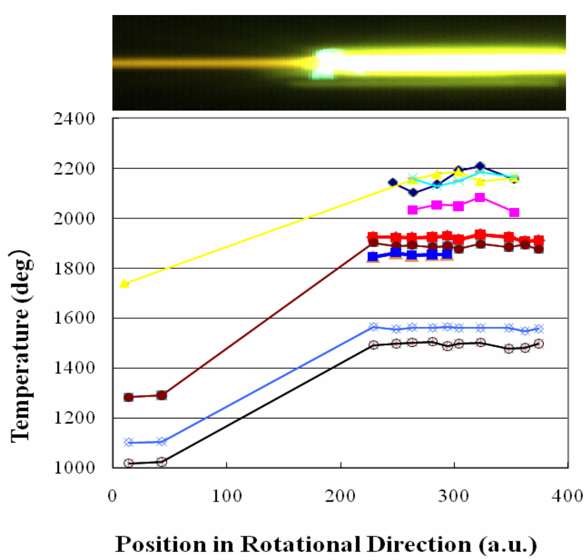


Figure 5: Temperature distribution of the target in rotational direction before and after irradiation.

The temperature near the irradiation area was observed by a two-colour type thermometer. The light for the measurement was taken out through a hole whose visible area on the target is 4.6mm x 6.5mm. The center of the visible area is the irradiation point and the takeout angle of the light is 65 degrees from the rotating surface. The antitarget of 10cm in diameter rotates with 6000RPM. Figure 6 shows examples of temperature distribution on the irradiated area. A visual picture near the irradiation area is shown on the top in Fig. 5.

## ENERGY DEPENDENCE

Cupper has large heat of fusion, which is very useful for suppressing the surface temperature raise caused by electron irradiation. This is one of features of our system in which high brilliant X-rays are safely generated in the range of the temperature over melting point.

In the case that the electron beam power would be fully used to melt the cupper surface, the temperature would be kept at melting point, where vapour pressure is negligibly small. Electrons with energy near the range of 50keV can, however, penetrate into the cupper in short distance; some micrometers. Therefore electrons can directly melt very limited volume near the surface.

In order to suppress the temperature raise, rotating antitargets are generally and widely adopted. The irradiated portion on the surface passes the electron beam cross section with a speed of rotation. Let us think the case that the antitarget is solid state before entering into the electron beam cross section, and in the middle of the passing period, the irradiated area has completely melted. But irradiation still continues. It would make the temperature easily higher to dangerous region since specific heat is too small to suppress.

It is obviously important to well utilize the phenomena, heat of fusion, for developing highly brighter X-ray generator. We have made an experiment to examine the energy dependence of temperature.

The rotating antitarget temperature would be thought to depend only on a rotating speed and the electron- beam power density. In our system, however, the electron energy has an important role, as having being pointed out from early stage by one of authors, N. Sakabe.

The penetrating depth of electron depends on the energy of electrons: higher the energy, deeper the depth. Then the higher-energy electrons can make larger volume melt, and more energy is absorbed for melting. As a result, it is expected that the temperature relatively goes down.

Figure 6 shows energy dependence of the temperature near the irradiated area of the rotating antitarget. The average temperature was measured by a thermometer of two-colour type in a region about 2mm apart from the beam center. This means that the data was taken in about 0.07μs after irradiation. Each connected set of data corresponds to a constant beam current. Energy dependence is obvious from the figure: higher the energy, lower the temperature, even if the beam power increases.

Each data set has a dotted line which was calculated by Eq. 4 with experimental parameters. They have a remarkable agreement.

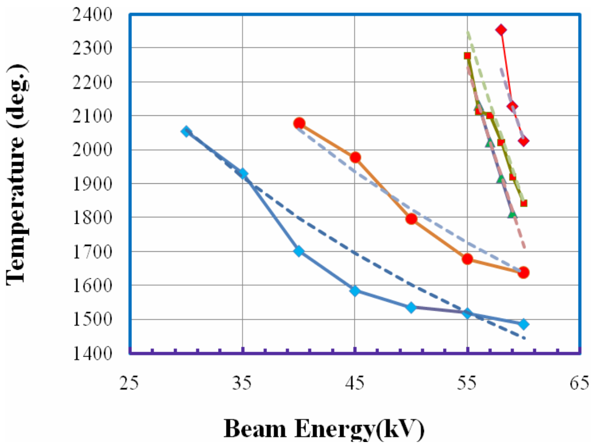


Figure 6: Energy dependence of the temperature at the irradiated area of the rotating antitarget.

## □□a□a□□□□□□□□□□□□a□□□

We can observe the antitarget area near irradiation from -4mm to +4mm in the rotational direction, which corresponds to the time range of 0.1ms before or after irradiation. In such a short time, heat conduction becomes negligibly small, so small that dissipated heat exists only in the area electrons reached. Therefore adiabatic approximation becomes useful. Let us think a case that electron energy increases by a tiny value of $\Delta□$, which is defined here to be measured in unit of Volt. From the energy conservation law we have

$$□\Delta□ = □\rho\Delta□□a\Delta□ + □\rho\Delta□□a□\Delta□, \tag{1}$$

where $□, □, \rho, \Delta□, □a, a□□, □$ are the electron beam current, heat of fusion, density, the beam spot size in the axial direction of rotation, and work correspondent of heat, respectively.

In the right side of Eq.1, the first term represents an increase of heat of fusion in a deeper region of $\Delta□$. Second term corresponds to amount of power increase which is used to raise temperature by a small value of $\Delta□$.

As for the electron penetrating range we assume the following empirical formula.

$$□ = a□^{\beta} \tag{2}$$

Then we have the following equation.

$$\frac{□□}{□□} = -\frac{□\beta}{□□}\frac{1}{□} + \frac{□}{□\rho□\Delta□□a□} \tag{3}$$

This gives us the relation, as follows.

$$□ - □_0 = -\frac{□\beta}{□□}\log\frac{□}{□_0} + \frac{□}{□\rho□(\beta-1)\Delta□□a}\left(\frac{□}{□} - \frac{□_0}{□_0}\right) \tag{4}$$

As for the right side terms, the first term comes from the cooling effect due to heat of fusion, and the second term corresponds to a temperature change in the power dissipating area due to the volume change. As our case of $\beta > 1$, the right side terms have both the same sign. Therefore both terms contribute to decrease temperature with energy up.

We should take attention to the following two facts: The first term contributes only when material melts by irradiation, and the second term depends on $□/\Delta□□a$ so that for small $\Delta□$ the second term becomes dominant as is the case of rapidly changing data in Fig. 6. Fortunately we have a free parameter such as $□a$, which is the rotating speed of anticathode. Others are all characteristic values of matter. By means of enlarging the value of $□a$, we would be able to suppress the second term's effect.

From Eq. 4, higher energy beams are obviously advantageous from a view of temperature.

## □□□□□□□□□□□□□□□□□□□□□□□□a□□□□□□□□

We also measured the X-ray strength shown in Fig. 7. It increases rapidly as is expected from a formula for radiation. As for the characteristic X-rays, however, other consideration would be necessary.

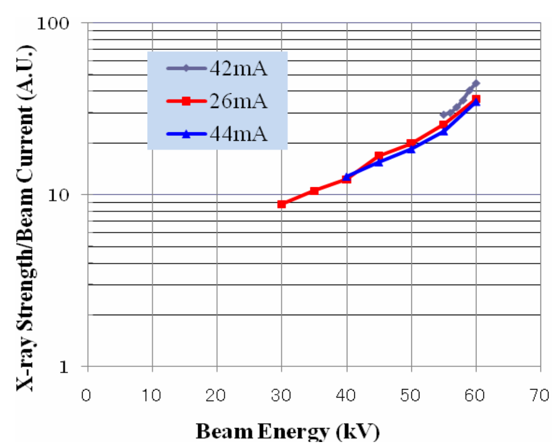


Figure 7: Energy dependence of X-ray strength.

## REFERENCES

[1] N. Sakabe, et al., "Highly bright X-ray generator using heat of fusion with a specially designed rotating anticathode", (2008), Journal of Synchrotron Radiation. 15, part3, 231-234.

[2] T. Sugimura, et al., "Performance of an electron gun for a high-brightness X-ray generator", (2008), Journal of Synchrotron Radiation, 15, part3, 258-261.

[3] S. Ohsawa, et al., "High Brightness Electron Gun for X-ray Source", Proceedings of PAC2005, Knoxville, U.S.A., 1488-1490, (2005).

# NUCLEAR REACTION ANALYSIS BY USING QUASI- ELASTIC SCATTERING OF ULTRA LOW INTENSITY ELECTRON BEAMS

Ryoichi Taniguchi, Ryoya Sasaki, Takao Kojima and Shuichi Okuda
Radiation Research Center, Osaka Prefecture University
1- 2 Gakuen- cho, Naka-ku, Sakai, Osaka, Japan

*Abstract*

High sensitivity nuclear reaction analysis method has been developed by the use of direct nuclear reaction (e,e') with electron bombardment. Huge X-ray burst caused by the bremsstrahlung could be suppressed by the use of ultra low intensity electron beams. Consequently, the neutron emitted by (e,e'n) reaction was measured successfully. The linearity between the neutron count and the concentration of target element was verified experimentally. The method is considered to be useful for the non-destructive analysis of heavy elements such as U and Th.

## INTRODUCTION

A beam pulse of an ordinary electron linear accelerator has about $10^{13}$electrons. In some cases, the radiation is too intensive. We have attempted to develop an ultra low intensity electron beam system by modifying an electron linear accelerator (1). The minimum beam charge about several aC/pulse has been generated (2). The accelerated electrons are basically mono-energetic, controllable, collimatable and synchronized with the accelerator, which are more favorable features compared with those of β-ray sources. In this study, a new analysis method has been developed by the use of the ultra low intensity electron beam developed.

## NUCLEAR REACTION INDUCED BY ELECTRON BOMBARDMENT

Energetic electron beams higher than several MeV occasionally induce direct nuclear reactions with the target nuclei. These processes are attributed to the quasi-elastic scattering of electrons (e,e') with the target nuclei and similar to the photo-nuclear reactions. Theoretically, the reactions are explained that the bremsstrahlung emitted near the nucleus with the electron bombardment (virtual photon) interacts to the same nucleus directly. The experimental results for heavy elements were few, because the reaction becomes to the competitive process with the normal photo-nuclear reaction by the bremsstrahlung emitted from neighboring nuclei. Figure 2 shows an experimental data of electron-disintegration (e,e'n)+(e,e'f) cross section for $^{238}$U (3) and photo-fission cross section of $^{238}$U (4). The figures show that the (e,e') cross section are about one order of magnitude small in comparison with that of the photo-nuclear reaction. However, the following advantages are considered for the purpose of developing a practical nuclear reaction analysis method.

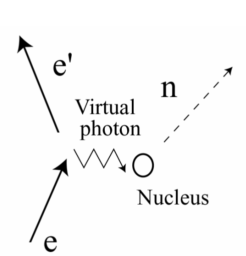


Figure 1: Quasi-elastic scattering of electron

1) The characteristics of the (e,e') reaction are similar to the photo-nuclear reaction. For instance, the both have the same threshold energy. Therefore, the nuclear reaction analysis by using (e,e') reaction has characteristics similar to that of the photo-nuclear reaction analysis. The (e,e') reactions are considered to be effective for analyzing of heavy elements such as U and Th.

2) In the case of the tracer level analysis, the total amount of X-ray burst is far less than that of the photo-nuclear reaction analysis. The X-ray burst is the most harmful phenomenon for the radiation measurement system used in the electron bombardment experiment. In the case of the photo-nuclear reaction analysis, the electron beams are completely transformed to X-rays by a X-ray target, while only partial electrons are transformed to X-rays in the case of the (e,e') analysis.

3) Electron beams are capable of focusing and scanning electrically. The method is considered to be easy of developing to a 2-dimensional analysis method only by the scanning of electron beam.

In the next section, the feasibility of the neutron detection with the electron bombardment are examined experimentally.

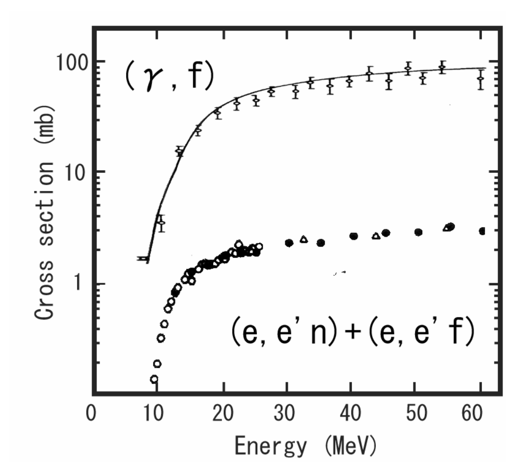


Figure 2: Photo-fission cross section (4) and electro disintegration cross section(3) of $^{238}$U.

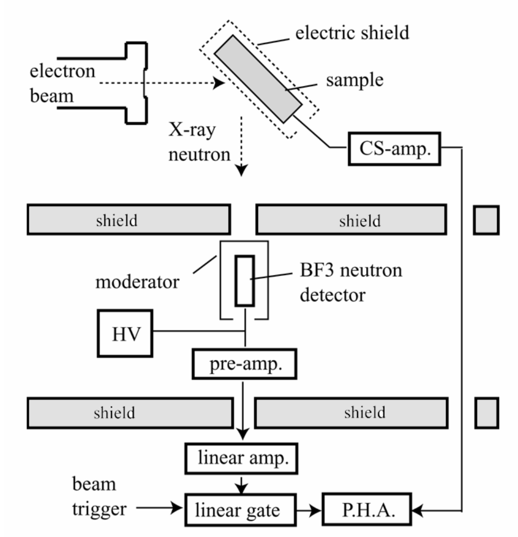


Figure 3: Experimental layout for the neutron detection accompanied with the (e,e') reaction.

## NEUTRON DETECTION

Figure 3 shows the experimental layout of the neutron detection system. The neutrons emitted by the electron irradiation passed through a collimator and injected a moderator at a distance of about 2 m from the target. The neutrons were thermalized in the moderator and measured by a $BF_3$ neutron detector centered in the moderator. The output signals of the pre-amplifier were sent to a linear amplifier set outside of the shielded room. Finally, the signals were analyzed by a multi-channel pulse-height analyzer (PHA). Simultaneously, the beam charges of electrons deposited in the target were monitored by a high sensitivity charge-sensitive amplifier.

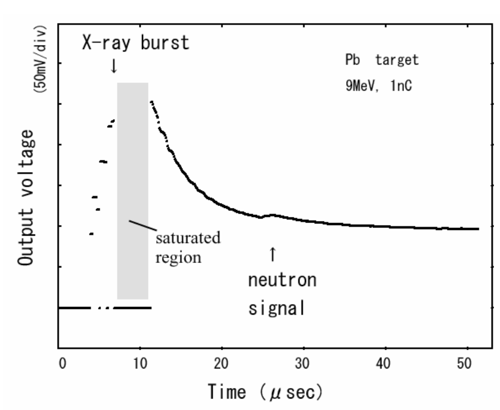


Figure 4: Output signal shape from the preamplifier of the $BF_3$ detector with electron irradiation.

### *X-ray Burst*

Generally, high energy electron irradiation accompanies with strong X-ray caused by bremsstrahlung. Especially in the case of pulse beam accelerator such as an electron linear accelerator, they appear as a huge X-ray burst. It has been severe problem for radiation measurement, even in the case of the ultra low intensity electron beam. First, the effect of the X-ray burst on the neutron detection system was tested experimentally. Figure 4 shows an example of the output pulse shape of the $BF_3$ pre-amplifier at Pb target irradiation. In the left side of the figure, a large and distorted pulse appeared and a tiny neutron signal was seen after the X-ray burst. The charge of electron beam irradiated was only about 1nC, which was about three order of magnitude low compared with that of the normal electron beam. Nevertheless, a neutron detection system was not considered to operate normally under the condition. Some method for reducing the large response of the X-ray burst was required. In this study, we tried to reduce them by the use of a linear gate technique. The generation timing of the X-ray burst was fixed at the time of electron irradiation, while the thermal neutron signal was delayed about few tens micro-second correspond to the thermalization time of the fast neutron. In the detection system used, the response of the X-ray burst could be reduced by the use of the linear gate circuit inserted between the linear amplifier and the PHA. Regretfully, the X-ray burst such as shown in Fig.4 could not be reduced completely by this method, since the large burst signals were distorted and unstable. Then, the electron beam was additionally weakened by about twenty times. Figure 5 shows the result. The horizontal axis indicates the pulse height and the vertical shows the counting rate in logarithm. Figure 5(a) is a pulse height distribution with opening the gate. The pulse height of X-ray burst was larger than that of neutron signals even for an ultra low intensity electron such as about 50pC beam. However, these events were completely eliminated by closing the gate (see Fig.5(b)), while the pulse height distribution of the neutron was not degraded.

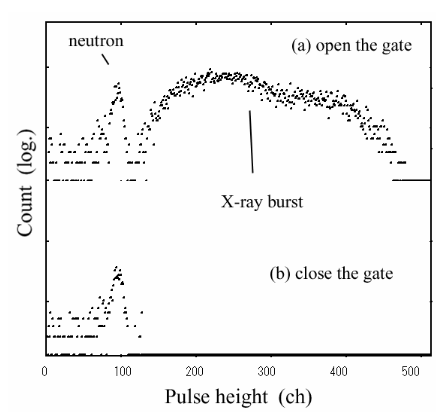


Figure 5: Effect of the linear gate operation.

### *Weakening of Electron Beam*

The linear gate method was effective for reduction of the X-ray burst signal at the thermal neutron detection. However, the method can not apply on the other radiation measurement without the delay time such as fast neutrons and prompt γ-rays. Then, the suppression of the X-ray burst was attempted only by weakening of electron beam. Figure 6 shows the results. The figure shows pulse height distribution of the $BF_3$ detector for Pb target irradiation with electron charge of , (a) 150pC, (b) 40pC, (c) 15pC, (d) 5pC respectively. The linear gate was opened in all cases. The pulse height of the X-ray burst seemed to be lower according to weakening of the electron beam. Finally, the response disappeared in the case of 5pC beam, while the neutron response was remained at the same position. These results suggested that the X-ray burst could be reduced only by weakening of electron beam. The fast neutron and secondary γ-ray accompanied with the electron bombardment would be measured by the use of this method.

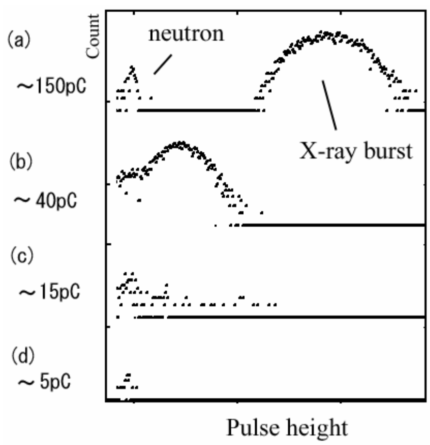


Figure 6: Effect on the pulse height of X-ray burst by weakening of electron beam without gating.

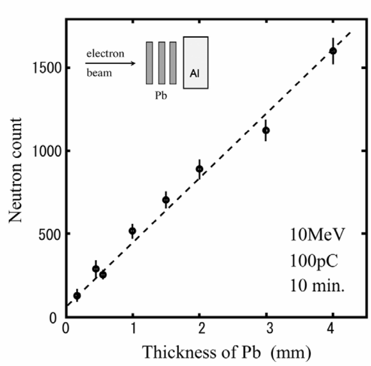


Figure 7: Relation between the neutron detection and the thickness of the Pb layer.

### *Detection Sensitivity*

The relation between the neutron detected and the mass of the target element was examined by the use of the same experimental setup. The diameter of the electron beam was estimated about 3mmφ. Pb thin sheets were used for the target. Figure 7 shows the results. Nearly linear relation was obtained between the neutron and the thickness of the Pb layer. By considering of the beam spot size, one neutron detected by the system corresponded to the 170µg of Pb in the target.

Next, the U and Th sensitivity was measured. The following two samples were prepared, (1) monazite powder, (2) power of refractory bricks respectively. By the use of γray analysis, the sample (1) was estimated to contain 9mg U, 15mg Th and the sample (2) was 0.8mg U, 0.31mg Th. The sample was put into a polyethylene pouch with the surface of 3.5×3 $cm^2$ and analyzed by the electron irradiation. The results show in Fig.8. The excess neutron could be measured only in the case of sample (1). The results show that one neutron count corresponded to the 8µg of U+Th in the target. The sensitivity was evaluated about 30µg for U+Th by considering of statistical uncertainty.

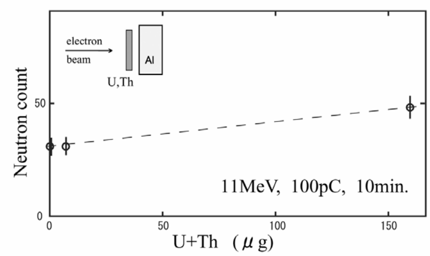


Figure 8 :Relation between the neutron and the mass of U and Th.

## CONCLUDING REMARKS

High sensitivity nuclear reaction analysis system by the use of direct nuclear reaction (e,e') has been developed. The effect of X-ray burst caused by bremsstrahlung could be eliminated by the use of the ultra low intensity electron beams. The linearity between the neutron count and the concentration of target element was verified experimentally. The sensitivity was evaluated about 30 µg for U,Th. The method is considered to be useful for the non-destructive analysis of heavy elements. In the next step, a two-dimensional analysis will be attempted by scanning of electron beam.

A part of our present work was carried out under the support project for accelerator study of universities of the High Energy Accelerator Research Organization (KEK).

## REFERENCES

[1] R. Taniguchi, T. Kojima, S. Okuda and Y. Tanaka. Proceedings of 2006 Linear Accelerator Conference (Aug.21-25, Knoxville, USA, 2006) pp58-60
[2] R. Taniguchi, T. Kojima, S. Okuda, Radia. Phys. Chem. 76, (2007) pp 1779-1782
[3] F.Gerab, M.N. Martins, Phys. Rev.C, Vol. 48, No.1 (1993) pp 105-108
[4] J.D.T. Arruda Neto, S.B. Herdade, B.S. Bhandari, I.C. Nascimento, Phys. Rev. C, Vol. 14, No.4 (1976) pp 1499-1505

# DEMONSTRATION OF MULTI-PULSE X-RAY GENERATION VIA LASER-COMPTON SCATTERING USING PULSED-LASER SUPER-CAVITY*

K. Sakaue,† M. Washio, Waseda University, Tokyo, Japan
S. Araki, M. Fukuda, Y. Higashi, Y. Honda, T. Taniguchi, T. Terunuma, J. Urakawa, KEK, Ibaraki, Japan
N. Sasao, Kyoto University, Kyoto, Japan

*Abstract*

A compact and high quality x-ray source is required for various field, such as medical diagnosis, drug manifacturing and biological sciences. Laser-Compton based x-ray source that consist of a compact electron storage ring and a pulsed-laser super-cavity is one of the solutions of a compact x-ray source. Pulsed-laser super-cavity has been developed at Waseda university for a compact high brightness x-ray source. The pulsed-laser super-cavity enables to make high peak power and small waist laser at the collision point with the electron beam. 357 MHz mode-locked Nd:VAN laser pulses can be stacked stably in a 420 mm long Fabry-Perot cavity with "burst mode", which means stacking of electron beam synchronized amplified pulses in our R& D. In view of this successful result, we have started an X-ray generation experiment using a super-cavity and a multi-bunch electron beam at KEK-LUCX. Recently, the demonstration experiment between the burst mode pulsed-laser super-cavity and the 100 bunch multi-bunch electron beam is successfully performed. Development of the super-cavity and the experimental results of X-ray generation will be presented at the conference.

## INTRODUCTION

Recently, x-rays from synchrotron radiation (SR) is widely used and produced a number of results in various fields, for example, medical diagnosis, biological sciences, material sciences and so on. However, SR x-rays is generated by the huge facility as SPring-8, therefore the use is limited by the operation schedule and the number of users. On these backgrounds, a compact x-ray source has been strongly required and studied in many laboratories. In 1997, Huang and Ruth proposed a compact laser-electron storage ring (LESR) for electron beam cooling or x-ray generation.[1] In this proposal, each electrons and photons storage in storage ring and super-cavity, respectively, and therefore electrons and photons continuously interact and generate a high flux x-rays through the laser-Compton process.

We have developed a laser cavity system as a laser-wire beam profile monitor for measuring the electron-beam emittance at KEK-ATF.[2] We proposed to apply this for pulsed-laser stacking to achieve the high peak power photon target. To use this super-cavity and an electron storage ring, the high peak power laser in super-cavity is scattered by the electron beam continuously, and generate a high quality and high flux x-rays up to $10^{14}$ photons/sec.[3] On the other hand, to use a multi-bunch electron linac and a "burst mode" super-cavity (see Sec. 3), high peak power laser target can be produced, which synchronized with a multi-bunch electron beam, so that linac based compact x-ray source is also readily achievable.

As the first step, we are performing a proof-of-principle experiment of laser-Compton scattering between pulsed-laser super-cavity and multi-bunch electron beam. We call this linac based x-ray source, "LUCX" (Laser Undulator Compact X-ray source).

## LUCX ELECTRON ACCELERATOR

LUCX multi-bunch electron linac is built by the side of the KEK-ATF accelerator. Figure 1 shows the beam line layout of LUCX. As shown in Figure 1, the accelerator consists of a photo-cathode RF-Gun and 3 m-long linac to generate and accelerate a multi-bunch electron beam up to 43 MeV. Beam loading effect in the accelerating structure is compensated by adjusting the timing of rf pulse and so the energy difference in a bunch train is compensated less than 1%.[4] The parameters of a multi-bunch electron linac is shown in Table 1.

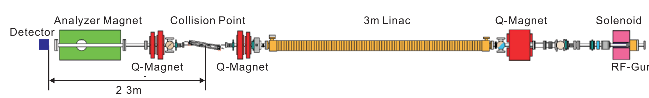


Figure 1: LUCX Electron Beam Line

Table 1: Parameters of Multi-bunch LINAC

| Bunch Charge | Energy | Num. Bunch | Rep Rate |
|---|---|---|---|
| 0.4 nC | 43 MeV | 100/Train | 12.5 Hz |

Laser-electron interaction point is located between the doublet quadrupole magnets to focus at the interaction point and to re-focus a diverging electron beam. At the interaction point, pulsed-laser super-cavity is installed at an angle of 20 deg with beam line, which can produce a high

* Work supported by a Grant-In-Aid for Creative Scientific Research of JSPS (KAKENHI 17GS0210) and a Grant-In-Aid for JSPS Fellows (19·5789)
† kazu-kazu-kazu@suou.waseda.jp

peak and high average power photon target. The detail parameters of the super-cavity are described in following section. Downstream of the interaction point, electrons are bended toward the earth by a right-angle analyzer magnet to separate from the scattered photons and damped after an energy monitor system. According to the distance between interaction point and x-ray detector and the aperture of Be window, x-rays within 10 mrad scattered angle can be extracted from the vacuum.

## PULSED-LASER SUPER-CAVITY

We have been developing the high finesse super-cavity to be used in this project.[5] In pulsed-laser case, the length of mode-locked cavity and super-cavity must be equal with less than nano-meter accuracy on more than 1000 finesse cavity. We have already succeeded in stacking 2.5 kW power in cavity and operating more than 1900 finesse super-cavity system over 10 hours without failing the resonant feedback.[6]

Taking over this successful result, we devised and developed a "burst mode super-cavity", that is a technique of pulsed amplified laser stacking in the super-cavity. Figure 2 shows a diagram of burst mode cavity and Figure 3 shows the timing diagram of burst mode cavity and LUCX multi-bunch electron beam. As shown in Figure 2, mode-locked

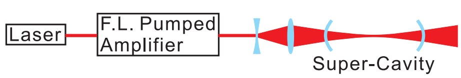


Figure 2: Diagram of Burst Mode Super-Cavity

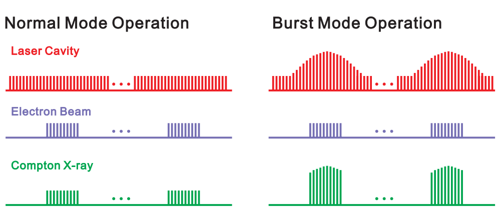


Figure 3: Timing Diagram of Burst Mode Cavity System

laser is amplified by the flash lamp pumped (pulse flash pumping) amplifier before injected to the super-cavity. To inject a pulse-amplified laser, laser power in cavity has high peak power at the pumping timing (Figure 3) and to synchronize a pumping timing to the electron beam timing, the number of x-ray will be enhanced by the gain of laser amplifier.

The measured parameters of burst mode super-cavity is shown in Table 2. We have already succeeded in the burst mode cavity operation and achieved 40 kW peak power in the cavity.

Table 2: Parameters of Burst Mode Super-Cavity

| Amp Gain | Finesse | Waist size | Peak Power in Cav. |
|---|---|---|---|
| 70 | 878.5 | 30.3 μm | 40 kW |

## X-RAY GENERATION EXPERIMENT

### *Expected X-ray at LUCX*

In LUCX, we are planning to generate 33 keV multi-pulse x-rays using 43 MeV multi-bunch electrons and 1064 nm laser light in the super-cavity. To scatter the laser photon off the electron beam at an angle of 20 deg, the generated x-rays in a front scattered angle have the energy of around 33 keV, that the attenuation coefficient of iodine is sharply changed (K-edge). In medical application, around 33 keV x-ray is used for a contrast diagnosis.

Considering the number of generating photons, to use burst mode super-cavity for laser-Compton collision at LUCX, the number of produced x-ray is multiplied by the peak power in the cavity. According to the parameters in Table 1, 2, the expected number of x-ray is $1.56 \times 10^4$ Photons/train in total. As the results of background measurement, this value is enough for x-ray detection.

### *Laser-Compton X-ray Detection*

**X-ray Detector** Figure 4 shows the setup of the x-ray detector at LUCX. Detection system consists of 5mm radius collimator and scintillation detector. We produced a 150 μm thick LYSO scintillation detector to detect x-ray signal, which is not sensitive for high energy photons and has relatively high time resolution (40ns). According to this detector setup, the aperture of detector is about 1 mrad and expected number of detected x-ray is $2.0 \times 10^2$ Photons/train.

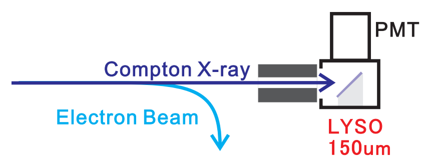


Figure 4: X-ray Detection System at LUCX

**Timing & Laser Power Correlation** We have already performed an x-ray generation experiment using a burst mode cavity, multi-bunch electron beam and a scintillation detector (Figure 4). The experimental results of x-ray detection are shown in Figure 5 and 6 As shown in Figure 6, the number of x-ray is certainly proportional to the laser power. On the other hand, Figure 5 shows the timing cross correlation between an electron beam and a laser pulse, to scan the laser timing at the collision point. The gaussian fit of the experimental result is also appeared in the figure (dotted line) and the rms of fitted line is 0.97 deg (7.5 ps) which is consistent of an electron bunch length. These two results indicate that this signal is exactly produced by the laser-Compton scattering between the multi-bunch beam and the pulsed-laser super-cavity. Concerning the number

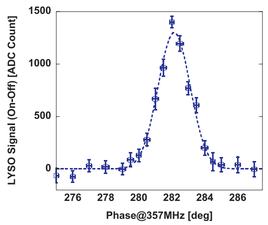


Figure 5: Timing Correlation

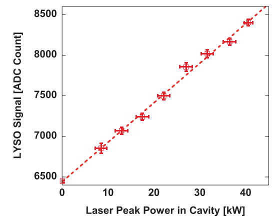


Figure 6: Laser Power Correlation

of produced x-rays, according to the calibration of LYSO scintillation detector, $1.65 \times 10^2$ Photons/Train have been detected at 40 kW peak laser power in super-cavity. This number is consistent with the expected number of x-rays of $2.0 \times 10^2$ Photons/Train

**Vertical Beam Size Measurement** The waist size of the laser target is precisely determined by the mirror curvature and the cavity length in super-cavity, so that scanning the position, measured x-ray profile can be used as the electron beam size measurement. Figure 7 shows the result of laser target position scan. The gaussian fit of the

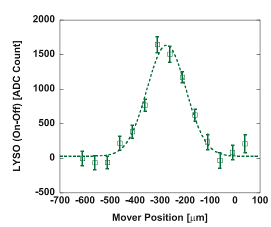


Figure 7: Vertical Laser Position Scan

result is shown by dotted line and the rms of x-ray profile is 77.6 μm. As described in previous section, laser waist size is measured as 30.3 μm. To consider the laser waist, beam size of the electron beam is calculated to 71.4 μm.

### *X-ray Energy Measurement*

After detecting the laser-Compton x-ray, we performed an x-ray energy measurement using a bragg reflector (periodic crystal). The setup of x-ray energy measurement is shown in Figure 8. HOPG (Highly Oriented Pyrolytic

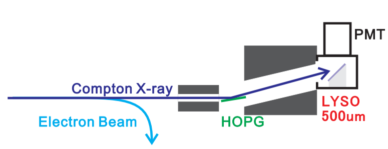


Figure 8: Setup of X-ray Energy Measurement

Graphite) is located after the collimator as the bragg reflector, which has the lattice period of $d = 3.356$ Å. Here, the x-ray energy can be decided by the bragg law (Eq. 1).

$$\lambda = 2d \sin\theta \tag{1}$$

where $\lambda$, $d$ and $\theta$ indicate the wavelength of x-ray, a lattice distance and a glancing angle at maximum reflectivity, respectively. Moreover, HOPG has another advantage, such as larger integrated reflectivity because of its mosaicity so that larger x-ray signal can be achieved at the LYSO detector.

The result of x-ray energy measurement is shown in Figure 9 as a function of electron beam energy. The energy

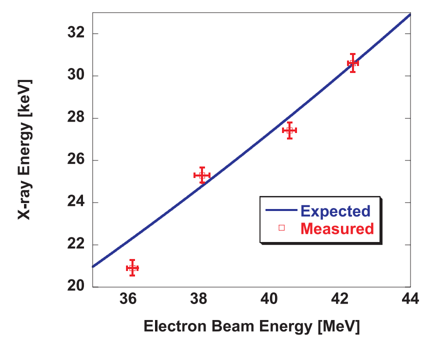


Figure 9: Result of X-ray Energy Measurement

measurement was performed at several electron beam energy, 36, 38, 40 and 42 MeV. The measured plots (red plots) show good agreement with the blue line which indicates the expected x-ray energy as a function of beam energy.

## CONCLUSIONS

We demonstrated a multi-pulse x-ray generation using pulsed-laser super-cavity and multi-bunch electron linac and confirmed the x-ray is certainly generated from the process of laser-Compton scattering by observing the correlation of laser-electron crossing. Further more, the energy of x-ray photon was measured by the reflection angle of bragg crystal and the results were consistent with the calculation.

In future, we will study about the effect of multi-bunch acceleration, and will design and construct a compact x-ray source for practical use, considering both warm and cold linac.

## REFERENCES

[1] Zh. Huang, R. D. Ruth, Phys. Rev. Lett. 80 (5) (1998) 976.

[2] Y. Honda et al., Nucl. Instr. and Meth. A, 538, (2005) 100.

[3] J. Urakawa et al., Nucl. Instr. and Meth. A, 532, (2005) 388.

[4] S. Liu et al., Nucl. Instr. and Meth. A, 584, (2008) 1.

[5] K. Sakaue et al., Proc. of EPAC2006 (2006) 3155.

[6] K. Sakaue et al., Proc. of PAC2007 (2007) 1034.

[7] K. Sakaue et al., Proc. of EPAC2008 (2008) 1872.

# COMMISSIONING OF 10-MEV L-BAND ELECTRON LINAC FOR INDUSTRIAL APPLICATIONS *

S. H. Kim#, H. R. Yang, Y. G. Son, S. D. Jang, S. J. Park, M. Cho, W. Namkung, POSTECH, Pohang 790-784, Korea

J. S. Oh, NFRI, Daejeon 305-333, Korea

*Abstract*

An intense L-band electron linear accelerator is now being commissioned for industrial applications in collaboration with POSTECH and KAPRA. It is capable of producing 10-MeV electron beams with the 30-kW average beam power. For a high-power capability, we adopted a traveling-wave structure operated with 2π/3-mode at 1.3 GHz. The structure is powered by the 25-MW pulsed klystron with the 60-kW average RF power. The RF pulse length is 8 μs while the beam pulse length is 7 μs due to the RF filling time into the accelerating structure. The accelerating gradient is 4.2 MeV/m at the beam current of 1.45 A, the fully-beam-loaded condition. In this paper, we present details of the accelerator system and commissioning results.

## INTRODUCTION

Recently, there are increase demands on electron linear accelerators for industrial applications [1]. In using electron beams as irradiation sources, the higher beam energy is favorable since the penetration depth is larger. However, the electron beam energy is limited by about 10 MeV due mainly to neutron production. For the clinical X-ray systems, a low current and a low repetition rate are required. The X-ray source for the container inspection requires 5-10 MeV with a few kilowatts of the average beam power [2]. On the other hand, the food or waste sterilization system requires relatively high average beam power to which the process speed is proportional [3].

A high average-power electron accelerator is being developed in the institutional collaboration with PAL/POSTECH and KAPRA. The accelerator is installed at CESC and it will be used for not only for sterilizing foods and medical products, but also reforming materials. The accelerator is required to provide an average beam power of 30 kW at the beam energy of 10 MeV. In order to treat such a high-power, an L-band RF system and accelerating column is adopted due to thermal stability compared with an S-band. A travelling-wave accelerating structure is adopted for industrial purposes due to the following reasons. It needs no circulator necessary for the standing-wave structure. It makes the system simpler and less expensive. Also the RF power coupling is insensitive to the beam-loading effect. It makes the operation of system easier. The design details are presented in table 1 and test results in the following sections.

Table 1: Accelerator Parameters

| Accelerator Parameters | |
|---|---|
| Operating Frequency | 1.3 GHz |
| Pulsed RF Power | 25 MW |
| RF Pulse Length | 8 μs |
| Repetition Rate | 300 Hz |
| Averaged RF Power | 60 kW |
| E-gun High Voltage | - 80 kV |
| Pulsed E-gun Current | 1.6 A |
| Beam Pulse Length | 7 μs |
| Beam Energy | 10 MeV |
| Output Beam Current | 1.45 A |
| Beam Transmission Rate | 90% |
| Averaged Beam Power | 30 kW |
| Shape of Accelerating Cell | Disk-loaded |
| Operating Mode of Accelerator | 2π/3 mode |
| RF Filling Time | 0.8 μs |
| Operating Temperature | 40°C ± 1°C |
| Averaged Accelerating Gradients | 4.2 MV/m |
| Beam Loading Factor | - 4.7 MeV/A |
| Temperature Shift Factor | - 2.3 MeV/1°C |

## RF MEASUREMENT

The Thales klystron tube (TV2022D) generates 25-MW pulsed RF with 8-μs pulse length and 300-Hz pulse repetition rate. It is powered by a matched pulse modulator, composed of a set of inverter power supplies, a pulse forming network and a thyratron switch.

The inverter power supplies are 8 units in total, each of 45 kV and average 30 kW. The PFN has 15 stages, each with a 50-nF capacitor and a 2.2-μH inductor. The EEV thyratron tube (CX2412X) switches pulsed power of 45 kV and 3 kA. The klystron tube with perveance of 1.6

*Work supported by KAPRA and POSTECH BK21 Program.
#khan777@postech.ac.kr

μPerv amplifies RF power to 25 MW when the beam voltage is 270 kV. The beam voltage is applied to the klystron with a 1:13 pulse transformer.

The L-band accelerating column is a travelling-wave structure, composed of 31 cells including 5 bunching-cells [4]. It is operated with $2\pi/3$-resonant-mode at 1.3 GHz. As a result of the low-power measurement of the column, the transmission coefficient of the cumulative phase shift per cell is phase advance of each cell is 120°±2° as shown in Figure 1.

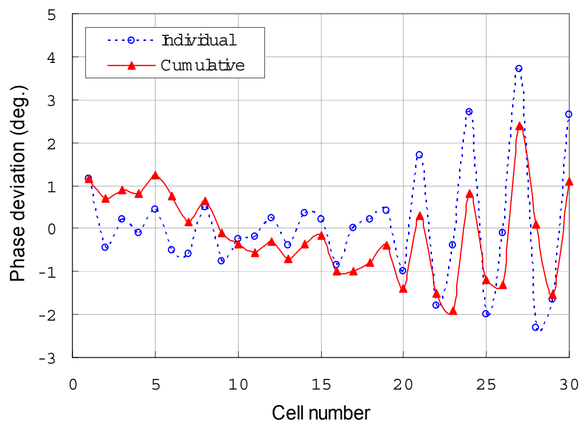


Figure 1: The cell-to-cell phase shifts with respect to 120°.

With an 8-μs pulse length, the klystron supplied peak RF power up to 25 MW. Figure 2 shows the klystron beam voltage, the resulting forward RF power into the accelerating column, and the transmitted RF power out from the column. The transmission is -1.6 dB consistent with the low-power measurement value of -1.5 dB, measured by using a network analyzer. The RF filling time in the column is 0.9 μs.

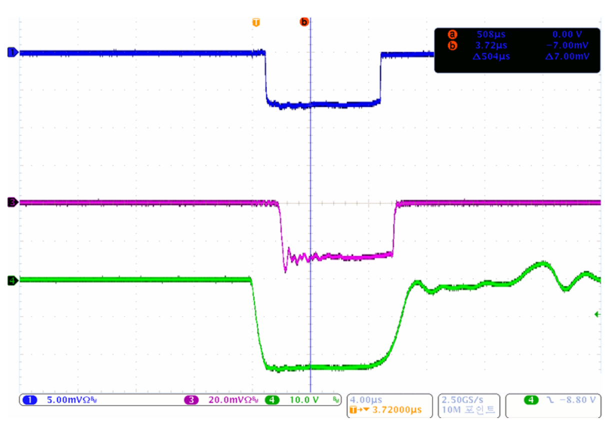

Figure 2: RF power waveform, from top: forward RF power into the column (23 MW), transmitted RF power out from column (16 MW), and klystron beam voltage (260 kV).

## BEAM ACCELERATION

A diode-type Pierce E-gun is used for an electron source, which is capable of emitting 3 A with 80-kV negative high-voltages. For an initial test of electron beam acceleration, the beam emission current was 1.6 A with the E-gun HV of 60 kV. The forward RF power into the accelerating column was 20 MW. With pre-buncher optimization, the accelerated beam current was 1.1 A which is measured at the downstream beam current transformer.

When the electron beam is accelerated by RF power, an electron is able to reach to the end of the accelerating column approximately in 10 ns. Since the RF filling time is almost $10^3$ times longer than the electron flight time, the electron beam was injected to the column immediately after the RF power had been filled through the column as shown in Figure 3.

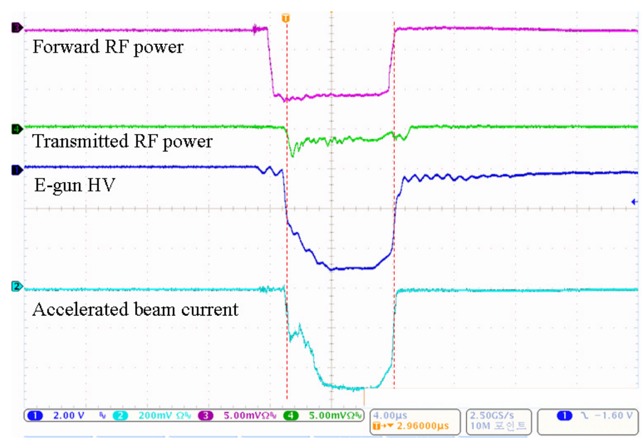


Figure 3: The synchronization of the RF and beam pulses (horizontal: 4 μs/division).

For the improvement of the beam transmission, the pre-buncher is optimized with the RF input power, called a pre-buncher power, and the relative RF phase difference from the accelerating column, called a pre-buncher phase. The changes of the transmission rate with respect to the pre-buncher phase are shown in Figure 4. At the phase of 207°, where the transmission rate is a maximum, the bunch center could slip into the synchronous phase of the RF in the accelerating column [5]. On the other hand, at the phase of 0~20° the RF could not be synchronized with the RF, therefore the transmission rate is a minimum.

With the phase of 207°, the transmission rate is saturated at the pre-buncher power of 0.7 kW, as shown in Figure 5. In the RF linac, the electrons within the acceptable phase are captured and accelerated, since the phase of the electrons can oscillate on the synchronous phase. Over the pre-buncher power of 0.7 kW, the phases of the electron beam are modulated within the acceptable phase [5].

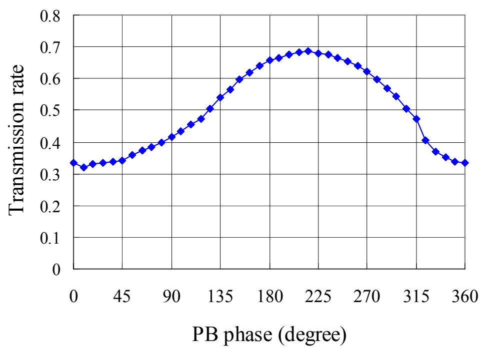


Figure 4: The beam transmission rate with the relative phase of the pre-buncher to the column. The input RF power into the pre-buncher is 0.9 kW.

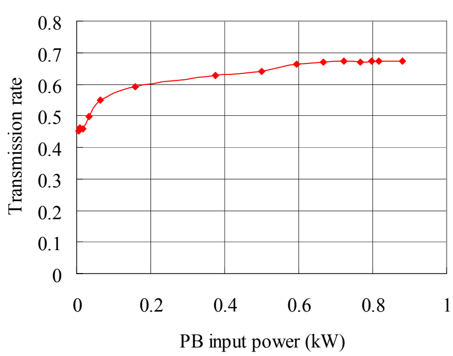


Figure 5: The beam transmission rate with the pre-buncher input power. The pre-buncher phase is 207°.

To measure the electron beam energy, we use an energy measurement tool which composed of 8-layered aluminium plates. The longitudinal length of the first plate is 13 mm as a low-energy filter and the final plate is 20 mm as a beam stopper. The length of the rest plates is 1 mm. The accelerated electron beam energy of 1.1 A with the 20-MW input RF is estimated to be 12.5 ± 0.5 MeV compared with the MCNP simulation on the deposit charge in the plates, as shown in Figure 6 [6].

## COMMISSIONING STATUS

The Operation condition of the RF conditioning without the beam is now as follows: 25-MW RF power, 8-μs pulse length, and 50-Hz repetition rate. After the RF conditioning, we will increase the beam duty factor to the nominal operation parameters.

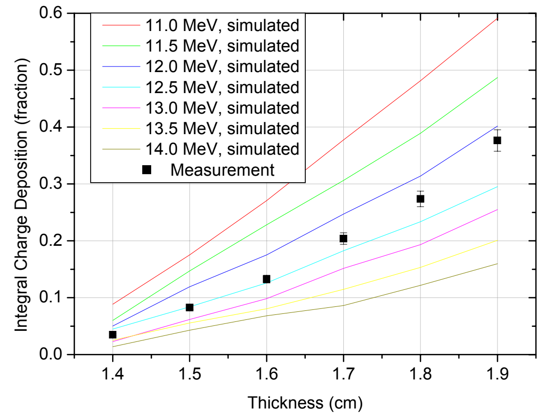


Figure 6: Integrated deposit charges for the electron beam penetrating aluminium plates, measurement values compared with MCNP simulation values.

## ACKNOWLEDGEMENT

This work is supported by Korea Accelerator and Plasma Research Association (KAPRA) and by Pohang Accelerator Laboratory (PAL). The authors express their appreciations to Prof. Luo Yingxiong at IHEP, Beijing for useful discussions.

## REFERENCES

[1] A. M. M. Todd, “Emerging Industrial Applications of Linacs,” in *Proc. Intl. LINAC Conf.* (Chicago, IL, August 23-28, 1998), 1036 (1998).
[2] V. Pirozhenko, et al., “Complex for X-ray Inspection of Large Containers,” in *Proc. of EPAC 2006* (Edinburgh, Scotland, June 26-30, 2006), 2388 (2006).
[3] Y. Kamio, “10-MeV 25-kW Industrial Electron Linacs,” in *Proc. Int. LINAC conf.* (Geneva, Switzerland, Aug. 26-30 1996), 836 (1996).
[4] S. H. Kim, B. Park, S. I. Moon, H. R. Yang, S. D. Jang, Y. G. Son, S. J. Park, J. S. Oh, M. H. Cho, and W. Namkung, J. Korean Phys. Soc. **50**, 1416 (2007).
[5] T. P. Wangler, *Principles of RF Linear Accelerators* (John Wiley & Sons, Inc., 1998), pp. 172 – 192.
[6] T. Tabata, R. Ito, S. Okabe, and Y. Fujita, Phys. Rev. B **3**, 572 (1971).

# PROJECT OF A NEUTRON SOURCE BASED ON THE SUB-CRITICAL ASSEMBLY DRIVEN BY ELECTRON LINEAR ACCELERATOR*

V. Azhazha, A. Dovbnya, I. Karnaukhov, A. Kostromin, V. Krasnorutzkiy, I. Neklyudov, S. Perezhogin, S. Soldatov, A. Zelinsky, NSC KIPT, Kharkov, Ukraine
M. Gohar, ANL, Argonne, IL 60439, U.S.A. I. Bolshinsky, INL, Idaho 83403, U.S.A.

*Abstract*

Today accelerator driven subcritical assembly is candidate for the next generation of energy-generating nuclear facility, which could provide safe energy production, burning of trans uranium elements and transmutation of the radionuclides. Use of the electron beam with particle energy up to 150-200 MeV secures several advantages. Electron linear accelerators are much cheaper compare to hadron accelerators. Homogeneous irradiation of the assembly with neutrons could be provided. NSC KIPT together with ANL develops the project of a neutron source based on the sub-critical assembly driven by electron linear accelerator. Energy of electrons is 100-200 MeV. The target and assembly design is optimized to maximize the neutron source intensity with subcriticality of 0.98. Accelerator on average beam power of 100 kW, with repetition rate up to 300 Hz and pulse duration of 3,2 μs is under development. Transportation line should provide beam transfer with minimal losses of electrons and should form homogeneous distribution of the particle density at the target. Maximal value of a neutron flux is $F_m=2.4\times10^{13}$ n/(cm$^2$s), and power of energy release in the result of nuclei fission is $P_m\approx$ 100 kW.

## INTRODUCTION

National Science Center "Kharkov Institute of Physics and Technology" (NSC KIPT, Kharkov, Ukraine) together with Argonne National Laboratory (ANL, USA) develops the conceptual project of a neutron source based on the sub-critical assembly driven by electron linear accelerator. The main functions of the subcritical assembly are to support of the nuclear industry and medical researches. Reactor physics and material researchs will be carried out at the facility. The goal of the development is to create in Ukraine the experimental basis for neutron research based on safe intensive sources of neutrons. The main facility components are an electron linear accelerator, a system for electron beam transportation from linear accelerator to the target, neutron production target, subcritical assembly, biological shield, neutron channels and auxiliary supporting systems.

Neutron source is a hybrid facility, which is composed from high-current electron accelerator and subcritical assembly. Photonuclear reactions, induced by hard electromagnetic radiation emerging at retarding of the beam of relativistic electrons in the target from heavy element, are used to generate primary neutrons. Two options of the target are under consideration: tungsten and natural uranium. Energy of electrons in driven beam is 100-200 MeV. The sectioned construction of a neutron-generating target has been selected based on depositing of energy and thermo-hydraulic calculations.

The core of the sub-critical assembly on thermal neutrons is made of fuel elements based on the enriched uranium with level of enrichment of 20% uranium isotope-235. Water is a neutron moderator and coolant. Graphite is used as neutron reflector. The target and subcritical assembly is designed to obtain neutron flux as high as possible with subcriticality of 0.98. Thus, possibility of chain reaction occurrence is excluded in the facilities of such a type. Maximal magnitude of neutron flux $F_m$, one of the main characteristics of the source, depends on beam parameters of the accelerated particles, efficiency of neutron yield from the neutron-generating target and characteristics of the sub-critical assembly. Magnitude of neutron flux is regulated by beam current and neutron field in the source disappears after shutting down the driving beam.

In the described facility the maximal meaning of middle plane of a neutron flux averaged by time using uranium target and nominal power of electron beam makes $F_m=2.4\times10^{13}$ n/(cm$^2$s), and power of energy release in the result of nuclei fission of $U^{235}$ makes $P_m\approx$ 250 kW. Considerable proportion of fast neutrons as well as of neutrons of intermediate energies is in energy spectra together with thermal neutrons.

This pater is the first publication inended to describe the main parameters and status of the facility.

The start of the described project can be marked as 2006. At the moment the conceptual design project of the neutron source are designen and egieniering development of the facility systems are began.

## SUB-CRITICAL ASSEMBLY BUILDING

The arrangement of the neutron source based on the accelerator-driven sub-critical assembly is shown in Fig. 1. The linear accelerator is located in the building of the former linear electron accelerator LUE-2000 (1). The electron beam is transported from the accelerator through the transport channel (2) to the sub-critical assembly (3). The sub-critical assembly is to be installed in the experiment room 24x36 m of a new building adjacent to the accelerator building. The sub-critical assembly building contains all the sub-critical assembly elements, neutron channels, neutron stations, and auxiliary systems. The three-storied part of the sub-critical assembly building (5) will host the control room, express laboratories, and all support systems.

The radial dimension of the heavy-concrete biological shielding with a density of 4.6 g/cm$^3$ is 1.8 m. The

*Work supported by STCU Project P-233
~~dovbnya@kipt.kharkov.ua~~

biological shielding contains neutron channels (4), which can be used for various purposes. The neutron channels have a biological shielding of heavy-concrete and steel key blocks, which contain vacuum neutron channels and neutron guides. The channels take neutrons to research stations, which have a biological shielding of their own. Each channel ends in an absorber of unused neutrons with an appropriate biological shielding. Some neutron stations have in-built neutron stoppers.

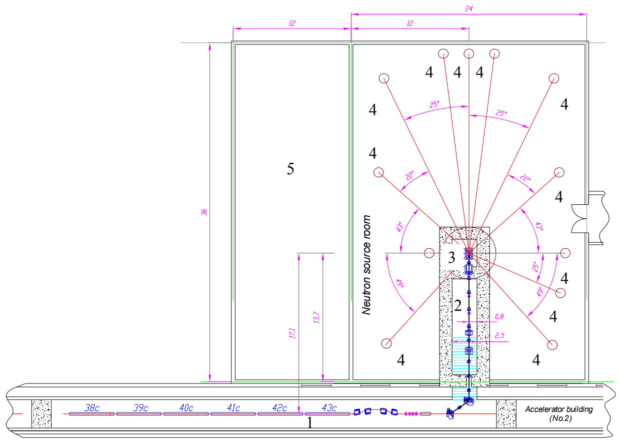


Figure 1. Layout of the Neutron Source Location: 1 – linear accelerator; 2 – electron beam transport channel; 3 – sub-critical assembly; 4 – neutron channels; 5 – express laboratories building.

## LINEAR ELECTRON ACCELERATOR

The use of linear electron accelerator (LEA) as a sub-critical assembly driver imposes a number of requirements. The accelerator output energy of electrons must be in the range of 100-200 MeV. It ensures a sufficient neutron yield, and on the other hand the volume of the neutron target will be sufficient to decrease the energy deposition density and thermomechanical target stress. The existing accelerating structures, sources of high-frequency power and injector systems allow getting an average current at such accelerator output in the required electron energy range approximating 1 mA. Thus, the average power in the beam reaches 100 kW. To minimize losses during beam transport to the target, the energy distribution must not exceed 1%.

The LEA will be installed in the bunker of the LU-2000 linear accelerator complex available at NSC KIPT. Such location of the complex will not require any significant capital construction efforts and will allow utilization of the available engineering infrastructure of the LU-2000 accelerator. New equipment will be installed after dismantling of the existing equipment and renovation of the premises. The main elements of the accelerator complex include an electron injector and five S-range accelerator sections. Section 1 is placed in a short solenoid. The accelerator sections are followed by a beam energy compression system (ECS) consisting of a magnetic debuncher and a compensator section. The system of RF power supply for the accelerator sections and the injector is based on using six SLAC-5045 klystrons.

Considering an average electron beam power of 100 kW at 100-200 MeV energy, the selected klystron type and beam parameters have prompted the accelerator system consisting of five accelerator sections in which the electron beam with 1 A pulse current, 3 µs pulse duration, and 300 Hz repetition rate should achieve the energy of ~ 130 MeV.

There has been selected a uniform regular S-range structure on a progressive wave with $2\pi/3$ type oscillations 4.3 m long. The time required to fill the accelerator structures with HF power is 0.4 µs. The accelerator sections have the following parameters: shunt resistance 46.3 MΩ/m; attenuation 0.0558 1/m; group velocity 0.0327 sec; Q factor 14300. The analyses also considered other accelerator section options for beam current pulse frequency 450 and 600 Hz and a corresponding shorter duration of the pulse current. The results of beam parameter analysis at the exit of LEA and ECS are provided in Table 1.

Table 1: Parameters of the Electron Beam at the Exit of The Linear Accelerator with Energy Compressing System

| $I_{out}$, A | $W_{out}$, MeV | d, mm | $\Delta_{rms}$, mm mrad | $\Delta\varphi°$ | ΔW/W % |
|---|---|---|---|---|---|
| 0.85 | 132.8 | | | | |
| 70% particles | | 1.6 | 21 | 16 | 0.098 |
| 95% particles | | 3.8 | 21 | 41 | 1 |

## TRANSPORTATION CHANNEL

The electron beam transportation channel from the electron linear accelerator to the target should meet the following requirements: transportation of the high current electron beam from the driving linear accelerator to the subcritical assembly with minimal particle losses, electron beam size at the subcritical assembly should be of about ±33 mm in both transversal directions with small value of the beam divergence, electron beam density distribution at the target should be uniform.

The detail description of the transportation channel is given in [1]. The layout of the transportation channel is shown in Fig. 2. After accelerator electron beam is bended with bending angle 90° (two bending magnets, 45° bend in each magnet). The first magnet is aligned with 45° angle to the horizontal plane, the second magnet is aligned in the same plane. Next, the beam is turned on 22.5° angle with two 11.25° bending magnets in vertical plane and turns in horizontal position. In the last turn the reference trajectory of the beam is bended with angle 90° in vertical plane by two 45° bending magnets and is aimed to the target straight from vertical direction.

The beam sizes at sections 1-3 are not bigger than 1 mm. Such focusing provides beam transportation to the section 4 without particle losses. In section 4 quadrupoles and octupoles of nonlinear objective for the beam density shape transformation are set. Increasing of beam sizes in sections 5, 6 can be explained by the requirements to the beam sizes at the target. Aperture of the channel at the sections 1-4 is ±20 mm and at section 5, 6 is ±70 mm. The total beam length is 27.542 m.

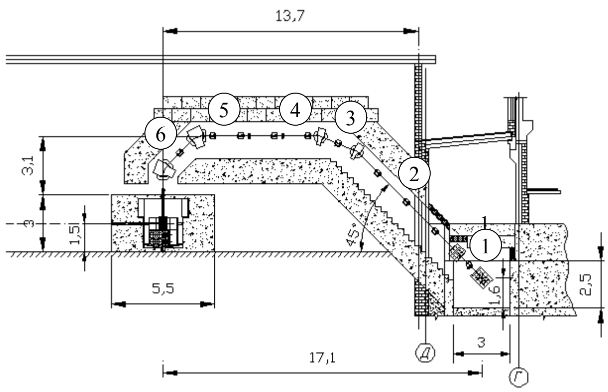


Figure 2. Layout of the transportation channel from the linear accelerator to the sub-critical assembly. Vertical plane.

In the transportation channel two octupole magnets, that are set in place 1 and 2 (Fig. 2), are used [2]. In the point 1 the octupole effects distribution function in horizontal direction. Octupole magnet in the point 2 transforms beam distribution in vertical direction. Initially, it was assumed, that electron beam at the entrance of the transportation channel has Gaussian beam density distribution functions in both horizontal and vertical directions with the same RMS sizes (1 mm and 1 mrad). One can see from the Fig. 3 that use of octupole magnets allows to realize pseudo-uniform distribution of particle density at the target.

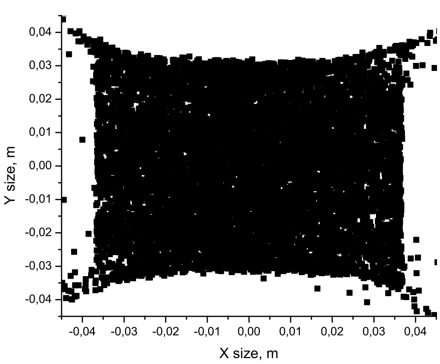


Figure 3. Transversal coordinate distribution of the driving electron beam at the target of the neutron source.

## TARGET AND SUBCRITICAL ASSEMBLY

Natural uranium and tungsten are considered as materials for the neutron generating target. Uranium and tungsten produce the highest neutron yield for electron energy in the range of 50-200 MeV. A single-section WWR-M2 fuel assembly has been selected as reference design of the sub-critical fuel assembly.

The sub-critical assembly is disposed in the redan filled with water. All components of the active zone of the sub-critical assembly are set up in the bottom grid plate, which has orifices for arrangement of fuel elements and rods of graphite reflector. Unusable orifices can be covered with taps to form water flux one needs. All assembling activity concerning fuel elements and reflector will be made with handling machine. Active zone pool circled with reactor tank. Height of the water reflector above active zone is set by the pool height and can not be bigger to excide increasing of multiplication factor of neutrons higher then 0.98. Cooling water of the subcritical assembly is entered the bottom of the active zone tank, cools fuel elements and reflector and through orifice in the very bottom of the outer tank exit trough the tubes to the cooling system of the sub-critical assembly. Neutron target is disposed in the center of the subcritical assembly. The main parameters of the designed sub-critical assembly are provided in Table 2.

Table 2. Parameters of the Sub-Critical Assembly

| N. | Parameter | Value |
|---|---|---|
| 1 | Electron beam power, kW | ~ 100 |
| 2 | Electron beam energy, MeV | 100 ÷ 200 |
| 3 | Neutron yield from the target (U/W), n/sec | $3.28\cdot10^{14}$/$1.91\cdot10^{14}$ |
| 4 | Target material | U238 / W |
| 5 | Fuel $U^{235}$ enrichment, w/o | ≤ 20 |
| 6 | Neutron flux density, n/cm$^2$ sec | ~ $2.4\cdot10^{13}$ |
| 7 | Total neutron flux density in the reflector region, n/cm$^2$ sec | ~ $2\cdot10^{13}$ |
| 8 | Maximum fast neutron flux density in the fuel region with E > 0.1 MeV, n/cm$^2$ sec | ~$1.3\cdot10^{13}$ |
| 9 | Moderator | $H_2O$ |
| 10 | Reflector material and, g/cm$^3$ | Carbon, 2.3 |
| 11 | Total power deposition in the fuel element region, kW | ~ 230 |
| 12 | Max power deposition in the reflector, kW | ~ 20 |
| 13 | Maximum power deposition in the sub-critical assembly, kW | ~350 |

The subcritical assembly is configured in such way to provide maximum flexibility of its operation as with square as well with round target and with various types of fuel elements and reflector to provide variation of neutron flux spectrum.

## CONCLUSION

A conceptual design of the "Neutron source based on the sub-critical assembly driven by the electron accelerator" which meets its primary functions has been developed. Implementation of the design will allow carrying out research with modern nuclear systems and provide ample opportunities for research using neutron beams.

## REFERENCES

[1] I. Karnaukhov, A. Zelinsky, “Transportation channel with uniform electron distribution for the Kharkov neutron source based on subcritical assembly driven by linear accelerator”, EPAC’08, Genova, June 2008, THPC077; http://www.JACoW.org.

[2] Y. Yuri et al. Uniformization of the Transverse Beam Profile by Means of Nonlinear Focusing Method, Phys. Rev. Special Topics, Accelerators and Beam, 10, 104001 (2007) 16 p.

# LOW ENERGY PHOTOEMISSION ELECTRON SOURCE FOR APPLICATIONS IN THZ RADIATION PRODUCTION AND TIME-RESOLVED ELECTRON MICROSCOPY*

N. Vinogradov, P. Piot, C. Prokop, Northern Illinois University, DeKalb, IL 60115, USA
J. Lewellen, J. Noonan, AST DoD Project Office, Argonne National Laboratory,
Argonne, IL 60440, USA

## Abstract

A simple, inexpensive, and compact low-energy (~20 KeV) photoemission electron source was designed, built and recently commissioned. It uses a commercial ultraviolet photocathode drive laser producing 3 ns (FWHM) pulse. The source will eventually be used to drive a table-top THz radiation source, based on the Smith-Purcell free-electron laser scheme, and could also have potential application to time-resolved electron microcopy. We present experimental measurements of the photoemitted electron beam and numerical simulations of the anticipated parameters. We also discuss the generation of flat beams required to efficiently drive the THz radiation source.

## INTRODUCTION

Generation of pulsed electron beams is essential for a variety of applications. In the electron sources based on thermionic and field emission effects it can be obtained by pulsing the extracting voltage, therefore, the temporal beam properties in this case are defined by the performance of the pulsed high voltage power supply. In the case of photoemission-based sources, the electron bunch mirrors the driving laser pulse that dictates the longitudinal and transverse properties of the bunch [1]. Low-energy pulsed electron beam can be generated using a simple, compact structure with dc accelerating field between anode and photocathode. This beam is characterized by very low transverse emittance because the initial transverse energy of the photoelectron is the same as its work function, i.e. a few eV. An additional advantage of photoemission-based sources is a possibility of producing spin-polarized electron beams that can be done, for instance, by impinging a circularly-polarized laser on a strained GaAs photocathode [2]. The time-resolved microscopy and spin-polarized electron microscopy are examples of promising applications for a low-energy photoemission electron gun. Besides, such a source can ideally serve as a driver for compact Smith-Purcell Free-Electron Laser in order to produce THz radiation [3]. In this approach a flat electron beam is propagated over metallic grating thereby producing radiation by periodical motion of the induced surface charge.

Recently we have constructed and commissioned the electron gun to study the physics and operation of a source based on the aforementioned conceptual framework [4]. The source generated >20 keV electron bunches with 1.3±0.1 ns RMS duration and 4±0.2 nC charge that corresponds to a peak current of about 1 A. The experimental results of the source commissioning along with detailed numerical model for the flat beam generation are subjects of this report.

## SOURCE DESIGN AND PERFORMANCE

The source structure consists of grounded anode with the beam aperture in the center and biased cathode shaped as a truncated cone for initial focusing of photoelectrons emitted from the central planar area of the electrode. Pure copper was chosen as a cathode material due to simplicity, low cost and modest vacuum requirements. The work function of copper is relatively high (4.65 eV) and requires an ultraviolet (uv) laser as a driver. We used a commercial frequency-quadrupled Nd:YAG laser from Continuum Inc. [5]. The laser operates at 266 nm wavelength (corresponding to a photon energy of 4.66 eV) and is specified to produce 1.3~2.1 ns RMS pulses with energy up to 4 mJ per pulse at repetition rate of 1 to 15 Hz. The quantum efficiency (ratio of number of emitted electrons over the number of photons in the incoming laser pulse) is typically low for pure metals and was reported to be in the range $10^{-6} \div 10^{-4}$ for copper. For the given laser beam energy, the expected total bunch charge of a photoemitted bunch is a few nC. The laser beam is transported using an optical system composed of uv lenses and mirrors to irradiate the cathode through a sapphire window at 45 deg incidence angle. Measurements of the laser pulse energy and duration are performed using a powermeter and a fast photodiode respectively. The transverse distribution of the laser intensity on the cathode is directly monitored using a combination of CCD camera and "virtual cathode" that is one-to-one optical image of the real cathode on a uv-sensitive screen located outside of the vacuum enclosure. The dc bias voltage applied to the cathode can reach 20 kV that corresponds to 0.5 MV/m for axial surface field in the center of cathode and 1.1 MV/m maximum field achieved approximately in the middle of anode-cathode gap. A fast Faraday Cup for bunch charge and length measurements was fabricated and installed on the source axis about 1 cm downstream the anode aperture. All components of the source are mounted inside the vacuum chamber equipped with various ports to connect the vacuum pumps, sapphire window, electrical feedthrough, etc. An overview of the experiment setup appears in the Fig. 1.

Extensive beam measurements have been carried out for a wide range of accelerating voltage, laser pulse energy, and size of the laser spot on the cathode. An

[1] Work supported by the Department of Education under contract P116Z010035 with Northern Illinois University.

example of measured bunch intensity distribution is shown on Fig. 2.

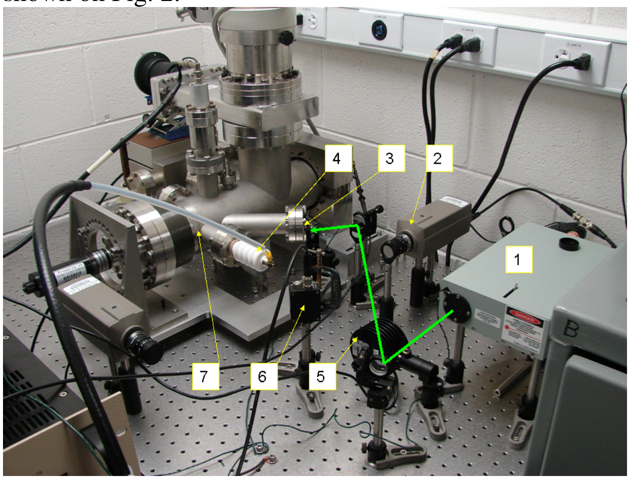


Figure 1. The experimental setup includes laser MINILITEII (1), CCD camera (2), UV viewport (3), high voltage feedthrough (4), powermeter (5), fast photodiode (6), vacuum chamber with pumps (7). The laser beam path is shown as a green line.

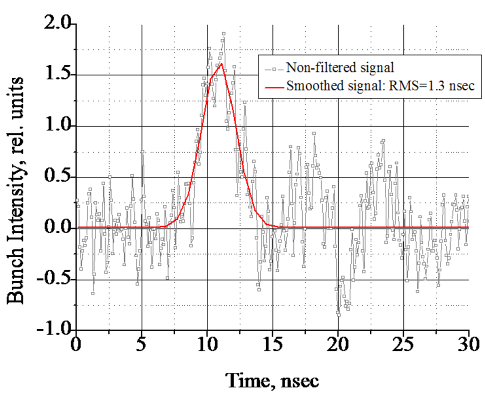


Figure2. Measured eletron bunch temporal distribution.

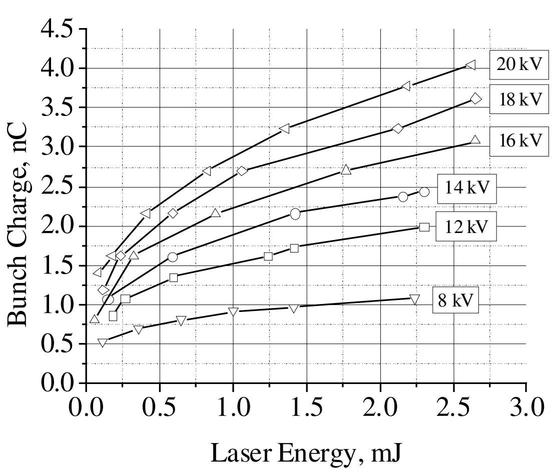


Figure 3. Extracted bunch charge as a function of laser beam energy for different values of extracting voltage.

The longitudinal space charge effects in the bunch have been found to be insignificant. Figure 3 shows an example of measured bunch charge as a function of laser pulse energy and accelerating voltage. Extrapolation of the quantum efficiency value to the zero laser energy limit inferred from these graphs gives $5 \cdot 10^{-5}$ for 20 kV accelerating voltage, which is consistent with previously reported results. The total extracted bunch charge of 4±0.2 nC corresponds to ~ 1 A peak current for the given bunch duration.

## GENERATION OF FLAT BEAM FOR SP-FEL APPLICATION

A promising application of the described source is the generation of copious amount of THz radiation via Smith-Purcell free-electron laser (SP-FEL) scheme. In a SP-FEL an electron beam propagate above a metallic grating and under certain condition can interact with a backward evanescent wave propagating in the grating [6]. A flat beam could enhance the interaction between the electrons and metal grating surface, thus reducing the gain length associated with the SP-FEL mechanism [7]. We plan to generate a flat beam starting from a magnetized beam as initially proposed in Reference [8]. The photocathode will be immersed in an axial magnetic field provided by a solenoid and a set of three quadrupole located downstream of the electron source will remove the angular momentum thereby generating a flat beam, i.e. a beam with high transverse emittance ratio

Numerical modeling of the proposed round-to-flat beam transformation has been performed using the ASTRA particle tracking code [9]. The transformation channel will be located approximately 70 cm downstream of the cathode and consists of three printed-circuit quadrupoles provided by University of Maryland [10]. An electrostatic lens (Einzel lens) will be installed 17 cm downstream of the cathode to adjust the transverse parameters of the photoemitted beam at the entrance of the first quadrupole. Start-to-end simulation of the beamline were performed with ASTRA following the procedure outlined in [11]. An example of simulated flat beam is shown on the Fig. 4; the achieved final transverse emittances ratio $\varepsilon_y/\varepsilon_x$=141.

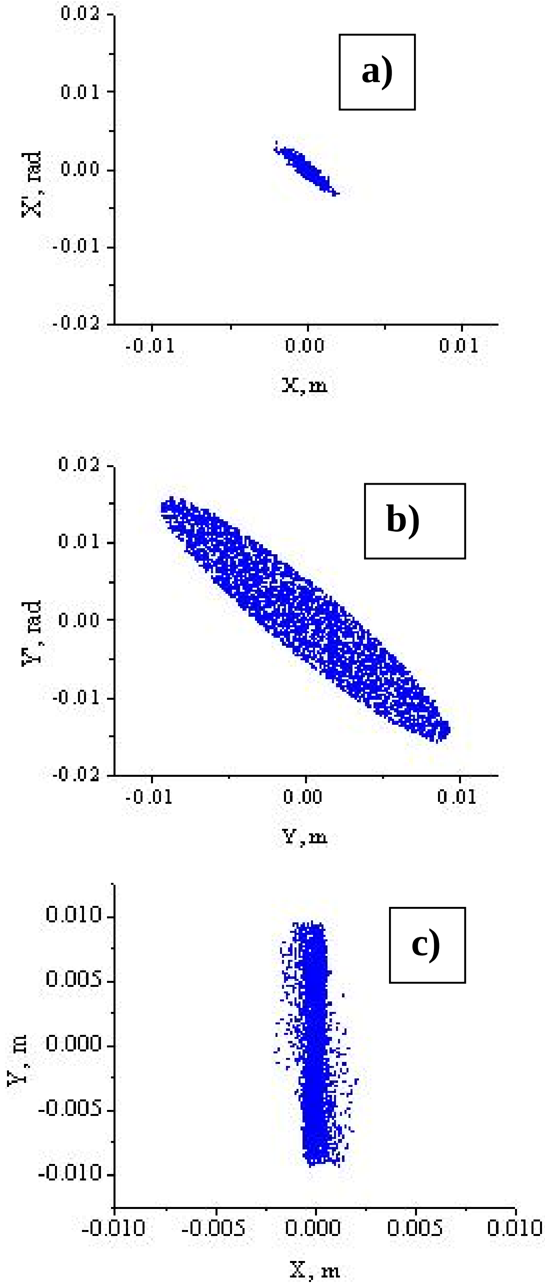


Figure 4. Simulated horizontal (a) and vertical (b) phase space distributions and the beam front view (c) at the exit of transformation channel.

Table 1. Flat Beam Parameters at the Entrance (IN) and at the Exit (OUT) of the Transformation Channel

| | IN | OUT |
|---|---|---|
| RMS X, mm | 2 | 0.4 |
| RMS Y, mm | 2 | 4.7 |
| RMS $\varepsilon_x$, mm mrad | 6.4 | 0.09 |
| RMS $\varepsilon_y$, mm mrad | 6.4 | 12.7 |

## SUMMARY

A new photoemission-based low-energy pulsed electron source has been commissioned. The source is capable of producing up to 4 nC bunches with RMS duration of 1.3 nsec that correspond to a peak cuurent of 1 A. We have also studied the application of the proposed source for production of Terahertz light via Smith-Purcell Free Electron Laser (SP-FEL) scheme. The numerical model has been developed to establish the parameters of transformation channel incorporating three quadrupoles in order to produce a flat beam required for SP-FEL. Experimental production of flat beams is foreseen in the nearest future.

## REFERENCES

[1] G. A. Westenskow, J. M. Madey, “Microwave electron gun”, Laser and Particle beams, 2, 223 (1984).

[2] D. T. Pierce, F. Meier, P. Zurcher, Appl. Phys. Lett. **26**, 670 (1975A.

[3] S. J. Smith, E.M. Purcell, Phys. Rev. **92**, 1069 (1953).

[4] N. Vinogradov et al., Proc. of PAC 2007 conf., Albuquerque, NM, June 25-29, 2007.

[5] www.continuumlasers.com

[6] J.Urata et al., Phys. Rev. Let., **80**, 516 (1998).

[7] C. Bohn et al. (unpublished), available at nicadd.niu.edu/presentations/BohnFNPLspeoi.doc

[8] Y.-E Sun et al., PRST(AB), v. 7, 123501 (2004).

[9] K. Flöttmann, “ASTRA: A Space Charge Tracking Algorithm,” user's manual available at http://www.desy.de/~mpyflo/Astra_dokumentation

[10] W.W. Zhang et al., PRST(AB), v. 3, 122401(2000).

[11] C. Bohn et al., Proc. of LINAC 2002 conf., Gyeongju, Korea, August 19-23, 2002.

# THE ISAC-II SC-LINAC OVER CURRENT MONITORING SYSTEM

A.K. Mitra, J. Drozdoff, K. Langton, R.E. Laxdal, M. Marchetto, W.R. Rawnsley, J.E. Richards, TRIUMF, Vancouver, Canada

*Abstract*

A personnel protection system is used to monitor the ion beam current into the experimental hall from the ISAC-II SC-linac. Two resonant capacitive pickups in the transfer line operate at 35.36 MHz, the third harmonic of the bunch rate. Ion charge, velocity and bunch width affect the sensitivity so calibration with dc Faraday cups is needed. Each monitor has a single conversion receiver with an active mixer. LO signals are provided by frequency synthesizers locked to the accelerator synthesizer. The 1250 Hz IF signals are amplified, filtered with a 100 Hz bandwidth and amplitude detected. An antenna in each monitor loosely couples a pulsed RF test signal to each pickup. These induced signals are mixed down to 11.875 kHz, filtered, detected and used to provide watchdog signals. The measured currents are displayed through our EPICS control system which allows setting of the gain ranges, trip levels and conversion factors. The signals are also processed independently by dedicated analog comparators and CPLDs to cause the Safety system to trip the beam if the current exceeds a nominal 5 to 10 nA.

## INTRODUCTION

A pair of Non-Intercepting beam current Monitors (NIMs) have been installed in the ISAC-II accelerator vault downstream of the SC-linac. Fig. 1 shows a recent calibration using dc Faraday cups downstream of each monitor. The sensitivity of less than 0.1 nA is sufficient for generating beam trips from 5 to 10 nA. The pickups have been described previously [1]. The electronics and Safety system aspects will be described here.

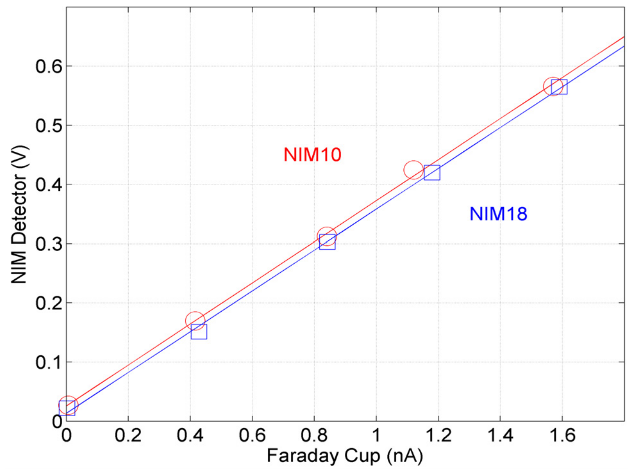


Figure 1: Calibration data using a $^{22}Ne^{+2}$ 2.7 MeV/u ion beam with straight line fits.

## SYSTEM

### *Front End Electronics*

The buffered NIM signals are brought out of the vault on Heliax solid shielded coax to the electronics racks, see Fig. 2. Each NIM signal passes through an Analog Devices AD8332 low noise amplifier. The Local Oscillator (LO), an Agilent N5181A frequency synthesizer, is locked to the 10 MHz reference from the accelerator synthesizer to minimize frequency drift. Its frequency is set to be offset from the signal frequency and multiplied by 4 to accommodate the AD8333 I/Q demodulator. The demodulator divides the LO down and

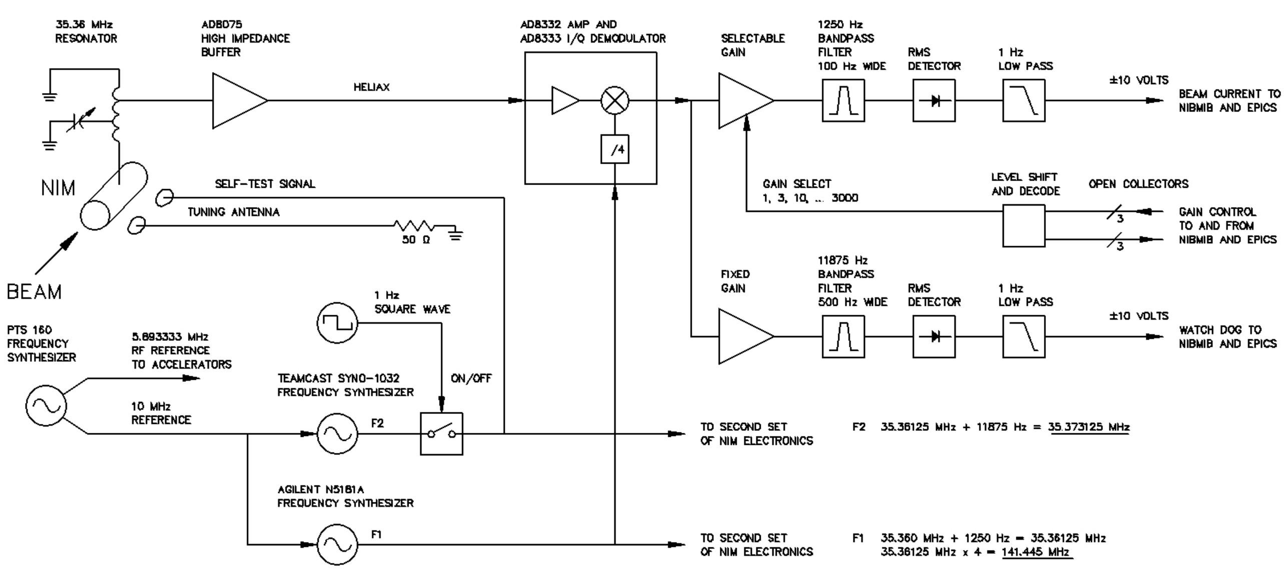


Figure 2: A block diagram of the front end electronics.

mixes it with the 35.36 MHz NIM signal to yield a 1250 Hz IF signal. Image rejection is not used as the background is due to leakage from the RFQ and bunchers which has the same frequency as the beam signal. LF356 op amps amplify the 1250 Hz signal. Wide dynamic range is provided by eight gain ranges which can be selected by the operator. The signal passes through a 100 Hz wide active bandpass filter. Amplitude detection is performed by an RMS converter followed by a low pass filter. The narrowband technique used here is similar to that of an earlier Atlas design [2].

A watchdog signal is provided by a TeamCast SYNO-1032 embedded frequency synthesizer. Its output is pulse modulated by a 1 Hz square wave and fed into the NIM by a small antenna near the capacitive pickup tube. The signal is mixed down to 11.875 kHz by the demodulator and amplified with a fixed gain. It is separated by a second bandpass filter and amplitude detected.

### *Interface to EPICS and Safety System*

The Non-Intercepting Beam Monitor Interlock Box (NIBMIB) monitors the beam current, watchdog, and gain control signals in parallel with the VME/EPICS system, Figs. 3 and 4. The NIBMIB provides a contact closure for the ISAC Safety System based on the monitored signals. The buffered beam current signal is compared to a bipolar threshold manually set by the operators via EPICS and the result of the comparison is fed to a Complex Programmable Logic Device (CPLD), an Altera EPM3256. The buffered watchdog signal is fed into two window comparators which detect acceptable states of the signal and the results are fed to the CPLD. The CPLD monitors the watchdog to determine that it is switching between the acceptable states at a 1 Hz rate. The beam current gain control signals (three bits) set by the operators via EPICS are compared in the CPLD to the actual gain setting returned from the front-end electronics. If the beam current threshold is exceeded, the watchdog is not switching states at the correct rate, or the gain settings don't match then the CPLD opens the contact initiating a beam trip by the ISAC Safety System. A manual reset from EPICS can restore the contact closure once a safe state is restored.

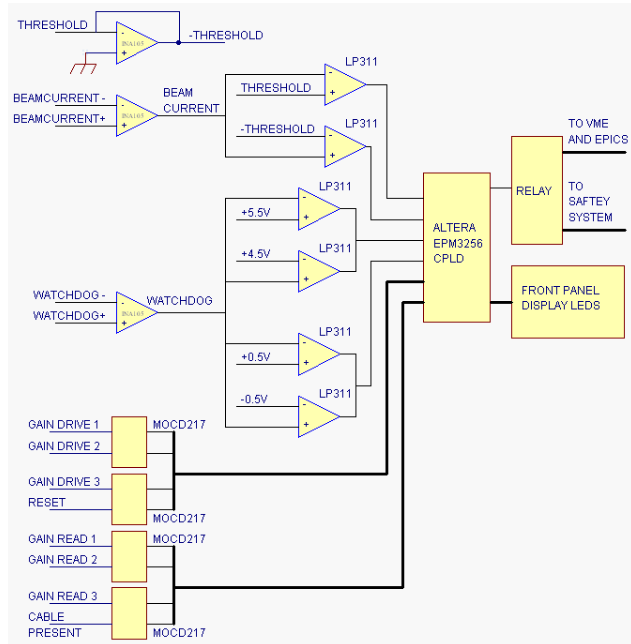


Figure 4: An Interlock Board.

The resolution of the VME ADCs is 11-bits plus sign while that of the DACs is 15-bits plus sign. The EPICS edm display for one of the monitors is shown in Fig. 5. For operator familiarity, it is very similar to that of a dc Faraday cup.

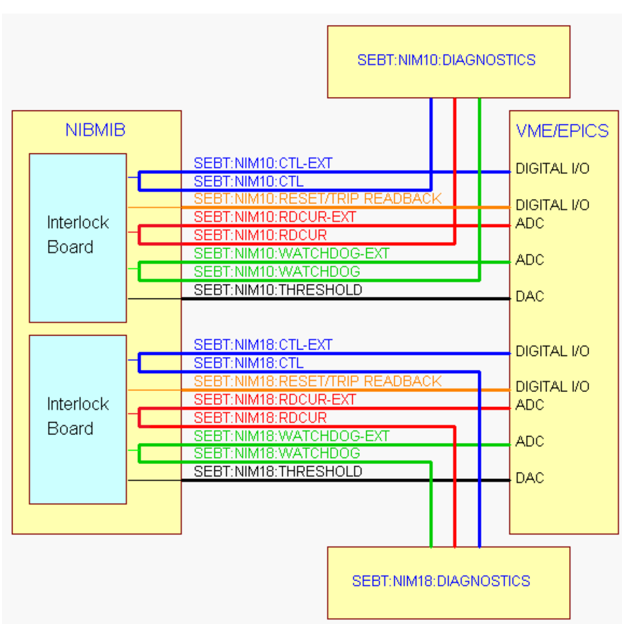


Figure 3: The system interconnections between the front end electronics, the NIBMIB and the VME/EPICS.

### *Safety System*

The ISAC Safety System (ISS) interlocks ensure that beams with parameter levels above pre-determined Vault NIM set points are not transported into the unshielded Experimental Area but are instead contained in the shielded SC-linac Vault. If any NIM set point is exceeded during beam delivery to the Experimental Area the ISS generates a NIM TRIP and drives in source Faraday Cups as well as a Vault Beamblocker downstream of the SC-linac. After the ISS receives indication that the downstream Vault Beamblocker has indeed reached its in limit, ISS interlocks will allow the source Faraday Cups to be driven out, allowing beam tuning to take place in the shielded Vault. Parameter levels above setpoints must be lowered to be below setpoints before the Vault Beamblocker can be driven out again, resuming safe beam delivery to the Experimental Area. A test of the NIM trip logic using the Safety system simulator is shown in Fig. 6.

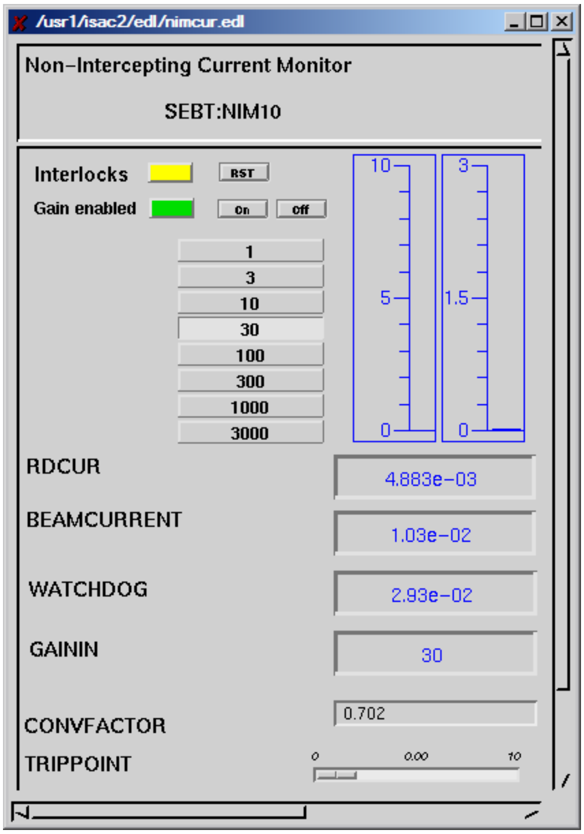


Figure 5: An EPICS edm display, beam off background.

## CONCLUSION

Though the NIM system has redundancy and self-test, an independent method of beam current measurement is still a licensing requirement. We have an 11.8 MHz buncher ahead of a 35 MHz RFQ which is followed by an 11.8 MHz chopper. Since the buncher works at the third sub harmonic the time structure after the RFQ has two main peaks spaced by 86 ns and two small satellites between them spaced by 28 ns. The chopper is used to clean the time structure by deflecting the satellites onto the side of a slit while the main peaks pass through. A pickup plate with nearby biased wires will be added to the slit to allow the deflected beam current to be measured. The new pickup will be tested this Fall to determine if the ~3% deflected beam can be reliably measured and used as an indication of total beam current.

## REFERENCES

[1] W.R. Rawnsley, R.E. Laxdal, A.K. Mitra, “A Non-intercepting Beam Current Monitor for the ISAC-II SC-Linac” PAC07, Albuquerque, June 2007

[2] J.M. Bogaty and B.E. Clifft, “A Low-Cost Non-Intercepting Beam Current and Phase Monitor for Heavy Ions” PAC’95, Dallas, May 1995, V4, pp. 2625-2627

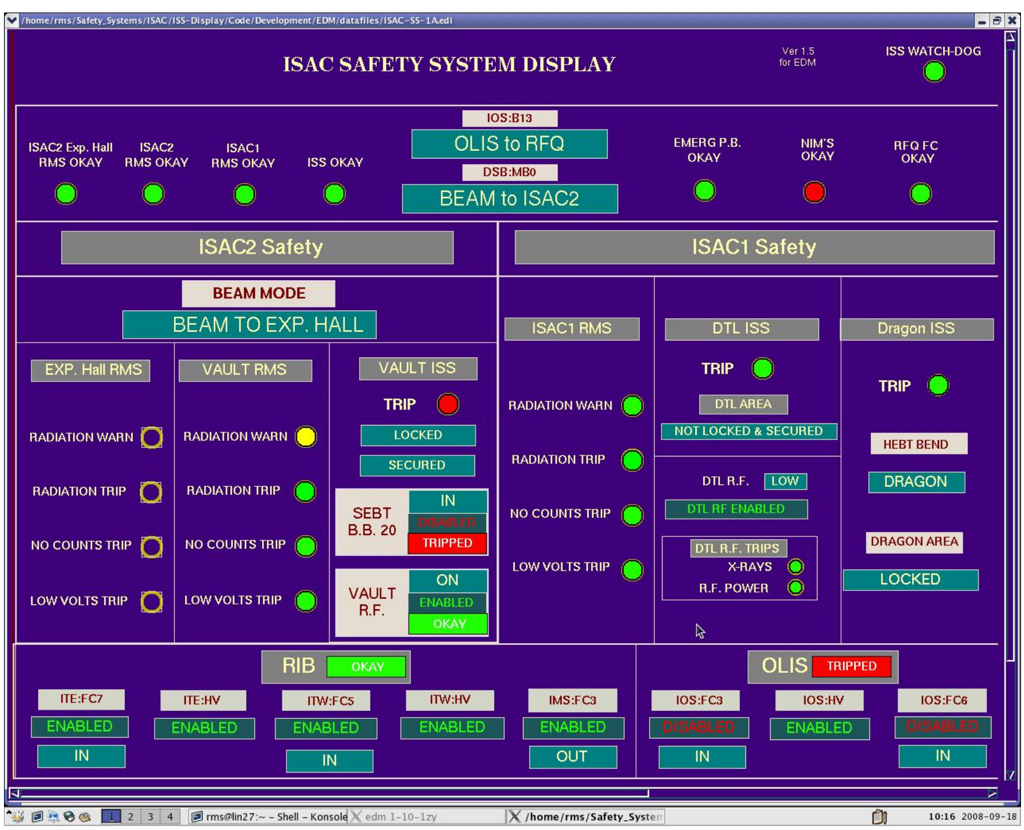


Figure 6: The ISAC Safety System simulator display screen while testing a NIM trip.

# AIRIX DIAGNOSTIC DEVICES FOR FOCAL SPOT SIZE AND DOSE MEASUREMENTS

O. Pierret, CEA, Pontfaverger-Moronvilliers


## Abstract

AIRIX is a 2 kA, 19 MeV, 60 ns, single shot linear accelerator that produces X-rays from the interaction between relativistic electrons and a Tantalum solid target (Ta). Focal spot size, integrated and temporal dose are the main characteristics that we need for the successful development of flash radiography at hydro test facilities. MTFX is a 12 bit Charge-Coupled Device (CCD) intensified camera which is equipped with a scintillator. It can give focal spot size measurements in two directions using a two dimensional wedge. By another way Mucaddix is a CVD Diamond detector which is integrated nearby the AIRIX X-ray beam source. It gives integrated dose, time resolve dose, temporal characteristics of the X-ray flash and timing of the flash respect to the start of object implosion. These two measurement systems are described and the quantified results are reviewed here.


**CONTRIBUTION NOT RECEIVED**

# TAILORING THE EMITTANCE OF A CHARGED PARTICLE BEAM WITH A TUNNEL EMITTANCE METER

Reinard Becker, Institut für Angewandte Physik der Goethe–Universität Frankfurt, Germany

*Abstract*

Based on the "tunnel" emittance used for electron beam focusing, a similar procedure is proposed to evaluate fractional emittances for ion beams using two pairs of slits with variable widths. A measurement starts with closing both slits (one after the other) until a specific fraction of the transmitted beam current is cut off. The emittance and brilliance can then be well defined for the transmitted beam. Formulae are given for the emittance as well as for the brilliance as a function of the slit widths and beam current. This emittance measurement technique is free from the background subtraction problem found in the classical density measurement of phase space(s). The measurement device is also at the same time an adjustable emittance/brilliance filter for the transmitted beam. The emittance and/or brilliance of a beam can thus be tailored to any value within the limits of the beam quality at the expense of transmitted beam current**.**

## INTRODUCTION

The emittance of ion sources is generally considered an important characteristic value, especially when the ion source will be used in combination with a beam line or the low energy transport (LEBT) section of an accelerator having a well-defined acceptance. Acceptances of beam lines and accelerators usually have the shape of ellipses with uniform density, characterized by the twiss parameters of these elliptical bounded phase spaces. While the matching conditions appear to be well defined by the accelerator expert, the ion source developer has great difficulty in satisfying these requirements for the following reasons:

- Ion source emittances, either measured or calculated, usually are not elliptically bounded but show wings of aberrations caused by the extraction system and the lenses.
- The emittance areas are not uniformly filled.
- Defining an exact value of the emittance is a matter of sophisticated background subtraction [1].

As a solution, we propose here a procedure to not only measure the emittance and brilliance of a beam in a simple and unambiguous way but to also define the beam quality by analysing its fractional emittance. This experimental procedure is based on the well-established experience of electron tube designers in the 1960's who characterized the quality of an electron gun by a "tunnel" emittance device. Recently this procedure has been modified [2,3] by replacing the tunnel with two pairs of slits for the x- and the y-direction.

## TUNNEL EMITTANCE

About 50 years ago the microwave industry developed GHz oscillators and rf-amplifiers called travelling wave tubes (TWT). A medium energy electron beam (similar to that of an EBIS) was focused in a strong solenoid (or an alternating permanent magnet structure) of some kilogauss and inside of a helical rf-structure, amplifying the velocity modulation on the beam by bunching. In order to measure the quality (=emittance) of such a gun and beam forming system a very practical experimental procedure has been developed. The beam is injected into a "tunnel" which is a cooled piece of copper with a hole drilled in it for the electron beam to pass through. Then the experiment shows that the smaller the hole and the higher the transmission at high current, the better the gun quality! [4]

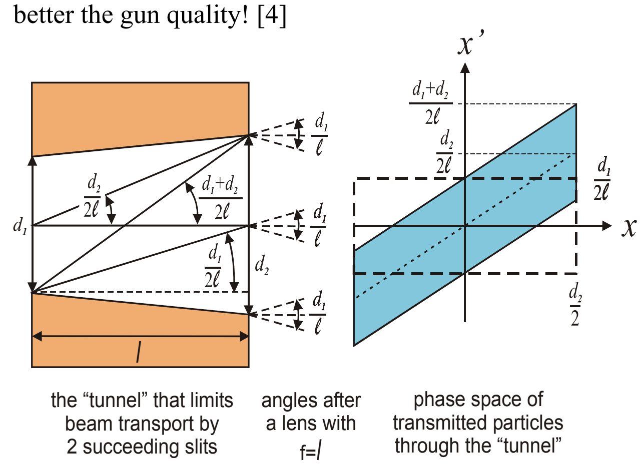


Figure 1: Definition of the tunnel emittance, showing how angles are defined by slit widths and the distance of the two apertures (left panel) and how this translates to the 2D phase space (right panel).

Referring to Fig. 1, assuming that the second aperture with width $d_2$ is fully illuminated by the beam passing through the first aperture with width $d_1$ we find the relations for the angles shown on the left characterizing the shaded phase space on the right. By focusing with a thin lens in the position of the second aperture with focal length $\boldsymbol{f} = \lambda$, the shaded parallelogram can be turned into the dashed rectangle. This produces the dashed rays found at the right side of the left panel. By definition the **full** emittance $\varepsilon_{full}$ then is calculated as the area of this rectangle with side lengths of $d_2$ and $d_1/\lambda$:

$$\varepsilon_{full} = \frac{d_1 d_2}{\lambda} \quad [m] \tag{1}$$

Quite naturally this emittance has the unit of length (m, cm, mm, yards, feet, inches, mils; however **microns** without any π or mrad are best!) [5]. It is seen from the dependence on the distance $\lambda$ between the slits that $1/\lambda^2$ enters into the error; hence a minimum distance is required for a given accuracy of the emittance determination. Sophisticated background subtraction, which is essential for emittance obtained by measuring the density distribution of the phase space(s) [1], is not needed for the tunnel emittance method. The measurement starts with both apertures fully open (see Fig. 2) and with a maximum signal on a Faraday cup located behind the slits. The 100% emittance is determined by reducing the width of both slits until a decrease of the beam intensity is just able to be observed. Then the slits are closed one after the other in succeeding steps to achieve a given transmitted beam fraction. This procedure can be continued until the slits are small enough to cut off most of the ion current. This will define the total and fractional emittances of the beam as a function of the current passing through both slits.

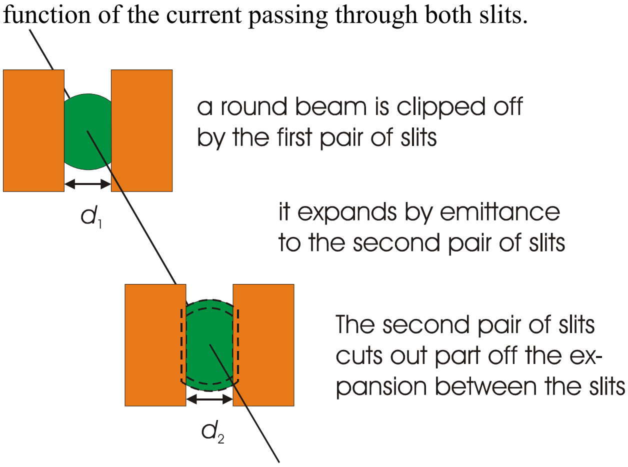


Figure 2: Measurement of full and fractional tunnel emittance by a pair of adjustable slits. For non-axisymmetric beams 2 pairs of slits in x and y-directions are needed. The transmitted beam then has a well defined, tailored emittance.

The tunnel emittances for the x- and y- directions are evaluated by 2 sets of perpendicular slits with widths $d_{x1}$, $d_{x2}$ and $d_{y1}$, $d_{y2}$ placed along the beam path at distances $\lambda_x$ and $\lambda_y$ apart:

$$\varepsilon_{x,full} = \frac{d_{x1} d_{x2}}{\lambda_x}, \quad \varepsilon_{y,full} = \frac{d_{y1} d_{y2}}{\lambda_y} \tag{2}$$

In the case of a round beam the pair of slits cutting out the beam in direction $y$ is not needed - all values may be taken from the emittance measurement in direction $x$. The brilliance then is defined as the current density in the right aperture of Fig. 1 divided by the solid-angle of the transmitted beam:

$$B = \frac{I}{d_{x2} d_{y2}} \times \frac{1}{\frac{d_{x1}}{\lambda_x}} \times \frac{1}{\frac{d_{y1}}{\lambda_y}} \qquad \left[\frac{A}{m^2}\right] \tag{3}$$

Using the expressions for $\varepsilon_{x,full}$ and $\varepsilon_{y,full}$ (Eqs. 2) this reproduces the well known expression for the brilliance:

$$B = \frac{I}{\varepsilon_{x,full}\ \varepsilon_{y,full}} \tag{4}$$

This formula demonstrates that the use of full emittances is more elegant than the common use of half-axis products. This argument is further enhanced by emittances, which have no point symmetry to the origin in phase space, such as those from ECR ion sources and all ion sources with a coma by misalignment.

## FRACTIONAL EMITTANCES

### *Beam with Rectangular Cross Section*

In order to analyse the quality of a given beam, we investigate the variation of emittances with the fraction of transmitted current through 2 slits. For a uniform beam with constant current density $j$ we use the relation between current density and beam current, assuming slit 1 is open and slit 2 is partially closed in the x-direction while both slits are open in the y-direction:

$$I^{fract}(d_{x2}) = j_2 D_{y2} d_{x2} \quad \text{and}$$

$$I^{total}(D_{x2}) = j_2 D_{y2} D_{x2} \tag{5}$$

This together with Eq. 2 gives the proportional relationship between the fractional emittance and current:

$$\frac{\varepsilon_{x,y}^{fract}}{\varepsilon_{x,y}^{total}} = \frac{I^{fract}}{I^{total}}\,. \tag{6}$$

Hence, for a beam with uniform current density, the fractional emittance is proportional to the current fraction. The same result is obtained if both slits were closed simultaneously.

### *Round Beam*

When closing a slit in a round beam (either x- or $y$-direction), the transmitted part becomes a function of the slit width $d$ only, as shown in Fig. 2, due to the circular shape of the beam cross section. For a beam of diameter $D$ and with uniform current density this translates directly to the transmitted current $I^{fract}$ in relation to the total current $I^{total}$:

$$\frac{I^{fract}}{I^{total}} = \frac{2}{\pi}\left\{\frac{d}{D}\sqrt{1-\left(\frac{d}{D}\right)^2} + \arcsin\frac{d}{D}\right\} \tag{7}$$

According to Eq. 1 the emittance of a beam passing through a constant slit width $d_1$ and a variable slit with width $d$ is given by

$$\varepsilon_{x,full}^{fract} = \frac{d_{x1}D}{\lambda_x} \times \frac{d}{D} \quad (8)$$

where the first fraction gives the total emittance if slit 2 is opened to width *D.* From this we get

$$\frac{\varepsilon_{x,full}^{fract}}{\varepsilon_{x,full}^{total}} = \frac{d}{D} \quad (9)$$

Inserting this into Eq. 7 we obtain an implicit relation for the dependence of the fractional emittance on the current fraction.

$$\frac{I^{fract}}{I^{total}} = \frac{2}{\pi}\left\{\frac{\varepsilon_{x,full}^{fract}}{\varepsilon_{x,full}^{total}}\sqrt{1-\left(\frac{\varepsilon_{x,full}^{fract}}{\varepsilon_{x,full}^{total}}\right)^2} + \arcsin\left(\frac{\varepsilon_{x,full}^{fract}}{\varepsilon_{x,full}^{total}}\right)\right\} \quad (10)$$

In the likely case that both slits are closed in the same way, the emittance will be reduced with the square of *d/D* and the fractional current will see the correction for the round beam (Eq. 7) twice. This gives

$$\frac{I^{fract}}{I^{total}} = \frac{4}{\pi^2}\left\{\sqrt{\frac{\varepsilon_{x,full}^{fract}}{\varepsilon_{x,full}^{total}}}\sqrt{1-\frac{\varepsilon_{x,full}^{fract}}{\varepsilon_{x,full}^{total}}} + \arcsin\sqrt{\frac{\varepsilon_{x,full}^{fract}}{\varepsilon_{x,full}^{total}}}\right\}^2 \quad (11)$$

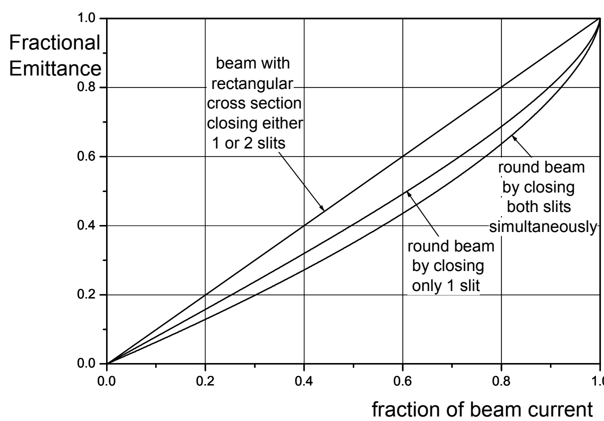


Figure 3: Theoretical variation of the fractional emittance on the transmitted current fraction for beams of uniform current density and rectangular or round cross section and for the cases of closing 1 slit only or 2 slits simultaneously.

The results of Eq. 6 for a beam with rectangular cross section and of Eq. 10 and Eq. 11 for round beams is shown in Fig. 3. The uniformly filled beam with rectangular cross sections will show a linear decrease of the emittance with the fraction of current, independent of whether only one slit is being closed or both slits are closed simultaneously. This is different for the round beam. If cut out by two slits simultaneously the round beam will exhibit a stronger decrease of the emittance for the associated loss of beam current.

## CONCLUSIONS

The tunnel emittance measured by 2 pairs of slits for the x- and the y- direction provides an easy method to test the "focusability" of ion beams, e.g. the matching into the acceptance of an accelerator or transport channel. In contrast to the classical method of measuring phase space densities, enclosing emittances are obtained. This eliminates the need for a careful background subtraction. In addition, fractional emittances can be determined which give useful information about the current density distribution inside the beam. This is especially important for emittance growth of high current ion beams by non-linear fields. For beams with uniform density distribution, formulae have been presented for the dependence of the fractional emittance on the current fraction, both for beams with rectangular cross sections and for round beams. Different relations are obtained for round beams if only one slit is closed or if both slits are closed simultaneously.

## ACKNOWLEDGMENTS

The careful reading of M. and R.W. Hamm and their important suggestions have greatly improved this paper.

## REFERENCES

[1] M. P. Stockli et al., AIP-CP**639** (2002) 135-159
[2] M. P. Stockli, private communication 2008
[3] M. P. Stockli, lecture, BIW-2006
[4] R. True, IEEE Trans. ED-**34**, (1987), p. 473-485.
[5] R. Becker and W. B. Herrmannsfeldt, Rev. Sci. Instrum. **77**, 03B907 (2006)

# COMMISSIONING OF THE HITRAP DECELERATOR USING A SINGLE-SHOT PEPPER POT EMITTANCE METER*

J. Pfister†, R. Nörenberg, U. Ratzinger
Institut für Angewandte Physik, Goethe-Universität Frankfurt, Frankfurt am Main, Germany
W. Barth, L. Dahl, P. Forck, F. Herfurth, O. Kester, T. Stöhlker
GSI, Darmstadt, Germany

*Abstract*

The Heavy Ion TRAP (HITRAP) project at GSI is in the commissioning phase. Highly charged ions up to $U^{92+}$ provided by the GSI accelerator facility will be decelerated and subsequently injected into a large Penning trap for cooling to the meV/u energy level. A combination of an IH- and an RFQ-structure decelerates the ions from 4MeV/u down to 6keV/u. In front of the decelerator a double drift-buncher-system is provided for phase focusing and a final de-buncher integrated in the RFQ-tank reduces the energy spread in order to improve the efficiency for beam capture in the cooler trap. This contribution concentrates on the beam dynamics simulations and corresponding measurements in the commissioning beam times up to the position of the entrance to the RFQ. Single-shot emittance measurements at higher energies using the GSI pepper pot device and construction of a new device using Micro Channel Plate technology for low energies as well as profile measurements are presented.

## HITRAP FACILITY AT GSI

The highly charged ions are accelerated in the heavy ion synchrotron to typically 400MeV/u, almost completely stripped and injected into the experimental storage ring (ESR). Here, they are first treated by stochastic cooling and decelerated to an intermediate energy level of 30 MeV/u. Then they are electron-cooled and further decelerated to 4 MeV/u. After another electron cooling cycle the ions are ejected from the ESR as a bunch of about $10^5 - 10^7$ ions depending on the element and a pulse length of 1-2 µs. Then they enter the linear decelerator of HITRAP. The final goal is the reduction of a deceleration cycle (filling the ESR, cooling, deceleration and ejection) down to 10-20s. Before the ion bunch enters the drift tube structure, the ion pulse is micro bunched by the double-drift buncher (DDB). After deceleration in the IH-structure as well as the RFQ, the ions enter the Cooler (Penning) trap with only 6 keV/u, where they can be confined by a combination of electrostatic and magnetic fields. By sympathetic cooling with cold electrons the trapped highly charged ions will reach a thermal energy corresponding to ~4K. The cold ions are then transported, with kinetic energies of only a few keV*q, to the different setups installed on top of the re-injection channel as a high-quality, low emittance, highly charged ion beam [1].

## LINAC COMMISSIONING

After deceleration and cooling of the ions down to 4MeV/u in the ESR, they were ejected via the transport line towards the HITRAP linac (see Fig. 1). The DDB is the first component of the HITRAP linac and is used for phase focussing. It was commissioned during two beam times in 2007 with an uncooled beam of the lighter ion species $^{64}Ni^{28+}$ and $^{20}Ne^{10+}$. The next structure is the IH-structure that decelerates the ions down to 500keV/u. Its initial commissioning took place in August 2008 with a partially cooled heavy $^{197}Au^{79+}$ beam and will be continued in October of this year [2]. For beam diagnostic measurements there are phase probes as well as beam diagnostic stations installed in the beamline. They house Faraday cups, grids and YAG-scintillation targets. Furthermore there were a single-shot pepper pot emittance meter and a diamond detector installed for transversal and longitudinal emittance measurements.

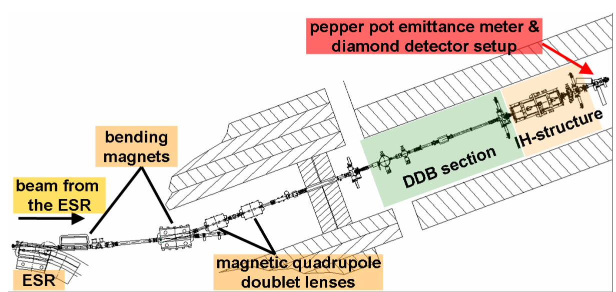


Figure 1: Overview of the transport beam line from ESR towards the position of the pepper pot emittance meter (later: position of the RFQ entrance).

### *Single-shot Emittance Measurements*

Since the HITRAP linac gets a bunch of ions only every 35-60 seconds from the ESR during commissioning the single-shot pepper pot emittance meter is the ideal choice for this task. The GSI pepper pot device has been adapted to the special needs at HITRAP and a new evaluation software has been developed [3].
In 2007 emittance measurements were done at the position of the entrance of the IH-structure whereas in August 2008

* work supported by BMBF under contract 06FY160I
† jpfister@gsi.de

the device was placed at the RFQ injection point. Measuring in front of or behind the IH-structure makes a big difference for evaluation, since the measurement behind the IH is much more influenced by noise mainly produced by secondary electrons and small angle scattering as it can be seen in Fig. 2.

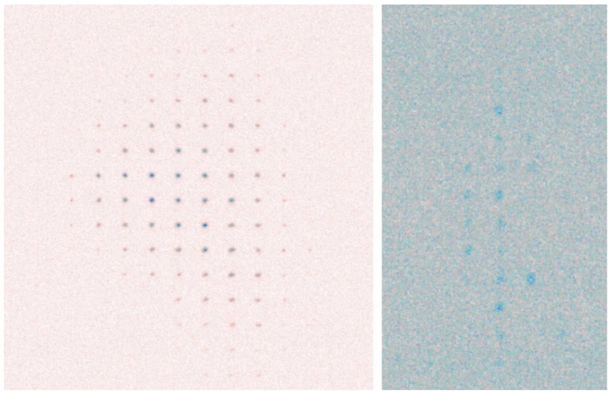

Figure 2: Typical pictures taken from the phosphor screen for emittance evaluation with Ne-beam in front of the IH (left) and Au-beam behind the IH-structure (right).

The emittance data has been evaluated with a new program written in MATLAB and ProEMI-PEDISP software as well as in profile measurements (2007 beam times only) using the "non-destructive" emittance evaluation method [4]. The evaluation data from MATLAB and ProEMI are in good agreement. Since the profile method is only a rough estimation of the emittance this value differs a little bit, but is still within the uncertainty limits. The emittance values are bigger than expected from prior calculations but this is due to the fact that cooling of the beam after deceleration in the ESR was not possible because of a limited beam lifetime. The emittance values and TWISS parameters calculated from the measurements were then used for the beam dynamics calculations backwards from the entrance of the IH-structure to the ESR.

Table 1: Comparison of emittances measured with uncooled Ne-beam and calculated with different software

| | $\varepsilon_{\text{rms,hor}}$ $[mm \cdot mrad]$ | $\varepsilon_{\text{rms,vert}}$ $[mm \cdot mrad]$ |
|---|---|---|
| MATLAB | 1.7 | 2.0 |
| ProEMI | 1.9 | 2.2 |
| profiles | 2.4 | 1.7 |

The evaluation of the $^{197}$Au$^{79+}$ data was done with MATLAB only. The quality of the pictures was not satisfying (see Fig. 2). The signal-to-noise ratio was approx. 1.7. In Fig. 3 a detailed evaluation screen is shown for one of the examples that was possible to evaluate. Evaluation of the complete set of measurements still has to be done. The data, which were evaluated so far show a horizontal rms-emittance of 0.6(3)mm·mrad and a vertical of 1.7(5)mm·mrad.

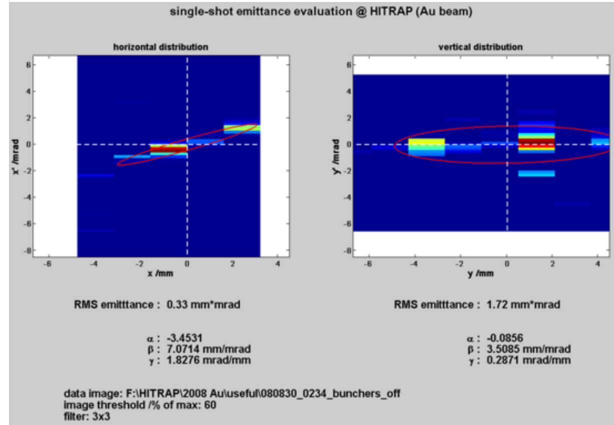


Figure 3: Data taken from the Au beam time with 60% noise cut.

## BEAM DYNAMICS CALCULATIONS

The lens settings, measured emittance values and TWISS parameters at the entrances of the IH-structure and RFQ were used to perform beam dynamics studies tracing the beam back from the point of measurement to the ejection point of the ESR. It was found that for the $^{20}$Ne$^{10+}$ beam the diameter in the dispersive plane of the bending magnets at the ESR is 40mm and 5mm in the lateral plane. But in the DDB cavities a beam with an approximately circular beam shape and a small divergence is required in order to avoid emittance growth. The corresponding envelopes of the beam calculated with COSY INFINITY [5] for both beam times are shown in Fig. 4. The beam size at the ESR exit corresponds approximately to the expected values due to the restricted aperture, but the divergence is larger due to the lack of cooling at 4MeV/u in the ESR during the 2007 run. However, the beam line tune reveals good beam transport properties with high transmission of 90%.

## LOW ENERGY PEPPER POT EMITTANCE METER

For measurements in the low energy section of HITRAP as well as in other applications it is advantageous to measure the emittance in one single shot at energies in the low keV-range. We proved that this is not possible with pure scintillator screens at low intensities [6]. The measured emittance value strongly depends on the used scintillator material. Therefore a Micro Channel Plate (MCP) with an amplification factor of about $10^4$ is placed in between the aperture plate and the scintillation screen. The resolution of the MCP (approx. 12 µm) is better than the resolution of the CCD camera, which is 1392×1040 pixels (1:1 transformation). Distributed to the size of the active area of the MCP the device will get an effective spacial resolution of 35 µm. Using a fixed focus lens no degradation of image quality is anticipated.

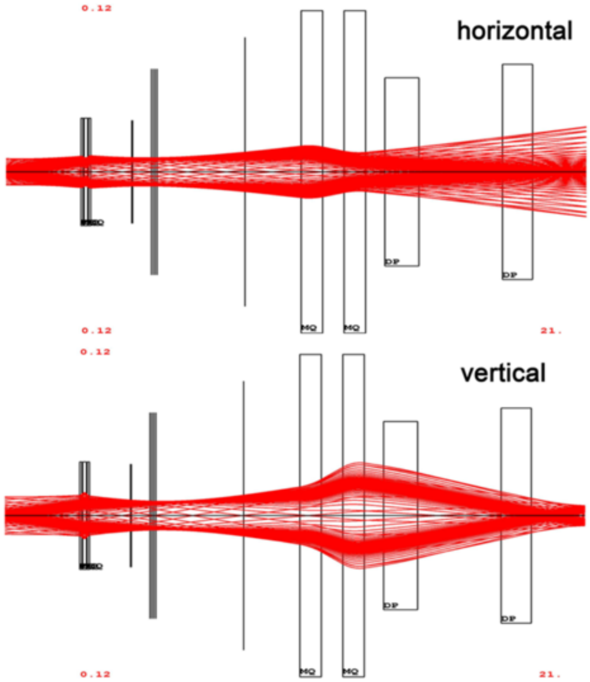


(a) 2007 Ne beam dynamics

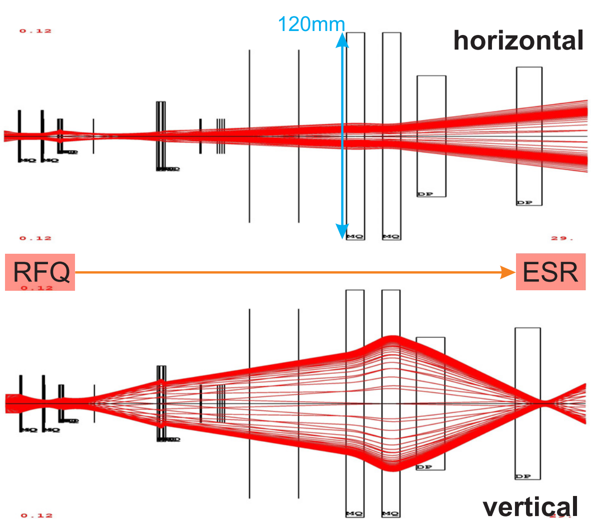


(b) 2008 Au beam dynamics

Figure 4: Envelopes of Ne and Au beam calculations using the beam optics settings and measured emittance values as input data.

With this new device the user will have all benefits like intensified images, online evaluation and phase space illustration of the measured beam. The device partly looks similar like the beam diagnostic monitors that were designed at KVI Groningen and are used for beam profile and current measurements in the low energy beam transport line of HITRAP. The system was upgraded and suited for its main purpose. It is equipped with the emittance meter and a Faraday cup. Determination of beam current and emittance can be done within seconds, nevertheless still two shots of ions are needed. The online readout of physical data within the scintillation effect on the phosphor screen that is the anode of the MCP takes place from a dedicated PC with special image acquisition software. The setup (see Fig. 5) with its fixed flange is mounted to a linear translator to move either the emittance meter or Faraday cup on beam axis or to remove it from the beam completely.

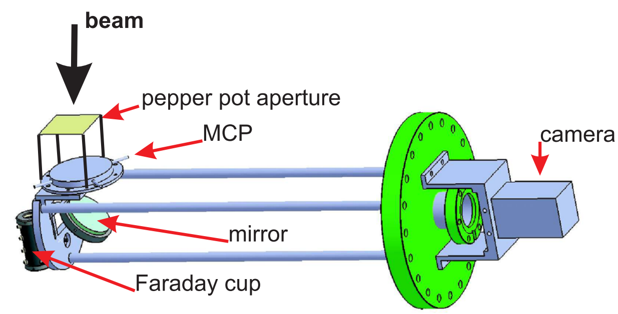


Figure 5: Design drawing of the new pepper pot emittance meter for low energies incorporating the device itself and a Faraday cup. Everything is mounted on a moveable CF-160 flange.

## OUTLOOK

Two more commissioning beam times are scheduled in October 2008 and beginning of 2009. The first beam time is forseen for final commissioning of the IH-structure and the re-buncher. After successful tuning the structure for deceleration down to 0.5MeV/u, emittance measurements are foreseen. The 2009 beam time is dedicated to the commissioning of the RFQ.

The new pepper pot device is almost completely designed and will be built this winter using a MCP instead of pure scintillators for emittance measurements. Using such a device, beam quality resp. emittance measurements in the low energy beam section of HITRAP will become possible.

## REFERENCES

[1] H.-J. Kluge et al., “HITRAP: A Facility at GSI for Highly Charged Ions”, Advances in Quantum Chemistry, Academic Press, 2008, Volume 53, pp.83-98.

[2] L. Dahl et al., “The HITRAP Decelerator Project at GSI - Status and Commissioning Report”, these conference proceedings, MOP019.

[3] J. Pfister et al., “A Decelerator for Heavy Highly Charge Ions at HITRAP”, EPAC08 Conference Proceedings, July 2008, pp.3449-3451.

[4] M. P. Stockli, “Measuring and Analyzing the Transverse Emittance of Charged Particle Beams”, AIP Conference Proceedings, November 2006, volume 868, pp.25-62.

[5] K. Makino and M. Berz, COSY INFINITY version 8, NIM A427 (1999), pp.338-343.

[6] H. Ernst, “Entwicklung eines Detektors für niederenergetische hochgeladene Ionen für HITRAP”, diploma thesis, Universität Mainz, Germany, 2007.

# DITANET: A EUROPEAN INITIATIVE IN THE DEVELOPMENT OF BEAM INSTRUMENTATION FOR FUTURE PARTICLE ACCELERATORS

C.P. Welsch
University of Heidelberg, GSI, Darmstadt and MPI-K, Heidelberg, Germany
on behalf of the DITANET consortium

*Abstract*

Without an adequate set of beam instrumentation, it would not be possible to operate any particle accelerator, let aside optimize its performance. In a joint effort between several research centres, Universities, and partners from industry, DITANET aims for the development of beyond-state-of-the-art diagnostic techniques for future accelerator facilities and for training the next-generation of young scientists in this truly multi-disciplinary field. The wide research program covers the development of beam profile, current, and position measurements, as well as of particle detection techniques and related electronics.

This contribution introduces this new Marie Curie Initial Training Network, presents the DITANET partner institutes, and gives an overview of the various research and training activities.

## INTRODUCTION

Marie Curie Initial Training Networks (ITN) are aimed at improving the career perspectives of researchers who are in the first five years of their career by offering structured training in well defined scientific and/or technological areas as well as providing complementary skills and exposing the researchers to other sectors including private companies.

The European Training Network DITANET - "DIagnostic Techniques for particle Accelerators – a Marie Curie initial training NETwork" - covers the development of advanced beam diagnostic methods for a wide range of existing or future accelerators, both for electrons and ions. It is the largest-ever education action for PhD students in the field of beam diagnostic techniques for future particle accelerators and officially started on 1.6.2008 with a total budget of up to 4.2 M€.

DITANET covers the development of advanced beam diagnostic methods for a wide range of existing or future accelerators, both for electrons and ions. DITANET consists of the following network participants:

University of Heidelberg (coordinator, Germany), CEA (France), CERN (Switzerland), DESY (Germany), GSI (Germany), HIT GmbH (Germany), IFIN-HH (Romania), Stockholm University (Sweden), Royal Holloway University of London (UK), and the University of Seville/Centro Nacional de Aceleradores (Spain).

The network is complemented by twelve associated partners from all over the world:

ESRF (France), idQuantique (Switzerland), INFN-LNF (Italy), Instrumentation Technologies (Slovenia), MPI for Nuclear Physics (MPI-K), PSI (Switzerland), THALES (France), Thermo Fisher Scientific (USA), TMD Technologies Limited (UK), TU Prague (Czech Republic), ViALUX (Germany), and WZW Optics (Switzerland).

## TRAINING

Beam diagnostics systems are essential constituents of any particle accelerator; they reveal the properties of a beam and how it behaves in a machine. Without an appropriate set of diagnostic elements, it would simply be impossible to operate any accelerator complex let alone optimize its performance. Beam diagnostics is a rich field in which a great variety of physical effects are made use of and consequently provides a wide and solid base for the training of young researchers. Moreover, the principles that are used in any beam monitor or detector enter readily into industrial applications or the medical sector, which guarantees that training of young researchers in this field is of relevance far beyond the pure field of particle accelerators.

Young researchers participating in DITANET will not only get the possibility to perform state-of-the-art research, they will also get a much wider training in the domain of beam diagnostics by interaction with other network participants and close collaboration with associated partners from the industrial sector. This includes regular exchanges of trainees between the partners that will thus get the possibility to participate in ongoing R&D work at linked institutes and universities.

This way, DITANET will provide a cohesive, flexible framework for the training and professional development of researchers in beam diagnostic techniques for particle accelerators, with a strong focus on possible applications of these principles in industry.

In addition, DITANET will organize one week courses on beam diagnostic techniques in spring 2009 at Royal Holloway University of London and in fall 2010 at Stockholm University that will be open to all network participants as well as to external participants. Details on these courses will be published on the DITANET web site [1].

## RESEARCH

Future accelerator projects will require innovative approaches in particle detection and imaging techniques to provide a full set of information about the beam characteristics. DITANET covers a wide range of future accelerators, ranging from the next generation of linear colliders (ILC, CLIC) and the most advanced high energy accelerators (LHC, FAIR), to innovative light sources (X-FEL) and novel low-energy storage ring projects (DESIREE, USR). A few examples of the research projects within DITANET are outlined in the following sections.

### *High-Intensity Klystrons*

The performance of high power electron devices is presently limited by the quality of the electron beam propagation along the interacting structures. These beams reach power densities as high as 5 MW/cm$^2$ and any interception of the beam with the structure risks damaging it.

Presently, simulation codes are commonly used to predict the behaviour of the electron beam, while very little has been achieved in the field of diagnostics for klystron applications. These physical measurements are necessary to validate and possibly improve the simulations codes, to rank limiting phenomena, and finally, to improve the design and performance of high power electron devices that will be used extensively in the future linear colliders like the ILC and CLIC.

In the frame of DITANET, the most pertinent instruments that can be adapted to the RF electron device problematic and geometry shall be identified. This work will be followed by the design and realisation of a set of diagnostics, including mechanics, control and signal processing.

This project will be realized in partnership with Thales Electron Devices, a world leading manufacturer of klystrons, and CEA Saclay.

### *Beam Diagnostics for CLIC*

One of the major decisions in particle physics over the next 3 years will be to decide on the next major accelerator to access the multi-TeV energy scale. The CLIC two-beam acceleration scheme [2] is one of the candidates for the next accelerator for the high-energy frontier, and the CLIC Test Facility (CTF3) at CERN [3] is the unique facility to test the CLIC acceleration principle and to prove the feasibility of associated RF systems.

In addition to the RF accelerating systems themselves, a host of beam diagnostics will need to be developed to cope with the challenging environment of CLIC. There exists space at the CLEX area of the CTF3 facility to build a new Instrumentation Test Beam (ITB). One of the first tasks of the trainee will be to design the machine optics for the ITB in collaboration with the CERN experts and to work with the CLIC diagnostics team to optimize the layout and functionality for future key diagnostics projects.

In addition to the ITB design, the Early Stage Researcher (ESR) with work with TMD technologies to assess the opportunities for RF system development and to identify a fruitful new line of R&D where the expertise of TMD can be combined with the expertise at RHUL and CERN to develop a new product of use to the CTF3/CLIC project.

The system design work will be complemented by frequent data taking and machine operation at CTF3. This combination of practical experience, beam-line design, and industrial collaboration, will provide a unique training opportunity.

### *A Beam Profile Monitor based on Light Emission from Rest Gas Atoms*

Many accelerator projects make use of high intensity ion beams, e.g. for the production of neutrons (ADS, IFMIF), at neutrinos factories, or in nuclear physics research (FAIR, SPIRAL 2). The transverse distribution of these beams needs to be accurately known to avoid any unwanted interaction with the vacuum chamber walls and to properly impact the target.

The power of these beams prevents using intrusive methods since any kind of screen would be rapidly destroyed by the temperature increase. One solution can be to use the neutral gas in the vacuum chamber which is excited by the beam. The light emitted by this gas may then be used to obtain a good representation of the beam itself.

Within DITANET the first focus will be the adaptation of this scheme to a particular accelerator project, including a theoretical description of the light emission, characterisation of the beam and an estimation of the required space in the vacuum chamber. Tomography algorithms will then be investigated to reconstruct the 2D transverse beam profile observed along various directions.

This work will then be followed by the design and realisation of the detector, followed by measurements on a specific ion beam and application of these measurements to fine-tune the accelerator.

### *Development of a CCC-based Current Monitor*

The FAIR storage rings have to be capable of the operation with very low ion currents, i.e. much below 1 μA. In particular, in the case of radioactive ion beams and antiprotons the amount of stored particles in the FAIR storage rings is too low for standard beam diagnostic devices. For the slow extraction from the SIS100 synchrotron the high-energy beam transfer-lines require diagnostic devices for the non-destructive measurement of ion currents down to the nA region. For this purpose, the installation of Cryogenic Current Comparators (CCC) is foreseen, offering a non-intercepting and absolute current measurement. The basic principle is the determination of the beam's magnetic field using a sensitive SQUID-based magnetic flux detector. A CCC prototype was realized at GSI already in 1996 [6] and an improved design is now planned to be used at DITANET participant DESY [7] for dark-current detection at the X-FEL acceleration cavities. The optimization, standardization and commissioning of a new CCC is the goal of the DITANET PhD work with the time frame of DITANET.

## INVOLVEMENT OF INDUSTRY

The participation of industry is an integral part of DITANET. As shown in the beginning of this article, a number of private companies are included as associated partners to the network. They are members of the supervisory board to ensure that industry-relevant aspects are covered in the different projects carried out within the network and to enhance knowledge transfer. In addition, one third of the DITANET Steering Committee members come from industry.

From the beginning, the DITANET management encouraged the involvement of these partners in the training program at the highest possible level. This led to the participation of HIT GmbH as a full network member with a PhD project that will be hosted by this company. In addition, the associated partner THALES, who is considered as a world-wide leader in the development of klystron technology, will host the trainee from CEA during up to 25% of the PhD project, thus taking over a considerable part of the training.

WZW Optics , Vialux, Thermo Fisher and idQuantique are among the leading companies in the field of optics, scientific cameras and detector systems. Instrumentation Technologies from Slovenia and TMD technologies from the UK have long-standing links to accelerator laboratories and have pushed the development of beam diagnostic techniques on various occasions in the past.

All companies as well as the other associated partners from academia (TU Prague, MPI for Nuclear Physics) and research (PSI, INFN, ESRF) have agreed to host the DITANET trainees during some weeks up to several months. This ensures that every trainee will get the possibility to realize an extended research stay at a leading partner institute from industry and to take part in its R&D efforts.

Thereby it is guaranteed that all trainees will be provided with a true multi-disciplinary and inter-sectorial training, where they will not only work on their main project, but learn about neighboring fields and get a view of possible applications and of the impact of their work in the industrial sector.

These measures will complement the scientific training and actively bridge between the academic and the industrial sectors within DITANET.

## IMPLEMENTATION

The DITANET Marie Curie Initial Training Network will form a consortium which comprises 10 network participants and a roughly equal number of associated partners. It is the goal of the management structure to profit from the individual expertise of the participating institutions while maintaining an effective decision making and controlling process.

The key bodies of the DITANET managerial structure are the Supervisory Board, the Network Coordinator assisted by the Management Office in scientific, management and financial matters, and the DITANET Steering Committee. Whenever required, a spin-off board will complement this structure.

## CONCLUSION

The largest ever coordinated EU education action for young researchers in the field of beam diagnostic techniques for particle accelerators has been awarded to a consortium of ten partners from all over Europe within the EU-Marie Curie program for initial training networks. The joint effort in setting up DITANET and the corresponding administrative and training-related boundary conditions will guarantee a continuous training of young researchers in this field. Close collaboration between the network participants and the associated partners with a very prominent role of industry, ensures that the basis for DITANET is laid in a true international approach with a clear long term perspective.

## REFERENCES

[1] http://www.ditanet.uni-hd.de.
[2] R.W.Assmann, et al., “A 3 TeV e+e- Linear Collider Based on CLIC Technology”, CERN 2000–008.
[3] G. Geschonke, A. Ghigo (ed.) et al., “CTF3 Design Report”, CERN/PS 2002-008 (RF).
[4] J. Dietrich et al., "Non-destructive beam position and profile measurements using light emiited by residual gas in a cyclotron beam line", Proc. Europ. Part. Acc. Conf., Genoa, Italy (2008).
[5] T. Kawakubo et al. “Non-Destructive Beam Profile Monitors in the KEK Proton Synchrotron”, KEK Preprint 91-23.
[6] A. Peters et al. “A cryogenic current comparator for nondestructive beam intensity measurements”, Proc. Europ. Part. Acc. Conf. (1994).
[7] W. Vodel et al. “SQUID-based cryogenic current comparator for measurements of the dark current of superconducting cavities”, Proc. DIPAC, Lyon, France (2005).

# DESIGN OF A BEAM HALO MONITOR WITH A HIGH DYNAMIC RANGE

J. Egberts[1], S. Artikova[1], E. Bravin[2], T.Chapman[3], T. Lefèvre[2], M.Pilon[3], C.P. Welsch[1,4,5]
[1]MPI-K, Heidelberg, [4]University of Heidelberg, [5]GSI, Darmstadt, Germany
[2]CERN, Geneva, Switzerland,[3]Thermo Fisher Scientific, Liverpool, NY USA

*Abstract*

A thorough understanding of halo formation and its possible control is highly desirable for essentially all particle accelerators. Limiting the number of particles in the halo region of a beam would allow for minimizing beam losses and maximizing beam transmission, i.e. the experimental output. Measurements based on either optical transition radiation (OTR) or synchrotron radiation (SR) provide an interesting opportunity for high dynamic range measurements of the transverse beam profile, since the signal is linear with the beam charge over a wide range and is routinely used in many diagnostic applications. In this contribution, first results on beam halo measurements obtained from a flexible core masking technique and an innovative CID camera system are summarized.

## INTRODUCTION

The detection and possible control of the beam halo is of utmost importance for high energy accelerators, where unwanted particle losses lead to an activation or even damage of the surrounding vacuum chamber [1], [2]. But also in low-energy machines, like the ultra-low energy storage ring (USR) [3] at the future facility for antiproton and ion research (FLAIR) [4], one is interested in minimizing the number of particles in the tail region of the beam distribution. Since most part of the beam is normally concentrated in the central region, observation techniques with a high dynamic range are required to ensure that halo particles can be monitored with sufficient accuracy. One option to monitor the beam halo is to use light generated by the beam, either through SR, OTR, or luminescent screens. In thus case, a special camera technology is required to allow for high dynamic range measurements.

But also for low energy accelerators and storage rings like the USR such measurements can be envisaged by e.g. exploiting the light from a phosphor screen.

In order to approximate a typical beam distribution as it is found in an accelerator we used a conventional laser beam in our lab. The open angle of the laser of 0.1 corresponds to SR/OTR emitted at some 100 MeV and can be regarded as a realistic approximation of a real particle beam.

## CID CAMERA

The charge injection device (CID) derives its name from its unique ability to clear individual pixel sites of photon-generated charge by injecting the charge directly into the substrate. The main features of this imager technology are its distinctive readout capabilities including inherent resistance to ionizing radiation, inherent resistance to charge blooming, true random pixel addressability, non-destructive pixel readout (NDRO), and on-sensor collective pixel readout and clear.

### *Architecture*

The on-sensor collective read feature allows the data acquisition routines to select contiguous pixel regions (e.g., a 3 by 3 pixel region) and interrogate those pixels with a single reading that is the electronic average of the signals on those pixels, thereby improving both readout speed and signal-to-noise ratio. This collective read feature is analogous to the binning that can be performed with certain CCD camera systems. However, unlike the CCD where the charge packets from the individual pixels are physically combined into a single larger charge packet, the CID collective read feature preserves the spatial integrity of the photon-generated charge in the pixels and the read process is non-destructive to that charge. The CID architecture also allows for the clearing of photon-generated charge from contiguous pixel regions with a single inject pulse. Similar to most micro-electronic devices built today, the CID is manufactured with silicon technology. A single crystal silicon wafer forms the substrate of the device. The insulating Si substrate is doped with boron to make it electrically conductive (p-type). Upon the substrate, an n-doped epitaxial layer is grown. As the thickness of the epitaxial layer is increased, the full well capacity and NIR response also increase. The epitaxial layer is slightly doped in such a manner as to cause minority signal carrier diffusion into the bulk silicon. Next, a thick field oxide is grown in a checker board pattern across the surface of the wafer. The field oxide is an isolating layer, a dielectric film, composed of silicon dioxide. A thin gate oxide of about 400 nm of $SiO_2$, is grown over the remaining exposed epitaxial layer. Conductive poly-silicon is then applied in thin strips that regularly crisscross the entire surface of the imager forming the row and column electrodes. The two orthogonal poly-silicon electrodes are electrically isolated and connect pixels to the processing electronics at the periphery of the device. One electrode is designated the column or sense electrode and the other is the row or drive electrode. The region at the intersection of the two electrodes under the thin gate oxide delineates the active charge-storage area for each pixel.

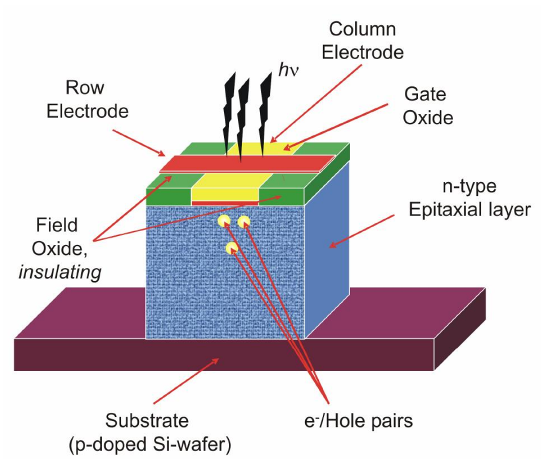


Figure 1: Layout CID pixel.

## *Readout*

Each pixel on the CID imager is individually addressable and allows for random access non-destructive pixel readout.

During charge generation, the row electrode is set on a high and the column electrode on a low potential. Since the photon generated charge is collected in the form of positively charged holes, the charge will pile up underneath the column electrode. The potential of the row electrode is measured and the column electrode is then set to an even lower voltage, which causes the holes to migrate toward the row electrode. When charge moves in or out of a capacitor, the electrode potential will change according to $dV = dQ/C$. Therefore, the change of the sense electrode potential is proportional to the amount of accumulated charge. After the readout of the pixel, the electrodes can either be set to their original potentials or the holes can be injected into the substrate layer where they will recombine with the electrons. The non-destructive pixel readout (NDRO) is one of the unique features of the CID camera [5].

Once the charge within a pixel exceeds a certain threshold value, the pixel can be read and thereby emptied independently from the others. Highly illuminated pixels will be emptied more often often than just slightly illuminated ones. Especially for very long exposure times, the number of readouts is a good mass for the light intensity. The ”Extreme Dynamic Range” (XDR) algorithm provided by the ”SpectraCam Racid Exposure” [6] software takes full advantage of this unique feature of the CID-camera and thereby maximises the achievable dynamic range [7].

Since the dark current would normally have a negative effect on the accumulated charges for long exposure times and low light intensities, the pixel array is down to -37°C by a thermoelectric cooling device. The heat is then transferred by water tubes to an external chiller. The dynamic range is therefore mainly limited by the readout frequency on the one hand, and the maximum acceptable light intensity on the other.

## *System Callibration*

In order to callibrate the camera system, a setup with a well-defined light source was used. It consists of the OSL1-EC [8] and a fibre illuminator with an adjustable light output of up to 100 W. At the end of the light guide, a little box with several diffusors was mounted to generate a homogeneous light distribution.

Behind the diffusors, a mask with different neutral density filters was attached. The homogeneous light that passes through the filters thus obtains a well-known intensity. By measuring the light transmission for various neutral density filters and light intensities, the specifications of the camera can be determined.

## *Measuring a Laser Profile*

Since the light intensity of the laser is too high for the CID-camera to handle, it was reduced by a neutral density filter. The laser beam profile was then obtained by directing the laser beam directly onto the pixel array without any objective lenses in between.

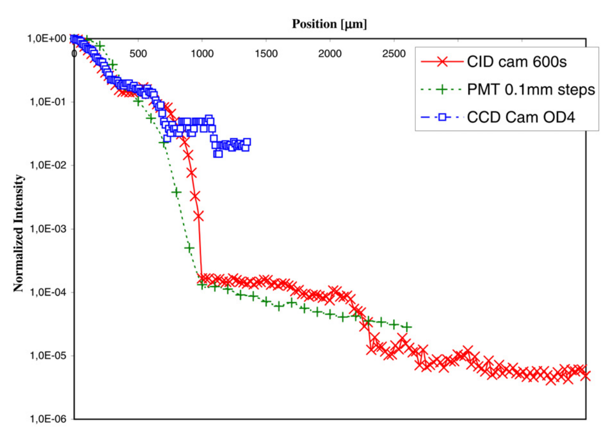


Figure 2: Beam profile of CCD (blue), CID (red) and PMT (green) [5].

In fig. 2 the normalised beam profile is shown as it was acquired by a CCD-camera (blue), a CID-camera (red) and a photomultiplier tube (green). By covering five orders of magnitude, the CID-camera grants the highest dynamic range combined with a high spatial resolution. Since it is possible to save the data in an ASCII-file, the data can be analysed by a C++ program which fits a Gaussian function to the data, determines the standard deviation $\sigma$, and on this basis, defines the beam halo as the amount of light outside of $n\sigma$.

## MASKING OUT THE BEAM CORE

Another option to measure the beam halo is to mask out the main beam core. If the intense light from the beam core is blanked out, a normal camera can monitor the halo without saturation and overexposure. An example of earlier measurements at CERN is given in fig. 3. In the first picture, a beam profile is shown through a 10% neural density filter, in the second, the beam core is masked out, and in the third, the neutral density filter is removed [9]. Again, one can clearly see the halo after the removal of the neutral density filter. Nevertheless, in contrast to the measurement with the CID-camera, this method does not grant a direct comparison between the halo and the beam core. On the other hand, it does not require the high dynamic range of a CID-camera but a normal 8 bit CCD-camera can be used. This yields the advantage of far lower costs for the camera and the option of an online beam halo monitoring since the large exposure time of the CID-camera is not required.

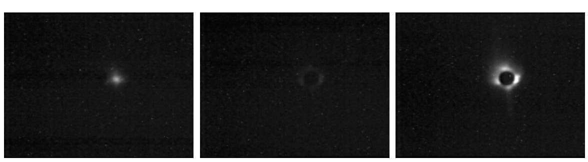

Figure 3: Masking out the beam core [9].

### *Micro Mirror Array*

A strong limitation in the first tests with the core masking technique was the fixed shape of the mask itself. For time dependent beam profile measurements a technique is required to generate a mask based on (online) measurements of the beam. In our setup, we realize a flexible mask by using a Micro-Mirror-Array (MMA).

An MMA consists of an array of $1024\times768$ micro mirrors of $13.68\mu$m$\times13.68\mu$m size which can be tilted by $12°$ in two directions. Each micro mirror can be steered individually and therefore the MMA can be used to display arbitrary shapes. If the beam core profile is displayed on the MMA and illuminated by the laser beam, the main beam core is deflected in another direction than the beam halo.

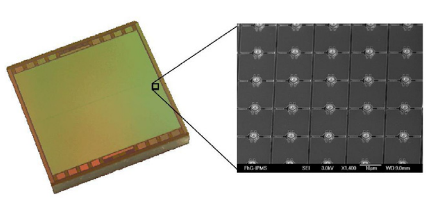

Figure 4: MMA with Enlargement of pixel structure[10].

A careful callibration of the overall optics is required to ensure that a pixel as measured by the camera system can be mapped on an MMA pixel. The correct adjustment of the image of the beam core on the MMA display is of critical importance. If the beam core does not fit to its image on the MMA, the MMA will not be able to properly mask out the beam core which will lead to an overexposure of the camera. Since the spatial resolution of the MMA and the CID-camera is in the micrometer regime, it is desirable to achieve an adjustment of laser, camera and MMA with comparable precision. In addition, the interference pattern generated by the MMA needs to be carefully investigated.

### *Outlook*

The Spectracam XDR is a next-generation CID camera which promises extreme dynamic ranges and will be tested in our optical laboratory within the next few months.

In contrast to this high-end camera technology, the Micro Mirror Array provides a relatively simple solution to generate spatially highly variable masks on very short time scales.

After successful tests in the lab, beam tests with both devices are foreseen which will allow for a direct comparison of the performances.

## REFERENCES


[1] E. Guignard et al, "A 3TeV e+ e- Linear Collider Based on the CLIC Technology", CERN-2000-008

[2] R. Schmidt et al, "Beam loss scenarios and strategies for machine protection at the LHC", Proc. 3rd HALO ICFA Advanced Beam Dynamic Workshop, Montauk, USA (2003)

[3] C.P. Welsch, M. Grieser, J. Ullrich, A. Wolf, "An ultra-low-energy storage ring at FLAIR", Nucl. Instr. Meth. A 546 (2005) 405417

[4] C.P. Welsch, H. Danared, "FLAIR: A Facility for Low-energy Antiproton and Ion Research", Proc. Europ. Part. Acc. Conf., Edinburgh, Scotland (2006)

[5] C.P. Welsch, E. Bravin, B. Burel, T. Chapman, T. Lefvre, M.J. Pilon, "Alternative Techniques for Beam Halo Measurements", Meas. Sci. Technol. 17 (2006) 2035c, CERN-AB-2006-23

[6] Thermo Scientific, http://www.thermo.com

[7] M.J. Pilon, private communication

[8] Thorlabs, Inc., http://www.thorlabs.com

[9] T.Lefèvre, H.Braun, E. Bravin, R. Corsini, D. Schulte, A. L. Perrot, "Beam Halo Monitoring at CTF3", Proc. EPAC, Lucerne, Switzerland (2004)

[10] Bakke, T., Völker, B., Friedrichs, M., Rudloff, D., "Micromirror Array of Monocrystalline Silicon", International Conference on Optical MEMS and their Applications 2006, pp: 128-129

# DEVELOPMENT OF SCREEN MONITOR WITH A SPATIAL RESOLUTION OF TEN MICRO-METERS FOR XFEL/SPring-8

K. Yanagida*, H. Tomizawa and A. Yamashita, JASRI, XFEL Joint Project /SPring-8
1-1-1 Kouto, Sayo-cho, Sayo-gun, Hyogo 679-5198
S. Inoue and Y. Otake, RIKEN, XFEL Joint Project /SPring-8
1-1-1 Kouto, Sayo-cho, Sayo-gun, Hyogo 679-5148

*Abstract*

A screen monitor with a resolution of less than 10 $\mu$m was developed for XFEL/SPring-8. It comprises a vacuum chamber with a metal (100 $\mu$m, SUS) foil to emit OTR, a lens for focusing and a CCD camera system. In order to realize this resolution, the lens is placed close to the foil, the distance between the lens and the foil is 100 mm, and the lens has a large diameter (2 in.). This optical-geometrical structure contributes much to increase the numerical aperture of a near-field image. Although the range of the observation wavelength is wide, such as from 400 to 800 nm, a resolution of 2.5 $\mu$m on the foil surface has been calculated. The experimental data of the developed optics also suggested the same resolution.

## INTRODUCTION

At SPring-8, the 8-GeV linac for an X-ray free electron laser (XFEL) is now under construction. In order to realize the XFEL, highly qualified electron beams are required. Especially in the undulator section the beam should have a size of several tens of micro-meters, a peak beam current of several kiro-amperes, a micro-bunch length comparable to the X-ray wavelength, and an emittance of less than 1 $\pi$mm·mrad [1].

In order to tune and realize such a beam, beam monitors are very important, and should have a comparable resolution to the beam parameters mentioned above. For a screen monitor (SCM), the required resolution is less than 10 $\mu$m. To achieve this resolution we have developed a prototype SCM using OTR and fluorescence radiation, based on the following design concept.

Generally a CCD camera with a ready-made zoom lens is used for SCM measurements. In this case we cannot have a precise parameter of the lens, such as the curvature, broadband property of dispersion, Abbe's number of glass and so on. This means that we cannot evaluate characteristics like aberrations, magnification and effective focal length using an optical design program. Therefore, we decided to know all of the design parameters so that we can evaluate the characteristics of the optical system. Consequently, a lens with published optical parameters was chosen, or a lens produced optimally by using an optical design program was selected. This paper gives a summary of the prototype SCM with the lens developed for transverse spatial structure measurements with a resolution of less than 10 $\mu$m.

* E-mail: ken@spring8.or.jp

## SYSTEM CONFIGURATION

### *Mechanical System*

The mechanical part of the SCM comprises a vacuum chamber with radiators, motorized stages that change the positions of a lens and a CCD camera.

The vacuum chamber has a shaft that links the upper and lower slide stages, as shown in Fig. 1. There are three holes along the shaft: an aperture of the beam passage and holes for two kinds of radiators.

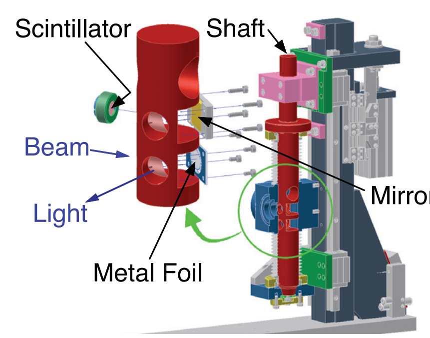


Figure 1: Structure around radiators.

One radiator is metal foil to emit OTR with a thickness of 100 $\mu$m. It is placed in the bottom hole where an electron beam hits the foil at an angle of 45°. The foil consists of nine apertured SUS foils (denoted by green foils in Fig. 2) and one SUS mirror foil without an aperture (denoted by the red foil in Fig. 2). The thickness of each foil is 100 $\mu$m. These ten foils are bonded by a diffusion bonding process, and form a single plate (see photograph in Fig. 2).

Figure 2: Metal foil.

The other radiator is a scintillator plate with a thickness of 100 $\mu$m, which is placed in the center hole where an electron beam hits the plate perpendicularly. The fluorescence from the plate is reflected at a mirror, and then led to the CCD camera.

The lens and the CCD camera are mounted on two different remote-controlled motorized stages. The position of the motorized stage with a lens is set for determining the magnification, and a motorized stage with a CCD camera is moved for focusing (see Fig. 3).

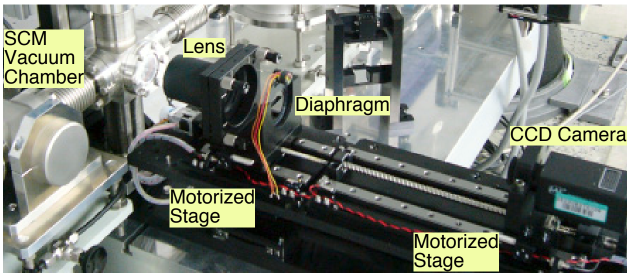


Figure 3: Developed prototype SCM installed in the SCSS test accelerator.

## *Optical System*

In order to obtain a bright and high-resolution optical system, the lens is placed close to the radiator, the distance between the lens and the radiator is 100 mm, and the lens has a large diameter (2 in.). This optical-geometrical structure contributes much to increases the numerical aperture (NA) of a near-field image. Table 1 summaries the principal specifications of the optical system. These parameters were calculated by the optical design program Zemax (ZEMAX DEVELOPMENT CORPORATION).

The lens structure is to be simple, like four elements in three groups, so as to reduce reflection on the glass surface. These three groups are installed into a single tube for easy alignment of the light axis. The bandwidth of the observation wavelength is wide, such as from 400 to 800 nm. The reason for the wide bandwidth is to obtain high light intensity. To realize this wide bandwidth, anomalous dispersion glass is used for the lens.

Geometrical and chromatic aberrations are minimized to be as small as possible by our design to reach down to a diffraction limit at 4 magnifications. The pixel size of the CCD is smaller than the image size due to diffraction. This means that the resolution of this optical system depends only on the image size, due to diffraction (diffraction-limted system).

# EVALUATION

In oder to evaluate the flatness of the metal foil, the positioning accuracy of the motorized stages and the resolution of the optical system following examinations were carried out.

## *Mechanical Evaluation*

The surface of the metal foil was measured, and found to be slightly concave. The concave depth is 3 $\mu$m in an area of 5$\phi$ mm. This value corresponds to only a $\sim$1 mrad difference from the light axis to the CCD camera, and is thought to be negligibly small compared to the tolerance of the optical system.

Table 1: Principal Specifications of Optical System

| | |
|---|---|
| Type of optical system | Object-space telecentric |
| Lens structure | 4 elements in 3 groups |
| Lens diameter | 50.8 mm |
| Lens effective focal length | 85.0 mm |
| Pupil radius of diaphragm | 1.0 $\sim$ 17.5 mm |
| M : Magnification | 1.2 $\sim$ 4.0 |
| Object-space NA at M = 4 | 0.010 $\sim$ 0.176 |
| Field of view at M = 4 | 2.2 $\times$ 1.7 mm (H $\times$ V) |
| Wavelength | 400 $\sim$ 800 nm |
| Resolution at object surface | 2.5 $\mu$m (HWHM) |

When the motorized stages moved from a position at 1.2 magnifications to a position at 4 magnifications, the positioning accuracy was measured. Checking the accuracy was done by analyzing the image acquired by a CCD camera. A transverse displacement errors along the movements of the motorized stages for focusing and zooming were 20 $\mu$m in the horizontal direction and 150 $\mu$m in the vertical direction. The cause of the vertical displacement error was a deformation of the bread board that mounted the motorized stages on it. The vertical displacement is sufficiently small compared with the size of the field of view.

## *Optical Evaluation*

The spacial resolution of the optical system was measured at 4 magnifications. A checking target used to evaluate the resolution is the Fixed Frequency Grid Distortion (FFGD) target (EDMUND OPTICS), as shown in Fig. 4. The diameter of dots on the target is 62.5 $\mu$m, and the center-to-center spacing of the dots is 125 $\mu$m.

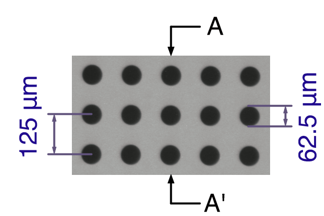


Figure 4: Pattern of the FFGD target.

In Fig. 5 the black line denotes the intensity proportional to contrast along the A-A' line in Fig. 4. The blue line expresses the differential of the intensity. The differential gives the resolution of the optical system. The HWHM (half width at half maximum) value of the differential data is 9.9 $\mu$m (2.5 $\mu$m on the object surface). This value is almost the same as the resolution calculated by Zemax.

# BEAM TEST

At the SCSS test accelerator [2], 250-MeV electron beams were targeted on the metal foil to observe the near-

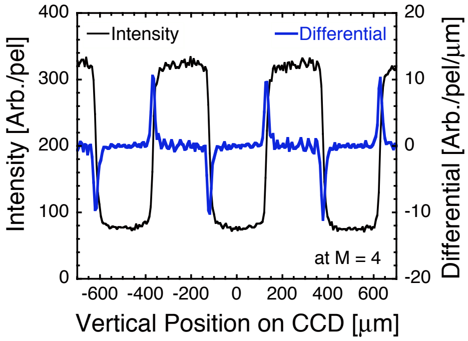


Figure 5: Intensity along the A-A' line in Fig. 4 and its differential.

field images of OTR at 4 magnifications. The images were analyzed to evaluate the image size of the OTR. This evaluation gives information on the resolution in the case of OTR emitted from an 8-GeV electron beam.

For the beam test, the electron beam size was kept minimized in the horizontal axis by quadrupole magnets, as shown in Fig. 6, and the numerical aperture ($NA_O$) of the object space was varied from 0.011 to 0.152 by changing the pupil radius. The measured image intensities and the horizontal image sizes are shown as circles in Fig. 7 and Fig. 8.

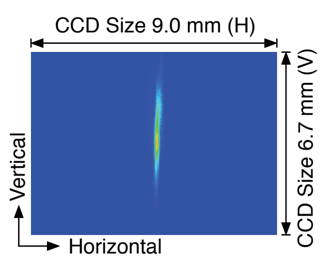


Figure 6: Near-field image of the OTR.

In order to compare the measured values and the theoretical ones, a calculation of the image intensity and the size of the OTR was carried out. The angular distribution of the OTR strength [3] is approximately expressed as

$$\frac{\theta^2}{(\gamma^{-2}+\theta^2)^2}\,, \tag{1}$$

where $\gamma$ is the Lorentz factor. The image intensity was calculated by integrating Eq. (1) in an integral range specified by $NA_O$. In Fig. 7 the calculated image intensity is indicated by the line. The line and circles exhibit the same tendency.

With this optical system, an image is formed by diffraction, and an object (beam profile). The image due to diffraction was calculated as follows: divide the OTR distribution of Eq. (1) into many sliced elements, specified by $NA_O$, calculate the image size and intensity of each element and integrate the image sizes and intensities of all elements into one image. In Fig. 8 the solid line expresses the calculated image size due to only diffraction. The dashed line

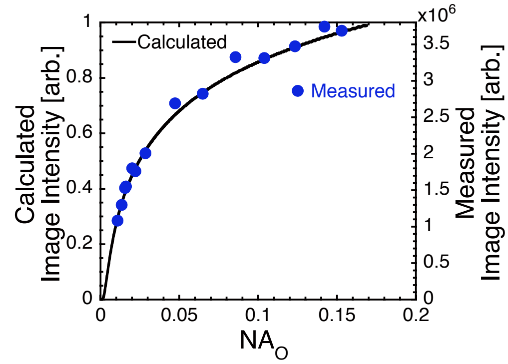


Figure 7: Measured and calculated image intensities.

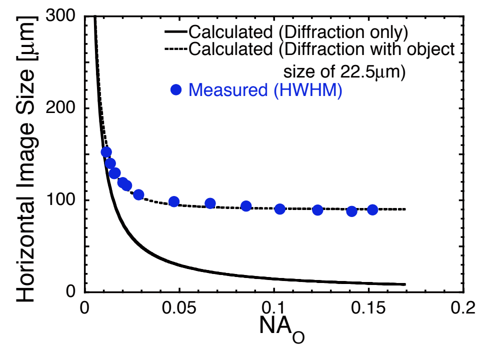


Figure 8: Measured and calculated horizontal image sizes.

expresses the root sum square of the calculated image sizes due to diffraction and an object with a size of 22.5 $\mu$m. The dashed line and the circles closely agree. This means that the electron beam size was surely measured down to 22.5 $\mu$m.

## SUMMARY

The development of a screen monitor has been completed. The resolution of the screen monitor was calculated and measured with 2.5 $\mu$m in length on an FFGD target surface. This resolution is sufficient to measure the transverse spatial structure of beams in an undulator section. The screen monitor was also evaluated by observing OTR emitted from a beam on a metal foil surface at the SCSS test accelerator. We must therefore check weather our developed OTR radiator works or not. The OTR radiator actually emitted light. The electron beam size was surely measured down to 22.5 $\mu$m.

## REFERENCES

[1] T. Tanaka et al., Nucl. Instrum. Meth. A 528, 172 (2004).

[2] T. Shintake et al, Nature Photonics, Vol. 2, pp. 555-559, (2008).

[3] P. Catravas et al., “Beam Profile Measurement at 30 GeV Using Optical Transition Radiation”, Proc. of the 18th Particle Accel. Conf. New York, March 1999, pp. 2111-2113.

# DEVELOPMENT OF INTEGRATOR CIRCUIT FOR CHARGE MONITORING

K. Yanagida*, S. Suzuki and H. Hanaki
JASRI, Accelerator Division /SPring-8
1-1-1 Kouto, Sayo-cho, Sayo-gun, Hyogo 679-5198

*Abstract*

At the SPring-8 1-GeV linac, an electric charge of a pulsed electron beam is measured by an integrator circuit. A signal from a current transformer is processed into an integrated voltage. To improve the resolution for future use, a low-noise integrator circuit was developed whose main elements are a gate switch (SW-283-PIN, M/A-COM) and an accumulator (coaxial cable). The resolution is 0.65 pC under conditions of a range of 2 nC and a gate width of 20 ns. The resolution of the developed integrator circuit is 1/12 of the resolution of the present integrator circuit. The nonlinearity of the output voltage is small, 0.14 % rms compared to the output full scale.

## INTRODUCTION

At the SPring-8 linac, eighteen current transformers (CTs) have been installed to observe macro longitudinal current structure or the electric charge of a pulsed electron beam by an oscilloscope. Beam charges are not recorded into the database except for two CTs; one is installed in the beam transfer line to the booster synchrotron, and the other is installed in the beam transfer line to the NewSubaru storage ring. These stored data are used to observe the beam charge and to calculate the injection efficiency to the booster synchrotron or the NewSubaru storage ring.

For top-up injection to the SPring-8 storage ring, about every 20 seconds the linac shoots an electron beam whose beam charge is about 1 nC. In the future the beam charge will be decreased due to more frequent beam injection to the storage ring. Presently Fast Gated Integrator and Boxcar Averager Modules (STANFORD RESEARCH SYSTEMS) are equipped as integrator circuits for signal processing. When the beam charge is decreased for the frequent beam injection, the resolution of the present integrator circuit will be worsened, too. To maintain or improve the resolution we developed a new integrator circuit to reduce the noise level to 1/10 of the present integrator circuit. The developed integrator circuits will be installed for all CTs in the linac instead of the present integrator circuits.

## PRINCIPLE

The principle of the developed integrator circuit is identical as the principle of the present integrator circuit [1]. The principal elements are a gate switch and an accumulator. The gate switch determines the integration time of the measurement. When the gate is open, the signal voltage is led to an accumulator (1 and 2 in Fig. 1) that is a delay line with a characteristic impedance of 50 Ω. A coaxial cable or a pulse forming network (PFN) is used as an accumulator. The signal voltage led into the accumulator is reflected at the opposite open end and returned to the gate switch (3 in Fig. 1). If the gate is closed before the reflected signal voltage arrives, both ends of the accumulator become open ends, and then the signal voltage is stuck in the accumulator (4 in Fig. 1). The stuck signal voltage is averaged as it goes back and forward (5, 6, and 7 in Fig. 1). This averaged voltage is proportional to the integral of the signal voltage while the gate is open.

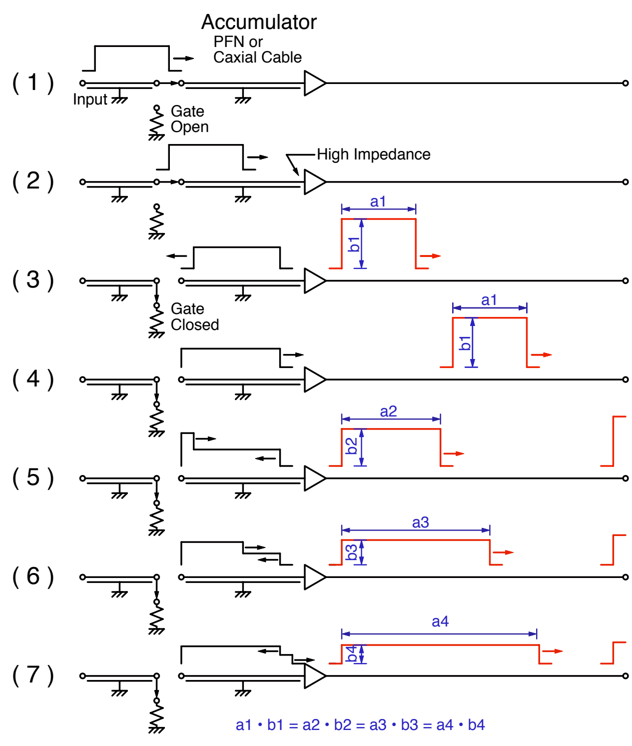


Figure 1: Principle of integrator circuit.

## DESIGN

The block diagram and exterior of the developed integrator circuit are shown in Figs. 2 and 3. In Fig. 2 "a:" denotes the parameter for a short (1 ns) pulsed beam measurement,

* E-mail: ken@spring8.or.jp.

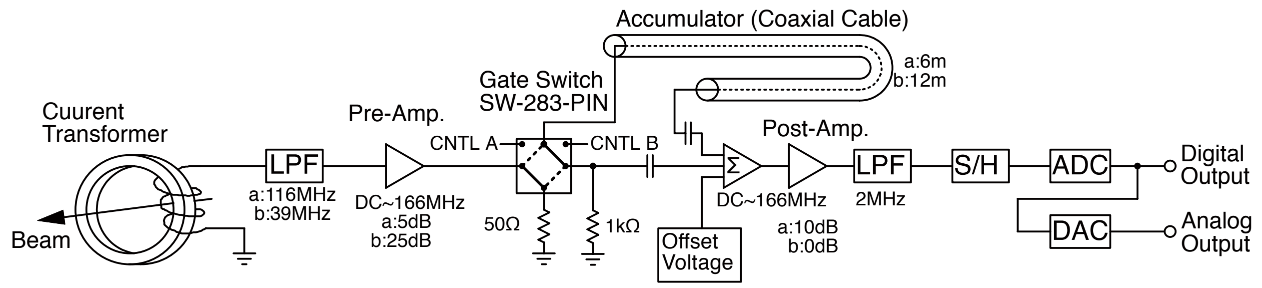


Figure 2: Block diagram of developed integrator circuit.

while "b:" denotes the parameter for a long (40 ns) pulsed beam measurement.

Two elements perform switching operations after receiving an external trigger: the gate switch and the sample-hold circuit in Fig. 2. The switching operation generates non-negligible fluctuation on its output voltage, and the typical amount of fluctuation is about 0.4 mV rms. Because this fluctuation dominantly affects the noise level of the output voltage of the integrator circuit, two amplifiers are installed to increase the input signal level to the switching elements: a pre-amplifier before the gate switch and a post-amplifier before the sample-hold circuit.

A low-pass filter, which is inserted between the CT and the pre-amplifier to avoid saturation of the pre-amplifier output, expands the pulse width and decreases the pulse height, but retains the time integral of the voltage.

The gate switch is a GaAs transfer switch SW-283-PIN (M/A-COM) (see Fig. 3). Its principal specifications are summarized in Table 1. A transfer switch was adopted to connect all ports with each other. If a port is not connected to another port, large switching noise appears in the port. The pre-amplifier becomes especially unstable due to this noise.

The SW-283-PIN has four ports and two control voltage inputs. The control voltages (denoted as CNTL A and CNTL B in Fig. 2) are complementary voltages that are inverted when the state of connection is switched. When the gate is open the ports of the pre-amplifier and the accumulator, and the ports of the 50 Ω and the 1 kΩ are connected. When the gate is closed the ports of the pre-amplifier and the 50 Ω, and the ports of the accumulator and the 1 kΩ are connected. The control voltages are -0.1 and -7.9 V, which are close to the limitation of the specified control voltage range.

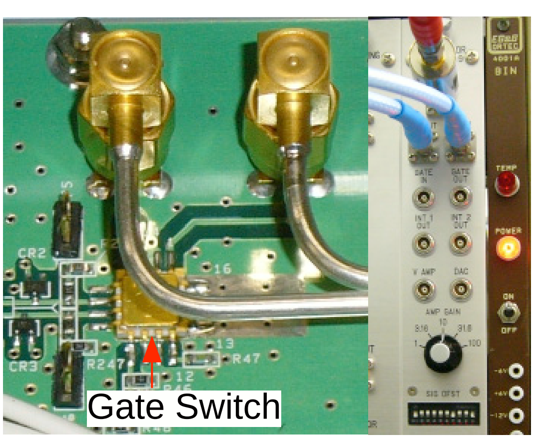


Figure 3: Gate switch on a base plate (left) and an exterior of developed integrator circuit (right).

Table 1: Principal Specifications of SW-283-PIN

| | | |
|---|---|---|
| Bandwidth [GHz] | | DC ∼ 3 |
| Isolation [dB] | DC ∼ 0.5 GHz | 45 |
| Rise/Fall time [ns] | 10 - 90% | 2 |
| 1dB Compression [dBm] | 0.05 GHz | +26 |
| Video Feedthru [mV] | | 30 |
| Control Voltages (Max) [V] | Low, High | 0, -8 |

The rise time of the gate switch is determined by the root sum square of the rise times of the SW-283-PIN and the control voltage. To avoid lengthening the rise time of the gate switch a fast circuit was developed to generate control voltages for the SW-283-PIN. The block diagram of the circuit is shown in Fig. 4. There are four fast transistor switches that consist of a bridge circuit and two kinds of DC voltages: +2 and -10 V. The control voltages are inverted instantaneously by the external gate pulse. The range of the control voltages is restrained between -0.1 and -7.9 V by clipping diodes. The merits for using clipping diodes include accuracy, stabilization , and the fast rise time of the pulsed control voltages.

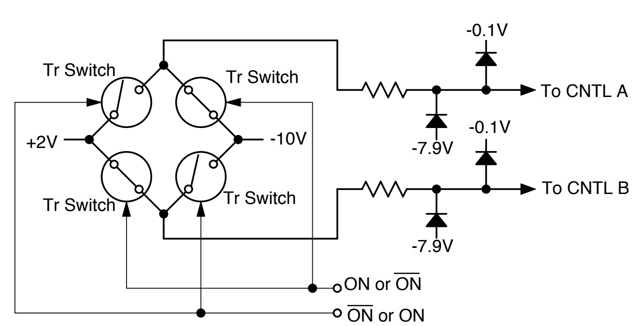


Figure 4: Block diagram of the circuit to generate control voltages for SW-283-PIN.

## PERFORMANCE

The following examination was carried out to evaluate the rise time of the gate switch. Pulsed voltages that passed through the gate switch were measured by an oscilloscope. Figure 5 is superimposed drawings of 61 waveforms. The initial pulse width and height were 1 ns and -1 V, and the pulses were successively delayed at 0.5 ns intervals. The measured pulse height is smaller than the initial pulse height because attenuation was caused by the internal resistance of the SW-283-PIN. The width of the superimposed waveforms expresses the width of the external gate pulse. Before and after the shape of the gate pulse, pulsed voltages don't appear, meaning that the pulsed voltage cannot completely pass through the gate switch when the gate is closed. The rise time is measured as 2 ns (10 → 90 %), 4 ns (10 → 95 %), or 8 ns (10 → 98 %), and these values are comparable to the SW-283-PIN specifications.

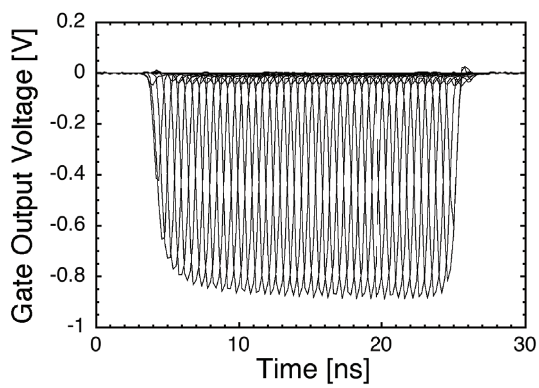


Figure 5: Superimposed 61 waveforms after passing gate switch.

When the gate is closed the accumulator is connected to the 1 kΩ termination and discharges with a time constant of $\sim 1\mu$ s. At this time the voltages that appear at both ends of the accumulator are summed by a summing amplifier. In Fig. 6 the red and blue lines express voltages that appear at the ends of the accumulator, and their pulsed voltages appear alternately. The height and width of the pulsed voltages decrease and widen as time elapses, until finally the voltages are averaged. The waveform of the 2 MHz LPF output is expressed as the green line, and the timing for the sample-hold is set around 700 ns in the figure.

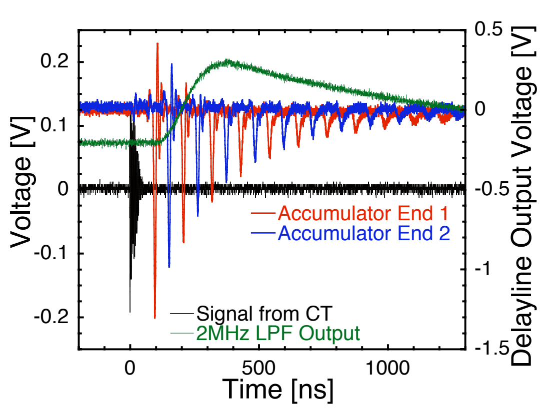


Figure 6: Voltages that appear at both ends of accumulator.

Resolution was measured as the standard deviation of the output voltage when the signal input is kept to 0 V (50 Ω termination). The resolution of the developed integrator circuit was measured as 0.65 pC under conditions of a range of 2 nC and a gate width of 20 ns, and the resolution of the present integrator circuit was measured as 2.9 pC under conditions of a range of 1.4 nC and a gate width of 10 ns. Because the resolution is proportional to the range and the gate width, the resolution of the developed integrator circuit has been significantly improved to 1/12 of the resolution of the present integrator circuit with the same range and gate width conditions.

The linearity of the output voltage to the time integral of the input voltage was measured with a gate width condition of 20 ns (Fig. 7). The output voltage shows good linearity, and its deviation 0.14 % rms, which is small compared to the output full scale (10 V).

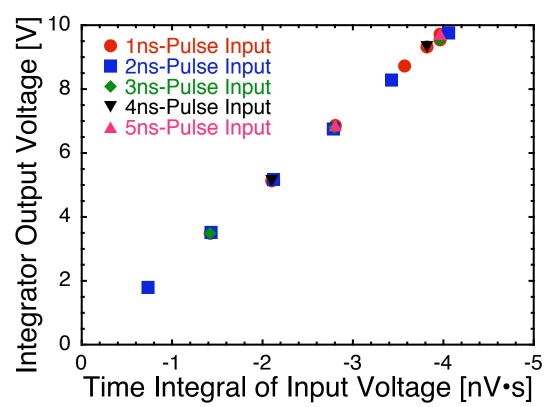


Figure 7: Output voltage to time integral of input voltage.

## SUMMARY

We developed an integrator circuit for the charge monitoring of the SPring-8 linac to improve resolution for future use. The main elements of the developed integrator are a gate switch and an accumulator. The rise time of the gate switch is 2 ns (10 - 90 %); this value is fast and comparable to the SW-283-PIN specifications. The resolution is 0.65 pC under conditions of a range of 2 nC and a gate width of 20 ns. This resolution is 1/12 compared to the resolution of the present integrator circuit with the same conditions. The nonlinearity of the output voltage is small, 0.14 % rms compared to the output full scale (10 V).

## REFERENCES

[1] Manual of Fast Gated Integrators and Boxcar Averagers, SANFORD RESEARCH SYSTEM S.

# OPERATIONAL PERFORMANCE OF A NEW BEAM-CHARGE INTERLOCK SYSTEM FOR RADIATION SAFETY AT THE KEKB INJECTOR LINAC

T. Suwada*, E. Kadokura, M. Satoh, K. Furukawa, KEK, Tsukuba, Ibaraki 305-0801, Japan

*Abstract*

A new beam-charge interlock system has been developed for radiation safety and machine protection at the KEKB injector linac. Although the previous software-based interlock system was working, it was replaced with the new hardware-based one to improve its operational performance and reliability. The new interlock system restricts the integrated amount of beam charges delivered to four different storage rings (KEKB $e^+$, KEKB $e^-$, PF, PF-AR) at six locations along the linac and the beam transport lines. The full-scale operation of the new interlock system has started in 27 March 2008 after elaborate beam tests. In this report we describe the beam tests, the technical improvements, and the operational performance of the new beam-charge interlock system.

## INTRODUCTION

A new injection scheme is under development for simultaneous and continuous injection delivered from the KEKB injector linac [1] to both the downstream storage rings (the KEKB electron/positron rings and the PF ring). The technical review was reported elsewhere in detail [2]. The new beam-charge interlock (BCI) system is one of the R&D subjects pertaining to the new injection scheme. The BCI system restricts the integrated amount of the beam intensity passing through the injector linac and the beam transport line to each storage ring. When it exceeds a certain threshold level prescribed at each location, the BCI system directly generates a beam-abort request to the safety control system of the linac for radiation safety and machine protection. Its technical review was reported in detail elsewhere [3-5].

The new BCI system also supplies a proper environment to advance the present accelerator complex towards the future projects. The following four subjects are underway,

(1) to increase of the injection beam intensity towards the next-generation B-factories,
(2) to perform the stable and continuous injection over an hour to the PF-AR,
(3) to enable easy beam tunings for the PF injection with a new beam dump,
(4) and to perform the new injection scheme for both the KEKB and the PF rings.

These subjects are strongly required for improving the stable and fast injection with higher-brightness (or higher-intensity) electron and positron beams into the downstream storage rings. In order to perform them, the instantaneous and integrated beam intensities must be controlled pulse-by-pulse at both the linac and each transport beam line. Therefore, the hardware-based BCI system with a higher reliability must have been developed for these purposes.

The new interlock system enables to relax the restrictions in the beam intensity for each injection mode. Table 1 shows the comparisons of the old and new beam-charge intensities prescribed at each location along the linac and each beam transport line.

Table 1: Comparisons of the Old and New Beam-charge Intensities Prescribed at Each Location

| Location | Old | | New | |
|---|---|---|---|---|
| | [nC/s] | [nC/h] | [nC/s] | [nC/h] |
| R0-01 | 1250 | - | 2500 | $4.50 \times 10^6$ |
| 22-44 | 625 | - | 1250 | $2.25 \times 10^6$ |
| Linac | 62.5 | - | - | $2.25 \times 10^5$ |
| KEKB | - | $5.76 \times 10^5$ | - | $5.76 \times 10^5$ |
| PF | - | - | - | $7.80 \times 10^4$ |
| PF-AR | - | $0.72 \times 10^4$ | - | $2.32 \times 10^4$ |

Based on this modification, the injection beam intensity can be controlled every an hour and every a second. In particular, the instantaneous beam intensity has been relaxed by two times. Thus, this modification has enabled to test high-intensity beam acceleration studies for the next-generation B-factories. On the other hand, the stable injection to the PF-AR over an hour has been realized. For the PF injection, the beam-intensity control has been available with a new beam dump. Thus, the flexible beam-intensity control has started and the highly reliable environment to advance the new injection scheme has been ready.

The development of the new BCI system has been finished after elaborate system tunings with beam tests during two years. The full-scale operation has started without any significant problems.

## FURTHER TECHNICAL IMPROVEMENTS

The designs of the new interlock system started in 2006, and the development of both the hardware and software system finished in October 2007. During two months since then, the operational tests were performed to check the technical functions, the reliability, and the stability in the nominal injection operation. We found several faults during the beam tests. Further the technical improvements have been performed step-by-step in order to increase the system reliability and flexibility. For the hardware system, metal doors were installed to shield a system rack to

*E-mail address: tsuyoshi.suwada@kek.jp.

further reduce electromagnetic noises mainly caused from high-power klystrons. An uninterruptible power supply (UPS) was also installed at each system rack to improve the operational reliability even for an unexpected power failure.

On the other hand, for the software system, the following subjects have been performed

(1) to add a clock time adjustment function for whole the system,
(2) to improve the stability of a serial communication line between the AR and the main control room of the linac,
(3) to connect the alarm system,
(4) and to improve the operational panels and the data transfer speed.

These improvements enabled to implement the flexible functions of the operation panels and to increase the speed of the data transfer and storage. The data transfer and the command controls were also stabilized without any problems. The function that automatically adjusts the clock time differences between the detector modules and the PLCs by communicating the UNIX-based host computer was added. It enabled to quickly let the linac operators know the abnormal system status. Thus, based on the software improvements, the operators can get easily and quickly the proper information and status of the BCI system.

## BEAM TESTS

The wall-current monitors are utilized for the beam-charge measurements in the new BCI system. They were calibrated with both bench and beam tests. The calibration system of the test bench was reported in detail elsewhere [4,6]. Here, the results of the beam tests are briefly described. The typical results with the KEKB positron beam are shown in fig. 1.

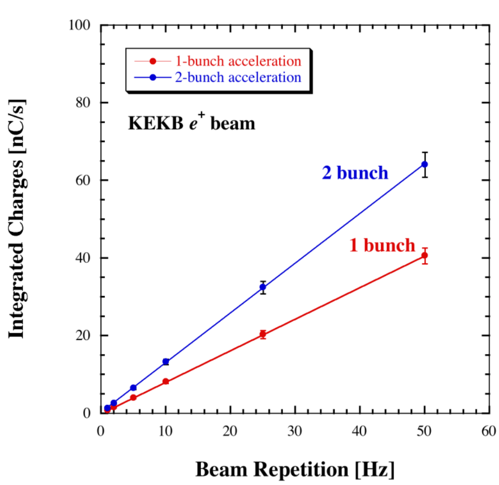


Figure 1: Linear relations of the beam charges integrated every a second interval as a function of the beam repetition rate obtained for one-bunch (red) and two-bunch (blue) acceleration mode.

The results show the linear relations of the beam charges integrated every a second interval depending on the beam repetition rate obtained for one-bunch and two-bunch acceleration mode. The results indicate a good linearity within 1% and with a dynamic range of ~20 dB although the obtained data include tiny beam intensity fluctuations.

Figure 2 shows the time trends of the beam charges integrated every a second interval measured for the nominal KEKB operation during a day. We can clearly see the variations in the differences on the KEKB electron and positron beam intensity, on the number of the accelerated bunches, and the repetition rate. The results also show that the beam charges are stably measured pulse-by-pulse without any significant signal noises.

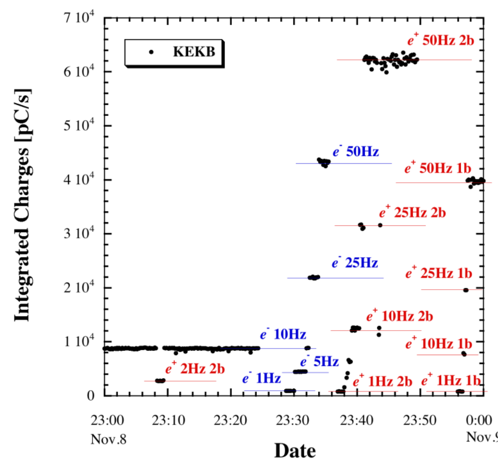


Figure 2: Time trends in the beam charges integrated every a second in the nominal KEKB operation. The repetition rate, the number of accelerated bunches (1b: 1 bunch, 2b: 2 bunches), and the charge sign are indicated at each data point.

Figures 3 (a) and (b) shows the typical time trends of the integrated charges integrated every an hour interval during a week and a day obtained for the nominal KEKB operation, respectively. As shown in fig. 3(a), the typical integrated intensities are ~3% to the prescribed beam charges (CL=$5.76\times10^5$ nC/h) at location KEKB while the maximum of the integrated intensity have attained up to ~10% (or $6\times10^4$ nC/h) level to it. This level (~3%) corresponds to the integrated beam charges in the stable continuous injection operation, in which the electron and positron injection has alternatively changed every a few minutes. The maximum level (~10%) corresponds to the injection with a maximum repetition rate. Thus, we can see that in the nominal operation condition the measured beam intensity is far enough away from the prescribed beam charges.

As shown in fig. 3(b), we can also see that the BCI system is properly reset every clock hour, and it successively continues the measurement after the reset without any time delay. It is also confirmed that the variations in the linear slope of the measured integrated charges depend on the change of the beam repetition rate.

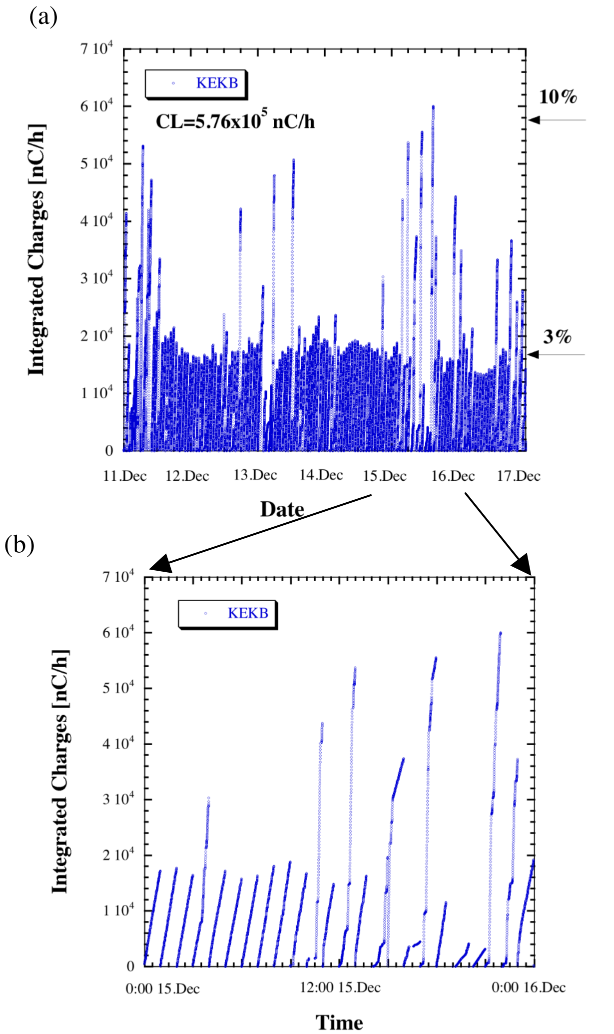


Figure 3: Time trends of the beam charges integrated every an hour during (a) a week and (b) a day in the nominal KEKB operation.

## OPERATIONAL PERFORMANCE

The successive full-scale operation of the BCI system has been stably implemented during three months without any significant problems while no abort-signal requests were generated in this operation. The typical charge-intensity levels measured in the nominal operation are summarized in Table 2. It should be noted that the unit is indicated by the ratio of the integrated beam charges to the prescribed ones at each location. The maximum of the beam charges integrated every a second (hour) at R0-01 was ~35% (~13%) for the primary high-intensity electron beam for positron generation.

Thus, it was confirmed that the beam intensity levels were much less than the prescribed beam charges in the nominal operation for each injection mode. The results clearly also show the good reliability and stability of the BCI system without any dangerous excesses on the beam intensity for all the beam modes.

Table 2: Integrated Amounts of the Beam Charges Normalized by Those Prescribed at Each Location Obtained in the Nominal Linac Operation

| Location | Beam Charges (1s interval) [%] | Beam Charges (1h interval) [%] |
|---|---|---|
| R0-01 | 8-35 | 3.5-13 |
| 22-44 | 1.5-5 | 2-12 |
| KEKB | - | 3.5-10 |
| PF | - | 0.2-0.6 |
| PF-AR | - | 2-5 |

The BCI system enabled to store other important data, that is, the beam charges and the shot numbers integrated during a day and a week at each location. The 1-week beam-charge data depending on the injection modes are required to radiation-safety records in the linac operation. We have no such kinds of data logging systems until now. It is expected that these data give an important operational history not only for radiation safety but also for the long-term stability and reproducibility of the injector linac operation.

## SUMMARY

The full-scale operation of the new beam-charge interlock system has started since 27 March 2008. The new BCI system highly improved its reliability and stability for radiation safety and machine protection for the KEKB injector linac and the downstream beam transport lines. It was confirmed that this new system has stably continued to work during three months until this summer shutdown (the end of June 2008) without any significant problems. An environment to advance several new activities for our future projects is ready now.

## REFERENCES

[1] I. Abe, *et al.,* Nucl. Instrum. & Methods. A499 (2003) pp.167-190.
[2] M. Satoh, *et al.*, *Procs. the 10th European Particle Accelerator Conference* (*EPAC'06*), p.855.
[3] T. Suwada, E. Kadokura, M. Satoh, K. Furukawa, *Procs. the 2006 International Linac Conference (LINAC'06)*, p.800.
[4] T. Suwada, E. Kadokura, M. Satoh, and K. Furukawa, Rev. Sci. Instrum. 79, 023302 (2008).
[5] E. Kadokura, T. Suwada, M. Satoh, and K. Furukawa, *Procs. of the Int'l Conf. on Accelerator and Large Experimental Physics Control Systems (ICALEPCS'07)*, p.149.
[6] T. Suwada, N. Kamikubota, H. Fukuma, N. Akasaka, and H.Kobayashi, Nucl. Instrum. & Methods. A396 Nos.1, 2 (1997) p.1.

# NUMERICAL STUDY OF A NEW BUNCH LENGTH MONITOR UTILIZING A DETECTION OF ELECTROMAGNETIC FIELDS IN MILLIMETER-WAVE REGION

T. Suwada* and M. Satoh, KEK, Tsukuba, Ibaraki 305-0801, Japan

*Abstract*

A new nondestructive bunch-length monitor has been numerically investigated in high-energy electron/positron linear accelerators. The monitor detects electromagnetic radiation emission generated in wave zone through a gap of a vacuum pipe when a relativistic bunched beam passes across the pipe gap. The frequency spectrum of the radiation emission spreads over microwave to a millimeter-wave region for the bunched beam with a bunch length of a picosecond region. The frequency spectrum strongly depends on the bunch length if the geometrical structure of the pipe gap is suitably fixed. The detection principle of the new bunch-length monitor and some numerical analysis results applied to a single-bunch electron beam at the KEKB injector linac are described in this report.

## INTRODUCTION

A bunch-length measurement of a bunched beam is one of important beam diagnostics in linear accelerators. There are several methods to measure the bunch length [1]. One is a standard method with a streak camera. It measures a pulse width of electromagnetic radiations in time domain, such as Cherenkov radiation and optical transition radiation generated through electromagnetic interactions between materials and the bunched beam. This method comes in useful for the bunch-length measurement in a picosecond region. Recently, a fast streak camera can makes the bunch-length measurement possible with a time resolution of sub-picoseconds [2].

These are well-known methods to measure the bunch length in a pico (or sub-pico) second region, and however, they have several drawbacks because they are basically based on destructive diagnostics, and they need expensive instrumentations with complicated systems.

Here, we propose an alternative new method to measure the bunch length in frequency domain by nondestructively detecting electromagnetic radiation emissions. They are shaken off the bunched beam by diffraction (or scattering) at a pipe gap of a beam line. This method requires only a pipe gap normally vacuum-sealed with a ceramic. It does not require any other devices in the beam line.

There are many pipe gaps vacuum-sealed with a conventional ceramic along the beam line of the KEKB injector linac in order to install other beam diagnostic devices. Such pipe gaps are available for the bunch-length measurement based on this new method at any locations of the entire beam line

In this report, the basic principle on this new method are presented. The characteristics of the electromagnetic radiation emitted from the pipe gap are also given, and some numerical results analyzed for a single-bunch electron beam at the KEKB injector linac are summarized.

*E-mail address: tsuyoshi.suwada@kek.jp.

## CHARACTERISTICS OF THE RADIATION EMISSION

When a charged particle with a relativistic energy passes through a vacuum pipe in linear accelerators, image charges with the inverse sign are induced on the inner surface of the pipe, and they also flow simultaneously through it. Electromagnetic fields (or self-fields) induced between the charged particle and the image charges are relativistically boosted in the longitudinal direction. When such pancake-like self-fields pass across the pipe gap, a part of the self-fields are emitted out of the pipe gap in wave zone because the self-fields must be met with the electromagnetic boundary conditions under which the charged particle is surrounded with both the pipe gap and the metal pipe.

The characteristics of the electromagnetic radiation emission from the charged particle are determined by depending on the geometrical structure of the pipe gap (see fig. 1(a)) if the charge and the energy of the charged particle are constant.

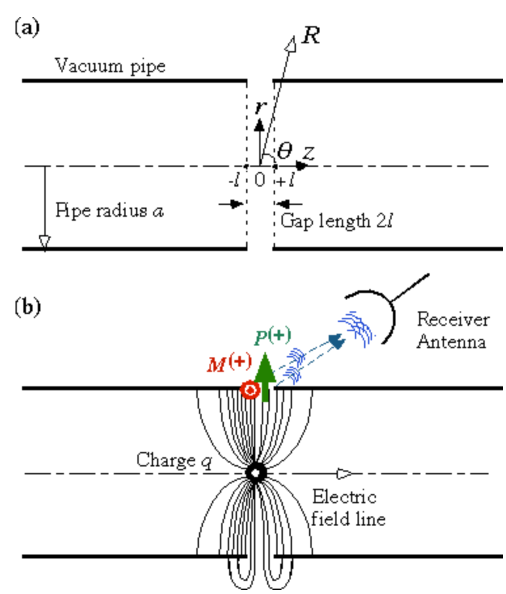


Figure 1: (a) Geometrical structure of the vacuum pipe and the pipe gap and (b) a schematic drawing of the electromagnetic radiation emission through the pipe gap.

On the other hand, when a bunched beam goes across the pipe gap, the characteristics of the electromagnetic radiation emission may be modified depending not only on the geometrical structure of the pipe gap, but also the geometrical charge distributions of the bunched beam.

Based on the Bethe's diffraction theory by small holes [3], a flow of electromagnetic radiations through such small holes may induce electric and magnetic dipole moments on the surface of the small holes. The vector directions of these dipoles correspond to those of the field vectors induced on the surface of the closed holes. The time oscillation of the induced dipoles can emit the electromagnetic radiations in wave zone out of the small holes. A schematic drawing on the radiation emission based on the dipole oscillations is shown in fig. 1(b). One of the characteristic features of the radiation emission is that the emission intensity becomes a maximum (minimum) in the direction of the beam axis ($r$ axis).

On the other hand, an emission of rf waves out of a finite open waveguide with an rf oscillator at one end was exactly investigated by Weinstein [4]. Based on the Weinstein's theory, when the relativistic bunch passes across the pipe gap, a large part of the self-fields transmits across the pipe gap, and however, a part of the self-fields reflects at both open ends of the pipe gap to be met with the electromagnetic boundary conditions. Thus, the multiple reflections of the self-fields occur between both the open ends, and a part of the interfered self-fields is emitted into free space out of the pipe gap due to diffraction (or scattering) (see fig. 1(b)).

It is generally very difficult to exactly solve these electromagnetic radiation emission problems. Palumbo [5] and Kheifets [6] give an analytical formula on an energy loss of the charged particle generated at such a pipe gap by approximately working out these problems based on the Weinstein's theory. The energy loss (or radiation power) per a solid angle $d\Omega$ is given by

$$\frac{dW(\theta)}{d\Omega}=\frac{\alpha\hbar\beta(q/e)^2\sin^2\theta\cdot J_0^2(ka\sin\theta)}{\pi(1-\beta\cos\theta)^2 I_0^2(ka/\beta\gamma)}\times$$

$$\left|\frac{L_-(\omega/v)\sqrt{1-\beta}}{L_-(k\cos\theta)\sqrt{1-\cos\theta}}e^{-jkl(1-\beta\cos\theta)/\beta}-j\frac{L_+(\omega/v)\sqrt{1+\beta}}{L_+(k\cos\theta)\sqrt{1+\cos\theta}}e^{jkl(1-\beta\cos\theta)/\beta}\right|^2 \quad (1)$$

Here, $\alpha$ the fine structure constant, $\hbar$ the reduced plank constant, $q$ the particle charge, $e$ the electron charge magnitude, $\beta=v/c$, $v$ the velocity of the charged particle, $\theta$ the spatial emission angle, $\omega$ the angular frequency of the electromagnetic radiation, $k=\omega/c$, $c$ the velocity of light, $\gamma$ the relativistic Lorentz factor, $J_0$ the Bessel function of the first kind, $I_0$ the modified Bessel function of the first kind. The other parameters are indicated in fig. 1(a). It should be noted that the higher-order multiple-reflection terms are neglected in Eq. (1) due to the smaller contribution. The right-hand side of Eq. (1) shows that the radiation spectrum mainly comprises two terms for which the first (second) term makes a contribution from the radiation emission generated at the left (right)-side end of the pipe gap (see fig. 1(b)). The functions $L_\pm$ are derived on the basis of the Wiener-Hopf factorization method [4] by

$$L_+(\alpha)=j\Gamma_+(\alpha)\sqrt{\alpha+k} \quad (2)$$

$$L_-(\alpha)=-j\sqrt{k-\alpha}/\Gamma_-(\alpha). \quad (3)$$

The functions $\Gamma_\pm$ are specified [7] by

$$\Gamma_\pm(\alpha)=[2\Sigma I_0(\Sigma)K_0(\Sigma)]^{\pm1/2}\exp\left\{\frac{\alpha a}{j\pi}\int_0^{ka}dt\frac{\ln\left[\pi\Sigma_1 J_0(\Sigma_1)H_0^{(1)}(\Sigma_1)\right]}{\alpha^2a^2-t^2}\right.$$

$$\left.+j\frac{\alpha a}{\pi}PV\int_{ka}^{\infty}dt\frac{\ln\left[2\Sigma_2 I_0(\Sigma_2)K_0(\Sigma_2)\right]}{t^2-\alpha^2a^2}\right\}. \quad (4)$$

Here, $H_0^{(1)}$ is the Hankel function of the first kind, $K_0$ is the modified Bessel function of the second kind, and the other parameters are given by

$$\Sigma^2=a^2(\alpha^2-k^2),\ \Sigma_1^2=k^2a^2-t^2,\ \Sigma_2^2=t^2-k^2a^2. \quad (5)$$

It should be noted that Eq. (1) gives the relativistic radiation emission formula in frequency domain.

## NUMERICAL STUDIES OF THE RADIATION EMISSION

In general, the radiation emission spectra from the bunched beam may be derived from the convolution of Eq. (1) with the spatial charge distributions. It is easy to numerically solve the integrations rather than to calculate them analytically. Assuming the longitudinal charge distribution of the bunched beam being expressed by a Gaussian function, several number of macro particles are arranged discretely at equal distance along the longitudinal direction.

Therefore, the radiation emission spectra can be numerically investigated by summing the imaginary amplitude contributions from all the macro particles following Eq. (1). Here, the number of macro particles was assumed to be 6 arranged within the total width of $\pm3\sigma_t$ ($\sigma_t$, one-sigma bunch length) of the longitudinal charge distribution. The gap length and the pipe diameter were fixed to be $2l$=12mm and $2a$=60mmϕ, respectively.

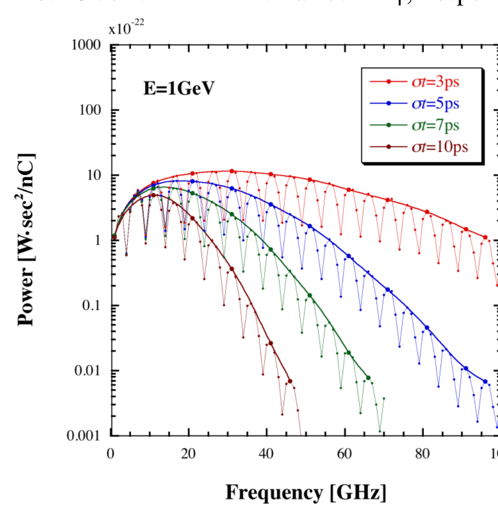


Figure 2: Radiation emission spectra as functions of the frequency and the bunch length.

The results at the beam energy of 1 GeV are shown in fig. 2. Here, for the sake of simplicity, the rf loss at a ceramic seal of the pipe gap and the energy spread of the single-bunch beam were neglected. The radiation emission angle was fixed to be $\theta=\pi/2$. As shown in fig. 2, the radiation emission powers are larger at the millimeter-wave region over the microwave region for the shorter bunch length in a picosecond region. The spectra also indicate periodical dip structures due to diffraction (or scattering). The frequency and the depth at the dip location are determined by the geometrical structure of the pipe gap. The solid curves in the figure are envelopes without the dip structures. The result (blue line, $\sigma_t$=5 ps) corresponds to that for the KEKB injection beam since the bunch length is ~10 ps in FHWM. The difference of each emission spectrum is so remarkable in millimeter-wave region (>~20 GHz) even for the bunch length difference of a few picoseconds.

The radiation emission spectra based on the envelopes depending on the beam energy are shown in fig. 3 while the bunch length is fixed to be $\sigma_t$=5 ps.

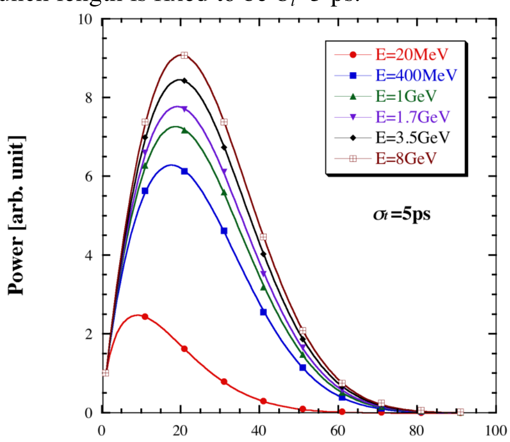


Figure 3: Radiation emission spectra as functions of the frequency and the beam energy.

It should be noted that the radiation power spectra are normalized with each power at the frequency of 1 GHz. It is understood that the energy dependence of the critical frequency is not very large at highly relativistic energies while the critical frequency giving the maximal power of each distribution increases with the increase of the beam energy. This may come from the relativistic Lorentz boost of the self-fields.

Figure 4 shows the variations in the normalized radiation power spectra as functions of the critical frequency, the bunch length, and the beam energy. The results indicate that the radiation power at the critical frequency increases with the increase of the beam energy, and the critical frequency largely shifts towards the higher frequency region for the shorter bunch length. It is of great benefit to this method for the shorter bunch-length measurement. The results also give the mapping curves as functions of the bunch length and the beam energy.

Assuming that the frequency resolution in the critical frequency measurement is attainable within $\delta f$ ~1 GHz over the millimetre-wave region ($f$=10-30GHz), the resolution of $\delta\sigma_t$~1 ps may be attainable enough although it is not easy to measure the precise beam energy with this method at highly relativistic energies.

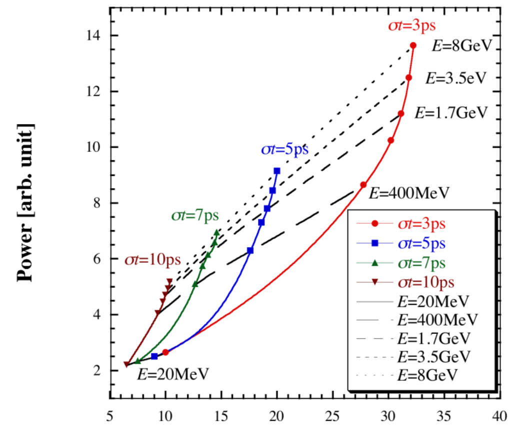


Figure 4: Relations (mapping curves) of the critical frequency to the radiation power as functions of the bunch length and the beam energy.

An example of the detection system is simply presented here. It comprises a receiver antenna, a tunable band-pass filter with a narrow bandwidth, and a peak-power meter. The millimetre waves are directly detected with the receiver antenna installed near the pipe gap. The power spectra are measured through the band-pass filter by sweeping the centre frequency over the frequency range of 5-40 GHz. The peak power obtained is ~54 dBm/nC, if the bandwidth of the detectable frequency is $\Delta f$~1 MHz. It seems to be possible by using a commercially available peak-power meter at millimetre-wave region.

## SUMMARY

A new nondestructive bunch-length monitor has been numerically investigated for a single-bunch beam of the KEKB injector linac. The numerical results show that the bunch length with a resolution of $\delta\sigma_t$~1 ps may be measured based on this new method with a suitable detection system.

## REFERENCES


[1] A.W.Chao and M.Tigner (eds.), Handbook of Accelerator Physics and Engineering (World Scientific, Singapore, 1999), p.547.

[2] http://jp.hamamatsu.com/en/index.html

[3] H.A.Bethe, Phys. Rev. 66, 163 (1944).

[4] L.A.Weinstein, *Theory of Diffraction and the Factorization Method* (The Golem Press, Colorado, 1969).

[5] L.Palumbo, CERN LEP-TH/84-4.

[6] S.Kheifets, *et al.*, CERN LEP-TH/85-23.

[7] B.W.Zotter and S.A.Kheifets, *Impedance and Wakes in High-Energy Particle Accelerators* (World Scientific, Singapore, 1998), p.267.

# TRANSIENT BEAM LOADING COMPENSATION IN CTF3

A. Dabrowski, S. Bettoni, H. H. Braun, E. Bravin, R. Corsini, S. Doebert, C. Dutriat, T. Lefèvre, M. Olvegård, P. K. Skowronski, F. Tecker
CERN, Geneva, Switzerland

*Abstract*

In the CLIC Test Facility 3 (CTF3), the strong coupling between the beam and the accelerating cavities (full beam loading) induces transient effects such that the head of the pulse is accelerated almost twice as much as the steady-state part of the pulse. The beam optics in the machine is tailored for the steady-state and not for the higher energy electrons, which are gradually lost. This can lead to inefficiency and contributes to the activation of the machine. A beam loading compensation scheme has been proposed to minimize this effect. By delaying appropriately the arrival time of the rf pulse in accelerating cavities with respect to the beam, the transient energy can be brought close to (within a few percent of) the steady-state one. This paper presents the measurements done on CTF3 using time resolved energy measurements.

## INTRODUCTION

In CTF3 an electron pulse of 3.5 A and 1.5 µs is accelerated using fully loaded 3 GHz accelerating structures [1]. The resulting energy spectrum shows a strong time dependency with higher energies in the first 50 nanoseconds of the pulse, followed by the steady state. Time-resolved spectrometry is therefore an essential beam diagnostic tool to correctly set the phase of the accelerating structures. Several spectrometer lines are installed along the CTF3 linac for this purpose. They consist of a bending magnet, which provides horizontal deflection to the electrons, followed by a transverse profile monitor measuring the beam position and its transverse width. The spectrometer lines are equipped with an optical transition radiation (OTR) screen [2] observed by a CCD camera with good spatial resolution and at the end of the line a novel segmented beam dump [3] for time resolved energy measurements.

This paper is devoted to the commissioning and utilization of the segmented beam dump. This device is composed of parallel metallic plates designed to measure a current, proportional to the number of stopped incident particles. By measuring the deposited charge in each segment, the beam energy profile can be reconstructed. The material and the dimension of the segments were chosen based on considerations of the beam parameters, in particular the beam energy and the energy spread, but also on the beam power absorbing efficiency and the radiation hardness requirements. The segments need to be deep enough to stop the particles; on the other hand, the segment thickness must be chosen to optimize the spatial resolution, which is eventually limited due to multiple Coulomb scattering [4]. After simulation studies with the Monte Carlo code FLUKA [5] as described in [3], the design was chosen as consisting of two devices; a passive 4 cm thick multi-slit (400 µm wide vertical slits) collimator made of iron which stops about 75% of the electrons and the active detector, which we refer to as the segmented dump that is installed just behind the collimator. It consists of tungsten plates of 2 mm transverse thickness, 5 cm depth and 5.5 cm height spaced by a 1mm thick radiation hard ceramic insulator as shown in Fig. 1. The role of the collimator is to capture as much beam power as necessary to ensure a good signal in the segmented dump, but to keep the deposited power low enough so that the segmented dump does not require water cooling.

The electronics, used to read the current drawn from each segment, consists of a direct connection to the segment with a 50 Ω impedance to ground. These signals are attenuated by 8 dB, and then digitised by a 100 MSa/s sampling ADC, which limits the time resolution of the post digitised signals to 10 ns, see Fig. 2.

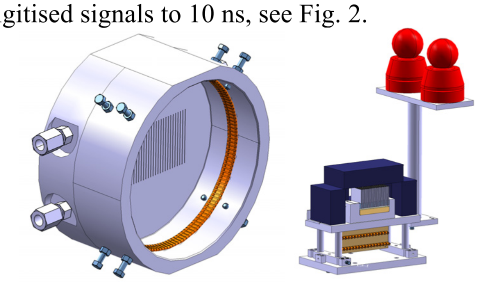

Figure 1: (a) Multi-slit collimator, (b) segmented dump.

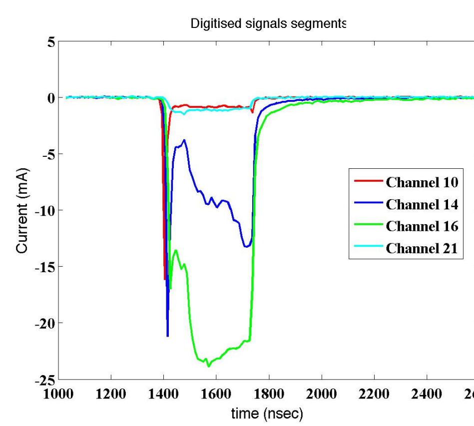


Figure 2: Typical digitised signals from segmented dump.

## COMMISSIONING OF THE SEGMENTED DUMP

The first part of the CTF3 drive beam linac is shown in the schematic of Fig. 3. The injector consists of a dc gun followed by a 3GHz bunching system. Two 3 GHz accelerating structures boosts then the beam energy up to approximately 20 MeV. A magnetic chicane equipped with a collimator provides the proper beam cleaning to get rid of the remaining low energy particles produced in the bunching cavities. The linac continues with standard accelerating modules composed of two 3 GHz accelerating structures fed by a single klystron. Two segmented dumps were installed in the spectrometer lines 4 and 10.

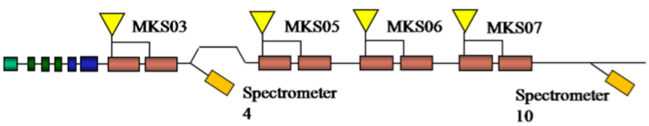


Figure 3: A schematic of the layout of the first part of the CTF3 injector and linac and the locations of the spectrometer lines used for energy measurement diagnostics.

The design of the two spectrometer lines are essentially the same with an acceptance in energy spread of about 15% for the spectrometer line 4 and 10% for the spectrometer line 10, as shown in Fig. 3.

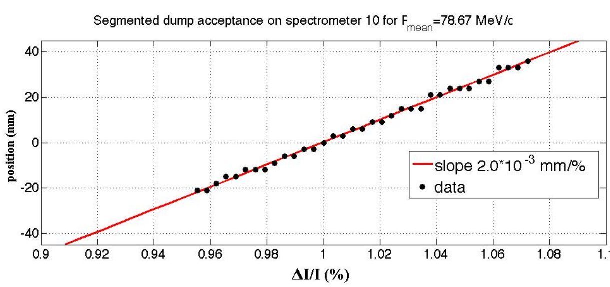


Figure 4: The horizontal dimension ±48 mm for the segmented dump in spectrometer 10 corresponds to an energy spread acceptance of about 10%.

The response of the segmented dump was measured by comparing the current read in each segment, with the beam current measured by the beam position monitor installed in front of the spectrometer line. By comparing the two devices, the amount of charge absorbed by the collimator can be estimated and also the response of each active segment. The total amount of absorbing material in front of each segment with respect to the beam path and any imperfections in the alignment of the detector with regard to the collimator and the beam axis could be measured and thus provide a calibration response for the detector. The calibration curve for each channel of the segmented dump installed in spectrometer line 10 is shown in Fig. 5. The triangular shape of the curve was expected based on Monte Carlo simulations [3], given that the segments, and the slits in the collimator are aligned parallel to the spectrometer axis. The calibration of the detector is implemented in the online analysis code used routinely in operation.

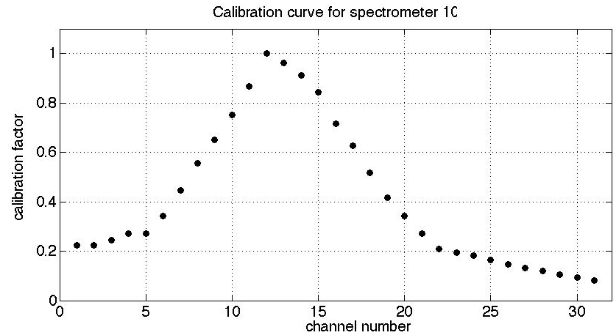


Figure 5: The calibration curve for the response of each segment of the segmented dump on spectrometer 10.

## MEASUREMENT OF TRANSIENT COMPENSATION USING THE SEGMENTED DUMP

The eight 3 GHz acceleration sections in the beginning of the CTF3 linac are fed by four klystrons, namely MKS03, MKS05, MKS06 and MKS07. In "full beam loading" [1] operation, the strong coupling between the beam and the accelerating cavities, generates transient effects such that the head of the pulse is accelerated almost twice as much as the steady-state part of the pulse, see Fig. 6.

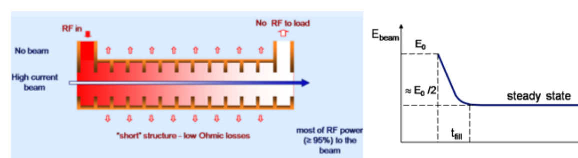


Figure 6: A schematic of the full beam loading concept.

Without compensating for the transient, the first 50 ns of the pulse experiences a much higher accelerating field than the steady state part of the beam. This effect can be seen in Fig. 7(a), which is the time resolved energy spectrum as measured by the segmented dump in spectrometer line 10. The transient is measured to have about a 40% higher energy than the steady state. In addition, since there was some residual dispersion in the linac, the transient was also seen reflected in the horizontal beam position monitor signals, just upstream of the dipole magnet used to bend the beam to the spectrometer line, see Fig. 7(c).

In order to reduce the transient, a technique has been proposed in order to accelerate the beam head less than the steady part of the pulse. It relies on the adjustment of the arrival time of the rf power in the accelerating structures with respect to the beam. The beam transient is initially generated in the first two accelerating structures on girder 3. The transient compensation is achieved by moving the timing of the next 3 klystrons pulses, namely MKS05, MKS06 and MKS07. The measurement of the evolution of the reduction in the transient is performed in the spectrometer line 10 and the results are depicted in Figs. 7-8.

The timing of MKS05 was adjusted to have the arrival of the rf, on the very edge of the arrival of the beam. Due to the filling time of the structure this meant that the transient saw less rf than the steady state, and hence was not accelerated as much as the steady state. The transient was reduced from 40% to approximately 20% of the steady state energy. Finally the arrival of the rf of MKS06 and MKS07 each were delayed by 550 and 250 ns, See Fig. 8(b) with regard to the nominal RF timings in Fig. 7(b). The final resulting transient was reduced to about 15%; see Fig. 8(a).

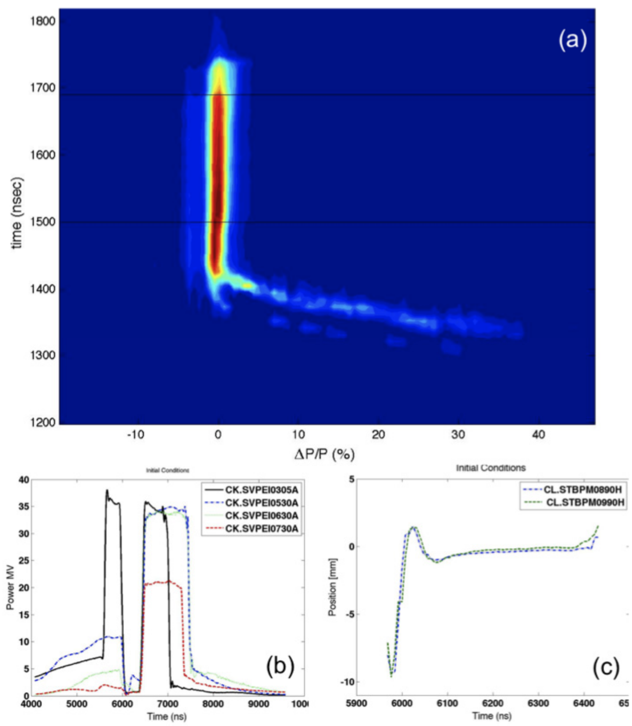


Figure 7: Initial Conditions. (a) The time resolved energy profile as measured with the segmented dump on spectrometer 10. (b) Output rf power measured from the accelerating structures (c) The horizontal position as measured with a beam position monitor on girders 8 and 9.

## CONCLUSION

A new radiation hard segmented dump was installed, calibrated and commissioned successfully with beam. Two devices have been installed in the CTF3 facility, and measure the time resolved beam energy and energy spread along the pulse with a 10 ns resolution. The devices are used routinely in CTF3 to optimise the beam energy along the pulse. By manipulating the arrival time of the rf, it has been shown that the transient can be reduced from an initial spread of 40% to a final spread of about 15%.

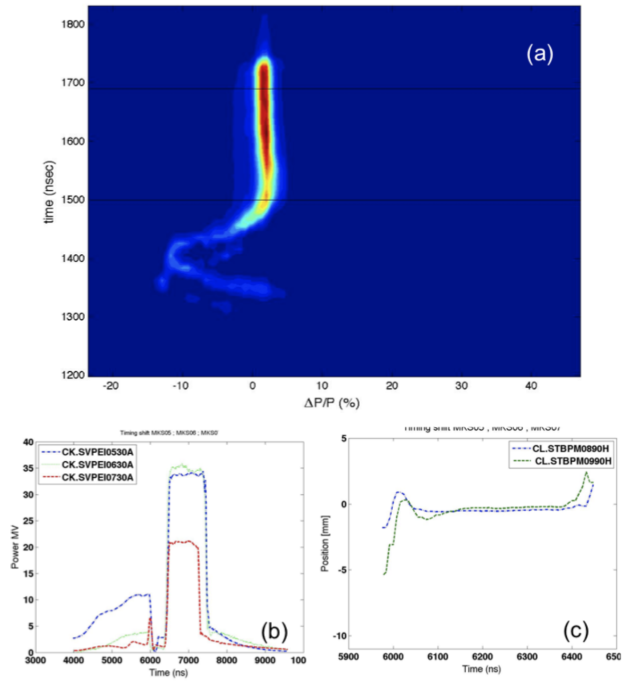


Figure 8: Delay arrival of rf from MKS05 by 400 ns; MKS06 by 550 ns and MKS07 by 250 ns with respect to the nominal conditions in Fig. 7. (a) The time resolved energy profile as measured with the segmented dump on spectrometer 10. (b) The output power measured from the accelerating structures. (c) The horizontal position as measured with a beam position monitor on girders 8 and 9.

## REFERENCES

[1] R. Corsini et *al*, "First Full Beam Loading Operation with the CTF3 Linac", EPAC 2004, Switzerland, p. 39

[2] C. P. Welsch et *al*, "Investigations of OTR Screen Surfaces and Shapes", EPAC 2006, UK, pp. 1220

[3] T. Lefevre *et al.*, "Segmented Beam Dump for Time resolved Spectrometry on a High Current Electron Beam", DIPAC'07, Italy

[4] J. W. Motz, H. Olsen and H.W. Koch, 'Electron scattering without Atomic or Nuclear Excitation', Review of Modern Physics 36**,** (1964), 881

[5] A. Fasso *et al*, "FLUKA: Status and Prospective for Hadronic Applications", Monte Carlo 2000, Conference, Lisbon, p. 955

# BUNCH LENGTH MEASUREMENTS IN CTF3

A. Dabrowski, S. Bettoni, H. H. Braun, R. Corsini, T. Lefevre, H. Shaker, P. Skowronski, S. Doebert, F. Tecker, CERN, Geneva, Switzerland
J. J. Jacobson, M. Velasco, Northwestern University, Illinois, USA

*Abstract*

The CLIC Test Facility CTF3, being built at CERN by an international collaboration, should demonstrate the feasibility of the CLIC two-beam technology by 2010. One of the issues addressed is the control of the electron bunch length in the whole complex. A bunch length measurement system, with a good resolution, is therefore paramount. Two different systems are presently used in CTF3 based on microwave spectroscopy and on transverse rf deflectors, respectively. In the paper we describe the two systems, we discuss the different experimental methods used and present the results of the latest measurement campaigns.

## INTRODUCTION

In the framework of the Compact Linear Collider (CLIC) project [1], a test facility named CTF3 [2] is constructed at CERN by an international collaboration. The CTF3 complex shall demonstrate by 2010 the key technological challenges for the construction of a high luminosity 3 TeV $e^+$-$e^-$ collider. The overall machine starts with a linac delivering a 3.7 A, 1.5 µs long electron beam with an energy of 150 MeV. The bunches are then injected in two consecutives rings [3] where the beam average current and the bunch frequency are multiplied by a factor 8. With a current of 30 A and 2.5 cm distance between bunches, the resulting beam is finally sent to the CLIC experimental area (CLEX) where it will be used to test all key CLIC RF components.

The performances of the accelerator depend directly on the control of the electron bunch length. In the linac the bunches must remain short (about 2 ps r.m.s.) to keep the energy spread as low as possible, but need to be stretched (6 - 10 ps r.m.s.) before the rings to minimize emittance dilution due to coherent synchrotron radiation. Therefore, two magnetic chicanes have been implemented, the first downstream of the injector and the second upstream of the first ring. A sketch of the second magnetic chicane, composed of 4 bending magnets, is presented in Fig. 1. Normally, bunch shortening or lengthening is obtained by changing the phase of the rf in the last accelerating structure. Bunch length measurements can be performed using Optical Transition Radiation screens coupled to a streak camera [4], but the present system limits the time resolution to 2 ps. Shorter bunches are measured with the 1.5 GHz rf deflector [5], normally used to inject the particles in the Delay Loop, but for the purposes of the bunch length measurement, it is used in conjunction with an Optical Transition Radiation screen. Recently, a new detector has been commissioned based on microwave spectrometry, which we commonly refer to as the "rf-pickup" [6]. In this paper, the rf deflector and the rf-pickup bunch length measurement techniques will be presented.

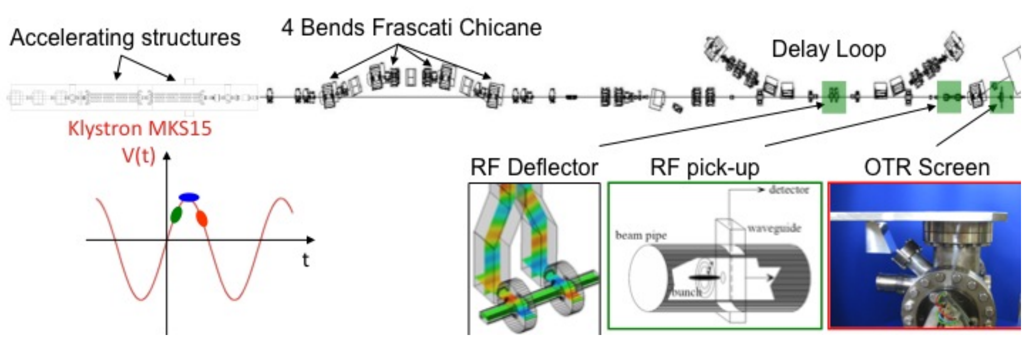


Figure 1: Layout of the Frascati chicane and locations of the bunch length monitors. By changing the Klystron MKS15 phase, the bunch length at the end of the chicane can get shorter (green), longer (red) or just be preserved (blue).

## MICROWAVE SPECTROMETER EXPERIMENTAL SETUP

A non-destructive single shot bunch length monitor was commissioned in CTF3 in 2006 [6]. This device, the "rf pick-up", measures the frequency spectrum of the electromagnetic field emitted by the particles and collected by a rectangular $K_a$ waveguide. The rf pickup was installed 50 cm upstream of the OTR screen, and hence cross calibrations can be performed between the rf deflector and the rf pickup monitor. This monitor has a sub-ps time resolution and the calibration is done in a self consistent manner. Moreover, this monitor has the advantage of being non destructive and relatively inexpensive compared to other techniques.

The rf pickup consists of a single WR-28 waveguide connected to the beam pipe as shown in Fig. 1. A 0.5 mm thick CVD diamond window [7] is used to isolate the vacuum in the beam pipe from the atmospheric pressure in the waveguide. Signal frequencies above the cut-off of the WR-28 waveguide (21.1 GHz) are transported in a

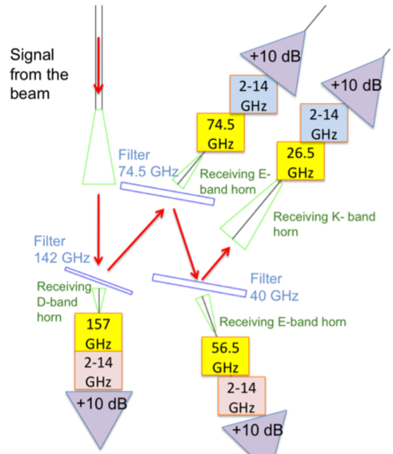


Figure 2: Schematic of the detection system.

continuous WR-28 waveguide for about 18 m to the detection station in a technical gallery.

At the detection station, the rf signal from the beam is emitted using a $K_a$ band horn antenna, as shown in Fig. 3. The detection system is designed to measure the amplitude of the rf signals from the beam, simultaneously in four frequency bands, namely 26.5-40 GHz, 45-69 GHz, 75-90 GHz and 142-170 GHz.

As shown schematically in Fig. 2, two down-mixing stages in series are required in order to measure the high frequency rf signals. The first down mixing stage has a fixed local oscillator frequency for each band , namely 26.5 GHz, 56.5 GHz, 75 GHz and 157 GHz. The second down mixing stage is in common to each of two of the four detection bands, obtained by using two synthesizers with a variable frequency range from 2-14 GHz. From this setup, measurements of the beam harmonics of 30 GHz, 33 GHz, 36 GHz and 39 GHz are made using the K-band detection, the beam harmonics of 60 GHz, 63 GHz, 66 GHz and 69 GHz are made using the first E-band detection stage, and the beam harmonics of 78 GHz, 81 GHz, 84 GHz and 87 GHz are made with the second E-band detection stage. The D-band detection stage provides signals only for beam conditions with very short bunches, which was not the case for the measurements presented in this paper. The signals are amplified by +10 dB after the second down mixing stage, and then digitized using a fast Acqiris digitizing scope with 2Gs/s per channel. The data acquisition is controlled remotely by a LabView program, which stores, displays and analyses the signals in real time.

## EXPERIMENTAL RESULTS

For each machine condition, which corresponds to a particular setting of the phase of the last Klystron (MKS15), 15 successive measurements are stored and their Fourier transforms performed. The mean height of the peak, corresponding to each beam harmonic is measured and used for the bunch length determination.

In order to extract the bunch length, the amplitude of each beam frequency measured as a function of the phase of MKS15 is used in the fitting procedure to extract the bunch length. The longitudinal distribution of the electrons is assumed to be single Gaussian distribution. A $\chi^2$ minimization fit, to the Gaussian function, is then performed, with the fit parameters being the r.m.s. bunch length at each machine setting, and the response factor of each frequency band. The extracted r.m.s. bunch length is shown in Fig. 6, and the evolution of the bunch length with respect to the phase of the last Klystron can be seen. The $\chi^2/\nu$ for the fit was $\chi^2/\nu$=1.08.

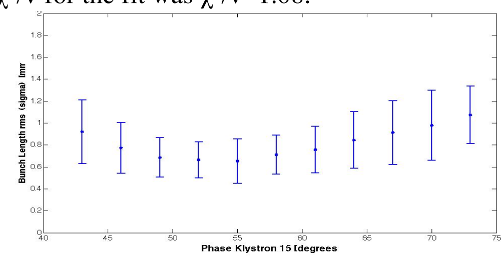


Figure 3: Evolution of the bunch length measured with the rf pickup as a function of the phase of Klystron 15.

## BUNCHLENGTH MEASUREMENT USING RF DEFLECTOR

Bunch length measurements were also performed using the 1.5 GHz transverse rf deflector and an Optical Transition Radiation screen installed downstream from the RF deflector kick position, see Fig. 1. As the bunch passes through the cavity, the field in the rf cavity induces a strong correlation between the particle's longitudinal position in the bunch and the transverse position after the kick. Hence the measurement of the transverse beam profile of the beam downstream of the cavity gives direct information about the bunch longitudinal length before the kick.

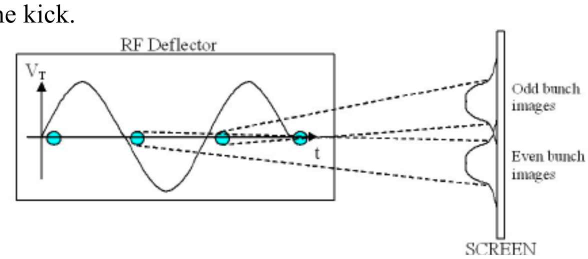


Figure 4: A schematic view of the rf deflector transverse kick on the bunches, a few degrees off the zero crossing†.

During the bunch length measurement, the beam bypassed the delay loop, and the rf deflector was powered and phased such that the beam arrived close to the rf zero crossing. In this configuration, the head and the tail of each bunch were then kicked in opposite directions. Because the 3 GHz bunching of the beam during this measurement campaign, and the rf deflector operating at 1.5 GHz, the phase of the rf deflector was adjusted

† Plot courtesy of Frascati note, CTF3-010

slightly off zero crossing, to image the two beam spots separately on the one screen, see Fig. 4.

Once the two beam spots were separated using the appropriate phase of the rf deflector, a horizontal corrector magnet was used in order to move one beam spot to the center of the screen, in order to maximize the light collection from the optical line. The second beam spot was therefore out of the acceptance of the screen. The increase in the observed transverse beam size, when the rf deflector was switched on was used to determine the bunch length, see Fig. 5.

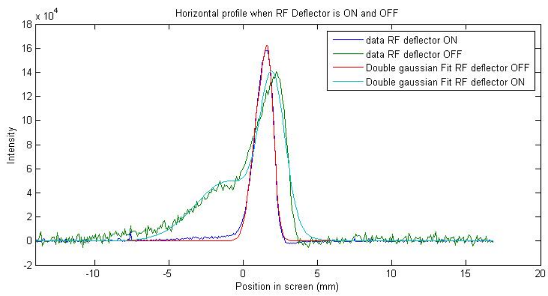


Figure 5. The transverse projection of the beam size with the rf deflector ON and OFF as imaged by the OTR screen.

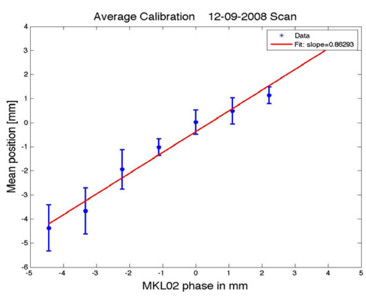


Figure 6: Typical calibration curve, showing the relationship between the phase of the MKL02 in units of longitudinal mm and the transverse position of the peak of the distribution on the screen.

In order to get a calibration of the system, which was independent of the transverse beam parameters, a calibration scan was done by measuring the position of the peak of the bunch distribution as a function of the rf phase of the deflector. A phase change of 1 degree of the 1.5 GHz rf deflector corresponds to a longitudinal distance of 200/360 mm. The calibration curve for a typical measurement is shown in Fig. 7, and the calibration constant is measured to be CAL=0.86±0.02 mm(screen)/mm(longitudinal).

To calculate the bunch length, quadratically the two rms transverse dimensions, measured when the rf deflector is on (and a few degrees off zero crossing) and when the rf deflector is OFF, are subtracted [8].

$$\sigma_{zrms} = \frac{1}{CAL} * \sqrt{\sigma^2_{x_{rms}(RFon)} - \sigma^2_{x_{rms}(RFoff)}}$$

In this approximation we extract the bunch length, as a function of the phase of MKS15, see Fig. 7. For this data taking the setting of the upstream compressor chicane,

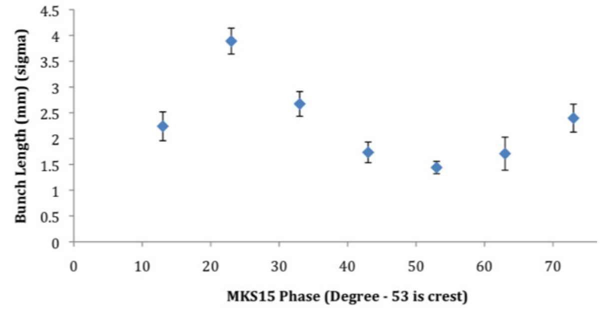


Figure 7: Evolution of the bunch length measured with the RF deflector as a function of the phase of the klystron MKS15.

R56 = 0.45, and the measured minimum of $\sigma_{zrms}$ = 1.5 mm seems to be in good agreement with expectations [9].

## CONCLUSIONS AND PERSPECTIVES

The rf-pickup monitor and the rf deflector were both used in the latest measurement campaign at CTF3 to measure bunch length. Both detectors measure the same shape response to the change in bunch length as a function of the phase of the last accelerating structure, however there seems to be a systematic difference between the results of the two techniques for these machine conditions, with the rf pickup measuring shorter bunches than the rf-deflector. More detailed studies in the future will be dedicated to understand the reason for this difference, in particular the effect due to the double Gaussian bunch shape and the enhanced sensitivity to high frequency components which seem to be biasing the rf-pickup detector to lower bunch length values.

## REFERENCES

[1] H.H. Braun *et al*, "Updated CLIC parameters 2005", CLIC note 627, (2005)
[2] G. Geschonke, "Status of the CLIC Test Facility 3 (CTF3)", Proceedings of LINAC 2006, USA, pp.11
[3] R. Corsini *et al*, "Commissioning Status of CTF3 the Delay Loop", Proceedings of EPAC 2006, UK, pp.771
[4] C. Welsch *et al*, "Longitudinal Beam Profile Measurements at CTF3 Using a Streak Camera", Journal of Instrumentation, 1, (2006), P09002
[5] A. Ghigo *et al*, "Commissioning and First Measurements on the CTF3 Chicane", Proceedings of PAC 2005, USA, pp.785
[6] A. Dabrowski *et al*, "Non Destructive Single Shot Bunch Length Measurements for the CLIC Test Facility 3", PAC 2007, USA, pp. 4069
[7] Brazinng done by S. Mathot, CERN TS/MME
[8] P. Emma, et al., "Transverse RF deflecting structure for bunch length and phase space diagnostics", 2000.
[9] H. Shaker *et al*, "Status of Longitudinal Beam Dynamics Studies in CTF3", to be published in proceedings of LINAC08, Victoria, Canada

# DIAGNOSTICS AND MEASUREMENT STRATEGY FOR THE CERN LINAC 4

K. Hanke, G. Bellodi, J.-B. Lallement, A. Lombardi, B. Mikulec, M. Pasini, U. Raich, E. Sargsyan, CERN, Geneva, Switzerland
M. Hori, Max-Planck-Institut für Quantenoptik, Hans-Kopfermann-Str. 1, D-85748 Garching, Germany, and Department of Physics, University of Tokyo, 7-3-1 Hongo, Bunkyo-ku, Tokyo 113-0033, Japan

*Abstract*

Linac4 is a 160 MeV $H^-$ linac which will become the new injector for CERN's proton accelerator chain. The linac will consist of 4 different RF structures, namely RFQ, DTL, CCDTL and PIMS running at 352.2 MHz with 2 Hz repetition rate and 0.4 ms pulse length. A chopper line ensures clean injection into the PS Booster. The combination of high frequency and a high-current, low-emittance beam calls for a compact design where minimum space is left for diagnostics. On the other hand, diagnostics is needed for setting up and tuning of the machine during both commissioning and operation. A measurement strategy and the corresponding choice of the diagnostic devices and their specific use in Linac4 are discussed in this paper.

## INTRODUCTION

Linac4, a 160 MeV $H^-$ linac, is the first step in re-building CERN's proton injector complex. The linac will consist of 4 different RF structures, namely a radio-frequency quadrupole (RFQ), a drift tube linac (DTL), a cell-coupled drift tube linac (CCDTL) and a pi-mode structure (PIMS). Figure 1 shows schematically the different sections of the linac. In a first phase, Linac 4 will inject into the existing CERN PS Booster and deliver beams for fixed-target physics and the LHC through the present accelerator chain. In a second phase, Linac4 will become the front-end of a superconducting linac (SPL), which will inject into a new proton synchrotron (PS2). In the operation of a high-power hadron linac as Linac4, beam loss is a critical issue. The specification of the instrumentation has therefore been driven by beam dynamics calculations. We will discuss in the following paragraphs the diagnostics specified for the commissioning of the different stages of the linac as well as for day-to-day operation.

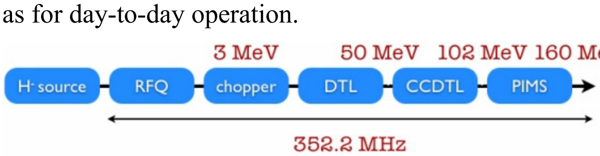


Figure 1: Linac4 layout.

## ALIGNMENT, STEERING STRATEGIES AND LOSS CONTROL

After the nominal layout of the machine had been defined, a series of runs (1000-2000) was made in order to evaluate beam losses and emittance growth under the effects of machine and beam errors. The results of these studies are reported in [1]. Starting from these results, a system composed of correctors (dipolar kicks) and diagnostics (beam position monitors) has been integrated in the Linac4 layout in order to minimise losses and to control emittance growth. A procedure has been implemented to find the value of the correctors which minimises orbit excursion at the location of the diagnostics, while maximising transmission. The aim is to have a sufficient number of correctors and monitors to be able to control routine beam loss to less than 1 W/m at the highest possible beam duty cycle (6%, foreseen for future operation of Linac4 as injector for the SPL operated at maximum beam power). These studies show that a correction system made of 15 horizontal and vertical steerers and monitors can correct the effects of quadrupole alignment errors within ±0.1 mm and ± 1 mrad and beam alignment errors of ±0.3 mm and ±0.3 mrad (all values are 1 sigma). The residual losses in the worst case scenario are shown in Figure 2.

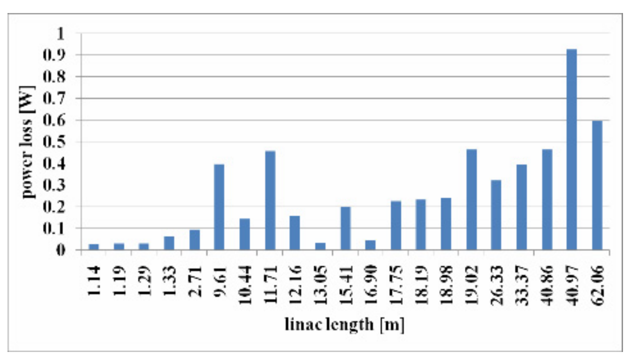


Figure 2: Power loss along Linac4 (40 mA, 6% duty cycle, and worst case out of 2000) for beam and machine alignment errors (quadrupoles 0.1 mm, 1 sigma, beam position ±0.3 mm/0.3 mrad Gaussian) applying the best correction achievable with the given diagnostic and steering system.

## DIAGNOSTICS CHOICES

### *Source and Low-Energy Beam Transport*

In order to characterise the $H^-$ source and the 2-solenoid low-energy beam transport (LEBT), measurements of the beam current (transmission), beam profile and emittance are required. During the commissioning phase the source and LEBT will be set up in two different ways: in the spectrometer configuration only one solenoid is used, followed by a diagnostics box which houses a Faraday cup (FC) and a secondary emission monitor (SEM) for profile measurements. Downstream of the diagnostics box there is a slit/spectrometer system followed by a SEM grid and a Faraday cup for measurement of the energy spread. In the emittance configuration, the LEBT is replaced by an emittance scanner consisting of a movable slit and SEM grid. In the operational linac the diagnostics box will be situated between the two solenoids. The beam current is measured by a beam current transformer (BCT) installed between the diagnostics box and the second solenoid.

### Chopper Line

The chopper line is equipped with two identical beam current transformers located between the first and the last pair of quadrupoles. Furthermore, there are two wire scanners (WS) upstream and downstream of the chopper structure. These devices measure beam profiles in both planes by scanning two orthogonal wires slowly through the beam. The moving range is large enough in order to measure both the deflected and undeflected beam. For commissioning of the chopper line we have developed a dedicated beam shape and halo monitor (BSHM) to verify the correct functioning of the chopper. The BSHM images secondary electrons generated by a thin carbon target inserted in the beam and is able to detect remaining beam current in chopped buckets down to an intensity of 1E3 particles per bunch. In the transverse plane, the detector can deliver an image of the beam and display simultaneously the beam core and beam halo thanks to its dynamic range of $>10^{-5}$. The detector has been successfully tested with a laser beam and with a 3 MeV proton beam [2].

### IPHI Measurement Line

The 3 MeV part of the linac including source, LEBT, RFQ and chopper line will be operated stand-alone and characterised with the IPHI (“Injecteur de Protons à Haute Intensité”) measurement line provided by the French CEA and IN2P3 laboratories in the frame of the IPHI-CERN collaboration. This temporary diagnostics line comprises measurement of the beam current, position, profiles, energy (time-of-flight) and energy spread. It has been described in detail in [3].

### Drift Tube Linac (DTL)

The Drift Tube Linac consists of three tanks accelerating to beam energies of 12, 32 and 50 MeV. Commissioning of the DTL is planned to take place in stages, where at each stage the beam is characterised using a movable diagnostics bench. This measurement bench comprises beam profile measurement devices (SEM grids), two pick-ups for position and time-of-flight (TOF) measurements, one beam current transformer as well as a spectrometer magnet for measurement of the energy spread, discussed in the following section. The transverse emittance is measured with a scanning slit/SEM device (modified from the source diagnostics) and the longitudinal profile and phase spread is measured by a bunch shape monitor (BSM) based on secondary electrons [4]. In the operational linac, there will be pick-ups after each of the three tanks. These pick-ups are specified to measure beam position, intensity and phase with a resolution of 0.1 deg, 0.1 mm and 0.5 mA. Due to space constraints, the pick-ups will be partly integrated into the magnets between the DTL tanks. At the exit of the last DTL tank a beam current transformer (resolution 0.5 mA) as well as a retractable SEM grid (resolution 0.5 mm) is foreseen.

### Spectrometer Line

Beam dynamics studies have been carried out to specify a layout for the diagnostics line on the movable bench and assess the feasibility of a slit/spectrometer/monitor technique for energy spread measurements of the DTL beam at the time of commissioning. Through the dispersion locally generated at the spectrometer magnet, the relative energy spread at the slit is converted into transverse beam size spread at the monitor according to a 1:1 ratio. Two quadrupole magnets are placed immediately after the end of the DTL tanks to produce a parallel beam at the slit. The slit itself needs to be positioned as close as possible to the beginning of the line to avoid an energy spread blowup due to space charge effects which could impair the measurements at low energy. Finally, a third quadrupole is placed after the slit for optical enhancement, followed by a 0.8 m long bending magnet with $\rho$=1 m bending radius and a magnetic B field varying between 0.5 and 1 T. The results of end-to-end beam dynamics simulations for the three separate DTL tank cases are summarized in Table 1.

Table 1: Results of beam simulations of the spectrometer line. From left to right: average tank output energy, 2.2σ beam energy spread at the tank output, 2.2σ beam size at the monitor and energy resolution.

| | W [MeV] | ΔW/W [%] | Δx [mm] I=65mA | resol. [keV/mm] |
|---|---|---|---|---|
| Tank 1 | 12.2 | 0.7 | 7.7 | 11 |
| Tank 2 | 31.8 | 0.5 | 4.0 | 37.5 |
| Tank 3 | 50.0 | 0.3 | 2.7 | 61 |

As shown by the last two columns, the performance of the scheme is rather satisfactory, though a 0.5 mm sampling monitor resolution might be needed to have better measurement sensitivity. The energy resolution per mm is also comparable to the precision that is required for the DTL tanks RF field and phase characterization at a 1%-1 deg level RF tolerance as specified in error studies [5]. The spectrometer diagnostics could hence complement TOF measurements when determining the RF set points. In conclusion however, despite a favorable assessment from the beam dynamics point of view, a few caveats remain on the suitability of such a beam diagnostics solution. Apart from cost considerations, the practicality of such an important installation for a temporary, movable bench is at present being evaluated, and has prompted a research into possible alternative solutions for comparison.

### Cell-Coupled Drift Tube Linac (CCDTL)

The cell-coupled drift tube linac consists of a total of seven modules accelerating the beam from 50 to 100 MeV. Its commissioning is planned to take place as a whole, where the beam is characterised using the diagnostics installed in the linac for operation. Furthermore, additional devices installed in the beam line between the end of Linac4 and the beam dump can also be used. In operation, the CCDTL will be equipped with two wire scanners (after modules 2 and 6), two SEM grids (after modules 4 and 7) and pick-ups after each of the seven modules. At the exit of the CCDTL there will be a beam current transformer.

### Pi-Mode Structures (PIMS)

The pi-mode structure linac consists of 12 cavities which accelerate the beam to the final energy of 160 MeV. For the PIMS we have foreseen a total of six pick-ups for measurement of position, intensity and phase after cavities 2, 4, 6, 8, 10 and 12. Measurement of the beam profile is accomplished by two wire scanners after cavities 3 and 9 as well as by two SEM grids after cavities 6 and 12. A beam current transformer at the exit of the linac provides an absolute measurement of the beam current. As the CCDTL, the PIMS will be commissioned using the diagnostics in the dump line.

### Dump Line

The beam line between the exit of the PIMS and the linac dump houses a number of diagnostics. Most of the equipment is located in a "diagnostics box" at the exit of the PIMS, which houses a transformer, a SEM grid and a pick-up. Furthermore diagnostics for the transverse and longitudinal emittance is required. As for the longitudinal plane, this will be accomplished by the bunch shape monitor [4]. For the transverse emittance, various techniques are currently being studied. The beam line will also contain two pick-ups and a beam current transformer. The whole linac will hence be commissioned stand-alone.

### Transfer Line and Booster Injection

A new transfer line will connect Linac4 with a part of the old Linac2 injection line. The transfer line will house a number of standard diagnostics tools according to Table 2. In order to characterise the beam emittance and energy before injection into the PS Booster, two existing measurement lines will be upgraded for Linac4 beam parameters. The Booster injection section is being redesigned for $H^-$ injection. The region around the stripping foil will also require dedicated diagnostics. It is proposed to use a radiation hard camera to monitor the injected and circulating beam size on the foil; foil temperature surveillance is also desirable. The dump behind the foil should be segmented in 2 parts to allow separate measurement of the $H^-$ and $H^0$ current via a resistance and will give an indication on potential foil degradation. View screens (VS) glued onto the dump will show the beam profiles. Matching could be optimized by installing SEM grids capable of multi-turn acquisition in the Booster ring; multi-turn acquisition is also a condition for the new pick-ups in the ring foreseen to measure the bump closure. Transformers and pick-ups will be used for beam current measurement and steering. In addition, beam loss monitors (BLMs) will be distributed along Linac4 and the transfer lines and installed preferably at positions with high dispersion, high potential losses and with a small aperture to beam size factor.

Table 2: Diagnostics Overview for Linac4 Operation

| Section | PU | BCT | FC | SEM | WS | VS |
|---|---|---|---|---|---|---|
| Source/LEBT | - | 1 | 1 | 1 | | |
| Chopper line | | 2 | | | 2 | |
| DTL | 3 | 1 | | 1 | | |
| CCDTL | 7 | 1 | | 2 | 2 | |
| PIMS | 6 | 1 | | 2 | 2 | |
| Dump Line | 3 | 2 | | 1 | | |
| Transfer Line | 15 | 11 | | 4 | | 2 |

## SUMMARY

The diagnostics specifications and choices for the new CERN Linac4 have been driven by beam dynamics simulations. Error studies have been performed to identify the measurement precision needed as well as the optimum location of beam monitors with respect to the correction elements. The results have been used to specify the beam instrumentation adapted to the Linac4 needs and to integrate it into the overall machine lay-out.

## ACKNOWLEDGEMENTS

We acknowledge the support of the European Community Research Infrastructure Activity under the FP6 "Structuring the European Research Area" programme (CARE, contract number RII3-CT-2003-506395).

## REFERENCES

[1] A.M. Lombardi et al, "Loss Control and Steering Strategy for the CERN Linac4", CERN AB-Note-2007-033 (ABP) (2007).

[2] M. Hori, K. Hanke, Nucl. Instr. Meth. A 588 (2008) 359-374.

[3] P. Ausset et al, "Beam Diagnostics Instrumentation for the High Energy Beam Transfer Line of IPHI", Dipac2005, Lyon, June 2005, POT013, p. 172 (2005); http://www.JACoW.org.

[4] A. Feschenko et al, "The First Results of Bunch Shape Measurements in the SNS Linac", Linac2004, Lübeck, August 2004, TUP63, p. 408 (2004); http://www.JACoW.org.

[5] G Bellodi et al, "End-to-end beam dynamics and RF error studies for Linac4", MOP086 this conference.

# EMITTANCE MEASUREMENT INSTRUMENT FOR A HIGH BRILLIANCE $H^-$ ION BEAM*

C. Gabor[†1], C.R. Prior[1], A.P. Letchford[2], J.K. Pozimski[2+3],
[1]STFC, ASTeC, Rutherford Appleton Laboratory (RAL), OX11 0QX, UK,
[2]STFC, ISIS, RAL, [3]Imperial College London, High Energy Physics Department, SW7 2AZ, UK


## *Abstract*

Among present challenges for beam diagnostics and instrumentation are issues presented by high beam intensity, brightness, resolution and the need to avoid inserting mechanical parts into the beam. This very often means applying non–destructive methods, which avoid interaction between ions and mechanical parts and, furthermore, allow on–line measurements during normal beam operation. The preferred technique for $H^-$ beams is the photo–detachment process where (laser) light within the range of 400. . . 1000 nm has a sufficient continuous cross section $\sigma_{PD}$ to neutralize negative ions. The actual diagnostics are then applied to either the neutrals produced or the electrons. The latter are typically used for beam profiles whereas neutrals are more suitable for emittances, and form the subject of the present paper. This provides an overview of the basic features of the diagnostic technique, followed by discussion about computing the missing second transverse projection view using a method called Maximum Entropy Method (MaxEnt, MEM).


## INTRODUCTION

The Front End Test Stand (FETS) project [1] at RAL, UK, makes high demands on the diagnostics because of its beam power (60 mA $H^-$, $\leq 3$ MeV beam energy, $\leq 10$ % duty cycle). Using a non–destructive method, i.e. no mechanical parts inside the ion beam, minimizes the influence on the ion beam with the advantage of an on–line diagnostic tool. The experimental set–up uses a Penning source with slit extraction, a solenoid LEBT, a four–vane RFQ who brings the beam from 70 keV up to 3 MeV and a MEBT consisting of quads, rebuncher and a fast/ slow chopper. Particularly the latter and the slit extraction results in a lack of symmetry which makes a 4D emittance measurement highly desirable.

The basic principle of the implemented Photo Detachment Emittance Instrument (PD–EMI) is illustrated in Fig. 1 and widely discussed in [2, 3]. Compared to more common devices like slit–grid/ harp (“slit–slit”) and pepperpot (“point–point”) instruments the laser acts like a slit whereas the particle detector takes the place of a pepperpot device, therefore the PD–EMI can be described as an instrument with a slit–point transfer function. The $yy'$ emittance in Fig. 1 can be measured in a direct way by gathering angle profiles for each laser position.

* Work supported by EU/FP6/CARE (HIPPI) RII3-CT-2003-506395
† c.gabor@rl.ac.uk

In principle it would be possible to measure in x–direction similarly to $yy'$ with a second set of mirrors. But it is technically a challenging problem to place the necessary movable stages inside a dipole. It is also not very attractive in price. A more physical drawback is the separation of the 4D emittance measurement into two projections. But a detector movable longitudinally along the drift length of the neutralized ions could help to overcome the problems: The laser will be moved several times through the ion beam and at each time the $z$ positions of the detector is moved along the drift of the neutrals. It is then possible to add up all detector signals for a given $z$ which results in a $\rho(x, y)_{z(n)}$ density distribution. Each extracted 1D profile is then mapped to the laser position by a drift matrix to calculate the $xx'$ emittance.

### *The Maximum Entropy Method MEM*

The best candidate to do the $xx'$ emittance reconstruction utilises a principle called maximum entropy method (MEM). This is a powerful and a extensively used technique for the deconvolution of data and the reconstruction of images (astronomy, tomography, neutron scattering). First applications in accelerator science are published in [5, 4] and a very good but general introduction is given in Sivia’s textbook [6].

The strengths of MEM are its generality and ability to deal with *noisy* and *incomplete* positive data. It is based on Bayes’ theorem and uses an entropy as described in information theory. The linear transformation between the

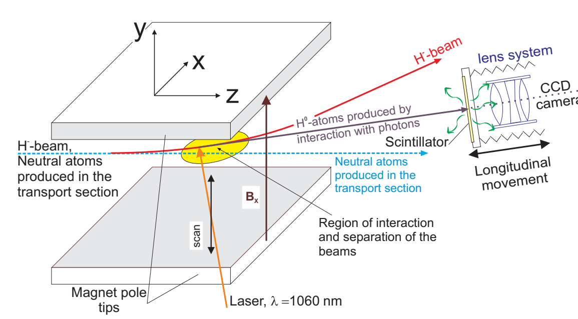


Figure 1: The negative ions penetrate the dipole and after some displacement a laser scans through the beam and neutralize a small amount of ions. The neutrals produced by photo detachment are guided to a detector system ($yy'$ emittance). The other transverse emittance can then be reconstructed by moving the scintillator and collecting $\rho(x, y)$ profiles along the drift.

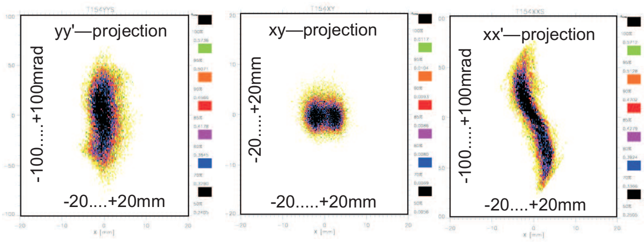


Figure 2: The three projected views of the chosen particle distribution from an ion source measurements. The distribution is scaled down in radius and angle to a level more likely downstream the RFQ.

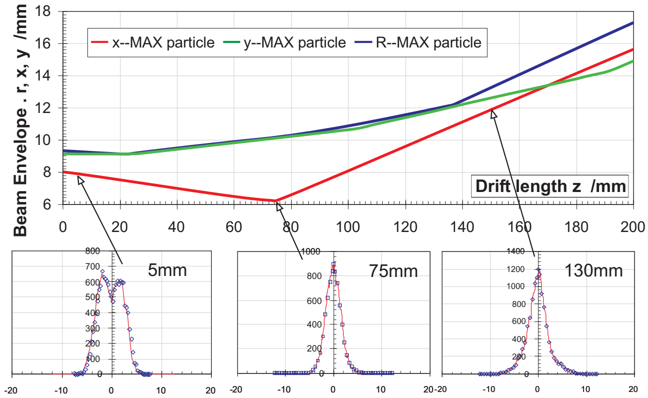


Figure 3: On the top the envelope of $x_{\max}$, $y_{\max}$ and $r_{\max}$ of the given entrance distribution. Below are three profiles $I(x_{z(n)})$ representing examples of the used projection data for the Maximum Entropy Method.

existing data and the reconstructed test object is important. Then the entropy $S$ can be seen as a regularization function which helps to stabilize the chosen procedure, like least–squares for a free–form solution, resulting in the "most probable" distribution which also satisfy all the observed constraints. For the phase space reconstruction a software called MemSys5 is chosen [8] originally written by J.Skilling and S.Gull.

### *Rotation Matrix*

If not other mentioned the whole paper uses a coordinate system as given in Fig. 1. But with rotating the orthogonal system it is possible to get emittances others than in x–or y–plane and does not affect the described MEM. The algorithm is applied to another projected view $\Theta_m$ of the 2D $\rho(x,y)_{z(n)}$ for all $n = 0 \ldots N$. Additionally to index $n$ which indicates the longitudinal position, index $m$ represents the rotation angle. For that purpose new coordinates $s, t$ can be introduced with $x = x_m(s,t)$ and $y = y_m(s,t)$. The m$^{\text{th}}$ pair of transformed coordinates for $\rho_m(x,y)_{z(n)}$ are specified by a rotation matrix like

$$\begin{pmatrix} s \\ t \end{pmatrix} = \begin{bmatrix} \cos\theta_m & \sin\theta_m \\ -\sin\theta_m & \cos\theta_m \end{bmatrix} \times \begin{pmatrix} x \\ y \end{pmatrix}.$$

## EMITTANCE RECONSTRUCTION

The ability of the described MaxEnt method has been investigated on an ion beam distribution measured downstream of the ion source with our pepperpot device. The three different views of projection xx$'$, yy$'$ and $xy$ are shown in Fig. 2. A Cartesian coordinate without any rotational offset was used to reconstruct the xx$'$ emittance. Furthermore the measured emittance was scaled down keeping the shape of each profile in the different subspaces constant to an expected value downstream the RFQ at a beam energy of 3 MeV.

In the next step the drift of the neutrals was simulated as illustrated in Fig. 3. The different development of the $x_{\max}$, $y_{\max}$, $r_{\max}$–envelopes represents the non–symmetric emittance. The deconvolution has been performed with maximal $8$ profiles at $z = 10, 25, 50, 60, 75, 90, 100\,150\,mm$ whereas Fig. 3 presents only three of them.

For the deconvolution a default model was used where starting with a homogeneous distribution for the test object and in accordance with the available data either the intensity will be increased or reduced after every iteration. Apart from the small influence of the chosen model any further assumptions not represented by known data are avoided. The emittances shown in Fig. 4 are reconstructed with 17 iterations which takes on a typical desktop less then 30 sec. Figure 4 compares three different reconstructions with the entrance emittance where number and position of the profiles vary. The results imply that not the number but the phase advance is critical. As long as the changes in between the profiles are small, increasing the number of profiles improve the emittance only very little. This is also visible in the difference of the blue covered areas at the edges of Fig. 4(A) and Fig. 4(B). These parts are not covered by any information of the profiles and therefore such low intensity levels represent the starting point of the default model. Example (A) covers the phase space more efficiently than (B) even with less profiles. Furthermore it is in better agreement with the original distribution and the reconstruction (C) with $8$ profiles.

It should also be mentioned that the fractional rms emittance of (A) and (B) does not diverge more than $\approx 20\%$ from the deconvolution with eight profiles if you consider only intensity levels $\leq 80\,\%$. For a more detailed study about the rms values of Fig. 4 (C) and Fig. 4 (D) in Fig. 5 graphs of both are shown. It was necessary to adopt the internal "phase space resolution" for each particle distribution on which then the rms formalism can be applied. To quantify this variation an intermediate step was introduced to test the smoothness of the graphs for each phase space resolution. The rms resolution is chosen to avoid erratic curves at high values and stepwise behaviour at low values. The deviation of each single emittance in between the described margins is of the same order $\Delta \approx 20\%$ as in the reconstruction with different number of profiles. The pos-

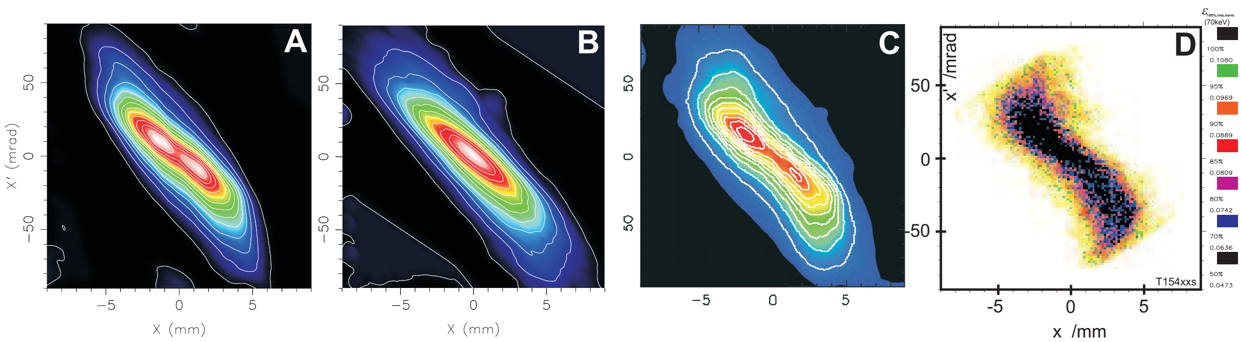


Figure 4: Different reconstructed emittances (A,B,C) in comparision with the original distribution **(D)**, all in same scale. The following profiles were used: **(A)**: $z = 25, 90, 150$ mm; **(B)**: $z = 75, 90, 100, 150$ mm; **(C)** $z = 10, 25, 50, 60, 75, 90, 100, 150$ mm.

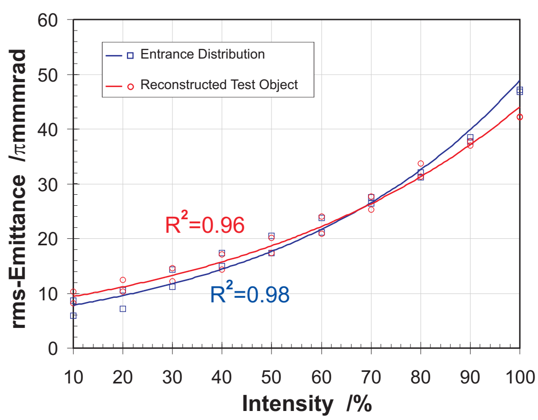


Figure 5: Comparison of the fractional emittance of both the entrance distribution and the reconstructed distribution (C). The phase space resolution for the applied rms–formalism is varied in a similar way for both distributions.

sible precision of a reconstruction with profiles with sufficient phase advance is in that context good enough.

In real measurements it would be reasonable to use the $yy'$ emitttance to compare this result with a reconstruction in the same plane. This might be helpful to specify the discussed problems like phase advance and correct phase space resolution for the rms formalism.

## SUMMARY & OUTLOOK

A method called Maximum Entropy (MaxEnt, MEM) is presented to reconstruct the $xx'$ emittance using a movable particle detector, the other transverse plane is measured according to a standard slit–slit principle. To generalize that concept a rotational matrix can be applied to be independent of the orthogonal coordinate system. The whole phase space information would then consist of a set of 2D projection views at different angles.

Further investigations about the MEM–limitations are necessary, e.g. beam noise and especially an estimation about the phase advance (i.e. alteration of profiles).

The paper does also not include a discussion about more technical aspects which are issues in the near future like magnet design, beam transport simulations through the dipole and experimental test of laser beam guiding and mirror movement concerning laser positioning.

## ACKNOWLEDGEMENT

The presented work benefited enormously from the generous help of Devinder Sivia, a lecturer at Oxford University and former member of the Computer Science Group at RAL. The author is grateful, not only for the fruitful discussion but also for the MemSys5 license and adopting the software to our demands.

## REFERENCES

[1] A.P. Letchford et al., "Status of the RAL Front End Test Stand", LINAC 2008, MOP009

[2] C. Gabor, "Untersuchungen zur zerstörungsfreien Emittanzmessung an einem Testaufbau für negative Ionen", Goethe–Universität Frankfurt, IAP, PhD–thesis, 2007

[3] C. Gabor, D.A. Lee, J.K. Pozimski, A.P. Letchford, "Laser–Based Beam Diagnostics for the RAL Front End Test Stand FETS", $11^{th}$ Int. Conf. on PNNIB, AIP Conf. Proc. 925, p.183, 2006

[4] U. Rohrer, "Introduction of 2–Dimensional Beam Tomography for Monitoring Transverse Beam Emittance at SIN", PSI Ann. Rep 1982, NL 5–6

[5] G.N. Minerbo, "MENT: A Maximum Entropy Algorithm for Reconstructing a source from Projection Data", Computer Graphics and Image Processing, 10 (1979), pp. 48. . . 68

[6] D.S. Sivia, J. Skilling, "Data Analysis — A Bayesian Tutorial", $2^{nd}$ edition, Oxford University Press, 2006

[7] R.C. Conolly, K.F. Johnson, D.P. Sandoval, V. Yuan, "A transverse phase-space measurement technique for high-brightness $H^-$ beams", Nucl. Instr. and Meth., A313, 1992, pages 414–419

[8] Maximum Entropy Data Consultants Ltd., J. Skilling, S. Gull, "MemSys 5" `http://www.maxent.co.uk`

# FOUR-DIMENSIONAL EMITTANCE METER FOR DC ION BEAMS EXTRACTED FROM AN ECR ION SOURCE*

S. Kondrashev[#], A. Barcikowski, B. Mustapha, P. N. Ostroumov, ANL, Argonne, IL 60439, U.S.A.
N. Vinogradov, Northern Illinois University, De Kalb, IL 60115, U.S.A.

*Abstract*

We have developed a pepper-pot, scintillator-screen probe to measure the emittance of low-energy DC beams extracted from ECR ion sources. Different scintillators have been tested, and CsI (Tl) was chosen due to its high sensitivity, wide dynamic range and long life-time. A fast vacuum shutter with a minimum dwell time of 18 ms has been employed to reduce the scintillator degradation by ion beam irradiation. A CCD camera with shutter speed adjustable from 1 μs to 65 s has been used to acquire pepper pot images. The linearity of both the scintillator and the CCD camera has been studied. On-line emittance measurements are performed by an application code developed on the LabVIEW platform. The sensitivity of the device is sufficient to measure the emittance of DC ion beams with current densities down to about 100 nA/cm$^2$. The emittance of all ion species extracted from the ECR ion source and post-accelerated to an energy of 75-90 keV/charge have been measured downstream of the LEBT. Because of the two-dimensional array of holes in the pepper-pot, this emittance meter can be used to observe and study four-dimensional emittance correlations in beams from ECR ion sources.

## INTRODUCTION

Ion beams extracted from ECR ion sources have a complicated structure in 4-D phase space [1]. The ion motion in the horizontal and vertical planes is strongly coupled due to the magnetic field configuration inside the source and extraction regions. Widely used slits and Alison type emittance scanners only provide 2-D projections of the beam emittance. A pepper pot emittance probe is the most suitable device to study 4-D ion beam emittance. Another significant advantage of the pepper pot probe is its short measurement time. 4-D emittance data can be obtained in less than 1 s on-line, allowing ECR ion source tuning to minimize emittance of the extracted ion beam. Previously, different scintillators were used to measure emittance of intense ion beams extracted from pulsed ion sources [2, 3]. However, there is almost no data on emittance measurements of DC ion beams with moderate intensities, which are typical for ECR ion sources, using a pepper-pot device coupled to a scintillator probe. The main challenge is the choice of a viewing screen that provides high sensitivity, a long life time, good linearity and a wide, dynamic range of measurements.

*This work was supported by the U.S. Department of Energy, Office of Nuclear Physics, under Contract No. DE-AC02-06CH11357.
[#]kondrashev@anl.gov

Our first tests of the pepper pot coupled to a CsI (Tl) crystal [4] have shown that the sensitivity of the probe is high enough to measure the emittance of DC ion beams with energy 75 keV per charge state for a variety of ion species from protons to heavy ions with current densities below 1 μA/cm$^2$.

## DESIGN OF THE EMITTANCE PROBE

The structure of the pepper pot emittance meter is shown in Fig. 1.

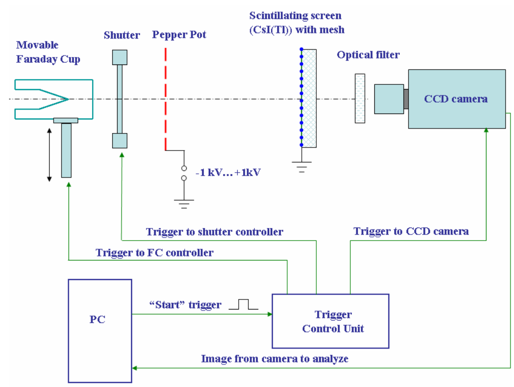


Figure 1: Emittance meter structure.

It consists of a movable Faraday cup (FC) equipped with a negatively biased suppression ring. The diameter of the FC input aperture is 46 mm. A compressed air cylinder drove the FC between two positions: in and out of the beam. The time required to complete the movement in both directions is about 1 s. The FC was used both as a detector of the ion beam current at the input of the emittance meter and as a beam blocker to protect the normally closed iris-type fast shutter from long time irradiation by a DC ion beam with a power of about 10 W. The normally closed iris-type UNIBLITZ-CS65S fast shutter with 65 mm aperture had an adjustable dwell time with a minimum of 18 ms and serves to protect the CsI (Tl) scintillator screen from possible degradation caused by DC ion beam irradiation. The tantalum pepper pot (PP) plate with a diameter of 70 mm and thickness of 380 μm had an aperture array over the whole area with 100 μm diameter holes with 3 mm spacing between them. An optical certification has shown that the diameters of all 415 holes were within the 100 – 104 μm range. The pepper pot plate was isolated from the ground and its potential can be varied in the range of ±1 kV to study the effect of secondary electrons on the emittance measurements. The CsI (Tl) scintillator screen with a diameter of 80 mm and thickness of 3 mm was placed at a distance of 100 mm downstream of the pepper pot plate.

To prevent charge build-up caused by the ion beam, a grounded fine nickel mesh with 88.6% transparency and 200 μm cell size was attached to the crystal surface being irradiated by ions. A CCD camera connected to a PC was used to acquire and save pepper pot images. Fig. 2 shows the time diagram of the FC, fast shutter and CCD camera triggering.

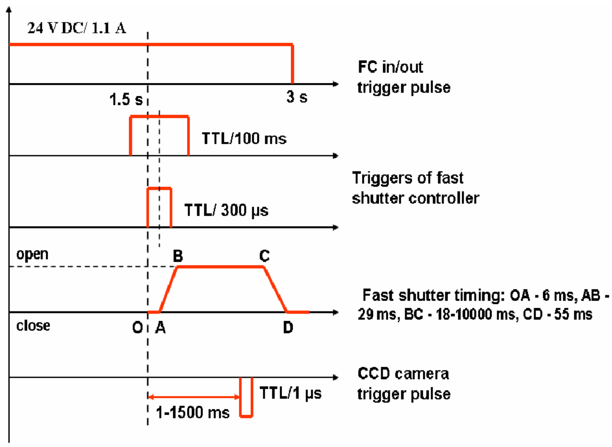


Figure 2: Emittance meter timing.

The operational cycle of the device consists of the following steps. First, the FC moves out of the beamline to allow the beam to pass to the closed iris of the fast shutter. Next, the shutter controller opens the iris for 100 msec to expose the PP plate. The image produced by the array of active beamlets on the crystal is acquired by the CCD camera and sent to the control PC for analysis. The cycle is completed by closing the fast shutter iris and returning the Faraday Cup back into the beam line. The overall cycle period is about 3 seconds and restricted by the time delay for moving the massive FC body. The actual time of acquiring the beam signal is defined by the camera settings (66 ms for the most of measurements). Processing of the acquired image is based on an algorithm similar to the one described in [5]. So far, two-dimensional codes are used for the data analysis while four-dimensional codes (x, y, x', y') will be developed in the future to take a full advantage of the 4-D pepper pot emittance probe.

The emittance probe has been used to measure the emittance of ion beams extracted from a high-intensity ECR ion source. The probe was placed at the end of the injector. The injector consists of an ECR ion source, a 100-kV platform and an achromatic LEBT system based on two 60° bending magnets [6]. The ECR ion source was built using all permanent magnets and is described elsewhere [7].

## CCD CAMERA AND SCINTILLATOR LINEARITY

The sensitivity of the emittance meter can be significantly enhanced by increasing the CCD camera gain and the shutter speed. The CCD camera shutter speed was normally kept unchanged during emittance measurements and the gain was varied depending on the ion beam intensity. The dependence of the emittance values on the CCD camera gain is shown in Fig. 3. The number of saturated CCD camera pixels depending on the CCD camera gain is plotted in Fig. 3 as well. One can see that the emittance increases with increasing CCD camera gain both below and above the saturation limit. The saturation limit corresponds to a CCD camera gain that is equal to 300 in Fig. 3. It is explained by the fact that low intensity tails of the ion beam phase space distribution become more and more visible to the emittance meter with increasing CCD camera gain. The emittance value will be not "true" in both regions below and above the saturation limit of the CCD camera. The most accurate emittance value should be found just at the boundary between saturated and non-saturated ranges (CCD camera gain is equal to 300 in Fig. 3). For all emittance measurement described below, a criteria for the number of saturated pixels to be between 1 and 10 was used.

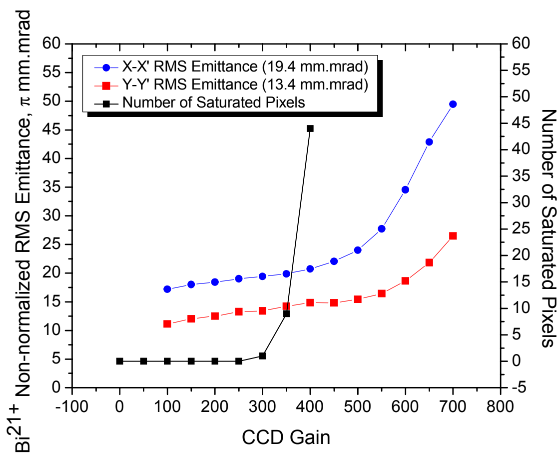


Figure 3: Emittance and number of saturated pixels as a function of CCD camera gain.

A special calibration PP plate was used to check the linearity of the CsI (Tl) scintillator. This plate has a 4x4 array of holes with diameters of 10 and 20 μm up to 300 μm (in 20 μm steps) with 5 mm spacing between them in both directions. If the diameters of the holes are much less than the diameters of their beam images (this condition was satisfied in our case) and ion beam distribution is homogeneous enough across the area occupied by the holes (15x15 $mm^2$ in our case), the diameters of the images are defined by the ion beam emittance and should be approximately the same for all holes. The ion current density at the scintillator surface should also be proportional to the square diameter of each hole. If the scintillator has a linear response, both maximum and integrated intensity of light recorded by the CCD camera should follow this relation too. The main challenge in these measurements was obtaining a homogeneous irradiation of the calibration PP plate. First the pepper pot with 100 μm holes was irradiated by beams of different ion species to study the homogeneity of the beams themselves. Very large spatial fluctuations in ion beam intensity (3 – 10 times over 15x15 $mm^2$ central area) were found for focused ion beams of different ion species. Homogeneity was improved to about 40 – 50% in the best cases by switching off all electrostatic quads along LEBT. At the same time, ion current density dropped by about a factor of 5 at the entrance of the emittance meter.

The dependence of integrated light intensity on the diameter of the calibration pepper pot holes for a $Bi^{20+}$ ion beam is presented in Fig. 4. As one can see, no evidence of saturation was found. Fluctuations around the expected curve are within homogeneity of irradiation. Similar dependence was found for an $O^{6+}$ ion beam. The obtained results also show that the CsI (Tl) crystal dynamic range is better than 50.

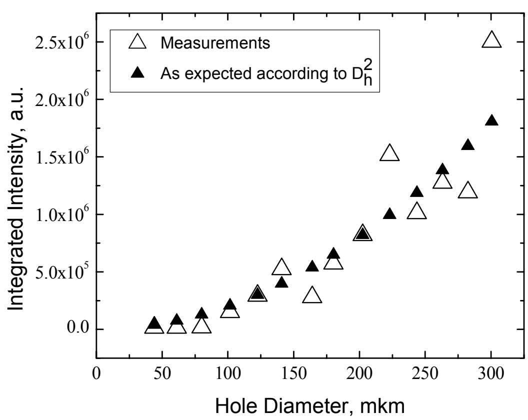


Figure 4: Integrated intensity as a function of hole diameter for $Bi^{20+}$ ion beam irradiation (energy – 1.5 MeV, current density at pepper pot plate – 0.4 $\mu A/cm^2$).

## EMITTANCE MEASUREMENTS FOR ALL ION SPECIES EXTRACTED FROM ECRIS

The dependence of the normalized x-x' and y-y' rms emittance on the mass to charge state ratio are presented in Fig. 5 for all ion species extracted from the source.

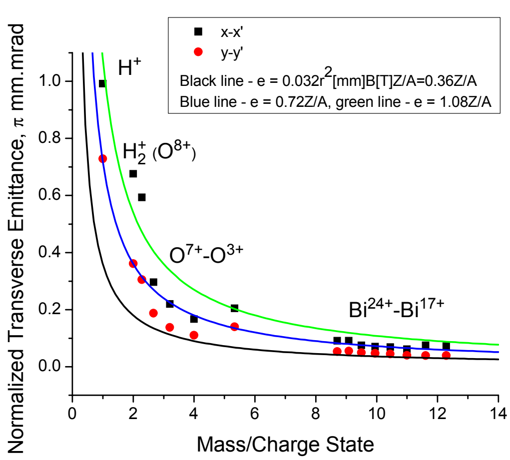


Figure 5: Normalized x-x' and y-y' rms emittance as a function of mass-to-charge-ratio for different ion species extracted from the source.

The black line in Fig. 5 shows the expected emittance dependence under the assumption that emittance is fully defined by beam rotation (angular momentum) induced by the ion source magnetic field [8]. The blue and green lines are the results of multiplication of this dependence by a factor of 2 and 3, respectively. The emittance significantly decreases with an increase in ion mass or a decrease in ion charge state and the measured values are typically ~2 times the angular momentum limit.

## CONCLUSION

A 4-D emittance meter based on a pepper pot - scintillator screen has been developed for on-line measurements and was used to study the emittance of DC ion beams extracted from an ECR ion source. Special attention was paid to the linearity of the emittance measurements:

- No saturation of the CsI (Tl) scintillator was found for typical ion current densities of ECR ion sources
- Emittance measurement errors can be minimized by choosing a CCD camera gain and shutter speed just at the boundary of CCD saturation.

The emittance was measured for several ion species extracted from the ECR ion source and it was found that:

- The dependence of emittance on ion mass-to- charge-state ratio follows qualitatively well the dependence due to beam rotation induced by a decreasing ECR axial magnetic field
- The measured emittance values can not be explained by angular momentum effects only; contributions due to ion temperature in the plasma, non-linear electric fields, or non-linear space charge are comparable
- The emittance increases with charge state for both oxygen and bismuth ions

## ACKNOWELEDGEMENT

The authors are grateful to R. H. Scott for his help with the ECR ion source operation, to M. Anthony, P. Wilt and S. I. Sharamentov for their electronics support, and to A. Pikin for discussions about the pepper-pot technique.

## REFERENCES

[1] P. Spadtke, et al., Rev. Sci. Instr. 79, 02B716 (2008).
[2] R. Scrivens, Extraction of an Ion Beam from a Laser Ion Source, Ph.D. thesis, Physics Department, University of Wales Swansea, May 1999.
[3] A. Sidorov, et al., Rev. Sci. Instr. 79, 02A313 (2008).
[4] S. Kondrashev, et al., "Experimental results on multi-charge-state LEBT approach," PAC'07, Albuquerque, June 2007, TUPAS003, p. 1658 (2007); http://www.JACoW.org.
[5] A. Pikin, A. Kponou, J. Ritter, V. Zajic, Pepper pot emittance meter, BNL note C-A/AP/#244, July 2006.
[6] P. N. Ostroumov, et al., Submitted to Phys. Rev. Lett.
[7] D. Z. Xie, Rev. Sci. Instr., 73(2), 2002, p.531.
[8] D. Leitner, et al., Nucl. Instr. And Meth. In Phys. Res. B, v. 235, 1-4, p. 486.

# INITIAL COMMISSIONING OF A DUAL-SWEEP STREAK CAMERA ON THE A0 PHOTOINJECTOR*

A.H. Lumpkin, J. Ruan, and T.W. Koeth, Fermilab, Batavia, IL U.S.A. 60510

*Abstract*

Characterization of the micropulse bunch lengths and phase stability of the drive laser and the electron beam continue to be of interest at the Fermilab A0 Photoinjector facility. Upgrades to the existing Hamamatsu C5680 streak camera were identified, and initially a synchroscan unit tuned to 81.25 MHz was installed to provide a method for synchronous summing of the micropulses from the drive laser and the optical transition radiation (OTR) generated by the e-beam. A phase-locked delay box was also added to the system to provide phase stability of ~1 ps over tens of minutes. Initial e-beam measurements identified a significant space-charge effect on the bunch length and other bunch length measurements supported the A0 emittance exchange experiments. Recent measurements with a re-optimized transverse emittance allowed the reduction of the micropulse number from 50 to 10 with 1 nC each to obtain a useful streak image. Installation of the recently procured dual-sweep module in the mainframe has now been done. Initial commissioning results and sub-macropulse display of the electron beam via OTR will be presented.

## INTRODUCTION

The opportunity for a new series of streak camera experiments at the Fermilab A0 photoinjector was recognized in the last year. The first enabling upgrade was adding the synchroscan option to the existing C5680 Hamamatsu streak camera mainframe. By locking this module to the 81.25 MHz subharmonic of the rf system, the synchronous summing of micropulses could be done with trigger jitter of <1.5 ps (FWHM) for both the UV drive laser component at 244 nm and the e-beam via optical transition radiation (OTR) measurements [1,2]. The synchronous summing of the low OTR signal from the 15-MeV electron beam micropulses allowed the needed bandpass filters to be utilized to reduce the chromatic temporal dispersion effects inherent to the broadband OTR source and the transmissive optics components. In addition, the C6768 delay module with phase feedback was also acquired, and this stabilized the streak camera sweep relative to the master oscillator so that camera phase drift was much reduced to the ps level over tens of minutes. This second enabling upgrade allowed a series of experiments to be done on the bandwidth effects and transit-time effects in the respective transport lines[3].

The third enabling upgrade involves our installation and initial commissioning of the horizontal deflection unit which allows dual-sweep streak camera operations. In this case we want to assess the phase jitter and/or slew at the ps level during the macropulse of the drive laser and the electron beam. In synchroscan mode we have synchronously summed over all the micropulses and the jitter and slew effects are included. After characterizing the UV laser bunch length, a series of e-beam experiments on the A0 beamlines was performed [3]. We report measurements of the beam transit time in a double-dogleg transport line as a function of the upstream 9-cell accelerator rf amplitude and the effects of emittance exchange in the x-z phase spaces. We then show our initial dual-sweep streak results on the e-beam.

*Work supported by U.S. Department of Energy, Office of Science, Office of High Energy Physics, under Contract No. DE-AC02-06CH11357.

## EXPERIMENTAL BACKGROUND

The tests were performed at the Fermilab A0 photoinjector facility which includes an L-band photocathode (PC) rf gun and a 9-cell SC rf accelerating structure which combine to generate up to 16-MeV electron beams [4]. The drive laser operates at 81.25 MHz although the micropulse structure is usually divided down to 9 MHz. Previous bunch length measurements of the drive laser and e-beam [2] were done with the fast single-sweep module of the Hamamatsu C5680 streak camera with an inherent shot-to-shot trigger jitter of 10 to 20 ps. Such jitter precluded synchronous summing of the short pulses. We have upgraded the camera by acquiring the M5676 synchroscan module tuned to 81.25 MHz with a trigger jitter of less than 1.5 ps (FWHM) and the C6878 phase-locked delay unit which stabilizes the camera phase over 10s of minutes. Due to the low, electron-beam energies and OTR signals, we typically synchronously summed over 50 micropulses with 1 nC per micropulse. The initial sampling station was chosen at Cross #9, and an optical transport system using flat mirrors and a parabolic mirror brought the light to the streak camera as indicated in Fig. 1. A short focal length quartz lens was used to focus the beam image more tightly onto the streak camera entrance slit. The quartz-based UV-Vis input optics barrel transferred the slit image to the Hamamatsu C5680 streak camera's photocathode. Alternatively, the 4-dipoles of the emittance exchange (EEX) line could be powered and experiments done at an OTR station, Cross #24, after the fourth dipole. A second optical transport line brings the OTR to the streak camera. In the EEX line the bunch compression effects were observed, and the shorter bunches were used to help delineate the chromatic temporal dispersion effects for various band pass, long pass, and short pass filters. The OTR converter is

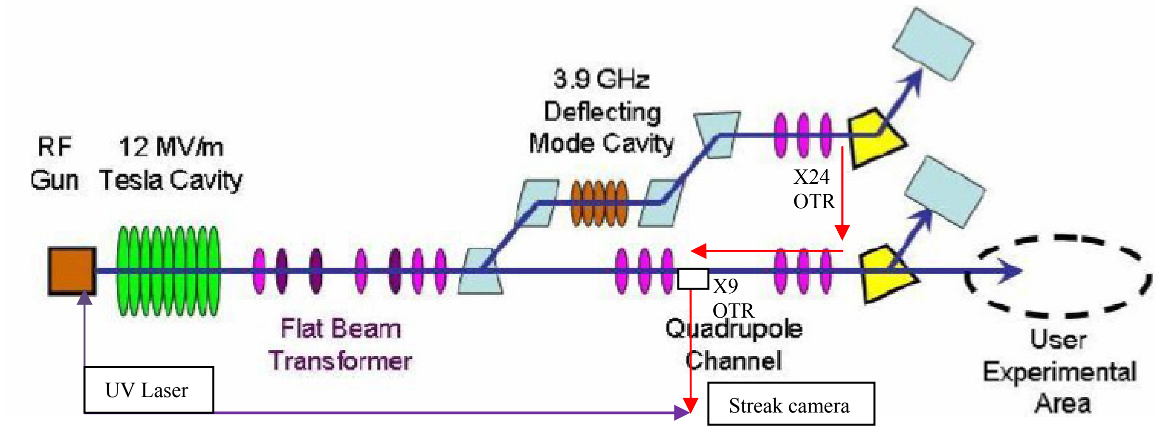


Figure 1: A schematic of the A0 photoinjector test area showing the PC rf gun, UV laser, 9-cell Tesla cavity, the OTR stations, the streak camera, and the second beamline when the two sets of dogleg dipoles are powered.

an Al-coated optics mirror that is 1.5 mm thick with a Zerodur substrate, and is mounted with its surface normal at 45 degrees to the beam direction on a stepper assembly. The assembly provides vertical positioning with an option for a YAG:Ce scintillator crystal position. We still suspect the larger beam sizes may have resulted in incomplete signal collection over angle space. A two-position actuator and a 4-position translation stage were used in the optical path in front of the camera to select band pass filters. The OTR streak readout camera images were recorded with a PCI-compatible video digitizer for both online and offline image analyses. The charge was monitored by an upstream current monitor.

## RESOLUTION AND BANDWIDTH EFFECTS

The calibration of the two fastest streak ranges, R1 and R2, using a laser pulse stacker was described previously [3]. Here we summarize that the calibration factors are 1.55 ps/ch for R2 and 0.32ps/ch for R1. With a limiting vertical spot size of about 4.7 ch (FWHM) in focus mode, the limiting tube resolution is about 1.5 ps FWHM. However, one of the practical issues we addressed was the chromatic temporal dispersion that occurred for the broadband OTR light as it was transported through the transmissive components of the optical transport line. Since the input optics barrel of the streak camera was actually UV transmitting, it consisted of quartz optical components. This material has less variation of index of refraction with wavelength than flint glass or other materials used in the other standard Hamamatsu input optics, but still results in a measurable effect that limits effective temporal resolution with broadband light. Our effect was shown to be smaller than the SSRL setup of 0.2 ps/nm reported at PAC07 [5]. The basic concept is expressed by the simple relationship for the transit-time change, $\Delta t = L\,(v_{g2}-v_{g1})/(v_{g1} \times v_{g2})$, due to the difference in group velocities $v_{g1}$ and $v_{g2}$ for two wavelengths through a characteristic material thickness, L [6].

This effect is represented in Fig. 2 where a 3-ps FWHM actual pulse is shown as arriving at different times for different wavelengths with a 4-ps shift across the bandwidth of the measurement. The resulting superposition of these Gaussian profiles can be fit to a single Gaussian of 4.21 ps (FWHM). In the actual MATLAB model, a series of over 1000 Gaussians was used. In our case the temporal shift was 8 to 9 ps within the 550-nm shortpass filter bandwidth and caused an effective limiting resolution term of about 4.4 pixels (FWHM) for range 2 in quadrature with the static spread function of 4.7 pixels.

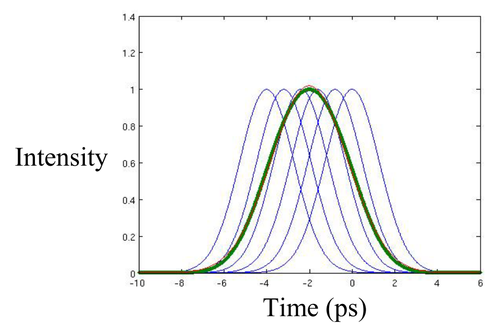


Figure 2: A simple representation of the group velocity dispersion effect on the streak image for a 3-ps FWHM initial pulse and a 4-ps temporal shift in the bandwidth used. The blue curves represent the series of Gaussians time shifted with wavelength. The resultant streak image profile has a 4.21 ps (FWHM) size (green curve).

We then can calculate the actual pulse length by subtracting from the total observed pulse width in pixels the contributing terms of static spread function, bandwidth, and trigger jitter. Since the jitter term appears to be small compared to our bunch lengths, we have absorbed it into the actual bunch length term for the time being. Then for range 2 and range 1 we would have with the 550 nm shortpass filter, respectively:

$$\delta t(FWHM) = \sqrt{Pixel^2 - 4.7^2 - 4.4^2} \times 1.55\,ps/pixel$$

$$\delta t(FWHM) = \sqrt{Pixel^2 - 4.7^2 - 22^2} \times 0.32\,ps/pixel$$

## STREAK CAMERA OTR RESULTS

The experiments were usually initiated by verifying the OTR-deduced spot sizes and centering of the beam on the screen centerline and the downstream rf BPM coordinates. We would optimize the signal transported through the entrance slit of the streak camera while in Focus mode. We then switched to either R2 or R1, set the delay for viewing the streak images, and phase locked the delay box. The initial investigations in the straight ahead line were reported elsewhere [3].

The next series of investigations was done in the other beam line that is setup for emittance exchange experiments [7]. A liquid-$N_2$-cooled, 5-cell $TM_{110}$ rf deflector cavity is positioned between two magnet transport doglegs. Additionally, the trajectory change with beam energy can be studied via the transit time changes through the doglegs as shown in Fig. 3. The phase-locked streak images allow the change in image time position to be used to track the arrival time change. One can see that a ±1% change in momentum causes an about ±6 ps change, respectively, in transit time through the bends. These data were used to evaluate one of the transport matrix elements of the emittance exchange line.

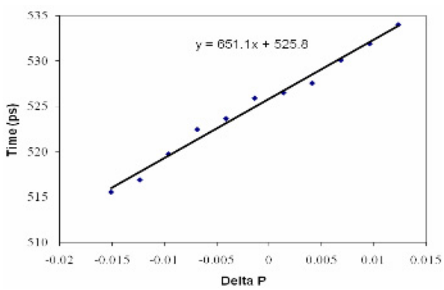


Figure 3: A plot of the change in transit time through the doglegs for different 9-cell rf amplitudes, and hence momentum changes, Delta P.

Critical measurements on one aspect of the x-z emittance exchange experiments were performed this year [7]. We observed the very clear reduction of the bunch length as a result of the exchange seen in Fig. 5. The 5-cell cavity-off data are clearly 4-5 times longer than the cavity-on data. The shortest bunches are close to the detection limit with a value of 1.4 ±0.9 ps (FWHM) when we use the 550-nm LP filter.

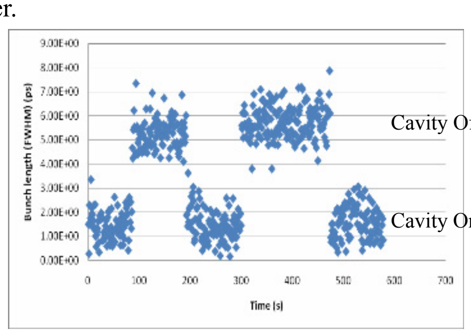


Figure 4: Direct measurement of the x-z emittance exchange and the bunch-length reduction with the 5-cell cavity power on versus cavity power off.

The dual-sweep measurements are in their initial stages. With the improved emittance, smaller beam sizes could be obtained and these resulted in improved photon statistics for the streak images. OTR from 10 bunches at X9 was first measured with synchroscan only as shown in Fig. 5 (left). Then the 10-μs range was selected for horizontal sweep. Due to the internal trigger delay of 5 μs, we see the last 5 of the 10 micropulses in the image at the right.

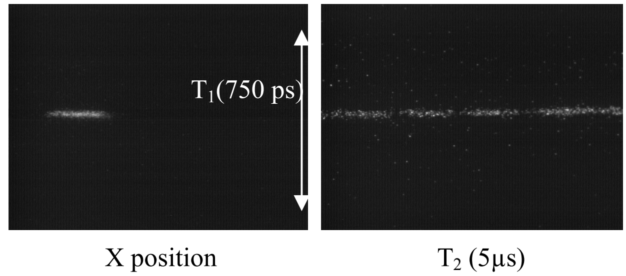


Figure 5: Examples of synchroscan image of 10 micropulses (L) and the dual-sweep image showing 5 of the individual micropulses across the horizontal axis (R). The vertical deflection range is R2 so it spans ~750 ps.

## SUMMARY

In summary, we have extended the investigations on streak camera imaging of the ~15-MeV electron beam in the transport lines of the A0 photoinjector using OTR as the conversion mechanism. The enabling steps for these measurements were the installations of the synchroscan module in the streak camera mainframe, the new phase-locked delay box, and the horizontal sweep unit. These allowed synchronous summing of micropulses with much lower jitter than the single sweep unit and with the phase stability locked over 10s of minutes. In addition sub-macropulse effects of the UV laser and the e-beam can now be evaluated with the dual-sweep mode.

## ACKNOWLEDGEMENTS

The authors acknowledge support from M. Wendt and H. Edwards of Fermilab and A0 technical assistance from J. Santucci, R. Fliller, and M. Davidsaver.

## REFERENCES

[1] Alex H. Lumpkin, "Synchroscan and Dual-Sweep Streak Camera Techniques," Nucl. Inst. and Meth. In Phys. Res., A304, 31 (1991).
[2] Tikohoplav Rodion, PhD thesis, "Low Emittance Electron Beam Studies", FERMILAB-THESIS-2006-04.
[3] A.H. Lumpkin and J. Ruan, "Initial Synchroscan Streak Camera Imaging at the A0 Photoinjector", subm. to proc. of BIW08, Tahoe, CA, May 4-8, 2008.
[4] R. P. Fliller, H. Edwards, W. Hartung, "Time dependent quantum efficiency and dark current measurements in an RF Photocathode injector with a high quantum efficiency cathode", proc. of PAC05, Knoxville, USA.
[5] J. Corbett et al., Proc. of PAC07, FRPMS065.
[6] H. Staerk, J. Ihlemann, A. Helmbold, Laser und Optoelektronik, **28**, 6 (1988) in english.
[7] T. Koeth et al., PAC 07, THPAS079, Albuquerque, NM, USA and these LINAC08 proceedings.

# SPECTRAL AND CHARGE-DEPENDENCE ASPECTS OF ENHANCED OTR SIGNALS FROM A COMPRESSED ELECTRON BEAM*

A.H. Lumpkin, Fermilab, Batavia, IL 60510, U.S.A.
N.S. Sereno, W.J. Berg, M. Borland, Y. Li, and S. Pasky,
Argonne National Laboratory, Argonne, IL 60439, U.S.A.

*Abstract*

Strong enhancements of the optical transition radiation (OTR) signal sampled after bunch compression in the Advanced Photon Source (APS) linac chicane have been observed as has been reported in LCLS injector commissioning. A FIR CTR detector and interferometer were used to monitor the bunch compression process of the PC gun beam down to sub-0.5 ps (FWHM) and correlate the appearance of spatially localized spikes of OTR signal (5 to 10 times brighter than adjacent areas) within the beam image footprint. Spectral-dependence measurements of the enhanced OTR were done initially at the 375-MeV station using a series of band pass filters inserted before the CCD camera. Tests with an Oriel spectrometer with CCD and ICCD readout have now been initiated to extend these studies. We also observed that a beam from a thermionic cathode gun with much lower charge per micropulse (but similar total macropulse charge as the PC gun) showed no enhancement of the OTR signal after compression. Reconstructions of the temporal profiles from the autocorrelations of both beams were performed and will be presented. Based on the available spectral and charge-dependent results, the results are consistent with a microbunching instability which results in broadband coherent OTR (COTR) emissions.

## INTRODUCTION

The interest in improved understanding of the strong enhancements in optical transition radiation (OTR) from bright linac beams following bunch compression is rapidly growing as evidenced by recent reports in workshops and conferences in the last year [1-4]. The observed features are attributed to a combination of longitudinal space charge (LSC) effects in a linac, coherent synchrotron radiation (CSR) effects, and a Chicane compression process [4]. There appears to be a microbunching instability such that broadband coherent OTR (COTR) is generated in the visible wavelength regime. During the commissioning of the LCLS injector in 2007, such unexpected enhancements of the signals in the visible light OTR monitors occurred after compression in a chicane [1]. Since the Advanced Photon Source (APS) injector complex includes a flexible chicane bunch compressor that is similar to that at LCLS, we have an option to use an rf photocathode (PC) gun, and we had experience with SASE-induced microbunching [5], a series of experiments was performed to explore the phenomena. We initially performed studies on OTR measured at three screens located after the bunch compressor [3]. We used focus-at-the-object or near-field imaging optics and established that there were clear enhancements of the OTR signals at maximum bunch compression. Such enhancements prevent the normal beam-profiling measurements with OTR monitors at LCLS and APS. On the other hand, it has now been suggested that such microbunching structures are favorable to startup of visible-UV light SASE FELs [6].

We also accelerated the compressed beam to the end of the linac and evaluated the enhancements at 375 MeV. The localized spikes in the beam distribution were still visible at this energy. At this latter station we have the light transported outside of the tunnel to a small optics lab that allowed us to perform additional spectral dependency measurements. Moreover, the use of a thermionic cathode gun pulse train with only 40 pC per micropulse did not show the OTR enhancements when the bunch length was compressed comparably to that of the PC gun beam. Discussions of the possible mechanisms will be presented for the APS case which is similar, but not identical to that of LCLS.

## EXPERIMENTAL BACKGROUND

The tests were performed at the APS facility which includes an injector complex with two rf thermionic cathode (TC) guns for injecting an S-band linac that typically accelerates the beam to 325 MeV, the particle accumulator ring (PAR), the booster synchrotron that ramps the energy from 0.325 to 7 GeV in 220 ms, a booster-to-storage-ring transport line (BTS), and the 7-GeV storage ring (SR). In addition, there is an rf photocathode (PC) gun that can also be used to inject into the linac as shown schematically in Fig. 1 of reference [3]. An extensive diagnostics suite is available in the chicane and after the chicane area. The tests were performed in the linac at the three imaging stations after the chicane bunch compressor and at the end of the linac where another beam imaging station is located. A FIR coherent transition radiation (CTR) detector (Golay cell) and Michelson interferometer [7] are located between the three-screen emittance stations. A vertical bend dipole and diagnostics screens in this short beamline allow the monitoring of tranverse x-beam size and energy following compression. The YAG:Ce and OTR were directed by

---

*Work supported by U.S. Department of Energy, Office of Science, Office of High Energy Physics, under Contract No. DE-AC02-06CH11357.

turning mirrors and relay optics to a Pulnix CCD camera located 0.5 m from the source. These Chicane stations also have options for low- and high-resolution imaging of the beam spot by selecting one of two lens configurations [8]. At the end of the linac, the imaging station (Sta-5) included the optical transport of the visible light out of the tunnel to a small, accessible optics lab where the CCD camera was located. This allowed the access for exploring the spectral dependency of the enhanced OTR. A set of bandpass filters with center wavelengths in 50-nm increments from 400 to 750 nm and 40-nm band width as well as a 500-nm shortpass filter and 500-nm long pass filter were used in the tests. Recently the spectral measurements were extended by adding an optional transport path to an Oriel UV-visible spectrometer with two readout ports. One port used a Vicon 2400 CCD, and the other used an ICCD. The OTR and YAG:Ce images were recorded with a Datacube MV200 video digitizer for both online and offline image analyses, and a video switcher was used to select the camera signal for digitizing. The beam energy was 375 MeV at this station.

## INITIAL FIR CTR RESULTS

The experiments were initiated by transporting the PC gun beam accelerated to 150 MeV to the chicane area. The rf phase of the L2 accelerator structure located before the chicane was used to establish the appropriate conditions for compression in the chicane. The degree of compression was tracked with the Golay cell signals. A very strong variation of the FIR signal with L2 phase was observed. There was almost no signal seen when uncompressed and 300 units seen at the peak compression. The autocorrelation scan was then done and showed a profile width of ~65 μm (FWHM) as shown in Fig. 3 of reference [3]. This would mean a roundtrip time of 130 μm, or about 430 fs (FWHM). The initial PC gun drive laser bunch length was 3 to 4 ps (FWHM). The PC gun beam bunch length may be a little longer.

The reconstruction of the time profile was performed by the standard practices as described previously [9]. A bunch length of less than 400 fs [FWHM] with a leading-edge spike was indicated for the PC gun beam. Subsequently the TC gun beam was also compressed and a similar autocorrelation was performed [3]. The zero phasing rf technique was also used to evaluate the compressed bunch length of the PC gun beam and a result of 550 fs rms was obtained. The leading edge spike however has a FWHM of ~440 fs as seen in Fig. 1.

## COTR AND OTR SPECTRAL RESULTS WITH PC AND TC RF GUN BEAMS

In order to assess the spectral dependency of the OTR enhancements, we accelerated the beam to 375 MeV and again imaged the beam spot with OTR at a downstream station. As described previously, this station included transport of the signal outside of the tunnel to a small optics lab. First, we still see enhanced localized spikes when we have compressed the beam such as shown in

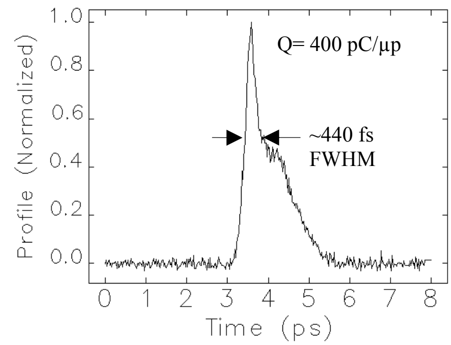


Figure 1: The time profile using the rf zero-phasing mode for the PC rf gun beam with maximum compression.

Fig. 2. We also confirmed that these spikes were present at even a compression level of ½ the CTR signal, although their intensity varied more from shot to shot.

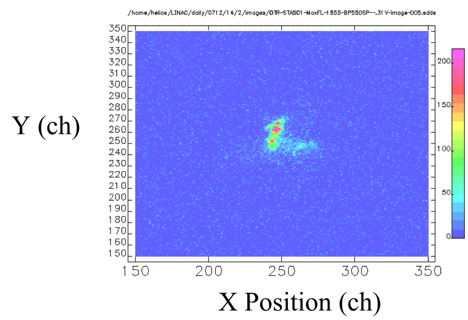


Figure 2: OTR image at 375 MeV showing the enhancements are still present after acceleration beyond the bunch compressor.

At full compression ($R_{56}$ = - 65 mm) we checked the spectral dependency of the enhancements by inserting the bandpass filters in front of the CCD camera. Our preliminary results are that the enhancements were seen at all central wavelengths from 400 to 750 nm (in steps of 50 nm), although relatively weaker in the 400 to 500-nm regime than at 550 nm. We checked the spectral dependence of incoherent OTR from the TC gun beam and saw an intensity rolloff in this short wavelength interval which we attribute to the CCD camera response to these different wavelengths. In Fig. 3 we show the image integrals and peak intensities normalized for CCD response and beam charge. The overall enhancement of the COTR from the PC gun beam is about four times the OTR from the TC gun beam, and the COTR has more red enhancements. This is corroborated by the spectrometer measurements shown in Fig. 4 where the x-localized emission point is shown in both images. It is noted that the YAG:Ce screen is normal to the beam with an Al mirror behind it at 45 degrees. This mirror is in the same plane as the Al OTR screen when it is inserted. The COTR spectral streak profile is more broadband than the YAG:Ce spectrum which is centered near 540 nm as shown in Fig. 5. The spectrometer wavelength span covers ~195 nm from 465 to 660 nm.

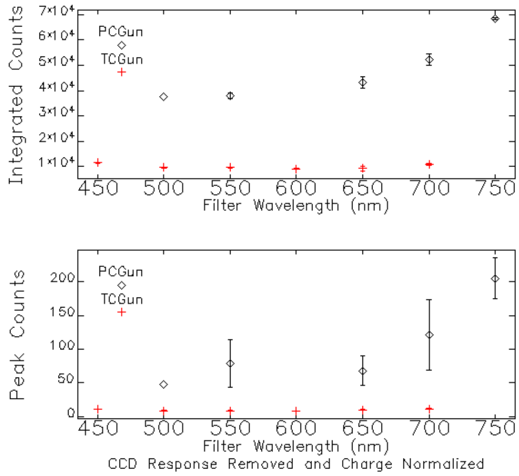


Figure 3: Evaluation of the OTR/COTR image intensities (top) and peak intensities (bottom) versus the bandpass filter center wavelength for the PC rf gun beam (◇) and TC rf gun beam (+). The COTR has a stronger red component than the incoherent OTR.

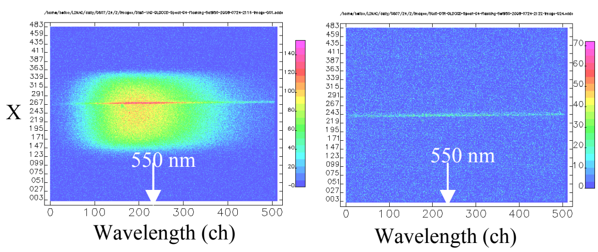


Figure 4: Imaging spectrometer results in x-λ space for YAG:Ce plus an Al mirror (left) and an Al mirror only (right). The localized x extent of the COTR streak in wavelength is evident in both configurations.

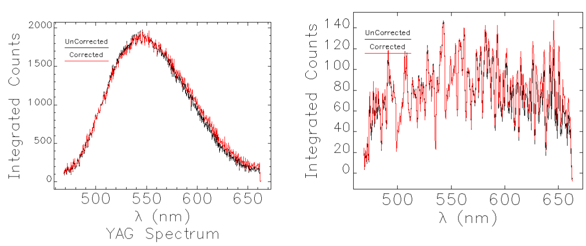


Figure 5: Imaging spectrometer profile results from the images in Fig. 4 for YAG:Ce only (left) and COTR only (right). The COTR spectral streak is more broadband and includes the longer-wavelength red end of the spectrum.

## CTR AND OTR RESULTS WITH TC RF GUN BEAM

In the course of our studies, we decided to test the effect with the TC rf gun beam. In this case we could generate about 40-70 pC per micropulse in a macropulse of 25 micropulses that contained about 1-2 nC total. So the integrated incoherent OTR signal should be larger than that of the PC gun beam. With the combination of compression in the alpha magnet of the TC gun system and the chicane, we were able to generate a similar autocorrelation FWHM. However, we observed no enhanced spatial structures or altered spectral content.

## SUMMARY

In summary, we have extended our investigations on enhancement of OTR signals in the visible light regime following bunch compression of our PC rf gun beam at APS. We have evidence that the spectral content of the COTR is redder than that of the incoherent OTR. Although the enhancements are not as high as that reported at LCLS, we do see order of magnitude signal increases in localized spatial spikes. At this time the coherent enhancement appears consistent with a fine spike(s) in the longitudinal distribution that develop after bunch compression or broadband microbunching. We did not see the effects in the TC gun beam when compressed similarly, but this involved only 70 pC per micropulse compared to 450 pC for the PC gun. Start-to-end simulations are warranted for the APS case. The growing interest in these COTR effects is indicated by the time allowed for discussion in the planned Microbunching Instabilities Workshop at Berkeley in October 2008 [10].

## ACKNOWLEDGEMENTS

The authors acknowledge support from R. Gerig and K.-J. Kim of the Argonne Accelerator Institute and M. Wendt of Fermilab. They also acknowledge the controls support by S. Shoaf of ANL for the relocated spectrometer and cameras and discussions with Z. Huang of SLAC.

## REFERENCES

[1] D.H. Dowell et al., “LCLS Injector Commissioning Results”, Proc. of FEL07, Aug. 26-30, 2007, Novosibirsk, Russia.
[2] Agenda for Mini Workshop on “Characterization of High Brightness Beams”, Zeuthen, May 26-30,2008.
[3] A.H.Lumpkin et al., “Observations of Enhanced OTR Signals from a Compressed Electron Beam”, submitted to proceedings of BIW08, May 4-8, 2008.
[4] Z. Huang et al., “COTR and CSR from Microbunched LCLS Beam”, Proc. of CHBB, Zeuthen, May 26-30, 2008.
[5] A.H. Lumpkin et al., “First Observation of z-dependent Microbunching using Coherent Transition Radiation,” Phys. Rev. Lett., Vol. 86(1), 79, January 1, 2001.
[6] A.H. Lumpkin, R.J. Dejus, and N.S. Sereno, “COTR and SASE from Compressed Electron Beams”, submitted to the Proc. of FEL08, Gyeongju, Korea, August 24-29, 2008.
[7] A.H. Lumpkin et al., Proc. of FEL05, JACoW/eConf C0508213, 608 (2005).
[8] B.Yang et al., BIW2002, AIP Conf. Proc. 648, 393 (2002).
[9] N.S. Sereno, M. Borland, A.H. Lumpkin, MOB17, Proc. of Linac 2000, Monterey, CA.
[10] Agenda for Workshop on “Microbunching Instabilities”, Berkeley, October 6-8, 2008.

# ELECTRON BEAM TIMING JITTER AND ENERGY MODULATION MEASUREMENTS AT THE JLAB ERL*

P. Evtushenko#, S. Benson, D. Douglas, D. Sexton, Jefferson Lab, Newport News, VA, USA

*Abstract*

When operating JLab high current ERL a strong reduction of the FEL efficiency was observed with the increase of the average current of the electron beam. Investigating the FEL efficiency drop-off with the electron beam average current we have measured the electron beam phase noise and the fast energy modulations. The phase noise is a variation of the time arrival of the electron bunches to the wiggler. It could be a very effective way of reducing the FEL efficiency especially when the driver accelerator for the FEL is operated with the RMS bunch length of about 150 fs. Under a fast energy modulation we denote a modulation which can not be followed by the FEL due to its time constant, defined by the net FEL gain. Such a modulation also could be a possible cause of the efficiency drop-off. Making the measurements we could rule out the FEL efficiency drop-off due either the fast energy modulation or the phase modulation. We also have learned a lot about instrumentation and techniques necessary for this kind of beam study.

## ELECTRON BEAM PHASE NOISE MEASUREMENTS

Investigating the FEL efficiency drop-off with the electron beam average current we have measured the electron beam phase noise and the fast energy modulations. The so-called phase noise is essentially a variation of the time arrival of the electron bunches to the wiggler. That could be a very effective way of reducing the FEL efficiency if one takes in to account that the accelerator is routinely operated with the RMS bunch length of about 150 fs [1]. Under a fast energy modulation we denote a modulation which can not be followed by the FEL due to its time constant, defined by the net FEL gain. Such a modulation also could be a possible cause of the efficiency drop-off. The two effects are strongly connected in the FEL driver accelerator due to the longitudinal phase space transformation, i.e., longitudinal bunch compression. The simplified view of the longitudinal phase space transformation is a rotation of a long and low energy spread beam at the injector by ~90 degrees in the longitudinal phase space so that the bunch length minimum is located at the wiggler [2]. Under such a transformation an energy modulation in the injector would get transferred in to a phase modulation at the wiggler and a phase modulation in the injector would gets transferred in to an energy modulation at the wiggler.

The technique we use for the phase noise characterization of the electron beam was originally developed for noise characterization of ultra fast lasers [3]. It was shown that both phase noise and amplitude noise information can be extracted from the power spectrum measurements of the electron beam intensity. The power spectrum of the electron beam is a comb with spectral lines separated by the frequency of the bunch repetition rate. The envelope of the spectrum is determined by the longitudinal profile of a single bunch. Both the amplitude (AM) and phase modulation (PM) (or noise) of the beam intensity manifest themselves in the power spectrum as the sideband modulations of the spectral lines of the comb spectrum. It was shown in [3] that amplitude of the sideband modulations seen relative to the carrier amplitude changes differently with the harmonic number for AM and PM. The relative amplitude of the sidebands due to the amplitude noise does not change with the harmonic number, whereas the relative amplitude of the phase noise increase as $\mu^2$, where $\mu$ is the harmonic number. Thus measurements of the sideband spectrum at the DC contain only the amplitude noise (modulations) and measurements made at very high harmonic number will be dominated by the phase noise (modulations).

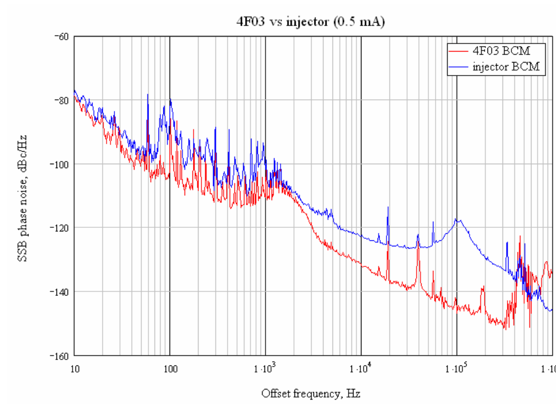


Figure 1a: Single sideband spectrum measured at 0.5 mA.

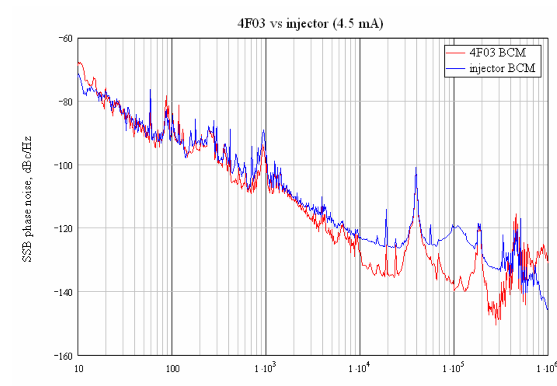


Figure 1b: Single sideband spectrum measured at 4.5 mA.

* Work supported by the U.S. DOE contract # DE-AC05-06OR23177
# Pavel.Evtushenko@jlab.org

Beam current monitor (BCM) cavities and Agilent E5052A Signal Source Analyzer were used for the electron beam phase noise measurements. The BCM is a pill box cavity with the fundamental mode tuned to 1497 MHz. Since the maximum repetition rate of the electron beam is 74.85 MHz the cavity is measuring at least 20$^{th}$ harmonic of the beam. Hence it is reasonable to assume that the sideband spectrum will be dominated by the phase noise. Two cavities used for the measurements are installed at the injector and upstream the wiggler. Signal of such a cavity is strong enough to be used for the phase noise measurements without additional amplification. The E5052A Signal Source Analyzer is a commercially available state of the art device designed for the phase noise measurements of RF sources.

In one set of the measurements the electron beam phase noise was measured as a function of average beam current in the range from 0.5 mA through 4.5 mA. As an example, Fig. 1 shows the phase noise spectra measured at the injector and in the vicinity of the wiggler side by side. Figure 1a shows the spectra measured with 0.5 mA beam current and Fig. 1b shows the spectra measured at 4.5 mA.

Figure 2 shows summary of the measurements made with the BCMs. Most critical question in the data interpretation is the question of the data “pollution” by the amplitude modulation. The signal source analyzer from its operational principal would not distinguish between phase and amplitude modulation. Even when we do the measurements at the relatively high harmonic number due to a very low phase modulation residual amplitude modulation could be present in the signal. We know from beam intensity measurements that there is AM present in the phase noise spectrum we measure and one should keep that in mind when evaluating the measurements results.

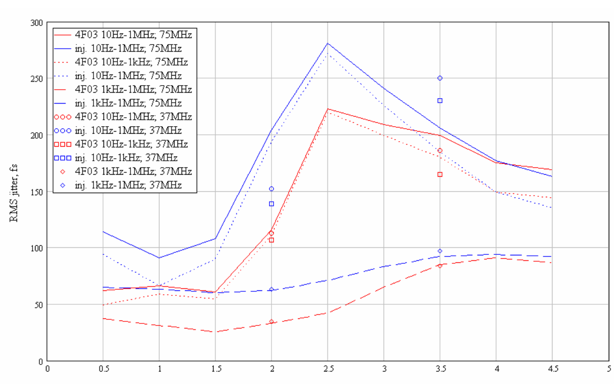


Figure 2: RMS phase noise as a function of the average beam current.

As one sees on the Fig. 2 we did measurements in three different ranges of the offset frequency, namely: 10 Hz ÷1 MHz, 10 Hz ÷1 kHz, 1 kHz ÷1 MHz. There are two reasons for doing the measurement this way. First of all in the preliminary measurements we saw a strong drop of the phase noise at 4.5 mA. On the spectrum one sees that the drop is due to the less noise at low frequency, i.e., below 1 kHz. But the higher frequency components did not went down, and if they reduce the FEL efficiency it could explain why the efficiency did not go up as the RMS jitter went down at the 4.5 mA. That was one reason to separate the range of the phase noise measurements in to two and also make the measurements in the whole range. The other reason is, when looking at the FEL noise data one sees that there are a lot of noise below ~1 kHz and much less above that. This is why we decided to separate the "low" and "higher" frequencies at 1 kHz.

Certainly it is important to compare the measured phase noise (modulation) with the specification. The spec derived from the requirement that the FEL intensity would be reduced not more than by 10 % due to the variation in the electron bunch time arrival can be summarized as following; the RMS jitter at frequency $f_m$ has to be less than $6 \cdot 10^{-9} / f_m$ [4].

Figure 3 shows the comparison of the spec and the measured phase spectra at 0.5 mA and 5 mA. The measured spectra are shown as the yellow curve; the spec is shown as the red line.

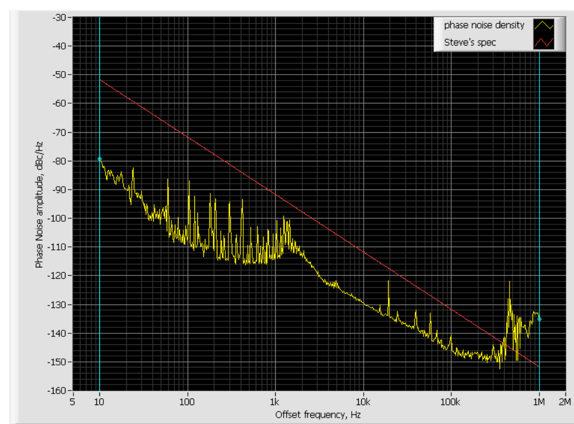


(a) measurements at the average current of 0.5 mA

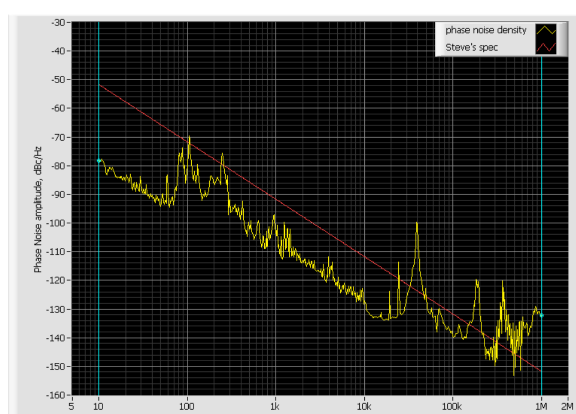


(b) measurements at the average current of 4.5 mA

Figure 3: Comparison of the measured phase noise spectrum with the requirements imposed by the FEL stability.

Comparison of the spec and the phase noise spectrum measured at 5 mA average beam current at first suggests that the measured phase noise exceeds the one allowed by the spec. However it was established that the peaks at ~100 Hz, ~250 Hz and ~ 40 kHz are due to amplitude modulation of the electron beam caused of by the amplitude modulation of the drive laser. The peaks do not represent the phase modulation of the electron beam and therefore our conclusion was that the measured phase noise does not exceed the required one.

## ENERGY MODULATION MEASUREMENTS

As was explained above the phase and energy modulation are strongly connected in the FEL driver due to the beam dynamics. Energy modulation can also originate from the LINAC, for instance due to misbehaving RF system. For this reasons we also did measurements of the "fast" up to 1 MHz electron beam energy modulation. The measurements were done at the injector and at the section with dispersion right upstream of the wiggler. Beam position monitors (BPM) were used for the measurements in a combination with the special set of the BPM electronics. The BPM electronics used for the measurements is essentially the analog part of the log-amp based BPM electronics [5], which we have been developing to upgrade our BPM system. The analog part of the electronics was used in a combination with high speed 4 channel simultaneously sampling ADC card. Essential part of the measurements was proper calibration of the electronics and making sure that the electronics will detect the beam position modulation properly. Such tests made in a lab have shown that this type of the BPM electronics would detect the modulation properly, thus our calculation and measurements in the lab were agreed on the 2 % level. The measurements in the lab also have shown that the system noise floor is at the level of 0.5 microns, which we consider to be quite remarkable. Figure 4 shows the lab noise floor measurements of the BPM electronics with the fast ADC. The peak in the X spectrum at the 20 kHz is our artificially introduced test modulation.

Our estimates are that the level of the energy modulation in the injector, which would lead to the phase modulation at the wiggler of a concern level, also would show up as a ~100 µm beam position jitter at the dispersion section in the injector. Thus we would be able to detect such a motion very easily. The first result of the measurements was that there is no significant change in the energy jitter in the injector when the average beam current is increased form 0.5 mA up to 5 mA, so that there is no correlation between the FEL efficiency drop-off and the injector energy modulation. The second result was that beam motion we are measuring in the injector dispersion section is on the level of ~ 1 micron, i.e., much less that the level of concern. The same system was used to measure the fast energy modulations in the dispersion section right upstream of the wiggler. Here again we could not see any dramatic change in the energy modulation with the average beam current. Also the beam energy modulation which we have measured was extremely low and several times smaller that the intrinsic beam energy spread.

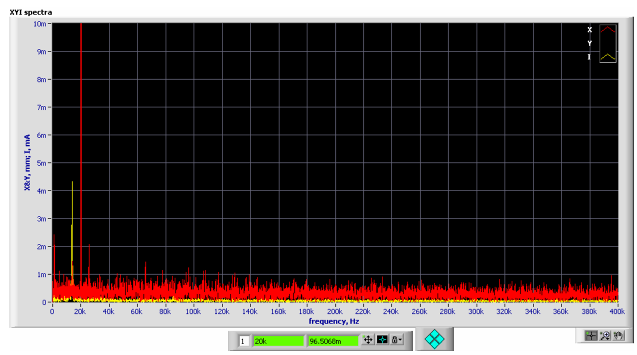

Figure 4: Noise floor in the fast beam position measurements and injected calibration signal.

## CONCLUSION

Making the above described measurements we could rule out the FEL efficiency drop-off due either the fast energy modulation or the phase modulation (timing jitter) of the electron beam. We also have learned a lot about instrumentation and techniques necessary for this kind of beam study. We think that it will have an impact not only on our future electron beam diagnostics and instrumentation but also on the instrumentation for other ERL accelerators.

## REFERENCES


[1] P. Evtushenko et al., Proceedings of 12th Beam Instrumentation Workshop, 2006, Fermilab, Batavia, IL, USA

[2] D. Douglas, Proceedings of PAC07, Albuquerque, New Mexico, USA

[3] D. von der Linde, Appl. Phys. B 39, 1986, p. 201

[4] Steve Benson, private communication

[5] D. Sexton et al., Proceedings of 12th Beam Instrumentation Workshop, Fermilab, Batavia, IL, USA

# OPTICAL DIFFRACTION RADIATION MEASUREMENTS AT CEBAF*

P. Evtushenko[#], A. P. Freyberger, C. Y. Liu, Jefferson Lab, Newport News, VA USA
A. Lumpkin, Fermilab, Batavia, IL USA

### Abstract

Optical diffraction radiation (ODR) is a promising technique, which could be used for non interceptive beam size measurements. An ODR diagnostic station was designed and installed on a CEBAF transfer beam line. The purpose of the setup is to evaluate experimentally the applicability range for an ODR based non interceptive beam size monitor and to collect data to benchmark numerical modeling. An extensive set of measurements were made at the electron beam energy of 4.5 GeV. The ODR measurements were made for both pulsed and CW electron beam of up to 80 μA. The wavelength dependence and polarization components of the ODR were studied using a set of insertable bandpass filters and polarizers. The typical transverse beam size during the measurements was ~150 microns. Complete ODR data, wavelength and polarization, were recorded for different beam sizes and intensities. The beam size was also measured with an optical transition radiation (OTR) as well as wire scanner located next to the ODR station. In this contribution we describe the experimental setup and present first results of the measurements with the comparison to the numerical simulations.

## INTRODUCTION

Optical diffraction radiation is generated when a charged particle passes near a conductor at a distance comparable or smaller than $\gamma \cdot \lambda / 2\pi$, where $\gamma$ is the relativistic Lorenz factor and $\lambda$ is the wavelength of the radiation. The theory of the diffraction radiation is well developed [1]. In the case of a highly relativistic particle beam with large $\gamma$, a conductor located at a distance bigger than the transverse beam size will generate a significant amount of diffraction radiation in the optical wavelength range. Several ODR based schemes were suggested for non-intercepting beam size measurements [2-6]. Some of them utilize the angular distribution of the ODR whereas others make use of imaging of the radiator surface, i.e., near-field measurements. The near-field ODR was observed experimentally previously [8, 9]. A common condition in such measurements was that the integrated charge used to generate the ODR was several nC.

The Continuous Electron Beam Accelerator Facility (CEBAF) is a multipass superconducting LINAC delivering CW electron beam with an energy up to 6 GeV and average current up to 100 μA for nuclear physics experiments on fixed targets [10]. A typical beam size in CEBAF at high energy is 100 μm. standard video camera uses to integrate one field of a video signal (16.6 ms) and when running 100 μA beam is 1.66 μC. The combination of the these parameters, GeV range energy, 100 μm beam size and μC charge integrated within 16.6 ms, makes CEBAF an ideal facility to study develop and implement an ODR based non-intercepting beam size diagnostic, as was pointed out previously [11]. From the operational point of view it is very desirable to have such a non-intercepting beam size monitor. It can be used to detect drifts leading to a change in the betatron match early and therefore can improve beam availability for the nuclear physics experiments. A set of such beam size monitors positioned properly along a transport beam line could also provide online emittance monitoring as well as emittance measurements.

## EXPERIMENTAL SETUP

The optical transition radiation (OTR) was used for reference beam size measurements. We have designed and built a radiator which could be used for both OTR and ODR measurements. The radiator is shown in Fig. 1. The ODR part of the radiator is a 300 μm thin silicon wafer optically polished and aluminized on one side. The thickness of the aluminum layer is about 600 nm. The wafer is mounted on an aluminum holder in such way that its edge does not have any frame underneath. This edge of the wafer was put close to the beam to generate the ODR. Minimizing the beam scattering in the OTR screen and reducing the beam losses downstream of the radiator is always desirable. Therefore next to the ODR radiator we have put a separate OTR radiator. The radiator is a 6 μm thin Kapton foil aluminized on one side and stretched on a frame so that it is flat. Surfaces of both radiators look as an optical mirror. The aluminization of both radiators is done to increase radiation yield.

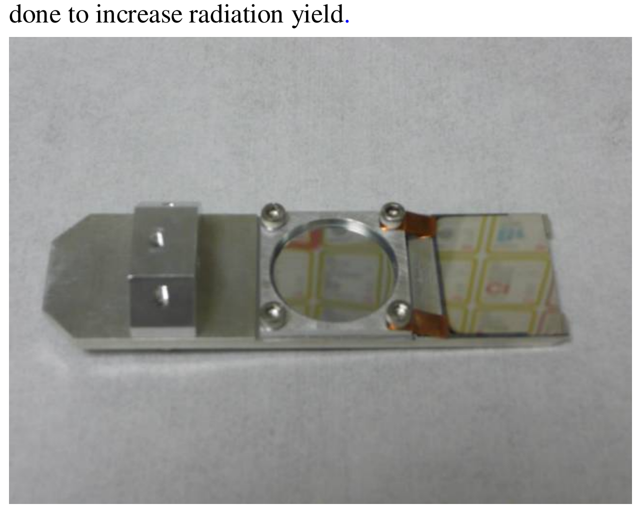

Figure 1: ODR-OTR radiator.

* Work supported by the U.S. DOE contract # DE-AC05-06OR23177
[#] Pavel.Evtushenko@jlab.org

The radiator is mounted on a stepper motor actuator with a lead screw. The actuator can position the radiator with accuracy better than 10 μm. The radiator is mounted on the actuator at an angle of 45 degrees relative to the direction of the beam propagation. Fig. 2 shows schematically the ODR diagnostic station. The setup was installed on an existing very stable girder in the beginning of the Hall-A beam line. The radiator is installed on the downstream side of the girder. An alignment laser was installed on the upstream side of the girder. The laser beam is coupled in to the beam line with the help of an insertable mirror. All optical components are mounted on two optical rails as can be seen in the Fig. 2. There are two 2″ mirrors on the vertical rail to redirect the OTR and ODR light to the horizontal rail. Two 2″ diameter achromatic lenses are used to image the surface of either radiator on a CCD camera. For the measurements we used a JAI-A50 CCD camera. The camera is neither cooled nor intensified. The most important feature of the camera is the signal to noise ratio (SNR) of 60 dB. There are two insertable polarizers, vertical and horizontal, installed in the optical system. There are also three motorized and remotely controlled filter wheels where band-pass and neutral density filters are installed. The video signal of the CCD camera was digitized with 10-bit frame grabber. Due to the SNR of the camera and the resolution of the frame grabber the dynamic range of our measurements was about $10^3$. There are two wire scanners installed on the same girder where the ODR diagnostic station was installed. This gave us the capability to cross check the ODR as well as OTR measurements with the wire scanners measurements.

## EXPERIMENTAL RESULTS

First the beam size was determined with the help of the OTR and the wire scanners. Unfortunately the thin Kapton OTR radiator surface happened to be somewhat misaligned with the surface of the ODR radiator. As a result the OTR image from the Kapton radiator was considerably dimmer and appeared somewhat shifted. For that reason we had to use the surface of the ODR radiator for the OTR measurements. Since our goal is to develop a non-intercepting beam size measurements technique, one of the measurements we did was to change the beam size

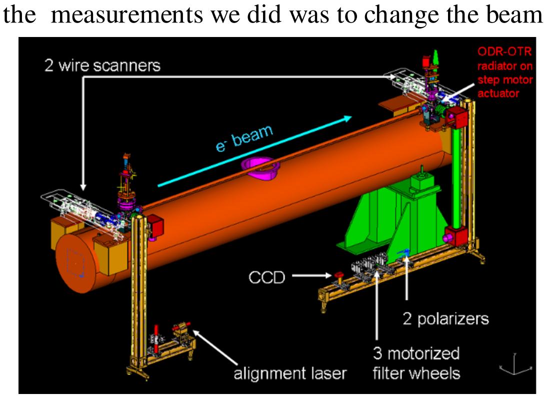


Figure 2: Schematic of ODR station.

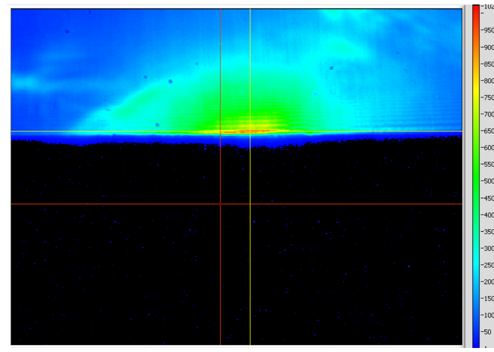

Figure 3: Unpolarized ODR pattern.

using upstream quadrupoles and measure the changes in the ODR pattern. The OTR and wire scanners were used to determine the beam size. We have observed that using polarizers made a difference for the measured beam size. If without polarizer we would measure the vertical and horizontal beam sizes of $\sigma_x$=149 μm and $\sigma_y$=157 μm, then when the horizontal polarizer was inserted we have measured $\sigma_x$=150 μm and $\sigma_y$=130 μm and when the vertical polarizer was inserted the measurements were $\sigma_x$=124 μm and $\sigma_y$=160 μm. That is for either polarization the beam size measured in perpendicular direction would appear to be smaller by about 20 % and the beam size measured in the direction of polarization essentially would not change.

Before inserting the ODR radiator close to the beam and running higher current beam the vertical beam size was reduced to 110 μm. The edge of the ODR radiator was positioned above the beam at 1.1 mm from the beam centroid, which is $10\times\sigma_y$. Gradually increasing the average beam current of CW beam at 10 μA we recorded the image shown in Fig. 3. No beam loss was detected with the ODR radiator inserted. The field of view of the image is 6.9 mm by 5.2 mm. Note that at this beam intensity we started to saturate the CCD camera at the maximum of the intensity of the ODR pattern. The measurements are made with the beam energy of 4.5 GeV. With the vertical polarizer inserted the ODR pattern appeared to be considerably narrower [7] and with the horizontal polarizer inserted we could clearly observe the double lobe pattern [7]. Both these observations are in agreement with the model prediction [8]. In an ODR image a small, approximately 100 μm wide, region of interest (ROI) close to the edge of the radiator was selected. The intensity of all lines in the ROI was added and normalized to the number of lines. Using a nonlinear least square fit, a best approximation of the normalized intensity profile in the ROI by a Gaussian function was found. The sigma of the Gaussian distribution found by the fit was taken as a measure of the ODR pattern. For the previously determined ten settings of the upstream quadrupole we have measured the width of the ODR patterns without any polarizers and with vertical polarizer inserted. Results of the measurements are shown in Fig. 4 where the horizontal axis is the beam size measured via vertically polarized OTR. For both unpolarized and vertically polarized ODR data a systematic increase of the ODR pattern width is measured when the horizontal beam size is increased. The same experimental observation was made previously in [8]. Ultimately we would like to be able to use ODR for beam size measurements without any cross-calibration. As a first step towards such measurements we need to see a good agreement between the measured data and the prediction of the model. The beam size measured with the OTR we also know the distance from the beam centroid to the edge of the ODR radiator, the expected ODR pattern distributions for these conditions can be calculated. We apply then the same procedure to the model data as we did with the experimental data. The results of this would be the expected sigma of the best Gaussian fit. We did such calculations for a horizontal beam size in the range 50 µm through 350 µm; the vertical beam size in the calculations was kept constant and equal to 150 µm. The calculations were made for four different wavelength 450 nm, 550 nm, 650 nm and 750 nm, for unpolarized and vertically polarized ODR. The results of the calculations are shown in Fig. 4 with the results of the measurements. Note that the measurements are broadband and the calculations are narrowband. It is reasonable to assume that when the quantum efficiency of the CCD camera is taken in to account the broad band data or calculations will be somewhere in the range between 450 nm and 750 nm. Comparing the calculation and the measurements in the Fig. 4 we can conclude that the unpolarized data are in reasonable agreement with the model predictions whereas the vertically polarized data agree less with the model. However, the disagreement between the vertically polarized ODR data and the model is only about 20 %. As can be seen in Fig. 3 there is a background present in the raw ODR data. Possible sources of the background are visible synchrotron radiation and visible edge radiation from the upstream dipole, which is located only 8 m upstream of the ODR radiator. The presence of the background in the data certainly affects the results of the Gaussian fits. We consider the background to be the main reason for the discrepancy between the model prediction and the experimental results. Note that at the maximum CW beam average current of 82 µA (the limitation factor was the quantum efficiency of the photocathode) no measurable beam loss was observed.

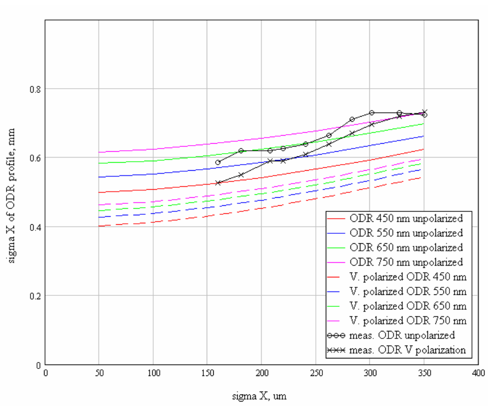


Figure 4: ODR data comparison with the model.

When measuring the ODR patterns with the horizontal polarizer inserted we were clearly observing the double lobe distributions. However the distributions we have observed were not symmetrical as the model predicts. One possible explanation for that can be a slightly misaligned polarizer. Another cause for the asymmetry can be a background intensity distribution which is not symmetric relative to the beam position at the ODR radiator.

## CONCLUSION

We have made measurements of the ODR patterns distribution using CW electron beam. We were able to run CW beam with an average current up to 82 µA with the ODR radiator edge placed at ten times the vertical beam size without measurable beam loss. We observe significant background in the ODR data that affects the data analysis and is considered to be the main reason for the discrepancy between the model and the experiment. We are planning to improve the experimental setup to mitigate or completely eliminate the background in the ODR data.

## ACKNOWLEDGMENTS

We would like to thank Lia Merminga, George Neil, Gwyn Williams and Steve Benson for stimulating and useful discussions. This work is supported by the U.S. Department of Energy under contract number DE-AC05-06OR23177.

## REFERENCES

[1] M. L. Ter-Mikaelian, High Energy Electromagnetic Processes in Condensed Media (Wiley/Interscience, New York, 1972)
[2] D.W. Rule and R. B. Fiorito "The Use of Transition Radiation as a Diagnostic for Intense Beams", NSWC Tech. Report 84-134, July 1984
[3] D.W. Rule , R. B. Fiorito and W.D. Kimura, Proc. of BIW , 7th Workshop, AIP Conf. Proc 390 pp. 51-517 (1997)
[4] M. Castellano, Nucl. Instrum. Methods Phys. Res., Sect. A394, 275 (1997).
[5] A. P. Potylitsyn, Nucl. Instrum. Methods Phys. Res., Sect. B 145, 169 (1998).
[6] P. Karataev et al., Phys. Rev. Lett. 93, 244802 (2004)
[7] P. Evtushenko et al., Proc. of BIW08
[8] A. H. Lumpkin, W. J. Berg, N. S. Sereno, D. W. Rule, and C.-Y. Yao, Phys. Rev. ST Accel. Beams 10, 022802 (2007)
[9] E. Chiadroni, et al., Proceedings of PAC07, Albuquerque, New Mexico, USA, p. 3982
[10] C.R. Leeman, D.R. Douglas, and G.A. Kraft, Annu. Rev. Nucl. Part. Sci. 51, 413-50 (2001).
[11] A. H. Lumpkin et al., Proceedings of PAC07, Albuquerque, New Mexico, USA, p. 4381

# EXTRACTING INFORMATION CONTENT WITHIN NOISY, SAMPLED PROFILE DATA FROM CHARGED PARTICLE BEAMS*: PART II

C.K. Allen#, W. Blokland, S.M. Cousineau, J.D. Galambos, ORNL, Oak Ridge, TN 38371 USA


## [illegible]

This is a continuation of work in [1]. The objective is to design a robust procedure for automating the analysis of beam profile data. In particular, we wish to extract accurate values for the beam position and beam size from profile data sets. These values may be then used to estimate additional beam characteristics such as the Courant-Snyder parameters.


## INTRODUCTION

Profile data are typically obtained from particle-beam diagnostic devices such as wire scanner, laser strippers, or wire harps. The beam distribution is projected upon various spatial axes the effect being marginalization of the beam distribution with all variables except the projection axis. We provide a model for the data collection process which includes random noise components. The goal is to design a robust, automated procedure for accurate estimation of beam position $\mu$ and RMS beam size $\sigma$. Additionally, we need a process for automatic identification of bad data sets (typically such a process requires human intervention, a tedious, time consuming, and expensive endeavor). This goal is the first requirement for automated procedures for Twiss parameter estimation, transverse matching, and halo identification and mitigation. To realize our current goal we must make real world considerations. Specifically, we consider information content, noise (randomness), and sampling theory. Information content was covered previously [1]; we briefly review sampling.

### [illegible]

Let [illegible] represent the profile distribution where [illegible] represents some spatial beam axis. Take the axis sampling locations to be equidistant so that $x_k = kh, k = 0, \ldots, N-1$, where $h > 0$ is the (constant) step length between measurements. Making the definition

$$f_k \triangleq f(x_k)$$

then $\{f_k\}$ is the sampling of the profile [illegible] Now denote the set of profile measurements as $\{m_k\}_{k=0}^{N-1}$. These ordered measurements correspond, respectively, to the set of sampling locations $\{x_k\}_{k=0}^{N-1}$.

### [illegible]

The $n^{th}$ moment $\langle x^n \rangle$ of a distribution $f$ is defined

$$\langle x^n \rangle \triangleq \frac{1}{Q} \int_{-\infty}^{+\infty} x^n f(x) dx, \tag{1}$$

where the constant $Q \triangleq \int f dx$ is the total beam charge. Because we are dealing with sampled data we can only approximate these values. The beam position μ and RMS size σ are the first two moments of the distribution

$$\mu \triangleq \langle x \rangle,$$
$$\sigma \triangleq \langle (x-\mu)^2 \rangle^{\frac{1}{2}}. \tag{2}$$

Because we are working with sampled data we normalize these quantities by [illegible] Specifically, the continuous approximations to beam position and RMS size are $h\mu$ and $h\sigma$, respectively.

We take two approaches for approximating μ and σ, 1) computing μ and σ directly from the measurements, and 2) fitting a Gaussian approximation for [illegible] from the measurements from which $\mu$ and $\sigma$ are determined.

### [illegible]

Each measurement $m_k$ is composed of both the actual beam profile $f_k$ plus a noise component $W_k$, where $W_k$ is part of a random process $\{W_k\}$. This noise introduces indeterminacy. Henceforth we can only generalize in terms of probabilities and stochastic (or "random") processes. Denote by $\mathrm{E}[\cdot]$ the expectation operator of the random variable $W_k$, averaging over its ensemble. Then $\Omega_k \triangleq \mathrm{E}[W_k]$ is the mean and the quantity $V_k \triangleq \mathrm{E}[(W_k - \Omega_k)^2]^{1/2}$ is the standard deviation, or variance. Although the values of a random process are not deterministic but their statistics are, specifically, $\Omega_k$ and $V_k$ can be measured through a calibration experiment. Most noise processes are modeled as random processes.

Take the process $\{W_k\}$ to be a Gaussian distributed white noise process with mean Ω and variance [illegible] then $W_k = W$ for all [illegible] and [illegible] is Gaussian distributed. We have

$$m_k = f_k + W, \qquad k = 0, \ldots, N-1 \tag{3}$$

where

$$Pr(W = w|\Omega, V) = \frac{1}{\sqrt{2\pi}V} e^{-\frac{(w-\Omega)^2}{2V^2}}. \tag{4}$$

The notation $\Pr(M_k = m_k|\Omega, V) = \Pr(W = m_k - \Omega - f_k|\Omega, V)$ indicates the probability that the measurement (random variable) $M_k$ at axial position $x_k$ has value $m_k$, given that the noise has mean Ω and variance [illegible]

## DIRECT MOMENT COMPUTATION

Because we are dealing with sampled data we can only approximate the moments $\langle x^n \rangle$. The simplest form of approximation would be to replace the integration in (1) with a finite summation. We begin with a definition to simply the sequel:

* This work supported by SNS through UT-Battelle, LLC, under contract DE-AC05-00OR22725 for the U.S. DOE.
#Corresponding author allenck@ornl.gov

$$S_n(\bar{k}) \triangleq \sum_{k=0}^{N-1} (k-\bar{k})^n f_k \tag{5}$$

Then, the $n^{th}$ discrete moment centered at $\bar{k}$ is given as

$$\langle (k-\bar{k})^n \rangle \triangleq \tilde{S}_n(\bar{k})/S_0(0) \tag{6}$$

where $\bar{k}$ is meant to identify the mean value of □

Computations involving random processes require that we properly observe their statistics. Considering the direct moment calculations based upon Eq. (5) we define

$$\tilde{S}_n(\bar{k}) \triangleq \sum_{k=0}^{N-1} (k-\bar{k})^n (m_k - \Omega), \tag{7}$$

the measurement central summations. Then

$$\begin{aligned} \bar{Q} &\triangleq \tilde{S}_0(0), \\ \bar{\mu} &\triangleq \frac{\tilde{S}_1(0)}{\tilde{S}_0(0)}, \\ \bar{\sigma} &\triangleq \tilde{S}_2(\bar{\mu})/\tilde{S}_0(0), \end{aligned} \tag{8}$$

are the computed values of the beam charge, position, and RMS size, respectively. The expected values for these quantities follow from Eq. (7), it is straightforward to show

$$E[\tilde{S}_n(\bar{k})] = \sum_{k=0}^{N-1} (k-\bar{k})^n E[(m_k - \Omega)] = S_n(\bar{k}) \tag{9}$$

since $E[\cdot]$ is a linear operator. This result is exactly that which we need. However, consider the variance of $\tilde{S}_n(\bar{k})$

$$E\left[\left(\tilde{S}_n(\bar{k}) - S_n(\bar{k})^2\right)\right]^{\frac{1}{2}} = N_n(\bar{k})V, \tag{10}$$

where $N_n(\bar{k}) \triangleq \sum_{k=0}^{N-1} (k-\bar{k})^n$ is a form of the Riemann zeta function. This function can become prohibitively large with relatively moderate values of □ and □ [1]. Ironically, increasing sample count □ provides more certainty in □ but less in $\tilde{S}_n(\bar{k})$. Yet, we can use Eq. (10) to compute the variances of Eq. (8). For two random variables □ and □ with means $\bar{x}$ and $\bar{y}$ and variances $\sigma_x$ and $\sigma_y$, respectively, the random variable $Z \triangleq X/Y$ has mean $\bar{z} = \bar{x}/\bar{y}$ and variance $\sigma_z = \bar{z}\sqrt{\sigma_x^2/\bar{x}^2 + \sigma_y^2/\bar{y}^2}$ [3]. Thus, we have (noting $N_0(0) = N$)

$$\begin{aligned} Var[\bar{Q}] &= NV, \\ Var[\bar{\mu}] &= \bar{\mu}\Delta_1(\bar{Q},\bar{\mu})V, \\ Var[\bar{\sigma}] &= \bar{\sigma}\Delta_2(\bar{Q},\bar{\mu},\bar{\sigma}), \end{aligned} \tag{11}$$

where

$$\Delta_1(\bar{Q},\bar{\mu}) \triangleq \sqrt{N^2/\bar{Q}^2 + N_1^2(\bar{\mu})/\bar{\sigma}^2},$$

Thus, the values of $\Delta_1(\bar{Q},\bar{\mu})V$ and $\Delta_2(\bar{Q},\bar{\mu},\bar{\sigma})V$ can be used to determine the order of magnitude to which $\bar{\mu}$ and $\bar{\sigma}$ are accurate.

## GAUSSIAN PROFILES

It can be shown in the limit of zero space charge the Gaussian profile is a stationary beam distribution [2]. Here we make that assumption. We need three parameters to identify a Gaussian profile: amplitude □, mean $\mu$, and standard deviation $\sigma$. The sampled Gaussian profile is

$$f_k(A,\mu,\sigma,B) = Ae^{-\frac{(k-\mu)^2}{2\sigma^2}}. \tag{12}$$

where, recall, $\mu$ and $\sigma$ are normalized by step length □

### □□□□□□a□□□□□□□

From Eq. (3) note again that $\Pr(M_k = m_k|\Omega, V)$ is equal to $\Pr(W = m_k - f_k|\Omega, V)$. From Eq. (4), and assuming that each measurement $m_k$ is independent, the probability of obtaining all the measurements $\{m_k\}$ is then

$$Pr(\{m_k\}|A,\mu,\sigma) = \prod_{k=0}^{N-1} Pr(m_k|\Omega,V) = \frac{e^{-\frac{\chi^2}{2V^2}}}{\left(\sqrt{2\pi}V\right)^N} \tag{13}$$

where

$$\chi^2(A,\mu,\sigma|\Omega) \triangleq \sum_{k=0}^{N-1} [m_k - \Omega - f_k(A,\mu,\sigma)]^2. \tag{14}$$

We can use the above equations to determine the most probable values of $(A,\mu,\sigma)$ which produce measurements $\{m_k\}$; this condition occurs when $\chi^2(A,\mu,\sigma|\Omega)$ is a minimum. Notice that noise variance □ does not explicitly occur in $\chi^2$. Consequently, we can take $\Omega$ as an additional free parameter in the minimization to avoid the separate calibration experiment for $\Omega$ and □

### □a□□□□a□□□□□□□

Bayes'theorem states that

$$Pr(A,\mu,\sigma|\{m_k\},\Omega,V) \propto Pr(\{m_k\}|A,\mu,\sigma)\, Pr(A,\mu,\sigma)$$

We know the first factor in the right hand side by Eq. (13). The final factor above is the □□□□□□□□□□□□ consisting of all the information we know about $A,\mu,\sigma$ prior to the measurements. Note that $\mu$ is independent but □ and $\sigma$ are correlated, their product proportional to beam charge □. Thus $\Pr(A,\mu,\sigma) = \Pr(A,\sigma)\Pr(\mu)$.

For the prior there are several other quantities we can infer from the data and our familiarity with the experiment. We can use the most reliable deterministic quantities in Eq. (8) and Eq. (11) to form the prior distribution, namely $\bar{Q}$ and $\bar{\mu}$. (If we find them unusable by inspecting variances, we must return to $\chi^2$ fitting.) The amplitude □ is correlated to the span of the measurements, however, we can say no more; that is, □ is uniformly distributed between the extremes. We have

$$Pr(Q|\Omega,V) = \frac{1}{\sqrt{2\pi}NV} e^{-\frac{(Q-\bar{Q})^2}{2N^2V^2}}$$

$$Pr(\mu|\Omega,V) = \frac{1}{\sqrt{2\pi}\Delta_1(\bar{Q},\bar{\mu})V} e^{-\frac{(\mu-\bar{\mu})^2}{2\Delta_1^2(\bar{Q},\bar{\mu})V^2}}$$

$$Pr(A|\Omega,V)=\begin{cases}\dfrac{1}{m_{max}-m_{min}} & A\in[m_{max}-m_{min}]\\ 0 & A\notin[m_{max}-m_{min}]\end{cases}$$

To find $\Pr(A,\sigma|\Omega,V)$ note that □ and □ are independent so $\Pr(A,Q)=\Pr(A)\Pr(Q)$. The random variables $A,\sigma$ and □ are related by $Q=\sqrt{2\pi}\sigma A$. Then $\Pr(A,\sigma)=\Pr(A)\Pr\big(Q(A,\sigma)\big)dQ/d\sigma$. The result,

$$Pr(A,\sigma)=\frac{A}{NV}e^{-\frac{\left(\sqrt{2\pi}A\sigma-\bar{Q}\right)^2}{2N^2V^2}}.$$

Putting it all together

$$Pr(A,\mu,\sigma|\{m_k\})$$

$$\propto\frac{\sqrt{2\pi}A}{\left(\sqrt{2\pi}V\right)^{N+2}}\frac{e^{-\frac{\chi^2}{2V^2}-\frac{\left(\sqrt{2\pi}A\sigma-\bar{Q}\right)^2}{2N^2V^2}-\frac{(\mu-\bar{\mu})^2}{2\Delta_1V^2}}}{N\Delta_1}$$

Taking the logarithm of the above, multiplying through by $2V^2$ and ignoring constant terms yields

$$J\triangleq\ln A-\chi^2-\frac{1}{N^2}\left(\sqrt{2\pi}\sigma A-\bar{Q}\right)^2-\frac{1}{\Delta_1^2}(\mu-\bar{\mu})^2.$$

Since the logarithm is a monotonic function, the maximum of $J$ is also a maximum of $\Pr(A,\mu,\sigma|\Omega,V)$. Maximizing $J$ with respect to our parameters yields the most probable values of $A,\mu,\sigma$.

## EXAMPLES

The first example is a profile with obvious (asymmetric) halo, shown in Figure 1. The second curve in Figure 1 is the Gaussian profile obtained when applying the parameters $\bar{A},\bar{\mu},\bar{\sigma}$ computed with the direct method.

Table 1: Example #1 Beam Parameter Comparison

| Method | $A$ | $\mu$ | $\sigma$ | $\Omega$ |
|---|---|---|---|---|
| Direct | 0.130 | 61.1±0.279 | 3.12±1.45 | 0.3e-3 |
| Bayes | 0.153 | 62.5 | 2.30 | 0.3e-3 |
| $\chi^2$ | 0.153 | 61.5 | 2.18 | 7.0e-3 |
| $l_1$ fit | 0.181 | 61.1 | 3.31 | 0.0 |

Table 2: Example #2 Beam Parameter Comparison

| Method | $A$ | $\mu$ | $\sigma$ | $\Omega$ |
|---|---|---|---|---|
| Direct | NaN | 53.6±21.2 | NaN±156 | 1.07e-3 |
| Bayes | 0.113 | 50.4 | 2.27 | 1.07e-3 |
| $\chi^2$ | 0.112 | 49.4 | 2.26 | 1.81e-3 |

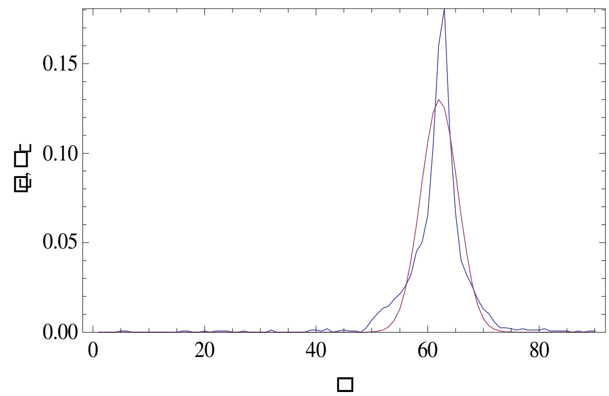


Figure 1: Example #1 profile with direct method Gaussian.

Table 1 provides a comparison for the different methods. In the table we have also included an $l_1$ fit to $\{m_k\}$ where the sum of the absolute values $|m_k-\Omega-f_k|$ is minimized. Interestingly enough this gives the same results as the direct method.

The second example is a pathological case involving extreme noise (not shown). Neither the direct method nor the $l_1$ fitting converge. 2 provides a comparison of the successful methods while demonstrating the failure of the direct method. Noise variances for the examples were $6.81\times10^{-5}$ and $2.23\times10^{-3}$, respectively.

## CONCLUSIONS

Accuracy for the direct computation of beam position and RMS size is quantified. When only the position and charge are accurate, they may be used in the Bayesian method. If both the position and sizes are inaccurate, then the $\chi^2$ approach is always available. Additionally, $\chi^2$ minimization does not require a calibration for noise mean and variance. Both $\chi^2$ minimization and Bayesian methods are robust with noisy data. The use of double-Gaussian profile has been suggested and would appear appealing for separating core and halo.

## REFERENCES


[1] C.K. Allen, W. Blokland, S.M. Cousineau, J.D. Galambos, High Brightness Workshop 2008, Nashville, TN, Aug. 25-29, 2008.

[2] M. Reiser, [illegible] (Wiley-VCH, 2008).

[3] D.S. Sivia, [illegible] (Oxford Press, Oxford, 1996).

# LASER-BASED PROFILE AND ENERGY MONITOR FOR $H^-$ BEAMS*

R. Connolly, J. Alessi, S. Bellavia, C. Dawson, C. Degen, W. Meng, D. Raparia, T. Russo and N. Tsoupas
Brookhaven National Lab
Upton, NY, USA

*Abstract*

A beam profile and energy monitor for $H^-$ beams based on laser photoneutralization was built at Brookhaven National Laboratory (BNL)* for use on the High Intensity Neutrino Source (HINS) at Fermilab. An $H^-$ ion has a first ionization potential of 0.75eV and can be neutralized by light from a Nd:YAG laser ($\lambda$=1064nm). To measure beam profiles, a narrow laser beam is stepped across the ion beam, removing electrons from the portion of the $H^-$ beam intercepted by the laser. These electrons are channeled into a Faraday cup by a curved axial magnetic field. To measure the energy distribution of the electrons, the laser position is fixed and the voltage on a screen in front of the Faraday cup is raised in small steps. We present a model which reproduces the measured energy spectrum from calculated beam energy and space-charge fields. Measurements are reported from experiments in the BNL linac MEBT at 750keV.

## INTRODUCTION

In 2002 we reported on a project at BNL to develop a beam profile monitor for $H^-$ beams using photoneutralization by a laser beam directed perpendicular to the ion beam [1]. That effort was in support of the Spallation Neutron Source being built at Oak Ridge National Lab [2]. Recently BNL was contracted by Fermi National Lab to build a laser-based $H^-$ beam-profile monitor for use on the HINS [3].

A pulse of electrons is removed from an $H^-$ beam by directing a 50mJ, 10ns light pulse from a Q-switched Nd:YAG laser through the ion beam. This electron pulse is channeled into a Faraday cup via a curved axial magnetic field produced by a series of coils. To measure transverse profiles, the trajectory of the focused laser beam is moved across the ion beam in small steps by small rotations of a mirror about 45°. At each mirror angle the electron current is integrated over the full laser pulse. A profile is produced by plotting total charge vs. mirror position.

In addition to transverse ion-beam profiles we measure the energy distribution of the signal electrons by ramping the voltage on a retarding grid in front of the cup. The energy of each electron is the sum of the initial kinetic energy and the energy it receives from the space-charge field as it is transported to the collector [4].

* This work was performed under the auspices of the U.S. Department of Energy.

In this paper we describe the detector and the measurements. We present a model which reproduces the measured energy spectrum from the beam current and transverse size, bunch length, and bunching fraction of the H- beam. The energy measurements are motivated by the desire to measure the energy spread of the $H^-$ beam. For the test beam energy of 750keV beam energy-spread information is buried in the space-charge effects, but we anticipate being able to measure beam energy spread in the BNL HEBT at 200MeV based on these experiments.

## DETECTOR

Figure 1 is a diagram of the detector from the side showing the signal-electron path. The neutralization chamber is a six-way cross with the laser beam passing through viewports either horizontally or vertically. A curved solenoidal magnetic field, generated by a series of coils, channels the signal electrons into the Faraday cup collector. A voltage grid in front of the collector provides secondary-electron suppression for profile scans and retarding voltage for energy scans. The Faraday cup charge signal passes to ground through a 1kΩ resistor. The resulting voltage pulse is digitized by a LeCroy LT584L oscilloscope.

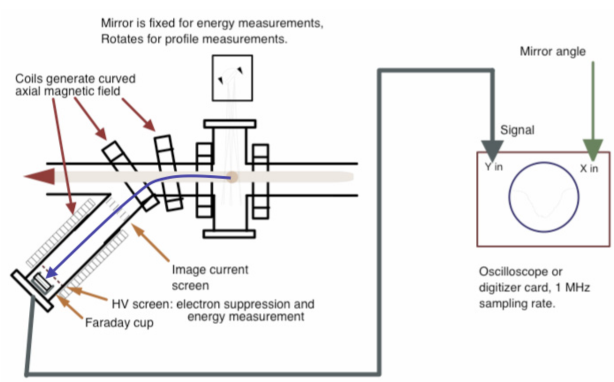


Figure 1: Longitudinal schematic. Electrons from the $H^-$ beam are guided by magnetic field through grid into cup.

A transverse diagram of the device is shown in Fig. 2. The 50mJ/pulse laser head [5] is mounted on an optics plate with a linear translation stage [6] to select scanning axis and two galvo-motors [7] to rotate mirrors about 45° to scan the laser beam. The optics platform and the full beamline installation in shown in Fig. 3.

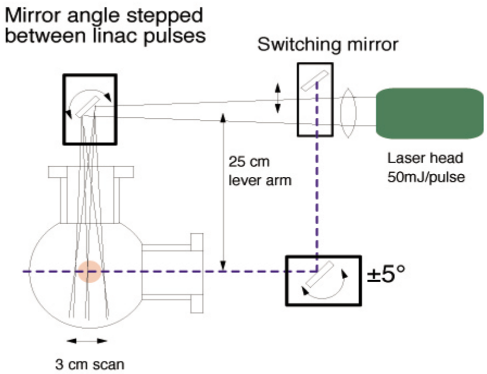


Figure 2: Transverse optical system.

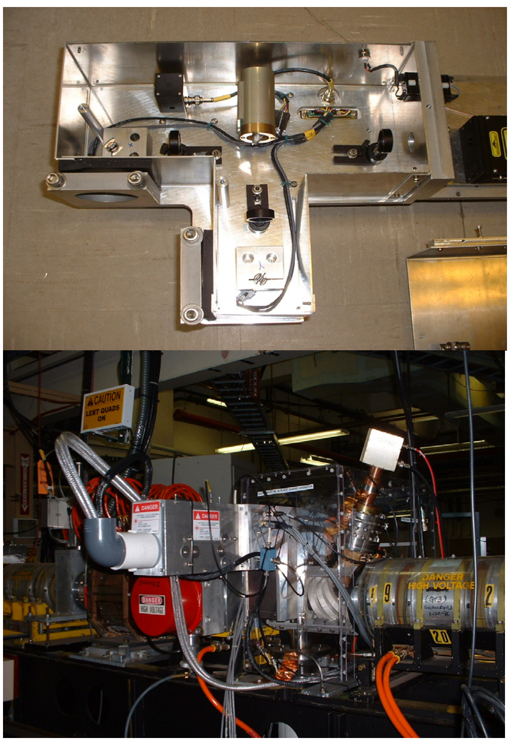

Figure 3: Optics platform (top) showing laser head at right and axis-switching actuator at top center. In beamline installation the ion beam travels left to right. The electron collector is top right. Field coils are right of center around the beamline.

The control system is a Labview program running on a dedicated PC with digital and analog I/O through a National Instruments USB-6229 BNC. The maximum firing rate of the laser is 20Hz so only one data point can be obtained per linac cycle (6.6Hz). A measurement cycle is initiated by a timing pulse from the linac which triggers the laser. The laser outputs a Q-switch synchronous pulse which triggers the scope. The signal pulse from the Faraday cup is passed through a 10MHz low-pass filter into the scope which does a baseline subtraction and integrates the pulse. Upon completion of this process, the scope signals the computer which reads the pulse.

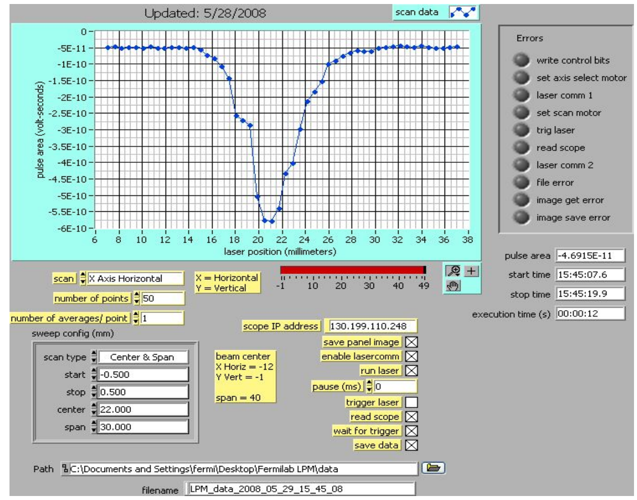


Figure 4: The Labview page showing a profile measurement.

## MEASUREMENTS

The laser-pulse length is about 10ns at the base and the ion-beam bunches are 5ns apart. It is not possible to lock the laser pulse to the rf structure of the beam so the laser timing is random with respect to the beam rf buckets. To compensate for the timing jitter a profile is built up by accumulating several pulses at each of several mirror angles. Figure 4 shows a profile taken with one measurement at each mirror position. The shot-shot jitter is evident in the jagged pulse edges. Averaging smoothes the edges.

An electron-energy spectrum is accumulated by keeping the mirror stationary and incrementing the voltage on the retarding grid. A signal electron is born with a kinetic energy of $T_{e0}= T_{H-}(m_e/M_H)=750,000/1838=408eV$, where $m_e$ and $M_{H-}$ are the masses of electron and H- ion respectively. As it is transported out of the beam along the magnetic field lines its energy is modified by the space-charge field.

A newly detached electron is moving with the $H^-$ beam. Electrons born in front of the bunch will experience an electrostatic force in the forward direction while the electrons born in back of the bunch will feel a force in the backward direction. Therefore the total energy of an electron born in the front of a beam bunch is $T_{e0}+\varphi$ and one in back of the bunch is $T_{e0}-\varphi$, where $\varphi$ is the space charge potential due to H- beam, Fig. 5.

This detector was located about 5m down stream from the RFQ. There are two buncher cavities in this space. PARMILA simulations show that for 70 mA beam, at this location about 50% of the beam is de-bunched due to space charge with the bunchers on and is debunched with them off. This 50% unbunched beam results in beam loss in DTL Tank1.

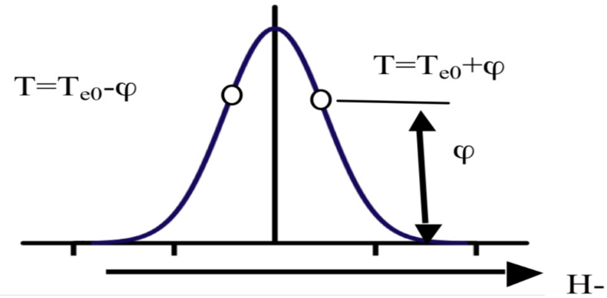


Figure 5: Illustration showing space-charge model used in simulation. Electrons in back of bunch lose the space-charge potential, φ, and those in front gain φ.

Figure 6 shows measured energy spectra from an unbunched beam and 35mA and 70mA bunched beams. The spectrum from the unbunched beam has a low-energy cutoff of 408eV and a high-energy cutoff of 600eV. The calculated space-charge potential on the axis of the unbunched beam is -200V.

The electrons from the bunched beams are born with 408eV and gain or lose energy from the space-charge potential. The low-energy of detected electrons should extend to near zero. However for all bunched-beam spectra the low-energy cutoff is about 250eV which is the time-of-flight cutoff from the integration window.

The high-energy cutoff is the initial kinetic energy plus the maximum space-charge potential in the bunch. For the 50% bunched 70mA beam the calculated potential at bunch center is -750V giving a calculated maximum electron energy of 1150eV. We measured 1025-1100eV. The 70%-bunched, 35mA beam gave a calculated maximum energy of 850eV and we measured 825eV. Also measured, but not on Fig. 6, was a 17mA beam producing a maximum electron energy of 700eV.

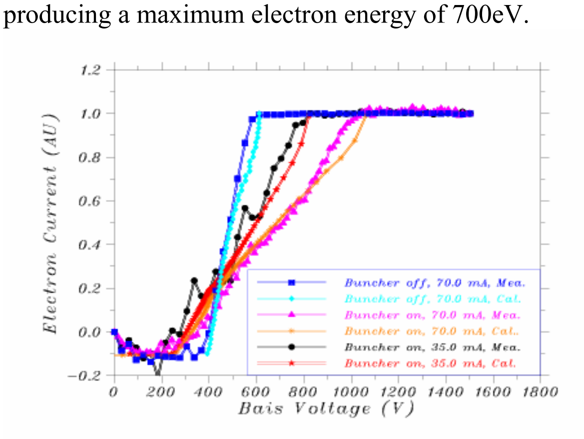


Figure 6: Electron current vs. screen voltage for buncher off and 35mA and 70mA with buncher on. Here the electron current is negative, zero is the top flat line.

Also shown on fig. 6 are calculated energy spectra from the three beam models given in Table I. The calculation models the beam as 3D Gaussian bunches with the transverse dimensions we measured and the longitudinal dimension as calculated by PARMILA riding on top of a DC beam.

Table 1: Beam Parameters used in the Calculations.

| Current mA | Buncher On/off | % of DC component | Bunched Length degrees |
|---|---|---|---|
| 70 | OFF | 100 | 360 |
| 70 | ON | 50 | 90 |
| 35 | ON | 30 | 70 |

## DISCUSSION

This detector provides accurate transverse profile measurements of an $H^-$ beam together with the energy spectrum of the signal electrons. At the low energy of this experiment an electrostatic model was used to fit the energy spectrum data. Using the measured beam current and transverse size, the bunch length and bunching fraction can be deduced. Extrapolation of these results indicates this method can be used to measure beam energy spread to 0.1% in the 200MeV HEBT.

The detector described here and the ones in refs. 1 and 2 use pulsed Nd:YAG lasers which allow one data point to be taken on each linac cycle. In a modern clean vacuum environment it should be possible to use a fiber-coupled diode laser with microchannel-plate (MCP) amplification to produce a profile with a 200µs scan of a single linac cycle [8]. This was our original design and the Faraday cup was a MCP detector with all surfaces connected in parallel. At the location of this experiment the gas-stripping signal [9] saturated the MCP.

## ACKNOWLEDGEMENTS

The authors thank Brian Briscoe, Tony Curcio, John Halinski, Steve Jao, Vinnie LoDestro, Brian Mullany, Craig Rhein, Joe Saetta, Walter Shaffer and Paul Ziminski for their many contributions.

## REFERENCES

[1] R. Connolly *et. al.*, "Laser Beam-Profile Monitor Development at BNL for SNS," Proc. 2002 Linac Conf., Gyeongju.
[2] S. Assadi *et. al.*, "SNS Transverse and Longitudinal Laser Profile Monitors Design, Implementation and Results," EPAC 2006, Edinburgh.
[3] http://www-td.fnal.gov/projects/hins.html
[4] S. Lee *et. al.*, "Direct Measurements of Space-Charge-Potential in High Intensity H- Beam with Laser Based Photo Neutralization Method," Proc. DIPAC 2005, Lyon.
[5] http://www.quantel-laser.com/industrial-scientific-lasers/uk/fiche_produit.php#
[6] http://www.bluehilloptical.com/Galvoline.htm
[7] http://www.cambridgetechnology.com/
[8] R. Connolly *et. al.*, "Photodetachment Profile Monitor Proposal for $H^-$ Beams at BNL," 11th ICFA Mini-Workshop on Diagnostics, SNS, Oak Ridge National Lab, 2002.
[9] R.E. Shafer, "Laser Diagnostic for High Current H- Beams", Proc. 1998 Beam Instrumentation Workshop (Stanford). A.I.P. Conf. Proceedings, (451), 191.

# ACTIVITIES ON HIGH BRIGHTNESS PHOTO-INJECTORS AT THE FRASCATI LABORATORIES, ITALY

R. Boni, D. Alesini, M. Bellaveglia, C. Biscari, M. Boscolo, M. Castellano, E. Chiadroni, A. Clozza, L. Cultrera, G. Di Pirro, A. Drago, A. Esposito, M. Ferrario, L. Ficcadenti, D. Filippetto, V. Fusco, A. Gallo, G. Gatti, A. Ghigo, B. Marchetti, A. Marinelli, C. Marrelli, M. Migliorati, A. Mostacci, E. Pace, L. Palumbo, L. Pellegrino, R. Ricci, U. Rotundo, C. Sanelli, M. Serio, F. Sgamma, B. Spataro, F. Tazzioli, S. Tomassini, C. Vaccarezza, M. Vescovi, C. Vicario, INFN-LNF, Frascati, RM, Italy
F. Ciocci, G. Dattoli, A. Dipace, A. Doria, M. Del Franco, G. P. Gallerano, L. Giannessi, E. Giovenale, G. Orlandi, S. Pagnutti, A. Petralia, M. Quattromini, A. Lo Bue, C. Ronsivalle, P. Rossi, E. Sabia, I. Spassovsky, V. Surrenti, ENEA C.R. Frascati, RM, Italy
A. Bacci, I. Boscolo, F.Broggi, F. Castelli, S. Cialdi, C. De Martinis, D. Giove, C. Maroli, V. Petrillo, A.R. Rossi, L. Serafini, INFN-Mi, Milano, Italy
M. Mattioli, M. Petrarca, M. Serluca, INFN-Roma I, Roma, Italy
L. Catani, A. Cianchi, INFN-Roma II, RM, Italy
J. Rosenzweig, UCLA, Los Angeles, CA, USA
M. E. Couprie, SOLEIL, Gif-sur-Yvette, France
M. Bougeard, B. Carré, D. Garzella, M. Labat, G. Lambert, H. Merdji, P. Salières, O. Tchebakoff, CEA Saclay, DSM/DRECAM, France.
J. Rossbach, Hamburg University and DESY

**Abstract**

An intense activity on high brightness photo-injectors for SASE-FEL experiments and facilities, is being carried out, since 2003, in the Research Site of the INFN Frascati Laboratory, Rome, in collaboration with CNR and ENEA. SPARC is the 150 MeV photo-injector, in advanced phase of commissioning at LNF. The electron beam, which drives a 530 nm FEL experiment, is being characterized in terms of emittance, energy spread, peak current. The matching with the linac confirmed the theoretical prediction of emittance compensation based on the "invariant envelope" matching. The demonstration of the "velocity bunching" technique is in progress too. The SPARC photo-injector is the test facility for the soft-X FEL project named SPARX [1], that is based on the generation of ultra high peak brightness electron beams at the energies of 1.2 and 2.4 GeV generating radiation in the 1.5-13 nm range. SPARX will be realized in the Tor-Vergata University campus. In this paper we report the experimental results obtained so far with SPARC and the design status of the SPARX project.

## THE SPARC TEST FACILITY

The INFN Frascati Laboratory (LNF) and the ENEA Frascati Research Center (CRF) are involved since 2003 in the development and the commissioning of the S-band photo-injector SPARC, aimed to generate high brilliance electron beams to drive SASE-FEL experiments in the visible and UV region, with a laser-seeding process. Moreover, SPARC will be the pre-injector of SPARX, the new high brightness electron linac to generate SASE-FEL radiation in the 40 to 0.6 nm wavelength range, that will be built in the campus of the Tor-Vergata (TV) Rome University, 4 km airline from LNF.

The SPARC research program is scheduled in two phases. The first one is concluded and consisted in characterizing the electron beam, photo-emitted at 5.6 MeV by the cathode of a S-band RF gun, illuminated by Ti-Sa Laser beam pulses [2]. The results of the first commissioning phase are reported in [3]. The second phase, still in progress, foresees a detailed analysis of the beam matching with the linac to confirm the emittance compensation theory, based on the "invariant envelope" matching [4] and to verify the emittance compensation with the "velocity bunching" (VB) experiment [5]. SASE and SEEDING experiments are also foreseen by the end of 2008. SPARC will also allow to study ultra-short beams physics, plasma wave-based acceleration, and to generate advanced X-ray beams via Compton back-scattering.

## SPARC COMMISSIONING

The installation of the whole machine, including six permanent magnet (pm) undulators and the by-pass diagnostic channel was completed after disassembling the emittance-meter in January 2007. Three S-band sections [6] have been power conditioned in short time and operate at 20-20-10 MV/m respectively, providing a final beam energy of 150 MeV. Digital based, low level RF (LLRF) controls [7] allow to monitor, synchronize and stabilize the accelerating section RF fields and the phase of the laser pulses on the photocathode. The beam energy stability achieved is less than 0.1%. Two solenoids with 0.18 T field, are wrapped around the first two accelerating sections, to provide additional focusing for matching the beam envelope with the linac.

The possibility to vary independently the input power to each RF section was foreseen by means of "in-vacuum" waveguide variable attenuators. This option would have allowed to operate the photo-injector in very flexible way. Unfortunately, the manufacturer, (the German company ) failed in developing such high power devices that discharged at a power level (≈ 20 MWpeak) much lower than the design one (≈ 60 MWp).

To estimate bunch length, long. phase-space and slice-emittance an RF deflector (RFD) is installed on the beam-line downstream the last RF section [8].

Six 1.2 m long undulators, manufactured by [9] and made of a pm section with 28 mm period, 6÷30 mm variable gap and k = 1.4, are aligned on the beam line. A drift space of 360 mm between each unit, hosts quadrupoles for horizontal focusing and radiation diagnostic boxes. The undulator vacuum chamber consists of a 20x10 mm rectangular copper guide.

The gun emitted beam was initially fully characterized with the emittance-meter [10]. Then, after the installation conclusion, bunches of 200÷700 pC, with photo-cathode QE of $10^{-5}$ and gaussian laser pulses 6÷8 ps FWHM long, have been accelerated up to 150 MeV with an energy spread of 0.1%. An unexpected degradation of the cathode QE, prevented us to achieve the nominal bunch charge of 1 nC. Main beam parameters like the rms spot-size and emittance [11], bunch charge, length and slice-emittance have been measured and compared with the simulations [12]. The emittance was measured at 500 pC and 8.5 psec FWHM Gaussian pulse. The best projected value is below 2 mm-mrad in both planes, in good agreement with the simulations. Optimal envelope matching conditions have not yet been achieved, but more improvements in beam quality are expected [12]. A preliminary measurement of slice emittance has been also performed, see Fig. 1. The bunch charge was 300 pC, 5.3 FHWM bunch length, at 145 MeV. The result is consistent with the projected emittance value. More details are reported in [8].

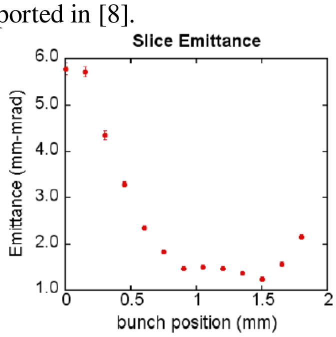


Figure 1: Slice emittance measurements. The slice length has been set to 150 µ i.e. about 0.5 ps.

Initial tests of beam longitudinal dynamics in the VB regime are shown in Fig. 2. The compression factor for 250 pC beam vs the phase of the first RF section is given. A bunch length reduction from 5 to 2.5 psec have been obtained, for $\Delta\Phi$ = 20 degrees.

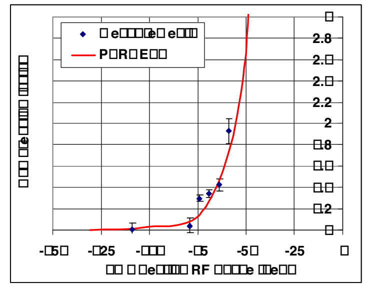

Figure 2: First velocity bunching: compression factor. Comparison between measurements and simulations.

The RFD together with a spectrometer dipole allows to obtain an image of the longitudinal phase space on a downstream screen as shown in Fig. 3.

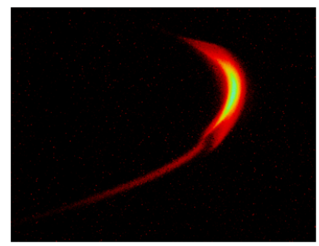

Figure 3: Imaging of long. phase space with the RFD. Beam energy: hor. axis; beam phase vert. axis.

## THE FREE ELECTRON LASER

The FEL will operate in SASE mode at a wavelength of about 500 nm with an expected saturation length of about 10-12 m. Shorter saturation length may be obtained in short e-pulse mode, where VB allows to test the single spike operation [14]. The flexibility offered by the variable gap configuration of the SPARC undulators and the natural synchronization of the electron beam with the laser driving the photoinjector, makes the SPARC layout particularly suited for a number of experiments where the FEL amplifier is seeded by an external laser source. The seed laser is driven by the same oscillator initiating the laser cascade which is used to run the photocathode and consists in a regenerative amplifier delivering 2.5mJ at 800 nm with a pulse duration shorter than 120 fs.

Different schemes of non-linear harmonic generation are then implemented to generate the shorter wavelength radiation for seeding the FEL. Second and third harmonic generation in LBO crystals will provide the powerful pulses required to reach saturation and study the non-linear pulse propagation in FELs and FEL cascades in superradiant regime, at 400 nm and 266 nm [17,18]. The other method considered for the frequency up-conversion of the Ti:Sa fundamental wavelength, is based on the non-linear higher order harmonics generation of the Ti:Sa laser in a gas-cell [19,20]. Injection is obtained with a chicane deflecting the beam from the linac axis and a periscope allowing the injection of the harmonic beam. The system has been aligned, with the laser and the injection periscope, and commissioned. A preliminary test was concluded with the observation of the third harmonic of the Ti:Sa beam with a CCD camera, shown in Fig. 4.

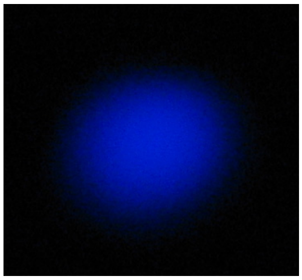

Figure 4: Spot of the UV radiation at the detection screen.

## THE SPARX PROJECT

The SPARX project is the natural continuation of the activity, undertook at LNF, on high brilliance photo-injectors. Supported by the Italian Minister of Reasearch (MIUR) and by the local government Regione Lazio, the project gathers the scientific know-how of three Italian research institutions, CNR, ENEA and INFN, together with the TV-University. SPARX will be an evolutionary project aiming to generate X-FEL radiation from 40 to 0.6 nm. It will be developed in two phases, corresponding to 1.5 GeV and 2.4 GeV, and realized on the grounds of the TV-University, not far from the LNF. SPARX, a user facility for applications in basic science and technology, will be housed in 2 underground 400 m. long overlaying tunnels. Construction and commissioning of the SPARX complex are planned in a 5 years schedule starting from the summer 2009. The 2008 is being dedicated to prepare a Technical Design Report that will be submitted to the funding authorities. The machine is a room-temperature S-band linac, with a 150 MeV SPARC-like pre-injector, followed by successive linac stages and undulator lines, as shown in Fig. 5, which also shows the RF layout consisting of '8+7' 60 MW klystron stations, each feeding three accelerating sections via SLED-type energy compressors. A travelling-wave 11.424 GHz accelerating structure, supplied by a 50 MW peak klystron, provides to linearize the beam longitudinal phase-space [x].

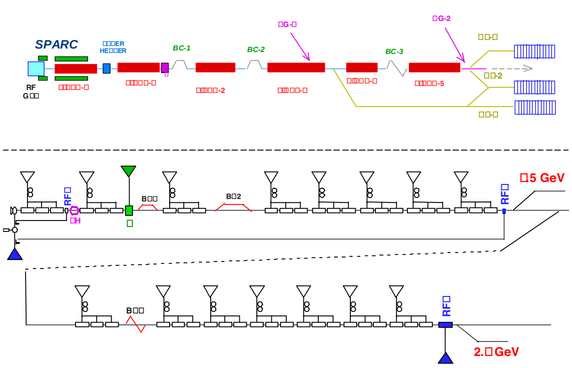


Figure 5: Layout and RF system of SPARX.

To keep the SASE saturation length within a reasonable value, magnetic bunch compressors (BC), between the linac stages, will be used to increase the bunch peak currents to 1÷2.5 kA at 1.5÷2.4 GeV respectively. A laser heater chicane [16] is also foreseen, after the pre-injector, to suppress microbunching instability generated by BC's.

Several operating schemes are being considered for SPARX [17]:

1) SASE operation with harmonic up-conversion;
2) Seeded, single step High Gain Harmonic Generation (HGHG), that is a new scheme for single pass FEL, more compact and capable of generating XUV radiation with better coherence and smaller energy fluctuations;
3) HHG + HGHG: an alternate way to get shorter wavelengths is to use a seed laser operating in VUV domain;
4) Multi stage HGHG cascade, in which the radiation from the first undulator is used as high-power seed for the successive stages;
5) Multi-bunch regenerative amplifier, either self-seeded or externally seeded, in a mirror resonator;. SPARX will be suited to accelerate multi-bunch trains at 357 MHz
6) Single spike operation with ultra-short, small charge beams that may have very high brightness and can drive the SPARX FEL producing ultra-short radiation pulses.

The SPARX Technical Design Report will be presented to the supporting Institutions within 2008. The civil works in the TV campus should start by the spring 2009 and the major contract procurements by the autumn 2009.

## REFERENCES

[1] L.Palumbo et al., "Status of the SPARX Project", EPAC2008.
[2] C.Vicario et al., "Drive Laser System for SPARC", PAC2007.
[3] M. Ferrario et al., Phys. Rev. Lett, 99, 234801 (2007).
[4] L.Serafini, J.Rosenzweig, Phys. Rev. E55 (1997) 7565.
[5] L.Serafini, M.Ferrario, AIP Conference Proceedings, 581, 87, (2001)
[6] R.Boni et al., "The RF System of SPARC", Linac Conf. 2006.
[7] A.Gallo et al., "Performances of the SPARC Laser and RF Synchronization Systems", EPAC2008
[8] C. Vaccarezza et al., "Slice Emittance Measurements at SPARC Photoinjector with a RF Deflector", EPAC2008.
[9] F. Ciocci et al. "SPARC undulator parameter set", SPARC-FEL-03/003.
[10] A. Cianchi et al., "Design Study of a Movable Emittance Meter Device for the SPARC Photoinjector", EPAC2004.
[11] A. Cianchi et al., "Preliminary Characterization of the Beam Properties of SPARC", EPAC2008
[12] C. Ronsivalle et al., "Simulations of the Emittance Compensation in Photoinjectors and Comparison with SPARC Measurements", EPAC2008.
[13] L. Poletto et al., EUROFEL-Report-2005-DS4-008.
[14] V. Petrillo et al., "Single spike operation in the SPARC SASE-FEL", 2008.
[15] O.Tcherbakoff et al., Proc. of FEL 2006 conference, BESSY, Berlin, Germany.
[16] E.Saldin et al., "Longitudinal space charge driven microbunching instability in the TESLA test facility linac", NIM A528 (2004) 355.
[17] R. Bonifacio, L.De Salvo Souza, P.Pierini, and N. Piovella, Nucl.Instrum. & Meth. A 296, 358 (1990)
[18] L. Giannessi, P. Musumeci, S. Spampinati, J. Appl. Phys. 98, 043110 (2005)
[19] T. Brabec, F. Krausz, Rev. Mod. Phys. 72, 545 (2000).
[20] D. Garzella et al., Nucl. Instrum. Methods Phys. Res. Sect. A 528, 502 (2004).

# DEVELOPMENT OF A PHOTOCATHODE RF GUN FOR AN L-BAND ELECTRON LINAC

S. Kashiwagi , R. Kato, G. Isoyama#, ISIR, Osaka University, Ibaraki, Osaka, 567-0047, Japan
H. Hayano, T. Muto, J. Urakawa, High Energy Accelerator Research Organization, Tsukuba, Ibaraki 305-0801, Japan
M. Kuriki, Graduate School of Advanced Sciences of Matter, Hiroshima University, Higashi-Hiroshima, Hiroshima 739-8511, Japan

*Abstract*

We have begun development of the L-band photo-cathode RF gun for the L-band linac at ISIR, Osaka University to advance studies with the high-intensity and low emittance electron beam, in collaboration with KEK and Hiroshima University. As the fist step, we plan to develop and commission the L-band RF electron gun for the Superconducting RF Test Facility at the High Energy Accelerator Research Organization. While waiting for delivery of an RF cavity and an input coupler from the Fermi National Accelerator Laboratory, we are preparing for the low lever RF measurement. Some results of the preparatory works are reported, including computer simulation for tuning of RF characteristics of the cavity, design of an input coupler for low level RF measurement, and computer simulation to evaluate characteristics of the accelerated electron beam.

## INTRODUCTION

We conduct experiments on radiation chemistry by means of pulse radiolysis and basic study on Self-Amplified Spontaneous Emission (SASE) in the far-infrared region using a high-intensity single-bunch electron beam from the 40 MeV, L-band electron linac at the Institute of Scientific and Industrial Research (ISIR), Osaka University. The linac is equipped with a DC 100 kV thermionic electron gun and can accelerate the single bunch electron beam with charge up to 91 nC.

A project to develop and use an L-band photo-cathode RF gun is being conducted at the Superconducting RF Test Facility (STF) at High Energy Accelerator Research Organization (KEK), which is a facility to develop accelerator technology necessary for construction of the main linac of the International Linear Collider (ILC). The aim of the project is to evaluate performance of superconducting accelerating structures using a multi-bunch electron beam that meets specifications given by ILC. A 1.5 cell L-band RF electron gun to produce such an electron beam is being fabricated currently at Fermi National Accelerator Laboratory (FNAL) in USA for the experiment.

In order to advance the studies at ISIR, Osaka University further in future, we joined the project in 2008 and began development of an L-band photo-cathode RF electron gun, which can produce a high-intensity and low emittance electron beam, in collaboration with KEK and Hiroshima University. We will evaluate RF performance of the cavity to be made at FNAL at a low RF level and then will conduct its high power test. In parallel with the activities, we plan to design an L-band RF electron gun optimized for the L-band linac at Osaka University based on results of the measurement and computer simulation for the FNAL gun.

We currently study how to tune the resonance frequency of the cavity, 1.3 GHz in the π mode, by calculating relations of the frequency and field balance between the half cell and the full cell with variations of the cavity shape and dimensions. We have also begun on design and fabrication of an RF coupler of the coaxial feed type to be used in the low level RF measurement. In this paper, we will report results of electric field calculation for the cavity of the electron gun being made at FNAL, progress of preparation for the low level RF measurement, and results of evaluation of electron beam characteristics calculated with PARMELA.

## L-BAND RF GUN

### *Cavity for Electron Gun*

We begin design study of a cavity for the L-band RF electron gun of the resonance frequency 1300 MHz, based on the design of the 1.5 cell RF cavity being fabricated at FNAL. The L-band RF cavity adopts the same design of the cavity used for the XFEL project in Europe, which has been designed by scaling the cavity for the S-band RF electron gun developed at BNL [1] up to the L-band. Cooling water channels of the cavity are reinforced to endure the high duty cycle RF power [2], and a coaxial RF coupler is adopted to make axial symmetry of the

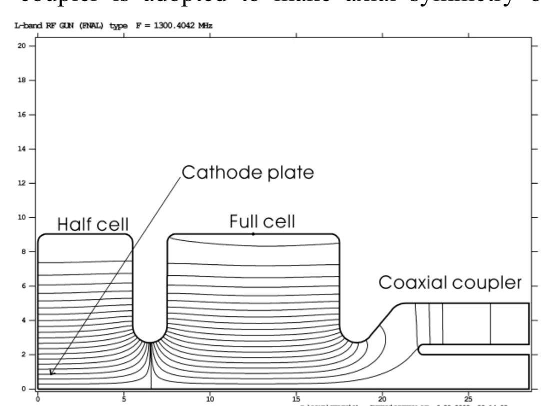


Figure 1: Electric field distribution of the π mode in the L-band RF electron gun.

#isoyama@sanken.osaka-u.ac.jp

electric field higher in the cavity. In any way, the side wall of the cavity is occupied with water channels for cooling and there is no space to install an RF coupler on the wall like the BNL design. Figure 1 shows the shape of the cavity of the L-band RF electron gun and the distribution of the electric field in the $\pi$ mode calculated with SuperFish [3]. The principal dimensions are as follows; lengths of the half and the full cells are 55 and 100 mm, respectively, the diameter of the cells (2b) is ~180 mm, and the radius of the disk (2a) and the downstream aperture of the full cell is ~54 mm.

## *Frequency Tuning*

The final tuning of the FNAL cavity will be made at KEK. The resonance frequency will be adjusted by varying the temperature of the cooling water and the ratio of electric fields in the half cell and the full cell is adjusted by mechanically pressing the cathode wall and the downstream wall of the full cell.

We calculate the frequency variation as a function of the cavity diameter (2b) with SuperFish. The resonance frequency becomes lower by ~15.02 MHz for increase of the radius (b) by 1 mm. The resonance frequency is inversely proportional to the cavity size, provided that the shape is similar, and the cavity size varies with its temperature due to thermal expansion. By taking into account the linear thermal expansion coefficient of copper of $\alpha = 1.6\times10^{-5}$ (1/K), it follows that increasing cooling water temperature by 1°C results in lowering the resonance frequency by 24 kHz. This temperature dependence of the frequency agrees well with the value –22 kHz/°C measured experimentally at DESY. Similarly,

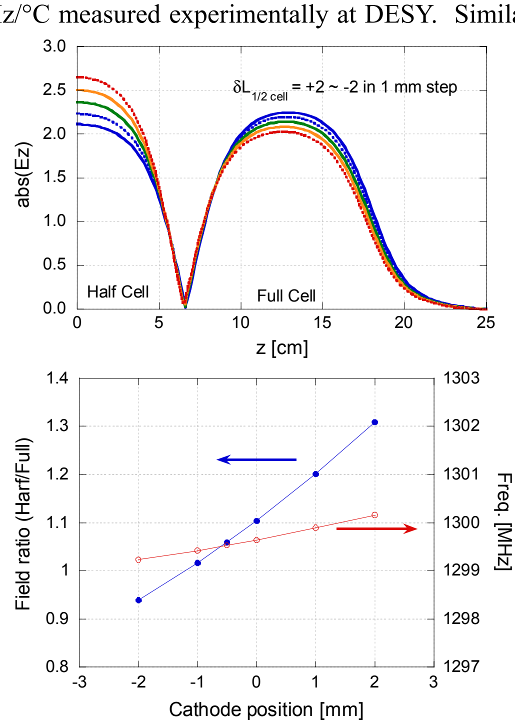


Figure 2: Electric fields on the beam axis for lengths of the half cell varied from –2 to +2 mm in a 1 mm step (top), and the field balance and the resonance frequency as a function of the cathode position (bottom).

we calculate how much the field balance can be changed by pressing the wall for the cathode. As can be seen in Fig. 2, the field ratio varies by 10 % when the length of the half cell is varied by 1 mm. Practically it is not possible to change the cell length more than a few 100 µm, so that the tunable range of the field balance is anticipated to be within a few %.

## *Coaxial Waveguide Converter*

As mentioned above, a coaxial type coupler is used to supply the RF power to the cavity of the RF electron gun. The RF power coming from a source through a rectangular waveguide in the TE01 mode is converted to the TEM mode in the coaxial waveguide using a doorknob type coaxial waveguide converter. The coaxial coupler including this converter will be made at FNAL, but delivery time will be later that that of the cavity, so that we have decided to make a coaxial waveguide converter for the low RF level measurement and the structure of the converter is studied with HFSS [2].

In the design of FNAL, he shorting plate of the waveguide is too close to the center of the coaxial line, so that a part of the doorknob is cut. To make machining of the coupler we will make for the low RF level measurement easier, we study another type of the converter, in which the shorting plate is set enough away

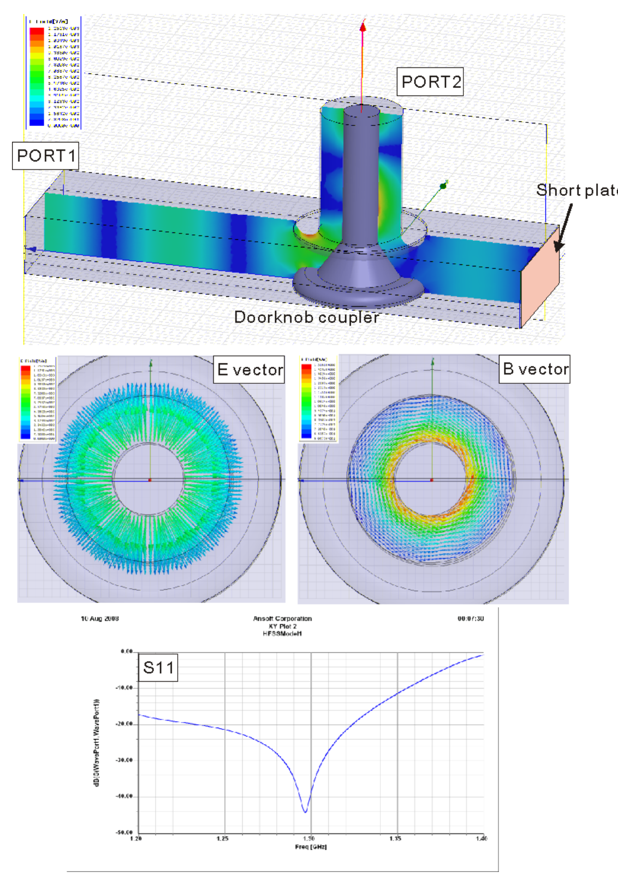


Figure 3: New design of the coupler (top), the electric and the magnetic field distributions at port 2 (middle), and the frequency dependence of S11 (bottom).

from the doorknob so that they do not interfere with each other. Figure 3 shows a three-dimensional drawing of the new type of the converter, the electric and the magnetic field distributions at port 2, and the frequency dependence of S11. In this calculation with HFSS, the shape and sizes of the doorknob are same as those of the FNAL design and the position of the shorting plate is determined to be 223 mm from the center of the coaxial waveguide so that reflection to the input is minimized or S11 becomes minimum. The function of the shorting plate as a capacitive stub is reduced because the plate is apart from the center of the coaxial waveguide, and it is conceivable that the plate works for reflection correction. Although the total length of the waveguide becomes slightly longer than that of the FNAL design, we will make the input coupler with the shorting plate apart from the coaxial waveguide as shown in Fig. 3.

## BEAM SIMULATION

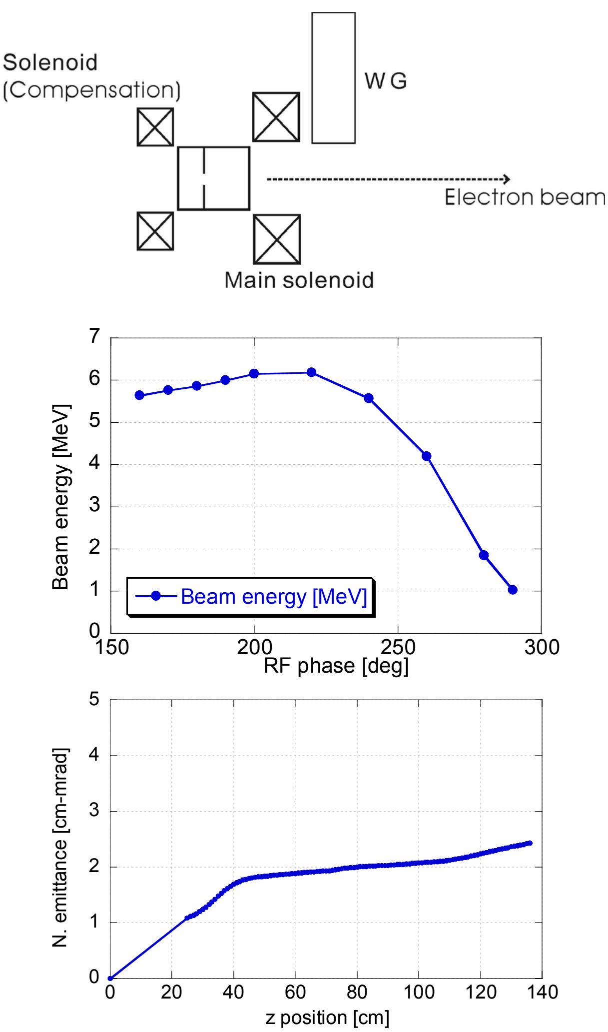


Figure 4: Schematic drawing of the beam line used for calculation with PARMELA (top), beam energy at the exit of the RF gun as a function of the injection phase of the laser (middle), and the normalized emittance in the horizontal direction along the beam line (bottom).

We conduct computer simulation of the beam acceleration with the designed L-band RF electron gun using the computer code, PARMELA. It is assumed that the beam line consists of the cavity for the RF gun, a solenoid coil for emittance correction, and a correction solenoid coil to cancel the magnetic field on the cathode, called as the backing coil, as shown at the top of Fig. 4.

When the electric field is assumed to be 60 MV/m at the cathode, the energy gain in the RF gun is calculated to be ~6.2 MeV at maximum. Figure 4 shows the relation between the injection phase of laser and the energy gain, and an example of the normalized emittance calculated along the beam axis, though parameters such as positions of the coils and strengths of their magnetic fields are not optimized. Values of the parameters used in the calculation are charge 1 nC, the radius of the laser beam 1 mm ($\sigma$), the pulse duration 10 ps ($\sigma$), the injection phase of the laser 220°, and the magnetic field in the solenoid coil 1400 G. It is reported that the normalized transverse emittance of 3 $\pi$ mm·mrad is realized for the charge 1 nC at PITZ (Photo Injector Test Facility at DESY Zeuthen) in Germany [2]. We plan to continue the calculation to optimize the parameters such as the beam size at the cathode, the pulse duration, the injection phase of the laser, and magnetic fields of the solenoid coils.

Because the coaxial coupler is adopted in this L-band RF electron gun, the bore radius of the solenoid coil for emittance correction becomes larger and consequently the gradient of the longitudinal magnetic field dBz/dz is significantly enhanced at ends of the solenoid coil, which deteriorates the emittance of the accelerated beam. It is also impossible to completely diminish and cancel the gradient of the radial magnetic field dBr/dr at the cathode using the backing coil. It is, therefore, important to optimize design and arrangement of the solenoid coils, and dimensions of the coaxial waveguide, especially the radius of the outer conductor. We will conduct thermal calculation of the RF cavity and study new arrangement of cooling water channels, and we will, based on these studies, investigate possibility to install a frequency tuner on the sidewall of the RF cavity.

## ACKNOWLEDGEMENTS

We thank Dr. Ken Watanabe of KEK for his advice on calculation with HFSS. This study is supported by the program of KEK in fiscal year 2008, "Comprehensive Support Program for the Promotion of Accelerator Science and Technology".

## REFERENCES

[1] X. J. Wang et al., Nucl. Instr. and Meth. A 375 (1996) 82-86.
[2] K. Abrahamyan et al., Nucl. Instr. and Meth. A 528 (2004) pp.360-365.
[3] http://laacg1.lanl.gov/laacg/services/serv_codes.phtml
[4] http://www.ansoft.com/products/hf/hfss/

# DEVELOPMENT OF A CS-TE CATHODE RF GUN AT WASEDA UNIVERSITY

Y. Kato[†], K. Sakaue, T. Suzuki, A. Murata, C. Igarashi, A. Masuda, T. Nomoto, A. Fujita, T. Hirose, Y. Hama, M. Washio, RISE, Tokyo, Japan
J. Urakawa, T. Takatomi, N. Terunuma, H. Hayano, KEK, Ibaraki, Japan
S. Kashiwagi, ISIR, Osaka, Japan
R. Kuroda, AIST, Ibaraki, Japan
Y. Kamiya, ICEPP, Tokyo, Japan
M. Kuriki, HU/AdSM, Higashi-Hiroshima, Japan

*Abstract*

A photo-cathode RF-Gun is one of the good alternatives for the electron source, because of its high gradient on the electron emitter causing small beam emittance, and tenability of initial beam profile especially for electron bunch length. Therefore, we are operating as a high brigh-tness short pulse electron source.

In last year, we have been developing a high quality electron source based on photo-cathode RF-gun which is newly designed RF cavity and has a Cs-Te cathode with high quantum efficiency [1] [2]. Improved RF-Gun cavity has four compact tuners on each half cell and full cell, which can be tuned the resonance frequency to deform the cavity wall. Also removing the Helicoflex seal and tuning holes, reduction of the dark current is expected.

According to these improvements, the Q value and shunt impedance of the new RF-Gun cavity increased 20% compared with the previous RF cavity. In addition, the dark current of cavity was reduced and the good electron beam parameters could be achieved compared with pre-vious RF-Gun with a Cu cathode.

## INTRODUCTION

At Waseda University, we have been developing a high quality electron source based on photo-cathode RF-gun and performing the application experiment using high quality electron beam. Until now, we have succeeded the soft X-ray generation via inverse-Compton scattering and pulse radiolysis system for studying the early processes of radiation chemistry using electron beams generated by copper cathode RF-gun as an electron beam application.

Cs-Te RF-gun is expected to generate higher charge electron bunches with a low emittance than a copper cathode because of its high quantum efficiency. Furthermore, its high quantum efficiency enables us to generate a multi-bunch electron beam and to extend the tenability of electron beam parameters for our application experiments [3]. However, a Cs-Te cathode has a relatively short life compared with a copper, so that it has to be exchanged occasionally, thus we have developed a new RF-gun cavity which can be attached the compact cathode load-lock system. Moreover, we improved the design of an existing RF-gun cavity for the reduction of the dark current and the higher electric field.

Figure 1 shows the picture of improved photo-cathode RF-Gun system at Waseda University.

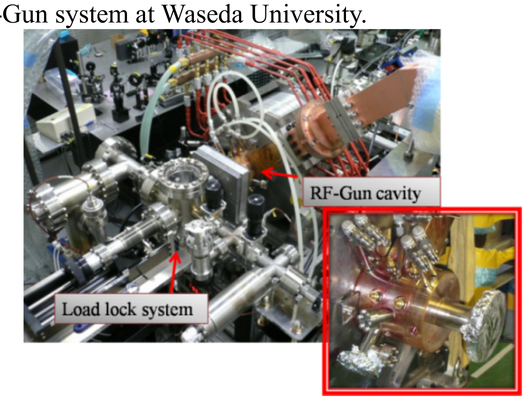


Figure 1: Improved photo-cathode RF-Gun system.

In this conference, the performance of the improved cavity, the results of electron beam generation experiments and the calculated results of beam loading effect of the multi-bunch electron beam generation will be reported.

## IMPROVED DESIGN OF PHOTO-CATHODE RF-GUN CAVITY

The design of a new RF-Gun cavity was based on the conventional type operated at Waseda University and KEK-ATF. Figure 2 (a) shows the previously RF-Gun cavity. It consists of the three components such as a half cell, a full cell, and end plate. The wall of end plate was polished as a Cu cathode and attached to the half cell through a SUS plate and a Helicoflex seal, which can be tuned the resonance frequency of the half cell by changing a torque provided to a Helicoflex seal. Concerning the full cell frequency tuning, each cells are brazed so that resonance frequency of the full cell is tuned by conventional tuner with a tuning hole.

However these tuning methods are considered to be the major cause of electrical discharge and dark current source and Q-value decrease. Therefore, as the improvement of RF-Gun cavity end plate is brazed to the half cell for removing the complicated structure around the

*Work supported by MEXT High Tech Research Project HRC707, JSPS Grant-in-Aid for Scientific Research (B) (2) 16340079
[#]katyu-spring@fuji.waseda.jp

Helicoflex seal and to simply the fabrication procedure. Figure 2 (b) shows improved RF-Gun cavity design.

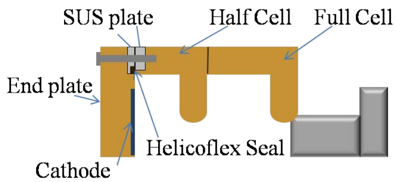


(a) Previously RF-Gun cavity design

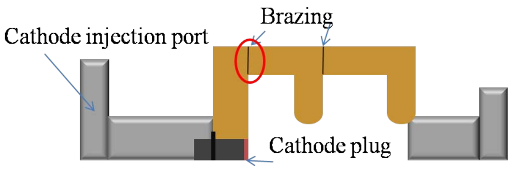


(b) Improved RF-Gun cavity design

Figure 2: Structure of the RF-Gun cavity.

In case of previously RF-Gun, the frequency tuning for the full cell is used by a tuning rod into the hole shown in Figure 3 (a). A new tuning method is also required for the half cell to tune the resonance frequency instead of Helicoflex based tuning method. Therefore, we have developed a new compact tuner using the mechanical deformation of the cavity wall. The new tuner shows Figure 3 (b). By pushing or pulling the cavity wall directly from outside, the inner wall is deformed, so resonance frequency can be tuned.

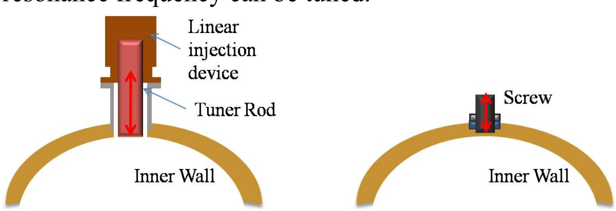


(a) Previously tuner diagram (b) New tuner diagram

Figure 3: Schematic drawings of frequency tuner.

## PARAMETERS OF THE NEW RF-GUN CAVITY

We performed a cavity parameter measurement such as Q-value, coupling constant β and shunt impedance R. Q value and coupling constant β were measured by Network analyzer and shunt impedance R was measured by bead perturbation method. The measured parameter of new RF cavity is shown in Table 1. With the bead perturbation method, R/Q is calculated by eq.1.

$$\frac{R}{Q} = \frac{\left|\int |\Delta f|\, dz\right|^2}{\pi f_0^2 \varepsilon \Delta V} \qquad (1)$$

where, $\Delta f$ is frequency change due to the perturbation, $\Delta V$ is volume of the bead, $\varepsilon$ is permittivity and $f_0$ is resonance frequency of $\pi$ mode.

As a result, effective shunt impedance and Q-value increased 20% compared with the previous RF cavity.

Table 1: RF-Gun Cavity Parameters (previous and new)

| | |
|---|---|
| Resonance frequency | 2854.9[MHz] |
| Q value | 12000<br>7900(previous) |
| Coupling factor β | 1<br>0.6(previous) |
| R/Q | 356[Ω]<br>240[Ω] (previous) |
| Shunt impedance [MΩ] | 4.4[MΩ]<br>1.87[MΩ] (previous) |

## EXPERIMENTS

### *Dark Current Measurement*

Dark current generated by the new cavity was measured by using Faraday cup. Figure 4 shows the comparison of dark current from each the previous RF cavity and the new RF cavity when 10MW power and 2.0μsec pulse was applied.(Typical operation parameters at Waseda University). It is much lower than that of the previous RF cavity with a Cu cathode at the same RF accelerating field. According to this result, we have successfully per-formed reduction of dark current at same RF power in the cavity. It is found that this effect make accelerating fields much higher.

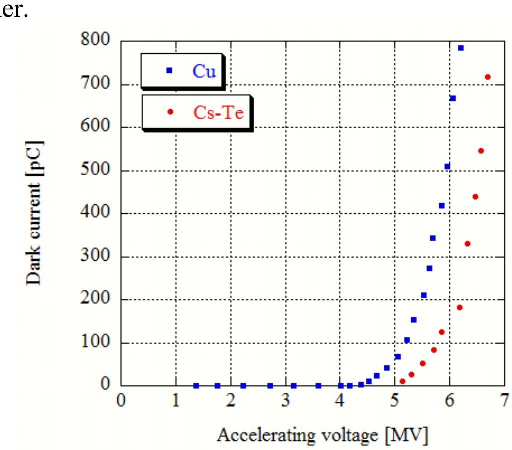


Figure 4: Result of dark current measurement.

### *Electron Beam Charge & Energy Measurement*

Figure 5 shows one of the results of electron beam charge and energy measurements. We were able to achieve the higher charge and energy than previous RF-Gun. Table 2 shows beam parameters with new RF-Gun with a Cs-Te cathode that is obtained significantly higher than that of previous RF-Gun with a Cu cathode. At Table 2, "*" means that will be measured in near future.

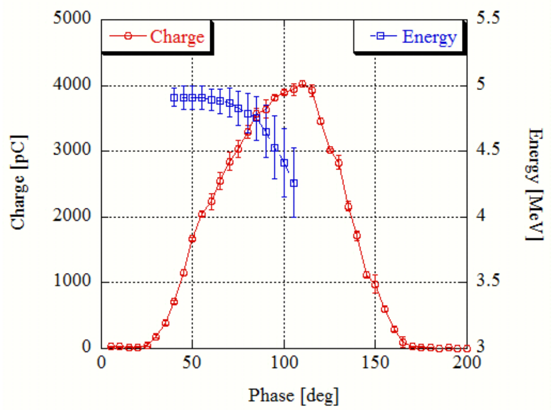


Figure 5: Charge and Energy Measurement as a function of laser injection RF phase.

Table 2: Electron Beam Parameters (previous and new)

| | Previous RF-Gun (Cu cathode) | New RF-Gun (Cs-Te cathode) |
|---|---|---|
| Charge | ~1[nC/bunch] | 4[nC/bunch] |
| Energy | ~4.6[MeV] | 5[MeV] |
| Energy spread | 1~[%] | 0.6[%] |
| Emittance | 3~[πmm mrad] | *[πmm mrad] |

## MULTI-BUNCH BEAM LOADING CALCULATION

In accelerating a multi-bunch electron beam, an electrical field which causing by the former electron bunches, decrease the accelerating field of latter electron bunches. So in accelerating multi-bunch beam at linac, energy difference should be caused between former bunch and latter bunch.

The beam loading effect which affects the Nth electron bunch is calculated as

$$V_{b,N} = \frac{\omega_0 Rsq}{2Q_0}\left(\frac{1-e^{-(N-2)\tau}}{1-e^{-\tau}} - \frac{1}{2}\right) \tag{2}$$

where $\omega_0$, Rs and $Q_0$ are the resonance frequency, the shunt impedance and unloaded Q-value of the acceleration cavity respectively. $\tau$ is expressed with the filling time of the cavity $t_f$ and bunch distance $t_b$ as

$$\tau = \frac{t_b}{t_f} \tag{3}$$

$$t_f = \frac{2Q_0}{\omega_0(1+\beta)} \tag{4}$$

where $\beta$ is the coupling constant of the input coupler. Flat energy multi-bunch electron beam is necessary for multi-pulse inverse Compton scattering [3]. So we have to compensate this effect. We are planning to com-pensate the effect by as adjusting the RF pulse timing.

$$V_{RF} = \frac{2}{1+\beta}\sqrt{\beta R s P_0}\left(1-e^{-\frac{t}{t_f}}\right) \tag{5}$$

where $P_0$ is the RF peak power. A numerical calculation of this method is shown in Figure 6 and calculation parameters are shown in Table 3. A red plots is a cavity voltage without beam loading effect. A blue plots shows the acceleration voltage of each electron bunch. Balancing the rising edge of RF and beam loading effect, energy difference in a pulse train is controlled to be 1.9%. If this method is not sufficient, we would consider modulating RF pulse wave shape.

Table 3: Parameters for Beam Loading Effect

| | |
|---|---|
| Filling time | 0.67[μsec] |
| Bunch distance | 8.4[nsec] |
| RF peak power | 10[MW] |
| Bunch Charge | 700[pC] |
| Number of electron bunches | 100bunches/train |

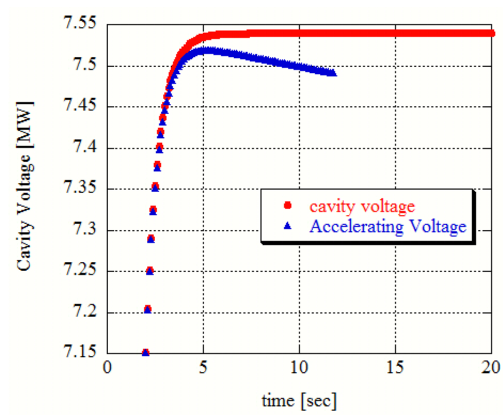


Figure 6: Numerical calculation of beam loading effect.

## CONCLUSIONS&FUTURE PLANS

According to our investigation of new design RF-Gun cavity, the Q-value and the shunt impedance improved 20% larger than previous RF-Gun cavity. As a result, reduction in the dark current has been successfully performed, and the electron beam parameters were also confirmed to be better by comparison with previous RF-Gun cavity.

As a future plans, emittance measurement of an electron beam emitted from improved RF-Gun and high quality multi-bunch electron beam generation will be performed.

## REFERENCES

[1] Y. Kamiya, et al., Proc. of EPAC'07, THPMN040 (2007)
[2] A. Murata, et al., Proc. of EPAC'08, MOPP074 (2008)
[3] A. Masuda, et al., Proc. of EPAC'08, MOPC043 (2008)

# RF GUN DEVELOPMENT WITH IMPROVED PARAMETERS

V. Paramonov *, Yu. Kalinin, INR RAS, Moscow,
M. Krasilnikov, T. Scholz, F. Stephan, DESY, Zeuthen,
K. Floettmann, DESY, Hamburg

During development and operation of DESY L-band RF gun cavities, desires for further improvements were formulated. The next step of development is based on the proven advantages of existing cavities, but includes significant changes. The L-band 1.6 cell RF gun cavity is intended for operation in pulse mode with electric fields at the cathode of up to $60\frac{MV}{m}$, RF pulse length of $\sim 1ms$ and average RF power higher than existing gun cavities. In the new design the cell shape is optimized to have the maximal surface electric field at the cathode and lower RF loss power. The cavity cells are equipped with RF probes. Cooling circuits are designed to combine cooling efficiency with operational flexibility. In the report, the main design ideas and simulation results are described.

## INTRODUCTION

In the development and optimization of the high brightness electron sources for Free Electron Lasers (FELs) and linear colliders several RF gun cavities, starting from TTF Gun [1] and differing mainly in the cooling circuit design, were constructed and studied. The last results for the Gun cavities developed can be seen in [2]. Experience of operation and results of various Gun cavity parameters study are the basement of desires and ideas for further improvements. In the next step of development more significant changes are required, starting from cavity RF shape. The influence of proposed improvements on different cavity parameters should be considered and analyzed carefully.

## RF CAVITY SHAPE

The profile of existing DESY 1.6 cell axial symmetrical RF Gun cavities [1] is shown in Fig. 1a together with electric field distribution. This cavity is considered further as the Reference Cavity (RC) and has the circular iris nose tip. The primary parameter of the RF Gun cavity is the RF electric field strength $E_c$ at the photo cathode surface. The maximal electric field at the cavity surface $E_{sm}$ in RC is at the iris tip and $E_{sm} \approx 1.2E_c$.

In the improved cavity, which is also 1.6 cell, Fig. 1b, the circular iris tip is replaced at the elliptical one. Dimensions are optimized to have $E_{sm} = E_c$. Together with $E_{sm}$ reduction by $\sim 20\%$, the elliptical nose shape results in increasing of the coupling coefficient between cavity cells and related mode separation. The iris nose shape has no influence at the cavity quality factor $Q_0$ and de-

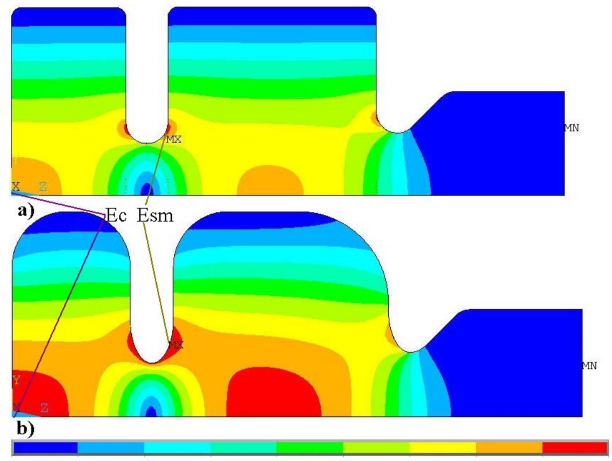


Figure 1: RF shape profile for the reference (a) and improved (f) cavity together with electric field distributions.

creases slightly $\frac{E}{\sqrt{W_0}}$ ratio, where $W_0$ is the stored energy. More RF power is necessary to get $E_c$ required with the same $Q$. Cavity $Q$ factor is increased by stronger rounding in the outer cell shapes. Different rounding combinations were considered. From practical reasons we chose the same outer radius for both cells and the same rounding radius in the first cell and in second cell near iris. The cavity operating frequency is adjusted by outer cell radius. The maximal field strength at the axis of the cells is equalized by adjusting the another radius of the second cell rounding. As the result, the cavity $Q$ factor is increased by $\sim 10\%$ and required RF pulse power is less by $\sim 4\%$. Even taking into account effects of RF pulsed heating effects and cavity parameters change during RF pulse, [3], lower RF pulse power is required for improved cavity to get required $E_c$ value.

## BEAM DYNAMIC

The cavity shape change results in small deviations of electric field distribution along the cavity and can change beam parameters. All combinations of shapes, discussed in cavity RF profile definition, were analyzed in simulations with the ASTRA code considering the European XFEL photo injector performance. Simulations revealed no essential difference for various cavity options, including RC and improved option, Fig. 1b. Optimized projected emittance for all cavity types is about the same, within simulations discrepancy. Slice parameters of the electron beam are also very similar. Optimum currents of main solenoid are within several $A$. Spread of optimum $rms$ sizes of the

* paramono@inr.ru

cathode laser is within $2\%$. The beam dynamic requirements are not a restrictions for the proposed cavity shape changes.

## PROBES

Each cavity cell has an antenna type RF probe, placed at the cavity cylindrical side. Longitudinal probe position is fixed by cavity and cooling circuit design. To minimize RF pulsed heating effect at the probe hole edges, and perturbation of azimuthal field symmetry, the probe hole radius $r_h$ should be as small as reasonable. Sharp hole edges are not acceptable and should be rounded with a radius $r_b = r_h/2$. For $E_c = 60\frac{MV}{m}$ the expected magnetic field near the cavity wall is $\approx 92\frac{kA}{m}$, corresponding to a pulse RF loss density $P_d \approx 3.8\frac{kW}{cm^2}$ and surface temperature rise $T_s \approx 34C^o$ after $\tau = 1ms$ RF pulse. In the vicinity of the probe hole the magnetic field distribution is perturbed with local increasing up to $P_d \approx 7.5\frac{kW}{cm^2}$ and $T_s \approx 67C^o$ for $r_h = 2mm$. Hole edges rounding is required both for local $P_d$ reduction and for smooth stress distribution. The stress values due to RF pulsed heating are proportional to $T_s$ [3] and after $\tau = 1ms$ RF pulse the maximal stress value is estimated below yield strength of OFC copper.

To cancel the dipole component in the field perturbation and to have as lowest component a quadruple one with zero field at the cavity axis, additional holes just opposite to existing are required. It looks attractive to use additional holes for vacuum probes. But consideration of sensitivity and response time for vacuum probes connected to cavity cells through narrow hole, optimized for RF probes, have shown vacuum sensors are not useful. Additional holes are foreseen as blind.

Required probe matching can be obtained without problems for a small probe hole radius, because for $\sim 1W$ RF signal at the probe we need attenuation $\approx 67dB$.

## COOLING CIRCUIT

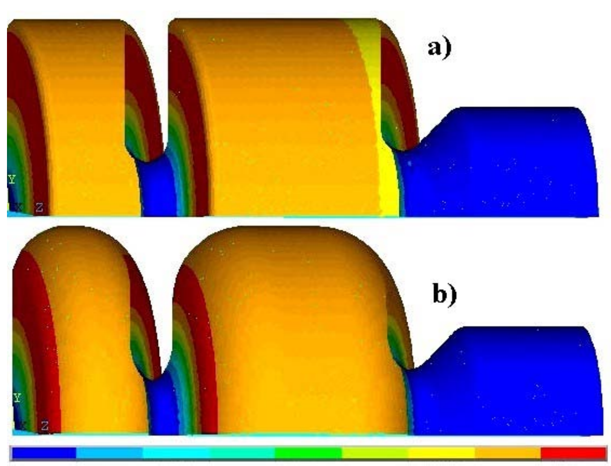


Figure 2: RF loss density distribution at the cavity surface for RC (a) and improved cavity (b). Arbitrary units.

Calculated pulse RF power values to get $E_c = 60\frac{MV}{m}$ are $P_i = 6.43MW$ for RC and $P_i = 6.18MW$ for improved cavity. For $10Hz$ repetition and $\tau = 1ms$ operation it results in average dissipated power $P_{av} \sim 65kW$ and the cavity should have an advanced cooling circuit. The distributions of RF loss density at the cavity surface are shown in Fig. 2a,b for RC and improved cavity. As one can see from Fig. 2, there is no essential qualitative difference in distributions. Cooling circuits for existing cavities are studied both in numerical simulations, see, for example [4], [5], and during cavities operation, generating ideas for improvement.

In cooling with turbulent flow a heat exchange between a cavity body and coolant takes place in a narrow boundary layer and the temperature near the center of the channel cross section is lower than near boundary. For efficient cooling we need a large amount of channels with large total surface area. The cavity surface temperature difference with respect input coolant temperature can be subdivided in three components - natural temperature drop in heat propagation from cavity surface to cooling channel surface, temperature rise in boundary layer in heat exchange with turbulent flow and bulk coolant temperature increasing in coolant motion. The distance from cavity surface to cooling channels is minimal to ensure the cavity rigid design. Large total surface area of channels is required to keep reasonable the second component. Cross section area of channels is important only to provide required flow to restrict the third component.

To have a large number of small cooling channels, we

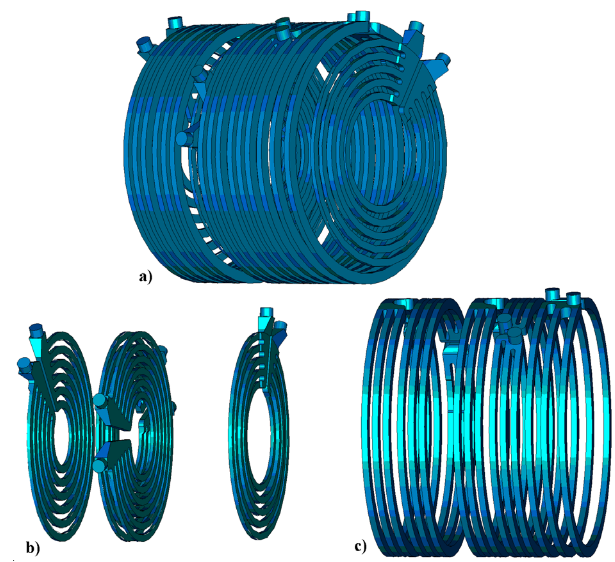


Figure 3: Proposed cooling circuit (a) consists from cooling channels for radial walls (b) and outer walls (c).

can have independent channels inside the cavity with large amount of input/output outlets and advanced distributing system outside the cavity. Proposed cooling circuit is shown in Fig. 3 and utilizes channels with flow distribution inside the cavity. The circuit has 9 cooling channels, divided in two groups. For outer wall cooling 5 channels are proposed, Fig. 3c, with three sub channel each. These channels are equalized in hydraulic resistance and equal flow velocities in sub channels. The pressure distribution at the channel surface for RF probe region is shown in Fig. 4. Four channels for radial walls cooling, Fig. 3b, have

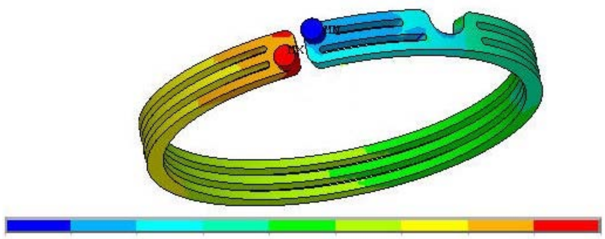

Figure 4: The pressure distribution at the surface of the channel for the RF probe region.

more complicated flow distribution. Pressure and flow velocity distributions in the channel for iris cooling are shown in Fig. 5. The flow velocities and flow rates in sub channels of channels for radial walls cooling are fitted to reflect the RF loss radial profile.

As second option for cooling channels, at least for comparison, we consider more conservative version without flow distribution within the cavity.

For cooling circuit simulations we use two approaches. In

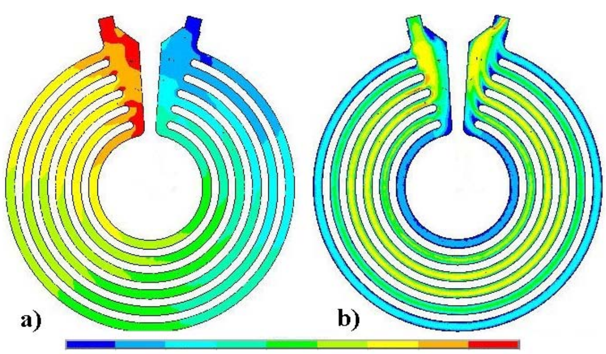


Figure 5: Pressure (a) and flow velocity (b) distributions in the channel for iris cooling.

the well known engineering approach, Fig. 6c,f, the cooling channels are considered at constant temperature and a heat exchange coefficient is defined from semi-empirical relations. In conjugated approach we specify coolant properties and pressure drop, simulate turbulent flow local parameters and solve heat exchange problem both for cavity body, Fig. 6b,e, and moving coolant flow, Fig. 6a,d. The conjugated approach provides a more logical physical picture for temperature distribution and allows to investigate in more detail particularities of flow distribution both in cooling channels itself and between connected channels, but is consuming much more in computer resources.

Comparison of calculated and measured data in DESY Gun 3 cavity have shown calculated results in temperature rise $\approx 25\%$ lower than measured. Extensive set of heat exchange experiments (hot water - cold water) has been performed to have the data for numerical model parameters calibration. This calibration now is in progress. The final results for temperature distributions in the gun cavity under development will be obtained with calibrated numerical models.

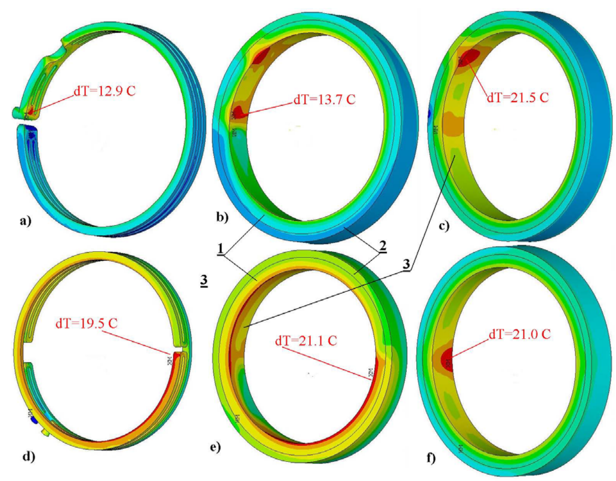


Figure 6: Temperature distributions at the surface of channels (a),(d) and at the composed ring, simulated with conjugated (b),(e) and engineering (c),(f) approaches. 1 - copper, 2 - stainless steel, 3 - surface with applied heat flux.

## CAVITY DESIGN

The cavity general design is strongly based on the proven advantages of existing cavities. The cavity consist from three parts to simplify parts fabrication. Cavity has a stainless steel jacket, also segmented in three parts. It improves cavity rigidity and decreases cavity expansion in radial direction due to cavity heating. It results in decreasing of the frequency shift due to both average and pulsed RF heating. Brazing technology is foreseen to connect cavity components without water - vacuum brazed joints. The technique for iris cooling channels placement in existing cavities is applied to all channels for radial walls cooling.

## REFERENCES

[1] B. Dwersteg, K. Floettmann, J. Sekutowicz, Ch. Stolzenburg. RF gun design for the TESLA VUV Free Electron Laser, NIM A 393, p.93-95, 1997.

[2] F. Stephan et al., New Experimental Results from PITZ. This Conference.

[3] V. Paramonov et al., Pulsed RF heating particularities in normal conducting L-band cavities. Proc. Linac2006, p. 646.

[4] F. Marhauser. Finite Element Analyses for RF Photoinjector Gun Cavities. TESLA FEL Report 2006-02, DESY, 2006.

[5] K. Floettmann et al., RF Gun Cavities Cooling Regime Study. TESLA-FEL Report 2008-02, DESY, 2008.

# MEASUREMENTS AND MODELING AT THE PSI-XFEL 500 kV LOW-EMITTANCE ELECTRON SOURCE

T. Schietinger, A. Adelmann, Å. Andersson, M. Dietl, R. Ganter, C. Gough, C.P. Hauri, R. Ischebeck, S. Ivkovic, Y. Kim, F. Le Pimpec, S.C. Leemann, K. Li, P. Ming, A. Oppelt, M. Paraliev, M. Pedrozzi, V. Schlott, B. Steffen, A.F. Wrulich,
Paul Scherrer Institut, CH-5232 Villigen PSI, Switzerland

*Abstract*

Paul Scherrer Institute (PSI) is presently developing a low-emittance electron source for the PSI-XFEL project. The electron gun consists of an adjustable diode configuration subject to pulses of 250 ns (FWHM) with amplitude up to 500 kV from an air-core transformer-based high-voltage pulser. The facility allows high gradient tests with different cathode configurations and emission processes (pulsed field emission and photo emission). In the first stage, the beamline consists of focusing solenoids followed by an emittance monitor. Selected beam characterization measurements from photo cathode operation driven by a 266 nm UV laser system delivering 4 μJ energy during 6.5 ps (RMS) are presented and compared to the results of 3D particle tracking simulations.

## INTRODUCTION AND MOTIVATION

The goal of the PSI-XFEL project is the realization of an X-ray Free Electron Laser (FEL) operating in the wavelength range between 1 and 100 Å and producing up to $10^{12}$ photons per pulse at a repetition rate of 100 Hz. To keep spatial and financial requirements within reasonable limits, the project foresees a compact design featuring a 6 GeV S-band main linac. This compact layout requires a high-brightness electron beam, which in turn calls for a low-emittance source. The strategy chosen for the PSI-XFEL project consists in utilizing a high-voltage pulsed diode providing fast acceleration with a special cathode optimized for low emittance (photo cathode or field emitter array). To evaluate various configurations and materials, a test stand has been set up at PSI consisting of a pulser, a laser system and a diagnostic beamline [1]. Figure 1 gives an overview of the pulser and beamline assembly.

An important aspect of the test facility, in particular in view of the further advancement of the PSI-XFEL project, is to improve the understanding of the space charge dominated electron beam by way of simulation. Indeed, one of the objectives of the test facility is the validation of our 3D particle tracking code against observations. In this paper we present a set of measurements taken at the test facility and compare it to the result of a 3D particle simulation.

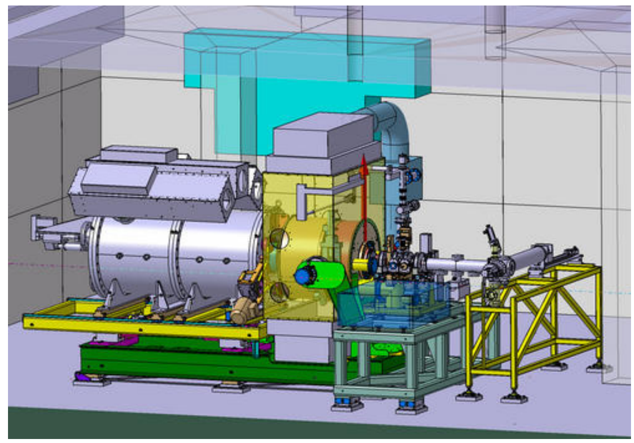

Figure 1: Schematic view of pulser (left) and diagnostic beamline, including the emittance monitor (right).

## EXPERIMENTAL SETUP

The air-core transformer-based high-voltage pulser delivers pulses of 250 ns (FWHM) with amplitude up to 500 kV [2]. The diode gap between two mirror-polished electrodes is adjustable between 0 and 30 mm. Electrodes manufactured from stainless steel have been found to withstand the highest gradients and generally to offer the most stable experimental conditions for beam measurements. The measurements described here were performed with hand-polished stainless steel electrodes separated by 7 mm at a voltage of 313 kV, corresponding to a gradient of 44.7 MV/m. The chosen gradient represents a compromise between high accelerating field and stable operation with this particular set of electrodes.

The metallic cathode is illuminated by laser pulses when the applied voltage across the anode-cathode gap is at maximum. The laser light enters the electron beamline from a side viewport and is reflected towards the cathode by a 5 mm × 5 mm mirror. The mirror edge is at least 5 mm away from the electron beam axis. The laser pulses, generated by a Nd:vanadate (Nd:VAN) passively mode locked picosecond system, feature a Gaussian time profile ($\sigma_t$ = 6.5 ps). The transverse profile is also Gaussian, with spatial dimensions controlled by a two-lens telescope assembly and monitored via a “virtual” cathode: a reflexion from the entrance viewport is monitored on a small optical table beside the beamline, at a distance equal to that between viewport and cathode. The maximum optical energy per pulse at the laser exit can reach about 12 μJ at laser exit and reduces to about 4 μJ at the pulser viewport entrance after ten meters of transport through an evacuated pipe and various optical components.

The diagnostic beamline includes five solenoid magnets, an emittance monitor and an additional YAG screen for transverse beam characterization upstream of the emittance monitor. A wall current monitor and a Faraday cup provide non-destructive and destructive bunch charge measurements, respectively. Only the first four solenoids were powered during the measurements described here.

The emittance monitor was specifically developed to cover the wide range of beam charges and energies [3]. Given the constraints of a space charge dominated, low-energy electron beam with possibly significant shot-to-shot fluctuations the pepper-pot measurement technique was chosen [4].

In our setup, the retractable pepper-pot mask is a laser-beam machined tungsten disk of 200 μm thickness. The 20 μm diameter holes are separated by 250 μm in both dimensions and extend over an area of 5 mm × 5 mm. An image of the beamlets is portrayed onto a 50 μm thick YAG screen, whose light is deflected by an out-coupling mirror under an angle of 90° into a telescope equipped with a firewire CCD camera. The optical resolution of the imaging system is about 10 μm. Both mask and screen are mounted on stainless steel sliders inside a 900 mm UHV chamber and can be moved individually over a distance of 600 mm along the beam axis, allowing for a wide range of experimental setups. The YAG screen of the emittance monitor can also be used for other measurements of transverse beam properties (beam envelope scans).

No longitudinal information such as beam energy and bunch length is obtained from this setup. For the simulation we assume that the electron bunch features the same Gaussian time profile as the laser pulse generating it.

## BEAM MEASUREMENTS

The transverse beam sizes are defined as the root-mean-square (RMS) of the particles' horizontal and vertical positions. For the observed beam, this is approximated by the widths obtained from Gaussian fits to beam image projections. The beam profile was measured with the first YAG screen at a distance of 498 mm from the cathode, and with the movable second YAG screen at distances ranging between 790 and 960 mm from the cathode.

The transverse beam emittance is estimated from images of the beam after its passage through the pepper-pot mask. The distance between mask and screen was kept at its minimum of 30 mm, for which the precision of the emittance measurements is highest. We perform 1D analyses on the two projections of the image. The resulting histograms are divided into bins covering one beamlet each. An evaluation of the RMS emittance requires beamlet centroids and widths. While the beamlet centroid is derived from the bin centroid, its width cannot simply be obtained from the RMS of the bin distribution due to the effects of background and overlapping beamlets. We therefore use full widths at various heights to estimate both the Gaussian width and the background level of an individual beamlet, after subtraction of a global background. The error on the resulting emittance is estimated by variation of all input parameters, including the background subtraction, within their respective uncertainties. Figure 2 shows the intensity pattern of a typical pepper-pot image. The emittance was measured at distances of 750, 830 and 890 mm from the cathode, with results around 1 mm mrad (see Fig. 3).

The bunch charge was determined to be about 20.7 pC by integration of the Faraday cup signal.

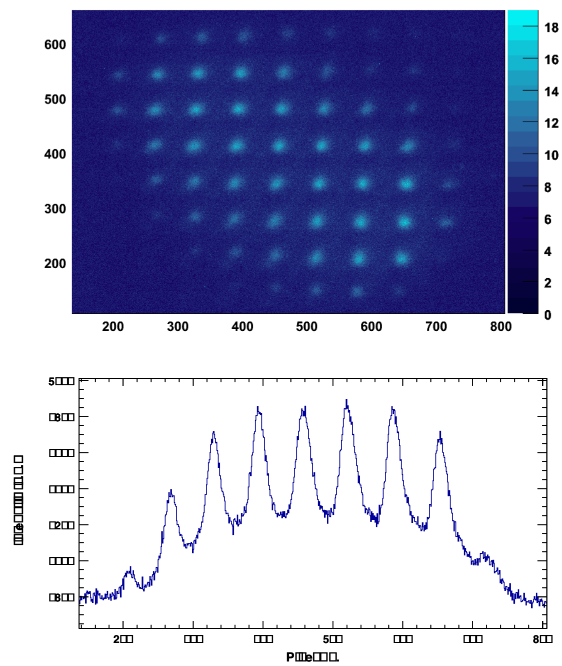


Figure 2: Detail of a typical pepper-pot raw image (top) with corresponding projection (bottom).

## SIMULATION TOOL

For the 3D particle simulation we use the Object-oriented Parallel Accelerator Library (OPAL) developed at PSI [5]. OPAL-T is a parallel time-dependent particle-in-cell code that uses a space charge solver based on an integrated Green function [6] and a set of easily adjustable beamline elements to compute trajectories of macro-particles in 3D space. Running in parallel on a distributed memory cluster it can handle the large particle numbers needed for detailed slice emittance and beam halo studies.

To simulate the beam generated at our test facility we track a minimum of $10^6$ particles on a $32\times32\times64$ moving mesh. Electrons with a Gaussian spatial distribution are emitted from the cathode with a Gaussian time profile, where the widths correspond to the measured values ($\sigma_x$ = 330 µm, $\sigma_x$ = 370 µm). The electrons leave the cathode in parallel with 1 eV kinetic energy, i.e., no microscopic properties of the cathode are taken into account. The beamline elements (diode and solenoids) are described by field maps, i.e., equally spaced samplings of the fields, which are then internally interpolated to the particle positions. The field maps for our setup were produced with Poisson/Superfish [7]. Inside the diode field the simulation advances in time steps of 0.1 ps, whereas in the ensuing beamline the time step is 1 ps. The solver parameters were derived from convergence studies observing RMS quantities such as beam size and emittance.

For the interpretation and visualization of the results we use H5Part [8], a portable high performance parallel data interface to HDF5 in conjunction with ROOT [9], an object-oriented data analysis framework developed at CERN.

## COMPARISON BETWEEN MEASUREMENTS AND SIMULATION

Small adjustments to the beam optics were necessary to match the observed beam sizes. Such adjustment is expected at some level, since the solenoid field measurements were not carried out *in situ* (in the presence of the beamline), but in an isolated environment. We found that lowering the field strengths of the first three solenoids by 5% while increasing that of the fourth by 9% brings measured and simulated beam sizes in reasonable agreement.

The emittance of the simulated beam features a prominent minimum of just above 2 mm mrad, near the waist in the region of the emittance monitor. The measured values are considerably lower, around 1 mm mrad, and their precision is insufficient to confirm the predicted minimum. Closer inspection of the simulated beam reveals a large halo in the region of the emittance monitor, the origin of which is still being studied. The large, but sparsely populated halo has a considerable effect on the RMS emittance. To exhibit the effect of the halo in the simulation we also plot the emittance as obtained considering only the central 90% particles (in the transverse plane). Figure 3 summarizes the comparison between measurements and simulation for the horizontal plane.

## CONCLUSION AND OUTLOOK

We have presented a first comparison between measurements made at the 500 keV PSI low-emittance gun test facility and the results of our own 3D particle tracking code. While there is reasonable agreement for the beam envelope, further study is needed to understand the details of both measured and simulated emittances.

The test facility is currently being upgraded with a two-cell RF cavity allowing acceleration of the beam up to an energy of 4 MeV. The upgrade includes various additional diagnostic elements, in particular an energy spectrometer.

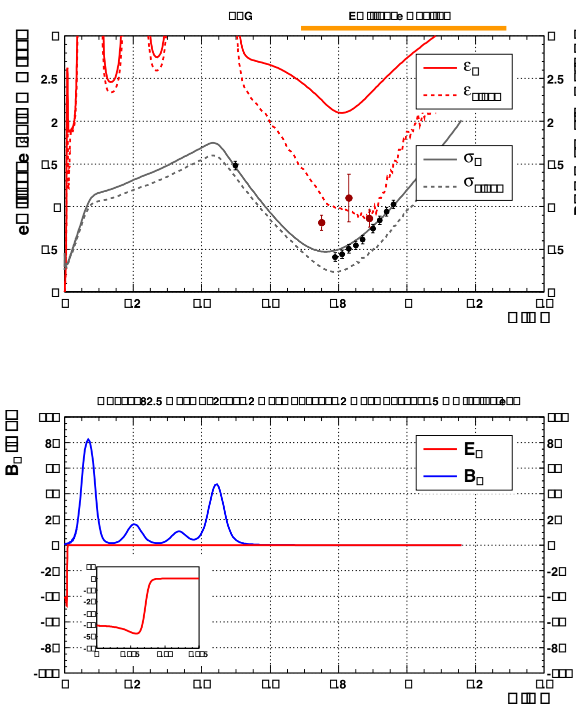

Figure 3: Top: Comparison of simulation results (solid and dashed lines) with measurements (points with error bars). See text for details. Bottom: Magnetic and electric field strengths entering the simulation drawn on the same horizontal scale.

## REFERENCES


[1] M. Pedrozzi et al., in Proceedings of the European Particle Accelerator Conference (EPAC), Genoa, Italy, 2008, p. 169.

[2] M. Paraliev, C. Gough, S. Ivkovic, in Proceedings of the IEEE International Power Modulator Conference, Las Vegas, NV, USA, 2008.

[3] V. Schlott et al., in Proceedings of the European Workshop on Beam Diagnostics for Particle Accelerators (DIPAC), Venice, Italy, 2007.

[4] C. Lejeune, J. Aubert, Adv. Electron. Electron Phys., Suppl. 13A (1980) 159.

[5] A. Adelmann, Y. Ineichen, Ch. Kraus, S. Russell, J. Yang, PSI report PSI-PR-08-02, unpublished.

[6] Ji Qiang, S. Lidia, R.D. Ryne and C. Limborg-Deprey, Phys. Rev. ST Accel. Beams 9 (2006) 044204.

[7] J.H. Billen and L.M. Young, Poisson Superfish V 7.06 User Guide, LANL Report No. LA-UR-96-1834, revised version (2003).

[8] A. Adelmann et al., in Proceedings of Particle Accelerator Conference (PAC), Albuquerque, NM, USA, 2007, p. 3396.

[9] ROOT, an object-oriented data analysis framework, `http://root.cern.ch`.

# LIENARD-WIECHERT POTENTIALS AND METHOD OF IMAGES IN RF FREE ELECTRON LASER PHOTOINJECTOR

W. Salah; The Hashemite University, Zarqa 13115, Jordan, R.M. Jones; Cockcroft Institute, Daresbury, WA4 4AD, UK; University of Manchester, Manchester, M13 9PL, UK.

*Abstract*

Based on Lienard-Weichert retarded potentials and the potential due to the image of charges on the cathode, a rigorous relativistic description of the beam transport inside the RF-photoinjector is presented. The velocity dependent effects are taken into account. Simulations are presented for parameters of the "ELSA" photo-cathode.

## INTRODUCTION

RF-photoinjectors are used as a source of low-emittance and ultra-high brightness electron beams. There are a limited number of codes which take wakefield effects into account in computing electron transport in photoemission. Although there are notable exceptions which do include these effects numerically [1]. The electromagnetic wake in a photoinjector is different from the standard case of a coasting ultrarelativistic beam due to the rapidly changing velocity. In this situation the influence of the acceleration-radiation field, or retardation, must be taken in to account in addition to the image charges on the cathode.

The aim of the present paper is to treat the wakefield of an intense electron beam strongly accelerated inside a cylindrical cavity similar to that of a photoinjector. We employ both Lienard-Weichert potentials and the method of images in order to derive an analytical expression for the field driven by the beam. Electromagnetic field expressions are computed for the "ELSA" photoinjector facility [2] schematized in Fig. 1. Furthermore, by applying the principle of causality we are able to simplify the effects associated with the actual cavity, illustrated in Fig. 1, to an analysis of the electromagnetic fields in a pill-box cavity.

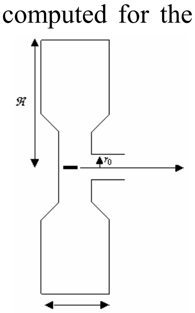

Figure 1: "ELSA" photoinjector (144 MHz cavity).

The beam pulse is assumed to be axisymmetric, of radius $a$, emitted by the cathode from $t = 0$ to $t = \tau$ (where $\tau$ is the time at which the photoemission ends), with a constant and uniform current density J. The acceleration RF-electric field $\vec{E}_0$ may be considered as constant and uniform provided, the beam pulse duration $\tau \ll 1/\nu$ (where $\nu$ is the RF frequency) and the beam radius $a$ is small compared to the cavity radius $\Re$. For the "ELSA" photoinjector $\nu$ = 144 MHz, $\Re$ = 60 cm, $\pi a^2 = 1$ cm$^2$; the first condition provides the pulse duration $\tau \ll 7$ ns. Under these conditions, the beam velocity $\vec{\beta}(z,t)$ and acceleration $\vec{\eta}(z,t)$ can be shown [3] to be parallel to $\vec{E}_0$ and independent of time:

$$\vec{\beta}(z,t) = \beta(z)\,\vec{u}_z \qquad \vec{\eta}(z) = \eta(z)\,\vec{u}_z \tag{1}$$

$$\beta(z) = \frac{\sqrt{(1+Hz(t))^2 - 1}}{1 + Hz(t)} \tag{2}$$

$$\eta(z) = 1 + Hz \tag{3}$$

$$z(t) = \frac{1}{H}\left(\sqrt{1 + (H\,c(t - t_z))^2} - 1\right) \tag{4}$$

$$H^{-1} = \frac{m\,c^2}{e\,E_0} \tag{5}$$

where: $m$ and $e$ are the rest mass and charge of the electron, respectively, $z(t)$ is the longitudinal coordinate of an electron at time $t$, and $t_z$ is the time at which an element z of the beam leaves the photocathode.

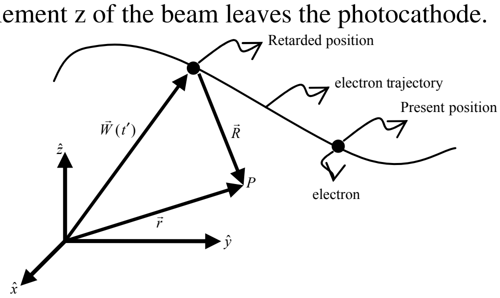


Figure 2: Field driven by an electron.

The electromagnetic fields $(\vec{E}, \vec{B})$ generated at time $t$ and point $P$, by an electron, that is moving on a specified trajectory depend on the position W(t') of the electron at time t' (Fig. 2). These fields are driven from the rebuilt scalar and vector potentials $\Phi$ and $\vec{A}$, respectively. Taking into account the boundary condition imposed on the cathode by the equipotential and causality, these fields are given by Lienard-Weichert expression as

$$\vec{E}(P,t|\,W) = -\frac{A}{c(R - \vec{R}\,.\,\vec{\beta}(t'))^3}\Big(c\frac{\left(\vec{R} - \vec{\beta}(t')R\right)}{\gamma(t')} + \vec{R}\times\{(\vec{R} - \vec{\beta}(t')R)\times\frac{\partial\vec{\beta}(t')}{\partial t'}\}\Big) \tag{6}$$

$$\vec{B}(P,t|W) = \frac{1}{c}\frac{\vec{R}}{R} \times \vec{E}(P,t|W) \qquad (7)$$

$$\gamma(t') = \left(1 - \beta(t')^2\right)^{-1/2} \qquad (8)$$

where $A = (4\pi\varepsilon_0)^{-1}$, $\varepsilon_0$ is the permittivity of free space, $R = W(t')P = c(t - t')$ is the magnitude of the vector from the retarded position *W* to the field point *P*, and $t'$ is the retarded time.

The first term in the parentheses in equation (6) is the velocity field while the second one is the acceleration or radiation field. The former falls off as $1/R^2$ while the later falls off as 1/*R*.

## DEVELOPMENT OF LIENARD - WIECHERT POTENTIALS

The components of the electromagnetic field driven by an electron within the beam and an image of the charge on the cathode can be obtained by the projection of Lienard-Wiechert fields given by equations (6) and (7) on the axes shown in Fig. 3. This projection is applied in the

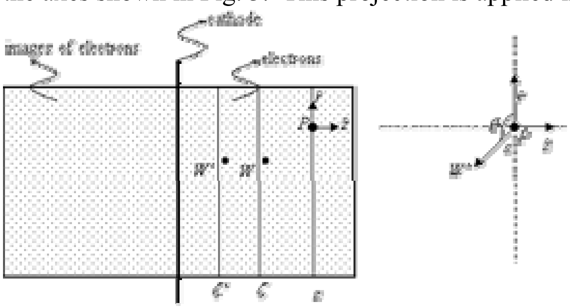


Figure 3: Cylindrical coordinates *s*, $\theta$ and *z*.

laboratory frame. The point where we observe the field will be taken as the origin of this frame. The cylindrical coordinates (*s*, $\theta$, *z*) of a $W'$ are defined in Fig. 3.

The vector from the retarded position of the electron *W* ($t'$) to the field point *p* is

$$\vec{R} = \begin{vmatrix} -s\cos\theta \\ -s\sin\theta \\ z - \zeta' \end{vmatrix} \qquad (9)$$

where the superscript ($'$) denotes that the values are taken at time t'. Since a paraxial approximation is used for the beam dynamics, the beam velocity $\beta(t)$ and the beam acceleration $\frac{\partial \beta(t)}{\partial t}$ are in the same direction. Therefore, the double cross product in equation (6) reads

$$\vec{R} \times ((\vec{R} - \vec{\beta}R) \times \frac{\partial \vec{\beta}}{\partial t}) = \frac{1}{R^2} \begin{vmatrix} -\frac{\partial \vec{\beta}}{\partial t} s(z - \zeta')\cos\theta \\ -\frac{\partial \vec{\beta}}{\partial t} s(z - \zeta')\sin\theta \\ \frac{\partial \vec{\beta}}{\partial t} s^2 \end{vmatrix} \qquad (10)$$

Using equations (10) and (6), the field components $E_z$, $E_r$ and $E_\theta$ on the axes of Fig. 3 are given as

$$E_{z,\beta}(P,t|W) = \frac{A(\zeta' - z + \beta' \sqrt{s^2 + (\zeta' - z)^2})}{\gamma'^2 (\sqrt{s^2 + (\zeta' - z)^2} + \beta'(\zeta' - z)^2)^3} \qquad (11)$$

$$E_{z,\dot{\beta}}(P,t|W) = \frac{A\dot{\beta}' s^2}{c(\sqrt{s^2 + (\zeta' - z)^2} + \beta'(\zeta' - z)^2)^3} \qquad (12)$$

$$E_{r,\beta}(P,t|W) = \frac{As\cos\theta}{\gamma'^2(\sqrt{s^2 + (\zeta' - z)^2} + \beta'(\zeta' - z)^2)^3} \qquad (13)$$

$$E_{r,\dot{\beta}}(P,t|W) = -\frac{A\dot{\beta}'(\zeta' - z)s\cos\theta}{c(\sqrt{s^2 + (\zeta' - z)^2} + \beta'(\zeta' - z)^2)^3} \qquad (14)$$

$$E_{\theta,\beta}(P,t|W) = \frac{As\sin\theta}{\gamma'^2(\sqrt{s^2 + (\zeta' - z)^2} + \beta'(\zeta' - z)^2)^3} \qquad (15)$$

$$E_{\theta,\dot{\beta}}(P,t|W) = -\frac{A\dot{\beta}'(\zeta' - z)s\sin\vartheta}{c(\sqrt{s^2 + (\zeta' - z)^2} + \beta'(\zeta' - z)^2)^3} \qquad (16)$$

where the indices $\beta$ and $\dot{\beta} = \frac{\partial \beta}{\partial t}$ denote the field components due to the velocity and acceleration; respectively. According to the cylindrical symmetry, the integration of the component $E_\theta$ over the whole beam gives zero.

## GENERATION OF GLOBAL FIELDS FROM INDIVIDUAL COMPONENTS

We generate the global fields driven by the beam using the field components driven by an individual electron and corresponding image charge. For seek of simplicity, we show how we can generate the longitudinal component $E_z$ of the global field, since the other components are identical to the longitudinal one. Consider a cylindrical beam pulse, with radius *a*, carrying a current *I*, emitted by the cathode with a constant and radially uniform current density *J*, moving along the z-axis with velocity $\beta(t)$ that varies with time. For seek of simplicity, we assume that the shape of the beam does not change during the acceleration. If n(*W*, *t*) is the density of electrons or image charge at time *t* then the longitudinal component of the global field at the point *P* is

$$E_z(P,t) = \int_D n(W,t)\, E_z(P,t|W)\, d^3W + \int_{\bar{D}} n(W,t)\, \bar{E}_z(P,t|\bar{W})\, d^3\bar{W} \qquad (17)$$

where $E_z(P,t\,|\,W)$ and $\bar{E}_z(P,t\,|\,\bar{W})$ are the field components due to an electron and image charge; respectively, D and $\bar{D}$ represent an ensemble of electrons and image charges; respectively having an antecedent at the retarded time t'and t''.

The components $E_z(P,t\,|\,W)$ and $\bar{E}_z(P,t\,|\,\bar{W})$ can be written in term of W(t) and $\bar{W}(t)$ using the following

$$W(t') = \Im_{z,t}(M) = \begin{cases} s' = s \\ \theta' = \theta \\ \zeta' = f(s,\theta,\zeta) \end{cases} \tag{18}$$

$$\bar{W}(t'') = \bar{\Im}_{z,t}(\bar{M}) = \begin{cases} s' = s \\ \theta' = \theta \\ \bar{\zeta}' = \bar{f}(s,\theta,\bar{\zeta}) \end{cases} \tag{19}$$

Hence

$$E_z(P,t) = \int_D n(W,t) E_z(P,t\,|\,W)\, \Im_{z,t}(W)\, d^3W + \int_{\bar{D}} n(W,t)\bar{E}_z(P,t\,|\,\bar{W})\bar{\Im}_{z,t}(\bar{W})\, d^3\bar{W} \tag{20}$$

Since the integral will be carried out with respect to $W' = W(t')$ and $\bar{W}' = \bar{W}(t'')$, we can write

$$d^3W = \Omega(\Im^{-1})\, d^3\,\bar{W} \tag{21}$$

$$d^3\bar{W} = \bar{\Omega}\,(\bar{\Im}^{-1})\, d^3\,\bar{W}' \tag{22}$$

with

$$\Omega(\Im^{-1}) = \frac{\beta}{\beta'}\left(1 - \frac{\beta'(z-\zeta')}{\sqrt{s^2 + (z-\zeta')^2}}\right) \tag{23}$$

$$\bar{\Omega}\,(\bar{\Im}^{-1}) = \frac{\bar{\beta}}{\bar{\beta}'}\left(1 - \frac{\bar{\beta}'(z-\bar{\zeta}')}{\sqrt{s^2 + (z-\bar{\zeta}')^2}}\right) \tag{24}$$

where $\Omega(\Im^{-1})$ and $\bar{\Omega}\,(\bar{\Im}^{-1})$ are the Jacobeans of $\Im^{-1}$ and $\bar{\Im}^{-1}$; respectively.

By means of equations (17-24), equation (17) becomes:

$$\begin{aligned} E_z(P,t) = {} & A \int_{D(P,\zeta,t)} \frac{J}{e\beta c}\Bigg(\frac{\zeta' - z + \beta'\sqrt{s^2 + (\zeta'-z)^2}}{\gamma'^2\left(\sqrt{s^2+(\zeta'-z)^2} + \beta'(\zeta'-z)\right)^3} \\ & + \frac{\dot{\beta}'\, s^2}{c\left(\sqrt{s^2+(\zeta'-z)^2} + \beta'(\zeta'-z)\right)^3}\Bigg)\frac{\beta}{\beta'} \times \\ & \left(1 - \frac{\beta'(z-\zeta')}{\sqrt{s^2+(z-\zeta')^2}}\right) s\, ds\, d\theta\, d\zeta' + \\ & A \int_{\bar{D}(P,\zeta,t)} \frac{J}{e\bar{\beta} c}\Bigg(\frac{\bar{\zeta}' - z + \bar{\beta}'\sqrt{s^2 + (\bar{\zeta}'-z)^2}}{\gamma'^2\left(\sqrt{s^2+(\bar{\zeta}'-z)^2} + \bar{\beta}'(\bar{\zeta}'-z)\right)^3} + \\ & \frac{\dot{\bar{\beta}}'\, s^2}{c\left(\sqrt{s^2+(\bar{\zeta}'-z)^2} + \bar{\beta}'(\bar{\zeta}'-z)\right)^3}\Bigg)\frac{\bar{\beta}}{\bar{\beta}'} \times \\ & \left(1 - \frac{\bar{\beta}'(z-\zeta')}{\sqrt{s^2+(z-\bar{\zeta}')^2}}\right) s\, ds\, d\theta\, d\bar{\zeta}' \end{aligned} \tag{25}$$

# APPLICATION OF METHOD

We apply the method to several emission regimes [4] from the photocathode. A particularly interesting case is that which occurs at the end of photoemission, corresponding to complete extraction of the beam (i. e at the instant $t = \tau = 30$ ps). This is illustrated in Fig 4. in which the axial electric field is displayed as a function of Z = Hz for the following parameters I =100 A, $E_0$= 30 MV/m. This field is compared to that due to the space charge (or self-field) and the image of charge on the cathode. At the centre of the cathode ($r$ = 0, $z$ = 0) the beam self field and the field driven by the image of charges on the cathode are similar. However, the field of

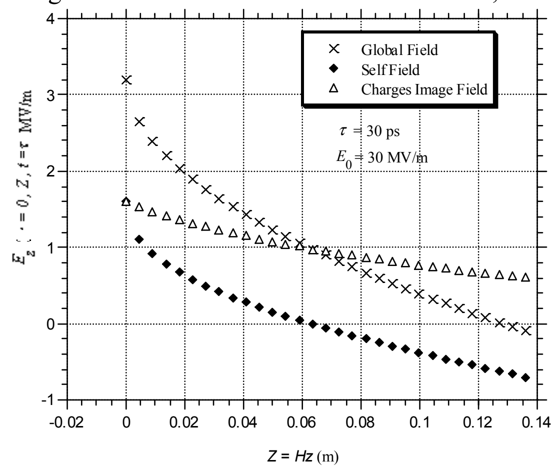


Figure 4: Axial electric field $E_z$ within beam at the end of photoemission.

the beam is dominated by that due to the image charges on the cathode as one moves from the tail to the head of the beam. Far from the cathode the self-field dominates.

# ACKNOWLEDGMENT

One of the authors, Wa'el Salah has benefited from a Cockcroft visiting fellowship. The majority of the research presented was completed during the tenure of this fellowship.

# REFERENCES

[1] A. Candel et al., MOP104, This conference.
[2] S. Joly and S. Striby, 1998, Revue Chocs n18, CEA.
[3] W. Salah and JM. Dolique, 1999, Nucl. Inst. and Meth. A431.
[4] W. Salah and R.M. Jones, to be published, 2008.

# DESIGN AND OPTIMIZATION OF AN S-BAND PHOTOINJECTOR

Jang-Hui Han, Diamond Light Source, Oxfordshire, United Kingdom


### Abstract

Several X-ray Free Electron Laser (XFEL) projects are under construction or are being proposed over the world. For successful XFEL operations photoinjectors with low transverse emittance are one of the key elements. For the European XFEL and LCLS projects, photoinjectors have been developed to reach their requirements, typically with a normalised emittance of 1 mm mrad for a 1 nC beam. Here, we make a further optimization of an S-band photoinjector to achieve 0.4 mm mrad for a 1 nC bunch in a structure that should permit high repetition rates operation. Optimizations for alternative operation conditions with a 0.2 nC bunch charge for lower emittance and a 10 pC charge for ultrashort pulse (< 100 fs) generation are also shown.


## INTRODUCTION

Two kinds of photocathode RF guns are successfully used as injectors for VUV or X-ray FELs. LCLS [1] uses a gun improved from the BNL/SLAC/UCLA guns which operate with a 2.856 GHz resonant frequency. The FLASH gun [2] operates at 1.3 GHz. Both gun cavities are composed of a first half cell and a second full cell. In the LCLS gun, RF power is coupled to the cavity through the side of the second cell and the focusing solenoid is located downstream of the cavity. In the FLASH gun, RF power is coupled coaxially through the exit of the second cell and the solenoid surrounds the cavity. In general, S-band guns provide a shorter pulse length and lower transverse emittance beam thanks to the higher accelerating field compared to L-band guns. Typically, the maximum field is 40 to 60 MV/m in L-band guns but 120 MV/m or higher in S-band guns. With a coaxial RF coupler, the RF field in the cavity is axisymmetric and the focusing solenoid can be located close to the cathode. In addition, the coaxial coupler allows more cooling-water channels around the cavity symmetrically. Here, we show a new design of an S-band photocathode RF gun with a coaxial coupler.

## GUN DESIGN AND OPTIMIZATION

In an RF gun cavity, an electron beam is generated by a drive laser pulse illuminated at a photocathode located on the back plane of the first cell. When the photon energy of the laser pulse excites electrons in the cathode so to overcome the potential barrier, the electrons are emitted into the vacuum. Depending on the direction of the RF field the electrons can be accelerated downstream. When the accelerated beam reaches the second cell the direction of the RF field is reversed and therefore the beam can be further accelerated. Since the beam starts at the first cell with almost zero velocity, there exists a large phase slippage. In order for the beam to get accelerated in sequence the beam must start earlier than maximum acceleration phase (90°) at the first cell depending on the first cell length and the accelerating field strength. For example, for a lower field strength or for a longer first cell length, the flight time in the first cell is longer, the phase slippage is higher, and the phase of beam emission for an optimum acceleration is shifted towards 0°. The beam dynamics (emittance and bunch length) of the beam strongly depends on the emission phase.

A new S-band gun was designed adopting the advanced features of the DESY gun [3], like the coaxial RF coupler and the cooling-water channels over the entire cavity surface. The resonant frequency was chosen as 2.998 GHz. Compared to the Eindhoven gun [4], which is another S-band gun with a coaxial coupler, the first cell length has been optimized for smaller emittance and the possibility of further cooling channel installation has been considered here. A focusing solenoid is located around the gun cavity (see Fig. 1). Another solenoid upstream of the gun compensates the magnetic field at the cathode. Even if the resonant frequency of the cavity is fixed as 2.998 GHz, the lengths of the first and second cells are slightly variable while keeping the cavity in resonance. The radii of the cells should be adjusted when the cell lengths are changed. The length of the first cell dramatically influences the beam dynamics while the length of the second cell does not visibly affect the beam dynamics. A shorter first cell length allows a higher acceleration field during beam emission at the cathode and a shorter electron flight time between the cathode and the second cell. A higher acceleration field minimize the beam quality degradation caused by the space charge force. The first cell length was set to 0.54 times a half of the RF wavelength and the second cell set to 0.98 times a half wavelength. The RF field in the cavity were calculated by SUPERFISH [5] (Fig. 2). After scaling down from the DESY L-band gun to the S-band, the iris thickness was changed thicker for allowing cooling channels inside the iris and the diameter of the coupler antenna was enlarged for a weaker interaction with electron beams. The $\pi$-mode of the RF is utilized for the beam acceleration. Even if the 0-mode is separated from the $\pi$-mode, the tail of the 0-mode peak is still activated at the resonant frequency of the $\pi$-mode, 2.998 GHz. When the 0-mode is activated, the electron beam is affected by the unwanted 0-mode field in a wrong phase. If the 0-mode is separated far from the $\pi$-mode, the unwanted effect is reduced. In this design, the mode separation is 18.25 MHz, which is larger than those of the other S-band guns [1, 4].

With this gun, the beam dynamics was calculated with ASTRA [6]. Parameters for optimization were the laser beam size and pulse length, the RF gun phase, and the solenoid field distribution and strength and the location.

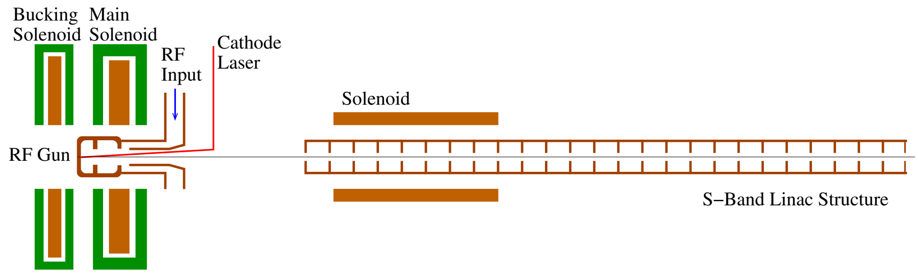


Figure 1: Injector layout. The injector consists of a gun and six 3.1 m long linacs. 1 m long solenoids are installed around first three linacs.

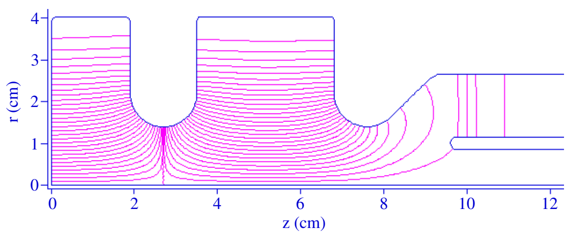


Figure 2: Gun cavity geometry and SUPERFISH calculation of the RF field.

The solenoid field was calculated with POISSON [5]. The center of the main solenoid was set to 9.5 cm from the cathode. The maximum field strength at the cathode was fixed as 120 MV/m which corresponds to an RF peak power of 7.5 MW in the cavity operating at 50 °C. In the case of 120 MV/m, a beam has a highest energy after the gun when the beam starts at a 50° RF phase at the cathode. The field strength at the emission phase is about 90 MV/m (120 MV/m $\times$ sin 50°). When a beam is emitted at the cathode, the beam is highly space-charge dominated and each slice of the beam experiences a different strength of the space charge force, which results in a misalignment of the beam slices in the phase space. With a solenoid field we are able to re-align the slices on a line in the phase space so that the projected emittance becomes small [7]. With the gun cavity only this alignment process takes place in the space-charge dominated region because the beam energy is not high enough. Therefore, the projected emittance blows up after a minimum (see Fig. 3).

A 1 nC beam with a 0.6 mm radius and a 10 ps fwhm length was numerically generated and tracked. The transverse and longitudinal electron distributions were assumed to be uniform. The rise/fall time of the pulse was 0.7 ps, which may be achievable with a Ti:Sapphire laser. The beam was emitted at 48° RF phase which is $-2°$ from the phase for the highest energy. The minimum emittance value is 0.51 mm mrad at z = 0.8 m. The minimum beam size is 0.094 mm at z = 0.73 m (Fig. 3). A 0.2 nC beam with a 0.28 mm radius and a 6 ps fwhm length was simulated also. The minimum emittance is 0.21 mm mrad at z = 0.96 m. The emission phase was 47 °. For this emittance simulation, the thermal emittance depending on the cathode material was included. Assuming a Cu cathode, the kinetic energy of emitted electron was set to 0.5 eV, which corresponds to 0.4 mm mrad per 1 mm beam radius. This thermal emittance estimation is about 30% higher than the theoretical value calculated in Ref. [8] for a bare Cu at a room temperature condition and a 90 MV/m field. A thermal emittance of 0.24 mm mrad was used for the 1 nC case and 0.11 mm mrad for 0.2 nC.

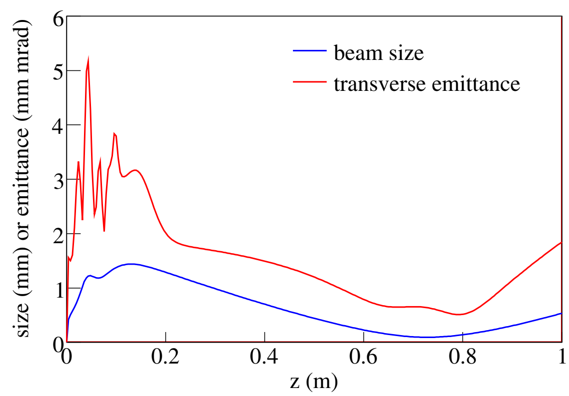


Figure 3: Beam size and transverse projected emittance evolution over the beam propagation for 1 nC beam.

## INJECTOR OPTIMIZATION

This photoinjector consists of a gun, gun solenoids, six 3.1 m long S-band RF linacs with a $2\pi/3$ mode travelling wave structure, and three 1 m long focusing solenoids for the first three linacs (Fig. 1). The first linac starts at z = 1.02 m and has a gradient of 12.44 MV/m. The other five linacs have a gradient of 18.3 MV/m. The six linac structures accelerate a beam up to 320 MeV. For the 1 nC case, a driving laser pulse with a 0.76 mm radius and a 10 ps fwhm length (0.7 ps rise/fall time) was used to generate a beam at the cathode. The beam starts at a 48 ° RF phase. For the 0.2 nC case, a driving laser pulse with 0.4 mm radius and 6 ps fwhm length was used. The emission phase was 47°. The field strength of the solenoids and the accelerating field of the linacs were optimized for a lowest transverse emittance after the sixth linac. Due to the further acceleration by the linacs, the emittance does not blow up (Fig. 4). The simulated beam parameters are summarized in Table 1. The slice emittance of the simulated beam is shown in Fig. 5 for both bunch charge cases. The slice and core emittances are shown in Table 1.

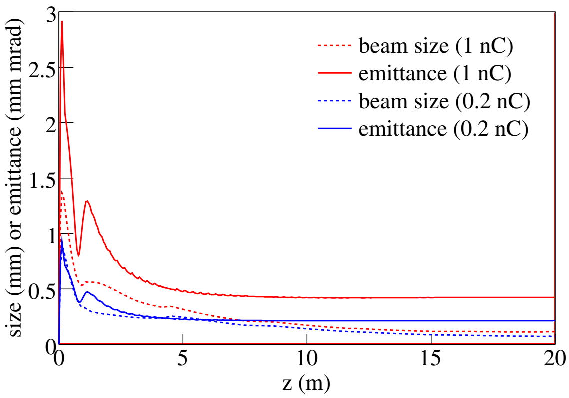


Figure 4: Beam size and transverse projected emittance including the linacs. ASTRA simulations for the 1 nC and 0.2 nC beam cases are shown.

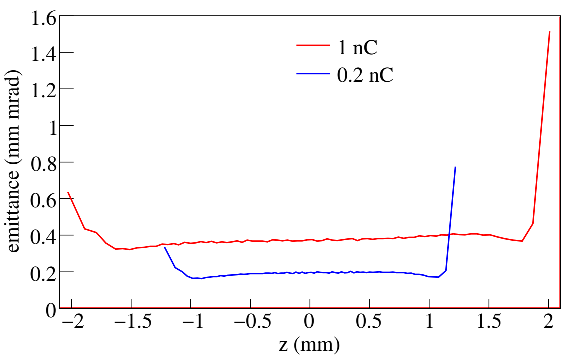


Figure 5: Slice emittances at the end of the injector.

## SUB-PS BEAM GENERATION

For the NLS project [9], a relativistic electron beam source synchronized with the FEL laser is of interest. Such beams should be ultrashort ($<$ 100 fs) and in a MeV range. This requirement may be satisfied by installing one more RF gun in the user hall. If a beam generated at the main injector driving the FEL is transported to the experiment station downstream of the undulator, the beam spreads due to the space charge force. When the drive laser of this gun is synchronised with the laser system for the FEL seeding, the generated beams by this gun can be synchronised with the FEL photons. According to a simulation, this gun is able to generate a bunch with an 90 fs rms length for a 10 pC and 5 MeV beam when a drive laser pulse has a 100 fs rms length and a 2 mm radius. A target for experiment should be at 0.6 m downstream of the cathode. At the target, the rms beam size is 1 mm and the energy spread is 7 keV.

Table 1: Initial parameters and simulated beam parameters. The average slice emittances of the central 95% are shown.

| **bunch charge** | **1 nC** | **0.2 nC** |
|---|---|---|
| **initial parameters** | | |
| laser radius | 0.76 mm | 0.40 mm |
| laser fwhm length | 10 ps | 6 ps |
| thermal emittance | 0.30 mm mrad | 0.16 mm mrad |
| **beam parameters at the end of the injector** | | |
| projected emittance | 0.42 mm mrad | 0.21 mm mrad |
| peak current | 90 A | 30 A |
| core emittances in 95/90/80% | 0.33/0.28/0.21 | 0.17/0.14/0.11 |
| 95% slice emittance | 0.37 | 0.19 |

## GUN CAVITY COOLING

For the temperature control of the cavity, cooling-water channels are distributed over the cavity surface (see Fig. 6). The channel distribution is similar as that of the DESY L-band guns. The new DESY gun is designed for an average power of 100 kW and tested up to 50 kW [10]. A simple scaling as $(1/f)^2$ estimates that 9.4 kW may be possible at 2.998 GHz which should allow operation up to 400 Hz at a 120 MV/m field and a 3 $\mu$s pulse length. Even if the gun is operated with a low repetition rate, e.g. 100 Hz, the high capacity of cooling has advantages so that it enables a fast recovery of RF operations after any kind of interlocks and a fast change of operation modes.

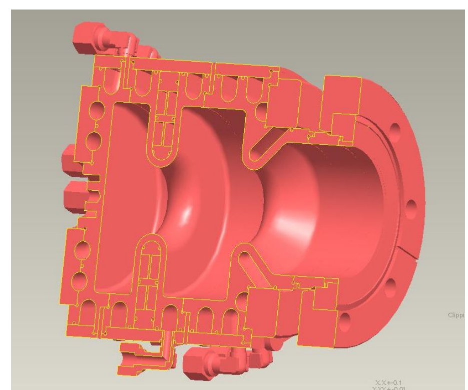

Figure 6: Designed gun cavity (drawing by L. Zaja).

## REFERENCES

[1] R. Akre et al., Phys. Rev. ST Accel. Beams **11**, 030703 (2008).
[2] S. Schreiber, Proceedings of FEL 2005, p. 545.
[3] B. Dwersteg et al., Nucl. Instr. and meth. A **393**, 93 (1997).
[4] B. van der Geer et al., Proceedings of FLS 2006.
[5] J. H. Billen and L. M. Young, Poisson Superfish, LA-UR-96-1834.
[6] K. Föttmann, `http://www.desy.de/~mpyflo`.
[7] B. E. Carlsten, Nucl. Instr. and Meth. A **285**, 313 (1989).
[8] K. L. Jensen et al., J. Appl. Phys. **102**, 074902 (2007).
[9] `http://www.newlightsource.org`.
[10] S. Rimjaem et al., Proceedings of EPAC 2008, p. 244.

# THE OPTIMIZATION OF A DC INJECTOR FOR THE ENERGY RECOVERY LINAC UPGRADE TO APS*

Yin-e Sun[1,2], Hairong Shang[1], Michael Borland[1], Yuelin Li[1], Katherine Harkay[1]
[1]Advanced Photon Source, Argonne National Lab., Argonne, IL 60439, USA
[2]Accelerator Physics Center, Fermilab, Batavia, IL 60510, USA

*Abstract*

An energy recovery linac based light source is a potential revolutionary upgrade to the Advanced Photon Source (APS) at Argonne National Laboratory. The concept relies on several key research areas, one of which is the generation of ultra-low emittance, high-average-current electron beams. In this paper, we present our investigation of a dc-gun-based system for ultra-low emittance bunches in the 20 pC range. A parallel multi-objective numerical optimization is performed in multi-parameter space. Parameters varied include experimentally feasible drive-laser shapes, the DC gun voltage, the thermal energy of the emitted photo-electrons and other electric or magnetic field strengths, RF cavity phase etc. Our goal is to deliver a $\sim$10 MeV, 20 pC bunch at the entrance of the linac with an emittance of 0.1 $\mu$m or lower, rms bunch length of $2 \sim 3$ ps, and energy spread no larger than 140 keV. We present the machine parameters needed to generate such an injector beam, albeit without a merger.

## INTRODUCTION

The APS is a storage-ring based light source. Fundamental physics principles governing a storage ring determine the electron beam emittance as well as its fractional energy spread. It is difficult to improve the beam quality dramatically solely by upgrading the storage ring[1], due to the requirement to keep the energy fixed at 7 GeV while accommodating the existing circumference and number of sectors. In contrast, the emittance of the electron beam in a linac is inversely proportionally to the beam energy, as the normalized emittance is constant. Therefore emittance much smaller than the APS storage ring is possible in a linac of the same beam energy. However, high average current (e.g., 100 mA) is needed for a facility to operate as a state-of-art light source. With 7 GeV beam energy, this corresponds to 700 MW beam power. The only feasible way to operate such a linac-based light source is to have the beam energy recovered [2] after it is used to generate light.

One of the most challenging aspects of the ERL design is the injector, as it requires unprecedented average current with extremely small normalized emittance. Currently there are several DC guns in operation for the ERLs, most notably at TJNAF [3]. However, none of these operating guns meets the requirements of the ERL upgrade at APS [4]. Some high performance dc-gun-based system have been investigated for ultra-low emittance beams [5, 6]. None of these analysis delivers the desired charge (20 pC or higher) while including the critical merger between the injector and the linac. In this paper, we present a first step in our efforts, namely, the design of a dc-gun-based injector without a merger system.

## OPTIMIZATION METHOD

This injector design is developed using the multi-objective optimization techniques, similar to those employed by Bazarov et al. [5]. At APS, a global parallel optimizer named GeneticOptimizer already existed[7]. Originally it accepted a single penalty function. For the present work, non-dominated sorting was incorporated to perform multi-objective optimization. The current version of GeneticOptimizer is able to do both single object and multi-objective optimization. For single objective optimization, the parents chosen by GeneticOptimizer are those who have the smallest penalty value, while for multi-object optimization, the parents are those with rank 1 after non-dominated sorting. The beam dynamics simulation program used is ASTRA [8], which includes space charge forces.

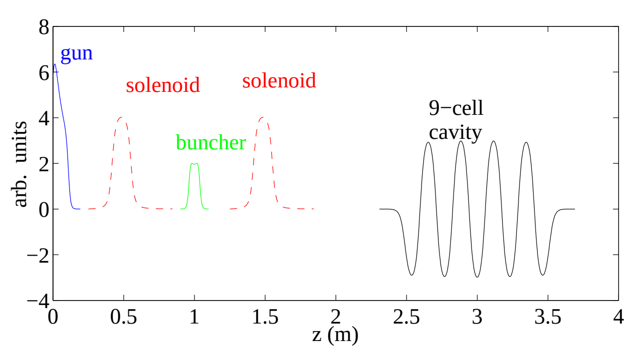


Figure 1: The field maps of the injector elements along the beamline.

## INJECTOR AND DRIVE-LASER

The photoinjector we considered is similar to the TJNAF FEL injector [9]. A DC photo emission electron source

* Work supported by the U.S. Department of Energy, Office of Science, Office of Basic Energy Sciences, under Contract No. DE-AC02-06CH11357.

(the DC gun) produces electron bunches. The bunches are compressed via ballistic bunching using a 1.3 GHz buncher cavity [10], and then further accelerated to $\sim$10 MeV in a TESLA type cavity [11]. The low energy section also incorporates two solenoidal lenses for the control of the beam's transverse envelope and emittance compensation [12]; see Fig. 1 for the relative positions of these elements in the beamline.

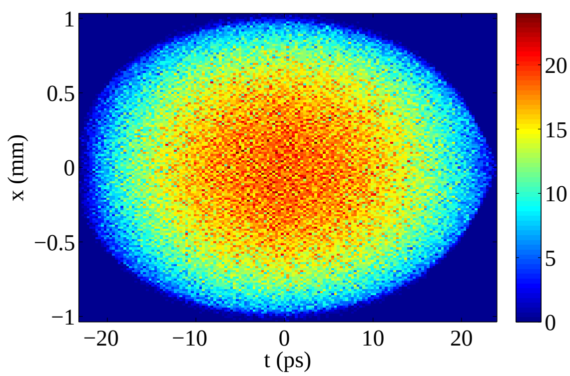


Figure 2: The (*x*,*t*) projection of the ellipsoidal drive-laser.

To achieve sub-micron beam emittances, the shaping of the photocathode drive laser pulse is critical. In our simulations, several drive laser distributions are explored: beer-can, pancake, and "egg" (which is a non-ideal ellipsoid). The beer-can has a transversely uniform, longitudinally flat distribution; the pancake is an ultra-short ( $\sim$10s of fs rms) pulse; for the egg distribution, a 3-D ellipsoidal surface is filled with uniform beam density. Both the beer-can [13] and pancake [14] shaped laser pulse have been experimentally demonstrated, while the ellipsoidal laser pulse is under developement [15, 16]. In Fig. 2, an example of the laser egg intensity profile is shown in the (*x*,*t*) plane; some structures exist in the two ends of the ellipse.

## OPTIMIZATION RESULTS

The optimization variables include the following: drive-laser transverse spot size and longitudinal pulse length, buncher cavity voltage and phase, booster cavity voltage, phase and position, solenoid strengths and positions.

In Fig. 3, we plot simulation results using the three types of photocathode drive laser pulses. We see the ellipsoidal laser pulse gives slightly smaller normalized transverse emittance than the beer-can. For the pancake case, the longitudinal phase space is much smaller but the transverse emittance is doubled; see Table. 1. In Luiten's scheme [17], to produce an ellipsoidal electron beam from a pancake laser, the following conditions are required

$$\frac{eE_0\tau_l}{mc^2} \ll \frac{\sigma_0}{\varepsilon_0 E_0} \ll 1, \qquad (1)$$

where $\varepsilon_0$ is the permittivity of free space. In our pancake simulation, the total emission time $\tau_l$ is about 80 fs, the accelerating gradient on cathode is about $E_0$=8.2 MV/m, therefore we have $\frac{eE_0\tau_l}{mc^2} = 3.9\times10^{-4} \ll \frac{\sigma_0}{\varepsilon_0 E_0} \simeq 0.5$. The right hand inequality of Eq. (1) is marginally satisfied. This explains the larger emittance from the pancake simulations, which is due to the fact that the accelerating gradient on the cathode is relatively low compared with a rf gun, and the transverse laser spot size cannot be arbitrarily increased as it is proportional to the thermal emittance [18]. In the simulation presented in Fig. 3, the thermal energy of the electron beam is assumed to be 40 meV at the cathode for all kinds of laser shapes.

Table 1: Optimized parameters for various drive laser

| | beer-can | egg | pancake |
|---|---|---|---|
| DC gun voltage (kV) | 740 | 748 | 728 |
| laser length $\sigma_t$(ps) | 9.7 | 10.4 | $13.2\times10^{-3}$ |
| laser spot $\sigma_0$ (mm) | 0.32 | 0.30 | 0.43 |
| thermal emit. $\varepsilon_{th}(\mu$ m) | 0.08 | 0.07 | 0.10 |
| norm. emit. $\varepsilon_x^n(\mu$ m) | 0.15 | 0.13 | 0.30 |
| bunch length $\sigma_z$ (mm) | 0.64 | 0.80 | 0.49 |
| uncor. energy spread (keV) | 4.69 | 4.93 | 0.83 |

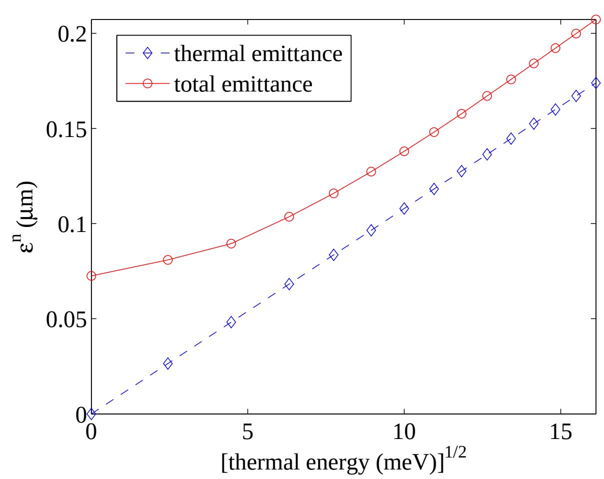


Figure 4: The normalized total beam emittance and the thermal emittance as a function of the thermal energy on the cathode; DC gun voltage is 735 keV.

As the thermal emittance depends on the choice of drive-laser and photocathode material, we have performed further injector optimizations for different initial thermal energies. Without repeating the optimized input variable results, we varied the input beam thermal energy and tracked the particles through the injector. The results are shown in Fig. 4.

The upper limit of the dc gun voltage in the optimization shown in Fig. 3 is 750 kV. However it should be noted that in dc guns under development, voltages have so far been limited to $\sim$350 kV due to technical issues. Several groups are working to improve this technology, including Cornell, TJNAF, and Daresbury. Nevertheless, we optimized the injector at several fixed DC gun voltage values using the

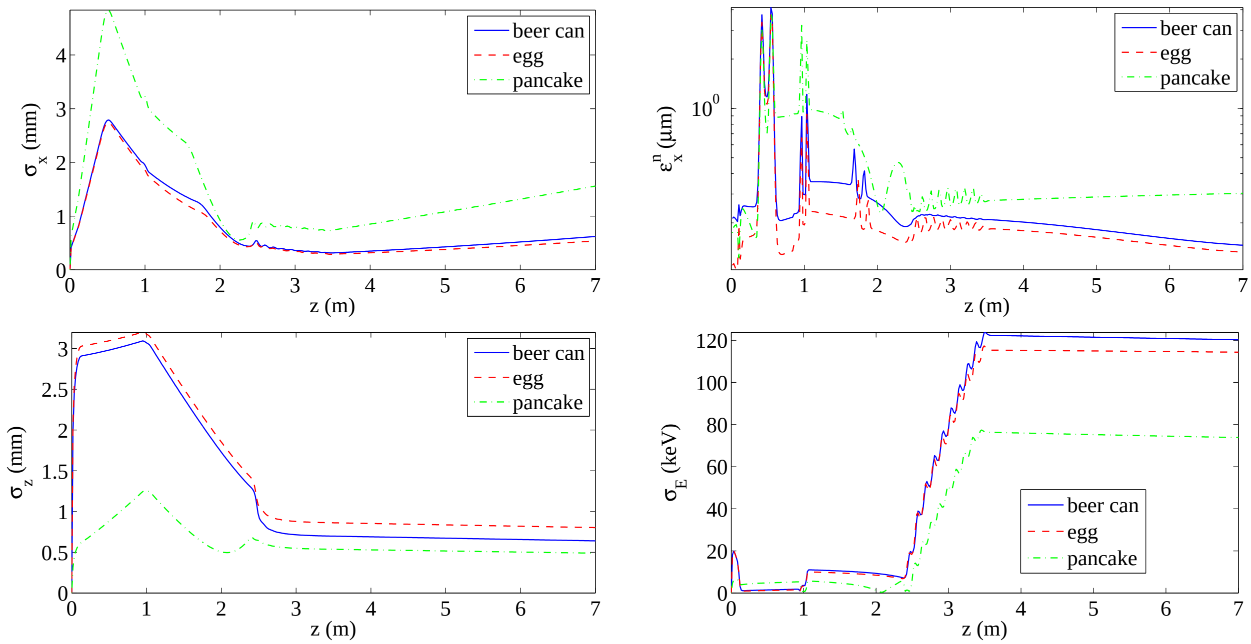


Figure 3: Beam parameter evolution along the injector beam line: the transverse beam size $\sigma_x$, normalized transverse emittance $\varepsilon_x^n$, rms bunch length $\sigma_z$ and the energy spread $\sigma_E$.

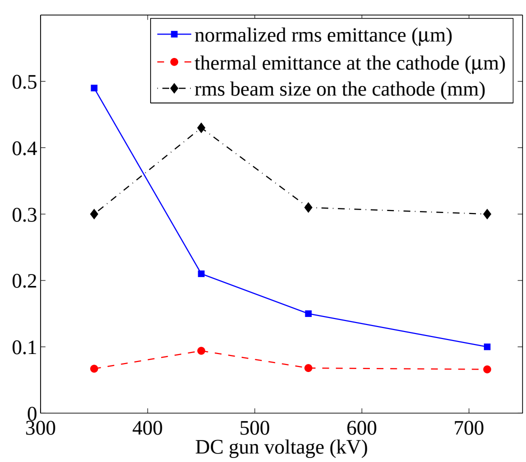


Figure 5: The normalized transverse emittance at various DC gun voltages.

ellipsoidal laser, as shown in Fig. 5. A significant drop in the beam emittance occurs between $350$ and $450$ keV gun voltage; further increase of the gun voltage leads to improved emittance at a slower rate.

The authors thank Philippe Piot for helpful discussions.

## REFERENCES

[1] A. Xiao *et al.*, in Proc. PAC 2007, pp. 3447-3449 (2007).

[2] M. Tigner, Nuovo Cimento **37**, pp 1228-1231 (1965).

[3] G. Neil *et al.*, Phys. Rev. Lett. **84**,662 (2000).

[4] M. Borland *et al.*, Nucl. Instrum. Methods A **582** (2007) 54-56 .

[5] I. Bazarov, and C. Sinclair, Phys. Rev. ST Accel. Beams **8**, 034202 (2005).

[6] R. Hajima, and R. Nagai, Nucl. Instrum. Methods A **557** (2006) 103-105.

[7] M. Borland, H. Shang, unpublished program.

[8] K. Flöttmann, http://www.desy.de/ mpyflo/

[9] P. Piot, in Proc. of EPAC 1998, pp. 1447 - 1449 (1998).

[10] I. Bazarov, *USPAS 2005: Recirculated and Energy Recovered Linacs*.

[11] B. Aune *et al.*, Phys. Rev. ST Accel. Beams **3**, 092001 (2000).

[12] C. K. Sinclair, Nucl. Instrum. Methods A **318** (1992) 410-414 .

[13] C. Vicario *et al.*, in Proc. of PAC 2007, pp. 1004-1006 (2007) .

[14] P. Musumeci *et al.*, Phys. Rev. Lett. **100**, 244801 (2008).

[15] Y. Li, and J. W. Lewellen, Phys. Rev. Lett. **100**, 074801 (2008).

[16] Y. Li, and S. Chemerisov, Opt. Lett. **33**, 1996 (2008).

[17] O. J. Luiten *et al.*, Phys. Rev. Lett. **93** ,094802 (2004).

[18] J. D. Lawson, “the physics of charged-particle physics”,Clarendon Press, Oxfod, 1988.

# PHOTOCATHODE R&D PROGRAM AT LBNL*

W. Wan#, E. Pedersoli, C. M. R. Greaves, C. Coleman-Smith, A. Polyakov, H. A. Padmore, ALS, LBNL, Berkeley, CA 94720, USA

S. Pagliara, A. Cartella, F. Lamarca, G. Ferrini, M. Montagnese, S. dal Conte, F. Parmigiani, Dipartimento di Matematica e Fisica, Università Cattolica, Via Musei 41, I-25121 Brescia, Italia

*Abstract*

The work of the photocathode R&D program at LBNL is presented. The quantum efficiency (QE) of Cu(111) is measured for different impinging light angles with photon energies just above the work function. We observe that the vectorial photoelectric effect, an enhancement of the quantum efficiency due to illumination of light with an electric vector perpendicular to the sample surface, is stronger in the more surface sensitive regime. This can be explained by a contribution to photoemission due to the variation of the electromagnetic potential at the surface. The contributions of bulk and surface electrons can then be determined. Angle-resolved photoemission data let us obtain the dispersion relation of the surface state, which in turn allows us to determine the thermal emittance of the electrons emitted from the surface.

## INTRODUCTION

The advances in diverse fields such as electron microscopy and the free electron laser drive demand for high brightness electron sources [1]. The photocathode R&D program at LBNL was established to explore ways of producing new generation of photocathode that can meet the demand. Our program is designed to study in detail the yield and the energy-momentum dispersion relation of the emitted electrons using angle-resolved photoemission spectroscopy (ARPES), as well as to develop new photocathode using nanotechnology. The capability of fully characterizing the photocathode in the ideal setting allows us to find out the physical limit of the performance of the material, as well as pointing to the direction of making better photocathode. In addition, the gap between the ideal setting and the realistic situation in a gun can be simulated to a certain extent in a controlled manner.

## EXPERIMENTS ON CU(111)

The first set of experiments were carried out in Brescia, Italy on Cu(111). New work is carried out using a similar system in the photocathodes lab at the ALS. Although copper has been widely used in RF photoguns [2], there are still a lot of questions remain unanswered, such as the origin of the emitted electrons and the lower bound of the transverse thermal emittance. Furthermore, Cu(111) was chosen as a sample due to its robust nature and its well known and experimentally verified band structure [3].

*Work supported by the U.S. Department of Energy under Contract No. DE-AC02-05CH11231.

#wwan@lbl.gov

An amplified Ti:Sapphire laser was used as the light source in this experiment, providing 150~fs 790~nm pulses with an average light power of 500~mW at 1~kHz repetition rate. The output was split into two beams: the first pumping a parametric amplifier that provided tunability in the near infrared, the second undergoing a process of third harmonic generation obtained with two stages of sum frequency generation in type I BBO crystals. After a delay line that provides temporal coincidence, the beams converge on a third crystal for sum frequency generation providing the desired wavelengths. The sample total current on a picoammeter and the light intensity of a beam reflection on a calibrated photodiode were measured to provide the experimental data.

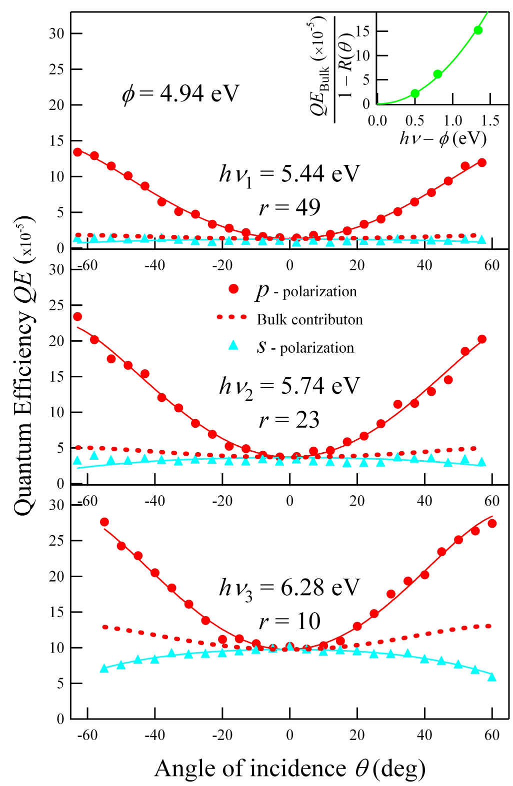


Figure 1: Quantum efficiency data as a function of the incident light angle θ for the three different photon energies are fitted using Eq. (1), (2); the bottom panel shows data from Ref. [4]. The red dotted lines represent the prediction for the bulk contribution, proportional to the absorbed part (1-$R$(θ)) of light energy. The top right panel shows the bulk quantum efficiency fitted by the Fowler law Eq. (3).

The experiment was performed in an ultrahigh vacuum chamber with the base pressure of 2e-10 mbar at room temperature on a Cu(111) crystal polished with cycles of $Ar^+$ sputtering at 1 keV kinetic energy and annealing at 750 K. The sample cleanliness was tested online by acquiring photoemission spectra through a time of flight analyzer and checking the sharpness of the L gap surface state and the work function value.

The quantum efficiency was measured as a function of the incidence angle θ of the impinging photons in the range $-63^\circ < \theta < 57^\circ$ with 5 steps ($\theta = 0^\circ$ indicates normal incidence) for two different values of the photon energy $h\nu_1$ = 5.44 eV and $h\nu_2$ = 5.74 eV; data are compared to results of Ref. [4], obtained with $h\nu_3$ = 6.28 eV.

The most widely applied theoretical model is the 3-step model [5], which assumes that the yield depends on the total absorbed photon energy. This is proportional to the incident light intensity and to (1-$R$(θ)), where $R$(θ) is the reflectivity calculated from the Fresnel laws [5]. Yet this prediction is not confirmed by Cu(111) data obtained for $p$ polarized light. From the phenomenological point of view, the dependence of the quantum efficiency on the $s$ and $p$ polarized light at a given incidence angle can be expressed as

$$\frac{QE_s(\theta)}{QE(0)} = \frac{\varepsilon_s(\theta)}{\varepsilon_s(0)} \tag{1}$$

$$\frac{QE_p(\theta)}{QE(0)} = \frac{\varepsilon_{p\|}(\theta)}{\varepsilon_{p\|}(0)} + r\frac{\varepsilon_{p\perp}(\theta)}{\varepsilon_{p\perp}(0)} \tag{2}$$

where $QE$(0) and $r$ are fit parameters. The parameter r is a measure of the ratio between the effectiveness of perpendicular and parallel light fields [6][4]. It is clear from Fig. 1 that $r$ increases as the photon energy decreases, which indicates that the contribution of the surface becomes more prominent (for details, see ref. [7]).

Another feature of Fig. 1 is that the bulk emission obeys the Fowler law, which is

$$\frac{QE_{bulk}(\theta)}{1-R(\theta)} = \frac{QE_{bulk}(0)}{1-R(0)} \propto (h\upsilon - \phi)^2 . \tag{3}$$

Yet the surface emission violates the Fowler law.

In addition to yield measurement, angle resolved time-of-flight spectrometer was used to measure the energy and momentum distribution of the photoelectrons. The data is presented in Fig. 2, which shows that, even at the photon energy of 5.71 eV, virtually all photoelectrons are from a surface state [8]. From the set of data, we obtain the effective mass of the electron, which is $0.45m_e$, where $m_e$ is the free electron rest mass. This is in excellent agreement with previous results, which is 0.46 $m_e$ [8].

With the knowledge that most photoelectrons are from the surface state and that the energy-momentum dispersion is known, we can compute the transverse emittance of the emitted electrons. Here we adopt the normalized emittance, which is definition as

$$\varepsilon_{x,rms} = x_{rms}\, p_{rms} /(m_e c) , \tag{4}$$

where $c$ is the speed of light. For uniform emission, we have

$$x_{rms} = \frac{1}{2}R , \tag{5}$$

where $R$ is radius of the emitting area. For free electron like dispersion relation, it is reasonable to assume that $d^2N/dp_x dp_y$ is constant. Hence we get

$$p_{x,rms} = \frac{1}{2}P_r . \tag{6}$$

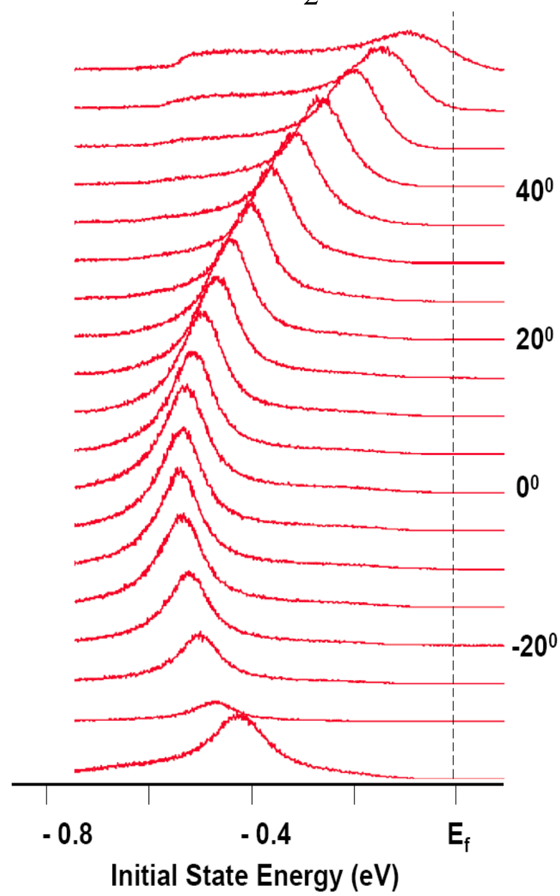


Figure 2: Energy spectrum of the photoelectrons for various angles of the electrons with respect to the norm of the surface. The photon energy is 5.71 eV. The ratio of the effective mass and the rest mass is 0.45.

As a result, the $rms$ transverse emittance is

$$\varepsilon_{rms} = \frac{1}{4}RP_r /(m_e c) . \tag{7}$$

For the surface state,

$$P_r = \hbar k_{\max}$$

and

$$P_r /(m_e c) = \hbar k_{\max} /(m_e c) = (\hbar c) k_{\max} /(m_e c^2) ,$$

where $\hbar c$ = 197 MeVfm and $m_e c$ = 0.511 MeV. For the Cu(111) surface state, $k_{max}$ = 0.225 Å$^{-1}$ and

$$P_r /(m_e c) = 0.87 \times 10^{-3} .$$

For R = 1 mm, $\varepsilon_{rms} = 0.22 \times 10^{-6}$ m, which is around 1/3 of the value measured in a RF gun [9].

## CURRENT STATUS AND FUTURE PLANS

The lab here at LBNL has been steadily built up for the past year and half. In addition to the standard equipment for a surface science lab, we purchased a 2D spatially resolved time-of-flight detector which will greatly speed up data acquisition time and reduce systematic errors generated from moving the sample. At present, all equipment have been set up and the first set of data on Cu(111) has been taken, which shows clearly the dispersion curve of the surface state. Commissioning of both the hardware and the software are well underway.

Once the system is calibrated, we will finish the experiments on Cu, with the hope of shedding some light on the origin of the electrons, especially for a copper cathode in the RF gun. Afterwards, we will focus our attention more and more on developing new photocathode that has the potential of increasing quantum efficiency and decreasing thermal emittance at the same time. One of the more promising candidates is nano-structured cathodes that couples light into the surface through the creation of surface plasmon.

## REFERENCES


[1] T. Shintake, "Review of the Worldwide SASE FEL Development," PAC'07, Albuquerque, June 2007, MOZBA01, p. 89 (2007); http://www.JACoW.org.

[2] C. Travier, "High-Brightness Photocathode Electron Sources", AIP Conf. Proc. 335 (1995) 57.

[3] A. Goldmann, V. Dose and G. Borstel, Phys. Rev. **B**. 32 (1985) 1971.

[4] E. Pedersoli, et. al. Appl. Phys. Lett. 87 (2005) 087112.

[5] H. Y. Fan, Phys. Rev. 68 (1945) 43.

[6] R. M. Broudy, Phys. Rev. **B**. 3 (1971) 3641.

[7] E. Pedersoli, et. al. Appl. Phys. Lett. (in press).

[8] S. D. Kevan and R. H. Gaylord, Phys. Rev. **B.** 36, (1987) 5809.

[9] D. H. Dowell, et. al. NIMA 507 (2003) 327.

# ANALYSIS OF HALO FORMATION IN A DC PHOTOINJECTOR

D. Mihalcea, P. Piot, Northern Illinois University, DeKalb, IL 60115, USA

*Abstract*

We discovered, by modeling the AES/JLab direct-current photoinjector with several beam-simulation codes, that nominal injector settings would create a large diffuse beam halo as a consequence of the internal space-charge force in the beam. The injector-induced halo is sensitive to the injector settings, but if the settings are judiciously chosen, it can be largely circumvented. We present an exploration of the parameter space for the AES/JLab photoinjector. Measurement of beam halo will be a crucial aspect of commissioning this machine.

## INTRODUCTION

The present driving accelerator for the Jefferson Lab 10 kW IR Free-Electron Laser (FEL) provides a 10 mA average current electron beam with energy up to 160 MeV and normalized transverse emittance less than 30 $\mu m$ [1, 2]. Since the gain of the laser increases with the electron beam current [3], to achieve megawatt-class FELs the injector should be upgraded to increase the average beam current at ampere level.

The normalized transverse emittance scales linearly with the laser wavelength and the relativistic factor $\gamma$ [4]:

$$\epsilon_N < \frac{\lambda\gamma}{4\pi} \quad (1)$$

Shorter laser wavelengths and/or more compact driving accelerators (lower energy) can be achieved by decreasing the emittance.

The next generation megawatt-class JLab FEL will require much improved quality of the electron beam. In particular the average beam current must be at ampere level and the transverse emittance not larger than a few microns. The upgraded photoinjector was designed at Advanced Energy Systems (AES) [5] and will be fabricated at Jefferson Lab.

In this paper we present some simulation results for this upgraded AES/JLab photoinjector. Due to the relatively large space charge forces, there is the potential for unwanted halo formation. The goal of our annalysis is to determine what are the photoinjector operating conditions that preclude halo formation and maximize the beam quality.

## AES/JLAB PHOTOINJECTOR

This new photoinjector [5] couples a normal-conducting DC gun a section of three 750 MHz superconducting RF single cells and a third harmonic 2250 MHz cavity. The schematic layout of the photoinjector is shown in Fig. 1.

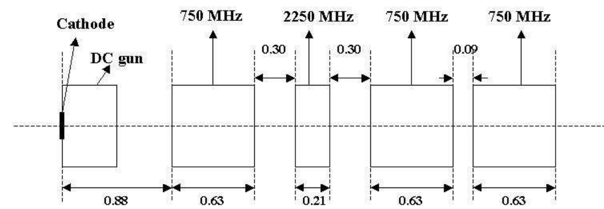


Figure 1: Schematic layout of the AES/JLab photoinjector. Emittance compensation solenoid is not shown. All dimensions are in meters.

Electron bunches of up to 1 nC charge and about 20 ps (rms) long are extracted from a photocathode illuminated with an infrared mode-locked Nd:YLF laser. The maximum accelerating gradient in the DC gun is 6 MV/m and the electron energy at the exit from the gun is about 1 MeV. At the end of the gun there is a solenoid to compensate the emittance growth due to space charge and external fields.

Three 750 MHz superconducting RF single cell cavities raise the energy of the electrons up to 6 MeV. A third harmonic cavity, located between first and second 750 MHz accelerating cavities, is used to linearize the energy dependence on longitudinal spatial coordinate.

## BEAM HALO FORMATION

Photoinjector parameters like cavities amplitudes and phases, solenoid magnetic field, gun accelerating voltage are optimized to minimize longitudinal and transverse emittances at the exit from the photoinjector. Fig. 2 shows the most important beam moments when the charge of the electron bunches is 1 nC (750 mA), the initial beam radius at the cathode is 3 mm, and the initial longitudinal bunch profile is gaussian with $\sigma_z = 20$ ps.

The results from Fig. 2 were obtained with Parmela [6] and Impact-T [7]. The most sensitive parameters in the optimization process were the magnetic field in the emittance compensation solenoid and the phase of the third harmonic cavity. The values of the most important beam moments are within the desired limits when the current is 100 mA and about 20% higher for transverse and longitudinal emittances when the current is increased to 750 mA.

Beam halo may develop if the size of the laser spot at cathode is decreased in an attempt to increase the electron bunch charge density. Figure 3 shows the transverse beam distributions at two locations downstream of the cathode when initial distribution has radius 2 and 3 mm respectively, the beam current is 750 mA, and the laser pulse duration is 20 ps. When the initial radius is 2 mm the halo has

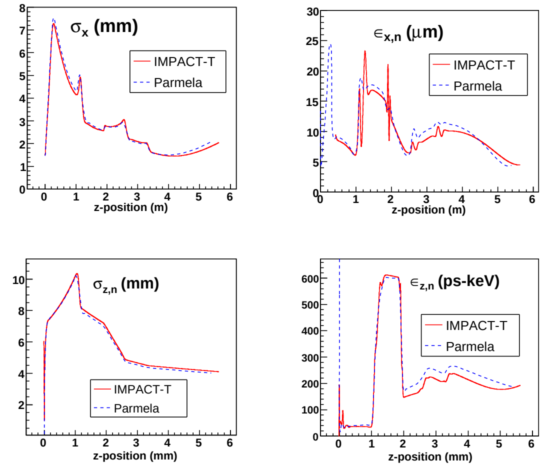


Figure 2: Beam moments as a function of the distance from the cathode. The average beam current is 750 mA and the radius of the beam at cathode is 3 mm.

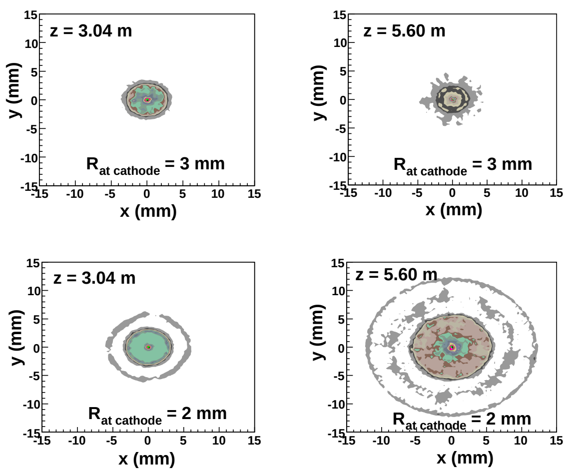


Figure 3: Transverse slices of the phase space at the entrance in the third accelerating cavity (left) and at the exit from the photoinjector (right). The radius of the beam at cathode was 3 mm (upper plots) and 2 mm (bottom plots).

the shape of cylindrical rings well separated from the core of the beam. There are two such rings at 5.62 m downstream of the cathode. The inner and outer rings contain 19% and 16% respectively, of the total bunch charge.

To identify the properties of the beam halo we tracked the outermost particles through the whole photoinjector. Figure 4 shows the distance between the outermost particle and beam axis, as well as beam radius and normalized transverse emittance as functions of laser spot size at the cathode. For 1 nC electron bunches halo may develop if laser duration is set at 20 ps and the initial transverse size is below 2.8 mm.

For the outermost particle (at the exit from photoinjector) Fig. 5 shows its radial position and velocity when ini-

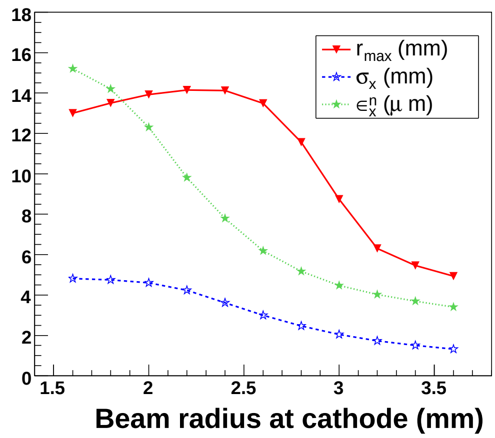


Figure 4: The distance between the outermost particle and the beam axis ($r_{max}$), the radius of the beam (rms), and the normalized transverse emittance as functions of the beam radius at cathode.

tial beam radius is 2 and 3 mm. For comparison, the non-realistic case when space charge forces are shutdown during the simulations is also shown in Fig. 5. When the spot size at the cathode is increased (from 2 mm to 3 mm) and the bunch charge is kept constant, the charge density decreases and consequently both radial electric field and radial velocity decrease. When space charge forces are turned-off there is still a small radial velocity (Fig. 5) due to the external electric field in the gun and accelerating cavities. The outermost particles at the exit from photoinjector (prime candidates for beam halo) originate from those particles that are farthest away from the beam axis at the generation level on the cathode's surface where space charge forces are maximal.

Our simulations show that transverse velocity and distance to beam axis are no longer linearly correlated when the initial beam radius is lowered to 2 mm. Figure 6 shows transverse velocity (in units of c) and distance from beam axis for all macroparticles when initial radius is 2 mm (upper plots) and 4 mm (bottom plots) and the z-location of the bunch is upstream (left plots) and downstream (right plots) of the first SRF cavity. Outermost particles have larger radial velocity moving toward the beam axis in the "2 mm" case (Fig. 6 top left plot) and they cross the beam axis after the reduction of the space charge forces due to the acceleration in the first SRF cavity (Fig. 6 top right plot). These particles, circled by the red marker in Fig. 6, break the laminar flow and depart from the core of the beam forming the ring-halo.

When the initial beam radius is increased from 2 mm to 4 mm (Fig. 6 bottom plots) the laminar flow is mostly restored but it is still true that the outermost particles originate from those with larger radial velocities at the entrance in the first SRF cavity.

By diminishing the space charge forces it is possible not

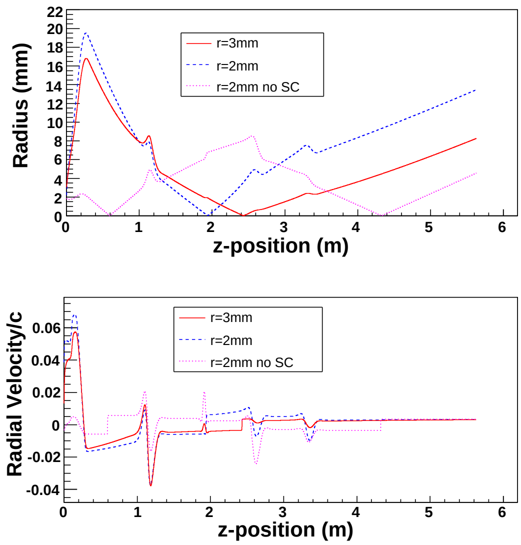


Figure 5: Top plot: the distance between the outermost particle and the beam axis as a function of the distance from cathode, when the initial beam radius was 2 mm, 3 mm, and 2 mm with space charge calculation turned off. Bottom plot: the radial velocity of the outermost particle as a function of the distance from cathode.

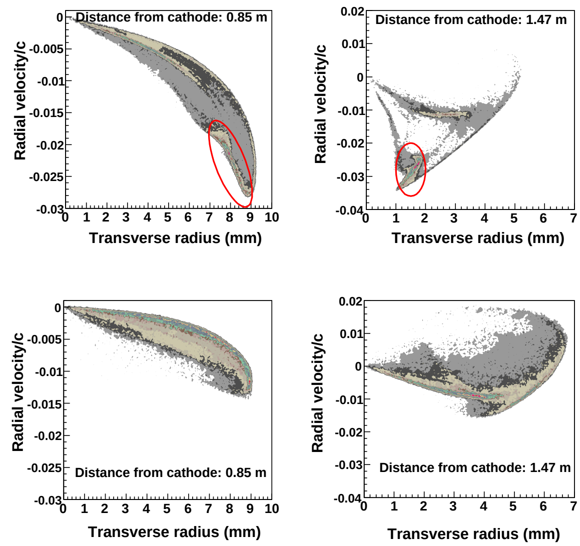


Figure 6: Slices of the phase space showing the radial velocity vs. the distance from the beam axis when the initial beam radius is 2 mm (upper plots) and 4 mm (bottom plots). For each case the plots correspond to two z-locations: upstream and downstream of the first SRF cavity. The red marker shows the location of the particles that generate the halo further downstream of the first SRF cavity.

only to improve the emittance but also to avoid the halo formation. In addition to increasing the laser spot at the cathode we investigated two more ways to reduce the space charge effects. The first was to use a flat longitudinal distribution (instead of the standard gaussian) [8] and the second was to use approximate ellipsoidal electron bunches [9]. Our simulations indicate that in both cases the halo formation can be avoided.

## CONCLUSIONS

We determine as cause for halo formation in electron beams the early tidal shock from space charge forces. The particles that experience the largest radial space charge forces in the vicinity of the cathode are the source for beam halo.

The simplest way to suppress halo is to increase the laser spot size at cathode. In the case of AES/JLab direct-current photoinjector beam halo at the exit from the photoinjector may be present when 1 nC electron bunches are generated with transverse size shorter than 2.8 mm. Other techniques to lower the space charge forces, like the use of electron bunches with flat longitudinal distribution or ellipsoidal shape, can also suppress the beam halo.

This work was supported by the Department of Defense under contract N00014-06-1-0587 with Northern Illinois University

## REFERENCES

[1] D. Douglas, *et al.*, "A 10 kW IR FEL Design for Jefferson Lab", PAC2001, p249-252, (2001).

[2] C. Hernandez-Garcia, *et al.*, "Performance and Modeling of the JLab IR FEL Upgrade Injector", Proceedings of the 2004 FEL Conference, p558, (2004).

[3] C. W. Roberson and P. Sprangle, Phys. Fluids B **1**, p3, (1989).

[4] L. H. Yu, *et al.*, NIM A272, p436, (1988).

[5] A. Todd, *et al.*, Proceedings of 2003 IEEE Particle Accelerator Conference, Portland, OR, p977 (2003).

[6] L. Young, LANL report LA-UR-96-1835.

[7] J. Qiang, *et al.*, Proceedings of 2005 IEEE Particle Accelerator Conference (PAC 05), Knoxville TN, p 3316 (2005).

[8] R. Tikhoplav, *et al.*, Proceedings of the 2006 Advanced Accelerator Concepts, p 694-700 (2006).

[9] O. J. Luiten, *et al.*, Phys. Rev. Lett., vol. **93**, 094802 (2004).

# A HIGH-BRIGHTNESS LOW-ENERGY PHOTOINJECTOR OPTION FOR THE FERMILAB ELECTRON ACCELERATOR FACILITY

P. Piot, Northern Illinois University, DeKalb, Illinois;
M. Church, Fermilab, Batavia;
D. Mihalcea, Northern Illinois University, DeKalb, Illinois;
S. Nagaitsev, Fermilab, Batavia;
I. V. Pogorelov, LBNL, Berkeley, California;
Y.-E. Sun, Fermilab, Batavia

## Abstract

Fermilab is currently constructing a GeV-scale electron accelerator test facility. The accelerator will serve as a backbone for several Fermilab R&D programs, e.g., to test subsystem associated to project-X, ILC and the muon collider program. It is also anticipated that this facility will support beam physics and accelerator R&D programs such as testing of novel acceleration techniques, beam diagnostics and radiation sources concepts. In this paper we describe a possible option for the electron injector based on a photoemission rf gun. Optimization and performance studies of this ~50 MeV photoinjector are performed with various tracking programs (Astra, GPT, Impact-T, Impact-Z). We explore the performances of the magnetic bunch compressor which is extremely challenging at 50 MeV due to strong phase space dilution via collective effects (space charge and coherent synchrotron radiation). We also investigate the generation of flat beams with very high transverse emittance ratio using a round-to-flat beam transformer.

**CONTRIBUTION NOT RECEIVED**

# SIMULATION OF THE UPGRADED PHOTOINJECTOR FOR THE 10 KW JLAB IR-FEL*

P. Piot, Department of Physics, Northern Illinois University, DeKalb, IL 60115, U.S.A.
and Accelerator Physics Center, Fermi National Accelerator Laboratory, Batavia, IL 60510, U.S.A.
D. Mihalcea, Department of Physics, Northern Illinois University, DeKalb, IL 60115, U.S.A.
C. Hernandez-Garcia, S. Zhang, Free-Electron Laser Group,
Thomas Jefferson Accelerator Laboratory, Newport News, VA 23606, U.S.A.

*Abstract*

The photoinjector of the JLab 10 kW IR FEL was recently upgraded: a new photocathode drive laser was commissioned and the booster section was replaced with new 5-cell cavities. In this paper we present numerical simulation and optimization of the photoinjector performances using ASTRA, IMPACT-T and IMPACT-Z beam dynamics codes. We perform these calculations for the nominal 350 keV operating voltage of the dc gun.

## INTRODUCTION

Jefferson Lab is currently operating a high average power infrared free-electron laser [1]. The driver accelerator is an upgraded version of the now decommissioned 1 kW IR-Demo FEL [2]. The facility also serve as a platform to explore beam dynamics phenomena and technologies associated with the realization of very high-average-power free-electron lasers. The driver accelerator comprises a $\sim 10$ MeV injector followed by a 80-200 MeV energy recovering superconducting RF linac that allows high average current operation with modest klystron power. To reach the 10 kW goal, the charge-per-bunch was increased from 60 pC to 135 pC and the bunch repetition rate from 37.425 MHz to 74.850 MHz. The requirements on beam quality at the wiggler location to lase with a 10 kW average power using 135 pC bunches are gathered in Table 1. The photoemission injector, whose block diagram is shown in Figure 1, is a key element in achieving the required beam quality. It basically consists of a 350 keV line coupled with a high gradient RF structure consisting of two CEBAF-type superconducting cavities that can accelerate the beam up to approximately 10 MeV. The accelerating section is followed by a 10 MeV injection line that includes a diagnostics suite.

## BEAM GENERATION & ACCELERATION

The low-energy line consists of a high-voltage DC photoemission gun for electron generation, a room-temperature buncher cavity and two solenoidal lenses (see Fig. 1). The gun uses a GaAs photocathode driven by a Nd:YLF laser [3] . The drive laser is mode locked to

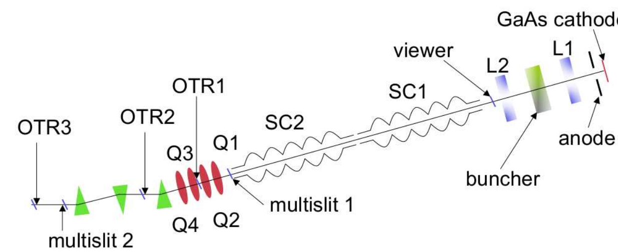


Figure 1: Overview of the Jlab IR-FEL photoinjector. The legend is ”L1” ”L2”: solenoidal magnetic lenses, ”SC1” ”SC2” superconducting 5-cell CEBAF cavities, ”Q1...4” quadrupoles, ”OTR1...3” optical transition radiation screen, ”multislit” emittance measurement stations. The green triangles indicate the locations of the sector dipoles composing the merger.

Table 1: Beam parameters specifications at the injection point (“multislit 2” in Fig. 1).

| parameter | value | units |
|---|---|---|
| bunch charge $Q$ | 135 | pC |
| transverse emit. $\varepsilon_{x,y}$ | $\leq 10$ | $\mu$m |
| $\beta_{x,y}$ | 10 | m |
| $\alpha_{x,y}$ | 0 | - |
| bunch duration $\sigma_t = \sigma_z/c$ | [1.5,2.5] | ps |
| longitudinal emit. $\varepsilon_z$ | $\leq 28$ | ps-keV |
| energy spread $\sigma_E$ | $\leq 15$ | keV |

37.425 MHz corresponding to the fortieth subharmonic of the rf fundamental frequency (1497 MHz) of the RF system. It can provide various micropulses shape and durations with a variable repetition rate ranging from 0.245 to 74.850 MHz. The gun is currently operated at 350 kV. Efforts to develop a gun capable of withstanding an accelerating voltage of 500 kV are underway. The beam is then ballistically bunched with a 1.5 GHz single-cell buncher [6] located $\sim$ 1 m upstream of the SCRF accelerating section. The accelerating section incorporate two modified CEBAF 5-cell cavities capable of maximum peak E-field of $\sim 20$ MV/m.

The performance of the beam generation and acceleration section was investigated with ASTRA [7]. The dc-gun

* Work supported by the Department of Defense under contract N00014-06-1-0587 with Northern Illinois University.

and the magnetic solenoid lenses are modeled by their axial electric or magnetic field obtained from POISSON simulations. The CEBAF cavities and buncher are described by their axial electric field simulated using SUPERFISH. In all the cases the electromagnetic structures are assumed to be cylindrical-symmetric and the radial electric and azimuthal magnetic fields are derived form a third order off-axis expansion. An evolutionary algorithm GENETICOPTIMIZER [8] was used in conjunction with ASTRA to seek a set of optimum operating parameters for the photoinjector such to minimize the longitudinal emittance downstream of the accelerating section. The transverse emittance, bunch duration, and energy spread were constrained accordingly to the specified range of values shown in Table 1. For fast throughput 2000 macroparticles were used to optimize the accelerator settings. The variable parameters for the optimization were: the transverse laser spot size, the solenoids magnetic field, the buncher and accelerating cavities electric field amplitudes and phases. The photocathode drive laser was assumed to have a uniform cylindrically-symmetric transverse distribution and three cases of temporal distributions were considered (Fig. 2). The evolution of beam parameters obtained for the best longitudinal emittance are shown in Fig. 3 for the three cases of the laser temporal distributions shown in Fig. 2. These simulations were performed using 200k macroparticles. The ”long” laser pulse does not meet the specified longitudinal emittance while the ”short” and ”flat top” shapes for the laser temporal distribution meet all requirements. The optimum settings for the short laser case call for a rather large laser spot size of $\sigma_c = 4$ mm (the maximum allowed – and twice of the spot size routinely used) on the photocathode. This, in turn, results in large transverse spot sizes in the low energy transport upstream of the accelerating cavities. However no particle loss are observed in our simulations (the beam pipe apertures are included). For these three sets of simulations the kinetic energy is within the specified range of $[9, 10]$ MeV.

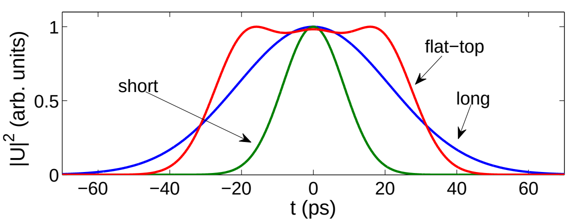


Figure 2: The three different photocathode drive laser intensity temporal distribution assumed for the optimization of the generation and acceleration section.

## 10 MEV SECTION

The 10 MeV accelerating section is followed by a quadrupole telescope and a “staircase” achromatic merger composed of three sector bending dipoles with bending angles $\theta = (+, -, +)\ 20°$. The dispersion function reaches a maximum in the second dipole ($|\eta_x| \simeq 56.38$ cm) and has a value of $|\eta_x| = 30$ cm at OTR2

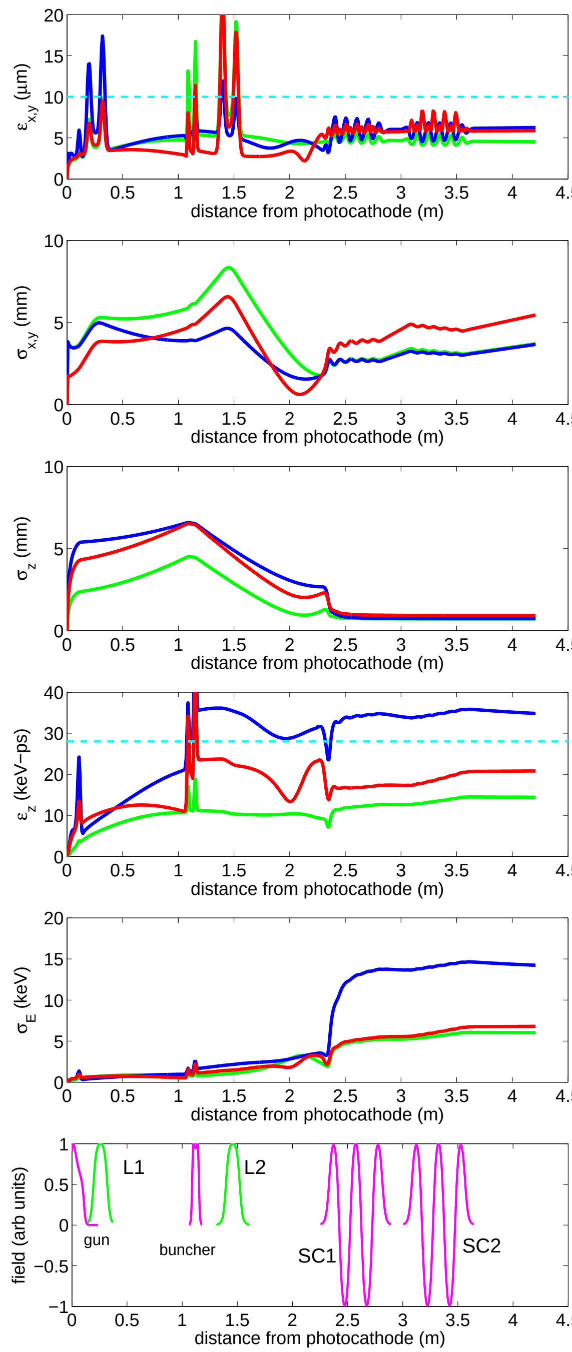


Figure 3: Rms beam parameters for the optimum injector settings that result in the smallest longitudinal emittance for the three different photocathode drive laser temporal distribution shown in Fig. 2 (same color coding is used). The bottom plot shows the field profile and location of each component. The symbols are defined in Table 1 and Fig. 1, $\sigma_{x,y}$ is the rms transverse beam size.

(see Fig. 1) thereby enabling energy profile measurement. The merger is non-isochronous with a longitudinal dispersion $R_{56} \simeq -19.25$ cm[1]. Therefore an incoming bunch with proper correlated energy spread can be further compressed. Two effects set the upper and lower limits on the bunch length downstream of the merger. On one hand a longer bunch length alleviates the detrimental effects of longitudinal space charge [10]. On another hand longer bunch lengths result in nonlinear (mainly quadratic) distortions of the longitudinal phase space as the bunch is accelerated in the downstream cryomodules. Such distortions yield significant longitudinal emittance growth. Simulations of the beam dynamics in the merger were

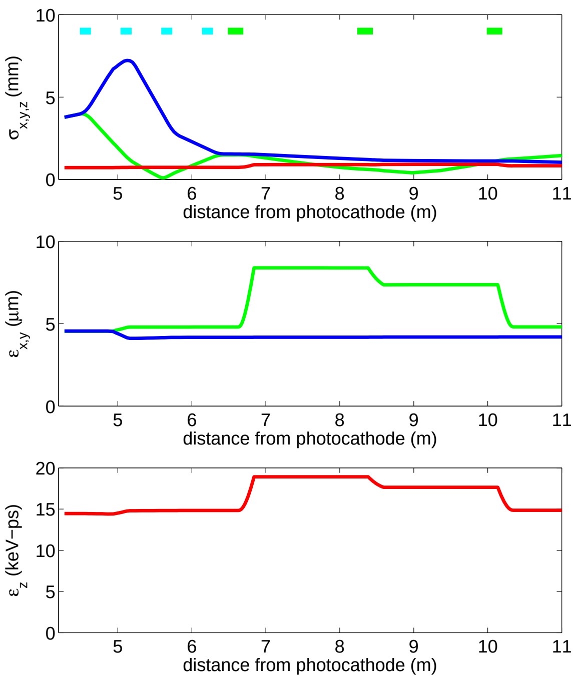


Figure 4: Rms beam properties along the 10 MeV section for the "short" laser pulse shape. The cyan and green rectangles on the upper plot respectively indicate the location of the quadrupoles and sector dipoles.

performed with IMPACT-T [11] which incorporates a 3-D poisson solver. Coherent synchrotron effects are neglected. The quadrupoles were varied to approximately achieve the desired Courant-Snyder parameters at the entrance of the main linac. The evolution of the rms beam parameters associated to the case of the short laser pulse shows minor emittances dilutions through the 10 MeV section; see Fig. 4. The corresponding longitudinal phase space at the injection point is shown in Fig. 5. Furthermore IMPACT-T simulations confirm that the bunch length can be tuned by varying the phase of SC2 without affecting the beam emittances (the final bunch length were $\sigma_z \in [0.5, 2]$ mm).

[1]In our matrix convention the $t > 0$ corresponds to the tail of the bunch

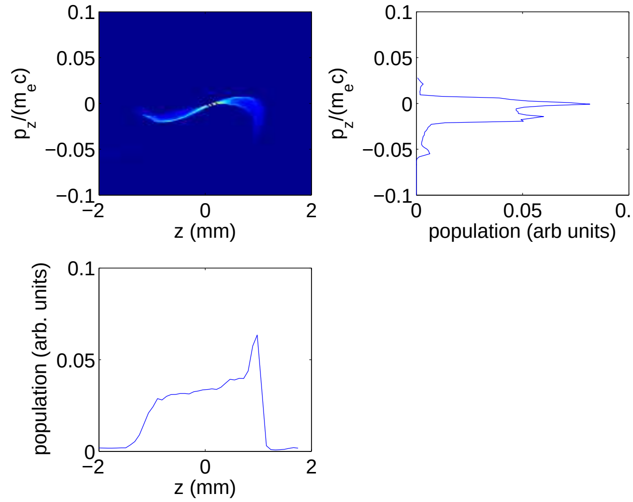


Figure 5: Longitudinal phase space and corresponding projections at the injection point for the "short" laser case.

## SUMMARY

Simulation and optimization of the injector currently in operation at the 10 kW JLab FEL have been performed for different scenarios of photocathode drive lasers. Optimum settings were found for two laser configurations that could provide beam parameters within the specified values. It is hoped that these simulations will serve as guidance to test and validate new settings of the photoinjector aimed at lowering the longitudinal emittance.

## REFERENCES


[1] S. V. Benson, *et al.*, Proceedings of the 2007 Particle Accelerator Conference, Albuquerque NM, 79 (2007).

[2] G. R. Neil, *et al.*, *Phys. Rev. Lett.*, **84**, 662 (2000).

[3] D. Engwall *et al.*, Proceedings of the 1997 Particle Accelerator Conference, Vancouver BC, 2693 (1997).

[4] H. Liu, D. Neuffer, Proceedings of the 1995 Particle Accelerator Conference, Dallas TX, 1867 (1995).

[5] P. Piot, *et al.*, Proceedings of the 1998 European Particle Accelerator Conference, Stockholm Sweden, 1447 (1998).

[6] B. C. Yunn, CEBAF internal report TN-94-021, available from Jefferson Lab (1994).

[7] K. Flöttmann, ASTRA: A space charge tracking algorithm, available from www.desy.de/˜mpyflo/Astra_dokumentation

[8] M. Borland and H. Shang, GENETICOPTIMIZER unpublished program (private communication, 2006).

[9] C. Hernandez-Garcia et al., Proceedings of the 2004 FEL conference, Triestre Italy, 558 (2004).

[10] C. Hernandez-Garcia et al., Proceedings of the 2004 FEL conference, Triestre Italy, 363 (2004).

[11] The IMPACT-Z / IMPACT-T suite of codes was provided by Ji Qiang of LBNL (2007).

# SIMULATION OF FIELD-EMISSION CATHODES FOR HIGH CURRENT ELECTRON INJECTORS

D. Mihalcea, P. Piot, Northern Illinois University, DeKalb, IL 60115, USA

*Abstract*

From the prospect of the high average current electron injectors, the most important advantage of the field-emission cathodes is their capability to generate very large current densities. Simulation of field-emission cathodes is complicated by the large range of spatial dimensions: from sub-micron scale, for a single field-emission tip, to millimeter scale, for a field-emitter array. To overcome this simulation challenge our numerical model is split in two steps. During the first step, only electrons emitted by a single tip are considered. In the second step, the beams originating from many single emitting tips are merged together to mimic the field-emitter array configuration. We present simulation results of injector based on field array emitters cathodes.

## MOTIVATION

Since the gain of a Free Electron Laser (FEL) increases with the electron beam current [1], to achieve megawatt-class FELs the injector should be upgraded to ampere level of average beam current. This can be done with standard photoinjectors but problems related to low quantum efficiency and limited lifetime of the photocathodes still need to be addressed. The upgrade of the Jefferson Lab IR FEL [2], requires a complete replacement of the old photoinjector. The new photoinjector [3] can deliver average beam current at ampere level, but, according to our simulations both transverse and longitudinal emittances exceed the specifications. New electron sources (like field-emitting cathodes) could eventually have better performances than standard photoinjectors. Diamond made field-emitters are mechanically robust, can carry large density currents, and because of the large external fields in the emitting area, the emittance growth due to space charge is diminished.

## THEORETICAL MODEL

Quantum tunneling allows extraction of electrons from atoms when large enough external electric field is present. The current density is given by Fowler-Nordheim (FN) equation:

$$j = \frac{K_1 E^2}{\phi} exp(-\frac{K_2 \phi^{1.5}}{E}) \quad (1)$$

where $E$ is the external electric field, $\phi$ the work function of the material and $K_1$, $K_2$ constants. Throughout this analysis we use the same values of the constants as in [4], $K_1 = 1.54 \times 10^{-6}$ A eV/V$^2$, $K_2 = 6.83 \times 10^7$ V/ (cm eV$^{3/2}$) and the work function for diamond $\phi = 4.15$ eV. The graph of the current density as a function of external electric field is shown in Fig. 1.

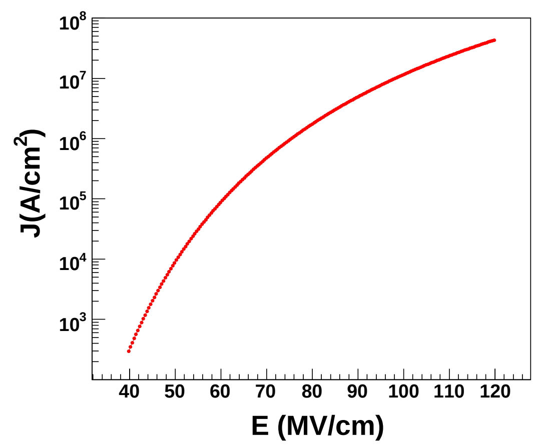


Figure 1: Fowler-Nordheim equation with the values of the constants indicated in the text.

In this paper we consider cylindrically symmetric diamond made field-emitters of conical shape. The tip of the cone is assumed spherical with a small curvature radius to favor a large external field enhancement in the region of the tip. The results shown in this paper are based on the assumption that the curvature radius of the field-emitting tip is 0.1 $\mu$m, but smaller tip radii of 0.05 $\mu$m and 0.01 $\mu$m were also considered. A field-emission cathode consists of an array of diamond made single field-emitters separated by distances of the order of a few tens of microns.

The simulation of electron beams from field-emission arrays is complicated by the large range of spatial dimensions: microns in the region of a single field-emitter and millimeters for the whole cathode. Therefore, as in [6], we split the simulation into two parts: first we simulate the electron beam from a single field-emitter and then in the second part the beamlets are merged together to mimic the beam extracted from the whole array of single field-emitters.

## SINGLE FIELD-EMITTERS

A typical single field-emitter consists of a conical shape diamond made cathode, an accelerating control electrode (gate) and at least one focusing layer (Fig. 2). To control the injection phase of the electrons into the gun, it is convenient to apply on the gate a time dependent voltage such that the electrons are emitted only during a narrow time window [5]. Since time constants to reach steady state inside the emitter are in the subpicosecond range, it is reasonable to assume that external fields are static [6].

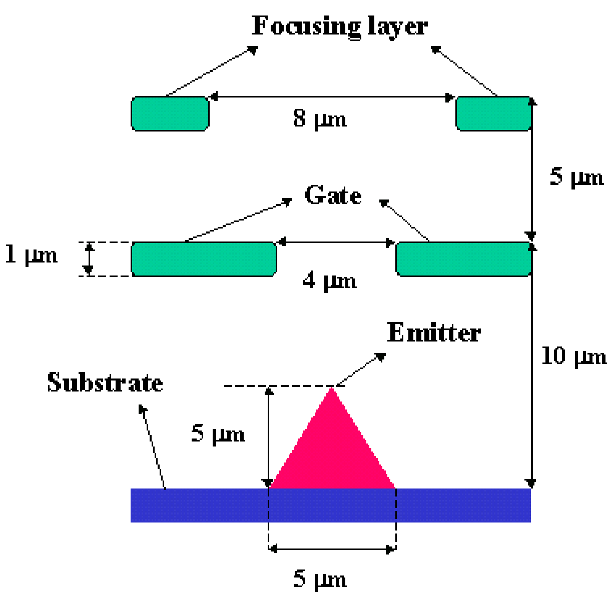


Figure 2: Geometry of single field-emitters.

In the first step of the simulation the map of the electric field is used to generate a particle distribution located just underneath the emitting surface. The electric field distribution (generated with LANL Poisson code [7]) depends on emitter geometry (Fig. 2) and on the constant voltages applied between the gate and cathode ($V_1$) and between the focusing layer and the gate ($V_2$). The accuracy of the field calculation is determined by the integration step used by Poisson software to evaluate the fields. This parameter was set at $10^{-2}\mu$m in both transverse directions for the most part of the integration domain. In the proximity of the tip, were the gradient of the electric field is significantly higher the integration step was lowered at $10^{-3}\mu$m.

The electric field at the tip of the diamond made cathode is a factor of $\beta \approx 30$ higher than the average accelerating field. An additional 4-5 enhancement factor is due to the surface roughness in the nanometer range [8]. To exemplify, the acceleration voltage should be about 530 V to obtain a total current of 57 $\mu$A if the surface roughness enhancement factor is conservatively assumed to be 4.

Our simulations show that the external electric field decreases rapidly with the radial distance from the emitter tip. In fact, external field is large enough to produce any significant field emission only in the region of the spherical portion of the field emitter. Figure 3 shows that the probability for field emission drops rapidly outside of the spherical region of the field-emitter. This observation may not be true

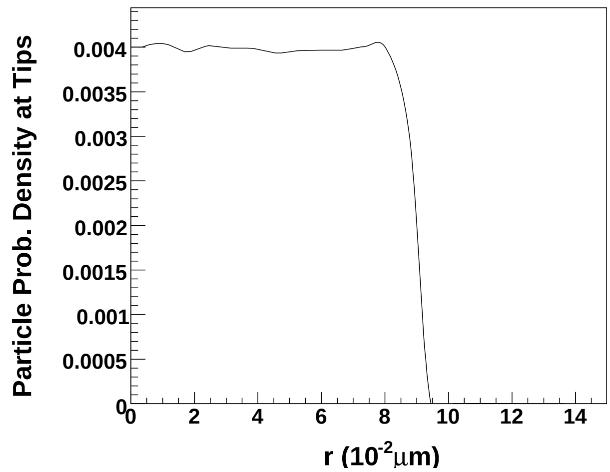


Figure 3: Probability of field emission as a function of the radial distance from the emitter tip.

in the case of pyramidal field-emitters because the electric field enhancement could be also large at the pyramid edges.

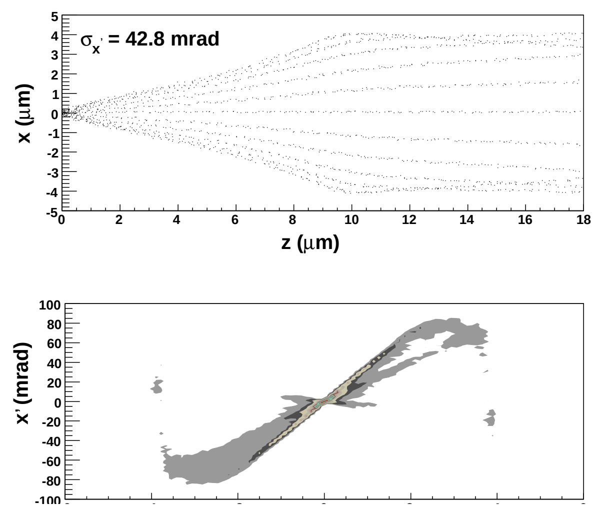


Figure 4: Top: electron trajectories when acceleration and focusing voltages are $V_1 = 530$ V and $V_2 = -400$ V respectively. Bottom: longitudinal phase space just after the focusing layer.

In the second step of the simulation the particle distribution generated in the first step is propagated from field-emitter to anode ($\approx 15\ \mu$m), with the particle tracking code Impact-T [9]. Slight modifications of the code were made to extract the particles from the beamlet once they arrive the anode and to store the new particle distribution. To focus the beam the voltage between the focusing layer and the gate ($V_2$) must be opposite to the accelerating voltage $V_1$. The lowest beam angular spread ($\sigma_{x'}$) is obtained when $V_2 \approx -0.75 \cdot V_1$ (Fig. 4).

For the case of $I = 57\ \mu$A, $V_1 = 530$ V and $V_2 =$

$-400$ V, the most important beamlet characteristics are: $(\epsilon)_{x,rms} = 8.3 \cdot 10^{-2}$ $\mu$m, $\sigma_x = 2.4$ $\mu$m, $\sigma_{x'} = 42.8$ mrad, $E = 0.34$ keV, and $\delta E/E = 4.5$ %.

Finally, the coordinates of the particles are translated in the transverse direction to mimic a distribution generated by an array of field-emitters. The longitudinal particle distribution depends on the accelerating and focusing voltages, but the pattern is similar to the initial distribution.

## COMPARISON WITH PHOTOEMISSION-CATHODES

The JLab IR FEL injector electron source consists of a DC-voltage GaAs photocathode gun driven by a mode-locked Nd:YLF laser. The electric field at the surface of the cathode is about 6 MV/m and the kinetic energy at the gun exit is 0.5 MeV. The typical electron bunch has 135 pC and its volume is relatively large in order to minimize the space charge effects. During normal operation the laser pulse duration is about 20 ps (rms) and the radius of the spot is 4 mm.

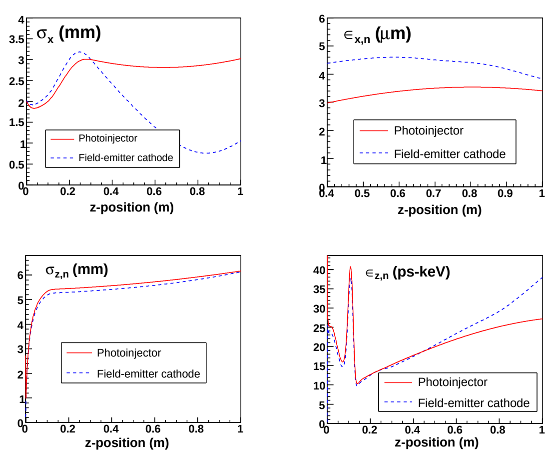


Figure 5: Beam moments at gun exit for a standard photoemission cathode and for a field-emitting cathode.

For comparison, we consider a field-emission array with individual emitters separated by 33 $\mu$m and with the same size as the regular photoemission cathode. To match the peak current of the standard photoemission cathode, each field-emitter should contribute with about 57 $\mu$A. The most important beam moments at the exit from the gun are shown in Fig. 5 for both standard photoemission cathode and field-emission array. The beam quality, measured by transverse and longitudinal emittances, is about the same in both cases.

## CONCLUSIONS

Since the field-emission effect occurs when the external electric field is of the order of several GV/m, the most challenging problem is to build field-emitting structures that do not break under such intense fields. Recent work [10] show that somewhat simpler field-emitting structures (array of field-emitting diamond made pyramids and just one metallic layer) are very reliable and the fluctuation of the extracted current is remarkably low.

A comparison based on simulations between the Jlab FEL DC-gun and the same gun equipped with a field-emission array shows that beam quality is about the same when the average current is set at the normal operating value of 100 mA. The next goal for the high current Jlab FEL injector is to deliver beam current at ampere level and this is out of reach with the existing photoemission cathode. An important candidate could be a field-emission cathode because even a small increase of the external field would lead to a substantial increase of the peak current. For the field-emitter arrays considered here, an increase of the external field from 50 to 60 MV/m would bring the peak current from 50 $\mu$A to milliamp range. A field-emitting array consisting of a few thousands single emitters can deliver beam current at the desired level.

This work was supported by the Department of Defense under contract N00014-06-1-0587 with Northern Illinois University.

## REFERENCES

[1] C. W. Roberson and P. Sprangle, Phys. Fluids B **1**, p3, (1989).

[2] C. Hernandez-Garcia, *et al.*, "Performance and Modeling of the JLab IR FEL Upgrade Injector", Proceedings of the 2004 FEL Conference, p558, (2004).

[3] A. Todd, *et al.*, Proceedings of 2003 IEEE Particle Accelerator Conference, Portland, OR, p977 (2003).

[4] A. Wisitsora-at, *et al.*, Journal of Vacuum Science & Technolgy B: Microelectronics and Nanometer Structures, **21**, p1671, (2003).

[5] J. W. Lewellen and J. Noonan, Pysical Review Special Topics - Accelerators and Beams, **8**, 033502, (2005).

[6] M. Dehler, A. Candel and E. Gjonaj, J. Vac. Sci. Tecnol. B 24(2), p 892, (2006).

[7] J. H. Billen and L. M. Young, LANL report LA-UR-96-1834.

[8] C. A. Spindt, I. Brodie, L. Humphrey, and E. R. Westerberg, J. Appl. Phys. **47**, 5248 (1976).

[9] J. Qiang, *et al.*, Proceedings of 2005 IEEE Particle Accelerator Conference (PAC 05), Knoxville TN, p 3316 (2005).

[10] C. A. Brau and J. L. Davidson, ANL TAWG presentation, May 2008.

# LONGITUDINAL BEAM DIAGNOSTICS FOR THE ILC INJECTORS AND BUNCH COMPRESSORS

P. Piot, Fermilab, Batavia, Illinois;
A. Bracke, Northern Illinois University, DeKalb, Illinois;
C.-J. Jing, Euclid TechLabs, LLC, Solon, Ohio;
T. J. Maxwell, D. Mihalcea, Northern Illinois University, DeKalb, Illinois;
J. G. Power, ANL, Argonne, Illinois;
M. M. Rihaoui, Northern Illinois University, DeKalb, Illinois

## Abstract

We present a diagnostics suite and analyze techniques for setting up the longitudinal beam dynamics in ILC electron injectors and bunch compressors. Techniques to measure first order moment and recover the first order longitudinal transfer map of the injector intricate bunching scheme are presented. Coherent transition radiation diagnotics needed to measure and monitor the bunch length downstream of the ~5 GeV bunch compressor are investigated using a vector diffraction model. We finally introduce a new diagnostics capable of measuring time-transverse correlation along a single bunch. Such a diagnostics should be valuable for controlling emittance dilution via transverse wakefield and for properly setting the crab cavities needed for maximizing luminosity for non-zero crossing angle at the interaction point.

**CONTRIBUTION NOT RECEIVED**

# INITIAL RF MEASUREMENTS OF THE CW NORMAL-CONDUCTING RF INJECTOR*

Frank L. Krawczyk#, Nathan A. Moody, Felix A Martinez, Gerald O. Bolme, Karen A. Young, Dinh C. Nguyen, Los Alamos National Laboratory, Los Alamos, NM 87545, USA
Lloyd M. Young, Advanced Energy Systems, Medford, NY 11763, U.S.A.

*Abstract*

The LANL 2.5-cell, normal-conducting radio-frequency (NCRF) injector has been fabricated [1]. We present initial results of low-power RF measurements (cavity Q, cavity field map, coupling beta, etc.) of the NCRF injector. The measured cavity Q and relative fields are found to be in good agreement with the design calculations and earlier measurements of Glidcop properties [2]. However, the coupling beta of the ridge-loaded waveguides is found to be significantly higher than the design point. The impact of these low-power measurement results on the planned high-power RF and electron beam tests will be discussed.

## INTRODUCTION

A 2.5 cell, π-mode, 700 MHz normal conducting RF-photoinjector cavity has been designed and built. It is seen as a crucial building block for low emittance high average current source for a 100 kW CW FEL. The operation at a gradient of 7, 7 and 5 MV/m in the three accelerating cells requires an RF-input in excess of 700 kW. While simulations show that the thermal management of this operation is feasible, the first step is to verify the operation of this prototype cavity without generating any beam. This thermal test is presently under preparation at LANL and is well under way to be started in September and completed by the end of CY2008. The pre-start activities and findings for the test will be reported here. They include vacuum and cooling passage integrity, bakeout and low-power rf-properties.

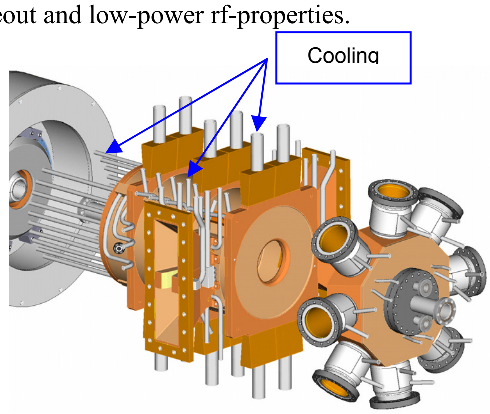


Figure 1: Exploded view of the photoinjector showing the cooling passages.

# fkrawczyk@lanl.gov

* This work is supported by the Office of Naval Research and the High-Energy Laser Joint Technology Office.

As the coupling from the ridge loaded waveguides to the cavity was different from the design point, a modification of the test setup for proper operation is provided also.

## STRUCTURAL AND VACUUM INTEGRITY

Besides the RF-performance, leak tightness of the cooling channels and proper vacuum sealing were of concern. Tests of all cooling channels indicated proper flow rates and showed no leaks into the cavity volume or to the outside.

The testing of the vacuum sealing required the installation of all vacuum pumps on the unexcited fourth cell, the cathode port in the first cell and the ridge loaded waveguide (RLWG) sections. A total of 9 ion pumps, a non-evaporative getter pump and five turbo pumps have been used. The total pumping speed is 600 l/s. The challenging seal between the waveguide (SST) and the RLWG (Glidcop) has been done with an AL/CU/Ni 90 Alloy Helicoflex seal. The system showed a good vacuum seal with a leak rate of less than 1 $10^{-10}$ Torr l/s.

## BAKEOUT INFORMATION

For a first cleaning of the RF-surfaces the cavity and all secondary ports have been baked out in a two-step process. In the first baking step all cavity parts were heated up to 175$^{o}$ C. The cavity was held at this temperature for 2 days. After cool-down the second bakeout period brought all parts of the cavity close to 150$^{o}$ C. For homogeneity the heating was controlled by 12 independent temperature zones. The base pressure after the bakeout was 2-3 $10^{-10}$ Torr. A cavity pressure in the low $10^{-10}$ Torr is needed for a good lifetime of future photocathodes.

Figure 2: Photoinjector wrapped in heating blankets for a bakeout that resulted in an excellent pre-test vacuum.

## LOW POWER RF-PROPERTIES

For the purpose of acceptance testing, all low power RF-properties of the cavity were measured before additional handling or installation of the cavity.

### *Cavity Q and Frequency*

For the $Q_0$ measurement antennas have been added for on-axis electric coupling on the cathode cell and the unexcited fourth (vacuum) cell. The probes have been successively shortened until the loaded Q did not change anymore with the presence of the probes. From the measured loaded Q and the corrections for the coupling βs $Q_0$ has been determined to be reasonably close to the expected value from the Superfish [3] simulations (in parentheses). The $Q_0$ value thus determined is 29108 (32600) at a center frequency of 700.2 (700.35) MHz.

### *Field Profile Measurement*

Another qualifying factor for the cavity is the proper ratio of field levels in the first 2.5 cells that needs to be 7, 7, and 5 MV/m, starting from the cathode cell. We set up a bead-pull measurement to obtain this ratio.

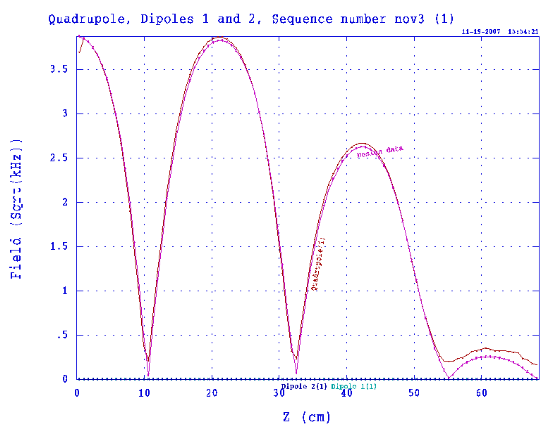


Figure 3: Comparison of the bead-pull measurement with the field distribution from Superfish. The agreement is better than 7%.

### *Waveguide Coupling*

The high power operation of the photoinjector requires accurate knowledge of the coupling of the ridge-loaded waveguides (RLWG) to the resonator volume. As this system has two strongly coupled waveguide couplers standard s-parameter measurement procedures do not apply. Any measurement through one port will measure the response of a system consisting of the resonator loaded by the RLWG connected to the second port. The configuration in Figure 4 requires two measurements to derive the unloaded coupling βs. It also allows calibration of the connections as close as possible to the cavity. While the original design planned for under-coupled waveguide couplers, the measured coupling was slightly above unity. This variation required a modification of the original test configuration of the photoinjector without beam. While the original plan assumed a symmetric RF drive through two couplers, the as-is coupling requires a single RF-feed with the second RLWG blanked off.

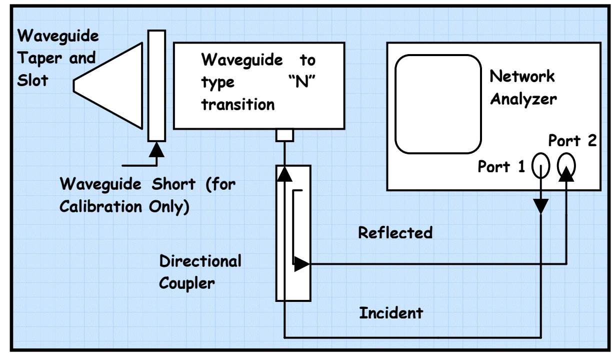


Figure 4: Calibration and coupling measurement for the waveguide couplers.

There are also some consequences for the operation with beam current. For the nominal current of 100 mA, a slightly larger reflected power than originally expected has to be handled.

### *Pick-up Probes*

Four RF-pickup probes have been placed in cells 2 and 3 of the photoinjector. As the power into the cavity is very high, extra care has been taken to have strongly attenuated signals to protect the probes from damage. All four probes show an attenuation of –55dB or larger.

## THERMAL TEST PREPARATION

Beyond the issues presented here, all facility preparations for the RF-test have been concluded. Pending the conditioning of the klystron, the test is scheduled to begin in the middle of September 2008.

## CONCLUSIONS

A novel RF-photoinjector for a high average current CW FEL has been built and installed in our test laboratory. Over the last year mechanical and RF-properties have been evaluated and the test stand was configured for a high power RF-test without beam. The photoinjector has passed all inspections prior to this high power test.

## REFERENCES

[1] Sergey S. Kurennoy et al., "Normal-conducting High Current Photoinjector for High-Power CW FEL", PAC05, Knoxville, USA

[2] Frank L. Krawczyk et al., "RF-Loss Measurements in an Open Coaxial Resonator for Characterization of Copper Plating", PAC07, Albuquerque, USA

[3] Los Alamos Accelerator Code Group Repository: http://laacg.lanl.gov/

# MODELING OF A LOW FREQUENCY SRF ELECTRON GUN FOR THE WISCONSIN FEL*

R. Legg#, UW-Madison/SRC, Madison, WI 53589, USA

*Abstract*

The Wisconsin FEL project is a 2.2 GeV, HHG seeded, FEL designed to provide six individual beamlines with photons from 5 to 900 eV. The FEL requires electron bunches with 1 kA peak bunch current and less than 1 mm-mrad normalized transverse slice emittance. To meet those requirements a low frequency, SRF electron gun is proposed which uses "blow-out" mode bunches [1]. Blow-out mode produces ellipsoidal bunches which are easily emittance compensated [2]. They also have a very smooth density and energy distribution. Results of the modeling of the injector and a diagnostic beamline are presented.

## INTRODUCTION

The Wisconsin FEL (WiFEL) project is a 2.2 GeV, HHG seeded, FEL designed to provide six individual beamlines with photons from 5 to 900 eV. The FEL requires electron bunches with 1 kA peak bunch current and less than 1 mm-mrad normalized transverse slice emittance. The injector for the WiFEL must supply the continuous stream of electron bunches which have the necessary transverse and longitudinal properties to support the compression system while minimizing the collective effects in the accelerator to the FEL. The bunch longitudinal profile must be optimized to avoid current spikes at the front and rear of the bunch charge density profile from wakefields [3]. At the same time, it must provide a bunch which reaches the kilo-amp level needed by the FEL for long enough to ensure overlap between the bunch and the seed laser in the undulator. It also must have a very smooth current density profile to prevent CSR or resistive wakefield microbunching in subsequent compressors. The 3D bunch profile which meets this requirement is a uniform ellipsoid [4].

To create an ellipsoidal bunch with uniform charge density, an ultra-short laser pulse with a hemispherical transverse profile is directed onto the photocathode. The charge pancake generated expands dynamically to form an ellipsoidal bunch under space charge forces. The limit on the dynamically formed bunch approach is that the charge density of the bunch is dependant on the peak electric field applied to the cathode. For a greater peak bunch current, either the electric field on the cathode must be increased or the emission radius must be enlarged with a consequent increase in thermal emittance; the limit for the FEL to operate, 1 mm-mrad, is reached at 1 mm rms radius for $Cs_2Te$ [5]. Twenty is about the maximum bunch compression ratio which can be easily achieved with two magnetic chicanes while preserving the beam parameters necessary to lase in a seeded FEL [6]. With that compression ratio 1 kA at the FEL requires 50 A peak from the gun. At the 1 mm rms emission radius the electric field on the cathode necessary to achieve 50 A peak is about 40 MV/m [7]. Such a CW field is too great for either a DC gun (field emission) or a CW normal conducting rf gun (thermal load), but is well within the reach of an SRF electron gun. For this reason, an SRF gun optimized to produce the smoothest maximum field on the cathode was selected.

The gun is to be built as part of the WiFEL R&D program along with a diagnostic beamline which can measure the bunch parameters. ASTRA [8] simulations of the beamline provided guidance in selection and placement of the diagnostic suite.

## ELECTRON GUN DESIGN

Table 1: Electron Gun Parameters

| | |
|---|---|
| Pulse frequency, MHz | 10 |
| Charge per bunch, pC | 200 |
| Average current, mA | <2 |
| $I_{peak}$ at first bunch compressor, Amps | 50 |
| Peak field in gun, MV/m | 41 |
| $\sigma_x$ at 100 MeV, mm | 0.34 |
| $\sigma_z$ at 100 MeV, mm | 0.34 |
| Transverse $\varepsilon$ at 100 MeV, mm-mrad | 0.9 |
| Longitudinal $\varepsilon$ at 100 MeV, keV-mm | 2.2 |

The electron gun design [9] uses a 200 MHz SRF half wave cavity with a warm, Cs2Te cathode mounted on a cathode stalk surrounded by a quarter-wave choke joint to

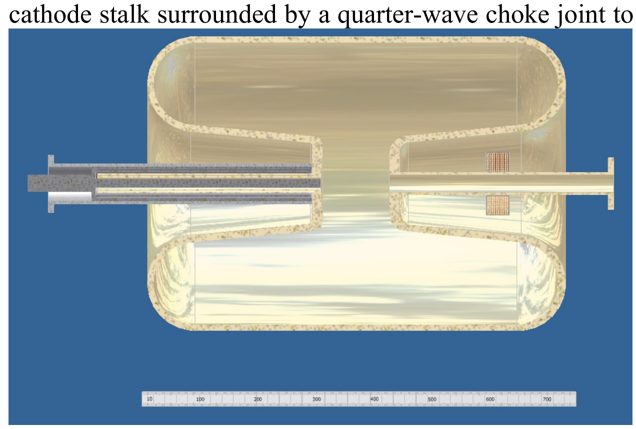

Figure 1: SRF gun cavity w/ cathode and solenoid.

isolate it from the rf in the cavity. The load lock system exploits the required choke joint with its low wall current point to mate the retractable Ti cathode stalk to the SRF

* This work is supported by the University of Wisconsin-Madison and MIT. SRC is funded by the US NSF under award No. DMR-0537588
#rlegg@src.wisc.edu

cavity. The entire assembly is contained in the nose cone of the cavity (Fig. 1). The entire cathode assembly can be retracted to an external cathode preparation chamber. The emittance compensation solenoid should be placed as closed to the cathode as possible for minimum emittance. The design used is a superconducting magnet placed on the Ti tube welded to the anode of the SRF cavity in the He bath. Cavity rf is fed from couplers in the sides of the cavities, allowing greater power input to the cavity. The cryomodule entrance is placed 1.9 meters from the cathode to be at the invariant envelope working point.

## MODELING RESULTS

The gun was modeled using ASTRA. The cathode emission was modeled as a 200 pC, 30 fsec long bunch with a hemispherical transverse charge distribution [9]. Figure 2 plots bunch development to the end of the first cryomodule in the WiFEL injector. The longitudinal ΔE induced by space charge cannot be corrected by running the low frequency cavity off-crest, as done with high

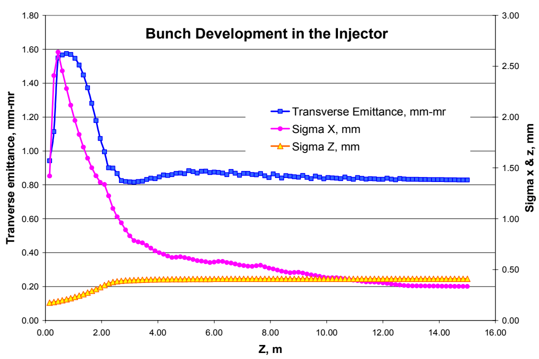


Figure 2: Space charge induced ΔE lengthens bunch.

frequency cavities [10]. Instead the module is moved closer to the cathode and the first cavity in the cryomodule is run off-crest to reverse the energy slew across the bunch and stop the blow out seen in sigma z. The phase and amplitude of the rf in the first cavity are calculated by looking at the amplitude of the energy chirp and the bunch length at the entrance to the module in the simulation and calculating the $\cos^{-1}$ (amplitude of energy chirp / amplitude of field in cavity) $\pm$ (the bunchlength in rf degrees) for the phase. The maximum cavity gradient is set to allow the emittance oscillation to be completed before the emittance is frozen. In practice, this value will need to be reduced to account for rf focusing in the cavity. This also converts the non-linear portion of the longitudinal energy distribution to a "U" shape (Fig. 3).

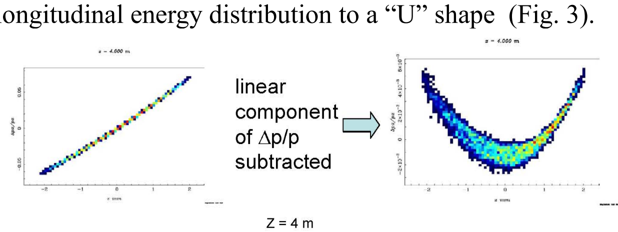


Figure 3: Longitudinal energy spread.

Figure 4 shows the simulated degradation of the transverse and longitudinal emittance at the entrance to the cryomodule versus an offset or error in field strength in the solenoid. The bunch is very sensitive to solenoid setting with a $\pm$1% change causing a 30% change in normalized emittance and a 50% change in transverse sigma. This also suggests that chromatic effects in the solenoid may have a large effect on the bunch. Figure 5 shows the sensitivity of the transverse emittance to $\pm$10% changes in bunch charge. Note that sigma z and the peak bunch current are also changing by $\pm$5% as the charge per

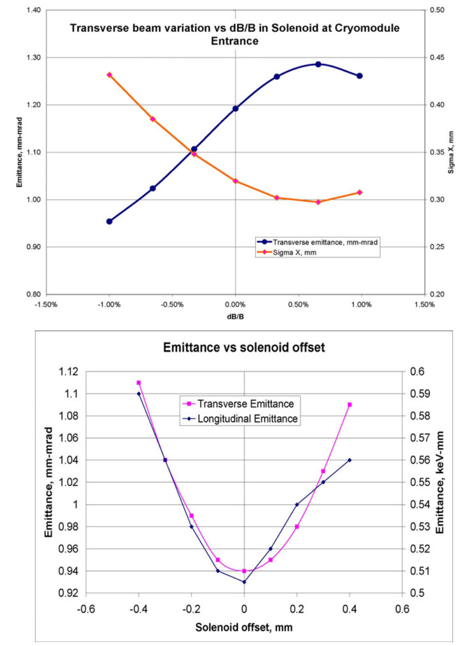


Figure 4: Sensitivity of ε working point to solenoid errors.

bunch is changed. This might effect subsequent compression and the lasing process.

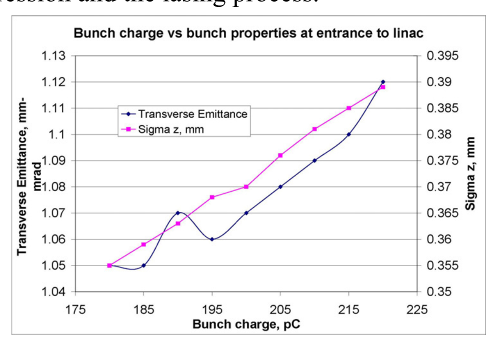


Figure 5: Sensitivity to bunch charge.

## WiFEL GUN TESTSTAND

The gun described above is to be built as part of the WiFEL R&D program. To test the properties of the gun and qualify it for use with the WiFEL, the diagnostic beamline shown in Fig. 6 has been proposed. The beamline is highlighted by a phosphor coated, 50 micron slit mounted between two bellows on a precision linear stage. This arrangement allows the slit to be moved plus or minus 0.5 meter from the working point of the

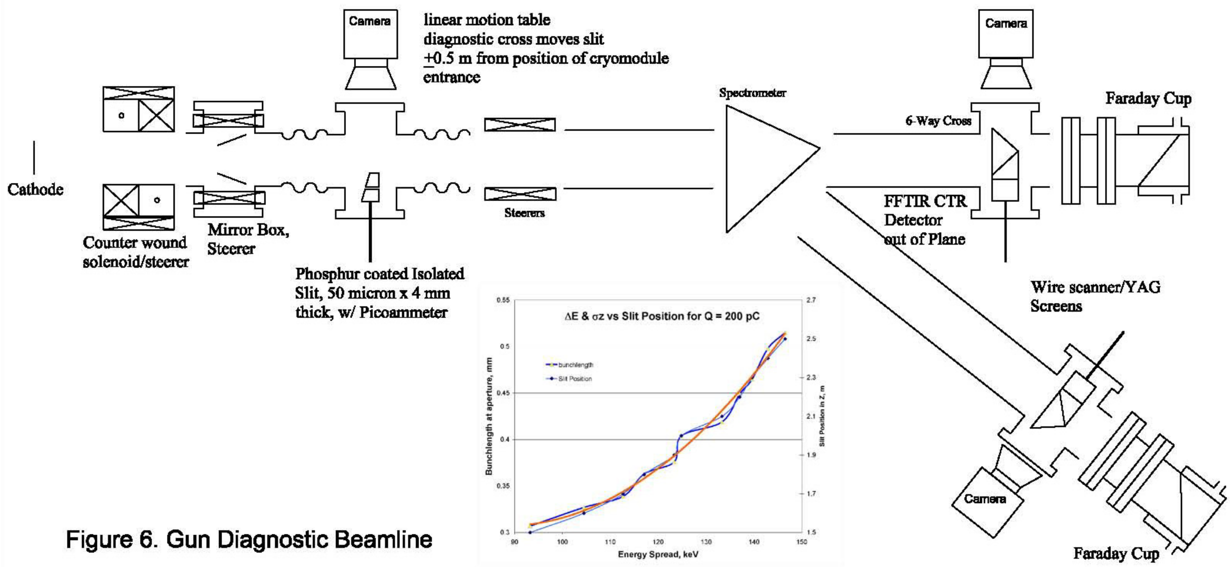


Figure 6. Gun Diagnostic Beamline

emittance compensation scheme. The slit acts to transform the bunch from a strongly space charge dominated regime to an emittance dominated regime [11] in which the development of the emittance envelope as a function of solenoid strength and position can be plotted. When the beamlet produced by the slit is allowed to drift through the spectrometer with no field, the rms emittance of the beam can be measured with the downstream slit/scanner using the technique described in [12]. Adjusting the longitudinal position of the aperture while measuring the downstream transverse emittance and beam sizes, the working point for the solenoid and placement of the linac section can be optimized experimentally.

The straight ahead line is also equipped with a Faraday cup to allow monitoring of the bunch charge throughout the measurements. Finally, an OTR (Optical Transition Radiation) screen and input to a FTIR (Fourier Transform InfraRed) detector is mounted on the other axis from the wire scanner. The FTIR allows the measurement of longitudinal modulation on the bunch by direct measurement of the 1.25 - 25 μm CTR (Coherent Transition Radiation) produced by the bunch. The FTIR diagnostic is looking for modulations on the beamlet which are of the scale to act as a seed for microbunching in compressors [6].

The spectrometer beamline after the dipole allows the momentum spread of the bunch to be measured at the wire scanner. Since the space charge increases the energy spread of the bunch as it moves away from the cathode in blow-out mode, measurements of energy spread in the spectrometer line can be correlated to a rough bunch length at the slit. To make the measurement even more precise, the slit can be moved longitudinally to vary the energy spread in the dump and the data fit to a curve of the simulated data (Fig. 6). The port on the spectrometer vacuum cross orthogonal to the harp contains a second mirror for transport to the FTIR spectrometer. The detector will measure longitudinal energy modulations converted to density modulation on the incoming bunch by the dispersion in the spectrometer leg. This pairing of energy spread and FTIR diagnostic will yield a rough bunch length along with the longitudinal high frequency content of the bunch. Discriminating the FTIR frequency content between the dispersive and non-dispersive measurements will yield both the longitudinal energy and density modulations. Both these measurements are key to the bunch compression process.

## CONCLUSIONS

A brief description of the proposed 200 MHz gun for the Wisconsin FEL and simulations showing bunch development are given. A diagnostic beamline is described. The transverse emittance and bunch sigmas will be measured to verify the solenoid strength and cryomodule placement.

## REFERENCES

[1] O.J. Luiten, et al., PRL **93**, 094802-1 (2004).
[2] C. Limborg-Deprey, P. Bolton, NIM-A, **557** (2006) 106-116.
[3] P. Emma, *Bunch Compression*, 17th Advanced Beam Dynamics Workshop on Future Light Sources, Argonne, Ill 1999.
[4] S.B.van der Geer, et al., PRST-AB **9**, 044203 (2006)
[5] V. Miltchev, *Investigations on the transverse phase space at a photo injector for minimized emittance*, Dissertation, University of Berlin, Feb 3, 2006.
[6] R. A. Bosch, SRC Technote 218, (2007).
[7] S.B. van der Geer, Proc of Future Light Sources 2006, DESY, Hamburg, Germany.
[8] K. Flottmann, http://www.desy.de/~mpyflo/.
[9] R. Legg, et al., Proc of EPAC 08, p 469.
[10] P. Musumeci, et al., PRL **100,** 244801 (2008).
[11] Anderson, et al., PRST-AB **5**, 014201 (2002).
[12] C.Lejeune and J. Aubert, Adv. Electron. Electron Phys., Suppl. **13A**, 159 (1980).

# LONGITUDINAL BUNCH LENGTHENING COMPENSATION IN A HIGH CHARGE RF PHOTOINJECTOR

S. Pei# and C. Adolphsen, Stanford Linear Accelerator Center, Menlo Park, CA 94025, USA

*Abstract*

In high charge RF photoinjectors for two-beam wakefield accelerators, bunch lengthening between the photocathode and photoinjector exit is a critical issue due to the strong longitudinal space charge forces. We present beam dynamics studies of bunch lengthening in an RF photoinjector for a high charge electron beam and describe methods to compensate the bunch lengthening to various degrees. In particular, the beam dynamics for bunch charge from 1 nC to 30 nC are studied for an S-band (2856 MHz) photoinjector.

## INTRODUCTION

RF photoinjector technology [1] is used world-wide in low emittance sources for linac-based free electron lasers [2] and in electron sources for electron storage rings [3]. It has been demonstrated that photoinjectors can produce high brightness and low emittance electron beams [4-6]. A particular challenge for high charge electron photoinjectors for two-beam wakefield accelerators is the longitudinal bunch lengthening that occurs due to strong space charge forces [7].

The longitudinal evolution of electrons in an RF injector can be divided into four steps as discussed in Ref. [8]: 1) initial launching and expansion; 2) RF compression inside the gun cavity; 3) drift space bunch compression or expansion; 4) longitudinal emittance compensation through the booster linac. To reduce the bunch lengthening in the first step, the laser pulse length can be reduced and beam radius increased, which usually results in transverse emittance growth. In the second step, one wants to accelerate the electron beam with as high a gradient as possible [9], which is constrained by the available klystron power and the maximum sustainable surface electric fields in the gun cavity. For the third step, appropriate tuning of the emittance compensation solenoid is needed to reduce the bunch lengthening. The fourth step, which ultimately determines whether the bunch is lengthened, preserved or shortened, appropriate phasing (off-crest acceleration to create an energy chirp along the bunch) is done in part of the booster linac and the electron beam focusing is adjusted along the entire injector.

Here we present two studies of longitudinal bunch lengthening compensation. In the first, we consider only increasing the RF gun acceleration gradient while optimizing the initial phase of the electron beam with the booster linac operated on-crest. The second study focuses on phasing both the RF gun and the first half booster linac for gun acceleration gradients ranging from 120 MV/m to 200 MV/m.

## PHOTOINJECTOR DESIGN

Fig. 1 shows the schematic layout of the photoinjector. Due to the strong space charge effect of a high charge beam (10 nC - 30 nC), the RF gun is immersed in the magnetic field of an integrated cathode solenoid. This magnet is composed of two symmetric solenoid coils whose symmetry plane is the cathode plane. The two coils are powered by separate supplies with opposite current flows so the magnetic field at the cathode surface can be easily adjusted to be near zero. The solenoid and the drift space just after the gun are used to compensate the linear space charge induced emittance growth in the gun region. For high charge, the combined axial magnetic field profiles of the cathode solenoid and the emittance compensation solenoid are shown in Fig. 2 (left) for a typical case. For low charge, only the emittance compensation solenoid is used, and a field profile example is shown in Fig. 2 (right, the two lines coincide with each other).

The basic parameters of the RF gun are listed in Table 1. The RF gun operates in π-mode, and Fig. 3 shows the 0-mode and π-mode electric field profiles for the geometry with a balanced π-mode at 2856 MHz.

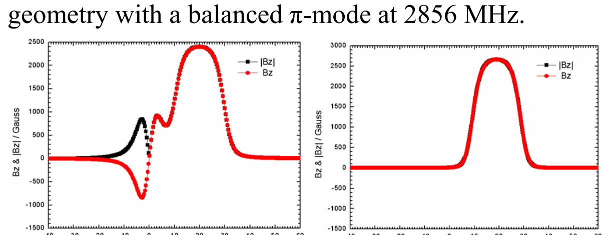


Fig. 2: Typical axial magnetic field profiles in the gun region for high charge (left) and low charge (right).

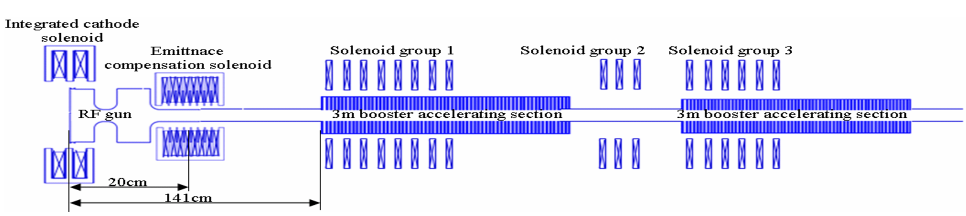


Fig. 1: Schematic layout of the photoinjector.

*Work supported by the DOE under contract DE-AC02-76SF00515.
#slpei@slac.stanford.edu

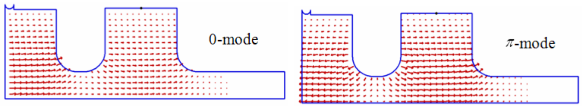


Fig. 3: 0-mode and π-mode electric field profiles for the balanced π-mode at 2856 MHz.

Table 1: Basic Parameters of the RF Gun

| parameter | SUPERFISH |
|---|---|
| Field balance ratio for π-mode (E2/E1) | 0.99960 |
| π-mode frequency / MHz | 2856.0 |
| π-mode quality factor | 15392 |
| π-mode shunt impedance / MΩ/m | 55.191 |
| Field balance ratio for 0-mde (E2/E1) | 0.57499 |
| 0-mode frequency / MHz | 2852.6 |
| 0-mode quality factor | 15764 |
| 0-mode shunt impedance / MΩ/m | 61.803 |
| Mode separation / MHz | 3.4127 |
| RF gun cavity length / cm | 12.611 |

## BEAM DYNAMICS SIMULATION

The beam dynamics were studied with SUPERFISH and PARMELA [10]. The beams at the photocathode have a uniform transverse distribution and their radii are 1.2 mm (1nC) and 5.4 mm (10 nC - 30 nC) [11][12]. The initial bunch in all simulations was assumed to have zero transverse emittance and a flat longitudinal distribution that is 10 ps long (~ 3 ps RMS). The beam injection phase, solenoid field position and amplitude, beam acceleration phase etc., were varied in each PARMELA simulation to optimize the final bunch length and the transverse emittance at the photoinjector exit. The beam dynamics of 1 nC beam was investigated first, through which the photoinjector layout shown in Fig. 1 was determined, and then high charge beams were studied.

### *Increasing the Gun Gradient*

For this case, the first 3-m long booster section was run on-crest (90°), which yields a beam energy of about 50 MeV, and the second booster section was not included in the simulation as it has little effect on the bunch length.

Fig's. 4-6 show the effect of the photocathode peak electric field on bunch length, emittance and energy spread for beams with different bunch charge. The solenoid current was adjusted to compensate the different space charge forces as the bunch charge was varied. The gun phase was about 12°, which is far off-crest to create a relatively big energy chirp. To preserve the initial 3 ps RMS bunch length, the RF gun should be run at ~ 140 MV/m for a 10 nC beam, and for each additional 5 nC of bunch charge, an 20 MV/m increase in gun accelerating gradient is needed. Running the gun at high gradient can also decrease the emittance and energy spread. Fig. 7 shows the emittance, energy, energy spread and bunch length as a function of distance from the photocathode for a 20 nC beam when the gun gradient was 160 MV/m.

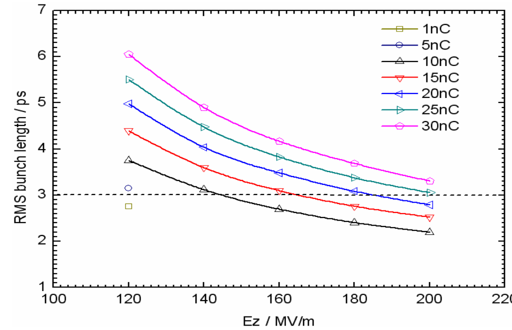


Fig. 4: RMS electron bunch length dependence on the photocathode peak electric field and bunch charge.

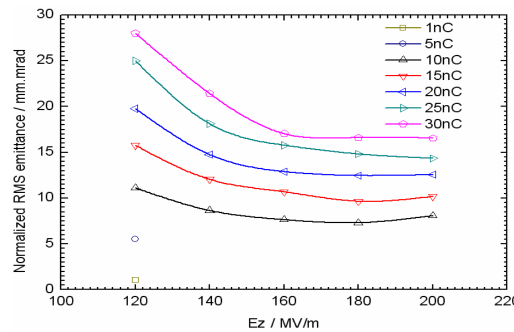


Fig. 5: Normalized RMS emittance dependence on the photocathode peak electric field and bunch charge.

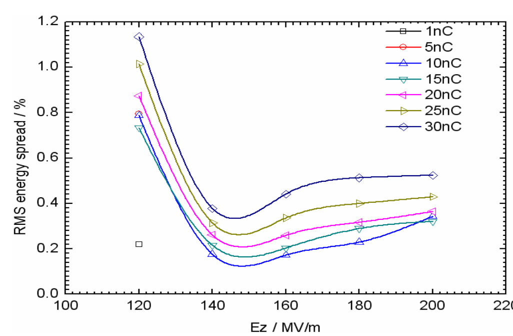


Fig. 6: RMS energy spread dependence on the photocathode peak electric field and bunch charge.

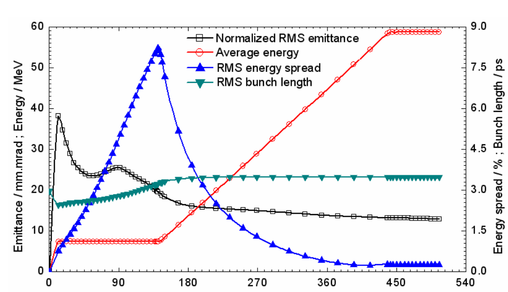


Fig. 7: Emittance, energy, energy spread and bunch length variation along the injector (20 nC, 160 MV/m).

### *Also Changing the Booster Linac Phase*

Fig's. 8-10 show the dependence of RMS bunch length, emittance and energy spread on the photocathode peak electric field when the first booster acceleration section was run off-crest to create an energy chirp along the bunch. The phases of the gun and first booster section were 25$^o$ and near 0$^o$, respectively, so the beam energy at the end of the first booster section was only several MeV. Adjusting the additional solenoids (i.e., solenoid group 2 and 3) was necessary to control the transverse emittance growth. In this case, the whole photoinjector including both booster sections was simulated and the final beam energy was larger than 50 MeV. Running the first booster section off-crest resulted in a shorter bunch length than just increasing the gun gradient with the drawback that the final energy spread was relatively large.

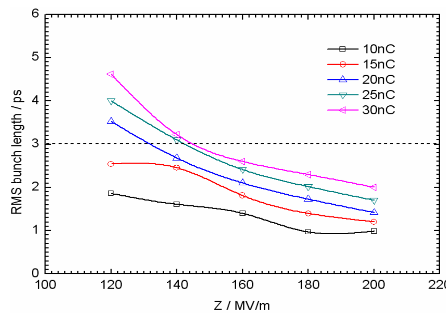


Fig. 8: RMS electron bunch length dependence on the photocathode peak electric field and bunch charge.

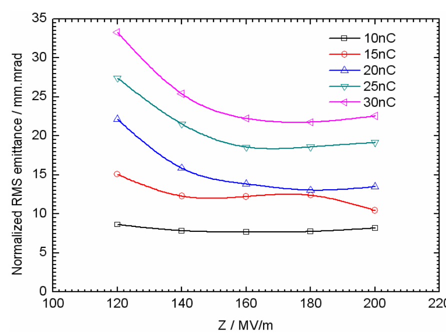


Fig. 9: Normalized RMS emittance dependence on the photocathode peak electric field and bunch charge.

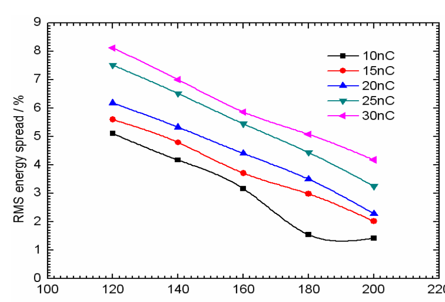


Fig. 10: RMS energy spread dependence on the photocathode peak electric field and bunch charge.

Fig. 11 shows the emittance, energy, energy spread and bunch length variation along the photoinjector for a 20 nC beam when the gun gradient was 160 MV/m. Fig. 11 is more complicated than Fig. 7 in that there are two more oscillations for emittance and one more for energy spread and bunch length; these are caused by the off-crest operation of the first booster section and the emittance re-compensation process in the middle of the booster linac. However, by the end of the photoinjector, the beam parameters were very stable with a smaller emittance and a shorter bunch length but a larger beam energy spread.

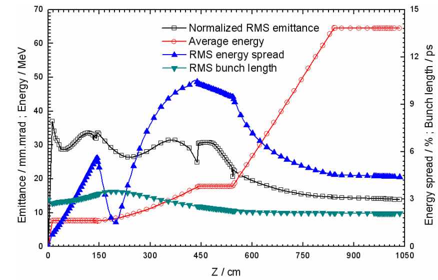


Fig. 11: Emittance, energy, energy spread and bunch length variation along the injector (20 nC, 160 MV/m).

## DISCUSSION AND SUMMARY

It has been shown that increasing the acceleration gradient in the RF gun and operating the gun and/or part of the booster linac off-crest to create an energy chirp along the beam can be used to compensate longitudinal space-charge induced bunch lengthening. In this way, a high current (a few tens of nano-Coulombs), short bunch length (few picoseconds), moderate transverse emittance (a few tens of mm-mrad) electron beam can be produced. The disadvantage of the off-crest operation to create an energy chirp is a larger final bunch energy spread. However, by appropriate design, the electron beam can meet both the low emittance requirements for free electron lasers and high charge requirements for two-beam wakefield accelerators.

## ACKNOWLEDGEMENT

Thanks to K. L. Bane and F. Zhou for reading the manuscript and helpful comments.

## REFERENCES

[1] Fraser J et al. IEEE Trans. Nucl. Sci. NS-32 (1985).
[2] LCLS CDR. SLAC-R-593. April 2002.
[3] Urakawa J, Hayano H et al. SLAC-PUB-9674, 2003.
[4] Akre R et al. SLAC-PUB-13014, 2007.
[5] Anderson S G et al. PAC07, 2007.
[6] Carneiro J P et al. PRST-AB, 8, 040101, 2005.
[7] Pei S et al. HPL&PB, accepted, 2008
[8] Wang X J, Chang X Y. NIM A 507 (2003) 310-313.
[9] Zhou F. Private communication.
[10] SUPERFISH and PARMELA, LANL. Report LA-UR-96-1834, 1997 and LA-UR-96-1835, 1996.
[11] Conde M E et al. PAC03, 2032, 2003.
[12] Gai W, Li X et al. NIM A, 1998, 410, 431-436.

# LASER TIMING JITTER MEASUREMENTS AT THE FERMILAB A0 PHOTOINJECTOR

Justin Kien Keung*, University of Pennsylvania, Philadelphia, PA, 19104, USA
Jinhao Ruan, Sergei Nagaitsev, FNAL, Batavia, IL, 60510, USA

*Abstract*

The Fermilab A0 Photoinjector is a 16 MeV high-intensity, low emittance electron linac used for advanced accelerator R&D. To achieve a high quality beam here it is important to maintain a stable laser in terms of both intensity and timing. This paper presents our measurement of the laser timing jitter, which is the random late or early arrival of the laser pulse. The seed laser timing jitter has been measured to be less than 200 fs, by examining the power spectrum of the signal of a fast photodiode illuminated by it. The pulsed and pumped laser timing jitter has been measured with limited resolution to be less than 1.4 ps, by examining the phase of a cavity impulsively excited by the signal from a fast photodiode illuminated by the laser pulse.

## INTRODUCTION

Photoinjectors are widely used in particle accelerators. They have uses from nuclear and high energy physics research in collider experiments (e.g. ILC), to biology and condensed matter research in light source experiments (e.g. XFEL).

The A0 Photoinjector [1] consists of a 1.3 GHz copper RF gun and a TESLA type RF cavity, and is a 16 MeV high-intensity, low emittance electron linac used for advanced accelerator R&D at Fermilab.

To achieve a high quality beam for advanced accelerator R&D it is important to maintain a stable laser in terms of both intensity and timing. Timing jitter of the laser is the unwanted random variation of the pulse arrival time. Low beam timing jitter is good because it increases collider luminosity (e.g. ILC nominal: 0.5ps RMS), and is necessary for Lasing in FEL (e.g. XFEL: 0.1ps RMS).

The laser timing jitter has been measured by examining the power spectrum of the seed laser at the 12th harmonic, and by examining the phase of a cavity impulsively excited by the signal of a fast photodiode illuminated by the pulsed laser shot. Our aim is to have a pulsed laser timing jitter measurement resolution of less than 200 fs.

## A0 LASER SYSTEM OVERVIEW

The A0 Laser System (Fig. 1) [2] consists of a seed laser, pumps, and two sets of doubling crystals. The laser begins as a continuous train having 5.5 nJ per FWHM 5 ps long infrared (1054 nm) laser pulses at 81.25 MHz. Some pulses (10 to 10000 out of 81.25 million) are allowed to pass through every second, to be pumped by a series of amplifiers. The amplified laser then passes through two sets of doubling crystals to become first green, then ultraviolet (UV). This UV laser having 5 $\mu$J per FWHM 5 ps long pulse is directed with only three turning corners to hit the $Cs_2Te$ photocathode to generate 10 nC of electrons per pulse to be accelerated to 16 MeV.

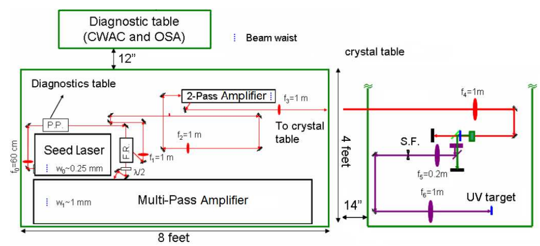


Figure 1: Layout of the A0 Laser System.

## SEED LASER TIMING JITTER

To study the laser timing jitter we begin at the seed laser (Time Bandwidth Products GE-100), which gives a continuous train having 5.5 nJ per FWHM 5 ps long infrared (1054 nm) laser pulses at 81.25 MHz. A high-speed photodiode with a rise/fall time of 12 ps (Fermionics Lasertech HSD-30) is illuminated by the seed laser, and the electrical output signal from the photodiode is analysed by a microwave spectrum analyzer (Agilent E4445A).

The power spectrum of the photodiode signal contains information both on the amplitude and timing jitter. The technique of calculating the timing jitter from the power spectrum is called the Power Spectral Density Technique. Amplitude jitter and timing jitter both show up as shoulders beside the spectral lines (Fig. 2). The RMS jitter is given by an integral of the power in the shoulders (Eq. (1)):

$$\text{RMS Jitter}_{f_1 to f_2} = \frac{1}{2\pi f_c}\sqrt{2\int_{f_1}^{f_2} 10^{\frac{L(f)}{10}} df} \quad (1)$$

Where the factor of 2 inside the square root uses the fact that the spectral shoulders are symmetric.

To separate the amplitude and timing jitter, we make use of the fact that amplitude jitter shoulder is constant, whereas the timing jitter shoulder is proportional to the square of the frequency [3], and measure the power spectrum of the 12th harmonic of the 81.25 MHz pulse rep rate. The timing jitter is measured to be 184 fs at 10 Hz to 10 kHz (Fig. 3).

* keungj@hep.upenn.edu

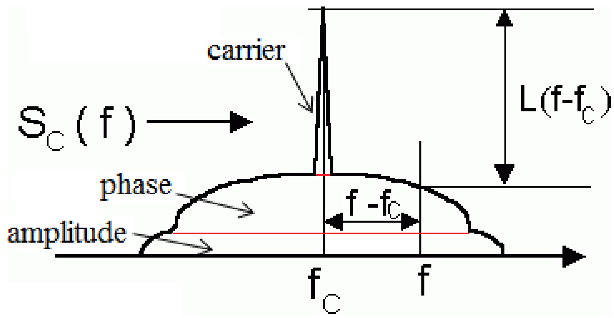


Figure 2: Sketch of a spectral line showing phase and amplitude shoulders.

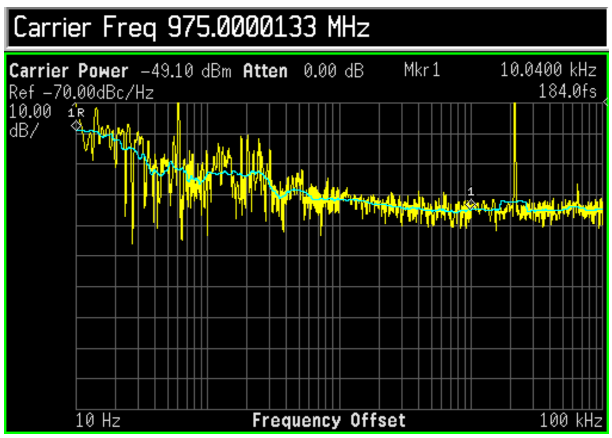


Figure 3: Timing jitter integral taken at 12th harmonic (975 MHz) from 10 Hz to 10 kHz gives 184 fs.

### *Seed Laser Timing Jitter Resolution*

To study the resolution of our application of the Power Spectral Density Technique, we measure the phase noise of the 1.3 GHz Master Oscillator (MO). The MO is the reference of our "Timing Distribution System", which has a very low jitter. Our resolution is 88 fs since the spectrum analyzer has an 88 fs jitter with respect to the MO (Fig. 4).

## PULSED LASER TIMING JITTER

Next we study the timing jitter of the pumped laser, which gives one train per second, consisting of 10 to 10000 infrared (1054 nm) pulses spaced by 1 $\mu$s, having 6 $\mu$J per pulse. This laser is attenuated to 1/1000 the original amplitude, then directed to illuminate the high-speed photodiode with a rise/fall time of 12 ps (Fermionics Lasertech HSD-30). The electrical output pulse from the photodiode is fed through a band pass cavity filter with a Q of 2600 and tuned to a center frequency at 1.28 GHz (EMR Corp. 6754/SBC). The photodiode causes the cavity to start oscillating (ringing) at a frequency of 1.28 GHz, which decays slowly (cavity energy reduces by 96% in 2600 oscillations). The phase of the ringing is measured to infer the timing of the laser pulse. We call this technique of measuring the phase of the ringing of the filter to get timing information the Ringing Filter Technique (Fig. 5).

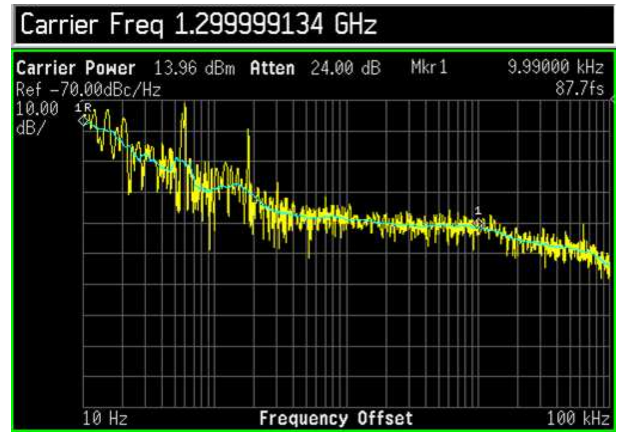


Figure 4: Timing jitter integral of the MO taken from 10 Hz to 10 kHz gives 88 fs. This is the resolution of our application of the Power Spectral Density Technique.

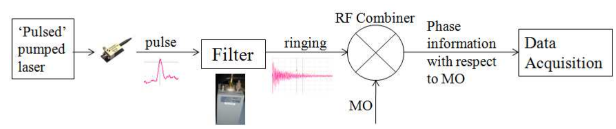


Figure 5: Sketch showing our application of the Ringing Filter Technique.

To measure the phase of the ringing we first feed it through an RF amplifier (ZHL-1042J), then superimpose it onto the 1.3 GHz Master Oscillator signal with an RF Combiner (RF Splitter Mini-Circuits ZX10-2-25, used in reverse). This superimposed signal is recorded by an oscilloscope (LeCroy Wavepro 7200A) using a single channel (avoiding the relative jitter between 2 channels). The superimposed signal has two main frequency components, 1.28 GHz (the cavity filter ringing) and 1.3 GHz (the MO reference) (Fig. 6). With an FFT done on the oscilloscope, one can find the phase of both the cavity ringing and the MO reference (Fig. 7).

The phases of the ringing and the MO are both dependent on the time which the oscilloscope has triggered, but the relative timing difference between them is not. The relative timing difference of each run modulo 770 ps (period of 1.3 GHz MO) is given by Eq. (2):

$$\Delta T_{filter} = \frac{\phi_{filter}}{\omega_{filter}} - \frac{\phi_{MO}}{\omega_{MO}} \quad (2)$$

Armed with the $\Delta T$ from 20 pulses, the RMS of this distribution gives us the pulsed laser timing jitter of 1.4 ps (Fig. 8).

### *Pulsed Laser Timing Jitter Resolution*

To study the resolution of our application of the Ringing Filter Technique, we measure the phase noise of the

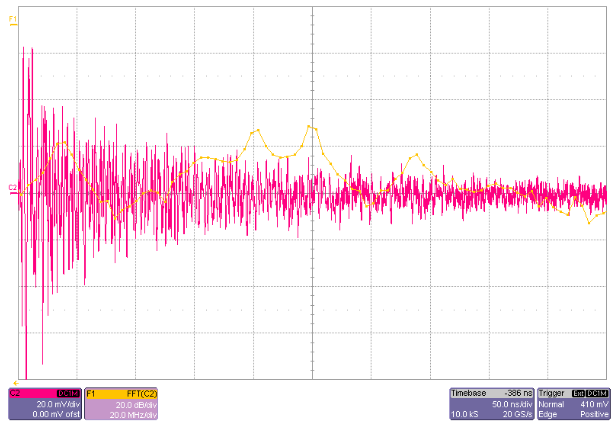

Figure 6: Red trace: superimposed signals of ringing and MO (time domain); Yellow trace: power spectrum showing 1.28 GHz ringing and 1.3 GHz MO components.

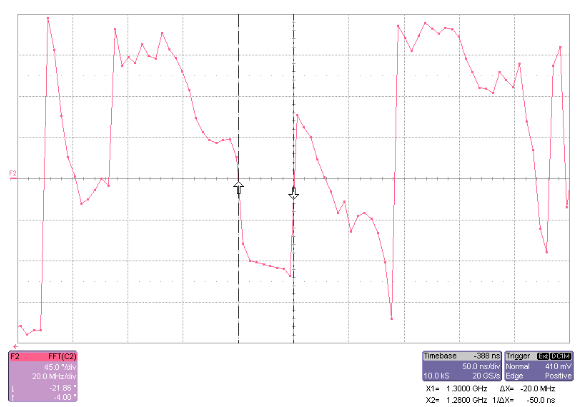

Figure 7: Phases of 1.28 GHz ringing (up arrow) and 1.3 GHz MO (down arrow).

1.313 GHz Local Oscillator (LO) with respect to the Master Oscillator (MO).

The LO, like the MO is part of our "Timing Distribution System", and as a result the timing jitter of the LO is much less than 1 ps with respect to the MO. This measurement therefore yields the resolution of our application of the Ringing Filter Technique. The distribution of $\Delta T_{LO}$ yields an RMS of 1.2 ps. Our data acquisition system therefore has a timing jitter of 1.2 ps.

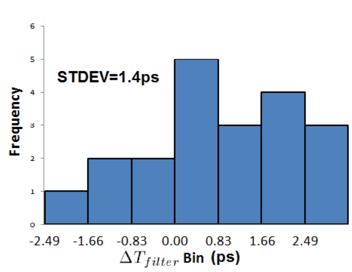


Figure 8: Histogram of $\Delta T$ from 20 pulses, STDEV = 1.4ps.

## POSSIBLE IMPROVEMENTS

One obvious improvement is to use a better data acquisition system, since the resolution is currently limited by our oscilloscope having a timing jitter of 1.2 ps. But beyond this, the challenge is that we want a short pulse from the photodiode: but the shorter the pulse, the less the excitation energy within the pulse. The difficulty is to accurately measure the phase of a decaying ringing signal with an initial amplitude on the order of mV.

The jitter of a pulse is 1% that of the rise time to a first approximation, and since we are aiming for a pulsed laser timing jitter measurement resolution of less than 200 ps, we need a photodiode with a rise time of less than 20 ps. We have not yet found a commercially available photodiode giving a pulse much larger than 1 V while having a rise time of less than 20 ps.

A potential solution is to put a matching optical cavity in front of the photodiode (Fig. 9). A matching optical cavity is two facing mirrors perfectly aligned, with the distance between the mirrors equal to half the wavelength of the filter downstream. This essentially is a delay line to excite the photodiode (and hence the filter) multiple times to obtain a higher ringing amplitude.

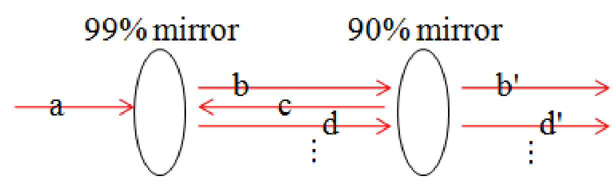


Figure 9: Sketch of an optical cavity.

## SUMMARY

We have presented our laser timing jitter measurements. The seed laser timing jitter has been measured to be less than 200 fs, by examining the power spectrum of the signal of a fast photodiode illuminated by it. The pulsed and pumped laser timing jitter has been measured with limited resolution to be less than 1.4 ps, by examining the phase of a cavity impulsively excited by the signal from a fast photodiode illuminated by the laser pulse. This resolution is limited by our oscilloscope, which has a timing jitter of 1.2 ps.

## REFERENCES

[1] http://www-a0.fnal.gov.

[2] Jian-Liang Li et al, "Performance of the upgraded laser system for the Fermilab-NIU photoinjector," Nucl. Instrum. Meth. A564:57-65, (2006).

[3] D. von der Linde, "Characterization of the Noise in Continuously Operating Mode-Locker Lasaers," Applied Physics B 39, 201-217 (1986).

# EMITTANCE EXCHANGE AT THE FERMILAB A0 PHOTOINJECTOR*

Timothy W. Koeth#, Rutgers University, Piscataway, New Jersey, USA

Helen Edwards, Raymond P. Fliller III†, Leo Bellantoni, Jinhao Ruan, Alex H. Lumpkin,Randy Thurman-Keup, Amber S. Johnson, Fermilab, Batavia, Illinois, USA

*Abstract*

An experiment to exchange the longitudinal emittance with the horizontal emittance has been installed at the Fermilab A0 Photoinjector. The exchange apparatus consists of a $TM_{110}$ deflecting mode cavity positioned between two magnetic doglegs as proposed by Kim & Sessler [1]. We report on the measurement of the emittance exchange beamline matrix elements and a direct measurement of emittance exchange.

## INTRODUCTION

A transverse to longitudinal emittance exchange (EEX) has been installed at the Fermilab A0 Photoinjector for a proof-of-principle demonstration through the exchange of a larger normalized longitudinal emittance, 30 mm.mrad, with that of a smaller normalized horizontal emittance, 10 mm.mrad, of a 14.3 MeV electron beam. In this paper we report on measurements of the emittance exchange beamline matrix elements as well as a preliminary measurement of an emittance exchange.

## EEX BEAMLINE & OPTICS

It is the goal of our emittance exchange experiment to exchange horizontal and longitudinal emittances of an electron beam. The apparatus that we have developed, which is a variant of Kim and Sessler's proposal, can be easily described through a linear optics treatment of the exchange beamline [1]. We describe the entire exchange apparatus by a typical 4x4 matrix relating the horizontal and longitudinal parameters, $\Delta x$, $\Delta x'$, $\Delta z$, $\Delta\delta$ ($\delta = \Delta p/p$) :

$$M_{EEX} = \begin{pmatrix} A_{11} & A_{12} & B_{11} & B_{12} \\ A_{21} & A_{22} & B_{21} & B_{22} \\ C_{11} & C_{12} & D_{11} & D_{12} \\ C_{21} & C_{22} & D_{21} & D_{22} \end{pmatrix}$$

A complete exchange matrix would be one in which the elements of the ***A*** and ***D*** sub-blocks become zero and the ***B*** and ***C*** sub-blocks become populated.

The A0 Photoinjector EEX apparatus, outlined in Fig. 1, consists of a 3.9 GHz $TM_{110}$ deflecting mode cavity located between two 'dogleg' magnetic channels. The $TM_{110}$ deflecting mode cavity is a $lN_2$ cooled, normal conducting, variant of a superconducting version previously developed at Fermilab [2]. The longitudinal electric field of the $TM_{110}$ mode is zero on axis and grows linearly off axis, the vertical magnetic field produces a time dependent transverse kick with respect to the synchronous particle. The $TM_{110}$ deflecting mode cavity's strength, *k*, is given by:

$$k = \frac{eV_{\perp}\omega}{Ec},$$

where $V_{\perp}$ is the peak deflecting field normalized to the beam energy, *E*, and $\omega$ is the resonant frequency.

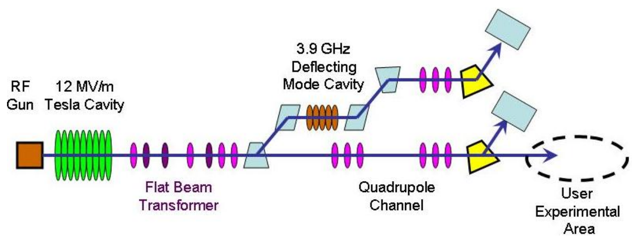


Figure 1: Layout of the A0 Photoinjector with straight ahead and EEX beamline sections.

Using a thin lens approximation of a cavity immediately between two magnetic doglegs, we can analytically express our EEX beamline matrix as:

$$\begin{pmatrix} 1+Dk & L+Dk+(1+Dk)L & kL & D+D(1+Dk)+\alpha DkL \\ 0 & 1+Dk & k & \alpha Dk \\ \alpha Dk & D+D(1+Dk)+\alpha DkL & 1+Dk & \alpha D+\alpha D^2k+\alpha D(1+Dk) \\ k & kL & 0 & 1+Dk \end{pmatrix}$$

where *L* is the drift between two magnetic dipoles that form a magnetic dogleg and *D* is the dispersion generated by one dogleg, and $\alpha$ is the magnitude of the bend angle.

It can easily be seen that in the special case where the $TM_{110}$ cavity strength, *k*, (defined 100% at 3.03 $m^{-1}$ in our case) equals the negative reciprocal of the dispersion, *D*, (0.33 m in our case) the diagonal sub-blocks of the matrix become zero while the off-diagonal sub-blocks become populated. Our bending angle is 22.5º.

$$M_{EEX} = \begin{pmatrix} 0 & 0 & \frac{-1}{\alpha} & 0 \\ 0 & 0 & \frac{-1}{D} & -\alpha \\ -\alpha & 0 & 0 & 0 \\ \frac{-1}{D} & -\frac{1}{\alpha} & 0 & 0 \end{pmatrix}$$

In practice, due to the finite length of our $TM_{110}$ deflecting mode cavity, several of the on-diagonal block elements are left non zero [3]. This, in addition to other higher order effects, such as space charge and CSR, will lead to an imperfect exchange and a coupling of the final emittances [4].

* This manuscript has been authored by Fermi Research Alliance, LLC under Contract No. DE-AC02-07CH11359 with the U.S. Department of Energy.

#koeth@physics.rutgers.edu

†Present address: NSLS II Project, Brookhaven National Laboratory, Upton, NY, 11973-5000NY

## EEX BEAMLINE DIAGNOSTICS

The EEX beam line is outfitted with ten Beam Position Monitors (BPM); the transverse beam profiles are measured by eight Optical Transition Radiation (OTR) viewing screens along the beamline. Two sets of tungsten slits and YAG viewing screen pairs measure the transverse beam divergence before and after the exchange beamline. EEX input and output central momenta and momentum spreads are measured by two spectrometer magnets and viewing screens. A single Hamamatsu C5680 streak camera outfitted with a synchroscan unit provides a measurement of the laser pulse length, electron bunch lengths at the input and output of the exchanger, and changes in bunch time-of-arrival at the picosecond level [5]. Finally, a Martin-Puplett interferometer is installed at the end of the EEX beamline to perform sub-picosecond bunch length measurements [6].

## EEX MATRIX MEASUREMENT

To verify the expected transport matrix, difference orbits have been used to measure the EEX beamline matrix. Diagnostic limitations required the measured matrix measured include the 2.1 m drift prior to the first EEX dipole magnet and the 0.2 m drift after the fourth EEX dipole. The procedure was to establish a nominal 14.3 MeV beam orbit through the EEX beamline and measure both the 6-D input and output vectors. Then one of the 6-D input vector's elements was varied; the change in the 6-D output vector was measured. To demonstrate the "turn-on" evolution of the EEX matrix, this procedure was repeated with the $TM_{110}$ deflecting mode cavity off, at the full strength for the complete EEX condition, and at three intermediate strengths. The BPM readings gave $\Delta x$, $\Delta x'$, $\Delta y$, and $\Delta y'$ data, while the streak camera provided the $\Delta z$ information, and finally the vertical bending spectrometer in conjunction with the subsequent vertical BPM position reading provided the output $\Delta\delta$ data.

Figure 2 graphically displays the 4x4 transport matrix as a function of the $TM_{110}$ deflecting mode cavity strength. The $TM_{110}$ cavity is completely off at 0% and is energized to the optimal level for EEX in our beamline at 100%. The measurements (circles) are compared to a simple linear optics model displayed by the red line. For the most part, we see close agreement. Although not shown, the full 6x6 transport matrix was measured. The corresponding vertical plane elements, as expected, displayed no dependence on the $TM_{110}$ cavity's state.

We consider the measurements of the second column "pure" in the sense that by use of a single correction dipole we can obtain an input angle without a transverse offset at a prescribed longitudinal location. However, due to the manual nature of setting two longitudinally spaced correctors to generate a horizontal input offset, $\Delta x$, it is impossible to avoid an input angle as well. By first measuring the respective input $\Delta x'$ dependencies and having the ability to measure the input angle, we subtract off the angular component from the input $\Delta x$ measurements. A similar circumstance occurs in the measurement of the third and fourth columns. The input $\Delta\delta$ is simply controlled by adjusting the Photoinjector's capture cavity gradient, and thus is also considered a "pure" measurement. The third column is a measure of the output vector's dependence on the input beams $\Delta z$ w.r.t. the synchronous bunch, i.e. time of arrival differences. To avoid the complexities of adjusting the Photoinjector's timed supply of electron bunches the phase of the $TM_{110}$ cavity was simply adjusted to affect differing bunch time-of-arrival. Except for the $TM_{110}$ cavity, all of the EEX components are static, thus a phase advance of 1° of the $TM_{110}$ cavity is equivalent to 0.7 ps earlier arrival time, or a 0.2 mm longitudinal offset.

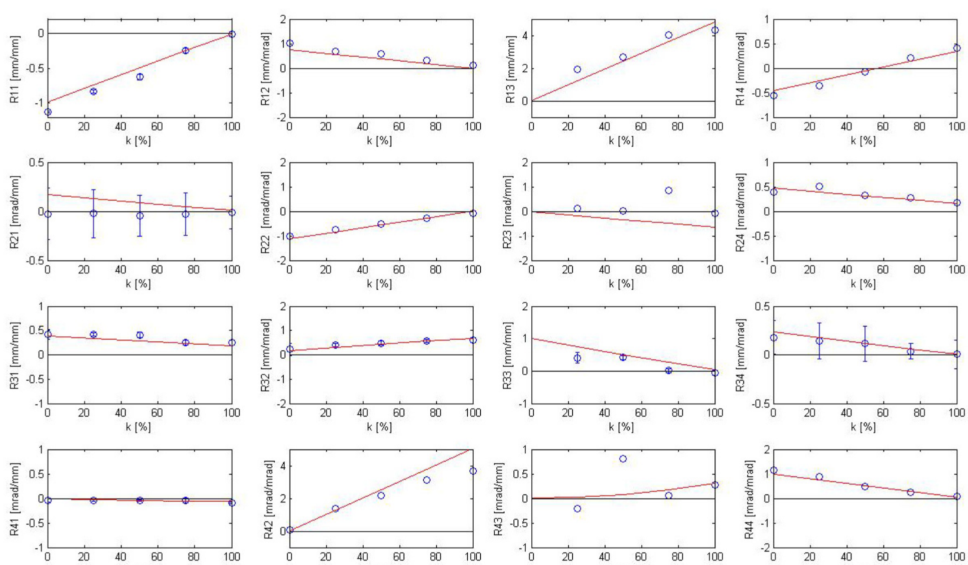


Figure 2: Measurement of 4x4 (horizontal and longitudinal) EEX matrix evolution as the $TM_{110}$ cavity strength is ramped from 0%, off, to 100%, full EEX strength. The red traces are expected values from a linear optics model. The analysis is presently still in progress thus not all measurements display error bars.

Simply adjusting the $TM_{110}$ deflecting mode cavity phase comes at the cost of losing the 0%, cavity off, data points. Several of the third column data points have large error bars as a result of the measurements relatively strong sensitivities to slight fluctuations of input parameters other than the one intentionally being adjusted. For instance the R43 element has a large uncertainty at the 50% data point. At the $TM_{110}$ cavity 50% level, any input momentum jitter is propagated through to the measurement point at half amplitude, and can swamp the signal sought. A future analysis will account for this energy jitter by using the horizontal BPM reading directly before the $TM_{110}$ deflecting cavity as a spectrometer, thus enabling us to remove the effect of the energy offset on a shot-to-shot basis.

## DIRECT EEX MEASUREMENT

A direct measurement of emittance exchange with a low charge 14.3 MeV beam consisting of 80 bunches per RF pulse was performed. The bunch charge of 250 pC was chosen as compromise between diagnostic requirements and space charge effects. Simulations provided an initial starting point for input beam conditions, including quadrupole settings and beam chirp [5]. The input horizontal parameter space was varied by adjusting two input quads while the output energy spread and bunch lengths were measured. Sub-picosecond bunch lengths, as well as very small energy spreads, ~ 10keV, could be obtained; however, not simultaneously. Several output parameters have been mapped against the input quads strengths. The first is a map of the interferometer's pyroelectric detectors sum signal, thus, an un-calibrated reference signal that is inversely proportional to bunch length, shown in Fig. 3.

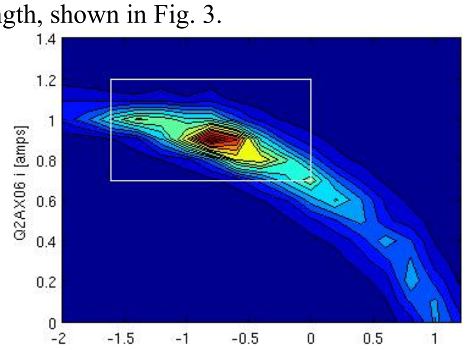


Figure 3: A relative output bunch length mapped against two input quad settings. (dark red is the minimum bunch length). The white box outlines Fig. 4 boundary.

Subsequent measurements at the location of the peak pyroelectric signal yielded a bunch length that was below the resolution limit of the streak camera and at which the interferometer revealed a bunch length of 0.40±0.04 ps rms. Output energy spread measurements at the same location yielded approximately 110keV.

An energy spread map near the peak pyroelectric signal was generated and is shown in Fig. 4.

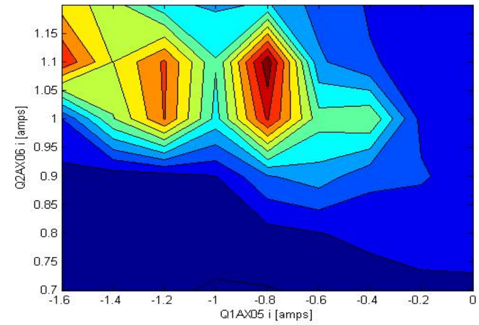


Figure 4: Output energy spread mapped against input quads. (dark blue are lowest energy spreads).

Guided by these maps, the input quads were empirically adjusted to find a location where the energy spread and bunch length product yielded a minimum output $\varepsilon_z$, at which an entire input and output emittance data set was taken; the normalized preliminary emittance exchange results are summarized in Table 1. We were unable to measure $TM_{110}$ cavity off $\varepsilon_x$ point as the output horizontal beam spot size is larger than the viewing screen. We are investigating the large increase in $\varepsilon_y$ in the $TM_{110}$ cavity on case.

Table 1: Preliminary EEX Data Set

| | $\varepsilon_x$ mm.mrad | $\varepsilon_y$ mm.mrad | $\varepsilon_z$ mm.mrad |
|---|---|---|---|
| INPUT | 9.2 | 7.2 | 32.5 |
| out $TM_{110}$ off | N/A | 11.4 | N/A |
| out $TM_{110}$ on | 38.4 | 18.2 | 13.3 |

## CONCLUSIONS

A measurement of our EEX transport matrix has been completed and demonstrates the desired properties of an EEX beamline. Additionally, an initial direct emittance exchange has been performed, but due to the large parameter space, will require further investigation.

## REFERENCES

[1] K.-J. Kim and A. Sessler, AIP Conf. Proc. **821**, 115(2006).

[2] T.W. Koeth, et. Al, "A Copper 3.9 GHz TM110 Cavity for Emittance Exchange" Proceedings of PAC 2007, Albuquerque, New Mexico, THPAS079.

[3] D. A. Edwards. Unpublished.

[4] R. P. Fliller III "Start to End Simulations of Transverse to Longitudinal Emittance Exchange at the A0 Photoinjector", EPAC08, Paper THPC014.

[5] A. H. Lumpkin, et al., "Initial Synchroscan Streak Camera Imaging at the A0 Photoinjector," Proceedings of 2008 Beam Instrumentation Workshop, Lake Tahoe, CA, USA.

[6] R. Thurman-Keup, et al., "Bunch Length Measurement at the Fermilab A0 Photoinjector using a Martin Puplett Interferometer", Proceedings of 2008 Beam Instrumentation Workshop, Lake Tahoe, CA, USA.

# BEAM TRANSPORT EFFECTS FOR ECRIS

P. Spädtke, R. Lang, J. Mäder, J. Roßbach, K. Tinschert, GSI Darmstadt, Germany

## ION BEAM EXTRACTION

Experimental results from ion beams, extracted from an Electron Cyclotron Resonance Ion Source (ECRIS) are compared with the model used for simulation, which has to taken into account that the energy of ions within the magnetically confined plasma in a trap of several T is in the eV-range. Electrons do have a different energy distribution: there are hot electrons up to MeV range, but also low energy electrons, responsible for charge neutrality within the plasma. Because the gyration radius of ions is within the sub-mm range, ions can be extracted only if they are located on a magnetic field line which goes through the extraction aperture. Ion-ion collisions are not important for the path of the ion. Because of the gradient dBz/dz of the mirror field only these ions can be extracted, which have enough energy in direction of the field line. These conditions are fulfilled for ions which are going to be lost through the loss cones created by the hexapole. The extracted beam shows a typical behavior for any ECRIS: when the beam is focused by a lens (here a solenoid) directly behind extraction, the initial round and hollow beam develops wings with a 120-degree symmetry. Because of these considerations, the magnetic flux density in the plane of extraction is a good approximation for the minimum required flux density from which ions can be extracted. This surface is shown in 2D-cuts for two different ECRIS types (see Fig. 2 to Fig. 6). It is assumed that the plasma generator is able to produce particles in the required charge state at these locations. The model has been tested for different existing ion sources, and for ion sources which are still under design or under construction.

### CAPRICE

This source, routinely in operation at GSI, has been used together with the technique of viewing targets, to proof our model for ion beam extraction. The ion source has two normal conducting coils for the mirror trap and a hexapolar device created by permanent magnets. Using different materials for these permanent magnets, we have had tested three differently strong hexapolar fields: 0.8 T, 1.0 T, and 1.2 T measured always at the plasma chamber. Whereas the transverse magnetic flux density is fixed when the hexapole has been installed, the mirror field for both mirror coils is variable up to 1.2 T on axis. By changing the current in the mirror field coils on injection side and extraction side, the location of extraction can be changed from the back side of the source to the radial location of the loss lines, starting at injection side and going to about the center between both coils. Because the allowed starting conditions are different for different magnetic settings, it is important for ECRIS extraction simulation to use the actual used magnetic fields. An example is shown in Fig. 9 for the 1 T hexapole.

### SUPERNANOGAN

This commercial available source[1] is much easier to simulate, because the magnetic flux density is frozen, which might be a disadvantage on the other side. The magnetic flux density has been calculated using the PANDIRA code[2]. This program calculates the cylinder symmetric mirror field, created by permanent magnets only. The hexapolar field has been added in the 3D-map required for the KOBRA3[3] simulation analytically. Because of the permanent magnets, the longitudinal flux density component changes sign within the extraction.

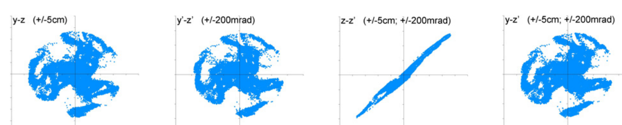


Figure 1: Different projections of the 6D phase space from left to right: beam cross section, momentum space, emittance, mixed phase space. Total current for the simulation 3 mA, shown is one charge state only.

### ARC-ECRIS

This is an already old idea from plasma-fusion science [4], using a curved coil to produce the required magnetic configuration. Because of this simple design, the idea has been re-invented [5] to check the performance of such a source. This device creates a minimum $|\vec{B}|$ structure with a quadrupole like loss cones, shown in Fig. 2. If the plasma generator provides a comparable charge state distribution as regular ECRIS it would be a promising alternative, see Fig. 3.

### MS-ECRIS

This source has been designed within a European collaboration[6]. It consists out of three solenoidal coils to produce the mirror field and a set of coils for the hexapole, designed to be 2.7 T at the plasma chamber. Depending on

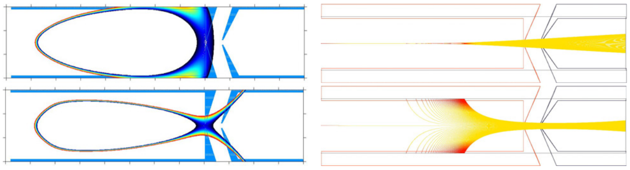

Figure 2: Magnetic structure of the arc-ecris: lines of constant $|\vec{B}|$ and magnetic field lines in horizontal and in vertical projection.

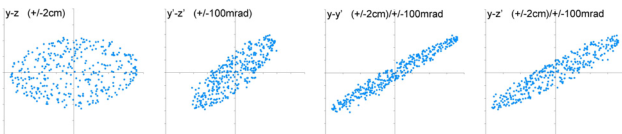


Figure 3: Different projections of the 6D phase space for the beam extracted from ARC-ECRIS: real space, momentum space, emittance, and a mixed phase space. In this solution, space charge effects are still neglected.

the polarity and strength of the middle solenoid, the extraction area can be changed from the back side of the source to the radial loss lines, see Fig. 4.

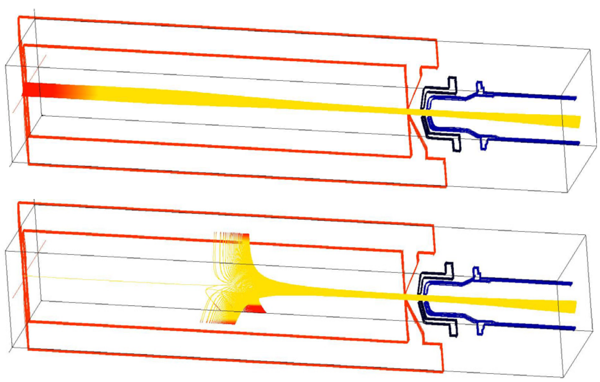

Figure 4: Magnetic field lines for different coil settings of the MS-ECRIS. Top: design value, middle coil switched off. Bottom: design values, injection field decreased to 60%. The red part of the field line indicates that the value of flux density is above that value at extraction aperture.

### *A-Phoenix*

This source[7] has a hybrid set up: two superconducting coils form the mirror field. The minimum between both coils can be slightly modified by an additional normal conducting coil. The hexapole is made by permanent magnets. For this simulation we have used the standard hexapole design with 1.83 T at 65 mm radius. The position of the extraction electrode is far away from the maximum field of the mirror coil on extraction side. This might have been enforced by the small diameter of the plasma chamber, see Fig. 5. Positioning of the electrode at that point lowers the magnetic flux density at extraction.

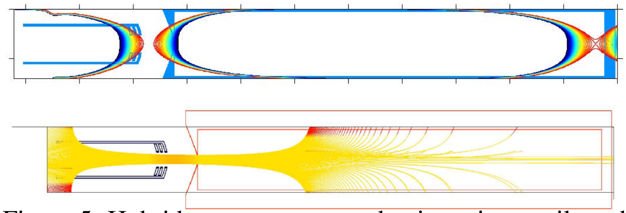

Figure 5: Hybrid source: superconducting mirror coils and permanent magnets for the hexapole.

### *SECRAL*

This source[8] has a reversed position between solenoid and hexapole. Here the hexapole is inside the solenoids. This was decided for technical reasons, especially due to the forces between solenoid and hexapole, extraction condition has been found to be very good, see Fig. 6.

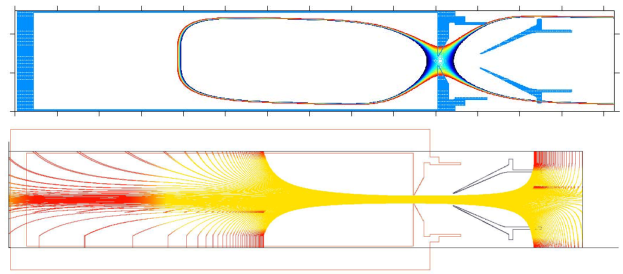

Figure 6: Magnetic field lines and magnetic flux density for the SECRAL ion source.

### *RIKEN 28 GHz*

The Riken version of a 28 GHz ECRIS[9] includes the possibility to bias the beam line, giving the opportunity to increase beam energy without having the source on extensive high potential, see Fig. 7. The advantage is the smaller emittance for the beam transport with higher energy, according to Liouville. The space charge compensation is not affected. When connecting the beam line again to ground, decelerating the beam, the emittance will increase again. Screening just before decelerating is required, otherwise the space charge compensation would be lost due to extracting electrons from the beam.

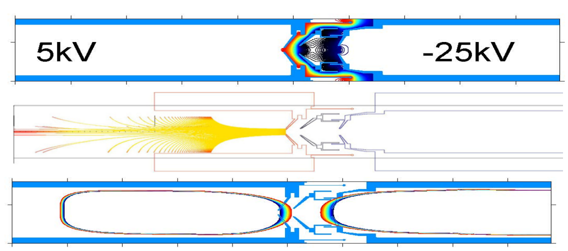


Figure 7: Superconducting ECRIS from Riken: top: electric potential, middle: magnetic field lines, bottom: lines of constant $|\vec{B}|$.

## BEAM LINE SIMULATION

Different numerical methods can be used to simulate the transport of an ion beam. The choice is from simple matrix formalism to time dependent particle in cell with exact calculation of forces. It depend on the specific problem to be investigated which type of program has to be used. If the computational results represent the experimental observations, it can be concluded that the applied model can describe the experimental observations sufficiently well. In the simulation for the beam line which has been described in [10], we use all phase space coordinates of each particle obtained from the extraction simulation. The beam transport is made by a matrix formalism using the full $6 \times 6$ matrix, including coupling elements for each particle individually[11].

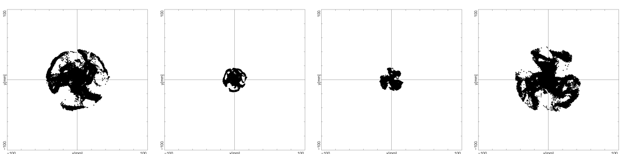

Figure 8: Beam cross sections from SUPERNANOGAN behind the beam line solenoid with increasing magnetic focusing strength from left to right.

The experimental results can be reproduced, using the linear transformation only and neglecting space charge effects. It seem that all peculiarities are defined by the initial particle distribution.

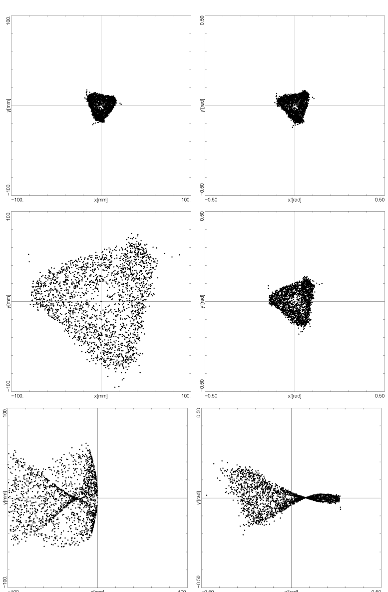

Figure 9: Beam profile (left) and momentum space (right) from CAPRICE with 1.0 T flux density hexapole, after extraction (first row), behind a focusing solenoid (second row), and after m/q separation (third row).

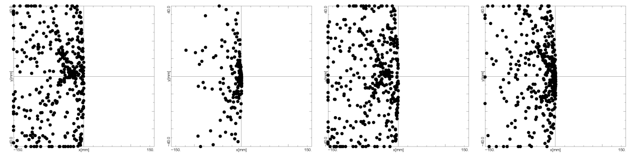

Figure 10: Expected beam cross sections behind the dipole for different magnetic settings of MG-ECRIS.

## CONCLUSION

Experimental results which have been described in [12] could be reproduced by the used model. One main result, which have been obtained with the CAPRICE, was that the cross section of each different extracted m/q ratio changes from a hollow triangular ring to a three-wing structure when the specific m/q becomes over-focused with decreasing m/q in the stray field of the source. The cross-section of each m/q ratio, starting with m/q= 1 focused by a beam line solenoid located directly behind extraction shows similar behavior. Behind the dipole a structure is obtained, which had already been defined inside the plasma chamber. We can conclude from that, that space charge of the dc beam along the beam line is compensated to a very high degree.

## REFERENCES


[1] C. Bieth, O. Tasset, S. Kantas, Pantechnik, Caen, France.

[2] Superfish program group `http://laacg1.lanl.gov`.

[3] KOBRA3-INP, INP, Junkernstr. 99, 65205 Wiesbaden.

[4] F. Cap, Einführung in die Plasmaphysik II, Wissenschaftliche Taschenbücher, Akademie Verlag Berlin, 1972.

[5] P. Suominen anf F. Wenander, Electron Cyclotron Resonance Ion Source with Arc-shaped Coils, RSI Vol. 79, Num. 2, 2008.

[6] G. Ciavola, A Status Report on the Multipurpose Superconducting Electron Cyclotron Resonance Ion Source, RSI Vol. 79, Num. 2, 2008.

[7] T. Thuillier et al., High Intensity Ion Beam Prospects for Acceleration with PHOENIX 28GHz, Proceedings of the EPAC Conference, Paris (2002).

[8] H.W. Zhao et al., Intense Beam Production of Highly Charged Heavy Ions by the Superconducting Electron Cyclotron Resonance Ion Source SECRAL, RSI Vol. 79, Num. 2, 2008.

[9] T. Nakagawa et al., New superconducting electron resonance ion source for RIKEN RI beam factory project, Rev. Sci. Intstrum. 79, 02A327 (2008).

[10] K. Tinschert et al.; Rev. Sci. Instr. 69 (1998) 709

[11] `http://mirko-optik.franczak.de`

[12] P. Spädtke, The Physics of Ion Beam Extraction from an Electron Cyclotron Resonance Ion Source, IEEE (2008).

# DEVELOPMENT OF VERY SMALL ECR ION SOURCE WITH PULSE GAS VALVE

M. Ichikawa#, H. Fujisawa, Y. Iwashita, T. Sugimoto, H. Tongu and M. Yamada, Kyoto University, Uji, Kyoto, Japan


*Abstract*

Neutrons are very interesting for scientists as new probes used for investigating inner structure of materials. But, there are few neutron science facilities available in the world for such purposes. To remedy a situation, we started to develop linear accelerator base small neutron source.

At present, we are working on a small $H^+$ ion source as the first step of development of a small neutron source. We have selected a type of ECR ion source with permanent magnets as a small and high intensity ion source.

A pulse gas valve made of a piezoelectric element was built-in in the ion source plasma chamber to reduce the loading of evacuation systems.

We have obtained in our test stand a beam current of 1.13 mA at RF frequency of 5.74 GHz and 25 W RF power. The ratio of $H^+$ to other ion species was also measured with an analyzing magnet.


## INTRODUCTION

We aim to develop a small and high intensity proton source for a compact accelerator based neutron source. Because this proton source shall be located close to RFQ for compactness, the ratio of $H^+$ to molecular ions such as $H_2^+$ or $H_3^+$ must be large. Therefore we have selected a type of ECR ion source with permanent magnet as a small and high intensity ion source. The ECR ion sources can provide high $H^+$ ratio because of their high plasma temperature. Using permanent magnets makes the ion source small and running cost low. Because there is no hot cathode, longer MTBF is also expected.

Usually, gas is fed into ion sources continuously, even if ion sources run in pulse operation mode. But, continuous gas flow becomes a load to the vacuum system. So, we decided to install a pulse gas valve directly to the plasma chamber. Feeding the gas only when RF power is enabled reduces the gas load to the evacuation system and the vacuum level can be kept high.

## PULSE GAS VALVE

We developed pulse gas valve with commercial piezoelectric element (Kyocera Co. KBS-20DA-7A) [1]. Fig. 1 shows the piezoelectric element, which is used for developing a pulse gas valve. Table 1 shows the specifications of the element. This valve utilize the piezoelectricity such that the elements warps by internal mechanical stress when a voltage is applied. As shown in Fig. 2, the application of a voltage opens a path under the element and the gas flow into the chamber.

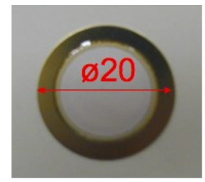


Figure 1: Piezoelectric element.

Table 1: Specifications of the piezoelectric element.

| | |
|---|---|
| Diameter of metal base | 20.0±0.1mm |
| Diameter of piezoelectric element | 14.2±0.1mm |
| Total thickness | 0.45±0.1mm |
| Thickness of metal base | 0.20±0.03mm |
| Resonance frequency | 6.6±1.0kHz |
| Capacitance | 10±0.3nF |
| Electric strength(catalogue spec.) | $30V_{p\text{-}p}$ |

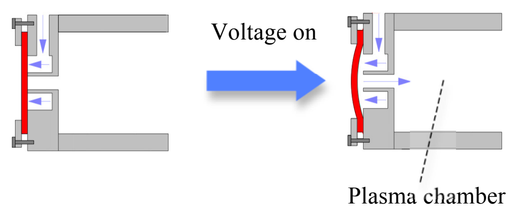


Figure 2: Operating principal of the valve .

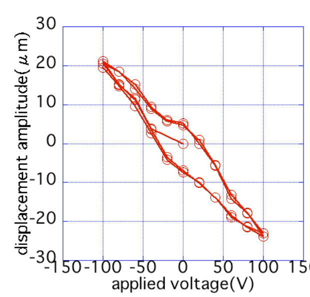


Figure 3: Hysteresis curve.

This piezoelectric element has a hysteresis characteristic like Fig. 3. When negative voltage is applied the valve opens and gas can flow. But because of hysteresis, applying only negative voltage reduce the displacement of the element or its warpage. Therefore, a bipolar voltage pulse generator was prepared for driving

#ichikawa@kyticr.kuicr.kyoto-u.ac.jp

the valve element. It reduces the quantity of leak gas in close position of the valve.

## DESIGN OF THE ECR ION SOURCE

### *Extraction Electrodes*

The optimal geometry of extraction electrodes were found by using a simulation soft PBGUNS[2]. Given extraction voltage was 25 keV. The optimal design of extraction electrode was like Fig 4. The density of plasma was $3.83\times10^{17}\mathrm{m}^{-3}$. This plasma density is proper for plasma frequency 5.56 GHz. The plasma has a property that if the frequency is lower than plasma frequency the RF can't penetrate into plasma. So, in order to supply RF power into plasma, RF frequency must be higher than plasma frequency. In this study we have chosen that RF frequency to be 6 GHz.

### *Magnets Arrangement*

The magnetic flux density optimal for ECR condition is given by a following formula:

$$B_{ecr}[\mathrm{T}] = \frac{m_e\omega}{e} = \frac{2\pi m_e}{e} f \cong \frac{f[\mathrm{GHz}]}{28} \tag{1}$$

where $B_{ecr}$ is magnetic flux density at ECR point, $m_e$ is mass of electron, $e$ is elementary charge, $f$ is frequency of RF, $\omega$ is angular frequency of RF [3]. RF frequency is 6 GHz, so the optimal magnetic flux density becomes 0.214 T. The optimization of permanent magnets and iron yokes arrangement is done with PANDIRA code [4]. Fig. 5 shows the distribution of axial magnetic field in the optimal arrangement. The magnet material we used is NEOMAX-48H, whose magnetic flux density is about 1.3 T. It is capable to adjust the strength of magnetic field by varying the distance between the permanent magnets.

### *Plasma Chamber*

We designed a plasma chamber so that the resonance frequency became 6 GHz. The resonance frequency of the $TE_{111}$ mode in a tube is expressed in the following expression:

$$f_{111} = \frac{1.841}{\sqrt{\varepsilon\mu}}\frac{c}{R}\sqrt{\left(1 + 2.912\frac{R^2}{d^2}\right)} \tag{2}$$

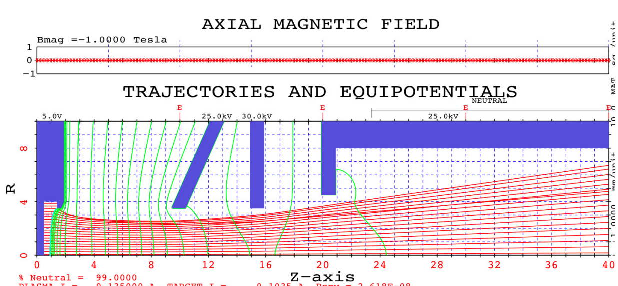


Figure 4: Result of PBGUNS simulation.

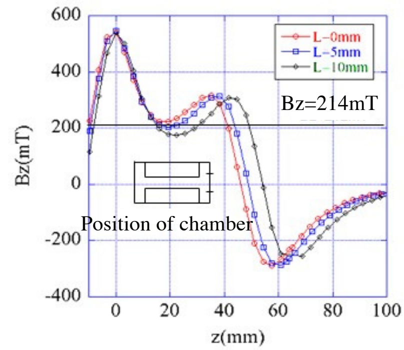


Figure 5: Distribution of axial magnetic field (L means variation of distance between magnets).

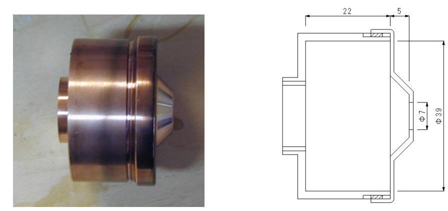

Figure 6: Plasma chamber.

where, $f_{111}$ is frequency of RF, $R$ is radius of plasma chamber, $d$ is length of plasma chamber. On the basis of this, the shape of plasma chamber was determined by HFSS simulation [5]. Fig 6 shows the plasma chamber designed by simulation. The size of this chamber is very small; being approximately f40mm×27mm.

### *Whole Ion Source*

Fig. 7 shows the schematic drawing of the ion source. In this ion source, the plasma chamber is at the high voltage potential and the iron yokes are electrically insulated by insulators. The ion source we developed has the whole size of only about f200 mm × 300 mm. To keep the vacuum in the ion source extraction region good, it has holes to evacuate (about f10 mm × 30 mm, 12 places). The total conductance of the holes and extraction hole is 27.3 l/s. The conductance was calculated by a following formula:

$$C\left[\frac{m^3}{s}\right] = 0.523\frac{r[cm]^3}{M^{\frac{1}{2}}L[cm]} \tag{3}$$

where r is radius of holes, M is the molecular weight of the gas particles (in this time, Hydrogen) and $L$ is length of holes. The pumping speed of our turbo molecular pump is 1500 l/s, so that the vacuum level in the plasma chamber is poorer by factor of about 100 than the pump head.

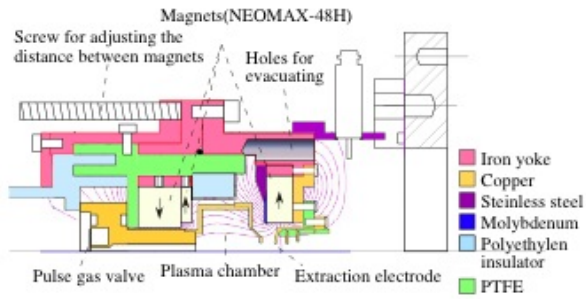


Figure 7: Schematic drawing of the ion source.

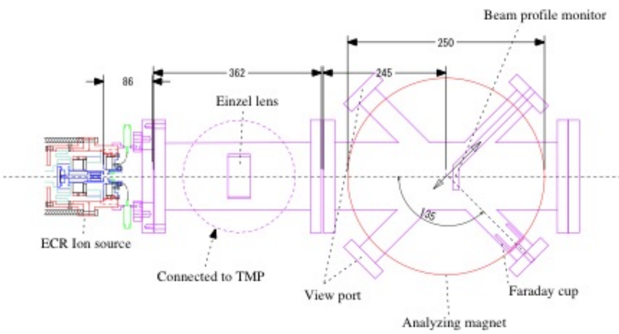


Figure 8: Horizontal profile of test bench (aperture of analyzing magnet is 60mm).

Table 2: Fixed parameters at total current measurement.

| | |
|---|---|
| RF frequency | 5.74 GHz |
| RF power | 25 W |
| Extraction voltage | 10 kV |
| Frequency of thepulse gas valve driving signal | 25 Hz |
| Duty of the pulse gas valve driving signal | 50% |
| Pressure of gas | 400 kPa |

## MEASUREMENT

The current from the ion source was measured. Fig. 8 shows the setup of test bench.

Total current including all ion species is measured with a Faraday cup set just downstream of the extraction electrode. Up to now, this ion source can supply ion beam of more than 1 mA. Table 2 shows the fixed parameters.

The current of each ion species was measured with analyzing magnet, while changing frequency of RF. Fig. 9 shows its result. In all case the ratio of $H^+$ to others is small. As RF frequency increases or gas flow decreases, the ratio of heavier ions decreases. Table 3 shows the fixed parameters. The variable parameters were the RF frequency and gas flow rate. When the gas flow rate was 0.25 sccm, plasma did not appear at the RF frequency lower than 5.7 GHz and higher than 5.78 GHz.

Table 3: Fixed parameters at each ion species' current measurement

| | |
|---|---|
| RF power | 25 W |
| Extraction voltage | 5 kV |
| Frequency of the pulse gas valve driving signal | 25 Hz |
| Duty of the pulse gas valve driving signal | 50% |

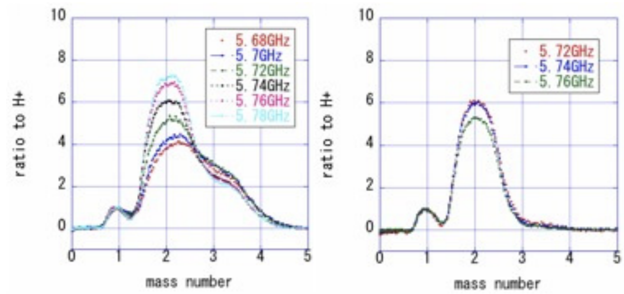


Figure 9: Ratio of each ion species current to $H^+$. Left: Gas flow rate was about 0.70 sccm. Right: Gas flow rate was about 0.25 sccm.

## CONCLUSIONS

We consider that to increase the ratio of $H^+$, the RF frequency should be higher and the gas flow as little as possible. Because in the current magnets arrangement we can't increase RF frequency a new magnets arrangement is being searched.

In the near future we'll develop a second model of the ion source to increase total beam current and the ratio of $H^+$ ions.

## REFERENCES


[1] M. Ichikawa, "Development of Piezoelectric Pulse Gas Valve", Proceedings of 4th Annual Meeting of Particle Accelerator Society of Japan and 32nd Linear Accelerator Meeting in Japan, August 2007, http://www.pasj.jp/

[2] J. E. Bores, "A digital computer code for the simulation of electron and ion beams on a PC", IEEE Cat. No. 93CH3334-0 (1993) 213.

[3] I. Blown, "The Physics and Technology of Ion Sources Second, Revised and Extended Edition", WILEY-VHC Verlag GmbH & Co. KGaA, 2004.

[4] Reference Manual for the POISSON/SUPERFISH Group of codes, No. LA-UR-8712.

[5] Ansoft, http://www.ansoft.com/products/hf/hfss/.

# DEVELOPMENT OF ULTRA-LOW EMITTANCE INJECTOR FOR FUTURE X-RAY FEL OSCILLATOR*

P.N. Ostroumov#, K.-J. Kim, ANL, Argonne, IL 60439, U.S.A
Ph. Piot, Northern Illinois University, DeKalb, IL, U.S.A.

*Abstract*

An XFELO proposed recently [1] requires a continuous sequence of electron bunches with ultra-low transverse emittance of less than 0.1 µm, a bunch charge of 40 pC, an rms energy spread of 1.4 MeV, repeating at a rate between 1 MHz to 100 MHz. The bunches are to be compressed to rms lengths less than 2 ps at the final energy of 7 GeV. Following the successful commissioning of the pulsed injector based on a thermionic gun [2] we discuss a concept for ultra-low emittance injector to produce 100 MHz CW electron bunches. The electron beam is extracted by ~ 1MV RF voltage using low frequency ~100 MHz room temperature RF cavity [3]. The injector also includes a chicane and slits to form a short ~0.5 nsec bunch, a buncher to form low longitudinal emittance of the bunched beam, an accelerating section to ~20 MeV using higher harmonic cavities, and an RF cosine-wave chopper to form any required bunch repetition rate between 1 MHz and 100 MHz. The results of initial optimizations of the beam dynamics with the focus on extracting and preserving ultra-low emittance will be presented.

## GENERAL LAYOUT

The 7 GeV electron beam must be delivered with the parameters listed in Table 1. We propose 7 GeV CW SC linac which includes Ultra-Low Emittance Injector (ULEI) based on a thermionic RF-gun as a solution to deliver an electron beam as specified in Table 1.

The proposed electron linac includes the following main systems:

- An RF-gun with a small diameter thermionic cathode to extract ultra-low emittance beam. The latter is possible primarily due to the low equivalent DC current which is ~80 mA for 0.5 nsec bunches and high extraction voltage.
- A low-frequency RF cavity capable to provide ~ 1.0 MV extracting voltage. The highest possible extraction voltage should suppress beam space charge in the following sections of the injector.
- An energy filter which includes a magnetic chicane and slits to form a short, ~ 0.5 nsec bunch.
- A 6th harmonic RF cavity (600 MHz) as a monochromator to minimize momentum spread of the electron beam.
- A velocity buncher (300 MHz) to form low longitudinal emittance of the bunched beam.
- A booster acceleration up to ~20 MeV using higher harmonic cavities (400 MHz).
- An RF cosine-wave chopper to form any required bunch repetition rate between 1 MHz and 100 MHz.
- Two chicanes along the linac for bunch compression.
- A final acceleration using SC ILC cavities (1300 MHz) with 20 MV/m accelerating field.

Table 1: Main Beam Parameters.

| Parameter | Value | Unit |
|---|---|---|
| Transverse rms emittance | <0.1 | µm* |
| Bunch charge | 40 | pC |
| Bunch rms time width | 2 | psec |
| Bunch rms energy spread | 1.4 | MeV |
| Bunch repetition rate | 1-100 | MHz |

*The emittance defined as the area must be multiplied by π.

The layout of the injector and the 1.6 GeV section of the linac is shown in Fig. 1.

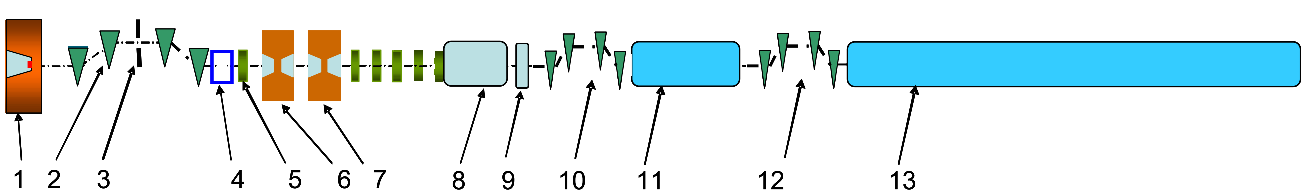


Figure 1: General layout of the linac for XFELO. 1 – RF cavity with thermionic cathode, 100 MHz, 1 MV; 2 – chicane and slits (3) as an energy filter; 4 – quadrupole triplet; 5 – focusing solenoid; 6 – monochromator of the beam energy, f=600 MHz; 7 –buncher, f=300 MHz; 8 – booster linac section, f=400 MHz; 9 –RF cosine-chopper to form rep. rate 1 MHz to 100 MHz; 10 – bunch compressor – I; 11 –SC linac section, 460 MeV, f=1300 MHz; 12 – bunch compressor – II; 13 – initial section of the SC linac, f=1300 MHz.

* This work was supported by the U.S. Department of Energy, Office of Nuclear Physics and Basic Energy Sciences, under Contract No. DE-AC02-06CH11357 . P.P is supported by U.S. Department of Education, under contract P116Z010035 with Northern Illinois University
#ostroumov@anl.gov

## THERMIONIC RF GUN

The normalized RMS emittance of an electron beam emitted from a hot cathode is described by the well-known formula $\varepsilon_{n,RMS} = \frac{r_C}{2}\sqrt{\frac{kT}{m_0 c^2}}$, where $r_C$ is the cathode radius and $T$ is the cathode temperature, $k$ is the Boltzmann constant, $m_0$ is the electron rest mass and $c$ is the speed of light. To obtain a low emittance beam, a small diameter cathode is required. Initial simulations of a 1 MeV DC electron beam produced by a thermionic cathode in a 100 MHz VHF gun similar to ref. [3] have been performed. The results, shown in Fig. 2, demonstrate that about a 50 mA DC beam can be extracted with an rms emittance less than 0.1 µm. These simulations are also consistent with the measurements performed at the Spring-8 injector [2].

In subsequent steps the cathode size was chosen to ensure that the slice (or uncorrelated) emittance is ~ 0.08 µm at the gun exit. The e-gun RF frequency and voltage were optimized from start-to-end simulations of the low energy transport line (including bunching and acceleration up to ~20 MeV) Among the considered frequency (50, 100 and 186 MHz), the 100 MHz case provided best results so far. The 100 MHz RF cavity creates ~20 MV/m across the accelerating gap with 1 MV total voltage. This cavity will require ~150 kW RF power.

Fig. 3 shows the electron beam momentum along the bunch for three different RF voltages. The energy filter will “chop” the top of the curve within the ±0.25 nsec time window to deliver 40 pC bunches from 80 mA DC beam.

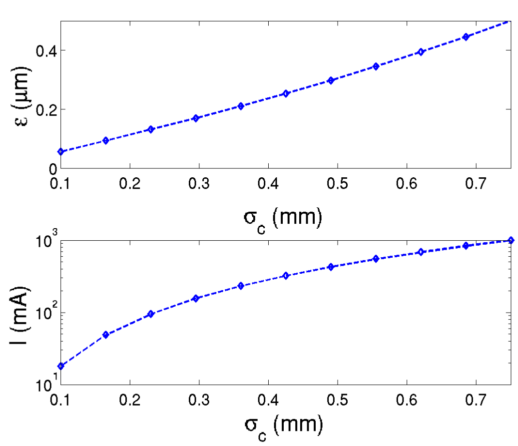


Figure 2: Electron beam slice emittance and current as a function of the cathode RMS radius ($\sigma_c$=$0.5r_C$) for the 100 MHz gun.

## PHYSICS DESIGN AND START-TO-END SIMULATIONS

The physics design of the injector and initial section of the main linac up to 1.6 GeV has been performed using

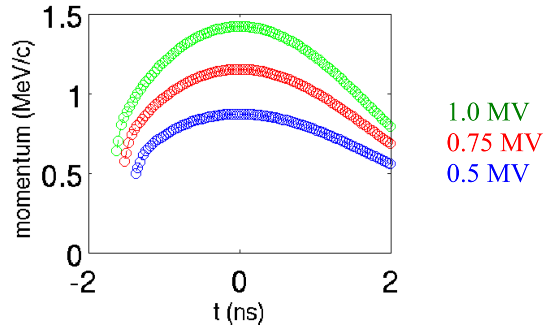


Figure 3: Electron beam momentum along the bunch for three different RF voltages in the 100 MHz cavity.

TRACK [4] and ASTRA [5] tracking codes. The simulations of 3D beam dynamics include space charge effects and realistic field distributions in all injector and linac elements. In addition, PARMELA is being used to verify the beam dynamics in some sections of the linac.

Originally the linac design has been performed by optimization of each subsystem such as the RF-gun, energy filter, monochromator, velocity buncher, booster acceleration and bunch compressors. For example, the monochromator, the velocity buncher and booster linac were optimized to minimize emittance growth due to space charge and chromatic aberrations.

The simulations indicate that all functional elements of the layout shown in Fig. 1 provide the expected performance. For example, the chicane and slits serve as a perfect energy filter and form 0.5 nsec bunch without any transverse emittance growth. The RF cavity (element 6 in Fig. 1) operating at 600 MHz can reduce the total energy spread down to 0.07%. The buncher and booster section reduce the rms bunch time width below 30 ps. The current configuration of the linac is not yet finalized: overall, we observe ~60% growth of the transverse rms emittance derived from 90% of particles.

The evolution of the RMS energy spread and bunch width along the 1.6 GeV linac is shown in Fig. 4. Although, the longitudinal emittance of the 1.6 GeV beam is within specifications, more optimization is required to reduce energy spread by the factor of 2. To achieve required bunch length, two magnetic chicanes are used. The final current distribution of the accelerated bunch is shown in Fig. 6.

We are developing a chopper system which allows us to produce a bunch sequence with any frequency between 1 to 100 MHz. The system is based on a combination of cosine-wave chopper [6] with a fast kicker (~20 nsec). The kicker can be used at low energy while cosine-wave chopper should be installed after the 20 MeV section to suppress any space charge effects.

## OPTIMIZATION VIA EVOLUTIONARY ALGORITHM

We have also started to use a genetic optimization code [7] in conjunction with ASTRA as done in ref. [8]. For the preliminary optimization (ASTRA does not yet include the space charge force in dipole magnets), a simplified approach was followed. The energy filter was idealized (by numerically chopping the distribution out of the gun), and the distribution was tracked in a cylindrical-symmetric beamline (to increase the simulation speed). Currently we considered the 100 MHz RF gun with an accelerating voltage of 1 MV and the ideal chopper was set such that 50 pC was transmitted. Our simplified beamline incorporates solenoids similar to the JLAB IR-FEL. The multi-objective optimization included the minimization of the transverse emittance and the bunch length. The positions and settings of all the elements in the beamline were optimization variables. The evolution of the transverse emittance along the optimized beamline is shown in Fig. 5, the 80 % rms emittance, i.e. corresponding to targeted 40 pC, is below 0.08 µm. The corresponding rms bunch length ~20 m downstream of the cathode is 27 mm (rms).

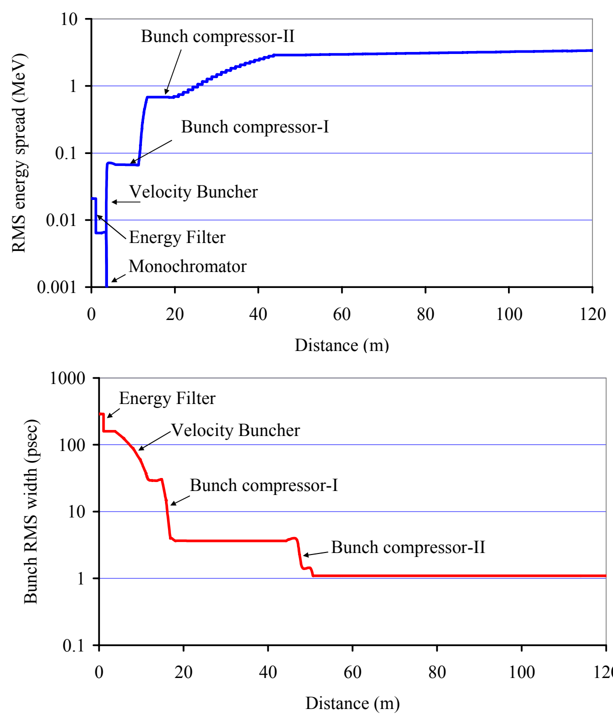


Figure 4: Evolution of RMS energy spread and bunch width along the linac.

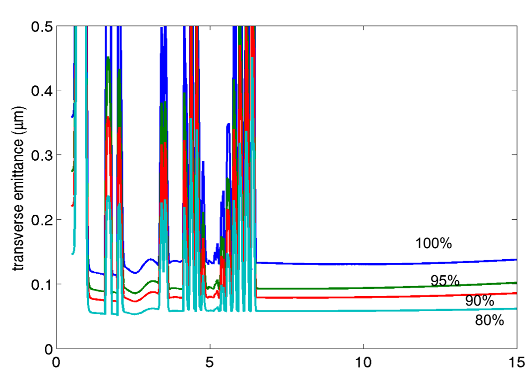


Figure 5: Electron beam emittance vs distance.

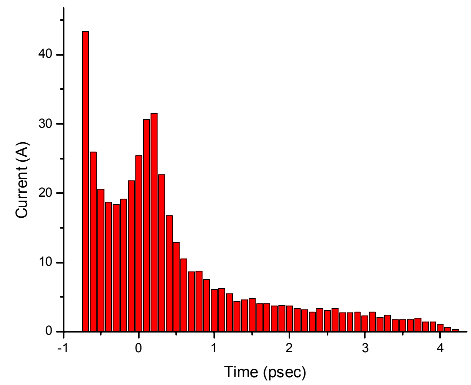


Figure 6: Current distribution in the accelerated bunch.

## CONCLUSION AND OUTLOOK

Preliminary "manual" design of the ULEI and CW accelerator has been developed without genetic optimization codes. 3D simulations show that the energy filter does not produce any transverse emittance growth. Two bunch compressors are required to achieve specified longitudinal beam parameters at the end of linac. Start-to-end simulations have been performed in realistic external and space charge 3D fields. These simulations show that the longitudinal emittance is within specifications while the transverse rms emittance (normalized and defined for 90% of particles) is 0.16 µm. Application of a genetic optimization code in a currently simplified injector section results in improved performance capable to maintain the emittance unchanged and equal to ~0.08 µm.

We plan to extend the genetic optimization of the injector and define cost-effective accelerating systems for the whole linac up to 7 GeV.

## REFERENCES

[1] K.-J. Kim, Y. Shvyd'ko, and S. Reiche, Phys. Rev. Lett., 100 244802 (2008).
[2] K. Togawa, et al., Phys. Rev. STAB 10, 020703 (2007)
[3] J.W. Staples, et al., Proceedings of the PAC 2007, p. 2990.
[4] http://www.phy.anl.gov/atlas/TRACK/
[5] K. Flottmann, ASTRA user manual available at: http://www.desy.de/ ˜mpyflo/Astra dokumentation/
[6] R. E. Laxdal, M. Pasini, L. Root, Proceedings of LINAC 2002, Gyeongju, Korea, p. 409.
[7] M. Borland, H.Shang, GeneticOptimizer unpublished program.
[8] I.V. Bazarov and C.K. Sinclair, PRST-AB, 8, 034202 (2005).

# EXTRACTION FROM ECR AND RECOMBINATION OF MULTIPLE-CHARGE STATE HEAVY-ION BEAMS IN LEBT*

P.N. Ostroumov#, A. Barcikowski, S.A. Kondrashev, B. Mustapha, R.H. Scott, and S.I. Sharamentov, ANL, Argonne, IL 60439, U.S.A.
N.E. Vinogradov, Northern Illinois University, DeKalb, IL 60115, USA

## ABSTRACT

A prototype injector capable to produce multiple-charge-state heavy-ion beams has been developed and constructed at ANL. The injector consists of an ECR ion source, a 100 kV platform and a Low Energy Beam Transport (LEBT). The latter comprises two 60-degree bending magnets, electrostatic triplets and beam diagnostics stations. Several charge states of bismuth ions from the ECR have been extracted, accelerated to the energy of 1.8 MeV, separated and then recombined into a high quality beam ready for further acceleration. This technique allows us to double heavy-ion beam intensity in high-power driver linac for future radioactive beam facility. The other application is the post-accelerators of radioactive ions based on charge breeders. The intensity of rare isotope beams can be doubled or even tripled by the extraction and acceleration of multiple charge state beams.

## INTRODUCTION

Ion accelerators worldwide use only single-charge state beams from the ion source. ECR Ion Sources (ECRIS) are widely used as injectors of highly charged ions. Current state of the art ECRIS built using superconducting (SC) magnets has recently demonstrated ~6 pμA of uranium ions with charge state 33+ or 34+ [1]. Taking into account the acceleration and stripping efficiencies, the ion source intensity must be doubled to meet the power requirements for the proposed Facility for Rare Isotope Beams (FRIB) [2] and other nuclear physics applications based on high-intensity ion linacs. Obviously, the intensity of single-charge state beams cannot be doubled in the near future and the appropriate solution is to simultaneously extract and accelerate multiple-charge states of the desired heavy-ions. This solution is not appropriate for light ions due to larger charge states separation in the phase space (large q/A separation, where q is the ion charge state and A is the mass number). Fortunately, ion sources produce enough single-charge state intensity for light ions. In addition to future facilities, existing facilities could benefit from the concept of multiple-charge state acceleration as well.

We have designed and built a prototype multiple-charge state injector system to demonstrate the possibility of extracting, analyzing and combining several charge states of a heavy-ion beam from the ion source to the point of injection to an RF accelerator. The injector consists of an ECRIS placed on a High-Voltage (HV) platform and an achromatic LEBT. The system was successfully tested for a two-charge state bismuth beam. This technique can be applied for both the driver and post accelerator in radioactive beam facilities. It is well recognized that the ECRIS and the Electron Beam Ion Source (EBIS) are effective charge breeders for radioactive beams [3]. The intensity of radioactive ions extracted either from an ECRIS or EBIS can be increased by combining several neighboring charge states into the same phase space area for further acceleration. This is especially important for rare isotope beams where doubling or tripling the intensity is critical for certain measurements.

## EXPERIMENTAL SET-UP

A 3D model of the injector is shown in Fig. 1. It consists of an ECR ion source, a 100-kV platform and an achromatic LEBT system based on two 60° bending magnets. The stand-alone ECR ion source is built using all permanent magnets, it is described in more detail elsewhere [4]. The HV platform was designed and constructed to accelerate all ion species extracted from the ECR source to higher energy to suppress space charge effects in the LEBT. The focusing is provided by electrostatic Einzel lenses and quadrupole triplets. Rotating wires are used for beam profile measurements. The beam emittance is measured by a specially developed scintillator-based pepper-pot emittance probe described in

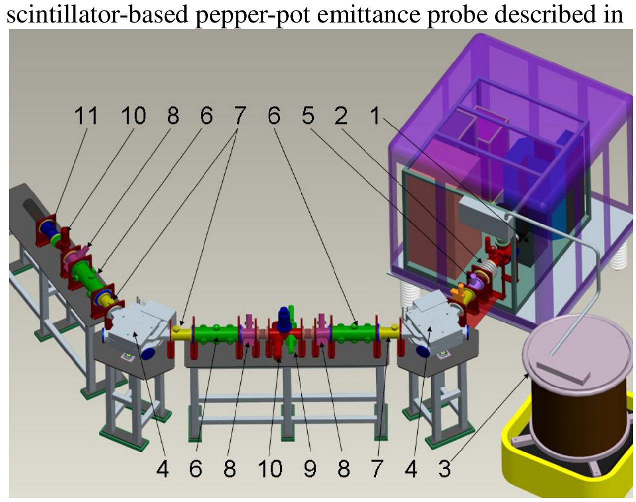


Figure 1: General view of the injector. 1 - ECRIS installed on HV platform, 2 - 75-kV accelerating tube, 3 - isolation transformer, 4 - 60° bending magnet, 5 - Einzel lens, 6 - electrostatic triplet, 7 - electrostatic steering plates, 8 - rotating wire scanner, 9 - horizontal jaw slits, 10 - Faraday cup, 11 - emittance probe.

* This work was supported by the U.S. Department of Energy, Office of Nuclear Physics Contract No. DE-AC02-06CH11357 . N.E.V. is supported by U.S. Department of Education, under contract P116Z010035 with Northern Illinois University
#ostroumov@anl.gov

[5]. Our injector differs from any other ECR source on a HV platform currently used in various applications worldwide. Specifically, we extract all ion species available form the ECR source and separate them after acceleration by the platform potential. For the purpose of these experiments, we use a bismuth ion beam which is relatively simple to produce using an oven heated to 550°C. The ECR is equipped with two RF amplifiers set to 12.8 GHz and 13.8 GHz with total RF power up to 1.5 kW. Oxygen is used as a support gas to produce higher charge states of $^{209}$Bi ions. The injector system allows us to accelerate all ion species up to q×100 keV total kinetic energy.

The bismuth ion beam is first extracted by applying a 15 kV potential to the source and then accelerated by a 75 kV platform potential. Fig. 2 shows the beam currents for the different charge states extracted from the source. Depending on the operational parameters, a total current of 4 mA is extracted from the ECR. In the scope of our experiment, we are interested to work with $^{209}$Bi$^{20+}$ and $^{209}$Bi$^{21+}$ to reduce charge spread. Our long-term operation experience has showed that the most stable operation of the ECR and the lowest beam emittances can be achieved for beam intensities of ~1.0 pμA for the charge states 20+ and 21+ of bismuth.

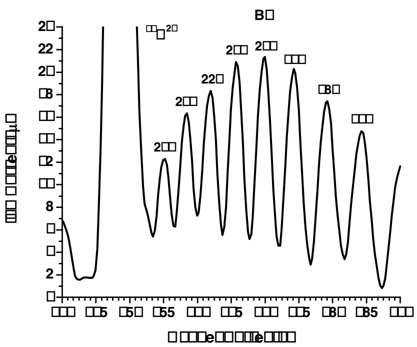

Figure 2: Bismuth beam intensities for different charge states.

## INJECTOR DESIGN AND SIMULATION

The ECR ion source generates multi-component ion beams with total intensity up to 4 mA. The main purpose of the LEBT is to select particular ion specie and match it into the following RF accelerator. The selection of the required ion specie is usually performed by adjustable horizontal jaw slits located in the high-dispersion area of the LEBT downstream of the first bending magnet. Several charge states of ion beam downstream of the selection slits can be re-combined into a beam with the same transverse phase space if the LEBT is an achromatic system.

The standard beam optics computer code COSY [6] was used to design and optimize the original layout of the LEBT by taking into account terms through third order. However, COSY does not include space charge effects. Therefore, numerical studies of beam dynamics in the LEBT have been performed using the multi-particle code TRACK [7]. TRACK can simulate a multiple-component ion beam through pre-calculated 3D fields taking into account space-charge effects. The magnetic field of the ECR extraction region and electrostatic fields in the initial part of the beam line that consists of a puller electrode, Einzel lens and grounded electrodes were calculated using the EM-Studio software. 3D representation of magnetic field including fringe fields was implemented using genuine configuration of the 60° bending magnet. Similarly, the electric fields of the triplets were implemented into TRACK. TRACK simulations have shown that the bending magnet must provide strong vertical focusing in order to compensate for space charge forces. The LEBT system shown in Fig. 1 is achromatic providing ~25 mm separation on the slits for neighboring charge states of bismuth beam tuned for 20+ as the central charge state.

The exact phase space distribution of ion beams extracted from the ECR is very complicated (see [8-9], for example) and can not be reproduced with any available computer code. For the initial design of the LEBT we have used simplified, axial-symmetric multi-component ion beams with the parameters best fitted to the measurements performed downstream of a 90° magnet [10]. For the tuning and operation of the actual LEBT system, we have developed and applied specific optimization algorithms within the code TRACK. These algorithms use the measured data such as the horizontal (H) and vertical (V) beam profiles from the wire scanners and H-profiles from the slits to adapt the computer model to the actual beam line. The first optimization step is to determine the beam emittance and Twiss parameters at the source that reproduce the measured beam profiles after the first bending magnet. The second step is to optimize the setting of nine quadrupoles to provide (a) no angular dispersion on the slits and (b) 100% beam transmission downstream of the slits.

## EXPERIMENTAL RESULTS

The measured beam profiles of a two-charge state bismuth beam (20+, 21+) on the wire scanner behind the first magnet have been used to fit the initial beam emittance and Twiss parameters at the source to use for further tuning and operation of the LEBT. For realistic beam dynamics simulations we track 17 beams simultaneously (O and Bi as in Fig. 2). The quadrupole settings were then optimized using TRACK to re-combine the $^{209}$Bi$^{20+}$ and $^{209}$Bi$^{21+}$ beams with [illegible] as the central charge state. Setting the values obtained by TRACK we noticed a very good agreement between the simulation and the actual measurements.

After we obtained initial beam parameters upstream of the first magnet, the LEBT was re-tuned to provide zero angular momentum dispersion at the separation slits placed at the mid-point of the LEBT. Figure 3 shows the linear and angular dispersions along the LEBT. We notice a good separation of the charge states, which is important to cleanly select a single- or a multiple-charge state beam.

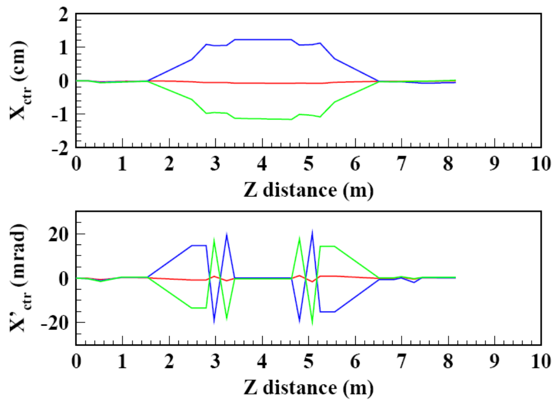


Figure 3: Linear and angular dispersions along the LEBT.

At the end of the LEBT, the beam emittance was measured for the following three different operation modes: 1) only $^{209}Bi^{20+}$ is selected by the slits; 2) only $^{209}Bi^{21+}$ is selected; 3) both $^{209}Bi^{20+}$ and $^{209}Bi^{21+}$ are selected. The beam parameters are given in Table 1. The focusing triplet upstream of the emittance probe is tuned to provide ~ 30 mm beam diameter on the emittance probe. Only several percent adjustment of quadrupole setting with respect to the pre-calculated values is required in order to combine the dual-charge state bismuth beam. 100 % beam transmission from FC-1 to FC-2 has been achieved with typical beam currents of: $I_{20+} = (20.9 \pm 0.2)\,\mu A$, $I_{21+} = (21.3 \pm 0.2)\,\mu A$, $I_{20+,21+} = (42.1 \pm 0.4)\,\mu A$

Figure 4 shows the H- and V-beam profiles on the wire scanner downstream of the second magnet while the pepper-pot images of single- and dual-charge state bismuth beam are shown in Figure 5. As can be seen from these figures, two charge states of bismuth beam are perfectly combined into the same phase space area. The emittances and Twiss parameters of the beam derived from the pepper-pot data for the three operation modes of the LEBT are listed in Table 1. As seen from this table, perfect recombination is achieved in the vertical plane while the horizontal Twiss parameters are slightly different. Further improvement of the phase space parameters of the dual-charge state beam can be achieved by providing better matching into the first magnet using an electrostatic doublet which will be installed upstream of the first bending magnet.

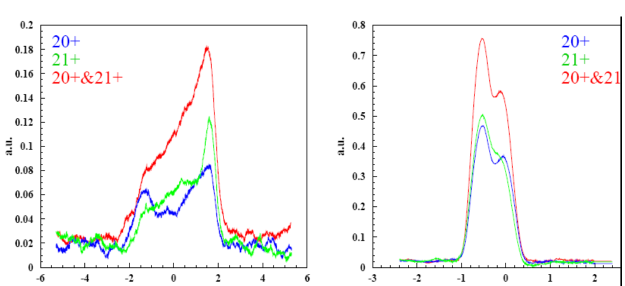


Figure 4: Measured bismuth beam profiles on the wire scanner downstream of the second bending magnet.

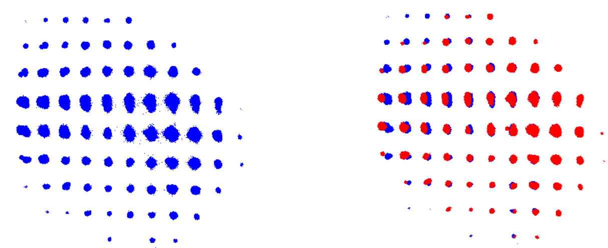

Figure 5: Pepper-pot image of the combined bismuth beam with charge states 20+ and 21+ (on the left) and superimposed images of $^{209}Bi^{20+}$ (blue) and $^{209}Bi^{21+}$ (red) beams transported individually (on the right).

Table 1: RMS normalized emittances and Twiss parameters of individual charge states (20+, 21+) and combined bismuth beams at the end of the LEBT.

| Parameter | $^{209}Bi^{20+}$ | $^{209}Bi^{21+}$ | $^{209}Bi^{20+}+^{209}Bi^{21+}$ |
|---|---|---|---|
| $\varepsilon_X$ (π μm) | 0.092 | 0.081 | 0.087 |
| $\alpha_X$ | 0.816 | -0.125 | 0.259 |
| $\beta_X$ (mm/mrad) | 2.93 | 3.17 | 2.68 |
| $\varepsilon_Y$ (π μm) | 0.055 | 0.059 | 0.057 |
| $\alpha_Y$ | -2.92 | -3.33 | -3.32 |
| $\beta_Y$ (mm/mrad) | 0.779 | 0.902 | 0.895 |

## CONCLUSION AND OUTLOOK

Several charge states of bismuth ions from an ECR ion source have been extracted, accelerated to an energy of 1.8 MeV, separated and then recombined into a high quality beam ready for further acceleration. This technique allows us to double the intensity of heavy-ion beams in high-intensity linacs for future radioactive beam facilities and other nuclear physics applications. Another important application of the concept of multiple charge state extraction and acceleration is in post-accelerators of radioactive ions based on charge breeders.

Currently we are modifying LEBT to improve transmission and recombination of three charge states of the bismuth beam. Also, the possibility to incorporate sextupoles into the LEBT is being investigated.

## REFERENCES

[1] D. Leitner et al., RSI, 79, 02C710 (2008).
[2] J. A. Nolen, Nucl. Phys. A787, 84c-93c (2007).
[3] T. Lamy, et al., RSI, 79, 02A909 (2008).
[4] D.Z. Xie, RSI, 73 (2), 2002, p. 531.
[5] S.A. Kondrashev, et al., in these proceedings.
[6] http://bt.pa.msu.edu/index_files/cosy.htm
[7] http://www.phy.anl.gov/atlas/TRACK/
[8] P. Spadtke et al, RSI, 79, 02B716 (2008).
[9] D.S. Todd et al, RSI, 79, 02A316 (2008).
[10] N.E. Vinogradov et al., in Proc. of the LINAC06, Knoxville TN, August 2006, p. 336.

# RAMPING UP THE SNS BEAM CURRENT WITH THE LBNL BASELINE H- SOURCE

Martin P. Stockli, B. Han, S. N. Murray, D. Newland, T. R. Pennisi, M. Santana, R. F. Welton,
Spallation Neutron Source, Oak Ridge National Laboratory, Oak Ridge, TN 37831, U.S.A..

Over the last two years the Spallation Neutron Source (SNS) has ramped up the repetition rate, pulse length, and the beam current to reach 540 kW, which has challenged many subsystems including the H- source designed and built by Lawrence Berkeley National Laboratory (LBNL). This paper discusses the major modifications of the $H^-$ source implemented to consistently and routinely output the beam current required by the SNS beam power ramp up plan. At this time, 32 mA LINAC beam current are routinely produced, which meets the requirement for 690 kW planned for end of 2008. In June 2008, a 14-day production run used 37 mA, which is close to the 38 mA required for 1.44 MW. A medium energy beam transport (MEBT) beam current of 46 mA was demonstrated on September 2, 2008.

## INTRODUCTION

LBNL designed and built the SNS baseline $H^-$ source, a mulicusp RF ion source [1]. Typically 250 W from a 600 W 13.56 MHz generator are matched into a 2.5 turn antenna loop inside the plasma chamber where it generates continuous, low-power hydrogen plasma. An additional 6%-duty-factor, 80-kW 2 MHz supply superimposes 40-70 kW for ≤1.23 ms at 60 Hz to boost the plasma density for beam production. As shown in Fig. 1, a transverse ~300 G filter field cools the plasma, which drifts towards the outlet aperture. The Cesium collar contains less than 30 mg of Cs in $Cs_2CrO_4$ cartridges [2]. Most of the negative ions form when bouncing from the Cs collar outlet aperture that is next to the source outlet.

A 1.6-kG dipole field, peaking 7 mm outside the source outlet, steers the co-extracted electrons toward one side of the e-dump, which is kept between +2 and +7 kV with respect to the -65 kV source potential. A fraction of the electrons impacts on the e-dump, while the other fraction ends on the extractor, where they generate thermal and radiation problems, especially when the extractor uses some of its +20 kV potential.

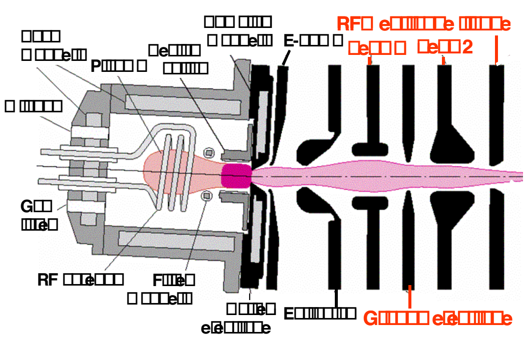

Figure 1: Schematic of the SNS H- source and LEBT.

Table 1: Duty factor, pulse length, unchopped MEBT beam current requirement and achievements, and the source and LEBT availability for neutron production runs. Run numbers reflect the calendar year.

| Production Run | Duty fator | Pulse length | mA required | mA in MEBT | %Avail ability |
|---|---|---|---|---|---|
| Run 2006-1 | | ~.1 ms | 20 | 20-28 | 99.9 |
| Run 2006-2 | 0.2 | ~.25ms | 20 | 14-30 | 99.98 |
| Run 2007-1 | 0.8 | ~0.4ms | 20 | 10-20 | 70.6 |
| Run 2007-2 | 1.8 | ~0.5ms | 20 | 11-20 | 97.2 |
| Run 2007-3 | 3.0 | ~0.6ms | 25 | 25-30 | 99.65 |
| Run 2008-1 | 3.6 | ~0.6ms | 25/30 | 25-37 | 94.9 |
| Run 2008-2 | 4.0 | 0.67ms | 32 | 32-35 | |

The extractor accelerates the beam into the 12-cm long, two-lens electrostatic low-energy beam transport (LEBT), which focuses the beam into the radio frequency quadrupole (RFQ). The compactness of the LEBT prohibits any characterization of the beam before it is accelerated to 2.5 MeV by the RFQ. The first beam current measurement is obtained from the first MEBT beam current monitor near the exit of the RFQ (BCM02).

This paper discusses the failures and successes in meeting MEBT beam current requirements as outlined in the SNS power ramp up plan [3] and listed in Table 1.

## LOW POWER PERFORMANCE

At the beginning of the SNS beam power ramp up, the short pulse length allowed the $H^-$ source to exceed the required 20 mA as seen in Fig. 2a. When the pulse length was increased to ~0.25 ms for the 2nd 2006 run, the source was at times unable to match the 20 mA requirement as seen in Fig. 2b.

Short beam pulses (<<0.2 ms) yield high beam currents when the matching network is matched without plasma. When the pulse length of short pulses is extended, a significant reduction in beam current is found, as seen in Fig. 3.

Long pulses yield the highest beam current when the matching network is tuned with the presence of plasma,

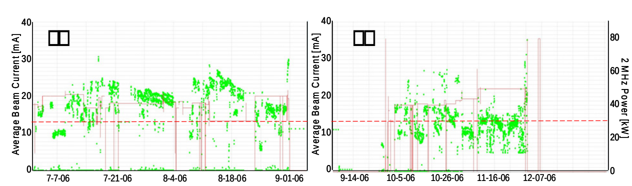


Figure 2: Requested 2 MHz peak power (solid line) and average chopped MEBT beam current (dots) compared with the required 13 mA (dashed line) for 2006.

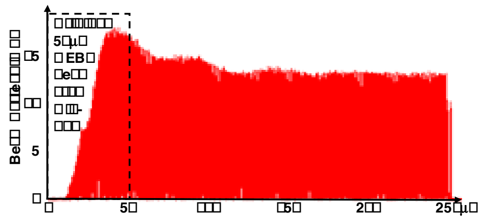

Figure 3: A 0.25 ms beam pulse optimized at 0.05 ms.

typically >0.2 ms after the start of the pulse. This, however, produces slow beam rise times, which often exhibit significant jitter. Or worse, sometimes the high-power plasma fails to ignite causing missing beam pulses. Mitigating efforts include compromise tunes, raising the 13 MHz and/or the 2 MHz RF power, and raising the $H_2$ flow. Raising the $H_2$ flow, however, reduced the beam current. Figure 4 shows this learning curve that yielded 20 mA beam current with maxed out 80 kW RF at the end of run 2007-2. There was no knob left that could meet the 25 mA required for the following run, starting 6 weeks later.

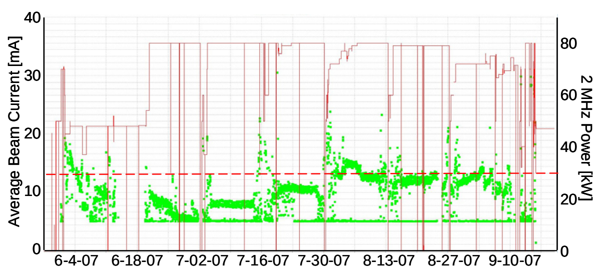


Figure 4: The learning curve of run 2007-2.

## LEARNING EFFECTIVE CESIATIONS

To reduce the risk of Cs induced arcing in the ultra compact LEBT and the nearby RFQ, LBNL implemented Cs cartridges [2], which contain $Cs_2CrO_4$ and St101, a getter made of 16% Al and 84% Zr. When heated to temperatures above 550 °C, the $Cs_2CrO_4$ reacts with the getter, releasing Cs while forming $Cr_2O_3$, $Al_2O_3$, and $ZrO_2$ [4]. The cartridges are contained in tight slots in the Cs collar that surrounds the ion source outlet. It can be cooled or heated to ~400°C with compressed air. The compressed air is shut off and the high-power plasma duty factor is adjusted to achieve and control the higher temperature required for releasing Cs.

Keeping the collar as cold as possible before cesiating at 550 °C for 30 minutes [5] yielded inconsistent results despite standardizing the conditioning and cesiation procedures: Very often, the cesiation process had to be repeated, and while the initial beam current could be quite high, it would decay in a matter of days (at low duty factor) or hours (at high duty factor) to much more modest levels as it can be seen in Figs. 2 and 4.

Being challenged to deliver 25 mA for run 2007-3, these problems were overcome with new methods that were deduced from a detailed study of manuals, records and new observations. All newly refurbished sources are evacuated and regularly vented with dry air and reevacuated to lower their water content. When needed the source is vented with dry air and quickly installed into the LEBT vessel that was vented with dry nitrogen. After evacuation, the Cs cartridges are being heated to ~100 °C before their temperature is ramped up to 350 °C over the last ~hour before cesiation. This degassing of the Cs cartridges seems to have eliminated the need for repeated cesiations. Apparently the degassed getter can more rapidly react with the $Cs_2CrO_4$ to release Cs.

While the Cs cartridges are degassed, the RF plasma is rapidly ramped up to a 6% duty factor with 50 kW of 2 MHz, where the source is conditioned for at least two hours. This appears to have eliminated the persistence problem. The likely cause is that Cs sputters easily from surfaces covered with water and other residues, while the Cs bonds well to clean metal surfaces.

Using the new methods, a single cesition of 30 minutes at 550 °C normally produces a performance level very close to the optimal performance, which is the best performance that can be achieved with any kind of subsequent cesiation(s) applied to its configuration.

## MODIFICATIONS TO REDUCE PERFORMANCE VARIATIONS

Despite standardizing all source dimensions, materials, refurbishments, preparations, and operations, significant, but apparently random variations were found from source to source. Being challenged to routinely produce 25 mA for run 2007-3 three significant problems were identified and mitigated.

Inadequate e-dump high voltage standoffs frequently arced and occasionally shorten out, which lowered temporarily or permanently the beam output. To improve the stability needed for the accelerator, the e-dump was often run near 2 kV, far below the optimal value. Newly designed standoffs appear to be arc-free.

Being heated, the cesium collar mounting legs would buckle, moving the collar by 1-3 mm either towards the ion source outlet aperture, which increases the beam current, or backward, which reduces the beam current. A new design yields a reduced, and consistently forward pushing force. This problem may explain source #2 to require ~50 kW for 25 mA in 11-07, while requiring only 35 kW for 25 mA in 12-07, as seen in Fig 5.

The Cs cartridges are 1.8 mm shorter than their slots, which allows for the Cs to be preferentially delivered either to the plasma chamber or to the Cs collar outlet

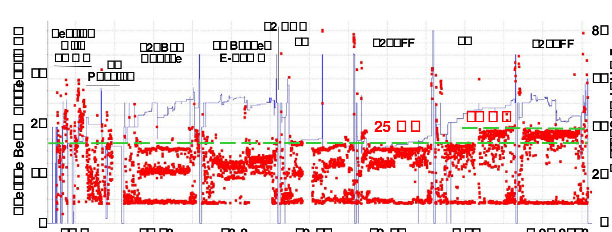

Figure 5: Measured (dots) and required (dashed line) average beam current with RF power (solid line) for run 2007-3.

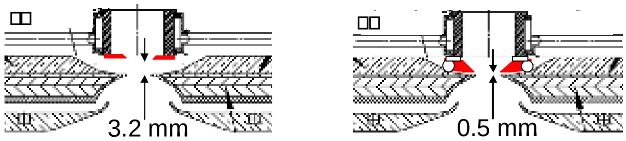


Figure 6: Original (a) and modified (b) Cs collar outlet.

aperture depending on the last tilt angle before the source was installed. Compression springs were installed to consistently deliver most of the Cs to the Cs collar outlet aperture.

## MODIFICATION INCREASING THE BEAM CURRENT

Being challenged to make 25 mA for run 2007-3, it was discovered that the 1-mm-thick, SS Cesium collar outlet aperture was 3.2 mm from the source outlet aperture, as shown in Fig. 6a. This was much more than the previously reported 1 mm gap [6] and the desired minimal gap [7]. Thirteen configurations tested within 6 weeks lead to a 4-mm-thick, Cs collar outlet aperture, which is tapered at 40°, made from Mo, and centered with ceramic balls, which maintain a distance of ~0.5 mm to the source outlet aperture, as shown in Fig. 6b.

When implemented for run 2007-3, this modification delivered more MEBT beam current than the integrated Cs collar [6] and the elemental Cs collar [8], both of which were tested between run 2007-2 and 2007-3.

The new Mo Cs collar outlet aperture and the associated learning curve have roughly doubled the MEBT beam current. It enabled routine production runs with MEBT beam currents in excess of 32 mA, including the two-week production run with 37 mA seen in Fig. 7. 38 mA MEBT beam current is sufficient for 1.44 MW.

It also allowed for a demonstration of 46 mA at 60 Hz and 0.65 ms seen in Fig. 8. This record current was demonstrated with a single cesiation during the source startup, then over 7 days of 32 mA production, followed by a retune and ramp up of the Cs-collar temperature and the 2 MHz power.

Typically the operators increase the power of the 2 MHz amplifier when the beam power or current appears to decrease. Accordingly a measure of the requested 2 MHz power allows for an estimate of the beam decay rate. The 3% increase for the recent 3 week production period seen in Fig. 9, is currently the best estimate for the beam decay rate after a single cesiation.

The major concerns with the modified LBNL H- source are the antenna defects found in ~30% of sources after a 2

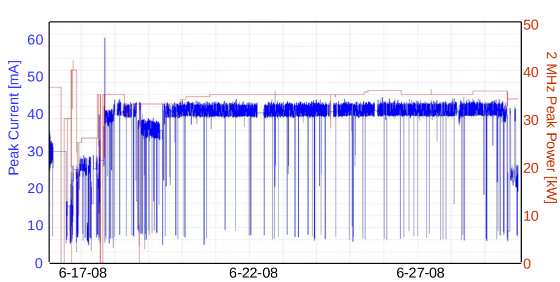


Figure 7: Two week production run with 37 mA.

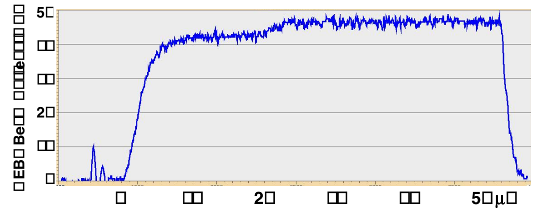

Figure 8: The 50-µs slice sampled by the RFQ 350 µs into the 650-µs 60-Hz pulses shows 46 mA.

or 3-week production period during 2008. Therefore we plan to use the external antenna source [9] in combination with the modified LBNL Cs collar for run 2009-1. This combination promises similarly high beam currents with a lower risk for antenna failures.

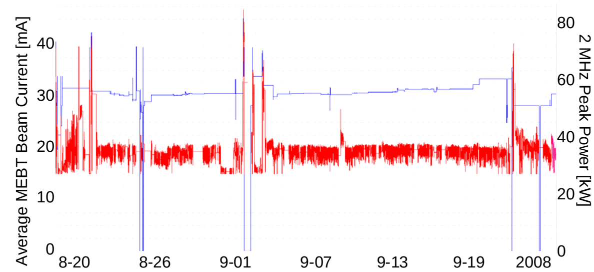


Figure 9: September 08 3-week run with ~32 mA MEBT beam current required a ~3% increase in RF power.

## ACKNOWLEDGEMENTS

The successful commissioning and beam power ramp up of the SNS baseline ion source would not have been possible without LBNL delivering a first-class Frontend on a very tight schedule. After implementing a series of modifications, at 4% duty factor the ion source appears to meet all important specifications, including the 3-week lifetime. The work at Oak Ridge National Laboratory, which is managed by UT-Battelle, LLC, was performed under contract DE-AC05-00OR2275 for the US Department of Energy.

## REFERENCES

[1] R. Keller et al, AIP Conference Proceedings CP639, M. P. Stockli, edt., American Institute of Physics, Melville, NY, 2002, p. 47.

[2] CS/NF/3.6/11 from SAES Getters S. p. A., Via Gallarate 215, 20151 Milano, Italy.

[3] S. Henderson, in [illegible] 2008, p. 2892.

[4] “Alkali Metal Dispensers” manual, SAES Getters, Via Gallarate 215, 20151 Milano, Italy.

[5] R. F. Welton at al, [illegible] Knoxville, TN, 2005, p. 472.

[6] R. F. Welton et al, in [illegible] 2002, p. 635.

[7] M. P. Stockli, Proceedings of the 2006 LINAC Conference, Knoxville, TN, 2006, p. 213.

[8] R. F. Welton et al., AIP Conference Proceedings CP925, M. P. Stockli, edt., American Institute of Physics, Melville, NY, 2007, p.87.

[9] R. F. Welton et al., in Proceedings of PAC07, Albuquerque, New Mexico, USA, 2007, p. 3774.

# EBIS PREINJECTOR CONSTRUCTION STATUS*

J. Alessi#, D. Barton, E. Beebe, S. Bellavia, O. Gould, A. Kponou, R. Lambiase, E. Lessard, R. Lockey, V. LoDestro, M. Mapes, D. McCafferty, A. McNerney, M. Okamura, A. Pendzick, D. Phillips, A.I. Pikin, D. Raparia, J. Ritter, J. Scaduto, L. Snydstrup, M. Wilinski, A. Zaltsman, BNL, Upton, Long Island, New York
U. Ratzinger, A. Schempp, IAP, Frankfurt am Main

*Abstract*

A new heavy ion preinjector is presently under construction at Brookhaven National Laboratory. This preinjector uses an Electron Beam Ion Source (EBIS), and an RFQ and IH Linac, both operating at 100.625 MHz, to produce 2 MeV/u ions of any species for use, after further acceleration, at the Relativistic Heavy Ion Collider, and the NASA Space Radiation Laboratory. Among the increased capabilities provided by this preinjector are the ability to produce ions of any species, and the ability to switch between multiple species in 1 second, to simultaneously meet the needs of both physics programs. Fabrication of all major components for this preinjector is in process, with testing of the EBIS and RFQ starting this year. The status of this construction is presented.

## INTRODUCTION

The layout for the new EBIS-based heavy ion preinjector is shown in Fig. 1. This preinjector, will be located at the high energy end of the existing 200 MeV H- linac building. Not shown in this figure is an additional 37 m long beamline which connects the preinjector to the heavy ion injection point of the Booster Synchrotron. This preinjector will replace two existing Tandem Van de Graaff accelerator and an 800 m transport line, as the heavy ion preinjector for both the Relativistic Heavy Ion Collider (RHIC) and NASA Space Radiation Laboratory (NSRL). It is designed to deliver milliampere currents of any ion species in short pulses, to allow single-turn injection into the Booster. With any of several external ion sources able to inject pulses of 1+ ions into the EBIS trap, species from EBIS can be changed on a pulse-to-pulse basis. The switching time for the magnets in the HEBT line will be 1 second. Some key parameters are given in Table 1. More details on the EBIS source and preinjector can be found in [1] and [2].

Table 1: Preinjector Parameters

| | |
|---|---|
| Ions | He - U |
| Q / m | ≥1/6 |
| Current | > 1.5 emA |
| Pulse length | 10 µs (for 1-turn injection) |
| Rep rate | 5 Hz |
| Output energy | 2 MeV / u |
| Time to switch species | 1 second |

## EBIS SOURCE

The design of the EBIS source is based on the very successful performance of the prototype Test EBIS at Brookhaven [1]. The primary changes in the present EBIS, relative to the prototype, is the increase of the source trap length from 0.7 to 1.5 m, which requires a superconducting solenoid with a length of 2m. Other changes relative to the Test EBIS are intended to allow operation at higher repetition rates, and improve reliability and maintainability. The source is shown schematically in Fig. 2. A brief status of some of the key components follows.

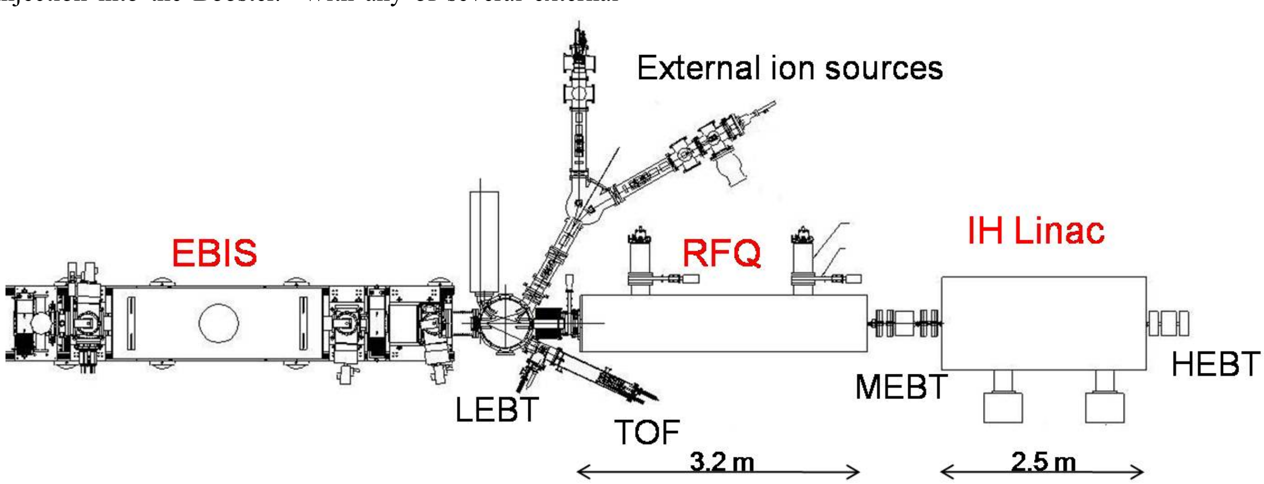


Figure 1: Layout of the EBIS-based heavy ion preinjector

*Work supported under the auspices of the US Department of Energy and the National Aeronautics and Space Administration.
#alessi@bnl.gov

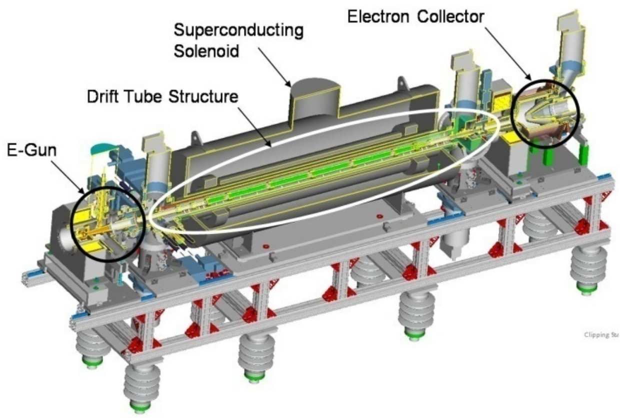


Figure 2: Drawing of the new RHIC EBIS.

### Electron Gun

The EBIS is planned to operate with a 10 A electron beam, but the electron gun is designed for up to 20 A operation. The cathode is a 9.2 mm diameter IrCe unit, made for BNL by BINP [3]. The electron gun has been fabricated, and successfully tested to 10 A on the Test EBIS.

### Electron Collector

The electron collector is designed to handle a nominal electron beam of 20 A, 15 kV dc, i.e. 300 kW, but since ionization times are typically < 50 ms, the electron beam can be pulsed at a duty factor < 25%, allowing the collector to handle lower average power. A collector fabricated from a Zr-Cr-Cu alloy in the Brookhaven shops, has been completed and is being installed on the Test EBIS for initial testing. A second collector is being made from a high conductivity Be-Cu (Hycon 3 HP). This should have somewhat better thermal fatigue lifetime. This collector is being fabricated by Brush-Wellman, and after some difficulties during the welding of the material, is now nearly complete as well.

### Superconducting Solenoid

The superconducting solenoid for the EBIS is 2 m long, and will have a 5.5 T field which is uniform to within ±0.25% over the 1.5 m trap length. The solenoid has a 204 mm diameter warm bore, to allow sufficient space for the vacuum pipe, which also has heating rods and water cooled shield for baking of the central trap region. The solenoid is being fabricated by ACCEL Instruments [4]. A failure during a quench test last year has delayed the delivery, but the magnet is now again ready for final acceptance testing.

### Central Trap

The central trap region consists of six cylindrical electrodes of ~42 mm diameter, each electrode capable of being individually biased. There is also NEG material running the length of the central vacuum pipe to provide extra pumping in this region. This assembly has been completed, and is being prepared for assembly on the RHIC EBIS.

## RFQ

The final design and fabrication of the RFQ was done through the Institute of Applied Physics at the University of Frankfurt, with most of the fabrication by NTG [5]. Some RFQ parameters are given in Table 2. Following vacuum testing and field measurement, the RFQ is now in transit to Brookhaven for initial testing with beam from the Test EBIS. More details on the RFQ can be found in [6]. The RFQ is shown during assembly in Fig. 3.

Table 2: Parameters of the RFQ

| | |
|---|---|
| Input Energy | 17 keV/u |
| Output energy | 300 keV/u |
| Q / m | > 1 / 6 |
| Frequency | 100.625 MHz |
| Length | 3.2 m |
| Power (with beam loading) | ~ 200 kW |

Figure 3: RFQ during assembly at IAP.

## IH LINAC

As with the RFQ, the final design and fabrication of the IH Linac is also being done through IAP, Frankfurt. The linac is designed for a beam current of up to 10 mA. The detailed design is completed, and fabrication of the cavity has started at PINK [7]. The internal quadrupole triplet will be built by Bruker [8]. The schematic of the linac is shown in Fig. 4, and parameters for the linac are given in Table 3. The cavity has ~ 5 cm thick walls, in order to reduce x-ray levels external to the linac. The linac is scheduled for delivery in the summer of 2009.

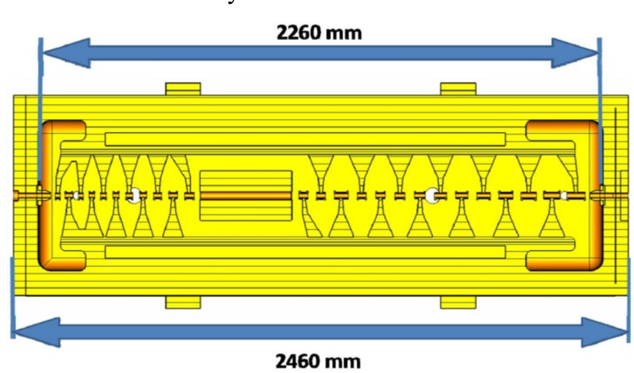


Figure 4: Schematic of the IH linac.

Table 3: Parameters of the IH Linac

| | |
|---|---|
| Input energy | 300 keV/u |
| Output energy | 2 MeV/u |
| Q / m | > 1 / 6 |
| Frequency | 100.625 |
| Cavity Length | 2.46 m |
| Power (with beam loading) | ~ 300 kW |

## BUNCHER CAVITIES

There are three spiral resonator cavities being built by IAP for the preinjector. A 20 cm long 4-gap rebuncher cavity will sit between the RFQ and linac. This cavity is presently being fabricated from Al, since it is very low power and low duty factor. In the HEBT line, there is a 4-gap debuncher cavity ~12 m from the end of the linac, and a 2-gap debuncher ~ 26 m from the end of the linac, to reduce the energy spread of the beam going into the Booster.

## RF AMPLIFIERS

The rf amplifiers for the RFQ and linac have been manufactured by Continental Electronics [9]. Each unit combines power from two 175 kW amplifiers which use a TH535 tetrode at the final stage, to produce 350 kW peak power at 100.625 MHz. These amplifiers were delivered to Brookhaven in August, and are now being installed in their final location.

## HEBT

The High Energy Beam Transport (HEBT) line transports the beam from the linac to Booster injection. There is a ~17 m section in the linac building, and then the beamline passes through a ~8 m thick shield wall and in to the Booster tunnel. Inside the Booster, there is ~12 m transport, including two dipoles, to inject beam into the Booster at the same location as beam coming from the Tandems. The final section of HEBT is shown in Fig. 5.

The two identical dipoles are laminated magnets to allow the required 1 second field changes. The magnets each have a bend angle of 72.5 degrees, a 13.5 cm gap, 1.3m bend radius, and 1T maximum field [10]. These magnets were manufactured by Sigmaphi [11], and were delivered on schedule in July, 2008.

The boring through the shield wall, and installation of the beampipe, occurred during the summer of 2007. During the summer of 2008, the dipoles were installed in the Booster tunnel (Fig. 6), and the remainder of the Booster-side beamline has been installed and is under vacuum.

## SUMMARY

There has been considerable progress in many areas in addition to those mentioned above. Hardware for LEBT and external ion injection is being fabricated. All power supplies for operation of the EBIS and LEBT line are now in hand and are being installed. Most hardware for the control system, vacuum, and beam diagnostics has been procured. The commissioning of beam into the HEBT and Booster is presently scheduled to start in January, 2010.

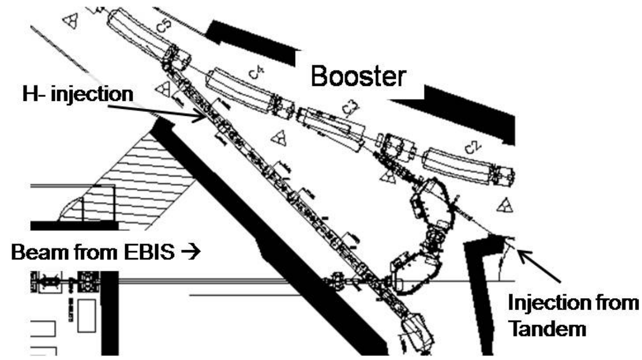


Figure 5: EBIS injection line into Booster.

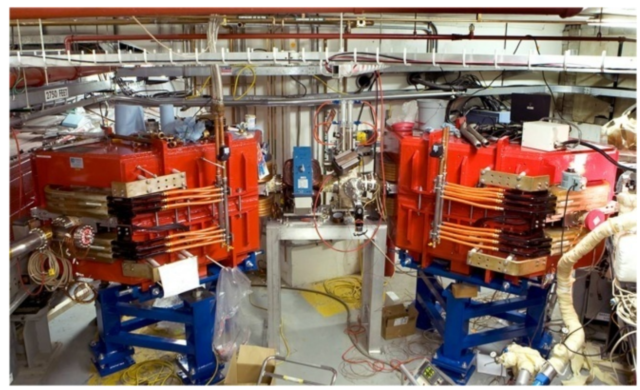

Figure 6: Dipoles installed in the Booster tunnel.

## REFERENCES

[1] J. Alessi, E.Beebe, O.Gould, A.Kponou, R.Lockey, A.Pikin, D.Raparia, J.Ritter, L.Snydstrup, "High performance EBIS for RHIC", PAC 2007, Albequerque, p. 3782 (2007).
[2] J. Alessi, et.al., "Status of the EBIS project at Brookhaven", Linac 2006, Knoxville, p. 365 (2006).
[3] G. Kuznetsov, Nuclear Instrum. & Meth. In Physics Res. A 340, 1994, p. 204.
[4] ACCEL Instruments GmbH, Bergisch Gladbach, Germany.
[5] NTG GmbH, Gelnhausen, Germany.
[6] M.Vossberg, B.Hofmann, A.Schempp, J.Alessi, D.Raparia, L.Snydstrup, "RF tuning of the EBIS-RFQ", these Proceedings.
[7] PiNK GmbH, Wertheim, Germany.
[8] Bruker Biospin S.A., Wissenbourg, France.
[9] Continental Electronics Corp., Dallas, TX.
[10] T.Kanesue, D.Raparia, J.Ritter, M.Okamura, J.Tamura, "Design study of the dipole magnet for the RHIC EBIS high energy transport line", PAC 2007, Albequerque, p. 3301 (2007).
[11] Sigmaphi, Vannes, France.

# ENERGY RECOVERED LINACS*

G. A. Krafft#, Jefferson Lab, Newport News, VA 23606, U.S.A.

*Abstract*

In the last decade, stimulated by the success of the energy recovered free electron lasers, many projects have been initiated exploring the applications and limitations of beam energy recovery in recirculated linear accelerators (linacs). In this talk the performance of many existing energy recovered linacs is briefly reviewed. Looking forward, potential applications of energy recovered linacs such as recirculated linac light sources, high energy beam electron cooling devices, and electron beam sources for high energy colliders have been pursued with varying degrees of effort. The types of new technology that must be developed for applications, and more broadly, some of the open issues regarding this technology, are discussed.

## RECIRCULATED AND ENERGY RECOVERED LINACS

Over the course of the last decade, there has been a growing interest in developing accelerators using the idea of beam energy recovery. This paper presents a review of the work done on energy recovery to date. In brief, applying the technique of beam energy recovery allows the construction of electron linear accelerators that can accelerate average beam currents similar to those provided by storage rings, but with the superior beam quality typical of linacs. Such an ability to simultaneously provide both high current and high beam quality can be broadly utilized. For example, high average power free electron laser sources may be built yielding unprecedented optical beam power, light sources extending the available photon brilliance beyond the limits imposed by present day synchrotron light sources may be designed, electron cooling devices may be possible which would benefit from both high average current and good beam quality to ensure a high cooling rate of the circulating particles in a storage ring collider, or, as a final theoretical possibility, the electron accelerator in an electron-ion collider intended to achieve operating luminosity beyond that provided by existing, storage-ring-based colliders may be based on an energy recovered linac (ERL).

In the following, we compare recirculating linacs to two more common types of accelerators: single pass linear accelerators and storage rings. We then discuss energy recovery conceptually, and review the work to date on this technique, primarily in the energy recovered free electron lasers. Most of this introductory material is a condensed paraphrase of material in an earlier review of energy recovered linacs [1]. Please consult this reference for a more detailed discussion.

*Authored by Jefferson Science Associates, LLC under U.S. DOE Contract No. DE-AC05-06OR23177. 

#krafft@jlab.org

In the past, two types of particle accelerators (Fig. 1) have been used. Among the electron accelerators, the first class of accelerators consists of the high-energy electron linacs. In such accelerators, the electron beam has a definite beginning and a definite end. Usually, the beam propagates along a nearly straight line, and there is a substantial length of RF beam-acceleration devices.

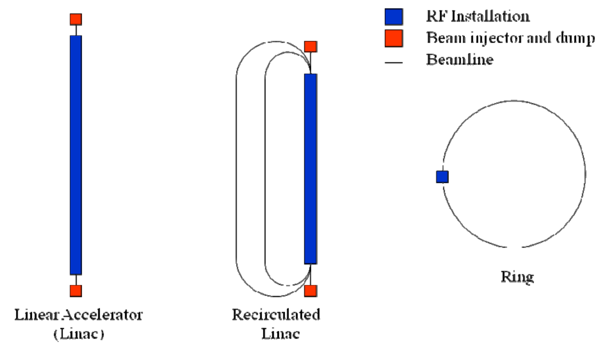


Figure 1: Main accelerator types.

Some main features of an electron linac are: first, an individual electron resides in the accelerator only briefly, certainly for times that are short compared to any relevant radiation damping times. Second, if a laser-driven photocathode gun is used as the electron source, it is relatively easy to load, or program, the beam current or beam polarization delivered to users by controlling the duration and polarization of the lasers that stimulate electron production at the gun. Third, the emittance, of the electrons in a typical beam tends to be set by phenomena in the low-energy electron source region, and this emittance may be well preserved during the acceleration to high energy. Fourth, the pulse duration, and more generally the longitudinal phase space distribution, is relatively easily manipulated by using standard beam-rf and electron beam optical techniques. Having long distance between the end of the linac and the beam dump is easy to arrange in a linear geometry.

The second class of high-energy electron accelerators is the synchrotron-like storage ring. In an electron storage ring, the electrons are bent on a roughly circular orbit. Because transversely accelerated electrons radiate copious amounts of electromagnetic radiation, to achieve a long-term equilibrium it is necessary to supply energy to the circulating electrons. Energy is supplied, as in linacs, with RF cavities but they subtend a small portion of the total machine circumference. After the beam is injected into the ring, the electrons rapidly settle into an equilibrium where the synchrotron radiation losses are made up by the energy transferred from RF to beam. The equilibrium characteristics point to the main limitations of storage rings. The equilibrium beam emittance, and hence the beam sizes in the storage ring, are given by a competition between the radiation damping, which tends to drive the electrons onto the closed orbit at the correct accelerating phase, and the quantized radiation emission, which tends to excite transverse and longitudinal oscillations. Formulas for the equilibrium size are well known [2]; here, it is sufficient to point out that both the emittances and the equilibrium pulse length in an electron storage ring can not be arbitrarily small.

Recirculating linacs are accelerators in which, as in linacs, there is substantial RF accelerating the beam and the beam has a definite beginning and ending (i.e., there is no closed or equilibrium orbit), but, as in a storage ring, the beam goes through the accelerating cavities more than once (Fig. 1). Such a hybrid arrangement, by applying beam energy recovery, allows one accelerator to feature some advantages of both of the usual arrangements.

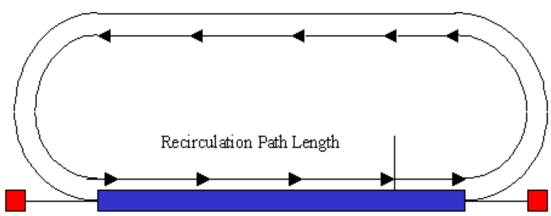


Figure 2: Traditional recirculation geometry.

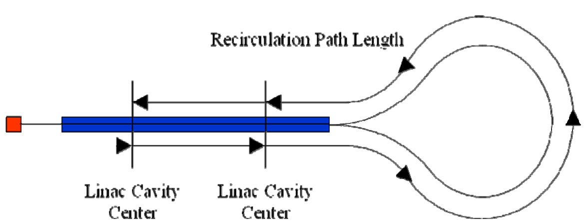


Figure 3: Reflex or herring-bone geometry.

Figures 2 and 3 define possible beam recirculation geometries. In the more traditional, and more utilized, geometry of Fig. 2, the recirculation path length is chosen to be approximately and integer plus one half RF wavelengths for energy recovery. By this choice, if the first pass beam is accelerated by the RF field, the second pass beam is decelerated by the same RF field because the RF phase has reversed sign when the second pass beam arrives. This geometry has the advantage of relatively easy phasing and no beam-beam collisions, but suffers from the fact that at most locations along the linac, two different beam energies exist. This shortcoming is solved in the reflex or herring-bone geometry of Fig. 3. Here both beam passes have nearly the same energy simplifying beam optical design. The downsides of this geometry are the possibility of beam-beam collisions and the fact that additional constraints must be placed on the linac geometry to ensure that the recirculation path length is nearly an integer number of RF wavelengths at each cavity. The earliest accelerator utilizing beam energy recovery was built at Chalk River in reflex geometry [3].

In the future, it is likely that electron recirculation will be applied to build recirculating linacs because of their superior beam quality. Recirculating linacs share with linacs the ability to accelerate and preserve the emittance of very-low-emittance injector beams. Because the transit time is short compared to a typical radiative emittance buildup time, no equilibrium is established as in a storage ring, implying that the emittance delivered to the end user may be smaller. Also, as in linacs, one can manipulate the longitudinal phase space of the electron beam to deliver very short beam pulses to the end user. The minimum pulse length is no longer set by radiative effects but by the ability to generate, and precisely manipulate, the longitudinal phase space of the electron beam, as shown many years ago at Jefferson Lab [4]. Applying energy recovery has allowed one to conceive of recirculating linacs with high average currents and efficiencies approaching those in storage rings.

## ENERGY RECOVERED FREE ELECTRON LASERS

The combination of high average current and good beam quality is highly desired when a high average power free electron laser is required. Therefore, the first purpose-built energy recovery linacs were constructed as free electron laser drivers. Presently, all the existing energy recovered linacs are FEL drivers.

### *Stanford Free Electron Laser*

The Stanford Superconducting Accelerator (SCA) was upgraded into a 5-pass recirculated linac for nuclear physics research in the late 1970s, and employed in that capacity for several years [5]. However, after free electron laser work was initiated at Stanford in the late 1970s and early 1980s, it was desired to increase the peak current in the beam bunches to increase FEL gain. The RECYCLOTRON bends were replaced with two sets of isochronous bends, one set being mounted on a movable table that allowed the path length of the recirculation arc to be adjusted throughout a full RF wavelength. This flexibility allowed RF power measurements to be performed comparing the RF power required to accelerate 1-pass beam, 2-pass beam in accelerating mode, and 2-pass beam in energy recovery mode. Such measurements convincingly demonstrated the possible efficiency enhancements permissible in a same-cell energy recovered beam [6].

The SCA had a long life as a FEL source of infrared radiation for two decades. Several papers in the proceedings document changes and upgrades to this venerable machine as it begins its new life in Monterey, CA as an energy recovered FEL [7].

### *Jefferson Laboratory 10 kW Free Electron Laser*

This devise represents the state of the art in high average current energy recovery in a superconducting linac. A parameter list for this device appears in Table 1. The free electron laser has, during conditions where the beam power was 1 MW, produced up to 14.2 kW optical power, a world record for continuous operation. The free electron laser presently employs moderate bunch charge, about 135 pC, and a relatively high repetition rate of 75 MHz to achieve high average power. Because the FEL operates in the IR region of the electromagnetic spectrum, the emittance requirement in this device is lax compared to some of the ERLs contemplated for the future. A new, 100 kW optical power free electron laser will be built by the U. S. Department of Defence and is being bidded on by U. S. industrial firms. Jefferson Lab scientists are assisting in proposal development for the bids and can be expected to have greater or less participation in the final projects, depending on the firm awarded the contract. It may be expected that a large portion of the power increase will be obtained by increasing the beam bunch repetition rate above 100 MHz. It is not expected that the energy recovered linac has to change much to support this jump to higher power operation.

Table 1: Jefferson Lab 10 kW FEL beam parameters.

| Electron Beam Parameters | IR FEL | UV FEL |
|---|---|---|
| Energy (MeV) | 80-150 | 150 |
| Accelerator Frequency (MHz) | 1500 | 1500 |
| Charge per Bunch (pC) | 135 | 135 |
| Bunch Repetition Rate (MHz) | 75 | 37.5 |
| Average Current (mA) | 10 | 5 |
| Beam Power (kW) | 1500 | 750 |
| Energy Spread (%) | 0.4 | 0.2 |
| Normalized Emittance (mm mrad) | <10 | <8 |
| Induced Full Energy Spread | 12% | 6% |

### *JAEA Free Electron Laser*

The JAEA Free Electron Laser consisted of a 230 keV thermionic cathode gun, acceleration by superconducting cavities to 2.5 MeV for injection, and 2 500 MHz 5-cell superconducting cavities for acceleration to 17 MeV in the beam reciculation loop. The recirculation arcs consisted of three bend achromats that could be adjusted to non-zero momentum compaction. Much recent work focussed on providing maximum bunch compression at the free electron laser by varying the compaction. Within a beam macropulse, the average power of this device was at the 1 kW level, but at a longer wavelengths than at Jefferson Lab. The three bend achromat could be tuned up to 15% energy acceptance, and the FEL extraction efficiency was measured to be up to 2.8%. After highly successful beam running, the facility was shut down in April of 2008 and the superconducting cavities were returned to KEK.

### *ALICE/ERLP*

Construction of the first energy recovered linac in Europe, the ERL Prototype (ERLP) at Daresbury, UK, is nearing completion. Because of the changing emphasis in the project away from ERL development and into experimental applications, the facility has been renamed to Accelerators and Linacs In Combined Experiments (ALICE) [8]. Gun commissioning is proceeding with the result that the longitudinal emittance of the extracted beam agrees well with ASTRA simulations. The transverse emittance has been higher than expected; present effort is focussed on understanding the discrepancies. First beam energy recovery experiments will be completed this fall, without the FEL. First light, and first energy recovery with the FEL completely in place will take place in Spring of 2009. A very complete review and status report was provided to the conference by D. Holder [9].

### *BINP Energy Recuperator*

The Budker Institute THz FEL is unique in several particulars of its design. Most prominently, the injector and linac consist of normal conducting 180 MHz accelerating cavities that are operated in CW mode. The linac provides approximately 15 MeV beam energy gain. The two-pass THz FEL is laid out on a vertically oriented plane with the accelerating cavities close to the ceiling and the THz optical cavity on the floor. Because low frequency cavities were utilized with very large apertures, this design is highly robust and reproducible. There is very little beam loss on recirculation, and this device has energy recovered the largest average current to date, at 40 mA beam current. Because of the large apertures, it is reasonable to upgrade to a multiple pass version of the accelerator. A four recirculation loop, eight-pass accelerator upgrade has recently been completed. On passes two and four there will be infrared free electron lasers; all of the recirculation beam lines are on a horizontal plane passing through the linac axis near the ceiling. As of the recent FEL conference, 9 mA beam had been transported and energy recovered through two loops of the upgraded machine, but without going through the FEL yet. During the coming months one anticipates completing the full 4-pass circuits and running the free electron lasers at high optical power.

## APPLICATION TO X-RAY SOURCES

Storage ring x-ray sources operate by having a high average current, high energy electron beam interact with the bend magnets of the ring, or with a series of insertion devices deployed throughout the ring where the x-rays are produced. The performance of these machines is constrained by fundamental processes, which ultimately limit the quality of the electron beam. Producing electron beams with superior characteristics for generating synchrotron radiation may be possible via photoinjector electron sources and a high-energy energy recovered linac. Relatively simple considerations lead to an understanding of the possible beam modes.

The brilliance of x-rays originating on a typical insertion device goes as

$$B = \frac{I}{\varepsilon^2} = \frac{fQ}{\varepsilon_{th}^2 + AQ^p}$$

where $I$ is the average current, $Q$ is the bunch charge, $\varepsilon_{th}$ is the beginning emittance, and a hypothetical power-law model for the emittance growth between source and insertion device is assumed. Because of the rapid increase with $Q$ of the denominator for a power law greater than ½, it is easy to show that the greatest brilliance occurs at a condition where the two terms in the denominator are of similar order. But usually the emittance at the insertion device is at least an order of magnitude beyond the beginning emittance. Thus, as a function of $Q$, the maximum brilliance occurs with high frequency low charge bunches. More thorough analysis of this problem including the diffraction effect of the x-rays leads to the conclusion that for 1300 MHz operation with every accelerating bucket filled, the optimal brilliance occurs at around 20 pC bunch charge [10], which has somewhat less average current than the comparable storage ring.

Table 2: ERL X-ray source beam parameters.

| Electron Beam Parameters | High Flux | High Coherence |
|---|---|---|
| Energy (GeV) | 5 | 5 |
| Accelerator Frequency (MHz) | 1300 | 1300 |
| Charge per Bunch (pC) | 77 | 19 |
| Bunch Repetition Rate (MHz) | 1300 | 1300 |
| Average Current (mA) | 100 | 25 |
| Beam Power (MW) | 500 | 100 |
| Energy Spread (%) | 0.02 | 0.02 |
| Normalized Emittance (mm mrad) | $<0.3$ | $<0.1$ |

Because of the smaller inherent energy spread in a recirculated linac beam [11] than in a storage ring, it is possible to raise brilliance by considering longer insertion devices with a larger number of magnetic periods. A rule-of-thumb that has been found useful in evaluating the brilliance of ERL x-ray sources is that the optimized brilliance of an ERL source is about 3 orders-of-magnitude above present day storage rings. About an order-and-a-half of this improvement is due to the superior beam emittance, and an order-and-a-half is due to the possibility of long undulators. To obtain conditions suitable for high-flux experiments, beam currents comparable to those in storage rings are supported by higher charge-per-bunch operation. Unfortunately, it may be difficult to arrange simultaneous high-flux and high brilliance running without some sort of RF beam separation system to divide the ERL beam to various users.

Since being initially proposed, and being strongly advocated by scientists from Novosibirsk [12], many groups considered the possibility of energy recovered x-ray sources. Cornell University is building and commissioning an ERL demonstration injector as a first step toward a follow-on many GeV light source. It is based on a DC photocathode source followed by beam bunching and acceleration to 10 MeV by 5 two-cell superconducting RF cavities. This prototype will demonstrate full current injection with the required beam properties, acceleration to 10 MeV, and if successful will be the first device to clearly demonstrate emittance compensation in a DC gun system [13]. It will also be highly influential for evaluating future projects because so much of the utility of the ERL light source idea is dependent on superior beam emittance being produced at low charges. New technology, especially in the area of drive laser pulse shaping, is being developed to meet this challange. Over the summer the ERL injector yielded its first beam. Presently, various commissioning studies are happening. The review talk at this conference provides much more on plans and recent accomplishments [14].

## APPLICATIONS TO HIGH ENERGY AND NUCLEAR PHYSICS

Energy recovered linacs are being considered for applications in high energy and nuclear physics because of their unique ability to provide high average current beams with superior beam quality. Two potential applications are as an electron source for beam cooling schemes and as an electron beam source for an electron-ion collider.

### *Electron Cooling*

In electron cooling, a relatively low-energy electron beam is merged with a relatively high-energy ion beam, the electron-beam energy being chosen so that the average longitudinal velocity of the two beams is the same. The electron beam acts as a heat sink, removing thermal energy from the ion beam. Collisions with cooled beams are possible at higher luminosity than in the same collider without cooling. The cooling rate is proportional to beam average current.

High-energy electron cooling with high cooling rates may be possible now that ERLs have demonstrated technical feasibility. Again, the main development is the high-average-current source. Such a design may be even more difficult than for the light sources because the bunch repetition rate, to match, for example the RHIC beams, must be reduced to 9 MHz, and to obtain the same average current, the charge per bunch must be increased to ~10 nC. Recent successes in utilizing stochastic beam cooling in RHIC have reduced interest in developing this device as a cooler for RHIC. But ERLs may find use as drivers for coherent electron cooling devices.

### *Electron-Ion Colliders*

Finally, energy recovered linacs have been studied for electron-ion colliders for nuclear and/or particle physics research. An ERL would replace the more typical electron storage ring. A *gedanken* experiment indicates why such an arrangement is advantageous and may produce higher luminosity. Assume for the moment that one has designed a stable ring-ring collider. If the electron ring is stable, any current-limiting instability growth rate must be slower than one ring damping time. Then, the electrons are confined to at least one damping time, or about 1000 revolutions.

Suppose now one designs an ERL collider with an identical ion-storage ring and an identical set of electron beam parameters to the ring-ring collider above. Because the electron-beam parameters are the same, the ion beam stability is assured, even if one increases the *ion* bunch charge and luminosity. Increasing the ion bunch charge will increase the disruption of the electron bunch by the beam-beam effect. However in the ERL it is no longer necessary to confine the electron beam for 1000 turns, only a few turns. Estimates of the emittance increase and the maximum deflection angle generated by a few beam-beam collisions show that there may be room to considerably increase the ion bunch charge, and the luminosity, before energy recovery becomes difficult.

Two projects have considered ERL collider drivers. The first is eRHIC, an electron-ion collider based at RHIC, and the second is ELIC, an electron--light-ion collider based at CEBAF. In the eRHIC proposal, one of the RHIC rings is used to contain the ions and a new ERL is built. In ELIC, CEBAF is upgraded to a higher-energy ERL, and a new ion-storage ring is constructed.

Table 3: BNL ERL prototype beam parameters.

| Electron Beam Parameters | High Current | High Charge |
|---|---|---|
| Energy (MeV) | 20 | 20 |
| Accelerator Frequency (MHz) | 700 | 700 |
| Charge per Bunch (nC) | 1.4 | 5 |
| Bunch Repetition Rate (MHz) | 700 | 9.4 |
| Average Current (mA) | 500 | 50 |
| Beam Power (kW) | 1000 | 150 |
| Energy Spread (%) | 0.5 | 1 |
| Normalized Emittance (mm mrad) | 2.3 | 5.3 |

The parameters required by these ERL proposals are an extrapolation from today's demonstrated performance by one to two orders of magnitude in average current. Because of the difficulty in constructing a high average current polarized electron source, the ELIC project has migrated back to a ring-ring design using the upgraded CEBAF accelerator as a full energy injector.

Supporting the development of very high average current ERLs, Brookhaven National Lab is assembling an ERL prototype. Potential operating modes of this device are shown in Table 3. D. Kayran presented a poster summarizing the status of this project [15].

## CONCLUSIONS

Energy recovered recirculated linacs are a new class of accelerators with the potential to produce unique beam properties. The field of ERL-based free electron lasers continues to grow and the performance of devices continues to improve. Higher peak and average brilliance may be possible in ERL-based x-ray sources than is possible in storage rings at the same beam current. Many new ideas are being explored in a broad range of applications. This field seems to be thriving and there is no shortage of interesting problems to work on.

## REFERENCES


[1] L. Merminga, D. R. Douglas, and G. A. Krafft, *Annu. Rev. Nucl. Part. Sci.*, 53, 387 (2003)

[2] M. Sands, "The Physics of Electron Storage Rings", SLAC-0121 (1970)

[3] S. O. Schriber, *et al.,* "Experimental Measurements on a 25 MeV Reflexotron", PAC77, Chicago, March 1977, p. 1061 (1977)

[4] D. X. Wang, G. A. Krafft, and C. K. Sinclair, *Phys. Rev. E,* **57**, 2283 (1998)

[5] C. M. Lyneis, *et al.,* "Unique Beam Properties of the Stanford 300 MeV Superconducting Recyclotron", PAC81, Washington, March 1981, p. 3445 (1981)

[6] T. I. Smith, *et al.,* Nucl. Inst. and Methods, **A259**, 1 (1987)

[7] J. Lewellen, *et al.,* "Status of the NPS Free-Electron Laser", LINAC08 proceedings

[8] The town of Daresbury was the boyhood home of one Charles Dodgson. As Lewis Carroll he wrote *Alice's Adventures in Wonderland* and other tales.

[9] D. J. Holder, Y. M. Saveliev, and S. Smith, "First Results from the ERL Prototype at Daresbury", LINAC08 proceedings.

[10] G. Hoffstaetter and M. Borland, private communication

[11] G. A. Krafft, *et al.,* "Measuring and Controlling Energy Spread in CEBAF", LINAC2000, Monterey, August 2000, p. 721 (2000)

[12] G. Kulypanov, A. Skrinsky, and N. Vinokurov, *Synchrotron Radiat.,* **5**, 176 (1998)

[13] I. V. Bazarov and C. K. Sinclair, *Phys. Rev. ST Accel. Beams,* **8**, 034202 (2005)

[14] B. Dunham, "First Tests of the Cornell University ERL Injector", LINAC08 proceedings.

[15] D. Kayran, *et al.,* "Status of High Current R&D Energy Recovery LINAC at Brookhaven National Laboratory", LINAC08 proceedings

# HIGH AVERAGE CURRENT SRF CAVITIES

T. Furuya, KEK, Ibaraki


## Abstract

Higher-order-mode (HOM) free superconducting (SC) single cell cavities were developed for the rf system of high luminosity storage ring colliders. Because of the successful results of these cavities under ampere-class beams, the components and technology of the SC cavities have immediately been applied to the middle sized storage rings upgrading the beam intensity by using a few SC cavities. Beside the storage ring rf, a SC based high intensity proton linac was commissioned for neutron physics. Recently, the feasibility study of energy recovery linacs has been carried at various laboratories aiming for the 4th generation light source. Status of these developments will be described.


**CONTRIBUTION NOT RECEIVED**

# FIRST RESULTS FROM THE ERL PROTOTYPE (ALICE) AT DARESBURY

D.J.Holder#, on behalf of the ALICE team at STFC Daresbury Laboratory, Warrington, UK.

*Abstract*

The energy recovery linac prototype at Daresbury is now called ALICE (Accelerators and Lasers In Combined Experiments). This paper presents the results obtained in the past year, including the fourth period of gun commissioning. Following the completion of gun commissioning in November 2007, the dedicated gun diagnostic line was removed and the electron gun attached to the booster cavity and hence the rest of the machine.

The paper outlines some of the challenges experienced during the commissioning of both the photoinjector system and the superconducting cavities and presents the current status of the project as well as the very latest results from commissioning during the summer of 2008.

## INTRODUCTION

Following the outcome of a review of synchrotron light sources in the UK, the proposed 4$^{th}$ Generation Light Source (4GLS) project was cancelled. The Energy Recovery Linac Prototype (ERLP), which was originally conceived as a prototype test-bed for the key concepts and technologies expected to feature in 4GLS, now has a broader role as an accelerator physics and technology test facility and for developing fourth generation light source science. Renamed ALICE (Accelerators and Lasers In Combined Experiments), the facility is being commissioned at present. The past year has been a frustrating combination of both progress and setbacks. A short productive period of gun commissioning has been book-ended with several vacuum problems with the gun. However in parallel to the commissioning work with beam, progress has also been made with the cryogenic and RF systems.

ALICE is based on a combination of a DC photocathode electron gun, a superconducting injector linac and a main linac intended to operate in energy recovery mode. These drive an IR-FEL, an inverse Compton Back-Scattering (CBS) x-ray source [1] and a terahertz beamline.

In addition, next year sees the start of construction the world's first non-scaling, Fixed-Field Alternating Gradient (FFAG) accelerator called EMMA, for which ALICE will act as an injector [2]. Fig. 1 shows the layout of both ALICE and EMMA.

## PROGRAMME

At the end of 2007, the dedicated gun diagnostic beamline, with which the gun was commissioned and characterised, was removed as the rest of the machine was ready to accept its first beam. It was expected that operation in energy-recovery mode (initially without the beam-disrupting effects of the FEL) would have been achieved, followed by installation of the FEL components and progress with the CBS source and terahertz beamline made. Unfortunately at the time of writing ALICE is still on the brink of this step. This paper will record both the successes and the lessons learnt during this sometimes painful period.

## OVERVIEW OF GUN COMMISSIONING

The first electron beam was obtained from the gun at 250 keV into a dedicated gun diagnostic beamline [3] in August 2006. Further operation of the electron gun was disrupted by various issues before the final (successful) period of operation at 350 keV towards the end of 2007.

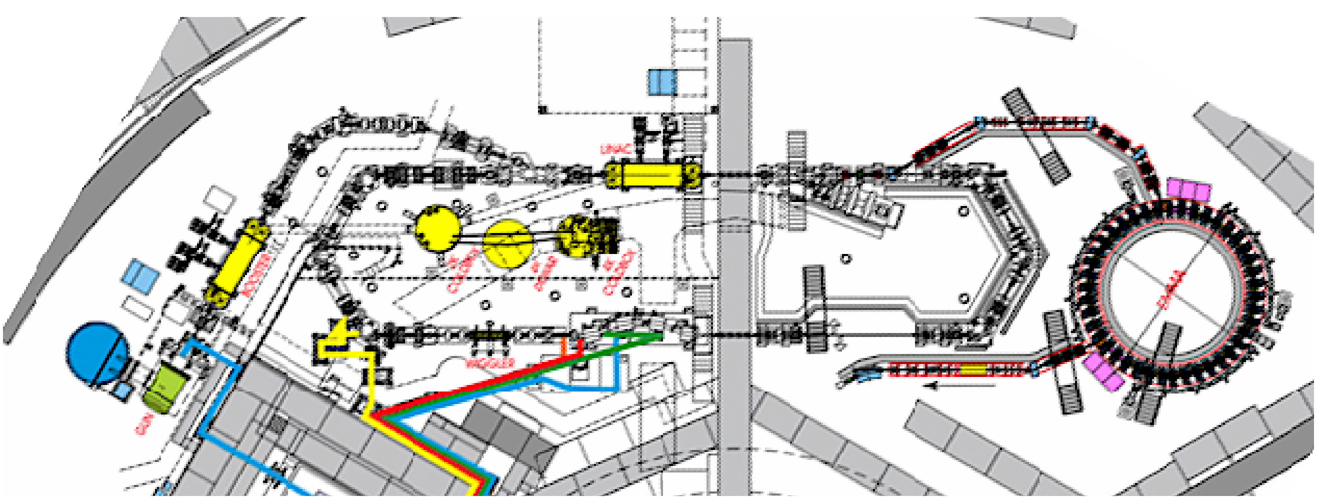

Figure 1: Layout of ALICE and EMMA.

#david.holder@stfc.ac.uk

These problems can be summarised as either:

- Physical problems, such as vacuum leaks at brazed joints, valves or vacuum flanges, and current leakage along the ceramic surface due to contamination from braze particles;
- Procedural problems, such as over-caesiation of the cathode leading to contamination of the gun, particulate contamination leading to Field Emission (FE) from the wafer and wafer overheating during heat cleaning leading to halo generation.

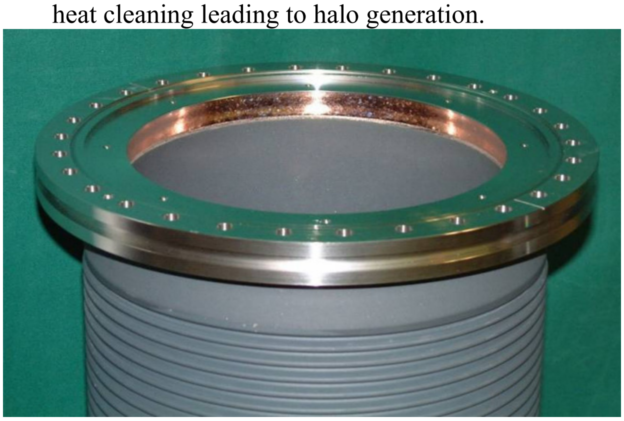

Figure 2: Gun ceramic showing problematic copper braze.

### *Vacuum Issues*

One end of the gun ceramic can be seen in Fig. 2. This ceramic is different to that used at TJNAF, to whose design the gun was produced. A single piece of ceramic with a bulk resistivity was employed, rather than two smaller sections with a conductive coating. Although there are advantages to this method (particularly with respect to producing a constant voltage gradient along the ceramic), there were also problems with its production. Producing a vacuum-tight braze of the metal flange to each end of a large ceramic caused major delays in its procurement, and would cause further problems after installation in the gun. There have been a number of failures in the vacuum integrity of this joint during the cool down from the 250 celsius bake of the gun required to achieve the desired gun vacuum. In addition failures of both 12 and 14 inch Conflat flanges have also occurred at this point in the bake cycle. In order to minimise future occurrences of this problem, the following steps were taken:

- Removal of conflat joints where possible by in-situ welding of the flanges;
- Replacement of all 14 inch flange seals with high-temperature gaskets seals (from silver-plated copper to silver-plated silver alloy);
- Replacement of all bolts on large flanges with high tensile steel, silver coated bolts;
- Tightening of bolts on large flanges to known torque and post-bake testing;
- Reduction of the maximum gun bake temperature to 220 celsius.

In addition to the vacuum problems associated with the large-diameter seals and the ceramic braze, the failure of a feedthrough for a vacuum gauge and of a valve in the gas line used during cathode caesiation have disrupted progress. It seems that repeated baking (to >200 celsius) of these gun components will always be a potential problem. Thus a load-lock system for cathode exchange is currently being designed which will significantly reduce the number of gun bake cycles required.

### *Ceramic Contamination Issues*

HV conditioning has also had to be aborted when the ceramic failed to hold off the voltage required for injector commissioning. The system was stripped down and an inspection of the ceramic indicated that the problem was due to contamination by particles of braze material on the ceramic surface.

### *Other Contamination Problems*

The second and third periods of gun commissioning ended when the problem of field emission (limiting high voltage operation to 250 kV rather than the nominal 350 kV) and beam halo became insurmountable. Fig. 3 illustrates the typical level of halo seen. The relatively poor vacuum environment thus generated also led to a poor cathode lifetime.

It was believed that contamination of the gun with excess caesium released during cathode activation was the cause of the field emission. Thus it was decided to strip down and clean the gun. Prior to this, a new cathode activation process was devised, using a pulsed light source and lock-in amplifier, which allowed the caesium ion current to be measured, thus minimising excess caesium generation.

A further strip-down, clean and rebuild of the gun was necessary following the detection of hydrocarbon contamination in the residual gas analysis of the gun vacuum. The source of the contamination was traced quickly to the vacuum cleaning/bake process and the assessment criteria used to accept the components for installation. This resulted in further delays.

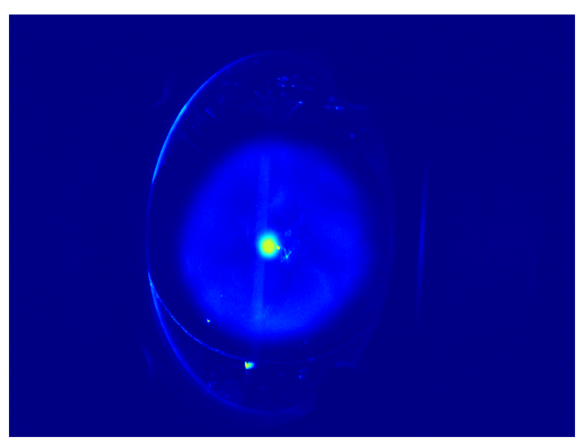

Figure 3. Screen image of the cathode showing laser-generated emission and the surrounding halo.

### *Commissioning Results*

With these problems overcome, and the new cathode activation process producing a quantum efficiency (QE) of 3.5%, a charge per bunch of over 100 pC was achieved. This allowed the performance of the injector to be measured at high bunch charge during the first few shifts with beam. Several weeks of productive measurements of the properties of the gun were made [4] until field emission from the cathode became a problem again. This had been managed up to that point by setting the solenoid parameters to less than optimum values. Table 1 lists the results obtained compared to their specification.

Table 1: Gun Commissioning Results

| **Parameter** | **Specification** | **Measured** | **Units** |
|---|---|---|---|
| Beam Energy | 350 | 350 | keV |
| Bunch Charge | 80 | >100 | pC |
| Train Length | 100 | 100 | µs |
| Train Repetition Rate | 20 | 20 | Hz |
| Quantum Efficiency | ~1 | 3.5 | % |
| RF-laser timing jitter | <1000 | 650 | fs |

In summary:

- The gun can now be routinely conditioned up to 450kV;
- The beam was fully characterised (emittance, bunch length and energy spectra) in a wide range of bunch charges from 1 to 80pC;
- A good agreement between the ASTRA simulations and experimental data was found for the energy spread (Fig. 4) and bunch length (Fig. 5);

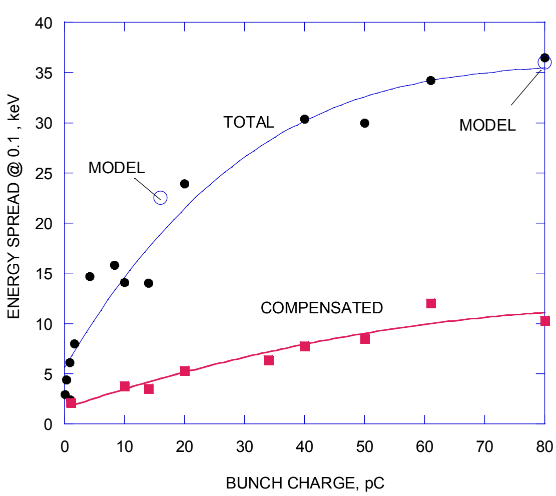


Figure 4: Comparison of the results from the ASTRA model with experimental measurements of the total and tilt-compensated energy spread as a function of the bunch charge, from [4].

- The emittance is however much larger than in simulations. This may be explained by the model lacking some factors and that the experimental conditions were not ideal (because of FE from the cathode, non-optimum setting of the solenoid fields, and macroscopically non-uniform QE on the cathode);
- A comparison of the bunch characteristics obtained with two different laser pulse lengths (7ps and 28ps), made at the modest bunch charge of 16pC. This indicates that there is little difference in bunch quality. The model indicates that there will be appreciable improvement in emittance with longer laser pulses at higher bunch charges, in the ideal case of a near flat-top laser pulse [5].

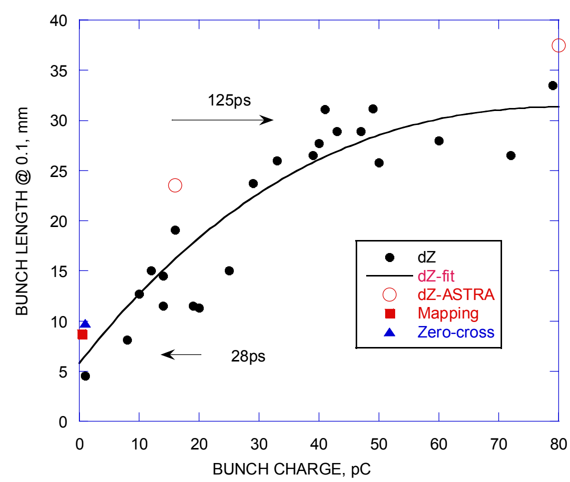


Figure 5: Bunch length at 10% of the peak value as a function of bunch charge from [4], comparing the results from the ASTRA model with three different measurement methods.

Fig. 6 shows the good agreement between the field in the first solenoid giving the minimum beamsize and the ASTRA model; Fig. 7 shows the slightly poorer results for the second solenoid.

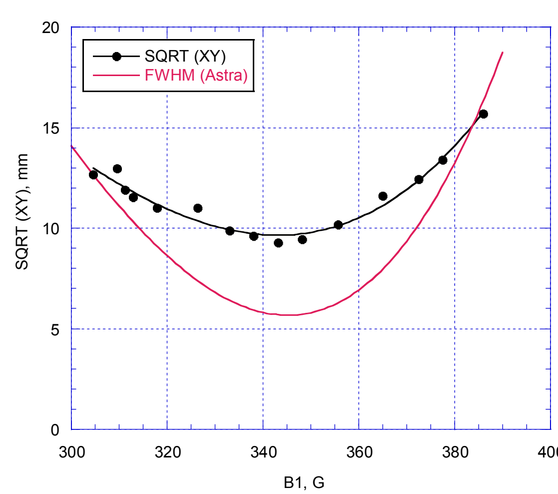


Figure 6: FWHM beam size at a bunch charge of 54 pC as a function of the first solenoid field compared to the results from the ASTRA model.

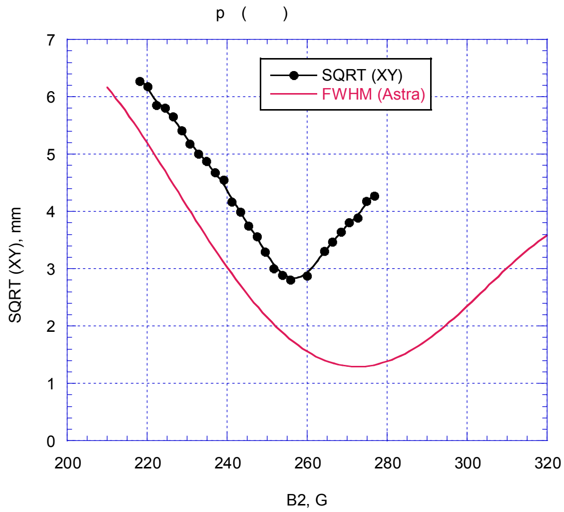


Figure 7: FWHM beam size at a bunch charge of 54 pC as a function of the second solenoid field compared to the results from the ASTRA model.

This is probably the first comprehensive investigation of the bunch parameters from this type of HV DC photogun.

## CRYOSYSTEM COMMISSIONING

As expected with such a complex system, a number of problems with the cryogenic system had to be overcome before it met its operational specification [6]. These included repeated failures of the heater used to warm up the returning helium gas flow, suspected heat leaks and a lack of capacity in the 2K stage. As well as now having ample cooling capacity to sustain ALICE operation, the system has been pushed beyond its specified operational temperature to 1.8K, as part of a series of cryogenic tests aimed towards developing a thorough practical understanding of the change in superconducting cavity performance at lower operating temperatures.

## SUPERCONDUCTING MODULES & RF SYSTEM

ALICE has two nominally identical superconducting modules, the first such devices to be obtained complete as commercial item, and manufactured by ACCEL. They consist of two 9-cell TESLA cavities in a cryomodule design from Stanford University and FZ Dresden. The two main issues with these modules have been:

- The reduction in performance between the vertical tests and when they are installed in ALICE;
- The very high levels of field emission (and therefore radiation) now being seen when operated at or below their intended gradient.

The test results from the cavities are summarised in Table 2, while the radiation measurements from the linac module can be seen in Fig. 8.

Table 2: Cavity Test Results

| | Booster | | Linac | |
|---|---|---|---|---|
| | Cavity 1 | Cavity 2 | Cavity 1 | Cavity 2 |
| **Vertical Tests at DESY** | | | | |
| **Eacc (MV/m)** | 18.9 | 20.8 | 17.1 | 20.4 |
| **Qo** | $5 \times 10^9$ | $5 \times 10^9$ | $5 \times 10^9$ | $5 \times 10^9$ |
| **Module Acceptance Tests at Daresbury** | | | | |
| **Eacc (MV/m)** | 10.8 | 13.5 | 16.4 | 12.8 |
| **Qo** | $3.5 \times 10^9$ @ 8.2 MV/m | $1.3 \times 10^9$ @ 11 MV/m | $1.9 \times 10^9$ @ 14.8 MV/m | $7 \times 10^9$ @ 9.8 MV/m |
| **Limit-ation** | FE Quench | FE Quench | RF Power | FE Quench |

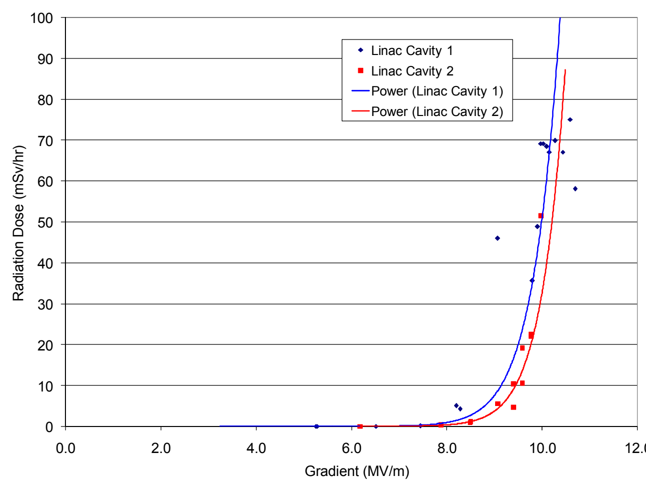


Figure 8: Radiation dose measured a short distance from the linac module.

The second issue has been mitigated by two strategies. The high radiation levels produced by operation of the booster (which requires a smaller gradient compared to the main linac) can be tolerated if some of the more sensitive equipment nearby is re-located. This module is planned to be replaced by the new module design currently being collaboratively developed [7] Secondly it was decided to surround the linac module with lead shielding to allow commissioning to continue in the short term. Further aggressive processing is now planned:

- Over longer conditioning periods;
- Varying frequency, pulse width and pulse repetition rate;
- CW conditioning (only possible at lower power levels);
- Possibly condition the cavity when warm;
- Introduce helium into the vacuum (this is risky as it is not always successful and would only be a last ditch attempt to improve the situation).

## NEXT STEPS

Installation of photon beam transport systems required for the FEL output, Compton backscattering & electro-optic longitudinal diagnostic laser and terahertz beamlines are continuing in parallel to all the other activities where possible.

As the electron beam transport system and the RF system are now ready for beam, the gun diagnostic beamline has been removed and the gun connected to the completed accelerator. Unfortunately, there is not a working ceramic at present, except for two on loan from Stanford University, which had already been prepared for use. Because these ceramics are smaller in diameter they cannot be operated at the nominal gun voltage of 350 kV, they will be adequate for achieving the significant next step of energy recovery. They have already been conditioned to more than 270 kV.

Work is also underway with the supplier to resolve the brazing issues with the gun ceramic; a tapered joint is being developed along with material changes to some of the components.

First beam into the circulating part of the accelerator is expected in October 2008. This will be followed by:

- Fine tuning of the machine (injector tuning for minimum emittance, optimisation of energy recovery at nominal beam parameters, extensive beam measurements);
- Short pulse commissioning stage (longitudinal dynamics, electro-optical diagnostics);
- Energy recovery with FEL (after installation of the FEL and getting the first IR light from FEL).

Simultaneously with ALICE commissioning, the terahertz and infrared FEL research programmes will start, as well as CBS, using head-on electron-photon collisions.

Looking further ahead, in addition to the gun upgrade (the installation of a the load-lock system for cathode activation and exchange [8]) the improved high-current cryomodule will be installed.

## SCIENCE PROGRAMME

In addition to the light derived directly from ALICE (mid-infrared FEL, CBS x-rays and terahertz radiation) an exciting research programme will also use combinations of these with a free-standing femtosecond tunable laser and the terawatt laser that is the photon source for the CBS, mostly for pump-probe experiments that will use one or another combination of light sources.

The ALICE capabilities will be extended into bioscience after completion of the Tissue Culture Laboratory.

## CONCLUSIONS

The prime motivation for the construction and operation of ALICE is to gain experience in designing and operating the technologies which are critical to the success of future UK light sources. In the short period since the start of this project, a huge amount has been learnt, with more still to come. This has now been extended to include an exciting science programme.

Once fully operational, ALICE will be one of the few true electron beam test facilities available in the world. It will be used for development of photoinjector guns, diagnostics, superconducting linacs, synchronisation and for benchmarking codes.

In addition to the IR radiation generated by the FEL and the x-rays produced by the Compton backscattering source, a third beamline to utilise terahertz radiation from a dipole magnet in the bunch compressor is being built.

## REFERENCES

[1] G. Priebe et al, Proc. of the SPIE, Soft X-Ray Lasers and Applications VII, Vol. 6702, CID 67020F (2007)

[2] R.Edgecock et al, "EMMA – The World's First Non-Scaling FFAG", EPAC'08, Genoa.

[3] D.J.Holder et al, "ERLP Gun Commissioning Beamline Design", LINAC'04, Lübeck, August 2004, p. 93.

[4] Y. M. Saveliev et al, "Results from ALICE (ERLP) DC Photoinjector Gun Commissioning", EPAC'08, Genoa.

[5] Y. M. Saveliev et al, "Characterisation of Electron Bunches from ALICE (ERLP) DC Photoinjector Gun at Two Different Laser Pulse Lengths", EPAC'08, Genoa.

[6] A.R.Goulden et al, "Installation and Commissioning of the Superconducting RF Linac Cryomodules for the ERLP", Advances in Cryogenic Engineering, 53B, 2007, p.1573.

[7] P McIntosh et al, "Realisation of a Prototype Superconducting CW Cavity and Cryo Module For Energy Recovery", SRF'07, Beijing.

[8] B.L. Militsyn et al, "Design of an Upgrade to the ALICE Photocathode Electron Gun", EPAC'08, Genoa.

# FIRST TESTS OF THE CORNELL UNIVERSITY ERL INJECTOR*

B. Dunham#, I. Bazarov, S. Belomestnykh, M. Billing, E. Chojnacki, Z. Conway, J. Dobbins, R. Ehrlich, M. Forster, S. Gruner, G. Hoffstaetter, V. Kostroun, M. Liepe, Y. Li, X. Liu, D. Ouzounov, H. Padamsee, D. Rice, V. Shemelin, C. Sinclair, E. Smith, K. Smolenski, S. Temnykh, M. Tigner, V. Veshcherevich, T. Wilksen, CLASSE, Cornell University, Ithaca, NY 14853, U.S.A.

*Abstract*

Cornell University is planning to build an Energy Recovery Linac (ERL) X-ray facility. For an ERL, it is well known that the x-ray beam brightness for the users is mainly determined by the initial electron beam emittance provided by the injector. To address technical challenges of producing very low emittance beams at high average current as required for an ERL, Cornell University has proposed a prototype injector with 5-15 MeV beam energy, 100 mA maximum average current and 77 pC/bunch. In this article, we describe the design, construction and initial results for an ERL injector prototype now under operation.

## INTRODUCTION

An electron injector for an ERL has many challenges. To provide the x-ray beam quality that users demand for the future, the injector needs to meet the requirements show in Table 1 [1].

Table 1: Injector Requirements (values in ( ) are goals for the prototype system of this paper)

| | |
|---|---|
| Beam Energy | 10-15 (5-15) MeV |
| Charge per bunch | 77 (77) pC |
| Average Current | 100 (100) mA |
| Bunch Length | 2-3 (2-3) ps |
| Transverse Emittance | 0.3 (2) μm |
| Operating Frequency | 1.3 (1.3) GHz |

At Cornell University, we have undertaken a program to develop and test such an injector (see Fig. 1) towards realization of this difficult set of requirements. The design was based on detailed simulations using genetic algorithms to find the optimum solutions to the multi-parameter design space [2]. The electron source is a DC photoemission gun using a GaAs cathode, providing a 1.3 GHz bunch train of 77 pC/bunch with a 20-40 ps 'beer can' distribution. This is followed by a short section for emittance compensation solenoids and a normal conducting buncher cavity [3]. The beam is then accelerated through a cryomodule containing five 2-cell niobium superconducting RF (SRF) cavities, each with individual control of phase and gradient. The cavities have two opposing 50 kW input couplers to feed in 100 kW per cavity. The available RF power allows for either 100 mA at 5 MeV or 33 mA at 15 MeV. After the SRF cavities, an extensive suite of diagnostics allows for a complete characterization of the transverse and longitudinal phase space of the beam. The beam is terminated in an aluminum dump with a capacity for disposing 600 kW of average power.

Each section of the injector will be described in detail, along with the current status of commissioning and beam tests.

## DC PHOTOEMISSION GUN

Based on the experience of other labs [4] and of the authors, DC photoemission guns provide the best chance of producing the low emittance, high average power beam to meet the needs of an ERL. The present record for average current belongs to the Boeing normal conducting RF (NCRF) gun [5] at 32 mA (25% duty factor), and while other projects continue to push for higher current with NCRF guns, no improvements have been realized. Work on SRF guns has made excellent progress recently [5], but the prospect of obtaining 100 mA average current is still many years away. The DC gun used for the Jefferson Lab FEL project [4] has reliably provided 135 pC bunches at an average current of ~9 mA, and an extension of that technology is the most likely path to meet the needs of an ERL injector in the near future.

### *High Voltage Gun*

Common sense dictates that high initial beam energy and high electric field at the cathode are necessary to overcome the space charge forces in bunched beams and obtain the best possible emittance. Simulations [2] show that higher gun voltage is important for obtaining low emittance up to a certain point, after which the improvement is relatively small. Thus, a DC gun operating in the range of 500-600 kV should meet the emittance goals with the appropriate cathode. To minimize dark current at the operating voltage, the gun must be processed to roughly 25% above the operating value, consequently the Cornell gun has been designed to withstand 750 kV maximum voltage.

A schematic cutaway of the Cornell DC photoemission gun is shown in Fig. 2, and was designed to meet the requirements in Table 2. The gun was operated for over a year using a test beamline to measure the performance of the gun and cathode before mating it to the rest of the injector. Details of these measurements have been published elsewhere [7, 8], with the main result that the emittance measurements at 77 pC/bunch and 250 kV beam energy match the simulations very closely, giving confidence that the simulations for the entire system are valid. Two difficulties observed involved the laser profile and laser stability. Tails in the phase space distribution were traced (through simulation) to non-uniformities

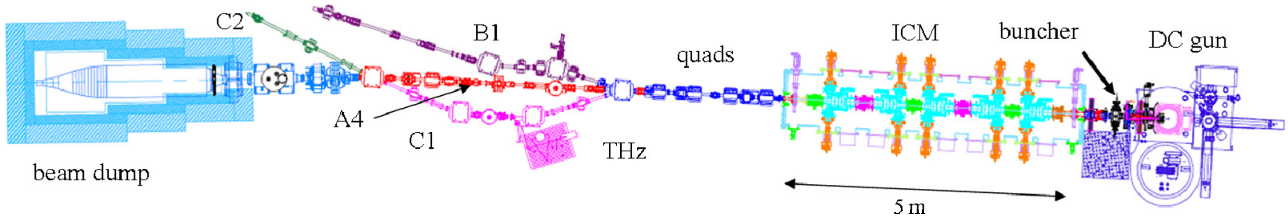


Figure 1: The layout of the Cornell prototype ERL injector.

across the 'flat-top' laser distribution and variations in the distribution over time. The pointing stability of the laser at the cathode was also an issue, causing jumps in the phase space measurements. The laser itself is stable to 20-30 μm rms, but this increases upon demagnification to the cathode. We have since purchased an active position stabilization device (MRC Systems GmbH) which will reduce the position jitter at the cathode to < 10 μm rms.

Table 2: DC Gun and Laser Requirements

| | |
|---|---|
| Operating voltage | 500-600 kV |
| Maximum voltage | 750 kV |
| Average Current | 100 mA |
| Vacuum during operation | $< 1\times10^{-11}$ Torr |
| External $SF_6$ pressure | 4 atm |
| Laser wavelength | 520 nm |
| Laser pulse shape | 'beer can' |
| Laser pulse length | 20-40 ps |
| Phase jitter | < 1 ps |

All guns of this type suffer from the problem of controlling field emitted electrons from the high voltage surfaces. These electrons can land on the insulator, and if the charge builds up punch-through can occur, causing a vacuum leak. We purchased an insulator with an internal resistive coating (CPI, Inc.) to bleed off these electrons, but it has only been successful up to 450 kV during processing, above which punch-throughs occur. In addition, the coating has not adhered well, leaving a layer of dust on the electrodes, certain demise for reaching 750 kV. Colleagues at Daresbury Lab [9] have built an insulator using a new material from Morgan Advanced Ceramics (AL-970CD) which is more resistant to field emitted electrons, at least up to 500 kV. We are in the process of obtaining a new insulator using this material, and are also investigating the use of segmented insulators [10] which completely block the line of sight between the electrodes and the insulator, but have a much more complicated mechanical structure. For now, we are limiting the gun voltage to 300 kV to reduce the chance of damage, until a spare is obtained.

If one can make electrodes that do not field emit, the insulator design is not so important – this is the Holy Grail for gun design (and for SRF cavities). We have built the present gun emulating the best techniques known for cavity cleaning, namely electro-polishing followed by high pressure rinsing. In a test chamber, gradients of 30 MV/m have been routinely reached on large area electrodes, but these results have not been reproduced in the real gun, most likely due to dust contamination from the insulator coating.

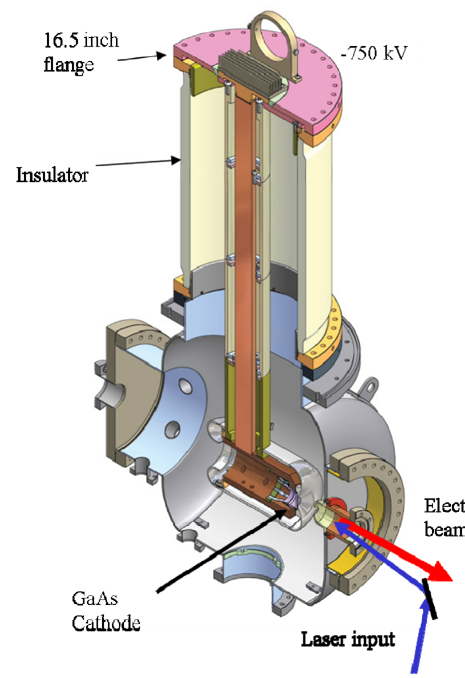


Figure 2: The Cornell Photoemission Gun.

## *Laser System*

To produce 100 mA from a GaAs cathode with a 1% QE, over 20 Watts of laser power at 520 nm is required at the cathode ( 2 W for 10% QE). Accounting for possible losses in the laser transport and beam shaping, a laser with 40 W of average power is desired. The system must provide pulses at a repetition rate of 1.3 GHz synchronized to the RF master clock (with a timing jitter < 1 ps), and a configurable pulse shape in time and space for minimizing the electron beam emittance.

We have chosen to use a Yb-doped fiber laser system to meet these requirements. Initially, the oscillator was made in-house, but difficulties were encountered in accurately synchronizing it to the RF system.

Subsequently, a commercial fiber laser 'clock' was purchased from PriTel Inc. They modified a standard product to work at our pulse repetition rate. The laser is triggered by the RF master clock signal, and the jitter between the output pulse the clock signal is less than 500 fs. The pulses are fed to a single mode fiber amplifier where the pulse energy is boosted to 150 nJ, low enough to prevent any nonlinear distortion. The pulse energy is further increased through amplification in a double clad large mode area fiber amplifier built to work in nearly single mode regime. Currently we have implemented only one such stage and achieved average power of 35 watts at 1040 nm (27 nJ pulse energy). The IR pulses are frequency doubled in a LBO crystal to produce pulses centered at 520 nm and energy of 9 nJ (12 W average power). Additional thermal management is needed to reach higher powers. Laser shaping of the pulses has been described in detail elsewhere [11].

### *Photocathode Materials*

A perfect photocathode for an accelerator electron source would have high efficiency at a convenient laser wavelength, fast response time, long lifetime and a low thermal emittance. Unfortunately, no such cathode exists today, although the search continues. A number of different photocathodes meet some of these criteria, so tradeoffs have to be made depending on the requirements of the particular system. For an ERL, obtaining 100 mA average current means high quantum efficiency (QE) photocathodes are a necessity.

Semiconductor photocathodes are currently the best choice for high QE and low emittance. Examples are GaAs, $Cs_2Te$, GaN, and $K_2CsSb$. Both $Cs_2Te$ and GaN show promise but require UV light but there are no laser systems available to produce enough average power in the UV. Both GaAs and $K_2CsSb$ have 5-10% QE for ~520 nm light, where high average power lasers are readily available. At Cornell, we have chosen to use GaAs, but are still considering other cathodes depending on the application.

As mentioned earlier, it is possible to recover the intrinsic thermal emittance from the cathode using a carefully designed emittance compensation scheme for the bunch charges of interest to an ERL [2]. Of all the cathodes available, GaAs has the lowest thermal emittance [6], so is the cathode of choice for an ERL. Unfortunately, the QE is near a minimum when the thermal emittance is smallest (close to the band gap), thus unsuitable for high average current. In addition, it is well known that at ~780 nm a fast laser pulse will generate an electron beam with a 20-40 ps tail, which is not acceptable for low emittance operation. For shorter wavelengths (~520nm) recent measurements [9] show that the response time is quite fast (~1 ps) as long as the QE is not too high (< 10%). This points out some of the tradeoffs one has to make even when using GaAs, and we have chosen an operating wavelength of 520 nm as the best compromise between QE, thermal emittance and response time.

The last important parameter is cathode lifetime. The cathodes described above are all sensitive to chemical poisoning to some extent, and require ultra-high vacuum. GaAs is the most sensitive, unfortunately, requiring vacuum levels < $10^{-11}$ Torr for successful operation. An additional lifetime limiter is ion back-bombardment which further reduces QE. The electron beam can ionize residual gas molecules anywhere along their path, which can then be accelerated back towards the cathode surface. Jefferson Lab [12] has carried out extensive measurements at 10 mA average current, and has measured cathode lifetimes as high as $10^6$ C/cm$^2$ (the amount of charge extracted per cm$^2$ when the QE has fallen by 1/e). One can use this data to estimate that a 10 W maximum power laser system should be able to provide 100 mA over 100 hours with a 1.8 mm diameter laser spot [13]. Such performance has not be demonstrated yet, and it is certainly an optimistic estimate.

## SRF AND RF SYSTEMS

There are many challenges in constructing an injector for an ERL, one of the most difficult being an injector cryomodule (ICM). The ICM RF system must transfer up to 500 kW to the beam (for the prototype system), damp out significant higher order modes (HOM) up to tens of GHz, and preserve the low emittance generated by the electron source. The specifications for the ICM RF system are shown in Table 3.

Table 3: Specifications of the ICM RF system

| Parameter | Value |
|---|---|
| Number of cavities | 5 |
| Accelerating voltage per cavity | 1 – 3 MV |
| 2-cell cavity length | 0.218 |
| R/Q (linac definition) | 222 Ohm |
| $Q_{ext}$ | $4.6\times10^4 - 4.1\times10^5$ |
| RF power per cavity | 100 kW |
| Maximum useful klystron power | ≥120 kW |
| Amplitude stability | $9.5\times10^{-4}$ (rms) |
| Phase stability | 0.1° (rms) |

The five 2-cell cavities were built at Cornell and vertical tested with $Q_0 > 1\times10^{10}$ at 15 MV/m and lower. One cavity was built into a horizontal test cryostat along with HOM loads [14] to verify the construction techniques before building the final ICM. The initial Q of the cavity was only $1\times10^9$, much lower than the vertical test results. On disassembly it was discovered that one of the ceramic HOM tiles had cracked and fallen, creating dust that reduced the cavity performance. The faulty tiles were removed and replaced with different material, then extensively cold tested before installing in the main ICM. Twin, opposing input couplers have been tested up to > 60 kW average power, more than the 50 kW needed for 100 mA operation. A complete description of the cryomodule construction and testing can be found in references [15,16] (see Fig. 3).

Figure 3: The ICM after final assembly.

So far all ICM operations have been at 1.8 K. The cavities have been processed in pulsed mode to >15 MV/m, and in all cases but one the limit was due to vacuum activity in the input couplers, so further processing should improve the maximum field. Cavity 4 quenched in pulsed mode (2 ms long pulses, 20 ms period) at 18 MV/m. In CW mode all cavities reached >2.8 MV/m when powered individually (see Table 4). Operation of cavity 1 was limited by excessive RF losses due to field emission (FE). While cavity 2 was limited by the input coupler vacuum, it also had rather significant FE. Operating at 1.8 K with two pump skids, the cryogenic system can handle all five cavities at gradients up to 10.4 MV/m (2.4 MV per cavity). Raising temperature to 2 K will allow for an increase of the cryogenic system heat handling capacity and hence higher gradient ICM operation.

Table 4: Cavity Performance Summary (IC = input coupler vacuum)

| Cavity | CW | Limit | Pulsed | Limit |
|---|---|---|---|---|
| 1 | 2.8 MV | Cryogenics | 4.35 MV | IC |
| 2 | 2.9 MV | IC | 3.75 MV | IC |
| 3 | 3.5 MV | Cryogenics | 3.66 MV | IC. |
| 4 | 3.4 MV | Cryogenics | 4.15 MV | Quench |
| 5 | 3.5 MV | none | 5.20 MV | IC |
| All 5 | 2.4 MV | Cryogenics | | |

## CRYOGENIC SYSTEM

The ICM requires cryogen delivery at three different temperatures: 1.8-2 K, 4-6 K, and ~80 K. The RF cavities are submerged in 1.8 K superfluid; supercritical helium streams at 4-6 K and 80 K intercept heat conducted down the internal supports from room temperature, as well as heat generated in the RF input couplers and higher-order-mode RF absorbers. The mass flow of 5-10 g/s is supplied by one of the helium compressors.

The helium refrigerator has no built-in capability to produce the superfluid liquid that cools the RF cavities. Instead, liquid from the 4.2 K pot is passed through a heat exchanger where it is pre-cooled by the low-pressure gas boiled off in ICM. It then goes to a JT valve where it is throttled to the 12 Torr pressure corresponding to 1.8 K liquid helium temperature. A 2 K heat exchanger greatly reduces the gas fraction of the stream emerging from the JT, and hence, the mass flow seen by the pump used to maintain the 12 Torr pressure above the 1.8 K liquid. The low-pressure gas is heated to near room temperature before being sent to the Roots blowers, the input stage of our pumping system. The 12 Torr pressure can be controlled to ± 0.01 Torr by means of a variable frequency (VFD) drive to the blower motor.

Heat absorbed at 1.8 K is a liquefaction load, since minimal use is made of the return gas. Thus, 1 g/s (~30 L/hour) boiled off there corresponds to about 20% of the capacity of one of the refrigerators. Our current estimate of the static heat load at 1.8 K is 10±3 Watts, complicated by the presence of a thermal oscillation associated with the cool-down plumbing.

## DIAGNOSTICS

The three diagnostics beamlines after the ICM are shown in Fig. 1. A matching section consisting of four quadrupoles resides between the ICM and the beamlines. Each beamline has a specific purpose along with the appropriate diagnostics to allow a full characterization of the beam phase space. Some of the diagnostics are only capable of handling 1-2 kW and thus must be used with pulsed beam (made by chopping the laser with a Pockels cell), while several of the devices can be used with the full beam power.

In the straight section (A4), a pair of slits with scanning magnets followed by a Faraday cup is used for transverse phase space measurements. An RF deflection cavity [17] downstream provides bunch length measurements with sub ps accuracy. By observing on a viewscreen at the end of the C2 line after a dipole, one can observe the time-resolved energy spread of the beam, or study slices of the beam in conjunction with the slits.

The B1 line geometry is similar to a method for merging the beam from the injector into the main ERL linac. After passing through the 3 dipole arrangement, another pair of (identical) emittance measurement slits allows for the measurement of the transverse phase space. This can then be compared to the straight ahead measurements to study the emittance growth in mergers. Other merger schemes can easily be studied.

The chicane (C1) line has several high power diagnostics as well as a viewscreen for cavity phasing. After the second dipole in the chicane, a copper mirror deflects THz radiation into an interferometer which can be used to monitor the bunch length [18]. In the straight arm, a custom made 'flying wire' that can handle the full beam power is available for beam size measurements. There is a similar flying wire in the A4 section. The high power diagnostics are meant for studying the beam properties under the influence of ions, wakefields, HOM's in the cavities and other high power RF effects.

Strip-line beam position monitors are used all along the beamlines to provide ~10 μm resolution.

## BEAM DUMP

The beam dump for the Cornell injector is based on a SLAC klystron collector [19] and is designed to absorb up to 600 kW average power for beams between 5 and 15 MeV. The beam is defocused using a pair of strong quadrupole magnets and rastered in a circle to reduce the instantaneous power on the dump walls. It is made using aluminum instead of the copper to reduce neutron production. The dump is made of two sections: the body and a outer shell to contain the cooling water. The body is 20 mm thick and the shell is 13 mm thick, with the total thickness enough to stop the beam. The sections are e-beam welded together and the welds are inspected for voids and cracks. The interior shape of the cone was designed using GEANT to distribute the scattered electrons (and thus the heat) as uniformly as possible around the cooled surface. A flow of 60 gpm is sufficient to extract ~40 W/cm$^2$ with a 600 kW heat load.

Metalex Mfg, Inc (Cincinnati, OH) is building the beam dump and delivery is expected at the end of September, 2008. It will be installed upon arrival along with extensive shielding.

## COMMISSIONING RESULTS AND PLANS

The entire injector has been installed with the exception of the high power beam dump, whose delivery is imminent. The gun has been processed only to 300 kV (as described earlier) so far, and we are not pushing the voltage higher until a backup insulator is acquired. The buncher cavity has been processed to ~50 kV peak voltage, limited by multi-pacting in the tuner area, which will be fixed by a new TiN coated tuner. The SRF cavities have been processed as described earlier, well enough to reach 12 MeV beam energy at 1.8 K, or 15 MeV at 2 K.

Beam has been accelerated to over 5 MeV so far, and threaded through each of the diagnostics beam lines. Initial checkout of the BPM's and the various diagnostics are just underway. Qualitatively, the phase stability between the laser and the RF is quite good as evidenced by a stable beam on the chicane (C1 line). The maximum current so far has been 20 μA, limited by the radiation shielding and the delivery of the final beam dump.

The near term plans include completing commissioning of the BPM's and other diagnostics, installing the final beam dump and shielding, testing the machine protection system and increasing the laser power. Once that is done an extensive set of phase space measurements will begin along with the push for 100 mA.

## REFERENCES


[1] S. M. Gruner and M. Tigner, Eds, "Study for a proposed Phase I Energy Recovery Linac (ERL) synchrotron light source at Cornell University", CHESS Technical Memo 02-003, Jefferson Laboratory Report No. JLABACT-01-04 (2001).

[2] I.V. Bazarov, *et al.*, "Multivariate optimization of a High Brightness DC Gun Photoinjector", PRST AB, **8**, 034202 (2005).

[3] S. Belomestnykh, *et al.*, "Commissioning of the Cornell ERL Injector RF Systems", 2008 European Particle Acc. Conf., Genoa, Italy, 832-834 (2008).

[4] C. Hernandez-Garcia, *et al.*, "A High Average Current DC GaAs Photocathode Gun for ERLs and FELs", 2005 Particle Acc. Conf., Knoxville, TN, 3117-3119 (2005).

[5] D. Dowell, *et al.*, Nucl. Instr. Meth. A **356**, 167 (1995).

[6] A. Arnold, *et al.*, "Development of a Superconducting RF Photoinjector", Nucl. Instr. Meth., A **577**, 440 (2007).

[7] I. Bazarov *et al.*, "Thermal emittance and response time measurements of negative electron affinity photocathodes", J. Appl. Phys., **103** (2008) 054901.

[8] I. Bazarov *et al.*, "Efficient temporal shaping of electron distributions for high brightness photoemission guns", PRST AB 11 (2008) 040702.

[9] R.J. Smith, Daresbury Lab, personal communication.

[10] J. Haimson, IEEE Trans. Nucl. Sci. **NS 22**, 1354 (1975.

[11] D. Ouzounov, *et al.*, "The Laser System for the ERL Electron Source at Cornell", 2007 Particle Acc. Conf., Albuquerque, NM, 530-532 (2007).

[12] J. Grames, *et al.*, "Ion Back-Bombardment of GaAs Photocathodes inside DC High Voltage Electron Guns, 2005 Particle Acc. Conf., Knoxville, TN 2875-2877 (2008).

[13] M. Furman and W. Chou, editors, "ICFA Beam Dynamics Newsletter, #46", 97-118 (2008).

[14] M. Liepe, *et al.*, "The Cornell ERL Superconducting 2-cell Injector Cavity String and Test Cryomodule", 2007 Particle Acc. Conf., Albuquerque, NM, 2572-2574 (2007).

[15] M. Liepe, *et al.*, "First Test Results from the Cornell ERL Injector Cryomodule," 2008 European Particle Acc. Conf., Genoa, Italy, 883-885 (2008).

[16] E. Chojnacki, *et al.*, "Design and Fabrication of the Cornell ERL Injector Cryomodule," 2008 European Particle Acc. Conf., Genoa, Italy, 844-846 (2008).

[17] S. Belomestnykh, et al., "Deflecting Cavity for Beam Diagnostics in an ERL Injector", 2007 Particle Acc. Conf., Albuquerque, NM, 2331-2333 (2007).

[18] G. Schneider, et al., "On using the coherent far IR radiation produced by a charge particle bunch to determine its shape", NIM A, **396(3)**, 283-292 (1997).

[19] Dieter Walz, SLAC, personal communication.

# RF CONTROL OF HIGH $Q_L$ SUPERCONDUCTING CAVITIES*

Curt Hovater#
Jefferson Lab, Newport News VA, USA

*Abstract*

In the last 20 years the requirements for RF Control have increased as the target use has broadened from electron/ion accelerators for Nuclear and Particle Physics to light sources such as Free Electron Lasers. The increasing requirement of cavity field control to meet the spectral and jitter performance specifications for light sources has led system designers to a more rigorous approach in designing the RF controls. Design attention must be applied not only to the hardware and control algorithms but also to the overall accelerating system to meet performance and cost requirements. As an example, cavity $Q_L$ in Energy Recovery Linacs (ERL) must be optimized such that the RF controls can accommodate the lowest possible RF power given the background cavity microphonics. This paper presents the status and future directions of high $Q_L$ superconducting RF control systems.

## INTRODUCTION

Recent proposals for energy recovering linacs (ERLs) at Cornell, Daresbury and Argonne have challenged the RF community to meet the field control requirements of the higher $Q_L$ cavities. It should be noted the operation of high $Q_L$ cavities is not new. Superconducting (sc) accelerating structures such as the types used in proton and ion accelerators have always operated with $Q_L > 10^7$. The difference is that beam requirements to meet the optical frequencies and line widths require them to be on the order of $< 0.1^o$ and $10^{-4}$ amplitude stability. Some of the techniques (Self Excited Loop) for operating these cavities can be applied to the ERLs. In addition to field control sc cavities can have large Lorentz coefficients making turn on or cavity recovery difficult. Fortunately, advances in electronics have made developing and designing RF control systems easier, where the designs have shifted from fairly rigid analog-centric hardware 20 years ago to a more flexible digital-centric software design.

RF control design starts at the beginning of the accelerator design. Depending on the application, energy spread and jitter specifications will directly correlate to the required cavity field control. Once this is known, the designer can begin modeling the receiver and feedback necessary to meet the field control requirement. Next, one must optimize the cavity $Q_L$ for the application. If the Linac is pulsed, some form of Lorentz detuning compensation must be considered.

Other control considerations include: multiple cavity control (i.e. vector sum) vs. single cavity control and Generator Driven Resonator (GDR) vs. Self Excited Loop (SEL).

## OPTIMIZING CAVITY $Q_L$

The RF system must be optimized for minimum power which ultimately sets the cavities loaded $Q$. The optimum coupling ($\beta_{opt}$) to a cavity can be derived from the steady state cavity equations and is given by

$$\beta_{opt} = \sqrt{(b+1)^2 + \left[\frac{2\delta f}{\Delta f_o}\right]^2} \qquad (1)$$

$$\text{where} \quad b = \frac{I_o (R/Q) Q_o}{V} \cos\phi$$

$V$ is the cavity voltage, $I_o$ is beam current, $R/Q$ is the shunt impedance, $Q_o$ is the cavity quality factor, $\phi$ is the beam phase, $f_o$ is the cavity frequency, $\delta f$ is the cavity detuning, and $\Delta f_o$ is the cavity bandwidth [1]. In the limit where the $Q_o >> Q_L$, one can make the approximation that $\beta \sim Q_o/Q_L$. In the case of a heavy beam loaded cavity such as one might find in an injector, the optimized loaded $Q$ is driven by beam loading (i.e. $b >> 1$) and eq. (1) reduces to

$$Q_{Lopt} \cong V / I_o (R/Q) \qquad (2)$$

In the case of an ERL where the vector sum of the two beams results in a net current that is less than a few tens of micro-amps, there is an incentive to increase the $Q_L$ [2]. $Q_L$ is limited by the amount of microphonic detuning the cavity exhibits under normal operating conditions (i.e. $2\delta f/\Delta f_o >> b+1$). In this case $Q_{Lopt}$ is given by

$$Q_{Lopt} \cong f_o / 2\delta f \qquad (3)$$

Figure 1 shows the optimizations on generator power for different beam loads.

If the cavity power requirement is driven by the microphonics, some consideration to cavity stiffening is necessary. At Jefferson Lab, we have operated both stiffened and un-stiffened cavities. The stiffening rings can have an effect on roughly similar cell shapes. Table 1 shows the microphonic detuning of elliptical cavities with and without stiffening. Included in the table is the klystron power required for the $Q_{Lopt}$ given the 6σ microphonic detuning.

* Notice: Authored by Jefferson Science Associates, LLC under U.S. DOE Contract No. DE-AC05-06OR23177. 
# hovater@jlab.org

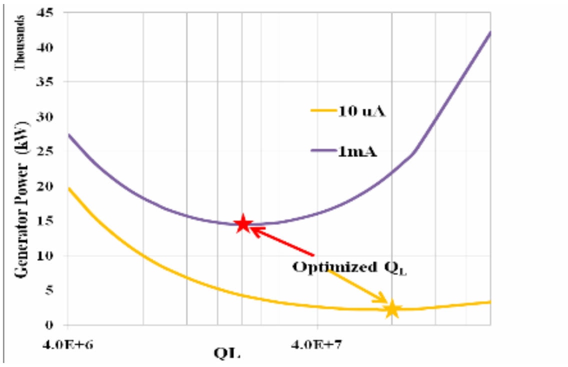


Figure 1: Forward power at 10 Hz detuning for a non-beam loaded and beam loaded sc cavity operating at 20 MV/m.

In the case of an ERL with complete energy recovery and improved microphonic damping, it may be possible to optimize the power to below 1 kW. For large installations (100+ cavities) where it is not beam current driven there is an incentive to keep the klystron power low for energy savings.

Table 1: Microphonic Detuning

| Microphonic Detuning | Renascence | C100 (Upgrade) |
|---|---|---|
| RMS (Hz) | 1.98 | 3.65 |
| 6 σ (Hz) | 11.9 | 21.9 |
| Stiffened | Yes | No |
| $Power_{OPT}$ (20 MV/m and 100 µA) | 3.3 kW | 5.3 kW |

## LORENTZ DETUNING

A concern with the increasing gradient and $Q_L$ in a superconducting cavity is the effect of the Lorentz detuning. Lorentz detuning is caused by the radiation pressure exerted on the cavity walls by an electromagnetic wave. The Lorentz force shifts the resonance frequency of the cavity by $\Delta f = - K\, E_c^2$, where the Lorentz coefficient, $K$, is typically ~ 2 for un-stiffened elliptical cavities (it can vary anywhere from 1.5 to 3 in CEBAF). Applying this to the cavity transfer function results in a folding of the curve as the gradient is increased. Figure 2 shows the expected resonance curve for the 7-cell cavity at design gradient and for a typical 5-cell cavity operating in CEBAF. The folding can lead to what is known as the monotonic ponderomotive instability, which has been a common feature in cavities for low-velocity, low-current beams and also for some high $Q_L$ elliptical cavities [4, 5]. This can be dealt with effectively by electronic control.

An additional constraint placed on any LLRF system is the Lorentz detuning of the cavity at turn-on. If the Lorentz detuning is beyond a bandwidth, a control system may have trouble reaching gradient without some fast tuner or slow gradient ramp (slow enough for the tuner to track the Lorentz detuning). In CW accelerators where the cavities trip off on the occasional arc or vacuum event, the system cannot always rely on electronic feedback (klystron power) to compensate for the turn on transient. An example of how large this detuning can be is the CEBAF 12 GeV upgrade cavities. They have a typical Lorentz detuning value, $K$, of ~ 2. At the required gradient of 20 MV/m this leads to a detuning of 800 Hz. Coupled with the large $Q_L$ (3.3 x $10^7$), this is 18 bandwidths away!

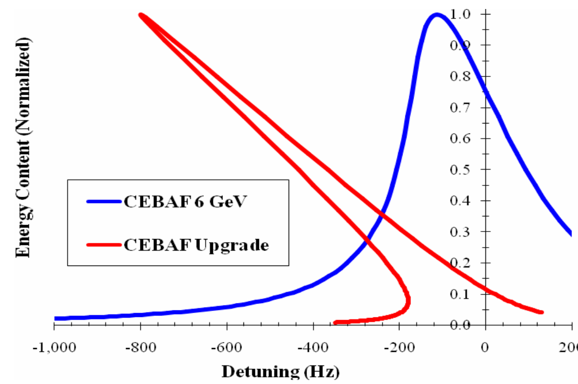


Figure 2: Resonance curves for a typical 5-cell cavity operating in CEBAF at 7.5 MV/m and $Q_L$ of 5 x $10^6$ and for the 7-cell upgrade cavity at design gradient of 20 MV/m and $Q_L$ of 2.2 x $10^7$.

## RF MODEL

Once the acceleration system (RF amplifier, distribution, and cavity) is specified, the RF control system can be modeled for the application. More often than not, control system models use Matlab/Simulink. At Jefferson lab we used a simple dc model. In this case the complex cavity representation as well as beam is simplified to quadrature components. The cavity can then be described by a low pass filter. Lorentz Force detuning, microphonics and tuners are incorporated as frequency modulators [6]. In addition to Jefferson Lab very good models exist for the cavity control [7, 8]. Whether to model in I and Q or phase and amplitude must be chosen and each has their advantages. While one can investigate many control algorithms (and they have), the simple Proportional, Integral, Derivative (PID) controller is often sufficient. From the background microphonics and required cavity field control, the feedback gain can be determined. This will drive the system latency (delay) requirement. Knowing that the klystron and distribution delay is set for the system, the only flexibility is in the signal processing and control algorithm.

## CAVITY CONTROL ALGORITHMS

There are two control algorithms now employed in high $Q_L$ operation; Generator Driven Resonator (GDR) and Self Excited Loop (SEL). In the case of the GDR, an external source drives the cavity, and control is maintained by comparing phase and amplitude to a reference. The cavity must be kept near the source frequency (within a few Hz) to keep the drive amplifier from saturating. Field control can be maintained using I and Q or its transformed companion, phase and amplitude. Presently CEBAF (old systems), XFEL, SNS and the proposed Cornell ERL use or intend to use the GDR method [2]. The advantage is that for pulsed systems the cavities are at a defined phase. GDR's are conceptually a traditional feedback system and therefore easier to model. Disadvantages are the cavity needs to be near resonance, and the system requires an automated search feature to find a detuned cavity.

An SEL uses the cavities own resonance in the same way an oscillator uses a tank circuit [5]. In this way it naturally tracks the cavity frequency (see Figure 3). Amplitude control is obtained by limiting the feedback amplitude, and then, providing an external set point which can be compared to the cavity signal. The circuit can be phase-locked to a reference (near the cavity frequency) by comparing the cavity signal to the reference. Optimally, for RF power reasons, this is less than half a cavity bandwidth. Heavy ion and electron accelerators have used analog versions of the SEL successfully for many years. The advantages for the SEL is that it can quickly energize a cavity regardless of frequency, which is useful at turn on where the Lorentz detuning can be large, minimizes or eliminating the need to use PZT devices on start up. The disadvantage is that for pulsed systems phase is arbitrary until locked to the reference. For cw machines this is not an issue, and the SEL should be considered for cavity recovery.

### *Digital Self Excited Loop*

At Jefferson Lab, we have developed a Digital SEL algorithm that can be configured in a modern FPGA based RF control system [9]. The idea of building a digital SEL has been around for some years. The Jefferson Lab system fully incorporates the SEL algorithm in a digital format. All algorithmic processing occurs at a multiple of the clock frequency, 56 MHz. Figure 4 shows a block diagram of the control logic. The control logic can be switched quickly, and various operational modes can be obtained (tone, SEL, and GDR).

The SEL algorithm was tested on numerous sc cavities including the 12 GeV upgrade cavity. In SEL mode, the system quickly (~ 10 ms) found (off to on) the cavity resonance with cavities detuned as much as 50 kHz away from the reference. The effective capture range of the SEL is only limited by the receivers digital filtering (typically > 100 kHz). Field control has been tested with both a microphonic compensation scheme and with traditional proportional feedback. Turning on the compensator and adjusting the proportional gain allowed us to reduce the phase error from 0.75$^o$ rms to 0.11$^o$ rms error. The utility of the digital SEL has not yet been fully realized. At the higher gradients (+20 MV/m) like those needed for future cw electron LINACs, the Lorentz detuning makes cavity turn-on (fault recovery) problematic without some tuner based compensation or other algorithmic solution. The digital SEL solves this problem.

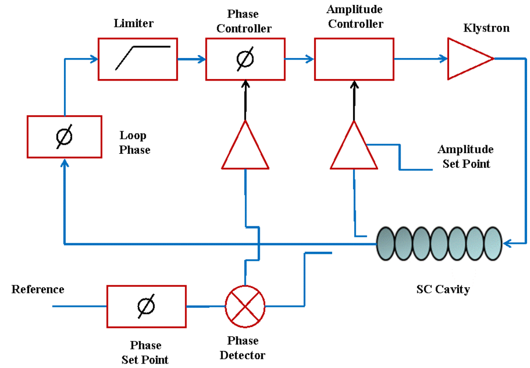


Figure 3: SEL block diagram.

## RF CONTROL HARDWARE

As has been presented in prior conferences, RF control has been simplified in the last 10 years to an embedded algorithm in a processor or a Field Programmable Gate Array (FPGA) [10]. The flexibility of having the algorithm programmed in the logic or software and being able to reconfigure quickly is a very desirable feature. Typical hardware consists of an RF receiver using a super heterodyne scheme (frequency mixer) to down convert the cavity signal down to a manageable intermediate frequency (IF). IF's are typically between 10 and 100 MHz. This is driven by the ADC's degrading S/N as the clock is increased. The IF is then digitized using a fast ADC clocked at quadrature (or near quadrature). A large FPGA then performs the necessary digital signal processing, and finally a control algorithm is applied to the signal. The feed forward portion is then processed similarly through a fast DAC, up converted through a mixer, applied to a power amplifier and finally driving the cavity.

Depending on the application, the basic system can take on various forms. For high $Q_L$ cw systems such as ERLs and nuclear physics accelerators, needed field control dictates one cavity/amplifier. In the case of the ILC or FLASH, where the footprint is multiple cavities/power amplifier, the receiver needs to have multiple cavity receiver channels [11].

Overall field control is ultimately determined by the front end receiver (mixer/LO, amplifiers, ADC/clock) and the reference jitter. This assumes delay and gain bandwidth are such that they do not interfere with the feedback controls. Figure 5 shows a receiver block diagram with pertinent information (S/N, Linearity) of the CEBAF Upgrade RF receiver. The selection of linear components (mixer, amplifiers) also plays into the design. Components that contribute to distortion can affect field control, especially if designing over a large gradient dynamic range. Amplitude control is driven by the cavities residual amplitude error requirement (~ $10^{-4}$ for light sources). Therefore the S/N must be better than this over the control bandwidth. It is possible to improve upon S/N digitally with processing gain (i.e. oversampling), but at the expense of either gain or stability margin [12].

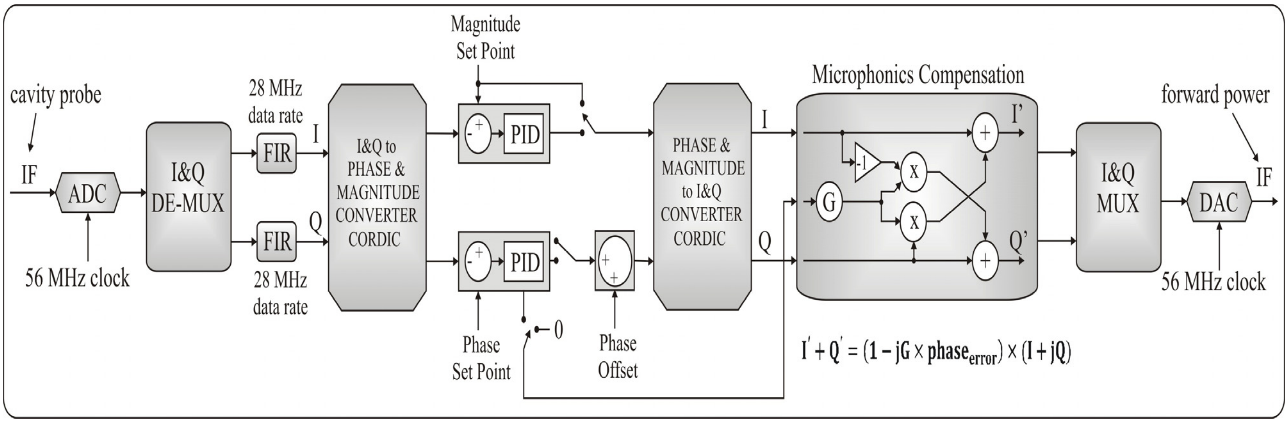


Figure 4: SEL algorithm logic block diagram.

Figure 6 shows the amplitude error of a digital receiver (14 bit) while controlling a superconducting cavity. In this case the receiver's S/N (Fig. 5.) has been improved by large over sampling (i.e. the receivers quantization noise has been improved by oversampling ~ $N^{1/2}$ ).

Cavity phase error largely depends on the reference jitter (phase noise), receiver components (mixer, amplifiers), the ADC aperture jitter, the PC board level clock/distribution, and loop gains [13, 14]. Therefore, the system needs to have a jitter budget from the master oscillator to the RF controller and ultimately to the beam. Clock circuitry and designing circuit boards to minimize sources of jitter is critical to meet the demands of light sources (< 0.1° residual phase noise). AM to PM contributions (component nonlinearities) can add to the phase uncertainty and some thought should be given to choosing linear receiver components. In addition, one can also use near quadrature sampling to improve the ADC linearity [15]

## *Digital Signal Processing*

With the conversion to all digital systems, signal processing becomes a large focus of the design. Modern digital communications has put filter, receiver designs, and DSP tricks at our finger tips. A typical front end receiver would consist of the I and Q muxing logic, followed by a digital filter such as a Cascaded-Integrator Comb (CIC) filter. Other filters and decimation may be added depending on the application. The feedback algorithm at this point is embedded in the process. Finally the output I and Q stream is demuxed and then applied to a DAC.

As simple as it sounds, it does require some thought. The latency between the ADC and DAC is really the only flexibility a designer has in the feedback. Sloppy, inefficient logic or poor filter choice can reduce the system stability by increased latency. Fortunately, FPGA tools can help synthesize and test the design.

Excitation of another cavity pass-band mode has always plagued RF control systems. In some cases the modes can be 1 MHz or less away from the accelerating mode. The made-to-order solution is a digital filter. One can potentially use creative ways of a digital filter's null to eliminate the need for a separate filter.

## *Resonance Control*

A subset of field control is the control of the cavities resonance frequency. In High $Q_L$ cavities, it is extremely important to keep the cavity near resonance (< ½ bandwidth). The RF system is optimized such that the power amplifier operates with a limited amount

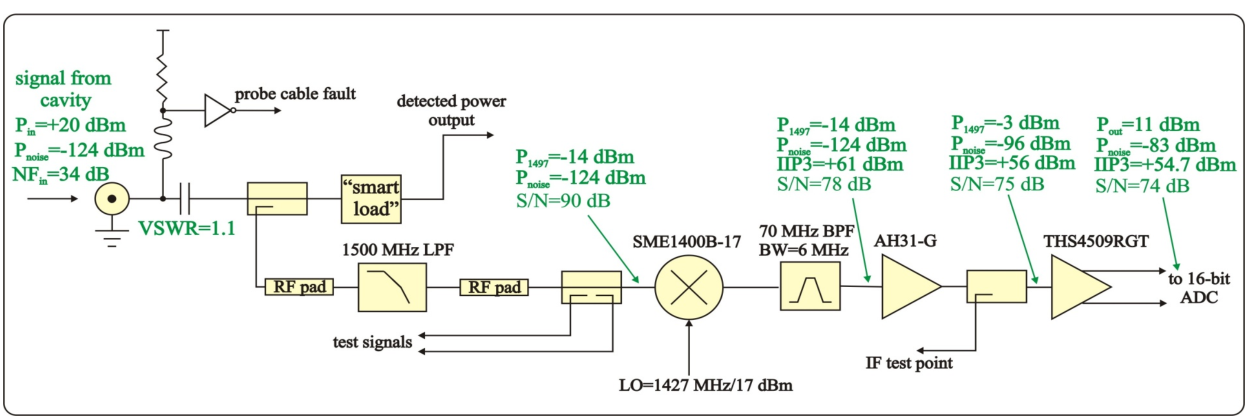


Figure 5: CEBAF upgrade receiver.

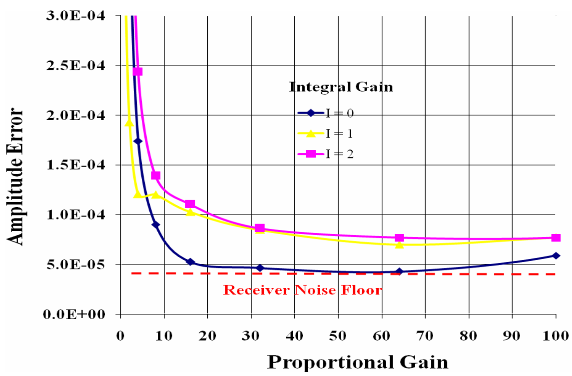


Figure 6: Measured amplitude error vs. proportional gain for a digital receiver (14 bit).

of control margin. In addition to the cw case, the pulsed (or during cavity recovery) system must account for Lorentz detuning. At the extreme, the detuning can be over 18 bandwidths between 0 and full gradient. For a pulsed accelerator to be practical, it needs a fast tuner to compensate for Lorentz detuning. Typically an accelerator will utilize both a slow and fast tuner. Some form (the actual mechanical mechanism can vary) of stepper motor is used. The CEBAF cryomodules have continuously used stepper motors for over 15 years with minimal down time. In this application, with $Q_L$'s ~ $6x10^6$ and average gradients around 7 MV/m, Lorentz effects on cavity recovery are small and can be handled by the klystron overhead.

For fast-finer control stepper motors are not adequate. For this, the accelerator community has turned to piezoelectric devices for tuning (PZT). The industrial utilization for Piezo devices is large, with many finding their way into fuel injectors and copiers/printers. PZT's were successfully demonstrated at DESY supporting the TESLA project [16]. In this application, the PZT was compensating the Lorentz detuning during each pulse. For the CEBAF upgrade, PZT's are intended to reduce detuning fluctuations due to He pressure in the cryo system. In addition to CEBAF, PZT's have been installed in the production cavities of the SNS [17] and are planned for the ILC and XFEL [11].

## SUMMARY

Operation of the next generation high $Q_L$ superconducting cavities will require precise RF control. The LLRF community has by in large answered this challenge using commercial solutions (modern digital receiver technology, Piezoelectric devices etc.) and novel methods (Digital Signal Processing) to meet the requirements. As more accelerators come on line, new control challenges, we are only now beginning to understand, such as ERLs with incomplete energy recovery [18] and light sources with tighter field control specifications, will have to be addressed. Given the flexibility of the digital RF systems, this will only be an increase in RF power and an algorithm change in the logic!

## ACKNOWLEDGEMENTS

The author wishes to thank Tomasz Plawski, John Musson, Trent Allison, Jean Delayen, Tom Powers and Brian Chase for many insightful discussions on the subject of RF control.

## REFERENCES

[1] L. Merminga, J. Delayen, "On the optimization of Qext under heavy beam loading and in the presence of microphonics", CEBAF-TN-96-022
[2] M. Liepe, et al, Proceedings of the 2005 Particle Accelerator Conference, Knoxville, USA
[3] K. Davis, T. Powers, "Microphonics Evaluation for the CEBAF Energy Upgrade", JLAB-TN-05-040
[4] D. Schulze, "Ponderomotive Stability of RF Resonators and Resonator Control Systems", KFK 1493, Karlsruhe (1971); ANL Translation ANL-TRANS-944 (1972).
[5] J. R. Delayen, "Phase and Amplitude Stabilization of Superconducting Resonators", Ph. D. Thesis, California Institute of Technology, 1978.
[6] T. Plawski, Proc.SPIE vol.7124, Wilga, Poland,
[7] A.S. Hofler et al, Proceedings of the 2004 Linear Accelerator Conference, Lubeck, Germany
[8] A. Neumann, et al, Proceedings of the 2004 European Particle Accelerator Conference, Lucerne, Switzerland.
[9] C. Hovater, et al, Proceedings of the 2007 Particle Accelerator Conference, Albuquerque NM, USA
[10] L. Doolittle, Proceedings of the 2007 Asian Particle Accelerator Conference, Indore, India
[11] S. Simrock, et al, Proceedings of the 2006 Linear Accelerator Conference, Knoxville, TN USA
[12] J. Musson, private conversations, musson@jlab.org
[13] F. Ludwig et al, Proceedings of the 2006 European Particle Accelerator Conference, Edinburgh
[14] U. Mavric and B. Chase, Microwave Journal, Vol. 51, No. 3, March 2008, page 94
[15] L. Doolittle et al, Proceedings of the 2006 Linear Accelerator Conference, Knoxville, TN, USA
[16] M. Liepe, et al, Proceedings of the 2001 Particle Accelerator Conference, Chicago, IL, USA
[17] K. Davis, J Delayen, Proceedings of the 2003 Particle Accelerator Conference, Portland USA
[18] T. Powers & C. Tennant, "Implications of Incomplete Energy Recovery in SRF-based Energy Recovery Linacs", JLAB-TN-07-069

# RF SYSTEMS FOR CW SRF LINACS

S. A. Belomestnykh, CLASSE, Ithaca, New York


## Abstract

The talk will provide an overview of the latest developments in rf systems for cw operated SRF linacs, such as CEBAF (in particular, 12 GeV Upgrade), Cornell ERL injector, ELBE, and ERLP at Daresbury.


**CONTRIBUTION NOT RECEIVED**

# OPERATIONAL EXPERIENCE WITH HIGH POWER BEAMS AT THE SNS SUPERCONDUCTING LINAC*

J. Galambos, on behalf of the SNS team, ORNL, Oak Ridge, TN, 37830, U.S.A.

*Abstract*

The Spallation Neutron Source (SNS) accelerator is in a period of rapid beam power ramp-up, with operation of over 0.5 MW achieved to date. SNS is the first high power proton pulsed superconducting linac (SCL), and has unique challenges. Beam tuning methods have been developed for setting the many independently powered SCL cavities, and recover from faults. The challenges and experience of minimizing beam loss at the high operational powers are also presented.

## INTRODUCTION

The Spallation Neutron Source provides a high power source of protons to drive a short pulsed spallation neutron source [1-5]. The beam acceleration is accomplished in a linac, with copper structures providing acceleration up to 186 MeV and superconducting RF structure providing acceleration to 1000 MeV. The linac design goal is a 1 msec long pulse of 26 mA average current provided at 60 Hz (~ 1.5 MW). This beam is injected into an accumulator ring and the pulse length compressed to ~ 1 μsec to provide a short pulse source of spallation neutrons. Many of the details of the power ramp-up over the last two years are provided in Ref [1-5]. Here we concentrate on the operational experience with beam of the Superconducting linac (SCL). Details of the operational experiences with the equipment are provided in Refs [6-7].

## POWER RAMPUP PROGRESS

To date the beam SCL has provided over 550 kW of production beam. Typical beam operating conditions at this power level are 60 Hz repetition rate, 18 (32) mA average (peak) current, 600 $\mu$sec pulse length and 890 MeV. For neutron production conditions, the beam energy is reduced to 890 MeV because of the SCL equipment issues discussed in Ref. 6, pulse length is limited by availability concerns for the High Voltage RF support systems, and peak current is limited by Ion Source capability and availability concerns. Figure 1 shows the history of the beam on Target power ramp-up (We note that the SCL beam power is ~ 5% higher than that provided on the neutron producing Target, because ~5% of the beam is lost at the Ring Injection.

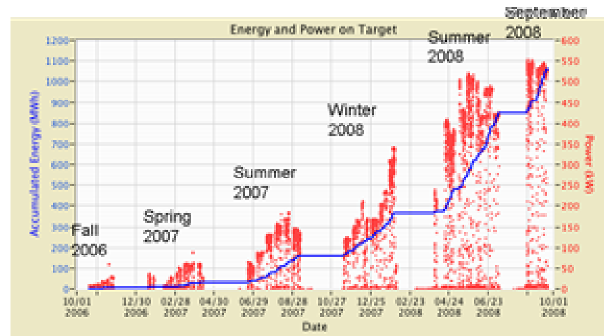


Figure 1. The beam on target power ramp-up progress since the start of neutron production at SNS.

## SCL RF SET-UP

One of the most striking features we have come to realize regarding the SCL operation with beam is its flexibility. The copper structures tend to be large, high power cavities (> 1 MW klystron power level), with many (~ 100) individual RF-gaps. For these large structures there is a significant change in the beam $\beta$, as well as significant phase advance of the beam bunch in longitudinal phase space. The copper cavity geometries are manufactured to match the expected energy gain and provide appropriate longitudinal focusing. Only one klystron RF phase and amplitude setting is correct. If one varies the phase and amplitude setting about the nominal set-point in the warm linac cavities, the resulting effect on the beam is complicated and each warm cavity has a unique output beam “response signature” [7]. Figure 2 shows the measured response of the beam Time-of-flight (TOF) downstream of the first Drift Tube Linac (DTL) tank in SNS, to perturbations in its phase and amplitude.

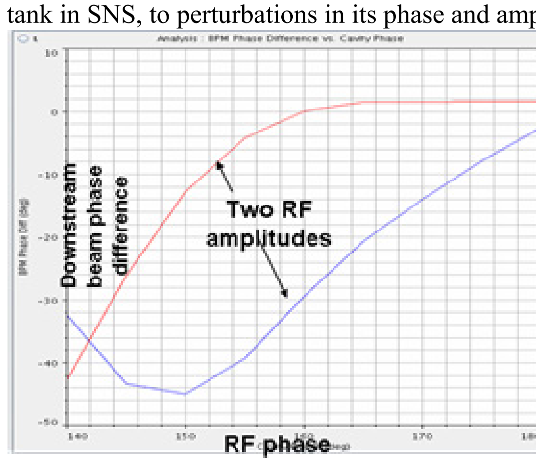


Figure 2. Measured change in the downstream beam velocity with changes to the RF phase and amplitude in the first DTL tank (Red is ~ 2 % below nominal amplitude; blue is ~ 2 % above).

* SNS is managed by UT-Battelle, LLC, under contract DE-AC05-00OR22725 for the U.S. Department of Energy

On the contrary, the SCL cavities are 6 cell elliptical cavities with independently controlled klystrons. The beam energy gain is ~ 10 MeV / cavity, for which the change in $\beta$ is small and also there is only a small longitudinal phase advance through each cavity. In this case, the beam response to the cavity is similar to that of an ideal RF gap. Figure 3 shows the measured response of the downstream beam TOF to the variation of the RF phase over a full 360 degrees. It is very similar to a sine-wave response as expected from an ideal RF-gap.

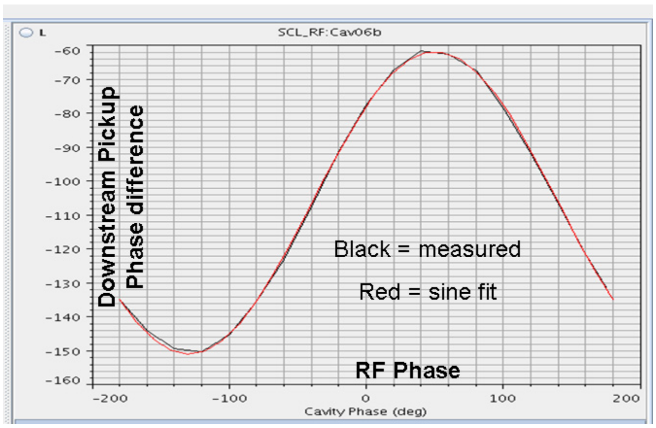


Figure 3. Response of the downstream beam TOF to a scan of the RF phase over 360 degrees.

This simple beam response to the RF set-up offers considerable flexibility. First, we tend to operate all our cavities at their maximum safe operating gradients, and only adjust the RF phase to the desired synchronous phase. Also it is simple to derive the input beam energy and calibrate the average cavity RF amplitude with this measurement [9].

Applying this scan technique to each cavity provides a measurement of the beam arrival time relative to the RF for each cavity (i.e. the synchronous phase setting for each cavity). This procedure takes 4-8 hours for the 75 SNS SCL cavities in use at present. If an upstream cavity phase and or amplitude is changed, the downstream cavity phases can change by 100's-1000's of degrees for the non fully relativistic SNS beam. However one can use a model to predict the change in downstream beam arrival time (or phase) to within a few degrees when an upstream cavity amplitude and/or phase is changed. Applying a model predicted perturbation to a beam based phase setpoint offers many possibilities. One can recover from a failed cavity without having to perform beam based measurements again. Also the technique can be used during beam studies to quickly test different longitudinal phase setupss. At SNS this scaling technique is is employed for multiple purposes. Figure 4 shows an example of the technique applied to resetting the RF phases of the SCL cavities when the operating temperature was changed from 4 to 2 K requiring change in almost ¼ of the cavity amplitude settings. The predicted RF phase settings changed by up to 2000 degrees (of 805 MHz RF cycles). Spot checks indicated the predicted phase changes to be accurate to within a few degrees. Beam loss – the primary indication of how well tuned RF systems are – is typically unchanged when applying this technique.

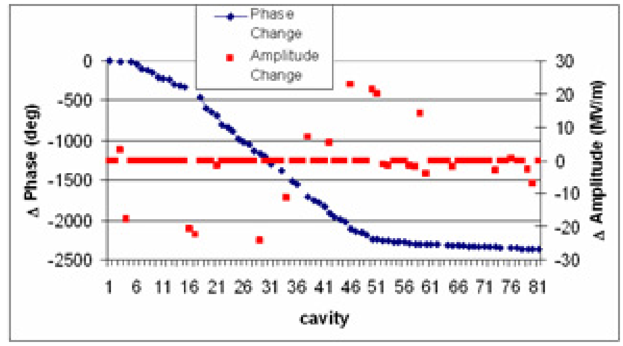


Figure 4. Change in the phase setpoints of the RF cavities (blue) resulting from changes in the cavity amplitudes (red).

The phase scaling techniques is also used in beam studies. One example is the beam acceptance measurement technique [12]. Figure 5 shows the longitudinal acceptance for the SNS linac, for two perturbations on the production setup. The linac beam emittance is much smaller than the area shown in Fig. 5. The phase scaling technique has been used to enable a raster scheme of the input beam across the longitudinal phase space. By measuring the beam transmission with downstream current toroids (or measuring beam loss with loss monitors) throughout this raster it is possible to experimentally measure the acceptance. An example of this is shown in figure 6 (taken from Ref. 12). Also use of the phase scaling techniques permits rapid testing of different RF setups, without having to perform beam based measurements for each cavity. Foe instance we have tried many different variants of constant focusing (adjusting the synchronous phase $\phi_s$, so that the product $E_0 \sin\phi_s$ is constant) and constant $\phi_s$ RF setups.

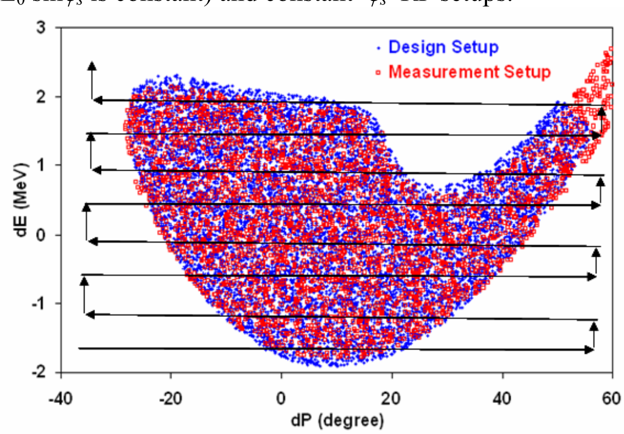


Figure 5. Model predicted longitudinal acceptance for the SNS SCL (taken from Ref. 12) with a superimposed path for rastering the input linac beam for experimental measurement.

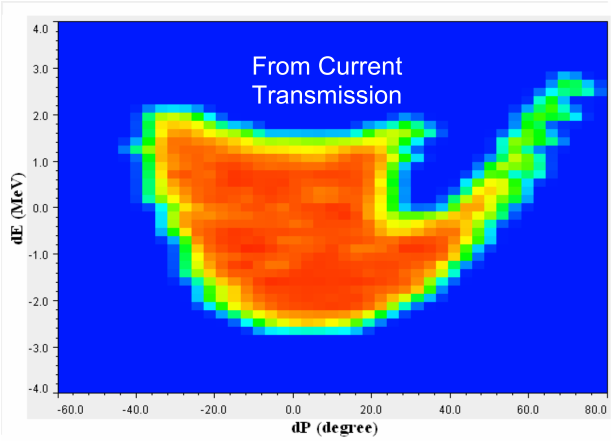


Figure 6. Measurement of the SNS SCL longitudinal acceptance using current transmission, taken from Ref. 12.

## BEAM LOSS

The SNS is expected to be a beam loss limited machine. The design basis is 1 W/m for uncontrolled beam loss, which is predicted to result in about 100 mrem/hr at 30 cm 4 hours after shutdown, and years of operation. This criteria was taken as a rough rule-of-thumb for hands-on-maintenance without significant dose to the workers. However, in the SCL region, losses were expected to be lower, due in large part to the large aperture associated with the SCL technology [13]. As the beam power exceeded about 50 kW, un-expected residual activation in the warm sections between the SCL cryomodules began to be measured after beam production. Subsequent movement of the loss monitors to within ~ 10 cm of the beam pipe in the warm sections verified measureable beam loss.

The magnitude of the beam loss appears to be small. We have performed controlled beam spills of small amounts of beam throughout the SCL to calibrate the loss monitors. Localizing the beam loss is difficult, resulting in large variability along the SCL for the calibrations (factors of $\pm$ 3 in our medium beta cavities (below 450 MeV) and factors of $\pm$ 2 in the high beta cavities). We estimate an upper bound of about $2\times10^{-6}$ fractional beam loss per warm section. The present warm section residual activation one day following a neutron production run is 10-60 mrem/hr at 30 cm. These values are consistent with < 1 W/m (or $< 2\times10^{-6}$ for the 500 kW power level). Measuring and modeling beam effects at this level are challenging. Presently, the beam loss monitor system is the only instrument sensitive enough to measure fractional beam at this level. To date the SCL residual activation has not significantly contributed to worked dose, nor is it expected to cause pre-mature end of component life [7].

Figure 7a shows the history of the buildup of the measured SCL warm-section activation following production runs of 1-2 weeks over the past year. There is some variability in the time between end of production and radiation surveys, with this time delay varying between one and two days. Also indicated are the beam power levels during these periods. The power is generally increased with time during each production run. There tends to be a saturation of the activation levels each run, despite the increase in operational beam power. Figure 7b shows the residual activation levels taken just downstream from the Ring injection foil (hottest region in the SNS which was expected and designed to have high beam loss). The Ring Injection area activation levels do not show the saturation. Beam pipe for both the SCL warm section and Ring Injection use 304 stain-less steel. Also we note that the SCL activation is much less than the Ring Injection (which is expected to be a high loss area).

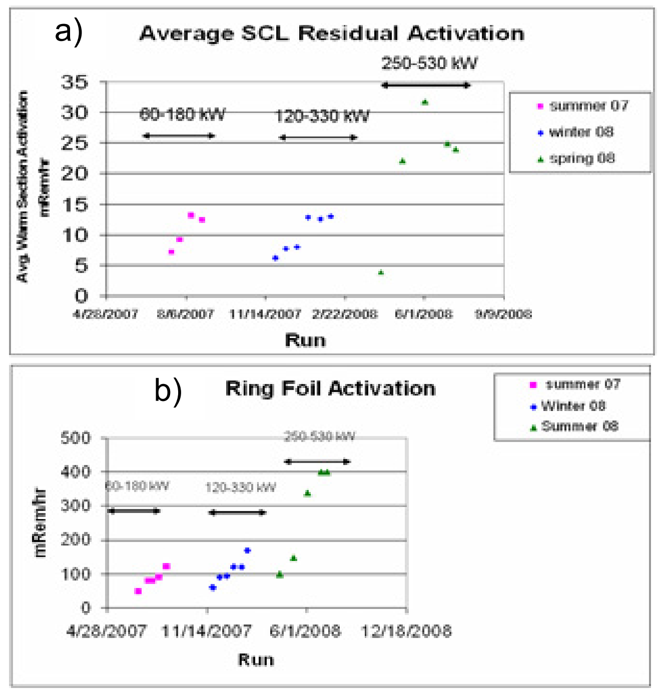


Figure 7. Buildup of the residual activation levels after production runs during the past year of power ramp-up for a) the average of all SCL warm sections, and b) the region downstream of the Ring injection foil.

At present the cause of the beam loss in the SCL is not well understood. Some of the sensitivities that have been experimentally addressed indicate that the loss is:

- Sensitive to upstream warm linac RF set-up
- Insensitive to the SCL matching quadrupole settings
- Insensitive to the SCL longitudinal tune scheme (constant phase or constant focusing)
- Sensitive to 5 mm upstream local trajectory bumps
- Insensitive to increase in the CCL background gas pressure.

## SUMMARY

The SNS SCL operational beam power has increased from a few kW to over 500 kW during the first two years of operation. The many independently powered cavities that comprise the SCL offer a flexible operational setup. A model based phase scaling method has been developed that facilitates quick adjustments of the RF phase settings for upstream cavity changes. This scheme is useful to quickly adapt to failed cavities as well as performing beam studies. There is also a low level (< 1 W/m) of beam loss in the SCL warm sections between cryo-modules, which is unexpected but not limiting beam power. The source of the loss is not understood.

## REFERENCES


[1] S. Henderson, “Spallation Neutron Source Progress, Challenges and Power Upgrade Paths”, Proceedings of EPAC08, Genoa, Italy, http://accelconf.web.cern.ch/AccelConf/e08/papers/thxg01.pdf .

[2] S. Henderson, “Status of the Spallation Neutron Source: Machine And Science”, Proceedings of PAC07, Albuquerque, New Mexico, USA, http://accelconf.web.cern.ch/AccelConf/p07/PAPERS/MOXKI03.PDF .

[3] S. Henderson, “Commissioning and Initial Operational Experience with the SNS 1 GeV Linac” , Proceedings of LINAC 2006, Knoxville, Tennessee USA, http://accelconf.web.cern.ch/AccelConf/l06/PAPERS/MO1002.PDF .

[4] A. Aleksandrov, S. Assadi, W. Blokland, P. Chu, S. Cousineau, V. Danilov, C. Deibele, J. Galambos, D. Jeon, S. Henderson, M. Plum, A. Shishlo, “SNS Warm Linac Commissioning Results”, Proceedings of EPAC 2006, Edinburgh, Scotland, http://accelconf.web.cern.ch/AccelConf/e06/PAPERS/MOPCH127.PDF .

[5] M.A. Plum, A.V. Aleksandrov, S. Assadi, W. Blokland, I. Campisi, C.P. Chu, S.M. Cousineau, V.V. Danilov, C. Deibele, G.W. Dodson, J. Galambos, M. Giannella, S. Henderson, J.A. Holmes, D. Jeon, S. Kim, C. Long, T. Pelaia, T. Shea, A.P. Shishlo, Y. Zhang, “SNS Ring Commissioning Results”, Proceedings of EPAC 2006, Edinburgh, Scotland, http://accelconf.web.cern.ch/AccelConf/e06/PAPERS/MOPCH131.PDF

[6] S. Kim et. al, these proceedings.

[7] J. Mammosser et.al., these proceedings.

[8] J. Galambos, a. Aleksandrov, C. Deibele, S. Henderson, “PASTA – An RF Phase Scan and Tuning Application”, , Proceedings of 2005 Particle Accelerator Conference, Knoxville, Tennessee, http://accelconf.web.cern.ch/AccelConf/p05/PAPERS/FPAT016.PDF

[9] J. Galambos, et. al., “Software Tools for Commissioning the SNS Linac”, Proceedings of PAC07, Albuquerque, New Mexico, USA , http://accelconf.web.cern.ch/AccelConf/p07/PAPERS/TUOCC01.PDF .

[10] J. Galambos, S. Henderson, A. Shishlo, Y. Zhang, „ A Fault Recovery System for the SNS SCL Linac”, Proceedings of LINAC 2006, Knoxville, Tennessee USA http://accelconf.web.cern.ch/AccelConf/l06/PAPERS/MOP057.PDF

[11] J. Galambos, S. Henderson, A. Shishlo, Y. Zhang, Proceedings Utilization and Reliability HPPA, (2007)

[12] Y. Zhang, J. Galambos, A. Shishlo, “ Measurement of Longitudinal Acceptance and Emittance of the Spallation Neutron Source Superconducting Linac”, Accepted for publication, Phys. Rev. Special Topics – Accelerators and Beams.

[13] N.Catalan-Lasheras (Editor) “Expected beam losses along the SNS accelerator facility during normal operation” , Internal SNS Report, SNS-AP17, 2001, http://neutrons.ornl.gov/APGroup/Papers/TechNotes/2001/losspattern.pdf


.

# FERMILAB'S PROJECT X

S. Nagaitsev, Fermilab, Batavia


## Abstract

The present status and plans for Fermilab's Project X will be reviewed.


**CONTRIBUTION NOT RECEIVED**

# IH-DTL AS A COMPACT INJECTOR FOR A HEAVY-ION MEDICAL SYNCHROTRON

Y. Iwata*, T. Fujisawa, S. Hojo, N. Miyahara, T. Murakami, M. Muramatsu,
H. Ogawa, Y. Sakamoto, S. Yamada, and K. Yamamoto,
NIRS, 4-9-1 Anagawa, Inage, Chiba 263-8555, Japan
T. Fujimoto and T. Takeuchi, AEC, 2-13-1 Konakadai, Inage, Chiba 263-0043, Japan.
T. Mitsumoto, H. Tsutsui, T. Ueda, and T. Watanabe, Sumitomo Heavy Industries (SHI), Ltd.,
1-1, Osaki 2-Chome, Shinagawa, Tokyo 141-6025, Japan

*Abstract*

Compact linacs, consisted of a Radio-Frequency-Quadrupole (RFQ) linac and an Interdigital H-mode Drift-Tube-Linac (IH-DTL) having the same operating frequency of 200 MHz, were designed for an injector of heavy-ion medical synchrotrons. For beam focusing of IH-DTL, the method of Alternating-Phase-Focusing (APF) was applied. The total length of the RFQ linac and the IH-DTL is as short as 6 m. With the two linacs, carbon ions of $^{12}C^{4+}$, produced by an ECR Ion-Source (ECRIS), are accelerated to 4.0 MeV/$u$ with the beam intensity of 380 eμA. The compact linacs were constructed and installed in NIRS. We have succeeded to accelerate carbon ions with the APF linac for the first time.

## INTRODUCTION

With development of accelerator physics and technology, number of compact linear accelerators as well as cyclotrons has been constructed around the world, and is utilized for medical and industrial applications. At the National Institute of Radiological Sciences (NIRS), cancer therapy using energetic carbon ions, as provided by the Heavy Ion Medical Accelerator in Chiba (HIMAC), has been carried out since June 1994 [1], and more than 4,000 patients have been treated until now. With the successful clinical results, projects of constructing these accelerator complexes, dedicated to the cancer therapy, are initiated over the world. To construct such the complex, construction costs as well as a size of the complex itself are issue, because existing complexes are costly and large in size. Therefore, the development of cost-effective and compact accelerators for a hospital-based complex is needed for the increased use of the heavy-ion therapy.

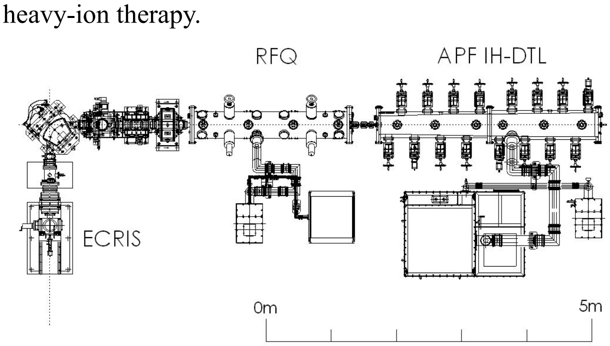


Figure 1: A schematic drawing of the compact injector.

* y_iwata@nirs.go.jp

In the development of the hospital-based accelerator complex, the design of an injector plays a key role, because the existing heavy-ion linacs such as Alvarez linacs are quite large. The size of the injector would affect the total size of the complex as well as total costs of construction. Therefore, we developed the compact injector for the heavy-ion medical synchrotrons.

The compact injector consists of the ECRIS and two linacs, which are the RFQ linac and the IH-DTL having the same operating frequency of 200 MHz. A schematic drawing and major parameters of the compact injector are shown in Figure 1 and Table 1, respectively. In this paper, design as well as performance of the compact injector is described.

Table 1: Major Parameters of the Compact Linacs

| Parameters | RFQ | IH-DTL | Units |
|---|---|---|---|
| Injection energy | 0.01 | 0.61 | MeV/$u$ |
| Extraction energy | 0.61 | 4.0 | MeV/$u$ |
| Operating frequency | 200 | 200 | MHz |
| q/m | 1/3 | 1/3 | - |
| Cavity length | 2.5 | 3.4 | m |
| Cavity outer diameter | 0.42 | 0.44 | m |

## DESIGN OF LINACS

### *Beam Dynamics*

Beam optics of the RFQ linac was designed by using the PARMTEQ code. By optimizing cell parameters for acceleration of $^{12}C^{4+}$, and using the rather high operating-frequency of 200 MHz, we could design the compact cavity; length and outer diameter of the cavity are 2.5 m and 0.42 m, respectively. The RFQ linac can accelerate carbon ions of $^{12}C^{4+}$ having 10 keV/$u$, as produced with the ECRIS, up to 608 keV/$u$. The normalized emittance of the extracted beam from the RFQ linac was calculated to be 0.68 π•mm•mrad.

Carbon ions, as extracted from the RFQ linac, are then accelerated with the IH-DTL up to 4.0 MeV/u. For beam focusing of the IH-DTL, the method of APF was applied [2]. This method utilizes the focusing and defocusing strengths as provided by the rf acceleration field by choosing the positive and negative synchronous phases alternately at each gap. By analogy with the principle of strong focusing, both longitudinal and transverse stability of beam motion could be obtained just with the rf acceleration field. By using this method, no additional focusing elements has to be installed in the cavity, making the cavity structure significantly simple as well as cost-effective. This also indicates that drift tubes can be designed smaller and shorter, and therefore allowed us to employ higher operating-frequency and lower injection-energy than ever before with conventional DTLs. Although the APF linacs have such the attractive features, it has never been practically used since it was first proposed in 50s, because the design of the synchronous phases is quite difficult, and focusing strengths of the rf field are generally weak.

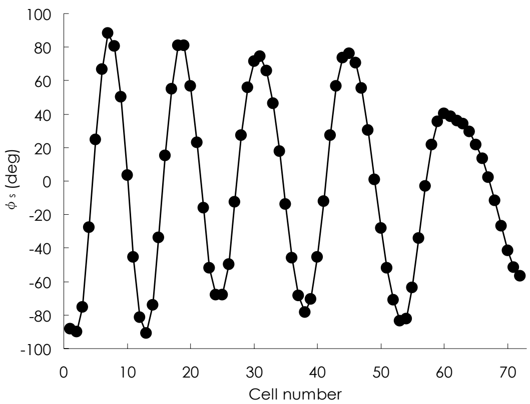


Figure 2: Synchronous phase as a function of the cell number.

Since the stability of beam motion for the APF linac relies only on the rf acceleration field, the entire characteristic of the beam dynamics depends strongly on a choice of the synchronous phase at each gap. Therefore, a major effort was devoted to optimize the phase array. By using a sinusoidal-like function to describe the phase array, as given in Figure 2, and performing beam dynamics simulations iteratively, we succeeded to optimize the phase array [3]. The calculated transmission was reached to as high as 99.6%. Parameters, calculated for the APF IH-DTL, are summarized in Table 2.

### *Cavity*

The RFQ linac has a conventional four-vane structure. Since the technology of this structure is well-established, no special R&D work had to be done, and the design of the cavity was made with the well-known Superfish code.

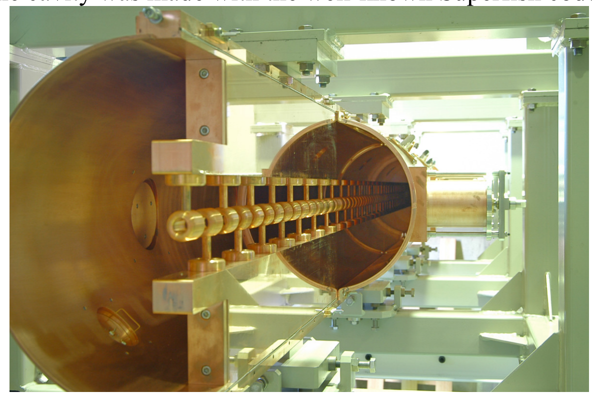

Figure 3: A picture of the model cavity (view from the downstream).

Table 2: Parameter Calculated for the APF IH-DTL

| Parameters | Valu | Units |
|---|---|---|
| Number of unit cell | 72 | - |
| Trans. 90% emittance of injected beam (normalized) | 0.68 | π•mm•mrad |
| Trans. 90% emittance of extracted beam (normalized) | 0.80 | π•mm•mrad |
| Long. 90% emittance of injected beam | 1.3 | π•keV/*u* •ns |
| Long. 90% emittance of extracted beam | 1.6 | π•keV/*u* •ns |
| Momentum spread | ±0.1 | % |
| Transmission | 99.6 | % |

For the APF IH-DTL, the IH structure was employed. The IH structure, which was first proposed in the 1950s, was known to provide high shunt impedance, and thus the rf power consumption would be significantly lower than that of Alvarez linacs at the energy range up to 10 MeV/*u* [4]. However, development of this structure was delayed against that of the Alvarez linacs, because the electric-field distribution could not be calculated precisely with existing two-dimensional electromagnetic-field solvers.

With the advent of three-dimensional field solvers, it became possible to calculate the electromagnetic field in the IH cavity. Although these solvers have recently been applied to design the cavities of linacs, the accuracy of the

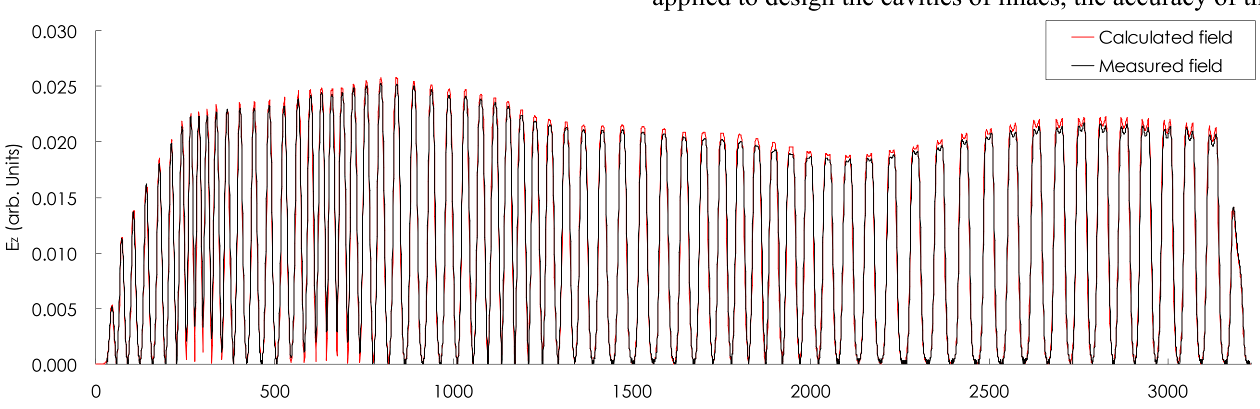


Figure 4: Electric field along the beam axis as functions of the beam coordinate, *Z*, for the model cavity. The black and red curves show the measured and calculated electric field with MWS, respectively.

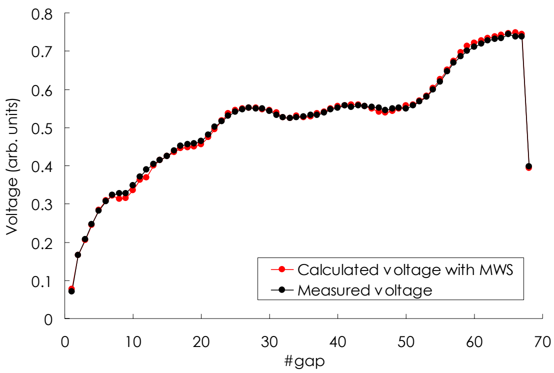


Figure 5: Gap voltages along the beam axis as functions of the gap number for the model cavity. The black and red dots show the measured and calculated gap-voltages, respectively.

solvers was not confirmed. Therefore, we constructed a full-scale model cavity of the APF IH-DTL, and compared its electric-field distribution with calculations.

A picture of the model cavity is presented in Figure 3. The length of the cavity is approximately 3.2 m, and the 67 drift tubes are installed on the upper and lower ridges. The cavity has four sections with different diameters to obtain a uniform electric field over the entire cavity. Fine adjustment of the electric field can be made with 15 inductive tuners, installed on the side wall, and end-ridge-cuts. All the cavity components were made with deoxidized copper.

The electromagnetic field of the model cavity was calculated with the three-dimensional solver, Micro Wave Studio (MWS) [5]. The calculated field is shown by the red curve in Figure 4. We see that the calculated distribution was rather uniform, although the field intensity around the first few gaps is lower than those for the rest of them.

The electric-field distribution along the center of the beam axis was measured using the perturbation method, and fine adjustments of the electric-field distribution with the tuners were made so as to reproduce the calculated field distribution. The measured field after the fine adjustments is shown by the black curve in Figure 4. We found that the measured field distribution agreed well with the calculated field with MWS.

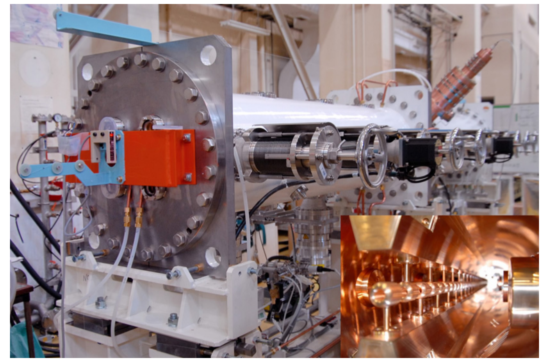

Figure 6: A picture of the APF IH-DTL during turning of the electric-field distribution in the cavity.

Having integrated the measured and calculated electric-field distributions, we could obtain the gap-voltage distributions as shown by the black and red dots in Figure 5, respectively. The overall voltages agreed with those calculated within an accuracy of ±2%. With these results of the comparisons, we concluded that the three-dimensional field solver would provide the sufficient accuracy in the calculated electric field.

The essential design of the model cavity was adopted to that for the cavity of the APF IH-DTL, although shapes of the drift tubes, ridges and structure of the tank were refined so as to accept the rf power for the acceleration of $^{12}C^{4+}$. To further obtain a uniform electric-field over the cavity, the inner diameter was designed to vary smoothly from 282.5 mm to 364.0 mm. Fine adjustments of the electric field were made with the 16 inductive tuners and the end-ridge-cuts as used in the model cavity.

A picture of the APF IH-DTL is shown in Figure 6. The electric-field distribution was measured with the perturbation method, and finely adjusted with the tuners so as to reproduce the designed electric-field distribution, which was calculated with MWS and used in the beam dynamics simulations as described previously. The measured and designed electric-field distributions are shown by the black and red curves in Figure 7, respectively. We see that the electric-field distributions are quite uniform as compared with that for the model cavity, because of the smooth change in the inner diameter. The measured and designed gap-voltage distributions, as calculated by integrating the electric-field, are shown by

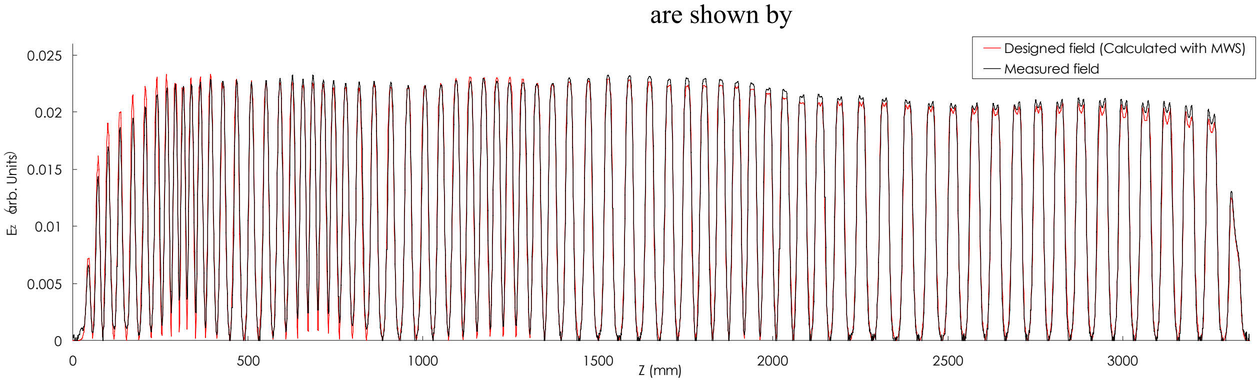


Figure 7: Electric field along the beam axis as functions of the beam coordinate, $Z$ for the APF IH-DTL. The black and red curves show the measured and designed electric field, respectively. The designed field was calculated with MWS.

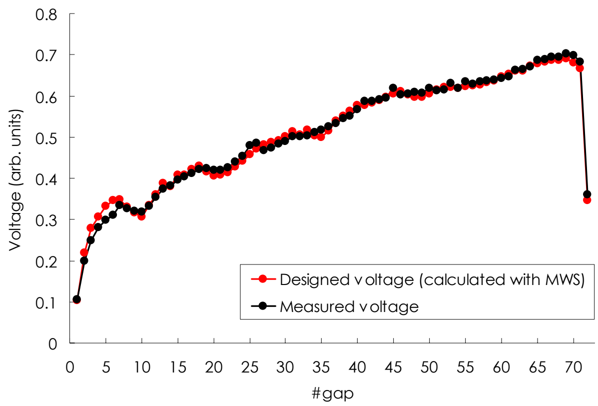


Figure 8: Gap voltages along the beam axis as functions of the gap number for the APF IH-DTL. The black and red dots show the measured and designed voltage, respectively.

the black and red dots in Figure 8, respectively. Although the measured and designed voltages around the first few gaps differ by 10%, most of the gap voltages were tuned to the designed voltages within a tolerable accuracy.

The quality factor of the cavity after the tuning of the electric-field distribution was measured to be $Q_m$=12,000, corresponding to 80% of the calculated value with MWS, $Q_c$=15,000 Considering the measured quality factor, the required rf power was estimated to be approximately 360 kW. The effective shunt-impedance was calculated to be 110 MΩ/m, which is remarkably higher than those of conventional linacs.

## BEAM ACCELERATION TESTS

### *ECRIS and RFQ Linac*

Prior to complete the entire compact-injector system, a beam acceleration test with the ECRIS and RFQ linac was made. The ECRIS and the RFQ linac were installed with the low-energy beam-transport (LEBT) line. To determine characteristics of the accelerated beam from the RFQ linac, a beam analyzing line, consisting of beam-transport and diagnostic devices, was placed downstream of the RFQ linac. In the test, the beam currents were initially measured with Faraday cups, FCN1 and FCN2, which located upstream and downstream of the RFQ linac, respectively. The measured currents of $^{12}C^{4+}$ with each cups were $I_{FCN1}$=412 eμA and $I_{FCN2}$=334 eμA. The corresponding transmission through the RFQ linac was

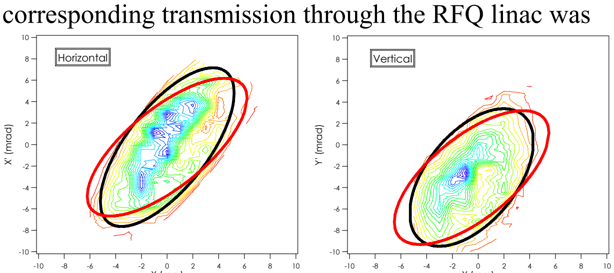


Figure 9: Contour plots show the horizontal and vertical phase-space distribution of a carbon beam from the RFQ linac (see text).

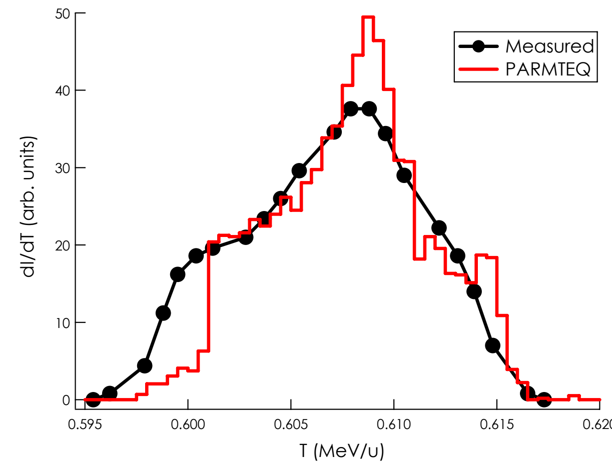


Figure 10: Kinetic energy distributions of a carbon beam from the RFQ linac. The filled dots and histogram show the results of the measurement and a PARMTEQ calculation, respectively.

estimated to be $\tau_{RFQ}= I_{FCN2}/ I_{FCN1}$=81%. Transverse phase-space distributions of the accelerated beam were measured using emittance monitors, installed in the beam analyzing line. The results are shown by the contour plots in Figure 9. The normalized values of horizontal and vertical 90% emittances were determined by fitting the distributions with an ellipse to be 1.02 and 0.954 π•mm•mrad, respectively, which are larger by 30% than those calculated with the PARMTEQ code. For a direct comparison, the calculated distributions showing the 90% emittance are also plotted by the red curves in Figure 9.

The accelerated beam was analyzed, and a kinetic-energy distribution was determined as shown in Figure 10. The result of the PARMTEQ calculation is also plotted by the histogram in the figure. The average energy was calculated with the measured distribution being $\langle E \rangle$=608.1 MeV/$u$, which is in good agreement with the designed value.

### *Entire Compact-Injector System*

Finally, the APF IH-DTL was installed downstream of the RFQ linac to perform the beam acceleration test of the entire compact-injector system. The beam analyzing line was realigned downstream of the APF IH-DTL. The beam current of $^{12}C^{4+}$ having 4.0 MeV/$u$ as accelerated with the APF IH-DTL was measured to be 380 eμA. With the known transmission of the RFQ linac, $\tau_{RFQ}$~81%, and

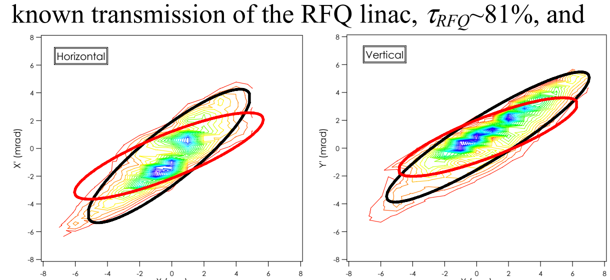


Figure 11: Contour plots show the horizontal and vertical phase-space distribution of a carbon beam from the APF IH-DTL (see text).

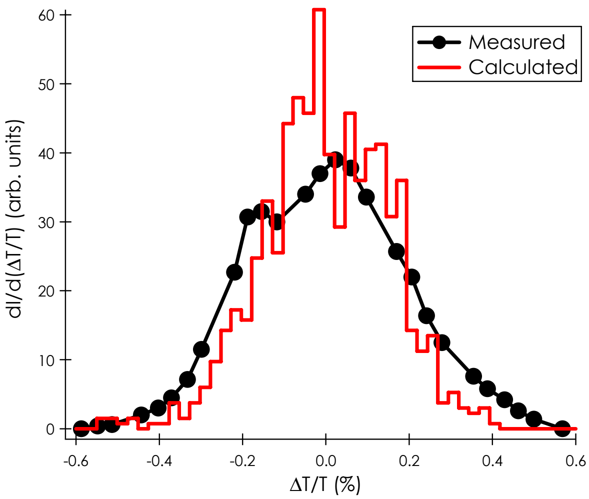


Figure 12: $\Delta T/T$ distributions of a carbon beam from the APF-IH-DTL. The filled dots and histogram show the result of the measurement and a tracking simulation, respectively.

measured current of the ECRIS during the test, $I_{FCN1}$=490 eμA, the transmission through the APF IH-DTL was estimated to be $\tau_{IH}$=380/($I_{FCN1}\times\tau_{RFQ}$ )~96%, which is comparable with the calculated value of 99.6%.

The phase-space distributions were measured as shown by the contour plots in Figure 11. For a comparison, the calculated distributions showing the 90% emittance are also plotted by the red curves in Figure 11. The normalized values of the horizontal and vertical 90% emittances were estimated to be 1.09 and 1.11 π•mm•mrad, respectively, which are larger than the calculated values; this might be attributed to the small emittance of the injected beam, as used in the calculation.

A kinetic energy distribution was measured, and the average energy was determined to be $\langle E\rangle$=4.000 MeV/$u$, which was slightly lower than the calculated energy of 4.029 MeV/$u$. However, as seen in the measured and calculated $\Delta T/T$ distributions, plotted in Figure 12, the measured energy spread of $\Delta T/T=\pm 0.4\%$ is comparable to that calculated with the simulation.

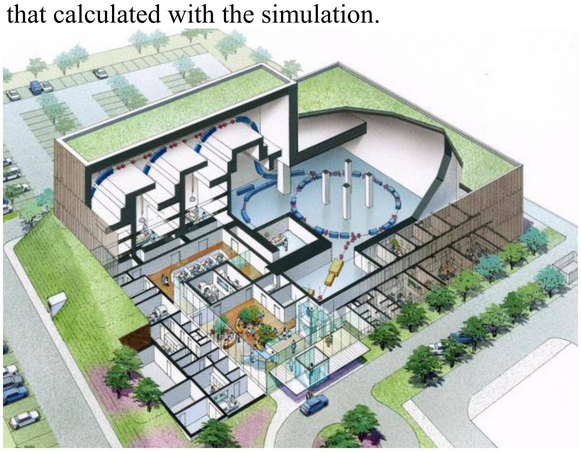

Figure 13: A schematic drawing of the compact therapy complex for the Gunma University.

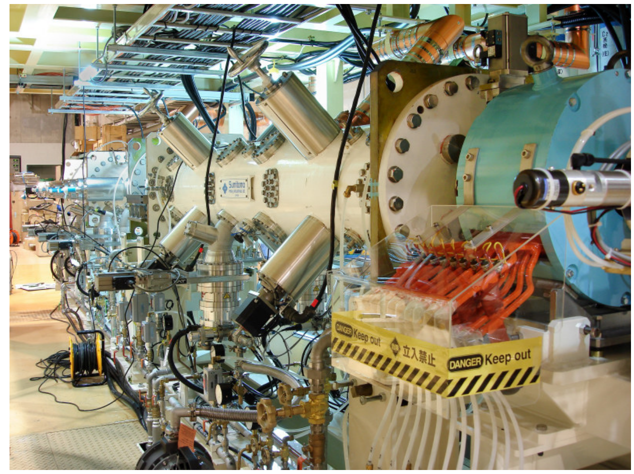

Figure 14: A picture of the compact injector system, as installed in the injector room of the HIMAC.

## PRESENT AND FUTURE PLAN

With these successful results of the beam acceleration tests, the design of the compact accelerator complex for the heavy-ion therapy had been completed, and the construction of the first compact complex started at the Gunma University. As shown in Figure 13, the compact complex consists of the injector, synchrotron ring and three treatment rooms. The design of the injector is identical to that, described here. Installation of the injector was completed, and we expect to have a first beam on the treatment rooms in next autumn.

Our compact injector was reinstalled in the injector room of the existing HIMAC complex, and will be used as a second injector. To provide carbon beams for the HIMAC synchrotrons, we are currently constructing a beam transport-line downstream of the APF IH-DTL.

## SUMMARY

The compact injector, consisting of ECRIS and two linacs, which are the RFQ and the APF IH-DTL, was designed and constructed. The acceleration tests were performed, and we have succeeded to accelerate carbon ions with the APF linac for the first time. The results of the tests demonstrated its excellent performance.

The total length of the two linacs was reduced to approximately 6 m, which is considerably shorter than that of the existing heavy-ion linacs. With this successful result, the construction of the first compact therapy complex had started at the Gunma University.

## REFERENCES


[1] Y. Hirao *et al.*, Ann. Rep. HIMAC, NIRS-M-89/HIMAC-001 (1992).

[2] M. L. Good, Phys. Rev. **92** (1953) 538.

[3] Y. Iwata *et al.*, Nucl. Instrum. and Meth. in Phys. Res. A **569** (2006) 685.

[4] J.P. Blewett, CERN Symposium (1956) 159.

[5] Computer Simulation Technology (CST), Micro Wave Studio Version 5. http://www.cst.de/.

# COMMISSIONING AND OPERATION OF THE INJECTOR LINACS FOR HIT AND CNAO

B. Schlitt, GSI, Darmstadt, Germany

The Heidelberg Ion-Beam Therapy Centre (HIT) is the first dedicated clinical synchrotron facility for cancer therapy using high energy proton and ion beams (C, He, and O) in Europe. The accelerator consists of a 7 MeV/u, 217 MHz injector linac and of a 430 MeV/u synchrotron. Installation and commissioning of the linac were performed in three phases for ion sources and LEBT, 400 keV/u RFQ, and 20 MV IH-type drift tube linac. The initial commissioning of the linac was finished successfully in December 2006, the commissioning of the synchrotron and the high energy beam lines was finished for both fixed-beam treatment places in December 2007. HIT intends to be ready for patient treatments by the end of 2008. The results of the linac commissioning are reported as well as the experience of more than one year of operation. To provide optimum conditions for patient treatment, an intensity upgrade program has been initiated for the linac. A copy of the HIT linac is presently being installed at the Centro Nazionale di Adroterapia Oncologica (CNAO) in Pavia, Italy. The status of the CNAO linac is also reported.

## INTRODUCTION

The number of accelerator facilities dedicated to radiation therapy using high energy proton and heavy-ion beams – also called hadrontherapy – is remarkably growing during the last years [1]. Since the first dedicated clinical centres started operation in Loma Linda, California, and at HIMAC / NIRS in Chiba, Japan, a number of technical improvements have been developed, namely raster-scanning techniques as well as compact synchrotron facilities for heavy-ion treatment and heavy-ion gantries. Also the role of industry has changed and turnkey hadrontherapy facilities are now offered by a number of commercial companies, e.g. IBA, HITACHI [2], ACCEL / VARIAN, or SIEMENS / DANFYSIK [3]. In particular for heavy-ion synchrotron facilities, size and

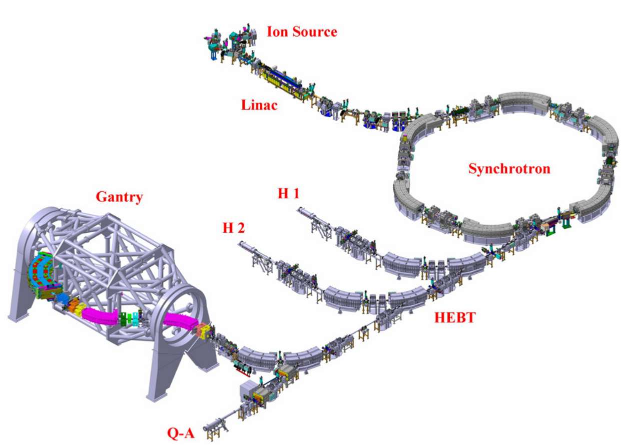


Figure 1: Layout of the HIT accelerator facility.

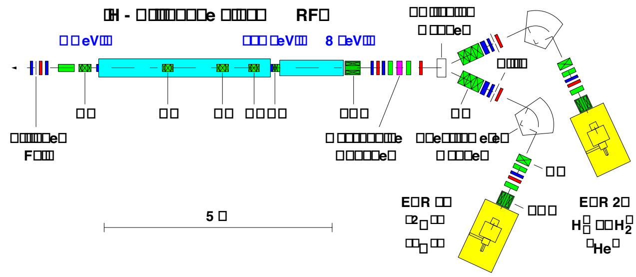


Figure 2: Layout of the HIT injector linac. QS, QD, and QT means quadrupole singulet, doublet and triplet, respectively, SOL means solenoid magnet; focusing and steering magnets (green), profile grids and viewing screens (red), and beam current monitors (blue).

Table 1: Main design parameters at the HIT linac exit

| | |
|---|---|
| Design ion | $^{12}C^{4+}$ |
| Operating frequency | 216.816 MHz |
| Final beam energy | 7 MeV/u |
| Beam pulse length | ≤ 300 µs |
| Beam repetition rate | ≤ 5 Hz |
| Pulse current after stripping | 100 µA ($^{12}C^{6+}$) |
| Transv. norm. emittances (95 %) [1] | 0.8 π mm mrad |
| Exit energy spread [1] | ±0.3 % |
| Total injector length [2] | ≈ 13 m |

[1] straggling effects in the stripper foil not included
[2] including ECRIS, LEBT and foil stripper

availability of suitable injector linacs are of major technical and economical interests. Whereas compact injector linacs are commercially available for proton synchrotron facilities [2], new compact heavy-ion injectors based on IH linacs have been developed at NIRS [4][5] and at GSI (in close collaboration with the Institute of Applied Physics (IAP) at Frankfurt University) [6][7][8] during the last ten years.

In Europe, two clinical heavy-ion facilities are currently being commissioned: the Heidelberg Ion-Beam Therapy Centre (HIT) [9][10] in Germany and the Centro Nazionale di Adroterapia Oncologica (CNAO) [11][12] in Pavia, Italy. An additional centre is being constructed by SIEMENS / DANFYSIK [3] in Marburg, Germany. All three centres will use the GSI linac design.

The HIT accelerator facility is shown in Fig. 1. It consists of two all permanent magnet ECR ion sources (ECRIS) of the SUPERNANOGAN type, a 7 MeV/u linac injector, and a compact synchrotron of about 65 m circumference to accelerate ions to final energies of 48 – 430 MeV/u. The beam is distributed by the high energy beam transport lines (HEBT) either to two fixed horizontal beam treatment places (H1, H2), to the isocentric heavy-ion gantry, or to a fixed horizontal beam quality-assurance place (QA) for dosimetry as well as

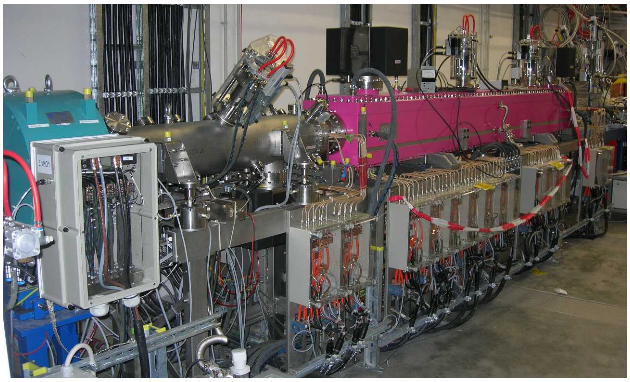

Figure 3: The HIT linac with solenoid magnet (left), RFQ, and IH linac during commissioning.

R&D activities. All four target stations are equipped with active raster-scanning beam delivery systems.

The linac injector (Fig. 2) comprises the ion sources, the low energy beam transfer lines (LEBT), a 400 keV/u Radio Frequency Quadrupole (RFQ) accelerator [13][14], and a 20 MV IH-type Drift Tube Linac (IH-DTL) [6][15][16][17]. Both, RFQ and IH-DTL, are operated at 216.8 MHz. Remaining electrons are stripped off the ions in a thin stripper foil behind the linac. Table 1 gives the design parameters for carbon ion beams, Fig. 3 shows the HIT linac. The linac (RFQ, intertank section, IH-DTL) has a length of about 5.4 m only, the complete injector including ion sources, LEBT, and the foil stripper tank a length of about 13 m.

## COMMISSIONING PHASES

After construction of the HIT building during 2004 and 2005 and installation of the accelerator infrastructure (water cooling systems, cables, etc.), the installation of the HIT accelerator started in November 2005. The commissioning of the linac injector was performed during 2006 [6][7] in three consecutive steps for ion sources and LEBT, RFQ, and IH-DTL, followed by synchrotron and HEBT in 2007 and 2008 [10] (Table 2). Beam performance of proton and carbon ion beams had reached a level enabling patient treatment at both fixed beam treatment places H1 and H2 in December 2007. Commissioning of the gantry is still ongoing [18].

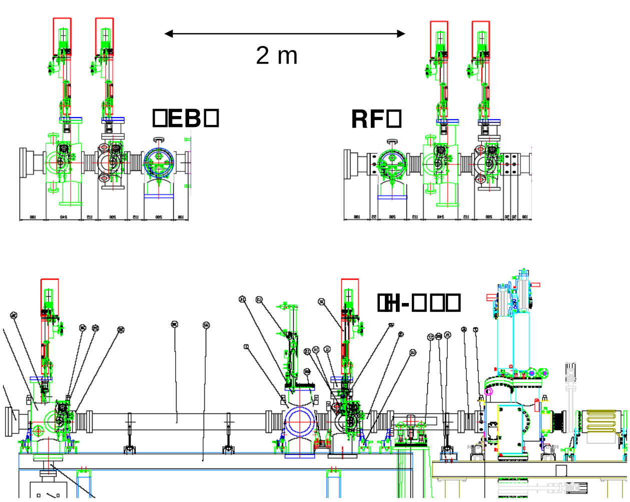


Figure 4: Mobile beam diagnostics benches used during beam commissioning of the different linac sections. The beam enters from the right.

In order to measure the beam parameters behind the different linac sections, a mobile beam diagnostics test bench was used for LEBT, RFQ, and IH linac commissioning. After installation of each section, this diagnostics bench was placed at the very end of this section. The bench was equipped with all instrumentation needed to measure the relevant beam characteristics, i.e. a beam current transformer, a horizontal and vertical slit-grid emittance measurement device, and a Faraday end-cup. After commissioning of a section, the test bench was removed, the subsequent section was installed, and the test bench was reinstalled in a new configuration.

For commissioning of RFQ and IH-DTL three phase probes were included to measure the beam energy via the time-of-flight (TOF) technique. To preserve the experimental resolution at higher beam energy, the IH-DTL setup was extended with respect to the RFQ set-up. The different test bench designs are shown in Fig. 4.

Table 2: HIT commissioning milestones

| | | |
|---|---|---|
| Nov 05 – Mar 06 | ECRIS, LEBT | installation, testing of components |
| April – May 06 | ECRIS | successful beam commissioning |
| May – July 06 | LEBT | |
| July – August 06 | RFQ | installation, rf commissioning |
| September 06 | | beam acceleration to 400 keV/u |
| October 06 | IH-DTL | installation |
| November 06 | | rf commissioning |
| December 06 | | beam acceleration to 7 MeV/u |
| February 7th, 2007 | LINAC, Synchrotron | 50 % Linac performance, 1st turn in synchrotron ($C^{6+}$) |
| March 23rd, 2007 | HEBT | 1st accelerated beam in treatment places |
| December 16th, 2007 | H1 & H2 | Beams in treatment quality (p + $C^{6+}$) |

## ION SOURCES AND LEBT

Each branch of the LEBT (Fig. 2) features a solenoid magnet behind the ion source, a single quadrupole lense to match into the 90° analyzing dipole, the analyzing slit, and a quadrupole triplet, which restores the cylindrical symmetry of the ion beams in front of the RFQ. Ion species can be quickly changed by a switching magnet. Since DC ion beams are extracted from the sources, up to 300 μs long beam pulses are formed by an electrostatic macropulse chopper. Finally, a second solenoid is used to focus the ion beams into the RFQ.

All specified analyzed ion currents were achieved during the on-site ion source acceptance tests at HIT in 2006 as listed in Table 3 [19]. During routine operation, about 140 μA are produced for $^{12}C^{4+}$ and more than 2 mA for $^{1}H_2^{+}$. Stable operation conditions and long runtimes

Table 3: Ion species, specified and measured analyzed electrical ion currents, and ion source potentials □source

| Ion | □ μA (spec.) | □ μA (meas.) | □source / kV |
|---|---|---|---|
| $^{1}H_2^{+}$ | 1000 | > 2000 | 16 |
| $^{1}H_3^{+}$ | 700 | ≈ 710 | 24 |
| $^{3}He^{1+}$ | 500 | ≈ 840 | 24 |
| $^{12}C^{4+}$ | 200 | ≈ 200 | 24 |
| $^{16}O^{6+}$ | 150 | ≈ 170 | 21.3 |

with only two maintenance periods per year are achieved. See Ref. [20] for details regarding ion source operation experience at HIT.

Many breakdowns of the ion sources occurred because of problems with the microwave generators. To reach long-term stable operation conditions with the oxygen beam, the original extraction system was revised by PANTECHNIK. The bias pipe caps of the ion sources were replaced by water-cooled ones.

Matched-beam settings were established for the LEBT during commissioning in 2006 [6]. After the 90° dipole the ion beams are transported to the end of the LEBT with transmissions ≥ 90 % (except for hydrogen beams).

A strong influence of the field strength of the solenoid for matched injection into the RFQ on beam steering and emittance was observed. An off-line field mapping revealed a strong transverse field bump with a relative strength up to 1.3 % with respect to the main solenoid field. A new solenoid magnet with better field quality was produced by SIGMAPHI and installed at HIT in August 2007 [21][22].

Transverse beam emittances up to 300 π mm mrad were measured at the LEBT exit in 2006 – depending on ion source and solenoid settings [6]. The design value is 180 π mm mrad. Because of severe problems at RFQ injection, additional measurements were performed in front of and behind the second solenoid in August 2007 for detailed investigations of the matching to the RFQ [20][22]. Emittances of 150 – 200 π mm mrad were measured for 150 μA $^{12}C^{4+}$ beams and for $^{3}He^{+}$, and 60 – 70 π mm mrad for $^{16}O^{6+}$. No severe dependence of the emittances on the solenoid field strength was observed at that time. In addition, beam profile measurements using a viewing screen were performed behind the second solenoid (Fig. 5). For low focusing strength of the solenoid a hollow beam was observed, whereas for larger focusing strength separated beam spots are visible. Simulations of ion beam extraction and transport can explain at least some of these observations [23][24].

## RFQ

The RFQ was designed, assembled and RF tuned in the group of Prof. Schempp at IAP. After first beam tests at IAP [13], rf tests with an rf power up to 200 kW were performed successfully at GSI as well as the final low-level tuning of the field flatness. Prior to the commissioning in Heidelberg an RFQ beam test bench using proton beams had been set up at GSI [14] in order to verify the output beam energy by TOF measurements and to check

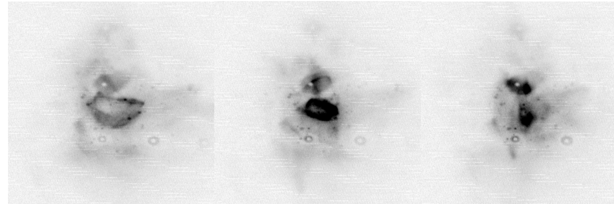

Figure 5: 2D beam profiles of a $^{12}C^{4+}$ beam behind the second solenoid, i.e. close to RFQ injection. The solenoid strength is 7, 10 and 12 1/m, respectively (from left to right). Nominal strength for operation is around 10 1/m.

the correct function of the two-gap rebuncher drift tube set-up integrated into the RFQ tank.

First $C^{4+}$ beams at 400 keV/u were observed at HIT in September 2006. Right after the RFQ a pair of steerers and a quadrupole doublet provide for transverse matching to the IH-DTL. The mobile diagnostics bench was directly installed behind the doublet during RFQ commissioning.

The RFQ working point was determined by measuring beam energy and transmission as functions of the applied rf input power. Figure 6 shows the beam energy measured behind the RFQ versus the tank voltage. The working point is defined by the tank voltage corresponding to the design beam energy of 400 keV/u. An rf pulse power of 190 – 200 kW is needed for $^{12}C^{4+}$ operation.

A strong dependence of the beam steering on the rf

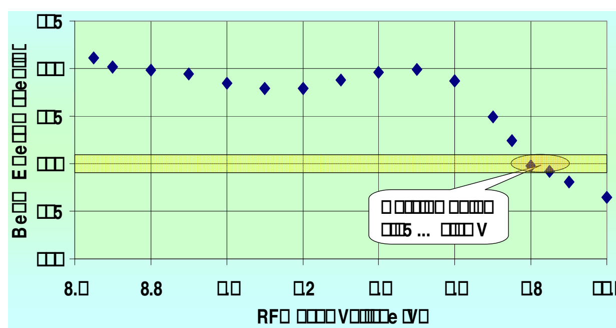

Figure 6: Measured RFQ output energy as function of the (scaled) tank voltage for $^{12}C^{4+}$ operation.

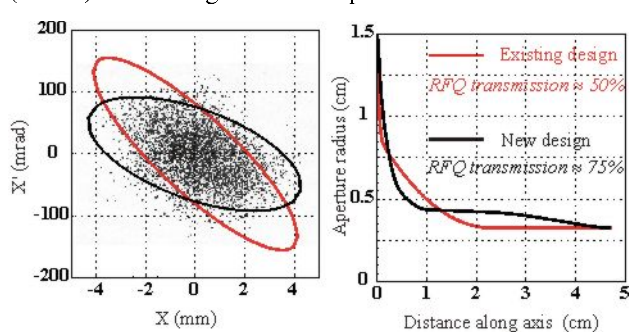


Figure 7: Results of beam dynamics simulations of the linac front-end using the DYNAMION code [22][25]. Left: RFQ acceptance for the original RFQ design (red) and for the new design of the input radial matcher (IRM) (black) together with a particle distribution deduced from beam measurements. Right: Comparison of the original and of the new design of the IRM.

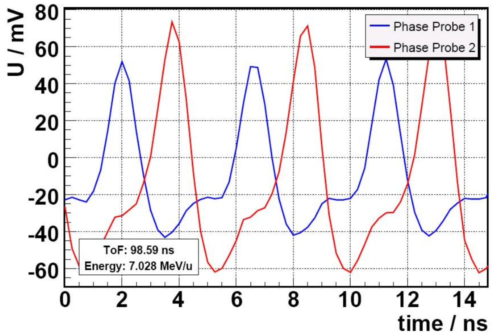


Figure 8: Phase probe signals of a $^{12}C^{4+}$ beam behind the linac [29]. The two probes are mounted at a distance of 3.61 m corresponding to a bunch number of 21. The signal resolution is limited by the acquisition electronics (1 GHz analogue bandwidth, 4 GS/s sampling rate, 8 bit).

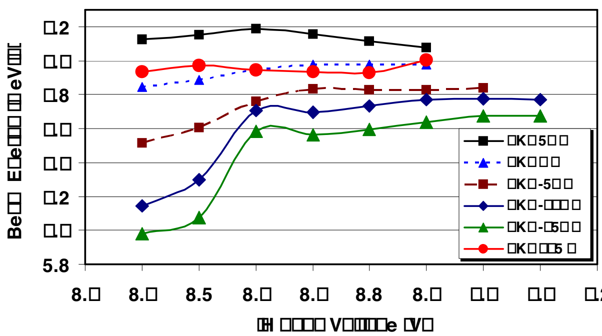

Figure 9: Final beam energy behind the linac as function of the (scaled) IH tank voltage for different settings of one of the RF plungers (for $^{12}C^{4+}$).

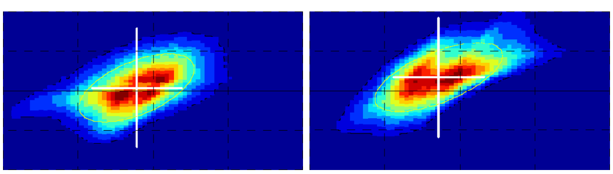

Figure 10: Measured horizontal (left) and vertical (right) beam emittances for a $^{12}C^{6+}$ beam behind the stripper foil. The coordinate axis range is ±10 mm in each plot and the range in x′ and y′ is ±4 mrad. The normalized 4 × rms emittance is 0.67 π mm mrad in the horizontal plane and 0.71 π mm mrad in the vertical plane, respectively. The measured emittance growth in the stripper foil was about 25 % (horizontally) and 9 % (vertically).

voltage was observed. Significant misalignment of the RFQ electrodes was partly corrected during RFQ commissioning but a deformation of the RFQ electrode structure observed by telescope measurements could not be corrected. An unsatisfying beam transmission as low as about 30 % was achieved during commissioning in 2006 for carbon and hydrogen ion beams.

Detailed beam dynamics simulations of the linac front-end, consisting of solenoid and RFQ, using the DYNAMION code and particle distributions deduced from emittance measurements at the LEBT revealed a considerable mismatch at RFQ injection [25]. In addition, as shown by these simulations, the deformation of the RFQ structure causes a significant reduction of the RFQ acceptance. To improve the matching and to prevent deformation of the RFQ structure, the RFQ design was revised at GSI applying a new shape of the input radial matcher (Fig. 7) as well as a more rigid RFQ tank with larger wall thickness and improved suspension [21][22]. The aim is an overall linac transmission above 60 %. This seems to be reasonable with the new RFQ design (Fig. 7). At present, beam tests of the new RFQ are being performed at DANFYSIK in Denmark [22]. Installation in Heidelberg is planned for 2009.

## IH LINAC

The 3.8 m long IH-cavity includes three internal magnetic quadrupole triplet lenses and applies the KONUS beam dynamics concept [26]. It was delivered to GSI in summer 2005 followed by copper plating, final drift tube assembly, and vacuum testing. After rf tuning especially with respect to field flatness [17][27][28], the cavity was installed at HIT in October 2006.

Figure 8 shows phase probe signals as used for high-precision measurements of the beam energy behind the linac. Figure 9 shows the measured beam energy as function of the IH tank voltage for different settings of the rf plunger in the last drift tube section. Since this plunger is highly effecting the voltage distribution along the drift tube structure, it has a significant influence on the final beam energy. Finally, the position of the plunger was fixed in the position used to measure the red spots in Fig. 9. An rf pulse power around 830 kW is needed for $^{12}C^{4+}$ operation.

The final normalized beam emittances measured as 0.7 π mm mrad (Fig. 10) agree well with the values expected from beam dynamics simulations [8][16]. During routine operation, $C^{4+}$ currents of 45 – 50 μA are achieved in front of the foil stripper, and up to 60 μA $C^{6+}$ at synchrotron injection. For protons, about 350 μA are typically achieved behind the foil stripper. By comparing the beam currents measured during RFQ and IH-DTL commissioning, respectively, a beam transmission above 90 % along the IH-DTL is estimated.

Similar measurements as shown in Fig. 8 are being performed during routine operation to check the linac beam energy as well as the energy loss in the stripper foil.

## CNAO LINAC STATUS

A contract between CNAO and GSI was signed in 2004 regarding the construction and commissioning of the CNAO injector linac, which is mainly a copy of the HIT linac. GSI delivers technical support for all linac components [27][30]. In particular, copper-plating, assembly, RF tuning, and pre-tests of RFQ, IH-DTL, and a debuncher cavity were performed at GSI. All components were delivered to CNAO and are ready for installation and commissioning in Pavia, which will be supported by GSI.

In contrast to the HIT linac, the CNAO linac will be installed inside the synchrotron ring [11][12]. The LEBT has been installed completely and first beam emittance measurements behind the LEBT have been performed recently using a special beam diagnostics test bench. After completion of the LEBT tests, RFQ installation and commissioning will start end of October this year.

The CNAO SUPERNANOGAN ion sources have been further improved with respect to the HIT sources [31]. In particular, an optimised extraction system and tuneable signal generators that drive the microwave amplifiers are used. Higher beam currents and very high beam stabilities have been achieved, and smaller beam emittances are expected.

## CONCLUSIONS AND OUTLOOK

The HIT linac was commissioned successfully with carbon and hydrogen ion beams in 2006. Parameter sets for routine operation were established. High linac reliability and availability as well as stable linac beam parameters provided stable conditions during commissioning of synchrotron, HEBT, and treatment systems. The achieved beam quality behind the linac allows for efficient beam injection into the synchrotron using a multi-turn injection scheme. Beam intensities of $4 \times 10^8$ ions per spill for $C^{6+}$ and $1 \times 10^{10}$ for protons are routinely available at the treatment places [10] – well suited to start patient irradiation.

Whereas installation and commissioning of the HIT accelerator were performed under the direction of GSI, routine operation is now done by the HIT operating team 7 days a week and 24 hours per day. The present activities at HIT focus on getting the treatment equipment ready for patient irradiation, in which process GSI is not involved. HIT intends to be ready for patient treatments by the end of 2008.

Ion beam intensities are currently limited by the performance of the linac front-end system (ECRIS, final solenoid, RFQ): low brilliances of the ECRIS beams accompanied by strong aberration effects of the solenoid focusing into the RFQ are causing significant mismatch to the RFQ acceptance. To overcome these limitations and to reach full design performance at the treatment stations ($1 \times 10^9$ ions per spill for $C^{6+}$ and $4 \times 10^{10}$ for protons), an intensity upgrade program has been initiated. A new RFQ has been designed and built and will be installed at HIT in 2009, and further improvements of the ion sources are planned [20].

## ACKNOWLEDGEMENTS

Numerous colleagues from GSI accelerator and central technical divisions as well as from HIT and from IAP have contributed significantly to the design, construction, installation, and commissioning of the HIT injector linac. The author would like to thank all of them for their support and for the fruitful cooperation. Special thanks to W. Barth, L. Dahl, H. Eickhoff, G. Hutter, C. Kleffner, M. Maier, A. Reiter, M. Schwickert, K. Tinschert, W. Vinzenz, H. Vormann and S. Yaramyshev (all GSI) as well as to R. Cee, E. Feldmeier, A. Peters and T. Winkelmann (HIT), and to U. Ratzinger (IAP). Many thanks to the colleagues at CNAO for the fruitful cooperation and for their kind hospitality at CNAO.

## REFERENCES

[1] E. Pedroni, Status of hadrontherapy facilities worldwide, talk presented at EPAC08, Genoa, TUZG02.
[2] K. Saito et al., Accelerator development for advanced particle beam therapy, Proc. EPAC08, p. 1827.
[3] S.P. Moeller et al., Status of the particle therapy accelerator systems built by DANFYSIK A/S, Proc. EPAC08, p. 1815.
[4] Y. Iwata, IH-DTL Linac as a compact injector for a heavy-ion medical synchrotron, these proceedings, WE204.
[5] Y. Iwata et al., Nucl. Instr. and Meth. A 572 (2007) 1007.
[6] B. Schlitt et al., Proc. LINAC 2006, p. 148.
[7] M. Maier et al., Proc. PAC07, p. 2734.
[8] B. Schlitt, A. Bechtold, U. Ratzinger, A. Schenpp, Proc. LINAC 2000, p. 226.
[9] H. Eickhoff, Th. Haberer, B. Schlitt, U. Weinrich, HICAT – The German hospital-based light ion cancer therapy project, Proc. EPAC 2004, p. 290.
[10] D. Ondreka, U. Weinrich, The Heidelberg ion therapy (HIT) accelerator coming into operation, Proc. EPAC08, p. 979.
[11] S. Rossi, Developments in proton and light-ion therapy, Proc. EPAC 2006, p. 3631.
[12] M. Pullia, Status report on the Centro Nazionale di Adroterapia Oncologica (CNAO), Proc. EPAC08, p. 982.
[13] A. Bechtold et al., First performance test of an integrated RFQ-drifttube-combination, Proc. LINAC 2006, p. 162.
[14] C. Kleffner et al., Testbench of the HIT RFQ at GSI, Proc. LINAC 2006, p. 791.
[15] B. Schlitt et al., Proc. LINAC 2004, p. 51.
[16] Y. Lu et al., The compact 20 MV IH-DTL for the Heidelberg therapy facility, LINAC 2004, p. 57.
[17] G. Clemente, H. Vormann et al., Assembly and RF tuning of the IH-DTL for the HIT linac, GSI Scientific Report 2006, p. 376.
[18] C. Kleffner, U. Weinrich, Proc. EPAC08, p. 1842.
[19] K. Tinschert, R. Iannucci and R. Lang, Rev. Sci. Instrum. **79**, 02C505 (2008).
[20] T. Winkelmann et al., Rev. Sci. Instrum. **79**, 02A331 (2008).
[21] R. Cee et al., Intensity upgrade programme for the HIT injector linac, Proc. EPAC08, p. 1788.
[22] M. Maier et al., Linac front-end upgrade at the cancer therapy facility HIT, these proceedings, MOP057.
[23] P. Spaedtke et al., Rev. Sci. Instrum. **79**, 02B716 (2008).
[24] P. Spaedtke et al., Beam transport effects for ECRIS, these proceedings, TUP115.
[25] S. Yaramyshev et al., Proc. ICAP 2006, p. 201.
[26] U. Ratzinger et al., Nucl. Instr. and Meth. A 415, (1998) 229.
[27] H. Vormann, B. Schlitt et al., Status of the linac components for the Italian hadrontherapy centre CNAO, Proc. EPAC08, p. 1833.
[28] Y.R. Lu, U. Ratzinger, B. Schlitt and R. Tiede, The general RF tuning for IH-DTL linear accelerators, Nucl. Instr. and Meth. A 582 (2007) 336.
[29] R. Cee et al., Proc. of the 6th Int. Workshop on Accelerator Operations, Trieste, Italy, September 2007, WEPMR02.
[30] B. Schlitt et al., GSI Scientific Report 2006, p. 383.
[31] G. Ciavola et al., Commissioning of the ECR ion sources at CNAO facility, Proc. EPAC08, p. 415.

# SUPERCONDUCTING RF R&D TOWARD HIGH GRADIENT*

C.M. Ginsburg#, Fermilab, Batavia, IL 60510, U.S.A.

*Abstract*

High-beta superconducting RF elliptical cavities are being developed in large numbers for several accelerator projects including the International Linear Collider (ILC). In recent years, the understanding of cavity performance limitations has improved significantly, leading to better than 40 MV/m in some cavities. However, further improvement is needed to reach reliably the 31.5 MV/m operating gradient proposed for the ILC Main Linac cavities. World-wide R&D on the cavity gradient frontier includes improved surface cleaning and smoothing treatments, development of alternative cavity shapes and materials, and novel cavity manufacturing techniques. Substantial progress has been made with diagnostic instrumentation to understand cavity performance limitations. Some highlights of the efforts in superconducting RF R&D toward achieving higher gradients in high-beta elliptical cavities are reviewed.

## INTRODUCTION

High-gradient superconducting radiofrequency (SRF) cavity technology is being advanced on many fronts because many cavities are needed for current and proposed projects: (1) the test/user facilities STF (KEK), NML (Fermilab), and FLASH (DESY), (2) the European XFEL currently under construction, (3) Project X at Fermilab, and (4) the International Linear Collider (ILC). The common requirements or choices for the high-gradient cavities in these projects are gradients of at least 23 MV/m, beta=1, elliptical shape and an accelerating mode frequency of 1.3 GHz. Recent studies intended to improve gradients in these cavities are reviewed.

First, the requirements for achieving high gradient and current standard cavity treatments are described. Second, some highlights of studies are shown: surface treatments to reduce field emission, alternative shapes to improve average performance, and new fabrication techniques and materials to reduce cost or improve performance. Third, one fundamental study into the cause of poor cavity quality factor ($Q_0$) at high gradients is shown. Finally, the cavity diagnostic instrumentation which has been used and/or developed within the last year to study cavity performance and sources of premature quenches is described.

## ACHIEVING HIGH GRADIENT

Because RF fields occupy the first ~40 nm of the inner cavity surface for these cavities, the quality of the innermost surface is critical and must be carefully controlled. For the niobium sheets which are used to make cavities, RRR of at least 300 is specified for the ILC[1]. Eddy current scanning (ECS) of all sheets is now done before cavity fabrication. ECS has proven to be a very useful technique to provide feedback to material vendors which has resulted in an overall improvement in the delivered material in recent years. The cavity inner surface has to be very smooth, with no inclusions of foreign particles, or topological defects such as bumps or pits or sharp grain boundaries. No dust or other microscopic contaminants may be introduced after the final surface preparation which could contribute to field emission.

Cavity cell shapes have been optimized for low peak surface magnetic field ($H_{peak}$) and low peak surface electric field ($E_{peak}$) relative to the gradient ($E_{acc}$), as well as ease of surface processing and fabrication.

Many cavities have reached 35 MV/m or more in the last decade, particularly single-cell cavities of varying elliptical shapes and 9-cell Tesla-shape cavities [2].

## SURFACE PROCESSING

The surface treatment intended to maximize cavity performance which was developed for the ILC [3] includes initial preparation steps to remove ~150 μm from the inner surface using electropolishing (EP). This initial removal step is also done with centrifugal barrel polishing (CBP) or buffered chemical polishing (BCP) at some labs, though the maximum gradients reached with BCP as the initial preparation step are lower than those achieved using the other methods. Cavities then undergo an 800°C annealing step, to drive hydrogen from the surface. The final preparation steps include degreasing with detergent, another light electropolishing (~20 μm), a high pressure rinse (HPR) with ultrapure water, drying in a class-10 cleanroom, and then evacuation and low-temperature baking (120°C) for about 48 hours after the final assembly with couplers. Additional treatments after the final EP are being studied to reduce field emission, and will be described later.

The primary methods for material removal during surface preparation are CBP, EP and BCP. CBP is a standard technique developed for cavities at KEK in which abrasive small stones are placed into a cavity with water to form a slurry and the cavity is rotated. As a centrifugal process, the material is preferentially removed from the equator region. Since standard cavities have an equator weld, CBP is very effective in smoothing the weld. EP is an electrolytic current-supported material removal, and has been developed for use on cavities by KEK in collaboration with industrial partners and adopted

* This manuscript has been authored by Fermi Research Alliance, LLC under Contract No. DE-AC02-07CH11359 with the U.S. Department of Energy. 

#ginsburg@fnal.gov

at most labs. In this case, the niobium cavity is the anode, and an aluminum cathode is inserted on the cavity axis. The electrolyte is HF(40%):$H_2SO_4$ in a ratio of 1:9 by volume. Some sulfur remains on the surface after EP and will cause field emission unless it is removed. The EP process is complementary to CBP because the material removal is preferentially on the iris. BCP is performed by filling a cavity with a combination of HF(40%): $HNO_3$ (65%):$H_3PO_4$(85%) in a 1:1:2 ratio by volume. BCP is known to cause hydrogen contamination at the surface; this problem can be mitigated by using the appropriate proportion of acid and buffer and by keeping the temperature below about 15°C. BCP is rather less expensive than EP and is often sufficient to produce cavities attaining gradients as high as about 25 MV/m. However, it tends to enhance grain boundaries which may degrade the performance of standard fine-grain cavities. A statistical improvement of maximum gradient was seen after the previous BCP standard was replaced with EP.

Although it is possible now to achieve gradients in 9-cell cavities higher than 35 MV/m, there are several factors which limit cavity performance.

## REDUCING FIELD EMISSION

Four field emission studies are described, which aim to improve cavity performance by reducing field emission: flash EP (also known as fresh EP), dry ice cleaning, degreasing, and ethanol rinsing.

In tests at KEK using six single-cell Ichiro-shape cavities, a 3 μm EP using fresh acid after the final EP was studied [4]. A gradient improvement to both average and rms was observed. Furthermore, the treatment was found to increase the gradient at which field emission turns on.

Dry ice cleaning is a less developed but promising alternative being developed at DESY [5]. It reduces or eliminates contaminating particles in several ways: they become brittle upon rapid cooling, they encounter pressure and shearing forces as $CO_2$ crystals hit the surface, and they are rinsed due to the 500 times increased volume after sublimation. Also, $LCO_2$ is a good solvent and detergent for hydrocarbons and silicones, etc. Dry ice cleaning is a dry process which leaves no residues, because the loosened contaminants are blown out the ends of the cavities by the positive pressure, and can be performed in a horizontal orientation. Dry ice cavity cleaning might be possible after coupler installation, a procedure likely to introduce field emission. Improved field emission characteristics have been seen in single-cell cavity tests, and an extension of the system to 9-cell cavities is planned.

One of several degreasing R&D studies is that of a KEK 9-cell Ichiro-shape cavity which was processed and tested at KEK and JLab [6]. In an initial test at JLab, the cavity produced substantial field emission which was observed at gradients above 15 MV/m. After the cavity was ultrasonically cleaned with a 2% Micro-90 solution and standard HPR, the field emission was substantially reduced or even eliminated.

An extensive study of ethanol rinsing after the final EP was carried out at DESY [7]. Out of 33 cavities used in the study, 20 were treated using the standard procedure and 13 with an additional ethanol rinse after the final EP. The number of tests in which field emission was observed was substantially reduced. In addition, the maximum gradient was somewhat improved. Since field emission was found to be reduced so substantially, the ethanol rinse is now part of the standard DESY cavity treatment.

## FUNDAMENTAL SRF STUDIES

Out of a rich field of fundamental SRF studies, one recent advancement regarding trapped vortices [8] is reported, which addresses the phenomenon of Q-drop, in which the cavity $Q_0$ drops precipitously at high gradients without field emission.

One hypothesis for Q-drop is trapped vortices, i.e., magnetic flux becoming trapped at surface defects or grain boundaries. The trapped vortices may cause excess power dissipation which can be observed as localized hot spots in a temperature map of the cavity external surface. An experiment performed at JLab involved gluing heaters to the outer cavity surface where a hot spot had previously been observed, and studying the temperature map before and after heating. After the application of a thermal gradient, the hot spot temperature was significantly reduced, and heating was redistributed more evenly over the cavity surface. Because a surface defect could not move, and trapped vortices would be subjected to a force from a temperature gradient, this study supports the hypothesis that trapped vortices may be one component of the heating, and therefore the Q-drop. An improved understanding of the Q-drop phenomenon may lead to reduced power consumption by the cavities.

## FUNDAMENTAL CAVITY STRUCTURE

The vast majority of cavities which have been processed and tested in the last decade are Tesla-shape fine-grain cavities [9]. Some fundamental changes to the standard Tesla-shape fine-grain cavities which have been under investigation include changes to the cavity shape, fabrication techniques, and material composition.

### *Alternative Cavity Shapes*

Cell accelerating length and equator diameter are fixed by beta and frequency respectively. However, the details of the shape may be optimized for low field emission (low $E_{peak}/E_{acc}$) and reduced sensitivity to the fundamental maximum surface magnetic field (low $H_{peak}/E_{acc}$); see, e.g., ref. [10].

Excellent results on single-cell elliptical cavities have recently been obtained. A re-entrant shape cavity built and tested by Cornell University recently reached 59 MV/m [11], setting a world record for the type of cavities described in this paper. Excellent results have also been achieved with an Ichiro shape cavity at KEK, with a record of 53.5 MV/m [2]. Furthermore, 46.7 ±1.9 MV/m was reached on six single-cell cavities with optimized surface treatment parameters [4]. Another low-loss shape single-cell cavity which was processed and tested by a DESY/KEK collaboration reached 47.3 MV/m [12].

It is rather more difficult to manufacture an excellent multi-cell cavity than an excellent single-cell cavity, and the very high gradients seen in single-cell alternative-shape cavities have not been achieved in 9-cell versions yet. One 9-cell Ichiro-shape cavity, without endgroups, which was processed and tested by a KEK/JLab collaboration reached up to 36 MV/m [13].

The conceptual design for a new cavity shape which simultaneously optimizes both $E_{peak}/E_{acc}$ and $H_{peak}/E_{acc}$ has been proposed [14].

### *Large-Grain and Single-Grain Niobium*

Material is wasted, and a lot of time is required, to roll sheets and stamp out the disks from which fine-grain cavities are made. In principle, it should be possible to save manufacturing costs by slicing an ingot directly into large-grain sheets. It may also be possible to achieve high gradients using BCP only, since the performance of large-grain cavities should be less sensitive to the grain boundary enhancement seen in fine-grain cavities, as long as the grain boundaries are strategically located in a low surface-field regions.

At a recent workshop [15], several issues associated with having large grains at the equator were discussed, such as ragged equator edges, material thinning or ripping at the equator, springback deforming half cells, etc. However, the companies involved in the fabrication work consider these problems surmountable. Effective large-grain ingot cutting methods are being pursued in industry.

Recent experience at DESY with large-grain cavities shows their performance is comparable to fine-grain cavities. It is still unclear whether BCP will be sufficient or whether EP will be necessary. Many 1-cell tests have shown high gradients, in a range comparable to fine-grain cavities. Recent tests on three 9-cell large-grain cavities [16] showed gradients of up to 30 MV/m with BCP only. Further processing with EP degraded the performance of two cavities, one because of field emission and one for an unknown reason, while the performance of the third was substantially improved to 37 MV/m.

Single-crystal niobium cavities have been difficult to produce, because it is difficult to produce large diameter single-grain ingots. Six single-cell single-grain cavities of varying shape and fabrication technique were fabricated, processed and tested recently by a JLab/DESY collaboration [17], with performance found to be comparable to that of fine-grain cavities. Unless substantial performance improvement is seen, the difficulty of producing the cavities may not justify the effort required.

In both the large-grain and single-grain cases, further study of crystal orientation effects is needed.

### *Hydroformed Niobium*

Because electron-beam welding is a substantial portion of the cavity fabrication cost, and may be a source of surface defects which cause premature quenches (described later), reducing the number of equator welds required in cavity fabrication would be advantageous.

Recently, a 9-cell cavity was fabricated using a hydroforming technique [18]. The cavity was built from three 3-cell hydroformed units, so it had only two iris welds and two beampipe welds. The surface was treated with the standard procedure including ethanol rinse. The cavity achieved 30.3 MV/m and was limited by quench without field emission. Because the $Q_0$ was poor at high gradient, the cavity will be baked at 120°C, which is likely to improve the performance in the next test.

### *Composite Niobium Material*

It may be possible to increase the RF breakdown magnetic field of superconducting cavities by creating a multilayer coating of alternating insulating layers and thin superconducting layers [19]. By using multilayers thinner than the RF penetration depth, the critical magnetic field can be increased from niobium Hc to one similar to high-Tc superconductors, thereby significantly improving the maximum gradient achievable.

Recently, a cavity was prepared with such a composite surface and tested [20]. A 10 nm layer of $Al_2O_3$ was chemically bonded to the niobium surface of an existing single-cell cavity using atomic layer deposition. The surface was then covered by a 3 nm layer of $Nb_2O_5$. The cavity was high pressure rinsed and tested, achieving 33 MV/m without Q-drop, restoring it to its best performance. A lack of Q-drop indicates good surface magnetic properties in these promising early results.

## UNDERSTANDING CAVITY BEHAVIOR

Quenches and field emission appear as hot spots on the outer cavity surface. Temperature mapping (T-map) systems have been used at nearly all of the labs active in this field for many years to study these phenomena [21]. The existing T-map systems primarily use Allen-Bradley carbon resistors as thermal sensors, as developed at Cornell [22]. T-map systems commonly in use for many years at DESY include a fixed type for single-cell cavities with 768 sensors [23], and a rotating system for 9-cell cavities with 128 sensors [24]. A fixed thermometry system for 9-cell cavities with four sensors around each equator and a few sensors on the endgroups has been developed at KEK and was used for tests of STF Tesla-like cavities [25]. Second sound detection has been used at ANL for quench location on split-ring resonators [26]. A selection of new hot spot detection systems are described; these systems vary in coverage, flexibility, and in the number of cavity tests required to extract useful T-map information.

### *Thermometry with Cernox Sensors*

A system of Cernox temperature sensors has been developed at Fermilab [27] and used for quench location. Up to 32 sensors may be attached as needed to suspect locations; therefore the system is very flexible but also time consuming to install, typically requiring several cavity test cycles to conclusively locate quenches. It is highly portable and suitable for any cavity shape.

### *Multi-Cell Fixed Thermometry Systems*

New multi-cell T-map systems have also been developed. A new 2-cell system at JLab was recently commissioned [28], with 160 Allen-Bradley sensors installed around each of the two equators. Understanding cavity behavior requires two cooldowns: one to measure the $TM_{010}$ passband modes and determine within two the limiting cells, then a second after the T-map installation to measure the temperature distribution of the limiting cell. At LANL, a new 9-cell T-map system has been developed [29] which employs 4608 Allen-Bradley sensors and a multiplexing scheme to map an entire 9-cell cavity in a single test yet limit the number of cables leaving the cryostat. The preliminary results are very promising. A 9-cell T-map system at Fermilab using 8640 diodes as a multiplexed thermometer array is under development [30]. All of these multi-cell T-maps are specifically designed for the Tesla cavity shape.

### *Second Sound*

Cornell has developed a new quench location system using second sound sensors [31]. Second sound is a thermal wave which can propagate only in superfluid helium. It is generated when a heat pulse is transmitted from a heat source, such as a quench, through superfluid helium. In this system, eight sensors detect the arrival of the temperature oscillation, and the location is determined from the relative timing of the arrival of the oscillation from different sensors. This simple system is suitable for any cavity shape or number of cells and can locate quenches in a single cavity test.

### *Optical Inspection*

A resurgence of interest in optical inspection occurred within the last year when several cavities with hard quench limitation in the 15-20 MV/m range, were observed to have surface defects correlated with hot spots, using a new optical inspection system developed by Kyoto University/KEK with a clever lighting technique and excellent resolution.

This optical system [32] consists of an integrated camera, mirror, and lighting system on a fixed rod; the cavity is moved longitudinally and axially with respect to the camera system. The lighting is provided by a series of electroluminescent strips, which provide lighting with low glare on the highly polished surface. These strips can be turned off and on, and the resulting shadows studied for an effective 3D image of the depth or height of the defect. The camera resolution is about 7 µm.

An optical inspection system employed regularly at JLab [13] includes a Questar long-distance microscope and mirror to inspect any cavity inner surface. This system uses electroluminescent lighting; the images are converted to black-and-white for clarity.

Additional optical inspection systems are in use or under development at other labs.

### *Improving Surface Quality*

Because many of the cavity-limiting surface defects found by thermometry and optical inspection are located in the heat-affected zone of the electron-beam welds, weld properties are under intense scrutiny. Understanding which weld parameters might contribute to creating such defects, and ultimately eliminating the defect occurrence, is critical to improving the yield of high-gradient cavities. Note that cavities with such defects are largely from new cavity manufacturers.

One group has attempted to reproduce these features by electron-beam welding high-quality niobium scraps, leftover from cavity fabrication, and electropolishing the samples using standard techniques [33]. Several such samples have been produced, and many have features which appear, with a 3D microscope, similar to those found in real cavities. It remains to be seen how similar these defects really are to those found on cavities. If the real defects are reproducible in the lab, they can be systematically studied and the information fed back to cavity fabricators. In time, the overall cavity surface quality may be improved in a manner similar to that of the niobium sheets resulting from eddy current scanning.

## CONCLUSIONS AND OUTLOOK

Highlights of the rich R&D activity in the quest for high gradient and reduced cost have been described. Very high gradients have been measured in niobium SRF cavities: more than 50 MV/m in single-cell cavities of various shapes, and more than 35 MV/m in several 9-cell Tesla-shape cavities. Several promising new results from large-grain 9-cell cavities and hydroformed cavities address the cost and reliability issues of these cavities. Several cavities which have been limited to 15-20 MV/m by hard quench have been studied using various techniques, and the outlook is good that useful information can be fed back to cavity manufacturers to improve the yield of high-gradient cavities over time. Surface treatment is crucial for optimum performance, and several promising studies on final preparation methods have been found to sharply reduce field emission. One study on trapped vortices may partially explain Q-drop, which causes poor cavity performance and high power dissipation at high gradient. Finally, a cavity made of bulk niobium and a layered composite at the RF surface has been proposed to break the critical magnetic field limitation of niobium and shows promising new results.

## ACKNOWLEDGMENTS

I am grateful to my colleagues for the hard work which provided the interesting content for this talk, as referenced. I especially thank those who graciously permitted me to show their unpublished data. I am indebted to G. Ciovati (JLab) and L. Lilje (DESY) for their kind assistance in the preparation of this talk.

## REFERENCES


[1] International Linear Collider RDR, 2007, http://ilcdoc.linearcollider.org/record/6321/files/ILC_RDR_Volume_3-Accelerator.pdf.

[2] K. Saito, “Gradient Yield Improvement Efforts for Single- and Multicells and Progress for Very High Gradient Cavities,” SRF2007, Beijing, Oct. 2007, TU202; http://www.pku.edu.cn/academic/srf2007/home.

[3] G. Ciovati et al., “Final Surface Preparation for Superconducting Cavities,” TTC-Report 2008-05, http://flash.desy.de/sites/site_vuvfel/content/e403/e1644/e2271/e2272/infoboxContent2354/TTC-Report2008-05.pdf.

[4] F. Furuta et al., “High Reliable Surface Treatment Recipe of High Gradient Single Cell Superconducting Cavities at KEK,” SRF 2007, Beijing, Oct. 2007, TUP10; http://www.pku.edu.cn/academic/srf2007/home.

[5] D. Reschke et al., “Dry-Ice Cleaning: The Most Effective Cleaning Process for SRF Cavities?” SRF 2007, Beijing, Oct. 2007, TUP48; http://www.pku.edu.cn/academic/srf2007/home.

[6] R.L. Geng, ILC SCRF Meeting at Fermilab, Apr.21-25, 2008; http://ilcagenda.linearcollider.org/getFile.py/access?contribId=1&sessionId=5&resId=1&materialId=slides&confId=2650.

[7] D. Reschke and L. Lilje, “Recent Experience with Nine-Cell Cavity Performance at DESY,” SRF 2007, Beijing, Oct. 2007, TUP77; http://www.pku.edu.cn/academic/srf2007/home.

[8] G. Ciovati and A. Gurevich, to be published in Phys. Rev. STAB.

[9] B. Aune et al., “The superconducting TESLA cavities,” Phys. Rev. STAB **3**,092001 (2000).

[10] J. Sekutowicz, “New Geometries: Elliptical Cavities,” ICFA Beam Dyn. Newslett. **39**, 112 (2006).

[11] R.L. Geng et al., “High Gradient Studies for ILC with Single-Cell Re-entrant Shape and Elliptical Shape Cavities Made of Fine-grain and Large-grain Niobium,” PAC’07, Albuquerque, Jun. 2007, WEPMS006, p.2337(2007), http://www.JACoW.org.

[12] F. Furuta et al., “Experimental Comparison at KEK of High Gradient Performance of Different Single Cell Superconducting Cavity Designs, EPAC’06, Edinburgh, Jun. 2006; http://www.JACoW.org.

[13] R.L. Geng, “High Gradient SRF R&D for ILC at Jefferson Lab,” LINAC08, Victoria, Sep. 2008, THP043; http://www.JACoW.org.

[14] Z. Li and C. Adolphsen, “A New SRF Cavity Shape with Minimized Surface Electric and Magnetic Fields for the ILC,” LINAC08, Victoria, Sep. 2008, THP038; http://www.JACoW.org.

[15] P. Kneisel, “Progress on Large Grain and Single Grain Niobium – Ingots and Sheet and Review of Progress on Large Grain and Single Grain Niobium Cavities,” SRF 2007, Beijing, Oct. 2007, TH102; http://www.pku.edu.cn/academic/srf2007/home.

[16] W. Singer (DESY), private communication.

[17] P. Kneisel et al., “Performance of Single Crystal Niobium Cavities,” EPAC’08, Genoa, Jun. 2008, MOPP136; http://www.JACoW.org.

[18] W. Singer et al., “Preliminary Results from Multi-Cell Seamless Niobium Cavities,” LINAC08, Victoria, Sep. 2008, THP043; http://www.JACoW.org.

[19] A. Gurevich, “Enhancement of rf breakdown field of superconductors by multilayer coating,” Appl. Phys. Lett. **88**, 012511 (2006).

[20] T. Proslier et al., “Tunneling Study of SRF Cavity-Grade Niobium,” ASC08, Chicago, Aug. 2008; 2LX05, submitted to IEEE Transactions on Applied Superconductivity.

[21] H. Padamsee, J. Knoboch and T. Hays, RF Superconductivity for Accelerators, (Wiley, New York 2008), pp.164-169.

[22] J. Knobloch, H. Muller, and H. Padamsee, “Design of a High-Speed, High-Resolution Thermometry System for 1.5-GHz Superconducting Radio-Frequency Cavities, Rev. Sci. Instrum. **65**, 3521 (1994).

[23] M. Pekeler et al., “Thermometric study of electron emission in a 1.3-GHz superconducting cavity,” SRF1995, Gif-sur-Yvette, Oct. 1995; Part. Accel. **53**, 35 (1996).

[24] Q.S. Shu et al., “A novel rotating temperature and radiation mapping system in superfluid He and its successful diagnostics,” CEC/ICMC 1995, Columbus, Ohio, Jul. 1995; Adv. Cryog. Eng. **41,** 895 (1996).

[25] Y. Yamamoto et al., “Cavity Diagnostic System for the Vertical Test of the Baseline SC Cavity in KEK-STF,” SRF 2007, Beijing, Oct. 2007, WEP13; http://www.pku.edu.cn/academic/srf2007/home.

[26] K.W. Shepard et al., IEEE Trans.Nucl.Sci.**24**, 1147 (1977); K.W. Shepard et al., IEEE Trans. Nucl. Sci. **30**, 3339 (1983).

[27] D. Orris et al., “Fast Thermometry for Superconducting RF Cavity Testing,” WEPMN105, PAC’07, Albuquerque, NM, USA, Jun. 2007.

[28] G. Ciovati et al., Jefferson Lab TN-08-012.

[29] A. Canabal et al., “Full Real-Time Temperature Mapping System for 1.3 GHz 9-cell Cavities,” EPAC’08, Genoa, June 2008, MOPP121; http://www.JACoW.org.

[30] N. Dhanaraj et al., “Multiplexed Diode Array for Temperature Mapping of ILC 9-cell Cavities,” ASC08, Chicago, Aug.2008; 3LPB07, submitted to IEEE Transactions on Applied Superconductivity.

[31] Z.A. Conway et al., “Oscillating Superleak Transducers for Quench Detection in Superconducting ILC Cavities Cooled with He-II,” TTC-Report 2008-06; http://flash.desy.de/reports_publications/ .

[32] Y. Iwashita et al., “Development of high resolution camera for observations of superconducting cavities,” Phys. Rev. STAB **11**, 093501 (2008).

[33] L. Cooley (FNAL), private communication.

# SRF DEVELOPMENTS FOR ION ACCELERATION

G. Olry#, CNRS/IN2P3, IPN Orsay, France

*Abstract*

This paper gives an overview of the recent Superconducting Radio Frequency developments on low and medium beta resonators, including Quarter-Wave Resonator, Half-Wave Resonator, Spoke and CH-type cavities, for ion accelerators.

We will describe the work done for the upgrade of some existing facilities, as well as the on-going developments on cavities for new projects.

## INTRODUCTION

SRF cavities (mainly low beta QWRs) are operating for many years in heavy-ions boosters [1-2]. Their successful operation leads to their integration into most of the new developments for ion acceleration: on existing facilities, such as ISAC-II, ATLAS or PIAVE-ALPI, and new facilities under construction like SARAF and SPIRAL2. Moreover, each driver of the future large-scale accelerators (HINS, FRIB in USA and EURISOL, EUROTRANS in Europe, for example) includes SRF low and medium beta cavities.

QWRs (and HWRS in a lesser extent) are mainly used for existing facilities upgrades and new facilities because of the need of a wide velocity acceptance in order to boost various ion species. Typical range of betas is from 0.001 to 0.15 and voltage gain per cavity around 1 MV.

Spoke resonators and CH-type cavities are studied in the frame of larger SC linacs for which, their multi-gap structure is a real advantage.

## UPGRADE OF EXISTING ION ACCELERATORS – UNDER CONSTRUCTION

### *TRIUMF/ISAC-II*

The ISAC-II superconducting linac is currently delivering beams since 2007. It boosts ion energy by 20 MV, thanks to 20 bulk Niobium QWRs housed in 5 cryomodules. The extension of that linac (called “Phase 2”) has started since one year and should end up, by the end of 2009, to the addition of twenty new 141 MHz, “high beta 0.11”, QWRs [3]. One can note that, besides the beta and frequency values, the inner conductor geometry has been modified (i.e. new “donut” shape) [SRF2007].

A local company, PAVAC, was chosen for the prototyping development and the series production. They built, at first, two copper models to test fabrication, assembly sequence and frequency tuning procedure then, two bulk Niobium prototypes (see photograph in Fig. 1). Final frequency of both cavities was well within 10 kHz of goal, demonstrating a good reproducibility of the fabrication.

Buffered Chemical Polishing (BCP) and High Pressure Water Rinsing (HPWR) were done in-house, at Triumf. Both resonators exceeded the ISAC-II specifications (Fig. 1) [4].

The 6 first cavities should be delivered at the end of October 2008.

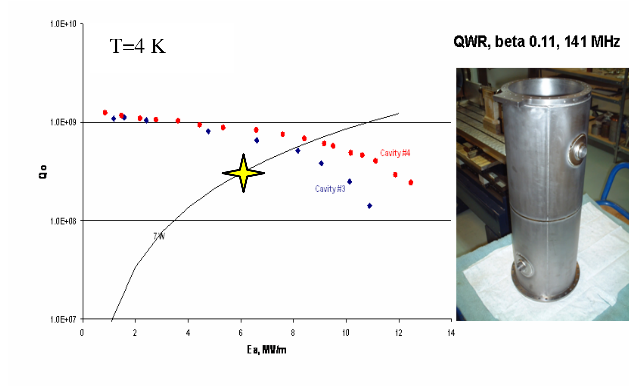


Figure 1: Vertical cold test results of the two first QWR prototypes. Yellow star: ISAC-II, phase 2 specifications.

### *ANL/ATLAS*

This upgrade calls for a total voltage boost between 12 and 14 MV (depending on ion species) thanks to the replacement of an “old” cryomodule by a new one. It will house seven 109 MHz, beta 0.14, QWRs made of bulk Niobium [5]. Cavities have been already qualified in vertical cold tests, giving a 25% higher average accelerating gradient than the design goal (Fig. 2). Details about the cavities’ fabrication and preparation can be found in [6].

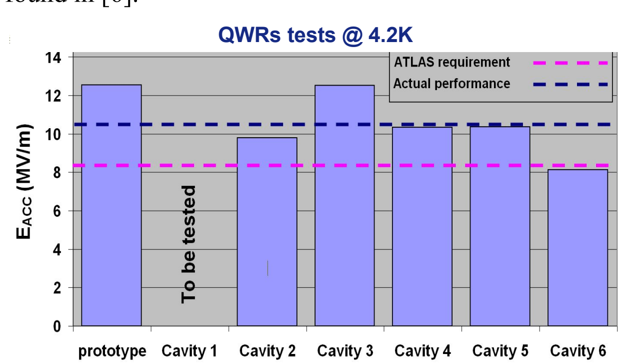


Figure 2: Vertical cold test results of the QWRs composing the new cryomodule for the ATLAS upgrade.

The cryomodule is currently under assembly in the ANL clean room. Its completion is foreseen by the end of 2008 and then, it shall be moved into the ATLAS tunnel.

#olry@ipno.in2p3.fr

### INFN-Legnaro/PIAVE-ALPI

The upgrade of the low-beta section of the superconducting linac PIAVE-ALPI will aim at a total voltage gain of about 10 MV, thanks to the addition of a new cryomodule (housing 4 new 80 MHz, beta 0.047, QWRs) and, among other things, replacements of RF amplifiers and couplers (see details in [7]).

The first resonator has been tested with its new tuning system (modified ISAC-II type which gives wider tuning range) and meets the specifications (Fig. 3) [8]. The second one is still under testing as they met some problems with the coupling antenna (preliminary results give a good Qo but a quench at 5.5 MV/m [9]). Remaining two cavities are waiting for testing.

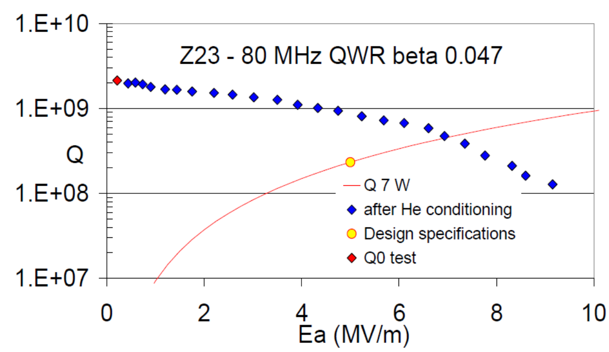


Figure 3: Vertical cold test results (T=4K) of the first QWR for the PIAVE-ALPI upgrade.

New cryostat should be operating in a couple of months while beginning for one year, the upgrade of the "old" cryomodules.

### IUAC New Delhi

Ion beams were successfully accelerates, by end of 2007, through the first superconducting linac module composed of 8 bulk Niobium QWRs (beta 0.08, 97 MHz) [10].

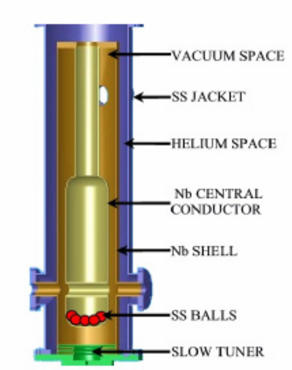


Figure 4: Stainless Steel balls (in red) inserted inside the inner conductor to damp mechanical vibrations.

However, some problems occurred while operating the cavities: lower accelerating gradient than expected, perturbations because of microphonics or leaks located near the tuning system. Important efforts were done to get rid of these problems. For example, Stainless Steel balls were inserted inside the inner conductor for reducing the perturbations due to microphonics (Fig. 4) and the fixture of the tuning system was changed to avoid leaks [11].

Now, these modifications are implemented for the 16 QWRs of the 2 next modules which are currently under fabrication at IUAC. They have developed all the necessary facilities to produce (EB welding machine) and prepare SC cavities (EP, HPWR and furnace for heat treatment).

## UPGRADE OF EXISTING ION ACCELERATORS – CAVITY DESIGN & PROTOTYPING

### MSU-NSCL/Re-Accelerator

A SC linac with 3 new cryomodules is proposed for the acceleration of ion beams up to a maximum energy of 3 MeV/u [12]. The cryomodules will house bulk niobium 80.5 MHz QWRs with beta of 0.041 and 0.085.

Two prototypes have been fabricated (one of each beta) in a close collaboration with INFN-Legnaro, and successfully tested at MSU in vertical cryostat [13-14]. Fig. 5 shows very good results of the beta 0.041 resonator with probably the highest peak surface electric field ever achieved in a QWR. The cavity preparation was done at MSU (BCP and HPWR).

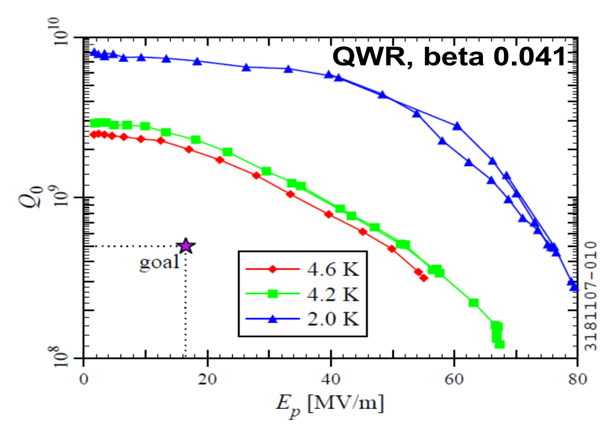


Figure 5: Vertical cold test results of the beta 0.041 QWR for the Re-Accelerator.

In parallel, a prototype cryomodule housing a beta 0.085 QWR cavity and a 322 MHz, beta 0.285, HWR, together with two focusing elements (one SC Quadrupole and one SC solenoid) has been assembled [15].

### CERN/HIE-ISOLDE

The energy upgrade of the REX-ISOLDE linac is an important part of the HIE-ISOLDE project at CERN [16]. This upgrade aims at a final energy of 10 MeV/u (= total boost of 37 MV) and will be realized in 2 stages:

- Stage 1: addition of 2 modules, housing 5 QWRs, beta 0.12, 101 MHz each, to get a final energy of 5.5 MeV/u.

- Stage 2: Reaching 10 MeV/u by adding 10 QWRs, beta 0.075, 101 MHz and 5 more QWRs, beta 0.12, 101 MHz.

"Classical well proven" technologies have been chosen for the cryomodule and QWR designs: common vacuum and Nb/Cu sputtered technology (Fig. 6) [17].

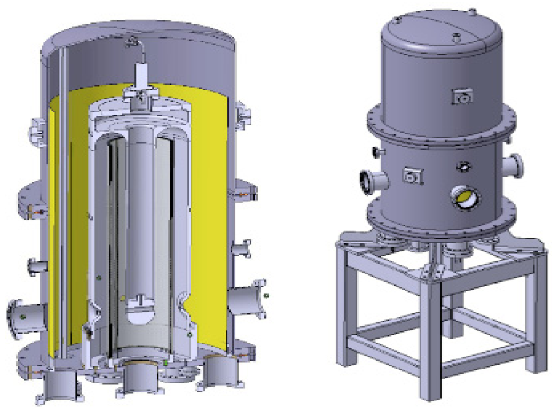

Figure 6: Sputtering chamber.

One copper model of the beta 0.075 resonator is currently under construction at CERN and should be completed by the end of October 2008.

## NEW FACILITIES – UNDER CONSTRUCTION

### *SOREQ/SARAF*

The SARAF "Phase 1" SC linac is getting close to the end after one year of commissioning [18]. Last element to be commissioned is the Prototype Superconducting Module (PSM) which hosts six 176 MHz, beta 0.09, bulk Niobium HWRs. Final expected energies are 4 MeV for protons and 5.2 MeV for deuterons beams.

While vertical tests performed at ACCEL showed that all cavities complied with the specifications ($Qo>5.10^8$ for Epk=25 MV/m), Q values of some cavities were much lower during the "off-line" PSM operation because of strong field emission. Nevertheless, as it is illustrated in Fig. 7, the average accelerating gradient is good and exceeds by 20% the design value (i.e. <Ea>=5 MV/m).

| Cavity | | vertical Test | | | 10/2007 PSM Test | | | 03/2008 PSM Test | |
|---|---|---|---|---|---|---|---|---|---|
| location | name | max field [MV/m] | losses at 25 MV/m [W] | Q at 25 MV/m | max field [MV/m] | losses at 25 MV/m [W] | Q at 25 MV/m | losses at 25 MV/m [w] | Q at 25 MV/m |
| HWR1 | LB-2 | 40 | 7,3 | 6,0E+08 | 30 | 6,3 | 7,0E+08 | 6 | 8,00E+08 |
| HWR2 | LB-3 | 43 | 7,3 | 6,0E+08 | 28 | 31,4 | 1,4E+08 | 9 | 5,00E+08 |
| HWR3 | LB-5 | 33 | 6,3 | 7,0E+08 | 32 | 22,0 | 2,0E+08 | 24 | 2,00E+08 |
| HWR4 | LB-7 | 46 | 6,3 | 7,0E+08 | 29 | 22,0 | 2,0E+08 | 39 | 2,00E+08 |
| HWR5 | LB-4 | 36 | 5,5 | 8,0E+08 | 31 | 11,0 | 4,0E+08 | 13 | 4,00E+08 |
| HWR6 | LB-6 | 38 | 7,3 | 6,0E+08 | 29 | 14,7 | 3,0E+08 | 42 | 1,00E+08 |
| | | sum | 40,0 | | | 107,3 | | 133 | |

Figure 7: Cold test results of the 6 beta 0.09, HWRs in the PSM [19].

Some cavities also suffered from ponderomotive oscillations (coupling between Lorentz Forces and Helium pressure fluctuations) while Epk was getting close to 16 MV/m. The phenomenon is now identified and piezo-tuners will be used to compensate this frequency detuning. Microphonics measurements were also performed and did not show up additional problems [18].

The PSM is now "on-line", ready to accelerate its first beam.

### *GANIL/SPIRAL2*

Major components of the SPIRAL2 SC linac are presently under construction [20] and among these; the two series of "low-beta" and "high-beta" resonators (88 MHz, QWRs made of bulk Niobium of two different betas 0.07 and 0.12).

Prototypes and qualifying cavities have been already tested in vertical cryostat and met the design specifications (results of beta 012 QWRs in Fig. 8) [21], excepted for the qualifying beta 0.07 cavity which low Qo value is not yet understood [22].

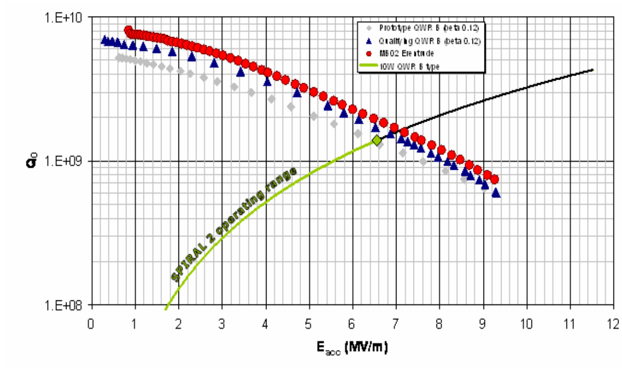


Figure 8: Vertical cold tests results of the beta 0.12 QWRs. Curves: Purple diamonds - prototype, blue triangles - qualifying cavity and red circles -1st series cavity.

The qualifying cavity has been set in its cryomodule and should be tested with its tuning system and RF power coupler in October 2008. The series fabrication of the two first beta 0.07 has started and delivery is expected in March 2009.

Series fabrication by ACCEL of the 16 "high beta 0.12" resonators is currently progress. The 3 first cavities have been delivered and one already tested with success (vertical cold results are presented in Fig. 8). This cavity and the qualifying one will be tested in cryomodule with their power coupler and tuning system. Last results of the tuning system by SC plunger used for beta 0.12 cavities are detailed in [23].

## NEW FACILITIES – CAVITY DESIGN & PROTOTYPING

### *Fermilab/HINS*

A SC linac with 325 MHz Single-Spoke (SSR) and Triple-Spoke resonators (TSR) is proposed to accelerate $H^-$ from 10 MeV to 400 MeV [24].

Two SSR with beta 0.22 have been fabricated (one by Zanon SpA, the other by Roark) and two more are presently under fabrication by the Inter University Accelerator Center in new-Delhi. The cavity produced by Zanon has been prepared in the ANL facility and tested at Fermilab. As shown Figure 9, a maximum gradient of 18 MV/m was reached (i.e. the highest Ea in a spoke cavity nowadays, see following Table 1). See more details in [25].

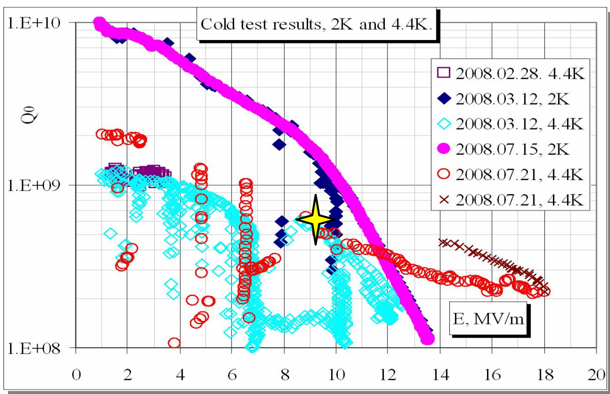


Figure 9: Vertical cold test results of the beta 0.22 Single-Spoke prototype.

## *INFN-Legnaro & IPN Orsay/EURISOL*

176 MHz, beta 0.15, HWRs and 352 MHz, beta 0.30, triple-spoke cavities are proposed for, respectively, the low and medium beta sections of the EURISOL driver [26]. HWR specified operating gradient is 5.5 MV/m and 8 MV/m for the spoke cavity.

The HWR design made by INFN-Legnaro and the Spoke cavity design made by IPN Orsay are finished (see Fig. 10) and the prototypes fabrication should begin in 2009. Both cavities are made of bulk niobium.

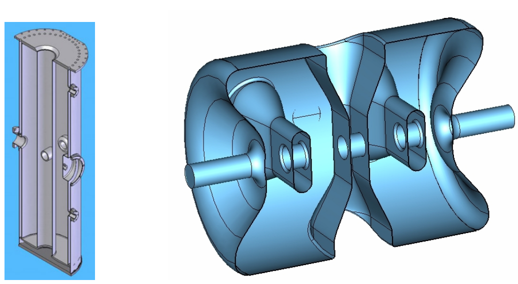

Figure 10: 176 MHz, beta 0.15, HWR (left) and 352 MHz, beta 0.30, Triple-Spoke cavity (right) for the EURISOL driver.

The RF tuning of the HWR will be done by cup deformation whereas a new RF tuning system by SC plunger will be tested with the triple-spoke cavity

## *IAP-Frankfurt & IPN Orsay/EUROTRANS*

Two different types of SC cavities (both operating at 352 MHz) are proposed for the proton driver of EUROTRANS between 5 MeV and 50 MeV.

- a beta 0.10, multi-gap, CH cavity between 5 and 17 MeV designed by IAP-Frankfurt..
- a beta 0.35, Single-Spoke resonator between 17 MeV up to 50 MeV designed by IPN Orsay.

A prototype of 19-gap, CH cavity has been successfully tested in vertical cryostat: Ea max of 7 MV/m, limited by field emission, for a design goal of 4 MV/m [27]. The cavity is now equipped with a tuning system and wait for a cold test in a refurbished horizontal cryostat. A new prototype, with 7 gaps, has been recently designed and should be fabricated in 2009.

Tests in horizontal cryostat are going on with the Single-Spoke beta 0.15. Piezo-tuners have been set on the tuning system and first test gave good results: expected sensitivity (100 Hz/µm) and good reproducibility of the full stroke (Fig. 11). A new version of the digital Low Level RF system is under fabrication. It will be used, together with the piezo-tuners tuning system, to get a frequency regulation.

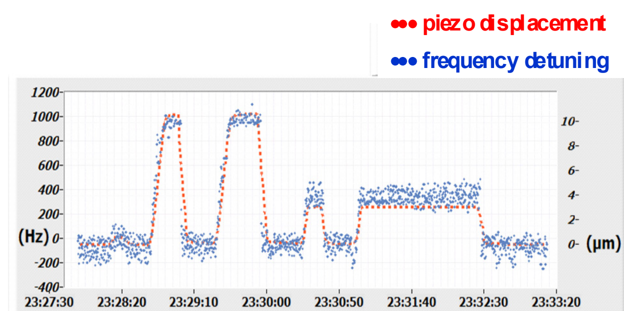


Figure 11: Frequency variation (blue dots) while moving the piezo-tuner (red dots).

# "ALL-AROUND-THE-WORLD" SPOKE COLD TESTS RESULTS

The table 1 summarizes the vertical test results of existing Spoke-type cavities at 4.2 K. One shall note that the accelerating gradient Ea is normalized with the following definition:

$$E_a = n\beta\lambda/2 \qquad (1)$$

with n the number of gaps.

Taking apart cavity performances below 5 MV/m, the mean values of Ea, Epk and Bpk are, respectively, 8.3 MV/m, 40 MV/m and 100 mT.

# ACKNOWLEDGEMENTS

The author would like to address many thanks to: B. Laxdal, L. Ristori, M.P. Kelly, W. Hartung, M. Doleans, R. Toelle, E. Zaplatin, A. Facco, I. Mardor, D. Berkovits, J. Rodnizki, H. Podlech, M. Pasini, H. Saugnac and P. Bosland.

Table 1: RF performances of existing Spoke-type cavities at 4.2 K.

| Lab | Type | Frequency [MHz] | Optimal beta (name) | Ea [MV/m] | Epk [MV/m] | Bpk [mT] | Voltage [MV] |
|---|---|---|---|---|---|---|---|
| IPN Orsay | Single | 352 | 0.20 | 4.77 | 32 | 69 | 0.82 |
| | Single | 352 | 0.36 | 8.14 | 38 | 104 | 2.49 |
| ANL | Single | 855 | 0.28 | 4.40 | 24 | 56 | 0.26 |
| | Single | 345 | 0.29 | 8.75 | 40 | 106 | 2.21 |
| | Single | 345 | 0.40 | 7.02 | 44 | 117 | 2.44 |
| | Double | 345 | 0.40 | 8.60 | 40 | 79 | 4.49 |
| | Triple | 345 | 0.50 | 7.65 | 28 | 88 | 6.65 |
| | Triple | 345 | 0.62 | 7.94 | 31 | 95 | 8.70 |
| FZ-Juelich | Triple | 760 | 0.20 | 8.63 | 42.8 | 87.2 | 1.36 |
| LANL | Single | 350 | 0.21 (EZ01) | 7.50 | 38 | 100 | 1.35 |
| | Single | 350 | 0.21 (EZ02) | 7.22 | 37 | 96 | 1.30 |
| Fermilab | Single | 325 | 0.21 (SSR1-01) | 12.00 | 69.5 | 112.5 | 2.43 |

## REFERENCES


[1] Den Hartog, P.K. et al., "Operational Experience of the ATLAS Accelerator," NIM in Phys. Rev. A 287, 1990, p. 235-239.

[2] L. Badan et al., "Review of ALPI", EPAC'94, London, June 1994

[3] R.E. Laxdal et al., "ISAC-II Superconducting Linac Upgrade - Design and Status", LINAC08, Victoria, September 2008.

[4] R.E. Laxdal et al., "Production and Testing of Two 141 MHz Prototype Quarter Wave Cavities for ISAC-II", LINAC08, Victoria, September 2008.

[5] J.D. Fuerst et al., "Status of the ATLAS upgrade cryomodule", SRF2005, Ithaca, July 2005, THP038

[6] J.D. Fuerst et al., "Progress on cavity fabrication for the ATLAS energy upgrade", SRF2007, Beijing, October 2007.

[7] D. Zenere et al., "Upgrade of the low-β section of the PIAVE-ALPI linac at LNL", SRF2007, Beijing, October 2007.

[8] D. Zenere et al., "Progress in the ALPI-PIAVE low-beta section upgrade", EPAC'08, Genoa, June 2008.

[9] Private communication.

[10] IUAC annual report 2007-2008, Chapter 2, http://www.iuac.ernet.in/publications/annualreport/AR07-08/annualreport.html

[11] S. Gosh et al., "Commissioning of superconducting linac at IUAC – initial challenges and solutions", EPAC'08, Genoa, June 2008.

[12] X. Wu et al., "MSU Re-Accelerator – the re-acceleration of low energy RIBs at the NSCL", SRF2007, Beijing, October 2007.

[13] W. Hartung et al., "Niobium Quarter-wave Resonator Development for the Rare Isotope Accelerator", SRF2003, Travemunde, September 2003.

[14] W. Hartung et al., "Niobium Quarter-wave Resonator development for a Heavy Ion Re-accelerator", SRF2007, Beijing, October 2007.

[15] W. Hartung et al., "Superconducting Quarter-Wave Resonator cavity and cryomodule development for a Heavy Ion Re-accelerator", LINAC08, Victoria, September 2008.

[16] http://hie-isolde.web.cern.ch/HIE-ISOLDE/HIE-ISOLDE_site/Welcome.html

[17] Report of the International Advisory Board for the REX-ISOLDE LINAC energy upgrade, May 2006

[18] C. Piel et al., "Phase 1 Commissioning Status of the 40 MeV Proton/Deuteron Accelerator SARAF", EPAC'08, Genoa, June 2008.

[19] D. Berkovits, "The 40-MeV Proton/Deuteron SC Linac at SARAF", HB2008, Nashville, August 2008.

[20] T. Junquera, "Status of the construction of the SPIRAL2 accelerator at GANIL", LINAC08, Victoria, September 2008.

[21] R. Ferdinand et al., "Status of the Cryomodules for the SPIRAL 2 Superconducting LINAC", PAC'07, Albuquerque, June 2007.

[22] R. Ferdinand et al., "The SPIRAL2 superconducting linac ", LINAC08, Victoria, September 2008.

[23] D. Longuevergne et al., "A novel frequency tuning system based on movable plunger for SPIRAL2 high-beta superconducting quarter-wave resonator", LINAC08, Victoria, September 2008,

[24] P.N. Ostroumov et al, "Front End Design of a Multi-GeV H-Minus Linac", Proc. Of the PAC-2005, Knoxville, Tennessee, May 2005.

[25] G. Apollinari et al., "High gradient test results of 325 MHz Single-Spoke cavities at Fermilab", LINAC08, Victoria, September 2008.

[26] A. Facco et al., "Beam dynamics studies on the EURISOL driver accelerator", LINAC08, Victoria, September 2008.

[27] H. Podlech et al., "Superconducting CH structure", Phys. Rev. ST Accel. Beams 10, 080101 (2007).

# DEVELOPING FACILITIES FOR SNS CRYOMODULE PERFORMANCE IMPROVEMENTS*

J. Mammosser,# SNS/ORNL, Oak Ridge, TN, U.S.A.

*Abstract*

Superconducting RF cavity facilities are currently being developed at SNS, aimed at addressing the limitations and availability of installed cavities and the direct support of the future power upgrade plans. Current efforts are directed towards development of in-situ repairs and developing processing techniques to increase available linac gradients. Procedures have been developed and implemented and the results will be presented for the repair of four cryomodules in the last year. Cryomodule testing facilities are being developed to further understand the collective limitations of installed cavities and spare cryomodule production is underway to develop and fabricate two high beta and one medium beta cryomodules. The direction and status of SRF facilities will be presented.

## SUPERCONDUCTING CRYOMODULE FACILITIES AT SNS

During the construction of the SNS accelerator, 11 medium beta (0.61) and 12 high beta (0.81) cryomodules were fabricated at Thomas Jefferson National Accelerator Facility, shipped to SNS and installed in the linac section of the accelerator. At this time there was no urgent need for SRF facilities with the exception of some clean work areas, portable cleanrooms, and limited utilities which were used for the installation effort. During this time the RF Test facility was installed but was not functional and the main focus was on commissioning and developing cryomodule operational experience as quickly as possible. Once the Superconducting Linac (SCL) was commissioned and operating, several limitations to cavity operating performance became known and further understanding of the operational limits was needed. The main concern was unusual higher order mode (HOM) signals, excessive fundamental power coupling out HOM couplers and breakdowns in cavities due to field emission and multipacting. Individual cavities operate to high gradients but must be turned down due to collective effects from electron heating [1]. Significant effort was spent understanding these problems and this knowledge was critical to setting optimal operating parameters. Today the SCL is one of the most stable operating systems in the accelerator [2].

Table 1: SRF Facilities at SNS

| SRF Facility | Classification | Details |
|---|---|---|
| **Cleanroom** | | |
| Small part cleaning/degreasing | ISO 7 (M 5.5) | $58m^2$ |
| Cleanroom- String assembly | ISO 5 (M 3.5) | $58m^2$ |
| Cleanroom – Cavity assembly | ISO 4 (M 2.5) | $2.5m^2$ |
| **Cryomodule Test Facility** | | |
| Horizontal Test Facility | | |
| | Space | 11m x 4m |
| | Cryogenic Connections | Supply transfer line<br>Shield transfer line<br>**Return transfer line |
| | **Test Facility Refrigerator | 200W 2K<br>200W Shield |
| ***Vertical Test Facility** | | Standard dewar/pit design |
| | Dewar | Depth -3.35m |
| | | Diameter – 71.1cm |
| | Cryogenic source | Separate helium refrigerator |
| ***DI water Plant** | E-1 | 2268 liter storage, 38 liter makeup |
| ***High Pressure Rinse Station** | | Cavity remains stationary |
| | Wand | Rotates and translates |
| | Nozzles | Water Fanjets |
| | | 2 opposed |
| | | Nitrogen gas Fanjets 2 opposed |
| | Pump | LEWA Teflon diaphragm -15 lpm |

Today there is the need to expand the SCL facilities to support linac maintenance on cryomodules, qualify subcomponents for repairs and for the development of spare cryomodules. Spare cryomodules will allow for the

*SNS is managed by UT-Battelle, LLC, under contract DE-AC05-00OR22725 for the U.S. Department of Energy.
#mammosserj@ornl.gov.

recovery and upgrading of problematic cryomodules in a recycling program.

The SRF facilities are located in the RF Test Facility building [3], where an installed cleanroom complex, horizontal test cave and the supporting utility infrastructure such as DI water plant and an RF test-stand are already located. The RF teststand consists of a 5MW, 805MHz RF klystron with full low level RF controls [4]. Although the existing facilities have adequately provided for limited servicing and repair of installed cryomodules, the plans are to extend and improve these facilities for compatibility with development and fabrication of in-house spares and to develop additional in-situ cryomodule performance improvements. In Table 1, SRF Facilities at SNS, are listed and brief details about them are provided. New facilities currently in design or construction are also listed and identified by the single asterisk *. Facilities that will be added as part of the power upgrade plan (PUP) are identified by double asterisk **. Currently there are several limitations to the existing facilities which prevent routine RF testing of cavities or components. The test facility support infrastructure has not yet been completed and is planned for installation when the PUP begins. Currently cryomodules can be tested in the test cave but only during operation's accelerator physics study periods or maintenance downs due to the lack of a separate helium gas return transfer line and an additional dedicated refrigerator supporting the test facility. These missing facilities will be completed during the power upgrade.

## CRYOMODULE REPAIR STRATEGY

With the requirements for high beam availability and high beam power at SNS, in-situ methods of repair and performance improvements are becoming more important. The cost and amount of time spent to rework a cryomodules is significant to operations. For SNS there is an additional burden in that there are currently no spare cryomodules and this makes developing new in-situ methods of repair a must to keep the installed components healthy while the spares are being designed and produced.

Currently, plans have been made to develop and apply in-situ RF processing to the installed superconducting cavities in parallel with redesign and fabrication of the first spare cryomodules. The processing techniques to be applied are helium and plasma processing. The helium processing method has been applied to installed cryomodules at various laboratories with some success. This helium processing method is easy to apply but has statistically provided only about 1 MV/m improvement to installed cavities limited by field emission. This method will be performed on the next cryomodule tested in the RF test facility and then will be applied to the linac. Additionally, we are pursuing the development of plasma cleaning, an industrially accepted method for cleaning of semiconductor wafers. A plasma cleaning setup has been assembled and commissioned in the RF test facility. This system has the same components necessary for helium processing and hardware will be used for both. The plasma setup consists of a high beta cavity with standard flange hardware and couplers, a gas mixing and metering manifold and a solid state 500 watt RF source. Niobium witness samples are mounted inside the cavity beam-line and will allow for surface analysis and the ability to understand how contaminants are being modified. To date, the system has been commissioned and plasma established in the cavity with two different gas mixtures. Figure 1, shows the plasma processing setup located in the RF test facility building.

Figure 1: Plasma processing setup with HB Cavity.

## PRODUCING SPARE CRYOMODULES

With the urgent need for producing a few spare cryomodules and the requirements by Department of Energy to comply with 10CFR851 it was decided to build these spares in-house. What the 10CFR851 document requires is that the new spare cryomodules will be designed and fabricated to be compliant with pressure vessel codes. The process of designing to pressure vessel code is straight forward but will take additional time to complete the module redesign and drawings before spares can be produced. The Oak Ridge National Laboratory (ORNL) is well suited for producing the few spare cryomodules in-house and handling pressure vessel fabrication already. ORNL has a code compliant machine shop, qualified welders and an X-ray weld analysis shop. All pressure vessel work in this shop is performed to ASTM standards. Along with these facilities at ORNL, there is significant material testing and surface science laboratories and expertise available for aiding progress and addressing problems. By choosing this path of building in-house, this will allow time for developing the new design into a production model and to train staff. The goal is to have the future nine upgrade cryomodules fabricated in industry and in-house expertise will be necessary to support the procurement contracts. This will also allow time for building staff expertise in-house to properly maintain these new cryomodules once received.

A decision was made on the new cryomodule design to establish the pressure boundary for all new cryomodules at the vacuum vessel and endcan envelop and not on the internal cavity and helium vessel envelop. This decision stems from the lack of code based materials within the cavity helium circuit design. Some of the materials used are recognized by the code board but are not listed materials and therefore would require code cases for each material to become a code listed material. Another difficulty is the ability to test materials at the operating temperatures. SNS has started the testing of materials for mechanical properties for all of the materials used in cavity helium vessel fabrication and have fully analyzed all electron beam welds on two of the spare six cell HB cavities.

The one facility that is missing at SNS is the chemical processing facilities for the niobium cavities. These facilities are necessary for removal of damaged niobium surface layers due to fabrication procedures. This removal is by acid etching of the cavity interior by one of two methods, buffered chemical polish or by electropolish. Both processes require chemical handling, processing equipment and first response hydrofluoric acid training for staff. Currently Thomas Jefferson National Accelerator (Jlab) is performing all the cavity processing, assembly and cryogenic testing of the cavities for the three spare cryomodules. The first four cavities have just completed qualification at JLab and will be used in the first HB spare cryomodule. The chemical facilities at ORNL, will be eventually needed for rework of cryomodules installed in the linac which are activated. Planning has begun to establish a limited cavity chemistry facility in the Nuclear Science and Technology Division at ORNL, to gain experience with these processes and to support future cavity processing needs for activated cavities.

## CRYOMODULE REPAIR SUMMARY

Although cryomodules are operating stably at SNS, currently there is one cavity not being operated in the linac due to HOM coupler damage and one cryomodule is removed from the SCL for repairs. To date several different SCL operating problems have been identified and over the last few years, repairs were attempted to recover performance to cavities in 4 of the 23 installed cryomodules. Cryomodule in linac position 19 (CM19) was removed due to excessive fundamental power coupling out a HOM coupler. This cryomodule was moved to the cleanroom and procedures were developed to vent and repair the cavity without extensive disassembling of the cryomodule. Repairs were performed through a 15.2cm access port with special tooling to remove both HOM coupling probes from the problem cavity. Cameras placed inside the cryomodule were extensively used during the repairs due to the small access hole and the location of the couplers. Repairs were completed on the cryomodule just as the test cave facilities were completing. CM19 was commissioned along with the new test cave facility and both were a big success. The procedures and tooling used in the repairs led to the first successful in-situ repair of a beam-line component through an access port, and no degradation to performance was experienced in commissioning of CM19. The cryomodule was then installed into the accelerator. Currently CM19 is the highest performing high beta cryomodule in the linac. At this time a decision was made to remove CM12 from the linac due to its suspected beam-line leak and because this cryomodule was limited by field emission and would be a good tool for further development of in-situ processing techniques. The testing of CM19 was important feedback on developed techniques and would allow us to proceeding with more aggressive repairs on installed cryomodules in the linac.

The next cryomodule identified for repair was CM10 which had a cavity with a noisy field probe signal, and CM09 cavity which had a tuner that was running excessively. CM10 was fully vented and access to the field probe identified the problem to be a loose cable. CM09 had the tuner motor, harmonic drive replaced and the piezo tuner removed. With CM10 the procedure used for venting 19 was utilized and this cryomodule is now fully recovered and being operated at its original gradient. CM09 was not successful however, after cooling down the cryomodule the tuner is still running excessively and therefore being operated at a lower gradient then its operational limit to reduce the tuner movements. Next work on CM12 began and it was moved to the cleanroom. During this repair three large beam-line to insulating vacuum leaks were discovered, all coming from failed HOM ceramic feed through. Suspicion is that during commissioning of cryomodules multipacting occurs in the HOM coupler detuning the notch filter and high fundamental power propagates through the feed through. These type or RF events can thermally shock the ceramic. Clear evidence of multipacting in the HOM coupler was identified during the commissioning of CM19 after the repairs. CM12 was then moved to the test-cave for commissioning and was cooled down. During the cool down it was identified that an additional cold leak on the helium circuit was appearing around when the piping reached 100 Kelvin. After much testing, suspicion is that the leak is located in the return end-can piping. Efforts are now focused on opening up the end-can to clearly identify the location of the leak and repair it.

## RADIATION LEVELS IN THE SCL

With increasing beam power, the activation levels of installed linac components are increasing. Activation is mainly due to beam loss, although the beam loss is small at <1 watt per meter [5]. The ability to perform quick repairs in the linac will increasingly be reduced to control personnel radiation exposures as the machine beam power increases and reaches its design goal of 1.4MW. Currently the beam power is between 500-600KW and is scheduled to be increased each run period until the

1.4MW level is reached. To better understand the radiation levels in the tunnel, several measurements have been made to quantify source terms, integrated doses to installed equipment and to measure decay rates to better predict personnel exposure rates and reduce them. First the isotopes from source terms were measured in the linac area of the machine between CM4-5. Table 2, shows the top ten source terms from the SCL, measured by the radiation control group. This spectrum differed significantly from the spectrum taken in the ring injection region in that the source terms were smaller and Nb-90 was not present. Next the radiation decay in the linac was measured as a function of time by increasing the sensitivity of neutron detectors to be sensitive to gamma emission. This provided a better understanding of the decay rates in the linac. Typically when the production run ends, The radiological control technicians (RCT's) perform a detailed radiation survey and the access into the SCL is delayed for one day to reduce exposure rates. This data is presented on Figure 2, Radiation Decay Measurement in The SCL [6]. Additionally High dose TLD's were placed on most of the cryomodules exiting gate valves. Here the total integrated radiation dose for the run period for an integrated beam power was determined for the linac components.

Table 2: SCL Radiation Source Terms

| Radiation Source Terms | | | |
|---|---|---|---|
| SCL | | Range | |
| uCi | Isotope | (keV) | |
| 1.31 | Mn-52 | 1329.23 | 1338.73 |
| 1.26 | Mn-52 | 1429.77 | 1439.27 |
| 1.01 | Cr-51 | 317.3 | 324.43 |
| 0.88 | Ni-57 | 1914.11 | 1924.39 |
| 0.82 | Na-24 | 2745.68 | 2758.32 |
| 0.78 | Sc-44m | 269.35 | 276.48 |
| 0.77 | Co-56 | 2590.73 | 2602.59 |
| 0.75 | Mn-52 | 931.32 | 940.03 |
| 0.67 | Nb-90 | 2311.6 | 2323.46 |
| 0.64 | Nb-90 | 2179.91 | 2190.98 |

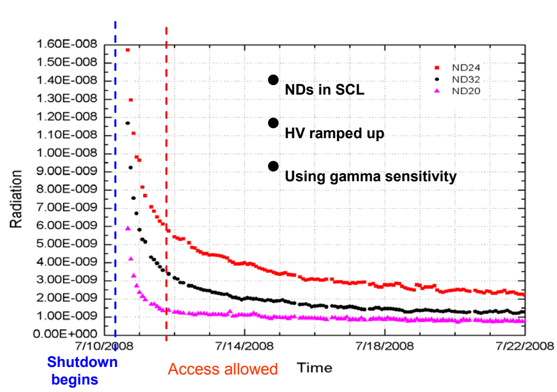


Figure 2: Radiation decay measurement in the SCL.

This data is presented in Figure 3, SCL Radiation Exposure. Through these series of measurements we are better able to plan and perform our maintenance duties.

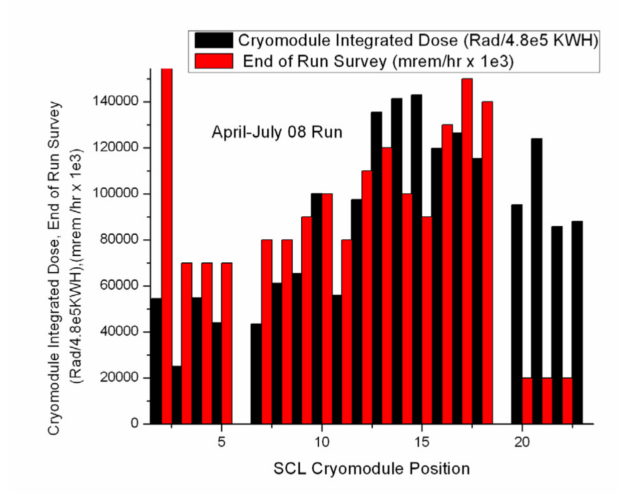


Figure 3: SCL radiation exposure.

## CRYOMODULE ACTIVATION

One of the complications of repairing cryomodules at SNS is that they are now all activated. Although the activation levels are still low, controls must be put in place, planning and procedures used to reduce exposures and all must be thought of well before the repairs can start. For cryomodules recently repaired in the RF test facility or the production cleanroom, control boundaries were established and the cryomodule was allowed to set for several weeks before work was started. RCT's, surveyed and tested for removable contamination throughout the repair process. So far no contamination has been detected in or on any cryomodule. As an example of how much activation, CM19 after setting for two months was measured around 30urem/hr on contact externally and around 3mrem/hr internally on the beam-line components. Clearly the stainless steel bellows between the cavities was the most activated component inside of the vacuum vessel. As the beam power increases in the linac, so will the levels of activation on the cryomodules making it even more important for planning and development of in-situ repair procedures and optimized tooling and shielding. The radiation exposure predicted for personnel for the removal of a cryomodule is higher then the in-situ repairs would incur.

For the repairs performed in the tunnel, the activation levels are much higher at around 40-100mrem/hr on contact of beam-line components. Therefore radiation shielding was designed and used on CM09 and CM10 repairs, recently repaired in July-August maintenance period. For the repairs to these two cryomodules, two different types of shielding was designed and used. The first type shielding was a roll around cart for shielding the vacuum work. This provided personnel protection from beam-line components directly in front as well as from the longitudinal sources down the linac from both directions. This was achieved by providing movable shielding doors. The shielding provided a reduction of a factor of two standing directly behind the cart and about one third for personnel standing in the tunnel walk way. The beam-line vacuum work can take hours to setup and perform and therefore must be shielded to reduce exposures. Further improvements have been identified for this cart to include better shielding for personnel standing adjacent to the cryomodule.

The second type of shielding developed was for the internal beam-line components inside the cryomodule. In this case the cryomodule insulating vacuum boundary was vented and the access ports removed. RCT's then surveyed and tested for contamination inside the cryomodule before shielding was wrapped around the beam-line components. This shielding reduced the exposure about a factor of two as well. Improvements were also identified for this shielding and the main one was to reduce the spacing around the components to reduce longitudinal sources. In both cases the shielding was successful but the first use discovered that the task that needed to be performed became more difficult because of the shielding barrier and it will take time for staff to become accustomed to working behind barriers. In total over the five week repair period the maximum integrated radiation exposure for a single person working on cryomodules was around 18mrem, whole body dose.

## ADDITIONAL CRYOMODULE REPAIRS IDENTIFIED

Plans are now being made to repair CM11 cavity b (the last remaining cavity not being operated in the SCL) failed HOM coupler during the February maintenance period 2009. The same methods and shielding will be used to gain more experience with this type in-situ repair.

Additionally during this maintenance period, an investigation into identifying and fixing cryomodule insulating vacuum leaks will begin in January. Currently there are seven cryomodules with known insulating vacuum leaks and have additional turbo pumps installed on them in the tunnel. Data suggests that four of the seven have outside to insulating circuit leaks, two are helium circuit to insulating circuit and one is unclear. Most leaks can be repaired in the tunnel but the helium circuit leaks will require an available spare cryomodule before they can be removed from the tunnel and repaired in the RF Test Facility.

## SUMMARY

The SRF facilities at SNS have been constantly evolving and improving over time and now plans are to expand the capabilities to support the building and testing of spare cryomodules and in-situ processing of installed SCL components. New facilities will be aimed at increasing the capability of processing and testing of cryomodule subcomponents and adding the additional refrigerator to support both the horizontal and vertical testing facilities. Along with these new facilities, upgrades to the cleanroom and DI water plant will complete the necessary facilities for supporting the cleaning of subcomponents for ultrahigh vacuum and particulate controlled work.

## ACKNOWLEDGEMENTS

The author would like to give credit to all the cryogenics and vacuum groups technical staff for supporting the cryomodule facility operations, developments and maintenance repairs that resulted in such high reliability while operating the SCL.

[1] S-H. Kim private communication, ORNL, September 2008.
[2] S-H. Kim, "SNS Superconducting Linac Operational Experience And Upgrade Path", Linac08, Victoria BC, September 2008, Mo103; http://www.JACoW.org.
[3] F. Casagrande, "Status of The Spallation Neutron Source Superconducting RF Facilities", EPAC08, Genoa, June 2008; http://www.JACoW.org.
[4] M. Crofford, "The Spallation Neutron Source Cryomodule Test Stand RF System", EPAC08, Genoa, June 2008; http://www.JACoW.org.
[5] J. Galambos, "Operational Experience With High Power Beams At The SNS Linac, Linac08, Victoria BC, September 2008; http://www.JACoW.org.
[6] A. Zhukov and S. Assadi, private communication, ORNL, September 2008.

# AN OVERVIEW OF LINAC ION SOURCES*

R. Keller,# LANL, Los Alamos, NM 87545, U.S.A.

*Abstract*

This paper discusses ion sources used in high-duty-factor proton and $H^-$ Linacs as well as in accelerators utilizing multi-charged heavy ions, mostly for nuclear physics applications. The included types are Electron Cyclotron Resonance (ECR) sources as well as filament and rf driven multicusp sources. The paper does not strive to attain encyclopedic character but rather to highlight major lines of development, peak performance parameters and type-specific limitations and problems of these sources. The main technical aspects being discussed are particle feed, plasma generation and ion production by discharges, and plasma confinement.

## INTRODUCTION

For the purpose of this presentation, the term Linac is narrowed down to include rf structures that accelerate ion beams with duty factors between about 5% and continuous operation. This group of Linacs includes high-current proton and $H^-$ machines as well as accelerators utilizing low- or moderate-current beams of multi-charged heavy ions, mostly for nuclear physics applications. Main types of ion sources serving these Linacs include Electron Cyclotron Resonance (ECR) sources, filament and rf driven multi-cusp sources, Penning (PIG) sources, duoplasmatrons and duopigatrons. However, the latter three source types have been in use for more than 50 years by now with more or less stagnant operational features, and for that reason they will not be discussed in the following even though they continue to produce beams for a number of Linac facilities.

This overview does not at all strive to attain encyclopedic character in terms of source varieties and performance results but rather to highlight the dominant design features, evolving performance parameters, major lines of development and general, as well as type-specific, limitations and problems. The main technical aspects being discussed are particle feeding methods, plasma generation and ion production by discharges, and plasma confinement.

## PARTICLE FEEDING METHODS

The simplest way of feeding particles into an ion source consists of letting gas flow into the discharge vessel, but sometimes a user needs to limit the overall gas flow into the subsequent Low-Energy Beam Transport (LEBT) structure of an injector and is forced to use a fast-pulsed valve, typically piezo-electrical driven [1].

The use of gaseous or liquid compounds with high-enough vapor pressure is the next best choice, with one note of caution: many of these substances contain a chemically aggressive component, and in the discharge plasma the reaction rates are typically much faster than at normal atmosphere. Erosion of source body and extraction electrodes and a significant increase of the sparking rate in the extraction system are typical consequences. A survey on this subject is given in Ref. 2; it is certainly a very good starting point to obtain information on specific feeding techniques and substance properties.

Many substances have sufficient vapor pressure at elevated temperatures to be fed into an ion source, but this option comes with its own design constraints: Once vapor of the desired pressure has been produced it should not be lost to condensation on any surface part of the conduit to the discharge vessel or that vessel itself. In other words, the oven where the solid feeding material is heated should be the coldest part of all internal ion source components. This condition suggests the installation of hot liners in the discharge vessel or even the use of dual heating elements for oven proper and conduit. A design example where the conduit is heated by the cathode filaments is given in Fig. 1. In many cases, the ion production will be much more stable when small amounts of an auxiliary gas such as argon are added into the discharge vessel.

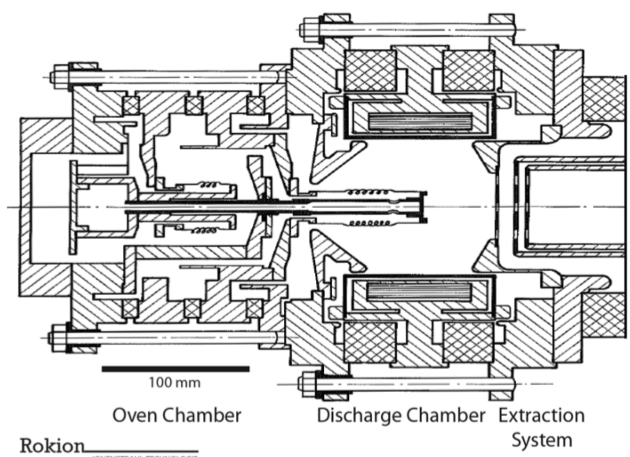


Figure 1. Hot-running multicusp ion source CHORDIS with oven and 18 cusp magnets [3]. Heat shields around the oven filaments are left out for the sake of clarity.

High-melting elements that cannot conveniently be fed into a source as part of a volatile compound can be released using the sputtering technique, adding an auxiliary gas such as argon. A dedicated sputter electrode may be inserted into the discharge vessel at a convenient location, or an existing electrode can be biased positively [3]. As with oven-equipped sources, use of sputtering benefits from the installation of hot-running liners or thinned-out electrodes to avoid re-condensation of the sputtered particles. Shares of the desired ion species typically do not exceed 10-20% of the entire extracted beam current.

Work supported by the US Department of Energy under Contract Number DE-AC52-06NA25396
#roderich@lanl.gov

## PLASMA GENERATION

Once a material has been introduced into the ion source it has to be ionized, and usually this process is performed by striking an electrical discharge. The often used term 'arc' discharge is a misnomer because arcs have a negative voltage/current characteristic and are associated with rather undesirable runaway conditions. The discharge is either sustained by dc power and thermionic cathodes (filaments) or by rf power and, as mentioned above, it may be continuous (dc/ cw) or pulsed.

The applied dc or rf current and voltage values depend on one hand on the ionization requirements of the dominant feeding substance, and on the other hand on the plasma density requirements imposed by the utilized extraction system, see below.

### *Filament Sustained Discharges*

Thermionic filaments are typically made from tungsten or tantalum wire or, when using hydrogen feeding gas, from a nickel mesh covered by an earth-alkaline oxide paste. The major problem with using refractory wire material is the finite time-between-services limited by erosion of the material. For example, the LANSCE $H^-$ ion source reaches 28-35 days with an average discharge power of 500 W (12 kW peak at 4.1% duty factor), utilizing two filaments in parallel. In a study of filament data from many production runs of this ion source [4], it was found that the relative increase in filament resistance, as compared to the initial value, is a good indicator of the expected lifetime as illustrated in Fig. 2.

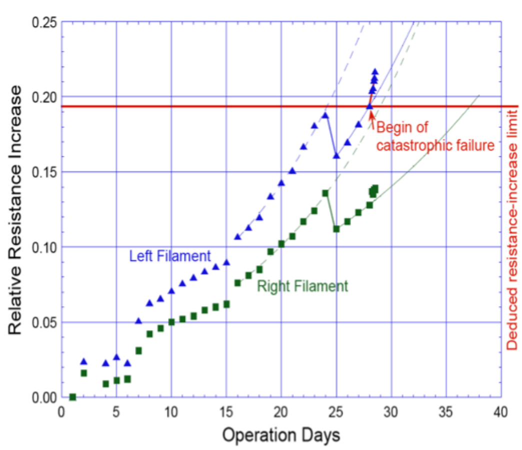


Figure 2. Resistance evolution of the two cathode filaments installed in the LANSCE $H^-$ source during a test run, showing the phases of initial shock (Days 1-7), exponential growth (Days 8-28), and catastrophic failure (left filament on Day 28). From Ref. 4.

Three distinct epochs of exponential growth are shown in Fig. 2 during Days 8-15 (less pronounced), 16-24, and 25-28; the latter two are fitted with exponential curves and extrapolated. The filament heating power values were different for each of these three phases; in fact, the close approach of the plotted data for the left filament on Day 24 led to reducing the heating power with the result that the filament lifetime could be extended by 4 more days. The catastrophic failure then occurred rapidly, once the value of 19% resistance increase had been reached.

In a theoretical and computational study of the filament failure mechanisms [5], two of the observed phenomena, i.e., exponential growth and catastrophic failure, could be well reproduced. This study proved that hot-spot formation is the dominant effect leading to excessive evaporation and failure; in addition it was found that very small diameter reductions (50 μm) of the wire can accelerate the time to failure by a factor of 2.

### *RF Sustained Discharges*

Rf sources are typically operated at 1-13.56 MHz frequency and are by design not suffering from the wear associated with hot filaments. The first aspect to take care of when driving an rf discharge is matching of the power source impedance to the plasma impedance inside the source, typically of the order of 1 Ohm. This is performed by an impedance-matching network [6]. Ignition of the discharge does not constitute a problem for filament-sustained discharges, but problems arise when rf power is utilized alone. The quick solution for the cw operation mode consists in raising the gas pressure inside the source to a level where ignition occurs at an acceptable rf power level and then reducing the pressure and possibly the rf power to their standard operating values before excessive discharge power results in damage to the vessel.

For pulsed rf operation, two ways have been successfully employed: One consists in maintaining a low-power discharge in cw mode and then applying the power pulse on top of it [7]. The two power sources need to be decoupled, for example, by choosing different rf frequencies, and the cw power source has to be protected against total reflection of its own power when the main rf pulse is applied and drastically changes the plasma impedance. This can be easily achieved by just using a cw power source with about 3 times higher nominal power rating than will actually be applied.

The other method is described in Ref. 1; it essentially consists of a spark gap that operates at significantly higher pressure than found in the discharge chamber. The gap chamber is fed with gas through the piezo-electric valve mentioned above, and a narrow opening conducts enough plasma to the discharge chamber to allow ignition of the main discharge but at the same time maintains the pressure difference between both chambers.

Rf power needs to be coupled into the discharge vessel by an antenna, and internal as well as external antennas are in use. Because of the fact that the antenna has to be shielded from the plasma by an insulating material to avoid arc-like runaway conditions, internal antennas are usually covered by single or multiple layers of porcelain, but the difference in thermal expansion coefficients of the antenna (normally copper) and the porcelain invariably leads to microscopic cracks in the porcelain, and the lifetime of these internal antennas is essentially unpredictable [8]. A rupture of the water-cooled copper tubing results in severe consequences for the vacuum system serving source and LEBT. For the same reason, water-cooled quartz tubes with inserted conductors are not offering a reliable operational solution.

An external rf antenna fulfills the operational needs much better in principle, but it requires a significant part of the discharge chamber to be made of an insulating material. $Al_2O_3$ is the most commonly used material, but for higher sustained discharge powers its thermal conductivity is insufficient, and the insulator has to be shielded from the major part of the discharge power by a slotted 'Faraday shield' [9]. Recently AlN has been employed as chamber material with an external rf antenna, and this material proved to be superior for the purpose, due to its high thermal conduction coefficient [10]. This ion source is shown in Fig. 3; recently, 100 mA $H^-$ beam current was obtained on a test stand from a 7-mm aperture at 1 ms pulse length and 60 Hz repetition rate.

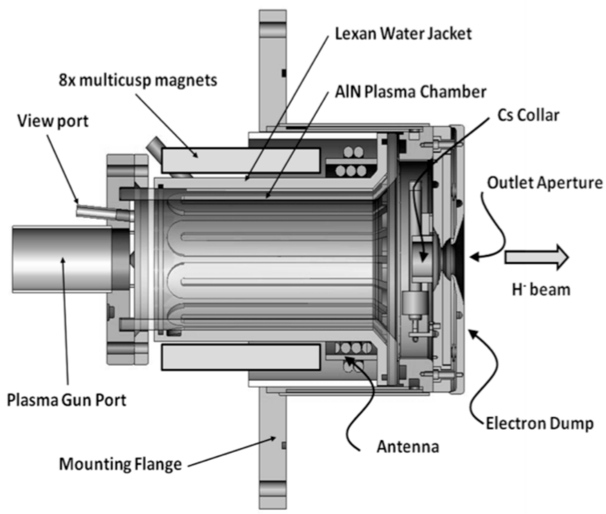


Figure 3. Developmental SNS $H^-$ rf ion source of 68 mm chamber diameter with external antenna [10]. The magnetic dipole filter (not indicated) vertically crosses the upstream end of the cesium collar.

## MULTICUSP SOURCES

Once a plasma is created, it is often convenient to restrict particle losses to the chamber walls, for the sake of power- and gas-efficiency as well as, in the case of multi-charged heavy ions, to increase the ionization probability for the plasma electrons and thus push the ion charge-state distribution to elevated values. Simple confinement of a plasma by a so-called magnetic bottle realized by two co-axial coils excited in parallel, however, leads in all rule to exciting plasma instabilities, with the undesired consequences of unstable ion beam intensity and loss of space charge-compensation in the transported beam.

Stable plasma confinement can be achieved by a minimum-B configuration where the magnetic field increases in strength with increasing distance from the center [11], and the configuration most frequently used in ion sources is the magnetic multipole, realized by lining the chamber wall(s) with either permanent magnets or electro-magnets.

These configurations generate cusped magnetic field lines, and sources with cylindrical discharge chambers and a higher number of magnets, between 10 and 20, are called multicusp or 'bucket' sources and are used to produce high-current ion beams, whereas sextupoles are most frequently used in combination with solenoid fields in ECR sources that produce highly charged beams, see below. The main effect is that only some energetic plasma particles can escape across the narrow, rectangular areas where the field lines cross a wall surface.

Examples of multi-cusp sources are shown above, in Fig. 1 (for high-current heavy-ion beams) and Fig. 3 (for high-current $H^-$ beams).

The higher the multipole number, the less do the magnetic fields penetrate towards the center of the discharge plasma, and a larger 'field-free' ($B < 10^{-3}$ T) cross sectional area allows the installation of wider extraction systems, such as the multi-aperture system depicted in Fig. 1, because the plasma density needs to be uniform across the entire outlet area.

Because of the increased collision probability for each individual electron with heavy particles, a larger discharge chamber will actually require less discharge power than a smaller one to create a plasma density value to match the applied beam extraction field [12].

The beam current I [mA] of a pure ion species with atomic weight A that can be extracted by a voltage U [kV] from a single, round outlet aperture of a multicusp source of matching plasma density is given with some margin by:

$$I = 0.5\, A^{-1/2}\, U^{3/2} \qquad (1)$$

This formula is based on a semi-empirical model that combines aberration-dominated optics effects of the beam formation process with empirical breakdown limits for the extraction gap [13]. Multi-aperture extraction systems with N apertures yield N times these values, but at the expense of a very significant emittance increase.

While the creation of positive, heavy ion beams in multicusp sources is straightforward and mostly raises issues of maximum plasma density, achievable charge-state distribution and time-between-services, hydrogen ions are somewhat more difficult to deal with. For protons and deuterons, the issue is the distribution among atomic and molecular ions ($H/D^+$ vs. $H/D_2^+$, $H/D_3^+$). The distribution cannot be pushed to enhancing the atomic ion shares by just raising the discharge voltage as one would do to get higher-charged heavy ions; instead, vibrational states of the neutral $H_2$ molecules have to be excited in greater numbers, and that requires copious low-energy electrons.

Apart from installing hot-running liners or certain insulators such as BN, the best method for enhancing atomic hydrogen ion shares consists in separating a part of the discharge chamber by a magnetic dipole filter-field from the main volume [14]. The filter keeps energetic electrons from passing into the $H/D^+$ production zone, whereas colder electrons can migrate through, due to their higher collision rates and the ExB drift effect. However, the primary plasma needs about 10 times higher electron densities than required for the extraction; hence the importance of carefully engineering the discharge chamber design with respect to high instantaneous and average power.

While negative hydrogen ion beams are transported by Linacs mainly for the purpose of utilizing charge-exchange injection into an accumulator ring, the high-duty-factor part of this group of ion sources is important enough to briefly be treated here as well.

There are two main principles of generating $H^-$ or $D^-$ ions: Volume and surface production [15]. Volume production follows similar principles as found with positive atomic ions, except that the optimum electron energy for $H^-$ creation is even lower and electrons with energies above 10 eV as well as positive ions and neutral atoms can easily destroy negative hydrogen ions once they have been formed. As a consequence, these ion sources include magnetic filters and are operated at the lowest possible neutral gas pressures.

Surface production occurs predominantly due to fast particles sputtering absorbed hydrogen atoms. For surface materials with low work function values, such as Cs-covered Mo or solid Ba, there is a fairly high probability for the released hydrogen particles to be $H^-$ or $D^-$. Two source types utilize these basic facts: Two-chamber multicusp sources as the one shown in Fig. 3 where the second chamber is made up by the walls of the cesium collar downstream of the dipole filter, and multicusp converter sources [16] that include a biased, Cs-covered converter electrode where negative ions are formed and accelerated towards the outlet electrode. A modern example of a converter source is shown in Fig. 4. To reduce the amount of electrons that are co-extracted with the $H^-$ ions, a permanent-magnet ‘repeller’ tube is installed in front of the outlet aperture.

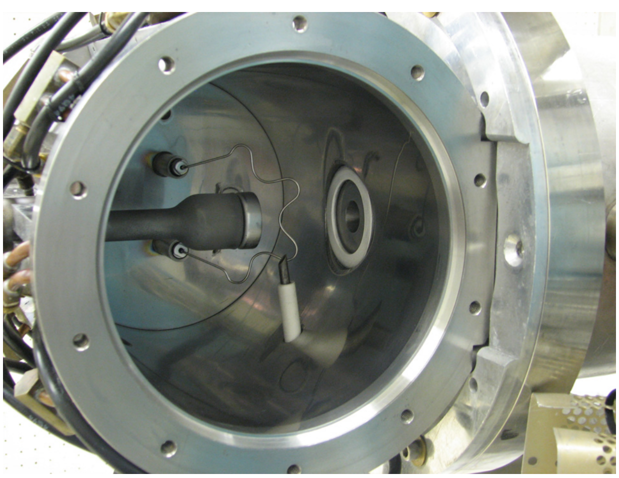

Figure 4. Multicusp converter source for $H^-$ with 192 mm inner chamber diameter. [4]. The converter electrode is at the center; cesium vapor is injected from the bottom, and the electron repeller is shown on the right, hiding the outlet aperture from view.

The peak result obtained with this ion source on a test stand from a 10-mm aperture at 0.835 ms pulse length and 60 Hz repetition rate is 24.5 mA.

## ECR ION SOURCES

ECR ion sources rely on the fact that electrons can gain substantial energies from microwave fields when their orbital motion around magnetic field lines created by two co-axial solenoids is in resonance with the microwave frequency f [17]:

$$B_{res}\,[\mathrm{T}] = 0.0354\, f\,[\mathrm{GHz}] \qquad (2)$$

When ECR discharges are operated at gas pressures around $1\times10^{-6}$ Torr the electron energy can exceed 1 keV, and at the same time recombination rates for the created ions are very low. These are optimal conditions for creating highly charged ions through step-by-step ionization processes. On the other hand, a line of ECR sources has been developed that operates around $2\times10^{-4}$ Torr, and these conditions are well suited for creating high-current beams. As with the rf driven multicusp sources, ECR sources are free from the wear associated with hot filaments, exhibit very long times-between-services and are typically operated in cw mode.

### *ECR Sources for Highly Charged Ions*

To obtain highly charged ions, one needs to minimize the operational gas pressure but also to increase the electron density in the plasma as much as possible, but there is a cut-off limit for the achievable density $n_e$ that depends on the applied microwave frequency [17]:

$$n_e\,[\mathrm{cm}^{-3}] \leq 1.25\times10^{10}\, f^2\,[\mathrm{GHz}^2] \qquad (3)$$

As a consequence, ECR sources for highly charged ions have been pushed to higher and higher microwave frequencies, and the top model VENUS [18], shown in Fig. 5, operates at 28 GHz. To satisfy Eqn. (2) for this frequency, a resonant magnetic field of 1 T (10 kG) is needed, and the peak field produced by superconducting magnets reaches 3.4 T. Modern ECR sources exhibit an asymmetric solenoid field with the higher peak being upstream of the lower peak (2.3 T for VENUS).

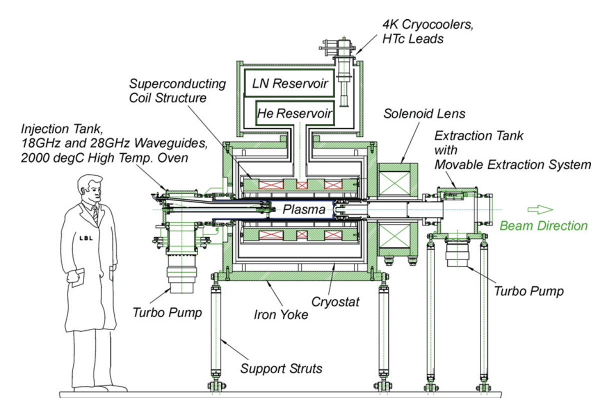


Figure 5. VENUS ECR ion source [18].

Apart from the longitudinal plasma confinement provided by the solenoids, ECR sources for highly charged ions also need a radial, minimum-B, confinement mechanism to enhance the ion persistence, and a sextupole is the most convenient choice. The needs for high magnetic fields to improve the ion confinement time (several ms are typical) contrast with the requirement for low fields near the outlet area to extract intense ion beams.

The VENUS sextupole field reaches 2.1 T at the chamber wall. Recent peak results [electrical μA] for beams created by VENUS are: $^{16}O^{6+}$- 2850; $^{16}O^{7+}$- 850; $^{129}Xe^{28+}$-222; $^{129}Xe^{38+}$- 7; $^{238}U^{35+}$- 175; $^{238}U^{47+}$- 5; $^{238}U^{50+}$- 1.9.

The 3-d field pattern created by the superimposed magnetic systems results in a cigar-like surface where the resonance condition, Eqn. (2), is fulfilled. The width of this surface is given by the Larmor radius of the circulating electrons, and it was discovered that this width could be substantially enlarged and thereby the power efficiency of an ECR source enhanced if microwave power of a somewhat lower frequency was fed into the source in addition to the main power, essentially doubling the effective ionization volume [19]. Another method of achieving the same goal consists in utilizing a broadband, Traveling-Wave-Tube-based amplifier that puts out microwave power over a wider frequency band [20]. The group in Ref. 20 recently reported about 30% power efficiency increase due to fine-tuning of the microwave frequency favoring resonance modes on the discharge vessel axis.

A major draw back associated with advanced ECR ion sources regards the emission of x rays at increasing intensities as electron density and microwave power are raised. This feature requires adequate external shielding to protect personnel and jeopardizes the source components themselves, especially the superconducting magnets.

### *ECR Sources as Charge Breeders*

ECR sources have become the tool of choice for a very specific task: the ionization to high charge states and formation into secondary beams of radioactive particles generated in a primary beam target of so-called Rare Isotope Accelerator facilities. Main aspects of this utilization are the comparatively high particle and ionization efficiencies of ECR sources and their modular design that lends itself to minimizing activated waste [21].

Two very recent examples of ECR-bred charge states obtained by the group quoted as Ref. 21 are: $^{133}Cs^{20+}$ at 3% particle efficiency and $^{85}Rb^{15+}$ at 3.6% efficiency.

### *ECR Sources for High-Current Beams*

A special condition for the propagation of microwaves allows their penetration into an overdense plasma [22], beyond the cut-off limit described by Eqn. (3). This effect is being exploited by high-current proton sources operated at 2.45 GHz frequency. The pioneering example of this type delivers more than 120 mA of transportable beam current in cw mode with a proton fraction of 90% from an 8.6-mm outlet aperture [23]. These high-current ECR sources do not use any transverse confinement device.

## REFERENCES

[1] J. Peters, Rev. Sci. Instrum. 69 (1998) 992.

[2] J. H. Freeman and G. Sidenius, Nucl. Instruments and Methods 107 (1973) 477.

[3] R. Keller, P. Spädtke and F. Nöhmayer, Proc. 1983 Int. Ion Engineering Congress, Kyoto, Inst. Electr. Engineers of Japan, Tokyo (1983) 25.

[4] R. Keller, O. Tarvainen, E. Chacon-Golcher, E. G. Geros, K. F. Johnson, G. Rouleau, J. E. Stelzer and T. J. Zaugg, Proc. 1st Int. Conf. on Negative Ions, Beams and Sources, Aix-en-Provence, France (2008).

[5] E. Chacon-Golcher, Internal Report LA-UR-08-05251, Los Alamos Nat. Lab., 12 Aug. 2008.

[6] J. W. Staples, Proc. *2001 Particle Accelerator Conf.,* Chicago, paper WPAH 014 (2001).

[7] T. Schenkel, J. Staples, R. Thomae, J. Reijonen, R. Gough, K. N. Leung, R. Keller, R. Welton and M. P. Stockli, Rev. Sci. Instrum. Meth. 73 (2002) 1017.

[8] R. F. Welton, M. P. Stockli, Y. Kang, M. Janney, R. Keller, R. W. Thomae, T. Schenkel and S. Shukla, Rev. Sci. Instrum. 73 (2002) 1008.

[9] P. McNeely, M. Bandyopadhyay, P. Franzen, B. Heinemann, C. Hu, W. Kraus, R. Riedl, E. Speth and R. Wilhelm, AIP Conf. Proc. 639, American Institute of Physics, Melville, NY (2002) 90.

[10] R. F. Welton, M.P. Stockli, S.N. Murray, D. Crisp, J. Carmichael, R.H. Goulding, B. Han, O. Tarvainen, T. Pennisia, Proc. 1st Int. Conf. on Negative Ions, Beams and Sources, Aix-en-Provence, France, 10-12 Sept. 2008.

[11] F. F. Cap, *Handbook on Plasma Instabilities*, Vol. 1, Academic Press, New York (1976) 149.

[12] R. Keller, GSI-Unilac-Int/88-1, Darmstadt (1988).

[13] R. Keller, Nucl. Instr. Meth. in Phys. Research A298 (1990) 247.

[14] T. S. Green, in A.K. Hyder, M. F. Rose and A. H. Guenther, eds., *High-Brightness Accelerators*, Plenum Press, New York and London (1988) 453.

[15] M. Bacal, Nucl. Fusion 46 (2006) S250.

[16] K. N. Leung and K. W. Ehlers, Rev. Sci. Instrum. 53 (1982) 803.

[17] R. Geller, *Electron Cyclotron Resonance Ion Sources and ECR Plasmas*, Institute of Physics, Bristol (1996).

[18] D. Leitner, J.Y. Benitez, D. R. Dietderich, M. Leitner, T.J. Loew, C.M. Lyneis, S. Prestemon, G. Sabbi, D.S. Todd, X. Wang, Proc. 2008 ECR Conf., Chicago.

[19] R. Vondrasek, R. Scott, R. Pardo, H. Koivisto, O. Tarvainen, P. Suominen and D. H. Edgell, AIP Conf. Proc. 749, American Institute of Physics, Melville, NY (2005) 31.

[20] L. Celona, S. Gammino, G. Ciavola, F. Consoli and A. Galatà, AIP Conf. Proc. 749, American Institute of Physics, Melville, NY (2005) 75.

[21] G. Savard, R. C. Pardo, E. F. Moore, A. A. Hecht,and S. Baker, AIP Conf. Proc. 749, American Institute of Physics, Melville, NY (2005) 75.

[22] T. Taylor and J. S. C. Wills, Nucl. Instrum. Methods Phys. Res. A 309 (1991) 37.

[23] J. D. Sherman, T. L. Figueroa, L. D. Hansborough, D. M. Kerstiens, J. D. Schneider, H. V. Smith, M. W. Stettler, R. R. Stevens, M. E. Thuot, D. S. Warren and T. J. Zaugg, Rev. Sci . Instrum. 73 (2002) 917.

# CHARGE STATE BOOSTERS FOR RADIOACTIVE ION ACCELERATION

F. Ames, TRIUMF, 4004 Wesbrook Mall, Vancouver, BC V6T 2A3, Canada

*Abstract*

For the post acceleration of radioactive ions produced at ISOL facilities the increase of the charge state is essential to fulfill the A/q requirements of the accelerators. Many of those existing or proposed facilities are relying on the performance of charge state boosters of EBIS or ECRIS type. Although, in principle both types of sources can be used in pulsed or continuous mode operation an EBIS is better suited for pulsed beams whereas an ECRIS is most efficient in a continuous mode. The first charge state booster of the EBIS type had been installed at CERN/ ISOLDE and is working in a routine way since several years. It has been constantly optimized and reaches efficiencies in the order of 10% for a single charge state. More recently ECRIS type devices with similar efficiencies for noble gas ions are being set up and put into on line operation at KEK and TRIUMF. The paper will discuss the present state of the art with respect to existing data of both sources and potential future developments.

## INTRODUCTION

At an ISOL type facility radioactive species are produced by the impact of an energetic beam of protons, heavy ions, electrons or photons on a solid or liquid target. The target is operated at high temperature to allow the products to diffuse out and into an ion source where an ion beam can be extracted. As those conditions, high radiation fields, high outgassing rates, are not very favorable for the operation of sophisticated ion sources normally only singly charged ions are produced. The isotope of interest can be selected by its mass and transported directly to the experiment or to an accelerator to boost its energy. In the later case increasing the charge state of the ions is essential. Transferring singly charged ions into highly charged ones can be achieved via collisions with electrons with total interaction energy higher than the ionization energy for the desired ionization state.

The simplest method to achieve this is accelerating the singly charged ions to a velocity higher than 100 keV/u and directing them through a thin stripper foil. For light ions this can lead to very high efficiency of about 25% in the maximum of the charge state distribution. As this distribution broadens for heavier elements and the cross sections for high charge states decrease the efficiency decreases. Furthermore, at those energies only low or moderate charge states can be reached and a second or third stripping at higher energy will become necessary, thus, reducing the total efficiency even more. Stripping is used at the ISAC I facility after a first acceleration to 150 keV/u. This is achieved with an RFQ accelerator capable of handling ions with a mass to charge ratio of A/q < 30.

So far all other facilities are using or are proposing an active system, where the charge state is increased before acceleration. The ions are injected into an ion source for highly charged ions where they interact with high energy electrons and their charge state is increased before they are extracted again. Two sources are being used for this: an electron beam ion source (or trap) EBIS/T and an electron cyclotron resonance ion source ECRIS. The charge state evolution in both systems can be described by a system of rate equations

$$\frac{dn_i}{dt} = n_e v_e \left[\sigma^{ion}_{i-1\to i} n_{i-1} - \left(\sigma^{ion}_{i\to i+1} + \sigma^{RR}_{i\to i-1}\right) n_i + \sigma^{RR}_{i+1\to i}\right]$$
$$- n_0 v_i \left[\sigma^{chex}_{i\to i-1} n_i - \sigma^{chex}_{i+1\to i} n_{i+1}\right]$$
$$- f_i^{coll} \frac{exp\left\{-\dfrac{ieU_w}{kT_{ion}}\right\}}{-\dfrac{ieU_w}{kT_{ion}}} n_i$$

with $n_i$, $n_e$, $n_0$ being the density of ions with charge q=i, electron and neutrals, $v_i$ and $v_e$ the velocity of ions and electrons, $\sigma^{ion}$, $\sigma^{RR}$, $\sigma^{chex}$, the cross sections for ionization, radiative recombination and charge exchange, $f_i^{coll}$ the coulomb collision frequency, $T_{ion}$ the ion temperature and $U_w$ the trapping potential. Only charge changes by +/- 1 are considered here. Especially at high electron energies or high charge states this may not be true, but there is only very little knowledge of charge changing cross sections in those cases. In principal the charge state distribution after a limited confinement time or in the equilibrium state can be calculated. As the cross section for ionization strongly depends on the electron energy the electron energy distribution function has to be known.

Charge breeding with both sources will be described in more detail in the following sections.

## EBIS

In an EBIS a high intensity electron beam with an energy up to several 10 keV is compressed within a strong magnetic field of usually several T in order to reach current densities of several hundred A/cm$^2$ or in some modern EBIT devices several 10 kA/cm$^2$. Ions injected can be confined radially inside the space charge potential of this beam and longitudinally by a superimposed electrostatic potential. They will be ionized to high charge states via collisions with the high energy electrons. The difference between EBIS and EBIT is mainly the length of the trapping region, which is much shorter in case of an EBIT allowing for a higher compression of the electron beam.

For charge state breeding singly charged ions are injected into the source and after some time the electrostatic potential is lowered to extract the ions at the same side; the other side is blocked by the cathode for the electron beam production. This allows only for pulsed beam operation. As the ion beam size has to match the electron beam size for an efficient capturing of the ions its transversal emittance has to be small. This requires bunching and cooling of the injected ion beam. The final charge state depends on the product of confinement time and electron density and on the electron energy.

The only operational system using an EBIS is also the first on line charge state booster for radioactive ions. It has been taken into operation in 2001 at the REX-ISOLDE facility at CERN [1]. It uses a relatively moderate electron beam intensity around 200 mA yielding to a current density of about 200 A/cm$^2$. Bunching and cooling of the ions is done with a gas filled Penning trap (REXTRAP) [2] in front of it. A broad variety of stable and radioactive ions covering the entire mass range from Li to U has been charge bred. A recent summary of the results can be found in [3]. The total efficiency, including the cooling and bunching, to reach charge states with a mass to charge ratio A/q <4.5 is around 10% with smaller values for the very light and the very heavy elements. The cooling and bunching efficiency is reported to be about 50%. In some selected cases like $^{39}K^{10+}$ where high beam intensity allows for a good optimization of the system the total efficiency can go up to 15%, which is close to the theoretical limit given by the charge state distribution and assuming 100% capture efficiency of the cooled ions. Breeding times vary between a few ms for the low charge state light elements to up to 500 ms for $U^{52+}$.

As an EBIS is operated at ultra high vacuum, $p < 10^{-8}$ Pa, the background from the ionization of residual gas ions is low. In case of the REXEBIS it is in the order of several 10 pA for the highest peaks in the spectrum. The maximum intensity the system can handle is given by the space charge capacity of both the EBIS and the cooler-buncher. In case of the REX-ISOLDE system the limit is given by the trap at about $10^9$ ions per bunch. Working with radioactive ions this is sufficient for most cases but the limit may be reached with strong molecular or stable isobaric contamination in the incoming beam. This will become more severe for future high intensity facilities.

## ECRIS

In an ECRIS a plasma is confined in the minimum of a magnetic field structure. In most designs the field is a superposition of a solenoid field in longitudinal direction with a minimum in the centre and a sextupole field for the radial confinement. The plasma is heated by an rf field at a frequency of several GHz and sustained by $O_2$ or He as support gas. The field strength of the magnet is chosen to allow a resonant energy transfer from the rf field to electrons at their cyclotron frequency on a closed surface around the centre of the source. The maximum of the magnetic field strength is about 2.5 times the field at the resonance. This allows heating and confining electrons up to several 100 keV. The maximum electron density and the maximum in the electron energy distribution mainly depend on the rf frequency. For a state of the art source operating at 14.5 GHz like the PHOENIX booster from Pantechnik [4], the density is about $10^{11} e^-/cm^3$ and the electron energy distribution reaches up to more than 500 keV with most of the intensity below 100 keV. The charge state distribution of the extracted ions depends on the electron density, energy distribution and confinement time. Eventually, equilibrium between the ionization and charge exchange with low charge states and neutral atoms or molecules is reached.

For charge state breeding singly charged ions are injected at one end of the source, captured and confined in the plasma and the highly charged ions extracted from the other side. The method has been developed at LPSC, Grenoble [5,6] and charge state boosters using an ECRIS have been set up at several places including TRIUMF [7], KEK-JAERI [8], ANL [9] and ISOLDE [10]. TRIUMF and ISOLDE are using the 14.5 GHz PHOENIX booster, whereas KEK-JAERI and ANL are using different sources operating at 18 GHz and 10.5 GHz respectively. First operation with radioactive ions has been reported from ISODE and KEK-JAERI. The TRIUMF set-up is expected to produce on line results in the end of 2008. The ISOLDE ECRIS charge breeder has not been used in conjunction with a following accelerator but for beam purification. Typical charge breeding efficiencies reported are 3-5% for condensable elements and more than 10% for noble gases at mass to charge ratios between 4 and 8 [6,7,8]. The efficiency for noble gases is higher because ions leaving the plasma to the wall of the chamber can be reemitted and enter the plasma again. The time necessary for the charge breeding can be measured by pulsing the incoming beam and recording the extracted highly charged ions as function of time after the start of the injection. Reported breeding times vary from some 10 ms up to several 100 ms. Though, in general they increase with charge state the values from different sources don't agree. Their dependence on the source parameters like rf frequency, plasma and neutral density and confinement time and also on the properties of the incoming beam is not well understood and needs some more detailed investigation.

Until now an ECRIS charge breeder is the only system working in true continuous operation mode as injection and extraction of the ions are clearly separated. Pulsed operation is possible if the afterglow mode is used. Here the source is run in a trapping mode with reduced extraction and all ions are extracted in a fast pulse following the switch off of the rf field. Until now only low repetition frequency, around 1 Hz and relatively long pulses, around 1 ms have been demonstrated [6].

A disadvantage of using an ECRIS is the high amount of total current extracted from the source. It mainly consists of ions from the plasma support gas and residual gas. It can be as high as several mA distributed over a broad spectrum of ions from different elements and at different charge states. This makes it difficult to separate the desired highly charged ions and can lead to high contamination of unwanted ions in the beam.

## FUTURE DEVELOPMENTS

There are some attempts for the acceleration of multiple charge states (see for example [11]) but common goals for developments for both sources is the increase in efficiency for the desired charge state and the decrease of the necessary breeding time as long delay time in the source reduces the efficiency for short lived radioactive isotopes.

### *EBIS*

A major point for increasing the efficiency of an EBIS system is to increase the acceptance for capturing the incoming ions. This will reduce efforts and also the losses from the beam preparation. It can be achieved by increasing the electron beam current and thus increasing the space charge potential for the ion confinement. At the moment there are several EBIT devices for charge state breeding planned or under construction with total electron beam current of several A and current density of several 10 kA/cm$^2$ (see for example [12,13]). Additionally, the high electron beam density will shorten the breeding time and allows for higher charge states and intensity.

Adapting the electron beam energy to the binding energy of an atomic shell and utilizing dielectronic recombination ions can be accumulated in a single charge state [14]. Theoretically this can increase the efficiency up to 90% [15].

There are several attempts of operating an EBIS in continuous mode. A semi continuous mode with a continuous injection only interrupted by a short time for extraction has been tested at the REXEBIS [16] with 2% efficiency for the breeding of $K^{10+}$. A further increase of this value with a precooled beam should be possible.

A new development at JINR, Dubna, [17] is the use of an electron in tubular geometry, with the electrons having undertaken a phase transition into an ordered “string” state yielding to very high current density. Such a tubular electron string ion source, TESIS, would allow a true continuous mode of operation. Both the injection and extraction have to be performed off axis but at different radial location. The proof of formation of electron strings has been done and a source based on the tubular geometry is being set up at the moment.

### *ECRIS*

The capture efficiency in an ECRIS is mainly determined by the plasma density. It can be increased by increasing the rf frequency or by using two different rf frequencies for the plasma heating. Due to the higher electron density this will shorten the breeding time as well.

Several attempts have been made to develop simulation codes for the capturing and further charge state increase in an ECR source (see for example [18]). The results obtained with these simulations will lead to a better understanding of the capturing and charge breeding process in an ECR and can be used for further optimization. Cooling of the incoming ion beam will help in the optimization of effective deceleration optics in front of the source.

In order to reduce the background from residual gas ions future sources will be designed in a UHV compatible way [19] and be operated with ultra pure support gases to sustain the plasma. As the maximum in the charge state distribution is mainly determined by the charge exchange with neutrals this may also lead to higher charge states.

## CONCLUSION

Charge state breeding for the post acceleration of radioactive ions at ISOL facilities can be performed with both EBIS and ECRIS. Though, the efficiency reached so far with an EBIS source is higher than with an ECRIS the later can be operated in continuous mode and at higher beam intensities. Until now only the EBIS system at ISOLDE is in routine operation and the ECRIS systems at KEK-JAERI, ANL and TRIUMF are being commissioned at the moment. Beside the common goal of increasing the efficiency future work aims to overcome the limitations of the specific systems, which in case of an EBIS is developing schemes for continuous mode operation and in case of an ECRIS reducing the amount of background ions and shortening the breeding time.

If it comes to choosing a specific system for a facility also operational aspects have to be considered. At the moment the complexity of an EBIS system is much higher as it includes the buncher and cooler for the beam preparations. This increases the set up time for a specific ion beam. ECR ion sources are more commonly used as ion sources for heavy ion accelerators but no extended experience for using them as charge breeders at such a facility exists so far. The complexity of new improved systems will increase as well with the use of superconducting magnets necessary to reach the high magnetic field strengths for higher frequency operation and UHV designs.

## REFERENCES


[1] B.H. Wolf, et al., Nucl. Instr. Meth. B 204 (2003) 428-32

[2] F. Ames, et al., Nucl. Instr. Meth. A 538 (2005) 17-32

[3] F. Wenander, Nucl. Instr. Meth. B (2008) in press

[4] http://www.pantechnik.fr

[5] C. Tamburella, et al., Rev. Sci. Instrum. 68 (1997) 2319-2321

[6] T. Lamy, et al., Rev. Sci. Instrum. 73 (2002) 717-719

[7] F. Ames, et al., Rev. Sci. Instrum. 79 (2008) 02A902

[8] S.C. Jeong, et al., Nucl. Instr. Meth. B 204 (2003) 420-427

[9] R.C. Vondrasek, Rev. Sci. Instrum. 79 (2008) 02A901

[10] T. Fritioff, et al., Nucl. Instr. Meth. A 556 (2006) 31-37
[11] B. Mustapha, P.N. Ostroumov, Phys. Rev. ST Accel. Beams 8 (2005) 090101
[12] S. Schwarz, et al., Rev. Sci. Instrum. 79 (2008) 02A706
[13] G. Sikler, et al., Eur. Phys. J. A25 (2005) 63-64
[14] J.R. Crespo Lopez-Urrutia, et al., Rev. Sci. Instrum. 75 (2004) 1560-1562
[15] S.Schwarz, et al., Nucl. Instr. Meth. B (2008) in press
[16] F. Wenander, et al., Rev Sci. Instrum. 77 (2006) 03B104
[17] E.D. Donets, et al., Rev Sci. Instrum. 75 (2004) 1566-1568
[18] J.S. Kim, et al., Rev Sci. Instrum. 79 (2008) 02B906
[19] T. Thuillier, et al., Rev Sci. Instrum. 79 (2008) 02A330

# HEAVY ION LINAC BOOSTER AT IUAC, NEW DELHI

Amit Roy

Inter-University Accelerator Centre, Aruna Asaf Ali Marg, New Delhi – 110067, India

*Abstract*

The first module of the booster superconducting linear accelerator that will have a total of three modules, each having 8 quarter wave coaxial line bulk Nb resonators, has been commissioned at IUAC. During initial operation of the first linac module, energy gain was found to be much lower due to various problems which are now identified and solved. After acceleration through the linac module and subsequent re-bunching using superconducting Rebuncher, 158 MeV Silicon beam having pulse width of 400 ps was delivered to conduct nuclear physics experiments. The other two linac cryostats and the required 16 resonators to be installed in those two cryostats are in the final stage of fabrication. Work has also progressed on a high current injector that would act as an alternate source of heavy ions for the super conducting Linac.

## INTRODUCTION

Currently the programmes for addition of superconducting linac boosters for increasing the energy of heavy ions from the Pelletron accelerator at Inter-University Accelerator Centre (IUAC), New Delhi is nearing completion. The accelerating structures for the linac is a quarter wave cavity resonators (QWR) made of bulk Niobium operating at 97 MHz and optimised for $\beta$ = 0.08 [1]. One module with eight cavities have been operated for beam acceleration and several problems faced with the drive coupler, slow tuner have been sorted out. A very novel method was found to reduce the microphonic noise in the cavity, which reduced the power required to amplitude and phase lock the cavities. Fields of the resonators obtained in the linac cryostat are in the range of 3 –5 MV/m at 6 watts of dissipated power at critically coupled condition of the power coupler. Fabrication of 15 more resonators for the next two modules is progressing according to schedule in the in-house resonator fabrication facility. In addition to the resonator production, several ANL built resonators have been repaired. It is also planned to design, develop and prototype a suitable low beta resonator around $\beta$ = 0.045 for the high current injector.

IUAC has also agreed to build two $\beta$ = 0.22, 325 MHz Single Spoke Resonators for the proton driver linac project of Fermi National Accelerator Lab (FNAL), USA. The resonators will be built at IUAC, and the final processing and testing will be carried out at FNAL.

## QUARTER WAVE RESONATOR

The Quarter Wave resonator is a coaxial structure operating in the TEM mode with beam accelerating gaps in a direction perpendicular to the symmetry axis. The QWR incorporates a few distinctive features viz., a pneumatic slow-tuner in the form of a niobium bellow provides a tuning range of approximately 100 kHz, substantially larger than in any working quarter wave resonators; the Nb cavity being jacketed by a stainless steel shell joined to the Nb cavity through explosively bonded Nb-SS transition flanges. A picture of completed QWR along with the Nb slow tuner bellows is given in Fig. 1.

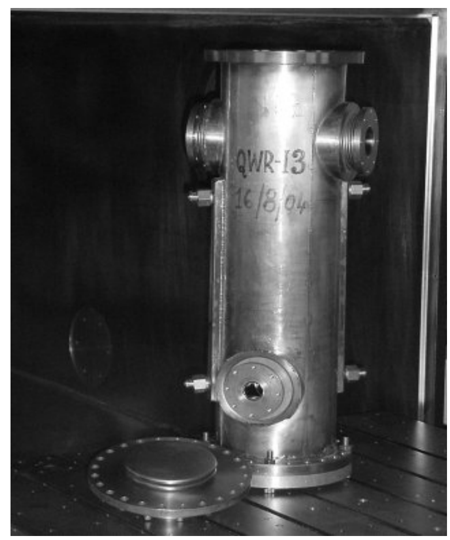


Figure 1: Indigenously built niobium quarter wave resonator with slow tuner bellows at IUAC.

The prototype QWR and twelve more resonators were fabricated in ANL and out of these, 8 resonators are used in the first linac module.

In order to fabricate the resonators in house, a Superconducting Resonator Fabrication Facility (SuRFF) has been set up and is fully functional. It consists of a 15 kW Electron Beam Welding machine, an automated Surface Preparation Laboratory for electro-polishing the cavities, a High Vacuum Furnace, and a dedicated test cryostat set-up.

Production of the superconducting niobium quarter wave resonators for the second and third linac modules has progressed sufficiently and nearing completion. There have been some problems faced in completing the (technically difficult) closure welds (the weld joining the top flange with the niobium housing as shown in Fig. 3) although several bare niobium resonators have been successfully welded and are ready for the stainless steel outer jacketing. After all the electropolishing was over, welding of the major sub-assemblies began for completing the bare niobium resonators. This work was done systematically to ensure that the RF resonance frequency scatter was kept to a minimum. The length of the Central Conductor primarily decides the RF frequency, therefore a single resonator was initially completed and its frequency was measured. Based on this data the Central Conductor length of two more resonators was adjusted and they were completed and their frequencies were measured. The Central Conductor length was further fine tuned and the remaining twelve resonators were completed. Although this took longer than if we had finished all the resonators together, it helped in achieving the desired RF frequency in most cases. Fabrication of the niobium mechanical Tuner Bellows began as the electropolishing work on the major resonator sub-assemblies neared completion. The tuner is mounted at the open end of the resonator. In order to determine the open-end length of the housing for providing appropriate capacitive loading and therefore the required tuning range from the tuner, we have decided to complete one tuner bellow assembly. This work is presently nearing completion. Simultaneously several components for the remaining tuner bellows have been machined and formed, and are being electron beam welded.

The stainless steel outer jackets (helium vessel) have been fabricated and electropolished (at a commercial vendor). They have been cut into two halves for the clamp shell assembly. Other items for the outer jackets, such as the top domes, CF flanges and pre-cool channels have also been fabricated. The measured Q curve for the first cavity fabricated at IUAC is presented in Fig. 2.

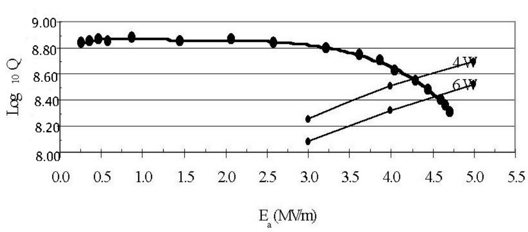


Figure 2: QWR-I1 cold test performance.

## *Repair Work on Existing QWRs*

In addition to resonator fabrication for the linac modules several critical repair jobs have also been undertaken. On several of the ANL built QWRs the transition assemblies, in which welded ss bellows were used, leaked when the resonators were loaded in the cryostat and filled with liquid/gas helium. This problem had not been encountered during the prototype resonator testing. The design of both the coupling and beam port transition flange assemblies were changed and formed stainless steel bellows are now being used. The leaking assemblies on several cavities have been successfully repaired by machining them out and replacing with the modified design.

## *Reduction of Microphonics Frequency Jitters*

During early on-line beam tests of linac, high RF power of about 300 watts was required to lock the resonators in over-coupled mode due to presence of microphonics. The high RF power caused melting of insulation of RF power cable, excessive heating of drive coupler and increased cryogenic losses. To reduce the requirement of RF power, a novel technique of damping the mechanical mode of the resonator by inserting stainless steel balls of suitable diameter inside the central conductor (Fig. 3) of the QWR has been adopted.

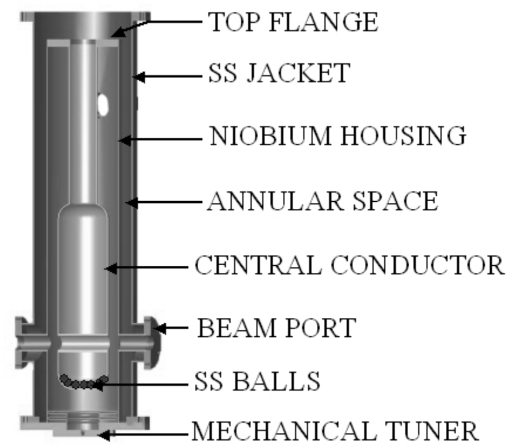


Figure 3. Schematic for the damping of vibrations of central conductor through stainless steel balls.

The dynamic friction between the balls and the niobium surface damps the vibration of the central conductor excited due to coupling of the mechanical mode to ambient noise. The frequency jitter of the QWR was measured at superconducting temperature without/with SS balls with the help of a cavity resonance monitor in phase lock loop and a reduction of microphonics by a factor of $\geq 2$ has been recorded with balls as damper. During phase and amplitude locking, a remarkable reduction of input RF power of about 50% (Fig. 4) has been achieved to lock the resonator [2].

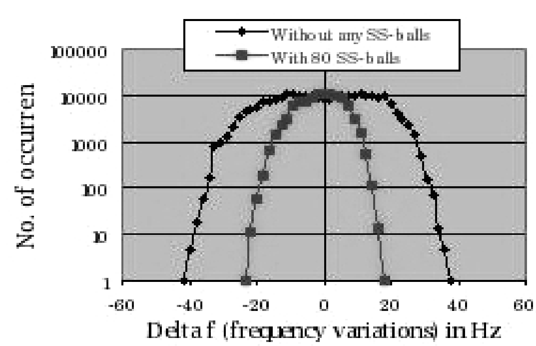


Figure 4. Damping in frequency jitter with ss balls in central conductor of resonator.

### *Modifications for Improvement f Liquid Helium Cooling Efficiency*

In our old design, at the top of the resonator, there used to be a flat flange (SS) with a 40 mm diameter bellows through which liquid helium enters into the resonator from helium vessel. Just below this flange, about 15 mm down, the resonator's niobium flange, which carries maximum current when the QWR is energised, is located.

To avoid trapping of bubbles at SS flat flange on the top of the resonator, the flat flange was replaced by a hemispherical structure. With these modifications, a number of cold tests were performed on different resonators in linac cryostat and improved electric fields comparable to the results in the test cryostat were obtained.

### *New Drive Coupler*

The Quarter Wave Resonators (QWR's) required nearly 300 Watts of RF power to generate field of ~4 MV/m in over coupled mode. Due to this high power requirement, in our first few tests, we found that the insulator of RF power cables were melting and a thin layer of material was deposited on to the cold surface of cavities. A detailed analysis of this thin film was done using Energy Dispersive X-Ray Analysis (EDX) at Solid State Physics Laboratory, Delhi. This showed Zn (96.5%)/Cu (2.49%) in atomic % as main peaks. The rack and pinion were made of brass and the excessive heating during powering of the cavities might have caused the coating. To eliminate any possibility of metal coating on niobium surface during the operation of the resonators in future, three new types of the drive coupler were fabricated. In the most successful design (Fig. 5), the rack and pinion made by brass was moved outside the resonator. During several off-line tests of the resonators with the new drive couplers, no coating was observed on niobium surface or on the inside portion of the drive coupler.

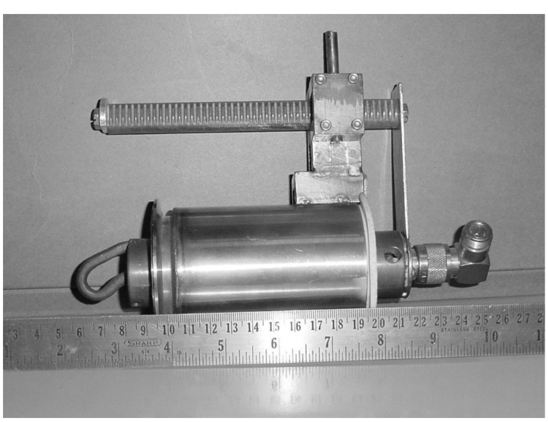

Figure 5. The final design of the power coupler

### *Slow Tuner*

During last few cold tests the original slow tuner bellows were observed to start leaking from welding joints. Though these leaks could be repaired, we decided to re-design the whole system of movement of the slow tuner. In new design, He gas is introduced in an stainless steel bellows and through a mechanical attachment linear motion is transferred to niobium bellows (Fig. 6). The new design was successfully tested in test and linac cryostat for frequency range and response measurements. Now the new arrangement has replaced the old one in all the resonators of superbuncher, linac and rebuncher cryostat.

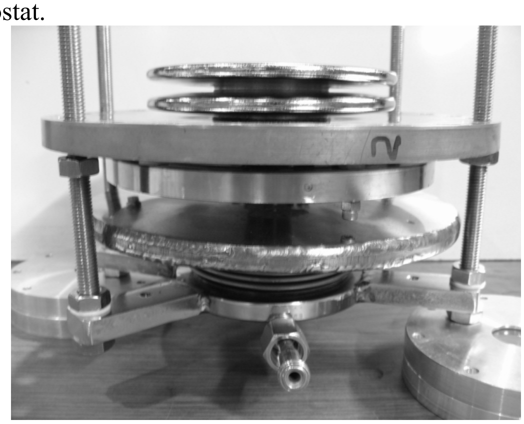

Figure 6. The mechanical tuner connected with the SS-bellow along with the gas line.

### *Rebuncher*

Two Quarter Wave Resonators (QWR) having accelerating field up to ~3.5 MV/m each have been installed in rebuncher cryostat. One of these resonators was fabricated in-house at IUAC. The rebuncher cryostat along with these resonators are shown in Fig. 7.

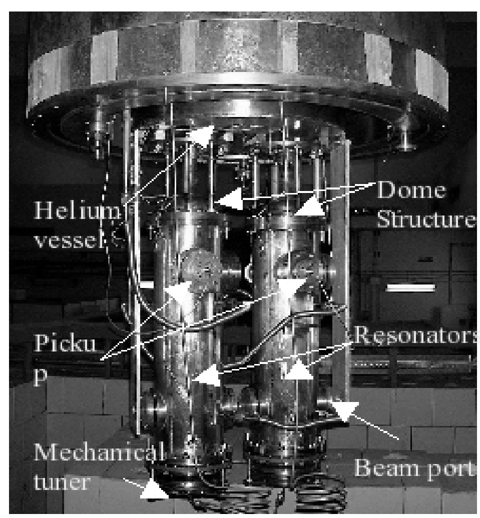


Figure 7. Two resonators (QWR) installed in rebuncher cryostat prior to cold test.

## ON-LINE TEST OF LINAC

After carrying out cold tests of the resonators in test cryostat, eight resonators and a superconducting solenoid has been installed and aligned in the first linac cryostat.

Initial off-line tests of the resonators in linac were carried out to understand the cool down times and check the field levels in the resonators.

Finally, dc and pulsed beam were accelerated through resonators in Linac cryostat. Three runs with $^{28}Si$ beam from the Pelletron have been successfully carried out. The beam bunching system of IUAC consists of a pre-tandem multiharmonic buncher (MHB) [3] and a post tandem high-energy sweeper (HES) [4]. A phase detector has been placed after analyser magnet of the Pelletron to sense the phase of the beam bunch. The bunched beam was transported to the superbuncher located about 25 metres downstream from the phase detector. The point of time focus of the superbuncher is ~ 9 metres from it and coincides with the entrance point of the first linac cryostat.

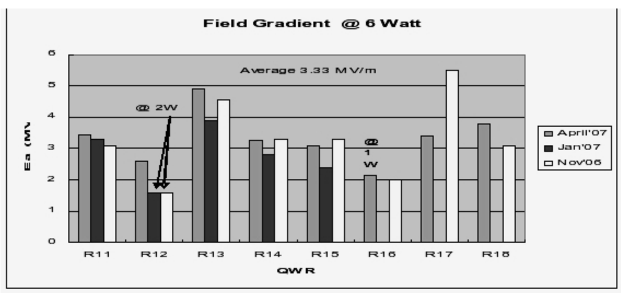


Figure 8. Field gradient achieved by 8 resonators on 3 on-line tests.

During these tests, the resonators could be maintained in phase locked condition for several hours. The field levels in the first test were quite low (1-2 MV/m) although field levels > 4 MV/m have been reached in previous tests [5]. The cause for the low field levels was coating of the resonator surface from overheated brass rack and pinion arrangement for movement of the RF coupler drive. The coupler design has been changed to avoid exposure of the brass portion to inside of the resonator. After these modifications, two runs of the linac with Si beam were performed. In these runs the field levels > 3 MV/m were maintained and the field levels were locked for 3-4 days for experiments to be done with the accelerated ions. The transmission of the beam through linac was close to 100%. The result of the accelerating field gradient of the linac resonators is shown in Fig. 8.

Towards the end of last year, all the modifications in the resonator accessories were tested and the resonators in SB, linac and RB cryostats, were made ready for beam acceleration. In November 2007, 130 MeV $^{28}Si^{+10}$ beam from Tandem was initially pre-bunched by the Multiharmonic buncher with the dark current removed by the high energy sweeper and a time width of ~ 1.1 ns was obtained at the entrance of the SB resonator. By carefully adjusting the phase and amplitude of the superbuncher resonator, a time width of ~ 250 ps had been measured at the entrance of linac cryostat with the help of a cooled thin (50 µm) surface barrier detector. The beam of 250 ps was then injected into the seven resonators of linac cryostat and a total energy gain of about 28 MeV was measured from all the resonators of linac cryostat by another thick surface barrier detector (300 µm) installed at the exit of linac. The energy spectrum of the beam from the Pelletron and after every resonator in linac is shown in Fig. 9.

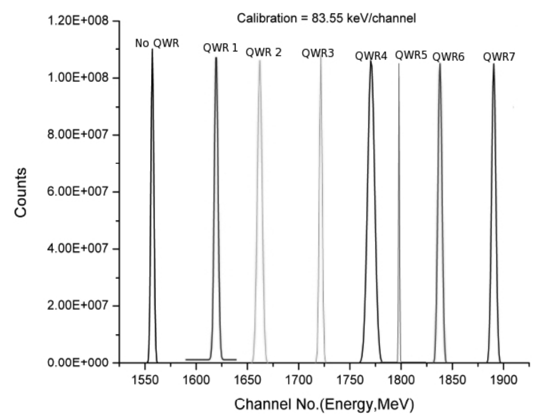


Figure 9. The energy spectrum of the beam from the Pelletron and after turning on the seven resonators one by one in linac cryostat.

The beam was then transported up to the rebuncher which was located at about 14 meters down the line from the first linac cryostat. With the help of the switcher magnet, beam was further tuned up to the location of an experimental scattering chamber, at about 13 meters from the rebuncher cryostat. A pair of thick (300 µm) and thin surface (40 µm) barrier detectors cooled to subzero temperature were installed in the scattering chamber to measure the energy and time width of the beam bunch.

By optimizing the reference phase of a single resonator of the RB cryostat and then by changing the amplitude of the accelerating field, a time width of the beam bunch measured by the detector at the scattering chamber could be compressed from 1.1 ns to ~400 ps (shown in Fig. 10). A nominal accelerating field of ~ 1.7 MV/m was found to be adequate from a single resonator of the rebuncher cryostat to re-bunch the beam at the experimental chamber. Due to shortage of time towards the end of the experiment, not much effort could be devoted to further reduce the time width. But with a more systematic approach to vary the bunching field of the rebuncher in smaller steps and proper adjustment of the nuclear electronics, the time width of the beam bunch could be matched with the value obtained at the entrance of linac by the SB.

In December 2007, 100 MeV $^{16}O^{+8}$ beam from Pelletron, pre-bunched by MHB and low energy chopper, a time width of ~1.0 ns was injected into SB. The resonator in SB had produced a time width of ~160 ps at linac entrance and finally after acceleration by seven resonators in linac, a total energy of 120 MeV was obtained at the exit of linac. The average field obtained from the resonators was ~ 3 MV/m from beam energy calibration. This beam was then re-bunched by a resonator in RBC and a time width of ~ 500 ps with 120 MeV was delivered at the experimental chamber. The beam was then used for about a week by an experimental group to study fusion-fission reaction dynamics using neutron multiplicity measurement.

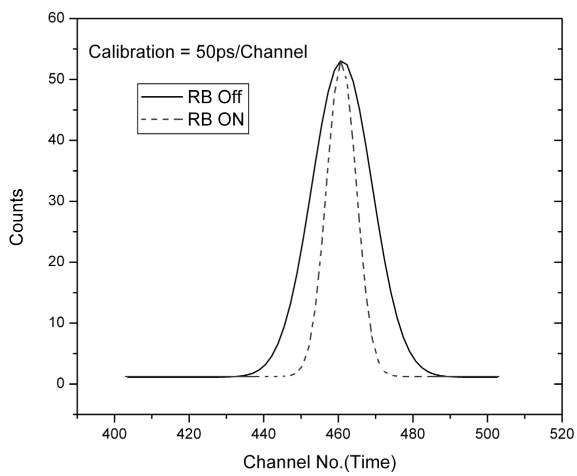


Figure 10. Beam pulse width with the rebuncher cavity on and off.

The operation of the one third of the complete linac with superbuncher, a single linac cryostat and rebuncher has thus been demonstrated and it is planned to deliver the linac beam to the user on a routine basis. The fabrication of the second and third linac modules with sixteen resonators are going on in full swing. These modules are expected to be installed in the beam line by the end of this year.

Two Nb Single Spoke Resonators operating at 325 MHz, β=0.22, is under fabrication at IUAC using in-house facilities for electon beam welding and electropolishing for the Proton Driver Linac of a High Intensity Neutrino Source at Fermi National Accelerator Laboratory, USA as a collaborative program. The resonators are designed by Fermilab.

In the high current injector project to provide an alternate injector to the superconducting linac, the high Tc superconductor based ECR source PKDELIS[6] parameters have been optimised and a prototype RFQ operating at 48.5 MHz has been fabricated and cold tested using bead-pull technique.

## ACKNOWLEDGMENT

The work from IUAC reported here is on behalf of the Phase II group of Inter-University Accelerator Centre.

## REFERENCE

[1] K.W.Shepard, P.N.Potukuchi and A. Roy, Proc. of the 1993 Particle Accelerator Conference, 17-20 May, 1993, Washington, DC,1045.

[2] S.Ghosh, P.N.Patra, B.K.Sahu, A.Rai, G.K. Chaudhuri, A.Pandey, D.Kanjilal and A.Roy, Physical Review STAB 10 (2007) 042002.

[3] A. Sarkar et al, Ind J. Pure and Appl. Phys. Vol 39(2001)15.

[4] S. Ghosh, A. Sarkar, S.S.K. Sonti, S. Rao, V.V. Sivakumar, A. Rai, P. Barua, S.K. Datta, R.K. Bhowmik and A. Roy, Rev. Sci Instr. Vol 77, (2006)076103.

[5] S.Ghosh, R. Mehta, P.N. Prakash, A. Mandal, G.K. Chaudhuri, S.S.K. Sonti, D. Mathuria, A. Rai, S. Rao, P. barua, A. Pandey, B.K. Sahu, A. Sarkar, G. Joshi, S.K. Datta, R.K. Bhowmik and A. Roy, Pramana Vol 59, No.5 (2002) 881.

[6] D.Kanjilal, G.Rodrigues, P.Kumar, A.Mandal, A. Roy, C.Bieth, S.Kantas and P.Sortais, Rev. Sci. Instr. Vol 77, (2006) 03A317.

# BEAM COMPRESSION IN HEAVY-ION INDUCTION LINACS*

P.A. Seidl[1#], A. Anders[1], F.M. Bieniosek[1], J.J. Barnard[2], J. Calanog[1],3, A.X. Chen[1,3], R.H. Cohen[2], J.E. Coleman[1,3], M. Dorf[4], E.P. Gilson[4], D.P. Grote[2], J.Y. Jung[1], M. Leitner[1], S.M. Lidia[1], B.G. Logan[1], P. Ni[1], P.K. Roy[1], K. Van den Bogert[1], W.L. Waldron[1], D.R. Welch[5],
[1]Lawrence Berkeley National Laboratory, Berkeley, CA 94720, USA
[2]Lawrence Livermore National laboratory, Livermore, CA 94550, USA
[3]University of California, Berkeley, CA 94720, USA
[4]Princeton Plasma Physics Laboratory, Princeton, NJ 08543-0451, USA
[5]Voss Scientific, Albuquerque, NM 87108, USA

*Abstract*

The Heavy-Ion Fusion Sciences Virtual National Laboratory is pursuing an approach to target heating experiments in the Warm Dense Matter regime, using space-charge-dominated ion beams that are simultaneously longitudinally bunched and transversely focused. Longitudinal beam compression by large factors has been demonstrated in the LBNL Neutralized Drift Compression Experiment (NDCX) experiment with controlled ramps and forced neutralization. The achieved peak beam current and energy can be used in experiments to heat targets and create warm dense matter. Using an injected 30 mA $K^+$ ion beam with initial kinetic energy 0.3 MeV, axial compression leading to ≈50x current amplification and simultaneous radial focusing to beam radii of a few mm have led to encouraging energy deposition approaching the intensities required for eV-range target heating experiments. We discuss experiments that are under development to reach the necessary higher beam intensities and the associated beam diagnostics.

## INTRODUCTION

To create a short (~ ns) pulse with duration suitable for the study of warm dense matter [1], our approach has been to modulate the energy of an initially much-longer non-relativistic beam. To achieve target temperatures around ~ 1 eV, the required beam intensity calls for space charge neutralization, which has been achieved with a background plasma through which the beam passes while it is focusing transversely and bunching longitudinally.

We are approaching the required beam intensities for heating targets toward warm dense matter conditions, and have arrived at this stage through a sequence of experiments over the past several years. The scaled final focusing experiment demonstrated the successful neutralization of an initially space-charge-dominated beam by a background source of electrons in order to achieve an emittance-limited focal spot [2]. The experiment was scaled from a design of a final focusing system for a heavy ion fusion driver using quadrupole magnets for beam transport (driver parameters: 10 GeV $Bi^+$ at 1.25 kA/beam). Following initial experiments with an emittance-limited 95 μA, 160 keV $Cs^+$ beam, the beam current was then increased to 400 μA with a perveance of 5 x $10^{-5}$; space-charge limited near the focal plane for an un-neutralized beam. The spot radius with neutralization was ~2X smaller, in agreement with models assuming 80% and 0% neutralization, respectively. LSP simulations [3] showed good agreement with the experiments.

Next, the Neutralized Transport Experiment, used a higher current (~25 mA) and higher energy (250-350 keV) $K^+$ beam. The beam perveance (~$10^{-3}$) was effectively neutralized with RF and cathodic-arc plasma sources [4]. This demonstrated the feasibility of neutralization of higher perveance beams, a precursor to the additional feature of axial bunching of the ion beam.

The axial compression is achieved with an induction bunching module (IBM) inserted after the matching section. Operating at ±80 kV, a ±12.5% velocity ramp is imparted to 150-200 ns subset of the several-microsecond beam pulse. The beam then drifts through a neutralizing plasma in a drift compression section a few meters in length (L). To establish a neutralizing plasma along most of the length of the drift compression section, the RF plasma used in NTX was replaced with a ferro-electric plasma source [5], and cathodic arc plasma sources injected a high-density plasma near the focal plane where the beam density is greatest. Current amplification of ≈ 50 was demonstrated in the first NDCX experiments [6].

A fundamental limit to the current amplification and pulse duration is the longitudinal energy spread (longitudinal phase space and emittance) of the injected beam, as shown in Eq. 1:

$$t_{\min} = \frac{L}{v^2}\sqrt{\frac{2kT}{M}} \tag{1}$$

where $v$ is the average ion velocity, $T$ is the effective longitudinal beam temperature and $M$ is the ion mass.

The energy spread was measured with an electrostatic energy analyzer. The measured energy spread is adequate for achieving nanosecond-duration bunches (see below). Other limits are set by the uniformity and density of the background neutralizing plasma, and imperfections of the bunching module waveform. In general, simulations have shown that if the background plasma density is greater than the local beam density, then the effectiveness of the neutralization is independent of the details of the plasma density distribution [7]. For near-term warm dense matter experiments, the beam density increases steeply and

* This work supported by the U.S. Dept. of Energy contracts W-7405-ENG-48, DE-AC02-05CH11231 and DE-AC02-76CH-O3073.
#PASeidl@lbl.gov

approaches $n_b = 10^{13}$ cm$^{-3}$ near the target plane. We have measured plasma densities in that range with cathodic-arc plasma sources. The plasma temperature should be low enough to not heat the beam and we have found that plasma temperatures in the few eV range have a benign influence on the beam. Depending on the beam and plasma densities, collective instabilities may limit the focused beam intensity, but for NDCX-I (based on both experiment and theory) and NDCX-II (based on theory) these instabilities appear to be benign.

## RESULTS AND DISCUSSION

We installed a short, high-field solenoid (B = 8 Tesla, 10-cm coil length) after the ferroelectric plasma source and before the target plane (Fig. 1) to impart a steep convergence angle on the beam before the focal plane. LSP modeling suggests that sub-mm radii might be possible, leading to a several-fold increase in the energy deposition. This assumes sufficiently high plasma density can be injected into the bore of the solenoid [8]. A target chamber and new target heating diagnostics have been installed at the end of the beamline [9].

### *Beam Diagnostics in the Target Chamber*

An improved Fast Faraday Cup has been installed in the new target chamber (See Fig. 1). The operating principle is the same as in ref. [10] and the electronic response still allows for ≈1 ns resolution of the ion beam current. This is established mainly by the 1-mm gap between the suppressor plate and the collector, since the incoming ion (v ≈ 1.2 m/μs) transit time of 1 ns will set the scale for the capacitive pickup of the ions approaching the collector. The new design enables variation of gaps between hole plates, and hole plate transparency, easier alignment of the front hole plate to middle (bias) hole plate, and a metal enclosure for shielding from the background plasma and electronic noise. Each hole plate has a hexagonal array of holes, extending over a circular area with 30-mm diameter. In the current version, the front hole plate (held at ground potential) has 0.23 mm diameter holes spaced by 1 mm, while the middle hole plate (suppressor grid, biased to -75 V) has 0.46 mm diameter holes spaced by 1 mm. The holes are larger on the middle plate to prevent scraping. This 95-mrad tolerance between the concentric front plate holes and the middle plate holes should compensate for non-zero ion trajectories and detector alignment imperfections. The collector plate is biased to +75 V.

The geometric transparency of the front hole plate results in a reduction of the beam current reaching the collector grid by a factor of 44. Figure 2 shows the response of the Faraday cup to the uncompressed head of the beam (30 mA $K^+$, 1 μs duration), and the compressed bunch at t ≈ 4.8 μs. The product of the collector signal amplitude and the hole plate transparency agrees (≈±5%) with the upstream measurement of the beam current before the IBM. The suppressor signal has a similar response to the collector, and is not as well understood at this time. We are modeling the detector response with WARP and LSP particle in cell simulations, including the effect of desorption and ionization of neutral atoms from the collector and front plate. The recognition of this latter effect as potentially significant is based on analytic estimates using known desorption coefficients, charge-exchange cross sections and ionization cross sections. We are also studying the possibility that ions are striking the middle plate due to detector misalignment, beam centroid misalignment, and large angle ion trajectories from the chromatic aberrations and also due to small angle scattering from the inside edge of the front plate holes.

Though simulations show that the collector should be effectively shielded from the plasma is by the front hole plate, a plasma background signal from the FCAPS has been measured on the collector. It is slowly varying and is subtracted during data analysis.

The transverse (spatial) distribution of the beam is measured by allowing the beam to strike a 100-micron thick alumina scintillator, and then detecting the beam induced light emission with an image-intensified gated-MCP camera. The optical system produced a resolution of 10 to 17 pixels/mm (depending on the choice of lens and

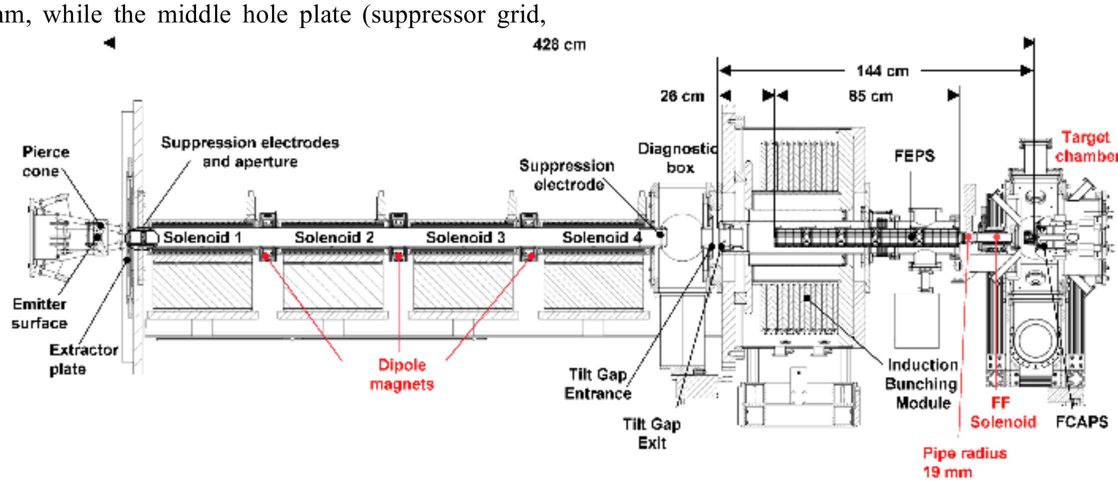


Figure 1: Elevation view of the Neutralized Drift Compression Experiment

optical setup). Image acquisition and processing software are then used to collect and analyze the time-gated images of the beam [11]. A steel mesh of transparency 28% is placed on the upstream side of the scintillator. The relatively low transparency reduces the flux onto the scintillator and the degradation of the scintillator. It is biased to -300 V, creating a supply of electrons to discharge the scintillator caused by the accumulation of charge from the positive ion beam. Using a phototube, photodiode, and streak camera, the time dependence of the light output from the scintillator has been recorded to measure the compressed pulse duration independently of the fast Faraday cup.

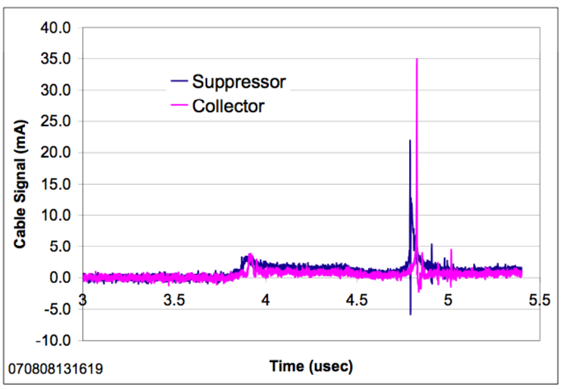


Figure 2: Faraday cup response to uncompressed beam and bunched portion ($t \approx 4.8$ μs).

## *Longitudinal Phase Space Measurements*

The energy spread, ΔE, of the non-relativistic ion beam is related to the longitudinal velocity spread $\Delta v_z$ by $\Delta E = mv\Delta v_z$. Assuming the velocity distribution is a one-dimensional Maxwellian about the mean beam velocity, the temperature, $T_z$, of that distribution is given by:

$$T_z = \frac{(\Delta E^2)}{2E_o} \tag{2}$$

The new electrostatic energy analyzer (EEA) was placed at the exit of the ferro-electric plasma source, to measure the longitudinal phase space and energy spread of the uncompressed beam with and without plasma neutralization [12, 13]. A special beam envelope tune was used for the un-neutralized beam to prevent particle loss in the 180-cm drift distance from the final matching solenoid to the entrance slit of the spectrometer. The entrance slit of the spectrometer was 0.1 mm x 5 mm, which allowed ~10 μA of the incident 30-mA $K^+$ beam to be transmitted through the spectrometer, a 90-degree sector design with a bending radius of 75 cm and a gap of 2.5 cm between concentric dipole electrodes. The focal plane detectors were a slit-Faraday cup and an alumina ($Al_2O_3$) scintillator with a gated CCD camera. For a 300 keV ion beam, deflection plate voltages were ±15 kV. The contribution of field quality to spectrometer resolution was estimated with ray tracing simulations with fields derived from the mechanical specifications of the field defining plates. The results suggest a resolution of $\Delta E/E \approx 5 \times 10^{-5}$ , while the contribution from the 0.1 mm entrance slit gives a resolution of $\Delta E/E = 2 \times 10^{-4}$ or $\Delta E =$ 60 eV. Thus, the choice of entrance slit width (motivated by detector signal-to-noise) is the dominant factor in determining the energy resolution for these data. The dispersion on the focal plane is 1.7 mm / keV and this is reflected in the data of Fig. 3, showing the profiles of a 500-ns slice of the 289 keV incident beam for several dipole plate voltages.

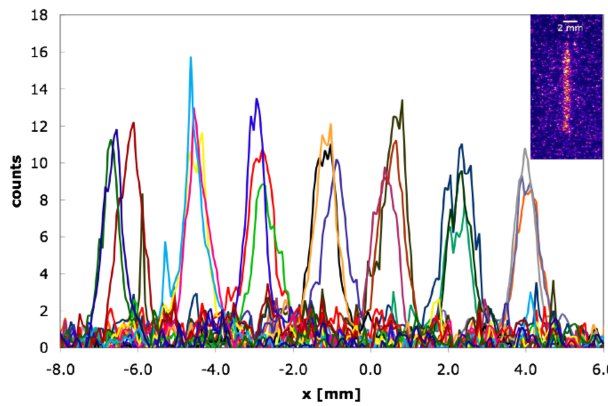


Figure 3: Beam image profiles as a function of deflection plate voltages. The incident beam energy was 289 keV, and the deflection plate voltages were scanned in 50-Volt steps around 14.5 kV, corresponding to beam energy variations of 1-keV steps. The inset shows one of the images from the scintillator (at $x \approx -1$ mm).

The data were measured with the scintillator and image-intensified CCD camera. The entire energy acceptance of the spectrometer is displayed, about 7 keV. The variation among repeated beam pulses (three per plate voltage setting) shows the shot-to-shot energy variation of the beam, <0.1 keV (rms). The measured width of the distributions, or the energy spread of the injected $E_o =$ 289-keV un-bunched beam is $\Delta E \approx 0.17$ keV. The measured energy spread corresponds to an axial temperature of $T_z = 0.05$ eV, which is adequate for compressing the beam to < 1 ns (Eq. 1). Other mechanisms may limit the pulse duration, such as incomplete neutralization of the compressed pulse, and waveform imperfections in the IBM. No significant difference was observed between the neutralized and un-neutralized beam cases, suggesting minimal heating of the beam from the FEPS plasma.

The time dependence of the energy distribution was recorded with a streak camera imaging the light emission from the scintillator (Fig. 4), and independently with a slit-Faraday cup. The results reflect the slight decrease (2-4 kV/μs) of the injector Marx voltage after the initial rise to peak voltage. Signal to noise limitations obscured the detection of the acceleration of ions near the head of the beam due to longitudinal space charge. Particle-in-cell simulations suggested this would be a difficult signal to detect due to low signal amplitude.

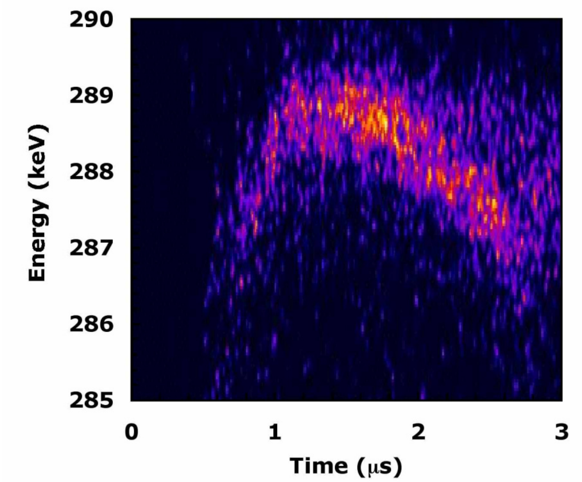


Figure 4: Streak camera image of the longitudinal phase space of the uncompressed beam near the beginning of the pulse.

### *Plasma Density Measurements*

The plasma density in the target chamber has been increased and now mostly exceeds the on-axis beam density to satisfy $n_p/n_b>1$, where $n_p$ and $n_b$ are the plasma electron density and ion beam density, respectively, and Z is the mean ion charge state of the plasma ions. This work consists of several segments. First the plasma density of two filtered cathodic arc plasma sources (two-FCAPS) was measured with an axially moveable Langmuir probe with a 4-Tesla solenoid magnetic field. Next, the two-FCAPS system was replaced by fabricating four cathodic arc plasma sources (four-FCAPS) with straight filters (vs the former $45^o$ bend in the two-FCAPS system) to increase the plasma density. The solenoid magnetic field was increased to 8 T. Results show that the new four-FCAPS system, with the short straight filters and driven with a 3x higher discharge current provides 9-60 times greater plasma density than the two-FCAPS system with the bent filters. Assuming a mean plasma velocity of $2x10^4$ m/s, the four-FCAPS system provided a peak plasma density 9 x $10^{12}$ – 6 x $10^{13}$ /cm$^3$. Finally, the axial and radial plasma distribution was measured with a specially designed array of 37 Langmuir probes. These new data shows that plasma forms a thin column of diameter ~5 mm along the solenoid axis when the Final Focus Solenoid (FFS) is energized. The results are described in [14].

### *Beam Compression and Focusing Results*

A new 8-Tesla pulsed Final Focus Solenoid (FFS) has been fabricated and installed at the target chamber entrance, and replaces the prototype solenoid that produced a 5-Tesla peak field. The peak field of the first solenoid was limited by high-voltage flashover near the magnet leads and later was limited to 4 Tesla peak field. The mechanical design and cooling system of the solenoid were improved, and the new solenoid consistently operates up to the design value of 8 Tesla.

The Faraday cup in the Diagnostic box has been used to measure the beam current transported to the entrance of the IBM. This measurement is used in a cross-normalization with the beam signal measured in the Target Chamber with the Fast Faraday Cup on a later pulse to establish the beam current and power impinging on the target plane. This shows that for 330 kV diode extraction voltage the beam current is 35.8 mA with a slight 0.7 mA/μs droop associated with the droop of the Marx voltage over this period. Thus, the beam is delivering 11.8 mJ/μs beam power over the flattop region. Several microseconds of this intensity has been used to commission new diagnostics that measure the transient temperature increase of thin foil targets.

In the induction bunching module (IBM) radial electric fields are generated in the gap across which the IBM voltage is applied that include a net radial defocusing effect on the bunching beam. Following an analysis of this effect [15], it was determined that tuning the initial beam envelope to compensate for the defocusing of the IBM enabled simultaneous transverse focusing and axial compression [16], as shown below.

For a tune that optimizes the compressed beam fluence, the variation of spot radius with beam current (and power) is shown in Fig 5. Here the changes to the spot radius and transverse distribution are evident in this time scan across the compression peak. The peak beam current is 1.5 A, and the peak fluence is ≈1 mJ/cm$^2$/ns At peak compression, 50% of the beam flux is within a radius of 1.5 mm. Higher peak beam current (2.6 A) was reported in [16], and the cause of the difference between the measurements is still being investigated. Topics under study include: diagnostic differences (new vs old fast Faraday cup), detector alignment, IBM waveform fidelity, and plasma density differences. Meanwhile, all the scintillator data and the fast Faraday cup data consistently show the bunch duration is ≈2.5 ns.

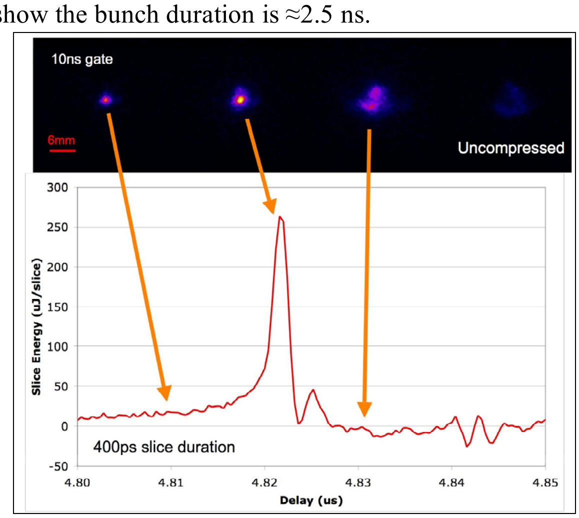


Figure 5: Time-dependent transverse beam distributions demonstrating the simultaneous transverse focusing at the time of peak compression. The peak is ≈2.5 ns FWHM.

Meanwhile, the spot size in these recent measurements is ≈2.1x smaller compared to ref. [16]. Two significant changes to the experiment are the transverse focusing supplied by the 8-Tesla final focusing solenoid and the modifications to the FCAPS described above. This is a significant improvement, though not as great as expected from PIC simulations assuming ideal neutralization. PIC simulations using the experimentally constrained plasma density distribution are underway which may lead to plasma injection modifications.

## FURTHER IMPROVEMENTS

Since mirroring of the plasma injected from outside the solenoid can limit the plasma density in the bore of the focusing element, we are exploring modification of the magnetic field topology near the target plane to allow more efficient plasma transport to the highest field region of solenoid while maintaining high plasma density near the target and in the fringe field of the solenoid. Modeling of plasma flow with auxiliary coils is underway. Also, more compact plasma sources are possible and are being designed. Smaller sources can be placed closer to the target plane, mitigating the limitations of cross-field plasma transport.

We have recently constructed a new IBM with 20 induction core units, or nearly twice the volt-seconds available compared to the present setup. The experiment design question is whether the increased capability should be used, for example, to impart a higher velocity tilt, $\Delta = \delta v/v_o$, (higher peak voltage), or keeping it unchanged for a shallower slope of the tilt and a correspondingly longer drift compression length. The trade-off is between a shorter bunch duration (and greater chromatic aberration), or a smaller spot size and longer pulse duration. The energy deposition on the target scales as [1]:

$$E \underset{\sim}{\propto} \frac{e\phi I\tau}{\varepsilon f\Delta} \tag{3}$$

where $e\phi$ is the ion kinetic energy, $I$ is the beam current before compression, $\tau$ is the initial pulse duration before compression, $\varepsilon$ is the un-normalized transverse emittance of the beam. This is based on assuming that all slices of the beam enter the solenoid at radius $r_0$ independent of velocity. Chromatic aberrations' influence on the spot radius scales as $(\Delta)^{1/2}$. Thus, keeping the focal length approximately the same in the experiment (attractive because of the simplicity) by increasing $\Delta$ and $\tau$ to use the additional volt seconds cancel in the above scaling. Conversely, doubling the $\tau$, keeping $\Delta$ fixed, and doubling the drift compression distance (distance from the IBM gap to the target plane) approximately doubles E, and doubles the compressed pulse duration under the assumption of conservation of longitudinal emittance. We tested these scaling arguments with a series of analytic approximations and LSP simulations [1]. It is advantageous to double the drift compression distance by (+1.44 m) via extension of the FEPS. The expected fluence on the target ($\approx$0.5 J/cm$^2$) is satisfactory for initial warm dense matter target experiments.

Time-dependent focusing to compensate for the large and limiting chromatic aberration in the bunched beam is desirable. Presently, chromatic aberrations increase the rms focal spot size by about a factor of two. Applying the correction over a longer timescale is technically easier to achieve, thus the correction should be applied near the IBM. A first examination of requirements for a time-dependent lens indicates that a pulsed electric einzel lens or quadrupole doublet with relatively low potentials (10-20 kV) meet the requirements. A quadrupole triplet would allow correction of non-axisymmetric rms-envelope parameters at injection to the bunching module to be brought to an axisymmetric distribution at the focal plane. These will be studied in numerical simulations.

## ACKNOWLEDGEMENTS

M. Dickinson, W. Greenway, T. Katayanagi, C. Lee and C. Rogers provided outstanding technical support.

## REFERENCES

[1] J.J. Barnard et al., these proceedings.
[2] S.A. MacLaren *et al.*, Phys. Plasmas, Vol. 9, No. 5, (2002), http://link.aip.org/link/?PHPAEN/9/1712/1
[3] D. V. Rose, *et al.*, PAC'01, Chicago, June 2001, RPAH068 http://accelconf.web.cern.ch/AccelConf/p01/PAPERS/RPAH068.PDF
[4] P.K. Roy et al. Nuc. Inst. & Meth. A 544 (2005) 225-235. E. Henestroza et al., PRST-AB 7, 083501 (2004), http://prst-ab.aps.org/abstract/PRSTAB/v7/i8/e083501
[5] P.C. Efthimion et al., PAC07, http://accelconf.web.cern.ch/AccelConf/p07/PAPERS/THPAS082.PDF
[6] P.K. Roy et al., Phys. Rev. Lett. 95, 234801 (2005).
[7] D.R. Welch, D.V. Rose, B.V. Oliver, R.E. Clark, Nuc. Instr. and Meth. A 464, (2001) 134.
[8] A.B. Sefkow and R.C. Davidson, PRST-AB 10, 100101 (2007), and references therein. http://prst-ab.aps.org/abstract/PRSTAB/v10/i10/e100101
[9] F.M. Bieniosek et al., To be published in Nucl. Inst. & Meth. A (NIM-A).
[10] A.B. Sefkow et al., PRST-AB 9, 052801(2006) http://prst-ab.aps.org/pdf/PRSTAB/v9/i5/e052801
[11] F.M. Bieniosek, et al., HIF'04, Nucl. Inst. & Meth. A (2005), 544, 268-276.
[12] F.M. Bieniosek and M. Leitner, PAC'07, Albuquerque, June 2007 FRPMS018, http://cern.ch/AccelConf/p07/PAPERS/FRPMS018.PDF
[13] J.E. Coleman, *Intense Ion Beams for Warm Dense Matter Physics,* PhD Thesis, Univ. of California at Berkeley (2008).
[14] P.K. Roy et al., To be published in Nuclear Instruments and Methods in Physics Research, Section A (NIM-A).
[15] D.R. Welch et al., Nucl. Instrum. Meth. Phys. Res. A 577, 231 (2007).
[16] J.E. Coleman; et al., PAC'07, Albuquerque, June 2007, THPAS004. http://accelconf.web.cern.ch/accelconf/p07/PAPERS/THPAS004.PDF

# STUDENT PRIZE WINNER TALK

# TWISTED STRUCTURES AND THEIR APPLICATION AS ACCELERATING STRUCTURES

J. L. Wilson, ORNL, Oak Ridge, Tennessee

## Abstract

Normally, reactive loading is employed to construct accelerating cavities in order to slow the phase velocity of the electromagnetic wave. However, due to their non-uniform cross section, they tend to be difficult to machine, requiring complicated welding or brazing processes which increase the total cost. Although empty straight waveguides can only support faster-than-light propagation, empty twisted waveguides can support propagation at or below c. Because twisted structures have a uniform cross section in the transverse plane, they offer several potential advantages over dielectric loaded structures or other types of periodic structures. Of particular interest are twisted structures whose longitudinal cross section has been selected to resemble well-known accelerating structures, such as the iris-loaded accelerating structure and the TESLA type elliptical cavity. Comparisons are drawn between these conventional cavities and their twisted counterparts. Specifically, the phase velocity and dispersion relationship are discussed, the accelerating mode is found and analyzed, and R/Q is calculated. Design guidelines for the design of twisted structures are given.

**SEE THE SLIDES OF THIS TALK AND PAPER THP045**

# BEAM DYNAMICS STUDIES OF THE 8 GeV LINAC AT FNAL*

P.N. Ostroumov†, B. Mustapha, ANL, Argonne, IL 60439 USA
J.-P. Carneiro‡, FNAL, Batavia, IL 60510, U.S.A.


## [illegible]

The proposed 8-GeV proton driver (PD) linac at FNAL includes a front end up to ~420 MeV operating at 325 MHz and a high energy section at 1300 MHz. A normal conducting RFQ and short CH type resonators are being developed for the initial acceleration of the H-minus or proton beam up to 10 MeV. From 10 MeV to ~420 MeV, the voltage gain is provided by superconducting (SC) spoke-loaded cavities. In the high-energy section, the acceleration will be provided by the International Linear Collider (ILC)-style SC elliptical cell cavities. To employ existing, readily available klystrons, an RF power fan out from high-power klystrons to multiple cavities is being developed. The beam dynamics simulation code TRACK, available in both serial and parallel versions, has been updated to include all known H-minus stripping mechanisms to predict the exact location of beam losses. An iterative simulation procedure is being developed to interact with a transient beam loading model taking into account RF feedback and feedforward systems.


## INTRODUCTION

Fermilab is developing the design for a high intensity proton driver 8 GeV superconducting (SC) $H^-$ linac. The principal mission of this proton driver (PD) linac is to increase the intensity of the Fermilab Main Injector for the production of neutrino superbeams. There are many other possible applications such as fixed target programs or acceleration of other species (e-, p, μ, etc…) as discussed in ref. [1] and [2].

To make the overall project cost-effective, the general approach was to adopt designs from existing accelerator or proposals. In particular we propose [3]:

- To directly apply the International Linear Collider (ILC) RF system (cavities, cryomodules and klystrons) operating at 1.3 GHz to accelerate the beam from 1.2 GeV to 8 GeV.
- To use Squeezed ILC (S-ILC) cavities operating at 1.3 GHz and designed for $\beta_G$=0.81 to accelerate the beam from ~420 MeV to 1.2 GeV.
- To operate the whole linac with only 2 frequencies in order to simplify the RF system. The front-end of the linac provides acceleration up to ~420 MeV operating at 325 MHz, the 4th sub-harmonic of the ILC frequency.

The front-end of this linac, up to 60 MeV, is currently being built by the High Intensity Neutrino Source (HINS) R&D Program to demonstrate some of the novel design concepts [4]. In the paper we discuss the beam dynamics design of the PD linac.

## LAYOUT OF THE FNAL PD LINAC

Based on the design published in 2006 [3], the proposed linac has the characteristics listed in Table 1. A schematic layout of the accelerator is shown in Fig. 1 together with the transport line to the Main Injector.

Table 1: Basic Parameters of the Linac

| Parameters | Value |
|---|---|
| Particle type (baseline mission) | $H^-$ |
| Beam kinetic energy | 8 GeV |
| Beam current avg. over the pulse | 25 mA |
| Beam current upstream of the chopper | 43 mA |
| Pulse repetition rate | 10 Hz |
| Pulse length | 1 msec |
| Number of protons per pulse | $1.56 \bullet 10^{14}$ |
| Beam pulsed power | 200 MW |
| Beam average power | 2 MW |
| Wall power (estimate) | 12.5 MW |
| Total length | ~678 m |

### [illegible]

As depicted in Fig. 1, the $H^-$ beam from the Ion Source is bunched and accelerated to 2.5 MeV by a Radio-Frequency Quadrupole (RFQ, [5]) operating at 325 MHz. At that energy, a Medium Energy Beam Transport (MEBT) provides the space for a fast beam chopper (<2 ns) that eliminates unwanted bunches and forms an optimal beam time structure for injection into the Main Injector. This chopping decreases the beam average current over the 1 msec pulse from ~45 mA to ~25 mA. Acceleration to ~100 MeV could be provided by Room temperature DTL cavities; however, a different approach was selected. Taking advantage of the development and excellent performance of SC Spoke cavities [6], it was decided to accelerate the beam from ~10 MeV to ~420 MeV using SC Single and Triple Spoke resonators (SSR and TSR). The Spoke resonators not only present the advantages of higher accelerating gradients and cost-effective operation but also allow one single klystron to power several cavities with the use of high-power ferrite vector modulators [7]. With this outstanding feature of the FNAL PD, only five J-PARC type 2.5 MW klystrons

* Work supported by the U.S. Department of Energy, under Contracts No. DE-AC-02-06CH11357 and DE-AC02-07CH11359.
† ostroumov@anl.gov
‡ carneiro@fnal.gov

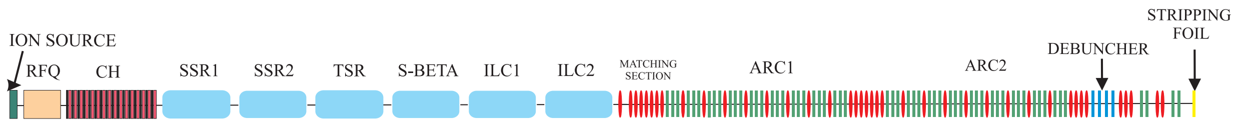


Figure 1: Schematic layout of the FNAL PD linac and High Energy Beam Transport to the Main Injector

Table 2: Main Parameters for each Section of the FNAL PD Linac with Focusing Type (S: Solenoid, R: Resonator, nR: n Resonators, F: Focusing quad. and D: Defocusing quad)

| Section No. | Section Name | Wout (MeV) | Cavities No. | Focusing Type | Period No. | Lf (m) | z (m) |
|---|---|---|---|---|---|---|---|
| 1 | CH | 10 | 16 | S1R | 16 | 0.49- 0.75 | 17 |
| 2 | SSR1 | 32 | 18 | S1R | 18 | 0.75 | 31.4 |
| 3 | SSR2 | 124 | 33 | S2R | 18 | 1.6 | 61.0 |
| 4 | TSR | 421 | 42 | FRDR | 21 | 3.8 | 142.2 |
| 5 | S-ILC | 1223 | 56 | F2RD2R | 14 | 6.1 | 226.7 |
| 6 | ILC1 | 2445 | 63 | F4RD3R | 9 | 12.2 | 336.5 |
| 7 | ILC2 | 8000 | 224 | F8RD8R | 14 | 24.2 | 678.1 |
| Total | | 8000 | 452 | | 110 | | ~678 |

are necessary to power the entire 420-MeV front-end of the linac. To boost the beam from 2.5 MeV to 10 MeV it was decided to use room-temperature cross-bar H-type (CH) cavities which have a higher shunt impedance (90 MOhm/m to 60 MOhm/m) than DTLs. Cavities of this type have been developed by Frankfurt University [8] as an accelerating structure for the future GSI proton synchrotron. For this energy range SC cavities are not an option as time-consuming and expensive development of several types would be required. Furthermore, the number of lattice transitions in the linac directly corresponds to the number of cavity types and must be minimized. As previously mentioned final acceleration to 8 GeV is provided by S-ILC and ILC type 1.3 GHz cavities. The frequency transition occurs at high energy (~420 MeV) which is favorable to the longitudinal beam dynamics.

### [illegible]

In the front-end, between the RFQ and TSR sections, SC solenoid magnets were selected as focusing elements for the following reasons:

- Axially-symmetric beam is less sensitive to space charge effects and helps mitigate the formation of halo (especially in the MEBT where long drifts are necessary to accommodate the chopper).
- Solenoids provide shorter length of the focusing period relative to quadrupole FODO which facilitates the use of the higher gradient offered by SC cavities.
- Solenoids can be made with bucking coils and do not require any additional shielding in the vicinity of the SC resonators. This results in a compact lattice which is very important in the low energy section.

Above ~100 MeV, focusing is provided with FODO quadrupole focusing. At these energies, the beam is less sensitive to spaces between the linac components and, moreover, focusing with ~6 T solenoids can result in stripping of the $H^-$ beam in the fringe fields.

The different sections of the linac with corresponding main parameters are presented in Table 2. The linac is made of 110 focusing periods with lengths varying from 49 cm to 24.2 m. As depicted in Fig. 1, the beam is transferred from the linac to the Main Injector by a High Energy Beam Transport (HEBT), a regular FODO lattice (60° phase advance per cell) made of two opposite sign arcs. A matching section with 6 transverse collimators is located upstream of the first arc and 4 debuncher cavities (necessary to reduce the momentum spread) downstream of the second arc. Downstream of the debuncher, the beam enters a matching section to get the desired beta function at the stripping foil. The total length of the linac and the transport line is ~1.7 km.

## LATTICE DESIGN

The design of the PD linac lattice has been performed following general design requirements for a high-intensity proton linac necessary to avoid RMS emittance growth [3]:

- The zero current phase advance of transverse and longitudinal oscillations should be kept below 90° per focusing period to avoid parametrically-excited instabilities at high current.
- The transverse and longitudinal wavenumbers [illegible] must change adiabatically along the linac. This feature minimizes the potential for mismatches and

helps assure a current independent lattice. The wavenumbers of particle oscillations are expressed as

$$k_{\square 0} = \frac{\sigma_{\square 0}}{L_{\square}}, \; k_{\square 0} = \frac{\sigma_{\square 0}}{L_{\square}}, \quad \text{where } \sigma_{\square 0}, \; \sigma_{\square 0} \text{ are}$$

the zero current transverse and longitudinal phase advances per focusing period of length $L_{\square}$.

- Avoid the $\square\square\square$ parametric resonance between the transverse and longitudinal motion. The condition for occurrence of an n-th order transverse motion parametric resonance is $\sigma_{\square 0} = \frac{\square}{2}\sigma_{\square 0}$. The strongest resonance is for n=1 and can occur particularly in SC linacs due to the availability of high accelerating gradients and relatively long focusing periods. It can be avoided by proper choice of operational tunes in the Kapchinskiy stability diagram.
- Avoid strong space charge resonances by selecting stable areas in the Hofmann's stability chart [9].
- Provide beam equipartitioning to avoid energy exchange between the transverse and longitudinal planes that can occur via space-charge forces.
- Provide proper matching in the lattice transitions to avoid appreciable halo formation.

In NC linacs these requirements can be fulfilled for peak currents up to ~150 mA [10]. Cost-effective SC linac solutions are more challenging. For example, cavities and focusing elements in SC linacs are combined into relatively long cryostats with an ineluctable drift space between them. Also there is a sharp change in the period length at transitions between the linac sections of different cavity types.

## BEAM DYNAMICS SIMULATIONS

The main tool used for the design of the PD linac is the code TRACK [11]. For benchmarking purposes the simulations have also been performed with the DESY code ASTRA [12]. Simulations presented in this paper start at the RFQ exit.

Figure 2 shows TRACK and ASTRA simulations of the PD linac at zero current. The transverse and longitudinal phase advances depicted in Fig. 2(a) present some strong but innocuous jumps due to changing length of the focusing periods at transitions between different types of cavities. Aside from few periods, the transverse and longitudinal phase advances are kept below 90°. The smooth evolution of the transverse and longitudinal wavenumbers shown in Fig. 2(b) is achieved by properly selecting the length of the focusing periods (as shown in Table 2) and adequately adjusting the synchronous phase $\varphi_{\square}$ of each cavity. Figure 3 shows the voltage gain per cavity. The Kapchinskiy stability diagram (Fig. 2(c)) presents the evolution of $\square\square\square\square_{\square}\square$ as a function of the defocusing factor $\gamma_{\square}$ for each one of the 110 periods. The gray area shows the boundary for the $\square\square\square$ parametric resonance to occur. The dashed line corresponds to the stability required for the particles near the separatrix boundary at a phase angle of -2|$\varphi_s$|. The majority of the

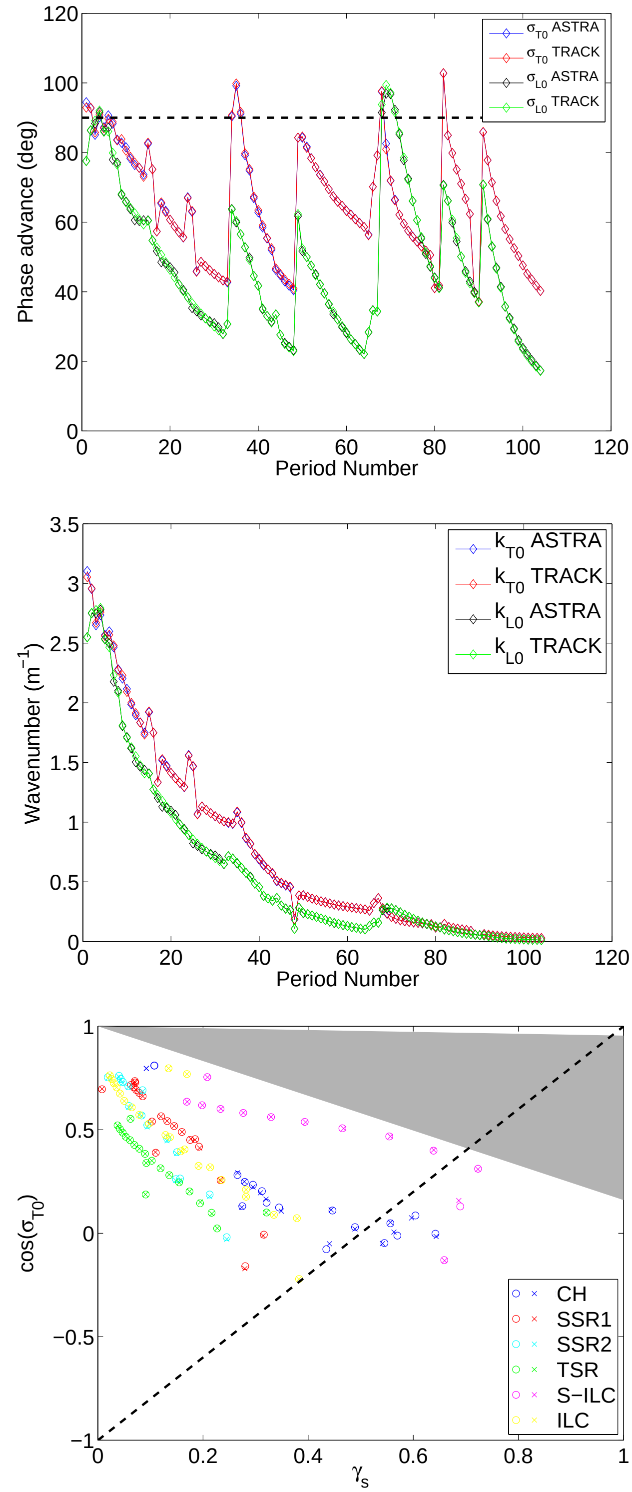


Figure 2: TRACK and ASTRA simulations of the FNAL PD linac at zero current: (a) trans. and long. phase advances, (b) trans. and long. wavenumbers and (c) Kapchinskiy stability diagram. The gray area in (c) shows the boundary of the $\square\square\square$ parametric resonance and the dashed line corresponds to the stability of particles located near the separatrix. In (c) the circles crosses represent TRACK and ASTRA, respectively.

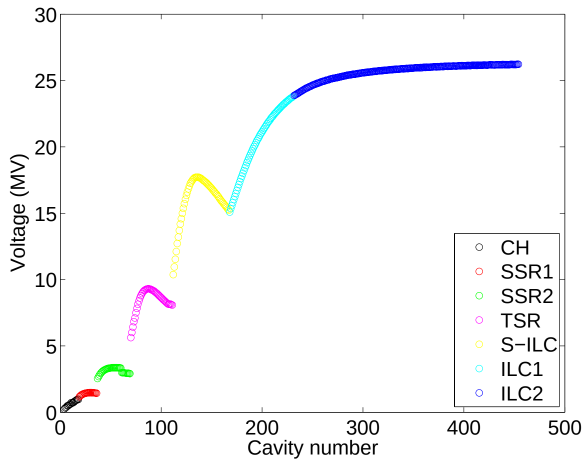


Figure 3: Voltage gain per cavity.

operating tunes are located in stable regions with few points lying on unstable ones. These tune points correspond to matching sections and are not expected to affect the beam since the susceptibility to instability exists for only a short distance compared to the betatron oscillation wavelength. Figure 4 presents Hofmann's stability chart (for details on the chart see for instance [13]) for the PD linac at the design current of 43 mA with a longitudinal to transverse emittance ratio of $\varepsilon_L/\varepsilon_T$=2.

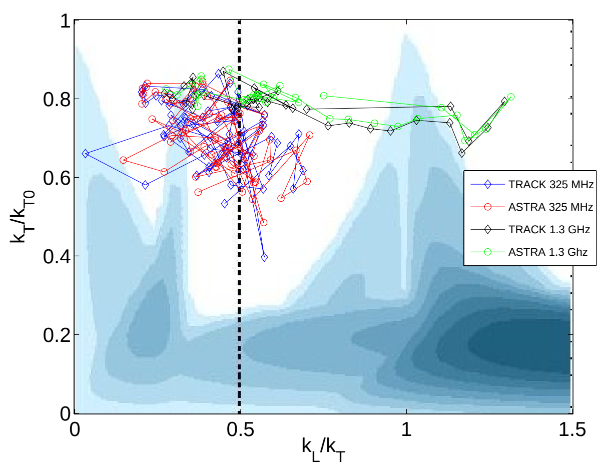


Figure 4: Hofmann's chart for a long. to trans. emittance ratio of 2. Courtesy of I. Hofmann.

As depicted on Fig. 4, both TRACK and ASTRA predict a moderate tune depression (0.5-0.8) along the linac with most of the operating tunes laying on stable (white) areas or fast-crossing the resonances. Therefore, space charge driven resonances are not a concern for this linac design.

Figure 5 shows TRACK and ASTRA simulations of the RMS transverse and longitudinal emittance growth factor along the PD linac at 43 mA. These are acceptable levels and are mainly attributed to imperfect matching between the different lattice transitions. Detailed beam loss studies along the PD linac have been performed with TRACK using $10^8$ macro-particles. Results are reported in Ref. [14]. These studies concluded that for typical values of misalignments and RF errors (±1° and ±1% RMS) the PD linac produces very limited total and peak power losses, respectively at $1\times10^{-4}$ and ~0.04 W/m for the linac operating at ~25 mA ($1.56\bullet10^{14}$ ppp) and 10 Hz.

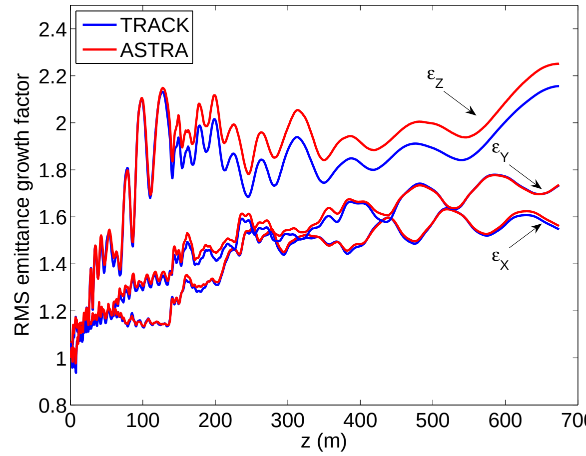


Figure 5: RMS trans. and long. emittance growth factor along the FNAL PD linac at 43 mA.

A parallel version of TRACK, PTRACK is being implemented on the BG/P supercomputer at ANL. With a 3D domain decomposition parallel Poisson solver, PTRACK can run on BG/P using more than $10^4$ processors. A novel advantage of this large scale computing is the possibility to perform simulations with a number of particles that equals the population of the bunch. A detailed description of PTRACK is presented in ref. [15]. Figure 6 shows a PTRACK simulation of the PD linac and HEBT with $10^8$ macro-particles on 4k processors and a total time of ~6.5 hours. PTRACK has successfully simulated 865 M (real bunch population for the current design of 43 mA) on the FNAL RFQ using 32k processors for a total time of ~6 hours. Start-to-end simulations with 865 M macro-particles are in progress and represent an ideal tool for studies of beam losses or halo formation.

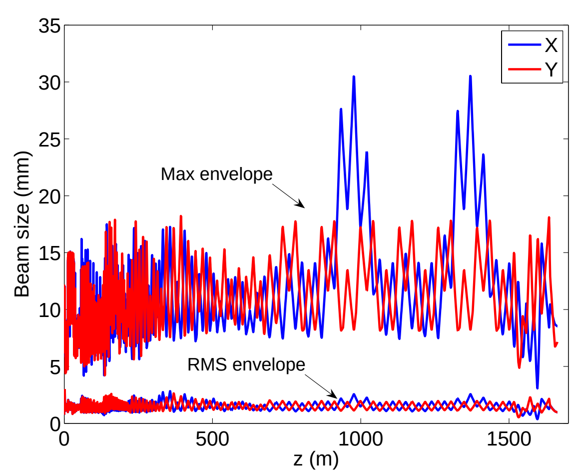


Figure 6: PTRACK simulation of beam envelope along the FNAL PD linac and HEBT at 43 mA with $10^8$ p.

### $H^-$ [illegible]

A potential source of uncontrolled losses in $H^-$ linacs is the stripping of the $H^-$ ion. $H^-$ ions have two electrons, one tightly bound at 13.6 eV binding energy and one loosely bound at 0.75 eV. During acceleration and transport, the ions suffer from blackbody radiation, electromagnetic fields, and residual gas any of which can strip the loosely bound electron. To quantify stripping losses, all three of these mechanisms have been recently implemented in the code PTRACK. A compilation of the $H^-$ stripping equations as implemented in the code is presented in ref. [16]. The code allows the user to set the temperature, pressure, and composition of the residual gas for any desired section of the linac. Concerning the residual gas, TRACK now supports stripping from $H_2$, $O_2$, Xe, Ar, He, Ne. $CO_2$, CO, $H_20$ will be implemented soon in the code.

Figure 7 presents PTRACK simulation of the stripping losses along the PD linac using $10^8$ macro-particles. For these simulations, typical temperature and pressure along the linac were setup in the code: SC linac (from SSR to ILC) at 4 K, $1\times10^{-10}$ T and the transport line at 150 K, $5\times10^{-9}$ T. Only $H_2$ has been considered as the residual gas for these simulations. Losses were computed for an average beam current of ~25 mA and 10 Hz. Figure 7 reports that for these conditions, the stripping losses along the linac remain below 0.1 W/m. Combined with the typical RF and misalignment errors previously mentioned, the peak power losses along the PD linac and HEBT remain below 0.1 W/m. This represents a safe margin from the 1W/m loss criterion widely adopted by the accelerator community.

### [illegible]

A new analytical approach is being developed to simulate LLRF system and determine optimized set point for the cavity operation in an RF unit where each cavity operates at a specific synchronous phase, accelerating field and under heavy beam loading. This method is described in ref. [17] and based on the cavity transient response in the presence of various imperfections, feedforward and feedback systems. It is our goal to implement the residual errors of the accelerating field parameters along the beam pulse into the TRACK code.

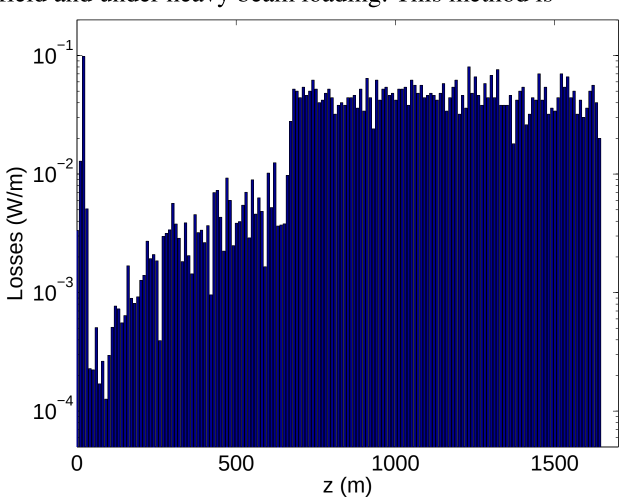


Figure 7: PTRACK simulation of the stripping losses along the FNAL PD linac and HEBT for typical operation.

## CONCLUSION

The simulated beam dynamics of the ~1.7 km FNAL 8 GeV PD SC linac and transport line show an excellent behavior of the current design in terms of emittance growth and beam losses. High-statistics simulations, with typical machine errors and $H^-$ stripping, show very low beam losses (<0.1W/m) along the linac and HEBT. Work is in progress to optimize the high energy section of the linac. Further development of PTRACK will include a realistic LLRF model and will enable even more precise beam dynamics simulations using the real bunch population.

## REFERENCES

[1] G.W. Foster and J.A. MacLachlan, "A multi-mission 8 GeV injector linac as a Fermilab booster replacement'', LINAC02.

[2] G.W. Foster (ed.), available at: http://protondriver.fnal.gov/#Technical_Design_Link

[3] P.N. Ostroumov, New J. of Physics, 8, 281, 2006.

[4] R.C. Webber et al. "Overview of the High Intensity Neutrino Source Linac R&D Program at Fermilab", LINAC08.

[5] P.N. Ostroumov et al., J. of Inst., P04002, 2006.

[6] K. W. Shepard, P. N. Ostroumov, and J. R. Delayen, Phys. Rev. ST – AB 6, 080101, 2003.

[7] R.L. Madrak et al., "A Fast Chopper for the Fermilab High Intensity Neutrino Source (HINS)", LINAC08.

[8] Z. Li, "Design of the RT CH-Cavity and Perspectives for a new GSI Proton Linac", LINAC04.

[9] I. Hofmann, Phys. Rev. E 57, 4713, 1998.

[10] G.P. Lawrence and T.P. Wangler, "Integrated Normal-Conducting/Superconducting High Power Proton Linac for APT Project", PAC97.

[11] V.N. Aseev et al. "TRACK : The new beam dynamics code", PAC05.

[12] K. Floettmann, ASTRA user manual available at : http://www.desy.de/~mpyflo/Astra_dokumentation/

[13] F. Gerigk, "Space charge and beam halos in Proton Linacs'', US-CERN-JAPAN-RUSSIA Accelerator School, November 2002.

[14] P.N. Ostroumov et al., "Beam dynamics studies of the 8-GeV superconducting H– linac", LINAC06.

[15] J. Xu et al. "Simulations of high-intensity beams using BG/P supercomputer at ANL'', HB2008.

[16] J.-P. Carneiro, FNAL Beams-doc 2741, April 2007.

[17] G. Cancelo and A. Vignoni, "Optimizing cavity gradients in pulses linacs using the cavity transient response'', LINAC08.

# TRANSPORT LIMITS IN PERIODIC FOCUSING CHANNELS

S. M. Lund, LLNL, Livermore, California

## Abstract

It has been empirically observed in both experiments and particle-in-cell simulations that space-charge-dominated beams suffer strong growth in emittance and particle losses in alternating gradient quadrupole transport channels when the undepressed phase advance increases beyond about 85 degrees per lattice period. Although this criterion has been used extensively in practical designs of strong focusing intense beam transport lattices, the origin of the limit has not been understood. We propose a mechanism for the transport limit resulting from strongly chaotic classes of halo particle resonances near the core of the beam that allow near-edge particles to rapidly increase in oscillation amplitude when the space-charge intensity and the flutter of the matched beam envelope are both sufficiently large. A core particle model is applied to parametrically analyze this process and the results are compared with extensive particle simulations.

**CONTRIBUTION NOT RECEIVED**

# TOWARDS A MODEL DRIVEN ACCELERATOR WITH PETASCALE COMPUTING*

B. Mustapha#, P.N. Ostroumov and J. Xu
Argonne National Laboratory, 9700 S. Cass Ave, IL 60439, U.S.A.

*Abstract*

Accelerator simulations still do not provide everything designers and operators need to deploy a new facility with confidence. This is mainly because of limitations preventing realistic end-to-end simulations of the beam from the source all the way through to a final interaction point and because of limitations in on-line monitoring that prevent a full characterization of the actual beam line. As a result, once a machine is built there can be a gap between the expected behavior of the machine and the actual behavior. This gap often corresponds to enormous work and significant delays in commissioning a new machine. To address the shortcomings of the existing beam dynamics simulation codes, and to fulfill the requirements of future hadron and heavy-ion machines, a starting point for a realistic simulation tool is being developed at ANL that will support detailed design evaluation and also fast turnaround simulations to support commissioning and operations. The proposed simulations will be performed on the fast growing computing facility at ANL with peta-scale capability.

## MODEL DRIVEN ACCELERATOR: CONCEPT & MOTIVATIONS

Presently, no accelerator in the world could fully rely on a computer model for its operations. The main reason is a discontinuity between the design and operation phases. Many factors contribute to this discontinuity: 1-Simulations in the design phase assume almost perfect conditions and cannot reproduce the real machine, 2-Actual elements specification and performance are usually different from their original design and in most cases 3-Not enough diagnostic devices to characterize the machine. The lack of a realistic model to support the commissioning and operations results in significant delay in the deployment of a new machine and a lot of time spent on machine tuning during operations. This usually leads to low availability and high operating cost of the machine. For example, a complex project such as the proposed FRIB facility [1], where primary beams from proton to uranium up to 600 MeV/u are used to produce beams of rare isotopes all over the map, cannot afford not to have a computer model to support its operations.

We here propose to bridge the gap between the design and operation phases and develop a realistic model of the machine. Among the benefits of such a model is fast tuning for the desired beam conditions and fast retuning to restore the beam after a failure. This should significantly improve the availability of the machine and reduce its operating cost. The requirements for the development of such a model and the realization of the concept of the model driven accelerator are discussed in the next sections.

*This work was supported by the U.S. Department of Energy, Office of Nuclear Physics, under Contract No. DE-AC02-06CH11357.

# mustapha@phy.anl.gov

## REQUIREMENTS TO REALIZE THE MODEL DRIVEN ACCELERATOR

The main requirements for the realization of the model driven accelerator could be summarized in the development of a 3D beam dynamics code with the appropriate set of optimization tools and large scale computing capabilities. A multi-particle beam dynamics code is more realistic than matrix-based and single-particle codes because it supports 3D fields, includes fringe fields and appropriate space charge calculations. It also allows more detailed simulations necessary to study eventual beam loss and produce data similar to the measured data. Such a code should also include a large set of optimization tools. Optimization tools are needed not only for design optimization but also to tailor the computer model to the actual machine to be useful for real-time operations. Multi-particle optimizations usually involve tracking a large number of particles for large number of iterations which is very time consuming and requires large scale parallel computing. Therefore the beam dynamics code should have parallel computing capabilities.

The beam dynamics code TRACK [2] is being developed at Argonne to meet these requirements. TRACK and a selected set of applications will be presented in the next section.

## A REALISTIC BEAM DYNAMICS CODE

The beam dynamics code TRACK is being developed over the last few years at the Physics Division of Argonne National Laboratory. Among the main features of TRACK are:

- A wide range of E-M elements with 3D fields
- End-to-end simulations from source to target
- Tracking multiple charge states heavy ion beams
- Interaction of heavy ion beams with strippers
- Automatic transverse and longitudinal beam tuning
- Error simulations: Static and dynamic errors
- Realistic transverse correction procedure
- Large number of particles for large number of seeds
- Beam loss analysis with exact location of the losses

And more recently:

- Possibility of fitting experimental data (profiles,…)
- H- Stripping: Black body, Residual gas and Lorentz

- The design and simulation of electron linacs
- Parallel version is fully developed with good scaling
- Simulating the actual number of particles in a bunch

A list of beam line elements supported by TRACK is given below:

- Any type of RF resonator (3D fields)
- Static ion optics devices (3D fields)
- Radio-Frequency Quadrupoles (RFQ)
- Drift Tube Linacs (DTL)
- Coupled Cavity Linacs (CCL)
- Solenoids with fringe fields (model or 3D fields)
- Dipoles with fringe fields (model or 3D fields)
- Electrostatic and magnetic multipoles
- Multi- Harmonic Bunchers (MHB)
- Axial Symmetric electrostatic lenses
- Entrance and exit of HV decks
- Accelerating tubes with DC voltage
- Transverse beam steering elements
- Stripping foils or films for heavy-ion beams
- Horizontal and vertical jaw slits

TRACK was extensively used in the design and simulations of the RIA/FRIB driver linac [3] and the FNAL-PD linac [4] and more recently in the end-to-end simulations of the SNS linac [5]. TRACK is now being used in the design and simulations of an electron linac for an X-FEL Oscillator [6].

### *Design and Simulations of the RIA/FRIB Linac*

The physics design and the results of large scale beam dynamics simulations of the FRIB linac proposed by Argonne were presented and discussed in detail at a previous conference [3].

### *Design and Simulations of the FNAL-PD Linac*

The physics design of the FNAL-PD linac was presented elsewhere [7]. Detailed beam dynamics simulations, including error and beam loss simulations for 100 seeds with million particles each, were presented at a previous conference [4]. The most recent results are presented in a separate paper at this conference [8].

### *End-to-end Simulation of the SNS Llinac*

The results of the first end-to-end simulation of the SNS linac are presented in a separate paper at this conference [5].

### *Design and Simulations of an Electron Linac*

Recently TRACK was used to design and simulate an electron linac for a future X-FEL Oscillator. This is discussed in more details in a separate paper at this conference [6].

## VERSATILE OPTIMIZATION TOOLS

As discussed in the previous sections, the realistic beam dynamics code should also have the appropriate set of optimization tools to be used to support accelerator commissioning and operations. A set of optimization tools developed for TRACK are presented in this section. This tools could be easily adapted to other codes such as IMPACT [9].

### *Automatic Tuning Procedures*

The automatic tuning procedures are developed to tune a given section of the linac to produce smooth beam dynamics by reducing the fluctuations in the rms beam size along a given linac section [10]. For the transverse tuning, the fit function is defined as:

$$F = X^0_{rms} + \sum_i \frac{(X^i_{rms} - X^0_{rms})^2}{\varepsilon^2_{X_{rms}}} + Y^0_{rms} + \sum_i \frac{(Y^i_{rms} - Y^0_{rms})^2}{\varepsilon^2_{Y_{rms}}}$$

where $X^0_{rms}$ and $Y^0_{rms}$ are the rms beam sizes at the entrance of the section, the sum index i runs over the focusing periods and $\varepsilon_{Xrms}$ and $\varepsilon_{Yrms}$ are the allowed errors on the rms beam sizes. The fit parameters are the field strengths in focusing elements. This method is general and should produce good results for periodic or non periodic accelerating structures. Applied for a two charge state uranium beam in the low-energy section of the RIA driver linac this method produced the results shown in Fig 1.

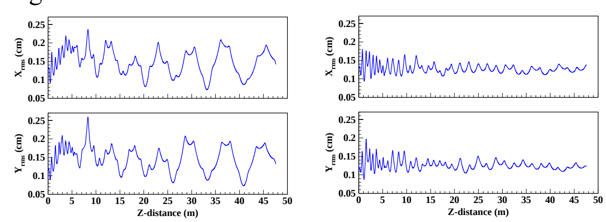


Figure 1: X and Y rms beam sizes before (left) and after (right) applying the automatic transverse tuning procedure. The beam is a two-charge state uranium beam in the low energy section of the RIA/FRIB driver linac.

Although developed for design optimization purpose this procedure could very well be applied to a real machine using beam profile measurements to reduce beam mismatch. A similar procedure was developed for the longitudinal rms envelopes.

### *Automatic Longitudinal FineTuning*

A longitudinal fine-tuning procedure was developed specifically for a multiple charge state beam to minimize its longitudinal emittance right before a stripper [11]. The beam should reach the stripper in the form of an up-right ellipse in the (Δφ, ΔW) plane to minimize the emittance growth from the energy straggling effect in the stripper. This could be realized by matching the beam centroids and Twiss parameters of the different charge state beams. The fit function in this case is:

$$F = \frac{(W_{q0} - W_0)^2}{\varepsilon_w^2} + \sum_{qi} \frac{\Delta W_{qi}^2}{\varepsilon^2_{\Delta w}} + \sum_{qi} \frac{\Delta \phi_{qi}^2}{\varepsilon^2_{\Delta\phi}} + \sum_{qi} \frac{\alpha_{qi}^2}{\varepsilon^2_{\alpha}} + \sum_{qi} \beta_{qi}$$

where $W_0$ is the desired beam energy and $\varepsilon_W$ is the associated error. $\varepsilon_{\Delta W}$, $\varepsilon_{\Delta\varphi}$ and $\varepsilon_\alpha$ are the allowed errors on the relative energy, phase and α shifts of the individual charge state beams from the central beam. The fit parameters in this case are the RF cavities phases and amplitudes in the section up-stream of the stripper. Figure 2 shows the results of the fit for a five charge state uranium beam in the medium energy section of the RIA driver linac. This optimization reduced beam losses in the high-energy section of the linac by a significant factor.

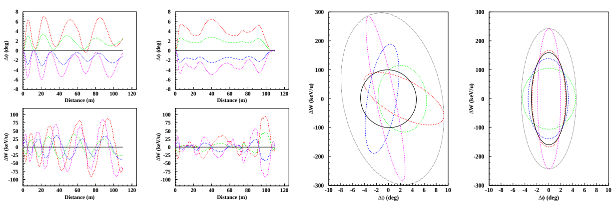

Figure 2: The left 4 plots show the phase and energy oscillations of the five charge states around the central charge state before and after applying the tuning procedure. The right 2 plots show the corresponding beam ellipses on the stripper before and after tuning.

This procedure could be used on a real machine but would require the measurements of energy and phase centers of individual charge state beams. More diagnostics development is needed to be able to measure and match the Twiss parameters.

### *Realistic Corrective Steering*

A realistic corrective steering procedure was developed to correct for misalignment errors. The procedure uses virtual beam position monitors and correctors including measurement errors. It was applied for the front-end of the FNAL-PD linac to optimize the number and locations of monitors and correctors and to determine the required correctors field strengths and monitors precision. Figure 3 shows the appropriate set of monitors and correctors required in the front-end of the FNAL-PD linac. Figure 4 shows the results of the correction procedure along with the required corrector strengths.

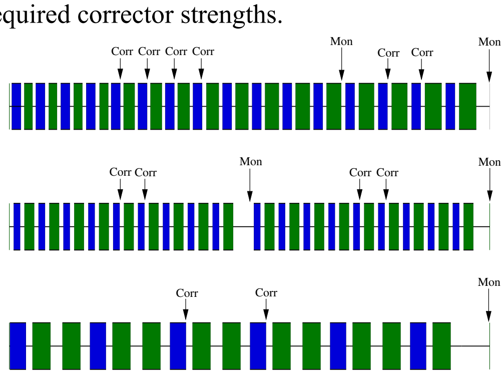


Figure 3: Monitors and correctors required for the front-end of the FNAL-PD linac.

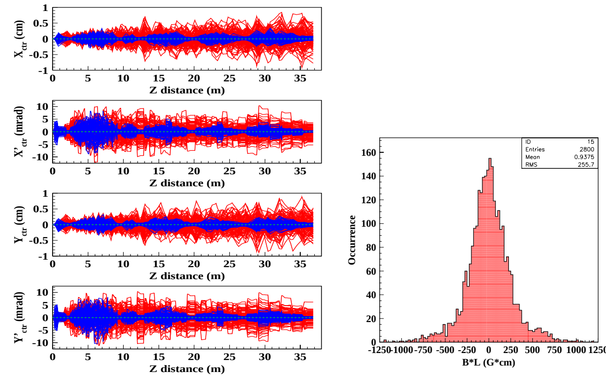


Figure 4: results of the correction procedure. On the right are beam centers in (x,x',y,y') before (red) and after (blue) correction. On the left is a distribution of required corrector strengths.

Figure 5 shows the effect of monitors precision on the correction procedure. The required precision should be 10-30 μ, much less than the misalignment error of 100 μ.

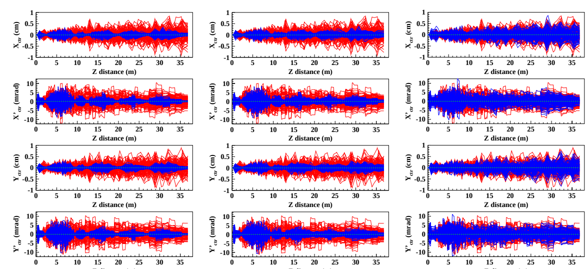

Figure 5: Effect of monitors precision on the correction: left: 10μ, middle: 30μ and right: 100μ.

This procedure could be easily implemented for a real machine using real beam position monitors and real beam steerers.

### *Operations of a Multi-Q Injector*

New optimization tools have been developed to support the operations of the prototype multiple charge state LEBT at Argonne. By fitting the measured beam profiles we were able to determine the initial beam conditions at the source which were later used to find the appropriate quadrupole settings to recombine a two charge states 90 kV bismuth beam (20+, 21+) at the end of the LEBT. Figure 6 shows the result of the profile fit from which the beam emittance and Twiss parameters at the source are extracted. Figure 7 shows a TRACK fit to produce symmetric beam dynamics in the LEBT which is necessary to recombine the two charge state beams at the end of the LEBT. The quadrupole settings obtained from this fit was used on the actual beam line for an almost perfect recombination of the two beams. Figure 8 shows the measured profiles at the end of the LEBT for the individual and combined beams. Figure 9 shows a pepper-pot image of the combined beam and a superposition of individual charge state beam images.

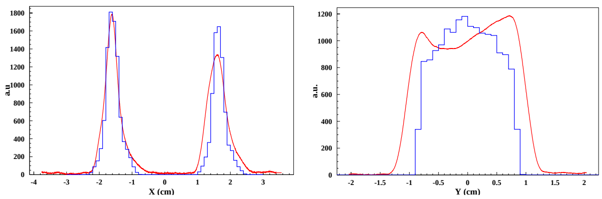


Figure 6: Horizontal (left) and vertical (right) beam profiles. The curves are the measured profiles and the histograms are the result of the TRACK fit.

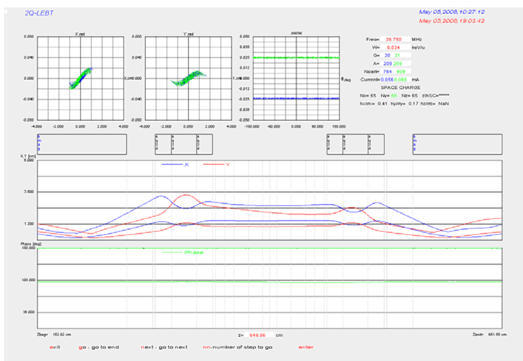

Figure 7: Result of a symmetric fit between the two LEBT magnets to recombine the two charge state Bi beams.

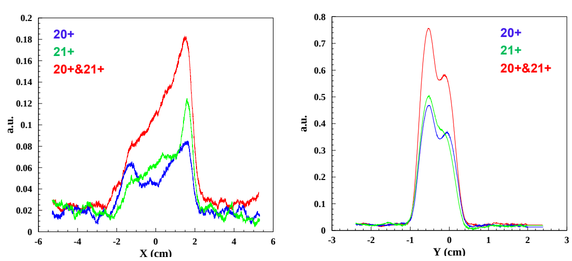


Figure 8: Measured beam profiles at the end of the LEBT for the individual Bi 20+ and 21+ beams and the combined beam.

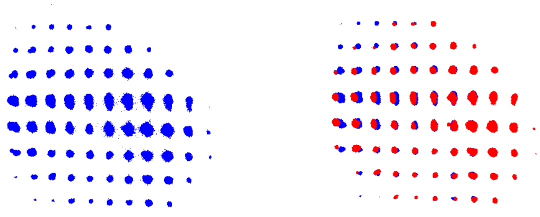

Figure 9: Pepper-Pot images of the combined beam (left) and the individual beams (right). Bi 20+ is in blue and 21+ is in red.

It is worth noting that without the support of the realistic TRACK simulations we would not be able to recombine the two charge state beams at the end of the LEBT.

## LARGE SCALE PARALLEL COMPUTING

As mentioned above multi-particle optimizations require large scale parallel computing to be useful for real-time machine operations.

The beam dynamics code TRACK was recently parallelized and successfully used on world-class computing facilities. The parallelization method is described in more detail elsewhere [12]. More recently TRACK was used for the simulations of very large number of particles on up to 32768 processors with very good scaling [13].

### *One to One RFQ Simulations*

We recently succeded to simulate the actual number of particles in a 45 mA proton beam bunch at 325 MHz accelerated in a RFQ from 50 keV to 2.5 MeV. That is 865 million particles simulated on 32768 processors in 6 hours on the Blue-Gene machine at Argonne. The benefits of simulating a large number of particles is first to suppress the noise from the PIC method with enough particles per cell and second to better characterize the beam especially halo formation. Figure 10 shows phase space plots in the RFQ for 865 M particles.

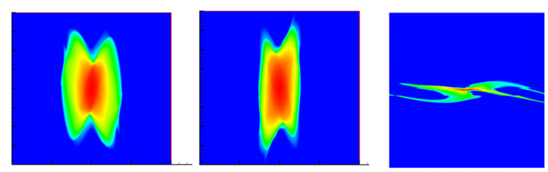

Figure 10: Phase space plots after 30 cells in the FNAL-PD RFQ. Left (x,x'), middle (y,y') and right (Δφ,ΔW/W).

### *Error Simulations With Large Number of Particles*

We simulated machine errors with 10M particles per seed in the FNAL-PD linac and transfer line with ~ 2000 elements and 1.7 km long. Included are misalignment errors and RF errors of (1%,1 deg) as well as H- stripping by three different processes, namely, black body radiation, residual gas interaction and Lorentz stripping. The benefit of simulating a very large number of particles is to study beam loss to the lowest possible level. Figure 11 shows beam envelopes and emittance for multiple seeds and Fig. 12 shows the beam loss in Watts/m along the linac.

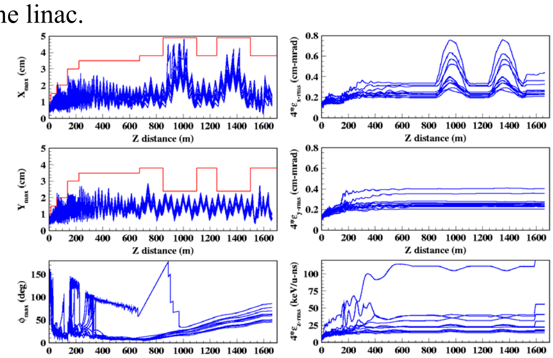


Figure 11: Beam envelopes (left) and emittances (right) along the FNAL-PD linac and transfer line for multiple seeds.

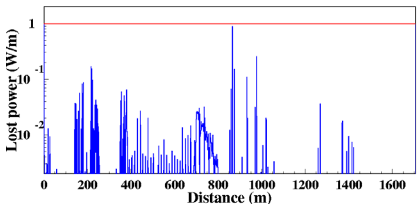


Figure 12: Beam loss in Watts/m in the FNAL-PD linac and transfer line. In red is the conventional 1 W/m limit.

We notice that by adding the H- stripping, the losses increased by an order of magnitude which suggest that the transfer line should be cooled to reduce the stripping by black body radiation.

## FUTURE DEVELOPMENTS

The tools developed so far were used only offline with the serial version of TRACK which is very time consuming. To be used online for real-time machine operations, we should be able to perform large scale optimizations on large number of processors (32768 processors or more). The parallel version of TRACK is now fully developed and scales reasonably well on very large number of processors. Parallel optimizations are now under development. We are investigating new parallel optimization algorithms such as the Toolkit for Advanced Optimization (TAO) developed at the Mathematics and Computer Science Division at Argonne [14].

More optimization tools need to be developed for the commissioning phase to tailor the computer model to the actual machine by fitting the measured data. For this purpose, interfaces between the beam diagnostic devices and the computer model are needed to calibrate and analyze the data to input to the code. Numerical experiments could be used to test and fine tune the tools before implementation to the real machine by producing detector-like data. Only after all these developments we can actually realize the model driven accelerator. As a full scale application, we are proposing to apply this concept to the superconducting linac ATLAS at Argonne and to other existing machines as a preparation exercise for the future FRIB facility.

## SUMMARY

Developing a realistic computer model to support real-time accelerator operations should significantly improve its availability and reduce its operating cost. The realization of this concept of model driven accelerator requires a realistic 3D beam dynamics code with the appropriate set of optimization tools and large scale computing capabilities. The beam dynamics code TRACK is being developed at Argonne to meet these requirements. Different optimization tools are needed for the different phases of an accelerator project namely, the design, commissioning and operations. For a new machine we should take advantage of the commissioning phase to bridge the gap between the original design and the actual machine by tailoring the computer to the machine. More developments are needed to realize the concept of the model driven accelerator.

## REFERENCES

[1] N. Ostroumov et al, Proceedings of PAC-07 Conference, Albuquerque, New Mexico, June 25-29, 2007.
[2] V.N. Aseev et al, Proceedings of PAC-05 Conference,
Knoxville, Tennessee, May 16-20, 2005.
[3] B. Mustapha, P.N. Ostroumov and J.A. Nolen, Proceedings of PAC-07 Conference, Albuquerque, New Mexico, June 25-29, 2007.
[4] P.N. Ostroumov, B. Mustapha and V.N. Assev, Proceedings of LINAC-06 Conference, Knoxville, Tennessee, August 21-25, 2006.
[5] B. Mustapha et al, this conference
[6] P.N. Ostroumov et al, this conference
[7] P.N. Ostroumov, V. N. Aseev, and A.A. Kolomiets, J. of Instr., JINST 1, P04002, 2006
[8] P.N. Ostroumov et al, this conference
[9] J. Qiang, R. D. Ryne, S. Habib, and V. Decyk, J. Comput. Phys. 163 (2000) 434.
[10] B. Mustapha and P.N. Ostroumov, Proceedings of LINAC-06 Conference, Knoxville, Tennessee, August 21-25, 2006.
[11] B. Mustapha and P.N. Ostroumov, Phys. Rev. ST. Accel. Beams 8, 090101 (2005).
[12] J. Xu, B. Mustapha, V.N. Aseev and P.N. Ostroumov, Phys. Rev. ST. Accel. Beams 10, 014201 (2007).
[13] J. Xu, B. Mustapha, V.N. Aseev and P.N. Ostroumov, Proceedings of the HB-2008 Workshop, Nashville, Tennessee, August 25-29, 2008.
[14] S. Benson, L. McInness, J. More, T. Munson and J. Sarich, "TAO User Manual (Revision 1.9)", Mathematics and Computer Science Division, Argonne National Laboratory, ANL/MCS-TM-242, and at http://www.mcs.anl.gov/tao.

# Nb-RRR SHEET INSPECTION BY MEANS OF ULTRASONIC MICROSCOPY

R. Grill, H. Traxler, L.S. Sigl, H. Kestler
PLANSEE SE, 6600 Reutte, Austria

*Abstract*

Nb-RRR sheet material is one of the key components of super-conducting linear particle accelerator projects (e.g. XFEL, ILC). The high quality requirements led to sophisticated quality systems in the manufacturing line. A major aspect is the development of non-destructive inspection methods for the detection of surface defects, delaminations, pores, inclusions and impurities. Up to now the standard inspection technologies for quality assurance of Nb-RRR sheet material are based on electromagnetic techniques, e.g. SQUID and eddy current. For these methods the detection limit is in the range of 0.1 mm.

Ultrasonic microscopy (USM) is a well established and economic technique for non-destructive surface inspection. For such applications strongly focused ultrasonic waves are applied. For volume inspection of sheet material the focal length of the ultrasonic transducer needs to be increased in order to enable constant defect resolution throughout the whole cross section of the material under inspection. For Nb-RRR sheets with typical thickness of 2.8 mm a detection limit of 0.1 mm is expected. First results of USM on Nb-RRR sheet material are presented.

## INTRODUCTION

Sheet material made of ultra-high-purity Niobium (so called Nb-RRR grade) is the key component for future linear accelerators, based on the superconducting RF technology. One is the XFEL (X-ray Free Electron Laser) whose construction started in 2007 at the German Electron Synchrotron in Hamburg. Based on the same technology is the ILC (International Linear Collider) which is currently in the design phase and will be the next major accelerator project in particle physics after XFEL realization.

Since 2004 Plansee SE (A) worked on the qualification as material supplier for the XFEL project. In co-operation with W. C. Heraeus (DE), which covers the raw material competence, Plansee SE established the industrial production of products made of Nb-RRR in various geometries and sizes. In December 2007 the qualification procedure at DESY could be successfully finished and Plansee SE was qualified as supplier for Nb-RRR 300 sheet material.

To be prepared for large production scale quantities for the XFEL project, activities for the installation of a Quality Assurance (QA) management system are ongoing. A major quality criterion for Nb-RRR sheets is the surface quality. For inspection of surface quality visual inspection and eddy current testing (ET) are established for pre-series production and future project realization as baseline. Both methods are commonly used for detection of defects and inclusions at the surface. For volumetric inspection SQUID (Superconducting Quantum Interference Device) was investigated during the last years and activities for establishment of a test standard are in work [1-4].

With ultrasonic microscopy (USM) an equivalent test procedure is available which allows a standardized surface inspection on industrial scale. For USM an automized visualization of surface defects and establishment of standardized test records is possible [5]. With adaptation of test setup the possibility of volumetric testing was assessed and first results will be presented.

## ULTRASONIC MICROSCOPY

Ultrasonic microscopy (USM) is established for the inspection of thin films in various industrial applications, e.g. electronics [6]. USM uses ultrasonic frequencies from 50 MHz to 2 GHz which is much higher compared to conventional ultrasonic NDT operating frequencies using about 1 to 20 MHz. This leads to enhanced defect resolution since the wavelength is reduced to the µm regime. An additional feature is the strong focussing of the ultrasonic wave which leads to lateral resolution in the magnitude of microns in the focused plane. For high resolution inspection in the volume the focus of the transducer is moved below the surface [7]. For inspection of the whole sample volume several scans need to be performed.

For the application described a device of the type Krämer Scientific Instruments, Vario III B is used. The inspection is performed in water immersion applying the pulse echo technique. A scanning mechanism moves the transducer and enables the generation of a C scan image. A sketch of the setup is given in Fig. 1.

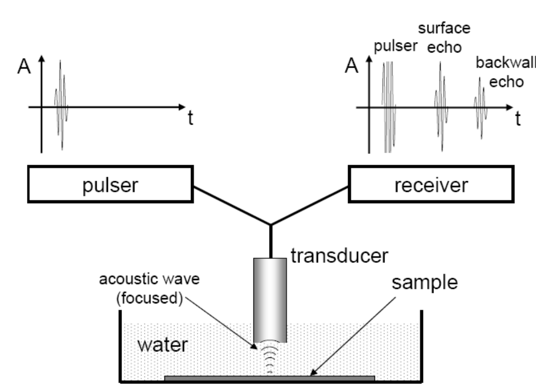


Figure 1: Sketch of the measurement chain of the USM.

## EXPERIMENTAL WORK

### *Nb-RRR Sheet Material*

Nb-RRR grade material is achieved by electron beam melting under high vacuum. Starting from premelted blocks with low content of metallic impurities (esp. Ta content) the material is remelted several times to reduce the impurities step by step. Especially the interstitial dissolved non-metal elements (C, O, N, and H) must be reduced to levels below 10 ppm to achieve RRR values > 300 on the semi finished products.

The melted cylinders were processed to plates by a multi-stage conversion process followed by sheet rolling. During processing the parameters must be carefully controlled to prevent reaction with the atmospheric gases. Due to the softness of the material and the cold-welding tendency of niobium a careful handling during processing is necessary to prevent surface defects like scratches, pinholes or metallic inclusion. To keep the high purity level over the whole production route, all processing steps must be well defined and controlled.

After sheet rolling to typical thickness of 2.8 mm, surface treatment and tailoring according customer specification is made. Small defects or inclusions on the surface can lead to severe problems in cavity performance. Therefore, beside the visual inspection, a test method which allows a standardized detection of surface defects is necessary for establishment of a QA management system for industrial production.

### *Test Results Surface Inspection*

For maximum resolution of the surface inspection the ultrasound frequency needs to be as high as possible. Fig. 2 compares the C scan of a defect indication obtained from a 75 MHz and a 150 MHz transducer detected on a Nb-RRR 300 sheet. The grey value code in the C scan gives the locally measured amplitude of the surface echo.

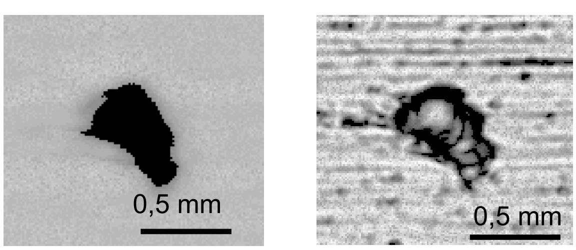


Figure 2: Comparison of the C scan obtained from a 75 MHz (left) and a 150 MHz (right) transducer showing a surface defect.

From Fig. 2 it is seen that the 150 MHz transducer displays the surface roughness which is within the specification (e.g. typical measured value: Rmax. = 17 µm). To allow an automized surface inspection the resolution needs to be reduced in order to discriminate the indications from the surface structure. This is possible by application of the 75 MHz transducer with a focal length of 8 mm; see Fig. 2 (left side).

The testing procedure was applied to 15 Nb-RRR sheets with dimension 265 x 265 x 2.8 mm. The material was produced under production conditions. USM testing was performed applying the 75 MHz transducer. An example for a C scan of the surface inspection is given in Fig. 3. The image is free of artefacts and enables a clear defect representation (see marked defect indication in Fig. 3).

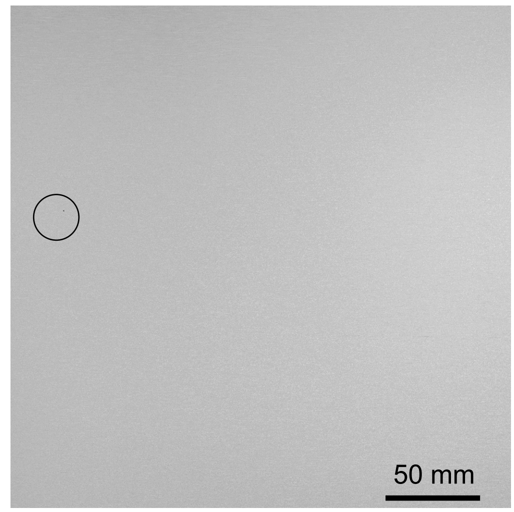


Figure 3: C scan of the surface inspection of a Nb-RRR sheet (265 x 265 x 2.8 mm, part no. C4 2.1-11). The location of a small defect is indicated by the black circle (detail see Fig. 3).

### *Test Body Preparation for Volume Inspection*

For first assessment of applicability of USM to volumetric inspection of Nb-RRR sheets and determination of the detection limit a test body was prepared. Corresponding to sheet thickness for cavity production on a Nb-RRR sheet with thickness 2,8 mm different holes with diameter 0.2 mm and depth between 0.2 and 1.4 mm were drilled on one side of the sheet. Simulating punctual volumetric defects (pores, inclusions) the tip of the blind holes has an angle of 118 °. Therefore the detection of the artificial defects is more challenging than for flat bottom holes commonly used for defect resolution determination in non destructive testing. In Fig. 4 the location and dimension of the artificial defects is shown schematically.

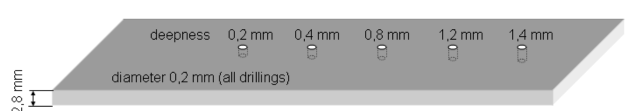


Figure 4: Schematic sketch of the test body for assessment of detection limit for volumetric defects (sheet thickness 2.8 mm).

### *Test Results Volume Inspection*

For volume inspection of the Nb-RRR sheets a 50 MHz ultrasonic transducer is used. The use of an increased ultrasonic frequency compared to standard ultrasonic inspection increases the defect detection capability. A focal length of 50 mm was chosen. This avoids multiple scanning with different focus adjustments which would be necessary for a focussed transducer. The result obtained from the inspection of the test body described above is given in Fig. 5.


Figure 5: C-scan representation of the defect echo obtained from the test body (see Fig. 4). The white points indicate the defect echo from the 0.2 mm drillings.

The artificial defects of the test body can be recognized in the C-scan image regardless of their depth location. Therefore the capability of volume inspection with a defect resolution of 0.2 mm is proven for the setup.

The volume inspection was also performed for the 15 Nb-RRR sheets of production lot "C4" described above. No volume defects were detected.

## DISCUSSION

For surface characterization Nb-RRR sheets prepared under production conditions with thickness of 2.8 mm and surface condition according to XFEL specification were used. USM was performed using a 75 MHz and a 150 MHz transducer with a focal length of 8 mm and 3.2 mm respectively. Using the 150 MHz transducer even the surface structure is displayed. Using the 75 MHz transducer the signal from the surface structure can be discriminated. Therefore this transducer is chosen for industrial application. The sensitivity of USM for surface defects is proven to be in the magnitude of 0.1 mm which is confirmed by light microscopy. To meet the specified detection limit the transducer frequency must be adapted individual according valid specification.

For determination of the defect resolution in the volume a test body of Nb-RRR sheet material was prepared. Blind holes with a diameter of 0.2 mm and a tooling angle of 118 ° were introduced in different depth. The use of a 50 MHz transducer with a focal length of 50 mm enables the detection of such point like defects through the body. Future work will focus on the detection of embedded material inclusions, e.g. Ta.

## CONCLUSIONS

USM was assessed as inspection tool for surface and volume inspection of Nb-RRR sheet material. With use of specific test setups the detected surface defects stand in good correlation with results from visual inspection. Concerning volumetric defects the resolution was demonstrated by means of artificial defects. A continuation of this activity is foreseen.

By use of transducers with long focal length a multiple scanning for volumetric inspection can be avoided. Therefore, reasonable scanning times for volumetric inspection can be realized.

For large production scale a standardized rating of the material quality under inspection is demanded. USM meets this requirement by an automized establishment of test records containing a clear display of defects.

## REFERENCES


[1] W. Singer et al.; "Diagnostic of Defects in High Purity Niobium", 8th Workshop on RF Superconductivity, Abano Terme, Italy (1997), Report LNL-INFN (Rep) 133/98, p850

[2] P. Kneissl, "State of the Art of Multicell SC Cavities and Perspectives", EPAC'02, Paris, TUXGB001, p. 139 (2002); www.JACoW.org

[3] W. Vodel et al.; "A new SQUID based Maesurement Tool for Characterization of Superconducting RF Cavities", EPAC'06, Edinburgh, TUPCH031, p. 1070 (2006), www.JACoW.org

[4] Q-S. Shu et al.; "SQUID Based Non-Destructive Testing Instrument of Dished Nb Sheets for SRF Cavities", PAC07, Albuquerque, WEPMS055, p. 2469 (2007), www.JACoW.org

[5] C.W. Hardin, J. Qu, A.J. Shih, "Fixed Abrasive Diamond Wire Saw Slieing of Single Crystal Silicon Carbide Wafers," *Materials and Manufacturing Processes,* 19(2), 2004: 357-369.

[6] A. Sutor-Dziedzic; "Scanning acoustic and X-ray microscopy as attractive tools for diagnostics of electronic components"; Electronika 12, 2007: 14-16

[7] S. Hirsekorn, U. Rabe, D. Bruche, J. Maurer, W. Arnold; „Prüfung von Nicht-Eisen-Metall-Druckgusskomponenten"; MP Materials Testing 50, 2008: 206-215.

# THE 1.3 GHz SUPERCONDUCTING RF PROGRAM AT TRIUMF

R.E. Laxdal, K. Fong, A. Grassellino, A.K. Mitra, I. Sekachev, V. Zvyagintsev,
TRIUMF*, Vancouver, BC, Canada,
R.S. Orr, W. Trischuk, U. of Toronto, Toronto, Ont., Canada

*Abstract*

TRIUMF is proposing to build a 50 MeV electron Linac as a driver to produce radioactive ion beams through photo-fission. The present design calls for the use of nine-cell 1.3 GHz Tesla type cavities. A 1.3 GHz Superconducting RF (SRF) program has been initiated with the goal to produce and test one nine cell cavity by the end of 2009. The program will use the existing clean room and SRF test facilities that support the ISAC-II heavy ion superconducting Linac. A vertical cryostat has been modified with a new insert to allow single cell testing. A single cell fabrication program is being initiated with a Vancouver company. A RRR measurement program is on-going to test cavity welds. The goal of the 1.3 GHz upgrade is to produce cavities for the 'in house' project as well as broaden TRIUMF's technical base for future potential collaborations.

## INTRODUCTION

### *Existing Program at 100 MHz*

A cavity testing program was initiated at TRIUMF in 2002 in support of the construction of a superconducting heavy ion Linac.[1] A test cryostat was used for single cavity characterizations, LLRF controls and RF ancillary development. Since then over 40 vertical cold tests have been completed to characterize a production series of twenty 106 MHz quarter wave bulk niobium cavities. In addition five full cryomodules have been assembled and ten cryomodule cold tests have been completed prior to installation of the modules in the Linac vault. TRIUMF has built a core competency in 100 MHz SRF technology while producing the ISAC-II heavy ion Linac. Due to the incorporation of modern processing techniques and clean room assembly, largely developed in the $\beta = 1$ community, the accelerating gradients achieved in the TRIUMF Linac are significantly higher than those found at other existing heavy ion machines. Presently a new series of cavities at 141 MHz is in production at PAVAC Industries of Richmond BC after a successful prototyping of two cavities.[2] Twenty cavities will be assembled in cryomodules for installation by the end of 2009.[3]

### *e-Linac Project*

The aim of the ISAC-III (ARIEL) proposal[4] is to generate additional radioactive ion beams (RIBs) on target to produce more physics. Presently a 500 MeV proton beam from the cyclotron at 100$\mu$A produces radioactive isotopes through fission and spallation from a thick target. It is proposed to increase the RIBs available by adding an independent and complimentary driver: a high-power 50 MeV electron Linac.[5] The electron linac would operate at 1.3 GHz and use, where possible, existing ILC technology to reduce development time.

* TRIUMF receives funding via a contribution agreement through the National Research Council of Canada

## EXISTING FACILITIES

The existing ISAC SRF facilities consist of the following areas as shown in Fig. 1:

- Preparation area: A staging area for receiving parts intended for use or assembly in the clean room. The room contains two large tanks one for ultrasound cleaning and one for rinsing. These tanks are used for cleaning of parts before sending to the assembly area.
- Clean room: This is divided up into sections depending on the level of particulate control required. The eastern area including the HPWR and assembly areas are cleanest (Class III). The cavity test area with an overhead crane has the next level of particulate control and protocol (Class II) and the RF measurement area is the third isolated area with a third protocol (Class I). The clean rooms are not commercial installations but home-made with large HEPA filter installations in the ceiling and return air ducts near the floor located around the room. Air pressure control is maintained to force HEPA filtered air to flow from the cleanest areas to the less clean areas. Particle counts are typically below 100 in Class III and below 1000 in Class II.
  - HPWR Rinse Area: Houses a fume hood for light chemical cleaning and a horizontal rinse stand to allow semi-automatic rinsing of quarter wave cavities. Filtered 18 MOhm water is delivered at high pressure as the cavities are rotated.
  - Assembly Area: Single cavities and whole cryomodules are assembled in clean conditions in preparation for cold tests.
  - RF measurement area: Houses the LLRF control racks and RF measurement equipment for cavity characterizations during vertical tests.
  - Cavity Test Area: Equipped with a test pit for x-ray shielding during RF tests. It is sufficient to contain both the single cavity test cryostat and the medium beta cryomodule, with dimensions 4m long x 2 m wide x 2.5m deep. An overhead crane is available for lifting the cold mass into

either the cryostat or the cryomodule. All signals from the test are gathered to the local racks and communicated to the EPICS control system.

- RF Controls Lab: Lab space for the development and production of the LLRF controls
- BCP Chemical Lab: A BCP facility with large walk-in fume hood allows full cavity etching for either the heavy ion cavities or a TESLA style nine-cell elliptical cavity.

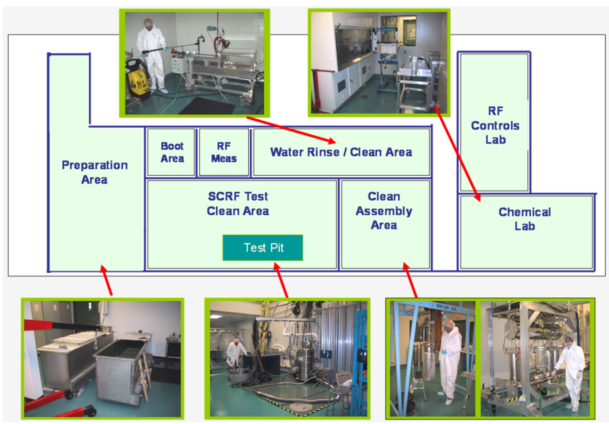


Figure 1: The SRF facilities in ISAC.

## 1.3 GHz PROGRAM

The cavities that will be developed for the e-Linac are 1.3 GHz elliptical cavities similar to those developed in DESY for the Tesla project and used at FLASH. We have presently received one single cell cavity as part of a collaboration with Fermilab. Two single cells and one nine-cell are also expected from DESY. The 1.3 GHz program will use the lab space already developed for the heavy ion cavity production. New vertical cryostats for both single cell and nine cell cavity testing are required. Presently a vertical cryostat from another application has been modified for single cell cavity testing. The cryostat consists of a vacuum chamber, an annular nitrogen bath just inside a vacuum chamber wall and a helium bath inside the nitrogen chamber with an inner diameter of 28 cm. The cryostat was first assembled for cryogenic and vacuum tests. In this case the top plate assembly consisted of temperature staging baffle plates, extension tubes to the cold mass, a Helium level sensor and cryogenic temperature sensors. The cold mass consisted of a copper plate with a 50 W heater. Hermetically sealed vacuum pumps were procured for sub-atmospheric pumping of the helium space. The pumping station consists of four interconnected pumps mounted in a metal frame and includes all the necessary power, control electronics, and valves. The pumps that are used are: (1) a Pfeiffer Balzers WKP 4000 SP roots pump, (2) a Pfeiffer Balzers WKP 500 A SP roots pump, (3) an Alcatel ZT 2060 H pump, and (4) an Alcatel 2063 H1 pump. The cryostat is first cooled with LN2 in the side shield before filling with LHe at atmospheric pressure. The bath pressure and helium temperature are then monitored as the pumps are activated (Fig. 2). The cryostat reached a temperature of 2°K after ∼25 minutes of pumping. A minimum temperature of 1°K (determined by pressure measurements) was reached after 45 minutes of pumping corresponding to a pressure of 130 mTorr. The helium level dropped by 8.5 inches, from 35.5 inches to 27 inches, corresponding to 13.6 liters in 15 minutes or 55 litres/hour. The variation in level was 23 litres/hour at 2°K corresponding to a gas evolution from a 17 W load. Since LHe has a density of 140 g/litre at 2°K this corresponds to a mass flow of 0.9 g/s. The static load on the cryostat was measured at 2.7 W. The pumping speed was further tested by activating the heater on the copper cold mass. The heater was raised until at ∼15 W active load the temperature reached an equilibrium near 2°K. The exhaust valve was also used to help throttle the pumping speed to control the temperature.

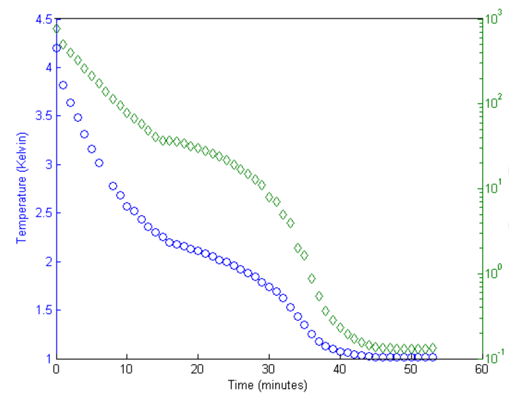


Figure 2: Temperature and pressure during pumpdown.

A top plate for single cell tests has been fabricated and assembled. A variable coupler has been designed to provide sufficient flexibility for single cell cavity rf tests. A capacitive coaxial coupler with antenna diameter 9.2 mm is equipped with a welded bellows to provide 74 mm travel and coupling in the range of $Q_{\rm ext} \sim$ 1e7 to 5e10. The test coupler is now being fabricated.

Additional test ancillaries include an RF amplifier, RF pickup, a low level RF system and diagnostic equipment. To avoid trapped flux significantly reducing the surface resistance the background field in the cavity should be suppressed to $<$10 mG. This will be accomplished by adding two layers of mu-metal; a warm layer of 1 mm thick material just inside the vacuum chamber and a cold layer of 1 mm Cryoperm material as a cylinder surrounding the cavity in the helium bath. In addition a steel pipe will be added around the cryostat to shield radiation but will also suppress environmental magnetic fields.

An apparatus for measurement of Niobium RRR has been assembled with electronics developed in house. It allows a fast measurement but is limited to only one sample per cool-down. The cryogenic hardware consists of a standard liquid helium 100 litre storage dewar. A sample is mounted into a cylindrical cartridge then introduced into the dewar using a long dipstick. The natural stratification of the He gas above the liquid surface and the insertion depth of the dipstick determine the sample temperature. Samples are typically 3 inches long and 1/4 inches wide. A four probe technique is used to measure the resistance just above the transition temperature of niobium, with the current injected at the ends of the sample and the voltage taps being located inwards. The samples are driven by a 100 mA, 3 Hz sine-wave current to average out thermally induced emf. The voltage across the sample is read through a nanovoltmeter designed in house and an AGILENT 35670 spectrum analyzer.

The 1.3 GHz cavity tests will be conducted in the existing test pit in the Class II area. An LHe feed from the central helium refrigerator is available. The vacuum pumps for sub-atmospheric operation at 2°K will be located in a nearby service room and connected to the EPICS controls system for remote start/stop. During initial operation the exhaust gas will be vented to atmosphere; in subsequent operation the exhaust will be first purified and then sent via return piping to the compressor.

Plans are in place to design and acquire a new vertically oriented HPWR facility and a tuning stand to allow plastic deformation of individual cells and field measurement with a bead pull. In addition a horizontal test cryomodule for testing fully dressed cavities will be designed and fabricated. After testing, the cavities will be assembled in horizontal strings for either single cavity tests in the horizontal test cryomodule or for installation in the e-Linac. These string assembly frames would reside in the Class III clean assembly area.

## CAVITY FABRICATION

The Tesla cavity consists of nine-cells with the entrance and exit cells welded to beam tubes and end flanges to make a continuous beam pipe. The entrance and exit beam tubes are also outfitted with ports for coupling in the RF power and coupling out a pick-up voltage for cavity regulation as well as coupling out HOMs from the cavity. The tubes for the beam pipes and the coupler ports are made by sheet rolling or back extrusion and are joined to the cavity by EB welds.

A cavity fabrication program has been initiated at PAVAC Industries, a local machining and EB welding firm in the Vancouver area. A set of forming dies has been sourced from RRCAT in India through a collaboration agreement with FNAL. The forming dies for the inner cells have been delivered and the two outer die sets are soon to arrive. Cavity fabrication will begin with forming studies on copper followed by the welding of copper half-cells into dumb-bells to establish weld fixtures and tooling and RF frequency defining steps. The plan is to complete two single cell niobium cavities by Spring 2009 and one nine cell cavity by the end of 2009.

## PROJECTS

The funding for the e-Linac may be announced in early 2010. In the meantime several initiatives allow us to move forward with the elliptical cavity program. We have recently signed an MOU with VECC in Kolkata. VECC also has plans to build an e-Linac for photo-fission and are working with TRIUMF on research and development towards that goal. An initial step will be the construction and beam test of an injector module capable of accelerating 10 mA of electrons to 5 MeV and reduced currents up to 10 MeV. The design, fabrication, installation and test of the injector module will test all technical aspects of the e-Linac program. A test area in the ISAC-II complex has been identified as a beam test area. An electron gun has been sourced from J-Lab and will be installed in the coming months followed by a room temperature buncher and matching optics. Beam dynamics and RF modelling studies of the e-Linac front-end will define the injector module by June 2009. Parallel cavity prototyping studies and cryomodule design and fabrication would continue through to the end of 2010 with a beam test scheduled for spring 2011.

TRIUMF has also entered into a collaboration with CERN on the Superconducting Proton Linac.[6] Two cavity types, a $\beta = 0.65$ and a $\beta = 1$ five-cell elliptical cavity are called for in the design. Both cavities will operate at 704 MHz. TRIUMF will initiate modelling, engineering and prototyping studies on the $\beta = 0.65$ cavity with the goal to produce a cavity in Canadian industry by the end of 2010.

## SUMMARY

A 1.3 GHz program for production of nine cell elliptical cavities has started at TRIUMF. Upgrades necessary for 1.3 GHz cavity fabrication and processing are underway in the existing SCRF infrastructure. Fabrication of a one cell in collaboration with PAVAC industries has begun with delivery and testing of a nine-cell cavity scheduled for the end of 2009.

## REFERENCES


[1] R.E. Laxdal, “Commissioning of the ISAC II SC-Linac”, LINAC06, Knoxville, USA.

[2] R.E. Laxdal, et al, “Production and Testing of Two 141 MHz Prototype Quarter Wave Cavities for ISAC-II”, these proceedings.

[3] R.E. Laxdal, et al, “ISAC-II Superconducting Linac Upgrade - Design and Status”, these proceedings.

[4] M. Marchetto, “ISAC-II Operation and Future Plans”, these proceedings.

[5] S. Koscielniak, et al, “ARIEL and the TRIUMF E-Linac Initiative, a 0.5 MW Electron Linac for Rare Isotope Beam Production”, these proceedings.

[6] A. Lombardi, et al, “The CERN Linac Upgrade Program”, these proceedings.

# PRODUCTION AND TESTING OF TWO 141 MHz PROTOTYPE QUARTER WAVE CAVITIES FOR ISAC-II

R.E. Laxdal, R.J. Dawson, K. Fong, A. Grassellino, M. Marchetto, A. K. Mitra, T. Ries, V. Zvyagintsev, TRIUMF*, Vancouver, BC, Canada,
R. Edinger, PAVAC Industries, Inc., Richmond, BC, Canada

*Abstract*

The medium beta section of the ISAC-II superconducting linac ($\beta$=5.7% and 7.1%) has been operational since April 2006 providing 20 MV of accelerating potential at 106 MHz. The 'high beta' extension to the linac, in progress, will see the addition of twenty 141 MHz quarter wave cavities at $\beta = 11\%$. The design specification calls for cw operation at a voltage gain of at least 1.1 MV/cavity for no more than 7 W of power dissipated in the cavity. This operation point corresponds to challenging peak surface fields of 30 MV/m and 60 mT. The cavity design is similar in concept to the medium beta cavities except for the addition of a drift tube to render symmetric the accelerating fields. A prototyping and qualification program was initiated with PAVAC Industries Inc. of Richmond, B.C. Two full size models in copper and two in niobium have been completed. The cold performance of both cavities exceeds the specification and the final frequency is within tuning range. The design, fabrication details and test results will be presented.

## INTRODUCTION

The high beta section will double the voltage gain of the ISAC-II superconducting accelerator by means of an additional twenty cavities[1]. These cavities will be housed in three cryomodules with common isolation and cavity vacuum. Two cryomodules will contain six cavities and the last one will contain eight cavities. The plan is to install the completed and tested cryomodules during an extended shutdown of ISAC-II starting in September 2009. The medium beta section is in operation since April 2006 and is reliably operating at an average acceleration gradient of 7 MV/m at 7 W cavity power, corresponding to peak electric and magnetic fields of 35 MV/m and 70 mT[2] and represent the highest values for an operating cw heavy ion linac. The medium beta design was accepted as a basis for the design of the high beta section.

## CAVITY DESIGN

The design of the new ISAC-II superconducting high beta cavity is presented in Fig. 1 and it is similar in structure to the medium beta 106 MHz cavities design[3]. The operational frequency is 141.44 MHz and $\beta_0 = 0.11$. It is a bulk niobium double wall structure $\sim$25% shorter than the medium beta cavity. The main difference is the donut shaped inner drift tube to provide higher geometric $\beta$ and transit time factor (TTF), and improved field symmetry. The acceleration gap is reduced from 40 to 35 mm and the grounded beam ports diameter is also reduced from 60 to 50 mm to achieve a 115 mm gap to gap distance with the 180/60 mm coaxial arrangement. The position of RF ports was optimized for coupler operation. A mechanical dissipator is inserted inside of the inner conductor of the cavity to dampen vibrations. The bottom plate of the cavity is modulated and slotted to provide a deformation of at least 3 mm for cavity tuning.

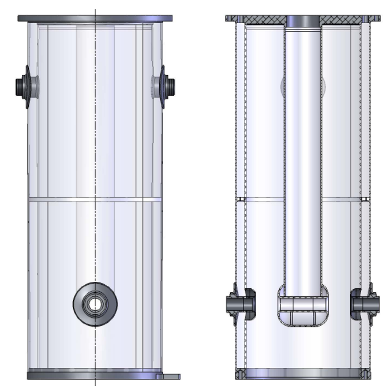

Figure 1: ISAC-II high beta cavity design.

CST 2008 Microwave Studio model and cavity parameters are shown in Fig.2. Virtual volumes in the model were used in the simulation to avoid errors from meshing. The models include a virtual cylinder around the beam tube donut and a virtual coaxial in the high magnetic field stem region. The peak electric field, $E_p$, is calculated from a donut geometry parameterization. $B_p$ is calculated assuming a cosine longitudinal, hyperbolic radial magnetic field distribution in the virtual coaxial and the value of magnetic field stored in this volume. Frequency sensitivity for beam ports and top and bottom flange displacements are calculated from surface densities of electric and magnetic fields by using the Slater theorem. The acceleration gradient definition is $E_a = V_a/D$ where $V_a$ is an acceleration voltage gain of the cavity at optimum velocity $\beta_0$ (including a transit time factor $\mathrm{TTF}_0$), $D$ is a conventional cavity length chosen as the cavity outer conductor diameter. The design goal is $E_a = 6$ MV/m and corresponds to $V_a = 1.08$ MV. The steering effect due to the electric and magnetic transverse rf fields can be largely compen-

* TRIUMF receives funding via a contribution agreement through the National Research Council of Canada

sated by shifting the cavity 1.3 mm downward relatively to the optical axis. The bottom tuning plate is removeable for easy cavity access with a metal to metal contact. The tuning plate position is optimized to have sufficient frequency sensitivity, ∼8 Hz/mm, while maintaining an acceptably low magnetic field ratio $B_c/E_a < 0.1$ mT/(MV/m) in the bottom tuning plate to flange non-welded contact.

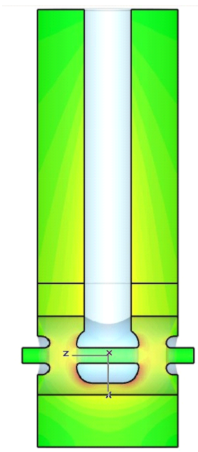

| | | |
|---|---|---|
| f | MHz | 141.44 |
| aperture | mm | 20 |
| gap | mm | 35 |
| drift | mm | 80 |
| Outer dia | mm | 180 |
| Inner dia | mm | 60 |
| Height | mm | 560 |
| bo | | 0.112 |
| TTFo | | 0.936 |
| U/Ea^2 | J/(MV/m)^2 | 0.067 |
| RsQo | Ohm | 26 |
| Ep/Ea | | 4.9 |
| Bp/Ea | mT/(MV/m) | 10 |
| Bc/Ea | mT/(MV/m) | 0.1 |
| Df/Dx | kHz/mm | |
| beam ports | | 120 |
| top | | -268 |
| bottom | | 8 |

Figure 2: CST model and cavity RF parameters.

## PRODUCTION

Initially two copper dummy cavities were produced at PAVAC Industries. This modelling period was useful in developing forming and welding fixtures and to develop frequency tuning steps and helped streamline the Nb production. Forming fixtures for rolling the inner and outer conductor were developed to roll and shape the 2mm Nb sheet. The donut beam tube was formed in three steps. The beam tube and end caps were machined from solid bar then welded into a sub-assembly. An outer shroud made from 1mm material was then rolled, machined and welded to the sub-assembly before final machining and welding to the inner conductor.

Frequency goals and tuning procedures during production were defined based on the data from the copper dummy cavities production, frequency sensitivities from CST cavity model and niobium welding trials. The sequence of tuning operations for the cavity production is the following:

- The inner and outer conductor length are trimmed before flanges welding with a sensitivity of -268 kHz/mm (data in Fig. 2).
- The acceleration gap adjustment is done by first determining the correct after weld gaps from rf frequency measurement then fixing the gaps with a welding jig with dimensions to compensate for the expected weld distortion. The beam ports sensitivity is 60 kHz/mm for total shift from both gaps.
- There is a final machining of the bottom flange after the initial cold test to set the final frequency; sensitivity is ∼8 kHz/mm.

BCP etching of parts prior to welding was done at TRIUMF with the standard 1:1:2 BCP with a typical etch rate of 1$\mu$m/minute. After all welds, tunings and pressure tests the cavities were BCP etched $\sim$ 80$\mu$m and high pressure rinsed with deionised water.

## CAVITY TESTS

Cavity tests were performed in the ISAC-II single cavity cryostat. The cavity is assembled and equipped with dissipator, coupler, tuning plate, pickup, temperature sensors and enclosed in mu-metal shield. After cavity pumping the frequency shift of +42 kHz corresponds to the air-vacuum shift (air dielectric constant=1.0005855) only and not due to alterations in the cavity volume. The cavity is pumped then baked for two days to achieve a temperature of 360°K at a vacuum of 1e-6 Torr. This is followed by two days of radiative cooling with LN2 in the thermal shields to reach 200°K before filling the cryostat with liquid helium. The estimate of frequency shift from room temperature to cold temperature was done based on previous experience with the medium beta ISAC-II cavities and Alpi cavities of INFN-LNL. To a good approximation the frequency shift is proportional to operational frequency. Following this scaling we predicted a 253 kHz frequency shift. This is just 4.5% less than the actual shift of 264 kHz. The resonant frequency of the superconducting cavities is within ±17 kHz of the goal operational frequency 141.44 MHz within the range of compensation allowed by small deformations of the tuning plate.

Table 1: Prototype cavities test results.

| Parameter | Prototype 1 | Prototype 2 |
|---|---|---|
| $f_o$ (MHz) | 141.423 | 141.456 |
| $Q_0$ | 1.10e09 | 1.20e09 |
| $E_a$ (MV/m) @ 7 W | 8.1 | 8.8 |
| $E_p$ (MV/m) @ 7 W | 40 | 43 |
| $B_p$ (mT) @ 7 W | 81 | 88 |
| $E_a$max (MV/m) | 10.9 | 12.5 |
| $E_p$max (MV/m) | 53 | 61 |
| $B_p$max (mT) | 109 | 125 |
| $df/dP$ (Hz/Torr) | 3.3 | 1.7 |
| $df/d(E_a)^2$ (Hz/(MV/m)$^2$) | -0.8 | -0.9 |
| $\Delta f$ (kHz) (300K-4K) | 263 | 265 |

RF conditioning of the cavity indicated the 1$^{st}$ level of multipacting at $E_a \sim 10$ kV/m, which according to Frequency-Gap Product in the Two Surface Multipactor model[4], corresponds to the 1$^{st}$ order of the acceleration gaps. There are also several higher levels. The multipactor levels process out in several hours using pulsed rf conditioning at strong coupling. Both prototypes exhibited strong field emission at ∼5 MV/m that could be eventually conditioned out by repeated conditioning. RF conditioning pulses varied from $\Delta T \sim 0.2$-$0.5$ s and $T \sim 1$ s at a forward power of 200-400 W with overcoupling to achieve fast cavity response with sufficient field level. Helium conditioning at ~1e-5 Torr was also employed. The calibration of the pickup voltage for acceleration gradient $E_a$ is calculated from the decay time constant and power dissipation during critically coupled cavity measurements.

The resulting Q-curves after conditioning of the prototype cavity cold tests are presented in Fig. 3 and the test summary data are presented in Table 1. A maximum cw acceleration gradient for one prototype of $E_a > 12$ MV/m is achieved, which corresponds to $E_p > 60$ MV/m and $B_p > 120$ mT. The limitation is from radiation levels produced in the test area. At 7 W power dissipation the cavities acceleration field $E_a = 8.5$ MV/m significantly exceeds the design goal of 6 MV/m. The measured quality factor $Q_0 = 1.2\mathrm{e}9$ corresponds to a residual resistance of $\sim 15$ n$\Omega$.

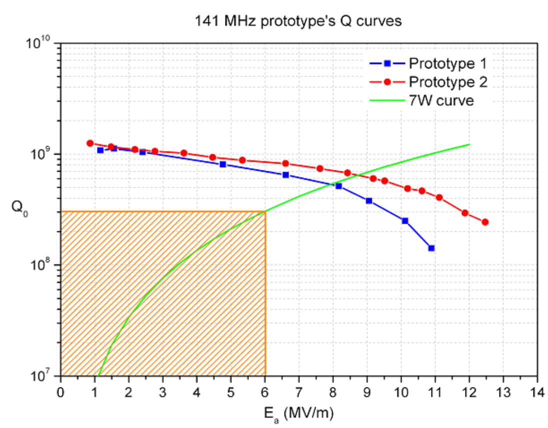


Figure 3: RF characterization results for prototype cavities.

A Q-disease test has been done for one of the cavities. The cavity was kept in the range 50-150 K for several days due to a cryogenic problem. The Q-curve taken after this is shown in Fig. 4. The quality factor drops an order of magnitude and the Q-curve shape becomes concave upward, a characteristic of Q-disease. After thermal cycling up to room temperature the Q-disease disappears.

The cavity lowest mechanical resonance frequency ~110 Hz is calculated and measured. Vibration measurements are taken with and without a mechanical dissipater in position. The peak phase error signal after a calibrated cavity excitation for the two cases is shown in Fig. 5. The dissipator helps reduce the forward power (reduce the overcoupling) required to provide a stable bandwidth for cavity operation.

## SUMMARY

Two superconducting bulk niobium ISAC-II high beta prototype cavities have been developed, produced and successfully tested. The acceleration gradient at nominal power dissipation 7 W is 8.5 MV/m corresponding to a

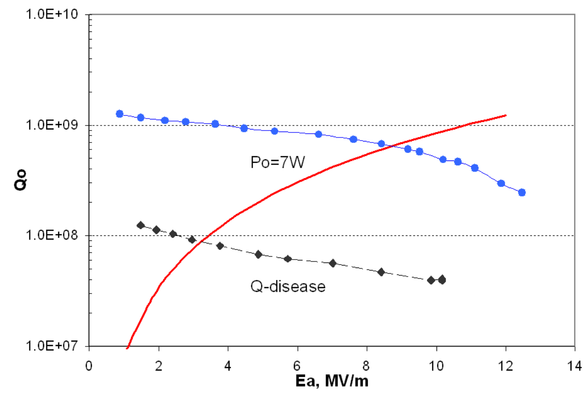


Figure 4: Prototype 2 with and without Q-disease.

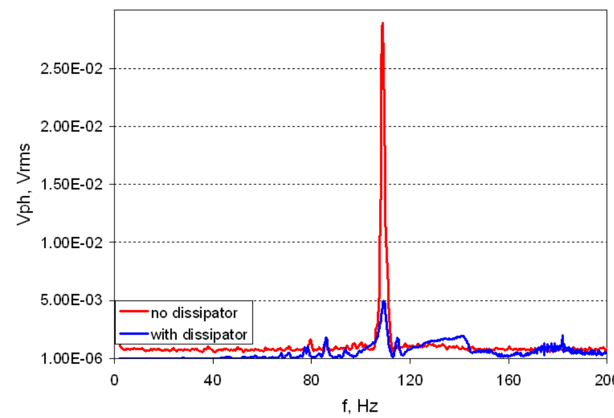


Figure 5: Phase noise with and without dissipator.

peak surface field in excess of 40 MV/m. The fabrication of twenty cavities are underway at PAVAC with the first six expected in October 2008. The Phase II extension is expected to be completed in Dec. 2009.

## ACKNOWLEDGEMENTS

The excellent technical assistance of Bhalwinder Waraich (TRIUMF) on the cavity assembly, Peter Harmer (TRIUMF) for the cavity etching and Bahman Latif (PAVAC) on the cavity fabrication are gratefully acknowledged.

## REFERENCES

[1] R.E. Laxdal et al, “ISAC-II Superconducting Linac Upgrade - Design and Status”, these proceedings.

[2] R.E. Laxdal et al, “Commissioning and Early Experiments with ISAC-II”, PAC 2007, Albuquerque, June 2005

[3] A. Facco et al, “The Superconducting Medium $\beta$ Prototype for Radioactive Beam Acceleration at TRIUMF”, PAC 2001, Chicago, May 2001.

[4] H. Padamsee et al, “RF Superconductivity for Accelerators”, Willey & Sons, 1998, p.191.

# PERFORMANCE OF THE ISAC-II 141 MHZ SOLID STATE AMPLIFIER

Amiya Kumar Mitra, Iouri Bylinskii, Ken Fong, Robert Edward Laxdal, Joseph Lu, Richard Shanks, Vladimir Zvyagintsev, TRIUMF, Vancouver, Canada

*Abstract*

The ISAC-II linac extension requires an additional 20 rf amplifiers to power twenty 141 MHz quarter wave superconducting cavities. Solid state amplifiers will be used for this extension as compared to tube amplifiers which have been employed for the existing ISAC-II linac section, operational since 2006. These solid state amplifiers are rated to an output power of 600 W. A prototype amplifier of the production series has been tested for gain and phase linearity. Phase noise of this amplifier has been measured on a 141 MHz superconducting cavity and compared with phase noise measured with a tube amplifier. The test results and general rf interlock and interface requirements are verified against tendered specification before series production of the remaining amplifiers can proceed. Benchmarking tests of the prototype amplifier will be reported.

## INTRODUCTION

An upgrade of the ISAC-II superconducting linac, operational since April 2006, is in progress. Additional 20 MV accelerating potential will be added to the ISAC Radioactive Ion Beam (RIB) facility by the end of 2009 [1]. The new installation consists of twenty 141 MHz quarter wave cavities at a design beta of 11%. The cavities will be housed in three cryomodules with six cavities in the first two cryomodules and eight cavities in the last. These additional 20 cavities will be powered by 20 solid state amplifiers which have been purchased from QEI Corporation, NJ, USA. The first amplifier of the production series is tested rigorously before production of final amplifiers can proceed. The medium beta linac which employs 20 quarter wave cavities operating at 106 MHz uses 20 triode tube amplifiers to power the cavities [2,3]. The limited tube life and marginal phase noise led to the option of using solid state amplifiers. Also, the tube amplifiers were rated for 1 kW however, only 600 watts was used for conditioning the cavities and around 200 watts was used for regular beam operation. The solid state amplifiers were therefore specified for maximum 600 watts output along with gain and phase linearity and phase noise requirements.

## GAIN AND PHASE MEASUREMENT

The amplifier output is terminated into a 50 ohms dummy load in order to measure the gain and phase characteristics and other basic functions. Figure 1 shows the gain and the phase characteristics which satisfy the specification outlined in table 1. Amplifier gain is measured to be 65 ± 0.75 dB (specified 55 ± 2 dB). Higher gain is acceptable since it can be lowered by addition of external 10 dB attenuator. The 1dB bandwidth is 8 MHz which is much higher than the specified 1 MHz bandwidth.

Table 1: Gain and Phase Linearity Requirement

| Parameter | value |
|---|---|
| Gain Linearity from 1 to 250 Watts | < ± 0.5 dB |
| Gain Linearity from 250 to 600 Watts | < ± 2.0 dB |
| Phase Linearity from 1 to 250 Watts | < ± 5° |
| Phase Linearity from 250 to 600 Watts | < ± 20° |
| Phase noise in 2 – 200 Hz range | < 0.3° rms. |

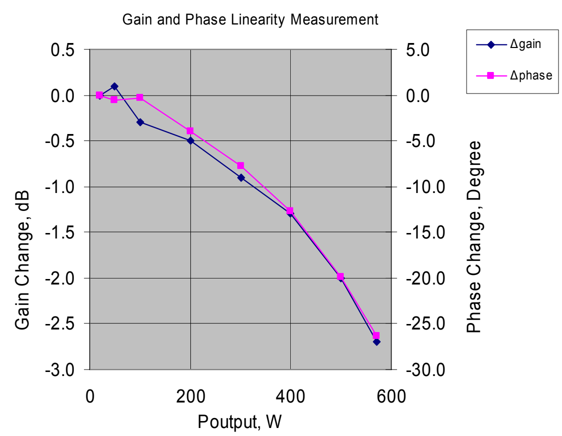


Figure 1: Gain and phase linearity measurement

## PROTECTION AND INTERFACE

The amplifiers are housed in the power supply room which is above the linac vault. These amplifiers are remotely operated from the control room via EPICS interface. These amplifiers are also interlocked with TRIUMF safety system which enables operation of the amplifiers when all safety requirements to operate the linac are satisfied. Table 2 outlines the alarm indications that are displayed on the front panel of the amplifier and are also sent to EPICS interface. Amplifier status and some of the rf parameters are also read by the EPICS system and are available at the EPICS page of the ISAC control system. This will help to debug the problems in the event of amplifier fault. This interface is similar to the existing 106 MHz amplifier. As an added new feature, these solid state amplifiers are protected for input over drive up to 10 dBm for a short period of time. If the maximum input power is exceeded a threshold comparator opens a fast RF GaAsFET switch at the RF input, which remains open until the operator resets the amplifier. The amplifier is also protected against excessive output forward and reverse power. The fast shut off of the DC supply to the amplifier modules against over voltage or over current at the transistor drains and case over temperature provides additional amplifier protection.

Table 2: Front Panel Alarm Indications

| Front Panel Alarm indication (LED) |
|---|
| High Input Power |
| High Output Forward Power |
| High Output Reflected Power (VSWR) |
| Power Amplifier Over Temperature |
| Power Amplifier Drain Voltage Alarm (summary) |
| Power Amplifier Drain Current Alarm (summary) |
| DC Power Supply Over Current |
| Loss of Cooling |
| Loss of External Interlock |

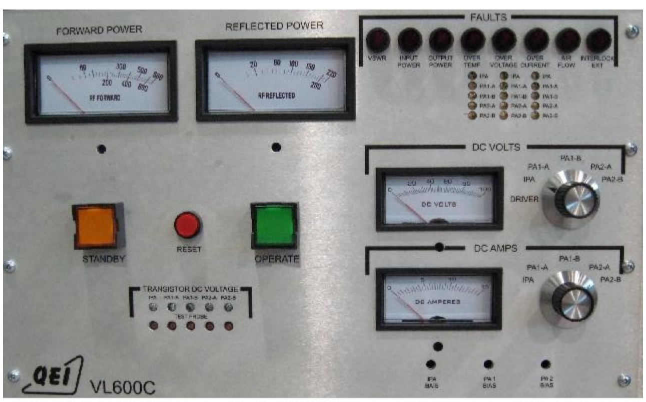


Figure 2. Photo of the front panel of the amplifier

## *Safety System*

The ISAC Safety System (ISS) ensures that the rf amplifiers are disabled when the linac is cold and vault door is open. The safety system provides a +24 vdc vault rf safety enable signal to the ISAC II rf amplifier only when all safety criteria are met. For external interlock a fail safe logic with Normally Open contacts is used. Only when these contacts are closed the amplifier can be put into the READY state. All amplifiers will be daisy chained through this contact. The safety system has already been implemented for the existing linac operating at 106 MHz. The new 20 solid state amplifiers will be daisy chained with the existing system.

# PHASE NOISE MEASUREMENT

The phase noise of the prototype amplifier was tested under two different conditions.

## *50 Ω Load*

The phase noise was measured with a 50 Ω load connected to the output of the amplifier. Figure 3 shows the basic scheme of the phase noise measurement. Similar measurement was done for a 141 MHz tube amplifier and results are compared. The signal generator output was set to provide +7 dBm signal level to the LO input of the double balanced mixer after the 3 dB power splitter. The attenuator before the input of the test amplifier was chosen such that the output of the power amplifier was at 200 watts. A -40 dB directional coupler and a suitable attenuator provides 0 dBm to the RF terminal of the double balanced mixer. The mixer sensitivity was measured with the same power levels that was used for measuring the phase noise voltage of the amplifier. The low pass filter cut off frequency was designed at 1 KHz.

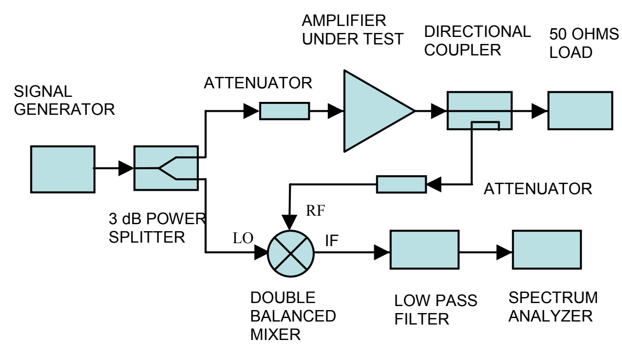


Figure 3: Basic block diagram of phase noise measurement

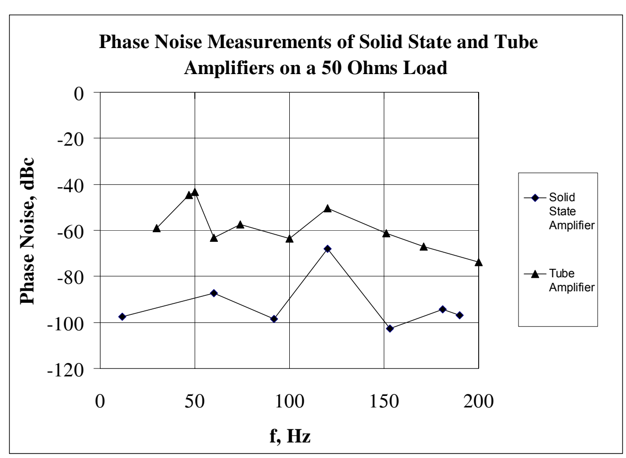


Figure 4: Phase noise measurement with a 50 ohms dummy load

Figure 5: Photo of 141 MHz superconducting cavity used for the test

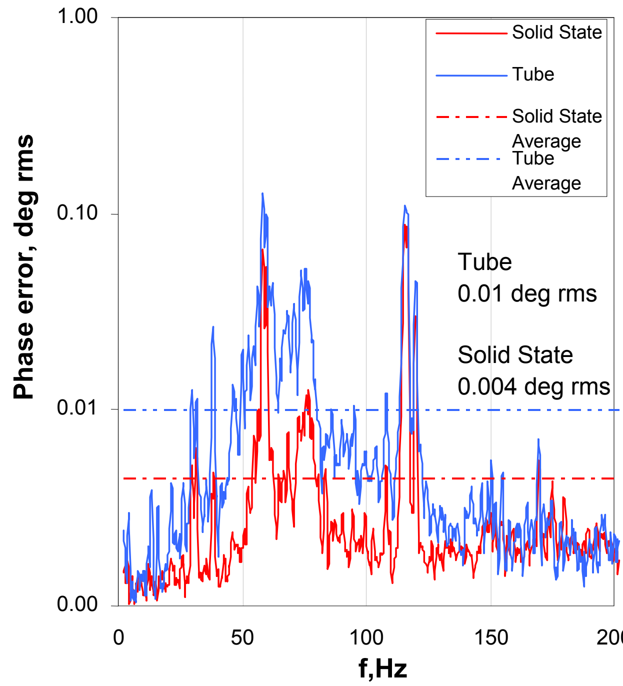


Figure 6: Phase noise measurements with the superconducting cavity

The spectrum analyzer measurement range was set from 1 Hz to 200 Hz. The tube amplifier was tested under same set up. The results of the phase noise measurements are shown in figure 4. The solid state amplifier has 20 dB less noise in the frequency range of 1 to 200 Hz. The noise at 120 Hz was most predominant.

### *High Q Load*

Phase noise measurement with the 141 MHz superconducting cavity [4] as a load for the amplifier was carried out with the rf control system which ran in closed amplitude and phase feedback loop. Figure 5 shows the photo of the 141 MHz cavity with coupling loop and pick up probe mounted. The same measurements were done with a 141 MHz tube amplifier and results were compared. Tests were done under the following cavity parameters:

Frequency, f =141.457 MHz
Unloaded Q, $Q_o$= $9e^8$
Loaded Q, $Q_l$ = $4.8e^6$
Forward power, Pf = 200 W
Loaded Bandwidth =f / $Q_l$ =30 Hz

Phase error signal was measured with a Spectrum Analyzer in the range 2-200 Hz and is shown in figure 6. 60 Hz and 120 Hz noise spectrum are due to ac power frequency and its second harmonic respectively. The other peaks in this frequency spectrum are due to mechanical resonances of the cavity, mechanical resonances in the cryovessel and cryogenic system. It can be seen from figure 6 that the solid state amplifier is significantly less noisy than tube amplifier. For the solid state amplifier the average noise value is 0.004° rms in the frequency range 2-200 Hz. The average noise for the tube amplifier in the same range is 0.01° rms.

## SUMMARY

The prototype solid state amplifier has been tested thoroughly and found to satisfy all the specifications requested. The solid state amplifiers provide lower phase noise by a factor pf 2.5 than tube amplifiers and at the same time will provide long device life than tube amplifiers. The long device life will lead to lower running cost of the linac. The ISAC linac will be equipped with two types of devices, tubes and solid state for all 40 quarter wave superconducting cavities. This will provide an unique opportunity to compare performance of these two types of amplifiers in the long run.

## REFERENCES

[1] R.E. Laxdal, et al, “ISAC-II Superconducting Linac upgrade- Design and Status”, this conference

[2] A.K. Mitra, et al, “Performance of rf amplifiers for ISAC-II medium beta linac operation”, 13th International workshop on RF Superconductivity (SRF 2007) Beijing

[3] I. Bylinskii, et al, “RF amplifier choice for the ISAC superconducting linac”, PAC2007, Albuquerque, New Mexico, USA, June 2007

[4] R.E. Laxdal, et al, “Production and Testing of Two 141 MHz Prototype Quarter Wave Cavities for ISAC-II”, this conference

# TESTS OF WIRE SUBLIMATIONS VERY CLOSE TO SPIRAL 2 SUPERCONDUCTING CAVITY

R. Ferdinand, J-L. Vignet, P. Robillard, E. Gueroult, GANIL, Caen, France
P. Ausset, H. Saugnac, G. Olry, D. Longuevergne, P. Szott, CNRS/IN2P3, IPN-Orsay, France.

*Abstract*

The construction of the new Spiral 2 facility has started in Caen (France) at the National Heavy Ions Accelerator Center (GANIL). The SPIRAL 2 project is based on a multi-beam Superconducting Linac Driver delivering 5 mA deuterons up to 40 MeV and 1 mA heavy ions up to 14.5 MeV/u delivering different Radioactive Isotope Beams (RIB). The LINAC is composed of 2 cryomodule families. The low energy family (cryomodules A) is composed of 12 cryomodules housing a single superconducting cavity at beta=0.07. The "high" energy family (cryomodules B) is composed of 7 cryomodules housing 2 cavities at beta=0.12. In between cryomodules are located the focalisation quadrupoles and the diagnostic boxes. Their multiplication may lead to cavity pollution. Strong believes forbid the use of interceptives diagnostics around superconducting cavities. We simulated the use of wires for diagnostics in the linac, sublimating 14 wires of tungsten, niobium and carbon while operating the cavity B at full performances. The results describe in this paper looks promising.

## DESCRIPTION

The objective for SPIRAL2 is to produce light ions (deutons, protons) up to 5 mA and a large diversity of heavy ions with intensities up to 1mA, including noble gases like $Ar^{12+}$ and metallic ions like Cr, Ni and Ca. The Injector, dedicated to protons, deuterons and ions of q/A=1/3, is mainly composed of two ECR ion sources with their associated LEBT lines, a warm RFQ and the MEBT line connected to the LINAC.

The LINAC is based on superconducting independently-phased resonators [1,2]. It is composed of 2 families of quarter-wave resonators (QWR) at 88 MHz, developed respectively by the CEA/DAPNIA and the IN2P3/IPNO teams: 12 resonators with $\beta$=0.07 (1 cavity/cryomodule) [3], and 14 resonators at $\beta$=0.12 (2 cavities/cryomodule) [4] (see Figure 1). The transverse focusing is ensured by means of room temperature quadrupole doublets located between each cryomodule. Additional dipolar coils are installed into the quadrupoles in order to compensate the steering effect of QWR cavities and eventually adjust the optimum beam position. These 20 “warm” sections (Figure 2), as opposed to the superconducting cavities, include also beam diagnostic boxes with different sensors types. The specifications require 20 Beam Monitors, 10 TOF and 6 phase length measurement devices and 20 vacuum pumping systems.

The multiplication of warm sections in such superconducting accelerator may lead to pollution problems and degradation of cavities performances.

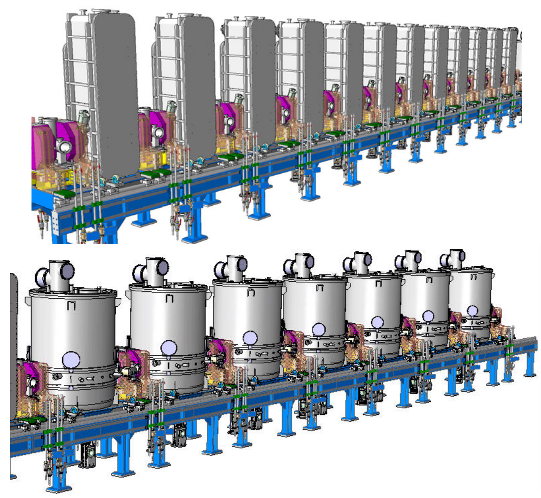

Figure 1: SPIRAL2 superconducting cryomodules (top: $\beta$=0.07, bottom: $\beta$=0.12).

One of the main beam diagnostic devices is the Beam Monitor (BM) which will measure more than the classical position of the centroid of the beam in the beam pipe of the accelerator. It plays a role of prime importance for the accelerator tuning and control. These capacitive sensors BM are located in the LINAC between the LINAC’s cryomodules and are mechanically integrated to the beam pipes into the quadrupole bore. The BMs give the classical beam positions, beam time of flight and possible phase information and current. Because of the non-cylindrical symmetry of the beam at this location, the signals return also information on quadratic moment related to the beam size. We expect CW operation as well as low duty factor pulsed mode operation. A $\pm$0.1mm resolution is foreseen and this criterion must be strongly taken in account for the mechanics and the electronics.

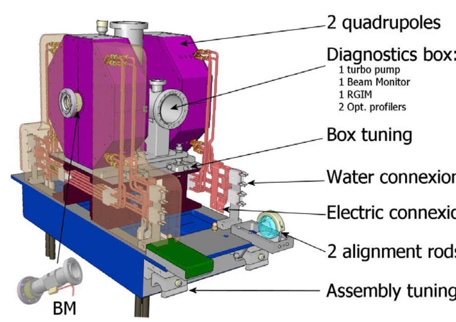


Figure 2 : Schematic of the “warm” section in between cryomodules.

The reference longitudinal diagnostics is the GANIL Residual Gas Ionization Monitor (RGIM) profiler [5] based on electron production resulting of the beam interaction with the residual gas (resolution 100 ps for a

10 mm beam, see Figure 3). They are equipped with micro-channel plate for amplification. This system does suffer of various difficulties like fixed errors, low response with a good vacuum, being fragile, but they are non interceptives.

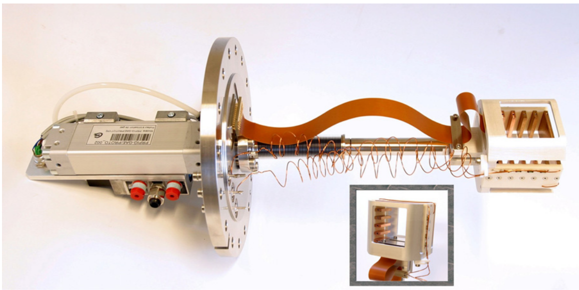

Figure 3 : RGIM diagnostic

Both the transverse and the longitudinal diagnostics will be difficult to build and tune and may suffer from low performances. Backup solution relies on interceptive wires used in pulse mode like S.E.M. Harp Profilers or wire scanners. This is not decided yet. We may be obliged to use them during the commissioning of the machine.

The use of interceptive diagnostics, located at about 70 cm from the superconducting cavities may result in serious malfunctions. Calculations showed that at these energies there are almost no sputtering from the beam on the wires. Nevertheless, from time to time the wires might be destroyed for various reasons: too long beam pulses, wrong beam focalisation, material fatigue etc... We fear quenches from such wires damages, permanent X-ray emission or overall degradation in cavities performances. The degradation of wires is not supposed to take place, and usually result from human errors. We count on none or low break frequency. It was decided to test the use of such wires during cavities operation at full power.

## TEST DESCRIPTION

The objectives of the test stand were multiples: analyse the influence of the wires close to a superconducting cavity, analyse the influence of the cryomodule (specially the X-rays emissions) on a RGIM device equipped with micro-channel plate, analyse the outgassing of the diagnostic box and its consequence on the cavities. Finally, a cohabitation test between the RGIM and an ionic pump was performed.

The cryomodule was assembled with two cavities, one with the power coupler and one with a $\beta$=1 coupling. The diagnostics box was put at its normal location, but without the quadrupoles and the BM. The cavity vacuum was pumped either through the diagnostics box or through the other end of the cryomodule. On the diagnostic box, 2 types of pumps were successfully installed: a turbomolecular pump with a dry primary pump or an ionic pump. A residual gas analyser (RGA) was installed on the diagnostics box, as well as a gas dosing valve for various gas injections. Schematics are given Figure 4.

For the wire sublimation tests, two sets of 7 wires were successfully inserted in the diagnostic box, in front of the cavities aperture. The distance between the sublimated wires and the center of the cavity was 70 cm, the distance being only 51 cm from the first superconducting surface. Each set included two 30 $\mu$m carbon wires, two 30 $\mu$m niobium wires, one 70 $\mu$m tungsten wire and two 150 $\mu$m tungsten wires. The wires were successfully sublimated with a controlled current power supply, while the cavity was working at full power (6.5 MV/m, about 1 kW RF power injected, 0.15 W transmitted). Every cavity parameters were recorded, as well as temperatures, helium consumption and un-calibrated X-rays emissions. The vacuum pressure was also recorded and images taken with a CCD camera (Figure 5).

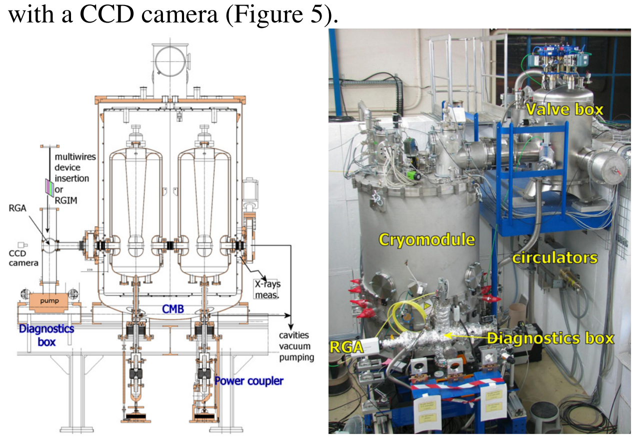


Figure 4 : Drawing and image of the setup.

## SUBLIMATION RESULTS

The multipactor barriers being easily passed with the power coupler, it was chosen to make the tests in front of the cavity with the power coupler.

As soon as a wire is warm to white, the X emission and the cavities vacuum increased slightly. The level of X-rays reached 1 to 5 mSv/h at 20 cm from the beam axis exit, and the pressure about 2 $10^{-6}$ hPa. A strong outgassing occurs when it breaks.

Unfortunately the first set of 7 wires was not very useful as a mix was observed between the wires. Also, some wires did short-circuit the others. Nevertheless the 7 sublimations did not induce any noticeable effect on the cryomodule performances, and the outgassing was of no noticeable effect on the set up.

The second set was used more carefully. We started with the 2 carbon wires, then the 3 tungsten ones and finally the 2 niobium wires. The 2 first sublimations did induce a quench in the cavity. The X-ray level went up by 50%, and stayed there, meaning that a carbon emitter was "glued" on the superconducting surface.

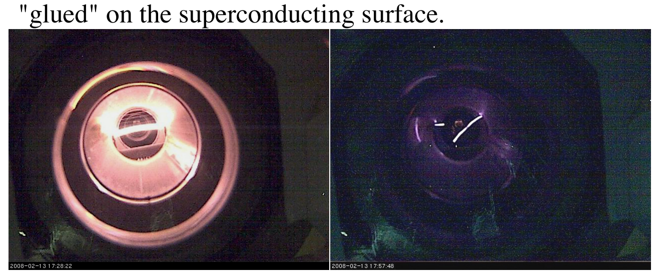

Figure 5: CCD camera views of a tungsten wire before sublimation (on the left) and during its breaking (right).

All the other wires induced a 2 to 20 times pressure increase for a short period (cf. Figure 6). None of the other cavity parameters evolved. We observed difference between the Nb wires and the W wires only on the pressure increase. It is most probably due to the wire diameter difference. The Nb wires were also extremely difficult to put in place, being easily broken. As they did not improve anything during the test, they will not be used for the drawback profiler solution.

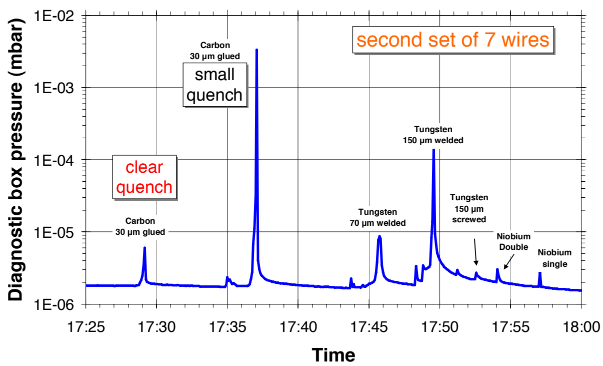


Figure 6: Outgassing during wire sublimation.

## RGIM RESULTS

The tests with the RGIM were made first with the ionic pump off, as well as the Residual Gas Analyser, in order to minimise the background noise. The superconducting cavities did not generate noise on the micro-channel plate of the RGIM, as soon as the multipactor barrier was over. The X-ray level dropped to about 30 mSv/h at the nominal cavity working point. Nevertheless this is not enough to validate the device, since the returning beam profile can also be modified by the electrostatic field of the cavity.

The ionic pump generates a lot of parasitic signals, making it incompatible with its use in a real machine. At a pressure level of $10^{-8}$ hPa, as it is expected in the machine, it should be kept acceptable, but it is a challenge.

## GAS POLLUTION RESULTS

The warm section will be backed at 150°C, and the expected outgasing will consist mostly of hydrogen. The multiplication of warm section compare to other linac design may result in more vacuum leak and hydrogen gas pollution than normally acceptable. The hydrogen at $10^{-8}$ hPa and 4.5K is not pumped. Hydrogen is pumped for a partial pressure of 1.3 $10^{-6}$ hPa for cavities at 4.4 K.

The pollution test consisted in injecting either hydrogen or filtrated room air for about an hour in the 2 cavities. The cavity performances were then tested, once the vacuum was good enough for RF injection. The injected gas quantity was equivalent to one year of continuous pollution. The pressure was about 2 $10^{-6}$ hPa with the hydrogen and 4 $10^{-8}$ hPa with the air.

The effect of the pollution was not evident. Just after injection the $Q_0$ was slightly degraded. After a week end at about 80k, the performances were up again (Figure 7). The resulting curves could also be in the errors bars.

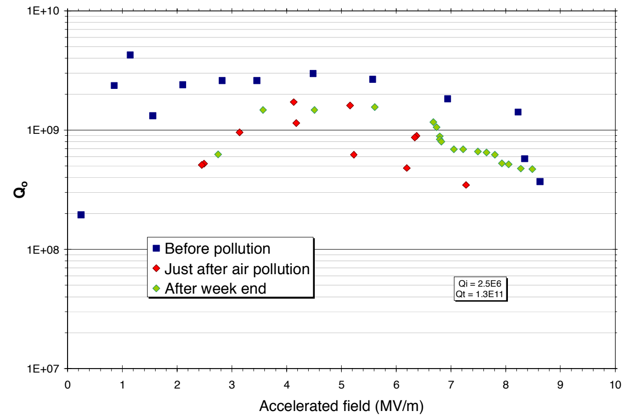


Figure 7: Cavity performance before and after pollution.

## CONCLUSION

First tests of the wire sublimation were very encouraging. If we clearly suffer from 2 carbon wires sublimations, 12 sublimations of tungsten and Nb wires did not induce any noticeable change in the cryomodule parameters. We need more statistics, but the use of wires for beam parameter measurements close to the cryomodules might be contemplate as a drawback solution if the other diagnostics do not provide the expected performances. It is foreseen to make such tests close to the first cryomodule family (β=0.07) in order to complete the statistics.

## ACKNOWLEDGEMENTS

Many thanks to the IPN-Orsay team which welcomed us and actively participated to these measurements. They did provide us a good support and many hours of their personal time.

## REFERENCES

[1] T. Junquera, “Status of the Construction of the SPIRAL2 Accelerator at GANIL”, this conference.

[2] R. Ferdinand and al., “The SPIRAL2 Superconducting Linac”, this conference.

[3] G. Devanz et al. “Status of the Low Beta Cryomodules for the SPIRAL 2 LINAC”, this conference.

[4] H. Saugnac et al. “RF cryogenic tests on the “qualifying” beta=0.12 SPIRAL2 cryomodule”, this conference.

[5] Beam profile and beam time structure monitors for the extracted beams from the GANIL cyclotrons (15 th conference and their application CAEN June 14-19 1998.

# 704 MHz HIGH POWER COUPLER AND CAVITY DEVELOPMENT FOR HIGH POWER PULSED PROTON LINACS

J. –P. Charrier, S. Chel, M. Desmons, G. Devanz, Y. Gasser, A. Hamdi,
P. Hardy, J. Plouin, D. Roudier, CEA, IRFU, F-91191 Gif-sur-Yvette, France

*Abstract*

In the framework of the European CARE-HIPPI program we develop components for superconducting high pulsed power proton linacs at 704 MHz. We have designed, fabricated and tested a beta 0.47 5-cell elliptical cavity with an optimized stiffening to reduce its sensitivity to Lorentz forces. A fast piezo tuner has been developed in order to be able to operate the cavity in pulsed mode in our horizontal test cryostat CryHoLab. We also have carried out the development of a fundamental power coupler. It is designed to transmit a power up to 1 MW at a 10 % duty cycle. A high power test area has been setup consisting of a 1 MW klystron, a pulsed high voltage power supply and a coupler test stand.

## INTRODUCTION

Elliptical superconducting (SC) cavities will be used in future high intensity proton linacs like SPL[1] for relative velocities β above 0.6. One goal of the CARE-HIPPI program is to build and test SC cavities for the lower energy section of pulsed proton accelerators. We have built and tested in vertical cryostat a 704 MHz 5-cell cavity optimised for pulsed operation at 2 K with a geometrical beta of 0.47, with a reduced sensitivity to Lorentz detuning [2]. The results of the vertical test are shown on figure 1. The measured static Lorentz coefficient $K_L$ is -3.8 Hz/(MV/m)$^2$.

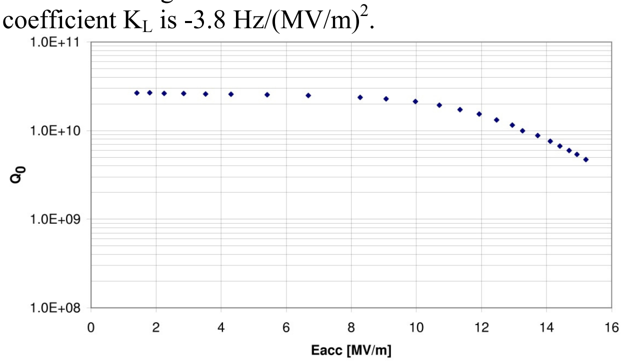


Figure 1: $Q_0(E_{acc})$ curve at 1.8 K.

The full test in pulsed mode in vertical cryostat requires developing of a fundamental power coupler (FPC) and setting up a pulsed power RF installation. Although the power needed for this type of cavity is limited to several hundreds of kW, the goal was to establish a 704 MHz test area enabling future developments demanding a higher power. In the higher energy section of SPL, a peak power of 1 MW must be transferred to the beam, this sets the target of our power coupler developments. The RF source has been commissioned reaching nominal parameters, 1 MW peak power, 2 ms RF pulse length at 50 Hz repetition rate [3]. The peak power can exceed 1.2 MW when the repetition rate is reduced. The circulator has been tested on a matched load at full power, filled with dry nitrogen. Tests have been performed in full reflection at all phases on a movable short, at nominal peak power and pulse length, but at the reduced repetition rate of 10 Hz. This limitation was due to a breakdown problem that occurred in the pulsed high voltage power supply which is being corrected.

Our horizontal test cryostat CryHoLab is being modified to accept the beta 0.47 cavity equipped with a FPC. The main changes are the larger FPC port, the LN2 copper thermal shield and the supporting systems for the cavities. Fig. 2 shows the new configuration with the cavity (mostly hidden by the magnetic shield) prepared for the low power measurements.

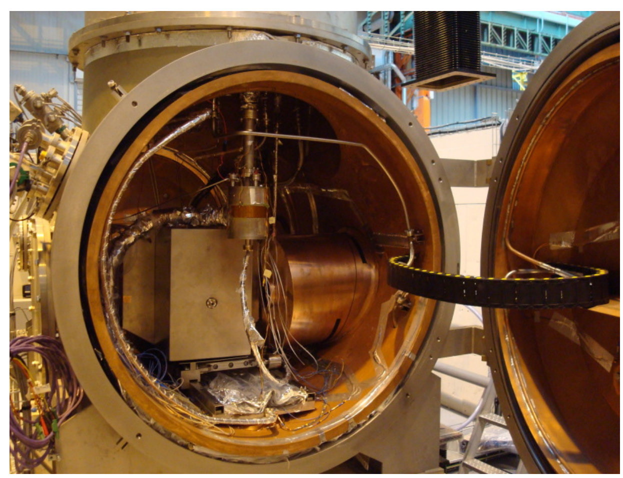

Figure 2: The new CryHoLab configuration.

## PIEZO TUNER

We have developed a fast piezo tuner based on the Saclay-II tuner design [4] built and qualified on a 1.3 GHz 9-cell Tesla type cavity. The main difference is the size of the system, and the piezo support which consists of a stainless steel elastic frame holding a single 30 mm piezo stack. It is designed in order to apply an adjustable preload on the piezo, limiting the influence of the spring constant of the cavity. The slow tuning range is +/-2.5 MHz. The tuner is attached between the He tank and the beam tube flange opposite to the power coupler side. With our optimized design, the tuner does not increase the overall length of the cavity (fig. 3).

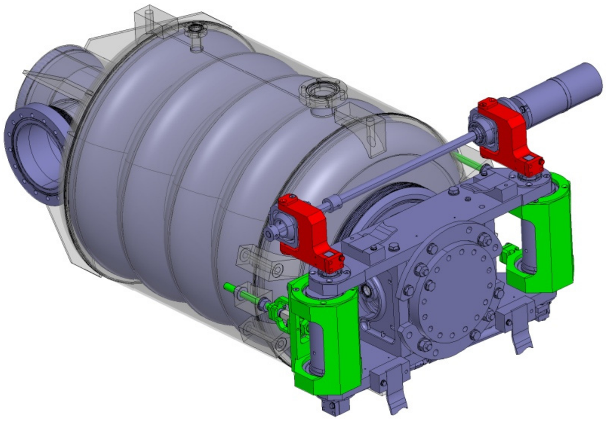

Figure 3: Cavity equipped with He tank and piezo tuner.

## MAGNETIC SHIELDING

The CryHoLab horizontal cryostat is only partially shielded therefore a magnetic shield for the cavity had to be designed. The average magnetic field in CryHoLab at its new location is 20 µT. The surface resistance measured on the cavity is 6 nΩ at 1.8 K at very low accelerating field in a vertical cryostat which is well shielded. An extra shielding factor of 33 is needed to reach a maximal residual field of 0.6 µT. With this value is possible to limit the extra superconductor surface resistance due to trapped magnetic flux below 2 nΩ. The shield has been designed with Vector Fields OPERA code. Much effort was done to reduce the magnetic field penetration due to the coupler port. The shield is operating at 1.8 K and surrounds both the cavity and the tuner. It has been fabricated out of 1.5 mm thick Cryoperm® alloy. It can be seen partially on figure 1. Extra parts are attached to the base of the FPC when it is connected to the cavity.

## FUNDAMENTAL POWER COUPLER

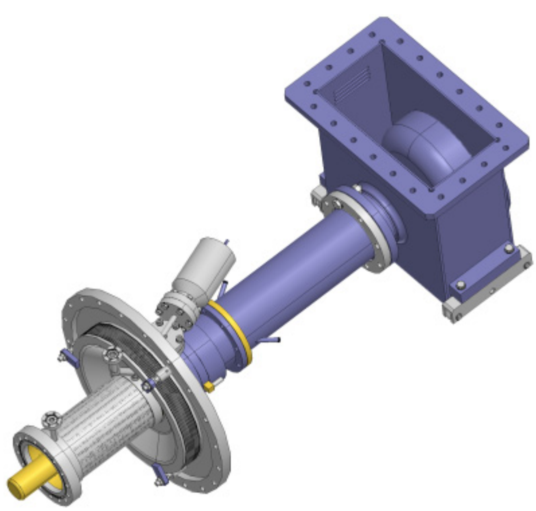

Figure 4: Overall view of the 704 MHz power coupler.

The peak power requirements to operate a cavity at 12 MV/m for typical beam current of 40 mA is around 120 kW. The power needed for the higher energy part of high intensity proton linacs such as SPL rises to 1 MW. We have aimed our design at this higher power levels. The duty cycle is targeted at 10% ( 100 kW average power). The design is similar to the KEK-B [5] and SNS [6] design, build around a coaxial disk window, and 100 mm coaxial line. The air part consists of a doorknob, which connects to a WR1150 waveguide (fig. 4).

The RF window is adapted from the KEK-B window, build around a ceramic disk. The RF adaptation is obtained using chokes on both inner and outer conductors. The coupler antenna is made of electropolished OFE copper to minimize thermal radiation on the Nb coupler port and beam tube and is electron beam welded to the window. Water cooling channels for the antenna are passing through the window core. The return channel is connected to the inner cooling channel of the ceramic. These coaxial cooling channels are connected to those of the inner conductor on the air-side, the inlet and outlets being at the doorknob. A prototype of the window with a shortened antenna has been built to check the RF transmission and the water tightness of the cooling channels connection.

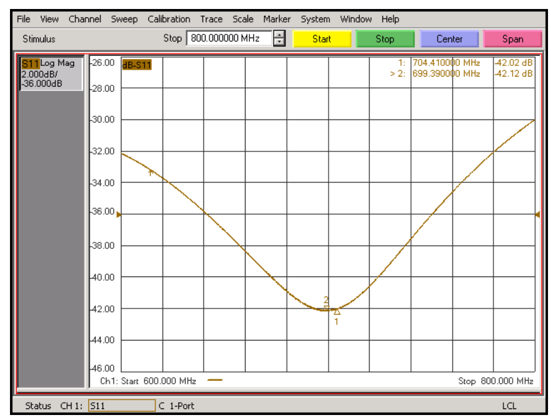


Figure 5: $S_{11}$ measurement of the window prototype.

A measurement of the $S_{11}$ is shown on figure 5, displaying a wide bandwidth of 200 MHz at -30 dB and a minimum reflection $S_{11}$=-42 dB at 700 MHz. Two complete windows have now been fabricated.

Figure 6: He cooled outer conductor.

The cold part of the coupler is a 100 mm in diameter, 50 Ω coaxial line. The outer conductor is a double walled stainless steel tube enclosing three separate spiral cooling channels. A counter-flow of He gas in used to adjust the temperature distribution along the conductor when operated in the cryomodule. The outer conductor has been plated with 10 microns copper at CERN, using microwave sputtering (fig. 6).

The length of the air side coaxial line is mostly constrained by the position of the cavity inside CryHoLab and the diameter of the vacuum vessel. The doorknob is made of aluminium (fig. 7). The knob itself is CNC machined to achieve mechanical tolerances. The junction between the antenna and the knob is of sliding type, so it can be electrically insulated to bias the inner conductor if needed during the conditioning. As expected, their bandwidth is only a few MHz.

Figure 7: Doorknobs with adaptors for RF measurements.

## COUPLER TEST STAND

The conditioning bench is designed around a coupler pair interconnected by a coupling waveguide (fig. 8). The first coupler is connected to the 1 MW power source, while the second is either connected to a load or a variable short, to process them in TW or SW respectively. The coupling waveguide was coated with electrolytic copper to limit RF losses to 80 W at 100 kW average power. It is equipped with a pumping port, and connected to a dedicated vacuum system comprising a 150 L/s turbomolecular pump, backed up with a dry primary pump. The vacuum parts will be assembled in our class 10 clean room.

The instrumentation ports on the RF windows are equipped with an arc detector, an electron pickup, and a vacuum gauge. The logic of the interlock and processing automation is adapted from our former 1.3 GHz coupler test stand [7].

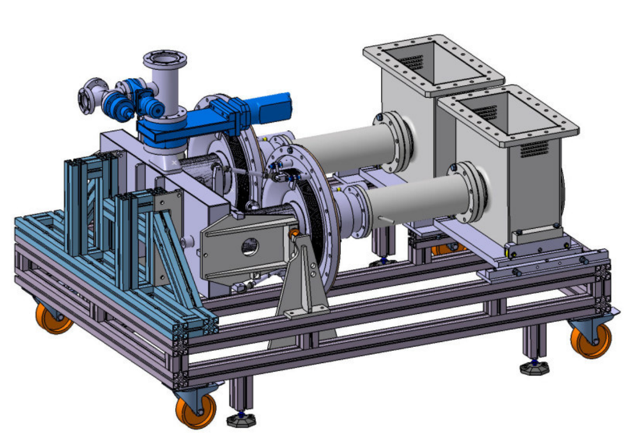

Figure 8: Coupler test bench.

Two couplers are now ready to be assembled and conditioned. One of the FPCs will then be connected to the $\beta$=0.47 cavity for the power tests in pulsed mode.

## AKNOWLEDGMENTS

We acknowledge the support of the European Community-Research Infrastructure Activity under the FP6 “Structuring the European Research Area” programme (CARE, contract number RII3-CT-2003-506395). Work carried out using the SUPRATech GIS infrastructures with the financial support from Region d’Ile de France.

We are grateful to S. Calatroni and H. Neupert from CERN for performing the copper deposition on the couplers.

## REFERENCES

[1] F. Gerick et al., ”Conceptual design of SPL II”, CERN-2006-006

[2] G. Devanz et al., “Experimental characterization of a 700 MHz $\beta$=0.47 5-cell superconducting cavity prototype for pulsed proton linac”, Proc. EPAC08, 2008 Genoa.

[3] S. Chel et al., “New 1 MW 704 MHz RF test stand at CEA-Saclay”, Proc. EPAC08, 2008 Genoa.

[4] G. Devanz et al., ”Compensation of Lorentz Force Detuning of a TTF 9-cell Cavity with a New Integrated Piezo Tuner”, Proc. EPAC06, 2006 Edinburgh.

[5] S. Mitsunobu et al., “High Power Input Coupler for KEKB SC Cavity,” Proceedings of the 9th Workshop on RF Superconductivity, Santa Fe, NM, 1999.

[6] K.M. Wilson et al., “The Prototype Fundamental Power Coupler for the Spallation Neutron Source Superconducting Cavities: Design and Initial Test Results”, Proc. SRF01, 2001 KEK.

[7] C. Travier et al., “Design and test of a 1.3 GHz travelling wave window”, Proc. 9th Workshop on RF Superconductivity, 1999, Santa Fe, NM.

# A NOVEL FREQUENCY TUNING SYSTEM BASED ON MOVABLE PLUNGER FOR SPIRAL2 HIGH-BETA SUPERCONDUCTING QUARTER-WAVE RESONATOR

D. Longuevergne, S. Blivet, G. Martinet, G. Olry, H. Saugnac,
CNRS/IN2P3, Institut de Physique Nucléaire, France

*Abstract*

SPIRAL2 aims at building a multi-purpose facility dedicated to nuclear physics studies, including the production of rich-neutrons isotopes. The multi-beam linear accelerator is composed of superconducting accelerating modules and warm focusing magnets. IPN Orsay is in charge of the high energy accelerating modules, each hosting two superconducting 88 MHz quarter-wave resonators operating at an accelerating field of 6.5 MV/m ($\beta$ = 0.12). The static and dynamic frequency tuning is achieved by the insertion and displacement of a niobium plunger into the magnetic field area. The efficiency of the tuning (1 kHz/mm) has been validated during the tests of the cryomodule. In this paper we discuss the impact of such a tuning system, based on experimental results on SPIRAL2 cavities, on the different aspects: maximum accelerating field, Qo slopes, quench, multipacting and microphonics.

## INTRODUCTION

The multi-purpose linear accelerator for SPIRAL2 has entered the construction phase since April 2006 [1]. Niobium quarter-wave resonators, composing the high energy part of the linac, have already been prototyped and qualified thanks to the construction of 2 cavities. These high-beta ($\beta$ = 0.12) cavities resonating at 88 MHz, contrary to the low-beta ones ($\beta$ = 0.07), are not tuned with a classical wall-deformation system due to the too low frequency shift versus the force applied [2]. The solution retained is the frequency tuning with a niobium movable plunger inserted into the magnetic field part of the cavity. This paper will present the full mechanism in the first part and then discuss the different results obtained with electromagnetic simulations and tests.

## DESCRIPTION

### *The Plunger*

The plunger, consists in a tube made of niobium (RRR = 250) with a length of 250 mm, a diameter between 30 and 20 mm (not yet defined) and a wall-thickness of 3 mm (see Fig. 1). It is totally filled with liquid helium when the cavity is operating. The plunger is maintained on the top cavity port through a stainless steel bellow stiffened by 3 guiding rods. A stainless steel bell, linking the rod coming from the motor and the plunger, closes the liquid helium circuit (See left Fig. 2). The bellows permit a total translation of about 5 mm. This kind of plunger achieves the static tuning as the plunger penetrates into the cavity of about 50 mm and the dynamic tuning thanks to its motion on a total range of about 4 mm.

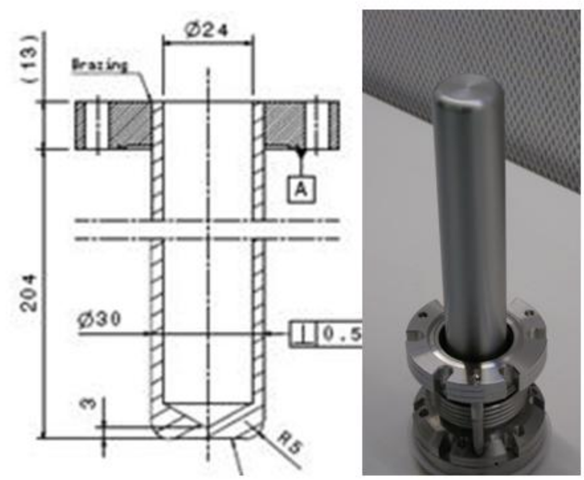


Figure 1: Picture and sketch of the plunger.

### *The Motion Controller*

The plunger is controlled by a stepping motor, installed on the top of the cryomodule. The stepping motor controller and the gear box provide a total reduction of about 0.125 μm/step. The motion is transmitted to the plunger through a rod fixed on the closing bell (See right Fig. 2).

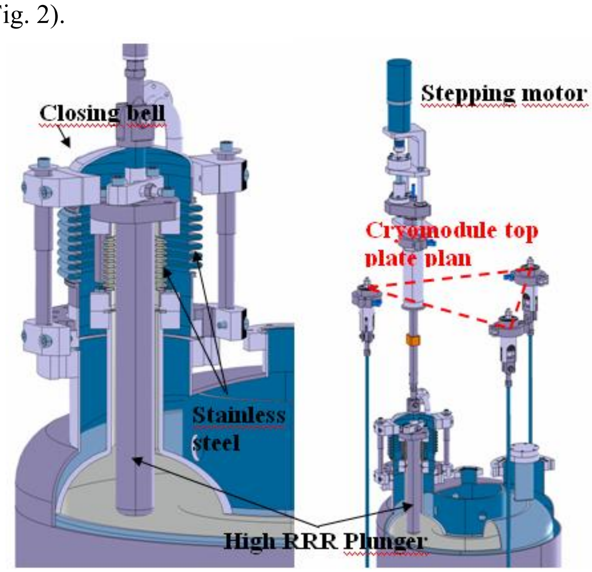


Figure 2: The system in its entirety.

## SIMULATIONS RESULTS

### *Frequency Sensitivity*

We performed all the simulations with CST Microwave Studio [4]. The aim is to evaluate frequency shift and dissipations versus penetration depth and plunger diameter. We calculate a constant frequency shift versus penetration depth of the plunger (See Fig. 3). For a diameter of 30mm, 25mm and 20 mm, the frequency shift is respectively around 1100 Hz/mm, 760 Hz/mm and 480 Hz/mm.

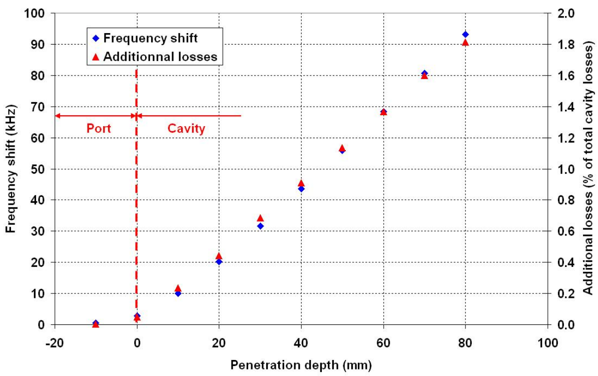


Figure 3: Frequency shift and additional losses versus penetration depth.

### *Dissipations*

As the total losses of the cavity have to be lower than 10W at 6.5 MV/m, dissipations added by the insertion of the plunger have to be evaluated.

The power dissipated on the whole surface of the plunger grows linearly with the penetration depth (See Fig 3). The Φ=30mm plunger increases the power dissipation of about 1% for a penetration depth of 50mm.

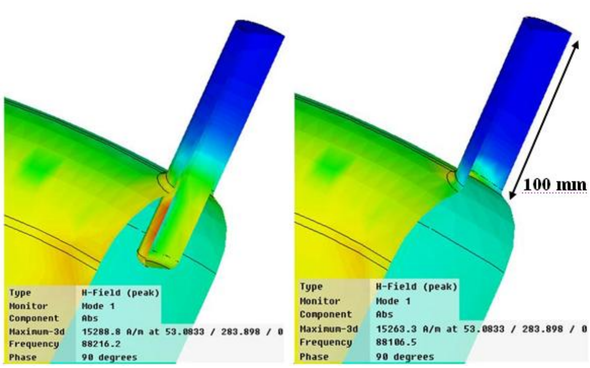


Figure 4: H-field distribution with and without the plunger.

Table 1 shows the additional losses for several plunger diameters and a penetration depth of 50mm.

We also have to take into account the power dissipated onto the stainless steel flange and bellow. In order to limit RF losses onto the flange, the port has been defined long enough.

Thus, with a 100mm long port, the magnetic field at the level of the flange is below 0.01% of the peak field in the cavity when no plunger is installed. The far-field onto the port seems greater when a plunger is installed (See Fig. 5). The magnetic field is multiplied by 100 at maximum!

Nevertheless, the power dissipation onto the flange and bellow is acceptable even for a Φ=30 mm plunger, leading to a increase of 11% of the total losses (See Table 1).

Table 1: Additional losses at 6.5 MV/m

| Diameter | Losses on plunger | Losses into the flange* |
|---|---|---|
| No plunger | 0 | ~ 0 W |
| 20 mm | 0.56 % | 0.2 W |
| 25 mm | 0.65 % | 0.4 W |
| 30 mm | 1 % | 1 W |

* Considering a decreasing field into a stainless steel tube

Moreover, the peak magnetic field of the plunger increases with plunger diameter (See Fig. 5).

Simulations show that the peak magnetic field on the plunger isn't higher than the peak field on the cavity (See Fig. 4). Thus the plunger shouldn't reduce the quench threshold of the cavity.

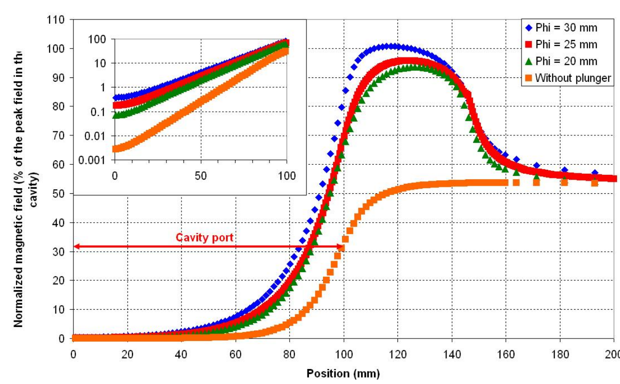


Figure 5: Magnetic field distribution along the plunger for different diameters.

## EXPERIMENTAL RESULTS

### *Mechanical Aspects*

The motion controller is clamp on the external vessel of the cryomodule, and the plunger fixed on the cavity. During cool down, a displacement of about 0.64 mm has been recorded due to thermal contractions. The plunger is, at rest, pushed up on the upper mechanical stop due to pressure difference between liquid helium bath and the vessel vacuum. The force is about 1000 N. This induces a mechanical hysteresis of about 20 µm when the plunger is moved up or down (See Fig. 6).

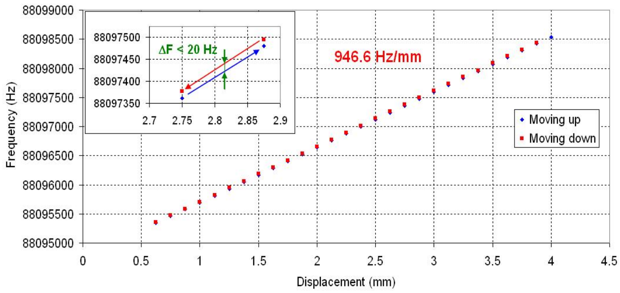


Figure 6: Frequency shift versus plunger. In the upper left corner, mechanical hysteresis when moving up and down.

This hysteresis can be a problem in the case of fast tuning. For the moment, no tests have been done to characterise the regulation efficiency. Only slow regulation (1.3 Hz/s ramp) have been tested, giving a frequency stability better than 4 Hz (See Fig. 7).

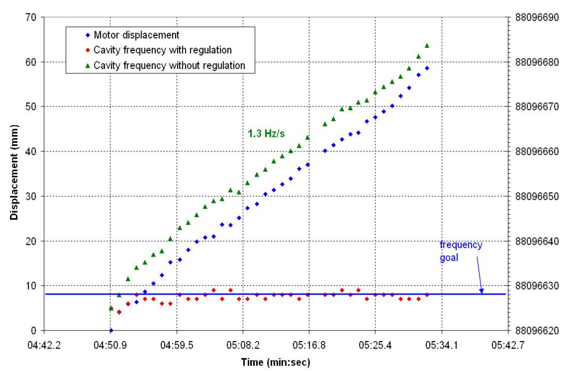


Figure 7: Slow frequency regulation test.

Preliminary tests have been performed to verify if the plunger causes microphonics perturbations. Results obtained [3] show no additional perturbations.

Nevertheless, slow frequency shift due to atmospheric pressure variations and temperature (day and night cycles) have been recorded and can be easily corrected.

### *Electromagnetic Aspects*

The frequency shift measured during the test is constant on the whole range (~ 4mm) and is about 950 Hz/mm (See Fig. 6). This result matches quite well with calculations. Qo versus accelerating field measurements have been plotted to verify whether or not the plunger is acceptable as a frequency tuner for the SPIRAL2 project.

Results obtained for the different tests are good (See Fig. 8). There is no effect visible on Qo value when a plunger is installed whatever its diameter. This was confirmed for two diameters 30 and 20 mm. The Qo drop due to the power dissipated on the plunger is within the measurement errors, estimated at 10%.

Furthermore, the Q-slope and quench limit are unchanged with or without plunger. The plunger doesn't induce more field emission. The same observation is made with multipacting barriers.

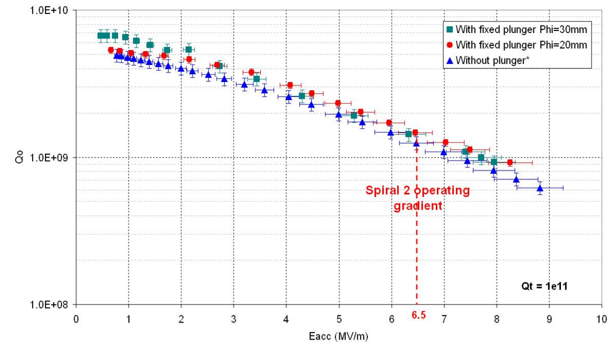


Figure 8: Qo versus accelerating field with $\Phi$ = 30mm and 20mm plungers and without plunger.

## CONCLUSIONS AND FUTURE WORKS

Preliminary results presented previously show that the movable plunger as the cold tuning system for the SPIRAL2 project is well suited. The frequency sensitivity and the range meet the requirements. The Qo and the accelerating field seem not affected. Neither multipacting barriers, nor field emission are observed with a plunger.

However, several tests have to be done to qualify other aspects:

- Reliability and long term effects of such a tuning system (dust released by the bellows during motion).
- The system must be tested in a frequency regulation loop to quantify how fast can regulate the system and if the mechanical hysteresis is changing during operations.

## REFERENCES


[1] T. Junquera et al., “Status of the Construction of the SPIRAL2 Accelerator at GANIL”, this conference.

[2] G. Olry and al., Development of a beta 0.12, 88 Mhz, quarter wave resonator and its cryomodule for the SPIRAL2 project”, SRF 2005, Ithaca, USA, July 2005.

[3] H. Saugnac and al., “RF Cryogenic Tests on the “Qualifying” beta = 0.12 SPIRAL2 Cryomodule”, this conference.

[4] http://www.cst.com.

# RF AND CRYOGENIC TESTS OF THE FIRST BETA 0.12 SPIRAL2 CRYOMODULE

H. Saugnac, C. Commeaux, C. Joly, J. Lesrel, D. Longuevergne, F. Lutton, G. Martinet, G. Olry
IPNO, Orsay, France

Y. Gomez Martinez, F. Vezzu LPSC, Grenoble, France

R. Ferdinand, R. Beunard, M. Souli GANIL, Caen, France

*Abstract*

The SPIRAL 2 project, installed in GANIL for Radioactive Ion Beam physics purposes requires the manufacturing of a multi beam driver. This driver is based on a superconducting LINAC [1] featuring two 88 MHz Quarter Wave Resonator (QWR) families. IPN Orsay is in charge of the study and the assembly of the 7 high energy (beta = 0.12) cryomodules. Each cryomodule is composed of two QWRs, specified to operate at 4.2 K at a nominal accelerating gradient of 6.5 MV/m. A first “qualifying” cryomodule has been manufactured and tested at the beginning of 2008 in order to validate the resonator and the cryostat design before launching the serial production of the 6 remaining cryomodules. The paper presents the main results of this test and the cryomodule design in its final version.

## INTRODUCTION

A first beta = 0.12 Cryomodule was manufactured [2] in order to qualify and validate the design of its different sub components: QWR resonator, Cold Tuning System (CTS), cryogenic circuits, power coupler, alignment procedure…. For this first test the cryomodule was not in its final configuration. Only one resonator was equipped with a power coupler and a cold tuning system and the cryomodule was not shielded against Earth’s magnetic field. The cryogenic feeding valves box, the power coupler as well as the solid state 10 kW RF amplifier are also “qualifying” units of the Spiral 2 superconducting LINAC components. The different results, concerning the cryogenic, mechanical and RF performances of the cryomodule are summarized below.

## CRYOGENIC PERFORMANCES

### *Cool Down Time*

For the test, the 60 K thermal shield was cooled with Liquid Nitrogen and the 4.2 K volume with Liquid Helium at around 1.3 bars. The thermal shield was first cooled during 9 hours and reached a temperature of about 80 K. Then the cavities were cooled from the bottom. Liquid appeared on the helium buffer situated on the top of the cavities after 4 hours. However the cool down time in the temperature range from 200 K to 20 K was below 1 hour which is fast enough to prevent from Q-disease. Both cavities were cooled in parallel with only one feeding valve. We noticed a small cooling time difference in the 70K/4K range of only 15 minutes between the two cavities.

Figure 1: Spiral 2 cryomodule test stand at IPN Orsay.

### *Cryomodule Static Losses*

Static losses (without RF) at 4 K are summarized in the Table 1. We note that for this test the cryomodule was not optimised in term of cryogenic losses and was not in the final configuration. For the cryomodule there are around 3 W more losses than expected. A part of these losses, 2 W, is explained by a lack of thermal interception sinks. For the final configuration the evaluated losses are 8.5 W.

Table 1: Static losses @ 4 K.

| Component | Calculated values | Measured values |
|---|---|---|
| "Qualifying" CM | **10 W** | **13 W** |
| Valve box | 5 W | 12 W |
| Connecting box | 3 W | |
| Single feeding line | 2 W | |

## CAVITY ALIGNMENT

The cavity alignment is performed using fiducials. A set of 2 fiducials, fixed on the side of the resonator gives the reference of the cavity axis. There are adjusted by measuring the cavity axis before the cryomodule assembly. Windows on the cryomodule vacuum vessel allow the optical measurements of these fiducials. Each cavity is laterally maintained by four antagonist rods and vertically maintained by three rods. These rods are made from titanium alloy.

The aim of this first test was to verify the displacement of the cavity relatively to the cryomodule vacuum vessel for different operation conditions (evacuation of vacuum vessel, cool down…).


Figure 2: Cavity and cryomodule alignment.

Four vacuum vessel 4 pumping cycles where done. We measured a vertical displacement (cavities go down) of 1.4 mm with a good reproducibility (below 0.1 mm). This displacement is due to the deformation of the cryomodule top plate. A value of 1.2 mm was calculated. We measured, as expected, a no significant (inside measurement errors) lateral displacement.

After cool down at 4.2 K the cavities go up of around 1 mm for an expected value of 1.2 mm. The vertical cavity position was then easily recovered using adjusting bolts situated on the outer side of the top plate vacuum vessel. On the lateral plane we measured a displacement of around 0.7 mm for an expected value of 0.6 mm. This displacement is due to the thermal contraction of the fiducial support and the cavity helium tank. It confirms that the horizontal antagonist rods maintain the cavity axis position during cool down.

Two additional tests are planned on this cryomodule to check the reproducibility after several cool down cycles and to check a possible relative displacement inside the cavity between the central stem and the two beam ports.

## COLD TUNING SYSTEM (CTS)

The tuning is performed by inserting superconducting plungers made from RRR250 niobium inside the cavity magnetic volume [3]. For the test only one cavity was equipped with one fixed plunger for static tuning and one movable plunger for static and dynamic tuning.


Figure 3: CTS with SC plunger insertion.

In the "qualification" configuration a total range of 4 mm was achieved with a tuning sensitivity of around 1 kHz/mm. A range of 8 mm is foreseen for the final version. The relation between the cavity frequency and the motors' steps shows a sufficient linearity for few millimetres range displacements. A non negligible hysteresis of around 23 Hz (The cavity bandwidth is around 70 Hz) has been measured. Its cause is currently under study. An optimization of the frequency regulation and the reduction of the hysteresis will be performed on the next test planned before the end of the year.

## CAVITY FREQUENCY STABILITY

### [illegible]

The pressure stability specification for the LINAC cryoplant is +/- 2 mbar, and 10 mbar/h for respectively short term and long term variations.

Frequency variations due to helium bath pressure fluctuations have been measured to -7 Hz/mbar which is acceptable taking into account the cryoplant specifications. The cold tuning system driving mechanism is installed at room temperature and the driving shaft has a heat sink at the thermal shield temperature. We have measured an important frequency shift of 60 Hz in 300 seconds caused by the thermal shield temperature variation. This variation is slow and can be compensated by the CTS regulation further more the thermal shield temperature may easily be adjusted with smaller temperature variation.

## MICROPHONICS

Microphonics measurements have been performed with a Cavity Resonance Monitor in a self oscillating loop. The excitation was done using a piezo-electric actuator situated on the cryomodule vacuum vessel top plate close to the CTS driving mechanism and one of the vertical cavity fixation rods. The excitation from 0 Hz to 450 Hz was only performed in the vertical direction. The magnitude of the excitation was not measured.

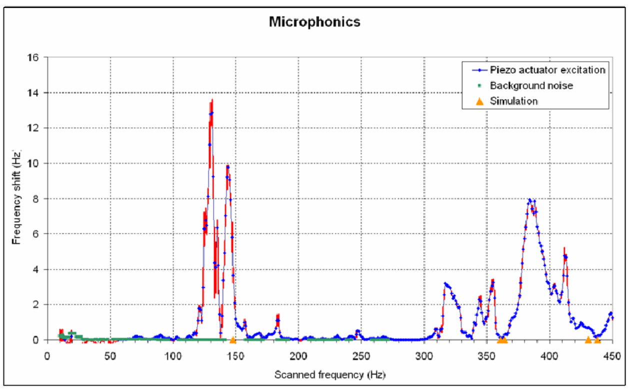


Figure 4: Microphonics measurements.

By comparison with similar measurements performed on the only cavity the mechanical modes appear to be well attenuated. This remains to be confirmed on the next test by using accelerometers to determine the excitation magnitude and performing excitation on different points of the vacuum vessel in the XYZ directions.

## RF PERFORMANCES

The specified main performances [4] are Eacc = 6.5 MV/m (normalized to $\beta\lambda = 0.41$ m) and dissipated power < 10 W @ 6.5 MV/m.

Only one cavity was equipped with a power coupler. Its maximum accelerating gradient was measured to 8.5 MV/m (normalized to $\beta\lambda = 0.41$ m) and was limited by a quench. The same value was previously measured in vertical cryostat. As the cavity was not equipped with magnetic shielding the measured quality factor was low, below $1\ 10^9$ at low field instead of $8\ 10^9$ in the shielded vertical cryostat. For the next test, the cavities will be shielded by a 1.5mm thick Cryoperm® sheet fixed on the resonators' helium vessel shell and by 3 active coils fixed on the cryomodule vacuum vessel outer shell. Several multipacting barriers where present inside the resonator (the power coupler was processed) at very low field (below 100 kV/m) but were easily passed after 30 minutes processing.

## VACUUM SYSTEM

The vacuum vessel is first evacuated from 1000 mbar to around $5\ 10^{-4}$ mbar using a standard Turbo-molecular pumping system with a pumping speed of 250 l/s. When the cryomodule is cold the vacuum is maintained by cryopumping. For the cavity vacuum one pumping port (coupler pumping tube c ~ 0.7 l/s) is used for maintenance purpose to evacuate or venting the cavity volume with a mobile dry Turbo-molecular pumping group and primary dry pump. Beam vacuum is maintained by the warm section (diagnostic box) pumping system. Choice is to be made between Turbo Molecular (250 l/s for N2, possibly magnetic bearing) or Ionic pump (75l/s for N2).

Due to the very small distance of the Cryomodule 300K/4K transition (95 mm) gas or vapour generated in the warm section may be a major concern for the cavity volume vacuum (H accumulation, generated by the warm section). First tests have been performed to study the effect of gas pollution (H2 and air) and interceptive beam diagnostics on the cavity performances [5].

## FUTURE WORK

In the short term a new "Qualification" cryomodule test is planned for November 2008. The Cryomodule will be completely equipped with 2 power couplers, 2 movable plungers and magnetic shielding.

The first serial resonator has been tested with success ($E_{acc\ max}$ = 9 MV/m with $P_{diss}$ = 6 W at 6.54 MV/m) in August 2008. The remaining 15 resonators will be delivered and tested up to January 2010.

The cryomodule (cryostat, CTS, MLI…) call for tender is in course (design review held in April 2008). The first Cryomodule unit delivery is planned for September 2009.

The 7th unit is to be assembled and tested for the beginning of 2011.

## REFERENCES

[1] R. Ferdinand and al., "The SPIRAL2 Superconducting Linac", this conference

[2] G. Olry and al., "Status of the beta 0.12 superconducting cryomodule development for the spiral 2 project", EPAC' 06, Edinburg, June 2006.

[3] D. Longuevergne and al., "A Novel Frequency Tuning System Based on Movable Plunger for SPIRAL2 High-Beta Superconducting Quarter-Wave Resonator", these proceedings.

[4] G. Olry and al., "Tests results of the beta 0.07 & beta 0.12 quarter waves resonators for the Spiral2 superconducting LINAC", EPAC' 06, Edinburg, June 2006.

[5] R. Ferdinand, "Tests of Wire Sublimations Very Close to SPIRAL 2 Superconducting Cavity", these proceedings.

# INFLUENCE OF PIEZO-HYSTERESIS AND RESOLUTION ON CAVITY TUNING*

O. Kugeler†, W. Anders, J. Knobloch, A. Neumann, BESSY, Berlin, Germany


## Abstract

All mechanical tuning systems are subject to hysteresis effects: For coarse tuning with a stepper motor, the exercised forces lead to a visco-elastic deformation of the tuner body. In piezo-based fine tuning, even if the smaller deformations of tuner and cavity can be regarded as fully elastic, the piezo-actuators themselves suffer from remanent polarisation effects. The extent of these nonlinearities has been measured in three different tuning systems (Saclay I, Saclay II and Blade Tuner) utilizing high-voltage as well as low-voltage piezo actuators. An estimate of the resulting tuner-resolution and performance degradation with respect to microphonics compensation is given. Experiments were performed at the HoBiCaT facility at BESSY.


## BACKGROUND

Future CW-LINAC driven light sources like the BESSY-FEL or ERL require an RF-phase stability better than $0.02°$. At an external quality factor of $3.2 \times 10^7$ and an LLRF feedback gain of 100 this corresponds to a maximum allowable detuning of 0.7 Hz. RF control systems are limited in gain or by phase noise of the RF reference system. Thus, it is a viable option to minimize the main error source, i.e. microphonic detuning. Microphonics compensation in cw-operated narrow-bandwidth (20-40 Hz FWHM) superconducting cavities has been demonstrated [1] with various different tuning systems [2, 3]. The maximum achievable compensation is limited by the resolution of the tuner system and hysteresis issues. The microphonics spectrum may be composed of a variety of small scaled detuning amplitudes. In order to compensate such a detuning, a piezo based system needs to resolve down to the centi-hertz regime, see Figure 1.

## PIEZO HYSTERESIS MEASUREMENT

Cavities were operated in a closed loop PLL, see Figure 2. In order to measure the dynamic hysteresis a piezo voltage history was imposed with a function generator (carrier signal). For simplicity, a periodic sawtooth wave with a small frequency was used. This signal was added to a low amplitude, high frequency sine-wave from a lock-in amplifier (modulator signal). The phase error signal from the cavity was measured with the lock-in amplifier yielding the true momentary piezo-voltage-history-dependent value of the transfer function at the modulator frequency.

* Work partly funded by the BMBF and the Land Berlin and the European Commission in the Sixth Framework Program, contract no. 011935 EuroFEL

† kugeler@bessy.de

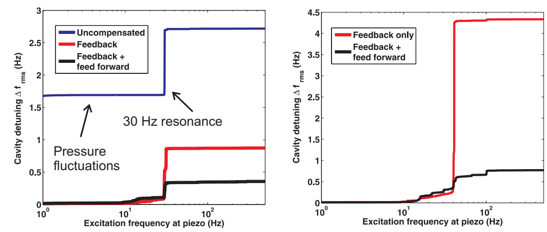


Figure 1: Microphonics compensation results: Integrated microphonics spectra of Saclay I (left) and Saclay II (right). By comparing feedback-only compensation with feedback/feedforward compensation, a resolution limit can be extracted: 0.1±0.05 Hz for the Saclay I tuner, and 0.2±0.05 Hz for the Saclay II tuner.

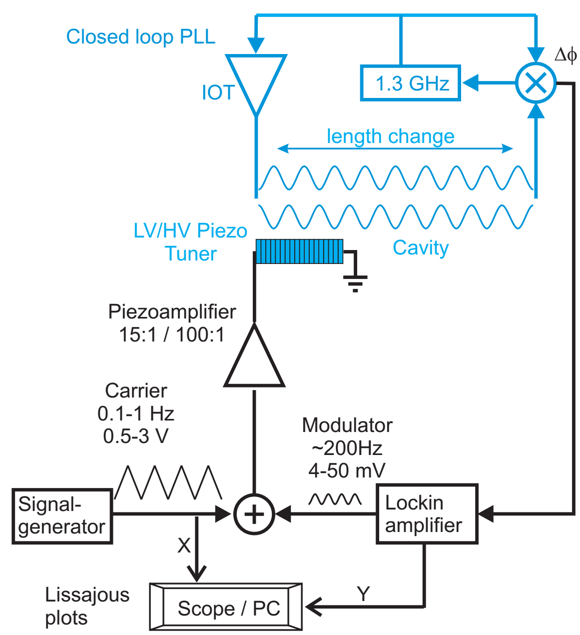


Figure 2: Experimental setup of the hysteresis measurements.

The dynamic response of the piezo to the controlling voltage is dependent on the history of the voltages, see Figure 3. The hysteresis effect can change the transfer function of the system: All resonances, or their Q-factors, respectively, are varied within an amplitude range defined by the maximum difference between the expanding and the contracting piezo. However, this viscoelastic nonlinearity of the piezo response is strongly deterministic, as can be seen from the shape of the hysteresis curves. With all the tuner modes mapped out properly, it can be incorporated into a feed forward based tuning algorithm.

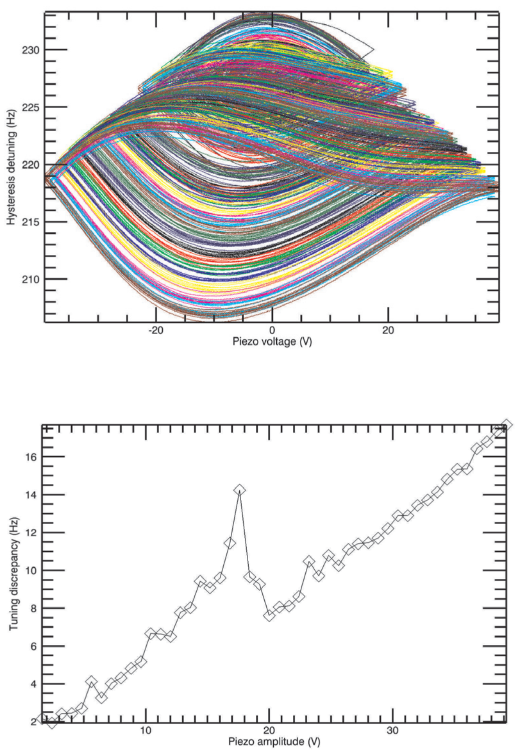


Figure 3: Dynamic hysteresis of piezo tuner. The measurement was done with the blade tuner at a modulator frequency of 205 Hz, a modulator amplitude of 1 V and a carrier frequency of 0.5 Hz. The carrier amplitude was varied from 1 V to 40 V. In the vertical direction, the variation of the phase-error signal in terms of detuning is plotted. The detuning obviously shows a hysteresis behavior. The asymmetrical shape of the hysteresis curve is caused by imperfect phase match of the PLL. In the lower plot, the maximum difference is plotted. The peak in the lower plot is due to manual phase correction during the measurement.

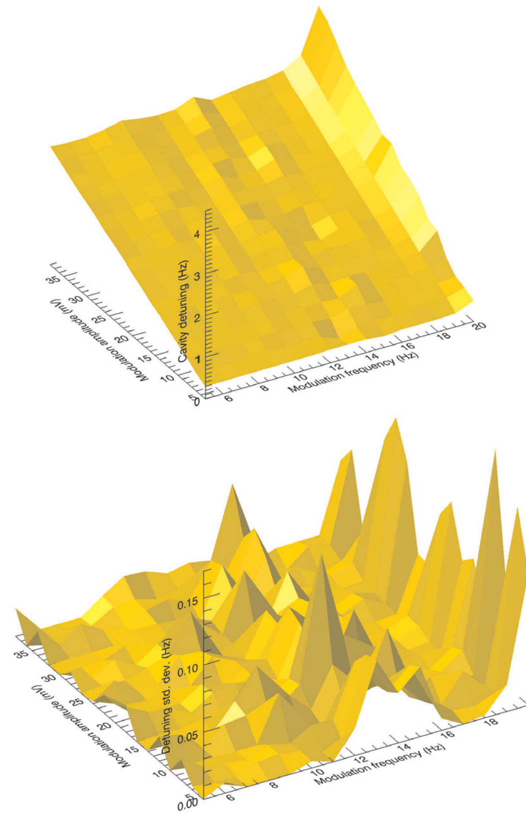


Figure 4: Measurement of piezo resolution without carrier (blade tuner, LV piezos). Upper picture: Low-frequency transfer function with amplitude scan. Lower picture: Standard deviation of the same measurement yielding estimates for the achievable piezo resolution. The measurement is overlapped by (very small scale) microphonics at 14 Hz and 20 Hz.

## PIEZO RESOLUTION

The piezo resolution was measured by taking regular transfer functions at low excitation frequencies. A series of those transfer functions was taken at different amplitudes. The average value from the lock-in amplifier yields the strength of the mechanical resonance. It is depicted in the upper part of Figure 4. In addition the standard deviation of lock-in amplifier value over time was recorded, see the lower part of Figure 4. We have identified this value as the piezo resolution, or rather the resolution including noise from all involved electronic components. The reason for this indirect approach was to minimize the impact of the ubiquitous microphonics.

We can extract a medium standard deviation of 0.016 Hz and a maximum value of 0.17 Hz from the data, which sets the limits for a successful detuning compensation of lines in the microphonics spectrum. These values are much lower than what would be expected from the curves in Figure 1 if the compensation limit was purely given by the piezo resolution. This observation suggests that it should in principle be possible to further optimize the compensation algorithm.

## OUTLOOK

In a next step we will attempt to incorporate the hysteresis into the feed forward tuning algorithm.

## REFERENCES

[1] A. Neumann "Control and Characterization of Narrow-Bandwidth CW Cavities for the BESSY Free Electron Laser Driver Linac" PhD thesis, Humboldt University, Berlin, Germany, 2008

[2] A. Bosotti et. Al. MOPP120, EPAC2008, Genoa, Italy

[3] P. Bosland, CARE-Note-2005-004-SRF, CEA-Saclay, Paris, 2005

# RECENT DEVELOPMENTS ON SUPERCONDUCTING CH-STRUCTURES AND FUTURE PERSPECTIVES

H. Podlech, M. Amberg, A. Bechtold, M. Busch, F. Dziuba, Ratzinger, C. Zhang
Institut für Angewandte Physik (IAP), Goethe Universität, Frankfurt am Main, Germany


## Abstract

Worldwide there is an increasing interest in new high intensity proton and ion driver linacs with beam powers up to several MW. A very challenging part of these accelerators is the low and medium energy section up to 100 MeV. Depending on the duty cycle room temperature or superconducting options are favoured. In both cases the Crossbar-H-mode (CH)-structure developed at the IAP in Frankfurt is an excellent candidate. Room temperature as well as superconducting prototype cavities have been developed and tested successfully. A superconducting 19 cell low energy CH-cavity at 360 MHz reached effective gradients of 7 MV/m corresponding to an accelerating voltage of 5.6 MV. This cavity could be used for high intensity, cw operated linacs like accelerator driven systems (ADS, EUROTRANS) or the international fusion material irradiation facility (IFMIF). Recent developments of this new type of a multi-cell drift tube cavity, tests of the prototypes and future plans will be presented.


## INTRODUCTION

The CH-cavity is operated in the $H_{21}$-mode and belongs to the family of H-mode cavities like the IH drift tube cavity and the 4-vane RFQ. Due to the mechanical rigidity of the CH-cavity room temperature (r.t.) as well as superconducting (s.c.) versions can be realized [1]. For higher duty cycles or even cw operation superconducting solutions become more favourable because of a lower plug power consumption and higher achievable gradients [2]. In many cases the rf linac efficiency and compactness can be increased significantly by the use of multi-cell cavities.

## 360 MHZ PROTOTYPE CAVITY

The superconducting CH-protoype cavity (f=360 MHz, $\beta$=0.1, 19 cells) has been tested successfully in Frankfurt. After a second chemical surface preparation gradients of 7 MV/m corresponding to an effective voltage of 5.6 MV have been achieved (Fig. 1). Presently the cavity is being prepared for tests in a horizontal cryostat which is equipped with a slow and a piezo based tuner system. The basic principle of the tuner is an elastic deformation of the cavity by applying an external force at the end flanges of the tank [3]. This changes the width $\Delta$x of the end gaps and the gap capacitance. Tests at room temperature have been

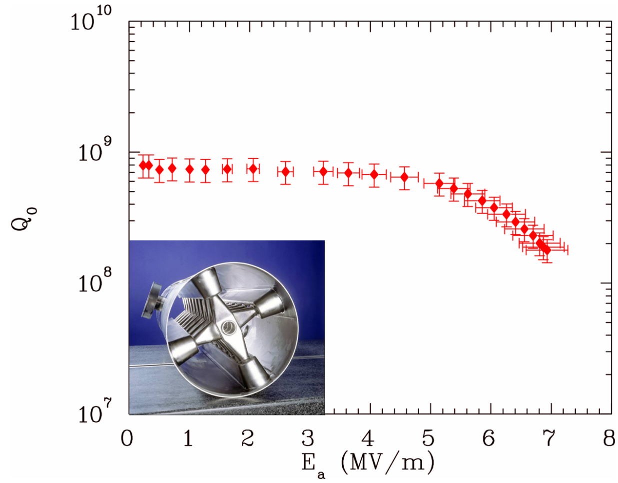


Figure 1: Measured Q-value of the superconducting CH-prototype cavity. Effecitve gradients of 7 MV/m have been achieved.

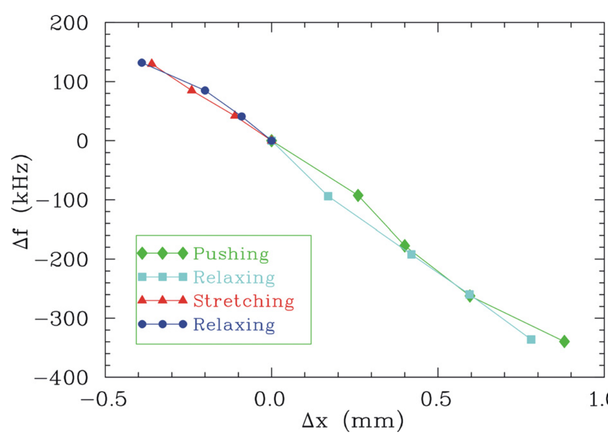


Figure 2: Measured frequency shift as function of the cavity deformation.

performed. The measured frequency tune shift is $\Delta f/\Delta x$ = 400 kHz/mm (see fig. 2). The change of field distribution according to the deformation of the tank has been measured by using the bead pull method. The experimental results are in good agreement with MWS simulations. The effect is mainly concentrated on the end cells of the structure, where a maintainable maximum field variation of 10% within the tuning range was observed [1]. The fast tuner will be used to operate the cavity at constant frequency. It

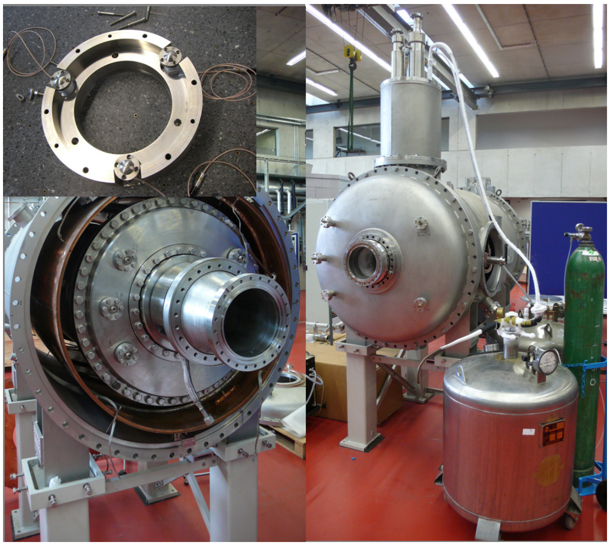

Figure 3: Horizontal cryostat with piezo tuner.

consists of three piezo elements with an expected stroke at 4 K of 3.5 $\mu$m which corresponds to a frequency shift of $\pm$700 Hz. Figure 3 shows the horizontal cryostat and the piezo tuner. First test with liquid nitrogen haven been performed for leak tests.

## A NEW 325 MHZ CH-CAVITY

The superconducting CH-cavity is an excellent candidate for high power applications because it reduces the drift space between cavities significantly compared to more conventinal solutions like Spoke-type cavities. To fullfil the requirements for high power applications the geometry of the sc CH-cavity has been optimized (Fig. 4). The stem orientation has been changed to accomodate sufficient large power couplers into the girder. The stems of the end cells are inclined. This increases the inductance in the end cells and increases the electric on-axis field without long end drift tubes which have been used before. This has great advantages for the beam dynamics of high intensity linacs. The drawback of inclined stems is an increased magnetic peak field of 13 mT/(MV/m). On the other hand, typical gradients of 5 MV/m lead to still modest values of 65 mT.
To reach the design frequency internal tuners it is planned to use cylindrical tuners. During the fabrication the frequency is measured and will be changed by 5 cylinders (r=15 mm). After this tuning process the tuners are welded into the girder. This procedure has been tested successfull with the first prototype cavity [1]. Additionally, two membran tuners with r=25 mm are foreseen. One tuner will act as a slow tuner to compensate temperature and pressure effects. The other tuner will be driven by a piezo to control fast frequency changes. Figure 5 shows the simulated frequency shift as function of the tuner height above the girder $H_T$ using all tuners simultaneously. The experience with the first prototype cavity showed that a good surface preparation is essential for the performance of the cavity.

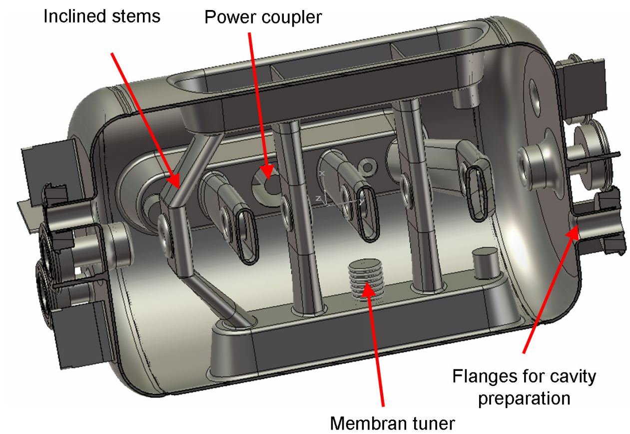


Figure 4: Geometry of the new superconducting 325 MHz CH-cavity.

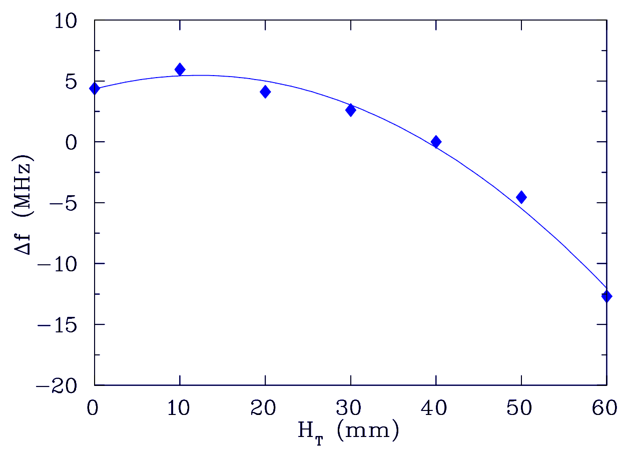


Figure 5: Frequency shift as function of the tuner height using all tuners simultaneously.

Therefore four additional flanges, two located at each end plate are foreseen now to improve the thoroughness of the surface preparation (BCP, HPR).
The cavity has 7 cells and will be operated at 325.224 MHz. The $\beta$ is 0.1585 which corresponds to 11.4 MeV/u. This gives the possibility to test the cavity with beam at GSI using the UNILAC as an injector. Figure 6 shows the distribution of the electric field along the beam axis. The cavity will be fully equipped with helium vessel and power coupler. It is expected to order the cavity at the end of this year. Table 1 summarizes the parameters of the cavity.

## EUROTRANS

EUROTRANS is the EUROpean research program for the TRANSmutation of high level nuclear waste in an accelerator driven system. The driver linac has to deliver a cw 2.5-4 mA, 600 MeV proton beam to a spallation target. In the present reference design a CH-DTL has been proposed. This 17 MV injector consists of a 3 MV 4-vane RFQ, a

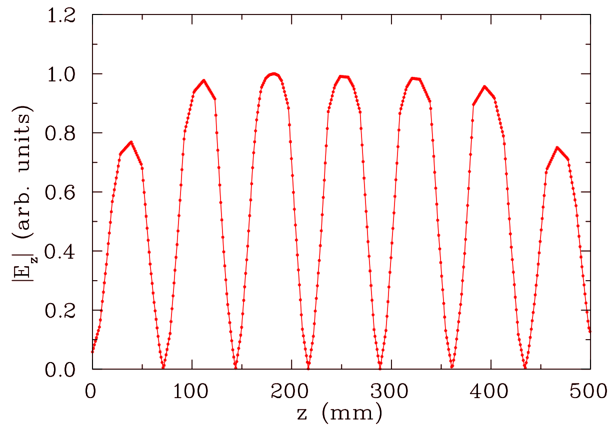


Figure 6: Simulated electric field distribution of the 325 MHz CH-cavity.

Table 1: Parameters of the sc 325 MHz CH-cavity

| | |
|---|---|
| f (MHz) | 325.224 |
| $\beta$ | 0.1585 |
| $L_{\beta\lambda}$ (m) | 0.55 |
| Aperture diameter (mm) | 30 |
| Accelerating cells | 7 |
| Tuner height (mm) | 0-60 |
| Tuner diameter (mm) | 30/50 |
| $E_p/E_a$ | 6 |
| $B_p/E_a$ [mT/(MV/m)] | 13 |
| G ($\Omega$) | 64 |
| $R_a/Q_0$ ($\Omega$) | 1265 |
| $R_aR_s$ ($\Omega^2$) | 80000 |

room temperature 2 MV CH-cavity and 4 superconducting CH-cavities operated at 352 MHz [4]. Figure 7 shows the schematic layout of the injector. Each superconducting CH-cavity provides about 3 MV effective accelerating voltage. Between the superconducting cavities a sc solenoid for transverse focusing is foreseen. The effective gradient is 4 MV/m which results in modest peak fields. The cavity geometry has been optimized using the ideas which will be realized first in the 325 MHz prototype cavity. This leads to a cost effective and very compact linac design with excellent beam dynamics properties. The simulated emittance growth is only about 10% at a current of 5 mA [4]. Figure 8 shows the geometry of the first superconducting CH-cavity (left) and the simulated field distribution (right).

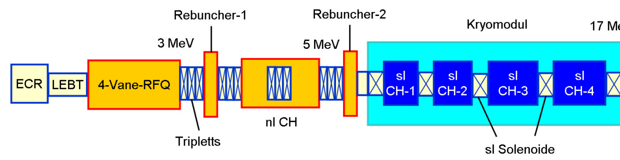


Figure 7: Schematic layout of the proposed 17 MV EUROTRANS injector which consists of a 4-vane RFQ, a room temperature CH-cavity and four superconducting CH-cavities.

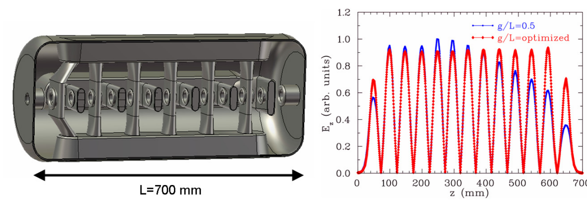


Figure 8: Geometry of the first superconducting CH-cavity for EUROTRANS (left) and the field distribution (right).

## ACKNOWLEDGEMENT

This work has been supported by Gesellschaft für Schwerionenforschung (GSI), BMBF contr. No. 06F134I. and EU contr. No 516520-FI6W. We acknowledge also the support of the European Community-Research Infrastructure Activity under the FP6 "Structuring the European Research Area" program (CARE, contract number RII3-CT-2003-506395) and EU contr. No. EFDA/99-507ERB5005 CT990061 between EURATOM/FZ Karlsruhe IAP-FU. The work was carried out within the framework of the European Fusion Development Agreement. The views and opinions expressed herein do not necessarily reflect those of the European Commission.

## REFERENCES


[1] H. Podlech, C. Commenda, H. Liebermann, H. Klein, U. Ratzinger, A. Sauer, Superconducting CH-structure, Physical Review Special Topics Accelerator and Beams, **10**, 080101(2007).

[2] H. Podlech, Entwicklung von Normal- und Supraleitenden CH-Strukturen zur effizienten Beschleunigung von Protonen und Ionen, Habilitationsschrift, Universität Frankfurt, in preparation.

[3] A. Bechtold, M. Busch, H. Liebermann, H. Podlech, U. Ratzinger, A Tuner for a Superconducting CH-Prototype Cavity, Proceedings of the 13th SRF Workshop (WEP54), Beijing, 2007.

[4] C- Zhang, M. Busch, H. Klein, H. Podlech, U. Ratzinger, R. Tiede KONUS Dynamics and H-Mode DTL Structures for EURОTRANS and IFMIF, Proceedings of the EPAC2008, pages 3239-3241.

# NONDESTRUCTIVE TESTING OF NIOBIUM SHEETS FOR SRF CAVITIES USING EDDY-CURRENT AND SQUID FLAW DETECTION

A. Brinkmann#, W. Singer, DESY, D-22607 Hamburg, Germany


## ABSTRACT

For more than 10 years DESY has been operating a high resolution Eddy Current scanning installation with rotating table for non destructive flaw detection on niobium sheets for SRF Cavities. About 2500 sheets have been examined up to now. Several types of defects have been detected and identified using different supplementary methods such as EDX, X-ray fluorescence, neutron activation analysis etc. In order to scan Niobium sheets needed for XFEL Cavity production, new scanning devices have to be built. One improvement of the Eddy Current installations could be the use of a more sensitive superconducting SQUID sensor. A SQUID based scanner system was built and is in evaluation at DESY. A status report will be given.


## INTRODUCTION

In 1996 the cavity D6 showed a strong temperature increasing during a RF test. The hotspot was located with a T-map system. Analysis with X-Ray radiograph, Synchrotron Radiation Fluorescence (SYRFA) and Neutron Activation Analysis (NAA) detected a tantalum inclusion 0.2 mm in diameter (Fig. 1). Due to this experience a non destructive testing device for niobium sheet inspection was designed.

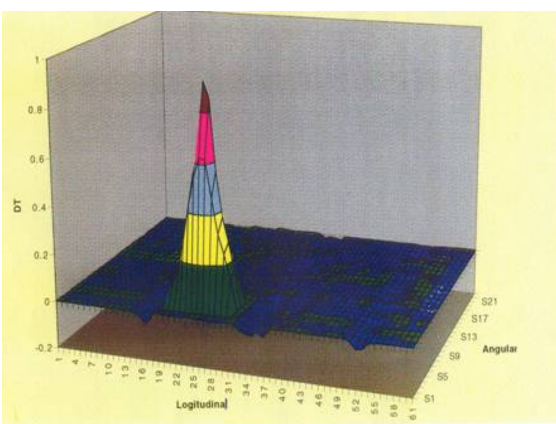


Figure 1: Hotspot found with T-Map.

## EDDY CURRENT INSPECTION SYSTEM

DESY and BAM (Bundesanstalt für Materialforschung und – prüfung, Berlin, Germany) developed an Eddy Current Inspection System. About 2500 Nb sheets were inspected up to now [1] (Fig.2).

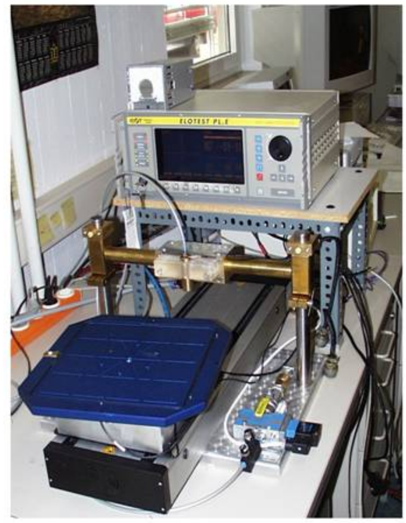


Figure 2: Eddy current inspection system.

Several kinds of flaws and imperfections were found with this system and could be analyzed with either EDX or SYRFA. For example: Fe inclusions (Fig.3-1), Si and Mg in small pits caused by grinding (Fig.3-2), imprints from rolling components (Fig.3-3), etching pits (Fig.3-4). Recently an image of the support frame in the 800° C furnace was found on a Nb sheet coming from evaporation or abrasion (Fig.3-5). On this niobium sheet Cr, Ni and W (1 %) could be detected on the surface using EDX.

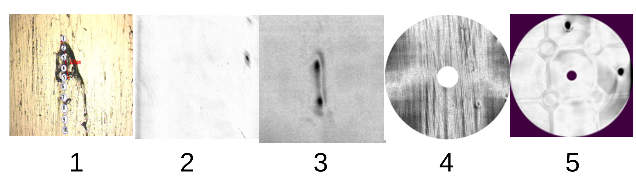


Figure 3: Several imperfections found with the Eddy Current Inspection System (explanation see text).

## SQUID SCANNER

New scanning devices are required for the XFEL cavity production. One option is to replace the pick up coil of the conventional device by a superconducting SQUID element. This sensor promises a much higher sensitivity [2]. Therefore a SQUID scanner was developed and built in collaboration between DESY and the Company WSK. An excitation coil induces eddy currents in the sample. But in the case of a SQUID scanner a superconducting SQUID detects the related magnetic field. A compensation coil close to the SQUID cancels the primary excitation field (Fig.4).

# arne.brinkmann@desy.de

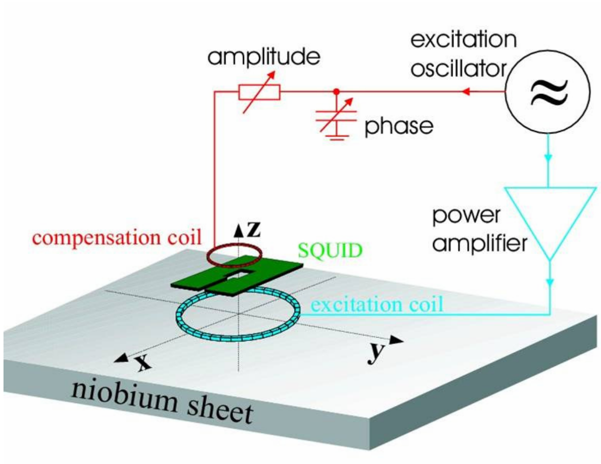


Figure 4: Measurement setup with SQUID.

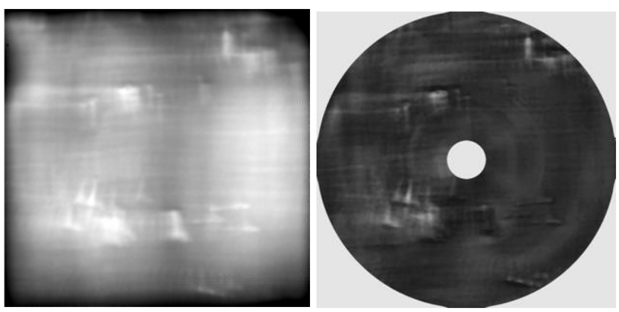

Figure 5: Scan images of SQUID (left) vs. EDDY-Current (right).

In addition the SQUID scanner uses more sophisticated image processing software. Compared to the conventional scanner SQUID images look more distinct (Fig.5). For twelve month the SQUID device is operational at DESY and shows promising results.(Fig.6).

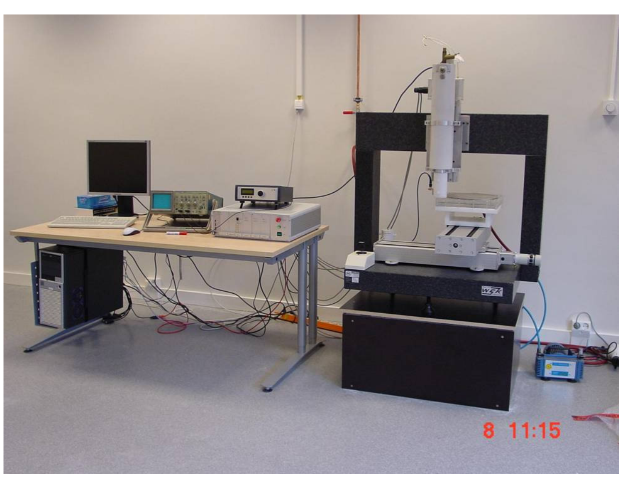


Figure 6: SQUID scanner at DESY.

## STATISTICS

Figure 7 shows the number of scanned sheets (in total 2451). Out of these, 231 sheets were declared as „suspicious“ after first scan. Due to this a second scan of the rear side of the sheet was carried out. A large number of these sheets was accepted. Real defects were found only in the first years of the scanning control, e.g. iron and tantalum inclusions. Therefore we conclude the scanning control has a benefit effect to the cleanliness of the later niobium sheet production. We will continue to use the quality control by the Eddy current/ SQUID scanning to assure the high quality of the industrial Nb production.

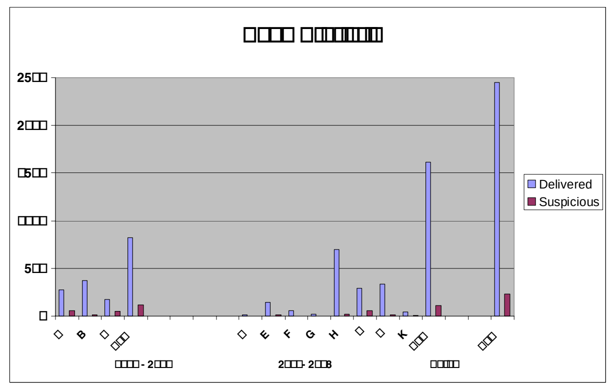


Figure 7: Statistic of scanned sheets, vertical axis shows the number of scanned sheets, horizontal axis batch number and production time of sheets.

## SUMMARY

| *PRO* | *CONTRA* |
|---|---|
| SQUID: More sensitive procedure compared to conventional setup. | SQUID: Only prototype available. |
| SQUID: Less Lift-Off effect -> no distance control needed. | SQUID: More complicated technique. For operating liquid Helium is required. |
| EDDY: well-established method. Ready to run systems available from industry. | SQUID: Limited frequency spectrum to 100 kHz. Signal penetrates through the sheet -> analysis is more complicated |

Table 1: Comparison of Eddy Current and SQUID Scanner

The eddy current setup has been in operation at DESY for more than ten years. The higher sensitivity of the SQUID element promises to detect smaller defects as compared to the normal conducting device. However, to exploit this benefit improvements of the present software and the cryogenic system are required. Table 1 lists the pros and cons of both systems.

## ACKNOWLEDGEMENT

We acknowledge the support of the European Community Research Infrastructure Activity under FP6 "Structuring the European Research Area" program (CARE, contract number RII-CT-2003-506395

## REFERENCES

[1] W.Singer, D.Proch, A.Brinkmann,"Diagnostic of Defect in High Purity Niobium". Proceedings of the 8th Workshop on RF Superconductivity, Abano Terme, Padua, Italy, Oct. 1997.

[2] W.Singer, A.Brinkmann (DESY),F.Schoelz, A.Farr, E.Wappler (WSK), M.Mueck (ez-Squid), "SQUID-Based Scanning System for Detecting Defects in Nb Sheets for RF Cavities". Proceedings of the 12th Workshop on RF Superconductivity, Cornell University, Ithaca, New York, USA, July 2005.

# VARIOUS APPLICATIONS OF DRY-ICE CLEANING IN THE FIELD OF ACCELERATOR COMPONENTS AT DESY

A. Brinkmann[#], D. Reschke, J. Ziegler DESY, D-22603 Hamburg, Germany

*Abstract*

Dry-Ice cleaning offers a dry and waterless cleaning option removing hydrocarbons and particles without residues. Complex excavations like Cu RF gun cavities and Nb multicell cavities in horizontal installation position can be cleaned in an effective way. In the recent past RF gun cathodes and cathode transport boxes could be cleaned satisfactory. A status report will be given.

## INTRODUCTION

Since recent 1-cell cavity RF-Tests showed acceptable behavior such as Eacc > 35 MV/m and promising results after RF conditioning a $CO_2$-cleaned RF gun cavity for the photo injector at PITZ (Photo Injector Test Facility Zeuthen) could be presented, the idea is to apply this cleaning method to other RF components and multicell Cavities.

A description of the cleaning process and the experimental setup for cleaning 1-cell niobium cavities has been given in [1, 2, 3].

Basic mechanical and chemical essentials for the cleaning effect are:

- Due to shock-freezing the contaminations become brittle.
- High pressure and a high momentum of snow crystals remove the contaminations. Particles down to 100 nm can be removed.
- Hitting the surface snow particles partially melt at the point of impact. Liquid $CO_2$ is a good solvent for hydrocarbons and silicones.

The major advantage of this cleaning method is the absence of water or other liquids which not evaporate in short time. Figure 1 illustrates the basic design of the device.

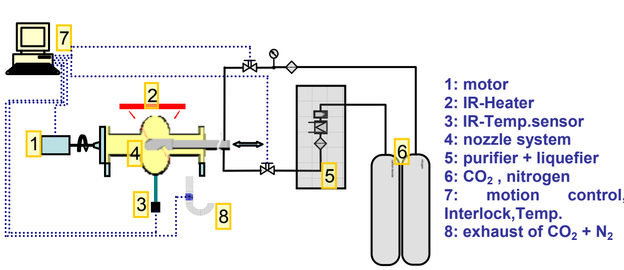


Figure 1: Basic design.

[#]arne.brinkmann@desy.de

For cleaning gun cavities a cleaning apparatus with a vertical nozzle exists. The principle setup is similar to the horizontal one shown in Figure 1.

The difference is the new rod with a gas supply and movable $CO_2$ nozzle, delivered from Fraunhofer Institute IPA, Stuttgart/Germany [4].

## CLEANED PARTS

### *2-Cell Cavity 2AC1 and 3-Cell Cavity 3AC1*

These two cavities were cleaned with the horizontal setup with additional heating from the IR-heater (Fig. 2).

Figure. 2: 3-cell cavity assembled to the horizontal cleaning setup with IR-heater above the cavity

The 2-cell cavity shows no field emission up to the thermal breakdown at ca. 23 MV/m (Fig. 3). The 3-cell cavity will be tested soon.

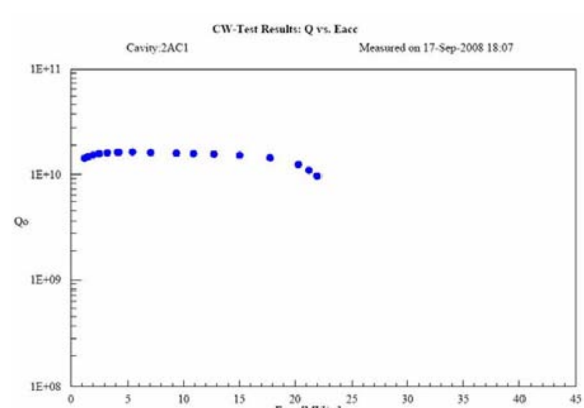


Figure 3: (Q/E)-Performance of cavity 2AC1.

### *RF Gun Cavity at PITZ*

The $C0_2$ cleaned gun cavity showed a factor of 10 less dark-current during a RF processing at DESY/Zeuthen compared to gun cavities cleaned with conventional water cleaning procedures (Fig. 4).

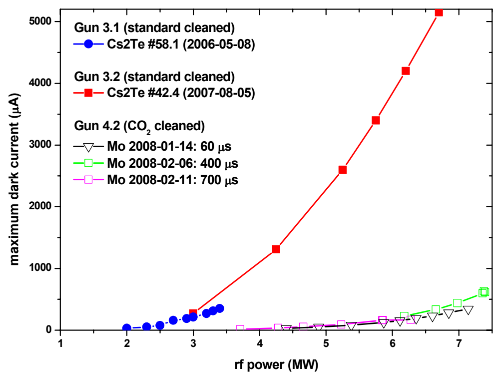


Figure 4: Comparison of dark-current for different cleaning methods. Different cathodes were used during these tests.

Figure 5 shows the gun cavity mounted to the vertical cleaning device. In order to avoid contaminations due to abrasion, the crossbar holding the cavity, moves up and down and turns the cavity along the way. The nozzle support does not move at all. Because of the complex outer surface of the gun cavity, we decided not to heat the cavity.

Figure 5: A gun cavity assembled to $CO_2$ cleaning device.

### *RF Gun Cathodes and Transport Frame*

Some cathodes and related components have been cleaned manually. Here the $CO_2$ nozzle from the horizontal setup was used (Fig. 6). An adequate cleaning was controlled by a particle counter. The counting decreased during the cleaning process. RF measurements are outstanding. However, the technical procedure is well-known. Figure 7 shows a cathode mounted to a transport frame.

Figure 6: $CO_2$ cathode cleaning by hand.

Figure 7: Cathodes in a transport frame.

### *Waveguide Connector*

A waveguide connector of the PITZ gun system was cleaned lately. In the near future RF tests will start at DESY/Zeuthen (Fig. 8 and Fig. 9).

Figure 8: Waveguide assembled to the vertical cleaning setup.

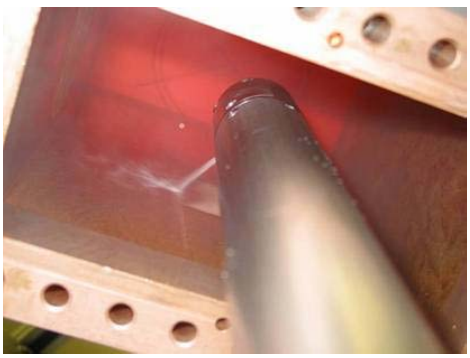

Figure 9: Nozzle and $CO_2$ - jet inside waveguide.

### *Input Coupler for Photo Injector*

First cleaning tests are done. Cleaned components will be mounted to the other photo injector parts and tested in the near future at DESY/Zeuthen (Fig. 10).

Figure 10: Input coupler in vertical device.

## SUMMARY

We could show that dry ice cleaning of complex structures is possible as a matter of principle. A movable gas nozzle helps to clean areas with limited accessibility. During the cleaning process of the RF gun no additional external heating was applied. The promising dark current measurements give an indication to omit the IR-heater in future. 2-cell and 3-cell cavities could be cleaned. Adjacent RF tests will follow in the near future.

## ACKNOWLEDGEMENT

We acknowledge the support of the European Community Research Infrastructure Activity under FP6 "Structuring the European Research Area" program (CARE, contract number RII3-CT-2003-506395).

## REFERENCES

[1] D. Reschke et al.; "First experience with dry-ice cleaning on srf cavities", Proc. Lin. Acc. Conf. LINAC2004, THP71, Luebeck, Germany (2004)

[2] D. Proch, D. Reschke, B. Günther, G. Müller, D. Werner, "Dry-ice cleaning for SRF applications", Proc. 10th Workshop on RF Superconductivity, Tsukuba, Japan, p. 463 (2001)

[3] A. Brinkmann et al., "Dry-ice cleaning on SRF cavities", Proc. of the Europ. Acc. Conf.; Edinburgh, Great Britain (2006)

[4] D.Reschke, A. Brinkmann, K.Floettmann, D.Klinke, J.Ziegler, D.Werner, A.Grimme, Ch.Zorn, "Dry-ice cleaning: The most effective cleaning process for SRF Cavities ?" Proc. 13th International Workshop on RF Superconductivity,Beijing,China (2007).

# RECENT RESULTS ON 1.3 GHz NINE-CELL SUPERCONDUCTING CAVITIES FOR THE EUROPEAN XFEL

L. Lilje#, D. Reschke, DESY, 22607 Hamburg Germany.

### [illegible]

The most recent production of superconducting nine-cell cavities of the TESLA [1] shape in preparation for the European XFEL [2, 3] is currently under test at DESY. The goals are training of companies in cavity preparation, streamlining the cavity preparation process and a better comparison of final treatments. The current measurements are compared to the previous production cycles.

## GOALS OF THE ONGOING XFEL NINE-CELL PROGRAMM

### [illegible]

The main goal is the training of industry. In previous production runs for the TTF at DESY, companies have fabricated the cavities. Additional quality control steps were introduced in the fabrication process. Most recently, a high resolution optical inspection system has been obtained from Kyoto University and KEK. This will be put into operation in the near future to further improve weld quality.

In the recent production run, the damage layer removal after fabrication was done by industrial companies. The process planned to be used in the XFEL production run is electropolishing (EP). So far, industrial electropolishing of multi-cell cavities was only available in Japan.

The final surface preparation (see below) for this production cycle was done at DESY. For the XFEL pre-series this process will also be transferred to industry.

### [illegible]

More efficient processes a desirable for the XFEL project in order to save cost. Several changes were introduced into the cavity preparation and assembly cycle.

Although the final treatment for the XFEL cavities has not yet been decided, tank welding at an early stage of the cavity process was considered a potential cost saving. The tank welding process was introduced after the furnace treatment and before the vertical test (For a detailed sequence of the assembly steps see next section).

The serious disadvantage of putting the tank on at such an early stage is that temperature mapping of the cavity is not possible anymore. In addition, a repair using EP is not viable either.

A second idea following along the same lines is to mount the HOM antennas already after the tank welding. The reason for this is, that a final cleaning. process i.e. high pressure rinsing with ultra-pure water can be done after the potentially particle-generating assembly processes.

It is a disadvantage, that assembled HOM antennas do not allow full passband mode measurements due to the narrow-band nature of the filter in the TESLA HOM couplers.

During vertical low-power continuous wave RF tests in some cavities Q-switches were observed. The effect disappears, when the HOM couplers are not equipped with antennas. During pulsed operation with HOMs these effects have never been observed. The nature of these effects is not fully understood yet, but is likely related to a temperature effect either at the feed-through or the antenna tip.

### [illegible]

The final surface treatment critically affects the cavity performance. The last treatment step is still under discussion for the XFEL. In the previous production run it turned out, that both a short final etch (10 µm) or a short EP (40 µm) followed by an ethanol rinse had good performance in terms of a reduction of field emission. The maximum gradient of the electropolished set of cavities seemed to be higher. To get a larger data set it was decided to test 10 cavities with each of the two choices of treatment.

## CAVITY PREPARATION

The 30 fine-grain niobium cavities in the recent program have been subjected to the following processes::

- Damage layer removal: 150µm EP inside
- 10µm etching (BCP) outside,
- Degassing: 800 C firing
- Frequency and field flatness tuning
- Tank-welding
- followed by either
    - final EP 50 µm, ethanol rinse
- or
    - final BCP (“EP+”) of 10µm
- HPR (High-pressure rinsing with ultra-pure water)
- Antenna assembly,
- HPR
- 130 °C bake
- Low-power Test

For simplification several additional cleaning steps like ultrasonic cleaning are not listed here.

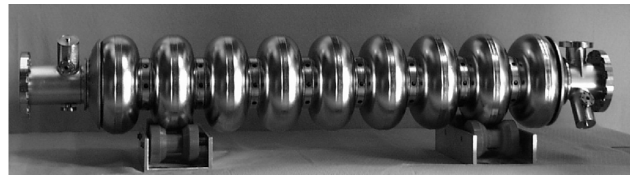

Figure 1: A TESLA 9-cell cavity with a length of about 1m.

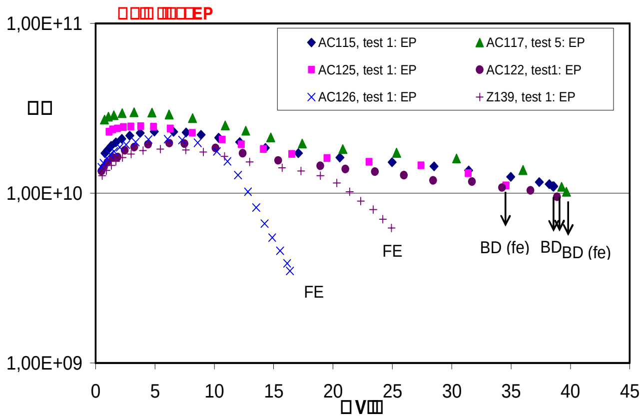


Figure 2 a): Vertical test results of most recent cavity production after EP as a final surface treatment. Strong field emission (FE) has been in two cavities causing a strong degradation of the quality factor. In two other cavities much smaller levels of radiation have been observed causing no significant degradation.

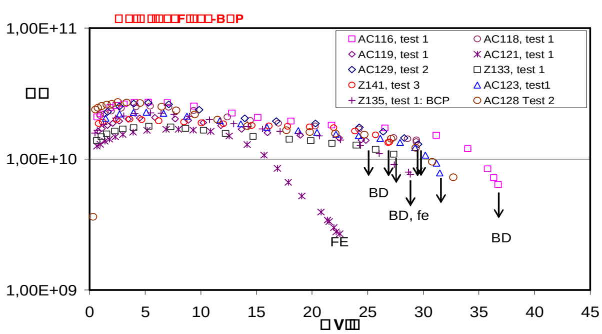


Figure 2 b): Vertical test results of most recent cavity production after etching (BCP=Buffered chemical polish) as a final surface treatment. One cavity shows strong FE.

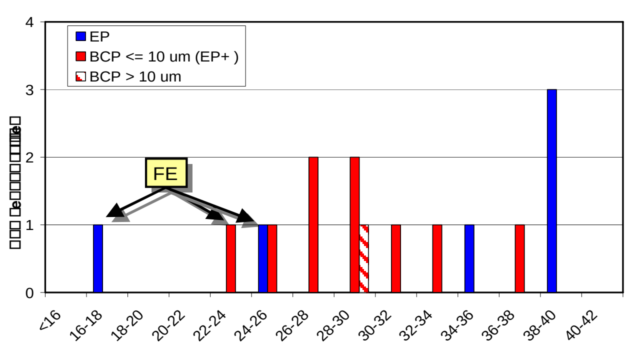


Figure 3: Comparison of the vertical test results for the final surface treatments.

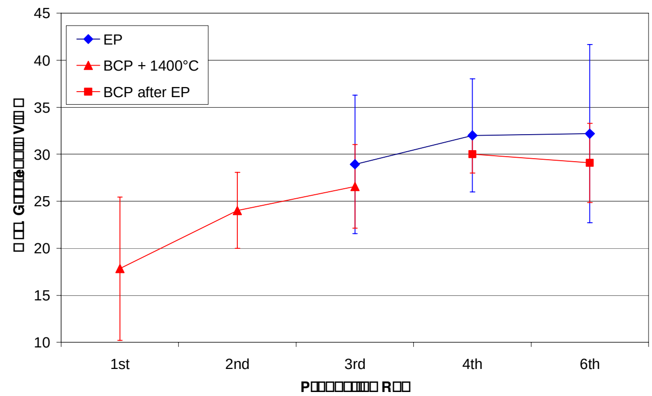


Figure 4: Comparison of final surface treatments for the cavity production runs at DESY. For comparison the maximum gradient in the last test of each cavity is shown. Note that data set for EP in 6th production is only six cavities so far. Re-tests of cavities with additional treatment have not yet been done. Other data sets include typically 10 – 20 cavities.

## RESULTS OF RF TESTS

The first cavities have now been tested. So far, three cavities have shown severe fabrication defects. They are not included in the data set in the following sections. The results are shown in figure 2 a) and b) for EP and the short BCP process, respectively.

Firstly, both processes have yielded three cavities in total that show strong field emission. These cavities will be re-treated with HPR only. In case this should not remove the field emitter, another short etching could be done without disturbing the field profile of the cavity too much.

The results of the two final treatment procedures are compared in figure 3. So far, the EP cavities show higher maximum gradients. This matches the experience from the previous productions (Figure 4). Due to the field emission loaded cavities, the standard deviation of the data sets is large.

The data in figure 4 indicates clearly, that there is no performance change from the 4th to the 6th production run. Therefore, main EP at the companies as not negatively affected the cavity performance.

## ETCHING AFTER ELECTROPOLISHING (ACCUMULATED DATA AT DESY):

Previous investigations at KEK [4] and DESY [5] have already shown that long etching of several ten µm after electropolishing deteriorates cavity performance. The reason for this deterioration is not finally understood. Grain boundary etching might play a role. At grain boundaries steps of several µm have been observed. It is not yet known, if topological defects or the chemical composition of the grain boundary area play a role.

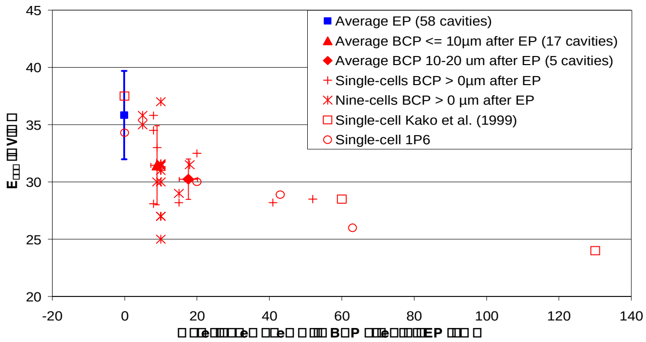


Figure 5: Cavity data for cavities with etching after electropolishing. Data includes both single- and nine-cell results as well as fine- and large-grain niobium material. For comparison older KEK data [4] is also shown. Cavities with field emission limitation and fabrication defects are excluded.

As early tank welding would exclude the option of a horizontal EP process for field emitter removal [6], other cleaning methods need to be explored. In case of field emitters sticking to the niobium surface, HPR in some cases might not be sufficient. The XFEL project therefore considers a short etching as a repair option for field emitter removal.

A critical question is whether a short etching (~10 µm) deteriorates cavity performance significantly. The results presented before indicate that already a BCP of only 10 µm is too much to get the full performance achieved with an EP final surface treatment.

To substantiate this finding we extend the cavity selection in this section to single-cells and nine-cells from both fine-grain and large-grain material after an initial full electropolishing of at least 100 µm followed either directly by an RF test or by a BCP with an RF test. Cavities with obvious fabrication defects and strong field emission loading have been de-selected from the data set. The data set includes roughly 60 cavities. Results are shown in figure 5.

A degradation of 4 MV/m is observed for a 10 µm etch after EP. For larger removal with etching a further reduction of the maximum gradient is found. Therefore field emitter removal using etching on cavities with helium tanks will degrade the maximum quench gradient.

The finding of this paper supports the choice of electropolishing as the final surface preparation process for the International Linear Collider (ILC). The current parameter set for the ILC requires a gradient of 35 MV/m at a $Q_0=10^{10}$.

For a better understanding of the performance difference between etched and electropolished surfaces additional measurements are needed. A more detailed investigation of the quench locations using high-resolution thermometry and optical inspection before and after etch processes is needed to identify the nature of the defects leading to a premature breakdown.

In previous investigations [4, 5] cavity performance could be recovered with electropolishing after etching. The amount of material removed was typically in the order of several ten µm. Whereas a typical BCP surface has a $R_a$ of 1µm, electropolishing will reduce surface roughness by a factor 10 after roughly 100 µm removal [7, 8]. To date it is not clear how much EP is needed minimally to fully recover from etching. A larger data set of cavities electropolished after etching would possibly allow distinguishing between a topological effect or the chemical composition of the surface.

## CONCLUSION

The XFEL project is being started at DESY now. The last cavity production before the XFEL production run of 800 cavities is under test. The main EP of 100 µm has been done at companies. Cavity performance has not changed. The training of companies in the preparation processes has successfully started.

A degradation of an EP surface due to subsequent etching has been observed starting already after 10 µm of etching. The mechanism of this deterioration is not understood so far. Systematic measurements using single-cells together with high-resolution temperature mapping would be highly desirable to understand the nature of the reduced magnetic peak fields.

## REFERENCES

[1] R. Brinkmann, et al. (editors), TESLA - Technical Design Report, volume II. DESY, March 2001. ECFA 2001-209, TESLA Report 2001-23.
[2] http://www.xfel.net
[3] M. Altarelli et al. (editors), The European XFEL Technical Design Report, DESY, July 2006, DESY 2006-097
[4] E. Kako et al. ; Improvement of Cavity Performance in Saclay/ Cornell/ DESY´s SC Cavities ; 9th Workshop on RF Superconductivity; 1999; Santa Fe; pp.179-186
[5] A. Brinkmann, Progress of the Test Cavity Program for the European XFEL, 13th Workshop on RF Superconductivity; 2007; Beijing, TUP74
[6] So far, there exists no experience of horizontal electropolishing niobium cavities with tank.
[7] K. Saito et al.,"R&D of Superconducting Cavities at KEK" , Proc. 4th SRF Workshop, Tsukuba (1990), p.651 ff.
[8] K. Saito, et al., Superiority of electropolishing over chemical polishing on high gradients, in: V. Palmieri (Ed.), Proceedings of the Eighth Workshop on RF Superconductivity, Vol. I+II, INFN, Abano Terme, 1997, pp. 759–813.

# OPEN 120°C BAKE IN ARGON ATMOSPHERE: A SIMPLIFIED APPROACH FOR Q-DROP REMOVAL

D. Reschke#, J. Ziegler, Deutsches Elektronen-Synchrotron DESY, 22603 Hamburg, Germany


### [illegible]

The removal of the Q-drop without field emission by a low temperature bake procedure (app. 120°C) is essential in order to achieve the full performance in both electropolished (EP) and chemically etched (BCP) high gradient SCRF Nb cavities. A simplified procedure applying an open 120°C bake in an Argon atmosphere is presented. The first successful cavity results are compared to the well-established bake procedure under ultra-high vacuum (UHV) conditions.


## INTRODUCTION

The low temperature annealing ("bake") at 100°C – 130°C is an essential preparation step following a chemical or electrochemical surface treatment in order to achieve high gradients (> 30 MV/m) at high Q-values [1, 2]. The standard bake procedure in UHV conditions is applied to the fully assembled cavity ready for its rf test (Fig. 1). The cavity itself is kept under vacuum during the bake, while the outside is an inert gas atmosphere in order to prevent oxidation (Fig. 1 shows the bake stand without its outer hood, which can be partially seen at the right-most of the picture). Typical parameters applied at DESY are (120 – 129)°C for 48 h. On single-cell cavities a modified process with (130 – 138)°C for 12 h has been applied successfully.


Figure 1: DESY bake stand for UHV bake.

In order to adapt the bake procedure for a large scale cavity production two alternatives have been proposed:

- a higher temperature (130 – 160)°C , but shorter time of (1 – 12) h [3, 4, 5]
- open bake in inert gas atmosphere or air with 110 – 120 °C for 12 h – 60 h or 145°C for 3 h

The latter using an inert gas atmosphere has been developed also at CEA Saclay [6].

## NEW BAKE PROCEDURE

### [illegible]

For the single-cell tests described below a commercial lab vacuum drying cabinet was used successfully (Fig. 2). The vacuum drying cabinet has a programmable temperature control unit with a stability of ± 3°C and excess temperature protection. The vacuum and venting installation is integrated, which allows an adjustable, permanent Argon flow with overpressure protection. A dry, oil-free diaphragm pump is used for the initial pump-and-purge cycles. Applied parameters are a temperature of 120°C for 24 h with an Ar flow of app. 250 l/h. The purity of the Ar gas is better than 99,999%. Typically, warm-up takes 2 h; cool-down takes 16 h.

Figure 2: Vacuum drying cabinet for single-cell cavities.

# detlef.reschke@desy.de

For the start-up experiments the vacuum drying cabinet could not be placed inside the cleanroom. It is located in a "grey" area close-by in order to avoid unnecessary contamination of the cavity. After the bake process the cavity is transported immediately back in the cleanroom, rinsed with ultrapure high pressure water (UHPW), assembled, again UHPW rinsed, finally assembled and evacuated.

The final technical design of a nine-cell bake cabinet is in preparation. It will be placed inside a cleanroom annex in order to allow the loading of cavities without contamination. Typical parameters and procedures will be based on the successful single-cell results, but matched to nine-cells, where necessary.

## CAVITY TESTS AFTER OPEN AR BAKE

One single-cell cavity fabricated of large grain Niobium was prepared and tested after a final electropolishing. The standard EP procedure at Henkel Co. consists of a 100 µm EP, high pressure rinse with demineralised water, hot ultra-pure water rinse, drying with pure nitrogen and final packing. After transportation to DESY, the cavity is stored until the final cleanroom UHPW rinse and assembly takes place. Open Ar bake was done with the procedure described above.

In Fig. 3 the Q(E)-performance of an earlier EP treatment followed by standard UHV-bake is compared to the recent EP + open Ar-bake. All Q(E)-curves are taken at 2 K. Both processes result in gradients around 40 MV/m at high Q-values limited by quench. The Q(E)-curve after open Ar-bake suffers from some field emission degrading the Q-value at gradients > 34 MV/m. This level of field emission occurs from time to time, and is most probably not related to the open Ar-bake process. The Q(E)-curve after UHV-bake shows no detectable x-rays until the quench field, which allows a Q-value of $1{,}4 \cdot 10^{10}$ at $E_{acc,max}$ = 40,5 MV/m.

Open Ar-bake removes the Q-drop of electropolished cavities as well as standard UHV-bake.

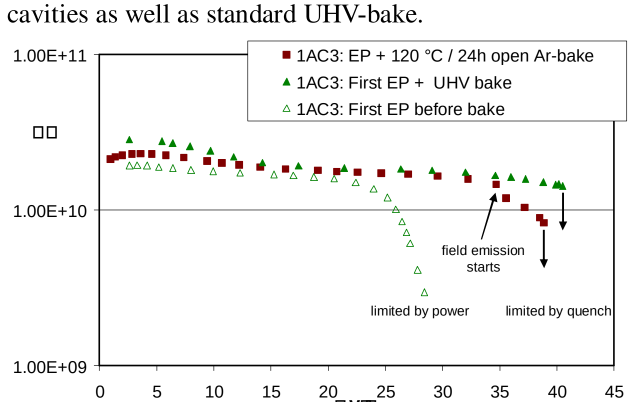


Figure 3: Effect of open Ar-bake and UHV-bake on an electropolished single-cell cavity made of large grain niobium (1AC3).

For the European XFEL project [7, 8] a final short BCP of app. 10 µm followed by the usual UHPW rinse, assembly and evacuation procedure is proposed as an alternative to a final EP treatment [9]. For two single-cell cavities fabricated of fine grain Nb a final short BCP of 8 µm was applied followed by the handling procedure described above.

Figure 4 shows the Q(E)-results at 2 K of both cavities before and after open Ar-bake. After Ar-bake both cavities are limited by quench and show no detectable x-rays indicating field emission. The Q-drop is significantly reduced and shifted towards higher fields. In addition, the Q-value at low and medium fields is higher. This is due to the typical reduction of the BCS the surface resistance after a low temperature bake procedure [2].

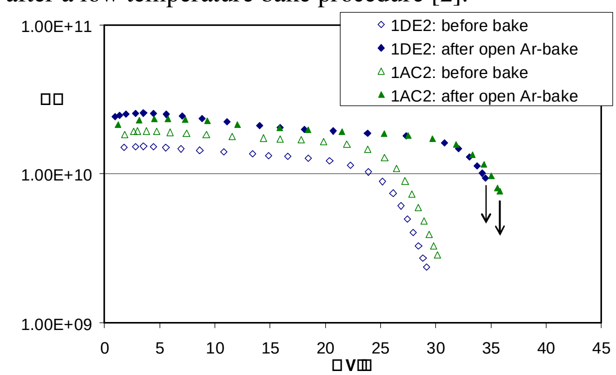


Figure 4: Effect of open Ar-bake after final short BCP on two single-cell cavities fabricated of fine-grain Nb.

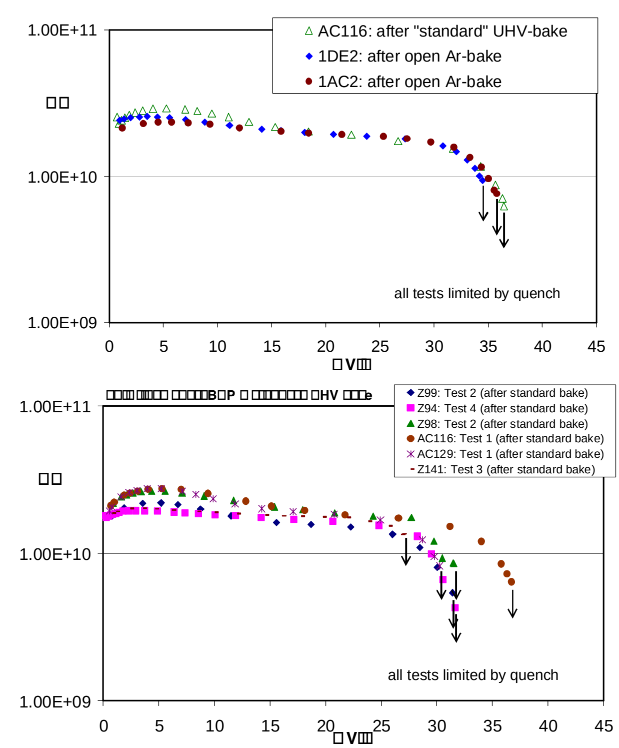


Figure 5 a+b: Comparison of open Ar-bake with standard UHV-bake after final short BCP (top); typical Q(E)-curves after final short BCP and UHV-bake (bottom).

In order to investigate the remaining Q-drop, Fig. 5a shows the comparison of the two single-cells (1AC2, 1DE2) with a nine-cell cavity (AC116) after comparable surface treatment (10 µm + UHPW rinse), but UHV bake applied. In addition, Fig. 5b gives typical Q(E)-performances of nine-cell cavities after final short BCP followed by standard UHV-bake.

Obviously, open Ar-bake is as effective as standard UHV removing the Q-drop for final short BCP surface treatment. The remaining Q-drop is a general effect of low temperature baked cavities after a final short BCP and not a specific negative impact of open Ar-bake. Moreover, it is reported in general for BCP treated cavities fabricated of fine grain Nb, that the Q-drop cannot be cured in all cases. An overview is given in [10].

## CONCLUSION

The new simplified open Argon bake procedure cures the Q-drop without field emission for final EP and final short BCP surface treatment. After final short BCP a remaining Q-drop is still present at gradients $E_{acc}$ > (25 – 30) MV/m, independent of the type of bake procedure.

Open Ar-bake is advantageous to standard UHV bake:

- The bake process can be simply implemented in the cavity preparation sequence before the final ultra-pure high pressure water rinse.
- No additional vacuum handling of the fully assembled cavity is necessary. There is no additional thermal stress of the cavity flange gaskets during bake.
- No additional UHV vacuum pump station necessary.
- The vacuum drying cabinet is commercially available instead of a special designed UHV-bake stand.

Open Ar-bake is a simplified practical solution for a mass preparation of cavities as e.g. for the upcoming European XFEL project with more than 800 nine-cell cavities.

## ACKNOWLEDGEMENT

The authors thank T. Cheung, K. Harries, J. Iversen, D. Klinke, M. Langer, L. Lilje, D. Proch, H. Remde, R. Ritter and all other involved colleagues for their technical support and many fruitful discussions.

## REFERENCES

[1] B. Visentin et al., “Improvement of Superconducting Cavity Performances”, Proc. of 6th EPAC, Vol. III, p. 1885, Stockholm, Sweden (1998)

[2] G. Ciovati et al., “Review of the Frontier Workshop and Q-slope results”, 12th Workshop on RF Supercond., Ithaca, USA (2005)

[3] B. Visentin et al., “First Results on Fast Baking”, 12th Workshop on RF Supercond., Ithaca, USA (2005) and Physica C Vol 441, Iss. 1-2, p. 66-69 (2006)

[4] B. Visentin et al., “Optimization of Baking Parameters for Electropolished Niobium Superconducting Cavities”, 13th Workshop on RF Supercond., Beijing, China (2007)

[5] P. Kneisel, “ Review of Progress on Large Grain and Single Grain Nb Cavities”, Lecture part II, 13th Workshop on RF Supercond., Beijing, China (2007)

[6] B. Visentin et al., “«Fast Argon-Baking» Process for Mass Production of Niobium Superconducting RF Cavities”; Proc. of the 10th EPAC, MOPCH141, Edinburgh, Scotland

[7] http://www.xfel.net

[8] M. Altarelli et al. (editors), The European XFEL Technical Design Report, DESY, July 2006, DESY 2006-097

[9] L. Lilje, D. Reschke, “Recent Results on 1.3 GHz Nine-Cell Superconducting Cavities for the European XFEL”, LINAC 2008, THP014, Victoria, Canada (2008)

[10] D. Reschke, “Limits in cavity performance”, Tutorial, 13th Workshop on RF Supercond., Beijing, China (2007)

# ANALYSIS OF QUENCHES USING TEMPERATURE MAPPING IN 1.3 GHz SCRF CAVITIES AT DESY*

D. Reschke#, Deutsches Elektronen-Synchrotron DESY, 22603 Hamburg, Germany.


## [illegible]

The local thermal breakdown (quench) behavior of one- and nine-cell SCRF Nb accelerator cavities is investigated systematically. For more than 50 cavities, in addition to the rf test results, temperature mapping data have been analyzed with respect to surface preparation, Nb material etc.. Results on rf properties, quench location and characteristic correlations are presented.


## T-MAPPING SYSTEMS AT DESY

Presently, three different T-mapping systems for superfluid Helium are in use at DESY.

- Fixed, high sensitivity T-mapping system for single-cell cavities with 768 sensors on 48 boards (= 7.5 ° angle spacing) (Fig. 1a) [1]
- Rotating nine-cell T-mapping system with 128 sensors for quench detection (Fig. 1b) [2]
- "Quick" fixed T-mapping with 72 sensors at 24 angle positions for equator region (Fig. 1c).

All sensors are based on carbon resistors [3]. The block diagram of the multiplexed data acquisition is shown in Fig. 1d. The off-line analysis is based on in-house programming using LINUX PC applications.

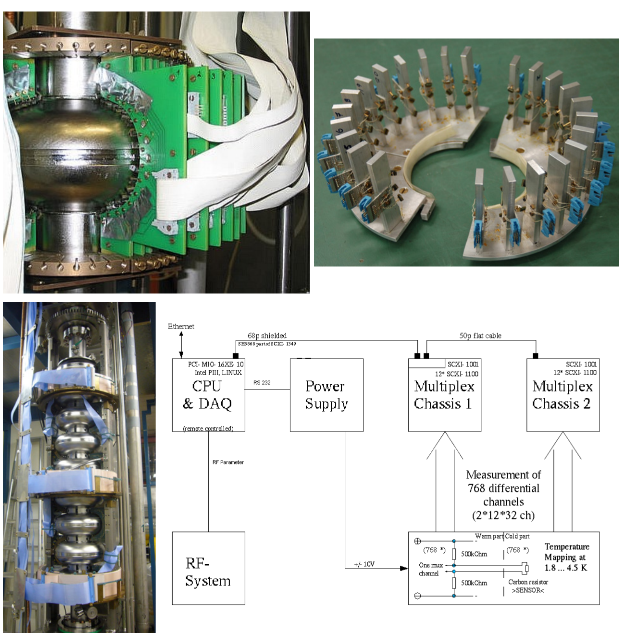


Figure 1: a) Single-cell T-map system (top left); b) rotating nine-cell T-map system (bottom left); c) "quick fixed" T-map (top right); d) data acquisition scheme (bottom right).

## LARGE GRAIN CAVITIES: ELECTRO-POLISHING vs. CHEMICAL ETCH

### [illegible]

Three nine-cell cavities (AC112 – AC114) [4] and five single-cell cavities [5] of TESLA shape were fabricated of two ingots of Large Grain (LG) Nb by W.C. Heraeus Co.. The cavities "AC" were machined and electron beam welded at Accel Instruments Co.; the cavities "DE" are DESY in-house production. Before the first cold rf test at least 120 µm of the surface have been removed by electropolishing (EP) or chemical etch (BCP) on all cavities. Also all cavities have been 800 °C vacuum annealed. After the final surface treatment by final EP or BCP, all cavities were assembled in a cl. 10/100 cleanroom and rinsed with ultrapure high pressure water of > 100 bar. Typical parameters of the low temperature bake procedure were (120 – 125) °C for 48 h for the nine-cells and (130 – 138) °C for 12 h for the single-cells. Both processes show comparable results. In Table 1 only the major preparations steps are shown; the full preparation and test summary can be found in [6].

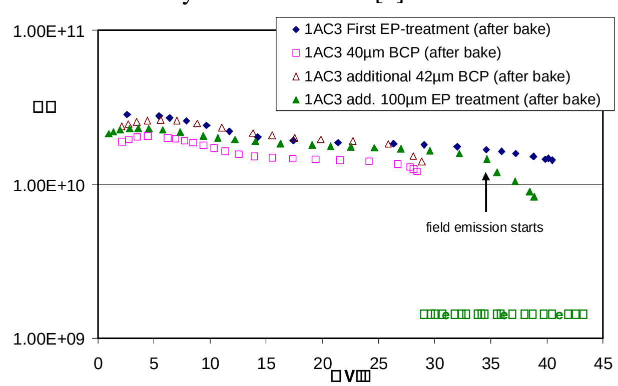


Figure 2: Q(E)-performance of an EP - BCP - BCP - EP preparation cycle of single-cell cavity 1AC3.

### [illegible]

As shown in Table 1 the influence of the final surface preparation of either > 40 µm removal by BCP or > 48 µm removal by EP on the Q(E)-performance has been investigated systematically. All test results of all 8 LG Nb cavities are given for $T_B = 2K$. Especially, the single-cells 1AC3 and 1AC4 went through full cycles of successive EP - BCP - EP treatments (Fig. 2). For both cavities a reproducible gradient gain of > 10 MV/m after EP compared to BCP is observed. A final BCP treatment applied on 6 cavities results in reproducible gradients of (25 – 30) MV/m limited by quench for all cavities. A final EP gives quench fields between (33 – 43) MV/m in 6 of 8 cavities. Two nine-cell cavities show low gradients

* We acknowledge the support of the European Community Research Infrastructure Activity FP6 "Structering the European Research Activity" program (CARE) contract number RII-CT_2003-506395
#detlef.reschke@desy.de

limited by field emission and quench. The reason for the unusual behaviour is not understood yet. New surface treatments of both cavities are in preparation.

### [illegible]

In Table 2 the characteristic rf properties of LG Nb cavities are compared to the well-known fine grain material. Obviously, the characteristic scrf parameters, especially the quench field, Q-drop without field emission and field emission behaviour, are identical within the available test results. For the quench gradient of fine grain Nb cavities, after 800 °C firing + final BCP, not sufficient data are available at DESY.

With the given identical rf performance of fine and large grain Nb, now a large scale accelerator application of LG Nb cavities (e.g. for the European XFEL) depends only on the availability of high quality LG Nb, its cost and the cost-effectiveness of the cavity production.

Table 1: Simplified summary of preparation and test history on large grain cavities (not all cavity preparations and tests shown; all rf test results at $T_B$ = 2 K).

| | | 1AC3 | 1AC4 | 1AC7 | 1DE20 | 1DE21 | AC112 | AC113 | AC114 |
|---|---|---|---|---|---|---|---|---|---|
| EP before bake | Eacc | 28 (FE) | 29 (pwr) | - | - | - | - | - | - |
| | Qo | 3e9 | 3e9 | - | - | - | - | - | - |
| + bake (+ HPR for 1AC3) | | 41 (BD) | 37 (BD,fe) | - | 33 (BD) | 39 (BD) | - | - | - |
| | | 1,4e10 | 6,3e9 | - | 1,4e10 | 1,1e10 | - | - | - |
| + BCP (~40µm or pure BCP ) + HPR | | 31 (pwr) | 30 (pwr) | 25 (BD) | | | 30 (BD) | 27 (BD) | 29 (BD,fe) |
| | | 2,2e9 | 2,2e9 | 1,5e10 | | | 6,6e9 | 1,7e10 | 7,3e9 |
| + bake | | 29 (BD) | 28 (BD) | | | | | | |
| | | 1,2e10 | 1,2e10 | | | | | | |
| + BCP (~40 µm) + HPR + bake | | 29 (BD) | | | | | | | +20 µm BCP: 27 (BD) |
| | | 1,4e10 | | | | | | | 1,6e10 |
| + EP (~100µm) + HPR + bake | | 39 (BD, fe) | 41 (BD) | 27 (BD, fe) | | | 20 (FE) | + 48 µm EP: 37 (pwr,fe) | 14 (BD) |
| | | 8,3e9 | 1,3e10 | 1,5e10 | | | 1,9e9 | 6,6e9 | 1,6e10 |
| + EP (~20µm) + HPR +bake | | | | 43 (BD) | | | +90 µm EP: 17 (FE) | - | |
| | | | | 1,4e10 | | | 1,5e9 | - | |

Table 2: Comparison of characteristic scrf properties for large grain vs. fine grain Nb cavities.

| | Quench gradient after final EP | Quench gradient after final BCP | **EP:** Q-drop before bake | **EP:** cure of Q-drop by bake | Characteristic rf parameters + residual resistance |
|---|---|---|---|---|---|
| Large grain Nb | (33 – 43) MV/m | (25 – 30 ) MV/m | Typically > 25 MV/m | yes | $R_{res}$, $R_{BCS}$, $\Delta/kT_c$, medium field Q-slope + field emission behaviour **identical** |
| Fine grain Nb | (36 ± 4) MV/m | Data not sufficient | Typically > 25 MV/m | yes | |

## T-MAP ANALYSIS OF SINGLE- AND NINE-CELL CAVITIES

### [illegible]

Most important is the localisation of fabrication and/or material problems in the TTF/FLASH nine-cell cavities. An example for the identification of a low gradient quench location at the equator is given in Fig. 3. The quench directly located on the equator weld indicates a problem during cavity fabrication, which requires further investigation of the weld procedure at the manufacturer. Furthermore, the improved optical surface inspection method has been applied to several nine-cell cavities recently [7, 8]. Many suspicious spots and surface anomalies have been found in the inspected cavities. Typically, correlations to the detected quench locations could be found. Next step will be the cutting-out of an identified defect region from a nine-cell cavity and material analysis of the defect.

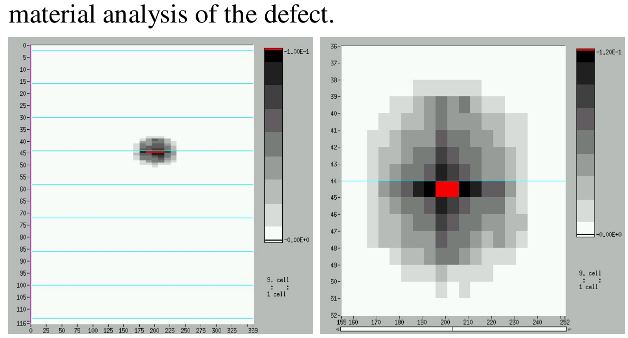

Figure 3: Identification of quench location at equator in cell 6 of nine-cell Z111 at 16 MV/m; left: Full rotating T-Map; right: Cell 6 with refined angle resolution.

### [illegible]

The analysed single- and nine-cell cavities fabricated of fine- and large-grain Nb with quench field > 25 MV/m , typically show the expected quench location in the high magnetic field region (Fig. 4 (right), Fig. 5 (left)). No systematic increased quench appearance on the equator weld could be found. In case of field emission, the characteristic heating of the iris region, often together with a trace to/in the equator region, is observed (Fig. 4(left)).

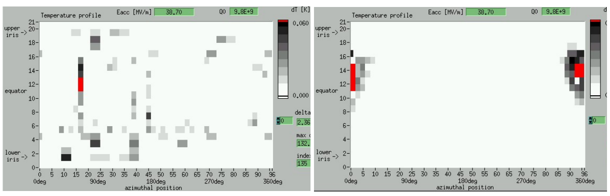

Figure 4: (left): Just below the quench field at 39 MV/m: typical field emission trace and heating at iris visible; (right): Quench at 39 MV/m located close above the equator (both T-maps taken in test 7 of single-cell 1AC3).

After an additional surface removal of several µm by EP or BCP, typically the quench location changes. In some cases the data are ambiguous or e.g. even after a 41 µm BCP the former quench location could be identified as a "hot spot" (Fig. 5 (right)).

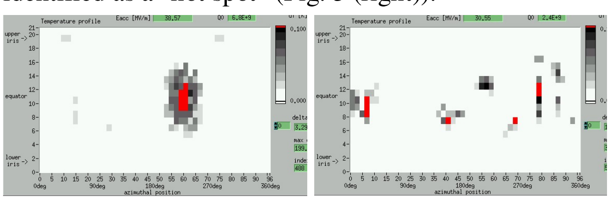

Figure 5: (left) Quench at 39 MV/m in single-cell 1AC4, test 6; (right): after 41 µm BCP a "hot spot" is visible at identical location in test 7, 1AC4.

Contrary to thermal conductivity model calculations based on the assumption of normal-conducting, lossy defects, often no clear pre-heating below the quench field could be observed at the quench location of single-cells (Fig. 4). Obviously, the nature of the defects responsible for the quench is not fully described by the above assumption and a more refined model is necessary.

### [illegible]

Rarely, the exciting observation of a changing or alternating quench position was made. By keeping the cavity in the self-pulsing quench and parallel continuous data sampling of the T-mapping system, in one single-cell three alternating quench locations at app. 40 MV/m could be found. This may be an indication of approaching the fundamental magnetic field limit, presumably combined with some magnetic field enhancement effects. As this measurement technique was not applied systematically to high gradient single-cells in the past, no information about the frequency of occurrence is available

## CONCLUSION

Systematic investigations on Large Grain Nb cavities show a typical gain in quench field of > 10 MV/m after final EP compared to final BCP. Comparing of LG Nb cavities with fine grain cavities, no difference in the characteristic scrf properties, especially in quench field, can be found.

Applying T-Mapping is essential for an effective quench analysis. An identification of field emission induced quenches is possible. In nine-cell cavities material and weld seam problems can be localized as a pre-condition for further (optical) investigation. High sensitivity T-mapping in single-cells allows a locally resolved analysis of thermal effects. Contrary to the expectation by thermal model calculation often no pre-heating below the quench is observed. Alternating quench locations may indicate, that the fundamental field limit is approached, possibly combined with field enhancement effects.

## ACKNOWLEDGEMENT

The author thanks all colleagues involved in the cavity fabrication, preparation and testing for their fruitful collaboration and manifold support.

## REFERENCES

[1] M. Pekeler et al., "Thermometric study of electron emission in a 1.3 GHz superconducting cavity", 7th Workshop on RF superconductivity, Vol.1, 79-93, Gif-sur-Yvette, France (1996) and
M. Pekeler, Ph.D. thesis, DESY-M-96-16 (1996).

[2] Q.S. Shu et al., "Experience in Design, Construction and Application of a Rotating T-R Mapping System in Superfluid He for TESLA 9-cell Cavities", ibid. ref. 1, Vol.2, p.523.

[3] M. Fouaidy et al., "Surface Scanning Thermometers for Diagnostic Purpose of the TESLA SRF Cavity", ibid. ref. 1, Vol.2, p. 559.

[4] W. Singer et al., "Advances in Large Grain/Single Crystal SC Resonators at DESY", Part. Acc. Conf 2007, THOKI01, Albuquerque, USA (2007).

[5] A. Brinkmann et al., "Progress of the Test Cavity Program for the European XFEL", 13th Workshop on RF Superconductivity, TUP74, Beijing, China (2007)

[6] http://tesla-new.desy.de/cavity_database

[7] Y. Iwashita et al., "Development of high resolution camera for observations of superconducting cavities", Phys. Rev. Special Topics – Acc. and Beams 11, 093501 (2008) and
Y. Iwashita et al., "Development of Inspection Systems for Superconducting Cavities", LINAC08, THP021, Victoria, Canada (2008) to be published.

[8] K. Watanabe, S. Aderhold, private communication.

# USE OF PIEZOELECTRIC ACTUATOR TO FREQUENCY LOCK SUPERCONDUCTING QUARTER WAVE RESONATOR

B.K.Sahu, S.Ghosh, R.Mehta, G.K.Chowdhury, A.Rai, P.Patra, A.Pandey, D.S.Mathuria, K. Singh, D.Kanjilal and A.Roy , Inter University Accelerator Centre (IUAC), Aruna Asaf Ali Marg, New Delhi – 110067, India

*Abstract*

The frequency control of the superconducting quarter wave resonator at Inter University Accelerator Centre (IUAC) is currently accomplished by mechanical and electronic tuners which are operated in the time scale in the range of a few seconds to a few microseconds. During operation, input RF power ≤ 100 W was required to control the resonator for a typical field of 3-5 MV/m for 6 watts of power dissipated in liquid helium. Though resonators are working fine at this power level, investigations are going on whether more reliable operation of the resonators is possible using a piezoelectric actuator to control the amplitude and phase of the accelerating fields. The piezoelectric tuner working in ~ milliseconds range with the dynamic phase control scheme will share a substantial load from the electronic tuner. In addition, in this new scheme, the resonator's phase lock loop will operate with lesser RF power than presently required. The test results of the piezoelectric tuner are presented in this paper.

## INTRODUCTION

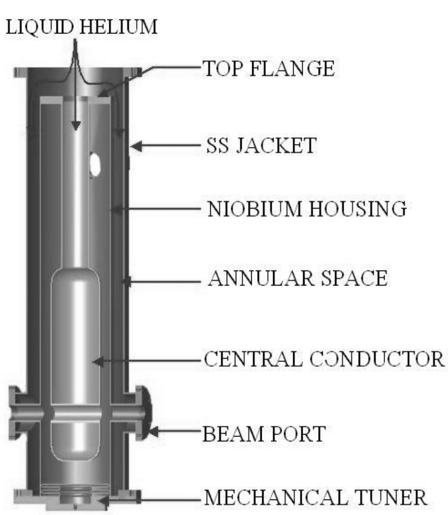


Figure 1: The schematic of the resonator and its mechanical tuner.

Presently, at IUAC, the commissioning of a superconducting (SC) linear accelerator (linac) based on niobium quarter wave coaxial resonator (QWR) is approaching completion [1,2]. The schematic of the resonator is shown in figure 1. The 15 UD Pelletron accelerator producing dc and bunched ion beam covering almost the entire periodic table, is used as the injector of the linac. Silicon and Oxygen beam from Pelletron accelerator has already been accelerated by the first accelerating module of linac and beam was delivered to conduct experiment.

The QWR of IUAC, is made from bulk niobium sheet and enclosed in a SS-jacket. Near the high voltage end of the central conductor, a pneumatically operated niobium bellows is placed to tune the resonator frequency. The complete resonator and the niobium bellow tuner are shown in figure 2 and 3.

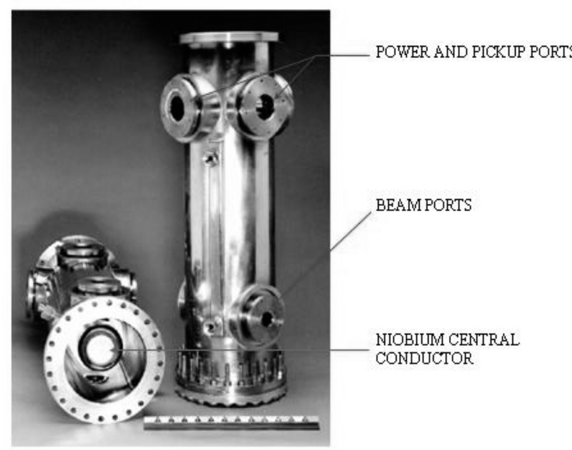


Figure 2: The photograph of two complete QWR.

The superconducting bulk niobium resonators have Quality factor in the range of $10^9$. For IUAC QWR with resonance frequency of 97 MHz, the bandwidth of resonator is around 0.1 Hz. Vibration induced fluctuations of the frequency are of the order of a few tens of Hz in these resonators. The frequency fluctuations have got two components – one happens in slow time scale (seconds) and the other happens in faster (a few tens to hundreds of μsec) time scale.

To arrest the fast drifts of frequency, the effective bandwidth is increased by overcoupling the resonator with respect to the RF amplifier and the resonator is supplied with the additional reactive power. By flexing the niobium bellows acting as the mechanical tuner, the slow drift of the frequency is controlled. This helps to reduce the overall power requirement of the fast tuner to control the frequency jitter.

The two tuning mechanisms working simultaneously are able to lock the phase and amplitude of the resonators with respect to master oscillator and beam was accelerated through the linac. However, since helium gas is used to flex the bellows sitting at a very low temperature (~ 40-60 K), the gas line got chocked a few times by traces of moisture in the past during cold tests. In addition, the slow tuning mechanism requires continuous supply of high purity helium gas inside the SS-bellow, for its operation.

With the recent growing usage of piezoelectric crystal in the tuning mechanism of SC resonators, efforts are on to make the tuning mechanism more reliable and cost effective. The aim of the work is to study and develop a piezoelectric tuning mechanism with our existing fast tuning control scheme based on Dynamic Phase Control (DPC) [3] method for the phase locking of the resonator.

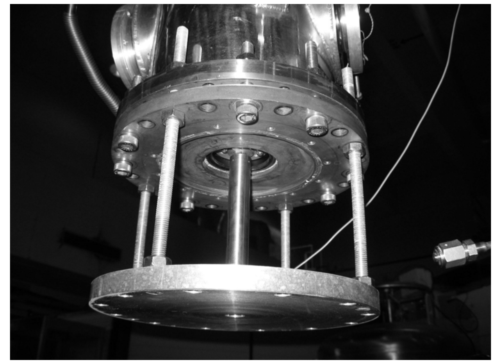

Figure 4: The mechanical tuner (hiding inside the resonator) along with the piezoelectric actuator prior to a cold test.

## TEST OF PIEZOELECTRIC ACTUATOR AT ROOM TEMPERATURE AND COLD CONDITION

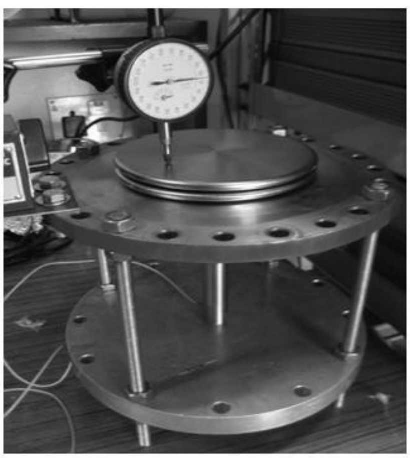

Figure 3: Measurement of the deflection of niobium bellows after powering the piezoelectric actuator.

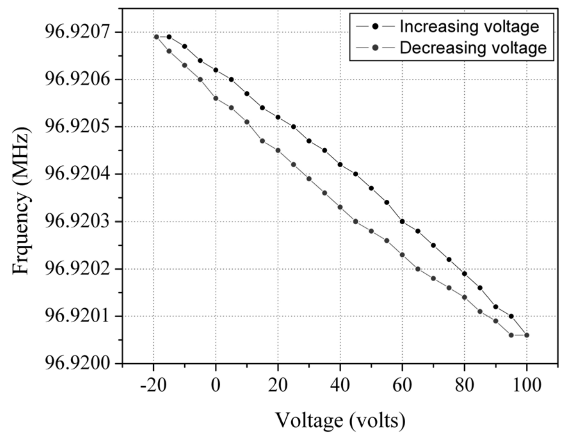


Figure 5: Hysteresis curve of the piezoelectric actuator.

Before connecting the niobium bellows loaded with piezoelectric tuner with the resonator, its effect on the niobium bellows was checked outside by measuring the deflection with dial gauge as shown in fig 3. One side of the piezoelectric is connected to the back of the niobium convolution of the tuner and the other side is clamped by fixing it on a aluminium flange. Biasing the piezoelectric actuator (Physik Instrumente (PI) make) [4] between -19 to 100 volts, the deflection measured by the dial gauge was 85 µm. The whole assembly shown in fig 3 was connected at the open end of a resonator (shown in figure 4) to test the performance at room temperature and cold condition. At room temperature, for a fixed distance between the top convolution of the slow tuner and the end of the central conductor, the frequency range of the resonator with full bias of the piezoelectric actuator (-19 to 100 Volts), was measured to be ~ 2.5 KHz. When the resonators were cold at 4.2 K, the frequency range had been reduced to 626 Hz. The hysteresis observed in the frequency change for increase and decrease of the bias voltage of the piezoelectric actuator is shown in figure 5.

## CLOSED LOOP OPERATION OF PIEZOELECTRIC ACTUATOR TO PHASE LOCK A SC RESONATOR

To keep the superconducting resonator phase locked with reference to the master oscillator in the dynamic phase control loop, the piezoelectric voltage should vary with phase error of the resonator controller. To achieve this, a PI based control scheme has been planned. The aim of this control scheme is to compensate the frequency drift around central frequency of the resonator and eliminate the hysteresis effects. The block diagram for the closed loop control of the piezoelectric actuator with existing dynamic phase control based resonator controller is shown in figure 6. In the existing resonator control electronics, the phase error calibration is set for ~ 100mV for 0.1 degree of phase difference. The high voltage amplifier for the piezoelectric actuator has open loop DC gain of 15. Within this range, piezoelectric control will also work along with the fast tuner but only for the frequency jitter occurring in the time range of ~ 100 msec. To get the piezoelectric control work efficiently, during operation, the error signal is reduced electronically by a factor of 10. So, for a phase error signal of ~ 1000 mV (to have a phase stability of ± 0.5 degree), a voltage of 1.5 Volts will appear at the piezoelectric crystal and this will change the frequency of the resonator by 7.8 Hz. As the total bias voltage of the piezoelectric is ~ 120 volts, the change of 7.8 Hz/1.5 Volts will be sufficient to cover the entire frequency window of 40 – 100 Hz required for the resonators in different cryostats. The P-I control is designed with variable proportional gain of 0.01 to 2 and with variable time constant of 3 msec to 300msec. However, at the time of experiment, a time constant of ~ 100 msec is kept for the time response of the piezoelectric actuator. The block diagram of P-I control is given below in figure 7.

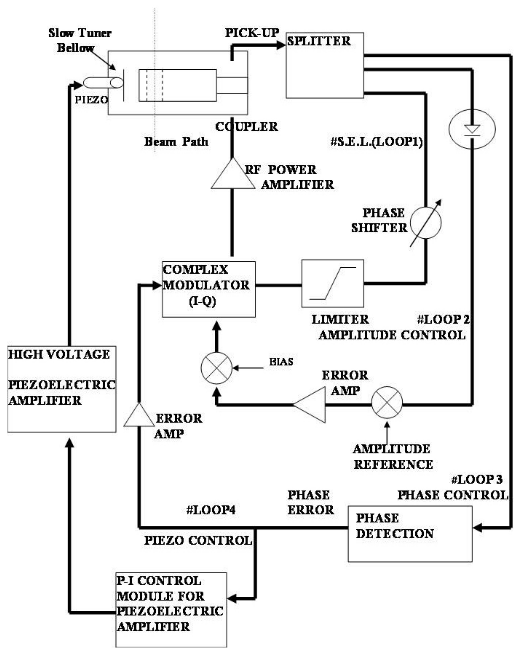


Figure 6: Block diagram of Piezoelectric close loop control scheme.

During the first test of a superconducting resonator in test cryostat along with the fast tuner and piezoelectric actuator acting as slow tuner, the overall locking mechanism worked very well. In this test, no mechanical arrangement for course tuning was available to tune the resonator frequency at 97.000 MHz. At a resonance frequency of 96.920 MHz, piezoelectric was kept at + 40 Volts to keep the phase error signal equal to zero by adjusting the reference of the P-I control. Then the control of phase and amplitude was put in close loop. It was observed that for both, large and small variation of resonance frequency from its central value, the piezoelectric voltage was kept on varying between a few volts to tens of volts. When the cryostat was banged to generate large vibrations, the resonator's frequency started fluctuating widely (>100 Hz), the controller drew lot of power (>250-300 watts) from RF amplifier and eventually the phase lock was broken. But within 5–10 seconds, the lock was recaptured with the help of piezoelectric tuner. During this extreme operation, the output from the high voltage amplifier to the piezoelectric actuator had gone up to a few tens of volts. The stability of the lock was observed for an hour at a moderate accelerating field of 2.2 MV/m. The amplitude and phase lock stabilities were measured to be 0.1% and ±0.4 degree respectively at this field level. The resonator was locked at 3.0 MV/m for a short duration, but due to lack of time, stability test at this field could not be accomplished for longer period.

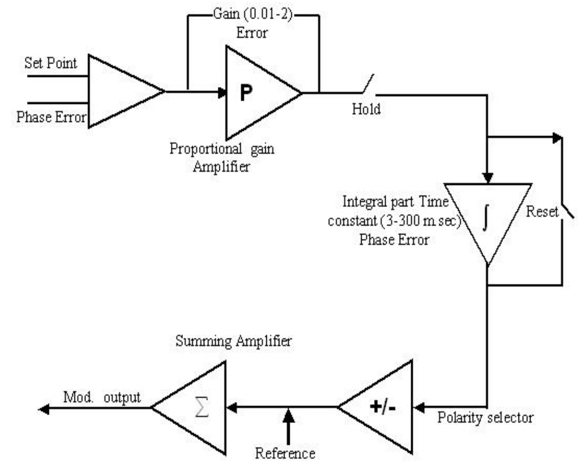


Figure 7: Block diagram of P-I control of piezoelectric actuator.

## CONCLUSION

Piezoelectric actuator based control scheme was demonstrated successfully to lock the phase and amplitude of the superconducting resonators of IUAC. A mechanical tuning mechanism with the piezoelectric actuator is under construction and will be tested along with the piezoelectric and the fast tuner in future. The mechanical tuning scheme, if required, can be integrated in the closed loop. After successful test of the new tuning and locking mechanism, it will be implemented on the resonators in all the resonators of linac.

## ACKNOWLEDGEMENT

Authors would like to acknowledge the help and cooperation received from the cryogenic group and resonator fabrication group of IUAC.

### REFERENCES

[1] S. Ghosh et al, Proc of tenth European Particle Accelerator Conference held during 23-27 June 2008 in Genoa Italy, page – 856.
[2] A. Roy, Proc. of this conference, TH202
[3] G. Joshi et al. Pramana, J. of Physics, Vol. 59, No.6, Dec 2002, page – 1035
[4] PI system product catalogue, http://www.pi.ws

# SUCCESSFUL QUALIFICATION OF THE COAXIAL BLADE TUNER

Angelo Bosotti, Carlo Pagani, Nicola Panzeri, Rocco Paparella, INFN/LASA, Segrate (MI)
Clemens Albrecht, Rolf Lange, Lutz Lilje, DESY, Hamburg
Jens Knobloch, Oliver Kugeler, Axel Neumann, BESSY GmbH, Berlin

*Abstract*

Cavity tuners are needed to precisely tune the narrow-band resonant frequency of superconducting cavities. The Blade Tuner is installed coaxially to the cavity and changes the resonator frequency by varying its length. Piezoceramic actuators add dynamic tuning capabilities, allowing fast compensation of main dynamic instabilities as Lorentz Forces, under pulsed operations, and microphonic noise. A prototype piezo Blade Tuner has been assembled on a TESLA cavity and extensively cold tested inside the horizontal cryostats CHECHIA (DESY) and HoBiCaT (BESSY). Then, as suggested by test results, few modifications have been implemented thus achieving the current Blade Tuner design. The introduction of thicker blades re-distributed along the circumference allows increasing its stiffness and fulfilling European and American pressure vessel codes, while ensuring the requested performances at the same cost. The paper will present the successful characterization tests performed on the prototype, the extensive mechanical analyses made to validate the final model and the results from qualification tests of first revised Blade Tuner produced, to be installed in the second module of ILCTA at FNAL.

## PROTOTYPE TESTS

The blade tuner working principle is to transfer azimuthal rotation, provided by a stepper motor into longitudinal motion by means of bending blades [1]. The device that has been tested inside CHECHIA and HoBiCaT is an enhancement of the TTF superstructures tuner, where the design has been simplified in view of the ILC requests, and completed with the insertion of the piezo for dynamic tuning operations.

Two prototypes of this device have been realized, one made from Titanium and the other from Stainless Steel (SS) with Inconel blades. The two new tuners where first tested at LASA at room temperature to check mechanical properties: after these tests we decided to use the SS – Inconel tuner for cold tests [2,3].

The first cold test inside horizontal cryostats has been performed, inside CHECHIA, at DESY, in pulsed RF regime. Then two other test sessions with CW RF have been done inside HoBiCaT, at BESSY. The tuner has been installed at DESY on the Zanon n°86 cavity (Z86), using a modified He tank, with the insertion of a central bellow, to allow for coaxial tuning operation. For the CHECHIA test, a stepper motor from Sanyo inc. has been installed, equipped with an harmonic drive component set. Two low-voltage, multilayer piezo from Noliac, 40 mm long and with 10x10 $mm^2$ cross section, have been installed as active elements.

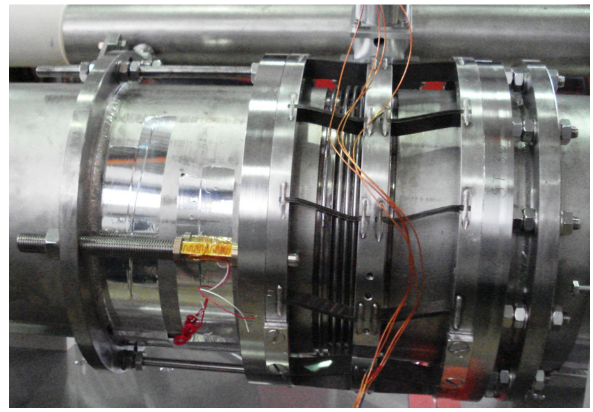

Figure 1: The Blade Tuner completely installed before cold test at BESSY; piezo actuators are in place and preloaded. The central bellow is also visible.

The correct preload to the piezo is given using the screws connected to the piezo supports. The goal pre-load value, about 1.5 kN on each piezo, is reached when the cavity is cooled at 2 K, taking into account all the cavity length changes, due to thermal contractions and pressure gradient sustained during the cooldown operation. During CHECHIA tests on September 2007, the entire Lorentz force detuning (LFD) shown by Z86 cavity at full gradient, about 300 Hz, has been successfully compensated in different load conditions. This was achieved using just one piezo, fed with one third of the nominal maximum driving voltage.

After the test in pulsed regime at DESY, the tuner was transferred to BESSY, to be tested from February to April 2008, inside the CW facility HoBiCaT. A Phytron stepper motor, provided with a planetary gear box, has been used in place of the former Sanyo stepper motor with harmonic drive gear (40000 half-steps per complete spindle turn instead of 35200). It must be remarked that this configuration was used for the first time for this application.

Among several other parameters (working point tuning range, piezo actuator DC tuning range, transfer functions and loading effect analyses), the whole tuning range has been extensively measured [2,3]. All the measurements are summarized in Figure 2, proving that the slow tuning performances meet expectations.

The cold tests inside CHECHIA and HoBiCaT facilities certified that the coaxial Blade Tuner has successfully overcome the prototype phase, providing a lot of useful information to optimize its design.

More than the required 600 kHz of tuning range has been achieved (Figure 2), with a tuning sensitivity of 1.5 Hz/half-step. The hysteresis of the first load cycle in the former test inside CHECHIA (red curve) has been almost cancelled in the successive cycles.

A static frequency shift of 5 kHz has moreover been obtained driving the piezo up to their maximum DC voltage, therefore a great margin for the active compensation of dynamic LFD is ensured also for high gradient pulsed operations [3].

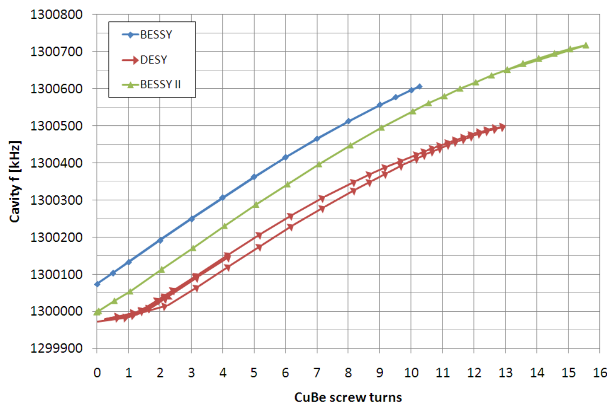


Figure 2: Tuning range tests in CHECHIA and HoBiCaT.

## FINAL TUNER DESIGN

In view of the construction of eight tuners to be installed in the new ILCTA_NML test facility, few modifications have been introduced allowing to increment the tuner strength and stiffness, in order to satisfy the requirement recently set by the XFEL project in terms of pressure vessels regulations. Taking into account all the possible load cases, both in work condition, transitory phases and accidental overpressures, the Blade Tuner is required to withstand at least 10.9 kN compressive load and 13.8 kN tensile load [4].

Moreover, the load acting on the tuner is applied in only two points, therefore breaking the original symmetry and over-loading the blades closer to the piezo position. The weight reduction has amplified the problem, therefore a non uniform distribution of the blade packs was introduced in order to avoid it. The final design has 2 packs of 4 blades, each positioned as near as possible to the piezo position, while 5 packs of 3 blades each are equally distributed along the remaining free space. Globally, 23 blades are used on 180° for a total of 92 blades on the whole tuner, 4 less than the previous design.

The actual configuration is reported in Figure 3. Moreover the need to increase the axial strength due to the requirement of the XFEL certification tests lead to thicker blades whose thickness is now increased from 0.5 mm to 0.8 mm. All these modifications have also a positive consequence on the stiffness of the tuner that now is higher than 30 kN/mm in almost the entire tuning range

Some finite elements analyses have been performed in order to simulate all the possible load cases and working conditions to which the tuner will be subject. This analytical model also allows obtaining the stresses in the tuner rings, blades, bolts and driving shaft [4].

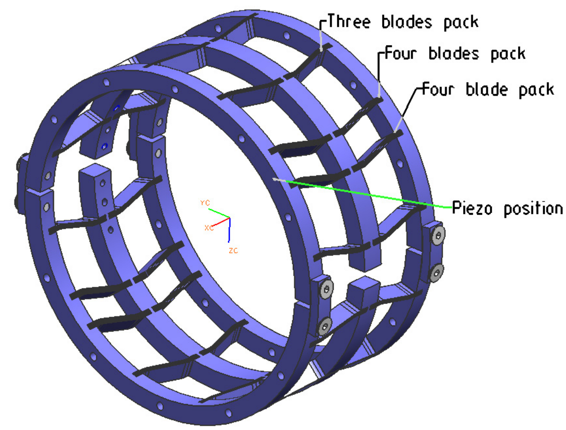


Figure 3: Improved blade tuner design with the upgraded blade positions and distribution.

For what concerns the compression load, the analyses account for the preload on the piezo, the moving of the tuner up to the maximum tuning range and an additional load growing up until the tuner collapse: a collapse load of 12.5 kN is achieved, higher than the required limit.

The tensile limit load has been determined applying four forces to the point corresponding to the safety bars. These are the elements that allow the force transfer between the helium tank and the tuner. For a traction force of 16 kN some plastic strains occurs in the blades, therefore this can be considered as the limit traction load, higher than the required one of 13.8 kN.

Finally, the force acting on the driving threaded spindle has been considered and used to evaluate the motor requirements. Given the piezo preload value, the tuner position and the friction (efficiency coefficient $\eta = 0.159$) the total maximum torque required is equal to 3.0 Nm. As a reference, a Phytron 2.5 A motor equipped with a 1:100 gearbox and operated at 1 A current is still able to drive the tuner with great margin, generating a nominal torque value of 12 Nm.

In conclusion, the final Blade Tuner design fulfils the requirements set by the XFEL and ILC projects both in terms of structural strength and tuning capabilities [4].

## ILCTA BLADE TUNER VALIDATION

A set of eight Blade Tuner units have been manufactured by Ettore Zanon S.p.A. (Italy) for CM2 and will be installed in the next months at the FNAL test facility ILCTA_NML (see Figure 4).

With the delivery of the eight units, an accurate process of validation started. It includes both a visual and dimensional check for all components and an experimental test procedure at room temperature based on an ad-hoc single cell test facility realized at LASA laboratory. At the time of writing the evaluation is not finished for all the devices and although the room temperature (RT) testing poses some limitations to the maximum displacements and forces to be applied (plastic strains can occurs in the blades from the $12^{th}$ screw turn), the tested models fulfill our expectations.

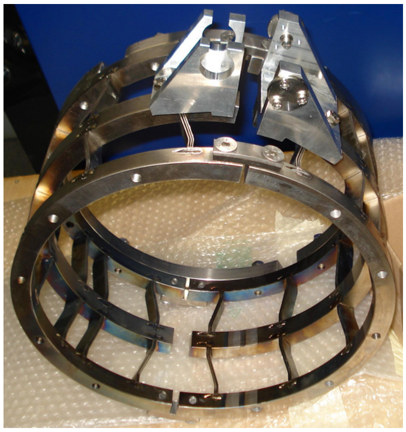

Figure 4: One of the Blade Tuner manufactured for ILCTA_NML facility at Fermilab.

The tuning range has been measured up to 11 turns of the driving screw, the maximum displacement safely achievable at RT. Experimental data are reported in Figure 5 and compared to the FEM simulations results.

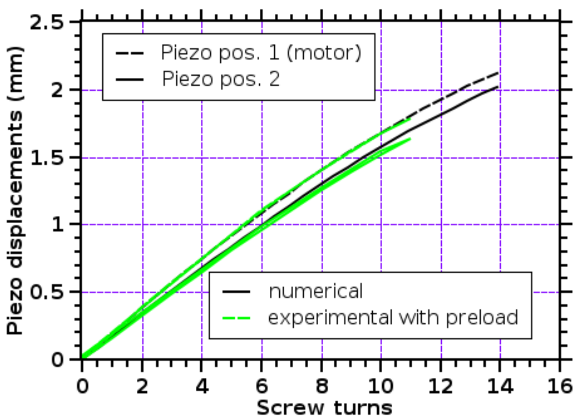


Figure 5: Tuning range results for ILCTA tuner, experimental vs. simulation at room temperature.

The strength of the Blade Tuners has also been verified applying a compressive load of 10 kN to the tuner, the maximum allowed in our test facility to safely operate it at room temperature. Results of this compressive load test are reported in Figure 6.

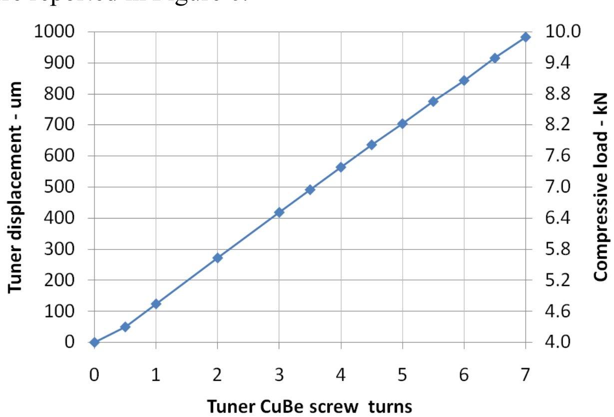


Figure 6: Compressive load test on ILCTA tuner

Moreover the tuner stiffness was evaluated in operative conditions, i.e. when the load is transferred through the piezo elements to the cavity. Also in this case the experimental results are positive, confirming the numerical simulation data where the estimated stiffness is greater than 30 kN/mm on the almost entire tuning range.

## CONCLUSIONS

After the cold tests inside CHECHIA and HoBiCaT facilities, it is possible to say that coaxial Blade Tuner has successfully passed the prototype test. More than 600 kHz of tuning range has been achieved at cold, with a total load of about 7 kN, successfully withstood by the tuner with no failure. Pulsed tests inside CHECHIA have shown the tuner high effectiveness in LFD compensation, this latter confirmed in the CW tests driving the piezo with DC voltages up to 200 V, where a static frequency shift superior to 5 kHz has been obtained. The analyses of the results allowed us to implement few improvements that have a significant impact on the strength and stiffness of the device. The new design fulfils the requirements set by the XFEL and ILC projects both in terms of structural strength and tuning capabilities.

This last version has been manufactured in eight units by Ettore Zanon S.p.A. (Italy) and will be installed in the next months at the FNAL test facility ILCTA_NML. Produced units have meanwhile been involved in a detailed acceptance test procedure at room temperature, still ongoing.

First results obtained confirm that their performances in terms of tuning range, hysteresis, stiffness and load bearing capability meet our expectations.

## ACKNOWLEDGMENTS

This activity has been partially supported by the EC-Research Infrastructure Activity under the FP6 "Structuring the European Research Area" program (CARE, contract number RII3-CT-2003-506395).

## REFERENCES

[1] D. Barni, A. Bosotti, C. Pagani, R. Lange, H.B. Peters, “A New Tuner For TESLA”, Proceedings of EPAC2002, Paris, France, p. 2205.
[2] A. Bosotti, C. Pagani, N. Panzeri, R. Paparella, “The Coaxial Blade Tuner – Final Report and Evaluation of Operation”, SRF CARE Report, 2008
[3] C. Pagani, A. Bosotti, N. Panzeri, R. Paparella; J. Knobloch, O. Kugeler, A. Neumann; C. Albrecht, K. Jensch, R. Lange, L. Lilje; “Full characterization of Piezo Blade Tuner for superconducting RF cavities”; Proceedings of EPAC 2008, Genoa, Italy
[4] C. Pagani, A. Bosotti, N. Panzeri, R. Paparella; “The Coaxial Tuner for ILCTA_NML at Fermilab”; Proceedings of EPAC 2008, Genoa, Italy.

# THIRD HARMONIC SUPERCONDUCTING CAVITY PROTOTYPES FOR THE XFEL

P. Pierini*, A. Bosotti, N. Panzeri, D. Sertore, INFN LASA
H. Edwards, M. Foley, E. Harms, D. Mitchell, FNAL
J. Iversen, W. Singer, E. Vogel, DESY

*Abstract*

The third harmonic cavities that will be used at the injector stage in the XFEL to linearize the bunch rf curvature distortions and minimize beam tails in the bunch compressor are based on the rf structures developed at FNAL for the DESY FLASH linac. The design and fabrication procedures have been modified in order to match the slightly different interfaces of XFEL linac modules and the procedures followed by the industrial production of the main (1.3 GHz) XFEL cavities. A revision of the helium vessel design has been required to match the layout of the cryomodule strings, and a lighter version of the tuner has been designed (derived from the 1.3 GHz ILC blade tuner activities). The main changes introduced in the design of the XFEL cavities and the preliminary experience of the fabrication of three industrially produced and processed third harmonic rf structures are described here.

## INTRODUCTION

The RF cavity design for the 3.9 GHz structures [1] has been performed by FNAL for the design of the FLASH 3rd harmonic section (ACC39) [2,3]. Several cavities have been fabricated and tested [4] with accelerating gradients up to 24 MV/m, well above the design value of 14 MV/m needed for the FLASH operation.

The design of the European XFEL project [6] foresees a third harmonic section in the injector linac, at the beam energy of 500 MeV, before a bunch compression stage.

Three modules of 8 cavities are currently envisaged in the XFEL TDR to provide a sufficient linearization of the RF field seen by the bunch [3].

In the context of the XFEL activities the production of three prototypical cavities of the FNAL design has been tendered to one of the qualified producers of the main linac RF structures, including the responsibilities for the subsequent processing needed before the vertical testing (BCP chemical etching and high pressure rinsing stages). Fabrication is ongoing and, although no changes have been performed to the RF characteristics of the cavities as designed by FNAL, a few interfaces have been modified in order to either profit from existing components developed for the 1.3 GHz cavities (HOM pickup antennas, RF pickups, slim blade tuner design) or to reflect the different physical layout of the cross section of the XFEL cryomodules. In addition, the production process has been revised and adapted to the consolidated vendor experience based on the production of the 1.3 GHz cavities.

* paolo.pierini@mi.infn.it

## XFEL CRYOMODULE LAYOUT

### *Type II and Type III Cryomodules vs XFEL*

The FLASH linac, previously known as the TESLA Test Facility, TTF, is currently composed of cryomodules of two types, with different cryogenic piping locations within cross-sections of different sizes. The changes were performed in "generations" after successive iterations aimed at design simplification and cost reduction [7]. Currently Type II and Type III cryomodules are located in the linac tunnel. The first accelerating section of the FLASH linac (ACC1), after which ACC39 will be placed, is of Type II, meaning a large vacuum vessel (1.2 m diameter) and an internal piping distribution different than in the standardized 38" vessel of the Type III. Since ACC39 is cryogenically connected to the ACC1, the transverse cross section of the FNAL module has been designed to match that of a Type II.

However, the XFEL module design has been derived from the Type III, in particular concerning the relative location of the He Gas Return Pipe (HeGRP, acting as a structural backbone for the entire cold mass), the 2-phase He pipe and the cavity string.

The XFEL third harmonic cryomodules, which are in the early design stage, need to reflect this change in the cross-section and, in particular, the ACC39 design of the dressed cavity package (cavity+He tank and 2 phase pipe) needs to be revised to account for these different interfaces.

### *Main Couplers Orientation*

Beam dynamics simulations of the entire XFEL linac suggests that, in order to obtain an on-axis cancellation of the RF coupler kicks, an alternating scheme for the coupler direction different from ACC39 needs to be used to limit emittance growth effects [8, 9]. This again has implications on the module design and requires the use of two types of dressed cavity assemblies, according to the coupler direction.

### *Slim Blade Tuner*

The coaxial tuner used on the FNAL ACC39 module has been derived from the INFN blade tuner originally proposed for the TESLA collider [10], scaled to the smaller size of the 3.9 GHz RF structures. Recent progresses at INFN on the blade tuner concept for ILC led to the development of a simpler, lighter and cheaper device, that has been extensively characterized [11]. Slim tuners of this kind will be installed in the second FNAL ILCTA cryomodule currently under construction.

For the XFEL third harmonic activities the “slim” tuner design has been scaled to the 3.9 GHz cavity dimensions.

Due to the much stiffer mechanical behaviour of the 3.9 GHz structures and the moderate accelerating gradients needed for their operation, no fast compensating tuning action is needed to handle Lorentz Force Detuning effects under pulsed operation.

Figure 1 shows a cavity, dressed with tank and tuner, located within the main boundaries of an XFEL main linac module cross-section.

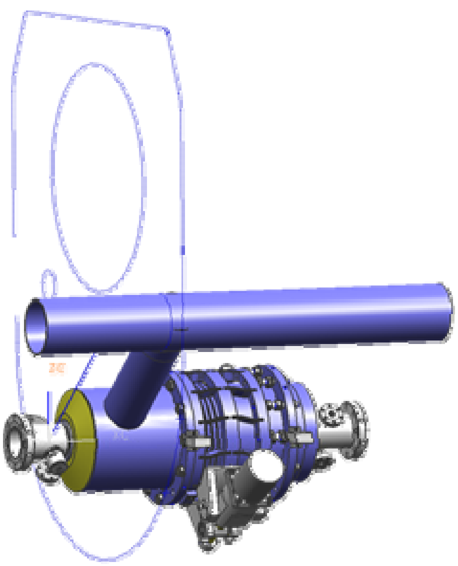

Figure 1: The XFEL third harmonic cavity dressed with the revised “slim” tuner, shown in the transverse cross section of the XFEL cryomodule (indicating HeGRP, 2 phase line and inner 4 K shield).

Work on the definition of a possible layout of the XFEL third harmonic cryomodules has just been started, along the guidelines expressed before. The final XFEL design will benefit from the many years experience gathered during the operation of the FLASH modules and from the ongoing FNAL ACC39 development.

The current XFEL third harmonic module foresees a string of eight cavities, a quadrupole/bpm package and an HOM beamline absorber, for a total module slot length of approximately 6 meter.

## PROTOTYPE XFEL CAVITY FABRICATION

### *Mechanical Design Changes*

Three nine cell cavities using the single-leg HOM coupler developed by FNAL [12] are currently under fabrication in Europe for the XFEL. A few variations have been made to the fabrication drawings or production steps in order to conform either to ancillaries developed for the XFEL (like HOM antennas and RF pickups) or to the consolidated expertise of a qualified vendor of the main linac structures:

- All the Conflat flanges in the original design of the cavity for the HOM antennas and RF pickups have been replaced with the same flanging system of the main linac (based on Al “diamond seals”). The same standard feedthrough components of the main XFEL linac for the HOM antenna pickup assemblies or the RF pickup will be used.
- In order to perform the last 9 equatorial welds in a single load of the Electron Beam Weld (EBW) machine, the end cones inclination of the tank has been changed, allowing access from the fixed electron beam gun to the end cells equatorial region. Weld lips have been machined at the equatorial plane of the cells, in order to ease the assembly process and to avoid the use of a temporary tooling to tack the assembly before performing the final EBW equatorial seams. Weld lips should also decrease the chance of niobium droplets from the EBW seam deposited on the RF surface.
- Similarly to what is being done for the XFEL 1.3 GHz cavities, alignment boreholes were placed on the cavity flanges to transfer the cavity alignment reference. A reference ring and plane are also machined at the cone transition in the end groups to assist mechanical survey.

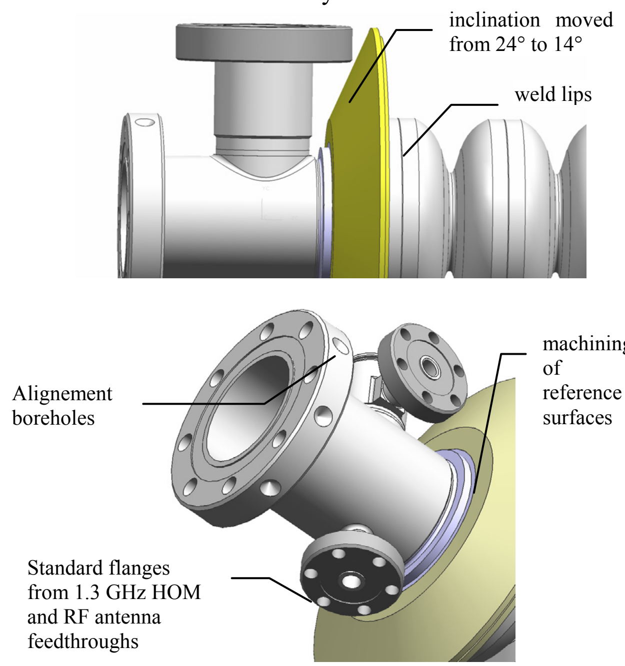


Figure 2: End group of the XFEL 3rd harmonic cavities (coupler side), showing some of the modifications.

### *EBW Parameters*

Batches of non RF-grade high RRR Nb provided by DESY, discarded after the sheet scanning QA process, have been used to fabricate an initial series of halfcells, then dumbbells, double dumbbells and end groups in order to determine the correct EBW parameters and toolings needed, and to experimentally determine the weld shrinkages to be taken into account in the fabrication drawings.

Figure 3 shows some of these parts during RF characterization. Halfcells and dumbells thus obtained were used to determine the experimental frequency coefficients for the trimming operations that need to be performed at the dumbbell stage and the effect of weld seams. This information is used to develop a consistent procedure, following closely that of the 1.3 GHz cavity fabrication, in order to meet the correct physical length and nominal frequency of the cavities. A field flatness tuning device to axially stretch or compress the individual cells is also being developed.

Figure 3: Equatorial weld lip preparation of the dumbbells (left) and samples (right) for equatorial EBW parameters.

### *RF Characterization of Subcomponents*

During the realization of the test parts using non RF grade Nb all the machining and welding tooling were debugged and improved when necessary. Frequency sensitivity coefficients were experimentally determined and compared with RF simulations. As an example Figure 4 shows the trimming sensitivity of the first series of 6 dumbbells produced. In the first 4 weld operation the spring load of the weld tooling caused excessive weld shrinkage of the structure, resulting in a global frequency offset. Nonetheless, the average longitudinal trimming sensitivity of -25.7 MHz/mm closely matches the value compute from SuperFish simulations (-24.7 MHz/mm).

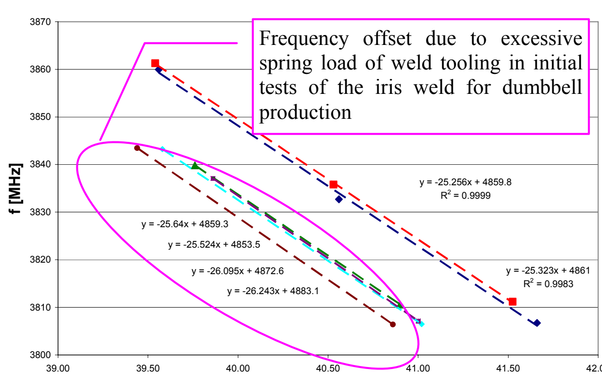


Figure 4: Frequency sensitivity for dumbbell trimming.

### *Status of the Prototype Fabrication*

After the weld tests performed to determine all weld parameters the three RF structures are now being fabricated. All main subcomponents have been prepared. All the production halfcells have been formed and their frequency spread is consistent with the achievable tolerances of the production process. Dumbbells and the main end group subassemblies are in the preparation stage. After the final trimming of the dumbbells to achieve the correct cavity length and frequency the final equatorial welds will be performed.

A copper RF mockup of the nine cell structure is under fabrication to test the field flatness measurement device under realization, and to provide a mechanical mockup for the test of the vertical inserts designed at INFN for the RF measurement of the cavities.

## CONCLUSIONS

The development of the main components of the superconducting 3.9 GHz system for the XFEL linac has started at INFN and DESY, and is relying on the extensive experience in the production of the main linac cavities and cryomodules and on the activities carried by FNAL for the FLASH ACC39 construction.

## REFERENCES

[1] N. Solyak et al., "Development of the third harmonic SC cavity at Fermilab", Proceedings of the PAC2003, Portland, Oregon, p. 1213.

[2] E. Harms et al., "Status of 3.9 GHZ Superconducting RF Cavity Technology at Fermilab", THP028.

[3] E.Vogel et al., "Status of the 3rd Harmonic Systems for FLASH and XFEL in Summer 2008", contribution TUP034, this Conference.

[4] T. Khabiboulline et al, "Vertical and horizontal test results of 3.9 GHz accelerating cavities at FNAL", in Proceedings of EPAC08, Genova, Italy,

[5] E. Harms et al. "Performance of 3.9-GHZ Superconducting Cavities", THP029.

[6] 'The Technical Design Report of the European XFEL', DESY Report DESY 2006-097 (July 2006), available from http://xfel.desy.de

[7] J. Weisend et al., "The TESLA Test Facility (TTF) Cryomodule: A Summary of Work to Date", Advances in Cryogenic Engineering, 45, Plenum Press, New York, 2000, p. 825.

[8] E. Vogel et al., "Considerations on the third harmonic rf of the European XFEL", Proceedings of the 13th International Workshop on RF Superconductivity, Beijing, 2007.

[9] M. Dohlus, private communication, material also available from the FEL Beam Dynamics Seminars, http://www.desy.de/xfel-beam/index.html.

[10] D. Barni, A. Bosotti, C. Pagani, R. Lange, H.B. Peters, "A New Tuner For TESLA", Proceedings of EPAC2002, Paris, France, p. 2205.

[11] A. Bosotti et al., "Full Characterization of the Piezo Blade Tuner for Superconducting RF Cavities", in Proceedings of EPAC08, Genova, Italy, p. 838.

[12] T. Khabiboulline, I. Gonin, N. Solyak, "New HOM Coupler Design For 3.9 Ghz Superconducting Cavities At FNAL", Proceedings of PAC2007, Albuquerque, p. 2259.

# DEVELOPMENT OF INSPECTION SYSTEMS FOR SUPERCONDUCTING CAVITIES

Yoshihisa Iwashita, Kyoto ICR, Uji, Kyoto
Hitoshi Hayano, Ken Watanabe, KEK, Ibaraki, Japan

*Abstract*

Development of inspection systems including high resolution camera for inner cavity surface, thermometry system for a cavity outer surface, and Eddy current scan for bare Nb plates are described. The cavity camera system revealed undiscovered defects at the inner sides of the locations predicted by passband-mode and thermometry measurements. A thermometry measurement system and an eddy current scan system are under development.

## INTRODUCTION

Inspections of superconducting (SC) RF cavities seem essential in achieving high accelerating gradient. The inspection of the interior surface with high enough resolution to find defects more than several tens microns is achieved by our high-resolution camera system. This system revealed undiscovered defects at the inner sides of the locations predicted by passband-mode and thermometry measurements (see Fig. 1)[1]. This system will help to improve cavity fabrication processes and their yield. We are planning to widen our activity in this field: developments of a new thermometry system with easy installation and less cabling, and high sensitivity eddy current surface inspection system for bare Nb sheets. The detailed systems and some preliminary data obtained from the systems are presented.

## HIGH RESOLUTION CAMERA

This high-resolution camera system is developed to search the defects and measure the shape of them for better yield of accelerating gradient of SC 9-cell cavities. As shown in Fig. 2, a black cylinder with EL (ElectroLuminescence) sheet as an illuminator on it having a camera inside is inserted into a cavity. The camera directs to the cylinder head and looks a reflected image of the cavity wall on a mirror installed in front of the camera [1]. The improvement of this system has been performed for the industrialization toward worldwide delivery. Figures 2-6 show the production model of our inspection system. The improvement points are listed as follows:

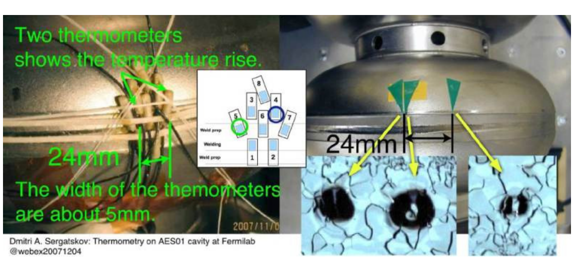


Figure 1: Positions of the two hot spots found at FNAL (left) and those found at Kyoto (right). The inset of left figure shows the location of the thermometers. The two thermometers (#4 and #5) that showed abnormal temperature rise are marked. (Courtesy of FNAL/JLAB.)

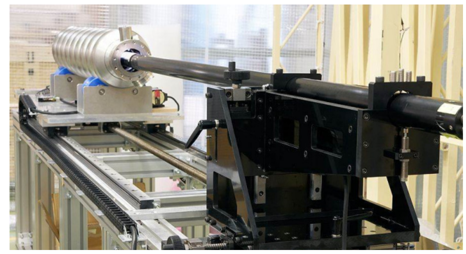

Figure 2: Production model of the inspection system.

1) The width of EL strip illumination is reduced from 10 mm to 7 mm for a better resolution in the shape measurement (see Fig. 3).
2) The EL illuminator is separated from the pipe unit, and all the electric wirings from the module are though two connectors for an easy replacement; its life may be up to a few thousand hours.
3) The EL illuminator unit slides with the mirror angle to keep the peephole on the sight line of the camera (see Fig. 4).
4) The half mirror for the coaxially illuminating LED is located before the tilting mirror to keep the illuminating direction and the sight line of the camera the same at any tilting angle.
5) The head assembly including the EL illuminator and mirror units is demountable from the camera cylinder. This modular structure also helps its maintenance. (see Fig. 5)
6) The camera lens is accessible by removing the head assembly and sending the camera all the way out. The magnification or even the lens itself can be changed at this position.
7) The damper against the vibration of the camera cylinder is installed on the cylinder support.
8) Better interface for the lighting control: each EL strip can be independently turned on/off. Any lighting pattern can be rotated right and left at a rate of about 2 Hz (see Fig.6).
9) The cavity table is retractable for easy shipping.

Figure 3: New EL stripe illuminator. The strip width is reduced from 10 mm to 7 mm; hence, the number of strips increases from 14 to 20. The camera looks through a peephole located at the center of strips.

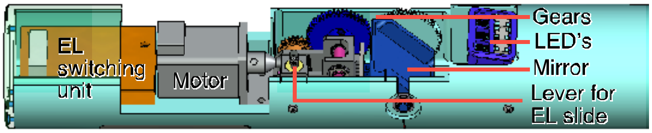


Figure 4: The new head assembly. The mirror is tilted by the pulse motor to change the sight line. Coaxially illuminating LED's located before the mirror enable us to observe a surface normal to the sight line of the camera at any mirror angle, where the EL strip is absent for the peephole. The EL sheet slides with the mirror angle by a lever to keep the peephole on the sight line.

Figure 5: The camera and new head assembly. They can be easily separated and all the electrical connections are through the pins, which makes the assemblage and maintenance easy. Left: Camera cylinder. Right: Head assembly.

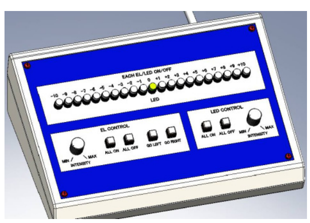

Figure 6: The EL controller box.

We are trying to track the cavity surfaces throughout the surface processes at STF with this camera to evaluate the correlation between the surface conditions and the hot spots quenching during vertical tests. This information will help to screen out bad cavities at early stages of the production line of the cavity. Figure 7 shows typical pictures of inner surface of before and after the electropolishing (EP) process taken by this camera system. It shows that the grain boundary becomes eminent with the EP process. Measurement of the shape of bosses or pits with the stripe illumination is not available before the first EP because the surfaces are not shiny. Preliminary results for AES001 and Zanon111 show bosses or pits of a few hundreds μm in diameter and a few tens μm around the hot spots at low accelerating gradients (Fig. 1). Further observations of many cavities will increase the statistics and clarify the correlation.

## THERMOMETRY SYSTEM

A thermometry measurement is a good tool for finding defects on the insides of superconducting cavities. It measures a temperature map of outer surfaces of the cavity under application of RF power during the horizontal

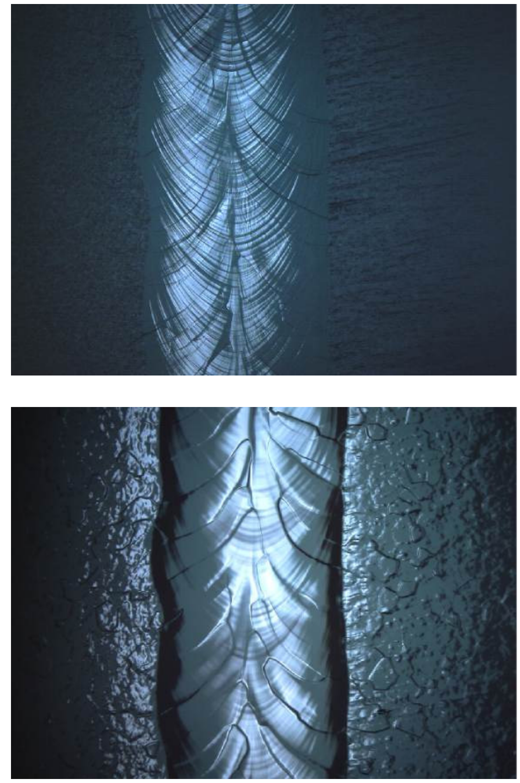

Figure 7: The inner surface (EBW seam) of SC cavity before (top) and after EP process (bottom, 125 μm removed.). The picture size is 13 mm x 9 mm.

test. Suppose that the total surface area is in the order of 1 $m^2$, and the spacing between the temperature sensors is 1 cm in both longitudinal and azimuthal directions, $10^4$ sensors are needed for a system. These massive signals have to be extracted from the cold region. Cabling such signals with separate wires will make the number of wires enormous, which increases the heat intrusion to the cold area and their installation becomes complicated.

The temperature sensors should have high sensitivity at the low temperature. Figure 8 shows a measured result of resistances of typical Ruthenium oxide based thick film resisters at low temperature regions. Although not many data points are available, they show high sensitivity at cryogenic temperature. In this experiment, the 10 kΩ resistor shows higher sensitivity than the 1 kΩ. This kind of device seems promising for the thermometry system because of its availability and low cost [2].

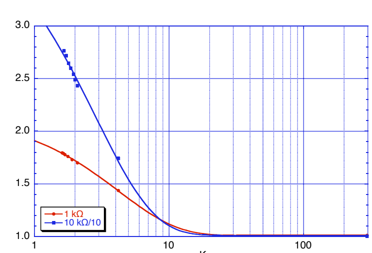


Figure 8: Measured resistances of 1kΩ and 10kΩ chip resisters as a function of temperature. The fitting curves are just guides for eyes.

Although many of circuit components do not work at the 2K regime, digital CMOS circuits such as inverters and analog switches worked fine in a preliminary test [3]. An 8-to-1 analog multiplexer (74HC4051) built from these elements should work at this temperature. Using these devices, we can construct a 512-to-1 multiplexer combining 512-sensor signals into one. The number of wires to be supplied would be eight for this system: three power supply lines, two output lines, two addressing lines and a ground line.

Installation of the sensors would be simplified by a concept shown in Fig. 9. The devices are mounted on a flexible printed circuit board (PCB). The resistive sensors are located on each separated strip (see Fig. 10) while the analog multiplexers are mounted at the common area (see Fig. 11). The sensors are mounted on the facing side of the PCB and pushed against the wall surface by squeezing the strip at the neck (see Figs. 10, 12). Because it was confirmed that the flexible PCB does not loose its flexibility at 77 K, it is supposed to hold the property even at 2 K. Further preliminary tests are under preparation. Since the density of the sensors on the cell is not enough, other PCB layout will be developed later to raise the sensor density.

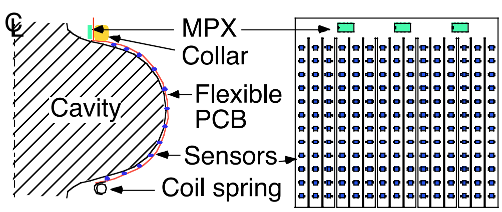


Figure 9: Conceptual sketch of an easy installation of sensors. The sensors are mounted on a flexible PCB that is wrapped around the cavity cell.

## EDDY CURRENT SCAN

Screenings of bulk Nb plates at the beginning would help to reduce the defects on the inner surfaces of cavities. This step has to be carried out before making the cups. We are seeking to use a special high-resolution eddy current scan for that purpose [2]. By setting exciting field perpendicular to the detecting coil, a detecting coil does not magnetically couple to it and only the disturbances from defects on the specimen surface are detected. Two excitation coils 90° rotated each other around the normal axis to the specimen surface with 90° excitation current will generate a rotating field and the detecting capability will be raised (see Fig. 13). About 0.1 mm diameter hole with 0.1mm depth can be detected so far.

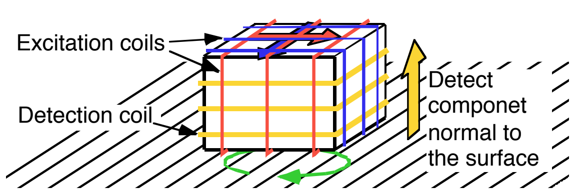


Figure 13: Excitation coil configuration. They generate a rotating magnetic field on the specimen surface.

Figure 10: The flexible PCB

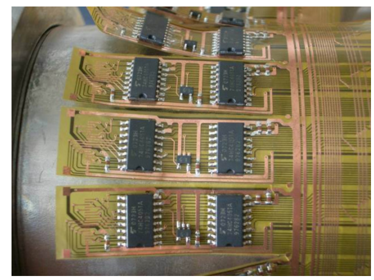

Figure 11: Analog multiplexers mounted on a demonstration setup.

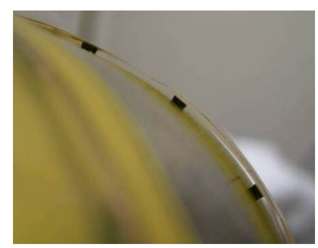

Figure 12: Sensors mounted on a flexible PCB are pushed against the wall surface.

## ACKNOWLEDGEMENT

The base model of the camera system was developed by Mr. Y. Tajima who is working for Toshiba Corporation after his graduation from Kyoto University. The authors thank Dr. H. Sato at RIKEN for his letting us to perform the low temperature experiments at RIKEN, Wako. The high-resolution eddy current sensors are developed by Dr. Hiroshima at Theta-Technology and Mr. Nakano at Hokuto Electronics.

## REFERENCES

[1] Y. Iwashita, Y. Tajima, and H. Hayano: Development of high resolution camera for observations of superconducting cavities, Phys. Rev., Special Topics Accelerators and Beams, **11**. 093501 (2008). http://prstab.aps.org/abstract/PRSTAB/v11/i9/e093501

[2] SCRF Meeting at FNAL, Monday 21 April 2008, http://ilcagenda.linearcollider.org/getFile.py/access?contribId=4&sessionId=5&resId=6&materialId=slides&confId=2650

[3] Michael Mück, Matthias Korn, C. G. A. Mugford and J. B. Kycia, Cryogenic direct current superconducting quantum interference device readout circuit, Review of Scientific Instruments **76**, 074701 (2005)

# SC Nb SPUTTERED QWRs FOR THE REX-ISOLDE ACCELERATOR AT CERN: PROTOTYPE DESIGN AND MANUFACTURING

M. Pasini*, S. Calatroni, L. M. A. Ferreira, D. Ramos, T. Tardy, F. Thierry, P. Trilhe
CERN, Geneva, Switzerland


## Abstract

The HIE-ISOLDE activity aims to construct a superconducting linac based on 101.28MHz niobium sputtered Quarter Wave Resonators (QWRs), which will be installed downstream of the present REX-ISOLDE linac. The current design considers two basic cavity geometries (geometric $\beta_0$ = 6.3% and 10.3%) for which a mechanical and a chemical treatment and niobium coating design study has been performed. We report here on the status of the high $\beta$ prototype cavity and sputtering chamber.


## INTRODUCTION

In the framework of a general upgrade activity, named HIE-ISOLDE [1], of the Radioactive Ion Beams (RIBs) facility ISOLDE at CERN, a new superconducting linac based on QWRs (see Fig. 1) is planned [2]. Presently, the REX linac is delivering beams with mass to charge ratio of $3 \leq A/q \leq 4.5$ at a final energy of 3 MeV/u by means of a combination of several normal conducting structures. The energy upgrade will happen in two stages; in a first stage the final energy will be limited to 5.5 MeV/u while for the second stage the required final energy will be 10 MeV/u. The superconducting linac will also replace part of the normal conducting one so the energy span covered by the SC cavities will be between 1.2 and 10 MeV/u. In order to efficiently accelerate the beams in this velocity range two cavity geometries have been studied, one with a geometrical $\beta_0 = 6.3\%$ and the other with a geometrical $\beta_0 = 10.3\%$ (units are in % with respect of the speed of light). These values were optimized in order to allow an optimum acceleration efficiency for the heaviest A/q ratio (A/q=4.5).

## CAVITY RF DESIGN

For the electromagnetic simulation of the two cavity geometries the MWS [3] code was used. The design aims at minimizing the peak surface electric field to accelerating field ratio ($E_{\mathrm{pk}}/E_{\mathrm{acc}}$), and the peak magnetic field to accelerating field ratio ($H_{\mathrm{pk}}/E_{\mathrm{acc}}$). The actual optimization is a trade-off between the RF performances and a simple shape that is better suited for the Nb sputtering. Another important aspect for this type of cavity is the magnetic steering effect due to a non-negligible magnetic field component at the beam axis. A special race-track shape, of the beam port (see Fig. 2) has been designed in order to minimize this effect. The beam axis position is in fact not centered vertically but shifted upwards by 4 mm. The vertical component of the electric field can in fact compensate the effect of the magnetic field on the beam so that the remnant steering kick is less then 0.1 mrad. The nominal gradient required is 6 MV/m over an active length of 195 and 300 mm respectively for the low and high $\beta$ cavity. A residual resistance $R_s$ of 50 n$\Omega$ is considered as a normally achievable value [4]. All the main cavity parameters are listed in Table 1

* matteo.pasini@cern.ch

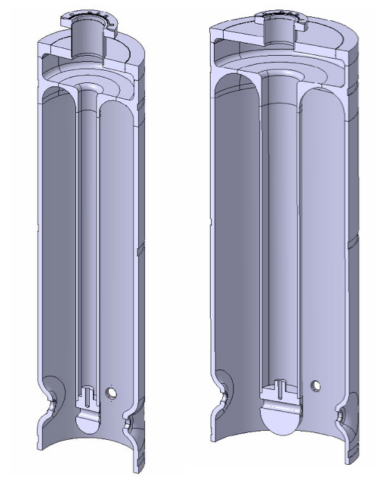

Figure 1: Low and high $\beta$ cavities.

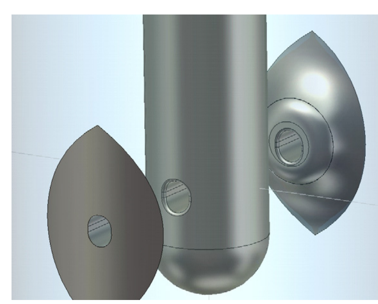

Figure 2: Details of beam port.

## CAVITY MECHANICAL DESIGN

The basic technological choice for the HIE-ISOLDE cavities lies in the use of the Nb/Cu sputtering technology [5] and [6]. Compared to bulk niobium cavities, copper ones can easily be made massive and stiff in order to reduce microphonics effects, and to prevent the deformations due to the mechanical actions of the tuning system,

Table 1: Cavity design parameters

| **Cavity** | **Low $\beta$** | **high $\beta$** |
|---|---|---|
| No. of Cells | 2 | 2 |
| f (MHz) | 101.28 | 101.28 |
| $\beta_0$ (%) | 6.3 | 10.3 |
| Design gradient $E_{acc}$(MV/m) | 6 | 6 |
| Active length (mm) | 195 | 300 |
| Inner conductor diameter (mm) | 50 | 90 |
| Mechanical length (mm) | 215 | 320 |
| Gap length (mm) | 50 | 85 |
| Beam aperture diameter (mm) | 20 | 20 |
| $U/E_{acc}{}^2$ (mJ/(MV/m)$^2$ | 73 | 207 |
| $E_{pk}/E_{acc}$ | 5.4 | 5.6 |
| $H_{pk}/E_{acc}$ (Oe/MV/m) | 80 | 100.7 |
| $R_{sh}/Q$ ($\Omega$) | 564 | 548 |
| $\Gamma = R_s \cdot Q_0$ ($\Omega$) | 23 | 30.6 |
| $Q_0$ for 6MV/m at 7W | $3.2 \cdot 10^8$ | $5 \cdot 10^8$ |
| TTF max | 0.85 | 0.9 |
| No. of cavities | 12 | 20 |

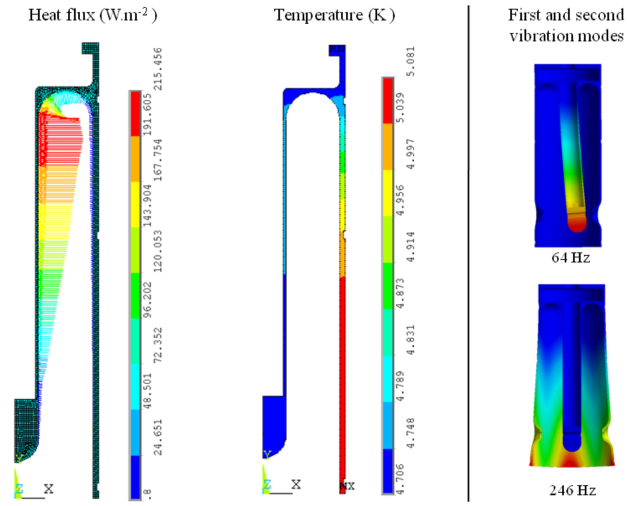


Figure 3: Heat flux input and resulting temperature distribution in the cavity, considering the thermal conductivity of copper RRR=100 and 4.5 K He I pool boiling cooling in convection and nucleate boiling regimes. First and second vibration mode shapes and corresponding frequencies.

at a fraction of the cost. This is done at the expense of the added complication of the sputtering of the niobium film, a technology that has been established for several years already. A further advantage of the thick copper substrate is that the liquid helium cooling circuits in the cryostat are simplified. The cavity can in fact be cooled only by pool boiling He I within the inner stem and over the top part, the thick external copper wall ensuring an adequate heat transfer by conduction. A thermal analysis has been carried out with a non-linear finite element model taking into account the dependence on temperature of the copper thermal conductivity and the helium film convection coefficient (Fig. 3). With the expected power dissipation distribution the temperature does not rise above 5.1 K, the design criterion being that the calculated temperature should always remain below 6 K, corresponding to an expected increment of surface resistance of about 20%. The study of the natural mechanical frequencies of the cavity also led to a choice of a thick-walled structure in order to increase the resonant frequencies, which should be beneficial in terms of RF operation.

Following CERN experience, the copper specifications used for manufacturing the cavity are Cu-OFE grade (UNS C10100), at least in the half-hard state, either in the form of rolled sheets or 3-D forged pieces, in order to minimize porosities which are harmful for the niobium film coating process. Common extruded pieces have an inferior degree of compaction, with pores aligned with the extrusion direction. Appropriate surface processes, which will be discussed later, must be applied prior to coating. Several critical manufacturing choices have been made in order to maximize the benefits of the cavity design such as not to perform any brazing on the main body of the cavity. Experience from INFN-LNL suggests in fact that the brazing alloy in the active RF regions may contaminate the niobium film. Second, copper softening due to the high temperature treatment would hinder the mechanical stability and accuracy of the cavity. Manufacturing the cavity from one single copper piece by turning or milling of the complete shape would be extremely expensive because of the cost of a 3-D forged billet of the required size. This leaves the option of using standard metal working techniques and then joining the pieces by e-beam welding. The chosen manufacturing sequence comprises the following main steps: rolling and e-beam welding of the external tube, together with the external half of the top plate, machining and welding of the central conductor with the internal half of the top plate, manufacturing of the beam ports by plastic deformation, joining of the two pieces by an internal e-beam welding (Fig. 4).

Figure 4: Manufacturing sequence of the cavity. The top half of the drawing illustrates the shape of the raw pieces, the bottom one the final shape. The arrow indicates the region of the final circular long-throw welding.

The manufacturing of the beam ports by drawing is a critical process that has been validated on flat copper test pieces. This is done by progressive deformation of copper with punches of different shapes into a fixed die, until the final shape is reached (Fig. 5). Development work has shown that with appropriate design of the tooling, the thickness of the wall is never reduced below 8 mm from the starting 10 mm. Local intermediate annealing steps are used in the process, the copper being cold worked at the final step thus recovering good mechanical properties. The e-beam welding of the top shorting plate needs to be done from the inner surface exposed to RF, in order to minimize porosities and projections of molten material, as the LEP/LHC experience has shown. It has been demonstrated in full scale simulation on test pieces that this can successfully be done with the e-beam gun kept outside the cavity, at a distance of about one meter. The quality of the welding has been monitored by ultrasound testing, and the surface roughness after 20 $\mu$m material removal by SUBU [5] chemical polishing was reduced to the expected value of 0.8 $\mu$m (average roughness $R_a$), common for this type of processing.

Figure 5: Sequence of the different drawing steps leading to the final form for the beam ports, and full scale test piece for the long-throw e-beam welding.

Surface preparation prior to coating will be carried out by SUBU chemical etching. Since all surfaces will be milled or turned with high accuracy, only minor material removal is necessary in order to achieve an optimum surface state. The treatment will benefit from the CERN existing infrastructure, with adaptations in order to make it compatible with the present goal. It is worth mentioning that dust-free water rinsing and clean room preparation will require only new tooling, without investments for modifications of the available basic infrastructure.

As already mentioned, the coating will follow generally the same bias diode sputtering procedure developed by INFN-LNL, which was itself based on previous CERN experience. A UHV coating system has been designed based on a vacuum jar of size sufficient to host both the low beta and high beta cavities. It is an all-metal system, compatible with standard vacuum bakeout, except for two Viton O-ring gaskets sealing the large diameter flanges (Fig. 6). Experience has already shown that such a configuration allows reaching vacuum levels in the $10^{-9}$ mbar range with standard turbomolecular pumping and bake-out while limiting heating of the gaskets in the 120 °C range. In order to keep the cold-worked copper state, the cavity will be cooled during coating by circulating a suitable coolant in the central stem. The study of the coating parameters will confirm whether this solution will bring all the benefits that are expected.

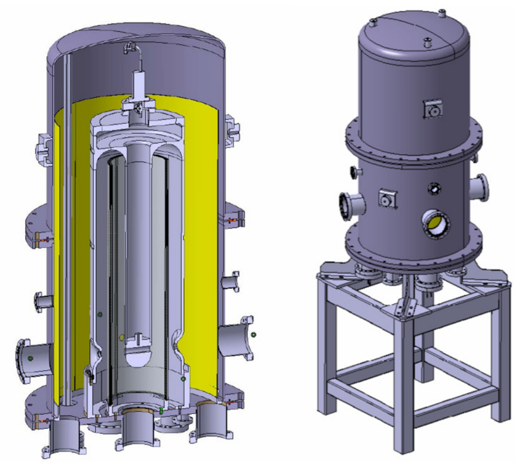

Figure 6: 3D views of the coating system.

Delivery of the first finished copper cavity and of the coating system vacuum components is expected by end of October 2008 and tests of surface treatments and of coating on small scale samples will follow immediately. The first coated cavity is expected to be tested for RF performance in early 2009, with the goal of delivering a prototype working at full specifications by end 2009.

## REFERENCES

[1] `http://hie-isolde.web.cern.ch`

[2] M. Pasini, et al., A SC Upgrade for the REX-ISOLDE accelerator at CERN, these proc.

[3] `http://www.cst.com`

[4] A. Facco, Tutorial on low beta cavity design, SRF2005 Workshop, Cornell University, Ithaca, New York, US

[5] C. Benvenuti, et al., Physica C 316 (1999) 153

[6] A. M. Porcellato et al., PRAMANA 59 (2002) pp. 871-880

# CRAB CAVITIES FOR LINEAR COLLIDERS

G. Burt, P. Ambattu, R. Carter, A. Dexter, I. Tahir, Cockcroft Institute, Lancaster University, Lancaster, UK, LA1 4YR
C. Beard, M. Dykes, P. Goudket, A. Kalinin, L. Ma, P. McIntosh, ASTeC, Daresbury Laboratory, Warrington, Cheshire, WA4 4AD, UK
D. Shulte, CERN, Geneva, Switzerland
R. Jones, Cockcroft Institute, Manchester University, Warrington, UK, WA4 4AD
L. Bellantoni, B. Chase, M. Church, T. Khabouline, A. Latina, FNAL, Batavia, Illinois, 60501
C. Adolphsen, Z. Li, A. Seryei, L. Xiao, SLAC, Menlo Park, California

*Abstract*

Crab cavities have been proposed for a wide number of accelerators and interest in crab cavities has recently increased after the successful operation of a pair of crab cavities in KEK-B. In particular crab cavities are required for both the ILC and CLIC linear colliders for bunch alignment. Consideration of bunch structure and size constraints favour a 3.9 GHz superconducting, multi-cell cavity as the solution for ILC, whilst bunch structure and beam-loading considerations suggest an X-band copper travelling wave structure for CLIC. These two cavity solutions are very different in design but share complex design issues. Phase stabilisation, beam loading, wakefields and mode damping are fundamental issues for these crab cavities. Requirements and potential design solutions will be discussed for both colliders.

## INTRODUCTION

Most linear collider concepts envision a crossing angle at the IP to aid the extraction of spent beams. This crossing angle will however reduce the luminosity of the collisions as the beam presents a larger effective transverse size. This loss in luminosity can be recovered by rotating the bunches prior to collision using the time dependant transverse kick of a crab cavity. In particular crab cavities are required for both the CLIC [1] and ILC [2] machines. The proposed solutions for these two colliders are very different and a comparison of the cavities will be the focus of this paper.

A crab cavity is a type of transverse deflecting cavity in which the RF is phased such that the centre of the bunch does not receive a net kick, and the head and tail of the bunch receive equal and opposite kicks [3]. Both travelling and standing wave solutions exist and the cavity can be either normal or superconducting depending on the bunch structure. As the cavity is typically positioned close to the IP before the final doublet their performance can be very sensitive to wakefields. Additionally as the separation between the incoming and extraction beam-lines are very close at this position, the cavities have to be transversely compact.

The voltage, $V_{cav}$, required to cancel the crossing angle of a bunch of energy, $E_0$, is given by equation 1,

$$V_{cav} = \frac{cE_0\theta_c}{2\omega R_{12}} \tag{1}$$

where $\theta_c$ is the crossing angle, ω is the cavity frequency and $R_{12}$ is the ratio of the bunch displacement at the IP to the divergence created by the crab cavity. The crab cavity is positioned at a location with a high $R_{12}$ to reduce the required voltage. The ILC has a crossing angle of 14 mrad and an $R_{12}$ of 16.2 m at the crab cavities location. This means a 3.9 GHz system requires a peak deflecting voltage of 2.64 MV at 1 TeV CoM. The CLIC has a crossing angle of 20 mrad and an $R_{12}$ of 25 m; hence a 12 GHz cavity will require a similar voltage of 2.39 MV at 3 TeV CoM.

## PHASE AND AMPLITUDE STABILITY

As both the ILC and CLIC machines have very small transverse bunch sizes at the IP, the phase and amplitude of the crab cavities have to be very stable, as the primary action of a crab cavity is to displace the head and tail of the bunch at the IP. The displacement of a bunch at the IP, Δx, due to a timing error Δt is given by,

$$\Delta x(\Delta t) = R_{12}\frac{V_{cav}}{E_o}\sin(\omega\Delta t) \tag{2}$$

and the luminosity reduction factor, S, is given by

$$S = \exp\left(-\frac{\Delta x^2}{4\sigma_x^2}\right) \tag{3}$$

The horizontal beam size in the ILC is around 500 nm giving a positron-to-electron arm phase tolerance of 80 fs which is around the state of the art level [4]. For the CLIC beam size of 60 nm the timing stability is much smaller at 5 fs which is a major challenge to be overcome and will certainly require all cavities to be driven by a single amplifier.

The amplitude tolerance of a crab cavity is set by the luminosity loss associated with beams colliding with crossing angles. The incorrect amplitude on a crab cavity will cause incorrectly bunch rotation for the crossing angle and the bunches will collide with a small angle between them. The tolerable amplitude stability is given in equation 4

$$\frac{\Delta V}{V_{cav}} = \frac{2}{\theta_c}\frac{\sigma_x}{\sigma_z}\sqrt{\frac{1}{S^2}-1} \quad (4)$$

This leads to an amplitude tolerance of 4.8 % for the ILC and 2.0 % for the CLIC crab cavities which should not prove difficult to achieve.

## BEAM LOADING

In transverse deflecting cavities the primary action of the RF fields is to kick the bunch transversely. This action has a very small exchange of energy between the electrons and the cavity fields as the electrons gain or loose very little energy. However if the beam traverses the cavity off-axis then the axial electric field component of the dipole fields can accelerate or decelerate the beam in it's direction of motion. This acceleration or deceleration of the bunch in the axial direction causes a large exchange of energy between the bunch and the cavity fields which can alter the amplitude and phase of the cavity fields. As the axial electric field is approximately proportional to the radial offset of the beam, the beam can either give or remove energy from the cavity depending on the exact beam position.

The RF fields induced by the beam have the longitudinal electric field in-phase with the beam, but the transverse voltage is always 90 degrees out of phase with the longitudinal field and hence the beam-loading is out of phase with the peak deflecting field which in turn means that beam-loading fields are in crabbing phase.. This means that crab cavities will have much higher beam loading than deflecting mode cavities which are only loaded by the beams self-field.

## MODAL DISTRIBUTION

The modal pass-band of a dipole cavity is not always sinusoidal due to the coupling between the upper and lower hybrid dipole modal pass-bands [5]. This effect often causes the group velocity to be reduced close to the π mode of the lower (operating) dipole pass-band, depending on the iris radius.

For a standing wave cavity like the design proposed for the ILC, the frequency separation between the π mode and its nearest neighbour is reduced. This can cause interference between these modes, restricting field flatness tuning and LLRF control of the cavity. This limits the number of cells to 9, in order to keep the separation greater than 2 MHz. The ILC cavity modal dispersion diagram is shown in Fig 1.

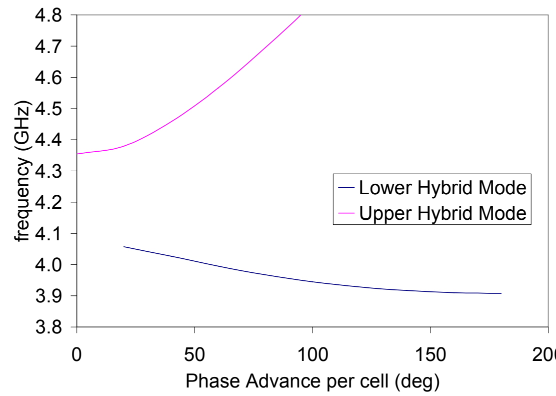


Figure 1: The modal distribution of the first two dipole passbands in the ILC Crab cavity.

For a travelling wave design a low group velocity will increase the effects of beam loading as the energy deposited will take longer to propagate out of the structure. This concern is likely to cause the design to call for the cavity to operate with a phase advance of around π/2 to 2π/3.

## HOM'S, LOM'S AND SOM'S

In any RF cavity there are a number of unwanted modes which may be excited by the beam and must be removed by RF dampers or couplers. In an accelerating cavity where the fundamental mode is the operating mode of the cavity, all the unwanted modes are classed as higher order modes (HOMs), however for a dipole cavity we also have other modes which must be removed. The fundamental mode pass-band of the cavity, which is a lower order mode (LOM), must also be removed to avoid unwanted energy spread. This is not always simple as the LOM is resonant at a lower frequency than the dipole mode and does not penetrate as far down the beampipe as the dipole mode does.

The dipole mode also has two polarisations, a vertical and a horizontal polarisation, which are fixed in place and separated in frequency by using polarising slots, rods or by squashing the cavity. The vertical polarisation of the operating mode, known as the same order mode (SOM) is particularly damaging to the beam due to the small vertical beam sizes and high shunt impedance of this mode (as it will have field shapes close to that of the operating mode).

In the ILC the LOM is damped by the use of a hook type coupler positioned vertically such that it doesn't couple to the operating mode. It is proposed that this coupler could also remove the SOM or a 2$^{nd}$ dedicated co-axial probe could be used. The HOM coupler is a co-axial F-probe type coupler similar to the design used in the ILC main linac [6]. The ILC couplers are shown in Fig 2.

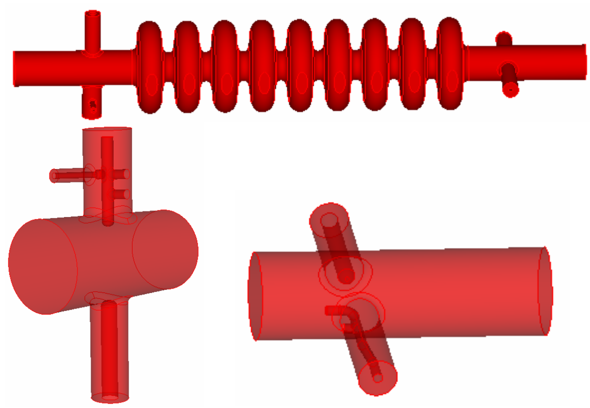

Figure 2: Model of the ILC deflecting mode cavity.

For the CLIC crab cavity a damped-detuned structure is proposed. A number of solutions have been proposed for the damping part; such as manifold damping or choke couplers combined with waveguide couplers at the end of each section. This could be combined with detuning of the SOM to provide very low wakefields for this mode.

## CAVITY FREQUENCY AND TECHNOLOGY CHOICES

For the ILC, a superconducting design was chosen at three times the frequency of the main linac to reduce its size. The size reduction was required to fit a cryostat that did not impinge on the extraction line 21 cm away from the crab cavity central axis. The superconducting design was chosen due to the high duty factor and high gradients required resulted in a very high average power required. The resulting thermal effects in a copper system could possibly cause problems in meeting the phase stability specification [7]. Additionally, the ILC design calls for very lengthy bunch trains and the larger iris of superconducting designs improves the beam-induced wakefield situation.

For the CLIC crab cavity the phase and timing stability requirements are much tighter than for the ILC. As the cavity voltage required decreases with frequency, the phase stability requirement loosens with increasing frequency. In addition it is obvious that with a fixed bunch separation, an increased cavity frequency means more RF periods between bunches. This means that the CLIC cavity should be at as high a frequency as possible. However the crab cavity is placed at the position with the largest beta function in the final focus, which places limits on the aperture size. This lead to the decision to use the main linac frequency of 11.9942 GHz for the crab cavity, which also allows a certain synergy between the two cavity designs [8].

At the frequency and bunch spacing chosen for the CLIC design, a normal conducting cavity is the only viable option.

## CONCLUSION

The crab cavities for the ILC and CLIC colliders are of very different design but they share a number of key similarities that differentiate them from accelerating cavities.

The ILC cavity has completed its design phase and is now moving into a prototyping phase. A single cell Nb prototype and a full 9 cell aluminium prototype including couplers has been fabricated and successfully used to validate the simulations..

The design of a crab cavity suitable for the CLIC collider has commenced and some basic design parameters have been investigated. It is proposed to test a prototype of this cavity at CTF3 in 2012.

## ACKNOWLEDGEMENTS

The authors would like to acknowledge the support and advice of A. Seryei and C. Adolphsen of SLAC. This work was supported by STFC through LC-ABD and the EU through the EUROTeV program.

## REFERENCES

[1] J. P. Delahaye, CLIC- A Two Beam Multi-TeV e+/- linear collider, XX International Linac Conference, MO201, Monterey 2000.
[2] C. Adolphsen et al, Design of the ILC Crab cavity System, EUROTeV-Report-2007-010
[3] R. B. Palmer, Energy scaling, crab crossing and the pair problem SLAC-PUB-4707, 1988
[4] G. Burt et. al, Effect of tolerances of the RF phase and amplitude errors in ILC crab cavity, EUROTeV-Report-2006-098
[5] M. McAshan and R. Wanzenberg, RF Design of a Transverse ModeCavity for Kaon Separation, FNAL TM 2144 (March 2001) and references therein.
[6] L. Xiao, HOM and LOM coupler Optimisation for the ILC Crab Cavity, PAC 07, Albuquerque
[7] G. Burt, Progress towards crab cavity solutions for the ILC, EPAC 06, Edinburgh
[8] P. K. Ambattu, Initial study on the shape optimization for the CLIC crab cavity, LINAC 08, Victoria

# INITIAL STUDY ON THE SHAPE OPTIMISATION OF THE CLIC CRAB CAVITY

P. K. Ambattu, G. Burt, R. G. Carter, A. C. Dexter, Cockcroft Institute, Lancaster University, Lancaster, UK, LA1 4YR
R. Jones, Cockcroft Institute, Manchester University, Warrington, UK, WA4 4AD
P. McIntosh, STFC, Daresbury Laboratory, Warrington, Cheshire, WA4 4AD, UK

*Abstract*

The compact linear collider (CLIC) requires a crab cavity to align bunches prior to collision. The bunch structure demands tight amplitude and phase tolerances of the RF fields inside the cavity, for the minimal luminosity loss. Beam loading effects require special attention as it is one potential sources of field errors in the cavity. In order to assist the amplitude and phase control, we propose a travelling wave (TW) structure with a high group velocity allowing rapid propagation of errors out of the system. Such a design makes the cavity structure significantly different from previous ones. This paper will look at the implications of this on other cavity parameters and the optimisation of the cavity geometry.

## INTRODUCTION

Deflection cavities were first proposed in 1988 for the rotation of particle bunches prior to the interaction point (IP) in the presence of a finite crossing angle. Efficient design of the crab cavity will lead to a flexible design of the interaction region. Unlike an accelerating cavity, a crab cavity is operated in the lowest dipole mode, which is $TM_{110}$-like in nature, as it has the highest transverse geometric shunt impedance defined as

$$\left(\frac{R}{Q}\right)_{\perp} = \frac{\left|V_z\right|^2}{\omega U}\left(\frac{c}{\omega r}\right)^2 \quad (1)$$

where U is the stored energy and $V_z$ is the longitudinal voltage measured at the radial offset of r from the cavity axis at the angular frequency of $\omega$ [1]. For a crossing angle of $\theta_c$, the peak transverse kick voltage required is given by

$$V_{\perp} = \frac{\theta_c E_{beam} c}{2\omega R_{12}} \quad (2)$$

where $E_{beam}$ is the beam energy and $R_{12}$ is the transfer matrix element representing the final focussing system, given by,

$$\Delta x_{ip} = R_{12} x_c' \quad (3)$$

where $\Delta x_{ip}$ is the vertical displacement of the bunch at the IP and $x_c$' is the angular direction of the bunch when leaving the cavity [2]. Eq. (2) shows that higher frequency operation of the cavity reduces the kick required to produce a given deflection angle. For 1.5 TeV beams crossing at 20 mrad and for $R_{12} = 25$ m, the maximum kick voltage required is 2.4 MV. For a transverse gradient of 20 MV/m, a structure length of 120 mm would be required to achieve the above kick. For a phase advance of $2\pi/3$ per cell, this requires about 15 cells. In addition to providing a kick at the operating frequency, the cavity should also suppress the wakefields that include monopole and higher order dipole modes in the cavity. However this aspect is not discussed here.

## CAVITY CELL SHAPE

The cavity cell shape is shown in Fig. 1. This is adopted from the basic disc-loaded waveguide structure, where the coupling between adjacent cells is achieved through a common iris. In the figure, L, R and C stands for the length, radius and curvature respectively and suffixes c, e and i stand for the cell, equator and iris respectively. The cell length (cavity + iris), is set by the phase advance per cell, $\Phi = k_{rf}(2L_c)$, where $k_{rf}$ is the free space phase constant in rad./meter. The iris edges are curved to avoid surface field enhancement and consequent field emission.

We studied the eigenmode characteristics of the single cell of an infinitely periodic copper structure as it can be used to infer the performance of a multi-cell structure. A $\Phi = 2\pi/3$ per cell structure, for which $2L_c = 8.337$ mm is modelled in Microwave Studio™ [3] as a first step.

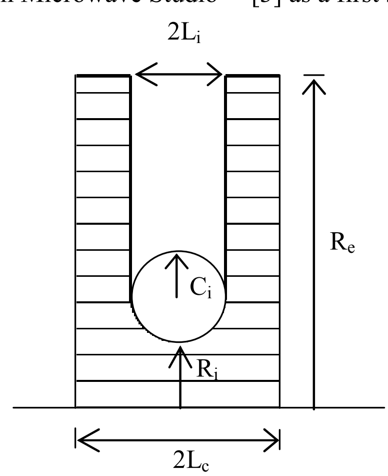


Figure 1: Cavity cell shape with dimensions.

Various cell shapes are simulated for the fixed operating frequency and the important figures of merit such as the transverse R/Q, group velocity and maximum surface fields are calculated.

## RESULTS

The frequency sensitivity of the dipole cavity to its dimensions is shown in table 1, which demand high fabrication tolerances for the dipole cavity. Fig. 2 shows the transverse R/Q for various cell shapes. For lower iris radii and lengths, R/Q is almost a constant with the iris radius, but falls as the iris dimensions increase.

Table 1: Frequency Sensitivity of the Dipole Cavity

| Dimension (mm) | Freq. sensitivity (MHz/mm) |
|---|---|
| $R_i$ | –231 |
| $R_e$ | –791 |
| $2L_i$ | –212 |
| $2L_c$ | 71 |

A maximum value around 4500 Ω/m is achieved at an iris radius of 2 mm and length of 1 mm. For the shunt impedance ≥ 67 % of the maximum value, the iris length is to be kept ≤ 75 % of the cell length. However, the minimum iris length is governed by good mechanical stability and effective heat removal.

Group velocities are calculated from the dispersion curves for a given cell shape and are shown in Fig. 3. A maximum value near 3 % of the velocity of light can be obtained with an iris radius of 4.25 mm and length of 1 mm. This is within the higher limit preferred for the X-band linacs [4]. This is because high group velocities enhance the impedance matching between the RF power and the breakdown spot. Also for a given iris radius, $v_{gr}$ varies inversely as the iris length. Also it was found that the cell with iris radii higher than 4.25 mm causes a coupling between the lower and upper dipole bands, hence changing the slope of the dispersion curve, thereby reducing the group velocity. The geometric dependence of group velocity is highly useful for the design of constant gradient TW structures [4] as long as its sign is not changed.

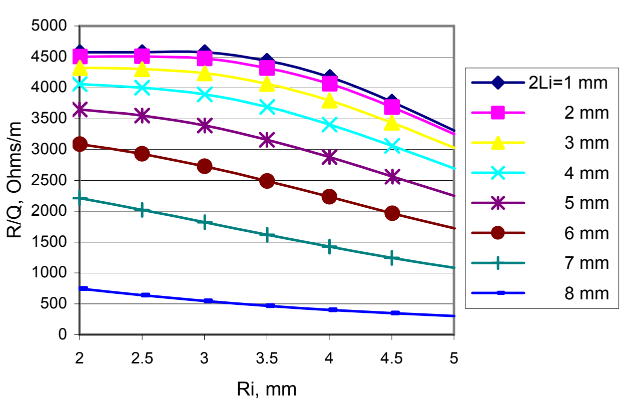


Figure 2: Iris radius × R/Q for different iris lengths.

## RF FIELD ERRORS AND BEAM LOADING

Amplitude and phase errors are unavoidable in any RF system, which for a crab cavity result in less efficient collisions. The amplitude error causes a residual

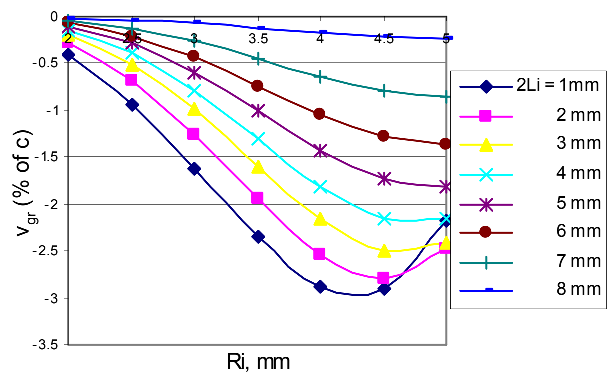


Figure 3: Iris radius × group velocity for different iris lengths.

crossing angle at the IP while the phase error causes a transverse offset of the bunch center at the IP. For the crab crossing scheme, these tolerances are given by,

$$\frac{\Delta V}{V} < \frac{2\sigma_x^*}{\sigma_z\theta_c}\sqrt{\frac{1}{S^2}-1} \qquad (4)$$

$$\Delta\Phi < \frac{4\omega_{rf}\sqrt{\sigma_x^*\ln(1/S)}}{c\,\theta_c} \qquad (5)$$

where $\sigma_x^*$ is the horizontal IP beam size, $\sigma_z$ is the bunch length and S is the luminosity reduction factor [2]. For 2 % luminosity loss (S = 0.98) and a crossing angle of 20 mrad, the CLIC scheme (11.994 GHz, $\sigma_x^*$ = 40 nm, $\sigma_z$ = 45 μm) requires the above tolerances as 1.8 % and 0.016° for the amplitude and phase respectively. For the ILC crab cavity (3.9 GHz, $\sigma_x^*$ = 640 nm, $\sigma_z$ = 300 μm) the values are obtained as 4.33 % and 0.085° and for the NLC cavity (11.424 GHz, $\sigma_x^*$ = 243 nm, $\sigma_z$ = 110 μm) these would be 4.49 % and 0.095° respectively. Thus the CLIC crab cavity necessitates tighter amplitude and phase control system than the existing ones which recommends a TW structure with a high group velocity since it allows rapid extraction and correction of the RF errors.

In a loaded cavity, the total field that the beam sees is the superposition of the generator induced and beam induced fields. For an ideal crab cavity, the fundamental component of the bunch current and the longitudinal cavity field ($E_z$) are in phase. If the beam doesn't arrive in phase with the cavity field, then a phase change will be introduced by the beam induced voltage. Also, the beam loading can cause amplitude errors; hence will be an assured source of the above stated errors in the CLIC crab cavity. The short bunch spacing (0.5 ns) of the CLIC structure makes the errors grow along the train (156 ns) causing displacement and/or uneven rotation of the bunches at IP. For a dipole cavity, the steady state beam loading is directly proportional to the ratio of geometric shunt impedance (R/Q) to the group velocity, the vertical offset from cavity center and the structure length. A lower $R/(Qv_{gr})$ can be realised with bigger coupling irises between the cells, to lower the beam loading in a constant impedance structure. In a constant gradient structure where the group velocity is lowered downstream along the structure, the beam loading may become even worse than that in a constant impedance structure.

## PEAK SURFACE FIELDS

In normal conducting cavities, the achievable peak surface electric field ($E_{max}$) is limited by field emission which can eventually lead to surface melting and breakdown. For such structures, the $E_{max}$ is expected to be around 100 MV/m which was the threshold of X-ray emission in normal conducting X-band TW cavity [5]. Peak surface magnetic field ($H_{max}$) is set by the limit at which the pulsed temperature rise on the structure (irises) is at around 40$^o$K. This is the threshold for forming micro cracks in OFE copper [6]. Since the peak fields are proportional to the gradient ($E_{trans}$), the quantities $E_{trans}/E_{max}$ and $H_{max}/E_{trans}$ are of importance and are plotted in Figs. 4 and 5, and can be considered as the normalised peak fields which depend only on the cell shape. As it is desired for the cavity to have lower surface fields at a given operating gradient, the $E_{trans}/E_{max}$ should be higher while the $H_{max}/E_{trans}$ should be lower. Though the surface fields are directly related to the iris dimensions, present results show that the fields have a higher dependence on the iris length than on the iris radius over the range of study. For the present dipole cavity, $E_{max}$ is concentrated on the equator faces (about half way on the $R_e$) while $H_{max}$ is concentrated on the iris. This makes the iris the hottest region in the cavity and should be provided with proper cooling channels.

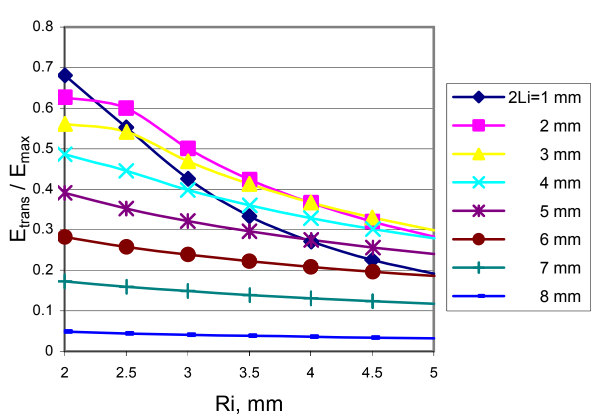


Figure 4: Iris radius × $E_{trans}/E_{max}$ for different iris lengths.

Assuming a 20 MV/m gradient structure, the peak surface fields for the present $2\pi/3$ cell were evaluated. It was found that $E_{max}$ was less than 100 MV/m for iris radii less than 4.5 mm and lengths below 7 mm. Similarly, the peak surface heating was below 40$^o$K for all iris radii with iris lengths below 8 mm. Further simulations showed that the peak fields can be drastically reduced if longer (higher phase advance) cells are used, which allows the use of longer irises. However this will reduce the group velocity.

Considering the above discussion, a range of 4 to 5 mm for the iris radius and 2 to 4 mm for the iris length for the $2\pi/3$ phase advance/cell structure could be a preferred choice.

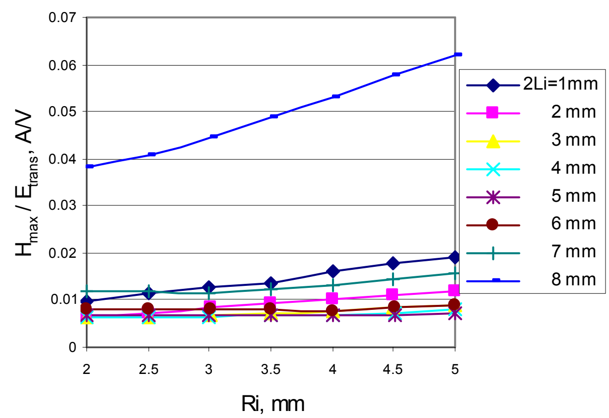


Figure 5: Iris radius × $H_{max}/E_{trans}$ for different iris lengths.

## CONCLUSION

The behaviour of a normal conducting cavity is highly sensitive to the cell shape when operated in the X-band. For a given gradient and a desired net kick, the cell shape can be optimised by the proper selection of the cell profile. The key parameters of concern are the geometric shunt impedance, group velocity and surface fields. A TW structure with a low shunt impedance and high group velocity is suggestive for reduced beam loading and efficient RF control. This can be achieved by using bigger coupling irises as long as the surface fields are in the safe limits.

## ACKNOWLEDGEMENT

The work is supported by the Science and Technology Facilities Council (STFC).

## REFERENCES

[1] H. Padamsee et.al, Crab cavity development for Cornell B-factory, PAC 91.
[2] G. Burt et.al, Effect of tolerances of the RF phase and amplitude errors in ILC crab cavity, EUROTeV-Report-2006-098.
[3] Microwave Studio™, CST, Germany.
[4] Z. Li et.al, Optimisation of the X-band structure for the JLC/NLC, SLAC-PUB-11916, 2006.
[5] V. A. Dolgashev et.al, High power tests of normal conducting single-cell structures, PAC 07.
[6] D. P. Pritzkau, RF pulsed heating, SLAC report-577, 2001.

# SUPERCONDUCTING QUARTER-WAVE RESONATORS FOR THE ATLAS ENERGY UPGRADE

M. P. Kelly, J. D. Fuerst, S. Gerbick, M. Kedzie, K. W. Shepard, G. P. Zinkann, P. N. Ostroumov
Argonne National Laboratory, Argonne, IL 60439, U.S.A

*Abstract*

A set of six new 109 MHz β=0.15 superconducting (SC) quarter-wave resonators (QWR) has been built at ANL as part of an upgrade to the ATLAS superconducting heavy-ion linac at Argonne National Laboratory. The final cavity string assembly will use most of the techniques needed for the next generation of large high-performance ion linacs such as the U.S. Department of Energy's FRIB project. Single-cavity cold tests at T=4.5 K have been performed for 5 of 6 cavities. Tests were performed with a moveable coupler, rf pickup, and VCX fast tuner as required for the full 5-meter cryomodule assembly. The average maximum accelerating gradient of 6 cavities (5 new + 1 prototype), is $E_{ACC}$=10.6 MV/m ($B_{PEAK}$=62 mT). Assembly of the clean cavity string has just begun using techniques which are fairly well developed based on many single cavity clean assemblies and one assembly of the entire string performed under non-clean conditions. Details on single cavity performance including high-field cw operation, microphonics and fast tuning are presented.

## INTRODUCTION

Advances in the last decade in SC cavity performance achieved using clean processing and assembly techniques at KEK, DESY and JLab for elliptical cavities have been adapted for TEM-cavities at Argonne and elsewhere. TEM cavity field performance with $B_{PEAK}$~100 mT or higher in single cavity tests is often achieved and is comparable to surface magnetic fields found in today's state-of-the-art elliptical cell cavity linacs. The ANL 7-cavity cryomodule, shown partially assembled in Figure 1, will be the first section of TEM-cavity linac incorporating all of the essential features found in clean elliptical cavity string assemblies. Features include electropolished high RRR bulk niobium cavities cleaned using high-pressure water rinsing and assembled in a clean room into a single sealed cavity string assembly. Isolation of the cavity rf volume from the cryomodule insulating volume greatly reduces the number of components assembled in the clean room and should help maintain cavity cleanliness.

## CAVITIES AND CRYOMODULE

### *Specifications*

Primary specifications for the upgrade cryomodule are shown in Figure 2. Initially the module was to hold seven β=0.15 quarter-wave resonators and one β=0.24 half-wave resonator, however, the half-wave requires additional work and will not be included in the initial assembly. This cw SC cryomodule is designed for a "real estate gradient" 3 MV/m which is now higher than achieved in pulsed normal conducting linacs for this velocity range.

### *Fabrication*

The quarter-wave prototype and six production cavities were fabricated from RRR~250 3-mm thick niobium sheet purchased from Wah Chang. Parts were die hydroformed at Advanced Energy Systems and then electropolished at ANL to remove at least 100 µm of niobium from the rf surface. To perform the initial rough tuning of the cavity, the niobium subassemblies were clamped together and the frequency was measured. The cavity housing and center conductor were then trimmed along the length using a wire EDM. Ref. [1] contains many additional details on fabrication and tuning. The niobium subassemblies were then electron beam welded together at Sciaky Inc. and the complete niobium cavity was enclosed in an integral stainless steel helium vessel. Details of the critical niobium-to-stainless steel braze transition have been presented [2]. In order to remove residues from electron beam welding, a final five minute

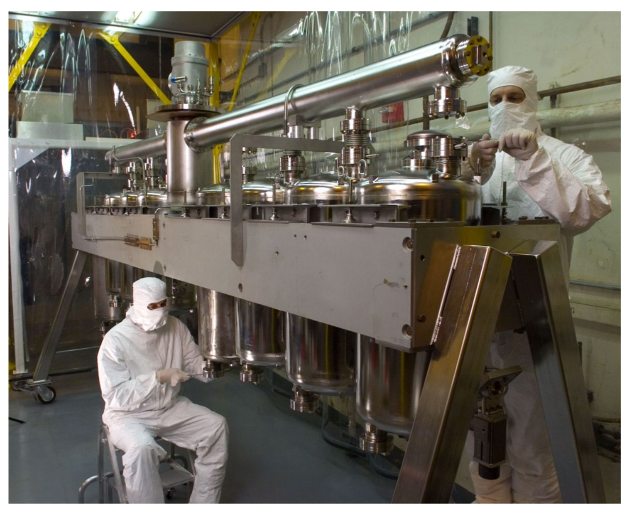

Figure 1: Partial assembly of the quarter-wave cavity string in the clean room.

| | |
|---|---|
| **physical length** | 4.62 meters |
| **# cavities** | 7 |
| **$L_{EFF}$/cavity** | 0.25 cm |
| **required gradient** | 8.4 MV/m |
| **total voltage** | 14.7 MV |
| **static load (4.5 K)** | 15 Watts |
| **rf load/cavity (4.5 K)** | 12 Watts |
| **total heat load (4.5 K)** | 100 Watts |

Figure 2: Primary specifications for the ATLAS upgrade cryomodule.

chemical etch was performed using standard 1:1:2 buffered chemical polish solution at T=15-17 °C.

### High-Pressure Rinsing and Clean Assembly

For single-cavity tests reported here, high-pressure water rinsing (HPR) was performed for each cavity. The rinsing system uses 0.04 μm filtered deionized water flowing at 16 liters/minute through a nozzle with eight jets at a pressure of 120 bar. HPR was done in a class 100 clean area using an automated spray wand and rinsing through each of the three cavity coupling ports for 45 minutes. By design, the coupling ports are located so that the high-pressure water spray has line-of-sight to the entire cavity rf surface.

Major subsystems including the rf power coupler, VCX fast tuner, rf pickup loop, and vacuum pumping lines were also high pressure rinsed in a class 100 clean area using a manual spray wand. The sealed cavity and subsystems were moved to a larger class-100 clean area for assembly. A model of a cavity, coupler and VCX tuner is shown on the left hand side of Figure 3.

### Clean Cavity String Assembly

Due to the cost and difficulty associated with assembly of hardware in a class-100 environment, a primary design goal was to minimize the number and complexity of the parts requiring clean assembly. A Pro/Engineer solid model of the clean assembly is shown on the right side of Figure 3. Major components include a pumping manifold to evacuate the cavity rf volume, the seven dressed cavities with coupler, VCX fast tuner and rf pickup. The string is supported on an anodized aluminum frame and a pair of gate valves (one is visible in Fig. 4) seals the string before it is removed from the clean room.

In order to avoid unforeseen difficulties during the first clean string assembly, a mock assembly was performed using all components with no high-pressure rinsing. The string has now been disassembled and is being reassembled after high-pressure rinsing. Manpower required for assembly was three man-months. An additional three man-months will be required for ultrasonic cleaning and high-pressure rinsing of all of the

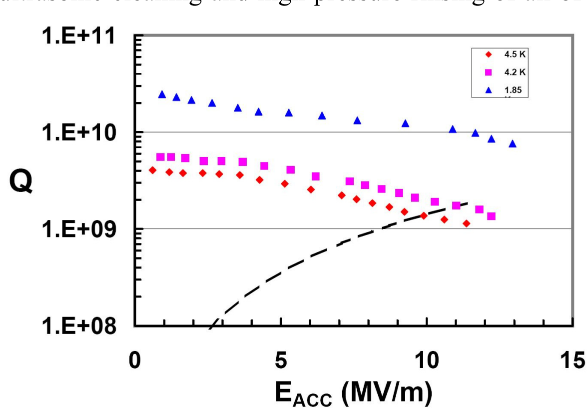


Figure 4: Q-curve measurements for the 109 MHz β=0.15 prototype quarter-wave cavity at T = 1.9, 4.2 and 4.5 Kelvin. The dashed line represents 8 Watts of rf power dissipated into the liquid helium cooling bath.

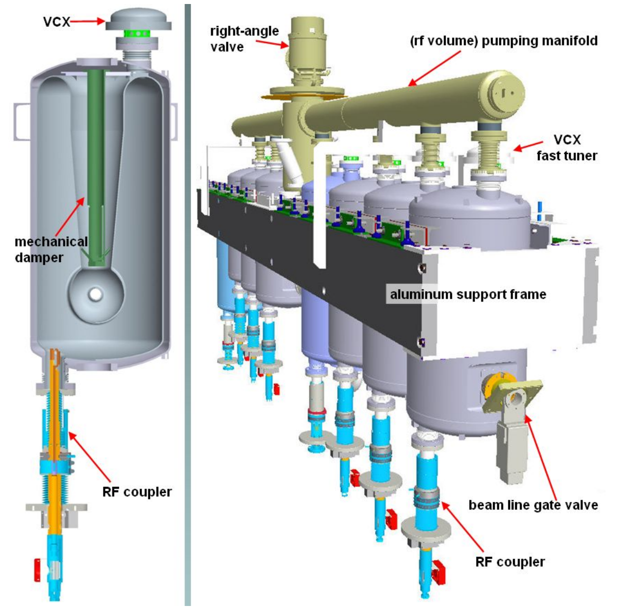


Figure 3: A 109 MHz quarter-wave resonator (left panel) as dressed in the clean room with rf power coupler and a VCX fast tuner. The right panel shows the sealed clean room cavity string assembly.

components based on experience from the single cavity testing work.

## COLD TEST RESULTS

### Prototype QWR Cavity

A prototype QWR cavity has been tested in the single-cavity test cryostat nearly a dozen times over a period of 4 years. In many tests the cavity operated with little or no field emission. An example is shown in Figure 5. The cavity has not been baked at high temperature in order to degas hydrogen, so it is necessary to cool rapidly (~1 hour) from 150 K to 80K in order to avoid hydride precipitation. The maximum gradient is limited to approximately $E_{ACC}$=12 MV/m by thermal-magnetic quench and is repeatable after cycling to room temperature.

The operating temperature for the upgrade cavities is set by the ATLAS refrigerator supply pressure of 20 PSIA, corresponding to T=4.5 K. Cavity performance at T=4.5 K is given by the red curve in Figure 4. Data in Figure 4 indicate there would be little benefit to 2 K operation in terms of wall plug power, however, hydrogen degassing, not performed here, would be likely to increase 2 K performance.

### Production Quarter-Wave Cavities

Five of the six production cavities have been cooled to 4.5 K in the ANL single-cavity test cryostat in order to measure cavity field performance and operation of the rf power coupler and VCX fast tuner. The last cavity has been cold tested in the upgrade cryomodule but with no high-pressure rinsing or clean assembly. The goal was to understand the operation of the helium and nitrogen cryogenics systems. Field testing of this cavity will be

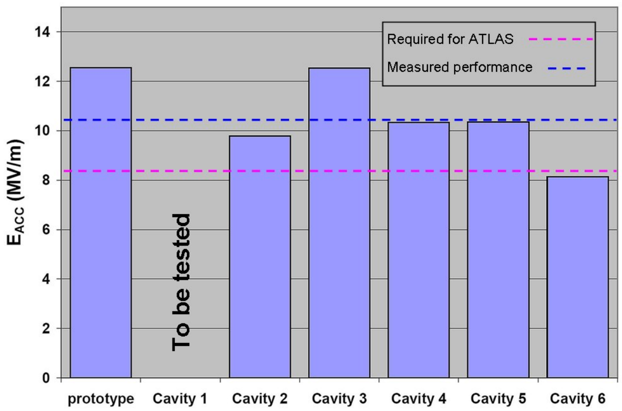


Figure 5: Measured maximum accelerating gradients at T= 4.5K in the vertical test cryostat for the prototype and five of the six production cavities.

performed with the cavity assembled onto the full clean cavity string.

Measured maximum accelerating gradients for 6 of the 7 cavities are shown in Figure 5 with average value of $E_{ACC}$=10.6 MV/m. Cavity #2, #3, #4 and #6 tests included a VCX fast tuner.

After several cold tests, a nominal VCX tuning window of 40 Hz with $Q_{EXT}$~2x$10^8$ was chosen for the upgrade. With these parameters the VCX was found to be thermally stable up to $E_{ACC}$=8 MV/m. In order to make use of the highest gradients achieved here, ~12 MV/m, future ion linacs may replace the VCX with a piezoelectric or magnetostrictive fast mechanical tuner.

The rf power coupler for the ATLAS upgrade is similar to the coupler reported on in Ref. [3], the primary difference being ~3X larger inductive loop area. The need for stronger coupling is due to the relatively low magnetic field at the quarter-wave cavity coupling port.

Coupler heating was experimentally measured using a silicon diode thermometer placed on the cavity coupling port flange and was not problematic under normal operating conditions. With the coupler positioned for β~1 (critically coupled) with $E_{ACC}$=10 MV/m and $P_{IN}$=70 Watts (10% into cavity walls, 90% in VCX $LN_2$), heating at the coupling port was ~1 degree Kelvin. Operation was stable over a period of several hours.

### *Microphonics*

Microphonics measurements have been made during many single cavity tests and one time in the upgrade cryomodule. In the test cryostat, rms frequency deviations of 2-4 Hz were observed mostly due to 10 Hz vibrations resulting from thermal-acoustic oscillations in the helium bath. Cryomodule test data, shown in Figures 6 and 7, had very low microphonics with $\sigma_{rms}$ ~1 Hz. Frequency deviations due to the peak at 80 Hz in Fig. 7 are well within the planned 40 Hz VCX tuning window.

## CONCLUSION

Assembly of a 5-meter 7 quarter-wave cavity clean string has begun. The new cryomodule is the first TEM

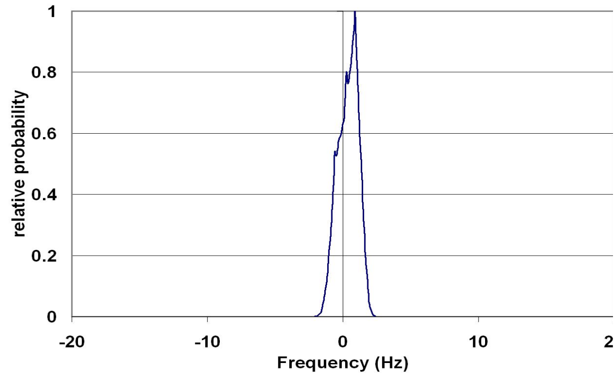


Figure 6: Probability density for eigenfrequency shifts for one of the six production cavities as measured in the upgrade cryomodule.

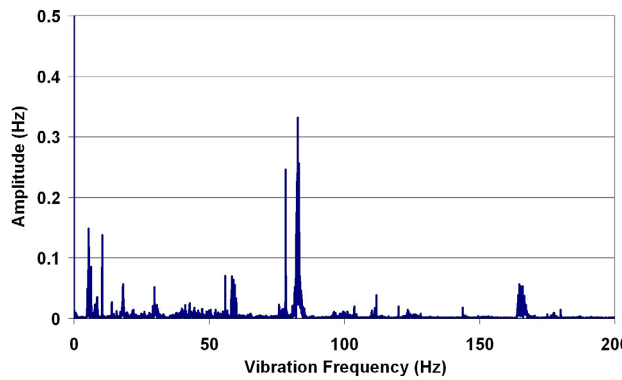


Figure 7: Power spectrum distribution of microphonics for one of the six production cavities as measured in the upgrade cryomodule.

cavity linac to use all of the essential clean techniques used in elliptical cavity linacs. Performance in single cavity tests shows $E_{ACC}$=10.6 MV/m, exceeding by 20% the requirement for ATLAS. Final assembly of the clean string is planned for late 2008 with installation of the module into the ATLAS tunnel in early 2009.

## ACKNOWLEDGEMENTS

This work was supported by the U. S. Department of Energy, Office of Nuclear Physics, under contract number DE-AC02-06CH11357.

## REFERENCES


[1] J. D. Fuerst, K. W. Shepard, M. P. Kelly, S. Gerbick, Z. Conway, G. P. Zinkann, "Progress on Cavity Fabrication for the ATLAS Energy Upgrade", Proceedings of the 13th International Workshop of RF Superconductivity, Beijing, China (2007).

[2] J. D. Fuerst, W. F. Toter, and W. Shepard, "Niobium to Stainless Steel Braze Transition Development", in Proc. 11th Workshop on RF Superconductivity, September 8-12, Lubeck, Germany (2003).

[3] K. W. Shepard, Z. A. Conway, J. D. Fuerst, M. P. Kelly, G. J. Waldschmidt, A.M. Porcellato, "Variable CW RF Power Coupler for 345 MHz Superconducting Cavities", Proc. Of the 2007 Particle Accelerator Conference, Albuquerque, NM (2007).

# SURFACE PROCESSING FACILITIES FOR SUPERCONDUCTING RF CAVITIES AT ANL

M.P. Kelly, S.M. Gerbick, ANL, Argonne, IL 60439
D. Olis, A. Rowe, FNAL, Batavia, Illinois, 60510

*Abstract*

New SRF cavity processing systems at ANL, including those for electropolishing (EP), high-pressure water rinsing (HPR), and single-cavity clean room assembly have been developed and operated at ANL for use with cavities for a range of electron and ion linac applications. Jointly with FNAL, systems for 1.3 GHz single- and multi-cell elliptical cavities for the linear collider effort have been developed. New systems for use with low-beta TEM-class cavities have also been built and used to process a set of six quarter-wave resonators as part of an upgrade to the ATLAS heavy-ion accelerator at ANL. All of the new hardware is located in a 200 $m^2$ joint ANL/FNAL Superconducting Cavity Surface Processing Facility (SCSPF) consisting of two separate chemical processing rooms, a clean anteroom, and a pair of class 10 and 100 clean rooms for HPR and cavity assembly. First cold tests results for elliptical cavities processed in these facilities are discussed.

## INTRODUCTION

A facility for processing superconducting (SC) niobium RF cavities has been built at Argonne National Laboratory (ANL) as part of an accelerator physics collaboration between ANL and Fermi National Accelerator Laboratory (FNAL). The facility will house in one location all hardware required to receive fabricated cavities as delivered from industry and, at the end of the process, yield a sealed cavity/coupler assembly ready for installation into a cold test cryostat. Overall costs and effort for construction of the facility are being shared approximately equally by ANL and FNAL. In addition to supporting upgrades for the ATLAS SC linacs at Argonne and linear collider R&D, the facility may also support development for the next-generation light source and proposed hadron linacs.

## FACILITY DESCRIPTION

The 200 $m^2$ surface processing facility contains two types of work areas: chemical processing rooms (see *e.g.* Fig. 1), and clean rooms for high pressure rinsing (see *e.g.* Fig. 2) and clean assembly. Details of the facility layout were presented previously [1]. Other major supporting hardware includes a 3000 scfm large air scrubber to remove hazardous airborne fumes from chemistry operations, a deionized water system with 4500 liter storage capacity for supplying up to 40 liter/minute of clean water to any of the work areas, and a high-pressure Teflon diaphragm pump from LEWA supplying 13 liter/minute of water for performing HPR.

### *Chemical Processing Rooms*

Two separate large chemical processing rooms, one administered by each laboratory is located at one end of the facility. The ANL administered chemistry room is presently configured for electropolishing of 1.3 GHz elliptical cell cavities. A nine-cell cavity, as positioned during electropolishing, is shown in Fig. 1. Previously, the same room has been used to perform electropolishing on six new production quarter-wave cavities for the ATLAS energy upgrade.

The FNAL administered chemistry room holds a buffered chemical polishing apparatus and automated


Figure 1: An electropolishing system for single- and multi-cell 1.3 GHz elliptical cavities at ANL

Figure 2: High-pressure rinsing system installed by Fermilab at the joint ANL/FNAL facility.

Table 1: Range of Operating Parameters for the Elliptical Cell Cavity Electropolishing System at ANL.

| Parameter | Unit | Value |
|---|---|---|
| Voltage | V | 0-20 |
| Current | A | 0-750 |
| Temperature | C | 20-35 |
| Temperature stability | C | +/- 1 |
| Acid flow rate | l/min | 0-25 |
| Cavity rotation speed | rpm | 0-5 |
| Air flow | scfm | 0-3 |

control system also for 1.3 GHz elliptical cell cavities. The system has been functional since 2007 but requires scheduling of safety review at ANL prior to operations.

## ELLIPTICAL CAVITY EP

### *Specifications*

Specifications (see Table 1) for the new 1.3 GHz single- and nine-cell cavity electropolishing system in the ANL portion of the processing facility are based upon the parameters discussed at the 2005 TTC meeting in Frascati [2]. Many other details were based on an EP design review at ANL in February 2007 attended by many of the world's experts on cavity EP.

A horizontal orientation for the cavity during EP was chosen based on the large experience with such systems at DESY, KEK and JLab. During EP the cavity is rotated slowly about the beam axis. After EP the system is rotated vertically in order to remove the acid and then rinse with water.

### *Materials*

Wetted materials used in the EP system have proven compatibility with the EP electrolyte and include: Teflon (PTFE), PFA, HDPE, and high-purity aluminum. Cathodes for single- and nine-cell cavities were fabricated from high-purity aluminum tubing provided by Jefferson Lab.

Non-acid-wetted structural materials located inside the chemistry room are constructed from chemical- and deionized-water-resistant materials including stainless steel, aluminum, HDPE and Type II PVC. Electrical leads and contacts are fabricated from copper, copper-graphite, aluminum and bronze. To the extent practicable electrical leads are coated or covered in order to prevent corrosion.

### *Acid Seals*

The horizontal EP system requires an acid tight seal between the rotating cavity assembly and the fixed cathode and EP end groups. ANL chose to use a double-Teflon lip seal available from industry and developed previously for automotive and petroleum industries. A section view of the EP system end group showing the location of the lip seal is shown in Fig. 3. After dozens of hours of operation using both water and EP acid solution no leaks have occurred. Additional acid seals for non-rotating connections include four flat Viton gaskets and a pair of Teflon-encapsulated Viton o-rings.

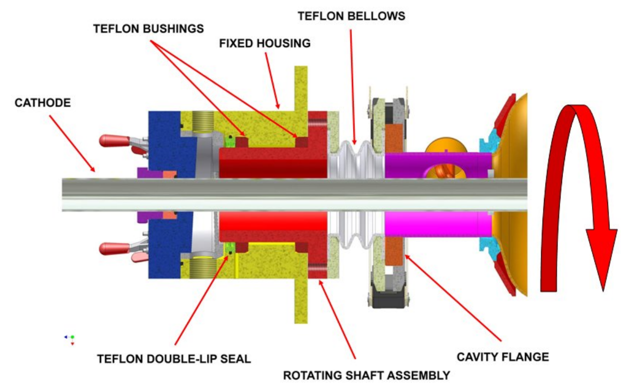


Figure 3: Section view of the electropolishing end group assembly.

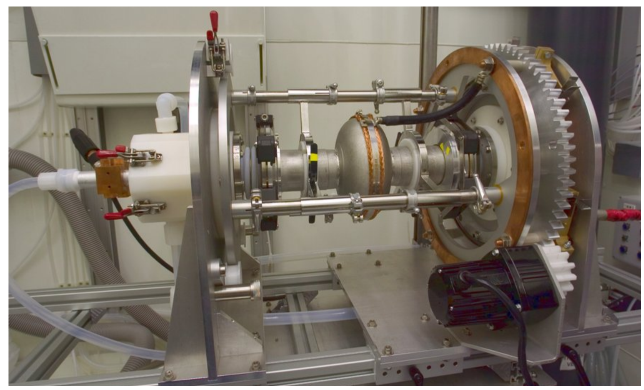

Figure 4: The electropolishing system re-configured for a 1.3 GHz single-cell elliptical cavity.

### *Heat Exchanger*

In order to maintain the acid temperature to within $^{+}/-1$ $^{o}$C of the nominal operating temperature during EP, a heat exchanger made of 30 meters of 1 cm diameter high-purity (3003) aluminum tubing is located inside an external acid cooling tank labeled "Acid Dump" in Fig. 1. The heat exchanger is similar to those used in the electropolishing of TEM cavities at ANL for more than three decades. A water chiller with a capacity of 10 kW at 5$^{o}$C is used to circulate cold water through the heat exchanger. Possible external (direct) water cooling to minimize temperature gradients across the cavity during EP was considered and may be added in the future.

### *First Cold Test Results*

Two 1.3 GHz cavities, a 1-cell and one 9-cell, have received a 20 μm EP at ANL. Cavities were tested at FNAL and JLab respectively with $E_{ACC}$~23 MV/m in each case. For the 1-cell cavity, performance was limited by field emission. More recently, a single-cell cavity received a 65 μm EP at ANL after having received heavy BCP at Cornell. Preliminary field tests at FNAL show $E_{ACC}$=33 MV/m after EP.

## ELLIPTICAL CAVITY HPR

A new high pressure rinse (HPR) apparatus and pump has been installed by Fermilab at the joint ANL/FNAL facility. The HPR tool, shown in Fig. 2, is based on a

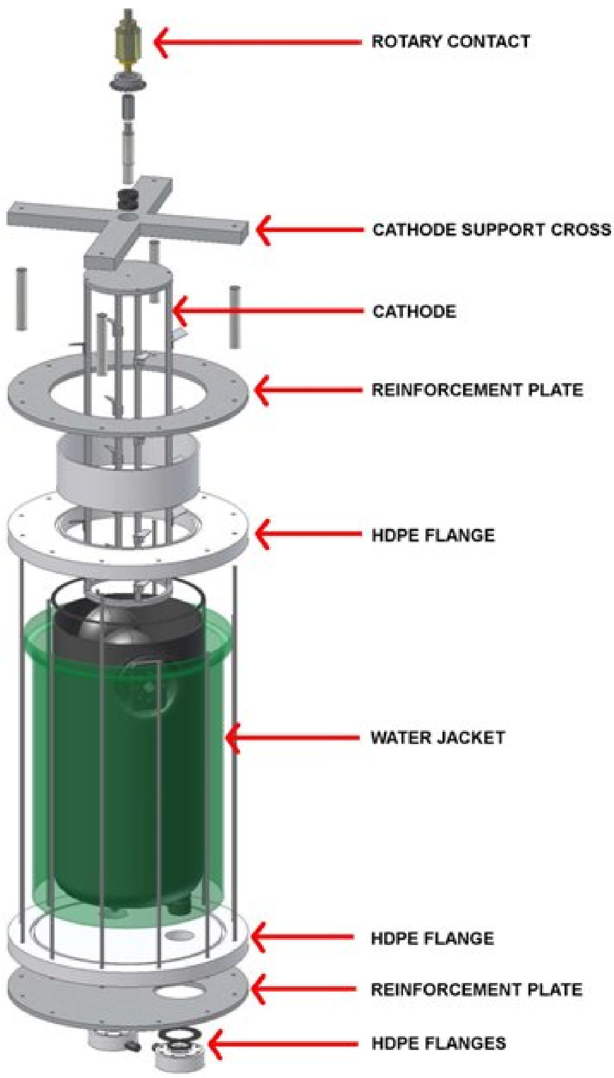


Figure 5: Exploded view of quarter-wave EP system.

system developed and operated at Cornell. During HPR the cavity is raised and lowered while a rinsing wand and nozzle is rotated inside the cavity.

Ultra-pure water will be supplied from a stainless steel body Teflon diaphragm pump manufactured by LEWA. The pump and deionized water plant are located on the service floor next to the processing facility. The HPR design operating pressure is 90 bar with a relief pressure set at 100 bar. A programmable and automated control system may be started from a pendant inside the clean room or from a control panel just outside the clean room.

## QUARTER-WAVE CAVITY EP

An EP system in the ANL chemistry area has been used with six quarter-wave resonators (QWR) as part of an upgrade of the ATLAS SC ion linac. EP was used to remove 100-150 μm of niobium from the cavities, the first to be processed in the joint ANL/FNAL facility.

Costs are reduced over previous systems by performing EP on only two major subassemblies prior to the final electron-beam closure weld. A model of the system for the larger subassembly is shown in Fig. 5. Both subassemblies after EP are shown in Fig. 6. To minimize temperature gradients in the electrolyte, which occur naturally in a vertical EP system, a rotating high-purity aluminum cathode with aluminum fins is used to mix the acid. Ref. [3] contains additional details on the system along with measured removal rates. Ref. [4] has first cold test results for these cavities.

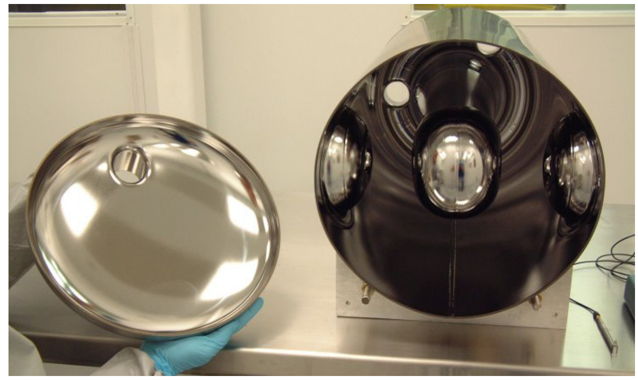

Figure 6: 109 MHz β=0.15 quarter-wave cavity after EP.

## CONCLUSION

A facility for processing superconducting niobium RF cavities has been built at Argonne in collaboration with Fermilab. The facility contains all of the systems to process, clean and assemble cavities for cold testing. To date, more than two dozen EP procedures on quarter-wave and elliptical cell cavities have been performed. High-pressure rinsing and clean assembly systems for linear collider elliptical cavities are nearly complete and will be operational before the end of 2008.

## ACKNOWLEDGEMENTS

This work was supported by the U. S. Department of Energy, Office of Nuclear Physics, under contract number DE-AC02-06CH11357.

## REFERENCES

[1] M.P. Kelly, K.W. Shepard, M. Kedzie ANL, Argonne, IL 60439, U.S.A., A. Rowe, Y. Terechkine, C. Boffo, L. Elementi, Fermi National Accelerator Laboratory, Batavia, IL, “A Joint ANL/FNAL Cavity Surface Processing Facility”, Proc. of SRF2005 (2005).
[2] T. Tajima, LANL, C. Boffo, FNAL, M.P. Kelly, J. Mammosser, JLab, ”Design of a New Electropolishing System for SRF Cavities”. Proc. of EPAC 2006 (2006).
[3] S.M. Gerbick, M.P. Kelly, J.D. Fuerst, “A New Electropolishing System at ANL for Superconducting Quarter-wave Resonators”, Proc. of SRF2007 (2007).
[4] M.P. Kelly, J.D. Fuerst, S. Gerbick, M. Kedzie, K.W. Shepard, G.P. Zinkann, P.N. Ostroumov, “Superconducting Quarter-wave Resonators for the ATLAS Energy Upgrade”, Proc. of LINAC08 (2008).

# WELDING HELIUM VESSELS TO THE 3.9 GHz SUPERCONDUCTING THIRD HARMONIC CAVITIES*

M. Foley, T. Arkan, H. Carter, H. Edwards, G. Galasso, C. Grimm, E. Harms, T. Khabiboulline, D. Mitchell, D. Olis, T. Peterson, P. Pfund, N. Solyak, D. Watkins, M. Wong
Fermilab, Batavia, IL 60510, U.S.A.

*Abstract*

The 3.9 GHz 3rd harmonic cavities are designed to serve as compensation devices for improving the longitudinal emittance of the free-electron laser FLASH at DESY. These cavities operate in the TM010 mode, and will be located between the injector and the accelerating cavities. Fermilab is obligated to provide DESY with a cryomodule containing four 3rd harmonic cavities. In this paper we discuss the process of welding helium vessels to these cavities. Included will be a description of the joint designs and weld preparations, development of the weld parameters, and the procedure for monitoring the frequency spectrum during TIG welding to prevent the cavity from undergoing plastic deformation. Also discussed will be issues related to qualifying the dressed cavities as exceptional vessels (relative to the ASME Boiler and Pressure Vessel Code) for horizontal testing and eventual installation at DESY, due to the necessary use of non-ASME code materials and non-full penetration electron beam welds.

## INTRODUCTION

The procedure for dressing a 3.9 GHz 3rd harmonic cavity with a helium vessel entails three welds in the following sequence: (1) Electron-beam (EB) weld of the helium vessel titanium shell to the large Nb55Ti conical disk, (2) EB weld of the titanium spacer ring to the small Nb55Ti conical disk, and (3) TIG fillet weld joining the titanium spacer ring to the titanium shell of the helium vessel. The weld joint geometry is shown in Figure 1. Full penetration EB welds are not allowed due to the possibility of vapor or weld debris deposition on the exterior surface of the cavity cells, thus potentially degrading the heat transfer rate from the cavity to the surrounding helium bath. The objective was to attain sufficient penetration to insure structural integrity and operational safety.

## WELD PARAMETERS

Weld samples were developed to generate final welding parameters. Each sample was cut, polished and etched. Figure 2 shows a final sample of the EB weld joining the helium vessel shell to the large conical disk. Penetration depth achieved is approximately 3 mm. Figure 2 also shows a final sample of the EB weld joining the titanium spacer ring to the small conical disk. Penetration depth is approximately 2.25 mm. Before TIG welding, a titanium filler ring will be inserted to span the gap between the

* Operated by Fermi Research Alliance, LLC under Contract No. DE-AC02-07CH11359.

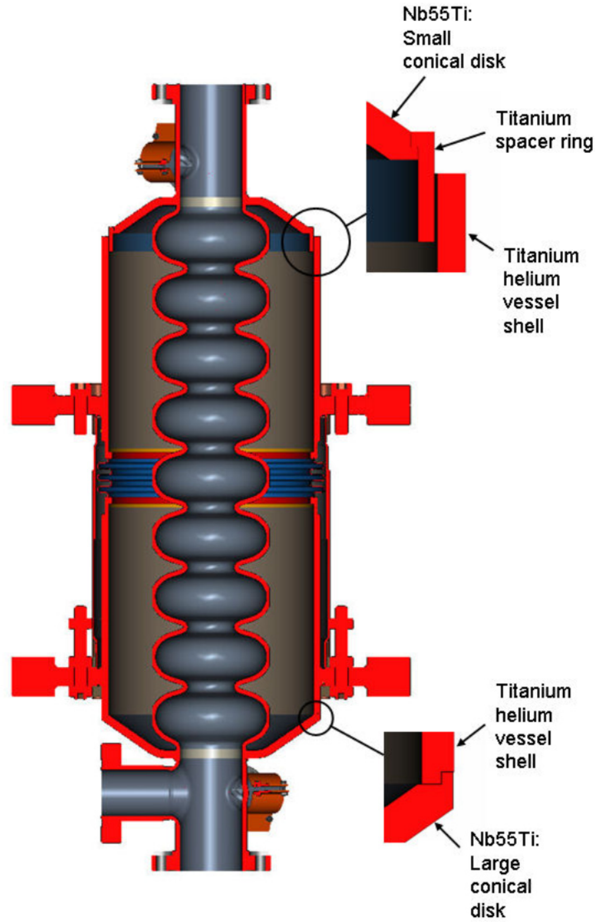


Figure 1: Breakaway view of dressed cavity showing the weld joint geometry.

spacer ring and the inner wall of the helium vessel shell. This is shown in Figure 3. The filler ring helps align the cavity and the helium vessel, and supplies material to augment the TIG fillet weld. The filler ring is fusion welded to the spacer ring on the cavity and the helium vessel shell, thus closing the entire circumferential gap between the helium vessel and the cavity. A TIG fillet weld will complete the process. Figure 3 shows the final sample for the TIG fillet weld.

## WELDING PROCEDURE

After all components are properly cleaned and no more than twenty-four hours before EB welding, the cavity and helium vessel are assembled in a specially designed welding fixture in a clean room environment as shown in Figure 4. The entire assembly is enclosed in a polyethylene bag, sealed, and backfilled with nitrogen for transportation to the EB welding site.

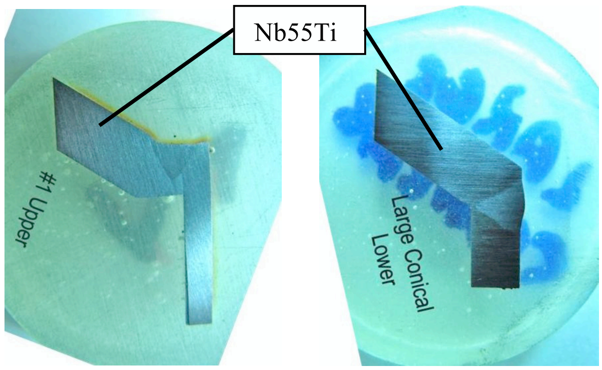


Figure 2: EB weld samples of helium vessel Ti shell to large conical disk (right), and Ti spacer ring to small conical disk (left).

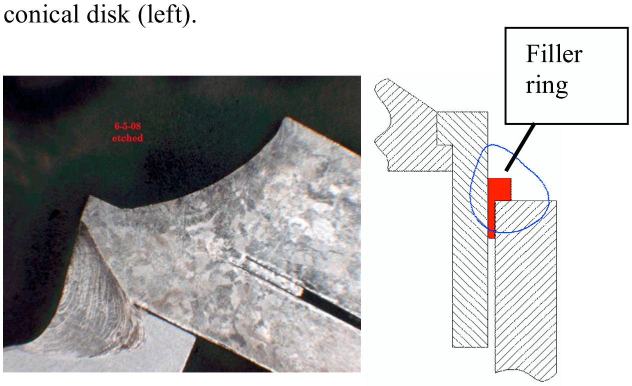


Figure 3: Drawing on the right shows titanium filler ring inserted in the gap between the spacer ring and the inner wall of the helium vessel shell. On the left is the TIG fillet weld sample generated using final weld parameters.

Following the completion of the EB welds the distance between the blade tuner flanges is measured at several locations to verify whether they are parallel. Nuts on the support rods connecting the blade tuner flanges (see Figure 4) can be adjusted for minor corrections. If the blade tuner flanges are significantly out-of-parallel, the cavity may have to be bent. At this point the titanium filler ring is inserted into the remaining gap between the cavity and the inner wall of the helium vessel shell.

## *TIG Welding*

TIG welding is done in a glove box purged with argon. The oxygen level is required to be less than 20 ppm for welding to proceed. Figure 5 shows the glove box configuration. Feedthroughs and hose lines are installed to pass a flow of argon through both the cavity and the helium vessel while TIG welding is in progress. Argon to the cavity passes through a 0.01 micron ceramic filter to avoid contamination. Once the helium vessel is tack welded to the cavity, the support rods are removed from the blade tuner flanges so that the bellows can relieve limited thermal expansion.

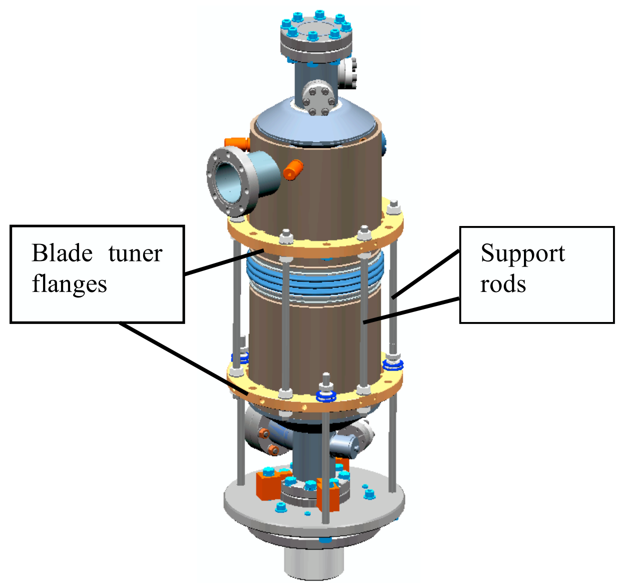


Figure 4: Cavity with helium vessel assembled in EB welding fixture.

TIG welding progresses in segments to avoid overheating and plastically deforming the cavity. A cool down period of ~ 15 minutes is allowed after each TIG weld segment. A continuous flow of argon gas is passed through both the cavity and the helium vessel during welding to facilitate cooling. The frequency spectrum of the cavity is monitored after every step of the welding process to insure the elastic limit of the cavity is not exceeded. Figure 6 shows a plot of the frequency response during TIG welding of cavity No. 7. A close-up view of a

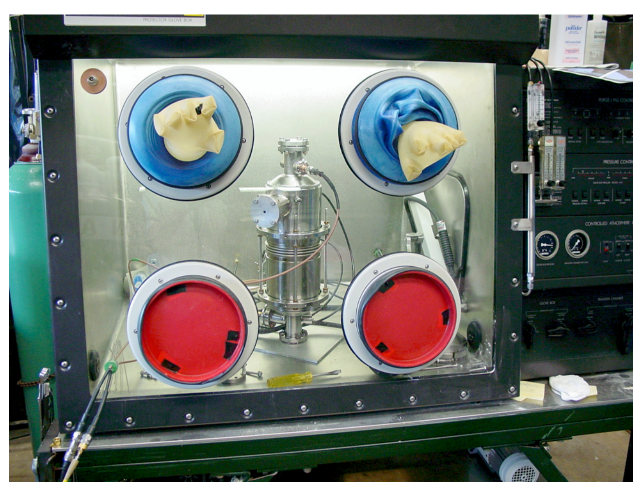

Figure 5: Glove box with cavity installed for TIG welding. Note the cables for monitoring the frequency spectrum of the cavity, and the lines for passing argon through the cavity and helium vessel during welding.

completed TIG weld on one of the cavities is shown in Figure 7.

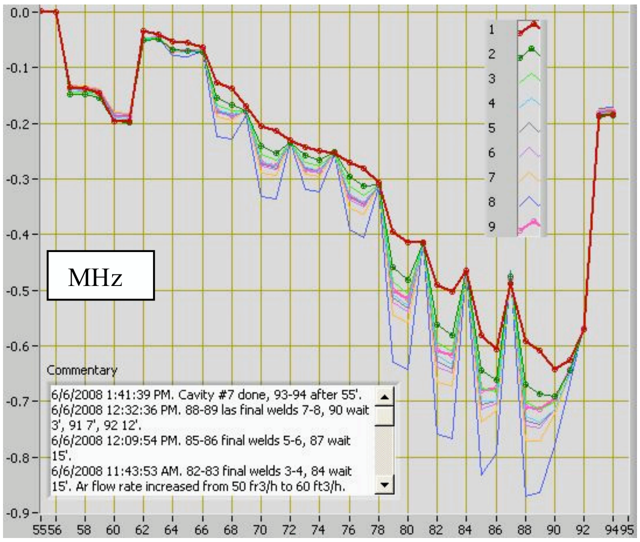


Figure 6: Frequency spectrum of cavity No. 7 recorded during TIG welding. The horizontal axis is time.

Figure 7: Close-up view of 3$^{rd}$ harmonic cavity with helium vessel after TIG welding is complete.

## RESULTS

A total of eight 3$^{rd}$ harmonic cavities have been fabricated, including one prototype. Five have been dressed (including the prototype). The two EB welds have had no significant effect on the tune of any of the five dressed cavities. This was expected because the cavities were not restrained during EB welding. Figure 8 shows plots of the field distribution for cavity No. 7 before and after TIG welding. Note that the field flatness is basically unaltered. This result is typical for the cavities that were TIG welded following the procedure described in the preceding section.

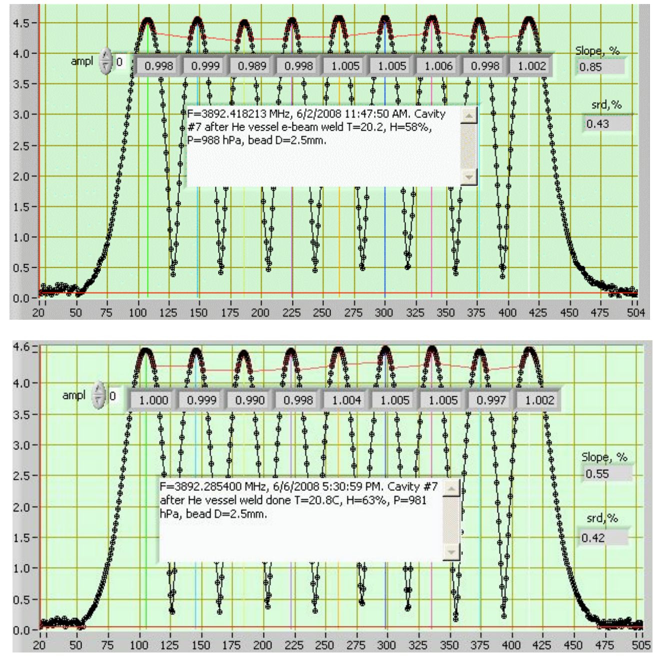


Figure 8: Field distribution of cavity No. 7 after EB welding and before TIG welding (top), and after TIG welding (bottom).

## PRESSURE VESSEL ISSUES

Each dressed cavity is defined by Fermilab safety standards as a pressure vessel. By definition, a pressure vessel follows the guidelines of the ASME Boiler and Pressure Vessel Code. As part of the Fermilab safety standard, an engineering note must be generated and submitted for approval to an internal Fermilab review committee. Once the note is approved, the dressed cavity is qualified for horizontal testing and eventual shipment to DESY. Because of the design and welding procedure of parts of the dressed cavity, these vessels are defined as “Exceptional Vessels” relative to the Fermilab safety standards. The major issues are: (1) Niobium and Nb55Ti are not ASME code certified materials, and (2) EB welds joining the helium vessels to the cavities are not full penetration. Furthermore, the published data on the mechanical properties of niobium and Nb55Ti at cryogenic temperatures are not entirely consistent at present. The objective in the engineering note is to demonstrate the vessels are safe at a level equivalent to the ASME code. The ASME Boiler and Pressure Vessel Code, Section VIII, Divisions 1 and 2 were used for guidance. FEA was done using the most conservative material properties in the published literature. Each dressed cavity will be pressure tested to 2.3 bar; i.e., 1.15 times the MAWP of 2.0 bar. To address these issues in the future, Fermilab has established an internal task force to discuss aspects of pressure vessel safety relative to the design, documentation, and review of SRF accelerating components.

# STATUS OF 3.9 GHz SUPERCONDUCTING RF CAVITY TECHNOLOGY AT FERMILAB*

E. Harms, T. Arkan, V. Bocean, H. Carter, H. Edwards, M. Foley, T. Khabiboulline, M. McGee, D. Mitchell, D. Olis, A. Rowe, N. Solyak, FNAL, Batavia, IL 60510, U.S.A.

*Abstract*

Fermilab is involved in an effort to design, build, test and deliver four 3.9 GHz superconducting rf cavities within a single cryomodule to be delivered to DESY as a 'third harmonic' structure for the FLASH facility to improve the longitudinal emittance. In addition to an overall status update we will present recent results from single 'dressed' cavity horizontal tests and shipping and alignment measurements.

## INTRODUCTION

Fermilab is constructing a cryomodule containing four superconducting radio frequency (SRF) cavities operating at 3.9 GHz for the Free electron LASer in Hamburg (FLASH) facility at the Deutsches Elektronen-SYnchrotron (DESY) laboratory. This cryomodule was proposed to linearize the energy distribution along a bunch upstream of the bunch compressor. The four 9-cell cavities were designed to operate at 2 K in the $TM_{010}$ $\pi$-mode at an accelerating gradient $E_{acc}$ = 14 MV/m. Table 1 contains a list of parameters.

Table 1: Cryomodule Parameters

| | |
|---|---|
| Number of Cavities | 4 |
| Active Length | 0.346 meter |
| Gradient | 14 MV/m |
| Phase | -179° |
| R/Q [$=U^2/(\omega W)$] | 750 Ω |
| $E_{peak}/E_{acc}$ | 2.26 |
| $B_{peak}$ ($E_{acc}$ = 14 MV/m) | 68 mT |
| $Q_{ext}$ | $1.3 \times 10^6$ |
| BBU Limit for HOM, Q | $<1 \times 10^5$ |
| Total Energy | 20 MeV |
| Beam Current | 9 mA |
| Forward Power, per cavity | 9 kW |
| Coupler Power, per coupler | 45 kW |

## CAVITY FABRICATION AND TESTING

Eight cavities have now been fabricated and undergone various levels of testing. A summary of test results and status of each is found in table 2. Details as to cavity performance can be found elsewhere [1] and at this conference [2].

*Operated by Fermi Research Alliance, LLC under Contract No. DE-AC02-07CH11359 with the United States Department of Energy.

Table 2: Cavity Fabrication and Testing Status

| Cavity | Assembled by | Completion date | Test results and status |
|---|---|---|---|
| #1: 2-leg HOM | Fermilab | January 2006 | - Never tested: HOM membrane break during cleaning<br>- Used as horizontal test prototype |
| #2: 2-leg HOM | Fermilab | February 2006 | - Best vertical test: 12 MV/m limited by HOM heating<br>- Fractured Formteils<br>- Awaiting repair |
| #3: 2-leg trimmed HOM | Fermilab JLab | August 2006 | - Best Vertical test: 24.5 MV/m, achieved after HOM trimming<br>- Welded into Helium vessel<br>- Dressed for Horizontal testing |
| #4: 2-leg trimmed HOM | Fermilab JLab | March 2007 | - Best Vertical test: 23 MV/m<br>- Final vertical test with HOM feedthroughs |
| #5: 2-leg trimmed HOM | Fermilab JLab | May 2007 | - Best Vertical test: 24 MV/m<br>- Welded into Helium vessel<br>- Horizontal testing complete: 22.5 MV/m<br>- Ready for string assembly |
| #6: 2-leg trimmed HOM | Fermilab JLab | May 2007 | - Best Vertical test: 22 MV/m<br>- Faulty welds repaired<br>- Awaiting final vertical test with HOM feedthroughs |
| #7 single-post HOM | Fermilab JLab DESY | November 2007 | - Best Vertical test: 24.5 MV/m<br>- Welded into Helium Vessel<br>- Awaiting dressing and horizontal test |
| #8 single-post HOM | Fermilab DESY | October 2007 | - Vertical test: 24 MV/m<br>- Welded into Helium vessel<br>- Awaiting dressing and horizontal test |

### *Fabrication*

Cavity fabrication has been reported previously [3]. Recently, Jefferson Lab expertise was called upon to repair broken welds found on cavity #6 ends during vertical testing. Cavity #2, which failed early in the test process, is now being fitted with replacement HOM bodies. At this time, weld samples are being evaluated prior to attempting this novel repair.

### *Helium Vessel Welding*

Once vertical test goals are met, each cavity is welded into a titanium helium vessel. Helium vessels have been welded on to five cavities (including one prototype) [4]. The frequency spectrum of each cavity was measured at appropriate intervals during the welding process to assess any changes. For the five vessels welded to date, the two electron beam welds have had no significant effect on the tune of any of the dressed cavities. This was expected because the cavities are not restrained during this welding step.

TIG welding is done in segments to avoid overheating and plastic deformation. Once the helium vessel is tack welded to the cavity, the support rods are removed from the blade tuner flanges so that the bellows can relieve limited thermal expansion. A cool down period of several minutes is allowed after each succeeding TIG weld segment. A continuous flow of argon gas is passed through both the cavity and the helium vessel during welding to facilitate cooling. The frequency spectrum of the cavity is monitored after every step of the TIG welding process to ensure the elastic limit of the cavity is not exceeded.

This critical assembly step can now be considered a mature and reproducible process. Detailed documentation exists to ensure that future welds are completed with the same care.

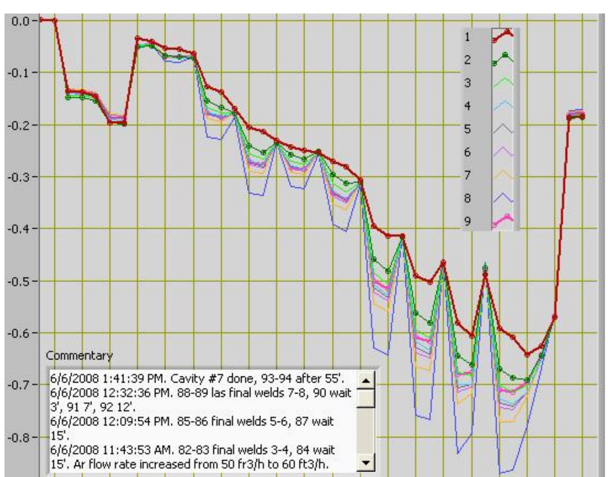


Figure 1: Frequency Spectrum for Cavity #7 during TIG welding. Time proceeds from left to right. Frequency spring-back due to cool down periods can be seen, particularly in later steps.

### *Dressing*

Following the helium vessel mating, each cavity receives a final 20 μ internal BCP etch, then is outfitted with its main input coupler, HOM coupler feed throughs, transmitted power probe, magnetic shielding, and blade tuner. Once this 'dressing' is completed a pressure vessel test is performed on the helium vessel to meet regulatory requirements. Assemblies are tested to 2.3 bar, 1.15 times the Maximum Allowable Working Pressure (MAWP) of 2.0 bar.

The resulting 'dressed' cavity is again RF tested, in a horizontal orientation, so as to ensure that the steps just completed have not compromised cavity performance. This test also provides the most realistic evaluation of single cavities prior to assembly as a string. As of this writing only one cavity, #5, has been subjected to this sequence. A description of the Horizontal Test stand and the test of #5 is described elsewhere [5].

### *String Assembly*

The 4-cavity string will be assembled in Fermilab's MP-9 clean room. Fit-ups with mockup cavities have helped to ensure that once a sufficient number of cavities are available, assembly will proceed in a relatively trouble-free manner.

## SHIPPING AND ALIGNMENT

Extensive modeling and studies have been carried out in preparation for transporting the entire 4-cavity module to DESY once completed. Much of this work has been documented elsewhere [6,7]. The design was peer reviewed verifying its fundamental soundness and providing valuable ideas based on past experience with transporting similar devices. This work has been carried out in four distinct phases:

- Modeling
- Transport studies utilizing a string of mock-up cavities driven around the Fermilab site
- Refinement of the transport/support scheme based on transport experience
- Transport from Fermilab to O'Hare International Airport to validate the transport scheme and document expected forces.

DESY has indicated the overall alignment tolerance requirement of the cold cryomodule for the TTF/FLASH accelerator to be 0.5 mm. An error budget analysis, including, among others, the referencing of the cavities centerline, thermal cycling (warm up cool down), cavity string alignment and referencing to the vessel, string misalignments due to shipping, gave a maximum tolerance for alignment and cavities shift during transport of 0.25 mm.

Analyses from the transport studies and follow-on alignment checks indicate that the cavities maintain their relative alignment of 0.1 mm with respect to a straight line within the cavity string; however, the alignment with respect to the vacuum vessel is only marginal to the allowable tolerance. During the early transport studies the cavity string was affected by transverse and longitudinal shock at low frequencies (beneath 10 Hz). Cavities moved coherently (as one) in the transverse direction, responding to shock and vibration.

After modifications to the base frame and isolation system, this effect was minimized. This deformation study indicates that the cavity string ensemble was subject to very small (less than 0.1 mm) displacements between subsequent tests while still maintaining their relative horizontal and vertical alignment with respect to a straight line within 0.1 mm. Also, the overall maximum transversal shift of the cavity string among those tests was less than 0.1mm horizontal and vertical.

## OTHER COMPONENTS

### *Input Couplers*

Three of the six procured input couplers have been assembled and conditioned on the test stand assembled for this purpose. Coupler design and early test stand experience is previously documented [8]. A conditioning protocol following the DESY experience is followed. Protection against damage is afforded by an interlock system using thermometry mounted close to the ceramic windows, electron and light detectors, and vacuum activity as inputs.

Couplers are conditioned in pairs. The first pair was conditioned as the stand was commissioned in late 2007. Only vacuum activity was noted, especially at higher powers, but this decreased over time. One of these couplers was mounted on Cavity #5 for horizontal testing and behavior here was similar during warm operation. For cold operation, no coupler-related trips were noted.

A second pair of couplers was mounted on the conditioning stand and operated in May 2008. One of these couplers was trimmed by an additional 1mm prior to conditioning based on the results of cold measurements on cavity #5 at HTS. This sequence, too, was fairly uneventful as evidenced by only seven ‘hard trips’ signifying excessive electron emission or visible sparks over the 3-day span of conditioning. The shorter of the two couplers conditioned here is now mounted on Cavity #3 for evaluation during the next horizontal test. The remaining couplers will be trimmed and conditioned once the proper coupler length is determined. As these couplers are of fixed length, it is obviously vital that this dimension is precisely known.

### *HOM Coupler Feedthroughs*

The HOM coupler feedthroughs mounted on the cavities for final vertical and horizontal testing are a 2$^{nd}$ generation design based upon Jefferson Lab experience with sapphire insulators. Each antenna probe is trimmed uniquely for the cavity and location to which it is placed. Extensive cold testing and vacuum leak checks ensure reliable feedthoughs. Some pieces have developed vacuum leaks following cool down to 2K and discarded. Of eighteen pieces received from the vendor, four have been deemed unusable.

## SUMMARY

Fermilab is in the process of providing a 4-cavity 3.9 GHz cryomodule to DESY for installation in the FLASH facility. A sufficient number of cavities have now passed vertical testing and have helium vessels welded onto them. Horizontal testing of dressed cavities is in progress and string assembly will commence shortly.

It is intended to ship the completed module to DESY and RF test it in the Cryo-Module Test Bed (CMTB) prior to installation in FLASH.

## ACKNOWLEDGEMENTS

The authors acknowledge the significant assistance and counsel received from numerous colleagues at DESY. Many people at Jefferson Lab have contributed to this effort as well. The dedicated efforts of the growing SRF staff at Fermilab, particularly members of the Accelerator and Technical Divisions, especially the A0 SCRF technical support group, have been critical to the progress made to date.

## REFERENCES

[1] T. Khabiboulline, et al, “Vertical and Horizontal Test Results of 3.9 GHz Accelerating Cavities at FNAL,” Applied Superconductivity Conference 2008, Chicago, August 2008, 2LPC07.

[2] E. Harms, et al, “Performance of 3.9 GHz Superconducting Cavities,” this conference, THP029.

[3] E. Harms, et al, “Status of 3.9-GHz Superconducting RF Cavity Technology at Fermilab,” LINAC 2006, Knoxville, TN, August 2006,THP051, p. 695 (2006); http://www.JACoW.org.

[4] M. Foley, et al, “Welding Helium Vessels to the 3.9 GHz Superconducting Third Harmonic Cavities,” this conference, THP027.

[5] E. Harms and A. Hocker, “Performance of 3.9 GHz SRF Cavities at Fermilab’s ILCTA_MDB Horizontal Test Stand,” Applied Superconductivity Conference 2008, Chicago, August 2008, 2LX08.

[6] M. McGee, et al. “Translantic Transport of Fermilab 3.9 GHz Cryomodule for TTF/FLASH to DESY,” EPAC08, Genoa, June 2008, MOPP022, p. 592 (2008); http://www.JACoW.org.

[7] V. Bocean and M. McGee, “Referencing and Stability Studies of the Fermilab 3.9 GHz (3$^{rd}$ Harmonic) Cryomodule for DESY TTF/FLASH,” The 10$^{th}$ International Workshop on Accelerator Alignment, Tsukuba, Feb. 2008, FR004.

[8] Li, et al, “ RF Design and Processing of a Power Coupler for Third Harmonic Superconducting Cavities,” Proceedings of PAC07, Albuquerque, WEPMN100, p. 2265; http://JACoW.org.

# PERFORMANCE OF 3.9-GHZ SUPERCONDUCTING CAVITIES*

E. Harms, H. Edwards, A. Hocker, T. Khabiboulline, N. Solyak,
Fermilab, Batavia, Illinois, 60510 USA

*Abstract*

We report on the performance of 3.9 GHz SRF cavities built and tested at Fermilab for use in the DESY FLASH facility. Comparisons of performance in various test scenarios are presented. We also report on analysis of expected maximum performance.

## INTRODUCTION

Four 3rd harmonic nine-cell 3.9 GHz superconducting cavities will operate at a gradient of 14 MV/m in the $TM_{010}$ mode and will be placed in TTF/FLASH. These cavities are designed to linearize the accelerating gradient of the accelerator, providing improved longitudinal emittance.

## TESTING SEQUENCE

Once fabricated, each 3.9 GHz cavity goes through a sequence of processing steps prior to high power RF being introduced to the cavity. This has been described previously [1]. Following initial processing, all cavities are tested vertically in the Fermilab's A0 North cave test area. This test area consists of a shielded enclosure, cryogenic system, LLRF, and traveling wave Tube amplifier capable of providing up to 150 watts CW. A basic controls system allows for Labview™ applications, electronic logbook, and file archival.

### *Vertical Tests*

More than fifty cold vertical tests have been conducted to date. Figure 2 shows the Q vs E slope for all such tests. Recently, cavities have been operated at the default operating temperature of 1.8K as well as the operating FLASH temperature, 2K. One can note that with few exceptions, cavities are able to achieve gradients well in excess of the goal of 14 MV/m. Several factors limit ultimate cavity performance in this stage. In best cases the limit is the available RF power. Excessive x-ray emission suggesting a need to re-rinse or, in isolated cases, repeat a BCP is not uncommon. Performance of cavities fitted with HOM feedthoughs tend to be limited by heating or quenching of one or both HOM's.

The number of tests per cavity have ranged from as few as 3 (for #7) to 14 (for #6) in the case of poor-performing cavities. All cavities destined for the next step in processing must achieve the cavity performance parameters and gradients at least 20% better than the goal of 14 MV/m. Figure 1 shows the Q vs E result for the four cavities passing the vertical test and welded into helium vessels.

Operated by Fermi Research Alliance, LLC under Contract No. DE-AC02-07CH11359 with the United States Department of Energy.

Table 2: Summary of Best Performance in Vertical Tests

| Cavity | # of tests | Emax (MV/m) | Status |
|---|---|---|---|
| #1 | n/a | n/a | Prototype; used as test bed |
| #2 | 6 | 12 | Fractured HOM formteils; to be repaired |
| #3 | 10 | 24.5 @ 1.8K<br>20.27@ 2K | Welded into helium vessel; dressed; being prepared for horizontal testing |
| #4 | 10 | 24.27 @ 1.8K | Final vertical testing in progress |
| #5 | 4 | 24 @ 1.8K<br>Horizontal test: 22.5 @ 2K | Welded into helium vessel; Horizontal testing completed; awaiting string assembly |
| #6 | 14 | 22.5 @ 1.8K | Weld repair, plasma processing attempted to improve vertical test performance |
| #7 | 3 | 24.5 @ 1.8K<br>19.17 @ 2K | Welded into helium vessel; awaiting dressing & horizontal testing |
| #8 | 5 | 24.5 @ 1.8K | Welded into helium vessel; awaiting dressing & horizontal testing |

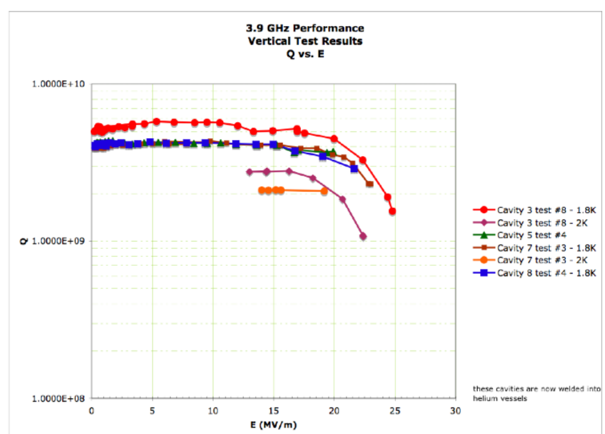


Figure 1: Q vs. E slope for 3.9 GHz cavities welded into Helium Vessels.

Recently, one cavity, #3, has undergone a final vertical test after being welded into a helium vessel, but prior to dressing. As the schedule permits, additional cavities may be subjected to this intermediate step.

Two production cavities, #4 and #6, remain to complete vertical testing owing to recent problems with vacuum system contamination and High Pressure Rinse system failures.

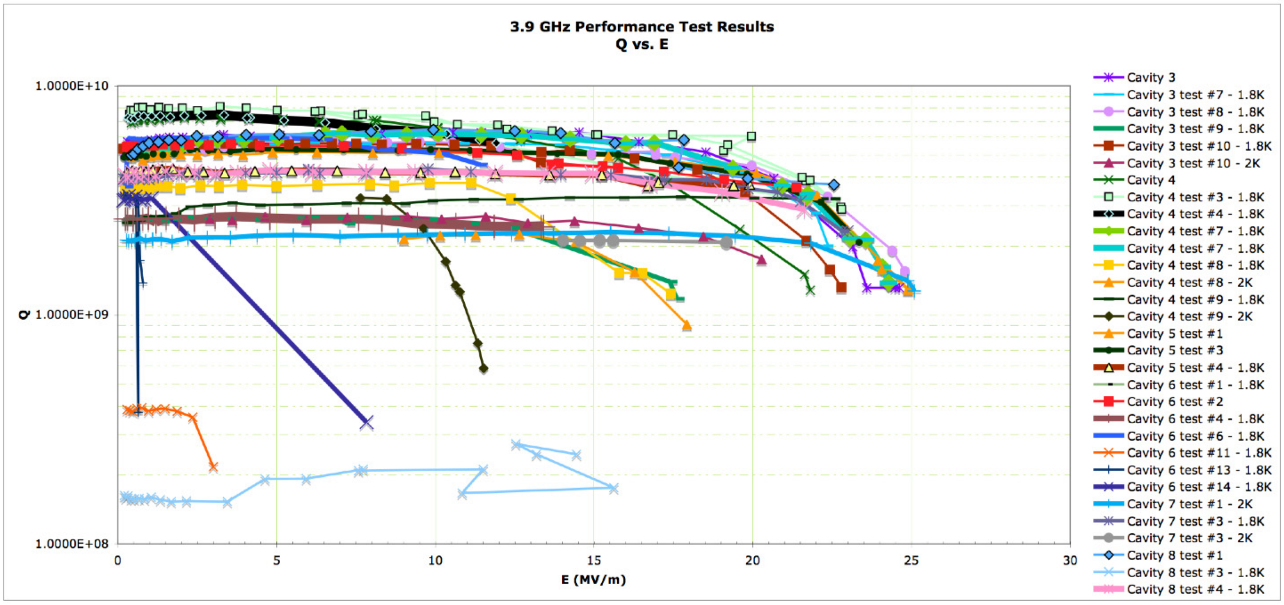


Figure 2: Vertical Test Performance of 3.9 GHz cavities. A handful, roughly 15%, indicate significantly poor performance.

## *Horizontal Testing*

After vertical testing is completed and a cavity dressed, it is subjected to additional RF testing in a horizontal configuration. As of this writing only one cavity, #5, has been completed this sequence. A description of the Horizontal Test Stand (HTS) and the test of #5 has been reported elsewhere [2].

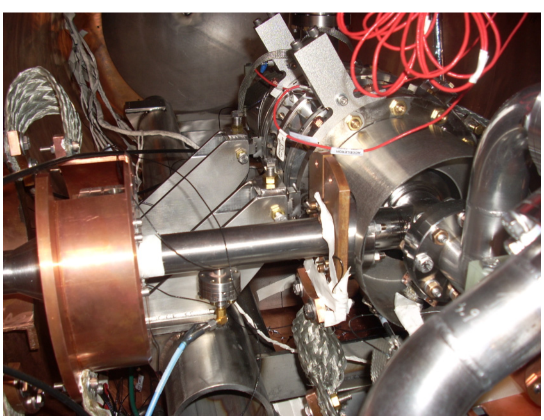

Figure 3: Cavity #5 mounted in the HTS.

This horizontal test with RF power was carried out over the period from early April through August 2008. Early on it was observed that 5 Hz operation led to unacceptable heating of the HOM coupler feed throughs. Various heat intercept schemes were attempted and each such iteration required a complete warm-up and cool down cycle. Future horizontal tests will benefit from this exercise.

Cavity #5 is now deemed ready for string assembly. Recently Cavity #3 was pressure tested and is being readied for horizontal testing.

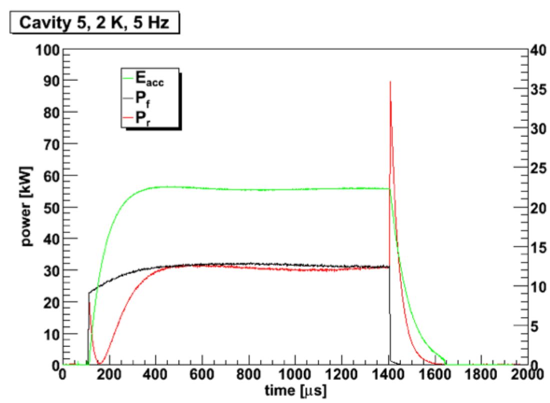


Figure 4: Cavity 5 performance in HTS just below its quench limit.

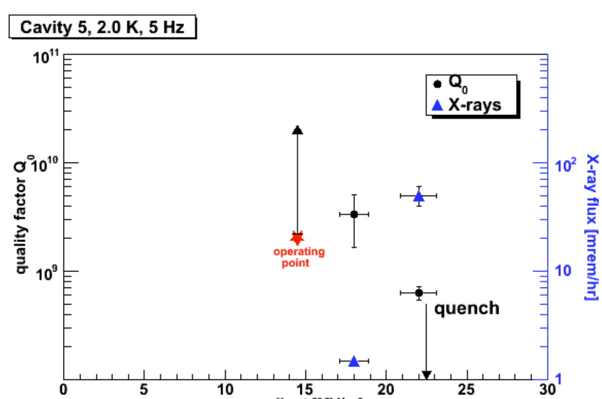


Figure 5: $Q_0$ vs. $E_{acc}$ and X-rays vs. $E_{acc}$ curves for Cavity #5.

## THERMAL ANALYSIS

The cavity performance data as shown here is quite reproducible and indicates a limit of about 24-25 MV/m for these cavities. It becomes interesting to try to perform a simple thermal analysis to compare with the measurements. Such an analysis might give an indication as to how close the global thermal breakdown limitation is being approached and is reported previously [4].

## SUMMARY

Fermilab is in the process of providing a 4-cavity 3.9 GHz cryomodule to DESY for installation in the FLASH facility. Most cavities perform well in excess of the design gradient of 14 MV/m. A sufficient number of cavities have now passed vertical testing and have helium vessels welded onto them. Horizontal testing of dressed cavities is in progress and string assembly will shortly commence.

## ACKNOWLEDGEMENTS

The authors acknowledge the significant assistance received from the staff of Jefferson Lab and particularly DESY. The dedicated efforts of the growing SRF staff at Fermilab, and especially the A0 SCRF technical support group, have been critical to the progress made to date.

## REFERENCES

[1] E. Harms, et al, “Status of 3.9-GHz Superconducting RF Cavity Technology at Fermilab,” LINAC 2006, Knoxville, TN, August 2006,THP051, p. 695 (2006); http://www.JACoW.org.

[2] E. Harms and A. Hocker, “Performance of 3.9 GHz SRF Cavities at Fermilab’s ILCTA_MDB Horizontal Test Stand,” Applied Superconductivity Conference 2008, August 2008, 2LX08.

[3] T. Khabiboulline, et al, “Vertical and Horizontal Test Results of 3.9 GHz Accelerating Cavities at FNAL,” Applied Superconductivity Conference 2008, Chicago, August 2008, 2LPC07.

[4] E. Harms, et al, “Status of 3.9 GHz Superconducting RF Cavity Technology at Fermilab,” 13th International Workshop on RF Superconductivity, Beijing, October 2007, WEP41.

# HIGH GRADIENT TESTS RESULTS OF 325 MHz SINGLE SPOKE CAVITY AT FERMILAB

I. Gonin, T. Khabibouline, G. Lanfranco, A. Mukherjee, J. Ozelis, L. Ristori, G. Romanov, D.A. Sergatskov, R. Wagner, R. Webber, G. Apollinari - FNAL, Batavia, IL 60510, U.S.A.
J. Fuerst, M. Kelley, K. Shepard - ANL, Argonne, IL 60439, U.S.A.

## Abstract

Eighteen β = 0.21 superconducting single spoke resonators comprise the first stage in the cold section of the 8-GeV $H^-$ Linac for Fermilab's proposed Project X. After Buffered Chemical Polishing and High Pressure Rinse, one resonator has undergone high gradient RF testing at 2.0 – 4.5 K in the Vertical Test Stand at Fermilab. We present measurements of the surface resistance as a function of temperature and the quality factor as a function of accelerating field. The resonator reached an accelerating field of 18.0 MV/m.

## SUPERCONDUCTING SPOKE RESONATORS IN PROJECT X AND HINS

Fermilab recently proposed Project X, a high intensity, 8-Gev, $H^-$ Linac based on independently phased superconducting resonators [1] to explore the Intensity Frontier. The High Intensity Neutrino Source (HINS) program is aimed at the demonstration of critical technologies for the low-energy front-end of the Linac.

Three superconducting spoke resonators comprise the low energy portion of the Linac cold section and operate at 325 MHz, one quarter of the frequency of the ILC type cavities that make up the high energy end. Two Single Spoke Resonators, SSR1 with β = 0.21 [2] and SSR2 with β = 0.4, will be built and operated as part of HINS.

Two SSR1 prototypes, SSR1-01 at Zanon [3] and SSR1-02 at Roark [4], have been fabricated. Figure 1, an exploded-view schematic of SSR1, shows the main features. The spoke spans the inner diameter of the shell, and two accelerating gaps are formed between the spoke and the endwalls. Liquid helium flows around the outer surfaces of the shell and endwalls and through the spoke.

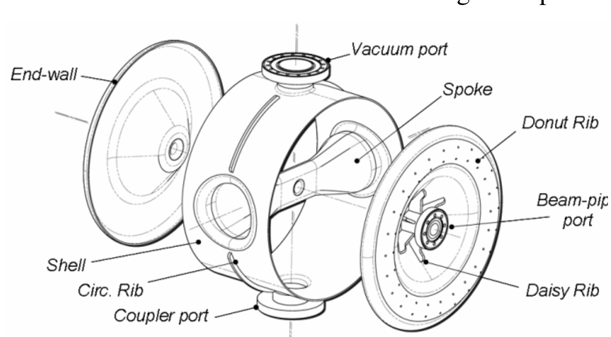


Figure 1: Exploded-view schematic of SSR1.

The cavity operates at a temperature T = 4.4 K, a nominal accelerating gradient $E_{acc}$ = 10 MV/m, and an intrinsic quality factor $Q_0 > 0.5\times10^9$ at the accelerating gradient of 10 Mv/m.

After the first prototype, SSR1-01, arrived at Fermilab from Zanon, low gradient RF measurements, including bead pulls, were made to check the resonant frequency and compare the field profile with the calculation of Microwave Studio (MWS) [5]. The agreement was very good, with a field flatness of 99.7%.

## BUFFERED CHEMICAL POLISHING AND HIGH PRESSURE RINSE

The interior surface of SSR1-01 was then prepared for testing at high gradient. The cavity was immersed in a bath of Ultra-Pure Water (UPW) with a degreasing agent and ultrasonically cleaned. It was then taken to the ANL G150 facility for Buffered Chemical Polishing (BCP), followed by a High Pressure Rinse (HPR).

The BCP used the standard $HF:HNO_3:H_3PO_4(1:1:2)$ acid mixture. During BCP, acid flow and temperature were controlled in the following manner. The cavity was immersed in a bath of UPW that was initially cooled to 7.5 ºC by a continuously operating chiller. The cavity interior, sealed from the water bath, was connected to a pump for acid circulation. The cavity was oriented with the power coupler port and the vacuum port along the vertical axis and the beam pipes along the horizontal axis. In order to begin etching, acid (earlier chilled to 14 ºC) was pumped up through the bottom port to fill the interior of the cavity plus an "overflow bucket" connected to the top port. After shutting off the source of acid, the closed loop circulation pump drew acid from the overflow bucket and sent it back to the cavity through flanges on both beam pipes. Heat generated by the etching was dissipated through the cavity walls (including the spoke walls) to the continuously cooled water bath.

In order to obtain a total etching of ~120 μm and keep the niobium content in the acid below 10 g/l, spent acid was replaced with fresh acid about half way through the etching. Given the asymmetry in the acid flow pattern, the cavity was flipped top to bottom between the two etching sessions. The reduction in wall thickness was monitored at 20 locations using an ultrasonic thickness gauge.

The wall thickness reduction averaged 119 μm after a total etching time of 160 minutes. The acid temperature averaged 15.9 ºC and ranged between 14.9 ºC and 17.0 ºC during the etching. The thickness reduction was not as uniform as hoped, and we have plans to distribute the acid flow more uniformly in the future.

After BCP, the SSR1-01 was moved to the G150 class

10 clean area for HPR. The UPW distribution consists of a long wand with a nozzle at the end that produces six water jets, two each at +45º, 90º, and –45º to the wand axis. The wand rapidly rotates about the axis and travels along the axis (into or out of the cavity) at ~3 cm/min. After completing the HPR (20 minutes at each of 6 orientations), the cavity was left in a good orientation for drainage and left to dry in the class 10 clean area overnight.

## HIGH GRADIENT MEASUREMENTS

The Fermilab Vertical Test Stand (VTS), a liquid helium dewar designed for high-gradient testing of bare 9-cell ILC cavities, was used for the first cold test of the bare SSR1-01. The SSR1-01 was mounted in the VTS dewar with the power coupler port up and the beam pipe along the horizontal axis.

There have been three test sessions in the VTS; Test 1 in February, 2008, Test 2 in March, 2008 and Test 3 in July, 2008. For Test 1 (the first cold test of the cavity) and Test 2, the VTS did not yet have a cavity vacuum system, so the SSR1 was evacuated (to $2\times10^{-6}$ Torr for Test 1) and sealed before installation into the dewar.

In Test 1, $Q_0$ was measured as a function of temperature, T, as the temperature was lowered from 4 K to 2 K at $E_{acc}$ = 2 MV/m. As shown in Fig. 2, this data was used to obtain the surface resistance, $R_s(T) = R_0 + R_{BCS}(T)$ with a fit residual resistance of $R_0$ = 5.1 nΩ.

In Test 1, the resonant frequency was measured as a function of the liquid helium bath pressure, as shown in Fig. 3. The measured pressure sensitivity agrees quite well with the value of –630 Hz/Torr predicted by the MWS simulation of the bare cavity (the simulation predicts a much smaller value of –30 Hz/Torr when the helium vessel is attached).

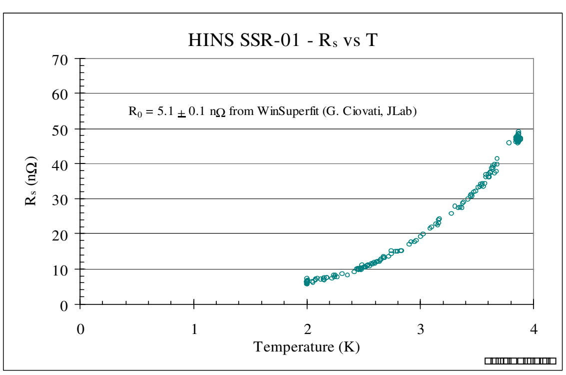


Figure 2: The measured variation of surface resistance with temperature.

In Test 2, the resonant frequency was measured as a function of $E_{acc}^2$, as shown in Fig. 4. The measured Lorentz force detuning coefficient of approximately –4 Hz/(MV/m)$^2$ agrees much better with the simulation's prediction of the cavity with the helium vessel attached, –3.8 Hz/(MV/m)$^2$, than bare, –13.4 Hz/(MV/m)$^2$. This is not yet understood.

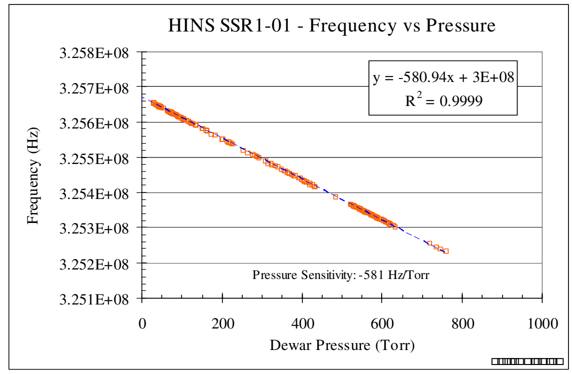


Figure 3: The measured variation of resonant frequency with liquid helium pressure.

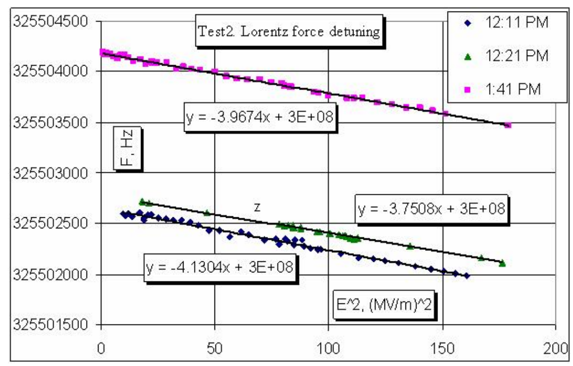


Figure 4: The measured variation of resonant frequency with $E_{acc}^2$. Change in dewar pressure accounts for the frequency shift with time.

### [illegible]

When increasing $E_{acc}$ at 2 K in Test 1, several multipacting barriers were encountered and we could not process beyond one near 6 MV/m. During Test 1, the SSR1-01 was instrumented with temperature monitors on the shell, around most of the circumference at the endwalls and around the ends of the spoke. The monitors indicated that the multipacting occurred only at the bottom of the cavity near the vacuum port.

After ending Test 1 and warming to room temperature, the cavity pressure was measured to be 1 to 2 orders of magnitude higher than expected if the cavity was just sitting on the shelf. An RGA indicated that the cavity contained water and hydrogen, but no detectable helium. The poor vacuum and evidence for multipacting predominately on the bottom indicated a possible problem with condensates forming during both the cool down and the multipacting.

Test 2 began with a cavity vacuum of $1.2\times10^{-7}$ Torr. The $E_{acc}$ scan of $Q_0$ at 2 K, shown in Fig. 5, reached 13.5 MV/m before field emission prevented further increase with our 200 W power supply. The multipacting barriers shown in the figure were also encountered upon subsequent $E_{acc}$ scans in Test 2. Figure 6 shows the X-ray intensity from a detector installed just above the VTS dewar's top plate. Field emission clearly became a significant power drain above ~8 MV/m in Test 2. An $E_{acc}$ scan of $Q_0$ at 4.4 K, shown in Figure 5, ended with a thermal quench at 12.5 MV/m.

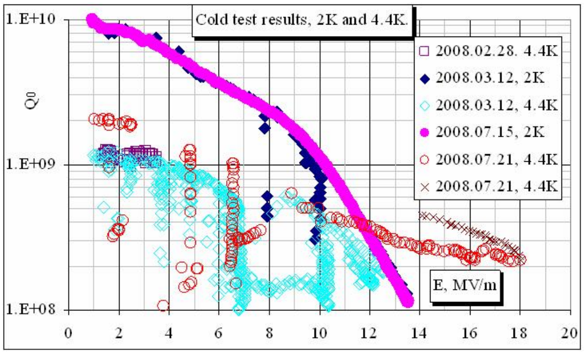


Figure 5: $Q_0$ versus $E_{acc}$ scans at 2 K and 4.4 K from the three tests. Test 1: 2008.02, Test 2: 2008.03, and Test 3: 2008.07. Data from the reverse scan at 4.4 K in Test 3 are indicated by X's.

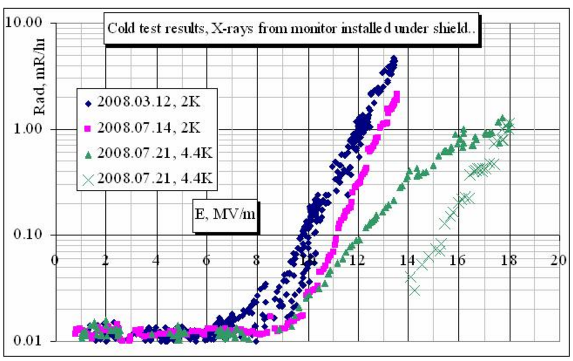


Figure 6: X-rays detected during the $Q_0$ versus $E_{acc}$ scans at 2 K and 4.4 K. Test 2: 2008.03, and Test 3: 2008.07. Data from the reverse scan at 4.4 K in Test 3 are indicated by X's.

With the presence of field emission at high $E_{acc}$, we hoped to do an improved HPR before the next VTS test, but the VTS scheduling allowed for a third test before another HPR could be arranged at ANL. Steps were taken to optimize the cavity vacuum throughout Test 3. A two day long 120 ℃ vacuum bake was performed shortly before the cavity was installed in the VTS. In addition, the newly commissioned cavity vacuum system of the VTS allowed a vacuum at the cavity of ~$8x10^{-8}$ Torr.

Test 3 started with an $E_{acc}$ scan of $Q_0$ at 2 K, and the result, shown in Fig. 5, was essentially identical to that from Test 2, with the important exception that after the initial scan, the cavity no longer fell into multipacting barriers near the operating gradient of 10 MV/m when raising the field. The VTS was left to warm to approximately 3.5 K overnight, and the following morning $E_{acc}$ could not be raised above 15 kV/m, indicating a helium leak. After warming up to room temperature, helium was clearly seen in an RGA, but efforts to isolate the source of the leak at that time were unsuccessful.

After cooling back down to 4.4 K, the field could again be raised, and the $E_{acc}$ scan of $Q_0$ shown in Fig. 5 was taken. In this case, data taken during the initial increase in field (including processing multipacting barriers) and data subsequently taken working backward from the maximum field are plotted with different symbols. There are several interesting features of this scan. $Q_0$ at low $E_{acc}$ is nearly a factor of two higher than that recorded in the 4.4 K scans in Tests 1 and 2. This corresponds to a reduction in surface resistance from 70 nΩ to 45 nΩ, and this may be due to the 120 ℃ bake. Note that an improvement was observed in $R_s$(4.4K), but not in $R_s(2K) \cong R_0$.

Up to 10 MV/m, the cavity behaved similarly to Test 2, but after 10 MV/m, the cavity properties started changing. The intensity of X-rays dropped (Fig. 6) and $Q_0$ increased (Fig. 5). It appears that helium processing of field emitters had occurred, allowing $E_{acc}$ to reach 18 MV/m, well beyond the earlier maxima of 12.5 MV/m at 4.4 K and 13.6 MV/m at 2 K. This scan could have continued to higher field levels, since power was not yet limited by field emission.

A backward scan in field was started to record any change in $Q_0$ after the initial processing. As evidenced by the reduced X-ray intensity, field emission was lower in the backward scan with a corresponding increase in $Q_0$ (Fig. 5). After recording the data point at 14 MV/m, the cavity again became inoperable, indicating further problems with the helium leak. Test 3 ended, and the leak was eventually isolated to the RF feed through for the power coupler antenna. The helium leak was probably a two-edged sword, sometimes preventing operation (possibly due to increased multipacting), but also allowing the processing of field emitters.

## ACKNOWLEDGEMENTS

The authors wish to acknowledge the efforts of S. Gerbick, M. Kedzie of ANL; T. Arkan, D. Arnold, D. Assell, J. Williams and B. Smith of Fermilab; and T. Roark and D. Osha of Roark.

## REFERENCES

[1] G. Apollinari, "Project X as a way to Intensity Frontier Physics", HB2008, Nashville, TN, Aug 2008 and references therein;
[2] S. Nagaitsev, these proceedings
[3] G. Lanfranco et al., "Production of 325 MHz single spoke resonators at FNAL", Proc. of PAC07, Albuquerque, New Mexico, USA.
[4] Ettore Zanon Spa - Via Vicenza 113 - 36015 Schio (Vi) Italy – www.zanon.com.
[5] C.F. Roark Welding & Engineering Co, Inc. - 136 N. Green St. - Brownsburg, IN 46112, USA – www.roarkfab.com.
[6] CST MICROWAVE STUDIO® (CST MWS), www.cst.com.

# SUPERCONDUCTING QUARTER-WAVE RESONATOR CAVITY AND CRYOMODULE DEVELOPMENT FOR A HEAVY ION RE-ACCELERATOR*

W. Hartung, J. Bierwagen, S. Bricker, C. Compton, J. DeLauter, P. Glennon, M. Hodek, M. Johnson, F. Marti, P. Miller, D. Norton, J. Popielarski, L. Popielarski, D. Sanderson, J. Wlodarczak, R. C. York, National Superconducting Cyclotron Laboratory, Michigan State University, East Lansing, Michigan, USA
A. Facco, Istituto Nazionale di Fisica Nucleare, Laboratori Nazionali di Legnaro, Legnaro, Italy
E. Zaplatin, Forschungszentrum Jülich, Jülich, Germany

*Abstract*

A superconducting linac is being planned for re-acceleration of exotic ions at the National Superconducting Cyclotron Laboratory. The linac will include two types of superconducting quarter-wave resonators (QWRs). The QWRs (80.5 MHz, optimum $\beta \equiv \beta_m = 0.041$ and 0.085, made from bulk niobium) are similar to existing cavities presently used at INFN-Legnaro. The re-accelerator's cryomodules will accommodate up to 8 cavities, along with superconducting solenoids for focussing. Active and passive shielding is required to ensure that the solenoids' field does not degrade the cavity performance. First prototypes of both QWR types have been fabricated and tested. A prototype solenoid has been procured and tested. A test cryomodule has been fabricated, containing one QWR, one solenoid, and two other beam-line elements. The QWR and solenoid have been operated successfully inside the cryomodule.

## INTRODUCTION

The National Superconducting Cyclotron Laboratory (NSCL) is building a re-accelerator for exotic ion beams [1, 2]. Stable ions are produced in an ion source and accelerated in the NSCL coupled cyclotron facility. The primary beam produces a secondary beam of exotic ions by particle fragmentation.

The re-accelerator will consist of a gas stopper to slow down the secondary ion beam, a charge breeder to increase the charge of the ions by removing electrons, a multi-harmonic buncher, a radio frequency quadrupole for initial acceleration and focussing, and a superconducting linac to accelerate the beam to a final energy of 3 MeV per nucleon. Additional cryomodules can be added to increase the energy to 12 MeV per nucleon.

The superconducting linac will consist of quarter-wave resonators (QWRs) optimised for $\beta = 0.041$ [3] and $\beta = 0.085$ [4]. The cavities will be housed in a rectangular box cryomodule. A test cryomodule [5] has been designed, assembled, and tested. This paper covers design and prototyping work on the $\beta_m = 0.041$ QWR, $\beta_m = 0.085$ QWR, and cryomodules for the re-accelerator.

*Work supported by Michigan State University.

## CAVITY DESIGN

The QWRs developed by Legnaro for ALPI and PIAVE [6] are the basis for the design of the QWRs for the re-accelerator (see Fig. 1). Some design modifications have been implemented. A larger aperture (30 mm) is used. Separation of cavity vacuum from insulation vacuum is implemented to reduce particulate contamination of cavity surfaces. Probe couplers [7] are used instead of loop couplers.

The cavity design has undergone some evolution since the first prototype cavity was fabricated and tested. For the second and third generation of QWRs, the shorting plate is formed from sheet niobium (3 mm thick) instead of being machined and the tuning plate (1.25 mm thick) is slotted to reduce the tuning force [7]. The shorting plate design is similar to designs used by Argonne [8] and SPIRAL 2 [9].

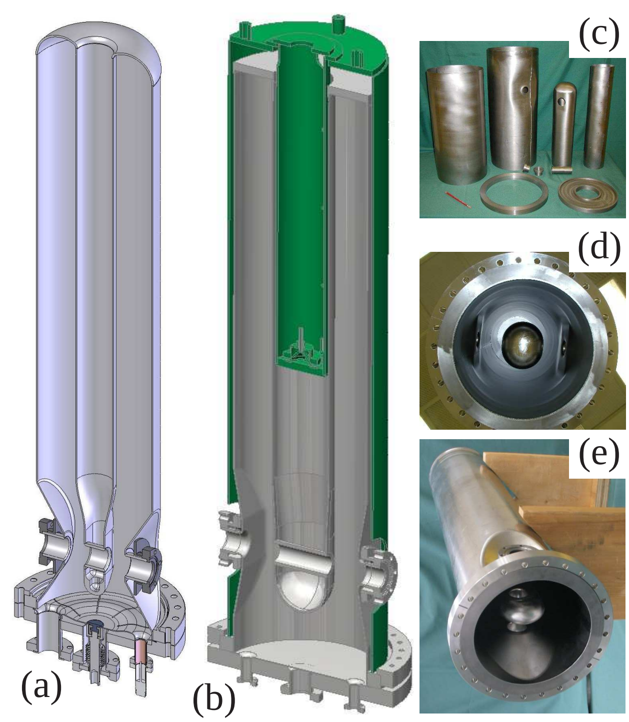


Figure 1: Drawings: (a) second generation $\beta_m = 0.041$ QWR; (b) first generation $\beta_m = 0.085$ QWR with damper and He vessel, shown in green. Photographs: (c) parts for first generation $\beta_m = 0.085$ QWR and (d) completed cavity; (e) completed second generation $\beta_m = 0.041$ QWR.

The tuning plate design is similar to designs for TRIUMF [10] and the ALPI upgrade [11].

The helium vessel is made of titanium. The vessel design includes a Legnaro-type frictional damper [6] inside the inner conductor to mitigate microphonic excitation of the cavity.

The design intrinsic quality factor is $Q_0 = 5 \cdot 10^8$ for both cavities at the operating temperature of 4.5 K. The design fields are $E_p = 16.5$ MV/m for the $\beta_m = 0.041$ cavity and $E_p = 20$ MV/m for the $\beta_m = 0.085$ cavity, where $E_p$ is the peak surface electric field. Detailed RF parameters for the cavities have been published previously [3, 4].

## PROTOTYPE CAVITY FABRICATION

Sheet Nb of thickness 2 mm and RRR $\geq 150$ was used. The tip of the center conductor and the beam tubes were machined from solid Nb. The Nb tuning plate on the bottom of the cavity is held by a Nb-Ti to stainless steel flange. Forming was done at NSCL and in the local area, while electron beam welding was done with industry. Indium joints were used to seal the bottom flange. Knife-edge seals were used for beam tube flanges. Between 120 and 150 $\mu$m was etched from the inner surface via buffered chemical polishing. High-pressure rinsing was done with ultra-pure water in a Class 100 clean room for 60 to 120 minutes.

## DEWAR TESTS

The Dewar test results have been reported previously for both the $\beta_m = 0.041$ QWR [3] and the $\beta_m = 0.085$ QWR [4]. Both cavities exceeded the design goals: at the design fields, the measured $Q_0$ exceeded $10^9$ in both cases. In the RF tests on the $\beta_m = 0.041$ QWR, the highest field reached at 4.2 K was $E_p \approx 65$ MV/m; at 2 K, the measured field was $E_p \approx 80$ MV/m. In the RF tests on the $\beta_m = 0.085$ QWR, the highest field reached at 4.2 K was $E_p \approx 31$ MV/m.

## TEST CRYOMODULE

A rectangular box cryomodule [5], shown in Fig. 2, was fabricated for testing of the cavities, magnets, and auxiliary elements as a unit. The test cryomodule contains one $\beta_m = 0.085$ QWR, one $\beta_m = 0.285$ half-wave resonator (HWR), one solenoid with a dipole steering coil, and one quadrupole. The QWR and HWR are both first generation prototypes without any stiffening elements. A Ti rail system is used for support and alignment. Active and passive magnetic shielding is implemented, consisting of reverse wound coils at the ends of the solenoid, a Meissner shield (Nb can) around the solenoid, and $\mu$ metal shields around the Meissner shield and the cavities.

Below 150 K, the cryomodule was cooled rapidly to minimise the risk of surface hydride formation ("$Q$ disease"). The measured static heat leak of the module at 4 K was 4.5 W $\pm$ 1.2 W; the predicted value was 5.2 W. No degradation in cavity performance was observed with the solenoid at full field. A decrease in the low-field $Q_0$ of the QWR was observed near the end of one cool-down, possibly due to the Meissner shield becoming warm with the solenoid energised. The cavity performance recovered after the cryomodule was warmed to room temperature and re-cooled.

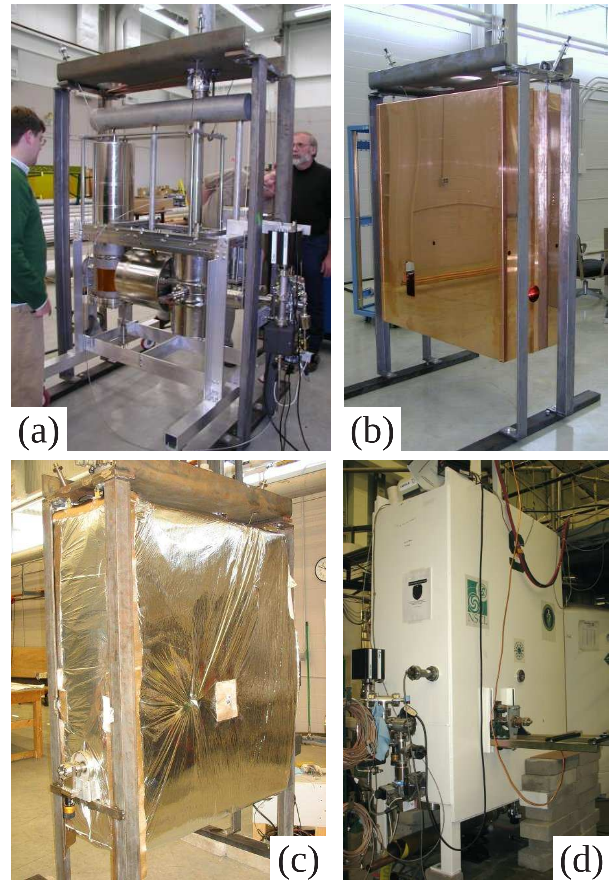


Figure 2: Construction of the low-$\beta$ test cryomodule: (a) cold mass hanging from top plate; (b) 77 K shield; (c) outer multi-layer insulation; (d) vacuum vessel.

RF testing of the cavities was done first with a direct connection from the RF amplifier to the coupler, and then with a sliding short to set up a standing wave on the rigid copper coaxial transmission line. The sliding short configuration provided less mismatch and made it easier to infer the intrinsic $Q$ of the cavity ($Q_0$) from the RF measurements; simple loop couplers were used to couple into the transmission line through the short and monitor the field in the line. The measured QWR input coupling strength was $Q_{ext} = 4.5 \cdot 10^6$ with a direct connection. With the sliding short set to minimise losses in the copper, the measured $Q_{ext}$ was $1.4 \cdot 10^9$. RF conditioning and helium processing were done to mitigate field emission. As can be seen in Fig. 3, the measured performance of the QWR after He processing is similar to its performance in the Dewar test.

The tuners were operated over their full range. The pressure sensitivity of the QWR was measured (see Table 1 below).

## CAVITY STIFFENING

Structural analyses of the QWRs are being done with ANSYS.[1] As shown in Fig. 4, stiffening methods are be-

[1]ANSYS, Inc., Canonsburg, Pennsylvania, USA.

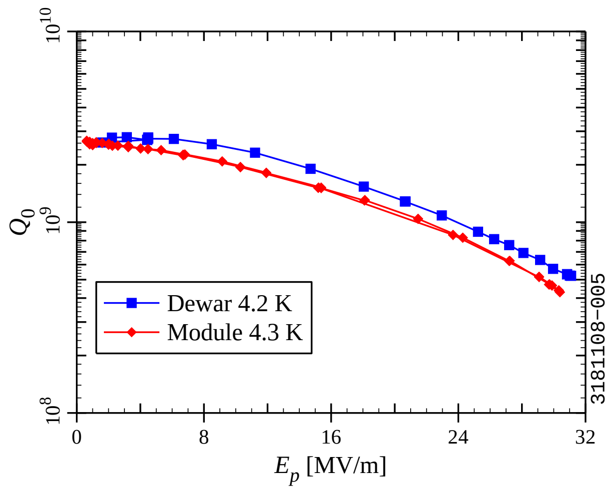


Figure 3: RF test results for the $\beta_m = 0.085$ QWR: comparison of Dewar test and cryomodule test (after solenoid operation, temperature cycling, and He processing).

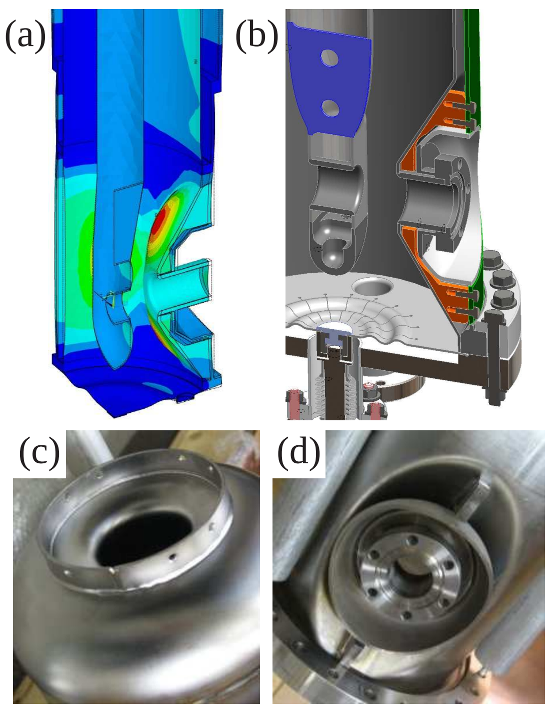


Figure 4: Stiffening of the $\beta_m = 0.041$ QWR: (a) ANSYS model showing the predicted deformation for a stiffened QWR; (b) drawing of QWR with center conductor rib (blue) and beam port buttresses (orange); (c) Nb ring welded to the top of the cavity; (d) Nb buttresses welded to the beam port region.

ing implemented for the $\beta_m = 0.041$ QWR to reduce the frequency shift due to bath pressure fluctuations. Some predicted and measured values of the frequency shift due to bath pressure are given in Table 1. The stiffening measures should reduce Lorentz detuning as well. Reduction in the pressure sensitivity of the $\beta_m = 0.085$ QWR is planned. After stiffening, it is anticipated that the QWRs' pressure sensitivities will be similar to those used elsewhere.

Table 1: Measured and predicted values of the shift in resonant frequency $f$ with bath pressure $P$ for the QWRs.

| $\beta_m$ | Stiffened | He vessel | $df/dP$ (Hz/mbar) Predicted | Measured |
|---|---|---|---|---|
| 0.041 | no | no | $-18.7$ | $-18.5$ |
| 0.041 | no | yes | $-11$ | |
| 0.041 | yes | yes | $-2.7$ | |
| 0.085 | no | no | | $-19.7$ |
| 0.085 | no | yes | $-6.8$ | $-7.3$ |

## CONCLUSION

Prototype cavities for the NSCL re-accelerator have been fabricated and tested. The design goals for the RF performance have been achieved in Dewar tests (for both cavity types) and a cryomodule test (for one cavity type so far).

The re-accelerator will require 3 cryomodules, with a total of 15 cavities and 8 solenoids. The cavities are being fabricated at NSCL, with electron beam welding done by industry. The 9 tesla superconducting solenoids are being fabricated by industry.

## ACKNOWLEDGMENTS

We wish to thank all of the people who helped with cavity and cryomodule design, fabrication, and testing. The NSCL cryogenics group, operations group, and electronics group provided valuable assistance with the prototyping and testing efforts.

## REFERENCES


[1] X. Wu *et al.*, "MSU Re-accelerator—The Re-acceleration of Low Energy RIBs at the NSCL," Presented at the 13th Workshop on RF Superconductivity, Beijing, China, 2007.

[2] X. Wu *et al.*, "The Status of the MSU Re-Accelerator (ReA3)," these proceedings.

[3] W. Hartung *et al.*, "Niobium Quarter-Wave Resonator Development for a Heavy Ion Re-Accelerator," presented at the 13th Workshop on RF Superconductivity, Beijing, China, 2007.

[4] W. Hartung *et al.*, in *Proceedings of SRF 2003: 11th Workshop on RF-Superconductivity: Travemünde, Germany*, DESY (2004), Paper TUP14.

[5] M. Johnson *et al.*, in *Proceedings of the 2005 Particle Accelerator Conference* (2005), p. 773–775.

[6] A. Facco & V. Zviagintsev, in *9th Workshop on RF Superconductivity: Proceedings*, LANL (2000), p. 203–206.

[7] J. Wlodarczak *et al.*, "Power Coupler and Tuner Development for Superconducting Quarter-Wave Resonators," these proceedings.

[8] M. P. Kelly *et al.*, in *Proceedings of the XXII International Linear Accelerator Conference: Lübeck, 2004*, DESY (2004), p. 605–607.

[9] G. Devanz, in *Proceedings of the 12th International Workshop on RF Superconductivity: Ithaca, 2005*, LEPP, Cornell (2007), p. 108–112.

[10] T. Ries *et al.*, in *Proceedings of the 2003 Particle Accelerator Conference* (2003), p. 1488–1490.

[11] D. Zenere, A. Facco & F. Scarpa, in *Proceedings of EPAC 2008, Genoa, Italy*, EPS-AG (2008), p. 3413–3415.

# CW RF SYSTEMS OF THE CORNELL ERL INJECTOR*

S. Belomestnykh#, Z. Conway, J. Dobbins, R. Kaplan, M. Liepe, P. Quigley, J. Reilly, J. Sikora, C. Strohman, V. Veshcherevich, CLASSE, Cornell University, Ithaca, NY 14853, U.S.A.

## Abstract

Two high power 1300 MHz RF systems have been developed for the Cornell University ERL Injector. The first system, based on a 16 kWCW IOT transmitter, is to provide RF power to a buncher cavity. The second system employs five 120 kWCW klystrons to feed 2-cell superconducting cavities of the injector cryomodule. The sixth, spare klystron is used to power a deflecting cavity in a pulsed mode for beam diagnostics. A digital LLRF control stem was designed and implemented for precise regulation of the cavities' field amplitudes and phases. All components of these systems have been recently installed and commissioned. The first operational experience with the systems is discussed.

## INTRODUCTION

A prototype of the ERL injector [1], under commissioning at Cornell University's Laboratory for Accelerator based Sciences and Education (CLASSE), is the first step toward the future X-ray light source based on the Energy Recovery Linac (ERL) [2]. The injector faces a challenging task of producing high-current, ultra-low-emittance beam. This, in turn, imposes very stringent requirements on its RF systems [3]. There are three different types of cavities, all operating at 1300 MHz: buncher cavity [4], five 2-cell superconducting (SC) cavities [5], and deflecting cavity [6]. Due to different power requirements for buncher and SC cavities, two different RF systems have been developed. The buncher RF is based on a 16 kWCW IOT transmitter. The injector cryomodule (ICM) RF system employs five 120 kWCW klystrons. The sixth, spare klystron is used to power a deflecting cavity in a pulsed mode for beam diagnostics. A new generation of the Cornell low level RF (LLRF) controls is used for precise cavity field regulation. All components of the RF systems have been recently installed and commissioned.

## RF FOR BUNCHER CAVITY

Specifications of the buncher RF system are listed in Table 1. As power requirements for this system are quite moderate, an IOT-based high power amplifier (HPA) was chosen. The HPA was manufactured by Thomson-BM. The system includes a 16 kWCW tube TH 713 (manufactured by Thales-ED) incorporated into a modified version of the DCX SIIA broadcast transmitter system. The high voltage power supply is manufactured by NWL. The block diagram of this system is shown in Figure 1. The HPA was tested at the factory and then at Cornell upon delivery [7].

A very small vacuum leaks were found in the buncher cavity tuners after the cavity installation. Vacuum dams were implemented to allow the injector operation while replacement tuners are being manufactured. After that the buncher was powered and commissioned up to 160 kV. A rather strong multipacting (MP) was observed during cavity processing. The multipactor exists at cavity voltages above 49 kV with the highest out-gassing between 60 and 70 kV. While the cavity body and input coupler are not susceptible to multipacting, it was found that the electric field in a small gap between the tuner plunger and the port is high enough to bring this area into the first order MP zone. It requires many hours to process this multipactor.

Table 1: Buncher RF Specifications

| | |
|---|---|
| Number of cavities | 1 |
| Nominal accelerating voltage | 120 kV |
| Maximum accelerating voltage | 200 kV |
| Shunt impedance, [illegible] | 2.1 MOhm |
| Maximum dissipating power | 9.6 kW |
| Maximum transmitter output power | 16 kW |
| Amplitude stability | $8\times10^{-3}$ (rms) |
| Phase stability | 0.1° (rms) |

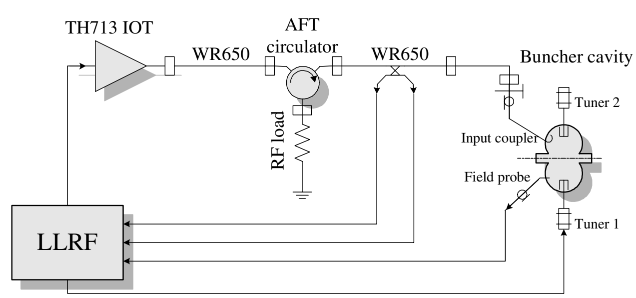


Figure 1: Block diagram of the buncher cavity RF system.

## INJECTOR CRYOMODULE RF SYSTEM

ICM houses five two-cell SC cavities, each delivering up to 100 kW of RF power to beam. As each cavity operates independently, the system consists of five identical channels. RF power is delivered to cavities via twin input couplers [8], each carrying up to 50 kWCW. Main parameters of this system are given in Table 2 and its block diagram is presented in Figure 2.

* Work is supported by the NSF grant PHY 0131508.
#s.belomestnykh@cornell.edu

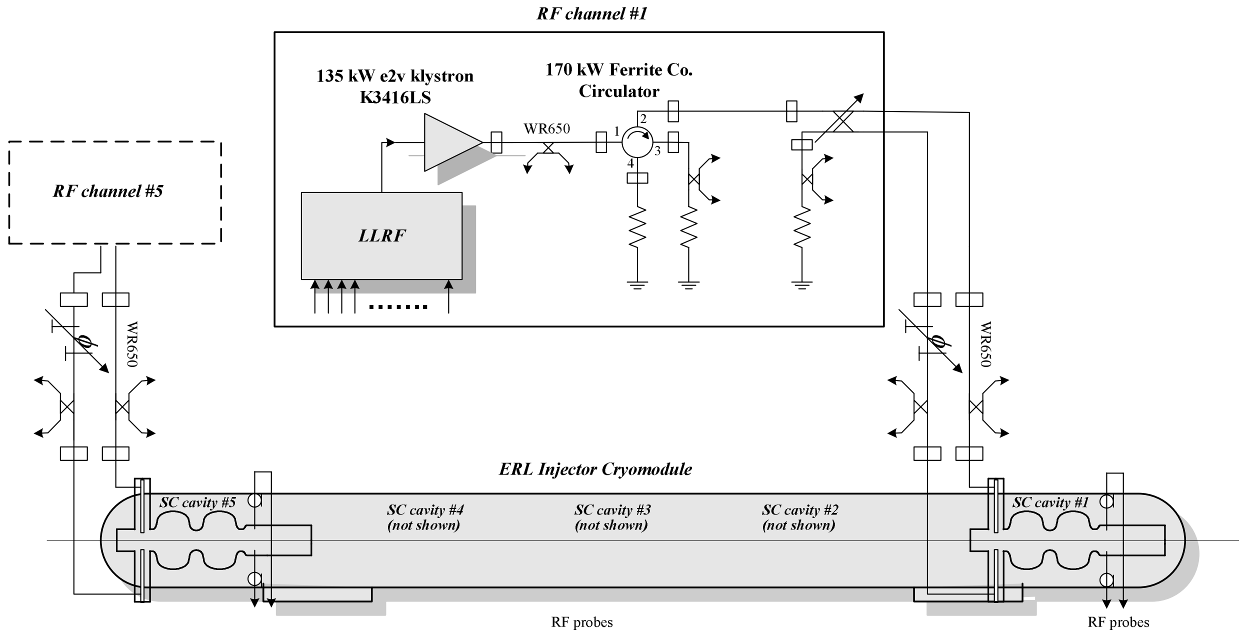


Figure 2: Block diagram of the ERL injector cryomodule RF system.

Table 2: Specifications of the ICM RF system

| | |
|---|---|
| Number of cavities | 5 |
| Accelerating voltage per cavity | 1 – 3 MV |
| 2-cell cavity length | 0.218 m |
| □□□ (linac definition) | 222 Ohm |
| □□□□ | $4.6\times10^4$ – $4.1\times10^5$ |
| RF power per cavity | 100 kW |
| Maximum useful klystron power | ≥ 120 kW |
| Amplitude stability | $9.5\times10^{-4}$ (rms) |
| Phase stability | 0.1° (rms) |

The twin-coupler cavity design requires an adjustable short-slot hybrid power splitter and a motorized two-stub phase shifter in one of the waveguide arms after the split [9]. Four input coupler were tested at high power in a specially designed liquid-nitrogen-cooled cryostat [10]. Maximum RF power level during the test of production input couplers was 61 kW. The test showed that couplers meet requirements of the ERL Injector.

The cryomodule RF system utilizes six klystrons K3415LS manufactured by e2v. The 7-cavity tube has saturated output power of about 160 kWCW. To provide very stable regulation of the cavity field, the klystron must have a non-zero gain and therefore cannot operate in saturation. The maximum useful output power for this tube was defined as a power with an incremental gain of 0.5 dB/dB of drive and specified to be no less than 120 kWCW. At this power level the efficiency should be at least 50% and the tube bandwidth not less than ±2 MHz at -1 dB level and not less than ±3 MHz at -3 dB level. All klystrons passed the factory acceptance test meeting the specs at 135 kW before shipping. The tubes were installed and tested again at Cornell.

So far all ICM operations have been at 1.8 K. The cavities have been processed in pulsed mode (2 ms long pulses, 20 ms period) to > 15 MV/m, and in all cases but one the limit was due to vacuum activity in the input couplers. Further processing of input couplers should improve the maximum cavity field. Cavity 4 quenched in pulsed mode at 18 MV/m. In CW mode all cavities reached accelerating voltages of at least 2.8 MV when powered individually (see Table 3). Operation of cavity 1 was limited by excessive RF losses due to field emission (FE). While cavity 2 was limited by the input coupler vacuum, it also had rather significant FE. Operating at 1.8 K with two pump skids, the cryogenic system can handle all five cavities at gradients up to 10.4 MV/m (2.4 MV per cavity). Raising temperature to 2 K will allow for increase of the cryogenic system heat handling capacity and hence higher gradient ICM operation. This operation will be tested soon.

Table 3: ICM Cavity Performance Summary (IC = input coupler vacuum)

| Cavity | CW | Limit | Pulsed | Limit |
|---|---|---|---|---|
| 1 | 2.80 MV | Cryogenics | 4.35 MV | IC |
| 2 | 2.90 MV | IC | 3.75 MV | IC |
| 3 | 3.50 MV | Cryogenics | 3.66 MV | IC. |
| 4 | 3.40 MV | Cryogenics | 4.15 MV | Quench |
| 5 | 3.50 MV | none | 5.20 MV | IC |
| All 5 | 2.40 MV | Cryogenics | — | — |

## RF FOR DEFLECTING CAVITY

A 1300 MHz deflecting cavity [6] is designed to be used for ERL injector beam diagnostics in conjunction with other instruments to measure low-emittance beam parameters. As all those measurements involve beam interception, the average beam current will have to kept low and hence the beam will be pulsed to keep the bunch charge high. The RF pulse length will be approximately 60 µs with the repetition rate up to 1 kHz. Specifications of RF system for this cavity are given in Table 4.

The block diagram of this RF system is presented in Figure 3. The RF system is identical to one of the ICM RF channels with the exception of RF power split and slightly modified FPGA and DSP codes of the LLRF control boards. The system is under commissioning at present.

Table 4: Specifications of the deflecting cavity RF system

| | |
|---|---|
| Number of cavities | 1 |
| Maximum transverse kick voltage | 200 kV |
| Shunt impedance, [illegible] | 5.3 MOhm |
| Maximum average dissipating power | 200 W |
| Pulsed RF power | 3.8 kW |
| RF pulse length | 60 µs |
| Maximum repetition rate | 1 kHz |

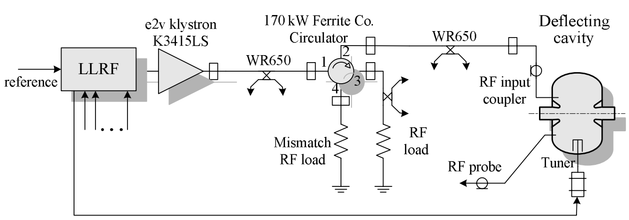


Figure 3: Block diagram of the deflecting cavity RF system.

## LOW LEVEL RF

The LLRF electronics for ERL injector is a new, improved generation of LLRF previously developed for CESR [11]. The new electronics, like the old one, uses VME form-factor. The ERL RF synthesizer is the master oscillator for the ERL injector. A low-noise ovenized oscillator provides the primary 10 MHz reference, which is used to stabilize a 200 MHz VCXO. 50 MHz and 12.5 MHz signals are then generated via appropriate dividers. These signals are used as sampling and clock signals by LLRF digital control boards. The 12.5 MHz signals are also sent to two high frequency PLL circuits, which generate the 1300 MHz RF and 1287.5 MHz LO signals. An Agilent E5052A Signal Source Analyzer was used to measure the phase noise and jitter. The 1300 MHz signal rms jitter integrated from 10 Hz to 100 kHz is 288 fs. The LO signal rms jitter is 294 fs.

During the first test of the new LLRF with one of the SC cavities the amplitude stability of $10^{-4}$ rms and the phase stability of 0.05° rms were achieved, exceeding the ERL injector requirements. More details about the LLRF system can be found in [10].

## SUMMARY

The 1300 MHz RF systems for the Cornell ERL injector have been installed and commissioned. ERL injector has begun operation with beam.

## REFERENCES

[1] I. Bazarov and C. Sinclair, "High Brightness, High Current Injector Design for the Cornell ERL Prototype," [illegible], pp. 2062-2064.
[2] G.H. Hoffstaetter, et al., "Progress toward an ERL Extension of CESR," [illegible], pp.107-109.
[3] M. Liepe and S. Belomestnykh, "RF Parameters and Field Stability Requirements for the Cornell ERL Prototype," [illegible], pp. 1329-1331.
[4] V. Veshcherevich and S. Belomestnykh, "Buncher Cavity for ERL," [illegible], pp. 1198-1200.
[5] V. Shemelin, et al., "Dipole-mode-free and kick-free 2-cell Cavity for SC ERL Injector," [illegible], pp. 2059-2061.
R. L. Geng, et al., "Fabrication and Performance of Superconducting RF Cavities for the Cornell ERL Injector," [illegible], pp. 2340-2342.
[6] S. Belomestnykh, et al., "Deflecting Cavity for Beam Diagnostics in ERL Injector," [illegible], pp. 2331-2333.
[7] S. Belomestnykh, et al., "High Power Testing RF System Components for the Cornell ERL Injector," [illegible], pp. 472-474.
[8] V. Veshcherevich, et al., "Design of High Power Input Coupler for Cornell ERL Injector Cavities," [illegible]
[9] S. Belomestnykh, et al., "Development of High RF Power Delivery System for 1300 MHz Superconducting Cavities of Cornell ERL Injector," [illegible], pp. 694-696.
[10] V. Veshcherevich, et al., "High Power Tests of Input Couplers for Cornell ERL Injector," [illegible]
[11] M. Liepe, et al., "A New Digital Control System for CESR-c and the Cornell ERL," [illegible], pp. 3347-3349.
M. Liepe, et al., "Experience with the New DIGITAL RF Control System at the CESR Storage Ring," [illegible], pp. 2592-2594.
[10] S. Belomestnykh, et al., "Commissioning of the Cornell ERL Injector RF Systems," [illegible], pp. 832-834.

# MULTIPACTOR IN MINIMUM ELECTRIC FIELD REGIONS OF TRANSMISSION LINES AND SUPERCONDUCTING RF CAVITIES*

S. Belomestnykh# and V. Shemelin, CLASSE, Cornell University, Ithaca, NY 14853, U.S.A.

*Abstract*

Multipactor in beam-pipe transitions of superconducting RF cavities can be explained using RF potential well theory [1]. In this paper we present simulation results supporting this explanation for both RF cavities and transmission lines.

## INTRODUCTION

Curved-shaped transition regions between a cavity and a beam pipe were thought to be multipactor-free. Thus recent experimental observations of multipactor (MP) in two such transitions in Cornell ERL injector cavity [2] and KEK Ichiro cavity [3] surprised experimenters. The possibility of multipacting in those geometries was later confirmed in computer simulations. Analyzing these cases we have noticed that the electric field along the cavity profile has a minimum at the locations of MP. We proposed an explanation based on the Gaponov-Miller theory [4]. According to the theory an electric field minimum is associated with the local potential well, thus attracting electrons. This creates conditions favorable for multipacting. More details can be found elsewhere [1]. To check this explanation, we performed MP simulations for cavity geometries with different transition shapes, which confirmed that multipactor is suppressed for transitions with no electric field minimum.

The potential well theory can be applied to transmission lines too. For example, Miller force was used in [5] to derive an analytic solution of electron motion in a coaxial line and also was invoked in discussion of MP in a waveguide iris [6]. This force can also explain drift of multipacting electrons from the waveguide midline to sidewalls, that was observed in computer simulations [7] and, in case of partial or full standing wave in a transmission line, migration of electrons toward the standing wave minimum. We explore electron migration in the latter case for coaxial line and rectangular waveguide later in this paper.

Simulation results presented here were obtained with computer codes MultiPac [8] (for cavity-to-beam-pipe transitions and a coaxial line) and XingRK4 [9, 10] (for a rectangular waveguide.)

## MP IN CAVITY-TO-BEAM-PIPE TRANSITIONS

Figure 1 shows MP trajectories at the electric field minimum in the transition form the Cornell ERL injector cavity end cell to a beam pipe. The contour line of the geometry, shown in Figure 2, consists of elliptic arcs connected with tangential straight segments. *Ae, Be, Ai, Bi* and so on are half-axes of the ellipses, *i* refers to the inner half of the cell, *e* refers to the outer half, *R* is the radius of the circle smoothening the transition; *Req* is the equatorial radius, *Rbp* is the radius of the beam-pipe.

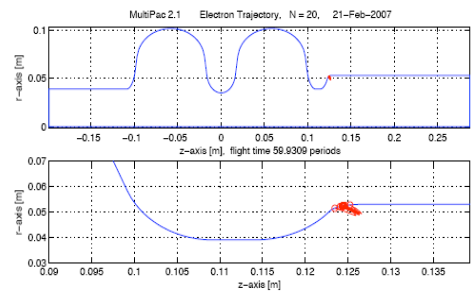


Figure 1: MP in the ERL injector cavity [2].

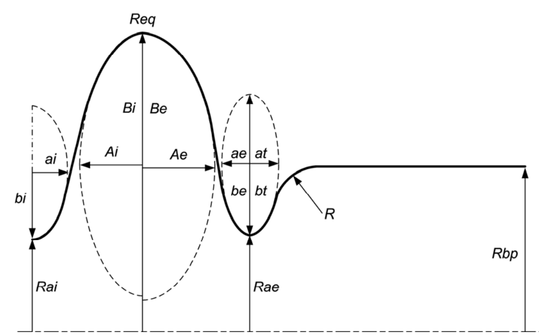


Figure 2: Geometry of the cavity-to-beam-pipe transition.

We have examined a transition from the end iris aperture *Rae* = 37 mm to the beam-pipe radius *Rbp* = 55 mm with different radii *R*. Half-axes of the end iris ellipses were *ae* = *at* = 12.53 and *bt* = *be* = 20.95 mm. Other dimensions of the cavity are chosen to tune its frequency to 1300 MHz and the ratio of the peak electric field to the accelerating field to $E_{pk}/E_{acc} = 2.0$.

Figures 3 and 4 show dependence of the maxima of the enhanced counter function *A* on the radius *R* and corresponding values of the peak electric field *E*. Three sets of points correspond to three different MP bands. Analyzed values of field levels were in the range from 25 to 35 MV/m as it has the most distinct maximum of the function *A*. Two points from Figures 3 and 4 corresponding to *R* = 12 mm are further looked at in Figure 5. Two maxima of the normalized enhanced function $e_{20}/c_0$ and corresponding impact energies and trajectories are presented. These trajectories can be related to two kinds of MP: three-periodic for 25 MV/m, and two-periodic MP for 33.5 MV/m (with some deviations from exact periodicity). Both are located in the flat minimum of the electric field.

* Work is supported by the NSF grant PHY 0131508.
#s.belomestnykh@cornell.edu

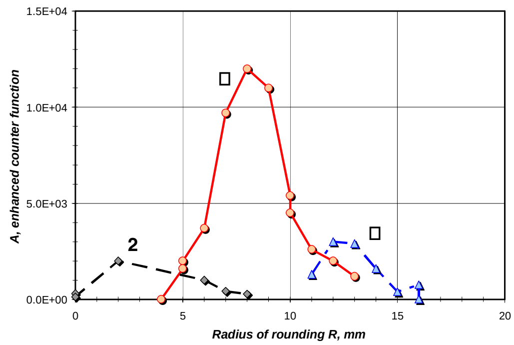


Figure 3: Dependences of maximum *A* on *R*.

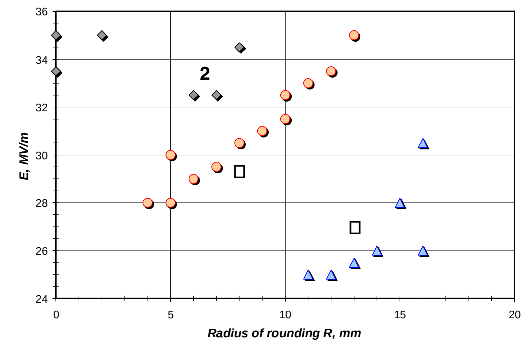


Figure 4: Dependences of *E* corresponding to max *A* on *R*.

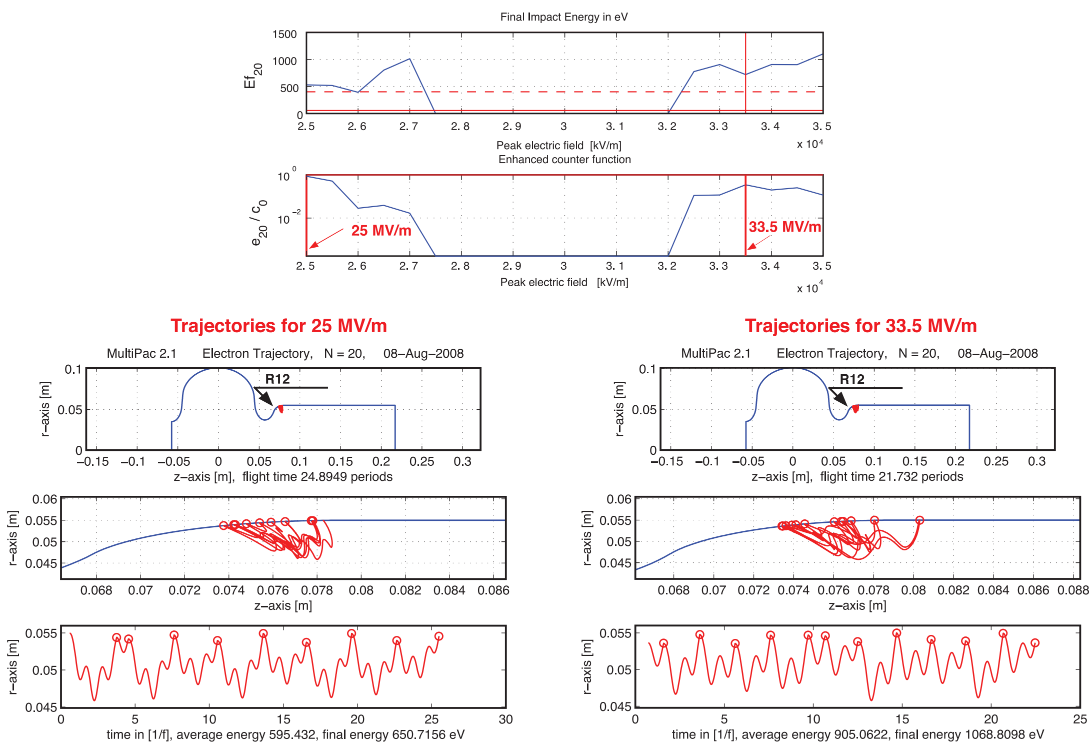


Figure 5: Three- and two-periodic MP at two different amplitudes of the peak electric field for $R$ = 12 mm.

## MP IN TRANSMISSION LINES

Two cases were studied: coaxial line and rectangular waveguide. With full standing wave conditions we have simulated trajectories of MP electrons along the transmission lines. In both cases particles were drifting toward the electric field minimum.

Multipactor in a half-wavelength long coaxial line with short boundary conditions at both ends was simulated at 1300 MHz in power ranges from 100 kW to 400 kW. One of these ranges is presented in Figure 6. A number of MP zones were found and for all simulated trajectories electrons were drifting from the maximum electric field in the middle of the line toward the minimum electric field at one of the ends. Figure 7 shows one of such trajectories.

A 1″ high by 5″ wide rectangular waveguide was simulated at 1500 MHz in the power range from 5 kW to 50 kW. Full standing wave was assumed with the electric field maximum at $z = 0$. Several MP zone were found and, as in the previous case, all electrons launched off the electric field maximum were drifting toward the minimum electric field. Figure 8 shows one of simulated trajectories.

## CONCLUSIONS

Attraction of MP electrons to the minimum of electric field can be explained in terms of the potential well created in the RF field [4]. We would like to point out that MP near the cavity equator also exists near the minimum (zero) of the electric field. This is usually one-periodic MP. In the cases analyzed in this paper, we see more complex trajectories of MP electrons in the region of minimal E.

The fact that the MP electrons are attracted to a minimum of electric field gives us an insight into how to avoid this phenomenon. Namely, the multipactor-free transitions between cavities and beam-pipes should have shapes designed to avoid local minima of the surface electric field. In such transitions electrons, instead of being attracted to "calm corners," will drift in the direction of decaying field.

Similarly, in transmission lines with full or partial standing wave MP electrons experience a force directed toward the electric field minimum. In transmission lines with a non-uniform cross-section MP particles will tend to move to locations where the electric field magnitude is smaller. One could say that there is an "electron wind" blowing in the direction of lower electric field along a transmission line. This electron wind can be gentle (the drift is slow) if the field has a small gradient, for example near the field maximum. In this case it does not inhibit MP in high-field areas but only increases susceptibility thresholds there while simultaneously enhancing MP in lower-field regions.

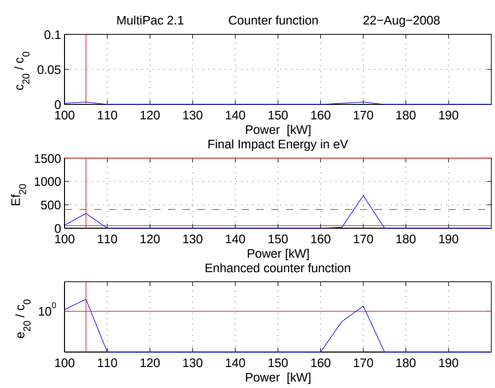


Figure 6: MP zones in power range from 100 to 200 kW.

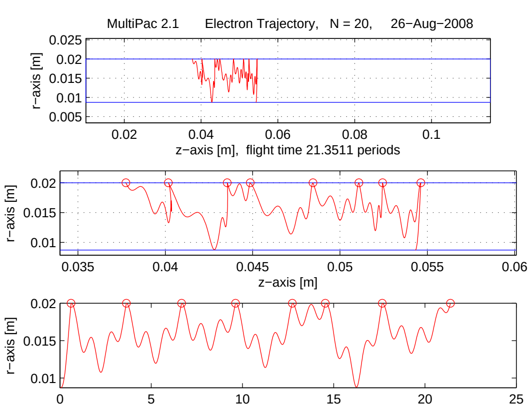


Figure 7: Trajectory of MP electrons in a coaxial line with full standing wave at 170 kW.

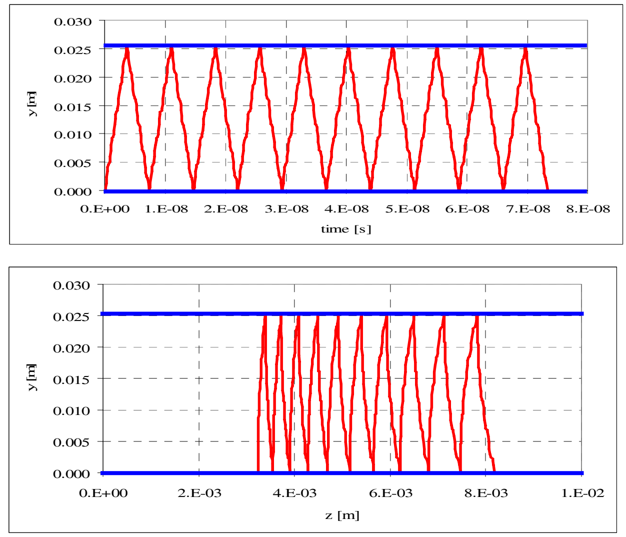


Figure 8: Trajectory of MP electrons in a rectangular waveguide with full standing wave at 36 kW.

## ACKNOWLEDGEMENT

The authors are thankful to Hasan Padamsee for helpful discussion and advice.

## REFERENCES


[1] S. Belomestnykh, V. Shemelin, "Multipacting-free transitions between cavities and beam-pipes," Nucl. Instr. and Meth. **A 595** (2008) 293-298,

[2] R.L. Geng, et al., "Fabrication and performance of superconducting RF cavities for the Cornell ERL injector," PAC 2007, Albuquerque, NM, WEPMS007, p. 2340 (2007).

[3] Y. Morozumi, "RF structure design and analysis," 18 May 2007; http://lcdev.kek.jp/ILC-AsiaWG/WG5notes.

[4] A.V. Gaponov, M.A. Miller, "Potential Wells for Charged Particles in a High-Frequency Electromagnetic Field," Sov. Phys. JETP **7** (1958) 168.

[5] R. Udiliak, et al., "Multipactor in a Coaxial Transmission Line. I Analytical Study," Phys. Plasmas **14** (2007) 033508.

[6] R. Udiljak, et al., "Multipactor in a Waveguide Iris," IEEE Trans. Plasma Sci. **35** (2007) 388.

[7] E. Chojnacki, "Simulation of a Multipactor-Inhibited Waveguide Geometry," Phys. Rev. ST Accel. Beams **3** (2000) 032001.

[8] P. Yla¨-Oijala, D. Proch, "MultiPac—Multipacting Simulation Package with 2D FEM field solver," 10th Workshop on RF Superconductivity, Tsukuba, Japan (2001).

[9] R.L. Geng, H. Padamsee, "Exploring Multipacting Characteristics of a Rectangular Waveguide," PAC 1999, New York, NY, p. 429 (1999).

[10] G. Miraglia, "Operation Manual for XingRK4" (2005).

# OSCILLATING SUPERLEAK TRANSDUCERS FOR QUENCH DETECTION IN SUPERCONDUCTING ILC CAVITIES COOLED WITH HE-II*

Z. A. Conway#, D. L. Hartill, H. S. Padamsee, and E. N. Smith
CLASSE, Cornell University, Ithaca, New York, USA

*Abstract*

Quench detection for 9-cell ILC cavities is presently a cumbersome procedure requiring two or more cold tests. One cold test identifies the cell-pair involved via quench field measurements in several 1.3 GHz $TM_{010}$ pass-band modes. A second test follows with numerous fixed thermometers attached to the culprit cell-pair to identify the particular cell. A third measurement with many localized fixed thermometers is necessary to zoom in on the quench spot. We report here on a far more efficient alternative method which utilizes a few (e.g. 8) oscillating superleak transducers to detect the He-II second sound wave driven by the defect induced quench. Using a 9-cell reentrant cavity we identified the quench location in one cold test by powering several modes of the fundamental pass-band. Results characterizing the defect location with He-II second sound detection and corroborating measurements with carbon thermometers will be presented.

## INTRODUCTION

Due to major R&D efforts by many laboratories within the TESLA Technology Collaboration (TTC) DESY has now successfully tested more than 12 cavities over 35 MV/m [1]. Nevertheless the means for reliably producing cavities which achieve accelerating gradients >35 MV/m with a high yield remains to be demonstrated as one of the ILC highest priority R&D goals. Frequently, the cavity gradients are limited by defects on the RF surface which quench at field levels well below 35 MV/m. Such quench limited cavities may be repairable but the process of locating defects in 9-cell cavities remains a lengthy and cumbersome process.

Many laboratories are developing large scale thermometry systems to pin-point the quench locations. Here, we present a cost-effective and simple method to determine quench locations. By testing a superconducting cavity in a superfluid helium bath it is possible to observe second-sound temperature waves driven by the conversion of stored RF energy to thermal energy at the defect [2, 3]. By measuring the time-of-arrival of the second sound wave at three or more detectors the defect location can be determined. Here, we use oscillating superleak transducers (OST), which measure the fluctuating counterflow velocity [4, 5, 6], to detect the time of arrival of second sound waves.

The remainder of this paper is split into four parts. First, we briefly discuss the RF performance history of the 9-cell reentrant cavity used in the experimental work. Next, we present the second-sound time-of-flight results used to locate the defect. Third, we show results of direct thermometric measurements of the cavity outer surface which corroborate the second sound defect location. Finally, we conclude with a few closing comments.

## RESONATOR TESTING

### *Resonator Processing and RF Performance*

After fabrication at AES (Medford, NY) the initial chemical processing of the 9-cell reentrant cavity was performed in early 2007 [7]. This included a final vertical EP of 25 μm and a bake at 110$^0$C for 48 hours. After cooling the cavity to 2 K, the RF performance shown in figure 1 was measured (July 2007 curve). The cavity operated cw at accelerating gradients up to 14.6 MV/m where the cavity quenched. This accelerating gradient corresponds to a peak surface magnetic field of 549 Oe and a peak surface electric field of 35 MV/m [8].

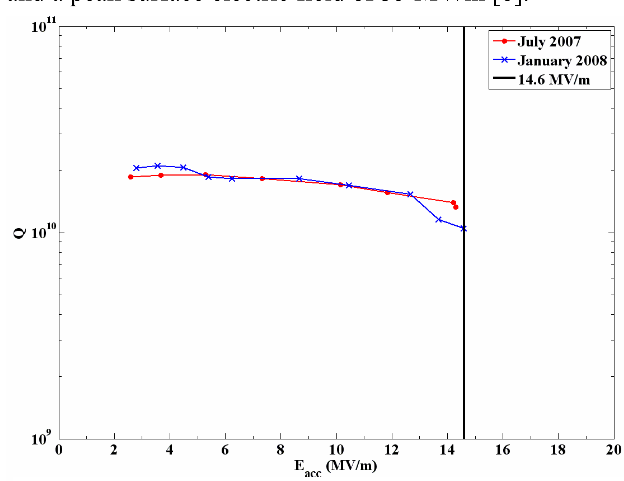


Figure 1: 9-cell reentrant cavity test results.

Immediately following the initial test which found the cavity RF field amplitude to be quench limited, two programs were implemented: 1) perform a heavy EP, to remove enough material to repair the cavity and 2) locate the defect should the EP repair prove ineffective.

First, the cavity received a series of heavy vertical electropolish procedures to remove 125 μm of material from the RF surface. The EP procedures were followed with a 48 hour 600$^0$C bake at FNAL. After another light EP etch (20 μm), HPR cleaning and 110$^0$C bake the cavity was again cooled to 2 K and tested. It was found that the cavity RF performance was unchanged (figure 1), requiring the determination of the defect location.

*Work supported by NSF and DOE
# zac22@cornell.edu

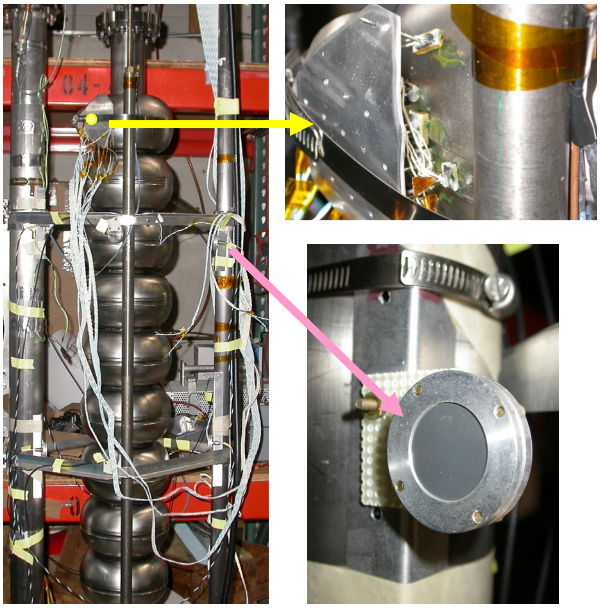

Figure 2: (Left) The 9-cell reentrant cavity ready for testing. 6 of the 8 OSTs and the fixed thermometer array are visible. The yellow circle corresponds to the defect location identified. (Top Right) A side view of the fixed thermometer array used to verify the accuracy of the second sound quench detection. (Lower Right) One of the 8 oscillating superleak transducers used to locate the defect.

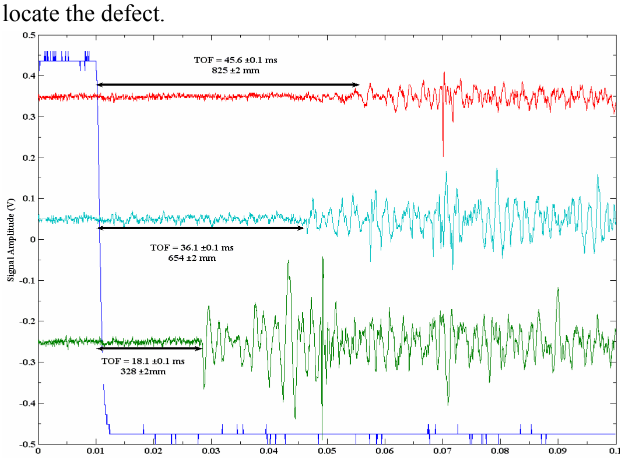


Figure 3: A representative quench event. The trace on the left (blue) shows the transmitted RF signal at quench. The upper three traces show the OST signals delayed by a time corresponding to their respective distances from the quench location.

## *Second Sound Defect Location*

The abrupt dissipation of the stored RF energy during quench is a symptom of a surface defect. To locate the defect an array of 8 OST were employed. The 8 OST were subdivided into two geometrically similar square arrays with one OST at each corner and ~17.2 cm from the cavity beam axis. One square array was located around the equator weld of the third cell and the OST of the second square array was ~11 cm above the equator weld of the sixth cell. Refer to figure 2 for details.

The measured time-of-arrival of the second sound wave is determined by the second sound wave time-of-flight from the defect heated region to the OST. By measuring the time-of-flight to three or more OST at different positions around the cavity, the location of the defect can be determined. It is important to note that this method requires only a single cavity test to locate, in three dimensions, surface defects which result in quench.

A single quench event at 1.94 K is shown in figure 3. The step-like trace on the left-hand side of the graph is the transmitted power signal output from an HP 423A crystal detector. The cavity $\pi$-mode was excited with an RF-pulse to a peak accelerating gradient of 14.6 MV/m, causing a cavity quench. The additional three traces display the output signal from three of the OST.

In addition, to the above event other modes of the cavity 1.3 GHz pass-band were excited at various He bath temperatures. In each case the cavity was found to quench at the same location.

## *Thermometric Defect Location*

Once the defect was located with second sound, another 2 K RF test focused on confirming the defect location with traditional carbon thermometers. A special plate, which conformed to the reentrant cell shape, was fitted with an array of 15 Allen-Bradley 100 Ω, 1/10 W, carbon resistors. This thermometer assembly was pressed with spring loaded contacts (pogo sticks) onto the cavity outer surface to map the temperature of the defect region.

Due to a failure of the input coupler feedthrough from very high power application during the previous test we were only able to weakly couple to the cavity during the fixed thermometry test. The maximum achievable accelerating gradient was limited to 8 MV/m in the cell with the defect. However, this was still sufficient for the measurement of a temperature map of the cavity surface around the defect location with 15 fixed thermometers. Four out of the 15 thermometers showed defect heating. The other thermometers showed no temperature rise as expected below quench.

Figure 4 shows the thermometer array spacing and the measured heating. The horizontal axis is the distance along the equator weld and the vertical axis is the distance away from the equator weld. Each square represents the measurement of a single thermometer. The maximum resistance change of 600 Ω corresponds to a thermometer

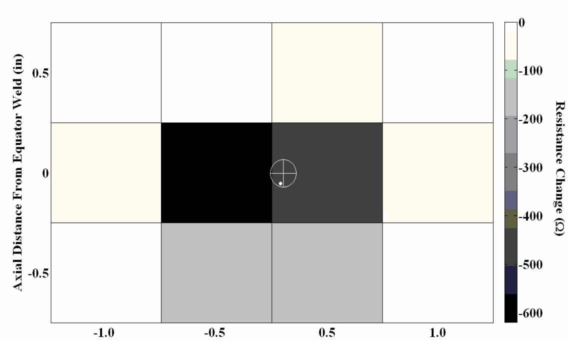


Figure 4: A thermal map of the cavity outer surface around the defect location. The horizontal axis corresponds to the distance along the weld and the vertical axis corresponds to the distance away from the weld. Each square represents one thermometer. The shading scale is shown on the right.

signal of about 50 mK during defect heating at 8 MV/m.

There are 3 distinct sets of data shown in figure 4: 1) the results of a direct thermometric measurement of the cavity temperature, 2) the results of the second sound quench location, and 3) the results of an optical inspection of the cavity RF surface (discussed in the next section). The second sound telemetry results for the quench location are highlighted with a cross and surrounded by a circle. The solid white circle in the lower left quadrant of the cross is centered over a pit located by optically inspecting the cavity RF surface, discussed in the next section. Notice the defect location determined by the thermometric measurement, the second sound time-of-flight measurements, and the optically located defect are in reasonably good agreement.

## INSPECTION

Optical inspection of the cavity RF surface using a Questar long-distance microscope found a small pit where the second sound telemetry located the defect, figure 5. The defect is elliptical in shape with a 0.12 mm major radius and a 0.06 mm minor radius. For reference, a large green circle was added to the figure where the second sound measurements located the defect.

Figure 6 shows the equipment used to optically inspect the cavity RF surface. The Questar long-distance microscope is on the left. Coaxial with the cavity is a white cylinder, which contains an integral mirror and light source for viewing the inner surface of the cavity.

## SUMMARY

We presented a method which can locate a quench site on the RF surface of a superconducting niobium 9-cell cavity which requires a single cold test. This was achieved by measuring the time-of-flight of He-II second sound waves, which are driven by the conversion of electrical to thermal energy at the defect. The quench location by second sound was confirmed by traditional thermometry and optical inspection.

The He-II second sound telemetry technique was verified with a direct thermometric mapping of the cavity

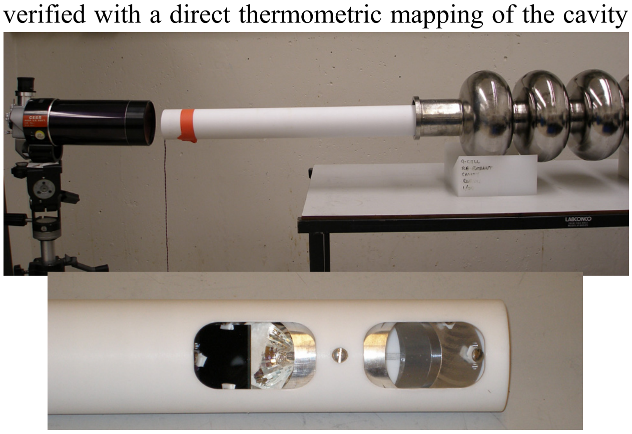

Figure 6: (Top)Questar long-distance microscope inspection equipment. (Top Left) Questar, (Top Middle) cylinder/mirror assembly (the mirror is not visible). (Bottom) Mirror and light used to view cavity interior.

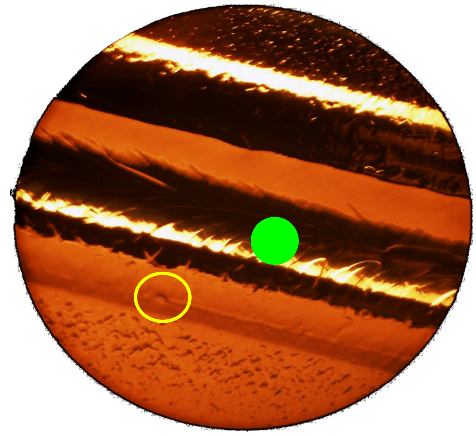

Figure 5: The defect found near the quench location is a 0.12 x 0.06 mm pit on the weld (inside yellow circle). The solid green circle corresponds to where the second sound measurement located the defect. The weld appears shiny in the middle and matt at the edge due to the lighting quality.

outer surface temperature. Subsequent optical inspections revealed a small pit on the equator weld. Future centrifugal barrel polishing will be employed to remove the defect and possibly others like it.

## ACKNOWLEDGEMENTS

Many thanks to Nick Szabo for his help in preparing and tesing the 2nd sound transducers and electronics in the Physics 510 teaching laboratory. A special thanks to Mathias Liepe and Grigori Eremeev for their late night help in RF tests.

## REFERENCES

[1] L. Lilje, "R&D In RF Superconductivity To Support The International Linear Collider," PAC 07, Albuquerque, NM, June 2007, Pg. 2559 (2007).

[2] K.W. Shepard, C.H. Scheibelhut, R. Benaroya, and L.M. Bollinger, "Split Ring Resonator For The Argonne Superconducting Heavy Ion Booster," IEEE Trans. Nuc. Sci., NS-24, Pg. 1147 June 1977.

[3] K.W. Shepard, C.H. Scheibelhut, P. Markovich, R. Benaroya, and L.M. Bollinger, "Development And Production Of Superconducting Resonators For The Argonne Heavy Ion Linac," IEEE Trans. Mag., MAG-15, Pg. 666, Jan. 1979.

[4] R.A. Sherlock and D.O. Edwards, "Oscillating Superleak Second Sound Transducers," Rev. Sci. Instrum. 41, Pg. 1603 (1970).

[5] R. Williams, S.E.A. Beaver, J.C. Fraser, R.S. Kagiwada, and I. Rudnick, "The Velocity Of Second Sound Near $T_{\lambda}$," Phys. Lett. 29A, Pg. 279 (1969).

[6] D. L. Hartill et al., To Be Published.

[7] H. Padamsee, et al., "Results On 9-Cell ILC and 9-Cell Re-Entrant Cavities," PAC 07, Albuquerque, NM, June 2007 ,WEPMS009, Pg. 2343 (2007).

[8] V. Shemelin and H. Padamsee, "Superconducting Multicell Cavity With Rentrant Cells," Cornell LEPP SRF Note SRF050808-06 (2005).

# RF DESIGN OF A SPOKE RESONATOR FOR HIGH POWER FREE-ELECTRON LASERS

F. L. Krawczyk, LANL, Los Alamos, New Mexico;
S. J. Cooke, NRL, Washington, DC;
D. C. Nguyen, LANL, Los Alamos, New Mexico;
B. Rusnak, LLNL, Livermore, California;
T. I. Smith, Stanford University, Stanford, Califormia;
E. L. Wright, Beam-Wave Research, Inc., Union City

## Abstract

We are investigating spoke resonators that originally were proposed for moderate energy proton acceleration for application in high-average-current free-electron lasers (FEL). This structure holds the promise of alleviating the BBU limitations of conventional rf structures. Spoke resonator have several advantages: 1) strong coupling simplifies the access to higher order modes (HOM), 2) at the same frequency a spoke resonator is about half the size of an elliptical resonator, 3) the spokes provide additional mechanical stability and stiffening , 4) the power and HOM couplers can be attached to the cavity body and do not take up additional space along the length of the accelerator, 5) the presence of the spokes limits the polarizations of the HOMs to two orientations which facilitates the selection of HOM coupler positions. The rf performance of a spoke resonator specifically designed for high-current electron applications (beta=1.0) will be presented and compared with the expected performance of elliptical resonators designed for such applications. Besides the structure's effectiveness for acceleration also HOM properties will be presented.

# CONTRIBUTION NOT RECEIVED

# A NEW SRF CAVITY SHAPE WITH MINIMIZED SURFACE ELECTRIC AND MAGNETIC FIELDS FOR THE ILC*

Zenghai Li and Chris Adolphsen, SLAC, Menlo Park, CA 94025, U.S.A.


*Abstract*

The TESLA TDR cavity has been chosen as the baseline design for the International Linear Collider (ILC) main linacs. There are continuous SRF R&D efforts to develop alternative cavity designs that can produce higher gradient which in turn could lead to significant cost savings in machine construction and operation. It is believed that the maximum gradient achievable in a superconducting cavity is limited by the critical magnetic flux Bc of the niobium, which is approximately 180 mT. Most of the new designs were focused on minimizing the surface magnetic field (Bs) while the requirement on electric field (Es) was relaxed. The Low Loss design was one of the optimized designs with a Bs reduction of more than 10% over the baseline design which could support a gradient as high as 50MV/m. The Es field in this design is however about 15% higher than the baseline design. Though it is not clear what undesirable effects the high Es field may induce at high gradient, it is advantageous in a design with both Bs and Es surface fields minimized. In this paper, we will present an optimized cavity shape that minimizes both the Bs and Es fields. The design of the HOM couplers for damping the wakefields will also be presented.


## INTRODUCTION

The TESLA TDR cavity shape [1], was proposed as the baseline design for the International Linear Collider (ILC) [2]. The cavity shape was optimized mainly with respect to Es/Ea, the ratio of maximum surface electric field to the accelerating gradient, and a ratio less than 2 was achieved. This low surface field ratio was considered advantageous in suppressing electron field emission at high gradients. Remarkable progresses have been made in understanding the limitations of field gradient in a superconducting cavity since the TDR was developed. It is believed that the maximum gradient achievable in a superconducting cavity is limited by the critical magnetic flux $B_c$ of the niobium which is approximately 180 mT [3]. The later works on the ILC cavity optimization were then aimed towards a lower Bs/Ea ratio. The Low Loss (LL) [4,5,6] cavity shape was then developed as an alternative design for the ILC. The geometry of the LL cavity is optimized to have a lower Bs/Ea ratio and a higher shunt R/Q by reducing the size of the iris and increasing the cavity volume in the high magnetic field region. As a comparison to the TDR shape, the iris radius of the LL cell is 30-mm, 5-mm smaller than TDR, and the side wall of the LL cell is more upright. These modifications resulted in more than 10% lower in Bs/Ea and 15% higher in R/Q and geometric factor G which make the cavity more efficient in acceleration and less cryogenics loss. However, the Es/Ea of the LL design is about 15% high than the TDR cavity. If the B field limitation is the dominant factor for reaching high gradient, the new LL shape could support an ultimate gradient of over 50 MV/m because of low Bs/Ea ratio. There are concerted efforts in various labs to fabricate and test the LL shape cavities [7,8] to realize such a gradient goal. Significant progresses have been made in high gradient testing of the LL 9-cell cavities in the past years. These efforts are on going to explore the gradient reach of such a design. Although it is not clear what undesirable effects the high surface electric field may induce at high gradients, it would be advantageous to have a cavity design that has both the Es/Ea and Bs/Ea minimized to alienate potential side effects of high surface fields. We have recently developed a Low Surface Field (LSF) cavity shape for the ILC. This shape could potentially improve the cavity performance since both the Bs and Es fields are lower. In this paper, we present the optimization results of the LSF shape, and the HOM coupler design to damp the harmful dipole modes.

* Work supported by DOE contract DE-AC02-76SF00515.

## CELL SHAPE OPTIMIZATION

### *Choice of Iris Aperture*

A small iris opening increases the shunt impedance thus reduces the stored energy in the cell for a given gradient, and in turn lowers the surface fields. It was found however that the cell-cell coupling quickly becomes undesirably small as the iris radius becomes much smaller than 30-mm as shown in Table 1. At a lower cell-cell coupling, the field imbalance becomes more sensitive to cell dimension errors as the figure of merit for the sensitivity is $N^2/k_{cc}$, where $N$ is the number of cells and $k_{cc}$ is the cell-cell coupling. In addition, a smaller iris opening will result in higher wakefields which would tighten the alignment tolerances. So the 30-mm iris radius is chosen for the LSF design.

Table 1: Monopole bandwidth versus iris opening

| iris radius (mm) | Bandwidth (MHz) |
|---|---|
| 25.0 | 9.6 |
| 27.5 | 13.0 |
| 30.0 (LL & LSF) | 19.2 |
| 35.0 (TDR) | 24.2 |

### *Cell Profile*

The new shape profile is similar to the LL shape except that the disk wall is straight up without a tilt angle. The cell contour is composed of an elliptical iris (*an, bn*) and an elliptical top (*at, bt*) connected by straight lines, as shown in Fig. 1. For a given disk thickness *T (an=T/2)*, *bn* and *bt* are optimized to minimize the surface E and B fields while cell radius "b" is adjusted to obtain a resonant frequency of 1.3-GHz. Fig. 2 shows the results of the surface field Bs/Ea and Es/Ea versus disk thickness. The TDR and LL cavity designs are also shown for comparison. The best surface field solution among these designs is the one that with an=11.8mm, which reduces the Bs/Ea by 11% and Es/Ea by 5% as compared with the TDR. However it was found that the dipole modes in this design are more trapped in the cell due to the thicker iris and are difficult to be damped. The next best solution is the design with an=10.5mm which is chosen as the LSF shape. This design has surface fields Bs/Ea 11% lower than the TDR and Es/Ea 15% lower than the LL. The cell profiles and the surface fields along the cell contours of the TDR, the LL, and the LSF designs are shown in Fig. 3 for comparison.

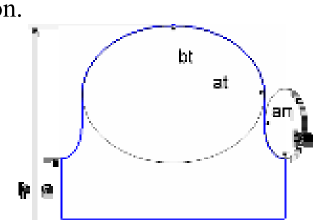


Figure 1: Cell parameters used for shape optimization.

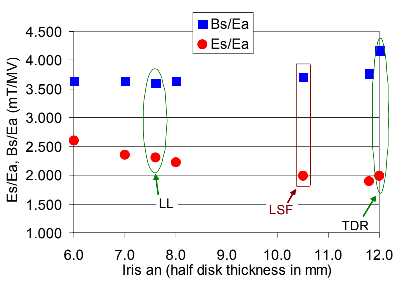


Figure 2: Surface fields vs disk thickness (an=T/2).

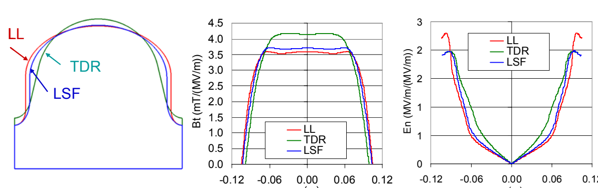


Figure 3: Cavity profile and surface field comparison between the LL (red), TDR (green), and the LSF (blue). "s" is the contour length of cell profile from the equator.

## SENSITIVITY TO CELL ERROR

Because of the thicker disk in the new LSF design, the monopole bandwidth is about 18% narrower than the LL cavity. The field flatness in the 9-cell cavity becomes more sensitive to the cell errors as the cell-cell coupling is reduced. The field amplitude deviation in cell "*i*" due to a frequency error $\Delta f_i$ in cell "*i*" can be estimated as

$$\frac{\Delta E_i}{E_i} = \frac{N^2}{k_{cc}} \cdot \frac{\Delta f_i}{f_i}$$

The cell frequency error $\Delta f_i$ and the coupled mode frequency errors of the 9-cell cavity due to an geometry error in cell "*i*" has little differences between the LL and LSF designs. The field imbalance due to the cell error is then inversely proportional to the cell-cell coupling $k_{cc}$. Fig. 4 compares the maximum field imbalance between the three designs for a 10-micrion single cell error, which corresponds to a $\Delta f_i$ of 150kHz, as functions of cell number. The LSF design is about 20% more sensitive than the LL design.

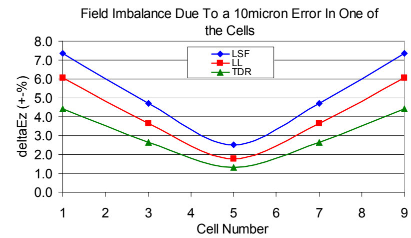


Figure 4: Field Imbalance due to a 10-µm error in cell radius.

## HOM COUPLER OPTIMIZATION

The mode spectrum and the R/Q values of the LSF design are shown in Fig. 5 up to the 3rd dipole band. The most important dipole mode is the 1pi/9 mode in the third band which has the highest R/Q. The 6pi/9 mode in the 1st band and the 5pi/9 mode in the 2nd band are also high in R/Q. The goal of the HOM coupler optimization is to damp the 3rd band high R/Q to a Qext bellow $10^5$, which is the ILC design requirement.

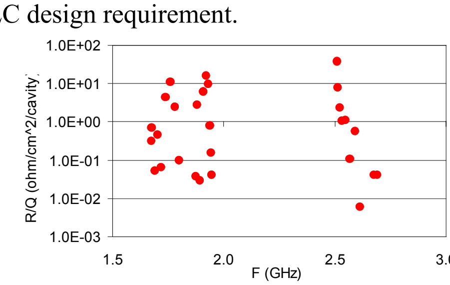


Figure 5: Dipole mode R/Q up to the third band.

### *End Beampipe*

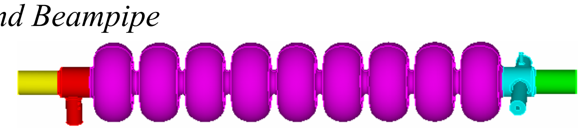

Figure 6: The 9-cell LSF cavity with coupler end-groups.

The end beampipe geometry of the LSF design is similar to the LL cavity. The beampipe radius is 38-mm in the HOM coupler region, and is tapered down to a smaller beampipe radius of 30-mm. The modes up to the 3rd band are cut off by the 30-mm beampipe (Fc=2.9 GHz). Thus the highest R/Q modes are damped "locally" by its own HOM couplers, not affected by adjacent cavities.

### *HOM Coupler*

The HOM coupler has the same basic design as the TDR and LL. However, the thicker disk in the new design shifted the frequency of the 3rd band high R/Q mode about

50-MHz higher. The fields of this mode are more concentrated in the cavity than that in the LL design, as compared in Fig. 7. The HOM damper needs to be modified in order to obtain effective damping.

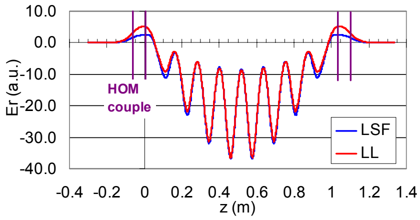


Figure 7: Field of the highest R/Q 3rd band mode.

**The loop shape:** The width of the loop was reduced to improve the match at the third band frequency. A nose-tip on the loop is included to enhance the electric coupling.

**The loop angle:** The loop angle is optimized to couple effectively to the high R/Q modes. This angle is 45 degrees with respect to the x-y plane with the hook side pointing to the cavity as shown in Fig. 8.

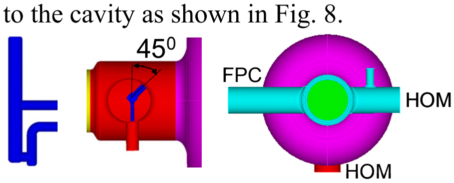


Figure 8: HOM coupler: loop shape and orientation.

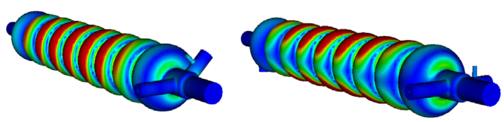

Figure 9: Mode polarization versus coupler orientations. Left) mode rotated with original LL coupler orientations; right) mode y-polarized with the new coupler orientations.

**The azimuthal location of HOM couplers:** The natural polarizations of the highest R/Q dipole modes in the LSF cavity are rotated about the z-axis, as shown in Fig. 9, if the HOM couplers are placed at the same azimuthal positions as in the LL design. These azimuthal positions were re-optimized for the LSF cavity such that the dominant modes, e.g. the 1pi/9 mode in the 3rd band, are polarized in the x or y directions. The new azimuthal positions of the HOM couplers are quite different from the LL design: the downstream HOM coupler is on the opposite side of the FPC coupler and the upstream HOM coupler is in the vertical plane as shown in Fig. 8. These new coupler orientations result in dipole modes naturally polarized in the x and y planes. An additional advantage of the new orientation is that the RF and short-range wakefield kicks due to the HOM and the FPC couplers at the downsteam end partially cancel. The upstream HOM coupler has a 180 degree azimuthal rotational symmetry in terms of the coupling to the dipole modes. One can alternate this orientation among the cavities in a cryomodule to minimize the wakefield and RF kicks in the y-plane.

### *Damping Results*

The Qext of the dipole modes were calculated using Omega3P [9] on the NERSC supercomputers. Optimized Qext for the first three dipole bands are shown in Fig 10. There are a few modes that have higher Qext, but the R/Q of these modes are low. The most important dipole mode to be damped is the 1pi/9 mode in the 3rd band. The Qext of this mode is bellow $10^5$ and satisfies the ILC requirement.

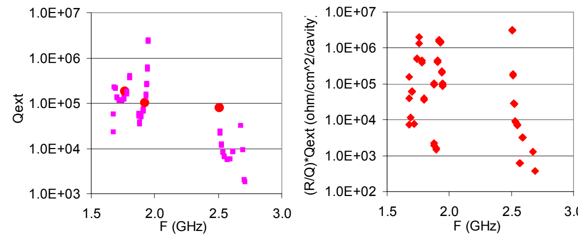


Figure 10: The damping results calculated using Omega3P: left) Qext; right) shunt impedance (R/Q)*Qext.

## SUMMARY

A Low Surface Field cavity shape was optimized based on the LL cavity design. The LSF shape provides a surface magnetic field 11% lower than the TDR design and the peak electric surface field 15% lower than the original LL design. This design could potentially support 10% higher gradient than the TDR and improve the cavity performance since both the electric and magnetic surface fields are low. The HOM coupler was re-optimized for the new LSF design to damp the dipole wakefields. The Qext of the highest R/Q mode in the 3rd band is bellow $10^5$ and satisfies the ILC requirement.

The simulation results presented in this paper was obtained using Omega3P running on NERSC computers.

## REFERENCES


[1] TESLA Collaboration.

[2] http://www.linearcollider.org

[3] K. Saito, “Fundamental RF critical Field Overview,” Proc. Workshop on Pushing the Limits of RF Superconductivity, ANL, Argonne, September 2004.

[4] J. Sekutowicz et al., “Low Loss Cavity for the 12 GeV CEBAF Upgrade“, JLAB, TN-02-023, 2002.

[5] J. Sekutowicz et al., “Design of a Low Loss SRF Cavity for the ILC,” Proc. PAC05, Knoxville, 2005.

[6] Z. Li et al., “Optimization of the Low Loss SRF Cavity for the ILC,” proc. Of PAC07, Albuquerque, New Mexico, June 2007.

[7] K. Saito et al., proc. of 12th Int. Workshop on RF Superconductivity, Ithaca, NY, July 10-15, 2005.

[8] P. Kneisel et al., proc. of 12th Int. Workshop on RF Superconductivity, Ithaca, NY, July 10-15, 2005.

[9] L. Lee et al., “Modeling RF Cavity with External Coupling,” 2005 SIAM Conference on Computational Science and Engineering, Orlando, Florida, 2005.

# SRF CAVITY IMPERFECTION STUDIES USING ADVANCED SHAPE UNCERTAINTY QUANTIFICATION TOOLS*

V. Akcelik, L-Q. Lee, Z. Li, C-K Ng, L. Xiao and K. Ko, SLAC, Menlo Park, CA 94536, USA


## Abstract

The deviations of a SRF cavity from the design shape may results in significant impact on cavity performance and wakefields that could lead to unexpected effects in beam dynamics. Yet, most of these deviations are unknown in the final cavity installation because of the complicated process of assembly and tuning. It is desirable to be able to infer for such distortions using measurable RF quantities. With these data, the cavity performance can be analyzed and realistic tolerance criteria may be implemented in the cavity design and manufacture for quality assurance. To perform such analyses, SLAC has developed advanced Shape Determination Tools, under the SciDAC support for high performance computing, that recover the real cavity shape by solving an inverse problem. These tools have been successfully applied to analyze shape deviations of many SRF cavities, and identified the cause of unexpected cavity behavior. The capabilities and applications of these tools are presented.


## INTRODUCTION

The SRF cavities differ from original shape due to manufacture error and the tuning for the accelerating mode to achieve the right frequency and flat field. The deformation of the cavity leads to changes in higher-order mode frequencies, field distribution and wakefield damping, and may result in beam instabilities. It is important to understand the shape deviations of the real cavity from the design shape so that undesirable side effects due to shape deviation can be minimized in the manufacture of new cavities. Although direct measurements of the cavity shape are not feasible after the cavity is installed in the cryomodule and tuned, some of the RF quantities can be measured and can be used to evaluate the cavity shape deviations. SLAC has developed a set of shape uncertainty quantification tools based on SLAC's parallel finite element software that can recover the real cavity shape by solving an inverse problem using measurable RF quantities as input data.

We formulate the shape determination problem as a PDE constraint optimization problem, where the constraint is the Maxwell eigenvalue problem, the objective function is the weighted summation of the least squares difference of the modeled and measured RF quantities, and the inversion variables are the unknown shape deviations.

We present capabilities of the shape uncertainty quantification tools on two real applications: 1) the shape determination of the TDR cavity; and 2) identifying the cause of the BBU in one of the CEBAF 12-GeV upgrade prototype cavities.

## METHODS

We pose the shape determination problem as a nonlinear least squares optimization problem

$$\begin{aligned} &\underset{\mathbf{e}_j,k_j,\mathbf{d}}{\text{minimize}} && \sum_i \alpha\left(f_i-\bar{f}_i\right)^2+\sum_i \beta\left(Q_i-\bar{Q}_i\right)^2 \\ &\text{subject to} && \mathbf{K}\mathbf{e}_j+ik_j\mathbf{W}\mathbf{e}_j-k_j^2\mathbf{M}\mathbf{e}_j=\mathbf{0} \\ & && \mathbf{e}_j^T\mathbf{M}\mathbf{e}_j=1 \end{aligned}$$

where α and β are weighting constants, $\mathbf{e}_j$ eigenvector, and $k_j$ eigenvalue for the $j$th mode, $f_i$ are mode frequencies, and $Q_i$ are external Q value for the $j$th mode, and **d** the represents the unknown shape parameters.

To solve the optimization problem, we follow a gradient based approach. The resulted nonlinear problem is solved using Gauss-Newton method, in which the required eigenvalue and eigenvector sensitivities are computed with a discrete adjoint approach. Inverse shape determination problem is generally ill-posed and rank deficient. To remedy this we use regularization methods such as truncated singular value decomposition (T-SVD), and Tikhonov regularization. The nonlinear optimization algorithm typically converges within a handful of nonlinear iteration. Each nonlinear iteration requires solutions of the forward eigenvalue problem, the adjoint problems, and evaluations of inversion equations. The forward eigenvalue problem is solved using Omega3P, and adjoint problems are solved using direct solvers such as MUMPS.

## SHAPE DETERMINATION OF TDR CAVITY

The shape determination tool is used to infer for the unknown cavity deviations of a TDR cavity (Fig. 1). The following RF quantities are used as input in the objective function: 9 monopole frequency value, 36 dipole frequency values, and normalized field values measured at the center of each cell for the 9 monopole modes. These input data were obtained from the TFF-III measurements [1].

* Work supported by the U.S. DOE ASCR, BES, and HEP Divisions under contract No. DE-AC02-76SF00515. The work used the resources of NCCS at ORNL which is supported by the Office of Science of the U.S. DOE under Contract No. DE-AC05-00OR22725, and the resources of NERSC at LBNL which is supported by the Office of Science of the U.S. DOE under Contract No. DE- AC03-76SF00098. Work used resources of NCCS/ORNL supported under US DOE Contract No. DE-AC05-00OR22725, and NERSC/LBNL supported under US DOE Contract No. DE-AC03-76SF00098.

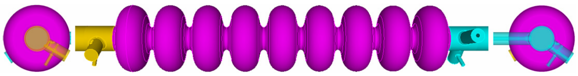

Figure 1: 3D CAD mode of TDR cavity.

The parametrization of each cell is shown in Fig. 2. There are five sections along each cell profile [illegible] each of these are unknown shape deviations parameters[illegible] In addition, changes in cell length ([illegible]) and changes in cell iris ([illegible]a[illegible] are also parametrized [2]. In total, inversion variable has 62 unknown parameters.

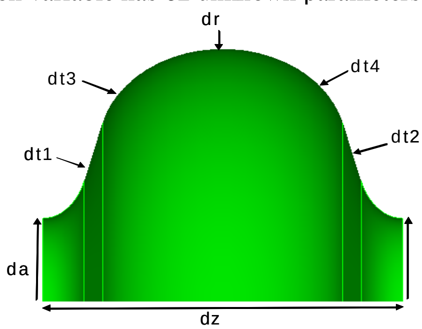


Figure 2: Definitions of shape parameters for a single cell.

The shape determination problem is solved using different regularization methods (Tikhonov regularization, and T-SVD), and different mesh discretization. In all of the inversion cases, the algorithm successfully reduced the error in the frequencies, and field values to the noise level. Figure 2 shows the frequency errors, which is the differences between calculated and measured, for the original design and the recovered cavity using the shape determination tools. The details of the analysis can be found in Ref. [3].

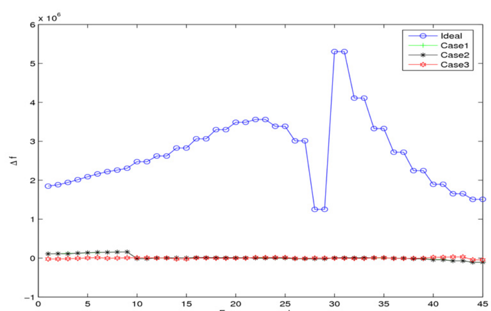


Figure 3: Frequency misfit for optimized and original cavities.

## JEFFERSON LAB HIGH GRADIENT PROTOTPYE CRYOMODULE

Beam based instability studies for JLab high gradient prototype cryomodule indicated that the beam breakup (BBU) threshold was well below the design value [4, 5]. Frequency spectrum peaked by the off-sided beam power shows that the cause is due to abnormal high Q modes in one of the cavities. The cause of this abnormality and future impact on the BBU couldn't be resolved due to limitations of information from the measurements. Omega3P [6] was used to compute $Q_{ext}$ values of these three HOM modes in an idea cavity shape, and they do not agree well with measurements of the real cavity. To understand the cause of this abnormality we used the shape determination tool developed as SLAC to solve for the unknown shape deviations.

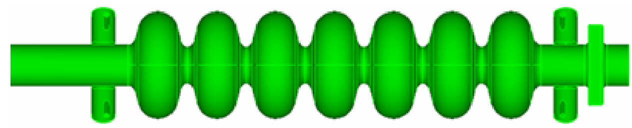

Figure 4: The 7-cell high gradient (HG) cavity model used for Omega3P simulations.

To descritize the unknown shape deviations we have used similar shape parametrization as in the TDR cavity shape determination problem. To recover the unknown shape, we used measured frequencies and $Q_{ext}$ values of the monopole modes and the first two dipole bands, which include the 7 monopole frequencies, 12 dipole frequencies, and 6 $Q_{ext}$ values.

Inversion algorithm successfully reduced the frequency differences between the recovered shape and the measurement of the real cavity to the noise level. Figure 5 shows the frequency error for the ideal and deformed cavities. Figure 6 shows the geometry difference of the deformed shape and ideal cavity. Although the inversion result is not unique due to ill-posedness and rank deficiency of the problem, inversion studies confirmed that the length of the deformed cavity is significantly shorter than the ideal cavity. The difference is found to be 8-mm. This result was confirmed by the cavity QC data.

Figure 7 shows the $Q_{ext}$ results of the deformed cavity. The deformed cavity not only reproduced high $Q_{ext}$ modes, it also reproduced the low $Q_{ext}$s for the modes around 2160 MHz which agree well with the measurements.

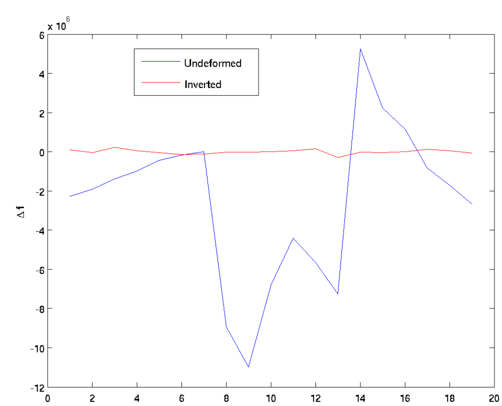


Figure 5: Frequency misfit for deformed and original cavities.

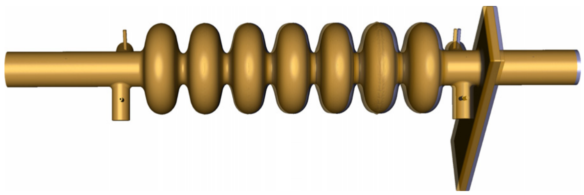

Figure 6: Deformed (goldenrod) and ideal (lightgrey) cavities.

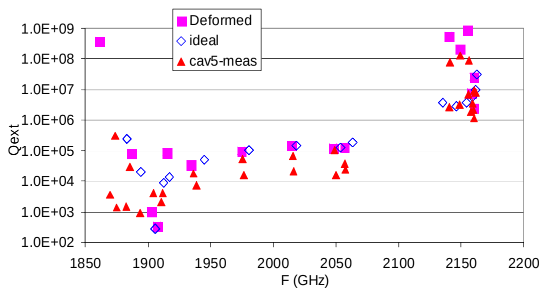


Figure 7: Qext for the ideal and deformed cavities.

The field distributions of the three abnormal modes in the deformed cavity are significantly different from that in the ideal cavity (Fig. 8). In the ideal cavity, fields are symmetrically distributed along the cavity, while in the deformed cavity they are heavily tilted toward the right side. The fields in HOM coupler region (left side) are more than one order of magnitude lower than the original cavity. This has resulted in ineffective damping. Because the fields of the other HOM modes were not altered as significantly by the deformation, no significant changes in the Qext of these modes were observed in the RF measurements.

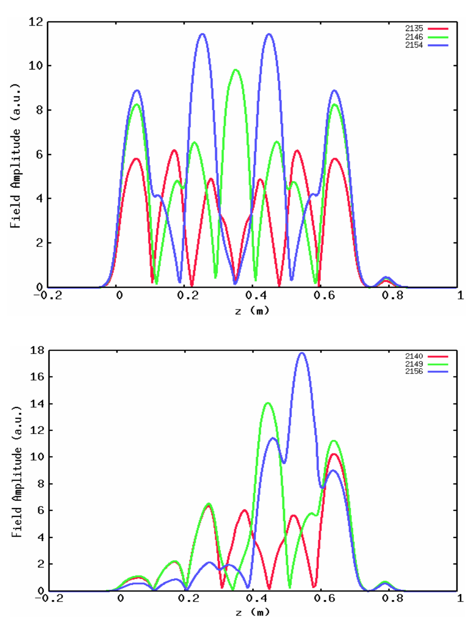


Figure 8: Comparison of electric field of the abnormal modes. Top: ideal design, bottom: deformed cavity with high $Q_{ext}$ modes.

## SUMMARY

Using the state of the art PDE constraint optimization techniques, and high performance computing tools, SLAC has developed shape uncertainty quantification tools to solve for the unknown shape deviations of the accelerator cavities using measurable RF quantities. We have used these tools to recover the unknown shape deviations of a TDR cavity from measured RF quantities. And these tools have been successfully used to determine the cause of the high abnormal $Q_{ext}$ values which caused unexpected BBU in one of the CEBAF 12 GeV upgrade cavities. It was found using the shape determination tool that the leading cause of the high Qext in that cavity was due to large errors in the cell lengths, which resulted in a total cavity length shortage of 8-mm. This result has been confirmed by the cavity QC data.

## REFERENCES

[1] http://tesla-new.desy.de

[2] L. Xiao et al. "Modeling Imperfections Effects on Dipole Modes in Tesla Cavity", in Proc. of 2007 Particle Accelerator Conference, Albuquerque, New Mexico.

[3] V. Akcelik et al, "Shape Determination for Deformed Electromagnetic Cavities", Journal of Computational Physics 227 (2008) `722-1738.

[4] E. F. Daly et al., "Improved Prototype Cryomodule for the CEBAF 12 GeV Upgrade," PAC03, p.1377, TPAB077.

[5] Z Li et al. "Analysis of the cause of high External Q modes in the Jlab High Gradient Prototype Cryomodule Renascence", SLAC-PUB-13266, June 2008.

[6] L.-Q. Lee, et al, "Advancing Computational Science Research for Accelerator Design and Optimization," Proc. Of SciDAC 2006 Conference, Denver, Colorado, June 25-29, 2006.

# A NEW TEM-TYPE DEFLECTING AND CRABBING RF STRUCTURE*

J. R. Delayen[1,2#] and H. Wang[1]
[1]Thomas Jefferson National Accelerator Facility, Newport News, VA 23606, U.S.A
[2]Old Dominion University, Norfolk, VA 23529, USA

*Abstract*

A new type of rf structure for the deflection and crabbing of particle bunches is introduced. It is comprised of a number of parallel TEM-resonant lines operating in opposite phase from each other. One of its main advantages is its compactness compared to conventional crabbing cavities operating in the $TM_{110}$ mode, thus allowing low frequency designs. The properties and characteristics of this type of structure are presented.

## INTRODUCTION

Rf cavities for the deflection or crabbing of particle beams have been developed for many years. Most of them are comprised of superconducting cavities operating in the $TM_{110}$ mode [1-4] although some are room temperature structures operating in a $\lambda/4$ mode [5] or are of *H*-type [6]. Crabbing rf structures have been of interest for the increase of luminosity in colliders [7,8], and more recently for the generation of sub-picosecond x-ray pulses [9,10].

The concept of the parallel-bar deflecting structure introduced here is shown in Fig. 1. It consists of 2 parallel $\lambda/2$ TEM resonant lines operating in opposite phase. The voltages generated are maximum and of opposite sign in the middle of the rods and generate a transverse electric field as shown in Fig. 2. The magnetic field is null in the mid-plane containing the beam line and is maximum where the bars meet the shorting planes, as shown in Fig. 3. Thus, unlike $TM_{110}$ structures where the deflection is produced by interaction with the magnetic field, in the parallel-bar structure, the deflection is produced by interaction with the electric field.

Figure 1: Concept of the parallel-bar deflecting structure.

* Authored by Jefferson Science Associates, LLC under U.S. DOE Contract No. DE-AC05-06OR23177. The U.S. Government retains a non-exclusive, paid-up, irrevocable, world-wide license to publish or reproduce this manuscript for U.S. Government purposes.
#delayen@jlab.org

In the absence of beam pipe apertures, and if the outer wall were made of flat planes, the deflecting π-mode would be degenerate with the accelerating 0-mode where the 2 bars are oscillating in phase. Because the π-mode has no electric or magnetic field where the beam line meets the entrance and exit walls, while the 0-mode has an electric field, the beam pipe apertures remove the degeneracy. The mode splitting is further increased by rounding all the corners as shown in Fig. 1.

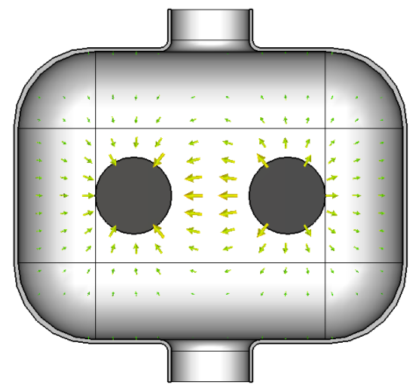

Figure 2: Electric field in the mid-plane of the parallel-bar structure operating in the π-mode.

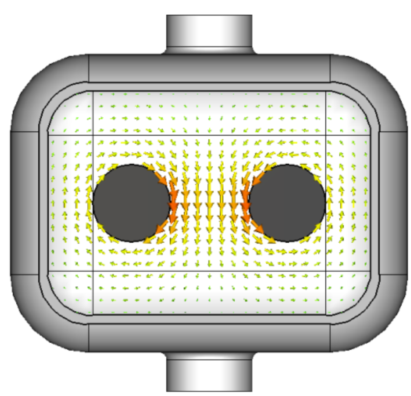

Figure 3: Magnetic field in the top-plate of the parallel-bar structure operating in the π-mode.

## ANALYTICAL MODEL

If the distance between the side walls and the rods is substantially larger than the distance between the rods and the vertical symmetry plane, then the walls' contributions to the electromagnetic properties will be small and the fundamental cell can be modeled by two parallel infinite planes separated by $\lambda/2$ and joined by two parallel cylinders of radius $R$ and of axis-to-axis separation $2A$. The properties of such a structure can be calculated exactly, and will be compared later to simulations.

### *Peak Surface Electric Field*

Defining the transverse electric field $E_t$ as $E_t = 2V_t/\lambda$, where $V_t$ is the transverse voltage acquired by an on-crest, velocity-of-light particle, the peak surface electric field $E_p$ is

$$\frac{E_p}{E_t} = \frac{1}{4\pi}\frac{\lambda}{R}\left(\frac{\alpha+1}{\alpha-1}\right)^{1/2} \exp\left[2\pi\frac{R}{\lambda}\sqrt{\alpha^2-1}\right], \quad (1)$$

where $\alpha = A/R$.

### *Peak Surface Magnetic Field*

Since this model is a uniform transmission line operating in a pure TEM mode, the peak magnetic field is related to the peak electric field by

$$B_p \text{ (in mT) } = \frac{10^9}{c} E_p \text{ (in MV/m)}. \quad (2)$$

### *Energy Content*

The energy content $U$ is related to the transverse gradient $E_t$ by

$$U = E_t^2 \frac{\varepsilon_0}{32\pi}\lambda^3 \cosh^{-1}\alpha \exp\left[4\pi\frac{R}{\lambda}\sqrt{\alpha^2-1}\right], \quad (3)$$

where $\varepsilon_0$ is the permittivity of the vacuum in SI units.

### *Geometrical Factor*

$$G = QR_s = 2\pi Z_0 \frac{R}{\lambda}\frac{\cosh^{-1}\alpha}{\frac{8R}{\lambda}\cosh^{-1}\alpha + \frac{\alpha}{\sqrt{\alpha^2-1}}}, \quad (4)$$

where $Z_0 = \sqrt{\mu_0/\varepsilon_0} \simeq 377\Omega$ is the impedance of the vacuum.

### *Transverse Shunt Impedance*

The transverse shunt impedance, defined as $R_t = V_t^2/P$ where $P$ is the power dissipation, is

$$R_t/Q = 4Z_0 \frac{\exp\left[-4\pi\frac{R}{\lambda}\sqrt{\alpha^2-1}\right]}{\cosh^{-1}\alpha}. \quad (5)$$

It can be noted that the electromagnetic properties can be expressed simply as functions of $R/\lambda$ and $\alpha = A/R$. Universal curves for the peak surface electric field and the product of the geometrical factor $G$ and $R_t/Q$ are shown in Figs. 4 and 5. The peak surface electric (and magnetic) field has a weak dependence on $R/\lambda$ and $A/R$ but is minimum for a rather large $R/\lambda$. $G*R_t/Q$, on the other hand, has a much stronger dependence on both and is maximum for smaller $R/\lambda$. Thus the final design will depend on which parameter to optimize, and in particular whether the structure will be normal or superconducting.

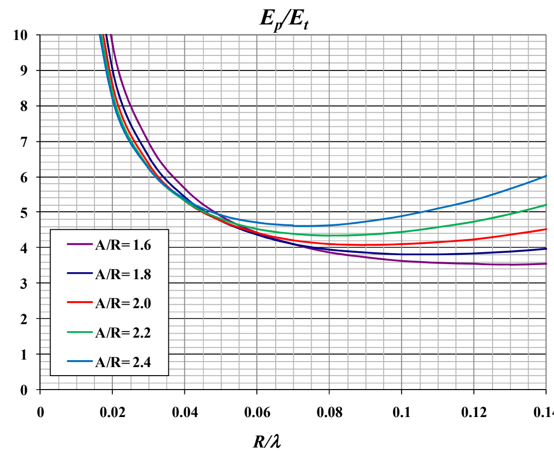


Figure 4: Ratio of peak to transverse electric field given by Eq. (1). $R$ is the radius of the cylindrical rods and $2A$ is the distance between their axes.

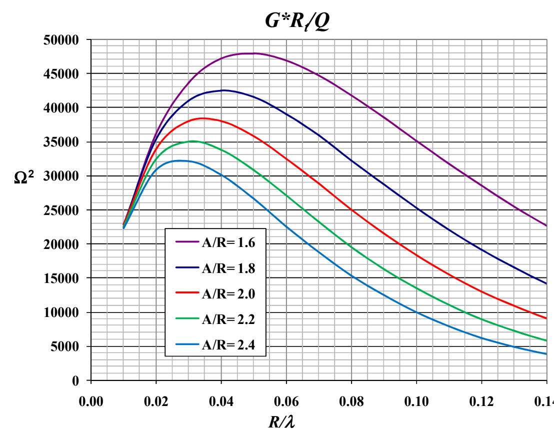


Figure 5: Product of the geometrical factor $G$ and the transverse shunt impedance $R_t/Q$ given by Eqs. (4)-(5).

## ELECTROMAGNETIC DESIGN

Since one of the main characteristics of this geometry is its small transverse size, it would be particularly attractive at low frequency, and preliminary design activities have focused on a 400 MHz single-cell cavity.

The lengths of the bars and of the outer box were, to first order, fixed at 375mm and the main design parameters were the radii and separation of the two parallel bars. Results of simulations using CST Microwave Studio® are shown in Fig. 6. They compare very favorably with the analytical results of the previous section. As was expected the transverse shunt impedance of this design is quite high compared to designs based on $TM_{110}$ modes. This is similar to the high shunt impedance of TEM accelerating structures compared to $TM_{010}$ structures [11].

For velocity-of-light applications TEM accelerating structures have peak surface fields larger that $TM_{010}$ structures [11]. The analytical model and these simulations show that this is not the case for deflecting cavities as peak surface fields for TEM structures are comparable to those in $TM_{110}$ structures.

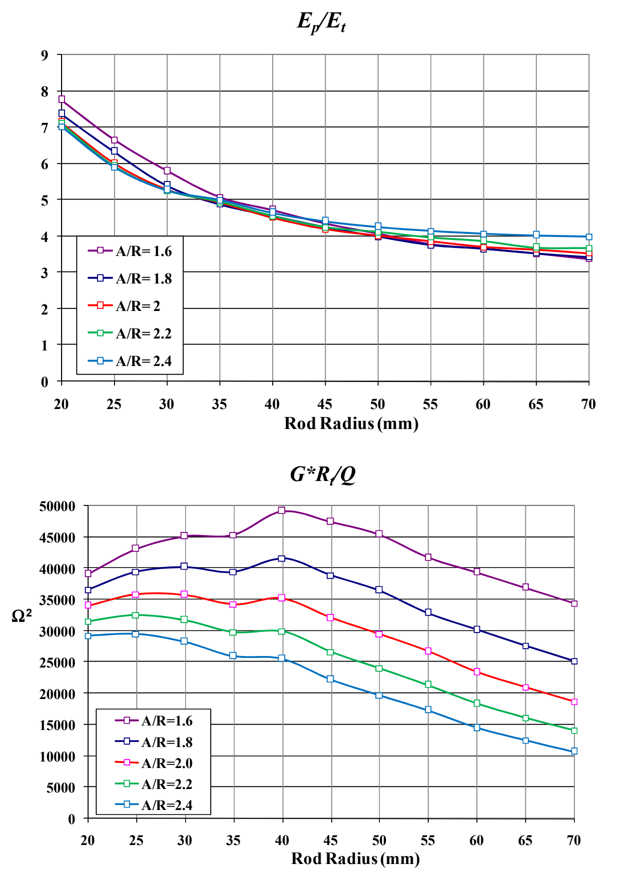


Figure 6: Ratio of peak to deflecting electric field (upper) and $G*R_t/Q$ (lower) for the 400 MHz structure shown in Fig. 1 obtained from CST Microwave Studio.

Properties of a preliminary design of a 400 MHz parallel-bar deflecting structure obtained from Omega3P are shown in Table 1. It can be noted that the deflecting π-mode is the lowest frequency mode, which would simplify the damping of all the other modes in high-current applications.

## EXTENSIONS AND OPTIMIZATION

The single-cell parallel bar structure discussed so far can be straightforwardly extended to a multicell structure by the addition of sets of parallel bars separated by $\lambda/2$ as shown in Fig. 7. In the relevant (deflecting) mode of operation each set of bars oscillates in opposite phase from its neighbors and each bar oscillates in opposite phase from the bar across the beam line. This will increase the degree of degeneracy since the number of TEM modes is equal to the number of bars, and splitting the (π,π) deflecting mode from all the others will need to be provided, for example by shaping the outer walls or introducing partial walls between the sets of bars.

All the above examples use straight circular cylinders for the bars. Further optimization can be obtained by deviation from a circular cross-section, deviation from a constant cross-section (hyperboloidal shape), deviation from a straight bar centerline. These modifications could yield geometries with lower surface magnetic field, for example, at the expense of added engineering complexity.

Table 1: Properties of Parallel-bar Structure shown in Figure 1 Calculated from Omega3P and Analytical Model

| Parameter | Ω3P | Analytical model | Unit |
|---|---|---|---|
| Frequency of π-mode | 400 | 400 | MHz |
| $\lambda/2$ of π-mode | 374.7 | 374.7 | mm |
| Frequency of 0-mode | 414.4 | 400 | MHz |
| Cavity length | 374.7 | ∞ | mm |
| Cavity width | 500 | ∞ | mm |
| Bars length | 381.9 | 374.7 | mm |
| Bars diameter ($2R$) | 100 | 100 | mm |
| Bars axes separation ($2A$) | 200 | 200 | mm |
| Aperture diameter | 100 | 0 | mm |
| Deflecting voltage $V_t$ * | 0.375 | 0.375 | MV |
| $E_p$ * | 4.09 | 4.28 | MV/m |
| $B_p$ * | 13.31 | 14.25 | mT |
| $U$ * | 0.215 | 0.209 | J |
| $G$ | 96.0 | 112 | Ω |
| $R_t/Q$ | 260 | 268 | Ω |
| * at $E_t$=1MV/m | | | |

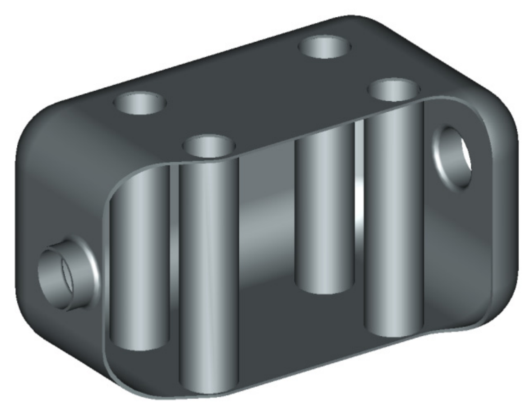

Figure 7: Concept for a 2-cell parallel-bar deflecting cavity. Each of the bars oscillates in opposite phase from its two nearest neighbors.

## REFERENCES

[1] A. Citron *et al.,* NIM **155** (1978), p. 93.
[2] H. Padamsee *et al.*, Proc. PAC91, p. 2423.
[3] K. Hosoyama *et al.*, Proc. APAC98, p. 828.
[4] T. W. Koeth, Proc. PAC99, p. 995.
[5] C. W. Leemann and C. G. Yao, Proc. LINAC90, p. 232.
[6] Yu. Senichev *et al.*, PRSTAB **9**, 012001 (2006).
[7] R. B. Palmer, SLAC-PUB 4707 (1988).
[8] K. Oide and K. Yokoya, Phys. Rev. **A40**, p. 315 (1989).
[9] A. Zholents, P. Heimann, M. Zolotorev, and J. Byrd, NIM **A425**, 385 (1999)
[10] J. Shi *et al.*, Proc. PAC05, p. 4287.
[11] J. R. Delayen, Proc. 2001 SRF Workshop, p. 152.

# ANALYSIS OF ELECTRONIC DAMPING OF MICROPHONICS IN SUPERCONDUCTING CAVITIES*

S. U. De Silva#1 and J. R. Delayen†1,2
[1]Old Dominion University, Norfolk, VA 23529, U.S.A.
[2]Thomas Jefferson National Accelerator Facility, Newport News, VA 23606, U.S.A.

*Abstract*

In low current applications superconducting cavities have a high susceptibility to microphonics induced by external vibrations and pressure fluctuations. Due to the narrow bandwidth of the cavities, the amount of rf power required to stabilize the phase and amplitude of the cavity field is dictated by the amount of microphonics that need to be compensated. Electronic damping of microphonics is investigated as a method to reduce the level of microphonics and of the amount of rf power required. The current work presents a detailed analysis of electronic damping and of the residual cavity field amplitude and phase errors due to the fluctuations of cavity frequency and beam current.

## INTRODUCTION

In superconducting cavities microphonics and ponderomotive effects are the major causes of the fluctuations in the cavity fields [1]. Microphonics are the changes in the cavity frequency caused by the connections to the external world, such as external vibrations, pressure fluctuations, etc., and the ponderomotive effects are changes in the cavity frequency caused by the electromagnetic field (radiation pressure). The amount of rf power required in controlling the cavity field–to maintain the amplitude and phase stabilized–is dominated in low-current superconducting cavities by the presence of microphonics.

Electronic damping may be an effective way of reducing microphonics; it requires an active modulation of the cavity field to induce ponderomotive effects that counteract the effects of external sources. The model developed to control the cavity field is to operate the superconducting cavity in a self excited loop with amplitude and phase feedback. This paper analyses the method of electronic damping of microphonics and presents a generalized analytical solution for the residual changes of the cavity field amplitude and phase with and without the presence of beam.

## MODEL AND EQUATIONS

The model, described in detail in [2-4], operates the cavity in a self excited loop. The transfer function diagram for the model described in [2-4] is given in Figure 1.

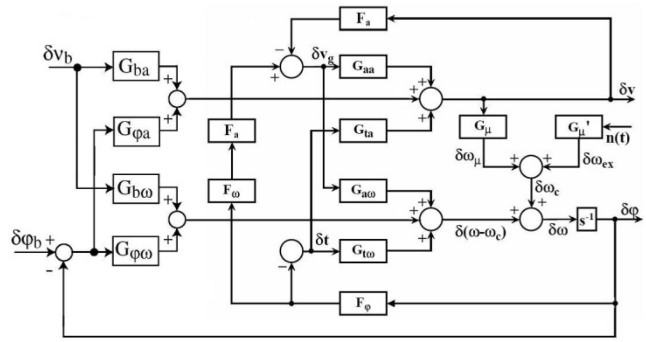


Figure 1: Transfer function representation of the system.

The corresponding transfer functions are as follows.

$$G_{aa} = \frac{\cos(\theta_l + \theta_f)}{\cos\theta_l}\frac{1}{1+\tau s},\ G_{ta} = -\frac{\sin(\theta_l + \theta_f)}{\cos\theta_l}\frac{1}{1+\tau s},$$

$$G_{a\omega} = \frac{1}{\tau}\frac{\cos(\theta_l + \theta_f)}{\cos\theta_l}\left[y - \frac{y_r}{1+\tau s}\right],\ G'_{\mu} = \frac{\Omega_\mu^2}{s^2 + \dfrac{2}{\tau_\mu}s + \Omega_\mu^2},$$

$$G_{t\omega} = \frac{1}{\tau}\frac{\cos(\theta_l + \theta_f)}{\cos\theta_l}\left[1 + \frac{y\, y_r}{1+\tau s}\right],\ G_{\mu} = -\frac{2\Omega_\mu^2\ k_\mu V_0^2}{s^2 + \dfrac{2}{\tau_\mu}s + \Omega_\mu^2},$$

$$G_{ba} = -\frac{m}{1+\tau s},\qquad G_{\varphi a} = -\frac{m\, y_0}{1+\tau s},$$

$$G_{b\omega} = \frac{m}{\tau}\left[-y_0 + \frac{y_r}{1+\tau s}\right],\qquad G_{\varphi\omega} = -\frac{m}{\tau}\left[1 + \frac{y_0 y_r}{1+\tau s}\right],$$

$$y = \tan(\theta_l + \theta_f),\ y_r = \frac{\tau_0(\omega_r - \omega_c)}{(1+\beta)} = \tau(\omega_r - \omega_c),\ y_0 = \tan\theta_0,$$

$F_a, F_\varphi, F_\omega$ : Amplitude, Phase and Frequency feedbacks,

$\tau = \dfrac{\tau_0}{1+\beta}$ : Loaded amplitude decay time,

$b = \dfrac{V_b \cos\varphi_0}{V_0}$ : Ratio of power absorbed by the beam to power dissipated in the cavity,

$m = \dfrac{b}{1+\beta}$ : Beam matching coefficient,

$\varphi_0$ : Nominal phase between the beam and the rf field,

$\tau_0$ : Intrinsic amplitude decay time,

$\beta$ : Coupling coefficient,

$\Omega_\mu$ : Frequency of the mechanical mode of the cavity,

*Authored by Jefferson Science Associates, LLC under U.S. DOE Contract No. DE-AC05-06OR23177. The U.S. Government retains a non-exclusive, paid-up, irrevocable, world-wide license to publish or reproduce this manuscript for U.S. Government purposes.
#pdesilva@odu.edu, †delayen@jlab.org

$\tau_\mu$ : Decay time of the mechanical mode of the cavity,

$k_\mu$ : Lorentz coefficient of the mechanical mode,

$\theta_l$ : Loop phase shift, $\theta_f$ : Feedback phase shift,

$V_0$: Cavity field amplitude.

$G_\mu$ represents the transfer function for ponderomotive effects that couples the cavity field amplitude and the cavity frequency. The transfer function $G'_\mu$ represents the coupling between the external sources and the cavity frequency. Fluctuations in the cavity frequency ($\delta\omega_c$) are a direct result of the frequency fluctuations due to ponderomotive effects ($\delta\omega_\mu$), and the frequency fluctuations due to external sources ($\delta\omega_{ex}$). Fluctuations in the cavity frequency are $\delta\omega_c = \delta\omega_\mu + \delta\omega_{ex}$ with $\delta\omega_\mu = G_\mu \delta v$ and $\delta\omega_{ex} = G'_\mu n(t)$. $\delta v$ is the residual amplitude error and $n(t)$ is the external source of vibration. The ponderomotive effects are used to counteract the effects of microphonics. The residual amplitude and phase errors due to the effects of microphonics ($\delta\omega_{ex}$) with absence of the beam are

$$\delta v = \frac{F_\varphi \left(F_a F_\omega G_{aa} - G_{ta}\right)}{D}\delta\omega_{ex}, \quad \delta\varphi = \frac{\left(1 + F_a G_{aa}\right)}{D}\delta\omega_{ex},$$

with

$$D = (1 + F_a G_{aa})(s + F_\varphi G_{t\omega} - F_a F_\varphi F_\omega G_{a\omega}) + F_\varphi (F_a F_\omega G_{aa} - G_{ta})(F_a G_{a\omega} - G_\mu).$$

## DAMPING BY FEEDBACK PHASE SHIFT

Electronic damping relies on the generation of ponderomotive effects that counteract the effects of externally-induced microphonics [4]. In this model, the feedbacks applied are simple proportional amplitude and phase feedback gains of $F_a = k_a$ and $F_\varphi = k_\varphi$. The system is analyzed on resonance ($\theta_l$) with a feedback phase shift ($\theta_f$) [3-5] producing a coupling between phase and amplitude feedback that acts as a damping mechanism for the mechanical mode. It is assumed that the cavity is operated with no frequency feedback, no beam loading $(G_{ba} = G_{\varphi a} = G_{b\omega} + G_{\varphi\omega} = 0)$, small feedback angle $(\theta_f \ll 1)$, large feedback gains $(k_a, k_\varphi \gg 1, \tau\Omega_\mu)$ and $\tau / \tau_\mu \ll 1$. The resultant residual amplitude and phase errors are

$$\delta v = \frac{\Omega_\mu^2 k_\varphi \theta_f}{A(s)} n(s), \quad \delta\varphi = \frac{\Omega_\mu^2 (1 + k_a + \tau s)}{A(s)} n(s),$$

with

$$A(s) = a_4 \left(\frac{s}{\Omega_\mu}\right)^4 + a_3 \left(\frac{s}{\Omega_\mu}\right)^3 + a_2 \left(\frac{s}{\Omega_\mu}\right)^2 + a_1 \left(\frac{s}{\Omega_\mu}\right)^1 + a_0$$

where the coefficients are

$$a_4 = \tau\Omega_\mu^4, \qquad a_3 = (1 + k_a + k_\varphi)\Omega_\mu^3 + \frac{2\tau\Omega_\mu^3}{\tau_\mu},$$

$$a_2 = \frac{(1 + k_a)k_\varphi \Omega_\mu^2}{\tau} + \frac{k_a k_\varphi \Omega_\mu^2 \theta_f^2}{\tau} + \frac{2(1 + k_a + k_\varphi)\Omega_\mu^2}{\tau_\mu} + \tau\Omega_\mu^4,$$

$$a_1 = \frac{2(1 + k_a)k_\varphi \Omega_\mu}{\tau\tau_\mu} + \frac{2k_a k_\varphi \Omega_\mu \theta_f^2}{\tau\tau_\mu} + (1 + k_a + k_\varphi)\Omega_\mu^3,$$

$$a_0 = \frac{(1 + k_a)k_\varphi \Omega_\mu^2}{\tau} + \frac{k_a k_\varphi \Omega_\mu^2 \theta_f^2}{\tau} + 2k_\varphi \Omega_\mu^2 k_\mu V_0^2 \theta_f.$$

The above system is analyzed by performing a frequency sweep of $\omega$ with $s = i\omega$, for several feedback phase shifts. The maximum response is found at

$$\Omega_r = \Omega_\mu \sqrt{1 + \frac{2\tau k_\mu V_0^2}{1 + k_a (1 + \theta_f^2)} \theta_f}.$$

This result is shown in Fig. 2 and reproduces the simulation of [5] where the same assumptions were used: $\tau = 6.4 \times 10^{-3}$ s, $k_a = 10^2$, $k_\mu = 3.69$ Hz/(MV/m)$^2$, $V_0 = 20$ MV/m.

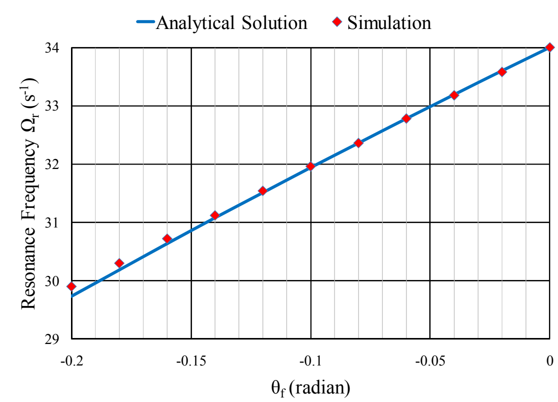


Figure 2: Resonance frequency ($\Omega_r$) as a function of feedback phase shift ($\theta_f$).

At maximum response, the residual phase and amplitude errors are

$$\delta v(\theta_f) = \tau\delta\omega \frac{\Omega_\mu}{\Omega_r} \frac{(1 + k_a)k_\varphi \theta_f}{\left[(1 + k_a + k_\varphi)\tau^2 \tau_\mu \Omega_\mu^2 k_\mu V_0^2 \theta_f - (1 + k_a)^2 k_\varphi\right]},$$

$$\delta\varphi(\theta_f) = \tau\delta\omega \frac{\Omega_\mu}{\Omega_r} \frac{(1 + k_a)\left[(1 + k_a)^2 + \tau^2 \Omega_r^2\right]^{1/2}}{\left[(1 + k_a)^2 k_\varphi - (1 + k_a + k_\varphi)\tau^2 \tau_\mu \Omega_\mu^2 k_\mu V_0^2 \theta_f\right]}.$$

As found analytically above and from simulations in [5] damping by amplitude to phase feedback coupling through the feedback phase shift is not very effective at damping broadband microphonics. However, since it is effective at shifting the resonant frequency, it might be useful in situations where the microphonics are due to a single frequency source close to a mechanical mode of the cavity.

## DAMPING BY FREQUENCY FEEDBACK

Another method is through frequency feedback where the signal driving the resonator is intentionally modulated to counteract the externally-induced microphonics [4].

The amount of modulation supplied at the generator is, $\delta v_\omega = F_a F_\varphi F_\omega \delta\varphi$ with $F_\omega = -\frac{k_\omega \Omega_\mu}{s}$ where $k_\omega$ is the frequency feedback gain. The resultant amplitude and phase errors are

$$\delta v = -\frac{k_a k_\varphi k_\omega \Omega_\mu^3}{B(s)} n(s), \quad \delta\varphi = \Omega_\mu^2 \frac{(1+k_a+\tau s)s}{B(s)} n(s),$$

with

$$B(s) = b_5\left(\frac{s}{\Omega_\mu}\right)^5 + b_4\left(\frac{s}{\Omega_\mu}\right)^4 + b_3\left(\frac{s}{\Omega_\mu}\right)^3 + b_2\left(\frac{s}{\Omega_\mu}\right)^2 + b_1\left(\frac{s}{\Omega_\mu}\right) + b_0$$

where the coefficients are

$$b_5 = \tau\Omega_\mu^5, \qquad b_4 = \frac{2\tau\Omega_\mu^4}{\tau_\mu} + \left(1+k_a+k_\varphi\right)\Omega_\mu^4,$$

$$b_3 = \tau\Omega_\mu^5 + \frac{2(1+k_a+k_\varphi)\Omega_\mu^3}{\tau_\mu} + \frac{(1+k_a)k_\varphi\Omega_\mu^3}{\tau},$$

$$b_2 = (1+k_a+k_\varphi)\Omega_\mu^4 + \frac{2(1+k_a)k_\varphi\Omega_\mu^2}{\tau\tau_\mu},$$

$$b_1 = \frac{(1+k_a)k_\varphi\Omega_\mu^3}{\tau}, \qquad b_0 = -2k_a k_\varphi k_\mu V_0^2 \Omega_\mu^3 k_\omega .$$

The above system is analyzed with the same frequency sweep as in the previous section for several frequency feedback gains ($k_\omega$). In this case the maximum response always occurs at the frequency of the mechanical mode. The maximum amplitude residual error and the normalized maximum residual phase error are

$$\delta v(k_\omega) = \frac{\tau k_\omega \delta\omega}{1+k_\mu V_0^2 \Omega_\mu k_\omega}, \quad \delta\varphi(k_\omega) = \frac{\delta\varphi(0)}{1+\tau\tau_\mu\Omega_\mu k_\mu V_0^2 k_\omega}.$$

and are shown in Fig. 4 with the values mentioned above and $\tau_\mu = 0.3$ s.

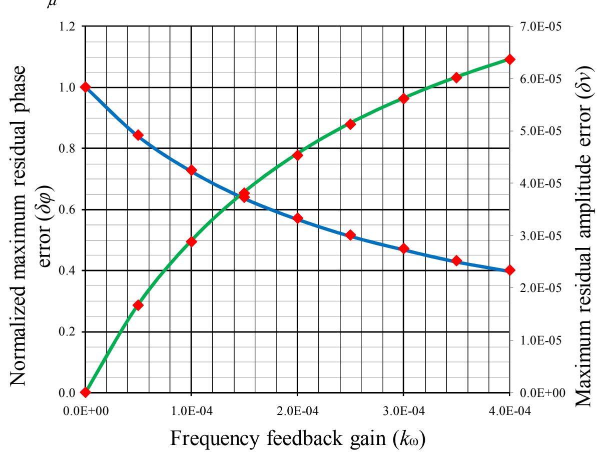


Figure 3: Maximum amplitude (green) and phase (blue) residual errors as a function of $k_\omega$. Simulation results are in red.

## *Frequency feedback with beam*

The frequency feedback method is further analyzed with light beam loading neglecting the fluctuations in the beam current ($\delta v_b = 0$) and beam phase ($\delta\varphi_b = 0$). The transfer function diagram is shown in Figure 1 with the corresponding transfer functions. The resultant residual amplitude and phase errors are

$$\delta v(k_\omega) = \frac{k_\varphi \tau\delta\omega\, k_\omega}{k_\varphi - m + k_\varphi\tau\tau_\mu\Omega_\mu k_\mu V_0^2\, k_\omega},$$

$$\delta\varphi(k_\omega) = \delta\varphi(0)\frac{k_\varphi - m}{k_\varphi - m + k_\varphi\tau\tau_\mu\Omega_\mu k_\mu V_0^2 k_\omega}.$$

In the presence of beam and with well matched coupling, the beam matching coefficient ($m$) varies in the range of (0,1) and does not produce a significant effect on residual errors. However, with the beam, the loaded amplitude decay time ($\tau$) reduces leading the term $\tau k_\omega$ in a decisive fashion in residual amplitude and phase errors. Subsequently $\tau k_\omega$ needs to be optimized to reduce the residual errors.

# CONCLUSIONS

Electronic damping can be effectively used to damp the effects of microphonics on the fluctuations of the cavity frequency. The method is analyzed in detail and analytical results are obtained for the residual amplitude and phase errors that are in confirmation with the simulations in [5]. In amplitude and phase feedback coupling method the feedback phase shift needs to be reduced in order to operate the system on resonance. Frequency feedback method is introduced as an effective way of damping the effects of microphonics. The analytical results show that with the increase in the frequency feedback gain, the residual amplitude error increases while the residual phase error decreases; hence feedback gain needs to be optimized to achieve optimal residual errors. Further analysis with the beam confirms that the frequency feedback gain requires controlling the factor $\tau k_\omega$ to reduce the residual errors.

# REFERENCES


[1] J. R. Delayen, "Ponderomotive Instabilities and Microphonics ", Physica C 441 (2006) p. 1.

[2] J. R. Delayen, "Phase and Amplitude Stabilization of Superconducting Resonators", Ph.D. thesis, California Institute of Technology, 1978.

[3] J. R. Delayen, "Phase and Amplitude Stabilization of Beam-Loaded Superconducting Resonators", Proc. LINAC92, p. 371.

[4] J. R. Delayen, "Electronic Damping of Microphonics in Superconducting Cavities", Proc. PAC 01, p. 1146.

[5] A. Hofler and J. R. Delayen, "Simulation Study of Electronic Damping of Microphonic Vibrations in Superconducting Cavities", Proc. PAC 05, p. 3916.

# HIGH-GRADIENT SRF R&D FOR ILC AT JEFFERSON LAB*

R.L. Geng#, A.C. Crawford, G. Ciovati, Jefferson Lab, Newport News, VA 23606, U.S.A.
M.S. Champion, D.A. Sergatskov, FNAL, Batavia, IL 60510, U.S.A.
F. Furuta, K. Saito, KEK, Tsukuba, Japan

*Abstract*

Jefferson Lab plays an active role in high-gradient SRF R&D in the frame work of the internationally coordinated International Linea Collider (ILC) S0 program. The S0 aim is to push the yield at 35 MV/m in 9-cell cavities. So far, twelve cavities have been electropolishing (EP) processed and RF tested by using the state-of-the-art recipes at JLab, in close collaboration with FNAL and KEK. Seven of them reached a best gradient of over 31.5 MV/m. Understanding gradient limiting mechanisms in real 9-cell cavities is an important component of our studies. Thermometry and high-resolution optical inspection are used to locate and understand the source of gradient limits. Experimenting with selective cavities is still a necessary method for process optimization. One example is the first demonstration of 35 MV/m without detectable Bremsstrahlung X-ray after a light EP is applied to a previously heavy chemical etched 7-cell cavity. Some new understanding has been gained with regard to quench behaviors, field emission behaviors as well as optimized processing. Progress has been made as a result, exemplified by the recent achievement of ≥ 35 MV/m in two cavities, each after the first light EP. Several exploratory studies are under way at JLab, aiming to covert the new understandings into further improved cavity gradient results.

## INTRODUCTION

A summary of our earlier high-gradient cavity R&D work for ILC was reported at SRF2007 and can be found in Ref. [1]. Seven 9-cell cavities (A6, A7, A8, AES1, AES2, AES3 and AES4) were reported therein. The present report focuses on the new results obtained after the 2007 SRF Workshop. These include continued studies of four old (AES2, AES3, AES4 and A8) cavities and new studies of ***five new cavities*** (I5, A11, A12, A15 and J2). Till the present time, twelve 9-cell cavities have been EP processed and tested. In addition, a previously chemically etched 7-cell cavity was electropolished for 30 micron surface removal and reached an excellent result. Over 100 hours of active EP time has been accumulated.

Improvements in many areas have been made toward optimized processing. Initial acid mixing is made using a volume ratio of 1:10 (HF(49%):$H_2SO_4$(96%)). Nominal voltage across the cavity and cathode is 14-15 V. Acid supplying holes in the cathode face upward. The optimal EP is done in the continuous current oscillation mode [2][3]. More active temperature control is accomplished by steering the cooling water in the heat exchanging loop. The minimum purging $N_2$ gas flow reduces HF loss. Sealing openings around the acid sump prevents water (moisture) addition into acid and also reduces HF loss. High pressure water rinsing (HPR) after bulk EP and before 600°C furnace heat treatment improves cleaning and avoids burning chemical residuals into surface.

A major enhancement of our cavity gradient studies is added instrumentation of T-mapping and high-resolution optical inspection (Fig. 1). We will give some examples of understanding cavity quench and field emission behaviors by using these new capabilities.

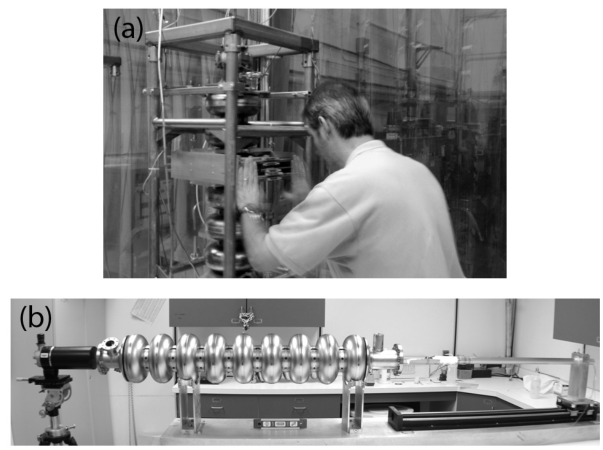


Figure 1: 9-cell cavity T-mapping (a) and high-resolution optical inspection (b) instruments used at Jefferson Lab.

## 9-CELL CAVITY RESULTS

Four (AES2, AES3, AES4 and A8) of the nine studied cavities were previously reported in Ref. [1]. Their further study results are reported herein. AES2 reached a best gradient of 32.8 MV/m. A8 reached a best gradient of 31.7 MV/m. AES3 was previously found [1] quench limited at 17-19 MV/m with the rough location of the quench origin determined. Finally, with 16 thermometers attached to the suspected region, the quench location was pinpointed by using FNAL's fast thermometry system. AES4 remained field emission limited at the gradient level of 27-29 MV/m despite further re-processing efforts.

Five of the nine cavities reported here are *new cavities*: three (A11, A12 and A15) are from the new batch of ACCEL procurement; one (I5) from KEK; one (J2) from the two new 9-cell cavities fabricated at Jefferson Lab.

A complete summary of all RF tests and associated surface processing histories is given in Table 1.

The best $Q(E_{acc})$ of cavities manufactured by "qualified" vendor (A8, A11, A12 & A15) and new

* Work supported by DOE and US-Japan Collaboration. Authored by Jefferson Science Associates, LLC under U.S. DOE Contract No. DE-AC05-06OR23177. 
#geng@jlab.org

vendors (AES2, AES3, AES4, I5 & J2) are given in Fig. 2(a) & (b), respectively.

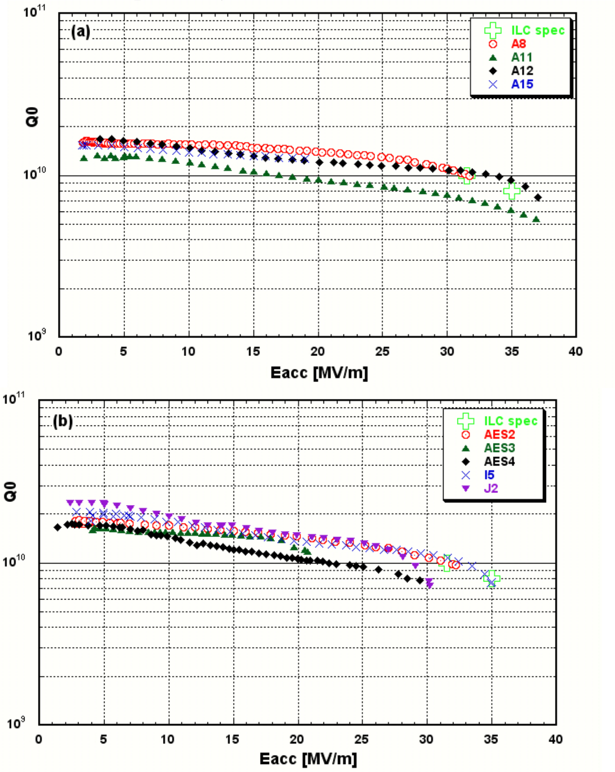


Figure 2: Best Q($E_{acc}$) of 9-cell ILC cavities EP processed and tested at Jefferson Lab. Cavities fabricated by "qualified" vendors (a) & new vendors (b). Note: low Q value of A11 is likely due to frozen flux effect and A11 will be re-tested; High field Q-slope in J2 is likely caused by non-optimal bulk EP and another light EP will follow.

## UNDERSTANDING QUENCH BEHAVIORS

We have two quench limited cavities further studied for understanding location and nature of responsible defects.

The first is AES3. Following previous studies [1], by using FNAL's fast thermometry system, the exact location of quench source in AES3 was finally determined to be near but outside of the equator EBW of the cell #4 (note: cell number is counted from side of input coupler port). The AES3 quench behavior is very close to that of AES1 (quench limited at gradient < 20 MV/m in fixed cell pairs despite repeated EP). In case of AES1, the location of quench source was determined and defects (pit/bump of 400-600 μm in diameter) were observed in the heat-affected zone of the equator weld of cell #3 [4].

A15 is the other successful example of finding responsible defects in a real 9-cell cavity. By using the combined technique and instrumentation of pass-band measurements, cavity cell thermometry, and high-resolution optical inspection of cavity RF surface, a "hot spot" (correlated to quench at 17-19 MV/m) was captured and a pit (with estimated depth of 50 μm) of 200-300 μm in diameter was discovered within 1cm distance from the hot spot (Fig. 3). The defect is located in the heat affected zone of the equator EBW of cell #3 of A15.

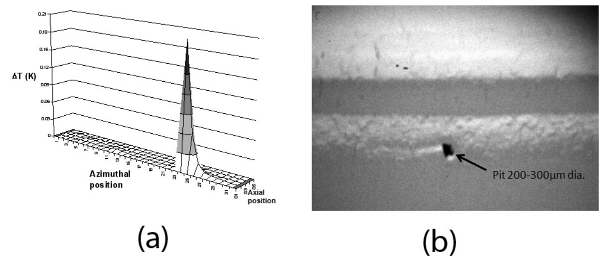


Figure 3: (a) hot spot captured by T-mapping near equator EBW of cell #3 of A15; (b) pit discovered on RF surface within 1cm distance from hot spot.

## UNDERSTANDING FE BEHAVIOR

FE remains an issue deserving attention, despite progress made recently. Here we report a FE behavior that can be generally characterized as FE turn on.

The first kind of FE turn on seems to be correlated to the presence of defects (sub-mm in diameter). Substantial Q-decline is resulted. It is observable in AES4 and I5 despite repeated EP processing. Fig. 4 gives some example defects discovered in these two cavities. These defects are located in the high electric field region of end cells, coinciding with the high FE cell pairs determined by pass-band measurements.

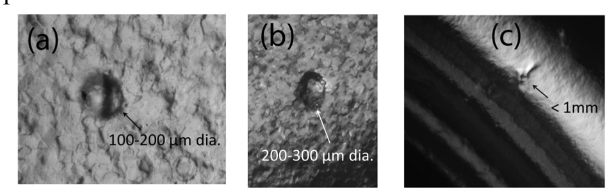


Figure 4: Defects observed in the high electric field region of high FE cells. (a) Circular defect in cell #9 of AES4 at radial location of stiffening ring. (b) Circular defect in cell #8 of AES4 near iris weld. (c) Linear defect near iris of end cell of I5.

The second kind of FE turn on is induced by low temperature bake. Only subtle Q decline is resulted. It was observed in A11 & A12. They were tested before low temperature bake with no detectable X-ray up to 28 & 30 MV/m, respectively. After low temperature bake, sudden FE turn on was observed during the first power rise at 25 & 23 MV/m, respectively. More details on this kind of FE behavior will be published in the future.

Re-processing by ultrasonic cleaning with detergent followed by HPR has been found effective in reducing FE in previously RF tested and heavily FE loaded cavities. A remarkably successful example is the $5^{th}$ RF test of I5 after re-processing with 2% micro-90 ultrasonic cleaning and HPR [6]. There was virtually no detectable Bremsstrahlung X-ray during the test up to 35 MV/m. The effectiveness of this re-processing technique has been further confirmed in two other cavities.

A related result worth mentioning is that a previously heavy BCP (buffered chemical polishing) etched 1.5 GHz 7-cell cavity (HG006) reaches a gradient of 35.3 MV/ without detectable Bremsstrahlung X-ray (Fig. 5). No low temperature induced FE turn on is observed, a clear contrast to FE behaviors of A11 & A12.

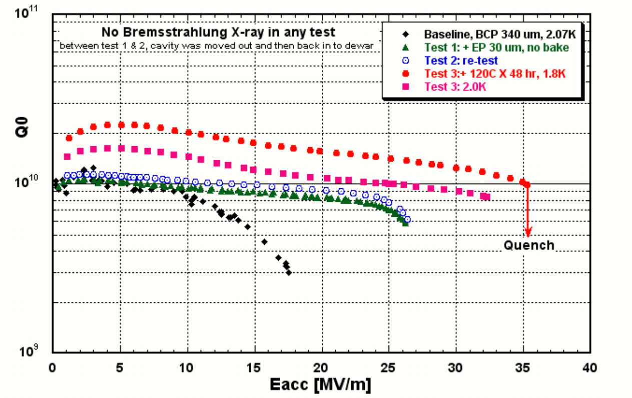


Figure 5: An example of initially BCP etched multi-cell cavity achieving 35.3 MV/m after a 30 µm EP. No detectable Bremsstrahlung X-ray up to 35.3 MV/m.

## SUMMARY

Progress has been made in understanding quench and FE behaviors in real 9-cell cavities. Some sub-mm sized defects in the heat affected zone of a niobium EBW are responsible to some observed quench and maybe even some observed FE turn on. Further studies are needed to understand the origin and evolution of these defects. An exploratory study is under way at JLab, aiming to remove these kinds of defect by local niobium re-melting technique. A baking induced FE turn on phenomenon was observed. Some positive sign has been demonstrated by applying HPR after bake, as shown by a preliminary experiment. Re-processing with detergent ultrasonic cleaning and HPR has been found effective in reducing/eliminating FE in previously RF tested cavities up to 35-39 MV/m. An example of a multi-cell cavity reaching 35 MV/m without detectable Bremsstrahlung X-ray has been demonstrated by applying a light EP to a previously heavy BCP etched cavity.

Twelve 9-cell cavities have been EP processed and tested at JLab. Eight of them exceeded a best gradient of 30 MV/m. Two of them exceeded 35 MV/m after the first light EP. We believe further improvement is possible by streamlined process of Integrated Cavity Processing (ICP) that is being conceived at JLab. Design studies and initial prototyping with a 1-cell cavity set-up is under way.

## ACKNOLEDGEMENTS

We thank the following colleagues for their important contributions to the presented work: Damon Bice of FNAL and Byron Golden, Pete Kushnick, Danny Forehand and Michael Morrone of Jefferson Lab.

## REFERENCES

[1] R.L. Geng et al., "Latest Results of ILC High-Gradient R&D 9-cell Cavities at JLAB", SRF2007, Beijing, China, October 2007, WEP28, (2007).
[2] H. Diepers et al., Phys. Lett., 37A (1971) p. 139-140.
[3] R.L. Geng et al., "Continuous current oscillation electropolishing and its application to half-cells", SRF2003, Travemünde/Lübeck, Germany, September 2003, TUP13, (2003).
[4] M.S. Champion et al., "Quench-limited SRF Cavities: Failure at the Heat-affected Zone", ASC2008, Chicago, USA, August 2008, 2LPR04, (2008).
[6] R.L. Geng, "Processing and Testing of ICHIRO5", SCRF Meeting, FNAL, April 2008, (2008).

Table 1: Summary of Cavity Processing and Testing. (EP = electropolishing; ER = ethanol rinsing; USC = ultrasonic cleaning with detergent solution; HPR = high pressure water rinsing; LTB = low temperature bake; FE = field emission; FEIQ = FE induced quench; FETO = FE turn on.)

| Cavity | Test | Processing | Max. $E_{acc}$ [MV/m] | Limit |
|---|---|---|---|---|
| AES2 | 3 | +EP 20µm | 26.0 | Quench |
| AES2 | 4 | +EP 20µm | 32.8 | Quench |
| AES3 | 5[#] | +EP 20µm | 21.0 | Quench |
| AES4 | 5 | +EP 20µm | 17.0 | RF cable |
| AES4 | 6 | +HPR | 23.0 | Quench |
| AES4 | 7 | +USC,HPR | 27.0 | FE |
| AES4 | 8[##] | +USC,ER,HPR | 29.4 | FEIQ |
| I5 | 1 | +USC,HPR | 30.0 | (note §) |
| I5 | 2 | (re-test) | 21.0 | FETO |
| I5 | 3 | (re-test) | 19.0 | FETO |
| I5 | 4 | +EP 30µm | 36.0 | FETO |
| I5 | 5 | +USC,HPR | 35.0 | Quench |
| I5 | 6 | +EP 40µm | 28.0 | FETO |
| I5 | 7 | +EP 20µm, ER | 29.0 | FE |
| A8 | 4 | +EP 20µm | 31.7 | Quench |
| A11 | 1[†] | EP 170µm[¥] | 28.0 | Q-drop |
| A11 | 2 | +LTB | 37.0 | Low Q |
| A11 | 3[††] | (re-test) | 36.0 | Low Q |
| A12 | 1[†] | EP 170µm[¥] | 30.0 | FE |
| A12 | 2 | +USC,HPR | 30.5 | Q-drop |
| A12 | 3 | +LTB | 36.6 | FE |
| A12 | 4 | +HPR | 37.0 | Q-drop |
| A15 | 1 | EP 170µm[¥] | 17.0 | Quench |
| A15 | 2[♣] | (re-test) | 19.0 | Quench |
| J2 | 1 | EP 170µm[¥¥] | 30.0 | Q-drop |

[#]Testing with FNAL's fast thermometry, found quench source location in cell #4.
[##] Testing with JLab's "2 of 9" thermometry, aiming for locating field emitters in end cells.
[§]Testing was limited by liquid helium and loose antenna.
[†]RF testing before low temperature bake.
[††]Re-testing after parking cavity at 70 - 140K for 16 hours. Test confirmed cavity had no Q-disease.
[¥]First RF test of original as-built cavity is after nominal total surface removal of 170 µm (150 µm from bulk EP and 20 µm from light EP). Cavity was NOT low temperature baked before first RF test.
[♣]Testing with JLab's "2 of 9" thermometry, found quench source location in cell#3.
[¥¥]HPR applied after low temperature bake and before 1st RF test.

# PRELIMINARY RESULTS FROM MULTI-CELL SEAMLESS NIOBIUM CAVITIES FABRICATED BY HYDROFORMING *

W. Singer, I. Jelezov, X. Singer, A. Matheisen, DESY, Hamburg, Germany
P. Kneisel#, G. Ciovati, M. Morrone, TJNAF, Newport News, VA 23606, USA

*Abstract*

The technology of forming multi-cell seamless niobium cavities has been developed at DESY within the European CARE (Coordinated Accelerator Research in Europe) program. Three-cell units have been manufactured successfully and a 9-cell cavity has recently been completed from three sub-sections and has been successfully tested at DESY.

Additionally, we have equipped two 3-cell units – one center unit of a 9-cell cavity and one end-unit – with niobium beam pipes, have tuned these units and carried out cryogenic radio-frequency (RF) tests after standard BCP surface treatments had been applied to these cavities.

In addition, we have taken temperature maps with JLab's two-cell thermometry system to compare with standard electron-beam welded cavities.

This contribution will report about the preliminary cryogenic test results and the T-mapping – this is an ongoing investigation.

## INTRODUCTION

Traditionally, rotational symmetric (elliptical) niobium accelerating cavities are fabricated by deep drawing of half-cells and, after machining to the length dimension, they are completed by electron beam welding (EBW) at the irises and the equators. Improved quality control procedures during the mechanical fabrication and the EBW resulted in cavity performances which, in some cases, came close to the fundamental limits of the high purity niobium. However, more recently improved inspection methods revealed that features in the weld and heat affected zone in a multi-cell cavity can and have contributed to limitations in cavity performance [1]. Therefore, electron beam welds have come again under scrutiny worldwide, mainly because the performance goals for cavities for the International Linear Collider (ILC) are quite close to the fundamental limitations of the material and any fabrication defects override the material properties.

Contrary to this experience, seamless cavities have no equator welds (the high magnetic field region in an "elliptical" cavity) and therefore an improved reliability could be expected. Additionally, cavity fabrication costs could be reduced, especially, if the end-groups of an accelerating cavity (these are the parts of the cavity, which are outside the cell structure and provide input coupling capability and higher order mode damping capability) can be flanged onto the cell structure [2]. Seamless cavity fabrication techniques have been pursued in the last years mainly at INFN Legnaro [3] – the chosen method was spinning – and at DESY (hydroforming) [4]. Both methods have produced single-cell cavities with high performance [5]. This contribution reports about an extension of the single-cell work to multi-cell cavities, 3-cell and 9-cell.

## CAVITY FABRICATION TECHNIQUE

The hydroforming technique, developed at DESY over several years, has been described in details in previous publications [4-6]. Here we will only summarize the essential steps in the process and describe the extension from the single-cell to the multi-cell hydroforming.

For hydroforming, one starts with a seamless tube of a diameter intermediate between iris and equator. During the computer controlled forming, a two-stage process takes place, namely a reduction of the tube diameter in the iris region and an expansion of the tube in the equator area. Considerations of surface roughness at the iris region for too much diameter reduction and work hardening at the equator for too much expansion determined a tube diameter of 130 mm to 150 mm to be the optimum for 1300 MHz TESLA/ILC type cavities.

The tube diameter reduction at the iris was optimized – after research into different methods such as hydraulic necking, electromagnetic strike necking and spinning – by using a specially profiled ring being moved in radial and axial directions. For this purpose a computer controlled hydraulic machine has been built, which is useable for up to 3-cell cavities.

During hydraulic expansion of the equator region an internal pressure is applied to the tube and simultaneously an axial displacement, forming the tube into an external mold. The hydraulic expansion relies on the use of the correct relationship between applied internal pressure and axial displacement under the assumption that the plastic limit of the material is not exceeded, which would result in rupture. Material uniformity of the tubing and the experimentally determined stress-strain characteristics as well as simulation calculations are essential and have led to a successful development of the hydroforming technology. A hydroforming machine was specially built for the tube expansion. Since no tubing with uniform material properties were commercially available, much effort was invested in researching – in collaboration with industrial partners and scientific institutions – several tube

* This manuscript has been authored by Jefferson Science Associates, LLC under U.S. DOE Contract No. DE-AC05-06OR23177. The U.S. Government retains a non-exclusive, paid-up, irrevocable, world-wide license to publish or reproduce this manuscript for U.S. Government purposes. We acknowledge the support of the European Community Research Infrastructure Activity under FP6 "Structuring the European Research Area" program (CARE, contract number RII-CT-2003-506395).
#kneisel@jlab.org

forming technologies (spinning, back extrusion, forward extrusion, flow forming and deep drawing). A combination of spinning or deep drawing with flow forming gave the best results. In Fig. 1 a set of hydroformed 3-cell cavities is shown.

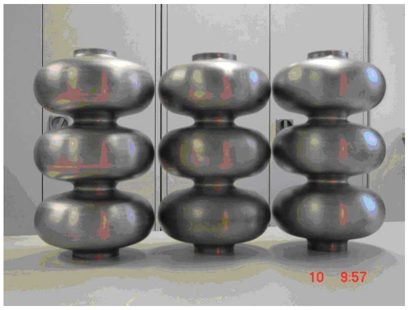

Figure 1: Hydroformed 3-cell niobium cavities.

## EXPERIMENTAL TEST PROCEDURES

### *Single 3-Cell Units*

After the hydroforming was completed at DESY, the 3-cell units as shown in Fig. 1 were barrel polished also at DESY removing approximately 100 μm and subsequently sent to JLab for completion with beam pipes and for evaluation. One unit (cavity #1) consisted only of center cells and the second unit (cavity #2) was an end-cell with two center cells.

Beam pipes were welded on at the outside irises and it was attempted to tune the cavities to a flat field profile. This turned out to be quite difficult, the cavities were quite stiff and "springy", most likely from the massive mechanical deformation during the forming process. A stress relieving annealing step at 600 °C for 10 h in high vacuum after app. 100 μm of material removal by BCP (Buffered Chemical Polishing: 1:1:1 ratio of nitric acid, hydrofluoric acid and phosphoric acid), softened the cavities appropriately and tuning could be accomplished.

For the cryogenic testing the cavities received standard BCP removing various amounts of niobium as indicated in the caption of Fig. 4. A high pressure rinsing (HPR) for two passes of 2 h each from the top of the cavity to the bottom followed after the BCP and subsequently the cavities were dried in a class 10 clean room for several hours prior to the attachment of input coupler/pump-out port and transmission probe port. The cavities were evacuated on the cryogenic test stand (Fig. 2) to a vacuum of typically < $10^{-8}$ mbar prior to cool-down to liquid helium temperature.

The cryogenic testing consisted of measuring in some cases the temperature dependence of the surface resistance, the pressure sensitivity of the cavity, the $Q_0$ vs. $E_{acc}$ performance in the π-mode and the Lorentz-force detuning.

Because the 3-cell seamless cavities have no stiffening rings between the cells, they were "externally" stiffened by an arrangement of Ti-rods/stainless steel threaded rods as shown in Fig. 2 to avoid a possible collapse under the vacuum load.

Figure 2: 3-cell cavity attached to test stand with external support rods. The cavity is located in the clean room in front of a horizontal laminar flow system.

### *9-Cell Cavity*

A 9-cell cavity was completed at Zanon, Italy, from three 3-cell units by electron beam welding from outside at the irises, then by adding stiffening rings and end-groups as for the conventional cavities.

Prior to tuning the cavity was "softened" by a 800 °C annealing step after removal of 40 μm by BCP. A "traditional" surface treatment of electropolishing (170 μm), ethanol rinsing, 800 °C heat treatment, electropolishing (48μm) and HPR at DESY preceded the cryogenic test.

## RESULTS AND DISCUSSION

The performance of the 9-cell cavity is shown in Fig. 3: the cavity reached a maximum gradient of $E_{acc}$ = 30.3 MV/m, limited by the Q-drop without field emission and no Q-disease. From mode measurements it was determined that individual cells had fields between 30 MV/m and 39 MV/m. The next step in the evaluation is an "in-situ" baking at 120 °C with the expectation of eliminating the Q-drop.

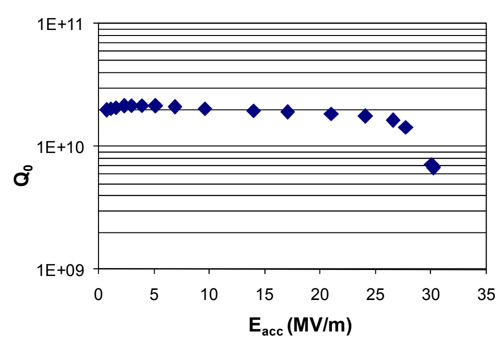


Figure 3: Performance of seamless 9-cell TESLA cavity.

We carried out three tests of the 3-cell units with different amounts of material removal on cavity 1 and two tests on cavity 2. The results are shown in Fig. 4. In addition, cavity 1 was re-tested with a 2-cell temperature mapping system after test 3.

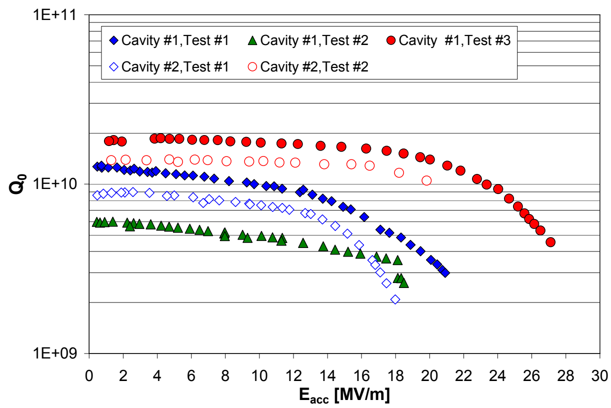


Figure 4: Summary of test results at 2 K from cavity 1 and 2. The total material removal was 150μm (test 1), 200μm (test 2) and 220 μm (test 3) for cavity 1; 200μm (test 1) and 250μm (test 2) for cavity 2.

Except for test 2 in cavity 1 no field emission was encountered. In this test a field emitter turned on at the highest field. Otherwise, the Q-degradations at the highest obtained gradients are caused by the "Q-drop", which starts at rather low gradients. As found earlier, heavy mechanical deformation of the niobium – without sufficient stress relieving – seems to be responsible for the low Q-drop onset [7]. More material removal might shift the onset fields to higher values; however, as is known, the Q-drop cannot be eliminated in poly-crystalline material after buffered chemical surface treatment only.

Test 2 of cavity 1 shows a rather low Q-value. This can be attributed to insufficient shielding of the Earth magnetic field (~ 150mG) in the dewar used for this test, due to a faulty power supply for the compensation coil. The additional resistance caused by the frozen-in flux amounts to ~50 nΩ, which would limit the Q-value at 2K to roughly $5\times10^9$. The first test of cavity 2 had a similar problem in another dewar, which had residual field of ~ 70 mG. In test 3 of cavity 1 a high Q-value was obtained after the magnetic shielding was improved to 5-7 mG over the cavity volume and an improvement of the onset field for Q-drop because of more removed material. Test 2 of cavity 2 was limited by a discharge due to poor vacuum in the cavity. In this test a "super-leak" was encountered caused by a crack in the cavity beamline flange. A re-test will be carried out after replacement of the defective flange.

The Lorentz-force detuning coefficient of the 3-cell, unstiffened cavity was determined to be $k_L$=-4.5 Hz/[(MV/m)$^2$], a factor of ~ 3 higher than for a cavity with stiffening rings. The sensitivity to the helium bath pressure in the configuration as shown in Fig. 2 was 185 Hz/mbar.

The 2-cell T-mapping system was assembled on the top and bottom cells of cavity 1. The sensors cover a region ~ 4 cm on each side of the equator. The T-maps show several "hot spots" in the equator (high magnetic field) region of both cells, although they appear to be more intense in the top cell (Fig. 5). The field dependence of the "hot-spots" temperature is nearly quadratic up to a peak surface magnetic field ($B_p$) of about 100 mT, when the Q-drop begins, above which the exponent *n* in the power-law dependence $\Delta T \propto B_p^n$ increases to about 6-10. Such dependence has been commonly observed in BCP-treated polycrystalline Nb cavities. More T-mapping measurements are planned, especially when the cavity reaches its quench field.

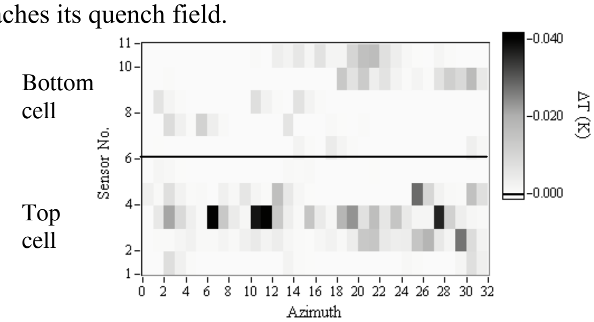


Figure 5: "Unfolded" T-map at the highest field achieved in cavity 1, test 3. The "azimuth" variable covers the cell's circumference, while "sensor no." covers a region ~ 4 cm on each side of the cells' equator (on rows no. 3 and 8). Hot-spots are visible in the equator area of both cells.

## SUMMARY

These preliminary results from the seamless 3-cell cavities give an indication of the soundness of the technology developed at DESY. The quench limitations of the cavities have not been reached because of the "Q-drop". Future experiments will incorporate post-purification heat treatments, electropolishing and "in-situ" baking, which most likely will improve the cavity performances. T-maps showed the presence of "hot-spots" with location and field dependence similar to those observed in standard BCP-treated polycrystalline cavities.

## ACKNOWLEDGEMENTS

We would like to thank our colleagues G. Slack, L. Turlington, B. Clemens, D. Forehand, R. Overtone, P. Kushnik, J. Davenport and T. Harris from JLab and J. Sekutowicz, B.Van der Horst, K.Tvarovski, G. Kreps and A. Ermakov from DESY for their support of this work.

## REFERENCES

[1] Y. Iwashita et al., EPAC'08, Genova, June 2008, paper WEOBM03.
[2] J. Sekutowicz et al., this conference, paper THP044A.
[3] V.Palmieri, SRF'03, Travemünde, Germany, September 2003, paper TuP26A.
[4] W. Singer et al., SRF'01, Tsukuba, Japan, September 2001, paper FA006.
[5] W. Singer, Physica 441 (2006), p.89-94.
[6] X. Singer, Materiaux&Techniques, No. 7-8-9 (2003), p. 28-32
[7] P. Kneisel et al., SRF'99, Santa Fe, USA, November 1999, p. 446-449.

# COAXIAL COUPLING SCHEME FOR FUNDAMENTAL AND HIGHER ORDER MODES IN SUPERCONDUCTING CAVITIES*

J. Sekutowicz, P. Kneisel, G. Ciovati, TJNAF, Newport News, 23606 Virginia, USA
L. Xiao, SLAC, Menlo Park, 94025 California, USA

*Abstract*

Higher Order Modes generated by a particle beam passing through a superconducting accelerating cavity have to be damped to avoid beam instabilities. A coaxial coupler located in the beam pipes of the cavities provides for better propagation of HOMs and strong damping in appropriate HOM dampers. The whole damping device can be designed as a detachable system. If appropriately dimensioned, the RF currents can be minimized at the flange position. Additionally, the coaxial system also provides efficient coupling of fundamental mode RF power into the superconducting cavity. Compared to presently available solutions for HOM damping, this scheme provides for several advantages: stronger HOM damping, attachable solution, and exchangeability of the HOM damping device on a cavity, less complexity of the superconducting cavity, possible cost advantages.

This contribution discusses modeling, which lead to an optimized layout of a cavity-coupler system and describes* results from the room temperature and first cryogenic temperature measurements .

## INTRODUCTION

The coaxial HOM couplers were originally developed for the 500 MHz HERA cavities in 1985 and later in the early 90's they were scaled to 1300 MHz and adapted for the TESLA cavities [1]. The scheme fulfills also the specification for the ILC project, which is the TESLA successor, and can be used for the superconducting cavities in the main accelerator. The coupling device we propose here (Fig. 1) takes advantage of the TESLA HOM damping scheme and combines it with the coaxial fundamental power coupler (FPC) used for the superconducting TESLA (ILC) cavities. In this scheme, all couplers are screened by the inner tube, which is supported by the Nb "donut" (disk) welded to it

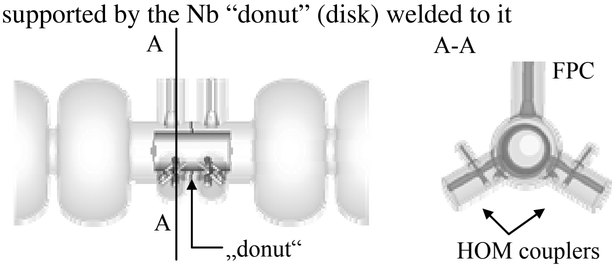


Figure 1: FPC and HOM couplers in two mirrored coaxial coupling devices placed between two cavities (left) and cross-section of the coupling device (right).

* This manuscript has been authored by Jefferson Science Associates, LLC under U.S. DOE Contract No. DE-AC05-06OR23177. The U.S. Government retains a non-exclusive, paid-up, irrevocable, world-wide license to publish or reproduce this manuscript for U.S. Government purposes.

and to the beam tube. The "donut" is an electric short in the coaxial line, which is formed by the inner and outer tubes, and thus separates electrically two mirrored coupling devices and neighboring cavities. The pair of mirrored coupling devices can be placed between two cavities.

### *Motivation*

This coaxial coupling scheme has the following advantages as compares to the standard TESLA scheme:

1. Field asymmetries and kicks from all couplers are minimized
2. The distance between two cavities can be shorter (higher real estate gradient); for the ILC, the difference is 9 cm.
3. The body of the cavity stays cylindrically symmetric, which enables its fabrication by hydro-forming as seamless device.
4. The interior of the coupling assembly and the cavities can be better cleaned before the final assembly.

## MODELING AND BENCH RF MEASUREMENTS

### *Modeling*

HOM damping and coupling to the fundamental mode have been modeled by the ACD team at SLAC. The RF model and HOM damping result for the 9-cell TESLA cavity is shown in Fig.2. For the accelerating mode, the computed $Q_{ext}$ for the FP coupler vs. its penetration depth, covered a wide range of values beginning at a lowest value of $10^5$.

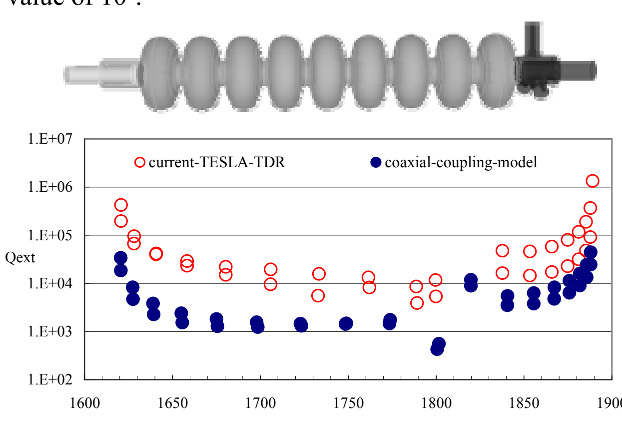


Figure 2: RF-model and damping ($Q_{ext}$) for the first two dipole passbands for the TESLA structure. The diagram compares the standard TESLA-TDR damping scheme with the scheme discussed in this paper.

### *Bench Measurements*

The second step in the verification of the concept was the HOM damping and FM coupling measurements for the copper model of the coupling device attached to the copper model of the TESLA cavity. The models, shown in Fig. 3, have been built and tested at JLab.

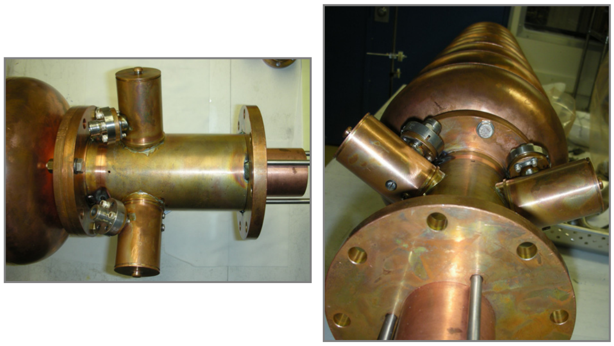

Figure 3: Pictures of the copper models built at JLab.

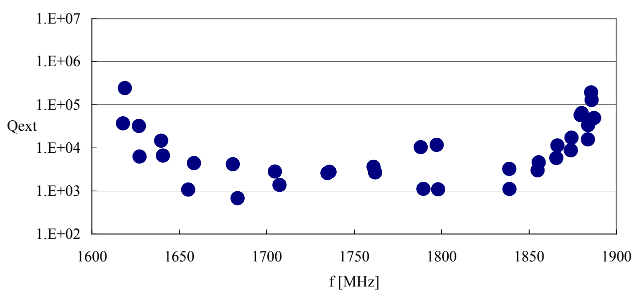


Figure 4: Measured $Q_{ext}$ values for the two lowest dipole passbands.

The HOM damping result for the two first dipole passbands is displayed in Fig. 4. The agreement with the modeled values is remarkable. More complete measured data and computed (R/Q) for three dipole passbands ($TE_{111}$, $TM_{110}$, and $TE_{121}$) and the lowest monopole passband ($TM_{011}$) is shown in Fig. 5. For all modes the damping specification for the ILC- $Q_{ext}$<2E5- is fulfilled.

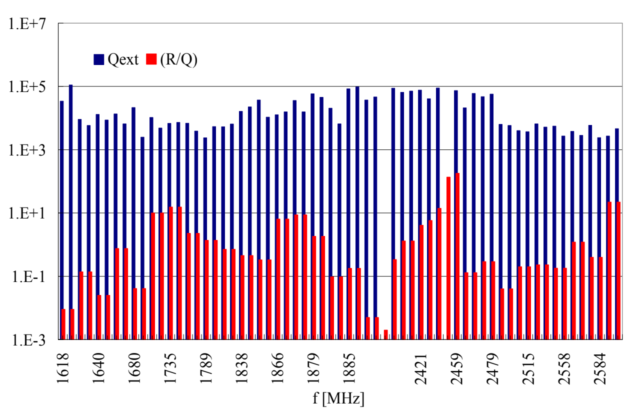


Figure 5: Computed (R/Q) and measured $Q_{ext}$ for the copper model of coupling device.

The data for the FM coupler, $Q_{ext}$ vs. distances to the end iris is shown in Fig. 6. These measurements have been carried out at DESY. By "x" and "y" the distances between the end iris and inner tube or end short are denoted respectively. Even for y=140.5 mm and short FPC antenna (tip hidden in the port tube) one can find "x" at which $Q_{ext}$ is as low as 2E5. Further retraction of the FPC antenna makes the $Q_{ext}$ value higher, roughly -1.5dB/mm when x < 90 mm. Smaller "x" and "y" make the $Q_{ext}$ lower, so these two

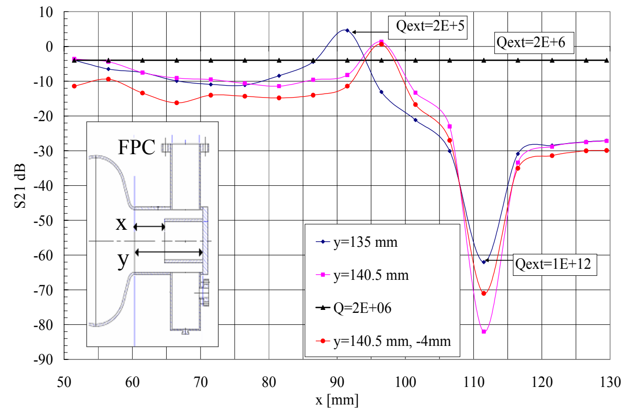


Figure 6: Measured $Q_{ext}$ for the coaxial FPC.

variables and the penetration allow for the proper adjustment of the FPC coupling strength, maintaining reflection free operation. For example, the ILC specification $Q_{ext}$=2E+6, can be obtained for x=50 mm, 87 mm and 94 mm, when y=135 mm.

## POSITIONING OF THE FLANGE CONNECTION

As mentioned above, the coupling device will be flanged to the cavity beam tube. Even though, super-conducting joints do not perform sufficiently for many other applications, due to their magnetic flux limitation to ~10 mT, one can make use of these connections for this coupling device. The reflected wave at the Nb short forms with the decaying field in the beam tube a standing wave pattern, having a B-field minimum ("notch") at 45 mm from the end iris. A superconducting connection made of a Nb gasket and NbTi or NbZr flanges, at that location will be exposed to a negligible residual magnetic flux. The B- field pattern in the beam tube for B = 150 mT on the equator (36 MV/m accelerating gradient) in the end-cell is shown in Fig. 7.

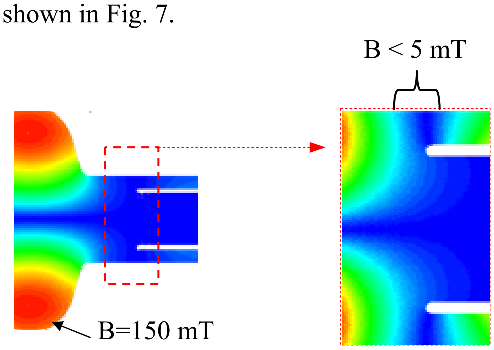


Figure 7: B-field pattern in the beam tube

## FUTURE COLD TEST

The first prototype of the coupling device has been fabricated and a cryogenic test is in preparation. The device will be attached to a large grain niobium prototype of a 1.6-cell photoinjector cavity built in the frame of another R&D project at JLab. The technical drawing and photograph of the cavity and the coaxial coupler are shown in Fig. 8. The cavity and coupling device will be

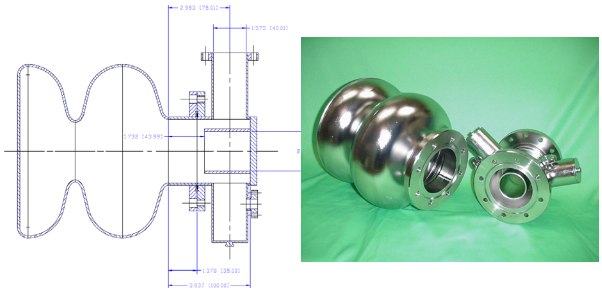

Figure 8: Technical drawing and photograph of the test cavity.

chemically cleaned ("Buffered Chemical Polishing") by standard processing techniques, high pressure water rinsed and assembled in a class 10 clean room prior to the test.

### *Objectives of the cold test*

There are three main objectives for the cold test.

- The first objective is to investigate multipacting (MP), which has been found in the coaxial part of the beam tube by means of the MP simulation calculations. This resonant phenomenon should take place at a field level of $E_{acc}$=2MV/m. The electron impact energy is in the range of 540~790 eV. The predicted MP is of 4-th order two-side and thus it should be possible to process.
- The second objective is to look at possible heating of the inner tube, which can be expected for cw operation because that tube is only cooled indirectly by heat conduction of the outer beam tube and the Nb "donut". This potential limitation may require an additional devoted cooling loop at that location for cw operation.
- Finally, one needs to verify the performance of the superconducting gasket in pulse and cw operation and explore the limitation in maximum achievable field level.

## SUMMARY

Model measurements at room temperature on a 9-cell TESLA/ILC-type copper cavity have shown, that a coaxial beam-line coupler for fundamental power and high order mode damping, flanged to the cell structure, can provide sufficient coupling and HOM damping to the cavity. The measurements are in agreement with model calculations and the HOM damping exceeds the obtainable $Q_{ext}$ values of the presently used couplers for the ILC. The flangeable design requires moderate performance of a superconducting connection between cell structure and coaxial coupler. Possibly, cost advantages can be realized by this design.

A niobium model of the coupler has been fabricated and a first cryogenic test will be carried out in the near future with a 1.6 cell photo-injector cavity. Most likely, further tests will be necessary to fully evaluate the suitability of this design.

## ACKNOWLEDGEMENT

We would like to thank our colleagues G. Slack, L. Turlington and D. Forehand from JLab and G. Kreps from DESY for their support of this work.

## REFERENCES

[1] J. Sekutowicz, Proc. $6^{th}$ Workshop on RF Superconductivity, TJNAF (JLab), Newport News, VA (1993), p.426.

# TWISTED STRUCTURES AND THEIR APPLICATION AS ACCELERATING STRUCTURES*

J. Wilson, Y. Kang, SNS, Oak Ridge, TN, USA
A.E. Fathy, EECS Department, University of Tennessee, Knoxville, TN, USA

*Abstract*

Normally, reactive loading is employed to construct slow-wave accelerating cavities. However, their non-uniform cross section, difficult machining, and complicated welding or brazing processes increase the total cost. Although straight hollow waveguides can only support faster-than-light propagation, twisted waveguides can support propagation at or below $c$. Because twisted structures have a uniform cross section in the transverse plane, they offer several potential advantages over dielectric loaded structures or other types of periodic structures. Of particular interest are twisted structures whose longitudinal cross section has been selected to resemble well-known accelerating structures, such as the disk-loaded accelerating structure and the TESLA type elliptical cavity. Comparisons are drawn between these conventional cavities and their twisted counterparts in terms of the phase velocity and dispersion relationship. The accelerating modes are found and analyzed, and R/Q's are calculated.

## INTRODUCTION

One very important consideration in the effective acceleration of particle beams is matching the velocity of an electromagnetic wave to the velocity of the particles traveling slower than $c$.

A conventional method for slowing the wave that is more well-suited for superconducting accelerators is to use a corrugated structure with nonuniform cross section. However, such corrugated structures have drawbacks. First, manufacturing is difficult due to the necessecity of very difficult machining and welding to create the smooth finish necessary. Secondly, trapped modes can exist in the structure because of the presence of stop bands in the dispersion characteristics. Finally, such corrugated structures tend to have zero group velocity when operating at $\pi-$mode, which causes problems for mode separation.

Therefore, we consider a uniformly twisted waveguide as a potential accelerating structure, consisting of a uniform cross section twisted about the beam axis. It has long been known that such a twisted structure can be a slow wave structure, and a preliminary investigation into the feasibility of twisted guides as accelerating structures was undertaken by Kang [1]. In this paper, we show that a twisted waveguide accelerating structure can be used to circumvent problems relating to trapped modes and mode separation. Also, tuning for a twisted structure could be done for the whole structure at once.

Any non-circular cross section will generate a nontrivial shape when twisted along the center axis, which has the potential to produce slow-wave effects. However, this paper concentrates on a few simple representative cross sectional shapes in order to describe the general nature of the slow-wave accelerating characteristics: a twisted structure whose longitudinal cross section is identical to that of a disk-loaded accelerating cavity, and a twisted structure with an elliptical cavity-like longitudinal cross section.

## PROPAGATION CHARACTERISTICS OF TWISTED STRUCTURES

When selecting a cross sectional shape for a twisted waveguide, an interesting choice would be one that would produce a structure with similar longitudinal cross section to an existing accelerating structure. The first structure we considered has the shape shown in Fig. 1. This figure shows that when this particular cross section is twisted, the shape of the longitudinal cross section is identical to a disk loaded structure. Table 1 gives relevant information for this structure based on simulation results.

Fig. 2 shows a CST Microwave Studio [2] simulation of the electric field in such a twisted structure subject to a periodic boundary condition. The simulation results clearly indicate a TM mode which could be useful for particle acceleration. Such a twisted analog can also be considered for the medium $\beta$ SNS superconducting cavity. Although the details are not given here, Fig. 2 shows the electric fields for such a structure. A clear similarity is seen between the fields of these twisted structures and the fields typically seen in rotationally symmetric (non-twisted) corrugated accelerating cavities.

Table 1: Parameters for twisted analog of disk-loaded accelerating cavity

| Parameter | Value | Unit |
|---|---|---|
| Frequency | 2.84 | GHz |
| Inner radius | 4.13 | cm |
| Outer radius | 5.493 | cm |
| Twist rate | 89.76 | Radians/m |
| Notch angle | 1.048 | Radians |
| Phase advance per cell | $\frac{2\pi}{3}$ | Radians |
| Phase velocity | $2.98 \times 10^8$ | m/s |

* This work has been sponsored by ORNL-SNS. The Spallation Neutron Source is managed by UT-Battelle, LLC, under contract DE-AC05-00OR22725 for the U.S. Department of Energy.

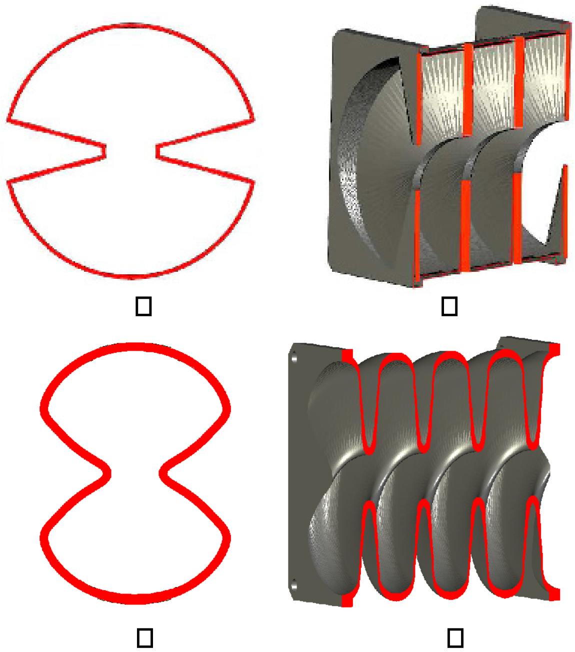

Figure 1: (a) “Notched” cross section of twisted disk-loaded analog. (b) 3D Cutaway view of twisted disk-loaded analog. (c) “Dumbell” cross section of elliptical twisted analog. (d) 3D Cutaway view of elliptical twisted analog.

This particular structure was designed to accelerate particles at relativistic velocities (i.e. electron accelerators). To do this, the dispersion properties were investigated in order to set the phase velocity equal to the speed of light $c$. The dispersion curves for this structure are shown in Fig. 3 for twist rates ranging from 67.3 $\frac{Rad}{m}$ to 337 $\frac{Rad}{m}$ . The dispersion curves were generated using the finite-difference frequency domain method discussed in [3], and they clearly indicate that for this particular TM accelerating mode, the phase velocity of the wave decreases as the twist rate increases. At the selected twist rate of 88.76 $\frac{Rad}{m}$ , the phase velocity was found to be $c$ at the design frequency of 2.84 GHz.

## TRAPPED MODES AND GROUP VELOCITY CONSIDERATIONS

One of the problems associated with reactively loaded corrugated accelerating structures is the tendency for trapped modes to develop. These occur when electromagnetic energy from the beam is deposited in a stop band where propagation in the cavity structure is not permitted.

The twisted guide is unique in that there exists a uniform straight waveguide equivalent (see [4]) to the twisted structure. A consequence of this equivalent waveguide is that the dispersion curves are continuous. In other words, in corrugated accelerating structures, it only makes sense to speak of phase constants between 0 and $\frac{\pi}{D}$, where $D$ is the length of a corrugation (single unit cell). However, in twisted structures, the dispersion curves continue indefi-

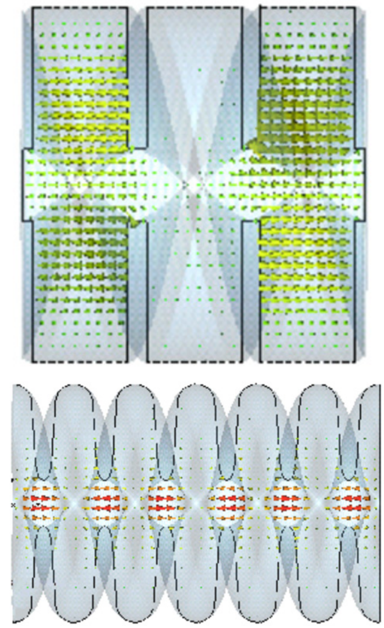

Figure 2: CST Simulation of Twisted disk loaded analog and SNS cavity analog: Electric field

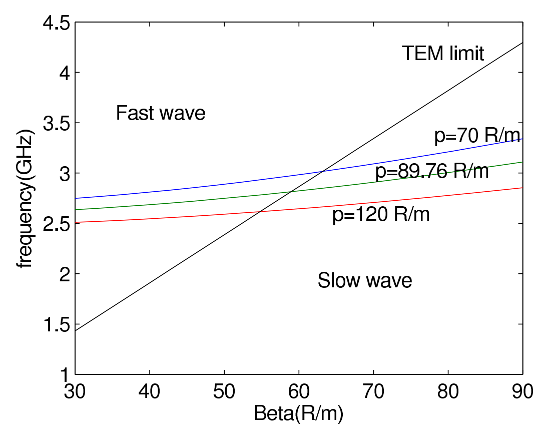


Figure 3: Dispersion diagram for twisted disk-loaded equivalent structure for several twist rates. (Twist rates in radians/meter.)

nitely because of the straight waveguide equivalent, meaning that the stop bands are eliminated. Therefore, the problem of trapped modes can be dealt with effectively.

Another common problem encountered with corrugated accelerating structures is vanishing group velocity near $\pi$ mode. In a cavity of finite length, this normally causes modes to be very closely spaced (so exciting the $\pi$ mode would likely cause other modes nearby to also be excited). However, the twisted guide does not have a point of vanishing group velocity, increasing mode spacing. Note that the “$\pi$ mode” of a twisted structure does not have the same precise meaning as it does for a corrugated accelerating structure – we simply mean the phase variation of the electromagnetic fields per $\frac{1}{2}$ twist. The fields will vary sinusoidally along the particle axis regardless of the mode designation.

## PERFORMANCE

The performance of the twisted guide was analyzed chiefly with respect to the $\frac{R}{Q}$ . We used the twisted analog of the disk-loaded accelerator described in Table 1 for our investigation. The twist rate $p$ was allowed to vary, and the frequency was readjusted at each value of $p$ to ensure that the phase velocity remained at $c$. The results are shown in Fig. 4

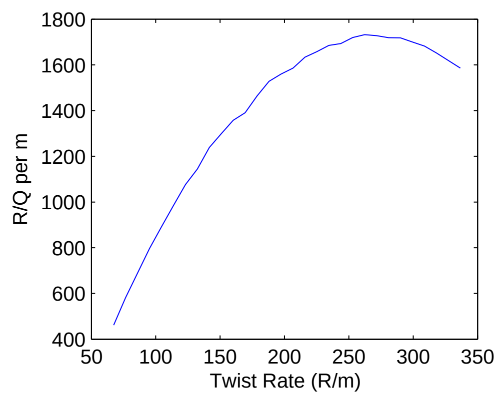


Figure 4: Simulated traveling wave $\frac{R}{Q}$ as a function of twist rate in a twisted analog of a disk-loaded accelerating structure.

This shows that the twist rate has a significant effect on $\frac{R}{Q}$ . In general, the twist rate should not be chosen to maintain a geometric similarity to an existing accelerating structure (such as a disk-loaded accelerating structure), but should rather be carefully chosen to optimize performance.

An example of a twisted elliptical cavity with particle $\beta = 0.61$ was printed using a 3D Stereolithography Apparatus (SLA) and electroplated with copper on the inner surface (Fig. 5). A beadpull measurement was then performed to measure the intensity of the electric field on the axis of the guide. The results of the beadpull are shown in Fig. 6, showing sinusoidal variation of the electric field in the center of the twisted cavity.

## CONCLUSION

We have examined twisted guides as an alternative to reactively loaded corrugated accelerating structures. Like corrugated structures, empty twisted waveguides can support slow wave operation. Twisted analogs to the disk-loaded accelerating structure and the TESLA-type elliptical cavity have been examined. Such twisted structures have a uniform cross section, meaning they could be easier to

Figure 5: Prototype of a twisted elliptical cavity.

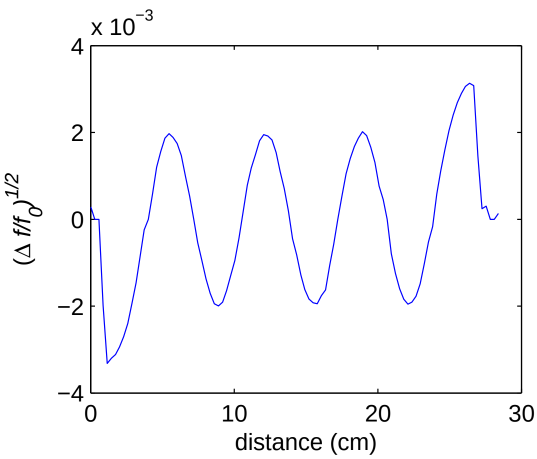


Figure 6: Measured (bead pull) results for elliptical twisted cavity prototype.

machine, eliminating complicated welding or brazing processes. The twisted structure can be tuned to a frequency as a single structure, and its field ditribution may have greater tolerance to internal dimensional error. The modes and field distributions in the twisted analogs are comparable to their nontwisted counterparts.

## REFERENCES

[1] Y. W. Kang, "Twisted waveguide accelerating structure," in *9th Workshop on Advanced Accelerator Concepts*, Aug. 2000.

[2] *CST Microwave Studio 2006 Users Manual.* CST Ltd., Darmstadt, Germany.

[3] J. Wilson, C. Wang, A. Fathy, and Y. Kang, "Analysis of rapidly twisted hollow waveguides," *Submitted to IEEE Transactions on Microwave Theory and Techniques*, Jun. 2008.

[4] D. Shyroki, "Exact equivalent straight waveguide model for bent and twisted waveguides," *IEEE Transactions on Microwave Theory and Techniques*, vol. 56, no. 2, pp. 414–419, 2008.

# PRELIMINARY DESIGN OF THE SLOW CHOPPER FOR THE SPIRAL 2 PROJECT

A. Caruso, A. Longhitano, D. Rifuggiato, G. Gallo, T. Spartà, E. Zappalà INFN/LNS, Catania, Italy
M. Di Giacomo, CEA/GANIL, Caen, France

*Abstract*

The Spiral 2 LEBT line uses a single chopper situated in the line section common to protons, deuterons and A/Q=3 ions. The paper describes the design and the test of the power circuits, based on standard components and working up to 10 kV, at a 1 kHz repetition rate.

## THE LOW ENERGY LINE

The low energy (LEBT) line of the Spiral 2 driver is designed to transport CW, high intensity, beams of protons (5mA), deuterons (5mA) and ions (1mA) with m/q=3 to the radiofrequency quadrupole (RFQ). The RFQ input energy is 20 keV/A and source voltages of 20, 40 and 60 kV are used for the 3 kind of particles. As shown in Figure 1, the chopper is located at the beginning of the common section just before the beam stop.

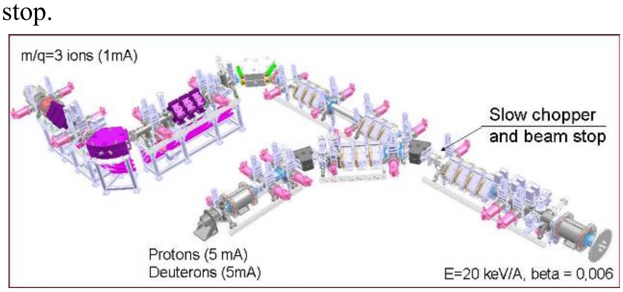


Figure 1: The injector low energy lines and the slow chopper position.

The chopper will be used to progressively increase the beam power during accelerator tuning, to rapidly remove the beam in case of failure detection, to avoid hitting the wheel spokes of rotating targets similar to the one shown in Figure 2 (FULIS or S3 experiences).

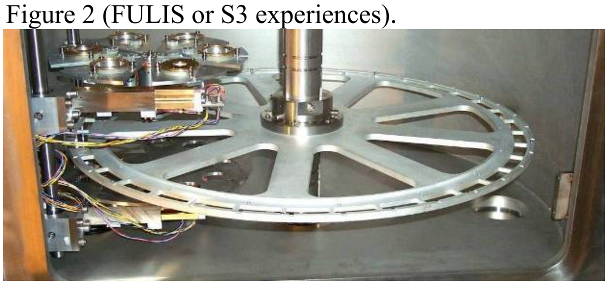

Figure 2: FULIS rotating target wheel (courtesy of C. Stodel).

## CHOPPER REQUIREMENTS

Accelerator tuning is performed at quite low frequency. Due to the high beam power: 200 kW, a very large range of duty cycles will be used, starting from very low fractions ($10^{-4}$). The rotating target asks for pulse repetition rates around 1 kHz. In both cases rapid transition times are required to avoid fractions of beam neither accelerated nor deviated to be lost through the linac.

The chopper voltage depends on the ion source voltage on the distance and length of the plates and on the beam stop location. Due to the LEBT line architecture and to the current intensity, the beam transversal section at the chopper location is quite large and relevant voltages have to be applied to the electrodes to compensate their distance.

In our case, the beam section has a diameter of 76 mm, the electrode hard-edge length considered in the beam dynamics simulations is of 160 mm, deflection at the end of the plates is of 10 mm. and a total deviating voltage of 17 kV has to be applied. Transient times for the pulse have to be shorter than 100 ns, and an amplitude stability of few percents is required.

High reliability and easy maintenance are also strong requirements of the devise.

## ELECTRODE GEOMETRY

The preliminary geometry shown in Figure 3 was designed to have a flat transversal field and to produce field maps for beam dynamic simulations. Two cases where simulated: a) one plate positively biased and one grounded and b) both plates biased with opposite voltages but no differences where observed.

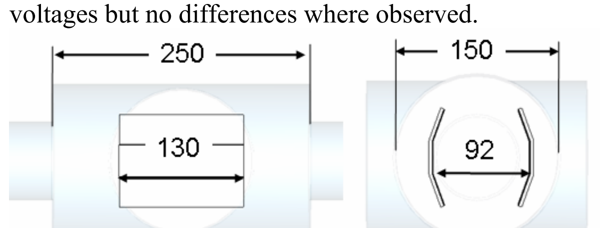


Figure 3: The simulated geometry, plate bending angle is 20°.

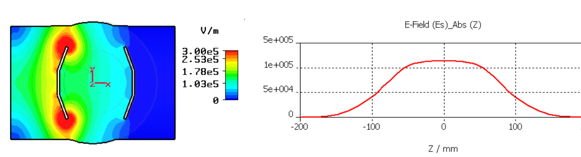


Figure 4: Electric field on the transversal plane and on the beam axis.

The first case, with positive voltage, was chosen, because it would let easier water cooling of the ground electrode if some beam was eventually lost. The deflection plane is horizontal because the beam section is smaller on this plane than on the vertical one. To obtain the deviating field, a pulse of 9.2 kV has to be applied to the electrode, whose capacitance is around 15 pF. The pulse duty cycle defines the attenuation on the beam.

## SLOW CHOPPER DEVELOPMENT

The development of the Spiral 2 device is foreseen in two years. In this first year, the power circuit, the feed-through and the assembling concept has been studied and tested on a prototype.

The design approach was strongly addressed towards reliability and decrease of the maintenance time, both being very important issues in high power accelerators. For the electrical parts, we have searched for standard commercial devices that are easy to check and to replace in case of failure. For the mechanical assembling concept, we chose to have no isolators between the plates, as Alumina could break and spread activated fragments. Each electrode is then supported by its flange.

### *Electrical Design*

The principle scheme of the chopper is represented in Figure 5.

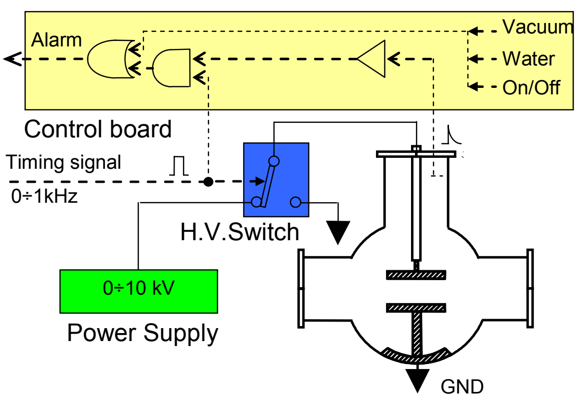


Figure 5: Principle scheme of the chopper.

The high voltage switch alternatively connects the electrode to ground or to the high voltage power supply following the timing signal repetition rate and duty cycle. A high voltage sealed connector is used as feed-through.

The power required to charge and to discharge the electrode equivalent capacitance Cplate, at the voltage V and repetition frequency f is approximately given by the formula [2]:

$$P = \frac{f \cdot C \cdot V^2}{2}$$

Numerical values considered for the design, are summarized in Table 1.

Table 1: Design parameters for the chopper power circuit.

| | |
|---|---|
| Maximum voltage: | 10kV |
| Rise/fall time under | 100ns |
| Duty cycle variable from | 0 to 100% |
| Repetition frequency | from few hertz to 1kHz |

where C includes Cplate but also the output internal capacity of the switch and the equivalent capacitances of the cable and of the vacuum connector This applies either for the power supply and the switch loss.

To fit the requirements, 10 Watt, off-the-shelf devices have been selected. A standard pulse/function generator AFG310 by Tektronix is used to drive the switch, while the main components of the system are:

- Power supply MPS10P10/24 by Spellman
- Solid state switch HTS151-03-GSM by Behlke
- Vacuum feed-through SHV-20 by Caburn
- Coaxial cable HTC-50-7-2 by Draka

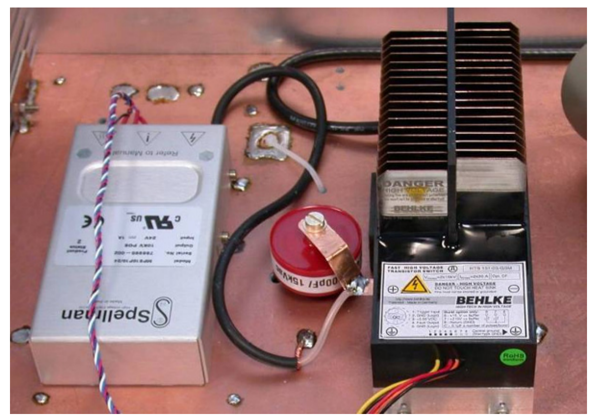


Figure 6: The power supply and the switch.

Figure 6 shows the high voltage switch, the power supply and the 1nF buffer capacitance in the rack. The solid state switch consists of two identical mosfet switching paths that form a so-called half bridge circuit configuration. Both switching paths are controlled by a common logic driver. The power supply can deliver up to 10kV, 1mA. The switch and the electrode are connected by a low loss coax cable. Great care was taken to assemble these modules into the rack. Special attention was given for grounding and shielding all the components.

### *Mechanical Design*

The mechanical assembling of Figure 7 was designed to test the feed-through in operating conditions and to verify the assembling concept and the plate alignment.

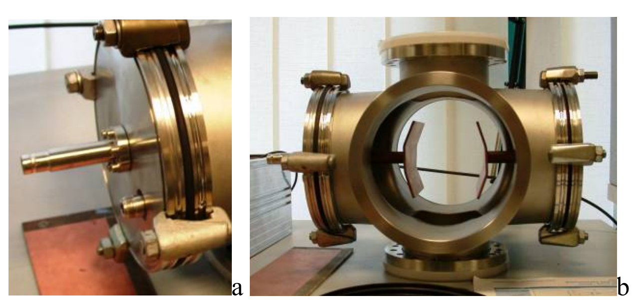


Figure 7: Feed-through and electrodes assembled in the cross section.

A standard beam line cross section with six gates was available at the Lab and was used to host the electrodes. Each electrode is constituted of a plate of 3mm thick cupper sheet supported by a cupper column. They are inserted from opposite sides and each one is supported by its vacuum flange. The ground electrode is connected directly to the flange while the polarized plate is brazed to the feed-through connector. The ceramic feed through is a standard 20kV single ended coaxial SHV connector, DN16CF already flanged. A capacitive pick-up is inserted near to the feed-through to be used to check the pulse presence, but the alarm board still has to be developed.

## EXPERIMENTAL RESULTS

A total capacitance of about 30pF was measured at the feed-through connector input. The cable adds some 70 pF and the data sheet gives a value of 30 pF for the switch output capacitance. With less than 150 pF, the system should reach a repetition rate of 1 kHz but the measured operating range (Figure 8) is smaller, and is limited by the current of the high voltage power supply.

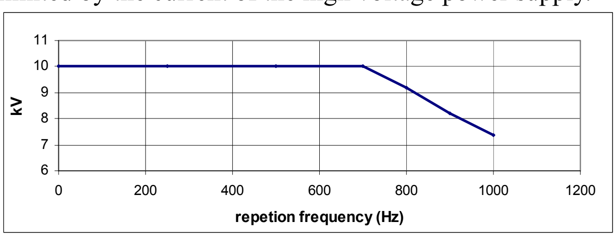


Figure 8: Prototype operating range.

A 20 W power supply will then be installed in the final rack, in order to reach the required repetition rate. No upgrade is foreseen for the switch as it had already been ordered with an option that let it dissipate up to 100 W.

Measurements of the transient times confirmed the data sheet performances: rise and fall times around 30 ns, as shown in Figure 9.

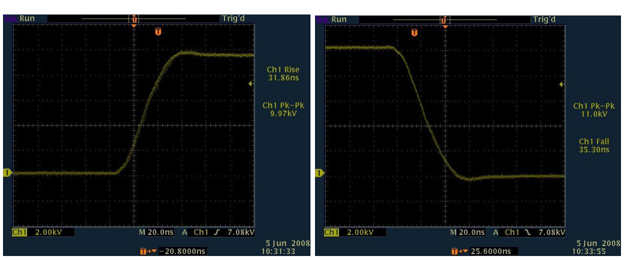

Figure 9: Rise and fall times.

A long time test of one week (@ 10kV, 800 Hz, 50% duty cycle) was also performed to check the circuit reliability and the stability of the pulse parameters. The amplitude stability is better then 1%, and no changes where observed in the delay between the driver and high voltage edges , which is of 160 ns as shown in Figure 10a, which also shows the 10 kV pulse shape at 700 Hz, 50% duty cycle and the pick-up response.

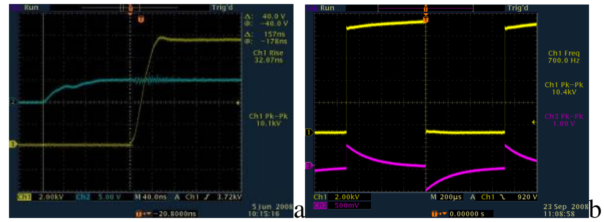


Figure 10: Pulse jitter (a) and shape (b yellow) @700 Hz, 50% dc, 10 kV. Pick-up response (b violet).

## CONCLUSION AND PERSPECTIVES

The pulse amplitude, jitter and transition time measured on the prototype fulfil the requirements, while a more powerful high voltage supply is required to achieve a 1 kHz repetition rate. A complete system (electronics and electrodes) is available today for beam tests and next efforts will be dedicated to the design of the alarm control card and of the computer control interface and to the manufacture of the final mechanical ensemble to be installed on the Spiral2 injector.

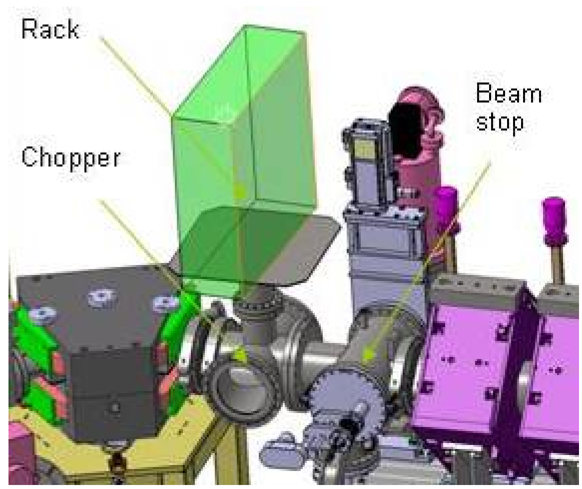


Figure 11: The chopper and beam stop line section with room reserved for the electronics rack.

## AKNOWLEDGEMENTS

We would like to thank F. Gobin and Ch. Contrepois who have studied the low energy line integration and defined all interfaces between different devices.

INFN LNS is member of the SPIRAL 2 Preparatory Phase. This work is supported by the European Commission within the 7$^{th}$ Framework Program: project n. 212692.

## REFERENCES

[1] Behlke, high voltage switch application note
[2] L. Calabretta et al: The radiofrequency pulsing system at INFN-LNS: Proceedings of Cyclotrons 2001, East Lansing, Michigan, USA

# DESIGN OF THE MEBT REBUNCHERS FOR THE SPIRAL2 DRIVER

M. Di Giacomo, JF Leyge, M. Michel, P. Toussaint, GANIL, Caen, France

*Abstract*

The SPIRAL2 project uses room temperature RFQ and rebunchers and a superconducting linac to accelerate high intensity beams of protons, deuterons and heavier ions. All cavities work at 88 MHz, the beta after the RFQ is 0.04 and 3 rebunchers are located in the MEBT line, which accepts ions with A/q up to 6. The paper describes the RF design and the technological solutions proposed for an original 3-gap cavity, characterised by very large beam holes (60mm) and providing up to 120 kV of effective voltage.

## INTRODUCTION

The SPIRAL2 [1] driver presents a quite long medium energy beam transport line (Figure 1) to insert a second beam line from a future RFQ for heavier ions: q/a=1/6, a single bunch selector and the corresponding beam dump. The line is seven and a half meters long and is equipped with three rebunchers to keep the beam longitudinal phase dimension.

Room requirements for all the devices are very tight and the cavities have to be compact on the beam axis direction. Moreover, the beam transverse section can be quite large in the line, then the beam aperture in the cavity drift tubes is much longer than the tube length and the gap electric fields interact with each other. The Transit Time Factor (TTF) is consequently quite low and voltages higher than usual have to be applied on the electrodes to obtain the required effective voltage.

## REBUNCHER REQUIREMENTS

The first and the last cavities will work at an effective voltage of 120 kV with the heaviest ions while the second one will work at 60 kV CW only. For the RFQ initial commissioning, only the first cavity will be installed before the diagnostic test bench and pulsed voltages up to 190 kV will be used for emittance measurements.

The line beta is 0.04 which is a reasonable figure with respect to the injector working frequency of 88,0525 MHz.

## RF DESIGN

To keep the longitudinal length of the cavity as small as possible and to handle reasonable values of RF power and electric field, a 3-gap structure has been chosen. The double quarter wave resonator of Figure 2 has been preferred to the more usual split ring, to have right stems with more homogeneous loss, easier cooling opportunities and better alignment guarantees. The central part of the tank has a square section to host the beam ports and the tuner (trimmer) while the rest of the tank is cylindrical. The stems are conical to progressively increase the diameter from the drift tube end (where it couldn't be bigger) to the short circuit. The drift tubes are spaced in order to obtain the required beta value and to limit the maximum electric field.

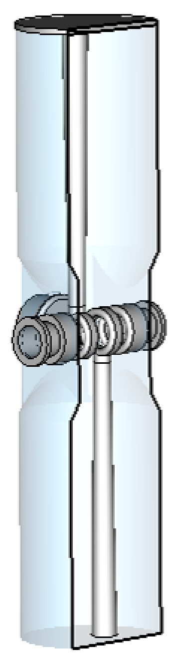

Figure 2: The RF structure.

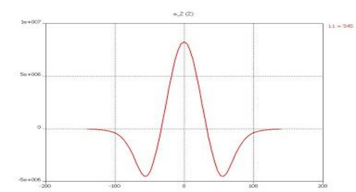

Electric field on the beam axis (@1 joule of stored energy)

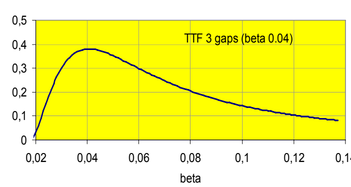


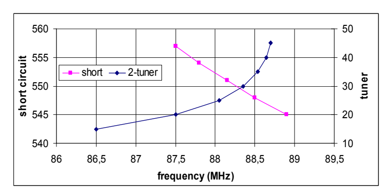


Tuner and shorting plate responses

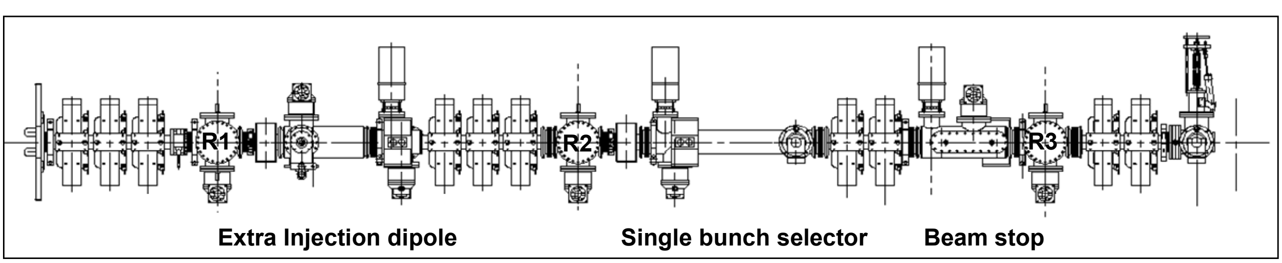


Figure 1: The medium energy beam transport line.

The cavity was simulated with Microwave Studio. Tables 1 and 2 recall geometrical dimensions and RF parameters.

Table 1: RF Cavity Simulated Geometry

| **Parameter** | **mm** |
|---|---|
| Beam diameter | 60 |
| Ring external diameter | 90 |
| Electrode ring length | 32 |
| Gap distances | 13, 30, 13 |
| Trimmer diameter | 130 |
| Trimmer stroke | 15 to 45 |
| Stem diameters | 32, 40 |
| Cavity central section sides | 180x180 |
| Cavity central section height | 2*152 |
| Cavity inner diameter | 260 |
| Cavity height | 2*545 |
| Flange to flange distance | 280 mm |

Table 2: Results of Simulation with Microwave Studio [2]

| | |
|---|---|
| Electrode voltage (@120 kVeff) | 79 kV |
| TTF | 0,38 |
| Q | 7600 |
| Rs (effective voltage^2/ power) | 3680 |
| Power loss (@120 kV) | 4 kW |
| Max E field (pulsed) | 11 MV/m |
| Max H field (pulsed) | 17,4 A/m |

### *Tuner*

Two capacitive panels are located on the side of the drift tubes. This solution has been preferred to an inductive plug on the short circuit area, where the stroke would have been longer and the sliding RF contacts more sophisticated due to the high magnetic field. Both panels are used to set the resonant frequency, in such a way that their position is symmetrical at 4 kW power level, but only one is motorised to be driven by the fine tuning loop. Their diameter has been designed in order to require a stroke of few centimetres. In this way, as shown in Figure 3, it has been possible to use flexible belts screw on both sides to transfer RF currents and heath.

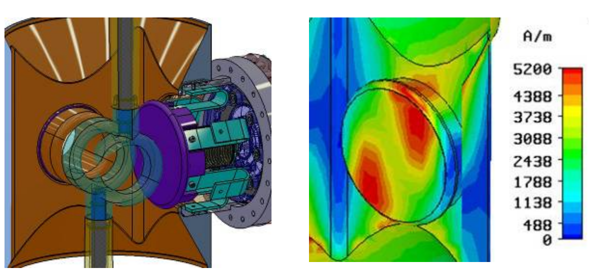


Figure 3: a) The tuner with flexible belts for RF and thermal contact; b) the current distribution.

RF Loss on each plate at maximum voltage depends on the position but is of the order of few tenth of watt. The maximum current density in the belts is around 12 A/cm.

### *Coupler*

A power loop situated on the bottom end of the tank matches the cavity to the 50 ohm transmission line from the amplifier. The presence of the coupler slightly changes the field symmetry but simulations have shown that field asymmetries introduced by the presence of the coupler and by a misalignment up to ±0.75 mm of the drift tubes don't perturb the beam dynamics.

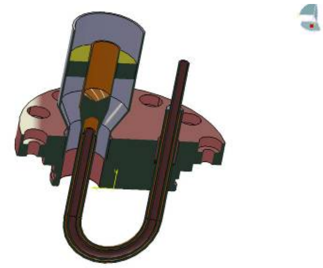

Figure 4: The coupling loop.

## THERMAL AND MECHANICAL STUDIES

External tanks made of thick copper or of copper plated stainless steel sheet have been studied. Use of steel was excluded in order to keep the possibility of plating the cavity again in case of problems after the first process. A minimum thickness of 5 mm was required for radiation protection. Thermal calculations were made with a margin factor of 1.5 applied to the loss distribution. In the case of the copper plated tank, special attention was paid to put the cooling channels along the warmest areas, while no special care was taken for the copper one. The temperature maps with input water at 26°C.are shown in Figure 5.

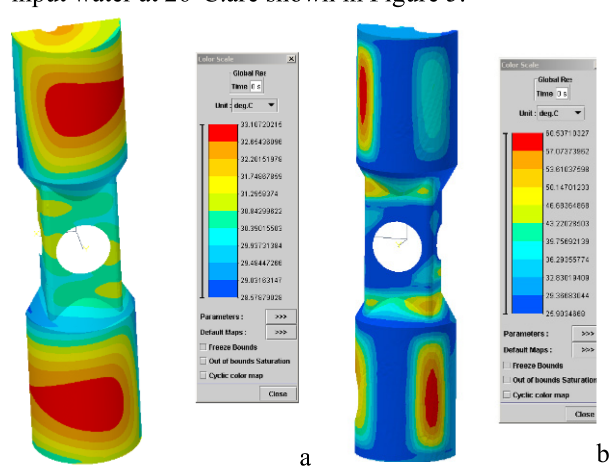


Figure 5: Temp. maps: a, solid copper, b: plated.

The copper structure stays very cold and maximum temperature difference is only of few degrees. The plated cavity warms up more but the hottest spots stay below 60 degrees. Displacements along the 3 axes of the points where the stems are connected stay below 0.1 mm.

Mechanically, the tank is built of three parts, welded before being copper plated. The central section is machined from a solid block for more precision, while the cylindrical parts are made of formed sheets. All other elements of the cavity are made of solid copper.

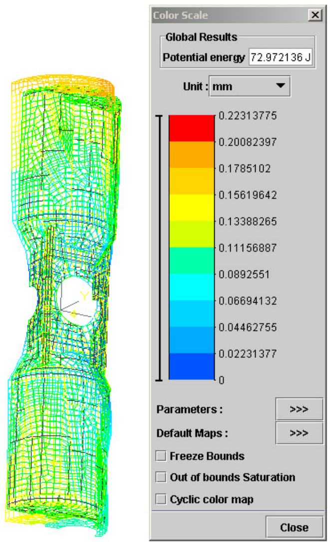


Figure 6: Deformations of the steel structure.

For the beam ports, the drift tubes and the trimmers; this is to avoid deterioration of the RF surface in case of sparks, while for the stems and short circuit plates this is to improve cooling and limit deformations. Figure 7 shows mechanical assembly of all elements.

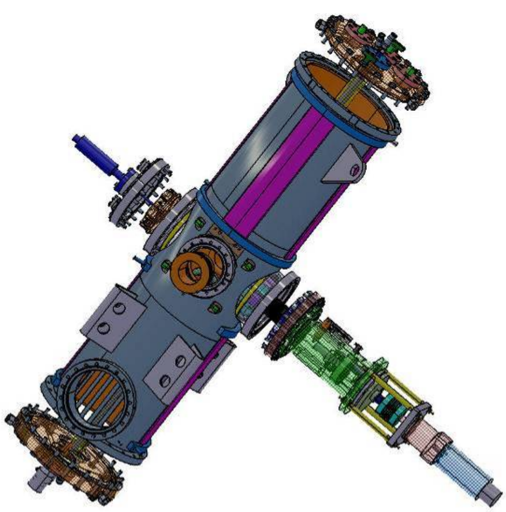

Figure 7: Cavity assembling.

The drift tubes and beam ports are cooled by thermal conduction through the stems or the tank. The stems are cooled by a continuous layer of water flowing inside the stem (Figure 8). Total displacements of the whole structure induce a misalignment of the electrode axis of only few tenths of mm. The tuner sensitivity around the nominal distance of 25mm gives good margins to lower the resonant frequency but not to increase it. Then the shorting plate is designed with an over-thickness to be adjusted after frequency measurements.

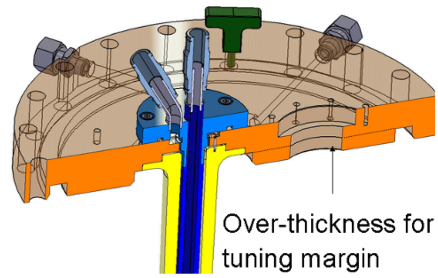


Figure 8: Stem cooling circuit and tuning margins.

## HIGHER FREQUENCY APPLICATION

In the framework of the collaboration between the projects, the application of the SPIRAL2 design to the Saraf linac has been studied. Saraf works at 176 MHz, beta 0.056, but the beam diameter is 100 mm and only 100 kV are required. The geometry on Figure 9 fits the requirements, with a total length on the line around 200 mm and losses of the order of 3 kW.

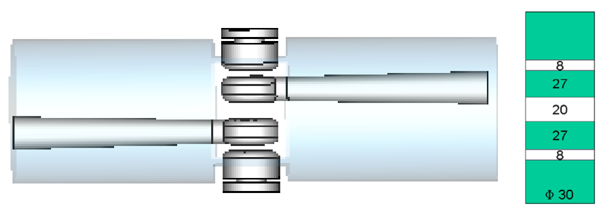


Figure 9: 176 MHz, beta 0.056 cavity and electrode geometry.

## CONCLUSION

An original RF structure has been designed to fit the SP2 requirement for the MEBT rebunchers. The proposed cavity grants high gradient, compactness along the beam axis, tight alignment tolerances. The cavity design is completed and a call for tender in progress.

## ACKNOWLEDGEMENTS

Many people have been involved in this work but we would particularly mention D. Uriot for beam dynamics simulations, G. Le Dem for field maps macros, M. Malabaila and T. Dettinger for their explanations about the copper plating process and M. Vretenar, H Vormann and their teams at CERN and GSI for their help and comments on the overall design.

## REFERENCES

[1] T. Junquera et al., Status of the construction of the SPIRAL2 accelerator at GANIL, Proc. Linac 08.

[2] MWS, Computer Simulation Technology, Darmstadt, Germany.

# RF POWER AMPLIFIERS FOR THE SPIRAL 2 DRIVER: REQUIREMENTS AND STATUS

Marco Di Giacomo, Bernard Ducoudret, GANIL, Caen, France


*Abstract*

The Spiral 2 project [1] uses a RFQ, normal conducting rebunchers and a superconducting linac to accelerate high intensity beams of protons, deuterons and heavier ions. All cavities work at 88 MHz, are independently phased and powered by amplifiers whose power ranges from few kilowatts to 250kW. The paper describes the amplifier requirements, the proposed solutions and their status.


## INTRODUCTION

The search of cost effective solutions has been one of the major aims of the project and studies about the RF power systems have begun since the very beginning phases. Concerning the linac frequency, the possibility of taking advantage of all developments from the FM market in the low level and power electronics, and the amount of RF power required by RFQ cavities at higher frequencies were among the major issues that lead to the choice of 88.0525 MHz.

Once the driver frequency was defined, two ranges of amplifiers were required: above 150 kW for the RFQ cavity and up to 20 kW for the linac cavities and the rebunchers of the medium energy line.

The solid state technology was investigated and definitely chosen for the second range. Security issues, modularity, quick trouble shooting, life time, have been privileged as already done in other accelerator projects and commercial fields.

Industrially available power at competitive cost being increasing quickly, the hope to have the same technology for the RFQ amplifiers too was kept for a while, but recently abandoned due to the amount of power finally required by the cavity.

## RFQ AMPLIFIER

### *Cavity Requirements*

Power loss in the RFQ cavity has been continuously upgraded as the contribution of different elements was calculated. Design study simulations, based on a 3D model of a 1-meter section including extremities, and 2D simulations of the other sections with changing beam aperture, had given some 130 kW. Power test on the prototype cavity (corresponding to the 3D model) revealed a Q factor 10% lower than expected which implies a correspondent increase of power loss. More recently, in the framework of the study for tuning procedure, manufacturing and positioning tolerances of the poles have been simulated and losses due to extreme tuner positions have been calculated. According to latest estimation, total loss in the cavity could reach some 180 kW [2].

Another important request from the RFQ team was to respect the quadrupolar symmetry of the RF structure. It was then decided to drive the cavity through four coupling loops, placed in the four quadrants of the same section as shown in Figure 1b.

### *Choice of the Amplifier Architecture*

Manufacturing considerations, as the cost of the power tube and the number of potential manufacturers, influenced the decision of using four different amplifiers too.

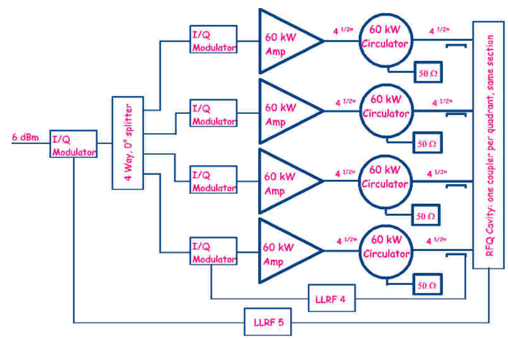


Figure 1a: Four amps and circulators scheme. The scheme shows the fast I/Q RFQ feedback loop (LLRF5) and one of the four local slower loops (LLRF4) to control the combining efficiency.

Up to several tens of kW, commercial, robust and non expensive power triodes working in the FM bandwidth are available and several broadcast companies are equipped with the ancillary systems for power tests. Behind the 30-40 kW threshold, the number of either power devices and potential manufacturers quickly decreases.

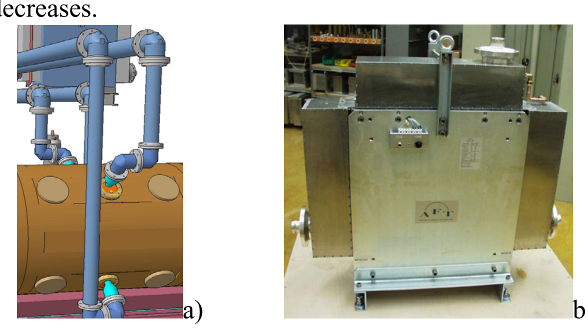


Figure 2: The four lines combined into the cavity and a 60 kW circulator.

Driving a cavity with more than one amplifier can easily be source of oscillation problems, unless they are isolated by circulators. Circulators present some percent of RF loss but match the amplifier load and handle the reflected power. The total balance is then highly positive as one doesn't need to oversize the amplifier power stage (tube and power supply) to work in mismatched conditions, like usual in accelerator applications.

These considerations, associated to the parallel request to drive the cavity keeping the 4-quadrant symmetry, lead to the scheme of Figure 1.

Four slow I/Q loops could be inserted to control the phase and amplitude of the signals at the entrance of the cavity, the amplitude being much more sensitive as shown in Figure 3.

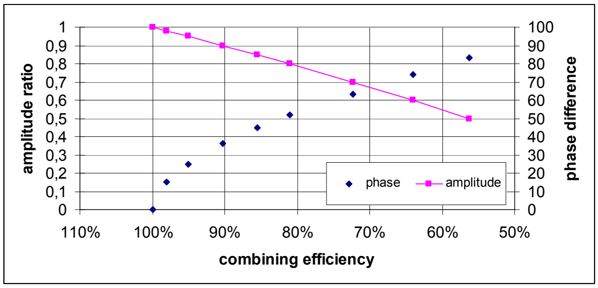


Figure 3: Effect of amplitude and phase difference in a 2-way combiner.

Taking into account circulator losses (.25 dB), combination efficiency and some margin for feedback and reliable operation, four 60 kW amplifiers were finally ordered.

## *The 60 kW Amplifier*

The amplifiers is built by the Italian broadcast company DB Elettronica. As shown in Figure 4, it is based on two stages: a compact, solid state 3 kW driver and a tube and cavity power stage, able to deliver up to 100 kW. The tube is the Thales tetrode TH535 and the cavity is the TH 18546.

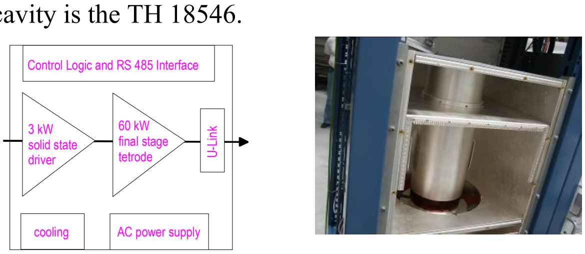


Figure 4: Scheme of the 60 kW amplifier and tube cavity.

Anode and grid supplies are designed for 65 to 70 kW. The driver, the tube anode and the anode voltage controller are water cooled while the tube filament, the cavity, the HV rectifiers and the grid and screen supplies are air cooled by dedicated fans. Filament and anode supply voltages are controlled by thirystor cards and can be set continuously in order to ramp the filament voltage during heating and the anode one at start up. Grid and screen voltages can be adjusted by 5% steps around nominal values.

The driver amplifier is the same 2.8 kW module used in the 10 and 20 kW solid state amplifiers and is described in [3].

A panel with U link integrated on the front face let switch the output on the circulator on to a dummy load. Everything is assembled in a very compact standing on a 2x1.2 meter area.

## *First Amplifier Test Results*

The first prototype was tested in July. It delivers up to 65 kW and performs very well in CW and pulsed modes. Pulsed mode is quite important for the SP2 RFQ as, due to the space charge compensation in the low energy line, it could be required to pulse the cavity to change the beam intensity. The amplifier was then tested from 1Hz to 1 kHz and no oscillation of the power supply filter appeared.

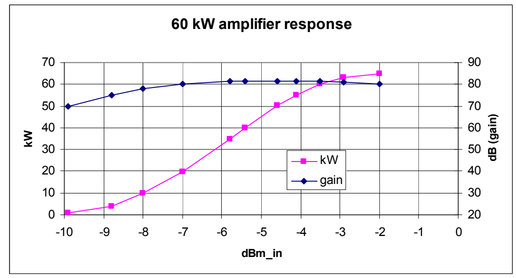


Figure 5: Amplifier response.

Electrical parameters of the final stage at maximum power are summarised in Table 1.

Table 1: Power Stage Electrical Parameters

| | | |
|---|---|---|
| Input power | 2.3 kW | |
| Filament V and I | 8.9 V | 192 A |
| Grid V and I | -140 V | 0.5 A |
| Screen V and I | 900 V | 0.5 A |
| Anode V and I | 10k V | 9.6 A |
| Efficiency | 65 % | |
| Gain | 14.5 | |

# SOLID STATE POWER AMPLIFIERS

## *Cavity Requirements*

Three normal conducting rebuchers [4] are used in the medium energy transport line. Two of them require 5 kW to work at 120 kV while the third one requires much less as it works up to 60 kV only.

Two families of superconducting cavities [1] are used in the SC linac: 0.07 and 0.12. Maximum accelerating field is 6.5 MV/m corresponding respectively to 1.5 MV and 2.6 MV effective voltages. First cavities ask for less power as they are not used at maximum voltage or accelerating phase, while the beam loading is mainly affected by the beta law for the following resonators

Maximum RF power requirements for the 29 cavities of the linac range from few to 13 kW, as shown by the blue curve of Figure 6.

LLRF requires some margin but microphonics could significantly increase this power levels. A 30% margin has then been taken, as represented by the green plot. Superconducting cavities require operation with total reflected power when the beam intensity is reduced, and during conditioning. This situation is the most demanding, as the coupler has to be conditioned above the maximum power it has to deliver.

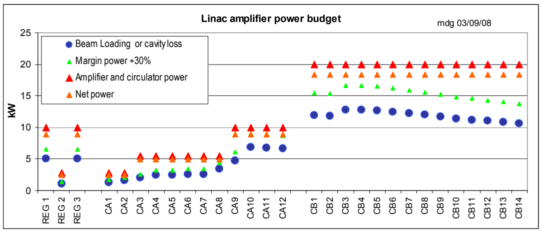


Figure 6: Requirements and choice of the linac amplifiers.

Finally, as some cavities will be operated over a very large range of voltages (factor 100), the amplifier have to be operated at very low power too.

### *Solid State Amplifiers*

To solve the different requirements, solid state amplifiers equipped with external circulators and dummy loads have been chosen, the circulator being placed as close as possible to the linac tunnel.

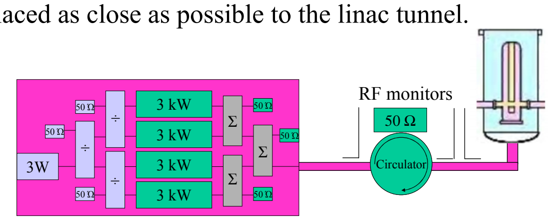


Figure 7 : Amplifier architecture. Circulators and dummy load are out of the amplifier cabinet, at the high power level. Green elements are water cooled.

This configuration was considered more reliable than distributed circulators at the output of the transistors as stands higher SWVR and protects the combiners and the transmission lines too. Measurements on the first prototypes performed on a 20 kW, variable VSWR, test bench[4], have shown that the way the reflected power is split back by the combiners, strongly depends on the phase of the RF, confirming our initial considerations.

b)

Figure 8 : Two 10 kW amplifiers installed at Orsay. Can be combined to obtain 20 kW. B) 10 and 20 kW circulators.

The architecture shown in Figure 7, based on 3 kW racks (2.8kW nominal value), seems the best compromise to fit our power level requirements, to optimise costs, and to let easy handling for maintenance. Roughly, 3, 5.5, 10 and 20 kW figures are available as shown on the red plot of Figure 6. This division covers quite well the requirements, even once loss in transmission line and circulators are considered (the orange curve).

The 10 kW prototype has already been successfully used for the power tests of the first high beta cryomodule at IPN-Orsay. The cavity was completely mismatched, no beam being present. As shown in Figure 9, it was detuned to condition the coupler at maximum power and then several measurements were performed at power levels of several kW, some 3 kW being required for nominal (6.5MV/m) gradient with no beam.[5]

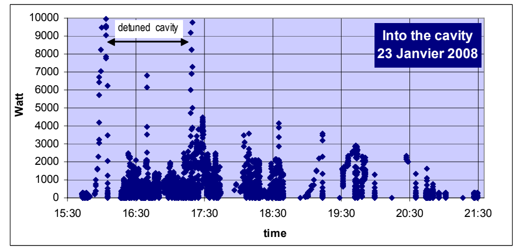


Figure 9: Power tests with the cryomodule.

Class C amplifier have been used by the moment as the digital LLRF should be able to compensate de gain variations. Tests with feedback loop still have to confirm this point.

## CONCLUSION

RF power requirements for the SP2 driver are well defined now. Four 60 kW, tube amplifiers are under construction for the RFQ, the first one of which has already been successfully tested. Solid state amplifiers are foreseen for the MEBT rebuncher and the SC linac. A 10 kW, class C prototype equipped with an external circulator has been successfully tested on the first cryomodule. Linearity issues still have to be tested, to confirm the transistor working class.

## ACKNOWLEDGMENTS

Many people have contributed to this work but we would particularly mention M. Desmons, F. Scarpa for all the improvements suggested during the design and test phases of the RFQ amplifier, Ti Ruan for useful discussion, P. Baret for his help during the solid state amplifier commissioning, JC. Deroy for the computer control interface and J. Lesrel and Ch. Joly for their work during tests on the cryomodules  Several papers describe Fabio's and Ti's works on solid state amplifiers and, should be added to the references list too.

## REFERENCES

[1] T. Junquera: *Status of the construction of the SPIRAL2 accelerator at GANIL*, Proc. of LINAC08,

[2] O. Piquet, Project Note

[3] M. Di Giacomo et al., *Design of the MEBT rebunchers for the SPIRAL 2 driver,* this conference.

[4] M. Di Giacomo et al., *The test bench for the power amplifiers of the Spiral-2 SC linac*, Proc. of SRF07

# OPTIMIZATION OF SPIRAL-LOADED CAVITIES USING THE 3D CODE OPERA/SOPRANO*

M. Schuh[1,2], K.U. Kühnel[2], C.P. Welsch[2−4]
[1]CERN, Geneva, Switzerland
[2]MPI for Nuclear Physics, Heidelberg, [3]GSI, Darmstadt, and [4]University of Heidelberg, Germany

*Abstract*

Rebunching cavities are today routinely used for matching a beam of charged particles between different accelerator structures, and thus optimizing the overall transmission and beam quality. At low resonance frequencies, unnecessary large dimensions of these cavities can be avoided by using spiral-loaded cavities. The optimization of these structures is a complicated process in which a wide range of different parameters have to be modified essentially in parallel. In this contribution, we investigate in detail the characteristics of a model structure with the 3D code OPERA/SOPRANO. This includes the optimization of the structure in terms of the spiral geometry for a given resonance frequency, the investigation of power losses on the inner surfaces, and the possibility of cavity tuning by means of a tuning cylinder.

## INTRODUCTION

Spiral-loaded cavities are today routinely used in many accelerator facilities around the world [1], [2]. Mainly as buncher and post accelerator elements to vary the temporal profile and the final energy of the beam [3]. The big advantage of this structure is its compact size as compared to quarter-wave resonators. These small structures allow changing the energy as well as the velocity distribution in a beam very efficiently and thus providing an efficient matching between different sections of an accelerator or shaping of the longitudinal beam profile in front of an experiment. Different types of spiral-loaded cavities have already been realized in the past, differing in number of accelerating gaps and in the winding of the spiral arms.

In this contribution, we consider a single arm normal conducting structures as it was already built up [4]. It consists of a cylindrical external tank and three drift tubes on the symmetry axis. The middle drift tube is attached to the spiral arm. A model of this structure is shown in Fig.1 and the design parameters for the initial model are found in Tab.1. A particularity of this type of structure is the ratio of the radii, where the small radius equals half of the large radius. In order to efficiently accelerate charged particles in such a structure, the distance between the midgaps needs to be an integer multiple of half an RF period. The geometry of this structure can be described by the following equation

$$L = \frac{n\beta\lambda}{2} \tag{1}$$

* Work supported by GSI and the Helmholtz Association of National Research Centers (HGF) under contract number VH-NG-328

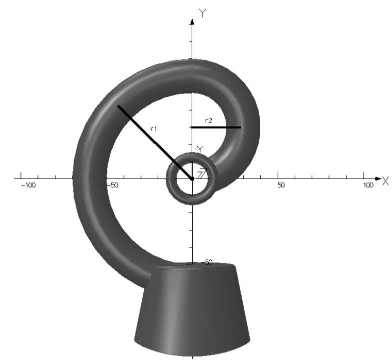


Figure 1: Model of the spiral arm with hidden tank walls and marked spiral radii.

where $\beta = \frac{v}{c}$, $\lambda$ the wavelength and $L$ is the distance between the middle of two gaps which is also referred to as the cell length.

Table 1: Design values of cavity tank and spiral arm

| Design Parameter | Size [mm] |
|---|---|
| Cavity length | 150 |
| Cavity radius | 100 |
| Cavity wall thickness | 5 |
| Drift tube length | 60 |
| Drift tube thickness | 10 |
| Gap width | 15 |
| Aperture radius | 10 |
| Blend radius | 2.5 |
| Spiral radius r1 | 60 |
| Spiral radius r2 | 30 |
| Spiral thickness | 20 |

In the frame of this study, we built up a model of a well-known cavity, which was then simulated and analyzed by using the different modules of OPERA [5]. This allowed us to benchmark the results of this code with previous data and results from other simulation codes. In our investigations, we used the eigenvalue solver SOPRANO to determine the relevant resonance frequencies. The solver can be used to find the different resonance modes of a cavity structure with either perfect conducting boundaries or realistic metal surfaces by solving the Helmholtz equation via the Galerkin method and subsequently solve the sparse generalized eigenvalue problem.

## FIGURES OF MERIT

In order to compare the simulation results with other structures several characteristic values are computed, which are defined according to [6]. First we define the quality factor Q as

$$Q = \frac{\omega U}{P} \tag{2}$$

where $\omega$ is the angular frequency of the mode, $U$ is the stored energy in the system and $P$ the average power loss.

$$U = \frac{1}{2}\mu_0 \int |\mathbf{H}|^2 \, dV \tag{3}$$

$$P = \frac{1}{2}R_s \int |\mathbf{H}|^2 \, dS \tag{4}$$

$R_s$ is the average surface resistance of the material. The quality factor indicates the power losses in the structure.

A second figure of merit that is independent of the excitation level of a cavity is the shunt impedance and the shunt impedance per unit length

$$r_s = \frac{V_0^2}{P}, \quad Z = \frac{r_s}{l} \tag{5}$$

where $V_0$ is the accelerating voltage

$$V_0 = \left| \int_{-L}^{0} E_z(z) dz \right| + \left| \int_{0}^{L} E_z(z) dz \right| \tag{6}$$

and $E_z$ is the the accelerating field. It expresses how much energy is needed establish a certain average E-field inside the cavity.

## SIMULATION RESULTS

For all simulations we used the same boundary conditions and mesh settings to allow for simple comparison of the results. In order to get a volume mesh error smaller than $10^{-6}$ around $10^5$ linear tetrahedrons were used to mesh the complete model body. A minimum of 1 GB RAM is required for running OPERA solver, which takes about 5 minutes at a CORE 2 DUO workstation using only one core.

### *Initial model*

The results of the first three modes of the initial model can be found in Tab.2 where the OPERA function to compute the Q value was used. The higher Q value at the second resonance is due to the surface resistance, which decreases with the square root of the frequency. At the third resonance the Q value increases more than expected from the change of the surface conductivity. That is on one hand due to a different field distribution in the cavity, which cannot be used for beam acceleration, because there is no change in sign between the two gaps. On the other hand the second modes is a $3\lambda/2$ oscillation which leads to much lower maximum fields. The accelerating field distribution on beam axis and the surface power losses of the first mode are shown in Fig.2 and Fig.3. It can clearly be seen that the main power losses are located along the spiral where the highest surface currents occur.

Table 2: Simulation results of initial model

| Mode | 1 | 2 | 3 |
|---|---|---|---|
| Frequency [MHz] | 234.283 | 607.945 | 838.894 |
| $Q$ (Copper) | 5,993 | 9,503 | 16,059 |
| $r_s$ [M$\Omega$] | 3.30 | 1.67 | 3.44 |
| $Z$ [M$\Omega$/m] | 22.02 | 11.12 | 22.19 |

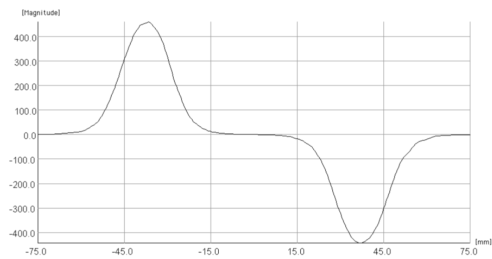


Figure 2: Accelerating field distribution on beam axis at the first resonance.

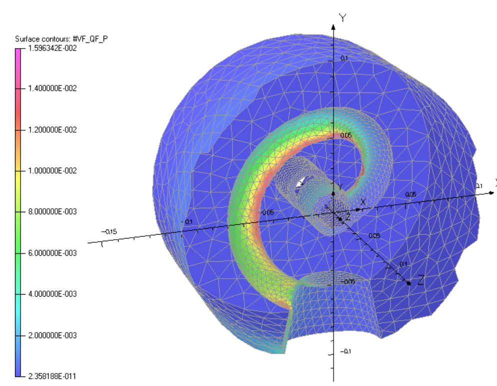


Figure 3: Power loss on surface at the first resonance frequency.

### *Rotation of the Spiral Arm*

The frequency tuning of spiral-loaded cavities is typically done by shortening of the spiral arm. In such an R-R/2 structure the drift tube remains centred in the cavity even after rotation, which allows for a simple tuning of the structure to the desired resonance frequency. In order to determine this dependency, we rotated the spiral arm in steps of one degree in the range of $-90°$ up to $90°$ and shortened it continuously. For each iteration step, we then calculated the effect on the resonance frequency. Thereby $-90°$ correspond to the longest spiral arm, $90°$ to the shortest one and zero degree to the initial model. By reducing the length of the spiral arm, the inductance of the system is reduced, which leads to a higher resonance frequency.

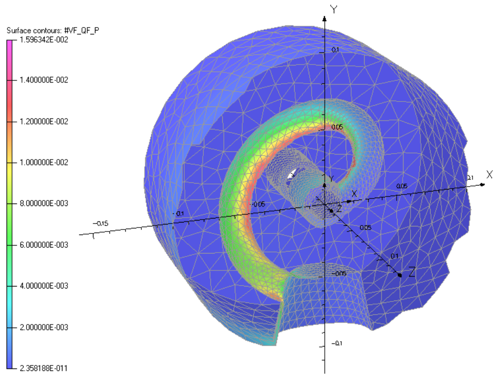

Figure 4: Resonance frequency as a function of the effective spiral arm length.

In Fig.4 the change of the first resonance frequency as a function of the rotation angle is displayed. The resonance frequency can be adjusted very smoothly over a range of more than 100 MHz, which underlines the flexibility of this structure.

### *Influence of a tuning cylinder*

During operation the resonance might get detuned by several effects like temperature drift, stress on the structure, aging processes or errors due to the driver. By introducing a tuning cylinder the resonance frequency can be fine-tuned to compensate these errors. The effect of a tune cylinder depends on its shape and insertion position. By introducing a tuning cylinder the resonance frequency can be fine-tuned over a range of aprox. 1 MHz to compensate these errors. During this process, the effective volume of the cavity is changed. Depending on the cylinder shape and its insertion position, a change in the inductance or capacity of the system is obtained. Depending on this coupling, the frequency can be changed according to $\omega \propto (LC)^{-1/2}$. In order to study these effects several simulations with different setups and varying insertion depths of up to 20 mm were performed. We concentrated on the following two parameters: cylinder radius (20, 25 and 30 mm) and the position of the cylinder. It can be seen that a strong influence of the tuning cylinder can only be found at the $0°$ position of the cylinder. Here, the resulting change is one order of magnitude higher than at the other two positions. This can be explained by the higher field level in this area, which is then displaced by the tuning cylinder. In total the frequency decreases to 7 MHz, which is more than enough to compensate detuning causes by heating or other effects. The change of resonance frequency as function of the insertion depth of the tune cylinder is shown in Fig.5 for the three different positions.

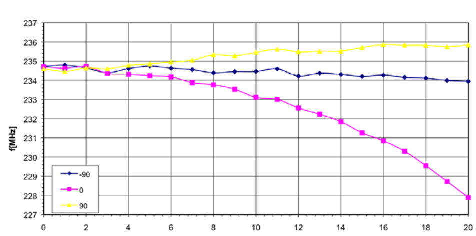


Figure 5: Resonance frequency as function of tune cylinder inserting depth at different positions and the same radius of 30 mm.

## COMPARISON OF THE RESULTS

The results of the shunt impedance of the initial model fit well with the simulation results and the built structure in [4]. Also the resonance frequencies found with SOPRANO are in the estimated range. Q values in the order of $10^4$ can be considered as typical for such copper structures as well as a shunt impedance of some M$\Omega$. In summary, these results are in very good agreement to earlier simulations and measurements and qualify OPERA for the design and simulation of such cavities.

## CONCLUSION AND OUTLOOK

OPERA/SOPRANO proved to be a useful tool to find resonance modes in complex 3D structures within a given frequency range and to investigate the properties of such structures in some detail. The code allowed us to analyze the 3D EM field distribution and in particular the influence of a tuning cylinder, which allowed for benchmarking against measurements.

The next step will be to develop a fully parameterized model of a spiral-loaded cavitiy which will allow for a flexible optimization of the whole structure to most different boundary conditions. By using OPERA's internatl optimizer we are aiming for substantially improving the layout of these structures.

## REFERENCES

[1] J. Häuser et al., "Properties of Spiral-Loaded Cavities" Proc. EPAC 1988, 1140.

[2] A. K. Mitra et al., "A 35 MHz Spiral Re-Buncher Cavity for the TRIUMF ISAC Facitlity", Proc. PAC 1999, 839.

[3] C.P. Welsch et al., "Development of Rebunching Cavities at IAP", Proc. LINAC 2000, 938.dc

[4] K. Kühnel, "Design und Aufbau eines Fingerdriftröhren-Beschleunigers", Dissertation, University of Frankfurt, 2005.

[5] Vector Fields Inc , `http://www.vectorfields.com/`

[6] T. Wangler, "RF Linear Accelerators", - 2., completely rev. and enl. ed.. - Weinheim : Wiley-VCH, 2008.

# DEVELOPMENT OF A HIGH-PRESSURE CHEMICAL ETCHING METHOD AS A SURFACE TREATMENT FOR HIGH-FIELD ACCELERATING STRUCTURES MADE OF COPPER

Hiromitsu Tomizawa, Tsutomu Taniuchi, Hideki Dewa, Akihiko Mizuno, Hirofumi Hanaki,
Accelerator Division, Japan Synchrotron Radiation Research Institute (JASRI/SPring-8),
Kouto, Sayo-cho, Sayo-gun, Hyogo 679-5198, Japan

### [illegible]

The acceleration gradient is limited by rf breakdown in accelerating rf structures, as well as by the surface condition of the inner wall. Surface treatment is an important technique for achieving the maximal acceleration gradient of accelerating rf structures. We chose chemical etching as a surface treatment method for accelerating rf structures made of copper (OFC). A maximum cathode surface field of 183 MV/m was achieved for an S-band (2856 MHz) pillbox-type single-cell rf gun cavity with this surface treatment under an rf-conditioning elapsed time of $1.9\times10^7$ shots (21 days) in 2004. Furthermore, we developed a high-pressure chemical etching method for complex inner structures in 2006. The results showed that the higher the pressure, the higher the cathode surface field (162 MV/m; 6 atm).

## INTRODUCTION

We have been developing a surface treatment method for optimizing the surface condition of the inner wall in order to achieve a maximum cathode surface field of ~200 MV/m. The acceleration gradient is limited by the rf breakdown in accelerating rf structures, as well as by the surface condition of the inner wall. Surface treatment is an important technique for achieving the maximal acceleration gradient in accelerating rf structures. It is necessary to realize chemically noncontaminated and physically smooth surfaces. In accelerator fields, oxygen-free copper (OFC) is widely used as a base material for normal conducting accelerators. Previously, we chose chemical etching as a surface treatment method for accelerating rf structures made of copper after several failed attempts involving high-pressure pure water rinsing [1]. In order to study rf breakdown and the effects of surface treatment [2], we used an S-band (2856 MHz) pillbox-type single-cell rf gun cavity. The highest cathode surface field (183 MV/m) of the rf gun cavity was achieved with this surface treatment under an rf-conditioning elapsed time of $1.9\times10^7$ shots (21 days) in 2004 [3]. The SPring-8 rf gun has been operating with the world's highest gradient of 190 MV/m [4]. This indicates that our treatment is remarkably effective in improving the properties of the inner cavity surfaces, which are made of copper (OFC). Furthermore, we developed a high-pressure chemical etching method for achieving more complex inner structures in 2006 [5]. Using a cartridge-type revolver photocathode rf gun [6], high-field experiments were performed with cathode plugs subjected to chemical etching at different pressure conditions. We found that the higher the pressure, the higher the cathode surface field. Here, we report these novel results regarding the highest gradient, which were obtained by using test copper (OFC) samples treated with high-pressure chemical etching.

## CHEMICAL ETCHING AND ITS OPTIMUM CONDITIONS

### [illegible]

Chemical etching entails a chemical reaction between an acid and a metal. We used an etching solution composed of sulfuric acid ($H_2SO_4$) and hydrogen peroxide ($H_2O_2$), each at 2 wt% standard concentration, in order to make the processing time loss negligible in relation to the etching rate at room temperature.

### [illegible]

Before etching, a copper test piece was dipped in Neos CM200C (5 wt%) solution at 40°C for 1.5 h as a degreasing preprocess. After rinsing in tap water for 5 min at room temperature, the copper test piece was etched with shaking to remove hydrogen bubbles from its surface. The etched copper test piece was then rinsed in pure water and then in ultrapure water for 1 min each at room temperature.

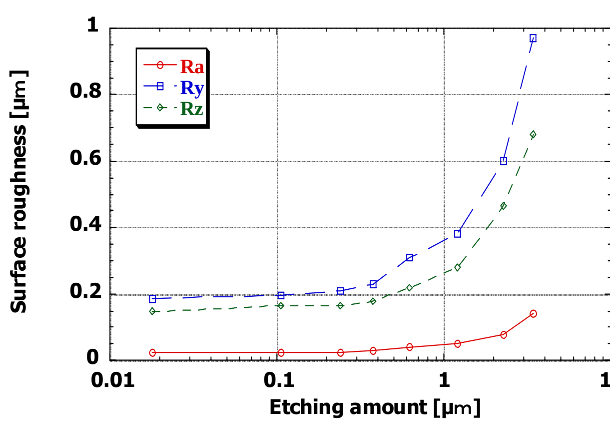


Figure 1: Dependence of the surface roughness on the etching amount in oxygen-free copper (OFC): After degreasing, Ra: 0.02 μm, Ry: 0.19 μm, Rz: 0.17 μm.

Chemical etching cleans the surface using a chemical reaction, resulting in physically rough metal surface. Therefore, we investigated the optimum etching conditions for copper test pieces. After a drying postprocess, the surface roughness of each test piece was measured with a chemical balance for the etching amount and Surftest SJ-301 (Mitutoyo). A laser microscope (VK-9500; KEYENCE) was used for measuring the grain size (see Figure 3) and for cross-checking surface measurements. Figure 1 shows that surface roughness does not increase in the region where the etching amount is less than 0.3 µm. Figure 2 indicates that the dipping time for our standard etching solution should be less than 2.5 min in order to keep the etching amount at less than 0.3 µm (Ra) at 20°C. It was ensured that the copper test pieces are comparable base materials in terms of grain size, impurities, and other properties. We observed the surface structures of each test piece with a laser microscope, and the obtained images are shown in Figure 3. For the etched copper test pieces, FTIR (IFS120HR; BRUKER) at SPring-8 BL43IR showed no significant chemical contamination (molecular bonding on the surface).

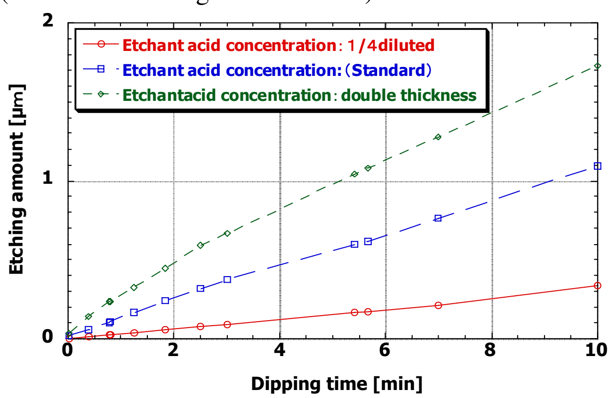


Figure 2: Dependence of the dipping time on the chemical etching amount at 20°C.

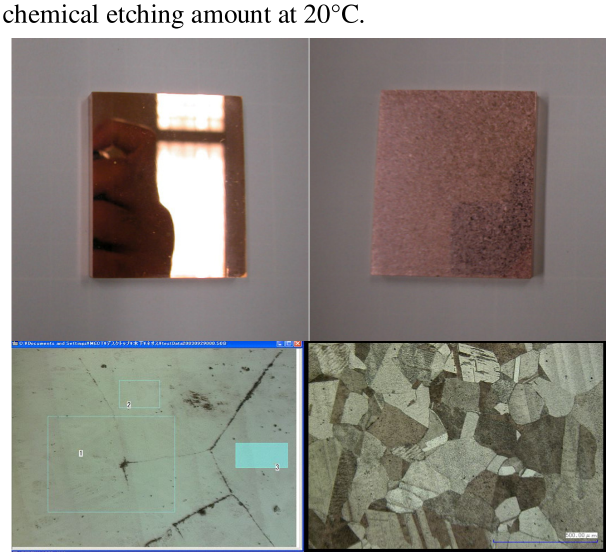

Figure 3: Effect on the structure of OFC due to chemical etching (Left: before etching; Right: after etching).

## FEASIBILITY TEST ON HIGH-FIELD ACCELERATION USING A CHEMICALLY ETCHED RF CAVITY

We performed experiments on high-field acceleration with an rf gun cavity using the etching process mentioned above. After the degreasing preprocess, the whole gun cavity made of copper (OFC) was dipped for 2.5 min in the etching solution of standard concentration at room temperature with shaking. Through a drying postprocess with nitrogen gas flow, the rf gun cavity was evacuated and installed in an aging test stand at SPring-8.

In the rf processing for 21 days ($1.9\times10^7$ shots), the maximum field gradient on the cathode reached 183 MV/m, as shown in Figure 4 [3]. Spark light spectrography showed that no significant rf breakdown occurred during this rf conditioning [2].

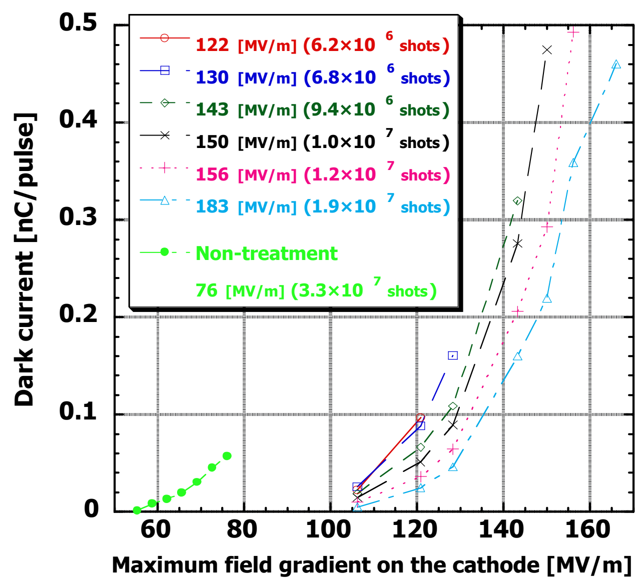


Figure 4: Dark current reduction during rf conditioning of an S-band pillbox-type single-cell rf gun cavity: In the figure, both the highest cathode surface field and the elapsed time of the rf conditioning are shown.

## HIGH-PRESSURE CHEMICAL ETCHING AND A TEST OF ITS FEASIBILITY

Using a simple single cell rf gun cavity, we proved that chemical etching is remarkably effective in improving the inner surface of cavities. Since the cavity structure was simple and relatively small, it was possible to simply shake the cavity during the process of dipping in the etching solution in order to remove hydrogen bubbles from the copper surface. However, in the case of accelerating structures longer than 1 m, the application of this method is not straightforward. In some parts of complex structures, hydrogen bubbles might serve as a masking layer against etching on the inner wall surface.

In order to apply our etching method even in complex rf structures, we developed a high-pressure chemical etching method [5]. In this method, remove hydrogen bubbles is performed by using high pressures and low temperatures during the etching process in order to dissolve hydrogen gas into the solution, in accordance with Henry's law. The first test was performed with a high-pressure chamber complex by using high-pressure argon gas, as shown in Figure 5. We performed experiments for high-field acceleration with a revolver-type of S-band rf gun system using a cartridge-type electric tube [6]. This system can accommodate 12 cathode tip plugs simultaneously, which can be replaced in vacuum. We performed high-pressure etching under different conditions on the OFC-cathode tips in the high-field acceleration test in comparable rf conditioning states. A high-pressure etching test stand was fabricated with multiple monitors in order to check the condition of the cathode tip surface (e.g., thermograph, manometers, and microscope cameras).

Figure 5: High-pressure (1~6 atm) chemical etching test stand for OFC-cathode tip plugs: the surface of the cathode tips was evaluated with a laser microscope.

Table 1: Maximum Surface Fields After rf Conditioning Under Different Conditions

HIP-[illegible]e[illegible]e[illegible] [illegible]e

| [illegible] | F[illegible]e[illegible] [illegible]e [illegible]e [illegible]e[illegible] | [illegible]e[illegible]e[illegible] e [illegible] [illegible] [illegible]e [illegible]e[illegible] |
|---|---|---|
| [illegible] | [illegible] [illegible]V/[illegible] | [illegible]2[illegible]e[illegible] ([illegible]) |
| [illegible] | [illegible] [illegible]V/[illegible] | [illegible]2[illegible]e[illegible] ([illegible]) |
| [illegible] | [illegible]5[illegible] [illegible]V/[illegible] | 2[illegible]8[illegible]e[illegible] ([illegible]2.[illegible]) |
| 5 [illegible] | [illegible]58.8[illegible] [illegible]V/[illegible] | 28[illegible]e[illegible] ([illegible]) |
| [illegible] | [illegible]2.[illegible] [illegible]V/[illegible] | 8[illegible]5[illegible]5[illegible]e[illegible] (22.[illegible]) |
| [illegible] e[illegible] | [illegible] [illegible]V/[illegible] | 2[illegible]e[illegible] ([illegible]2[illegible]) |
| [illegible] e[illegible] | [illegible] [illegible]V/[illegible] | [illegible]e[illegible] (2[illegible]) |
| [illegible] e[illegible] | [illegible]2[illegible] [illegible]V/[illegible] | [illegible]2[illegible]5[illegible]e[illegible] (2[illegible]2[illegible]) |
| [illegible] e[illegible] | [illegible] [illegible]V/[illegible] | 82[illegible]2[illegible]e[illegible] (22.8[illegible]) |

[illegible]-HIP-[illegible]e[illegible]e[illegible] [illegible]e

| [illegible] | F[illegible]e[illegible] [illegible]e [illegible]e [illegible]e[illegible] | [illegible]e[illegible]e[illegible] e [illegible] [illegible] [illegible]e [illegible]e[illegible] |
|---|---|---|
| [illegible] | [illegible]58 [illegible]V/[illegible] | [illegible]e[illegible] (8[illegible]) |
| [illegible] | [illegible] [illegible]V/[illegible] | [illegible]2[illegible]e[illegible] ([illegible]) |
| [illegible] | [illegible]5[illegible] [illegible]V/[illegible] | 2[illegible]8[illegible]2[illegible]e[illegible] ([illegible]) |
| [illegible] | [illegible]5[illegible] [illegible]V/[illegible] | 258[illegible]8[illegible]e[illegible] ([illegible]) |
| [illegible] e[illegible] | [illegible]25.[illegible] [illegible]V/[illegible] | 82[illegible]5[illegible]e[illegible] (22.[illegible]) |
| [illegible] e[illegible] | [illegible]28.[illegible] [illegible]V/[illegible] | 8[illegible]e[illegible] (2[illegible]2[illegible]) |
| [illegible] e[illegible] | [illegible]2[illegible] [illegible]V/[illegible] | [illegible]52[illegible]e[illegible] ([illegible]2.[illegible]) |

H[illegible]e[illegible]e[illegible]e e[illegible] [illegible] [illegible]e[illegible].

In Table 1, 1 atm indicates atmospheric pressure without additional pressure. We conducted a feasibility study of the effect of high-pressure chemical etching on the non-HIP-treated OFC-cathode surface condition with high-field acceleration. Before testing the etched cathodes, rf conditioning was performed on non-etched cathode plugs. Table 1 shows that the highest cathode surface field could not exceed 135 MV/m without etching. The test was performed with a blind check in order to avoid biased interpretation. The results show that the higher the pressure, the higher the cathode surface field. The effect of HIP-processed base materials on the realization of the highest cathode field is not highly significant from a statistical point of view.

## SUMMARY

We chose chemical etching as a surface treatment method for accelerating rf structures made of copper (OFC). In this paper, we studied the effects of etching on the copper surface by using OFC test samples subjected to chemical etching under different pressures. In order to study the effects of the surface treatment through high-field acceleration, we first used an S-band pillbox-type single-cell rf gun cavity. After rf processing for 21 days ($1.9\times10^{7}$ shots), the maximum field gradient on the cathode reached 183 MV/m [3]. This indicates that chemical etching is remarkably effective in improving the inner surface of cavities made of OFC. The result of high-pressure chemical etching indicates that the higher the pressure, the higher the cathode surface field. The highest field achieved with the above method was 162 MV/m in the case of the HIP-processed sample subjected to chemical etching under a pressure of 6 atm.

We are currently preparing a high-pressure chemical etching test facility for rf accelerating structures (Figure 6). In this system, a 1-m-long accelerator tube can be directly etched under a pressure of up to 10 atm.

Figure 6: High-pressure chemical etching test facility for rf accelerating structures made of OFC.

## REFERENCES

[1] H. Tomizawa, et al., Proc. of the 28th Linear Accelerator Meeting in Japan, 2003, p. 132.
[2] H. Tomizawa et al., Applied Surface Science, 2004 235/1-2, 2003, p. 214.
[3] H. Tomizawa, et al., Proc. of the 29th Linear Accelerator Meeting in Japan, 2004, p. 147.
[4] H. Tomizawa, the 3rd PASJ Prize Award for Young Scientists, Proc. of the 4th Annual Meeting of Particle Accelerator Society of Japan, 2007, p. 130.
[5] H. Tomizawa and H. Ohtsuka, Japan Patent Application No. 2007-84245.
[6] J. Sasabe, et al., NIM A 528, 2004, p. 382.

# THE STATUS OF NEXTEF: THE X-BAND TEST FACILITY IN KEK

S. Matsumoto*, M. Akemoto, S. Fukuda, T. Higo, N. Kudoh, H. Matsushita, H. Nakajima, T. Shidara, K. Yokoyama, M. Yoshida, Accelerator Lab, KEK, Tsukuba, Ibaraki 305-0801, Japan

*Abstract*

Nextef is the 100MW-class X-band (11.424GHz) RF test facility in KEK. By combining the power from two klystrons, 100MW RF power is produced. While the facility was originally planned to conduct fundamental research programs of RF breakdown issues, it will be used as the one of the high power station for new international research collaboration on the study of future high gradient linear accelerators. A series of high gradient test structures are being tested at the facility. The gradient is as high as 100MV/m.

## INTRODUCTION

XTF (X-band Test Facility) was the test facility for X-band accelerator structures in KEK which had run during 2003~2007. It was eventually evacuated in May 2007 due to the termination of R&D program of normal conducting linear collider (LC) project. Most of the key equipments and essential components of XTF were selected and moved into the "new place", KEKB Injector test area, to be reassembled them as Nextef (stands for NEw X-band TEst Facility), based on the plan originally proposed to use this new facility for small size fundamental research programs for the development of high gradient normal conducting linear accelerator and its applications. The new place for Nextef is chosen since the facility can be jointly operated with KEKB Injector. This enables 6,000 hrs of annual operation of this facility.

In December 2006, a decision was made on Compact Linear Collider (CLIC). They optimized the operating frequency of the main linac from 30GHz to 12 GHz and relaxed the accelerating gradient from 150MV/m to 100MV/m [1]. In order to establish the feasibility of this parameter choice, we organized new international research collaboration with CERN and SLAC on the X-band accelerator structures in June 2007 [2].

To demonstrate such a high gradient (~100MV/*m*) accelerator structure, at least several tens MW RF power is necessary and Nextef meets this requirement. Although the construction of Nextef was still ongoing when the collaboration started, KEK has agreed to run this new facility for testing a series of X-band structures (T18 series) newly developed and prepared in this collaboration. There have been some active X-band test facilities at SLAC and Nextef plays a role of their new counterpart in this collaboration research.

The commissioning of Nextef has been done and the facility currently runs for its first testing of the structure, named T18_vg2.4_Disk #2 shown in Fig.1. As we will see below, we will conduct the tests of T18 structures at this facility for next two years. Our fundamental research program originally supposed to be done here, such as the study of high gradient RF breakdowns in narrow waveguides [3], is now being done at another X-band test station (Klystron Test stand). It is an individual 50MW RF station driven by a single klystron, located adjacent to Nextef, originally prepared for the X-band klystron tests. Although the available power is half to that of Nextef, this station is usable for small size experiment.

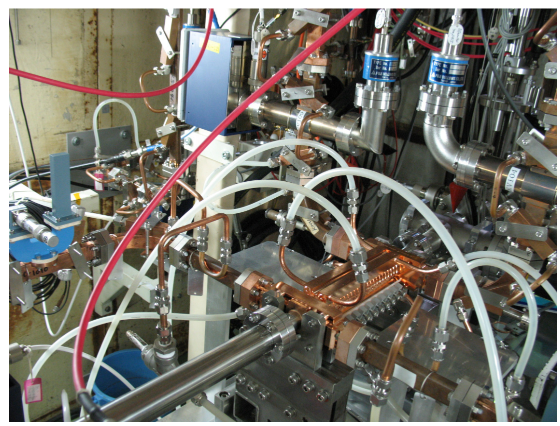

Figure 1: T18_vg2.4_Disk installed in Nextef.

## FACILITY

The configuration of Nextef is shown in Fig.2. The modulator drives two klystrons simultaneously. By combining the power from two klystrons, the maximum RF power of 100MW for 400ns can be produced. We employ twin PPM (Periodic Permanent Magnet) klystrons. The structures to be tested are installed in the bunker. The distance from the klystrons to the test area is about 16*m* [4]. About half of the distance, a circular waveguide is used to reduce the power loss. Two SLAC mode converters are mounted at both ends of the circular waveguide to transform rectangular WR90 TE10 mode ↔ circular TE01 mode. Measurement shows there is about 25% power loss in the power transmission. The specification of the facility is given in Table.1. For the details of each component, refer to [5].

Table 1: Nextef Nominal Specifications

| | |
|---|---|
| Frequency | 11.424GHz |
| Max power production | 100MW |
| Max power for test* | 75MW |
| Pulse width | 400ns |
| Repetition rate | 50pps |

* 25% power loss in the waveguide.

*shuji.matsumoto@kek.jp

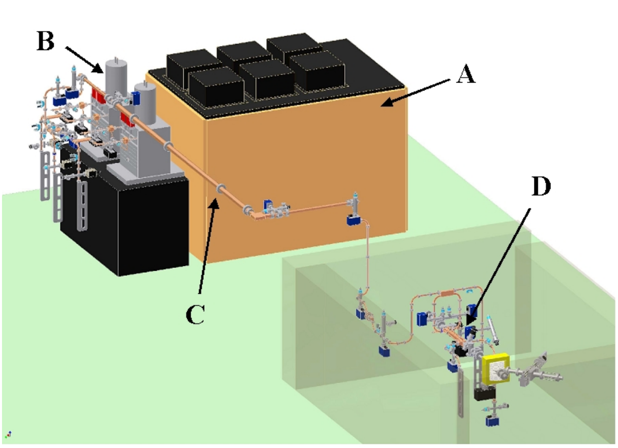


Figure 2: Configuration of Nextef. A: Modulator B: Klystrons C: Circular Waveguide D: Accelerator Structure in the Bunker. The control hut is not shown explicitly in the figure.

The PLC mounted on the modulator, which primarily controls the modulator, plays the central role in the control of whole facility. It monitors the status of the modulator as well as that of other devices such as the klystrons and waveguide. Remote access is also through this PLC. The data such as the charging voltage or RF power vacuum and temperature are logged in the storage area linked to those of KEKB Injector. Some oscilloscopes are used to monitor high voltage and RF pulse waveforms and a local PC collects and stores these waveforms regularly.

The beam-line (although we have no beam here) setup in the bunker is shown in Fig. 3. Several crystal detectors monitor the RF pulses propagating into or from the test structure. In order to identify the location of breakdown, we use X-ray detectors, consisting of scintillators and photomultipliers, as well as the acoustic sensors on the structure. The dark current is detected and monitored by the profile monitors and the Faraday cups placed along the beam line. The energy spectrum of the dark current can be measured with the analyser magnet.

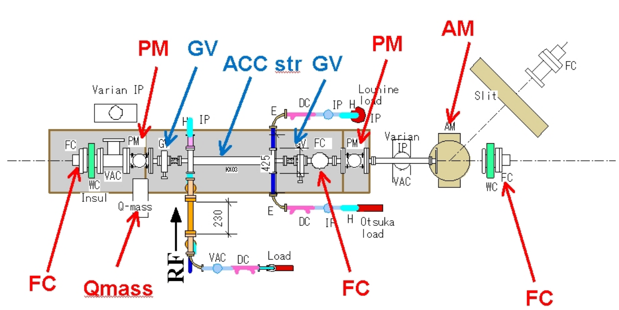


Figure 3: Plan view of Nextef beam-line setup. ACC: Space for Accelerator Structure to be tested. FC: Faraday Cup, PM: Profile Monitor, AM: Analyser magnet, GV: Gate Valve.

## COMMISSIONING

After the construction work being finished, we begun to run Nextef, starting with the diode operations of the klystrons. From November 2007, we started the operation with RF. We conditioned the waveguide terminated with RF load before the accelerator structure being installed. In the run from May 23 to June 4 2008, we have achieved 90MW RF production (equivalent to 65MW feed to the structure) with 210ns pulse width and 25pps repetition rate. Though this power is smaller than the specification of the facility, it suffices for T18 series structure tests.

Before we install the structure to be tested, we installed an old structure KX03 instead in June 2008. (KX03 is a 60cm-long X-band structure which is the latest model of the series of prototype LC accelerator structures, achieved the unloaded accelerating gradient of 65MV/*m* with the breakdown rate of ~$10^{-6}$ per pulse at XTF [6].)

From June 11 we started the run with KX03 to commission the detectors and data acquisition system for the breakdowns and to confirm the way to identify the breakdown event, which is crucial for the structure tests. A typical example of the RF waveforms recorded at a structure breakdown event is shown in Fig. 4.

The video signal from the crystal detector monitoring the reflected power can be used for the breakdown identification. Also do the signals from the Faraday cups. Actually those signals are used for the system interlock to inhibit the next RF trigger once the breakdown is detected. Disappearance of transmitted power through the structure also looks usable but is not included in the interlock.

We will prepare fast pulse-to-pulse RF waveform analysis, which is important for the breakdown study, by Tektronix 7054. It can store the waveforms consecutively over several pulses inside and put them out when the breakdown occurs. We have the data of waveforms not only the pulse with breakdown but those of previous pulses.

The power needed to produce 100mV/m gradient in T18_vg2.4_Disk structure is about 60MW with 300ns pulse width. This power was established in this run as shown in Fig. 5.

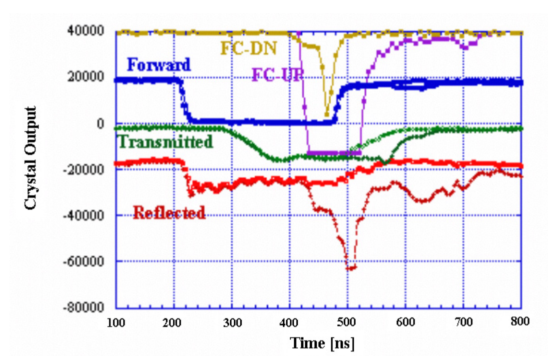


Figure 4: RF waveforms at a breakdown event. Crystal detectors monitor the power of forward to, transmitted through and reflected from KX03 structure. Faraday cups (FC) of both DN (downstream) and UP (upstream) detect anomalous current.

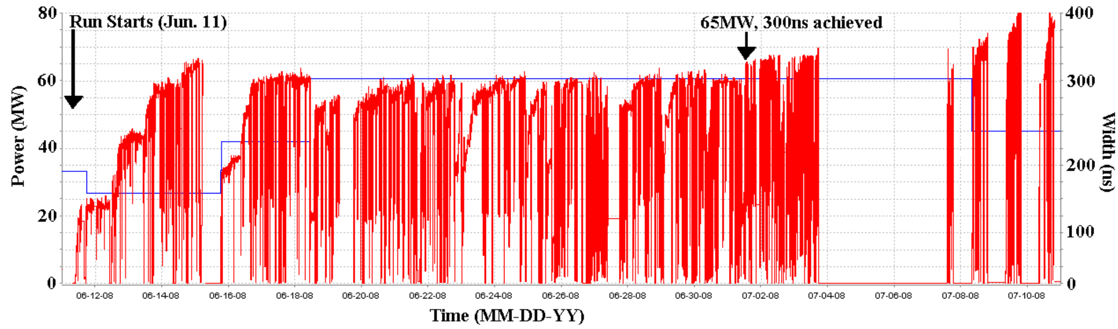


Figure 5: The RF input power to KX03 accelerator structure (red line) and pulse width (blue). One-month history plots of these values in commissioning run starting Jun. 11 2008 with KX03 structure installed. The power of 65MW with 300ns was achieved on Jul.1. Note that Nextef operation was done on daytime after July 4, since KEKB Injector was in scheduled long-term shutdown from this date.

## STRUCTURE TEST & FUTURE PLAN

T18_vg2.4_Disk is the first accelerator structure to be tested at Nextef. This is a disk loaded 18-cell structure without HOM damping slots, designed vg /c varies from 2.6 to 1.0. Its design and fabrication was done during 2007-2008 in the collaboration among KEK, CERN and SLAC. It was planned to make four identical T18_vg2.4_Disk structures (#1-#4) under the same fabrication process. This enables us to check whether the same fabrication process can reproduce the same structure. The high power test of structure #2 has just started at Nextef while that of #1 has already been done at SLAC NLCTA[7]. Both test results of #1 and #2 will be compared.

As shown in Fig. 6, we are going to test a series of structures at least in next two years. Some structures are currently under fabrication process and already on the list to be tested at Nextef. TD18_vg2.4_Quad is a CLIC type structure consists of four quadrants and TD18_vg2.4_Disk is a disk-loaded structure with damping slots.

Here are a few comments on our other future plans.

1) C-band: We have a C-band accelerator program for KEKB Injector and we need to test a few C-band structures in next a few years. The bunker of Nextef will be used for these tests. X-band structure test may be stopped during the C-band tests since C-band test is not compatible with that of X-band (Nextef). The extension of the bunker is now under examination to find a way to do both tests individually.

2) Pulse compression: The maximum power available in Nextef for the structure is currently 75MW (50MW * 2 * 75%). This may not enough for the future structures to be tested at Nextef. A plan to install a pulse compression system is now under examination. The goal of the power is 150MW with 300ns by the compression rate is about 3. Design works for this project has just started. The installation of the system may be in the end of next year.

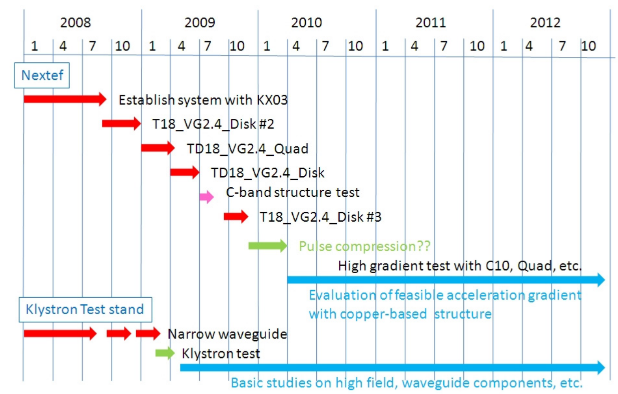


Figure 6: Planned schedule of the testing of structures in Nextef.

## REFERENCES


[1] H. H. Braun, “Toward a Multi-TeV linear collider Drive Beam generation with CTF3”, APAC’07, Indore, India, Feb 2007.

[2] The X-Band Accelerating Structure Design and Test-Program Workshop, June 18-19, 2007, CERN, Geneva, Switzerland; http://indico.cern.ch/conferenceDisplay.py?confId=15112.

[3] K. Yokoyama et al., “Characteristics of Different Materials on High-Gradient Experiments”, these proceedings.

[4] The power attenuation in WR90 rectangular waveguide is -0.1dB (-2.3%)/m @11.424GHz.

[5] S. Matsumoto et al., “Nextef: 100MW X-Band Test Facility in KEK”, Proceedings of EPAC2008, Genova, Italy, June 2008.

[6] T. Higo, et al., “High Gradient Study at KEK on X-Band Accelerator Structure for Linear Collider”, PAC’05, Knoxville, Tennessee, USA, May 2005.

[7] S. Doebert, “Status and Future Prospects for CLIC”, these proceedings.

# STATUS OF RF SOURCES IN SUPER-CONDUCTING RF TEST FACILITY(STF) AT KEK

S. Fukuda#, M. Akemoto, H. Hayano, H. Honma, H. Katagiri, S. Kazakov, S. Matsumoto, T. Matsumoto, S. Michizono, H. Nakajima, K. Nakao, T. Shidara, T. Takenaka, Y. Yano, M. Yoshida, KEK, Ibaraki, 305-0801, Japan.

*Abstract*

The super-conducting RF test facility (STF) at KEK has been functional since 2005, and the STF phase-I, which involves the testing of a cryomodule with four superconducting cavities, is now under way. Furthermore, KEK will conduct the S1-global test and the STF-II project in the future. The S1-global test aims at evaluating the performance of the superconducting cavities provided by Japan and the international collaborators, USA and Europe. The phase-II project aims at testing RF unit of the proposed ILC. In this paper, we describe the current status of the RF sources in the STF phase-I and the development of RF source for future projects.

## INTRODUCTION

The superconducting RF test facility (STF) at KEK comprises two phases, as shown in figure 1, and has been operational since 2005 [1]. The STF Phase-I consists of a cryomodule with a four-cavity structure having a gradient of 35 MV/m and is being tested. In Phase-I, the high level RF (HLRF) team is planning to install two types of power distribution systems (PDSs) and conduct the associated R&D. The low level RF (LLRF) team is planning to test the digital feedback with vector sum control. The STF Phase-II employs one RF unit, which is similar to the ILC baseline configuration design (BCD) layout. Phase-II employs beam acceleration to evaluate the entire linac system. The construction of STF-II is delaying and it is scheduled from 2012 to 2015. Recently, an S1-global phase was proposed; this phase will be completed before Phase-II of the STF. The S1-global phase will include two cryomodules with eight super-conducting cavities provided by Japan and international collaborators, USA and Europe. A different RF PDS scheme is tried to be used for evaluating the performance of the cavities, and currently, our efforts are focused on meeting the requirement to optimized operation of the cavities. In this paper, we describe the current status of the RF sources in the STF-I phase and the preparation of RF sources for future projects.

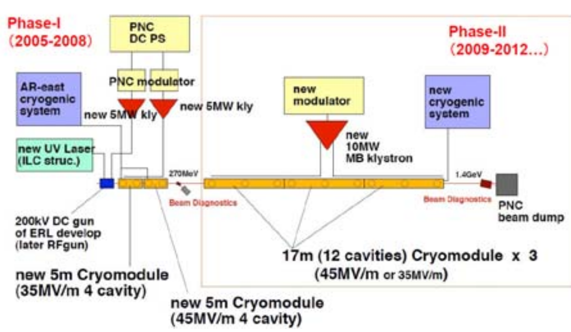


Figure 1: STF layout.

#Shigeki.fukuda@kek.jp

## HLRF

### Modulator and Klystron

The current STF RF sources comprise two stations. In the first station, a bouncer-type insulated gate bipolar transistor (IGBT) modulator is used along with a pulse transformer with a step-up ratio of 1:6. A 5-MW Thomson klystron, TH2104C, is used in this station; this klystron was previously used in the JAPAN HADRON PROJECT (JHP). The maximum available power of this station is 3.0 MW [1]. The power limitation is come from fast over-voltage protection for the IGBT switch which comprises 36 IGBT devices connected in series. The maximum voltage applied to a IGBT in the switch comes when the switch is turned off for a klystron gun spark, and must not exceed the maximum rating of 1200 V. The maximum IGBT switch operating voltage is 21.5 kV at the primary of the pulse transformer, which corresponds to a klystron voltage of 120 kV[2]. The RF source used in station no. 1 is utilized for conducting coupler processing tests and the STF-I experiment. Station no. 2 uses another bouncer-type IGBT modulator with a pulse transformer having a step-up ratio of 1:15 [3]. A 5-MW Thales klystron, TH2104A, is used in this station. The performance of the bouncer circuit in both modulators was excellent and a flat-top of less than ±0.8% was achieved in both modulators. A breakdown failure of the IGBT modulator in station no. 2 occurred due to a water leak in the pulse transformer; therefore, we have been checking the protection system for the shorting the undesired load ever since. The layout of the STF is shown in figure 1. We will introduce a third modulator and a 10-MW multi-beam klystron in the STF phase-II. We will select this modulator from two candidate modulators—the bouncer-type modulator and a Marx modulator.

### PDS for STF-I

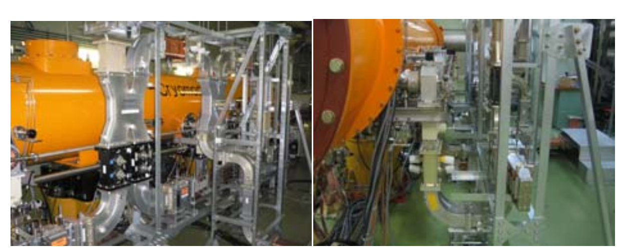

Figure 2: Tree type PDS connected to cryomodule.

As described in ref [1], we prepared two types of PDSs: a tree-like PDS using 3 dB hybrids and a TESLA test facility (TTF)-like linear power distribution network. Although a 5-MW circulator is installed at the output waveguide of the klystron, both PDSs utilize circulators at the upstream of the cavity couplers; four circulators were developed by SPA Ltd., Russia and four were developed by Nihon Kosyuha, Japan, as described later in this paper. Two systems will be tested in the STF Phase-I this year. Figure 2 shows the tree-type PDS connected to the STF cryomodule. PDS is evaluated by investigating several themes. The tree-like PDS employs 3-dB hybrids with a variable tap-off (VTO), which the power dividing ratio is adjusted by the depth of the button of the hybrid divider. This enables us to vary the power dividing ratio from 2.5 to 3.5 dB. If the cavities accept different allowable powers, it is possible to vary the power of each cavity within this range. STF Phase-I tests are performed using circulators for all cavities; in the same testing period, performance tests without circulators are also planned. The 3-dB hybrid with a VTO also changes the isolation between the two splitting waveguides, from 25 to 40 dB. We expect to study the effects of crosstalk between the reflections from the adjacent cavity with the function of the isolation when we eliminate the isolator. The total performance is evaluated under the condition of the vector sum control of LLRF. The cost impact of eliminating the circulator in the ILC design is large, and the circulator issues are important for investigating the HLRF performance in the STF. These tests will be conducted in November 2008.

## *Developed Waveguide Components*

In order to perform the planned tests for S1-global, STF-I, and STF-II, we developed the key waveguide components such as the phase shifter and reflector that allow us to change either the power level or the loaded Q

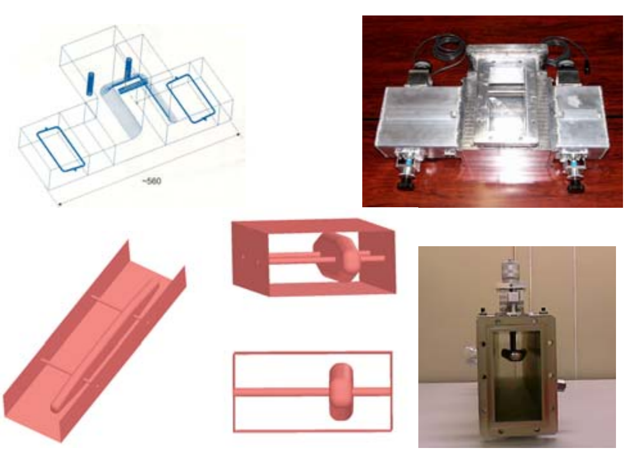

Figure 3:Top shows phase-shifter with two reflectors: top left, schematic drawing and top right, outer view. Bottom shows phase shifter with a plate; bottom left and middle shows schematic draw and bottom right shows outer view.

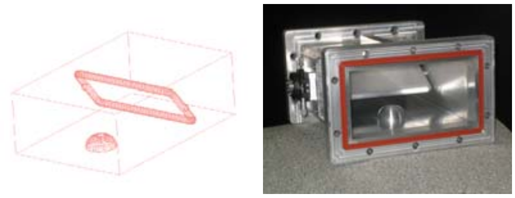

Figure 4: Left shows the schematic draw and right shows the outer view of reflector.

value of the cavity. The 3-dB hybrid with a VTO is an example of a simple power-varying component and is used in the tree-like PDS. We purchased four circulators from Russia, which are used in DESY and also developed the equivalent circulators at the Nihon Kosyuha Corp. in Japan. The circulators would be operated successfully up to 500 kW with a pulse width of 1.5 ms and a pulse repetition rate of 50 pps. The Japanese circulator has an insertion loss of 0.15 dB, which is slightly larger than that in the Russian circulator. Apart from the phase shifter used in DESY, KEK developed several different types of phase shifters, as shown in figure 3. We manufactured three phase shifters with a moving plate, as shown in figure 3, and used them in the liner PDS. Another important component is a reflector, which varies the power and the loaded Q value. Figure 4 shows a schematic representation of a reflector. A reflector can be used in combination with a phase shifter as shown in figure 5. All components described here are successfully tested up to 2 MW with a pulse width of 1.5 ms and a pulse repetition rate of 50 pps.

## *PDS Layout for S1-global Plan*

If the cavities under test show a large variation in their parameters, an adjustment is required to ensure that all

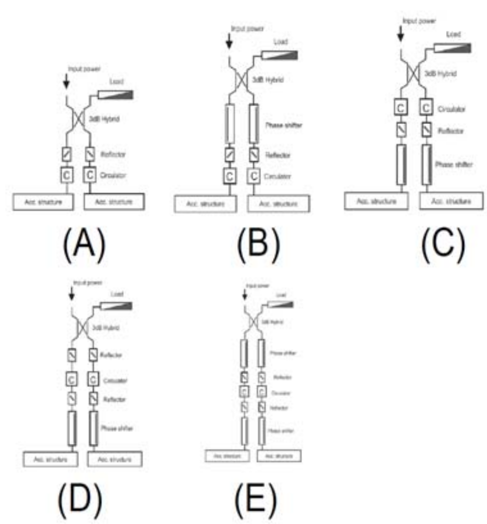


Figure 5: Schematic concept for changing a power, a phase and a loaded Q ($Q_L$) for the cavity in the PDS. (A) Power control, (B) power and phase control,(C) $Q_L$ control, (D)power and $Q_L$ control, and (E) power, phase and $Q_L$ control.

cavities have matched parameters. Figure 5 presents the techniques for changing the parameters such as the loaded Q, phase, and the power in the linear PDS. In the case of the proposed S1-global plan—in which superconducting cavities manufactured in three regions in the world will be evaluated—a large variation in the cavity parameters may exist. We plan to add a phase shifter and a reflector between the circulator and the cavity in the linear PDS to change the loaded Q value of the four cavities in the cryomodule. It is possible to vary the available power of the four cavities in another cryomodule by using a 3-dB hybrid with a VTO in the tree-like PDS. The schematic layout of the PDS for the S1-global plan is shown in figure 6. Figure 6 shows the two different PDS connected to the different cryomodules.

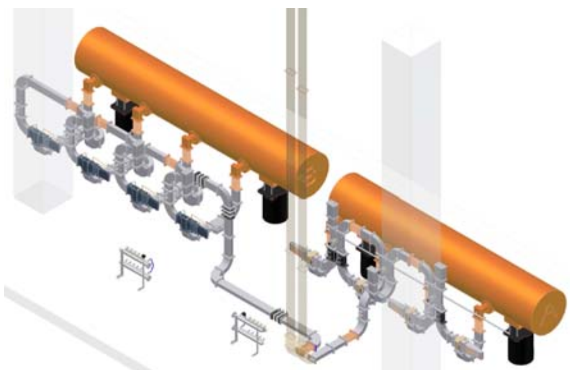

Figure 6: PDS planned in the S1-global. The right cryomodule is connected to the tree-like PDS with 3dB hybrid with a VTO. The left cryomodule is connected to the linear PDS having phase-shifters and reflectors in the down stream of the circulators.

### *PDS Layout for Phase-II*

Since phase-II aims at the construction and evaluation of one RF unit of the ILC BCD, a basic layout is the same as the layout shown in the RDR [4]. On the other hand, the GDE of the ILC is discussing more efficient and cheap layout. Though recently an RF cluster scheme is proposed, in which 35 to 37 RF stations in the surface combined the power up to 350 MW and this power is delivered to the linac, PDS in the tunnel seems to be basically the same. Circulator elimination and VTO components are R&D items. We are tentatively preparing for PDS based on the BCD.

## LLRF

After the LLRF evaluation using cavity simulator, several studies are conducted using super conducting cavity in STF-0.5. Feed forward control to vary the RF power with the step function in the 1.5ms pulse width were also done for cavity processing. For digital feedback control, the measured RF stabilities of the digital LLRF system at the STF were 0.04% in amplitude and 0.02°. in phase, respectively [4] and performance is shown in figure 7. The RF waveforms obtained using the digital LLRF system are utilized for the evaluation of cavity parameters such as microphonics and for determining Lorentz force detuning. Several studies related LLRF were performed. A digital LLRF control system with four intermediate frequencies was successfully operated [5]. Measurements of the feedback-instability by 8/9π and 7/9π modes were conducted to check the mode-mixing other than π mode [6]. Direct sampling test to input 1300 GHz signal to ADC by connecting fast-speed FPGA board was performed [7].

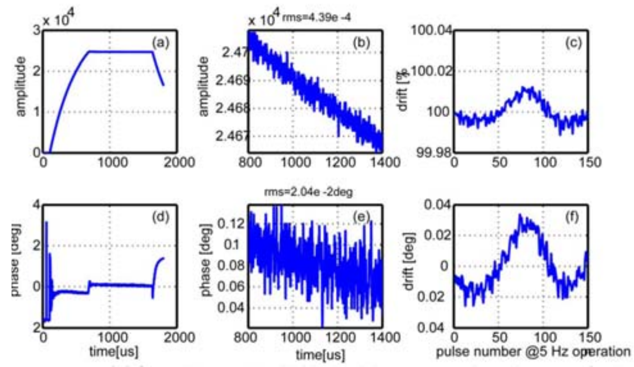


Figure 7: Performance of the llrf field regulation. Amplitude (a) and (b), drift of the amplitude during 30 seconds (150 pulses) (c), phase stability (d) and (e), drift of the phase during successive 150 pulses.

## SUMMARY

The STF at KEK has been operational since 2005; currently, the STF-I phase is being carries out. The operations of HLRF and LLRF for a single cavity have been successfully performed. The operation of four superconducting cavities is scheduled for November 2008, and further studies on HLRF and LLRF will be conducted: these studies will include the possibility of circulator elimination. Several waveguide components have been designed and tested up to two MW to achieve the requirements of phase-I and the S1-global cavity testing. The layout and the scheme of PDS for the achievement of requirements are described in this report.

### REFERENCES

[1] S. Fukuda, et al., “RF sources of Super-conducting Test Facility (STF) at KEK”, PAC05, Knoxville, TN, USA, 2006.
[2] M. Akemoto, et al., “Long-Pulse Modulator for the STF at KEK”, Proc. of 2007 IEEE Pulsed Power Conference, 2007
[3] H. Mori, et al., “Developments of Long-pulse Klystron modulator for KEK Super-conducting RF Test Facility”, PAC07, Albuquerque, NM, USA, 2007.
[4] http://www.linearcollider.org
[5] S. Michizono, “Performance of the Digital LLRF System for STF in KEK”, LINAC08.
[6] T. Matsumoto et al., “Performance of Digital LL RF Control System with Four Intermediate Frequencies”, LINAC08.
[7] T. Miura et al., “Measurements of the Feedback-Instability by 8/9π and 7/9 π modes at the KEK-STF”, LINAC08
[8] H. Katagiri et al., “Application of FPGA to Low Level RF Measurement and Control”, LINAC08.

# CHARACTERISTICS OF DIFFERENT MATERIALS ON HIGH-GRADIENT EXPERIMENTS

K. Yokoyama#, T. Higo, S. Fukuda, S. Matsumoto, Y. Higashi, N. Kudoh, Y. Watanabe, KEK, Ibaraki, Japan


### *Abstract*

RF breakdown is one of the major problems encountered in the development of accelerating structures that operate at high fields since the acceleration field is limited by the damage caused to metal surfaces. We examine electrical discharge characteristics such as breakdown rates and conduct surface observations of various materials in order to investigate the possibility of the stable operation of accelerating structures for high-field accelerations; a similar fundamental research has also been conducted at CERN and SLAC [1, 2,]. High-gradient RF breakdown studies have been in progress at Nextef (New X-band Test Facility at KEK) since 2006 [3, 4, 5]. In order to investigate the characteristics of various materials at high-gradient RF breakdown, we have performed high-gradient experiments by using narrow waveguides having a field of around 200 MV/m at a power of 100 MW. Copper (OFC) and stainless-steel (AISI-316L) waveguides were tested in order to perform high-gradient experiments at Nextef. The result of the experiment conducted at XTF (Old X-band Test Facility at KEK) suggested that the stainless-steel waveguide had a better performance than the copper waveguide, and it exhibited a lesser number of RF breakdowns at a higher electric field. This paper reports the results of breakdown rates and observations of the surface of stainless-steel waveguide subjected to high-gradient experiments.


## HIGH-GRADIENT EXPERIENTS

### *Narrow Waveguide*

A narrow waveguide was designed to obtain a group velocity of around 0.3 *c*, which is used to drive an LC accelerating structure, and a field gradient of approximately 200 MV/m at an RF power of 100 MW at the centre, as shown in Fig. 1. The geometry was transformed from the X-band rectangular waveguide (WR90). The height and the width were reduced from 10.16 mm to 1 mm and from 22.86 mm ($\lambda_g$ ~ 32.15 mm) to 14 mm ($\lambda_g$ ~ 76.59 mm), respectively. A narrow waveguide was constructed from four parts in the manufacture. After annealing in a hydrogen furnace, the narrow waveguide was processed by milling. The parts were chemically polished in an acid solution by 10 μm, following which they were brazed in a hydrogen furnace. A narrow waveguide having a voltage standing wave ratio (VSWR) of less than 1.1 is required for our experiments.

#kazue.yokoyama@kek.jp

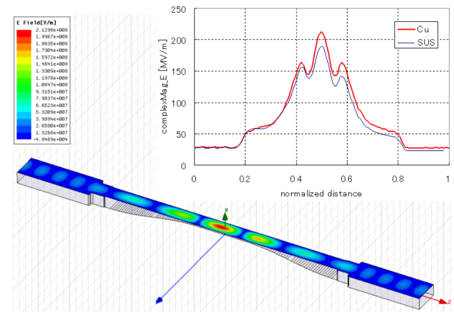


Figure 1: Electric field in a narrow waveguide at an input power of 100 MW obtained by the HFSS calculation.

### *Experimental Setup*

The setup for the high-gradient experiment is shown in Fig. 2. RF power is supplied to the narrow waveguide from a PPM-focused klystron that is operated at 11.424 GHz with a pulse width of 400 ns, pulse repetition rate of 50 Hz, and peak output power of approximately 50 MW. Transmitted and reflected RF waveforms are observed for breakdown events. An RF pulse is detected by using a crystal diode and a digital oscilloscope is used to calculate the power, VSWR, and power loss. All RF pulses are measured, and the digital data for 10 successive pulses is saved in order to analyze the RF waveforms when some interlock controls such as HV, Trig, and RF are tripped. In order to distinguish a breakdown in the narrow waveguide from one that occurs at another location, photomultipliers (PMTs) and acoustic sensors are placed along the waveguide.

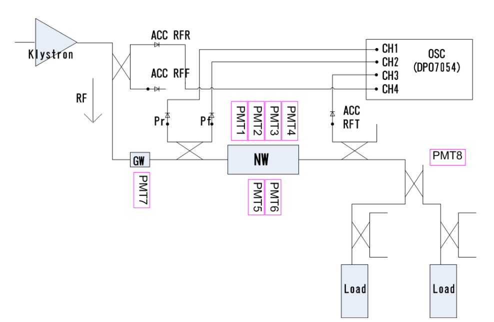


Figure 2: Setup of a high-gradient experiment conducted at Nextef.

During waveguide processing, the RF pulse width is increased from 50 ns to 400 ns, and an RF power of up to 50 MW at a repetition rate of 50 pps is supplied. The increase in the output power and the duration of incremented power are controlled by a computer in accordance with the past processing history depending on the experienced power and the pressure. When the pressure in the waveguide increases, the processing power is maintained constant until the pressure reaches a normal level. However, in case where the pressure increases significantly, the processing power is decreased, and processing is repeated from a lower power level in order to avoid serious breakdown damages to the waveguide.

## RESULTS

### *RF Processing*

The processing history and accumulated data for breakdown events that occur during the processing of #CU002 (copper) and #SUS003 (stainless-steel) waveguides are shown in Figs. 3(a) and (b), respectively. The first high-gradient experiment was conducted over a period of one month at the XTF using the #CU002 waveguide. The RF processing time was restricted to approximately 250 h due to a fixed XTF schedule. Therefore, we could not confirm whether the numbers of break down events were saturated or not but we could not keep operating of #CU002 due to a lot of breakdown. The second high-gradient experiment was conducted at Nextef using the #SUS003 waveguide. The existing interlock controls for RF processing and breakdown measurement systems were replaced with improved interlock controls during the processing of the #SUS003 waveguide. Almost half a year was required to complete the RF processing of RF components such as guard windows, directional couplers, and dummy loads. The RF processing time of the #SUS003 waveguide reached up to approximately 1200 h.

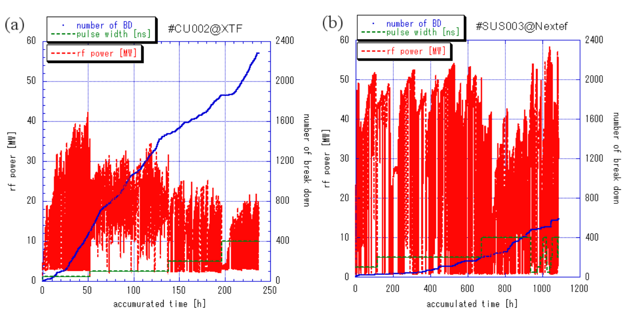


Figure 3: Power history of (a) #CU002 and (b) #SUS003 waveguides during processing.

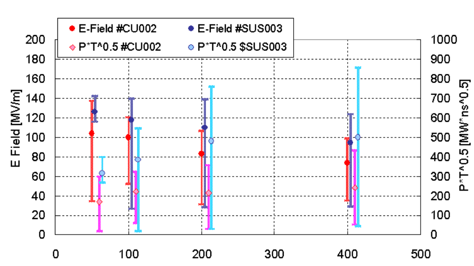


Figure 4: Experienced E-field and $P*T^{1/2}$ for #CU002 and #SUS003 waveguides.

Figure 4 shows the electric field and the temperature-related parameter $P*T^{1/2}$ (the product of the RF power and the square root of the pulse width) as the function of the pulse width of #CU002 and #SUS003. The results of these experiments indicated that the #SUS003 waveguide had a better performance than the #CU002 waveguide in that it exhibited a lesser number of RF breakdowns at a higher electric field. Figure 4 indicates that a higher RF power might be required in order to perform RF processing and to determine the power limit for sustaining a high electric field.

### *Breakdown Rates*

After RF processing, breakdown rates (BDRs) of the waveguide were measured as a function of the RF power and the pulse width in order to investigate their dependence on the material characteristics. A constant power was supplied for approximately 24 h, and the number of breakdown events was recorded. Figure 5 shows the BDRs of the #SUS003 waveguide as a function of the RF power. BDRs for a pulse width less than 100 ns are very low. Although the number of breakdown events fluctuates, it is observed that the BDR increases with power, and the relationship between the BDR and the input power is exponential, as shown in Fig. 5.

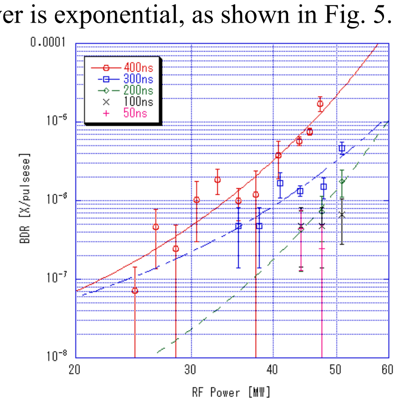


Figure 5: Breakdown rate as a function of pulse width of #SUS003 waveguide.

### *Surface Observations*

The material surfaces were observed using a laser microscope and a SEM. Figure 6 shows a drawing of the waiveguide and a overall picture of #CU002 and #SUS003 after cutting structures for surface observation after high-gradient experiments. Many breakdown (BD) damages were observed in areas that produced a high field on the E-plane surface. Figures 7 (a) and (b) show the laser microscope view and (c) shows the concavoconvex-view of #CU002 by laser scanning around the area. Similarly, Figs. 8 (a), (b), and (c) show the corresponding images of the #SUS003 waveguide. The magnification factor for both figures is the same; (a) 200, (b) 1000, and (c) 1000. Many peaks and valleys (~ 30 μm in height) are detected on the material surface in a high-field region, although details of the peaks observed using the laser microscope are different for the #CU002 and #SUS003 waveguides. In the wider hight region, we observed traces of a single BD and several single-BD patterns. The narrower-height region suffered extensive breakdown damage as a result of which it melted. We believe that #SUS003 melts more than #CU002; however, their peak heights are similar, althogh the fine structure of these surfaces differ significantly, as shown in Figs. 7(c) and 8(c). Examples of breakdown spots observed on the surfaces of (a) #CU002 and (b) #SUS003 by SEM are shown in Fig. 9. Under an SEM magnification factor of 1000, the breakdown spots in both materials are observed to have a similar melting pattern. Since the surface finishing and processing process of #CU002 differ from those of #SUS003, a precise comparison between the two remains difficult. In the future, we plan to conduct experiments using copper (#CU004) having the same machine-finished surfaces as stainless-steel (#SUS003) in order to obtain a more accurate comparison.

## SUMMARY

An experimental setup for conducting RF breakdown studies has almost been established at Nextef in KEK. Breakdown diagnoses including waveform analysis are being developed, and these will be useful for obtaining more reliable measurements of materials. Breakdown tests on different materials are also being performed. The prototypes #CU002 and #SUS003 have been tested under different systems, and their material surfaces have been observed after testing. Initial test results indicate that stainless-steel (#SUS003) probably has higher breakdown durability than copper (#CU002). In the future, we plan to test a narrow waveguide composed of #CU004 using the same system parameters and fabrication method as #SUS003 to validate the results obtained in the case of #CU002.

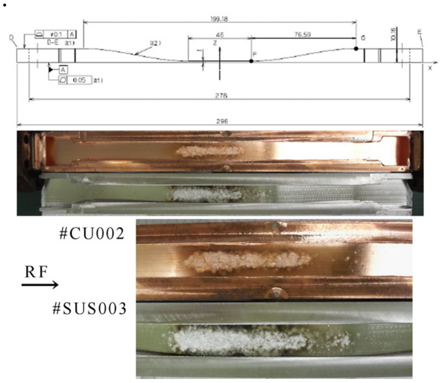


Figure 6: Waveguide drawing and surface #CU002 and #SUS003 after processing.

## REFERENCES

[1] A. Descoudre, et. al., "DC Breakdown Experiments for CLIC", Proc. of EPAC08, Genoa, Italy, June 23-27, 2008, pp.577-579.

[2] V. A. Dolgashev, S. G. Tantawi, "RF Breakdown in X-band. Waveguides," TUPLE098, EPAC'02, 3-7 June, 2002, Paris,. France, pp. 2139-2141.

[3] S. Matsumoto, et al., "The Status of Nextef; The X-band Test Facility in KEK", Proc. of LINAC08, Victoria, British Columbia, Canada.

[4] K.Yokoyama, et al., "High Field Performance in Reduced Cross-Sectional X-band Waveguides made of Different Materials", Proc. of PAC07, Albuquerque, NM, USA, pp.2119-2121.

[5] K. Yokoyama, et. al., "High-Gradient Experiments with Narrow Waveguides", Proc. of EPAC08, Genoa, Italy, June 23-27, 2008, pp.2758-2760.

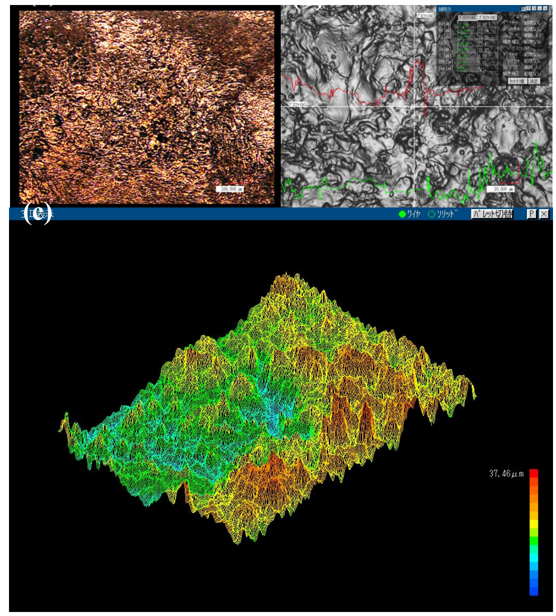


Figure 7: Surface observation of #CU002 by laser microscope. (a) and (b) show examples of the breakdown area at different scales, and (c) provides the birds eye view of laser scanned (b).

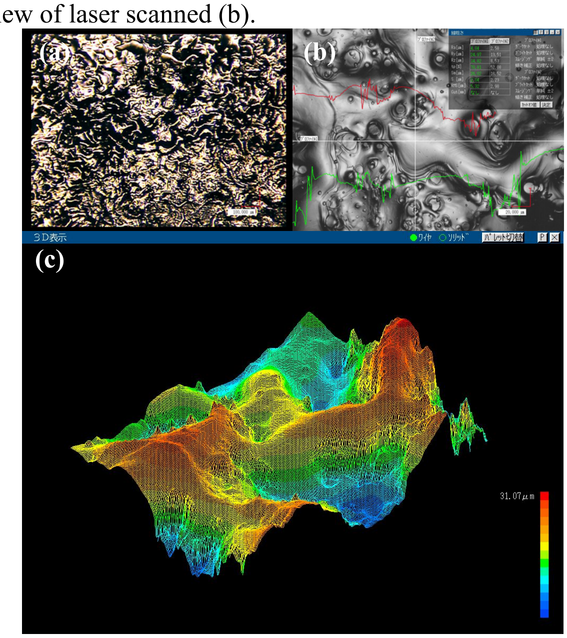


Figure 8: The same as Figure 7 for #SUS003.

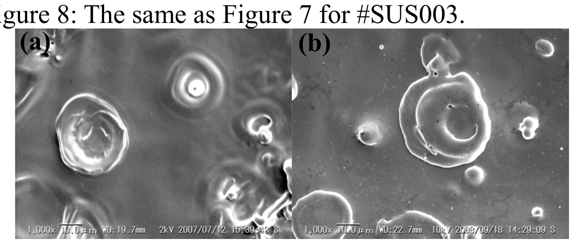


Figure 9: Examples of breakdown spots observed on the surfaces observation of (a) #CU002 and (b) #SUS003 by SEM.

# IMPROVEMENT IN THE ACS CAVITY DESIGN FOR THE J-PARC LINAC ENERGY UPGRADE

H. Ao*, K. Hirano, H. Asano, T. Morishita, A. Ueno, K. Hasegawa, J-PARC, JAEA, Ibaraki, Japan
F. Naito, M. Ikegami, Y. Yamazaki, J-PARC, KEK, Japan, V. Varamonov, INR, Moscow, Russia

*Abstract*

The ACS is the accelerating structure for the J-PARC Linac from 190-MeV to 400-MeV. The mass production of the ACS with a tight time schedule is now an issue. This paper mentions two main issues. The first one is that the coupling slot machining especially needed much long time on the fabrication process. We simplify the finishing of the coupling slot, comparing the surface roughness and the machining time. From the low-level measurements with the test cells, the simplified slot machining is judged to be acceptable for the practical cavity. The second one is that the coupling mode frequency has about 0.5 MHz error after the final brazing, because that the frequency shifts by the brazing are not stable. Thus, we consider the coupling mode frequency tuning by the fixed tuner after the final brazing. The equivalent circuit analysis shows that the -0.5 MHz accelerating mode error and +1 MHz coupling mode error brings the 3.7 % electric field error under the correction with the 12 coupling cells.

## INTRODUCTION

The ACS (Annular-ring Coupled Structure) cavities were under development for the J- PARC Linac [1, 2] from 190-MeV to 400-MeV. We have fixed the cavity specification, taking into account the results of the high-power conditioning [3] and the fabrication experience.

The mass production of the ACS with a tight time schedule is now an issue, since the user community strongly requests the beam power upgrade as early as possible. Therefore, the design and the fabrication process of the ACS cavity have been reexamined on the basis of the experience, stored during the course of the fabrication and the tuning of the prototype ACS tanks.

Here, we also discussed about the key issues on the mass production with a manufacturer. The cavity shape, that required complicated machining, was simplified to some extent, while the frequency tuning strategy was reconsidered to reduce the production period.

The present paper mentions two main issues about the recent progress of the ACS developments. The first one is the simplification of the coupling slot machining, and the other is the coupling mode frequency tuning after the final brazing. The following sections describe these results in detail with the background of these issues.

* hiroyuki.ao@j-parc.jp

## SIMPLIFY COUPLING SLOTS

### *Background*

The ACS cavity consists of many half-cell parts (cell), and vacuum brazing connects these cells. The 1300 cells are required for mass production (18.5 modules$\times$2 tanks$\times$17 cells$\times$2 parts/cell=1258), so that it is very important to reduce the machining time of the cell.

On the cell machining process through the several R&D modules, the coupling slot machining especially needed much long time. Although the modules brought good results through the high-power conditioning, one slot machining required 3 hours 20 minutes with a 5-axis processing machine, thus one cell (4 slots) needed more than 13 hours only for the slot machining.

We, therefore, simplify the finishing of the coupling slot, comparing the surface roughness and the machining time for each machining step.

The four test cells are machined with the reexamined process. And then, the RF properties are measured to compare frequencies and Q-values before and after the simplification.

### *Machining Process*

The new slot machining (See Fig.1) takes only 46 minutes that is much shorter than the original of 3 hours 20 minutes. The total machining time with a 5-axis processing machine will be reduced from 1.5 day/cell to 1 day/cell. It means that, at a rough estimate, the 1300 cells require two years and two months. It seems that it is the acceptable period for the mass production.

In this new machining process, we also restrict the movement of the tool within XYZ-axes and a rotation around the beam-axis. This restriction for the 5-axis "simultaneous" processing allows the machining process without the input programs that have been developed more than one month. It also makes very easy for an operator to input and change parameters, even though we use a 5-axis processing machine.

It is another great advantage to skip the programming process other than the machining time. The main reason for the long time development is not only the complicated structure of the ACS, but also the inefficient machining as, for example, it takes much more time for the surface finishing in a very small area.

Continuously, we are interested in simplifying the machining process for the other parts to optimize the balance between the machining time and the cavity properties.

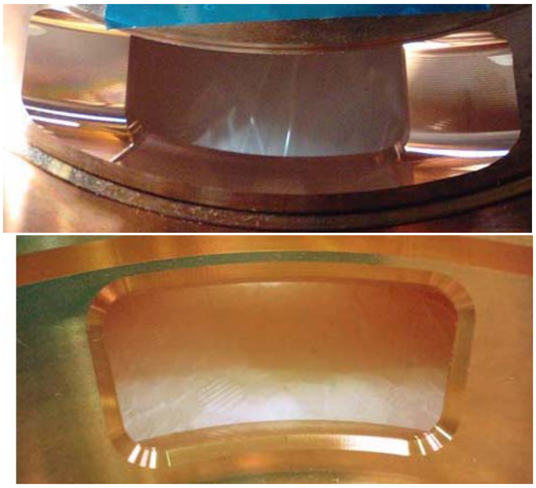

Figure 1: Simplified machining slots. The top is the coupling cell side view, the bottom is the accelerating cell side view.

### *Test Cell Measurements*

The four test cells (#B, #C, #D and #E) are fabricated and measured to compare the frequencies. Table 1 summarizes these results.

Table 1: Frequency and Q-value of the original machining and simplified test machining

| | Average freq. of the original cells (Q) | |
|---|---|---|
| Acc.mode | $973.52 \pm 0.08$ MHz $(8300 \pm 900)$ | |
| Coup. mode | $978.56 \pm 0.02$ MHz $(5000 \pm 1800)$ | |
| Coupling | $5.931 \pm 0.006$ % | |
| | Test E+B | Test C+D |
| Acc.mode | 974.27 (8290) | 974.29 (8170) |
| Coup. mode | 983.54 (3620) | 983.57 (4570) |
| Coupling | 5.776 % | 5.796 % |

The test cell Q-values of the accelerating cell are as same as the original error range of $8300 \pm 900$. Although the test cell Q-values of the coupling cell are a little smaller than the original of $5000 \pm 1800$, they are acceptable change.

From these low-level measurements, the simplified slot machining is judged to be acceptable for the practical cavity, although the small corrections are required for the frequency tuning about the accelerating and coupling mode frequencies.

## FREQUENCY TUNERS ON THE COUPLING CELL

### *Background*

The accelerating and coupling cell frequencies of the ACS cavity are tuned with the additional machining before the brazing process. Although the frequency tuning includes the frequency shifts by the brazing, these shifts are not stable and they bring the error of 0.1 MHz for the accelerating mode frequency and 0.5 MHz for the coupling mode frequency after the final brazing.

In the present design, the accelerating mode frequency can be tuned to the operating frequency by the movable tuner, the coupling mode frequency, however, has no tuning method after the final brazing.

The coupling mode frequency error reduces the recovering effect from the tilt of the electric field distribution.

Thus, we consider the coupling mode frequency tuning by the fixed tuner after the final brazing. The number of tuners should be minimized for the cost reduction in the mass production.

In the following section, the equivalent circuit analysis [4] simulates the error correction for the coupling mode frequency. This simulation evaluates the fluctuation of the electric field amplitude under the assumed frequency errors, a tuner arrangement and the corrected coupling mode frequency.

### *Equivalent Circuit Analysis*

Table 2 shows the parameters for these simulations. We assume that the accelerating mode and the coupling mode errors are -0.5 MHz and +1 MHz respectively. This accelerating mode error of -0.5 MHz is based on the experience of the R&D modules of $\pm 0.3$ MHz. The coupling mode error of 1 MHz includes not only the brazing shift of 0.5 MHz, but also the more large tolerance for the frequency tuning in the future. This error is also assumed to be the reversed sign of the accelerating one, which intends to be more critical situation for the field tilt.

Table 2: Accelerating cell (AC) and coupling cell (CC) parameters for the simulation

| | | |
|---|---|---|
| Number of total cell | 77 | Acc. tank (17 ACs+17 CCs)×2 + Bri. tank (5 ACs+ 4 CCs) |
| ACs error | -0.5 | MHz |
| CCs error | +1 | MHz |
| Coupling | 6 | % |

As the first step of the simulation to see the trend of the electric field, we evaluate the two type corrections: corrected by the every two coupling cells, and by the every four coupling cells. Figure 2 shows these results. The correction amount of the frequency is so adjusted that the electric field amplitudes at the both end-accelerating cells (#1 and #17) are equal in the one accelerating tank. The corrections are uniform for the all coupling cells in this simulation.

Here, this amplitude error is defined as (Max.-Min.)/Average, so that the two errors are 3.7 % for the every two cells correction (red) and 10 % for the every four cells (blue) as shown in Fig. 2. In this case, the correction amounts of the frequency are -0.8 MHz for the every two cells correction (red) and -2.3 MHz for every four cells correction (blue) respectively.

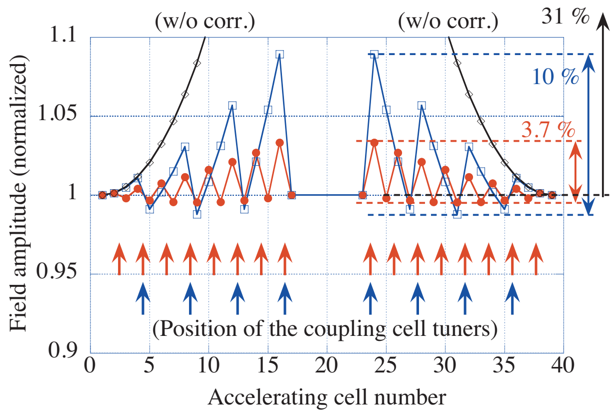


Figure 2: Simulated electric field distribution after the coupling mode frequency correction. The vertical axis is normalized at the first cell (#1). The arrows indicate the tuner position for the coupling cells. The red plot shows the case of the every two cells correction, the blue plot shows the every four cells correction, and the black plot shows the without correction.

This result indicates the small and distributed coupling cell tuners are suitable for the small fluctuation of the electric field more than the large and localized tuners.

The above result also shows that the electric field error is accumulated from the end cell to the center cell. Thus, the other solutions are expected for the small error of 3.7 % with less number of tuners.

For the next step, we rearrange the tuner and readjust the correction amounts of the frequency for the target of the 3.7 % error. Fig. 3 shows this results.

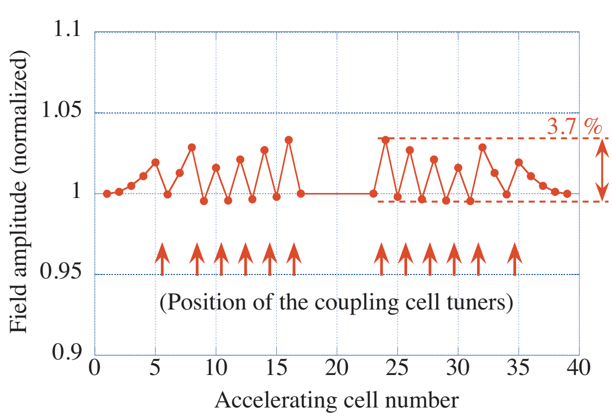


Figure 3: Simulated electric field distribution after the coupling mode frequency correction. The vertical axis is normalized at the first cell (#1). The arrows indicate the tuner position for the coupling cells. The total 12 coupling cells are corrected mainly around the center part of the module.

As shown in Fig. 3, this solution can suppress the electric field error under 3.7 % with reducing four tuners from the solution of Fig. 2. In this case, the amounts of the frequency tuning are -1.8 MHz for the two outside tuners (#5, #8, #31 and #34) and -0.8 MHz for the other tuners.

### *Tuner design*

Based on the results in the previous section, this section describes the basic concept of the fixed coupling cell tuner. Figure 4 shows the draft design of the tuner.

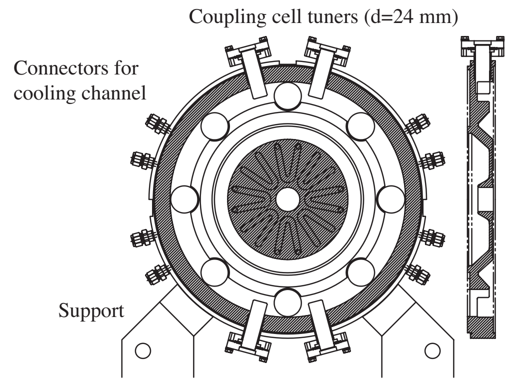


Figure 4: Draft design of the fixed coupling cell tuner. The four tuners are able to be attached for the maximum case.

The two tuners will be sufficient to correct the assumed frequency errors.(See Table 2) This reason is as follows. The tuner with 24 mm diameter in Fig. 4 can change the frequency up to 2 MHz evaluated from the MW-Studio (microwave studio). The required correction amount of the frequency is less than $\pm 1.8$ MHz, so that the two tuners can cover this correcting range.

Consequently, we fix that the baseline design has total 24 tuners on 12 coupling cells, and that the one coupling cell has the two tuners.

## SUMMARY

It was found that the simplified slot machining is acceptable for the practical cavity through the test cell measurement.

The equivalent circuit analysis shows that the coupling mode frequency error of +1 MHz brings the 3.7 % electric field error under the correction. For this correction, we consider that the baseline design has 24 tuners.

An R&D module including these improvements will be fabricated to confirm the properties under the high-power operation. The detail design and the further optimization for the mass production also will be developed with this module.

## REFERENCES


[1] Y. Yamazaki ed., "Accelerator Technical Design Report for J-PARC", KEK Report, 2002-13 (2002).

[2] V. V. Paromonov, "The Annular Coupled Structure Optimization for JAERI/KEK Joint Project for High Intensity Proton Accelerators", KEK Report 2001-14, 2001

[3] H. Ao et al. "First High-Power ACS Module for J-PARC Linac", Proc. of the 2006 Linac Conf., August 2006, p.725-727

[4] D. E. Nagle et al. "Coupled Resonator Model for Standing Wave Accelerator Tanks", Rev. Sci. Instr., 38 (1967), p.1583

# DEVELOPMENT OF RF CAVITIES FOR THE SHB SYSTEM OF THE L-BAND ELECTRON LINAC AT OSAKA UNIVERSITY

R. Kato, S. Kashiwagi, Y. Morio, S. Suemine, G. Isoyama[#]
Institute of Scientific and Industrial Research, Osaka University, Ibaraki, Osaka 567-0047, Japan

*Abstract*

Two 108 MHz and one 216 MHz RF cavities are developed for the subharmonic buncher system of the L-band electron linac at Osaka University. They are quarter-wavelength coaxial RF cavities made only of oxygen-free copper. Special care is taken to make their operation stable by keeping their temperature constant with cooling water. The cavities are successfully fabricated and commissioned.

## INTRODUCTION

A sub-harmonic buncher (SHB), which operates at a sub-harmonic of the RF frequency of a linac, is used to produce a single-bunch electron beam by preliminary bunching of electrons. The 40 MeV L-band linac at Osaka University operating at a 1.3 GHz frequency in the L-band is equipped with a three-stage SHB system and it is optimized to produce a high-intensity single-bunch electron beam. When constructed in 1978, it was equipped with a single 216 MHz quarter-wavelength coaxial RF cavity, frequency of which is a sixth sub-harmonic of 1.3 GHz, and afterward two 108 MHz, or 12th sub-harmonic RF cavities of the same type were added between the electron gun and the 216 MHz cavity, comprising a three-stage SHB system. The charge in a single bunch beam is higher than 30 nC/bunch in ordinary operation and the maximum charge so far realized reaches 91 nC/bunch with the SHB system.

The SHB system is turned on in the single bunch mode and the multi-bunch mode of operation of the L-band linac. The single bunch mode is used for laser-synchronized pulse radiolysis experiments in the time range down to femto-seconds and for basic study on Self-Amplified Spontaneous Emission (SASE) in the far-infrared region, and the multi-bunch mode is used for free electron laser experiments in the same wavelength region. These experiments require stable operation of the linac. Problems of the linac in these experiments were that it took three to four hours to warm up the linac after start-up in the morning and that a beam condition suddenly and sometimes changed, and their causes are found to be due to the SHB system. The RF cavities of the SHB system are made of clad plates of copper on stainless steel and they are cooled with water flowing through a copper pipe wound on the outside wall of the cavity, which is the stainless steel side of the outer conductor. The area of heat generation and the cooling part are away and cooling is made only by heat conductivity through a thin clad plate of copper and stainless steel, which makes the warm-up time longer, and when temperature of the clad plate varies, the cavities slightly change their shapes and sizes due to difference in thermal expansion coefficients of the two metals, which produces sudden changes of the beam condition. To solve these problems, we have fabricated new RF cavities for the SHB system that have higher temperature stability; two 108 MHz cavities and one 216 MHz cavities, which are designated from the upstream side as cavity #1 through #3. We will report design, fabrication, and commissioning of the RF cavities.

## DESIGN

Basic design concept of the new RF cavities is as follows. The new cavities will be substituted for the present ones, so that physical sizes must fit with the present environments. Longitudinal lengths of the cavities between the entrance and the exit flanges should be same as the present values and transverse sizes should be smaller than the inner size of the Helmholtz coils, 253 mm. The physical aperture for the beam should not be smaller than the present value, 50 mm in diameter. The new cavities should be made of pure copper to realize higher temperature stability. The cavities will be cooled with water, temperature of which is precisely controlled to be 38 ± 0.03°C, so that water channels should be equally distributed over bodies of the cavities, including the outer and the inner conductors, in order to make the temperature of the cavities uniform and constant and not to rely on thermal conductivity of copper too much. Routes of the water channels should be designed so that heat is taken away by water at the place it is generated.

The mechanical design of the cavities are made by referring to a similar SHB cavity used for the electron and positron linac at KEK, which is a quarter wavelength coaxial cavity of a resonance frequency of 114 MHz made of copper. The physical design is made using the computer code, SUPERFISH. The main parameters calculated for the cavities #1 and #2, and the cavity #3 are listed in Table 1.

Table 1: Calculated Main Parameters of the Cavities

| | Cavity#1, #2 | Cavity#3 |
|---|---|---|
| Resonance freq. (MHz) | 108.4 | 216.8 |
| Unloaded Q-value $Q_0$ | 8765 | 11642 |
| Shunt impedance R (MΩ) | 1.45 | 2.07 |
| $RT^2$ (MΩ) | 0.844 | 0.871 |
| $RT^2/Q$ (Ω) | 96.3 | 74.8 |
| Transit time factor (β=0.55) | 0.764 | 0.649 |

[#]isoyama@sanken.osaka-u.ac.jp

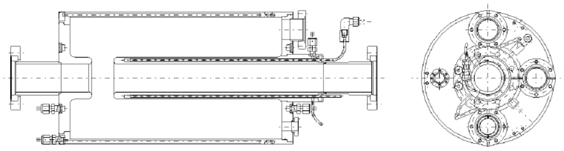

Figure 1: Mechanical design of the 216 MHz cavity.

Fig. 1 shows a mechanical design of a 216 MHz RF cavity. It has the circular symmetry around the central axis. The diameters of surfaces of the inner and the outer conductors are 76 mm and 220 mm, respectively, and the longitudinal lengths between the inner surfaces of the end plates are 733 mm for 108 MHz cavities and 386 mm for the 216 MHz cavity. The gap between the two electrodes is 40 mm. The inner and the outer cylinders are 13 and 10 mm thick, respectively, while the end plates are 20 mm thick. Fig. 2 shows a distribution of heat generated on the surface of the cavity calculated for the KEK cavity. The heat is generated mainly around the conjugation between the end plate with the long inner conductor and the heat generation quickly falls off as it goes away from the conjunction to both directions, so that the conjunct part as well as the end plate and the inner conductor should be efficiently cooled. To realize this and the other requirements for cooling, four long holes of 6 mm in diameter are drilled along the inner conductor from the base towards the gap but not to the end. A stainless steel pipe of 4 mm in diameter is inserted in each hole to make a water circuit. Water comes in through the pipe and goes out through the hole and the four water channels for the inner conductor are connected in series. A circular trench from the outside of each end plate is made near the inner conductor and it is covered with a plate to make a water channel in order to effectively cool the area of heat generation. Similar to the inner conductor, 16 long holes of 6 mm in diameter are drilled along the outer conductor from the base towards the gap side but not to the end. These holes are connected with trenches from outside of the outer conductor, and the trenches are covered with copper plates to make a water channel serially connecting 16 holes.

The end plate on the gap side is equipped with four ports for an input coupler, a tuner, a pick-up monitor, and a vacuum pump, and the other end plate is occupied by piping and connection for cooling water. The input coupler is a loop for magnetic coupling, the tuner is a copper block, and the pick-up monitor is a thin rod plated with copper.

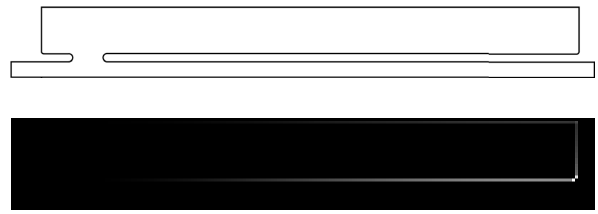

Figure 2: Cross section of the 114 MHz quarter-wavelength RF cavity of the KEK linac (top) and calculated heat generation on its wall (bottom). The brightness of the white line in the bottom figure shows intensity of heat generated on the surface of the inner conductor and the end plate of the RF structure illustrated above.

## FABRICATION

The cavity consists of three major parts, that is, an inner conductor with an end plate, an outer conductor, and an end plate with a short electrode, as shown in Fig. 3. They are machined from oxygen-free copper cylinders and plates. The outer conductor is made slightly longer than a design value to make the frequency tuning afterwards. All the welding is made with silver brazing, including welding between copper and stainless steel. After smaller parts are welded to the three main components, they are temporarily assembled with O-rings and the resonance frequency is measured at room temperature. Then it is evacuated with a scroll pump or rotary pump and a shift of the resonance frequency is measured at room temperature and then it is measured at the temperature determined by cooling water, 38°C. The frequency drift ceases in 13 minutes after opening valves of the cooling water system, which means that the cavity temperature becomes uniform and constant in the time. These frequency shifts for the 216 MHz cavity are $\Delta f = +55$ kHz by evacuation and $\Delta f = -70$ kHz with cooling water, and those for the 108 MHz are +30 kHz by evacuation and -30 kHz with cooling water. When the resonance frequency is tuned, the input coupler and the tuner are installed. The cavity is evacuated to make RF contact between the major parts firm and the frequency is measured at room

Figure 3: Three major components of the 216 MHz cavity. From left to right: short electrode with the end plate, inner conductor with the end plate, and the outer conductor.

temperature. By taking the frequency shift due to cooling water into account, the resonance frequency is tuned to be the designed value under the normal operating conditions. The resonance frequency is determined mainly by the length of the long inner conductor and weakly by the gap, so that there are four possible places to be machined to change the frequency. For a larger change, shaving of the inner conductor end makes the frequency higher while saving of the inner surface of the end plate with the long inner conductor makes it lower. For fine frequency tuning, shaving of the outer conductor end makes the frequency low and shaving of the short nose at the gap makes it higher. At first, the inner conductor is made longer than a design value to save margins for frequency tuning because it is easier to shave the end of the inner conductor than to do the inner surface of the end plate, and then the resonance frequency is measured. The measured frequency is corrected for the shift owing to the cooling water and compared with a calculated frequency. The amount of machining is determined by the calculation and it can be repeated until the target value is realized. However, one trial is usually enough to reach the design frequency by a little help of the tuner except for the case where a mistake is found in machining of the nose cone of the long inner conductor. After the frequency tuning, the three major parts are welded to be a coaxial RF cavity by silver brazing.

The 216 MHz cavity was fabricated first, because the cavity is short and easier to fabricate. Then two 108 MHz cavities were fabricated by making good use of experience gained in the first cavity.

## COMMISSIONING

After completing fabrication of the cavity, we measured characteristics of the cavity at the low RF power level. The measured characteristics are listed in Table 2. The calculated values of the unloaded Q-value listed in Table 1 are 8765 for the 108 MHz cavities and 11,642 for the 216 MHz cavity, while the measured values listed in Table 2 are ~8,200 for the 108 MHz cavities and ~10,300 for the 216 MHz cavity, which are 94 % and 89 % of the calculated values, respectively. These measured Q-values should be compared also with those measured for the previous cavities, which are ~5,500 for the 108 MHz cavities and ~5,900 for the 216 MHz cavity, indicating that the new cavities have RF characteristics better than the previous ones and close to the ideal ones. The unloaded Q-values of the cavities are too high to obtain constant RF voltage in the pulse duration of the RF power 40 μs produced with the independent RF amplifiers. The rise time of the RF voltage in the cavity has to be reduced while the same peak voltage is produced with the RF amplifier. This is realized by setting input couplings to be ~4 for the 108 MHz cavities and ~4.4 for the 216 MHz cavity, as can be seen in Table 2, which make filling times of the RF power 4.8 and 2.4 μs, respectively. Owing to space limitations, we can use linear motion feedthroughs with a stroke of only 20 mm for the tuners. A copper cylinder of 29 mm in diameter is attached on the rod of a linear motion feedthrough. Lengths of the cylinders are adjusted so that the resonance frequencies become close to the design values, 108.42 MHz and 216.88 MHz, as listed in Table 2 when they are inserted by 10 mm. The cylinder lengths are 30, 22, and 34 mm for cavities #1, #2, and #3, respectively.

Table 2: Measured Parameters of the Cavities

| | Cavity#1 | Cavity#2 | Cavity#3 |
|---|---|---|---|
| Res. freq. (MHz) | 108.423 | 108.426 | 216.881 |
| Tuning range (kHz) | 83 | 73 | 327 |
| Loaded Q-value $Q_L$ | 1626 ± 6 | 1612 ± 6 | 1899 ± 17 |
| Unloaded Q-value $Q_0$ | 8232 ± 35 | 8187 ± 35 | 10297 ± 128 |
| Input coupling $\beta_1$ | 4.06 | 4.08 | 4.42 |
| Filling time (μs) | 4.8 | 4.8 | 2.8 |

After completing the measurement and tuning of the cavities at the low RF level, we proceed to the high power test and conditioning of the cavities. A cavity is mildly baked with tape heaters and then evacuated with an ion pump through the beam pipe. The RF power is fed to the cavity at a very low repetition rate like 0.1 Hz while the monitor waveform and the vacuum level are being watched. We are afraid of multipactoring but it does not occur when the high power RF power is fed at once instead of increasing the RF power gradually from a low level. The condition of the cavity is made by gradually increasing the repetition frequency while keeping the vacuum high, until normal operation conditions of the 60 Hz repetition rate and the 20 kW input RF power with the pulse duration up to 100 μs are realized.

The high power test and the conditioning of the cavities are conducted one by one and then the three cavities are installed on the linac in place of the previous ones. The linac is successfully operated with the new cavities for the SHB system without any problems. The overall start-up time of the linac with the SHB system is reduced from some hours to one hour, which is same as the time necessary for the other operation modes without the SHB system and the linac can be operated long time without readjustment.

## ACKNOWLEDGEMENTS

The authors would like to thank Professors S. Ohsawa, M. Isawa, H. Hayano, and J. Urakawa of KEK for their valuable suggestions and advice about this work. The mechanical design and fabrication of the cavities are conducted by Meisho Kiko Co. Ltd. This work is partly supported by the program of KEK, “Comprehensive Support Program for the Promotion of Accelerator Science and Technology”.

# ACCELERATING STRUCTURE FOR C-BAND ELECTRON LINEAR ACCELERATOR OPTIMIZATION

S.V. Kutsaev, N.P. Sobenin, A.A. Anisimov, Moscow Engineering-Physics Institute (State University), Moscow, Russian Federation
M. Ferderer, A.A. Zavadtsev, A.A. Krasnov, Identification Beam Systems LLC, Atlanta, USA

*Abstract*

This paper presents the results of a survey study that analyzed and compared several linear accelerator designs operating in the range of 5 to 20 MeV for use in advanced cargo inspection systems. These designs were based on klystron generated RF power input of 3.2 and 4.5 MW at 5712 MHz. Several different accelerating structures were considered including standing wave (SW) and travelling wave (TW) structures. In addition several hybrid structures, composed of a SW buncher sections and TW accelerator sections, were included in the study. Cells geometries and beam dynamics parameters, for these accelerating structures, were calculated using advanced numerical simulation methods. Accelerating structures and input couplers for SW and hybrid structures were designed.

## INTRODUCTION

Cargo inspection systems should be simple, compact and highly reliable. Historically S-band liner accelerators have been used for this application. By using a higher frequency structure we can significantly increase the shunt impedance and therefore provide necessary energy gain with a shorter structure length. The effective shunt impedance of a 5712 MHz biperiodic structure is 30% greater than a 2856 MHz structure while the external diameter is approximately half the diameter. In addition to the cavity being significantly smaller waveguides and other RF components are as well. To facilitate large capture coefficients, without using an external focusing magnet, SW biperiodic structure bunchers were used. Along with the SW biperiodic structures, hybrid structures are of particular interest for this type of application.

Modern cargo systems need to generate more than a black and white image to be effective in solving the cargo security problem that the world is facing. To be effective the systems must also generate material based information. In particular, Z-function and density information needs to be presented to the operators. To obtain Z-function and density information the accelerator must be able to vary output energy from pulse to pulse.

## SW STRUCTURE

In designing SW biperiodic accelerating structures it is important to ensure that the necessary beam parameters are met without requiring unrealistic manufacturing tolerances. To satisfy this requirement the coupling coefficient ($k_c$) was increased to 11 percent from the more traditional range of 4 to 5 percent.

Cell tuning to the required frequency and field distribution was performed using the resonant models. In Figure 1 a resonant model for the regular cell and the distribution of longitudinal component of electric field on axis are illustrated.

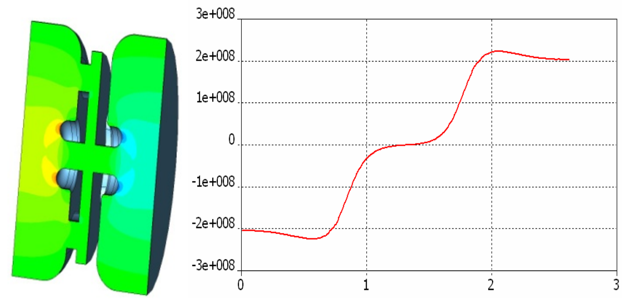


Figure 1: Resonant model of the regular cell and the distribution of electric field in it.

For constructional convenience the RF power is input into the first cell. Two WR187 waveguides are connected to the first cell symmetrically to provide symmetry of the field in this cell. One of these waveguides is short-circuited by the metal pin and is used for vacuum pumping. Figure 2 shows the model of this coupler as well as electric field intensity.

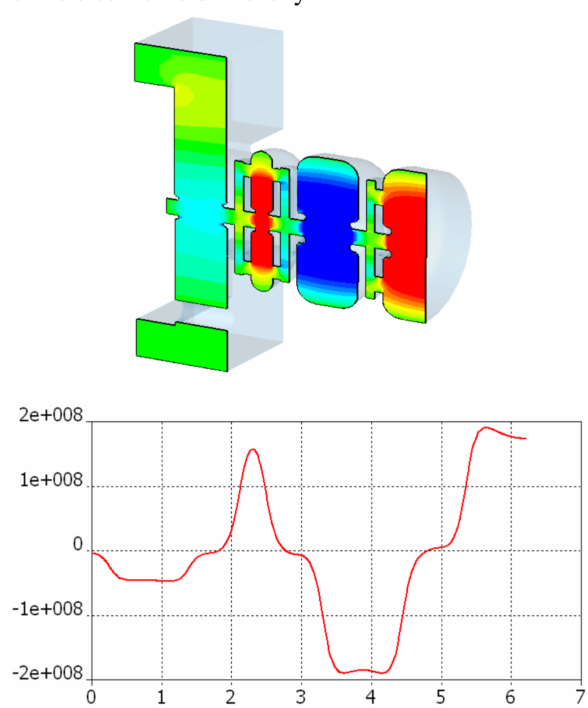


Figure 2: Distribution of electric field in SW buncher.

Table 1: SW Structure Parameters

| Cell number | Phase velocity | Effective shunt impedance, MOhm/m | Coupling coefficient, % | Q-factor |
|---|---|---|---|---|
| 1 | 0.67 | 50.3 | 38.9 | 5540 |
| 2 | 0.42 | 28.2 | 13.5 | 5680 |
| 3 | 0.78 | 97.6 | 10.9 | 6800 |
| 4, 5… | 0.99 | 114.2 | 11.0 | 9770 |

The calculations for two C-band structures, with a different number of accelerating cells, were performed. In addition, energy variation capability was evaluated for these two structures. The first accelerator had output energies in the range of 3-7 MeV while the second one had output energies in the range of 11-15 MeV. Energy variation capability was evaluated by adjusting the injected current. The results of beam dynamics calculations for these accelerators are presented in Table 2 ($W_{av}$ is average energy of accelerated electrons, $I_{out}$ is output beam current, $I_{in}$ is injected beam current, $k_c$ is capture coefficient, L is structure length, $P_b$ is beam power, $P_{in}$ is input RF power.). The dependency of output energy as function of input current for these two accelerator structures is illustrated in Figure 3.

Table 2: Results of Particle Dynamics Calculations

| L, m | $k_c$, % | $P_{in}$, MW | $W_{av}$, MeV | $I_{out}$, mA | $k_c$, % | $P_b$, MW |
|---|---|---|---|---|---|---|
| 0.97 | 57.2 | 4.5 | 15 | 86 | 57.2 | 1.43 |
| 0.97 | 51.5 | 4.5 | 11 | 195 | 51.5 | 2.48 |
| 0.44 | 50.6 | 3.3 | 7 | 230 | 50.6 | 1.82 |
| 0.44 | 38.6 | 3.3 | 3 | 730 | 38.6 | 2.92 |

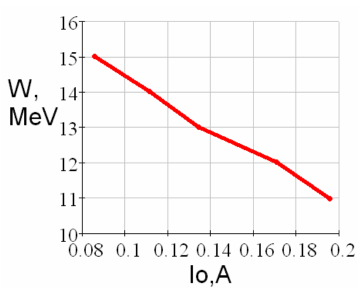


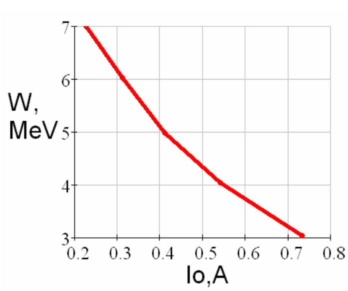


Figure 3: Output energy of 11-15 MeV structure (left) and 3-7 MeV structure (right) as functions of current.

## HYBRID STRUCTURE

Along with SW structure presented above several hybrid structures were considered. The analyzed hybrid structures consisted of a SW-buncher section combined with TW accelerating sections. Accelerating cells in the TW sections can be coupled by electric field through on-axis wholes (disk-loaded structure – DLS) [1-3] or by magnetic field through periphery slots (Figure 4) with negative (NDS) or positive (PDS) dispersion [4].

Calculated PDS electro-dynamic characteristics depending on operating mode Θ are shown in Table 3 (a is aperture diameter, λ is wave length, $R_{sh}$ is shunt impedance, α is attenuation factor, $\beta_{gr}$ is relative group velocity, τ=αL).

Table 3: Parameters of PDS Hybrid Structure

| Θ | a/λ | $R_{sh}$, MOhm/m | Q | α, 1/m | $\beta_{gr}$, % | τ |
|---|---|---|---|---|---|---|
| 3π/2 | 0.1 | 95 | 11130 | 0.059 | 9.1 | 0.11 |
| 4π/3 | 0.1 | 123 | 10310 | 0.096 | 6.3 | 0.12 |
| 5π/4 | 0.1 | 92 | 9420 | 0.146 | 4.4 | 0.18 |
| 6π/5 | 0.1 | 96 | 9072 | 0.171 | 3.9 | 0.19 |

Main electro-dynamic characteristics of DAL, PDS and NDS as a functions of a/λ at relative phase velocity 0.999 are presented in Table 4. It can be seen that shunt impedance of the structures decreases as the aperture diameter is increased. τ corresponds to TW section for $W_{av}$=10 MeV, $P_{in}$=4.1 MW, $I_{out}$=0.1 A.

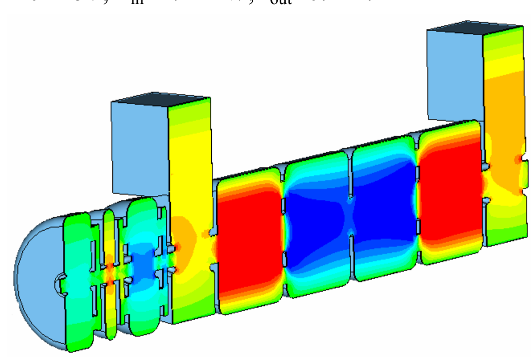

Figure 4: Magnetic coupled TW structure with SW Buncher.

Common input coupler is used for SW buncher and for TW accelerating structure.

If TW accelerating structure is based on DLS or PDS, input coupler in coupled with last cell of the buncher and with first cell of the TW accelerating structure. Input waveguide is located between the buncher and the TW accelerating structure.

If TW accelerating structure is based on NDS, input coupler in coupled with last cell of the TW accelerating structure. RF power, passing through the whole TW accelerating structure, comes into the buncher through coupling whole between first cell of the TW accelerating structure and last cell of the buncher.

Table 4: Parameters of Different TW Sections

| a/λ | Type | Θ | $R_{sh}$, MOhm /m | Q-factor | α, 1/m | $\beta_{gr}$, % | τ |
|---|---|---|---|---|---|---|---|
| 0.04 | PDS | 5π/4 | 122 | 9750 | 0.121 | 4.5 | 0.11 |
| | NDS | 3π/4 | 86 | 7400 | 0.145 | 5.9 | 0.18 |
| 0.07 | PDS | 5π/4 | 111 | 9950 | 0.126 | 4.5 | 0.12 |
| | NDS | 3π/4 | 73 | 7520 | 0.151 | 5.5 | 0.16 |
| 0.10 | PDS | 5π/4 | 92 | 9420 | 0.146 | 4.5 | 0.14 |
| | NDS | 3π/4 | 56 | 7130 | 0.156 | 5.7 | 0.19 |
| | DLS | 2π/3 | 87 | 9070 | 0.660 | 1.0 | 0.35 |
| 0.12 | PDS | 5π/4 | 84 | 9430 | 0.150 | 4.4 | 0.15 |
| | NDS | 3π/4 | 49 | 7300 | 0.148 | 5.7 | 0.20 |
| | DLS | 2π/3 | 65 | 9000 | 0.330 | 1.9 | 0.27 |
| 0.14 | PDS | 5π/4 | 69 | 8700 | 0.156 | 4.4 | 0.17 |
| | NDS | 3π/4 | 39 | 6700 | 0.173 | 5.4 | 0.25 |
| | DLS | 2π/3 | 65 | 9000 | 0.200 | 3.2 | 0.20 |

Using the parameters from Tables 3 and 4, the beam dynamics calculations were done for two structure types: DLS and PDS. In both accelerators the buncher is the same to the one used for the SW accelerator. All calculations were done for 10 MeV energy and 100 mA beam current. The accelerating sections are considered to be with constant impedance. The results of these calculations are presented in Table 5.

Table 5: Results of Particle Dynamics Calculations

| Structure | $W_{av}$, MeV | $I_{out}$, mA | $k_c$, % | L, m | $P_{in}$, MW |
|---|---|---|---|---|---|
| DLS | 10 | 99 | 65.8 | 0.8 | 4.5 |
| PDS | 10 | 96 | 63.8 | 1.1 | 4.5 |

## CONSTRUCTION

3D engineering design of SW accelerating structure is shown in Figure 5.

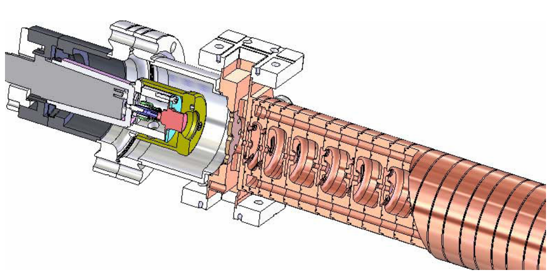

Figure 5: SW accelerating structure with the injector.

3D engineering design of irradiator of the accelerator is shown in Figure 6.

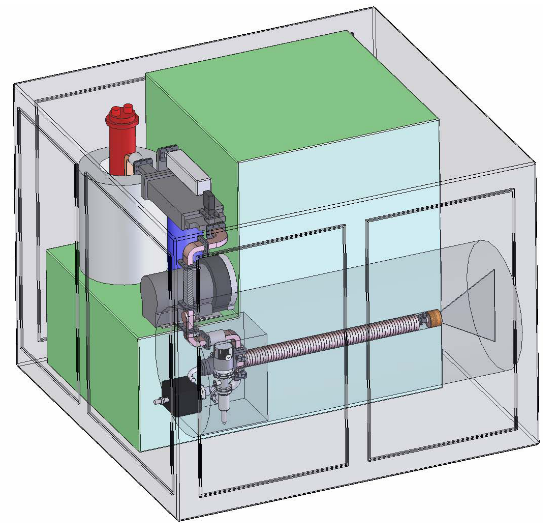

Figure 6: Irradiator.

The irradiator includes SW accelerating structure, injector, W-target, klystron, circulator, directional coupler, waveguide window, vacuum system, modulator and lead local shielding (shown transparent). Overall dimensions of the irradiator are 1.8x1.8x1.4 m.

## CONCLUSIONS

Several linear electron beam accelerator structures for cargo inspection applications have proposed. Electro-dynamic characteristics for a pure SW structure and different types of Hybrid (SW buncher plus TW accelerating section) structures were calculated. Variable energy control was studied for the SW structure. Particle dynamics for the SW structure and Hybrid structures (PDS and DLS) was calculated. A common input coupler and bunching sections was designed for the SW and Hybrid structures. The use of compact C-band accelerating structure allows us to build very compact and effective irradiator for cargo inspection system.

## REFERENCES

[1] O.A.Valdner, N.P.Sobenin, B.V.Zverev, I.S. Shedrin, "Disk-Loaded Waveguides", 3rd Edition, 1991, Energoatomizdat.

[2] N.P.Sobenin, B.V.Zverev, "Electrodynamical characteristics of accelerating cavities", 1999, Foundation of International Scientific and Educational Cooperation, London, England.

[3] Yu.V.Zuev, M.A.Kalinichenko, A.V.Ryabtsov, I.V.Chetverikov, "Accelerating structure of electron linear accelerator UELV-10/5-15C", Preprint CNIIAtomInform, 2001.

[4] D.Tronc, "Linac accelerating structures", Proceeding EPAC'94.

# THE CUT DISK STRUCTURE PARAMETERS FOR MEDIUM PROTON ENERGY RANGE

V. Paramonov *, INR RAS, 117312 Moscow, Russia


## Abstract

For intense proton beam acceleration the structure aperture diameter should be $\approx 30mm$. With such aperture room temperature coupled cell accelerating structures have the maximal effective shunt impedance $Z_e$ value at operating frequency $\approx 650MHz$. For this frequency well known Side Coupled Stricture (SCS), Disk and Washer Structure (DAW), Annular Coupled Structure (ACS) have large transversal dimensions, leading to essential technological problems. The Cut Disk Structure (CDS) has been proposed to join both high $Z_e$ and coupling coefficient $k_c$ values, but preferably for high energy linacs. In this report parameters of the four windows CDS option are considered at operating frequency $\approx 700MHz$ for proton energy range $80MeV \div 200MeV$. The outer diameter $\approx 30cm$ and $kc \approx 0.12$ result naturally, but $Z_e$ value is of $(0.7 \div 0.9)$ from $Z_e$ value for SCS ($k_c = 0.03$). Small cells diameter opens possibility of CDS applications for twice lower frequency and structure parameters at operating frequency $\approx 350MHz$ are estimated too. Cooling conditions for heavy duty cycle operation are considered.


## INTRODUCTION

The scaling relation for effective shunt impedance of a structure $Z_e \sim \sqrt{f}$, where $f$ is an operating frequency, is widely known and is frequently used for fast $Z_e$ estimations at different $f$ values. It means, that we simultaneously scale all dimensions of the structure. It is not perfectly correct for practical case.

Let us consider typical $\Omega$-shaped accelerating cell geome-

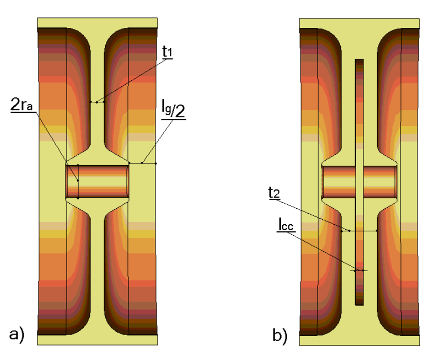


Figure 1: Typical cells geometries for structures with ECC (a) and ICC (b).

tries, shown in Fig. 1 for structures with External Coupling Cells (ESS), such as SCS, ACS, Fig. 1a, and for Internal Coupling Cells (ISS), for example, On-Axis Coupled Structure (OSC), Fig. 1b. The aperture diameter of the structure $2r_a$, Fig. 1a, is defined by a transverse beam size and safety margins. These parameters are not related directly with operating frequency. We can not reduce $2r_a$ for high operating frequency, but there are no reasons for $2r_a$ increasing for lower $f$. As it is known well, $Z_e$ value increases with $r_a$ decreasing. A septum thickness $t_1$, Fig. 1a, for ESS, is defined by cooling channels placing and rigidity requirements. From these requirements a reasonable $t_1$ value is $(10 \div 15mm)$. We also can not reduce $t_1$ at higher $f$ values and there are no reasons for $t_1$ increasing for lower operating frequency. And $Z_e$ increases with relative $\frac{t_1}{L}$ increasing, where $L_p = \frac{\beta\lambda}{2}$ is the period length, $\beta$, $\lambda$ are the relative particle velocity and the operating wavelength, respectively. For the ICC case we should have two septa with the thickness $t_1$ and coupling cell with the length $l_{cc}$ in between with effective septum thickness $t_2 \approx 2 \cdot t_1 + l_{cc}$.
To find a frequency for the maximal $Z_e$ value we have the contradiction - for higher frequencies skin effect leads to RF losses reduction, but we have to increase ratio $\frac{r}{\lambda}$ and $\frac{t_1}{\lambda}$. For lower frequencies it are conversely.

## CDS ADVANTAGES

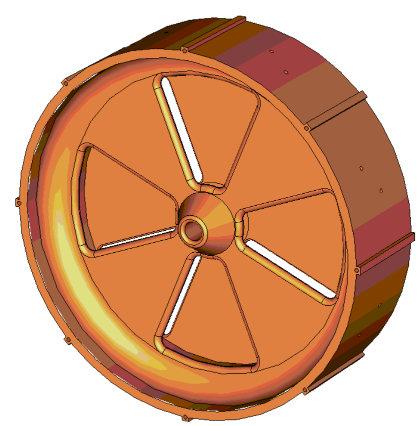

Figure 2: Four windows CDS option.

The CDS was proposed for high energy linacs $\beta \approx 1$ and L-band operating frequency [1]. CDS is topologically similar to OCS, but realizes quite different coupling concept - coupling mode has no own space for magnetic field, which should penetrate strongly through coupling windows (slots) in an accelerating cell, resulting in the high coupling coefficient value $k_c \sim 0.12 \div 0.25$. Coupling windows in CDS have not so strong magnetic field enhancement at windows ends, as compared to coupling slots in OCS, ACS, SCS and a high coupling coefficient is not connected with $Z_e$

* paramono@inr.ru

reduction. Windows are placed in the region of the maximal magnetic field for accelerating mode, resulting in RF loss reduction. Calculated and measured $Z_e$ value for CDS is even higher, than for similar structure without windows (zero coupling). High order modes problem for CDS is absent. Further CDS development [2] has shown preference of the four windows CDS option, Fig. 2, as compared to two or three windows - sufficient value $k_c \approx 0.1 \div 0.15$, a higher vacuum conductivity, a simpler cooling scheme, slightly higher $Z_e$ value, absence of transversal field for coupling mode, strongly reduced multipactoring possibility in coupling cells. But for L-band operating frequency the relative septum thickness $\frac{t_2}{L}$ is still high for $(\beta \sim 0.4 \div 0.5)$ and CDS loses in $Z_e$ value to another structures. With the operating frequency reduction the ratio $\frac{t_2}{L}$ decreases, providing CDS competitiveness for medium proton energies.

### [illegible]

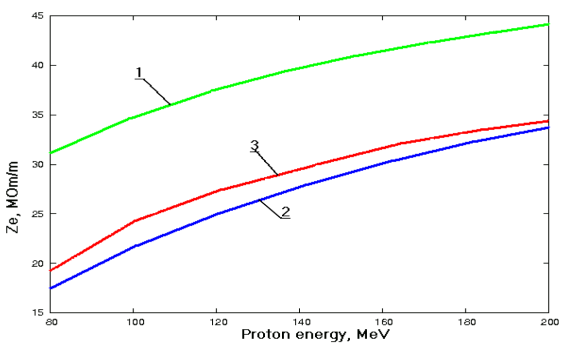


Figure 3: Effective shunt impedance at operating frequency $f = 704MHz$ for structures: 1 - with ECC ($k_c = 0$), 2 - ICC ($k_c = 0$) and 3 - CDS.

CDS parameters were estimated for operating frequency of $f = 704MHz$ with aperture diameter of $2r_a = 32mm$ and proton energy range $W_p = (80 \div 200)MeV$. Reference cell geometries, both for ICC and for ECC, Fig. 1, were optimized in 2D approximation following procedure, described in [3]. The septum thickness is fixed at $t_1 = 14mm$ for ECC, and at $t_2 = 36mm$ for ICC. Effective shunt impedance is defined as:

$$Z_e = \frac{(E_0 T)^2 L_p}{P_s}, \quad \text{MOm/m} \qquad (1)$$

where $E_0$ is the average electric field along the structure axis, $T$ is the transit time factor, $P_s$ is the RF loss power at the period.

For each proton energy the optimal gap ratio $\alpha = \frac{l_g}{L}$, where $l_g$ is the gap length, has been defined for the maximal $Z_e$ value. An optimal $\alpha$ essentially depends on septum thickness and to have the maximal $Z_e$ value structures with ECC and ICC have a different gap length for the same $\beta$. The optimal cell geometry with ICC were modified in CDS and simulated in 3D approximation with MWS [4]. Results of simulations are plotted in Fig. 3.

Comparing curve 1 and curve 2 in Fig. 3, one can see, that the effectively thick septum directly leads to lower $Z_e$ value for the structures with ICC. The CDS utilizes the same reference geometry with the same thick septum but, due to design idea, partially regains initial $Z_e$ defeat. But calculated $Z_e$ value is still $\sim 75\%$ from similar value for structures with ECC ($k_c = 0$). The coupling coefficient $k_c \approx (0.14 \div 0.12)$ obtains for CDS naturally, together with the shown $Z_e$ value. Such $k_c$ values are not reachable for SCS and ACS - for that structures $k_c$ increasing at $1\%$ is coupled with $Z_e$ reduction at $\approx 2.5\%$. For CDS we have to take into account only $Z_e$ reduction due to surface roughness. Low RF level measurements show for [2] quality factor $Q_0$ and $Z_e$ values are of $95\%$ from calculated in 3D approximation. Outer CDS cell diameter is $\approx 305mm$ and CDS transverse dimensions do not provide problems for brazing technology.

For medium proton energy range CDS at operating frequency $704MHz$ has in times higher coupling coefficient and smaller transverse dimension, as compared to structures with ESS. But CDS effective shunt impedance is of $\approx 10\% \div 15\%$ lower, as compared to SCS or ACS with $k_c \sim 0.03 \div 0.05$.

### [illegible]

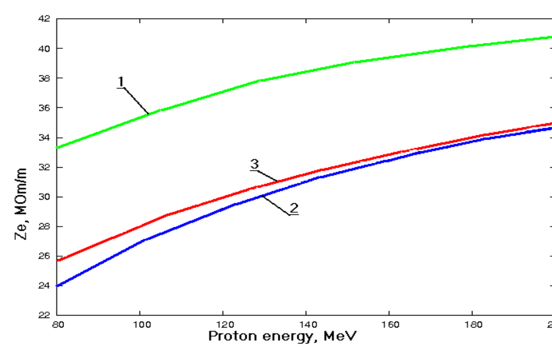


Figure 4: Effective shunt impedance at operating frequency $f = 352MHz$ for structures: 1 - with ESS ($k_c = 0$),2 - ICC ($k_c = 0$), and 3 - CDS.

Small transverse dimensions make it attractive to consider CDS parameters for twice lower operating frequency of $352MHz$. Similar simulations were performed with the same aperture diameter of $2r_a = 32mm$. The septum thickness is fixed at $t_1 = 16mm$ for ECC, and at $t_2 = 46mm$ for ICC. Results are plotted in Fig. 4.

For operating frequency of $352MHz$ a relative difference in $Z_e$ value between ECC and ICC structures decreases, but remains essential. CDS remains in $Z_e$ value higher than ICC structures, but $\approx 15\%$ lower than structures with ECC ($k_c = 0$). We can not consider ECC structures, which became not practical due to large $(> 1200mm)$ transverse dimensions. At this frequency we can consider only ICC structures with outer diameter of $\approx 590mm$, defined by

$TM_{010}$ mode frequency, definitely have lower, than CDS, $Z_e$ value.
Another possible competitor is a simple chain directly coupled accelerating cells in $\pi$-mode. Sufficient $k_c$ value can be provided only by coupling slots in the septum between cells. In $\pi$-mode a low $Q$ element - the coupling slot, is excited with a twice higher amplitude, as compared $\frac{\pi}{2}$ mode. This case the magnetic field enhancement and related RF loss density increasing at the ends of coupling slot is larger. It leads to a larger rate of $Z_e$ decreasing with $k_c$ increasing, as compared to $\frac{\pi}{2}$ structures. Even with careful coupling slot shape definition ($k_c$ increasing with the slot height increasing entails with a smaller $Z_e$ decreasing, [5]) and slots rounding such $k_c \approx (0.15 \div 0.13)$ for directly coupled $\pi$-mode structure will be connected with very large $Z_e$ reduction. For lower $k_c \approx 0.05$ values in $\pi$-mode structure the careful comparison should be performed - $Z_e$ for CDS can be higher.

## COOLING CONDITIONS

Cooling problem for CDS is not difficult. Differing from structures with ECC, heat dissipates from one one side of each web. A typical RF loss density distribution at the CDS cell surface is shown in Fig. 5. With the appropriate choice of shape and rounding of windows end magnetic field enhancement at the window ends is smaller, than at the ends of usual coupling slots.
Assuming CDS operation with $E_0$ of $4\frac{MV}{m}$ and duty factor of $4\%$, average RF power, dissipated in CDS period ($\beta = 0.4282$) is of $\approx 2.4kW$ for $f = 704MHz$ and of $\approx 4.75kW$ for $f = 352MHz$. The temperature distributions at the surface of CDS cells ($f = 704MHz$), calculated according [6] with ANSYS, [7], are shown in Fig .6 for cooling water velocity of $\approx 2\frac{m}{sec}$ and two options of internal cooling channels. A simple $V$-like internal channels in the septum are better adjusted with RF loss density profile and the maximal temperature difference at the surface, with respect incoming cooling water temperature of $27^oC$, is of $\approx 8.8^oC$. With $V$-like channels the drift tube region has a maximal temperature, Fig. 6a. Intersecting internal cooling channels are realized in [2] for effective drift tube cooling at the expense of some temperature increase at outer CDS part. For small CDS radius at frequency $704MHz$ intersecting internal channels are realistic and lead to maximal temperature difference $\approx 10.3^oC$.
For operating frequency of $352MHz$ and outer CDS radius of $\approx 300mm$ intersecting internal channels may be difficult in manufacturing and $V$-like channels look preferable. The calculated maximal temperature difference is estimated as of $\approx 11.9^oC$.

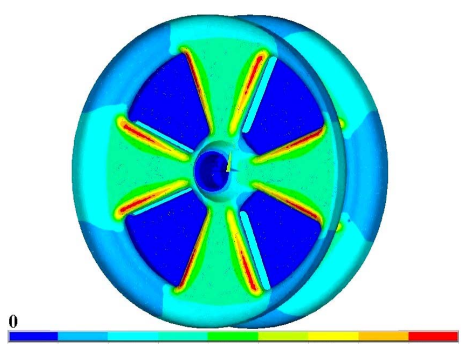


Figure 5: RF loss density distribution at the CDS cell surface, relative units.

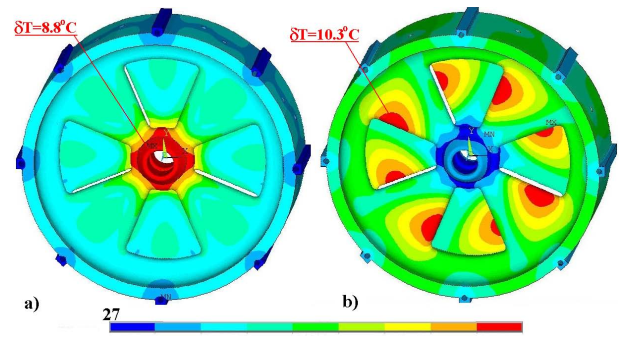


Figure 6: Temperature distribution at the surface of CDS cells ($f = 704MHz$) for $V$-like (a) and intersecting (b) internal channels.

## SUMMARY

Application at operating frequencies of $\sim 700MHz$ and lower smoothes the CDS disadvantage in medium $\beta \sim 0.4$ region - the effective shunt impedance decreasing due to necessity of thick septum. CDS advantages - the high coupling coefficient value, small transverse dimensions come in front in escort of competitive $Z_e$ value. This case CDS is a reasonable candidate for proton accelerations in the medium energy range of $(80 \div 200MeV)$.
The author thanks DESY for providing conditions for this work.

## REFERENCES

[1] V.V. Paramonov. The Cut Disk Accelerating Structure for High Energy Linacs. Proc. 1997 PAC, v.3, p.2959, 1997.

[2] V.V. Paramonov et al., Design Parameters of the NC Booster Cavity for PITZ-2 Test Stand. Proc. Linac2004, p. 204, 2004.

[3] V.V. Paramonov. The Data Library for Accelerating Structures Development. Proc. 1996 Linac Conf., v.2, p. 493, 1996.

[4] http://www.cst.com

[5] V.V. Paramonov. Methods of coupling coefficient increasing in periodical structures. Proc. RuPAC 1996, Protvino, v.1, p. 161, 1996 (in Russian).

[6] A. Skassyrskaya et al., The complete 3-D coupled rf-thermal-structural-rf analysis procedure for normal conducting structures. Proc. 2002 Linac Conf., p. 216, 2002.

[7] http://www.ansoft.com.

# ROOM TEMPERATURE ACCELERATING STRUCTURE FOR HEAVY ION LINACS

V. Paramonov *, V. Moiseev, INR RAS, Moscow, Russia,
Yu. Bylinskii, TRIUMF, Vancouver, Canada


## Abstract

In this report we consider room temperature DTL structure for heavy ions acceleration from $150\frac{keV}{u}$ to $400\frac{keV}{u}$. The structure design is based on known and proven solutions. The structure has no end wall problem. It allows flexible segmentation in RF cavities to place transverse focusing elements between cavities. As compared to well known IH DTL, considered structure has smaller transverse dimensions and is designated for lower operating frequency. The structure promises high RF efficiency: calculated effective shunt impedance value is higher than $1.0\frac{GOm}{m}$ for operating frequency $\sim 70MHz$ and particle energy $E \sim 150\frac{keV}{u}$.


## INTRODUCTION

Interdigital H-type Drift Tube (IH DT) structure, see, for example [1], [2] and related references, is now well developed and widely used for heavy ion acceleration. Idea of Interigital Structure (IS) is in two steps. First one is to generate RF voltage between two conductors, placed along the beam line, providing a transverse electric field. At the second step with drift tubes, connected in turn to opposite conductors, transverse field transforms into longitudinal accelerating one. Efficiency of such structure depends on number of drift tubes per unit length and a zero order estimation for effective shunt impedance $Z_e$ is $Z_e \sim \frac{1}{\beta^2}$, where $\beta$ is the relative particle velocity.
Similarly we can consider another classical device - Radio Frequency Quadrupole (RFQ). With some RF geometry one should provide RF voltage between four conductors, placed along the beam line. Every RF circuit for quadruple RF voltage distribution can be adopted for dipole one to be the IS basement. Basing on this approach, several RF circuit, used for RFQ, were considered in [3] for IS at operating frequency $f = 105MHz$. The Split Ring (SR) RF circuit, applied in TRIUMF RFQ [4] at $f = 35MHz$ and adopted in [3] for IDS with $f = 105MHz$, Fig. 1, have shown attractive properties - the small cavity outer diameter and calculated $Z_e \sim 1.0\frac{GOm}{m}$ for $\beta = 0.015$.
The lower operating frequency for DTL part of the heavy ion linac [5] results in the higher linac acceptance. In this report we consider the parameters of Split Ring Drift Tube (SR DT) structure for operating frequency $f = 70MHz$.

* paramono@inr.ru

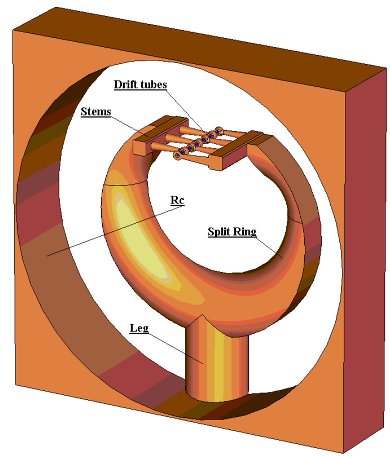


Figure 1: Proposed structure with Split Ring RF circuit and Drift Tubes. Half of the structure period.

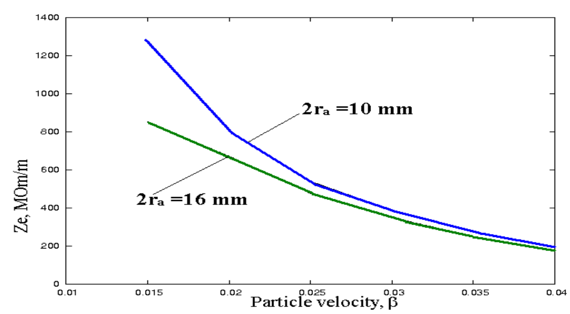


Figure 2: $Z_e$ dependence on $\beta$ for aperture diameters $2r_a = 10mm$ and $2r_a = 16mm$, $\alpha = 0.5$ .

## PERIODICAL STRUCTURE

RF parameters of the proposed structure at operating frequency $70MHz$ can be estimated in consideration of one half of ideal periodical structure shown in Fig. 1. For $Z_e(\beta)$ dependence estimation the gap ratio $\alpha = \frac{l}{L} = \frac{2l}{\beta\lambda}$, where $l_g$ is the accelerating gap length, $L_p$ is the period length, $\lambda$ is the operating wavelength, was fixed to $\alpha = 0.5$. Effective shunt impedance $Z_e$ is defined as:

$$Z_e = \frac{(E_0T)^2 N_p L_p}{P_s}, \quad \text{MOm/m} \qquad (1)$$

where $E_0$ is the average electric field along the structure axis, $T$ is the transit time factor, $N_p = 6$ is the number of accelerating periods in the half structure, $P_s$ is the RF loss power in the half structure.

Calculated $Z_e(\beta)$ dependence is plotted in Fig. 2 for two values of the beam aperture radius, $r_a = 5mm$ and $r_a = 8mm$. At low $\beta = 0.015$ SR DT shows very high $Z_e$ value, $Z_e \approx 1300\frac{MOm}{m}, 2r_a = 10mm$, but drops as $Z_e(\beta) \sim \frac{1}{\beta^2}$. In our consideration the structure has been optimized in $Z_e$ for $\beta = 0.015, 2r_a = 10mm$ and dimensions obtained were applied for another $\beta$, except ring radius, changed for operating frequency adjustment. The dependence $Z_e(\beta) \sim \frac{1}{\beta^2}$ is not a low and can be weakened by dimensions optimization for another $\beta$. As one can see from Fig. 2, for $2r_a = 16mm$ this dependence is not valid and structure $Z_e$ value for $\beta > 0.015$ can be improved by optimization distance between stems, gap ratio $\alpha$ and drift tube radius $r_t$. To improve $Z_e$ value we have to reduce capacitative load in the structure. A typical $Z_e(\alpha)$ and $T(\alpha)$ dependences are shown in Fig. 3 for $\beta = 0.015, 2r_a = 10mm$. The optimal number of drift tubes, supported by one ring, should be defined for each cavity. If we suppose the same number of periods $N_p \sim 12$, supported by one ring, at high $\beta > 0.25$ one will see the tilt in $E_0T$ distribution. The length of stems becomes large and there is a natural cosine filed tilt as at open end of line, formed by two conductors (stems). To avoid this tilt, stems should be shorter and one ring should support less number of drift tubes at higher $\beta$.

At the frequency $f = 70MHz$ Kilpatrick limit is $E_k = 10\frac{MV}{m}$. In modern linacs operation with electric field $1.5E_k$ is usual. For SR DT the ratio $\frac{E}{E_0T} \sim (4.6 \div 5.3)$, depending on the drift tube shape, is for $\beta = 0.015$ and decreases with $\beta$ increasing. Assuming the maximal electric field at the surface $E_{smax} = 15\frac{MV}{m}$, accelerating rate tolerable is $E_0T \sim (2.8 \div 5.3)\frac{MV}{m}$. To define the operating accelerating gradient, one has to take into account the cooling conditions of the structure.

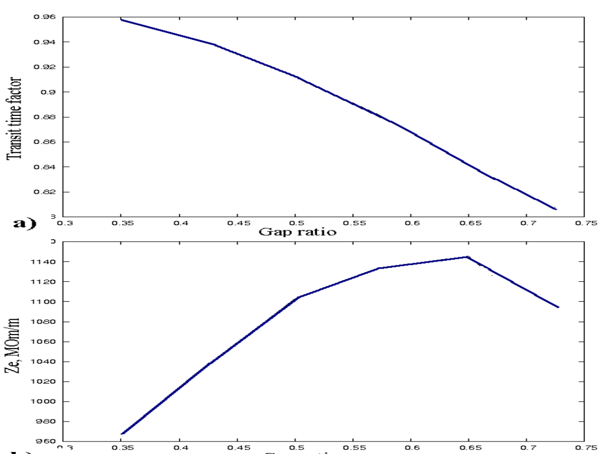


Figure 3: $T(\alpha)$ and $Z_e(\alpha)$ dependences for $\beta = 0.015, 2r_a = 10mm$.

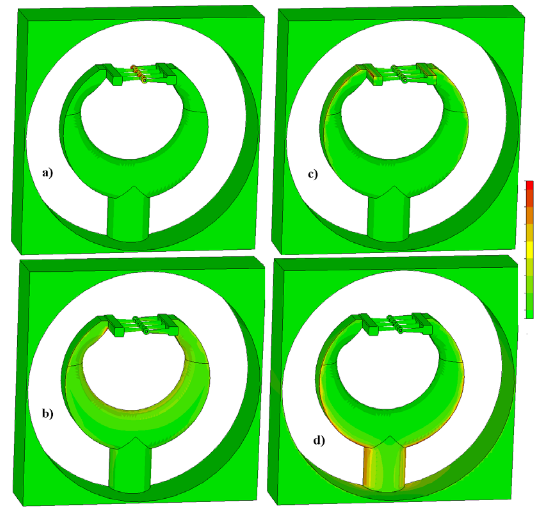


Figure 4: Electric $\epsilon_0 E^2$ (a),(c) and magnetic $\mu_0 H^2$ (b),(d) energy density distribution at the structure surface for operating (a),(b) and parasitic (c),(d) modes.

## [illegible]

In the vicinity of operating mode SR DT has the parasitic mode. Operating mode has zero RF potential in the bottom of the ring and there is no RF current at the leg, Fig. 4a. Stems have $\pm V$ RF potential with respect to cavity wall and voltage difference between neighbor drift tubes is $2V$. The parasitic mode has the same potential at the stems and strong RF current at the leg. Distributions of the energy density for electric $W_e = \epsilon_0 E^2$ and magnetic $W_m = \mu_0 H^2$ for operating and parasitic modes are shown in Fig. 4. With different choice of structure dimension, we can have parasitic mode both lower and higher than operating one. As one can see from Fig. 4, operating and parasitic modes have quite different $E^2$ and $H^2$ distributions and required reasonable frequency difference between these modes can be obtained by appropriate dimensions correction without strong deterioration of operating parameters.

## SR DT CAVITY

Due to design idea, the structure has no end wall problem and can be easy segmented into cavities. To have more equalized capacitative load for both stems, it is preferable to have the same number of drift tubes at both stems and odd total number of accelerating gaps in the cavity. The cavity can be short, with one supporting ring, for lower $\beta$ range and with number of periods $N_p \sim 13$ or less. In Fig. 5 such short cavity is shown just for illustration, with variable period length ($\beta \sim 0.01797 \div 0.02017, \alpha = 0.5, N_p = 13$), corresponding to ion acceleration with $E_0T = 2.4\frac{MV}{m}$. Electric field distribution for operating mode is shown in Fig. 6. Because potential difference between cavity wall and end tubes is a half from potential difference between regular tubes, electric field amplitude

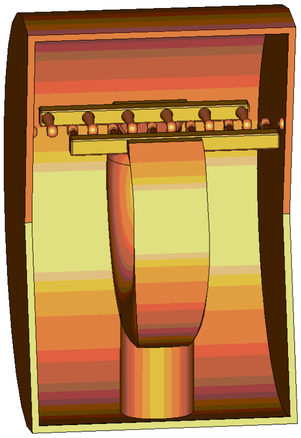

Figure 5: Short SR DT cavity with one supporting ring.

in end gaps is reduced. If required, the field in end gaps can be enlarged by appropriate gap length decreasing, as it is realized for the triple gap bunchers [6].

Also one can see a regular field reduction from lower $\beta$

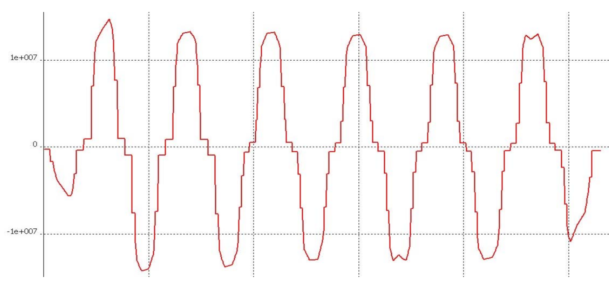


Figure 6: Electric field distribution along the beam axis in the short SR DT cavity.

periods to higher $\beta$ ones. The potential difference between stems is constant, and with growing period length $L_p = \frac{\beta\lambda}{2}$ the average electric field decreases. Without any correction the field tilt is $\frac{\Delta E}{E} = \frac{\Delta\beta}{\beta}$. This tilt can be corrected either by easy gap ratio decreasing, or, more complicated, by drift tubes radii change. The short SR DT cavity, shown in Fig. 5, has the inner diameter of $853mm$ and length of $531mm$. Calculated $Z_e$ value is of $619\frac{MOm}{m}$. RF power losses in both end walls are of $4.7\%$ from the total dissipated power. To provide flat electric field distribution, SR DT cavities with a larger number of accelerating gaps should have several supporting rings. The long SR DT cavity with two supporting rings and variable period length, ($\beta \sim 0.02383 \div 0.02748, \alpha = 0.5, N_p = 13$), is shown in Fig. 7. The cavity has the inner diameter of $860mm$ and length of $1153mm$. Calculated $Z_e$ value is of $420\frac{MOm}{m}$. RF power losses in both end walls are of $1.6\%$ from the total dissipated power.

For parasitic mode frequency, both in short, and in long SR DT cavities, the stem terminations near ens walls are important. At the stem ends parasitic mode has the largest $W_e$ value. With easy cavity segmentation, magnetic elements for transverse beam foquing can be placed outside cavities for easy mantainance. Such elements of the real cavity as fixed tuners, movable tuners and so on, can be easyly adopted from the same elements, developed, tested [2] and proven in operation. The structure is designated for CW operation and cooling problem is very important. For SR DT we can naturaly adopt the concept and parts of design of split ring RFQ [4], which are well tested in operation.

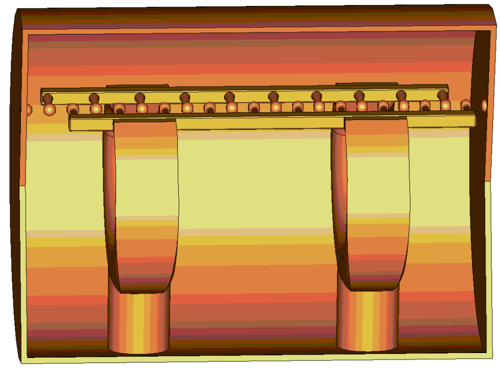

Figure 7: Long SR DT cavity with two supporting rings, $N_p = 21$.

## SUMMARY

Considerations shows for the proposed SR DT structure also attractive properties at the operating frequency $f = 70MHz$ - expected $Z_e$ value higher than for IH DTL and definitely smaller cavity diameter. SR DT parameters at frequency $70MHz$ are comparable with IH DTL ones at frequency $105MHz$, but lower frequency results in the higher linac acceptance. In case of RFQ at frequency $70MHz$ [7], assuming Split Ring RFQ, SR DT application will also provide technological unity in the the line Split Ring RFQ - Split Ring DTL, opening possibility for linac cost reduction.

## REFERENCES

[1] U. Ratzinger, Interdigital IH structure. Proc. Linac1990, p.525, 1990.

[2] A.K. Mitra et al., RF Measurements Summary of ISAC DTL Tanks and DTL Bunchers. Proc. PAC2001, p. 951.

[3] V. Paramonov, Effective Compact Accelerating Structures for Heavy Ions. Proc PAC1997, p. 2959, 1999.

[4] R.L Poirier et al., CW Performance of the TRIUMF 8 Meter Long RFQ for Exotic Ions. Proc. Linac2000, p.1023, 2000.

[5] ISAC-II - a Project for Higher Energies at ISAC. TRIUMF, TRI-99-1, 1999.

[6] Y. Bilinsky at al., A Triple Gap Resonator for the Separated Function DTL at TRIUMF. Proc. PAC 1997, p.1135, 1997.

[7] R. Laxdal et al., The Proposed ISAC-III Upgrade at TRIUMF. Proc. EPAC 2008, p. 3636, 2008.

# HIGH POWER TEST OF A LOW GROUP VELOCITY X-BAND ACCELERATOR STRUCTURE FOR CLIC

S. Döbert, A. Grudiev, G. Riddone,M. Taborelli, W. Wuensch, R. Zennaro, CERN, Geneva, Switzerland
S. Fukuda, Y. Higashi, T. Higo, S. Matsumoto, K. Ueno, K. Yokoyama, KEK, Tsukuba, Japan
C. Adolphsen, V. Dolgashev, L. Laurent, J. Lewandowski, S. Tantawi, F. Wang, J. W. Wang, SLAC, Menlo Park, USA

*Abstract*

In recent years evidence has been found that the maximum sustainable gradient in an accelerating structure depends on the rf power flow through the structure. The CLIC study group has consequently designed a new prototype structure for CLIC with a very low group velocity, input power and average aperture ($<a/\lambda> = 0.13$). The 18 cell structure has a group velocity of 2.6 % at the entrance and 1 % at the last cell. Several of these structures have been made in a collaboration between KEK, SLAC and CERN. A total of five brazed-disk structures and two quadrant structures have been made. The high power results of the first KEK/SLAC built structure is presented which reached an unloaded gradient in excess of 100 MV/m at a pulse length of 230 ns with a breakdown rate below $10^{-6}$ per meter active length. The high-power testing was done using the NLCTA facility at SLAC.

## INTRODUCTION

The CLIC study [1] aims to demonstrate a prototype accelerating structure suitable for a linear collider with an average loaded gradient of 100 MV/m at 12 GHz. To reach a sufficient luminosity for the collider a bunch train of 312 bunches with 3.7 $10^9$ electrons each has to be accelerated with a reasonable rf-to-beam efficiency. Therefore the structure needs to be equipped with heavy higher order mode damping and the gradient should be sustainable for 230 ns. The present structure is the result of a sophisticated optimization procedure to maximize the overall collider luminosity taking into account rf constraints like surface fields, input power, pulse length dependence and pulse heating as well as beam dynamics constraints for short and long range wake fields [2]. The rf constraints used in the optimization are the result of a comprehensive analysis of the available data mostly from the NLC/GLC program [3] and from 30 GHz tests at CERN. The rf power flow characterized by $P/C*\tau^{1/3}$ (P= input power, C= circumference of the first iris, $\tau$ = pulse length) was identified in this analysis as a possible limitation [4] and is therefore limited to previously demonstrated values in the optimization. The structure obtained is strongly tapered resulting in a quasi constant gradient with beam loading and a constant ratio of power over circumference along the structure. The unloaded gradient rises linearly towards the end of the structure due to this design. The structure needs only 55 MW for an average unloaded gradient of 100 MV/m due to its low group velocity- starting at 2.6 % and reaching 1% in the last cell. The detailed parameters of this structure can be found in table 1 and [5].

Table 1: Design and Measured Parameters of T18_vg2.6_disk (1)

| | |
|---|---|
| Frequency: | 11.424 GHz |
| Cells: | 18+2 matching cells |
| Filling Time: | 36 ns |
| Length: active acceleration | 18 cm |
| Iris Dia. a/λ | 0.155~0.10 |
| Group Velocity: vg/c | 2.6-1.0 % |
| S11/ S21 | 0.035/0.8 |
| Phase Advace Per Cell | 2π/3 |
| Power for <Ea>=100MV/m | 55.5MW |
| Unloaded Ea(out)/Ea(in) | 1.55 |
| Es/Ea | 2 |
| Pulse Heating ΔT: (75.4MW@200ns) | 16 - 25 K |

Four of these structures have been made in collaboration between KEK and SLAC using the NLC/GLC fabrication technique which comprises single crystal diamond turning of the cells, high temperature bonding (1000 C°) in a hydrogen furnace followed by extensive vacuum baking at 650 C° . CERN has made one more of this structure out of disks but using a vacuum furnace just above 800 C° for the bonding. In addition two structures with HOM damping are being prepared made out of clamped quadrants, one by CERN in OFC Copper and one by KEK in CuZr. More information about structures made out of clamped quadrant can be found in [6]. The aim is to compare different fabrication technologies and preparation techniques. A photo of the first structure tested made by KEK/SLAC is shown in figure 1. The high-power prototypes made out of disks do not include high order damping which will be added in subsequent versions. The higher order mode damping for this structures consists out of four damping waveguides in each cell which change the rf parameters slightly but in particular enhances the pulsed heating temperature rise by about a factor 2.

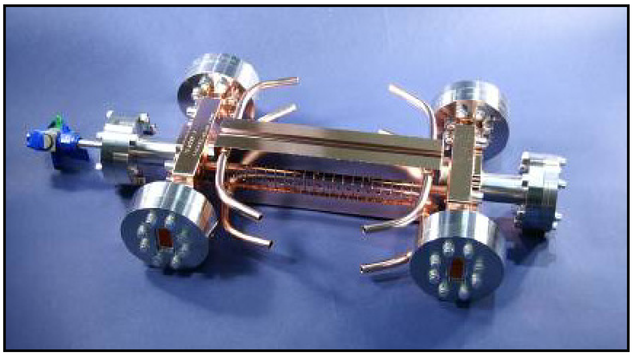

Figure 1: Photo of a KEK/SLAC made x-band accelerating structure called T18_vg2.6_disk (1).

## EXPERIMENTAL RESULTS

The results reported here are from the first structure out of the KEK/SLAC production which was tested in NLCTA [7] at SLAC. The structure was high power tested for a total of 1400 hours using an automated conditioning system which detects missing transmitted energy pulse by pulse and switches off the rf input in case of a breakdown. A total of 2148 breakdowns were accumulated during the entire experiment. The initial conditioning started with 50 ns pulses up to just above 110 MV/m. The pulse length was then extended in several steps to a maximum pulse length of 230 ns. This pulse length corresponds to the flattop pulse length needed for the structure to accelerate 312 bunches and happens to be the length of the available SLED 2 pulse compressor used in NLCTA. After roughly 250 hours of conditioning breakdown rate measurements were started in order to characterize the performance of the structure. The main result of the experiment is summarized in figure 2 where the breakdown probability is plotted as a function of the average unloaded gradient along the structure for a pulse length of 230 ns. The breakdown probability has been normalized by the active length of the structure. The CLIC goal for a 3 TeV machine is a trip rate of 3 10-7 per meter at 100 MV/m loaded gradient. An average unloaded gradient of 109 MV/m corresponds to a loaded gradient of 100 MV/m for the present CLIC beam parameters [1]. The breakdown rate at a fixed working point continued to improve almost until the end of the experiment with a time-dependence proportional to t-2.

The data taken at NLCTA allows determining the location of breakdowns in the structure by analysing the timing of the reflected rf and the pulse shortening of the transmitted rf signals. About half of the breakdown events have been recorded and analyzed. The distribution of the breakdown along the structure is shown in figure 3. During the first 750 hours where more than 80% of the breakdowns occurred, the number of breakdowns per cell rises linearity towards the end of the structure. This rise is consistent with the rise in surface field (see figure 4). The last 650 hours of the experiment during which less than 20 % of the breakdown occurred the distribution changed suggesting a ‘hot spot’ in cell No. 7 or 8. The breakdown rate actually went up slightly in the last 200 hours of the experiment (not shown in figure 2) due to this hot spot. For completeness the distribution of all recorded breakdown is shown as well. The suspicious cells will be inspected to understand this behaviour. Apart from these curious events the distribution indicates that the structure was limited by the end cells which reach surface fields above 300 MV/m. The pulse heating is also highest in the end cells but is only around 25 C°. The effect of pulse shape on gradient was studied with a special experiment using a 200 ns pulse and varying the power during the first 100 ns. This experiment showed a sudden increase in breakdown rate when in the first 100 ns the gradient exceeded 80% of the gradient in the second 100ns. The breakdown then happened more often during the first 100 ns indicating that the change in gradient is more relevant than the change in pulsed heating. These results can be found in more detail in [8].

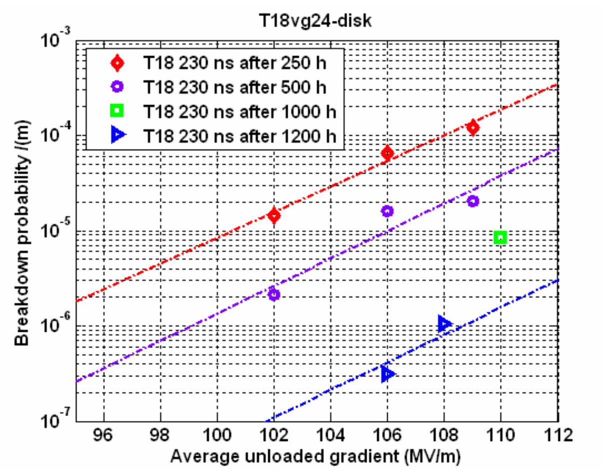


Figure 2: Normalized breakdown probability as a function of the average unloaded gradient measured different times during the experiment. The CLIC goal is a trip rate below 3 $10^{-7}$ per meter.

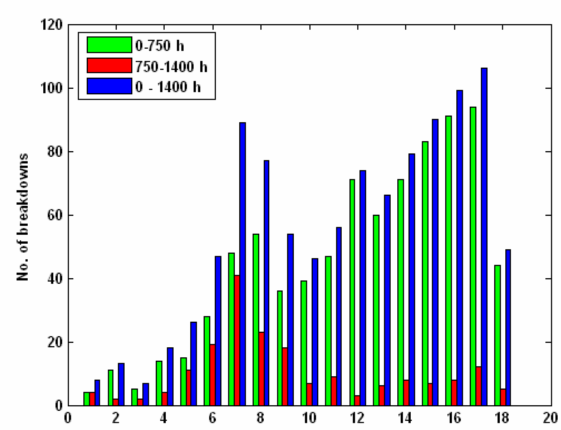


Figure 3: Breakdown distribution along the accelerating structure after 750 hours (green), for all recorded breakdowns (blue) and in the second half of the experiment (red).

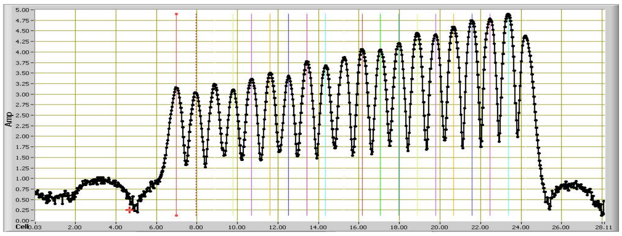

Figure 4: Bead pull field measurement along the structure. The accelerating field is increasing from 100 MV/m in the first regular cell to 155 MV/m in the last cell corresponding to an average unloaded gradient of 109 MV/m.

## CONCLUSIONS AND OUTLOOK

Design, construction and testing of this accelerator prototype for CLIC is the result of a very successful collaborative effort between KEK, SLAC and CERN. The high power test of this low group velocity X-band structure for CLIC demonstrated an unloaded gradient in excess of 100 MV/m with a breakdown rate below the CLIC goal of 3 $10^{-7}$. The structure seems to be limited at the far end of the taper where several rf parameters like the electrical and magnetic surface fields have their maximum. Even so pulsed heating originating from the magnetic field seems not to be the critical parameter. The complex pointing vector at the surface combining magnetic and electrical fields has recently been found to describe well the limits of several test structures [9] and it rises also towards the end of the structure. The former power flow parameter ~P/C originally used to design the structure is constant along the structure and seems therefore less relevant. However the general concept to optimize for low input power and low group velocity in the CLIC structure design proved to be very successful. The fabrication techniques developed by the NLC/GLC program has once again been very reliable and further test in this structure series should give much more insides in the issues of fabrication technology.

This prototype structure for a high-gradient test does not include yet the necessary features for HOM damping. Therefore the next step therefore is clearly to test a similar structure but which has HOM damping. In addition the mode launcher type couplers used are not compatible with the desired filling factor for CLIC and therefore need to be replaced by shorter couplers. The present high-power test structure would have an rf to beam efficiency of ~ 17% when used with CLIC parameters. These issues have to be addressed in the next generation of test structures already under preparation.

A second structure which has seen an identical preparation will be tested soon at KEK in the Nextef [10] facility. The aim is to check the reproducibility of the results for different structures and test facilities. Two more sets of cells have been machined and will be assembled using slightly different preparation techniques. For one structure the time consuming high-temperature vacuum bake after bonding will be skipped. In addition two structures with the same rf circuit made out of quadrants are under construction. The quadrants will be clamped together and installed in a vacuum tank for testing. This technique allows for more flexibility in the choice of materials and does not need a heating cycle for joining the parts together which might compromise the otherwise favourable properties against fatigue from pulsed heating. One particular interesting material is CuZr. However several accelerating structures have been tested already using this technique and showed inferior results compared to similar structures made out of brazed disks.

The latest version of the CLIC accelerating structure is the result of optimizing with lower surface field constraints (Es < 250 MV/m) and trying to keep the local complex pointing vector below a critical value [2]. This new design has a superior rf to beam efficiency of 27 % and is expected to exceed even the results reported in this paper.

## REFERENCES


[1] http://clic-study.web.cern.ch/CLIC-Study/.

[2] F .Tecker, ‘CLIC 2008 Parameters’, CLIC-Note 764, (2008).

[3] S. Doebert, ‘High Gradient Performance of Prototype NLC/GLC X-band Accelerator Structures’, Proc. PAC2005, Knoxville, Tennessee, USA (2005).

[4] W. Wuemsch, ‘The Scaling of the travelling-wave rf breakdown limit’. CLIC-Note-649, 2006.

[5] R. Zennaro, ‘Design and Fabrication of CLIC test structures’, this conference.

[6] S. Doebert, ‘High Power Test of an x-band slotted-iris Accelerator Structure at NLCTA’, Proc. PAC 2007, Albuquerque, New Mexico, USA (2007).

[7] C. Adolphsen, ‘ Normal-Conducting RF Structure Test Facilities and Results’, Proc. PAC 2003, Portland, Oregon, USA (2003), 668.

[8] F. Wang, ‘Breakdown Study on the CLIC designed T18 x-band structure’, Proc. AAC08 workshop, Santa Cruz, California, USA (2008).

[9] A. Grudiev, ‘A new local field quantity describing the high gradient limit of accelerating structures’, this conference.

[10] S. Fukuda, ‘The Status of Nextef; The X-band Test Facility in KEK’ this conference.

# DESIGN OF AN X-BAND ACCELERATING STRUCTURE FOR THE CLIC MAIN LINAC

A. Grudiev, W. Wuensch, CERN, Geneva, Switzerland

*Abstract*

The rf design of an accelerating structure for the CLIC main linac is presented. The 12 GHz structure is designed to provide 100 MV/m average accelerating gradient with an rf-to-beam efficiency as high as 27.7 %. The design takes into account both aperture limitations and HOM-suppression requirements coming from beam dynamics as well as constraints related to rf breakdown and pulsed surface heating.

## INTRODUCTION

Recently the CLIC study has changed the operating frequency and accelerating gradient of the main linac from 30 GHz and 150 MV/m to 12 GHz and 100 MV/m respectively. This major change of parameters has been driven by the results of a main linac cost and performance optimization [1]. A new set of overall CLIC parameters is under preparation [2]. In this report, the rf design of the new X-band accelerating structure for the CLIC main linac is presented.

## RF DESIGN AND OPTIMIZATION

Frequency and gradient are the key parameters for any accelerating structure. Following their major change fundamental issues ranging from the basic rf design of the cell to the structure rf design and optimization procedure have been revisited.

### *Basic Cell Geometry and HOM Damping*

The basic cell geometry and heavy damping developed for 30 GHz CLIC structures have been carried over into the X-band CLIC structures. However the reduction in frequency by factor 2.5 and, even more importantly, the gradient reduction by factor 1.5 results in an overall reduction of the pulsed surface heating temperature rise $\Delta T^{max}$ of $1.5^2{\cdot}2.5^{1/2} \approx 3.6$ in a scaled structure at the same pulse length. Because of this the old structure design, which was based on hybrid slotted iris plus waveguide damping, was not simply scaled [3] to the new frequency keeping pulse length the same. Instead the decrease in the pulsed surface heating was used to eliminating the iris slots, and compensating by opening the damping waveguide coupling aperture. The first measure reduces the maximum surface fields on the iris and consequently increases the high gradient potential, on one hand, but degrades the HOM damping because of the absence of slots, on the other hand. The second measure improves the waveguide damping to the required level but reduces the surface of the outer cell wall and thus increases the temperature rise which, nevertheless, still remains acceptable. The basic cell geometry after these modifications is shown in Fig. 1. The wakefield damping waveguides result in a lowest dipole-band Q of below ten. The cell has an elliptical cross section iris and convex elliptical cross-section outer walls in order to minimize surface fields. The four damping waveguides are terminated with broadband loads which are not shown in Fig. 1. This geometry is very close to the one which has been already proposed as the nominal CLIC accelerating structure design [4].

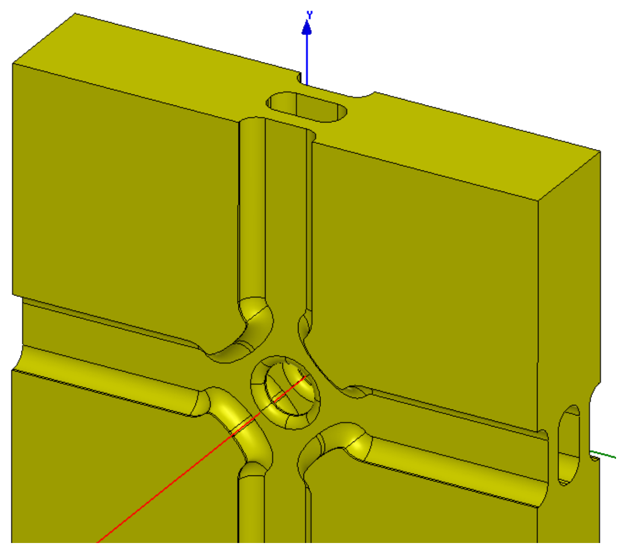

Figure 1: Basic cell geometry of the accelerating structure with strong waveguide HOM damping.

### *RF Constraints for X-band Copper Structures*

A significant effort has been made to collect as many additional X-band experimental data points as possible beyond those that have been used in [1] in order to refine the rf constraints for copper structures. Based mainly on the NLC/JLC X-band program [5] many new unpublished data points have been collected via private communications with SLAC colleagues [6]. All the collected data is summarized in [7]. Based on the high gradient performance of X-band travelling-wave accelerating structures with rf phase advance per cell of 120 and 150 degree the two rf constraints (1) and (3) used in [1] have been updated to:

1. Surface electric field: $E_{surf}^{max} < 260$ MV/m
2. Pulsed surface heating: $\Delta T^{max} < 56$ K
3. Power: $P_{in}/C{\cdot}\tau_p^{1/3} < 18$ MW/mm$\cdot$ ns$^{1/3}$

Here $E_{surf}^{max}$ refers to maximum surface electric field in the structure, $P_{in}$ refers to input power and $\tau_p$ refers to pulse length. $C$ is the circumference of the first regular iris. This set of rf constraints has been used in the rf design and optimization of the CLIC X-band accelerating structure which is described in the next section.

### *Structure Optimization*

Essentially the same optimization procedure as used in [1] has been applied for the final structure optimization except the frequency and the gradient were fixed and the values used for two of the high-power constraints were changed as described in the previous section. Fixing frequency and gradient allowed a significant reduction in the step size by which the other free parameters of the structure were varied. These parameters include first and last iris radius and thickness, structure length and pulse length. In addition 120 and 150 degree per cell phase advance were compared. The optimisation was made twice, once with performance and once with cost as the final criterion. No advantage was observed both in performance and in cost for 150 degree phase advance so the classical value of 120 degree has been chosen. On the other hand, the choice of the structure length was not so clear because the optimum length of for cost was 18 cm and the optimum length for performance was 30 cm. A structure active length of 23 cm was chosen as a compromise.

## STRUCTURE PARAMETERS

Table 1: CLIC_G Structure Parameters

| | |
|---|---|
| Average loaded accelerating gradient | 100 MV/m |
| Frequency | 12 GHz |
| RF phase advance per cell | $2\pi/3$ rad. |
| Average iris radius to wavelength ratio | 0.11 |
| Input, Output iris radii | 3.15, 2.35 mm |
| Input, Output iris thickness | 1.67, 1.00 mm |
| Input, Output group velocity | 1.66, 0.83 % of $c$ |
| First and last cell Q-factor (Cu) | 6100, 6265 |
| First and last cell shunt impedance | 89, 112 MΩ/m |
| Number of regular cells | 24 |
| Structure length including couplers | 230 mm (active) |
| Bunch spacing | 0.5 ns |
| Bunch population | $3.7\times10^9$ |
| Number of bunches in the train | 312 |
| Filling time, rise time | 62.9, 22.4 ns |
| Total pulse length | 240.8 ns |
| Peak input power | 63.8 MW |
| RF-to-beam efficiency | 27.7 % |
| Maximum surface electric field | 245 MV/m |
| Maximum pulsed surface heating temperature rise | 53 K |

After a few iterations of the optimization which also took into account feed-back from other CLIC sub-systems, a final set of parameters for main linac accelerating structures emerged under the name CLIC_G.

The main parameters of the structure are presented in Table 1. Several issues are worth emphasising. Firstly, following beam dynamics requirements, the optimum average aperture radius to wavelength ration is 0.11 resulting in the group velocity reaching in the last cell 0.83 % $v_g/c$. At this rather low group velocity, the bandwidth of the structure sets a lower limit to the rise time of the field level in a cell in the same way as in a high Q cavity. This rise-time limit is also shown in the Table 1 together with the conventional filling time of a travelling-wave structure. The consequence of the limited bandwidth is that two ramps are necessary at the beginning of the pulse to simultaneously compensate for the structure bandwidth and for the beam loading induced bunch to bunch energy spread. The input pulse shape is shown in Fig. 2.

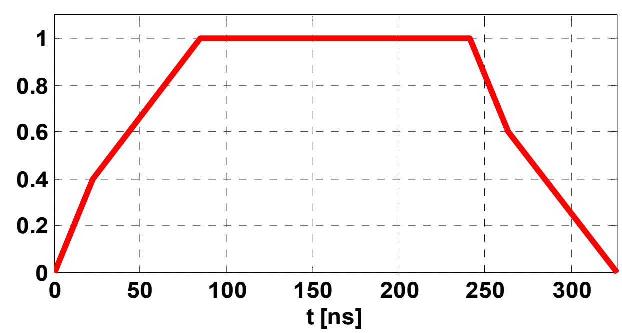


Figure 2: Schematic shape of the input pulse for CLIC_G.

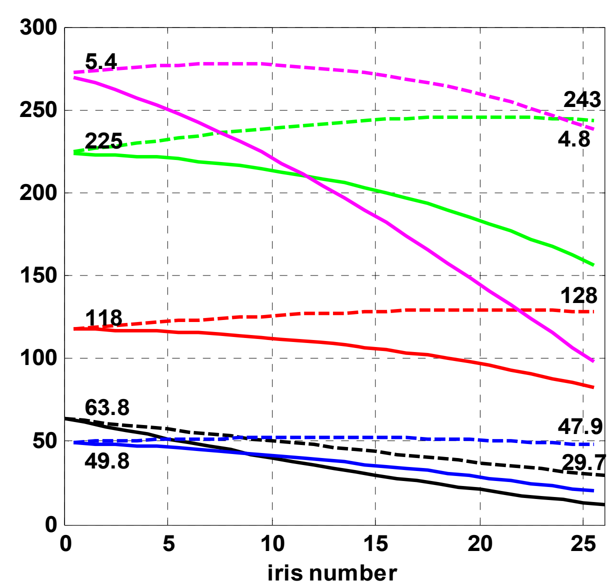


Figure 3: The fundamental mode properties of the nominal CLIC accelerating structure, CLIC_G. The traces from top to bottom are: $S_c$ *40 [W/μm$^2$](pink), surface electric field [MV/m](green), accelerating gradient [MV/m](red), power [MW](black), pulse surface temperature rise [K](blue). Dashed traces are unloaded and solid are beam loaded conditions.

Secondly, both the iris radius and thickness are tapered linearly in order to provide an optimum distribution of various high-power parameters and to avoid the hot spots along the structure. Distributions of these parameters are shown in Fig. 3. The unloaded structure gradient and the surface electric field rise slightly towards the end. The temperature rise is made to be constant because it is the dominant high-power constraint for the present type of HOM damping. In Fig. 3, the pink line shows the distribution of a new field quantity $S_c$ [7] which serves as a limit for high gradient performance and to certain extent combines both the power and the surface electric field constraints. Though it was not directly implemented in the optimization algorithm, its distribution looks reasonable and its maximum value of 5.5 W/μm$^2$ is rather close to experimental observations summarized in [7]. Several prototypes of the CLIC_G structure without and with damping features are currently under fabrication and planned to be tested soon [8].

Table 2: Parameters of the lowest dipole-band modes in CLIC_G

| Cell | First | Middle | Last |
|---|---|---|---|
| Q-factor | 10 | 7.7 | 6.3 |
| Amplitude [V/pC/mm/m] | 117 | 140 | 156 |
| Frequency [GHz] | 16.74 | 17.21 | 17.67 |

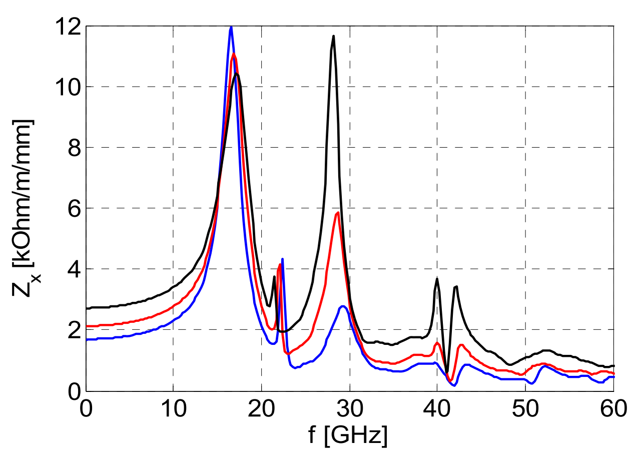


Figure 4: Transverse impedances of the first (blue), middle (red) and last (black) cells of the CLIC_G structure.

The taping also provides detuning of the higher order modes which is an important effect even for heavily damped structures. The relative contributions of the heavy damping and detuning to the transverse wakefield spectrum is shown in Fig. 4. Parameters of the lowest dipole-band modes calculated from the fitting to the impedance curves are listed in Table 2. The transverse wake of the full structure was computed in time domain using parallel code GdfidL [9] is the result is shown in Fig 5. One can see that the wake at the position of the second bunch is below the 7 V/pC/mm/m, as required for beam dynamics.

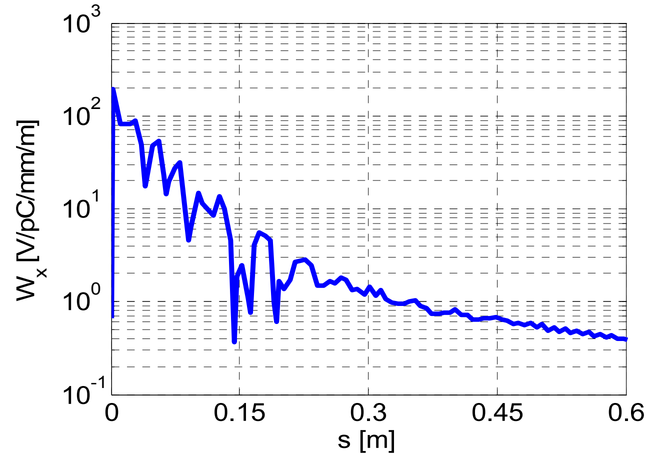


Figure 5: The envelope of the transverse wake of the CLIC_G structure. The CLIC bunch spacing is 0.15 m.

## CONCLUSIONS

A new X-band CLIC main linac accelerating structure has been designed taking into account complex interplay between beam dynamics, rf performance and the overall machine cost. The new structure provides rf-to-beam efficiency of 27.7 % and strong HOM damping which has been validated by full scale time domain simulations.

## REFERENCES


[1] A. Grudiev et al., “Optimum Frequency and Gradient for the CLIC Main Linac Accelerating Structure”, This conference.

[2] The CLIC Study Team (edited by F. Tecker), “CLIC 2008 Parameters”, CLIC-Note-764, to be published.

[3] A. Grudiev and W. Wuensch, “Design of High Gradient Accelerating Structure for CLIC”, In: AIP Conf. Proc.: 807 (2006), pp.439-446.

[4] J.-Y. Raguin et al., “Progress on the Design of a Damped and Tapered Accelerating Structure for CLIC”, PAC’03, Portland, May 2003.

[5] S. Doebert et al., “High Gradient Performance of Prototype NLC/GLC X-band Accelerator Structures”, PAC’05, Knoxville, May 2005.

[6] C. Adolphsen, S. Doebert, Private communications.

[7] A. Grudiev and W. Wuensch, “A new local field quantity describing the high gradient limit of accelerating structures”, This conference.

[8] R. Zennaro et al., “Design and Fabrication of CLIC Test Structures”, This conference.

[9] W. Bruns, www.gdfidl.de.

# A NEW LOCAL FIELD QUANTITY DESCRIBING THE HIGH GRADIENT LIMIT OF ACCELERATING STRUCTURES

A. Grudiev, W. Wuensch, CERN, Geneva, Switzerland

*Abstract*

A new local field quantity is presented which gives the high-gradient performance limit of accelerating structures in the presence of vacuum rf breakdown. The new field quantity, a modified Poynting vector $S_c$, is derived from a model of the breakdown trigger in which field emission currents from potential breakdown sites cause local pulsed heating. The field quantity $S_c$ takes into account both active and reactive power flow on the structure surface. This new quantity has been evaluated for many X-band and 30 GHz rf tests, both travelling wave and standing wave, and the value of $S_c$ achieved in the experiments agrees well with analytical estimates.

## INTRODUCTION

Limitations coming from the rf breakdown in vacuum strongly influence the design of a high gradient accelerating structures. Rf breakdown is a very complicated phenomenon involving effects which are described in different fields of applied physics such as surface physics, material science, plasma physics and electromagnetism. No quantitative theory to date satisfactorily explains and predicts rf breakdown levels in vacuum. In the framework of CLIC study [1] a significant effort has been made to derive the high-gradient limit due to rf breakdown and to collect all available experimental data both at X-band and at 30 GHz to use to check the validity of the limiting quantity. The quantity has been used to guide high gradient accelerating structure design and to make quantitative performance predictions for structures in the CLIC high power testing program [2].

## EXPERIMENTAL DATA

The quest to accumulate high-gradient data in a coherent and quantitatively comparable way focused on two frequencies: 30 GHz, the old CLIC frequency, and 11.4 GHz which is the former NLC/JLC frequency and is very close to the new CLIC frequency of 12 GHz. To our knowledge only at these two frequencies has a systematic study been done where the structure accelerating gradient was pushed up to the limit imposed by the rf breakdown and where relevant parameters were measured. In particular all available data where the breakdown rate (BDR), the probability of a breakdown during a pulse, was measured at certain gradient and pulse length was collected. Data from structures where the performance was limited by an identified defect or by some other area of the structure such as the power couplers which are not directly related to the regular cell performance were not included. The main parameters of the structures are summarized in the Table 1 which shows the rather large variation in group velocity (from 0 up to ~40 % of the speed of light), rf phase advance (from 60 to 180 degree per cell) and iris geometry which is available for analysis. The experimentally achieved value of the gradient scaled to pulse length of 200 ns and breakdown rate of $10^{-6}$ per pulse as described below is presented together with the corresponding references.

In a typical high-gradient experiment, the BDR is measured at fixed value of accelerating gradient and pulse length. On the other hand, it is most convenient to compare performance with the achieved gradient at a fixed value of the pulse length and BDR. To do this the measured data has had to be scaled. This involves two steps - first scaling the gradient versus pulse length and then scaling the gradient versus BDR. Both of these scaling behaviours have been measured in a number of structures but not systematically in all cases. In order to scale the data for the structures where these scaling laws have not been measured a general scaling law which us consistent with all measured data has been applied.

The dependence of gradient on pulse length at a fixed BDR has well established scaling law observed in many experiments (see for example [3]):

$$E_{acc} t_p^{1/6} = const \tag{1}$$

where $E_{acc}$ denotes the gradient and $t_p$ the pulse length. It was also confirmed by fitting the data for the structure numbers 3, 4, 8, 9, 10, 12, 13, 18, 20 in Table 1.

For the gradient versus BDR dependence at a fixed pulse length the different scaling laws which have been used are exponential (see for example [3]) and a power law. In this paper, we have used a power law:

$$E_{acc}^{30} \big/ BDR = const \tag{2}$$

It was also confirmed by fitting the data for the structure numbers 3, 8, 10, 12, 13, 18, 20, 21 in Table 1.

Finally, (1) and (2) can be combined into,

$$E_{acc}^{30} t_p^{5} \big/ BDR = const \tag{3}$$

This general scaling law has been used to scale the collected experimental data to the pulse length of 200 ns and BDR of $10^{-6}$ per pulse. The results are presented in the last column of Table 1.

## RF BREAKDOWN CONSTRAINTS

For a long time, the surface electric field was considered to be the main quantity which limits accelerating gradient because of its direct role in field

Table 1: Structure Parameters Used in the Analysis. From left to right: number for references in the following figures, name, frequency, rf phase per cell, group velocity and first iris radius, thickness and tip ellipse ratio (except for T18vg2.6-Out, where $v_g/c$, $a$, $d$ and $e$ are given for the last regular cell), and the accelerating gradient (average or single cell depending on the structure type) scaled to the pulse length of 200 ns and BDR of $10^{-6}$ per pulse.

| N | Name | $f$ [GHz] | Δφ [°] | $v_g/c$ [%] | $a$ [mm] | $d$ [mm] | $e$ | $E_{acc}$ [MV/m] @ 200 ns, $10^{-6}$ 1/pulse |
|---|---|---|---|---|---|---|---|---|
| 1 | DDS1 | 11.424 | 120 | 11.7 | 5.7 | 1.0 | 1 | 52.9 (average) [4] |
| 2 | T53vg5R | 11.424 | 120 | 5.0 | 4.45 | 1.66 | 1 | 72.0 (average) [4] |
| 3 | T53vg3MC | 11.424 | 120 | 3.3 | 3.9 | 1.66 | 1 | 91.1 (average) [4] |
| 4 | H90vg3 | 11.424 | 150 | 3.0 | 5.3 | 4.2 | 1 | 69.2 (average) [4] |
| 5 | H60vg3 | 11.424 | 150 | 2.8 | 5.3 | 4.4 | 1 | 72.0 (average) [4] |
| 6 | H60vg3S18 | 11.424 | 150 | 3.3 | 5.5 | 4.6 | 1.15 | 67.7 (average) [3, 4] |
| 7 | H60vg3S17 | 11.424 | 150 | 3.6 | 5.3 | 3.7 | 1.34 | 74.2 (average) [3, 4] |
| 8 | H75vg4S18 | 11.424 | 150 | 4.0 | 5.3 | 3.04 | 1.36 | 90.0 (average) [4] |
| 9 | H60vg4S17 | 11.424 | 150 | 4.5 | 5.68 | 3.65 | 1.37 | 73.6 (average) [3, 4] |
| 10 | HDX11 | 11.424 | 60 | 5.1 | 4.21 | 1.45 | 2.4 | 49.3 (first cell) [5] |
| 11 | CLIC-X-band | 11.424 | 120 | 1.1 | 3.0 | 2.0 | 1 | 107.3 (first cell) [6] |
| 12 | T18vg2.6-In | 11.424 | 120 | 2.6 | 4.06 | 2.79 | 1.21 | 114.5 (average) [7] |
| 13 | T18vg2.6-Out | 11.424 | 120 | 1.0 | 2.66 | 1.31 | 1.15 | 114.5 (average) [7] $v_g/c$, $a$, $d$, $e$ for last cell |
| 14 | SW1a5.65t4.6 | 11.424 | 180 | 0 | 5.65 | 4.6 | 3.4 | 92.2 (single cell) [8] |
| 15 | SW20a3.75 | 11.424 | 180 | 0 | 3.75 | 2.6 | 1.7 | 67.0 (average) [4] |
| 16 | SW1a3.75t2.6 | 11.424 | 180 | 0 | 3.75 | 2.6 | 1.7 | 135.6 (single cell) [8] |
| 17 | SW1a3.75t1.66 | 11.424 | 180 | 0 | 3.75 | 1.66 | 1 | 135.2 (single cell) [8] |
| 18 | 2π/3 | 29.985 | 120 | 4.7 | 1.75 | 0.85 | 1 | 61.1 (first cell) [9] |
| 19 | π/2 | 29.985 | 90 | 7.4 | 2 | 0.85 | 1 | 43.3 (first cell) [10] |
| 20 | HDS60L | 29.985 | 60 | 8.0 | 1.9 | 0.55 | 2.5 | 40.5 (first cell) [11] |
| 21 | HDS60S | 29.985 | 60 | 5.1 | 1.6 | 0.55 | 2.4 | 49.7 (first cell) [11] |
| 22 | PETS9mm | 29.985 | 120 | 39.8 | 4.5 | 0.85 | 1 | 14.6 (last cell) [12] |

emission. The magnetic field was considered to be unimportant. However, as more data has become available, it is clear that the maximum surface electric field could not serve as an ultimate constraint in the rf design of high gradient accelerating structures because the large variation of achieved surface electric field as shown in Fig. 1(top).

Recently, new ideas have appeared about the importance of power flow in the accelerating structures. The proposal that the ratio of the input power to the iris circumference, *P/C*, is the parameter which limits gradient in travelling-wave structures (TWS) is presented in [13]. The square root of *P/C* (to be linear in field quantity) is plotted in Fig. 1(middle). It is evident that P/C shows much smaller spread than surface electric field and therefore is a better constraint to be used in rf design. Nevertheless, there are shortcomings which limit its applicability:

- Structure number 8 exceeds significantly all the others.
- Standing-wave structures (SWS) are not described by definition as there is essentially no power flow through the iris aperture.
- Data achieved at different frequencies must be scaled inversely with frequency.

The last point is also confirmed by an observation that scaled structures achieve the same gradient at the same pulse length and BDR [5, 11]. This observation also favours an idea that it is a combination of local electric and magnetic fields which sets a limit to achievable gradient rather than an integral parameter which must then be scaled with frequency.

## A NEW QUANTITY

The new proposed field quantity is based on the following considerations. First, at very low values the BDR is determined mainly by processes which accumulate over many pulses rather than during a single pulse. Local pulsed heating of future breakdown sites by the field emission currents is consistent with this

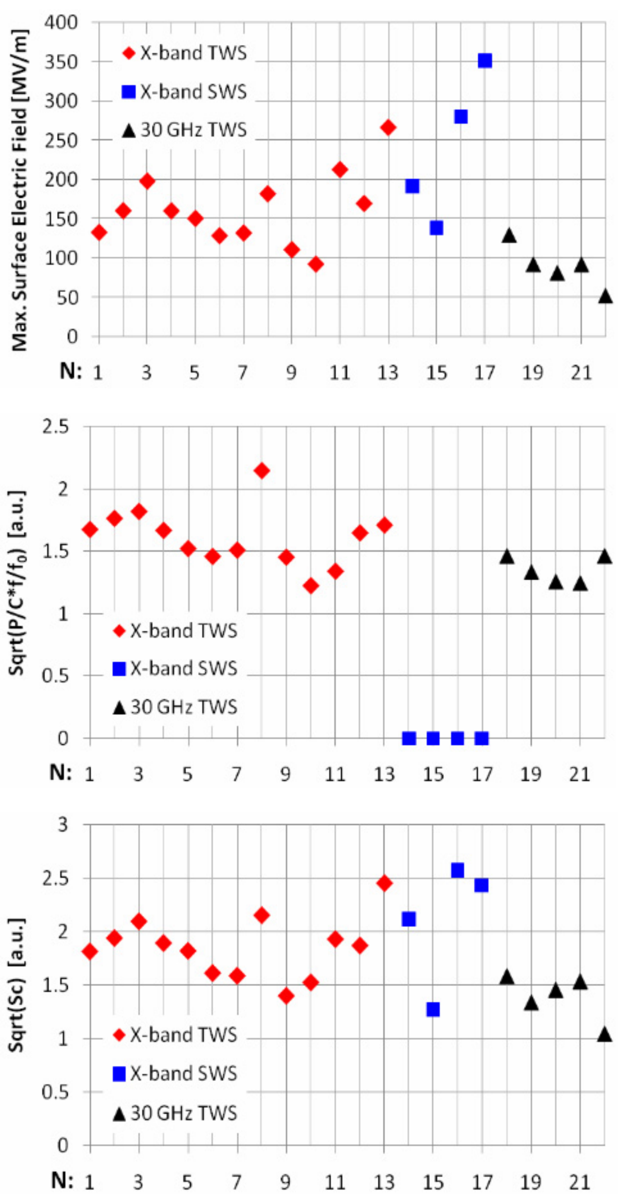


Figure 1: Maximum surface electric field (top), square root of P/C (middle) and square root of $S_c$ (bottom) are scaled to pulse length of 200 ns and BDR of $10^{-6}$ per pulse and plotted for the structures presented in Table 1. For P/C, 30 GHz data scaled by factor 30/11.4.

postulate. The actual trigger of a breakdown can be via many mechanisms and its combinations - mechanical fatigue and fracture, melting, gas desorption – the details of which are not relevant for further considerations. Second, any heating requires power and there is no other source of power other than rf power flow on the surface. This is naturally described by the complex Poynting vector $S$. The real part, $\mathrm{Re}\{S\}$, describes active power flow along TWSs. It is however zero in SWSs. $\mathrm{Im}\{S\}$ describes reactive power flow inside the cells and is non-zero in all rf structures. Electric and magnetic fields are in phase in $\mathrm{Re}\{S\}$ 90 degree out of phase in $\mathrm{Im}\{S\}$. Thus the reactive power flow couples much more weakly to the field emission current than active power flow. Taking this into account along with the exponential dependence of emission current on electric field the new quantity, the modified Poynting vector:

$$S_c = \mathrm{Re}\{S\} + \mathrm{Im}\{S\}/6 \qquad (4)$$

is proposed. The square root of $S_c$ is plotted in Fig. 1(bottom) and demonstrates rather good agreement between the structures from Table 1. It effectively combines the surface electric field and P/C limits and can be used as a single rf breakdown constraint in rf design. Its numerical value should not exceed 5.5 W/μm$^2$ in order to have BDR below $10^{-6}$ 1/pulse at pulse length of 200 ns.

## ACKNOWLEDGEMENTS

The authors would like to thank S. Calatroni for many inspiring discussions and encourage the reader to study the closely related calculations he has made on breakdown.

## REFERENCES


[1] F. Tecker (ed.), “CLIC 2008 Parameters”, CLIC-Note-764, to be published.

[2] R. Zennaro et al., “Design and Fabrication of CLIC Test Structures”, This conference.

[3] S. Doebert et al., “High Gradient Performance of Prototype NLC/GLC X-band Accelerator Structures”, PAC’05, Knoxville, May 2005.

[4] C. Adolphsen, S. Doebert, Private communications.

[5] S. Doebert et al., “High Power Test of an X-band Slotted-Iris Accelerator Structure at NLCTA”, PAC’07, Albuquerque, June 2007.

[6] J.W. Wang et al., “SLAC/CERN High Gradient Tests of an X-band Accelerating Section”, PAC’95, Dallas, May 1995.

[7] S. Doebert et al., “High Power Test of a Low Group Velocity X-band Accelerator Structure for CLIC”, This conference.

[8] V. Dolgashev et al., “Status of High Power Tests of Normal Conducting Single-Cell Structures”, EPAC’08, Genoa, June 2008.

[9] R. Corsini et al., “A High-Gradient Test of 30 GHz Copper Accelerating Structure”, LINAC’06, Knoxville, August 2006.

[10] S. Doebert et al., “High-Gradient Test Results”, CLIC’07, Geneva, October 2007.

[11] J. Rodriguez et al., “30 GHz High-Gradient Accelerating Structure Test Results”, PAC’07, Albuquerque, June 2007.

[12] C. Achard et al., “30 GHz Power Production in CTF3”, PAC’05, Knoxville, May 2005.

[13] W. Wuensch, “The Scaling of the Travelling-Wave RF Breakdown Limit”, CLIC-Note-649, 2006.

# DEVELOPMENT STATUS OF THE PI-MODE ACCELERATING STRUCTURE (PIMS) FOR LINAC4

P. Bourquin, R. De Morais Amaral, G. Favre, F. Gerigk, J-M. Lacroix, T. Tardy, M. Vretenar, R. Wegner, CERN, Geneva, Switzerland

*Abstract*

The high-energy section of Linac4, between 100 and 160 MeV, will be made of a sequence of 12 seven-cell accelerating cavities of the Pi-Mode Structure (PIMS) type, resonating at 352 MHz. The cell length is the same within a cavity, but changes from cavity to cavity according to the beam velocity profile. Compared to other structures used in this energy range, $\pi$-mode cavities with a low number of cells have the advantage of simplified construction and tuning, compensating for the fact that the shunt impedance is about 10% lower because of the lower frequency. Field stability in steady state and in presence of transients is assured by the low number of cells and by the relatively high coupling factor of 5%. Standardising the linac RF system to a single frequency is considered as an additional economical and operational advantage.

The mechanical design of the PIMS will be very similar to that of the 352 MHz normal conducting 5-cell LEP (Large Electron Proton collider at CERN) accelerating cavities, which have been successfully operated at CERN for 15 years. After reviewing the basic design principles, the paper will focus on the tuning strategy, on the field stability calculations and on the mechanical design. It will also report the results of measurement on a cold model and the design of a full-scale prototype.

## RF DESIGN

The PIMS replaces a Side Coupled Linac (SCL), which was originally foreseen in the high energy section of Linac4 [1]. The SCL was using a total of 468 cells (220 accelerating cells plus coupling cells) operating at 704 MHz to accelerate beam from 90 to 160 MeV, while the PIMS now covers 102 to 160 MeV using only 84 cells (12 cavities of 7 cells). Since the construction and tuning of $\pi$-mode cavities is already well known at CERN, and since the SCL entails the use of 2 different RF frequencies in Linac4 it was decided to give preference to the PIMS [2] despite the $\approx$ 12% lower shunt impedance (see Fig. 1).

The basic design is a scaled (in geometrical $\beta$) version of the normal conducting LEP accelerating structure [3], which was then modified for higher cell-to-cell coupling. The accelerating gradient in the first 10 cavities has been adjusted to a relatively high value of 4 MV/m, resulting in a maximum power of $\approx$ 1 MW per cavity. Using a high gradient limits the number of cells per cavity to 7, and thus makes it easier to obtain a flat field distribution. The last 2 cavities are used not only for acceleration but also for energy painting for injection into the subsequent Proton Synchrotron Booster (PSB). In order to achieve a high ramping speed in these cavities ($\approx$ 2 MeV/10 $\mu$s), the nominal accelerating gradient was lowered to 3.1 MV/m. An overview of the main parameters is given in Table 1. The basic design was made with Superfish and the 3D calculations to determine the coupling coefficients, shunt impedance degradation (due to coupling, tuners, etc), end-cell tuning were made with GdfidL [4] (see Fig. 2).

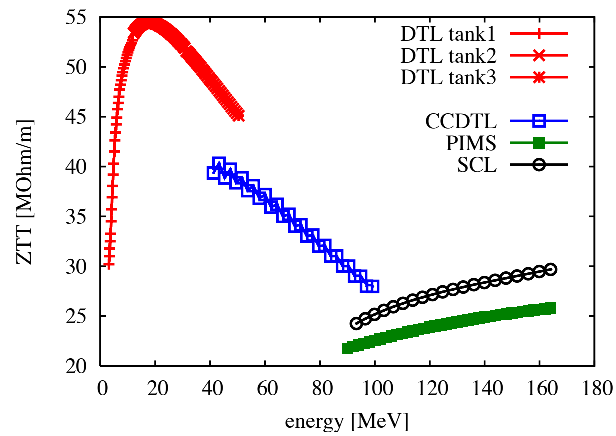


Figure 1: Shunt impdance ($ZT^2$) for the Linac4 accelerating structures (80% of simulated values, including additional losses on stems, coupling holes, tuning rings).

Table 1: Main Parameters

| parameter | | value |
|---|---|---|
| frequency | MHz | 352.2 |
| input energy | MeV | 102 |
| output energy | MeV | 160 |
| electric gradient | MV/m | 4 |
| peak power/cav.* | MW | 1 |
| max. surface field | kilpatrick | 1.8 |
| design duty cycle | % | 10 |
| max. expected d.c. | % | 6 |
| Linac4 d.c. | % | 0.1 |
| cells/cavity | | 7 |
| number of cavities | | 12 |
| beam aperture | mm | 40 |

* including beam loading

Using a coupled circuit model one can evaluate the voltage error due to the exptected spread in cell frequencies, which is linked to the production tolerances and the tuning precision. Assuming the same frequency scatter ($\pm$25 kHz)

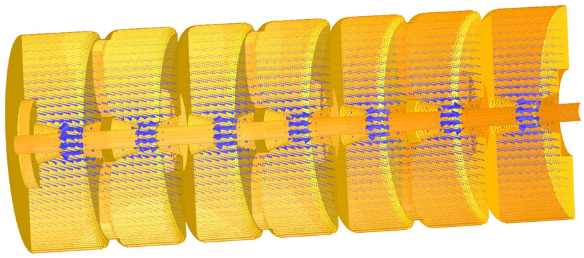

Figure 2: GdfidL simulation of the 7-cell structure.

as for the LEP cavities one can calculate the expected voltage error versus coupling factor as shown in Fig. 3.

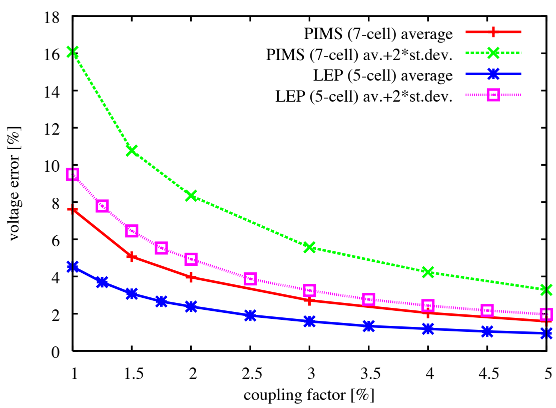


Figure 3: Voltage error versus coupling factor (3000 error cases per point).

One can see that we can achieve the same level of voltage errors (av. + 2x st. dev:6.5%) as in LEP (5 cells, 1.5% coupling), when increasing the coupling to 2.7% for a 7-cell structure. After calculating the loss in shunt impedance for various coupling factors, we decided to use 5% coupling, for which we expect a 11% reduction in $ZT^2$. Further reductions in shunt impedance are coming from: surface roughness ($\approx -7\%$), RF coupler ($\approx -2\%$), increased volume of end cells ($\approx +4\%$), heating during high-duty cycle operation ($\approx -3.5\%$), welding grooves ($\approx -2\%$), tuning rings and tuners ($\approx -4\%$). For Linac4/SPL operation this means a total reduction of $\approx 22/26\%$ with respect to Superfish. For power calculations we use an additional safety margin and reduce the calculated values by 30%.

The frequency tuning of the structure is done in 2 steps: i) Before the joining of the discs and cylinders the machined cells are clamped together and the cell frequencies are measured. Deviations are then corrected by machining the "tuning islands", which are shown in Fig. 4, taking into account the expected frequency shifts due to vacuum, welding, heating, etc, which are listed in Table 2. ii) Each cell is equipped with a tuner, which can change the cell-frequency by $\pm 0.5$ MHz. Cells 2 and 6 have movable tuners and all other cells have fixed tuners, which are cut to length after the assembly of the complete cavities.

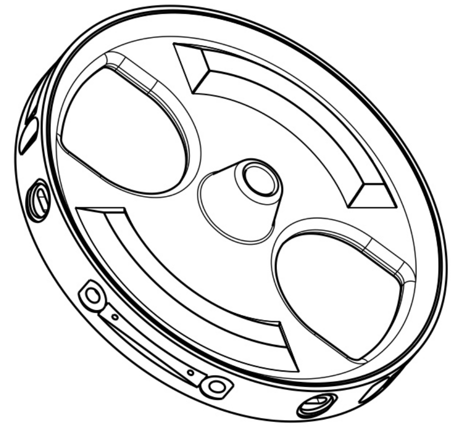

Figure 4: 3D disc geometry with tuning islands.

Table 2: Expected Frequency Shifts for the Full Cavity

| **effect** | **Δf [kHz]** |
|---|---|
| machining tolerances | $\pm 200$ |
| thermal expansion | $-200$ |
| welding rings | -190 |
| weld shrinkage (disc/cylinder weld)* | -310 |
| air to vacuum | +114 |

* assuming 0.2 mm shrinkage per weld (to be confirmed)

## COLD MODEL MEASUREMENTS

A scaled (to 704 MHz) 7-cell aluminium cold model was constructed at CERN to test the RF design procedure for cell frequencies, coupling factor, end-cell tuning, and field flatness. Two cells of the model are shown in Fig. 5 and a field profile measured via bead-pull is shown in Fig. 6. The measured field flatness was better than expected and is within 0.8% ($\Delta E/E_0$).

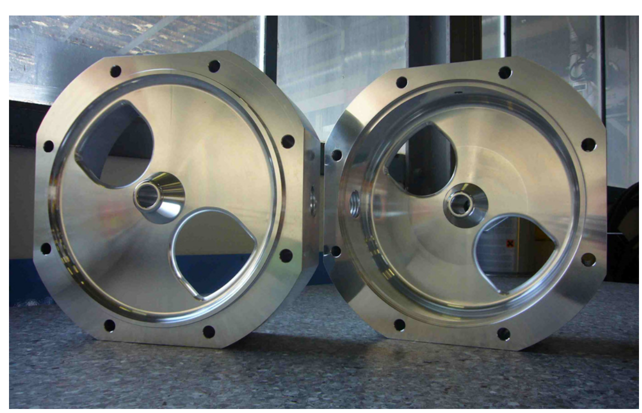

Figure 5: Aluminium cold model.

When detuning the end cells the coupled circuit model predicts a tilt sensitivity of 66%/MHz (at 352 MHz), which could be confirmed by measurements.

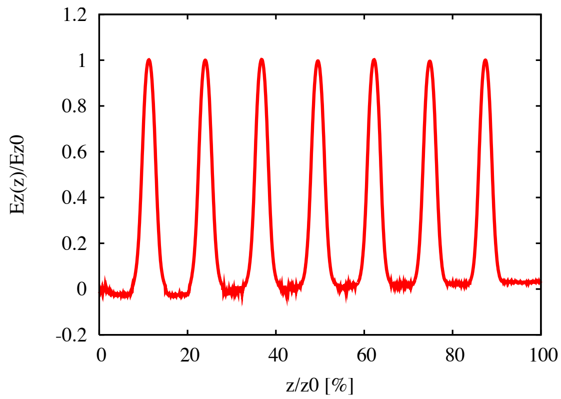


Figure 6: Measured field profile of cold model (bead-pull).

## SERIES CONSTRUCTION

The structure is composed of discs (as in Fig. 4) and cylinders, which are joined via electron-beam (EB) welding around the circumference. The welding is applied from the outside with full penetration as shown in Fig. 7.

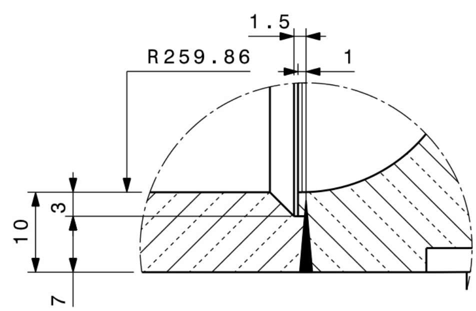


Figure 7: Electron-beam welding joint between discs (right) and cylinders (left).

Discs and cylinders are machined out of pre-shaped 3D forged OFE copper. The option of using copper plated steel was abandoned after cooling simulations showed excessive heating of the structure. All copper ports (including the brazed steel vacuum flanges) are EB welded onto the cylinders before joining the whole structure. The only exception is the RF port together with its cooling channels, which are machined out of a thick cylinder. In this case, in order to braze the 316 LN vacuum flanges onto the RF and tuner ports, the whole cylinder is put into the brazing oven. All other discs and cylinders do not undergo any heat treatment and thus maintain their original material properties.

For the cooling of the cells water channels are drilled from the outside into the discs as shown in Fig. 8. Due to the high heat load around the edges of the coupling slots additional channels were introduced to avoid any deformation of the coupling slot shape due to increased temperatures during operation. In contrast to the LEP cavities no cooling channels are used on the cylinders. ANSYS© simulations, which assume a constant water temperature of 21 $\mathrm{deg}$ and an average normal flow velocity of 1.4 m/s, show maximum temperatures of $\approx 60\,\mathrm{deg}$ at the nose tips and the inner corner radius of the slots for a 10% duty cycle (see Fig. 9).

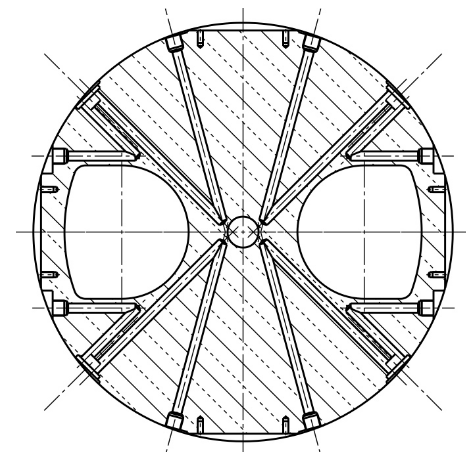

Figure 8: Cooling channels in the discs.

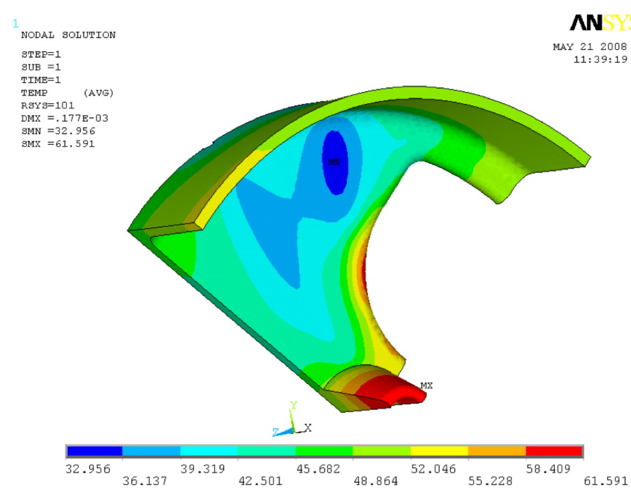


Figure 9: Cooling simulation with ANSYS©, assuming constant average water temperature of 21 $\mathrm{deg}$, average normal flow velocity of 1.4 m/s, and a duty cycle of 10%.

The stress values due the structures own weight, the weight of attached wave-guide and the cooling thermal stresses, are well below the limits for plastic deformation, following the von Mises criterion. The construction of a "hot" prototype starts in October in the CERN workshops and high-power tests are expected in summer 2009.

## REFERENCES

[1] F. Gerigk, M. Vretenar (Editors), "Linac4 technical design report", CERN-AB-2006-084, December 2006.

[2] F. Gerigk *et al.*, "RF structures for Linac4", PAC07, Albuquerque, USA.

[3] I. Wilson and H. Henke, "The LEP main ring accelerating structure", CERN 89-09, November 1989.

[4] W. Bruns, "GdfidL: a finite difference program with reduced memory and CPU usage, PAC97, Vancouver, Canada.

# SHUNT IMPEDANCE STUDIES IN THE ISIS LINAC

C. Plostinar, STFC/RAL/ASTeC, Harwell, Didcot, Oxfordshire, UK
A. Letchford, STFC/RAL/ISIS, Harwell, Didcot, Oxfordshire, UK


## Abstract

The ISIS linac consists of four DTL tanks that accelerate a 50 pps, 20 mA H⁻ beam up to 70 MeV before injecting it into an 800 MeV synchrotron. Over the last decades, the linac has proved to be a stable and reliable injector for ISIS, which is a significant achievement considering that two of the tanks are more than 50 years old. At the time the machine was designed, the limited computing power available and the absence of 3D electromagnetic (EM) simulation codes, made the creation of a linac optimized for power efficiency almost impossible, so from this point of view, the ISIS linac is quite simple by today's standards. In this paper, we make a shunt impedance comparison study using the power consumption data collected from ISIS and the results obtained when simulating each of the four DTL tanks with 2D and 3D EM codes. The comparison will allow us to check the accuracy of our simulation codes and models and to assess their relative performance. It is particularly important to benchmark these codes against real data, in preparation for their use in the design of a proposed new linac, which will replace the currently aging ISIS injector [1].


## THE ISIS INJECTOR

The ISIS facility at Rutherford Appleton Laboratory (RAL), has been the world leading pulsed neutron source for over two decades, delivering neutrons for users from all over the world and proving to be a very stable and reliable machine. It consists of a 70 MeV $H^-$ injector, an 800 MeV synchrotron and two target stations [2]. The injector starts with an $H^-$ ion source, followed by a low energy beam transport line and a 665 keV RFQ operating at 202.5 MHz. The energy is then raised to 70 MeV by four Drift Tube Linac (DTL) tanks. Tanks 2 and 3 were built in the 1950s for the RAL Proton Linear Accelerator [3] and have been in operation ever since, while tanks 1 and 4 were built in the 1970s originally intended for the Nimrod accelerator, but first used in ISIS. A layout of the DTL section of the linac can be seen in Figure 1 and a list of parameters is given in Table 1.

Table 1: ISIS Linac Parameters

| | | |
|---|---|---|
| Energy | 70.4 | MeV |
| Frequency | 202.5 | MHz |
| Pulse Length | 200 – 250 | μs |
| Peak Current | 25 | mA |
| Repetition Rate | 50 | Hz |
| Total Length | 55 | m |
| Duty Cycle | 1 – 1.25 | % |

## ELECTROMAGNETIC MODELLING

The choice of accelerating structures is essential for every linac. In ISIS, the DTL structure is used for the entire length of the linac with small geometry variations between the tanks. The synchronous phase is kept constant at -30° in the four tanks, while the accelerating gradient varies: 1.6 – 2.2 MV/m in tank 1, 2.45 – 2. 55 MV/m in tank 2, 2.3 – 2.4 MV/m in tank 3 and 2.6 MV/m in tank 4. The geometry of a single DTL cell is very simple and it is not fully optimised for power efficiency resulting in a longer linac structure. In modern linac designs, the overall length of every tank is reduced by choosing a higher accelerating gradient and synchronous phase, optimising the cell geometry and by increasing the transit time factor by shortening the cell gap lengths [4].

The figure of merit which will be used to characterize the accelerating cavities is the effective shunt impedance per unit length, $ZT^2$, which is a measure of the effectiveness of producing an axial voltage $V_0$ for a given power dissipated, P [5]:

$$ZT^2 = \frac{(E_0 T)^2}{P/L}$$

T – transit time factor
$E_0 = V_0/L$ – average axial electric field
L – cell length

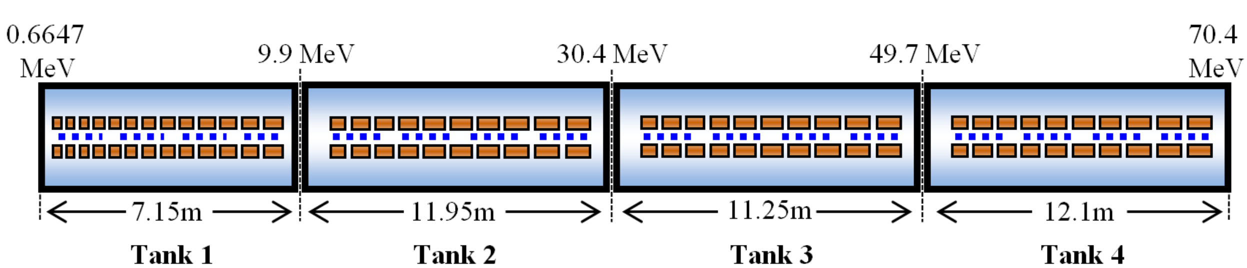


Figure 1: Layout of the DTL section of the ISIS Linac.

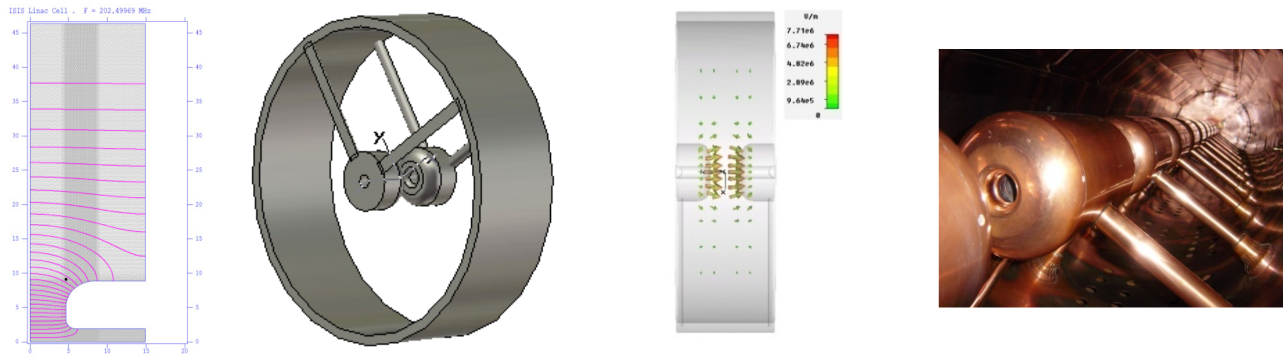

a. b. c. d.

Figure 2: DTL cell operating at 20 MeV and 202.5 MHz. a) 2D Superfish model. b) 3D cell geometry in Microwave Studio. c) Electric field vectors. d) Tank 3 of the ISIS linac.

Using the exact cell dimensions as in the ISIS linac, an accurate 2D model of the four DTL tanks has been prepared using Superfish, a tool used widely by linac designers [6]. The code evaluates RF cavities with cylindrical symmetry, but it can make corrections to take into account the effect of the stems, or the end plates on frequency and shunt impedance. A model of a single accelerating cell operating at 20 MeV can be seen in Figure 2a, while Table 2 details the input parameters for each individual tank.

The 148 cells have also been modelled in CST Microwave Studio [7], a 3D EM code normally used in linac design for problems that lack cylindrical symmetry, like the effect of tuners, post-couplers, stems, vacuum pumping ports, etc. but also to check the results calculated by the 2D codes. The geometrical model of a single cell can be seen in Figure 2b, and 2c, together with the electric field vectors as computed by Microwave Studio while Figure 2d is a picture inside tank 3.

## RESULTS

In Figure 3 the evolution of the effective shunt impedance per unit length along the linac is presented as predicted by the two models. The agreement between the two codes is reasonably good, although the 3D results seem to be more sensitive to the choice of mesh. As it can be seen, Microwave Studio predicts a constantly higher shunt impedance than Superfish in each of the four DTL tanks by up to 6%, although the two curves follow a very similar path. A big jump in shunt impedance can be seen at the transition between the tanks, due to the effects of the end plates, but also a lower average value in tanks 2 and 3. This is due to the fact that these tanks being quite old have been designed and built with an emphasis on reliability rather than power efficiency. Tanks 1 and 4 being of a later generation have a slightly different cell geometry and a higher shunt impedance indicating a different design approach.

Table 2: DTL Main Parameters

| | | **Tank 1** | **Tank 2** | **Tank3** | **Tank4** |
|---|---|---|---|---|---|
| Input Energy | MeV | 0.6647 | 9.90 | 30.4 | 49.7 |
| Output Energy | MeV | 9.90 | 30.4 | 49.7 | 70.4 |
| Accelerating Gradient ($E_0$) | MV/m | 1.6 – 2.2 | 2.45 – 2. 55 | 2.3 – 2.4 | 2.6 |
| Synchronous Phase | Deg | -30 | -30 | -30 | -30 |
| Max. Surface Electric Field | Kilpatrick | 0.67 | 0.81 | 0.84 | 0.87 |
| Number of Cells | | 56 | 41 | 27 | 24 |
| Tank Diameter | cm | 93.4 | 92.71 | 81.28 | 88 |
| Drift Tube Diameter | cm | 18 | 17.78 | 17.78 | 16 |
| Aperture Diameter | cm | 2.5 | 3.81 | 3.81 | 3 |
| Stems/Cell | | 1 | 2 | 2 | 1 |
| Total Length | m | 7.15 | 11.95 | 11.25 | 12.1 |

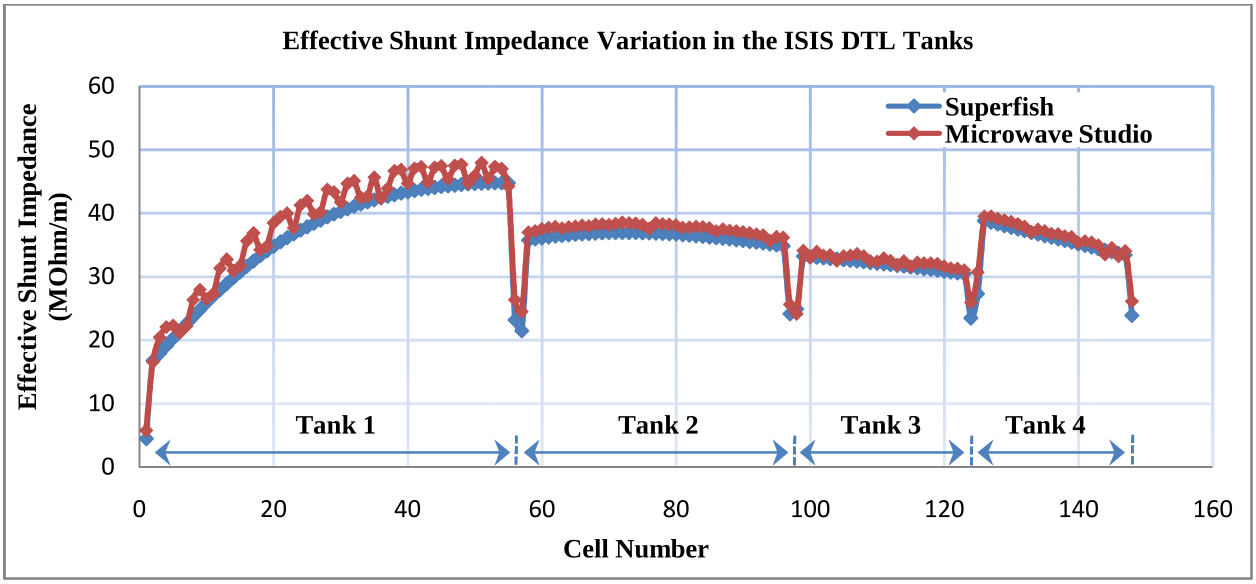


Figure 3: Effective shunt impedance variation in the ISIS DTL tanks.

However, a comparison between the shunt impedance calculated by the two models and the actual power levels measured in each of the four DTL tanks shows a mixed picture. As it can be seen in Figure 4, for tank 1, the measured power level is 0.49 MW, while Superfish and Microwave Studio predict 0.43 and 0.4 respectively, thus requiring a ~13% adjustment for Superfish and ~20% for Microwave Studio. The best agreement seems to be for tank 3 where the predicted shunt impedance has to be reduced by only ~10% for Superfish and ~12.5% for Microwave Studio. On the other hand, for tanks 2 and 4, the models overestimate the shunt impedance by a much higher fraction: 32%/37% for tank 2 and 23%/28% for tank 4. We believe that the significant disagreement between simulations and measurements for tanks 2 and 4 can be explained if we assume that these tanks are being operated at a higher electric field gradient than the design value. However, this assumption is very difficult to verify as in the current DTL setup, the electric field gradient cannon be accurately measured.

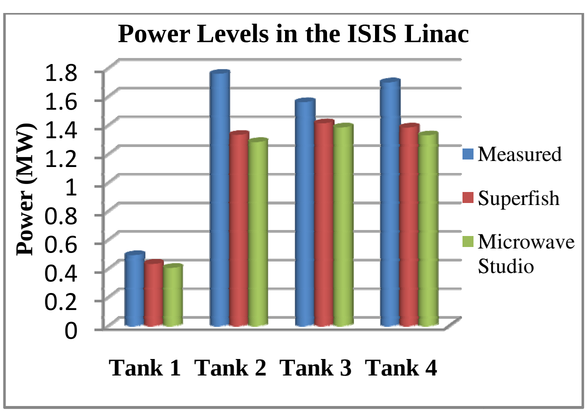


Figure 4: Power levels in the ISIS DTL tanks.

## CONCLUSIONS

Two computer models for the four ISIS DTL tanks have been created and the predicted shunt impedance has been compared with the power levels measured in the ISIS linac. While the 2D and the 3D simulation codes show a good agreement throughout the linac, the actual power dissipation is constantly underestimated by an average of ~20% by Superfish and ~25% by Microwave Studio. This difference is normal, and it is due to the effects of surface imperfections, coupling holes, post-couplers, tuners and other auxiliary equipment. However, one can note a relatively high discrepancy for tanks 2 and 4, which we believe is caused by operating the tanks at a higher electric field gradient than the design value.

## REFERENCES

[1] J. Thomason et al., “Megawatt Upgrades for the ISIS Facility”, Proc. of EPAC’08, Genoa, Italy, June 2008.

[2] I. Gardner, “ISIS Status Report”, Proc. of EPAC’94, London, UK, June 1994.

[3] “Proposal for a Spallation Neutron Facility”, UK Science Research Council, October 1978.

[4] F. Gerigk et al., “Conceptual Design of the SPL II”, CERN-2006-006, Geneva, Switzerland, July 2006.

[5] T. Wangler, “RF Linear Accelerators”, John Wiley & Sons, New York, 1998, p. 47.

[6] K. Halbach and R. F. Holsinger, "SUPERFISH - A Computer Program for Evaluation of RF Cavities with Cylindrical Symmetry", Particle Accelerators 7, 1976, pp. 213-222.

[7] “CST Microwave Studio” – http://www.cst.com.

# BREAKDOWN IN PRESSURIZED RF CAVITIES*

R. Sah#, M. Alsharo'a, M. Neubauer, R. P. Johnson, Muons Inc., Batavia, IL, USA
D. Li, J. Byrd, LBNL, Berkeley, CA, USA
M. BastaniNejad, A. Elmustafa, G. Wang, ODU, Norfolk, VA, USA
D. V. Rose, C. Thoma, and D. R. Welch, Voss Scientific, LLC, Albuquerque, NM, USA

*Abstract*

The performance of many particle accelerators is limited by the maximum electric gradient that can be realized in RF cavities. Recent studies have shown that high gradients can be achieved quickly in 805-MHz cavities pressurized with dense hydrogen gas, because the gas can suppress, or essentially eliminate, dark currents and multipacting. In this project, two new test cells operating at 500 MHz and 1.3 GHz will be built and tested, and the high pressure technique will be used to suppress the vacuum effects of evacuated RF cavities, so that the role of metallic surfaces in RF cavity breakdown can be isolated and studied as a function of external magnetic field, frequency, and surface preparation. Previous studies have indicated that the breakdown probability is proportional to a high power of the surface electromagnetic field, in accordance with the Fowler-Nordheim description of electron emission from a cold cathode. The experiments will be compared with computer simulations of the RF breakdown process.

## INTRODUCTION

RF cavities pressurized with hydrogen gas are being developed to produce low emittance, high intensity muon beams for muon colliders, neutrino factories, and other applications. The high-pressure gas suppresses dark currents, multipacting, and other effects that are complicating factors in the study of breakdown in usual RF cavities that operate in vacuum. In the studies reported here, various metals were tested in a pressurized cavity where RF breakdown is expected to be due only to the interaction of the metallic surfaces with the electromagnetic fields. After exposure to the RF fields, metallic Be, Mo, Cu, and W samples were examined using a Hirox microscope and a scanning electron microscope (SEM) to measure the distribution of breakdown events on the electrode surfaces [1].

### *Apparatus*

A schematic of the 805 MHz Test Cell (TC) geometry is shown in Figure 1. The TC is a cylindrical stainless steel pressure vessel. RF power is fed into the chamber via a coaxial line. A solenoid magnet (not shown in the figure) provides an axial magnetic field of up to 3 T, which is used in some of the data sets. Replaceable hemispherical electrodes of various materials (Cu, Mo, Be, W) are separated by a 2 cm gap.

*Supported in part by the US DOE under grants DE-FG02-08ER86350, -08ER86352, and -05ER86252
#rol@muonsinc.com

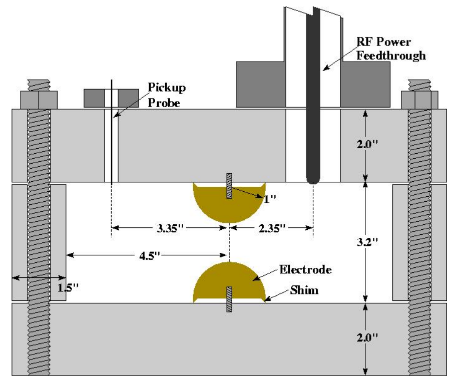


Figure 1: Cross section of the 805-MHz test cell showing the replaceable one inch radius Cu, Be, Mo, or W, hemispherical electrodes. The top and bottom plates and the cylinder are copper-plated stainless steel (the gas input/exhaust port is not shown in the figure).

## EXPERIMENTAL RESULTS

### *RF Breakdown*

Increasing gas density reduces the mean free collision path for ions giving them less chance to accelerate to energies sufficient to initiate showers and avalanches. As shown in Figure 2, it is found that Cu and Be electrodes operated stably with surface gradients near 50 MV/m, Mo near 63 MV/m, and W near 72 MV/m [2].

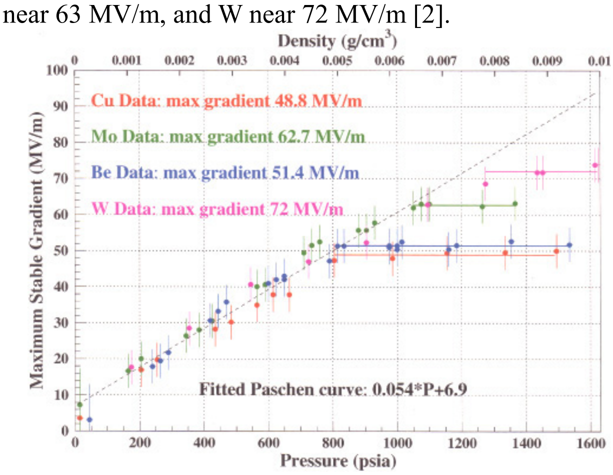


Figure 2: Maximum stable TC gradient as a function of hydrogen gas density or pressure for Cu, Be, Mo, and W with no external magnetic field.

## EXPERIMENTAL DATA ANALYSIS

To investigate the correlation of breakdown and the electric field, the local surface density of breakdown remnants was compared with the maximum expected surface electric field, which was calculated using an ANSYS model. Least squares fits of the data to a power of the predicted maximum electric gradient at the surfaces of the electrodes show good agreement for high values of the exponent. Figure 3 shows the predicted maximum surface gradient (dashed), the data (black with error bars) as described above, and the best least squares fit (red) to the data $y=0.34E^7$ versus zenith angle for Be. Figures 4 and 5 show the experimental data, the ANSYS model data, and best fits for Mo and W respectively.

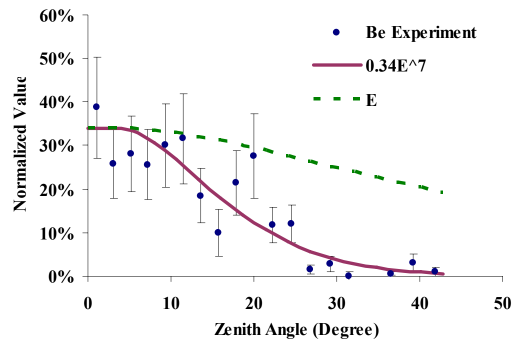


Figure 3: Be breakdown area fraction vs. zenith angle.

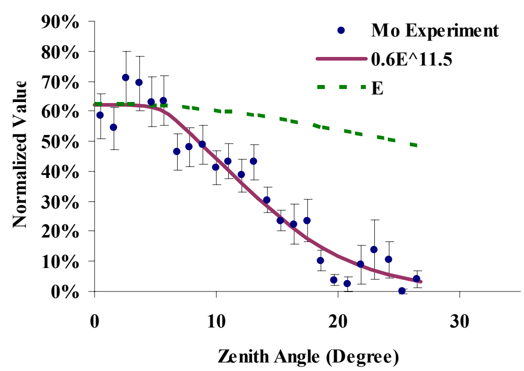


Figure 4: Mo breakdown area fraction vs. zenith angle.

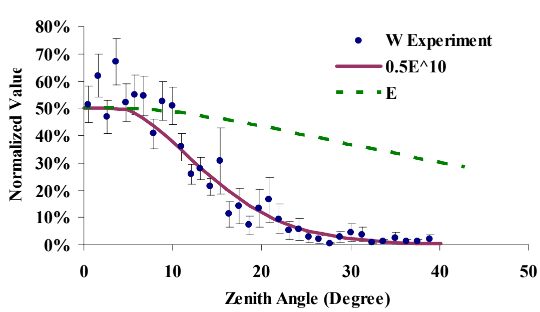


Figure 5: W breakdown area fraction vs. zenith angle.

The plots also show that the breakdown data correlate with a high power of electric field: 7 for Be, 11.5 for Mo and 10 for W. This suggests that the breakdown is a quantum mechanical effect described by the Fowler-Nordheim theory of field emission [3] by tunnelling of electrons through a barrier in the presence of a high electric field.

## MELTING OR BOILING POINTS

The maximum stable gradient for each of the four electrode materials is shown on figure 6. For these data, the 805 MHz TC was operated at 5 Hz repetition rate with 100 microsecond long pulses. The maximum gradients that were achieved show a correlation with the melting points and with the boiling points of the electrode metals.

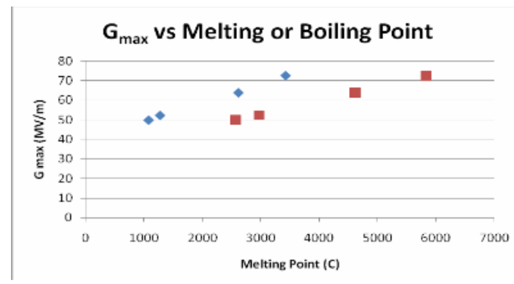


Figure 6: Maximum stable gradient as a function of metallic melting point (blue diamonds) or boiling point (red squares). From left to right, the four data points correspond to Cu, Be, Mo, and W.

Table 1: Material Properties

| Metal | Cu | Be | Mo | W |
|---|---|---|---|---|
| Melting point [C] | 1083 | 1278 | 2617 | 3422 |
| Boiling Point [C] | 2567 | 2970 | 4612 | 5828 |
| Heat of fusion [KJ/mol] | 13.05 | 12.20 | 32 | 35.40 |
| Heat of vaporization [KJ/mol] | 300.3 | 292.4 | 598.0 | 824.0 |

## FIRST COMPUTER SIMULATIONS

The first computer simulations of RF Breakdown have begun.

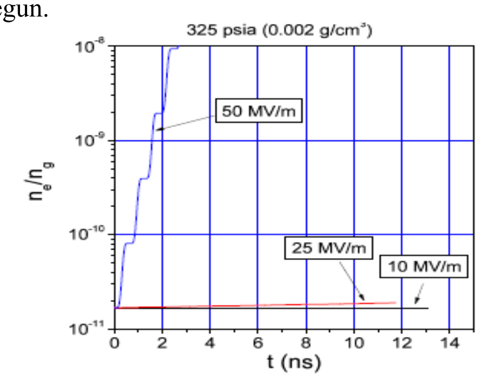


Figure 7: Electron density as a function of time at 805 MHz and gas density 0.002 g/cm$^{-3}$.

Computer calculations to simulate the behaviour of breakdown in helium-filled spark-gap switches have been extended to the case of the hydrogen-filled Muons, Inc. test cell [4]. Figure 7 shows the simulation results for three electric field strengths, where the electron density is stable below the Paschen curve (10 MV/m), slightly unstable at the curve (25 MV/m), and very unstable for values above the curve (50 MV/m). These simulation results agree with the experiments.

## SIMPLE MODEL OF BREAKDOWN

The correlation of maximum gradient with melting and boiling points, the SEM and optical pictures, and the Fowler-Nordheim dependence of the observed breakdown probability argue for a simple breakdown model for pressurized RF cavities that should apply to some aspects of vacuum cavity breakdown as well.

1. A feature on the metal surface (perhaps a bump, a grain boundary, or an inclusion) is a source of a strong Fowler-Nordheim field emission current.
2. The electrons flow through the metal below the source and heat the metal, before they are emitted from this source. The resistivity increases locally, and a runaway temperature occurs.
3. When the metal becomes hot enough locally, it can weaken or melt, so that the metal surface deforms into more or enhanced peaks with larger local fields and more local current. These peaks can be blown off and vaporized.
4. Alternatively, the metal can just boil to vent vapor into the gap. Pictures of the Be electrodes show this behavior.
5. A third possibility is that explosive boiling at the metal surface could expel some of the melted metal. Some of the W data show this behavior.
6. In any case, it appears likely that deformed metal surfaces, melted metal in the gap, or metal vapor in the gap may be the initiating events that lead to RF breakdown in pressurized cavities.

## FUTURE PLANS FOR THIS STUDY

We have begun a new phase of investigations of RF breakdown in pressurized cavities. It is a multi-institutional study that will include the construction of two new test cells that will operate at 500 MHz and 1.3 GHz. The goal is to use the pressurized cavity to isolate the role of the metallic surfaces in RF breakdown, and breakdown will be studied as a function of external magnetic field, radiofrequency, the metal chosen for the electrodes, and surface preparation. Progress on this study is reported as follows.

1. A brief set of experiments is being carried out with the 805-MHz test cell at Fermilab. New electrode metals and new gas mixtures are being investigated. One important result is the successful operation of the test cell using nitrogen gas, because future experiments using nitrogen will avoid some of the safety concerns of high-pressure hydrogen gas.
2. The next set of experiments will be carried out at LBNL using the 500-MHz test stand. Therefore, a 500-MHz test cell is being designed and fabricated, and it will be assembled and tested at LBNL with nitrogen gas.
3. Details of the 500-MHz RF breakdown studies are being worked out, including metal selection for the electrodes, methods to study the metal surfaces, and other aspects of the experimental design.
4. Numerical simulation efforts have begun, and the goal will be to develop a consistent theoretical model of RF breakdown in pressurized cavities, a model that can be applied to the behavior of metal surfaces in vacuum RF cavities as well.
5. A follow-on experiment has been tentatively defined as the construction and test of a third test cell, one that will operate at 1.3 GHz at a test stand at ANL.

## CONCLUSIONS

A series of experiments with an 805 MHz test cell has provided a great deal of data on the characteristics of RF breakdown in pressurized RF cavities. At high gas pressures, the maximum test cell gradient reaches a plateau that reveals properties of the metal surface during RF breakdown. Examination of the metal electrode surfaces reveals evidence of locally high temperatures (melting and boiling), and a study of the local surface density of breakdown remnants suggests that the breakdown process is a quantum mechanical effect described by the Fowler-Nordheim theory of field emission by tunnelling of electrons through a barrier in the presence of a high electric field.

These studies are being extended in a new phase of experimentation that will include the use of a number of metal electrodes in two new test cells designed to operate at 500 MHz and 1.3 GHz. In addition, the numerical simulation of the RF breakdown process will be extended in an effort to develop a consistent and more complete model of RF breakdown in pressurized RF cavities. It is likely that this model will apply to some aspects of RF breakdown in vacuum RF cavities as well.

## REFERENCES

[1] M. Bastaninejad et al, proceedings of EPAC08, http://jacow.org/e08/papers/mopp080.pdf
[2] P. Hanlet et al., in Proceedings of EPAC06, Edinburgh, Scotland (2006), p. 1364.
[3] R. H. Fowler and L. Nordheim, “Electron emission in intense electric fields,” in Proc. Roy. Soc. (London), A119, pp. 173–181, 1928.
[4] V. Rose, C. Thoma, D. R. Welch, and R. E. Clark, Low Emittance Muon Collider Workshop, Fermilab, 2008,http://www.muonsinc.com/lemc2008/presentations/ROSE_LEMC2008.ppt

# DESIGN AND TEST OF THE TRIPLE-HARMONIC BUNCHER FOR THE NSCL REACCELERATOR*

Q. Zhao†, V. Andreev, J. Brandon, G. Machicoane, F. Marti, J. Oliva, J. Ottarson, J. Vincent
NSCL, East Lansing, MI 48823, U.S.A.

**Abstract**

A unique triple-harmonic buncher operating at the fundamental frequency of 80.5 MHz upstream the Radio Frequency Quadrupole (RFQ) linac has been designed, manufactured and tested at the National Superconducting Cyclotron Laboratory (NSCL) to meet the requirement of a small output longitudinal beam emittance from the reaccelerator. The buncher consists of two coaxial resonators with a single gridded gap. One cavity provides both the fundamental and the third harmonic simultaneously with λ/4 and 3λ/4 modes respectively, while the other provides the second harmonic in λ/4 mode. This buncher combines the advantages of using high quality factor resonator and only a pair of grids. Details on design considerations, electromagnetic simulations, and primary test results are presented.

## INTRODUCTION

The National Superconducting Cyclotron Laboratory (NSCL) at Michigan State University is developing a facility named ReA3 to demonstrate the technical feasibility and performance characteristics for stopping and reaccelerating rare-isotope beams, as an important step towards a next-generation rare-isotope facility in the United States [1]. Beams of rare isotopes will be produced and separated in-flight at the NSCL Coupled Cyclotron Facility and subsequently stopped by a novel gas stopper, breeded by a state-of-the-art electron beam ion trap based charge-breeder, and reaccelerated by a modern linear accelerator. The linac consists of a low energy beam transport line, a cw radio-frequency quadrupole, a quarter wave resonator based superconducting linac, and a high energy beam transport line [2]. ReA3 will delivery various exotic beams with charge-to-mass ratios (Q/A) of 0.2 – 0.4 and variable energies of about 0.3 to 3 MeV/u.

Nuclear experimental programs require a beam on target with an energy spread of ~1 keV/u and a bunch length of ~1 ns simultaneously. Therefore, a longitudinal beam emittance of less than 0.3 π·ns·keV/u from ReA3 is demanded. Since the intensities of the rare-isotope beams will be low, the scheme of using an external multi-harmonic buncher upstream of the RFQ has been adopted to produce a small longitudinal emittance beam from RFQ with high bunching efficiency [3-6]. A unique triple harmonic buncher using two high quality factor resonators with one pair of grids has been designed, fabricated and tested at NSCL for this application.

## DESIGN CONSIDERATIONS

The buncher is designed to operate with three harmonics, a fundamental frequency of 80.5 MHz and two additional harmonics of 161 and 241.5 MHz, respectively. The fundamental frequency, same as that of the downstream RFQ and superconducting cavities, is mainly determined by the small longitudinal beam emittance requirement. Since beams from the charge breeder will have a larger intrinsic energy spread (e.g. ΔE ~ ±25eV/u for Q/A = 0.25), the beam micro-bunch frequency should not be lower than ~80 MHz, otherwise the longitudinal emittance of the bunched beam will be too large to achieve the required time and energy resolution on target. Considering the higher bunching efficiency and lower output longitudinal emittance needed, a total of three harmonics are chosen for the operation of the buncher [6]. A high quality factor resonator was proposed, which needs a lower power amplifier to drive it. This buncher consists of two coaxial cavities, as shown in Fig. 1. One cavity provides both the fundamental and the third harmonics. The other cavity provides the second harmonic with a λ/4 mode. The dual frequency cavity will operate simultaneously at the λ/4 and 3λ/4 modes, as was done at PIAVE in Legnaro [5]. The buncher bunches beams with a nominal relativistic velocity $\beta$ = 0.00507 (beam energy of 12keV/u), so the $\beta\lambda$ is small especially for harmonics. For example, $\beta\lambda$ = 9.4 mm for second harmonic. On the other hand, the beam diameter is about 30mm at the buncher position in order to match it into RFQ. Therefore gridded electrode tubes are necessary to achieve uniform field distributions and thus satisfactory transit time factors. We proposed to design the buncher in such a way that all three harmonics are applied in one single gridded gap. This configuration with only one pair of grids minimizes the beam losses on grids and makes the buncher longitudinally more compact as well.

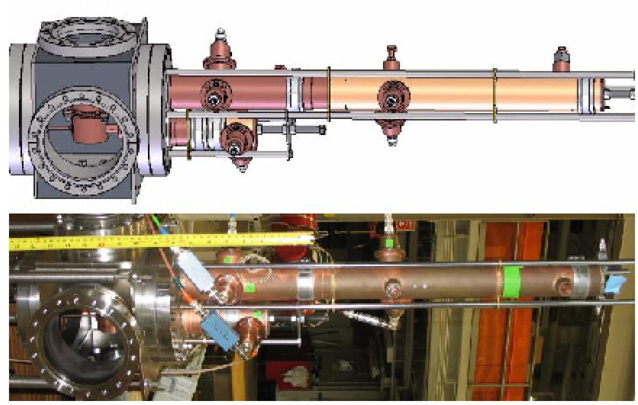

Figure 1: Triple harmonic buncher with two coaxial resonators and a single gridded gap: design drawing (top), photograph (bottom).

*Work supported by Michigan State University.
†zhao@nscl.msu.edu

## ELECTROMAGNETIC SIMULATIONS

Although the required bunching voltage is not high (<1kV) and the design of λ/4 resonators is conventional, cross-talk between the two cavities due to the coupling through the gridded gap must be evaluated. MAFIA code was used to simulate the resonators and determine the electromagnetic properties of the triple harmonic buncher.

A schematic layout of the buncher is shown in Fig. 2. Both of the resonators have a shorter length than those in ideal λ/4 cases to achieve the desired resonant frequencies. The lengths of the dual and single frequency cavities were reduced about 20% and 40% respectively. These reductions are mainly due to the capacitive load from the gridded gap, the dielectric vacuum isolators and the tube supports. As a result, a strong coupling was observed between the two resonators, which not only decreased the effective voltage across the gap but also made the tunings much difficult especially for the third harmonic.

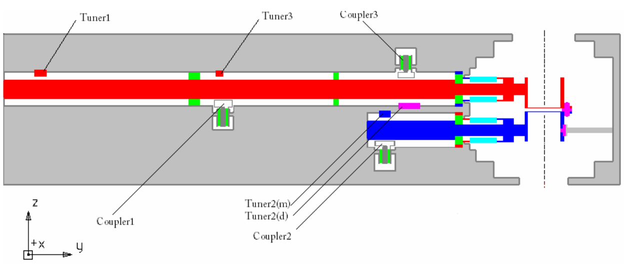


Figure 2: Layout of the triple harmonic buncher.

One of the solutions currently adopted in the design is to add an rf filter on the electrode that connects to the second harmonic cavity. This filter is only for the third harmonic (very small impedance for third harmonic and very large for others). MAFIA simulation showed the effective voltage across the gap for the third harmonic increased significantly with the filter. The calculated quality factors are 2020, 3170, 4140 for 80.5, 161, 241.5 MHz, respectively. Simulation also found the 50mm diameter of the tube is large enough not necessary to use conic electrodes to deal with the fringing fields.

An adjustable magnetic power coupler is used for each harmonic to provide critical coupling. Each harmonic also has an adjustable pickup and the pickups are carefully positioned to reduce the interference between different modes of oscillations, as shown in Fig. 2.

## MECHANICAL DESIGN

Standard size copper tubes were chosen for both the inner and outer conductor of the resonators. One side of the outer conductors is directly welded on the vacuum chamber while the inner conductor welded on the chamber through a ceramic. The inner and outer conductors are welded each other on the other side. Two Teflon washes were installed between the inner and outer conductors to improve the stiffness for the dual frequency resonator. Both resonators are placed in air without water-cooling. A pair of copper tubes with grids on one end is used as the electrodes. Each 50mm diameter electrode is directly connected to the inner conductors of the two coaxial resonators and housed in a 20cm cubic stainless steel vacuum chamber.

The buncher grid has a 50mm diameter, made by ThinMetalParts (Colorado Spring, CO). Both the thickness and width of the copper grid is 0.005” with square meshes spaced 1mm apart, as shown in Fig. 3. The grids are clamped 4mm apart and self aligned on pins in the copper electrodes so that the grids on each grid are also aligned to minimize the interception of beam.

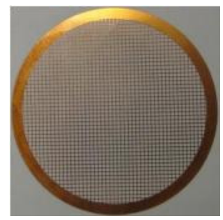

Figure 3: The 0.005” thickness and 50 mm diameter copper grid. Square mesh with grid width of 0.005” spaced 1mm apart.

A 4 mm diameter cylindrical copper rod that connects the bottom of the housing chamber and the electrode of the second harmonic cavity is used as a filter for third harmonic. The rod is electrically isolated to the electrode by a dielectric spacer. This filter can also be used to tune both the third and second resonant frequencies by changing of the thickness of the dielectric spacer.

There is a movable finger sleeve connecting inner and outer conductors for the dual frequency cavity for coarse frequency tuning. The fine frequency tuners for the fundamental and second harmonics are placed close to their maximum magnetic fields, while that for the third harmonic near its maximum electric field. Cylindrical coppers with diameters of 12, 10, and 6 mm are used for the fundamental, second and third harmonic, respectively, which provides about total 100kHz tuning range.

## EXPERIMENTAL TESTS

After assembly, this buncher was measured with low rf and then beam tested on the electron cyclotron resonance ion source (ECRIS) test stand at the NSCL. Fig. 3 is a photo of the test stand beam line showing various beam diagnostic tools and instruments. Two solenoids upstream the buncher provide transverse focusing. A fast Faraday cup (FFC) approximately 75cm downstream the buncher is used to measure the longitudinal beam temporal profile after the buncher. The FFC is a 50 Ohm coaxial cone with a grounded copper grid in front of the collector similar to that in Legnaro [5]. This output of the FFC is sent into an oscilloscope .

An oscillator (Frequency Synthesizer PTS 500, Programmed Test Source Inc.) generates an 80.5MHz signal. This frequency is doubled and tripled by the Triple Harmonic Module developed at NSCL. Each frequency signal is then send into a separate amplifier (PTEK 100W 10-100MHz, Worldwide 20W, Model Kaw 1040 MI, 1-512MHz) through an individual RF Voltage Regulator (developed at NSCL for cyclotron rf control). There is a phase shift between the voltage regulator and amplifier for both second and third harmonics. Each amplifier is connected its coupler on the buncher through a directional coupler. Signals from the pickups are then send back to the voltage regulators. RG142 double shield cables are used for all the connections.

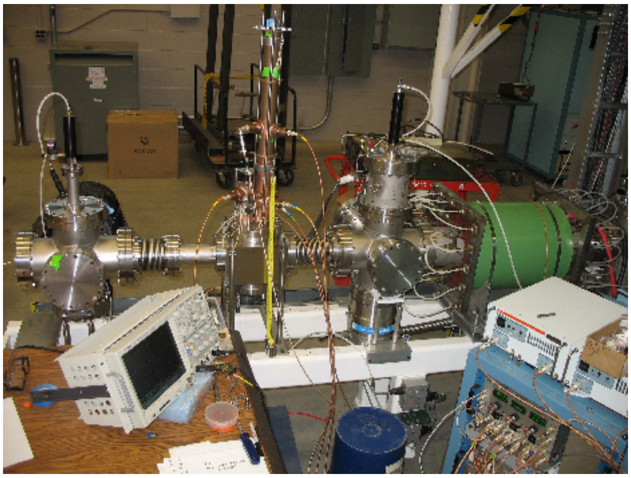

Figure 4: Experimental setup for the beam test of the triple harmonic buncher.

A low intensity single-charge state helium beam was produced with 20kV ECRIS extraction voltage. This 5keV/u beam was tuned to pass through the buncher grids and collected by the FFC. For the initial beam tests, only fundamental frequency was applied. The buncher voltage was scanned in a wide range so we observed the bunching and over-bunching processes on the oscilloscope. However, the direct signal obtained from the oscilloscope, as shown in Fig. 5, indicated that the temporal durations were much longer than anticipated. We believe that the time resolution of our FFC may be not as high as we expected. Therefore, a Matlab based code was written to quantify various impacts. This code includes the simulation of the beam bunching process with different input conditions, variable time response of the FFC. We first conducted beam simulations to obtain the longitudinal temporal profiles with different buncher voltages and different initial beam energy spreads. Then we introduced a time response constant ($\tau$) for the FFC and recalculate the simulated temporal distributions based on the time constant $\tau$ and tried to fit the traces recorded from the scope. As an example, Fig. 5 shows the temporal distributions at the entrance of buncher vs. at the FFC in the left, and simulated temporal distributions and the real trace recoded from oscilloscope. From the data analyses, we determined the time response constant $\tau$=1.6ns that is close to our estimation, and the initial beam energy spread $\Delta$E=11.5eV/u that also agrees with other measured from ECRIS. We are going to test the buncher with all three harmonics in the next step.

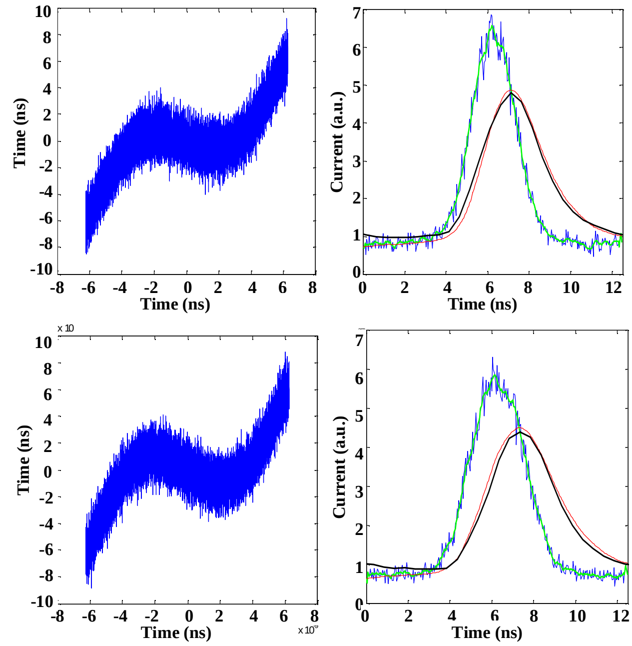


Figure 5: Temporal distributions at the entrance of buncher vs. at the FFC (left), projected temporal profiles (right): raw data (blue), smoothed data (green), trace from scope (black), fitted distribution (red), with initial beam energy spread $\Delta$E=11.5eV/u and FFC time response constant $\tau$=1.6ns. Buncher voltage Vb=174V (tops) and Vb=205V (bottoms).

## SUMMARY

The unique triple harmonic buncher consisting of two coaxial resonators with a single gridded gap for ReA3 was designed, fabricated and tested at NSCL. The results of the primary tests confirmed our design goals. Further experiment measurements on the test stand together with beam simulations are planed to develop the procedures on how to tune and operate the triple-harmonic buncher optimally. This buncher will be installed in the ReA3 and started commissioning in Spring 2009.

## REFERENCES

[1] http://www.er.doe.gov/np/program/FRIB.html
[2] X. Wu, et al., "The Status of MSU Re-Accelerator (ReA3)", these proceedings.
[3] J.W. Staples, Part. Accel., 47(1994)191; J. Staples, "Reducing RFQ Longitudinal Emittance", LINAC'94, p.755.
[4] S. Koscielniak, "Reducing Longitudinal Emittance Growth in RFQ Accelerators", LINAC'94, p.526; S. Koscielniak, et al., "Beam Dynamics of the TRIUMF ISAC RFQ", LINAC'96, p.402.
[5] A. Facco, et al., "Status of the Non-RFQ Resonators of the PIAVE Heavy Ion Linac", EPAC'00, p.2037
[6] Q. Zhao, et al., "Design studies of the reaccelerator RFQ at NSCL", PAC'07, 1772.

# SURFACE-LOSS POWER CALCULATIONS FOR THE LANSCE DTL

Sergey S. Kurennoy, LANL, Los Alamos, NM 87545, U.S.A.

### Abstract

The surface losses in the drift-tube linac (DTL) tanks 3 and 4 of the LANSCE linear accelerator are calculated using 3-D electromagnetic modeling with the CST MicroWave Studio (MWS). The results are used to provide more realistic power estimates for the 201.25-MHz RF upgrade design within the LANSCE-R project. We compared 3-D MWS results with those from traditional 2-D Superfish computations for DTL cells and their simplified models and found differences on the level of a few percent. The differences are traced to a 3-D effect consisting in a redistribution of the surface currents on the drift tubes (DT) produced by the DT stem. The dependence of MWS results on the mesh size used in computations is also discussed.

## INTRODUCTION

There are some disagreements between the existing results on the surface-loss power in the LANSCE DTL tanks 3 and 4 [1]. In particular, the power values cited in the book [2], respectively 2.745 and 2.674 MW, are noticeably higher than the historical maxima in 1994-1998, 2.090 and 2.493 MW, as well as the values found in old design reports, 2.33 and 2.33 MW [1].

More accurate values of the power loss in the DTL tanks 3 and 4 are important for finalizing a design of the 201.25-MHz RF system upgrade within the LANSCE-R project. The surface losses in the DTL tanks 3 and 4 were recalculated using both 3-D electromagnetic modeling with MicroWave Studio (MWS) [3] and the traditional approach with Superfish (DTLfish) [4]. This paper summarizes our results.

## CALCULATION METHOD AND RESULTS

We used a piece-wise approach to calculate the surface losses in the DTL tanks, performing MWS computations separately for a few selected cells in the tank, with electric boundary conditions on the cell end walls. The standard DTLfish approach is essentially the same: 2-D Superfish (SF) computations are performed for a few selected half-cells and the results are interpolated [4]. The parameters of the DTL tank cells were taken from the LANSCE online database and post-coupler tuning tables. Figure 1 shows the MWS model of the DTL cell DT98, the first cell in the tank 3. The cell is about 43 cm long and has 44-cm radius. The MWS model includes a drift tube (DT), stem with bellows, and post-coupler. The picture inset shows the post-coupler with two tab rotations, at 22.5 and 45°. These two virtual tab shapes are vacuum-filled and not used in this particular calculation; however, their presence influences the MWS mesh.

Figure 2 shows the surface currents calculated by MWS in the model of the DTL cell DT165, the last cell in the tank 4. Its length is 55.6 cm, and the DT is almost 35 cm long. The highest current density is on the DT stem near its connection to the DT.

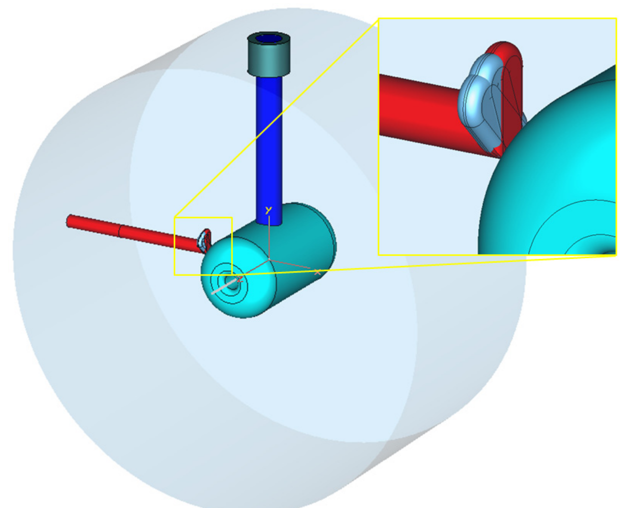

Figure 1: MWS model of DTL cell: drift tube (cyan), stem (dark-blue), bellows (sea-green), and post-coupler (red).

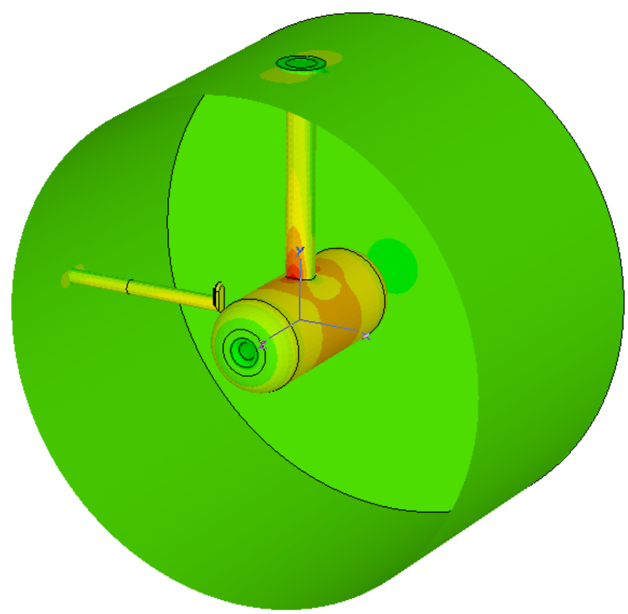

Figure 2: Surface-current magnitude in DT165 cell (red corresponds to the highest value, dark-green to zero).

In the Superfish approach, 2-D computations are performed for an axisymmetric model of the (half-)cell that includes only the cavity and DT. After that a theoretical perturbation correction is added to include the DT stem effect [4], but post-couplers are usually not taken into account. In the MWS 3-D models with post-couplers, we impose the electric boundary conditions on the side walls and find the modes with the MWS eigensolver. Such an approach is justified when the post-couplers are in the neutral position, at 0°. The effects due to post-coupler tab rotations will be discussed below.

The MWS computation results for the surface losses in a few representative cells of the DTL tank 3 with 38 cells are summarized in Table 1. The MWS computations were performed for cells 1, 10, 19, 28, and 38, both with rough meshes of 0.7-0.8 million mesh-points over the full cell, and with fine meshes of 4-4.2M points (Table 1). The cell power values are scaled to the tank nominal electric field gradient □$_0$ = 2.4 MV/m, given at 100% duty, and assume the surface conductivity of copper σ = 5.8·10$^7$ (Ω·m)$^{-1}$. SF results for the same cells with the stem corrections (and without post-coupler ones) are shown for comparison at the bottom.

Table 1: Loss power in tank 3 cells from MWS & SF

| Cell # (DT #) | 1 (98) | 19 (116) | 38 (135) |
|---|---|---|---|
| □-factor | 71046 | 70348 | 69712 |
| Power □$_c$, kW | 42.91 | 49.94 | 56.95 |
| □$_c$ distr.,: wall, %% | 46.2 | 46.0 | 45.2 |
| : DT, %% | 40.7 | 42.2 | 43.9 |
| : stem, %% | 7.82 | 7.23 | 6.85 |
| : bellows, %% | 1.53 | 1.32 | 1.17 |
| : post-c. at 0°, %% | 3.72 | 3.23 | 2.86 |
| Superfish □-factor | 70231 | 69570 | 68817 |
| Superfish □$_c$, kW | 42.97 | 50.08 | 57.26 |

Figure 3 shows the interpolation of the loss-power results to the other cells in tank 3. The MWS results with fine meshes (marked MWS2) and the Superfish ones are within 1% of each other for all cells, even though the post-coupler losses (3-4% of the cell surface-loss power) are not included in the SF results. The MWS power values with rougher meshes (MWS1) are lower by about 4%, while the □-factors are 4-5% higher. In all cases the power distribution along the tank is close to linear.

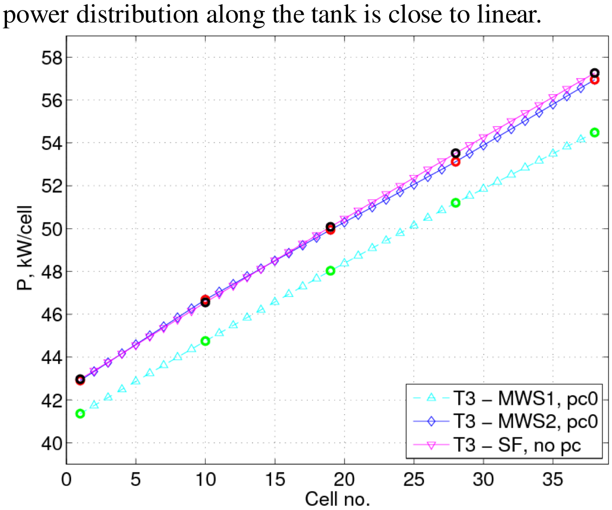


Figure 3: MWS and Superfish result interpolation for surface losses in the DTL tank 3.

Summing the interpolated power values □$_c$ for the fine meshes (blue diamonds in Fig. 3 marked MWS2) and adding two end-wall contributions (28.04 kW and 34.12 kW at the upstream and downstream end of the tank), we obtain an estimate of the total dissipated power in the DTL tank 3: □$_{T3}$ = 1964.1 kW. Interpolating □-values from the MWS calculations gives the tank □-factor as □$_{calc}$ = Σ□$_c$□/□$_{T3}$ = 68088. The sum of the DTLfish results gives an estimate 1907.8 kW, without the end-wall contributions. One important observation here is that the product □$_{T3}$□$_{calc}$ remains practically the same for both MWS calculations, with the fine and rough meshes: the difference is less than 0.5%.

Similar computations were performed for the DTL tank 4 with 30 cells; Fig. 4 shows the power-loss interpolation. The Superfish results are higher than the MWS ones with fine meshes of 5M points (marked MWS2) by 1%, while the □-values are about 2% lower. The MWS results with meshes of about 3M points (MWS1) are 2% above the SF results; the corresponding □s are about 3% lower than for MWS2. Again, the power distribution along the tank is close to linear, which simplifies the result interpolation. Summing the interpolated MWS power values (MWS2 in Fig. 4) and adding two end-wall contributions (34.33 kW and 39.35 kW), we obtain an estimate of the total dissipated power in the DTL tank 4: □$_{T4}$ = 1942.7 kW. Interpolating □-values allows us to find the □-factor of the tank 4: □$_{calc}$ = Σ□$_c$□/□$_{T4}$ = 66576. The sum of the DTLfish results provides an estimate 1888.2 kW, without the end-wall contributions.

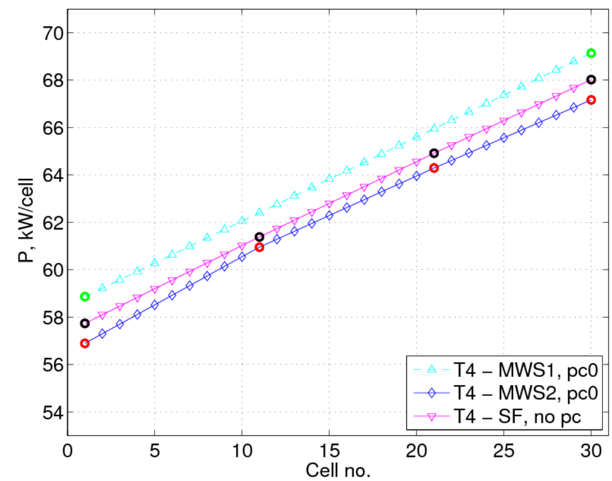


Figure 4: MWS and Superfish result interpolation for surface losses in the DTL tank 4.

## DISCUSSION

**MWS versus SF.** The fact that Superfish (SF) results for the surface-loss power are higher than those from MWS is unexpected: the opposite would be natural since the MWS models include post-coupler losses, in addition to the elements taken into account by SF. To understand this difference, we compared three different MWS models of the same cell, the last cell in the tank 4 (DT165), with the SF model in detail [5]. The first model calculates exactly the same problem as SF does: only the cavity with a DT, no stem, and no post-coupler. In the second model, we added a simple stem. The third one is the model used for MWS computations above, with the post-coupler at 0°, see Fig. 2. When the problem solved by MWS and SF is exactly the same – an axisymmetric layout with a DT – the calculated power values are close (0.5-1.5%

difference). In the SF approach, when the stem perturbation correction is added, the losses on the cavity wall and DT are assumed unchanged. 3-D MWS computations show redistributed currents on the DT surface. Overall, the SF result for this layout is 2-3% higher than the MWS-calculated results. The difference becomes smaller, ~1%, for the complete cell (MWS model with post-coupler, Fig. 2; SF – without); the post-coupler adds ~2.5% of the total cell power loss. If the post-coupler correction were added to the SF result, it would be even higher, 3-4% above the MWS value. Note that MWS computations for such a comparison must be performed with very fine meshes; otherwise, the MWS result inaccuracy can be larger than the effect, see below.

**Tab rotation effect.** An important question is what happens when post-coupler tabs are rotated. A few MWS runs were performed to compare the tab at 0° and 45° imposing both electric and periodic boundary conditions (BC) on the cell side walls. For electric BC, in tank 3 cells with post-couplers at 0° the power dissipated on the post-coupler is 3-4% of the cell power dissipation, cf. Tab. 1; in tank 4, it is below 3%. When the tabs are rotated to 45°, the power dissipated on the post-coupler jumps to 10-20% of the total cell power loss for the cells near the tank ends.

Unfortunately, the surface-loss results even in these cells are misleading and cannot be trusted because of the strong mixing between the accelerating mode and post-coupler mode. The mixing is much stronger in a short resonator (a cell with electric BC on its end walls) than it would be in a long tank. This becomes especially obvious when MWS calculations with the tabs at 45° are performed for the tank central cells where the accelerating and post-coupler modes are very close in frequency: the mixing is so strong that most of the cell power dissipation occurs at the post-coupler, e.g. 54% in the cell 28 (DT 125) of tank 3. The relative field difference between two gaps in that case is very large: $\Delta E/E_{av}$ = 0.36, many times higher than in a long tank with one post-coupler rotated.

On the other hand, when periodic BCs are imposed on the cell end walls, the calculated losses are almost the same for the tabs at 0° and 45°. Of course, when the tab is not rotated (0°), the results with periodic or electric BC should be identical due to the cell symmetry. In a long tank with a flat electric field, the situation in a particular cell is close to periodic BC due to almost equal fields on the cell “end walls”. Because of that and the fact that for periodic BC the losses are the same with rotated and non-rotated tabs, we believe that the calculations above with the post-coupler tabs at 0° give the correct results.

**Dependence of MWS results on mesh size.** The values of $P$ and $Q$ vary by a few percent (as much as ±8% for rough meshes in the results above) depending on the MWS mesh size, but in opposite directions, so that their product $PQ$ remains practically unchanged (the maximal deviation was below 1%) [5]. One possible explanation is that the secondary resonator parameters like $Q$ are derived based on the definition $Q = \omega W/P$, where $W$ is the field energy and $\omega$ is the mode frequency, using the fields computed by the eigensolver. The MWS eigensolver solves for the electric field (eigenvector) and frequency (eigenvalue), thus naturally $W$ and $\omega$ are calculated more accurately. The surface-loss power – a surface integral of the squared magnetic field – is likely less accurate. From the above definition, slightly lower values of $P$ give higher $Q$s and vice versa, while their product $PQ = \omega W$ remains more accurate.

## SUMMARY

The surface losses in the DTL tanks 3 and 4 are calculated both in 3D with the MicroWave Studio and using the traditional 2-D Superfish approach. For practical estimates, it is usual to increase the calculated power values by 15% or even 20% to account for the difference in the theoretical and real surface conductivities. In the case of the LANSCE DTL tanks, we can use the measured values of the tank $Q$-factors. The calculated power value should be multiplied by factor $k = Q_{calc}/Q_{meas}$, the ratio of the calculated $Q$-factor of the tank to the measured one. The measured value for the DTL tank 3 is $Q_{meas}$ = 59460; for tank 4, different measurements give results from 53400 to 57780 [1]. The summary of our calculation results (the averaged power for the nominal electric field gradient $E_0$ = 2.4 MV/m, 100% duty, post-couplers at 0°, end-walls included) is presented in Tab. 2.

Table 2: Surface-loss power in the DTL tanks 3 and 4

| | $P_{calc}$, MW (MWS) | Scaling factor $k = Q_{calc}/Q_{meas}$ | $P$, MW ($kP_{calc}$) |
|---|---|---|---|
| Tank 3 | 1.964 | 1.145 | 2.249 |
| Tank 4 | 1.943 | 1.152–1.247 | 2.238–2.423 |

If the MWS results with rougher meshes for tank 3 ($P_{calc}$ = 1.890 MW and $Q_{calc}$ = 71069) were used, the scaling factor would be different, $k$ = 1.195, but the power estimate would remain almost the same, $P$ = 2.259 MW

From comparison of the surface losses calculated by MWS and Superfish (SF), we see that SF overestimates the losses in DTL cells by a few percent. This is due to the surface-current redistribution – a purely 3-D effect that cannot be taken into account in 2-D calculations. This result is important since SF results are widely used in surface-loss calculations.

The author would like to acknowledge useful discussions with G. Bolme, J. Lyles, and L. Rybarcyk.

## REFERENCES

[1] J.T. Lyles and G.O. Bolme, Private communications, Los Alamos, April 2008.

[2] T.P. Wangler, [illegible], J. Wiley & Sons, NY, 1998, p. 99.

[3] CST MicroWave Studio 2008, http://www.cst.com.

[4] J.H. Billen and L.M. Young. “Poisson/Superfish,” LA-UR-96-1834, Los Alamos, 1996 (rev. 2005).

[5] S.S. Kurennoy. “Surface-loss power calculations for LANSCE DTL tanks 3 and 4,” Tech. note AOT-ABS: 08-008 (TN), Los Alamos, 2008.

# EFFICIENT LOW-BETA H-MODE ACCELERATING STRUCTURES WITH PMQ FOCUSING

S.S. Kurennoy, J.F. O'Hara, E.R. Olivas, L.J. Rybarcyk, LANL, Los Alamos, NM 87545, U.S.A.


*Abstract*

We are developing high-efficiency room-temperature RF accelerating structures for beam velocities in the range of a few percent of the speed of light by merging two well-known ideas: H-mode cavities and the transverse beam focusing with permanent-magnet quadrupoles (PMQ). Combining electromagnetic 3-D modeling with beam dynamics simulations and thermal-stress analysis, we have found that the H-mode structures with PMQ focusing provide a very efficient and practical accelerator for light-ion beams of considerable currents. Such accelerating structures following a short RFQ can be used in the front end of ion linacs or in stand-alone applications such as a compact deuteron-beam accelerator up to the energy of a few MeV.


## INTRODUCTION

Room-temperature H-mode resonators – inter-digital (IH) or cross-bar (CH) – provide effective acceleration at low beam velocities, $\beta=v/c<0.3$-$0.4$, e.g. [1]. IH structures are especially efficient at very low velocities, $\beta<0.1$. Transverse focusing options used in H-structures include electric RF quadrupoles in RFQ at very low $\beta$ and magnetic focusing by quadrupole triplets inserted into the structure [1]. The triplet insertions interrupt the structure reducing its acceleration efficiency. On the other hand, small sizes of the drift tubes (DTs) required to achieve high shunt impedances in H-structures prevent placing usual electromagnetic quadrupoles inside DTs. Using permanent-magnet quadrupoles (PMQs) placed inside H-structure small DTs was suggested [2], which promises both efficient beam acceleration and beam focusing.

Here we focus on a particular application: using IH structures with PMQ beam focusing for a compact deuteron-beam accelerator from 1 to 4 MeV at the RF frequency around 200 MHz, with the peak current up to 50 mA and duty factor of 10%. Such an accelerator can serve in a mobile intense neutron and gamma source for interrogation of special nuclear materials for homeland defense. Requirements of the system mobility and ease of use favor the room-temperature (RT) option. For higher energies and/or higher RF frequencies using CH-PMQ structures can be beneficial.

## PMQ FOCUSING IN IH STRUCTURES

Deuteron kinetic energies from 1 to 4 MeV correspond to the beam velocity range of $\beta=0.033$-$0.065$. The cell length $L_c=\beta\lambda/2$ – equal to a half-period in IH structures – is very short at the low-energy end, only about 2.5 cm. To keep the DT length $L_{DT}$ as long as possible, we consider first the IH structure with narrow gaps $g$ between DTs by fixing the ratio $g/L_c=0.15$. A 2-cm long PMQ with the bore radius 5 mm can readily provide the field gradient $G$=200 T/m, even if the PMQ outer radius is only 11 mm. Such PMQs fit into DTs even at the lower end of the IH accelerating structure, with geometrical value $\beta_g=0.034$, where the DT length is $L_{DT}$=2.16 cm. In Ref. [3, 4] we explored the beam transverse focusing structure F*n*OD*n*O, where the focusing period consists of one focusing (F) and one defocusing (D) PMQ separated and followed by $n$ empty DTs, $n$=0,1,2,… We denote such structures as IH 1-(n+1), with one PMQ per (n+1) cells. Initial beam dynamics calculations were performed with the envelope code TRACE-3D; the results for the beam sizes and phase advances are summarized in [3, 4]. Long focusing periods are excluded because of large phase advances $\sigma_{0x/y}$ per focusing period, above 90°. All configurations IH1-2 to IH1-4 were found acceptable, and the differences between them were not very significant. Overall, IH1-3 ($n$=2), cf. Fig. 1, where PMQs are inserted in every third DT, provided the smallest beam size.

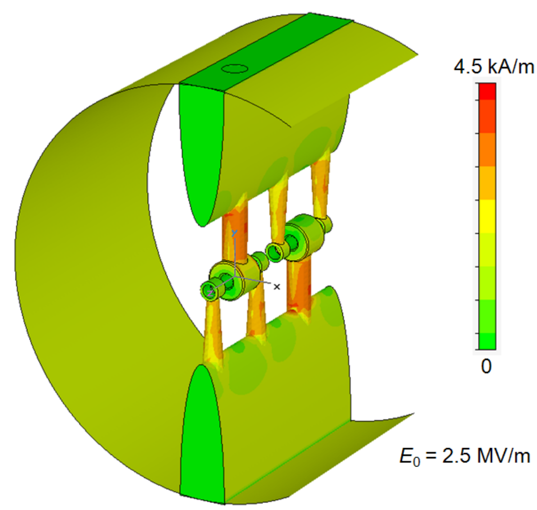


Figure 1: Surface current magnitude in the modified IH1-3 structure for $\beta_g$ = 0.04 (the cavity wall is partially cut).

Still, the beam size was rather large in all the cases, which can lead to undesirable beam losses. We plan to perform multi-particle beam-dynamics simulations next. Should they indicate significant beam losses, we will apply stronger transverse focusing using PMQ pairing, e.g. FFODDO (IH2-3); the structure is illustrated in Fig. 2. Such focusing schemes make the matched beam size smaller and reduce losses. TRACE-3D envelope calculations were performed also for the high energy end, $\beta_g$=0.065. There are more options there since the DT lengths are longer. For example, using longer PMQ while simultaneously increasing the PMQ and DT apertures to prevent beam losses gives good results [3]. Preventing beam losses is especially important at the high-energy end of the deuteron linac.

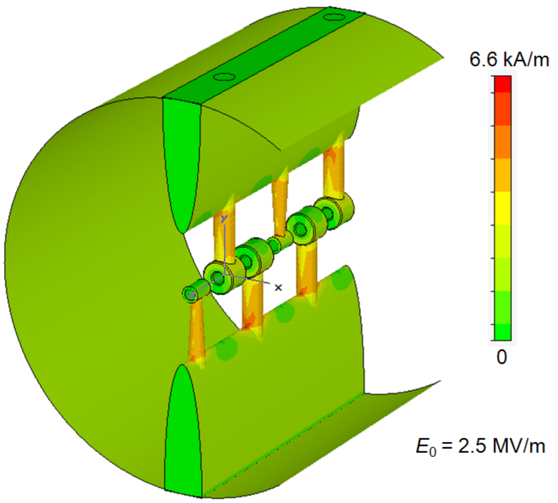


Figure 2: Surface current magnitude in the modified IH2-3 structure for $\beta_g = 0.06$ (the cavity wall is partially cut).

Overall, the transverse focusing structure IH1-3 (FOODOO, $n$=2), where PMQs are inserted only in every third DT, appears to be the best choice. It provides an acceptable beam transverse size while reducing the number of the required PMQs by a factor of three compared to the maximum equal to the number of DTs – a significant cost saving. It also gives us an opportunity to use DTs of different sizes – increasing the transverse size of DTs with PMQ while reducing the sizes of empty DT, as shown in Fig. 1 – to keep or even increase the high accelerating efficiency of the IH structure.

## IH STRUCTURE CHARACTERISTICS

It is known that IH room-temperature structures have high accelerating efficiency, an order of magnitude higher than the DTL structures, in the beam velocity range $\beta$ = 0.033-0.065, and small cavity transverse size (3-4 times smaller than DTL) [1]. Relatively homogeneous surface loss distributions compared to DTL (no hot spots) can simplify cooling. Our previous results [2] found the IH structures with DTs supported by stems on two vanes the most effective in this velocity range. We explore the characteristics of such IH structures for $\beta$ = 0.033-0.065 using EM modeling with the CST MicroWave Studio (MWS) [5]. The MWS eigensolver finds the modes in one period of the structure with periodic boundary conditions imposed at the ends.

### *Structures with Identical DTs and Narrow Gaps*

For the regular IH structures (identical DTs) with vanes and narrow gaps, $g/L_c$ = 0.15, the transit-time factor $T$ slowly increases from 0.9 to 0.96, while the shunt impedance $Z_{sh}$ decreases with $\beta$ [3]. The effective shunt impedance $Z_{sh}T^2$ ranges from 360 at low $\beta$ to 300 MΩ/m at high $\beta$, well above $Z_{sh}T^2$ of the DTL structure, which increases from 22 to 34 MΩ/m in this velocity range. Here we assume the copper surface with $\sigma = 5.8\cdot10^7$ $(\Omega\ \mathrm{m})^{-1}$.

A few designs of the 1 to 4 MeV deuteron accelerator based on the regular IH structures with vanes were evaluated [4]. We found only small differences between various design options, from one with gradually increasing cell lengths to the three-step design that includes only three types of cells, with $\beta_g$ = 0.04, 0.05, 0.06. In all these cases, assuming the average on-axis electric field $E_0$=2.5 MV/m and the RF synchronous phase -30°, the accelerator consists of 19-20 IH periods (38-40 cells) and has the total length 1.45-1.5 m. The surface-loss power is about 25 kW at 100% duty, small compared to the beam power 150 kW at 50 mA CW. Using a phase ramp to better capture the RFQ beam longitudinally would slightly increase the linac length.

One potential concern for the considered IH structures with narrow gaps was the maximal electric field $E_{max}$ exceeding for $\beta_g \geq 0.05$ the conservative safe level of $1.8E_K$, where $E_K$=14.8 MV/m is the Kilpatrick field at 201.25 MHz. In fact, the RF breakdown level can be even lower due to high magnetic fields near the PMQ surface. The surface loss per cell $P_{loss}$ and the maximal surface power density $(dP/ds)_{max}$ also increase as $\beta$ increases.

### *Structure Improvement Options*

One possible way to reduce $E_{max}$ for a fixed gradient is increasing the gap length between DTs by making the DTs shorter. This is an attractive option at $\beta_g \geq 0.05$, since the DTs are relatively long and can accommodate PMQs even with reduced DT length. For regular IH structures $L_{DT}$ should remain longer than the PMQ length, $L_q$=2 cm, which limits the gap width by $g/L_c$= 0.25, 0.35, 0.45 for $\beta_g$ =0.04, 0.05, 0.06, respectively. Apart from a small drop in the $T$-factor values (3-8%), the structure parameters improve significantly with the gap width increase: the effective shunt impedance $Z_{sh}T^2$ increases by ~50%, from 300-360 MΩ/m to ~500 MΩ/m; $E_{max}$ is reduced to safe levels around 20 MV/m with wider gaps [3, 4].

Another option for the IH structure improvement is to use DTs of different transverse sizes depending on whether they house PMQ inside or not. In IH1-3 structure, the transverse size of the DT with PMQ can be increased to facilitate the PMQ placement inside it, while the outer diameter of empty DTs can be reduced to keep the shunt impedance high. One can go a step further and reduce also the lengths of empty DTs to have wider gaps. One period of the modified IH1-3 structure for $\beta_g$ = 0.04 is shown in Fig. 1. The DTs with PMQ have large $r_{out}$ = 14 mm and length 24 mm; the empty DTs are short and slim, $r_{out}$ = 7 mm and length near 12 mm; the aperture radius is 5 mm. The resulting $Z_{sh}T^2$ is 712 MΩ/m; it decreases at the high-energy end but still is above 500 MΩ/m for $\beta_g$ = 0.06 [4].

For wider gaps in IH structures, a noticeable transverse on-axis electric field was observed, the known effect [1]. Asymmetric bulges on DT outer surface were used for its mitigation. The bulges reduce the dipole field but also reduce $Z_{sh}$. We considered an alternative measure – slanted ends of the empty DTs – that can compensate the integral transverse kick completely [4]. It keeps $Z_{sh}$ high but increases $E_{max}$ more than the bulges. The effects of the transverse on-axis electric field on the beam will be studied using Parmela multi-particle beam dynamics simulations with the MWS calculated 3-D fields for the modified IH structures.

## ENGINEERING ANALYSIS

We have developed a procedure [6] to transfer surface-loss power data calculated by MWS to finite-element (FE) engineering codes COSMOS and ANSYS. The important feature is that the MWS fields are extracted not exactly at the cavity surface points but with a small offset into the cavity along the normal to each FE out of the FE center point. This helps avoiding errors in the surface fields due to hexahedral MWS meshes as well as in the cases when the FE central points are located inside convex metal walls. Thermal and stress analysis was performed for the regular IH structures with cooling channels in the vanes.

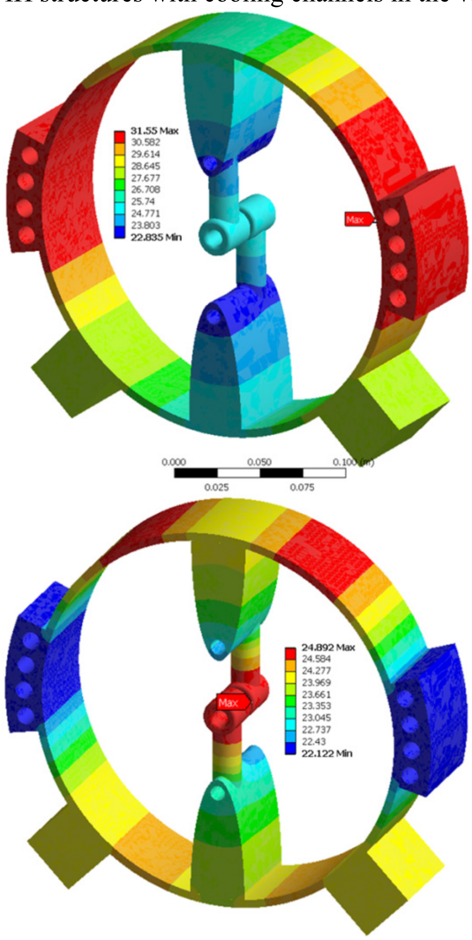


Figure 3: Temperature distribution in regular IH structure.

For the nominal 10% duty, the temperature distributions calculated by ANSYS are shown in Fig. 3. In the top picture, the water cooling is only in the vanes (4.4-m/s flow, 22°C inlet temperature); the maximal temperature (red) is 31.6°C, while the minimal (blue) one is 22.8°C. With the side-wall manifold cooling added at 10% duty (Fig. 3, bottom), the temperature range is from 22.1°C to 24.9°C. This option may be needed at higher duty factors. This important result – PMQ temperatures can be kept low by cooling only the vanes – confirms the IH-PMQ RT concept feasibility. The DT relative vertical displacements for 10% duty are between 15 and 35 μm depending on the cooling scheme, below typical manufacturing tolerances. The stresses at 10% duty are practically the same as in the cold state due to the atmospheric pressure, below 8 MPa, and even at 100% duty they do not exceed 28 MPa, which is still very far from the copper yield stress of 57 MPa. The transient thermal-stress analysis did not show any stresses above the static ones.

## SUMMARY

We are developing RT IH accelerating structures with PMQ beam focusing for low beam velocities using 3-D electromagnetic modeling combined with beam dynamics simulations and thermal-stress analysis. The modified IH1-3 structures, like the one shown in Fig. 1, where PMQs are inserted in every third (larger) DT followed by two short and slim empty DTs, provide both high accelerating efficiency – $Z_{sh}T^2$ from 700 to 500 MΩ/m in the beam velocity range $\beta$ = 0.033-0.065 – and good transverse beam focusing. Detailed multi-particle beam dynamics simulations are planned next. Should they indicate noticeable beam losses, we will switch to stronger focusing by pairing PMQs – see an example of the modified IH2-3 structure in Fig. 2 – and/or increase the DT apertures.

A compact 1-4 MeV deuteron linac based on IH-PMQ structure with the accelerating gradient $E_0$=2.5 MV/m has the total length of about 1.5 m. The surface-loss power in the accelerator is below 3 kW at the nominal 10% duty, which is less than 20% of the power delivered to the 50-mA deuteron beam, 15 kW. High efficiency of the described compact deuteron linac opens new options for RF. One of them is using inductive output tubes (IOT) instead of expensive custom grid tubes or klystrons as RF power sources; it would lead to both cost savings and an increased mobility of the system.

The authors gratefully acknowledge useful discussions with D. Barlow, F. Neri, and T. Wangler. This work is supported by the DOE NNSA via LANL LDRD program.

## REFERENCES

[1] U. Ratzinger, NIM A464 (2001) 636; Proceed. CAS 2000, CERN 2005-003, p. 351 (2005).
[2] S. Kurennoy, L. Rybarcyk, and T. Wangler, "Efficient Accelerating Structures for Low-Energy Light Ions," PAC'07, Albuquerque, NM, p. 3824 (2007).
[3] S. Kurennoy, S. Konecni, J. O'Hara, & L. Rybarcyk, "IH Accelerating Structures with PMQ Focusing for Low-Energy Light Ions," EPAC08, Genoa, p. 3428 (2008).
[4] S. Kurennoy, Technical notes AOT-ABS: 07-032, 08-008, 08-017; LA-UR-08-03795, Los Alamos, 2008.
[5] CST MicroWave Studio 2008, http://www.cst.com.
[6] S. Kurennoy, S. Konecni, J. O'Hara, & L. Rybarcyk, "Heating and Stress in the LANSCE Side-Coupled Linac RF Cavities," EPAC08, Genoa, p. 3431 (2008).

# PERFORMANCE OF A 1.3 GHZ NORMAL-CONDUCTING 5-CELL STANDING-WAVE CAVITY*

Faya Wang, Chris Adolphsen and Juwen Wang, SLAC, Menlo Park, CA 94025, U.S.A

*Abstract*

A 5-cell, normal-conducting, 1.3 GHz, standing-wave (SW) cavity was built as a prototype capture accelerator for the ILC positron source. Although the ILC uses predominately superconducting cavities, the capture cavity location in both a high radiation environment and a solenoidal magnetic field requires it to be normal conducting. With the relatively high duty ILC beam pulses (1 msec at 5 Hz) and the high gradient required for efficient positron capture (15 MV/m), achieving adequate cavity cooling to prevent significant detuning is challenging. This paper presents the operational performance of this cavity including the processing history, characteristics of the breakdown events and the acceleration gradient witnessed by a single bunch at different injection times for different rf pulse lengths.

## INTRODUCTION

Due to high radiation levels and the need of a solenoidal magnetic field for focusing, the 1.3 GHz pre-accelerator that follows the ILC positron target will be normal conducting. A half-length (5-cell) prototype standing-wave (SW), cavity was built at SLAC to verify that the gradient (15 MV/m in 1.0 ms pulses) can be achieved stably and without significant detuning from the RF heat load (4 kW per cell). Details of the design can be found in [1, 2], and the cavity cross-section is shown in Fig. 1 [3].

Fig. 2 is a plot of the cold test measurement of the mode frequencies (dots); the solid line is the fitted dispersion curve, expressed as,

$$f_n^2 = \frac{f_0^2}{1 + k_1 \cos(\phi)}$$

with $f_0$= 1291.8 MHz and $k_1$= 0.01249. The unloaded Q of the cavity is ~ 29000 and the operating frequency (at π phase advance) is 1299.7 MHz. The time constant of this critically-coupled cavity ($0.5Q_o/\omega$) is 1.8 us.

So far, the cavity has been rf processed at the π-mode for about 530 hrs and it has incurred about 6200 breakdowns. The gradient goal of 15 MV/m with 1 ms pulses has been achieved. Fig. 3 shows the breakdown rate history during processing. For these data, the pulse repetition rate was 5 Hz except for 1 ms pulses where it was lowered to 1 Hz to reduce the detuning as the reflected power was causing waveguide breakdowns (the source of these breakdowns has since been eliminated and 5 Hz operation is expected to be possible in the future).

The goal when designing the cavity cooling system was to have about 25% reflected power when the cavity was turned on 'cold' that then dropped to zero in steady state with full rf power dissipation (20 kW at 15 MV/m). In this way, a cavity temperature control system is not needed (at least for testing). However, the flow rate that was achieved (due to a limited supply of temperature-regulated water) was 86 gpm compared to the 140 gpm desired, which increased the cavity temperature by about 50% (to 0.13 degC per kW dissipated). Also, the detuning (-2.7 kHz/kW) was about 25% larger than expected from simulations using the actual temperature rise and led to an overall reflection of about 50% when cold with the appropriate choice of rf frequency to minimize the reflection at full power in steady state.

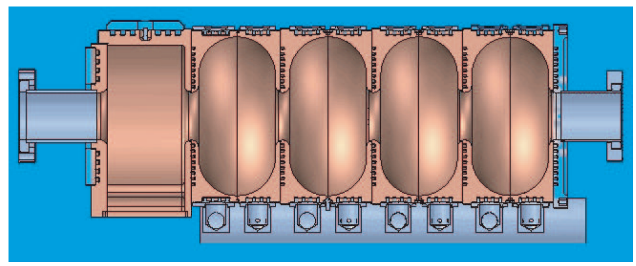

Figure. 1: Cross sectional view of the 5-cell cavity where the coupler cell is on the left. Water circulates through rectangular grooves in the irises and outer cavity walls.

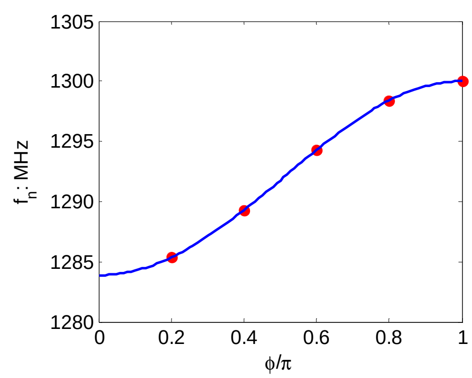


Figure 2: The 5-cell SW cavity dispersion curve.

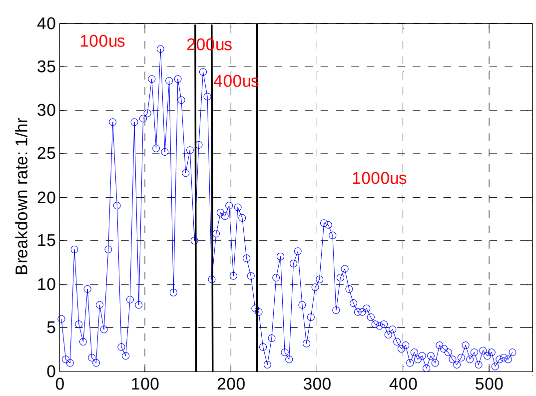


Figure 3: Breakdown rate history of the cavity for various pulse lengths (in red).

* Work Supported by DOE Contract DE-AC03-76F00515.

## CAVITY BREAKDOWN STUDIES

After hundreds of hours of conditioning, the breakdown rate was measured as a function of unloaded gradient (G). A $G^{21}$ dependence was found, which is less steep than the $G^{32}$ dependence recently observed for a CERN-designed, low a/λ, TW, X-band (11.4 GHz) structure [4]. However, the gradient exponent is within the 20-30 range measured for NLC/GLC X-band prototype structures and close to the 19.5 value measured for the FNAL 805 MHz injector linac cavities.

The breakdowns fall into two types, which we call 'hard' and 'soft' depending on the decay profile of the cavity stored energy as measured by a pick-up probe in the beam pipe on the non-coupler end of the cavity. For hard events the stored energy drops quickly (in < 2 us) after a breakdown as illustrated in Fig. 4; for soft events it decays slowly (in 10-20 us), with a 'beating' pattern as illustrated in Fig. 5 (note: the actual beating frequency is higher than seen in the plot due to the low waveform sampling frequency, and the klystron power is shut off within 2 us after a breakdown is detected).

Although the cause for these two types of events is not known, one guess is that a breakdown effectively splits the cavity into two isolated parts, and the breakdown induced currents load the two parts differently in the two cases. That is, if the currents load down the non-coupler end, both the reflected power and stored energy fall rapidly (the reflected power because of the lower loaded *Q* and the stored energy because of the loading). If the currents load down the coupler end, however, the reflected power falls quickly, but the stored energy in the non-coupler end behaves as if it is in a shorter, higher *Q* cavity. In this case the stored energy drops slower, and because the energy is partitioned into more than one mode, there is a beating pattern as the energy decays.

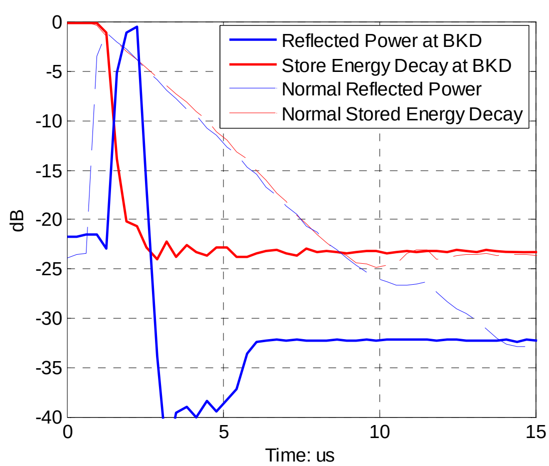


Figure 4: An example of a hard event. The red and blue dashed lines are the stored energy and reflected power, respectively, when the cavity turns off at the end of the pulse (no breakdown), and the solid lines are these waveforms for a breakdown event where the time scale has been shifted to match the initial drop in stored energy for the normal turn-off case.

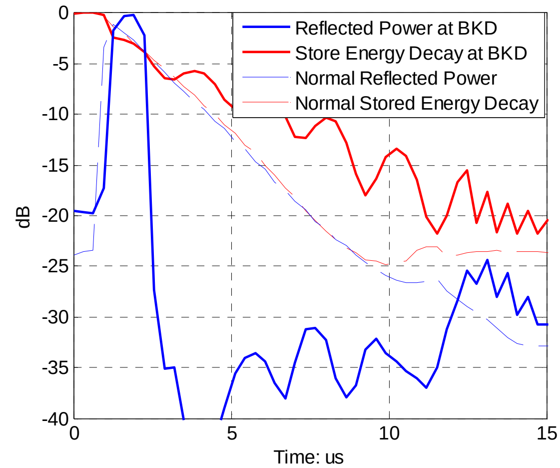


Figure 5: An example of a soft event. The waveforms are the same as described in the Fig. 4 caption.

To explore this further, an equivalent circuit model was used to analyze the transient response of the two cavity parts. The model shows that the stored energy remaining in each part will excite all possible modes in that part to some degree. For the coupler-end part, the loaded *Q* is quite low because of the coupler, so it is hard to see the oscillation in the reflected power after a breakdown. For the soft events, Fig. 6 shows the FFT of the simulated stored energy waveform when different irises are blocked (zero coupling through the iris) in the equivalent circuit model. By comparing the measured beating frequency with the peak values predicted, the breakdown iris should be identifiable. Since the waveforms shown were sampled at 3.125 MHz and there was some cross talk between the phase and amplitude, it is hard to extract the correct mode beating frequency from these data. In the future, a much higher sampling frequency will be used to study the breakdown waveforms. Finally, it is interesting to note how the fraction of hard and soft events changed during processing (see Fig.7).

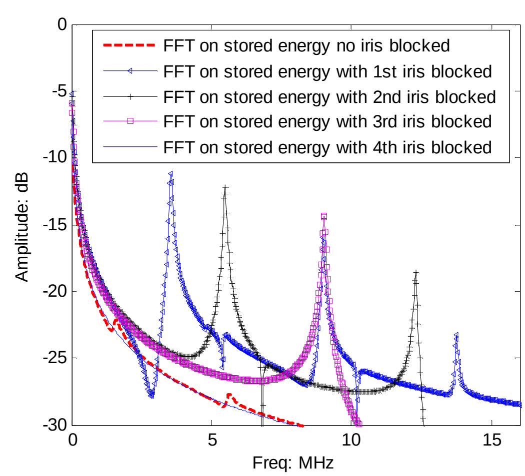


Figure 6: Predicted stored energy frequency spectrum at the non-coupler end of cavity when different irises are blocked.

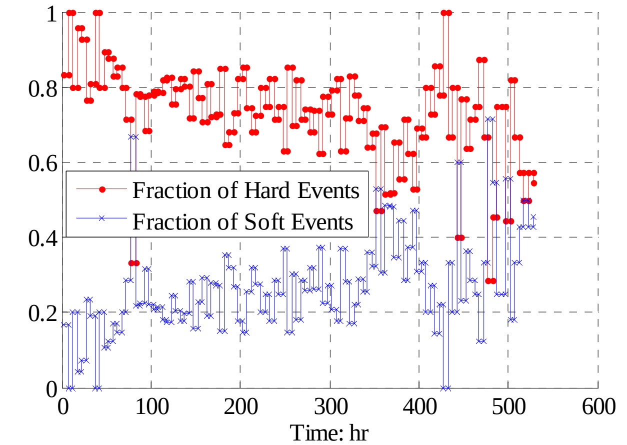


Figure 7: Hard and soft event fractions during conditioning.

## DETUNING EFFECTS

To study how the detuning from average heating (up to 45 kHz at 15 MV/m) and intra-pulse heating (up to 4 kHz at 15 MV/m) affects the cavity gradient, the cell field distributions as a function of the detuning were computed using an equivalent circuit model. These data are shown in Fig. 8 together with the relative average gradient that a speed-of-light particle would see if the rf phase is optimized. This latter curve shows that the gradient is fairly independent of the frequency shifts in the range that are expected.

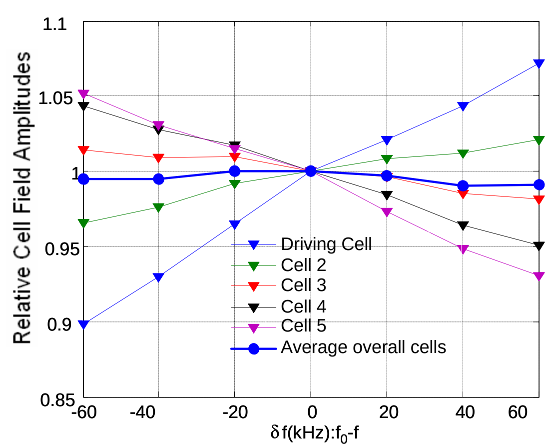


Figure 8: Simulated relative cell field amplitudes versus cavity detuning for a fixed net power into the cavity.

To explore the detuning effect experimentally, a single bunch was accelerated at 5 Hz in the cavity at NLCTA at different injection times (85 us and 900 us) during rf pulses with different widths (100 us and 1100 us). These combinations were chosen to distinguish detuning effects from low average heating, high average heating and intra-pulse heating. The gradients inferred from the bunch energy gains are plotted in Fig 9 versus the net cavity input power (problems with the klystron modulator at the time prevented > 2 MW operation). These measurements were done at a fixed rf frequency and the bunch charge was about 20 pC so the beam loading was very small. For low average heating, the cavity detuning was about -20 kHz and for high average heating, it was about -4 kHz at the beginning of the pulse and around - 6 kHz by the end of the pulse. The gradient versus power fits agree to within the roughly 4% systematic errors so no significant gradient changes were observed as expected from Fig 8. These measurements will be repeated for power levels up to 4 MW (15 MV/m gradients).

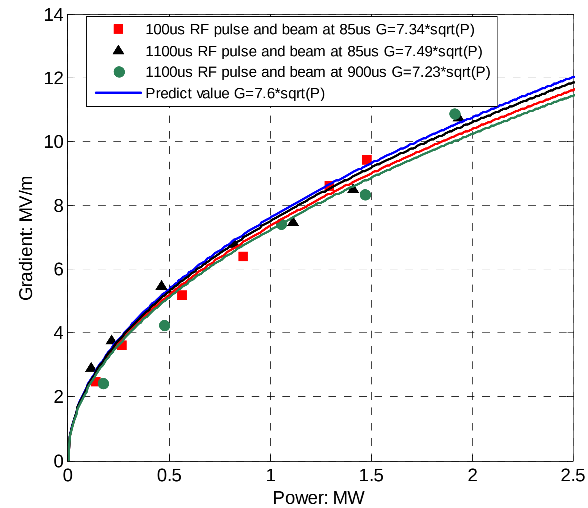


Figure 9: Single bunch acceleration gradient versus the net cavity input power (forward – reflected) for different pulse widths and bunch injection times.

## SUMMARY AND OUTLOOK

A 5-cell SW cavity has been conditioned to 15 MV/m with 1ms pulses although the ultimate breakdown rate has yet to be fully characterized. As expected, detuning from average and inter-pulse heating had a small effect on the gradients achieved during single bunch operation.

In the ILC, the positron capture cavity will need to operate in a 0.5 T solenoidal magnet. Such a magnet has been installed around the 5-cell prototype to gauge its effect on the cavity performance. Although the outgassing and breakdown rate initially increased, the performance improved with rf processing. In the next few months, rf conditioning in the presence of the magnetic field will continue, breakdown location studies will be done, and the breakdown dependence on pulse width will be measured.

## REFERENCES

[1] J.W. Wang, C. Adolphsen, et al., 'Studies of Room Temperature Accelerator Structures for the ILC Positron Source', SLAC-PUB-11767.

[2] J.W. Wang, C. Adolphsen, et al., 'Positron Injector Accelerator and RF System for the ILC', SLAC-PUB-12412.

[3] G. Bowden, 'L-Band Accelerator Cooling', SLAC ILC ME Note 2-05, Aug. 2005.

[4] F. Wang, 'Breakdown Characteristics Study of an 18 Cell X-band Structure', AAC08.

# PROGRESS IN L-BAND POWER DISTRIBUTION SYSTEM R&D AT SLAC*

Christopher Nantista, Chris Adolphsen and Faya Wang, SLAC, Menlo Park, CA 94025, U.S.A.

*Abstract*

We report on the L-band RF power distribution system (PDS) developed at SLAC for Fermilab's NML superconducting test accelerator facility. The makeup of the system, which allows tailoring of the power distribution to cavities by pairs, is briefly described. Cold test measurements of the system and the results of high power processing are presented. We also investigate the feasibility of eliminating the expensive, lossy circulators from the PDS by pair-feeding cavities through custom 3-dB hybrids. A computational model is used to simulate the impact on cavity field stability due to the reduced cavity-to-cavity isolation.

## INTRODUCTION

In high energy particle accelerators, particularly in high-gradient linear collider designs, there is generally a significant mismatch between the peak power and pulse length in which RF can be efficiently produced and that in which they can be efficiently used for acceleration. The waveguide network connecting the sources to the structures, or power distribution system (PDS), is thus often less straight-forward than might be thought. Sources might be combined for convenient transport, sometimes compression techniques are used to trade pulse width for peak power, and power division at the accelerator for feeding multiple structures is usually required.

For L-band (1.3 GHz) superconducting linacs, state-of-art klystrons can produce 10 MW in 1.6 ms pulses, and state-of-the-art cavities can sustain gradients corresponding to about 300 kW of input power. Thus one source can drive quite a few cavities, 26 in current ILC plans, with allowance for losses and overhead for low-level RF control. The most direct approach to implementing this, adopted at DESY's TTF, is to use a set of hybrid directional couplers connected in series, each with a different coupling. Another approach, less compact, would be to use successive splitting in a branching arrangement.

In an inter-lab R&D collaboration, SLAC is providing RF system components for the test accelerator under construction in Fermilab's NML building, eventually a full system including couplers, but initially a PDS for the first cryomodule. The layout we chose [1] uses two levels of splitting (as does that chosen for the European XFEL), so that an appropriate portion of the power flowing in a main waveguide line is tapped off and then evenly split for each successive pair of cavities.

The two unique features of our PDS are the use of a novel variable tap-off (VTO), a four-port directional coupler with mechanically adjustable coupling [2], and the use of a four-port hybrid rather than a simple "T" for the binary split. The former allows uniform fabrication of the main line tap-offs as well as the ability to better optimize the overall gradient by tailoring the power distribution to accommodate a spread in sustainable gradient among the cavities [3]. The use of a 3-dB hybrid, standard for feeding standing-wave normal conducting accelerator structures, for the final split allows the reflected power from each cavity pair to be directed to a load. We hope thus to eliminate the need for an expensive and lossy circulator for each cavity.

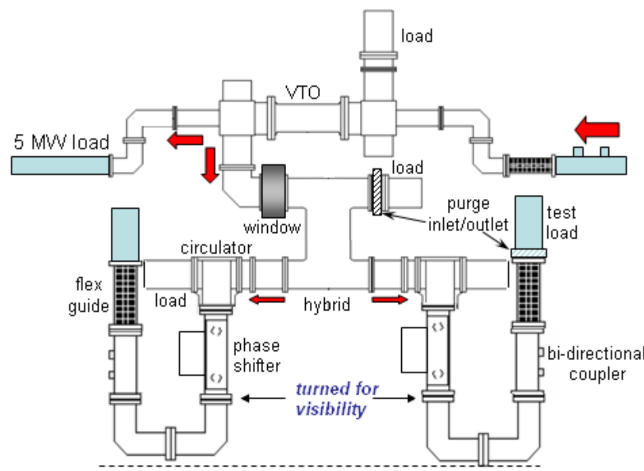


Figure 1: A two-feed sub-unit of the power distribution system. Blue components belong to the test setup, not the unit. The U-bends at the bottom are actually perpendicular to the page.

## THE PDS UNIT

The pair-wise feeding in our approach is well suited to standard 8-cavity cryomodules. The local PDS along such a cryomodule consists of four, two-feed modular units connected in series. Fig. 1 shows a diagram of one such unit as built for FNAL. The VTO and the hybrid are SLAC designs, machined from aluminum and dip-brazed. The WR650 waveguide bends, spool pieces and semi-flexible sections are supplied commercially with custom lengths, many thick-walled for pressurizability. The remaining components were developed for DESY's L-band program by commercial vendors. They include a modified pillbox window to separate pressurized and non-pressurized regions, 1 MW loads, circulators (isolators), phase shifters and diagnostic directional couplers. Most flange connections employ aluminum gaskets combining knurled contact surfaces with rubber pressure seals.

The assembly is supported for testing and shipping in an aluminum box frame as shown in Fig. 2. Only one wall of this frame will remain after anchoring it in the accelerator enclosure. The upper waveguide, which would

*Work supported by the U.S. Department of Energy under contract DE-AC02-76SF00515.

transport up to 3.5 MW in the ILC, is to be filled with pressurized $N_2$ to 2 bar absolute (14.5 psig) to suppress RF breakdown. The lower power region after the window is to be lightly purged with $N_2$ to avoid oxidation.

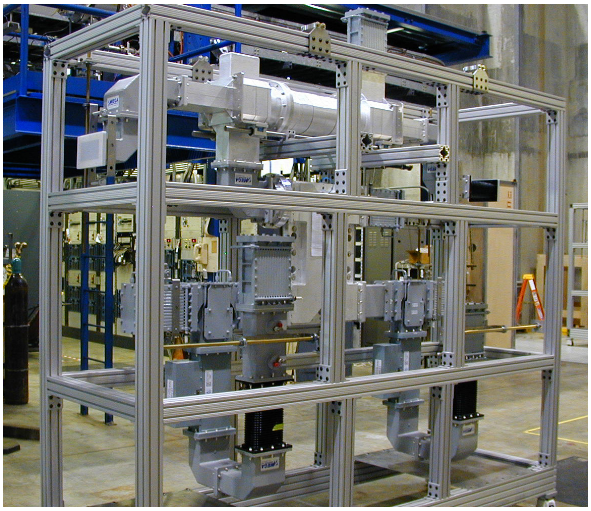

Figure 2: A two-feed sub-unit of the power distribution system in its support frame. When installed, the front wall of the frame will be removed, and the U-bends reversed to go under the remaining wall.

## TESTING

The modularity of our PDS makes it convenient to individually test the two-cavity units. One unit has been completely tested and received by Fermilab; three more are in queue to be connected to our 5 MW klystron.

### *Low Power*

The first unit tested has the VTO set for roughly 50% extraction. Cold test measurements were made first with a network analyzer. Fig. 3 shows the S matrix parameters between the input port and the other ports; 50.7% is transmitted, and 23.4% and 23.6% are extracted to the cavity feeds. The return loss is -43 dB (-38 dB from the output end. Of the approximately 2.3% missing power, most can be attributed to the corrugated flex guides and the circulators. The match at the two cavity feed ports is -23–26 dB and the isolation between them -69 dB.

The phases of the extracted signals differ by less than 2°, and the error in the through-signal phase (designed to be zero) is ~-6.7°. Such errors are easily corrected by the phase shifters.

### *High Power*

After RF leak checking and connecting the cooling water circuits, the unit was configured for high-power operation by adding loads to the output ports and a directional coupler to the input port, as shown in Fig. 1. The lower region was N2 purged and the upper region pressurized to 12 psig.

To limit breakdown damage, the RF power was interlocked to trip off on a reflected signal from the unit. The VTO and hybrid had both been previously high-power tested successfully above 4 MW under 3 bar absolute pressure down to atmospheric pressure. We were more concerned about the circulators and phase shifter since we had not tested them and were pushing them somewhat beyond the level where they been reported to breakdown on occasion at DESY. Since the circulators absorb any reflected power from downstream break-downs, we also interlocked on missing energy signals formed by comparing the forward signals at the feed directional couplers with the forward signal into the unit.

Power was gradually stepped up to at least 1.5 MW in 1.2 ms long pulses (our maximum pulse width) so each feed saw at least 360 kW (~10% more than needed for 35 MV/m, 9 mA acceleration at ILC). At this power, each phase shifter was run over its full 100° range. The dummy loads representing the cavities were then replaced with shorts to simulate worst case full reflection, and the above procedures were repeated. The feed arms have different lengths so the standing wave pattern in one arm was shifted a ¼ wavelength relative to that in the other, and any weak points in the components were guaranteed to see field. Finally ~24 hours of operation (at 5 Hz) were logged in this configuration to test reliability. No RF breakdowns in the PDS unit were detected during any of these tests (which we attribute in large part to having good RF connections between flanges).

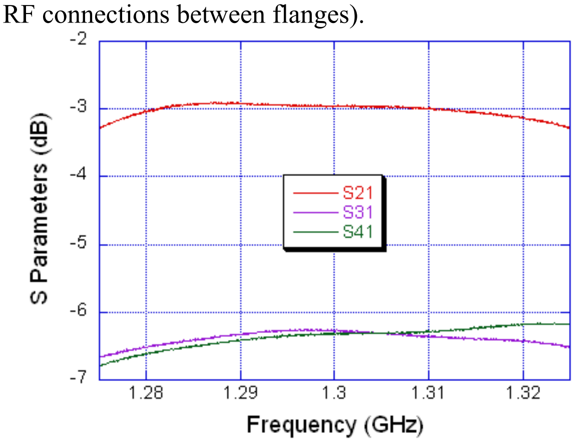


Figure 3: Network analyzer measurements of the coupling from the input port to the through port (S21) and to each cavity feed port (S31 and S41) for the first two-feed unit tested.

## VTO SETTINGS

The four VTO's have been set for roughly the nominal tap-off ratios, i.e. 1/4, 1/3, 1/2, and 1. To account for transmission loss between one unit and the next, and to tailor the distribution for a given set of cavities, it can be shown that the couplings should be reset according to

$$C_n = \frac{G_n T^{N-n}}{\sum_{m=0}^{N-n} G_{N-m} T^m} , \quad (1)$$

where $T$ is the power transmission factor per sub-unit (not counting the tapped-off power), estimated from measure-ments to be ~ 0.986 for our system, and the $G_n$'s are the relative gradients or powers at which each pair of cavities is to be run (lowest of the two thresholds). This is done by setting the angle of each VTO central section relative to the end sections to

$$\alpha_n = \frac{1}{2}\sin^{-1}\sqrt{C_n} \, . \qquad (2)$$

Such adjustment can be done in situ, with power locked out and the system depressurized, by loosening the two rotatable flange joints flanking the central section until it can be turned. This may also require unbolting the joint between E-plane bends at the VTO input end. The power distributed to each cavity pair is given by $P_1 = P_0 T_E C_1$ and

$$P_n = P_0 T_E \prod_{m=1}^{n-1} (1 - C_m) T^{n-1} C_n \quad , n > 1 \, , \qquad (3)$$

where $P_0$ is the power at the PDS input end and $T_E$ the power transmission factor for the extracted power from the sub-unit input to cavity coupler (not counting through power).

## OPERATION WITHOUT CIRCULATORS

Because the cavity spacing in the first FNAL cryomodule does not allow for both beam acceleration and combining reflections in the terminated hybrid port (the phase requirements conflict), circulators had to be included in this PDS. We have, however, procured custom H-plane bends to replace the circulators for an experiment powering the cavities without them (no beam). For this, the E-plane bends composing the U-bends in the feeds (see Figs. 1&2) will be reconfigured (one long and one short, rotated 90°) to produce equal phase lengths.

In addition to the reflection cancellation, which will require setting the cavity couplers for identical loaded quality factors, we can check the stability of the cavity fields. One concern with such operation is that the cavities won't be as isolated as with circulators and resulting coupling between cavities will cause beating of the field amplitudes.

To allay such fears, we have simulated the effect of coupling between a pair of cavities driven through a hybrid with imperfect isolation. The cavities are assumed to be identical, with nominal ILC parameters, and the transient behavior of the field amplitudes was numerically computed from a set of coupled differential equations, including beam loading. The amplitude of the coupling was varied with zero and π/2 relative phases, and the resulting cavity gradients are shown in Fig. 4. The deviations from flatness along the bunch train tend to cancel between the two cavities, especially for the π/2 phase case, where they are largest. Similar results were reported in [4].

Measurements of the SLAC hybrids show isolations of -45.5–48.2 dB, while that in a commercial hybrid was measured to be -42.5 dB. With isolations better than -40 dB readily achievable, the affect on the cavity gradients should be negligible. Indeed, the fractional net gradient spread at this coupling level ranges from 0.9–$6.5\times10^{-5}$, depending on phase.

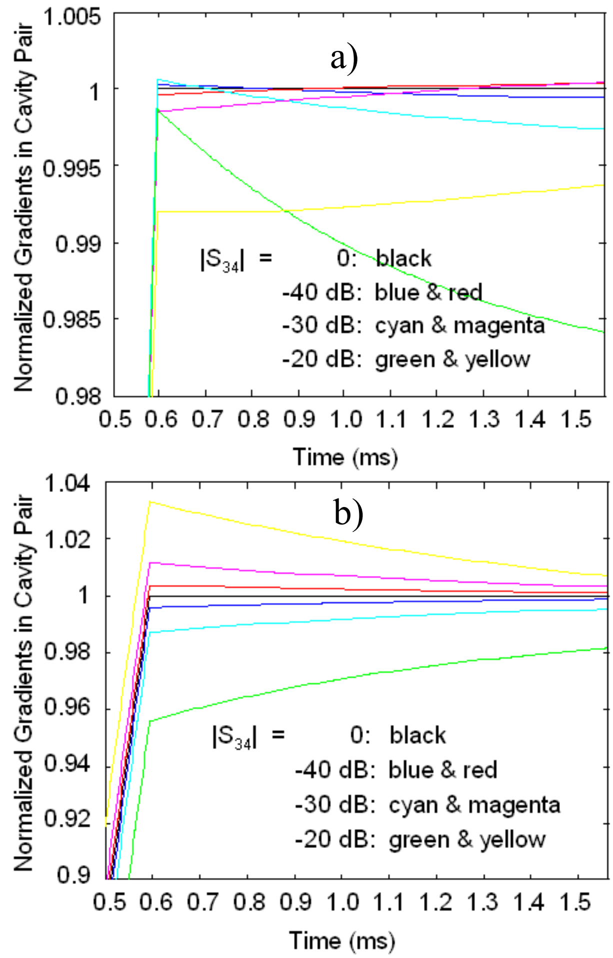


Figure 4: Simulations of cavity field amplitude "flat-tops" with imperfect isolation between hybrid-coupled cavities at coupling phases a) 0 and b) π/2. Pairs of colors represent the pair of cavities.

## REFERENCES

[1] Christopher Nantista *et al.*, "An RF Waveguide Distribution System for the ILC Test Accelerator at Fermilab's NML," presented at the 2007 Particle Accelerator Conference, Albuquerque, New Mexico, June 25-29, 2007; SLAC-PUB-12626.

[2] Christopher D. Nantista and Chris Adolphsen, "A Variable Directional Coupler for an Alternate ILC High-Power RF Distribution Scheme," presented at the 2006 Linear Accelerator Conference (LINAC06), Knoxville, TN, August 21-25, 2006; SLAC-PUB-12372.

[3] K.L.F. Bane, C. Adolphsen, and C. Nantista, "RF Distribution Optimization in the Main Linacs of the ILC," presented at the 2007 Particle Accelerator Conference, Albuquerque, New Mexico, June 25-29, 2007; SLAC-PUB-12628.

[4] Justin Keung, "Application Note: Effects of an Alternative RF Distribution Configuration on Flattop," Sept., 2007.

# A NEW ACCELERATOR STRUCTURE CONCEPT: THE ZIPPER STRUCTURE*

Christopher Nantista, SLAC, Menlo Park, CA 94025, U.S.A.

*Abstract*

I introduce a novel normal-conducting accelerator structure combining standing wave and traveling wave characteristics, with relatively open cells. I describe the concept and geometry, optimize parameters, and discuss the advantages and limitations this new structure presents.

## INTRODUCTION

A number of different geometries have been employed over the years in accelerating structures. Currently, efforts continue toward finding the optimal design for use in a normal conducting TeV-scale electron-positron linear collider. The key general structure parameters of shunt impedance and quality factor relate to the RF-to-beam power transfer efficiency. Also rising to prime importance for a linear collider are the sustainable accelerating gradient, which drives the overall linac length, and the HOM wakefields, which impact beam dynamics and emittance preservation. To maximize the former, generally limited by RF breakdown or pulsed heating, variation of geometrical parameters has been tried, including group velocity, phase advance per cell, and iris tip shape, as well as different materials, surface preparations, and frequencies. Standing-wave structures have also been considered as perhaps offering advantages over traveling-wave structures in regard to breakdown. The deleterious effects of wakefields have been addressed by techniques such as damping into external manifolds, radiating out through chokes or channeling through slots into absorbers.

I present below an idea for a radically different structure with features that may recommend it over perturbations of more conventional geometries. It has not yet been tested, but is currently in the design stage. I will attempt to motivate its conception, describe its features, and suggest reasonable parameters for an X-band prototype.

## MOTIVATING CONSIDERATIONS

Large iris apertures, for large group velocity (traveling-wave structures) or mode spacing (standing wave structures), seem to exacerbate breakdown problems. They tend to increase the ratio of the peak surface electric field to the accelerating gradient and reduce shunt impedance. If we decouple power flow/cell coupling from the beam irises, we can keep the latter as small as short-range wakefield considerations allow.

Coupler cells (and those near them) have proven to be particularly prone to gradient limiting RF breakdown. Even if pulsed heating of the waveguide coupling iris is minimized, squeezing the full structure power through such cells seems inadvisable. We can eliminate the bottleneck presented by coupler cells if we couple to all cells identically.

Long range wakefields must be suppressed by removing HOM power deposited by the bunch train. What if all the cells were heavily coupled, with a fairly wide-open geometry, into an easily damped volume? One might then avoid pulsed heating and high electric field problems associated with slots and chokes.

A π/2 phase advance per cell might offer improved R/Q, though perhaps lower Q, compared to larger phase advances, since the cell transit time factor can be significantly larger (0.90 *vs.* 0.64 for a π mode in a simple pillbox). For traveling-wave structures, variations from the 2π/3 traditional SLAC choice that have been tried range from π/3–5π/6. For a standing-wave structure, a π/2 mode leaves every other cell empty, thus killing the effective shunt impedance. This problem is often dealt with by employing a bi-periodic structure with the empty cells either collapsed in length or moved off axis (side-coupled).

What if, instead, we excited the set of empty cells in their own independent resonance π/2 out of phase with the first set, so that the beam is synchronously accelerated throughout?

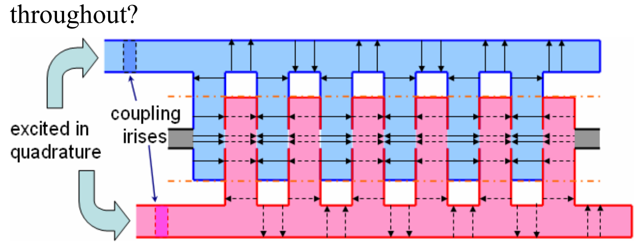


Figure 1: Basic waveguide circuit and field pattern of the zipper structure with degenerate orthogonal resonances driven π/2 out of phase.

## THE ZIPPER CONCEPT

Consideration of the above issues eventually led to the zipper-like structure geometry suggested by Fig.1. With normal, axial cell coupling, the tuning of the end cells would determine whether one, the other, or neither π/2 mode was a resonance in the fundamental mode passband of the structure. If the cells are decoupled on axis, or such coupling is overwhelmed by heavy side coupling between sets of every other cell through a waveguide, as shown, one might imagine driving both degenerate resonances.

The structure is essentially a pair of interleaved combs of stubbed waveguide. The regions comprising the actual cells are, as envisioned here, square, rather than axially symmetric. One wall of each cell is removed, perfectly substituted for by a null in the standing-wave field pattern

*Work supported by the U.S. Department of Energy under contract DE-AC02-76SF00515.

of the stub. The alternate stubs are connected at the center of their field lobes by a beam hole.

As the normal guide wavelength in the coupling waveguide is greater than the free space wavelength, coupling periodically to a speed-of-light structure might seem problematic. The key to this solution was extending the stub length between the waveguide wall and the virtual short represented by the null at the missing cavity wall. By adjusting this length, the periodic structure represented by the (short-)stubbed waveguide could be made to have the same phase advance as required by the accelerating structure. (In practice, the phase advance is set by boundary conditions and the stub adjusted to set the frequency.)

Each waveguide comb resonates in a standing-wave π-mode pattern. When excited in quadrature, they present to the beam what appears to be a traveling-wave π/2-mode structure. This "zipper" structure* can thus be considered a virtual- or pseudo-traveling-wave structure.

## FEEDING

To obtain the proper relative phase, the two sides of the structure can be powered from a single feed waveguide split through a hybrid or asymmetric magic T. A benefit of this split feeding, is that the reflections from the two sides combine into the fourth port of the hybrid or magic T, which would terminate in a load. The standard technique of pairing up standing-wave structures to isolate the source from reflections this way is not necessary; the structure is itself a pair of resonators.

At the input of each side waveguide, a mismatch can be incorporated into a transition to reduced height to achieve the proper coupling for the desired β. The waveguide, being so strongly coupled to each of its cells, is itself part of the resonant circuit.

In the two waveguide coupling irises and the load port can be seen further similarities to a traveling-wave structure, though they are all at the same end.

## CELL DESIGN

After a simulation check of the concept, an attempt was made to develop reasonable, somewhat optimized parameters for an initial 11.424 GHz design. The iris radius was fixed at 2.887 mm, or a/λ at 0.11, following recent CLIC designs [2]. For the zipper geometry, only short range wakefield considerations limit how small this can be. Structure performance can be improved with smaller apertures where applications allow.

As shunt impedance for the square π/2 accelerating region tended to improve with decreasing iris thickness, a value of 0.050" (1.27 mm) was chosen as mechanically feasible. To reduce the peak surface field, the iris tip shape was morphed to an ellipse with an aspect ratio of 3. The cell side, and thus the waveguide width, came out to be 0.7591". The waveguide height was set at 0.1875" (4.7625 mm), half the height of the WR75 standard. The corners at the stub intersection are points of high electric field and had to also be elliptically blunted (with semi-axes 0.100" along and 0.050" perpendicular to the waveguide) to bring the field down to about the level of that at the iris tips.

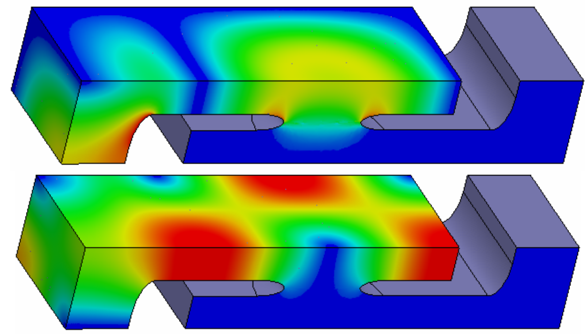

Figure 2: Half geometry of one period from mid-cell to mid-cell. The top image shows the electric field pattern and the bottom one the magnetic field pattern for one of the two symmetric, out-of phase modes.

The resulting geometry of one period of this zipper structure is shown in Fig. 2, along with HFSS plots of the fields for one of the two resonances, solved by imposing electric and magnetic boundary conditions on the top and bottom faces, respectively. The longitudinal cuts here suggest how the structure might be fabricated from machined stack-and-braze cells. Structure parameters were calculated from these field solutions. To account for the other mode, the voltage across this period is doubled, as is the stored energy, so that r/Q (=$V^2/(\omega UL)$) is also doubled.

Table 1: Structure Parameters

| Parameter | Zipper 1 | Zipper 2 | Circ (π) 1 |
|---|---|---|---|
| $f_r$ (GHz) | 11.424 | 11.424 | 11.424 |
| a/λ | 0.11 | 0.11 | 0.11 |
| r/Q (kΩ/m) | 10.90 | 11.73 | 11.28 |
| $Q_0$ | 6,370 | 6,193 | 8,949 |
| r (MΩ/m) | 69.41 | 72.65 | 100.9 |
| $E_p/E_a$ | 1.75 | 1.98 | 3.20 |
| $\eta_{CLIC}$ | 0.2831 | 0.2964 | 0.3310 |

Structure characteristics are listed in Table 1 (Zipper 1). The last row gives the calculated RF-to-beam efficiency,

$$\eta \equiv \frac{T_b}{T_f + T_b} \frac{I_b G}{P_{RF} / L}, \quad (1)$$

using the CLIC parameters: $I_b$=1.192 A, $T_b$=155.5ns, and $G$=100 MV/m [1]. $T_f$ is the fill time and $P_{RF}/L$ the input power per unit length. These are set, along with $\beta$, to give flat acceleration and zero reflection during the beam.

* This name, previously applied to an unrelated W-band structure (see Kroll, *et al.*,"PLANAR ACCELERATOR STRUCTURES FOR MILLIMETER WAVELENGTHS," PAC '99), is appropriated with the permission of the late Prof. Robert H. Siemann.

A second design was made with the focus more on increasing efficiency than minimizing surface electric field. The iris was thinned slightly to 0.045” (1.143 mm), with the tip blended into a 0.0522” (1.326 mm) diameter bulb. This allowed the side to be held at exactly 0.750” (19.05 mm) to match WR75. The side waveguide was slightly reduced in height to 4 mm to reduce stored energy, and the stub corner rounded to 1.5 mm.

The characteristics of this design (Zipper 2) are also shown in Table 1. For comparison, a third set of values is given for a circular π-mode standing-wave cell of the same iris as the first zipper design. This standard structure wins here in efficiency, but at the cost of much higher surface field. Further, it has no HOM damping and would be limited in length by narrow pass band. The latest traveling-wave CLIC structure has an efficiency of 0.277 [1].

Based on calculated 0-π mode frequency separation for the two regions, the period-to-period coupling of the stubbed waveguide region of the first design was found to be ~16.4 times greater coupling than that of the square cell region (k=0.197 vs. 0.012) and should dominate. An S-parameter simulation using two periods to eliminate the need for an artificially imposed magnetic boundary verified isolation between the two side waveguides of better than -30 dB. This decoupling of the combs without the need for cell-isolating nose cones is required by field symmetry, as well as by the fact that the π/2 mode leaves every other cell empty.

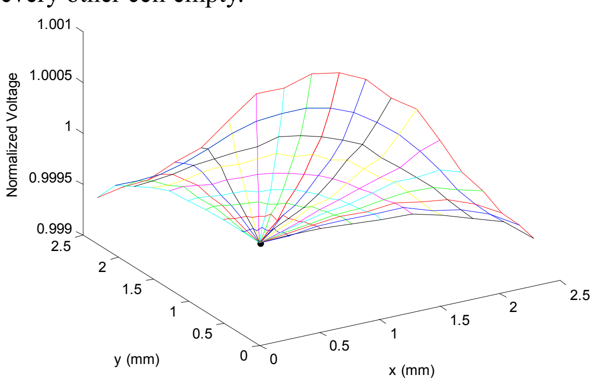


Figure 3: Integrated acceleration as a function of transverse displacement from the axis calculated from HFSS fields.

## ACCELERATION FLATNESS

To avoid HOM-trapping constrictions and for symmetry with the standing wave electric field null, the effective accelerating cell region in the zipper structure is given a square shape. For a standard structure with circular cells, it can be shown that the longitudinal acceleration experienced by the beam is constant across the iris aperture. That is, it has no dependence on transverse position. This does not hold when the azimuthal symmetry is broken.

For the fields obtained in simulation of the first zipper design, the effective voltage (including transit time effect) was calculated at various radii and azimuths over 45°. The results are plotted in Fig. 3. For a centered perfect square, there are no dipole or quadrupole components. There is, however, a slight octupole variation in the kick. Fitting the data to the function

$$G(r,\phi) = G_0\left(1 - \alpha r^4 \cos 4\phi\right) \qquad (2)$$

yields a value of $\alpha$ = ~$1.46\times10^{-5}$mm$^{-4}$. Across a centered beam 100 microns wide, the fractional variation in acceleration would be only on the order of $1.5\times10^{-9}$.

## HOM DAMPING AND TUNING

Higher-order cell modes excited by the beam should be well coupled into the side waveguide through the missing cell wall. This is like an extreme case of the damping manifolds included in NLC structures. Of course, the power could likewise couple back into the other cells. The overall mode structure of a zipper structure needs to be explored.

To dissipate higher-frequency power, the shorted ends of the side waveguides (opposite the coupling ends) could be extended in narrower waveguides, cutoff to the operating frequency and loaded with absorber. If necessary, a second set of stubs, opposite and offset from the first, could be added to each side waveguide. These would contain absorbers and have smaller narrow dimension. The accelerating mode would be prevented by symmetry from coupling to these, but they would serve also to damp all other longitudinal modes in the passband.

If cell tuning is needed to flatten the field profile in conjunction with a bead-pull, dimpling pins can be included in the two exposed walls of the cells. For phase adjustment, tuning pins can also be added between cells in the side waveguide.

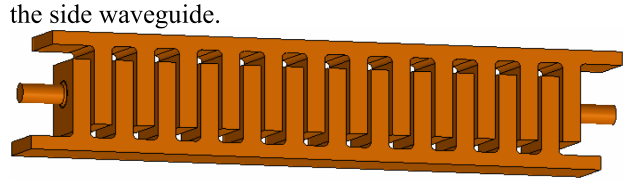

Figure 4: Example of a 24 cell, 15.75 cm zipper structure.

## CONCLUSION

This novel structure geometry has attractive features, such as good efficiency, easy fabrication and damping, no coupling cell and a built-in circulator. It has been likened to an inter-digital slow-wave structure, and a similar idea for an interwoven SCRF accelerator, of more complicated construction, was presented in [2]. More study and design is needed to develop a complete, optimized zipper structure. Fig. 4 gives an indication of how it might look.

## REFERENCES


[1] Alexej Grudiev, “Update on structure optimization procedure, input and results. CLIC reference structure,” CLIC-ACE meeting, Jan. 16, 2008.

[2] P. Avrakhov, *et al.*, “Superconducting Accelerating Structure with Gradient as 2 Times Higher as TESLA Structure,” presented at LINAC 04, Lubeck, Germany, Aug. 16-20, 2004.

# X-BAND TRAVELING WAVE RF DEFLECTOR STRUCTURES *

J. W. Wang[#] and S. Tantawi., SLAC, Menlo Park, CA 94025, USA

*Abstract*

Design studies on the X-Band transverse RF deflectors operating at $HEM_{11}$ mode have been made for two different applications. One is for beam measurement of time-sliced emittance and slice energy spread for the upgraded LCLS project, its optimization in RF efficiency and system design are carefully considered. Another is to design an ultra-fast RF kicker in order to pick up single bunches from the bunch-train of the B-factory storage ring. The challenges are to obtain very short structure filling time with high RF group velocity and good RF efficiency with reasonable transverse shunt impedance. Its RF system will be discussed.

## INTRODUCTION

The RF deflectors were developed from 1960's for high energy particles separation using the interaction with a transversely deflecting mode. As a measure of the deflecting efficiency, the transverse shunt impedance $r_\perp$ is defined as:

$$r_\perp = \frac{\left(\frac{c}{\omega}\frac{\partial E_z}{\partial r}\right)^2}{\partial P/\partial z} \quad , \qquad (1)$$

where z and r is structure longitudinal and transverse axis respectively, $E_z$ is the electrical field amplitude for the dipole mode with angular frequency ω and P is the RF power as function of z. Using the simulation codes for electromagnetic field in RF structures, the transverse shunt impedance can be calculated from:

$$r_\perp = \frac{QV_\perp^{\ 2}}{\omega UL} = \frac{c^2 QV_z^{\ 2}}{\omega^3 r_0^2 UL} \quad , \qquad (2)$$

where Q is quality factor, $V_\perp$ and $V_z$ are integrated potential change in r and z direction for a particle traversing through structure along a trajectory with $r=r_0$ and length of L, U is stored energy within the structure with the length of L.

Traveling wave X-Band deflector structures have many advantages: their RF systems are simpler without the requirement of circulators for standing wave structures and their shunt impedances (proportional to the square root of frequency) are higher than structures working at lower frequencies. In addition, SLAC is well advanced in the art of high power X-Band RF source [1] including klystrons and pulse compression systems. In recent years, many new applications of RF deflectors have been developed. Here we will mainly discussion the deflector applications for measurement of bunch length as well as longitudinal phase space and super fast RF kicker for future light sources, which could not be realized by conventional charged particle deflecting devices.

## DEFLECTOR FOR BEAM MEASUREMENT

If a charged particle beam is at the zero-crossing phase of the deflecting mode, the bunch is given a strong correlation between longitudinal coordinate and transverse position due to RF kick.

Recently at SLAC, a 2.4 m long S-Band deflector built in 1960's was used in LCLS beam line for commissioning. [2] The bunch length in the order of 100 fs was successfully measured and the tuning of the bunch compressor was performed based on the bunch measurement data.

In the future, in order to characterize the extremely short bunch of the LCLS project, we need to extend the time-resolved electron bunch diagnostics to the scale of 10-20 fs. We have to consider a new RF deflector with much powerful deflecting capability. The peak deflecting voltage necessary to produce a temporal bunch resolution of $\Delta t$ is: [3],[4]

$$eV_\perp \approx n\frac{\lambda}{2\pi c\Delta t}\sqrt{\frac{\varepsilon_N Emc^2}{\beta_d}} , \qquad (3)$$

where $E$ is the electron energy and the transverse momentum of the electron at time $\Delta t$ (with respect to the zero-crossing phase of the RF) is $p_y = eV_\perp/c$, $n$ is the kick amplitude in the unit of nominal rms beam size, λ is the RF wavelength, $\varepsilon_N$ is the normalized rms vertical emittance, $c$ is the speed of light, and $\beta_d$ is the vertical beta function at the deflector. This is for an RF deflector, which is $\pi/2$ in betatron phase advance from a downstream screen.

As a practical estimation, in order to create an offset of roughly double rms beam size with 10 fs temporal separation, for the LCLS beam parameters with full beam energy of 13.6 GeV and vertical normalized rms emittance of 1 μm, the necessary peak vertically deflecting voltage for a X-band (11424 MHz) deflector is 33 MV.

For the accelerator structure design, we have to consider to use the available peak power from an X-Band klystron and to obtain higher RF efficiency and reliability at acceptable maximum electric field for RF breakdown and maximum magnetic field for RF pulse heating. Making effort in optimization, the designed deflector is a single section $2\pi/3$ mode backward wave structure with length of 1.5 m. Its main parameters are listed in the Table 1.

*Work supported by U.S. Department of Energy, contract DE-AC02-76SF00515.
[#] jywap@slac.stanford.edu

Table 1: RF Specification of a Deflector for the LCLS Beam Measurement

| Structure type | TW DLWG |
|---|---|
| Mode | 2π/3 Backward wave |
| Aperture 2a | 10.00 mm |
| Cavity diameter 2b | 29.74m |
| Cell length d | 8.7475 mm |
| Disk thickness | 1.45 mm |
| Quality factor Q | 6400 |
| Kick factor k | $2.986 \times 10^{16}$ V/C/m/m |
| Transverse shunt impedance r⊥ | 43.17 MΩ/m |
| Group velocity Vg/c | - 3.165 % |
| Total length L | 1.5 m |
| Filling time $T_f$ | 158 ns |
| Attenuation factor τ | 0.885 |
| Input peak RF power | 30 MW |
| Maximum electric field | 129 MV/m |
| Maximum magnetic field | 0.45 MA/m |
| Deflecting voltage | 38.9 MV |

## DEFLECTOR USED AS A SUPER FAST RF KICKER

It has been proposed to convert the SLAC B-factory to be a very strong FEL light source.[5] In order to pick up single bunches from the bunch-trains, we need to have an ultra-fast RF kicker. There are 1746 bunches circulating in an orbit with 2200 meters circumference in the B-factory. The bunch spacing is two RF periods with 1.26 m in space or 4.2 ns in time. Therefore, the most challenging design issues are to obtain less than 6 ns RF filling time and more than 5 MV vertical deflecting voltage.

For higher RF efficiency, most deflectors of the disc-loaded waveguide structures were designed in the "backward wave" region of dispersion curves as shown by a dashed line circle in Figure 1,[6] where the group velocity is negative and the RF energy propagates in the opposite direction with particle beam. In order to obtain fast group velocities for fast kicker under discussion, it is necessary to design the deflector structures in the region shown by a solid line circle in Figure 1, where the group velocity is positive with value of more than 30% of the speed of light, the RF energy propagates in the same direction with particle beam. For a disc-loaded waveguide structures with aperture radius a, cell radius b, every dispersion curve in Figure 1 was calculated for certain ratio of a/b. The region with higher group velocities corresponds to the structures with larger iris apertures, they have lower shunt impedances and high RF power requirements. In order to optimize the RF design, the group velocities and transverse shunt impedances were calculated as the function of the ratio a/b, which were shown in Figure 2.

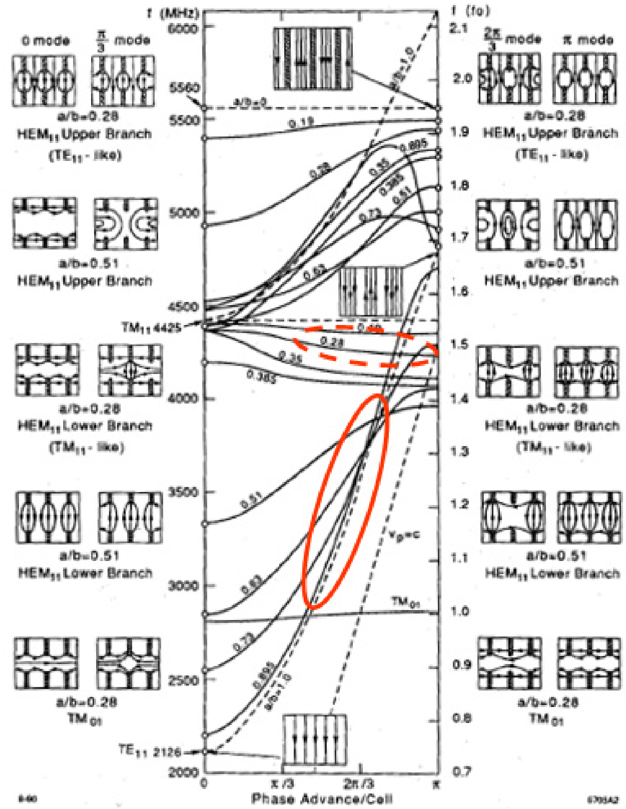


Figure 1: Dispersion diagram and E-field configurations of TM01 and HEM11 modes for some X-Band structures with various ratio of aperture radius with cell radius a/b.

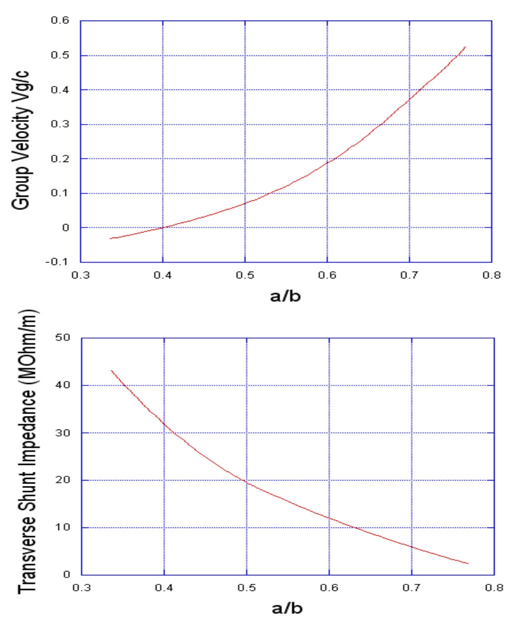


Figure 2. Group velocity (top) and transverse shunt impedance (bottom) as the function of the ratio of cell aperture radius with cell radius (a/b).

Table 2 lists all most important parameters for a 0.75 m ultra-fast X-Band 11424 MHz RF kicker with filling time 4.8 ns and the deflecting voltage is 5MV at 400 MW input power.

Table 2: RF Specification of a Deflector as a Fast Kicker for the PEP-X

| | |
|---|---|
| Structure type | TW DLWG |
| Mode | 2π/3 Forward wave |
| Aperture 2a | 27.0 mm |
| Cavity diameter 2b | 35.33 mm |
| Cell length d | 8.7475 mm |
| Disk thickness | 1.45 mm |
| Quality factor Q | 9763 |
| Kick factor k | $1.052 \times 10^{16}$ V/C/m/m |
| Transverse shunt impedance r⊥ | 2.39 MΩ/m |
| Group velocity Vg/c | 52.4 % |
| Total length L | 0.75 m |
| Filling time $T_f$ | 4.77 ns |
| Attenuation factor τ | 0.0176 |
| Input peak RF power | 400 MW |
| Maximum electric field | 121 MV/m |
| Maximum magnetic field | 0.19 MA/m |
| Deflecting voltage | 5 MV |

Figure 3 shows a schematic diagram for the SLED-II system and Figure 4 shows the waveforms of the input and output power in high power system tests. This system will provide a reliable RF source to power the fast kicker under designing.

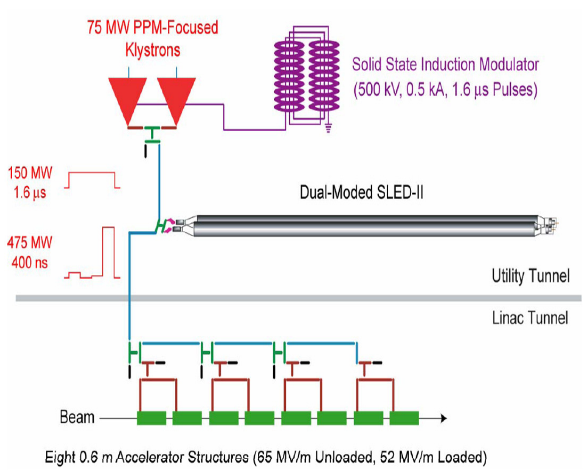


Figure 3: Schematic diagram of the SLED-II System.

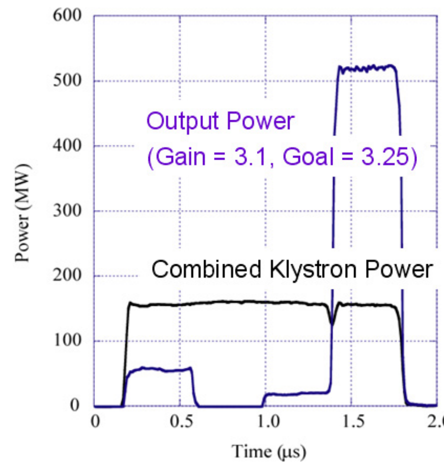


Figure 4: Waveforms of the input and output power for a SLED-II system.

## REFERENCES

[1] Sami G. Tantawi, Christopher D. Nantista, Valery A. Dolgashev, Chris Pearson, Janice Nelson, Keith Jobe, Jose Chan, Karen Fant, and Josef Frisch, "High-power multimode x-band rf pulse compression system for future linear colliders," Physical Review Special Topics - Accelerator and Beams, No. 8, 2005.

[2] R. Akre, L. Benson, P. Emma, P.Krejcik, "Bunch Length measurements Using a Transverse RF Deflecting Structure in the SLAC Linac", SLAC-PUB-9241, May 2002, EPAC2002.

[3] P. Emma, J. Frisch, P. Krejcik, "A Transverse RF Deflecting for Bunch Length and Phase Space Diagnostics", LCLS-TN-00-12, Aug. 2000.

[4] P. Emma, An X-Band Transverse RF Deflector for the LCLS, A Technical Note, October, 2006.

[5] R. Hettel et al., "Ideas for a Future Pep-X Light Source," Proceedings of EPAC08, June, 2008, Genoa, Italy.

[6] J.W. Wang and G.A. Loew, "HEM-11 Modes Revisited", SLAC-PUB-5321, September 1990, LINAC1990.

# LAST SPIRAL 2 10 KW CW RF COUPLER DESIGN

Y. Gómez Martínez, T. Cabanel, J. Giraud, D. Marchand, R. Micoud, F.Vezzu,
LPSC (UJF-CNRS/IN2P3-INPG), Grenoble, France.

*Abstract*

RF tests of the SPIRAL 2 coupler were done successfully in the cryomodules of the LINAC. Weakness during the transport has led to an updated mechanical design. We present here the results of the RF tests as well as the new design.

## INTRODUCTION

SPIRAL 2 is a 40 MeV-5mA deuterons and a 14.5MeV/u-1mA heavy ions superconducting LINAC under construction at GANIL. The SPIRAL 2 superconducting LINAC consists of 19 cryomodules, 12 of them called A (including 1 Quarter-Wave Resonator (QWR) at beta=0.07) and the other 7 cryomodules called B (including 2 QWR at beta = 0.12).

The coupler transfers the power into the two types of cavities and keeps the vacuum into the accelerator. The RF couplers have to provide 10 kW Continuous Wave (CW) nominal power to the cavities at 88.05 MHz for an accelerating field of 6.5 MV/m. The coupler must handle 100% reflected power at maximum incident power.

The Laboratory of Subatomic Physics and Cosmology (LPSC) realized the design, the simulation and the test of the disc shape ceramic coupler. [1].

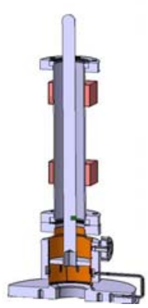

Figure 1: The RF coupler prototype.

Four coupler prototypes were manufactured and conditioned [2] and two of them were mounted in each cryomodule type. For the B-cryomodule, high power tests are finished and they were done successfully.

Figure 2: Coupler prototype.

## TESTS OF THE COUPLER PROTOTYPE IN THE B-CRYOMODULE

Figure 3: Coupler in the B-cryomodule.

We measured a reflected coefficient $S_{11}$ = -50 dB, and a quality factor $Q_{ext} = 1.1*10^6$ (beam dynamic quality factor choice).

At the resonance frequency of the cavity, the maximal accelerating field has been reached; the cleanness of the coupler is confirmed.

Outside the resonance, the coupler has been conditioned till 10 kW CW at room temperature and also at 4.2 K. During this test, weak multipactor (0.2mA) has been found only at low power (less than 300W).

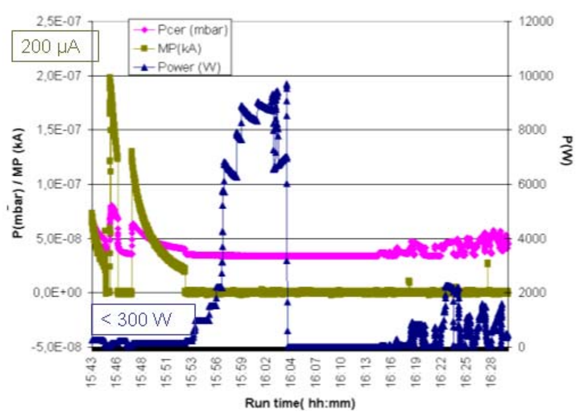


Figure 4: First conditioning at 4.2K (out of the resonance).

After those tests the RF design of the coupler was validated.

## MAIN DESIGN CHANGES

The reasons of the mechanical changes were to obtain a more robust coupler especially during the transports.

### *The Antenna*

To minimise the risks of deviation of the antenna during the transport we designed a hollow antenna. For this purpose we also have chosen a long internal support of the antenna.

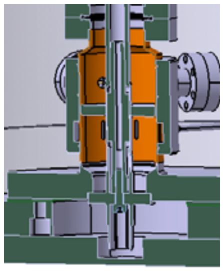

Figure 5: Connection with the internal support.

### The Air Cooling Tube & the Stitchings

We increased their diameter to make them more robust.

The air cooling tube is now shorter also, to protect it from possible shocks.

### Choice of Material

The initial Kovar material that was surrounding the ceramic was later excluded; it was changed by copper. Indeed, Kovar magnetic properties can disturb the good operation of the cavities.

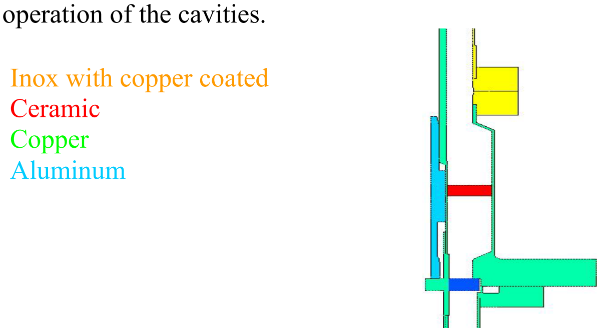


Figure 6: Materials of the updated RF coupler.

## UPDATED RF COUPLEUR DESIGN

An updated RF coupler design was manufactured in 3 examples, conditioned and two of them are being mounted on the cryomodules.

Figure 7: Updated design of the RF coupler.

## UPDATED SIMULATIONS

Simulations were made with the updated design and compared with the results obtained previously with the first prototype.

### RF Simulations

RF performances were not changed with the new design.

The antenna penetration is not adjustable but its length was adjusted (7.5 mm for the A-cryomodule and 16.6mm for the B-cryomodule in order to minimize the RF mismatch in nominal conditions for all beams and also for all the cavities).

### Mechanical Simulations

The finite element SAMCEF code is used.

- The modal frequencies of the coupler are far away of the typical motor frequency (50Hz). The design modifications of the antenna (full to hollow) had a positive effect on its modal frequencies.

Table 1: Modes (Hz) / design

| Design | Mode | Frequency (Hz) |
|---|---|---|
| Prototype | 1 – 2 | 59.5 |
| Prototype | 3 – 4 | 387 |
| Updated | 1 – 2 | 73.5 |
| Updated | 3 – 4 | 467.7 |

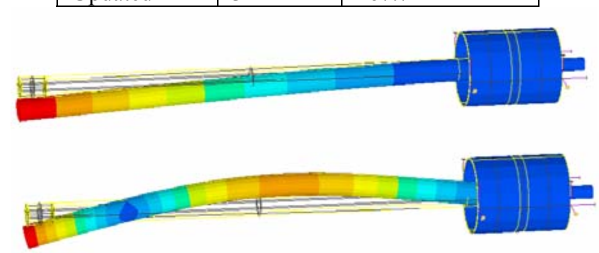

Figure 8: The mode 1-2 (up) and 3-4 (down).

- For the harmonic responses, harmonic simulations were performed with a fixed displacement of 0.01 mm on the frequency range from 0 Hz to 700 Hz. At 73.5 Hz frequency, we found the maximal displacement of the end of the antenna (0.375 mm). A displacement of 0.375 mm corresponds to a main stress of 33 MPa located at the internal radius of the ceramic window. In this range of frequency (0 → 700 Hz) the endurance stress limit of the material is never reached.

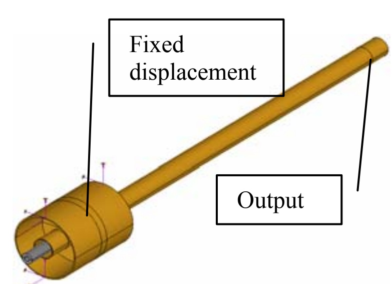


Figure 9: Imposed displacement and output in the harmonic response.

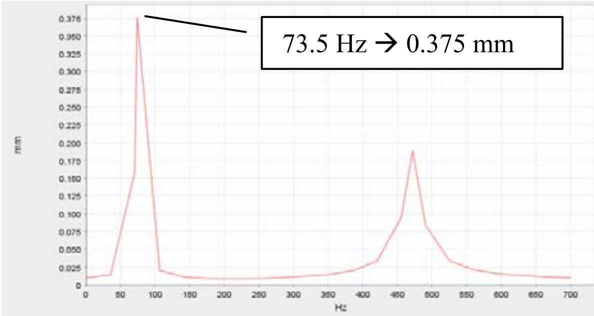


Figure 10: Displacement of the end of the antenna versus the frequency (0-700Hz)

- During the transport, the maximum acceptable acceleration is 10 g to avoid any lamination. A special transport is operated.

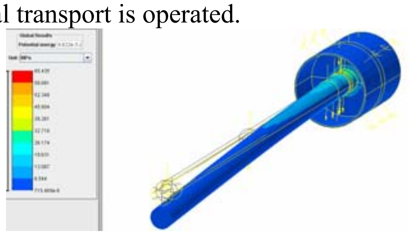

Figure 10: Stress of the coupler in the transports at 10g

### *Thermal Simulations*

The results are very similar to the results of the prototype simulations.

Each cryomodule is set at a fixed temperature according to its thermal load limitations.

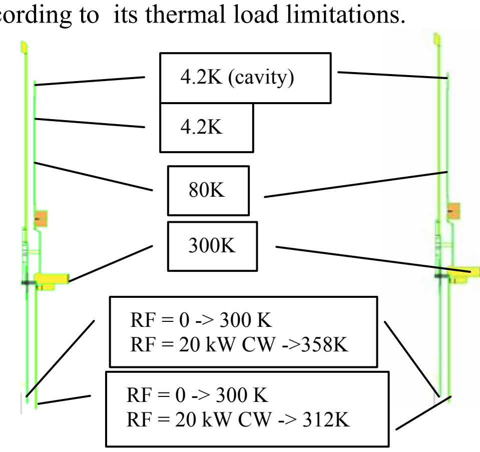


Figure 11: Thermal boundaries conditions for the coupler in the cryomodules A (left) and B (right).

Table 2: Temperatures (K) of the Coupler. Cu RRR10

| Cryomodule | RF power | $T_{tip}$ antenna | $T_{Max}$ ceramic |
|---|---|---|---|
| A | 0 kW | 296 K | 296.8 K |
| A | 20 kW | 349.4 K | 320 K |
| B | 0 kW | 295 K | 296.7 K |
| B | 20 kW | 347.6 K | 320 K |

One goal is to keep the temperature of the ceramic at a level higher than the water condensation temperature.

To control the ceramic window temperature an air cooling system is installed.

Table 3: Thermal Loads (watts) of the Coupler. Cu RRR10

| Cryomodule | RF power | Thermal load at 4.2K link | Thermal load at the cavity (estimation) |
|---|---|---|---|
| A | 0 kW | 0.98 W | 0 W |
| A | 20 kW | 1.28 W | 0.17 W |
| B | 0 kW | - | 0.59 W |
| B | 20 kW | - | 0.934 W |

The goal, a thermal load input at the cavity less than 1 W, is obtained.

During the cool down, there is a displacement of the end of the antenna. It was taken into account to have the antenna penetration of 7.5 mm for the A-cryomodule and 16.6mm for the B-cryomodule.

Table 4: Thermal Radiation from the End of the Antenna to the Cavity and the Cool Down Displacement. Cu RRR10

| Cryomodule | RF power | Radiation thermal load at the cavity | Displacement |
|---|---|---|---|
| A | 0 kW | -0.08 W | 0.52 mm |
| A | 20 kW | -0.16 W | 0.746 mm |
| B | 0 kW | -0.18 W | 0.54 mm |
| B | 20 kW | -0.34 W | 0.758 mm |

## CONCLUSION

The RF coupler is validated.

The kicking off of the SPIRAL 2 coupler was done the 2nd of september 2008. The production of 30 couplers is under way by SCT company .

The goal is the conditioning of the last accelerator couplers at the end of 2010.

## AKNOWLEDGMENTS

Special thanks to M.Baylac (LPSC, France) for her help.

Many thanks to the cryomodule B team (H. Saugnac, G.Olry, J.Lesrel, D.Longuevergne, T. Junquera…) (IPNO, France), who did the B-cryomodules tests.

Thanks to R.Ferdinand (GANIL, France), and A – cryomodule team (CEA Saclay, France), for their comments.

## REFERENCES

[1] Y. Gómez Martínez et al., “Theoretical Study and Experimental Result of the RF Coupler Prototypes of SPIRAL 2”, EPAC 06, Edinburgh, Scotland.

[2] Y. Gómez Martínez et al., “SPIRAL 2 coupler preparation and RF conditioning”, SRF07, Beijing, Chine.

# STUDIES ON INPUT COUPLERS FOR SUPERCONDUCTING CAVITIES *

H. Jenhani#, A. Variola, L. Grandsire, T. Garvey, M. Lacroix, W. Kaabi, B. Mercier, C. Prevost, S. Cavalier, LAL, Univ Paris-Sud, CNRS/IN2P3, Orsay, France.

*Abstract*

We have recently demonstrated a dramatic reduction in conditioning time for TTF-III couplers [1]. This was carried out by a systematic study of the different parameters that play a role in the conditioning process. In addition, many investigations have been made in order to have a better understanding of the couplers' behaviour. These activities represent some aspects of a larger technology program that we are developing to study power couplers and their multipacting. This paper will give an overview of some of these studies, our future experiments on couplers and the development of the associated technology program.

## INTRODUCTION

An ambitious R&D program on power couplers for superconducting cavities has been established at LAL. The LAL-DESY collaboration, which aims to study the behaviour of the TTF-III prototype couplers for the European XFEL and the reduction of their conditioning time, was at the origin of these activities. In this context, successful results, with a dramatic reduction in conditioning time, were achieved and good experience was acquired concerning the behaviour of these couplers under RF power [1]. However, much R&D effort has still to be made in order to face many other challenges. The TTF-III couplers have a very complex geometry and are composed of many sub-parts. To understand the influence of some of these parts on the coupler behaviour, multipacting (MP) simulations are being performed. This allows some correlation between the simulation results and the measured signals during the coupler power tests. Furthermore, many difficult industrial processes are needed for coupler manufacturing. Thin layer deposition of Titanium-Nitrogen (TiN) on ceramic windows is one of the processes which needs to be mastered and optimized. The TiN sputtering deposition processes is currently studied at LAL using a reactive DC magnetron sputtering bench [2]. This device will also strongly contribute to experimental MP studies. Technological solutions have also to be found for the power couplers that would be needed for the ILC in order to increase their operating RF power, while decreasing their cost. We have designed, built and tested two coupler prototypes, TTF-V and TW60, for this purpose.

A short overview on our coupler activities, including realisation of our proto-types and their test results will be presented in this paper.

* We acknowledge the support of the European Community-Research Infrastructure Activity under the FP6 "Structuring the European Research Area" programme (CARE, contract number RII3-CT-2003-506395)

# Corresponding author: jenhani@lal.in2p3.fr

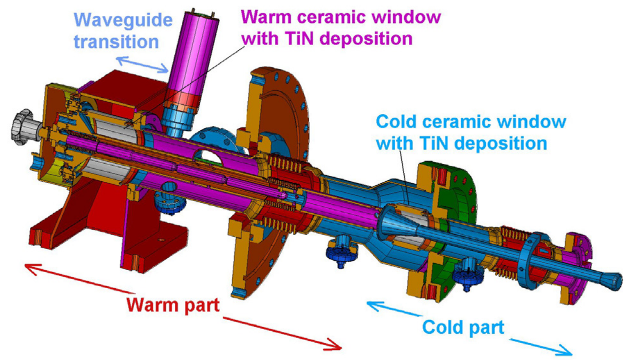


Figure 1: TTF-III power coupler (DESY design).

## MULTIPACTING CALCULATION

Much effort is needed in order to understand the coupler behaviour during processing. Therefore, we have tried to find a correlation between $e^-$ currents measured during standard TTF-III coupler conditioning and the calculation results using the 2D MP simulation program for axi-symmetric geometries named MultiPac 2.1 [3].

During TTF-III coupler conditioning, we observe that the power levels corresponding to $e^-$ current enhancement in the cold parts are generally the same for most of the couplers. However, these similarities were not noticeable for the warm coupler parts. This may be due to the higher geometrical complexity of this part (figure 1). To perform MP simulations, we initially considered a model for the cold part that was composed of the RF window geometry and a simple coaxial line geometry. The effect of the bellows on MP levels was neglected in this approach. Consequently, simulation shows that, for a pure RF travelling wave, there is no MP on the cold ceramic window. Nevertheless, the presence of many MP levels in the coaxial line geometry was confirmed. Some incoherence between the calculated MP levels and the measured $e^-$ currents during conditioning was noticed. In fact, we usually measure a relatively high e- current in the cold part for a forward RF power of about 700 kW. Our simulations show complete absence of a MP threshold in this power range. In order, to see if the bellows are at the origin of this MP we integrated them into the model and made new calculations. The new results show a good correlation between the calculated MP levels and the measured $e^-$ currents from several conditioning tests (figure 2). As a consequence, the bellows appear to be the origin of the MP power level taking place at 700 kW. Nevertheless, electron trajectory calculations show that this MP level is not built up within the bellow undulations but rather in their neighbourhood.

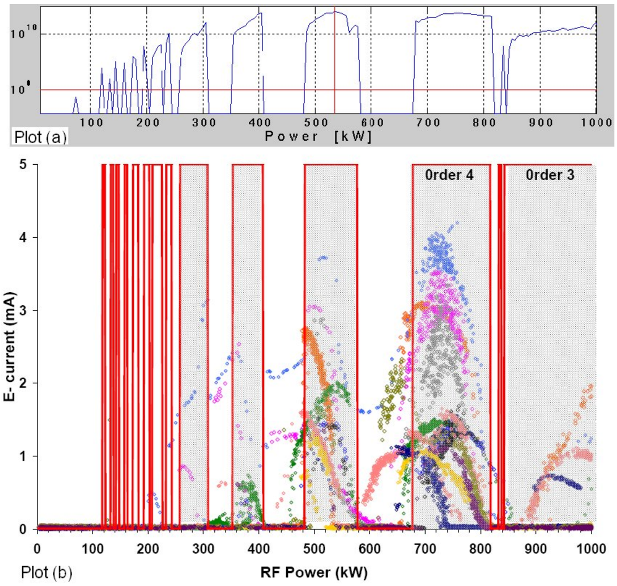


Figure 2: Comparison between MP simulation and e$^-$ current measurements in the TTF-III coupler cold part. Plot (a) shows the MP thresholds given by simulation. In plot (b) the differently coloured dots represent e- current acquisitions coming from different coupler tests and conditioning steps. The rectangular grey zones correspond to the MP power levels given by simulation.

## TIN SPUTTERING ACTIVITIES

A thin layer of TiN coating on coupler ceramic windows is the most common technique used to prevent MP on these components. Made from Alumina ($Al_2O_3$), they have a relatively high secondary emission coefficient (SEC) which favours the appearance of MP and can cause irremediable damage to the coupler. A suitably thick TiN deposition on these components reduces the SEC sufficiently without causing RF mismatch due to the ceramic surface metallization. A coating thickness of around 10 nm has been found to be a good compromise.

In the framework of our R&D program on power couplers, a new activity, aimed at mastering the TiN deposition technique, has been established in order to optimize the surface properties of TiN coated ceramic windows and to study their response and evolution under MP. This is possible by producing well characterised, coated samples for processing studies using a MP resonator.

Reactive magnetron sputtering technology was chosen for the TiN deposition. A coating bench was developed and delivered to LAL at the end of 2007. The machine configuration allows a uniform deposition of TiN on both sides of disk or cylindrical ceramic window shapes. Surface cleaning of the sample inside of the sputtering machine is also feasible using an RF etching system [2]. The deposition of Ti is achieved by activation of the magnetron creating an argon plasma on the Ti target. Titanium atoms are then sputtered onto the sample and associated with injected nitrogen to give the TiN layer. A crystal-quartz micro-balance is used to survey the deposited thickness and deposition rate during the process. Stoechiometry can be obtained by controlling the gas inlet flows.

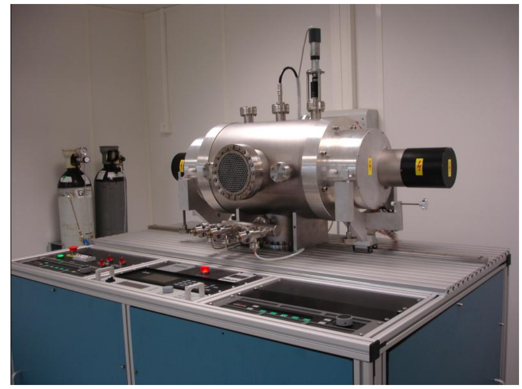

Figure 3: The TiN sputtering machine.

The first aim of the TiN deposition activities was to obtain a stoechiometric layer on small quartz substrates. XRD analysis of some relatively thick layers showed that this aim was fulfilled as we obtained $TiN_{x=1.022}$ [2]. The next step will be the achievement of stoechiometry for layer thicknesses of about 10 nm only. The rate of carbon and oxygen contamination of the TiN deposited layer have also to be found using XPS analysis.

## COUPLER PROTOTYPES

We have designed two new coupler prototypes named TTF-V and TW60 (figure 4). To validate these couplers it was decided to use the TTF-III coupler conditioning procedure [1]. The next step will be the test of these couplers using a conditioning procedure with enough RF power constraints to make them competitive for the ILC project. However, these prototypes are still not optimized for cryogenic operation. At present, only the validation studies of these two prototype concepts using the TTF-III coupler processing procedure have been performed.

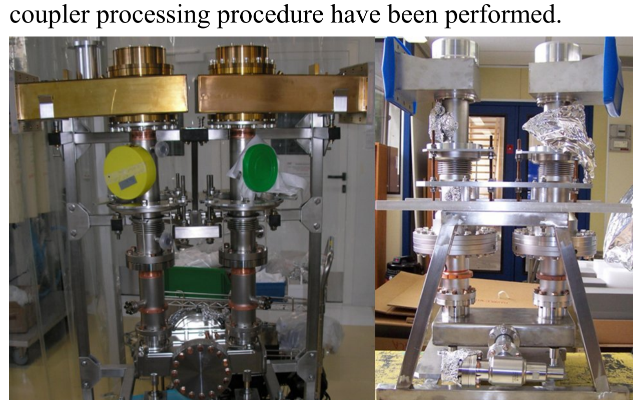

Figure 4: Coupler prototypes at LAL: TW60 at the left side and TTF-V at the right side.

TTF-V and TW60 have two very different designs. TTF-V is very similar to the TTF-III coupler, but has a larger cold part diameter in order to reduce MP effects. This geometrical modification imposed also some new design considerations for the cold window geometry. The warm part of TTF-V is almost the same as for the TTF-III coupler. However, the TW60 coupler has a very different design. It has coaxial disk warm and cold windows, a different DC bias system for its inner conductor and a new waveguide transition design with a movable stub allowing an adjustable matching of the coupler pair assembly. This coupler also has a large cold part compared to TTF-III. Accordingly, TW60 has simpler design than TTF-III and should be less expensive.

For simplification and cost reasons, the coupler versions that are used to validate the design concepts do not have adjustable antenna penetration unlike the case of TTF-III.

Both of the coupler prototypes have been produced by ACCEL.

## *TW60 Coupler Prototype*

An RF processing of a TW60 coupler pair was carried out after some assembly difficulties. The conditioning progress was limited by $e^-$ current peaks correlated with vacuum bursts during the first step of the processing procedure, using 20 µs pulses. As a consequence, it was necessary that an operator assisted the monitoring program during this step to choose adequate conditioning parameters in order to go through some MP thresholds. 1 MW RF power was reached for the first time after 54 h. After this, the following conditioning steps, using larger pulses, were performed rapidly and fully automated conditioning was possible. Finally, the coupler pair was fully conditioned (950 kW with 400 µs pulses and 500 kW with 1.3 ms pulses using a repetition rate of 2 Hz). The total conditioning time was 67 h with some long interruptions. After conditioning, the $e^-$ currents were very low.

The conditioning difficulties may have been caused by some surface anomalies that we have noticed. Coupler dis-assembly and inspection will allow further interpretation.

## *TTF-V Coupler Prototype*

One TTF-V coupler pair was processed successfully. The total RF conditioning was achieved after only 24 h. Many $e^-$ current interlocks were noticed during the first step of the conditioning. The origin of these interlocks was generally the high $e^-$ current detected with the pick-up located on the cold part of the upstream coupler (figure 5). This current was particularly enhanced between 200 kW and 300 kW. Its fluctuations were high enough to exceed the $e^-$ current interlock level several times. No vacuum bursts were correlated with these interlocks. The maximum power of 1 MW was reached for the first time after about 17 h. Afterwards, the conditioning was continued using larger pulses (50 µs, 100 µs, 200 µs, 400 µs to reach 1 MW and 800 µs, 1300 µs to reach 500 kW with a repetition rate of 2 Hz). These conditioning steps were relatively short and only one $e^-$ current interlock occurred.

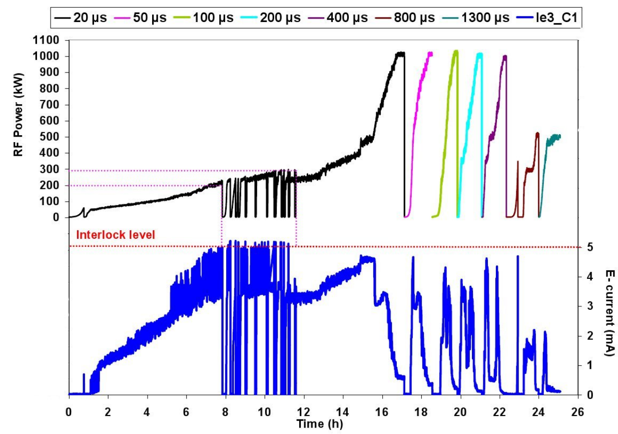


Figure 5: Power variation during the RF conditioning test of TTF-V. Ie3_C1 curve shows the $e^-$ current measured in the cold part of the up-stream coupler.

# CONCLUSION

Many activities are taking place at LAL in the framework of the R&D on power couplers and new results have been obtained. MP simulation results are in good agreement with the $e^-$ current measurements in the cold part of the TTF-III coupler and show the strong influence of the bellows on the MP levels. The TiN sputtering bunch built in the context of a LAL-INFN collaboration was tested with success and a stoechiometric coating has been obtained. Two power couplers prototypes were realised and tested successfully.

# ACKNOWLEDGMENTS

The authors thank A. Thiebault, T. Chabaud, Y. Peinaud and B. Mouton from LAL for their help and contributions to this work.

Thanks are due to DESY, especially D. Proch and A. Brinkmann for authorization to use MultiPac 2.1.

We also thank V. Palmieri and G. Keppel for their strong collaboration for the TiN sputtering bench.

# REFERENCES

[1] H. Jenhani, et al., Nucl. Instr. and Meth. A (2008), doi:10.1016/j.nima.2008.07.111

[2] A. Variola, W. Kaabi et al., “Titanium nitride coating of RF ceramic windows by reactive DC magnetron sputtering”, EPAC’08, Genoa, Italy, June 2008

[3] P. Yla-Oijala, “MultiPac – Multipacting simulation package with 2D FEM field solver”, SRF conference, KEK, Tsukuba, Japan, 2001

# HIGH POWER RF SUPPLIES FOR THE FAIR INJECTOR LINACS

W. Vinzenz, G. Schreiber, L. Groening, W. Barth, M. Hoerr, H.-L. Dambowy
GSI, Darmstadt, Germany

*Abstract*

The operating frequency of the FAIR proton linac was fixed to 325.224 MHz two years ago. Even though the six coupled CH-structures need slightly different RF levels, the proton linac will be equipped with identical RF power sources. That applies also for the RFQ structure.

To supply the FAIR accelerators with a good beam quality by the UNILAC as the high current heavy ion injector for FAIR as well as a high duty factor accelerator for nuclear physics experiments, different upgrades and modifications have to be made at the RF components.

The provision of an excellent RF operation for the next years postulates some general renewals. This paper describes the actual status of the proton linac RF system and the future requirements for the existing UNILAC RF systems.

## INTRODUCTION

In the context of the dedicated proton linac within the FAIR project seven high power RF amplifiers up to 2.5 MW at 325 MHz have to be installed. The Toshiba E3740A klystrons selected meanwhile can provide enough power for the overall RF pulse length of 200 µs at a repetition rate of 4 Hz with sufficient margin.

For the UNILAC altogether eight high power RF tube amplifiers at 36 MHz (3 up to 2 MW) and at 108 MHz (5 up to 1.6 MW) will be involved in the future beam operation for high current beams (up to 800 kW beam load in addition at HSI) and a so-called long pulse mode (up to 50% beam duty cycle for a/q ~ 6). The FAIR requirements will meet or exceed the present capabilities in maximum power and duty factor. This leads to detailed improvements of the existing amplifiers and power supplies involved.

## FAIR PROTON LINAC

Choosing an operating frequency of 325,224 MHz was triggered by an existing prototype of a coupled CCH-Structure [1] and the presence of high power klystrons used at the J-PARC facility. Following these facts, the number of RF power sources for the DTL could be reduced to six. Even though the RFQ needs less than half the RF power with respect to one CH-structure we decided to stay at the same amplifier type. This makes sense due to spare part storage and reduces the diversity of amplifier types. Two more identical amplifiers will supply the bunching cavities at the same frequency with an expected RF power of 15 and 50 kW, respectively.

### *Test Bench*

For tests with all infrastructure components of one klystron section a test bench is mandatory. Also the first CCH-Structure has to be tested in an X-ray shielded cave. In February 2008 the first Toshiba klystron was successfully tested at manufacturer's site in Japan and delivered to GSI in April. A 100 W driver amplifier was ordered and delivered by RES Ingenium (Italy) in 2007. At present a test bench [Fig. 1] is under construction, offers for additional technical equipment are available. All power supplies will be developed by the GSI power supply group. Because of the very low duty factor a crowbar-less solution has been developed [2]. The prototyping of the LLRF is made by GSI, based on a system that will be installed at the GSI/FAIR synchrotrons using IQ detection and digital control FPGA/DAC solutions. After some technical revision the measurement and data acquisition system used at the High Current Injector (HSI) RF section will be also implemented at the proton linac.

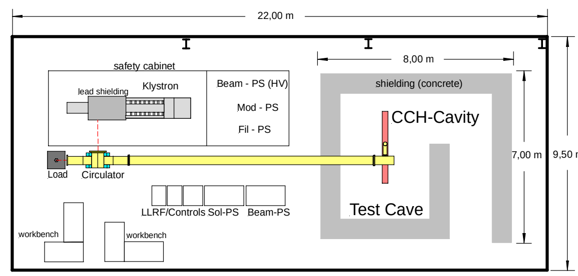


Figure 1: Layout of the test bench.

Some special features on behalf of pulse forming and tube protection purposes will be updated from the UNILAC LLRF system and functionally included in the new digital control system. There are established and approved methods for pulsed RF operation at high power levels reducing faults and off-times as well as enormous time savings during cavity conditioning. Due to the higher demands for the proton linac, the existing analogue value measurement was meanwhile improved. The standard LLRF layout is shown in [Fig. 3]; an overview of the special functions is shown in [Fig. 6].

### *Proton LINAC RF System*

The layout of a klystron driven high power RF system has been sufficiently described in conference proceedings. Building restrictions e.g. the maximum length of the klystron gallery as well as the cost optimised infrastructure of the building has to be taken into account, however. As [Fig. 3] shows seven klystrons will be installed inside the RF-Gallery at ground level. Each klystron is feeding one cavity, which makes the variation of the linac output energy very simple. Further more all electronic devices and supply units are arranged in the meaning of this solution. The RF power transportation is made by waveguides (WR2300), for klystron protection an isolator is installed at each output. The calculated progression of the output power is shown in [Fig. 2]. At a repetition rate of 4 Hz the RF ON time will be maximum 200 µs whereas the BEAM ON time is 40 µs. The remaining time is for cavity filling and safety margin.

Two identical amplifiers will supply the rebunching cavities, one in-between the RFQ and the first CCH-structure, the 2nd one at the end of the proton linac. These amplifiers will be placed at the 2nd floor of the LINAC building. The decision whether to use either tube (e.g. TH 571) or solid-state amplifiers has to be made as soon as possible.

Considering that the proton linac is part of the FAIR project, which includes more than forty high power RF systems, some 'generic specifications' have been fixed [3]. These standards widely affect the power supplies, PLC soft- and hardware, LLRF systems, and the interface to the main control system.

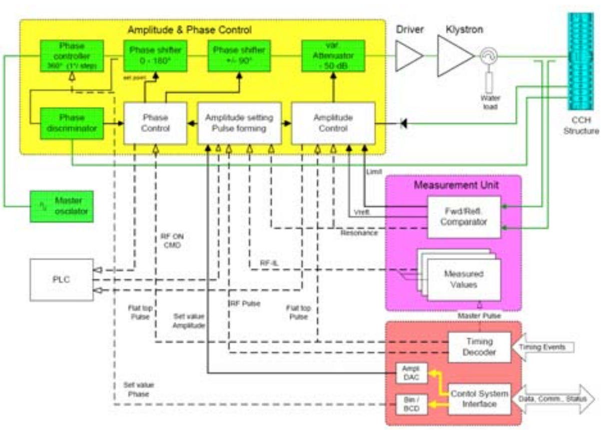


Figure 2: LLRF System

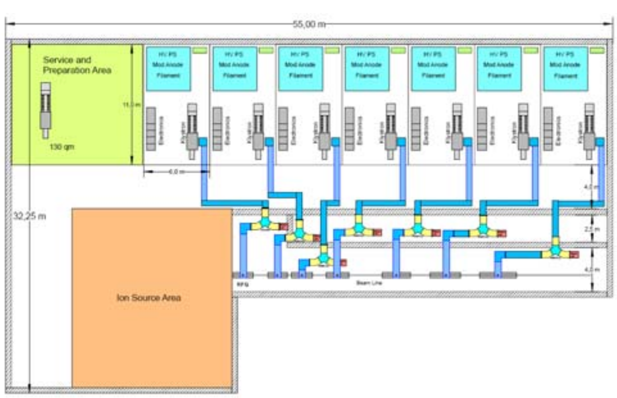


Figure 3: Layout klystron gallery.

## NEW UNILAC RF REQUIREMENTS

The future requirements for the FAIR operation are directly affecting each of the three existing GSI injectors in different manners:

High Current Injector [HSI]
- Higher beam load up to 18 mA
- Additional copper losses at the RFQ

High Charge Injector [HLI]
- Increased duty factor (50%) at 120 kW RF Pulse power
- 60 kW CW for future operation

Post Stripper Section [Alvarez]
- Additional beam load up to 15 mA at the high beam current mode
- Increased beam duty factor (50%) for a mass to charge ratio of 6

To ensure a safe and stable operation of all the involved accelerating and bunching structures for the next three decades a bundle of additional upgrade steps has to be planned, calculated and realized:

Modification of the involved power supplies
- PLC implementation
- Enlarging of the capacitor battery

Upgrade of all LLRF equipment at 108 MHz
- Modification of the bandwidth
- Renewal of measurement equipment
- Improvement of the pulse rise time

Amplifier replacement at 108 MHz (partly)
- Exchange of the pre amplifier chain within the 200 kW amplifiers towards 8 kW solid-state-amplifiers

## UNILAC RF UPGRADE

### *High Current Injector [HSI] 36 MHz*

After electrode replacement at the RFQ of the High Current Injector (HSI) higher beam transmission will increase the beam current about 20 %. That leads to beam loads of 180 kW at the RFQ and 800 kW at IH1 and IH2 each. Additional copper losses at approximately 300 kW at the RFQ have to be fed. Based on the fact that the three 2 $MW_{peak}$ final stages at this accelerator section are DC supplied by one common power source, the storage capacitor has to be enlarged by 135 µF (currently 880 µF) to stay below 4 % voltage drop during a 3 ms RF pulse. Therefore the DC power supply will be extended with two capacitor cabinets. The design of the electrical and mechanical reconstruction is on the way and the capacitors are at hand. Work can be started by beginning of the planned shut down for the electrode replacement in February 2009 and has to be finished before commissioning of the RFQ tank in May 2009.

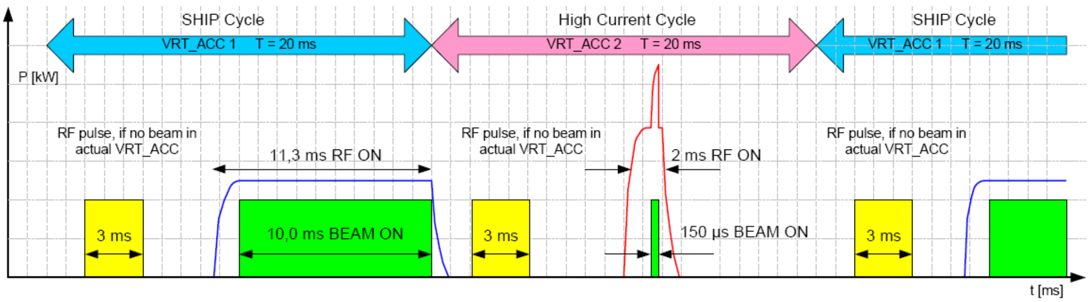


Figure 4: Example of the planned pulse train at the UNILAC.

## *High Charge Injector [HLI] 108 MHz*

A completely new RFQ, designed by A. Schempp (IAP Frankfurt), will be installed in September 2009. The cavity needs 120 kW RF pulse at 50 % duty factor corresponding to 60 kW CW. The performance of the amplifiers (equipped with RS1084CJ) has been tested on dummy load in 2007.

## *Post Stripper Section [Alvarez] 108 MHz*

The UNILAC RF amplifiers supplying Alvarez 1 and Alvarez 2 have to provide additional beam load by approximately 400 kW at 150 µs pulse length at 5 Hz repetition rate, alternating with a RF power level of roughly 600 kW at 57 % RF duty factor and 50 Hz repetition rate. This mode will push the amplifiers to the limits of the tube operation possibilities. During the UNILAC design more than thirty-five years ago, both operating modes have not been taken into account (standard operation 5ms at 50 Hz). The connected power supplies have to be upgraded for the long-pulse mode. Performance measurements have shown that the final stage at Alvarez 1, running the RS2074HF, is able to provide the requested long pulse power only up to 45 % RF duty factor in maximum after optimised tuning. To reach the required gap voltage the amplifier has to deliver approximately 700 kW output power. This means more than 350 kW CW, whereas the average anode dissipation is 320 kW. Under best conditions the maximum output of the RS2074HF is about 1,6 MW pulse power at 108 MHz with a repetition rate of 20 ms and a pulse length of 4 ms.

It has to be pointed out that a safe and stable operation has to be ensured. In consideration of the above-mentioned operating conditions, it is obvious that the existing equipment is not qualified to work in a pulse-to-pulse operation with alternating requirements shown in [Fig. 4].

To reach the expected requirements means a jump to the next power level in RF tubes, which can be a Thales TH526B, Eimac 8973, or equivalent. In case of changing the tube type a new design of the final stages for at least one of the Alvarez stages is required. The remaining final stages at Alvarez 2a, 2b, 3 and 4 have to be upgraded in that way that there is a full inspection of the RF circuits. The complete LLRF equipment has to be improved in the sense of extending the over-all-bandwidth, timing aspects and measurement.

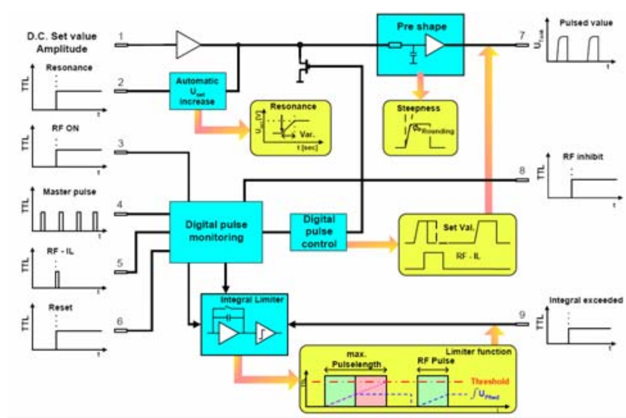


Figure 5: Pulse forming and operating automation.

## *Single-Gap-Cavities*

Due to the age of the 200 kW driver amplifiers of 35 years for the Alvarez structures, and the identical amplifiers for the single-gap cavities and some bunchers, problems arose on the procurement of spare parts. Special components for the input circuits of the RS2024CW tube-pre-driver–stage and electronic components for the R&S solid-state amplifiers are no longer available. A study, established in 2007, follows the idea to replace these 50 W, 300 W and 10 kW (tube) amplifiers in a row against one 8 kW solid-state amplifier. A very helpful design and construction idea came from RES Ingenium (Italy). If this study ends successfully, we will have to upgrade about 25 amplifiers in that way. This means removal of the wiring, mechanical realignment, as well as the new installation of LLRF, PLC and control equipment.

## REFERENCES

[1] G. Clemente "The Room Temperature CH-DTL and its application for the FAIR p-Injector" Thesis 2007

[2] H. Ramakers "Common Remarks Power Converters", GSI Internal Note 2006

[3] Dr. H. Klingbeil et al. "FAIR Standardization RF Systems", GSI Internal Note 2006

# OPERATION EXPERIENCE WITH THE FLASH RF WAVEGUIDE DISTRIBUTION SYSTEM AT DESY

S. Choroba, F. Eints, T. Froelich, A. Gamp, T. Grevsmühl, V. Katalev, DESY, Hamburg, Germany


### Abstract

The RF stations for the FLASH linear accelerator at DESY provide RF up to 10MW for 1.3ms and 10Hz at 1.3GHz for forty-eight superconducting cavities grouped into six cryogenic modules and for one normal conducting RF gun. A WR650 waveguide distribution system distributes the power generated by five RF stations using 5MW single beam and a 10MW multibeam klystron to the cavities and the gun. Since FLASH is based on the Tesla Test Facility, TTF, a number of different distribution layouts for the different modules and the gun have been developed and used over the years in terms of type of components and distribution scheme. This paper presents the layout and summarizes the experience with the existing waveguide distribution system.


## INTRODUCTION

FLASH bases upon the TESLA Test Facility at DESY which has been constructed since the early 1990 in order to test all components required to construct a linear collider using superconducting cavity technology. Over the years the test facility has undergone many changes in order to meet the demands of different test options and operation conditions. Today FLASH serves as a user facility for synchrotron radiation research as well as a test facility for the European XFEL and for ILC studies.

FLASH accelerates an electron beam of 1nC bunches up to 1GeV which is used to generate laser light in the VUV regime. The electrons are produced in a RF gun and are accelerated in forty-eight superconducting nine-cell niobium cavities which are grouped in six cryogenic modules. The cavities are operated in a range between 12MV/m and 32MV/m. The RF power required by the RF gun and the cavities is generated by three 5MW klystrons and one 10MW multibeam klystron. The RF power distribution based on WR650 type waveguide distributes the power between the RF sources and the RF gun or the superconducting cavities. Due to different requirements and state of the art at a certain point of time a number of waveguide components and layouts have been developed, installed and operated over the years.

## RF STATION LAYOUT

Each FLASH RF station consists of a HV pulse modulator with pulse transformer, a high power klystron, which generates the power required by the RF gun and the cavities, and a number of additional components. The HV pulses modulator converts AC line voltage to pulsed high voltage up to 130kV at a pulse duration of 1.5ms and 10Hz repetition rate. The klystrons convert pulsed power into pulsed RF power by amplifying an input RF drive power of 200W to the 5MW or 10MW output level with pulse durations up to 1.3ms of which 500µs required to fill the cavities with RF power and 800µs to accelerate the beam. More detailed information of the RF station layout can be found in [1].

## RF DISTRIBUTION LAYOUTS

### [illegible]

Six RF stations have been installed at TTF and are labelled by #1 to #6. Station #1 is not in regular use for FLASH. It serves as power source for superconducting cavity tests but could be used as spare for FLASH which has not been required during the years. Station #3 provides RF power to the RF gun of FLASH, #2 to the first cryogenic module ACC1 with eight cavities, #5 supplies RF power for the modules ACC2 and ACC3 with sixteen cavities in total. Station #4 supplies power to the three modules ACC4, 5 and 6 with twenty-four cavities in total. Station #6 serves as spare for the other stations and, in case this is not required, is used for experiments and tests of waveguide elements. Figure 1 shows the actual RF distribution.

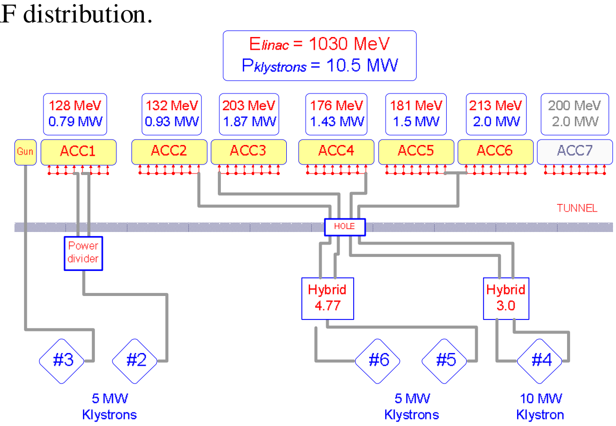


Figure 1: FLASH RF System.

All waveguide distributions between the klystrons and the superconducting cavities comprise the following sections. A section of typical 2m between the klystron window and an additional window with circulator in between filled with SF6 of typical 1.2bar, a module distribution for eight cavities at the cryogenic module either of linear or of combined (tree like and linear) type, and several meters of WR650 waveguide filled with air between these two sections. The module distributions with the exception of the distribution for ACC6 are of linear type. Equal amounts of power are branched off by hybrids. Therefore the operation gradient of these modules is limited by the maximum gradient of the weakest cavity in the module. Optimization is only possible in coarse steps by insertion of hybrids of completely other coupling ratio than for equal power branching ratio or by insertion of an attenuator in front of the weak cavity. The module distribution for ACC6 is of combined type. The power for a pair of cavities is branched off by asymmetric shunt tees. By adjusting the position of the tuning posts in the shunt tees the coupling ratio can be adjusted so that each pair of cavities is operated at its maximum possible gradient. Waveguide isolators (circulators with load) capable of 400kW in front of each cavity are used to absorb the power reflected from the cavities during the filling time of 500µs or in case of arcing or quenching. In case of the linear module distributions three-stub tuners between circulator and cavity are used to adjust the phase and $Q_{ext}$. In case of the combined system piston phase shifters which are integrated in the shunt tees which divide the power for a pair of cavities are used to adjust the phase. Adjustment of $Q_{ext}$ is done by adjustable cavity couplers of ACC6. The $Q_{ext}$ in all cases is $3{\cdot}10^6$. The module distribution in front of each module is filled with normal air at atmospheric pressure. The typical power loss in the circulators and long waveguides between the klystron and the cavity is of the order of 25%. Total length of the FLASH waveguides is about 300m. More detailed information about the different module distributions can be found in [2-4].

## [illegible]

The 5MW THALES TH2104C klystron of station #2 provides about 1MW of power for the eight superconducting cavities of the cryogenic module ACC1. This module distribution of ACC1 has a specific feature. The first four cavities are operated at a gradient of 12MV/m and the second four at 20MV/m, with the exception of one at 14MV/m, thus 50kW, 140kW and 70kW, respectively of input power per cavity are required. Therefore the power between the first and second four cavities is split unequally and then branched off by a linear type system. The total accelerating voltage is 128MV.

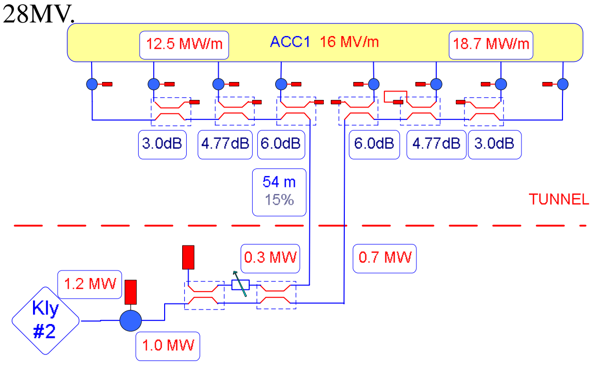


Figure 2: Distribution for ACC1.

The 5MW THALES TH2104C klystron of station #5 provides about 4MW of power for the sixteen superconducting cavities of the cryogenic modules ACC2 and 3. The cavities of ACC2 are operated an average gradient of 16MV/m, the cavities of ACC3 at 24MV/m, thus the average power per cavity is 90kW and 210kW, respectively. Two cavities in ACC2 are operated with an attenuator in front of the cavity because their maximum possible gradient is only 15MV/m and 17MV/m. Since the klystron has only one output arm, the power is split in a 4.77dB hybrid and transmitted in two 65m long waveguides to the two module distributions. The total accelerating voltage of the two modules is 132MV and 203MV.

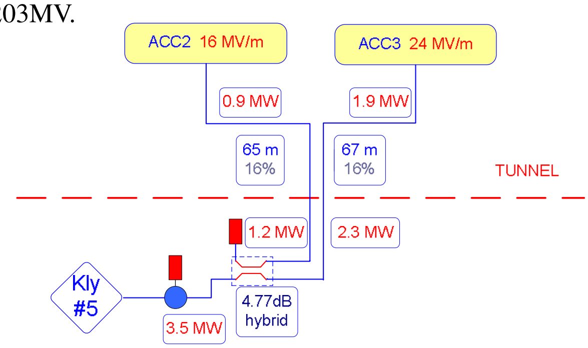


Figure 3: Distribution for ACC2 and ACC3.

The 10MW THALES TH1801 multibeam klystron of station #4 provides up to 7MW of power for the twenty-four superconducting cavities of the cryogenic modules ACC4, 5 and 6. The cavities of ACC4, 5 and 6 are operated at an average gradient of 21MV/m, 22MV/m and 26MV/m, thus an average input power of 160kW, 169kW and 241kW per cavity is required. Since ACC6 uses a combined waveguide distribution with asymmetric shunt tees the coupling ratio could be optimized for maximum possible gradient in each cavity. Four of the cavities receive 350kW which is sufficient for 32MV/m. Since the klystron has two output arms, the power is combined in a section of two 3dB hybrids with phase shifter.

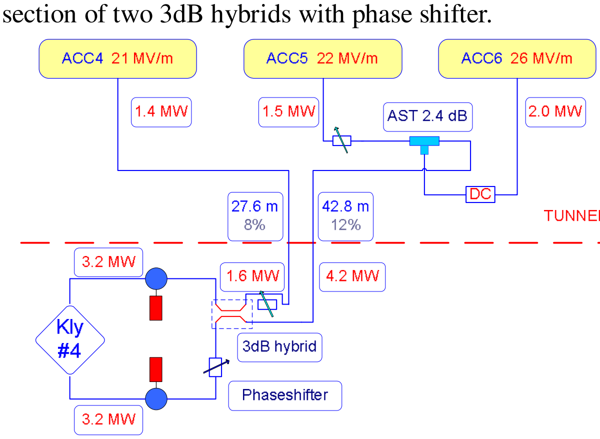


Figure 4: Distribution for ACC4, ACC5 and ACC6.

This allows adjustment of the power for two arms. Power for ACC4 is transmitted in a 27m long section between the output port of the hybrid to the module distribution, whereas the other output arm is connected to another 42m long waveguide which is connected via a shunt tee to the distributions of ACC5 and 6. The total accelerating voltage of the three modules is 176MV, 181MV, 213MV.

### □□*G*□□□*D*□□□□□□□□□

The 5MW THALES TH2104C of station #3 generates RF power of 5MW for the one-and-a-half-cell normal conducting RF gun. Since this cavity is normal conducting the filling time is some microseconds only and the total RF pulse duration is 800µs at 10Hz repetition rate. The electrons for the accelerator beam are produced in the RF gun by firing a laser onto the photocathode located at the position of maximum electrical field of some 40MV/m. Since the klystron requires SF6 at the klystron window a section of about 2m length between the klystron window and an additional window is filled with SF6 of typical 1.2bar. A four-port circulator is located in the tunnel in front of the input window in order to protect the klystron from reflected power from the RF gun. This section of ca. 2m between the RF gun window and an additional window is filled with SF6 at 1.2bar, too, in order to protect the RF gun window and to enhance the power capability of the circulator. The waveguide length between the klystron and the RF gun is about 40m. Because of losses in the waveguides and the circulator only 3.5MW of power are reaching the RF gun.

## MAIN COMPONENTS

Many waveguide components have been developed at DESY and in cooperation with or by industrial companies. Some of them are described in the following briefly. The 5MW four-port circulators which protect the klystrons from reflected power have been manufactured by Ferrite SPA, St. Petersburg, Russia. They must be filled with SF6 at typical 1.2bar in order to enhance the breakdown level, just filled with air at atmospheric pressure this level is only 800kW. In order to decrease losses in the ferrite material the magnetic field must be carefully adjusted. No active tuning circuit either by cooling water or electromagnetic adjustment of the magnet field exists. The insertion losses depend on the temperature of the ferrite material, thus losses depend on operation conditions. The 400kW isolators in front of each cavity are required to absorb power reflected from the cavities during filling time. They can be operated in air. Some of the circulators are only capable of 350kW whereas others are capable of 450kW. The specification is 400kW at full reflection and any phase for 1.5ms and 10Hz repetition rate.

The asymmetric shunt tees of the combined distribution have two posts inside. By adjusting the position of the posts the coupling ration can be adjusted in order to optimize the power distribution for a given maximum gradient distribution in a cryomodule. This is not possible in the linear distribution because the hybrids used there can not be tuned to a specific coupling ratio. The integrated phase shifters of the new combined distribution are capable of 4MW and allow the adjustment of phase by 90 degree. The three-stub tuners in the linear distribution have similar tuning range and in addition allow the tuning of $Q_{ext}$. The three-stub tuners limit the maximum power which can be transmitted to a cavity. This is due to the reduced breakdown capability in case a stub reaches too far inside the waveguide. Under normal operation condition this usually is not a problem but during conditioning of the cavity couplers it might be.

Although the theoretical power limit of WR650 waveguides in air is 58MW the practical limit is much lower. It is near the 5MW operation level of some of the waveguides and even less in some of the components in the module distributions. This limitation is mainly due to limited size inside some of the components, due to higher order modes, which are generated in the klystrons and built up to high electrical field strength in the waveguides because they are not well terminated for these frequencies, and also due to imperfect VSWR of waveguide components at the fundamental frequency, thus leading to high electrical field in the standing wave parts. Most critical are three-stub tuners, hybrids, circulators and windows. The use of the new combined module distribution has improved the situation.

## OUTLOOK AND SUMMARY

During the next FLASH shutdown another module will be installed. Module ACC7 will be supplied together with ACC6 by one klystron. The use of the new combined module distribution has improved the operation conditions with respect to power limitation and to optimization for maximum gradient. This type of distribution will be used in the XFEL too.

## ACKNOWLEDGEMENTS

The authors would like to acknowledge the work of all persons of the FLASH and XFEL RF group contributing to testing, installation and commissioning of the waveguide distributions for FLASH.

## REFERENCES

[1] S. Choroba., “Design and Status of the XFEL RF System”, Proceedings of PAC07, Albuquerque, New Mexico, USA, June 25-29, 2007, p. 841.

[2] V. Katalev, S. Choroba, “RF Power Distributing Waveguide System for TESLA”, Proceedings of the Russian Particle Accelerator Conference, Rupac 2002, Obninsk, Russia, October 1-4, 2002, p 79.

[3] V. Katalev, S. Choroba, “Tuning of External Q and Phase for the Cavities of a Superconducting Linear Accelerator”, Proceedings of the XXII International Linear Accelerator Conference, Linac 2004, Lübeck, Germany, August 16-20, 2004, p 724.

[4] V. Katalev, S. Choroba, “Compact Waveguide Distribution with Asymmetric Shunt Tees for the European XFEL”, Proceedings of the 22nd Particle Accelerator Conference, PAC07, Albuquerque, USA, June 25-29, 2007, p. 176.

# ELIMINATION OF PARASITIC OSCILLATIONS IN RF TUBE AMPLIFIER FOR HIGH POWER APPLICATION

E. Feldmeier, Heidelberg Ion Beam Therapy Center, Universitätsklinik Heidelberg, Germany
G. Hutter, W. Vinzenz, B. Schlitt, GSI, Darmstadt, Germany

*Abstract*

For the heavy ion therapy center HIT in Heidelberg a 1.6 MW power amplifier for 217 MHz was built to supply the 7 MeV/u IH cavity. The inherent parasitic oscillations of the RF tube increases rapidly the anode current until the system switches off. For the elimination of those parasitic oscillations ferrite material is used. The electro magnetic fields are simulated to find an optimal positioning of the ferrite material in the anode cavity such that only the parasitic oscillations are attenuated without affecting the fundamental mode.

## INTRODUCTION

A dedicated clinical cancer therapy center designed by GSI was built at the Universitätsklinik in Heidelberg, Germany [1,2]. The facility is designed to treat about 1200 patients per year using the intensity controlled raster scan method developed by GSI. Since 1997 more than 400 patients have been successfully treated with carbon ions at GSI.

During the last two years the HIT accelerator and its subsystems were commissioned [3]. In December 2007 the carbon beam reached therapy quality in the treatment rooms. The start of the clinical operation is planned for December 2008.

The facility consists of the 7 MeV/u injector linac, a 430 MeV/u synchrotron, an experimental area, two treatment rooms with horizontally fixed beam lines and one treatment room with an isocentric gantry.

The injector linac consists of a 400 keV/u RFQ and a 7 MeV/u IH drift tube linac with an effective acceleration length of 5.5 m.

The RF system of the compact injector operates at 216.816 MHz. It consists of three RF tube amplifier working in pulsed operation at 200 kW (RFQ) and 120 kW/1.4 MW (IH) with a pulse length of 500 µs and a duty cycle of 0.5%. The 200 kW tube amplifier and the preamplifier for the 1.6 MW final stage was built commercially by THALES/THOMSON. The final stage of the 1.6 MW amplifier was designed and manufactured by BERTRONIX, Munich. This stage was mechanically assembled in Munich and delivered to GSI for the commissioning and RF tests. For the clinical application a very stable and reliable operation is mandatory. To get more options the stage is constructed for two different tube types, the THALES TH 526 and the EIMAC E 8973. In the beginning of the project it was not decided which tube would be used for standard operation. During the commissioning the TH 526 was chosen.

## PARASITIC OSCILLATIONS

One of the main problems during the commissioning was the parasitic oscillations of the TH526 which appear with different strengths at 478 MHz, 818 MHz, 875 MHz, 1024 MHz, 1240 MHz, 1468 MHz and 1680 MHz.

Parasitic oscillations occur even without RF when the tube is pulsed to the A-working point. Using the control grid voltage the tube should be set to a working point with an anode current of 6 A. When increasing the anode current to more than 2 A the parasitic oscillations set in and lead to an uncontrollable operation in which the tube cannot be locked by the control grid anymore. The problems occur mainly with the parasitic oscillations at 875 MHz and 1240 MHz.

It was shown earlier [4] that oscillations can be suppressed successfully by using ferrite material in the anode circuit and between grid 1 and grid 2. This paper proposes a new method find an optimal position for the ferrite material.

## FIELD SIMULATIONS

The ferrites have to be positioned at locations where the H-field of the parasitic mode is large in order to suppress these modes most effectively. To find the optimal position for the ferrite rods and slabs the electro magnetic field distribution within the cavity is numerically calculated using CST Microwave Studio. It is sufficient to calculate the fields in the anode cavity of the amplifier. One part of the anode cavity is the amplifier tube which however is an active component that cannot be simulated within the used FIT method [5].

The electron flux in the tube represents a conductive area in the active system of the tube. In the simulation this area is represented by a conductive material with a conductivity σ which can be calculated as

$$\sigma = \frac{1}{2\pi \cdot L} \cdot \frac{I_A}{U_A} \cdot \ln \frac{R_2}{R_1}.$$

L denotes the length of the active system, $R_2$ and $R_1$ are the outer and inner radii of the cylindrical cavity, respesctively. The anode current $I_A$ and voltage $U_A$ are measured.

First one has to verify that one gets the correct frequency of 216.816 MHz for the fundamental mode. To correct for uncertainties in the geometrical dimensions and inaccuracies in the mapping of the active tube system, for example the leakage of the field through the grid, one may move the position of the cavity bottom slightly.

The next step is to verify that besides the fundamental mode also the higher eigenmodes coincide with the measured frequency spectrum. This test assures the quality of the calculated fields.

In Fig. 1 the input reflection parameter $S_{11}$ at the RF 50 Ω output line is shown as a function of frequency. The fundamental mode appears at 216.7 MHz while higher modes are at 247.6 MHz and 345.6 MHz. The accuracy is sufficient as the corresponding measured modes are located at 216.816 MHz, 248 MHz and 343 MHz.

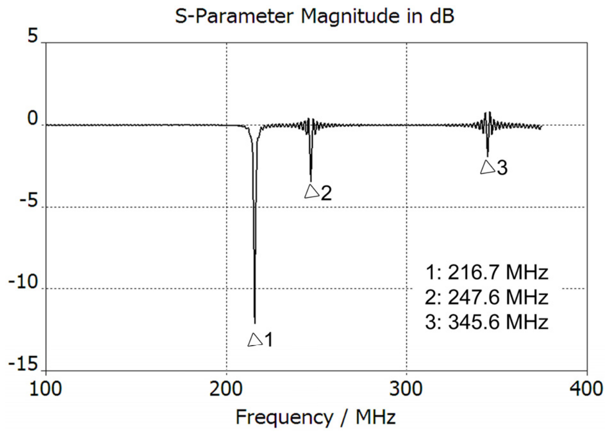


Figure 1: simulated |S11| as function of frequency.

Now the H-field distribution is calculated at the parasitic mode frequencies of 875 MHz and 1240 MHz. Fig. 2 displays the geometry of the amplifier including the tube on top. The red cylinder in the upper part of the model indicates the active system of the tube where the conductive material is placed. The lower part of the model represents the anode cavity. At the bottom the outcoupling loop to the 50 Ω RF line can be seen.

The parasitic frequencies which originate from the tube do not correspond to eigenmodes of the complete amplifier structure. Therefore the structure is stimulated with 875 MHz and 1240 MHz to calculate the H-field distribution of the parasitic mode. The field distributions for the fundamental mode as well as for the parasitic mode are shown in Fig 2. One can see that in the areas denoted by 1 the parasitic fields are large whereas the fundamental mode is weak, so that one expects to suppress the mode at 1240 MHz.

The photograph displayed in Fig. 3 shows the actual setup that has been devised based on the simulations. The area denoted by 1 correspond to the 6 ferrite slaps that are positioned on teflon tubes.

The more dangerous mode is however at 875 MHz. Without any ferrites this mode grows exponentially and triggers the safety shutdown sequence. The H-fields of this mode are displayed in Fig. 2b. There are no obvious locations for the ferrites because in the areas of large H-fields the fundamental mode also has large fields (Fig. 2a). Previous experiments have shown that ferrite rods at positions indicated by 2 and 3 damp the 875 MHz mode without too much effect on the fundamental mode.

Area 2 corresponds to the 16 ferrite rods held by small teflon bricks at the bottom. At area 3 a teflon ring with 72 holes to hold further ferrite rods is placed next to the tube ceramic. For the first test all 72 places were filled. It turned out that the fundamental mode was suppressed too much. Using only 36 ferrites the effect on the fundamental mode was insignificant.

As it is often not possible to find locations where large H-fields of parasitic modes coincide with small fields of the fundamental mode one has to find a compromise.

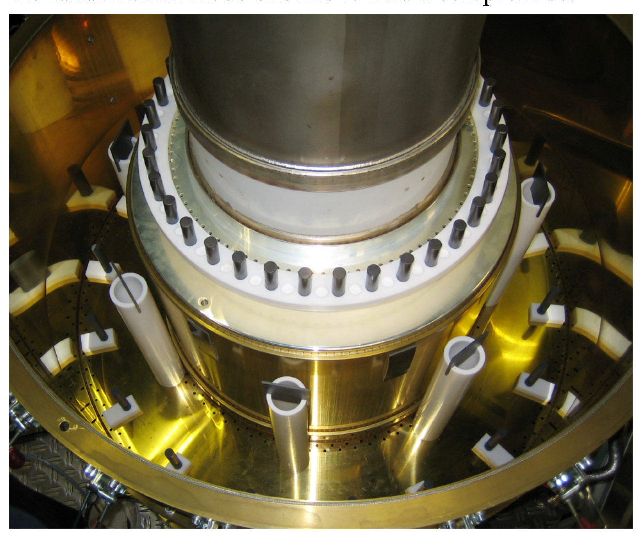

Figure 3: Ferrite arrangement as result of considerations based on the theoretical simulated H-field distribution.

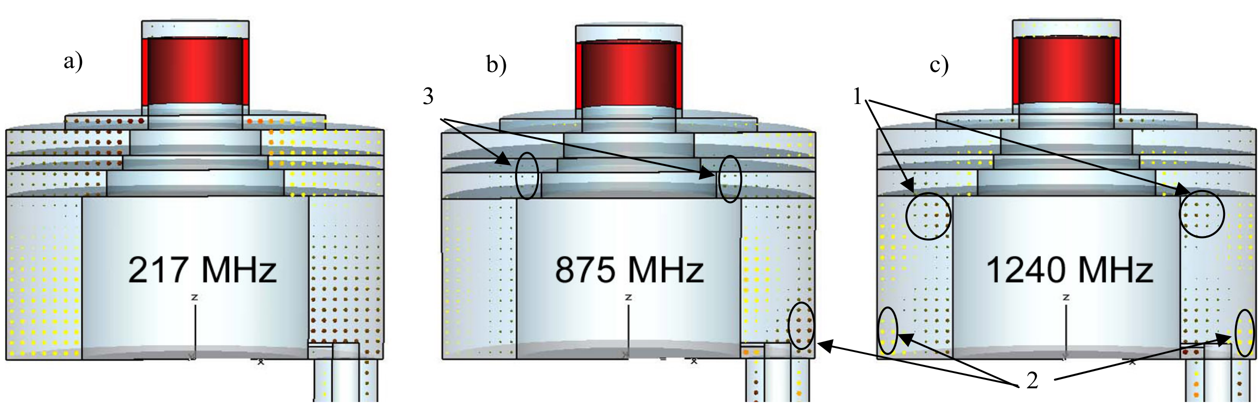


Figure 2: (a) H-Field distribution for the operating frequency 216,816MHz, (b) for the parasitic mode at 875MHz, and (c) for the parasitic mode at 1240MHz.

It is also helpful to select ferrite material that has a higher permeability at the parasitic frequency than at the operating frequency.

## RESULT

Fig. 4 shows the spectrum measured with a small coupling loop in the anode circuit when only 36 ferrite rods are placed in area 3 on the teflon ring, all other ferrites are removed. The first strong peak denotes the fundamental peak and is followed by its equidistant harmonics. The other strong peak is the parasitic mode at 1240 MHz. At the dangerous frequency 875 MHz no signal is seen. Thus the ring of 36 ferrite rods suppresses this mode sufficiently.

After introducing the ferrite slaps at area 1 and additional rods at area 2 the spectrum shown in Fig. 5 is obtained. As expected from the simulation the parasitic mode at 1240 MHz is completely suppressed. Furthermore, the amplitudes of the harmonics decay more rapidly.

It should be mentioned that at the area 3 the electric field is rather strong so that the ferrites have to be manufactured with rounded edges to avoid sparking.

Before optimization anode currents larger than 2 A lead to an uncontrollable operation. After optimization the anode current can be increased up to 60A without excitation of the parasitic modes. A stable and dependable operation is therefore guaranteed.

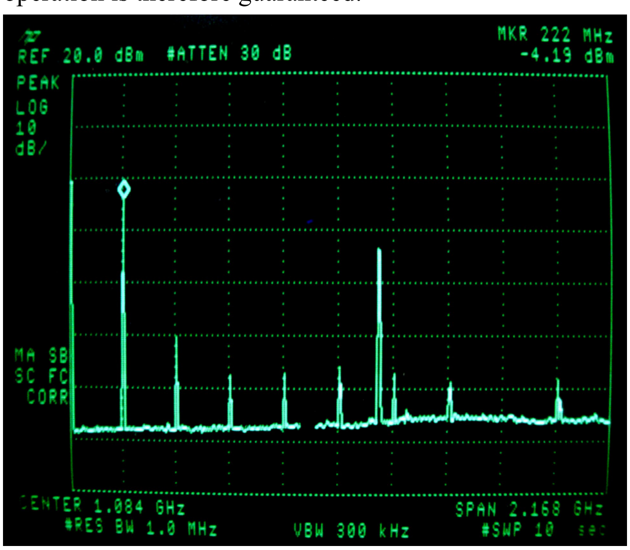


Figure 4: Measured spectrum with a coupling loop in the the anode circuit with ferrites only in area 3.

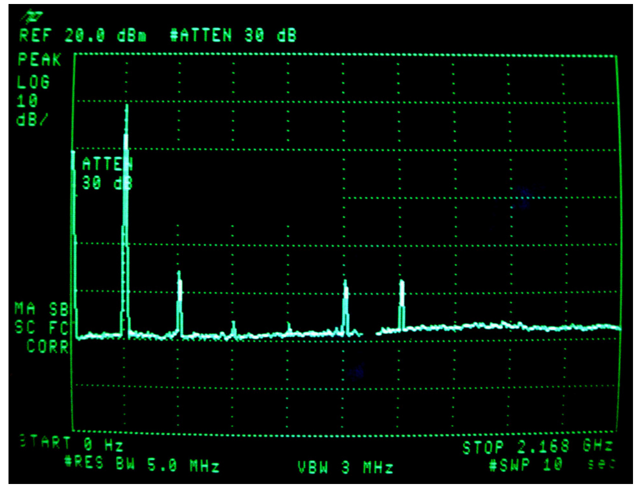


Figure 5: Measured spectrum with the new optimized ferrite setting.

## OUTLOOK

To commission the 1.4 MW final stage amplifier for the second designated tube type EIMAC E8973 new calculations have to be performed as this tube has a different geometry and thus different parasitic modes. It remains to be seen in how far the present arrangement has to be modified to allow also the operation with this tube.

It is desirable to perform systematic investigations of available ferrite material with respect to its properties and to study the possibility to produce new ferrite material optimized for this application.

## REFERENCES

[1] H. Eickhoff, D. Böhne, Th. Haberer, B. Schlitt, P. Spiller, J. Debus and A. Dolinskii, “The proposed dedicated ion beam facility for cancer therapy at the clinic in Heidelberg”, Proc. EPAC 2000, Vienna, p. 2512, and references therein.

[2] H. Eickhoff et al., “HICAT - The German Hospital Based Light Ion Cancer Therapy Project”; EPAC 2004, p. 290.

[3] B. Schlitt et al., “Commisioning of the 7 MeV/u, 217 MHz injector linac…”, Proc. LINAC 2006, Knoxville, p. 150.

[4] G. Hutter et al., “The 101 MHz amplifier system of the new CERN lead injector”, PAC 97, p. 3123.

[5] T. Weiland, “A discretization method for the solution of Maxwell's equations for six-component fields”, Electronics and Communications AEUE, vol. 31, no. 3, pp. 116-120, 1977.

# DEVELOPMENT OF ALL SOLID STATE BOUNCER COMPENSATED LONG PULSE MODULATORS FOR LEP 1MW KLYSTRONS TO BE USED FOR LINAC4 PROJECT AT CERN*

Purushottam Shrivastava#, J. Mulchandani, V.C. Sahni
Raja Ramanna Centre for Advanced Technology, Indore, India
Carlos A. Martins, Carlo Rossi, Frédérick Bordry, CERN, Switzerland.

## ABSTRACT

CERN is building a 352.21 MHz 3 MeV RFQ based test stand as first part of LINAC4. Extending its earlier collaboration with RRCAT, India, CERN had approached it to design and develop a high voltage pulsed modulator for 1 MW LEP klystrons, planning their reuse. RRCAT proposed three design schemes out of which an all solid state bouncer compensated modulator was chosen for follow up development work. The main considerations for the design were to avoid gas tube crowbar on the HV side, to have low rise and fall times and to realize high voltage stability of the flat top. The output voltage and current are rated up to 110 kV/24 A, with pulse duration 800 µs, repetition rate of 2 Hz, <1% droop and <0.1% ripple on pulse top with energy restricted to 10 J in case of klystron arc. Based on these principles, a modulator has been developed and constructed at CERN and is currently undergoing tests with a klystron while another one with similar development is in the final stages of integration/evaluation at RRCAT. The present paper describes the topology, simulation results, protection strategy and briefly summarizes the results achieved.

## INTRODUCTION

The 3 MeV test stand will enable to explore the beam dynamics issues at the low energy end and comprises of 352.21 MHz, 3 MeV, 3-meter long RFQ, (part of SPL Front End) as the first part of the LINAC4 [1], a new PS Booster injector proposed to improve the proton beam quality and availability for CERN users in the LHC era.

LEP 352.21 MHZ, 1 MW CW klystrons will be operated in pulsed mode with maximum average power up to 2 kW, to feed the RF sections of the linear accelerators. This requirement necessitated the development of new high voltage pulsed modulators tailored for operation at duty cycle of 0.1%.

## DESIGN CONSIDERATIONS

The following issues were considered in the design:

- Crow-bar-less (no ignitron or thyratron) protection of klystron against arcing. The protection is assured by a) switching-off the main series switch very swiftly b) absorbing and dissipating the maximum of energy stored in the parasitic elements (stray capacitances, inductances, etc) inside the damping networks
- Low rise and fall time to limit the amount of wasted power
- High voltage stability of the flat top to assure the necessary phase stability of the RF output
- High reliability, minimum maintenance efforts and high lifetime due to solid-state construction.
- Modular structure to facilitate higher repetition rate up to 15 % duty at a later stage.
- The power supply interlock system able to be integrated into the CERN control and interlock system

## TECHNICAL SPECIFICATIONS

The major requirements are listed in Table 1.

Table 1: List of modulator main parameters

| **Parameter** | **Design Targets** |
|---|---|
| Klystron modulator type | Bouncer |
| High Voltage pulse amplitude | -10 kV to -110 kV |
| High Voltage pulse width measured at 70% to 70 % of peak. | 800 µsec |
| Minimum Flat top available | 600 µsec |
| Maximum current during pulse | 24 A |
| Pulse repetition rate | 2 Hz |
| Acceptable voltage drop | ≤ 1.0% |
| Allowed ripple on flat top (≥ 10 kHz) | ≤ 0.1% |
| Rise time/fall time | <100 µsec |
| Energy dissipated in klystron during klystron arc | <10 J |

## TOPOLOGIES CONSIDERED

At RRCAT we have designed and commissioned several modulators for klystrons based on the PFN topologies with step up pulse transformers, which have peak pulse power up to 15 MW and mean power up to 90 kW[2]. Few solid state switched modulators were also developed using RRCAT built stacked MOSFET/IGBT solid state switches, operating at 5 kV/0.5 A@10 µsec/ 1 Hz and 50kV/2A@10µsec/300Hz for pulsing driver klystrons and LINAC electron guns respectively. Looking into large reservoir of experience gathered on various topologies RRCAT took up the present project for CERN. Out of several schemes three options were found to be suitable and therefore an initial evaluation was restricted to: 1) Hard switched klystron modulator with high voltage programmable power supply for droop correction (active

#purushri@rrcat.gov.in
*work supported by DAE of India under aegis of DAE CERN NAT Protocol

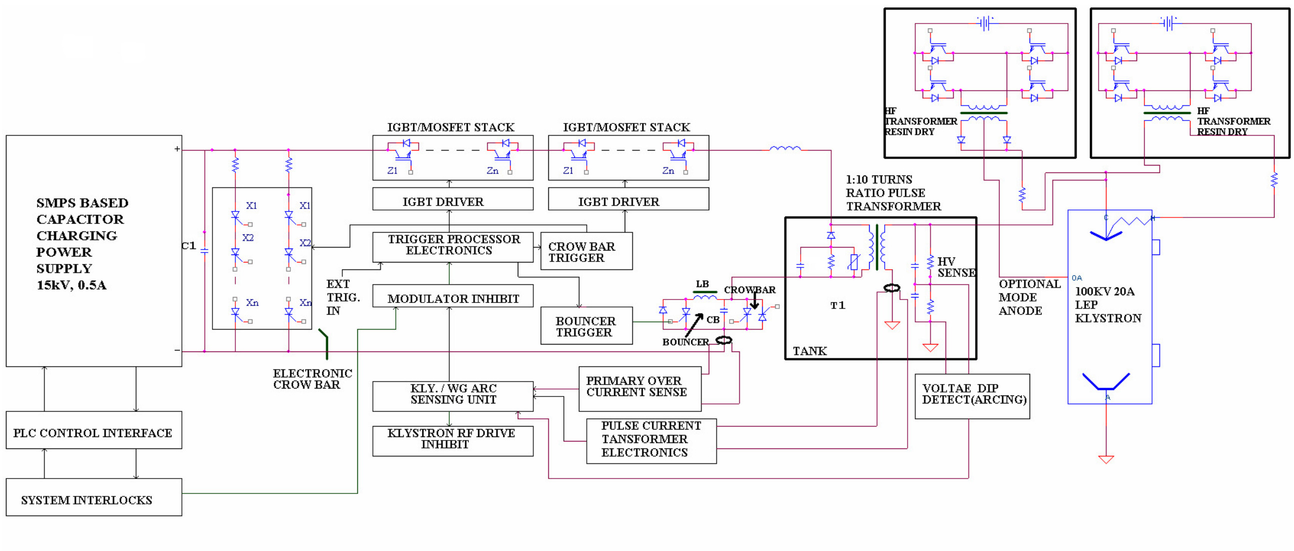


Figure 1: Solid state bouncer compensated pulse modulator schematic for LEP klystrons.

droop compensation) with step up pulse transformer; 2) Hard switched klystron modulator with bouncer circuit for droop compensation with step up pulse transformer [4][5]; 3) Pulse forming network based line type pulse modulator with step up pulse transformer. Finally option 2 was chosen for further development of the modulator.

## ADOPTED TOPOLOGY USING SOLID STATE TECHNOLOGY

To meet the specifications, we have chosen a bouncer compensated all solid state klystron modulator (Fig. 1). The main capacitor bank C1, is charged to ~10% higher voltage than required for the nominal output voltage. The bouncer capacitor $C_B$ is charged to ~10% of the required output voltage. During the generation of output pulse the pulse transformer sees the difference of main capacitor and bouncer voltage at its primary[4][5]. As the two voltages fall at the same rate due to proper designing and setting, the output voltage is constant during the pulse with <1% droop. The use of Capacitor switching with droop compensation overcomes the difficulties as normally encountered with PFN topologies and also reduces the size of energy storage device. The low loss LC bouncer circuit is chosen for better efficiency over other droop compensation techniques. The solid-state construction avoids bulky energising supplies and also improves the reliability and lifetime.

To assess the performance of this scheme a full simulation study was conducted at RRCAT whose results are shown at Fig. 2. The circuit simulation was done with basic elements of Pulse Modulator. In our actual simulation the series switch was modelled using IGBT devices in series and an ideal Pulse transformer has been connected along with equivalent circuit components transformed to primary side. As a step further a proof of principle a solid state bouncer modulator was assembled at RRCAT to demonstrate the droop compensation of 20% to 1% at a pulse width of 50 microsec with 12 kV, 0.5A output. This modulator used RRCAT made MOSFET Switches and 1:10 pulse transformer.[3][6]

The modulator comprises of charging supply, main storage capacitor, series switch, 1:10 pulse transformer and crowbar switch. A 15 kV DC capacitor charging supply with 7500 J/s is used for linear charging of storage capacitor comprising of 4 Nos. of 50 MFD, 20 kV capacitors. For series switch IGBT/IGCT based stacked assembly with 20 kV operating voltage rating and 300 A peak current is chosen.

The droop compensation is produced by series resonant LC circuit made of $L_B$ and $C_B$ bouncer inductor and capacitor respectively (Fig. 1). This bouncer circuit is triggered ON to start its cycle before the start of the main pulse of the modulator. Values of both components can be chosen to account for any variations in practice and to tune the pulse shape. To achieve the desired 1% droop the linear part of the bouncer cycle is subtracted from the drooping main capacitor bank. It has been considered to allow the main capacitor bank voltage droop to 20% so as to reduce capacitance value further. We start the bouncer waveform earlier than the modulator pulse, by triggering the bouncer switch SB1 first at a predetermined time with respect to that of the main modulator switch SW, such that the net positive energy is stored in the bouncer.

***The Bouncer Switch SB1***: Since we expect a 10% of nominal primary voltage across the bouncer capacitor this leads to the 1 kV voltage at the capacitor. A 3 kV switch with peak current of 1500 Amp is used.

***The Bouncer Crowbar BCB1***: The bouncer crowbar switch is rated for 4 kV and 2 kA.

The limit of the energy to be dissipated in an arc is <20 J. We limit it to 10 J in our design. During arcing the primary current will rise, limited only by the leakage inductance of the pulse transformer. The series switch is opened and the crowbar at the main capacitor bank as well as the bouncer circuit are fired simultaneously. A series back up switch is provided in case the main switch fails to open up due to any reason. The energy stored in the leakage inductance is 36 J and this energy is removed before it is dissipated in arc. The dip in the output pulse voltage as well as increase in the primary current above a threshold value is detected and the series switch is opened and the primary crowbar is triggered. The main switch and the back up switch are opened simultaneously to assure the removal of the voltage from the pulse transformer in few microsecond. Due to this there is an inversion of voltage at the primary up to few hundred volts, which is controlled by a circuit connected to the primary of the pulse transformer. This circuit has been realized with a parallel combination of resistor, capacitor and a MOV-resistor assembly, all connected to a back diode. The values of the capacitor and resistor are 100 µF and 50Ω.

## RESULTS

Figure 2 shows the results of the simulation. Modulator built at RRCAT is shown in Fig. 3 & 4. The preliminary test was done for modulator up to 5 kV output pulse. The waveforms of tests are shown in Fig. 5. Both the simulated and tested results show <1% droop in output voltage.

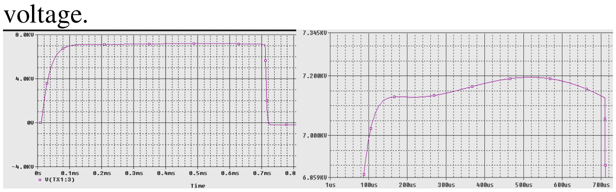

Figure 2: Simulated waveforms (referred to primary) (left) full pulse and; (right) Zoomed at flat-top.

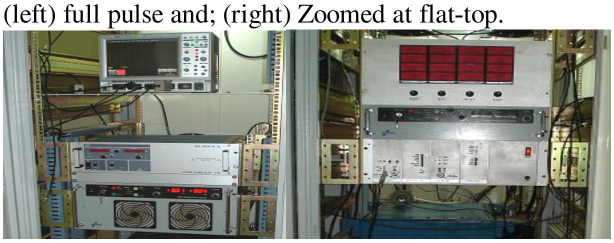

Figure 3: (left) Photo of Charging/Filament; (right) photo of trigger, controls and interlock system of modulator at RRCAT.

Figure 4: (left) resistive load in oil tank (@110kv) connected to modulator; (right) bouncer circuit elements pictures at RRCAT

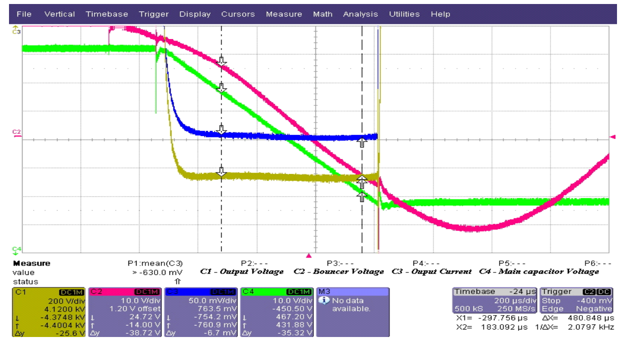


Figure 5: Obtained output during initial run, at resistive load, representing klystron impedance. Waveforms represent C1:Output voltage C2: Bouncer voltage C3: Output Load current C4: Main Capacitor voltage

## CONCLUSION

We have presented design of an all-solid state bouncer compensated modulator evolved at RRCAT for LEP klystrons to be used in LINAC4 project. One modulator has been assembled at RRCAT and another at CERN and testing has been started on a dummy load at RRCAT, equivalent to klystron impedance. The performance of the systems built agrees with simulation results. After further evaluation and tests on resistive load the systems will be integrated for final use in 3 MeV test stand of LINAC4.

## REFERENCES

[1] M. Vretenar, C. Carli, R. Garoby, F. Gerigk, K. Hanke, A.M. Lombardi, S. Maury, C. Rossi, "Status of the Linac4 Project at CERN", this Conference.

[2] Purushottam Shrivastava at el., "Performance of 6 MW peak, 25 kW Average power Microwave system for 10 MeV, 10 kW electron LINAC," APAC 07, RRCAT, Indore, India

[3] V.C. Sahni, "Cheers to Indian Science and Technology Community Engaged in building Large Research and Development Facilities and the Challenges Ahead", PRAMANA Journal of Physics, Vol. 67, No.1, pp 243-245 July 2006

[4] Shekar Mishra, Chris Jensen, FNAL, private communication.

[5] H. Pfeffer, L. Bartelson, K. Bourkland, C. Jensen, Q. Kerns, P. Prieto, C. Saewert, D. Wolff, "A Long Pulse Modulator for Reduced Size", 21st International Power Modulator Symposium, Costa Mesa, CA, June 27 - 30,1994.

[6] V. Bhanage et al., V.C. Sahni, et al, Purushottam Shrivastava, et al., "Indian Participation in LHC, SPL and CTF3 projects at CERN SWITZERLAND", Proceedings of APAC 07, RRCAT, Indore, India.

# COOLING SYSTEM DESIGN OF COMPACT KLYSTRON MODULATOR POWER SUPPLY IN THE XFEL PROJECT AT SPring-8

Chikara Kondo, Takahiro Inagaki, Katsutoshi Shiarasawa, Tatsuyuki Sakurai, Tsumoru Shintake,
RIKEN SPring-8, 1-1-1 Koto, Sayo, Hyogo, Japan

*Abstract*

XFEL project at SPring-8 requests the high performance modulator power supply for klystron i.e., low pulse-to-pulse fluctuation, low parameter drift, low noise, compact size, and easy maintenance [1]. To meet these requirements, we developed the compact klystron modulator power supply which stores the high voltage components in single steel tank. In order to obtain the practical heat transfer efficiency, we measured the heat transfer efficiency for various cooling panels in the model tank. Based on the results, we designed the optimum cooling system for the actual modulator power supply. We installed the cooling system to the modulator power supply, and confirmed the cooling efficiency was as expecting, and the oil temperature was under 45 °C.

## THE KLYSTRON MODULATOR POWER SUPPRY AT XFEL/SPRING-8

In the XFEL/SPring-8 project, the electron beams are accelerated by 128 of C-band accelerating structures. Since the accelerator is compact thanks to the acceleration gradient as high as 35 MV/m, the interval lengths of the modulator power supply for klystron become narrow. Therefore, the size of the modulator should be more compact than traditional one. Consequently, we developed the compact modulator power supply for klystron, which stored the PFN condensers, a thyratron, and a pulse transformer in an oil-filled tank. The specification of the modulator is listed in table 1.

The insulation oil enabled the tank to be compact, and isolate the performance from dust and humidity. Otherwise, the cooling system of the oil is one of the most important points for the requirement of stable operation and maintenance-free. The modulator dissipates the heat mainly coming from a thyratron cathode heater, a klystron cathode heater, a pulse transformer, and electrical resistors. The excessive increase of the oil temperature by the heat generation leads the problems as written blow;

- The drifts of the electrical properties of the components.
- The drift of the air temperature by the heat dissipation from the modulator to the air.
- The deterioration of the insulation oil and the heat dissipation to the air.

To avoid the problems, we need the efficient cooling system which transfers the heat from the oil to the cooling water. We aimed for the cooling system not only efficient but also compact and maintenance-free. We chose the natural convection cooling, i.e. fan-less cooling.

In this paper, we described the review of the oil cooling, the efficiency of the fan-less cooling system, and the results of the oil temperature of the modulator in our prototype modulator.

Table1: Klystron modulator specifications

| | |
|---|---|
| PFN charging voltage | 45 kV |
| Output voltage | 350 kV |
| Output current | 316 A |
| Transformer step up ratio | 1 : 16 |
| Pulse width<br>(at 70% of the voltage peak ) | 4.2 μsec |
| Peak output power | 110 MW |
| Maximum repetition rate | 60 pps |

## HEAT TRANSFER IN NATURAL CONVECTION

The oil flows by natural convection which occurs due to the heat transfer between oil and object. Around the heat sources, such as electric resistors or cathode heaters, the oil is heated and starts to rise. When the hot oil reaches to the cooling material, such as a water pipe or panel, the heat moves to the water and the oil sinks down.

The heat transfer rate $q$ between the oil and the object can be written as,

$$q = hA(T_h - T_c) \tag{1}$$

where $h$ is the heat transfer coefficient, $A$ is area of the cooling material, $T_h$ and $T_c$ are the temperature of the hot object and the cold object, respectively. The heat transfer coefficient represents the cooling efficiency. The practical value of the coefficient is difficult to be calculated analytically, because it depends on not only the property of the oil but also the geometry of the panel and the detail flow around the object [2].

There are a few reports for the heat transfer coefficient for the insulation oil [3]. But, the conditions of the report differ from our condition in the oil type and the cooling panel geometry. Therefore, we performed the experiment to measure the coefficients.

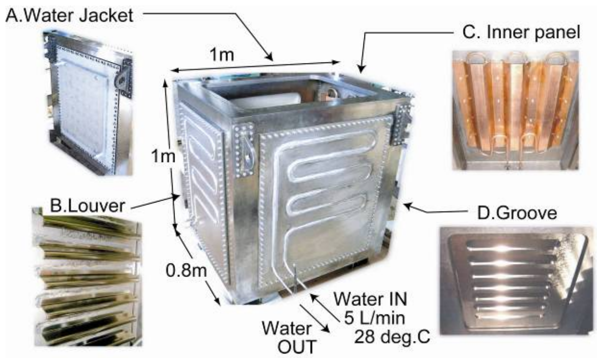


Figure 1: The model tank and the cooling panels.

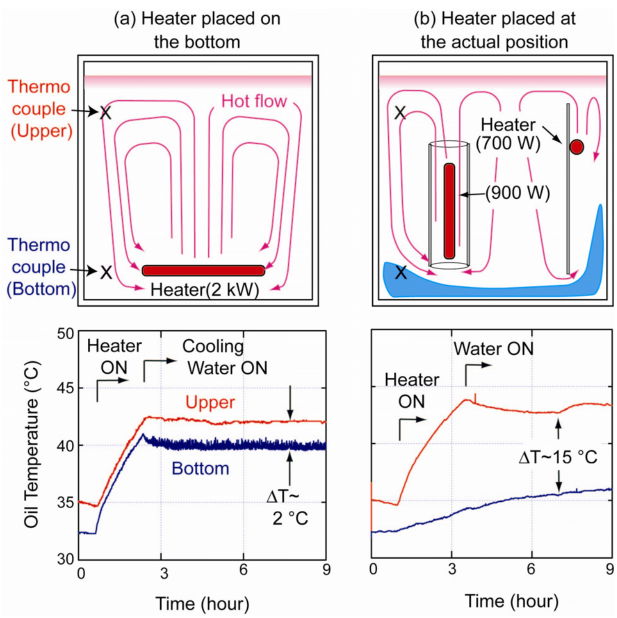


Figure 2: Upper figures show the schematic layouts of the experiments, and lower figures show the oil temperatures at the upper area and the bottom area of the model tank.

## EXPERIMENTS OF THE COOLING PANELS IN THE TEST TANK

To obtain the practical heat transfer coefficient, the dimensions of the tank and the cooling panel demand to be close to the actual modulator. Consequently, we fabricated the model tank with the comparable size as the modulator. We designed the four cooling panels as shown in Fig. 1. The characteristic features for the panels are written below.

A) **Jacket type**; the water jacket on the plate is attached on whole area of the SUS flat panel.

B) **Louver type**; water pipe is built in a steel panel and copper louver is attached on inside of the panel. The louver mixes cold oil falling on the plate, and prevents the build-up of the layer of the cold viscous oil [3].

C) **Inner panel type**; the corrugated copper board jointing with the water pipe is installed inside of the tank.

Table 2: Heat transfer and heat transfer coefficient between the four cooling panels and the water.

| Panel | Area ($m^2$) | Heat transfer (W) | Heat transfer Coefficient ($W/m^2K$) |
|---|---|---|---|
| A) Jacket | 0.35 | 350 | 75 |
| B) Louver | 0.38 | 315 | 62 |
| C) Inner Panel | 0.42 | 665 | 130 |
| D) Groove | 0.42 | 385 | 69 |
| Air | 3.6 | 285 | 4.5 |

D) **Groove type**; water pipe is attached on the outside of the panel, and the inside surface is grooved. The groove mixes the oil and advances the heat transfer as same as the louver type.

In Fig. 2, we show the schematic layout of the experiments and the measurements oil temperature. At the setup (a), we placed the electric heater on the bottom of the tank, and heated the oil with 2 kW heat power. The flow rate of the cooling water was 10 L/min, and the water temperature was 28 °C. The heat transfer coefficients of the four cooling panels were estimated in the thermal equilibrium state; we estimated the heat flow from the oil to the panels by measuring the temperature difference between the water at enter and at exit, and assumed the cooling water temperature as the mean temperature between enter and exit, and the oil temperature as that in the upper oil. In table 2, the estimated heat transfer coefficients are summarized. The heat transfer coefficients of the panels with external water pipe, such as (A) Jacket, (B) Louver, and (D) Groove, are about 60-75 $W/m^2K$. The coefficient of the inner panel is 130 $W/m^2K$, which is twice as large as the others. It is assumed that the inner panel have the larger area contacting the oil than others.

At the setup (b), we measured the coefficients and the oil temperature in the situation similar to the actual modulator; one heater assumed the thyratron was placed vertically and heated up with 900 W, and the another heater assumed the EOL resistor was placed on the similar height and heated up with 700 W. In this experiment, the difference of the temperature between upper and bottom of the oil was larger than the previous experiments (setup (a)). It was explained that the oil flow was restricted around the heater and the upper of the tank. And the cold oil was fixed around the lower area because of the large viscosity of the oil. Therefore, the heat transfer between the oil and the panels was occurred only upper area, and the total heat transfer became small. The heat transfer coefficient of the inner panel was estimated to be about 91 $W/m^2K$, which was smaller than the previous setup.

This result shows that the cooling efficiency depends on not only the design of the cooling panel but also the position of heater. To enhance the cooling efficiency, the heater should be placed on the bottom. The heat transfer from oil to air was estimated to be 4.5 $W/m^2K$.

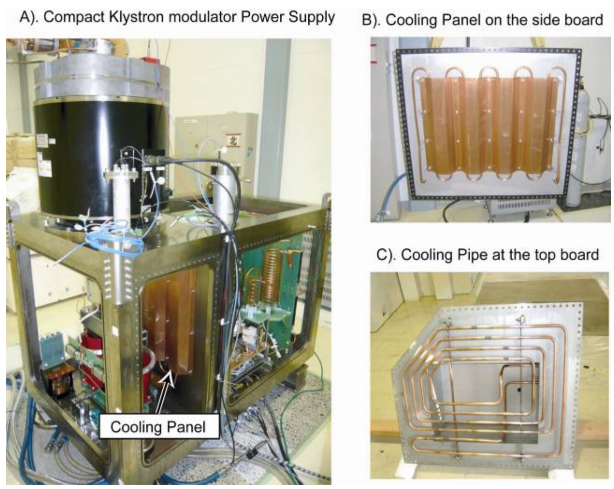


Figure 3: View of the compact klystron modulator, and the cooling system.

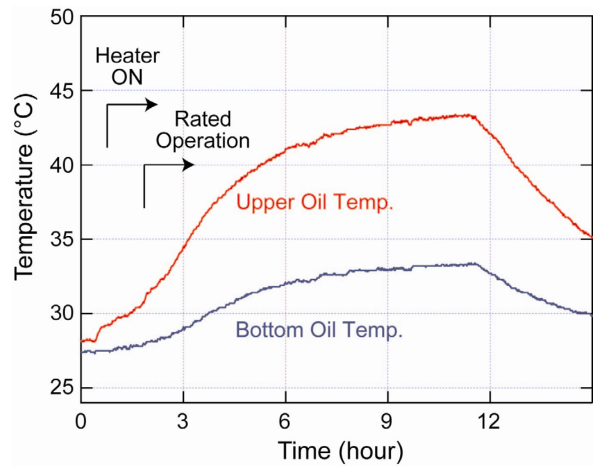


Figure 4: Oil temperature in the rated operation.

## DESIGN OF THE COOLING SYSTEM FOR THE NEW MODULATOR

We designed the cooling system for the actual modulator based on the result of the test experiment. The heat generation in the modulator was estimated to be about 3 kW [4]. We aimed to suppress the oil temperature below 45 °C. The requirement cooling power which assumed the product of the heat transfer coefficient and the area, is calculated to be 178 W/K in the condition of the water flow rate is 8 L/min and the water temperature is 26 °C. Using the coefficient 91 $W/m^2K$, the total area is needed to be 2.2 $m^2$.

We designed the simple cooling system to satisfy the above request and to keep the easy maintenance. We installed it into the actual modulator. In Fig. 3, the view of the modulator and the cooling panel are represented.

1. Two inner panels (type C) attached on inside of the side panel
2. Two inner type panels (type C) attached both side of the partition wall.
3. One water pipe installed inside of the top panel.

The total cooling power was calculated as 210 W/K using the heat transfer coefficient and the total areas. The oil temperature in the actual modulator was predicted to be about 42 °C.

## MEASUREMENTS OF THE TEMPRETURE OF THE MODULATOR

During the rated operation of the modulator, we measured the oil temperature of the oil. The temperature of the insulation oil is represented in figure 4. The temperature reached 43 °C in the upper area, and 34 °C in the lower area. The heat transfer from the oil to the water was calculated about 3 kW from the water temperature difference. Therefore, the total cooling power was estimated to be 214 W/K, which was nearly equal to the expected ability.

In addition, we also measured the temperature of the HV components. surface temperatures of the EOL resistance was 50 °C, thyratron anode was 45 °C and the outer case of thyratron cathode are 80 °C. Expect the out case of the thyratron cathode, the surface temperatures of these components were below the deteriorated temperature of the insulation oil. For the thyratron, we are going to improve the heat transfer.

The heat transfer to the air was calculated to be about 200 W at 26 °C air temperature. This heat dissipation is much smaller than that from other components.

## SUMMARY

We performed the experiment to measure the heat transfer coefficients between the insulation oil and the cooling panels using the model tank. Based on the result, we designed the cooling system of the new modulator in XFEL/SPring-8. In the rated operation of the modulator, we confirmed the oil temperature was under 45 °C, and the cooling system performed as our expected. The modulator is in operation without problems.

## ACKNOWLEDGMENTS

We thank to Kotobuki Iron Works Co., Ltd. for the mechanical design and fabrication of the model tank and the first modulator power supply. We also thank to the technical staff members in SCSS group for their support to the experiment, and Dr. S. Takahashi for his helpful advices to the heat transfer theory.

## REFERENCES

[1] T. Inagaki, et. al., "8-GeV C-band Accelerator Construction For XFEL/SPring-8", LINAC'08, Victoria, Sept. 2008, FR101.
[2] JSME, Heat Transfer, Maruzen, 2005.
[3] E2V report TR108, "The cooling of oil-filled electrical equipment, with special reference to high power line-type pulse generators," presented at the International Pulsed Power Conference, Lubbock, Texas, November, 9-11, 1976.
[4] J. S. Oh, Internal information.

# COLD CATHODE ELECTRON TUBE TOWARD PLENTY MULTI BEAM TUBE

M. Yoshida, KEK, Ibaraki, Japan
T. Hioka, K. Someya, Tokyo University of Science, Chiba, Japan
K. Utsunomiya, University of Tokyo, Tokyo, Japan

*Abstract*

The multi beam electron tube with a lot of beam pipes is required for the lower applied voltage and the higher frequency because the efficiency has a limit according to the perveance. However, the total heater power consumption becomes too high if many thermal cathodes are used. Thus the cold cathode such as the carbon nano tube (CNT) is suitable for such a multi beam electron tube. Further the cold cathode has the advantage to work as a switching device since the metal grid close to the cathode can be used. The design and the fundamental test of the partial model will be presented.

## ELECTRON TUBE USING COLD CATHODE

If we attempt to design the hundred or thousand multi beam electron tube, the following problems were occurred:

- Huge power consumption of thermal cathodes.
- Complicated gain cavity system using higher mode.
- Huge solenoid magnet.
- Parallel switching device adopting higher current is required for the pulse operation.

To avoid them, the grid triode [1] like the inductive output tube (IOT) using the field emission cathode has a possibility as a solution of such a plenty multi beam electron tube.

The advantages using the field emission cathode compared with the thermal cathode are as followings:

- No power consumption for the cathode.
- Very thin metal wire grid can be used and long life time is expected since the life time described in reference [1] is mostly caused by the high temperature of the thermal cathode.
- No resonant frequency change is occurred.
- Shorter grid gap and higher surface field makes to operate at higher frequency.
- Shorter bunch caused by the E-I curve of the field emitter can operate as the frequency doubler as shown in Fig. 1. Fig. 1 (left) shows the expected emission current according to the E-I curve of the carbon nano tube (CNT). Fig. 1 (right) shows the comparison of the frequency component between the CNT cathode and the thermal cathode

Further the grid tube has many advantages as followings:

- Huge solenoid magnet is not required since the beam trajectory is shorter.
- No switching device is required for the pulse operation.
- Simple cavity system

The disadvantages using the field emission cathode are as followings:

- Much higher surface field is required for the emission.
- Since it causes the lower gain, multi stage tube has to be considered to get higher gain.
- Proper ageing process is required for the field emission cathode.
- Special treatment is required to reduce the ununiformity of the cathode emission. One candidate for this is that the field emitter is arranged on the high resistance plate.

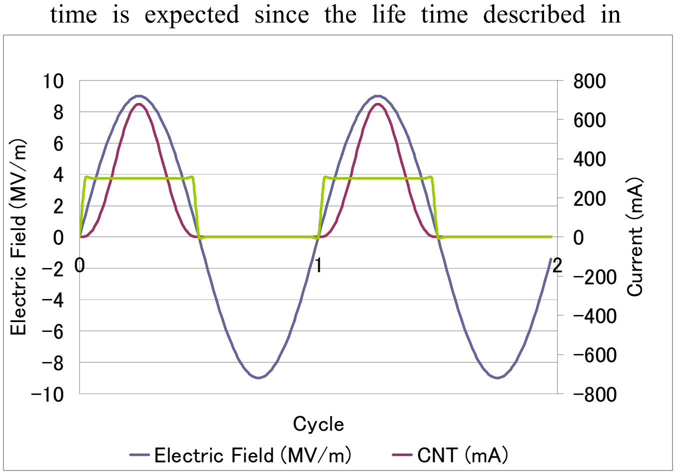


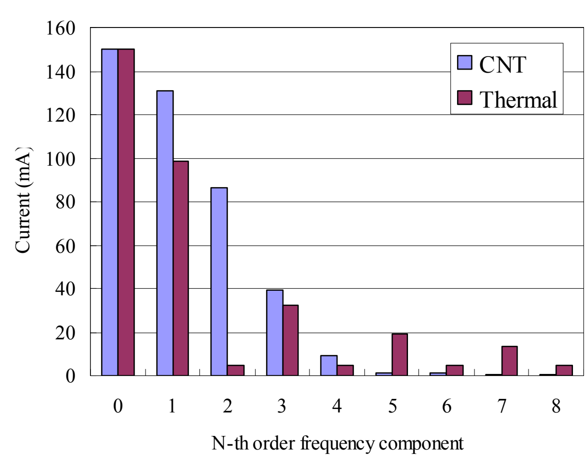


Figure 1: The emission current and its frequency component.

## TEST TUBE

The test tube was designed to obtain the fundamental characteristics of the RF response of the field emitter. The inductive output tube is a good candidate for such a test. Further the test tube was designed to work as the frequency multiplier of the input and the output frequency of C-band and X-band respectively since the higher efficiency for the frequency multiplication shown in Fig.1 is an important feature.

### *Field Emitter*

The multi-wall carbon nano tube (MWCNT) which is strongly bonded on the titanium plated surface is used for the field emission cathode. Its bonding procedure is written in reference [2]. Further some DC pulse experiments show that the CNT emitter can produce higher current than the expected current of the simple field emitter. This seems to be caused by the thermal effect. One purpose of this test tube is the estimation of such an effect since higher current is expected due to the microwave heating.

### *Input Cavity and Metal Wire Grid*

The C-band input cavity is designed to use the $TM_{01}$ like mode extended to the TEM mode and excited by the coaxial line. The $TM_{01}$ like mode has thin gap whose top is the wire grid and bottom is the CNT emitter. Fig. 2 left and right top, right bottom show the mechanical drawing of the input cavity and the simulation model overlapping the electric field, the assembled input cavity respectively. The grey part of the top of the cavity is the dielectric substance to adjust the resonant frequency.

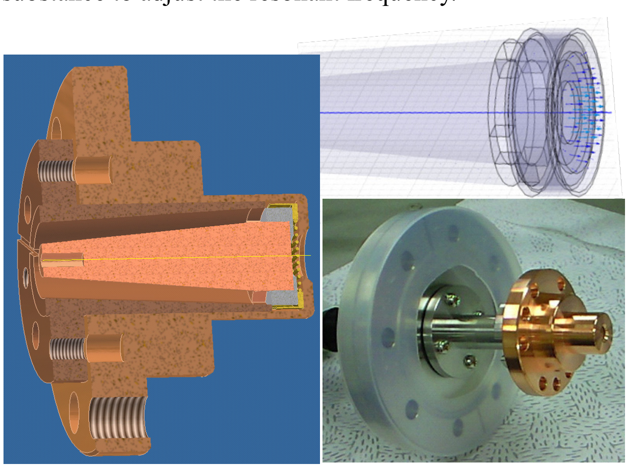

Figure 2: The C-band input cavity of the test tube.

### *Output Cavity*

The output cavity is designed to work at X-band frequency. Fig.3 left and right show the simulation model and the assembled cavity respectively. There is the matching section to connect to the waveguide of WR-90.

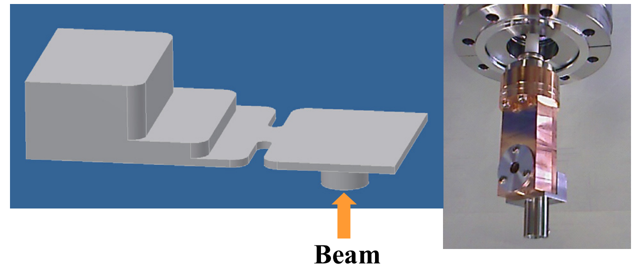


Figure 3: The output cavity of the test tube.

### *Dielectric Waveguide*

It is arbitrary which is selected the anode side or the cathode side for the high voltage. Both have respective advantage. In case of this test tube, the power consumption is enough small not to use the cooling liquid. Thus anode side was selected for high voltage to simplify the cathode side. Further the dielectric waveguide [3] is used to combine the microwave propagation and the high voltage insulation since high frequency cavity including the insulator is difficult. Fig. 4 top and bottom show the simulation model and the mechanical drawing of the X-band dielectric waveguide. The dielectric waveguide is consist of 10 mm diameter alumina rod brazed by Hitachi Haramachi Electronics Co., Ltd and the matching cavity to connect the WR-90 waveguide.

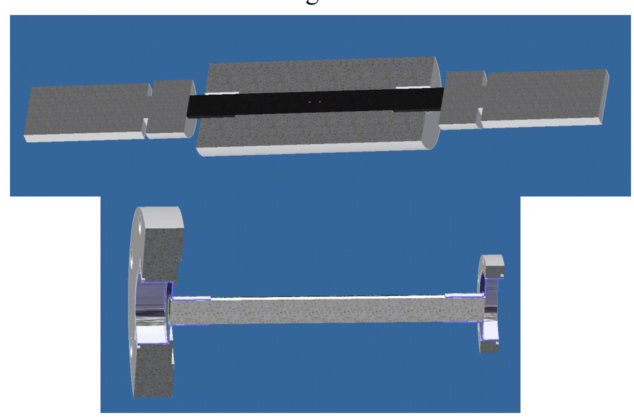

Figure 4: The X-band dielectric waveguide for the insulation.

### *Beam trajectory*

The beam trajectory of the test tube is calculated using the code CST Particle Studio (TM) as shown in Fig.5. The beam is focused well only by the electric field.

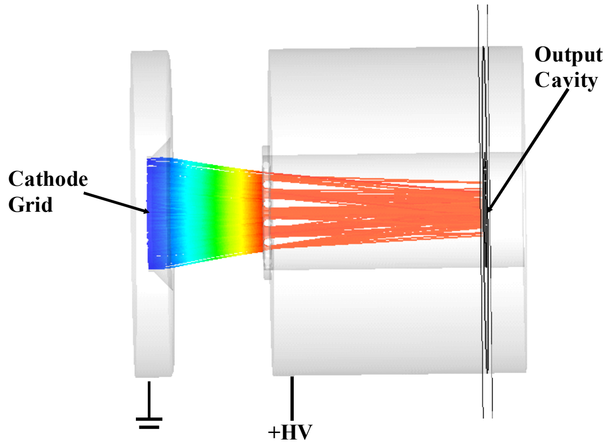


Figure 5: The beam trajectory of the test tube.

### *Mechanical Design*

Fig. 6 shows the overview of the test tube. The C-band input cavity is placed at the left side. And the X-band output is connected to the top of the test tube. The high voltage is applied for the bottom and connected to the output cavity using the central rod. The coaxial feedthrough for the input and the dielectric waveguide using the alumina ceramic for the output are used to avoid the vacuum leak.

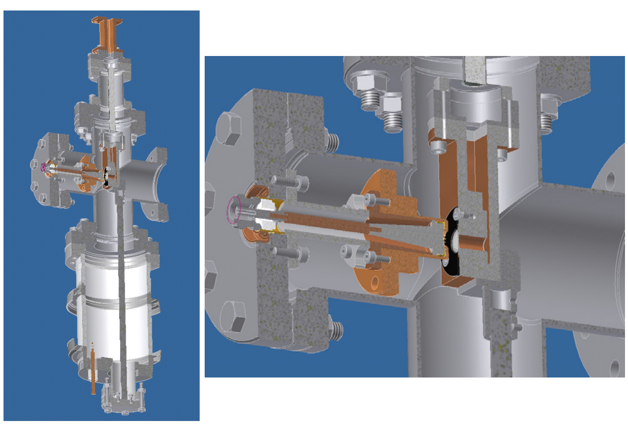

Figure 6: The overview of the test tube.

### *Experiment*

The preliminary experiment was done for the test tube as shown in Fig. 7 (left). The vacuum pressure is approximately $10^{-5}$ Pa and the applied voltage was +20 kV. Further a capacitor of 3 μF is used to make the pulsed high current. Fig. 7 (right) shows the waveform of the C-band input power and the X-band output power using the crystal detector.

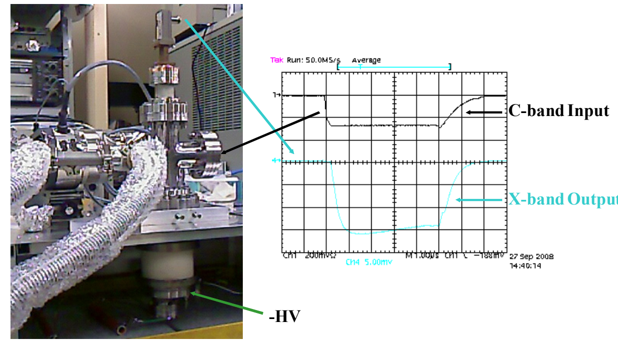


Figure 7: Experiment and result of the test tube.

In this preliminary experiment, the CNT cathode has only 2 mm square size. Further the input power is limited by the output power of preamplifier and the gap between the grid and the CNT cathode of the input cavity becomes longer than the designed value. Thus the output power is much less than the designed power.

## SUMMARY AND FUTURE PLAN

The test tube of the grid triode using the CNT emitter was tested. The parameter optimization will be done soon.

After the fundamental characteristics are obtained by this test tube, the multi beam electron tube using such a CNT emitter will be designed.

## ACKNOWLEDGEMENT

This work was supported by KAKENHI (60391710).

## REFERENCES

[1] Lundstrom, Oscar C. Nuclear Science, IEEE Transactions on Volume 12, Issue 3, June 1965 Page(s):222 – 226.

[2] Noguchi. T, et al., Nanotechnology, 2005. 5th IEEE Conference on Volume, Issue, 11-15 July 2005 Page(s): 669 – 672.

[3] “Foundations for Microwave Engineering" by R. E. Collins, McGraw-Hill, Inc., 1966, N.Y., N.Y., pp. 266-271.

# QUARTER-WAVE-STUB RESONANT COUPLER

Donald A. Swenson, Linac Systems, LLC, Albuquerque, NM

*Abstract*

Most small proton and other ion linacs involve two different linac structures, namely an RFQ linac section and some other, more efficient, linac structure, such as the Drift Tube Linac (DTL), the interdigital (Wideröe) linac, or the Rf Focused Interdigital (RFI) linac. Such linacs can benefit a lot by being resonantly coupled into a single resonant unit. The resonantly coupled structures can be driven by a single rf power system, through single rf drive loop, at a single rf frequency. The relative phase and relative amplitude of the fields in the two structures are locked by the resonant coupler. Such systems require no control of phase of the rf power. By designing the rf power system to track the resonant frequency of the combined structures, the control of the resonant frequencies of the two structures is greatly simplified. A simple, compact, resonant coupler, based on a quarter-wave-stub, will be described. Models of this resonant couple have been tuned and adjusted, and are scheduled to be tested at operating powers in the fourth quarter of 2008.

## BACKGROUND

Resonantly coupled linac structures have been around for 50 years. In the mid-60s, the Side Coupled Linac (SCL) structure was developed at Los Alamos for use in the Los Alamos Meson Physics Facility (LAMPF), and subsequently in thousands of today's electron linacs. Later in that decade, the post coupled Drift Tube Linac (DTL) was developed, which stabilized the amplitude and phase of the fields in these structures. Resonant coupling and operation in the $\pi/2$ mode are essential to modern linac technology.

The same technology that stabilizes linac structures can be used to couple any two resonant structures that operate at the same frequency. The bridge couplers of LAMPF are prime examples. They are not resonant couplers themselves, but rather resonant structures that are resonantly coupled to adjacent linac structures. The first 8 modules of LAMPF are built as 4 SCL linac tanks and 3 bridge couplers. The last 36 modules of LAMPF are built as two SCL linac tanks and one bridge coupler. In all cases, the SCL tanks are resonantly coupled to the bridge coupler by a minor modification of the side coupling cell. The "bridge coupler" name comes from the fact that these devices bridge the resonant properties of the structure around the required beam focusing quadrupoles.

For proton and ion linac applications, where the relative amplitude and phase of the fields are so important, the resonant coupling of the resonant units in a linac system is very important. The resonant couplers operate in the $\pi/2$ mode. They are nominally unexcited while the units that they couple are excited. The $\pi/2$ mode is unique in that it is the only mode in the mode spectrum where no changes are required in the amplitude or phase of the excited cells to accommodate changes in power flow through the structure. The resonant couplers lock the relative amplitude and phase of the fields in the excited cell of the structures. They stand by to support power flow in whichever direction is required to keep the fields in the excited structure at their design value.

For the theory of resonant coupling go to the Nagle, Knapp, and Knapp[1] or the Knapp, Knapp, and Potter[2] papers of the late 60's.

## INTRODUCTION

Particle accelerators employ electromagnetic resonators to produce high electric fields that can be used to accelerate charged particles to higher energies. Particle accelerators involving a single resonator have a requirement that the amplitude and distribution of the fields in the resonator be appropriate for the acceleration process. Particle accelerators involving two or more resonators have an additional requirement that the relative phase of the fields in adjacent resonators be controlled. Control of the relative phase of the fields requires that the frequency of the electromagnetic excitations in the all resonators be the same or harmonically related.

The conventional solution to these requirements is to control the resonant frequency of all resonators to the required accuracy, to control the amplitude of the fields in all resonators to the required accuracy, and to control the phase of rf fields in all cavities to some phase reference to the required accuracy.

The use of a resonant coupler greatly simplifies the controls problem for two-resonator particle accelerators. The resonant coupler provides a single frequency at which the pair of resonators can be excited, even when the resonant frequencies of the individual resonators are slightly different. The resonant coupler locks the relative amplitudes and relative phases of the field in the two resonators. Consequently, the resonant coupler reduces the controls problem for two-resonator accelerators to that of controlling the frequency of the drive power to the single frequency offered by the resonant coupler and controlling the amplitude of either resonator to the required accuracy.

Two-resonator accelerators are common in low energy range of ion accelerators, where the first resonator is a radio frequency quadrupole (RFQ) linac structure, with its superb very low energy capabilities, followed by some other low energy linac structure with better acceleration properties. This resonant coupler offers significant advantages to this important class of low energy ion accelerator.

A block diagram of two generic resonators that are resonantly coupled by a generic coupling resonator is shown in Fig. 1.

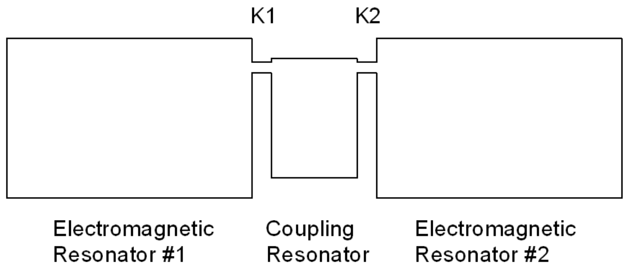


Figure 1: Diagram of resonantly coupled resonators.

The coupling between resonators can be either between the magnetic fields of the resonators or the between the electric fields of the resonators as shown in Fig. 2. Here the dots represent magnetic fields coming out of the paper, the pluses represent magnetic fields going into the paper, and the arrows represent electric fields in the plane of the paper.

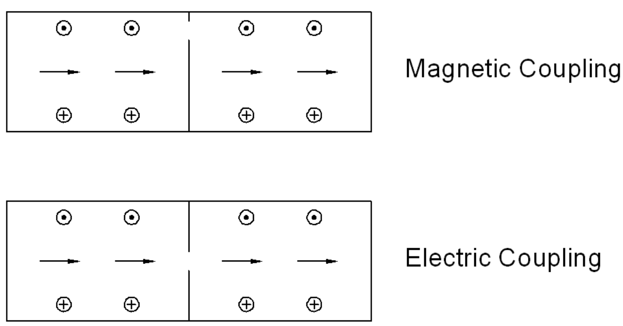


Figure 2: Examples of magnetic and electrical coupling.

The properties of the three basic electromagnetic modes of a three resonator configuration are shown in Fig. 3, where in the "0" mode, the electric fields in adjacent resonators are "in phase" (same direction), where in the "π" mode, the electric fields in adjacent resonators are π radians (180°) "out of phase" (opposite directions), and where in the "π/2" mode, the first and last resonators are excited "out of phase" and the coupling resonator is nominally unexcited;

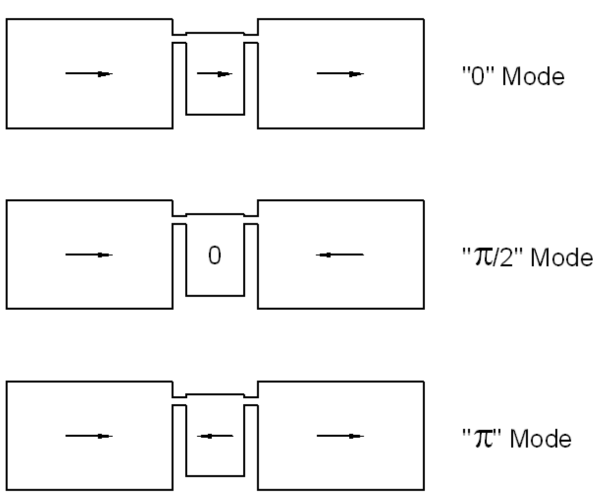


Figure 3: Basic modes of three coupled resonators.

The generic quarter-wave-stub resonator is shown in Fig. 4. It comprises a cylindrical outer conductor with a concentric quarter wave length cylindrical post along the axis. The magnetic fields are primarily at one end and the electric field are primarily at the other end.

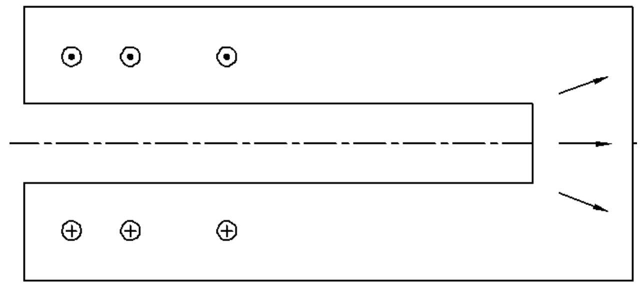

Figure 4: Generic quarter-wave stub resonator.

Most linac structures have their strongest electric fields on the axis of the linac structure for particle acceleration, and their strongest magnetic fields off the axis near the outer extremities of the linac structure. A favourable configuration for coupling two resonators with a quarter-wave resonator is shown in Fig. 5, which employs magnetic coupling between the two resonators and the resonant coupler. As there is a 180° shift in the direction of the magnetic fields across the resonant coupler, the field directions shown here are correct for the π/2 mode. The resonant coupler is nominally un-excited.

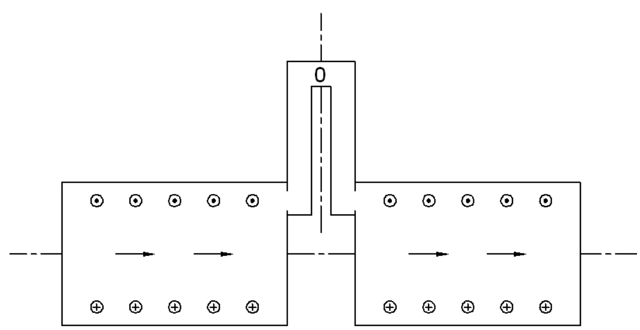


Figure 5: Quarter-wave-stub resonant coupler.

The common linac structures include the RFQ linac, the drift tube linac (DTL), the coupled cavity linac (CCL), the side coupled linac (SCL), the disk and washer (DAW) linac, the rf focused interdigital (RFI) linac[3], the alternating phase focused interdigital (APF-IH) linac. The DTL, CCL, SCL, and DAW linac structures employ transverse magnetic (TM) electromagnetic modes, which have strong transverse magnetic fields near the ends and outer extremities of the structure. The RFQ, RFI, and APF-IH linac structures have primarily longitudinal magnetic fields for most of the structure, which turn around at the ends of the structure, resulting in a transverse components of the magnetic fields. In the RFQ, there are four azimuthal locations at each end of the structure that suitable for magnetic coupling to a resonant coupler. In the RFI, there is one azimuthal location at the each end of the structure that is suitable for magnetic coupling to a resonant coupler. In the APF-IH, the best coupling to a resonant coupler may be through electric coupling to the off-axis electric fields near the ends of the structure.

## EXAMPLE

A 1.1-MeV RFQ linac structure resonantly coupled to a 3.5 MeV RFI linac structure is shown in Fig. 6. The resonante coupler is the horizontal projection at the interface between the two structures.

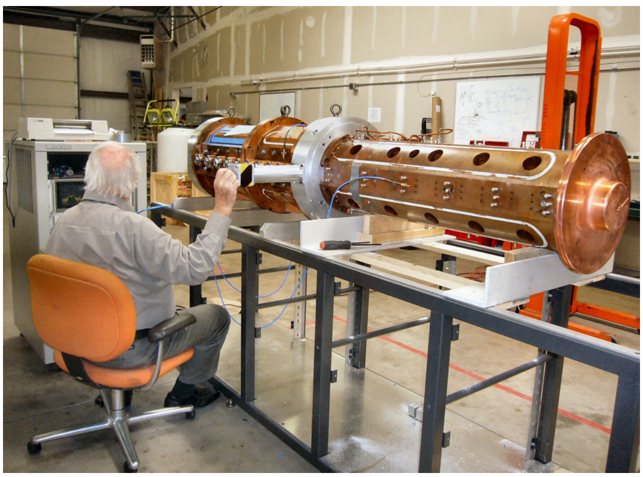

Figure 6: A 1.1-MeV RFQ linac resonantly coupled to a 3.5-MeV RFI linac with a quarter-wave-stub resonant coupler.

Two views of the resonant coupler are shown in Fig. 7, one looking downstream (upper) showing the RFQ coupling slot, and one looking upstream (lower) showing the RFI coupling slot. In the downstream view, the resonant couple cavity has been sectioned to show the quarter wave stub. In the upstream view, you can see a rectangular slot cover plate held in place with four screws. Initially, this cover plate was flush on the left (no cut back), which resulted in a very small coupling to the RFI structure. In the course of the adjustment of the ratio of cavity powers in the two accelerating structures, this cover plate was machined to the shape show here, which resulted in a significant coupling to the RFI structure.

The mode spectrum of the three modes (0, $\pi/2$ and $\pi$) of this three cavity system are shown in Fig. 8, with a total width of 2.3-MHz. The knob at the end of the Resonant Coupler moves a tuning slug in and out to adjust the resonant frequency of the resonant coupler. Using this knob, it is possible to achieve the symmetrical distribution of mode frequencies, which is important for proper operation.

## ACKNOWLEDGEMENTS

The author wishes to acknowledge interactions with Darragh Nagle, Ed Knapp and Jim Potter, who whetted my appetite for linac structures and resonant coupling.

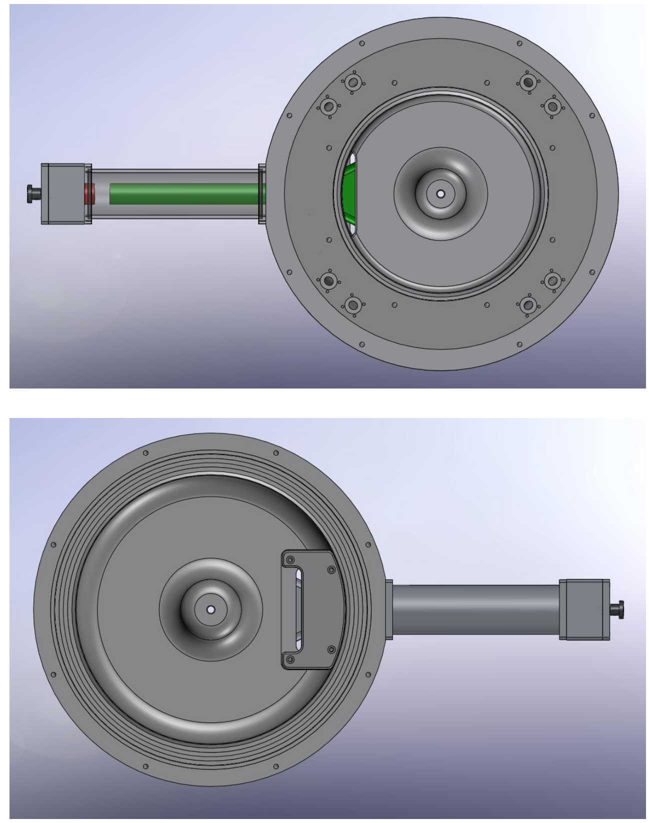

Figure 7: Two views of the resonant coupler.

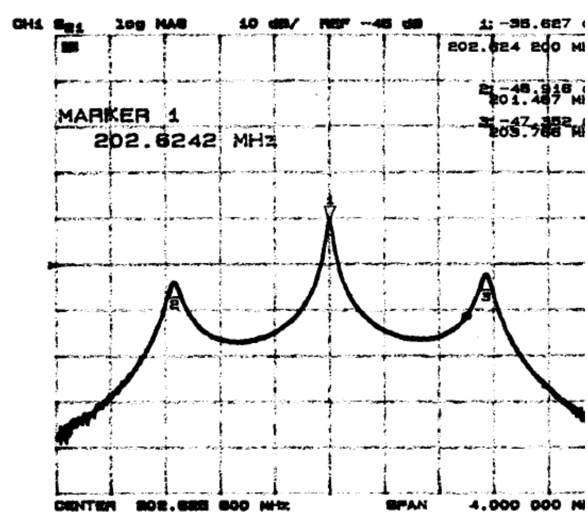


Figure 8: Mode spectra for resonantly coupled structures shown in Fig 6.

## REFERENCES

[1] D. Nagle, E. Knapp and B. Knapp, 1967, Rev. Sci. Instr. 38, 1538.
[2] E. Knapp, B. Knapp, and J. Potter, 1968, Rev. Sci. Instr. 39, 979.
[3] D.A. Swenson and W.J. Starling, CAARI 2002 Conference, Denton, TX.

# HIGH POWER 325 MHZ VECTOR MODULATORS FOR THE FERMILAB HIGH INTENSITY NEUTRINO SOURCE (HINS)*

Robyn Leigh Madrak and David Wildman
Fermilab, Batavia, IL 60510, U.S.A.

*Abstract*

One of the goals of the low energy 60 MeV section of the HINS $H^-$ linac [1] is to demonstrate that a total of ~40 RF cavities can be powered by a single 2.5 MW, 325 MHz klystron. This requires individual vector modulators at the input of each RF cavity to independently adjust the amplitude and phase of the RF input signal during the 3.5 ms RF pulse. Two versions of vector modulators have been developed; a 500 kW device for the radiofrequency quadrupole (RFQ) and a 75 kW modulator for the RF cavities. High power tests showing the vector modulator phase and amplitude responses will be presented.

## INTRODUCTION

The first high power microwave phase shifters using ferrite-loaded coaxial structures were first described more than forty-five years ago [2,3]. Recently, there has been renewed interest in the field with advances in technology and materials. The possibility of powering multiple RF cavities from a single RF source has become a viable alternative to the traditional single RF source per cavity [4,5]. At Fermilab we are in the process of building a 60 MeV $H^-$ linac to be used as the front end of a future High Intensity Neutrino Source (HINS). The linac is designed to accelerate 20 mA of beam current in either 1 ms pulses at a 10 Hz rate or 3 ms pulses at a 2.5 Hz rate. The first 30 MeV section of this new linac will have a 2.5 MeV RFQ, two bunching cavities, 16 room temperature CH type (3 & 4 spoke) cavities, and 18 superconducting single spoke cavities all being driven by a single 2.5 MW, 325 MHz klystron (Toshiba E3740AFermi.) Here there will be one vector modulator between the klystron and each cavity to independently control the phase and amplitude of the RF drive signal to its coupling loop. For the room temperature cavities these vector modulators will serve two purposes. First, they will be used to correct for cavity tuning errors caused by cavity heating and cooling water temperature fluctuations. Second, they will provide a means of compensating the effects of beam loading. To meet these goals we have developed two versions of high power vector modulators using fast ferrite loaded coaxial phase shifters. A 75 kW version will be used for all of the room temperature RF cavities. The RFQ which requires a larger 500 kW model.

* Operated by Fermi Research Alliance, LLC under contract with the U.S. Department of Energy

## VECTOR MODULATORS

A photograph of one of the 75 kW vector modulators is shown in Figure 1. The 325 MHz signal from the klystron enters port 1 of a –3 dB quad hybrid (Dielectric Communications) where it is equally split with a 90° phase difference between ports 2 and 3. Two shorted 1.625″ OD coaxial, ferrite-loaded phase shifters, described below, are attached to ports 2 and 3 and provide full reflections with phase shifts φ2 and φ3 respectively. The desired phase shift is produced by a variable solenoidal magnetic field along the axis of the coaxial line which is used to adjust the permeability, μ, of the ferrite. These reflected signals are recombined at the output (port 4) of the quad hybrid with a resulting output phase of (φ2 + φ3)/2 and power proportional to $\cos^2$ (φ2 - φ3)/2. A 3 port 75 kW circulator (D & M Co. Ferrit-Quasar) with a 5 kW water cooled RF load (Altronic) is connected between the quad hybrid output and the RF cavity to isolate the phase shifters from any power being reflected from the cavity during the cavity filling time or under cavity detuning conditions.

The higher power vector modulator to be used with the RFQ is similar to the one described above except that the components are physically larger. The –3 dB quad hybrid (Micro Communications) has a coaxial design with 6″ EIA flanges and is filled with $SF_6$ to prevent sparking. The two phase shifters are 3.125″ OD, ferrite-loaded, shorted coaxial lines and are also filled with $SF_6$. A high power 3 port coaxial/stripline circulator (D & M Co. Ferrit-Quasar) is used to prevent the reflection of power back to the phase shifters.

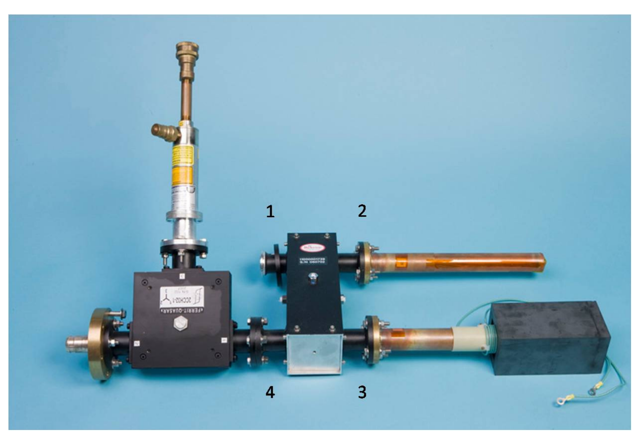


Figure1: Photograph of a 75 kW vector modulator.

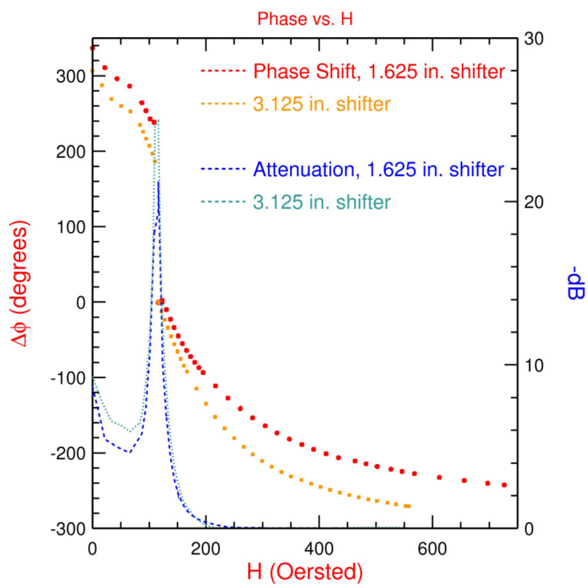


Figure 2: Phase shifter attenuation and phase shift vs. internal bias field, H, inside the garnet cores.

## PHASE SHIFTERS

The phase shifters are OFHC copper shorted coaxial lines filled with a 5″ long section of aluminum doped yttrium-iron garnet (TCI Ceramics type AL-400) which has a saturation magnetization ($4\pi Ms$) of 400 gauss. The 75 kW version uses a 1.5″ OD x 0.65″ ID x 5″ long garnet cylinder at the shorted end over a 0.65″ diameter center conductor. The center conductor diameter is then increased to 0.880″ for a quarter of a wavelength (9.08″) to form a $Z_0$ = 33 Ω matching section between the garnet filled region and the standard $Z_0$ = 50Ω port of the quad hybrid. The OFHC copper center conductor/garnet cylinder is assembled using a shrink fit technique where the center conductor is first cooled to $LN_2$ temperature and then inserted into the garnet cylinder. The phase shifter coaxial line outer conductor is a standard 1.625″ OD, 50Ω line (1.527″ ID) whose OD has been reduced to 1.567″ over the 9″ length closest to the short. Both this 9″ section and the bottom copper shorting plate have a 0.0197″ wide slot machined through the copper to reduce eddy current effects. The shorted end of the phase shifter containing the garnet cylinder is surrounded by a solenoid wound from 47 turns of 12 AWG stranded copper THHN wire on a 1.812″ OD G10 form. A magnetic flux return made from 0.75″ thick ferrite blocks (TCI Ceramics material G4) helps to increase the phase shifter frequency response.

The larger version phase shifter uses a 3.0″ OD x 0.65″ ID x 5″ long AL-400 garnet cylinder along with a $Z_0$ = 46Ω matching section. Here also, the outer conductor has a 0.020″ thick wall and a 9″ long slot. The biasing solenoid is 62 turns of 12 AWG wire on a 3.316″ OD G10 form with a G4 ferrite flux return. Each solenoid is

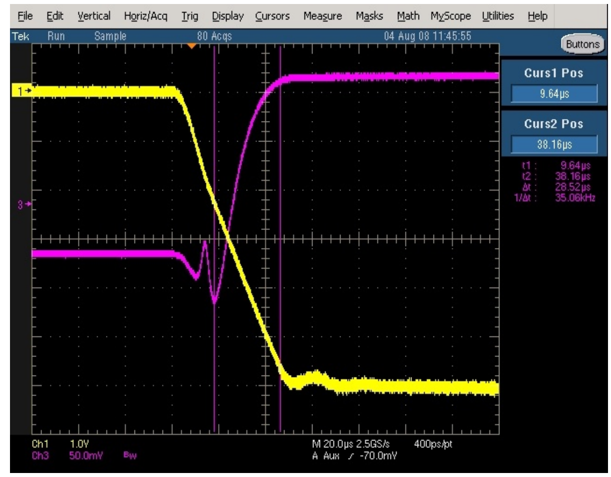


Figure 3: Time response of the 75 kW phase shifter biasing solenoid current (CH1 @ 50A/div.) and reflected phase (CH3 @ ~30 deg./div.) to a fast step (risetime< 1 µs) in the current program. The time scale is 20µs/div.

independently powered by a 300V, 300A, 2 quadrant switching supply with a switching frequency of 250 kHz. A Praeg [6] style filter on the supply output, currently set to roll off at 40 kHz, is necessary to reduce the 250 kHz ripple that would otherwise be seen on the vector modulator outputs.

## TUNING RANGE

Figure 2 shows a low power measurement of the round trip phase shifts and RF losses at 325 MHz for the 1.625″ OD and 3.125″ OD shifters plotted as a function of the internal biasing field, H. The maximum solenoid current for both cases was 300A during the 4ms pulse. The abrupt step in phase shift corresponds to the garnets going through gyromagnetic resonance. In Figure 2 the scale of H is normalized so that the gyromagnetic resonance at 325 MHz corresponds to the theoretical value of 2.8 MHz/oersted or H = 116 oersted. Below and at resonance the RF losses at 325 MHz are large which makes this region unsuitable for high power operation. However, above H ~ 200 oersted RF losses drop below -0.2 dB (typically < -0.1 dB) and high power operation becomes practical. Using –0.2 dB loss as an acceptable figure, the useable phase shift range is seen to be ~120 degrees.

## FREQUENCY RESPONSE

Figure 3 is a scope trace showing the low power phase shifter response to a fast step used as the input program (0 to 300A) to the solenoid pulsed power supply. The rate of rise of the solenoid current is seen to be limited by the 300V maximum output of the supply and the ~45 µH inductance of the solenoid coil. The measured phase shift was obtained with an HP 86205A directional bridge and HP 10514A mixer, used as a phase detector at 325 MHz, comparing the input and reflected RF signals. Above resonance the average phase slew rate is ~ 6°/µs.

The small signal (+/- 10°) frequency response of the 1.625″ OD and 3.125″ OD shifters, centered at midrange, is shown in Figure 4. The open loop case (triangles) can be compared to a case with feedback (squares). The feedback error signal was obtained by comparing the measured reflected phase to a reference. The error signal was then amplified and summed back into the bias solenoid current program. The 1.625″ OD shifter open loop bandwidth is seen to be ~ 15 kHz which was extended to > 35 kHz with the phase feedback.

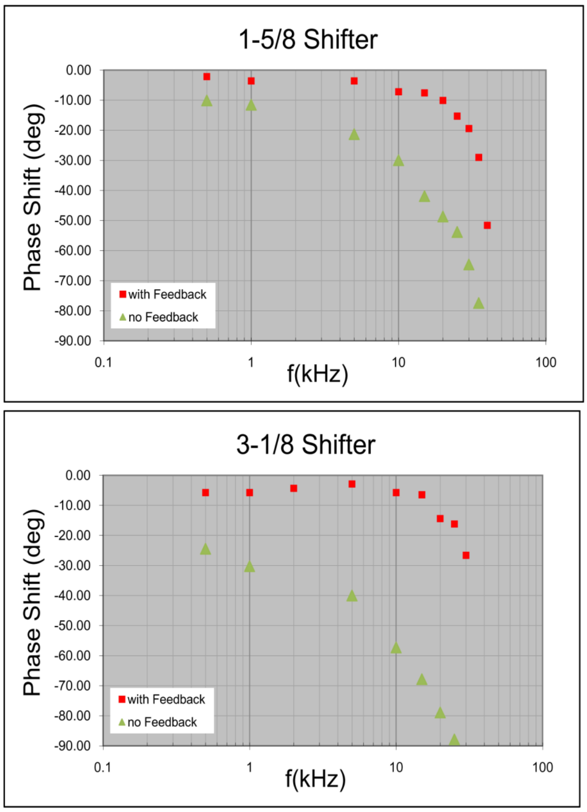


Figure 4: Phase shifter frequency responses with and without feedback.

## HIGH POWER OPERATION

Figure 5 illustrates the amplitude modulation capability of the 75 kW vector modulator during a 2 ms RF pulse without any phase feedback. With a constant 50 kW input power to the vector modulator, the output power is stepped from 25kW ( $\varphi 2 - \varphi 3 = 90°$) to the full 50 kW ($\varphi 2 - \varphi 3 = 0°$). During the first portion of the pulse, the 25 kW of unwanted power is directed back towards the circulator at the output of the 2.5 MW klystron where it is absorbed in the circulator load.

Both the 75kW and 500 kW phase shifters have successfully operated at their design power levels along with the 75 kW circulators. However; we have encountered some breakdown problems at the ~ 400 kW power level in the larger circulator. This circulator is currently being modified to reach the full 500 kW level.

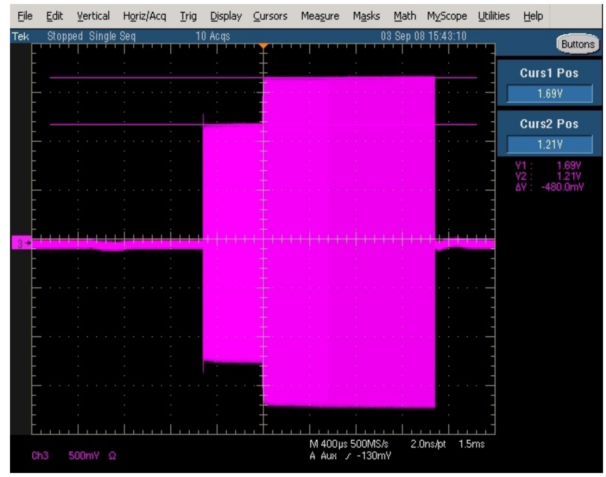


Figure 5: Vector modulator 325 MHz RF output amplitude being increased from 25 kW to 50 kW during a 2 ms pulse without any phase feedback. The time scale is 400µs/div.

## ACKNOWLEDGEMENTS

The authors would like to thank the Fermilab Accelerator Division EE Support Group, specifically, B. Claypool. S. Hays, and H. Pfeffer for providing the solenoid pulsed power supplies used in this work.

## REFERENCES

[1] SCRF Linac Proton Driver Study Group, “An 8 GeV SCRF Linac Proton Driver,” http://protondriver.fnal.gov/#Technical_Design_Link
[2] A.S. Boxer, S. Hershenov, and E.F. Landry, IRE Trans. Microwave Theory Tech. 9 (1961) 577.
[3] A. S. Boxer and R.S. McCarter, J. Appl. Phys. 33 (1962) 1263.
[4] R. Madrak et. al, “ New Materials and Designs for High-Power, Fast Phase Shifters,” LINAC 2006, Knoxville, FR2003, p.829 (2006).
[5] J.L. Wilson et. al, “ Development of High –Power RF Vector Modulator Employing TEM Ferrite Phase Shifters,” LINAC 2006, Knoxville, TUP083, p.451 (2006).
[6] W.F. Praeg, IEEE Trans. Industrial Electronics and Control Inst., IBECI-1 (1970) 16.

# HIGH POWER L-BAND FAST PHASE SHIFTER*

I. Terechkine#, T. Khabiboulline, N. Solyak, FNAL, Batavia, IL 60510, U.S.A.


### *Abstract*

A design of a waveguide-based, L-band, fast, high-power phase shifter is proposed. The shifter uses two magnetically biased blocks of Yttrium Iron Garnet (YIG) positioned in contact with the side walls of a rectangular waveguide. The cross-section of the waveguide is chosen to suppress unwanted RF modes that could otherwise compromise performance of the phase shifter. Static bias field in the YIG blocks is created by permanent magnets. Low inductance coils in the same magnetic circuit excite changing component of the bias field. Design of the device ensures effective heat extraction from the YIG blocks and penetration of the fast magnetic field inside the waveguide with minimum delay. This paper summarizes main steps in this development and gives brief description of the phase shifter.


## INTRODUCTION

The attractiveness of using devices that control phase and amplitude of input RF power of superconducting accelerating cavities of a high-power linac is widely recognized [1]. Once implemented, this approach will result in significant savings in number of klystrons. This motivates multiple efforts towards building a high-power, fast phase and amplitude modulator, also known as vector modulator [2], [3]. At Fermilab, a prototype of a waveguide-based phase shifter was built and tested to demonstrate high power handling capability: up to 2 MW at 1300 MHz [4]. The phase shift range of this device was limited by the onset of sparking in the ferrite-loaded waveguide. Understanding the nature of the this effect was considered crucial for improvement of the performance, and a study was conducted that connected the sparking with the excitation of one of several resonant modes in the ferrite-loaded part of the waveguide [5]. The resonant modes could exist due to imperfections in positioning of the YIG blocks inside the waveguide or due to some difference in the levels of the bias field in the blocks. Variations in the magnetic properties of the YIG blocks can also result in resonances. Following this phase shifter performance study, a way to design a resonance-free system was proposed [6].

In the end, the answer to the question of whether the use of vector modulators in RF distribution system of a linac is advantageous in comparison with the "one transmitter per cavity" approach is in the complexity of a power system needed to activate the device. An impact of possible design solutions on requirements for the power supply must be closely watched.

This paper summarizes results of the phase shifter prototype performance study and presents a design concept of a fast, high-power phase shifter. The operating frequency (1.3 GHz) and the transmitted power requirement (~125 kW per one phase shifter) were chosen having in mind an elliptical (TESLA-type), nine-cell superconducting cavity.

## PHASE SHIFTER PERFORMANCE

Dynamic range of the phase shifter prototype described in [4] depended on the input power. It was ~90º at 100 kW and reduced to ~30º at 1500 kW due to onset of sparking in the gaps between the YIG blocks and the walls of the waveguide. The sparking could be stopped by partial filling the waveguide with $SF_6$. The sparking was the result of RF electric field increase when one of trapped RF modes in the ferrite-loaded waveguide was close to resonance and got coupled with the main $TE_{10}$ mode.

In the regular section of the prototype's waveguide (165.1 mm x 50.8 mm), the modes $TE_{11}$, $TM_{11}$, $TE_{20}$, $TE_{21}$, etc. have critical frequencies higher than 1300 MHz. Only $TE_{10}$ mode can propagate along the waveguide – the critical wavelength of this mode is 330.2 mm versus the free space wavelength at 1.3 GHz of 230.8 mm. In the ferrite-loaded section of the waveguide, critical frequencies for all modes shift to lower values; as a result, these modes can propagate in this section. Each high-order mode can be excited if there is a coupling with the main $TE_{10}$ mode. If the coupling is small, corresponding mode can have a quality factor high enough for the electric field to exceed the breakdown threshold setting off the sparks.

The following subsections show which high order modes exist in the ferrite-loaded section and how they are coupled with the main mode.

### *$TE_{20}$ Modes*

If the two YIG blocks of the phase shifter are identical, positioned in the same longitudinal space, and have equal magnetic bias, $TE_{20}$ mode is not coupled with the main mode: coupling with one of the blocks is cancelled by coupling with another one. By introducing bias asymmetry, or moving one of the blocks longitudinally, the coupling through electric and magnetic field is made possible. As a result, trapped resonance condition can exist for $TE_{202}$ or $TE_{203}$ mode. To ensure the absence of the coupling, the bias field in the blocks must be equal.

### *$TE_{11}$ Modes*

The presence of the YIG blocks makes it possible for the RF modes with variations along the short side of the waveguide to exist. In this case, the section of the waveguide between the YIG blocks is impassible for the modes. Each block supports its own oscillation mode, and these modes can be excited independently. It means that we will observe not a pure $TE_{11}$ mode, but two separate

*Work supported by the U.S. Department of Energy under contract No. DE-AC02-07CH11359.
#terechki@fnal.gov

quarter-wave $TE_{11}$-like modes. If there is symmetry in the vertical position of one of the blocks, no coupling with the main $TE_{10}$ mode exists for corresponding modes. Shifting the block up or down relative to this symmetry position results in coupling.

### [illegible]

If direction of the bias field is the same in the two YIG blocks, additional resonances could take place because of circular polarization of the magnetic field vector in the blocks. In case of circular polarization, the wavelength at given frequency depends on direction of wave propagation. For the $TE_{10}$ mode, the polarization is opposite for the two sides of the waveguide, and significant phase difference can exist between the two sides of the ferrite-loaded section, which can result in resonant condition.

In [5] it was shown by modeling and proved by making direct RF measurements how resonances appear in a ferrite-loaded waveguide and what measures help to avoid them. Certain recommendations were made there on how to improve RF properties of the tested phase shifter. Based on these recommendations, a design has been proposed, which is described below.

## PHASE SHIFTER DESIGN

Following recommendations of [5], the next changes in the prototype design have been made to improve the performance of the phase shifter. First, the width of the loaded waveguide was made smaller, which increased the cut-off frequency of the $TE_{20}$ modes. Second, the height of this section was made smaller, which resulted in higher cut-off frequency of the $TE_{11}$ modes and relaxed requirements for the fast bias power supply. Finally, the thickness of the YIG blocks was reduced, which allowed lower bias field and simplified heat management. Fig. 1 shows main features of the proposed design.

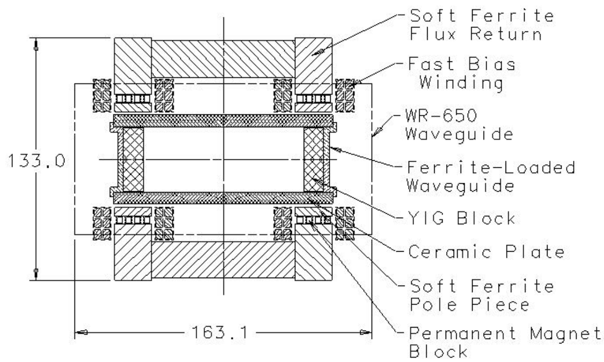


Figure 1: Design concept of a fast phase shifter.

Two YIG blocks, 11 mm wide and 35 mm high each, are placed inside a rectangular waveguide (110 mm wide and 36 mm high) in close contact with the side walls. Heat generated in the blocks is removed by cooling the walls. The magnetic system, built around the waveguide, is made to ensure needed bias field in the blocks. There are two components of the bias: static and dynamic. Static bias is created by using blocks of permanent magnets with the help of pole pieces and a flux return. The direction of this bias field is opposite in the two YIG blocks. To generate fast changing bias field, copper windings are used. Because the permanent magnets and the fast bias windings share the same magnetic circuit, spatial shape of the bias field in the absence of the waveguide is essentially the same for the static and dynamic magnetic field components. Eddy currents in the walls of the waveguide affect the dynamic component of the magnetic field; special design measures are needed to ensure the field penetration inside the waveguide. To handle both the static and dynamic components of the magnetic flux, the pole pieces and the flux return must be made of soft magneto-ceramic.

### [illegible]

RF design of the phase shifter provides a framework for configuring the rest of the device. The phase shifter must handle certain levels of peak and average power and provide required phase shift. The geometry of the ferrite-loaded section and range of the bias field change define performance of the device and configuration of the magnetic circuit. On the other hand, magnetic circuit imposes some limitations on the RF design, and several iterations in the design were made before reasonable convergence was achieved. The optimization goals were to get greater phase shift in combination with smaller bias field and its range and to lower power dissipation in the system. As it was mentioned earlier, uncertainties in the bias field symmetry and accuracy of the block placement in the waveguide can result in the appearance of unwanted resonances with corresponding increase in the power loss. The geometry of the ferrite-loaded waveguide and the level of the static bias in the YIG blocks were chosen after analyzing sensitivity of the system to these uncertainties. The bias field of ~700 G was found to be optimal.

Fig. 2 shows phase shift and power loss diagram for the final version of the RF design.

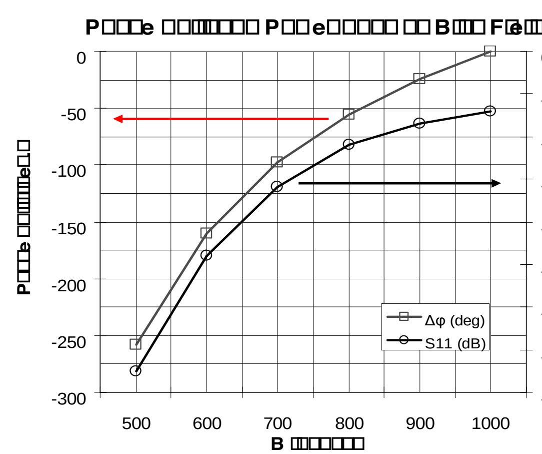


Figure 2: Power loss and phase shift diagram of the phase shifter. 110 mm x 36 mm ferrite-loaded waveguide.

The loss of power becomes more significant at lower bias, although it does not exceed 0.37 dB at 500 G. If the maximum allowed power loss is 0.3 dB, the magnetic bias change from 550 G up to 850 G (±150 G relative to the static bias value of 700 G) results in the phase shift of ~170º.

As a result of the RF stage of the design, the geometry of the ferrite-loaded waveguide, the static bias field level, and the fast bias field change range were chosen. Using this data as an input, magnetic circuit design was made, which is summarized in the next subsection of the paper.

### [illegible]

The static bias field in the YIG blocks is created by permanent magnets; so, only the dynamic bias circuit, which uses copper windings to generate fast changing bias field, will require a power supply. To ensure penetration of the fast bias field in the YIG blocks, the walls of the ferrite-loaded waveguide are made by applying 5-µm copper coating on the surfaces of ceramic plates that form the top and the bottom of the waveguide in Fig. 1. Also, because the permanent magnet material of choice (SmCo-2:17) has electrical resistance similar to that of stainless steel, each permanent magnet block is made of several smaller blocks separated by gaps.

Six-turn fast bias windings are placed around each pole of the device and connected in series. The current in the winding of ±100 A is needed to create the required fast bias field swing of ±150 G. Parameters of the fast bias excitation circuit in Table 1 are shown for the frequencies 1 kHz and 20 kHz. The difference in the parameter values at different frequencies is due to skin effect.

Table 1: Fast Bias Current Circuit Parameter

| f (Hz) | 1000 | 20,000 |
|---|---|---|
| R (mOhm) | 50 | 900 |
| L (µH) | 56 | 36 |
| ωL/R | 6.77 | 5 |
| U (V) @ 100 A | ~40 | ~480 |

The inductance in the fast bias circuit limits the current change rate, which depends on the applied voltage. Based on the inductance data from Table 1, the phase shift rate per 1 V is ~0.02 º/µs. Besides, even with the 5-µm thin waveguide walls, penetration of the magnetic field inside the waveguide will be delayed relative to the current pulse. The field penetration analysis for realistic geometry shows that the time constant of the field diffusion is ~25 µs. Combined phase change delay relative to the voltage pulse is ~10 µs and almost does not depend on the level of the applied voltage. The maximum phase shift rate at 100 V is ~2 º/µs. A higher voltage must be used if a greater phase shift rate is needed.

### [illegible]

Two factors must be taken into account while trying to define the ultimate power the device can handle: the heating of the YIG blocks and electrical breakdown in the ferrite-loaded section of the waveguide. Requirements to the device naturally depend on the power requirements to the accelerating system; they also depend on details of the phase shift algorithm in the low level RF control system. If a superconducting, TESLA-type, nine-cell cavity is used with 25 MV/m accelerating gradient and 10 mA beam current, the required input RF power is ~250 kW. As it was pointed out in [3], accelerating structure must be separated from a vector modulator by a circulator. In this case, each phase shifter in the vector modulator sees only half of the power, or ~125 kW. For this power level and with 3.3% duty factor, the temperature rise in the hottest spot of the YIG blocks is ~10ºC [6].

In our previous work [4] the trapezoidal shape of the YIG blocks was used to avoid the sparking. Other solutions can also be used, e.g. encapsulating the blocks in polyethylene (the absence of gaps between the top of the block and the wall of the waveguide must be ensured), or increasing the air pressure in the waveguide, or filling the waveguide with $SF_6$. Without using any of these measures, in our case, with the input power of 125 kW, the electric field in the 0.5-mm air gap between the YIG block and the waveguide wall reaches ~22.5 kV/cm, which seems marginally OK.

## CONCLUSION

Following the power test of a conceptual prototype of a waveguide-based phase shifter, a design study was undertaken that have resulted in a concept of high power, fast, L-band waveguide-based phase shifter. This concept can be used as a base for future attempts to configure an RF distribution system with the set of parameters different from what was used in this exercise. To complete this development, a prototype of a vector modulator must be built and tested.

## REFERENCES


[1] J. Tuckmantel, “Proposal for the Control of a Multi-Cavity RF System with One Transmitter”, CERN, AB-Note 2003-055, Geneva, Switzerland, 2003.

[2] Y. Kang, “Fast RF Ferrite Phase Shifter for High-Power Applications”, LINAC-2000, Monterey, Ca, Aug. 21-25, 2000, Proceedings, pp. 1012 – 1014.

[3] D. Valuch, High CW Power, Phase, and Amplitude Modulators Realized with Fast Ferrite Phase Shifters, PhD Thesis, Slovak University of Technology, Bratislava, 2004.

[4] B. Foster, et al, “High Power Phase Shifter,” PAC-05, Knoxville, TN, 2005, Proceedings, pp. 3123 – 3125.

[5] I. Gonin, et al, “Waveguide-Based Phase Shifter Performance Study”, FNAL TD Note TD-08-011, April 2008.

[6] T. Khabiboulline, N. Solyak, I. Terechkine, “L-Band, Waveguide-Based, Fast, High Power Phase Shifter”. FNAL TD Note TD-08-025, Sept. 2008.

# MARX BANK TECHNOLOGY FOR ACCELERATORS AND COLLIDERS

J. Casey, R. Ciprian, I. Roth, M. Kempkes, M. P.J. Gaudreau, F. Arntz
Diversified Technologies, Inc., 35 Wiggins Avenue, Bedford, MA 01730 USA

*Abstract*

Diversified Technologies, Inc. (DTI) has developed high power, solid-state Marx Bank modulators for a range of accelerator and collider designs. We estimate the Marx topology can deliver equivalent performance to conventional solid state modulator designs, while reducing system acquisition costs by 25-50%.

In this paper DTI will describe the application of Marx based technology to two different designs, built under two separate DOE Phase II SBIR grants: a long-pulse ILC focused design (140 kV, 160 A, 1.5 ms), and a short-pulse design (500 kV, 265 A, 3 μs). These designs span the known requirements for future accelerator modulators. For the ILC design, the primary challenge is minimizing the overall size and cost of the storage capacitors in the modulator. For the short-pulse design, the primary challenge is high speed operation, to limit the energy lost in the pulse rise-time while providing a very tight (+/-3%) voltage flattop. Each design demands unique choices in components and controls, including the use of electrolytic capacitors in the ILC Marx design.

## INTRODUCTION

In the last decade, advances in high voltage, solid state switches have enabled a new class of Marx modulators, using "opening switch" technology for the basic building blocks. Three key advances are enabled by using this class of switches. First, the switches may open under fault conditions with sub-microsecond response, minimizing the energy discharged into a load arc, and the need for arc protection crowbars. Second, the capacitors may be sized for an arbitrarily small droop during the pulse duration, eliminating the need for pulse forming circuitry. Last, the triggering of the individual stages may be staggered, with the non-triggered stages bypassed via a diode, allowing programmable waveform synthesis within a single high voltage pulse.

We are nearing completion of two Marx development projects funded under the U.S. Dept. of Energy SBIR program. Although both of these projects are inspired by advanced accelerator requirements, the detailed engineering requirements of each are quite different.

## COMMONALITIES TO MARX MODULATORS

The Marx cell is fundamentally composed of an energy storage capacitor and a pulse switch, with a bypass diode spanning them both (Figure 1). When the pulse switch is closed, the capacitor is added in series to the circuit, erecting the high voltage pulse. If the switch remains open, but other cells are closed (and pulse current is flowing), the bypass diode is pulled into conduction and the cell contributes nothing to the series voltage.

This choice – to fire or not to fire the pulse switch – is the key to synthesizing a desired waveform during the pulse. The usual application is to compensate for capacitor droop by firing additional cells as the voltage falls. We can also use such waveform synthesis to actively compensate for transient effects, such as leading edge ringing due to parasitic capacitance.

Between pulses, the energy storage capacitors must be recharged. At very low repetition rates, this charge can be dribbled in with high impedance resistance or high inductance daisy-chain wiring, which carries little current during the erection of the pulse. For short pulse durations, a common-mode choke topology can be used, with differential leads to recharge the capacitors at low impedance, while providing common-mode impedance during the pulse. This technique becomes impractical for long pulse durations, however, as the choke core becomes prohibitively large to avoid saturation. Instead, the technique of choice for long pulses is to use a second string of high voltage switches to supply a charging chain, firing these switches with gating complementary to the pulse switches (Figure 1).

Diversified Technologies has over a decade of experience building series arrays of IGBTs that act as single high voltage switching elements, and are sufficiently robust to use as hard switches in systems over 100 kV. These arrays are ideal for sizing the individual cells of a Marx modulator to optimize the overall system performance. The use of such series arrays can yield further advantage – since IGBTs generally fail short, a properly sized system can lose a single IGBT and

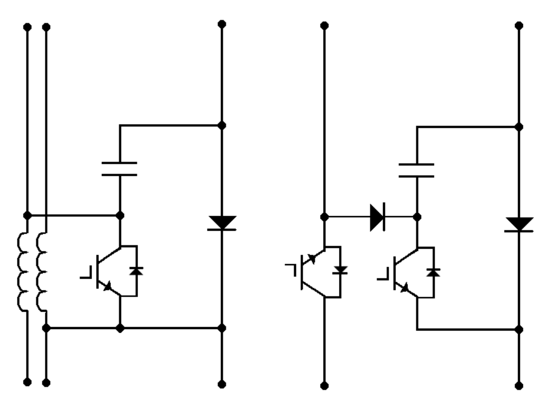

Figure 1: (left) A single Marx cell, recharged via common mode choke, is suitable for short pulses. (right) Long pulses require prohibitively large choke cores, thus recharge is better served via a second switch.

continue to operate at full specification. In order to achieve this capability, there must be a reasonable number (at least five or six) of series IGBTs comprising each cell. Failure of the modulator thus requires double failures within a single cell.

## SHORT PULSE HIGH VOLTAGE MARX MODULATOR

We recently completed a solid state Marx Modulator originally designed for the Next Linear Collider (NLC). After the 2004 decision to back a "cold" machine (the superconducting International Linear Collider, or ILC), this project was orphaned, and later redirected to support the Yale Magnicon development – at similar voltage and pulsewidth (500 kV, 1.5 us), but less current.

The charging topology for the short pulse Marx was naturally chosen to be a common-mode choke scheme. In addition to carrying the two-in-hand conductors for charging the capacitors, this choke carried two additional conductors – one with +400V for local housekeeping power, and one to carry a continuous current for core reset. This last winding comprised fewer turns per coil relative to the common return lead, thus a continuous current feed through the stack biased all cores to offset magnetization current.

The system for NLC was originally designed to be air-insulated, to minimize the effects of parasitic capacitance. In addition, the arrangement of the modules was used to "self-shield" the overall system as much as practical, to further reduce parasitic capacitance. For the Yale Magnicon, power efficiency was no longer critical, but compactness (to meet the existing facility constraints) became essential. As a result, we redesigned the system layout for a highly compact, oil-immersed system.

Our optimization calculations settled on a 12.5 kV cell size for this system, which we implemented with a single 0.6 μF capacitor and a six-stage series switch (Figure 2). Each cell was powered via the common-mode choke, and triggered via fiber-optics. An additional optical feed from each cell reported diagnostic information to ground-based controls.

SPICE models for a 500 kV pulse with a 0.625 μP load, 270 pF load capacitance, and 50 cells showed that we could maintain better than +/-1% flatness of the pulse. We included a small amount of *LR* compensation within each module, yet intentionally underdamped this compensation to decrease risetime. We then eliminated the ringing by firing only 44 stages initially, with several more timed to cancel the ring-up, and the remainder spaced out for the duration of the pulse to cancel capacitor droop. SPICE model runs with a wide variety of load and parasitic changes showed that the authority of the waveform synthesis through timing changes was sufficient to maintain a flat pulse over all reasonable conditions.

The physical layout of the cells included significant Faraday shielding (Figure 2), to protect the control logic, diagnostics, internal power, and gate drives from

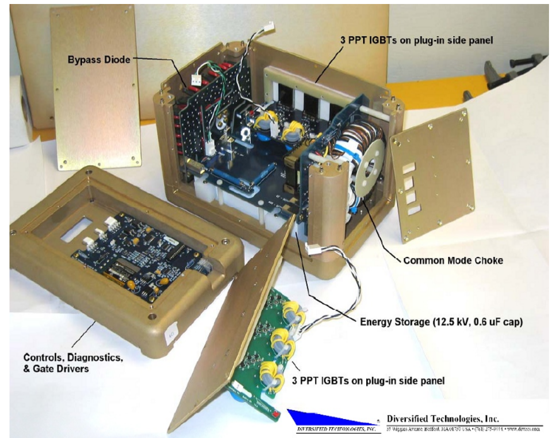


Figure 2: Exploded photograph of a single cell for the short-pulse Marx modulator. This cell has 0.6 uF energy storage, 12.5 kV switching, housekeeping and diagnostics, mounted in a tight Faraday shield.

Figure 3: Nine cells of the short-pulse Marx mounted in a rack for system testing.

transients as other modules are pulsed. We have completed the design, and assembled 9 stages into one rack (Figure 3). With this assembly, we were able to test the controls and pulse output at about 20% voltage (Figure 4). The programmatic delays and scope redirections, as well as the unforeseen expense in machining the Faraday enclosures, precluded completing the full system under the SBIR budget. Completion of the modulator awaits further funding.

## LONG PULSE (ILC) MARX MODULATOR

Our second Marx project was directed towards the ILC, with specifications of 140 kV, 160 A, 1.5 ms, and 5 Hz. Unlike the short pulse system, which gravitated towards Marx topology to attain high speed and avoid 500 kV DC infrastructure, we found that the ILC modulator engineering was completely dominated by the long pulse, and the very large delivered energy per pulse.

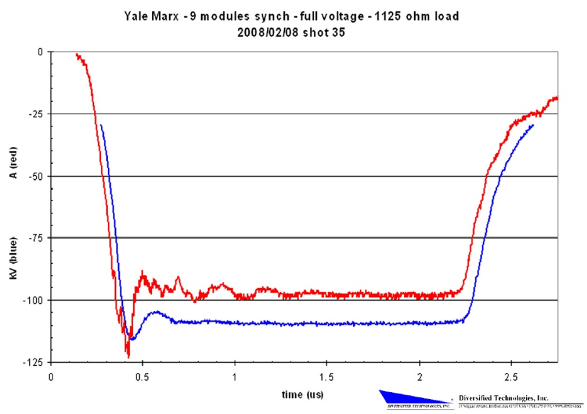


Figure 4: A test pulse of the nine-stage (20%) short pulse Marx has initial charging voltage of 12.5 kV, resulting in 110 kV into 1125 ohms. (Lower/blue: voltage in kV; upper/red: current in amps).

A simple hard switch – or a Marx modulator with simultaneous firing of all cells – would need an energy storage capacitor bank of ~ 1.5 MJ to maintain the specified 1% flattop. This is prohibitive, for reasons of physical size as well as cost. Our preference for a Marx topology is motivated primarily by its capability for waveform synthesis, which allows us to reduce the capacitor bank nearly 10x without sacrificing the 1% flattop specification.

The key to achieving this without unwieldy requirements of high charging currents is to use a dual cell approach. We chose a 6-7 kV cell size for the core cells – each with 8.2 kJ of series electrolytic capacitors and a six stage IGBT switch for pulsing. A second identical switch is used for the charging circuit, eliminating the need for a common mode choke. All of the core modules are fired simultaneously to erect the initial pulse voltage, with high reliability ensured by the *N+1* redundant design.

A hot deck at the top of the core module stack houses a small buck regulator, which steps the 6-7 kV charging supply down to 900VDC. This is passed to the next array of modules, which correct the pulse waveform in 900V steps, ensuring that the 1% pulse flatness specifications are met. No synthesis is necessary for transients – only for droop remediation. We can merely stack the modules in an oil tank, as we do for conventional hard switch modulators at similar voltages (Figure 5).

This project is nearing completion. The corrector modules are completed and tested, and the core modules are in assembly and testing (Figure 6). Full-width pulses have been obtained at partial voltage (Figure 7), and assembly of the tank is complete. Delivery of the full specification system to a DOE laboratory is planned in early 2009.

Figure 5: The ILC Modulator is presently being assembled into a compact unit, for immersion in a 7' x 5.5' oil tank, with controls on top and coax cable pulse output.

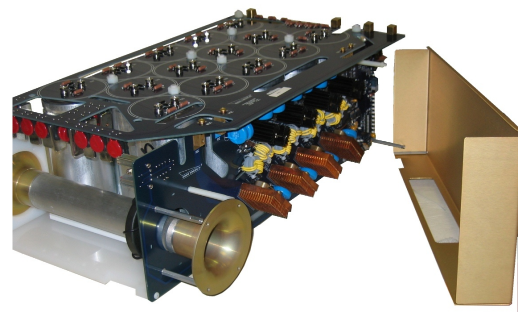

Figure 6: Photo of a long pulse "core" module shows the 8.2 kJ electrolytic capacitor bank and the two four-stage 7kV IGBT switch arrays.

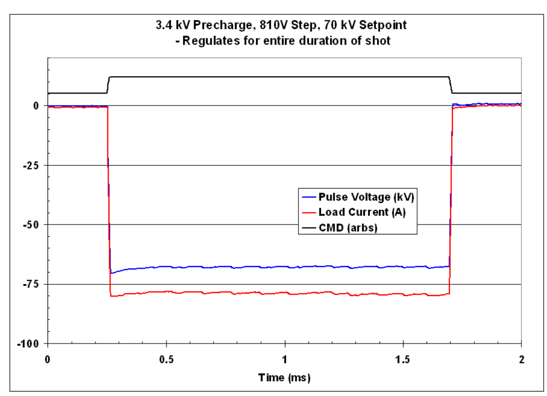


Figure 7: Full 1.5 ms pulse with corrector regulation atop the main high voltage pulse (70 kV into 900 Ohms). The main pulse is constructed through 20 core modules at 3.4 kV each; with the correctors charged to 810 V (+/- 0.6% regulation).

## ACKNOWLEDGEMENT

We gratefully acknowledge the U.S. Department of Energy, and our colleagues at Stanford Linear Accelerator Center, for SBIR funding and fruitful collaboration.

# POWER COUPLER AND TUNER DEVELOPMENT FOR SUPERCONDUCTING QUARTER-WAVE RESONATORS*

J. Wlodarczak#, P. Glennon, W. Hartung, M. Hodek, M. J. Johnson, D. Norton, J. Popielarski,
National Superconducting Cyclotron Laboratory, Michigan State University, East Lansing, Michigan, USA

## Abstract

The construction of a re-accelerator for secondary ion beams is currently underway at the National Superconducting Cyclotron Laboratory (NSCL). The re-accelerator linac will use superconducting quarter-wave resonators (QWR) operating at 80.5 MHz with $\beta = 0.041$ and $\beta = 0.085$. A coaxial probe-type RF fundamental power coupler (FPC) will be used for both QWR types. The power coupler makes use of a commercially available feedthrough to minimize the cost. The FPC has been simulated and optimized for operation at 80.5 MHz using a finite element electromagnetics code. Prototype FPCs have been fabricated and conditioned with traveling wave and standing wave power using a 1 kW amplifier. A niobium tuning plate is incorporated into the bottom flange of the QWR. The tuner is actuated by a stepping motor for slow (coarse) tuning and a stacked piezoelectric element in series for fast (fine) tuning. A prototype tuner for the $\beta = 0.041$ QWR has been tested on the cavity at room temperature.

## INTRODUCTION

NSCL is building a re-accelerator, currently titled ReA3, which will create rare isotope beams (RIBs) for experiments in nuclear science [1]. Stable ions will be produced in an ion source and accelerated by the NSCL Coupled Cyclotron Facility. Particle fragmentation will be used to create a secondary beam. The secondary beam will then be stopped and re-accelerated. This will allow measurements on the exotic beams to be done with higher precision than other techniques.

The first phase of the re-accelerator will accelerate the RIBs up to 3 MeV per nucleon. The superconducting linac will consist of three cryomodules, containing a total of 15 QWRs for either $\beta = 0.041$ or $\beta = 0.085$ [2-4]. Both QWR cavities will utilize similar methods for frequency tuning and RF coupling. Tuning will be done using a slotted tuning plate made from sheet niobium, similar to the designs used at TRIUMF and Legnaro [5,6]. One feature of the NSCL QWRs is the use of separate cavity and insulation vacuum, as opposed to common vacuum, which affects the design of the tuning plate assembly. This plate will provide approximately 20 kHz of tuning for the $\beta = 0.041$ cavities. A fixed probe-type power coupler will penetrate through the tuning plate to transmit power to the cavity. This differs from the adjustable loop-type couplers used at Legnaro and TRIUMF.

This paper will cover the design, prototyping, and testing of both the fundamental power coupler and the tuner for the ReA3 QWRs.

*Work supported by Michigan State University
#wlodarcz@nscl.msu.edu

## COUPLER DESIGN

The FPCs for ReA3 will be coaxial, operating at 80.5 MHz, with fixed coupling and continuous wave (CW) power, with 400 to 800 watts of forward power, depending on the cavity type [7]. A key component of the power coupler is the RF power feedthrough, which will isolate the cavity vacuum and allow cavity pressures of less than $10^{-8}$ torr. The feedthrough is based on a power feedthrough readily available in industry, which helps reduce cost and production time.

A prototype low-$\beta$ cryomodule [8] has been built and tested. The coupler used for the prototype cryomodule test has a small diameter inner conductor and a thin ceramic window [9]. This coupler was designed for lower forward power than needed for ReA3. The updated design incorporates a larger diameter center conductor, thicker alumina window, and less obtrusive air side geometry. These improvements increase the durability, especially during assembly, and power handling capacity of the coupler. The addition of diagnostic ports on the coupler allows the condition of the ceramic window to be monitored. The diagnostic devices consist of a vacuum gauge, current probe, and spark detector. Additionally, a sealed adapter flange is used on the air side, which will be filled with argon gas. In the event of a window failure, the cavity vacuum will be less vulnerable, and the increase in argon can be detected using a residual gas analyzer (RGA).

Several iterations of feedthrough configurations were modeled using Analyst[1], a finite element solver, until an acceptable geometry was found. The S-parameters were also modeled. The final design utilizes a semi-custom feedthrough to allow a more compact size.

After the feedthrough configuration was chosen, an analysis of the mechanical modes of the copper inner conductor was performed. Fundamental modes were found near 30 Hz, and were verified experimentally. Several inner conductors with various lengths of stainless steel liners were modeled, in an attempt to increase this frequency. With an 11 inch (279.4 mm) liner, the frequency was shifted up approximately 7 Hz. Other methods are being investigated to increase the fundamental frequency above 100 Hz.

The heat load to liquid helium from the coupler is a major concern. The total load of the coupler can be

[1] Simulation Technology & Applied Research, Inc., Mequon, Wisconsin, USA.

estimated from the sum of the conducted heat, radiated heat, and RF heating for both the inner and outer conductors. The design specifies that the static heat load should be less than 1 watt. Stainless steel has a much lower thermal conductivity than copper, so the outer conductor is made from 0.035 inch (0.89 mm) wall AISI 316 stainless steel tubing. In order to minimize RF heating, the interior surface of the outer conductor was plated with approximately 8 µm of copper. The location of the 77 K intercept was chosen to produce a total heat load of 1.8 watts and a static heat load of 1 watt to the helium bath.

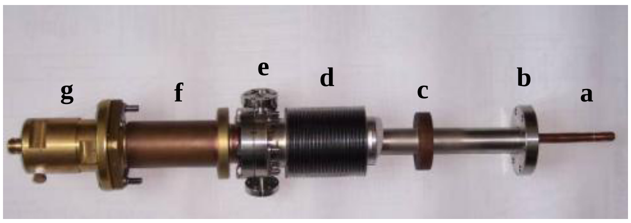


Figure 1: Assembled fundamental power coupler: (a) vacuum side inner conductor, (b) vacuum side outer conductor, (c) 77 K intercept, (d) bellows, (e) diagnostic ports, (f) air side outer conductor, (g) adapter to type N.

## COUPLER TESTING

Four prototype coupler assemblies have been manufactured, as shown in Figure 1. Two of those couplers were assembled tip-to-tip, placed under vacuum, and conditioned using both standing and traveling wave power.

The vacuum components of the FPCs were ultrasonically cleaned and rinsed in class a 10,000 clean room. The feedthroughs were leak tested, and then ultrasonically cleaned and rinsed separately in a weaker cleaning solution. The components were assembled end-to-end with a copper barrel connecting the tips of the two inner conductors. This allowed two couplers to be conditioned simultaneously.

Once the assembly was under vacuum, it was removed from the clean room and baked out. The outer surface of the vacuum section was heated to a temperature of 200° C and baked for 36 hours, until the vacuum no longer showed much improvement. After baking, the vacuum inside the conditioning assembly improved by an order of magnitude.

Standing wave conditioning was done using two sliding shorts, for two reasons. First, this allowed the couplers to be conditioned at higher power than the amplifier could apply alone: the equivalent power in the standing wave was 20 dB higher than the forward power. Second, the moveable shorts allowed the entire surface of both couplers to be subjected to both high voltage and high current. Input power was slowly ramped up to 50 dBm. The system was then left for a period of time to condition. The shorts were then shifted 3 inches (76.2 mm) each, to maintain a frequency of 80.5 MHz, and the process was repeated until the entire length of both couplers was completely conditioned.

The conditioning set-up was next reconfigured for traveling wave to perform a high power endurance test. A power of 1 kW, the amplifier limit, was applied through the couplers and into a matched load for seven days. The temperature of one inner conductor was measured twice using thermal labels: it did not exceed 54° C. The outer conductors reached approximately 50° C.

The assembly was transferred back into the clean room, where it was backfilled with dry nitrogen and stored for future reconditioning tests. The reconditioning will determine how well the conditioning holds after venting.

## TUNER DESIGN

Tuning of the QWRs is done using a thin niobium plate mounted at the base of the cavity. The cavity is tuned by mechanically adjusting the distance between the bottom plate and the tip of the inner conductor. Mechanical actuators apply force to the center of the tuning plate to adjust the position. The plate's outer edge is beveled and pinched between a Nb45-Ti flange (electron beam welded to the outer conductor) and the stainless steel plate which provides the RF contact; an indium seal is used for vacuum, placed just outside the bevel.

Initially, the tuning plate was a flat sheet of niobium. This design was very stiff and limited the tuning range. Two new tuning plates were made from 1.25 mm thick sheet niobium. Concentric convolutions are stamped into the plates and up to 20 slots are EDM cut to reduce the tuning force. The final design is shown in Figure 2. This configuration gives the tuning plates a ± 3 mm range of motion. Modeling was performed on the two slotted designs using ANSYS[2] in order to locate the high stress areas and estimate the forces necessary to actuate the tuner, as shown in Figure 3.

Figure 2: Niobium tuning plate with convolutions, slots, and RF ports.

## TUNER MEASUREMENTS

Room temperature measurements were performed on the new tuning plates, and cold tests were performed on the initial flat tuning plate. The forces necessary to actuate through the full tuning range and the

[2] ANSYS, Inc., Canonsburg, Pennsylvania, USA

corresponding frequency shift were measured. An S-beam load cell was used to measure the force. Some hysteresis was found, as shown in Figure 4, however more analysis will be needed to find the cause. Actuation of the tuner the full ±3 mm range provides approximately 28 kHz of tuning with a maximum force of 600 N. This experimental data agrees with the simulated results.

Actuation of the tuning plate will be provided via a linear stepper motor for coarse tuning and a stacked piezoelectric (PZT) element for fine tuning. Both actuators are at room temperature and feed into the vacuum vessel via bellows. The force is transmitted through concentric tubes, producing a push-pull action between the tuner plate and the cavity flange. Both tubes are 77 K intercepted to reduce the cavity heat load to 0.13 W. The stepper motor has a range of ± 25 mm, and a maximum force of ± 900 N. It has a resolution of nearly 0.04 mm, which equates to approximately 13 Hz per step. The PZT actuator has a range of 0.09 mm and can apply forces of +3000 N to –700 N. The PZT has a closed-loop resolution of 1.8 nm and can shift the frequency approximately 300 Hz total.

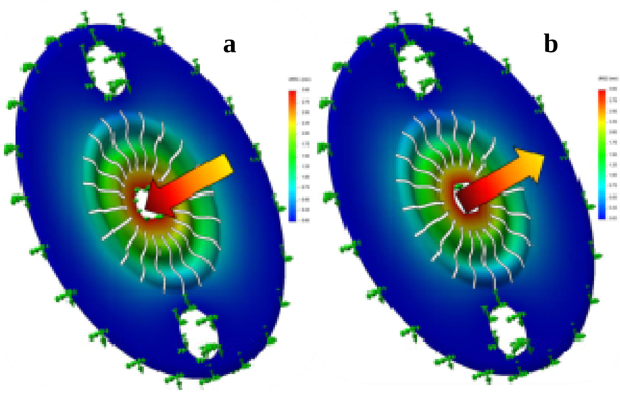


Figure 3: Simulations for a 3 mm displacement (red) of the final tuning plate, (a) pulling and (b) pushing.

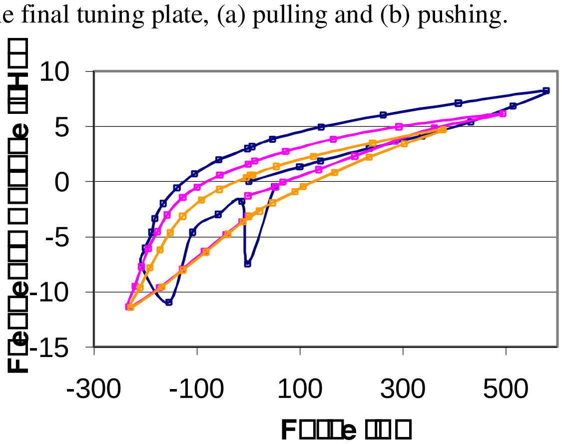


Figure 4: Measured frequency change versus force for the full ±3 mm actuation of the final tuner design.

## CONCLUSION

Prototype tuners and power couplers have been designed and individually tested for the re-accelerator at NSCL. The results show that both components meet their respective design goals. The construction of the cryomodules for ReA3 is underway. The first module will contain a single $\beta = 0.041$ QWR. This will allow the components to be assembled as shown in Figure 5, and tested together in an operational environment.

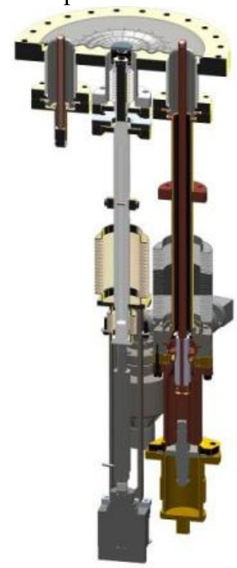

Figure 5: Power coupler and tuner assembly.

## ACKNOWLEDGMENTS

We would like to thank all of the people who helped with the design, fabrication and testing of the tuner and FPC. L. Popielarski, J. Bierwagen, S. Bricker, L. Hodges, J. Vincent, A. Facco (Legnaro) and M. Champion (ORNL) provided valuable assistance with the work done in developing these designs.

## REFERENCES

[1] X. Wu, Presented at [illegible], Paper MO304.
[2] W. Hartung [illegible], in [illegible], Paper TuP14.
[3] W. Hartung [illegible], Paper TUP67.
[4] W. Hartung [illegible] Paper THP033, these proceedings.
[5] T. Ries [illegible], in [illegible], p. 1488-1490.
[6] D. Zenere [illegible], Presented at [illegible], Paper THPP020.
[7] J. Wlodarczak, [illegible], M.S. Thesis, Michigan State University, East Lansing, Michigan, 2008.
[8] M. Johnson [illegible], in [illegible], p. 4317-4319.
[9] A.D. Moblo, [illegible], M.S. Thesis, Michigan State University, East Lansing, Michigan, 2004.

# LEVERAGING THE LEDA HIGH VOLTAGE POWER SUPPLY SYSTEMS FOR THE LANSCE REFURBISHMENT PROJECT*

J. Bradley III, D. Rees, W. Roybal, K. A. Young, LANL, Los Alamos, NM 87545, U.S.A.

*Abstract*

The LANSCE Refurbishment Project (LANSCE-R) will revitalize the LANSCE accelerator infrastructure. Much of the equipment has been in use for over 39 years and is approaching the end of its design lifetime. As obsolescence issues make like-for-like replacements increasingly more expensive, modern systems with lower costs become a reasonable alternative. As part of the LANSCE-R project, four of the seven HV power supplies for the 805 MHz RF klystrons will be replaced. The present and future requirements for these power supplies influence the selection of replacement options. Details of the HV power supply replacement requirements and the different replacement options will be discussed. One option is to use four 95 kV, 21 A DC power supplies originally installed nearby as part of the Low Energy Demonstration Accelerator (LEDA) project. Significant material and labor cost savings can be achieved by leaving these supplies installed where they are and building a HV transport system to bring high voltage power from the existing LEDA facility to the LANSCE facility. The different replacement options will be compared based on material and labor costs as offset by long-term energy savings.

## OVERVIEW OF THE EXISTING LANSCE HVPS SYSTEMS

The LANSCE facility uses seven sectors of 805 MHz klystrons to drive a side coupled 800-MeV proton linac capable of delivering up to 800 kW of beam power. The klystrons require pulsed High Voltage (HV) DC power to operate. The High Voltage Power Supply (HVPS) systems regulate the incoming AC power and convert it to regulated HV DC power. Each sector has a HVPS located just outside the north wall of the klystron gallery and a capacitor room located within the klystron gallery. Underground HV cables transmit the power from the HVPS system to the capacitor room. All of the klystron modulators in a sector draw pulsed HV DC power from that sector's capacitor room.

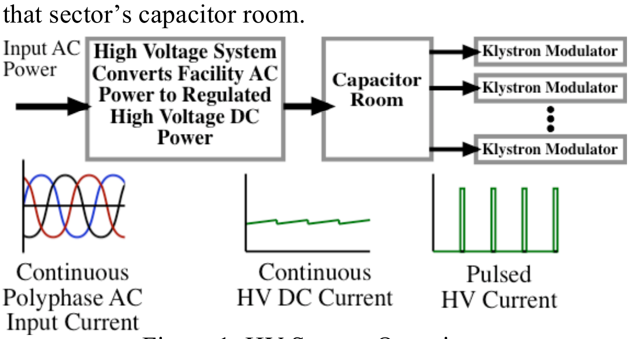


Figure 1: HV System Overview.

*Work supported by the NNSA, U. S. Department of Energy under contract DE-AC52-06NA25396.

Fig 1 diagrams the power flow in the HV system. When the klystron modulators are pulsed on, the peak klystron beam current is provided by the charge stored within the capacitor bank. During the interpulse period when the klystrons are off, the HVPS system recharges the capacitor bank to the nominal 85 kV level.

The existing LANSCE HVPS systems consist of two sub units: an Inductrol® Voltage Regulator (IVR) and a HV step-up Transformer/Rectifier (T/R). The IVR can vary the three phase 4160VAC input power by ±33%. The output of the IVR feeds T/R. Adjustment of the IVR varies the T/R output voltage from 47 to 90 kV. The standard IVR and T/R sub units are both oil filled devices and are shown in Fig 2 . The existing HVPS systems for the seven sectors (B-H) at LANSCE were installed during the late 1960s and early 1970s.

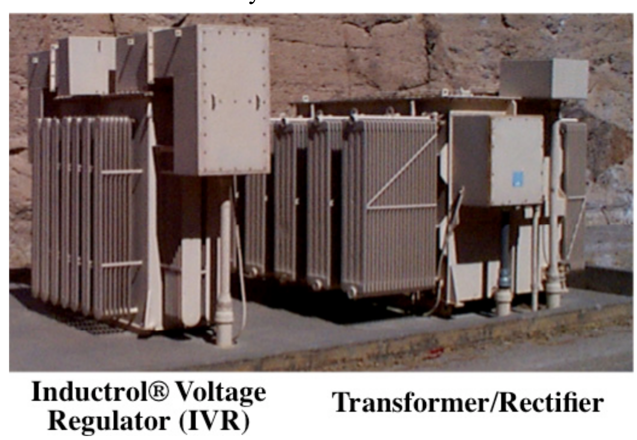


Figure 2: IVR and T/R sub units in the existing LANSCE HVPS systems.

## NEED FOR HVPS REPLACEMENT

The LANSCE HVPS systems are in excess of 30 years old and it is well known in the literature that systems of this age are approaching end of life [1]. Dissolved gas analysis has been adopted as a tool for assessing the status of the LANSCE HVPS systems. The transformer oil is typically sampled on a yearly prior to any reprocessing (cleaning). Because the level of dissolved gases in the oil and the gas evolution within the transformers varies with hours of operation and operating parameters, we use the level of dissolved gas not as an absolute quantitative indicator of health but as a qualitative indicator of which units are experiencing the highest level of age related degradation. The status of the LANSCE HVPS systems is inferred from the dissolved gases within the oil in accordance with the following list [2]:

- Methane, Ethane, Ethylene, and Hydrogen are produced from high temperature thermal heating of oil.

- Acetylene is produced only at the very high temperatures that occur in the presence of an arc.
- $CO_2$ is produced from low temperature thermal degradation of cellulose products.
- CO is produced from high temperature thermal degradation of cellulose products.

IEEE standard C57.104-1991 establishes recommended limits for the types of gases found in the LANSCE transformers. These limits are 2500 ppm for $CO_2$, 350 ppm for CO, 50 ppm for Ethylene and 35 ppm for Acetylene [3]. Table 1 shows how the measured values compare to the IEEE standard. This data indicates thermal degradation of cellulose products in the transformers for Sectors B, D, E and G. Ethylene indicates high temperature heating in Sectors B and E. Acetylene in Sector F transformer indicates arcing may be indicated. Based on the results of the analysis, a minimum of 4 units should be replaced.

Table 1: Existing LANSCE HVPS in FY 2004.

| Location | Gas-in-oil in ppm and Analysis |
|---|---|
| Sector B | $CO_2$ – 8986, CO – 367, Ethylene – 59. $CO_2$ , CO, and Ethylene above IEEE limit. |
| Sector C | All gas levels good. |
| Sector D | $CO_2$ – 3897, CO – 247. $CO_2$ above IEEE limit. |
| Sector E | $CO_2$ – 10607, CO – 440, Ethylene – 109. $CO_2$ , CO, and Ethylene above IEEE limit. |
| Sector F | Acetylene – 84 |
| Sector G | $CO_2$ – 4323, CO – 229. $CO_2$ above IEEE limit. |
| Sector H | All gas levels good. |

## HIGH EFFICIENCY KLYSTRON ENERGY SAVINGS

New high efficiency klystrons have been developed in the four decades years since the first LANSCE klystrons were designed. These high efficiency klystrons increase the RF-to-DC conversion efficiency from approximately 40% with the existing klystrons to approximately 65% with the new klystrons. This will decrease the amount of AC power required to produce the RF power delivered to the cavities by roughly 40%, reducing the four sectors' electricity costs by approximately $650k (US$) per year.

The klystrons will be modulating anode klystrons operating at a maximum cathode voltage of 95 kV, a nominal peak RF output of 1.2 MW, and a nominal duty factor of 10% (120 Hz RF pulse train with 800 microsecond pulses). In order for the klystrons to achieve high efficiency at the LANSCE-R peak power requirement, the HVPS nominal system voltage must be increased from the present 85 kV to 95 kV.

## HVPS REPLACEMENT OPTIONS

The high voltage systems represent the single most expensive component of the LANSCE-RF systems. Four options were considered. The first two options involved the procurement of new HVPS systems. The last two options involved the use of existing HVPS systems left over from a recent project.

### *Procure New HVPS Options*

The first option was replacing the old LANSCE HVPS systems with nearly identical units that could produce the required 95 kV. This option is not viable because not only are the units no longer made by their original manufacturers, but the entire technology of controlling voltage with megawatt sized mechanical variable inductors (Inductrol®s) is obsolete. The risks would include re-engineering old technology that will not be supported in the future.

The second option was to replace the old LANSCE HVPS systems with modern SCR controlled HVPS systems that could produce the required 95 kV. The cost of removing the old systems would be added to the cost of building and installing the new systems. This made removing the old systems and replacing them with the latest technology less cost effective.

### *Utilize LEDA HVPS Options*

Four new SCR controlled HVPS systems were installed across the street from the LANSCE accelerator as part of the Low Energy Demonstration Accelerator (LEDA) that was a part of the Accelerator Production of Tritium (APT) program in the mid 1990's. Table 2 shows how the LEDA HVPS systems are of similar output power ratings to the original LANSCE HVPS systems. While the total output power of the LEDA HVPS systems is less than the output power of the original LANCSE HVPS systems, the increased efficiency of the 95 kV klystrons allows us to generate the same RF power with the lower DC current.

Table 2: Comparison of Original LANSCE HVPS Systems and LEDA HVPS Systems.

| Parameter | HVPS System | |
|---|---|---|
| | Old LANSCE HVPS | New LEDA HVPS |
| Max Output Voltage (kV) | 90 | 95 |
| Max Output Current (A) | 26 | 21 |
| Max HV Output Power (MW) | 2.34 | 2.00 |

The third option was to uninstall the four new LEDA HVPS systems and move them to the unit substations north of the accelerator where the old LANSCE HVPS systems were installed. This is impractical given that the old LANSCE HVPS systems required three-phase 4160V input power feeds and the LEDA HVPS systems require six-phase 1500V input power feeds. The facility transformers to convert three-phase power to six-phase power are extremely large, so it is not economical to move these transformers across the street to the LANSCE accelerator. In addition, the cost of removing the old systems would be added to the cost of installing the new systems.

The fourth option was to leave the four LEDA HVPS systems in place and run HV cables under the road to the klystron galleries 50 meters to the north, as shown in Fig 3. This allows the existing hardware to be reused without the cost of moving it or relocating the input power feeds. The original LANSCE HVPS system could be left in place to serve as a backup system, eliminating the cost of disposal and offering an opportunity for improving reliability through redundancy. The reduced costs allows us to make more of an impact towards addressing other obsolescence and reliability issues within the LANSCE complex. For these reasons we chose the fourth option.


Figure 3: HV cable routing from LEDA power supplies to LANSCE capacitor rooms.[4]

The new LEDA HVPS systems will need to be modified to provide positive fail-safe control from racks located outside the capacitor rooms, 250 meters from the physical HVPS system. Emergency OFF buttons will be located on the T/R sets south of the road and at the four capacitor rooms at LANSCE. Pressing any Emergency OFF button shall open the main circuit breakers at the LEDA substation. The emergency OFF function shall be implemented such that it operates independently of computer control. It must also fail to a safe condition in the event of loss of control power either at the substation or in the klystron gallery.

### *Benefits of Maintaining the Existing LANSCE HVPS Systems as Backup Systems*

The LEDA HVPS systems were designed to be ultra reliable, even when operated continuously at their maximum rated output voltage and current. This reliability was required for the APT accelerator design where over one hundred of the supplies would be simultaneously in use. Even though we expect the new HVPS systems to be much more reliable than the old HVPS systems, failures of the new systems are still possible. The failure of an oil-filled portion of an any HVPS system is typically a very long down time event. Usually specialized rigging and cranes need to be brought on site to remove the T/R subunit. The transformer then needs to be sent to a vendor for rework and repair. Weeks to months of downtime can result.

We intend to connect the LEDA HVPS systems to the first four sectors in a redundant configuration with the existing LANSCE HVPS systems. Nominal operation will be with the LEDA power supplies, but if a power supply should fail, we will be able to reconfigure to the existing sector supply within hours and continue to operate. The new high efficiency klystrons will be able to operate at the reduced voltage capability (90 kV) of the existing supplies at a reduced efficiency. Because the existing LANSCE klystrons are so low in efficiency, it is likely that we will still be able to support full beam operations if we lose a power supply from one of the 6-klystron sectors. If we need to reconfigure a power supply in a 7-klystron sector, we will likely be able to support the full peak beam current after reconfiguration but will probably need to reduce the duty factor by 10 – 20%. This approach should improve the overall reliability of the LANSCE HVPS systems and will also defer the disposal costs for the existing HVPS systems.

### *Challenges of Maintaining the Existing LANSCE HVPS Systems as Backup Systems*

High voltage cables from both new and old HVPS systems will be brought into the capacitor rooms, but only one cable will be connected to the capacitor bank. The unused set will be terminated in a short rated for the maximum output current of the power supply feeding the cable. Engineered controls including captured-key interlock systems will be used to ensure the desired power supply configuration is maintained and to mitigate safety issues.

## CONCLUSIONS

The LANSCE Refurbishment project will replace obsolete equipment that is nearing the end of its design lifetime. The replacement of this equipment can significantly increase the overall electrical efficiency of the AC to RF conversion systems. New, high efficiency klystrons require higher voltages than the existing LANSCE HVPS systems can provide. Completely replacing the existing LANSCE HVPS systems with similar or new technologies was found to be cost prohibitive. Therefore we devised a way to reuse existing 1990s LEDA HVPS systems that were installed at LANL as a part of the APT project. Leaving the new supplies installed in place 50 meters to the south and running the HV output cables under the road to LANSCE was found to be the most cost effective way of upgrading the accelerator. The annual electrical cost savings resulting from the upgrade of four sectors of klystrons and HVPS systems is estimated to be $650k (US$).

## REFERENCES

[1] *Review of Condition Assessment of Power Transformers in Service,* IEEE Electrical Insulation Magazine, Vol: 18, Issue: 6, Nov-Dec 2002, pp. 12 – 25.

[2] *Diagnostic Techniques for Assessing Insulation Condition in Aged Transformer*, IEEE Transactions on Dielectrics and Electrical Insulation, Vol.10, No. 5, October 2003.

[3] IEEE, ''IEEE Guide for the Interpretation of Gases Generated in Oil-immersed Transformers'', IEEE Standard C57.104-1991, 1991.

[4] Satellite view of LANSCE, retrieved July, 2007 from website www.google.com.

# PROGRESS TOWARDS THE LANSCE RF SYSTEM REFURBISHMENT

D. Rees, J. T. Bradley III, S. Kwon, J. T.M. Lyles, M. T. Lynch, M. S. Prokop, W. Reass, K. A. Young,
LANL, Los Alamos, New Mexico

## Abstract

The Los Alamos Neutron Science Center (LANSCE) is in the conceptual design phase of a refurbishment project that will sustain reliable facility operations well into the next decade. The LANSCE accelerator was constructed in the late 1960s and early 1970s and is a national user facility that provides pulsed protons and spallation neutrons for defense and civilian research and applications. The refurbishment will focus on systems that are approaching "end of life" and systems where modern upgrades hold the promise for significant operating cost savings. The current baseline consist of replacing all the 201 MHz rf amplifiers, replacing greater than 75% of the 805 MHz rf systems with a combination of high efficiency klystrons and new klystrons of the existing style, replacing four high voltage systems, and replacing all the low level rf cavity field control systems along the accelerator. System designs and requirements will be presented and the project plan will be discussed.

**CONTRIBUTION NOT RECEIVED**

# NEXT GENERATION IGBT SWITCH PLATE DEVELOPMENT FOR THE SNS HIGH VOLTAGE CONVERTER MODULATOR*

Mark A. Kemp, Craig Burkhart, Minh N. Nguyen, SLAC, Menlo Park, CA, U.S.A.
David E. Anderson, ORNL, Oak Ridge, TN, U.S.A.


## *Abstract*

The RF source High Voltage Converter Modulator (HVCM) systems installed on the Spallation Neutron Source (SNS) have operated well in excess of 200,000 hours, during which time numerous failures have occurred. An improved Insulated Gate Bipolar Transistor (IGBT) switch plate is under development to help mitigate these failures. The new design incorporates two significant improvements. The IGBTs are upgraded to 4500 V, 1200 A, press-pack devices, which increase the voltage margin, facilitate better cooling, and eliminate explosive disassembly of the package in the event of device failure. The upgrade to an advanced IGBT gate drive circuit decreases switching losses and improves fault-condition response. The upgrade design and development status will be presented.


## BACKGROUND

### *SNS HVCM*

The topology of the SNS HVCM is shown in Fig. 1 [1]. There have been numerous upgrades to the original design which have greatly improved the reliability [2]. However, to further improve reliability and to provide voltage regulation of the output pulses at full average power, additional improvements are required. Work is underway at SLAC to develop a new H-bridge switchplate, a part of the modulator which has caused many of the modulator failures. The new design incorporates higher power IGBTs, improved fault current control and an advanced fault-detecting IGBT gate drive.

### *Press-Pack IGBTs*

The press-pack IGBTs selected to replace the flat-pack devices used in the present switchplate, offer several advantages. First, the new IGBTs will have an increased voltage margin (3.3 kV vs 4.5 kV). Second, these IGBTs can be cooled on two sides, which will aid in heat removal. Third, press-pack IGBTs have been shown to have increased reliability in pulsed-power applications [3]. Lastly, unlike the flat-pack devices, the press-pack will not explosively disassemble in the event of an IGBT failure.

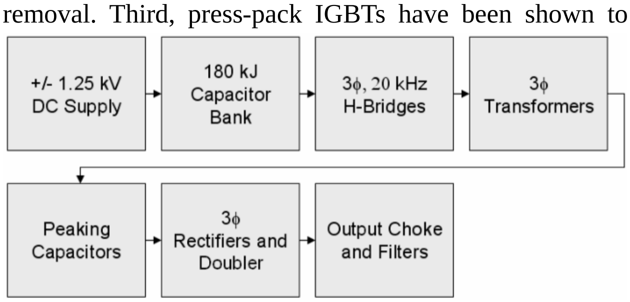


Figure 1: Simplified diagram of the SNS HVCM.

*Work supported by the U.S. Department of Energy under contract DE-AC05-00OR22725. SLAC-PUB-13385
e-mail: mkemp@slac.stanford.edu

## DESIGN

### *Press-Pack Switchplate*

A photograph of the current switchplate is shown in Fig. 2 and the simplified circuit schematic is shown in Fig. 3. The flat-pack IGBTs utilized in the present switchplate design have an advantage in being relatively straightforward to implement mechanically. The anti-parallel diode is in the same package as the IGBT, further simplifying the assembly.

A drawing of the SLAC press-pack switchplate is shown in Fig. 4. Compared to the current design, the press-pack based design has several key advantages in addition to those mentioned above:

- The bottom heat-sink is at the same potential as the

Figure 2: Photograph of one SNS H-bridge card on the SLAC single phase test stand.

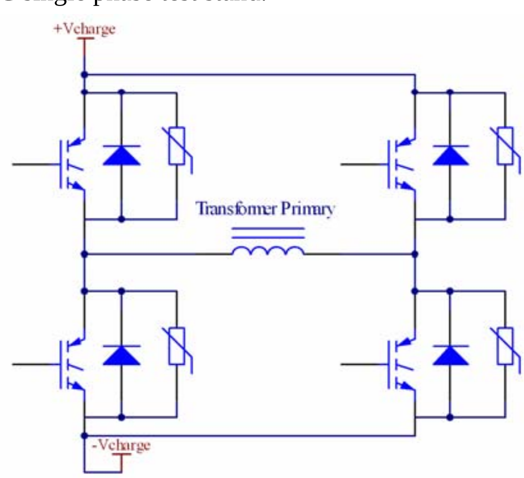


Figure 3: Simplified circuit model of the SNS H-bridge. In the original design, the IGBTs and diodes are in one, flat-pack package and there is no parallel MOV.

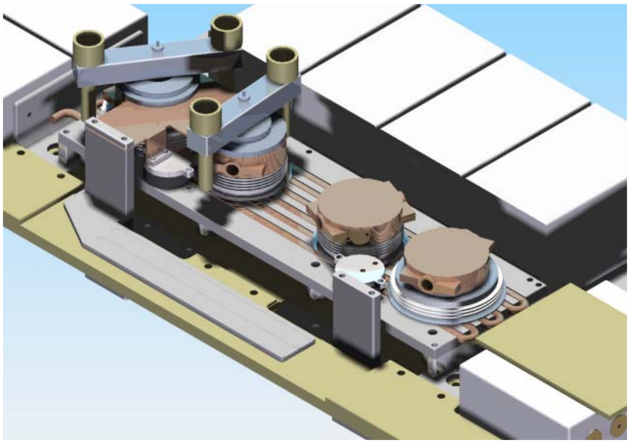

Figure 4: Rendering of the designed press-pack switchplate. Some parts are omitted for clarity.

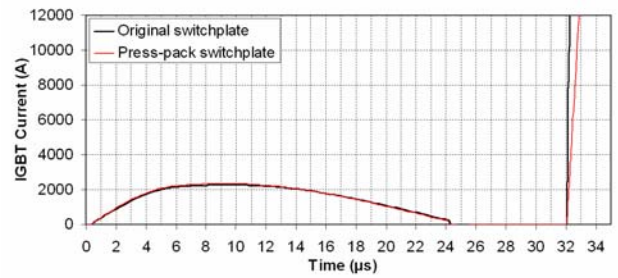


Figure 5: Simulated IGBT current during a shoot-through fault. The opposing IGBT is triggered at ~32 µs.

nearby bus, unlike the current design, which relies on the liberal use of dielectric insulating sheets between the heat sink and bus, which suffer coronic degradation over time.

- The diode will be packaged separately from the IGBT. Diode failure cannot be differentiated from IGBT failure in the flat-pack and a fault in either results in the loss of the entire package.
- A MOV is incorporated to clamp voltage transients.
- The IGBT drivers will be mounted over the side snubber capacitors to improve accessibility.

Finite Element (FE) simulations were used to estimate the inductance of the normal conduction path and the shoot-through fault path (both IGBTs on one side of the H-bridge in conduction) of both designs, as shown in Tab. 1. The inductance of the press-pack plate's normal conduction path is slightly higher, which will increase the transient voltage during switching. This is offset by the increased IGBT breakdown voltage and the MOV that is co-located with the switch and diode. Conversely, the shoot-through inductance of the new design is about twice as large as the original. This increase in inductance will lower the di/dt during a shoot-through fault, decreasing the fault current and increasing the probability that the IGBT can be commutated after a fault is detected.

The FE program generated a matrix of inductance values for each design. These details were added to the model of the SNS modulator that is used for circuit simulation. One simulation result is shown in Fig. 5. The period from zero to ~24 µs on the plot is the normal conduction current through the IGBT. At ~32 µs, a shoot-through condition was induced. The calculated di/dt for the press-pack switchplate is 10 kA/µs, as compared to 45 kA/µs for the original switchplate. For the estimated fault detection and IGBT commutation time of 1 µs, this corresponds to an estimated decrease in commutation current from 45 to 10 kA. Future experiments will be conducted to confirm whether or not this value is low enough to allow detected faults to be suppressed.

Table 1: Values from FE simulation of the total inductance for the shoot-through and normal conducting paths for one leg of the H-bridge. The defined paths are from the +HV to -HV snubber capacitors and ignore the inductance of the transformer, snubber capacitors, and internal IGBT connections.

| Design | Total Path Inductance during Shoot-through | Total Path Inductance during Normal Conduction |
|---|---|---|
| **Original** | 77 nH | 123 nH |
| **Press-Pack** | 153 nH | 171 nH |

### *Gate Driver*

One of the primary motivations for the advanced gate drive development is to improve fault suppression. The existing gate driver has a "fault out" signal which indicates either a power dip or a tripped klixon. The new gate driver will add spurious trigger, excess di/dt, and excess $V_{ce,sat}$ detection. The spurious trigger fault is caused whenever a trigger signal is sent to two IGBTs in a shoot-through path. The gate drivers send a "handshake" enable signal to each other during operation.

The excess di/dt is indicative of a fault that has lowered the impedance of the current path, e.g. a shoot-thru fault. It is detected by a differential voltage measurement between the emitter and a nearby point. The inductance between the two points will induce a voltage proportional to the IGBT di/dt. If the measured voltage is above a preset level, a fault will be indicated.

A second check for excess current through the IGBT is made by monitoring $V_{ce}$, which will increase dramatically if the IGBT current exceeds the saturation value. The new gate driver incorporates a commercial gate driver chip with integral $V_{ce,sat}$ detection. The occurrence of any of the monitored faults will be indicated by a latching LED indicator, and if so configured, terminate modulator triggering.

## EXPERIMENT

### *Single Phase Test Stand*

A test stand was developed at SLAC to simulate the switching conditions of a single SNS H-bridge switchplate. It was designed to match the switching voltage as well as the peak and commutation currents through the IGBTs. An example waveform is shown in

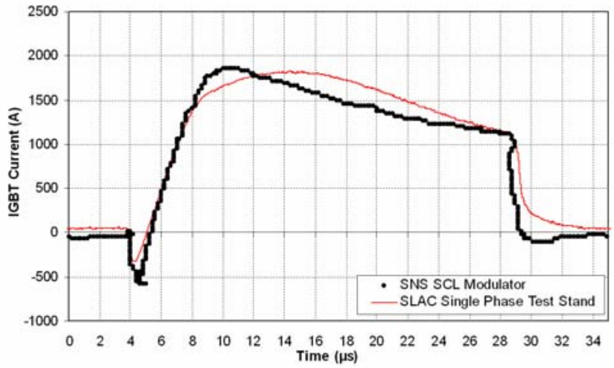


Figure 6: Comparison of the measured IGBT current in a SNS SCL modulator to the SLAC single phase test stand.

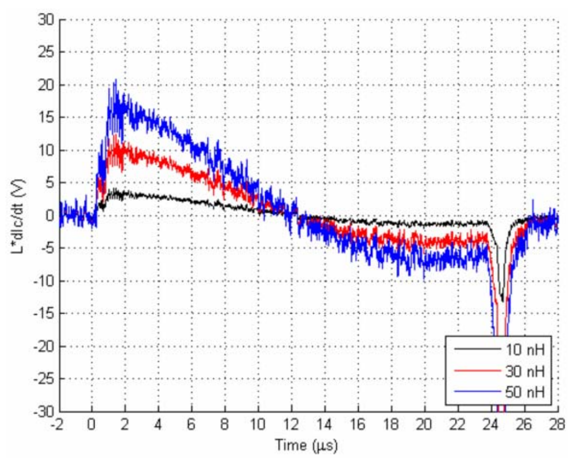


Figure 7: Calculated L*dI/di using measured IGBT collector current values and three estimated inductance values.

Fig. 6. This test stand provides a convenient platform to evaluate the impact of switchplate modifications. Additionally, fault conditions can be simulated in a controlled environment.

The test stand has been used to evaluate the efficacy of using a di/dt measurement to detect the onset of a current fault condition, e.g. shoot-thru. Using the test stand, the IGBT collector current was measured and di/dt was calculated. Fig. 7 illustrates the expected diagnostic response for three different inductance values. The preliminary estimate of the diagnostic's differential voltage measurement path inductance is 30nH. Therefore, the normal signal, ~10V maximum, is large enough for good signal-to-noise, but significantly less than expected under fault conditions, 30 V for 1 kA/µs. Future, measurements using the single phase test stand will confirm nominal and fault condition behavior.

### *Single Device Test Stand*

The SLAC 2-pack test stand was modified to provide a platform to evaluate candidate IGBTs and gate drivers for the switchplate upgrade. The IGBT emitter is ground referenced in the test stand to simplify the measurement of gate and collector voltages coincident with emitter current under switching, normal conduction, and fault conditions. The test stand inductively couples the IGBT

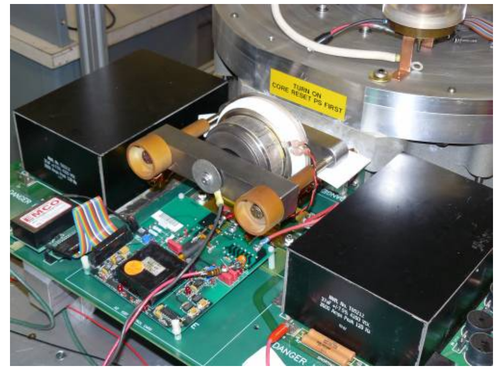

Figure 8: Photograph of the single device test stand with a press-pack IGBT.

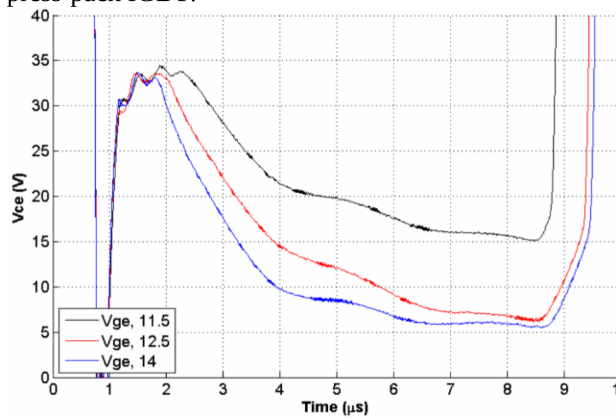


Figure 9: Vce values measured on the single device test stand for various values of Vge.

under test to a 1 ohm load. A photograph of part of the test stand with a press-pack IGBT is shown in Fig. 8.

One preliminary test result is shown in Fig. 9. The $V_{ce}$ voltage was measured for a range of applied gate voltages. The gate voltage should be low to minimize the IGBT saturation current, for protection during a fault condition. However, low gate voltage increases the IGBT losses during normal operation. The test stand aids in identifying the appropriate levels.

## SUMMARY

An advanced switchplate for the SNS HVCM, incorporating press-pack IGBTs and improved gate drivers, is under development at SLAC. Test stands to evaluate the improved switchplate and key components under nominal and fault conditions have been developed and commissioned at SLAC. The switchplate design has been finalized and commissioning is currently underway. Future work will include further testing of these devices under nominal and fault conditions.

## REFERENCES

[1] W.A. Reass, *et al.*, IEEE Trans. Plasma Sci. 33 (2005) 1210.

[2] D.E. Anderson, *et al.*, Power Modulator Symposium 2006, p. 427.

[3] F. Wakeman, *et al.*, Pulsed Power Plasma Science Conference 2001, p. 1051.

# ILC MARX MODULATOR DEVELOPMENT PROGRAM STATUS*

C. Burkhart#, T. Beukers, R. Larsen, K. Macken, M. Nguyen, J. Olsen, T. Tang,
SLAC, Menlo Park, CA 94025 USA, U.S.A.

*Abstract*

Development of a first generation prototype (P1) Marx-topology klystron modulator for the International Linear Collider is nearing completion at the Stanford Linear Accelerator Center. It is envisioned as a smaller, lower cost, and higher reliability alternative to the present, bouncer-topology, "Baseline Conceptual Design." The Marx presents several advantages over conventional klystron modulator designs. It is physically smaller; there is no pulse transformer (quite massive at ILC parameters) and the energy storage capacitor bank is quite small, owing to the active droop compensation. It is oil-free; voltage hold-off is achieved using air insulation. It is air cooled; the secondary air-water heat exchanger is physically isolated from the electronic components. The P1-Marx employs all solid state elements; IGBTs and diodes, to control the charge, discharge and isolation of the cells. A general overview of the modulator design and the program status are presented.

## INTRODUCTION

The International Linear Collider (ILC) will require 576 RF stations. Each 10 MW L-band klystron will require a modulator capable of; 120 kV, 140 A, 1.6 ms (27 kJ) at 5 Hz repetition rate. The existing Baseline Conceptual Design (BCD) is a transformer-based topology. The large size, weight, and cost of this transformer, owing to the long pulse length, have motivated research into alternative topologies that do not employ power magnetics.

The P1-Marx [1] modulator uses solid-state switches and isolation elements to connect capacitors in parallel while charging but in series during discharge to generate high voltage output without the use of a transformer.

## DESIGN OVERVIEW

The topology is illustrated in Fig. 1. A diode string provides a path for charging the 50 μF capacitor of each of the 16 Marx cells to 11 kV and isolation between the cells during erection. Likewise, a second diode string provides a path for auxiliary power to each cell. A charge switch in each cell provides a common return path for both power sources.

Closure of a fire switch will produce a -11 kV output pulse from the cell; closure of additional switches will increase the output by -11 kV for each cell that is fired. The by-pass diode provides a conduction path to the load through the cells that have not been fired. The series inductor limits dI/dt of the output current.

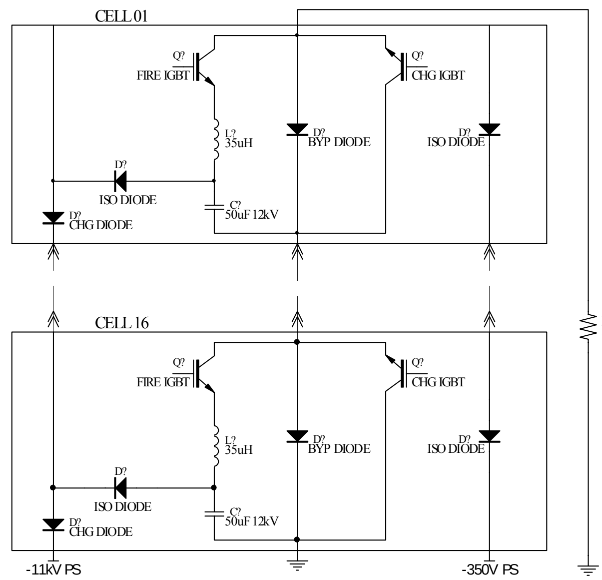


Figure 1: Simplified schematic diagram of the SLAC Marx.

Eleven cells are triggered to produce the required output voltage. As the energy storage capacitors discharge, the output voltage drops. Once it has decreased by 11 kV, in ~0.35 ms, an additional cell is triggered to bring the output back to 120 kV. This proceeds sequentially through the remaining five cells to provide coarse, ±5%, pulse flattening.

The output will be further regulated to ±0.5% by a second Marx, the vernier regulator, in series with the main Marx. The topology of the vernier is similar to the main Marx, however each of the 16 cells is charged to 1.2 kV. These are fired sequentially to generate a stair-step waveform, which is added to the main Marx to maintain an approximately constant output voltage.

### *Marx Structure*

Fig. 2 is a photo of the P1-Marx modulator. A steel structure supports the modulator components and the control system (not visible, outside the enclosure in the front of the support structure). A hollow, cantilevered beam supports the individual Marx cells, forms a duct to direct the forced air coolant, and houses the control system fiber optic cables. It also supports a PCB backplane that provides the electrical interconnections between cells. When a cell is installed, it hangs from the beam, plugs into connectors on the backplane, and aligns the fiber optic lenses with those in the beam to transmit and receive optical control and diagnostic information.

*Work supported by the U.S. Department of Energy under contract DE-AC02-76SF00515
#burkhart@slac.stanford.edu

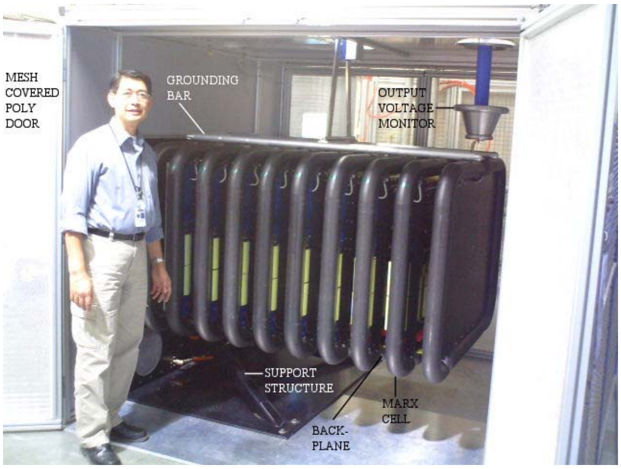


Figure 2: Photo of the P1- Marx.

A grounding bar is lowered from supports above the modulator to ground out all cells for personnel protection during servicing. A high voltage divider is used to monitor the modulator output.

The design is intended to simplify maintenance. A cell is removed by lifting it off the backplane and a replacement cell is then set in place; there is no wiring to remove or install. Ambient air provides high voltage insulation. The polycarbonate panels in the enclosure door allow visual observation during developmental testing, while the internal mesh provides a bonded electrostatic enclose. The 0.38 m spacing between the cell structure and enclosure walls provides sufficient insulation for the Marx voltage.

## Marx Cell Design

The Marx is a fundamentally modular topology, with inherent cost and maintenance advantages. The P1-Marx design fully exploits this trait. A Marx cell, shown in Fig. 3, consists of a PCB motherboard on which connectorized, modular components are mounted. The motherboard is supported by a backing frame that also supports the equipotential ring that surrounds the cell. The energy storage capacitor, capacitor discharge relay and resistor, and series inductor are permanently mounted on the motherboard; all other major components are modular.

The charge and fire switches are each an array of IGBTs, five modules connected in series. Each module uses three parallel IGBTs that are controlled by a common driver. During transient conditions, the voltage distribution between the series switches will be non-uniform. To protect the IGBTs from damage, over-voltage protection is incorporated into each switch module. The isolation boards translate auxiliary power and control signals from the reference potential to the emitter potential of each switch module. The control board, auxiliary power, and equipotential ring are referenced to the cell output potential.

The diodes; charge, charge isolation, by-pass, and auxiliary (on the same PCB as the by-pass) are each an array of eighteen series 1200 V ultra-fast soft-recovery devices with a parallel MOV to assure uniform voltage distribution.

A CPLD on the control board sequences the firing of the charge and fire switches; the charge switch is gated off 10 μs before the fire switch is gated on and then back on 10 μs after the fire switch is gated off. The delays eliminate the shoot-through condition that would occur if both switches were on simultaneously. Both switches are monitored for an over current condition, which if detected remove the gate pulse from the switch.

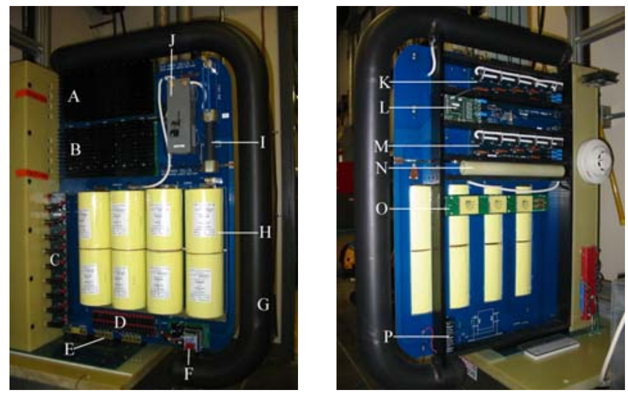


Figure 3: Photo of Marx cell, front (left) and rear (right), noting major elements. A: Charge IGBT module, B: Fire IGBT module, C: Charge diode, D: By-pass diode, E: Backplane connector group, F: Auxiliary power dc-dc converters, G: Equipotential ring, H: Energy storage capacitor, I: Discharge resistor, J: Discharge relay, K: Isolation board for charge switch, L: Control board, M: Isolation board for fire switch, N: Series inductor, O: Charge isolation diode, P: Auxiliary power storage capacitor

## Control System

The Marx employs a FPGA-based control system. A diagnostic module, with a jumper configurable address, is attached to the control card in each cell. Communication to the system ground station is over 60 Mb/s fiber optic data lines using point-to-point serial protocol. In the ground station, a FPGA communicates with a ColdFire processor, which provides the system's RTEMS-based EPICS IOC. The EPICS database contains the timing information, entered by the operator, and status and diagnostic information communicated from the Marx cells.

The diagnostic module passes timing information to the control board CPLD to coordinate the timing of the Marx cells. The diagnostic module also has four analog input channels to monitor voltages and currents on the Marx cell. The channels are monitored at 20 kS/s with a resolution of 16 bits. A fast transient recorder can also be triggered to capture each of the channels at 30 MS/s with an 8-bit resolution into a 2 kS buffer.

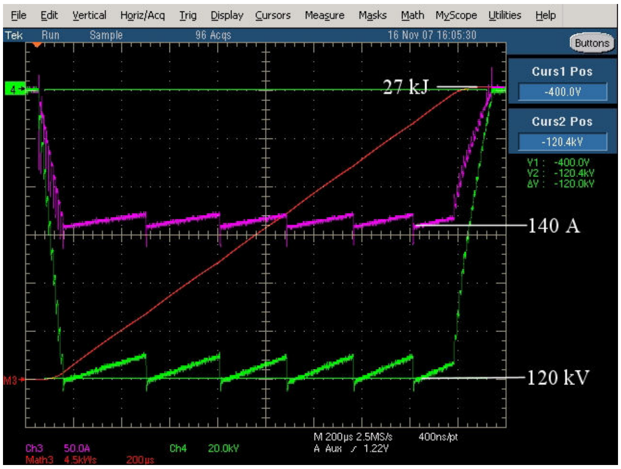


Figure 4: Marx output with coarse flattening, Ch3 is load current, Ch4 is load voltage, and Math3 is load energy.

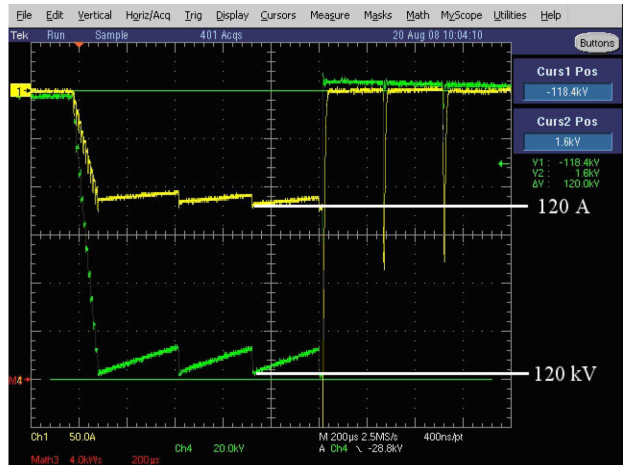


Figure 5: Arc-down test of Marx during full voltage operation, Ch1 is load current and Ch4 is load voltage.

## TEST RESULTS

Individual modules are extensively tested for quality control purposes. Qualified modules are assembled into Marx cells, which are individually tested to 12 kV and 150 A. Cells are tested under normal operating conditions and short-circuit conditions. The over-current protection circuitry gates off the fire switches if the cell current exceeds 180 A. The turn-off delay is ~1.4 µs, which limits the peak cell current to ~600 A.

Once cells have been qualified, they are assembled as a Marx. The vernier regulator is still under development, so the modulator is run with only coarse pulse flattening at present. Infrastructure issues currently prevent operation at full power, the modulator is run at either 1.6 ms pulse width and reduced PRF or at 5 Hz and reduced pulse width. The former is illustrated in Fig. 4. The turn on, and off, of the cells is staggered to reduce the peak current into the long cable that connects the modulator to the load in the test configuration. In the ILC implementation the cable would be eliminated, as could be the triggering delays, shortening the rise and fall times.

Arc-down tests were performed to simulate modulator behavior during a klystron arc. A spark-gap switch was installed in parallel with the test load. The switch was self-triggered, approximating the random nature of a klystron arc. Typical data for a 16-cell test is presented in Fig. 5 and 6. This event occurred ~15 µs after the third delay cell was triggered. The voltage rapidly collapses and the current rises. The maximum dI/dt is inductively limited, ~0.5 mH internal inductance in the modulator and ~0.3 mH at the load to protect the klystron from the energy stored in the cable from the modulator. The peak fault current, ~0.5 kA is consistent with the test results for individual cells. The energy deposited into a klystron from such an event would be limited to a safe level, ~10 J. At present, the cells individually detect and react to the over-current condition. Hence, delay cells 4 and 5 subsequently turn on, detect the fault, and turn off. System over-current detection will be added to the controls to provide a back-up and prevent these additional

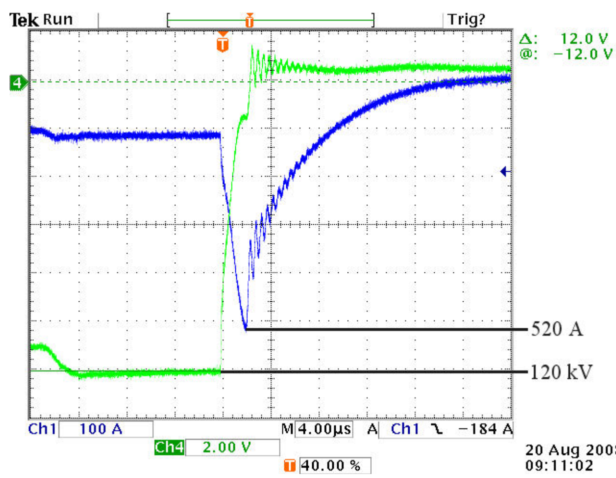


Figure 6: Detail of full voltage arc-down test, Ch1 is load current and Ch4 is load voltage.

pulses. Detailed examination of the voltage waveforms indicates good voltage sharing between cells under this transient condition.

The P1-Marx developmental testing is nearing completion. During the next quarter, it will be installed in a new L-band test facility at SLAC. The test facility will provide a platform for extensive life testing of the modulator and the new Toshiba 10 MW L-band klystron during FY09.

## ACKNOWLEDGMENT

The authors wish to acknowledge the significant contributions of D. Anderson, C. Brooksby (LLNL), R. Cassel, E. Cook (LLNL), G. Leyh, D. Moreno, P. Shen, and A. Viceral to the SLAC Marx development program.

## REFERENCES

[1] G.E. Leyh, “Development and Testing of the ILC Marx Modulator,” Proc. of PAC07, Albuquerque, NM, pp. 849-851, 2007.

# RF VECTOR CONTROL FOR EFFICIENT FAN-OUT POWER DISTRIBUTION *

Y. W. Kang, Oak Ridge National Laboratory, Oak Ridge, TN, USA


*Abstract*

Distributing RF power of a generator to many cavity loads is often considered in RF linacs for possible cost reduction and simplification of system. If the amplitude and phase of the power delivered to individual cavity have to be controlled precisely, using fixed power splitting system may not be satisfactory. An approach for fan-out RF power distribution using transmission line circuit parameters for achieving full vector control and maximum power efficiency is considered. This fan-out distribution approach can provide required RF power to the cavities by adjusting the transmission line phase delays between the cavities and reactive loads at the cavity inputs. In this approach, the phase delays and the reactive loads become the RF control parameters for delivering a set of required cavity RF voltages for an entire system.


## INTRODUCTION

Many high power RF accelerators may have to drive one cavity with one RF generator if independent and accurate RF vector control is required. Fan-out power distribution system feeding many cavities with a high powered generator can be useful for large scale high powered systems, especially for SRF ion accelerators, to reduce construction costs and save on operating costs. Various RF power distribution systems have been used and proposed in [1] and often pulse compression is combined for short pulse systems. Mechanically variable directional couplers are employed for an adjustable distribution [2]. RF distribution systems using high power vector modulators have been considered for fast control [3]. Using a vector modulator at a cavity input with a fixed power splitting requires more power than the power required in the cavity to enable adequate RF control.

A fan-out distribution presented in this paper can use only the power required to maintain right RF voltages in the cavities with a transmission line network. This approach can maximize the RF power to beam efficiency of a fan-out system. The multi-cavity system is controlled as a whole for various operation condition of the accelerator. The vector control is done by adjusting phase delays between the load cavities and reactive loads at cavity inputs. The reactive loads and transmission line phase delays can be realized using high power RF phase shifters.

Figure 1(a) shows an arbitrary fan-out power distribution system for a particle accelerator with N cavities. There can be various ways to construct a fan-out power distribution system using a transmission line network: one approach is shown in Figures 1(b) with the loads connected in parallel to the transmission line and 1(c) with the loads connected in series. The two types of connections may be mixed if construction and operation can benefit.

* SNS is managed by UT-Battelle, LLC, under contract DE-AC05-00OR22725 for the U.S. Department of Energy.

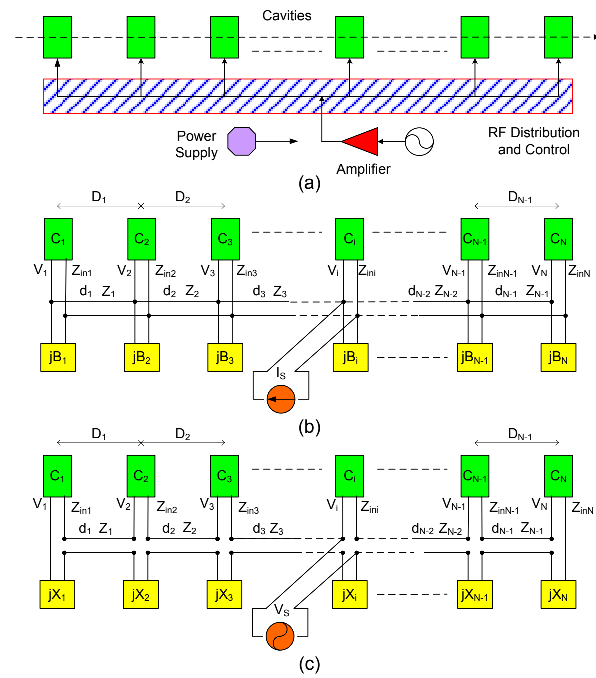


Figure 1: (a) Generalized high power RF distribution in a multi-cavity accelerator, (b) using transmission line network with loads and control elements connected in parallel, (c) using transmission line network with loads and control elements connected in series.

## DEVELOPMENT

The transmission line network shown in Figure 1(b) can be synthesized and analyzed using short-circuit admittance parameters and the network in Figure 1(c) can be treated using open-circuit impedance parameters similarly [4]. Although either one of the approaches can be used, it seems the parallel connection can be more practical in using various transmission lines. The design in Figure 1(b) using the short-circuit admittance parameters is discussed in the following.

Generally, in an accelerator, the cavity input impedances and the required load voltages are known for an operating condition. Therefore, in a network shown in Figure 1(b), any two of the three unknown parameters, transmission line characteristic impedance, $Z_i$, electrical length between the two neighboring loads, $d_i$, and the reactive loads, $B_i$ can be varied for having the required voltages at the cavities. Among the above possibilities, the most practical way of having adjustable transmission line network is to have a uniform characteristic impedance $Z_o$ ($Z_i = Z_o$ *for* $i=1,.., N-1$) and find $d_i$ and $B_i$.

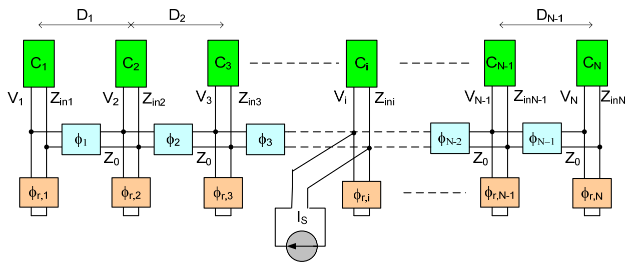


Figure 2 – A fan-out power distribution system in Figure 1(b) realized using phase shifts in transmission line phase delays and reactive loadings

In Figure 1(b), N cavities are fed by a single generator at the *i-th* terminal through a transmission line network. $D_i$ is the physical spacing between two neighboring cavities, $V_i$ is the voltage delivered to the cavity input, $Z_i$ is the transmission line characteristic impedance, and $Z_{in,i}$ is the cavity input impedance. If $[V^P]$ is a set of voltages for a specific cavity excitation at a time, the phase delays through the transmission line sections between the cavities and the reactive loads that can deliver $[V^P]$ can be found. The transmission line delays (lengths) and reactive loads can be realized by using phase shifters as shown in Figure 2 with phase shifts $\phi_n^T = \beta d_n$ and $\phi_n^L = \cot^{-1}(-B_n/Y_o)$, respectively.

## *Formulation*

Using the short-circuit admittance parameters [Y], the whole network admittance matrix $[Y^S]$ can be constructed and the terminal currents $[I^S]$ and the terminal voltages $[V^P]$ are related as

$$[I^S] = [Y^S][V^P] \tag{1}$$

where $[Y^S]$ is the short-circuit terminal admittance matrix of the whole system that can be expressed as

$$[Y^S] = [Y^P] + [Y^T] + [Y^L] \tag{2}$$

where $[Y^P]$ is the input port admittance matrix for the cavities, $[Y^T]$ is admittance matrix of the transmission line network, and $[Y^L]$ is reactive load admittance matrix.

The voltage vectors that are required to maintain a specific voltage distribution over the cavities are

$$[V^P]^t = [V_1 \quad V_2 \quad V_3 \quad \cdots \quad V_N] \tag{3}$$

$[I^S]$ contains all zero elements except for the *n-th* terminal that is connected to the generator. The current for the feed terminal is found as

$$Z_f = V_f / I_f \tag{4}$$

where the input impedance $Z_f$ can be found by selecting the element $Z_{ii}$ in the impedance matrix $[Z^S]=[Y^S]^{-1}$. For a system shown in Figure 2, the port admittance matrix for the cavity inputs

$$[Y^P] = \begin{pmatrix} Y_{in,1} & 0 & \cdots & 0 & 0 \\ 0 & Y_{in,2} & \cdots & 0 & 0 \\ \vdots & \vdots & \ddots & \vdots & \vdots \\ 0 & 0 & \cdots & Y_{in,N} & 0 \\ 0 & 0 & \cdots & 0 & 0 \end{pmatrix} \tag{5}$$

which is simply a diagonal matrix with $Y_{in,ii} = 1/Z_{in,ii}$ since no mutual coupling is assumed between the cavities. The reactive load admittance matrix

$$[Y^L] = \begin{pmatrix} jB_1 & 0 & \cdots & 0 \\ 0 & jB_2 & \cdots & 0 \\ \vdots & \vdots & \ddots & \vdots \\ 0 & 0 & \cdots & jB_{N+1} \end{pmatrix} \tag{6}$$

The transmission line admittance matrix

$$[Y^T] = \begin{pmatrix} -jY_1 \cot\beta d_1 & jY_1 \csc\beta d_1 & 0 & \cdots & 0 \\ jY_1 \csc\beta d_1 & -j(Y_1 \cot\beta d_1 - Y_2 \cot\beta d_2) & jY_2 \csc\beta d_2 & \cdots & 0 \\ 0 & jY_2 \csc\beta d_2 & -j(Y_2 \cot\beta d_2 - Y_3 \cot\beta d_3) & \cdots & 0 \\ \vdots & \vdots & \vdots & \ddots & \vdots \\ 0 & 0 & 0 & \cdots & -jY_N \cot\beta d_N \end{pmatrix} \tag{7}$$

A system of equations can be established with Eqs (5) – (7) in Eq. (1) and solved for $d_i$ and $B_i$ with a set of given cavity voltages $[V^P]$. The total power delivered to the loads is the sum of real power flow to the loads and must be equal to the output power of the generator. This enables the complete impedance matching of the generator at the feed terminal. Detailed solution procedure for this fan-out approach was outlined in [5].

Note that there can be several different methods to achieve the impedance matching at the *i-th* terminal for the generator input: $C_i$ is connected to the port with the generator as in Fig. 1(b), $C_i$ is removed to construct a simple Y-type connection to the generator, or with $C_i$ one more reactive loading is used at the generator output.

## *Load Condition*

The above solution includes all mutual couplings associated with the multiple transmissions and reflections at and between the cavity terminals. Note that $V_k = 0$ if no power is applied at the *k-th* cavity input. This can be the case for a disabled or a detuned cavity in practical systems.

If a cavity is connected through a transmission line section and not impedance matched, the connecting line section can be included with an additional short-circuit admittance matrix [Y]. Or the mismatch through the transmission line section between the cavity and the terminal can be included by considering the standing wave with a reflection coefficient Γ(z). For a mismatched cavity load, the port admittance matrix at the terminal before the input of a cavity is

$$Y_{in,i} = Y_o \frac{Y_i^c \cos\beta d_i^c + jY_o \sin\beta d_i^c}{Y_o \cos\beta d_i^c + jY_i^c \sin\beta d_i^c} \qquad (8)$$

where $Y_o$ and $d_i^c$ are the characteristic impedance and the length of the transmission line section connects the cavity to the network, respectively; $Y_i^c$ is the cavity input impedance, and $\beta$ is the phase constant. The voltage standing wave in the transmission line section between the cavity and the terminal is $V(z) = V_o^+ e^{-j\beta z}\{1+\Gamma(z)\}$ where voltage reflection coefficient is related to load reflection coefficient $\Gamma(0)$ as $\Gamma(d_i^c) = \Gamma(0)e^{-2j\beta d_i^c}$. The knowledge of the reflection and the field inside the cavity can define the voltage vectors that need to be satisfied for an operating condition.

### *Example*

An example case of the fan-out power distribution system with uniformly spaced 14-cavity loads with a generator connected at the center of the network (at $i$=8) is considered. No cavity is connected to the terminal with the generator. Each cavity has 50-ohm input impedance and all the transmission line sections have 50-ohm characteristic impedance. All physical distances between two neighboring cavities are set to 1.5m. Two sets of voltages are used and results are compared: (1) a set of voltages for excitation of the cavities are specified for this example and (2) the same voltages except $V_{10}$=0 to simulate a disconnected or a disabled cavity. The specified voltages and resulting computed phases to achieve the $d_i$ and $B_i$ are shown in Table 1. The frequency of operation is 805 MHz. For $B_i$ a short circuit is assumed at the end of the phase shifter.

Table 1: An example case with 14 loads

| Cav | $V_i$ (V) | $\phi$ for $d_i$ (deg) | $\phi$ for $B_i$ (deg) | Cav | $V_i$ (V) | $\phi$ for $d_i$ (deg) | $\phi$ for $B_i$ (deg) |
|---|---|---|---|---|---|---|---|
| 1 | 1.0000/09.90° | 195.31 | 53.58 | 1 | 1.0000/09.90° | 195.31 | 53.58 |
| 2 | 1.1892/22.74 ° | 189.22 | -89.33 | 2 | 1.1892/22.74 ° | 189.22 | -89.33 |
| 3 | 1.3161/37.00 ° | 186.81 | -71.85 | 3 | 1.3161/37.00 ° | 186.81 | -71.85 |
| 4 | 1.4142/52.75 ° | 185.45 | -59.54 | 4 | 1.4142/52.75 ° | 185.45 | -59.54 |
| 5 | 1.4953/68.30 ° | 184.58 | -49.99 | 5 | 1.4953/68.30 ° | 184.58 | -49.99 |
| 6 | 1.5651/85.00 ° | 184.01 | -42.51 | 6 | 1.5651/85.00 ° | 184.01 | -42.51 |
| 7 | 1.6266/102.27 ° | 133.68 | 46.97 | 7 | 1.6266/102.27 ° | 136.19 | 44.40 |
| (8) | 6.1352/0 ° | 162.95 | 11.27 | (8) | 5.8718/0 ° | 161.21 | 11.90 |
| 9 | 1.7321/138.27 ° | 177.34 | 4.45 | 9 | 1.7321/138.27 ° | 179.95 | 0.02 |
| 10 | 1.7783/156.90° | 176.66 | 24.98 | 10 | 0.0000 | 179.95 | 0.00 |
| 11 | 1.8212/175.92 ° | 175.60 | 30.31 | 11 | 1.8212/175.92 ° | 175.60 | 0.02 |
| 12 | 1.8612/195.28 ° | 173.86 | 37.91 | 12 | 1.8612/195.28 ° | 173.86 | 37.91 |
| 13 | 1.8988/214.96 ° | 170.48 | 49.66 | 13 | 1.8988/214.96 ° | 170.48 | 49.66 |
| 14 | 1.9343/234.96 ° | 160.05 | 70.94 | 14 | 1.9343/234.96 ° | 160.05 | 70.94 |
| 15 | 1.9680/255.24 ° | | 86.94 | 15 | 1.9680/255.24 ° | | 86.94 |

The specified cavity input voltages in this example have fairly large variations both in amplitude and in phase. It is seen that setting a zero voltage for a cavity changes the $d_i$ and $B_i$ only around the affected terminals between the cavity and the generator. The voltage at the feed terminal, $V_8$ shows the voltage for the total power from the generator.

## DISCUSSION AND CONCLUSION

In this fan-out distribution, one control system needs to govern all cavities in a network as a whole. Since the system is designed to deliver only the power needed in the cavities, the output power of the generator needs to be controlled. If the cavities are excited with beam and thus the beam induced voltages appear at the cavity input couplers, the required voltage vectors can be redefined accordingly. The approach can be applied to various multi-cavity accelerators including the energy recovery linacs.

Although the power density in the transmission line becomes greater if it is closer to the generator input in the network, the maximum power allowed in the transmission lines are usually comparable to the maximum power available from the high power generators. For practical transmission line junctions at the network nodes, modification of the system admittance matrices will be needed. The phase delays and reactive loadings can be realized by using fast high power fast phase shifters for fast vector control of RF voltages. The control can still be done using any mechanical phase shifters if it is acceptable for a system. For a practical multi-cavity system using the proposed fan-out distribution, matching low-level RF control system needs to be developed.

The proposed system can eliminate the requirement of extra power in fixed power distribution systems so that operation efficiency can be maximized. The method presented here can also be used with more than one single generator, making the system more redundant in certain applications.

## ACKNOWLEGEMENTS

The author thanks S.-W. Lee for assistance and the SNS project for the encouraging the work and allowing contribution to this conference.

## REFERENCES

[1] V. Katalev, S. Choroba, “RF Power Distributing Waveguide Systems For Tesla,” Presented At The XVIII Russian Part. Accel. Conf., Oct. 1-4, 2002.

[2] C. Nantista, et. al., “A Variable Directional Coupler For An Alternate ILC High-Power RF Distribution Scheme,” Linac 2006, Knoxville, TN, USA.

[3] D. Valuch, H. Frischholz, J. Tückmantel, C. Weil, “First Results With a Fast Phase and Amplitude Modulator For High Power RF Application,” EPAC 2004, Lucerne, Switzerland.

[4] R. E. Collin, “Foundations for Microwave Engineering,” 2nd Ed. Mcgraw-Hill, 1992.

[5] Y. Kang, “Efficient Fan-out RF Vector Control Algorithm,” EPAC 2008, Genoa, Italy.

# SPALLATION NEUTRON SOURCE SUPERCONDUCTING LINAC KLYSTRON TO CAVITY MISMATCH EFFECTS AND COMPENSATION*

M. McCarthy, M. Crofford, S. Kim ORNL, Oak Ridge, TN 37831, USA

*Abstract*

Observations of several of the 81 klystron output waveforms into their respective superconducting cavities do not correspond with their rectangular klystron inputs in open loop mode. This can't be completely explained by a drooping high voltage power supply especially when the waveform is parabolic. Some possible causes and effects of these anomalies are presented.

## DISTORTED WAVEFORMS

While optimizing the superconducting linac (SCL) cavity fields of the SNS linac [1] we noted that some of the 81 cavity input power waveforms were not linearly tracking the shape of the input signal (Figure 1). This caused concern that this would be an additional error source that the low level RF (LLRF) control system must compensate.

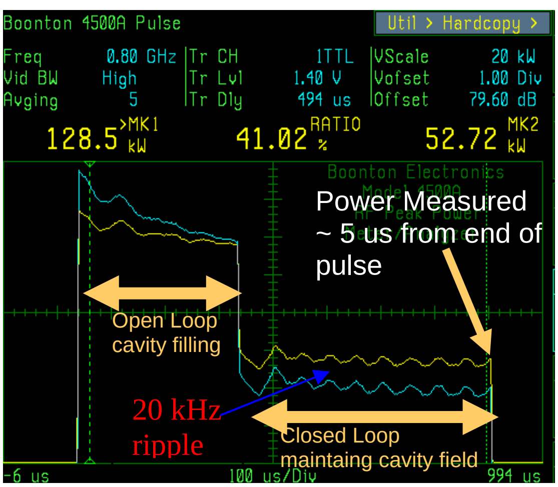


Figure 1: SCL Klystron RF Out and Cavity RF In.

Other sources of error include the phase and amplitude changes that occur during the 1ms RF pulse caused by drooping klystron cathode voltage and the resulting increased delay of the electron beam through the klystron. Also contributing are 20 kHz ripple, cavity resonance drift, beam loading and cable tolerances. Typical cathode voltage droop is ~3%. Klystron power follows cathode voltage to the 5/2 power so we expect an 8% power droop without LLRF feedback (open loop). However, some droops were as high as 32% (Figure 2).

Possible causes of the distortion were:

1) Non-linear measurement device or mis-calibration.
2) Solid State Amplifier (SSA) distortion.

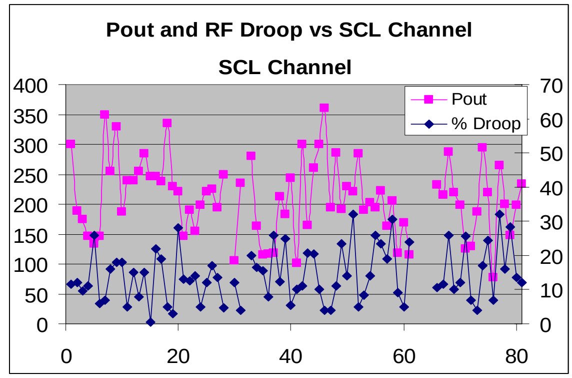


Figure 2: Klystron power and droop by SCL cavity.

3) Impedance mismatch between klystron and circulator caused by:
   a) Bad water-load match.
   b) Harmonics from klystron.
   c) Misadjusted TCU (circulator Temperature Compensating Unit)
   d) Waveguide discontinuity (bent).
   e) Bad circulator matching during full reflected power from cavity.
   f) Heating of the circulator ferrites changing their H-field during the pulse.

These possible causes were investigated; the measuring instrumentation was in calibration and two of the directional couplers were checked on the bench, the SSA met its <1% droop specification, and the waster load had a good 1.05 VSWR. A calculation of the estimated heat deposited in the circulator ferrites over the time of an RF pulse indicated insignificant temperature change. A mismatch between the circulator and the klystron appeared to be the primary candidate for the distortion.

Each TCU is factory matched to a circulator with specific internal look-up tables that compensate for changes in ferrite characteristics as a function of temperature. Over the past five years of SNS commissioning and operation, seven TCUs and two circulators have failed. Because the circulator weighs 250 lbs and hangs 13 feet above the floor, it was not changed when its matching TCU failed. The replacement TCU was tuned in-situ with a factory (AFT: Advanced Ferrite Technologies) proprietary program using a laptop. Because we couldn't vary water temperature while monitoring reflected power, the circulator was optimized for minimum reflected power to the klystron at the nominal temperature and cavity operating field.

*SNS is managed by UT-Battelle, LLC, under contract DE-AC05-00OR22725 for the U.S. Department of Energy

These Y-junction circulators function by cancellation of waves propagating from the input port over two different paths about the ferrite disks in the center magnetic field [2]. A standing wave is formed and then rotated about the circulator Y-axis by the magnetic field. There is a standing wave node at the mouth of one waveguide output port and an anti-node at the other output port, providing isolation and throughput at the respective ports. The circulator ferrites are externally biased with both electro- and permanent magnets.

The permanent magnets in the circulators may be degrading over time. Physical changes like developing cracks or loosened adhesion to the circulator could make the whole device behave differently [3]. Without a baseline measurement of their magnetic fields it is difficult to determine if changes have occurred. In addition, internal inspections of the circulators are very labor intensive and impractical.

If the ferrite is heated over the Curie temperature (over 120~200-deg-C depending on the composition) characteristics might change. That is a possibility if water cooling to the circulator were lost, but the TCU would alarm and the transmitter cooling cart would indicate a low flow, which hasn't happened.

## ERRONEOUS READINGS

Our standard waveguide directional coupler couples -63 dB of the forward and reflected power to the LLRF detectors (Figure 3a) with a nominal directivity of 26 dB.

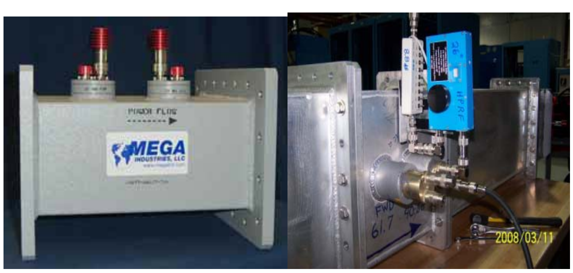


Figure 3 a, b: Waveguide Directional Coupler and 60 dB directivity modified unit.

An average circulator might only reflect 0.5 kW of 200 kW forward power. Thus the signal at the reflected directional coupler is comprised of the forward power (down 63 + 26 dB) and the reflected power (down 63 dB). These two signals are of the same order in amplitude. The signals combine with phases which depend on the physical location of the coupler with respect to the circulator and its distance from the klystron. All 81 systems are physically different. If two signals were in phase it appeared as high reflected power and if they were out of phase it appeared as a perfect well-matched circulator. So our reflected power measurements used to adjust the TCU were based on inaccurate coupler values.

To accurately measure the reflected power with near 1% accuracy a directional coupler (DC) with 47 dB directivity or better was needed. The waveguide coupler has two N-type connectors; one is the output, the other a standard 50 ohm load. The accuracy and part-to-part variation of this standard load is what limits the directivity. This load was replaced with a circuit containing a variable attenuator and variable phase shifter (Figure 3b). These were adjusted to optimize the directivity at 805.0 MHz using a network analyzer. 60-dB directivity (Figure 4) was achieved using this technique and two units were constructed to test on an SCL RF system. With these units we observed that when the reflected power was truly minimized, the klystron output was still distorted.

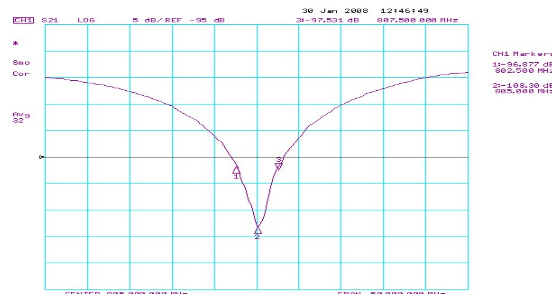


Figure 4: Directivity optimized.

Measurements were made to observe the effect of pulse width and rf power on the distortion with no attributable link. Spectrum analysis showed no significant power outside the band regardless of distortion. However circulator bias coil adjustments did affect circulator port to port isolation, as expected.

## KLYSTRON SENSITIVITY TO LOAD

By observing the klystron output power and the cavity input power waveforms simultaneously on either side of the circulator, with a Boonton 4500 power meter, the differences were quite clear. The TCU circulator bias current was adjusted so the waveforms were nearly identical in shape with allowances for differences in coupler calibrations that affect amplitude. This appeared to reduce the slope of the power curve to what was expected but not minimize it. The power reflected from the circulator back to the klystron was five times higher than minimum.

When reviewing the klystron data sheets, the factory (CPI, Palo Alto, CA) measurements indicated that the klystron output varied markedly when driving into a load with a 1.20 VSWR and variable phase. Some of the outputs were considerably higher than the nominal rated output. This would explain why the minimized reflected power point wasn't optimum. A paper from LANL [4] corroborated this observation as well as an AFT technical note [5].

## OPERATIONAL ADJUSTMENTS

The physical arrangement of instruments used to make these measurements required turning off the klystron while connections were made. This made the adjustment of the TCU during operations impractical. The adjustment during a maintenance period was also impractical because the RF systems must be off while the linac tunnel is accessible. Fortunately a subset of the measurement appeared to give enough information to make the adjustment during short non-beam periods. Both the SCL klystron output power and cavity input power are recorded by the LLRF High Power Protect Module (HPM) [6]. This is accessible from the control room. The TCUs can be adjusted in-situ with a laptop and auxiliary connection. The problem with using the HPM readouts is the arbitrary scales on each waveform. The actual values can't be read directly. This wasn't a large impediment when it was shown empirically that if the two forward power measurements on the input and output of the circulator had the same slope, the klystron/circulator/cavity match would be satisfactory.

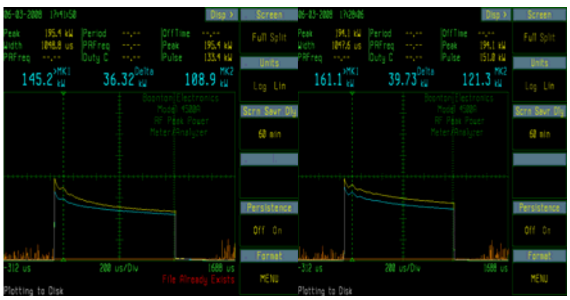

Figure 5: Before (left) and after bias current adjustment with pulse power meter.

## AUTOMATIC SLOPE GENERATION

A Perl script was written to automatically compute the slope and ratio of the klystron forward power and cavity input power waveforms. This information was used to adjust the bias current for the TCU for the optimal match among the klystron, circulator, and cavity during one of the RF development time slots with good results. The script allows the operator to select the klystron/cavity pair to be tested and three sample points to measure across the RF pulse (beginning, middle, and end). The RF measurement itself is accomplished in the LLRF system by reading the pulsed power with the HPM.

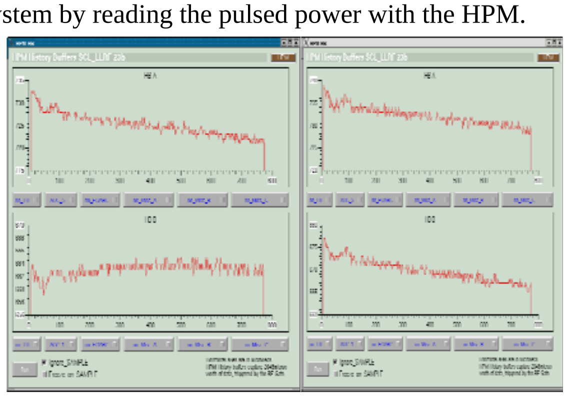

Figure 6: Before and after bias adjustment with HPM.

The slope is calculated utilizing selected beginning and end points and the ratios of all three points are used to determine if the waveform has an unusual shape. In addition to the results from the script, the HPM provides history buffers (figure 6) that allow the operator to visually look at the waveforms of the klystron and cavity to determine if the slopes are grossly different. Typical bad slope values were 6-8% apart, with good values being $\leq$ 2% apart. When a system was found with bad slope values, the TCU current was adjusted locally with a laptop operating the proprietary tuning software until the system was within tolerance. During a recent shift, eight TCUs were successfully adjusted with this technique.

## FUTURE UPGRADES

Presently there is no communication with the TCU. A status transfer to the transmitter that includes fault alarms will be implemented. While it is desirable to be able to monitor and adjust the circulator routinely and automatically, this would require a development effort to interface with the TCU and perhaps monitor the actual internal magnetic field rather than inferred ferrite temperatures. A simple feedback circuit could then adjust the bias to maintain that constant magnetic field.

## CONCLUSION

The waveguide circulators must be matched to their klystrons for undistorted power transmission. The lowest reflected power between circulator and klystron doesn't provide the best match for the klystron output cavity. Adjusting circulator coil bias until the power waveform slopes into and out of the circulator are equal yields a sufficient match.

## ACKNOWLEDGEMENTS

The authors wish to thank J. Ball, M. Cardinal, D. Heidenreich, S. Jones, M. Middendorf, C. Phibbs, V. Patania and the very patient Operations staff for their help with the measurements.

## REFERENCES

[1] D. Rees, "The SNS Linac High Power RF System Design, Status, and Results" PAC'03, Portland, OR.
[2] C.L. Hogan, "The Ferromagnetic Faraday Effect at Microwave Frequencies and its Applications" Review of Modern Physics, Vol 25-1, Jan 1953
[3] Y. Kang, ORNL, personal communication; 9/08
[4] K. Young et al, LANL, "5MW 805MHz SNS RF System Experience," Proceedings PAC'05, Knoxville, TN, July 2005
[5] AFT Technical Note:"Analysis of Directional Coupler Performance in High Power Waveguide Measurement Applications"; AFT996B.DOC [2/03]
[6] M. Crofford,et al, ORNL, "SNS Low Level RF System High Power Protection," Proceedings PAC'05, Knoxville, TN, July 2005

# SELF-TUNING REGULATOR FOR ISAC 2 SUPERCONDUCTING RF CAVITY TUNER CONTROL

K. Fong, M. Laverty and Q.W. Zheng, TRIUMF, Vancouver, Canada

*Abstract*

The ISAC 2 superconducting RF cavities use the self-excited, phase-locked mode of operation. As such the microphonics are sensitive to the alignment of the phase control loop. Although initial alignment can minimize the effect of microphonics, amplitude-dependent phase shift and long term drift, particularly in the power amplifiers, can cause the control loop misalignment and an increase in sensitivity to microphonics. The ISAC 2 control system monitors several points in the control loop to determine the phase alignment of the power amplifiers as well as the RF resonant cavities. Online adaptive feedback using Self-Tuning Regulator is employed to bring the different components back into alignment.

## INTRODUCTION

Figure 1 shows the block diagram of a self-excited system. In this type of system amplitude control is achieved by feedback regulation of the In-phase channel, while frequency and phase control are achieved by feedback regulation of the Quadrature-phase channel.

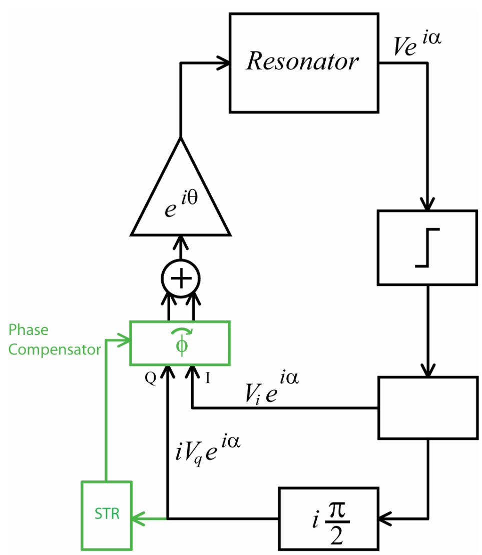


Figure 1: Phase-locked Self-excited loop with Self-Tuning phase compensator.

The feedback signal is derived by comparing the phase of the self-excited signal with an external reference frequency. In ISAC 2, the I/Q feedback controller functions are performed by a single digital signal processor[1], while the phase comparison is done by a FPGA[2]. Proper phase-locked operation and the amount of residual microphonics in the feedback system depends on its alignment[3]. This includes the phase delays of the cables, the amplifier system as well as the resonant cavity. Phase delay changes in all these components can be caused by cryogenic helium pressure, thermal effects and long term deterioration such as power tube emissivity. To counter act these changes a digital phase shifter, coloured in green in Figure 1, is incorporated into the feedback controller DSP. This phase shifter is essentially a rotation matrix operating on the In-phase and the Quadrature-phase channel outputs of the DSP. The phase sifter is controlled by a self-tuning regulator for automatic phase noise reduction. The self-tuning regulator monitors the original Q channel output, then calculates the optimum drive to modify the rotation angle.

## THEORY

The equation for the voltage of the cavity is [1]

$$\ddot{v} + 2\frac{1}{\tau}\dot{v} + \omega_c^2 v = 2\frac{\gamma}{\tau}\dot{V}_g \qquad (1)$$

Using the I and Q components of the input voltage $V_g$ as the independent variables and the amplitude and phase of the output voltage $v$ as the dependent variables for a phase-locked self-excited system, the equation of state is

$$\begin{bmatrix}\delta V\\ \delta\omega\end{bmatrix} = \gamma\cos\theta \begin{bmatrix} \dfrac{1}{s\tau+1} & -\dfrac{\tan\theta}{s\tau+1} \\ \dfrac{1}{\tau V_0}\left(\tan\theta - \dfrac{\tan\phi}{s\tau+1}\right) & \dfrac{1}{\tau V_0}\left(1-\dfrac{\tan\phi\tan\theta}{s\tau+1}\right)\end{bmatrix}\begin{bmatrix}\delta v_i\\ \delta v_q\end{bmatrix} \qquad (2)$$

The phase shift $\phi$ of the RF cavity is given by

$$\phi = \tan^{-1}\left(\omega_c - \omega\right)\tau \qquad (3)$$

and the I/Q modulator produces a phase shift $\rho$ given by

$$\rho = \tan^{-1}\frac{V_q}{V_i} \qquad (4)$$

The phase relation in a self-excited loop must obey

$$\theta+\rho+\phi=2n\pi \qquad (5)$$

In order to minimize the power requirement, $\phi$ should be set to zero. While $\phi$ can be measured directly from the phase difference between the input and the output of the cavity, $\theta$ is a dynamic variable, namely the amplifier phase shift. In self-excited mode $\theta$ and $\phi$ are not independent variables since they must obey Equation 5. Therefore when $\phi$ is set to zero by the tuner, and when $\theta = 0$ , $q \equiv V_q = 0$. This is operationally desirable since it eliminates cross-talk between the I and the Q channels. Another important reason for $\theta = 0$ is that when this condition is not met, the cross-talk between the I and Q channel outputs can in some cases trip the built-in limiters in the PID controllers and causes both the amplitude and the phase loops to lose regulation.

Although $q$ can be measured quite easily, it is contaminated with noise due to microphonics in the cavity. In addition, the relationship between $q$ and $\theta$ is variable depending on the misalignment and the drive level. Therefore for these reasons a self-tuning regulator (STR) with recursive least square estimator is used to control $\theta$.

## IMPLEMENTATION

### *Phase Rotator*

In ISAC 2 RF systems, a single DSP performs both the I and Q channel feedback control. Output limiting on the I and Q channels is implemented to prevent integrator wind-up. The DSP then accepts 4 parameters from the supervisory PC and performs the matrix multiplication on the I and Q outputs

$$\begin{pmatrix} I_1 \\ Q_1 \end{pmatrix} = \begin{pmatrix} A & B \\ C & D \end{pmatrix} \begin{pmatrix} I_0 \\ Q_0 \end{pmatrix} \tag{6}$$

With an input parameter of $\theta$, the supervisory PC supplies these 4 parameters as

$$A = D = \cos\theta \tag{7a}$$

and

$$C = -B = \sin\theta \tag{7b}$$

The rotated digital outputs are converted into analogue signals for the complex modulator. There are 2 ADC's that monitors the I and Q inputs to the complex modulator. Since the phase rotator has already been applied with the DSP, the supervisory PC reads these 2 ADC's and apply the inverse of the rotation matrix to get the original I and Q output.

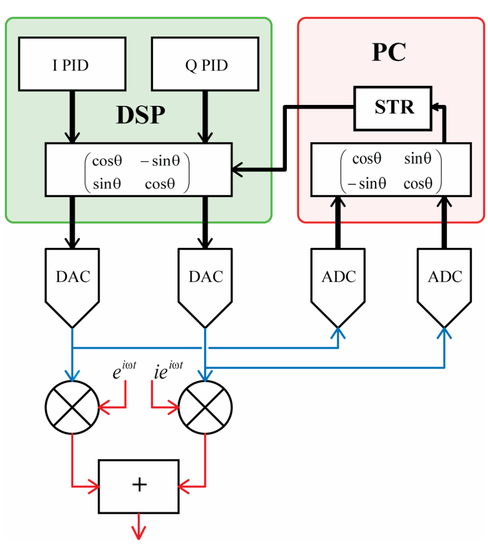


Figure 2: Implementation of phase rotator.

### *Self Tuning Regulator*

Since the sampling frequency of the STR is much lower than the frequencies of the harmonics, $q$ will be filtered to prevent aliasing before it is used as the input to the STR. Therefore the STR as shown in Figure 3 is assumed to have a first order system equation:

$$q(t) = b_0 + b_1\theta(t) + n(t) \tag{8}$$

where $n(t)$ is a zero mean Gaussian noise, $b_0$ and $b_1$ are the process parameters. $b_0$ is the misalignment and $b_1$ depends on $V_o$. Their estimates $\hat{b}_0$, $\hat{b}_1$ are obtained from a Recursive Least Square Estimator. Defining

$$\Phi^T(t) = [1 \quad \theta(t)] \tag{9a}$$

and

$$\Theta^T(t) = [b_0 \quad b_1] \tag{9b}$$

As we are trying to minimize $q(t)$, the residue is simply

$$\varepsilon(t) = q(t) \tag{10}$$

The Recursive least-squares estimation $\hat{\Phi}(t), \Theta^T(t)$ then satisifies the recursive equations [4]

$$\Theta^T(t) = \Theta^T(t-1) + K(t)q(t) \tag{11a}$$

With exponential forgetting factor $\lambda$ to account for slow varying drifts,

$$K(t) = P(t-1)\Phi(t)\left(\lambda + \Phi^T(t)P(t-1)\Phi(t)\right)^{-1} \tag{11b}$$

$$P(t) = \left(I - K(t)\Phi^T(t)\right)P(t-1)/\lambda \tag{11c}$$

with the initial conditions on the covariance $p$_matrix

$$P(0) = \left(\Phi^T(0)\Phi(0)\right)^{-1} \tag{12a}$$

and estimated process-parameter vector

$$\Theta^T(0) = P(0)\Phi^T(0)q(0) \tag{12b}$$

The STR then has the following control law,

$$\theta(t) = \frac{q(t) - \hat{b}_0}{\hat{b}_1} \tag{13}$$

where the static misalignment is accounted for by $\hat{b}_0$, which has been internally integrated by the Kalman filter[5] within the Recursive Least Square Estimator.

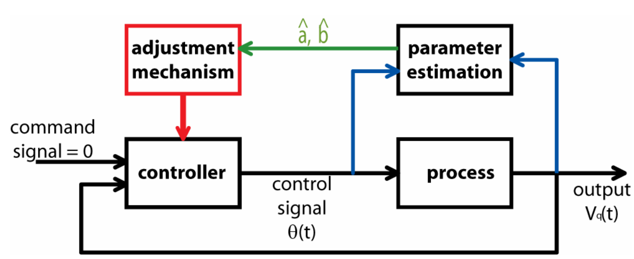


Figure 3: Block diagram of a self-tuning regulator.

The bulk of the self-tuning regulator is implemented in the supervisory PC for three reasons: First- the misalignment drift is a very slow process, and a fast sampling rate is not necessary, second- the DSP employed in ISAC 2 control is a fixed-point DSP, whereas the supervisory PC can perform 64-bit floating-point operations, and in addition has practically unlimited memory resources. The third reason is that the PC is programmed in C++ while the DSP is programmed in Assembler (optimized for speed).

## RESULT

The phase rotators were implemented in all ISAC 2 RF control systems in 2007, and a self-tuning regulator is being tested on the test cryostat in the ISAC 2 test facility. Figure 4 shows the phase noise of the RF field voltage at various degrees of misalignment. The peaks at 58 Hz are due to external excitations such as pumps and fans. As can be seen in the figure, phase noise increases for progressively with misalignment in one direction, while it has little effects in the opposite direction.

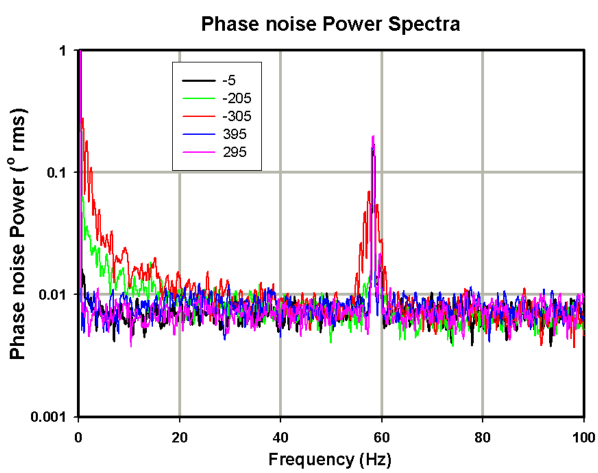


Figure 4: Phase noise of ISAC 2 cavity at different degrees of misalignment.

Figure 5 show a computer simulation of the self tuning regulator in action. A series of curves were superimposed on each other to represent the same initial misalignment but with different random noises of the same level. These noises are zero-mean Gaussian noise with a standard deviation of 50 units. The red curves represent the Q drives, corrupted by the noise, required to compensate a misalignment. For all cases, within 20 time steps the Q drives have been reduced from a high value of 1000 to close to 0, where the required phase shift to compensate the misalignment is taken over by the phase rotator (blue curves). After the regulator has converged, there are still some control movements due to the random noise. This noise actually prevents the covariance *p*_matrix from winding-up. In an actual implementation there should be a dead-band on the control to prevent unnecessary control inputs. This dead-band control would simply stop the updating of the self-tuning regulator but continue to monitor *q*. As soon as *q* exceeded a pre-determined threshold the covariance *p*_matrix would reset and the self-tuning regulator re-activated.

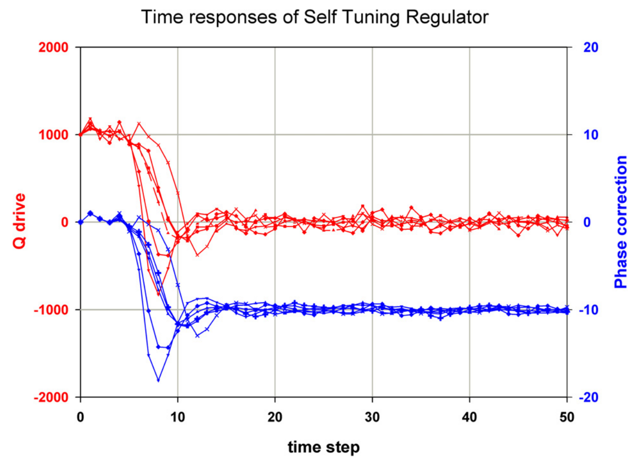


Figure 5: Simulation of Self Tuning Regulator for misalignment compensation.

## CONCLUSION

Accurate alignment is very important to the performance of the ISAC 2 superconducting cavities, particularly to the suppression of phase noise. Long term phase drift in the system can adversely affect this alignment. A self-tuning regulator can be implemented with no hardware change to compensate for this slow varying drift in alignment. The regulator can provide optimum control in the presence of phase noise and with varying system parameters. The recursive least-square estimator is the heart of the regulator. Using the proper least-square error function, the regulator is able to track change in system parameters online and automatically bring the system back to the optimum alignment.

## REFERENCES

[1] K. Fong, M. Laverty and Q.W. Zheng, “Adaptive Tuner Control in TRIUMF ISAC 2 Superconducting Linac using Kalman Filter”, Proc. Linac 06, p. 592.

[2] K. Fong, M. Laverty and S. Fang, “Status of RF Control System for ISAC II Superconducting Cavities”, Proc. Linac 04, p. 450.

[3] H. Rasmussen, “Automatic Tuning of PID-regulators”, Aalborg University, 1993.

[4] K.J. Astrom and B. Wittenmark, “Adaptive Control”, Second Edition, Addison Wesley, 1995.

[5] R.E. Kalman, “A New Approach to Linear Filtering and Prediction Problems”, Trans. ASME-J. Basic Engineering, p. 35 (March 1960).

# AM-PM CONVERSION INDUCED INSTABILITY IN AN I/Q FEEDBACK CONTROL LOOP

K. Fong, M. Laverty and Q.W. Zheng, TRIUMF, Vancouver, Canada

*Abstract*

Most RF feedback control systems today use the I/Q demodulation and modulation scheme because of its simplicity. Its performance, however, depends on the alignment of the feedback loops. If the loop contains elements that have a high AM-PM conversion factor such as a class C amplifier or a high power klystron, then the misalignment is dynamic and power dependent. In most systems the phase noise is increased, and in some cases the I/Q loops become unstable and the system settles into a limit-cycle oscillation.

## INTRODUCTION

The 92MHz RF Booster has been in operation in the TRIUMF cyclotron for more than 15 years[1]. The original system was an analogue system that used amplitude/phase modulation. When the control system was replaced in 2005 with a digital signal processor system, the control algorithm was converted into I/Q modulation. After the conversion the feedback system would operate satisfactory at 90% nominal power, but at 100% nominal power, on some occasions, the I/Q loops and the tuner loop would jump into limit cycle oscillations. It was also determined that the booster RF amplifier chain has a large phase shift that is power dependent. In an I/Q system, detuning of the resonant cavity will introduce cross-talk between the I and the Q channels. Normally the detuning will be suppressed by the tuning feedback loop but in the TRIUMF RF Booster the tuning motor movement is relatively slow and is unable to correct the detuning within a few seconds. During this crucial time the cross-talk is enhanced by the dynamic phase shift of the amplifier chain. Its growth rate, depending on the initial detuning, can sometimes exceed the damping rate provided by the tuner loop and cause the collapse of this RF system.

## BOOSTER RF POWER AMPLIFIER

The Booster RF power amplifier chain consists of a three-stage amplifier: a 10W solid state driver amplifier, a 10kW tube pre-amplifier and a 100kW final tube power amplifier. The final stage amplifier is a grounded grid power amplifier for the booster cavity of the TRIUMF cyclotron, operating at the frequency 92MHz. The configuration is shown in Figure 1.

A huge phase shift in the Booster PA was detected which was dependent on RF output power, possibly due to a thermal effect. Phase changes from 0 to -15 degrees with power going from 0 to 15 kW and then from -15 to 40 degrees when output ramping up to full power (40kW) as indicated in Figure 2. Bipolar phase shift response is most likely caused by alternate behaviour of the FM transmitter and final PA, and is difficult to suppress with a phase compensation circuit inside the Booster RF power amplifier.

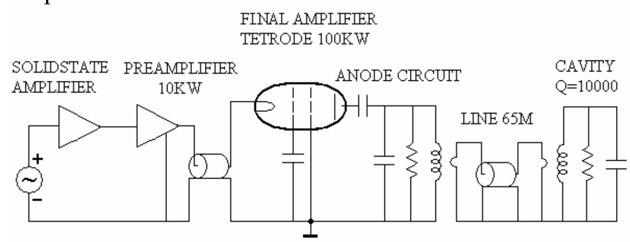


Figure 1: TRIUMF RF booster amplifiers.

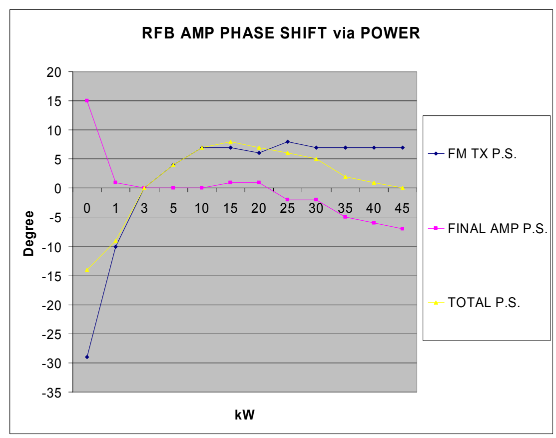


Figure 2: Phase shift vs. power.

This high AM-PM conversion phase shift enhances I/Q loop cross-talk, eventually making the Booster RF system operation unstable.

## THE BOOSTER RF TUNING SYSTEM

The automatic frequency tuning system keeps the RF cavity at its resonant frequency. This achieves the desired RF voltage with minimum RF power input and minimum reflected RF power. The TRIUMF booster tuning unit uses two DC motors to move the upper and lower shorting plates in the root region of the cavity to accomplish the Booster cavity frequency tuning. To prevent wearing out of mechanical contacts due to constant movement of the tuner, a bang-bang controller is used for the booster tuning control. The motors are also heavily geared down in order to have enough force to move the tuning plate. All these factors contribute to the slow response of the tuning control system.

## LINEAR THEORY OF AM-PM CONVERSION INDUCED INSTABILITY

In this section we will develop the linear theory for instability caused by AM to PM conversion. Figure 3 shows a typical I/Q driven mode feedback control system.

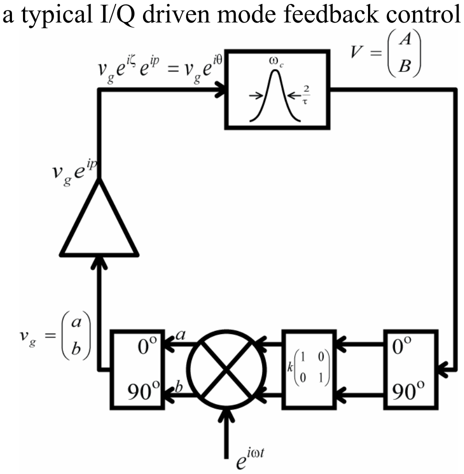


Figure 3: Basic I/Q driven mode with proportional feedback system.

The equation for the voltage of the cavity is [2]

$$\ddot{v} + 2\frac{1}{\tau}\dot{v} + \omega_c^2 v = 2\frac{\gamma}{\tau}\dot{V}_g \tag{1}$$

Using the I and Q components of the input voltage $V_g$ as the independent variables and the I and Q component of the output voltage $v$ as the dependent variables,

$$v = Ve^{i\alpha} = \begin{pmatrix} \cos\alpha & -\sin\alpha \\ \sin\alpha & \cos\alpha \end{pmatrix}\begin{pmatrix} A \\ B \end{pmatrix},$$

$$V_g = v_g e^{i(\theta+\omega t)} = \begin{pmatrix} \cos(\theta+\omega t) & -\sin(\theta+\omega t) \\ \sin(\theta+\omega t) & \cos(\theta+\omega t) \end{pmatrix}\begin{pmatrix} a \\ b \end{pmatrix}$$

where $\omega_c$ is the resonant frequency of the cavity and $\gamma$ is the coupling coefficient into the cavity.

The phase shift $\phi$ of the RF cavity is

$$\phi = \tan^{-1}(\omega_c - \omega)\tau\,. \tag{2}$$

By eliminating slowly varying terms and applying the Laplace transform, Equation 1 becomes

$$(1+s\tau)V + i\tan\phi V = \gamma e^{i\theta} v_g \tag{3}$$

where $\theta$ is the total phase shift from the control output to the cavity input. It can be separated into static phase shift $\zeta$ and an amplitude dependent phase shift $\rho$ such that

$$(1+s\tau)V + i\tan\phi V = \gamma e^{i\zeta} e^{i\rho} v_g \tag{4}$$

where $\rho$ is a function of $v_g$.

The equation is non-linear due to the dependency of $\rho$ on $v_g$. A good approximation of $\rho$ is

$$\rho = \eta v_g v_g^* = \eta P \tag{5}$$

where $P$ is the output power.

To linearize Equation 3, take the variations of both the dependent and independent variables

$$(1+s\tau)\delta V + i\tan\phi\delta V = \gamma e^{i\theta}\left(iv_g\delta p + \delta v_g\right) \tag{6}$$

With $\mathrm{P} \equiv \dfrac{d\rho}{dv_g} v_g = 2\eta a^2$ and $\varphi \equiv \dfrac{b}{a}$. Therefore

$$\left(iv_g\delta p + \delta v_g\right) = \begin{bmatrix} 1-\mathrm{P}\varphi & -\mathrm{P}\varphi^2 \\ \mathrm{P} & 1+\mathrm{P}\varphi \end{bmatrix}\begin{bmatrix} \delta a \\ \delta b \end{bmatrix} \tag{7}$$

Equation 6 becomes

$$\begin{bmatrix} \delta A \\ \delta B \end{bmatrix} = \frac{\gamma}{\sigma^2 + \tan^2\phi}\begin{bmatrix} \sigma & -\tan\phi \\ \tan\phi & \sigma \end{bmatrix}\begin{bmatrix} \cos\theta & -\sin\theta \\ \sin\theta & \cos\theta \end{bmatrix}\begin{bmatrix} 1-\mathrm{P}\varphi & -\mathrm{P}\varphi^2 \\ \mathrm{P} & 1+\mathrm{P}\varphi \end{bmatrix}\begin{bmatrix} \delta a \\ \delta b \end{bmatrix} \tag{8}$$

where $\sigma = 1 + s\tau$.

Equation 8 shows that the phase shift of the transfer function of the system is the result of the three "rotation" matrices. The left-hand most matrix is the phase shift due to cavity detuning, the second matrix is the phase shift due to total cable length. These two matrices can be reduced to rotation matrices and represent actual rotations of the input phasor, albeit time-dependent due to the dependence of $\sigma$ on $s$. The last matrix $\begin{bmatrix} 1-\mathrm{P}\varphi & -\mathrm{P}\varphi^2 \\ \mathrm{P} & 1+\mathrm{P}\varphi \end{bmatrix}$ is due to amplitude-dependent phase shift of the amplifiers. Since it is not an orthogonal matrix, the stability of a feedback system involving power dependent phase shift is not guaranteed.

For small misalignment and detuning and keeping only first order terms

$$\begin{bmatrix} \delta A \\ \delta B \end{bmatrix} = \frac{\gamma}{\sigma}\begin{bmatrix} 1-\mathrm{P}\varphi-\mathrm{P}\theta-\mathrm{P}\dfrac{\phi}{\sigma} & -\theta-\dfrac{\phi}{\sigma} \\ \theta+\dfrac{\phi}{\sigma}+\mathrm{P} & 1+\mathrm{P}\varphi \end{bmatrix}\begin{bmatrix} \delta a \\ \delta b \end{bmatrix} \tag{9}$$

Consider symmetric P controllers, the controller gain matrix is

$$F = fI \tag{10}$$

where $I$ is the identity matrix. The feedback transmission is simply

$$H = hI \tag{11}$$

A new variable $\gamma' \equiv \gamma fh$ incorporates the controller gain $f$ and the feedback gain $h$ into the coupling coefficient $\gamma$ of the cavity. Then the characteristic equation of the system is the determinant of the return difference

$$\left|\begin{bmatrix} 1 & 0 \\ 0 & 1 \end{bmatrix} + \frac{\gamma'}{\sigma}\begin{bmatrix} 1-\mathrm{P}\varphi-\mathrm{P}\theta-\mathrm{P}\dfrac{\phi}{\sigma} & -\theta-\dfrac{\phi}{\sigma} \\ \theta+\dfrac{\phi}{\sigma}+\mathrm{P} & 1+\mathrm{P}\varphi \end{bmatrix}\right| = 0 \tag{12}$$

or

$$\frac{s^2\tau^2}{\gamma'^2} + \frac{s\tau}{\gamma'}\left(\frac{2}{\gamma'} + 2 - \mathrm{P}\theta\right) + \frac{1}{\gamma'^2} + \frac{2}{\gamma'} - \frac{\mathrm{P}\theta}{\gamma'} + 1 - \frac{\mathrm{P}\phi}{\gamma'} = 0 \tag{13}$$

under negative feedback the controller will adjust $\varphi$ such that

$$\theta + \phi = 0\,. \tag{14}$$

Therefore

$$s\tau = \gamma' \frac{\Delta - 2 \pm \sqrt{\Delta^2 - 4\Delta}}{2} \text{ with } \Delta \equiv P\theta \qquad (15)$$

where $\Delta$ can be viewed as the damping factor.
The following plot is the root loci of Equation 15.

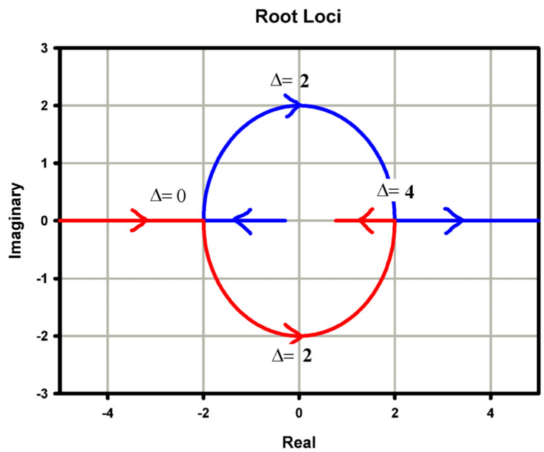


Figure 4: Root loci showing regions of stability.

The root loci plot indicates the system becomes unstable for $\eta a^2\theta > 2$ or $\left(\frac{d\rho}{dP}P\right)\theta > 2$. The system actually becomes under-damped for $\frac{d\rho}{dP}\theta > 0$. The system quickly becomes non-linear and the stability margin decreases further.

This instability has a simple explanation. Since in an I/Q driven system quadrature power is used to achieve a change in $\theta$, the amplitude-dependent phase shift at one side of the misalignment causes $\theta$ to change in the opposition direction to that required. At higher power levels, or when misaligned, more quadrature power is required to create the same phase shift, so the feedback system becomes more susceptible to instability. Although the proportional gain does not affect the instability regime, it does affect the growth rate.

The above calculations were developed using small-signal variations, a proportional controller and a very simple amplitude dependent phase shift. The stability requirement will be more stringent as misalignment increases, system Q increases, amplitude dependent phase shift becomes more non-linear or more complicated poles and zeros are included in the feedback path. For the TRIUMF RF booster, using the data from Figure 2, $\frac{dp}{dP}P \approx 0.8$. The stability is marginal and instability did occur occasionally, particularly when the tuner dead band caused $\phi$ to become more negative and thus $\theta$ to become more positive. There are many ways to eliminate or suppress this form of instability. We can reduce $\frac{dp}{dP}$ by operating the amplifier in the linear region. We can try to operate the system in the region where $\frac{d\rho}{dP}\theta < 0$ by purposing misaligning the tuner, or we can operate using amplitude and phase modulation.

## MODIFIED BOOSTER RF OPERATION

As the mechanism of the instability of the booster operation became evident due to AM-PM conversion, the RF control system was modified to eliminate this instability. Method 1 mentioned above is expensive since it involved rebuilding the amplifier chain. The operating frequency of the booster is phase-locked to the frequency of the cyclotron, which changes with its tune. This eliminates Method 2. An ISAC-2 controller which uses phase-locked self-excited mode of operation [3], was modified from I/Q modulation to Amplitude/Phase modulation by adding an electronic phase shifter. This modified controller changes the control algorithm from driven operation with I/Q modulation and demodulation, to phase-locked self-excited operation with amplitude/phase modulation and demodulation. By doing so the AM-PM conversion instability is completely eliminated. Powering up the cavity also becomes much easier. Previously, the tuner position had to be adjusted to match the cyclotron frequency before RF power could be applied. Now the self-excited loop automatically adjusts its frequency to match the resonant frequency of the booster, regardless of the tuner position. The problem of loss of synchronization with the main RF cyclotron has also been eliminated, since the phase locking can be turned off and the RF booster can operate in self-excited mode whenever the synchronization signal is lost.

## CONCLUSION

Three conditions are required to AM-PM conversion instability to happen: amplitude dependent phase shift, operation at $\frac{d\rho}{dP}\theta > 0$, and the feedback system uses I/Q modulation. The RF booster happened to have these three conditions after the conversion from an amplitude/phase modulator to I/Q modulator, and its operation became unstable. After the the mechanism of the instability was understood, the control system was changed from I/Q driven mode to phase-locked, self-excited mode with Amplitude/Phase modulation. This eliminated the last condition for AM-PM instability and the RF booster has since been running satisfactorily.

## REFERENCES

[1] K. Fong, M. Laverty, “RF Control System for TRIUMF Booster Cavity”, Proc. EPAC, Berlin, 1992, p. 1176.

[2] J. Delayen, “Self Excited Loop”, LLRF Workshop, 2001.

[3] K. Fong, M. Laverty and S. Fang, “RF Control System for ISAC II Superconducting Cavities”, Proc. EPAC 2002, Paris, p. 2226.

# EVALUATION OF FAST ADCS FOR DIRECT SAMPLING RF FIELD DETECTION FOR THE EUROPEAN XFEL AND ILC

Z. Geng[#], S. N. Simrock, DESY, Hamburg, Germany

*Abstract*

For the LLRF system of superconducting Linacs, precision measurements of the RF phase and amplitude are critical for the achievable field stability. In this paper, a fast ADC (ADS5474) was employed to measure the 1.3 GHz RF signal directly without frequency down conversion. In the laboratory, the Signal to Noise Ratio (SNR) of the ADC was studied for different RF input levels, and the temperature sensitivity of the ADC has been determined. A full bandwidth phase jitter of 0.2 degree (RMS) and amplitude jitter of 0.2% (RMS) was measured. For field control of superconducting cavities with a closed loop bandwidth up to 50 kHz, one can expect to achieve a phase stability close to 0.01 degree. The main limitation will be the jitter of the external clock. We represent measurements of the cavity fields at FLASH and compare the result with the existing system with down converter.

## INTRODUCTION

The superconducting Linacs in facilities such as European XFEL and ILC, require significant RF field stability up to 0.01 degree in phase and 0.02% in amplitude [1], which are guaranteed by the LLRF system. Precision measurements of the RF phase and amplitude are critical for the achievable field stability for the LLRF system.

Most of the superconducting cavities of European XFEL and ILC work on the frequency of 1.3 GHz, which until recently could not be directly measured by commercially available ADCs. The most widely used way for measurement is to convert the 1.3 GHz RF signal to an intermediate frequency and then sample by ADCs.

Though ADCs with a bandwidth of a few GHz are available since a few years, their resolution was limited to 8 or maximum 10 bits. Recently, ADCs with 12 or even 14 bits are available, making it possible to measure the RF signal directly without frequency down conversion. Direct sampling ADC gets rid of the down converter and makes the RF measurement circuit much simpler and smaller, but will be sensitive to the clock jitter. The ADS5474 is an ADC with 14-bit resolution, 400 MSPS and 1.4 GHz bandwidth, which is suitable to sample the 1.3 GHz signal directly with under sampling scheme. This ADC was evaluated both in the laboratory and for the injector RF system at FLASH.

[#]zheqiao.geng@desy.de

## RF FIELD DETECTION

The ADC sampling frequency (400 MSPS) is much smaller than the RF frequency (1.3 GHz), so under sampling is used, and the RF signal is measured in a higher Nyquist band. In order to derive the phase and amplitude directly from the sampling, the clock frequency should be synchronized with the RF frequency and chosen based on the non-IQ sampling scheme [2]. The possible sampling frequency $f_s$ is

$$f_s = \frac{f_0}{k + \frac{m}{n}}, \quad k = 0,1,2... \tag{1}$$

where $f_0$ is the RF frequency, $m$ and $n$ represent the phase difference between two adjacent samples

$$\Delta\varphi = \frac{m}{n} \cdot 2\pi \tag{2}$$

The $I$ and $Q$ baseband components can be calculated by the ADC sampling according to the formula below

$$I = \frac{2}{n}\sum_{i=0}^{n-1} x_i \sin(i\Delta\varphi)$$
$$Q = \frac{2}{n}\sum_{i=0}^{n-1} x_i \cos(i\Delta\varphi) \tag{3}$$

where $x_i$ is the ADC sampling data.

The non-IQ demodulation by equation (3) can separate and suppress the harmonics of the carrier frequency.

During testing, the sampling frequency is chosen to be 178.8990825 MHz ($m$ = 4 and $n$ = 15), and the RF frequency is mapped to 47.7064225 MHz.

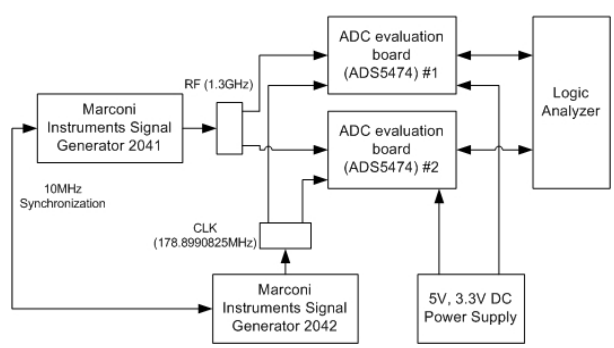


Figure 1: ADC testing stand in laboratory.

## NOISE CHARACTERISTICS

The ADC evaluation board is measured in laboratory for estimating the noise characteristics. The testing stand is shown in Fig. 1. Two synchronized low noise signal generators are used for clock and RF signals. The ADC sampling data are recorded by a logic analyzer. The second ADC evaluation board is installed for the temperature sensitivity measurements for phase and amplitude.

For different RF input power, the SNR and noise floor of the ADC are measured by Fourier transform (see Fig. 2). It is seen from the figure that when the RF input power gets larger, the noise floor becomes larger, but the SNR becomes more constant.

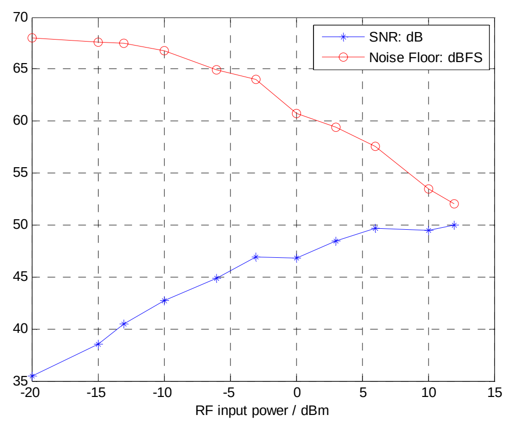


Figure 2: Signal to noise ratio and noise floor of the ADC with different RF input power.

For the direct sampling ADC, when the RF input power is large, the noise will be dominated by the external clock jitter effect. The limitation to SNR based only on clock jitter can be determined by the equation

$$SNR_{jitter} = -20\log_{10}\left(2\pi f_{RF}\Delta t\right) \tag{4}$$

where $f_{RF}$ is the RF frequency and $\Delta t$ is the RMS clock jitter. For the signal source (Marconi Instruments 2042) used for clock, the typical single sideband (SSB) phase noise is shown in Table 1 [3].

Table 1: SSB Phase Noise of Marconi Instruments 2042

| **Offset Frequency** | **SSB Phase Noise (dBc/Hz)** |
|---|---|
| 100 Hz | -81 |
| 1 kHz | -121 |
| >= 20 kHz | -140 |

From Table 1, the time jitter of the clock signal is estimated to be 0.3 ps (RMS), which corresponds to a SNR of 52 dB according to equation (4) when the RF frequency is 1.3 GHz. This is the limitation of the SNR with the setup shown in Fig. 1.

The spectrum of the sampled RF signal is shown in Fig.3, with the RF power of 12 dBm, and the SNR of 50.5 dB.

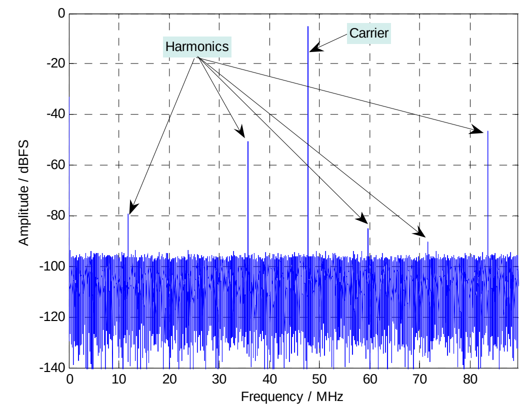


Figure 3: Spectrum of the sampled RF signal.

The phase and amplitude of the RF signal can be derived from equation (3). For the data shown in Fig. 3, the measured phase jitter is about 0.05 degree (RMS) and amplitude jitter 0.06% (RMS), where equation (3) can be viewed as a bandpass filter with a bandwidth of about 10 MHz. With the full Nyquist bandwidth of 89.45 MHz, one can estimate a phase jitter of about 0.2 degree (RMS) and amplitude jitter 0.2% (RMS).

For the LLRF system of European XFEL, the direct sampling ADC can be used for measuring the cavity probe signals, which acts as the input to the feedback loop. The TESLA typed superconducting cavity has a bandwidth of about 200 Hz, so with a feedback gain of 250, the closed loop bandwidth will be about 50 kHz. The ADC noise will be low pass filtered by the feedback loop, so the phase and amplitude jitter will be lowered by the factor of

$$C = \sqrt{\frac{f_{BW,closed\_loop}}{f_{BW,Nyquist}}} = \sqrt{\frac{50kHz}{89.45MHz}} \tag{5}$$

So, even with the feedback gain high as to 250, one can expect a phase stability of better than 0.01 degree and amplitude stability of better than 0.01%, which can meet the requirements for the main Linac of the European XFEL.

## TEMPERATURE STABILITY

The temperature sensitivity of the ADC is important for the long term stability. The phase and amplitude drifts due to the ADC temperature change are measured in the laboratory. The testing stand is shown in Fig. 1; one ADC chip is cooled by cold spray while another ADC is used for measuring the RF signal as phase reference.

The measured phase and amplitude drifts according to the ADC chip surface temperature are shown in Fig. 4. The phase temperature coefficient is 0.14º/ºC and the gain temperature coefficient is -0.03 %FS/ºC, which are acceptable for the accelerator environment. The phase and amplitude drifts with temperature are quite linear, which can be compensated by measuring the ADC temperature.

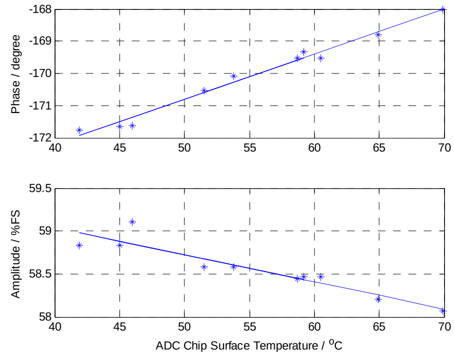


Figure 4: Phase and amplitude drift measurements.

## MEASUREMENTS AT FLASH

The ADC boards are evaluated by measuring the probe signals in ACC1 at FLASH. The measurement setup is similar to Fig. 1, except that the RF signals to the ADC boards are replaced by a cavity probe signal and master oscillator signal respectively. Because the clock signal is not synchronized with the FLASH RF, we need a master oscillator signal as reference measured with a second ADC to compensate the phase slope.

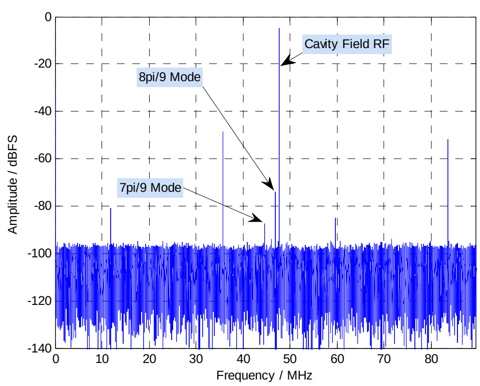


Figure 5: Spectrum of the probe signal of cavity 8 in ACC1.

Fig. 5 shows the spectrum of the probe signal of cavity 8 in ACC1 measured by the ADC. Comparing to Fig. 3, there are two additional frequency components except for the harmonic frequencies, which show the excitation of the $8\pi/9$ and $7\pi/9$ modes of the cavity.

The amplitude and phase of the probe signal of cavity 8 in ACC1 are derived from non-IQ demodulation, see Fig. 6, and the measurements from the monitoring ADCs with down conversion to 250 kHz IF are also shown for comparison.

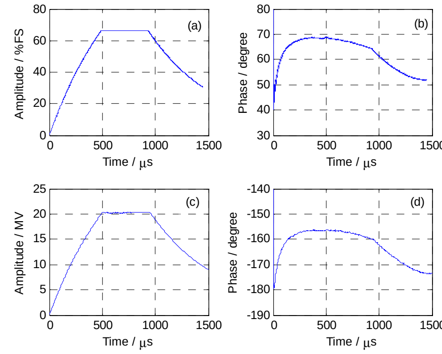


Figure 6: Amplitude and phase measurements. (a),(b): Measured by direct sampling ADC; (c),(d): Measured by monitoring ADC in ACC1 at FLASH.

During the flat top of the RF pulse, the direct sampling ADC exhibits a phase jitter of 0.05 degree and amplitude jitter of 0.054% (with a bandwidth of about 10 MHz); while the monitoring ADC gives a phase jitter of 0.09 degree and amplitude jitter of 0.078% (with a bandwidth of about 500 kHz).

## SUMMARY

In this paper, a high bandwidth ADC (ADS5474) was evaluated both in laboratory and FLASH. A full bandwidth phase jitter of 0.2 degree (RMS) and amplitude jitter of 0.2% (RMS) was achieved. The temperature stability of the ADC was also measured and as the results, the sensitivity for the phase is 0.14º/ºC and for the amplitude -0.03 %FS/ºC. During the test at FLASH, the direct sampling ADC demonstrated even better noise characteristics than the existing monitoring ADC.

*The authors would like to thank Tomasz Jezynski for the setup of the data acquisition system based on a logic analyzer, Matthias Hoffmann for the support and advice in the analysis of the data, and Mariusz Grecki for his recommendation concerning the best choice for the rf and clock frequency for the non-IQ demodulation.*

## REFERENCES

[1] S.N. Simrock, "Measurements for Low Level RF Control Systems", Meas. Sci. Technol. 18 (2007) 2320–2327

[2] M. Grecki, T. Jezynski and A. Brandt, "Estimation of IQ Vector Components of RF Field - Theory and Implementation", 12th Int. Conf. Mixed Design of Integrated Circuits and Systems, MIXDES 2005, p.783-788

[3] ftp://ftp.testequity.com/pdf/2040.pdf

# LLRF SYSTEM REQUIREMENT ENGINEERING FOR THE EUROPEAN XFEL

S.N. Simrock#, G. Ayvazyan, Z. Geng, M. Grecki, DESY, Hamburg, Germany
B.Aminov, CRE, Wuppertal

*Abstract*

The LLRF system of the European XFEL must fulfill the requirements of various stakeholders: Photon beam users, accelerator operators, rf experts, controls system, beam diagnostics and many others. Besides stabilizing the accelerating fields the system must be easy to operate, to maintain, and to upgrade. Furthermore it must guarantee high availability and it must be well understood. The development, construction, commissioning and operation with an international team requires excellent documentation of the requirements, designs and acceptance test. For the RF control system of the XFEL the new system modelling language SySML has been chosen to facilitate the system engineering and to document the system. SysML uses 9 diagram types to describe the structure and behavior of the system. The hierarchy of the diagrams allows individual task managers to develop detailed subsystem descriptions in a consistent framework.

We present the description of functional and non-functional requirements, the system design and the test cases.

## CONCEPT OF SYSTEM ENGINEERING

Systems Engineering signifies both an approach and, more recently, as a discipline in engineering. The aim of education in Systems Engineering is to simply formalize the approach and in doing so, identify new methods and research opportunities similar to the way it occurs in other fields of engineering. As an approach, Systems Engineering is holistic and interdisciplinary in flavor.

Systems engineering is a robust approach to the design, creation, and operation of systems. In simple terms, the approach consists of identification and quantification of system goals, creation of alternative system design concepts, performance of design trades, selection and implementation of the best design, verification that the design is properly built and integrated, and post-implementation assessment of how well the system meets (or met) the goals.

- Understand the whole problem before you try to solve it.
- Translate the problem into measurable requirements
- Examine all feasible alternatives before selecting a solution.
- Make sure you consider the total system life cycle. The birth to death concept extends to maintenance, replacement and decommission. If these are not considered in the other tasks, major life cycle costs can be ignored.
- Make sure to test the total system before delivering it.
- Document everything.

#stefan.simrock@desy.de

The seven-task process defined above is an excellent representation of systems engineering as is presently practiced and should serve to avoid most of the problems that have plagued the development of large, complex systems in the past.

## SYSML LANGUAGE

The Systems Modeling Language (SysML), is a Domain-Specific Modeling language for systems engineering. It supports the specification, analysis, design, verification and validation of a broad range of systems and systems-of-systems. SysML was originally developed by an open source specification project, and includes an open source license for distribution and use. SysML is defined as an extension of a subset of the Unified Modeling Language (UML) using UML's profile mechanism. SysML uses seven of UML 2.0's thirteen diagrams, and adds two diagrams (requirements and parametric diagrams) for a total of nine diagram types. SysML also supports allocation tables, a tabular format that can be dynamically derived from SysML allocation relationships.

Table 2: Diagram Types

| SysML Diagram | Purpose |
|---|---|
| Activity | Show system behavior as control and data flows. Useful for functional analysis. |
| Block Definition diagram | Show system structure as components along with their properties, operations and relationships. Useful for system analysis and design. |
| Internal Block diagram | Show the internal structures of components, including their parts and connectors. Useful for system analysis and design. |
| Parametric diagram | Show parametric constraints between structural elements. Useful for performance and quantitative analysis. |
| Requirement diagram | Show system requirements and their relationships with other elements. Useful for requirements engineering. |
| Sequence diagram | Show system behavior as interactions between system components. Useful for system analysis and design. |
| State Machine diagram | Show system behavior as sequences of states that a component or interaction experience in response to events. Useful for system design and simulation/code generation. |
| Use case diagram | Show system functional requirements as transactions that are meaningful to system users. Useful for specifying functional requirements. (Note potential overlap with Requirement diagrams.) |

## LLRF SYSTEM

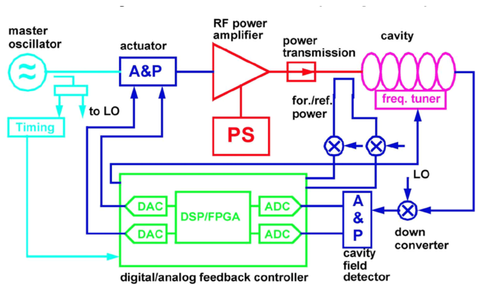

Figure 1: LLRF System Architecture

The architecture of the RF system for the European XFEL is shown in Figure 1. A power amplifier provides the rf power necessary for establishing the accelerating fields in the cavities. The cavity field is measured and the compared to a set-point. The resulting error signal is amplified and filtered and drives a controller for the incident wave to the cavity. A frequency and phase reference system provides the necessary rf signals.
Frequency tuner (motor and piezo) are used for slow and fast resonance control. The timing system provides triggers for pulsed operation and clocks for data acquisition.

## LLRF DIAGRAMS

Several types of diagrams are used to describe the LLRF system:

- Requirement diagrams
- Structural diagrams
- Behavioral digrams
- Parametric diagrams

In the following we describe some examples of diagrams which represent the view of the llrf project team. A view is a representation of a whole system from the perspective of a single viewpoint.

### *Context Diagram*

A System Context Diagram (SCD) is the highest level view of a system, similar to Block Diagram, showing a (normally software-based) system as a whole and its inputs and outputs from/to external factors. The best System Context Diagrams are used to display how system

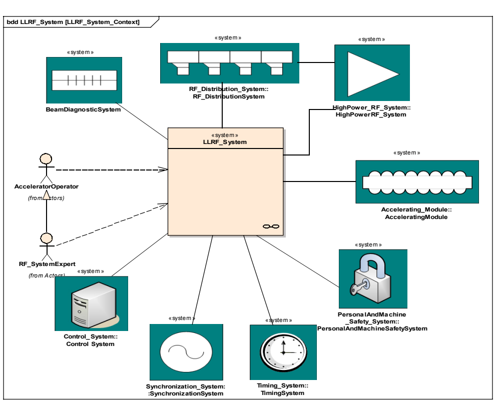
Figure 2: System context diagram

inter operates at a very high level or how systems operate and interact logically. The system context diagram is a necessary tool in developing a baseline interaction between systems and actors; actors and system or systems and systems.

### *LLRF Use Cases*

The use case technique is used in software and systems engineering to capture the functional requirements of a system.

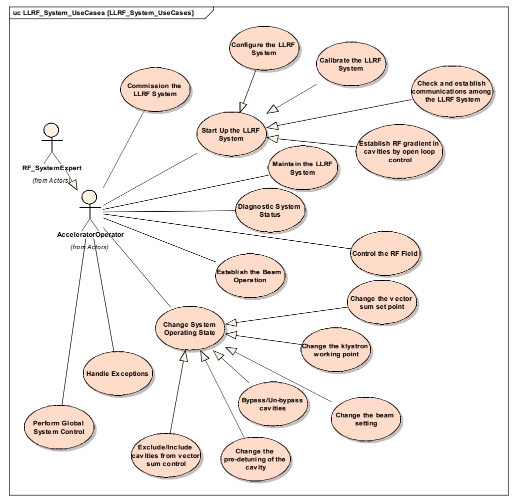

Figure 3: Use cases for the LLRF system

Use cases describe the interaction between a primary Actor (the initiator of the interaction) and the system itself, represented as a sequence of simple steps. Actors are something or someone which exist outside the system under study, and that take part in a sequence of activities in a dialogue with the system to achieve some goal. They may be end users, other systems, or hardware devices. Each use case is a complete series of events, described from the point of view of the Actor.

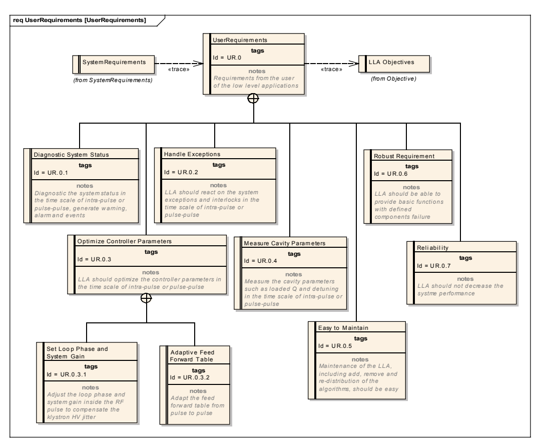
Figure 4: Requirements for an LLRF Subsystem

### *Requirements*

In engineering, a requirement is a singular documented need of what a particular product or service should be or do. It is most commonly used in a formal sense in systems engineering or software engineering. It is a statement that identifies a necessary attribute, capability, characteristic, or quality of a system in order for it to have value and utility to a user.

In the classical engineering approach, sets of requirements are used as inputs into the design stages of product development. Requirements show what elements and functions are necessary for the particular project.

The requirements development phase may have been preceded by a feasibility study, or a conceptual analysis phase of the project. The requirements phase may be broken down into requirements elicitation (gathering the requirements from stakeholders), analysis (checking for consistency and completeness), specification (documenting the requirements) and verification (making sure the specified requirements are correct)

### *Block Definition Diagram*

Block diagram is a diagram of a system, in which the principal parts or functions are represented by blocks connected by lines, that show the relationships of the blocks. They are heavily used in the engineering world in hardware design, software design, and process flow diagrams.

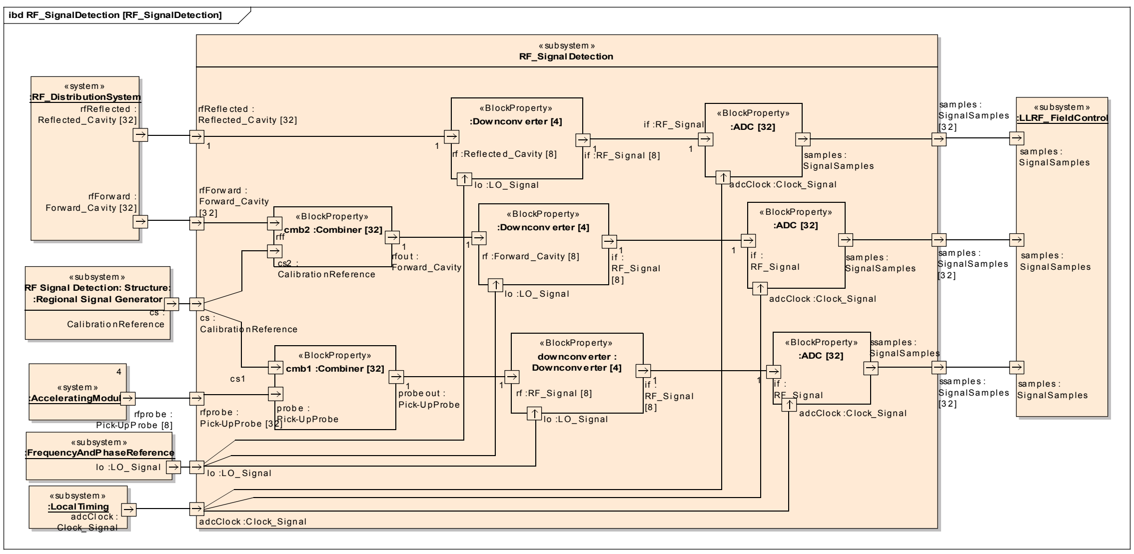

Figure 5: Example for an internal block diagram showing the interfaces and item flow between the LLRF subsystems.

### *Activity Diagram*

An activity diagram is a diagram that shows activities and actions to describe workflows. In the Unified Modeling Language an activity diagram represents the business and operational step-by-step workflows of components in a system. An activity diagram shows the overall flow of control.

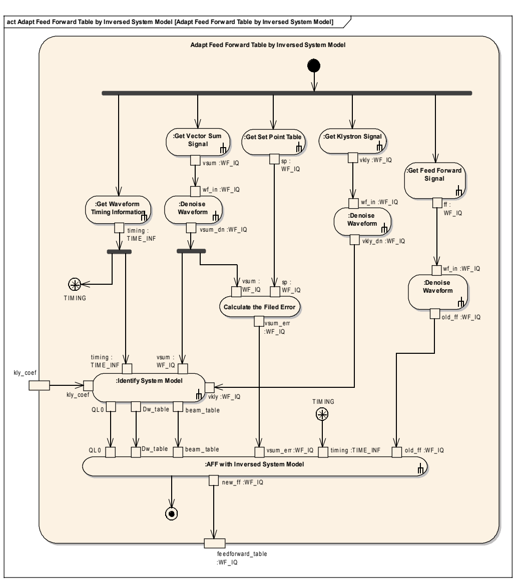

Figure 6: Example for an activity diagram.

In SysML the activity diagram has been extended to indicate flows among steps that convey physical element or energy. Additional changes allow the diagram to better support continuous behaviors and continuous data flows.

## SUMMARY

Complex systems such as the LLRF control for the European XFEL require work-processes and tools to guarantee a successful outcome. The attempt to combine of modern system engineering methodologies with the modeling language SysML and the SysML Modeling tool Enterprise Architect (EA) has proven to be very promising in a large international collaboration between research labs, universities and industry.

## REFERENCES

[1] (1995) NASA Systems Engineering Handbook. NASA. SP-610S.

[2] Weilkiens, T. , "Systems Engineering with SysML/UML", 1st edition, 2008, Morgan Kaufmann Publishers Inc., ISBN 0123742749

# LOW LEVL RF AND TIMING SYSTEM FOR XFEL/SPRING-8

T. Ohshima[a,#], N. Hosoda[a], H. Maesaka[a], K. Tamasaku[a], M. Musha[b], Y. Otake[a]
[a]RIKEN, XFEL project/SPring-8, 1-1-1 Kouto, Sayo, Hyogo, 679-5148, Japan
[b]Institute of Laser Science, Univ. Electro-communications, 1-5-1 Chofugaoka, Chofu, Tokyo, 182-8585, Japan

*Abstract*

The construction of XFEL/SPring-8 is progressing. In this accelerator, it is needed to obtain stabilities of 50 fs and 1E-4 in time and amplitude of the acceleration voltage. To satisfy these requirements, rf components, such as a reference rf oscillator with low phase noise, IQ modulators and so on, were developed. These modules were installed to an SCSS test accelerator. Their performance was confirmed by monitoring the beam arrival timing compared with the reference rf signal. The measured time jitter of the arrival timing was 46 fs, which implies that the rf modules have a potential to control the timing of the accelerator within several 10 fs. Using these modules, the SCSS test accelerator is operated stably and offers EUV light to user experiments. The compression factor of the XFEL is about 10-times larger than that of the test accelerator. Thus special care is taken for the XFEL to keep the temperature of rf modules constant. For delivery of the reference rf signals, an optical system is adopted instead of coaxial cables, because signal transmission loss with coaxial cable is not allowed for the long distance for the XFEL..

## INTRODUCTION

Construction of the XFEL/SPring-8, Japan is in progress. Fig. 1 shows a schematic view of the rf components of the XFEL. An electron beam with an energy of 500 keV and a current of 1A is extracted from a thermionic gun. Velocity bunching is done by using 238 MHz, 476 MHz, and 1428 MHz (L-band) sub harmonic cavities, which increase the beam energy and compress the bunch length. Then, the beam is passed through cavities with frequencies of 2856 MHz (S-band) and 5712 MHz (C-band) and three magnetic bunch compressors (BC 1 ~ 3). Two correction cavities are used to compensate for the non-linearity of the sine wave, and to give a linear energy chirp to the beam. The peak current is increased very carefully as the beam energy is increased.

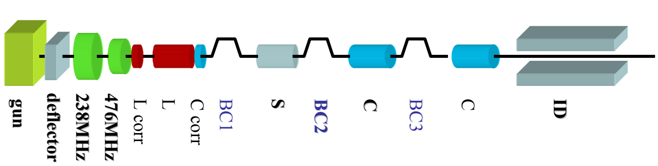


Figure 1: Schematic view of the rf components in the XFEL.

[#]ohshima@spring8.or.jp

This is because the beam emittance is easily blown up by a strong space charge force. Thus the allowable amplitude and phase fluctuations of the accelerating cavity voltages at the bunch compressor section are very severer: 50 fs and 1E-4 [1]. At the crest acceleration section the requirement to the rf phase stability is relaxed: 240 fs because dV/dt is nearly zero. Finally, the expected peak current at the insertion device is 3 kA with a beam energy of 8 GeV. To obtain saturated self-amplified spontaneous emission (SASE) light, it is important to maintain a very high peak current, i.e., a very high bunch compression ratio. The phases and amplitudes of the rf cavities should be stable within their tolerances, as mentioned above.

To satisfy these requirements, the rf components, such as a reference rf oscillator with low phase noise and an IQ (In-phase and Quadrature) modulator / demodulator have been developed [2]. Their performances measured at a test accelerator, issues concerning temperature stabilization of the rf modules, and the delivery system of the reference signal for the XFEL are shown in the following.

## PERFORMANCE OF THE LLRF SYSTEM AT THE SCSS TEST ACCELERATOR

The SCSS test accelerator was constructed in 2005. Its beam energy is 250 MeV. The machine length is about 70 m. Components shown in Fig.1 with bold face are installed in the test accelerator. To drive all of the high power rf sources of the test accelerator, and to realize stable SASE generation, a low-noise reference signal oscillator was developed. The phase noise of 5712 MHz signal is -140dBc/Hz at an offset frequency of 1 MHz to the carrier signal. The sub-harmonic signals for velocity bunching are generated by dividing the 5712MHz signal. The reference signals are transmitted to 19" racks located along the klystron gallery of the test accelerator through coaxial cables. There, the reference signal is modulated by an IQ modulator controlled by a high-speed 14-bits DAC, and fed to a high-power klystron. It excites the accelerating cavity. The phase and the amplitude of the accelerating voltages are monitored by an IQ demodulator and high-speed 12-bits ADCs.

As described in the previous section, the phase and amplitude of the 238MHz sub-harmonic cavity voltage are sensitive to the lasing stability. Thus, a feedback process to stabilize the rf phase and amplitude of the cavity voltage is introduced. Fig. 2 shows the set and measured values of (a) the phase and (b) the amplitude of the pickup signal of the 238MHz cavity. The setting

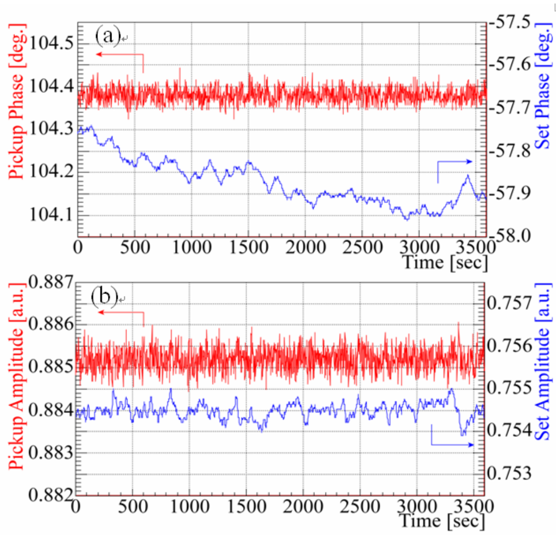


Figure 2: Set and measured value of (a) the phase and (b) the amplitude of the 238 MHz cavity pickup signal at the test accelerator.

resolutions are 0.01 degree and 1E-4 in phase and amplitude. Fluctuations of the phase and amplitude are 0.02 degree and 3E-4 in r.m.s. [3].

To evaluate the total performance of the rf system of the test accelerator, the beam arrival time to a reference rf signal was measured. The signal from the cavity of an RF BPM located after a C-band accelerating structure has a frequency component of 4760 MHz. The phase difference between this signal and the 4760 MHz reference rf signal was measured. The r.m.s. value of the phase fluctuation was 0.08 degree, which corresponds to 46 fs in time. This implies that our rf control systems, including the master oscillator, the delivery system of the reference rf signals, and the cavity phase and amplitude controls with the IQ modulators and demodulators, have a potential to achieve a time jitter of less than several 10 fs. Fig. 3 shows trend of the arrival time for one week during a user run. There is a small drift of the arrival time each day. It has a strong correlation to the beam energy measured at a dispersive section of the BC of the test accelerator. This implies that a change of the beam energy leads to an arrival time change through the R56 parameter of the BC. The main source of this drift may be caused by a temperature change due to a daily machine operation cycle: starting in the morning and stopping in the night. This thermal cycle may cause a voltage change in the high-voltage power supply of the electron gun, a length change of the cavity pickup cables used for rf monitoring, the gain or offset change of detection in the IQ demodulator modules and so on. Although there are still small drifts in the arrival timing, the laser intensity is almost constant, as shown in Fig. 3. The r.m.s. value of the fluctuation of the laser intensity is about 10%. The test accelerator is operated stably, and provides stable EUV light to experimental users [4, 5].

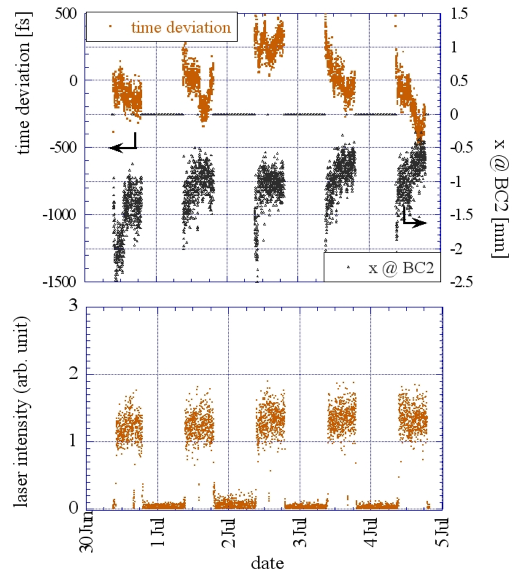


Figure 3: Trend of the arrival time (top), horizontal beam position measured at a dispersive section of the BC (middle) and the observed EUV laser intensity (down) for one week.

## IMPROVEMENTS OF THE LLRF SYSTEM FOR THE XFEL

Here, two topics describing improvements in the low-level rf system of the test accelerator to extend to the XFEL/SPring-8 are shown. One is a temperature-control issue to overcome the drift problem described in the previous section. The other is a delivery issue of the reference rf signals to adapt for the long machine length of the XFEL.

### *Temperature-Control Issue*

Because the bunch compression factor of the XFEL is about 10-times larger than that of the test accelerator, the temperature drift allowed in the test accelerator may not be sufficient at the XFEL. Special care should be taken for the temperature control in the low-level rf system for the XFEL. A water-cooled 19” rack was developed to stabilize the temperature around rf modules, such as a receiver module for the reference rf signal, an IQ modulator, an IQ demodulator, a preamplifier for driving a klystron and so on. The rack has a heat exchanger and blowers to stabilize the temperature inside the rack. The heat exchanger is cooled by water whose temperature is kept constant within +/- 0.2 degree. The performance test of this cooling rack with a constant heat load of 1 kW was carried out. A step change of 4 K to the ambient temperature was applied at the test. This is because the temperature stability of the large klystron gallery of the XFEL is designed to be within +/- 2K in a specification of the air conditioner. The temperature stability inside the rack was within 0.4 degree at this test.

A software feedback control process is used to stabilize the rf phases and the amplitude of all the accelerating cavities (238, 476, 2856, 5712 MHz cavities) along the test accelerator. This feedback works with preconditions, which include that the low-level rf system has a stable rf reference and a minimum drift of the rf phase and amplitude detection. Thus the lengths of a reference signal line and a pickup cable from the rf cavity to the rf detector included in the rack should be stabilized. For this purpose, the reference cable and the pickup cables of the XFEL will be equipped with thermal insulation and water cooling.

### *Delivery of Reference rf Signals and the Trigger Signal*

Because of the long delivery length, we use an optical-fiber link to distribute reference rf signals and a trigger signal at the XFEL [6]. Fig. 4 shows a schematic diagram of a system used to deliver the signals. We have the reference signals of the several sub-harmonic frequencies, and the trigger signal, as mentioned previously. To reduce the number of fiber cables for delivering signals, we apply a wavelength division multiplexing (WDM) for the system. Prototype modules of an optical transmitter and a receiver for a 5712 MHz signal transmission were fabricated. The phase noise of the signal before and after optical transmission was checked in a test. A slight increase of the phase noise of a 5712 MHz signal was observed above an offset frequency of 1 MHz. However the value of the phase noise integrated along the region was small, and corresponds to about 7 fs, which is an allowable level for the XFEL requirement.

We use a phase-stabilized optical fiber with a thermal-expansion coefficient of 5 ps/km/K to prevent rf phase drift in the reference signals. Even if we use this stabilized fiber, the time delay could be as much as 500 fs with conditions of 1km length and a temperature change of 0.1 K. This change of the delay time is not allowable for the XFEL, and thus a feedback control circuit is prepared to stabilize the optical length of the fiber. This circuit is based on a Michelson interferometer. A preliminary test of the circuit was carried out by using an existing 2 km optical fiber cable placed along the circumference of the SPring-8 ring accelerator. The test result showed that the stability of the optical length controlled by the circuit was within 2 μm in a frequency range below 100 Hz.

## SUMMARY

We have developed low-level rf components for XFEL. The basic components are used in the SCSS test accelerator. A phase jitter of 0.02 degree and an amplitude fluctuation of 3E-4 in r.m.s at a 238 MHz cavity were obtained with these components. The total performance of the low level rf system was confirmed by measuring the beam arrival time, whose jitter was less than 46 fs in r.m.s, For temperature stabilization of the rf components, a water-cooled 19" rack was developed. For distributing of the reference signal of the XFEL, an optical transmission system with WDM and an optical length control system for the fiber cable were developed. Their test results show that an increase of the phase noise in the transmission system was suppressed down to 7 fs, and the optical length of a fiber cable was controlled to within 2 μm for a 2 km fiber. The total performance satisfies the requirements for the XFEL.

## REFERENCES

[1] H. Tanaka, private communication.
[2] Y. Otake et al., "SCSS RF Control Toward 5712 MHz Phase Accuracy of One Degree", proc. of APAC'07.
[3] H. Maesaka, et. al., "Precise RF Control System of the SCSS Test Accelerator", proc. of EPAC08, pp 1944-1946, (2008).
[4] H. Tanaka et al., "Operation Status of the SCSS Test Accelerator", proc. of EPAC08, pp 1944-1946, (2008).
[5] T. Tanaka et al., "SASE Saturation at the SCSS Test Accelerator Ranging from 50 nm to 60 nm", proc. of FEL08, (2008).
[6] H. Maesaka, et al., ""Development of the Optical Timing and RF Distribution System for XFEL/SPring-8", proc. of FEL08, (2008).

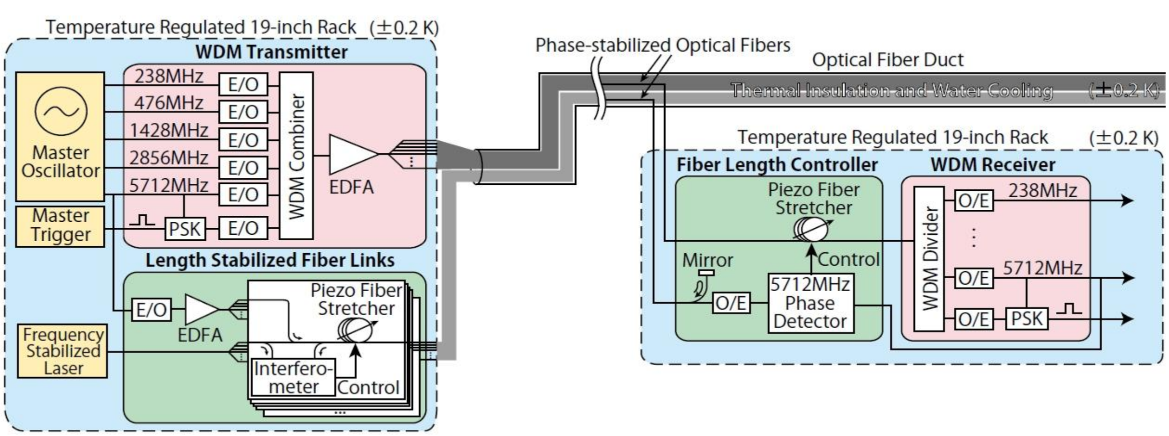


Figure 4: Schematic view of reference rf signals and the trigger-signal delivery system.

# LLRF CONTROL SYSTEM OF THE J-PARC LINAC

Z. Fang, S. Anami, S. Michizono, S. Yamaguchi, KEK
T. Kobayashi, H. Suzuki, JAEA

*Abstract*

In the J-PARC proton LINAC, each klystron drives two RF cavities. The RF amplitude and phase of the cavities are controlled by an FPGA-based digital feedback control system. The test results show that the variations in the cavity amplitude and phase are less than 0.1% and 0.1° without beam loading, or 0.3% and 0.2° with beam loading. The tuning of each cavity is also controlled by a DSP of this control system. The cavity auto-tuning is successfully controlled to keep the detuned phase within ±1 degree. In our RF system, the tuning information including detuned frequency and phase, and Q-value of each cavity are measured in real-time and displayed in the PLC touch panel of the control system.

## INTRODUCTION

The RF sources of the J-PARC 181-MeV proton LINAC consist of 4 solid-state amplifiers and 20 klystrons with operation frequency of 324 MHz. The RF fields of each RF source are controlled by an FPGA-based digital RF feedback system installed in a compact PCI, which consists of the CPU, IO, DSP with FPGA, Mixer & IQ modulator, and RF & CLK boards [1-5]. Besides, the tuning of each accelerator cavity including 3 DTLs and 15 SDTLs is also controlled by this feedback system through a cavity tuner.

## FEEDBACK PERFORMANCE

High-power tests were performed for the 24 RF systems of the J-PARC LINAC. A very good stability of the accelerating fields has been successfully achieved about ±0.1% in amplitude and ±0.1° in phase without beam loading, or ±0.3% in amplitude and ±0.2° in phase with beam loading, much better than the requirements of ±1% in amplitude and ±1° in phase. Fig. 1 shows an example of the cavity outputs with FB ON at SDTL7 with full power operation, when the RF amplitude is set to 4000 and the phase is set to 0°.

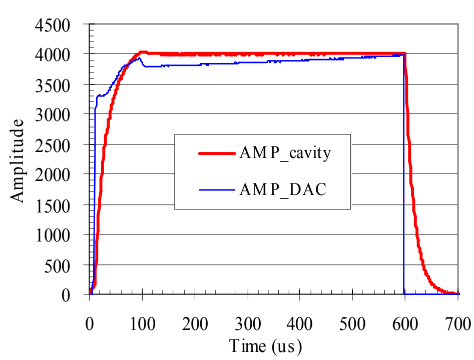


a) full scale of cavity and DAC amplitude waveform.

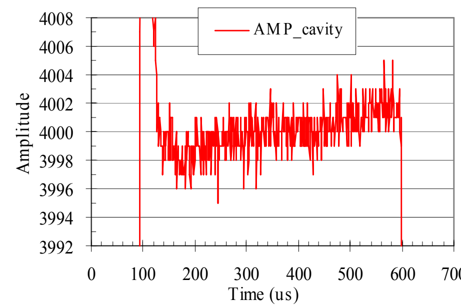


b) expansion of flat top of cavity amplitude.

Figure 1: Amplitudes of cavity and DAC outputs with FB ON at SDTL7.

## THREE METHODS OF $F_0$ SETTING

By adjusting the tuner position, we tune the RF cavity with a resonant frequency of 324 MHz, and register the phase difference between picked-up signal from cavity and cavity input signal, which will be used in the auto-tuning control of the RF cavity. This process is called as $f_0$ setting of RF cavity.

We have investigated three methods of $f_0$ setting of RF cavity with FB OFF. With the cavity tuner moved, we take data of 1) cavity amplitude, 2) reflection from cavity, and 3) phase slope during field decay. Then the tuner positions for 1) the maximum cavity amplitude, 2) the minimum reflection, and 3) the flat cavity-phase decay, are obtained, which correspond to the positions for $f_0$ setting of the three methods.

Figure 2 shows an example of $f_0$ setting data by the three methods at S1A; cavity amplitude normalized by input signal (red curve), reflection amplitude from cavity (green curve), and cavity phase slope during field decay (blue curve), as function of tuner position. We can see that, the $f_0$ setting tuner positions of the three methods are different from each other.

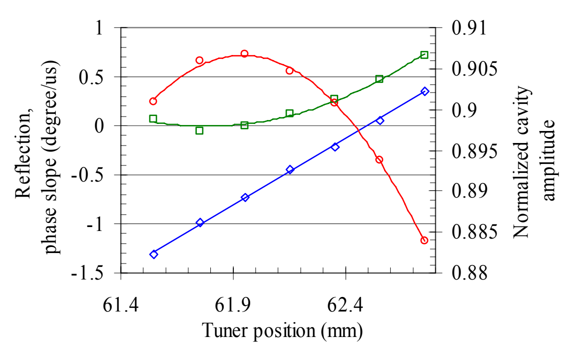


Figure 2: Cavity amplitude (red curve), reflection from cavity (green curve), and cavity phase slope during field decay (blue curve), as function of tuner position for S1A.

## AFFECTING BETWEEN TWO CAVITIES

At the SDTLs of the J-PARC LINAC, one klystron drives two cavities, as shown in Fig. 3. However each component in the waveguide systems is not an ideal device. For examples, there are reflections from cavities and dummy loads; the hybrid has a finite isolation between the two outputs; and also the direction couplers have a finite directivity. Due to the hybrid isolation and dummy reflection, the reflection from one cavity will affect the RF amplitude and phase of the other cavity.

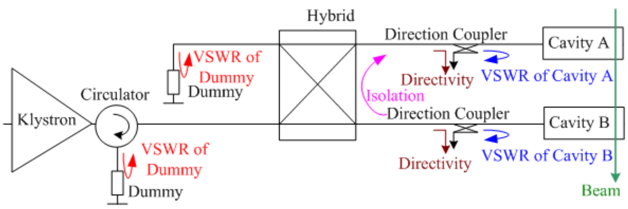


Figure 3: Setup of RF systems at the SDTLs of the J-PARC LINAC.

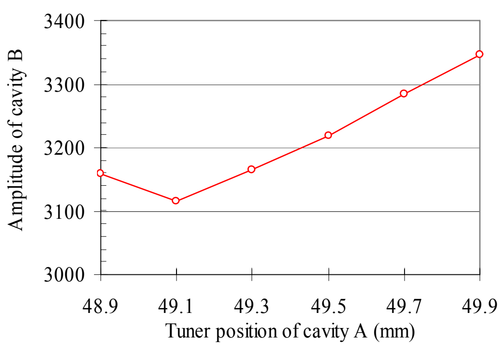


(a) Amplitude of cavity B

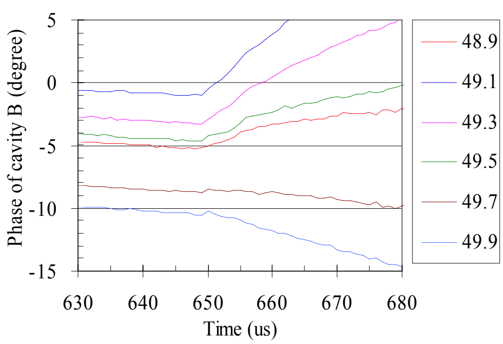


(b) Phase of cavity B

Figure 4: Amplitude and phase of cavity B as function of tuner position of cavity A.

Figure 4 shows an example of test results of affecting between the two cavities at S14. We can see that, when the tuner of cavity A is moved, both the amplitude and phase of cavity B change much.

The maximum amplitude method for $f_0$ setting is not good in the case with large affecting between the two cavities, since it will result in a large system error. On the other hand, the minimum reflection method by using a directional coupler is not good either. Two reasons, the affecting between the two cavities and directivity (about -35dB) of directional coupler, will result in a worse system error.

Only by using the method with flat cavity-phase decay, the cavity will be exactly tuned at 324 MHz, because the phase decay is just determined by the frequency difference of the cavity itself from the sampling frequency (324 MHz).

However, with FB OFF, the cavity power will be affected when the other cavity tuner is moved, so the resonant tuner position will be changed too. Therefore we should take the data of the resonant tuner position corresponding to a fixed cavity power with FB ON.

## CORRECT $F_0$ SETTING METHOD

From the above discussion of $f_0$ setting by the three methods, we know the correct method is the flat phase decay method with FB ON. This conclusion has been proved by late experiments, in which it was confirmed that the cavity resonant tuner position by flat phase decay method is only dependent on cavity power, even with interactions between cavities.

Figure 5 shows the test results of resonant tuner position of cavity B at S14 with flat phase decay method, when the tuner of cavity A is moved to change the interactions between the two cavities.

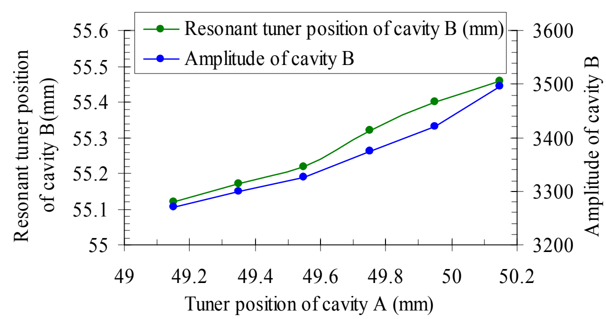


(a) Cavity A and B are set with FB OFF.

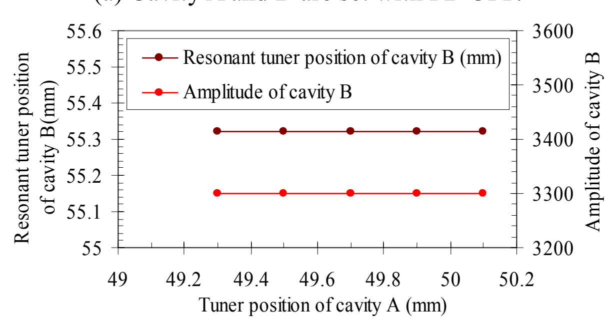


(b) Only Cavity B is set with FB ON.

Figure 5: Resonant tuner position of cavity B as function of tuner position of cavity A at S14.

From the above experiments, we can see that, 1) in case of FB OFF, both the cavity power and the resonant tuner position are changed when the other cavity tuner is moved; and 2) in case of FB ON, both the cavity power and the resonant tuner position are fixed even when the other cavity tuner is moved.

Finally, the $f_0$ setting method using flat phase decay with FB ON is adopted in the actual operation of the J-PARC LINAC. We pre-defined the cavity resonant states with the tuner adjusted to obtain a constant phase during the cavity field decay. The cavity auto-tuning is successfully controlled to keep the detuned phase within ±1 degree.

## GENERAL DISCUSSION ON $F_0$ SETTING

From the above analysis and experiments, it is concluded that:

1) In case of one cavity without cavity interactions, both the maximum amplitude method and flat phase decay method should be correct, and the results from the two ways should be same. This point has been confirmed by experiments at BUN1, BUN2, and DEB2. The resonant tuner positions from the two methods are exactly same as shown in Fig. 6.

2) In case of two cavities with cavity interactions, the maximum amplitude method is not good, while only the flat phase decay method is correct.

3) In any cases, due to the directivity of directional coupler, the minimum cavity input method with FB ON is not good.

4) Again, in any cases, due to the directivity of directional coupler, the minimum cavity reflection method is not good either.

The $f_0$ setting methods for different cases of cavity interactions are summarized in Table 1.

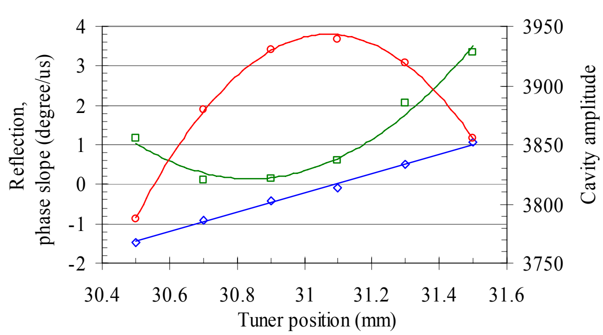


Figure 6: Cavity amplitude (red curve), reflection from cavity (green curve), and cavity phase slope during field decay (blue curve), as function of tuner position for BUN2.

Table 1: $F_0$ Setting Methods for different Case of Cavity Interaction

| Case of cavity interaction | Maximum amplitude method | Flat phase decay method |
|---|---|---|
| one cavity without cavity interactions | Correct | Correct |
| two cavities with cavity interactions | Not good | Correct |

For the maximum amplitude method, it can only be used in case of one cavity with FB OFF. For the flat phase decay method, it can be used in any cases, one or two cavities, with FB ON or FB OFF. We just need to take care of the cavity power at the moment of resonance measuring. The flat phase decay is the absolute standard of cavity resonance.

## AUTO-TUNING AND Q-VALUE MONITORING

In our RF system, the detuned phases of RF cavities are successfully controlled within ±1 degree, and the tuning information including detuned frequency and phase, and Q-value of each cavity are measured in real-time and displayed in the PLC touch panel.

From the amplitude waveform during the cavity field decay, the time constant of decay is calculated out by measuring the amplitude at two sampling points:

$$T_d = \frac{t_2 - t_1}{\ln(AMP_1) - \ln(AMP_2)}\,.$$

Then, the Q-value of cavity is carried out:

$$Q_L = \frac{\omega_{rf}}{2} \times T_d\,.$$

In the meantime, from the phase waveform during the cavity field decay, the detuning frequency and phase of each cavity are calculated out:

$$\Delta f = \frac{d\theta}{2\pi \times dt}\,, \quad \Delta\varphi = \tan^{-1}(2Q_L \frac{\Delta f}{f_0})\,.$$

All of those parameters are monitored in real-time in the PLC touch panel of the control system.

## SUMMARY

By using developed FPGA-based RF feedback control systems, a very good stability of the accelerating fields has been successfully achieved about ±0.2% in amplitude and ±0.2 degree in phase.

The three methods of $f_0$ setting of RF cavity, 1) maximum cavity amplitude, 2) minimum reflection, and 3) flat cavity-phase decay, have been discussed. Finally, the $f_0$ setting method using flat phase decay with FB ON is adopted in the actual operation of the J-PARC LINAC. The cavity auto-tuning is successfully controlled to keep the detuned phase within ±1 degree.

The tuning information including detuned frequency and phase, and Q-value of each cavity are measured in real-time and displayed in the PLC touch panel in our RF system.

## REFERENCES

[1] S. Anami et al., "Control of the Low Level RF System for the J-PARC Linac", LINAC 2004, 739–741, Germany.

[2] S. Michizono et al., "Performance of Digital LLRF Field Control System for the J-PARC Linac", LINAC 2006, USA.

[3] Z. Fang et al., "Stabilization of Accelerating Field Using FPGA for J-PARC Linac", Proceedings of the 3rd Japan Particle Accelerator Conference and the 31st Linear Accelerator Meeting in Japan, 2006.

[4] T. Kobayashi et al., "Performance of J-PARC Linac RF System", Proceedings of the 4th Japan Particle Accelerator Conference and the 32nd Linear Accelerator Meeting in Japan, 2007.

[5] H. Suzuki et al., "PLC control of J-PARC LowLevel RF System", Proceedings of the 4th Japan Particle Accelerator Conference and the 32nd Linear Accelerator Meeting in Japan, 2007.

# HIGH SPEED DATA ACQUISITION SYSTEM USING FPGA FOR LLRF MEASUREMENT AND CONTROL

H. Katagiri, S. Fukuda, T. Matsumoto, T. Miura, S. Michizono, Y. Yano, M. Yoshida
High Energy Accelerator Research Organization
1-1 Oho, Tsukuba, Ibaraki 305-0801, Japan

*Abstract*

Currently, FPGA (Field Programmable Gate Array) technology is being widely used for accelerator control owing to its fast digital processing capability. We have recently developed a high-speed data acquisition system that combines a commercial FPGA board (ML555) with a fast ADC (ADS5474; 14 bit; maximum sampling rate: 400 MS/s; bandwidth: 1.4 GHz). This system enables direct measurements of 1.3-GHz RF signals at a sampling frequency 270 MHz. This direct sampling method does not require a down-converter, and hence, the calibration step can be avoided. These results are analyzed and compared with those obtained with the conventional measurement method.

## INTRODUCTION

Plans for the construction of an STF (Superconducting RF Test Facility) for the ILC (International Linear Collider) are currently in progress [1,2]. An LLRF (Low Level RF) control system based on a compact PCI has been installed in the STF at KEK in order to achieve the required amplitude and phase stability (0.3% and 0.3°) during RF pulse (1300 MHz, 1.5 ms) generation [3]. A customized FPGA board, which is built into the PCI crate, conducts feedback and feedforward control. The amplitude and phase, measured using the intermediate frequency (IF) conversion method, have been adopted in the LLRF control system. An RF signal is converted into a 10-MHz IF signal using a down-converter. The FPGA board (equips 10 16-bit ADCs) samples the IF signal at a 40-MHz clock signal and calculates IQ elements for the collection of amplitude and phase data. Recently, a high-speed and wideband ADC, which that can sample RF signal directly, 1300 MHz RF signal is available. A high-speed data acquisition system using a fast ADC has been utilized for evaluating the efficiency of the direct sampling method.

## CONSTRUCTION OF HIGH-SPEED DATA ACQUISITION SYSTEM

The high-speed data acquiring system is composed of an ADC board (ADS5474EVM) and an FPGA board (ML555). The FPGA board stores the raw data acquired by the ADC board in its internal memory. This data is then transmitted and analyzed by the host PC (Fig.1). Figure 2 shows the ML555 installed in a PCI-Express slot on the host PC. ML555 and ADS5474EVM are connected by LVDS cables via adaptors, as shown in Fig.3.

### *ADS5474*

ADS5474EVM is an evaluation board equipped with an ADS5474 ADC manufactured by Texas Instruments. Its features are as follows:

- Resolution: 14 bit
- Maximum sampling rate: 400MSPS
- Analog bandwidth: 1.4 GHz
- Data output: LVDS compatible

### *ML555*

ML555 is a commercial FPGA board manufactured by Xilinx and is equipped with a Virtex-5 (XC5VLX50T).

Its features are as follows:

- PCI-Express/PCI/PCI-X card-edge connector
- DDR2-SDRAM
- LVDS interface with SAMTEC connector

USB port

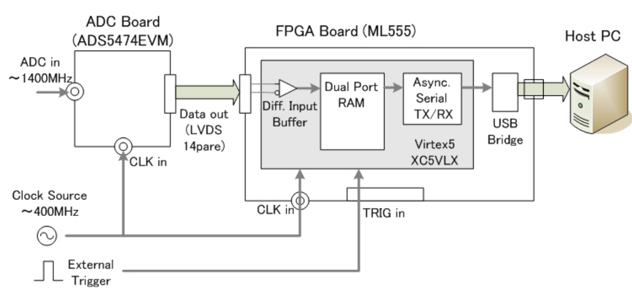


Figure 1: Block diagram of the high-speed data acquisition system.

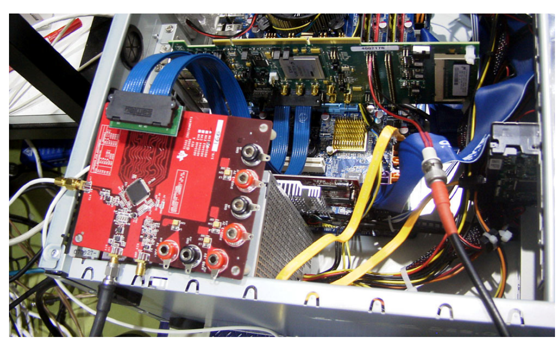

Figure 2: ML555 and ADS5474EVM on host PC.

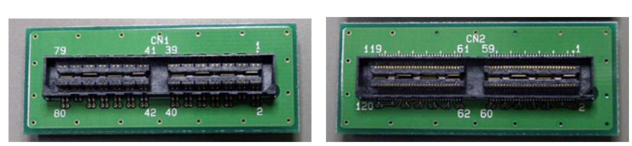


Figure 3: SAMTEC connector adaptor.

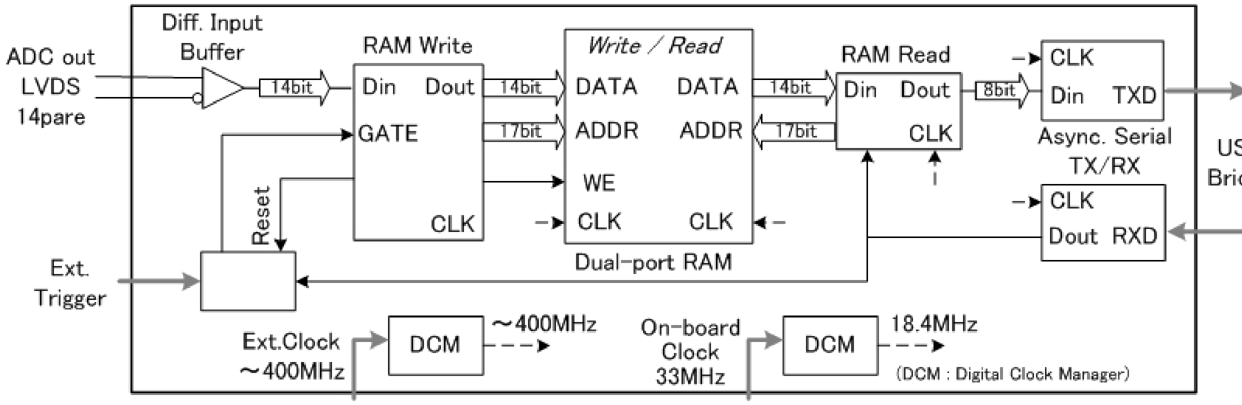


Figure 4: Block diagram of the FPGA logic.

## DESIGN OF FPGA LOGIC

Figure 4 shows the construction of an FPGA logic. Xilinx ISE9.2, an integrated development tool, has been utilized for designing the FPGA logic.

### *LVDS Interface*

Virtex5 has input-buffers and output-buffers which can handle single-end signal and differential signals.

ML555 is equipped with two SAMTEC connectors as the LVDS interface.

### *Data Acquisition and Storage*

A built-in memory block Virtex-5 has been used to accumulate the acquired data. A dual-port RAM (width: 14 bit; 131,072 words) designed by CoreGenerator is included in the designing software developed by Xilinx (ISE9.2). At a sampling frequency of 400 MHz, the memory block can accumulate data of around 327 μs. The data accumulation time is controlled by the external trigger signal.

### *Host Interface*

A USB-UART (Universal asynchronous receiver-transmitter) bridge is equipped with ML555. ML555 has been identified to be connected with the serial port on the host computer upon installation of the bridge driver software. An asynchronous serial communication circuit, which was developed for another FPGA board, is used to reduce the development time. A communication program on the host PC is designed using LabVIEW. The entire data in the FPGA can be transferred in approximately 4 seconds.

## EVALUATION OF DIRECT SAMPLING IN STF

### *Direct Sampling Method*

The high-speed data acquisition system is applied to electric field measurement of the superconducting cavity in STF. The direct sampling method has the following advantages. Because a sampling clock is faster, events that cannot be acquired by the IF conversion method might be detected. Since a down-converter is unnecessary, construction of the RF measurement circuit becomes significantly simple. Moreover, measurement errors that depend on the characteristics of the down-converter will be eliminated. However, because the sampling frequency is lower than the RF frequency, it is necessary to obtain an average of the data accumulated over several cycles in order to calculate the IQ elements. Therefore, selection of proper sampling frequency is important.

The clock divider and IQ modulator manufactured by Analog Devices were combined to distribute the clock signal to the data acquisition system. The frequency of the generated clock signal is calculated as follows:

$$f = \frac{1}{M}\left(f_0 + \frac{f_0}{N}\right) = \frac{N+1}{MN} f_0, \tag{1}$$

*where* $f_0$ is the input frequency (1.3GHz), and M and N are parameters of the frequency divider.

The data acquired in this method can be separated into I and Q elements by the following expressions [4,5]:

$$I = \frac{2}{L}\sum_{K=1}^{L} x(k) \times \cos\left(\frac{2\pi M N}{N+1} k\right) \tag{2}$$

$$Q = \frac{2}{L}\sum_{K=1}^{L} x(k) \times \sin\left(\frac{2\pi M N}{N+1} k\right) \tag{3}$$

The chosen parameters are M = 24, and N = 5 (sampling frequency: 270.83 MHz). In this case, the RF signal is sampled five times over 24 cycles.

### *Results*

The RF output signal obtained from the STF superconducting cavity was measured by the fast data acquisition system. Figure 5 shows the raw data recorded during the rising of the pulse signal using LabVIEW. The memory capacity of the FPGA was insufficient for acquiring the complete pulse width at 270.83 MHz. Hence, the measurements were repeated six times by adjusting the trigger time.

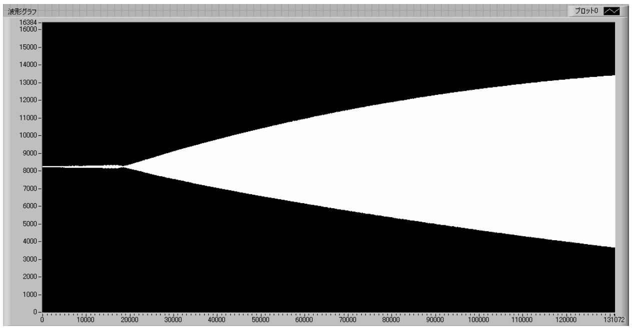

Figure 5: Amplitude and phase data obtained from direct sampling method.

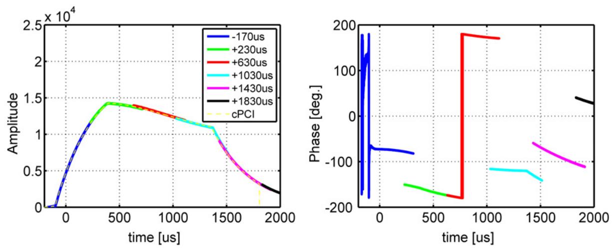


Figure 6: Amplitude and phase data obtained from direct sampling method.

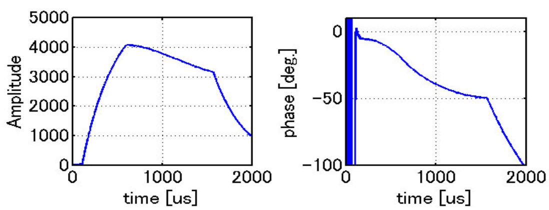


Figure 7: Amplitude and phase measured by IF convert method.

Figure 6 shows the amplitude and phase data of the complete pulse width converted by MATLAB. Though the reference point of the phase was different for each measurement, it was stable within the given range for a single measurement.

The amplitude and phase data obtained using the conventional IF conversion method are shown in Fig. 7. It is confirmed that the results of the direct conversion method agree well with those obtained with the conventional data acquisition system.

## CONCLUSION

A high-speed data acquisition system comprising ML555 and ADS5474 was employed to measure RF signals in STF by the direct sampling method. The effectiveness of this method was confirmed by verifying results of the measurement.

## REFERENCES

[1] "ILC Reference Design Report (RDR)," http://www.linearcollider.org/cms/?pid=1000437.

[2] S. Fukuda et al., "Status of RF Sources in Superconducting RF Test Facility (STF) at KEK," Linac08.

[3] S. Michizono et al., "Performance of Digital LLRF system for STF in KEK," Linac08.

[4] T. Matsumoto et al., "Performance of Digital Low-Level RF Control System with Four Intermediate Frequencies," Linac08.

[5] T. Matsumoto et al., "Low-level RF System for STF," Linac06, Knoxville, Aug 2006, p.586.

# PERFORMANCE OF DIGITAL LOW-LEVEL RF CONTROL SYSTEM WITH FOUR INTERMEDIATE FREQUENCIES

T. Matsumoto*, S. Fukuda, H. Katagiri, S. Michizono, T. Miura, Y. Yano, KEK, Tsukuba, Japan

*Abstract*

In superconducting accelerators, an FPGA-based low-level RF (LLRF) system is employed with a digital feedback control system to satisfy the stability requirement of the accelerating field. In the digital LLRF systems, an RF signal picked up from a cavity is down-converted into an intermediate frequency (IF) signal to estimate the I and Q components of the RF signal. A new digital LLRF system that uses four different IFs has been developed to decrease the number of analog-to-digital converters (ADC) required during the feedback operation of the RF sources.

In this study, the digital LLRF system with four different frequencies is examined and the feedback operation using a superconducting cavity is performed at the Superconducting RF Test Facility (STF) at KEK. The performance of the digital LLRF system is reported by measuring the stabilities of the accelerating fields.

## INTRODUCTION

A single RF system of the International Linear Collider (ILC) consists of three accelerating cryomodules (two of these are composed of nine superconducting cavities each and one is composed of eight cavities) and a klystron that generates RF power [1]. In the ILC, an accelerating field stability of 0.07% in amplitude and 0.24° in phase is required for its operation. In order to meet this requirement, the RF field is controlled with vector-sum feedback (FB) and feedforward (FF) mechanism using a digital low-level RF (LLRF) system based on an FPGA/DSP board.

In the digital LLRF system, the RF signal picked up from a cavity is down-converted into an intermediate frequency (IF) signal while retaining the amplitude and phase information of the RF signal. The IF signals are sampled by analog-to-digital converters (ADCs) with a constant sampling rate (SR) and the amplitude and phase information (or I and Q components) of the RF signal are determined by digital signal processing.

In the case of vector-sum FB control, the number of ADCs required for field detection is equal to the number of cavities, as shown in Figure 1(a). In the case of the ILC, one RF station requires 26 ADCs to operate the RF field with FB control. It is difficult to construct an FPGA board that can hold such a large number of ADCs because the number of lines between the FPGA and the ADCs increases as the number of ADCs increases.

Currently, a digital LLRF control system using a new IF-mixture technique is being developed in order to decrease the number of ADCs required for field detection. In this technique, the RF signals from different cavities are down-converted into different IF signals and these IF signals are then combined using a combiner, as shown in Figure 1(b). The I and Q components of each IF signal are evaluated from the combined IF signal sampled by ADC. By employing two IFs in the digital LLRF system, the number of ADCs can be reduced to half the original value.

*toshihiro.matsumoto@kek.jp

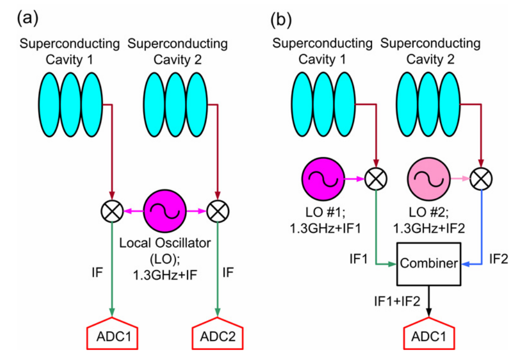


Figure 1: Schematic diagram of the digital LLRF system: a) conventional and (b) IF-mixture technique.

A digital LLRF system employing the IF-mixture technique on two IF signals has been developed and the performance of FB operation has been evaluated by using two cavity simulators [2]. In this study, we developed a digital LLRF system with four IF signals that operated a superconducting cavity [3] at the Superconducting RF Test Facility (STF) at KEK.

## IF-MIXTURE TECHNIQUE

The down-converted IF signal is expressed as follows:

$$x(t) = I(t)\cdot\cos(\omega_{IF}t+\varphi) + iQ(t)\cdot\sin(\omega_{IF}t+\varphi)$$

where $I(t)$, $Q(t)$, and $\varphi$ are the I and Q components and the loop phase of the cavity, respectively, and $\omega_{IF} = 2\pi\cdot IF$. When the sampling rate of the ADC and the frequency of the IF signal satisfy the condition M • *IF* = N • *SR* (N is an integer and M is an integer greater than 3), the I and Q components of the IF signals can be numerically calculated using the following equations for averaging consecutive signal samples [4, 5].

$$I = \frac{2}{M}\sum_{n=1}^{M} x_i(n)\cdot\cos\left(\frac{2\pi\cdot N}{M}\cdot n\right)$$
$$Q = \frac{2}{M}\sum_{n=1}^{M} x_i(n)\cdot\sin\left(\frac{2\pi\cdot N}{M}\cdot n\right) \quad (1)$$

It is expected that the influence of noise and jitter caused by the ADC sampling can be reduced by averaging the signal samples.

A specific set of I and Q components are evaluated and the remaining I and Q components are cancelled by selecting the appropriate N and M values in the IQ algorithm (1) such that the combined IF signal can be expressed as a combination of frequencies with (N1/M) ・ *SR*, (N2/M) ・ *SR*, and so on. In this experiment, we choose 40.625 MHz as the sampling rate of the ADC and as the FPGA clock rate. The combinations of (M, N1, N2, N3, N4) = (9, 1, 2, 3, 4) and (24, 3, 4, 6, 8) are selected to demonstrate the IF-mixture technique using four IFs.

## DIGITAL FEEDBACK SYSTEM

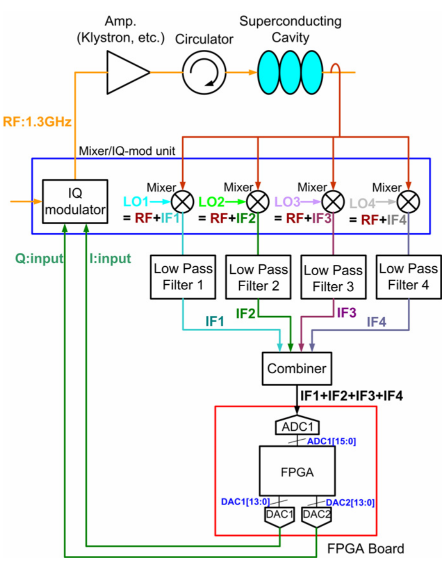


Figure 2: Schematic of system configuration.

The configuration of the digital LLRF system employing the IF-mixture technique consists of an FPGA board, a mixer/IQ-mod unit, and a signal distribution system. The block diagram of the configuration is shown in Figure 2. The FPGA board consists of an FPGA chip (VirtexIIPro30), ten 16-bit ADCs (LTC2204), and two 14-bit DACs (AD9764). This board is installed in a CompactPCI to control the RF field. The mixer/IQ-mod unit consists of ten active mixers (AD8343) and two IQ modulators (AD8349). These units were developed for the STF [6].

The DACs on the FPGA board are connected to the IQ modulator. The RF signal outputted from IQ modulator is amplified by a klystron and is used to drive a cavity. The RF-probe signal from the cavity is divided into four RF signals, and each RF signal is down-converted into the corresponding IFs. These IF signals are filtered by using an appropriate low-pass filter to eliminate the harmonics and then combined using a combiner (Mini-circuits, ZMSC-4-3). The combined IF signal is directly transmitted to the ADC and processed by the FPGA.

### *Signal Distribution System*

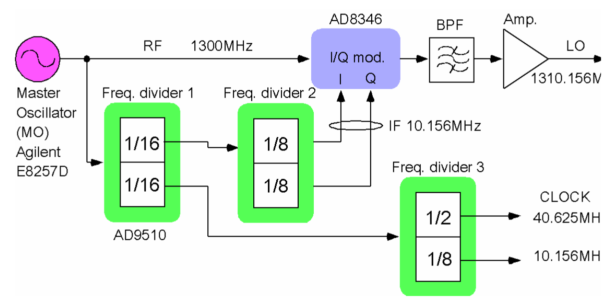


Figure 3: Schematic of signal distribution system.

The signal distribution system consists of a master oscillator (MO, Agilent E8257D), evaluation board containing programmable clock distribution ICs (AD9510/PCB), IQ modulator (AD8346) and a band-pass

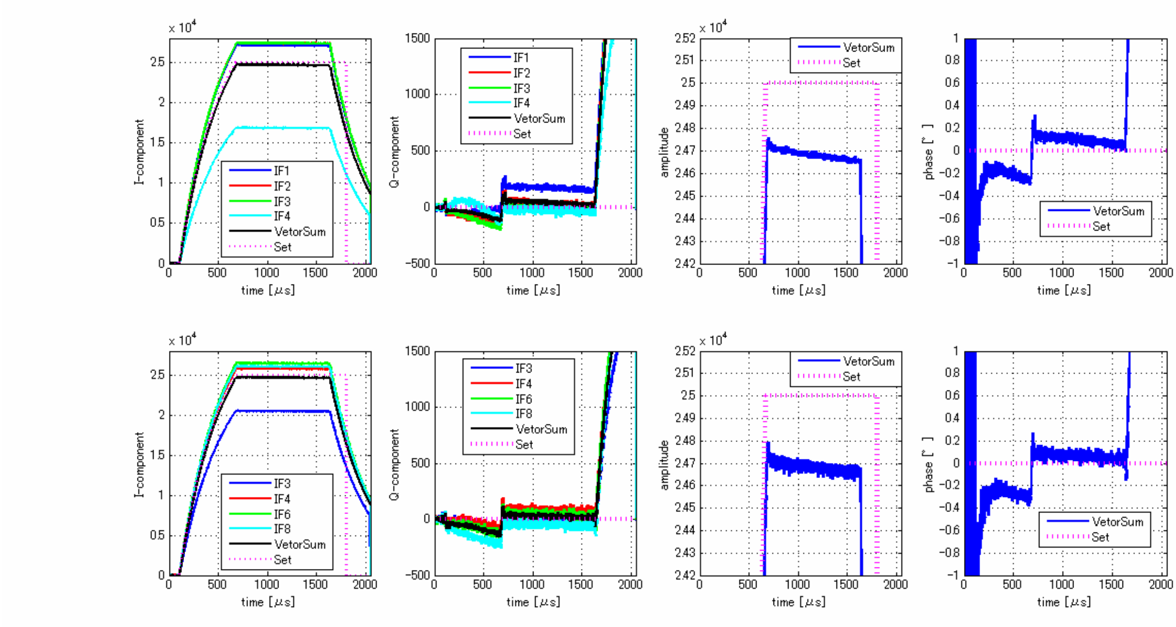


Figure 4: Measured I/Q and amplitude/phase components with FB operation for (M, N1, N2, N3, N4) = (9, 1, 2, 3, 4) and (24, 3, 4, 6, 8).

filter, as shown in Figure 3. This system generates a 40.625 MHz clock signal for the FPGA board along with several different local oscillator (LO) signals; these signals are synchronous with the 1.3 GHz RF signal. The phase noise of each frequency is measured using Agilent E5052A; the root mean square (RMS) phase noises estimated by integration over 10Hz to 10MHz were found to be 0.015° for MO and 0.02° for LO, respectively.

## FEEDBACK PERFORMANCE

The feedback performance of this digital LLRF system using the IF-mixture technique is evaluated using a superconducting cavity at the STF at KEK.

Figure 4 shows the result obtained at the set point of 25,000 under P control for a gain of 80 (without FF) in the case of (N, M1, M2, M3, M4) = (9, 1, 2, 3, 4) and (24, 3, 4, 6, 8). As shown in Figure 4, the feedback loop of the system is closed and the I and Q components of the cavity signal are separated from those of the combined IF signal. In both combinations of (M,N1～N4), the corresponding errors in the amplitude and phase observed at the flat top from 750 to 1600 μs are 0.08% (RMS) and 0.03° (RMS), respectively.

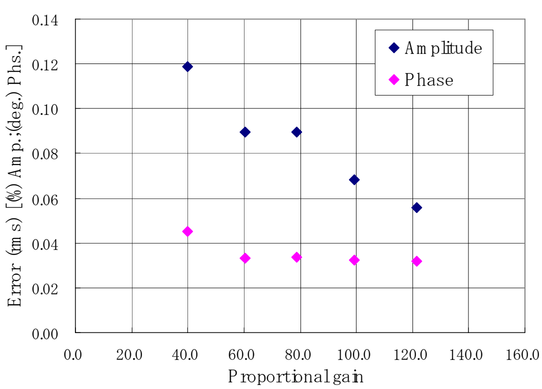


Figure 5: Errors in amplitude and phase at flat top.

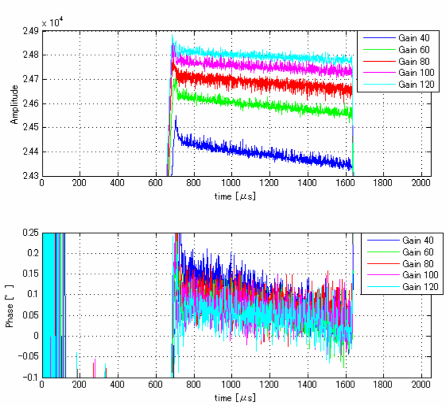


Figure 6: Amplitude and phase at the flat top with different proportional gain.

Figure 5 shows the relation between the proportional gain (P-gain) and the amplitude and phase stabilities at flat top. The P-gain is calculated from the difference between the set point and the average of the measured flat top. The FB operation becomes unstable when the P-gain is greater than 140.

In the region of stable FB operation, the error in the phase is constant at 0.03° (RMS), but the error in the amplitude depends on the P-gain. Figure 6 shows the observed amplitude and phase at the flat top. By adopting an appropriate feed-forward table, the slope in the amplitude at the flat top is expected to disappear. On neglecting the effect of sag, the errors in the amplitude and phase over the period between 1000 μs and 1050 μs, are found to be 0.03% (RMS) and 0.02° (RMS), respectively.

## SUMMARY

At the STF, a digital LLRF system employing the IF-mixture technique was operated over a superconducting cavity. In order to demonstrate the IF-mixture technique with the cavity, we developed a signal distribution system that can generate several LO signals. The phase noise of the signals were measured and estimated to be 0.015° (RMS) for MO and 0.02° (RMS) for LO by integration over 10Hz to 10MHz. The FB performance of the system was examined under several P-gains and the stabilities of the amplitude and phase were evaluated. At the flat top, the stabilities of the amplitude and phase were expected to be 0.03% (RMS) and 0.02° (RMS), respectively, by adopting the appropriate feed-forward table.

A cryomodule that installs four superconducting cavities is planned to operate this winter with the demonstration of the digital LLRF system employing the IF-mixture technique.

## REFERENCES

[1] http://www.linearcollider.org/cms/?pid=1000437

[2] T. Matsumoto, et al., “Development of Digital Low-level RF Control System using Multi-intermediate Frequencies”, PAC2007, Albuquerque, USA, pp. 2110–2112.

[3] T.Saeki et al., “The First Measurement of Low-Loss 9-Cell Cavity in a Cryomodule at STF”, EPAC08, Genoa, Italy, pp. 610-612.

[4] M. Grecki, et al., “Estimation of IQ Vector Components of RF Field - Theory and Implementation”, MIXDES 2005, Cracow, Poland, pp. 783–788.

[5] S. Simrock, et al., “Considerations for the Choice of the Intermediate Frequency and Sampling Rate for Digital RF Control”, EPAC2006, Edinburgh, Scotland, pp. 1462–1464.

[6] S. Michizono, et al., “Status of the Low-level RF System at KEK-STF”, PAC2007, Albuquerque, USA, pp. 2113–2115.

# PERFORMANCE OF DIGITAL LLRF SYSTEM FOR STF IN KEK

S. Michizono#, H. Katagiri, T. Matsumoto, T. Miura, Y. Yano and S. Fukuda, KEK, Tsukuba, Japan
.

*Abstract*

RF operations were carried out at the STF (Superconducting RF Test Facility) in KEK. The digital feedback system was installed in order to satisfy the strict rf-field requirements. The rf field stabilities under various feedback parameters are presented in this report. Cavity detuning measurements (microphonics, quench detection, etc.) were among the various studies that were conducted. Results of these studies are also summarized.

## INTRODUCTION

The STF is a test facility for pulsed superconducting cavities aiming for ILC (International Linear Collider). An amplitude of 0.07% and a 0.24° phase are required for rf stability in the ILC in order to satisfy the collision luminosity [1]. In order to satisfy these requirements, a digital llrf (low-level radio frequency) system has been developed.

The STF started its operation in July 2007 [2], and several llrf studies have been carried out. Some of the topics studied are as follows:

(1) Study of cavity field stability
(2) IF mixture method: This method enables us to reduce the number of ADCs by combining intermediate frequency (IF) signals. This method has been validated by using electrical cavity simulators. This is the first time a study has been conducted using a real super-conducting cavity [3].
(3) Instability evaluation: An evaluation of the feedback performance under all fundamental modes such as the 8/9π mode was performed. This evaluation was carried out by eliminating the analog low-pass filter that was inserted between the IQ modulator and the DACs [4].
(4) Direct rf detection using a fast 14-bit ADC: In order to develop next-generation future rf detection systems, we examine a 14–bit fast ADC with a bandwidth of more than 1.3 GHz. This method allows the detection of the rf signal without the use of a downconverter [5].
(5) Analysis of the rf monitor: llrf monitors are used for the evaluation of cavity characteristics such as microphonics and for quench detection.

In this report, we summarize the results of the above studies.

## DIGITAL LLRF SYSTEM

The digital llrf system comprises an rf signal generator (RF & CLK), downconverters, and a DSP/FPGA board having ten 16-bit ADCs and two 14-bit DACs. The

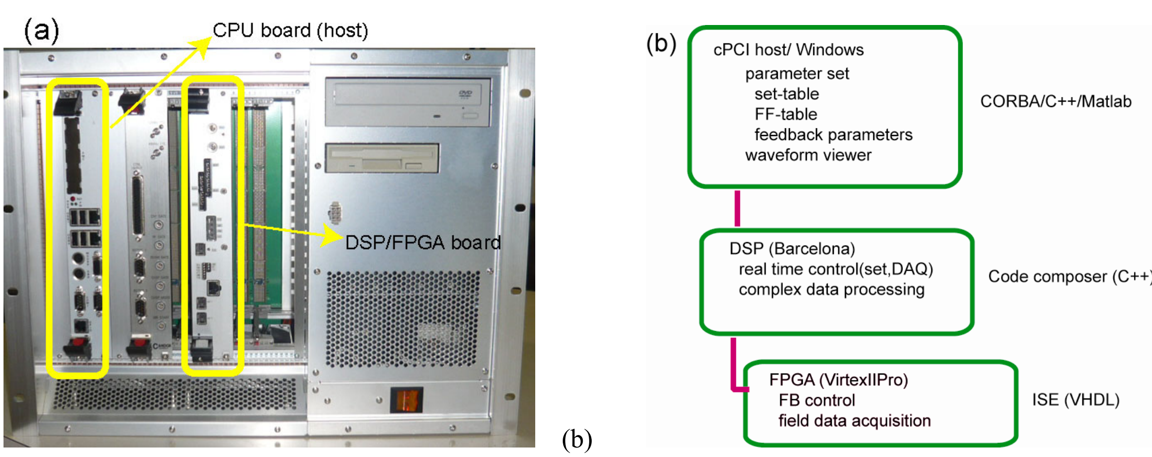


Figure 1: Photograph of cPCI system (a), and system layers inside cPCI (b).

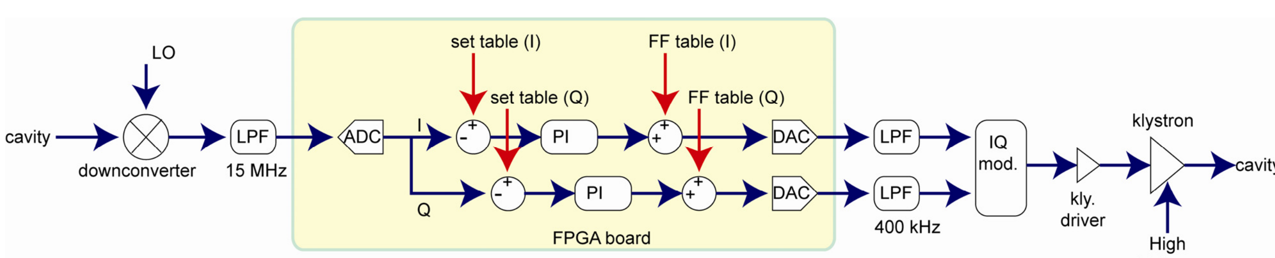


Figure 2: Block diagram of digital llrf system in case of a single cavity operation.

#shinichiro.michizono@kek.jp

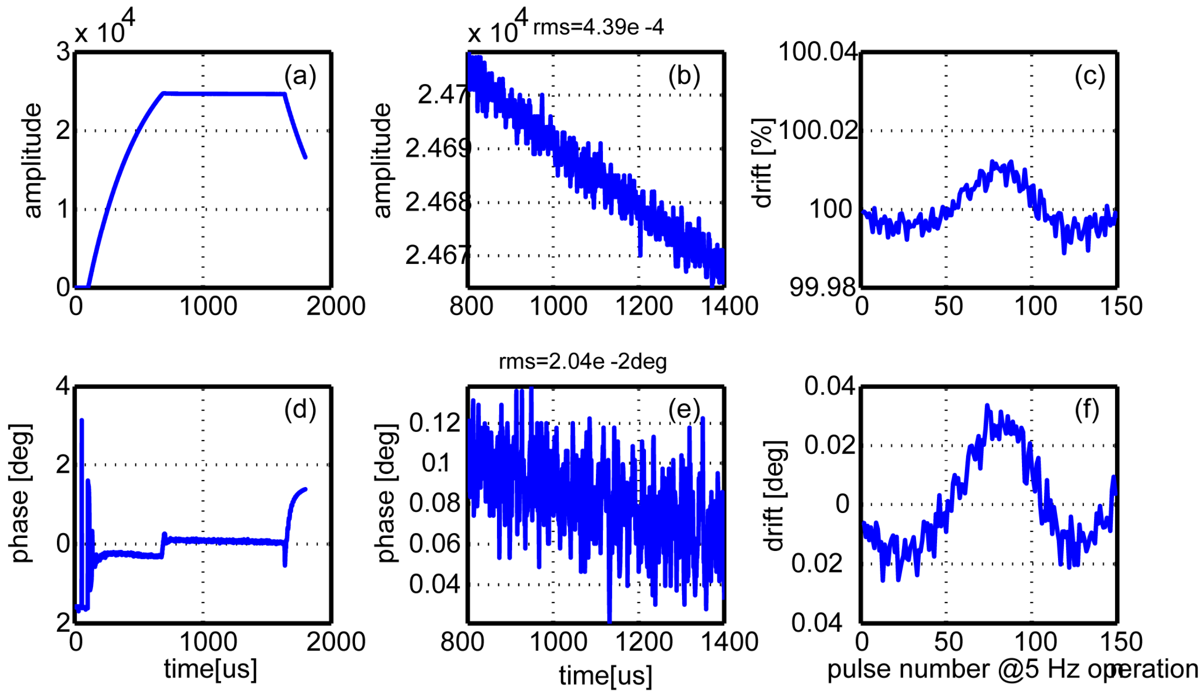


Figure 3: Performance of the llrf field regulation. Amplitude (a) and (b), drift of the amplitude during 30 seconds (150 pulses) (c), phase stability (d) and (e), drift of the phase during successive 150 pulses.

DSP/FPGA board is installed in the cPCI, which is the same as the J-PARC linac system [6]. Figure 1 (a) shows an image of the cPCI.

RF & CLK are used to deliver the local oscillator (LO; 1.31 GHz) signal and the clock (40 MHz) signal generated by the clock distribution chips (AD9510) and IQ modulators (AD8346) [3].

The FPGA board is a mezzanine card made up of a commercially available DSP board (Barcelona by Spectrum Inc.), and it facilitates fast feedback; DSP board is used for running complicated algorithms such as those for detuning and loaded-Q calculations. System developments are carried out using electric cavity simulators, which are installed in commercial FPGA boards and are capable of deferring beam loading and microphonics and Lorentz force detuning [7].

Figure 1 (b) shows the system configuration of the cPCI. The waveforms generated by each ADC are stored in a block RAM (2048 deep) in the FPGA board. The stored data in the block RAM is expandable like a digital oscilloscope (max. 40 MHz) and it can be accessed via the cPCI host. Windows operating system is installed in the CPU board of the cPCI (Host), and the Matlab library helps the online analysis of the llrf performance. The host records the waveforms generated in the last 30 seconds, which are highly useful for the evaluation of phenomena such as microphonics and cavity quench.

Fig. 2 shows the sequence of the digital feedback system. The rf pickup signal is downconverted to an intermediate frequency (IF) signal of 10 MHz (additional IFs were introduced in the case of IF-mixing [3]). Active mixers (AD8343) are used for downconversion. In order to eliminate the higher-order modes of the mixers, the output of the downconverters is filtered using low-pass filters with a 15-MHz bandwidth. The 16-bit ADCs (40 MHz clock) sample the IF signal directly, and proportional-integral (PI) control is performed. Two 14-bit DACs drive the IQ modulator (AD8349) via low pass

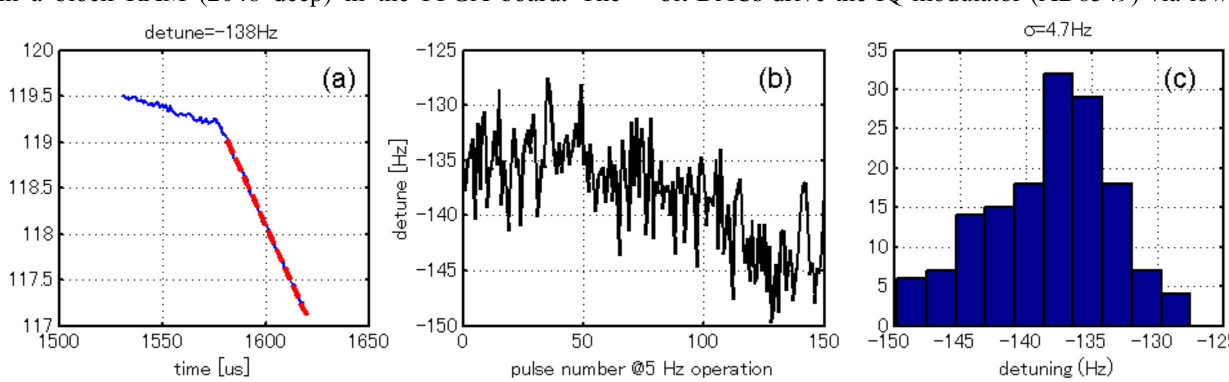


Figure 4: Phase change during the decay time (a), detuning change (b) and histogram of the detuning (c).

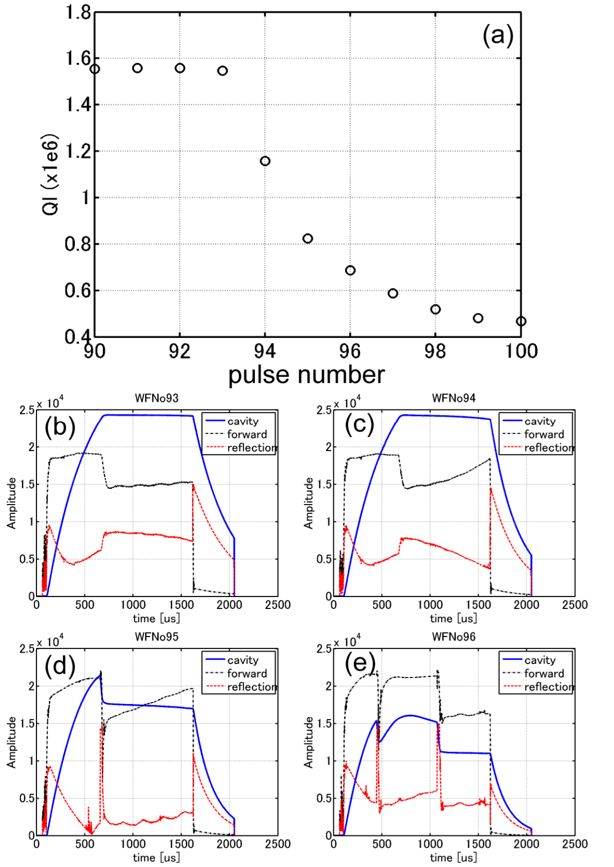

Figure 5: Decrease in loaded Q values (Ql) at quench (a) and waveforms just before and after quench (b)~(e). Blue: cavity field, black: drive power, red: reflection power.

filters that have a bandwidth of 400 kHz. The rf signal is amplified by a klystron driver (max. 500 W) and a klystron (TH2104A, 1.5 ms, max 5 MW, 5 pps).

## PERFORMANCE OF THE LLRF SYSTEM

The rf waveforms produced during the feedback operation are shown in Fig. 3. The amplitude of the rf field is an arbitrary value (corresponding to the output of the 16-bit ADC). Only proportional feedback control was applied (without feed-forward) with a feedback gain of 80. The amplitude and phase stabilities are 0.04% rms and 0.02°, respectively. In general, the performance depends on perturbations such as pulse-to-pulse fluctuation of the klystron's high voltage, gain of the klystron driver, and cavity detuning induced by microphonics or Lorentz force detuning. The observed decrease in the amplitude can be attributed to the non-linear characteristics of the klystron driver. The drifts in 150 successive pulses are +/–0.01% and +/–0.02°. Although these results were obtained without using a beam, They satisfy the ILC requirements.

The rf waveforms can be used for online/offline analysis of the cavities. The microphonics of the cavities were evaluated by using cavity detunings, which were calculated from the phase changes when the rf field decayed (Fig. 4 (a)). Figure 4 (b) shows detuning changes during the application of 150 successive pulses. The histogram of detuning (Fig. 4 (c)) indicates that the microphonic values are approximately 4.7 Hz rms, which is similar to those of FLASH (4 Hz) [8].

Another example of llrf off-line analysis is the observation of waveforms when quench occurs. Figure 5 (a) shows the loaded Q values, which were calculated from the time constants of field decay, along with the waveforms. Figure 5 (b)~(e) show the waveforms before and after quench took place. When quench occurs (pulse #94), the cavity field decreases, despite an increase in the klystron drive power. The loaded Q values of successive pulses (#95, #96, etc.) decrease rapidly. Since the quench spreads fast (in one rf pulse), the rf power should be cut off immediately in order to minimize the heat load of the cryogenic system during quench (or decrease in loaded Q). New software is being developed to facilitate quench detection and the instant stopping of the rf if quench occurs.

## SUMMARY

The measured rf stabilities of the digital llrf system at the STF were 0.04% in amplitude and 0.02°. in phase. The rf waveforms obtained using the digital llrf system are utilized for the evaluation of cavity parameters such as microphonics and for determining Lorentz force detuning. The operation of 4 superconducting cavities is scheduled for November 2008 and methods such as vector sum control method will be examined.

## REFERENCES


[1] "ILC Reference Design Report (RDR)", http://www.linearcollider.org/cms/?pid=1000437.

[2] S. Fukuda et al., "Status of RF Sources in Super-Conducting RF Test Facility (STF) at KEK", LINAC08.

[3] T. Matsumoto et al., "Performance of Digital Low-Level RF Control System with Four Intermediate Frequencies", LINAC08.

[4] T. Miura et al., "Measurements of the Feedback-Instability by 8/9π and 7/9π modes at the KEK-STF", LINAC08.

[5] H. Katagiri et al., "Application of FPGA to Low Level RF Measurement and Control", LINAC08.

[6] S. Michizono et al., "Performance of a Digital LLRF Field Control System for the J-PARC Linac", LINAC06, Knoxville, Aug.2006, p.574.

[7] T. Matsumoto et al., "Low-level RF system for STF", LINAC06, Knoxville, Aug.2006, p.586.

[8] T. Schilcher, Ph.D. thesis, "Vector Sum Control of Pulsed Accelerating Fields in Lorentz Force Detuned Superconducting Cavities", University of Hamburg, 1998; (TESLA Report No. TESLA 1998-20, 1998).

# MEASUREMENTS OF FEEDBACK-INSTABILITY DUE TO 8/9π AND 7/9π MODES AT KEK-STF

T. Miura#, H. Katagiri, T. Matsumoto, S. Michizono, Y. Yano, S. Fukuda, KEK, Ibaraki, Japan

*Abstract*

At the superconducting RF test facility (STF) at KEK, high-power tests of the superconducting nine-cell cavity for the International Linear Collider (ILC) have been performed. The cavity was driven by an RF of 1.3GHz which corresponds to the π mode with zero beam acceleration. Feedback instabilities due to the 8/9π and 7/9π modes were observed when the other modes were not filtered. The intensities of the 8/9π and 7/9π modes were measured by varying the feedback loop delay, and the stable/unstable regions appeared at regular intervals as expected.

## INTRODUCTION

The superconducting RF test facility (STF) at KEK is the research and development facility of the International Linear Collider (ILC). At the STF, high-power tests of the superconducting nine-cell cavity have been performed. The cavity is driven by an RF of 1.3 GHz with a pulse duration of 1.5 ms and a repetition rate of 5 Hz. A stability of 0.3% amplitude and 0.3° phase is required at the flat-top region where beam acceleration is performed. To achieve this stability, we adopt a high-speed digital feedback control system using a field programmable gate array (FPGA) in the low-level RF (LLRF) system [1,2]. The cavity is operated in the π mode which has the highest efficiency for beam acceleration. However, Vogel [3] has pointed out the occurrence of the feedback control instability due to the passband of $TM_{010}$ mode except for the π mode. Therefore, we measured the instability in the STF.

## MODE FREQUENCIES

Table 1: Frequency differences the π mode and other modes for each cavity

| | cav#1@2K $f$-$f_\pi$ (MHz) | cav#2@2K $f$-$f_\pi$ (MHz) | cav#3@2K $f$-$f_\pi$ (MHz) | cav#4@RT* $f$-$f_\pi$ (MHz) |
|---|---|---|---|---|
| 8/9π | −0.70 | −1.11 | −0.88 | −0.83 |
| 7/9π | −3.53 | −3.45 | −3.39 | −3.04 |
| 6/9π | −7.31 | −6.98 | −7.08 | −6.27 |
| 5/9π | −11.69 | −11.62 | −11.50 | −10.00 |
| 4/9π | −16.47 | −16.37 | −16.31 | −14.05 |
| 3/9π | −20.83 | −20.94 | −20.63 | −17.86 |
| 2/9π | −24.54 | −24.52 | −24.20 | −21.14 |
| 1/9π | −27.25 | −26.68 | −26.64 | no-data |

*RT: Room Temperature

Table 1 shows the frequency differences between the π mode and other modes for each cavity in the STF. For a given mode, the frequency is different for different cavities due to fabrication error. When performing vector-sum control, we have to pay attention to many frequency components in comparison with the control for only one cavity. Figure 1 shows the band-pass characteristics of a TH2104A klystron used at the STF. The peak is observed at 1294 MHz. Therefore, it is easier for frequencies of modes in the range 6/9π - 8/9π to pass through the klystron as compared to π mode.

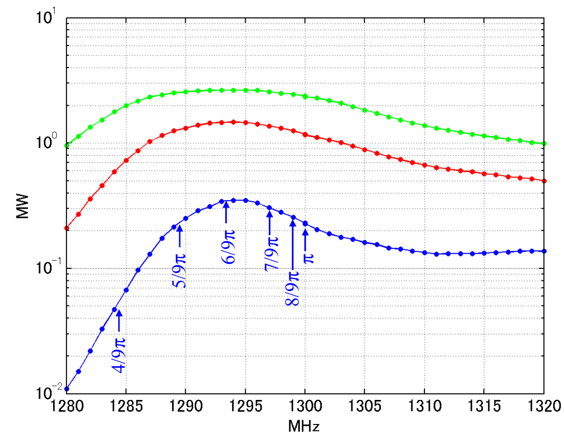


Figure 1: Band-pass characteristics of klystron (TH2104A).

## ESTIMATION OF GAIN MARGIN

In order to estimate the feedback instability, the gain margin of each mode, except the π mode, was calculated. A more detailed description of the calculation is presented by Vogel [3]. The open-loop transfer function (TF) of the system is represented as follows:

$$H(s) = Gp\, H_{delay}(s)\, H_{cav}(s)\, H_{kly}(s), \qquad (1)$$

where $Gp$ is the proportional gain of the feedback, $H_{delay}(s)$ is the TF of the feedback loop delay, $H_{cav}(s)$ is the TF of the cavity, and $H_{kly}(s)$ is the TF of the klystron. In this calculation, $H_{kly}(s)$ is approximated by a low-pass filter with a 3 dB bandwidth of 3 MHz in a manner similar to that employed by Vogel [3]. $H(s)$ is converted to a discrete system of 40 MHz, which is the sampling frequency in analog-to-digital converter (ADC), and the gain margin is calculated from the Nyquist stability criterion. The gain margins for different feedback loop delays are shown in Fig. 2. In the figure, the area shaded grey indicates a stable region, while that shaded white denotes an unstable region. Even when $Gp$ is small, the feedback system becomes unstable for modes in the range of 8/9π – 5/9π. The stable and unstable regions appear at regular intervals with the intervals depending on the difference between their frequencies and the frequency of the π mode. On the other hand, low-order modes such as the 2/9π and 1/9π modes are stable for large values of $Gp$.

#takako.miura@kek.jp

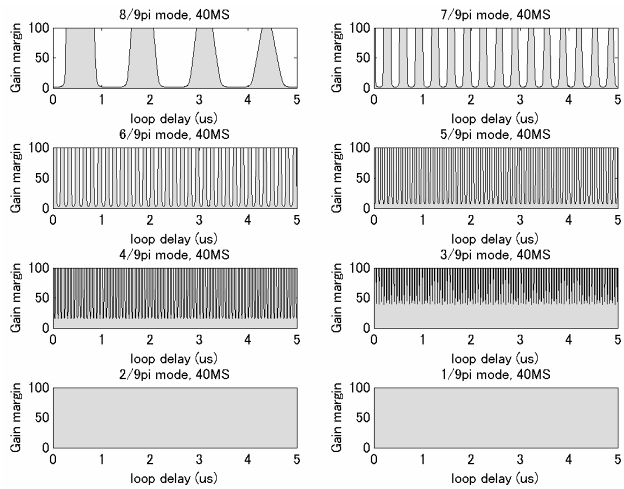


Figure 2: Calculation of gain margins for feedback loop delay (grey : stable; white : unstable).

## MEASUREMENT

Figure 3 shows the LLRF control system in the STF. The pick-up signal (1.3 GHz) from the cavity is down-converted to an intermediate frequency (IF) of 10.156 (1300/128=10.156) MHz. The IF signal is sampled by a 16-bit ADC whose sampling rate is four times the IF (40.625 MHz). Separation of I/Q components and feedback calculation using proportional control are performed in the FPGA. The calculation yields baseband I/Q signals as an output from the 14-bit digital-to-analog converter (DAC). In the IQ modulator, these baseband signals are modulated using an RF of 1.3GHz generated by the master oscillator. In our typical LLRF system, a 0.4-MHz low-pass filter (LPF) is installed between the DAC and the IQ modulator in order to reject the signals corresponding to modes other than the π mode. In this study, the LPF was removed in order to measure the raw intensities of the signals of the other modes. A digital delay system (0.0246 μs/tap) was introduced in the FPGA in order to observe the relation between feedback loop delay and instability. The digital delay was varied between 1 tap and 200 tap at each step. In this study, the cavity that is labelled #4 in Table 1 was employed and *Gp* was set to 11.5. The power was set at a low level, so that it did not quench even when the feedback became unstable condition due to large oscillations.

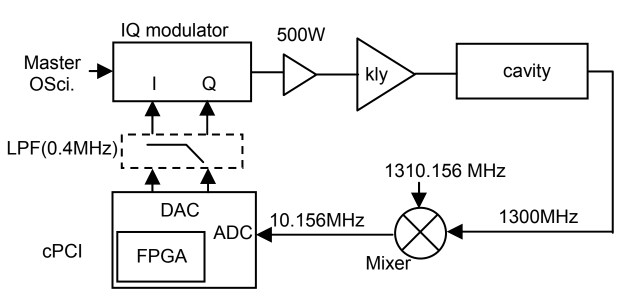


Figure 3: Schematic view of the LLRF system.

IF signal of the electric field in the cavity was sampled at 40.625 MHz. The frequency spectra of the klystron and the cavity were calculated by using Fourier transform algorithm using 2048 data points obtained from the region of the flat-top. The frequency resolution was 0.02 MHz.

## RESULTS

### *Results of Waveform Spectrum*

The feedback became stable or unstable depending on the duration of the digital delay, and the shape of the spectrum for the electric field in the cavity also varied. Figure 4 shows an example of variations in the intensity of the electric field in the cavity and the frequency spectra of the klystron and the cavity. In the case of stable feedback, only one IF (π mode) was observed; this is shown in Fig. 4 (a). Figure 4 (b) shows the instance when the feedback just turns unstable due to the 8/9π mode.

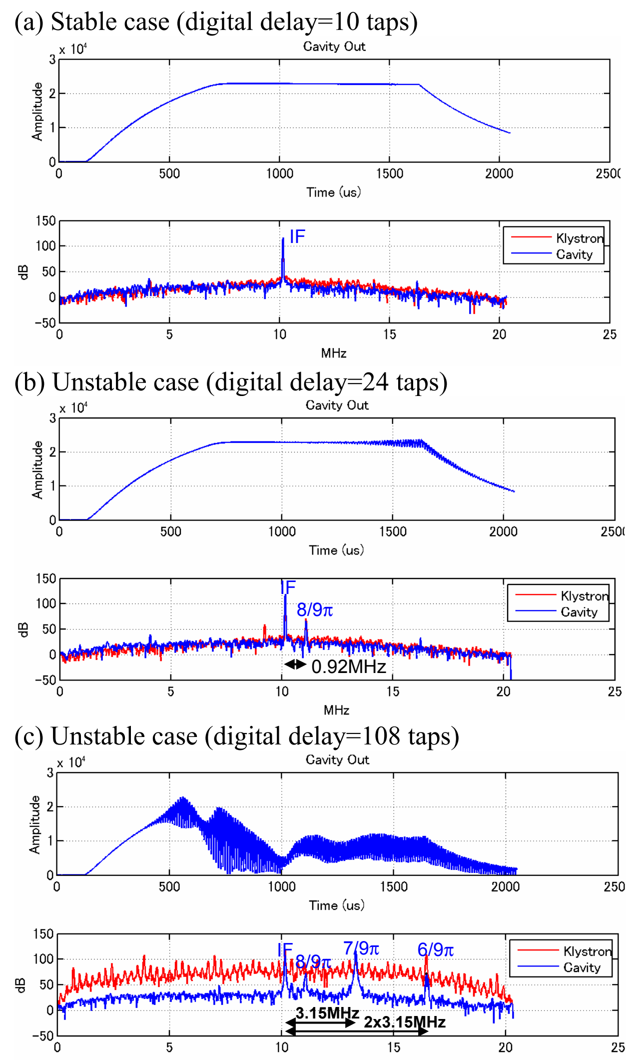


Figure 4: Electric field in the cavity (up) and frequency spectra of the klystron and cavity in the flat-top region (down).

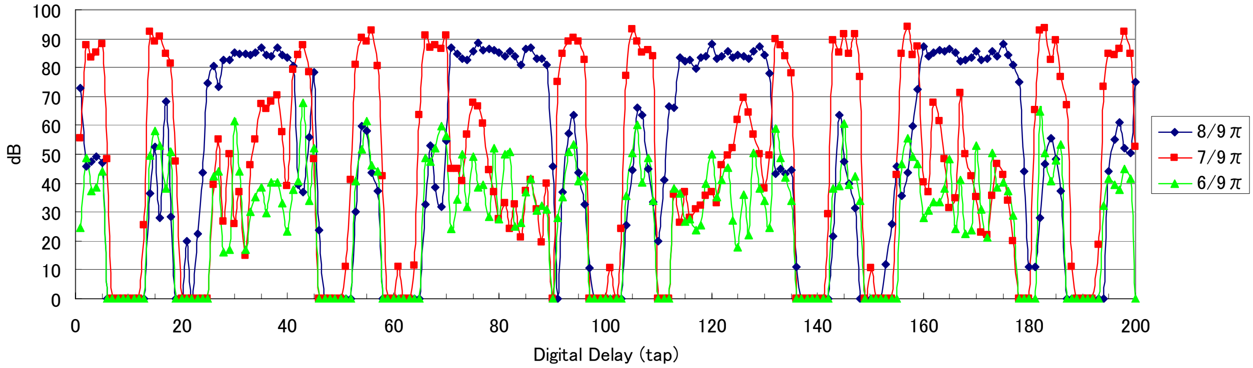


Figure 5: Intensities of the 8/9π, 7/9π, and 6/9π modes for each digital delay.

Incrementing the digital delay by a few more taps led to an increase in the instability. Figure 4 (c) shows a large oscillation due to the 7/9π mode. In this case, several frequencies were output from the klystron and the 8/9π and 6/9π modes were also excited in the cavity. Frequency differences ($\Delta f$) between the π mode and the 8/9π and 7/9π modes are 0.92 MHz and 3.15 MHz, respectively. Further, $\Delta f$ between the π mode and the 6/9π mode was 6.35 MHz ($\Delta f_{(8/9\pi)} \times 7$) or 6.29 MHz ($\Delta f_{(7/9\pi)} \times 2$) depending on whether the 8/9π mode or the 7/9π mode excited to a greater extent.

### *Results of Digital Delay Scan*

Figure 5 shows the intensities of the 8/9π, 7/9π and 6/9π modes with digital delays introduced in the feedback loop. For a digital delay in the range 0 – 200 taps (4.9μs), the stable region is extremely narrow: the unstable region extends across a large part of the plot. Severe instabilities are produced mainly by the 8/9π and 7/9π modes, while the 6/9π mode does not induce instability by itself. Therefore, we suggest that occurrence of the 6/9π mode is associated with the large instabilities caused by the 8/9π or 7/9π mode. The periodicity of stability for feedback loop delays for the 8/9π and 7/9π modes is determined by using points that do not overlap the 8/9π and the 7/9π modes. The resulting periodicities are 44 taps (1.08 μs) for the 8/9π mode and 13 taps (0.32 μs) for the 7/9π mode, respectively. These values are approximately equal to those calculated from the expression $1/(f_\pi - f_{n/9\pi})$.

### *Estimation of Feedback Loop-Delay*

If the feedback loop delay is 0, the feedback control is unstable for the 8/9π mode and stable for the 7/9π mode (see Fig. 2); this is because the initial stability condition of each mode is based on the direction of the electric-field vector at the end cell of the cavity. The original feedback loop delay of this system was evaluated by comparing the patterns in Fig. 2 and Fig. 5. For the 8/9π mode in Fig. 5, the 25$^{th}$ tap, where the leading edge of 8/9π mode occurs, is used as the reference point. The point of zero digital delay is obtained by subtracting the half period, which is 22 taps, from the reference point. Since the 25th tap was designated as the reference point, the point with zero digital delay would be the 3$^{rd}$ tap from the end of unstable region. By comparing this delay with that obtained from Fig. 2, the feedback loop delay is estimated as 1.22 μs or 2.3 μs (1.22μs + 1 cycle). In addition, integration in order to obtain the delay of each component, DAC (~10ns) + IQ modulator (~160ns) + wave guide · coaxial cable of 100m (~500ns) + Mixer (130 ns) + ADC (6 clock, 150 ns) + FPGA (16 clock, 400 ns), was also estimated. This integration yielded a value of ~1.35 μs. Therefore, a feedback loop delay of ~1.22 μs would be reasonable for this system.

## SUMMARY

In the STF at KEK, the feedback instability due to $TM_{010}$ passband modes, except for the π mode, was measured under the conditions of low *Gp* and zero beam acceleration. The RF was predominantly destabilized by the 8/9π and 7/9π modes. A component of the 6/9π mode also appeared; however, it did not destabilized the system by itself. By varying the feedback loop delay through the introduction of a digital delay in the FPGA, the stable/unstable regions appeared at regular intervals. The period for each mode was almost equal to that obtained from the expression $1/(f_\pi - f_{n/9\pi})$. The original feedback loop delay was also estimated by using the periodic pattern. If feedback is employed by using a large *Gp*, the 6/9π mode or 5/9π mode will destabilize the system, and the stable region will shrink further. Therefore, a filter is required for stable operation. In our typical LLRF system, a 0.4 MHz LPF inserted between the DAC and the IQ modulator would ensure the stable operation of the RF system.

## REFERENCES


[1] S. Michizono et al., "Performance of the Digital LLRF System for STF in KEK", Linac08.

[2] T. Matsumoto et al., "Low-level RF system for STF", LINAC 2006, Knoxville, Aug. 2006, THP010, p.586 (2006).

[3] E. Vogel, "High gain proportional rf control stability at TESLA cavities", Phys. Rev. ST Accel. Beams 10, 052001 (2007).

# PULSE-BY-PULSE SWITCHING OF BEAM LOADING COMPENSATION IN J-PARC LINAC RF CONTROL

T. Kobayashi#, E. Chishiro, H. Suzuki, JAEA, Tokai, Naka, Ibaraki, Japan
S. Anami, Z. Fang, S. Michizono, S. Yamaguchi, KEK, Tsukuba, Ibaraki, Japan

*Abstract*

For the J-PARC linac low level RF system, a new function that switches the feed-forward control parameters in every pulse was installed into the digital accelerating-field control system, in order to compensate beam-loading change by pulses in the operation of 25-Hz repetition.

The linac provides a 50-mA peak current proton beam to a 3-GeV rapid-cycling synchrotron (RCS). Then the RCS distributes the 3-GeV beam into a following 50-GeV synchrotron (main ring, MR) and the Materials and Life Science Facility (MLF), which is one of the experimental facilities in the J-PARC. The 500-us long macro pulses from the ion source of the linac should be chopped into medium pulses for injection into the RCS. The duty (width or repetition) of the medium pulse depends on which facility the RCS provides the beam to the MR or MLF. Therefore the beam loading compensation needs to be corrected for the change of the medium pulse duty in the 25-Hz operation.

## INTRODUCTION

J-PARC will be one of the highest intensity proton accelerators, which consists of a 181 or 400-MeV Linac, a 3-GeV rapid-cycling synchrotron (RCS) and a 50-GeV synchrotron (main ring, MR) [1]. The beam is applied to several experimental facilities, for example, the Materials and Life Science Facility (MLF), the Hadron Physics Facility and the Neutrino Facility (See Fig. 1). The MLF is aimed at promoting materials science and life science using the world highest intensity pulsed neutron and muon beams which are produced using 3-GeV protons with a current of 333micro-amps and a repetition rate of 25 Hz.

The beam commissioning has progressed steadily, since the linac beam commissioning was started in October 2006. Then the first neutron production was succeeded at the MLF, and in the MR the 3-GeV beam was captured by RF and extracted to the beam dump after 1000 turns in this year. Now more detail beam sturdy is in progress.

As described in above, the RCS has to distribute the beam to the MLF and the MR. This switching of the beam destination (MLF or MR) influences the beam intensity of the linac. Therefore the parameters of the beam-loading compensation need to be switched due to the destination of the beam in the 25-Hz pulse operation. Accordingly, a new function that switches the feed-forward control parameters in every pulse was installed into the digital accelerating-field control system.

For high quality and high intensity beam acceleration, the stability of the accelerating field is one of the most important issue. Because the momentum spread (Δp/p) of the RCS injection beam is required to be within 0.1%, the accelerating field error of the linac must maintained within ±1% in amplitude and ±1 degree in phase. To realize this stability, a digital feedback (FB) control is used in the low level RF (LLRF) control system, and a feed-forward (FF) technique is combined with the FB control for the beam loading compensation [2]. In the 181-MeV acceleration of the linac, the 24 LLRF systems are operated in a frequency of 324 MHz and the stability of ±0.2% in amplitude and ±0.2 degree in phase is achieved including the beam loading [3]. This RF stability makes high reproducibility of the injection beam and then contributes to the steady commissioning progress of the J-PARC.

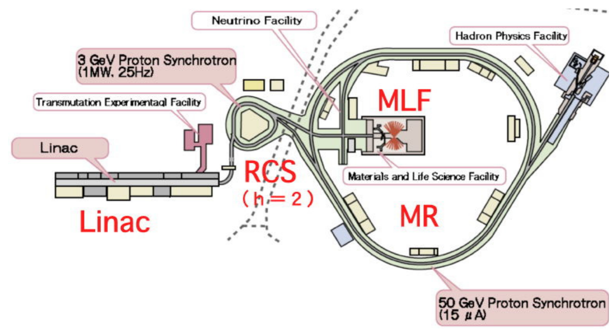


Figure 1: Layout of J-PARC accelerator.

## BEAM STRUCTURE AND RF SYSTEM

The beam structure of the J-PARC linac is shown in Fig. 2. Maximum peak current will be 50 mA. Macro-pulses of 500-$\mu$s widths are accelerated in 25-Hz repetition. The macro-pulse is chopped by a RF-chopper into medium pulses as synchronized with the RCS RF

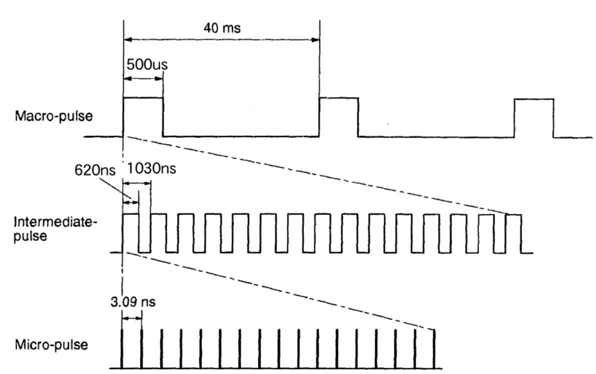


Figure 2: Beam Structure of the J-PARC linac.

# tetsuya.kobayashi@j-parc.jp

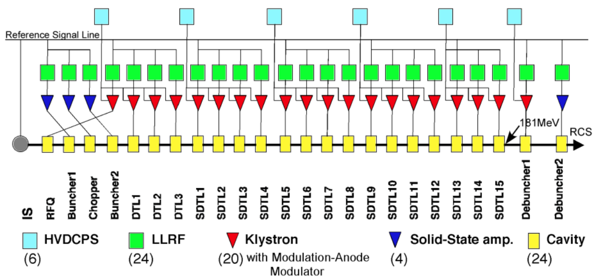


Figure 3: Overview of the J-PARC linac RF system.

frequency of about 1 MHz. In the linac commissioning the macro-pulse beam is 50-$\mu$s width and 30-mA peak current.

The harmonic number of the RCS is 2 (h = 2). The medium pulses shown in the Fig. 2 correspond to two-bunch (full bucket) acceleration in the RCS. In this case, the beam is distributed to the MLF. On the other hand, when the beam is distributed to the MR, the RCS operation changes to the one-bunch acceleration. In the case of the one-bunch acceleration, the train of the medium pulses of the linac is alternative; the macro pulse is chopped in about 500 kHz.

The overview of the J-PARC linac RF system and cavities is shown in Fig. 3. There are totally 24 cavity units including bunchers/debunchers, and the 24 LLRF systems control the each cavity field. An accelerating frequency is 324 MHz, and the RF pulse width is 650 $\mu$s. Twenty 324-MHz klystrons are used for the 181-MeV acceleration. One DC high-voltage power supply drives four klystrons.

The RF chopper is located between two bunchers in the medium energy beam transport line (MEBT). It is driven by a 30-kW solid-state amplifier and it chops the macro pulse beam into the medium pulse beam [4]. The LLRF for the chopper drive generates the chopped RF pulse as synchronizing with the RCS injection RF signal, which is received from the RCS through an optical link. This chopping frequency (1 MHz or 500 kHz) depends on the beam destination (the MLF or the MR). Accordingly, the beam loading changes twice when the beam is distributed to the MLF.

## FB CONTROL SYSTEM AND BEAM LOADING COMPENSATION

For stabilization of cavity field, a digital feedback (FB) control system, which acts on a cPCI crate system, is applied. The FB control is programmed on a FPGA as shown in Fig. 4. The cavity filed monitor signal (324 MHz) is down-converted into a 12-MHz IF signal by a 312-MHz LO; The 312-MHz optical signal is received by an O/E in the cPCI as the phase reference. The I and Q components of the field are obtained by sampling the IF signal in 48 MHz with 14-bit ADC on the FPGA. The I/Q

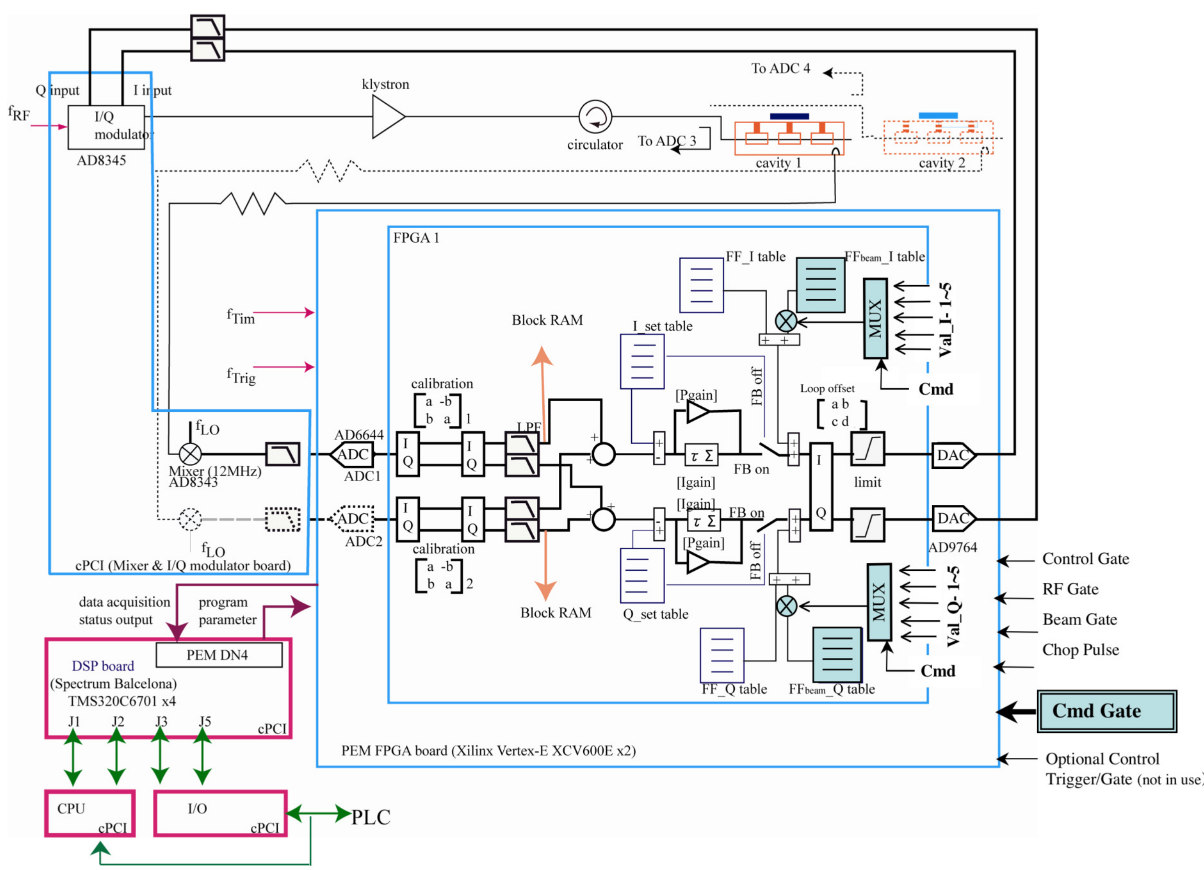


Figure 4: FPAG block diagram of the digital FB and FF control system for the J-PARC linac LLRF.

components are controlled to be set values by PI control and output to an IQ-modulator through a DAC.

Cavity-tuners are controlled from the cPCI by way of a program logic controller (PLC) [2], and the auto-recover sequence from the fault down is processed by the PLC.

The beam-loading ripple at the rising/falling of macro beam pulse could not be compensated enough by only the FB control. Therefore FF control is combined with the FB control for the beam loading compensation. FF-control values are added to the I/Q-component outputs during the external beam gate (See Fig. 4). As shown in Fig. 5, by using the FF control with FB, the field change due to the beam loading (26-mA peak current and 50-$\mu$s width) was vanished almost perfectly. If the FF control is not adopted, the amplitude and phase change due to the beam loading is about ±3% and ±1.5 degrees, respectively. The beam current decay of about 3% was observed in 181-MeV acceleration without the FF control. By applying the FF control to all cavities, the current decay and the energy dispersion in the macro pulse decrease obviously [5].

For the FF-control, it is necessary to adjust a timing of a beam-synchronized gate signal in precision of 0.1-µs. Furthermore, optimum values of the FF amplitude and phase depend on beam intensity, therefore the FF parameters are need to be changed with beam intensity changes. As described above, the beam intensity changes due to the destination of the RCS extraction beam. Therefore a function that can switch the feed-forward control parameters in every pulse is required. In addition, when the beam is stopped due to some faults, the FF control has to be stopped in order to prevent the cavity from being damaged by overloading.

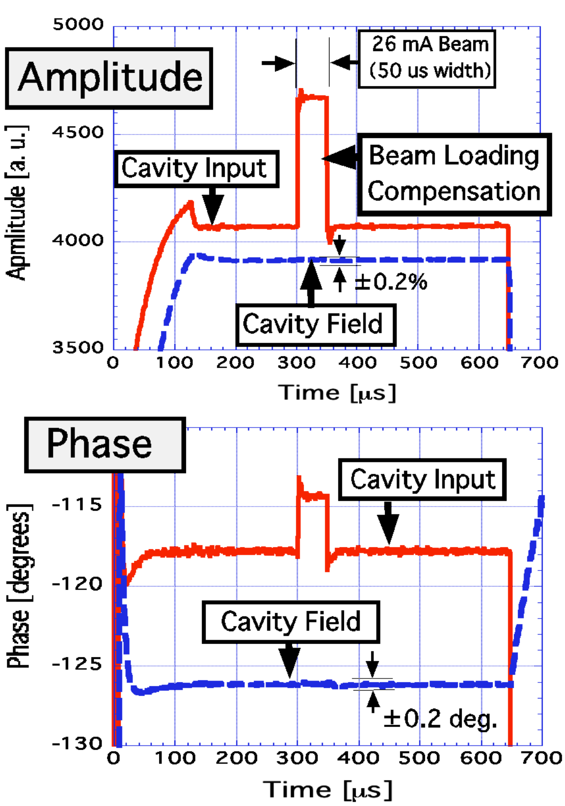


Figure 5: Beam Loading Compensation

## PULSE-BY-PULSE SWITCHING OF BEAM LOADIN COMENSATION

The FPGA program was modified, and the new function for pulse-by-pulse switching of the beam-loading compensation parameters is installed into the LLRF control system. As shown in the Fig. 4, FF-control preset values of the I/Q component are switched by an external command gate signal. The width of the command gate controls selection of the preset values as shown in Table 1. This command gate signal is generated by the timing system of the J-PARC and it is switched automatically in accordance with the operation mode. This switching command affects an immediate RF pulse in 25-Hz repetition. Presently, 5 sets of the preset value are available as shown in the Table. One set of the preset values is set zero, so that the beam loading compensation is to be stopped when the beam is stopped.

The operation test for the new function was performed and it was succeeded in low power operation. This new function in planned to be used from December 2008 for the J-PARC.

Table 1: Preset values for the FF control switching.

| Gate Width | | Preset Value | |
|---|---|---|---|
| 5 | (04∼06) | Val1_I, Val1_Q | I and Q = 0 |
| 10 | (09∼11) | Val2_I, Val2_Q | I and Q = 1024 |
| 15 | (14∼16) | Val3_I, Val3_Q | |
| 20 | (19∼21) | Val4_I, Val4_Q | |
| 25 | (24∼26) | Val5_I, Val5_Q | |

## SUMMARY

Because the linac beam intensity changes depending on the destination of the RCS beam extraction, a new function that can switch the beam-compensation parameters in every pulse was installed into J-PARC linac LLRF control system. The test operation was succeeded, and this new function will be used from December 2008 for the J-PARC.

## REFERENCES

[1] URL: http://www.j-parc.jp/
[2] S. Michizono, et al., "Performance of a Digital LLRF Field Control system for the J-PARC Linac", Proc. of LINAC2006, pp. 574-576, 2006.
[3] T. Kobayashi, et al., "Performance of J-PARC Linac RF System", Proc of PAC07, pp. 2128-2130, 2007.
[4] S. Wang, S. Fu and T. Kato, "The development and beam test of an RF chopper system for J-PARC", Nuclear Instruments and Methods in Physics Research A 547, pp. 302–312, 2005.
[5] M. Ikegami, "Progress in the Beam Commissioning of the J-PARC Linac and Its Upgrade Path", Oral talk in this conference (MO201), 2008.

# LLRF CONTROL SYSTEM USING A COMMERCIAL BOARD*

Han-Sung Kim#, Hyeok-Jung Kwon, Kyung-Tae Seol, and Yong-Sub Cho
Korea Atomic Energy Research Institute, Daejeon 305-353, Korea

*Abstract*

The requirements for the field amplitude and phase stability of the PEFP linac are 1% and 1 degree, respectively. To achieve the requirements, a digital LLRF control system has been developed using a commercial digital board for general purpose (FPGA). The feedback with PI control and feedforward are implemented in the FPGA. The LLRF control systems are currently used for the linac test. In this paper, test results and discussion on the advantage and disadvantage of the LLRF system based on a commercial board are presented.

## INTRODUCTION

In the 100 MeV proton linear accelerator for PEFP (Proton Engineering Frontier Project), the RF source will power an RFQ cavity and DTL tanks operated at a frequency of 350 MHz [1]. The low level RF(LLRF) system for 100 MeV proton linear accelerator provides field control including an RFQ and DTL tanks at 350 MHz. In our system, an accelerating field stability of ±1% in amplitude and ±1 deg. in phase is required for the RF system. The digital RF feedback control system using the FPGAs and PowerPC Embedded Processor is adopted in order to accomplish these requirements and flexibility of the feedback and feed-forward algorithm [2]. The analog front-end also developed which contains the IQ modulator, RF mixer, attenuators etc. To check the performance of the digital feedback control system, low power test with a dummy cavity has been performed with an intentional perturbation and has shown that the feedback system rejected the perturbation as expected. High power RF test with 3 MeV RFQ and 20 MeV DTL has been performed and the accelerating field profiles were measured and the pulse-to-pulse stability was checked by pulse operation with 0.1 Hz repetition rate. In addition, the LLRF system can be used for resonant frequency observer. Measured frequency offset from resonance condition is converted to analog voltage signal, which can be used as an error input signal for RCCS (Resonance Control Cooling System).

## LLRF SYSTEM DESCRIPTIONS

The main hardware components of the digital RF feedback system are ADC for sampling of the RF signal, FPGA for the signal processing and DAC for driving the IQ modulator. A ICS-572B commercial board which is shown in figure 1 is adopted for the ADC/DAC and FPGA board. ICS-572B is a PMC module with 2-channel 105 MHz ADC, 2-channel 200 MHz DAC and with 4 million gate onboard Xilinx FPGA.

* This work is supported by the Ministry of Education, Science and Technology of the Korean government.
#kimhs@kaeri.re.kr

The board uses two 14-bit ADCs (Analog Devices AD6645) with a maximum sampling rate of 105 MHz. The sampling clock can be either internally or externally generated. The minimum ADC sample rate is 30 MHz. Both input channels are simultaneously sampled and transformer-coupled with turn rato of 4:1.

The outputs of the ADCs are connected to a Xilinx FPGA for direct processing of the ADC data. The ICS-572B includes a Xilinx Virtex-II FPGA (XC2V4000) that can be programmed by the user via a JTAG port or PCI communication.

On the output side, the ICS-572B uses two 14-bit high speed DACs (Analog Devices AD9857). The maximum simultaneous conversion rate is 200 MHz. The DAC has a built-in quadrature up-converter that allows the user to provide complex baseband input which is up-converted to a programmable IF (up to 100 MHz). The DAC also provides a programmable clock multiplier.

The communication between the ICS-572B board and host system is made using PCI bus. The QL5064 QuickPCI chip from QuickLogic is used for PCI interface solution. The performance of the QL5064 is 64 bit/66 MHz and automatically backwards compatible to 33 MHz or 32 bit

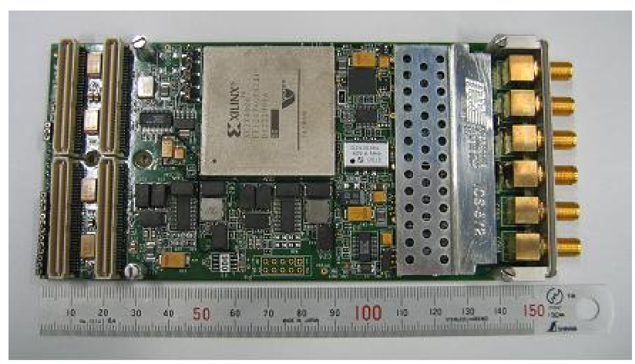

Figure 1: ICS-572B PMC Board.

For the host system of the ICS-572B FPGA board, a Motorola VME processor module, MVME5100, is adopted. The main roles of the host system are the configuration of the FPGA board and the data acquisition.

The feedback logic based on the PI control is implemented in the FPGA by using VHDL. The I and Q component of the cavity field signal is fed into the FPGA using the ADC, which samples the RF signal four times during one period. The sampled I and Q components of the cavity signals are compared with the set value, which generates the error signal. The calculated proportional and integral control values are added then converted to an analogue signal by using DAC.

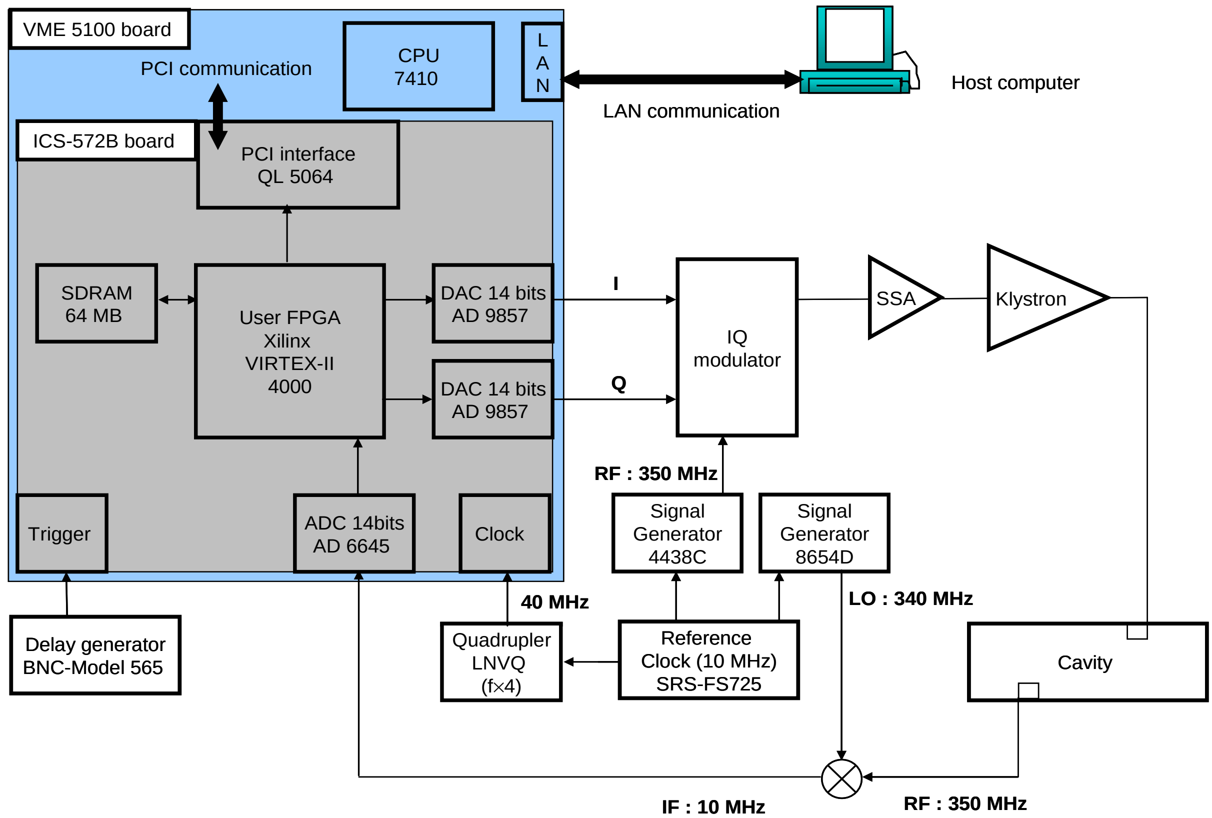


Figure 2: Schematic of the overall control system and experimental set-up.

The analogue signal from the DAC drives the IQ modulator. The set values and each gain value are written into the register in the FPGA by the host processor through a PCI communication. Therefore the set values and gains can be changed during the operation. The measured I and Q components of the RF signals are uploaded to the host board by using a PCI communication.

## PERFORMANCE TEST RESULTS

The schematic block diagram for the overall LLRF control system is shown in figure 2. The shot-to-shot RF stability was measured and we found that the feedback control improved the shot-to-shot stability by an order of a magnitude compared with an open loop control [3].

For the high power RF test, the RF system was operated in pulse mode with 200 μs duration and 0.1 Hz. The measured RF amplitude variation and phase variation during a single RF pulse without beam were less than 0.2% and 0.3˚, respectively as shown in figure 3. The RF amplitude and phase of DTL cavity for 600 shots are recorded and the results are summarized in Table 1. For 600 shots, the RF amplitude and phase were kept within ±0.7% and ±0.9˚ respectively, which meet the RF requirements of the LLRF control system.

For the feedback and feed-forward test, we established the experimental setup by using a dummy cavity. As can be seen in figure 4, the PI control has shown a good performance in perturbation rejection. In addition, the feedback control with feed-forward could improve the transient response significantly.

We performed a test for monitoring the frequency offset from the resonance by using the developed LLRF system and dummy cavity. Figure 5 shows the measured results for frequency offset as a function of the dummy cavity temperature. We analyzed the results by linear fitting. The error bars represent the maximum and minimum values at given temperature.

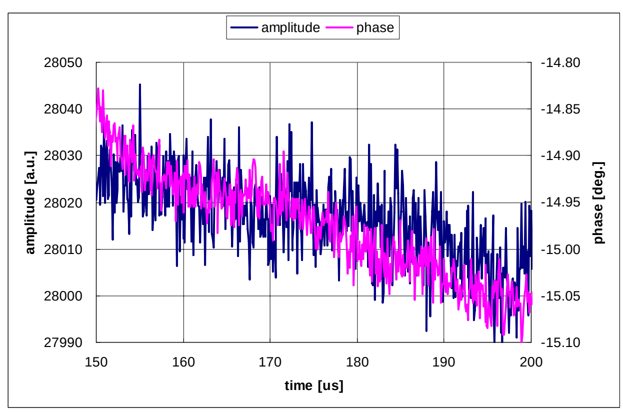


Figure 3: RF amplitude and phase in DTL cavity.

Table 1: Statistics for 600 shots measurements results.

| | amplitude | phase [deg.] |
|---|---|---|
| average | 28139.1 | -14.109 |
| sigma | 121.2 | 0.323 |
| max error | 0.79% | 0.904 |
| min error | -0.63% | -0.744 |

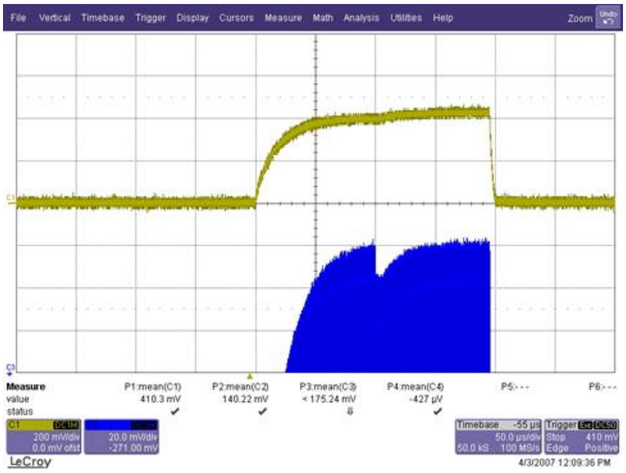

Figure 4(a): Cavity field response for feedback control. (upper: Forward RF power, lower: Cavity field)

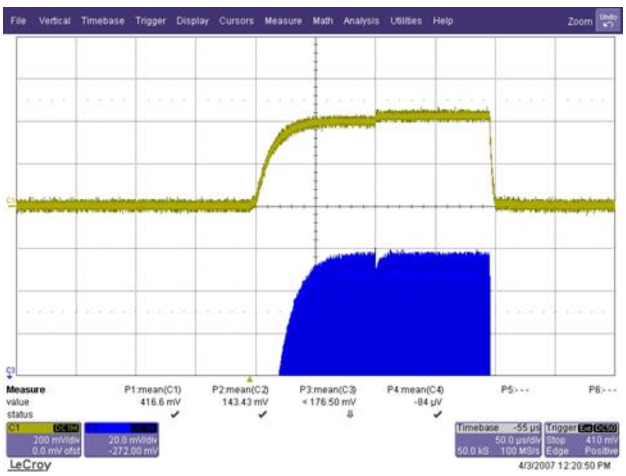

Figure 4(b): Feedback control with Feed-forward. (upper: Forward RF power, lower: Cavity field)

One of reasons for large scatter in measured data by network analyzer is that the dummy cavity has a low quality factor. In addition, the fluctuation in temperature measurement system is another reason for data scatter shown in figure 5. The frequency offsets measured by network analyzer and by LLRF were slightly different by about 6 kHz, which is about 3 % of bandwidth of the dummy cavity. This discrepancy is still under investigation. However, the gradients are almost same, which means that the frequency sensitivity to the temperature measured by using LLRF system is reliable.

The measured frequency offset is converted to analog voltage signal through the DAC in the multi-functional IO board mounted on the VME host board, which will be used for the error signal input for RCCS. The DAC was programmed to have output ranging from -10 V to +10 V for frequency offset from -20 kHz to +20 kHz. The DAC output behaved as expected as shown in figure 6, which shows the recorded DAC output during the frequency offset measurement experiment.

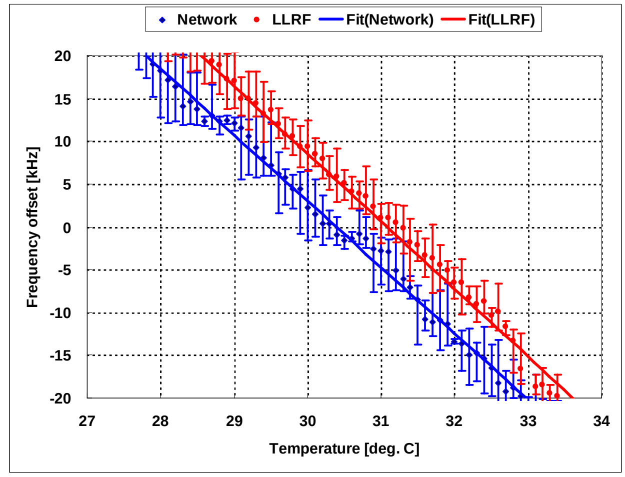

Figure 5: Frequency offset from resonance measured by network analyzer and LLRF system.

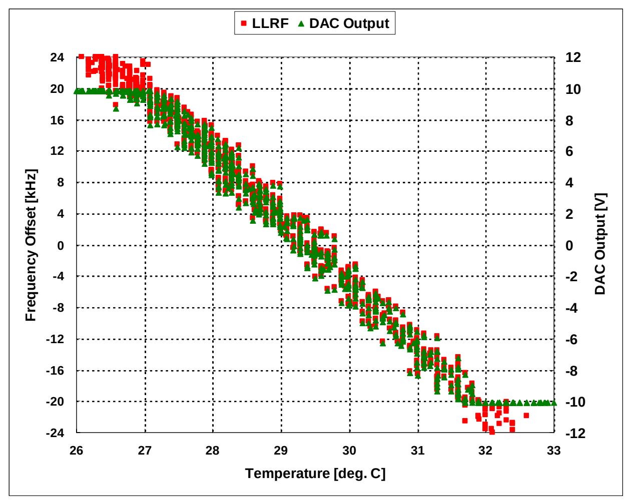

Figure 6: DAC output based on the measured frequency offset from the resonance.

## CONCLUSIONS

The digital LLRF control system has been developed and tested by using a commercial FPGA board. The test results showed that the control system meets the requirements. In addition, the frequency offset from the resonance can be monitored by using the LLRF system. Use of the commercial board can reduce the development time considerably. But the limitations in flexibility such as fixed IO channel number and the operation mode are main drawbacks.

## REFERENCES

[1] H. S. Kim, et al, “RF Characteristics of the PEFP DTL”, Proceedings of EPAC 2006, Edinburgh.

[2] M. E. Angoletta, “Digital Low Level RF”, Proceedings of EPAC 2006, Edinburgh.

[3] H. S. Kim, et al, “Development of the PEFP Low Level RF Control System”, Proceedings of PAC 2007, Albuquerque.

# NUMERICAL SIMULATION OF THE INR DTL A/P CONTROL SYSTEM

A.I.Kvasha, Institute for Nuclear Research, RAS, Moscow, Russia

*Abstract*.
Stabilization of amplitude and phase in linear accelerator cavities can be realized by means of control systems, operating both in polar (A/P) and rectangular (I/Q) coordinate. In analyzing of linear control systems, as a rule, transfer functions are used, which, in turn, are the symbolic representation of the linear differential equation, connecting the input and output variables. It's well known that generally in A/P coordinate it is impossible to get two separate linear differential equations for amplitude and phase of RF voltage in a cavity except for estimating of the control system stability "in the small" near steady state values of variables [1]. Nevertheless, there is a possibility of numerical simulation of nonlinear A/P control system using up-to-date programs. Some results of the simulation are presented.

## INTRODUCTION

In contrast to A/P, in I/Q coordinates it is succeeded in separating of both variables in two linear differential equations even for detuned cavity. That is why I/Q control systems became so popular last years, particularly, in connection with successful development of digital feedback systems. Despite obvious advantages of I/Q control system, its real application in pulse DTL RF system, operating at frequencies below 300 MHz, meets some difficulties. In this case RF amplifiers, as a rule, are based on application of vacuum tubes. The vacuum tube RF amplifiers construction inevitably contains bypass capacitors, which always are sources of RF parasitic radiation. Since I/Q control systems basically use standard integrated circuits: mixers, I/Q modulators and demodulators, working at low RF power level, its operation due to interferences from vacuum tube RF amplifiers, can be disturbed. That is why application of I/Q control systems is preferable for stabilization of accelerating field in cavities with klystron RF supply or with the low gain vacuum tube amplifiers in a case of CW accelerators.

Since at INR linear accelerator output RF power amplifier (PA) is connected with the DTL cavity (tank) by means of coaxial transmitting line (CTL) without circulator, the PA and the tank can be considered as a common high quality oscillating system [1]. At that, processes in the system are described by the first order linear differential equation with complex coefficients, which appear in result of two admissions:

- Transients in the high quality cavity are so slow that changing of amplitude and phase for the RF period can be not taken into account.
- Transients in the output RF power amplifier circuits and CTL are so fast in comparison with transients in the accelerator high quality cavity that steady-states are available in these circuits (including CTL) at every instant of amplitude and phase transients in the cavity.

These admissions allow simplifying not only the calculation of transients in the high quality tank, but also estimating parameters of control systems, stabilizing amplitude and phase of RF voltage in the DTL tank. As it was shown in [1] the first order - linear at complex variable plane, Differential Equation (DE) for a "complex envelope" of RF voltage in a high quality accelerator cavity can be presented in the following way:

$$T_n \frac{d\overline{U}_c(t)}{dt} + (1 - j\xi_c)\overline{U}_c(t) = \frac{T_n}{T_0} R_S(\bar{I}_g - \bar{I}_b)\,, \tag{1}$$

where $\bar{U}_C$ is a complex amplitude of accelerating voltage in the high-quality cavity; $\xi_c = (\Delta\omega_g + \Delta\omega_0)T_n$; $\Delta\omega_0, T_0, R_s$ are the own cavity detuning, cavity time constant and cavity shunt impedance; $\Delta\omega_g, T_n$ are the cavity "detuning" and "time constant" of the cavity, determined by the RF system parameters, such as internal resistance of the PA vacuum tube, coupling with CTL both from the side of the output RF power and from the cavity, length of the CTL [1,2]; $\bar{I}_g$ is a complicated function of RF supply parameters, listed above; $\bar{I}_b$ is a complex amplitude of the beam current resonance harmonic. So, one could say that Eq. (1) determines transient in common "PA-cavity" oscillating system. Moreover, as evident from Eq. (1), application of the complex envelope of RF in the cavity notably simplifies an analysis of control systems since both RF channel with the cavity and the feedback circuits are arranged in the same low-frequency domain. In polar A/P coordinates the complex amplitude $\overline{U}_c(t) = a_c(t)\exp(j\varphi_c(t))$. Substituting this expression in Eq. (1) and taking into account that $\bar{I}_g = I_g e^{j\varphi_g}$, $\bar{I}_b = I_b e^{j\varphi_b}$ it is easy to get from Eq. (1) the next system of the nonlinear differential equations for the real and imaginary parts of the Eq. (1):

$$\begin{aligned} T_n \frac{d\varphi_c}{dt} - \xi_c &= \frac{T_n R_s}{a_c T_0}(I_g \sin(\varphi_g - \varphi_c) - I_b \sin(\varphi_b - \varphi_c)) \\ T_n \frac{da_c}{dt} + a_c &= \frac{T_n}{T_0} R_s (I_g \cos(\varphi_g - \varphi_c) - I_b \cos(\varphi_b - \varphi_c)) \end{aligned} \tag{2}$$

In turn, in rectangular coordinate $\overline{U}_C = X_C + jY_C$ and Eq. (1) can be represented by the following system of two differential equations:

$$\begin{pmatrix} sT_n + 1 & \xi_c \\ sT_n + 1 & -\xi_c \end{pmatrix} \begin{pmatrix} X_c \\ Y_c \end{pmatrix} = \frac{T_n}{T_0} R_S \begin{pmatrix} \cos\varphi_g & -\cos\varphi_b \\ \sin\varphi_g & -\sin\varphi_b \end{pmatrix} \begin{pmatrix} I_g \\ I_b \end{pmatrix} \quad (3)$$

Expressing $X_C$ from the second DE and substituting it in the first one it is not difficult to get the linear DE of the second order for $Y_C$. Repeating the procedure for $Y_C$ one can get the similar DE for $X_C$.

## MODELLING OF A/P CONTROL SYSTEM

In the INR DTL cavity (tank) stabilization of the accelerating RF voltage is realized by means of the feedback RF signals from the tank pickup loops, controlling values of $I_g$ and $\varphi_g$ in Eq. (1), so that to support unchangeable values of amplitude and phase of the accelerating voltage. The feedback RF signals are transformed in the phase and amplitude error signals as result of comparison with phase (in phase detector) and amplitude (after amplitude detector) set points signals. The gained phase error signal controls phase shifter at RF pulse power level ~1Wt; the gained amplitude error signal controls the value of PA pulse plate voltage. For the A/P control system modelling was chosen the Matlab Simulink program. The main result of control system modelling by means of Matlab Simulink is a possibility of immediate observation of transients in any point of control system, following after changing of outside or inner parameter values. At that, for modelling of the A/P control system both systems of Eq. (2) and Eq. (3) are available, but the system Eq. (3) is simpler and more suitable, taking into account a possibility of conversion from polar system of coordinate to rectangular one and vice versa. The main blocks of the A/P control system Model are described below.

### *DE (differential equations) Block*

First of all the system Eq. (3) has to be transformed to the form suitable for modelling in Matlab Simulink. The point is that because integration is a more numerically stable operation than differentiation, in Matlab ordinary differential equations are transformed into ones that use integration operators. It follows then that the number of Simulink *Integrator* block equals the order of the highest derivative. Hence, the system of Eq. (3) has to be transformed in the following way:

$$X_C = \frac{1}{sT_n}\left(R_S \frac{T_n}{T_0}(I_g \cos\varphi_g - I_b \cos\varphi_b) - X_C - \xi_C Y_C\right)$$

$$Y_C = \frac{1}{sT_n}\left(R_S \frac{T_n}{T_0}(I_g \cos\varphi_g - I_b \cos\varphi_b) - Y_C + \xi_C Y_C\right) \quad (4)$$

In Fig.1 the model of the system Eq. (4) is presented. As the A/P control system is the subject of present investigation, the Simulink Extras Transformation blocks "Polar to Cartesian" and "Cartesian to Polar" are input. The blocks allow using the system of linear DE for analysis of the nonlinear A/P control system. It is obvious that without the Extras Transformation blocks the model in Fig. 1 can be used for I/Q control systems analysis too.

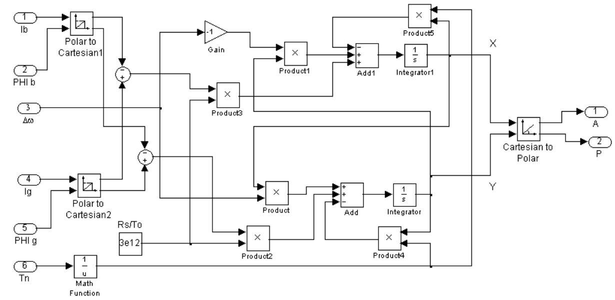


Figure 1: Model of nonlinear differential equations system.

### *Block "Feedback"*

In Fig. 2 the block Feedback is presented. It consists of two separate networks. In amplitude control system feedback there are anode pulse modulator transfer function, time delay TD and limiter AD for positive signals, which ensures opening of the feedback only if pickup signal from the tank exceeds the amplitude set-point.

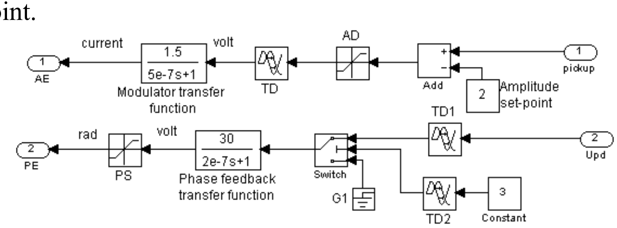


Figure 2: Model of the block "Feedback".

In phase control system except of the feedback transfer function, time delay TD1 and limiter PS, determining the phase shifter, the block "Switch" is input. It serves for creating of time delay (TD2) between the moments of the simulation beginning and the phase feedback closing.

### *Block "Timer"*

The block transforms DC input signals $I_g$, $\varphi_g$, $I_b$, $\varphi_b$ in pulse form and attaches the beam phase to the set-point phase $\varphi_g$ and tank phase detuning $atan\xi_c$ (see Fig. 3).

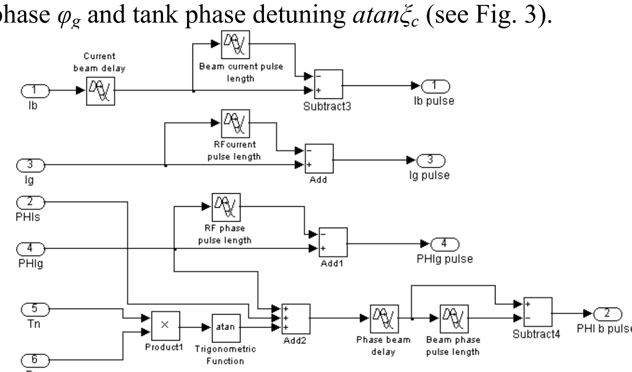


Figure 3: Block "Timer".

### *Block "RF Channel"*

The block presents a transformer function of the series RF amplifiers, tuned at the master oscillator frequency.

The transformer function is input in Cartesian coordinates by means of two Simulink blocks “Polar to Cartesian” and “Cartesian to Polar” (see Fig. 4).

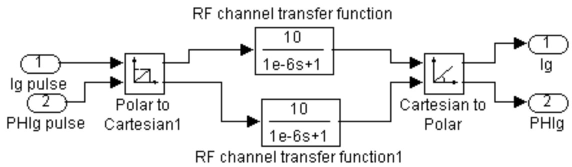


Figure 4: Block “RF channel”

Except of the subsystem blocks, listed above, there are a few additional math operation blocks: *block “PD”* (phase detector), which corresponds to well-known expression for the PD output signal:

$$U_{PD} \equiv \frac{U_C U_{SP}}{\sqrt{U_C^2 + U_{SP}^2}} \sin(\varphi_C - \varphi_g)\,, \qquad (5)$$

where Uc, $\varphi_C$ – amplitude and phase of RF voltage in the tank; $U_{SP}$, $\varphi_g$ – amplitude and phase of the set-point signal and block “PSS” (slow phase stabilization system), which compensates a constant phase shift due to tank detuning.

## SOME RESULTS OF MODELLING

In Fig. 5 the common view of the Model is shown. All numerical data in the Model correspond to the third cavity of the INR DTL.

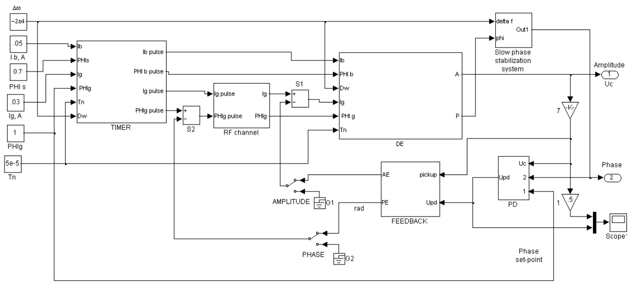

Figure 5: Common view of the control system Model

As can be seen from the blocks, presented above, numerical calculation of the control systems demands determination of the input values of cavity time constant $T_n$ and detuning $\Delta\omega_g + \Delta\omega_0$, amplitude and phase of the beam current $\bar{I}_b$. As a rule, at INR DTL RF system a coupling of the CTL with the tank is chosen so that to minimize the VSWR value and, hence, value of the tank detuning $\Delta\omega_0 \sim 0$. Nevertheless, without a circulator between PA and tank, a value of $\Delta\omega_g$ is really always takes place, since its value, as and $T_n$ value, depends on the CTL length, coupling PA anode-grid cavity with CTL and the PA supply. In turn, during RF channel operation all cited above parameters are optimized so that to achieve a maximum efficiency of the PA without a danger of overvoltage in the PA cavity [2], but not to minimize $\Delta\omega_g$ value. However, there is a possibility to estimate values of $T_n$ and $\Delta\omega_g$, analyzing the amplitude and phase transients in the tank at the open fast amplitude and phase feedbacks. At that, sign and amplitude of the phase transients at the front edge of the phase pulse can be used for determination of the tank detuning value and a tangent to the RF envelope in the tank – for determination of the loaded tank quality.

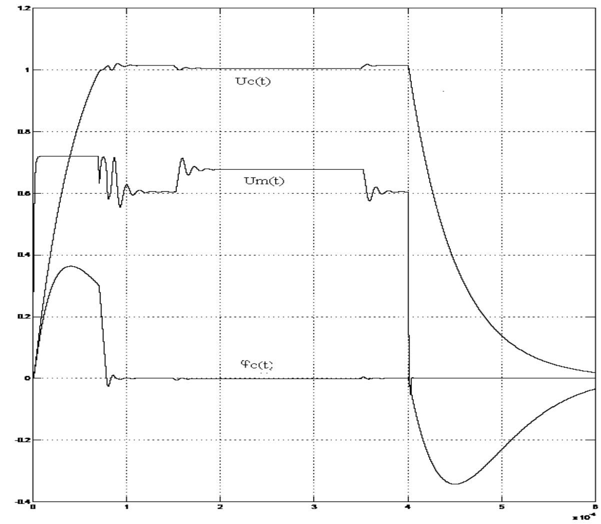


Figure 6: Envelope of RF voltage Uc(t), phase $\varphi_C(t)$ in the tank and anode modulator pulse Um(t)

As an example in Fig. 6 pictures of the signals in different points of the Model are shown. Parameters of the feedback transfer functions, tank ($T_n$ and $\Delta\omega_g$), RF channel are pointed in Figs. 1-5. Beam loading is ~ 24%. Hidden parameters are following: transport delay in the amplitude feedback TD=2μs, in the phase feedback TD1=.5μs, time delay of the phase feedback closing is 70μs, $T_n$ /$T_0$ =.5. The results of modelling are in good agreement with real measurement data, which have been done at the third DTL cavity. Certainly, results of modelling depend on specific parameters of RF channel and feedback networks, but some common peculiarities it is worthy to mention:

- Closing of the phase feedback near the flat top of RF pulse in the tank allows avoiding a danger of the amplitude degradation due to self exciting of the phase system at the leading edge of RF pulse.
- At $\Delta\omega_g \neq 0$ opening of the phase feedback as a rule makes poor quality of the amplitude stabilization system.
- At $\Delta\omega_g \neq 0$ the feedback gain in the amplitude or phase control systems, taken separately, is always higher than that of when both systems are closed.

## REFERENCES

[1] V.V. Balandin et al. "Conceptual Design of a Positron pre-Accelerator for the TESLA Linear Collider", August 1999, TESLA 99-14.

[2] A.I.Kvasha “Investigation of overvoltages in the anode-grid cavity of the 200MHz pulse power amplifier of the MMF”, Proceedings of the PAC2001, p. 1225.

# OPTIMAL COUPLER AND POWER SETTINGS FOR SUPERCONDUCTIVE LINEAR ACCELERATORS*

J. Branlard†, B. Chase, S. Nagaitsev, O. Nezhevenko, J. Reid
Fermi National Accelerator Laboratory, Batavia, IL, U.S.A.

*Abstract*

The modeling analysis presented in this paper addresses the question of how to achieve the highest vector sum gradient for all beam currents when individual cavities operate at different gradients due to their inherent quenching limitations. The analytical method explained here constitutes a step forward toward the operability of the International Linear Collider (ILC), Project X [8], or XFEL [7]. Unlike previously proposed methods [1, 2], this approach prevents cavities from quenching should the beam current be lower than its maximum value.

## INTRODUCTION

Ideally, all superconducting cavities of a linear accelerator RF station operate at the target gradient (31.5 MV/m for the ILC). Practically however, cavities show a certain disparity in their gradient performance. Based on the experience acquired at DESY XFEL [6], we know that some cavities quench or exhibit a $Q$ drop behavior when operating above 22 MV/m while others will sustain an accelerating gradient of 34 MV/m. This disparity among cavities raises challenging issues related to conditioning and operations of linear accelerators using one klystron per RF station. More precisely, this paper presents an analytical solution to the following question: for $N$ cavities with a given maximum gradient distribution (i.e. quenching limits), what is the highest vector sum gradient that can be maintained for the entire flat top duration with beam or in the absence of beam, while ensuring that no cavity quenches? Currently, one approach has been proposed [1, 2] to address this issue but it only guaranties maximum gradient operability when the beam current is maximum. A second approach implemented at DESY for XFEL [7] only guaranties maximum gradient without beam current. In contrast, the method presented here predicts the maximum vector sum gradient that can be reached for a given cavity distribution, independently of the beam loading.

## $Q_L$ AND $P_K$ SETTINGS

The present model consists of a low level RF (LLRF) controller driving a single klystron, providing the RF forward power to multiple cavities. The amplitude and phase of the klystron drive signal can be adjusted from the LLRF controller, the proportion of forward RF power delivered to individual cavities can be adjusted at the wave guide level by tuning the wave guide couplers, (referred to as $P_k$ setting) and at the cavity level by changing the loaded $Q$ of each cavity's input coupler, (referred to as $Q_L$ settings). Several techniques have been suggested to adjust the forward power distributed to a pair of cavities: variable tap off splitters [5], or phase shifters [9]. Either of these techniques requires hardware replacement and interrupting accelerator operations for an extended period of time. Hence, this tuning is considered to be set once and not changed again. Setting the external $Q$ at the cavity input coupler is an operation which does not require shutting down the RF station. It is nonetheless a time consuming procedure and is not practical for large scale machines. Finally, the LLRF drive signal can dynamically (i.e. during the RF pulse) control and adjust the amplitude and phase of the klystron drive signal. The goal of this study is to find the optimal configuration of these parameters to achieve the highest vector sum gradient, while respecting the operational and security constrains listed above.

The approach described in [4] consists of choosing $Q_L$ and $P_k$ settings specific to each cavity so as to match every cavity with maximum beam loading. One major issue associated with this scheme is that the individual $Q_L$ and $P_k$ need to be readjusted every time the beam loading is less than maximum which can become a real operation bottleneck for large scale accelerators. Alternatively, lowering the klystron forward power for less than maximum beam current operations can prevent cavities from quenching but will significantly degrade the vector sum gradient. In the DESY approach [7], all cavities are set to the same $Q_L$ but some cavities will quench when the beam is on unless the vector sum gradient is lowered. The approach presented here addresses these issues.

## ANALYTICAL INSIGHT

### *Flat Top without Beam*

The voltage inside a superconducting cavity, on resonance and with on-crest beam loading can be modeled as follows [3]:

$$V_C(t) = 2R_L \left[ I_{g0}(1 - e^{--}) - I_{b0}(1 - e^{-\frac{-\ 0}{}}) \right] \quad (1)$$

where $R_L$ is the loaded resistance of the cavity, $I_{b0}$ is the nominal DC beam current, $\tau = \frac{2Q}{\omega_0}$ is the cavity time constant and $t_0$ is the duration of the fill time of the cavity, after which the forward power is dropped by four when no beam is present. Achieving a flat top in the absence of beam

* work supported by Fermi Research Alliance, LLC under Contract No. DE-AC02-07CH11359 with the United States Department of Energy
† branlard@fnal.gov

is equivalent to a null time-derivative of the cavity voltage which is obtained when $t_0 = \tau \ln 2$. The steady state cavity voltage is then $V_{SS}^{nobeam} = R_L I_{g0}$, where $I_{g0} = 2I_{bo}$ is the nominal generator current. This flat top condition under no beam is solely function of $\tau$, (i.e indirectly function of $Q_L$). So, setting all cavities to the same $Q_L$, and setting the fill time $t_0 = \tau \ln 2$ will guarantee a flat top for all cavities hence for their vector sum.

### *Flat Top with Beam*

Setting all cavities to the same $Q_L$ will result in all $R_L$ and all $\tau$ being equal. The vector sum can then be simplified to the following expression:

$$V_S(t) = 2R_L(1 - e^{-\frac{t}{\tau}})\frac{1}{N}\sum_i I_{gi} - 2R_L I_{b0}(1 - e^{-\frac{t-t_0}{\tau}}) \tag{2}$$

The flat top for the vector sum is achieved by annulling the time derivative of $V_S(t)$, which is equivalent to setting $\frac{1}{N}\sum_i I_{gi} = 2I_{b0}$. Using the notation $I_{gi} = \alpha_i I_{g0}$, the flat top condition for the vector sum with beam becomes

$$\frac{1}{N}\sum_i \alpha_i = 1 \tag{3}$$

### *The No-quench Guarantee*

When the beam is on, a cavity which receives less (more) than the nominal generator current, $\alpha_i < 1$, ($\alpha_i > 1$) sees its voltage drop (increase) during beam loading. Comparing the cavity voltage at the beginning (end) of the beam loading against the cavity quenching gradient can determine whether the quenching limit has been exceeded, as illustrated in Fig.1. From Eq.1, and by introducing the following notation for the flat top duration $T_{FT} = t_1 - t_0 = \tau \ln \beta$, the cavity voltage at the beginning and at the end of the beam loading are $V_{Ci}(t_0) = 2R_L \alpha_i I_{b0}$ and $V_{Ci}(t_1) = 2R_L I_{b0}\left[\alpha_i(2 - \frac{1}{\beta}) - (1 - \frac{1}{\beta})\right]$. For cavities operating below (above) the vector sum, the no-quenching condition is equivalent to having $V_{Ci}(t_0) \leq V_{qi}$, ($V_{Ci}(t_1) \geq V_{qi}$), where the $V_{qi}$'s are the cavity quenching limits. Introducing the following notation,

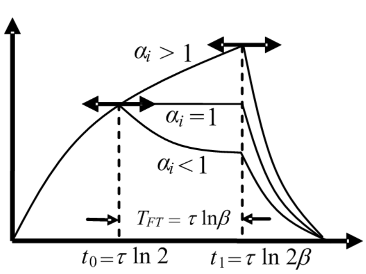


Figure 1: Quenching limits as a function of $I_{gi}$.

$$\alpha_i^- = \frac{V_{qi}}{2R_L I_{b0}} \tag{4}$$

$$\alpha_i^+ = \left[\frac{V_{qi}}{2R_L I_{b0}} + (1 - \frac{1}{\beta})\right]\frac{\beta}{2\beta - 1} \tag{5}$$

the maximum gradient corresponding to the critical quenching case is reached when the cavities operating below (above) the vector sum have $\alpha_i = \alpha_i^-$ ($\alpha_i = \alpha_i^+$). One can note that $\alpha_i^-$ and $\alpha_i^+$ are monotonous in $V_{qi}$ and that for a cavity operating at the vector sum gradient, we have $\alpha_i^- = \alpha_i^+ = 1$. Hence, choosing $\alpha_i^{lim} = \min\{\alpha_i^-, \alpha_i^+\}$ for every cavity will guaranty that no cavity quenches. Normalizing all $\alpha_i$'s by $\bar{\alpha} = \frac{1}{N}\sum_i \alpha_i^{lim}$ will guaranty that their arithmetic mean is unity. Assuming $\bar{\alpha} \geq 1$, the normalized $\alpha_i = \frac{\alpha_i^{lim}}{\bar{\alpha}}$ now verify Eq.3, 4 and 5, resulting in a flat vector sum and no quench. With this choice of $\alpha_i$'s, the steady state vector sum with beam is $V_{SS}^{beam} = 2R_L I_{b0}$, also equal to the flat top gradient in the absence of beam. Furthermore, the critical case of $\bar{\alpha} = 1$ corresponds to the maximum flat vector sum without a cavity quench.

## RESULTS

In the ILC baseline design, each RF station comprises of 26 cavities in pairs. Unless specified otherwise, the simulations in this work follow the gradient distribution introduced in [4] consisting of 13 cavities with maximum gradients uniformly distributed between 22 and 34 MV/m. The amplitude plot of Fig. 2 is obtained maximum beam current (a) and no beam (b). Individual quenching gradients are indicated with dashed lines, while the vector sum gradient is shown with a thicker trace. As this result illustrates the critical case of $\bar{\alpha} = 1$, under maximum beam, Fig. 2(a), the cavities with a gradient below (above) the vector sum reach their quench limit at the beginning (end) of the beam time. In the no-beam case, Fig. 2(b), the cavities operating below the vector sum are at their quenching limit while the cavities above do not reach their own limit. These two plots illustrate the extreme cases. Any intermediate beam current would result in all cavities running below their quenching limits at all time. The maximum vector sum gradient $V_S$ is a function of the cavity gradient distribution and of the beam time duration. In the example of Fig. 2, a maxium vector sum of 27.1 MV/m is found. This is approximately 97% of the intrinsic limit gradient of 28 MV/m. A higher maximum vector sum gradient can be reached as the cavity spread decreases. A uniform spread of 6 MV/m centered around 28 MV/m yields a vector sum of 27.6 MV/m (or 98.6% of the limit gradient). The distribution of the cavity gradients within a given range also has an impact on $V_S$. A more realistic distribution than that used in the previous example would be where the larger portion of the cavities has a quenching limit close to the average of 28 MV/m, while a few "extreme" cavities would perform at the lower or higher end of the distribution. A such "gaussian-like" cavity gradient distribution for the same spread yields a vector sum typically above 98% of the limit gradient. This is illustrated in the first two rows of Table 1, showing the maximum vector sum gradient obtained for two cavity gra-

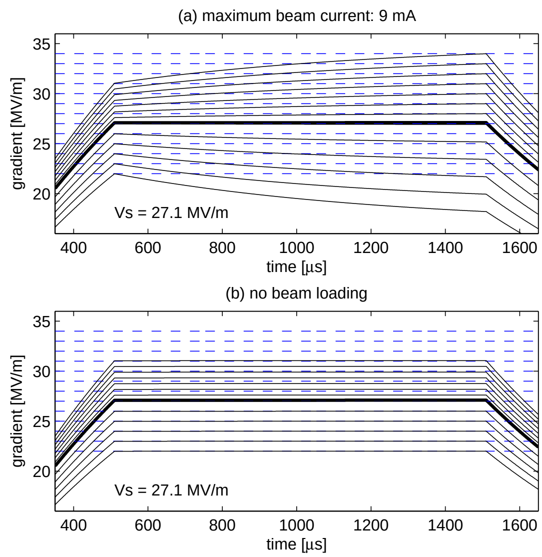


Figure 2: Amplitude plot for 13 cavities with (a) and without (b) beam.

Table 1: Impact of the distribution of cavity gradients

| | uniform | gaussian | |
|---|---|---|---|
| $V_S$ | 27.1 | 27.5 | [MV/m] |
| $V_S/V_{lim}$ | 96.8 | 98.2 | [%] |
| $P^*_{fwd}$ | 6.65 | 6.62 | [MW] |
| $P^*_{ref}$ | 0.039 | 0.020 | [MW] |

$^*$*power calculated for 26 cavities*

dient distributions, spread between 22 and 34 MV/m.

A significant improvement of this present scheme with respect to [1, 2] is the reduced reflected power during the beam time. For 26 cavities, the reflected power is reduced by more than 400 kW compared to that calculated with the previous scheme. The plot of Fig. 3 shows the variations of the maximum vector sum gradient as a function of $Q_L$. As $Q_L$ is increased the vector sum improves until the quenching limit is reached. Setting the cavities to a higher $Q_L$ is possible so long the overall forward power is reduced to avoid a cavity quench. However, this has a negative impact on the vector sum gradient $V_S$ which starts to decrease once the critical $Q_L$ value is passed. Also shown in Fig. 3 is the total reflected power $P_{ref}$ summed for 13 cavities and over the duration of the flat top. As can be seen, the $Q_L$ value maximizing the vector sum is also the optimal $Q_L$ minimizing the reflected power.

## CONCLUSION

A method to calibrate $N$ superconducting cavities with any gradient disparity is proposed in this report. This approach provides the optimal coupler and power settings and is applicable for any large scale linear accelerator where a single-klystron/multiple-cavities scheme is used. The complete analytical derivation for this method is exposed and explained in details. For a given distribution of quenching limits, choosing the optimal $Q_L$ for all cavities provides the highest vector sum gradient, guaranties that it will remain flat under any beam or no beam condition, and that no cavity will quench during operation. Depending on the cavity distribution, accelerating gradients over 98% of the intrinsic limit can be reached. As a by product, the reflected power is greatly reduced during the beam time. This constitutes a more efficient way of accelerating the beam.

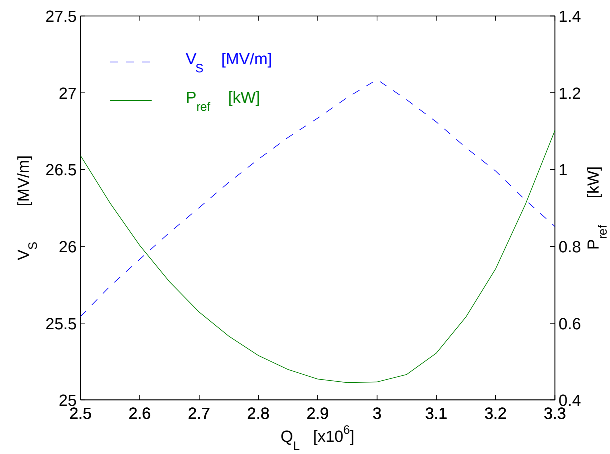


Figure 3: Variations of the vector sum gradient $V_S$ and the total reflected power $P_{ref}$ as a function of $Q_L$.

## REFERENCES


[1] J. Branlard, "Coupling Adjustments for Cavities with Gradient Disparities", FNAL, 2006, ILC database document no.442.

[2] K. Bane *et al.*,"RF Distribution Optimization in the Main Linacs of the ILC", SLAC, 2007, Technical Note

[3] T. Schilcher, "Vector Sum Control of Pulsed Accelerating Fields in Lorentz Force Detuned Superconducting Cavities", DESY, 1998, PhD Thesis.

[4] K. Bane, C. Adolphsen, C. Nantista, "RF Distribution Optimization in the Main Linacs of the ILC", Proceedings of PAC07, Albuquerque, New Mexico, USA.

[5] C. Nantista, C. Adolphsen, G. Bowden, R. Swent, B. McKee, "An RF Waveguide Distribution System for the ILC Test Accelerator at Fermilab's NML", Proceedings of PAC07, Albuquerque, New Mexico, USA.

[6] S. Choroba *et al.*, "XFEL High Power RF Status", SCRF Workshop presentation, April 2008.

[7] "DESY XFEL Technical Report", July 2007, ISBN 978-3-935702-17-1,Notkestrasse 85, 22607 Hamburg, Germany.

[8] "Accelarator Physics and Technology for Project X", Workshop Report, FNAL, November, 2007.

[9] V. Katalev, S. Choroba, "Compact waveguide distribution with asymmetric shunt tees for the European XFEL", Proceedings of PAC07, 2007, Albuquerque, New Mexico, USA.

# NEW LLRF SYSTEM FOR FERMILAB 201.25 MHZ LINAC

Trevor A. Butler, Lawrence J. Allen, Julien Branlard, Brian Chase, Ed Cullerton, Paul W. Joireman, Michael Kucera, Vitali Tupikov, Philip Varghese, Fermilab, Batavia, IL 60510, U.S.A.

*Abstract*

The Fermilab Proton Plan, tasked to increase the intensity and reliability of the Proton Source, has identified the Low Level Radio Frequency (LLRF) system as the critical component to be upgraded in the Linac. The current 201.25 MHz Drift Tube Linac LLRF system was designed and built over 35 years ago and does not meet the higher beam quality requirements under the new Proton Plan. A new VXI based LLRF system has been designed to improve cavity vector regulation and reduce beam losses. The upgrade includes an adaptive feedforward system for beam loading compensation, a new phase feedback system, and a digital phase comparator for cavity tuning. The new LLRF system is phase locked to the 805 MHz reference line, currently used as frequency standard in the higher energy accelerating section of the Linac. This paper will address the current status of the project, present the advancements in both amplitude and phase stability over the old LLRF system, and discuss commissioning plans.

## INTRODUCTION

The RF control system that is presently implemented in low energy (LE) Linac was first commissioned in the late sixties. Although it received minor modifications in 1994, it does not meet the present amplitude and phase stability requirements. During the last seven years, the types and number of beam pulses that are being accelerated in the Linac have risen tenfold, resulting in an increase in activation of the Linac enclosure. As a result, the Proton Plan was developed to fund projects that could either improve beam quality or reduce enclosure activation due to beam loss [1]. In order to meet these demands, a new LLRF for the LE Linac system has been designed and prototyped. The design goal for the new LLRF system is to reduce amplitude variations to < 0.2% and to reduce the beam setting time to < 2 μs. The current LLRF system (see Fig. 1) is only able to achieve 2% amplitude stability. During the first 10 μs of beam, both the RF amplitude and phase errors have the largest excursion. These errors cause momentum drift in the beam, which in turn, creates matching problems into the downstream Booster accelerator. A beam drift of 2 mm, both vertically and horizontally was measured at the downstream end of Linac. In order to reduce this mismatch into Booster, the first 10 μs of beam is presently chopped off and sent to a dump line. With the increased repetition rate of the Linac, this wasted beam has steadily increased the activation of both the dump line and the accelerating structure. By reducing the beam settling time from 10 μs to less than 2 μs, and by improving beam loading compensation and regulation, the beam loss and resulting activation can be greatly reduced [2].

## LINAC LLRF SYSTEM

In order accomplish the goals of the Proton Plan, a new LLRF system has been designed and implemented to replace the present LLRF system (see Fig. 1). The new system consists of three parts, a slot 0 controller, a multi-channel field control (MFC) module, and an analog RF module (see Fig. 2). The slot 0 controller is used to connect the Fermilab controls network (ACNET) with the

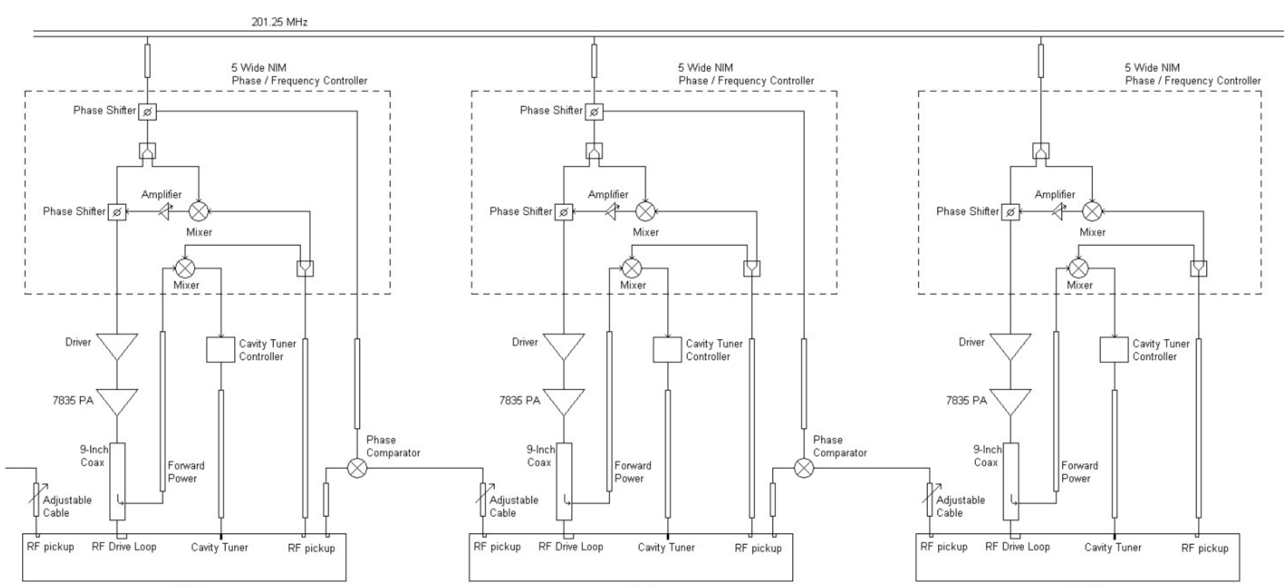


Figure 1: Simplified low energy (LE) linac RF block diagram of the present LLRF control system.

LLRF system. The MFC Board uses a modern Digital Signal Processor (DSP) and Field Programmable Gate Arrays (FPGA) to implement the phase loop, perform feed-forward calculations, and execute other digital control loops. The RF module is responsible for all of the analog RF signal processing and control. Working together, the new VXI based LLRF system provides the following features:

- Digitally controlled phase feedback system that replaces the present analog RF phase feedback
- Adaptive feed-forward for both amplitude and phase control to improve beam loading compensation
- 201.25 MHz RF reference generated from the HE Linac 805 MHz reference line
- Phase loop regulation from the reference line replacing the present inter-tank phase reference
- Digital phase detection for the cavity resonant control system

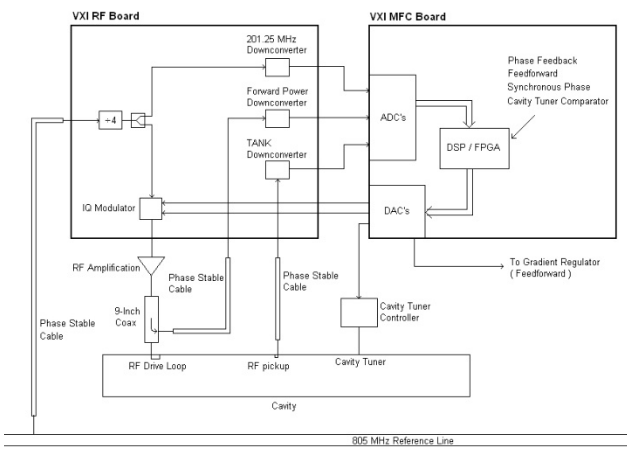


Figure 2: Block diagram of the new VXI LLRF system.

## *Multichannel Field Control Module*

The MFC is modern Low Level RF Controller designed to handle from one to 32 cavities driven from a single RF power amplifier. This allows it to be used in many applications such as Project X or the International Linear Collider (ILC). The MFC module has 32 12-bit ADC's that can operate up to 65 MHz, one 14-bit ADC that can operate up 105 MHz, four 14-bit DAC's that operate up to 240 MHz, an Altera Cyclone II FPGA and a 400 MHz SHARC Digital Signal Processor (DSP). The clock distribution is programmable and there is 64 Mbytes of DDRAM as well as ample flash memory. It is packaged in a one wide VXI module. The Altera Cyclone II FPGA (EP2C70F672C6) functions as the primary signal processor [3].

## *RF Control Module*

Unlike the MFC module, the VXI RF control module was designed specifically for the Linac LLRF upgrade (see Fig. 3). The RF module down converts RF signals to an intermediate frequency (IF) of 12.578 MHz for processing by the MFC module. This module also takes the 805 MHz reference line and divides it by 4 to generate the 201.25 MHz reference at each accelerating cavity. This 201.25 MHz reference signal provides the RF drive for the cavity. An in-phase/quadrature (IQ) modulator on board allows vector control of the magnitude and phase of the RF drive. The module also performs analog RF signal processing tasks, such as RF gating, clock division, phase comparison, and other signal conditioning.

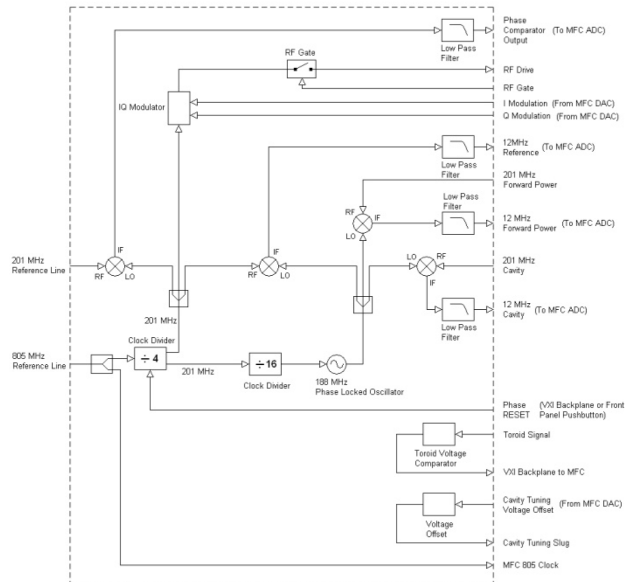


Figure 3: Block diagram of VXI RF module.

## *RF Phase Reference*

The main reason for using the 805 MHz reference line in the new LLRF system is to provide an independent, phase stable RF drive for each accelerating cavity (see Fig. 4). This new system allows the phase of each cavity to be adjusted independently. The present LLRF system uses an inter-tank phase comparator that holds the cavity phase constant relative to each other (see Fig. 1).

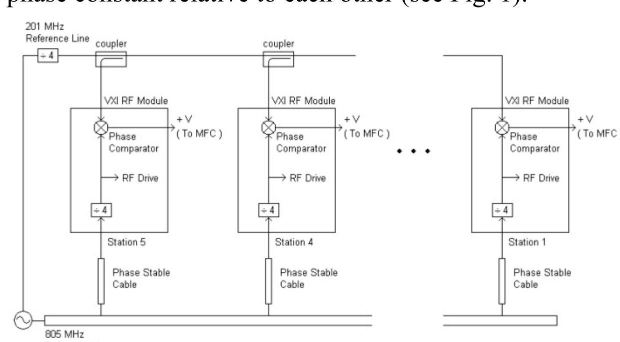


Figure 4: Block diagram of synchronous phase system.

To maintain phase stability of the new LLRF system, phase matched, phase stabilized 3/8" Heliax cable have been installed for each LLRF station. The new cables carry the 805 MHz reference line, the cavity pickup, and the forward power from the accelerator tunnel to each respective RF system. These cables are bundled together so that temperature drifts do not affect the RF system phase. Phase drift problems are very noticeable in the present LLRF system and need constant accelerator tuning to keep beam losses to a minimum.

### *RF Phase Feedback Control*

RF phase modulation is done using the IQ modulator on the RF Board, controlled by the MFC. The IQ modulator is capable of providing both phase and amplitude modulation. Since the main power amplifier, the Burle 7835 power triode, operates in saturation, the amplitude of the cavity vector is controlled by the modulator voltage, not the LLRF drive amplitude. The IQ modulator amplitude is used to adjust the proper output level for the driver amplifier stage.

To control the phase of the LLRF system, the 201.25 MHz reference and the 201.25 MHz cavity pickup signals are both down-converted to an IF of 12.578 MHz. These signals are sent to the analog-to-digital converters (ADC's) on the MFC board (see Fig. 3). The 201.25 MHz reference is generated by dividing the 805 MHz reference input by four on the RF board. The 12.578 MHz IF reference and cavity signals are then digitally down converted to baseband on the MFC board. Using the IF of 12.578 MHz eliminates the problems associated with down converting to baseband in the analog domain.

After down conversion to baseband, the MFC board performs phase feedback calculations which are sent out to the IQ modulator on the RF Board to modulate the RF drive phase. This configuration allows for a complete 360° of phase rotation on the RF drive. This phase modulation is used to regulate the phase of the RF relative to the reference line and uses RF phase feedback to keep the phase of the RF drive consistent throughout the pulse. Using digitally phase feedback also allows the user to easily control the feedback gain of the system.

### *RF Amplitude Feed-Forward Control*

Since the LE Linac RF amplifiers run in saturation, amplitude control cannot be done effectively using direct RF feedback. Instead, amplitude of the RF is controlled by regulating the modulator voltage applied to the anode of the Burle 7835 power amplifier. There are two loops that are presently used to regulate the field in the cavity. The first loop, coded into the Fermilab computer controls network, is used to keep the overall RF field strength consistent on a pulse-to-pulse basis by sampling the field during beam time and making amplitude adjustments to the modulator waveform. This modulator waveform is then input into a second feedback loop to control the overall shape and amplitude of the RF gradient (see Fig. 5). If only the modulator waveform pulse is used as input to this loop, when beam enters the cavity, significant beam loading occurs, dropping the accelerating field in the cavity by more than 10%. The present system compensates for this beam loading by adding the beam toroid pulse into the feedback loop along with the modulator waveform pulse. The problem with using the beam toroid pulse is that it arrives to the LLRF system after beam has already started loading down the cavity. Although adding the beam toroid pulse to the feedback loop reduces the beam loading down to 2%, it still does not meet the proton plan design criteria. In the new LLRF system, instead of using the beam toroid pulse, a feed-forward pulse is added to the modulator amplitude control loop. By summing in this feed-forward input pulse, amplitude stability of 0.1% has been accomplished, which exceeds the design goal of 0.2% beam loading amplitude stability. The vast improvement is a result of the ability for the new LLRF system to precisely control the timing of this feed-forward pulse before beam loading occurs and the ability for precise waveform shaping. Both the modulator and toroid pulse system can add up to 9 µs and 1 µs of delay respectively, which can then be compensated for by timing the feed-forward pulse up to 10 µs before beam arrives [2].

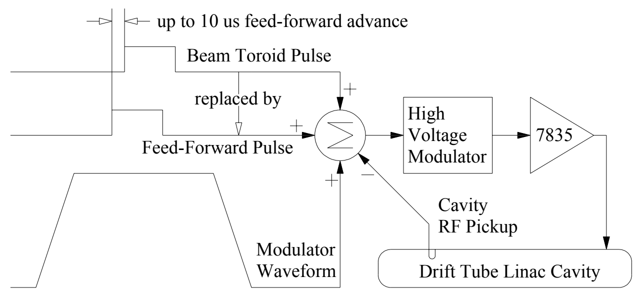


Figure 5: Modulator control system.

## COMMISSIONING PLANS

This new LLRF design was prototyped and installed at the LE Linac RF end station. After extensive fine tuning on phase and amplitude control parameters, the design goals of the Proton Plan where exceeded, with amplitude variations < 0.2% and beam setting time < 2 µs. The plan is to have the prototype LLRF system in operation by the end of the year, with full implementation by mid 2009.

## ACKNOWLEDGEMENTS

The authors would like to thank Barry Barnes, Ken Hartman, Dan Klepec, Joshua Moua, Ken Quinn, Brian Stanzil, Lester Wahl, and Johnathan Walters for their advice and help in assembling, testing, and installation of the LLRF system.

## REFERENCES

[1] L. Allen, 2005 Proton Plan Review, Available: www-accel-proj.fnal.gov/Proton_Plan/index.html
[2] T. Butler et al., "Proposed LLRF Improvements for Fermilab 201.25 MHz Linac", LINAC2006, Knoxville, August 2006, THP058, p. 713.
[3] P. Varghese et al., "Multichannel Vector Field Control Module for LLRF Control of Superconducting Cavities", PAC'07, Albuquerque, June 2007, WEPMN112, p. 2298.

# OPTIMIZING CAVITY GRADIENTS IN PULSED LINACS USING THE CAVITY TRANSIENT RESPONSE*

G. Cancelo#, A. Vignoni, Fermi National Accelerator Laboratory, Batavia, IL 60510, U.S.A.

*Abstract*

In order to achieve beam intensity and luminosity requirements, pulsed LINAC accelerators have stringent requirements on the amplitude and phase of RF cavity gradients. The amplitude and phase of the RF cavity gradients under heavy beam loading must be kept constant within a fraction of a % and a fraction of a degree respectively. The current paper develops a theoretical method to calculate RF parameters that optimize cavity gradients in multi cavity RF units under heavy beam loading. The theory is tested with a simulation example.

## INTRODUCTION

Modern pulsed LINAC accelerators are being designed taking advantage of the cost reduction that can be achieved powering a string of cavities from one klystron. At 70% peak power utilization a 10 MW klystron can power 24 superconducting cavities at an average gradient of 31.5MV/m and a beam current of 9 mA. The XFEL main LINAC klystrons at DESY will power 32 cavities at 23.6MV/m and an average beam current of 5mA. As multiple cavities are connected to a single klystron the RF system parameters and control become more complex. A typical low level RF (LLRF) control loop controls the amplitude and the phase of the klystron's RF power, however, the loop cannot dynamically control individual cavity amplitude and phases. Typically, the control is done over the vector sum of all cavity gradients within the RF unit. The problem is further complicated by the need to obtain the maximum possible acceleration from the RF unit, pushing cavity gradients up close to their quenching limits. These cavity maximum gradients are different within a certain spread. Proton LINACs such as HINS [5] and Project X [6] add extra complexity to the RF system. A RF unit may need cavities operating at different synchronous phases (Φs). Secondly, particles travel cavities at increasing (non-relativistic) velocities, which implies different beam loading conditions from cavity to cavity.

Most of the literature available on cavity field dynamics follows a steady state approach [1-4]. The cavity is modeled by a 2nd order ODE (ordinary differential equation) and later approximated by a 1st order ODE model due to the high loaded Q of the cavity. The steady state approach determines optimality conditions for minimum generator power as a function of the cavity coupling parameter βopt and cavity tuning angle φopt. The steady state analysis works well for continuous

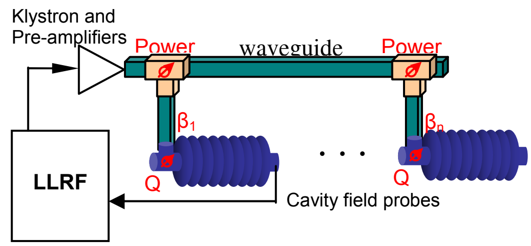


Figure 1: RF system block diagram.

waveform (CW) machines. A similar steady state assumption is assumed about the beam, and these models use the average beam current.

The steady state analysis applied to pulsed RF Linacs does not provide optimum operation parameters for all cases. For cavities operating "on crest" (Φs=0) under heavy beam loading and strong RF coupling an exact calculation of the forward power and beam injection time can set constant cavity gradients (flattops) and minimize or zero out the reflected power. For "on crest" operation, gradient flattops can still be maintained for cavities operating at different gradients with one time optimization of the coupling parameter. Unfortunately, this is not longer valid when cavities in the same RF unit need to be operated at different synchronous phases. Moreover, as is the case for pulsed RF proton beam Linacs such as HINS [5] and Project X [6], cavities have different beam loading conditions. To exemplify the theory that will be developed in this paper we use one RF unit from the Project X proposal. The RF unit has 3 cryomodules with a total of 21 cavities operating with synchronous phases and beam loadings as described in Table 1. A typical ±10% Vcav spread is assumed.

Table 1: Example Using a Project X RF Unit

| Cavity Number | Beam Beta In | Beam Beta Out | Cavity Phase (degrees) | Cavity voltage (MV/m) |
|---|---|---|---|---|
| 182 | 0.9196 | 0.9208 | -20 | 23.22 |
| 183 | 0.9208 | 0.9220 | -20 | 25.62 |
| 184 | 0.9220 | 0.9232 | -20 | 24.90 |
| 185 | 0.9232 | 0.9243 | -20 | 27.30 |
| 186 | 0.9243 | 0.9255 | -20 | 23.46 |
| 187 | 0.9255 | 0.9266 | -19 | 26.34 |
| 188 | 0.9266 | 0.9277 | -19 | 24.66 |
| 189 | 0.9277 | 0.9288 | -19 | 24.18 |
| 190 | 0.9288 | 0.9299 | -19 | 26.58 |
| 191 | 0.9299 | 0.9309 | -19 | 22.74 |
| 192 | 0.9309 | 0.9320 | -18 | 27.54 |
| 193 | 0.9320 | 0.9330 | -18 | 25.38 |
| 194 | 0.9330 | 0.9340 | -18 | 24.42 |
| 195 | 0.9340 | 0.9350 | -18 | 26.82 |
| 196 | 0.9350 | 0.9360 | -18 | 25.86 |
| 197 | 0.9360 | 0.9370 | -17 | 22.98 |
| 198 | 0.9370 | 0.9380 | -17 | 23.94 |
| 199 | 0.9380 | 0.9389 | -17 | 25.14 |
| 200 | 0.9389 | 0.9398 | -17 | 23.70 |
| 201 | 0.9398 | 0.9407 | -17 | 26.10 |
| 202 | 0.9407 | 0.9416 | -16 | 27.06 |

*Work supported by Fermi Research Alliance, LLC. under Contract No. DE-AC02-07CH11359 with the United States Department of Energy.
#cancelo@fnal.gov

The steady state optimization minimizes the klystron reflected power during beam-on time using [1-4]:

$$\beta_{opt} = 1 + \frac{2RI_{b0}}{V_{cav}}\cos\phi_s \qquad \text{and} \qquad \varphi_{opt} = -\phi_s$$

Table 2 introduces the RF system parameters. For a description of these parameters see [1-4];

Table 2: RF System Parameters

| Symbol | Definition |
|---|---|
| □ | RF Coupling coefficient |
| □□ | Cavity detuning |
| $\square_{12}$ | Cavity half bandwidth |
| R | Cavity shunt impedance |
| $R_L$ | Loaded resistance |
| Ig | Generator current |
| Ib | Beam current |
| □ | Generator current phase |

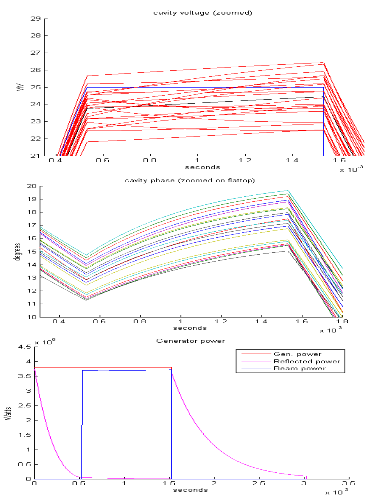


Figure 2: a) Cavity, vectorsum and vectorsum setpoint amplitude voltages, b) cavity phases, c) RF forward, reflected and beam powers.

A simulation of the steady state optimum parameters using the RF unit example described above gives gradients and powers as shown in Fig. 2. The simulator used is based on the 1st order dynamic models described in [1-4]. Also a ±10% uniformly distributed maximum cavity gradient spread has been assumed around the required average cavity gradient for the RF unit. We observe that although the reflected power is small the individual cavity amplitudes and phases are neither constant nor close to the set-point values. Also the vectorsum (Fig. 2a black trace) is far away from the vectorsum set-point (Fig. 2a blue trace). As a consequence, when the feedback loop is closed the individual cavity gradients are further distorted to accommodate the vectorsum to the setpoint. The LLRF closed loop is unable to control cavity voltages to individual set-points because the system is uncontrollable at the individual set point level.

## TRANSIENT ANALYSIS

The RF system voltages and currents are modeled by

$$V(t) = V_A(t)\cdot e^{(j\omega + \phi(t))} = (V_r(t) + jV_i(t))\cdot e^{j\omega} \quad (1)$$
$$I(t) = I_A(t)\cdot e^{(j\omega + \phi(t))} = (I_r(t) + jI_i(t))\cdot e^{j\omega}$$

The RF voltages and currents in (1) are modulated in amplitude and phase. The LLRF controls the slow dynamics of the RF amplitude and phase called the RF envelope. The RF envelope is typically modeled by a 1st order ODE in the complex space $\mathbb{C}^1$ [4].

$$\dot{V}_{cav}(t) = AV_{cav}(t) + BI_{tot}(t), \qquad (2)$$

As said, V and I are complex numbers, and

$$A = \begin{pmatrix} -\omega_{12} & -\Delta\omega \\ \Delta\omega & -\omega_{12} \end{pmatrix}, \qquad B = \begin{pmatrix} R_L\omega_{12} & 0 \\ 0 & R_L\omega_{12} \end{pmatrix}$$

Since the system is linear, the cavity voltage is the superposition of the cavity response to the generator and beam currents (power) $I_g e^{j\theta}$ and $I_b e^{j\pi}$. The current equations assume the convention that the phase is zero for the negative of the beam current.

The solution to equation (2) is given by:

$$\begin{aligned}\begin{pmatrix} V_r \\ V_i \end{pmatrix} = \frac{\omega_{12}R_L}{\omega_{12}^2+\Delta\omega^2}\Bigg\{ & e^{-\omega_{12}t} I_g \begin{pmatrix} -\omega_{12}\cos(\Delta\omega t+\theta)+\Delta\omega\sin(\Delta\omega t+\theta) \\ -\Delta\omega\cos(\Delta\omega t+\theta)-\omega_{12}\sin(\Delta\omega t+\theta) \end{pmatrix} u(t) + I_g \begin{pmatrix} \omega_{12}\cos\theta-\Delta\omega\sin\theta \\ \Delta\omega\cos\theta+\omega_{12}\sin\theta \end{pmatrix} u(t) - \\ & e^{-\omega_{12}(t-t_o)} I_b \begin{pmatrix} -\omega_{12}\cos\Delta\omega(t-t_o)+\Delta\omega\sin\Delta\omega(t-t_o) \\ -\Delta\omega\cos\Delta\omega(t-t_o)-\omega_{12}\sin\Delta\omega(t-t_o) \end{pmatrix} u(t-t_0) - I_b \begin{pmatrix} \omega_{12} \\ \Delta\omega \end{pmatrix} u(t-t_0) \Bigg\}\end{aligned} \qquad (3)$$

Where u(t) is the Heaviside function (i.e. u(t)=1 t≥0 and 0 otherwise).

To obtain a flattop at the injection time $t=t_0$ we must eliminate the time dependency in equation (3). That is achieved by making

$$I_g = e^{\omega_{12}t_o} I_b \quad (4) \qquad \text{and} \qquad \Delta\omega = -\theta/t_0 \quad (5)$$

Equations (4) and (5) guarantee a flattop for $t \geq t_0$. The appropriate value for the flattop amplitude and phase can be obtained from equation (3) at $t=t_0$-. This is given by

$$\begin{pmatrix} V_r \\ V_i \end{pmatrix}_{t=t_o} = \frac{\omega_{12}R_L}{\omega_{12}^2+\Delta\omega^2}\left\{ e^{-\omega_{12}t_o} I_g \begin{pmatrix} -\omega_{12} \\ -\Delta\omega \end{pmatrix} + I_g \begin{pmatrix} \omega_{12}\cos\theta - \Delta\omega\sin\theta \\ \Delta\omega\cos\theta + \omega_{12}\sin\theta \end{pmatrix} \right\} \qquad (6)$$

Using the tuning angle equation $\tan\psi = \frac{\Delta\omega}{\omega_{12}}$, the complex cavity voltage in (6) can be by its amplitude and phase

$$\begin{aligned}|V_c| = \frac{R_L I_b}{1+\tan^2\psi}\sqrt{\left(-1+e^{\omega_{12}t_o}(\cos\theta - \tan\psi\sin\theta)\right)^2 + \ldots} \\ \overline{+\left(-\tan\psi + e^{\omega_{12}t_o}(\tan\psi\cos\theta+\sin\theta)\right)^2}\end{aligned} \qquad (7)$$

$$\phi_s = \tan^{-1}\left(\frac{\tan\psi\cos\theta + \sin\theta - \tan\psi e^{-\omega_{12}t_o}}{\cos\theta - \tan\psi\sin\theta - e^{-\omega_{12}t_o}}\right) \qquad (8)$$

Equations (7) and (8) have 3 degrees of freedom in the RF system phase space θ (or ψ), β and $t_0$. Both $R_L$ and the half bandwidth of the cavity $\omega_{12}$ are a function of β. In a multi cavity RF unit, individual cavity flattops can be set calculating individual cavity values $\theta_{cav}$ and $\beta_{cav}$ that satisfy (7) and (8) with (constrains (4) and (5) for a given $t_0$. However, $t_0$, the beam-on time, is unique for the RF unit and constrains the generator (reflected) power. Hence, to minimize the overall power requirements in an N cavity RF unit a system of 2·N equations with 2·N+1 unknowns must be solved.

## RF POWER OPTIMIZATION

The reflected power is given by

$$P_{ref} = P_{gen} - \frac{dW}{dt} - P_{beam} - P_{diss}, \quad \text{where}$$

$P_{ref}$: reflected power.
$P_{gen}$: generator power
$P_{beam}$: power transferred to the beam.
dW/dt: change of stored energy in the cavity.
$P_{diss}$: cavity cryogenic losses.

For superconducting cavities $P_{diss}$ is very small compared to the other members and can be neglected. If (6) and (7) are able to achieve a good flattop then dW/dt is also very small. Then we can approximate Pref ≈ Pgen – Pbeam and the reflected power is given by the mismatch between the RF system characteristic impedance and the cavity-beam impedance reflected to the waveguide (Fig 2).

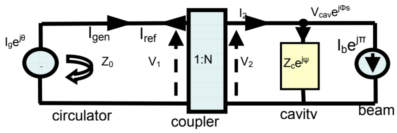


Figure 3: Power-impedance block diagram.

The cavity-beam impedance is given by the parallel

$$Z_{eq} = Z_{cav} // Z_{beam} = Z_c e^{j\psi} // \frac{V_{cav} e^{-j\phi_s}}{I_b} \qquad (9)$$

Minimizing the reflected power implies $Z_{eq}/N^2$ that should be a close match of $Z_o$. Given that $Z_o$ is real, the imaginary part of $Z_{eq}$ should be minimized and the real part of $Z_{eq}$ reflected to the waveguide side should match $Z_o$.

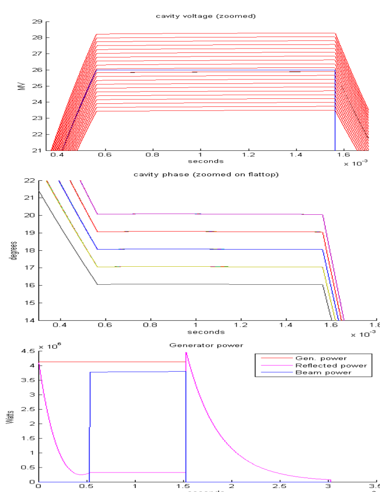


Figure 4: a) Cavity, vectorsum and vectorsum setpoint amplitude voltages, b) cavity phases, c) RF forward, reflected and beam powers.

## OPTIMIZATION AND SIMULATION EXAMPLE

The nonlinear system given by (7), (8) and (9) with constrains given by (4) and (5) for each cavity can be solved to find an optimum set of parameters $\beta_i^{opt}$, $\psi_i^{opt}$ (or $\theta_i^{opt}$), and $t_0^{opt}$. As an example of the method described above we have used the same Project X RF unit described in Table 1. The nonlinear system of equations has been solved using a numerical solver from Matlab. The optimized parameters were fed to the same RF unit simulator used to generate Fig. 2. Figure 4 shows that the cavity gradients using the transient approach have been substantially improved both for amplitude and phase. This improvement to the individual cavity gradients is done at the cost of increasing the reflected power with respect to the steady state approach during the beam-on to about 4% of the beam power.

## CONCLUSIONS

The transient analysis allows optimum cavity gradient flattops across the RF unit, in particular when those cavities are operated at different synchronous phases ($\Phi_s$) and with different beam loading conditions. The optimum RF parameters $\beta_i^{opt}, \psi_i^{opt}$ only need to be set once during the RF and beam commissioning and are not coupled with parameters in other cavities in the RF unit. The beam-on time $t_0^{opt}$ can be used to minimize the RF generator power. For the sake of comparison Table 3 shows the optimization parameters obtained by each method.

Table 3: Optimization Parameters

| Cavity Number | Steady state | | Transient | |
|---|---|---|---|---|
| | Beta | Theta | Beta | Theta |
| 182 | 2942 | -20.00º | 3473 | -35.54º |
| 183 | 2692 | -20.00º | 4184 | -34.77º |
| 184 | 2797 | -20.00º | 3881 | -35.10º |
| 185 | 2574 | -20.00º | 4540 | -34.40º |
| 186 | 3021 | -20.00º | 3257 | -35.79º |
| 187 | 2731 | -19.00º | 4109 | -33.11º |
| 188 | 2940 | -19.00º | 3515 | -33.72º |
| 189 | 3022 | -19.00º | 3292 | -33.96º |
| 190 | 2770 | -19.00º | 3993 | -33.23º |
| 191 | 3262 | -19.00º | 2663 | -34.66º |
| 192 | 2728 | -18.00º | 4151 | -31.33º |
| 193 | 2981 | -18.00º | 3439 | -32.03º |
| 194 | 3119 | -18.00º | 3071 | -32.40º |
| 195 | 2858 | -18.00º | 3781 | -31.69º |
| 196 | 2982 | -18.00º | 3436 | -32.03º |
| 197 | 3395 | -17.00º | 2398 | -31.28º |
| 198 | 3278 | -17.00º | 2691 | -30.98º |
| 199 | 3140 | -17.00º | 3049 | -30.63º |
| 200 | 3348 | -17.00º | 2516 | -31.16º |
| 201 | 3055 | -17.00º | 3272 | -30.41º |
| 202 | 2977 | -16.00º | 3515 | -28.40º |

## REFERENCES


[1] Wilson, P.B. "High energy Linacs: Application to storage ring RF systems and linear colliders", SLAC-PUB-2884 Nov. 1987.

[2] Schilcher, T. "Vector Sum Control of Pulsed Accelerating Fields in Lorentz Force Detuned Superconducting Cavities", Ph.D thesis, DESY, Hamburg, August 1998.

[3] Padamsee, H., Knobloch, J., Hays, T., *RF Superconductivity for Accelerators*, John Willey & Sons, Inc., New York, 1998, p.381-401.

[4] T.P. Wangler. *Principles of RF Linear Accelerators*, John Wiley&Sons, Inc., NY, 1998.

[5] P.N. Ostroumov et al, "Front end design of a multi-GeV H-minus Linac", Proc. PAC-2005 (Knoxville, TN), 2005, ed. C. Horak p 3286.

[6] P.N. Ostroumov, "Physics Design of the 8-GeV H-minus Linac". New Journal of Physics, New J. Phys. **8** 281, 2006. http://stacks.iop.org/1367-2630/8/281

# REAL TIME RF SIMULATOR (RTS) AND CONTROL*

G. Cancelo#, C. Armiento, K. Treptow, A. Vignoni, T. Zmuda, FNAL, Batavia, IL 60510, U.S.A.

*Abstract*

The multi-cavity RTS allows LLRF algorithm development and lab testing prior to commissioning with real cavities and cryomodules. The RTS is a valuable tool since it models the functions, errors and disturbances of real RF systems. The advantage of a RTS over an off-line simulator is that it can be implemented on the actual LLRF hardware, on the same FPGA and processor, and run at the same speed of the LLRF control loop.

Additionally the RTS can be shared by collaborators who do not have access to RF systems or when the systems are not available to LLRF engineers. The RTS simulator incorporates hardware, firmware and software errors and limitations of a real implementation, which would be hard to identify and time consuming to model in off-line simulations.

## RTS ARCHITECTURE

The RTS simulates the amplitude and phase dynamics of the RF carrier in the RF system. It does not simulate the RF behavior of RF components such as up and down converters, klystron, waveguides and cavities. However, since the LLRF control is performed over the RF envelope, most errors and disturbances are incorporated. As shown in Figure 1 the multi-cavity simulator and the LLRF control are connected in a loop. The RTS can be operated in any combination of feedforward (FF) and feedback (FB) modes.

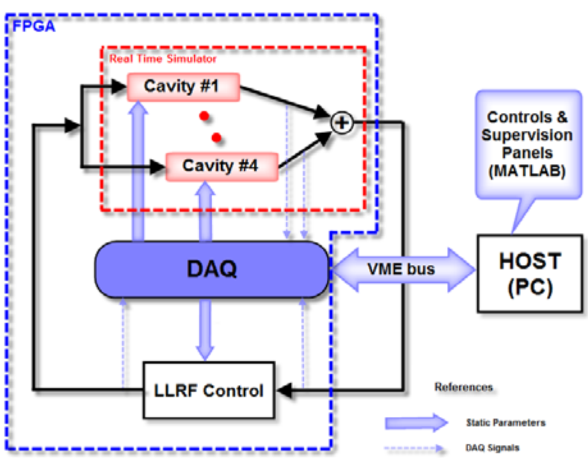


Figure 1: RTS and LLRF control basic scheme.

The RTS and the LLRF control interface to a host computer via a real-time DAQ. The computer server hosts the control software and applications so as perform the RTS and LLRF control initialization, acquire statistics and perform data analysis. The DAQ acquires data during the simulation/control pulse. The data is locally stored into a memory which is readout by the Control server in between RF pulses.

*Work supported by Fermi Research Alliance, LLC. under Contract No. DE-AC02-07CH11359 with the United States Department of Energy.
#cancelo@fnal.gov

## RTS MODELS

### *Cavity Models*

The RTS models some of the electrical and mechanical fundamental cavity modes. The electrical model is a 1st order approximation of the cavity's Π mode in the complex plane (1) [1,3]. The mechanical mode, models the Lorentz force detuning [3]. The total detuning from the mechanical model is the linear sum of three mechanical resonances (2). The differential equations for such behaviours are:

$$\begin{bmatrix}\dot{V}_r(t)\\ \dot{V}_i(t)\end{bmatrix} = \begin{bmatrix}-\omega_{1/2} & -\Delta\omega(t)\\ \Delta\omega(t) & -\omega_{1/2}\end{bmatrix}\begin{bmatrix}V_r(t)\\ V_i(t)\end{bmatrix} + \begin{bmatrix}\omega_{1/2}R_L\\ \omega_{1/2}R_L\end{bmatrix}\begin{bmatrix}I_r(t)\\ I_i(t)\end{bmatrix} \quad (1)$$

$$\frac{d^2(\Delta\omega_m)}{dt^2} + \frac{\omega_m}{Q_m}\frac{d(\Delta\omega_m)}{dt} + (\omega_m)^2\,\Delta\omega_m = (\omega_m)^2\,2\pi K_m V^2(t)$$
$$\Delta\omega_m = \sum_{m=1}^{3}\Delta\omega_m \qquad m = 1,2,3 \quad (2)$$

The electrical and mechanical cavity models combined behave as a linear time variant system. The detuning coefficient in the electrical model's transition matrix is a function of the mechanical model's dynamics, which has the cavity gradient as an input. The RTS can also simulate the cavity's 8/9Π mode whose response is added to the Π mode response.

## BEAM LOADING

The beam loading is implemented by a table, which is preloaded by the Control server before run time. Each cavity has its own table allowing individual cavity beam loading conditions. This feature is particularly important when the RTS simulates a beam traveling at non relativistic velocities, with β changing at each cavity or when the synchronous phase between the cavity and the beam changes along the simulated cavities.

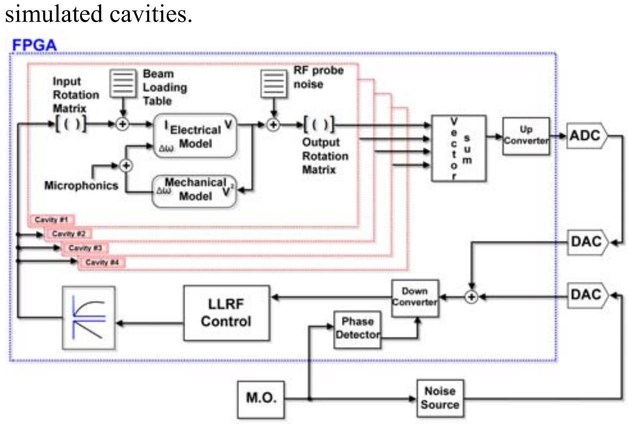


Figure 2: Real time simulator.

## KLYSTRON AND RF COUPLERS

Klystron characteristics have a nonlinear behavior in amplitude and phase as a function of the input drive. The RTS models the klystron's nonlinear behavior with amplitude and phase tables. Since a typical klystron bandwidth is on the order of 5 MHz, at least an order of magnitude faster than the cavity closed loop bandwidth, its dynamic behavior has not been modeled.

The distribution of RF power into each cavity is a function of the waveguide tuners and RF couplers. The RTS simulates those functions with a 2x2 input matrix per cavity. The input matrices set the amplitude and phase of each cavity. The numbers in the input matrices represent a fixed RF configuration, and are usually kept constant during an individual run.

## OUTPUT MATRICES AND TABLES

The RTS also implements a matrix and a table at the output of each cavity. These matrices and tables are used to introduce noise, disturbances and misalignments of the RF output system such as RF cavity probes, down converters, cables, LO jitter, etc.

### *RF Pickup Probe*

Cavity gradient levels are measured by RF probes whose transfer function gains exhibit notable dispersion from probe to probe.

The output matrices can also account for random static errors in gains, phase rotations and reflections in attenuators and down-converters. These errors along with simulated microphonics can be used to test vector sum calibration algorithms.

## CAVITY FIELD VECTOR SUM AND DIGITAL UP CONVERTER

The Vector Sum adds the field of each cavity. Then, is up converted in frequency to an intermediate frequency (IF). The IF, currently set to 13 MHz, is tuned from a Control panel. Different IF values can be used to determine an optimum one in terms of ADC, DAC and filter noise.

## ADC AND DAC NOISE

The system formed by the multi-cavity simulator and LLRF control can be entirely implemented inside of an FPGA. Alternatively, the simulator's output, after the up converter (Figure 2), is sent to a DAC and looped back into an ADC. The loopback add the DAC and ADC noises and limitations into the RTS and LLRF control loop.

The RTS also features a noise input connected to an ADC channel. This input can be used to simulate external disturbances, correlated and uncorrelated noise, such as high harmonic content from the down converter which is aliased back into the control bandwidth.

## HARDWARE IMPLEMENTATION

The RTS core has been implemented in a Xilinx Virtex4 FPGA (XC4VLX80) using the tools provided by Simulink/Matlab/System Generator and the Xilinx ISE compiler. The RTS can be easily compiled for other Xilinx FPGAs. An Altera based implementation would require more work, although now similar interfaces to Simulink/Matlab do exist. The current version of the RTS runs on the VME based ESECON LLRF controller [2]. The ESECON (Figure 3) is connected to a VME processor running the Control server and applications (Figure 1).

## DAQ AND COMMUNICATION

At runtime the DAQ saves the status of simulator and control variables on the ESECON local RAM. The data is retrieved by the host processor between RF pulses and displayed using the Control and RTS simulator panel applications. The Control and Simulator panels are also used to initialize the hardware, and firmware. The parameters of the RTS cavity models and other variables can be manually set using the panels or loaded from a CSV type file.

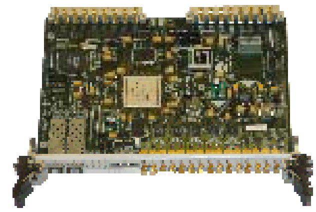

Figure 3: ESECON board.

## RTS AND LLRF CONTROL EXAMPLE

In order to illustrate the RTS with an example we have configured 4 cavities using the values in Table I [5]. Notice that the cavities are configured with different synchronous phases and beam loadings. Each synchronous phase will determine the values of the cavity input rotation matrix, each beam loading condition will translate into a different beam loading table per cavity (Figure 2).

The Feed Forward (FF) and PID controls are set to the Control Panel values as shown in Figure 6. The ESECON Control Panel is used to initialize the ESECON board, set the FF and PID controller values, set the IF reference channel, etc. The Control Panel also allows opening the cavity parameters panel editor and displaying individual cavity responses as shown in Figure 5.

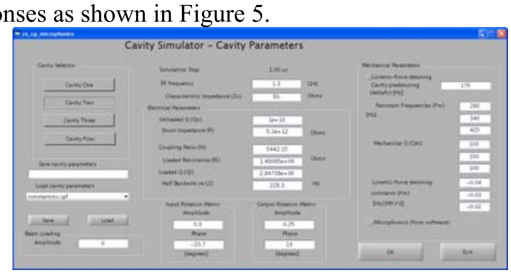


Figure 4: Cavity parameters panel.

Figure 5 shows the amplitudes and phases of 4 simulated cavities when only FF control is applied. During this simulation the Lorentz force detuning has been turned off. Figure 7 shows real time oscilloscope traces of the simulator's vectorsum in IF domain (yellow) along with the I (purple) and Q (green) components using the DAC output.

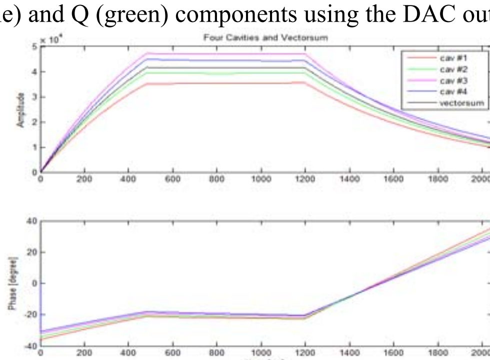


Figure 5: Individual response of the four cavities .

Table 1: Set Cavities Parameters

| Cav N° | Amplitude | Phase | TTF | N_coupler | Beta | Rl | Ql | w12 | delta_fo | Ig | theta |
|---|---|---|---|---|---|---|---|---|---|---|---|
| **182** | 23.22 | -20 | 0.7358 | 5471.6 | 3473.8 | 1.50E+09 | 2.87E+06 | 225.8 | -186 | 14.8678 | -35.54 |
| **188** | 24.66 | -19 | 0.7762 | 5438.92 | 3515.67 | 1.48E+09 | 2.84E+06 | 228.52 | -176 | 15.8279 | -33.72 |
| **195** | 26.82 | -18 | 0.8156 | 5244.08 | 3781.76 | 1.38E+09 | 2.64E+06 | 245.81 | -165 | 17.6222 | -31.69 |
| **201** | 26.1 | -17 | 0.844 | 5637.16 | 3272.75 | 1.59E+09 | 3.05E+06 | 212.73 | -159 | 16.3261 | -30.41 |

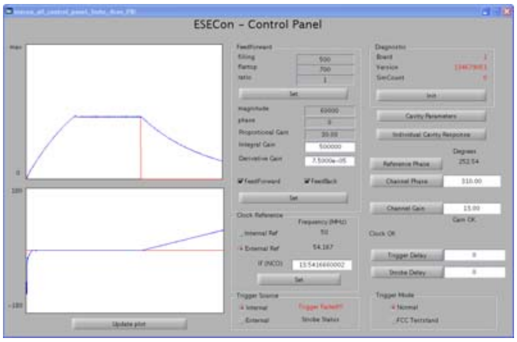


Figure 6: ESECON control panel showing vectorsum in amplitude and phase in closed loop.

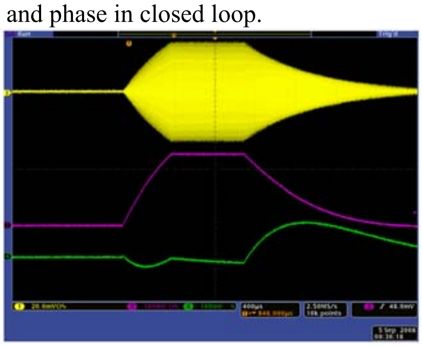

Figure 7: Scope plot of Vectorsum (I and Q) and IF signal (yellow).

### *Real Time Simulation and Control including Lorentz Force Detuning*

Figures 8 and 9 show the Lorentz force detuning effect on the amplitudes and phases of the simulated cavities and vectorsum respectively. The detuning steers the amplitudes and phases away from their goals and flattops. Figure 9 shows the mixed I and Q effects caused by the increased detuning ($\Delta\omega$) due to the Lorentz force.

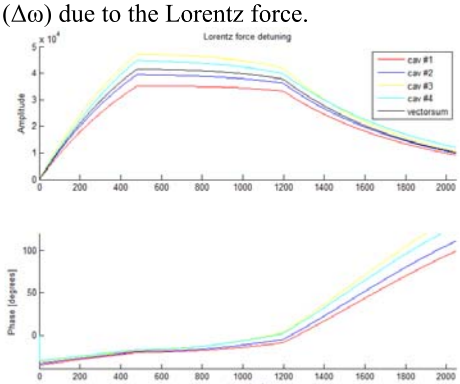


Figure 8: Individual response of each cavity with Lorentz force detuning.

Figure 10 shows the amplitudes and phases of the simulated cavities when the PID feedback control is applied. The controller has been set with the parameters shown on Figure 6. The PID compensates for the Lorentz force detuning restoring the flattops and bringing the amplitudes and phases close to their goals.

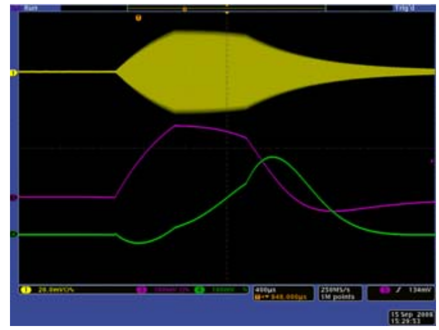

Figure 9: Vectorsum and IF signal for the Lorentz force detuned cavities

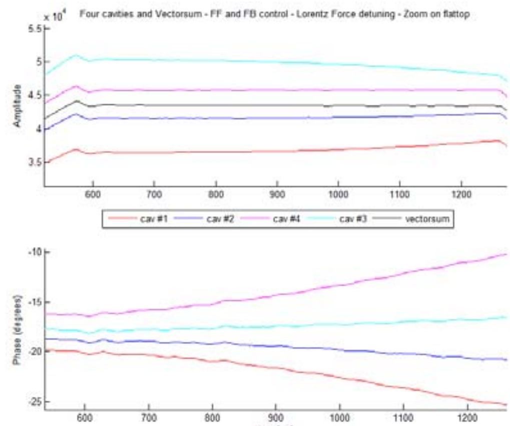


Figure 10: Close loop (PID) with Lorentz force detuning response.

## CONCLUSION

The multi cavity RTS is still a work in progress but it has matured enough to be an interesting tool to help in the development and testing of LLRF algorithms. The RTS can also help understanding some of the noise components in the control loop and suggest mitigation techniques.

## REFERENCES

[1] T. Schilcher, “Vector Sum Control of Pulsed Accelerating Fields in Lorentz Force Detuned Superconducting Cavities”, DESY, Hamburg, August 1998.

[2] G. Cancelo, T. Zmuda, K.Treptow, N.Wilcer, "ESECON, 14-channel LLRF Controller ", LLRF Workshop 2007, Knoxville, Tennessee, October 22-25, 2007, paper 031.

[3] T. Czarski, S. Simrock, K. Poźniak, R. Romaniuk, “Cavity Control System Advanced Modeling and Simulation for TESLA Linear Accelerator and Free Electron Laser”, Tesla Technical Notes 2003.

[4] C. Armiento, “Real-time SRF cavity simulator”, Fermilab Internal Report, October 2007.

[5] G. Cancelo, A. Vignoni, “Optimizing cavity gradients in pulsed Linacs using the cavity transient response”, LINAC08, this proceedings, Victoria, British Columbia, Canada, September 2008.

# DESIGN AND EVALUATION OF THE LOW-LEVEL RF ELECTRONICS FOR THE ILC MAIN LINAC*

U. Mavric#, B. Chase, J. Branlard, V. Tupikov, B. Barnes, D. Klepec, Fermilab, Batavia, IL 60510


### *Abstract*

The proposed 30 km long ILC electron/positron collider is pushing the limits not only in basic physics research but also in engineering. For the two main LINACs, the pulsed RF power that is feeding the high number of SC RF cavities (~ 17 000) must be regulated to app. 0.1% for amplitude and 0.2° for phase. This guarantees the required energy spread (0.1%) at the interaction point in the detector. The regulation of phase and amplitude is carried out by the analog/digital electronics also denoted as the low-level RF control system. Besides meeting the regulation specifications, the low-level RF must be reliable, robust and low cost. In the paper we present a possible hardware solution that addresses these issues. The system is evaluated on a cavity emulator implemented on the FPGA. We also present measurement carried out at AØ photo injector.


## INTRODUCTION

The two main LINACs for the proposed ILC, will accelerate electrons and positron from 15 MeV up to 250 GeV with the goal luminosity of $2 \cdot 1034\ cm^{-2}s^{-1}$. The energy spread of the beam, introduced by the RF system will be mitigated by the low-level RF (LLRF) control system. The lowest achievable energy spread is ultimately defined by the disturbances introduced by the electronics that is controlling it. Besides regulation requirements, the LLRF electronics for the ILC main LINACs must address also reliability, price, low power consumption, mechanical robustness and ease of automation. It is worth noting that the LLRF will have to process over 50 000 RF channels (pick-up probes, reference signals, reflected power, forward power, beam signals, interlocks etc.) coming from both LINACs.

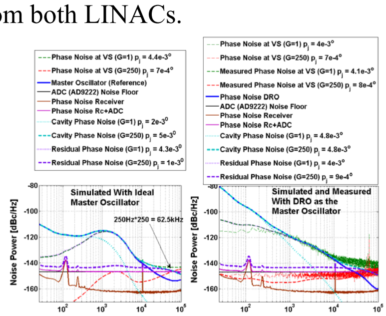


Figure 1: Analysis of close-in noise at various loop gains (>250). The analysis is done at the vector sum, at the output of the cavity and as a relative measurement of the beam compared to the cavity phase uncertainty.

### *Regulation Requirements*

According to [1], the correlated error at the interaction point should be lower than 0.5\% for amplitude and 0.24° for phase. The unanswered question at this point is what is the allowed contribution of the LLRF system to this error budget? Ultimately, the measurement of the residual phase (meaning the relative fluctuation of beam compared to the cavity field) is limited by the noise added in the receiver. After various measurements on-the-bench we proved that a 12 bit (-147dBc/Hz noise floor, AD9222) ADC meets the regulation requirements for the ILC main LINACs. Fig.1 shows a theoretical analysis of the expected regulation at very high gains.

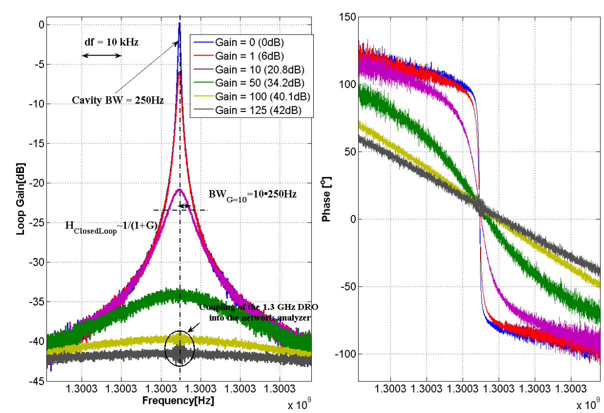


Figure 2: Transfer function of disturbance injected before the cavity to the output of the cavity.

Further on we will present the practical implementation of the LLRF and the evaluation of the system by using a cavity simulator and on an operating machine (AØ photo injector at Fermilab).

## THE LLRF SYSTEM FOR THE ILC MAIN LINACS

The system presented in this paper is composed of the 33 channel digital board (Multichannel Field Controller - MFC) and the nine channel analog receiver/transmitter board. The 1.3GHz RF signal is first downconverted by mixing with the LO at 1.313GHz to get the IF at 13MHz. The LO is generated in a separate chassis. The processing of the signal in digital domain is shown in Fig.3. The analog downconversion is done by using the 8 channel receiver/transmitter presented in [2].

*Work supported by …
# mavric@fnal.gov

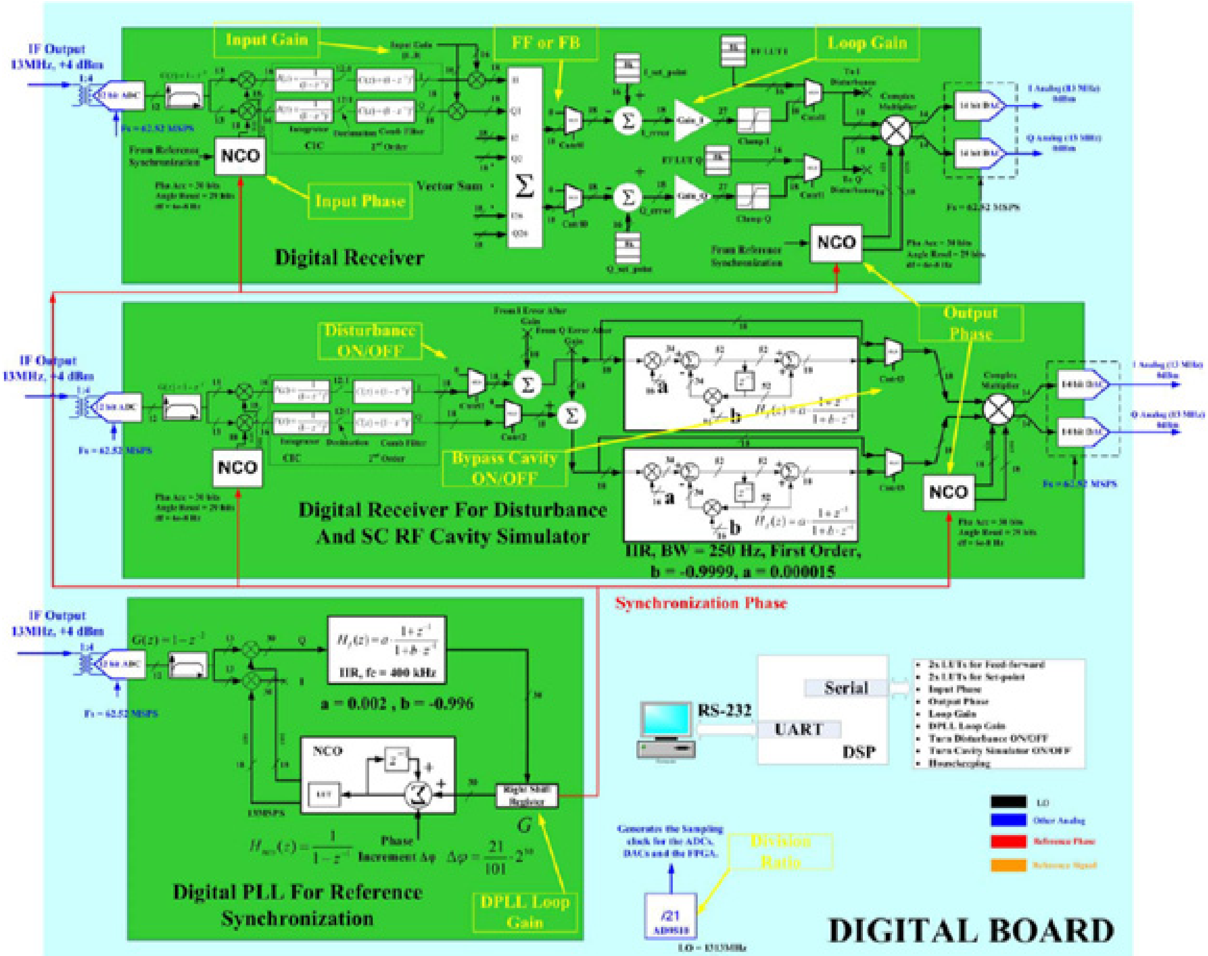


Figure 2: Block diagram of the firmware implemented on the FPGA. The main building blocks are the digital downconverter, the digital PLL synchronization with the reference, the digital upconverter, the controller, the cavity simulator and the disturbance channel.

## ON-THE-BENCH MEASUREMENTS

We simulated the superconducting (SC) cavity with a narrowband (half bandwidth 250Hz) IIR filter. An additional RF input allowed us to inject an arbitrary disturbance. By using the disturbance channel we also measured the transfer function of the disturbance to the output of the cavity as shown in Fig.3.

## MEASUREMENTS AT AØ PHOTO INJECTOR

We used the presented LLRF system to control capture cavity I, which is a 9-cell SC RF cavity with half bandwidth close to 100Hz and loaded QL ~ $6 \cdot 10^6$. Fig.4 shows the transient at the flat-top after perturbing the closed loop with an impulse superimposed on the feed-forward drive signal. We managed to increase the loop gains up to 1000 (closed loop bandwidth close to 100 kHz) before noticeable instabilities could be seen. The first instabilities we noticed were caused by the 8π/9 mode.

### *Phase and Amplitude Uncertainty*

Fig.5 shows amplitude (in %) and phase (in °) uncertainty as function of loop gain. The minimum amplitude and phase standard deviations we are able to achieve is 0.016% and 0.016 ° over 1 MHz bandwidth. Calculations of the theoretical limitations (-147dBc/Hz over the same bandwidth) of the ADC give integrated uncertainty 0.0044% and 0.0026°. However, the phase noise before the subtraction in the feedback loop is twice the residual phase noise generated by the receiver. The reason lays in the reference receiver, which synchronizes the 1.3GHz reference signal and applies a phase correction to all the down and up converters in the design. Consequently, there is approximately a factor of ~3.6 for the amplitude and a factor of ~3 for phase discrepancy between the measured and calculated values.

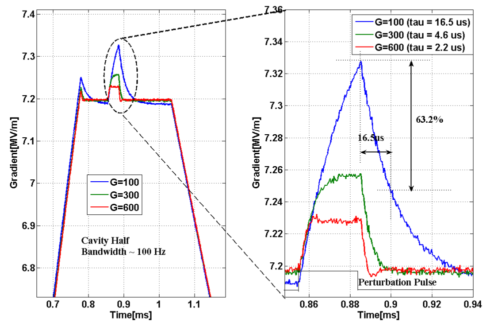


Figure 4: Response of the system measured before the subtraction after an impulse perturbation of the closed loop. Out of the exponential characteristic one can calculate the loop gain (half bandwidth is $100Hz).

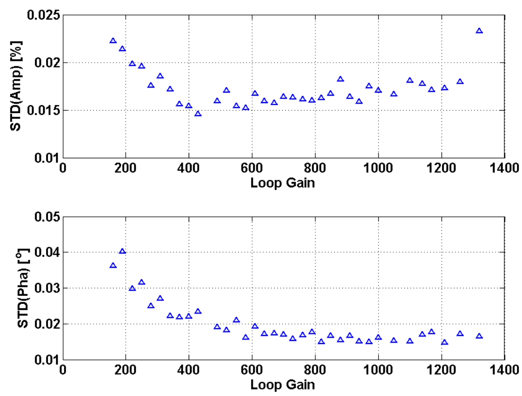


Figure 5: Amplitude and phase uncertainty measured before the subtraction as a function of loop gain. At gain larger than 1000 the system becomes unstable.

## *Energy Dispersion Measurements*

Measurements of the energy spread were done by using a spectrometer. A bending magnet steers the particle by an angle, which depends on the energy of the particle. The beam position monitor located after the bending magnet detects the horizontal and vertical position of the beam. This information can be used to calculate the energy spread of the beam. Fig.7 shows the energy spread as a function of the loop gain. We repeated the measurements at different phase locations of the accelerating curve. Acceleration at 5 ° off-crest is less susceptible to phase deviations than at 26 ° off-crest acceleration.

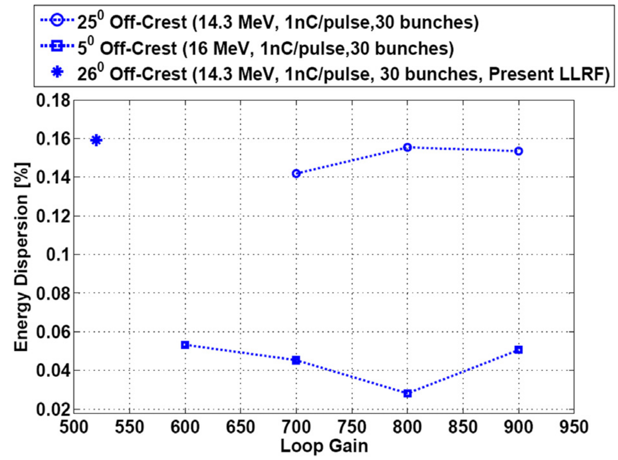


Figure 7: Energy spread measurements at AØ on CCI using a spectrometer. The present LLRF system is achieving twice that good performance at loop gain close to 520. However it is not capable of larger closed loop bandwidths due to the instabilities.

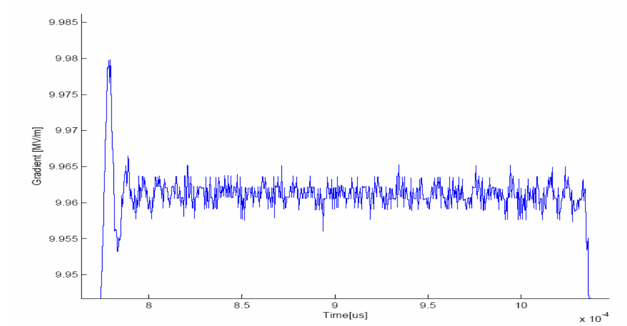


Figure 6: Regulation of flat-top region at loop gain of 970.

## CONCLUSIONS

The presented LLRF system is a cost effective solution for RF systems where a large number of channels needs to be processed. At the same time the performance meet the ILC main LINACs specifications. In the future we intend to do more research on the factor of 3 discrepancies between the measured and expected regulation uncertainty. Also, we believe there is a significant contribution of the energy spread of the beam coming from the sections that proceed (RF gun, laser etc.) the cavity we are controlling.

## REFERENCES

[1] Global Design Effort, ``International Linear Collider Reference Design Report - Volume 3" August 2007; http://www.linearcollider.org/cms/?pid=1000437.

[2] U. Mavric, B. Chase and M. Vidmar., "Design and evaluation of a low-level RF control system analog/digital receiver for the ILC main LINACs", Nuclear Instruments & Methods in Physics Research Section A, August 2008, vol. 594, no. 1, pp. 90-96.

# A FEMTOSECOND-LEVEL FIBER-OPTICS TIMING DISTRIBUTION SYSTEM USING FREQUENCY-OFFSET INTERFEROMETRY*

J. W. Staples, J. Byrd, L. Doolittle, G. Huang and R. Wilcox, LBNL, Berkeley, California, USA


## *Abstract*

An optical fiber-based frequency and timing distribution system based on the principle of heterodyne interferometry has been in development at LBNL for several years. The fiber drift corrector has evolved from an RF-based to an optical-based system, from mechanical correctors (piezo and optical trombone) to fully electronic, and the electronics from analog to fully digital, all using inexpensive off-the-shelf commodity fiber components. Short-term optical phase jitter and long-term phase drift are both in the femtosecond range over distribution paths of 2 km or more.


## *Future Accelerator Timing Requirements*

The next generation of accelerators, spread over an area measured in kilometers, will require femtosecond-level synchronization of RF cavities, lasers, photoinjectors and diagnostic devices. Phase-stabilized optical fiber is well-suited for this, along with its immunity to electrical interference, gigaHertz bandwidth, low loss and easy installation in wireways.

Commodity-level single-mode glass fiber, such as Corning SMF-28, optimized for 1300-1550 nm wavelength, exhibits about the same phase velocity dependence on temperature as copper, although the mechanism is temperature dependence of the glass dielectric constant. All fiber components used are inexpensive off-the-shelf devices developed for the telecommunications industry.

The stabilization system developed at LBNL uses the technique of frequency-offset interferometry.

As shown in Figure 1, the optical output of a 1550 nm CW laser is split between the short arm of a Michaelson interferometer and the long fiber to a remote receiver. The short arm of the interferometer is temperature-controlled to a variation of less than 0.01 C. At the end of the long fiber arm, an acousto-optical modulator (AOM) excited at 50 MHz up-shifts the 195 THz laser frequency by 50 MHz, where it is then reflected by a 50% Faraday rotator mirror. The shift of the laser frequency is phase coherent with the 50 MHz RF drive of the AOM. The reflected laser signal is again upshifted by 50 MHz by its return passage through the AOM, resulting in a 100 MHz total frequency shift where it returns along the long fiber, and combines with a sample of the original laser frequency from the interferometer short arm in the splitter.

The variation of the phase length of the fiber is phase coherent to the phase variation of the 100 MHz upshifted return signal. The original laser frequency, from the short arm and the upshifted laser frequency are transmitted along a second fiber, the error signal fiber, to a photodiode at the stabilizer where they produce a 100 MHz beat note which is compared to the 100 MHz reference oscillator. Any change in the phase length of the long fiber is reflected in a phase shift of the 50 MHz signal to the AOM, derived from the 100 MHz reference oscillator, which adds or subtracts the same number of optical cycles in the AOM. The resulting error signal is integrated, the integral representing the change of phase length of the fiber, which shifts the phase of the 50 MHz drive signal to the AOM. All these function are combined in a single chip field-programmable gate array (FPGA) controller.

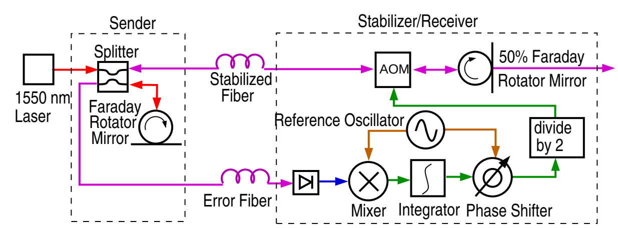


Figure 1: Frequency-offset stabilizer configuration.

The fiber that carries the error signal to the stabilizer needs no stabilization itself, as it is providing optical phase information down-converted to 100 MHz. The 100 MHz beat note is phase-coherent with changes in optical phase in the stabilized fiber, but the frequency ratio of 195 THz (1550 nm wavelength) and 100 MHz is $2 \times 10^6$, so a 1 nanosecond change in the error signal fiber produces an error of only 0.5 femtosecond to the correction.

In previous implementations of the stabilizer, the AOM phase was fixed, and mechanical phase shifters (piezo and motor-driven optical trombone) were placed in series with the stabilized fiber. These suffered from a finite range of correction and the usual problems with devices using moving parts. The transition to an all-electronic system significantly simplified the system with a smaller parts count, essentially unlimited range of correction, and increased reliability.

The frequency reference for the system is the 195 THz laser frequency itself, which must be stabilized to 1 part in $10^9$ for the system to provide 1 femtosecond stability with with variations of the long fiber of 1 nanosecond. The CW laser is stabilized by taking a sample of the laser, doubling its frequency, and locking it to a saturated absorption line in a Rubidium cell using a Pound-Drever-Hall (PDH) [2]

* This work is supported by the Director, Office of Science, U.S. Dept. of Energy under Contract No. DE-AC02-05CH11231

stabilizer configuration. To verify its operation, two independent PDH-stabilized 1550 nm lasers were beat against each other with measured drifts in the 200 kHz range.

To measure the effectiveness of the stabilizer itself, two independent stabilizers were built, operating from a common laser, and the out-of-loop optical beat note measured between the outputs of the 50% Faraday mirrors at the far end of the long fibers of the independent stabilizers. The AOMs may operate by shifting the laser light either upward or downward, so one channel has an up-shifting AOM and the other uses a down-shifting AOM, giving a 100 MHz difference in the laser light between the two channels (the one-way shift in each channel is up or down 50 MHz). The resultant difference in optical frequency of the laser light exiting each of the 50% Faraday mirrors in the independently stabilized channels is then compared directly to the 100 MHz reference oscillator and represents the residual differential optical phase error between the two channels.

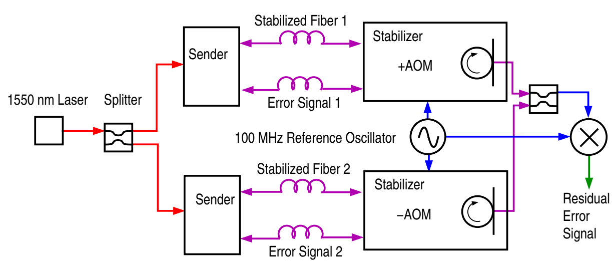


Figure 2: Two independent channels with out-of-loop monitor.

We tested the stabilizer performance in two venues: the long fiber at LBNL is a 2 km loop, part of the LBNL data network backbone which runs under roads and through several buildings, and a 2.8 km fiber loop in the SLAC klystron gallery, exposed to full ambient temperature variation and the acoustic perturbation of the klystron modulators. Measurement were taken with a stabilized reference short fiber in one channel and the long fiber in the other. Figure 2 shows a block diagram of the differential phase measurement setup, with a long fiber in channel 1 and a short fiber in the channel 2. Figure 3 shows the results for a 232 hour data run of the 2.8 km fiber in the SLAC klystron gallery. The black trace shows the phase length change of the gallery fiber, 2184 picoseconds peak-to-peak due to diurnal temperature variation, and the red trace is the residual error after correction, drifting 31.5 femtoseconds in 232 hours, or less than 0.14 fsec per hour. The p-p short-term jitter is less than 2 femtoseconds.

Figure 4 shows the noise spectrum on the stabilized klystron gallery fiber, measured on the 50 MHz drive to the AOM, from 10 Hz to 100 KHz with the loop open (red) and closed (black). The noise suppression at 10 Hz is 60 dB. The feedback loop consists of a simple integrator with a $1/f$ gain curve. As the correction is phase-coherent to the optical frequency, the integration of the power spectrum from 10 Hz to 1 MHz gives an rms jitter of the optical carrier of 0.95 femtosecond.

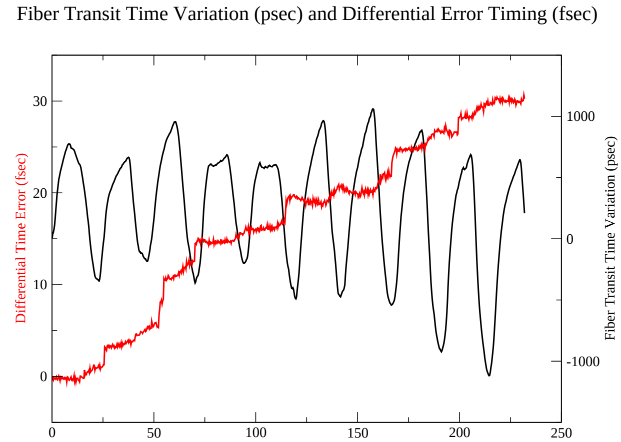


Figure 3: 2.8 km SLAC klystron gallery phase variation (black trace, right-hand scale), and residual error after correction (red trace, left-hand scale) for a 232 hour data run.

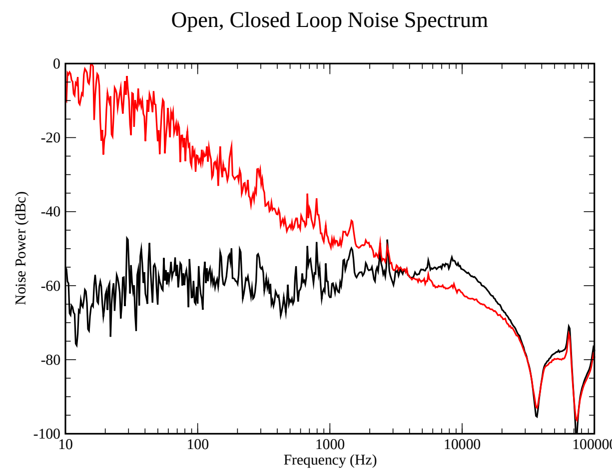


Figure 4: Loop noise with control loop open (red) and closed (black).

## *Group-Phase Velocity Correlation*

The system corrects the *phase* variation of the fiber. To transmit a stabilized RF signal, the *group* velocity must also be stabilized. There is a monotonic relationship between the two, which is experimentally determined. [3] This requires the modulation of the laser by RF, recovery of the RF at the far end of the fiber with a photodiode and measuring the group velocity variation, and comparing it to the optical phase velocity variation of the fiber. The optical level to the photodiode is set to the level that minimizes the phase-amplitude characteristic of the photodiode itself. The ratio of group velocity to phase velocity variation of the fiber due to temperature variation is approximately 1.02.

## *Stabilized RF Phase Detectors*

To maintain better than 10 femtosecond stability in the RF domain, phase detectors operating at S-band (2856 MHz) must have a stability of better than 0.01 degrees. In a configuration where RF is transmitted over a stabilized fiber, closed-loop controllers will include high-precision phase detectors operating in the RF domain. This requires active stabilization of the RF phase detector itself.

To maintain the high precision offered by stabilization in the optical domain, a technique that continually injects a calibration signal into the RF circuits is used [4]. As this is a CW rather than a pulsed RF transmission system, a double-sideband suppressed-carrier (DSSC) calibrate signal is injected into the RF chain, immediately following the RF recovery photodiode and carried through the entire RF closed-loop phase corrector. The frequency offset of the sidebands in an S-band system is on the order of 1 MHz.

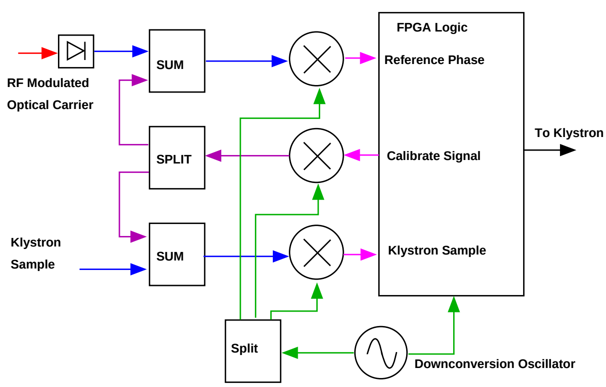


Figure 5: Phase detectors stabilized by injection of a DSSC calibrate signal.

Figure 5 shows an example where a stabilized fiber link carries an S-band modulated carrier to a photodiode, which recovers the S-band phase reference signal. The system's goal is to use the phase of that reference to stabilize the phase of the cavity field, and the feedback actuator is the phase of a klystron drive signal. The FPGA generates a DSSC signal and injects it as close to the photodiode and the cavity sensor as possible. All phase shifts (including those that vary with temperature) in the components after the summing junctions will apply equally to the reference and calibration signals, and can therefore be detected and corrected digitally by the FPGA. The downconversion mixers convert S-band signals to 50 MHz that are digitized by the FPGA circuit board.

### *Modulation-Demodulation Noise Performance*

The additional noise generated by the modulation-demodulation process of transmitting RF over an optical link is measured. The RF carrier is impressed onto the laser light with a Mach-Zehnder (M-Z) modulator. The AM modulated carrier is then amplified with an erbium-doped diode-pumped fiber amplifier (EDFA) and transmitted through the stabilizer. The modulation of the laser signal does not affect the operation of the stabilizer. Figure 6 shows two overlaid plots of the noise power spectrum of a 1 GHz oscillator that modulates the laser light through the M-Z modulator, and of the output of the photodiode.

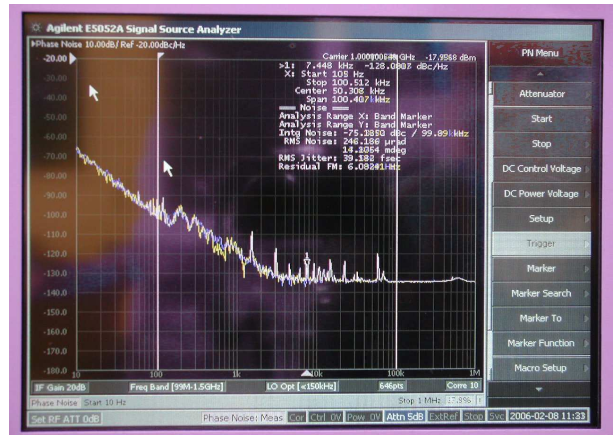


Figure 6: Noise spectrum of original RF generator (yellow), and of photodiode output of RF modulated onto laser and demodulated (blue).

In this case, the phase noise jitter of the 1.0 GHz test signal was 31 femtosecond, integrated over the range of 100 Hz to 100 kHz, as was the recovered 1 GHz signal from the photodiode. The modulation-demodulation process does not add significant phase noise to the original RF signal.

### *Synchronizing Mode-Locked Lasers*

This system is particularly well-suited to locking a remote mode-locked (M-L) laser to a local reference standard. Two widely separate (for example, 5 THz) comb lines of the M-L laser spectrum synchronize two CW lasers, which are each transmitted over individually stabilized fibers, which then lock the same two lines in a slave laser. This preserves the carrier-envelope-offset conditions of the slave M-L laser to that of the reference laser. In this application, only phase stabilization of the fiber stabilizers is needed, not group velocity correction as only the unmodulated optical carrier frequency is used. [5]

## REFERENCES

[1] R. B. Wilcox and J. W. Staples, Systems Design Concepts for Optical Synchronization in Accelerators, PAC2007, p.3807, Albuquerque, USA.

[2] Eric. D. Black, An introduction to Pound-Drever-Hall laser frequency stabilization, Am. J. Phys. 69, 79 (2001).

[3] J. M. Byrd et al, Timing Distribution in Accelerators via Stabilized Optical Fiber Links, Linac06, p. 577, Knoxville, USA.

[4] L. R. Doolittle, Low-Level RF Control System Design and Architecture, APAC 2007, Indore, India.

[5] J. W. Staples, R. Wilcox and J. Byrd, Demonstration of Femtosecond-Phase Stabilization in 2 km Optical Fiber, PAC07, p. 494, Albuquerque, USA.

# CONCEPT DESIGN STUDIES OF THE REX-ISOLDE CRYOMODULES AT CERN

V. Parma, S. Calatroni, N. Delruelle, C. Maglioni, M. Modena, M. Pasini, P. Trilhe, J.Hansen, CERN, Geneva, Switzerland
S. Pattalwar, STFC, Daresbury Laboratory, UK

[illegible]

The High Intensity and Energy (HIE) proposal plans a major upgrade of the existing ISOLDE and REX-ISOLDE facilities at CERN [1], with the objective of substantially increasing the energy and the intensity of the delivered radioactive ion beams. In the frame of this upgrade activity, a superconducting linac, based on Nb sputtered Quarter Wave Resonators (QWRs) is proposed to be installed downstream the existing normal conducting machine. The present design of the accelerator lattice features housing of five high-beta cavities (β=10.3%) and a superconducting solenoid in a common cryomodule. In most of the existing low-energy heavy-ion installations worldwide, insulation and beam vacuum are in common, with the risk of cavity surface contamination in case of accidental leak of the cryostat vessel. Following a concept study, we report in this paper on three design options, namely cryo-modules with [illegible] vacuum, with [illegible] or with [illegible] vacuum systems (the latter having a low conductance between insulation and beam vacuum) and compare them in terms of technical complexity, performance, reliability and maintainability.

## INTRODUCTION

QWRs are commonly used in linacs for the acceleration of heavy ion beams in the range of 5-10 MeV/u, due to their high velocity acceptance allowing the coverage of a wide variety of nuclei and beam energies. Examples of heavy ion accelerators based on similar superconducting resonators are the ISAC-II at TRIUMF (Vancouver, Canada) [2], in operation since 2007, the ALPI at LNL (Legnaro, Italy) [3], in operation since several years, ATLAS at Argonne national laboratory [4], in operation since 1992 (Argonne, Illinois, US), the QWR superconducting linac for the 15 UD Pelletron at IUAC (New Delhi, India) [5], and the SPIRAL II at Ganil (Caen, France) [6], now in the construction phase.

In most of the projects, a single vacuum system was chosen both for beam and thermal insulation of the cryo-modules, essentially because it leads to simpler mechanical design and assembly of the cryo-modules; despite the required cleanliness, the number of components is generally smaller and complex flanged connections in the usually compact inter-cavity spacing can be avoided. But, as a consequence, in order to preserve the superconducting surface from contamination, a high level of cleanliness of all internal surfaces is needed, and the use of Multilayer Insulation protection (MLI) and of volatiles like lubricants and brazing fluxes is precluded.

The choice of single vacuum carries a number of drawbacks, the main one being the risk of contamination in case of accidental break of the insulation vacuum leading to particulate contamination of the cavity surface at any stage of the preparation of the cryo-modules outside clean-room or during machine operation. Similar events have been reported and discussed on existing linacs [7], and in some cases the disassembly of the cavities for reconditioning was the only alternative to recover performance. A failure in one of the cryo-module would also propagate through the adjacent units affecting an entire SC linac, unless a sound protection system with fast-closing interlocked vacuum valves is capable of isolating the leak.

Single-vacuum cryo-module is also subject to higher radiation heat loads due to the absence of MLI protection, only in part compensated by low-emissivity surface plating of cold surfaces, and therefore lead to larger cryo-plants, capital and cryogenic operating costs.

Spiral II has made the choice of cryo-modules with separate vacuum, despite the higher complexity of the design, considering contamination of the cavities a major risk for reliability and the heaviness of repair interventions would hinder the machine availability.

## THE REX-ISOLDE SC LINAC

In the present REX-ISOLDE facility the radioactive ion beams are accelerated to higher energies with a compact normal conducting linac where, with a complex scheme of several acceleration stages and re-bunching, the energy at extraction is of 3 MeV/u. For the increase in energy, a SC linac is proposed, designed to achieve a final energy of at least 10 MeV/u, delivering an effective accelerating voltage of at least 39.6 MV.

The linac requires a total of 20 high β and 12 low β cavities, and 8 SC solenoids, cooled by boiling helium at 4.5 K.

### [illegible]

The possibility of making use of an existing refrigerator at CERN, formerly used for the ALEPH experiment during the LEP operation, would allow substantial cost saving in the HIE upgrade; keeping the heat load budgets well below the refrigeration capacity of 630 W at 4.5 K and 2700 W at 55-75 K (measured capacities during commissioning in 1998), is mandatory to leave overcapacity for cool-down in a reasonable time. A 35-m dedicated transfer line from the plant to the linac will provide independent feeding of the cryomodules and operational flexibility allowing warm-up and removal of individual cryomodules in case of need.

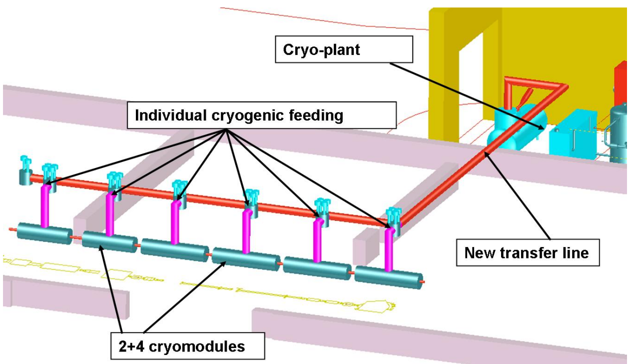


Figure 1: Cryoplant and cryogenic distribution line. Each SC cavity module is independent from the others.

## CRYO-MODULE CONCEPTS

The high β cavities are grouped into 4 cryomodules of 5 cavities and 1 solenoid each, while the low β cavities are grouped into 2 cryomodules with 6 cavities and 2 solenoids each. This arrangement yields comparable overall dimensions of the low β and high β cryomodules, offering the advantage that a standardised solution for the main cryostat parts, in particular the vessel, can be envisaged. For the sake of clarity, only the high β cryomodules (for which the main parameters are described in Table 1.), will be discussed hereafter, but similar considerations can be extended to the low β cryomodules.

Table 1: Main parameters of high β cryomodule

| Parameter | Value |
|---|---|
| No. cavities | 5 |
| Mechanical length of cavity | 320 mm |
| Beam aperture diameter | 20 mm |
| No. of SC solenoids | 1 |
| Solenoid max field, current | 9 T, 900 A |
| Vacuum vessel (approximate dimensions) | Length: 2.5 m; width: 1 m; height: 2 m |
| Cavity/solenoid operating temperature | 4.5 K |
| Helium vessel volume (preliminary) | 150 l |
| Thermal shield temperature | 50 K (gaseous helium) |

Figure 2 illustrates the two concepts of cryomodules with single or separate vacuum. In the former, the cavities and solenoid beam tubes are open to the cryostat envelope which would contain only clean equipment, all assembled in a clean room of class 100.

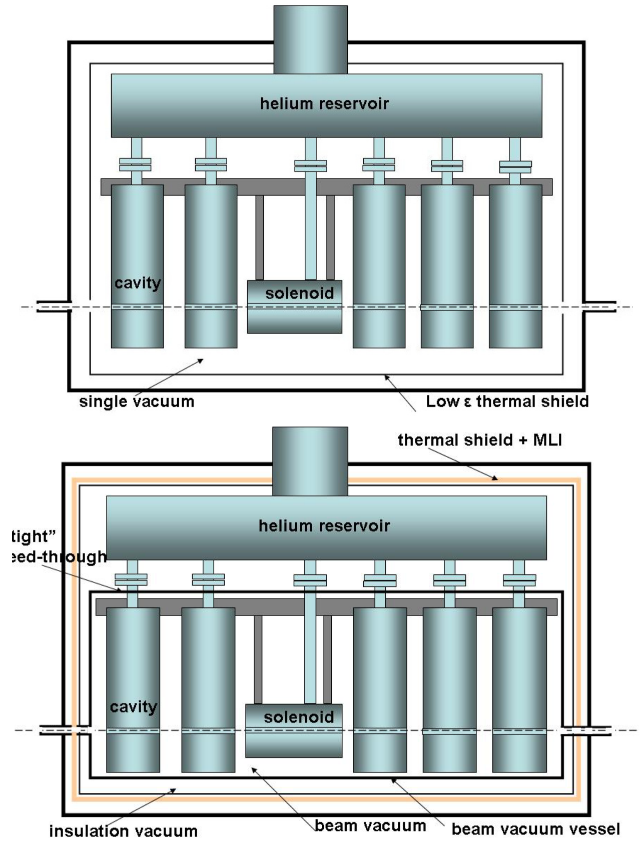


Figure 2: Single vacuum (top) and separate vacuum (bottom) concepts.

The thermal shield would require a low emissivity surface (lower than 0.06), resulting for example from nickel plating.

The separate vacuum concept features an additional vessel, so-called [illegible], creating a second vacuum envelope around the cavities and the solenoid, thus limiting the extent of the clean equipment to a strict minimum. The insulation vacuum vessel and the thermal shield can be made of more conventional materials and levels of cleanliness. MLI could be used on the thermal shield thus improving thermal performance. Adopting a beam vacuum vessel presents the major advantage that it allows making use of cavities developed for a single vacuum application (as those developed by INFN-LNL for example) with only minor modifications; a more conventional solution with a beam tube interconnecting cavities and solenoid would require a considerable redesign of the cavities. The separate vacuum concept is nevertheless technically more complex. A number of leak-tight feed-through passages to the cavities are needed for the tuners (externally operated), the coaxial cables of the couplers, and the electrical feeding of the solenoid. Also, the beam vacuum vessel needs a dedicated pumping system and an appropriate overpressure protection (burst disk or valve). Cold-to-warm transitions between the beam vessel and the room temperature insulation vacuum vessel are also needed.

An intermediate concept, the □□□□□□ one, has been taken into consideration. By hybrid we intend essentially a separated vacuum concept with no leak tight separation between the beam and insulation vacuum. It was decided to investigate this option since, in our case, the basic design choices for the cavity were already assessed and integration at the cavity level of the separate vacuum would have been very difficult at this moment. A not perfect separation (typically in the order of $10^{-1}$mbar.l/s at RT) would anyhow allow a better preservation of the cleanliness of the cavity surface in case of vacuum leak from the outside world into the insulation vacuum. Assuring this, the advantage is a shorter down-time, as it would not require a reprocessing (rinsing, conditioning) of the cavities. In addition MLI could be used and reduce as well the heat load at 50-75 K.

A preliminary comparison of heat loads between the single and separate solutions, is presented in Table 2, shows identical heat loads at 4.5 K in both cases, these being dominated by RF loads. The single vacuum solution presents a heat load at 55-75K which is about 6 times the one of separate vacuum, which would reduce the cooling overcapacity of the existing cryoplant.

Table 2: Linac heat load (HL) estimates

| Source | Type | HL at 4.5 K [W] | HL at 55-75 K [W] | |
|---|---|---|---|---|
| | | | Single vacuum | Separate vacuum |
| Cavities | dynamic | 420 | - | - |
| Solenoids | dynamic | 8 | - | - |
| Cryostats | Static | 42 | 1620 | 210 |
| Transfer line | Static | 35 | 140 | 140 |
| Valves | Static | 72 | - | - |
| **Totals** | | **580** | **1760** | **350** |

For the evaluation of the three concepts we look at different aspects of the design issues of the cryomodules. These issues are not of the same importance; some of them are linked to the running cost of the cryomodules, others have an impact on the schedule, resources and capital cost, others concerns the availability of the machine and others bring along technical risks. We have given the maximum importance to the availability of the machine, and a weighted factor has been considered when comparing the different cryomodules concepts. In Table 3 are listed all the items considered for the comparison and our rating ("+" is an advantage, "-" is a drawback). A common vacuum system can be seen as the one that better covers all the aspects taken into consideration.

## SUMMARY

A first analysis among the three concepts has been made, highlighting their relative advantages and drawbacks. For the purposes of the REX-ISOLDE cryomodules the common vacuum solution seems to provide the best compromise. Further analysis will follow together with a more detailed design of the cryomodule.

Table 3: Comparison between the three concepts

| Issue | Com. Vacuum | Sep. vacuum | Hyb. vacuum |
|---|---|---|---|
| Heat loads | - | + | + |
| Risk of cavity pollution | --- | +++ | ++ |
| On-site cryomod. intervention | + | +++ | ++ |
| Size of clean room infrastructure | - | ++ | ++ |
| Disassembly cav. for maintenance | +++ | + | + |
| Design/construction/ assembly complexity | ++ | - | + |
| Cryostat cleanliness requirements | - | ++ | + |
| Alignment at assembly | ++ | - | - |
| Longitudinal space requirements | ++ | - | - |
| Capital cost | ++ | - | + |
| Development | ++ | - | + |
| Learning curve and construction time | ++ | - | + |

## REFERENCES


[1] M. Pasini □□a□'A SC upgrade for the REX-ISOLDE accelerator at CERN," these proceedings.

[2] G. Stanford, R.E. Laxdal, C.Marshall, T.Ries and I.Sekashev. Proceedings CEC-ICMC 2003, p.552, Vol 49, 2004.

[3] A. M. Porcellato □□a□□'Production, installation and test of Nb-sputtered QWRs for ALPI", Pramana journal of physics, Vol.59, No.5 November 2002, pp.871-880.

[4] http://www.phy.anl.gov/atlas/facility/index.html

[5] P. E. Bernaudin □□a□□"Design of the low-beta, QWRs and its components for SPIRAL 2". Proceedings EPAC'04, Lucerne, p.1276, (2004)

[6] S. Gosh □□a□□'Commisioning of SC linac at IUAC-Initial challenges and solutions". Proceedings of EPAC'08, Genoa, Italy, p.856. (2008)

[7] R.E. Laxdal, "Commisioning and early experiments with ISAC-II", Proceedings of PAC07, Albuquerque, USA.

# OVERVIEW OF THE FIRST FIVE REFURBISHED CEBAF CRYOMODULES*

M. Drury, E. F. Daly, G. K. Davis, J. Fischer, C. Grenoble, J. Hogan, F. Humphry, L. King, J. Preble, K. Worland, Jefferson Lab, Newport News, VA 23606, USA

*Abstract*

The Thomas Jefferson National Accelerator Facility is currently engaged in a cryomodule refurbishment project known as the C50 project. The goal of this project is robust 6 GeV, 5 pass operation of the Continuous Electron Beam Accelerator Facility (CEBAF). The scope of the project includes removing, refurbishing and replacing ten CEBAF cryomodules at a rate of three per year. Refurbishment includes reprocessing of SRF cavities to eliminate field emission and increase the nominal gradient from the original 5 MV/m to 12.5 MV/m. New "dogleg" couplers between the cavity and helium vessel flanges will intercept secondary electrons that produce arcing at the 2 K ceramic window in the fundamental Power Coupler (FPC). Modifications of the external Q (Qext) of the FPC will allow higher gradient operations. Other changes include new ceramic RF windows for the air to vacuum interface of the FPC and improvements to the mechanical tuner. Any damaged or worn components are replaced as well. Currently, six refurbished cryomodules are installed in CEBAF. Five have completed testing and are operational. This paper will summarize the test results and operational experience for the first five cryomodules.

## INTRODUCTION

The first of the refurbished cryomodules (C50-01) was installed in the North Linac of CEBAF in January, 2007. The fifth refurbished CEBAF cryomodule (C50-05) was installed in the South Linac of CEBAF in February, 2008. All five of these cryomodules had previously been in service in the accelerator tunnel since 1992. During the refurbishment process, each cryomodule was disassembled and its cavities removed. Improved processing methods were used to eliminate field emission and increase the gradient from the original 5 MV/m to an average of 12.5 MV/m. "Dogleg" waveguides were installed between the cavity and helium vessel flanges to intercept the secondary electrons that produce arcing on the cold ceramic window of the FPC. Improved warm ceramic windows were added as well. Improvements were made to the mechanical tuners to reduce backlash. Components that were subject to mechanical wear or radiation damage over the years were replaced.

As these cryomodules are installed, they are subjected to a commissioning process prior to being released for operation in the accelerator. During the commissioning process, each cavity is tested individually to determine the maximum gradient (Emax), and the maximum operating gradient (Emaxop). Measurements of the unloaded Q (Qo) and of field emission are made across the available gradient range. This paper compares the results of commissioning after refurbishment to the results of the original commissioning in 1992. This paper also takes a brief look at the operational history of the refurbished cryomodules.

* This manuscript has been authored by Jefferson Science Associates, LLC under U.S. DOE Contract No. DE-AC05-06OR23177. T he U.S. Government retains a non-exclusive, paid-up, irrevocable, worldwide license to publish or reproduce this manuscript for U.S. Government purposes.

## GRADIENT IMPROVEMENT

One of the goals of the refurbishment project is to increase the energy gain from 20 MV to a nominal 50 MV. This goal required an increase in the nominal cavity gradient from 5 MV/m to 12.5 MV/m. Improvements in cavity processing are used to increase the quench gradient and eliminate field emission. The dogleg waveguides are designed to eliminate arcing as a limitation on gradient. The improved RF window design reduces FPC operating temperatures and allows higher forward power levels.

Figure 1 shows the distribution of Emax before and after rebuilding. Emax is defined as the highest gradient that can be reached without quenching the cavity or activating one of the machine protection interlocks. These interlocks include arc detectors looking at the waveguide vacuum space, warm window temperature, or beamline and waveguide vacuum set points.

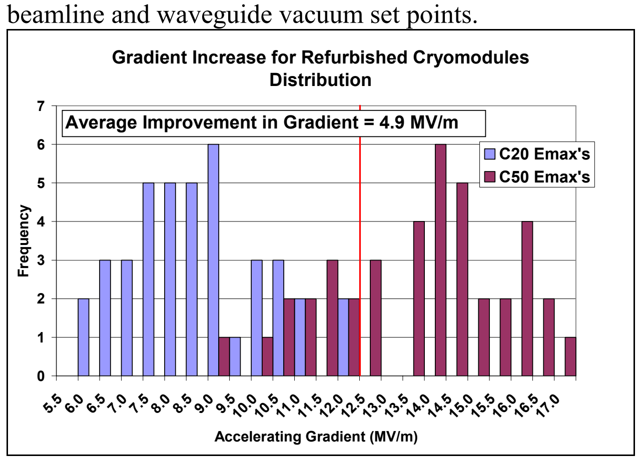


Figure 1: Gradient Improvement

Before reprocessing, these cavities had an average Emax of 8.5 MV/m. The average maximum gradient for the forty cavities has increased to 13.4 MV/m, an increase of 4.9 MV/m or 58%.

Table 1 lists the gradient limits for these cryomodules. The majority of cavities are quench limited. Nine cavities were limited by the warm window temperature. An older style of window had been installed temporarily because of window production delays. These windows were recently replaced with the correct type of ceramic window and the cryomodule (C50-05) is waiting for a retest. It is expected that window-heating will no longer limit gradient in this cryomodule.

Table 1: Gradient Limits

| Limit | Number of Instances |
|---|---|
| Cavity Quench | 27 |
| Waveguide Vacuum Fault | 2 |
| Warm Window Temp Fault | 9 |
| Waveguide Arcs | 1 |
| Forward Power Limit | 1 |

While the increase in Emax is a useful indicator of increased performance, Emaxop, is a better measure of the usable gradient. Once Emax has been determined, a stable operating gradient must be determined. In the case of the CEBAF cryomodules, a one-hour run is completed at the highest possible gradient below Emax. This gradient is defined as Emaxop. The average value for Emaxop is 12.5 MV/m, 0.9 MV/m lower than the average for Emax.

Finally, Table 2 shows the predicted energy gain based on the determinations of maximum operating gradient.

Table 2: Energy Gain

| Cryomodule | Energy Gain (MV) |
|---|---|
| C50-01 | 51.0 |
| C50-02 | 53.3 |
| C50-03 | 52.4 |
| C50-04 | 49.8 |
| C50-05 | 43.1 (window temp. limited) |

## FIELD EMISSION

Improved processing techniques, such as high pressure rinsing, are applied to the cavities in the C50 cryomodules to eliminate or reduce field emission and increase operating gradients. Figure 2 is a comparison of the onset gradients for detectable X-rays from field emission before and after refurbishment.

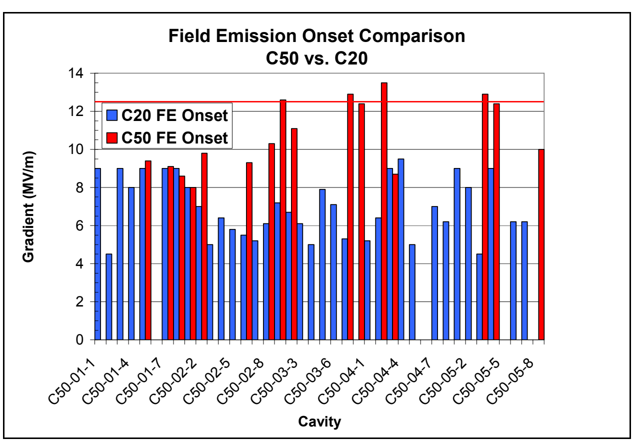


Figure 2: Field Onset Comparison

This graph illustrates several points. First, all but three of the forty cavities originally exhibited field emission. After processing, only sixteen cavities generated any measurable field emission. Second, the average gradient at which field emission turns on, for those cavities that generated field emitted X-rays, has increased from 6.9 MV/m to 10.7 MV/m.

## $Q_O$ AND HEAT LOAD

The goal for RF heat dissipated by C50 cryomodules in the 2 K helium circuit is 100 Watts at 50 MV or 12 Watts per cavity at 12.5 MV/m. This implies that Qo for these cavities must be greater than or equal to $6.8\times10^{9}$.

For cavities installed in a cryomodule, Qo is measured calorimetrically. The cryomodule is isolated from the cryogenic system and the RF heat load is determined from the rate of rise of the helium bath pressure. The results of these measurements are shown in Figure 3.

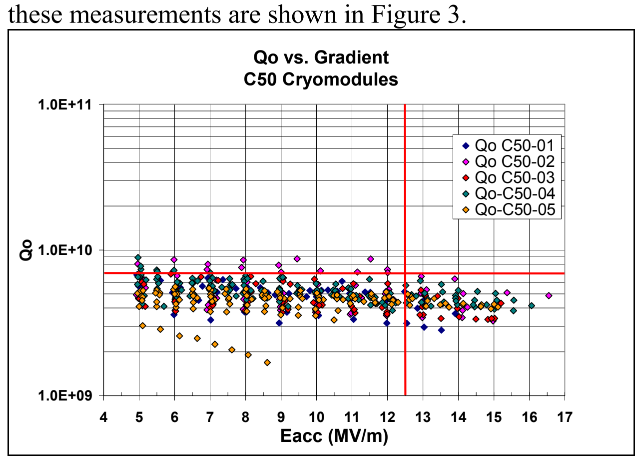


Figure 3: Qo Results

The two red lines on the graph indicate the gradient and Qo requirements. It is obvious from the figure that the cavities are not meeting the goal for Qo and therefore are dissipating more heat than is desired. Figure 4 shows the Qo values for the cavities at their respective Emaxop's.

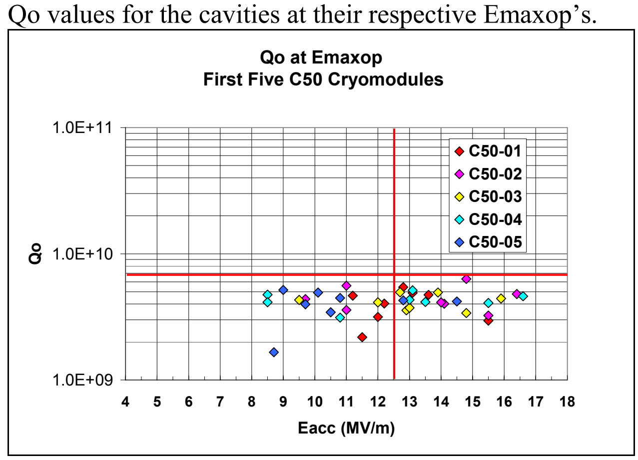


Figure 4: Qo at Emaxop

Table 3 lists the expected 2 K heat load for the cryomodules with all cavities operating at Emaxop. The heat load also includes the average static 2 K heat load of 13.2 Watts.

Improving the unloaded Q of these cavities is one of the biggest challenges facing the C50 project.

Table 3: Overall Heat Load

| Cryomodule | Total RF Heat Load (W) |
|---|---|
| C50-01 | 198 |
| C50-02 | 190 |
| C50-03 | 191 |
| C50-04 | 198 |
| C50-05 | 145 |

After the cavities are reprocessed, they are tested in a dewar in the Vertical Test Area (VTA). This happens before the cavities are installed in a cryomodule. Figure 5 shows the typical disparity between Qo as measured in the VTA and Qo as measured after the cavities are installed in a cryomodule. Generally, Qo's of $1\times10^{10}$ or better are measured in the VTA, followed by a reduction of as much as 50% after the cavities are installed in a cryomodule.

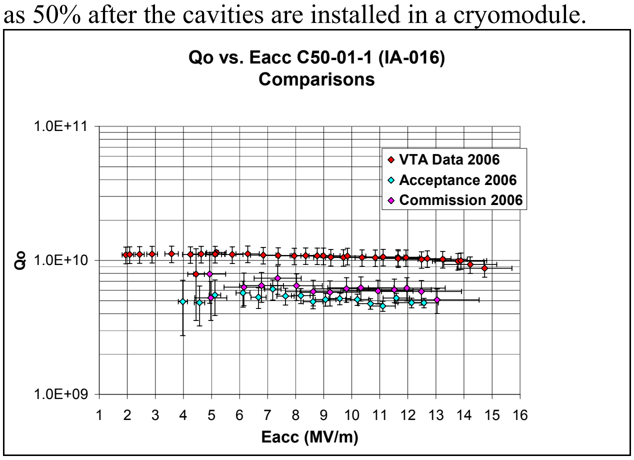


Figure 5: Qo Discrepancy

Several possible reasons for this reduction have been or are being investigated. The presence of unaccounted for magnetic components near the cavities is viewed as a likely reason for the reduction in Qo performance. One magnetized component in the tuner assembly has so far been identified. During the reconstruction of the sixth C50 cryomodule, magnetic shielding was wrapped around the magnetized components associated with four of the cavities. This cryomodule is still under test and so is not covered in any detail in this paper. However, Figure 6 shows the initial results of the attempted mitigation.

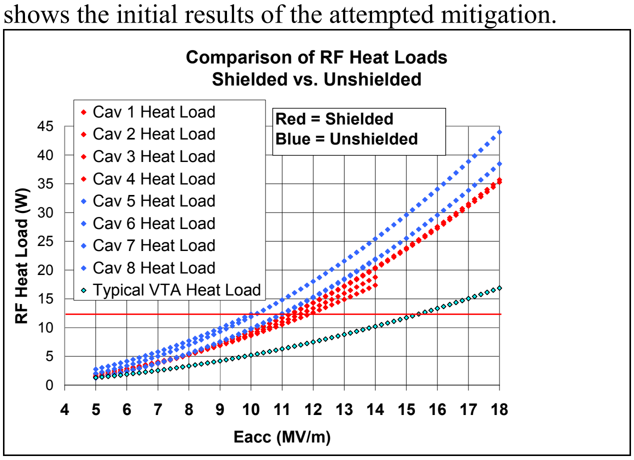


Figure 6: Effects of Magnetic Shielding

Figure 6 shows that the shielded cavities have a reduced RF heat load (increased Qo). However, the reduction was not enough to account for all of the discrepancy between the VTA measurements and the cryomodule measurements. The investigation will continue.

## OPERATIONAL EXPERIENCE

The first of the refurbished cryomodules has been in operation in the accelerator, except for maintenance periods, since May 2007. The last two of this group have been in operation since March 2008. Table 4 compares the predicted energy gain with the best energy gain achieved during beam operations since installation.

Table 4: Energy Gain Comparison

| Cryomodule | Predicted Energy (MV) | Best Actual (MV) |
|---|---|---|
| C50-01 | 51.0 | 45.8 |
| C50-02 | 53.2 | 45.5 |
| C50-03 | 52.3 | 49.6 |
| C50-04 | 49.8 | 46.8 |
| C50-05 | 43.1 | 39.6 |

Among the reasons for the lower actual energy gains are issues that occur with run times longer than an hour, such as waveguide vacuums that degrade over longer time periods.

Figure 7 shows RF trip totals for the five cryomodules over time. The graph shows a decrease in total trips for the first of the cryomodules. The slow cleanup of the waveguide vacuum spaces is responsible for most of that reduction. The graph also shows a big increase in faults for C50-03 during the latest run. The cavities in this cryomodule had not been pushed to their gradient limits until the most recent run. When they were finally pushed to their limits, an increase in vacuum trips would be expected.

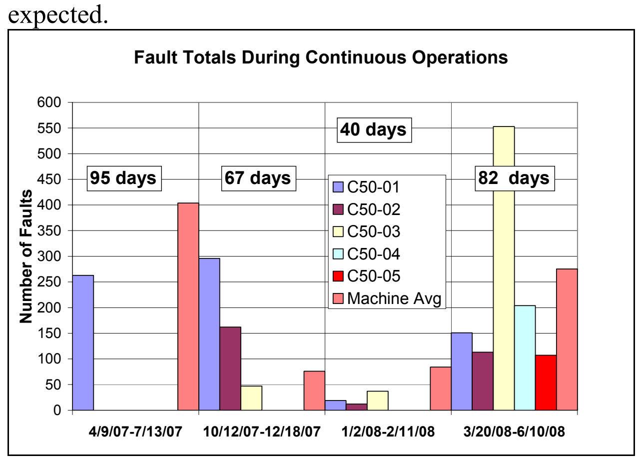


Figure 7: RF Fault Totals

## CONCLUSION

The C50 project, so far, has, met the goals for increased gradient and reduced field emission. The project has not met the goal set for Qo. We are investigating how to meet that specification in future C50 cryomodules.

# CONSTRUCTION OF THE MAGNETS AND SUPPORTS FOR THE LINAC COHERENT LIGHT SOURCE (LCLS) UNDULATOR SYSTEM*

M. White#, J. Collins, M. Jaski, G. Pile, B. Rusthoven, S. Sasaki, S. Shoaf, J. Stein, E. Trakhtenberg, I. Vasserman, and J. Xu, ANL, Argonne, IL 60439, U.S.A.

*Abstract*

The LCLS [1], nearing completion at the Stanford Linear Accelerator Center (SLAC) in California, will be the world's first x-ray free-electron laser when it comes online in mid-2009. Design and production of the undulator system was the responsibility of a team from the Advanced Photon Source (APS) at Argonne National Laboratory. Forty 3.4-m-long precision undulators, 37 laminated quadrupole magnets, and 38 precision support and motion systems with micron-level adjustability and stability were constructed and delivered to SLAC for tuning, fiducialization, final assembly, and installation in the LCLS tunnel. In addition to the magnets and supports, Argonne provided vacuum and diagnostics systems for the undulator line and a computer control and monitoring system that enables undulator girders and all components mounted on them to be accurately positioned [2]. An overview of the magnet and support construction is presented herein.

## INTRODUCTION

The LCLS construction project is nearing completion at the Stanford Linear Accelerator Center (SLAC) in California, and LCLS will be the world's first x-ray free-electron laser when it comes online in mid-2009. LCLS design and construction were accomplished primarily by a partnership of three U. S. national laboratories: Argonne National Laboratory (ANL), Lawrence Livermore National Laboratory (LLNL), and SLAC. A team from Argonne's Advanced Photon Source was responsible for design and construction of the high-precision undulator system, including the undulator and quadrupole magnets, vacuum system, beam diagnostics, ultra-stable support and motion system, and computer control and monitoring of the undulator system. At the time of this paper, the magnets and supports, vacuum system, and undulator controls system are all delivered, and component installation in the LCLS tunnel is well underway.

## MAGNETS AND SUPPORTS

### *Undulators*

Forty planar-hybrid, fixed-gap precision undulators were designed for LCLS by the Argonne team [3,4], and were optimized for efficient, cost-effective industrial mass production. The magnets are made of NdFeB, and poles are vanadium permendur. Magnets and poles are installed on an aluminum structure that defines their precise locations; the aluminum structure is bolted into a strong titanium housing. The most important undulator physics requirements are listed in Table 1. Undulator assembly was accomplished ahead of schedule and with significant cost savings. Bidders on the fabrication and assembly contracts were prequalified to ensure that they were capable of performing the job safely and correctly. The Argonne team devoted time up front to procedure development, vendor safety training, and completion of the necessary documentation. Vendor oversight, communication, and QA were continuous and thorough throughout the duration.

Table 1: Undulator Physics Requirements

| Parameter | Value | Units |
|---|---|---|
| # of 3.4-m-long und. segments | 33 + 7 | |
| Total installed undulator length | 131.520 | m |
| Min. expected undulator sys. life | 20 | years |
| Undulator period length | 30.00±0.05 | mm |
| Undulator gap height | ≥ 6.8 | mm |
| Wiggle plane | horizontal | |
| Horiz. und. seg. good field region | ±5.0 | mm |
| Vert. und. seg. good field region | ±200 | μm |
| Total pole cant angle | 4.5 | mrad |
| Phase slippage distance of 113×2π | 3.656 | m |
| Phase slip. tolerance (@ 1.5 Å) | ±175 | mrad |
| Max. acc. seg. ph. err. (@ 1.5Å) | ±175 | mrad |
| Abs. $1^{st}$ field int. along und. seg. | $<40\times10^{-6}$ | Tm |
| Abs. $2^{nd}$ field int. along und. seg. | $<50\times10^{-6}$ | $Tm^2$ |
| Undulator system temp. range | 20.00±0.56 | °C |

The final undulator was ready 27 months after award of the first long-lead contract. The first undulator from each of the assembly vendors [5,6] was magnetically tuned and mechanically verified at Argonne. All other undulators were delivered directly to SLAC for final tuning and fiducialization. Average peak fields of all undulators were measured at factory acceptance using a portable Hall probe. Results for 38 devices are shown in Figure 1.

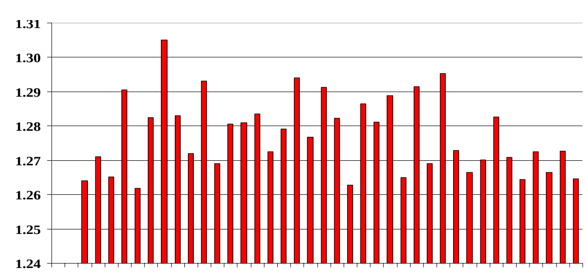


Figure 1: Average peak fields measured during factory acceptance of LCLS undulators.

*Work at Argonne was supported by the U. S. Department of Energy, Office of Science, Office of Basic Energy Sciences under Contract No. DE-AC02-06CH11357.

# mwhite@aps.anl.gov

### *Support and Motion System (SMS)*

The undulator system SMS is shown in Figure 2 [7]. It consists of three main elements: pedestals; intermediate plates with camshaft movers; and a girder with two translation stages onto which the undulator, vacuum chamber, quadrupole, beam position monitors, and various other vacuum and diagnostic components are mounted. Figure 3 is a photo of the girder cross section.

An undulator is ~305 mm in diameter, 3400 mm long, and weighs 1000 kg. The 1000-kg weight of the undulator is transferred through its feet to the translation stages and then directly to the girders. The weight is then transferred to the hardened-steel wedges that are attached to the underside of the girder directly below the stages, and then to the camshaft mover (CSM) bearings, beneath which adjustable screws direct this load to the pedestal. The five camshaft movers, with eccentricity of ~1.5 mm, allow for precise horizontal and vertical positioning and adjustment of the girder. The pedestal's intermediate plate is attached to the pedestal with rods that allow for initial height adjustment. A double CSM and a single CSM are located adjacent to each other on the upstream pedestal. Two single CSMs, acting as a double CSM—where the cams are spread apart for added stability—are located on the intermediate plate of the downstream pedestal, as shown in Figure 4.

Undulators can be remotely retracted out of the beamline by 80 mm using the translation slides. The tolerances on precision, short- and long-term stability, and reproducibility are quite stringent, as shown in Table 2. The complete SMS was tested for many hundreds of hours to ensure that stability, repeatability, and reproducibility met specifications.

Table 2: Major Support and Motion System Requirements

| SMS Requirements | Value | Unit |
|---|---|---|
| Quad. position repeatability | ±7 | μm |
| Short-term BPM & quad stability | ±2 | μm |
| Long-term BPM & quad stability | ±5 | μm |
| Min. quad motion range radius | 1.0 | mm |
| Quad center man. adj. range | ±2 | mm |
| Quad center man. adj. resolution | 2 | μm |
| Quad position change in roll-out | ±25 | μm |
| Quad reproducibility after roll-out | ±2 | μm |
| BPM transverse change in roll-out | ±25 | μm |
| BPM reproducibility after roll-out | ±2 | μm |
| Horiz. und. repeatability in roll-out | ±10 | μm |
| Vert. und. repeatability in roll-out | ±5 | μm |
| Maximum und. roll-out duration | 60 | s |

A complete undulator module was assembled from prototype and first-article components, including pedestals, intermediate plates with camshaft movers, controls rack, cabling, electronic components, a girder with translation stages, a quadrupole, an RF-BPM, a wire position monitor (WPM), and an undulator with mu-metal shield. The module was thoroughly tested for hundreds of hours at the Advanced Photon Source at Argonne in order to demonstrate that the system, as designed, met all specifications. Some adjustments were made to the final production supports to make them even more rigid. Figure 5 is a photograph of the final undulator module and controls system at Argonne, assembled from first-article production components.

### *Control and Monitoring*

The LCLS undulator control system is responsible for micron-accuracy positioning of each undulator segment within the undulator hall. The undulator system controls rack can be seen below the girder in Figure 5.

Each control module controls five camshaft movers and two translation slides. Together, they enable positioning of the girder to micron accuracy with five degrees of freedom, including x and y, pitch, roll and yaw, where the z-axis is oriented along the undulator axis.

Undulators are protected against over-travel by redundant sets of software limits, limit switches, and hard stops. Transverse undulator motion is constantly monitored by software and two long-travel potentiometers to ensure synchronicity of the two translation stages within 50 microns. Motion control is supported by six 0.5-inch-travel spring-loaded potentiometers with a resolution of 0.13 microns. Four potentiometers provide vertical position data and two provide horizontal position data.

The undulator control system is also responsible for monitoring the temperature at 12 points along each undulator and for controlling the beam finder wire diagnostic.

Undulator system installation is progressing extremely well at SLAC and should be complete in the next couple of months.

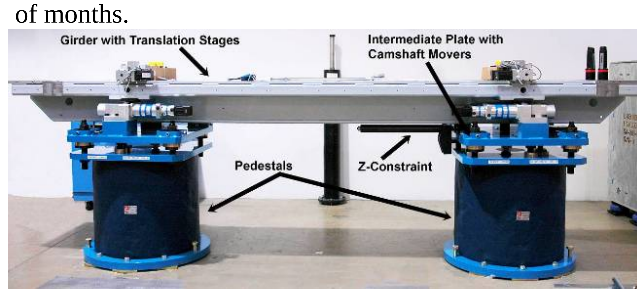


Figure 2: The SMS with pedestals, intermediate plates with camshaft movers, and girder with translation stages.

Figure 3: A cross section of the support girder mounted on the intermediate plate.

Figure 4: The undulator is mounted on a translation slide that is attached to the girder. The double CSM is shown below the girder, mounted on the intermediate plate.


Figure 5: The single-undulator module at Argonne.

### *Quadrupole Magnets*

A quadrupole magnet with horizontal and vertical correctors is installed on each girder. The magnet was designed for excellent field quality and mechanical stability, and is laminated to permit fast beam-based alignment operations. It is air-cooled to avoid the need to supply water in the undulator tunnel. The quadrupole magnet and support parameters are listed in Table 3 and Figure 6 shows the magnet and support stage.

Table 3: Major Quadrupole Magnet Parameters

| Quadrupole Parameter | Value | Unit |
|---|---|---|
| Nominal integrated quad gradient | 3.00±0.03 | T |
| Maximum integrated quad gradient | 4.0 | T |
| Trim strength range | $\pm 3\times 10^{-4}$ | Tm |
| Trim stability | $\pm 3\times 10^{-7}$ | Tm |
| Trim settability | $\pm 1.5\times 10^{-6}$ | Tm |
| Center stability after fiducialization | ±10 | µm |
| Center stability @ ±20% grad. chng | ±3 | µm |
| Center stability - short term (1h) | ±1 | µm |
| Center stability - long term (24h) | ±3 | µm |
| Grad. stability - long term (24h) rms | 0.25 | % |
| Roll tolerance | ±20 | mrad |
| Pitch tolerance | ±15 | mrad |
| Yaw tolerance | ±15 | mrad |

The quadrupole was also designed for low power dissipation, since the total dissipated-power budget from all sources is 50 W/meter, including lighting. The 29.5-kg quadrupole is supported by a stable, compact, rigid stage that provides for vertical and transverse adjustment of the magnet. The stage has a travel range of ±3 mm in both directions and a precision of 2 microns.

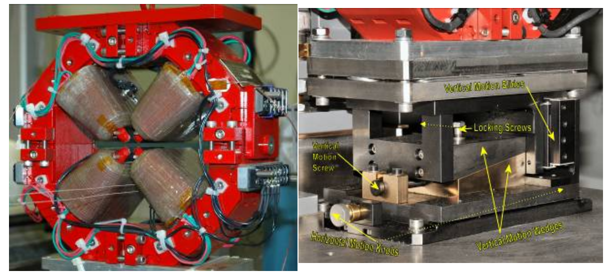


Figure 6: End view of the quadrupole magnet (left) and support and translation stage (right).

## SUMMARY

Forty undulators, 37 laminated quadrupole magnets, 38 precision support and motion systems, and complete undulator system controls were designed, prototyped, tested, and constructed by Argonne. All components were delivered to SLAC. Final undulator tuning and fiducialization are ongoing at SLAC, and component installation in the LCLS tunnel is well underway.

## ACKNOWLEDGEMENTS

We gratefully acknowledge Y. G. Amer, T. Barsz, K. Boerste, D. Capatina, J. Chan, J. Q. Chan, E. Chang, F. Clark, L. Cokeley, R. A. Conley, F. Coose, R. Dejus, P. Den Hartog, F. DePaola, S. Doran, C. Doose, M. Erdmann, C. Eyberger, F. Fisher, H. Friedsam, M. Givens, J. Grimmer, S. Hahn, S. Hanuska, B. S. Hoster, J. Ingraffia, W. Jansma, M. Kasa, R. T. Kmak, K. Knight, J. W. Lang, R. Lanham, G. Lawrence, P. Mast, K. Meitsner, M. Merritt, E. Moog, D. Nocher, H. D. Nuhn, M. Oprondek, T. Powers, C. Rago, D. Schafer, J. Schneider, D. Schultz, L. Skubal, J. TerHaar, R. Voogt, S. Wesling, D. Wilkinson, and J. M. Wozniak for their critical contributions to this effort.

## REFERENCES

[1] Linac Coherent Light Source (LCLS) Project homepage: http://www-ssrl.slac.stanford.edu/lcls/

[2] G. Pile et al., "Design and Production of the Undulator System for the Linac Coherent Light Source (LCLS)," Proc. of FEL08, to be published at http://www.JACoW.org.

[3] E. Trakhtenberg et al., Proc. of PAC07, Albuquerque, NM, USA, July 2007, TUPMN100, p. 1148-1150 (2007); http://www.JACoW.org.

[4] I.B. Vasserman et al., Nucl. Instrum. Methods A575 (2007) 22.

[5] Hi-Tech Mfg., 4637 N 25th Ave, Schiller Park, IL, 60176, USA.

[6] Metalex Mfg., 5750 Cornell Rd., Blue Ash, OH, 45242, USA.

[7] E. Trakhtenberg et al., Proceedings of the 2008 MEDSI Conference, to be published in NIMA.

# 8-GeV C-BAND ACCELERATOR CONSTRUCTION FOR XFEL/SPring-8

Takahiro Inagaki#, on behalf of the members of the XFEL/SPring-8 project,
XFEL joint project of RIKEN and JASRI,
1-1-1 Kouto, Sayo-cho, Sayo-gun, Hyogo, 679-5148, Japan

*Abstract*

The C-band (5712 MHz) accelerator is used as the main accelerator of the X-ray free electron laser (XFEL) facility in SPring-8. We will use 64 units of them for the 8 GeV XFEL accelerator. Since the C-band generates a high accelerator gradient, as high as 35 MV/m, it makes the accelerator compact. Since May 2008, we have operated one of the C-band units in the SCSS test accelerator with a high accelerator gradient of 37 MV/m. We have experienced no trouble, no serious rf discharge, and no degradation of FEL performance. We confirmed high reliability of the C-band accelerator at high-gradient.

Mass-production of high-power rf components was started in 2007. They have been delivered on schedule. In order to maintain the production quality, we constructed a high-power rf test bunker.

For the power supply, special design was taken to improve stability. The new high-voltage charger has extremely high stability, which satisfies the requirement for the XFEL.

## INTRODUCTION

The Japanese X-ray free electron laser (XFEL/SPring-8) is under construction at the SPring-8 site [1,2]. It aims to achieve excellent laser performance with a compact, low-cost, highly reliable machine. It is based on three key technologies; 1) a low-emittance injector using the thermonic electron gun, 2) a C-band high-gradient accelerator, 3) an in-vacuum short-period undulator. The frequency of C-band is 5712 MHz, which is double of conventional S-band accelerator. Higher frequency is chosen due to the higher power efficiency, which makes the accelerator compact. Since the C-band generates a high accelerator gradient, as high as 35 MV/m, the total length of the accelerator fits within 400 m, including the injector and three bunch compressors. The C-band uses normal conducting rf technology, thus it runs in the pulse mode at 60 pps, which is well suited for XFEL operation, and is less expensive.

Figure 1 shows a computer image of our facility. The total length of the FEL facility is 700 m, which fits with available length in our site.

Figure 2 shows the accelerator layout. After the injector and S-band sector, the first C-band sector with 12 C-band units accelerates an electron beam from 415 MeV to 1.45 GeV. At this sector, the rf phase is set at 42 degrees from the crest, which makes energy chirp for the bunch compression chicane (BC3). After BC3, 52 C-band units accelerate the beam to 8 GeV.

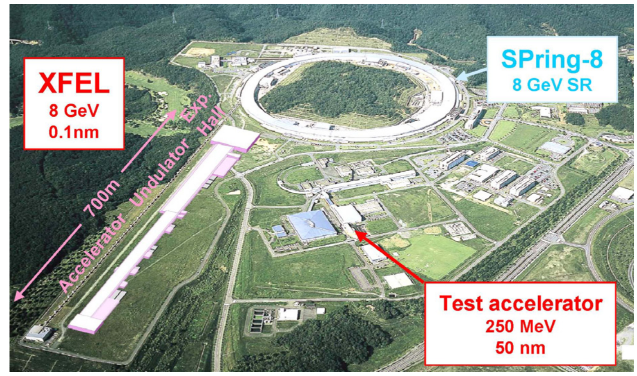


Figure 1: Computer image of the XFEL facility in SPring-8 site.

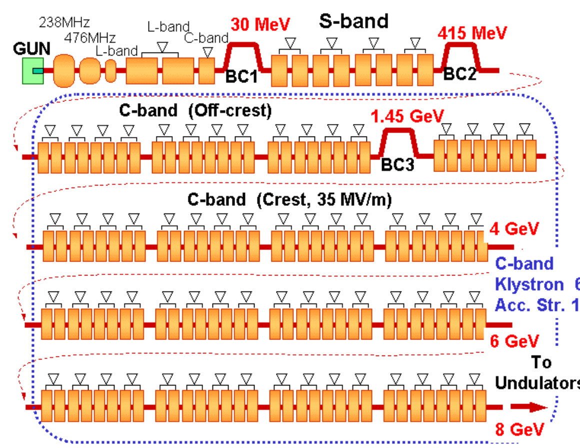


Figure 2: Accelerator layout of XFEL/SPring-8.

## C-BAND ACCELERATOR SYSTEM

Figure 3 shows one unit of the C-band accelerator system. The rf source is the 50 MW pulse klystron. An rf pulse compressor compresses a 50 MW, 2.5 μs square pulse to a 150 MW, 0.5 μs pulse. It is then fed to two 1.8 m accelerating structures.

The C-band accelerator was initially developed for the $e^+e^-$ linear collider project. At KEK, the first model of the accelerating structure, the rf pulse compressor, waveguide components, and the klystron were developed [3,4,5,6]. We adopted C-band technology for XFEL. XFEL is the first practical application of the C-band accelerator in a large facility..

#inagaki@spring8.or.jp

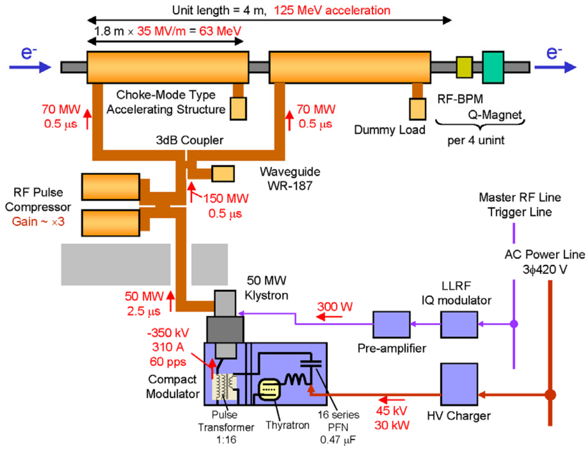


Figure 3: C-band accelerator system.

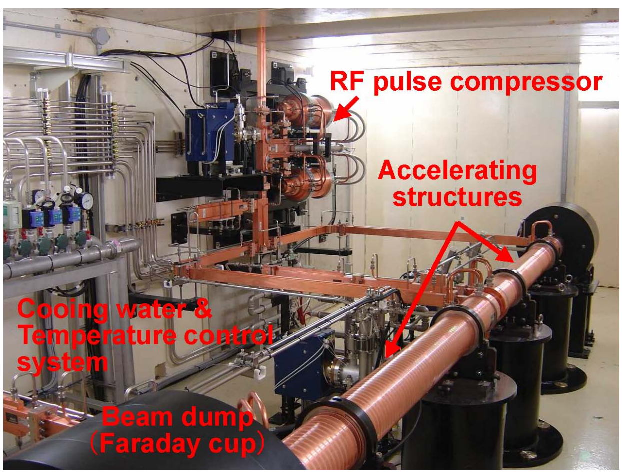


Figure 4: Two accelerating structures and the rf pulse compressor are installed at a high-power test bunker, which is the exact model of 8 GeV accelerator.

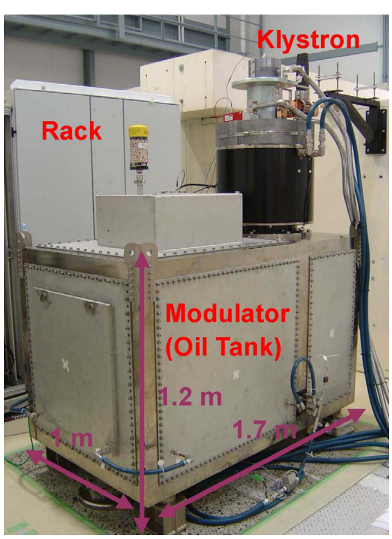


Figure 5: The first model of new oil-filled modulator, where the klystron is attached directly on the modulator.

### *Choke-Mode-Type Accelerating Structure*

Figure 4 shows the C-band accelerator unit. The 1.8 m long accelerating structure is formed 91 cells, quasi-CG structure. The rf mode is $3\pi/4$ traveling wave. The shunt impedance is 54 MΩ/m on average. The attenuation parameter is 0.53. The filling time is 300 nsec. A unique feature is "choke-mode-structure". It eliminates the wakefield of electron beams for future multi-bunch operation [4].

The cavity structure is made of high-purity oxygen-free copper with hot isostatic pressing (HIP). Each cavity cell is carefully shaped on a high-precision lathe, in order to adjust the cavity frequency. After rf measurements, they are brazed. Fabrication of this accelerating structure is well established by MITSUBISHI HEAVY INDUSTRIES, LTD [7].

Since the C-band accelerator generates high-gradient, it has higher heat dissipation. In order to compensate the heat dissipation, we prepare a precise temperature-control system [8]. Measuring the body temperature, the feedback system controls the heater of the cooling water. Thanks to this feedback loop, we can easily change the pulse repetition. At the test accelerator, this system controls the temperature to within ±0.04 degree.

### *RF Pulse Compressor*

SLED-type rf pulse compressor is used. It consists of one pair of high-Q cavities and one 3-dB coupler. The rf mode of the cavity is $TE_{0,1,15}$. The measured $Q_0$ is 190,000, and $\beta$ is 9.5. A unique feature is that each cavity has an rf mode converter [5]. It converts the waveguide mode ($TE_{10}$) to the cylindrical mode ($TE_{01x}$). The rf pulse compressor is also fabricated by MITSUBISHI HEAVY INDUSTRIES, LTD.

The cavity frequency is tuned at the factory. After installation in the accelerator tunnel, the frequency can be finally adjusted by a precise temperature-control system.

### *50-MW Pulse Klystron*

The maximum output power is 50 MW, 2.5 µsec. We use model E37202 of TOSHIBA ELECTRON TUBES & DEVICES CO., LTD. The design and the development are presented in [6]. The compatible klystron is available at MITSUBISHI ELECTRIC CORP.

### *Compact, Oil-Filled Modulator*

The 110 MW modulator supplies a pulsed high-voltage of -350 kV, 310 A to the klystron. Last year we developed a new compact modulator. Figure 5 shows an outer view of the modulator. In a steel tank (1.7m×1.0m×1.2m), all of the high-voltage components, including an 16 series PFN circuit, a thyratron tube, and a pulse transformer, are immersed in insulating oil. The steel tank works as an EM shield against thyratron noise. Insulating oil eliminates any trouble due to humidity or dust. Cooling is performed by natural convection of oil, without a fan [9]. Oil is cooled by water running through copper pipe and copper plate.

Last year, the first prototype of this modulator was fabricated by NIHON KOSHUHA CO., LTD. So far, it has worked well for more than 600 hours. A previous model of the oil-filled modulator is used at a test accelerator [10]. Four modulators have worked for more than 3,000 hours without any serious problem. We conclude that the concept of the oil-filled modulator has been realized.

### *PFN High-Voltage Charger*

We use an inverter-type high-voltage power supply for PFN charging. The maximum charged voltage is 50 kV. The averaged charged current is about 2 A.

The XFEL accelerator requires very high stability on the accelerating rf field. According to a beam-optics consideration, the stability of the acceleration energy of each unit should be on the order of $10^{-4}$ [2]. The jitter of the PFN charged voltage is one of the largest sources of pulse-to-pulse instability. Our requirement concerning the PFN voltage jitter is about 100 ppm (0.01%), although a conventional inverter-type high-voltage charger has a one-order larger jitter.

We have been developing a high-voltage charger with stability better than 100 ppm. The charger has a feedback control of the PFN voltage using a high-voltage probe attached to the modulator. A new 50 kV high-voltage probe with a fast time response and a low thermal drift was developed by JAPAN FINECHEM COMPANY, Inc. [11]. For the high-voltage charger, special design was taken to improve stability. The charger is equipped with two switching power supply units in parallel. One is the "main charger" with 2 A output, and the other is the "sub charger" with a two-order smaller output. After the main charger charges up to about 99.7% of the target voltage, the sub charger precisely charges the remaining voltage. Last year NICHICON CORPORATION made a high-precision charger [12]. Figure 6 shows a typical waveform of the charging cycle. The voltage jitter is measured as 60 ppm in peak-to-peak (10 ppm in standard deviation). This stability satisfies the requirement for the XFEL.

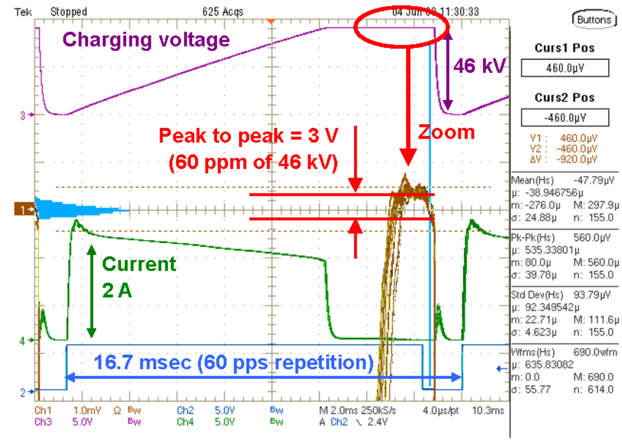


Figure 6: Typical waveform of the PFN voltage and the charging current using the high-precision charger. Tens of the waveforms are overlapped. The left blue histogram shows the stability of the PFN voltage accumulated during 1 minute operation.

### *Low-Level rf System and Timing System*

The rf phase and amplitude are precisely controlled by the low-level rf system. It consists of IQ modulators / IQ demodulators and VME waveform generators / digitizers. It is also used for pulse shaping and phase reversal for rf pulse compression. A precise timing system, which is synchronized to the master rf is developed. Details of the low-level rf system and the timing system are described in [13].

## HIGH-GRADIENT OPERATION AT THE SCSS TEST ACCELERATOR

In order to demonstrate SASE-FEL in the EUV range, the SCSS (SPring-8 Compact SASE Source) test accelerator was constructed in 2005 [14]. We built the 250 MeV accelerator and two in-vacuum undulators in a 60 m tunnel. After careful beam commissioning, we successfully observed SASE amplification at 49 nm wavelength with a 250 MeV beam energy in June, 2006. In 2007, laser amplification reached to the SASE saturation, which was verified by a measurement of the radiation characteristics [14]. Since 2007, several scientific experiments have started. The test accelerator stably supplies FEL radiation to the users.

In the test accelerator, two C-band accelerator units (named CB1 and CB2) are used. Until April 2008, the acceleration gradient of CB1 and CB2 was set at 29 MV/m (100 MeV gain per one unit), which is sufficient to obtain 250-MeV at the end. Besides the operation, we conducted 500 hours of rf processing. We measured the trip rate and confirmed that we sustain a high electric field gradient. We performed a beam acceleration test, and confirmed the field gradient [15].

Since May 2008, we have increased the rf power of CB2. Final energy is limited to 250 MeV due to the radiation safety. Therefore, we decreased the power of CB1 to adjust the final energy to 250 MeV.

Figure 7 shows the typical waveform during high-gradient operation at CB2. The pulse width of the klystron output is 2.5 μsec, with phase reversal at 2 μsec. In order to suppress the spike peak at the pulse compressor output, amplitude modulation makes a roughly flat pulse for over 200 nsec. Phase reversal and amplitude modulation are performed with the IQ modulator. The klystron output is about 50 MW. After the rf pulse compressor, the peak power is about 200 MW, and the average power in the 300 nsec filling time is about 150 MW. Therefore, the power gain using the rf pulse compressor is about 3.

The acceleration energy at CB2 was measured with a bending magnet, which is located 3 m after CB2. By comparing the beam energy with/without CB2, the acceleration energy was measured to be 131 MeV. Dividing by the active length of 3.6 m, the accelerating gradient was determined to be 37 MV/m.

After beam commissioning, we achieved that FEL lasing was easily obtained as same as before. We maintain CB2 in high-gradient (37 MV/m) for FEL operation for daily user run.

Figure 8 shows the trend graph of the vacuum pressure during high-gradient operation. The base pressure was on the order of $10^{-8}$ Pa. Small spikes were observed at a rate at one per hour. But it was much lower than the interlock level of $2\times10^{-5}$ Pa. During 300 hours (10 pps) of the user run, we had only 2 interlock stops due to the rf discharge at CB2. We confirmed that we can practically use the C-band accelerator with high-gradient of nominal 35 MV/m in XFEL.

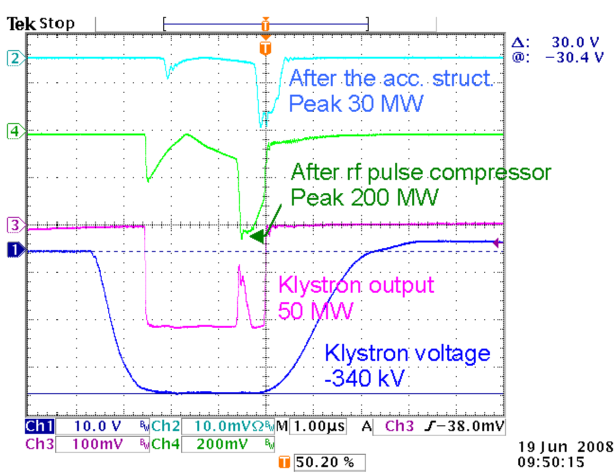


Figure 7: Typical waveform of the klystron voltage and the rf pulse at CB2.

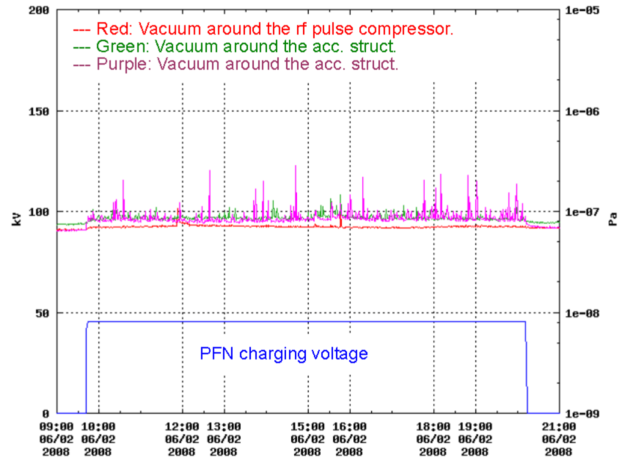


Figure 8: Typical trend graph of the vacuum pressure in the CB2 system. The accelerator operation started at 9:40, and ended at 20:10, with 10 pps repetition.

## HIGH-POWER RF TEST BUNKER

In order to check the quality of many high-power rf components delivered from the factory, we constructed a test bunker. Figure 4 and 5 are photos of the test bunker. The first set of rf components were installed. In order to perform complete tests of the C-band accelerator, we also installed vacuum components, water pipes, and the support structures with almost the same layout in XFEL,

We started rf processing at the end of July. The rf processing is in progress. After a certain period, we have a plan to replace another set of the accelerating structures and the rf pulse compressor. We expect that about ten sets of rf components can be tested before installation to the XFEL tunnel. It is a reasonable number as sample checks of 64 units.

## SUMMARY AND SCHEDULE

In the SCSS test accelerator, we have operated one of the C-band units with a high accelerating gradient of 37 MV/m. Nominal acceleration gradient of 35 MV/m is well confirmed.

High-power rf components, which include the accelerating structure, the rf pulse compressor, waveguide components, and the klystron, have been produced on schedule. So far, roughly 30 % of the 64 units have been delivered. Concerning the modulator and the PFN high-voltage charger, the prototype model has extremely high stability, which satisfies the requirement for the XFEL. The first models for XFEL are being fabricated at the company.

The XFEL building will be completed in April 2009. We plan to install the C-band units from 2009 to 2010. After rf processing, we plan to start commissioning by the early period of 2011.

## REFERENCES

[1] T. Shintake et. al., “SPring-8 Compact SASE Source (SCSS)”, SPIE, Optics for Fourth-Generation X-ray Sources, Bellingham, August 2001, P. 12.

[2] Y. Otake et al., “Construction status of XFEL/SPring-8”, FEL’08, Aug. 2008.

[3] H. Matsumoto et al., “The KEK C-band RF System for a Linear Collider”, LINAC’04, 2004.

[4] T. Shintake et al., “The First Wakefield Test on the C-band Choke-mode Accelerating Structure”, PAC’99, 1999.

[5] T. Shintake et al., “Development of C-band RF Pulse Compression System for the e+e- Linear Collider”, PAC’97, 1997.

[6] Y. Ohkubo, et. al., “The C-band 50MW Klystron using Traveling-wave Output Structure”, LINAC’98, 1998.

[7] H. Matsumoto et. al., “Fabrication of the C-band (5712 MHz) choke-mode type damped accelerator structure”, LINAC’98, 1998; S. Miura et al., “Fabrication of the C-band Choke-mode-type Accelerating Structure” (In Japanese), Linear Accelerator Meeting in Japan, 2004.

[8] S. Takahashi, et. al., “Precise Temperature Regulation System for C-band Accelerating Structure”, APAC’04, 2004.

[9] C. Kondo et al., “Cooling System of Klystron Modulator Power Supply for XFEL Project at SPring-8”, LINAC’08, Victoria, Sept. 2008, THP085.

[10] T. Inagaki et al., “A Compact oil-filled modulator for C-band klystrons”, IEEE Pulse Power Conf’05, June 2005.

[11] K. Okada et al., “High voltage probe filled fluorinert for XFEL/SPring-8” (In Japanese), Particle Accelerator Society of Japan, Aug. 2008.

[12] A. Kawasaki et al., “Development of high voltage capacitor charger for XFEL/SPring-8” (In Japanese), Particle Accelerator Society of Japan, Aug. 2008.

[13] T. Ohshima et al., “Low Level RF and Timing System for XFEL/SPring-8”, LINAC’08, Victoria, Sept. 2008, THP104.

[14] T. Shintake et al., “A compact free-electron laser for generating coherent radiation in the extreme ultraviolet region”, Sept. 2008, Nature photonics Vol.2 No.9, p555-559;
T. Tanaka et al., “SASE saturation at the SCSS test accelerator ranging fro0m 50 nm to 60 nm”, FEL’08, Aug. 2008.

[15] K. Shirasawa et al., “High gradient tests of C-band accelerating system for Japanese XFEL project”, PAC’07, June 2007.

# COMMISSIONING OF THE LCLS LINAC*

H. Loos†, R. Akre, A. Brachmann, F.-J. Decker, Y. Ding, D. Dowell, P. Emma, J. Frisch, S. Gilevich, G. Hays, Ph. Hering, Z. Huang, R. Iverson, C. Limborg-Deprey, A. Miahnahri, S. Molloy, H.-D. Nuhn, J. Turner, J. Welch, W. White, J. Wu, SLAC, Menlo Park, CA 94025, USA
D. Ratner, Stanford University, Stanford, CA 94305, USA

*Abstract*

The Linac Coherent Light Source (LCLS) X-ray free electron laser project is currently under construction at the Stanford Linear Accelerator Center (SLAC). A new injector and upgrades to the existing accelerator were installed in two phases in 2006 and 2007. We report on the commissioning of the injector, the two new bunch compressors at 250 MeV and 4.3 GeV, and transverse and longitudinal beam diagnostics up to the end of the existing linac at 13.6 GeV. The commissioning of the new transfer line from the end of the linac to the undulator is scheduled to start in November 2008 and for the undulator in March 2009 with first light to be expected in July 2009.

## INTRODUCTION

The Linac Coherent Light Source (LCLS) [1] is an X-ray free electron laser project aimed at generating coherent radiation at wavelengths from 15 Å to 1.5 Å using the final third of the existing SLAC 2-mile accelerator to deliver electrons with an energy of up to 13.6 GeV into an undulator with a length of 130 m. The requirements of a small transverse normalized emittance of 1.2 $\mu$m and a peak current of 3 kA to achieve saturation within the length of the undulator are met with the addition of a high brightness photo-injector at the 2/3 point in the linac and two subsequent magnetic chicane bunch compressors. The photo-injector and first bunch compressor was constructed in 2006 and commissioned from April to August 2007 [2, 3]. The second bunch compressor was installed in the fall of 2007 and the second phase of commissioning took place from January to August of 2008 [3].

The layout of the LCLS is depicted in Fig. 1, showing the injector oriented at 35° to the main linac, the two bunch compressors, and some of the diagnostics (LTU and undulator not shown). The main design parameters of the LCLS linac and the achieved values are listed in Table 1.

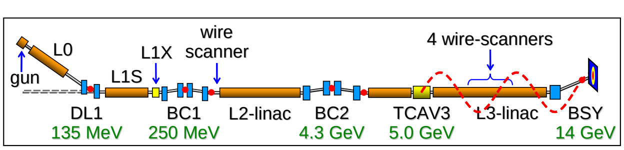


Figure 1: Layout of the LCLS accelerator.

Table 1: LCLS Accelerator Specifications

| | Design | Meas. | Unit |
|---|---|---|---|
| Repetition rate | 120 | 30 | Hz |
| Energy | 13.6 | 13.6 | GeV |
| Charge | 1 | 0.25 | nC |
| Bunch length | 20 | 8-10 | $\mu$m |
| Peak current | 3 | 3 | kA |
| Emittance (injector) | 1.2 | 0.7-1 | $\mu$m |
| Slice emittance (inj.) | 1.0 | 0.6 | $\mu$m |
| Emittance (linac end) | 1.5 | 0.7-1.6 | $\mu$m |
| Laser energy | 250 | 20-150 | $\mu$J |
| Gun field at cathode | 120 | 115 | MV/m |
| Quantum efficiency | 6 | 0.7-7 | $10^{-5}$ |

Most of the diagnostics for the electron beam were commissioned in the first phase with some additions during the second phase. New beam position monitors in the injector and bunch compressors and upgraded ones in the existing linac achieve between $5 - 10\,\mu$m resolution. Images of the beam are obtained with YAG screens in the gun and low energy area of the injector, and OTR foils with up to 10 $\mu$m resolution throughout the rest of the machine. Their functioning is presently compromised by the occurrence of coherent optical transition radiation and are expected to become reliable with the installation of a laser heater in the injector, which will suppress coherent effects in the beam. Projected transverse emittance can be measured with OTR screens and wire scanners located in the injector at 135 MeV and after BC1 at 250 MeV with 3-screen or quadrupole scan technique. Four wire scanners halfway in the third linac (L3) at 9 GeV are used to obtain the emittance after the second bunch compressor.

A transverse deflector cavity in the injector and one after BC2 make it possible to measure the longitudinal bunch profile and longitudinal phase space on OTR screens in the injector and a phosphorus screen in a dispersive section downstream of the main linac. The vertically deflecting cavity is also used to obtain the horizontal slice emittance in the injector. A number of phase cavities in the injector and after each bunch compressor give the bunch arrival time. Two relative bunch length monitors after BC1 and BC2 which detect coherent edge radiation from the bunch compressor dipoles provide a non-interceptive signal related to the bunch length. The signals are calibrated against an absolute measurement with the transverse cavity.

* Work supported by US DOE contract DE-AC02-76SF00515.
† loos@slac.stanford.edu

The following sections describe the performance of the drive laser and photo injector, the commissioning of the bunch compressors and the observation of coherent effects of the compressed electron bunch.

## PHOTO-INJECTOR

The drive laser system for the photo-injector uses a regenerative Ti:Sapphire amplifier and frequency tripling to the UV at 255 nm to generate electrons in the copper cathode. With most controls and diagnostics remotely available the laser beam now has an uptime of over 99%.

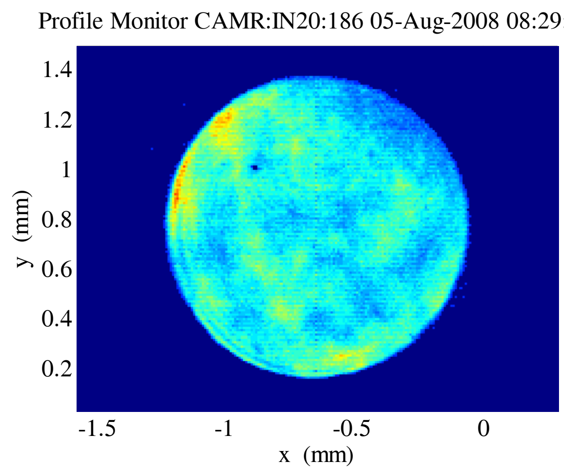


Figure 2: Laser distribution on the virtual cathode.

A typical flat-top transverse distribution of the laser beam on the virtual cathode is shown in Fig. 2 with about 10% rms intensity variation. The UV pulse shape can be seen in Fig. 3, as measured by a cross-correlation with the oscillator pulse. The pulse to pulse rms transverse stability of the laser on the cathode was 30 $\mu$m in the original installation, but could be since be improved to 10 $\mu$m rms by implementing changes to the laser transport line.

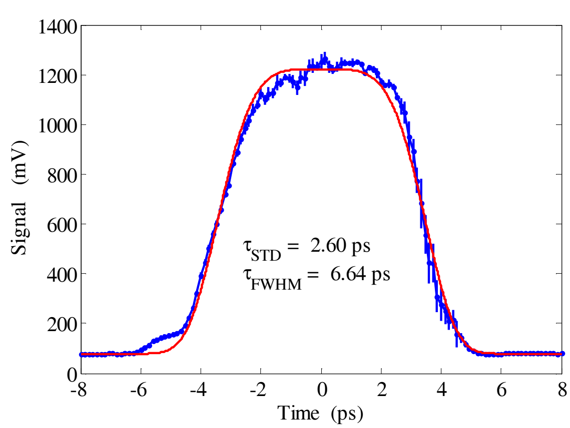


Figure 3: Temporal distribution of the UV-drive laser measured by a cross-correlation with the Ti:Sapphire oscillator.

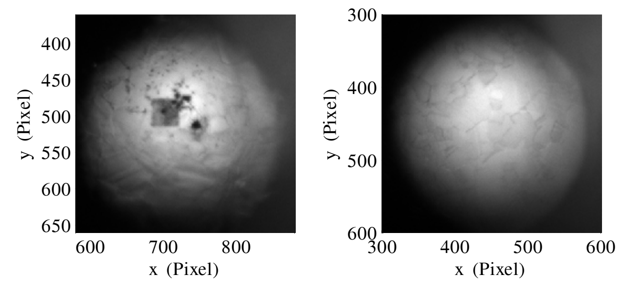


Figure 4: White-light image of the cathode before (left) and after (right) replacement.

While the first year of operation had shown a steady increase of the quantum efficiency (QE) of the copper cathode, it began to steadily drop after a scheduled vacuum break. Initially, a laser cleaning procedure helped to recover the QE, but after repeated cleaning it remained low at $0.75 \times 10^{-5}$ which limited the bunch charge to 200 pC at full laser power. The laser cleaning also damaged the cathode surface as can be seen in Fig. 4. The cathode was subsequently replaced and the QE measured to $7.6 \times 10^{-5}$ as pictured in Fig. 5. The QE is obtained from a linear fit at small laser energy in the range denoted by the dotted line. The charge rolls off at higher laser power due to space charge shielding [4].

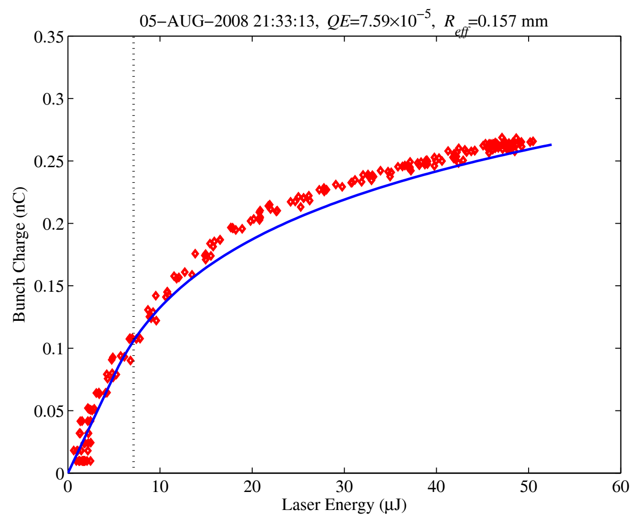


Figure 5: Cathode quantum efficiency obtained from measurement of electron bunch charge vs. laser energy.

The operation of the main linac and the FEL requires stable and repeatable beam parameters from the photo-injector for varying machine configurations such as desired bunch charge and bunch length, as well as for changes in the laser transverse and longitudinal profile and uniformity of the cathode. A procedure has been established to set up the injector magnets to optimize the projected emittance. In an iterative and semi-automated way, the steering or focusing magnet is varied and the projected emittance measured at each step with a quadrupole scan on an OTR screen downstream of the first two accelerating structures. The magnet is then set to the minimum of the measured emittance. The procedure includes the gun solenoid, a normal and a skew quad embedded within the solenoid, correctors in the gun region to find the optimum trajectory through the first accelerating structure and subsequent matching of the transverse beam phase space to the design Twiss parameters at the OTR screen location with the upstream injector quadrupoles.

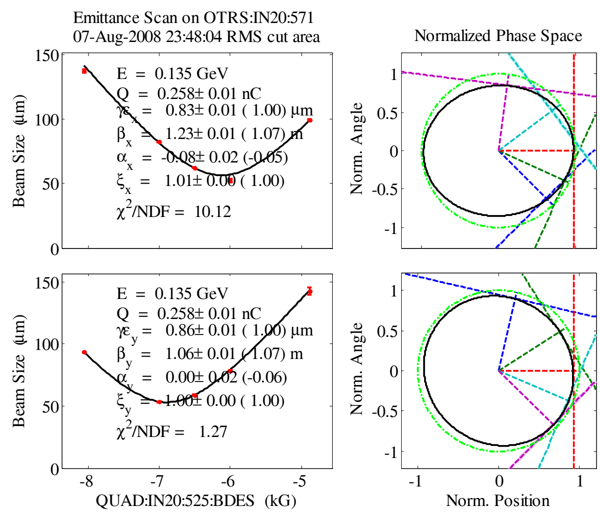


Figure 6: Emittance at OTR screen downstream of first two acceleration structures at normal operating conditions of 250 pC and 135 MeV measured by scanning an upstream quadrupole.

This procedure enables the injector to meet the performance requirements for the emittance, as can be seen in Fig. 6 for a 250 pC bunch charge. The left part shows the horizontal and vertical beam size of the central 95% of the beam distribution as a function of the quadrupole strength. The phase space ellipse from a fit to the data is on the right part and shown in units of the design ellipse at 1 $\mu$m. The measured projected emittance is 0.85 $\mu$m in both planes with nearly optimum match to the design ellipse.

The emittance as a function of temporal slices within the bunch can be measured in the horizontal plane by streaking the beam vertically with the transverse deflecting cavity upstream of the OTR screen. Measurements with as low a charge as 10 pC are possible on the OTR screen to measure the thermal contribution to the emittance. Figure 7 shows the horizontal slice emittance for 20 pC bunch charge and 400 $\mu$m rms bunch length from a 0.6 mm diameter laser spot on the cathode. The emittance is almost constant at 0.14 $\mu$m within the FWHM of the bunch. Measurements at 250 pC and 1.2 mm laser diameter give a slice emittance of 0.6 $\mu$m.

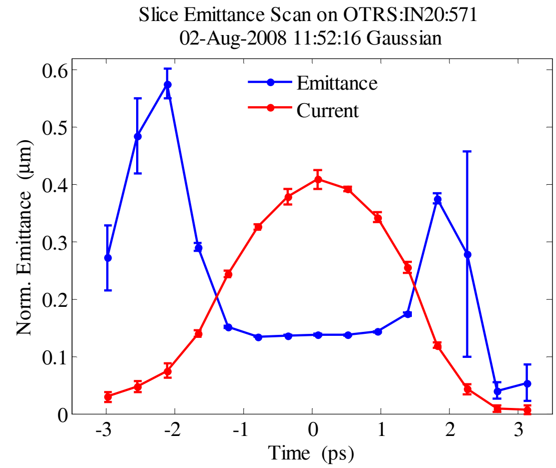


Figure 7: Slice emittance of low charge beam at 19 pC with a 0.6 mm diameter laser spot.

## BUNCH COMPRESSORS

The two 4-dipole magnetic chicane bunch compressors BC1 and BC2 in the LCLS linac are designed to compress the injector bunches from nominally 800 $\mu$m by a factor of 4 and 10 to 200 $\mu$m and 20 $\mu$m, while preserving the emittance from the injector. During the first commissioning phase it was not possible to transport the chirped beam through the BC1 chicane without deterioration of the emittance from about 1 $\mu$m to 2 $\mu$m. This was attributed to insufficient field uniformity of the two center dipoles where the dispersed beam is about 25 mm wide. Prior to the second commissioning phase the pole width was increased and with subsequent shimming the field error could be reduced to better than 0.03% within the chirped beam width. Emittance measurements after this modification confirm that the emittance can be preserved through BC1.

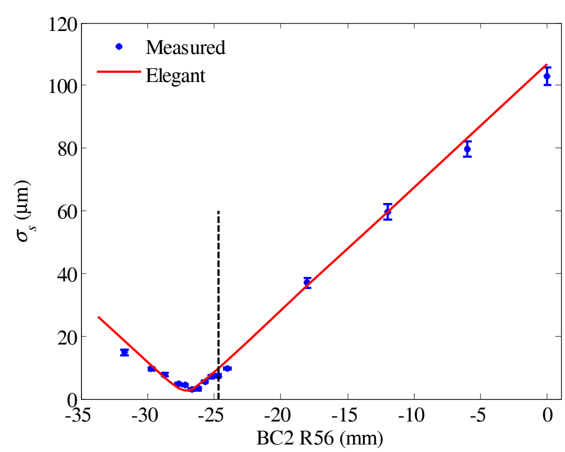


Figure 8: Bunch length after BC2 vs. $R_{56}$ of the bunch compressor. The black line indicates the normal operating point at -24.7 mm and the red arrow the minimum bunch length.

The bunch compression and effects of coherent synchrotron radiation (CSR) on the beam were studied with both bunch compressors as a function of energy chirp from the preceding linac (BC1) or chicane $R_{56}$ (BC2) and compared with tracking simulations [5] in Elegant [6]. The bunch length after BC1 was measured by turning off the magnets of BC2 and imposing a vertical transverse-time correlation on the bunch with the transverse cavity downstream of BC2. The beam was monitored on a phosphorescent screen in the beam switch yard downstream of L3 and the measurement calibrated by changing the transverse cavity phase while observing the vertical beam position on the screen. The bunch length after BC2 was measured in a similar way and is shown in Fig. 8 for the low charge configuration at 250 pC. The bunch length is 8 $\mu$m at the nominal chicane $R_{56}$ of -24.7 mm and L2 phase at -37° and has its minimum at 2 $\mu$m. This short bunch length is at the limit of the method given by the RF-power of the transverse cavity and the resolution of the screen.

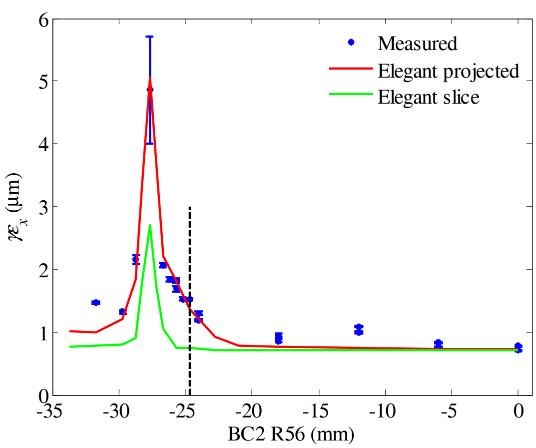


Figure 9: Horizontal normalized emittance after BC2 vs. $R_{56}$ of the bunch compressor. The black line indicates the normal operating point at -24.7 mm.

The projected horizontal emittance as a function of BC2 chicane $R_{56}$ was measured with the four wire scanners in L3 and is shown in Fig. 9. It illustrates the emittance growth related to the bunch compression. The large error bar of the data point at the peak in the emittance is due to the sensitivity to phase jitter at maximum compression. The simulation of the projected emittance with Elegant agrees well with the measured data and predicts in particular the doubling of the projected emittance from the value of 0.7 $\mu$m for the straightened chicane to 1.5 $\mu$m at the normal operating point, suggesting that the emittance growth can be entirely attributed to CSR. Although a measurement of the slice emittance which is critical for the FEL performance is not yet available downstream of the bunch compressors, a simulation of the slice emittance shows no emittance growth at the normal operating point.

## FEEDBACK SYSTEM

A number of beam based feedback systems [7] have been developed to control the most critical electron beam parameters and are based on signals from beam position monitors and coherent signals from the two bunch length monitors. The charge feedback measures the bunch charge after the gun and controls the laser power to keep the charge within 1.5% of the set point. Several independent feedback loops steer the beam after the gun, in the injector, through the X-band cavity, and into the L2 and L3 linac. The transverse beam jitter measured after BC1 is 4% of the rms beam size and $10\% - 15\%$ (see Fig. 10) near the end of the linac [8], which is near the goal of 10% set from the requirements of FEL operation.

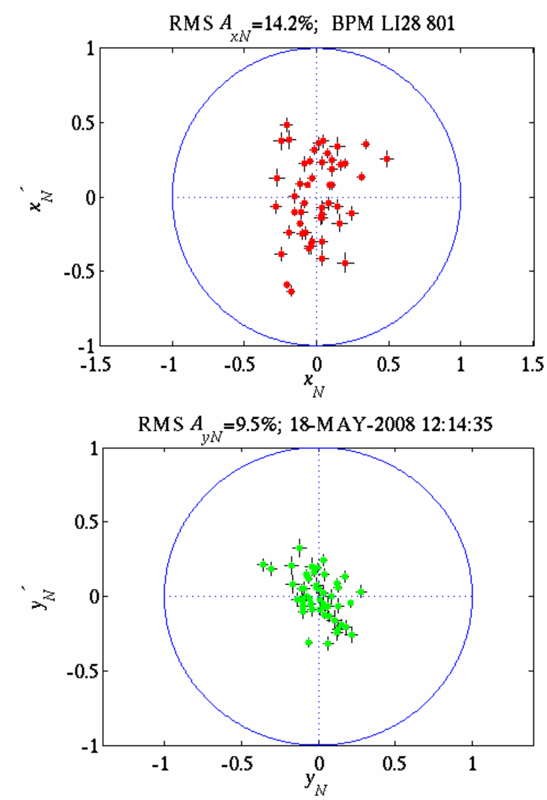


Figure 10: Shot to shot beam position and angle near the end of the linac in units normalized to the transverse beam phase space.

The feedback for the longitudinal coordinates is a combined loop for the beam energy measured with beam position monitors in DL1 and in the center of both bunch compressors as well as the bunch lengths after BC1 and BC2 measured with the relative bunch length monitors based on coherent edge radiation [9]. The feedback controls the amplitude of the L0, L1, and L2 linac for energy and the phase of L1 and L2 for bunch length. The measured energy jitter at the final energy with feedbacks in place is 0.03%. With the installation of the undulator beam line the final energy after L3 will be added to the feedback.

## ULTRA-SHORT BUNCH OPERATION

The normal operating modes of the accelerator are at 200 pC and 1 nC with bunch lengths after BC2 of 8 $\mu$m and 20 $\mu$m while maintaining a small emittance of 0.8 $\mu$m and 1.2 $\mu$m. Initial tests and simulations [10] have been done to utilize the small thermal emittance in a low-charge mode for ultra-short bunch generation. The low charge enables ultra-short bunches without adverse effects on the emittance due to CSR effects. In the experiment, a 20 pC bunch from a 4 ps FWHM laser pulse was accelerated at a -15° gun phase to a 260 $\mu$m bunch length after the injector. The emittance of 0.2 $\mu$m in the injector could mostly be preserved through the bunch compression with $0.2 - 0.3\,\mu$m after BC2. Although it was not possible to measure the absolute bunch length due to insufficient measurement resolution with transverse cavity, it was likely to be about 1 $\mu$m according to Elegant simulations. Such a short bunch length is also supported by the observation of strong near infrared COTR light at maximum compression.

## COHERENT RADIATION OBSERVATIONS

An unexpected result of the high brightness of the LCLS electron beam was the observation of coherent effects from the OTR screens along the main linac [2, 11]. The effect of this coherent optical transition radiation (COTR) is observed from the uncompressed beam after the first dogleg [12] to the compressed beam after BC2. It ranges from a small intensity enhancement of a factor 4 and about 20% changes in the beam size in the uncompressed case to an increase by a factor of up to $10^5$ in light intensity and complex transverse distributions for highly compressed bunches.

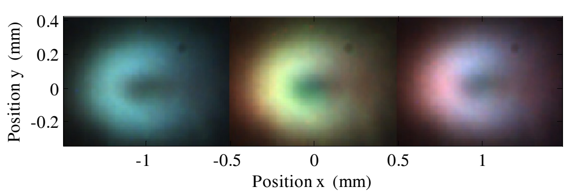


Figure 11: Coherent optical transition radiation observed with a color camera downstream of BC2.

This can be seen in Fig. 11 showing three shots of COTR images taken within one minute with a color CCD downstream of BC2. The uniformity of the spectrum within a single shot indicates transverse coherence in the microstructure radiating at optical wavelengths. The doughnut shape is caused by destructive interference in the light emitted from the beam center [11].

## SUMMARY

The two commissioning phases of the LCLS injector and linac have succeeded in generating an electron beam that meets all the requirements needed to operate the X-ray FEL at energies of up to 14 GeV. Figure 12 shows the projected FEL performance based on measured electron beam parameters for a period of one week. The blue curve is the simulated gain length, and saturation of the FEL is achieved for gain lengths shorter than the dashed line at 1/20th of the undulator length.

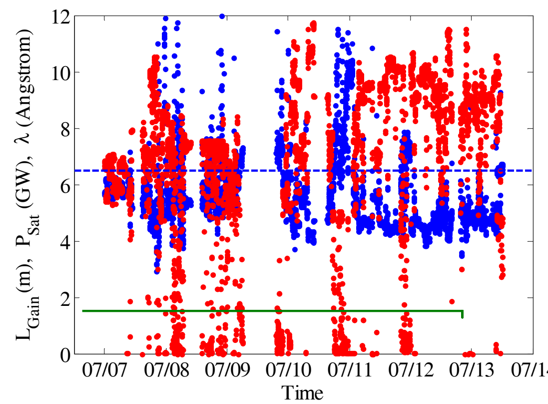


Figure 12: Simulated FEL performance based on measured electron beam parameters. The gain length is shown in blue, the saturation power in red and the wavelength in green. The dashed line represents the maximum gain length to achieve saturation.

The upcoming third phase of the LCLS commissioning starting in November 2008 will focus on the transfer line to the undulator and beginning March 2009 on the undulators with first light expected in June 2009. The installation of the laser heater in the injector is expected to mitigate the COTR effects on the OTR diagnostics and additional diagnostics to measure $\mu$m long bunches with spectral methods are under consideration.

## REFERENCES


[1] J. Arthur et al., "Linac Coherent Light Source (LCLS) Conceptual Design Report", SLAC-R-593.

[2] R. Akre et al., Phys. Rev. ST-AB 11 (2008) 030703.

[3] R. Akre et al., FEL'08, Gyeongju, August 2008, FRAAU04.

[4] D. H. Dowell et al., Phys. Rev. ST-AB 9 (2006) 063502.

[5] K.L.F. Bane et al., FEL'08, Gyeongju, August 2008, TUPPH027.

[6] M. Borland, ANL/APS LS-287 (2000).

[7] J. Wu et al., FEL'08, Gyeongju, August 2008, MOPPH052.

[8] R. Akre et al., FEL'08, Gyeongju, August 2008, MOPPH051.

[9] H. Loos et al., PAC'07, Albuquerque, August 2008, FRPMS071, p. 4191 (2007).

[10] Y. Ding, personal communication

[11] H. Loos et al., FEL'08, Gyeongju, August 2008, THBAU01.

[12] D. Ratner, A. Chao, Z. Huang, FEL'08, Gyeongju, August 2008, TUPPH041.

# OPERATION OF FLASH AS AN FEL USER FACILITY

K. Honkavaara*, DESY, Hamburg, Germany †

*Abstract*

FLASH, the FEL user facility at DESY, is operated with an electron beam energy up to 1 GeV corresponding to a photon wavelength down to 6.5 nm. The full year 2008 is dedicated to beam operation: about half of the time is scheduled for FEL users, and the rest for accelerator and FEL physics studies. Operational experience gathered at FLASH is very important not only for further improvements of the FLASH facility itself, but also for the European XFEL and for the ILC R&D effort. This paper reports our experience to operate FLASH as a user facility.

## INTRODUCTION

FLASH is a free-electron laser (FEL) user facility at DESY (Hamburg, Germany). It is a high-gain single-pass FEL based on self-amplified spontaneous emission (SASE). FLASH is a world-wide unique light source providing ultrashort radiation pulses (femtosecond range) with an unprecedented brilliance.

FLASH is based on the TTF-FEL [1] operated at DESY until end of 2002 with a photon wavelength range from 120 nm to 80 nm [2, 3]. The first lasing of FLASH at 32 nm was achieved in January 2005 [4]. Since summer 2005, FLASH is an FEL user facility. The first two years it provided FEL radiation for user experiments with photon wavelengths from 47 nm to 13 nm [5]. An energy upgrade to 1 GeV in summer 2007 extended the wavelength range down to 6.5 nm. The second user period started end of November 2007.

The complete year 2008, as well as the first half of 2009, is dedicated to beam operation. About half of the time is scheduled for FEL user experiments. The other half is shared between accelerator and FEL physics studies, and maintenance periods.

The experience gathered at FLASH is important not only for further improvements of the FLASH facility itself, but also for the European XFEL project [6] and for the R&D effort of the International Linear Collider (ILC) [7]. We report here our experience to operate FLASH as a user facility. Part of this material has already been presented in [8] and [9].

## PRODUCTION OF ELECTRON BUNCHES

Figure 1 shows a schematic layout of the FLASH linac.

A laser driven pulsed RF-gun provides up to 800 electron bunches per bunch train. The macro-pulse repetition rate is 5 Hz. The photocathode laser is based on a mode-locked pulse train oscillator synchronized to the 1.3 GHz of the accelerator. A chain of single-pass Nd:YLF amplifiers provides enough power to convert the initial infra-red wavelengths to ultraviolet (262 nm). The laser beam is guided to a $Ce_2Te$ cathode, which is inserted to the backplane of the RF-gun. The RF-gun is a 1.5 cell normal conducting L-band cavity (1.3 GHz). The maximum accelerating gradient on the photocathode is 46 MV/m, and the electron beam energy at the gun exit ∼5 MeV.

The number of bunches in the bunch train as well as the bunch spacing can be varied: the standard spacing is 1 MHz, other spacings like 500 kHz, 250 kHz, or 100 kHz have been realized as well. The electron bunch charge is variable to a certain extend. During FEL operation, a charge between 0.5 nC and 1 nC is used. Some main electron beam parameters are listed in Table 1.

Table 1: Some FLASH Parameters

| | | |
|---|---|---|
| **Electron beam** | | |
| Energy | MeV | 370 - 1000 |
| Peak current | kA | 1-2 |
| Emittance, norm. (x,y) | $\mu$mrad | 1.5 - 2 |
| nb. of bunches / train | | 1 - 800 |
| Bunch train length | ms | up to 0.8 |
| Rep. rate | Hz | 5 |
| **Undulator** | | |
| Period | cm | 2.73 |
| Gap | mm | 12 |
| Peak magnetic field | T | 0.48 |
| K | | 1.23 |
| Total length | m | 27.3 |
| **FEL radiation** | | |
| Wavelength | nm | 47 - 6.5 |
| Average pulse energy (typ.) | $\mu$J | 10 - 50 |
| Average pulse energy (max) | $\mu$J | 70 |
| Bandwidth (fwhm) | % | ∼1 |
| Pulse duration (fwhm) | fs | 10 - 50 |
| Peak power | GW | 1 - 5 |
| Peak spectral brilliance | * | $10^{29}$ - $10^{30}$ |

* photons/s/mrad$^2$/mm$^2$/(0.1% bw)

FLASH uses TESLA type accelerating modules. Each module contains eight superconducting niobium 9-cell cavities, a quadrupole doublet with integrated steerers and a beam position monitor. The first accelerating module boosts the electron beam energy to 130 MeV. In order to reduce space charge effects, its first four cavities are operated with a moderate gradient (12-15 MV/m). The first bunch compressor is followed by two modules (ACC2 and

* katja.honkavaara@desy.de
† for the FLASH team

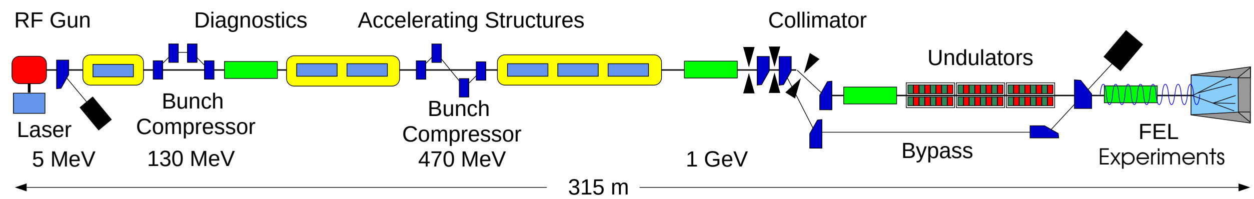


Figure 1: Layout of the FLASH linac including the experimental hall (not to scale).

ACC3), which accelerate the beam energy up to 470 MeV. After the second bunch compressor, three modules (ACC4, ACC5, and ACC6) further increase the electron beam energy up to 1 GeV.

The accelerating module at the position ACC6 is a new module installed in summer 2007. At the same time, the module at position ACC3 was replaced by a new one. The performance of both new accelerating modules is excellent. Both of them reach an average gradient of 25 MV/m, and four cavities of the sixth module even more than 30 MV/m.

## PRODUCTION OF SASE FEL RADIATION

In the SASE process the radiation amplification starts from shot noise in the electron beam. The interaction of the electron bunch with the undulator magnetic field leads to a periodic charge density modulation of the electron bunch. Once this “micro-bunching” is induced, many electrons within the bunch start to radiate coherently with the resonant wavelength. This wavelength depends on the electron beam energy and the properties of the undulator (period, gap, magnetic field).

A high-gain single-pass SASE FEL like FLASH requires a long undulator system. Six 4.5 m long undulator modules consisting of a periodic structure of permanent NdFeB magnets are installed after the collimation section. The undulator has a fixed gap of 12 mm. Some main undulator parameters are listed in Table 1.

The most relevant electron beam parameters for the SASE process are peak current and transverse emittance: the peak current has to be high enough and the emittance simultaneously small enough.

Two magnetic chicane bunch compressors are used to achieve the required peak current of 1-2 kA. The compression process requires a linear energy chirp along the bunch introduced by off-crest acceleration. However, to optimize the transverse emittance in the RF-gun, the initial electron bunch is relatively long (∼2 mm), and when it is accelerated off-crest by the sinusoidal RF field of the first accelerating module, a non-linear energy chirp is produced. Therefore, the compression leads to a longitudinal bunch shape with a leading spike of a high peak current and a long tail. The shape of the spike can be adjusted to some extend by varying the compression ratio between the two bunch compressors.

The RF curvature can be removed by third harmonic accelerating cavities (3.9 GHz). In summer 2009, it is planned to install a module with four superconducting 3.9 GHz cavities [10] upstream of the first bunch compressor. With this third harmonic module, it is expected to achieve a more regular longitudinal shape of the compressed bunch. The advantage will be a better and easier control of the SASE process together with a significant increase in SASE FEL radiation energy (a factor of 10 is predicted [11]). However, the FEL pulse duration is expected to increase simultaneously from the present value of a couple of 10 fs to ∼200 fs [11]. When the third harmonic module is switched off, FLASH can still be operated in the femtosecond mode, and also intermediate modes are anticipated.

The transverse emittance is optimized in the injector: the photocathode laser parameters are carefully adjusted, the accelerating gradient on the cathode is as high as possible, the transverse space charge effects are compensated by a solenoid magnet, and the steering of the electron beam through the first accelerating module is optimized. A typical transverse emittance of a 1 nC bunch (on-crest acceleration) is around 2 mm mrad [12].

In the present operation mode (femtosecond mode) with a leading spike and a long tail, the slice emittance of the high peak current spike, not the projected emittance of the entire bunch, is the relevant parameter for the lasing process. A description and results of the slice parameter measurements at FLASH can be found in [13].

The produced SASE FEL radiation is transported from the accelerator tunnel to the experimental hall via a specially designed beam line including photon diagnostics devices to determine the photon pulse energy, the transverse position, and the wavelength. In the experimental hall, where the user experiments are placed, the radiation can be guided to five different beam lines. However, only one line can be served at a given time.

### *SASE Performance*

Some typical FEL radiation parameters are listed in Table 1. The performance is different for each photon wavelength: each wavelength has different beam optics and – more important – a different bunch compression scheme. Therefore, the parameter range shown in Table 1 should be taken as an indication of the overall span of the performance. A complete characterization of the SASE radiation at 13.7 nm can be found in [5].

With the present undulator design having a fixed gap, the photon wavelength can only be varied by changing the electron beam energy. After the energy upgrade in summer 2007, electron beam energies up to 1 GeV are now available corresponding to photon wavelengths down to 6.5 nm. The lasing with this world record wavelength of SASE FELs was observed in the beginning of October 2007 for the first time [8, 9].

An other milestone was also achieved in October 2007: lasing with a complete bunch train of 800 bunches. The electron beam energy was 685 MeV corresponding to a photon wavelength of 13.4 nm. The average power of the photon beam was 56 mW.

Some of the operational highlights of this user period have been an experiment using the fifth harmonic of 7.97 nm (1.59 nm), and a continuous running of five days at 7 nm with a bunch train of 100 bunches for two experiments.

## OPERATIONAL ISSUES

FLASH is operated 24 hours per day, 7 days per week. The FEL user experiments are grouped into blocks of four weeks. Between two user blocks, a block of three weeks is reserved for improvements of the FLASH facility, and for FEL physics studies. Three times per year a dedicated beam time of 2-3 weeks is scheduled for general accelerator physics studies and technical developments.

During the period from November 26, 2007 (beginning of the second user period) to September 7, 2008 (end of the fifth user block within the second period), 49 % of the time has been scheduled for user experiments, 38 % for accelerator and FEL physics studies, and the rest for maintenance, including a maintenance period of 3 weeks in May 2008.

During the user blocks, FEL radiation has been delivered in average 73 % of the time to experiments. The rest of the up-time is used to tune FEL radiation properties (17 %) and to start-up the accelerator after maintenance or failures (1 %). The total downtime due to technical failures or other incidents is 6 %. The scheduled weekly maintenance takes 3 % of the time.

The time distribution of individual user blocks differs from each other (Table 2). For example, during the second user block the FEL radiation was delivered 79 % of the time, when in the fourth block its proportion was only 67 %. The difference is partly due to different amounts of the downtime, but more important due to different requirements of the user experiments. The more demanding the experiments are, the more time is needed for tuning.

Stability is an important issue to ensure continuous delivery of high quality FEL radiation. Many measures, like installation of low noise magnet power supplies, replacement of the old master oscillator, as well as temperature stabilization and reduction of electro-magnetic interference of the injector low level RF (LLRF) system racks, have already been taken. Several other actions are on-going including, for example, improvements of the LLRF phase and amplitude regulation, and developments of feedbacks to compensate drifts of electron beam parameters (energy, charge, arrival time, bunch compression, orbit).

Table 2: Time distribution between SASE FEL radiation delivery, tuning, linac set-up, maintenance, and downtime during the user blocks from November 26, 2007 to September 7, 2008. Each block has a length of four weeks.

| Block | SASE (%) | Tuning (%) | Set-up (%) | Maint. (%) | Down (%) |
|---|---|---|---|---|---|
| 1 | 71 | 14 | 2 | 4 | 9 |
| 2 | 79 | 13 | 1 | 4 | 3 |
| 3 | 75 | 16 | 1 | 2 | 6 |
| 4 | 67 | 24 | 1 | 2 | 6 |
| 5 | 69 | 18 | 2 | 1 | 10 |
| Total | 73 | 17 | 1 | 3 | 6 |

### *Downtime*

Downtime discussed here considers the five user blocks since November 2007. During FEL and accelerator study periods, the linac is often operated in unusual conditions. Therefore, the study periods are not representative for a standard FEL operation, and thus excluded from the downtime statistics.

About one third of the downtime (31 %) is related to failures of RF-stations (modulators, transformers, klystrons, preamplifiers, waveguides). Presently, four RF-stations are used to operate the FLASH linac: the RF-gun and the first accelerating module (ACC1) are operated by a 5 MW klystron each, ACC2 and ACC3 have a common 5 MW klystron, and the other three accelerating modules are fed by one 10 MW klystron. The modulators and transformers of RF-gun and ACC1 have been in operation already more than ten years. The two other RF-stations are of a newer type and have been in operation since 2004. During the last two years, the downtime due to RF-stations has been reduced significantly: in 2006-2007 it still caused more that 50 % of the total downtime. The reduction to the present 31 % is achieved especially by improving the start-up and reset procedures. A further improvement is expected, when the two aged modulators will be replaced during the shutdown in 2009.

Infrastructure failures, especially power cuts and disturbances of cooling water, air conditioning and temperature stabilization systems, have caused 11 % of the downtime. Magnet power supplies have been the source for 8 % of the downtime. In order to reduce the downtime due to failures of the photocathode laser (presently 7 %), a second laser system is in preparation.

Other downtime sources are low level RF regulation (5 %), and occasional failures of photon beamline components (7 %) and control (4 %) and cryogenic (3 %) systems. About 17 % of the downtime is caused by single incidents happening only once or very rarely. For example, operational and maintenance mistakes, and technical interlocks of the RF-gun and accelerating cavity couplers belong to this category.

The RF-system for the normal conducting RF-gun is especially demanding in terms of power transmitted to the gun cavity and reflected from it. During one of the user blocks, substantial amount of the downtime was caused by spikes in the reflected RF-power detected at the RF-gun klystron.

### *User Experiments*

Every user experiment has its own demands on the properties of the FEL radiation in terms of photon wavelength, pulse energy, pulse repetition rate, spectrum bandwidth, and stability. As mentioned above, 17 % of the time during the five user blocks has been used for tuning of these properties.

Usually, two user experiments, placed at different photon beam lines, run in parallel. The photon beam is changed from one experiment to another typically every 12 hours. In order to minimize the time required for tuning, the experiments are scheduled – whenever possible – to have similar FEL radiation properties. However, even with this, the change of, for example, the photon wavelength or the bunch pattern is often required between user shifts.

More than half of the total tuning time is needed for wavelength changes (57 %). Since FLASH has a fixed gap undulator, a change of the photon wavelength requires a change of the electron beam energy. In addition to adjustments of the gradients and phases of the accelerating modules, the wavelength change procedure includes an adjustment of the beam optics and a correction of the orbit through the undulator. Different wavelengths may also require different bunch compression schemes. A standard wavelength change with well-known accelerator settings takes in average two hours. Substantially longer tuning times are needed for wavelengths delivered for the first time, as well as for short wavelengths, especially if high photon pulse energy is required simultaneously. During the five user blocks the wavelength has been changed more than 60 times, and totally 24 different wavelengths between 7 nm and 27 nm have been delivered to the experiments.

Every now and then tuning is required to increase the FEL radiation energy, or to correct the transverse position of the photon beam. 15 % of the tuning time is used for this kind of standard tuning. A typical average FEL pulse energy delivered to user experiments is between 10 and 30 $\mu$J. Occasionally even higher pulse energies (up to 50 $\mu$J) has been provided.

Some experiments have special demands concerning the FEL radiation quality, like an exact wavelength or a narrow bandwidth of the wavelength spectrum. This kind of quality tuning takes presently 8 % of the tuning time, but its amount is likely to increase with the increasing demands of the experiments.

About half of the experiments request a single bunch operation (5 Hz FEL pulse repetition rate). The majority of the other experiments uses 10 to 30 electron bunches per bunch train. A couple of experiments have been carried out with longer bunch trains ($\sim$100 bunches). Setting up the long bunch train lasing have taken 4 % of the total tuning time.

Tuning is also required after technical failures (5 %) and after weekly maintenance (7 %).

## SUMMARY AND OUTLOOK

FLASH is a world-wide unique light source providing ultrashort FEL pulses with a high brilliance.

After the energy upgrade in summer 2007, the design electron beam energy of 1 GeV was reached in September 2007, and two other milestones in October 2007: lasing at a wavelength of 6.5 nm – a new world record for a SASE FEL – and lasing with a complete bunch train of 800 bunches.

The second FEL user period started end of November 2007, and since then FEL user experiments with more than 20 different wavelengths between 27 nm and 7 nm have been successfully performed.

During user experiments FEL radiation has been delivered in average 73 % of the time. Tuning of FEL radiation parameters has taken 17 % of the time. The downtime due to technical failures or other incidents has been 6 %. The rest of time has been used for weekly maintenance (3 %) and start-up (1 %).

A long shutdown is scheduled for the second half of 2009. Several modifications of the FLASH facility are planned to take place during the shutdown. A third harmonic module with four 3.9 GHz superconducting cavities will be installed in the injector. An other major modification is the installation of an experiment for seeded VUV radiation (sFLASH) [14] requiring a modification of the complete 40 m long electron beam line between the collimators and the SASE undulators. In addition, it is planned to exchange the RF-gun, and to install a seventh accelerating module to further increase the electron beam energy. Upgrades for the RF-stations and waveguide systems are scheduled as well. After a commissioning period, the third FEL user period is expected to start in spring 2010.

## ACKNOWLEDGMENT

We like to thank all colleagues, both at DESY and at the collaborating institutes, who are participating in the development, operation, and maintenance of FLASH.

## REFERENCES

[1] J. Rossbach, Nucl. Instrum. Meth. A **375** (1996) 269.

[2] J. Andruszkow *et al.*, Phys. Rev. Lett. **85** (2000) 3825.

[3] V. Ayvazyan *et al.*, Phys. Rev. Lett. **88** (2002) 104802.

[4] V. Ayvazyan *et al.*, Eur. Phys. J. D **37** (2006) 297.

[5] W. Ackermann *et al.*, Nature Photonics **1** (2007) 336.

[6] M. Altarelli *et al.* (Eds.), "XFEL: The European X-Ray Free-Electron Laser: Technical Design report", DESY Report DESY 2006-097, July 2006.

[7] http://www.linearcollider.org.

[8] S. Schreiber, B. Faatz, K. Honkavaara, "Operation of FLASH at 6.5 nm wavelength", Proc. EPAC 2008, Genoa, Italy, 23-27 June, 2008.

[9] K. Honkavaara, B. Faatz, S. Schreiber, "Status of FLASH", Proc. FEL 2008, Gyeongju, Korea, 24-29 Aug, 2008.

[10] E. Vogel *et al.*, "Status of the 3rd harmonic systems for FLASH and XFEL in summer 2008", these proceedings.

[11] The TTF FEL team, "SASE FEL at the TESLA Test Facility, Phase 2", DESY Report TESLA-FEL 2002-01, June 2002.

[12] F. Löhl *el al*, PRST-AB **9** (2006) 092802.

[13] M. Röhrs, "Investigation of the Phase Space Distribution of Electron Bunches at the FLASH-Linac using a Transverse Deflecting Structure", Ph. D. Thesis, DESY Report DESY-THESIS 2008-012, June 2008.

[14] S. Khan *et al.*, "sFLASH: an experiment for seeding VUV radiation at FLASH", Proc. FEL 2008, Gyeongju, Korea, 24-29 Aug, 2008.

# REVIEW OF ADVANCED LASER TECHNOLOGIES FOR PHOTOCATHODE HIGH BRIGHTNESS GUNS

H. Tomizawa, H. Dewa, T. Taniuchi, A. Mizuno, and H. Hanaki,
Accelerator Division, Japan Synchrotron Radiation Research Institute (JASRI/SPring-8),
Kouto, Sayo-cho, Sayo-gun, Hyogo 679-5198, Japan

*Abstract*

We developed an adaptive 3D shaping UV pulse laser system (based on a Ti:S laser) as an ideal light source for yearlong stable generation of low-emittance electron beams with a charge of 1 nC/bunch. From 2005 onwards, the laser's pulse-energy stability was continuously kept at <1.4% for THG (263 nm) for several months (flashlamp lifetime). In addition, in order to suppress the emittance growth caused by the space charge effect, the 3D cylindrical "beer-can" shape of the laser pulse was optimized spatially as a top-hat (flattop) and temporally as a square stacked chirped pulse. We utilized a deformable mirror that automatically shapes the spatial profile with a feedback routine, which is based on a genetic algorithm, and an UV pulse stacker consisting of three birefringent Alpha-BBO crystal rods for temporal shaping at the same time. Using this "beer-can" 3D-shaped laser pulse, so far we have obtained a minimum horizontal normalized emittance of 1.4 π mm mrad. In 2006, we proposed a laser-induced Schottky-effect-gated photocathode gun for the realization of a water bag beam in Luiten's scheme by using Z-polarization of the laser on the cathode. A hollow laser incidence was applied with convex lens focusing after passing the beam through a radial polarizer. According to our calculations (NA=0.15), a Z-field of 1 GV/m needs 1.26 MW at peak power for the fundamental wavelength (790 nm) and 0.316 MW for the SHG (395 nm).

## INTRODUCTION

Since 1996, we have been developing a stable and highly effective UV laser pulse as the light source for a photo-cathode RF gun [1] which in turn provides high-brightness electron beams for future X-ray light sources at SPring-8. The electron source for several X-ray FEL projects [2-4] requires electron beams with very low emittance (high brightness), often as low as 1 π mm mrad, and a charge of 1 nC/bunch. One of the most reliable candidates for this high-brightness electron source is a photocathode RF gun. This type of gun generates an electron beam pulse from a photocathode illuminated by a laser pulse. The development of this gun is oriented toward the creation of a yearlong stable system for user facilities. Since we started developing the laser test facility in 2001, two issues related to the source of laser light have arisen. One is the energy stability of the UV laser light source. In this regard, we successfully stabilized the third-harmonic generation (THG) of a CPA (chirped pulse amplification) Ti:Sapphire terawatt laser system as the laser light source for the SPring-8 RF gun. From 2005 onwards, the laser's pulse-energy stability was continuously kept at <1.4% for THG (263 nm) for several months limited by flashlamp lifetime. This improvement reflects the ability to stabilize the laser system in the pumping sources (Q-switched YAG) of the amplifiers with a temperature-controlled base plate in a clean room where the relative humidity was maintained at 55%. This system keeps dust particles away from the charged optical elements (typically insulator) and thus avoids burn-out damage with the laser incidence.

The other problem concerns the spatial and temporal laser profiles. In order to minimize the beam emittance of a photocathode RF gun, the laser pulse shape should be optimized in three dimensions. One of the candidates for a reliable 3D laser pulse shape has been the cylindrical "beer-can" shaped (spatially top-hat and temporally square) pulse. Over the past seven years, at the test facility for photocathode laser light sources at SPring-8, several 3D shaping systems in the UV region have been developed from combinations of spatial (transverse: x-, y-axes) and temporal (longitudinal: z-axis) pulse-shaping methods (Fig. 1). It was necessary to modify the spatial profile with a microlens array [5] or a deformable mirror (DM) [6], as well as to alter the temporal profile with a spatial light modulator (SLM) [6] or a pulse stacker. In its current form, we have applied a deformable mirror which automatically shapes the spatial profile with a feedback routine based on a genetic algorithm and a UV pulse stacker consisting of three or four birefringent Alpha-BBO crystal rods for temporal shaping at the same time [7]. In 2006, we demonstrated a cylindrical 3D UV laser pulse with the shaping system described above. By precisely optimizing the 3D shape of the laser pulse, we are striving toward the generation of a beam with as high a brightness and as low an emittance as possible. The perfect homogeneity of temporal stacking is automatically optimized with a feedback routine between a AOPDF UV pulse measurement (spectral phase interferometry in the UV region) and a high-resolution DAZZLER as a micro pulse shaper. Using this "beer-can" 3D-shaped laser pulse (diameter: 0.8 mm; pulse duration: 10 ps), so far we have obtained a minimum horizontal normalized emittance of 1.4 π mm mrad [7].

Recently, another candidate for the generation of a reliable 3D pulse shape was proposed for even lower emittance values [8], which comprises an ellipsoid with equivalent fluence along the temporal axis. Such uniform 3D ellipsoidal distributions of charge are one of the ultimate goals in high-brightness beams due to their linear internal force fields. O. J. Luiten simulated a method for the actual production of such bunches, which are based on photoemission by femtosecond laser pulses [9]. In 2006, we proposed a laser-induced Schottky-effect-gated photocathode gun in order to realize a water bag beam in Luiten's scheme by using Z-polarization of the laser on the cathode [10,11]. A hollow laser incidence is applied with convex lens focusing after passing the beam through a radial polarizer. According to our calculations (NA=0.15), a Z-field of 1 GV/m needs 1.2 MW at peak power for the fundamental wavelength (790 nm) and 0.31 MW for the SHG (395 nm) [11]. This concept of laser-induced Schottky emission can be applied to photocathode RF and DC guns.

## 3D UV LASER PULSE SHAPING SYSTEM

The 3D UV laser pulse shaping system combined with a deformable mirror (transverse: 2D) assisted by a genetic algorithm and a chirped pulse stacker (longitudinal: 1D) is shown in Fig. 1. By utilizing the long-term stable UV laser source described above, this system can generate a "beer can" laser pulse. Note that the shape and pulse duration of the original micro chirped pulse is optimized with DAZZLER (AO-modulator) at the fundamental wavelength. We describe the pulse stacking rods consisting of three birefringent Alpha-BBO crystals below.

## SPATIAL SHAPING WITH A DEFORMABLE MIRROR

The laser spatial profile was automatically optimized with self-developed genetic algorithms for a deformable mirror. We measured the profile with a laser profile monitor (Spiricon, Inc.: LBA300-PC) whose analyzing program can provide many parameters of beam profiles. We chose useful parameters to evaluate flattop profiles and made a fitting function for the developed genetic algorithm to optimize the profile toward an ideal flattop. These parameters for flattop shaping and their meaning are shown in Table 1. The value of this fitting function is returned as feedback to control the deformable mirror with the genetic algorithm.

As a result, the laser profile on the cathode surface was spatially shaped as a quasi-flattop profile (see in Fig.1). The laser spatial profile was remarkably improved by this shaping technique.

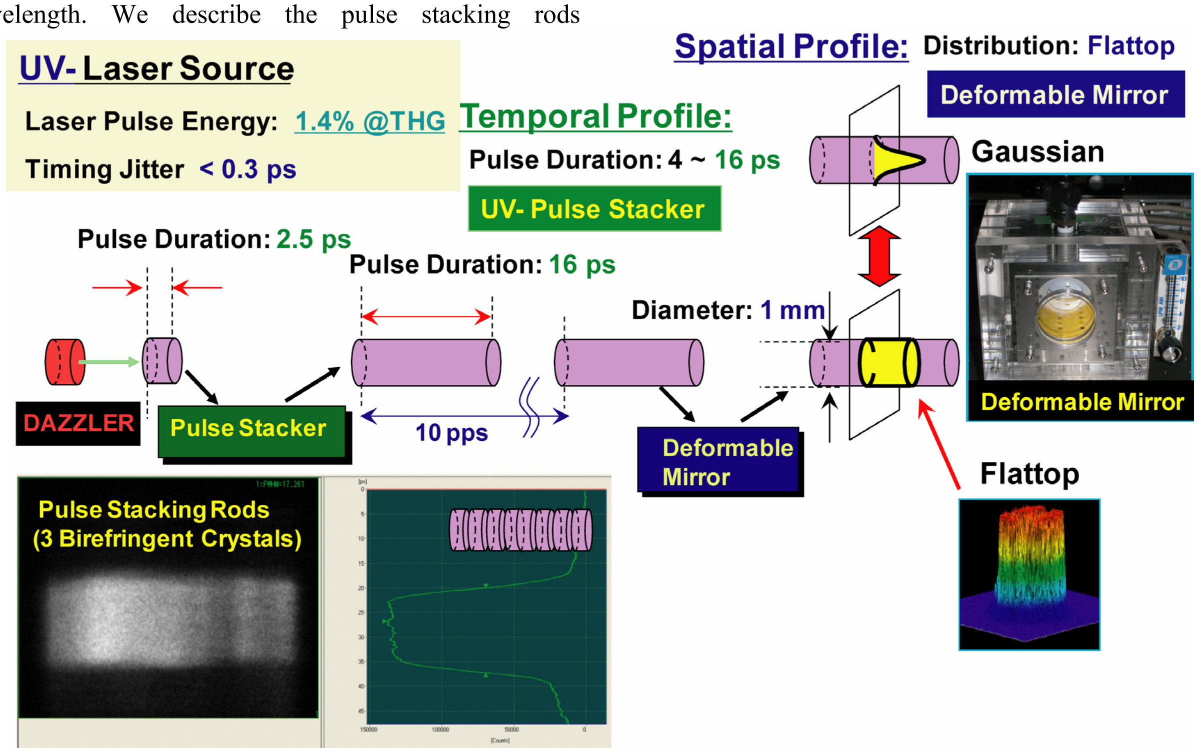


Figure 1: Three-dimensional UV-laser pulse shaping system: the 3D shaping system consists of a deformable mirror (DM) and chirped pulse stacking rods. These two shaping techniques can be optimized independently because there is no interference between them. The schematic drawing of pulse stacking shows 16-ps pulse generation by stacking eight 2.5-ps micro chirped pulses. The chirped pulse duration of THG (263 nm) depends on the group delay dispersion (GDD) introduced by AO-modulator (DAZZLER: FASTLITE) after the stretcher (790 nm). To obtain a homogeneous square pulse by stacking chirped pulses in pulse stacker, the micro pulse duration is stretched 1.2~1.3 times longer than the optical delay between neighboring micro pulses at the cathode by the total amount of GDD during transport through transparent optical elements. Here 16-ps square pulse generated with three birefringent crystals in pulse stacking rods measured by streak camera (Fesca-200, Hamamatsu Photonics K.K.) is shown.

Table 1: Set Parameters and Usages for Fitting Function to Evaluate Spatial Profile Optimization [6]

| Fitting function parameters for flattop shaping | |
|---|---|
| Beam Centre | Minimize differences from initial centre position (x, y) |
| THF [4] | Maximize Top Hat Factor (0~ 1) (Flattop: THF=1.0; Gaussian: THF=0.5) |
| Effective Area | Maximize integrated energy within set circle area |
| Effective Diameter | Minimize differences from diameter of set circle |
| Flatness | Minimize standard deviation divided by the average in a flattop area |
| Peak-to-peak | Minimize differences between max. and min. in a flattop area |
| Beam Diameter | Minimize differences from set diameter |
| Hot Spot (max.) | Minimize max. in a flattop area |
| Dark Spot (min.) | Maximize min. in a flattop area |

## SQUARE TEMPORAL SHAPING (CHIRPED UV PULSE STACKING)

### *Chirped Pulse Stacking Rods with Fixed Optical Delays*

In order to avoid interference caused by stacking, the orthogonally polarized chirped pulses are alternatively stacked with the optical delay for a period of time as long as the micro pulse duration in generating a homogeneous electron bunch at the cathode. This method with introducing additional chirp to avoid interference as shown in Fig. 2 is referred to as "chirped pulse stacking". In 2007, in order to fix the optical delays between neighbouring micro chirped pulses in the previously developed mechanical pulse stacker [8], we installed a new UV pulse stacking system consisting of three birefringent α-BBO crystal rods. The angle of rotation of each crystal rod against the incident polarization $E_{in}$ is 45 degrees, as shown in Fig. 3.

A birefringent crystal works similar to a conventional retardation plate. This type of crystal introduces a certain temporal delay between two orthogonally polarized components of a linearly polarized incident beam. In polarized order to realize this temporal delay, the linearly incident beam $E_{in}$ should meet the crystal surface with normal incidence. $E_{in}$ is divided into two components being orthogonally polarized to each other (see Fig. 4). The first component E1 is polarized parallel to the x-axis, the second component E2 is polarized parallel to the y-axis. While propagating through the crystal, components E1 and E2 propagate extraordinary refractive index $n_e$ and ordinary refractive index $n_o$, respectively. Due to the difference of the refraction indexes there will be a temporal delay Δt between E1 and E2 depending on the thickness d of the crystal and on the difference between the refraction indexes $\Delta n = n_e - n_o$. This temporal delay is given by the formula $\Delta t = d\, \Delta n / c$, where c is the speed of light. A very important constraint in our application is that there is no beam displacement between the two components E1 and E2, i.e. the two components should propagate collinearly inside and outside of the crystal without any spatial separation. They should propagate along the same path. This means that the crystal's optical axis must be located in the xy-plane.

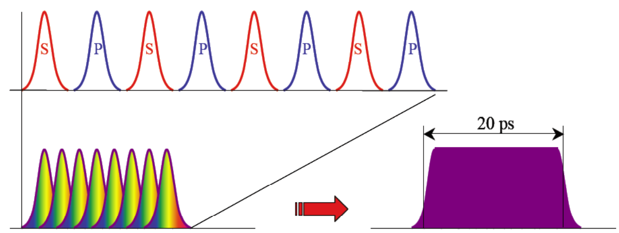


Figure 2: Principle of chirped pulse stacking (8 pulses: three birefringent crystal rods): For the purpose of avoiding interference, the orthogonally polarized chirped pulses are alternatively stacked with the optical delays in each birefringent crystal for a period of time as long as the micro pulse duration in generating a homogeneous electron bunch at the cathode.

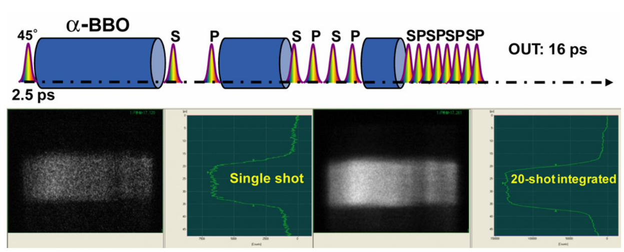


Figure 3: UV laser pulse stacking rods: The angle of rotation of each crystal against the incident polarization is 45 degrees. The drawings are shown in the case of three birefringent α-BBO crystal rods. This pulse stacking kit is commercially available (http://www.luminex.co.jp/) under a license from SPring8 /JASRI.

To generate a long square pulse without any timing gap or overlap, optical delays in each birefringent crystal, which are ~20% shorter than the micro pulse duration, are applied to generate a homogeneous electron bunch at the cathode. To obtain longer square laser pulses of 16 ps with three birefringent crystals, each crystal should generate temporal delays of Δt = 2.0 ps, 4.0 ps, and 8.0 ps, respectively. In order to realize these values, the difference Δn of refraction indexes and the thickness d of the crystal must be adapted to each other. Even if a 4-, 8-

or 16-ps squarely combined pulse is generated by rotating crystal axis parallel to the incident polarization at each corresponding crystal.

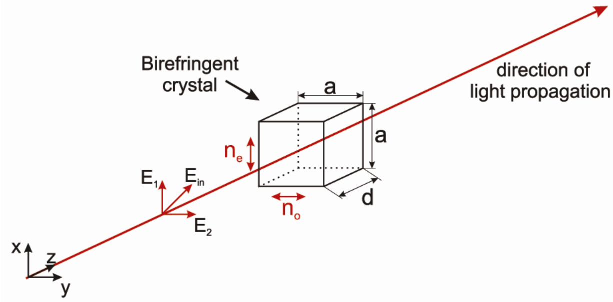


Figure 4: Optical delay in a birefringent crystal.

### *Homogeneous Connection at the Cathode*

In order to generate a long pulse without any timing gap or overlap, optical delays in each birefringent crystal which are as long as the micro pulse duration are applied in generating a homogeneous electron bunch at the cathode. The stretching factor due to the total amount of GDD during the transport through transparent optics should be taken into account. We checked the homogeneity of the electron bunch by measuring the electron energy spectra. The energy of the electron beam is measured on the basis of the beam positions on a florescence profile monitor after they pass through a bending magnet downstream of the RF gun cavity. Introducing a second dispersion with DAZZLER, the micro chirped pulse duration is optimized in order to make the electron beam profile at the dispersion section homogeneous (lower right in Fig. 5).

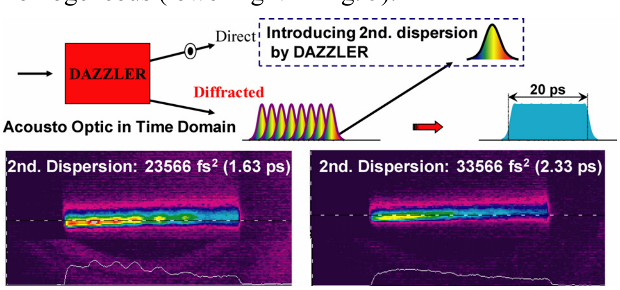


Figure 5: Generating homogeneous electron bunch: we optimized GDDs to roughly stretch the micro pulses with DAZZLER (HR-800, FASTLITE) and then additionally micro pulse shape for fine tuning with the depth and position of the dip in the spectra and the higher order dispersions up to the 4th.

## FUTURE Z-POLARIZATION SCHOTTKY EMISSION GUN WITH HOLLOW LASER INCIDENCE

We propose a laser-induced Schottky-effect-gated photocathode gun using the Z-polarization of the laser source [10, 11]. The existence of radial polarized laser propagation modes has been theoretically predicted, and such modes were recently demonstrated. Focusing a radial polarized beam on the photocathode, the Z-polarization of the laser is generated at the focal point. The generated Z-polarization field can easily exceed an electrical field of 1 GV/m with the fundamental wavelength from compact femtosecond Ti:Sa laser systems. According to our calculations (NA=0.15, 60% hollow ratio, inside-out Gaussian beam), a Z-field of 1 GV/m needs 1.3 MW of peak power for the fundamental wavelength (790 nm) and 0.32 MW for the second harmonic generation (SHG). In a 1 GV/m field, the work function of the copper cathode decreases by ~2 eV [10,11]. This Schottky effect can be used as a gate of the photo-emission process, as shown in Fig. 6.

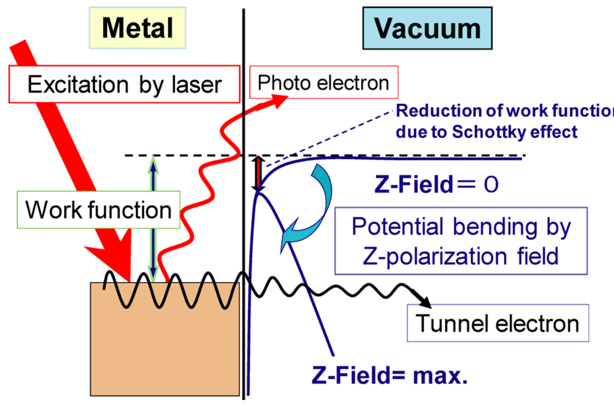


Figure 6: The principle of laser-induced Schottky-effect-gated photocathode gun: The important question was whether a femtosecond temporal response of the cathode is possible. Due to this temporal response issue, we started the feasibility tests with several metal cathode candidates.

We performed the investigation with a plane-field emitter assisted by laser radiation field and obtained indirect evidence of such laser field effects through comparison between normal and oblique incidences to the cathode. It is well known that the oblique incidence produces higher QE than normal incidence. This fact cannot be explained only with Brewster's angle. However, multi-photon absorption should be taken into account in the case of intensive laser focusing on the cathode. The Z-field component exists in the case of P-polarization incidence, but not in S-polarization, as shown in Fig. 7. This indicates that the laser field can assist the Schottky effect on the cathode.

Up to now, we have only discussed focusing radial polarization for maximizing the Z-field on the photocathode. On the other hand, the Z-polarization becomes zero if an azimuth polarized beam is focused. We conducted a feasibility study of this laser-induced Schottky effect on the photocathode with a comparison between radial and azimuth polarization shown in Fig. 8. In this experiment, the linear polarization of the incidence laser switches only from vertical to horizontal direction. In this method, we can check the Z-field effect separately from the multi-photon process. Comparing the photo-emission process with these polarizations, we demonstrate the feasibility of this new conceptual photocathode.

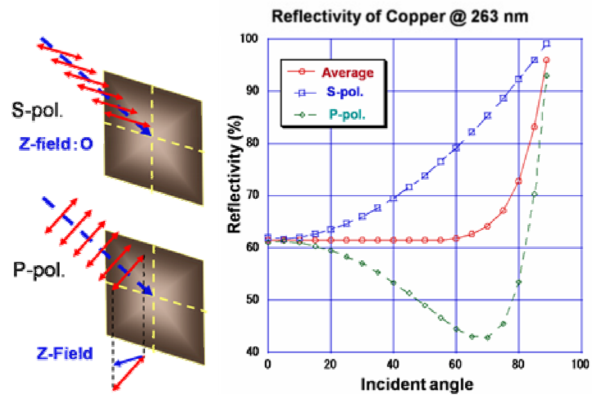


Figure 7: Incident angle dependency of reflectivity (Cu)

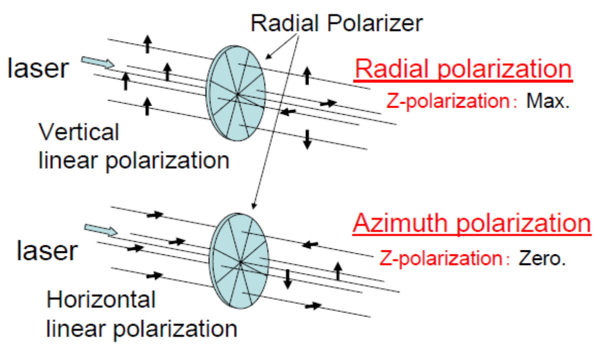


Figure 8: Concept of feasibility test for Schottky effect due to Z-polarization at focus point with the comparison of Z-fields between radial and azimuth polarization

## SUMMARY

At present, if the oscillator is stable without mode-locking failure, the overall laser system can remain stable during yearlong operation with the energy stability described in this paper. We reviewed a short pulse (5~20 ps) laser beam subjected to 3D cylindrical "beer-can" shaping (both temporal (1D) and spatial (2D)) as an ideal UV light source for the generation of yearlong stable low-emittance electron beams with a high charge. In its current form, it comprises a deformable mirror that automatically shapes the spatial UV laser profile with a feedback routine, which is based on a genetic algorithm, and a pulse stacker for temporal shaping at the same time. The 3D shape of the laser pulse is spatially top-hat (flattop) and temporally a square stacked pulse.

Using this "beer-can" 3D-shaped laser pulse, so far we have obtained a minimum horizontal normalized emittance of 1.4 $\pi$ mm mrad. This high-brightness electron source has maintained its emittance at levels which are almost sufficiently low for meeting the X-ray FEL requirements during a yearlong continuous operation. However, the vertical emittance was around 1.5 times greater than the horizontal emittance. It was found that the last mirror in the vacuum chamber which generates the normal incidence presents an obstacle (wake field and charged-up by dark current) for the electron beam. In order to solve this problem, we developed two methods for generating laser incidence. One method involves the generation of a new hollow laser incidence with a final focusing to suppress the asymmetrical wake field effect, and the other method involves a quasi-normal incidence with an angle of 4 degrees without the reflecting mirror in vacuum (the mirror is located outside the vacuum chamber).

Our next laser shaping goal is the generation of a uniform 3D ellipsoidal distribution. In 2006, we proposed a laser-induced Schottky-effect-gated photocathode gun for realizing water bag beams in Luiten's scheme by using the Z-polarization of the laser on the cathode [7]. We apply the hollow laser incidence with a convex lens focusing after passing the laser through a radial polarizer. According to our calculations (NA=0.15), a Z-field of 1 GV/m needs 1.26 MW at peak power for the fundamental wavelength (790 nm) and 0.316 MW for the SHG (395 nm) [10]. This concept of laser-induced Schottky emission can be applied to photocathode RF and DC guns. In the first feasibility test run, we prepared a radial polarizer (8-way segmented half-waveplate) for SHG (395 nm) or THG (263 nm) to generate the radial and azimuthal polarizations. The metal cathode candidates are platinum, gold, silver, and copper. Comparing the photo-emission process with these polarizations, we demonstrate the feasibility of this new conceptual photocathode.

## REFERENCES

[1] T. Taniuchi et al., Proc. of FEL'96, 1996, p. 137.
[2] "TESLA Technical Design Report, PART V, The X-Ray Free Electron Laser", ed. G. Materlik and Th. Tschentscher, March 2001.
[3] "Linac Coherent Light Source (LCLS) Conceptual Design Report", SLAC-R-593, April 2002.
[4] J. Rivers, "SCSS X-FEL Conceptual Design Report", RIKEN, May 2005.
[5] H. Tomizawa et al., Proc. of EPAC02, 2002, p. 1819.
[6] H. Tomizawa et al., Proc. of FEL05, 2005, p. 138.
[7] H. Tomizawa et al., Proc. of FEL07, 2007, p. 298.
[8] C. Limborg-Deprey et al., NIMA 557, 2006, p. 106.
[9] O. J. Luiten et al., Phys. Rev. Lett. 93, 2004, p. 094802.
[10] H. Tomizawa and M. Kobayashi, Japan Patent Application No. 2007-197232.
[11] H. Tomizawa et al., Proc. of FEL07, 2007, p. 382.

# BILLION PARTICLE LINAC SIMULATIONS FOR FUTURE LIGHT SOURCES*

J. Qiang#, R. D. Ryne, M. Venturini, A. A. Zholents, LBNL, Berkeley, CA 94720, U.S.A.

*Abstract*

In this paper we report on multi-physics, multi-billion macroparticle simulation of beam transport in a free electron laser (FEL) linac for future light source applications. The simulation includes a self-consistent calculation of 3D space-charge effects, short-range geometry wakefields, longitudinal coherent synchrotron radiation (CSR) wakefields, and detailed modeling of RF acceleration and focusing. We discuss the need for and the challenges associated with such large-scale simulation. Applications to the study of the microbunching instability in an FEL linac are also presented.

## INTRODUCTION

The electron beam quality at the entrance to FEL undulators plays a crucial role for the success of next generation X-ray light sources. In order to achieve good performance of X-ray output with reasonable cost, the emittance of the electron beam and the energy spread of the electron beam need to be controlled within the tolerance level subject to a high peak current. However, collective effects such as the microbunching instability driven by space-charge, wakefields, and CSR can pose a particular challenge that leads to irreversible degradation in beam quality. In order to accurately predict the beam properties at the end of linac subject to those collective effects and to optimize the linac design, large-scale self-consistent simulation is needed. As will be shown, the use of on the order of a billion macroparticles or close to real number of electrons per bunch in self-consistent particle tracking helps to correctly simulate the shot noise inside the electron beam that can be amplified by the microbunching instability.

## COMPUTATIONAL AND PHYSICAL MODELS

In this study, we have used the IMPACT code [1], a parallel beam dynamics macroparticle tracking code, as our major simulation tool. The IMPACT code is an object-based parallel particle-in-cell code to simulate high intensity, high brightness beam transport in a beam delivery system. It uses a split-operator method to separate the particle advance subject to the given external fields from the particle advance subject to the collective self-consistent space-charge or wakefield forces. The space-charge forces are calculated from the solution of the 3D Poisson equation in the beam frame using a convolution of the charge density with the Green function for open boundary conditions (in most applications). This convolution is calculated numerically on a 3D grid using an integrated Green function method [2] with FFT calculation of a cyclic summation in a doubled computational domain [3]. The space-charge fields are Lorentz transformed back to the laboratory frame to advance particle momentum. The wakefield forces are calculated in the laboratory frame using a convolution of the wake function and the particle density. This convolution is also computed using the FFT based method. The CSR effects inside a chicane are calculated using a one-dimensional longitudinal CSR wake model [4]. As a test of our space-charge model, we computed the energy modulation amplitude of an initial 120 MeV round uniform electron beam with 120 A current, 5% modulation, and zero initial temperature propagating through a drift space. Figure 1 shows the amplitude of energy modulation as a function of distance in comparison with an often used analytical model of longitudinal space-charge impedance [5]. This analytical model presupposes that the longitudinal component of the electric field across the beam is uniform and equal to the value on the beam axis. This is a good approximation if the wavelength of the perturbation as measured in the beam commoving frame is large compared to the beam transverse radius (or $k^*r_b/\gamma \ll 1$, where $k=2\pi/\lambda$ is the perturbation wavenumber in the lab frame.) However, as shown in the picture at smaller wavelengths the analytical model tends to overestimate the energy modulation when this is averaged over the beam tranasverse density. See also [6].

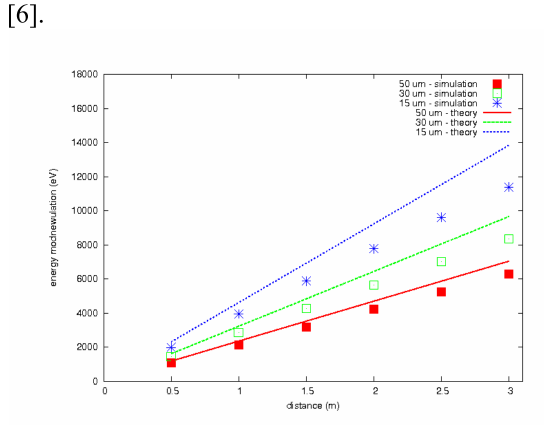


Figure 1: Energy modulation amplitude as a function of distance with initial 5% current modulation at 15 um, 30 um and 50 um wavelength.

The code is implemented on parallel computers using both a domain-decomposition method and a particle-field decomposition method. In the domain-decomposition method, the spatial physical domain is decomposed

*Work supported by the U.S. Department of Energy under Contract No. DE-AC02-05CH11231.
#jqiang@lbl.gov

among processors. The particles located inside a physical domain are assigned to the processor containing that physical domain. The particle movement is controlled through a particle manager using neighboring communication. Dynamic load balance is used periodically to adjust the size of each domain. In the particle-field decomposition method, all particles and computational domain grids are uniformly distributed among all processors. Global communication is used to collect the particle charge density distribution on each physical domain. The Poisson equation is solved in parallel in both approaches. The particle-field decomposition method has the advantage of good load balance without resorting to any dynamic load balance. Its disadvantage is to use global communication to collect the charge density distribution.

The linac simulation starts with an initial distribution generated by the photoinjector. In most cases, this initial macroparticle distribution is generated by some other photoinjector simulation code such as ASTRA or IMPACT-T. The number of macroparticles in this initial distribution can be as small as a few hundred thousand or a few million. In order to suppress the sampling noise in that initial distribution, up-sampling is used with many more macroparticles, e.g. one billion macroparticles. In this study, a six-dimensional box centered at the original particle phase space location is used to up-sample the initial distribution. A uniform distribution is assumed in four-dimensional transverse phase space with box size set by external users. Within the box, a linear current density distribution is assumed using the current profile from the original particle distribution. The energy-position correlation is obtained from the original distribution using a cubic spline. Each new particle inside the box assumes the same uncorrelated energy spread as the original particle plus a Gaussian or uniformly sampled uncorrelated energy spread and a correlated energy from the new longitudinal position. The box size is chosen to produce sufficient smoothness of the resulting particle distribution while maintaining similar global properties (rms emittance, current profile, etc) of the original distribution. Figure 2 shows the initial peak current profile of a Gaussian distribution from direct one billion macroparticle sampling and from one billion macroparticle up-sampling of a two million Gaussian particle distribution. It is seen that the direct sampling and the up-sampling described above have a good agreement between each other. Figure 3 shows the final longitudinal phase space from the direct sampling and the up-sampling. Again, the up-sampling method used here gives a good reproduction of the direct sampling results.

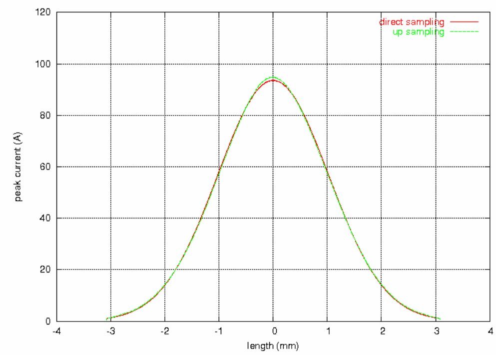


Figure 2: Initial current profile from direct sampling and up sampling.

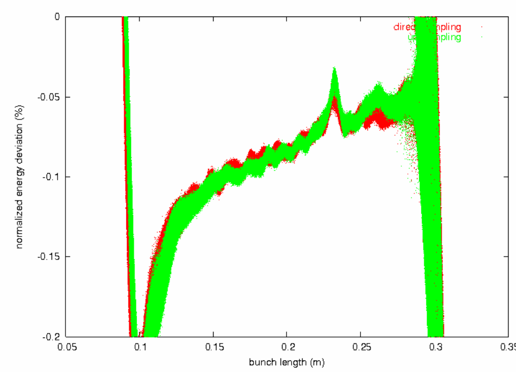


Figure 3: Final longitudinal phase space from direct sampling and up sampling.

## NUMERICAL PARAMETER SETTINGS

The choice of numerical parameters in the self-consistent macroparticle simulation can significantly affect the final results due to the fact that the microbunching instability is highly sensitive to initial noise level. Figure 4 shows the final energy spread at the end of the linac as a function of number of macroparticles used in the simulation.

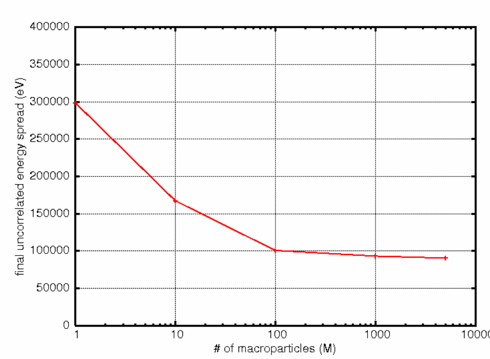


Figure 4: Final electron beam energy spread as a function of number of macroparticles.

It is seen that the final energy spread starts to saturate beyond 100 million macroparticles. Using a smaller number of macroparticles will lead to an unphysically larger energy spread. As the number of macroparticles approaches to the real number of electrons in the beam, the finite number of numerical grid points being used may present some unphysical smoothness of the electron beam. Figure 5 shows the power spectrum of the initial current profile from using 1024, 2048, 4096, and 8192 grid points. It is seen that the increasing number of grid points will mostly increase the initial current noise level at high frequency.

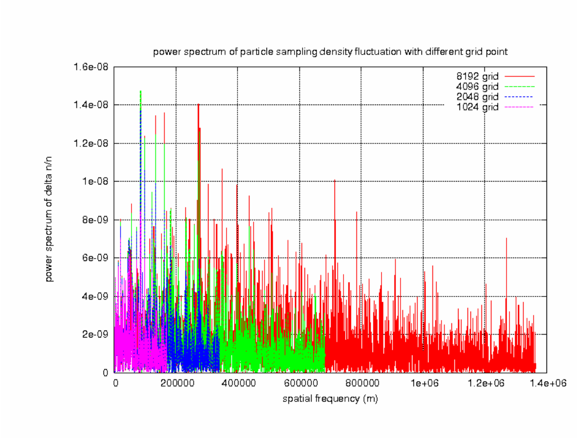


Figure 5: Power spectra of the initial current profile using different number of grid points.

Near the low frequency level, there is not much difference in the noise level for grid points beyond 2048. This suggests that keeping on increasing the number of grid points will not lead to an increase of noise level near low frequency. From the linear theory calculation, the gain of the microbunching instability decreases quickly at high frequency and has a peak near the low frequency in our linac study (around 300 um) [6]. This suggests that keeping on increasing the number of grid points will not change the final energy spread driven by the microbunching instability that is peaked near the low frequency level. Figure 6 shows the final energy spread with 2048 and 4096 grid points. It is seen that both cases give nearly the same final energy spread.

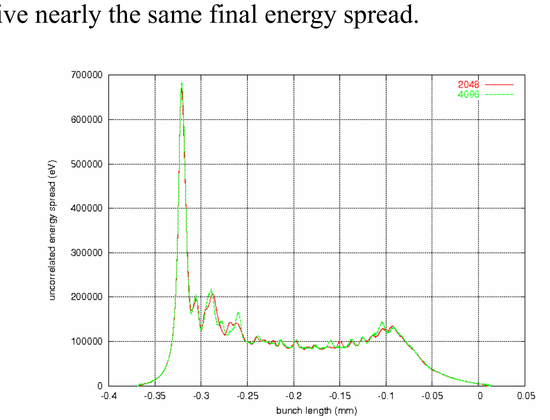


Figure 6: Final energy spread from simulations using 2048 and 4096 grid points.

## APPLICATIONS

Using one billion macroparticles, we carried out self-consistent particle tracking of the electron transport subject to the microbunching instability in a linac planned for a soft X-ray free electron laser at Berkeley [7]. Given the same rms bunch length and similar peak current, the detailed shape of the initial current profile can have significant effects on final beam quality. Figure 7 shows the final energy spread for four different initial current distributions. Here, Litrack 1 and Litrack 2 are two initial distributions obtained from the back track of an ideal current profile at the end of the linac using the Litrack code.

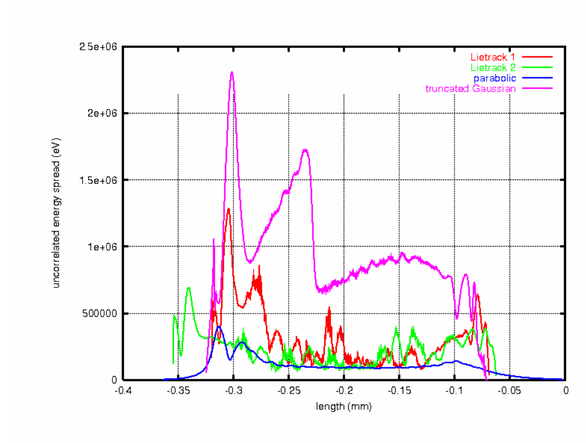


Figure 7: Final energy spread from using different initial current distributions.

It appears that the parabolic distribution with the same rms bunch length produces the best beam quality at the end of the linac. Using five billion macroparticles that is close to the real number of electrons in 0.8 nC charge, we simulated the electron beam transport through the linac for an array of soft X-ray FELs. The initial peak current is about 70 A with a parabolic density distribution and 5 keV uncorrelated rms energy spread. Figure 8 shows the longitudinal phase space distribution at the end of linac. The final rms energy spread is on the order of 0.01%. Figure 9 shows the horizontal and vertical slice emittance at the end of the linac. No slice emittance growth is seen from the simulation. Figure 10 shows the final current profile at 2.4 GeV energy. This current profile is reasonably flat enough for generating coherent soft X-ray radiation.

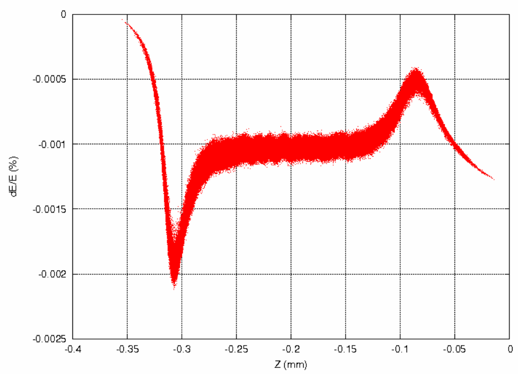

Figure 8: Longitudinal phase space distribution at the end of the linac from a five billion macroparticle simulation.

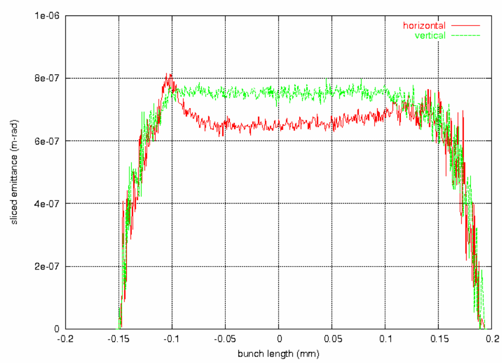

Figure 9: Transverse slice emittance at the end of the linac.

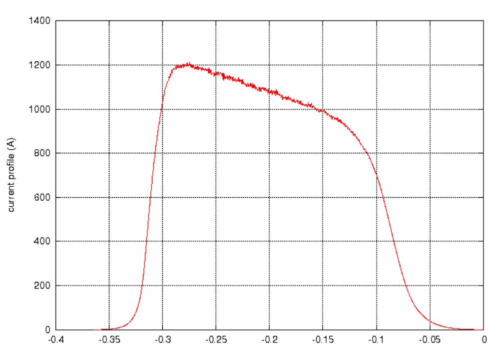

Figure 10: Current profile at the end of the linac.

The initial uncorrelated energy spread in an electron beam can smear the coherent growth of the microbunching instability. A larger initial energy spread leads to less growth of the microbunching instability. Figure 11 shows the final uncorrelated rms energy spread as a function of initial energy spread. It is seen that beyond 5 keV initial energy spread, the final energy shows a linear dependence of the initial energy spread due to the bunch compression. The microbunching instability has been sufficiently suppressed by the incoherent motion of electrons with different initial energy spread.

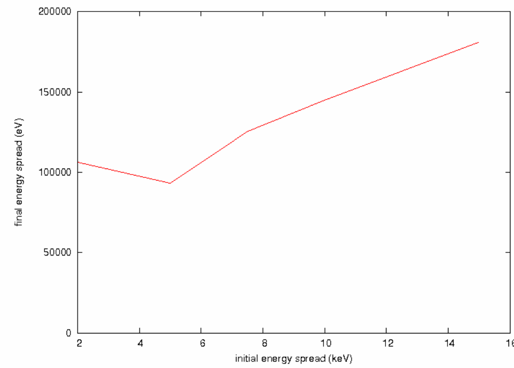

Figure 11: Final energy spread as a function of initial energy spread.

In conclusion, we have shown that a large number of macroparticles is needed for self-consistent particle tracking of high brightness electron beams subject to the microbunching instability in order to accurately predict the electron beam properties at the end of the linac. Applications of large-scale simulation with billions of macroparticles to the planned Berkeley FEL linac show that a reasonably good beam quality can be achieved to satisfy performance requirements for the soft x-ray FEL array.

## REFERENCES

[1] J. Qiang, *et. al.*, J. Comp. Phys. **163**, 434 (2000).
[2] J. Qiang, *et. al.*, PRST-AB, **9**, 044204 (2006).
[3] R. W. Hockney and J. W. Eastwood, *Computer Simulation Using Particles* (Hilger, New York, 1988).
[4] I. Pogorelov, *et. al.*, Proc. ICAP 2006, Chamonix, France, 182 (2006).
[5] Z. Huang, *et. al.*, PRST-AB, **7**, 074401 (2004).
[6] M. Venturini, LBNL Report LBNL-63111, Berkeley (2007), unpublished.
[7] A. Zholents, *et. al.*, these proceedings.

# THE IFMIF 5 MW LINACS

A. Mosnier, CEA, IRFU, F-91191 Gif-sur-Yvette, France.

*Abstract*

The International Fusion Materials Irradiation Facility (IFMIF) is based on two high power cw accelerator drivers, each delivering a 125 mA deuteron beam at 40 MeV to the common lithium target. The present design of the 5 MW IFMIF Linacs, as well as the description of the prototype accelerator to be built in Japan are presented: the injector including the 140 mA ion source and the magnetic focusing LEBT, the RFQ for the bunching and acceleration to 5 MeV, the MEBT for the proper injection into the Drift-Tube-Linac where the beam is accelerated to the final energy of 40 MeV. Recently, the Alvarez type DTL was replaced by a superconducting Half-Wave Resonator Linac to benefit from the advantages of the SRF technology, in particular the rf power reduction, plug power saving, ability to accelerate high intensity cw beams with high flexibility and reliability. Last, a HEBT section transports and tailors the beam as a flat rectangular profile on the flowing Lithium target. The design and technology choices will be validated during the EVEDA phase, which includes the construction of one full-intensity deuteron linac, but at a lower energy (9 MeV) at Rokkasho Mura in Japan.

## INTRODUCTION

The International Fusion Materials Irradiation Facility (IFMIF) is an accelerator driven neutron source for the investigation of the fusion plasma facing materials [1]. The accelerator consists of two high power linacs, each delivering 125 mA deuteron beams at the energy of 40 MeV to the common lithium target. The Engineering Validation and Engineering Design Activities (EVEDA), launched in the framework of a bilateral agreement between Euratom and the Government of Japan in the middle of 2007 aims at producing the detailed design file enabling the further construction of IFMIF, as well as the construction and test at full current of the low energy part of one accelerator at Rokkasho in Japan. The components of the prototype accelerator are provided by European institutions (CEA, INFN, CIEMAT): the injector, the RFQ, the transport line to the 1.2 MW beam dump, the 175 MHz RF systems, the matching section and the DTL, the local control systems and the beam instrumentation, required for tuning, commissioning and operation of the accelerator. The building constructed at Rokkasho Broader Approach site, the supervision of the accelerator control system, as well as the RFQ couplers, are provided by JAEA. From the IFMIF Conceptual Design Report [2], technical updates have been brought in order to optimise the design of the entire linac. In addition to the RFQ, which looks now shorter, the major change is the switch from the room temperature DTL to superconducting technology for the high energy portion of the linac and a linked complete redesign of the RF system.

## INJECTOR

The injector has to deliver a 140 mA, low emittance deuteron beam with high reliability. An ECR type (Electron Cyclotron Resonance) ion source has been selected owing to its intrinsic high efficiency, high availability and limitless lifetime. Starting from the SILHI source, developed at CEA-Saclay, with a frequency of 2.45 GHz at 875 Gauss, the extracted energy has been increased from 95 keV to 100 keV, then the extracted intensity from 150 mA to 175 mA in order to meet the 140 mA $D^+$ requirement (26 mA $D_2^+$, 9 mA $D_3^+$). Simulations have been carried out to optimize the electrode number, electrode shape, aperture diameter and to minimize the electric field (Figure 1). A four electrode extraction system was finally chosen since it allows an easy tuning with minimum beam losses and back-streamed electrons. In order to decrease the risk of sparking, the maximum electric field has been kept around 100 kV/cm.

The Low Energy Beam Transport (LEBT) is a dual solenoid transport system with space charge compensation. The total length was minimized to about 2 m to restrain the emittance growth, but even so it allows to include classical diagnostics (movable Faraday cup and insulated screens associated with cameras, current transformers, emittance measurement unit) as well as non destructive optical diagnostic based on residual gas fluorescence to measure steadily the species fraction by Doppler shift analysis. Numerical simulations [3], using a back-and-forth process between the TRACEWIN code and a specially developed code, capable of calculating the space charge compensation, showed that the emittance at the RFQ entrance could come close to the challenging requirement (0.25 $\pi$.mm.mrad for the total current of 175 mA) provided that a Krypton gas is injected in addition to deuterium in order to better compensate the space charge effect ($P_{D2}$ = $1.10^{-5}$ hPa, $P_{Kr}$ = $4.10^{-5}$ hPa). The loss rate of the incoming $D^+$ beam by neutralization on the gas is about 2.4% under these pressure conditions.

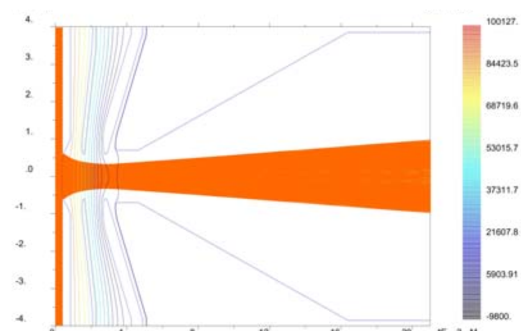

Figure 1: Plot of trajectory simulation for the 4 electrode extraction system (175 mA, 100 kV).

## RADIOFREQUENCY QUADRUPOLE

The RFQ is a four vane structure – due to the high beam current and CW operation – and is developed by INFN. It has to bunch the dc beam from the injector and to accelerate the beam from 100 keV to 5 MeV. The optimisation of the 175 MHz RFQ [4] resulted in reduced length (9.8 m) and power consumption, with beam losses along the RFQ under control. The criteria chosen for the shaper, gentle buncher and accelerator sections are:

- Analytic law for the voltage with a smooth increase in the accelerator section
- Larger acceptance in the accelerator section to reduce losses at high energy
- Physical aperture "a" minimal at gentle buncher end playing the role of beam collimation to prevent for beam loss downstream
- High focusing factor $B = qV\lambda^2 / mc^2 r_0^2$ to keep the beam in the linear part of the focusing fields.
- Peak surface electric field limited to the reasonable value of 1.8 x Kilpatrick's criterion.

The resulting parameters, modulation, vane voltage, average aperture and physical aperture along the RFQ are plotted in Figure 2.

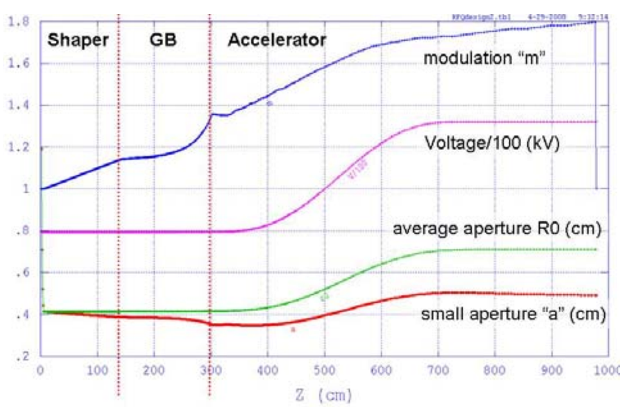


Figure 2: Main parameters along the RFQ.

As activation of the RFQ cavity is of main concern for maintenance, extensive multi-particle simulations [4] have been performed to evaluate the loss of particles along the RFQ. Assuming an input beam of 0.25 π.mm.mrad rms emittance with waterbag distribution, the output rms transverse and longitudinal emittances are 0.29 π.mm.mrad and 0.27 deg.MeV, respectively. The transmission is about 98.5% and the losses above 1 MeV are kept at a very low level (Figure 3). Any deviation from these ideal conditions will increase the losses in the RFQ and spoil the emittance. If one consider for example an input beam, of Gaussian distribution and 20% larger in emittance, the transmission drops to 92%, still acceptable.

An overall view of the RFQ with the location of the RF couplers and vacuum ports is shown in Figure 4. Although it offers a lower stiffness under vacuum, a square transversal section instead of circular shape was chosen because it presents some advantages, as a lower total amount of required RF power, large free surfaces for the positioning of all vacuum lines and tuning plungers, reduced request of raw material to obtain the final shape of the components.

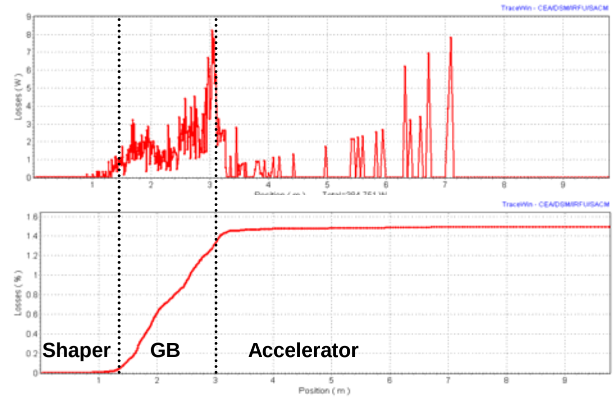


Figure 3: Beam losses along the RFQ with a waterbag input beam (130 mA @ 0.25 π mm.mrad).

The structure is made of 9 modules of 1.1 m each. The brazing technique has been chosen for the assembling of the different modules.

The total RF power required is about 1.6 MW and will be delivered by eight 200 kW RF power sources. Field stability should be provided by segmentation and finger dipole correctors. However, since simulations do not show a large gain from segmentation, mesurements will be made on a full scale cold model.

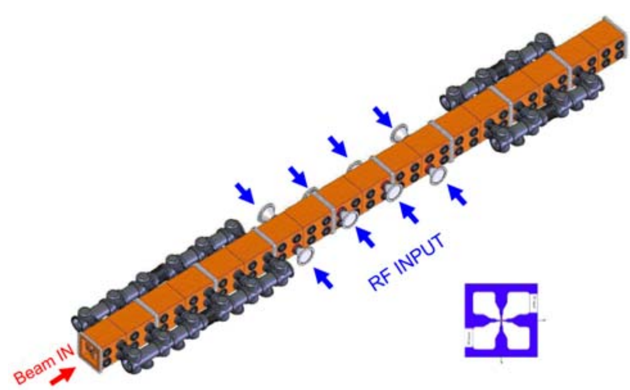


Figure 4: Overall view of the RFQ.

## DRIFT TUBE LINAC

A Drift Tube Linac (DTL) has to accelerate the beam from 5 MeV to the final energy 40 MeV. While intensive activities on conventional Alvarez DTL have been carried out all around the world in the past decade, all these developments were done for lower beam intensity and pulsed operation, and therefore for much lower average dissipated power. Two options based on superconducting technology have been under investigation [5] since they offer many technological and financial advantages, as:

- RF power reduction, leading to 6 MW saving;
- higher flexibility and reliability;
- mature technology and better suited to existing teams and industries;
- less sensitive to all machining and assembly errors.

The proposal, based on Half Wave Resonators (HWR) and close to existing and widely used technology, was finally selected for the EVEDA phase. The baseline design is the result of a conservative approach for both resonators and focusing lattice. Moderate gradient at 4.5 MV/m and large aperture in the 40-50 mm range were chosen. As a result, the peak surface fields (Epk < 30 MV/m, Bpk < 50 mT) are much lower than the ones that can be achieved today by using well-tried methods developed in the last ten years, such as high-pressure rinsing, high-purity niobium and clean conditions. The phase advance per lattice period is always lower than 90° in order to avoid any structure instability. Four cryomodules for an overall length of 22 m housing a total of 42 resonators are used to cover the acceleration from 5 MeV to the final energy 40 MeV (Figure 8). Table 1 lists the main parameters of the HWR Linac and Figure 5 shows an overview of a possible cryomodule design.

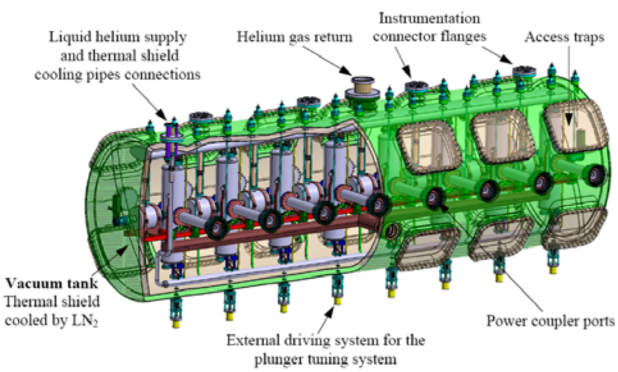


Figure 5: Overview of a possible cryomodule design.

Table 1: Main Parameters of the HWR Linac

| Cryomodule | 1 | 2 | 3 & 4 |
|---|---|---|---|
| Cavity β | 0.094 | 0.094 | 0.166 |
| Cavity length (mm) | 180 | 180 | 280 |
| Beam aperture (mm) | 40 | 40 | 48 |
| Nb cavities / period | 1 | 2 | 3 |
| Nb cavities / cryostat | 1 x 8 | 2 x 5 | 3 x 4 |
| Nb solenoids | 8 | 5 | 4 |
| Cryostat length (mm) | 4.64 | 4.30 | 6.03 |
| Output energy (MeV) | 9 | 14.5 | 26 – 40 |

Particle tracking simulations [6] have shown that the HWR scheme can sustain very conservative alignment and field errors, up to 1 mm misalignment and 10 mrad solenoid tilt while keeping a large safety margin between the beam occupancy and the pipe aperture (Figure 6).

The beam orbit correction relies on beam position monitors and steering coils located at the solenoid package. The beam phase space distribution at the exit of the linac is shown in Figure 7. After the linac, the beam has to be transported to the target through a long HEBT line, with very stringent beam footprint and homogeneity requirements on the liquid Li target. It was checked that, by injecting the beam output from the s.c. HWR linac into the present IFMIF HEBT, the beam footprint and homogeneity were similar to the results obtained with the room temperature DTL.

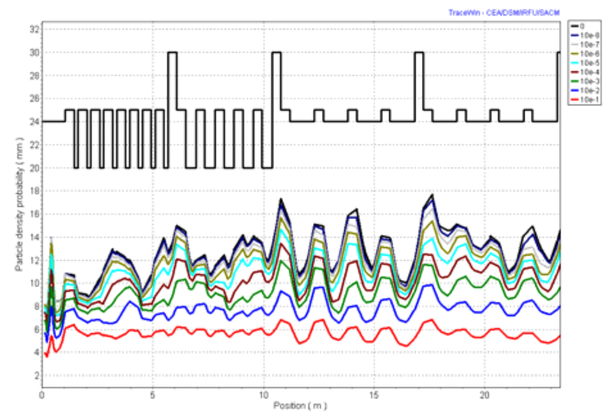


Figure 6: Plot of contour lines encircling 90% to 100% of Particles, with errors and beam orbit correction.

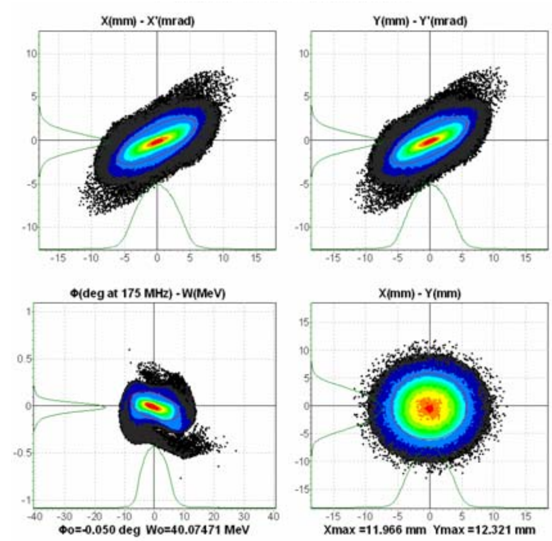


Figure 7: Beam space phase distribution at linac exit.

Further beam dynamics simulations are required to include a matching section between the RFQ and the cryomodule with realistic dimensions and to optimise the focusing scheme, as well as matching between sections.

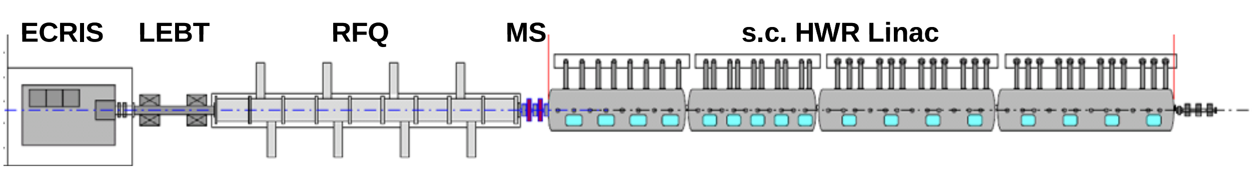


Figure 8: Layout of the superconducting Linac for IFMIF.

## RF POWER SYSTEM

Following the change from normal to superconducting DTL, the RF Power System [7] can be made simpler and more reliable, based on smaller and more conventional power units using tetrodes: 18 units of 105 kW and 24 units of 220 kW (Figure 9).

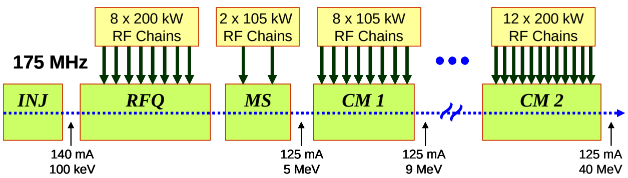


Figure 9: Identical RF power stations for the accelerator.

As a positive side effect, these 220 kW units will also be used for the RFQ, standardizing the whole accelerator. In addition, the same RF chain is used for all power sources, only the high voltage power supply changes: one 400 kW HVPS feeds one 220 kW RF amplifier or two 105 kW RF amplifiers. In order to optimize space, maintenance and availability, a symmetric modular system, composed by removable modules with 2 complete RF chains each, has been proposed (Figure 10).

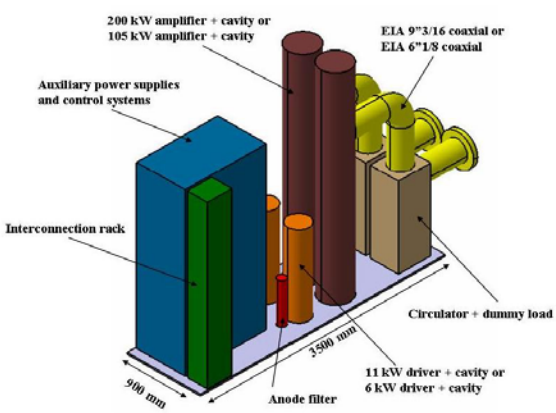


Figure 10: Removable RF power module.

The LLRF system is designed for CW mode operation but also for pulsed mode operation, needed during the commissioning and tuning of the prototype accelerator. The main requirements of the LLRF system are :

- Field error 1% in amplitude, 1deg. in phase
- Field ramp up with a predefined time profile
- Switch off the RF power in case of abnormal operation or upon request from other subsystem.
- RF signals monitoring to control performance and prevent failures.

## HIGH ENERGY BEAM TRANSPORT

The 50 m long HEBT transports the 40 MeV, 125 mA beam to the target. The present design from the CDR [2] includes two twenty degree achromatic bends, FODO lattice, a final focus and a final 9° achromatic bend before reaching the lithium target, in order to avoid neutron back-streaming into the accelerator beam pipe. The required beam spot on target, a rectangle of 20 x 5 $cm^2$, with a uniform distribution is achieved by a nonlinear focusing beam expander scheme (Figure 11). The main issues (uncontrolled beam losses in the non-linear magnets, complex beam tuning procedure requires a robust nonintercepting beam profile monitor for tuning the 2 x 5 MW beams, beam-on-target jitter due to dynamic errors, very sensitivity to the input beam distribution) remain to be studied. An alternative solution could be the raster-scanning technique, widely used in medical applications, but the impact of the high power beam sweeping on the target (risk of shock-wave excitation) and on the condition of material irradiation has to be carefully analysed.

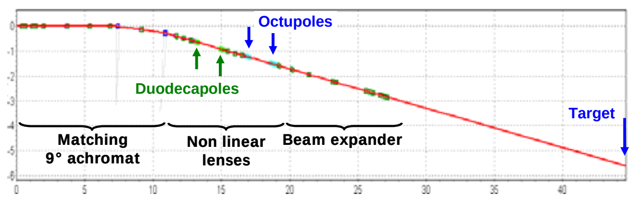


Figure 11: Layout of the HEBT (nonlinear focusing beam expander scheme).

## PROTOTYPE ACCELERATOR

In order to test and to validate the technical options, the prototype accelerator is identical to one IFMIF accelerator running at full beam current (125 mA) but the high energy portion includes only the first cryomodule, resulting in the lower output energy of 9 MeV. It will comprise the ion source and LEBT, the RFQ, the matching section and the DTL, the transport line to a 1.2 MW beam dump, as well as the 175 MHz RF system and the beam instrumentation, required for the tuning, commissioning, operation. The layout of the prototype accelerator integrated in the IFMIF/EVEDA accelerator building of the Rokkasho BA site is shown in Figure 12. The figure shows also the implementation of the high voltage power supplies and RF amplifiers of the RF Power system, the cryogenic plant and the water cooling circuits.

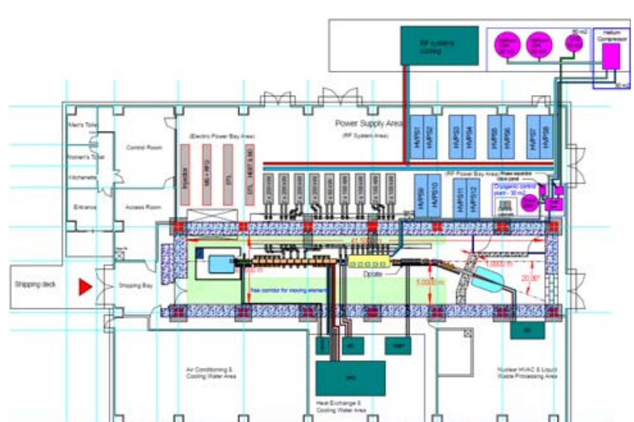

Figure 12: Layout of the prototype accelerator in the IFMIF/EVEDA accelerator building.

### HEBT and Beam Dump

The High Energy Beam Transport [8] of the prototype accelerator has to transfer the beam to the beam dump with the required beam spot (rms size of 40 mm rms divergence of 16 mrad) while enabling the full beam characterization by means of the so-called Diagnostics Plate (Figure 13). A first triplet focuses the beam through the 3 m diagnostics plate; a doublet is able to compensate the variations of the first triplet during the emittance measurement with the quad-scan method; a bending magnet (angle 20°) prevents neutron from streaming back into the accelerator and can be used as spectrometer for the energy spread measurement; the last triplet expands the beam towards the downstream beam dump.

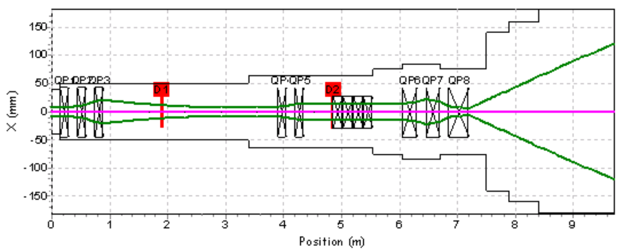


Figure 13: Layout of the HEBT of the P.A.

The EVEDA beam dump has to stop deuteron beams with a maximum power of 1.125 MW. Figure 14 shows the profile of the beam power deposition on the wall facing material, assuming a 2.5 m long Cu cone. This choice was infered from thermal stresses calculations [9].

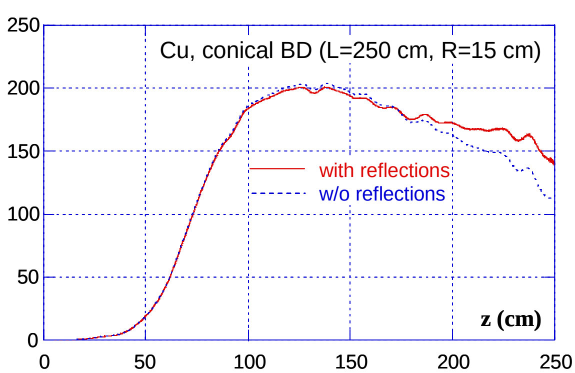


Figure 14: Power density at BD surface (W/cm$^2$).

### Diagnostics

Beam instrumentation is essential to tune the linac and monitor the beam from the ion source to the beam dump, to minimize the beam loss and to characterize the beam properties. Furthermore, a complete set of diagnostics will be implemented at the exit of the HWR Linac on the Diagnostics Plate, for the measurement of the main beam parameters [10]: current, phase, position, transverse profile, energy, transverse halo, transverse emittance and longitudinal profile. Non interceptive transverse profile monitors, based on fluorescence and ionization of the residual gas, are specially developed for the prototype accelerator [11] and will be the first step towards the IFMIF diagnostics, required for the proper characterization of the beam shape near the target.

## CONCLUSION

One year after the start of the project, substantial technical updates have been brought in order to optimise the design of the entire linac. In addition to the RFQ, which looks now shorter and less prone to beam loss, the major change is the switch from the room temperature DTL to superconducting technology for the high energy portion of the linac and a linked complete redesign of the RF system, based on conventional RF amplifiers.

The beam dynamics studies, even if they are far from being completed (next steps: optimisation of the linac focusing, end-to-end simulations with errors, beam tuning strategy, analysis of the IFMIF HEBT line, etc), have shown that the acceleration of the full beam looks feasible with reasonable emittance growth and beam loss.

The components of the prototype accelerator, starting with the injector, the RFQ and the RF power system, enter now into the manufacturing phase. Most of them will be tested in Europe before the shipping, installation, check-out, commissioning and operation at Rokkasho.

## REFERENCES

[1] P. Garin, "IFMIF: Status and Developments", Proc. of EPAC08, Genoa, Italy.
[2] IFMIF Comprehensive Design Report, An activity of the International Energy Agency, January 2004.
[3] N. Chauvin et al, "Beam Dynamics Simulations of the Low Energy Beam Line for IFMIF/EVEDA", these proceedings.
[4] M. Comunian, A. Pisent, E. Fagotti, "The IFMIF-EVEDA RFQ: Beam Dynamics Design", these proceedings.
[5] F. Grespan, A. Palmieri, A. Pisent, "RF Design of the IFMIF-EVEDA RFQ", these proceedings.
[6] N. Chauvin et al, "Alternative Designs and Beam Dynamics Simulations of the Superconducting HWR Cavities Section of the IFMIF Linac", these proceedings.
[7] I. Kirpitchev, "RF power system for the IFMIF-EVEDA prototype accelerator", proc. of EPAC08, Genoa, Italy.
[8] C. Oliver, "High energy Beam transport line for the IFMIF-EVEDA accelerator", Proc. EPAC08, Genoa, Italy.
[9] B. Brañas, "Beam Dump Design for the IFMIF-EVEDA Accelerator", Proc. EPAC08, Genoa, Italy.
[10] I. Podadera et al, "A Diagnostics Plate for the IFMIF-EVEDA Accelerator" , Proc. EPAC08, Genoa, Italy.
[11] J. Marroncle et al, "Beam Transverse Profile Monitor for IFMIF-EVEDA Accelerator" , BIW 2008, Lake Tahoe, May 2008.
[12] P. Nghiem et al, "Parameter Design and Beam Dynamics Simulations for the IFMIF-EVEDA Accelerators", these proceedings.

# LINACS FOR FUTURE MUON FACILITIES*

S.A. Bogacz#, Jefferson Lab, Newport News, VA, USA
R.P. Johnson, Muons, Inc., Batavia IL, USA.

*Abstract*

Future Muon Colliders (MC) and Neutrino Factories (NF) based on muon storage rings will require innovative linacs to: produce the muons, cool them, compress longitudinally and 'shape' them into a beam and finally to rapidly accelerate them to multi-GeV (NF) and TeV (MC) energies. Each of these four linac applications has new requirements and opportunities that follow from the nature of the muon in that it has a short lifetime ($\tau$ = 2.2 μsec) in its own rest frame, it is produced in a tertiary process into a large emittance, and its electron, photon, and neutrino decay products can be more than an annoyance. As an example, for optimum performance, the linac repetition rates should scale inversely with the laboratory lifetime of the muon in its storage ring, something as high as 1 kHz for a 40 GeV Neutrino Factory or as low as 20 Hz for a 5 TeV Muon Collider. A superconducting 8 GeV Linac capable of CW operation is being studied as a versatile option for muon production [1] for colliders, factories, and muon beams for diverse purposes. A linac filled with high pressure hydrogen gas and imbedded in strong magnetic fields has been proposed to rapidly cool muon beams [2]. Recirculating Linear Accelerators (RLA) are possible because muons do not generate significant synchrotron radiation even at extremely high energy and in strong magnetic fields. We will describe the present status of linacs for muon applications; in particular the longitudinal bunch compression in a single pass linac and multipass acceleration in the RLA, especially the optics and technical requirements for RLA designs, using superconducting RF cavities capable of simultaneous acceleration of both $\mu^+$ and $\mu^-$ species, with pulsed linac quadrupoles to allow the maximum number of passes. The design will include the optics for the multi-pass linac and droplet-shaped return arcs.

## MUON PRODUCTION AND COOLING

### *Proton Driver Linac*

The first linac in the accelerator chain for intense muon beams is for the proton driver. Proposals for various types of linacs and synchrotrons for this purpose have been to use charge exchange injection of $H^-$ ions to overcome the Laslett space charge tune spread. The ultimate expression of this idea is to eliminate acceleration in the synchrotron, such that it becomes an accumulation and bunching ring, and provide all of the acceleration in an 8 GeV linac [1]. To provide sufficient muon flux for a collider of acceptable luminosity will require over 4 MW of beam power at some energy greater than 6 GeV [3].

*Work supported in part by DOE STTR grant DE-FG02-08ER86251
#bogacz@jlab.org

### *Multi-Megawatt Target*

Once the intense proton bunches have been formed at 8 GeV they are tightly focused onto a target capable of many MW operation [4] to produce an intense pion beam. The pions are captured in a strong solenoidal field where they decay into muons (and neutrinos). At the end of the 40 m pion decay channel the muon beam has transverse normalized emittances of around 40,000 mm-mr and is spread in time over tens of ns. The transverse dimensions of the beam must be cooled to be small enough and bunches must be formed to fit into reasonable accelerating structures, depending on their intended NF or MC use.

### *Ionization Cooling and Emittance Exchange*

The only method fast enough to cool a muon beam is ionization cooling in which the muons pass through a low Z material to lose energy in all three directions, have only the longitudinal component replenished by RF, and thereby reduce their angular divergence. Doing the same thing after ninety degrees in betatron phase advance allows the transverse dimensions of the beam to be reduced, but to reduce the bunch length by ionization cooling requires the longitudinal emittance to be exchanged with the transverse emittance. This exchange can be accomplished by placing the energy absorbing material in a dispersive region, either as a wedge-shaped absorber or as a continuous homogeneous absorber [5].

### *Linacs for Bunching and Cooling*

The reduction in each transverse emittance by a factor of 1/e from ionization cooling requires that the energy lost in the absorber be equal to the energy of the beam. Thus for a 250 MeV beam, a linac of about 7×250 = 1750 MeV energy would be needed to achieve a factor of a thousand in each transverse plane, or a factor of a million in six-dimensional emittance reduction as is required for a MC. In muon ionization cooling, intense magnetic fields are required which imply either sequential energy absorption and RF segments or the use of normal conducting RF filled with high-pressure gas [6].

## CHOICE OF ACCELERATION TECHNOLOGY

Since muons are generated as a tertiary beam they occupy large phase-space volume and the accelerator must provide very large transverse and longitudinal acceptances. The above requirements drive the design to low RF frequency, as low as 200 MHz for the initial bunching and cooling sections. If normal-conducting cavities were used, the required high gradients of order of ~15 MV/m would demand uneconomically high peak power of RF sources. Superconducting RF (SRF) cavities are a much more attractive solution. RF power can then be delivered to the cavities over an extended time, and thus RF source peak power can be reduced. Another important advantage of SRF cavities is that their design is not limited by a requirement of low shunt impedance and therefore their aperture can be significantly larger.

Muon survival practically excludes use of conventional circular accelerators and demands either a high-gradient conventional or recirculating linac. While recirculation provides significant cost savings over a single linac, it cannot be used at low energy since the beam is not sufficiently relativistic and will therefore cause a phase slip for beams in higher passes, thus significantly reducing acceleration efficiency for subsequent passes.

## LONGITUDINAL BUNCH COMPRESSION

Initial pre-acceleration in a single-pass linac (to about 3 GeV) is necessary to make the beam sufficiently relativistic, so that further acceleration in RLA is possible. In addition, the muon's longitudinal phase space volume is adiabatically compressed in the course of acceleration.

The large acceptance of the accelerator requires large aperture and tight focusing at its front-end. The above requirement combined with necessity of strong focusing in both planes at moderate energy makes the solenoidal focusing superior to the quadrupole one and hence has been chosen for the entire linac [7]. To achieve a manageable beam size at the linac front-end short focusing cells are used for the first 12 cryo-modules. The beam size is adiabatically damped with acceleration, and that allows one to replace short cryo-modules with 18 intermediate-length cryo-modules and then, with 22 long cryo-modules as illustrated in Figure 1.

The initial bunch length and energy spread are very large, so that the bunch length is more than half a wave length ($\Delta\phi$=±89 deg) and the momentum acceptance is about ±21%.

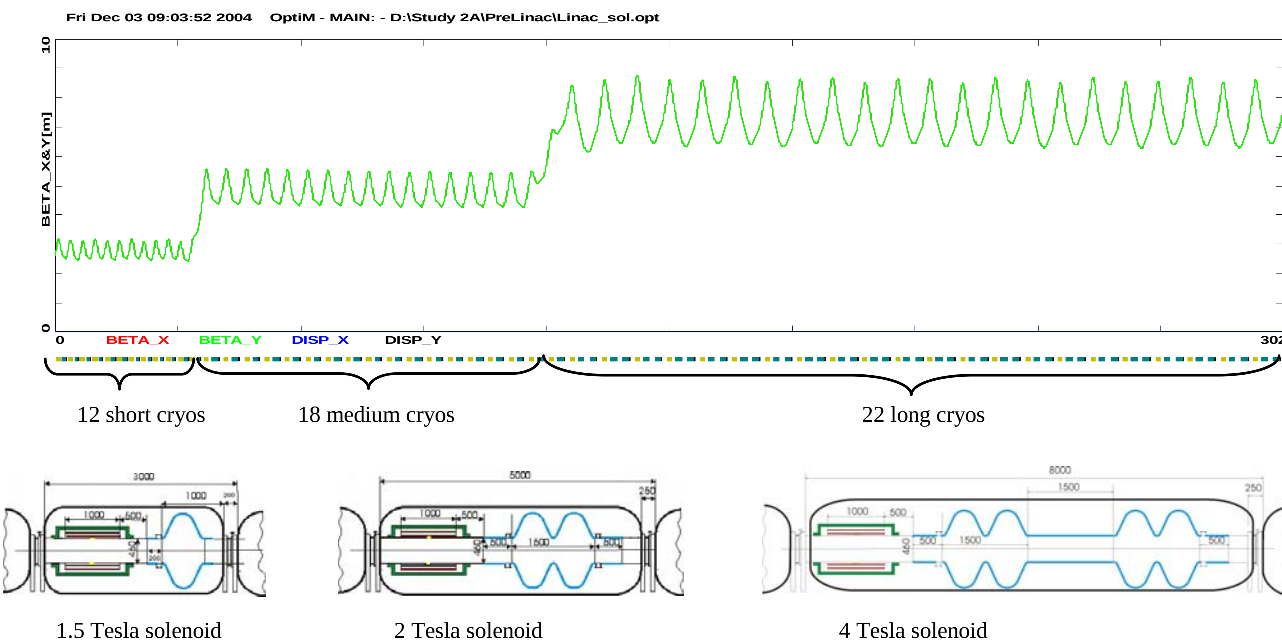


Figure 1: Top, transverse optics of the linac – uniform periodic focusing with three styles of cryo-modules. Below, layout of short, intermediate and long cryo-modules along with the required solenoid fields for each style.

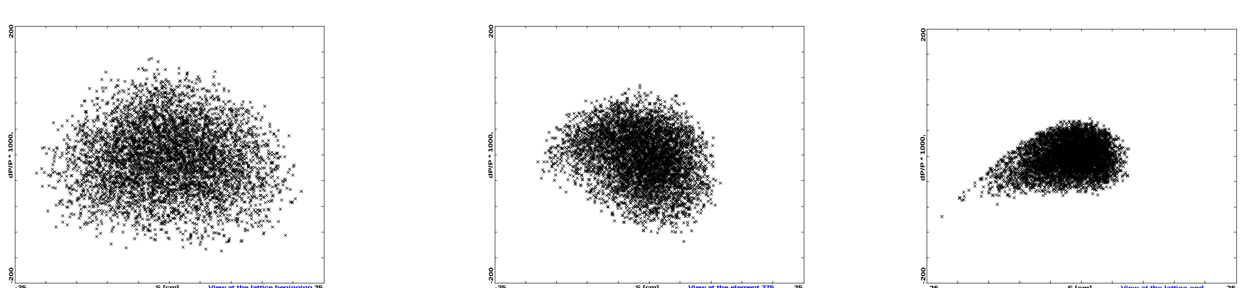

Figure 2: Adiabatic bunch compression along the linac – Longitudinal phase-space (s, Δp/p): at the beginning, half-way through and at the end of the pre-accelerator, as illustrated by particle tracking, axis range: s = ±25 cm, Δp/p = ±0.2 .

To perform adiabatic bunching, the RF phase of the cavities is shifted by 72 deg at the beginning. of the pre-accelerator and gradually changed to zero by the linac end. In the first half of the linac, when the beam is still not sufficiently relativistic, the offset causes synchrotron motion, allowing bunch compression in both length and momentum spread to $\Delta p/p$=±7% and $\Delta\phi$=±29 deg. The synchrotron motion also suppresses the sag in acceleration for the bunch head and tail. Figure 2 illustrates adiabatic bunch compression along the linac.

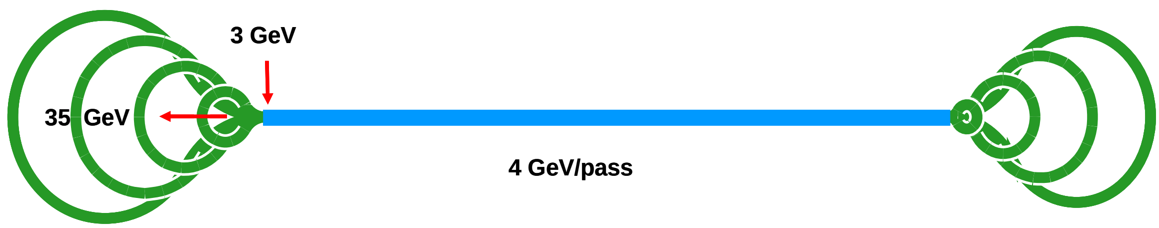


Figure 3: Layout of an 8-pass 'Dogbone' RLA with the top-to-injected energy ratio of 12.

## MULTI-PASS LINAC OPTICS

The superconducting accelerating structure is by far the most expensive component of the accelerator complex. Maximizing the number of passes in the RLA has significant impact on cost-effectiveness [8] of the overall acceleration scheme.

There are two notable advantages of the 'Dogbone' configuration compared to the 'Racetrack':

- Better orbit separation at the linac ends resulting from larger (factor of two) energy difference between two consecutive linac passes.
- Favorable optics solution for simultaneous acceleration of both $\mu^{\pm}$ species can be supported by the 'Dogbone' topology, which allows both charge species to traverse the RLA linac in the same direction while passing in the opposite directions through the mirror symmetric optics of the return 'droplet' Arcs.

The key element of the transverse beam dynamics in a 'Dogbone' RLA is an appropriate choice of multi-pass linac optics. The focusing profile along the linac (quadrupole gradients) need to be set, so that one can transport (provide adequate transverse focusing for given aperture) multiple pass beams within a vast energy range. Obviously, one would like to optimize the focusing profile to accommodate maximum number of passes through the RLA. The RLA layout illustrated in Figure 3, features a 'Dogbone' based on a 500 meter long (20 FODO cells with 8 RF cavities/cell) 4 GeV linac with the injection energy of 3 GeV. The alternative structure is called a racetrack, where the CEBAF machine at Jefferson Lab is an example.

Two styles of linac focusing lattice (FODO and Triplet) were studied for the lattice design of the RLA [9]. The focusing symmetry between the horizontal and vertical planes in the FODO lattice guarantees uniformly decreasing betatron phases in both planes while the energy increases in higher linacs passes. This yields a linac optic design that is well balanced in terms of Twiss functions and beam envelopes, which supports twice as many passes through the 'Dogbone' RLA.

Pass 1 (3-7 GeV)

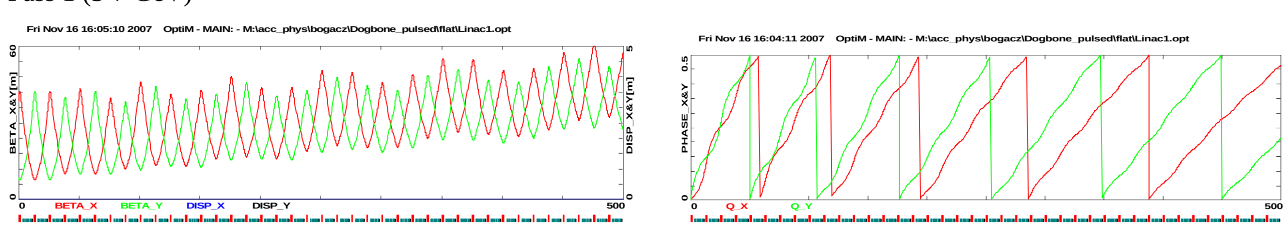


Pass 8 (31-35 GeV)

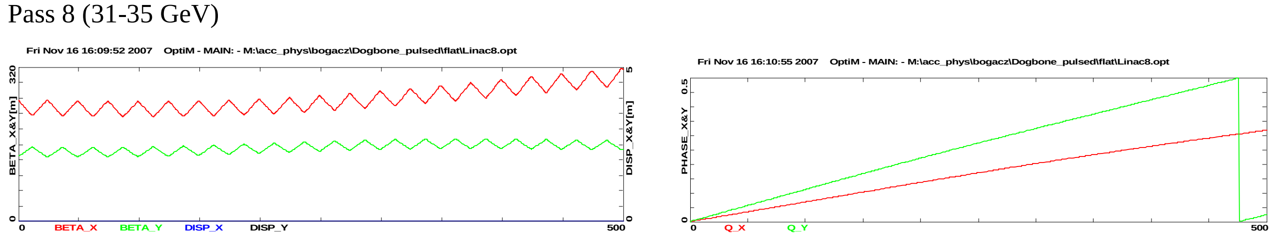


Figure 4: The first pass and the last one (8-th) of a FODO based multi-pass linac optics. In each set, the left plot represents beta functions, and the right plot describes betatron phase advance. Red is horizontal and green is vertical.

Since the beam is traversing the linac in both directions throughout the course of acceleration, the best choice is a 'flat' focusing profile for the entire linac. That is, the quads in all cells are set to the same gradient. This gradient was chosen to correspond to a 90° phase advance per cell as determined for the injection energy. There is no scaling of the quad gradients for increasing energy along the linac as this scaling would be incorrect for subsequent passes. Figure 4 illustrates the multi-pass optics case, which supports a maximum number of 8 passes through the RLA. The highest pass is limited by the linac phase advance falling below 180 deg.

Now we consider a 'Pulsed' linac Optics for the same RLA layout. Here we assume a time varying quad strength in the RLA linac described in the previous section. A feasible quad pulse would assume 500 Hz cycle ramp with the top pole field of 1 Tesla. That would translate to a maximum quad gradient of $G^{max}$ =2 kGauss/cm (5 cm bore radius) ramped over $\tau$ = 1 ms from the initial gradient of $G_0$ =0.1 kGauss/cm. We have used a fairly conservative rise time based on similar applications for ramping the new corrector magnets for the Fermilab Booster that have 1 kHz capability [10].

Pass 8 (31-35 GeV)

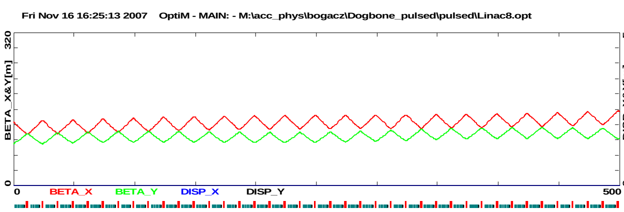


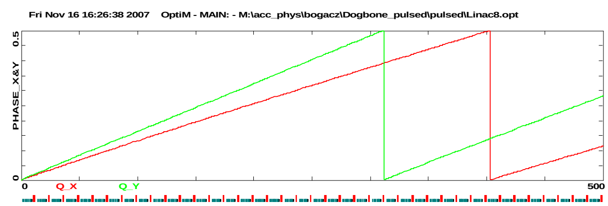


Pass 12 (47-51 GeV)

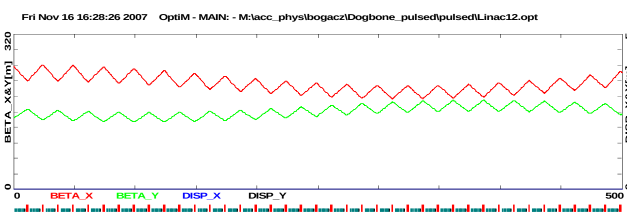


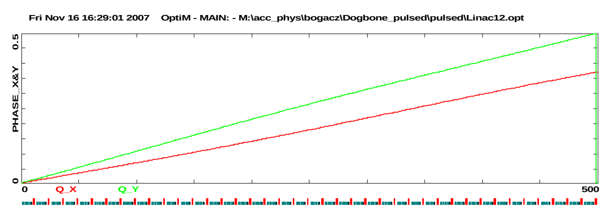


Figure 5: The 8-th pass and the last one (12-th**)** of the pulsed linac optics. By pulsing the focusing quads as described in Eq.(3), the additional 4 passes increase the output energy from 35 to 51 GeV. In each set, the left plot represents beta functions, and the right plot describes betatron phase advance. Red is horizontal and green is vertical**.**

For simplicity, we consider a linear ramp according to the following formula:

$$G(t) = G_0 + \frac{G^{max} - G_0}{\tau} t \qquad (1)$$

A single bunch travelling with a speed of light along the linac with quads ramped according to Eq.(1), 'sees' the following quad gradient passing through i-th cell along the linac (i = 1,…20)

$$G_i = G_0 + \frac{G^{max} - G_0}{\tau} \frac{\ell_{cell}}{c} i \qquad \textbf{(2)}$$

where $\ell_{cell}$ is the cell length and i defines the bunch position along the linac.

For multiple passes through the linac (the index n defines the pass number) the above formula can be generalized as follows:

$$G_i^n = G_0 + \frac{G^{max} - G_0}{\tau c} \left[ (n-1)\left( \ell_{linac} + \frac{n}{2} \ell_{arc} \right) + i \ell_{cell} \right] \qquad (3)$$

where $\ell_{linac}$ is the full linac length and $\ell_{arc}$ is the length of the lowest energy droplet arc. Here we also assume that the energy gain per linac is much larger than the injection energy. Figure 5 illustrates the multi pass optics for the pulsed linacs. As one can see, there is sufficient phase advance to support up to 12 passes.

## 'DROPLET' ARCS

In a 'Dogbone' RLA one needs to separate different energy beams coming out of a linac and to direct them into appropriate 'droplet' arcs for recirculation [7]. For multiple practical reasons horizontal rather than vertical beam separation was chosen. Rather than suppressing horizontal dispersion created by the Spreader it is smoothly matched to the horizontal dispersion of the outward $60^0$ arc. Then by appropriate pattern of removed dipoles in three transition cells one 'flips' the dispersion for the inward bending $300^0$ arc, etc. The entire 'droplet' Arc optics architecture is based on $90^0$ betatron phase advance cells with uniform periodicity of Twiss functions. The resulting 'droplet' Arc optics based on FODO focusing [8] is illustrated along with its 'foot print' in Figure 6.

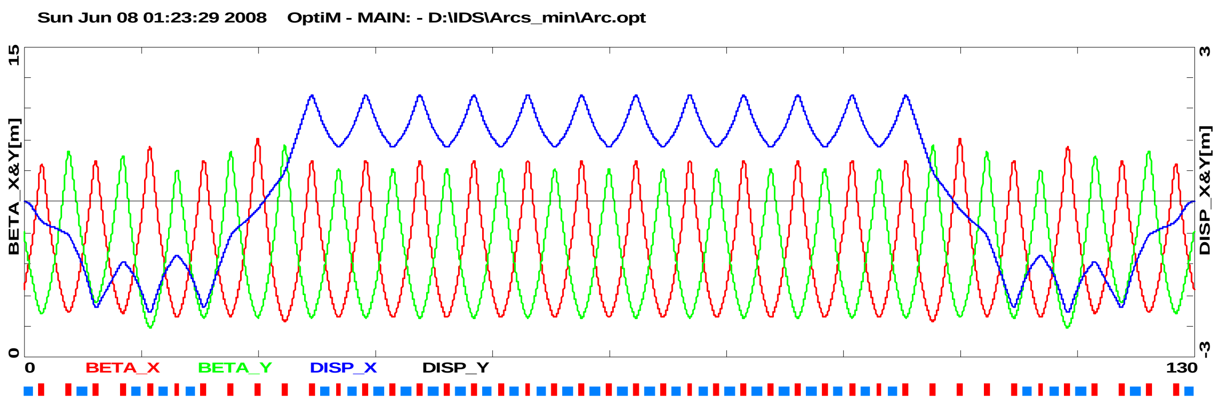


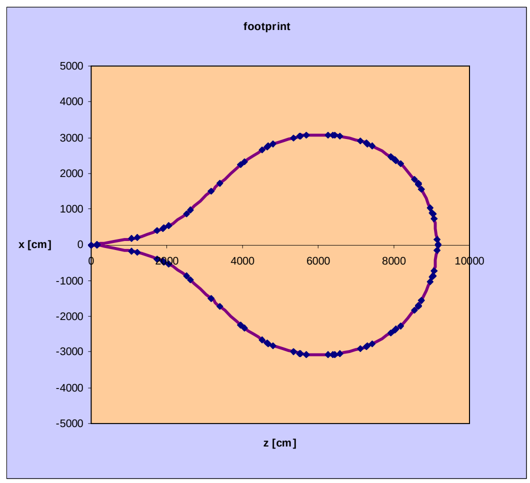


Figure 6: Top plot, 'Droplet' Arc optics – uniform periodicity of beta functions and dispersion. Bottom**,** horizontal layout of a 'Droplet' Arc – outward bending 60 deg. arc followed by 300 deg. inward bending arc.

## CONCLUSIONS

Intense muon beams for Muon Colliders, Neutrino Factories, and other physics and commercial ventures demand extensive use of linac technologies for their production, cooling, capture, beam formation/shaping and acceleration. The short muon lifetime drives the technology to the highest possible gradients for a wide range of frequencies. Furthermore, the accelerator must provide very large transverse and longitudinal acceptances. The above requirements drive the design to low RF frequency. If normal-conducting cavities at that frequency were used, the required high gradients would demand unachievably high peak power RF sources.

A TeV scale muon accelerator would consist of a single-pass linac that captures large muon phase space coming from the cooling channel and accelerates them to relativistic energies, while adiabatically decreasing the phase-space volume. It would be followed by an RLA that uses International Linear Collider (ILC) SRF structures in a single linac and 'droplet' return Arcs. The so called 'Dogbone' RLA can provide exceptionally fast and economical acceleration to the extent that the focusing range of the RLA quadrupoles allows each muon to pass several times through each high-gradient cavity. In addition a new concept of rapidly changing the strength of the linac quadrupoles as the muons gain energy is being developed to further increase the number of passes, leading to greater cost effectiveness.

## REFERENCES

[1] M. Popovic et al., this conference
[2] R.P. Johnson, LINAC 2004
[3] C.M. Ankenbrandt and R. P. Johnson, HB 2008
[4] H. Kirk et al. EPAC08
[5] R.P. Johnson, COOL 2007
[6] M. Bastaninejad et al., this conference
[7] S.A. Bogacz, Nuclear Physics B, Vol **149**, 309, (2005)
[8] J.S. Berg et al., Physical Review Special Topics – Accelerators and Beams, **9**, 011001 (2006)
[9] S.A. Bogacz, Nuclear Physics B, Vol **155**, 334, (2006)
[10] V.S. Kashikhin et al., PAC 2005

# NEUTRONS AND PHOTONS: PROBES OF CONDENSED MATTER

W. G. Stirling, ESRF, Grenoble


## Abstract

Synchrotron X-rays and neutrons provide unique microscopic information on the structures and dynamics of condensed matter. These probes are essential tools for biologists, chemists, physicists and materials scientists and have become increasingly important in a remarkably wide range of disciplines, from palaeontology to medicine. The electron storage rings producing synchrotron radiation, and fission reactor or spallation neutron sources, are usually situated at major national or international laboratories. Such central research facilities are exemplified by the two international laboratories in Grenoble, the European Synchrotron Radiation Facility and the Institut Laue-Langevin. After a discussion of the sources used to produce synchrotron radiation and neutron beams, some of the instrumentation and methods used in the investigation of materials will be described, with illustrative examples of recent research. Finally, some major X-ray and neutron sources under construction or at the planning stage will be described, including several where linac technology plays an important role (e.g. the XFEL at DESY and the SNS at ORNL).


**CONTRIBUTION NOT RECEIVED**

# THE HIGGS BOSON
# HOLY GRAIL OF PARTICLE PHYSICS

Nigel Lockyer, TRIUMF, 4004 Wesbrook Mall, Vancouver, BC Canada V6T 2A3

*Abstract*

The most sought after particle in history is the Higgs Boson. Arguably, the Large Hadron Collider (LHC) at CERN has been built to find the Higgs. Some kind of Higgs mechanism is needed in the Standard Model to give mass to the intermediate vector bosons, the carriers of the weak force. The same mechanism gives mass to the quarks and leptons as well. An elementary introduction to the Higgs Boson is presented.

## INTRODUCTION

There are several motivating questions that drive research in particle physics and for more than half of these it can be argued the Higgs boson sheds some light on the question.

1. Are there undiscovered new symmetries or laws in nature?
2. Are there extra dimensions of space? (small or large)
3. Do all the forces become one?
4. How can we solve the mystery of Dark Energy?
5. What is Dark Matter?
6. Where is all the anti-matter?
7. How to combine quantum mechanics & gravity?

Items 1) and 2) motivated by new physics to stabilize Higgs mass calculation-no fine tuning assumption. Item 3) Hints exist & needs spontaneous symmetry breaking. Item 4) Higgs may be part of the puzzle. Items 5) 6) require experimenters to get more data since theory cannot lead. Item 7) String theory has much to say about this since it is the only theory to include gravitational interactions and particle physics.

In this paper we'll discuss: What is the Higgs Boson? What is the Higgs Mechanism? Why are weak interactions weak? Connections to Nuclear Physics & Astrophysics? Higgs Search Status at Tevatron and a few words about the ILC as a Higgs Factory.

Peter Higgs is a theoretical physicist from the University of Edinburgh. He did his seminal work over 40-years ago. He was motivated by the work of Schrieffer and Nambu amongst others, who had been studying superconductivity. It was recognized that the Higgs field was a form of superconductivity in vacuum, a relativistic quantum fluid that fills all of space.

In a superconductor, Cooper pairs form a condensate which breaks the electromagnetic gauge symmetry and expels magnetic fields from inside the superconductor, a phenomena called the Meisner Effect. One interpretation of the Meisner effect is that the electromagnetic fields in the superconductor are short range and therefore cannot penetrate the surface more than a short distance. In an ordinary metal, we know electric fields inside the conductor are zero due to a rearrangement of the electric charges on the surface of the conductor. However, magnetic fields can fully penetrate a conductor. In a superconductor, the photon becomes massive and consequently has a short range, inversely proportional to the mass.

The Higgs mechanism is a form of superconductivity in vacuum. The Higgs field fills all space and prevents the weak force from propagating over infinite distance. In the simplest case, the Higgs field consists of 2 neutral and 2 charged components. When the Higgs acquires a non-zero vacuum expectation value, the Higgs field then has a non-zero value throughout space. The value is given in the standard model as 246 GeV. Three of the fields, the two neutral and one charged field mixes with the three W and Z bosons, giving them mass, and the other remaining field is the scalar Higgs boson. The weak force range is inversely proportional to the mass of the W and Z bosons.

Now for a few simple definitions to set the stage for further discussion. A particle is a disturbance in a field. An example of a field, such as a temperature field, is a number at every point in space that describes the temperature at that point. If one number describes each point, it is called a scalar field. If two numbers are required, such as with a wind field or a magnetic field, where you need a number and a direction, it is a vector field. The Higgs field is a neutral scalar field that fills the entire universe. Particles travelling through the universe interact with the field and become massive. Importantly, the W and Z become massive and the photon must have a mass identical to zero in the standard model.

We wish to introduce the concept of spontaneous symmetry breaking in a non-rigorous manner. Firstly, symmetry is a concept we are all familiar with, especially in art. M.C. Escher is a good example. It is however more precisely defined in physics and this leads to some confusion. Often, non-scientists think a snow-flake has a great deal of symmetry (6-fold) and yet steam does not. However, if we define a perfectly symmetric system as one where every direction for example, is identical, then steam is more symmetric than a snow flake. Therefore, steam, after it cools, loses symmetry. The original symmetry is broken.

Steam

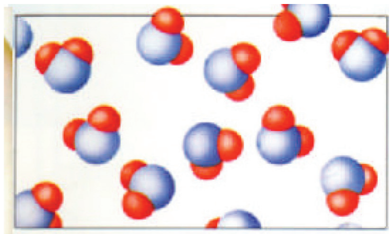

Figure 1: Steam is fully symmetric.

Ice

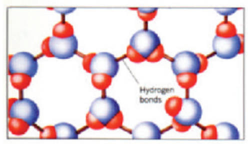


Figure 2: The snowflake has less symmetry than steam.

Iron is an excellent example. Above the critical temperature, iron is non-magnetic. Below the critical temperature, the spins of the iron atoms (actually domains) spontaneously align, and the symmetry is decreased. Above the critical temperature, the spins are not aligned, and iron is in a state of greater symmetry.

In the example with the Mexican hat potential, the system starts out in a fully symmetric state when the ball (or Higgs Boson) is at the top of the hat. The ball is in a state of unstable equilibrium and will fall down eventually. When the ball rolls down, a random direction is chosen (or in the case of the Higgs a random phase is chosen), which spontaneously breaks the symmetry. This ball rolling down the hat happens when the universe cools for the massive Higgs boson, in which case the Higgs rolls down a potential. A very similar potential describes the breaking of gauge symmetry in a superconductor when the Cooper pair condensate forms.

Ferromagnetism above the Curie temperature is spatially invariant and there is no magnetic field in space. Below the Curie temperature, the symmetry is spontaneously broken, and there is a magnetic field created in space. This is called a phase transition. One can demonstrate this effect by heating an iron nail with a blow torch. Once red hot, the nail is

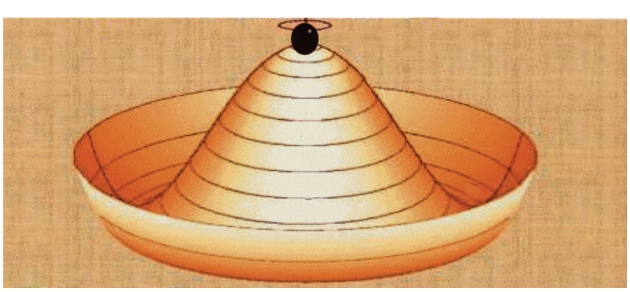

Figure 3: Mexican hat potential. The ball rolls down into the brim breaking the initial “symmetric state”.

above the Curie temperature and will not stick to a simple bar magnet. As the nail cools, the spins align at the critical temperature, the symmetry being spontaneously broken, a net magnetization is created and the nail sticks to the magnet.

This is in analogy to the universe cooling, and at the critical electroweak temperature, there is a phase transition and the electroweak symmetry is broken and the Higgs field is created in space. The electroweak phase transition occurs about one pico-second after the Big Bang. This is the time (or energy or temperature) scale being explored by the Large Hadron Collider (LHC). Above this temperature there is no Higgs field, and below this temperature there is a Higgs field. The electroweak symmetry breaks into electromagnetic and weak fields (in analogy to the rotational symmetry breaking in the ferromagnetism example). The W & Z gain mass and have finite range whilst the photon remains mass-less and has infinite range.

When the universe was created, all four forces, gravity, electromagnetic, weak, and strong force are thought to be identical. The universe was fully symmetric. However, as the universe expanded and cooled, at the temperature of the Planck scale, gravity breaks away from the other three forces, and then at the Grand Unification scale of $10^{16}$ GeV, the strong nuclear force and the electroweak force go through a phase transition and separate. Observing the spontaneous electroweak symmetry breaking at the LHC will give us more confidence we are on the right track for unification (maybe).

Why are we excited about the LHC? The LHC will substantially increase the energy scale we study in particle physics by a factor of seven. This is a big jump and we cannot possibly predict what will be seen. The LHC is an exploratory machine. Importantly, if the idea of electroweak symmetry is correct, the LHC will prove it and thus explain why the weak interactions are weak.

The Higgs is different. All matter particles are spin-1/2, while all forces are carried by particles with spin-1. Higgs particles are spin-0. The Higgs is neither matter or a force carrier. The Higgs is its own antiparticle. The Higgs is just different. It would be the first fundamental scalar observed. All extensions of the standard model contain scalar fields, such as the inflaton of inflation or the radion of extra dimensions. Discovering the first fundamental scalar will indicate we are perhaps on the right track with these other ideas. The Higgs will also be a powerful probe of new physics. The standard model constrains the couplings to the quarks, and measuring those couplings precisely will be a powerful test of the standard model and whether new physics is leaking in. In principal, the Higgs will couple to other scalars in any broader theory, and this could show up in the couplings.

It is interesting to note the Higgs mechanism does not give the proton or neutron most of their mass. Most of the mass of the proton or neutron comes from the chiral symmetry breaking in QCD. However, the mass of the quarks is important because it is the Higgs interaction that determines which of the up or down quarks is heavier. The proton (uud) is lighter than the neutron (udd) because the mass of the down quark is greater than that of the up quark. If the quarks had equal mass, the proton would be slightly heavier than the neutron because of its charge, and the proton would decay to the neutron. Furthermore, since the electron would be massless without the Higgs mechanism, the Bohr radius of the electron, inversely proportional to mass, would be infinite and there would be no chemistry. The lightest nuclei would be neutral and atoms would not exist. The universe would be quite different. The Higgs is very important to how we understand our visible universe.

The best experimental limits on the Higgs come from the Tevatron. Figure 4 shows the exclusion plot using 3 fb$^{-1}$ of data, CDF and D0 combined. The data are sensitive enough to just about exclude masses around 170 GeV/c$^2$. The lower mass range, 115-150 GeV/c$^2$, has sensitivities about three times the standard model cross section.

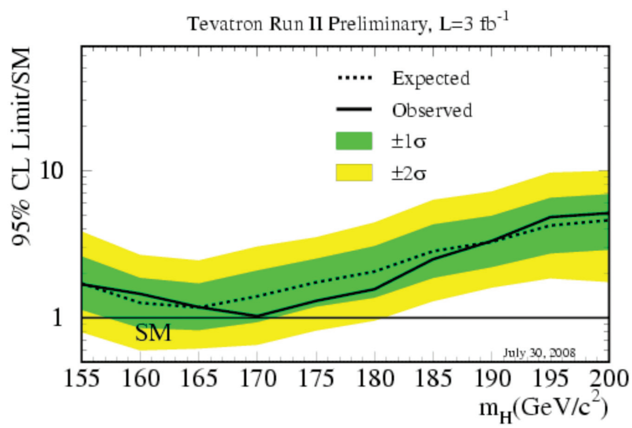


Figure 4: Exclusion plot for SM Higgs boson.

There are several systems in nature that exhibit phenomena that is similar to superconductivity, the Higgs mechanism being just one such system. A well known example is Helium-3, which is a p-wave superfluid at low temperatures. The system is an example of fermionic atoms, not electrons as in metals, that exhibit pairing properties.

Another example, less dense that helium-3, is a quantum fermionic gas, such as Li-6 gas. When trapped and cooled below a critical temperature Tc, the system exhibits superfluid vortices. If the system is placed in an external magnetic field, the inter-atomic attraction can be adjusted, hence varying the strength of the coupling. This makes it possible to create cold Fermi gases with a high Tc. Figure 5 shows superfluid vortices in a quantum gas [1].

In the nucleus, neutrons can pair with neutrons and protons can pair with protons. Since the interaction between nucleons is strong, it is not necessary to cool the nucleus in order to observe super-effects. Therefore in nuclei with an even number of protons, *superconductivity* behaviour is observed and nuclei with an even number of neutrons *superfluid* behaviour is observed. This is exhibited by the excitation energy-gap of about one MeV in even-even nuclei.

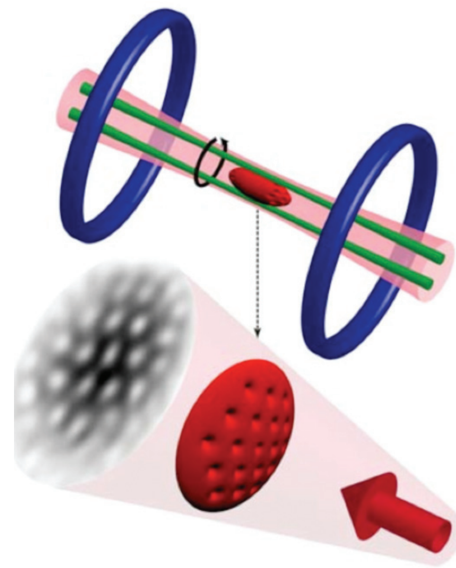

Figure 5: Superfluid vortices in trapped ultra cold atoms[1].

In even-odd nuclei, the excitation energy is a factor of ten less. This discovery was made one year after the discovery of BCS theory.

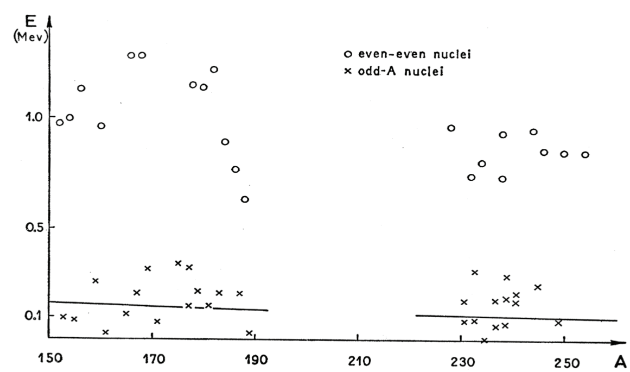


Figure 6: Excitation energy-gap in even-even nuclei compared to odd-mass nuclei[2].

Neutron stars are very interesting laboratories for many studies. The crust contains neutron-rich nuclei in a sea of neutrons. Initially, once the neutron star is born, the temperature of the star is too high to allow a superfluid, but quickly the neutrons in the crust form an s-wave superfluid. In the core, the neutrons may form a p-wave superfluid and the protons an s-wave superconductor. These condensates impact the cooling of the neutron star. It is known that roughly in the first $10^6$ years, cooling is primarily due to neutrino emission. The processes are neutron decay and electron capture on protons. If the neutrons or protons are paired, extra energy is needed to break the Cooper pairs and therefore superfluid/ superconducting neutron stars cool slower.

In some X-ray bursts in accreting neutron stars, it is possible to observe the cooling of the crust in real-time. The

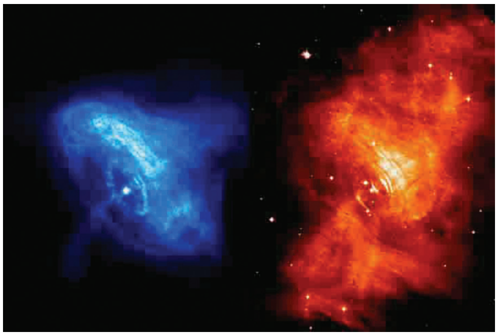

Figure 7: Crab pulsar in X-ray and optical: Superfluidity/superconductivity impacts cooling of neutron stars.

light curve time constant is affected by whether the crust is a superfluid. In pulsars, there is angular momentum stored in superfluid vortices in the crust in a similar manner to a superfluid that has been rotated. As the neutron star rotation period slows down, it is possible for these vortices to transfer their angular momentum to the stars rotation. This suddenly increases the rotation rate of the star, and these spin ups are observed as glitches in the period[3].

## CONCLUSION

Particle physicists at Fermilab and CERN are in hot pursuit of the Higgs boson. If found it will be the last missing particle in the standard model. The Higgs boson will be the first fundamental scalar observed and will give credence to proposed models beyond the standard model that have scalar fields, including inflation. The precision study of the Higgs may reveal new physics beyond the standard model. The Higgs mechanism is one of several phenomena in nature that connects to superfluidity and superconductivity. The International Linear Collider may be the ideal new machine to explore the properties of the Higgs.

## ACKNOWLEDGEMENT

I would like to thank Matt Hearndon (CDF and Wisconsin), Marcela Carena (Fermilab), Edward Witten (IAS), Chris Quigg (Fermilab), Achim Schwenk (TRIUMF) and all my CDF colleagues.

## REFERENCES

[1] W. Ketterle and M.W. Zwierlein,"Making, probing and understanding ultracold Fermi gases", to appear in Ultracold Fermi Gases, Proceedings of the International School of Physics "Enrico Fermi", Course CLXIV, ed. M. Inguscio, W. Ketterle, and C. Salomon (IOS Press, Amsterdam, 2008).

[2] A. Bohr, B.R. Mottelson and D. Pines, Phys. Rev. 110, (1958) 936.

[3] P.W. Anderson and N. Itoh, Nature (London) 256, (1975) 25.

## List of Authors

*Italic* papercodes indicate primary authors

## — C —

## — D —

## — L —

## — N —

## — Q —



## — R —

## — U —



## — V —



## — W —

# List of Institutes

- Beebe, E.N.
- Bellavia, S.
- Ben-Zvi, I.
- Blaskiewicz, M.
- Brennan, J.M.
- Burrill, A.
- Calaga, R.
- Cameron, P.
- Chang, X.
- Connolly, R.
- Dawson, W.C.
- Degen, C.
- Drees, K.A.
- Ganetis, G.
- Gassner, D.M.
- Gould, O.
- Grimes, J.G.
- Hahn, H.
- Hammons, L.R.
- Hershcovitch, A.
- Hseuh, H.-C.
- Jain, A.K.
- Kayran, A.
- Kponou, A.
- Kusche, K.
- Lambiase, R.F.
- Lederle, D.L.
- Lessard, E.T.
- Litvinenko, V.
- LoDestro, V.
- Lockey, R.
- Mahler, G.J.
- Malitsky, N.
- Mapes, M.
- McCafferty, D.R.
- McIntyre, G.T.
- McNerney, A.
- Meng, W.
- Murphy, J.B.
- Nehring, T.C.
- Oerter, B.
- Okamura, M.
- Pai, C.
- Park, J.H.
- Pate, D.
- Pendzick, A.
- Phillips, D.
- Pikin, A.I.
- Pozdeyev, E.
- Qian, H.J.
- Rao, T.
- Raparia, D.
- Reich, J.
- Ritter, J.
- Roser, T.
- Russo, T.
- Scaduto, J.
- Segalov, Z.
- Seletskiy, S.
- Sharma, A.K.
- Shen, Y.
- Smedley, J.
- Smith, K.
- Snydstrup, L.
- Srinivasan-Rao, T.
- Tsoupas, N.
- Tuozzolo, J.E.
- Wang, G.
- Wang, X.J.
- Weiss, D.
- Wilinski, M.
- Williams, N.
- Wu, Q.
- Yakimenko, V.
- Yang, X.
- Yip, K.
- Zaltsman, A.

**Beam-Wave Research, Inc.**
Union City
- Wright, E.L.

**Bilbao, Faculty of Science and Technology**
Bilbao
- Bermejo, F.J.

**CASA**
newport news
- Liu, C.

**CEA**
Bruyeres-le-Chatel
- Guilhem, D.
- Lemaire, J.-L.
- Millerioux, M.M.
- Lemaire, J.-L.
- Pichon, S.J.
- Balleyguier, P.
- Flament, J.-L.
- Le Flanchec, V.
- Bernaudin, P.-E.
- Bogard, D.
- Bosland, P.
- Bougeard, M.
- Carré, B.
- Cazaux, S.
- Charrier, J.-P.
- Chauvin, N.
- Chel, S.
- Cheymol, G.
- Contrepois, P.
- Curtoni, A.
- Delferriere, O.
- Desmons, M.
- Devanz, G.
- Dispau, G.
- Dorlot, M.
- Duperrier, R.D.
- Farabolini, W.

- Fontaine, M.
- France, A.
- Garzella, D.
- Gasser, Y.
- Girardot, P.
- Gobin, R.
- Granelli, R.
- Hamdi, A.
- Hardy, P.
- Harrault, F.
- Jannin, J.L.
- Labat, M.
- Lahonde-Hamdoun, C.L.H.
- Lambert, G.
- Leboeuf, D.
- Lerch, T.
- Leroy, P.-A.
- Luong, M.
- Merdji, H.
- Mosnier, A.
- Nghiem, P.A.P.
- Orsini, F.
- Peauger, F.
- Piquet, O.
- Plouin, J.
- Roudier, D.
- Salieres, P.
- Simon, C.
- Tchebakoff, O.
- Uriot, D.
- Pierret, O.

**CERN**
Geneva

- Adli, E.
- Alharbi, N.
- Bellodi, G.
- Bettoni, S.
- Bordry, F.
- Bourquin, P.
- Braun, H.-H.
- Bravin, E.
- Brunner, O.
- Calatroni, S.
- Carli, C.
- Chamizo, R.
- Chritin, N.C.
- Ciapala, E.
- Corsini, R.
- Curt, S.
- Cuvet, Y.
- Dabrowski, A.E.
- De Almeida Martins, C.
- De Michele, G.
- De Morais Amaral, R.
- Delruelle, N.
- Doebert, S.
- Dutriat, C.
- Elsener, K.
- Eshraqi, M.
- Favre, G.
- Fedosseev, V.
- Ferreira, L.M.A.
- Garoby, R.
- Gerigk, F.
- Grenier, D.
- Grudiev, A.
- Hanke, K.
- Hansen, J.
- Kadi, Y.
- Lacroix, J.-M.
- Lallement, J.-B.
- Lanzone, S.
- Latina, A.
- Lefevre, T.
- Lindroos, M.
- Lombardi, A.M.
- Losito, R.
- Maglioni, C.
- Massidda, L.
- Mathot, S.J.
- Maury, S.
- McMonagle, G.
- Mikulec, B.
- Modena, M.
- Mourier, J.
- Olvegaard, M.
- Otto, Th.
- Parma, V.
- Pasini, M.
- Petrarca, M.
- Raich, U.
- Ramberger, S.
- Ramos, D.
- Riddone, G.
- Rinolfi, L.
- Rocca, R.
- Rossat, G.
- Rossi, C.
- Rugo, E.
- Samoshkin, A.
- Sargsyan, E.Zh.
- Schuh, M.
- Schulte, D.
- Shaker, H.
- Skowronski, P.K.
- Stulle, F.
- Taborelli, M.
- Tardy, T.
- Tecker, F.
- Thierry, F.
- Timeo, L.
- Timmins, M.A.
- Tomas, R.
- Trilhe, T.
- Tuckmantel, J.
- Urschütz, P.
- Vandoni, G.
- Voulot, D.
- Vretenar, M.
- Wegner, R.
- Weingarten, W.

- Floettmann, K.
- Froelich, T.
- Gamp, A.
- Geng, Z.
- Gerth, C.
- Golubeva, N.
- Grecki, M.K.
- Grevsmuehl, T.
- Hoffmann, M.G.
- Honkavaara, K.
- Huening, M.
- Iversen, J.
- Jelezov, I.
- Jensch, K.
- Katalev, V.V.
- Kot, Y.A.
- Kreps, G.
- Lange, R.
- Lederer, S.
- Lilje, L.
- Limberg, T.
- Matheisen, A.
- Moeller, W.-D.
- Rehlich, K.
- Reschke, D.
- Rossbach, J.
- Schmidt, A.
- Schmitz, M.
- Sekutowicz, J.K.
- Simrock, S.
- Singer, W.
- Singer, X.
- Vogel, E.
- Ziegler, J.

**Department of Energy Sciences, Tokyo Institute of Technology**
Yokohama
- Tamura, J.

**Diamond**
Oxfordshire
- Bartolini, R.
- Christou, C.
- Han, J.H.
- Huang, H.C.
- Kay, J.
- Kempson, V.C.
- Singleton, S.J.

**Diversified Technologies, Inc.**
Bedford, Massachusetts
- Arntz, F.O.
- Casey, J.A.
- Ciprian, R.
- Gaudreau, M.P.J.
- Kardo-Sysoev, A.
- Kempkes, M.K.
- Krasnykh, A.
- Roth, I.

**ELSA**
Bonn
- Boldt, O.
- Hillert, W.
- Klarner, F.

**ENEA C.R. Frascati**
Frascati (Roma)
- Ciocci, F.
- Dattoli, G.
- Del Franco, M.
- Dipace, A.
- Doria, A.
- Gallerano, G.P.
- Giannessi, L.
- Giovenale, E.
- Lo Bue, A.
- Orlandi, G.L.
- Pagnutti, S.
- Petralia, A.
- Quattromini, M.
- Ronsivalle, C.
- Rossi, P.
- Sabia, E.
- Spassovsky, I.P.
- Surrenti, V.

**ESRF**
Grenoble
- Stirling, W.G.

**Elytt Energy**
Madrid
- Lucas, J.

**Euclid TechLabs, LLC**
Solon, Ohio
- Jing, C.-J.

**FZJ**
Jülich
- Zaplatin, E.N.

**Fermilab**
Batavia
- Allen, L.J.
- Ankenbrandt, C.M.
- Apollinari, G.
- Arkan, T.T.
- Barnes, B.
- Bellantoni, L.
- Bocean, V.T.
- Branlard, J.
- Butler, T.A.
- Cancelo, G.I.
- Carneiro, J.-P.

- Carter, H.
- Champion, M.S.
- Chase, B.
- Church, M.
- Cullerton, E.
- DiMarco, J.
- Edwards, H.T.
- Fliller, R.P.
- Foley, M.H.
- Ginsburg, C.M.
- Gonin, I.G.
- Grimm, J.
- Hanna, B.M.
- Harms, E.R.
- Hays, S.
- Hocker, A.
- Huang, Y.
- Johnson, A.S.
- Joireman, P.W.
- Khabiboulline, T.N.
- Klepec, D.W.
- Koeth, T.W.
- Kucera, M.J.
- Lackey, S.L.
- Lanfranco, G.
- Lumpkin, A.H.
- Lunin, A.
- Madrak, R.L.
- Mavric, U.
- McGee, M.W.
- Mitchell, D.V.
- Moretti, A.
- Mukherjee, A.
- Nagaitsev, S.
- Nezhevenko, O.A.
- Nicol, T.H.
- Olis, D.R.
- Orris, D.F.
- Ozelis, J.P.
- Page, T.M.
- Patrick, J.F.
- Peoples, E.
- Peterson, T.J.
- Pfund, P.A.
- Piekarz, H.
- Piot, P.
- Popovic, M.
- Rabehl, R.
- Reid, J.
- Ristori, L.
- Romanov, G.V.
- Ross, M.C.
- Rowe, A.M.
- Ruan, J.
- Schmidt, C.W.
- Sergatskov, D.A.
- Solyak, N.
- Steimel, J.
- Sun, Y.-E.
- Tam, W.M.
- Tartaglia, M.A.
- Terechkine, I.
- Thurman-Keup, R.
- Tompkins, J.C.
- Treptow, K.R.
- Tupikov, V.
- Varghese, P.
- Vignoni, A.
- Wagner, R.L.
- Watkins, D.J.
- Webber, R.C.
- Wildman, D.
- Wong, M.
- Yakovlev, V.P.
- Yonehara, K.
- Zmuda, T.J.

**Fundación TEKNIKER**
Eibar (Gipuzkoa)
- Enparantza, R.

**Fundación Tekniker**
Elbr (Guipuzkoa)
- Alonso, J.

**G.H. Gillespie Associates, Inc.**
Del Mar, California
- Gillespie, G.H.
- Hill, W.

**GANIL**
Caen
- Bertrand, P.
- Beunard, R.
- Di Giacomo, M.
- Ducoudret, B.
- Ferdinand, R.
- Gueroult, E.
- Leyge, J.F.
- Michel, M.
- Robillard, P.
- Souli, M.
- Toussaint, P.
- Vignet, J.L.

**GSI**
Darmstadt
- Barth, W.
- Bayer, W.B.
- Clemente, G.
- Dahl, L.A.
- Dambowy, H.-L.
- Forck, P.
- Franchetti, G.
- Gerhard, P.
- Groening, L.
- Herfurth, F.
- Hoerr, M.

- Hofmann, I.
- Hutter, G.
- Kaiser, M.
- Kester, O.K.
- Kluge, H.J.
- Koszudowski, S.
- Kozhuharov, C.
- Lang, R.
- Maeder, J.
- Maero, G.
- Maier, M.T.
- Mickat, S.
- Orzhekhovskaya, A.
- Quint, W.
- Riehl, G.A.
- Rossbach, J.
- Schlitt, B.
- Schreiber, G.
- Schuh, M.
- Sokolov, A.
- Spaedtke, P.
- Stoehlker, T.
- Tinschert, K.
- Vinzenz, W.
- Vormann, H.
- Vorobjev, G.
- Winters, D.F.A.
- Yaramyshev, S.

**GUAS/AS**
Ibaraki
- Kazakov, A.

**HIT**
Heidelberg
- Cee, R.
- Feldmeier, E.

**HU/AdSM**
Higashi-Hiroshima
- Kuriki, M.

**IAP**
Frankfurt am Main
- Amberg, M.
- Bartz, U.
- Bechtold, A.
- Becker, R.
- Busch, M.
- Chau, L.P.
- Dziuba, F.D.
- Heilmann, M.
- Hofmann, B.
- Kolb, P.
- Liebermann, H.
- Meusel, O.
- Mäder, D.
- Noerenberg, R.
- Pfister, J.
- Podlech, H.
- Ratzinger, U.
- Sauer, A.C.
- Schempp, A.
- Schmidt, J.S.
- Volk, K.
- Vossberg, M.
- Wiesner, C.
- Zhang, C.

**ICEPP**
Tokyo
- Yoshioka, T.

**IHEP Beijing**
Beijing
- Cheng, Y.
- Fu, S.
- Gong, K.Y.
- Lei, G.
- Li, J.
- Ouyang, H.F.
- Pei, G.
- Peng, J.
- Sun, Z.R.
- Xu, G.X.
- Yin, X.

**IHEP Protvino**
Protvino, Moscow Region
- Belyaev, O.K.
- Budanov, Yu.A.
- Maltsev, A.
- Zvonarev, I.A.

**IIT**
Chicago, Illinois
- Huang, D.

**IKP**
Mainz
- Aulenbacher, K.

**ILL**
Grenoble
- Geltenbort, P.

**IN2P3-CNRS**
Orsay
- Grandsire, L.

**INFN-Roma II**
Roma
- Catani, L.
- Cianchi, A.

**INFN-Roma**
Roma
- Mattioli, M.
- Petrarca, M.
- Serluca, M.

**INFN/LASA**
Segrate (MI)
- Bosotti, A.
- Michelato, P.M.
- Monaco, L.
- Pagani, C.
- Panzeri, N.
- Paparella, R.
- Pierini, P.
- Sertore, D.

**INFN/LNF**
Frascati (Roma)
- Alesini, D.
- Bellaveglia, M.
- Biscari, C.
- Boni, R.
- Boscolo, M.
- Castellano, M.
- Chiadroni, E.
- Clozza, A.
- Cultrera, L.
- Di Pirro, G.
- Drago, A.
- Esposito, A.
- Ferrario, M.
- Ficcadenti, L.
- Filippetto, D.
- Fusco, V.
- Gallo, A.
- Gatti, G.
- Ghigo, A.
- Marchetti, B.
- Marinelli, A.
- Marrelli, C.
- Migliorati, M.
- Mostacci, A.
- Pace, E.
- Palumbo, L.
- Pellegrino, L.
- Ricci, R.
- Rotundo, U.
- Sanelli, C.
- Serio, M.
- Sgamma, F.
- Spataro, B.
- Tazzioli, F.
- Tomassini, S.
- Vaccarezza, C.
- Vescovi, M.
- Vicario, C.

**INFN/LNL**
Legnaro, Padova
- Balabin, A.I.
- Bisoffi, G.
- Carlucci, D.
- Comunian, M.
- Facco, A.
- Fagotti, E.
- Grespan, F.
- Palmieri, A.
- Paparella, R.
- Pisent, A.
- Poggi, M.
- Posocco, P.A.
- Roncolato, C.
- Zenere, D.

**INFN/LNS**
Catania
- Caruso, A.C.
- Gallo, G.
- Rifuggiato, D.
- Spartà, A.
- Zappalà, E.

**INRNE**
Sofia
- Asova, G.
- Staykov, L.

**IPM**
Tehran
- Shaker, H.

**IPN**
Orsay
- Ausset, P.
- Biarrotte, J.-L.
- Blivet, S.
- Bousson, S.
- Commeaux, C.
- Joly, C.
- Junquera, T.
- Lesrel, J.
- Longuevergne, D.
- Lutton, F.
- Martinet, G.
- Olry, G.
- Perrot, L.
- Ponton, A.
- Saugnac, H.
- Szott, P.

**ISIR**
Osaka
- Isoyama, G.
- Kashiwagi, S.
- Kato, R.
- Morio, M.
- Suemine, S.

**ITEP**
Moscow
- Kolomiets, A.
- Minaev, S.

**IUAC**
New Delhi
- Chowdhury, G.K.
- Ghosh, S.
- Kanjilal, D.
- Mathuria, D.S.
- Mehta, R.
- Pandey, A.
- Patra, P.
- Rai, A.
- Roy, A.
- Sahu, B.K.
- Singh, K.

**IUCF**
Bloomington, Indiana
- Tam, W.M.

**Idaho National Laboratory**
Idaho
- Bolshinsky, I.

**Illinois Institute of Technology**
Chicago, Illinois
- Kaplan, D.M.

**Imperial College of Science and Technology, Department of Physics**
London
- Al Sari, S.M.H.
- Jolly, S.
- Kurup, A.
- Lee, D.A.
- Pozimski, J.K.
- Savage, P.

**Introscan**
Moscow
- Zavadtsev, A.A.

**Istituto Nazionale di Fisica Nucleare**
Milano
- Bacci, A.
- Boscolo, I.
- Broggi, F.
- Castelli, F.
- Cialdi, S.
- De Martinis, C.
- Giove, D.
- Maroli, C.
- Petrillo, V.
- Rossi, A.R.
- Serafini, L.

**J-PARC, KEK & JAEA**
Ibaraki-ken
- Namekawa, Y.
- Ohkoshi, K.
- Yamazaki, Y.

**JAEA**
Ibaraki-ken
- Chishiro, E.
- Hori, T.
- Ohkawa, T.
- Oku, T.
- Pirozhkov, A.
- Sakai, K.
- Shinohara, T.
- Suzuki, H.
- Suzuki, J.
- Suzuki, T.
- Yamazaki, M.
- Yoshikawa, H.
- Sakaki, H.

**JAEA/J-PARC**
Tokai-Mura, Naka-Gun, Ibaraki-Ken
- Asano, H.
- Hasegawa, K.
- Ikegami, M.
- Ito, T.
- Itoh, Y.I.
- Kato, Y.
- Kawase, M.
- Kobayashi, T.
- Kondo, Y.
- Morishita, T.
- Oguri, H.
- Sako, H.
- Shen, G.B.
- Takahashi, H.
- Ueno, A.

**JAEA/Kansai**
Kizu-machi Souraku-gun Kyoto-fu
- Daido, H.
- Ikegami, M.
- Kiriyama, H.
- Mori, M.
- Nishiuchi, M.
- Ogura, K.
- Orimo, S.
- Sagisaka, A.
- Yogo, A.

**JAEA/LINAC**
Ibaraki-ken

- Ao, H.
- Hasegawa, K.
- Hirano, K.
- Morishita, T.
- Ueno, A.

**JASRI/SPring-8**
Hyogo-ken
- Dewa, H.
- Hanaki, H.
- Mizuno, A.
- Suzuki, S.
- Taniuchi, T.
- Tomizawa, H.
- Yamashita, A.
- Yanagida, K.

**JINR**
Dubna, Moscow Region
- Balalykin, N.
- Boudagov, Ju.
- Denisov, Yu.N.
- Donets, E.D.
- Donets, E.E.
- Govorov, A.
- Kobets, A.G.
- Kobets, V.
- Meshkov, I.N.
- Minashkin, V.
- Monchinsky, V.
- Shirkov, G.
- Sidorin, A.O.
- Sidorov, G.I.
- Sissakian, A.N.
- Trubnikov, G.V.

**JINR/LHE**
Moscow
- Shabratov, V.

**JLAB**
Newport News, Virginia
- Benson, S.V.
- Bogacz, S.A.
- Ciovati, G.
- Crawford, A.C.
- Daly, E.
- Davis, G.K.
- Delayen, J.R.
- Douglas, D.
- Drury, M.A.
- Evtushenko, P.
- Fischer, J.F.
- Freyberger, A.
- Funk, L.W.
- Geng, R.L.
- Grenoble, C.
- Hernandez-Garcia, C.
- Hogan, J.
- Hovater, C.
- Humphry, F.
- King, L.K.
- Kneisel, P.
- Krafft, G.A.
- Morrone, M.
- Phillips, H.L.
- Preble, J.P.
- Rimmer, R.A.
- Sekutowicz, J.K.
- Sexton, D.W.
- Wang, H.
- Worland, K.
- Zhang, S.

**KAERI**
Daejon
- Cho, Y.-S.
- Hong, I.-S.
- Jang, J.-H.
- Kim, D.I.
- Kim, H.S.
- Kwon, H.-J.
- Park, B.-S.
- Seol, K.T.
- Song, Y.-G.
- Yun, S.P.

**KEK**
Ibaraki
- Akemoto, M.
- Akikawa, H.
- Anami, S.
- Araki, S.
- Chin, Y.H.
- Fang, Z.
- Fukuda, M.K.
- Fukuda, S.
- Fukui, Y.
- Furukawa, K.
- Furuta, F.
- Furuya, T.
- Hayano, H.
- Higashi, Y.
- Higo, T.
- Honda, Y.
- Honma, H.
- Iida, N.
- Ikeda, M.
- Ikegami, K.
- Ikegami, M.
- Ino, T.
- Kadokura, E.
- Kakihara, K.
- Kamitani, T.
- Katagiri, H.
- Kawamura, M.
- Kazakov, S.
- Kikuchi, M.

- Kudoh, N.
- Matsumoto, S.
- Matsumoto, T.
- Matsushita, H.
- Michizono, S.
- Mimashi, T.
- Mishima, K.
- Miura, T.
- Muto, T.
- Mutou, S.
- Naito, F.
- Nakajima, H.
- Nakao, K.
- Nanmo, K.
- Ogawa, Y.
- Ohnishi, Y.
- Ohsawa, S.
- Saito, K.
- Satoh, K.
- Satoh, M.
- Shidara, T.
- Shirakawa, A.
- Sugimura, T.
- Suwada, T.
- Takatomi, T.
- Takenaka, T.
- Tanaka, H.
- Taniguchi, T.
- Tauchi, T.
- Terunuma, N.
- Ueno, K.
- Urakawa, J.
- Watanabe, K.
- Watanabe, Y.
- Yamaguchi, S.
- Yano, Y.
- Yokoyama, K.
- Yoshida, M.
- Morishima, T.
- Sakabe, N.
- Shimizu, H.M.
- Taketani, K.

**KEK/JAEA**
Ibaraki-Ken
- Ishiyama, T.
- Ueno, A.

**KIP**
Heidelberg
- Welsch, C.P.

**Kentech Instruments Ltd.**
Wallingford, Oxfordshire
- Dymokde-Bradshaw, A.K.L.
- Hares, J.D.
- Kellett, P.A.

**Kyoto IAE**
Kyoto
- Higashimura, K.
- Kii, T.
- Kinjo, R.
- Masuda, K.
- Ohgaki, H.
- Zen, H.

**Kyoto ICR**
Uji, Kyoto
- Fujisawa, H.
- Ichikawa, M.
- Iwashita, Y.
- Kazama, I.
- Noda, A.
- Souda, H.
- Sugimoto, T.
- Tongu, H.
- Wakita, A.
- Yamada, M.

**Kyoto University**
Kyoto
- Sasao, N.
- Seki, Y.

**Kyushu University, Department of Applied Quantum Physics and Nuclear Engineering**
Fukuoka
- Ishibashi, K.
- Kanesue, T.
- Yonemura, Y.

**LAL**
Orsay
- Cavalier, S.
- Garvey, T.
- Jenhani, H.
- Kaabi, W.
- Lacroix, M.
- Mercier, B.M.
- Prevost, C.
- Roux, R.
- Variola, A.

**LANL**
Los Alamos, New Mexico
- Abeyta, E.O.
- Aragon, P.
- Archuleta, R.D.
- Barraza, J.
- Bishofberger, K.
- Bolme, G.O.
- Bradley III, J.T.
- Carlsten, B.E.
- Cook, G.V.

- Dalmas, D.
- Ekdahl, C.
- Erickson, J.L.
- Esquibel, K.
- Faehl, R.
- Fernandez, J.C.
- Gallegos, R.J.
- Garnett, R.W.
- Gregory, W.L.
- Harrison, J.F.
- Jacquez, E.B.
- Johnson, J.B.
- Jones, K.W.
- Keller, R.
- Krawczyk, F.L.
- Kurennoy, S.S.
- Kwon, S.
- Lyles, J.T.M.
- Lynch, M.T.
- Marroquin, P.S.
- Martinez, F.A.
- McCuistian, B.T.
- Mitchell, R.R.
- Montoya, N.
- Moody, N.A.
- Nath, S.
- Nguyen, D.C.
- Nielsen, K.
- O'Hara, J.F.
- Olivas, E.R.
- Oro, D.
- Ortiz, R.M.
- Pieck, M.
- Prokop, M.S.
- Reass, W.
- Rees, D.
- Rowton, L.J.
- Roybal, W.
- Rybarcyk, L.
- Sanchez, L.
- Sanchez, M.
- Scarpetti, R.D.
- Schauer, M.
- Schoenberg, K.
- Seitz, G.J.
- Smith, H.V.
- Strevell, M.W.
- Temple, R.
- Young, K.A.

**LBNL**
Berkeley, California

- Anders, A.
- Bieniosek, F.M.
- Byrd, J.M.
- Chen, A.X.
- Coleman, J.E.
- Coleman-Smith, C.E.
- Doolittle, L.R.
- Greaves, C.M.R.
- Huang, G.
- Jung, J.-Y.
- Leitner, M.
- Li, D.
- Lidia, S.M.
- Logan, B.G.
- Ni, P.N.
- Ogata, D.
- Padmore, H.A.
- Panasenko, D.
- Pedersoli, E.
- Penn, G.
- Pogorelov, I.V.
- Polyakov, A.
- Qiang, J.
- Roy, P.K.
- Ryne, R.D.
- Seidl, P.A.
- Staples, J.W.
- Van den Bogert, K.
- Venturini, M.
- Waldron, W.L.
- Wan, W.
- Wells, R.P.
- Wilcox, R.B.
- Zholents, A.
- Zisman, M.S.

**LEBRA**
Funabashi

- Hayakawa, K.
- Hayakawa, Y.
- Nakao, K.
- Nogami, K.
- Takahashi, Y.
- Tanaka, T.

**LLNL**
Livermore, California

- Anaya, R.
- Barnard, J.J.
- Caporaso, G.J.
- Chambers, F.W.
- Chen, Y.-J.
- Cohen, R.H.
- Falabella, S.
- Grote, D.P.
- Guethlein, G.
- Lund, S.M.
- Raymond, B.A.
- Richardson, R.A.
- Rusnak, B.
- Watson, J.A.
- Weir, J.T.

**LPSC**
Grenoble

- Cabanel, T.
- Giraud, J.
- Gómez-Martínez, Y.

- Marchand, D.
- Micoud, R.
- Vezzu, F.

**Linac Systems, LLC**
Albuquerque, New Mexico
- Swenson, D.A.
- Willis, C.A.

**MELCO SC**
Tsukuba
- Fukuta, S.F.
- Kudou, T.
- Kusano, S.

**MEPhI**
Moscow
- Anisimov, A.
- Gusarova, M.
- Kaminsky, V.I.
- Kutsaev, S.V.
- Lalayan, M.V.
- Makarov, V.A.
- Shapovalov, A.
- Sobenin, N.P.

**MIT**
Middleton, Massachusetts
- Graves, W.

**MPI-K**
Heidelberg
- Artikova, S.T.
- Egberts, J.
- Kuehnel, K.-U.
- Welsch, C.P.

**MPQ**
Garching, Munich
- Hori, H.

**MSU**
Moscow
- Shvedunov, V.I.

**Muons, Inc**
Batavia
- Alsharo'a, M.
- Enchevich, I.B.
- Johnson, R.P.
- Neubauer, M.L.
- Sah, R.

**NFRI**
Daejon
- Oh, J.-S.

**NIIEFA**
St. Petersburg
- Svistunov, Y.A.
- Vorogushin, M.F.

**NIRS**
Chiba-shi
- Fujisawa, T.
- Hojo, S.
- Iwata, Y.
- Miyahara, N.
- Murakami, T.M.
- Muramatsu, M.
- Ogawa, H.
- Sakamoto, Y.
- Shirai, T.
- Yamada, S.
- Yamamoto, K.

**NPS**
Monterey, California
- Colson, W.B.
- Lewellen, J.W.
- Niles, S.P.

**NRL**
Washington, DC
- Cooke, S.J.

**NSC/KIPT**
Kharkov
- Ayzatskiy, M.I.
- Azhazha, V.
- Bomko, V.A.
- Boriskin, V.N.
- Dovbnya, A.N.
- Dyachenko, O.F.
- Karnaukhov, I.M.
- Khodak, I.V.
- Kobets, A.P.
- Kononenko, S.G.
- Kostromin, A.S.
- Krasnorutzkiy, V.E.
- Kushnir, V.A.
- Lesnykh, M.S.
- Mytrochenko, V.V.
- Neklyudov, I.M.
- Pavlij, K.V.
- Perezhogin, S.A.
- Ptukhina, Z.O.
- Reshetnikov, V.N.
- Soldatov, S.
- Tishkin, S.S.

- Tur, Y.D.
- Yegorov, A.M.
- Zabotin, A.V.
- Zajtsev, B.V.
- Zelinsky, A.Y.
- Zhuravlev, V.G.
- Zinchenko, B.N.

**NSCL**
East Lansing, Michigan

- Andreev, V.
- Bierwagen, J.
- Brandon, J.
- Bricker, S.
- Chouhan, S.
- Compton, C.
- DeLauter, J.
- Doleans, M.
- Glennon, P.
- Gorelov, D.
- Hartung, W.
- Hodek, M.
- Johnson, M.J.
- Lawton, D.
- Machicoane, G.
- Marti, F.
- Miller, P.S.
- Norton, D.
- Oliva, J.C.
- Ottarson, J.
- Popielarski, J.
- Popielarski, L.
- Portillo, M.
- Sanderson, D.
- Vincent, J.J.
- Wlodarczak, J.
- Wu, X.
- York, R.C.
- Zeller, A.
- Zhao, Q.

**NSTec**
Los Alamos, New Mexico

- Bender, H.
- Broste, W.
- Carlson, C.
- Frayer, D.
- Johnson, D.
- Tom, C.-Y.
- Trainham, C.P.
- Williams, J.T.

**NU**
Evanston

- Jacobson, J.J.
- Velasco, M.

**Nihon University, Advanced Research Institute for the Sciences and Humanities**
Funabashi

- Inagaki, M.
- Kuwada, T.
- Sakai, T.
- Sato, I.

**Niowave, Inc.**
Lansing, Michigan

- Bogle, A.E.
- Grimm, T.L.

**Northern Illinois University**
DeKalb, Illinois

- Bracke, A.
- Maxwell, T.J.
- Mihalcea, D.
- Piot, P.
- Prokop, C.R.
- Rihaoui, M.M.
- Terzic, B.
- Vinogradov, N.

**ODU**
Norfolk, Virginia

- De Silva, S.U.
- Wang, G.M.

**ORNL RAD**
Oak Ridge, Tennessee

- Newland, D.J.

**ORNL**
Oak Ridge, Tennessee

- Aleksandrov, A.V.
- Allen, C.K.
- Anderson, D.E.
- Blokland, W.
- Cousineau, S.M.
- Crofford, M.T.
- Galambos, J.
- Han, B.
- Jeon, D.
- Kang, Y.W.
- Kim, S.-H.
- Mammosser, J.
- McCarthy, M.P.
- Murray, S.N.
- Pennisi, T.R.
- Santana, M.
- Stockli, M.P.
- Welton, R.F.
- Wilson, J.L.

**Old Dominion University**
Norfolk, Virginia

- BastaniNejad, M.
- Elmustafa, A.A.

**Osaka Prefecture University**
Sakai
- Kojima, T.
- Okuda, S.
- Sakamoto, Y.
- Sasaki, R.
- Taniguchi, R.

**PAL**
Pohang, Kyungbuk
- Jang, S.D.
- Park, S.J.
- Son, Y.G.

**PAVAC**
Richmond, B.C.
- Edinger, R.

**PKU/IHIP**
Beijing
- Chen, J.E.
- Fang, J.X.
- Gao, S.L.
- Guo, Z.Y.
- Kang, M.
- Liu, K.X.
- Lu, Y.R.
- Nie, Y.C.
- Peng, S.X.
- Wang, Z.
- Yan, X.Q.
- Zhang, M.
- Zhao, J.
- Zhu, K.

**POSTECH**
Pohang, Kyungbuk
- Cho, M.-H.
- Kim, S.H.
- Namkung, W.
- Yang, H.R.

**PPPL**
Princeton, New Jersey
- Dorf, M.
- Gilson, E.P.

**PSI**
Villigen
- Adelmann, A.
- Andersson, Å.
- Beutner, B.
- Dehler, M.M.
- Dietl, M.
- Ganter, R.
- Garvey, T.
- Gough, C.
- Hauri, C.P.
- Ischebeck, R.
- Ivkovic, S.
- Kim, Y.
- Le Pimpec, F.
- Leemann, S.C.
- Li, K.B.
- Ming, P.
- Oppelt, A.
- Paraliev, M.
- Pedrozzi, M.
- Raguin, J.-Y.
- Reiche, S.
- Rivkin, L.
- Schietinger, T.
- Schlott, V.
- Steffen, B.
- Streun, A.
- Wrulich, A.F.

**Plansee Metall GmbH**
Reutte
- Grill, R.
- Kestler, H.
- Sigl, L.S.
- Traxler, H.

**RAS/INR**
Moscow
- Kalinin, Y.Z.
- Kravchuk, L.V.
- Kvasha, A.I.
- Moiseev, V.A.
- Paramonov, V.V.
- Tarasov, S.G.

**RFNC-VNIITF**
Snezhinsk, Chelyabinsk region
- Naumenko, M.Y.

**RIKEN Nishina Center**
Saitama
- Haba, H.
- Koyama, R.
- Kuboki, H.
- Okuno, H.
- Sakamoto, N.S.
- Sato, Y.
- Yano, Y.
- Fujimaki, M.K.
- Fujinawa, T.
- Fukunishi, N.
- Goto, A.
- Higurashi, Y.
- Ikezawa, E.
- Kamigaito, O.
- Kase, M.
- Kidera, M.
- Komiyama, M.
- Kumagai, K.

- Maie, T.
- Nagase, M.
- Nakagawa, T.
- Ohnishi, J.
- Suda, K.
- Watanabe, T.
- Yamada, K.
- Yokouchi, S.

**RIKEN Spring-8 Harima**
Hyogo
- Kondo, C.
- Tamasaku, K.

**RIKEN**
Wako, Saitama
- Hirota, K.
- Otake, Y.
- Sato, H.

**RIKEN/SPring-8**
Hyogo
- Hosoda, N.
- Inagaki, T.
- Inoue, S.I.
- Maesaka, H.
- Ohshima, T.
- Otake, Y.
- Sakurai, T.
- Shintake, T.
- Shirasawa, K.

**RISE**
Tokyo
- Fujita, A.
- Hama, Y.
- Hirose, T.
- Igarashi, C.
- Kato, Y.
- Masuda, A.
- Murata, A.
- Nomoto, T.
- Sakaue, K.
- Suzuki, T.
- Washio, M.

**RLNR**
Tokyo
- Hattori, T.
- Hayashizaki, N.
- Ishibashi, T.
- Ito, T.
- Kobori, R.
- Lu, L.

**RRCAT**
Indore (M.P.)
- Mulchandani, J.
- Sahni, V.C.
- Shrivastava, P.

**Rutgers University, The State University of New Jersey**
Piscataway, New Jersey
- Koeth, T.W.

**SAIC**
Los Alamos, New Mexico
- Prichard, B.A.
- Schulze, M.E.

**SHI**
Tokyo
- Mitsumoto, T.
- Tsutsui, H.
- Ueda, T.
- Watanabe, T.

**SLAC**
Menlo Park, California
- Adolphsen, C.
- Akcelik, V.
- Akre, R.
- Beukers, T.G.
- Brachmann, A.
- Burkhart, C.
- Candel, A.E.
- Chao, A.
- Colocho, W.S.
- Decker, F.-J.
- Ding, Y.T.
- Dolgashev, V.A.
- Dowell, D.
- Emma, P.
- Frisch, J.C.
- Gilevich, A.
- Hays, G.R.
- Hering, P.
- Hogan, M.J.
- Huang, Z.
- Iverson, R.H.
- Jones, R.M.
- Kabel, A.C.
- Kemp, M.A.
- Ko, K.
- Kotturi, K.D.
- Krasnykh, A.
- Larsen, R.S.
- Laurent, L.
- Lee, L.
- Lewandowski, J.R.
- Li, Z.
- Limborg-Deprey, C.
- Loos, H.
- MacNair, D.J.
- Macken, K.J.P.
- Miahnahri, A.
- Molloy, S.

- Nantista, C.D.
- Ng, C.-K.
- Nguyen, M.N.
- Nuhn, H.-D.
- Olsen, J.J.
- Pei, S.
- Ratner, D.F.
- Schussman, G.L.
- Seryi, A.
- Tang, T.
- Tantawi, S.G.
- Turner, J.L.
- Uplenchwar, R.
- Wang, F.
- Wang, J.W.
- Welch, J.J.
- White, W.E.
- Wu, J.
- Xiao, L.
- Yeddulla, M.

**SOLEIL**
Gif-sur-Yvette
- Couprie, M.-E.

**STFC/DL/ASTeC**
Daresbury, Warrington, Cheshire
- Bate, R.
- Beard, C.D.
- Dykes, D.M.
- Goudket, P.
- Holder, D.J.
- Jackson, F.
- Kalinin, A.
- Ma, L.
- McIntosh, P.A.
- McKenzie, J.W.
- Militsyn, B.L.
- Pattalwar, S.M.

**STFC/RAL**
Chilton, Didcot, Oxon
- Faircloth, D.C.
- Pasternak, J.
- Pozimski, J.K.

**STFC/RAL/ASTeC**
Chilton, Didcot, Oxon
- Gabor, C.
- Plostinar, D.C.
- Prior, C.R.

**STFC/RAL/ISIS**
Chilton, Didcot, Oxon
- Clarke-Gayther, M.A.
- Faircloth, D.C.
- Findlay, D.J.S.
- Lawrie, S.R.
- Letchford, A.P.
- Romano, P.
- Wise, P.

**SUT**
Noda-shi, Chiba
- Hioka, H.
- Someya, S.

**Saint-Petersburg State University**
Saint-Petersburg
- Kolevatov, R.S.

**ScanTech**
Atlanta, Georgia
- Ferderer, M.A.
- Krasnov, A.A.
- Zavadtsev, A.A.

**Soreq NRC**
Yavne
- Berkovits, D.
- Gertz, I.
- Mardor, I.
- Nagler, A.
- Rodnizki, J.
- Weissman, L.

**Stanford University**
Stanford, Califormia
- Ratner, D.F.
- Smith, T.I.

**TEMF, TU Darmstadt**
Darmstadt
- Ackermann, W.
- Franke, S.
- Müller, W.F.O.
- Steiner, B.
- Weiland, T.

**TRIUMF**
Vancouver
- Ames, F.
- Baartman, R.A.
- Bylinskii, I.V.
- Chao, Y.-C.
- Dawson, R.J.
- Drozdoff, J.T.
- Fong, K.
- Grassellino, A.
- Hurst, A.
- Keitel, R.
- Koscielniak, S.R.
- Langton, K.
- Laverty, M.P.
- Laxdal, R.E.

- Lockyer, N.S.
- Lu, J.
- Mammarella, F.
- Marchetto, M.
- Merminga, L.
- Mitra, A.K.
- Rawnsley, W.R.
- Reiniger, K.W.
- Richards, J.E.
- Ries, T.C.
- Ruegg, R.
- Sekachev, I.
- Shanks, R.W.
- Stinson, G.M.
- Trinczek, M.
- Verzilov, V.A.
- Yan, F.
- Zheng, Q.
- Zvyagintsev, V.

**TU Darmstadt**
Darmstadt
- Araz, A.
- Barday, R.
- Bonnes, U.
- Brunken, M.
- Conrad, J.
- Eckardt, C.
- Eichhorn, R.
- Enders, J.
- Gräf, H.-D.
- Hertling, M.
- Hessler, C.
- Hug, F.
- Klose, C.
- Konrad, M.
- Kuerzeder, T.
- Liebig, C.
- Platz, M.
- Poltoratska, Y.
- Richter, A.
- Roth, M.
- Sievers, S.T.
- Weilbach, T.

**The Hashemite University**
Zarka
- Salah, W.

**Thermo**
Liverpool, New York
- Chapman, T.
- Pilon, M.J.

**Total Saport System Corp.**
Naka-gun, Ibaraki
- Sawa, S.S.

**U. Sapientia**
Targu Mures
- Hollanda, D.
- Kenez, L.

**UCB**
Berkeley, California
- Calanog, J.A.
- Kur, E.

**UCLA**
Los Angeles, California
- Muggli, P.
- Rosenzweig, J.B.

**UMAN**
Manchester
- Fraser, M.A.
- Glasman, C.J.
- Jones, R.M.
- Khan, V.F.
- Shinton, I.R.R.

**USC**
Los Angeles, California
- Kallos, E.

**UW-Madison/SRC**
Madison, Wisconsin
- Bisognano, J.
- Bosch, R.A.
- Kleman, K.J.
- Legg, R.A.

**Uni HH**
Hamburg
- Roensch, J.

**University of Oslo**
Oslo
- Adli, E.

**University of Pennsylvania**
Philadelphia, Pennsylvania
- Keung, J.K.

**University of Pisa and INFN**
Pisa
- Armiento, C.

**University of Tennessee**
Knoxville, Tennessee
- Fathy, A.E.

**University of Tokyo**
Tokyo
- Kamiya, Y.
- Kawasaki, S.
- Komamiya, S.
- Otono, H.
- Utsunomiya, U.
- Yamashita, S.

**University of Toronto**
Toronto, Ontario
- Orr, R.S.
- Trischuk, W.

**University of Udine**
Udine
- Galasso, G.

**University of Warwick**
Coventry
- Back, J.J.

**University of electro-communications**
Tokyo
- Musha, M.

**Università Cattolica-Brescia**
Brescia
- Ferrini, G.
- Montagnese, M.
- Pagliara, S.
- Parmigiani, F.

**Università degli Studi di Milano**
Milano
- Grespan, F.

**Victoria University**
Victoria, B.C.
- Karlen, D.

**Visual Information Center, Inc.**
Ibaraki-ken
- Ikeda, H.

**Voss Scientific**
Albuquerque, New Mexico
- Genoni, T.C.
- Hughes, T.P.
- Rose, D.
- Thoma, C.H.
- Welch, D.R.

**YerPhI**
Yerevan
- Hakobyan, L.
- Khojoyan, M.K.

# List of Participants

| | | |
|---|---|---|
| Abo-Bakr, Michael | BESSY | Germany |
| Adli, Erik | U. Oslo / CERN | Switzerland |
| Adolphsen, Chris | SLAC | USA |
| Aleksandrov, Alexander | ORNL-SNS | USA |
| Alessi, James | BNL | USA |
| Allen, Christopher | ORNL-SNS | USA |
| Allen, Lawrence | Fermilab | USA |
| Alton, Bill | The Ferrite Company | USA |
| Ames, Friedhelm | TRIUMF | Canada |
| Ao, Hiroyuki | JAEA | Japan |
| Apollinari, Giorgio | Fermilab | USA |
| Archuleta, Rita | LANL | USA |
| Baartman, Richard | TRIUMF | Canada |
| Bajwa, Bill | Apple Canada | Canada |
| Balkam, Adam | Communications & Power Industries | USA |
| Bane, Karl | SLAC | USA |
| Bardorfer, Ales | Instrumentation Technologies | Slovenia |
| Baricevic, Borut | Instrumentation Technologies | Slovenia |
| Barnard, John | LLNL | USA |
| Barth, Winfried | GSI | Germany |
| Beard, Carl | STFC/DL/ASTeC | UK |
| Beauvais, Pierre-Yves | CEA, IRFU, Gif-sur-Yvette | France |
| Bechtold, Alexander | IAP, Goethe U. Frankfurt | Germany |
| Becker, Reinard | IAP, Goethe U. Frankfurt | Germany |
| Bedau, Juergen | Bruker Biospin Corp. | USA |
| Bellodi, Giulia | CERN | Switzerland |
| Belomestnykh, Sergey | Cornell U. | USA |
| Berg, William | ANL | USA |
| Bertrand, Patrick | GANIL | France |
| Bethuys, Stephane | Thales Components Corporation | France |
| Birney, Paul | U. Victoria | Canada |
| Bishofberger, Kip | LANL | USA |
| Bisoffi, Giovanni | INFN/LNL | Italy |
| Bocchetta, Carlo | Instrumentation Technologies | Slovenia |
| Bogacz, Alex | Jefferson Lab | USA |
| Bogle, Andrew | Niowave, Inc. | USA |
| Bojechko, Casey | U. Victoria | Canada |
| Boni, Roberto | INFN/LNF | Italy |
| Borland, Michael | ANL | USA |
| Boyle, Michael | L-3 Communications Electron Devices | USA |
| Bradley III, Joseph | LANL | USA |
| Branlard, Julien | Fermilab | USA |
| Brinkmann, Arne | DESY | Germany |
| Brinkmann, Reinhard | DESY | Germany |
| Burkhart, Craig | SLAC | USA |
| Burt, Graeme | Lancaster U. | UK |
| Butler, Trevor | Fermilab | USA |
| Bylinskii, Iouri | TRIUMF | Canada |
| Cancelo, Gustavo | Fermilab | USA |
| Candel, Arno | SLAC | USA |
| Chakrabarti, Alok | DAE/VECC, Calcutta | India |
| Chamizo, Rocio | CERN | Switzerland |
| Champion, Mark | Fermilab | USA |
| Chan, Kwok-Chi | LANL | USA |

| | | |
|---|---|---|
| Charron, Lorraine | U. Victoria | Canada |
| Chautard, Frederic | GANIL | France |
| Chauvin, Nicolas | CEA, IRFU, Gif-sur-Yvette | France |
| Chen, Yu-Jiuan | U. California | USA |
| Chin, Yong Ho | KEK | Japan |
| Cho, Yanglai | ANL | USA |
| Chohan, Vinod | CERN | Switzerland |
| Choroba, Stefan | DESY | Germany |
| Chrin, Jan | PSI | Switzerland |
| Christou, Chris | Diamond Light Source Ltd. | UK |
| Clausen, Juergen | Linde | Switzerland |
| Colson, William | Naval Postgraduate School | USA |
| Comunian, Michele | INFN/LNL | Italy |
| Comyn, Martin | TRIUMF | Canada |
| Conde, Manoel | ANL | USA |
| Cours, Alexander | ANL | USA |
| Dabrowski, Anne | CERN | Switzerland |
| Dahl, Ludwig | GSI | Germany |
| De Almeida Martins, Carlos | CERN | Switzerland |
| De Caire, Lynn | TRIUMF | Canada |
| Decker, Franz-Josef | SLAC | USA |
| Delayen, Jean | Jefferson Lab | USA |
| Devanz, Guillaume | CEA, IRFU, Gif-sur-Yvette | France |
| Di Giacomo, Marco | GANIL | France |
| Doebert, Steffen | CERN | Switzerland |
| Dolgashev, Valery | SLAC | USA |
| Douglas, David | Jefferson Lab | USA |
| Dovbnya, Anatoly | National Science Centre | Ukraine |
| Drury, Michael | Jefferson Lab | USA |
| Duffin, Sean | Varian Canada, Inc. | Canada |
| Dunham, Bruce | Cornell U. | USA |
| Dunkel, Kai | ACCEL Instruments GmbH | Germany |
| Dupire, Pascal | Bruker Biospin Corp. | USA |
| Dutto, Gerardo | TRIUMF | Canada |
| Edinger, Ralf | PAVAC Industries Inc. | Canada |
| Eichhorn, Ralf | TU Darmstadt | Germany |
| Einarson, Steve | Communications & Power Industries | USA |
| Ekdahl, Carl | LANL | USA |
| Emhofer, Stephan | Siemens AG | Germany |
| Erickson, John | LANL | USA |
| Evtushenko, Pavel | Jefferson Lab | USA |
| Facco, Alberto | INFN/LNL | Italy |
| Fagotti, Enrico | INFN/LNL | Italy |
| Favale, Anthony | Advanced Energy Systems, Inc. | USA |
| Fazio, Michael | LANL | USA |
| Fejfar, Jeremy | CST of America, Inc. | USA |
| Feldmeier, Eike | HIT, Heidelberg | Germany |
| Ferdinand, Robin | GANIL | France |
| Fernandez, Juan | LANL | USA |
| Fitzgerald, Mark | The Ferrite Company | USA |
| Fleming, Gordon | PAVAC Industries Inc. | Canada |
| Foley, Mike | Fermilab | USA |
| Fong, Ken | TRIUMF | Canada |
| Franke, Sylvain | TEMF, TU Darmstadt | Germany |
| Frigola, Pedro | Radiabeam Technologies | USA |
| Fu, Shinian | IHEP Beijing | PR China |

| | | |
|---|---|---|
| Fukuda, Shigeki | KEK | Japan |
| Furuya, Takaaki | KEK | Japan |
| Gable, Ian | U. Victoria | Canada |
| Gabor, Christoph | STFC/RAL/ASTeC | UK |
| Galambos, John | ORNL-SNS | USA |
| Gardner, Phil | AAPS | Canada |
| Garnett, Robert | LANL | USA |
| Garoby, Roland | CERN | Switzerland |
| Geng, Rong-Li | Jefferson Lab | USA |
| Geng, Zheqiao | DESY | Germany |
| Gillespie, George | AccelSoft Inc. / G.H. Gillespie | USA |
| Ginsburg, Camille | Fermilab | USA |
| Gomez-Martinez, Yolanda | LPSC, Grenoble | France |
| Gorelov, Dmitry | Michigan State U. | USA |
| Grassellino, Anna | U. Pennsylvania / TRIUMF | Canada |
| Grevsmuehl, Torsten | DESY | Germany |
| Grill, Robert | PLANSEE SE | Austria |
| Grimm, Terry | Niowave, Inc. | USA |
| Groening, Lars | GSI | Germany |
| Grudiev, Alexej | CERN | Switzerland |
| Guy, Frank | Linac Systems, LLC | USA |
| Haeuser, Juergen | Neue Technologien GmbH | Germany |
| Hale, Jim | Linac Systems, LLC | USA |
| Hamm, Robert | Ramtech Enterprises | USA |
| Han, Jang Hui | Diamond Light Source Ltd. | UK |
| Hanke, Klaus | CERN | Switzerland |
| Hapke, Mindy | TRIUMF | Canada |
| Harms, Elvin | Fermilab | USA |
| Hartung, Walter | Michigan State U. | USA |
| Harwood, Leigh | Jefferson Lab | USA |
| Hasegawa, Kazuo | J-PARC | Japan |
| Hattori, Toshiyuki | RLNR, Tokyo IT | Japan |
| Henderson, Stuart | ORNL-SNS | USA |
| Holder, David | STFC/DL/ASTeC | UK |
| Honkavaara, Katja | DESY | Germany |
| Hopkins, Steve | Lambda Americas / Test Force | USA |
| Horak, Charlie | ORNL-SNS | USA |
| Hott, Thomas | DESY | Germany |
| Hovater, Curt | Jefferson Lab | USA |
| Huang, Dazhang | Illinois IT | USA |
| Huang, Perry | TRIUMF | Canada |
| Huening, Markus | DESY | Germany |
| Ibarra, Angel | CIEMAT, Madrid | Spain |
| Ichikawa, Masahiro | ICR, Kyoto U. | Japan |
| Iizuka, Minoru | Toshiba - TETD | Japan |
| Ikegami, Masanori | JAEA / J-PARC | Japan |
| Inagaki, Takahiro | RIKEN/SPring-8 | Japan |
| Ishibashi, Takuya | RLNR, Tokyo IT | Japan |
| Isoyama, Goro | ISIR, Osaka | Japan |
| Iwashita, Yoshihisa | ICR, Kyoto U. | Japan |
| Iwata, Yoshiyuki | NIRS | Japan |
| Jacob, Jeremy | RadiaBeam Technologies, LLC | USA |
| Jacquez, Edward | LANL | USA |
| Jaeschke, Eberhard | BESSY | Germany |
| Jaggi, Vinder | AAPS | Canada |
| Jamet, Christophe | GANIL | France |

| | | |
|---|---|---|
| Jenhani, Hassen | LAL, Orsay | France |
| Jeon, Dong-o | ORNL-SNS | USA |
| Jin, Kai | U. Science and Technology | PR China |
| Johnson, Rolland | Muons, Inc. | USA |
| Jones, Emily | ZTEC Instruments | USA |
| Jones, Kevin | LANL | USA |
| Jones, Roger | Cockcroft Institute | UK |
| Junquera, Tomas | IPN, Orsay | France |
| Jurkovic, Anto | Instrumentation Technologies | Slovenia |
| Kaesler, Wolfgang | Puls-Plasmatechnik GmbH | Germany |
| Kamigaito, Osamu | RIKEN | Japan |
| Kamitani, Takuya | KEK | Japan |
| Kang, Yoon | ORNL-SNS | USA |
| Karlen, Dean | U. Victoria | Canada |
| Kase, Edwin | Tech-X Corporation | USA |
| Kato, Yuta | RISE, Waseda U. | Japan |
| Kawai Parker, Yoko | AccSys Technology, Inc. | USA |
| Kayran, Dmitry | BNL | USA |
| Keller, Roderich | LANL | USA |
| Kelly, Michael | ANL | USA |
| Kemp, Mark | SLAC | USA |
| Kempkes, Michael | Diversified Technologies, Inc. | USA |
| Kephart, Robert | Fermilab | USA |
| Keung, Justin | U. Pennsylvania | USA |
| Kii, Toshiteru | IAE, Kyoto U. | Japan |
| Kim, Han-Sung | KAERI | Korea |
| Kim, Sang-Ho | ORNL-SNS | USA |
| Klarner, Fabian | Bonn U. | Germany |
| Klein, Horst | IAP, Goethe U. Frankfurt | Germany |
| Kneisel, Peter | Jefferson Lab | USA |
| Knight, Charles | L-3 Communications Electron Devices | USA |
| Knobloch, Jens | BESSY | Germany |
| Kobets, Anatoliy | National Science Centre | Ukraine |
| Koch, Stuart | Amuneal Manufacturing Corp. | USA |
| Koeth, Timothy | Rutgers U. / Fermilab | USA |
| Kolda, Peter | Communications & Power Industries | USA |
| Kondo, Chikara | RIKEN/SPring-8 | Japan |
| Kondrashev, Sergei | ANL | USA |
| Koscielniak, Shane | TRIUMF | Canada |
| Kosicek, Andrej | Instrumentation Technologies | Slovenia |
| Kost, Corrie | TRIUMF | Canada |
| Kot, Yauhen | DESY | Germany |
| Krafft, Geoffrey | Jefferson Lab | USA |
| Krawczyk, Frank | LANL | USA |
| Kuenzi, Creston | ZTEC Instruments | USA |
| Kugeler, Oliver | BESSY | Germany |
| Kurennoy, Sergey | LANL | USA |
| Kurup, Ajit | Imperial College, London U. | UK |
| Kurzydlo, John | Toshiba - TETD | Japan |
| Kutsaev, Sergey | MEPhI | Russia |
| Kvasha, Adolf | RAS/INR | Russia |
| Lackey, Sharon | Fermilab | USA |
| Langstaff, Roy | U. Victoria | Canada |
| Lauder, Laurie | Amuneal Manufacturing Corp. | USA |
| Laverty, Michael | TRIUMF | Canada |
| Laxdal, Robert | TRIUMF | Canada |

| | | |
|---|---|---|
| Legg, Robert | U. Wisconsin-Madison | USA |
| Lemaire, Jean-Louis | CEA, Bruyères-le-Châtel | France |
| Len, Lek | U.S. DOE | USA |
| Lenckowski, Mark | U. Victoria | Canada |
| Letchford, Alan | STFC/RAL/ISIS | UK |
| Lewellen, John | Naval Postgraduate School | USA |
| Li, Zenghai | SLAC | USA |
| Lilje, Lutz | DESY | Germany |
| Lockyer, Nigel | TRIUMF | Canada |
| Lombardi, Alessandra | CERN | Switzerland |
| Lombardi, Augusto | INFN/LNL | Italy |
| Longuevergne, David | IPN, Orsay | France |
| Loos, Henrik | SLAC | USA |
| Lu, Yuanrong | Peking U. | PR China |
| Lund, Steven | LBNL | USA |
| MacNair, David | SLAC | USA |
| Madrak, Robyn | Fermilab | USA |
| Maier, Michael | GSI | Germany |
| Maltin, Larry | Amuneal Manufacturing Corp. | USA |
| Maltin, Meira | Amuneal Manufacturing Corp. | USA |
| Mammosser, John | ORNL-SNS | USA |
| Marchetto, Marco | TRIUMF | Canada |
| Mardor, Israel | Soreq NRC | Israel |
| Matsumoto, Toshihiro | KEK | Japan |
| Mavric, Uros | Fermilab | Slovenia |
| McCarthy, Michael | ORNL-SNS | USA |
| McDonald, Steven | TRIUMF | Canada |
| McGill, John | McGillWork, LLC | USA |
| McIntosh, Peter | STFC/DL/ASTeC | UK |
| McVea, Jim | Thales Components Corporation | USA |
| Merminga, Lia | TRIUMF | Canada |
| Meusel, Oliver | IAP, Goethe U. Frankfurt | Germany |
| Michizono, Shinichiro | KEK | Japan |
| Mihalcea, Daniel | Northern Illinois U. | USA |
| Militsyn, Boris | STFC/DL/ASTeC | UK |
| Miller, Sandi | TRIUMF | Canada |
| Mishra, Shekhar | Fermilab | USA |
| Mitra, Amiya | TRIUMF | Canada |
| Miura, Akihiko | JAEA | Japan |
| Monsarrat, Mark | Apple Canada | Canada |
| Mosnier, Alban | CEA, Gif-sur-Yvette | France |
| Muehlegger, Marco | Linde | Switzerland |
| Muggli, Patric | U. Southern California | USA |
| Muller, Wolfgang | TEMF, TU Darmstadt | Germany |
| Mulvaney, Joan | AccelSoft Inc. / G.H. Gillespie | USA |
| Mustapha, Brahim | ANL | USA |
| Mytrochenko, Viktor | National Science Centre | Ukraine |
| Nagaitsev, Sergei | Fermilab | USA |
| Namkung, Won | PAL | Korea |
| Nantista, Christopher | SLAC | USA |
| Nath, Subrata | LANL | USA |
| Neumann, Axel | BESSY | Germany |
| Nezhevenko, Oleg | Fermilab | USA |
| Nghiem, Phu Anh Phi | CEA, IRFU, Gif-sur-Yvette | France |
| Niles, Sean | Naval Postgraduate School | USA |
| Noda, Akira | ICR, Kyoto U. | Japan |

| | | |
|---|---|---|
| Ohnishi, Yukiyoshi | KEK | Japan |
| Ohsawa, Satoshi | KEK | Japan |
| Ohshima, Takashi | RIKEN/SPring-8 | Japan |
| Okamura, Masahiro | BNL | USA |
| Okuda, Shuichi | Osaka Prefecture U. | Japan |
| Olry, Guillaume | IPN, Orsay | France |
| Ostroumov, Peter | ANL | USA |
| Padamsee, Hasan | Cornell U. | USA |
| Pagani, Carlo | INFN/LASA | Italy |
| Panasenko, Dmitriy | LBNL | USA |
| Paparella, Rocco | INFN/LASA | Italy |
| Paramonov, Valentin | RAS/INR | Russia |
| Pasini, Matteo | CERN | Switzerland |
| Peauger, Franck | CEA, IRFU, Gif-sur-Yvette | France |
| Pei, Guoxi | IHEP Beijing | PR China |
| Pepato, Adriano | U. Padova | Italy |
| Petit-Jean-Genaz, Christine | CERN | Switzerland |
| Pfister, Jochen | IAP, Goethe U. Frankfurt | Germany |
| Pieck, Martin | LANL | USA |
| Piel, Christian | ACCEL Instruments GmbH | Germany |
| Pierini, Paolo | INFN/LASA | Italy |
| Piermarini, Graziano | INFN/LNF | Italy |
| Pierret, Olivier | CEA, Pontfaverger-Moronvilliers | France |
| Pisent, Andrea | INFN/LNL | Italy |
| Plostinar, Ciprian | JAI / STFC/RAL/ASTeC | UK |
| Podlech, Holger | IAP, Goethe U. Frankfurt | Germany |
| Poirier, Roger | TRIUMF | Canada |
| Popovic, Milorad | Fermilab | USA |
| Posocco, Piero Antonio | INFN/LNL, Consorzio RFX | Italy |
| Powers, Tom | Jefferson Lab | USA |
| Pozimski, Jurgen | Imperial College, London U. | UK |
| Preble, Joseph | Jefferson Lab | USA |
| Preston, Alisa | U. Victoria | Canada |
| Prior, Christopher | STFC/RAL/ASTeC | UK |
| Qiang, Ji | LBNL | USA |
| Ramberger, Suitbert | CERN | Switzerland |
| Raparia, Deepak | BNL | USA |
| Rathke, John | Advanced Energy Systems, Inc. | USA |
| Rauh, Andrea | attocube systems AG | Germany |
| Ravindran, Murali | National Instruments | USA |
| Rawnsley, William | TRIUMF | Canada |
| Rees, Grahame | STFC/RAL/ASTeC | UK |
| Reeve, Shirley | TRIUMF | Canada |
| Repic, Borut | Instrumentation Technologies | Slovenia |
| Reschke, Detlef | DESY | Germany |
| Richards, Dave | Goodfellow Corporation | USA |
| Robinson, Dennis | Diversified Technologies, Inc | USA |
| Romanov, Gennady | Fermilab | USA |
| Rosenthal, Glenn | Alpha Source | USA |
| Ross, Marc | Fermilab | USA |
| Rossi, Carlo | CERN | Switzerland |
| Roux, Raphael | LAL, Orsay | France |
| Roy, Amit | IUAC, Delhi | India |
| Ruf, Marcel | U. Erlangen-Nurnberg LHFT | Germany |
| Rusnak, Brian | LLNL | USA |
| Sah, Richard | Muons, Inc. | USA |

| | | |
|---|---|---|
| Sajaev, Vadim | ANL | USA |
| Sakai, Takeshi | Nihon U. | Japan |
| Sakaue, Kazuyuki | RISE, Waseda U. | Japan |
| Sako, Hiroyuki | J-PARC | Japan |
| Satoh, Masanori | KEK | Japan |
| Schaa, Volker | GSI | Germany |
| Schempp, Alwin | IAP, Goethe U. Frankfurt | Germany |
| Schietinger, Thomas | PSI | Switzerland |
| Schlitt, Bernhard | GSI | Germany |
| Schmickler, Hermann | CERN | Switzerland |
| Schmor, Paul | TRIUMF | Canada |
| Schulze, Martin | Science Applications International | USA |
| Seidl, Peter | LBNL | USA |
| Senti, Mark | Advanced Magnet Lab, Inc. | USA |
| Sharamentov, Sergey | ANL | USA |
| Sheffield, Richard | LANL | USA |
| Shen, Xiaofeng | Canadian Light Source Inc. | Canada |
| Skowronski, Piotr | CERN | Switzerland |
| Smith, Terry | ANL | USA |
| Spaedtke, Peter | GSI | Germany |
| Spataro, Bruno | INFN/LNF | Italy |
| Speer, Eileen | ETM Electromatic Inc. | USA |
| Staples, John | LBNL | USA |
| Stephan, Frank | DESY | Germany |
| Stirling, William | ESRF | France |
| Stockli, Martin | ORNL-SNS | USA |
| Strehar, Mojca | Instrumentation Technologies | Slovenia |
| Sugimoto, Takanori | ICR, Kyoto U. | Japan |
| Sun, Yin-E | Fermilab | USA |
| Svistunov, Yuri | NIIEFA, St. Petersburg | Russia |
| Swenson, Donald | Linac Systems, LLC | USA |
| Talman, Richard | Cornell U. | USA |
| Tam, Wai-Ming | Indiana U. / Fermilab | USA |
| Taniguchi, Ryoichi | Osaka Prefecture U. | Japan |
| Terechkine, Iouri | Fermilab | USA |
| Terrasi, Paula | The Ferrite Company | USA |
| Terzic, Balsa | Northern Illinois U. | USA |
| Teytelman, Dmitry | Dimtel, Inc. | USA |
| Thomson, Jana | TRIUMF | Canada |
| Tomizawa, Hiromitsu | JASRI/SPring-8 | Japan |
| Trischuk, William | U. Toronto | Canada |
| Trubnikov, Grigoriy | JINR | Russia |
| Ueno, Akira | J-PARC | Japan |
| Urbin, John | Linde | USA |
| Uriot, Didier | CEA, IRFU, Gif-sur-Yvette | France |
| Ursic, Rok | Instrumentation Technologies | Slovenia |
| Vaccarezza, Cristina | INFN/LNF | Italy |
| Variola, Alessandro | LAL, Orsay | France |
| Vescovi, Mario | INFN/LNF | Italy |
| Vetter, Arthur | Boeing Company | USA |
| Vinzenz, Wolfgang | GSI | Germany |
| Vogel, Elmar | DESY | Germany |
| Vossberg, Markus | IAP, Goethe U. Frankfurt | Germany |
| Vretenar, Maurizio | CERN | Switzerland |
| Wan, Weishi | LBNL | USA |
| Wang, Guimei | Jefferson Lab | PR China |

| | | |
|---|---|---|
| Wang, Jingsong | CST of America, Inc. | USA |
| Wang, Juwen | SLAC | USA |
| Weise, Hans | DESY | Germany |
| Welsch, Carsten | MPI-K, Heidelberg | Germany |
| White, Marion | ANL | USA |
| Wildman, David | Fermilab | USA |
| Willis, Carl | Ohio State U. | USA |
| Wilsen, Craig | L-3 Communications Electron Devices | USA |
| Wilson, Joshua | U. Tennessee / ORNL-SNS | USA |
| Wlodarczak, Jon | Michigan State U. | USA |
| Wu, Juhao | SLAC | USA |
| Wu, Xiaoyu | Michigan State U. | USA |
| Xiao, Aimin | ANL | USA |
| Yamada, Masako | ICR, Kyoto U. | Japan |
| Yamazaki, Yoshishige | J-PARC | Japan |
| Yan, Fang | TRIUMF | Canada |
| Yanagida, Kenichi | JASRI/SPring-8 | Japan |
| Yang, Xi | BNL | PR China |
| Yeddulla, Muralidhar | SLAC | USA |
| Yokoyama, Kazue | KEK | Japan |
| Yoshida, Mitsuhiro | KEK | Japan |
| Yoshikawa, Hiroshi | J-PARC | Japan |
| Yushiro, Osamu | Toshiba - TETD | Japan |
| Zeisler, Stefan | AAPS | Canada |
| Zennaro, Riccardo | CERN | Switzerland |
| Zhao, Qiang | Michigan State U. | USA |
| Zheng, Qiwen | TRIUMF | Canada |
| Zholents, Alexander | LBNL | USA |
| Zhou, Zilu | Schlumberger Doll Research | USA |